ENOC 2022 - Book of abstracts

10th European Nonlinear Dynamics Conference

July 17-22, 2022
Lyon, France

ORGANIZERS

Local Organizing Committee (LOC)

Claude Henri Lamarque (Chair)
Régis Dufour (Co-Chair)
Fabrice Thouverez (Co-Chair)
Louis Jézéquel (Honorary Chairman)
Sébastien Baguet (Secretary General)

Administrative support (INSAVALOR)
Muriel Personne
Secretarial support
Zahia Achoui, Cécile Demornex
Local organizing committee
Sébastien Besset
Laurent Blanc
Emmanuel Gourdon
Alain Le Bot
Lionel Manin†
Lyes Nechak
Joel Perret-Liaudet
Didier Rémond
Emmanuel Rigaud
Jean-Jacques Sinou
Alireza Ture Savadkoohi

† Lionel left us in may 2021. We would like to acknowledge his memory and his dynamic involvement in the organizing committee.

European Nonlinear Oscillations Conference Committee (ENOCC)

Gaëtan Kerschen (Chair)
University of Liege, Belgium
Katrin Ellermann
University of Graz, Austria
Alexander Fidlin
Karlsruher Institut für Technologie, Germany
Oleg Gendelman
Technion, Israel Institute of Technology, Israel
Ivana Kovačić (Co-chair)
University of Novi Sad, Faculty of Technical Sciences, Serbia
Claude-Henri Lamarque
University of Lyon, France
Stefano Lenci
Università Politecnica delle Marche, Italy
Andrei Metrikine
Delft University of Technology, The Netherlands
Ekaterina Pavlovskaia
University of Aberdeen, UK
Gabor Stepan
Budapest University of Technology and Economics, Hungary

Front page:
Photo credits
L'église Saint-Georges et les quais de Saône, Lyon 5e © Tristan Deschamps
Opéra de Lyon - Place Louis Pradel - Lors du Festival Street Day 2011 ©www.b-rob.com
Le Cube Orange de la Confluence ©Jakob + MacFarlane architectes/©www.b-rob.com

Scope of the conference

Although the brand name ENOC is still used as the historical abbreviation, the present European Nonlinear Dynamics Conferences organized by EUROMECH aim at covering the complete field of Nonlinear Dynamics, including Multibody Dynamics and coupling to Stability, Identification, Control and (Structural) Optimization.

Presently, ENOCs are the largest, high-quality, scientific events in the broad area of nonlinear dynamics not only in Europe but on a worldwide basis. Indeed, parallel important events organized by other Societies often cover partial aspects of the whole scientific area, for being either more theoretically or more engineering oriented.

In contrast, ENOC encompasses many diverse topics ranging from dynamical systems theory to different engineering applications, and collects scholars from theoretical and applied mechanics as well as from applied mathematics and physics, within an actually cross-disciplinary framework.

The 10th European Nonlinear Dynamics Conference (ENOC 2022) is held in Lyon, France and is organized by the University of Lyon at the Lyon Convention Centre.

ENOC History

Since 1992, EUROMECH organizes European Nonlinear Oscillations Conferences through the European Nonlinear Oscillations Conference Committee (ENOCC). Actually, these events have a much longer tradition, since they are successors of the former ICNO (International Conference on Nonlinear Oscillations) series held from 1961 to 1990 in East-European countries. Starting from the 1st International Conference on Nonlinear Oscillations in Kiev, 1961, twelve ICNOs were organized till 1990. Then, starting with the 1st European Nonlinear Oscillations Conference in Hamburg, 1992, nine ENOCs were organized till 2017 (Prague, Copenhagen, Moscow, Eindhoven, St. Petersburg, Rome, Wien and Budapest).

Both the ICNO and ENOC series of conferences intend to be a meeting place for nonlinear dynamics' scientists from all over the world, where in particular "East meets West"

ENOC 2022 - Program overview

July 17-22, 2022 - Lyon, France

		room **Auditorium**	room **Rhône 1**	room **Rhone 2**	room **Rhone 3A**	room **Rhone 3B**	room **St Clair 1**	room **St Clair 2**	room **St Clair 3A**	room **St Clair 3B**
Sunday, July 17, 2022										
17.00-21.00	Early registration									
19.00-21.00	Welcome reception									
day, July 18, 2022										
09:30-10:30	Opening ceremony									
10:30-11:00	Coffee break									
11:00-12:00	Plenary lecture	I. Kovačić								
12:00-13:30	Lunch									
13:30-15:30	Parallel MS sessions		MS-15	MS-14	MS-03	MS-04	MS-05	MS-07	MS-10	MS-20
15:30-16:00	Coffee break									
16:00-18:20	Parallel MS sessions		MS-15	MS-14	MS-03	MS-04	MS-05	MS-07	MS-10	MS-20
Tuesday, July 19, 2022										
08:30-10:30	Parallel MS sessions	MS-09	MS-15	MS-14	MS-03	MS-04	MS-16	MS-21	MS-13	MS-01
10:30-11:00	Coffee break									
11:00-12:00	Plenary lecture	E. Schöll								
12:00-13:30	Lunch									
13:30-15:30	Parallel MS sessions	MS-09	MS-15	MS-14	MS-12	MS-08	MS-16	MS-21	MS-13	MS-01
15:30-16:00	Coffee break									
16:00-18:20	Parallel MS sessions	MS-09	MS-15	MS-14	MS-06	MS-08	MS-05	MS-07	MS-10	MS-01
Wednesday, July 20, 2022										
08:30-10:30	Parallel MS sessions	MS-09	MS-18	MS-16	MS-03	MS-08	MS-22	MS-21	MS-17	MS-19
10:30-11:00	Coffee break									
11:00-12:00	Plenary lecture	A. Vakakis								
12:00-13:30	Lunch									
14:00-18:00	Excursion									
Thursday, July 21, 2022										
08:30-10:30	Parallel MS sessions	MS-09	MS-18	MS-16	MS-12	MS-08	MS-02	MS-11	MS-17	MS-19
10:30-11:00	Coffee break									
11:00-12:00	Plenary lecture	W. Lacarbonara								
12:00-13:30	Lunch									
13:30-15:30	Parallel MS sessions	MS-09	MS-18	MS-14	MS-12	MS-08	MS-02	MS-11	MS-17	MS-19
15:30-16:00	Coffee break									
16:00-18:00	Poster session									
19:00	Conference banquet									
Friday, July 22, 2022										
08:30-10:30	Parallel MS sessions	MS-09	MS-18	MS-14	MS-12	MS-08	MS-02	MS-11	MS-17	MS-19
10:30-11:00	Coffee break									
11:00-12:00	Plenary lecture	B. Cochelin								
12:00-13:00	Closing ceremony									

Mini-Symposia (MS)

MS-01	Reduced-Order Modeling and System Identification
MS-02	Asymptotic Methods
MS-03	Computational Methods
MS-04	Experiments in Nonlinear Dynamics and Control
MS-05	Slow-Fast Systems and Phenomena
MS-06	Fractional Derivatives
MS-07	Dynamics and Optimization of Multibody Systems
MS-08	Nonlinear Phenomena in Mechanical and Structural Systems
MS-09	Nonlinear Dynamics in Engineering Systems
MS-10	Non-Smooth Dynamics
MS-11	Systems with Time Delay
MS-12	Micro- and Nano-Electro-Mechanical Systems
MS-13	Nonlinear Dynamics in Biological Systems
MS-14	Nonlinear Dynamics for Engineering Design
MS-15	Energy Transfer and Harvesting in Nonlinear Systems
MS-16	Random Dynamical Systems - Recent Advances and New Directions
MS-17	Time-periodic systems
MS-18	Control and Synchronization in Nonlinear Systems
MS-19	Fluid-Structure Interaction
MS-20	Wave Propagation in Mechanical Systems
MS-21	Nonlinear Dynamics in Acoustics
MS-22	Special session dedicated to L.I. Manevitch

KEYNOTE LECTURES

Auditorium Lumière - 11:00-12:00

Monday, July 18, 2022
On Exact Analytical Solutions for Free and Forced Discrete and Continuous Nonlinear Oscillators
Ivana Kovačić
University of Novi Sad, Faculty of Technical Sciences, Serbia

Tuesday, July 19, 2022
On the role of nonlinear dynamics in the installation, operation and monitoring of offshore wind turbines
Andrei Metrikine
Faculty of Civil Engineering, TU Delft

Wednesday, July 20, 2022
Engineering Nonlinearity
Oleg Gendelman
Technion - Israel Institute of Technology, Haïfa, Israel

Thursday, July 21, 2022
High damping metamaterials with hysteretic resonators
Walter Lacarbonara
Department of Structural and Geotechnical Engineering, Sapienza University of Rome, Italy

Friday, July 22, 2022
Computing nonlinear modes in complex continuum mechanical models
Bruno Cochelin
École Centrale de Marseille, University of Marseille, France

Mini-Symposia (MS) Co-organizers

MS-01 Reduced-Order Modeling and System Identification
Lawrence A. Bergman, University of Illinois at Urbana-Champain, USA
Mehmet Kurt, Stanford University, USA
Keegan Moore, University of Nebraska-Lincoln, USA

MS-02 Asymptotic Methods
Jan Awrejcewicz, University of Lodz, Poland
Igor V. Andrianov, Aachen University, Germany
Leonid I. Manevitch†, Russian Academy of Sciences, Russia
Livija Cveticanin, University of Novi Sad, Serbia
† Leonid Manevich left us in the summer of 2020. We would like to pay tribute to him.

MS-03 Computational Methods
Jan Sieber, University of Exeter, UK
Harry Dankowicz, University of Illinois at Urbana-Champaign, USA
Themistoklis Sapsis, Massachusetts Institute of Technology, USA

MS-04 Experiments in Nonlinear Dynamics and Control
Hiroshi Yabuno, University of Tsukuba, Japan
Walter Lacarbonara, University of Rome, Italy
Guilhem Michon, University of Toulouse, France

MS-05 Slow-Fast Systems and Phenomena
Jon Juel Thomsen, Technical University of Denmark, Denmark
Anatoly Neishtadt, Loughborough University, UK
D. Dane Quinn, The University of Akron, USA

MS-06 Fractional Derivatives
Pierre Melchior, Bordeaux Institute of Technology, France
Dana Copot, Ghent University, Belgium

MS-07 Dynamics and Optimization of Multibody Systems
Felix L. Chernousko, IPMech RAS, Russia
József Kövecses, McGill University, Canada
Werner Schiehlen, University of Stuttgart, Germany

MS-08 Nonlinear Phenomena in Mechanical and Structural Systems
Jerzy Warmiński, Lublin University of Technology, Poland
Bala Balachandran, University of Maryland, USA
Sotirios Natsiavas, Aristotle University of Thessaloniki, Greece

MS-09 Nonlinear Dynamics in Engineering Systems
Yuri Vladimirovich Mikhlin, National Technical University “Kharkov Polytechnical Institute”, Ukraine
Matthew Cartmell, The University of Strathclyde, Scotland, UK
Konstantin Vitalievich Avramov, NAS of Ukraine, Ukraine
Francesco Pellicano, University of Modena and Reggio Emilia, Italy

MS-10 Non-Smooth Dynamics
Remco Ingmar Leine, University of Suttgart, germany
Vincent Acary, INRIA, France
Olivier Brüls, University of Liège, Belgium

MS-11 Systems with Time Delay
Zaihua Wang, Nanjing University of Aeronautics and Astronautics, China
Tamas Insperger, Budapest University of Technology and Economics, Hungary
Gabor Orosz, University of Michigan at Ann Arbor, USA

MS-12 Micro- and Nano-Electro-Mechanical Systems
Slava Krylov, Tel Aviv University, Israel
Anil Bajaj, Purdue University, USA
E.M. Abdel-Raman, University of Waterloo, Canada

MS-13 Nonlinear Dynamics in Biological Systems
Gert van der Heijden, University College London, UH
Gergely Röst, University of Szeged, Hungary
Soheil Fatehiboroujeni, UC Merced, USA

MS-14 Nonlinear Dynamics for Engineering Design
Marco Amabili, McGill University, Canada
Stefano Lenci, Università Politecnica delle Marche, Italy
Bogdan Epureanu, University of Michigan, USA

MS-15 Energy Transfer and Harvesting in Nonlinear Systems
Alexander Vakakis, University of Illinois at Urbana-Champaign, USA
Oleg Gendelman, Technion, Israel Institute of Technology, Israel

MS-16 Random Dynamical Systems - Recent Advances and New Directions
Rachel Kuske, School of Math, Georgia Tech, USA
Daniil Yurchenko, Heriot-Watt University, UK

MS-17 Time-periodic systems
Tamas Kalmar-Nagy, Budapest University of Technology and Economics, Hungary
Thomas Pumhössel, Johannes Kepler Universität, Austria
Zoltán Dombóvári, Budapest University of Technology and Economics, Hungary

MS-18 Control and Synchronization in Nonlinear Systems
Nathan van de Wouw, Eindhoven University of Technology, The Netherlands
Bernard Brogliato, INRIA Grenoble Rhône-Alpes, France
Alexey Pavlov, Norwegian University of Science and Technology (NTNU), Norway

MS-19 Fluid-Structure Interaction
Andrei Metrikine, Delft University of Technology, The Netherlands
Oded Gottlieb, Technion - Israel Institute of Technology, Israel
Kerry Hourigan, Monash University, Australia

MS-20 Wave propagation in Mechanical Systems and Nonlinear Metamaterials
Francesco Romeo, Sapienza University of Rome, Italy
Yuli Starosvetsky, Technion, Israel Institute of Technology, Israel
Marco Lepidi, University of Genova, Italy

MS-21 Nonlinear Dynamics in Acoustics
Cyril Touzé, ENSTA ParisTech, France
Olivier Thomas, ENSAM Lille, France
Jose Antunes, Instituto Superior Técnico, University of Lisbon, Portugal
Stefan Bilbao, University of Edinburgh, UK

MS-22 Special session dedicated to L.I. Manevitch
Yuri V. Mikhlin, National Technical University «Kharkiv Polytechnic University», Ukraine
Igor V. Andrianov, Aachen University, Germany
Oleg V. Gendelman, Technion, Israel Institute of Technology, Israel

ENOC 2022 MS Sessions

Monday, July 18, 2022

13:30 - 15:30 MS-04 Experiments in Nonlinear Dynamics and Control (Rhone 3B) 11
13:30 - 15:30 MS-15 Energy Transfer and Harvesting in Nonlinear Systems (Rhone 1) 26
13:30 - 15:30 MS-07 Dynamics and Optimization of Multibody Systems (Saint Clair 2) 36
13:30 - 15:30 MS-14 Nonlinear Dynamics for Engineering Design (Rhone 2) 63
13:30 - 15:30 MS-03 Computational Methods (Rhone 3A) 76
13:30 - 15:30 MS-05 Slow-Fast Systems and Phenomena (Saint Clair 1) 89
13:30 - 15:50 MS-10 Non-Smooth Dynamics (Saint Clair 3A) 105
13:30 - 15:30 MS-20 Wave propagation in Mechanical Systems and Nonlinear Metamaterials (Saint Clair 3B) 120

16:00 - 18:20 MS-04 Experiments in Nonlinear Dynamics and Control (Rhone 3B) 134
16:00 - 18:00 MS-15 Energy Transfer and Harvesting in Nonlinear Systems (Rhone 1) 155
16:00 - 18:20 MS-14 Nonlinear Dynamics for Engineering Design (Rhone 2) 164
16:00 - 18:20 MS-03 Computational Methods (Rhone 3A) 179
16:00 - 18:20 MS-05 Slow-Fast Systems and Phenomena (Saint Clair 1) 195
16:00 - 18:20 MS-07 Dynamics and Optimization of Multibody Systems (Saint Clair 2) 204
16:00 - 18:40 MS-10 Non-Smooth Dynamics (Saint Clair 3A) 228
16:00 - 18:20 MS-20 Wave propagation in Mechanical Systems and Nonlinear Metamaterials (Saint Clair 3B) 250

Tuesday, July 19, 2022

08:30 - 10:30 MS-21 Nonlinear Dynamics in Acoustics (Saint Clair 2) 272
08:30 - 10:30 MS-04 Experiments in Nonlinear Dynamics and Control (Rhone 3B) 289
08:30 - 10:30 MS-01 Reduced-Order Modeling and System Identification (Saint Clair 3B) 304
08:30 - 10:30 MS-14 Nonlinear Dynamics for Engineering Design (Rhone 2) 319
08:30 - 10:30 MS-13 Nonlinear Dynamics in Biological Systems (Saint Clair 3A) 338
08:30 - 10:30 MS-16 Random Dynamical Systems - Recent Advances and New Directions (Saint Clair 1) 349
08:30 - 10:30 MS-03 Computational Methods (Rhone 3A) 358
08:30 - 10:30 MS-15 Energy Transfer and Harvesting in Nonlinear Systems (Rhone 1) 375
08:30 - 10:30 MS-09 Nonlinear Dynamics in Engineering Systems (Auditorium Lumiere) 388

13:30 - 15:30 MS-01 Reduced-Order Modeling and System Identification (Saint Clair 3B) 406
13:30 - 15:30 MS-21 Nonlinear Dynamics in Acoustics (Saint Clair 2) 420
13:30 - 15:30 MS-13 Nonlinear Dynamics in Biological Systems (Saint Clair 3A) 439
13:30 - 15:30 MS-08 Nonlinear Phenomena in Mechanical and Structural Systems (Rhone 3B) 453
13:30 - 15:30 MS-16 Random Dynamical Systems - Recent Advances and New Directions (Saint Clair 1) 478
13:30 - 15:30 MS-12 Micro- and Nano-Electro-Mechanical Systems (Rhone 3A) 496
13:30 - 15:30 MS-14 Nonlinear Dynamics for Engineering Design (Rhone 2) 503
13:30 - 15:30 MS-15 Energy Transfer and Harvesting in Nonlinear Systems (Rhone 1) 514
13:30 - 15:30 MS-09 Nonlinear Dynamics in Engineering Systems (Auditorium Lumiere) 525

16:00 - 18:20 MS-01 Reduced-Order Modeling and System Identification (Saint Clair 3B) 536
16:00 - 18:20 MS-10 Non-Smooth Dynamics (Saint Clair 3A) 556
16:00 - 18:00 MS-07 Dynamics and Optimization of Multibody Systems (Saint Clair 2) 571
16:00 - 18:20 MS-05 Slow-Fast Systems and Phenomena (Saint Clair 1) 584
16:00 - 18:20 MS-08 Nonlinear Phenomena in Mechanical and Structural Systems (Rhone 3B) 603
16:00 - 18:20 MS-06 Fractional Derivatives (Rhone 3A) 618
16:00 - 18:20 MS-14 Nonlinear Dynamics for Engineering Design (Rhone 2) 627
16:00 - 18:20 MS-15 Energy Transfer and Harvesting in Nonlinear Systems (Rhone 1) 636
16:00 - 18:20 MS-09 Nonlinear Dynamics in Engineering Systems (Auditorium Lumiere) 649

Wednesday, July 20, 2022

08:30 - 10:30 MS-22 Special session dedicated to L.I. Manevitch (Saint Clair 1) 663
08:30 - 10:30 MS-16 Random Dynamical Systems - Recent Advances and New Directions (Rhone 2) 677
08:30 - 10:30 MS-21 Nonlinear Dynamics in Acoustics (Saint Clair 2) 692
08:30 - 10:30 MS-08 Nonlinear Phenomena in Mechanical and Structural Systems (Rhone 3B) 726
08:30 - 10:30 MS-03 Computational Methods (Rhone 3A) 739
08:30 - 10:30 MS-18 Control and Synchronization in Nonlinear Systems (Rhone 1) 754
08:30 - 10:30 MS-09 Nonlinear Dynamics in Engineering Systems (Auditorium Lumiere) 773
08:30 - 10:30 MS-17 Time-periodic systems (Saint Clair 3A) 792
08:30 - 10:30 MS-19 Fluid-Structure Interaction (Saint Clair 3B) 808

Thursday, July 21, 2022

08:30 - 10:30 MS-19 Fluid-Structure Interaction (Saint Clair 3B) . . . 826
08:30 - 10:30 MS-17 Time-periodic systems (Saint Clair 3A) . . . 837
08:30 - 10:30 MS-11 Systems with Time Delay (Saint Clair 2) . . . 852
08:30 - 10:30 MS-02 Asymptotic Methods (Saint Clair 1) . . . 863
08:30 - 10:30 MS-08 Nonlinear Phenomena in Mechanical and Structural Systems (Rhone 3B) . . . 875
08:30 - 10:30 MS-12 Micro- and Nano-Electro-Mechanical Systems (Rhone 3A) . . . 891
08:30 - 10:30 MS-16 Random Dynamical Systems - Recent Advances and New Directions (Rhone 2) . . . 904
08:30 - 10:30 MS-18 Control and Synchronization in Nonlinear Systems (Rhone 1) . . . 909
08:30 - 10:30 MS-09 Nonlinear Dynamics in Engineering Systems (Auditorium Lumiere) . . . 920

13:30 - 15:30 MS-17 Time-periodic systems (Saint Clair 3A) . . . 931
13:30 - 15:30 MS-11 Systems with Time Delay (Saint Clair 2) . . . 942
13:30 - 15:30 MS-02 Asymptotic Methods (Saint Clair 1) . . . 955
13:30 - 15:30 MS-12 Micro- and Nano-Electro-Mechanical Systems (Rhone 3A) . . . 965
13:30 - 15:30 MS-18 Control and Synchronization in Nonlinear Systems (Rhone 1) . . . 978
13:30 - 15:30 MS-14 Nonlinear Dynamics for Engineering Design (Rhone 2) . . . 993
13:30 - 15:30 MS-09 Nonlinear Dynamics in Engineering Systems (Auditorium Lumiere) . . . 1002
13:30 - 15:30 MS-08 Nonlinear Phenomena in Mechanical and Structural Systems (Rhone 3B) . . . 1020
13:30 - 15:30 MS-19 Fluid-Structure Interaction (Saint Clair 3B) . . . 1033

16:00 - 18:00 Poster Session (Foyer Lumiere) . . . 1053

Friday, July 22, 2022

08:30 - 10:30 MS-11 Systems with Time Delay (Saint Clair 2) . . . 1110
08:30 - 10:30 MS-09 Nonlinear Dynamics in Engineering Systems (Auditorium Lumiere) . . . 1123
08:30 - 10:30 MS-18 Control and Synchronization in Nonlinear Systems (Rhone 1) . . . 1124
08:30 - 10:30 MS-14 Nonlinear Dynamics for Engineering Design (Rhone 2) . . . 1133
08:30 - 10:30 MS-12 Micro- and Nano-Electro-Mechanical Systems (Rhone 3A) . . . 1153
08:30 - 10:30 MS-08 Nonlinear Phenomena in Mechanical and Structural Systems (Rhone 3B) . . . 1164
08:30 - 10:30 MS-02 Asymptotic Methods (Saint Clair 1) . . . 1165
08:30 - 10:30 MS-17 Time-periodic systems (Saint Clair 3A) . . . 1179
08:30 - 10:30 MS-19 Fluid-Structure Interaction (Saint Clair 3B) . . . 1194

Author index . . . 1201

Monday, July 18, 2022

13:30 - 15:30

MS-04 Experiments in Nonlinear Dynamics and Control

Rhone 3B

Chair: Guilhem Michon

13:30 - 13:50
Analysis of nonlinear gear dynamics based on visualization of vibro-impact regimes
RIGAUD Emmanuel*, PERRET-LIAUDET Joel
*Laboratoire de Tribologie et Dynamique des Systèmes (Ecole Centrale de Lyon. 36 avenue Guy de Collongue. 69134 ECULLY cedex France)

13:50 - 14:10
Ensemble Models for Identification of Nonlinear Systems with Stick-Slip
PIRES Macedo Oliveira Dos Santos Ingrid*, AYALA Helon, WEBER Hans
*Pontifical Catholic University (Marquês de São Vicente Street, 225 Brazil)

14:10 - 14:30
Experimental bifurcation analysis of a self-excited system exhibiting a subcritical Hopf bifurcation using control-based continuation
LEE Kyoung Hyun*, BARTON David, RENSON Ludovic
*Department of Engineering Mathematics, University of Bristol (Department of Engineering Mathematics University of Bristol Merchant Venturers Building Woodland Road Bristol, BS8 1UB, England, UK United Kingdom)

14:30 - 14:50
Experimental Dynamics of Composite Bistable Cantilever Shells
MITURA Andrzej*, WARMINSKI Jerzy, BRUNETTI Matteo, ROMEO Francesco
*Department of Applied Mechanics, Lublin University of Technology (Nadbystrzycka 38D, 20-618 Lublin Poland)

14:50 - 15:10
Exploration of edge states by bubbles in a constricted Hele-Shaw channel
KEELER Jack, GAILLARD Antoine, **THOMPSON Alice***, HAZEL Andrew, JUEL Anne
*Manchester Centre for Nonlinear Dynamics (University of Manchester, Oxford Road, Manchester, M13 9PL United Kingdom) - Department of Mathematics, University of Manchester (Oxford Road, Manchester, M13 9PL United Kingdom)

Analysis of nonlinear gear dynamics based on visualization of vibro-impact regimes

Emmanuel Rigaud, Joël Perret-Liaudet
Tribology and Systems Dynamics Laboratory, LTDS UMR 5513
Université de Lyon, Ecole Centrale de Lyon, ENISE, ENTPE, CNRS
36 avenue Guy de Collongue, F-69134, ECULLY, France
Corresponding author: emmanuel.rigaud@ec-lyon.fr

Summary. Nonlinear gear dynamic response and rattle noise induced by vibroimpacts between gear teeth are investigated using a specific experimental set-up allowing the visualization of impacts thanks to a high-speed camera. The control parameters during the experiment are the drag torque, the mean drive gear rotational speed, and the velocity fluctuation amplitude and frequency. Most of the time, an almost 1*T*-periodic response is observed with 2 impacts per period. A contact phase between gear teeth is observed after each impact instead of an instantaneous rebound. The number of successive tooth pairs crossing the meshing zone without any contact between gear teeth varies according to the ratio of the excitation frequency to the rotation frequency. Analytical and numerical works performed using a gear rattle model show good agreement with the experiments. Finally, the sound pressure emitted from the gear pair is measured. The acoustic power imputable to gear rattle is found to be proportional to the total kinetic energy transferred per second to the system by the successive impacts.

Introduction

Many geared systems, are subjected to such external excitations that contact losses between gear teeth may occur under some particular operating conditions (e. g. manual automotive gearbox [1], roots vacuum pump [2]). The nonlinear gear dynamic response is then characterized by impacts between the active and/or the reverse tooth flanks, leading to a broadband noise emitted from the mechanical system known as gear rattle noise. In this study, a specific experimental set-up is designed to analyse the rattle behaviour of a spur gear. Most of the key parameters governing the nonlinear dynamics are controlled during the experiments, that is to say the velocity fluctuation amplitude and frequency of the drive gear, the inertia of the output gear, the drag torque, and the gear backlash. Unlike most systems and experimental studies, the vibratory level of the drive gear is controlled independently of its mean rotational speed. Operation is performed without oil lubrication in order to allow simple modelling of the elastic and damping characteristics during impacts and easy direct visualization of the meshing zone, thanks to a high-speed camera. The occurrence of successive impacts between gear teeth obtained from video post-processing are then coupled with the gear dynamic transmission error measurement thanks to high resolution optical encoders. Finally, the sound pressure generated by successive impacts between gear teeth is also measured thanks to a microphone.

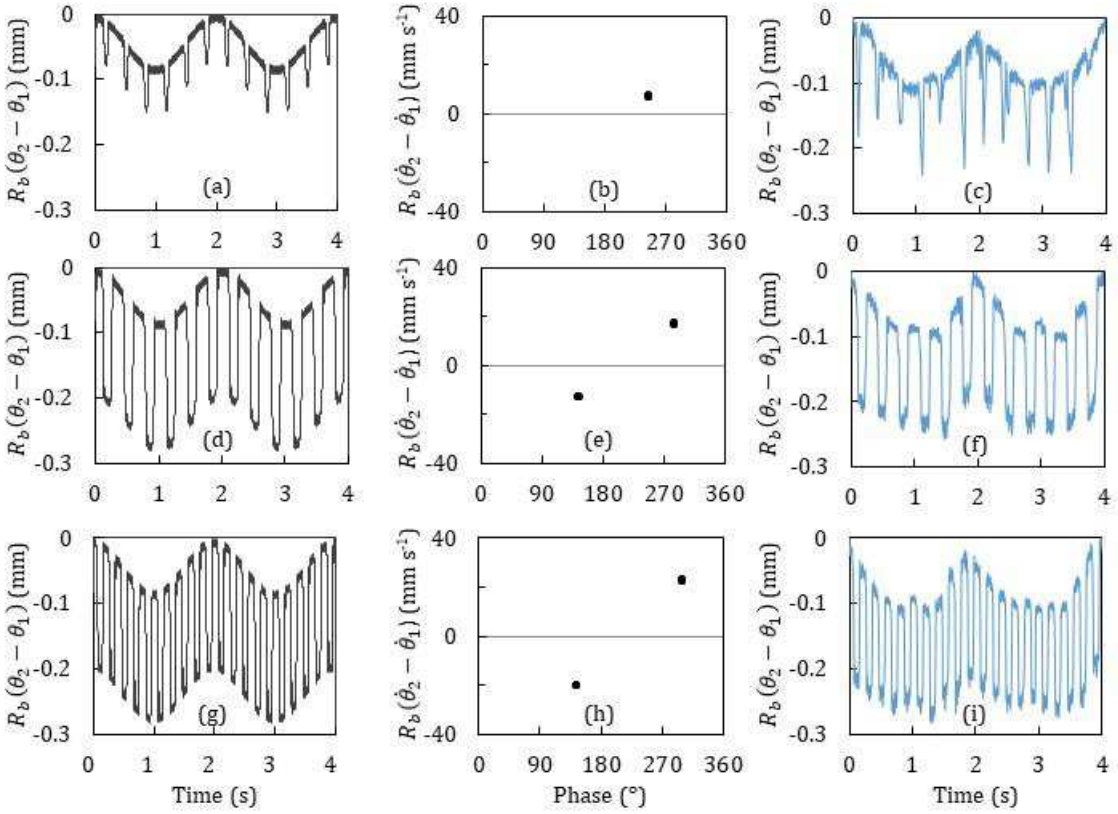

Figure 1: Impact response (numerical transmission error, Poincaré section, experimental transmission error) for several velocity fluctuation frequency and amplitude.

Nonlinear gear dynamic responses

The instantaneous drive gear velocity is:

$$\Omega(t) = \Omega_0 + \Delta\Omega \sin(\omega t) \quad (1)$$

The piloting allows increasing and decreasing sweeps of the mean rotational speed Ω_0, the velocity fluctuation amplitude $\Delta\Omega$ and frequency ω. Parameters are controlled independently. First, the effect of velocity fluctuation amplitude $\Delta\Omega$ is analysed for a chosen excitation frequency ω. Second, the effect of the excitation frequency ω is analysed for a chosen velocity fluctuation amplitude $\Delta\Omega$. For a very low excitation, an almost permanent contact between the active flanks is observed. When the amplitude is increased, the rattle threshold is reached. Video post-processing (see figure 2) and dynamic transmission error response (see figure 1) show noticeable contact losses and impacts. First, impacts only occur between the active flanks with a low impacting velocity, because the excitation amplitude is still too low to cross the gear backlash. Larger excitation amplitude leads to successive impacts alternating between the active and the reverse flanks. The output gear crosses the gear backlash forward and backward. Each impact is followed by a persistent contact phase between the gear teeth. The free flight period and the following persistent contact phase show a duration of the same order of magnitude. Considering the period of the excitation $T = 2\pi/\omega$, the gear dynamics corresponds to a $1T$-periodic response with 2 impacts per period. Poincaré sections show that impact phases and impacting velocities are almost constant for all the successive impacts between the active flanks, as well as for all the impacts between the reverse flanks. Visualization confirms that the number of successive tooth pairs in contact and the number of successive tooth pairs crossing the meshing zone without any contact between gear teeth vary according to the ratio of the excitation frequency to the rotation frequency.

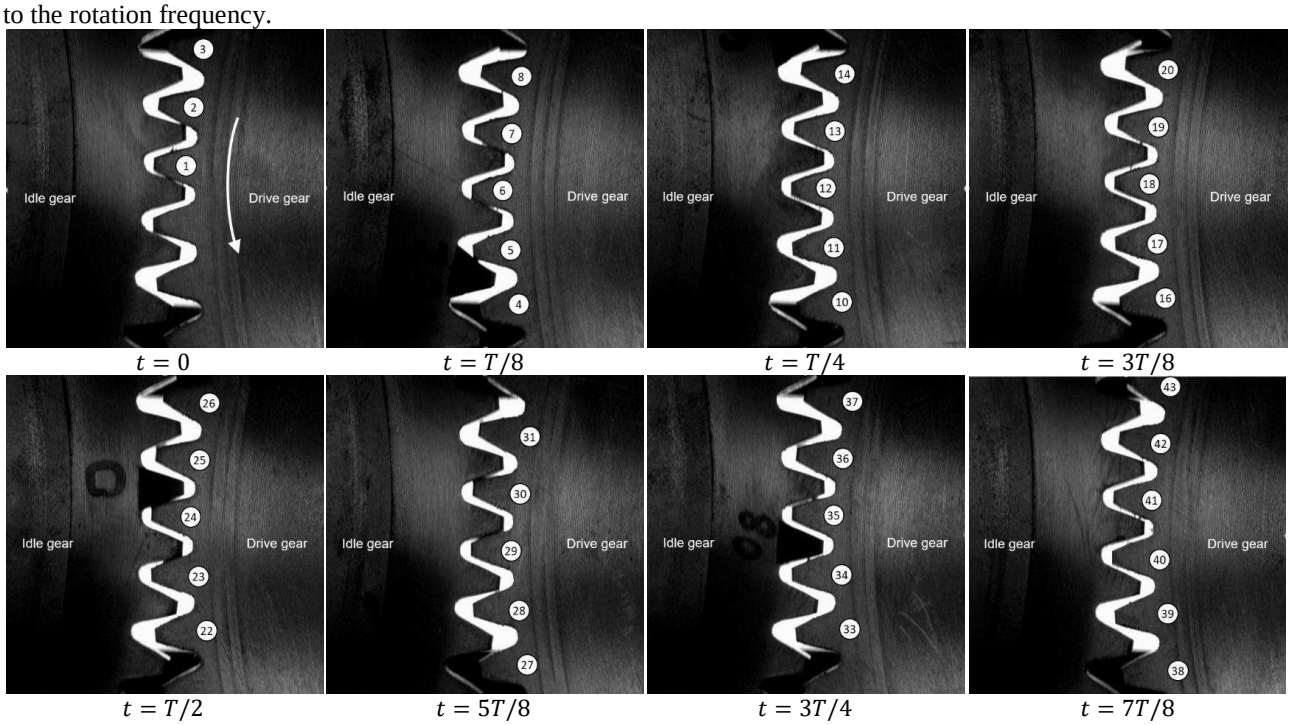

Figure 2: Sequence of images of the contact along a period of excitation.

The gear rattle dynamics is modelled with a SDOF bouncing ball with two moving walls excited by the velocity fluctuation. After adjustment of the restitution coefficient modelling the damping characteristics during impacts, a very good agreement between experimental and numerical results is observed. A slight difference is confirmed between active flanks impacts and reverse flanks impacts for which the impacting velocity is slightly lower. The squared impacting velocity transferred to the system, shows a linear relationship with the product $\omega\Delta\Omega$. It is proportional to the impacting kinetic energy which is entirely transferred to the system, because of the persistent contact observed after the impact. Taking account of the number of impacts per second proportional to ω, the assumption that the acoustic power generated by the successive impacts is proportional to the energy transferred to the system per second i.e. parameter $\omega^2\Delta\Omega$, is validated by rattle noise measurement. For low amplitude of parameter $\omega^2\Delta\Omega$, the successive impacts are clearly audible once they occur, but the sound pressure radiated from the system is mainly due to the gear whining noise. For larger amplitude of parameter $\omega^2\Delta\Omega$, the rattle noise induced by the successive impacts becomes the main source of acoustic nuisance.

References

[1] Kadmiri Y., Rigaud E., Perret-Liaudet J., Vary L. (2012) Experimental and numerical analysis of automotive rattle noise. Journal of Sound and Vibration 331(13), 3144-3157, 2012.

[2] Mason J., Homer M., Wilson R. (2007) Mathematical models of gear rattle in roots blower vacuum pumps. Journal of sound and vibration, 308 (3–5), 431-440.

[3] Rigaud E., Perret-Liaudet J. (2020) Investigation of gear rattle noise including visualization of vibro-impact regimes. Journal of sound and vibration, 467, (article 115026, online version: https://doi.org/10.1016/j.jsv.2019.115026).

Ensemble Models for Identification of Nonlinear Systems with Stick-Slip

Ingrid Pires*, Helon Vicente Hultmann Ayala* and Hans Ingo Weber*
*Department of Mechanical Engineering, Pontifical Catholic University, Rio de Janeiro, Brazil

Summary. The nonlinear interactions between the drilling equipment and the rock formation result in torsional, axial, and lateral oscillations in oil drilling routines. Concerning torsional oscillations, the stick-slip phenomenon is the most severe stage. This kind of self-sustained vibrations compromise the performance of mechanical systems. Accordingly, adequate mathematical models are required to analyze these vibrations. In this work, we study two different ways of combining system identification techniques. We employ time-domain data of an experimental setup to build ensemble models. Then we simulate the system and compare their effectiveness in enhancing the accuracy of model predictions and reproducing the stick-slip phenomenon.

Introduction

The nonlinear interactions between the drilling equipment and the rock formation result in torsional, axial, and lateral oscillations in oil drilling routines. The stick-slip phenomenon is the most severe stage of torsional oscillations. In these drilling processes, the phenomenon of stick-slip is the alternation of two phases: the stick phase, in which the drill bit remains stopped by the resistive torque, and the slip phase, which begins when the stored energy overcomes the resistive torque, and the bit is set in motion.
Stick-slip oscillations compromise the performance of mechanical systems [1], therefore proper mathematical descriptions are required to simulate and analyze the system. Extensive surveys on drill string modeling and dynamics can be found in [2, 3].
A common practice is to model the nonlinear interaction between the drill string and rock as dry friction. Regarding the stick-slip phenomenon, the complexity of the analysis lies in the fact that two different friction mechanisms govern the motion. During the stick phase, the static friction rules the motion, while velocity-dependent kinetic friction governs it during the slip phase [1].
Practical limitations of analytical analysis motivate the application of system identification, which comprises a set of techniques for building data-based models. The author of [4] classifies system identification techniques in white, gray, and black-box. They differ from each other by the amount of prior knowledge employed in the construction of mathematical models.
This paper explores two different methods of building ensemble models for an experimental drill string setup. The ensemble model, in this context, consists of a combination between grey and black-box approaches. The test rig used in this study uses dry friction contact to simulate the nonlinear interactions present in drilling routines. We employ time-domain data to build the ensemble models and compare their effectiveness in enhancing the accuracy of model predictions and reproducing the stick-slip phenomenon. The main contribution of this work is the investigation of the suitability of the ensemble of gray and black-box approaches for the identification of systems with friction-induced vibrations.

Experimental system

The test rig employed in this study is a horizontal apparatus composed of a DC motor connected to two solid discs by a low stiffness shaft. The shaft transmits torque and motion from the DC motor to the discs, which are free to rotate. Figure 1 displays a picture of the experimental setup.

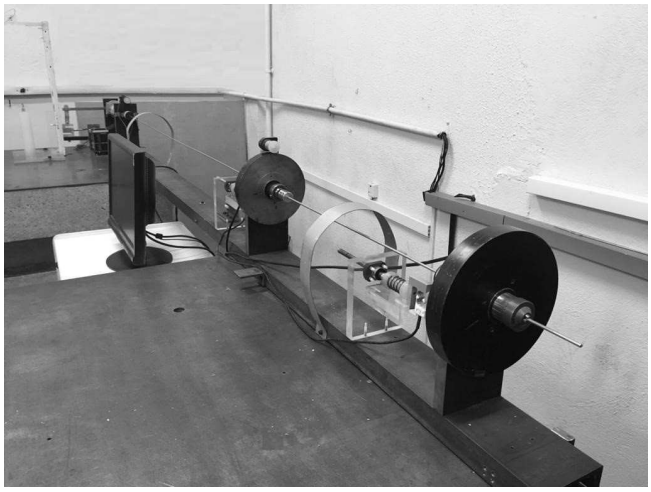

Figure 1: Experimental test rig composed of DC motor, solid discs, and low stiffness shaft.

The rig can replicate the undesired torsional vibrations present in drilling routines. Two braking devices act on the solid

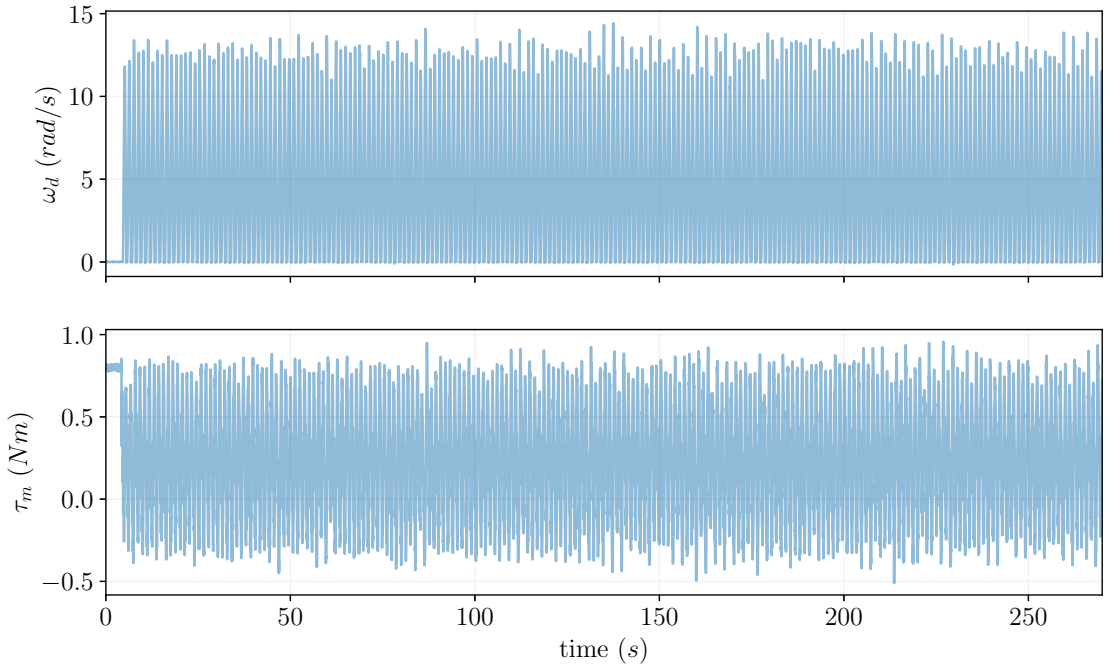

Figure 2: Measured time history of (top) disc angular velocity, ω_d; and (bottom) motor torque, τ_m.

discs to induce friction torque, leading the system to exhibit torsional oscillations and stick-slip. Only the subsystem composed of one of the discs, the intermediary one, and the shaft connecting it to the DC motor is considered in this work.

The dynamical model

Assuming that the subsystem composed of the intermediary disc and the shaft connecting it to the DC motor behaves as a torsional pendulum and that the only resistive torque in the system is caused by the friction torque induced by the braking device, we modeled it as:

$$\begin{aligned} J_d\ddot{\theta}_d + c(\dot{\theta}_d - \dot{\theta}_m) + c_d\dot{\theta}_d + k(\theta_d - \theta_m) &= -T_f, \\ J_m\ddot{\theta}_m + c(\dot{\theta}_m - \dot{\theta}_d) + c_m\dot{\theta}_m + k(\theta_m - \theta_d) &= \tau_m, \end{aligned} \tag{1}$$

where the moments of inertia of the disc and the motor are J_d and J_m. The shaft stiffness is denoted by k and the internal damping by c. c_d and c_m are the external dampings. θ, $\dot{\theta}$, and $\ddot{\theta}$ are the angular displacement, angular velocity, and angular acceleration of the inertias, respectively. The resistive friction torque on disc D2 is denoted by T_f, and the torque transmitted to the mechanical subsystem is denoted by τ_m.

The experimental data

We utilized a LabView-based Data Acquisition System (DAQ) to measure forces, displacements, and velocities. Figure 2 shows the time histories of the disc angular velocity (top) the motor torque (bottom). The motor torque is the system input, and the disc angular velocity is the system output.

We acquired these records for a nominal angular velocity of $5.76\ rad/s$ and an average normal contact force between pin and disc of $50\ N$. As we can observe in Fig. 2, this combination of nominal angular velocity and normal force leads the system to exhibit stick-slip oscillations. The signals were recorded for 270 seconds.

Methodology

This analysis employs the test rig physical description in two different ensemble models to improve the precision of the predictions. There are three approaches for system identification: white, gray, and black-box. The techniques differ from each other by the amount of prior knowledge used in the mathematical models' construction. The white-box approach applies only physical insight, the gray-box uses less physical information, and the black-box does not involve a priori knowledge. The ensemble models studied in this paper are combinations of gray and black-box components.

This study compares two different methods of building ensemble models. According to [5], one method to build an ensemble model is to use a white-box as a mean function and fit the model residuals using a black-box algorithm. Instead, in this study, we used the gray-box model as a mean function and modeled the residuals with a black-box algorithm:

$$\hat{y_e} = \overbrace{f(x,u)}^{\text{gray-box}} + \overbrace{g(\hat{e},u)}^{\text{black-box}} \tag{2}$$

where $\hat{y_e}$ is the predicted output of the ensemble model. $\hat{y_e}$ is a sum of the predicted system model output $\hat{y_m} = f(x,u)$ and the predicted model residual $\hat{e} = g(\hat{e},u)$. The predicted system output $\hat{y_m}$ is a function of the system input u, and space states x, and the predicted error $\hat{e}$ is a function of the system input u and itself. Another way to construct an ensemble model is to use the information encoded in a white or a gray-box model as an additional input to the black-box. Here, we used the gray-box model output as an input to the black-box as follows:

$$\hat{y_e} = \overbrace{h(e, \underbrace{f(x,u)}_{\text{gray-box}})}^{\text{black-box}} \tag{3}$$

h is a function of the model residual, e, and the output of the gray-box model $f(x,u)$. For simplicity, we name (2) Model 1 and (3) Model 2 in the analysis. Figure 3 gives a general overview of the methodology employed for the formulation of Model 1 and Model 2.

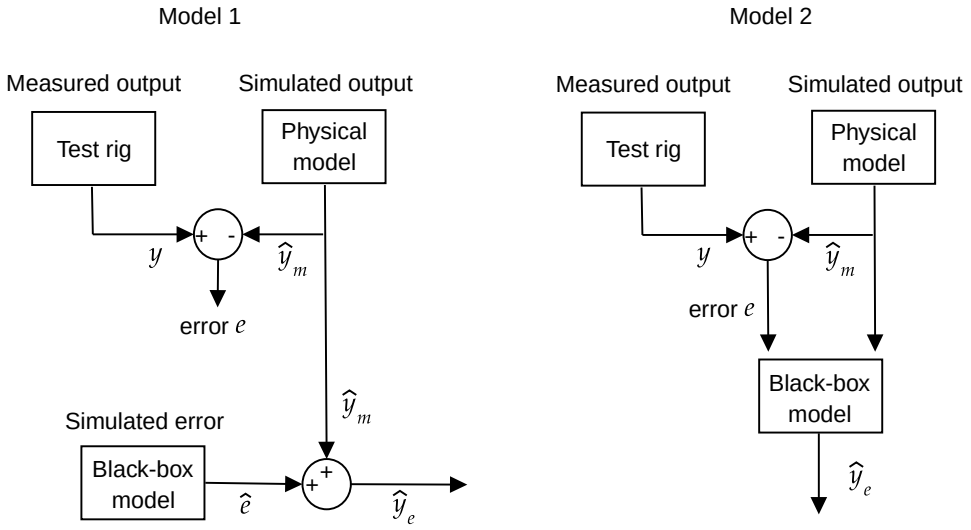

Figure 3: Methodological formulations for (right) Model 1, and (left) Model 2.

Gray-box model

Physical and semi-physical models are particular cases of gray-box models and are related to the estimation of the physical parameters of a system. To estimate the physical parameters of the test rig described by (1), we defined the following state-variables:

$$\mathbf{x} = \begin{bmatrix} \delta & \dot{\theta_d} & \dot{\theta_m} \end{bmatrix}^T,$$

where $\delta = \theta_d - \theta_m$ is the angular difference. Therefore, (1) can be rewritten as a state-space system as follows:

$$\begin{aligned} \dot{\mathbf{x}} &= \begin{bmatrix} 0 & 1 & -1 \\ -k/J_d & -(c+c_d)/J_d & c/J_d \\ k/J_m & c/J_m & -(c+c_m)/J_m \end{bmatrix} \mathbf{x} + \begin{bmatrix} 0 & 0 \\ -1/J_d & 0 \\ 0 & 1/J_m \end{bmatrix} \begin{bmatrix} T_f \\ \tau_m \end{bmatrix} \\ y_m &= \begin{bmatrix} 0 & 1 & 0 \end{bmatrix} \mathbf{x} \end{aligned} \tag{4}$$

where y_m is the output of our gray-box model. The system of (4) is nonlinear since resistive friction torque T_f is a nonlinear function of the disc angular velocity ω_d. T_f is given by:

$$T_f = F_f a, \tag{5}$$

where a is the distance between the disc center and the disc-pin contact point. F_f is the friction force.

The Coulomb friction model states that friction opposes the relative motion between contacting surfaces, and its magnitude is proportional to the normal contact force. The classical Coulomb friction model presents a velocity dependence by the sign function that introduces a discontinuity in the system of ODEs. The regularized Coulomb friction model, instead,

considers the hyperbolic tangent with the transition velocity, v_t, approximation for this study to avoid discontinuities. The following equation defines the regularized model:

$$F_f = F_C \tanh\left(\frac{v}{v_t}\right). \tag{6}$$

where F_f is the friction force, $F_C = \mu_k F_N$ is the magnitude of the Coulomb friction, v is, from the perspective of the body, the relative tangential velocity between the contacting surfaces, F_N is the normal force, and μ_k is the kinetic friction coefficient. For simplicity, we consider $T_C = F_C a$ as the resistive torque related to the kinetic Coulomb friction.

Black-box model

Black-box models are constructed without a priori information. Data acquired from experimentation is used to capture the system dynamics in this modeling. Regarding black-box, we utilized the AutoRegressive eXogenous (ARX) model and the Nonlinear AutoRegressive eXogenous (NARX) model. The ARX structure is:

$$\begin{aligned} y(k) = -(a_1 y(k-1) + a_2 y(k-2) + ... + a_n y(k-n_y)) + \\ (b_1 u(k) + b_2 u(k-1) + ... + b_{n+1} u(k-n_u)), \end{aligned} \tag{7}$$

where $y(k)$, $u(k)$ are the system output and input, respectively; and n_y and n_u are the maximum lags at the system output and input, respectively.

The NARX models are a nonlinear extension of the ARX models [6, 7].The NARX structure is:

$$\begin{aligned} y(k) = F(y(k-1), y(k-2), ..., y(k-n_y), \\ u(k-d), u(k-d-1), ..., u(k-d-n_u)), \end{aligned} \tag{8}$$

F is some nonlinear function, and d is a time delay.

Results and Discussion

We evaluated the performance of the proposed identification methodology via simulation. First, we integrated (4) utilizing the 5th-order Runge-Kutta numerical method with a time step equal to $0,01$ in Matlab. The simulations employed the experimental data for input τ_m. The data set employed for the identification is composed of experimental data from 30 to 90 seconds. And the one used for the validation analyses is composed of experimental data from 120 to 180 seconds.

Table 1 gives the set of estimated parameters obtained employing the system dynamics forward simulation. Using the estimated parameter depicted in Table 1, we simulated the system and calculated the error of prediction to build the ensemble models.

Table 1: Estimated parameters values

$k\ (Nm/rad)$	0.1614
$c\ (Ns/m)$	0
$c_d\ (Ns/m)$	0
$c_m\ (Ns/m)$	0.0071
$T_C\ (Nm)$	0.2278

For Model 1, the NARX model with motor torque τ_m as input, and error e as output was built as follows:

$$e(k) = \alpha_1 e(k-1) + \alpha_2 e(k-2) + \beta_1 \tau_m(k-1) + beta_2 \tau_m(k-2) +_1 e(k-1)\tau_m(k-1), \tag{9}$$

where α_1, α_2, β_1, β_2, and γ_1 are the parameters of the NARX model. We trained the black-box model with the recorded input and output data of the time interval from 30 to 90 seconds of the recording in Fig. 2 and validated it by employing the recorded input and output data of the time interval from 120 to 180 seconds. We constructed the ensemble model as displayed in (2).

For Model 2, the ARX model with error e and y_m as input, and ensemble model y_e as output was built as follows:

$$y_e(k) = -(a_2 e(k-2) + b_1 y_m(k-1) + b_2 y_m(k-2)) + c_1 y_e(k-1), \tag{10}$$

where a_2, b_1, b_2, and c_1 are the parameters of the ARX model. We trained the black-box model with the recorded input and output data of the time interval from 30 to 90 seconds of the recording in Fig. 2 and validated it by employing the recorded input and output data of the time interval from 120 to 180 seconds. We constructed the ensemble model as displayed in (3).

Figure 4 depicts the free-run prediction obtained with Model 1 (top) and Model 2 (bottom), plotting the direct comparison of experimental and estimated time histories of the disc angular velocity for the validation set. The two ensemble models can reproduce the torsional oscillations with the stick-slip phenomenon observed in the experimental results. Figure 5 shows us one interval of the stick phase, comparing measurements and estimations for the two models.

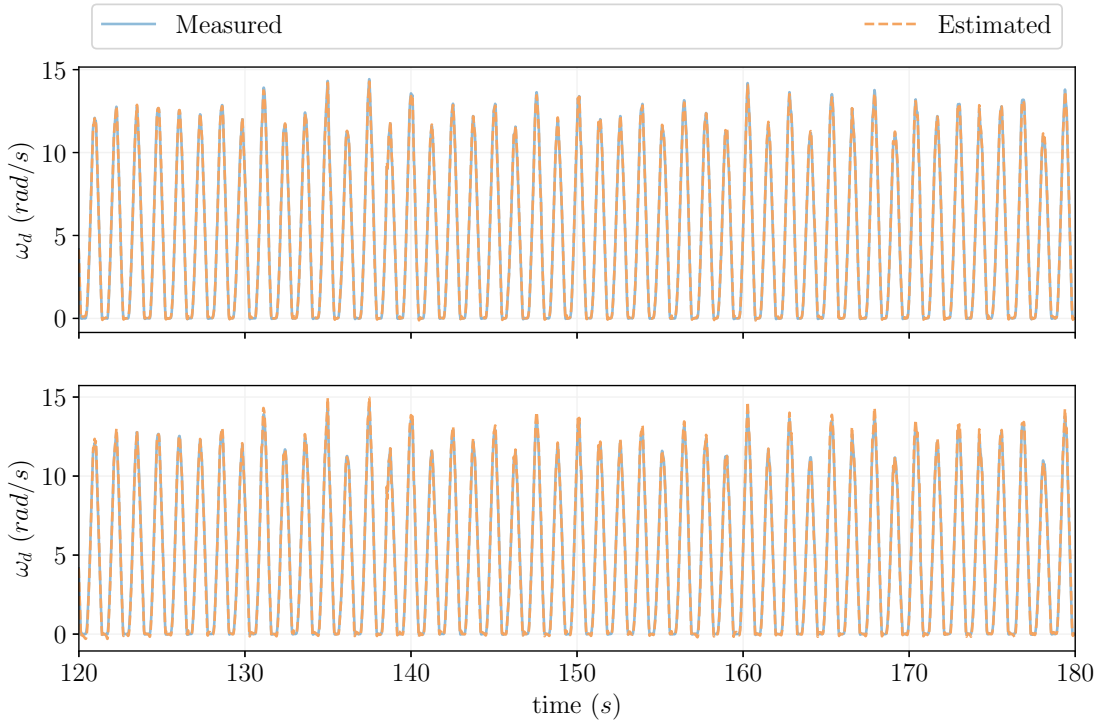

Figure 4: Comparison of measured and predicted disc angular velocity using: (top) Model 1, and (bottom) Model 2.

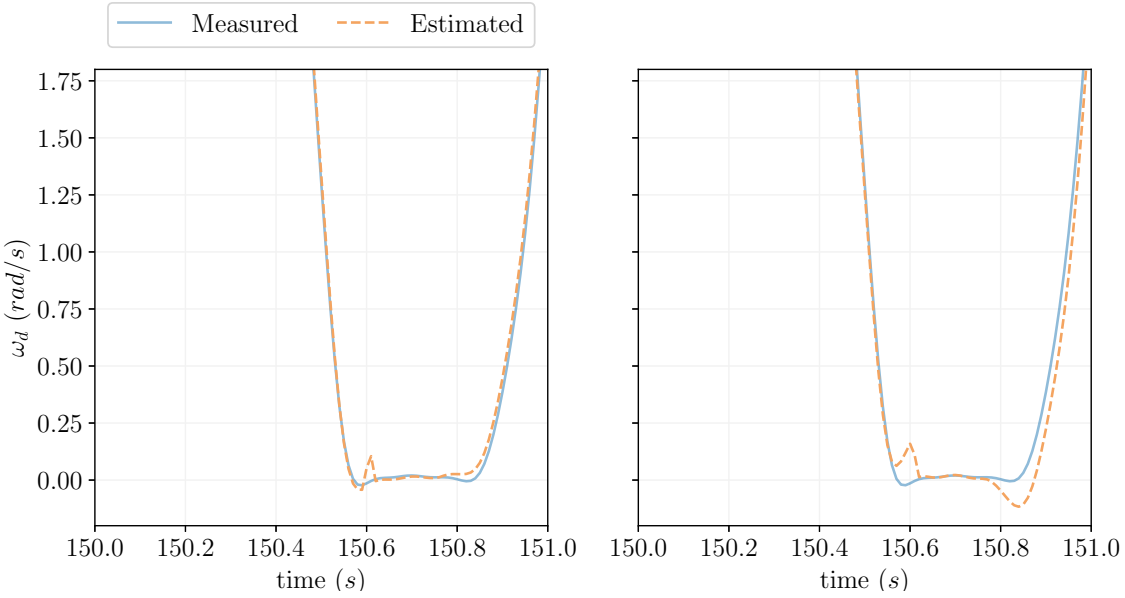

Figure 5: Comparison of measured and predicted disc angular velocity, one stick phase interval, using: (top) Model 1, and (bottom) Model 2.

Figure 6 plots the histogram of the prediction errors for both Models. From the graph of Fig. 6, we can conclude that Model 2 presents the higher prediction errors. Table 2 presents the Root Mean Squared Error (RMSE) and the maximum error for the two ensemble models. From Tab. 2, we see that the ensemble Model 1 presented the lowest RMSE score and the lowest maximum error.

Table 2: RMSE and maximum error scores

	RMSE	max error
Model 1	0.0897	0.3065
Model 2	0.1514	0.4741

As we are interested in the accuracy of predictions and the reproduction of the dynamical phenomenon observed in experimental tests, we also evaluate the average duration of the stick intervals. Table 3 presents the estimated mean stick

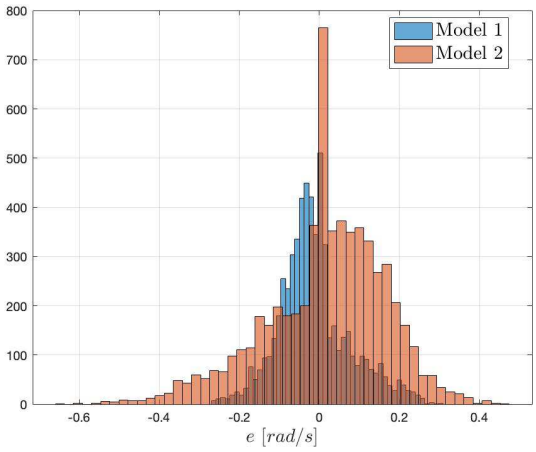

Figure 6: Histogram of prediction errors for Model 1 and Model 2.

duration for the two ensemble models studied. The mean stick interval duration predicted with Model 1, $0.3715s$, is the one that gets closer to the calculated from experimental measurements, that is $0.3770s$.

Table 3: Mean stick duration

Model 1	0.3715
Model 2	0.3913

We chose the RSME, the maximum errors, and the average duration of the stick intervals to compare the model's effectiveness in enhancing the accuracy of predictions and reproducing the stick-slip phenomenon. From the results presented in Table 2 and Table 3, we can say that the ensemble Model 1 performs better in reproducing the test rig experimental data when compared to the ensemble Model 2.

Concluding Remarks

In this work, we compared two different methods of combining system identification techniques. The investigated system is a laboratory test rig that reproduces the torsional vibration of a drill string in drilling operations. We estimated the mechanical parameters and dry contact friction parameters utilizing measured data. With the estimated parameters, we built the ensemble models. Model 1 uses the gray-box model as a mean function and adds the black-box modeled residuals; Model 2 uses the information encoded in the gray-box model as an input to a black-box model.
The proposed ensemble models combine the physics-based approach and ARX or NARX formulations to capture the aspects of the dynamical response missed by the physical model alone. The hybrid formulations were proposed to increase the accuracy of the predictions without losing interpretability.

Acknowledgments

This work has been supported by Brazilian research agencies: CAPES and CNPq.

References

[1] Leine R.I., Van Campen D.H., De Kraker A. (1998) Stick-Slip Vibrations Induced by Alternate Friction Models. *J. Nonlinear Dynamics* **16**:41-54.

[2] Ghasemloonia A., Rideout D.G., Butt S.D. (2015) A review of drillstring vibration modeling and suppression methods. *Journal of Petroleum Science and Engineering* **131**:150-164.

[3] Saldivar B., Mondié S., Niculescu S.I., Mounier H., Boussaada I. (2016) A control oriented guided tour in oilwell drilling vibration modeling. *Annual Reviews in Control* **42**:100-113.

[4] Aguirre L.A. (2015) Introdução à Identificação de Sistemas. editora UFMG, Belo Horizonte, Brazil.

[5] Worden K., Barthorpe R.J., Cross E.J., Dervilis N., Holmes G.R., Manson G., Rogers T.J. (2018) On evolutionary system identification with applications to nonlinear benchmarks. *Mechanical Systems and Signal Processing* **112**:194-232.

[6] Billings S.A., Chen S., Korenberg M.J. (1989) Identification of MIMO non-linear systems using a forward-regression orthogonal estimator. *Journal of Control***6** : 2157-2189.

[7] Aguirre L.A., Billings S.A. (1995) Retrieving dynamical invariants from chaotic data using NARMAX models. *International Journal of Bifurcation and Chaos***2**:449-474.

Experimental bifurcation analysis of a self-excited system exhibiting a subcritical Hopf bifurcation using control-based continuation

K.H. Lee*, D.A.W. Barton* and L. Renson †
* *Department of Engineering Mathematics, University of Bristol, United Kingdom*
† *Department of Mechanical Engineering, Imperial College London, United Kingdom*

Summary. In this paper, control based continuation (CBC) is exploited to systematically characterise in a controlled manner the LCOs of an airfoil during wind tunnel tests. Limit cycle oscillations (LCOs) are found in a wide range of engineering systems such as aircraft, valves, towed wheels and machine tools. The development of corresponding mathematical models that can accurately predict the region where LCOs exist is challenging, especially when the LCOs coexist with the stable equilibrium of the system. Experimental validation is also challenging as the LCOs that can be observed during tests can have large amplitudes. Contrary to previous applications of CBC, the present system is autonomous and the frequency of oscillation is therefore a priori unknown. A phase-plane (geometric) control approach is used to overcome this difficulty. Experimentally measured bifurcation diagrams are then exploited for parameter estimation and model validation.

Introduction

Limit cycle oscillations (LCOs) are found in a wide range of engineering systems such as aircraft, valves, towed wheels and machine tools. In those systems, LCOs emerge from a Hopf bifurcation which can either be super- or sub-critical. The latter is particularly problematic as the stable equilibrium of the system will coexist with LCOs that have potentially large amplitudes. A transition from the equilibrium to such a large-amplitude LCO could cause unacceptable oscillation amplitudes and even lead to catastrophic failures.

The development of mathematical models that can accurately capture the region where the equilibrium and the LCOs coexist is key to the proper operation and safety of those engineering systems. However, this is very difficult task as it often entails capturing complex nonlinear physical phenomena such as fluid-structure interactions (see example here below). Furthermore, parameter estimation and model validation may not be able to exploit LCO data as it would be unsafe to operate the system in this regime of motion.

In this paper, we overcome these difficulties using control-based continuation (CBC). CBC is an experimental scheme that combines feedback control with path following techniques to systematically investigate the dynamic behaviour of physical systems. CBC was applied to a wide range of mechanical experiments such as a impact oscillators, nonlinear energy harvesters, and a cantilever beam with a nonlinear mechanism at its free tip [3, 2, 4]. Here, CBC is exploited to characterise the dynamics of a two-degree-of-freedom airfoil exhibiting LCOs through a subcritical Hopf bifurcation. Testing such a system with a feedback controller provides numerous advantages compared to classical open-loop experiments. If properly designed, the controller maintains the response of the system around a prescribed operating point, avoiding untimely transitions to other, potentially dangerous behaviours. The controller also modifies the linearization of the dynamical system such that unstable responses are stable and hence observable. The unstable LCOs correspond to smaller oscillation amplitudes which can be safely measured and exploited for parameter estimation and model validation.

Application of CBC to LCOs

The fundamental idea of CBC is to find a suitable target signal for the controller such that it becomes *non-invasive* and does not modify the position in parameter space of the responses of the open-loop experiment of interest. The target signal is usually described by a finite sum of Fourier modes whose coefficients can be found iteratively. Until now, the frequency of the target signal was known a priori and identical to the frequency of the external excitation applied to the system (see, for instance, [2]). This is no longer the case here where the system is autonomous.

To overcome this difficulty and obtain the appropriate frequency for the target signal, the fundamental component of the target signal $z^*(t)$ is phase locked with the measured response of the system $z_1(t)$. This is equivalent to locking the phase between force and the response of the forced Hopf bifurcation. For simplicity, the target signal is also limited to a single Fourier mode. Assuming that the measured signal z_1 is analytic, it and it's time derivative can be expressed as

$$\begin{aligned} z_1(t) =& A(t)\cos(\phi), \\ z_2(t) =& \dot{z}_1(t) = -\dot{\phi}A(t)\sin(\phi) \end{aligned} \tag{1}$$

where, $A(t)$ is the instantaneous amplitude, ϕ is the instantaneous phase of the response, $\dot{\phi}$ is the frequency of the response. The target signal can then be set as

$$z^*(t) = \hat{A}\cos(\phi) \qquad \text{where} \qquad \phi = \tan^{-1}\left(\frac{-z_2(t)}{\dot{\phi}z_1(t)}\right) \tag{2}$$

and $\hat{A}$ is the unknown amplitude of the control target. The amplitude coefficient $\hat{A}$ is found such that the controller becomes non-invasive. This is achieved by solving the zero problem $\Xi = \hat{A} - A(\hat{A})$ where A is amplitude of the measured

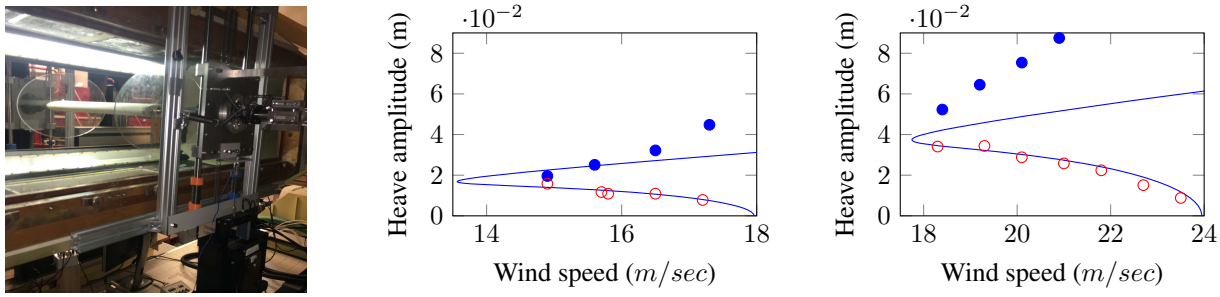

(a) (b) (c)

Figure 1: Picture of the flutter rig and CBC results of two systems. (a) Picture of the rig (b) CBC result and numerical computation of LCO of the model (system 1) (c) CBC result and numerical computation of LCO of the model (system 2). (●) is measured stable LCO, (○) is measured unstable LCO, (——) is computed LCO from the model.

response. This one-dimensional problem can be solved using Newton-like algorithms or, more simply, by testing a range of target amplitudes and taking the one for which $|\Xi_k| < \delta$, where δ is a user-defined tolerance.

Experimental results

CBC was applied to a flutter rig (Figure 1(a)) with a rigid NACA-0015 wing profile and two degrees of freedom (heave and pitch). The heave motion was measured using a laser displacement sensor and the control force was applied to the heave motion using an APS Electro-Seis Shaker. The CBC algorithm were run on a laptop computer connected to a real-time controller (RTC). The RTC consists of a BeagleBone Black on which is fitted with a custom data acquisition board [1] in which the real-time feedback controller was implemented. Measurement and actuation was performed with a sampling frequency of 5 kHz.
The bifurcation diagram obtained using CBC is presented in Figure 1 (b)-(c). LCOs measured at different wind velocities represent either unstable (○) or stable (●) LCOs of the underlying uncontrolled experiment. The location of the sub-critical Hopf bifurcation and the LCOs represent valuable information that was exploited to estimate the nonlinear parameters of the mathematical model. This models accounts for the presence of linear and nonlinear stiffnesses in heave and pitch. It also includes an unsteady representation of the aerodynamics. The bifurcation diagrams found for this model are shown in Figure 1(b)-(c) for two diffrent configurations. The agreement between the model and the unstable responses is very good. The significant difference observed at high amplitudes between the model and the experimentally-measured stable LCOs is thought to be due to complex aerodynamic phenomena that are not included in the model.

Conclusions

Control-based continuation was exploited to characterise the limit cycle oscillations of a flutter rig in wind tunnel tests. The control target signal was phase-locked with the response of the system to find and match the frequency of oscillation. Identified LCOs were exploited to estimate parameters of a model and reproduce numerically the bifurcation diagram of the system.

Acknowledgements

KHL is funded by a University of Bristol Scholarship, D.A.W.B. is funded by the EPSRC grant EP/K032738/1 and LR is funded by a Research Fellowship from the Royal Academy of Engineering (RF1516/15/11). The University of Bristol, the EPSRC and the Royal Academy of Engineering are gratefully acknowledged.

References

[1] D. A. W. Barton. *A real-time controller (RTC) based on the Beaglebone Black (https://github.com/dawbarton/rtc)*, 2018 (accessed Sep, 2018).

[2] David AW Barton and Stephen G Burrow. Numerical continuation in a physical experiment: investigation of a nonlinear energy harvester. *Journal of Computational and Nonlinear Dynamics*, 6(1):011010, 2011.

[3] Emil Bureau, Frank Schilder, Ilmar Ferreira Santos, Jon Juel Thomsen, and Jens Starke. Experimental bifurcation analysis of an impact oscillator—tuning a non-invasive control scheme. *Journal of Sound and Vibration*, 332(22):5883–5897, 2013.

[4] L Renson, AD Shaw, DAW Barton, and SA Neild. Application of control-based continuation to a nonlinear structure with harmonically coupled modes. *Mechanical Systems and Signal Processing*, 120:449–464, 2019.

Experimental Dynamics of Composite Bistable Cantilever Shells

Andrzej Mitura[*], Jerzy Warminski[*], Matteo Brunetti[**] and Francesco Romeo[**]
[*]*Department of Applied Mechanics, Lublin University of Technology, Lublin, Poland*
[**] *Dipartimento di Ingegneria Strutturale e Geotecnica, Sapienza University of Rome, Rome, Italy*

Summary
Bistable cantilever shells subjected to harmonic base excitation have been experimentally investigated with the aim of extending previous quasi-static studies [1] and characterizing their nonlinear dynamic behavior. The tested shells have rectangular planform and almost cylindrical shape. Their shorter edge, flattened by means of a specifically designed clamp, has been excited using an electrodynamic shaker. Sensors and dedicated interface electronics for forward and backward frequency sweeping and control have allowed the identification of the nonlinear resonance curves. Such curves describe the intrawell nonlinear dynamics around the stable equilibrium configurations of the tested shells and have clearly exhibited the expected softening behaviour. Moreover, the experimental campaign provided insights on the dynamic regimes enabling to trigger snap-through mechanisms.

Introduction

The possibility to design and manufacture bi- or multi-stable structures is interesting for both technological and scientific reasons. As an example, a bistable device consisting of a ferromagnetic cantilever elastic beam and two fixed magnets has been proposed in [2]; for such a system the bistability is the result of the interaction between the magnetic field yielded by the magnets and the beam. The authors found the occurrence of nonlinear phenomena, including chaos; in this case the bistability has been exploited to harvest energy from the beam motion. More complicated bistability or multistability systems are presented in the doctoral dissertation [3], where potential applications in aircraft and aerospace industries are suggested. A special class of cantilever composite shells exhibiting multi-stability has been presented by the authors in [1]. Finite element numerical simulations confirmed by experimental tests demonstrated the existence of two or four stable equilibrium configurations, depending on the shape of the natural stress-free configuration of the shell. While therein the research was limited to quasi-static analysis, in this contribution the aim is to perform experimental tests for characterizing the nonlinear dynamics of the multi-stable shells.

Tested composite shells and experimental setup

The manufactured shells are made of carbon-epoxy unidirectional eight-layers composite with stacking sequence [45/-45_2/45/-45/45_2/-45]. Each prototype has been manufactured using autoclave technology; we refer to [1] for all the details about the shell geometry and the constitutive properties. During the manufacturing process different moulds have been used to obtain the two shapes chosen for the prototypes. These latter have an almost cylindrical shape and differ only in length; we label A the longer shell, B the shorter. The natural stress-free configuration of A and B shells is shown in Figure 1. After flattening and clamping one of the shorter edges both shells turn out to be bi-stable, with I or C stable shape configurations (see reference [1]).
The shells are clamped into a special holder and then mounted on the electrodynamic shaker armature. The structure is then kinematically excited with the shaker controller set in sine mode with a constant acceleration of amplitude a_{shaher}. The excitation frequency *f(t)* has been swept forward and then backward and the shell response has been measured by a piezoelectric triaxial accelerometer (a_x,a_y, a_z). Based on the measured signals, the experimental resonance characteristics have been identified.

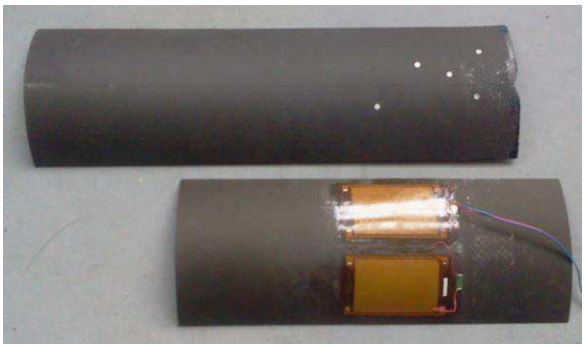

Figure 1: Shell shape before clamping, variant A and B.

Experimental results

The experimental results for the (longer) shell A are shown in Figure 2 for I (Figure 2 a) and C stable shapes (Figure 2b), respectively (accelerometer at the free end). For the I stable shape the softening effect is clearly visible: when incrementing the excitation amplitude the resonance is shifted towards lower frequencies. In contrast, for the C stable shape the resonance shifting is not so evident.

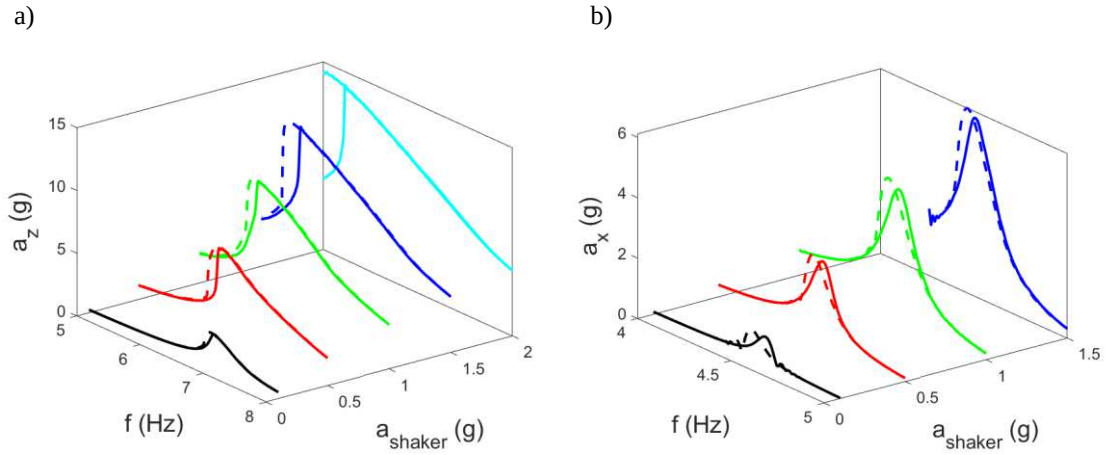

Figure 2: Resonance characteristics of A shell; a) I stable configuration, b) C stable configuration solid line - frequency sweep forward, dashed line - frequency sweep backward

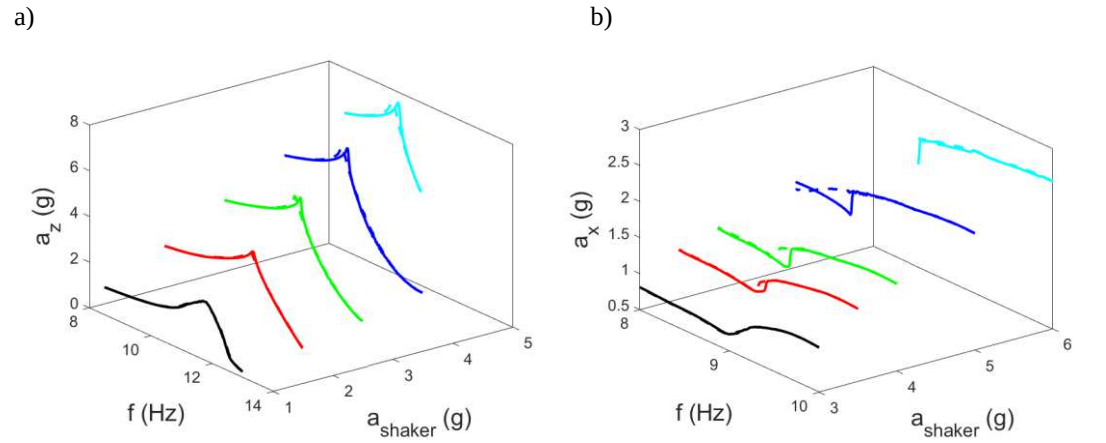

Figure 3: Resonance characteristics of B shell; a) I stable configuration, b) C stable configuration solid line - frequency forward, dashed line - frequency backward

The experimental curves for the (shorter) shell B are shown in Figure 3 (accelerometer at the clamped end). As expected, the resonance frequencies of the shorter shell are higher than those of the longer shell. For example, the natural frequency of the I stable configuration is about 11 Hz for the shell B (Figure 3a) and about 7 Hz for the shell A (Figure 2a). In this case the softening effect is evident on both Figures 3a and 3b: for the shorter shell, as the excitation amplitude is increased, the resonance frequencies for both the I and C stable shapes are shifted towards lower values.

Conclusions

In this contribution the nonlinear dynamics of bi-stable composite shells has been experimentally investigated. The intrawell dynamics around the stable configurations has shown a softening behaviour for both the manufactured prototypes. While the snap-through phenomenon has not been found in the present experimental set-up, further on-going tests are devoted to trigger a shape jump between the I and C stable configurations. The obtained data will be used to validate numerical models as well as reduced order semi-analytical models.

Acknowledgment
The project is financially supported from grant PO19MO15 and co-financed by the Polish National Agency for Academic Exchange PPN/BIL/2018/2/00076.

References

[1] Brunetti M. Kloda L. Romeo F. Warminski J. (2018) Multistable cantilever shells: Analytical prediction, numerical simulation and experimental validation. *Compos Sci Technol* **165**:397-410.
[2] Erturk A. Inman D.J. (2011) Broadband piezoelectric power generation on high-energy orbits of the bistable Duffing oscillator with electromechanical coupling. *J Sound Vib* **330**:2339-2353.
[3] Cui Y. (2015) Adaptive multistable flexible composite structures. *PhD Thesis*, ICL Dept. Aeronaustics, Londyn.

Exploration of edge states by bubbles in a constricted Hele-Shaw channel

Jack Keeler*, Antoine Gaillard†, Alice Thompson*, Andrew Hazel*, and Anne Juel †
*Department of Mathematics and Manchester Centre for Nonlinear Dynamics, University of Manchester, UK
†Manchester Centre for Nonlinear Dynamics and Department of Physics & Astronomy, University of Manchester, UK

Summary. We study experimentally and numerically the propagation of an air bubble through a fluid-filled, geometrically-perturbed Hele-Shaw channel; a system which supports several stable modes of steady bubble propagation. During its transient evolution, a bubble may undergo several topological changes in the form of breakup and coalescence, depending on both initial conditions and control parameters. Long-term, either a single asymmetric or symmetric bubble is recovered or else multiple bubbles remain, whose relative separation increases with time. We explore how the transient and long-term evolution is controlled by edge states available to the bubble, which may change with each new topological configuration.

Introduction

Two-phase displacement flow in a confined geometry is a fundamental problem in fluid mechanics with applications in biomechanics, geophysics and industry. A canonical example is the viscous fingering instability which occurs when air displaces a viscous fluid in a Hele-Shaw channel of width much greater than its depth. An initially flat interface evolves into a single finger of air, symmetric about the centreline of the channel [1]. When the nondimensional driving flux is above a threshold, which depends on the roughness of the channel, this finger is observed to become unstable to tip-splitting leading to the emergence of complex patterns [2]. As the steady solution is linearly stable for all computed flow rates [3], these further instabilities must arise subcritically. For both air fingers (i.e. of semi-infinite extent) and bubbles (with fixed volume), models of the system also contain alternative, weakly-unstable families of multiple-tipped symmetric solutions and asymmetric solutions in addition to the linearly stable solution branch [4].
The system can be perturbed by introducing a small depth-perturbation to the channel cross section (see figure 1a, b) (termed a 'rail') which discourages propagation in the centre of the channel. The perturbed system is axially uniform and can support invariant propagation modes, which are broadly similar to those in the Hele-Shaw channel of rectangular cross-section. However, their stability is altered so that multiple linearly stable steady solutions occur for the same driving parameters (figure 1c). Hence, several long-term outcomes are possible for a bubble propagated from a centred initial position. For small flow-rates the bubble will readily settle on a stable off-rail state (see figure 1c) but for larger flow-rates the bubble shape will become increasingly deformed and a large range of transient behaviour is observed, including tip-splitting, and oscillatory behaviour [5]. Our previous studies have focused on a single-bubble configuration, where we showed that the bubble evolution is guided by transient exploration of the stable manifolds of weakly unstable edge states of the system [5]. In this paper, we explore in particular the behaviour at flow rates where the propensity for bubble breakup and topological changes can have a profound effect on the governing dynamics and lead to the bubble exploring multiple topological configurations before reaching its final state.

Experiment

The experimental channel is shown schematically in figure 1a,b. An air bubble of controlled volume is injected at one end of the channel and propagated by infusing silicone oil at a constant flow rate. We impose different initial conditions corresponding to bubbles of different initial widths by allowing a controlled relaxation period prior to flow initiation. The channel aspect ratio is fixed at 40, and the rail occupies 25% of the channel width and 2.4% of its height.

Numerical model

We use a depth-averaged model for bubble propagation in this large-aspect ratio channel. This model, which qualitatively captures all observed modes of finger propagation in the constricted Hele-Shaw channel [6], was recently extended to

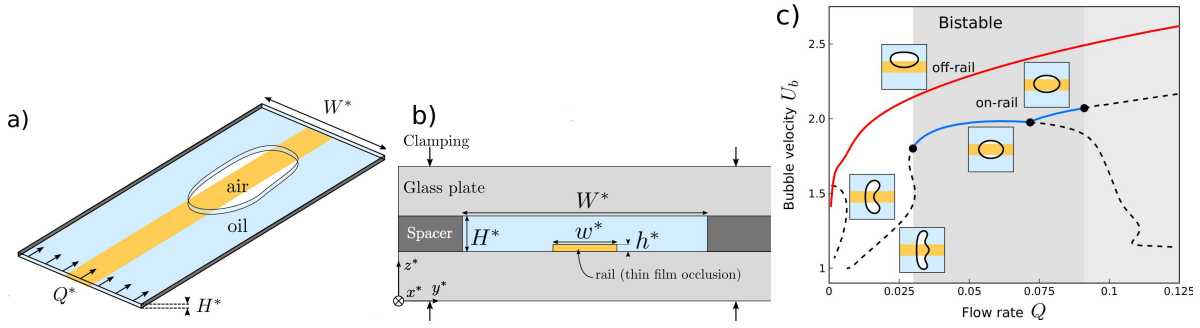

Figure 1: (a) Top-view of the experimental channel with an axially uniform, centred rail. (b) Cross-section of the channel. (c) Numerical bifurcation diagram depicting the steady modes of bubble propagation in terms of the bubble velocity as a function of the flow rate [5]. Stable and unstable modes are indicated by solid and dashed lines, respectively.

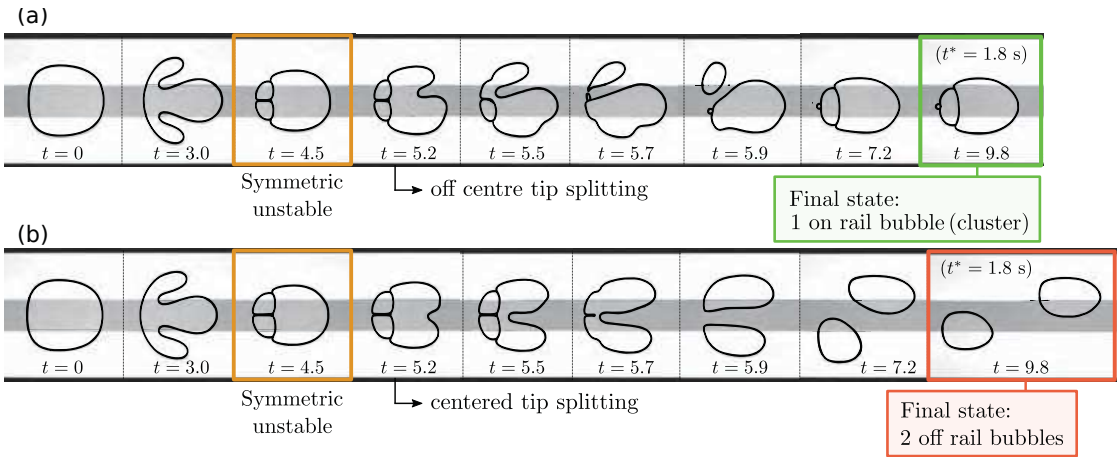

Figure 2: Examples of experimentally-observed transient bubble dynamics showing bubble breakup and recombination, leading to distinct outcomes (a) the compound bubble will eventually recombine to a single bubble and (b) two asymmetric bubbles which will eventually drift apart.

include bubble breakup and coalescence and to describe the motion of one or more bubbles. The use of a simplified model allows the computational effort to be concentrated on capturing the 2D interface as viewed in the experiment, enables a much wider range of computations, and also allows us to directly isolate different physical mechanisms. We solve our model equations using a finite-element method in the open-source library `oomph-lib`, and have access to steady solutions, bifurcation tracking, initial value problems, linear stability and weakly nonlinear stability analysis.

Results

An initially centred bubble may eventually reach the on-rail or off-rail single-bubble steady solutions, or else form two or more bubble fragments which drift away from each other as they propagate. These long-term outcomes can be reached via a surprisingly rich range of transient evolution scenarios, with the transient evolution depending on both control parameters and the initial bubble width. Only for the smallest flow rates does the bubble always remain simply connected throughout its evolution. Above a threshold flow rate, initially slender bubbles evolve towards on-rail steady states, while initially wide bubbles will break up into two or more separating bubbles. For example, figure 2 shows scenarios for two very similar bubbles. In each case the bubble first splits into three smaller bubbles, which then undergoes a complicated sequence of recombination and splitting, and eventually reach two different outcomes.

In order to explore the interactions between multiple bubbles and how these select the eventual fate, we concentrate on situations where the first topological change usually involves the bubble breaking into two near-equal size fragments. The subsequent evolution depends on the volume ratio selected by breakup and the relative position of each bubble, along with the driving parameters. We calculate steady solutions for the two-bubble configuration numerically using our depth-averaged model. Nearly all of these states are weakly unstable, but we find strong evidence that they act as edge states controlling whether the newly-formed bubbles remain on different sides of the rail (and hence usually separate) or whether they migrate across the rail to recombine.

Conclusion

This system exhibits rich transient evolutions, some of which involving bubble breakup into two or more bubbles, and can be followed by other topological reorganisations of the system. The problem is amenable to experiments and numerical simulations using a simplified model. We provide evidence that the dynamics of both single and multiple bubble systems are organised by weakly unstable solutions or "edge states", and can calculate these using our simplified model. As the flow rate increases, transient bubble shapes are increasingly deformed and the number of breakups and recombinations undergone by the bubble increases. We suspect that this increase in complexity is due to a subcritical transition to disorder above a threshold that depends on the roughness of the occlusion, reminiscent of the transition to turbulence in shear flow.

References

[1] Saffman, P.G. & Taylor, G.I. (1958) The penetration of a fluid into a porous medium or Hele-Shaw cell containing a more viscous liquid. *Proc. R. Soc. A* **245** 312-329.

[2] Tabeling, P., Zocchi, G. & Libchaber, A. (1987) An experimental study of the Saffman-Taylor instability. *J. Fluid Mech.* **177**, 67-82.

[3] Bensimon, D. (1986) Stability of viscous fingering. *Phys. Rev. A* **33** 1302-1308.

[4] Franco-Gómez, A., Thompson, A. B., Hazel, A. L. & Juel, A. (2016) Sensitivity of Saffman-Taylor fingers to channel-depth perturbations. *J. Fluid Mech* **794**, 343-368.

[5] Keeler, J.S., Thompson, A.B., Lemoult, G., Juel, A. & Hazel, A.L. (2019) The influence of invariant solutions on the transient behaviour of an air bubble in a Hele-Shaw channel. *Proc. R. Soc. A* **475**, 20190434.

[6] Thompson, A. B., Hazel, A. L. & Juel, A. (2014) Multiple bubble propagation modes in Hele-Shaw channels of variable depth. *J. Fluid Mech* **746**, 123-164.

Monday, July 18, 2022
13:30 - 15:30

MS-15 Energy Transfer and Harvesting in Nonlinear Systems
Rhone 1

Chair: Mohammad AL-Shudeifat

13:30 - 13:50
A Nonlinear Piezoelectric Shunt Absorber with 2:1 Internal Resonance
SHAMI Zein Alabidin*, THOMAS Olivier, CHRISTOPHE Giraud-Audine
*Laboratoire d'Ingénierie des Systèmes Physiques et Numériques (F-13617 Aix-en-Provence F-71100 Chalon-Sur-Saône F-59000 Lille France)

13:50 - 14:10
A numerical study on passive suppression of vortex-induced vibration (VIV) using an elastic rotative non-linear vibration absorber
FRANZINI Guilherme*
*Escola Politecnica da Universidade de Sao Paulo [Sao Paulo] (Av. Prof. Luciano Gualberto, 380 - Butantã, São Paulo - SP, 05508-010 Brazil)

14:10 - 14:30
Broadband vibration energy harvesting based on a weakly coupled nonlinear periodic system
AOUALI Kaouthar, BOUHADDI Noureddine, **KACEM Najib***
*Univ. Bourgogne Franche-Comté, FEMTO-ST Institute, Department of Applied Mechanics (25000 BESANCON France)

14:30 - 14:50
Determination of performance parameters of nonlinear galloping energy harvesters using Jacobi elliptic functions
SARBINOWSKI Filip*, STAROSTA Roman
*Poznań University of Technology, Institute of Applied Mechanics (Jana Pawła II 24, 60-965 Poznań, Poland Poland)

14:50 - 15:10
Dynamic instability mitigation using a single nonlinear energy sink in a friction system with two unstable modes
BERGEOT Baptiste*, BELLIZZI Sergio, BERGER Sébastien
*Institut National des Sciences Appliquées - Centre Val de Loire (campus de Blois) (3 rue de la chocolaterie, CS 23410, 41034 Blois cedex France)

A Nonlinear Piezoelectric Shunt Absorber with 2:1 Internal Resonance

Zein A. Shami*, Christophe Giraud-Audine **, and Olivier Thomas*
* *Arts et Métiers Institute of Technology, LISPEN, HESAM Université, Lille, France*
** *Arts et Métiers Institute of Technology, L2EP, HESAM Université, Lille, France*

Summary. This abstract presents the design of a new nonlinear vibration absorber that aims to attenuate the vibration of an elastic structure near its resonance frequency. This absorber is formed by connecting the elastic structure via a piezoelectric patch to an electrical shunt circuit consisting of a resonant shunt (R-L circuit), combined in series with a quadratic voltage component. The 2DOF reduced order model showed that, for suitable tuning, a 2:1 internal resonance could be generated leading to a creation of an anti-resonance in the response of the elastic structure at the resonance frequency of the mode to be attenuated. The anti-resonance amplitude is shown to remain constant after a threshold excitation level giving this absorber an advantage over the linear absorbers.

Nonlinear Piezoelectric Shunt Absorber Design

The shunt absorber is designed by connecting an electric shunt circuit, consisting of a resistor R and an inductor L in series with a quadratic nonlinear voltage component, to an elastic structure through a piezoelectric patch, as shown in Fig. 1. The quadratic nonlinear term is set to be proportional to the square of the voltage across the piezoelectric patch V_p by a gain equals to β. By introducing this quadratic non-linearity in the shunt circuit and by tuning the electrical resonance

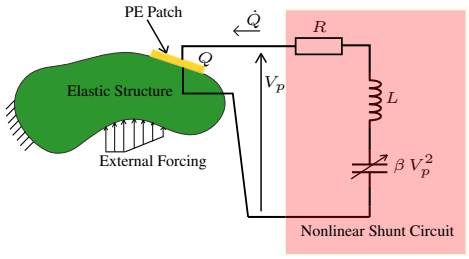

Figure 1: Nonlinear shunt circuit schematic

frequency to be at one half of the resonance frequency of the structure mode to be attenuated, a 2:1 internal resonance would occur. Such an internal resonance, when forcing above a threshold level, leads to an energy transfer from the mode to be attenuated to an electrical mode at the first sub-harmonic frequency. As a result, a kind of anti-resonance at the resonance frequency of the structure is created and the amplitude of the anti-resonance is shown to be independent of the excitation level, leading to a saturation phenomenon [1, 2].

Reduced Order Model and Numerical Results

The main equations governing an elastic system subjected to harmonic excitation and connected to a nonlinear resonant shunt circuit through a piezoelectric patch as shown in Fig. 1, are: (see [3])

$$\mathbf{M}\ddot{\mathbf{u}} + \mathbf{D}\dot{\mathbf{u}} + \mathbf{K}\mathbf{u} + \mathbf{K}_c V_p = \mathbf{F}\cos(\Omega t)\,, \tag{1a}$$

$$C_p V_p - Q - \mathbf{K}_c \mathbf{u} = 0\,, \tag{1b}$$

$$V_p + L\ddot{Q} + R\dot{Q} + \beta V_p^2 = 0\,, \tag{1c}$$

where $\mathbf{M}$, $\mathbf{K}$, and $\mathbf{D}$ are the mass, stiffness, and damping matrices respectively. $\mathbf{K_c}$ is the electro-mechanical coupling coefficients vector, C_p is the piezoelectric patch capacitance, and $\mathbf{F}$ is the excitation force vector. A reduced order model is constructed by performing two modal expansions. The first one is obtained by expanding the displacement vector denoted by $\mathbf{u}$ on the basis of the N linear modes. This would lead to a linearly coupled 2DOF system in terms of the charge Q and the modal displacement q_i, by truncating the displacement at the i-th mode to be attenuated. Then, a second modal expansion is done, on a basis of two modes to obtain the following fully quadratic differential system:

$$\ddot{x_1} + 2\mu_1\dot{x_1} + \omega_1^2 x_1 + \Lambda_1 x_1^2 + \Lambda_2 x_1 x_2 + \Lambda_3 x_2^2 = f_1 \cos\Omega t\,, \tag{2a}$$

$$\ddot{x_2} + 2\mu_2\dot{x_2} + \omega_2^2 x_2 + \Lambda_4 x_1^2 + \Lambda_5 x_1 x_2 + \Lambda_6 x_2^2 = f_2 \cos\Omega t\,. \tag{2b}$$

Eq. (2) is solved using the Multiple Scales Method (MSM) to have a closed form solutions that are used to study the effect of each design parameter on the response, so an optimized parameters selection could be established to achieve the highest attenuation. In addition, the Harmonic Balance Method (HBM), coupled with a numerical continuation procedure based on the Asymptotic Numeric Method (ANM) [4, 5], is used for results validation. Then, the results could be transferred back to the physical coordinates, which are plotted in Fig. (2). It can be observed that the stable solution of q_i stems from the principal resonance curve through a branching point bifurcation, reaching a minimum at the resonance frequency.

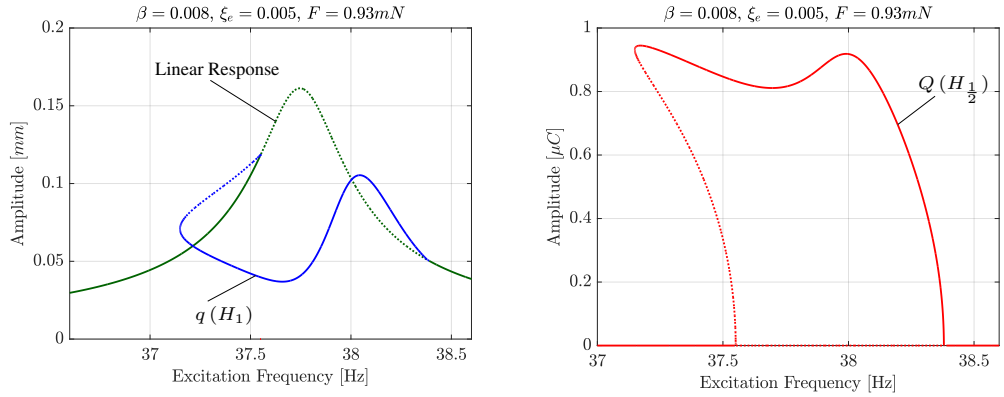

Figure 2: Numerical Results of the amplitudes of q_i (left) and Q (right) based on HBM. Solid line for stable solution and dotted line for unstable solution.

Experimental Setup and Results

Experimental tests are conducted on a cantilever beam to attenuate the first bending mode by connecting the nonlinear shunt circuit through a piezoelectric patch glued at the beam bottom. The excitation is done on the beam tip by inducing a current in a coil-magnet system, as shown in Fig. 3. The nonlinear shunt circuit consisted of an Antoniou synthetic inductor, to achieve a high inductance value, in series with a multiplier circuit composed of a set of Op-Amps and a signal

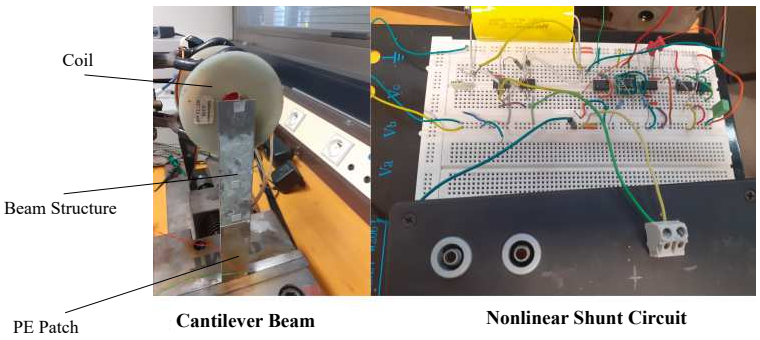

Figure 3: Experiment Setup

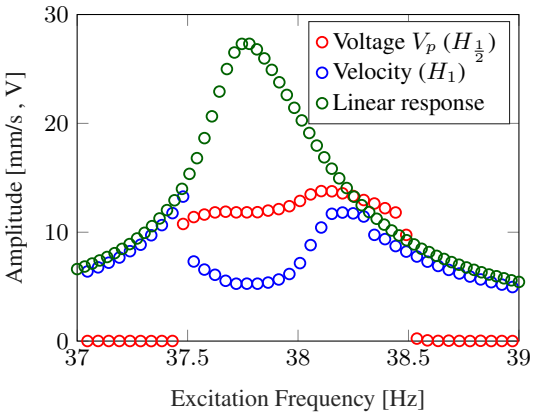

Figure 4: Experimental Results

multiplier, to generate the quadratic voltage behaviour. The time signal of the velocity is measured also at the beam tip using a laser vibrometer, and the voltage across the piezoelectric patch is measured using a voltage probe, which is then fed back to the input of the multiplier circuit. The harmonics amplitude could be extracted from the time signal, and the experimental results are shown in Fig. 4, which clearly validate the numerical results in Fig. 2.

Conclusions

In this study, a semi-passive nonlinear piezoelectric shunt absorber is designed for the first time to attenuate the vibration level using the 2:1 internal resonance features. A 2DOF reduced order model has been constructed, in which the numerical and experimental results appeared to be in full accordance. In addition, when connecting the absorber to a cantilever beam, a high attenuation is achieved near the resonance frequency of the first bending mode.

References

[1] P.F. Pai, B. Wen, A.S. Naser, and M.J. Schulz. Structural vibration control using pzt patches and non-linear phenomena. *Journal of Sound and Vibration*, 215(2):273 – 296, 1998.

[2] A.H. Nayfeh and D.T. Mook. *Nonlinear Oscillations*. Pure and Applied Mathematics: A Wiley Series of Texts, Monographs and Tracts. Wiley.

[3] O. Thomas, J.-F. Deü, and J. Ducarne. Vibrations of an elastic structure with shunted piezoelectric patches: efficient finite element formulation and electromechanical coupling coefficients. *International Journal for Numerical Methods in Engineering*, 80(2):235–268, 2009.

[4] Louis Guillot, Bruno Cochelin, and Christophe Vergez. A Taylor series-based continuation method for solutions of dynamical systems. *Nonlinear Dynamics*, May 2019.

[5] Louis Guillot, Arnaud Lazarus, Olivier Thomas, Christophe Vergez, and Bruno Cochelin. A purely frequency based floquet-hill formulation for the efficient stability computation of periodic solutions of ordinary differential systems. *Journal of Computational Physics*, 416:109477, 2020.

A numerical study on passive suppression of vortex-induced vibration (VIV) using an elastic rotative non-linear vibration absorber

Guilherme Rosa Franzini
Offshore Mechanics Laboratory, Escola Politécnica, University of São Paulo, Brazil

Summary. The focus of this contribution is to present a numerical study on passive suppression of the vortex-induced vibration phenomenon (VIV) using an elastic rotative non-linear vibration absorber (ERNVA). The cylinder (structure to be controlled) is constrained to oscillate only in the cross-wise direction (i.e., the direction orthogonal to the direction of incoming flow). The hydrodynamic loads are modeled using a wake-oscillator model. Curves showing the efficiency of the device are presented and discussed.

Introduction

Vortex-induced vibration (VIV) is a particular flow-induced vibration phenomenon particularly important on risers' dynamics. Phenomenlogical aspects of the phenomenon can be found in the surveys [1] and [2]. Its self-excited and self-limited character plays a role in the structural lifespan due to fatigue. Hence, VIV suppression is of interest for both industrial and academic communities.

A number of studies focusing on VIV suppression can be found in the literature. For the sake of conciseness of this extended abstract, focus is placed on investigations using rotative non-linear vibration absorbers (RNVAs) or non-linear energy sinks (RNES). A rotative NVA is composed of a rigid arm fitted with a tip-mass, linked to the main structure by means of a linear dashpot in which energy is dissipated.

References [3, 4] bring numerical studies focusing on the behavior of a cylinder fitted with a RNVA subjected to VIV. In both papers, the cylinder was constrained to oscillate in the cross-wise direction and the forces applied by the fluid to the solid are computed using computational fluid dynamics (CFD) techniques. In these references, the authors point out the existence of strongly modulated responses for the cylinder and a decrease in the cylinder response. [5] also deals with the passive suppression of VIV using a RNVA, but using reduced-order models based on wake-oscillators for calculating the hydrodynamic load. The latter reference numerically investigates the cases in which the cylinder is constrained to oscillate in one or two directions of the horizontal plane. Due to the lower computational cost compared to the CFD, [5] presents maps showing the sensitivity of the response with respect to the RNVA parameters.

This paper extends the work presented in [5]. Instead of considering a rigid arm, an elastic linear spring allows motion of the suppressor mass in the radial direction. This type of suppressor is herein defined as elastic non-linear vibration absorber (ERNVA). At least to the author's knowledge, this is the first application of such device for VIV suppression.

Mathematical model and results

Consider the problem sketched in Fig. 1. The rigid cylinder has mass M, length L, diameter D and is immersed in a fluid of specific mass ρ and characterized by an uniform free-stream velocity U_∞. The cylinder is assembled onto a viscoelastic support of stiffness k_y and damping constant c_y and its cross-wise displacement is Y. The ERNVA is composed of a point mass m_N placed at the tip of an elastic arm of axial stiffness and damping constant of constant k_r and c_r respectively. The elastic arm is hinged to the cylinder by means of a dashpot of constant c_θ. The instantaneous radial position of the point mass is $r_0 + r(t)$, r_0 being the unstretched length of the arm. Two reference frequencies can be defined, namely $\omega_{n,y} = 2\pi f_{n,y} = \sqrt{k_y/(M + m_N + m_a)}$ (m_a is the potential added mass) and $\omega_r = \sqrt{k_r/m_N}$. Now, consider the dimensionless quantities defined in Eq. 1.

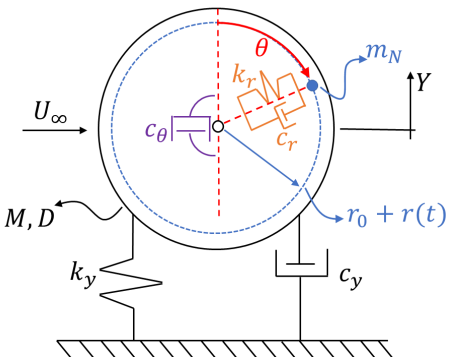

Figure 1: Schematic representation of the problem. The cylinder is constrained to oscillate in the cross-wise direction.

$$y=\frac{Y}{D},\eta=\frac{r}{D},\tau=\omega_{n,y}t,\hat{r}=\frac{r_0}{D},\hat{m}=\frac{m_N}{M+m_N},\zeta_r=\frac{c_r}{2m_N\omega_r},\zeta_y=\frac{c_y}{2(M+m_N+m_a)\omega_{n,y}},\hat{\omega}=\frac{\omega_r}{\omega_{n,y}}$$
$$U_r=\frac{U_\infty}{f_{n,y}D},m^*=4\frac{(M+m_N)}{\rho\pi D^2L},C_a=4\frac{m_a}{\rho\pi D^2L} \quad (1)$$

In addition to the above quantities, the mathematical model also depends on the Strouhal number St, the amplitude of the lift coefficient obtained for a fixed cylinder $\hat{C}_L$ and the mean drag coefficient (also for a fixed cylinder) C_D. Following the wake-oscillator model proposed in [6], the loads due to the fluid-structure interaction can be obtained by coupling a van der Pol equation to the structural oscillator by means of empirically calibrated parameters, namely A_y and ϵ_y. Using this approach, the mathematical model is governed by the following dimensionless mathematical model:

$$\ddot{y}+2\zeta_y\dot{y}+y=\frac{1}{2\pi^3}\frac{U_r^2}{(m^*+C_a)}\sqrt{1+\left(\frac{2\pi\dot{y}}{U_r}\right)^2}\left(\frac{q_y}{\hat{q}_y}\hat{C}_L-C_D\frac{2\pi\dot{y}}{U_r}\right)=\varepsilon\left[2\sin\theta\dot{\eta}\dot{\theta}-\ddot{\eta}\cos\theta+(\hat{r}+\eta)\frac{d}{d\tau}(\dot{\theta}\sin\theta)\right] \quad (2)$$

$$(\hat{r}+\eta)^2\ddot{\theta}+(2\zeta_\theta\hat{r}^2+2(\hat{r}+\eta)\dot{\eta})\dot{\theta}=(r+\eta)\ddot{y}\sin\theta \quad (3)$$

$$\ddot{\eta}+2\zeta_r\hat{\omega}\dot{\eta}+(\hat{\omega}^2-\dot{\theta}^2)\eta=\hat{r}\dot{\theta}^2-\ddot{y}\cos\theta \quad (4)$$

$$\ddot{q}_y+\epsilon_y StU_r(q_y^2-1)\dot{q}_y+(StU_r)^2q_y=A_y\ddot{y} \quad (5)$$

where $\varepsilon=(\hat{m}m^*)/(m^*+C_a)$. Equations 2 - 5 are numerically integrated using the Mathematica® NDSolve function during $\tau_{max}=1000$. For the sake of limitation on the number of pages of this extended abstract, just one set of parameters is tested. The chosen parameters for the cylinder and the ERNVA are $m^*=2.6$, $\zeta_y=0.0001$, $\zeta_r=\zeta_\theta=0.10$, $\hat{\omega}=1$, $\hat{r}=0.5$ and $\hat{m}=0.07$. The investigated reduced velocity is $U_r=5.5$, a favorable scenario for VIV. Only two non-trivial initial conditions are considered, namely, $\theta(0)=\pi/6$ and $q_y(0)=0.10$.

Fig. 2(a) shows two displacement time-histories $y(\tau)$, one of them being labeled as "Pure VIV" and corresponding to the condition in which no suppressor is attached to the cylinder. From this figure, one clearly notice that the presence of the ERNVA decreased the characteristic oscillation amplitude from $\hat{A}_y\approx0.94$ ("Pure VIV" case) to $\hat{A}_y\approx0.65$, a reduction close to 33%. The complete curve of characteristic oscillation amplitude as a function of reduced velocity is depicted in Fig. 2(b), which shows that the ERNVA is able to suppress VIV for a certain range of reduced velocities corresponding to the lock-in.

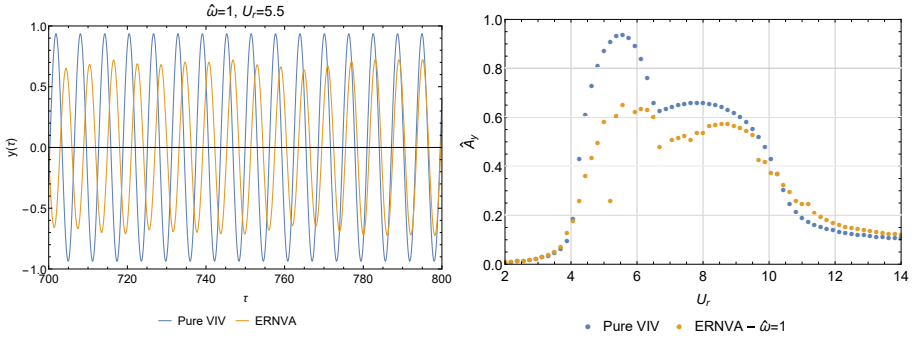

(a) $y(\tau)$. (b) $\hat{A}_y(U_r)$.

Conclusions

This extended abstract presented a numerical investigation on passive suppression of VIV using an elastic rotative non-linear vibration absorber (ERNVA). Considering the ERNVA mass equal to 7% of the total oscillating mass, it was found that a decrease in the characteristic oscillation amplitude has been achieved, specially close to $U_r=5.5$. In the full paper and at the conference, more comprehensive studies will be presented.

Acknowledgments

The author thanks FAPESP and CNPq for the grants 2019/27855-2 and 305945/2020-3.

References

[1] T. Sarpkaya (2004) A critical review of the intrinsic nature of vortex-induced vibrations. *J. Fluids and Structures.* **19**:389-447.

[2] C.H.K. Williamson C.H.K., R. Govardhan (2008) A brief review of recent results in vortex-induced vibrations. *J. Wind Eng. and Ind. Aerodyn.* **96**: 713-735.

[3] A.B. Blanchard, O.V. Gendelman, L.A. Bergman, A.F. Vakakis (2016) Capture into a slow-invariant-manifold in the fluid-structure dynamics of a sprung cylinder with a nonlinear rotator. *J. Fluids and Structures.* **63**:155-173.

[4] A.B. Blanchard, L.A. Bergman, A.F. Vakakis (2019) Vortex-induced vibration of a linearly sprung cylinder with an internal rotational nonlinear energy sink in turbulent flow. *Nonlinear Dynamics.* :1-17.

[5] T. Ueno, G.R. Franzini (2019) Numerical studies on passive suppression of one and two degrees-of-freedom vortex-induced vibrations using a rotative non-linear vibration absorber. *Int. J. of Non-Lin. Mech.* **116**: 230-249.

[6] R. Ogink, A. Metrikine (2010) A wake oscillator with frequency dependent coupling for the modeling of vortex-induced vibration. *J. Sound and Vibr.* **329**:5452-5473.

Broadband vibration energy harvesting based on a weakly coupled nonlinear periodic system

Kaouthar Aouali, Najib Kacem and Noureddine Bouhaddi
Univ. Bourgogne Franche-Comté, FEMTO-ST Institute, CNRS/UFC/ENSMM/UTBM, Department of Applied Mechanics, 25000 Besançon, France

Summary. In this work, a broadband vibration energy harvester based on a weakly coupled nonlinear periodic N-Dofs system is proposed. In order to enlarge the frequency bandwidth of the harvester, the multimodal property induced by the system periodicity and the nonlinear hardening and softening behaviors are functionalized.

Over the past decades, many efforts have been made to harvest energy from ambient vibrations. Various techniques for vibration energy harvesting (VEH) based on different energy conversion mechanisms have been achieved and proved their potential to enhance the output performances of the harvesters. Although the conversion's mechanisms are various and the development of harvesters is continuous, VEHs still have limitations. In fact, most devices have a narrow operating bandwidth. Consequently, their implementation is limited in real-life applications where energy prevails over a wider bandwidth. To overcome this limitation, several approaches have been proposed namely the adoption of multimodal configurations and the introduction of nonlinearity.
In the following, we are interested in the enhancement of the performances of a vibrating energy harvester based on electromagnetic transduction. The present work investigates the benefits of the multimodal approach and the introduction of the nonlinearity. The multimodal approach involves operating multiple modes in a periodic N-Dofs discrete system. This technique proves its potential to enlarge the frequency bandwidth [1,2,3]. Concerning the nonlinearity, it is used also to extend the frequency bandwidth and diverse works have shown the remarkable improvement of the bandwidth while using this method [4,5,6]. In this work, we functionalized simultaneously the nonlinear softening and hardening behaviors of different Dofs.
Numerical simulations on 5 and 10-Dofs systems have been performed to highlight the benefits of the proposed approach.

References

[1] Abed, I., Kacem, N., Bouhaddi, N., & Bouazizi, M. L. (2016). Multi-modal vibration energy harvesting approach based on nonlinear oscillator arrays under magnetic levitation. *Smart Materials and Structures*, *25*(2), 025018.Icer D.F., Adams J.A. (1977) Mathematical Elements for Computer Simulation. McGraw Hill, NY.
[2] Roundy, S., Leland, E. S., Baker, J., Carleton, E., Reilly, E., Lai, E., ... & Sundararajan, V. (2005). Improving power output for vibration-based energy scavengers. *IEEE Pervasive computing*, *4*(1), 28-36.
[3] Shahruz, S. M. (2006). Design of mechanical band-pass filters with large frequency bands for energy scavenging. *Mechatronics*, *16*(9), 523-531.
[4] Mahmoudi, S., Kacem, N., & Bouhaddi, N. (2014). Enhancement of the performance of a hybrid nonlinear vibration energy harvester based on piezoelectric and electromagnetic transductions. *Smart Materials and Structures*, *23*(7), 075024.
[5] Mann, B. P., & Sims, N. D. (2009). Energy harvesting from the nonlinear oscillations of magnetic levitation. *Journal of Sound and Vibration*, *319*(1-2), 515-530.
[6] Daqaq, M. F., Stabler, C., Qaroush, Y., & Seuaciuc-Osório, T. (2009). Investigation of power harvesting via parametric excitations. *Journal of Intelligent Material Systems and Structures*, *20*(5), 545-557.

Determination of performance parameters of nonlinear galloping energy harvesters using Jacobi elliptic functions

Filip Sarbinowski*, Roman Starosta *
*Institute of Applied Mechanics, Poznan University of Technology, Poznan, Poland

Summary. In the work, through analytical considerations, the peak efficiency of three different variants of galloping energy harvester was defined. For this purpose, the authorial method based on elliptic harmonic balance was employed, consisting of comparison of impossible to analyze, accurate high order solutions, and simplified solutions of a linearized model. Research has shown that the peak efficiency of the hardening and bistable devices is greater by 17% and 30% respectively in regards to the linear device, while application of softening stiffness always leads to a loss of efficiency.

Introduction

In the era of the idea of the Internet of Things, the desire of scientists, engineers, medics, and even not-professionals is to continuously measure countless physical phenomena that occur both in our surroundings and at great distances beyond direct human reach. This increases the requirements for measuring devices and thus for their power supply – if access to the operating device is limited, it may not be possible to route the power cables or periodically exchange the batteries. The solution to this problem may be the application of autonomous devices - equipped with their generator harvesting ambient energy. An example of such a generator is the galloping energy harvester (GEH) - the device that allows to harvest the energy of vibrations induced by the flow.
In its simplest version, the GEH can be considered as a body (resonator) mounted on the elastic element, coupled to the piezoelectric (Fig. 1.), described by the mathematical model (1) – (2). If an appropriately shaped body is used, the geometry of which is represented by the coefficients a_1 and a_3, at a certain flow velocity, called the critical velocity, negative damping will be induced in the system and thus stability of the system will be lost.

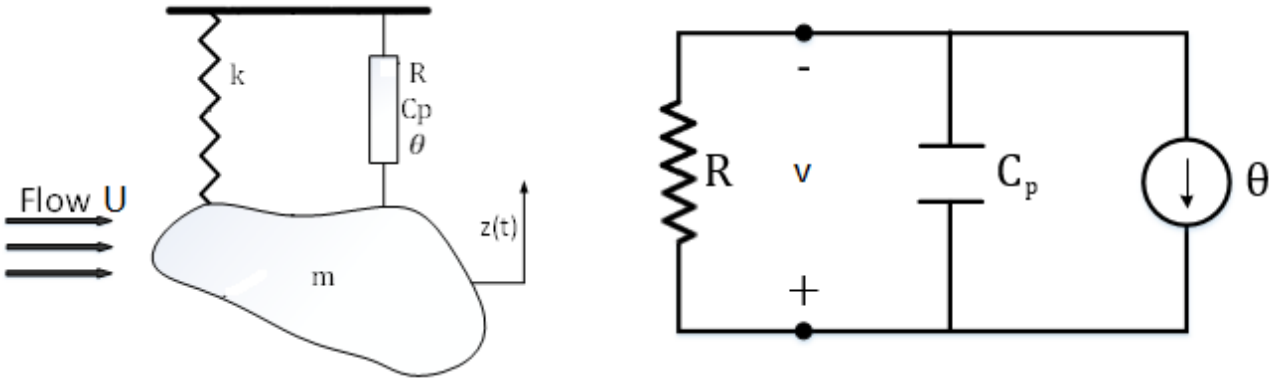

Figure 1: Model of the aeroelastic energy harvester

$$m\,\ddot{z}(t) + S\big(z(t)\big) - \theta\, v(t) = -\frac{1}{2}\rho h\left(a_1\, U\, \dot{z}(t) + a_3 \frac{\dot{z}(t)^3}{U}\right) \tag{1}$$

$$C_p \dot{v}(t) + \frac{v(t)}{R} + \theta \dot{z}(t) = 0 \tag{2}$$

where: m – mass of the body, $S(z(t)) = k\, z(t)$ – restoring force, $z(t)$ – displacement, $\dot{()}$ and $\ddot{()}$ – first and second time derivative, h – characteristic length of the body, ρ – fluid density, U – flow velocity, $a_1,\ a_3$ – experimentally determined coefficients, $v(t)$ – voltage, θ – piezoelectric coefficient, R – circuit resistance, C_p – circuit equivalent capacity.

The efficiency of the device

One of the most important parameters describing energy generators is peak efficiency η_{peak}. In [1], the maximum efficiency was derived for the simplified linear GEH model, in which the harvested was defined as structural damping. In work [2], we confirm the validity of the obtained results also for the full electromechanical model. These results indicate that the peak efficiency of such a device depends only on the geometry of the resonator and has a form:

$$\eta_{peak} = -\frac{{a_1}^2}{6\, a_3} \tag{3}$$

The natural path of exploring this matter are studies of the possibilities offered by the application of a system with different types of non-linear stiffness characteristics. Although there already studies that compare different GEH variants, e.g. [3], but none of them have defined the efficiency of the devices.
Our earlier studies proved that the analytically formulated limit cycle of the model of the device can be obtained through the harmonic balance assuming some form of the model solution. In the case of devices with a more complex structure, the solutions obtained with this method are, however, too complicated to draw appropriate conclusions from them. Preliminary studies indicate that an excellent alternative may be the elliptic harmonics balance method, where the solution of the model is assumed in the form of elliptic Jacobi functions. Because of that, in the paper, we propose a method of solving this problem based on a comparison of a linearized, easy-to-analyze solution and a very precise one, obtained with elliptic harmonic balance method. The analytical forms of both solutions are very similar, and the value of the factors by which they differ can be strictly defined at extreme points.

Results and conclusions

Employing the elliptic harmonics balance, the expressions describing the efficiency of various variants of devices were obtained as a function of the flow velocity in the form of $\eta_N = \eta_L \Psi$, where $\eta_L = \eta_L(U)$ is the efficiency of linear device and $\Psi = \Psi(m)$ (Fig. 2) is the coefficient that describes the impact of nonlinearity on the efficiency of the device in function of the modulus of elliptic function m. Depending on the nature of the nonlinearity, the value modulus is bounded in the following ranges: for hardening stiffness $0 < m < 0.5$, for softening stiffness $0 < m < 1$ and for bistable system $0.5 < m < 1$, it is therefore, possible to strictly determine the value of the Ψ coefficient at extreme its extreme values.

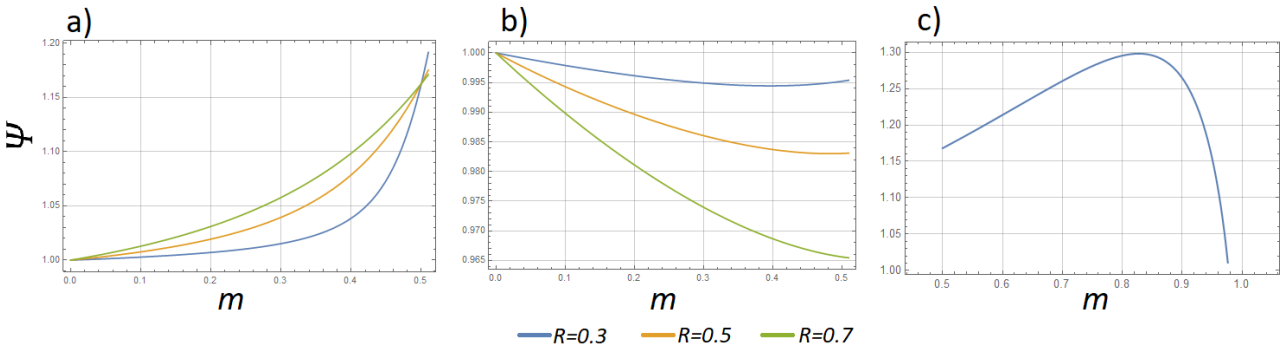

Figure 2: Ψ values as a function of m for different R values and different stiffness variants: a) hardening, b) softening, c) bistable

Based on the above information, it can be concluded that: a) the function $\Psi(m)$ for the system with hardening stiffness depends on the values of the system parameters, but for the $m = 0.5$ it always has the same, maximum value $\Psi(0.5) \approx 1.17$, b) maximum value of $\Psi(m)$ for the system with softening stiffness is reached for $m = 0$ and $\Psi(0) = 1$ therefore, the softening stiffness will lead to a decrease in peak efficiency, c) regardless of the system parameters, the peak value of $\Psi(m)$ for the bistable system is $\Psi(0.83) \approx 1.30$.

References

[1] Barrero-Gil, A., Alonso, G., and Sanz-Andrés, A. (2010) Energy harvesting from transverse galloping. *Journal of Sound and Vibration*, 329(14), 2873– 2883.
[2] Sarbinowski F., Starosta R., (2020) Minimization of critical flow velocity of aeroelastic energy harvester via delayed feedback control, *Vibrations in Physical Systems*, 31(2).
[3] Bibo A., Alhadidi A. H., Daqaqa, M. F. (2015) Exploiting a nonlinear restoring force to improve the performance of flow energy harvesters, *Journal of Applied Physics*, 117.

Dynamic instability mitigation using a single nonlinear energy sink in a friction system with two unstable modes

Baptiste Bergeot*, Sergio Bellizzi† and Sébastien Berger*
*INSA CVL, Univ. Orléans, Univ. Tours, LaMé EA 7494, F-41034, 3 Rue de la Chocolaterie, CS 23410, 41034 Blois Cedex, France
†Aix Marseille Univ, CNRS, Centrale Marseille, LMA UMR 7031, Marseille, France

Summary. This work studies a problem of passive mitigation by means of one nonlinear energy sink (NES) of a dynamic instability arising from two unstable modes of a primary structure. For that, a phenomenological friction model with four-degrees-of-freedom (DOF) having two unstable modes (the primary structure) is coupled to a NES. We investigate analytically, using an asymptotic analysis, the response regimes resulting from the interaction between the two unstable linear modes of the primary structure and the NES. The analytical results are compared and complemented by direct numerical simulations of the coupled system. In each situation, a good agreement is observed which allows us to validate the presented asymptotic analysis.

Introduction

In the context of passive control of dynamic instabilities, the Nonlinear Energy Sinks (NESs) are now well-known means. For example, NES have been used to suppress aeroelastic instability [1], regenerative chatter in machine tool vibrations [2], helicopter ground resonance instability [3] or friction-induced vibrations due to mode coupling instability [4].
The NES operate on the basis of Targeted Energy Transfer (TET) concept. In general, a NES consists of a light mass, an essentially nonlinear spring (here cubic) and a viscous linear damper. Because of its essentially nonlinear stiffness, a NES can adjust its frequency to that of the primary system and therefore engage in resonance over a large frequency range. Whether for a system under impulsive, harmonic or broadband frequency excitation or whether for an auto-oscillating system, TET results from nonlinear mode bifurcations. In general, the phenomenon of TET can be described as a 1:1 resonance capture [5].
In this work a friction system is considered as a primary system, it consists in a simple four-DOF (two linearly coupled well-known Hultèn's models, see Fig. 1) [6]. The model has two unstable modes, i.e. the associated eigenvalues have positive real parts with also the same order of magnitude. Moreover, the imaginary parts (the frequencies) are chosen to be incommensurable. We study the mitigation by means of a single NES of the friction-induced vibrations resulting of the presence of two unstable modes and having therefore two frequency components. Moreover, because the system (without NES) is linear, it undergoes, when it is unstable, an exponential growth of its amplitude.
Preliminary numerical simulations of the coupled system show that the single NES is effectively capable to interact with the two unstable modes and mitigate the double instability. Inter alia, the mitigation may be performed through periodic regimes (see Fig. 2(a) where ϵ is a small parameter related to the mass ratio between the NES and the primary structure) or Strongly Modulated Responses (SMR, see Fig. 2(b)).
In order to understand these interactions and the mitigation processes, based on the procedure presented by the authors [7], an analytical framework is presented. The obtained results are compared and completed by direct numerical integration of the coupled system. The method and the major results of the study are summarized below.

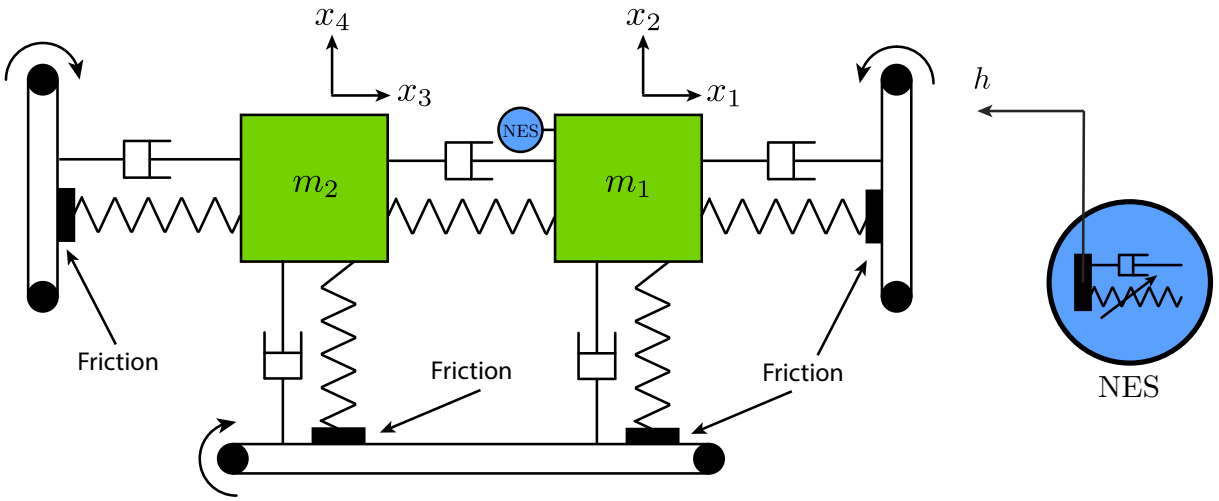

Figure 1: The phenomenological system under study.

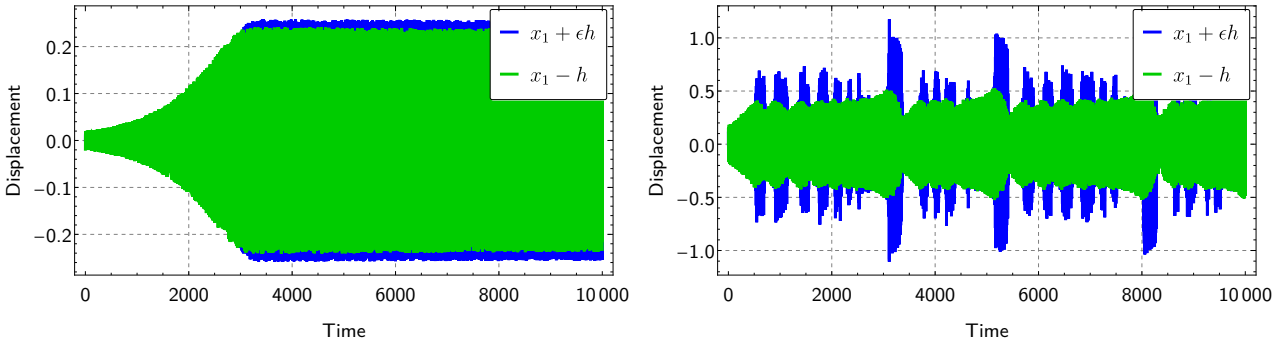

(a) Periodic refime

(b) SMR

Figure 2: Possible mitigation responses obtained from direct numerical integration of the coupled system.

Method and results

The analytical method begins with the so-called biorthogonal transformation to diagonalize the primary friction system. Then, the resulting diagonalized system is reduced keeping only the two unstable modes and ignoring the two stable modes. Afterwards, the slow-flow motion of the system is obtained using the complexification-averaging (CA-X) method within the assumption of two simultaneous 1:1-1:1 resonances to the natural frequencies of the two unstable modes. The slow-flow, which also depends on the small parameter ϵ, is analyzed in the framework of the Geometric Singular Perturbation Theory (GSPT) [8] in which it is defined as a $(4, 2)$-fast–slow system. Each of the two slow variables characterizes one of the two unstable modes of the primary system whereas the four fast variables describe the NES motion (amplitude and phase of each of the two frequency component).
The Critical Manifold (CM) of the slow-flow is obtained, it is a two-dimensional parametric surface (with respect to two of the four fast variables) which evolves in the six-dimensional variable space. The shape of the CM and its stability properties allow us to contemplate some mitigated responses, in agreement with the preliminary numerical simulations. Indeed, the critical manifold appears as the union between a normally hyperbolic attracting domain with four closed normally hyperbolic saddle type domains.
First, equilibrium positions of the slow-flow are deduced from the knowledge of the CM. A stable equilibrium position (which is on the attractive part of the CM) characterizes a mitigation regime through a periodic response of the initial system if one of the frequency component is completely suppressed, otherwise the response is quasi-periodic with two frequency components. Secondly, because two of the normally hyperbolic saddle type domains meet the attracting part at fold curves, mitigation regimes through Sustained relaxations oscillations of the slow-flow - i.e SMR for the initial system - are possible. Contrary to the case with only one unstable mode, because of the two-dimensional CM, multiple SMR scenarios are possible with different levels of complexity. Fig. 2(b) show an example of a "complex" SMR.
The analysis also suggests that the system may have simultaneous stable attractors (two stable equilibrium positions, one stable equilibrium position with stable sustained relaxations oscillations . . .).

Numerical simulations valid the possibility of a competition between two stable attractors and allowing us to study their basins of attractions. In each considered situation, a good agreement has been observed between theoretical results and numerical simulations which validates the proposed asymptotic analysis.

To conclude, this study confirms that a NES is able to mitigate simultaneously two unstable modes.

References

[1] O. Gendelman, A. Vakakis, L. Bergman, D. McFarland, Asymptotic analysis of passive nonlinear suppression of aeroelastic instabilities of a rigid wing in subsonic flow, SIAM Journal on Applied Mathematics 70 (5) (2010) 1655–1677. doi:10.1137/090754819.

[2] E. Gourc, S. Seguy, G. Michon, A. Berlioz, Chatter Control in Turning Process with a Nonlinear Energy Sink, Advanced Materials Research 698 (2013) 89–98. doi:10.4028/www.scientific.net/AMR.698.89.

[3] B. Bergeot, S. Bellizzi, B. Cochelin, Analysis of steady-state response regimes of a helicopter ground resonance model including a non-linear energy sink attachment, International Journal of Non-Linear Mechanics 78 (2016) 72 – 89. doi:http://dx.doi.org/10.1016/j.ijnonlinmec.2015.10.006.

[4] B. Bergeot, S. Berger, S. Bellizzi, Mode coupling instability mitigation in friction systems by means of nonlinear energy sinks : numerical highlighting and local stability analysis, Journal of Vibration and Control 24 (15) (2017) 3487–3511. doi:10.1177/1077546317707101.

[5] O. Gendelman, L. I. Manevitch, a. F. Vakakis, R. M'Closkey, Energy Pumping in Nonlinear Mechanical Oscillators: Part I—Dynamics of the Underlying Hamiltonian Systems, Journal of Applied Mechanics 68 (1) (2001) 34. doi:10.1115/1.1345524.

[6] E. Denimal, L. Nechak, J.-J. Sinou, S. Nacivet, Kriging surrogate models for predicting the complex eigenvalues of mechanical systems subjected to friction-induced vibration, Shock and Vibration Hindawi Publishing Corporation ID 3586230 (2016) 22 pages.

[7] B. Bergeot, S. Bellizzi, Steady-state regimes prediction of a multi-degree-of-freedom unstable dynamical system coupled to a set of nonlinear energy sinks, Mechanical Systems and Signal Processing 131 (2019) 728–750.

[8] C. Jones, Geometric singular perturbation theory, in: R. Johnson (Ed.), Dynamical Systems, Vol. 1609 of Lecture Notes in Mathematics, Springer Berlin Heidelberg, 1995, pp. 44–118. doi:10.1007/BFb0095239.

Monday, July 18, 2022
13:30 - 15:30

MS-07 Dynamics and Optimization of Multibody Systems
Saint Clair 2

Chair: József Kövecses - Marek Wojtyra

13:30 - 13:50
Application of the ODE Integration Methods for Multibody Systems With and Without Redundant Constraints
PĘKAL Marcin[*], WOJTYRA Marek
[*]Warsaw University of Technology, Institute of Aeronautics and Applied Mechanics (Nowowiejska 24, 00-665 Warsaw Poland)

13:50 - 14:10
A rockfall simulation scheme which preserves the stability properties of rotating rocks
LEINE Remco[*], CAPOBIANCO Giuseppe, BARTELT Perry, LU Guang
[*]Institute for Nonlinear Mechanics (Pfaffenwaldring 9, 70569, Stuttgart Germany)

14:10 - 14:30
A Three-Dimensional and Nonlinear Virtual Test Car
RILL Georg[*]
[*]OTH Regensburg (Galgenbergstr. 30, 93053 Regensburg Germany)

14:30 - 14:50
Abscissa minimization for self-stability of bicycles and nonholonomic acceleration when riding out of the saddle
KIRILLOV Oleg[*]
[*]Northumbria University (Northumbria University Mathematics, Physics and Electrical Engineering Ellison Building, D219 Newcastle upon Tyne NE1 8ST United Kingdom)

14:50 - 15:10
An original walking composed of a ballistic single-support and a finite time double-support phases
AOUSTIN Yannick[*], FORMALSKII Alexander
[*]LS2N, Université de Nantes (1 rue de la Noë, 44321 Nantes France)

Application of the ODE Integration Methods for Multibody Systems With and Without Redundant Constraints

Marcin Pękal* and Marek Wojtyra*
*Institute of Aeronautics and Applied Mechanics, Faculty of Power and Aeronautical Engineering, Warsaw University of Technology, Warsaw, Poland

Summary. The multibody approach is commonly used in analyzing complex mechanical systems. Simulation of multibody systems (MBSs) may be a challenging task. Some problems are present for both overconstrained and non-overconstrained MBSs. The other difficulties concern only overconstrained MBSs. Various formulations and numerical solution approaches may be used to simulate MBSs. Some of them allow us to transform the DAEs into ODEs and have different computational properties, especially in the presence of redundant constraints. These methods are investigated in this paper. The numerical methods were compared with respect to the integration method used. The following methods are considered: the Zero Eigenvalue Method, the Pseudo Upper Triangular Decomposition method (two forms—with the Householder Transformation and the Gauss Decomposition), the Schur Decomposition Method, the SVD Method, the QR Decomposition Method, the Direct Integration Method, the Coordinate Partitioning Method, the Udwadia-Kalaba Formulation, the Least-squares Block Solution (two forms), the Udwadia-Phohomsiri Formulation, and the Wang Huston Formulation. For these methods, both the non-stiff ODE solvers (ode45, ode23, ode113) and stiff solvers (ode15s, ode23t, ode23tb, ode23s) of MATLAB® were considered. The methods were tested on two exemplary MBSs described in absolute coordinates—overconstrained and non-overconstrained robotic manipulators.

Introduction and motivation

The method of multibody systems (MBSs) may be used in many areas, e.g., to describe robots, mechanisms, machines, and vehicles. It may also be used for less common applications, e.g., molecular modeling, biomechanical systems, or modeling of contact or impact. The analysis of MBSs may cause some problems.
During simulations of MBSs, various numerical difficulties may occur. One source of the problems may be related to the type of equations to solve. Usually, the MBSs are described by differential-algebraic equations (DAEs). In this set, the algebraic equations describe the constraint equations that represent loop closing kinematic pairs—in the case of relative joint coordinates—or all kinematic pairs—in the case of absolute coordinates.
The DAEs are usually more challenging to solve than ordinary differential equations (ODEs). Depending on the multibody formulation employed, DAEs may have a different index, which determines the computational complexity of the equations. Large DAEs may also be challenging to integrate. Some methods allow us to transform the DAEs into ODEs. These methods are investigated in this paper.
A significant group of MBSs is the group of systems with redundant constraints. The introduction of redundant constraints into the structure of the system is usually the result of a conscious decision of the designer, made after considering the advantages (e.g., greater strength) and disadvantages (e.g., the requirement of greater accuracy of manufacturing of the bodies and the introduction of assembly stresses) of such systems.
Redundant constraints cause further problems in the simulation of the system. In the case of overconstrained MBSs, additional numerical issues result from the fact that the Jacobian/constraint matrix of the considered MBS is rank-deficient. These problems may be reduced by using the appropriate methods to analyze overconstrained MBSs (see, e.g., [2, 1, 5, 6]). Some publications compare selected ODE approaches that are applicable to simulate multibody systems with or without redundant constraints, e.g., [4, 2, 1, 6, 5]. However, a limited number of integration methods were tested in these publications. Hence, a natural question arises: **will the obtained results regarding the relative effectiveness of these methods be the same when other integration schemes are used, and will all integration algorithms give the results at all?** This paper presents the preliminary results of research conducted in this research field.

Numerical methods

In this paper, selected approaches used for the simulation of the MBSs are considered. These methods allow for the integration of the DAEs by using methods for ODEs. The following methods are used: the Zero Eigenvalue Method [4, 6, 2, 1], the Pseudo Upper Triangular Decomposition method (two forms—with the Householder Transformation and the Gauss Decomposition) [4, 6, 2, 1], the Schur Decomposition Method [4, 6, 2, 1], the SVD Method [4, 6, 2, 1], the QR Decomposition Method [4, 6, 2, 1], the Direct Integration Method [5], the Coordinate Partitioning Method [4, 6, 2, 1], the Udwadia-Kalaba Formulation [4, 5, 2, 1], the Least-squares Block Solution (two forms) [5, 2, 1], the Udwadia-Phohomsiri Formulation [5, 2, 1], and the Wang Huston Formulation [6, 2, 1].
Several integration schemes were considered for these methods, i.e., the non-stiff ODE solvers (ode45, ode23, ode113) and stiff solvers (ode15s, ode23t, ode23tb, ode23s) of MATLAB®. The ode45 is the Runge-Kutta method based on the Dormand-Prince (4,5) pair [7], which is frequently the first-choice method [3]. The ode23 is the Runge-Kutta method based on the Bosacki-Shampine (2,3) pair [7]. The ode113 is an application of the Adams-Bashforth-Moulton approach [7]. The ode15s is quasi-constant step size NDFs/BDFs method [7]. The ode23t is trapezoidal rule method [8]. The ode23tb is the Runge-Kutta method with a trapezoidal rule and second-order BDF (TR-BDF2 method) [3]. The ode23s is modified Rosenbrock code [7].

Examples and results

Two MBSs described by absolute coordinates are studied—redundantly constrained and non-redundantly constrained robotic manipulators (see Fig. 1). Both the systems are spatial. The non-overconstrained manipulator was created by removing the redundant body no. 7 of the other MBS. The Euler angles (zxz) are used for the orientation description of the systems to allow us to consider the numerical methods that do not work in the case of a singular mass matrix.
The manipulators are built from the bodies of the same parameters, i.e., length $l = 0.5\ m$, mass $m = 5\ kg$, and moments of inertia $J_x = 0.025\ kgm^2$, $J_y = J_z = 0.12\ kgm^2$. Revolute joints connect the bodies. The gravity acts in the negative direction of axis z_0, and its acceleration $|g| = 9.80665\ m/s^2$. During the simulations, the manipulators were loaded with forces.

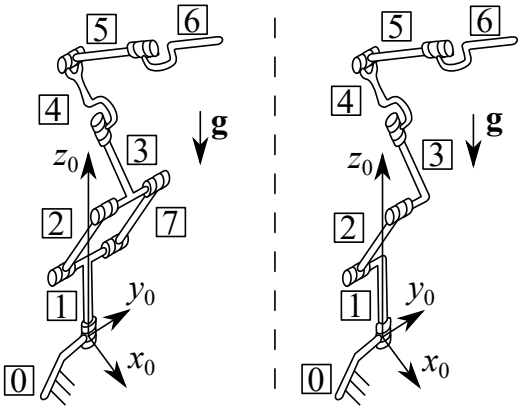

Figure 1: Considered robotic manipulators—overconstrained (on the left) and non-overconstrained (on the right)

The 10-second simulations of motion were performed for selected error tolerance values. MATLAB® run in single-thread mode during the calculations to obtain more reliable time results (which are not disturbed by the time needed to exchange data between multiple threads).

Conclusions

It turns out that the efficiency of the methods depends not only on the selected integration method but also on the structure of MBS. The non-stiff ODE solvers gave results for both the overconstrained and non-overconstrained manipulators. In contrast, the stiff solvers had trouble getting a solution, especially (but not only) in the case of the redundantly constrained manipulator. In addition, not all the methods had produced results in a reasonable time. Some simulations were interrupted when no result was obtained within approximately 15 minutes. It should be emphasized that the obtained results cannot be considered valid for all MBSs. However, based on this work, it can be supposed which of the studied simulation methods will be better for the other systems. This work also provides a reasonable basis for further research in numerical methods for MBSs.

Acknowledgements

This work has been supported by the Warsaw University of Technology under a grant awarded by the Scientific Council for the Discipline of Automatic Control, Electronics and Electrical Engineering.

References

[1] Mariti L., Belfiore N.P., Pennestrì E., Valentini P.P. (2011) Comparison of solution strategies for multibody dynamics equations. *International Journal for Numerical Methods in Engineering* **88(7)**:637-656.

[2] Mariti L., Pennestrì E., Valentini P.P., Belfiore N.P. (2010) Review and Comparison of Solution Strategies for Multibody Dynamics Equations. *The 1st Joint International Conference on Multibody System Dynamics*, Lappeenranta, Finland.

[3] MATLAB® help.

[4] Pennestrì E., Valentini P.P.(2007) Coordinate reduction strategies in multibody dynamics: A review. *Proceedings of the Conference on Multibody System Dynamics*: 1-17.

[5] Pękal M., Frączek J. (2016) Comparison of selected formulations for multibody system dynamics with redundant constraints. *Archive of Mechanical Engineering* **63(1)**:93-112.

[6] Pękal M., Frączek J. (2016) Comparison of natural complement formulations for multibody dynamics. *Journal of Theoretical and Applied Mechanics* **54(4)**:1391-1404.

[7] Shampine L.F., Reichelt M.W. (1997) The MATLAB ODE Suite. *SIAM Journal on Scientific Computing* **18(1)**:1-22.

[8] Shampine L.F., Reichelt M.W., Kierzenka J.A. (1999) Solving Index-1 DAEs in MATLAB and Simulink. *SIAM Review* **41(3)**:538-552.

A rockfall simulation scheme which preserves the stability properties of rotating rocks

Remco Leine[⋆], Giuseppe Capobianco[⋆], Perry Bartelt[†], Guang Lu[†]
[⋆]*Institute for Nonlinear Mechanics, University of Stuttgart, Germany*
[†]*WSL Institute for Snow and Avalanche Research SLF, Davos Dorf, Switzerland*

Summary. The stability properties of a freely rotating rigid body are governed by the intermediate axis theorem, i.e. rotation around the major and minor principal axes is stable whereas and rotation around the intermediate axis is unstable. The stability of the principal axes is of importance for the prediction of rockfall. Current numerical schemes for 3D rockfall simulation, however, are not able to correctly represent these stability properties. In this paper we give a proof using Lyapunov functions of an extended intermediate axis theorem, which not only involves the angular momentum equations but also the orientation of the body. Inspired by the stability proof, we present an novel scheme which respects the stability properties of a freely rotating body and which can be incorporated in numerical schemes for the simulation of rigid bodies with frictional unilateral constraints.

Introduction

A full 3D simulation technique for rockfall dynamics, taking rock shape into account and using the state-of-the-art methods of multibody dynamics and nonsmooth contact dynamics, has been developed in [3]. The rockfall simulation technique is based on the nonsmooth contact dynamics method with hard contact laws. The rock is modeled as an arbitrary convex polyhedron and the terrain model is based on a high resolution digital elevation model. The developed numerical methods have been implemented in the code RAMMS::ROCKFALL, which is being actively used in the natural hazards research community, and is to date the only 3D code which takes rockshape into account [2].
Field observations of natural rockfall events as well as high precision measurements with instrumented experimental rocks [1] have shown that platy disk-shaped rocks have the tendency to roll and bump down the slope around their major principal axis[1]. Simulations with the present implementation of RAMMS::ROCKFALL, however, fail to represent the observed rolling phenomenon.
The intermediate axis theorem is a result of the Euler equations describing the movement of a rigid body with three distinct principal moments of inertia. The theorem describes the following effect: rotation of a rigid body around its minor and major principal axes is stable, while rotation around its intermediate principal axis is unstable. The classical intermediate axis theorem, however, only involves the Euler equations for the three components of the angular velocity. In this paper, we describe the dynamics of a freely rotating body in state-space form using as states the three angular velocity components and an arbitrary parametrization of the orientation of the body with respect to the inertial frame. Using the method of Lyapunov functions we rigorously prove an extended version of the intermediate axis theorem in the full state-space.
In this paper we will show that the present scheme, which is fully explicit during flight phases of the rock, does not respect the intermediate axis theorem. Furthermore, we will present an alternative implicit scheme which correctly describes the stability properties of a freely rotating body.

Equations of motion of a free spinning body

Let $\mathcal{V}$ be the Euclidean vector space. To describe the orientation of the rock, we will use a body-fixed frame $K = (\vec{e}_x^K, \vec{e}_y^K, \vec{e}_z^K)$ as well as an inertial frame $I = (\vec{e}_x^I, \vec{e}_y^I, \vec{e}_z^I)$. An arbitrary vector $\vec{a} \in \mathcal{V}$ can be expressed in the K-frame through the tuple ${}_K\vec{a} \in \mathbb{R}^3$, which is related to its representation ${}_I\vec{a}$ in the inertial frame through

$$\vec{a} = \boldsymbol{A}_{IK}\, {}_K\vec{a}, \tag{1}$$

where $\boldsymbol{A}_{IK} = \begin{pmatrix} {}_I\vec{e}_x^K & {}_I\vec{e}_y^K & {}_I\vec{e}_z^K \end{pmatrix} \in \mathrm{SO}(3)$ is the transformation matrix describing the orientation of the rock. Let ${}_K\vec{\boldsymbol{\Omega}}$ denote the angular velocity of the body expressed in the body-fixed frame K. The spin of the body is defined by

$$\vec{\boldsymbol{N}}_S = \boldsymbol{\Theta}_S\, \vec{\boldsymbol{\Omega}} \tag{2}$$

where $\boldsymbol{\Theta}_S$ is the inertia tensor. The inertia tensor takes a constant form in the body-fixed frame, which we choose to be aligned along the principal axes of inertia, such that

$$\boldsymbol{\Theta} := {}_K\boldsymbol{\Theta}_S = \begin{pmatrix} A & 0 & 0 \\ 0 & B & 0 \\ 0 & 0 & C \end{pmatrix} \tag{3}$$

where $A, B, C > 0$ are the principal moments of inertia around the minor, intermediate and major axis respectively. We will denote $\boldsymbol{\Theta} := {}_K\boldsymbol{\Theta}_S$ as inertia matrix to have a short-hand notation. During flight, the rotational motion of the rock is decoupled from the translational motion and fully described by the spin invariance $\dot{\vec{\boldsymbol{N}}}_S = \vec{\boldsymbol{0}}$, yielding

$${}_K\dot{\vec{\boldsymbol{N}}}_S + {}_K\vec{\boldsymbol{\Omega}} \times {}_K\vec{\boldsymbol{N}}_S = \vec{\boldsymbol{0}} \tag{4}$$

[1] https://youtu.be/oWkTfTGeAEo

in the body-fixed frame, which lead to the Euler equations for a freely rotating rigid body

$$\boldsymbol{\Theta}\dot{\boldsymbol{\omega}} + \boldsymbol{\omega} \times (\boldsymbol{\Theta}\boldsymbol{\omega}) = \mathbf{0}. \tag{5}$$

Herein, we used the short-hand notation $\boldsymbol{\omega} = {}_K\vec{\boldsymbol{\Omega}}$. The evolution of the orientation of the body is described by

$$\dot{\boldsymbol{A}}_{IK} = \boldsymbol{A}_{IK}\tilde{\boldsymbol{\omega}}, \tag{6}$$

where $\tilde{\boldsymbol{\omega}}$ is the skew-symmetric matrix such that $\tilde{\boldsymbol{\omega}}\boldsymbol{c} = \boldsymbol{\omega} \times \boldsymbol{c}$ for all $\boldsymbol{c} \in \mathbb{R}^3$. The orientation of the body may be freely parameterized using for instance unit-quaternions $\boldsymbol{q} \in \mathbb{R}^4$ or axis-angle notation ($\boldsymbol{n}$,χ). The matrix differential equation (6) results in a set of ordinary differential equations for the chosen parametrization. If a quaternion $\boldsymbol{q} = (p_0, \boldsymbol{p}^{\mathrm{T}})^{\mathrm{T}}$ representation is used then the rotation matrix is parametrized as

$$\boldsymbol{A}_{IK} = \boldsymbol{I} + \frac{2}{p_0^2 + \boldsymbol{p}^{\mathrm{T}}\boldsymbol{p}}(\tilde{\boldsymbol{p}}\tilde{\boldsymbol{p}} + p_0\tilde{\boldsymbol{p}}) \tag{7}$$

resulting in

$$\dot{\boldsymbol{q}} = \boldsymbol{F}(\boldsymbol{q})\boldsymbol{\omega} \tag{8}$$

with

$$\boldsymbol{F}(\boldsymbol{q}) = \frac{1}{2\|\boldsymbol{q}\|}\begin{pmatrix} \boldsymbol{p}^{\mathrm{T}} \\ \tilde{\boldsymbol{p}} + p_0\boldsymbol{I} \end{pmatrix}. \tag{9}$$

Invariants of motion of the Euler equations

The body has the rotational kinetic energy

$$T = \frac{1}{2}\boldsymbol{\omega}^{\mathrm{T}}\boldsymbol{\Theta}\boldsymbol{\omega} \tag{10}$$

being a constant of motion as, using (5),

$$\frac{\mathrm{d}}{\mathrm{d}t}T = \boldsymbol{\omega}^{\mathrm{T}}\boldsymbol{\Theta}\dot{\boldsymbol{\omega}} = -\boldsymbol{\omega}^{\mathrm{T}}\big(\boldsymbol{\omega} \times (\boldsymbol{\Theta}\boldsymbol{\omega})\big) = 0\,. \tag{11}$$

A second invariant follows from the spin

$${}_I\vec{\boldsymbol{N}}_S = \boldsymbol{A}_{IK}\boldsymbol{\Theta}\boldsymbol{\omega}, \tag{12}$$

which is constant in the inertial frame, i.e.

$$\frac{\mathrm{d}}{\mathrm{d}t}\left({}_I\vec{\boldsymbol{N}}_S\right) = \dot{\boldsymbol{A}}_{IK}\boldsymbol{\Theta}\boldsymbol{\omega} + \boldsymbol{A}_{IK}\boldsymbol{\Theta}\dot{\boldsymbol{\omega}} = \boldsymbol{A}_{IK}\left(\boldsymbol{\omega} \times (\boldsymbol{\Theta}\boldsymbol{\omega})\right) - \boldsymbol{A}_{IK}\left(\boldsymbol{\omega} \times (\boldsymbol{\Theta}\boldsymbol{\omega})\right) = \mathbf{0}. \tag{13}$$

When expressed in the body fixed frame, the spin ${}_K\vec{\boldsymbol{N}}_S$ is not constant but keeps a constant magnitude

$$\frac{\mathrm{d}}{\mathrm{d}t}||{}_K\vec{\boldsymbol{N}}_S||^2 = \frac{\mathrm{d}}{\mathrm{d}t}({}_K\vec{\boldsymbol{N}}_S^{\mathrm{T}}\,{}_K\vec{\boldsymbol{N}}_S) = 2(\boldsymbol{\Theta}\boldsymbol{\omega})^{\mathrm{T}}\boldsymbol{\Theta}\dot{\boldsymbol{\omega}} = -2(\boldsymbol{\Theta}\boldsymbol{\omega})^{\mathrm{T}}\big(\boldsymbol{\omega} \times (\boldsymbol{\Theta}\boldsymbol{\omega})\big) = \mathbf{0}\,. \tag{14}$$

Stationary motion

A rigid body may undergo a stationary motion for which its angular velocity is constant, i.e. $\dot{\boldsymbol{\omega}} = \mathbf{0}$. We will denote such a stationary motion in state-space as $(\boldsymbol{A}_{IK\star}(t), \boldsymbol{\omega}_\star)$. From the Euler equations (5) we infer that stationary motion is only possible if the term $\boldsymbol{\omega} \times (\boldsymbol{\Theta}\boldsymbol{\omega})$ vanishes. Stationary motion therefore implies that $\boldsymbol{\omega}_\star$ is in an eigendirection of $\boldsymbol{\Theta}$, resulting in three stationary directions of motion ${}_K\vec{\boldsymbol{e}}_x^K, {}_K\vec{\boldsymbol{e}}_y^K, {}_K\vec{\boldsymbol{e}}_z^K$. Without loss of generality, let $\boldsymbol{\omega}_\star = \Omega\boldsymbol{e}_\star$, where $\boldsymbol{e}_\star = \boldsymbol{e}_3 = \begin{bmatrix}0 & 0 & 1\end{bmatrix}^{\mathrm{T}}$ agrees with ${}_K\vec{\boldsymbol{e}}_z^K$. The vector $\boldsymbol{e}_\star$ may be complemented by $\boldsymbol{e}_1 = \begin{bmatrix}1 & 0 & 0\end{bmatrix}^{\mathrm{T}}$ and $\boldsymbol{e}_2 = \begin{bmatrix}0 & 1 & 0\end{bmatrix}^{\mathrm{T}}$ to form an orthonormal basis. The evolution of the orientation of the body during stationary motion

$$\boldsymbol{A}_{IK\star}(t) = \boldsymbol{A}_{IK\star}(0)\mathrm{e}^{\tilde{\boldsymbol{\omega}}_\star t} \tag{15}$$

follows from the closed form solution of the matrix differential equation (6). Without loss of generality, we set $\boldsymbol{A}_{IK\star}(0) = \boldsymbol{I}$. From

$${}_I\vec{\boldsymbol{e}}_z^{K\star}(t) = \boldsymbol{A}_{IK\star}(t)\boldsymbol{e}_3 = \mathrm{e}^{\tilde{\boldsymbol{\omega}}_\star t}\boldsymbol{e}_\star = \boldsymbol{e}_\star = {}_I\vec{\boldsymbol{e}}_z^I \tag{16}$$

it follows that $\vec{\boldsymbol{e}}_z^{K\star} = \vec{\boldsymbol{e}}_z^I$ for all t. The stationary motion $(\boldsymbol{A}_{IK\star}(t), \boldsymbol{\omega}_\star)$ itself cannot be stable, irrespective of the principal axis which is considered, because a small error $\Delta\Omega$ in the magnitude of the angular velocity $\boldsymbol{\omega} = (\Omega + \Delta\Omega)\boldsymbol{e}_\star$ will cause $\boldsymbol{A}_{IK}(t)$ to diverge from $\boldsymbol{A}_{IK\star}(t)$. Hence, instead of the stationary motion we need to study the stability of the axis of rotation, or, more precisely, of a manifold in state-space related to that. Hereto, we consider the distance between the axes

of rotation $\vec{e}_z^{K\star} = \vec{e}_z^{I}$ of the stationary motion and $\vec{e}_z^{K}$ of an arbitrary motion, which we express in the K-frame using the quantity

$$\boldsymbol{d}(t) = {}_K\vec{e}_z^{K\star} - {}_K\vec{e}_z^{K} = {}_K\vec{e}_z^{I} - {}_K\vec{e}_z^{K} = \boldsymbol{A}_{KI}(t)\boldsymbol{e}_\star - \boldsymbol{e}_\star. \tag{17}$$

Furthermore, to parametrize the transformation matrix $\boldsymbol{A}_{IK}(t)$, we also introduce the time-dependent quantities

$$\boldsymbol{h}_1(t) = \boldsymbol{A}_{KI}(t)\boldsymbol{e}_1 - \boldsymbol{e}_1, \tag{18}$$

$$\boldsymbol{h}_2(t) = \boldsymbol{A}_{KI}(t)\boldsymbol{e}_2 - \boldsymbol{e}_2. \tag{19}$$

The transformation matrix may therefore be expressed as

$$\begin{aligned} \boldsymbol{A}_{IK}^{\mathrm{T}}(t) &= \boldsymbol{I} + \begin{bmatrix}\boldsymbol{h}_1(t) & \boldsymbol{h}_2(t) & \boldsymbol{d}(t)\end{bmatrix}\begin{bmatrix}\boldsymbol{e}_1 & \boldsymbol{e}_2 & \boldsymbol{e}_\star\end{bmatrix}^{-1} \\ &= \boldsymbol{I} + \begin{bmatrix}\boldsymbol{h}_1(t) & \boldsymbol{h}_2(t) & \boldsymbol{d}(t)\end{bmatrix}. \end{aligned} \tag{20}$$

Furthermore, we introduce the quantity

$$\boldsymbol{\alpha}(t) = \boldsymbol{\omega}(t) - \boldsymbol{\omega}_\star \tag{21}$$

to express the difference in rotation speed, which is being governed by the Euler equations (5)

$$\boldsymbol{\Theta}\dot{\boldsymbol{\alpha}} + (\boldsymbol{\omega}_\star + \boldsymbol{\alpha}) \times (\boldsymbol{\Theta}(\boldsymbol{\omega}_\star + \boldsymbol{\alpha})) = \boldsymbol{0}. \tag{22}$$

Having introduced the quantities $\boldsymbol{d}$ and $\boldsymbol{\alpha}$, we can define the manifold of stationary rotation in a straightforward way

$$\mathcal{M} = \left\{(\boldsymbol{A}_{IK}, \boldsymbol{\omega}) \in \mathrm{SO}(3) \times \mathbb{R}^3 \mid \boldsymbol{d} = \boldsymbol{0}, \boldsymbol{\alpha} = \boldsymbol{0}\right\}. \tag{23}$$

The dynamics of the distance to the axis of stationary rotation is given by

$$\begin{aligned} \dot{\boldsymbol{d}}(t) = \dot{\boldsymbol{A}}_{KI}(t)\boldsymbol{e}_\star &= \left(\boldsymbol{A}_{IK}(t)\tilde{\boldsymbol{\omega}}(t)\right)^{\mathrm{T}}\boldsymbol{e}_\star \\ &= -\tilde{\boldsymbol{\omega}}(t)\boldsymbol{A}_{KI}(t)\boldsymbol{e}_\star \\ &= -\left(\tilde{\boldsymbol{\omega}}_\star + \tilde{\boldsymbol{\alpha}}(t)\right)\left(\boldsymbol{d}(t) + \boldsymbol{e}_\star\right) \\ &= -\tilde{\boldsymbol{\omega}}_\star\boldsymbol{d}(t) - \tilde{\boldsymbol{\alpha}}(t)\left(\boldsymbol{d}(t) + \boldsymbol{e}_\star\right) \end{aligned} \tag{24}$$

being only dependent on $\boldsymbol{d}$ and $\boldsymbol{\alpha}$. It holds that $\dot{\boldsymbol{d}}(t) = \boldsymbol{0}$ if $\boldsymbol{d} = \boldsymbol{\alpha} = \boldsymbol{0}$ and $\dot{\boldsymbol{\alpha}}(t) = \boldsymbol{0}$ if $\boldsymbol{\alpha} = \boldsymbol{0}$. Hence, the manifold $\mathcal{M}$ of stationary rotation is invariant. The differential equations (24) and (22) can be gathered using $\boldsymbol{y}(t) = \begin{pmatrix}\boldsymbol{d}^{\mathrm{T}} & \boldsymbol{\alpha}^{\mathrm{T}}\end{pmatrix}^{\mathrm{T}}$ in the system of ordinary differential equations

$$\dot{\boldsymbol{y}}(t) = \boldsymbol{f}(\boldsymbol{y}(t)), \tag{25}$$

which is time-autonomous. The stability of the axis of rotation now bears down to the stability of the invariant manifold $\mathcal{M}$, i.e. the stability of the equilibrium $\boldsymbol{y}^\star = \boldsymbol{0}$ of system (25). The stability properties of stationary rotation in the 6-dimensional state-space $\boldsymbol{y}$ will be referred as the extended intermediate axis theorem.

Extended intermediate axis theorem

Stability of rotation around the major principal axis

We consider motion in the vicinity of the stationary rotation $\boldsymbol{\omega}_\star = \Omega\boldsymbol{e}_\star$, $\Omega > 0$, and $C \geq \max(A, B)$ such that $\boldsymbol{e}_\star$ is the major principal axis of inertia. Herein, the $K\star$-frame is the body fixed frame of stationary motion, whereas we will reserve the K-frame for the body fixed frame of an arbitrary motion in the vicinity of the stationary motion. The frames are related through $\boldsymbol{A}_{KK\star} = \boldsymbol{A}_{KI}\boldsymbol{A}_{IK\star} = \boldsymbol{A}_{IK}^{\mathrm{T}}\boldsymbol{A}_{IK\star}$ and it therefore holds that

$$\boldsymbol{A}_{KK\star}\boldsymbol{e}_\star = \boldsymbol{A}_{KI}\boldsymbol{A}_{IK\star}\boldsymbol{e}_\star = \boldsymbol{A}_{KI}\boldsymbol{e}_\star = \boldsymbol{d} + \boldsymbol{e}_\star. \tag{26}$$

In order to set up a Lyapunov function, we consider the function

$$\bar{V}(\boldsymbol{d}, \boldsymbol{\alpha}) = \|{}_I\vec{\boldsymbol{N}}_S - {}_I\vec{\boldsymbol{N}}_{S\star}\|^2 = \|{}_K\vec{\boldsymbol{N}}_S - {}_K\vec{\boldsymbol{N}}_{S\star}\|^2. \tag{27}$$

The spin $\vec{\boldsymbol{N}}_{S\star}$ can be easily expressed in the $K\star$-frame as ${}_{K\star}\vec{\boldsymbol{N}}_{S\star} = \boldsymbol{\Theta}\boldsymbol{\omega}_\star = C\Omega\boldsymbol{e}_\star$, which can be cast in the K-frame through

$${}_K\vec{\boldsymbol{N}}_{S\star} = \boldsymbol{A}_{KK\star}\,{}_{K\star}\vec{\boldsymbol{N}}_{S\star} = C\Omega\,\boldsymbol{A}_{KK\star}\boldsymbol{e}_\star = C\Omega(\boldsymbol{d} + \boldsymbol{e}_\star). \tag{28}$$

Using ${}_K\vec{\boldsymbol{N}}_S = \boldsymbol{\Theta}\boldsymbol{\omega} = \boldsymbol{\Theta}(\boldsymbol{\alpha} + \boldsymbol{\omega}_\star) = \boldsymbol{\Theta}\boldsymbol{\alpha} + C\Omega\boldsymbol{e}_\star$ we arrive at

$$\bar{V}(\boldsymbol{d}, \boldsymbol{\alpha}) = \|\boldsymbol{\Theta}\boldsymbol{\alpha} - C\Omega\boldsymbol{d}\|^2 = (A\alpha_x - C\Omega d_x)^2 + (B\alpha_y - C\Omega d_y)^2 + (C\alpha_z - C\Omega d_z)^2. \tag{29}$$

Furthermore, we introduce the function

$$\hat{V}(\boldsymbol{\alpha}) = 2C\,T(\boldsymbol{\omega}) - \|\vec{\boldsymbol{N}}_S(\boldsymbol{\omega})\|^2 + \frac{1}{\Omega^2}(2\,T(\boldsymbol{\omega}) - 2\,T(\boldsymbol{\omega}_\star))^2\,, \tag{30}$$

which can be expressed as

$$\begin{aligned}\hat{V}(\boldsymbol{\alpha}) &= C\boldsymbol{\omega}^{\mathrm{T}}\boldsymbol{\Theta}\boldsymbol{\omega} - \boldsymbol{\omega}^{\mathrm{T}}\boldsymbol{\Theta}^2\boldsymbol{\omega} + \frac{1}{\Omega^2}(\boldsymbol{\omega}^{\mathrm{T}}\boldsymbol{\Theta}\boldsymbol{\omega} - \boldsymbol{\omega}_\star^{\mathrm{T}}\boldsymbol{\Theta}\boldsymbol{\omega}_\star)^2 \\ &= (\boldsymbol{\alpha}+\boldsymbol{\omega}_\star)^{\mathrm{T}}(C\boldsymbol{\Theta}-\boldsymbol{\Theta}^2)(\boldsymbol{\alpha}+\boldsymbol{\omega}_\star) + \frac{1}{\Omega^2}\left((\boldsymbol{\alpha}+\boldsymbol{\omega}_\star)^{\mathrm{T}}\boldsymbol{\Theta}(\boldsymbol{\alpha}+\boldsymbol{\omega}_\star) - \boldsymbol{\omega}_\star^{\mathrm{T}}\boldsymbol{\Theta}\boldsymbol{\omega}_\star\right)^2 \\ &= \boldsymbol{\alpha}^{\mathrm{T}}(C\boldsymbol{\Theta}-\boldsymbol{\Theta}^2)\boldsymbol{\alpha} + \frac{1}{\Omega^2}\left(\boldsymbol{\alpha}^{\mathrm{T}}\boldsymbol{\Theta}\boldsymbol{\alpha} + 2C\boldsymbol{\omega}_\star^{\mathrm{T}}\boldsymbol{\alpha}\right)^2 \\ &= A(C-A)\alpha_x^2 + B(C-B)\alpha_y^2 + \frac{1}{\Omega^2}(A\alpha_x^2 + B\alpha_y^2 + C\alpha_z^2 + 2C\Omega\alpha_z)^2\end{aligned} \tag{31}$$

To prove stability of the trivial equilibrium of (25) for $C \geq \max(A,B)$, we consider the Lyapunov candidate function

$$V(\boldsymbol{y}) = \bar{V}(\boldsymbol{d},\boldsymbol{\alpha}) + \hat{V}(\boldsymbol{\alpha}), \tag{32}$$

which purely consists of the invariants of motion $\vec{\boldsymbol{N}}_S = \text{const.}$ and $T(\boldsymbol{\omega}) = \text{const.}$ and is therefore constant, i.e. $\dot{V} = 0$ along solutions of the system. The (local) positive definiteness of V remains to be investigated in the following.
First, we show that $\hat{V}(\boldsymbol{\alpha})$ is a local positive definite function in $\boldsymbol{\alpha}$. We infer that $\hat{V}(\boldsymbol{\alpha}) \geq 0$ for arbitrary $\boldsymbol{\alpha} \in \mathbb{R}^3$ as it is a sum of squares with positive coefficients for $C \geq \max(A,B)$. Moreover, the points where $\hat{V}(\boldsymbol{\alpha}) = 0$ are characterized by $\alpha_x = 0$, $\alpha_y = 0$ and $\alpha_z(\alpha_z + 2\Omega) = 0$. This implies that $\hat{V}$ vanishes at the origin and at the point $\boldsymbol{\alpha} = (0\ 0\ -2\Omega)^{\mathrm{T}}$ and is strictly positive for all other $\boldsymbol{\alpha} \in \mathbb{R}^3$, proving that $\hat{V}(\boldsymbol{\alpha})$ is locally positive definite.
As V is the sum of $\bar{V}(\boldsymbol{d},\boldsymbol{\alpha}) \geq 0$ and $\hat{V}(\boldsymbol{\alpha}) \geq 0$, it may only vanish if $\bar{V}(\boldsymbol{d},\boldsymbol{\alpha})$ and $\hat{V}(\boldsymbol{\alpha})$ vanish simultaneously. From the local positive definiteness of $\hat{V}(\boldsymbol{\alpha})$ it is clear that, in the neighborhood of the origin, V may only vanish for $\boldsymbol{\alpha} = \boldsymbol{0}$. Now we consider $\bar{V}(\boldsymbol{d},\boldsymbol{\alpha})$ and note that $\bar{V}(\boldsymbol{d},\boldsymbol{0}) = C^2\Omega^2\|\boldsymbol{d}\|^2$ can only vanish if $\boldsymbol{d} = \boldsymbol{0}$. This proves local positive definiteness of V and, thereby, that rotation around the major principal axis is stable. This result may be viewed as an *extended* intermediate axis theorem, as it not only proves that the angular velocity $\boldsymbol{\omega}$ remains close to $\boldsymbol{\omega}_\star$ (i.e. the classical intermediate axis theorem), but also proves that $\boldsymbol{d}$ remains small, i.e. the orientation of the axis of rotation is stable.

Stability of rotation around the minor principal axis
We now consider the stability of stationary rotation around the minor principal axis by setting again $\boldsymbol{\omega}_\star = \Omega\boldsymbol{e}_\star$, $\Omega > 0$ with $\boldsymbol{e}_\star = \boldsymbol{e}_3$ but assuming $C \leq \min(A,B)$. The proof of the stability of stationary rotation around the minor principal axis is completely analogous to the proof for the major principal axis.
We consider again the Lyapunov candidate function of the form

$$V(\boldsymbol{y}) = \bar{V}(\boldsymbol{d},\boldsymbol{\alpha}) + \hat{V}(\boldsymbol{\alpha}), \tag{33}$$

where the function

$$\bar{V}(\boldsymbol{d},\boldsymbol{\alpha}) = \|\boldsymbol{\Theta}\boldsymbol{\alpha} - C\Omega\boldsymbol{d}\|^2 = (A\alpha_x - C\Omega d_x)^2 + (B\alpha_y - C\Omega d_y)^2 + (C\alpha_z - C\Omega d_z)^2 \tag{34}$$

is defined as before, but $\hat{V}(\boldsymbol{\alpha})$ is chosen as

$$\begin{aligned}\hat{V}(\boldsymbol{\alpha}) &= -C\boldsymbol{\omega}^{\mathrm{T}}\boldsymbol{\Theta}\boldsymbol{\omega} + \boldsymbol{\omega}^{\mathrm{T}}\boldsymbol{\Theta}^2\boldsymbol{\omega} + \frac{1}{\Omega^2}(\boldsymbol{\omega}^{\mathrm{T}}\boldsymbol{\Theta}\boldsymbol{\omega} - \boldsymbol{\omega}_\star^{\mathrm{T}}\boldsymbol{\Theta}\boldsymbol{\omega}_\star)^2 \\ &= A(A-C)\alpha_x^2 + B(B-C)\alpha_y^2 + \frac{1}{\Omega^2}(A\alpha_x^2 + B\alpha_y^2 + C\alpha_z^2 + 2C\Omega\alpha_z)^2\end{aligned} \tag{35}$$

The Lyapunov function is constant along solutions and is locally positive definite for $C \leq \min(A,B)$, proving stability of rotation around the minor principal axis.

Fully explicit scheme

We briefly discuss the fully explicit scheme (or pseudo-implicit scheme) which is currently implemented in RAMMS:rockfall. Let $\boldsymbol{\omega}^k$ denote the angular velocity of the rock at time instant t^k. The present scheme calculates the angular velocity $\boldsymbol{\omega}^{k+1}$ at time instant $t^{k+1} = t^k + \Delta t$ (in the absence of contact with the terrain) through

$$\boldsymbol{\Theta}(\boldsymbol{\omega}^{k+1} - \boldsymbol{\omega}^k) + \frac{\Delta t}{2}\boldsymbol{G}(\boldsymbol{\omega}^k)(\boldsymbol{\omega}^{k+1} + \boldsymbol{\omega}^k) = 0\ , \tag{36}$$

where $\boldsymbol{G}(\boldsymbol{\omega}) = \boldsymbol{\Theta}\tilde{\boldsymbol{\omega}} + \tilde{\boldsymbol{\omega}}\boldsymbol{\Theta}$, resulting the explicit velocity update

$$\boldsymbol{\omega}^{k+1} = \left(\boldsymbol{\Theta} + \frac{\Delta t}{2}\boldsymbol{G}(\boldsymbol{\omega}^k)\right)^{-1}\left(\boldsymbol{\Theta} - \frac{\Delta t}{2}\boldsymbol{G}(\boldsymbol{\omega}^k)\right)\boldsymbol{\omega}^k = \boldsymbol{\omega}^k - \left(\boldsymbol{\Theta} + \frac{\Delta t}{2}\boldsymbol{G}(\boldsymbol{\omega}^k)\right)^{-1}\boldsymbol{G}(\boldsymbol{\omega}^k)\boldsymbol{\omega}^k, \tag{37}$$

where the last step is a simplification explained in [5]. The rotation matrix is parametrized using a quaternion $\boldsymbol{q}^k$ with a midpoint update rule

$$\boldsymbol{q}_{\text{pre}}^{k+1} = \boldsymbol{q}^{k+\frac{1}{2}} + \frac{\Delta t}{2}\boldsymbol{F}(\boldsymbol{q}^{k+\frac{1}{2}})\boldsymbol{\omega}^{k+1}, \qquad \boldsymbol{q}^{k+1} = \frac{\boldsymbol{q}_{\text{pre}}^{k+1}}{\|\boldsymbol{q}_{\text{pre}}^{k+1}\|}, \tag{38}$$

where $\boldsymbol{q}^{k+\frac{1}{2}} = \boldsymbol{q}^k + \frac{\Delta t}{2}\boldsymbol{\omega}^k$.
The rationale behind the explicit scheme is that it preserves the kinetic energy. The change in kinetic energy over the time step is

$$\begin{aligned} T(\boldsymbol{\omega}^{k+1}) - T(\boldsymbol{\omega}^k) &= \frac{1}{2}(\boldsymbol{\omega}^{k+1})^{\mathrm{T}}\boldsymbol{\Theta}\boldsymbol{\omega}^{k+1} - \frac{1}{2}(\boldsymbol{\omega}^k)^{\mathrm{T}}\boldsymbol{\Theta}\boldsymbol{\omega}^k \\ &= \frac{1}{2}(\boldsymbol{\omega}^{k+1} + \boldsymbol{\omega}^k)^{\mathrm{T}}\boldsymbol{\Theta}(\boldsymbol{\omega}^{k+1} - \boldsymbol{\omega}^k). \end{aligned} \tag{39}$$

Substitution of the explicit scheme (36) yields

$$T(\boldsymbol{\omega}^{k+1}) - T(\boldsymbol{\omega}^k) = -\frac{\Delta t}{4}(\boldsymbol{\omega}^{k+1} + \boldsymbol{\omega}^k)^{\mathrm{T}}\boldsymbol{G}(\boldsymbol{\omega}^k)(\boldsymbol{\omega}^{k+1} + \boldsymbol{\omega}^k) = 0 \tag{40}$$

due to the skew-symmetry of $\boldsymbol{G}(\boldsymbol{\omega})$ which shows that the kinetic energy is conserved. A stationary solution $\boldsymbol{\omega}_\star = \boldsymbol{\omega}^k = \boldsymbol{\omega}^{k+1}$ of the scheme respects

$$\boldsymbol{G}(\boldsymbol{\omega}_\star)\boldsymbol{\omega}_\star = \boldsymbol{\omega}_\star \times (\boldsymbol{\Theta}\boldsymbol{\omega}_\star) = 0\ , \tag{41}$$

and corresponds to a stationary rotation of the Euler equations around principal axes.
Let $\boldsymbol{\alpha}^k$ be the perturbation of the angular velocity with respect to the stationary rotation $\boldsymbol{\omega}_\star = \Omega \boldsymbol{e}_\star$ around the principal axis $\boldsymbol{e}_\star = \boldsymbol{e}_3$. The perturbation dynamics is obtained using $\boldsymbol{\omega}^k = \boldsymbol{\omega}_\star + \boldsymbol{\alpha}^k$ as

$$\boldsymbol{\Theta}(\boldsymbol{\alpha}^{k+1} - \boldsymbol{\alpha}^k) + \frac{\Delta t}{2}\boldsymbol{G}(\boldsymbol{\omega}_\star)(\boldsymbol{\alpha}^{k+1} + \boldsymbol{\alpha}^k) + \frac{\Delta t}{2}\boldsymbol{G}(\boldsymbol{\alpha}^k)(\boldsymbol{\alpha}^{k+1} + \boldsymbol{\alpha}^k) + \Delta t\boldsymbol{G}(\boldsymbol{\alpha}^k)\boldsymbol{\omega}_\star = 0\ , \tag{42}$$

where the linearity of $\boldsymbol{G}$ and (41) have been used. For small perturbations we can neglect higher order terms in $\boldsymbol{\alpha}^k$ giving the linearized perturbation dynamics

$$\begin{aligned} \boldsymbol{0} &= \boldsymbol{\Theta}(\boldsymbol{\alpha}^{k+1} - \boldsymbol{\alpha}^k) + \frac{\Delta t}{2}\boldsymbol{G}(\boldsymbol{\omega}_\star)(\boldsymbol{\alpha}^{k+1} + \boldsymbol{\alpha}^k) + \Delta t\boldsymbol{G}(\boldsymbol{\alpha}^k)\boldsymbol{\omega}_\star \\ &= \left[\boldsymbol{\Theta} + \frac{\Delta t}{2}\boldsymbol{G}(\boldsymbol{\omega}_\star)\right](\boldsymbol{\alpha}^{k+1} - \boldsymbol{\alpha}^k) + \Delta t\big(\boldsymbol{G}(\boldsymbol{\alpha}^k)\boldsymbol{\omega}_\star + \boldsymbol{G}(\boldsymbol{\omega}_\star)\boldsymbol{\alpha}^k\big)\ . \end{aligned} \tag{43}$$

The linearized perturbation dynamics can be solved for $\boldsymbol{\alpha}^{k+1}$ explicitly. Hereto, the second term is reformulated as

$$\begin{aligned} \boldsymbol{G}(\boldsymbol{\alpha}^k)\boldsymbol{\omega}_\star + \boldsymbol{G}(\boldsymbol{\omega}_\star)\boldsymbol{\alpha}^k &= \boldsymbol{\Theta}\tilde{\boldsymbol{\alpha}}^k\boldsymbol{\omega}_\star + \tilde{\boldsymbol{\alpha}}^k\boldsymbol{\Theta}\boldsymbol{\omega}_\star + \boldsymbol{\Theta}\tilde{\boldsymbol{\omega}}_\star\boldsymbol{\alpha}^k + \tilde{\boldsymbol{\omega}}_\star\boldsymbol{\Theta}\boldsymbol{\alpha}^k \\ &= \tilde{\boldsymbol{\alpha}}^k\boldsymbol{\Theta}\boldsymbol{\omega}_\star + \tilde{\boldsymbol{\omega}}_\star\boldsymbol{\Theta}\boldsymbol{\alpha}^k \\ &= \boldsymbol{\alpha}^k \times (\boldsymbol{\Theta}\boldsymbol{\omega}_\star) + \boldsymbol{\omega}_\star \times (\boldsymbol{\Theta}\boldsymbol{\alpha}^k) \\ &=: \boldsymbol{A}\boldsymbol{\alpha}^k\ , \end{aligned} \tag{44}$$

where $\boldsymbol{A} = -\widetilde{(\boldsymbol{\Theta}\boldsymbol{\omega}_\star)} + \tilde{\boldsymbol{\omega}}_\star\boldsymbol{\Theta}$. Next, the matrix $\boldsymbol{B} = \boldsymbol{\Theta} + \frac{\Delta t}{2}\boldsymbol{G}(\boldsymbol{\omega}_\star)$ in (43) has the inverse

$$\boldsymbol{B}^{-1} = \frac{1}{\det \boldsymbol{B}}\begin{pmatrix} BC & \frac{\Delta t}{2}\Omega C(A+B) & 0 \\ -\frac{\Delta t}{2}\Omega C(A+B) & AC & 0 \\ 0 & 0 & \frac{\det \boldsymbol{B}}{C} \end{pmatrix}\ , \tag{45}$$

where the determinant of $\boldsymbol{B}$ is given by $\det \boldsymbol{B} = ABC + \frac{\Delta t^2}{4}C(A+B)^2$. Hence, the linearized perturbation dynamics can be given in the explicit form

$$\boldsymbol{\alpha}^{k+1} = \left(\boldsymbol{I} - \Delta t\boldsymbol{B}^{-1}\boldsymbol{A}\right)\boldsymbol{\alpha}^k = \boldsymbol{D}\boldsymbol{\alpha}^k\ , \tag{46}$$

in which the matrix $\boldsymbol{D}$ has the non-zero components

$$\begin{aligned} &D_{11} = 1 - \frac{\Delta t^2}{2\det \boldsymbol{B}}\Omega^2 C(A+B)(A-C), \quad D_{12} = -\frac{\Delta t}{\det \boldsymbol{B}}\Omega AC(A-C), \\ &D_{21} = -\frac{\Delta t}{\det \boldsymbol{B}}\Omega BC(C-B) \qquad\qquad D_{22}, = 1 + \frac{\Delta t^2}{2\det \boldsymbol{B}}\Omega^2 C(A+B)(C-B), \\ &D_{33} = 1. \end{aligned} \tag{47}$$

The stability of rotation around the major principal axis is determined through the eigenvalues of $\boldsymbol{D}$, being the roots of the characteristic polynomial

$$\begin{aligned}\det(\lambda\boldsymbol{I}-\boldsymbol{D}) &= (\lambda-1)\left[(\lambda-D_{11})(\lambda-D_{22})-D_{12}D_{21})\right] \\ &= (\lambda-1)\left[\lambda^2-(D_{11}+D_{22})\lambda+(D_{11}D_{22}-D_{12}D_{21})\right]\end{aligned} \tag{48}$$

given by

$$\lambda_{1/2}=\frac{b\pm\sqrt{b^2-4c}}{2} \quad \text{and} \quad \lambda_3=1. \tag{49}$$

Herein, the parameters $b=D_{11}+D_{22}$ and $c=D_{11}D_{22}-D_{12}D_{21}$ can be calculated as

$$b=2-\frac{\Delta t^2\Omega^2}{2\det\boldsymbol{B}}C(A+B)(A+B-2C), \quad c=1+\frac{\Delta t^2\Omega^2}{2\det\boldsymbol{B}}C\left((A+B)\left(A+B-2C\right)-2\left(A-C\right)\left(C-B\right)\right) .$$

The eigenvalues $\lambda_{1/2}$ in (49) take the form

$$\lambda_{1/2}=1-\frac{d}{2}\pm\frac{\sqrt{d^2+4e}}{2} \tag{50}$$

with

$$d=\frac{\Delta t^2}{2\det\boldsymbol{B}}\Omega^2C(A+B)(A+B-2C), \qquad e=\frac{\Delta t^2}{\det\boldsymbol{B}}\Omega^2C(A-C)(C-B) \tag{51}$$

For rotation around the major principal axis it holds that $C\geq\max(A,B)$ from which follows that $d<0$. Therefore, at least one of the eigenvalues has a magnitude larger than unity which proves instability of rotation around the major principal axis, contrary to the intermediate axis theorem. Hence, the explicit scheme cannot correctly represent the stability properties of a freely rotating body.

A stability preserving implicit scheme

Here, we propose an alternative scheme for rockfall simulation with RAMMS:rockfall which preserves the stability properties of the principal axes of rotation in accordance with the intermediate axis theorem. The alternative scheme consists of two parts:

1. as update rule for the angular velocity, we use the implicit scheme proposed by [5]
2. as update rule for the orientation parametrization, we propose a novel scheme which preserves the spin.

The implicit scheme for the angular velocity calculates $\boldsymbol{\omega}^{k+1}$ at time instant $t^{k+1}=t^k+\Delta t$ during a flight phase as

$$\boldsymbol{\Theta}(\boldsymbol{\omega}^{k+1}-\boldsymbol{\omega}^k)+\Delta t\boldsymbol{\omega}^{k+\frac{1}{2}}\times(\boldsymbol{\Theta}\boldsymbol{\omega}^{k+\frac{1}{2}})=0 \quad \text{with} \quad \boldsymbol{\omega}^{k+\frac{1}{2}}=\frac{1}{2}(\boldsymbol{\omega}^k+\boldsymbol{\omega}^{k+1}) . \tag{52}$$

Substitution of the scheme (52) in the kinetic energy expression (39) yields

$$T(\boldsymbol{\omega}^{k+1})-T(\boldsymbol{\omega}^k)=-\frac{\Delta t}{2}(\boldsymbol{\omega}^{k+\frac{1}{2}})^{\mathrm{T}}\left[\boldsymbol{\omega}^{k+\frac{1}{2}}\times(\boldsymbol{\Theta}\boldsymbol{\omega}^{k+\frac{1}{2}})\right]=0 . \tag{53}$$

showing that the kinetic energy is preserved by the implicit scheme. The magnitude of the spin $\|\vec{\boldsymbol{N}}_S\|=\|_K\vec{\boldsymbol{N}}_S\|=\|\boldsymbol{\Theta}\boldsymbol{\omega}\|$, defined by (12), is only dependent on the angular velocity. The implicit scheme for the angular velocity also conserves the magnitude of the spin as follows from

$$\begin{aligned}||\vec{\boldsymbol{N}}_S^{k+1}||^2-||\vec{\boldsymbol{N}}_S^{k}||^2 &= (\boldsymbol{\Theta}\boldsymbol{\omega}^{k+1})^{\mathrm{T}}\boldsymbol{\Theta}\boldsymbol{\omega}^{k+1}-(\boldsymbol{\Theta}\boldsymbol{\omega}^{k})^{\mathrm{T}}\boldsymbol{\Theta}\boldsymbol{\omega}^{k} \\ &= (\boldsymbol{\Theta}\boldsymbol{\omega}^{k+\frac{1}{2}})^{\mathrm{T}}\boldsymbol{\Theta}(\boldsymbol{\omega}^{k+1}-\boldsymbol{\omega}^{k}) \\ &\overset{(52)}{=} -\Delta t(\boldsymbol{\Theta}\boldsymbol{\omega}^{k+\frac{1}{2}})^{\mathrm{T}}\left[\boldsymbol{\omega}^{k+\frac{1}{2}}\times(\boldsymbol{\Theta}\boldsymbol{\omega}^{k+\frac{1}{2}})\right]=0 .\end{aligned} \tag{54}$$

We now propose an update rule for the orientation parametrization. The update of the orientation $\boldsymbol{A}_{IK}^{k+1}$ is chosen such that the spin remains constant, i.e.

$${}_I\vec{\boldsymbol{N}}_S^{k+1}={}_I\vec{\boldsymbol{N}}_S^{k}, \tag{55}$$

and such that the kinematic equation is correctly approximated in the sense that

$$\lim_{\Delta t\downarrow 0}\frac{\boldsymbol{A}_{IK}^{k+1}-\boldsymbol{A}_{IK}^{k}}{\Delta t}=\dot{\boldsymbol{A}}_{IK}(t^k) \tag{56}$$

where $\dot{\boldsymbol{A}}_{IK} = \boldsymbol{A}_{IK}(t)\tilde{\boldsymbol{\omega}}$. We choose an update of the form

$$\boldsymbol{A}_{IK}^{k+1} = \boldsymbol{A}_{IK}^{k}\mathrm{e}^{\tilde{\boldsymbol{\omega}}^{k+\frac{1}{2}}\Delta t}\boldsymbol{B}(\boldsymbol{\omega}^k, \boldsymbol{\omega}^{k+1}) \tag{57}$$

where the matrix $\boldsymbol{B}$ depends on $\boldsymbol{\omega}^k$ and $\boldsymbol{\omega}^{k+1}$ and needs to fulfill $\boldsymbol{B}^{\mathrm{T}}\boldsymbol{B} = \boldsymbol{I}$ to ensure that $(\boldsymbol{A}_{IK}^{k+1})^{\mathrm{T}}\boldsymbol{A}_{IK}^{k+1} = \boldsymbol{I}$. Furthermore, we demand that $\boldsymbol{B}(\boldsymbol{x}, \boldsymbol{x}) = \boldsymbol{I}$ for all $\boldsymbol{x}$ such that

$$\lim_{\Delta t \downarrow 0} \boldsymbol{B}(\boldsymbol{\omega}^k, \boldsymbol{\omega}^{k+1}) = \boldsymbol{B}(\boldsymbol{\omega}^k, \boldsymbol{\omega}^k) = \boldsymbol{I} \tag{58}$$

from which follows the kinematic consistency (56).
To ensure the conservation of spin we demand

$$\boldsymbol{A}_{IK}^{k+1}\boldsymbol{\Theta}\boldsymbol{\omega}^{k+1} = \boldsymbol{A}_{IK}^{k}\boldsymbol{\Theta}\boldsymbol{\omega}^k \tag{59}$$

which, after substitution of the update rule, gives

$$\boldsymbol{A}_{IK}^{k}\mathrm{e}^{\tilde{\boldsymbol{\omega}}^{k+\frac{1}{2}}\Delta t}\boldsymbol{B}(\boldsymbol{\omega}^k, \boldsymbol{\omega}^{k+1})\boldsymbol{\Theta}\boldsymbol{\omega}^{k+1} = \boldsymbol{A}_{IK}^{k}\boldsymbol{\Theta}\boldsymbol{\omega}^k. \tag{60}$$

The matrix $\boldsymbol{B}$ will now be chosen such that

$$\mathrm{e}^{\tilde{\boldsymbol{\omega}}^{k+\frac{1}{2}}\Delta t}\boldsymbol{B}(\boldsymbol{\omega}^k, \boldsymbol{\omega}^{k+1})\boldsymbol{\Theta}\boldsymbol{\omega}^{k+1} = \boldsymbol{\Theta}\boldsymbol{\omega}^k \tag{61}$$

and therefore

$$\boldsymbol{B}(\boldsymbol{\omega}^k, \boldsymbol{\omega}^{k+1})\boldsymbol{\Theta}\boldsymbol{\omega}^{k+1} = \mathrm{e}^{-\tilde{\boldsymbol{\omega}}^{k+\frac{1}{2}}\Delta t}\boldsymbol{\Theta}\boldsymbol{\omega}^k \tag{62}$$

from which we see that it is indeed only dependent on $\boldsymbol{\omega}^k$ and $\boldsymbol{\omega}^{k+1}$. The matrix $\boldsymbol{B}$ is a pure rotation.
Using Rodrigues formula, every pure rotation $\boldsymbol{R}$ around the unit vector $\boldsymbol{k}$ with rotation angle θ can be represented as

$$\boldsymbol{R} = \boldsymbol{I} + \sin\theta\boldsymbol{K} + (1 - \cos\theta)\boldsymbol{K}^2 \tag{63}$$

where $\boldsymbol{K} = \tilde{\boldsymbol{k}}$. If $\boldsymbol{k}$ and θ are chosen as

$$\boldsymbol{k} = \frac{\boldsymbol{b} \times \boldsymbol{c}}{\|\boldsymbol{b} \times \boldsymbol{c}\|}, \quad \cos\theta = \frac{\boldsymbol{b} \cdot \boldsymbol{c}}{\|\boldsymbol{b}\|\|\boldsymbol{c}\|} \tag{64}$$

then it holds that $\boldsymbol{R}\boldsymbol{b} = \boldsymbol{c}$ if $\|\boldsymbol{b}\| = \|\boldsymbol{c}\|$. Furthermore, it holds that $\boldsymbol{R} \to \boldsymbol{I}$ for $\boldsymbol{b} \to \boldsymbol{c}$.
Hence, we choose $\boldsymbol{B} = \boldsymbol{I} + \sin\theta\boldsymbol{K} + (1 - \cos\theta)\boldsymbol{K}^2$ with

$$\boldsymbol{k} = \frac{\boldsymbol{\Theta}\boldsymbol{\omega}^{k+1} \times (\mathrm{e}^{-\tilde{\boldsymbol{\omega}}^{k+\frac{1}{2}}\Delta t}\boldsymbol{\Theta}\boldsymbol{\omega}^k)}{\|\boldsymbol{\Theta}\boldsymbol{\omega}^{k+1} \times (\mathrm{e}^{-\tilde{\boldsymbol{\omega}}^{k+\frac{1}{2}}\Delta t}\boldsymbol{\Theta}\boldsymbol{\omega}^k)\|}, \quad \cos\theta = \frac{\boldsymbol{\Theta}\boldsymbol{\omega}^{k+1} \cdot (\mathrm{e}^{-\tilde{\boldsymbol{\omega}}^{k+\frac{1}{2}}\Delta t}\boldsymbol{\Theta}\boldsymbol{\omega}^k)}{\|\boldsymbol{\Theta}\boldsymbol{\omega}^{k+1}\|\|\boldsymbol{\Theta}\boldsymbol{\omega}^k\|}. \tag{65}$$

To prove that the proposed scheme has the desired stability properties of the principal axes of rotation, we use the Lyapunov functions $V(\boldsymbol{y}^k)$ for the major and minor principal axes as presented before. As the proposed scheme conserves the kinetic energy and the spin by construction it holds that $V(\boldsymbol{y}^{k+1}) = V(\boldsymbol{y}^k)$, whereas positive definiteness has already been shown. The proposed scheme therefore preserves the stability properties of the principal axes of rotation in accordance with the extended intermediate axis theorem.

Numerical results

We compare the explicit and the implicit scheme on a numerical example. We consider a cuboid of mass $m = 1$ kg with length $a = 3$ m, width $b = 2$ m and height $c = 1$ m in the $\vec{\boldsymbol{e}}_x^K$, $\vec{\boldsymbol{e}}_y^K$ and $\vec{\boldsymbol{e}}_z^K$) direction, respectively. The principal moments of inertia are therefore $A = \frac{m}{12}(b^2 + c^2)$, $B = \frac{m}{12}(a^2 + c^2)$ and $C = \frac{m}{12}(a^2 + b^2)$ such that $A < B < C$. Rotation in the neighborhood of stationary rotation $\boldsymbol{\omega}_\star = \Omega\boldsymbol{e}_\star$ around the major principal axis $\boldsymbol{e}_\star = \boldsymbol{e}_3$ is considered. As initial conditions we choose $\boldsymbol{A}_{IK}(0) = \boldsymbol{I}$ and $\boldsymbol{\omega} = \begin{pmatrix}\omega_x & \omega_y & \omega_z\end{pmatrix}^{\mathrm{T}} = \begin{pmatrix}10^{-3} & 10^{-3} & 10\end{pmatrix}^{\mathrm{T}}$ rad/s. We simulate 20 s using a time-step of $\Delta t = 0.01$ s using the explicit and implicit scheme. The results of both schemes are shown in Figures 1 and 2. The body initially rotates in the vicinity of the major principal axis with angular velocity $\omega_z = \Omega = 10$ rad/s, which is stable as follows from the extended intermediate axis theorem. However, in the numerical solution of the explicit scheme, the body deviates from stationary rotation around the major principal axis (approximately at $t = 10$ s) and tends to stable rotation around the minor principal axis with angular speed $\omega_x = -\sqrt{\frac{C}{A}}\Omega$. If a smaller time-step is taken in the explicit scheme, then the change of axis will be slower and will take place at a later point in time. The solution of the implicit scheme remains very close to the major principal axis, both in angular velocity and in the distance $\boldsymbol{d}(t) = {}_K\vec{\boldsymbol{e}}_z^{K\star} - {}_K\vec{\boldsymbol{e}}_z^K$ and is therefore much more accurate.

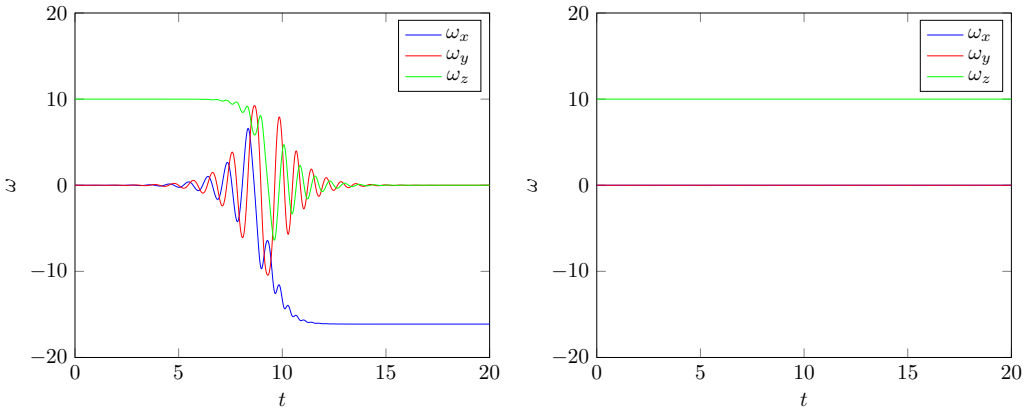

Figure 1: Angular velocities: left the explicit scheme, right the implicit scheme

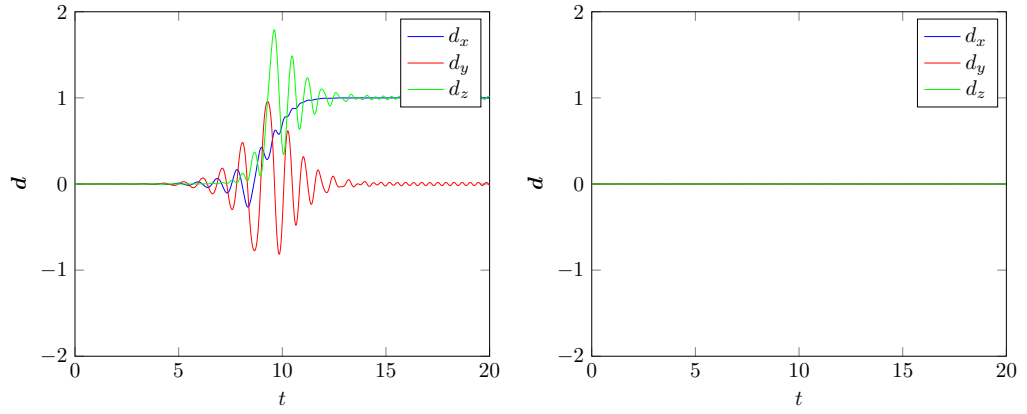

Figure 2: Distance $\boldsymbol{d}(t) = {}_K\vec{\boldsymbol{e}}_z^{K\star} - {}_K\vec{\boldsymbol{e}}_z^{K}$: left the explicit scheme, right the implicit scheme

Simulation results with RAMMS::ROCKFALL

In rockfall events the rotation of platy disk-shaped rocks around their major principal axis is a remarkable phenomenon which has been recently precisely measured in experiments [1]. In order to capture these rock dynamics, we have fully implemented the newly proposed implicit scheme into RAMMS::ROCKFALL and have performed simulations in both idealized and actual rockfall environments. As a control group, the original explicit scheme employed in the current RAMMS:ROCKFALL version has been utilized to obtain rockfall simulations under the same boundary conditions.
The first group of simulations was performed with a disk-shaped rock going downward an idealized inclined slope of 40°. The rock has a uniformly distributed mass of 1000 kg and has a geometry size of 1.16, 1.14 and 0.35 m along its three principal axes, respectively (see Tab. 3). In total 300 simulations were performed with only changing the initial rock orientation. The same initial rock orientation set and time step (0.002 s) was employed for both the explicit and the implicit scheme [4]. Fig. 3 compares for both numerical schemes the kinetic rock energy using the statistic mode of RAMMS::ROCKFALL (first row). The trajectory mode (second row) shows for a single simulation the development of rock rotations along its principal axes. The implicit scheme tends to give significantly lower and much more homogeneous values of the kinetic energy. Furthermore, it takes a much shorter distance for rocks calculated with the implicit scheme to enter the mode rotating around their major principal axes, which remains stable until the rock reaches the horizontal deposition zone. Tab. 1 compares the corresponding mean and standard deviation values obtained for the both numerical schemes. The second group of simulations was performed with a so-called EOTA-shaped rock (see Tab. 3) which was used in rockfall experiments with instrumented rocks at Chant Sura in Davos, Switzerland [1]. The rock mass is 780 kg, homogeneously distributed in a rigid body of 0.93, 0.93 and 0.47 m along the three principal axes. Also 300 simulations

Table 1: Comparison of 300 rocks behavior on an idealized slope for the explicit and the implicit schemes.

Parameter	**Explicit**		**Implicit**	
	Mean	Standard Deviation	Mean	Standard Deviation
kinetic energy (kJ)	127.95	107.25	78.13	43.08
translational velocity (m/s)	13.35	6.29	10.59	3.48
rotational velocity (rot/s)	3.01	1.39	2.47	0.77
jump height (m)	1.23	1.24	0.87	0.84

Table 2: Comparison of 300 rocks behavior at Chant Sura for the explicit and the implicit schemes.

Parameter	**Explicit**		**Implicit**	
	Mean	Standard Deviation	Mean	Standard Deviation
kinetic energy (kJ)	64.60	46.50	76.48	47.79
translational velocity (m/s)	10.74	4.58	11.64	4.45
rotational velocity (rot/s)	2.71	1.10	2.98	1.03
jump height (m)	1.07	0.85	1.10	0.84

Table 3: Comparison of the computational time for the explicit and the implicit schemes (300-rock simulation).

Simulation case		**Explicit**	**Implicit**
idealized slope (ramp)	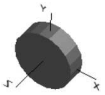	47 s	57 s
actual slope (Chant Sura)		9 s	15 s

were carried out here, setting the same initial rock orientations and time step (0.002 s) for both the explicit and the implicit schemes. The implicit scheme gives a more concentrated run-out zone for the rocks, see the first row in Fig. 4 and the distribution of rock kinetic energy looks “smoother” when compared with the explicit scheme. Most interestingly, the implicit scheme captures well the fast rotation of the flat rock during the entire trajectory while the explicit scheme cannot reproduce the rock’s stable rotation around its major principal axis. Tab. 2 lists the mean and standard deviation values for both the numerical schemes. Finally, Tab. 3 displays the computational time recorded for the 300-rock simulations under the explicit and the implicit schemes. The implicit scheme is a bit slower in comparison to the explicit scheme, which is expected as the updating of rock rotations requires more computational effort. However, the former does respect the stability properties of rotating 3D objects, which is a key improvement for RAMMS::ROCKFALL. Future simulations will be carefully validated against the real rockfall events and experiments. It is anticipated that for extremely long rolling phases of platy rocks the differences between the explicit and the implicit schemes could be even larger.

Conclusions

In this paper an extended intermediate axis theorem has been proven using Lyapunov functions. Using the same Lyapunov functions, we have given a rigorous proof that the implicit scheme presented in [5] respects the extended intermediate axis theorem. The computational cost per time-step is larger for the implicit scheme than the explicit scheme, as Newton iterations are needed to solve the implicit equations. However, numerical simulations show that the implicit scheme is far more accurate as it respects both the energy conservation and the invariance of the spin. The implicit scheme therefore allows to take larger time-steps without excessive error, making it a suitable scheme for 3D rockfall simulation.
Numerical simulations with RAMMS::ROCKFALL using the newly developed implicit scheme show that for the downward motion of a platy rock on an actual slope the rotation around the major principal axis is stable, even in the presence of intermediate collisions and contact phases with the slope. This is in correspondence with data from field experiments.

Acknowledgement

The authors are indepted to Marc Christen and Andrin Caviezel of the WSL Institute for Snow and Avalanche Research SLF for support with the RAMMS::ROCKFALL simulations and visualization.

References

[1] CAVIEZEL, A., DEMMEL, S., RINGENBACH, A., BÜHLER, Y., LU, G., CHRISTEN, M., DINNEEN, C., EBERHARD, L., VON RICKENBACH, D., AND BARTELT, P. Reconstruction of four-dimensional rockfall trajectories using remote sensing and rock-based accelerometers and gyroscopes. *Earth Surface Dynamics 7*, 1 (2019), 199–210.

[2] CHRISTEN, M., BÜHLER, Y.AND BARTELT, P., LEINE, R., GLOVER, J., SCHWEIZER, A., GRAF, C., MCARDELL, B., GERBER, W., DEUBELBEISS, Y., FEISTL, T., AND VOLKWEIN, A. Integral hazard management using a unified software environment: numerical simulation tool "RAMMS" for gravitational natural hazards. In *Proceedings 12th Congress INTERPRAEVENT* (2012), G. Koboltschnig, J. Hübl, and J. Braun, Eds., vol. 1, pp. 77–86.

[3] LEINE, R. I., SCHWEIZER, A., CHRISTEN, M., GLOVER, J., BARTELT, P., AND GERBER, W. *Multibody System Dynamics 32* (2014), 241–271.

[4] LU, G., CAVIEZEL, A., CHRISTEN, M., DEMMEL, S., RINGENBACH, A., BÜHLER, Y., DINNEEN, C., GERBER, W., AND BARTELT, P. Modelling rockfall impact with scarring in compactable soils. *Landslides* (2019), 2353–2367.

[5] SCHWEIZER, A. *Ein nichtglattes mechanisches Modell für Steinschlag*. PhD thesis, ETH Zurich, 2015.

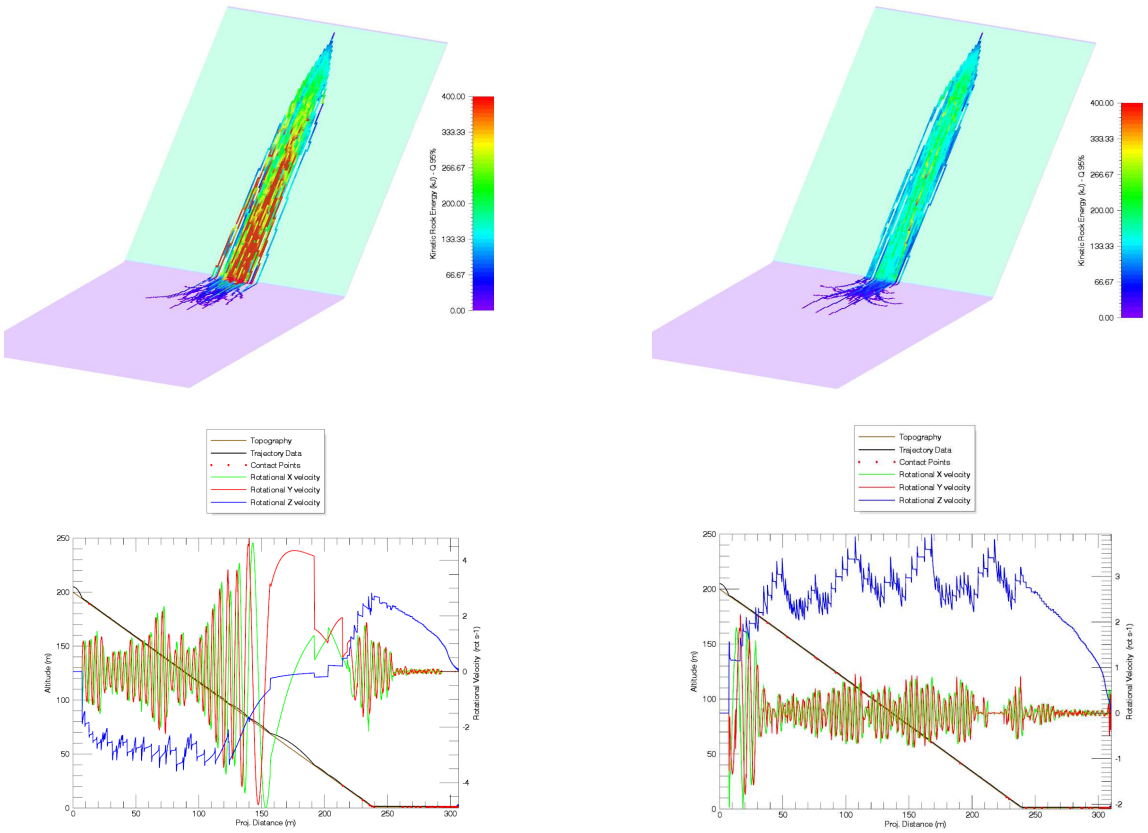

Figure 3: Disk-shaped rock rolling down an idealized inclined slope: left the explicit scheme, right the implicit scheme.

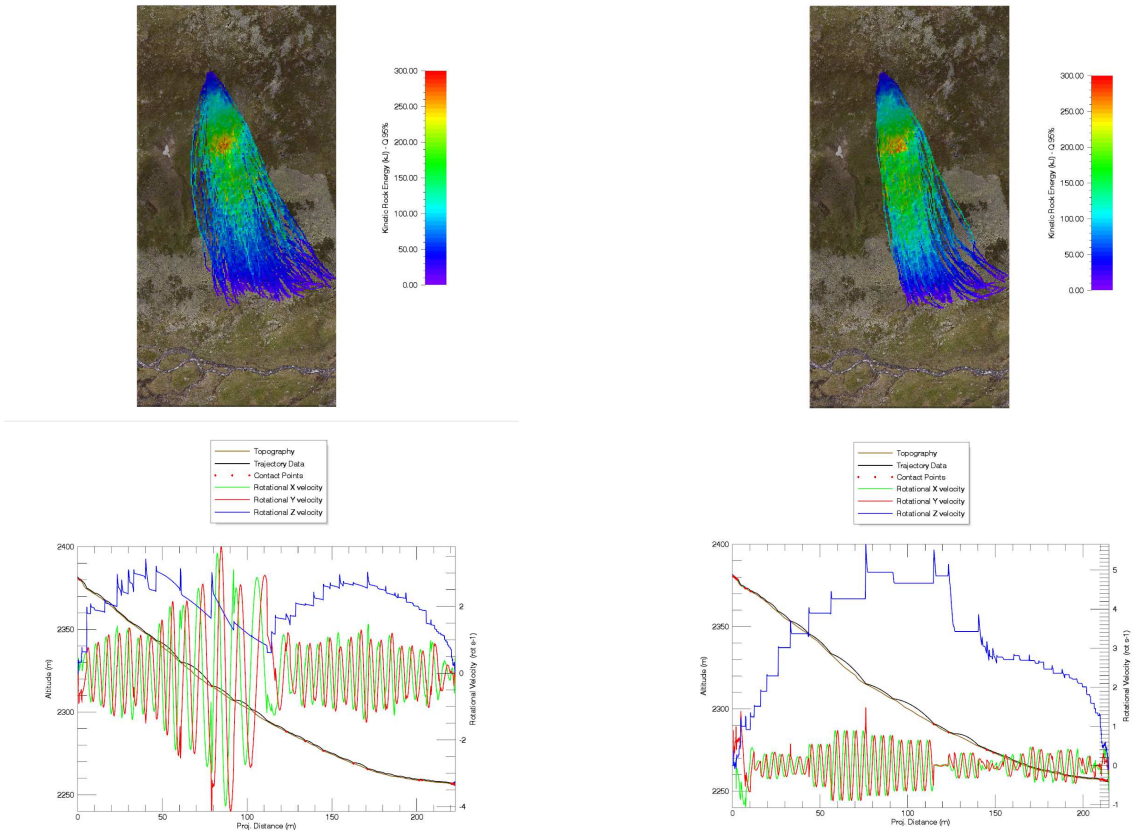

Figure 4: EOTA-shaped rock rolling down an actual slope at Chant Sura (Davos, Switzerland): left the explicit scheme, right the implicit scheme

A Three-Dimensional and Nonlinear Virtual Test Car

Georg Rill*
*Department of Mechanical Engineering, OTH Regensburg, Germany

Summary. Virtual testing procedures have become a standard in vehicle dynamics. The increasing complexity of driver assistance systems demand for more and more virtual tests, which are supposed to produce reliable results even in the limit range. As a consequence, simplified vehicle models, like the classical bicycle model or 4-wheel vehicle models, have to be replaced by a fully three-dimensional and nonlinear vehicle model, which also encompasses the details of the suspension systems. This paper presents a passenger car model, where the chassis, the four knuckles, and the four wheels are described by rigid bodies, the suspension system is modeled by the generic design kinematics, and the TMeasy tire model provides the tire forces and torques in all driving situations.

Keywords: Virtual Test Car (VTC), Design Kinematics, TMeasy, Equations of Motion, Transient Response

Introduction

The multibody approach has become a standard in vehicle dynamics [1]. General multibody software packages, like Adams/Car [2], ReCurDyn [3], or SIMPACK [4] make it possible to assemble vehicle models of different complexities. Commercial products, like CarSim [5], CarMaker [6], or DYNA4 [7] provide ready to use vehicle models, which are real-time capable and may be used in Hardware-in-the-Loop (HIL) test rigs, in driving simulators, or for all kind of virtual driving tests including parameter optimization or autonomous drive. A basic multibody model of a standard passenger car is usually supplemented by a handling tire model, like Pacejka [8] or TMeasy [9], and it is extensible by subsystems for the steering system and the drive train [10]. Sophisticated model approaches combined with an efficient and robust solver provide an excellent runtime performance [11]. Nevertheless, simplified and rather crude three-dimensional vehicle models are still applied in the context of lap-time optimization [12] and autonomous driving [13]. However, this reduces such investigations to the level of basic studies, because the impact of the suspension properties and the road roughness on vehicle dynamics is not taken into account. This paper demonstrates, that a virtual test car (VTC), properly modeled by a three-dimensional and nonlinear multibody system, is able to achieve a much faster-than-real-time performance even on standard personal computers, although it includes the nonlinear suspension kinematics and the wheel/tire dynamics.

The VTC-Model

Model Structure

A virtual test car, valid for typical passenger cars in all driving situations, is represented by a three-dimensional multibody model which consists at least of the chassis, four knuckles, and four wheels, Figure 1. The virtual test car (VTC) is

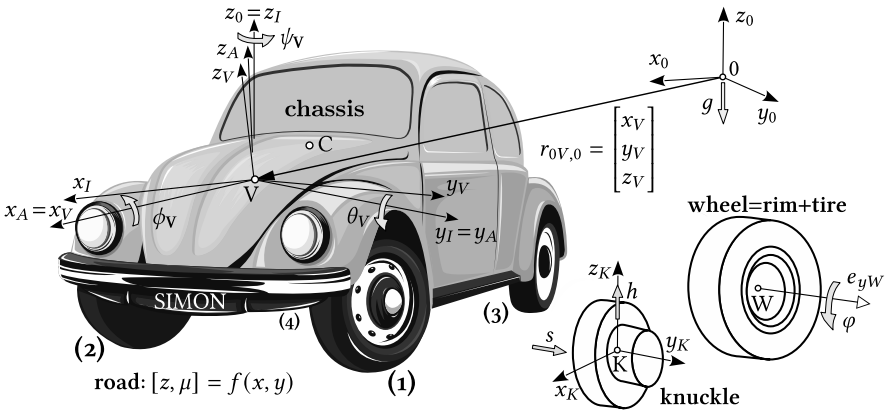

Figure 1: Multibody model structure of a passenger car

operated with the TMeasy tire model, which represents a handling model, where the tire acts as a massless force element. The suspension kinematics allows each knuckle to perform relative to the chassis a hub motion h and a steer motion s. This generic model approach makes it possible to investigate the influence of different suspension designs, including all-wheel steering, on the handling and dynamics of a vehicle. The steer motions of passenger car front wheels are typically coupled by a rack and pinion steering system and the rear suspension often incorporates no active steer motions at all.
Each of the four wheels, consisting of the rim and the tire, rotates with the angle φ about a knuckle-fixed axis, defined by the unit vector e_{yW}. The generalized coordinates x_V, y_V, z_V, ψ_V, θ_V, and ϕ_V describe the momentary position and orientation of the vehicle-fixed, within the VTC model also chassis-fixed, reference frame V with respect to an earth-fixed frame 0. The points C and K denote the gravity centers of the chassis and the knuckle. In practice, the wheels of passenger cars are sufficiently balanced. Then, the wheel center W will be located on the wheel rotation axis and is fixed to the knuckle as a consequence.

The multibody system, providing the basis of three-dimensional passenger car model, has up to $f = 6 + 4 * 2 + 4 = 18$ degrees of freedom if each of the four knuckles is modeled with a hub and a steer motion. The total number of degrees of freedom is reduced to $f = 16$ if the rear wheels are not actively steered. More complex but still real-time capable vehicle models including the drive train, the steering system, and dynamic force elements are described in [11] and [14]. Appropriate road models provide the road height z and the friction coefficient μ as a function of the contact point coordinates x and y [15].

Reference Frame and Nontrivial Generalized Velocities

The momentary position and orientation of the chassis-fixed or vehicle-fixed reference frame V is provided by the position vector $r_{0V,0}$ and the rotation matrix A_{0V} defined in the VTC model as

$$r_{0V,0} = \begin{bmatrix} x_V \\ y_V \\ z_V \end{bmatrix} \quad \text{and} \quad A_{0V} = \begin{bmatrix} \cos\psi_V & -\sin\psi_V & 0 \\ \sin\psi_V & \cos\psi_V & 0 \\ 0 & 0 & 1 \end{bmatrix} \begin{bmatrix} \cos\theta_V & 0 & \sin\theta_V \\ 0. & 1 & 0 \\ -\sin\theta_V & 0 & \cos\theta_V \end{bmatrix} \begin{bmatrix} 1 & 0 & 0 \\ 0 & \cos\phi_V & -\sin\phi_V \\ 0 & \sin\phi_V & \cos\phi_V \end{bmatrix} \tag{1}$$

where x_V, y_V, z_V, ϕ_V, θ_V, and ψ_V serve as generalized coordinates. The comma separated index 0 indicates that the components of the vector r_{0V} pointing from 0 to V are expressed in the earth-fixed reference frame 0.
The components of the velocity vector v_{0V} and the angular velocity vector ω_{0V} can both be expressed in the vehicle-fixed frame. The set of kinematical differential equations

$$\begin{bmatrix} \dot{x}_V \\ \dot{y}_V \\ \dot{z}_V \end{bmatrix} = A_{0V}^T \underbrace{\begin{bmatrix} v_x \\ v_y \\ v_z \end{bmatrix}}_{v_{0V,V}} \quad \text{and} \quad \begin{bmatrix} \dot{\phi}_V \\ \dot{\theta}_V \\ \dot{\psi}_V \end{bmatrix} = \frac{1}{\cos\theta} \begin{bmatrix} \cos\theta & \sin\phi\sin\theta & \cos\phi\sin\theta \\ 0 & \cos\phi\cos\theta & -\sin\phi\cos\theta \\ 0 & \sin\phi & \cos\phi \end{bmatrix} \underbrace{\begin{bmatrix} \omega_x \\ \omega_y \\ \omega_z \end{bmatrix}}_{\omega_{0V,V}} \tag{2}$$

provides then the time derivatives of the generalized coordinates $\dot{x}_V$, $\dot{y}_V$, $\dot{z}_V$, $\dot{\phi}_V$, $\dot{\theta}_V$, $\dot{\psi}_V$ as a function of the generalized velocities v_x, v_y, v_z, and ω_x, ω_y, ω_z. As shown in [16] this particular choice of nontrivial generalized velocities reduces the complexity of the equations of motion significantly.

Relative Kinematics

The vehicle model, shown in Figure 1, consists of $n = 9$ rigid bodies: the chassis, four knuckles, and four wheels. The absolute position and orientation of an arbitrary body j is defined by

$$r_{0j,0} = r_{0V,0} + A_{0V}\, r_{Vj,V} \quad \text{and} \quad A_{0j} = A_{0V}\, A_{Vj} \tag{3}$$

where $r_{0V,0}$ and A_{0V} are defined by (1) and $r_{Vj,V}$ and A_{Vj} describe the position and orientation of body j relative to the vehicle-fixed reference frame V.
The vector of the absolute body velocity v_{0j} can be expressed in the vehicle-fixed frame

$$v_{0j,V} = v_{0V,V} + A_{0V}^T \frac{d}{dt} \left(A_{0V}\, r_{Vj,V}\right) = v_{0V,V} + \omega_{0V,V} \times r_{Vj,V} + \dot{r}_{Vj,V} \tag{4}$$

where according to (2) the components of the vectors $v_{0V,V}$ and $\omega_{0V,V}$ are entirely defined by the nontrivial generalized velocities v_x, v_y, v_z, ω_x, ω_y, ω_z. The movements of body j relative to the vehicle-fixed frame V can be characterized by a certain set of generalized coordinates, which may be collected in the vector y_j. Then, the vector $r_{Vj,V}$ describing the momentary position of body j relative to V depends on this set of generalized coordinates, $r_{Vj,V} = r_{Vj,V}(y_j)$ and its time derivative with respect to frame V results in

$$\dot{r}_{Vj,V} = \frac{d}{d\,t} r_{Vj,V}(y_j) = \frac{\partial\, r_{Vj,V}}{\partial\, y_j}\, \dot{y}_j = t_{j,V}(y_j)\, \dot{y}_j \tag{5}$$

where the term $t_{j,V}$ represents the partial velocity of the body j motions. Similarly, the vector of the absolute body angular velocity, expressed in the vehicle-fixed frame V, reads as

$$\omega_{0j,V} = \omega_{0V,V} + \omega_{Vj,V} = \omega_{0V,V} + d_{j,V}(y_j)\, \dot{y}_j \tag{6}$$

where the term $d_{j,V}$ describes the partial angular velocity of the body j motions.
The absolute acceleration and the absolute angular acceleration of body j, both expressed in the vehicle-fixed frame V, are at first provided by

$$\begin{aligned} a_{0j,V} &= A_{0V}^T \frac{d}{dt} \left(A_{0V}\, v_{0V,V}\right) = \omega_{0V,V} \times v_{0j,V} \;+\; \dot{v}_{0V,V} + \tilde{r}_{Vj,V}^T\, \dot{\omega}_{0V,V} + \omega_{0V,V} \times \dot{r}_{Vj,V} + \ddot{r}_{Vj,V} \\ \alpha_{0j,V} &= A_{0V}^T \frac{d}{dt} \left(A_{0V}\, \omega_{0V,V}\right) = \omega_{0V,V} \times \omega_{0j,V} \;+\; \dot{\omega}_{0V,V} + \dot{\omega}_{Vj,V} \end{aligned} \tag{7}$$

where the cross product $\dot{\omega}_{0V,V} \times r_{Vj,V}$ was transferred via $\dot{\omega} \times r = -r \times \dot{\omega} = -\tilde{r}\,\dot{\omega} = \tilde{r}^T \dot{\omega}$ to the multiplication of a transposed skew-symmetric matrix with a vector. The velocity $v_{0V,V}$ and the angular velocity $\omega_{0V,V}$ depend entirely on the generalized velocities. The relative velocity $\dot{r}_{Vj,V}$ and the relative angular velocity $\omega_{Vj,V}$ are provided in (5) and (6). Their time derivatives result in

$$\ddot{r}_{Vj,V} = t_{j,V}(y_j)\,\ddot{y}_j + \dot{t}_{j,V}(y_j)\,\dot{y}_j \qquad \text{and} \qquad \dot{\omega}_{Vj,V} = d_{j,V}(y_j)\,\ddot{y}_j + \dot{d}_{j,V}(y_j)\,\dot{y}_j \tag{8}$$

The trivial choice $z_j = \dot{y}_j$ of generalized velocities is always possible. Then (7) reads as

$$\begin{aligned} a_{0j,V} &= \begin{bmatrix} \mathrm{I}_{3\times3} & \tilde{r}^T_{Vj,V} & \dots t_{j,V} \dots \end{bmatrix} \dot{z} \;+\; \omega_{0V,V} \times (v_{0j,V} + \dot{r}_{Vj,V}) + \dot{t}_{j,V}\dot{y}_j \;=\; \frac{\partial\, v_{0j,V}}{\partial\, z}\,\dot{z} \;+\; a^R_{0j,V} \\ \alpha_{0j,V} &= \begin{bmatrix} 0_{3\times3} & \mathrm{I}_{3\times3} & \dots d_{j,V} \dots \end{bmatrix} \dot{z} \;+\; \omega_{0V,V} \times \omega_{0j,V} + \dot{d}_{j,V}\,\dot{y}_j \;=\; \frac{\partial\, \omega_{0j,V}}{\partial\, z}\,\dot{z} \;+\; \alpha^R_{0j,V} \end{aligned} \tag{9}$$

where the vector

$$z = \begin{bmatrix} v_x\, v_y\, v_z & \omega_x\, \omega_y\, \omega_z & \dot{y}_1 \dots \dot{y}_n \end{bmatrix}^T \tag{10}$$

collects the generalized velocities of the vehicle model. The symbols $\mathrm{I}_{3\times3}$ and $0_{3\times3}$ represent 3×3 matrices of identity and zeros. The $3 \times f$ matrices $\partial\, v_{0j,V}/\partial\, z_j$ and $\partial\, \omega_{0j,V}/\partial\, z_j$, where f denotes the number of degrees of freedom, represent the partial velocities and partial angular velocities of the absolute body j motion. The symbols $a^R_{0j,V}$ and $\alpha^R_{0j,V}$ abbreviate the remaining acceleration and the remaining angular acceleration terms, which do not explicitly depend on the time derivatives of the generalized velocities.

Passenger car suspensions force the knuckles to perform rather complex nonlinear but smooth motions relative to the chassis or the vehicle-fixed reference frame V respectively. In addition, the damper elements in a vehicle suspension systems reduce the relative velocities $\dot{y}_j$ to moderate values. As a consequence, the terms $\dot{t}_{j,V}\,\dot{y}_j$ and $\dot{d}_{j,V}\,\dot{y}_j$ can be neglected compared to the other terms in the remaining acceleration and the remaining angular acceleration which results in a non-perfect multibody model, but safes a significant amount on computation effort and still provides an acceptable accuracy [17].

Chassis

The first body, the chassis, represents a special case, because the vehicle-fixed reference V frame is fixed to the chassis. As a consequence, the position vector $r_{V1,V} = r_{VC,V}$ is constant and the rotation matrix is simply defined by the 3×3 matrix of identity, $A_{V1} = A_{VC} = \mathrm{I}_{3\times3}$. Then

$$\frac{\partial\, v_{0C,V}}{\partial\, z} = \begin{bmatrix} \mathrm{I}_{3\times3} & \tilde{r}^T_{VC,V} & 0_{3\times f_r} \end{bmatrix} \qquad \text{and} \qquad \frac{\partial\, \omega_{0C,V}}{\partial\, z} = \begin{bmatrix} 0_{3\times3} & \mathrm{I}_{3\times3} & 0_{3\times f_r} \end{bmatrix} \tag{11}$$

provide the partial velocities and the partial angular velocities of the chassis, where $f_r = f - 6$ denotes the degrees of freedom of the motions relative to the chassis.

Generic Suspension

The kinematics of standard suspension systems, like the double wishbone, the MacPherson, or the multi-link suspension, can be solved online or approximated by lookup tables or more efficiently by smooth two-dimensional functions [18]. Regardless of the type of an independent suspension the position and orientation of the knuckle fixed reference frame K relative to the chassis or vehicle-fixed frame V can be described by a position vector and a rotation matrix

$$r_{VW,V} = r_{VW,D} + \begin{bmatrix} \xi \\ \eta \\ \zeta \end{bmatrix} \quad \text{and} \quad A_{VK} = A_\gamma\, A_\alpha\, A_\beta \tag{12}$$

where $r_{VW,D}$ describes the design position of the wheel center W, which on a balanced wheel is located on the wheel rotation axis and hence fixed to the knuckle. The rotation matrix is composed of three elementary rotations, where γ describes the steer motion, α the wheel camber, and β the pitch motion of the knuckle.

In particular at kinematic and compliance (KnC) tests, the wheel center W is used as a reference point to monitore and measure the knuckle/wheel movements. The coordinates $\xi = \xi(h, s)$, $\eta = \eta(h, s)$, $\zeta = \zeta(h, s)$ as well as the rotation angles $\alpha = \alpha(h, s)$, $\beta = \beta(h, s)$, $\gamma = \gamma(h, s)$ depend on the hub and steer motions h and s. In general, the hub motion can be described by the vertical displacement of the wheel center, $\zeta = h$. A least square approximation of measured or computed KnC tests delivers the design kinematic parameters, which for a typical double wishbone suspension on the left front wheel are listed in Table 1. It provides column by column the parameter sets required for the two-dimensional design kinematic functions $f = f(h, s)$, where h and s represent the hub and the steer motion. The columns hold for the constraint knuckle motions $\xi = \xi(h, s)$ to $\gamma = \gamma(h, s)$, the spring and damper displacements $u_S = u_S(h, s)$ and $u_D = u_D(h, s)$, as well as the vertical movement $z_{arb} = z_{arb}(h, s)$ of the anti-roll bar attachment point. Each parameter set consists of the range limits (`dh`, `ds`), the initial inclinations (`dfdh0`, `dfds0`), as well as the four center (`fp0`, `f0p`, `f0n`, `fn0`) and the four corner points (`fpp`, `fpn`, `fnp`, `fnn`) as defined in [18].

Table 1: Design kinematics parameters for a typical double wishbone front left suspension including force element displacements

ξ	η	α	β	γ	u_S	u_D	z_{arb}	
+0.08096	+0.08096	+0.08096	+0.08096	+0.08096	+0.08096	+0.08096	+0.08096	dh
+0.07240	+0.07240	+0.07240	+0.07240	+0.07240	+0.07240	+0.07240	+0.07240	ds
-0.02765	-0.07112	+0.44734	-0.32329	+0.11453	+0.89260	+0.89323	+0.67524	dfdh0
+0.30806	-0.14963	+1.20972	+1.20120	-8.21459	-0.19082	-0.16794	-0.01680	dfds0
+0.01559	-0.03140	+0.11704	+0.10749	-0.57684	+0.01238	+0.05418	+0.05251	fpp=f(+dh,+ds)
-0.00218	-0.01604	+0.05305	-0.02603	+0.00908	+0.07213	+0.07291	+0.05257	fp0=f(+dh, 0)
-0.03338	-0.01630	-0.12277	-0.11642	+0.78398	+0.01970	+0.07544	+0.05581	fpn=f(+dh,-ds)
+0.01826	-0.01635	+0.06099	+0.10629	-0.61014	-0.04529	-0.01864	-0.00030	f0p=f(0 ,+ds)
-0.03167	+0.00089	-0.14875	-0.05932	+0.79015	-0.04802	+0.00026	+0.00311	f0n=f(0 ,-ds)
+0.02081	-0.02134	+0.02840	+0.11802	-0.63890	-0.10653	-0.08846	-0.05699	fnp=f(-dh,+ds)
+0.00224	-0.00420	-0.02389	+0.02663	-0.00885	-0.07249	-0.07190	-0.05673	fn0=f(-dh, 0)
-0.02946	-0.00217	-0.14831	-0.02219	+0.78449	-0.11015	-0.07223	-0.05396	fnn=f(-dh,-ds)

The Matlab function provided in the following Listing computes the kinematics of a generic suspension modeled by the design kinematics. It provides the orientation of the knuckle-fixed reference frame, the momentary position of the wheel center which serves as a reference point for the knuckle motion, as well as the corresponding partial velocity and partial angular velocity. The 3×1-vector `ufe` collects the displacements of the spring u_S, the damper u_D, and the vertical movement z_{arb} of the anti-roll bar. The 3×2-matrix `dufedyf` contains the changes of `ufe` with respect to the hub and steer motions collected in the 2×1-vector `yk = [h; s]`. They are used within the VTC environment to compute the contribution of the suspension forces to the vector of generalized forces directly via the virtual power. The additional 5×1 output vector `ao` collects the constraint motions resulting from the Matlab function `dk_fun`, which evaluates the two-dimensional functions as described in [18].

Listing: Matlab function computing the kinematics of a generic suspension via the design kinematics

```
function ...     % v t c   u t i l i t y
[ avk ...        % orientation of knuckle fixed frame
, dkv ...        % part. angular velocities knuckle
, rvwv ...       % position of wheel center
, twv ...        % partial velocities wheel center
, ufe ...        % force element displacements
, dufedyf ...    % change of ufe due to yf
, ao ...         % additional output
] = dk_susp ... % generic suspension via design kinematics
( yk ...         % generalized suspension coordinates yk = [ h; s ]
, rvkd ...       % design position of wheel center
, dkin ...       % matrix of design kinematics parameter
)

% constraint wheel motions ( yk(1) = hub, yk(2) = steer )
[ xw,dxwdyf(1),dxwdyf(2) ] = dk_fun( yk(1), yk(2), dkin(:,1) );
[ yw,dywdyf(1),dywdyf(2) ] = dk_fun( yk(1), yk(2), dkin(:,2) );
[ al,daldyf(1),daldyf(2) ] = dk_fun( yk(1), yk(2), dkin(:,3) );
[ be,dbedyf(1),dbedyf(2) ] = dk_fun( yk(1), yk(2), dkin(:,4) );
[ ga,dgadyf(1),dgadyf(2) ] = dk_fun( yk(1), yk(2), dkin(:,5) );

% sine- and cosine functions as well as combinations
sal = sin(al);  sbe = sin(be);  sga = sin(ga);
cal = cos(al);  cbe = cos(be);  cga = cos(ga);
salsbe = sal*sbe; salcbe = sal*cbe; calsga = cal*sga; calcga = cal*cga;

% rotation matrix of chassis -> knuckle (elementary rotations: ga-al-be)
avk(1,1) =  cbe*cga - salsbe*sga;
avk(2,1) =  cbe*sga + salsbe*cga;
avk(3,1) = -sbe*cal;
avk(1,2) = -calsga;
avk(2,2) =  calcga;
avk(3,2) =  sal;
avk(1,3) =  sbe*cga + salcbe*sga;
avk(2,3) =  sbe*sga - salcbe*cga;
avk(3,3) =  cal*cbe;

% partial angular velocities due to hub and steer
dkv = zeros(3,2);
for j=1:2
  dkv(1,j) = cga*daldyf(j) - calsga*dbedyf(j);
  dkv(2,j) = sga*daldyf(j) + calcga*dbedyf(j);
  dkv(3,j) =                    sal*dbedyf(j)  +  dgadyf(j);
end

% actual position of wheel center
rvwv = [ rvkd(1)+xw; rvkd(2)+yw; rvkd(3)+yk(1) ];

% partial velocities  due to hub and steer
```

```
twv = [ dxwdyf(1)  dxwdyf(2) ; ...
        dywdyf(1)  dywdyf(2) ; ...
            1          0     ];

% displacements and partial derivatives of force elements
[ ufe(1),dufedyf(1,1),dufedyf(1,2) ] = dk_fun( yk(1), yk(2), dkin(:,6) );
[ ufe(2),dufedyf(2,1),dufedyf(2,2) ] = dk_fun( yk(1), yk(2), dkin(:,7) );
[ ufe(3),dufedyf(3,1),dufedyf(3,2) ] = dk_fun( yk(1), yk(2), dkin(:,8) );

% provide constraint motions as additional output
ao  =  [ xw; yw;  al; be; ga ];

end
```

The generic suspension model provides the position of the wheel center rvwv $\rightarrow r_{VW,V}$ and the orientation of the knuckle avk $\rightarrow A_{VK}$ relative to the vehicle-fixed reference frame V as well as the 3×2-matrices dkv $\rightarrow d_{K,V}$ and twv $\rightarrow t_{W,V}$ which provide the partial angular velocities of the knuckle and the partial velocity of the wheel center. The velocity of the wheel center and the angular velocity of the wheel are then determined by

$$v_{0W,V} = v_{0V,V} + \omega_{0V,V} \times r_{VW,V} + t_{W,V} \begin{bmatrix} \dot{h} \\ \dot{s} \end{bmatrix} \quad \text{and} \quad \omega_{0W,V} = \omega_{0V,V} + d_{K,V} \begin{bmatrix} \dot{h} \\ \dot{s} \end{bmatrix} + e_{yW,V}\, \dot{\varphi} \tag{13}$$

where $e_{yW,V} = A_{VK}\, e_{yW,D}$ provides the knuckle-fixed wheel rotation axis and $\omega_{KW,V} = e_{yW,V}\, \dot{\varphi}$ describes the angular velocity of the wheel rotation relativ to the knuckle. The momentary position of the knuckle center K and its partial velocities are defined by

$$r_{VK,V} = r_{VW,V} + A_{VK}\, r_{WK,D} = r_{VW,V} + r_{WK,V} \quad \text{and} \quad t_{K,V} = t_{W,V} + d_{K,V} \times r_{WK,V} \tag{14}$$

where $r_{WK,D}$ denotes the design position of the knuckle center K relative to the wheel center W.

Equations of Motion

The state of a generic VTC model, as proposed here, is defined by $f = 18$ generalized coordinates and $f = 18$ generalized velocities collected in the vectors

$$\begin{aligned} y &= \left[\begin{array}{cccccccccccccccccc} x_V & y_V & z_V & \phi_V & \theta_V & \psi_V & h_1 & s_1 & h_2 & u_2 & h_3 & u_3 & h_4 & u_4 & \varphi_1 & \varphi_2 & \varphi_3 & \varphi_4 \end{array} \right]^T \\ z &= \left[\begin{array}{cccccccccccccccccc} v_x & v_y & v_z & \omega_x & \omega_y & \omega_z & \dot{h}_1 & \dot{s}_1 & \dot{h}_2 & \dot{u}_2 & \dot{h}_3 & \dot{u}_3 & \dot{h}_4 & \dot{u}_4 & \dot{\varphi}_1 & \dot{\varphi}_2 & \dot{\varphi}_3 & \dot{\varphi}_4 \end{array} \right]^T \end{aligned} \tag{15}$$

Jourdain's principle of virtual power delivers the equations of motion as a set of two first order nonlinear systems of differential equations

$$\dot{y} = K(y)\, z \quad \text{and} \quad M(y)\, \dot{z} = q(y,\, z,\, u,\, w) \tag{16}$$

where the vectors u and w collect all model inputs and additional dynamic states, required for dynamic tire and dynamic suspension forces. A kinematic matrix K which does not coincide with the matrix of identity, makes it possible to define non-trivial generalized velocities, as done here in (2) for the overall vehicle motions. The elements of the mass matrix M and the vector of generalized forces and torques q applied to the vehicle are generated for the $n = 9$ bodies of the VTC model via

$$M = \sum_{j=1}^{n} \left\{ \left(\frac{\partial v_{0j,V}}{\partial z} \right)^T m_j \, \frac{\partial v_{0j,V}}{\partial z} + \left(\frac{\partial \omega_{0j,V}}{\partial z} \right)^T \Theta_{j,V} \, \frac{\partial \omega_{0j,V}}{\partial z} \right\} \tag{17}$$

$$q = \sum_{j=1}^{n} \left\{ \left(\frac{\partial v_{0j,V}}{\partial z} \right)^T \left[F^a_{j,V} - m_j\, a^R_{0j,V} \right] + \left(\frac{\partial \omega_{0j,V}}{\partial z} \right)^T \left[T^a_{j,V} - \Theta_{j,V} \alpha^R_{0j,V} - \omega_{0j,V} \times \Theta_{j,V} \omega_{0j,V} \right] \right\} \tag{18}$$

where m_j and $\Theta_{j,V}$ describe the mass and inertia of body j, $F^a_{j,V}$ and $T^a_{j,V}$ represent the resulting vectors of the forces and torques applied to body j. Equations (6) and (9) provide the angular velocities $\omega_{0j,V}$, the partial velocities $\partial v_{0j,V} \partial z$, the partial angular velocities $\partial \omega_{0j,V} / \partial z$, as well as the remaining acceleration $a^R_{0j,V}$ and the remaining angular acceleration $\alpha^R_{0j,V}$. The partial velocities of the front right knuckle (K2) and the front right wheel (W2) are, for example, defined by

$$\begin{aligned} \frac{\partial\, v_{0K2,V}}{\partial\, z} &= \left[\begin{array}{cccccccccc} \mathrm{I}_{3\times3} & \tilde{r}^T_{VK2,V} & 0_{3\times2} & t_{K2,V} & 0_{3\times2} & 0_{3\times2} & 0_{3\times1} & 0_{3\times1} & 0_{3\times1} & 0_{3\times1} \end{array} \right] \\ \frac{\partial\, \omega_{0K2,V}}{\partial\, z} &= \left[\begin{array}{cccccccccc} 0_{3\times3} & \mathrm{I}_{3\times3} & 0_{3\times2} & d_{K2,V} & 0_{3\times2} & 0_{3\times2} & 0_{3\times1} & 0_{3\times1} & 0_{3\times1} & 0_{3\times1} \end{array} \right] \end{aligned} \tag{19}$$

$$\begin{aligned} \frac{\partial\, v_{0W2,V}}{\partial\, z} &= \left[\begin{array}{cccccccccc} \mathrm{I}_{3\times3} & \tilde{r}^T_{VW2,V} & 0_{3\times2} & t_{W2,V} & 0_{3\times2} & 0_{3\times2} & 0_{3\times1} & 0_{3\times1} & 0_{3\times1} & 0_{3\times1} \end{array} \right] \\ \frac{\partial\, \omega_{0W2,V}}{\partial\, z} &= \left[\begin{array}{cccccccccc} 0_{3\times3} & \mathrm{I}_{3\times3} & 0_{3\times2} & d_{W2,V} & 0_{3\times2} & 0_{3\times2} & 0_{3\times1} & e_{yW2,V} & 0_{3\times1} & 0_{3\times1} \end{array} \right] \end{aligned} \tag{20}$$

The TMeasy model [9] provides the tire forces $F_{T1,0}$ to $F_{T4,0}$ and the torques $T_{T1,0}$ to $T_{T4,0}$ applied to the four wheel centers. In particular, the slip based longitudinal and lateral tire forces strongly depend on the velocity state v_{0W} and ω_{0W} of the wheel. The velocity state of the wheel depends, according to (13), on the velocity state of the vehicle ($v_{0V,V}$ and $\omega_{0V,V}$) and on the kinematical properties of the suspension systems represented by the symbols $t_{W,V}$, $d_{K,V}$, and $e_{yW,V}$, which describe the partial velocity of the wheel center, the partial angular velocity of the knuckle, and the position of the wheel rotation axis. Hence, neglecting the suspension kinematics partly or completely, as done in simplified vehicle models, inevitably results in poorly modeled tire forces and tire torques.
The vehicle dynamics represented by (16) is driven by the vector of generalized forces and torques. The contribution of front right tire, part of the front right knuckle (K2) and wheel (W2) combination, to the vector of generalized forces and torques is, for example, provided by

$$\begin{aligned} \text{overall vehicle:} \quad & q_{1:6} = q_{1:6} + \begin{bmatrix} F_{T2,V} \\ T_{T2,V} + r_{VW2,V} \times F^T_{T2,V} \end{bmatrix} \\ \text{hub and steer motions front right:} \quad & q_{9:10} = q_{9:10} + t^T_{W2,V}\, F_{T2,V} + d^T_{K2,V}\, T_{T2,V} \\ \text{wheel rotation front right:} \quad & q_{16} = q_{16} + e^T_{yW,V}\, T_{T2,V} \end{aligned} \tag{21}$$

The relations $F_{T2,V} = A^T_{0V}\, F_{T2,0}$ and $T_{T2,V} = A^T_{0V}\, T_{T2,0}$ transform the resulting tire force vector and the resulting tire torque vector from the earth-fixed into the vehicle-fixed frame. The amount of contribution depends on the partial velocity of the wheel center $t_{W2,V}$, the partial angular velocity of the knuckle $d_{K2,V}$, and the wheel rotation axis $e_{yW,V}$. Tire forces, which support and guide the vehicle, may change very quickly and can increase to considerable values, in particular in critical driving situations. That is why, even rather small changes in the kinematical suspension properties, represented by the symbols $t_{W,V}$, $d_{K,V}$, and $e_{yW,V}$, result in significant contributions to the vector of generalized force and torques. Which magnifies the error in neglecting the specific properties of the suspension kinematics.

Example: Braking in a Turn

The numerical solution of differential equations, like the ones in (16), is discussed in [19]. A straightforward implementation of the virtual test car (VTC) entirely realized in MATLAB provides an easy to use simulation environment including plotting and animation facilities, Figure 2. As typical for standard passenger cars on dry road, the left plot in Figure 2

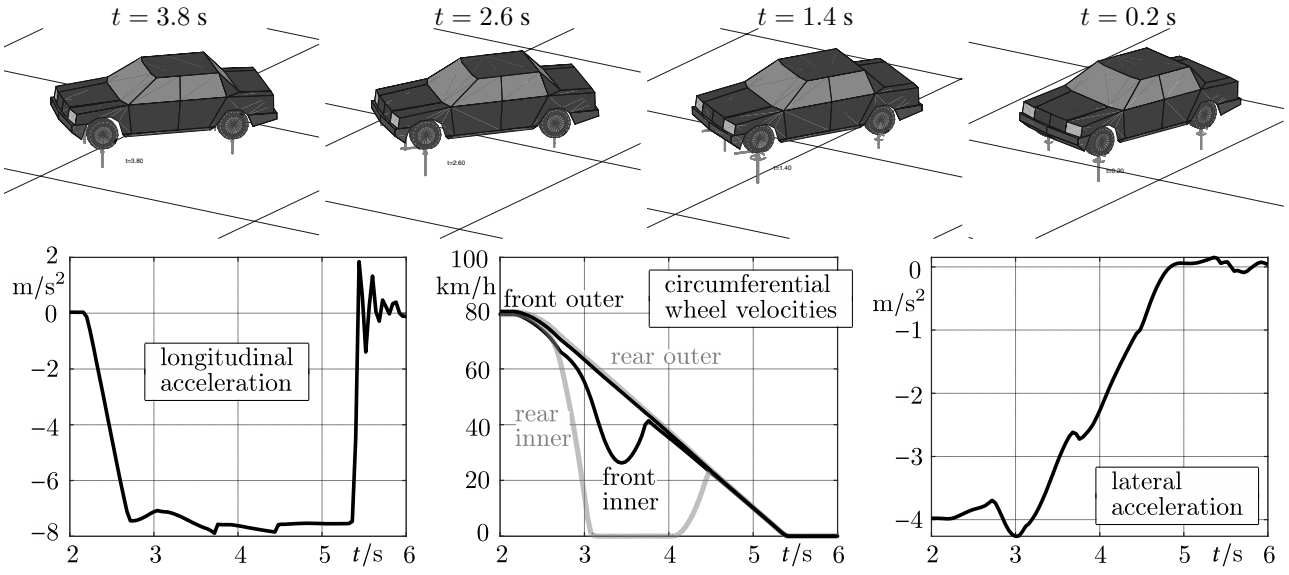

Figure 2: Emergency braking in a turn without ABS of a typical midsize passenger car illustrated by animation screenshots and plots.

indicates a maximum deceleration of approximately 8 m/s^2. The wheel load transfer from inner to outer during cornering and from rear to front when braking causes the inner rear wheel to lock in the time interval $t \approx 3$ s to $t \approx 4$ s, center plot in Figure 2. The VTC model handles wheel lock without any problems and the TMeasy tire model provides a smooth transition to stand still in addition.
The numerical integration in the time interval $2 \leq t \leq 6$ s performed with the standard MATLAB solver ode45, an explicit Runge-Kutta formula of order 4 and 5 with step size control, took a 2,7 GHz Quad-Core Intel Core i7 just 4.72 seconds. This is already close to real-time performance $(6-2)/4.72 = 0.85$ even in the comparatively slow MATLAB interpretation mode.

Influence of the Suspension Kinematics on the Vehicle Dynamics

From a Standard to a Simplified Suspension Kinematics

Table 1 provides the design kinematics parameter matrix for the front left suspension of a typical passenger car. The initial inclinations $d\alpha/dh$ = `+0.44734` rad(m, $d\beta/dh$ = `-0.32329` rad(m, and $d\beta/dh$ = `+0.11453` rad(m indicate that the knuckle performs significant rotations induced by the hub motion. As typical for front axle suspensions, the first, second, and third rotation produces a partial camber compensation, counteracts the brake pitch, and generates a slight self-steering effect. The axis of the knuckle-fixed coordinate system are parallel to the corresponding axis of the vehicle-fixed reference frame. That is why, the design kinematics takes `f00=f(0,0)=0` for granted. Then, center points with different absolute values at vanishing steering angles (`s=0`), like $\texttt{fp0}_\alpha = \alpha(+dh, 0)$ = `+0.05305` rad and $\texttt{fn0}_\alpha = \alpha(-dh, 0)$ = `-0.02389` rad specify a nonlinear behavior, which in general is not a simple side effect but a well design feature of the suspension kinematics. The design kinematics approach makes it easy to tune or design the suspension kinematics. Replacing the first row in the parameter matrix of Table 1 by

```
+0.00000   +0.00000   +0.00000   +0.00000   +0.00000   +0.08096   +0.08096   +0.08096   dh
```

just switches off the influence of the hub motion h on the constraint motions ξ, η, α, β, and γ by leaving the force element displacements u_S, u_D, and z_{arb} unchanged. Simple 4-wheel vehicle models just take the steer motions into consideration by neglecting the vertical suspension motions in addition, thus providing a far worse approximation.

Transient Vehicle Response

The DIN ISO directive 7401 lists the step steer input as one of the standard open loop maneuvers to reveal insight into the transient response of vehicles. In practice, an ideal step input is not possible. The VTC environment realizes the steer input s at the front and optionally at the rear axle via the rack displacements. Table 2 provides the time history of the

Table 2: Define step steer input within the VTC environment via lookup tables

```
0.0000   0.5000    0.6000    6.0000     time sample points τ_Si in s
0.0000   0.0000   -0.0050   -0.0050     steer input front left ϱ1(t_Si) in m
0.0000   0.0000   -0.0050   -0.0050     steer input front right ϱ2(t_Si) in m
```

steer inputs at the front axle which correspond here to the rack displacement $\varrho_1 = \varrho_2 = \varrho$ of a standard rack and pinion steering system. The rear wheels are not steered in this example $\varrho_3 = \varrho_4 = 0$. The steering forces applied to the knuckles 1 to 4 are defined by

$$F_{Si} = c_{Si}\,(\varrho_i - s_i) + d_{Si}\,(\dot{\varrho}_i - \dot{s}_i)\,, \quad i = 1(1)4 \tag{22}$$

The constants c_{Si}, d_{Si} summarize the stiffness and damping properties of the tie rods and the steering lever. The time histories of the steer inputs deliver also their time derivatives $\dot{\varrho}_1$ to $\dot{\varrho}_4$. The steer motions of the knuckles s_1 to s_4 and their derivatives $\dot{s}_1$ to $\dot{s}_4$ are part of the vectors of generalized coordinates y and generalized velocities z as defined in (15).
Table 2 approximates the step by a continuous ramp, where the rack is moved in the time interval $0.5 \le \tau_S \le 0.6$ s from its center position $s_1 = s_2 = 0$ to the right $s_1 = s_2 = -5$ mm and then ($\tau_S > 0.6$ s) kept constant. This input generates the wheel steering angles displayed as dotted black and dotted grey lines in plot (a) of Figure 3.

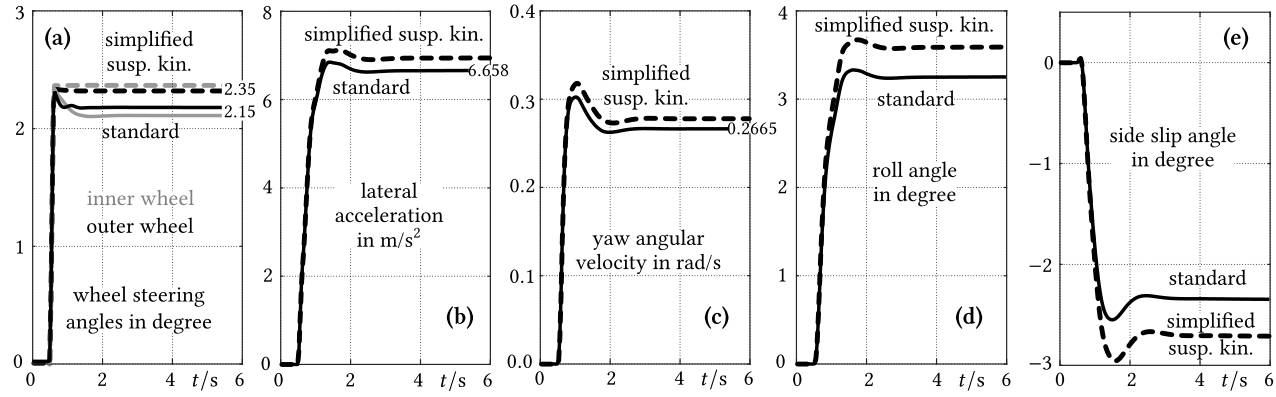

Figure 3: VTC step steer results, where solid and broken lines characterize vehicles with standard and simplified suspension kinematics

The VTC model represents here a fullsize passenger car with a wheel base of $a = 2.9$ m, a track width of $s \approx 1.5$ m, and wheel loads of $F_{z1} = F_{z2} = 5.39$ kN and $F_{z3} = F_{z4} = 5.06$ kN at the front and rear. The steady state values of the lateral acceleration $a_y = v^2/R = 6.658$ m/s^2 and the yaw angular velocity $\dot{\psi} = v/R = 0.2665$ rad/s deliver a cornering radius of $R = 94$ m and a vehicle velocity of $v = 25$ m/s in this example. A PI-controller keeps the vehicle velocity constant during the whole manuever by generating appropriate drive torques applied to the rear wheels.

The plots in Figure 3 compare the results of the VTC model with standard double wishbone suspensions at the front and the rear to a VTC model where the influence of the hub motion on the constraint suspension motions is completely switched off. As a consequence, the wheel steering angles of the simplified VTC model, represented by the dotted gray and dotted black lines in plot (a) of Figure 3, correspond perfectly to the step or more precisely to the ramp steer input. The nonlinear suspension kinematics of the front wheels incorporates a roll steering which reduces the steering angles with increasing body roll. That is why the steering angles drop down in the average from 2.35 to 2.15 degree when the roll angle, solid line in plot (c) of Figure 3, increases from 0 to 3.25 degree. This roll steer effect is a well designed feature of the suspension kinematics. It automatically reduces the impact of the steer input at fast cornering but keeps the maneuverability in the lower lateral acceleration range.
For a fair comparison of the standard vehicle to a vehicle with simplified kinematics the steer input of the standard vehicle is increased such that both VTC models end up in the same lateral acceleration. The results are displayed in Figure 4, where the steering wheel angles, plotted on the left, are zoomed to the interesting range from 2.0 to 2.5 degrees. In general, the kinematics of passenger car steering linkages is designed according to the Ackermann geometry which results in larger steering angles at the curve inner wheel compared to the curve outer wheel. The roll steering effect of the VTC model with the standard suspension kinematics even counteracts the Ackermann geometry, solid black and grey lines in the left plot of Figure 4. This is a smart suspension design, because during fast cornering the outer wheels are much more loaded than the inner ones and hence the steering angle of the outer wheel is the one that counts.

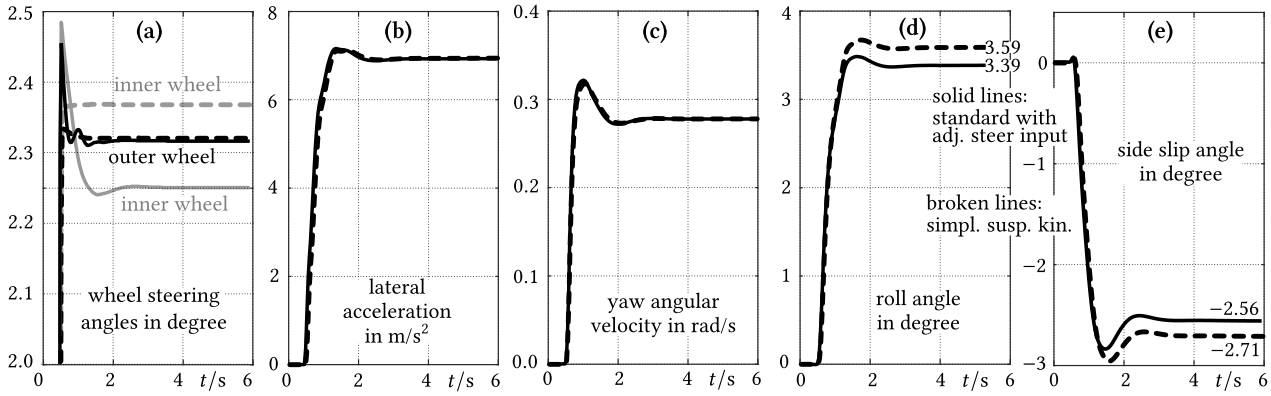

Figure 4: VTC step steer results with simplified and standard suspension kinematics with adjusted steer input

Both VTC models end up now in the same lateral acceleration and the same yaw angular velocity, plots (b) and (c) in Figure 4. But, the time histories of the roll angle and the side slip angle still differ in their steady state values, plots (d) and (e) in Figure 4.

Standard Versus Simplified Kinematics

In practice, the suspension kinematics of a passenger car is carefully designed to meet certain requests arising from the longitudinal and lateral dynamics [20]. The Figures 5 and 6 show the three-dimensional motions of the front left knuckle for the VTC model with the simplified suspension kinematics and for the VTC model with the standard suspension kinematics.
At real passenger car suspension systems a steer motion causes the knuckle to rotate about the inclined kingpin axis which in addition has a longitudinal and lateral offset to the wheel center. That is why, the centers 1 and 2 of the steered front wheels perform longitudinal ξ and lateral η motions as well as elementary rotations α, β, γ about the x-, y-, and z-axis which in case of the simplified suspension entirely depend on the steer input s, Figure 5. The vertical displacements of the wheel centers are unconstrained and described by the hub motion $\zeta = h$. Bump stops in the suspension systems restrict the jounce motions ($h > 0$) at the curve outer wheels 2 and 4, upper right plot in Figures 5 and 6. The plots in Figure 6 reveal the complexity of standard passenger car suspension systems. The distinct longitudinal motions ξ of the wheel center 3 and the distinct pitch rotations β of the knuckle 3 indicate for example the ability of the rear suspension to reduce a brake pitch. The lateral motions η and the rotations α about the x-axis provide the roll support and a partial camber compensation. The former brings down the roll angle from 3.59 to 3.39 degrees, plot (d) of Figure 4. The roll support and the camber compensation at the front and rear wheels, which are carefully coordinated to each other, reduce further on the side slip angle from -2.71 to -2.56 degrees, plot (e) of Figure 4.
The steering forces $F_S = [F_{S1}\ F_{S2}\ F_{S3}\ F_{S4}]^T$ and the driving torques $T_D = [T_{D1}\ T_{D2}\ T_{D3}\ T_{D4}]^T$ as well as the braking torques $T_B = [T_{B1}\ T_{B2}\ T_{B3}\ T_{B4}]^T$ define the inputs of the VTC model. The steering forces are directly applied to the knuckles. Each of the driving torques acts between the chassis and the corresponding wheel at conventional drive trains or between knuckle and wheel in case of wheel motors. The braking torques specify the maximum torques usually defined by the braking pressures distributed to the wheels. An enhanced dry friction model, as described in [20], generates the individual braking torque acting between knuckle and wheel. All inputs may be defined as simple feed forward time

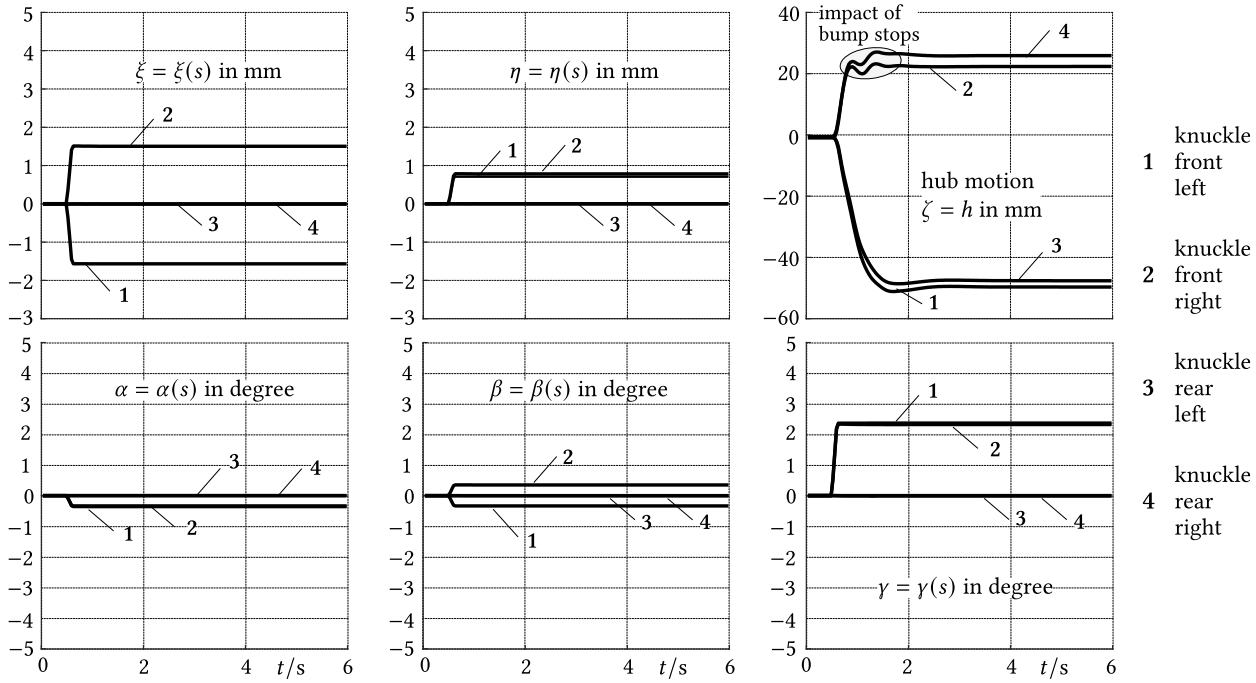

Figure 5: Simplified suspension kinematics neglecting hub influence

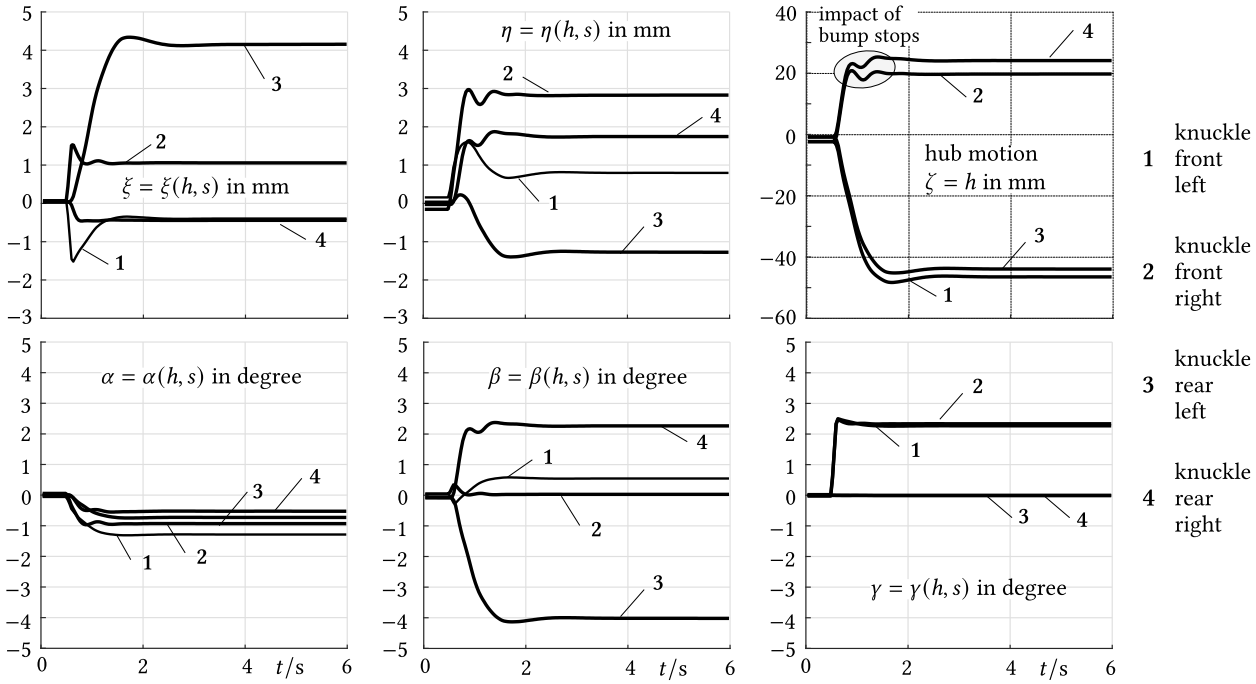

Figure 6: Standard suspension kinematics with adjusted step steer input

histories or provided by external controllers or by the output of additional subsystems. Hence, the VTC environment is able to simulate vehicles with all kind of steering, driving and braking modes.
Jourdain's principle combined with non-trivial generalized velocities and the idea of a non-perfect multibody system approach result in equations of motion of minimal complexity. A partial implicit solver, as described in [21], provides an extremely fast numerical solution of sufficient accuracy and stability.

Consequences

Human drivers and automated drivers too are very sensitive to the roll angle and to the side slip angle, in particular. Hence, a vehicle model which neglects some or all properties of the suspension kinematics is not able to reproduce the dynamics of a real passenger car with reliable accuracy. Virtual tests to investigate the dynamics and the stability of vehicles as well as the development and further improvement of driver assistance systems require at least vehicle models which incorporate the nonlinearities of the suspension kinematics. Otherwise just basic studies will be possible, which of course may serve as starting points for further and reliable investigations.

Conclusion

Simplified vehicle models, like the classical bicycle model, 4-wheel vehicle models, or even three-dimensional vehicle models neglecting the specific kinematical properties of the suspension systems, are not able to reproduce the dynamics of vehicles properly. Such models are restricted to basic studies. The VTC environment takes the three-dimensional motions of the chassis, four knuckles, and four wheels into account. The generic design kinematics suspension model is able to describe the nonlinear properties of standard passenger car suspension systems with sufficient accuracy and with a minimum of computation effort. The VTC model operated with the TMeasy tire model is valid in any driving situation. A straightforward implementation of the virtual test car (VTC) entirely realized in MATLAB provides an easy to use simulation environment including plotting and animation facilities. A VTC implementation coded in C achieves on a standard personal computer with a 2,7 GHz Quad-Core Intel Core i7 a real-time factor (real-time/cpu-time) of 160 which is magnitudes faster than real-time. Thus making the Virtual Test Car to an ideal platform for modern simulation tasks.

References

[1] . Bruni S. et al. (2020) State-of-the-art and challenges of railway and road vehicle dynamics with multibody dynamics approaches. *Multibody System Dynamics 49, 1-32*.

[2] Adams/Car. https://www.mscsoftware.com/de/product/adams-car, last accessed on March 11, 2022.

[3] RecurDyn. https://www.functionbay.org, last accessed on March 11, 2022.

[4] SIMPACK. https://www.3ds.com/products-services/simulia/products/simpack/, last accessed on March 11, 2022.

[5] CarSim. https://www.carsim.com, last accessed on March 11, 2022.

[6] CarMaker. https://ipg-automotive.com/en/products-solutions/software/carmaker/, last accessed on March 11, 2022.

[7] . DYNA4. https://www.vector.com/int/en/products/products-a-z/software/dyna4/, last accessed on March 11, 2022.

[8] Pacejka, H. B. (2002) Tire and Vehicle Dynamics, Butterworth-Heinemann, Oxford.

[9] Rill, G. (2013) TMeasy – The Handling Tire Model for all Driving Situations. *Proceedings of the XV International Symposium on Dynamic Problems of Mechanics (DINAME)*

[10] Rill, G. (2006) Vehicle Modeling by Subsystems. *Journal of the Brazilian Society of Mechanical Sciences & Engineering - ABCM 4, 431-443*.

[11] Rill, G. (1997) Vehicle Modeling for Real Time Applications. *Journal of the Brazilian Society of Mechanical Sciences - RBCM XIX.2 , pp. 192-206*.

[12] Gabiccini, M. et al. (2021) Analysis of driving styles of a GP2 car via minimum lap-time direct trajectory optimization *Multibody System Dynamics 53 pp. 85-113*. https://doi.org/10.1007/s11044-021-09789-7 last accessed on March 11, 2022.

[13] Vu, T. M. et al. (2021) Model Predictive Control for Autonomous Driving Vehicles. Electronics 2021, 10, 2593. https://doi.org/10.3390/electronics10212593.

[14] Rill, G. et al. (2019) VTT – a virtual test truck for modern simulation tasks. *Vehicle System Dynamics 0, 1-22*.

[15] Rill, G. (2019) Sophisticated but quite simple contact calculation for handling tire models. *Multibody System Dynamics 2, 131-153*.

[16] Rill, G. (1994) Simulation von Kraftfahrzeugen. Vieweg, Braunschweig/Wiesbaden. Reprint at https://www.researchgate.net/publication/317037037_Simulation_von_Kraftfahrzeugen#fullTextFileContent

[17] Rill, G. and Schaeffer, Th. (2017) Vehicle Modeling by non-perfect Multibody-Systems. *88th GAMM Annual Meeting, Weimar*. https://www.researchgate.net/publication/328049816_Vehicle_Modeling_by_non-perfect_Multibody_Systems#fullTextFileContent last accessed on March 11, 2022.

[18] Rill, G., Castro, A. A. (2020) A Novel Approach for Parametrization of Suspension Kinematics. *Advances in Dynamics of Vehicles on Roads and Tracks, 1848-1857*.

[19] Arnold, M. et al. (2011) Numerical methods in vehicle system dynamics: State of the art and current developments. *Vehicle System Dynamics 49, 1159-1207*.

[20] Rill, G. and Castro, A. A. (2020) Road Vehicle Dynamics: Fundamentals and Modeling with MATLAB® *CRC Press, Ed. 2*.

[21] Rill, G. (2006) A modified implicit Euler Algorithm for solving Vehicle Dynamic Equations. *Multibody System Dynamics, 15(1) 1-24*.

Abscissa minimization for self-stability of bicycles and nonholonomic acceleration when riding out of the saddle

Oleg Kirillov*
*Northumbria University, NE1 8ST Newcastle upon Tyne, UK

Summary. The model of a two-mass-skate (TMS) bicycle is reconsidered from the point of view of optimization of its self-stability, i.e. asymptotic stability of its vertical position in a uniform straight motion with respect to small perturbations of its leaning and steering angles. The critical Froude number for the onset of the self-stability is found explicitly. Minimization of the spectral abscissa is then performed yielding a new scaling low that links together the geometric and the mass parameters of the TMS bicycle. The scaling law fits well the relations between the geometric and mass parameters of a recent experimental realization of the TMS bicycle. Modification of the TMS model by including into it a mass moving periodically in the direction perpendicular to the frame of the bicycle is discussed as a step to understand nonholonomic acceleration of bicycles when riding out of the saddle.

Self-stability of bicycles and its optimization

The bicycle is easy to ride, but surprisingly difficult to model. Refinement of the mathematical model of a bicycle has continued over the last 150 years with contributions from Rankine, Boussinesq, Whipple, Klein, Sommerfeld, Appel, Synge and many others [1, 2, 3]. The canonical, nowadays commonly-accepted model goes back to the 1899 work by Whipple [1, 4, 5]. The Whipple bike is a system consisting of four rigid bodies with knife-edge wheels making it non-holonomic, i.e., requiring for its description more configuration coordinates than the number of its admissible velocities.

Self-stability of a riderless bicycle is a well-known empirical phenomenon that can be easily reproduced in an experiment with the majority of known practical designs of bicycles. Namely, a bicycle in its uniform motion along a straight path keeps the vertical position of the plane of its frame under small perturbations if its forward speed is high enough. Moreover, perturbations of its leaning and steering angles die out, so that one can say about asymptotic self-stability of the vertical position of the bicycle. The fact of the asymptotic self-stability has been theoretically supported already by Whipple [1]. The self-stability has a number of important practical implications. For instance, the bicycle designs that do not present the self-stability are difficult for a person to ride; in other words, more stable bikes handle better. Hence, deeper understanding of the passive stabilization can provide new principles for the design of more safe and rideable bicycles, including compact and foldable models. Furthermore, it is expected to play a crucial part in formulating principles of the design of energy-efficient wheeled and bipedal robots [6].

However, the theoretical explanation of the self-stability has been highly debated throughout the history of bicycle dynamics to such an extent that a recent news feature article in Nature described this as "the bicycle problem that nearly broke mathematics" [7]. The reason as to why "simple questions about self-stabilization of bicycles do not have straightforward answers" [8] lies in the symbolical complexity of the Whipple model that contains 7 degrees of freedom and depends on 25 physical and design parameters [2]. In recent numerical simulations [1, 4, 5], self-stabilization has been observed for some benchmark designs of the Whipple bike. These results suggested further simplification of the model yielding a reduced model of a bicycle with vanishing radii of the wheels (which are replaced by skate blades), known as the two-mass-skate (TMS) bicycle [3, 9, 10]. Despite the self-stable TMS bike having been successfully realized in recent laboratory experiments [3], its self-stability still awaits a theoretical explanation. In this lecture we find explicitly the critical Froude number for the onset of-self-stability of the TMS bicycle and will show how minimization of the spectral abscissa [11, 12] allows one to find hidden symmetries in the model, suggesting further reduction of the parameter space and, finally, providing explicit relations between the parameters of stability-optimized TMS bikes [13, 14].

Nonholonomic acceleration due to honking or riding out of the saddle

Honking means cycling out of the saddle. Cyclists use this way of riding to accelerate. In this process, the body of the cyclist moves rhythmically side to side with respect to the plane of the bicycle, while the frame of the bicycle rocks or sways with respect to the vertical position. It is known, however, that the commonly accepted modern bicycle models, stemming from the Whipple model of 1899, are non-holonomic and conservative. On one hand, this implies the conservation of energy, and on the other, non-conservation of the phase volume, which results in the possibility of the asymptotic stability of a straight vertical position of a bicycle that is riding along a straight path if the forward velocity is high enough, which is a well-known empirical fact [2, 3]. A natural question is: where the energy of dying leaning and steering motions flows? Actually, the energy in the lean and steer oscillations is transferred via a nonlinear coupling to the forward speed rather than being dissipated, as it was shown in numerical simulations in [2]. This effect suggests a method of acceleration of the bicycle due to periodic movements of a mass in the direction perpendicular to the plane of the frame of the bicycle. It can therefore be conjectured that when cycling out of the saddle, the periodical movement of the cyclist's mass pumps energy into the forward motion leading to the desired acceleration.

Recently, acceleration due to a periodic motion of an internal mass has been theoretically discovered in a non-holonomic

Chaplygin sleigh model [15, 16] and linked to the mechanism of acceleration of particles moving between periodically oscillating walls in the Fermi-Ulam model [17]. In the present talk we will discuss the ways of extending the model of a TMS bicycle to take into account a periodically moving mass for investigation of the nonholonomic Fermi-like acceleration during cycling out of the saddle.

References

[1] Whipple F.J. (1899) The stability of the motion of a bicycle. *Quart. J. Pure Appl. Math.*, **30**(120): 312-348.

[2] Meijaard J.P., Papadopoulos J.M., Ruina A., Schwab A.L. (2007) Linearized dynamics equations for the balance and steer of a bicycle: a benchmark and review. *Proc. R. Soc. A* **463**: 1955–1982.

[3] Kooijman J.D.G., Meijaard J.P., Papadopoulos J.M., Ruina A., Schwab A.L. (2011) A bicycle can be self-stable without gyroscopic or caster effects. *Science* **332**: 339–342.

[4] Boyer F., Porez M., Mauny J. (2018) Reduced dynamics of the non-holonomic Whipple bicycle. *J. Nonlinear Sci.* **28**: 943–983.

[5] Xiong J., Wang N., Liu C. (2019) Stability analysis for the Whipple bicycle dynamics. *Multibody. Syst. Dyn.*

[6] Ruina A., Collins S., Tedrake R., Wisse M. (2005) Efficient bipedal robots based on passive-dynamic walkers. *S*cience **307**: 1082–1085.

[7] Borrell B. (2016) Physics on two wheels. *Nature* **535**: 338–341.

[8] Sharp R.S. (2008) On the stability and control of the bicycle. *Appl. Mech. Rev.* **61**, 060803.

[9] Perantoni G., Limebeer D.J.N. (2013) Optimal control of a two-mass-skate bicycle without steering. 2013 IEEE International Conference on Industrial Technology (ICIT), Cape Town, 2013, pp. 134–139.

[10] Ricci F., Frosali G. A symbolic method for the analysis of a nonlinear Two-Mass-Skate model. arXiv 2016,arXiv:1611.07796.

[11] Blondel V.D., Gurbuzbalaban M., Megretski A., Overton M.L. (2012) Explicit solutions for root optimization of a polynomial family with one affine constraint. *IEEE Trans. Autom. Control* **57**: 3078–3089.

[12] Kirillov O.N., Overton M.L. (2013) Robust stability at the swallowtail singularity. *Frontiers in Physics* **1**: 24

[13] Kirillov O.N. (2018) Locating the sets of exceptional points in dissipative systems and the self-stability of bicycles. *Entropy* **20**(7):502.

[14] Bigoni D., Kirillov O.N. (2019) Dynamic Stability and Bifurcation in Nonconservative Mechanics, CISM International Centre for Mechanical Sciences 586, Springer, Berlin.

[15] Bizyaev I.A., Borisov A.V., Kuznetsov S.P. (2017) Chaplygin sleigh with periodically oscillating internal mass. *EPL* **119**: 60008

[16] Bizyaev I.A., Borisov A.V., Mamaev I.S. (2017) The Chaplygin sleigh with parametric excitation: chaotic dynamics and nonholonomic acceleration. *Reg. Chaot. Dyn.* **22**(8): 955–975

[17] Bizyaev I.A., Borisov A.V., Kozlov V.V., Mamaev I.S. (2019) Fermi-like acceleration and power-law energy growth in nonholonomic systems. *Nonlinearity* **32**: 3209–3233.

An original walking composed of a ballistic single-support and a finite time double-support phases

Yannick Aoustin*, Alexander Formalskii†
*Laboratoire des Sciences du Numérique de Nantes, CNRS UMR6004, Université de Nantes, France
†Institute of Mechanics, Lomonosov Moscow State University, Moscow, Russia

Summary. The paper aim is to define an original walking for a 2D biped with a trunk, two identical legs with knees and massless feet. This walking is composed of a ballistic single-support phase and a distributed in time double-support phase. The ballistic movement in single support is defined by solving a boundary value problem with initial and final biped configurations and velocity conditions. These conditions ensure that at the beginning of the single support the toe of the rear leg rises without touching the ground again and at the landing of the heel there is no impact. In the double-support phase, the orientation of the two feet and other generalized coordinates which are used to define the configuration of the biped, are chosen as Bezier functions of time. The torques and ground reaction forces resulting from this double-support phase are determined by solving for the biped the inverse dynamic problem.

Statement of the problem

The walking motion

We design biped periodic walking, which consist of distributed in time single- and double-support phases. Ballistic single-support motion is designed. During this motion the torques in all joints are zeroes except the torque in the ankle-joint of the stance leg. The torque in the ankle-joint of the stance leg is applied in order to keep its foot in the equilibrium. During double-support motion the torques are applied in all the six joints; during this time both feet rotate: foot of the rear leg - around its toe, foot of the front leg - around its heel. To explain our statement of the problem more clearly, we show Fig. 1 with several stick-figures, which results from our numerical investigations.

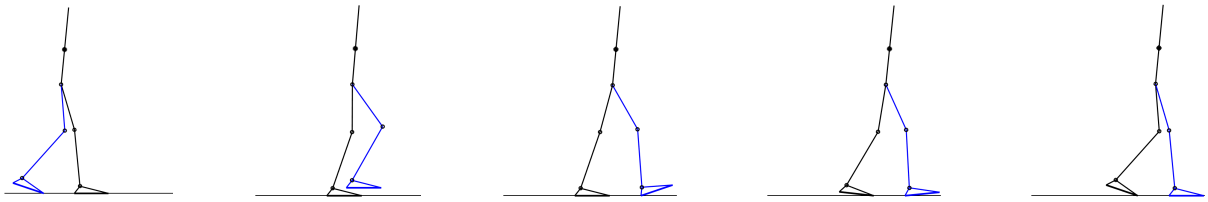

Figure 1: a) Initial configuration of biped in single support. b) Intermediate configuration in single support. c) Final configuration in single support − initial one in double support. d) Intermediate configuration in double support. e) Final configuration in double support − initial one in the next single-support motion.

Mathematical model and design of the walking

The absolute orientation of the shins and thighs are defined with angles q_1, q_2, q_3, q_4 (see Fig. 2). The orientation of the trunk is defined by angle q_5. Cartesian hip-joint coordinates are x and y. The orientation of both feet are described by angles q_{p1} and q_{p2}. It is assumed that there are no sliding motion and no take-off of the support legs. In real human walking, the double-support motion is distributed in time, and consequently the configuration of the human at the beginning of the double support differs from the configuration at the end of this double support. Consequently for the human walking the configurations at the beginning and at the end of the single-support motion are also different. Vector $\mathbf{x}$ of the generalized coordinates for the biped with massless feet is $\mathbf{x} = [q_1, q_2, q_3, q_4, q_5, x, y]^\top$. Superscript $^\top$ means transposition. The mathematical model of the biped is:

$$\mathbf{A}(\mathbf{x})\ddot{\mathbf{x}} + \mathbf{h}(\mathbf{x}, \dot{\mathbf{x}}) = \mathbf{D}\boldsymbol{\Gamma} + \mathbf{J}_{\mathbf{r}_1}^\top \mathbf{r}_1 + \mathbf{J}_{\mathbf{r}_2}^\top \mathbf{r}_2, \tag{1}$$

where $\mathbf{A}(\mathbf{x})$ is a 7×7 symmetric positive definite inertia matrix, $\mathbf{h}(\mathbf{x}, \dot{\mathbf{x}})$ is a 7×1 vector, which groups the centrifugal, Coriolis, and gravity forces. $\boldsymbol{\Gamma}$ is 6×1 vector of the joint torques applied by the biped. We consider six torques applied in the hip-, knee- and ankle-joints. Vectors $\mathbf{r}_i = (r_{ix}, r_{iy})^\top$, with $i = 1,\ 2$, are the ground reactions applied to the massless feet and consequently to the ankle-joints. The following constraint equations are correct when the front or/and rear leg is/are on the bearing surface.

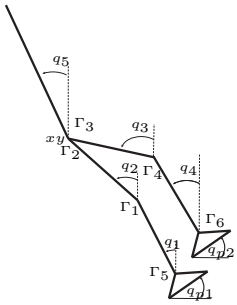

Figure 2: Generalized coordinates, and inter-link torques.

$$\mathbf{J}_{\mathbf{r}_i}\ddot{\mathbf{x}} + \dot{\mathbf{J}}_{\mathbf{r}_i}\dot{\mathbf{x}} = \mathbf{0} \qquad \text{for } i = 1 \text{ or/and } 2. \tag{2}$$

Single-support motion: Boundary value problem

In the single-support phase, the ballistic movement takes place on the supporting leg with a flat-foot contact, Fig. 1. A torque is applied only in the ankle-joint of this stance leg in order to maintain the equilibrium of its foot. Let a_2, t_2, and h_2 refer to the ankle, toe and heel of the transferred leg (shown in Fig. 1 by blue color). The five initial velocities $\dot{q}_i(0)$,

length of the step d and duration T_{SS} of the single-support motion are calculated to reach the final configuration from the initial one and to satisfy the two following velocity conditions $V_{a_2}(0) \cdot \mathbf{a_2 t_2} = 0$ and $V_{a_2}(T_{SS}) \cdot \mathbf{a_2 h_2} = 0$. They respectively ensure that the toe t_2 of the rear foot rises from the ground without touching the ground again and there is an impactless landing of the heel h_2 on the ground at the end of the single-support motion.

Double-support motion: problem definition

At the end of the single-support phase, the landing massless foot touches the ground with its heel, Fig. 1 c). The other foot keeps contact with the ground through its toe. In double-support phase both feet rotate, Fig. 1 d), the double support motion is ended when the foot of the front leg touches the ground with the toe and the rear foot rises. At this instant, the single-support motion of the next step starts. Variables q_{p1}, q_{p2}, q_1, q_2, q_5 and r_{1x} are defined with Bezier polynomial functions $P_j(\tau)$ with five control point p_j $(j = 0, \cdots, 4)$ and $\tau = (t - T_{SS})/T_{DS}$, T_{DS} being the duration of the double-support motion. At each sampling time the knowledge of $P_j(\tau)$ allows us to calculate the trajectory of x, y, x_{a1}, x_{a2}, q_3 and q_4, by using geometric and kinematic models, (2), and thus the left term of (1).

Numerical results

Figure 3 a) shows that the evolutions of angles q_{p1} and q_{p2} are synchronized during the double-support phase. Figure 3 b) shows that the magnitude of the torque in the ankle-joint of the rear leg is much greater than the magnitude of the torque in the ankle-joint of the front leg. This seems physically coherent because the biped pushes on the rear leg to move forward during the double-support phase.

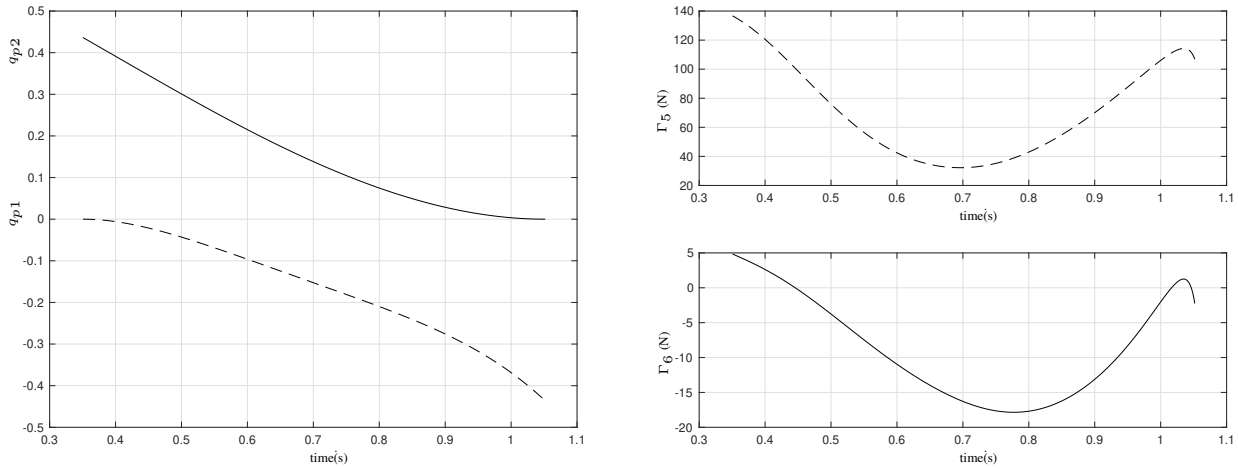

a) b)

Figure 3: Front leg (solid lines) and rear leg (dashed lines) in double-support phase: a) Orientation angles of feet . b) Ankle torques.

Conclusions

The definition of a walking with a distributed in time double support is a complex problem, [4]. In the papers [1–3], we studied ballistic single-support motion coupled with *instantaneous* double-support phase. The torques in the biped joints at the instantaneous double support are impulsive one. The *distribution in time* of the double support allows to get a cyclic gait with the torques of finite magnitude. The future objective is to increase the time of the single-support motion and decrease the time of double-support motion in order to get biped walking closer to human one.

References

[1] AOUSTIN, Y., AND FORMALSKII, A. Walking of biped with passive exoskeleton: evaluation of energy consumption. *Multibody System Dynamics 43*, 1 (2016), 71–96.

[2] FORMAL'SKII, A. M. Motion of anthropomorphic biped under impulsive control. In *Proc. of Institute of Mechanics, Moscow State Lomonosov University: "Some Questions of Robot's Mechanics and Biomechnics"* (1978, (In Russian)), pp. 17–34.

[3] FORMAL'SKII, A. M. Ballistic walking design via impulsive control. *ASCE, Journal of Aerospace Engineering 23*, 2 (2010), 129–138.

[4] MIOSSEC, S., AND AOUSTIN, Y. A simplified stability study for a biped walk with underactuated and overactuated phases. *International Journal of Robotics Research 24*, 6 (June 2005), 537–551.

Monday, July 18, 2022
13:30 - 15:30

MS-14 Nonlinear Dynamics for Engineering Design
Rhone 2

Chair: Stefano Lenci

13:30 - 13:50
Optimal design and tuning of an SMA-assisted PTMD system
MUCCHIELLI Paul*, GOGOI Ankush, HAZRA Budhaditya, PAKRASHI Vikram
*University College Dublin [Dublin] (Belfield, Dublin 4 Ireland)

13:50 - 14:10
Coupling of bio-inspired, nonlinear acoustic sensors for sound pre-processing and bandwidth tuning
VED Kalpan*, LENK Claudia, HÖVEL Philipp, ZIEGLER Martin
*Technische Universität Ilmenau (G.-Kirchhoff-Str. 1, 98693 Ilmenau Germany)

14:10 - 14:30
Dynamic loads produced by swinging bells ? experimental and numerical investigation of the novel yoke-bell-clapper system with variable geometry
BURZYŃSKI Tomasz*, BRZESKI Piotr, BALCERZAK Marek, PERLIKOWSKI Przemysław
*Division of Dynamics, Lodz University of Technology (90-924 Łódź, ul. Stefanowskiego 1/15 K-13, bud. A22 Poland Poland)

14:30 - 14:50
Experimentally validated geometrically exact model for nonlinear dynamic analysis of cantilevers undergoing extreme motions
FAROKHI Hamed*, XIA Yiwei, ERTURK Alper
*University of Northumbria at Newcastle (Newcastle City Campus, 2 Ellison Pl, Newcastle upon Tyne NE1 8ST, United Kingdom United Kingdom)

14:50 - 15:10
Model order reduction of nonlinear piezoelectric microstructures through direct parametrisation of invariant manifolds
OPRENI Andrea, VIZZACCARO Alessandra, TOUZÉ Cyril, **FRANGI Attilio***
*Politecnico di Milano (Piazza Leonardo da Vinci, 32 20133 Milano Italy)

15:10 - 15:30
Modeling Nonlinearities in MEMS Micro Mirrors: From Single Chip to Wafer Level
NABHOLZ Ulrike, MEHNER Jan, **DEGENFELD-SCHONBURG Peter***
*Robert Bosch GmbH, Corporate Research (71272 Renningen Germany)

Optimal design and tuning of an SMA-assisted PTMD system

Paul Mucchielli*, Ankush Gogoi*, Budhaditya Hazra† and Vikram Pakrashi*
*UCD Centre for Mechanics, Department of Mechanical and Materials Engineering, Univeristy College Dublin, Dublin, Ireland
†Indian Institute of Technology, Guwahati, India

Summary. This work presents a first step to using a phenomenological model of an SMA spring as an auxiliary damping mechanism in a Pendulum Tuned Mass Damper (PTMD) setup under stochastic excitation. An SMA superelasticity model was considered to approach the hysteretic behaviour of an SMA material. In provision for susbsequent simulations, this model's optimal damping parameters were derived with particular care for the implicit relationship between the SMA model parameters and system mean square response.

Introduction

In the field of Pendulum Tuned Mass Dampers (PTMD), many damping modalities have been investigated. This paper presents a novel way of using hysteretic aspects of Shape Memory Alloy (SMA) spring as a damping mechanism in a PTMD system. This investigation looks into damping for a single SMA spring, allowed to move in a one-dimensional space along the horizontal displacement of the pendulum mass. It presents the results of the optimal parameters corresponding to maximum structure displacement variance reduction. The methods address the derivation of moment equations through symbolic computing and solving. These are then used to optimise the system parameters through numerically solving implicit relationship between the SMA parameters and the system's mean square response through an iterative process proposed in [2].

Methods

The system under consideration is presented in Fig. 1. The main structure was assumed to move only along the x-axis. The pendulum is attached to the structure at point A and has length L and angle of inclination θ. The SMA spring is attached at the bottom of the ball mass and at the side floor of the structure. The top floor and wall were assumed to move as a rigid body and the excitation, applied along the x-direction, is modeled as a white noise excitation.

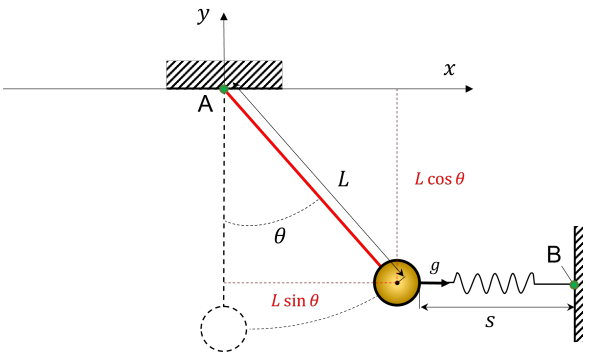

Figure 1: Schematic of the system under consideration

The elongation of the spring, denoted by s, has a minimum length of s_0. The restoring force g of the SMA spring is here assumed to behave according to the Yan-Nie equivalent linearization model [3],

$$g(s, \dot{s}) = \alpha k s + (1 - \alpha) k z \tag{1}$$

where,

$$z = c_e \dot{s} + k_e s \qquad c_e = \frac{b-a}{\sqrt{2\pi}\sigma_{\dot{s}}} \left[1 - \text{erf}\left(\frac{a}{\sqrt{2}\sigma_s}\right)\right] \qquad k_e = \frac{a+b}{\sqrt{2\pi}\sigma_s} e^{-\frac{a^2}{2\sigma_s^2}} \tag{2}$$

Here a and b are constants defining the phase transition lengths of the SMA material. Note that in order to use this linearized model for the restoring force, the standard deviations σ_s and $\sigma_{\dot{s}}$ of the elongation displacement and velocity must be known. In this case, according to the law of cosines, the elongation displacement s and velocity $\dot{s}$ could be expressed as,

$$s = s_0 - L \sin\theta \tag{3}$$

$$\dot{s} = L \cos\theta \dot{\theta} \tag{4}$$

This system's dynamics under white noise excitation can be described by,

$$\begin{pmatrix} M+m & mL\cos\theta \\ mL\cos\theta & mL^2 \end{pmatrix}\begin{pmatrix}\ddot{x}\\ \ddot{\theta}\end{pmatrix} + \begin{pmatrix} C & -mL\sin\theta\dot{\theta} \\ 0 & (1-\alpha)kc_eL^2\cos\theta^2 \end{pmatrix}\begin{pmatrix}\dot{x}\\ \dot{\theta}\end{pmatrix}\begin{pmatrix} K & 0 \\ 0 & 0 \end{pmatrix}\begin{pmatrix}x\\ \theta\end{pmatrix} = \begin{pmatrix} 0 \\ -mgL\sin\theta - (\alpha k + (1-\alpha)kk_e)(L^2\sin\theta\cos\theta + Ls_0\cos\theta)\end{pmatrix} \quad (5)$$

where M, C and K are the primary structure mass, damping and stiffness, respectively. The constant m represents the pendulum mass. Here, $k = \frac{F_0 mg}{b}$ where g is the acceleration due to gravity. F_0, the normalized transformation strength, therefore drives the SMA stiffness. It was chosen to investigate the system with a mass ratio $\frac{m}{M} = 0.2$, a frequency of oscillation of 1.5 Hz and a damping ratio of 0.017. The SMA parameters were chosen to be $a = 0.005\text{m}$, $b = 0.08\text{m}$ and $\alpha = 0.06$.

Throughout the study, all the state variables (the structure displacement x and pendulum angle θ) were assumed to be zero-mean stationary Gaussian random variables. The following quantities were therefore determined using a small-angle approximation,

$$\sigma_s^2 = L^2E[\theta^2] \qquad \sigma_{\dot{s}}^2 = L^2E[\dot{\theta}^2] \quad (6)$$

Since the relationship between Eqs. (2) and (6) is implicit, it was proposed to use the iterative process described in [2] to determine adequate values for c_e and k_e upon convergence. This was allowed by first deriving the moment derivatives of this system, derived using principles devised in [1]. Additionally, this system's optimal operating point in a domain $L \in [0,1]$, $F_0 \in [0.1, 0.95]$ was determine through the optimization of a performance index defined by the ratio of the optimized variance (σ^2_{optim}) and the determined uncontrolled primary structure's variance (σ_r^2). For the purpose of optimization, the MATLAB® *fmincon* function was used. Namely,

$$\begin{aligned} \min_{L,F_0} \quad & \frac{\sigma^2_{optim}}{\sigma_r^2} \\ s.t. \quad & 0 \le L \le 5 \quad (m) \\ & 0.1 \le F_0 \le 0.95 \end{aligned} \quad (7)$$

Results

Figure 2 demonstrates the results of a parameter sweep performed for the described range of values of L and F_0. It also presents the optimal operating point for this system with $L = 0.4932\ m$, $F_0 = 0.2066$ with an optimal reduction of the variance to 13.88% of the uncontrolled structure's variance.

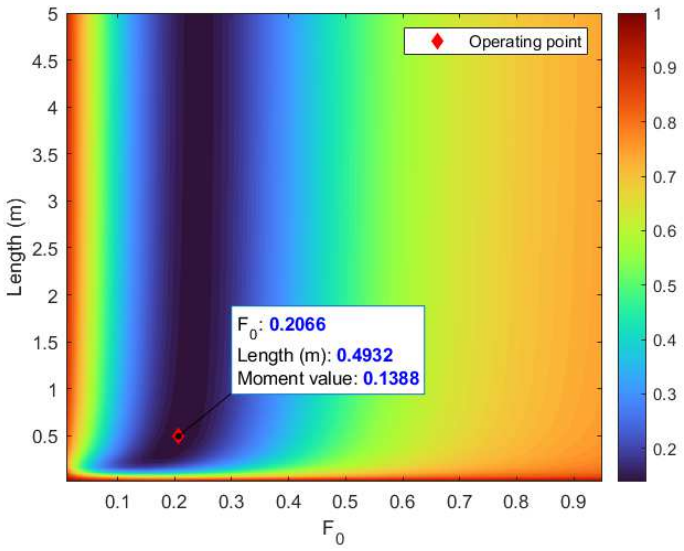

Figure 2: Contour plot of the ratio of derived variance to uncontrolled variance as a function of length and normalized transformation strength

References

[1] L. Socha. *Linearization Methods for Stochastic Dynamic Systems*. 2008.

[2] N. D. Tiwari, A. Gogoi, B. Hazra, and Q. Wang. A shape memory alloy-tuned mass damper inerter system for passive control of linked-SDOF structural systems under seismic excitation. *Journal of Sound and Vibration*, 494:115893, 2021.

[3] X. Yan and J. Nie. Response of SMA superelastic systems under random excitation. *Journal of Sound and Vibration*, 238(5):893–901, dec 2000.

Coupling of bio-inspired, nonlinear acoustic sensors for sound pre-processing and bandwidth tuning

Kalpan Ved[*] , Philipp Hövel[**], Martin Ziegler[*], Claudia Lenk[*]

[*]*Department of Micro- and Nanoelectronic Systems TU Ilmenau, Ilmenau, Germany*
[**]*School of Mathematical Sciences, University College Cork, Cork, Ireland*

Summary: Most sensory systems in biology exhibit properties that resemble the behaviour of nonlinear dynamic systems [1]. The auditory sensing system is no exception with its nonlinear transfer characteristics enabling amplification and selection features [2]. It was suggested that biological auditory sensing can be modelled as a system tuned near/at a Hopf bifurcation [2]. Theoretical studies showed that the tuning to the bifurcation point can be achieved also if sub-threshold Hopf oscillators are coupled via their output signals [3]. Here, we study experimentally and numerically the properties of a nonlinear cantilever-based acoustic sensing system in dependence of the coupling strength. We show that coupling not only yields a transition between linear and nonlinear characteristics and increases sensitivity but it can be used for bandwidth enhancement of the system as well, enabling coverage of larger frequency ranges.

Introduction

Introducing bio-inspired signal pre-processing into speech and sound processing system strongly increases the performance, as recently shown by Araujo et al [4]. The main pre-processing components are thereby frequency decomposition of the signal, nonlinear (compressive) amplification, and adaptation of sensing properties to different inputs. Nevertheless, software-based implementations prevent real-time performance and high efficiency. Thus, hardware-based implementations are required. These can further improve the signal-to-noise ratio and the above mentioned properties if implemented into the sensing stage directly. We developed an acoustic sensing system with integrated bio-inspired pre-processing based on a silicon cantilever beam with real-time feedback [5]. Thereby, frequency decomposition is obtained using resonant operation. We demonstrated that nonlinear operation similar to a Hopf oscillator can be obtained using certain real-time feedback mechanism [5]. Since the linear or nonlinear characteristics are controlled by the feedback loop, dynamic adaptation of sensor properties can be introduced easily.

The exact mechanism, generating nonlinear dynamics in the inner ear, is still under discussion [6]. However, one proposed mechanism is coupling of the receptor cells and/or the hair bundles on top of these cells. This coupling increases the tolerance against noise and improves the range of non-linear regime [6]. Gomez et al. [3] theoretically showed that coupling of sub-threshold Hopf oscillators can induce a bifurcation as well. This yields an increase of the parameter range for the occurrence of the Hopf bifurcation and improves the sensitivity of the complete system. Here, we study the influence of output-signal coupling on the properties of our acoustic sensing system, consisting of nonlinear cantilevers. In particular, we analyse (i) if a Hopf bifurcation can be achieved due to the coupling, (ii) how the critical coupling strength depends on the sensor properties, and (iii) how the coupling affects sensor properties like sensitivity and bandwidth.

Implementation

Figure 1 schematically shows the coupled cantilever system. We use micro-electro-mechanical systems (MEMS)-based silicon beams with integrated deflection sensing and actuation [7]. After a first amplification stage and decomposition of the sensing signal x into an AC and a DC part using a high-pass and low-pass filter, respectively, feedback and output-signal coupling are realised using the FPGA structure of a STEMLAB-125 board. Two cantilevers with different characteristic frequencies ω are coupled and analysed. Coupling is implemented by first multiplying the sensing signal x_1 of one cantilever by the coupling factor $C_{f,}$ then adding an offset u_{DC}, and finally using the resulting signal $y_2 = C_{f,1}x_1 + u_{DC}$ to drive the actuation of the second cantilever (see figure 1). Similarly, the signal x_2 from the second cantilever drives the actuation y_1 of the first cantilever. The coupling between both cantilevers is symmetric, i.e. $C_{f,1} = C_{f,2}$. Furthermore, self-feedback given by a_1x_1 is added to the actuation signal, yielding $y_1 = C_{f,1}x_2 + a_1x_1 + u_{DC}$. In this work, the critical coupling strength $C_{critical}$, at which the bifurcation is observed, is determined in dependence of the characteristic frequencies $\omega_{1,2}$ of the sensors and the distance $\mu = a_{crit} - a_{1,2}$ of the feedback strength a from its critical value a_{crit} at the Hopf bifurcation. Then, the response of the sensing system to sound stimuli of various frequencies and amplitudes is analysed.

Results

Figure 2 shows the critical coupling strength $C_{critical}$ in dependence of the ratio of characteristic frequencies ω_1/ω_2 of the two coupled cantilevers and the distance μ from the Hopf bifurcation. It is observed that $C_{critical}$ increases, if ω_1/ω_2 or μ increase, as was expected from the theoretical studies of Gomez et al. [3]. However, for a fixed ω_1/ω_2 and increasing μ, the slope of $dC_{critical}/d\mu$ is decreasing in the experiment while it is increasing for the theoretical prediction by Gomez etal., which is based on a normal form for the Hopf oscillators. To study, if this deviation arises from the coupling mechanism or the oscillator model, we will compare the experimental results with simulations of the system, using a sensor-specific model, and simulations of an adapted Gomez system.

Regarding the sensing properties, we observe higher sensitivities for the coupled system, as expected from the theoretical predictions. Nonlinear transfer characteristics occur, if the system of both cantilevers is tuned near the bifurcation point. Additionally, the range of frequencies, for which the system is sensitive, increases strongly (up to 10 times larger bandwidth). In this case, both sensors do not only show a stronger response to sound frequencies at the two characteristic frequencies, but also in the frequency range in between. This enables bio-inspired acoustic sensing systems covering the auditory frequency range with only a few cantilevers with nonlinear characteristics.

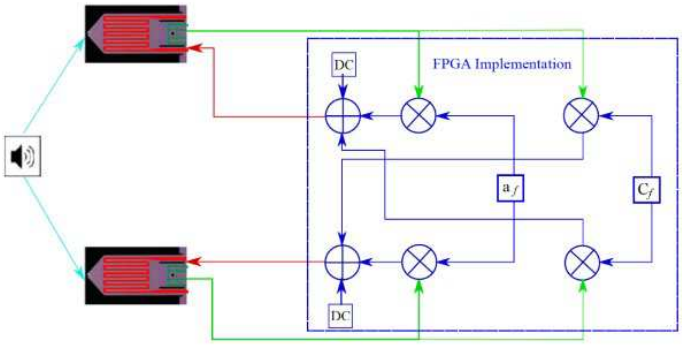

Figure 1: Schematic for feedback and coupling mechanism

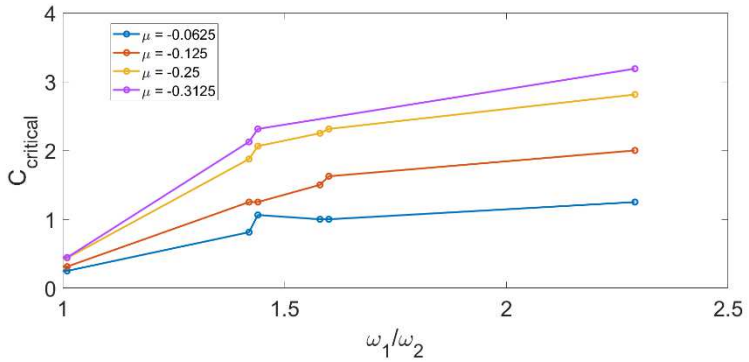

Figure 2: $C_{critical}$ as a function of ω_1/ω_2 and μ for different pairs of coupled cantilevers obtained from experiments.

Acknowledgment: Funded by the Deutsche Forschungsgemeinschaft (DFG. German Research Foundation) – Project-ID 434434223 – SFB 1461 and the Carl-Zeiss-Stiftung through the project 'Memristive Materials for Neuromorphic Engineering (Memwerk)'.

References

[1] Kandel E. R. (2013), *Principles of Neural Science*. McGraw-Hill Education Ltd.
[2] Hudspeth A.J., Jülicher F., Martin P. (2010). A critique of the critical cochlea: Hopf-a bifurcation is better than none. *J. Neurophysiol.* **104**(10): 1219-1229.
[3] Gomez F., Lorimer T., Stoop R. (2016) Signal-coupled subthreshold Hopf-type systems show a sharpened collective response. *Phys. Rev. Lett.* **116**(10): 108101.
[4] Araujo F.A., et al. (2020). Role of non-linear data processing on speech recognition task in the framework of reservoir computing. *Sci. Rep.* **10**(1):1-11.
[5] Lenk C., et al. (2020). Enabling Adaptive and Enhanced Acoustic Sensing Using Nonlinear Dynamics. *2020 IEEE International Symposium on Circuits and Systems (ISCAS)*.
[6] Ashmore J., et al. (2010). The remarkable cochlear amplifier. *Hearing research* **266**(1-2):1-17.
[7] Rangelow I.W. et al. (2017). Active scanning probes: A versatile toolkit for fast imaging and emerging nanofabrication. *JVST* B **35**(6):10.116.

Dynamic loads produced by swinging bells – experimental and numerical investigation of the novel yoke-bell-clapper system with variable geometry

Tomasz Burzyński*, Piotr Brzeski* , Marek Balcerzak* and Przemysław Perlikowski*
*Division of Dynamics, Lodz University of Technology, Lodz, Poland

Summary. Dynamics of the swinging bells is a timely problem considered when the bell's supporting structures are designed or monitored. The geometry of the yoke and the magnitude of excitation force are the crucial parameters determining the yok-bell-clapper system response for a given size and shape of the bell. In this paper we present novel yoke-bell-clapper system with variable geometry and adjustable excitation force. We introduce mathematical model based on the existing prototype. We validate the mathematical model and then assess the influence of the yoke geometry and excitation force on the system response. The simulations are done using sample-based approach. The system that undergoes investigation in the paper is non-linear, piecewise and discontinuous. Created numerical tool can reliably predict the ringing scheme of the bell and associated reaction forces in the supports.

Introduction

Dynamics of the swinging bells is a timely problem that is recently widely considered by scientific community. The phenomena that are the most widely investigated are the bell to the clapper impact modeling, different bell's working regimes, the dynamics of bell towers and the magnitudes of forces transferred between the bells and their supporting structures. The loads generated by swinging bells are in special interest because they may have severe consequences on the bell's supporting structure as recently reported by [1,2,3]. For a given size and shape of the bell, the crucial parameter that determines it's dynamics are the geometry of the yoke and magnitude of excitation force. In the existing studies, when modeling the dynamics of the bell supporting structure the loads generated by swinging bells are either measured by accelerometers placed on the existing constructions or estimated according to some semi-empirical formulas [4].

In this paper we present novel yoke-bell-clapper system with variable geometry and adjustable excitation force. We introduce the mathematical model of the system that is based on the existing prototype and validate it. Our goal is to assess the influence of the yoke's geometry and the excitation force on the bell's and clapper's oscillations amplitude and associated reaction forces in the supports. The simulations are done using sample-based approach, values of system parameters are randomly sampled from the analyzed set of parameter values. As a result we obtain an effective and robust numerical tool that can trustworthy predict the bell's ringing scheme and produced loads.

Experimental stand and mathematical model validation

Figure 1 presents the experimental rig based on the project and patent of the Lodz University of Technology. The rig consists of the yoke, the bell, the clapper, the moving beam and the supporting frame. The idea behind the moving beam is that we can alter the geometry of the yoke, therefore reproduce different bell mounting types and analyze the influence of the parameters describing the yoke's geometry on the system response. The rig is equipped with sensors that measure the kinematics and the dynamics of the system.

The mathematical model representing the yoke-bell-clapper system is build based on the physical model that is also schematically presented in the figure 1. It is a four degree of freedom (DoF) system accommodating the yoke with the bell, the clapper and the yoke's supports. The clapper to the bell collisions are described using a discrete mathematical model based on the coefficient of restitution. The analyzed yoke-bell-clapper system is propelled with a linear motor activated when the bell goes through its stable equilibrium position. The excitation mathematical model is therefore piece-wise and depends on the period of the system.

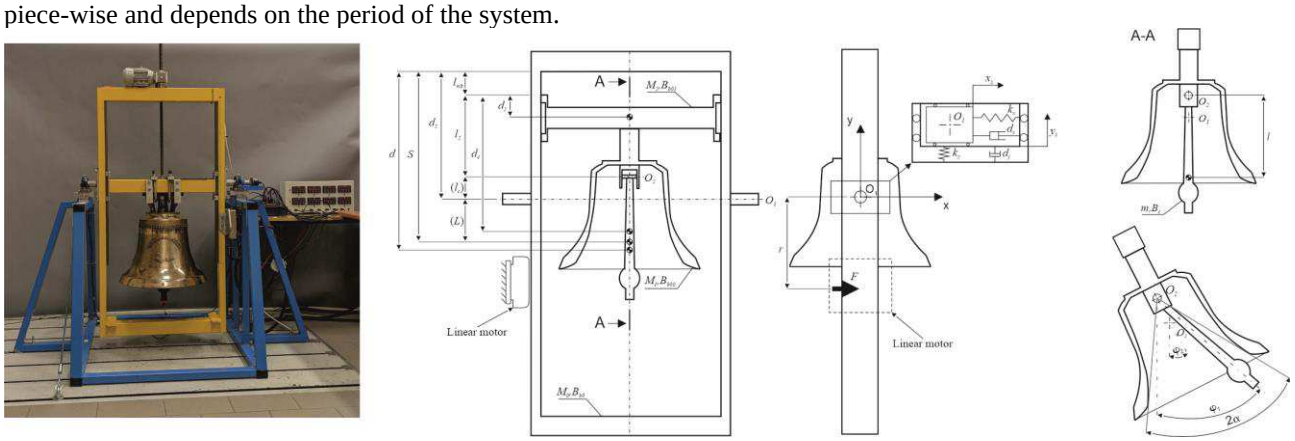

Figure 1: Experimental rig and schematic model of the experimental rig along with its physical and geometrical quantities involved in the mathematical model of the system.

The mathematical model is validated by performing the series of simulations for chosen yokes' geometries. Each time numerical results were compared with data obtained experimentally. Good matching between experimental data and numerical results is achieved in all scenarios. It shows that our model can accurately represents reality regardless of the yoke's geometry. Important aspects from engineering point of view including: The period of the system, its dynamics, reaction forces, and ringing scheme of the bell are reliably determined.

The influence of the yoke geometry and excitation on the system response

Using validated mathematical model we investigate the influence of the yoke geometry and the excitation force magnitude on the system response. In the analysis we focus on the aspects crucial from practical point of view namely: working regime, amplitude of the bell and clapper motion and dynamical loads acting on the supporting structure. We perform a series of 100,000 simulations using sample-based approach. The results are presented in a form of two parameters color maps. In each map on the horizontal axis there is a parameter determining the yoke's geometry and on the vertical axis the excitation force amplitude. Figure 2(a) shows the variety of ringing schemes that can be obtained depending on the geometry and excitation. Figures 2(b) and 2(c) present the amplitudes of dynamic reaction forces in the yoke supports in the horizontal and vertical direction consecutively.

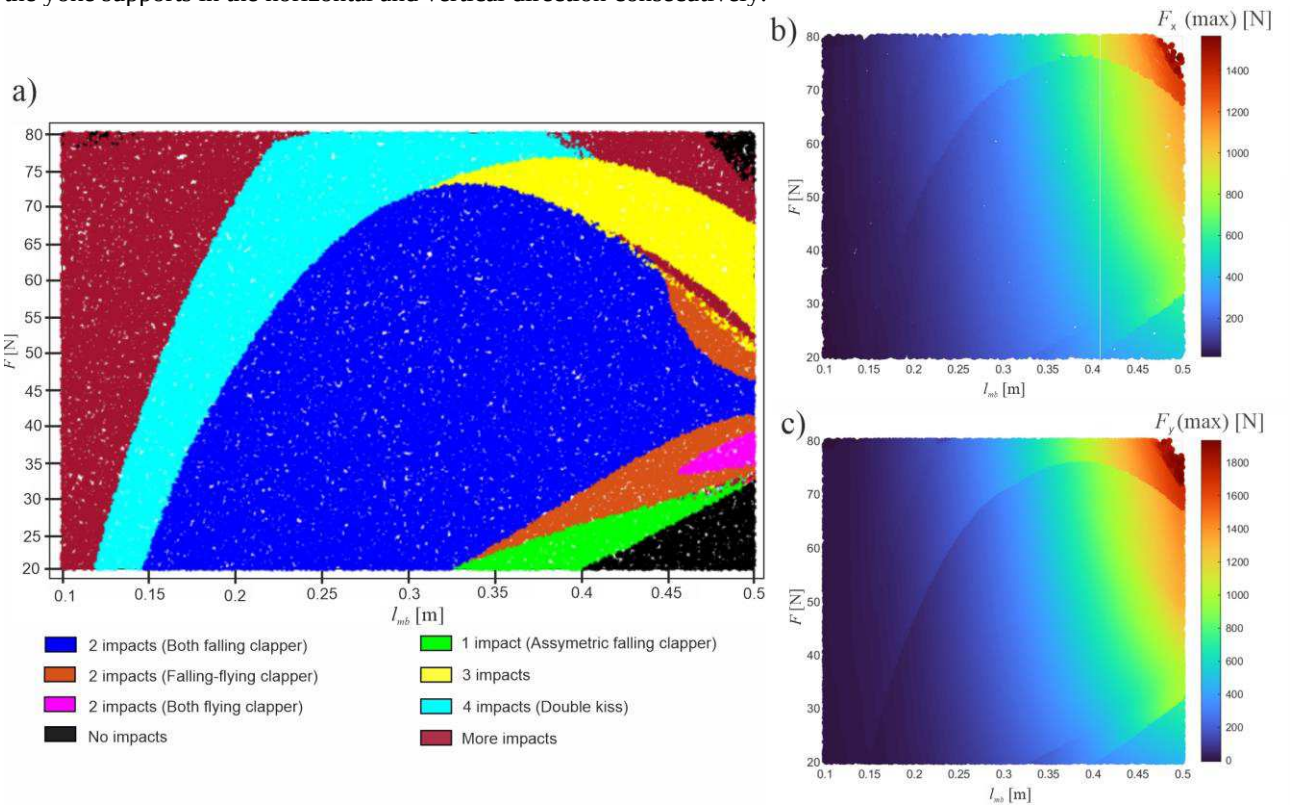

Figure 2: Two parameters colormaps showing a) the behavior of the system after reaching its attractor, amplitude of the reaction force in the supports in the a) horizontal and b) vertical direction.

Conclusions

We present that transition from one ringing scheme to another is usually associated with a step change of produced reaction forces and oscillations amplitude. We also show that for a given yoke's geometry different ringing schemes are possible depending on the excitation force.

Developed numerical algorithm can serve as a reliable tool for engineers during the design phase of the bells, yokes and their supporting structures.

References

[1] Ivorra, S., Palomo, M., Verdú, G. and Zasso, G. (2006) Dynamics forces produced by swinging bells. *Mechanica*, 41:47-62.

[2] Pallarés, F., Betti, M., Bartoli, G. and Pallarés, L. (2021) Structural health monitoring (shm) and non-destructive testing (ndt) of slender masonry structures: A practical review. *Construction and Building Materials*, 297:123768.

[3] McCombie, P. F. (2019) Rocking of a bell tower – investigation by non-contact video measurement. *Engineering Structures*, 193:271-280.

[4] Ivorra, S., Foti, D., Diaferio, M., Vacca, V. and Bru, D. (2018) Resonance detected on a historical tower under bell's forced vibrations. *Frattura ed Integrita Strutturale*, 12:203-215.

[5] Brzeski, P., Kapitaniak, T. and Perlikowski, P. (2015) Experimental verification of a hybrid dynamical model of the church bell. *International Journal of Impact Engineering*, 80:177-184.

Experimentally validated geometrically exact model for nonlinear dynamic analysis of cantilevers undergoing extreme motions

Hamed Farokhi*, Yiwei Xia† and Alper Erturk†
*Department of Mechanical and Construction Engineering, Northumbria University, Newcastle upon Tyne NE1 8ST, UK
†George W. Woodruff School of Mechanical Engineering, Georgia Institute of Technology, Atlanta, 30332, USA

Summary. A unique characteristics of cantilevered beams is their capability of undergoing very large-amplitude oscillations, which has been used in various applications such as energy harvesting and bio-inspired actuation. To examine cantilever motions of extremely large amplitudes, the third-order inextensible nonlinear model cannot be used, hence requiring the application of a geometrically exact model. This study presents an experimental and theoretical investigation on nonlinear extreme dynamics of cantilevers under base excitation. A rotation-based geometrically exact model is developed using Euler-Bernoulli beam theory and inextensibility assumption to examine the cantilever response at extreme motion amplitudes. Precise experiments are conducted using a state-of-the-art in vacuo base excitation experimental set-up to drive the cantilever to extremely large motion amplitudes, and a high-speed camera is used to capture the motion. Extensive comparisons are conducted between experimental and theoretical results and it is shown that the proposed exact model can be used reliably to capture cantilever motions of extreme amplitudes.

Introduction

Cantilevered beams are present in different engineering applications such as vibration energy harvesters, micro gyroscopes, and piezoelectric sensors and actuators. Owing to have one end free, they can undergo large-amplitude vibrations. However, analysing large-amplitude vibration is a difficult task, not only due to the presence of different sources of nonlinearity, but also the fact that the amplitude could grow extremely large, rendering nonlinear truncated models inaccurate and requiring a geometrically exact model. Many investigators have examined the vibrations of cantilevers over the last few decades, starting with the well-known third-order model developed by Crespo da Silva and Glynn [1, 2], which was later further examined by Nayfeh and Pai [3, 4]. Many other studies utilised the third-order model to examine the behaviour of cantilevers, namely Dwivedy and Kar [5] and Mahmoodi et al. [6]. Farokhi et al. [7] continued the studies on this topic by developing a dynamical version of the rotation-based exact nonlinear cantilever model, originally used for static buckling of an elastic continuum [8], capable of capturing motions of extreme amplitudes. This study reports detailed experimental results on extremely large vibrations of a cantilever and shows comparisons between experimental and theoretical results.

Model Development

To derive the rotation-based geometrically exact equation of motion, a cantilevered beam is considered of length L, cross-sectional area A, second moment of area I, Young's modulus E, mass per unit length m, and material damping coefficient η, under harmonic excitation in the form of $z_0 \sin(\omega_z t)$. Making use of the inextensibility assumption, and in the context of the Euler-Bernoulli beam theory, the longitudinal (u) and transverse (w) displacements of the cantilever (the latter with respect ot the clamped end), can be formulated in terms of the centreline rotation ψ as

$$u(s,t) = \int_0^s \Big(\cos\psi(\xi,t) - 1\Big)\,\mathrm{d}\xi, \qquad w(s,t) = \int_0^s \sin\psi(\xi,t)\,\mathrm{d}\xi. \tag{1}$$

Assuming a vertical configuration for the cantilever with the clamped end at the bottom (see Fig. 1(a)) and taking into account the gravity, the geometrically exact equation of motion for centreline rotation of the cantilever can be derived as

$$\begin{aligned} &J\partial_{tt}\psi + m\sin\psi \int_s^L \int_0^{s^*} \Big(\partial_{tt}\psi(\xi,t)\sin\psi(\xi,t) + \Big(\partial_t\psi(\xi,t)\Big)^2\cos\psi(\xi,t)\Big)\,\mathrm{d}\xi\,\mathrm{d}s^* \\ &+ m\cos\psi \int_s^L \Big[-z_0\omega_z^2\sin(\omega_z t) + \int_0^{s^*}\Big(\partial_{tt}\psi(\xi,t)\cos\psi(\xi,t) - \Big(\partial_t\psi(\xi,t)\Big)^2\sin\psi(\xi,t)\Big)\,\mathrm{d}\xi\Big]\,\mathrm{d}s^* \\ &- EI\partial_{ss}\psi - \eta I\partial_{tss}\psi - mg(L-s)\sin\psi = 0. \end{aligned} \tag{2}$$

in which $J = \rho I$ with ρ being the mass density, g is the acceleration due to gravity, and $\partial_s \equiv \partial/\partial s$. Equation 2 is then nondimensionalised and discretised into a 6-degree-of-freedom system using the Galerkin technique while keeping all terms geometrically exact. The resultant set is solved using a continuation technique.

Results

Figure 1(b) shows the in vacuo base excitation experimental set-up used to excite the cantilever in the primary resonance region and to drive it to extremely large amplitude. A high-speed camera system was used to capture vibration response of the cantilever. An image processing code was then developed to extract the beam deformed shape and the motion amplitudes from the videos. In order to examine oscillations of extremely large amplitudes, the cantilever was excited

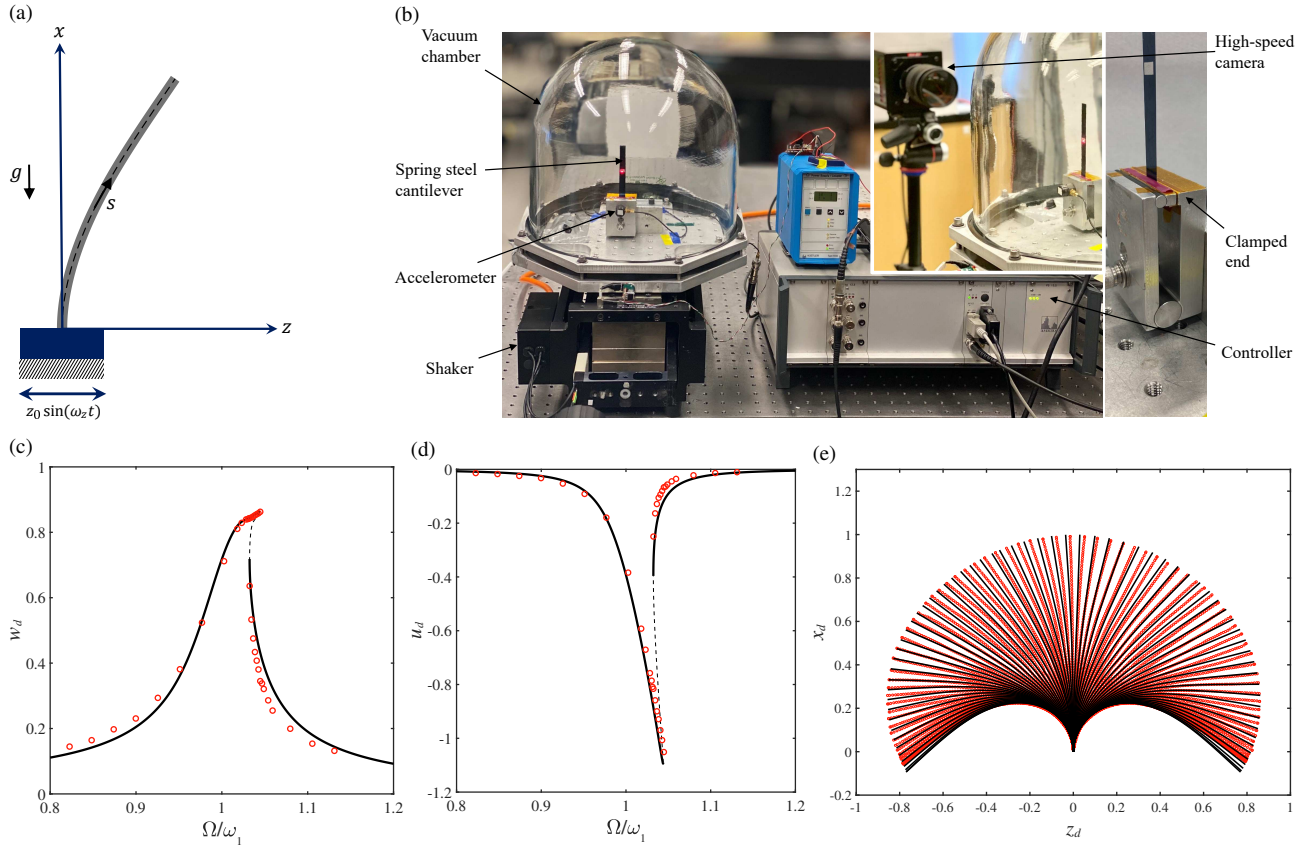

Figure 1: (a) Schematic of the cantilever. (b) In vacuo base excitation experimental set-up. (c, d) Frequency response of the cantilever tip transverse and longitudinal vibration at 0.5g RMS acceleration level, respectively. (e) Motion of the cantilever at peak amplitude in one period of oscillation. In sub-figure (c)-(e), circles denote experimental results and lines show geometrically exact model predictions.

at base acceleration of $0.5g$ RMS under near-vacuum conditions (i.e. 9% atmospheric pressure). The theoretical and experimental frequency responses of the cantilever are illustrated in Fig. 1(c) and 1(d), and the oscillation of the cantilever at its peak resonance amplitude in one period of oscillation is shown in Fig. 1(e). It is seen in Fig. 1(c, d) that the exact model works very well even at this extreme oscillation amplitude and predicts a frequency response amplitude very close to the experimental one. Additionally, as shown in Fig. 1(e), the exact model does an excellent job at capturing the extreme vibrations of the cantilever, even when the tip of the cantilever bends backwards, as confirmed by the experimental observations. Hence, these results prove the validity of the proposed geometrically exact model and that it can be used reliably for studying cantilever vibrations of extremely large amplitudes.

Conclusions

Nonlinear extreme dynamics of a cantilever was examined experimentally and theoretically. For the experimental part, an in vacuo experimental set-up was used to excited the cantilever in the primary resonance region and to drive the cantilever vibration to extremely large amplitudes, and for the theoretical part, a geometrically exact model based on Euler-Bernoulli beam theory was developed. Comparisons between experimental and theoretical results showed that the proposed exact model is fully capable of capturing vibrations of extremely large amplitudes reliably.

References

[1] MRM Crespo da Silva and CC Glynn. Nonlinear flexural-flexural-torsional dynamics of inextensional beams. i. equations of motion. *Journal of Structural Mechanics*, 6(4):437–448, 1978.

[2] MRM Crespo da Silva and CC Glynn. Nonlinear flexural-flexural-torsional dynamics of inextensional beams. ii. forced motions. *Journal of Structural Mechanics*, 6(4):449–461, 1978.

[3] Ali H. Nayfeh and Perngjin F. Pai. Non-linear non-planar parametric responses of an inextensional beam. *International Journal of Non-Linear Mechanics*, 24(2):139–158, 1989.

[4] Perngjin F Pai and Ali H Nayfeh. Non-linear non-planar oscillations of a cantilever beam under lateral base excitations. *International Journal of Non-Linear Mechanics*, 25(5):455–474, 1990.

[5] SK Dwivedy and RC Kar. Nonlinear dynamics of a cantilever beam carrying an attached mass with 1: 3: 9 internal resonances. *Nonlinear Dynamics*, 31(1):49–72, 2003.

[6] S. Nima Mahmoodi, Nader Jalili, and Siamak E. Khadem. An experimental investigation of nonlinear vibration and frequency response analysis of cantilever viscoelastic beams. *Journal of Sound and Vibration*, 311(3):1409–1419, 2008.

[7] Hamed Farokhi and Mergen H Ghayesh. Geometrically exact extreme vibrations of cantilevers. *International Journal of Mechanical Sciences*, 168:105051, 2020.

[8] Z. J. Bažant and Luigi Cedolin. *Stability of structures: elastic, inelastic, fracture and damage theories*. World Scientific, 2010.

Model order reduction of nonlinear piezoelectric microstructures through direct parametrisation of invariant manifolds

Andrea Opreni*, Alessandra Vizzaccaro†, Cyril Touzé‡, and Attilio Frangi*
*Dipartimento di Ingegneria Civile e Ambientale, Politecnico di Milano, Milan, Italy
†Department of Engineering Mathematics, University of Bristol, Bristol, United Kingdom
‡Institute of Mechanical Sciences and Industrial Applications (IMSIA) ENSTA Paris - CNRS - EDF - CEA - Institut Polytechnique de Paris, Paris, France

Summary. Piezoelectric actuation represents the most effective out-of-plane actuation mechanism for resonant microstructures as scanning micromirrors and piezoelectric ultrasonic transducers. Nevertheless, predicting the dynamic response of such devices at their design stage is often impractical since numerical computation of periodic orbits from finite element systems is computationally demanding. In this work, we propose a model order reduction strategy based on the direct parametrisation for invariant manifolds tailored for nonlinear piezoelectric structures. The innovative aspect of the method is the introduction of nonlinear terms that arise due to piezoelectric coupling in the reduction procedure.

Introduction

Among the actuation techniques available for the development of micro-electro-mechanical systems (MEMS), piezoelectric actuation is the most effective to achieve large out-of-plane displacements in resonant actuators as scanning micromirrors and piezoelectric ultrasonic transducers. Indeed, its enhanced linearity, fast feedback response, and high exerted forces provide a mean to achieve high performance with moderate power consumption and easy control of the device. However, the large amplitudes developed by devices as scanning micromirrors are still affected by geometric nonlinearities and by the hysteretic behaviour of piezoelectric materials, which in turn makes the dynamic response of the device nonlinear. Such effects need to be predicted at the design stage of MEMS components, hence making numerical methods of paramount importance for their design. Since full-order numerical simulations are computationally demanding for performing parametrised analyses of mechanical components, dimensionality reduction techniques are essential [1, 2]. Within the context of vibratory systems, the Direct Parametrisation for Invariant Manifolds (DPIM) [3, 4] represents the most effective method for deriving accurate reduced models of structures actuated at resonance. In the present work, we derive an extension of the method initially introduced for systems subjected to geometric nonlinearities to account for the nonlinear converse piezoelectric effect as modeled by the Landau-Devonshire theory of ferroelectrics. The proposed approach is applied to predict the nonlinear dynamic response of MEMS micromirrors and its results are compared with experimental data.

Method

The dynamic response of piezo-MEMS undergoing large displacements and subjected to converse piezoelectric effect is governed by the conservation of linear momentum formulated as follows [5]:

$$\int_\Omega \rho\, \ddot{\mathbf{u}} \cdot \mathbf{w}\, d\Omega + \int_\Omega (\mathbf{S}^e - \mathbf{S}^p) : \delta\mathbf{e}\, d\Omega = 0, \tag{1}$$

where all quantities are reported in material configuration Ω. ρ is the density, $\mathbf{w}$ is the test function, $\delta\mathbf{e}$ is the first variation of the Green-Lagrange strain tensor. The second Piola-Kirchhoff stress tensor is decomposed in elastic $\mathbf{S}^e$ and inelastic components $\mathbf{S}^p$, which in the present framework are given by the following constitutive models [6]:

$$\mathbf{S}^e = \mathcal{A} : \mathbf{e}, \quad \mathbf{S}^p = \mathcal{Q} : \mathcal{A} : (\mathbf{p} \otimes \mathbf{p}), \tag{2}$$

with $\mathcal{A}$ elasticity tensor, $\mathcal{Q}$ electrostrictive tensor, and $\mathbf{p}$ polarisation vector. In general $\mathbf{p}$ is time-dependent and with non-zero average value. Upon finite element discretisation of Eq. (1) and addition of damping the following discrete system of ordinary differential equations is retrieved:

$$\mathbf{M}\ddot{\mathbf{U}} + \mathbf{C}\dot{\mathbf{U}} + \mathbf{K}\mathbf{U} + \mathbf{G}(\mathbf{U},\mathbf{U}) + \mathbf{H}(\mathbf{U},\mathbf{U},\mathbf{U}) = \mathbf{F}^p(\mathbf{U},\mathbf{p}), \tag{3}$$

with $\mathbf{p}$ function of time. Dimensionality reduction of Eq. (3) is achieved by parametrising the motion of the system along an invariant-based span of the phase space. We recast Eq. (3) in first order by introducing the velocity $\mathbf{V} = \dot{\mathbf{U}}$ and we introduce a nonlinear coordinate change between the normal coordinates $\mathbf{z}$ that describe the motion of the system along the embedding and the nodal degrees of freedom of the model [7, 8]:

$$\mathbf{U} = \mathbf{\Psi}(\mathbf{z}), \quad \mathbf{V} = \mathbf{\Upsilon}(\mathbf{z}). \tag{4}$$

The dynamics along the defined subspace is expressed as:

$$\dot{\mathbf{z}} = \mathbf{f}(\mathbf{z}), \tag{5}$$

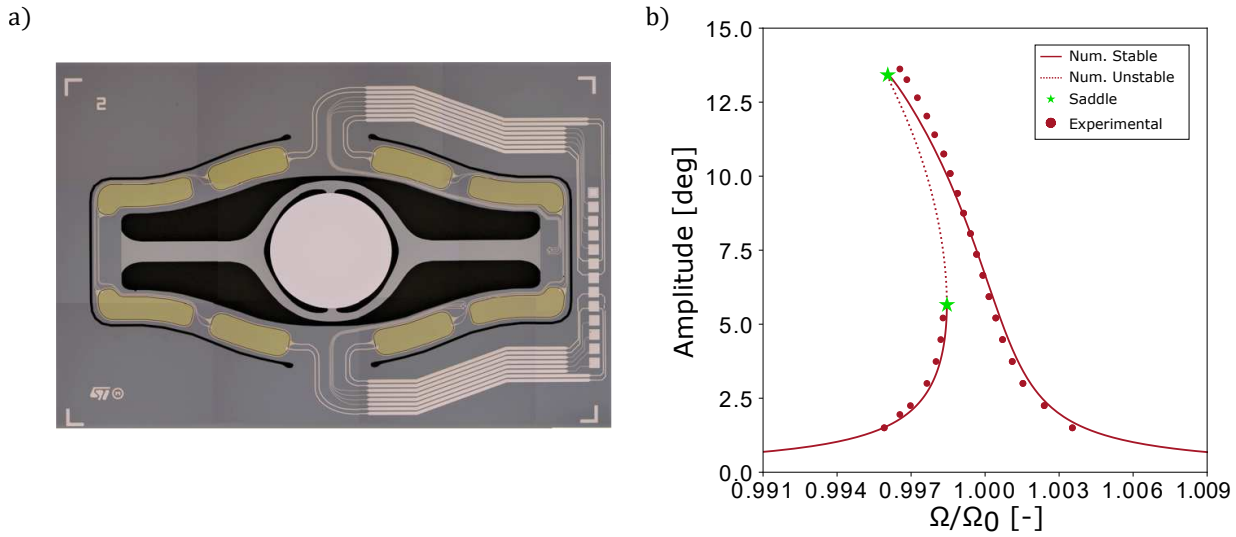

Figure 1: (a) optical microscope image of the tested device. (b) Preliminary comparison between experimental data and numerical frequency response curves. Numerical curves are obtained using a complex normal form style parametrisation.

with $\mathbf{f}(\mathbf{z})$ reduced dynamics. An important remark of the presented formulation is that the polarization field $\mathbf{p}$ is assumed as known. In the present work, the polarisation is measured from experimental data and fed to the model to compute the piezoelectric forces $\mathbf{F}^p(\mathbf{U}, \mathbf{p})$ beforehand. This provides an efficient modeling approach as already evidenced in past works. When combined with the proposed model order reduction strategy it provides an efficient framework for predicting the nonlinear dynamic response of piezoelectrically actuated microstructures.

First results reported on a MEMS device are reported in Fig. 1. Fig. 1(a) reports the device under consideration, which is a MEMS micromirror developed by STMicroelectronics. In Fig. 1(b) a preliminary comparison between numerical simulations and experimental data is reported, highlighting the remarkable agreement of the proposed approach.

Conclusion

We here reported a model order reduction method for nonlinear piezoelectric structures based on the direct parametrisation for invariant manifolds. The starting equation is the conservation of linear momentum for structures subjected to finite transformations and to converse piezoelectric effect, the latter modeled using the Landau-Devonshire theory of ferroelectrics. The resulting system exhibits a follower force controlled by the polarization of the piezoelectric material and by the displacement of the structure, which in turn modifies the vibratory response of the system. Preliminary results obtained on a real MEMS device show promising results both in terms of computational performance and accuracy.

References

[1] G. Gobat, A. Opreni, S. Fresca, A. Manzoni, and A. Frangi. Reduced order modeling of nonlinear microstructures through Proper Orthogonal Decomposition. Accepted in *Mechanical Systems and Signal Processing*, 2021

[2] S. Fresca, G. Gobat, P. Fedeli, A. Frangi, A. Manzoni. Deep learning-based reduced order models for the real-time simulation of the nonlinear dynamics of microstructures. *arXiv*, 2111.12511, 2021

[3] A. Vizzaccaro, A. Opreni, L. Salles, A. Frangi, C. Touzé. High order direct parametrisation of invariant manifolds for model order reduction of finite element structures: application to large amplitude vibrations and uncovering of a folding point. *arXiv*, 2109.10031, 2021

[4] S. Jain and G. Haller. How to compute invariant manifolds and their reduced dynamics in high-dimensional finite element models. *Nonlinear Dynamics*, in press, 2021.

[5] A. Opreni, N. Boni, R. Carminati, and A. Frangi. Analysis of the Nonlinear Response of Piezo-Micromirrors with the Harmonic Balance Method. *Actuators*, vol. 10(2), pp. 21, 2021

[6] A. Frangi, A. Opreni, N. Boni, P. Fedeli, R. Carminati, M. Merli, G. Mendicino. Nonlinear Response of PZT-Actuated Resonant Micromirrors. *Journal of Microelectromechanical Systems*, vol. 29(6), pp. 1421 - 1430, 2020

[7] A. Vizzaccaro, Y. Shen, L. Salles, J. Blahoš, C. Touzé. Direct computation of nonlinear mapping via normal form for reduced-order models of finite element nonlinear structures. *Computer Methods in Applied Mechanics and Engineering*, vol. 384, pp. 113957, 2021

[8] A. Opreni, A. Vizzaccaro, A. Frangi, and C. Touzé. Model order reduction based on direct normal form: application to large finite element MEMS structures featuring internal resonance. *Nonlinear Dynamics*, vol. 105, pp. 1237-1272, 2021.

Modeling Nonlinearities in MEMS Micro Mirrors: From Single Chip to Wafer Level

Ulrike Nabholz*, Jan E. Mehner† and Peter Degenfeld-Schonburg*
*Robert Bosch GmbH Corporate Research, 71272 Renningen, Germany
†Chemnitz University of Technology, 09107 Chemnitz, Germany

Summary. The performance requirements for MEMS sensors and actuators, such as scanning micro mirrors, are increasing as emerging applications in the fields of highly-automated driving or augmented reality are in increasing demand. During final testing, a device is rejected as soon as it does not fulfil the performance specifications which decreases yield and thus increases the overall cost. In many cases, unexpected device failure or performance issues can be traced back to nonlinear system behaviour. This entails the need for system models which take nonlinear sensor dynamics into account and a fundamental understanding of the underlying nonlinear physics is often essential for an improved MEMS design. Here, we present a comprehensive analysis of nonlinear dynamics in scanning MEMS micro mirrors ranging from careful measurements and modeling of nonlinear system behaviour on the level of individual chips up to wafer-level testing of several hundred devices. The underlying nonlinear mode-coupling phenomenon, known as spontaneous parametric down-conversion (SPDC) exhibits a sudden transition from mostly linear to nonlinear system behaviour. The threshold amplitude or rather critical point only lies within the operational amplitude of a device, when a specific frequency resonance condition (a 1:1:1 internal resonance) for the mechanical modes of the device is closely matched. Due to fabrication imperfections of MEMS process technologies small deviations in the geometry between several devices of the same design occur which consequently influences the frequency spectrum strongly influence the frequency spectrum of each individual device and therefore decide about the fulfilment of the resonance condition. We demonstrate the benefits that can be achieved by employing the insights gained from single-chip measurements and models to the analysis of a large number of devices on wafer level and suggest a possible path towards successful design iterations. Moreover, above the threshold we show that the micro mirror displays fundamental nonlinear behavior ranging from stationary state bifurcations to dynamical instabilities.

Introduction

One main requirement for scanning MEMS micro mirrors for automotive as well as for consumer applications is the reachable deflection angle. Yet, our experimental observations show that even micro mirrors of the same design layout often show drastic differences in their maximum deflection [3]: Some devices reach the required deflection angle while others exhibit instabilities in their deflection and sometimes even fracture.
These drastic differences in the device behaviour can be attributed to small differences in the mode spectrum caused by geometry variations due to the process tolerances of surface micromachining. In the case of the scanning MEMS micro mirror at hand, the nonlinear dynamic behaviour which occurs in some cases is due to a fundamental nonlinear model, more prominently known from nonlinear optics, namely spontaneous parametric down-conversion (SPDC). In the mechanical domain, where the nonlinear mode coupling originates from geometric nonlinearities, SPDC or three-wave mixing has only been studied in recent years [1, 3].
For SPDC, a model of an externally driven, damped Duffing oscillator with a cubic nonlinearity is used for the drive mode. Additionally, two so-called parasitic modes of the same type are coupled to the drive mode through a three-wave coupling term. In addition, as discussed in [2], a nonlinear damping term needs to be included.

Full Model for Single Chips

With the a simple model of three nonlinearly coupled ordinary differential equations, the observed effects can be simulated and thus explained physically. They include bifurcations and hysteresis, as well as unstable behaviour caused by a resonant actuation of parasitic modes and thus amplitude depletion of the drive mode. Additionally, critical slowing-down and limit cycles can explain the observed phenomena.
The system parameters needed to emulate the behaviour can be measured directly using laser doppler vibrometry. They can also be obtained from simple optical measurements, where the deflection angle is measured during the undisturbed and during the disturbed operation of the mirror.
Fig. 1 shows the modelled behaviour of a micro mirror that shows SPDC behaviour. As mentioned above, SPDC is a spontaneous process and thus, the figure shows the behaviour below threshold (identical to the nonlinearly damped Duffing oscillator) as well as the behaviour above threshold, where the two parasitic modes gain amplitude and disturb the oscillation of the drive mode. The critical point model represents the threshold deflection angle, that is the transition from uncoupled behaviour to SPDC behaviour with the two additional parasitic modes. This model is of vital importance for the large scale application and wafer level testing that will be elaborated on in the next section.

Critical Point Model for Wafer Level

The simple analytical model for the critical deflection angles that was shown as a red line in Fig. 1, becomes relevant when measurements need to be carried out for a larger number of devices in order to assess their nonlinear behaviour.

Thus, it is especially important for engineering applications, since it allows for a differentiation between devices that lie within the specifications and devices that lie outside

As we show in [3], mode coupling can be predicted with low computational effort. The result of the prediction only includes at what angle mode coupling occurs in a specific mirror and does not characterize the full range of nonlinear dynamic effects as was the case for the full model above. Yet, this prediction is sufficient for the decision on whether or not a device meets the requirements pertaining to the deflection angle. It points out the individual chips with critical deflection angles below a certain threshold. Apart from this, it increases knowledge about the design and thus provides input for design iterations and optimization.

Fig. 2 show the results of the critical point model [4]. The design parameter $\delta = f_{0,d} - f_{0,p_1} - f_{0,p_2}$ on the horizontal axis gives the relation of the linear mode frequencies of the three coupled modes, where $f_{0,0}$ denotes the frequency of the drive mode and f_{0,p_1} and f_{0,p_2} the frequencies of the two parasitic modes. In other words, δ represent the 1:1:1 internal resonance condition.

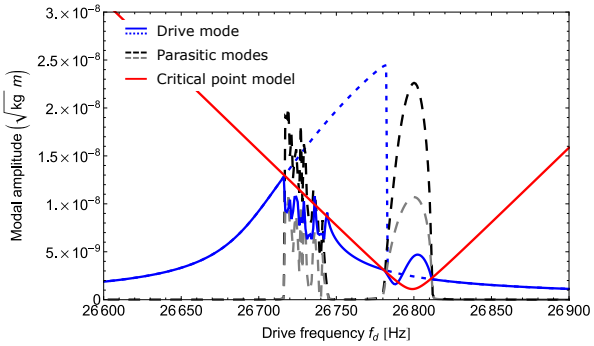

Figure 1: Transient representation of a sweep with increasing frequency. The drive mode is shown in blue, for the case of mode coupling, the line is solid. For comparison, the dotted blue line represents the behaviour of the drive mode without any mode coupling. The dashed lines in grey and black show the two parasitic modes during mode coupling. The red line denotes the critical point model which depicts the onset of SPDC and will be of great importance in the following section.

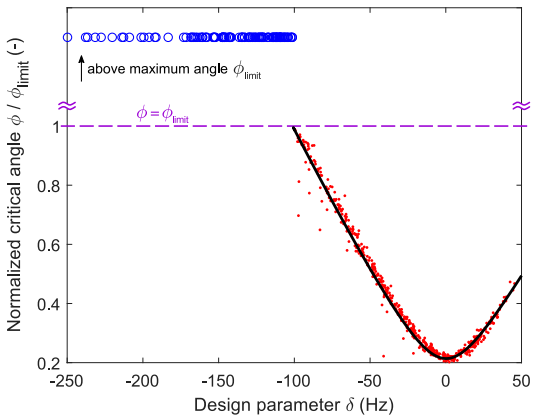

Figure 2: Validation of the critical point model: The measured critical deflection angles (631 points) which mark the onset of mode coupling, where red dots and blue circles distinguish critical angles below and above the specified deflection angle, are compared to the prediction from the critical point model, shown as a black line.

Conclusion

We showed that when the modes of a mechanical structure fulfil an internal resonance condition and show a large coupling strength, nonlinear phenomena such as SPDC can occur. The behaviour of single chips was modelled using the full model for three coupled equations of motion with the relevant nonlinear terms from structural mechanics. Wafer level testing of the critical threshold for the onset of mode coupling was successfully matched with the prediction of the much simpler critical point model. The design parameter δ provides leverage for adjusting the mode coupling of a MEMS design. Thus, we explained both the underlying nonlinear dynamics effects and their implications for unwanted nonlinear system behaviour. Connecting these two parts is highly relevant for the development of not only MEMS micro mirrors, but any resonant MEMS sensor or actuator. A range of similar coupling mechanisms due to geometric nonlinearities is also conceivable.

References

[1] Adarsh Ganesan, Cuong Do, and Ashwin Seshia. Phononic Frequency Comb via Intrinsic Three-Wave Mixing. *Physical Review Letters*, 118:033903, Jan 2017.

[2] U. Nabholz, W. Heinzelmann, J. E. Mehner, and P. Degenfeld-Schonburg. Amplitude- and Gas Pressure-Dependent Nonlinear Damping of High-Q Oscillatory MEMS Micro Mirrors. *Journal of Microelectromechanical Systems*, 27(3):383–391, June 2018.

[3] U. Nabholz, F. Schatz, J. E. Mehner, and P. Degenfeld-Schonburg. Spontaneous Parametric Down-Conversion Induced by Non-Degenerate Three-Wave Mixing in a Scanning MEMS Micro Mirror. *Scientific Reports*, 9(1):2045–2322, 2019.

[4] Ulrike Nabholz, Florian Stockmar, Jan E. Mehner, and Peter Degenfeld-Schonburg. Measurement Series for Validation of Critical Point Model in 600 Scanning Micro Mirrors Affected by Three-Wave Down-Conversion. Preprint, 2019. arXiv:1912.06189.

Monday, July 18, 2022
13:30 - 15:30

MS-03 Computational Methods
Rhone 3A

Chair: Jan Sieber

13:30 - 13:50
A fast, efficient algorithm for quantification of rare events in dynamical systems
BLANCHARD Antoine*, SAPSIS Themistoklis
*Massachusetts Institute of Technology (77 Massachusetts Ave, Cambridge, MA 02139 United States)

13:50 - 14:10
A Multi-Dimensional Atlas Algorithm for Variable-Mesh Boundary-Value Problems
DANKOWICZ Harry*, WANG Yuqing, SCHILDER Frank, HENDERSON Michael
*University of Illinois at Urbana Champaign (University of Illinois at Urbana-Champaign, The Grainger College of Engineering, Department of Mechanical Science and Engineering, 1206 W. Green St, Urbana, IL 61801 United States)

14:10 - 14:30
A new co-simulation approach for mechanical systems with nonlinear components
NATSIAVAS Sotirios, **KOUTRAS Evangelos***, PARASKEVOPOULOS Elias
*Aristotle Un. (Thessaloniki Greece)

14:30 - 14:50
A numerical package for model order reduction of large dimensional finite element systems of nonlinear vibrating structures based on invariant manifold theory
OPRENI Andrea*, VIZZACCARO Alessandra, MARTIN Adrien, TOUZÉ Cyril, FRANGI Attilio
*Politecnico di Milano [Milan] (Piazza Leonardo da Vinci, 32 20133 Milano Italy)

14:50 - 15:10
A port-Hamiltonian formulation for the full von-Kármán plate model
BRUGNOLI Andrea*, MATIGNON Denis
*University of Twente (Drienerlolaan 5, 7522 NB Enschede Netherlands)

15:10 - 15:30
Analysis of Stable and Unstable Pedestrian Flow Situations in Particle Simulations and Evacuation Experiments
STARKE Jens*, PANAGIOTOPOULOS Ilias, SIEBER Jan, JUST Wolfram
*University of Rostock (Ulmenstr. 69, Haus 3 18057 Rostock Germany)

A fast, efficient algorithm for quantification of rare events in dynamical systems

Antoine Blanchard*, Themistoklis P. Sapsis*
*Department of Mechanical Engineering, Massachusetts Institute of Technology, USA

Summary. We introduce a fast, efficient algorithm for quantification of rare events in dynamical systems. The algorithm iteratively learns the "black-box" relationship between parameters (the inputs) and extreme observations (the outputs). To keep the number of black-box evaluations to a minimum, the algorithm cleverly selects the "next-best point" that it should sample based on how much that point will improve our estimate of the output statistics. "Improvement" is quantified by the so-called Q-criterion whose computation (and that of its gradient) can be done analytically, which allows for the possibility of the input space being high-dimensional. We show that the proposed sampling algorithm outperforms other standard sampling approaches.

Background

Extreme events may be thought of as short-lived episodes during which an observable (e.g., drag force, temperature, or stock price) significantly deviates from its mean value. They often have disastrous consequences, as with rogue waves, avalanches, wildfires or extreme weather conditions (see figure 1 and [1]). Quantification of extreme events is particularly difficult because they often arise in complex, high-dimensional, nonlinear systems, and give rise to heavy-tail probability density functions (pdf). The fact that extreme events occur with very low probability means that reliable quantification of the statistics requires an unfathomable amount of data. If the data is collected from a large-scale experiment or a computer simulation with millions of degrees of freedom, the task of extreme-event quantification is virtually hopeless. Thus, the challenge is to come up with a way to estimate the heavy-tail statistics of the system using as few samples as possible.

(a) Rogue waves (b) Avalanches (c) Wildfires (d) Hurricanes

Figure 1: Examples of extreme events arising in nature.

Mohamad & Sapsis [2] recently proposed a sampling strategy for quantification of extreme events in dynamical systems. The basis for their approach was to approximate the unknown "black box" $y = F(x)$ as the realization of a Gaussian process. Specifically, starting from an initially small dataset, their algorithm uses Gaussian process (GP) regression [4] to construct a surrogate map, and then determines the next-best sample for which evaluation of the black box will most improve knowledge of the statistics. At each iteration, the sought-after pdf can be approximated using the posterior distribution of the surrogate map. In their work, the criterion used to determine the next-best point is problematic for two reasons. First, it takes the form of an integral over the input space, which is intractable in high dimensions. Second, there is no closed-form expression for the gradient of their criterion, which forces them to use non-gradient-based optimizers.

Overview of the algorithm

Our algorithm is inspired by that of Mohamad & Sapsis [2], but considerably improves its scope and efficiency. Assuming that we have available a dataset of input–output pairs $\mathcal{D}_n = \{x_i, F(x_i)\}_{i=1}^n$, we proceed iteratively as follows:

Step 1. Train a GP regressor on $\mathcal{D}_n$, and compute surrogate mean f_n and covariance σ_n^2.
Step 2. Determine the next-best point by solving the minimization problem

$$x^* = \operatorname*{argmin}_x Q(x; f_n, \mathcal{D}_n). \tag{1}$$

Step 3. Evaluate the expensive map F at the new point, and append $\{x^*, F(x^*)\}$ to $\mathcal{D}_n$. Then, go back to Step 1.

To compute the criterion $Q(\tilde{x}; f_n, \mathcal{D}_n)$ at some candidate point $\tilde{x}$, we proceed as follows:

Step Q1. Construct $\tilde{\mathcal{D}}_n$ by appending $\{\tilde{x}, f_n(\tilde{x})\}$ to $\mathcal{D}_n$. (Note that we use the surrogate map f_n rather than F.)
Step Q2. Predict the covariance $\tilde{\sigma}_n^2$ using the GP regressor trained on $\mathcal{D}_n$, and return

$$Q(\tilde{x}; f_n, \mathcal{D}_n) = \int \frac{\tilde{\sigma}_n^2(x) p_x(x)}{p_n(f_n(x))} \, \mathrm{d}x. \tag{2}$$

In the above, $p_x(x)$ and $p_n(f_n(x))$ respectively denote the joint pdf of the inputs (which is assumed to be known) and the approximate pdf of the output as predicted by the surrogate map. Criterion (2) is already an improvement over the

A Multi-Dimensional Atlas Algorithm for Variable-Mesh Boundary-Value Problems

Harry Dankowicz*, Yuqing Wang*, Frank Schilder†, and Michael E. Henderson‡
*Department of Mechanical Science and Engineering, University of Illinois at Urbana-Champaign, Urbana, Illinois, USA
†Technical University of Denmark, Roskilde, Denmark
‡IBM Research, T.J. Watson Research Center, Yorktown Heights, New York, USA

Summary. In development since 2007, the MATLAB-based, object-oriented, software platform COCO provides general-purpose support for construction of nonlinear constraints and, in applications to optimization, the corresponding adjoint conditions. COCO atlas algorithms implement continuation strategies that grow constraint manifolds successively from an initial solution guess. Until recently, an alpha implementation in COCO of the multi-dimensional MULTIFARIO package in the `atlas-kd` atlas algorithm was unable to handle problems with changing dimension and/or interpretation of variables and constraints, e.g., boundary-value problems with adaptive meshes. This paper describes a recent upgrade to the `atlas-kd` atlas algorithm that not only provides a resolution to this conundrum, but makes problem-dependent implementation straightforward and consistent with the existing COCO paradigm for construction of constraints and monitor functions. Here, in lieu of a definition of an inner product on an underlying infinite-dimensional vector space, the manifold geometry is characterized using the Euclidean inner product on a suitably-defined finite-dimensional projection. Several examples are considered from the theory of periodic orbits in autonomous and periodically-excited nonlinear dynamical systems.

Fundamentals

The trajectory collocation problem

Following [1], consider the autonomous differential equation $\dot{y} = f(y,p)$ on the interval $[0,T]$ for some positive real number T. Here, the vector field $f : \mathbb{R}^n \times \mathbb{R}^q \mapsto \mathbb{R}^n$ is parameterized by a vector of problem parameters $p \in \mathbb{R}^q$. Choose the integers N and m and the sequence $\{\kappa_j\}_{j=1}^N$ such that $\sum_{j=1}^N \kappa_j = N$. Let $u = \big(\upsilon_{bp}, T, p\big) \in \mathbb{R}^{Nn(m+1)+1+q}$, where

$$\upsilon_{bp}^\top = \begin{pmatrix} \cdots & \upsilon_{(m+1)(j-1)+1}^\top & \cdots & \upsilon_{(m+1)j}^\top & \cdots \end{pmatrix} \tag{1}$$

and j ranges from 1 to N. Then,

$$\tilde{y}(t) = \sum_{i=1}^{m+1} \mathcal{L}_i\left(\frac{2N}{T\kappa_j}\left(t - \frac{T}{N}\sum_{k=1}^{j-1}\kappa_k\right) - 1\right)\upsilon_{(m+1)(j-1)+i} \tag{2}$$

is a candidate approximant for $y(t)$ on the interval $\frac{T}{N}\left(\sum_{k=1}^{j-1}\kappa_k + [0,\kappa_j]\right)$ for every $j = 1,\ldots,N$. Here, $\mathcal{L}_i$ is the i-th Lagrange polynomial of degree m defined on the uniform partition of $[-1,1]$. We obtain a system of $(N-1)n + Nnm$ nonlinear equations by imposition of continuity on $\tilde{y}$ and the collection of collocation conditions

$$0 = \frac{d\tilde{y}}{dt}\left(\frac{T}{N}\left(\sum_{k=1}^{j-1}\kappa_k + \frac{\kappa_j}{2}(1+z_l)\right)\right) - f\left(\tilde{y}\left(\frac{T}{N}\left(\sum_{k=1}^{j-1}\kappa_k + \frac{\kappa_j}{2}(1+z_l)\right)\right), p\right) \tag{3}$$

for $j = 1,\ldots,N$ and $l = 1,\ldots,m$, where z_l is the l-th root of the Legendre polynomial of degree m on the interval $[-1,1]$. Provided that a solution u^* to these equations is regular, there exists an $n+q+1$-dimensional manifold through u^* so that every local solution lies on this manifold. The imposition of up to $n+q+1$ additional constraints (satisfied by u^*) then reduce consideration to lower-dimensional submanifolds of the original solution manifold. The conditions

$$\upsilon_1 - \upsilon_{N(m+1)} = 0 = \tilde{\upsilon}^\top \cdot \upsilon_{bp} \tag{4}$$

for some suitably constructed $\tilde{\upsilon}$ reduce consideration to a local q-dimensional manifold of periodic orbits.

Continuation with a variable mesh

The periodic-orbit problem in the previous section is characterized by the integers N and m, corresponding to the number of mesh intervals and polynomial degree, respectively, the sequence $\{\kappa_j\}_{j=1}^N$ of scaled interval widths, and the reference discretization $\tilde{\upsilon}$, all of which may change during analysis of the collection of solutions obtained for different values of the problem parameters p. Indeed, $\tilde{\upsilon}$ is usually updated before each new solution is sought, using a discretization υ_{bp} from a previously located, nearby solution. Similarly, N and $\{\kappa_j\}_{j=1}^N$ (and, less often, m) may be updated every so often in order to satisfy a desired error tolerance. Each such choice restricts attention to a particular variable space, with its unique interpretations and numbers of problem variables and problem constraints (but identical manifold dimension). As long as one is not concerned with global comparisons between solutions obtained at different stages of the analysis, sequences of solutions may be generated iteratively through a predictor-corrector framework as implemented in an *atlas algorithm*, wherein

interpolation is used by the predictor to accommodate changes to N or $\{\kappa_j\}_{j=1}^{N}$. When global comparisons are of concern, as is the case for closed one-dimensional manifolds and all manifolds of dimension ≥ 2, these may additionally be implemented on the approximant $\tilde{y}$ rather than on the problem discretizations (cf. [2]). Alternatively, as proposed recently in [3], comparisons may be performed in a projected space in terms of invariantly defined solution properties, sufficient in number to ensure a regular embedding of the solution manifold for the underlying infinite-dimensional problem.

A software implementation

The COCO (https://sourceforge.net/projects/cocotools/) software development originates in an effort to provide general-purpose, problem-independent support for i) the construction of *composite continuation problems* (i.e., decomposable into glued-together subproblems with an excess of unknowns relative to the total number of constraints) without concern for the sought manifold dimensionality, and ii) the subsequent analysis of the solution manifold for a given choice of dimension. COCO's construction paradigm allows for solution properties to be defined in terms of subsets of problem variables defined at different stages of construction, for example, the difference between the periods of the individual solutions to two coupled periodic-orbit problems. For variable-mesh problems, such solution properties are said to be invariantly defined if they correspond to a discretized evaluation of a property of the solution to the underlying infinite-dimensional problem, e.g., the mean of a variable or the magnitude of a complex-valued Fourier coefficient. In a recent upgrade to COCO, an implementation of the MULTIFARIO (https://sourceforge.net/projects/multifario/) package for multi-dimensional continuation [4] in the `atlas-kd` atlas algorithm that previously offered no support for variable-mesh continuation problems now provides such support, independently of the nature of the original problem. This functionality is achieved by performing global comparisons in a projection onto a finite-dimensional Euclidean space in terms of invariantly defined solution properties that may be constructed solely in terms of individual discretizations. As an example, Fig. 1 depicts the two-dimensional frequency-amplitude response surface of a hardening Duffing oscillator obtained with `atlas-kd` by performing all global comparisons in the five-dimensional projection onto the excitation period T, excitation amplitude A, first-harmonic Fourier coefficients (scaled by $T/2$), and first-harmonic Fourier amplitude $|c_1|$ (scaled by $T/2$).

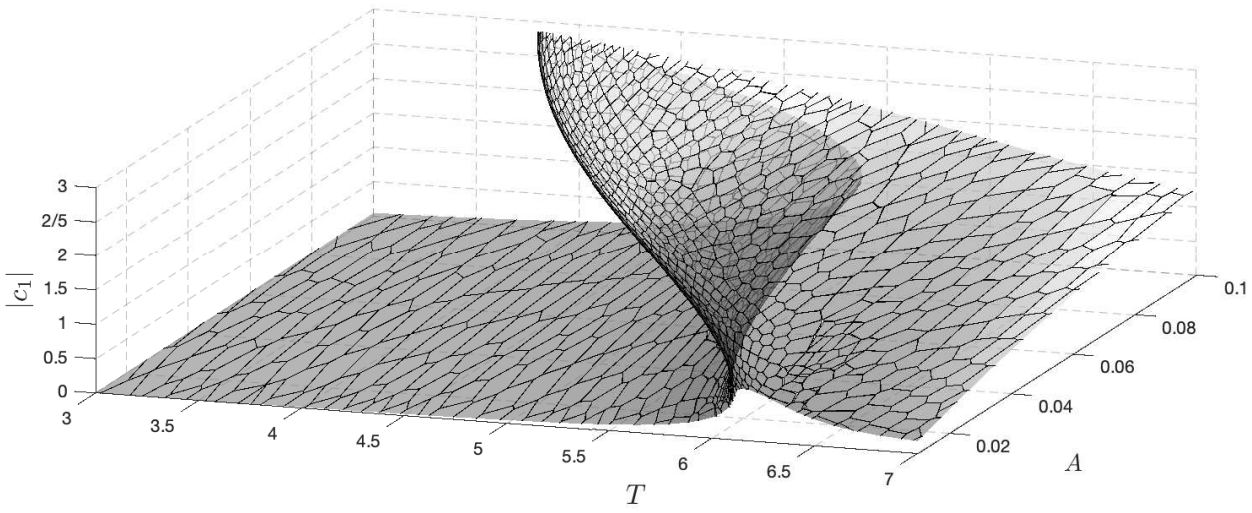

Figure 1: Two-dimensional frequency-amplitude response surface for a hardening Duffing oscillator.

Conclusions

The COCO construction paradigm provides general-purpose support for the definition of small numbers of solution properties that can be used for detecting special points during continuation. Remarkably, the same functionality supports a low-complexity approach for multi-dimensional continuation of variable-mesh boundary-value problems without requiring a user-defined inner product in terms of pairs of discretizations with different interpretations and numbers of problem variables and constraints. The COCO-compatible `atlas-kd` atlas algorithm implements this new paradigm with only minimal modifications to the algorithms inherited from MULTIFARIO.

References

[1] Dankowicz, H., Schilder, F. (2013) Recipes for Continuation. SIAM.

[2] Gameiro, M., Lessard, J.-P., Pugliese, A. (2016) Computation of Smooth Manifolds Via Rigorous Multi-parameter Continuation in Infinite Dimensions. *Foundations of Computational Mathematics*, **16(2)**:531-575.

[3] Dankowicz, H., Wang, Y., Schilder, F., Henderson, M. E. (2019) Multi-Dimensional Manifold Continuation for Adaptive Boundary-Value Problems. In review.

[4] Henderson, M. E. (2002) Multiple Parameter Continuation: Computing Implicitly Defined k-Manifolds. *Int. J. Bifurcation Chaos*, **12(3)**:451-476.

A new co-simulation approach for mechanical systems with nonlinear components

Evangelos Koutras, Elias Paraskevopoulos and Sotirios Natsiavas
Department of Mechanical Engineering, Aristotle University, 54124 Thessaloniki, Greece

Summary. Co-simulation is used to enable global simulation of a coupled system via the composition of simulators. Within this work, a new co-simulation approach is developed for mechanical systems with nonlinear components. Specifically, a model two-degree-of-freedom oscillator, including Duffing type nonlinearities, was investigated first by applying the method of multiple scales. This provided reliable information on its dynamics under primary external resonance. Moreover, the new co-simulation approach was presented and compared with the classical co-simulation methods from the literature. Here, the main focus is placed on mechanical subsystems. However, the new methods have general validity and can be applied to couple arbitrary solvers.

Introduction

Co-simulation or solver coupling has already been applied extensively to various engineering fields [1, 2]. The basic idea consists in a decomposition of the global model into two or more sub-models. The different subsystems are connected by coupling variables, which are exchanged only at the macro-time points (also called communication points). Between these points, the subsystems integrate independently from each other, using their own solver. Generally, the subsystems can be coupled by physical force/torque laws (applied forces/torques) or by algebraic constraint equations (reaction forces/torques) [3, 4].
Two well-known co-simulation approaches are used: a parallel and a sequential, known as Jacobi and Gauss-Seidel, respectively, as their properties are similar to the respective linear iterative solvers. Furthermore, co-simulation approaches can be subdivided into explicit, implicit and semi-implicit methods. Finally, concerning the decomposition of the overall system into subsystems, three different possibilities can be distinguished. Namely, force/force, force/displacement and displacement/displacement decomposition.

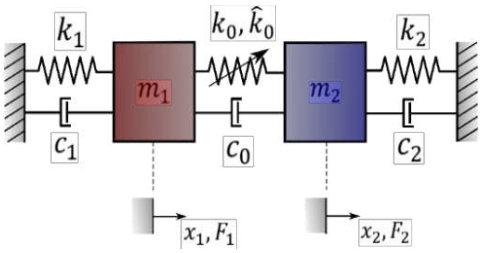

Figure 1: Example mechanical model

Description of the new co-simulation method

Within this work, emphasis is placed on the proper decomposition of the original system into two (or more) subsystems. Specifically, the decomposition takes place only at constraints of the initial model, which are artificially introduced through auxiliary bodies, in case they do not exist. The previously described procedure for the original mechanical model, shown in Figure 1, is depicted in Figure 2. Moreover, following recent work of the authors, the constraint equations and the equations of motion of each sub-model are formulated as a system of exclusively second-order ordinary differential equations (ODEs), bypassing numerical challenges associated with differential-algebraic equations [6, 7]. The distinct difference of the proposed approach, in comparison to the formerly developed co-simulation methods, lies in the dynamic nature of the master/orchestrator, which is now treated as a separate subsystem. Finally, through an appropriate weak formulation, the constraint equations and the OEMs of interface (master) model are expressed in a convenient and consistent first order ODE form, which carries over all the advantages of the corresponding second order ODE form [8].

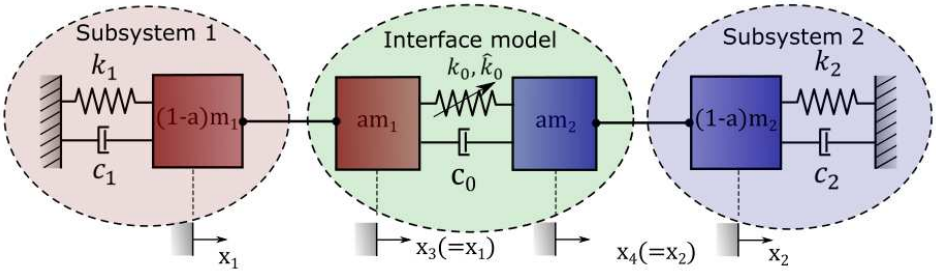

Figure 2: Equivalent model of initial mechanical model (Figure 1)

Numerical results and discussion

Here, a mechanical system with nonlinear components is examined [9, 10]. Specifically, the dynamic behavior of a two-degree-of-freedom oscillator involving stiffness characteristics modelled by linear and cubic terms is investigated by applying the method of multiple scales (see Figure 1). In the cases examined, the external forcing possesses a component with frequency close to one of the natural frequencies of the linearized model (for typical results, see Figure 3). A detailed analysis of the convergence and the numerical error behavior is carried out in order to examine the different properties of the new co-simulation scheme developed, in comparison to the already existing approaches. A set of characteristic results are presented in Figure 4. Despite the fact that the models examined are simple and purely mechanical, the techniques used can also be extended and applied to arbitrary multibody or structural dynamics systems.

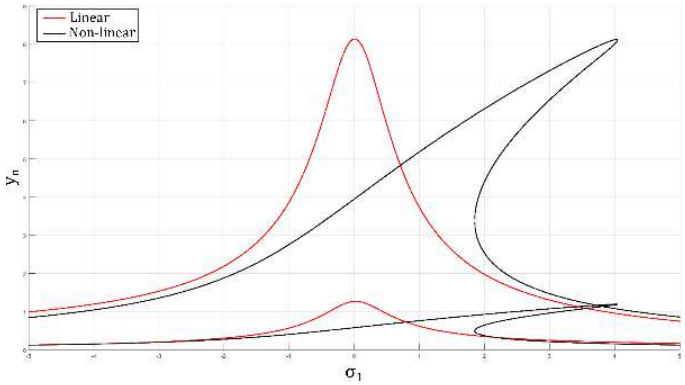

Figure 3: Normalized displacement amplitude for linear and non-linear system

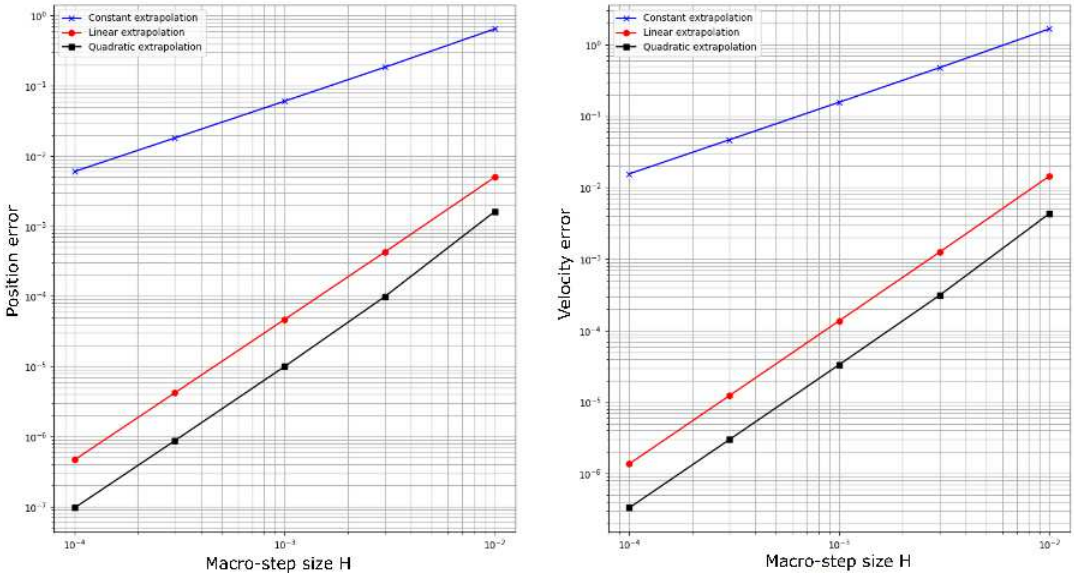

Figure 4: Convergence plots for Jacobi communication pattern, explicit scheme and force-force decomposition (classical approach)

References

[1] Gomes C., Thule C., Larsen P.G., Vangheluwe H. (2017). Co-simulation: State of the art. *arXiv preprint arXiv:1702.00686*.

[2] Paraskevopoulos, E., Stefanidou, S., Natsiavas, S. (2019). A novel approach for the analysis of a coupled train-railway bridge system: Basic principles and methodology. *COMPDYN2019*.

[3] Schweizer, B., & Lu, D. (2014). Semi-implicit co-simulation approach for solver coupling. *Archive of Applied Mechanics*, *84*(12), 1739-1769.

[4] Schweizer, B., & Lu, D. (2015). Predictor/corrector co-simulation approaches for solver coupling with algebraic constraints. *ZAMM - Journal of Applied Mathematics and Mechanics*, 95(9), 911-938.

[5] Sicklinger, S.A. (2014). Stabilized co-simulation of coupled problems including fields and signals. Doctoral dissertation, Technische Universität München.

[6] Paraskevopoulos, E., Natsiavas, S. (2013). On application of Newton's law to mechanical systems with motion constraints. *Nonlinear Dynamics*, 72(1-2), 455-475.

[7] Natsiavas, S., Paraskevopoulos, E. (2015). A set of ordinary differential equations of motion for constrained mechanical systems. *Nonlinear Dynamics*, 79(3), 1911-1938.

[8] Paraskevopoulos, E., Natsiavas, S. (2015). Weak formulation and first order form of the equations of motion for a class of constrained mechanical systems. *International Journal of Non-Linear Mechanics*, 77, 208-222.

[9] Natsiavas, S. (1995). Modal interactions in self-excited oscillators under external primary resonance. *Journal of Sound and Vibration*, *184*(2), 261-280.

[10] Natsiavas, S., Metallidis, P. (1997). External primary resonance of self-excited oscillators with 1:3 internal resonance. *Journal of Sound and Vibration*, *208*(2), 211-224.

A numerical package for model order reduction of large dimensional finite element systems of nonlinear vibrating structures based on invariant manifold theory

Andrea Opreni*, Alessandra Vizzaccaro†, Adrien Martin‡, Cyril Touzé‡, and Attilio Frangi*
*Dipartimento di Ingegneria Civile e Ambientale, Politecnico di Milano, Milan, Italy
†Department of Engineering Mathematics, University of Bristol, Bristol, United Kingdom
‡Institute of Mechanical Sciences and Industrial Applications (IMSIA) ENSTA Paris - CNRS - EDF - CEA - Institut Polytechnique de Paris, Paris, France

Summary. Dimensionality reduction through parametrisation of the system motion along a low dimensional invariant-based span of the phase space represents the most efficient technique for deriving reduced order models (ROM) of structures vibrating with large amplitudes. In this work we present the first release of an efficient software for deriving reduced models of structures based on the Direct Parametrisation of Invariant Manifolds (DPIM). The package exploits an algorithmic implementation of the method tailored for mechanical systems, hence achieving low memory consumption and unprecedented speed. Examples of large scale systems of industrial interest are shown and comparisons with experimental data and full order numerical simulations are reported.

Introduction

The computation of periodic orbits in large scale finite element models of vibrating structures represents a major challenge from a numerical standpoint. Indeed, full order simulations have computational times and memory requirements that make numerical integration schemes directly applied to finite element models rarely applicable at an industrial level [1]. As a result, dimensionality reduction techniques need to be applied. In this framework, the lack of invariance of modal subspaces hinder the applicability of linear projection methods as the modal decomposition or the proper orthogonal decomposition [2], since the embedding defined by this class of techniques is not invariant. Furthermore, the identification of coupled modes, that need to be accounted for in order to define a proper ROM, is generally impossible. As a result, nonlinear reduction methods are expected to provide higher accuracy and cheaper computational demands [3]. Among this class of techniques, the Direct Parametrisation Method for Invariant Manifolds [4, 5] allows deriving invariant subspaces together with the dynamics along such sets in an efficient manner. In this work, we report a numerical package that exploits a specific implementation of the method tailored for vibratory systems. Examples of structures of industrial relevance analysed with the proposed method are reported, together with validation against full order numerical simulations.

Method

Nonlinear vibrations of continuous structures discretised by the finite element method and featuring geometric nonlinearities are considered. In this framework, the discretised equations of motion stemming from the FE procedure leads to the following system of differential equations:

$$\begin{aligned} &\mathbf{M}\dot{\mathbf{V}} + \mathbf{C}\mathbf{V} + \mathbf{K}\mathbf{U} + \mathbf{G}(\mathbf{U},\mathbf{U}) + \mathbf{H}(\mathbf{U},\mathbf{U},\mathbf{U}) = \mathbf{F}, \\ &\dot{\mathbf{U}} = \mathbf{V}, \end{aligned} \tag{1}$$

with $\mathbf{M}$ mass matrix, $\mathbf{C}$ damping matrix, $\mathbf{K}$ stiffness matrix, $\mathbf{U}$ nodal displacement, $\mathbf{V}$ nodal velocity, $\mathbf{G}(\mathbf{U},\mathbf{U})$ quadratic nonlinearity tensor, $\mathbf{H}(\mathbf{U},\mathbf{U},\mathbf{U})$ cubic nonlinearity tensor, and $\mathbf{F}$ external forcing vector. $\dot{(\cdot)}$ denotes the time derivative operator. The number of degrees of freedom of Eq. (1) typically between 10^3 and 10^9. Dimensionality reduction is performed using the DPIM. To this aim, we introduce a nonlinear change of coordinates aimed at parametrising the system motion along a low dimensional invariant based-span of the phase space. The mappings introduced to parametrise nodal displacement and velocity are defined as [6]:

$$\mathbf{U} = \boldsymbol{\Psi}(\mathbf{z}), \qquad \mathbf{V} = \boldsymbol{\Upsilon}(\mathbf{z}), \tag{2}$$

where $\mathbf{z}$ are normal coordinates, i.e. the coordinates that describe the system motion along the embedding. The reduced dynamics is given as:

$$\dot{\mathbf{z}} = \mathbf{f}(\mathbf{z}). \tag{3}$$

Both mappings $\boldsymbol{\Psi}(\mathbf{z})$, $\boldsymbol{\Upsilon}(\mathbf{z})$ and reduced dynamics $\mathbf{f}(\mathbf{z})$ are obtained upon their substitution into Eq. (1), operation that yields the following invariance equations:

$$\begin{aligned} &\mathbf{M}\nabla_{\mathbf{z}}\boldsymbol{\Upsilon}(\mathbf{z})\mathbf{f}(\mathbf{z}) + \mathbf{C}\boldsymbol{\Upsilon}(\mathbf{z}) + \mathbf{K}\boldsymbol{\Psi}(\mathbf{z}) + \mathbf{G}(\boldsymbol{\Psi}(\mathbf{z}),\boldsymbol{\Psi}(\mathbf{z})) + \mathbf{H}(\boldsymbol{\Psi}(\mathbf{z}),\boldsymbol{\Psi}(\mathbf{z}),\boldsymbol{\Psi}(\mathbf{z})) = \mathbf{0}, \\ &\mathbf{M}\nabla_{\mathbf{z}}\boldsymbol{\Psi}(\mathbf{z})\mathbf{f}(\mathbf{z}) = \mathbf{M}\boldsymbol{\Upsilon}(\mathbf{z}). \end{aligned} \tag{4}$$

The resulting reduced model can then be solved to retrieve the frequency response curve of the associated structure.

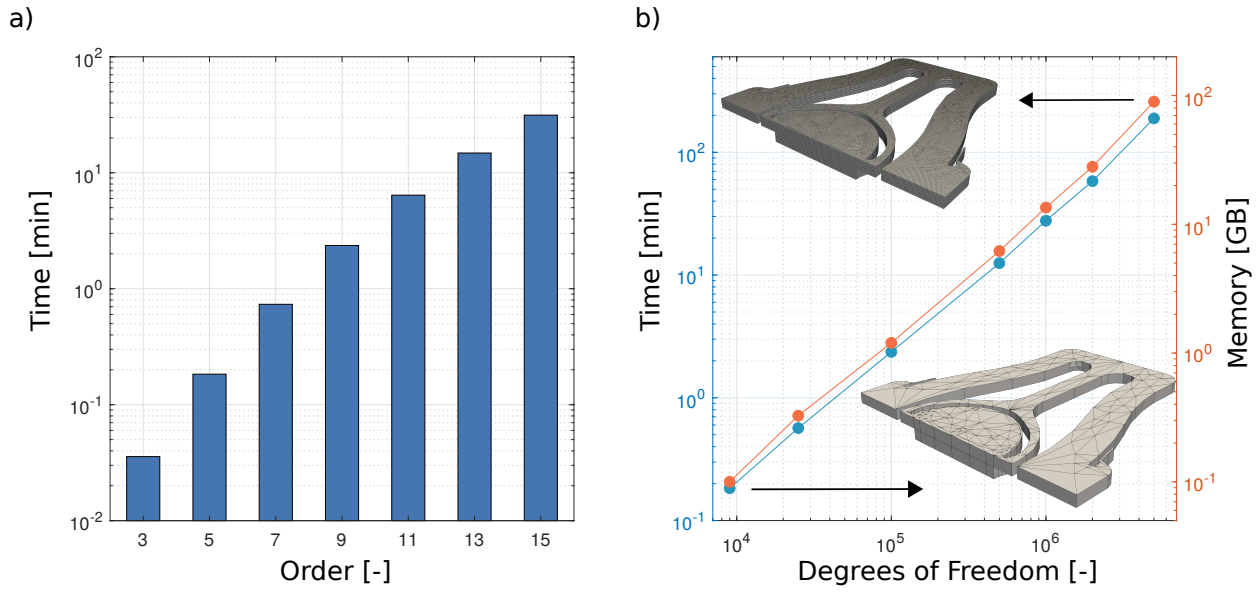

Figure 1: (a) Computing times required to reach a given parametrisation order, for a mesh of 9732 degrees of freedom. (b) Computing times required to perform an order 5 parametrisation for meshes of increasing refinement. All the analyses were performed on a desktop workstation with an AMD®Ryzen 5950X processor and 128GB RAM.

Mappings and reduced dynamics are polynomial functions of the normal coordinates and for each monomial the linear system of the associated homological equation needs to be solved. The DPIM is formulated from the general theory provided by the parametrisation method for invariant manifold, see [7], and has been applied to FE structures in [5] and [4]. In the proposed software, the homological equations are solved at the elementary level for 3D elements, which in turn allows avoiding the computation of the full nonlinearity tensor of the system beforehand, leading to very important savings in memory consumption. Furthermore, we leverage the symmetries of the formulation to avoid computing all monomials associated to the expansion, the latter extensively detailed in [4]. This in turn allows deriving an efficient formulation and yields a technique applicable to large finite element models.

The resulting algorithm has been implemented in a Julia package that provides a mean to identify frequency response curves of structures actuated at resonance with high accuracy and performance. An example of the performance provided by the technique is reported in Fig. 1, where results obtained for a single master mode reduction are highlighted. Fig. 1(a) reports the expected time required to parametrise a system of 9732 degrees of freedom up to an asymptotic development of order 15. Fig. 1(b) details the computational time and memory required to parametrise finite element systems of increasing number of degrees of freedom.

Conclusions

In the present contribution we provide an overview of algorithms and results provided by an open-source model order reduction package. This software aims at providing a tool for fast and accurate analysis of nonlinear structures, hence accelerating the design of structural components. Example applications highlight how the proposed package can play a major role in several fields as the semiconductor industry.

References

[1] A. Opreni, N. Boni, R. Carminati, and A. Frangi. Analysis of the Nonlinear Response of Piezo-Micromirrors with the Harmonic Balance Method. *Actuators*, vol. 10(2), pp. 21, 2021

[2] G. Gobat, A. Opreni, S. Fresca, A. Manzoni, and A. Frangi. Reduced order modeling of nonlinear microstructures through Proper Orthogonal Decomposition. Accepted in *Mechanical Systems and Signal Processing*, 2021

[3] C. Touzé, A. Vizzaccaro, and O. Thomas. Model order reduction methods for geometrically nonlinear structures: a review of nonlinear techniques. *Nonlinear Dynamics*, vol. 105, pp. 1141-1190, 2021.

[4] A. Vizzaccaro, A. Opreni, L. Salles, A. Frangi, C. Touzé. High order direct parametrisation of invariant manifolds for model order reduction of finite element structures: application to large amplitude vibrations and uncovering of a folding point. *arXiv*, 2109.10031, 2021

[5] S. Jain and G. Haller. How to compute invariant manifolds and their reduced dynamics in high-dimensional finite element models. *Nonlinear Dynamics*, in press, 2021.

[6] A. Opreni, A. Vizzaccaro, A. Frangi, and C. Touzé. Model order reduction based on direct normal form: application to large finite element MEMS structures featuring internal resonance. *Nonlinear Dynamics*, vol. 105, pp. 1237-1272, 2021.

[7] A. Haro, M. Canadell, J.-L. Figueras, A. Luque, and J.-M. Mondelo. The parameterization method for invariant manifolds. From rigorous results to effective computations. *Springer*, Switzerland, 2016

A port-Hamiltonian formulation for the full von-Kármán plate model

Andrea Brugnoli[†], Denis Matignon[*]
[†]*University of Twente, Netherlands*
[*]*ISAE-SUPAERO, Université de Toulouse, France*

Summary. In this contribution, a port-Hamiltonian reformulation of the full von-Kármán dynamical model for geometrically non-linear plates is detailed, including the collocated boundary control and observation. Starting from the canonical equations, a set of variables is chosen so as to make the total energy quadratic. The model, reformulated in these variables, highlights a port-Hamiltonian structure ruled by a state-modulated interconnection operator.

Classical model

The classical full von-Kármán dynamical model is presented in Bilbao et al. [2015]. The problem, defined on an open connected set $\Omega \subset \mathbb{R}^2$, takes the dimensionless form

$$\begin{aligned} \ddot{\boldsymbol{u}} &= \operatorname{Div} \boldsymbol{N}, & \boldsymbol{N} &= \boldsymbol{\Phi}(\boldsymbol{\varepsilon}), & \boldsymbol{\varepsilon} &= \operatorname{Grad} \boldsymbol{u} + 1/2 \operatorname{grad} w \otimes \operatorname{grad} w, \\ \ddot{w} &= -\operatorname{div} \operatorname{Div} \boldsymbol{M} + \operatorname{div}(\boldsymbol{N} \operatorname{grad} w), & \boldsymbol{M} &= \boldsymbol{\Phi}(\boldsymbol{\kappa}), & \boldsymbol{\kappa} &= \operatorname{Grad} \operatorname{grad} w, \end{aligned} \tag{1}$$

where $\boldsymbol{u} \in \mathbb{R}^2$ is the in-plane displacement, w is the vertical displacement, $\boldsymbol{\varepsilon}$ is the in-plane strain tensor, $\boldsymbol{\kappa}$ is the curvature tensor, $\boldsymbol{N}$ is the in-plane stress resultant and $\boldsymbol{M}$ is the bending stress resultant. The notation $\boldsymbol{a} \otimes \boldsymbol{b} = \boldsymbol{a}\boldsymbol{b}^\top$ denotes the dyadic product of two vectors. The div operator is the divergence of a vector field, and grad the gradient of a scalar field. The operator $\operatorname{Grad} = \frac{1}{2}\left(\nabla + \nabla^\top\right)$ designates the symmetric part of the gradient (i. e. the deformation gradient in continuum mechanics). For a tensor field $\boldsymbol{U} : \Omega \to \mathbb{R}^{2\times 2}$, with components U_{ij}, the divergence $\operatorname{Div}(\boldsymbol{U})$ is a vector, defined column-wise as

$$\operatorname{Div}(\boldsymbol{U}) := \sum_{i=1}^{2} \partial_{x_i} U_{ij}, \qquad \forall j = \{1, 2\}.$$

The linear tensor mapping $\boldsymbol{\Phi}$ is positive and preserves symmetry:

$$\boldsymbol{\Phi}(\boldsymbol{A}) = \nu \operatorname{Tr}(\boldsymbol{A})\mathbf{1} + (1-\nu)\boldsymbol{A}, \qquad \boldsymbol{A} = \boldsymbol{A}^\top \implies \boldsymbol{\Phi}(\boldsymbol{A}) = \boldsymbol{\Phi}(\boldsymbol{A})^\top, \qquad \text{where} \qquad \mathbf{1} = \operatorname{Diag}(1, 1).$$

The total energy of the model (Hamiltonian functional)

$$H = \frac{1}{2} \int_\Omega \left\{ \|\dot{\boldsymbol{u}}\|^2 + \dot{w}^2 + \boldsymbol{N} : \boldsymbol{\varepsilon} + \boldsymbol{M} : \boldsymbol{\kappa} \right\} \mathrm{d}\Omega, \qquad \text{where} \qquad \boldsymbol{A} : \boldsymbol{B} = \operatorname{Tr}(\boldsymbol{A}^\top \boldsymbol{B}) \tag{2}$$

consists of the kinetic energy and both membrane and bending deformation energies. This model proves conservative, see Bilbao et al. [2015]. Indeed, this implies that a port-Hamiltonian realization of the system exists. We shall demonstrate how to construct a port-Hamiltonian realization, equivalent to (1).

The equivalent port-Hamiltonian system (pHs)

To find a suitable port-Hamiltonian system, we first select a set of new energy variables to make the Hamiltonian functional quadratic. The selection is the same as for both the linear plate problems in Brugnoli et al. [2019a,b]:

$$\boldsymbol{\alpha}_u = \dot{\boldsymbol{u}}, \qquad \alpha_w = \dot{w}, \qquad \boldsymbol{A}_\varepsilon = \boldsymbol{\varepsilon}, \qquad \boldsymbol{A}_\kappa = \boldsymbol{\kappa}. \tag{3}$$

The energy is quadratic in these variables

$$H = \frac{1}{2} \int_\Omega \left\{ \|\boldsymbol{\alpha}_u\|^2 + \alpha_w^2 + \boldsymbol{\Phi}(\boldsymbol{A}_\varepsilon) : \boldsymbol{A}_\varepsilon + \boldsymbol{\Phi}(\boldsymbol{A}_\kappa) : \boldsymbol{A}_\kappa \right\}. \tag{4}$$

By computing the variational derivative of the Hamiltonian, one obtains the so-called co-energy variables:

$$\boldsymbol{e}_u := \delta_{\boldsymbol{\alpha}_u} H = \dot{\boldsymbol{u}}, \qquad e_w := \delta_{\alpha_w} H = \dot{w}, \qquad \boldsymbol{E}_\varepsilon := \delta_{\boldsymbol{A}_\varepsilon} H = \boldsymbol{\Phi}(\boldsymbol{A}_\varepsilon), \qquad \boldsymbol{E}_\kappa := \delta_{\boldsymbol{A}_\kappa} H = \boldsymbol{\Phi}(\boldsymbol{A}_\kappa). \tag{5}$$

Before stating the final formulation, consider the operator $\mathcal{C}(w)(\cdot) : L^2(\Omega, \mathbb{R}^{2\times 2}_{\text{sym}}) \to L^2(\Omega)$ acting on symmetric tensors

$$\mathcal{C}(w)(\boldsymbol{T}) = \operatorname{div}(\boldsymbol{T} \operatorname{grad} w). \tag{6}$$

Proposition 1 *The formal adjoint of the $\mathcal{C}(w)(\cdot)$ is given by*

$$\mathcal{C}(w)^*(\cdot) = -\frac{1}{2} \left[\operatorname{grad}(\cdot) \otimes \operatorname{grad}(w) + \operatorname{grad}(w) \otimes \operatorname{grad}(\cdot) \right]. \tag{7}$$

Proof 1 *Consider a smooth scalar field $v \in C_0^\infty(\Omega)$ and a smooth symmetric tensor field $\boldsymbol{U} \in C_0^\infty(\Omega, \mathbb{R}^{2\times 2}_{sym})$ with compact support. The formal adjoint of $\mathcal{C}(w)(\cdot)$ satisfies the relation*

$$\langle v,\, \mathcal{C}(w)(\boldsymbol{U})\rangle_{L^2(\Omega)} = \langle \mathcal{C}(w)(v)^*,\, \boldsymbol{U}\rangle_{L^2(\Omega,\mathbb{R}^{2\times 2}_{sym})}\,. \tag{8}$$

The proof follows from the computation

$$\begin{aligned}
\langle v,\, \mathcal{C}(w)(\boldsymbol{U})\rangle_{L^2(\Omega)} &= \langle v,\, \operatorname{div}(\boldsymbol{U}\operatorname{grad} w)\rangle_{L^2(\Omega)}\,, && \textit{Integration by parts,}\\
&= \langle -\operatorname{grad} v,\, \boldsymbol{U}\operatorname{grad} w\rangle_{L^2(\Omega,\mathbb{R}^2)}\,, && \textit{Dyadic product properties,}\\
&= \langle -\operatorname{grad} v\otimes\operatorname{grad} w,\, \boldsymbol{U}\rangle_{L^2(\Omega,\mathbb{R}^{2\times 2}_{sym})}\,, && \textit{Symmetry of } \boldsymbol{U},\\
&= \langle -1/2(\operatorname{grad} v\otimes\operatorname{grad} w + \operatorname{grad} w\otimes\operatorname{grad} v),\, \boldsymbol{U}\rangle_{L^2(\Omega,\mathbb{R}^{2\times 2}_{sym})}\,.
\end{aligned} \tag{9}$$

This means

$$\mathcal{C}(w)^*(\cdot) = -\frac{1}{2}\left[\operatorname{grad}(\cdot)\otimes\operatorname{grad}(w) + \operatorname{grad}(w)\otimes\operatorname{grad}(\cdot)\right], \tag{10}$$

leading to the final result.

The pH realization is then given by the following system

$$\frac{\partial}{\partial t}\begin{pmatrix}\boldsymbol{\alpha}_u\\ \boldsymbol{A}_\varepsilon\\ \alpha_w\\ \boldsymbol{A}_\kappa\end{pmatrix} = \begin{bmatrix}\mathbf{0} & \operatorname{Div} & \mathbf{0} & \mathbf{0}\\ \operatorname{Grad} & \mathbf{0} & -\mathcal{C}(w)^* & \mathbf{0}\\ 0 & \mathcal{C}(w) & 0 & -\operatorname{div}\operatorname{Div}\\ \mathbf{0} & \mathbf{0} & \operatorname{Grad}\operatorname{grad} & \mathbf{0}\end{bmatrix}\begin{pmatrix}\delta_{\boldsymbol{\alpha}_u}H\\ \delta_{\boldsymbol{A}_\varepsilon}H\\ \delta_{\boldsymbol{\alpha}_w}H\\ \delta_{\boldsymbol{A}_\kappa}H\end{pmatrix}, \tag{11}$$

The second line of system (11) represents the time derivative of the membrane strain tensor. To close the system, variable w has to be accessible. For this reason, its dynamics has to be included. The augmented system reads

$$\frac{\partial}{\partial t}\begin{pmatrix}\boldsymbol{\alpha}_u\\ \boldsymbol{A}_\varepsilon\\ w\\ \alpha_w\\ \boldsymbol{A}_\kappa\end{pmatrix} = \underbrace{\begin{bmatrix}\mathbf{0} & \operatorname{Div} & \mathbf{0} & \mathbf{0} & \mathbf{0}\\ \operatorname{Grad} & \mathbf{0} & \mathbf{0} & -\mathcal{C}(w)^* & \mathbf{0}\\ 0 & 0 & 0 & 1 & 0\\ 0 & \mathcal{C}(w) & -1 & 0 & -\operatorname{div}\operatorname{Div}\\ \mathbf{0} & \mathbf{0} & \mathbf{0} & \operatorname{Grad}\operatorname{grad} & \mathbf{0}\end{bmatrix}}_{\mathcal{J}}\begin{pmatrix}\delta_{\boldsymbol{\alpha}_u}H\\ \delta_{\boldsymbol{A}_\varepsilon}H\\ \delta_{w}H\\ \delta_{\alpha_w}H\\ \delta_{\boldsymbol{A}_\kappa}H\end{pmatrix}. \tag{12}$$

Given the results in Brugnoli et al. [2019a,b] and Proposition 1, the operator $\mathcal{J}$ is formally skew-adjoint. If only the kinetic and deformation energies are considered, it holds $\delta_w H = 0$. In general this terms allows accommodating other potentials, for example the gravitational one. Suitable boundary variables are then obtained considering the power balance

$$\dot{H} = \langle \gamma_0\boldsymbol{e}_u,\, \gamma_\perp\boldsymbol{E}_\varepsilon\rangle_{\partial\Omega} + \langle \gamma_0\boldsymbol{e}_w,\, \gamma_{\perp\perp,1}\boldsymbol{E}_\kappa + \gamma_0(\boldsymbol{E}_\varepsilon\boldsymbol{n}\cdot\operatorname{grad} w)\rangle_{\partial\Omega} + \langle \gamma_1\boldsymbol{e}_w,\, \gamma_{\perp\perp}\boldsymbol{E}_\kappa\rangle_{\partial\Omega}\,, \tag{13}$$

where $\gamma_0\boldsymbol{e}_u = \boldsymbol{e}_u|_{\partial\Omega}$ is the Dirichlet trace, $\gamma_\perp\boldsymbol{E}_\varepsilon = \boldsymbol{E}_\varepsilon\boldsymbol{n}|_{\partial\Omega}$ is the normal trace ($\boldsymbol{n}$ is the outward normal vector), $\gamma_{\perp\perp,1}\boldsymbol{E}_\kappa = -\boldsymbol{n}\cdot\operatorname{Div}\boldsymbol{E}_\kappa - \partial_{\boldsymbol{s}}(\boldsymbol{n}^\top\boldsymbol{E}_\kappa\boldsymbol{s})|_{\partial\Omega}$ is the effective shear force at the boundary ($\boldsymbol{s}$ is the tangent versor at the boundary), $\gamma_1\boldsymbol{e}_w = \partial_{\boldsymbol{n}}\boldsymbol{e}_w|_{\partial\Omega}$ is the normal derivative trace and $\gamma_{\perp\perp}\boldsymbol{E}_\kappa = \boldsymbol{n}^\top\boldsymbol{E}_\kappa\boldsymbol{n}$ is the normal to normal trace. The boundary conditions are consistent with the ones assumed in Puel and Tucsnak [1996] for deriving a global existence result for this model.

Conclusions

We have presented a pHs formulation of the full von-Kármán model. The dynamics of the system exhibits a state modulated interconnection operator, while the energy remains quadratic in the chosen variables. Of particular interest is the discretization of such a model for simulation and control purposes. The Partitioned Finite Element Method (PFEM), an extension of mixed finite elements to pHs, seems to be particularly suitable to achieve a structure-preserving discretization of this model, as in Cardoso-Ribeiro et al. [2020] for the 2D Shallow Water Equation, which exhibits the same kind of polynomial nonlinearity.

References

S. Bilbao, O. Thomas, C. Touzé, and M. Ducceschi. Conservative numerical methods for the full von kármán plate equations. *Numerical Methods for Partial Differential Equations*, 31(6):1948–1970, 2015. doi: 10.1002/num.21974.

A. Brugnoli, D. Alazard, V. Budinger, and D. Matignon. Port-Hamiltonian formulation and symplectic discretization of plate models Part I: Mindlin model for thick plates. *Applied Mathematical Modelling*, 75:940–960, 2019a.

A. Brugnoli, D. Alazard, V. Budinger, and D. Matignon. Port-Hamiltonian formulation and symplectic discretization of plate models Part II: Kirchhoff model for thin plates. *Applied Mathematical Modelling*, 75:961–981, 2019b.

J. P. Puel and M. Tucsnak. Global existence for the full von kármán system. *Applied Mathematics and Optimization*, 34(2):139–160, Sep 1996. ISSN 1432-0606. doi: 10.1007/BF01182621.

F.L. Cardoso-Ribeiro, D. Matignon, and L. Lefèvre. A partitioned finite element method for power-preserving discretization of open systems of conservation laws. *IMA Journal of Mathematical Control and Information*, pages 1 – 41, 2020. doi: https://doi:10.1093/imamci/xxx000. In Press.

Analysis of Stable and Unstable Pedestrian Flow Situations in Particle Simulations and Evacuation Experiments

Jens Starke*, Ilias Panagiotopoulos*, Jan Sieber† and Wolfram Just‡
*Institute of Mathematics, University of Rostock, Germany
†College of Engineering, Mathematics and Physical Sciences, University of Exeter, UK
‡School of Mathematical Sciences, Queen Mary University of London, UK

Summary. Methods to analyze the macroscopic behaviour of systems which are either given as discrete agent-based model or as laboratory experiments are discussed. For demonstration, we address a challenging real-live experiment as application problem within the social sciences: a simplified evacuation scenario is considered where pedestrians have to pass a corridor manoeuvring around a triangular obstacle either left or right. Their decision is influenced by the shortest route to the exit and the route choice of nearby pedestrians. The route choice is investigated under varying the position of the obstacle and by this the length of each route. The macroscopic measure defined as difference of the pedestrian flux left and right from the obstacle shows bistability and a hysteresis behaviour. The branch of unstable flow situations separating the two stable branches where all pedestrians pass the obstacle either left or right was succesfully detected by using a control based continuation. In addition to the analysis of stable and unstable pedestrian flow situations in the pedestrian experiments with humans, a particle model is presented for which the control based continuation algorithm computed the branch of unstable flow situations and reproduced the findings of the pedestrian experiments.

Control-Based Continuation for Laboratory Experiments and Microscopic Simulations

Typically, information from laboratory experiments or microscopic simulations is restricted to ω-limit sets, in the simplest case to stable stationary states. By definition, a system state is moving away from unstable states which can therefore not be directly observed in laboratory experiments or direct simulations. Furthermore, a detailed understanding of the parameter dependent behavior is missing as this would require exhaustive experimental runs or microscopic computations scanning the parameter space. In contrast to this, macroscopic mathematical models successfully formulated for many problems in science and engineering, often allow for a detailed understanding of parameter dependencies of the dynamical behaviour as there are tools available for low-dimensional mathematical models to perform an analytical or numerical bifurcation analysis.

In the present work a method is presented which allows to perform a continuation of stable as well as unstable stationary states in laboratory experiments or microscopic simulations. This approach stabilizes unstable states by adding a non-invasive control which vanishes at the stationary state. The non-invasive control doen't change the stationary state itself but its neighborhood and by this its stability proporties. Often, the dynamic properties of the macroscopic behaviour of a considered laboratory experiment or microscopic simulation system depends on one or several parameters and it is of interest to explore the dynamics depending on such a parameter and to perform a continuation of e.g. stationary states. This approach is called control based continuation [1, 2, 3, 4, 5] and allows to detect also branches of unstable states in addition to the stable branches of the bifurcation diagram.

Suppose the system of interest is represented by

$$\dot{x} = f(x), \tag{1}$$

where the function $f : \mathbb{R} \to \mathbb{R}$ is not explicitly given but the system can be explored by experimental observations measuring the time series $x(t)$.

A non-invasive feedback control is added to the system (1) so that a stationary state of the system with control is also a stationary state of (1) but unstable states are changed to stable ones. This requires that the laboratory experiment and the microscopic simulation is accessible by a control altering the original set-up slightly. The control algorithm used follows a suggestion of [6] and is a feedback control with state observer:

$$\dot{x} = f(x) + a \cdot (y - x) \tag{2}$$

$$\dot{y} = b \cdot (y - x) \tag{3}$$

Equation (2) consists of the original system (1) by adding a control term $a \cdot (y - x)$ which forces for $a > 0$ and a large enough the system to the control target y. The aim is to choose y as unknown unstable stationary state and to stabilize this state with the control. In [2, 3, 4, 5] the unknown target y is computed by using a Newton-method which requires derivative information of suitable quality. The second equation (3) finds this state automatically and for a suitable parameter b unstable stationary states are changed to stable ones.

Varying now a parameter crucial for the system dynamics by changing its value using predictor-corrector methods and adding ideas like pseudo-arclength continuation it is possible to perform a control-based continuation along branches of the bifucation diagram consisting of stable as well as unstable states and also passing saddle-node bifurcation points.

Pedestrian Evacuation Scenario: Real Experiment with Humans and Particle Simulations

The above described approach for control based continuation is demonstrated and tested for a simplified evacuation scenario for pedestrian crowds. In this set-up, pedestrians have to pass a corridor maneuvering around a triangular obstacle

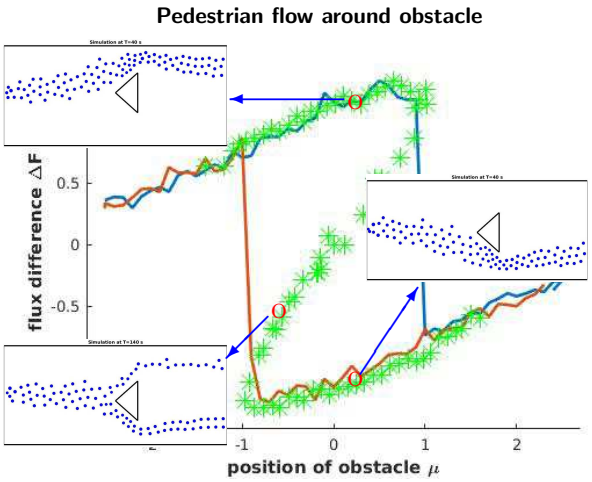

Figure 1: Macroscopic measure of pedestrian flux difference left and right from the obstacle. The insets show the microscopic pedestrian flow situation. The upper and lower branch are stable ones which basins of attraction are separated by an unstable branch. The control-based continuation detected also the unstable branch.

either left or right [7]. The pedestrian's decision is influenced by the shortest route to the exit and the route choice of other pedestrians in a certain neighborhood. The symmetry of the set-up is broken by changing the position of the obstacle and by this the length of each route. The macroscopic measure to be investigated is defined as the difference of the pedestrian flux left and right from the obstacle using the obstacle position as parameter.
As result, the considered pedestrian evacuation scenario shows bistability and a hysteresis behaviour both for the particle model as well as for a real pedestrian experiment with humans. The bifurcation diagram of the particle simulation is shown in Fig. 1. The control-based continuation detects in addition to the two stable branches where all pedestrians pass the obstacle either left or right also an unstable state of the pedestrian flow separating the two stable branches. The insets show the microscopic particle configuation of the observes stable and unstable states of the pedestrian flow.

Conclusion and Outlook

The presented approach is applicable to a wide range of applications in complex systems given by microscopic models or experiments. It extends the gained insight one gets by direct simulations and experiments by adding information about unstable states and by computing the branches of bifurcation diagrams effecively summing up parameter dependent macroscopic system information.

References

[1] Siettos, C. I. ; Kevrekidis, I. G. ; Maroudas, D. (2004). *Coarse bifurcation diagrams via microscopic simulators: A state-feedback control-based approach*. International Journal of Bifurcation and Chaos, **14**(1), 207-220.

[2] Sieber, J., Krauskopf, B. (2008). *Control based bifurcation analysis for experiments*, Nonlinear Dynamics **51**(3), 365–377.

[3] Bureau, E., Schilder, F., Santos, I., Thomsen, J., Starke, J. (2013). *Experimental Bifurcation Analysis of an Impact Oscillator – Tuning A Non-Invasive Control Scheme*. Journal of Sound and Vibration **332**(22), 5883-5897.

[4] Bureau, E., Schilder, F., Elmegård, M., Santos, I., Thomsen, J., Starke, J. (2014). *Experimental Bifurcation Analysis of an Impact Oscillator – Determining Stability*. Journal of Sound and Vibration **333**(21), 5464-5474.

[5] Schilder, F., Bureau, E., Santos, I., Thomsen, J., Starke, J. (2015). *Experimental Bifurcation Analysis – Continuation for Noise-Contaminated Zero Problems*. Journal of Sound and Vibration **358**, 251-266.

[6] Pyragas, K., Pyragas, V., Kiss, I. & Hudson, J. (2002). *Stabilizing and tracking unknown steady states of dynamical systems*. Physical Review Letters **89**, 244103.

[7] Starke, J., Thomsen, K. B., Sørensen, A., Marschler, C., Schilder, F., Dederichs, A., Hjorth, P. (2014). *Nonlinear Effects in Examples of Crowd Evacuation Scenarios*. Pages 560-565. Proceedings of *17th International IEEE Conference on Intelligent Transportation Systems (ITSC 2014)*, Qingdao, China.

Monday, July 18, 2022

13:30 - 15:30

MS-05 Slow-Fast Systems and Phenomena

Saint Clair 1

Chair: Valery Pilipchuk

13:30 - 13:50
Adiabatic phenomena in particle accelerators
BAZZANI Armando*, CAPOANI Federico, GIOVANNOZZI Massimo
*Department of Physics and Astronomy University of Bologna and INFN sezione di Bologna, Italy (via Irnerio 46 40126 Bologna Italy)

13:50 - 14:10
A surface of connecting orbits between two saddle slow manifolds in a return mechanism of mixed-mode oscillations
KRAUSKOPF Bernd*, MUSOKE Elle, OSINGA Hinke M.
*Department of Mathematics, The University of Auckland (38 Princes Street, Auckland CBD, Auckland 1010 New Zealand)

14:10 - 14:30
Analysis of a Singularly Perturbed Continuous Piecewise Linear System
KAROUI A. Yassine*, LEINE Remco
*Institute for Nonlinear Mechanics, University of Stuttgart (Pfaffenwaldring 9 70569 Stuttgart Germany)

14:30 - 14:50
Bursting and Excitability in Neuromorphic Resonant Tunneling Diodes
JAVALOYES Julien*, IGNACIO Ortega-Piwonka
*Universitat de les Illes Balears (Cra. de Valldemossa, km 7.5. Palma Illes Balears Spain) - Departament de Fısica [Palma de Mallorca] (Universitat de les Illes Balears, E-07122 Palma de Mallorca, Spain Spain)

14:50 - 15:10
Delayed loss of stability in multiple time scale models of natural phenomena
SENSI Mattia*
*MathNeuro Team, Inria at Université Côte d'Azur (2004 Rte des Lucioles, 06410 Biot, France France)

Adiabatic phenomena in particle accelerators

Armando Bazzani*, Federico Capoani† and Massimo Giovannozzi ‡
* *Department of Physics and Astronomy University of Bologna and INFN sezione di Bologna, Italy*
†*Department of Physics and Astronomy University of Bologna and Beams Department, CERN, Esplanade des Particules 1, 1211 Geneva 23, Switzerland*
‡ *Beams Department, CERN, Esplanade des Particules 1, 1211 Geneva 23, Switzerland*

Summary. In the hadron colliders the transverse dynamics of a charge particle in a magnetic lattice is well modeled by a Hamiltonian formalism and the Poincaré map of the system is a polynomial symplectic map with a elliptic fixed point (reference orbit) in two or three degrees of freedom. The presence of fast-slow variables or slow modulations in the dynamics has been considered to estimate the dynamic aperture (i.e. the transverse phase space region that guarantees a long term stability of the orbits) or to perform the beam shaping in the synchroton motion. Recently, the possibility of slowly modulating the linear frequencies of the reference orbit (linear tunes) in presence of non-linear resonances in the phase space has been proved to provide a very efficient mechanism for beam extraction by means of the adiabatic resonance trapping phenomenon (Multiturn Extraction). The multiturn extraction has been verified in real experiments at PS (CERN). Here, we propose a new approach for adiabatic extraction by considering time dependent symplectic maps, where the adiabatic trapping is induced by a modulated dipole or quadrupole kicker. This approach can be particularly relevant when the modulation of the linear tunes is not workable. We discuss the extension of the adiabatic theory results to the symplectic map models and the possible applications to leptonic collider where the dissipation and fluctuations effects are not negligible. We illustrate the results by numerical simulations.

Multi-turn extraction in hadron storage rings using modulated dipole or quadrupole

The adiabatic trapping phenomenon into a nonlinear resonance and the possibility of adiabatic transport in the phase space have been experimentally proven to provide an very efficient extraction mechanism (Multi Turn Extraction (MTE) in high energy hadron storage rings [2, 3]. In the experiments, sextupole and octupole magnets are used to excite a non-linear resonance in transverse phase space [4] and the linear frequencies (linear tunes [4]) are slowly modulated crossing the resonance value and performing the adiabatic trapping of particles. The transverse beam dynamics is described by the one-turn symplectic map (Poincaré map) and the main issues are to extend the adiabatic theory results for Hamiltonian systems to the case of slowly modulated symplectic map in the neighborhood of an elliptic fixed point where the dynamics is almost integrable and the perturbation theory applies. The application to the beam extraction problem requires to optimize and control the trapping efficiency and the quality of the extracted beams [5]. To extend the applicability of this techniques to hadron accelerators, where the change of the linear tunes and the multipolar components in a magnetic lattice can be a complex procedure, we consider the possibility of controlling the adiabatic trapping in the phase space using a dipole or quadrupole 'kicker' in the magnetic lattice whose frequency is slowly modulated to excite a resonance condition with the linear tunes and whose amplitude can be used to optimize the trapping efficiency. The optimization of the MTE is a key issue since the loss of particles in the phase space decreases the luminosity of the beam and create parasitic losses in the accelerator. One of the goal of MTE is to divide the original beam into a fixed number of beamlets with the almost the same number of particle and a defined emittance [1]. The advantage of introducing a modulated kicker is twofold: from one hand it allows to introduce new control parameters in the dynamics that can be easily varied to optimize the efficiency of MTE; from the other hand, the changes of the kicker parameters are easily implemented in a magnetic lattice. The simplest, though non-trivial, model of betatron motion in a hadron storage ring is the 2-dimensional symplectic map

$$\mathcal{M}\begin{pmatrix} q_n \\ p_n \end{pmatrix} = \begin{pmatrix} q_{n+1} \\ p_{n+1} \end{pmatrix} = R(\omega_0)\begin{pmatrix} q_n \\ p_n + k_3 q_n^2 + k_4 q_n^3 + \varepsilon(n)\cos\omega(n)n \end{pmatrix} \tag{1}$$

where $R(\omega_0)$ is the rotation matrix evaluated at the frequency ω_0 (linear tune), n is the turn number and $\varepsilon(n)$ and $\omega(n)$ are the amplitude and the frequency of a dipole kicker that can be adiabatically varied as a function of n. The kicker frequency crosses a resonance value with the linear tune ω_0 (i.e. $\omega = m\omega_0 + \delta$ with δ varying adiabatically in the interval $\delta \in [-\delta_0, \delta_0]$). Using the perturbation theory it is possible to prove that the adiabatic trapping phenomenon in the phase space of the map (1) is described by an interpolating Hamiltonian provided by the Birkhoff Normal Forms Theory

$$\mathcal{H} = \omega_0\, J + \frac{\omega_2}{2} J^2 + \varepsilon\, \mathcal{A}_m J^{3/2} \cos(m\,\theta - \omega t) \tag{2}$$

and to give an explicit correspondence among the parameters of the modulated map (1) and that of the interpolating Hamiltonian (2). According to the results of adiabatic theory [6], we have explicitly computed the trapping probability in the nonlinear resonance for the Hamiltonian system (2) and we have pointed out the dependence of this probability from the kicker parameters. We have numerically checked the applicability of trapping probability estimates in the case of the map (1) (see next section) and that could be extended to more realistic models of the betatron motion defined by 4-dimensional symplectic maps, under suitable conditions.

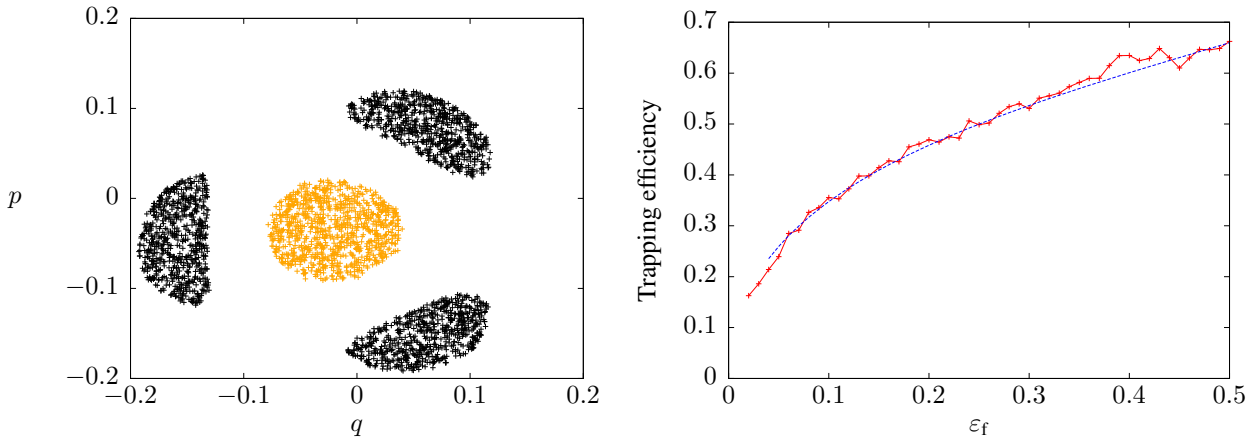

Figure 1: Left: example of the beam splitting obtained by modulating adiabatically the parameters of a dipole element. Right: efficiency of the trapping mechanism as a function of the final dipolar perturbation strength (see Eq. 3) evaluated numerically together with the analytical formula.

Numerical simulations and results

We have performed accurate numerical simulations of the map (1) to study the adiabatic trapping into a 3-order resonance and to check the validity of the trapping probability analytic estimate obtained from the Hamiltonian (2). In Fig. 1 (left) we show an example of the beam splitting obtained modulating adiabatically the parameters of a dipole element according to the following equations

$$\varepsilon(n) = \begin{cases} \varepsilon_f\, n/N & n < N \\ \varepsilon_f & N \le n \le 2N \end{cases} \qquad \omega(n) = \begin{cases} \omega_i & n < N \\ \omega_i + (\omega_f - \omega_i)(n-N)/N & N \le n \le 2N \end{cases} \tag{3}$$

whereas in Fig. 1 (right) we plot the efficiency of the trapping mechanism (i.e. the fraction of particles trapped in the resonance region with respect to the total number of particles in the initial beam given the initial particle distribution) comparing the numerical results with the analytical formulas.
Using the results of the Birkhoff Normal Forms theory for symplectic maps near an elliptic fixed point, we propose a theoretical approach that justifies the use of the interpolating Hamiltonian for a modulated map and point out the applicability conditions of the adiabatic theory results to symplectic maps in a neighborhood of an elliptic fixed point.

Conclusions

The adiabatic trapping into resonance for Hamiltonian systems is a robust phenomenon that can be extended to modulated symplectic maps in the neighborhood of an elliptic point when a resonance condition is satisfied in the phase space. Even if a rigorous proof is not yet available, our results show that it is possible to get estimates of the trapping probability for a particle distribution and to apply the adiabatic theory to realistic model of particle dynamics in hadron colliders. This step is not only relevant in itself, but it is also an essential one in view of applications. Indeed, recently, it has been possible to make adiabatic theory the basis of a successful and novel operational beam manipulation that splits the beam transversely into several beamlets to enable loss-free multi-turn extraction. The new results presented here allow extending the capabilities of performing beam splitting beyond what is know today, thus opening new scenarios for accelerator physics. The ultimate goal of this research is to open the possibility of performing these novel beam manipulations in lepton circular rings.

References

[1] Cappi, R. and Giovannozzi, M. (2002), Novel method for multiturn extraction: Trapping charged particles in islands of phase space, *Phys. Rev. Lett.* **88** 104801.

[2] A. Huschauer, A. Blas, J. Borburgh, S. Damjanovic, S. Gilardoni, M. Giovannozzi, M. Hourican, K. Kahle, G. Le Godec, O. Michels, G. Sterbini, and C. Hernalsteens (2017), Transverse beam splitting made operational: Key features of the multiturn extraction at the CERN Proton Synchrotron, Phys. Rev. Accel. Beams **20**, 061001.

[3] S. Abernethy, A. Akroh, H. Bartosik, A. Blas, T. Bohl, S. Cettour-Cave, K. Cornelis, H. Damerau, S. Gilardoni, M. Giovannozzi, C. Hernalsteens, A. Huschauer, V. Kain, D. Manglunki, G. Métral, B. Mikulec, B. Salvant, J.-L. Sanchez Alvarez, R. Steerenberg, G. Sterbini, and Y. Wu (2017), Operational performance of the CERN injector complex with transversely split beams, Phys. Rev. Accel. Beams **20**, 014001.

[4] Wiedemann, H. (2007), Particle accelerator physics. Springer, Berlin.

[5] Bazzani, A., Frye, C., Giovannozzi, M., and Hernalsteens, C. (2014), Analysis of adiabatic trapping for quasi-integrable area-preserving maps, *Phys. Rev. E* **89** 042915.

[6] Neishtadt, A. I., Vasiliev, A. A., and Artemyev, A. V. (2013), Capture into resonance and escape from it in a forced nonlinear pendulum, *Regular and Chaotic Dynamics* **18** 686.

A surface of connecting orbits between two saddle slow manifolds in a return mechanism of mixed-mode oscillations

Bernd Krauskopf*, Elle Musoke* and Hinke M. Osinga*
*Department of Mathematics, University of Auckland, Auckland, New Zealand

Summary. We employ a Lin's method set-up to compute a surface of heteroclinic connections between two saddle slow manifolds in the four-dimensional Olsen model for peroxidase-oxidase reaction. As will be shown, this surface organises the return mechanism of mixed-mode oscillations that involve a slow passage through a Hopf bifurcation.

We consider a model for peroxidase-oxidase reaction first introduced by Olsen [6], which we study here in the scaled form presented in [4]; it is given as the system of ordinary differential equations

$$\begin{cases} \dot{A} &= \mu - \alpha A - ABY, \\ \dot{B} &= \varepsilon(1 - BX - ABY), \\ \dot{X} &= \lambda(BX - X^2 + 3ABY - \zeta X + \delta), \\ \dot{Y} &= \kappa\lambda(X^2 - Y - ABY), \end{cases} \tag{1}$$

for the vector of chemical concentrations $(A, B, X, Y) \in \mathbb{R}^4$. The system parameters are fixed here, as in [4], to $\alpha = 0.0912$, $\delta = 1.2121 \times 10^{-4}$, $\varepsilon = 0.0037$, $\lambda = 18.5281$, $\kappa = 3.7963$, $\mu = 0.9697$, and $\zeta = 0.9847$. For this choice, the three concentrations A, X, and Y can be considered as fast and B as slow. System (1) has been of interest because it exhibits mixed-mode oscillations (MMOs), which are characterised by a mixture of small-amplitude oscillations (SAOs) that usually arise locally in phase space and large-amplitude oscillations (LAOs) that are generally associated with a global return to the region of SAOs. To date, mechanisms for MMOs are quite well understood in slow-fast systems of dimension three; see, for example, the survey paper [5] as an entry point to the literature on MMOs. For four-dimensional slow-fast systems, on the other hand, new mechanisms and types of MMOs may arise. The case study of the Olsen model (1) presented here shows that the return mechanism of the MMOs involves heteroclinic connecting orbits between two saddle slow manifolds. It follows on from earlier work in [1], where the same parameter regime was considered but a model reduction to a three-dimensional system (via a quasi-steady-state assumption) was performed. In contrast, we now consider and compute all relevant objects in the full (A, B, X, Y)-space of system (1).

In the spirit of geometric singular perturbation theory [3], we start with the limit of $\varepsilon = 0$ and consider the three-dimensional fast subsystem for the fast variables A, X, and Y, where the slow variable B is now a parameter. The equilibria of the fast subsystem, which are parametrised by B, form the critical manifold C in the (A, B, X, Y)-space of system (1). A linear stability analysis shows that C consists (in the physically relevant region of positive A, B, X, and Y) of four branches of hyperbolic equilibria of the fast subsystem: a branch denoted C^4_+ of stable equilibria; a branch C^3 of saddle equilibria with one unstable eigenvalue; a branch C^2 of saddle equilibria with two unstable eigenvalues; and a second branch C^4_- of stable equilibria. These branches connect at points F_1 and F_2 of fold bifurcation and H of Hopf bifurcation, and the superscipts indicate the dimensions of their stable manifolds in (A, B, X, Y)-space.

Our specific interest is in the two branches C^3 and C^2 because they are saddle objects with different dimensions of stable and unstable manifolds. While C^3 and C^2 only exist for $\varepsilon = 0$, according to Fenichel threory [3], they persist as locally invariant slow manifolds S^3 and S^2 for sufficiently small $\varepsilon > 0$; note that orbit segments on a slow manifold remain slow for $O(1)$ time. Moreover, the one-dimensional manifolds S^3 and S^2 lie $O(\varepsilon)$ close to C^3 and C^2, and they have stable and unstable manifolds of the same dimensions as those of C^3 and C^2. Hence, S^3 has a three-dimensional stable manifold $W^s(S^3)$, consisting of orbit segments that, in forward time, approach S^3 along a fast direction and then remain slow while following S^3; similarly, S^2 has a three-dimensional unstable manifold $W^u(S^2)$ consisting of orbit segments that, in backward time, approach S^3 along a fast direction and then remain slow while following S^3.

The two three-dimensional objects $W^s(S^3)$ and $W^u(S^2)$ are expected to intersect generically in a two-dimensional surface $\mathcal{H}$ of connecting orbits between S^3 and S^2; in forward time, any such connecting orbit first slowly follows the curve S^2, makes a transition across to the curve S^3, and then follows it slowly. In order to find $\mathcal{H}$, we use two ingredients: firstly, we adapt the technique in [2] for the computation of one-dimensional slow manifolds and their (un)stable manifolds to the four-dimensional setting of system (1) and, secondly, we employ a Lin's method approach [7] to define two orbit segments, in $W^s(S^3)$ and $W^u(S^2)$, respectively, that have end points in a chosen three-dimensional section. Closing the gap between them along a specified direction, by continuation of solutions to an overall boundary value problem, allows us to find a first heteroclinic orbit, which is then swept out in a further continuation run to obtain the surface $\mathcal{H}$.

Figure 1 shows the two-dimensional surface $\mathcal{H}$ in projection onto the three-dimensional (B, A, X)-space of system (1), together with the critical branches C^4_+ , C^2, C^4_- and C^3. Notice that $\mathcal{H}$ spirals out from the saddle branch C^2 and then approaches the saddle branch C^3 in a non-spiralling fashion; here, S^2 and S^3 (not shown) are indistinguishably close to

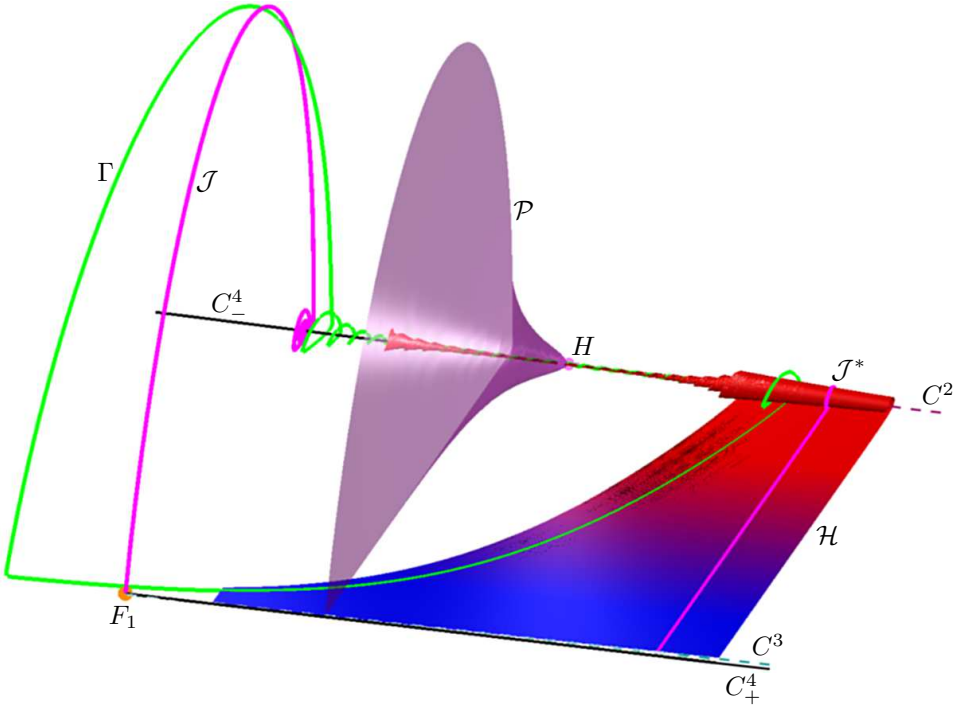

Figure 1: Three-dimensional projection onto (B, A, X)-space of the MMO periodic orbit Γ and the surface $\mathcal{H} = W^s(S^3) \cap W^u(S^2)$ (red-blue faded) of system (1) for $\varepsilon = 0.0037$, shown in relation to the following objects for $\varepsilon = 0$: the curves C^4_+ (black), C^2 (dashed raspberry), C^4_- (black) and C^3 (dashed teal) of the critical manifold; the fold point F_1 (orange dot) and the Hopf bifurcation point H (pink dot); the singular jump branch $\mathcal{J}$ from F_1 to C^4_- and its counterpart $\mathcal{J}^*$ (magenta curves) from the counterpoint on C^2, at equal distance from H, to C^3; and the surface $\mathcal{P}$ (transparent midnight grape) of periodic orbits arising from H.

C^2 and C^3 on the scale of Fig. 1. The surface $\mathcal{H}$ consists of orbit segments of an intermediate timescale in both $W^s(S^3)$ and $W^u(S^2)$, namely those that "make it all the way across" in forward time from near C^2 (where $\mathcal{H}$ is shaded red) to near C^3 (where $\mathcal{H}$ is shaded blue). As we checked, orbit segments close to but not on $\mathcal{H}$ quickly diverge from this surface in both forward and backward time in the X- and Y-directions.

Figure 1 is for $\varepsilon = 0.0037$ when one finds a stable MMO periodic orbit Γ, which is also shown. Starting near the attracting branch C^4_-, observe the SAOs of decreasing and then increasing amplitude that are generated by a slow passage through the Hopf bifurcation point H. Well past H and the surface $\mathcal{P}$ of periodic orbits of the fast subsystem, Γ leaves the branch C^2 by following the surface $\mathcal{H}$ very closely to a vicinity of the critical branch C^3. Somewhat past the fold point F_1, it subsequently has a sudden excursion in the X- and Y-directions to return back to C^4_-; the process then repeats.

We conclude that the surface $\mathcal{H}$ of connecting orbits is a crucial part of the return mechanism that is responsible for a single LAO per period of Γ. We further observe that Γ returns to C^4_- very near where the critical jump orbit $\mathcal{J}$ from F_1 for $\varepsilon = 0$ returns (this point is given by the B-value of F_1). Similarly, the take-off point on C^2 is close to that of the counterpart $\mathcal{J}^*$ of $\mathcal{J}$, which lies on the other side of $\mathcal{H}$ at the same B-distance. The suggestion from Fig. 1 is, hence, that the concatenation of $\mathcal{J}$ and $\mathcal{J}^*$ with the respective parts of C^4_-, C^2 and C^3 acts as a singular limit of Γ as ε approaches 0. Indeed, how the MMOs of the Olsen model (1) depend on parameters is a subject of our ongoing research.

References

[1] Desroches, M., Krauskopf, B., Osinga, H.M. (2009) The geometry of mixed-mode oscillations in the Olsen model for peroxidase-oxidase reaction. *Discrete & Continuous Dynamical Systems* **2**:807–827.

[2] Farjami, S., Kirk, V., Osinga, H.M. (2018) Computing the stable manifold of a saddle slow manifold. *SIAM Journal on Applied Dynamical Systems* **17**:350–379.

[3] Fenichel, N. (1979) Geometric singular perturbation theory for ordinary differential equations. *Journal of Differential Equations* **31**:53–98.

[4] Kuehn, C., Szmolyan, P. (2015) Multiscale geometry of the Olsen model and non-classical relaxation oscillations. *Journal of Nonlinear Science* **25**:583–629.

[5] Desroches, M., Guckenheimer, J., Krauskopf, B., Kuehn, C., Osinga, H.M., Wechselberger, M. (2012) Mixed-mode oscillations with multiple time scales. *SIAM Review* **54**:211–288.

[6] Olsen, L. (1983) An enzyme reaction with a strange attractor. *Physics Letters A* **94**:454–457.

[7] Krauskopf, B. & Rieß, T. [2008] A Lin's method approach to finding and continuing heteroclinic connections involving periodic orbits. *Nonlinearity* **21**: 1655–1690.

Analysis of a Singularly Perturbed Continuous Piecewise Linear System

A. Yassine Karoui* and Remco I. Leine*
*Institute for Nonlinear Mechanics, University of Stuttgart, Germany

Summary. The dynamics of piecewise linear systems can often be reduced to lower dimensional invariant cones using an appropriate Poincaré map. These invariant cones can be understood as a generalization of the center manifold concept to nonsmooth systems. In this paper, we show that the singular perturbation technique applied to a slow-fast continuous piecewise linear system can deliver a good approximation of the invariant cone. The proposed approximation approach is demonstrated on an oscillator with a unilateral spring as an example of a continuous piecewise linear system in $\mathbb{R}^3$.

Introduction

Recently, there has been a greater focus placed upon piecewise linear systems, due to their ability to model many complex physical phenomena. Typical applications range from mechanical systems involving dry friction [10], to neuron models [5], electronic circuits [2] and control systems [11]. Furthermore, continuous piecewise linear systems (hereafter, CPWL) are widely used to reproduce and understand various bifurcation phenomena of smooth nonlinear dynamical systems. The dynamics of CPWL systems can exhibit very interesting effects, which are impossible to observe in smooth systems [4]. A prominent example of this rich dynamic behavior was reported in [4], where the continuous matching of two stable subsystems can result in an unstable dynamics. The authors show that this behavior is possible, only if the CPWL system has an invariant cone, which is characterized by a fixed point of a corresponding Poincaré map and serves as a reduced system to investigate the stability and bifurcations of the full system. Therefore, the existence and computation of invariant cones for systems lacking smoothness are of interest. Unfortunately, the generation of invariant cones requires the numerical solution of a system of nonlinear equations and is therefore not suitable as a constructive reduction method towards a lower-dimensional dynamical model. However, the invariant cones can be understood as a generalization of center manifold theory to piecewise linear systems with an equilibrium on the switching manifold. Moreover, the long-term behavior of the full system can be described by a lower-dimensional model obtained from reducing the system to its dynamics on the invariant cone, if the latter is attractive. This perspective shows a clear similarity between invariant cones of piecewise linear systems and smooth invariant manifolds, which are used to obtain reduced order models for general differentiable systems.

For smooth nonlinear systems, projections to linear subspaces are usually used for model reduction, even though these are not invariant with respect to the original nonlinear dynamics. A reduced dynamics on an attractive invariant set, however, constitutes a mathematically more justifiable model reduction, since the trajectories of the reduced system on the invariant set are actual solutions of the full system. Relying on smoothness properties of the system, the existence and uniqueness of smooth invariant manifolds, seen as an extension of the underlying linear subspaces, have been addressed in the framework of spectral submanifolds (SSMs) [6]. The idea of model reduction in the framework of SSMs is based on a specific choice of slow variables, which determine the steady-state behavior of the system and are used as master coordinates to enslave the remaining state variables, therefore giving birth to a reduced model containing the long term characteristics of the full system. This fundamental idea emanated originally from a slow-fast decomposition using singular perturbation theory for smooth nonlinear systems. Therefore, the investigation of slow-fast CPWL systems using perturbative approximations could pave the way for the development of novel reduction methods for systems with nonsmooth nonlinearities.

The aim of this paper is to derive an approximation in closed form of the eigenvector defining the invariant half-lines of the cone for a specific homogeneous CPWL mechanical system using the theory of singular perturbations. This allows to obtain a reduced order model, for which the switching plane is modified such that the reduced dynamics is also of CPWL nature.

This paper is organized as follows. A brief overview on invariant cones along with an important result from [4] on their existence and stability are presented in next section. Then, the theory of singular perturbations is described with a focus on piecewise linear systems. In the last section, a slow-fast oscillator in $\mathbb{R}^3$ with a unilateral spring is analyzed. An explicit expression for its invariant half-lines is derived using singular perturbation theory, and a reduced model with a modified switching condition is obtained.

Invariant cones of continuous piecewise linear systems in $\mathbb{R}^3$

Without loss of generality, we consider a CPWL system with a single switching plane $\mathbf{\Sigma} = \{\mathbf{x} \in \mathbb{R}^3 : y = 0\}$ written as:

$$\dot{\mathbf{x}} = \mathbf{F}(\mathbf{x}) = \begin{cases} \mathbf{A}^+\mathbf{x} & \text{for } y \geq 0 \\ \mathbf{A}^-\mathbf{x} & \text{for } y < 0 \end{cases}, \tag{1}$$

where $\mathbf{x} = \begin{pmatrix} x_1 & x_2 & y \end{pmatrix}^{\mathrm{T}} \in \mathbb{R}^3$ and $\mathbf{A}^{\pm}$ are 3×3 real constant matrices satisfying the continuity condition $\mathbf{A}^+ - \mathbf{A}^- = (\mathbf{A}^+ - \mathbf{A}^-)\mathbf{e}_3\mathbf{e}_3^{\mathrm{T}}$, with $\mathbf{e}_3$ being the third vector of the standard basis of $\mathbb{R}^3$. Therefore, both matrices are only different in the third column.

For the sake of brevity, we will use the compact form

$$\Upsilon(\eta) = \Upsilon^{\pm} = \begin{cases} \Upsilon^{+} & \text{if } \eta \geq 0 \\ \Upsilon^{-} & \text{if } \eta < 0 \end{cases}, \tag{2}$$

where $\Upsilon^{\pm}$ are either matrices or scalars. Hence, system (1) can be written as $\dot{\mathbf{x}} = \mathbf{A}(y)\mathbf{x} = \mathbf{A}^{\pm}\mathbf{x}$. The origin is always an equilibrium point of system (1), and it is the unique equilibrium if $\mathbf{A}^{\pm}$ are both nonsingular. Suppose that an initial condition $\mathbf{x}_0$ lies in one of the domains $\boldsymbol{\mathcal{U}}^{\pm} = \{\mathbf{x} \in \mathbb{R}^3 : y \gtrless 0\}$, and that the corresponding trajectory remains in the same domain for any given time $t \in (0, \infty)$ and therefore does never reach the switching plane $\boldsymbol{\Sigma}$. In this case, the system behaves purely in a smooth fashion and the conventional theory for differentiable systems can be applied. The interesting behavior occurs, however, if the trajectory crosses $\boldsymbol{\Sigma}$ at a finite time, which can lead to various dynamical behaviors in general piecewise linear systems, such as direct crossing, sliding, grazing or jumping. In this work, we consider the class of CPWL systems, for which the dynamics can only include direct crossing behavior and the uniqueness of solutions for every initial condition is ensured. To understand the composed motion of both subsystems, we consider the following subsets of $\boldsymbol{\Sigma}$:

$$\boldsymbol{\Sigma}_{>} := \{\mathbf{x} \in \boldsymbol{\Sigma} : \mathbf{e}_3^{\mathrm{T}}\mathbf{A}^{+}\mathbf{x} = \mathbf{e}_3^{\mathrm{T}}\mathbf{A}^{-}\mathbf{x} > 0\}, \quad \boldsymbol{\Sigma}_{<} := \{\mathbf{x} \in \boldsymbol{\Sigma} : \mathbf{e}_3^{\mathrm{T}}\mathbf{A}^{+}\mathbf{x} = \mathbf{e}_3^{\mathrm{T}}\mathbf{A}^{-}\mathbf{x} < 0\}$$

For $\mathbf{x}^* \in \boldsymbol{\Sigma}_{<}$ or $\mathbf{x}^* \in \boldsymbol{\Sigma}_{>}$, the flow transitions from one domain into the other through $\mathbf{x}^*$. In the following, we will assume that initial values $\mathbf{x}_0$ are chosen from the set $\mathbf{x}_0 \in \boldsymbol{\Sigma}_{<}$. A trajectory is then given by $\boldsymbol{\varphi}(\mathbf{x}_0, t) = e^{\mathbf{A}^{-}t}\mathbf{x}_0$ and enters $\boldsymbol{\mathcal{U}}^{-}$ by means of the flow of the system $\dot{\mathbf{x}} = \mathbf{A}^{-}\mathbf{x}$. It reaches the switching plane again for the first time at $\mathbf{x}_1 \in \boldsymbol{\Sigma}_{>}$. Hence, there is a positive finite time $t^{-}(\mathbf{x}_0) = \min\{t > 0 : \mathbf{e}_3^{\mathrm{T}}e^{\mathbf{A}^{-}t}\mathbf{x}_0 = 0, \mathbf{e}_3^{\mathrm{T}}e^{\mathbf{A}^{-}t}\mathbf{A}^{-}\mathbf{x}_0 > 0\}$. Similarly $t^{+}(\mathbf{x}_1)$ can be defined for $\mathbf{x}_1 \in \boldsymbol{\Sigma}_{>}$. Since the flow is piecewise linear, one can see that t^{-} and t^{+} are constant on half-lines, i.e. $t^{\pm}(\lambda\mathbf{x}) = t^{\pm}(\mathbf{x})$ with $\lambda \in (0, \infty)$. For initial conditions $\mathbf{x}_0 \in \boldsymbol{\Sigma}$, the following half-maps are defined:

$$\begin{aligned} P^{-} :& \boldsymbol{\Sigma}_{<} \to \boldsymbol{\Sigma} & \qquad P^{+} :& \boldsymbol{\Sigma}_{>} \to \boldsymbol{\Sigma} \\ \mathbf{x}_0 \mapsto& e^{\mathbf{A}^{-}t^{-}(\mathbf{x}_0)}\mathbf{x}_0 =: P^{-}(\mathbf{x}_0) & \qquad \mathbf{x}_1 \mapsto& e^{\mathbf{A}^{+}t^{+}(\mathbf{x}_1)}\mathbf{x}_1 =: P^{+}(\mathbf{x}_1) \end{aligned}$$

Hence, the Poincaré map reads:

$$P(\mathbf{x}_0) := P^{+}(P^{-}(\mathbf{x}_0)) = e^{\mathbf{A}^{+}t^{+}(P^{-}(\mathbf{x}_0))}e^{\mathbf{A}^{-}t^{-}(\mathbf{x}_0)}\mathbf{x}_0 \tag{3}$$

Since system (1) is positively homogeneous and the vector field satisfies $\mathbf{F}(\mu\mathbf{x}) = \mu\mathbf{x}, \forall\mathbf{x} \in \mathbb{R}^3, \mu > 0$, the Poincaré map P transforms half-lines contained in $\boldsymbol{\Sigma}$ and passing through the origin into half-lines contained in the same plane, also passing through the origin. A more general construction is given by the following theorem stated in [7]:

Theorem 1 *Let $\overline{\mathbf{x}} \in \boldsymbol{\Sigma}$ be an eigenvector of the nonlinear eigenvalue problem $P(\overline{\mathbf{x}}) = \mu\overline{\mathbf{x}}$, with some real positive eigenvalue μ. Then there is an invariant cone for system* (1)*. Moreover,*

- *If $\mu > 1$, then the origin is an unstable equilibrium.*
- *If $\mu = 1$, then the cone consists of periodic orbits.*
- *If $\mu < 1$, then the stability of the origin is dependent of the stability of P w.r.t. the complimentary directions.*

Therefore, system (1) has an invariant cone if there exists a half-line contained in $\boldsymbol{\Sigma}$ that is invariant for the Poincaré map P. The nonlinear eigenvalue problem $P(\overline{\mathbf{x}}) = \mu\overline{\mathbf{x}}$ determines the invariant cone and involves the six independent variables $\overline{\mathbf{x}} \in \mathbb{R}^3, \mu, t^{-}(\overline{\mathbf{x}})$ and $t^{+}(P(\overline{\mathbf{x}}))$, which can be obtained numerically as solution of the nonlinear equation system given by:

$$0 = \mathbf{G}(\mathbf{x}, t^{-}, t^{+}, \mu) = \begin{pmatrix} e^{\mathbf{A}^{+}t^{+}}e^{\mathbf{A}^{-}t^{-}}\mathbf{x} - \mu\mathbf{x} \\ \mathbf{e}_3^{\mathrm{T}}e^{\mathbf{A}^{-}t^{-}}\mathbf{x} \\ \mathbf{e}_3^{\mathrm{T}}\mathbf{x} \\ \mathbf{x}^{\mathrm{T}}\mathbf{x} - 1 \end{pmatrix} \tag{4}$$

This system of equations includes the definition of the Poincaré map, the first return to $\boldsymbol{\Sigma}$ at the time t^{-}, the location of the initial condition on $\boldsymbol{\Sigma}$ and a normalization. The zeros of $\mathbf{G}$ can be solved numerically to obtain the 6 independent unknows characterizing the invariant cone. Although the problem of existence and number of invariant cones in general piecewise linear systems is still open, it has been proved that there exists at most one invariant cone for some degenerate CPWL cases in [3] and [4] and at most two invariant cones for observable three dimensional CPWL cases in [1]. For the sake of completeness, we recall here an important result from [4] (Theorem 2 - Statement (a)) on the number and stability of invariant cones for a specific case, which is considered in the mechanical system studied in this work.

Theorem 2 *Suppose that system* (1) *satisfies the observability condition, i.e. the observability matrix*

$$\mathbf{O} = \begin{pmatrix} \mathbf{e}_3^{\mathrm{T}} \\ \mathbf{e}_3^{\mathrm{T}}\mathbf{A}^- \\ \mathbf{e}_3^{\mathrm{T}}(\mathbf{A}^-)^2 \end{pmatrix}$$

has full rank. Further, assume that the eigenvalues of matrices $\mathbf{A}^\pm$ *are* $\lambda_1^\pm = \lambda^\pm$ *and* $\lambda_{2,3}^\pm = \alpha^\pm \pm i\beta^\pm$*, with* $\beta^\pm > 0$ *and introduce the parameters*

$$\gamma^+ = \frac{\alpha^+ - \lambda^+}{\beta^+}, \quad \textit{and} \quad \gamma^- = \frac{\alpha^- - \lambda^-}{\beta^-}.$$

Then the following statement holds: If $\gamma^+\gamma^- > 0$*, then system* (1) *has only one invariant cone, which is two-zonal (i.e. lives in the two linear zones) and hyperbolic, asymptotically stable for* $\gamma^+ + \gamma^- > 0$ *and unstable for* $\gamma^+ + \gamma^- < 0$*.*

Note that due to the continuity condition, the observability matrix is independent of the chosen matrix, $\mathbf{A}^+$ or $\mathbf{A}^-$.
In the next section, a brief introduction to singular perturbation theory with an emphasis on CPWL system is given.

Singular perturbation theory for CPWL systems

For an n-dimensional smooth system having s slow variables and a small perturbation parameter ε, which is responsible for a time-scale separation, classical geometric perturbation theory can be used to obtain a reduced-order model. The limiting case $\varepsilon \to 0$ gives an f-dimensional critical manifold $\boldsymbol{\mathcal{M}}_c$, where $f = n - s$. According to Fenichel's theorem, if $\boldsymbol{\mathcal{M}}_c$ is normally hyperbolic, then there exists an f-dimensional slow invariant manifold $\boldsymbol{\mathcal{M}}_s$, on which the dynamics is a perturbation of order $\boldsymbol{\mathcal{O}}(\varepsilon)$ of the dynamics on $\boldsymbol{\mathcal{M}}_c$. This theorem can be applied to slow-fast CPWL systems only on the subsets of the state space that do not include the switching manifold. This yields two linear locally invariant slow half-manifolds $\boldsymbol{\mathcal{M}}_s^\pm$, each aligned with the slow eigenspaces of $\mathbf{A}^+$ or $\mathbf{A}^-$. Furthermore, a forward invariant neighborhood enveloping the linear critical manifold, which is continuous at the switching manifold, has been shown to exist under suitable conditions [9]. For this, the critical manifold $\boldsymbol{\mathcal{M}}_c$, which is not normally hyperbolic on $\boldsymbol{\Sigma}$, has to be attracting.
Consider a slow-fast ODE system of the form:

$$\begin{aligned} \dot{\mathbf{x}} &= \begin{cases} \mathbf{f}^+(\mathbf{x},\mathbf{y};\varepsilon) & \text{for } h(\mathbf{x},\mathbf{y}) \geq 0 \\ \mathbf{f}^-(\mathbf{x},\mathbf{y};\varepsilon) & \text{for } h(\mathbf{x},\mathbf{y}) < 0 \end{cases} \\ \varepsilon\dot{\mathbf{y}} &= \begin{cases} \mathbf{g}^+(\mathbf{x},\mathbf{y};\varepsilon) & \text{for } h(\mathbf{x},\mathbf{y}) \geq 0 \\ \mathbf{g}^-(\mathbf{x},\mathbf{y};\varepsilon) & \text{for } h(\mathbf{x},\mathbf{y}) < 0, \end{cases} \end{aligned} \tag{5}$$

where $\mathbf{x} = \begin{pmatrix} x_1 & \cdots & x_s \end{pmatrix}^{\mathrm{T}} \in \mathbb{R}^s$ are the slow variables, $\mathbf{y} = \begin{pmatrix} y_1 & \cdots & y_f \end{pmatrix}^{\mathrm{T}} \in \mathbb{R}^f$ are the fast variables, $0 \leq \varepsilon \ll 1$ is the small parameter and $\dot{(\cdot)} := \frac{\mathrm{d}(\cdot)}{\mathrm{d}t}$ denotes the derivative with respect to the "slow" time scale t. The switching manifold is therefore given by the scalar function $h(\mathbf{x},\mathbf{y}) = 0$. We assume that the functions $\mathbf{f}^\pm, \mathbf{g}^\pm$ and h are linear with respect to $\mathbf{x}$ and $\mathbf{y}$ and that the system is continuous at the switching manifold. Furthermore, suppose that $h(\mathbf{0},\mathbf{0}) = 0$. At the origin, we also assume that the switching manifold is not tangent to all fast directions, which means that ∇h has at least one non-zero component. Without loss of generality, one can assume $\frac{\partial h}{\partial y_1} \neq 0$. This assumption leads to a more general configuration, where both the slow and fast dynamics contain a switch. Otherwise, a degenerate system is obtained, where only the slow dynamics has a switch and the fast dynamics is $\mathbf{g}^\pm = \mathbf{g}$. In order to simplify the switching condition, an invertible transformation $(\mathbf{x},\mathbf{y}) \to (\tilde{\mathbf{x}},\tilde{\mathbf{y}})$ is introduced, with a new set of coordinates $\tilde{\mathbf{x}} = \mathbf{x}$ and $\tilde{\mathbf{y}} = \begin{pmatrix} h(\mathbf{x},\mathbf{y}) & y_2 & y_3 & \cdots & y_f \end{pmatrix}^{\mathrm{T}}$. Since $\tilde{y}_1$ is a new fast variable, the slow-fast system has the same form as (5) except that the switching manifold is determined by $\tilde{y}_1 = 0$. Taking the new coordinates and setting the small parameter $\varepsilon = 0$ in (5) yields the critical system

$$\dot{\mathbf{x}} = \mathbf{f}^\pm(\mathbf{x},\mathbf{y};0) \tag{6}$$

$$0 = \mathbf{g}^\pm(\mathbf{x},\mathbf{y};0) \tag{7}$$

where the $\tilde{(\cdot)}$ is dropped for simplicity, and the $\pm$ switch is governed by equation (2) with $y_1 = \eta$.
The critical manifold is obtained as $\boldsymbol{\mathcal{M}}_c = \{(\mathbf{x},\mathbf{y}) \in \mathbb{R}^{s+f} : \mathbf{y} = \mathbf{h}_c^\pm(\mathbf{x})\}$, where $\mathbf{y} = \mathbf{h}_c^\pm(\mathbf{x})$ are the solutions of the two algebraic constraints (7) and describe the behavior of the fast variables as a function of the slow variables. Note that $\mathbf{h}_c^\pm$ are both linear functions of $\mathbf{x}$ and that the matching from both linear subsystems is continuous. The dynamics on $\boldsymbol{\mathcal{M}}_c$ is governed by

$$\dot{\mathbf{x}} = \mathbf{f}^\pm(\mathbf{x},\mathbf{h}_c^\pm(\mathbf{x});0). \tag{8}$$

The Jacobians $\frac{\partial \mathbf{g}^\pm}{\partial \mathbf{y}}(\mathbf{x})\Big|_{\mathbf{y}=h_0^\pm,\varepsilon=0}$ along both critical manifolds are assumed to fulfill the stability condition, so that a relevant reduction to the slow dynamics can be obtained. For CPWL systems, the existence of a forward invariant neighborhood around the critical manifold has been shown in [9], if $\boldsymbol{\mathcal{M}}_c$ is globally exponentially stable. Therefore, and for the

sake of brevity, we assume global exponential stability of the critical manifold, which is naturally given for the specific example considered in this work. We refer to [9] for more details on the stability properties of $\boldsymbol{\mathcal{M}}_c$ and the proof of the existence of a forward invariant neighborhood. For systems of the form (1), the singular perturbation technique is performed on each linear subsystem to obtain the linear locally invariant slow half-manifolds. This is described in the following, where the $\pm$ switching is dropped for simplicity and only the linear region defined by $y_1 \geq 0$ is considered. Obviously, the approach is analogous for the other linear region. The matching of both linear invariant half-manifolds and the corresponding switching condition are discussed explicitly for the example in the next section.
The s-dimensional, locally invariant slow manifold is defined as $\boldsymbol{\mathcal{M}}_s^+ = \{(\mathbf{x}, \mathbf{y}) \in \mathbb{R}^{s+f} : \mathbf{y} = \mathbf{h}_s^+(\mathbf{x})\}$. Since the state space is decomposed into two linear parts, the invariance property of $\boldsymbol{\mathcal{M}}_s^+$ must be understood in a local way. Inserting $\mathbf{y} = \mathbf{h}_s^+$ and $\dot{\mathbf{y}} = \frac{\partial \mathbf{h}_s^+}{\partial \mathbf{x}}\Big|_{\mathbf{x},\varepsilon} \dot{\mathbf{x}}$ into the fast dynamics $\varepsilon\dot{\mathbf{y}} = \mathbf{g}^+(\mathbf{x}, \mathbf{y}, \varepsilon)$ yields:

$$\varepsilon \frac{\partial \mathbf{h}_s^+}{\partial \mathbf{x}} \mathbf{f}^+(\mathbf{x}, \mathbf{h}_s^+; \varepsilon) = \mathbf{g}^+(\mathbf{x}, \mathbf{h}_s^+; \varepsilon). \tag{9}$$

In each linear region, the asymptotic expansion given by

$$\mathbf{h}_s^+(\mathbf{x}) = \mathbf{h}_0^+(\mathbf{x}) + \varepsilon \mathbf{h}_1^+(\mathbf{x}) + \boldsymbol{\mathcal{O}}(\varepsilon^2) \tag{10}$$

is used in the invariance equation (9). By equating the coefficients of powers of ε one can see that $\mathbf{h}_c^+(\mathbf{x}) = \mathbf{h}_0^+(\mathbf{x})$, which means that the critical manifold is the zero-order approximation of the slow manifold. Moreover, the first order term $\mathbf{h}_1^+(\mathbf{x})$ is obtained as:

$$\mathbf{h}_1^+ = \frac{\partial \mathbf{g}^+}{\partial \mathbf{y}}\Big|_{\mathbf{y}=\mathbf{h}_0^+;\varepsilon=0}^{-1} \left[\frac{\partial \mathbf{h}_0^+}{\partial \mathbf{x}} \mathbf{f}^+(\mathbf{x}, \mathbf{h}_0^+; 0) - \frac{\partial \mathbf{g}^+}{\partial \varepsilon}\Big|_{\mathbf{x},\mathbf{h}_0^+;0} \right]. \tag{11}$$

Three-dimensional oscillator with a unilateral spring

The approximation of the invariant cone by means of singular perturbation theory is demonstrated on the CPWL system shown in Figure 1. The system consists of a mass m and a massless rod, each coupled to the environment by a spring-damper element. In addition, the mass is connected to the rod by one linear and one unilateral spring, with stiffnesses k_3 and k_{N3}, respectively. The unilateral spring is active only when the relative displacement $q_1 - q_2$ is positive, where q_1 and q_2 are the displacements of the mass and the massless rod, respectively. Let $\mathbf{x} = \begin{pmatrix} x_1 & x_2 & y \end{pmatrix}^{\mathrm{T}} \in \mathbb{R}^3$ be the state vector, where the components are defined as follows:

$$x_1 = q_1, \quad x_2 = \dot{q}_1, \quad y = q_1 - q_2. \tag{12}$$

In this set of coordinates, the equations of motion have the form of system (1), where $\mathbf{A}^{\pm}$ are constant matrices given by

$$\mathbf{A}^{\pm} = \begin{pmatrix} 0 & 1 & 0 \\ -\frac{k_1}{m} & -\frac{c_1}{m} & -\frac{k_3^{\pm}}{m} \\ \frac{k_2}{c_2} & 1 & -\frac{k_2 + k_3^{\pm}}{c_2} \end{pmatrix} \quad \text{with} \quad \begin{cases} k_3^+ = k_3 + k_{N3} & \text{for} \quad y \geq 0 \\ k_3^- = k_3 & \text{for} \quad y < 0 \end{cases}, \tag{13}$$

with all damping and stiffness coefficients assumed to be non-negative. The switching manifold is defined as $\boldsymbol{\Sigma} = \{\mathbf{x} \in \mathbb{R}^3 | y = 0\}$ and the state space consists of two half-spaces $\boldsymbol{\mathcal{U}}^{\pm} = \{\mathbf{x} \in \mathbb{R}^3 | y \gtrless 0\}$. By statement (a) of Theorem 2 and after performing simple calculations for fixed sets of parameters which fulfill the assumptions on the matrices $\mathbf{A}^{\pm}$, we deduce that this system has only one invariant cone which is hyperbolic and asymptotically stable. As the existence of a stable invariant cone is now established, the next step is to apply singular perturbation theory to approximate the cone. In order to bring the system to a singularly perturbed form, the damping constant c_2 is assumed to be a small parameter ($c_2 = \varepsilon$). Next, we split the state vector $\mathbf{x}$ into slow variables $\mathbf{x}_s = \begin{pmatrix} x_1 & x_2 \end{pmatrix}^{\mathrm{T}} \in \mathbb{R}^2$ and a scalar fast variable y.

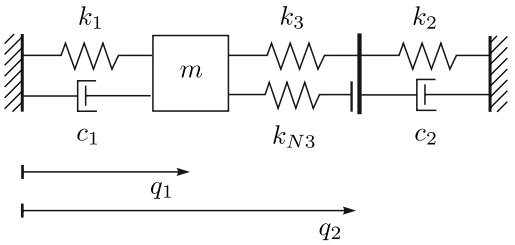

Figure 1: Mechanical system of a slow-fast oscillator in $\mathbb{R}^3$.

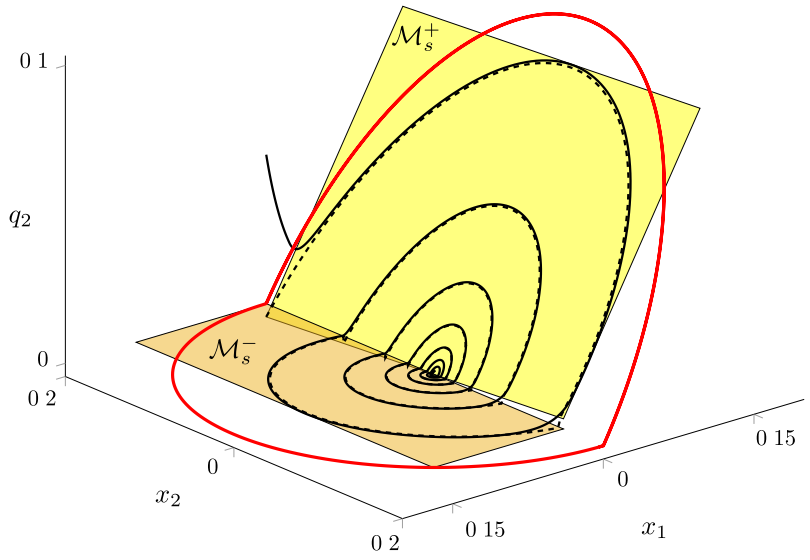

Figure 2: Illustration of the attracting invariant cone approximated by two half-planes $\boldsymbol{\mathcal{M}}_s^{\pm}$ with a switch at $x_1 = 0$ for the parameter set $\varepsilon = c_2 = 0.1, c_1 = 0.4,\ m = 1, k_1 = k_2 = 1, k_3 = 0, k_{N3} = 2$. A general trajectory of the full system (solid line) is attracted to the half-planes and synchronizes with a trajectory of reduced dynamics (dashed line). The critical manifold gives a conservative periodic orbit (red line) and is therefore not suitable as an approximation of the full system.

The equations of motion in the slow-fast form read as:

$$\dot{\mathbf{x}}_s = \mathbf{f}^{\pm}(\mathbf{x}_s, y) = \begin{pmatrix} x_2 \\ -\frac{k_1}{m}x_1 - \frac{c_1}{m}x_2 - \frac{k_3^{\pm}}{m}y \end{pmatrix} \tag{14}$$

$$\varepsilon\dot{y} = g^{\pm}(\mathbf{x}_s, y, \varepsilon) = k_2 x_1 + \varepsilon x_2 - (k_2 + k_3^{\pm})y. \tag{15}$$

The critical manifolds in the half-spaces $\boldsymbol{\mathcal{U}}^{\pm}$ are obtained as isolated solutions $h_0^{\pm}(\mathbf{x}_s)$ of the equations $g^{\pm}(\mathbf{x}_s, h_0^{\pm}(\mathbf{x}_s), 0) = 0$ and read as:

$$h_0^{\pm}(\mathbf{x}_s) = \frac{k_2}{k_2 + k_3^{\pm}} x_1 \tag{16}$$

Herein, $h_0^+(\mathbf{x}_s)$ is only applicable for $h_0^+(\mathbf{x}_s) \geq 0$, which in view of $k_2, k_3^+ \geq 0$ comes down to $x_1 \geq 0$. Similarly $h_0^-(\mathbf{x}_s)$ is only applicable for $x_1 < 0$. Hence, we may define the critical manifold by

$$h_0(\mathbf{x}_s) = \begin{cases} h_0^+(\mathbf{x}_s) & \text{for} \quad x_1 \geq 0 \\ h_0^-(\mathbf{x}_s) & \text{for} \quad x_1 < 0 \end{cases} \tag{17}$$

The Jacobians $\frac{\partial g^{\pm}}{\partial y}(\mathbf{x}_s)\Big|_{y=h_0^{\pm},\varepsilon=0}$ along the critical manifold are strictly negative and fulfill the stability condition, and the dynamics on this manifold is given by $\dot{\mathbf{x}}_s = \mathbf{f}^{\pm}(\mathbf{x}_s, y = h_0(\mathbf{x}_s); 0)$. For the special choice $c_1 = 0$, this dynamics is purely conservative and yields a periodic orbit, which does not reflect the dissipative nature of the original system ($\varepsilon \neq 0$) and therefore cannot be used to approximate the long time behavior of the full system, as shown in Figure 2. Thus, terms of $\boldsymbol{\mathcal{O}}(\varepsilon)$ must be included to obtain a dissipative reduced-order model. Using the equations (10) and (11), the locally invariant slow half-manifolds of the two linear subsystems read as:

$$y_{\text{slow}} = h_s^{\pm}(\mathbf{x}_s) = \frac{k_2}{k_2 + k_3^{\pm}} x_1 + \frac{\varepsilon k_3^{\pm}}{(k_2 + k_3^{\pm})^2} x_2 + \boldsymbol{\mathcal{O}}(\varepsilon^2), \quad \text{with} \quad k_3^{\pm} = \begin{cases} k_3 + k_{N3} & \text{for} \quad y_{\text{slow}} \geq 0 \\ k_3 & \text{for} \quad y_{\text{slow}} < 0 \end{cases}. \tag{18}$$

The dynamics of the 2-dimensional system, reduced to the linear locally invariant slow manifolds in both regions, is governed by $\dot{\mathbf{x}}_s = \mathbf{f}^{\pm}(\mathbf{x}_s, h^{\pm}(\mathbf{x}_s))$. The switching condition in this case is not trivial anymore, since the stiffness $k_3^{\pm}$ depends on y_{slow} itself. This problem is illustrated in Figure 3. The colored areas and their corresponding limits are obtained from (18) by solving the inequalities $y_{\text{slow}} \geq 0$ (yellow region for h_s^+) and $y_{\text{slow}} < 0$ (orange region for h_s^-), which matches the physical switching condition. In the white area, none of the inequalities are satisfied, whereas the dark area shows the region where both inequalities are fulfilled. To circumvent this problem of switching between $h_s^{\pm}$, one could take $x_1 = 0$ as a switching plane, since the x_2 terms in (18) are of order ε. At this modified switching plane, the linear slow manifolds, obtained as two half-planes $\boldsymbol{\mathcal{M}}_s^{\pm} = \{\mathbf{x} \in \mathbb{R}^3 | y = h_s^{\pm}(\mathbf{x}_s)\}$, are askew and meet only at the equilibrium point. This leads to a reduced system containing a jump at $x_1 = 0$. However, the trajectories of the reduced system are still a good approximation and follow the trajectories of the full system, which converge asymptotically towards $\boldsymbol{\mathcal{M}}_s^{\pm}$ as shown in Figure 2. In order to obtain a continuous reduced system, $\boldsymbol{\mathcal{M}}_s^{\pm}$ can be continued up to their intersection line. This leads to the avoidance of jumps in the reduced dynamics at $\boldsymbol{\Sigma}$.

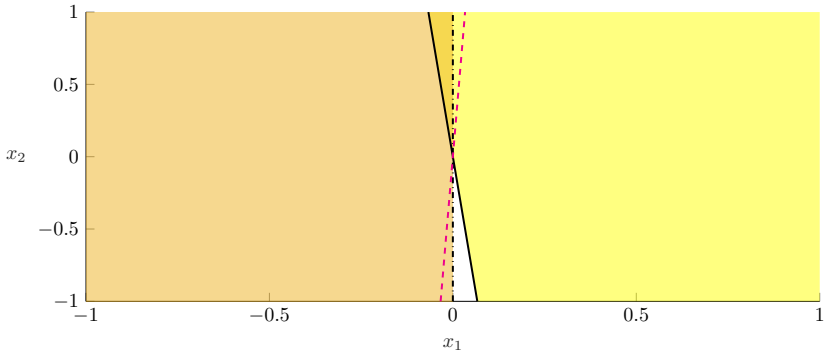

Figure 3: Illustration of the admissibility regions for h_s^+ (yellow area with the solid black line as limit) and h_s^- (orange area with the dash-dotted black line as limit). The white area is the region for which both $h_s^\pm$ are not admissible. The magenta dashed line shows the intersection of the two linear slow manifolds. Example for the parameter set $\varepsilon = c_2 = 0.1, c_1 = 0, m = 1, k_1 = k_2 = 1, k_3 = 0, k_{N3} = 2$.

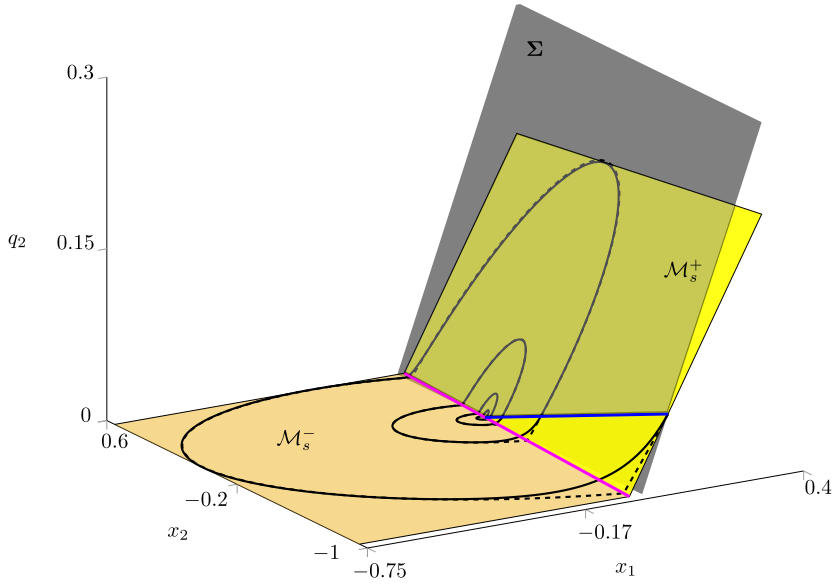

Figure 4: Illustration of the invariant cone for $\varepsilon = c_2 = 0.1, c_1 = 0.4, m = 1, k_1 = k_2 = 1, k_3 = 0, k_{N3} = 2$. The magenta line shows the intersection line of the two locally invariant half-planes. The blue line is the intersection line of $\boldsymbol{\mathcal{M}}_s^+$ with the switching manifold $\boldsymbol{\Sigma}$, which lies exactly on the direction of the eigenvector from the numerical solution of equation (4).

Continued reduced slow dynamics

The main disadvantage of taking $x_1 = 0$ as a switching plane in (18) is that the reconstruction of the fast variable y contains a jump leading to a Filippov system [8] for the reduced dynamics. For the purpose of obtaining a continuous matching of the two locally invariant half-planes, the switching plane can be modified and fixed at the intersection line defined by $\boldsymbol{\mathcal{M}}_s^+ \cap \boldsymbol{\mathcal{M}}_s^-$. Setting $h_s^+ = h_s^-$ yields:

$$\left(-\frac{k_2}{k_2 + k_3^+} + \frac{k_2}{k_2 + k_3^-}\right) x_1 + \left(\frac{k_3^-}{(k_2 + k_3^-)^2} - \frac{k_3^+}{(k_2 + k_3^+)^2}\right) x_2 = 0. \tag{19}$$

This condition $h_s^+ = h_s^-$ is then used in (18) as switching condition instead of y_{slow}. Even though this line does not lie on the physical switching plane $\boldsymbol{\Sigma}$, defined by $y = 0$, the reduced dynamics gives a better approximation of the dynamics of the full system. This is illustrated in Figure 4, where the reduced dynamics on the slow manifolds (dashed line) contains only a kink at the switching instead of a jump. The trajectory of the reduced system follows the solution of the full system more closely than trajectories containing a jump at $x_1 = 0$. Figure 5 compares the time histories of the displacements q_1 and q_2 over some periods of decaying oscillations from the full system (black), the reduced system with a jump (blue) and the reduced model from the continued invariant half-planes (red). The continued reduced dynamics shows a closer agreement with the full system than the reduced model containing jumps.

Approximation of the invariant half-lines

Since the global stability of the continuous critical manifold $\boldsymbol{\mathcal{M}}_c$ is ensured and the two slow manifolds $\boldsymbol{\mathcal{M}}_s^\pm$ are locally invariant and attracting, a typical trajectory in $\boldsymbol{\mathcal{U}}^+$ would cross $\boldsymbol{\Sigma}$ from right to left at a point that can be assumed in the $\mathcal{O}(\varepsilon)$ neighborhood of $\boldsymbol{\mathcal{M}}_s^+$. For sufficiently small ε, the trajectory would then approach $\boldsymbol{\mathcal{M}}_s^-$ and follow it closely

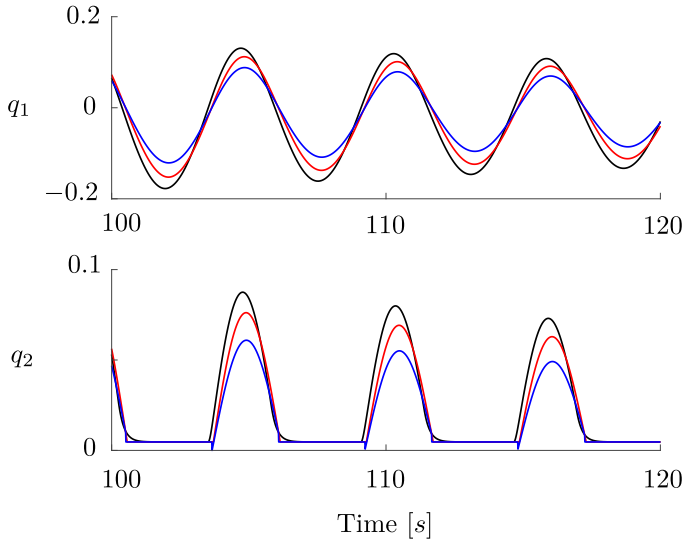

Figure 5: Time histories for $\varepsilon = c_2 = 0.2, c_1 = 0, m = 1, k_1 = k_2 = 1, k_3 = 0, k_{N3} = 2$. The black, blue and red lines show the displacements from the full system, the reduced system with a jump and the continued reduced system, respectively.

until the next crossing with $\boldsymbol{\Sigma}$. Hence, we can assume that every transition from right to left through $\boldsymbol{\Sigma}$ is in a $\boldsymbol{\mathcal{O}}(\varepsilon)$ neighborhood of $\boldsymbol{\mathcal{M}}_s^+$. Consequently, the intersection line of $\boldsymbol{\mathcal{M}}_s^+$ and $\boldsymbol{\Sigma}$ presents a good approximation of an invariant half-line of the invariant cone and can be obtained by setting $y_{\text{slow}}^+ = 0$ in (18) as :

$$\mathbf{r}_{\text{inv}} = \{x_1 = -\varepsilon \frac{k_3^+}{k_2(k_2 + k_3^+)} x_2, y = 0\}. \tag{20}$$

Using the definitions in (12), this half-line is visualized as the blue line in Figure 4 in the original coordinates of the system $(q_1, \dot{q}_1, q_2)^{\mathrm{T}}$. For ε sufficiently small, this simple closed form approximation matches the invariant half-lines obtained from the numerical solution of (4). Obviously, this argumentation is analogous if we assume trajectories starting near the intersection of $\boldsymbol{\mathcal{M}}_s^-$ and $\boldsymbol{\Sigma}$ and leads to an approximation of the other invariant half-line, which corresponds to a Poincaré map defined as $P = P^-(P^+)$.

Conclusion

This study set out to explore the connection between singular perturbation theory applied to a slow-fast CPWL system and its invariant cones. The results show that the invariant half-lines of the corresponding invariant cone can directly be approximated in a closed form from a geometric perspective by computing the intersection of the locally invariant slow manifolds and the switching plane. Moreover, this work has also highlighted that trajectories of the reduced dynamics with a modified switching condition, which was obtained from the intersection line of the two slow manifolds, can closely approximate trajectories of the full system. Further research might explore the applicability of these findings for higher dimensional CPWL systems.

References

[1] V. Carmona, , E. Freire, and S. F.-G. and. Periodic orbits and invariant cones in three-dimensional piecewise linear systems. *Discrete and Continuous Dynamical Systems - A*, 35(1):59–72, 2015.

[2] V. Carmona, E. Freire, E. Ponce, J. Ros, and F. Torres. Limit cycle bifurcation in 3D continuous piecewise linear systems with two zones: Application to Chua's circuit. *International Journal of Bifurcation and Chaos*, 15(10):3153–3164, 2005.

[3] V. Carmona, E. Freire, E. Ponce, and F. Torres. Invariant manifolds of periodic orbits for piecewise linear three-dimensional systems. *IMA Journal of Applied Mathematics*, 2004.

[4] V. Carmona, E. Freire, E. Ponce, and F. Torres. Bifurcation of invariant cones in piecewise linear homogeneous systems. *International Journal of Bifurcation and Chaos*, 15(08):2469–2484, 2005.

[5] S. Coombes, R. Thul, and K. C. Wedgwood. Nonsmooth dynamics in spiking neuron models. *Physica D: Nonlinear Phenomena*, 241(22):2042–2057, 2012.

[6] G. Haller and S. Ponsioen. Nonlinear normal modes and spectral submanifolds: existence, uniqueness and use in model reduction. *Nonlinear Dynamics*, 86(3):1493–1534, 2016.

[7] T. Küpper. Invariant cones for non-smooth dynamical systems. *Mathematics and Computers in Simulation*, 79(4):1396–1408, 2008.

[8] R. I. Leine and H. Nijmeijer. *Dynamics and Bifurcations of Non-Smooth Mechanical Systems*, volume 18 of *Lecture Notes in Applied and Computational Mechanics*. Springer Verlag, Berlin, 2004.

[9] D. J. W. Simpson. Dimension reduction for slow-fast, piecewise-smooth, continuous systems of O.D.E. 2018.

[10] D. Weiss, T. Küpper, and H. Hosham. Invariant manifolds for nonsmooth systems with sliding mode. *Mathematics and Computers in Simulation*, 110:15–32, apr 2015.

[11] Z. T. Zhusubaliyev and E. Mosekilde. *Bifurcations and chaos in piecewise-smooth dynamical systems*, volume 44. World Scientific, 2003.

Bursting and Excitability in Neuromorphic Resonant Tunneling Diodes

Julien Javaloyes* and Ignacio Ortega-Piwonka†
* *Departament de Física & Institute of Applied Computing and Community Code (IAC-3), Universitat de les Illes Baleares, C/ Valldemossa km 7.5, 07122 Mallorca, Spain*

Summary. We study in this paper the dynamics of quantum nanoelectronic resonant tunneling diodes (RTDs) as excitable neuromorphic spike generators. We disclose the mechanisms by which the RTD creates excitable all-or-nothing spikes and we identify a regime of bursting in which the RTD emits a random number of closely packed spikes. The control of the latter is paramount for applications in event-activated neuromorphic sensing and computing. Finally, we discuss a regime of multi-stability in which the RTD behaves as a memory.

Introduction

Spike information processing and transmission in the form of events that occur at continuous times has numerous advantages over digital encoding and signaling [1]. It is a key mechanism in the dynamics of neurons and the brain, which suggests its value in the development of biologically-inspired artificial intelligence. Neurons are *excitable systems*; they respond to an external stimulus by realizing a large amplitude response, typically in the millisecond and millivolt range, before returning to their rest state, provided that said stimulus is larger than a certain threshold. Several neuromorphic circuits have been proposed which attempt to emulate the transmission of information in the brain and the nervous systems [2,3,4], including the IBM TrueNorth chip and the Intel Quark SE chi. These approaches are still based on adapting the conventional Complementary Metal Oxide Semiconductor architecture, and have some drawbacks, such as low frequency (kHz) and much higher power consumption than the brain.

Results

In this work, we provide a detailed analysis on the performance of quantum nanoelectronic resonant tunneling diodes (RTDs) as neuromorphic spike generators. Resonant tunneling diodes are promising candidates and are the fastest electronic oscillators up to date, reaching frequencies in the order of the hundreds of GHz, with a world record of 1.98 THz. Double barrier quantum well RTDs exhibit a nonlinear current-votage characteristic with regions of negative differential conductance (NDC) [1] (fig. 1). This property is key for the potential configuration of RTDs as excitable spike generators [5]. Excitable systems respond to an above-threshold stimulus by realizing a large amplitude response, typically in the millisecond and milivolt range, before returning to their rest state. For the duration of the response, known as lethargic time, the system is unable to respond to any other stimulus, irrespective of its amplitude [6]. Here, a theoretical model is proposed following the first-principle calculations of [5] accounting for an RTD with a single NDC connected to a DC voltage source (see fig. 1 inset).

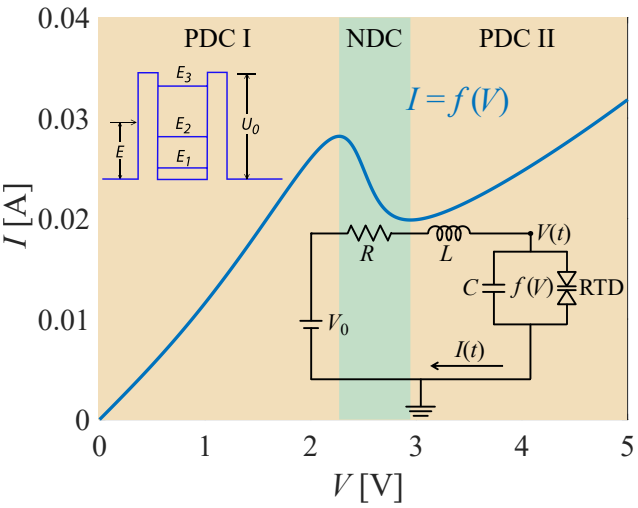

Figure 1: DBQW RTD connected to DC voltage.

The system of two first-order differential equations for the current and voltage derived from Kirchoff laws reads

$$\mu \dot{V} = I - f(V), \tag{1}$$
$$\mu^{-1} \dot{I} = V_0 - V - RI. \tag{2}$$

Here, $V(t)$ is the voltage across the RTD and $I(t)$ is the total current. V_0 is the bias DC voltage, R is the circuit intrinsic resistance and the parameter μ is the stiffness coefficient defined as $\mu = \sqrt{\frac{C}{L}}$, where L and C are the equivalent inductance and capacitance, respectively, which sets the circuit's natural frequency. The system's response depends on three parameters: the bias voltage, the circuit's resistance and a parameter accounting for the stiffness of the dynamics. Provided that this stiffness coefficient is sufficiently small, the system exhibits an adiabatic limit cycle with stages of slow and fast dynamics when biased in the NDC region and a stable fixed point when biased elsewhere (fig. 2.b). If the bias is set in the proximity to the NDC region and the system is perturbed with a perturbation above a certain threshold, it responds with a spike reminescent of the slow-fast limit cycle. If the system is subjected to noise instead of a single perturbation, it randomly generates spikes depending on the noise intensity. If the bias is set in the proximity to the I-V curve valley, the spikes appear agglomerated in bursts (fig. 2.c), which has already been observed in experiments [5].

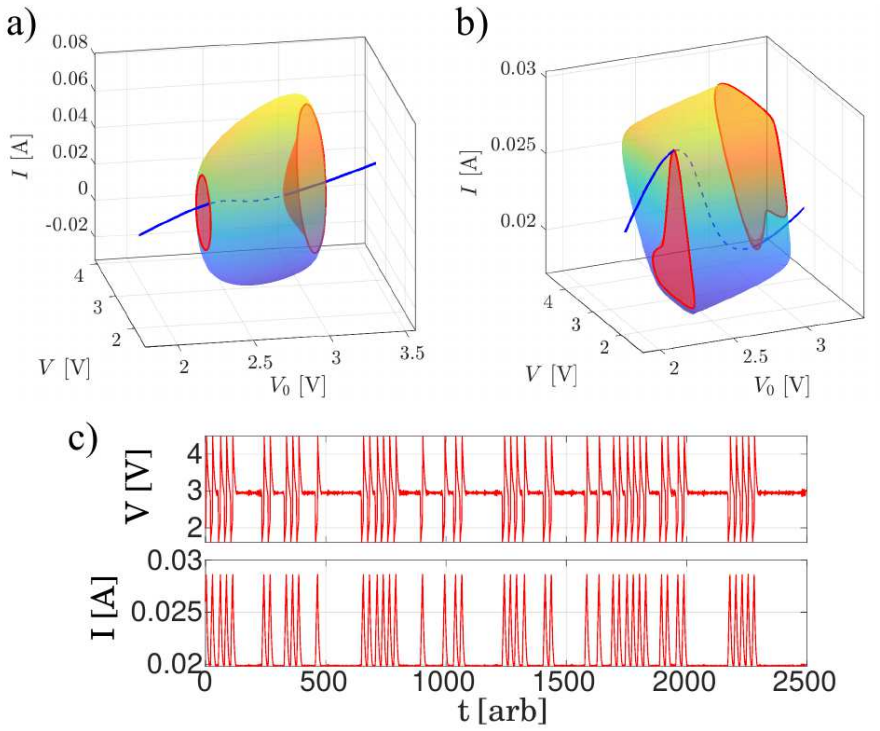

Figure 2: a,b) RTD response as a function of the bias voltage. Limit cycles are smooth (a) or stiff (b) depending on the stiffness coefficient. c) RTD response to external noise in the form of bursts of spikes.

An extensive study on the system's responses in terms of the parameters mentioned above is performed. Depending on the I-V characterisic, there may be narrow ranges of bias voltage at each side of the NDC region where the system is bistable. A critical value for the resistance is also found, above which the system exhibits a rich variety of multistabilities, with multiple fixed points and homoclinic curves. The bistability ranges and the lethargic time are measured as functions of the stiffness coefficient and the resistance, and they are found to be mainly dependent on the former, with little influence by the latter. In particular, the lethargic time is found to be inversely proportional to the circuit's inductance.

Conclusions

A Liénard-type nonlinear oscillator was proposed to model the dynamics of a double barrier quantum well resonant tunneling diode (DBQW RTD) connected to an electrical DC input.The configurations where the circuit behaves as an excitable spike generator were disclosed in a perspective to design and fabricate optoelectronic, nanoscale devices able of transmission, reception and storage of spike-coded information. The RTD oscillator may exhibit one or more equilibrium solutions in the form of a fixed point or a limit cycle. In particular, the stiffness coefficients determines whether or not the system behaves as a smooth oscillator or a spike generator.

References

[1] Eugene M. Izhikevich. *Dynamical systems in neuroscience : the geometry of excitability and bursting. Computational neuroscience*. MIT Press, Cambridge, Mass., London (2007).

[2] P. A. Merolla, et al. "A million spiking-neuron integrated circuit with a scalable communication network and interface". *Science*, **345** (668) (2014).

[3] Y. Shen et al. "Deep learning with coherent nanophotonic circuits". *Nature Photonics*, **11**: 441-446 (2017).

[4] P. Stark et al. "Opportunities for integrated photonic neural networks". *Nanophotonics*, **9** (13): 4221-4232 (2020).

[5] J. N. Schulman, H. J. De Los Santos, and D. H. Chow. "Physics-based rtd current-voltage equation". *IEEE Electron Device Letters*, **17** (5): 220-222 (1996).

[6] B. Romeira, J. Javaloyes, C. N. Ironside, J. M. L. Figueiredo, S. Balle, and O. Piro. "Excitability and optical pulse generation in semiconductor lasers driven by resonant tunneling diode photo etectors". *Opt. Express*, **12** (8): 20931-20940 (2013)

Delayed loss of stability in multiple time scale models of natural phenomena

Mattia Sensi*
*MathNeuro Team, Inria at Université Côte d'Azur, Biot, France

Summary. Numerous real-world phenomena exhibit mechanisms evolving on greatly different time scales. In this talk, we focus on delayed loss of stability in two classes of mathematical models, namely epidemics and neuroscience, specifically synaptic transmission, and comment on the possible asymptotic, and in one case transient, behaviour of such systems.

Introduction

Numerous natural phenomena exhibit mechanisms evolving on greatly different time scales, e.g. days against months or even years. The presence of multiple time scales gives rise to complex phenomenon, such as the focus of this talk, i.e. the so-called delayed loss of stability [1, 7]. Geometric Singular Perturbation Theory (GSPT) [2, 6] is a powerful tool to analyze such systems: by considering each time scale separately, GSPT allows to deduce information on the behaviour of the original model.
In this talk, we present various multiple time scale systems, both in standard and non-standard form [9], and describe their behaviour using different techniques from GSPT. In particular, we showcase the delayed loss of stability of orbits passing nearby critical manifolds (the sets of equilibria of the fast limit) of such systems. We focus on the entry-exit relation (also known as way-in/way-out, delayed loss of stability, or Pontryagin delay) which we use to analyze the passage of orbits near the critical manifolds.
In its simplest form, the entry-exit function is applied to planar systems of the form

$$\begin{aligned} x' =& \epsilon f(x, z, \epsilon), \\ z' =& z g(x, z, \epsilon), \end{aligned}$$

with $0 < \epsilon \ll 1$, $x, z \in \mathbb{R}$, $f(x, 0, 0) > 0$ and $\text{sign}(g(x, 0, 0)) = \text{sign}(x)$.
As shown in Figure 1, one can derive a Poincaré map $x_0 \mapsto p_\epsilon(x_0)$ from a horizontal line $\{z = z_0\}$ to itself. The x-axis $z = 0$ changes stability, from attracting to repelling, at $x = 0$. Orbits which are attracted towards it at a point $(x, z) = (x_0, z_0)$, with $x_0 < 0$, will eventually leave a neighbourhood of the x-axis and re-intersect the line $\{z = z_0\}$ at a point with $(x, z) = (p_\epsilon(x_0), z_0)$, with $p_\epsilon(x_0) > 0$. As $\epsilon \to 0$, the exit point $p_\epsilon(x_0)$ approaches the value $p_0(x_0)$ given implicitly by the following integral:

$$\int_{x_0}^{p_0(x_0)} \frac{g(x, 0, 0)}{f(x, 0, 0)} \mathrm{d}x = 0.$$

Such a formula can be generalized to higher-dimensional systems, at the cost of additional assumptions which, as we explain, are not always trivially satisfied.

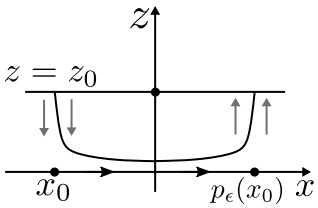

Figure 1: A visualization of the entry-exit map for a planar system.

The models

Compartmental epidemics models

The first models we present are the compartmental models, in non-standard GSPT form, studied in [3]. In all the models, the fast processes are the ones related to infection and recovery, whereas the slow processes are the ones related to loss of immunity or demography. The passage of an orbit close to the critical manifold, represented in all cases by the absence of infectious individuals in the population, allows us to bring the system in standard form through a rescaling of the variables, and to predict the beginning of another "wave" through the entry-exit function.
We analyzed three epidemics models given as slow-fast SIR (Susceptible-Infected-Recovered) and SIRS compartmental models, and proved that when the basic reproduction number R_0 is greater than 1, the system will converge to an endemic equilibrium characterized by an $\mathcal{O}(\epsilon)$ fraction of the population still in the infected compartment.
Then, we studied an SIRWS (where the "W" represents individuals in a Waning immunity phase), and we applied a geometrical argument, sketched in Figure 2, to prove the asymptotic convergence towards a unique endemic equilibrium or towards a limit cycle.

Finally, we present the SIRS compartmental model on homogeneous networks studied in [4]; one fundamental difference with the SIRS model studied in [3] is the existence of stable limit cycles. All the results obtained in the aforementioned papers heavily rely on the entry-exit function, and one critical assumption needed in order to use this tool (namely, separation of eigenvalues of the linearization of the systems along the critical manifold) is not always satisfied along solutions of the SIRS model on networks. We comment on such a limitation, and provide a possible solution to overcome such an issue.

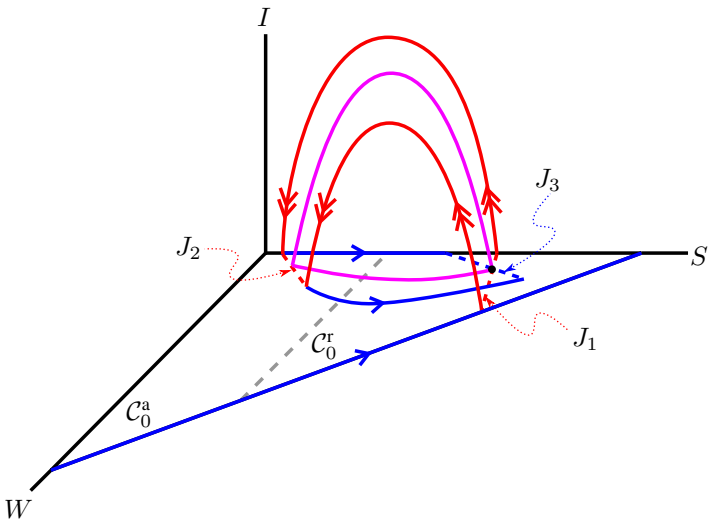

Figure 2: Concatenation of slow and fast orbits, giving rise to a limit cycle.

A short theoretical digression

As a follow-up to the criticality emerging from the model studied in [4], we shortly describe an ongoing project [5] which aims at generalizing the possibilities of application of the entry-exit function.
Specifically, we consider a class of 1-fast/2-slow systems of ODEs, and provide entry-exit relations for systems whose linearizations do not exhibit separation of eigenvalues on the critical manifold. We argue that such an approach could be generalized to higher-dimensional systems.

Synaptic transmission via neurotransmitter release

Then, we showcase the application of the entry-exit function to a planar system in standard GSPT form studied in [8]. The entry-exit function can be used, in this context, to compute the delay between subsequent spikes in the neural activity and capture possible response of a post-synaptic neuron to an input (formed by one or several spikes) received by a pre-synaptic neuron. This response always incurs a minimal delay (diffusion time to cross the synaptic cleft, the space in between the two neurons) but can increase substantially depending on the neural type and possible pathological behaviour of the underlying neural population. The entry-exit function hence allows to fine-tune the model so as to capture all these scenarios within a parsimonious framework, and fit to data of both excitatory and inhibitory synapses.
Lastly, we propose a generalization of the previous system, in which the quadratic component of the critical manifold is replaced with a quartic curve. We study how the shape of the quartic, as well as other parameters of the system, may affect both the transient and asymptotic behaviour of the system, since both are of interest in such applications.

References

[1] De Maesschalck P., Schecter S. (2016) The entry–exit function and geometric singular perturbation theory. *Journal of Differential Equations* **260(8)**:6697-6715.

[2] Fenichel N. (1979) Geometric singular perturbation theory for ordinary differential equations. *Journal of differential equations* **31(1)**:53-98.

[3] Jardón-Kojakhmetov H., Kuehn C., Pugliese A., Sensi M. (2021) A geometric analysis of the SIR, SIRS and SIRWS epidemiological models. *Nonlinear Analysis: Real World Applications* **58**:103220.

[4] Jardón-Kojakhmetov H., Kuehn C., Pugliese A., Sensi M. (2021) A geometric analysis of the SIRS epidemiological model on a homogeneous network. *Journal of mathematical biology* **83(4)**:1-38.

[5] Kaklamanos P., Kuehn C., Popović N., Sensi M. (2022) Entry-exit functions: beyond eigenvalue separation. *In preparation*.

[6] Kuehn C. (2015) Multiple time scale dynamics. Springer, Berlin.

[7] Neishtadt A. I. (1987) On delayed stability loss under dynamical bifurcations I. *Differential Equations* **23**:2060-2067.

[8] Rodrigues S., Desroches M., Krupa M., Cortes J. M., Sejnowski T. J., Ali A. B. (2016) Time-coded neurotransmitter release at excitatory and inhibitory synapses. *Proceedings of the National Academy of Sciences*, **113(8)**:E1108-E1115.

[9] Wechselberger M. (2020) Geometric singular perturbation theory beyond the standard form. Springer, NY.

Monday, July 18, 2022
13:30 - 15:50

MS-10 Non-Smooth Dynamics
Saint Clair 3A

Chair : Vincent Acary - Remco Leine

13:30 - 13:50
A new explicit CD-Lagrange scheme with redistributed mass for structural dynamics with impacts
DI Stasio Jean*, DUREISSEIX David, GRAVOUIL Anthony, GEORGES Gabriel, HOMOLLE Thomas
*Laboratoire de Mécanique des Contacts et des Structures [Villeurbanne] (Bâtiment Sophie Germain27b, avenue Jean CapelleF69621 VILLEURBANNE CEDEX France) - Centre de Technologie de Ladoux (Place des Carmes-Déchaux 63000 Clermont-Ferrand France)

13:50 - 14:10
Bifurcations in Piecewise Smooth, Delay Differential Systems
SHUKLA Amit*, STRIJBOSCH Nard, NIJMEIJER Henk
*Miami University (650 East High Street, Oxford, Ohio 45056 United States)

14:10 - 14:30
Coexistence of conservative and dissipative dynamics in forced vibro-impact oscillator with Amonton-Coulomb friction
KRAVETC Pavel*, GENDELMAN Oleg, RACHINSKII Dmitrii
*Department of Mechanical Engineering [Haifa] (Technion - Institute of Technology Haifa 32000 Israel Israel)

14:30 - 14:50
Compact weighted residual formulation for periodic solutions of systems undergoing unilateral contact and frictional occurrences
LEGRAND Mathias*, PIERRE Christophe
*Structural Dynamics and Vibration Laboratory, McGill University (Department of Mechanical Engineering, Room 122, McConnell Engineering Building, McGill University, 817 Sherbrooke St West, Montréal QC H3A 0C3 Canada)

14:50 - 15:10
Dynamic non-smooth fold bifurcations influenced by oscillations and noise
KUSKE Rachel*, BUDD Chris, GRIFFITH Cody
*Georgia Institute of Technology (Atlanta United States)

15:10 - 15:30
Effect of dry friction on a parametrically excited nonlinear oscillator
BENACCHIO Simon*, GIRAUD-AUDINE Christophe, THOMAS Olivier
*Arts et Metiers Institute of Technology, LISPEN, HESAM Université (F-59000 Lille France)

15:30 - 15:50
Experimental Verification of Stability Theory for a Planar Rigid Body with Two Unilateral Frictional Contacts
OR Yizhar*, VARKONYI Peter
*Department of Mechanical Engineering, Technion - Institute of Technology Haifa 32000 Israel (Technion - Institute of Technology Haifa 32000 Israel Israel)

A new explicit CD-Lagrange scheme with redistributed mass for structural dynamics with impacts

Jean Di Stasio[*,†], David Dureisseix[*], Anthony Gravouil [*], Gabriel Georges[†] and Thomas Homolle[†]
[*]*Univ Lyon, INSA-Lyon, CNRS UMR5259, LaMCoS, France*
[†]*Centre de technologie de Ladoux-Manufacture française de pneumatiques Michelin, France*

Summary. This work aims to apply mass redistribution method to explicit schemes in non-smooth contact dynamics, especially the CD-Lagrange scheme. New properties are being investigated to better address the issues of impact for structural transient dynamics. Mass redistribution method improves energy balance and stability for CD-Lagrange scheme. Results for a simple contact problem are presented.

Non-smooth Contact Dynamics and mass redistribution method

In structural transient dynamics, problems with impact belong to the family of Non-Smooth Contact Dynamics (NSCD) problems. An impact causes a discontinuity in velocity, and therefore a non-defined acceleration. Integrating in time requires thus dedicated schemes. A first family, event-driven schemes, adjust the time-step to set impact times at discrete times. They fail in case of numerous and close impacts leading to a high computation time. A second family, time-stepping schemes, can deal with multiple impacts between two discrete times keeping time-step constant. Time-stepping schemes are thus more robust for practical finite elements problems.
The first NSCD time-stepping scheme is Moreau-Jean's scheme [1, 2]. It introduces a new contact formulation written in terms of velocity and impulsion. It allows stability at impact and a better energy balance, and is equivalent to classical Signorini's condition. But writing contact in terms of velocity does not solve exactly position. A residual penetration remains during contact. Chen, Acary et al. [5] extend Moreau's velocity formulation to Newmark's family. All these schemes are implicit.
A first family of NSCD explicit schemes is Paoli-Schatzman's one [3]. They use a contact formulation in terms of position, and central difference method for time-integration. For velocity/impulse contact formulation, the only explicit scheme is CD-Lagrange [4]. It uses the central difference method too for time-integration, but preserves properties of Moreau-Jean's family.
A active research field in NSCD is currently the mass redistribution method. Following the work of Khenous, Laborde and Renard [6], new spatial discretizations appear with massless node for contact. This improves the energy balance, and velocity stability for contact nodes after release. Dabaghi [7] applies this technique to Paoli-Schatzman's schemes leading to similar improvements.
In the present work redistribution mass method is applied to CD-Lagrange scheme. The purpose is to exhibit the interest of mass redistribution method to velocity/impulse contact formulation and a explicit scheme. This new scheme would be well suited to non-linear impact dynamics involved in tire simulations.

CD-Lagrange scheme with redistributed mass : a 1D example

Figure 1: Redistributed mass on a discrete bar

Here a one-dimensional problem is presented to illustrate the main features of mass redistribution on a CD-Lagrange scheme. The impacting bar problem is chosen. It is a common benchmark case for NSCD integration schemes [4, 5, 7, 8]. This case is a discrete bar impacting on a rigid barrier, with a linear elastic material law.
Here the skin is defined as being the last element of the bar. Modifying mass consists of removing mass of contact node and distributing it uniformly on other nodes. It results in two problems : one for the bulk, and one for the skin. The bulk problem is dynamic with kinetic and internal stresses. The skin problem is similar to a static one. The contact node having no mass, no kinetical term is involved in equation of dynamic.
This leads to a difficulty for schemes with velocity as main unknown (like CD-Lagrange): the contact node velocity can not be determined by the equation of dynamic. The solution is to set the normal velocity depending on state of contact. It is fixed to zero for an active contact, and to the normal velocity of preceding mass node otherwise. This means that the skin deforms only when the contact is active. After release, a deformed state can thus persist. In such a case the skin force acting on bulk domain is set to zero. As a consequence the contact problem no longer contains kinetic terms, but only forces based on stresses in skin.

Figures 2 and 3 show respectively the contact node position and velocity over time for analytical, classical CD-Lagrange and redistributed mass CD-Lagrange solutions.
The analytical solution of the continuous problem is known. The bar gets closer to the barrier with constant speed and impacts it (around $t = 0,5 \times 10^{-4} s$). The contact persists until the compression wave reaches the free end and returns.

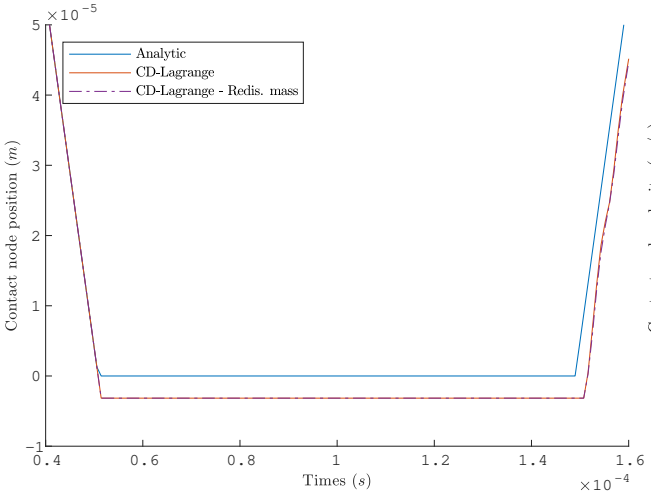

Figure 2: Contact node position

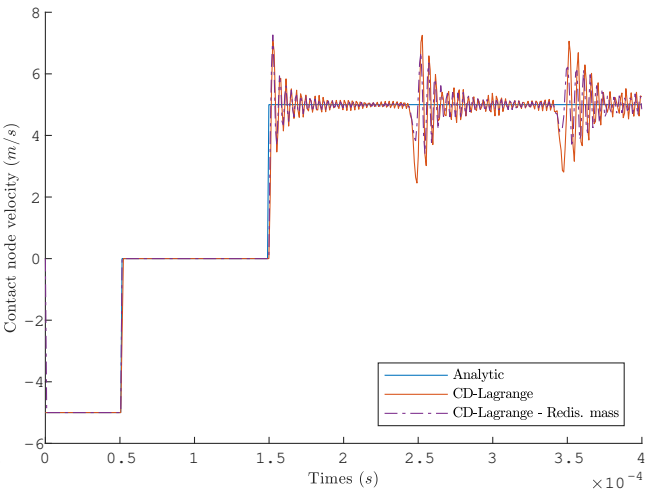

Figure 3: Contact node velocity

Then the bar releases contact (around $t = 1.5 \times 10^{-4}s$) and moves away with the same constant speed as before impact.

Time-integration schemes compute discrete solutions with commons features : a residual penetration remains after impact, because of the velocity contact condition. This residual penetration is the same for both CD-Lagrange schemes. Redistributing mass has no influence on discrete position. For velocity, if the discrete solutions stay close from analytic one before the contact release, spurious oscillations appear after. For redistributed mass CD-Lagrange, they vanish slightly faster.

Discrete energy over time is depicted on figure 4. This energy contains only conservative terms: kinetic, internal and complementary energy. At impact time the loss of energy for CD-Lagrange is the kinetic energy of contact node, as its velocity is set to zero. For CD-Lagrange with redistributed mass, no energy is lost as the node is massless. But at contact release, some energy is injected.

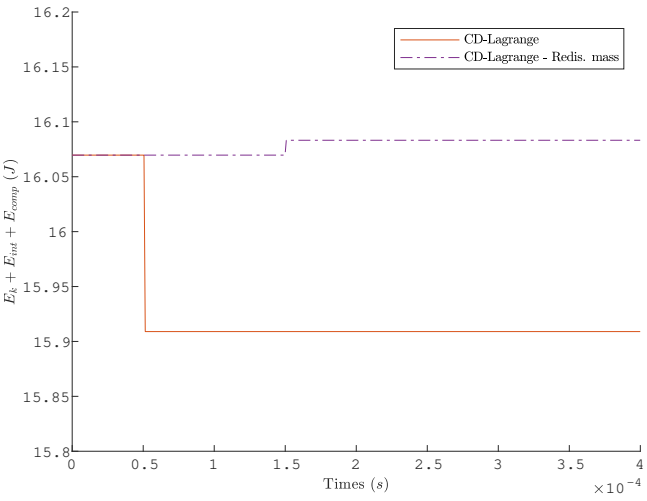

Figure 4: Energy : conservative terms

Conclusion and future work

Embedding mass redistribution in CD-Lagrange scheme allows to improve three features: a new contact problem, simpler without kinetic terms; a conservative impact; a weakening of spurious oscillations slightly improved.

The next step of this work is to extend it to three-dimensional problems. A major issue is dealing with incompatible meshes, that leads to a higher complexity for the impact problem.

References

[1] Moreau J. J. (1999) Numerical aspects of the sweeping process. *Comput. Methods Appl. Mech. Eng.* vol. 177, no. 3-4, pp. 329-349

[2] Jean M.(1999) The non-smooth contact dynamics method. *Comput. Methods Appl. Mech. Eng.* vol. 177, no. 34, pp. 235-257

[3] Paoli L., Schatzman M. (2002) A Numerical Scheme for Impact Problems I: The One-dimensional Case. *SIAM J. Numer. Anal.* vol. 40, no. 2, pp. 702-733

[4] Fekak F. E. , Brun M., Gravouil A., Depale B. (2017) A new heterogeneous asynchronous explicit-implicit time integrator for nonsmooth dynamics. *Comput. Mech.* vol. 60, no. 1, pp. 1-21

[5] Chen Q., Acary V., Virlez G., Brüls O. (2013) A nonsmooth generalized-α scheme for flexible multibody systems with unilateral constraints. *Int. J. Numer. Methods Eng.* vol. 96, no. 8, pp. 487–511

[6] Khenous H. B., Laborde P., Renard Y. (2008) Mass redistribution method for finite element contact problems in elastodynamics, *Eur. J. Mech. A/Solids* vol. 27, no. 5, pp. 918-932

[7] Dabaghi F., Petrov A., Pousin J., Renard Y. (2016) A robust finite element redistribution approach for elastodynamic contact problems *Appl. Numer. Math.* vol. 103, pp. 48-71

[8] Di Stasio J., Dureisseix D., Gravouil A., Georges G., Homolle T. (2019) Benchmark cases for robust explicit time integrators in non-smooth transient dynamics, *Adv. Model. Simul. Eng. Sci.* vol. 6, no. 2

We gratefully acknowledge the French National Association for Research and Technology (ANRT, CIFRE grant number 2017/1555). This work was supported by the Manufacture Française de Pneumatiques Michelin.

Bifurcations in Piecewise Smooth, Delay Differential Systems

Amit Shukla*, N.W.A. Strijbosch† and Henk Nijmeijer †
*Department of Mechanical and Manufacturing Engineering, Miami University, Oxford, Ohio, USA
†Department of Mechanical Engineering, Eindhoven University of Technology, The Netherlands

Summary. This paper presents bifurcation study of piecewise smooth differential delay equations (PWS-DDEs) where the state variable determines which differential delay equation is active. This paper aims to add to the existing research performed on bifurcation studies of PWS-DDEs by developing an algorithm to perform bifurcation studies of a general form of PWS-DDEs, such that it can be used for any bifurcation study of a PWS-DDEs system. Bifurcation studies are performed using a simplified model of a controlled inverted pendulum to study the effect of parameters. During the bifurcation studies, new type of bifurcations that arise for PWS-DDEs are defined.

Introduction

The ability to predict the stability of periodic behavior can be of importance in the research into for instance Parkinson [2] or other balance disorders. Methods to determine periodic solutions for differential delay equations (DDEs) or piecewise smooth (PWS) systems are well described. To find periodic solutions of DDEs the collocation method is often used [3, 4, 5, 6]. In [1] the collocation method as used for DDEs is extended such that it is able to find periodic solutions of PWS-DDEs.This paper presents bifurcation studies of a general form of PWS-DDEs. We study the influence of smooth switching manifold on the parametric bifurcations for a controlled inverted pendulum. Bifurcation studies are presented for systems with smooth switching manifolds using the algorithm developed.

Model

The state space model of the inverted pendulum is given by

$$\begin{bmatrix}\dot{x}_1\\ \dot{x}_2\end{bmatrix} = \begin{bmatrix}x_2(t)\\ \sin x_1(t) - x_2(t) - u(x(t-\tau))\end{bmatrix} \tag{1}$$

where $x_1 := \theta$ and $x_2 := \dot{\theta}$, where θ is the angle and u is a torque determined by a controller. Delays in for instance the sensors or computational delays are modeled by using the delayed values of the angle and angular velocity to determine the torque u.The parameters (mass, length, and damping coefficient) in this model are scaled to unity.Some studies suggest that central nervous system uses control switching strategies that deactivate the controller in certain (stable) subspaces of the state space, to minimize control effort [7]. The switching strategies are a function of these delayed values, hence one way to describe the control input on the system can be:

$$u(x(t-\tau)) = \begin{cases}0 & \text{when } x(t-\tau) \in \chi_{unctrl}\\ K_p x_1(t-\tau) + K_d x_2(t-\tau) & \text{when } x(t-\tau) \in \chi_{ctrl}\end{cases} \tag{2}$$

with $\chi_{unctrl} \bigcup \chi_{ctrl} = \mathbb{R}^2$, with K_p and K_d the proportional and derivative gain, respectively. The switching strategy studied here is to only control the system if magnitude of the angle is large. The subspaces $\chi_{unctrl} = \{x \in \mathbb{R}^2 | \, |x_1| \leq e\}$ and $\chi_{ctrl} = \{x \in \mathbb{R}^2 | \, |x_1| > e\}$ define this switching strategy where e is the value of $|\theta(t-\tau)|$ which defines the switching plane.

Bifurcation studies

A bifurcation study along parameter K_p is performed to study the effect of switching manifold. The bifurcation behavior is characterized by appearance of topologically nonequivalent phase portraits under variation of the parameter μ. The bifurcation studies are performed using the switching plane with $e = 0.1$. The parameters of the model are $K_p = 2$, $K_d = 1$ and $\tau = 0.5$, if not mentioned differently. The bifurcation diagram along the bifurcation parameter K_p is depicted in Figure 1. The whole branch consist of stable periodic solutions and the unstable equilibrium point at the origin. The evolution of a branch at $K_p = 1$ is given in Figure 2. Due to the sudden periodic solutions that originate similar to a Pitchfork bifurcation this phenomena will be referred to as the *Pseudo-pitchfork bifurcation*. There are two differences between pseudo-pitchfork bifurcation and the pitchfork bifurcation:the periodic solutions do not originate from the main branch and stability along the main branch does not change at the bifurcation point. For phase portrait C in Figure 1 one side has a stable periodic solution, and the other side there are two stable periodic solutions and on each side of the bifurcation point the solutions are stable. To study the behavior that causes the bifurcation, a section of the whole branch around the bifurcation point is depicted in Figure 3. In this case, for $\mu < \mu_0$, with μ_0 the bifurcation point, there is one unstable equilibrium one periodic solution, and for $\mu \geq \mu_0$ there is still one unstable equilibrium and two stable periodic solutions. This is called an *X-bifurcation*. The most challenging part of these studies is an inherent inability to capture all bifurcations at any critical point due to an inherent numerical approach and this remains part of future work for authors.

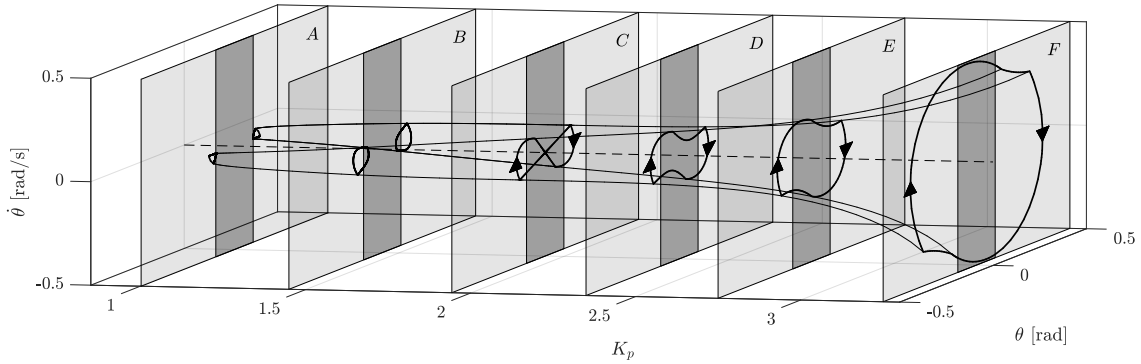

Figure 1: Bifurcation diagram along parameter K_p with the magnitude switching manifold

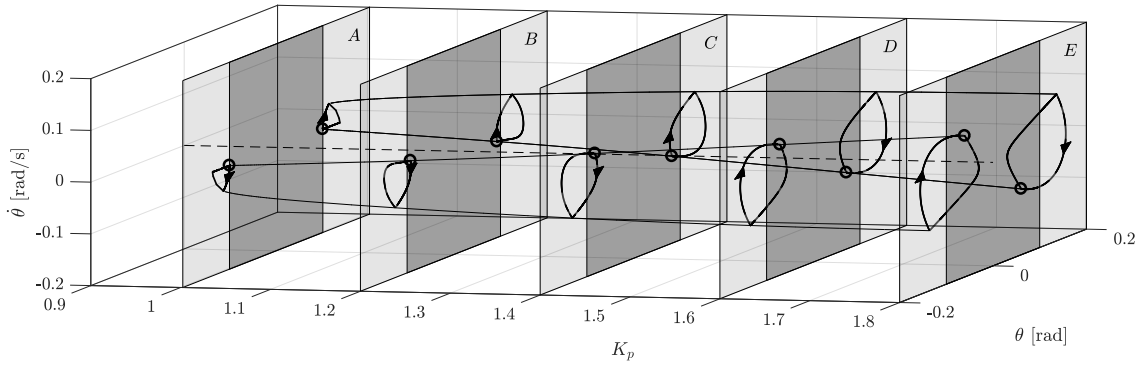

Figure 2: Evolution of periodic solutions close to Pseudo-pitchfork bifurcation

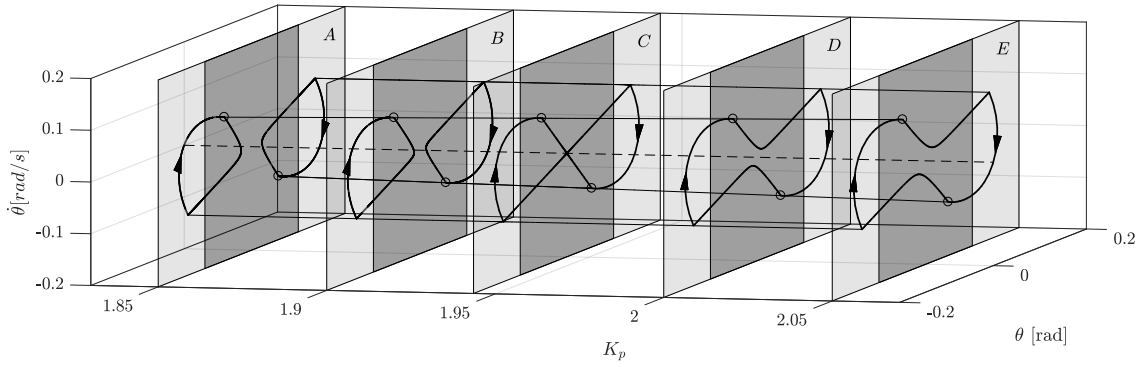

Figure 3: Evolution of periodic solutions close to X-bifurcation

Conclusions

Two new bifurcations are observed for the system using a smooth switching control strategy for a PWS-DDE system.

References

[1] D.A.W. Barton. Stability calculations for piecewise-smooth delay equations. *International Journal of BIfurcation and Chaos*, pages 19(2):639–650, 2009.

[2] C. Ramaker, J. Marinus, and A.M. Sitgelbout andB.J. van Hilten. Systematic evaluation of rating scales for impairment and disability in parkinson's disease. *Movement disorders*, 17 (5):867–876, 2002.

[3] K. Engelborghs, T. Luzyanina, and D. Roose. Numerical bifurcation analysis of delay differential equations. *Journal of Computational and Applied Mathematics*, 125 (I):265–275, 2000.

[4] K. Engelborghs and E.J. Doedel. Stability of piecewise polynomial collocation for computing periodic solutions of delay differential equations. *Numerische Mathematik*, 91(4):627–648, 2002.

[5] D. Roose and R. Szalai. *Continuation and Bifurcation Analysis of Delay Differential Equations*, pages 359–399. Springer Netherlands, Dordrecht, 2007.

[6] K. Verheyden and K. Lust. A newton-picard collocation method for periodic solutions of delay differential equations. *BIT Numerical Mathematics*, 45(3):605–625, 2005.

[7] I.D. Loram, H. Gollee, M. Lakie, and P.J. Gawthrop. Human control of an inverted pendulum: Is continuous control necessary? is intermittent control effective? is intermittent control physiological? *The Journal of Physiology*, 589(2):307–324, 2011.

Coexistence of conservative and dissipative dynamics in forced vibro-impact oscillator with Amonton-Coulomb friction

Pavel Kravetc*, Oleg Gendelman* and Dmitrii Rachinskii †
*Faculty of Mechanical Engineering, Technion – Israel Institute of Technology, Haifa, 3200003, Israel
†Department of Mathematical Sciences, The University of Texas at Dallas, Richardson, Texas, 75080, USA

Summary. The qualitative differences in the behaviors of Hamiltonian and dissipative systems are profound. In particular, in Hamiltonian systems the existence of asymptotically stable solutions is impossible due to the Liouville's theorem. By contrast, dissipative systems usually exhibit eventual attraction of all phase trajectories to ω-limit sets such as fixed points, (quasi-) periodic or strange attractors. In this work we present a class of dissipative mechanical systems which demonstrate mixed global dynamics, i.e., coexistence of both attracting and Hamiltonian-like behaviors. Our main model is a well-known system of harmonically forced vibro-impact oscillator with Amonton-Coulomb friction. In a vast majority of previous studies, it also includes viscous friction, and the global dynamics of its state space is governed by the aforementioned attractors. However, if we omit viscous friction, we observe that the state space is divided into regions with "regular" attraction, as well as regions with profoundly Hamiltonian dynamics, e.g., KAM-like tori. We show that such local Hamiltonian behavior occurs for the phase trajectories with non-vanishing velocities. The stability analysis of the periodic solutions confirms the above statement. We also demonstrate that similar mixed global dynamics can be observed in a broader class of models including systems with x-dependent potentials as well as multi-particle systems.

Introduction

Model formulation

We consider a single-degree-of-freedom unit mass particle which displacement is constrained by two rigid walls ($l < x(t) < r$). The particle is subject to external sinusoidal forcing of period $T = 2\pi/\omega$ and the Amonton-Coulomb dry friction [1, 2]. The equation for motions $l < x(t) < r$ is

$$\ddot{x} + f\,\mathrm{sgn}\,(\dot{x}) = F\cos(\omega t). \tag{1}$$

We assume that $F > f$, since otherwise any motion comes to stop. When $x(t) = r, l$ the following impact rule [3] is applied:

$$\dot{x}(t^-) = -\dot{x}(t^+). \tag{2}$$

Dynamics of system (1)–(2), and its dependence on parameters, will be illustrated by the global phase portrait of the stroboscopic time T map $\Phi : (x(0),\ \dot{x}(0)) \mapsto (x(T),\ \dot{x}(T))$. In particular, a fixed point of Φ corresponds to a periodic solution of system (1)–(2).

Numerical investigations

A typical phase portrait of Φ with $f = 0$ is shown on Figure 1a. It presents an invariant island containing a fixed point and periodic orbits which are surrounded by invariant curves representing quasiperiodic motions. Another region of quasiperiodic motions is observed for large velocities. Between these two regions there is a chaotic sea (gray dots). Furthermore, a horizontal segment of fixed points represents periodic solutions without impacts $x(t) = -\frac{F}{\omega 2}\cos(\omega t) + C$.

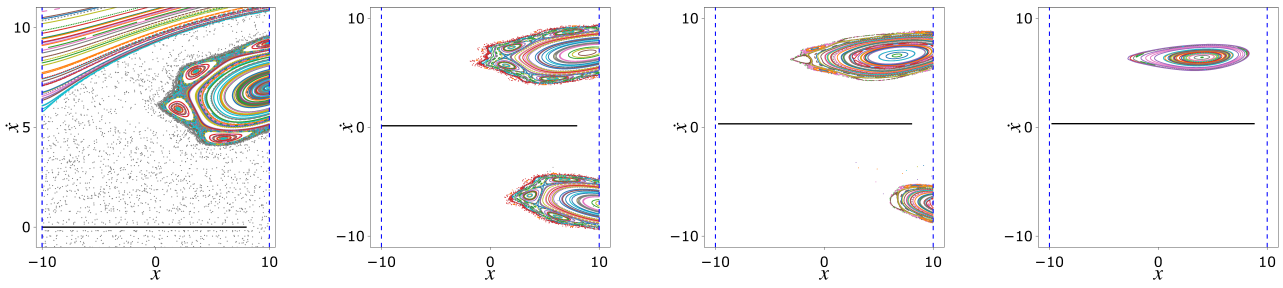

(a) $f = 0$ (b) $f = 0.1$ (c) $f = 0.3$ (d) $f = 0.5$

Figure 1: Evolution of the phase portrait with increasing friction. Other parameters are the following: $F = 1, \omega = 1, R := r - l = 20$.

Introducing friction drastically changes the phase portrait (Figures 1b–d). In particular, the segment of fixed points corresponding to periodic solutions without impacts becomes an attractor. However, the invariant island of Hamiltonian dynamics persists, thus, we observe coexistence of dissipative and conservative behaviors. The trajectories from the invariant island have a non-vanishing velocity, and, therefore, we call such solutions *non-sticking*.

Analysis

Hamiltonian dynamics of system (1)–(2) can be explained by lifting it to the unconstrained Hamiltonian system

$$\ddot{q} + \frac{\partial V}{\partial q} = \frac{f}{R}, \qquad V(t,\ q) = \frac{F}{R}\cos(\omega t)W(q), \qquad W(q) = \begin{cases} q, & 0 \le q < 1, \\ 2-q, & 1 \le q < 2, \end{cases} \qquad W(q+2) = W(q). \tag{3}$$

Any non-sticking solution of (3) is mapped to a non-sticking solution of (1)–(2) by the simple relationship

$$x = R \cdot W(q) + l. \tag{4}$$

Therefore, if all solutions starting from a domain Ω of the state space of system (1)–(2) are non-sticking and Ω is invariant for the time T map Φ of this system, then Ω is a region of Hamiltonian dynamics. In particular, at least a small invariant region Ω of Hamiltonian dynamics exists around every fixed point of non-degenerate non-resonant center type.

Stability analysis

Stability and type of a fixed point and the corresponding periodic solution is determined using the Floquet theory as follows. Any trajectory of (1)–(2) can be represented as a sequence of motions and events of the following types: *free flight* ($\dot{x} \neq 0$), *sticking* ($\dot{x} = 0$ over a nonzero interval of time), *reflection from the wall* ($x = r, l$) and *a turning point* (change of sign of $\dot{x}$). Thus, the Jacobi matrix Φ' can be obtained as a product of corresponding matrices (matrix related to an instantaneous event is known as *saltation matrix* [4]). In particular, it is easy to show that matrices for free flights and reflections of the walls have unit determinants. Thus, non-sticking trajectories, $\det(\Phi') = 1$ which corresponds to the phase area preservation.

Extensions

Mixed global dynamics can also be observed in systems with x-dependent potentials as well as systems with higher degrees of freedom. For instance, one can consider system of $n \geq 2$ elastically colliding particles with masses m_i placed between the same two walls. Again, in order to spot regions of Hamiltonian-like behavior we should check non-sticking periodic trajectories of non-resonant center type. The linear stability analysis can be easily extended to the case of many particles, however, in order to be volume-preserving the Jacobian Φ' should be symplectic. It turns out that the saltation matrix S related to the particle collision is not necessary symplectic. However, if the product of velocities of the two colliding particles has the same sign before and after the collision, then the corresponding saltation matrix (for $n = 2$)

$$S = \begin{bmatrix} A^T & 0 \\ B & A \end{bmatrix} \quad \text{with} \quad A = \frac{1}{m_1+m_2}\begin{bmatrix} m_1-m_2 & 2m_1 \\ 2m_2 & m_2-m_1 \end{bmatrix} \quad \text{and} \quad B = \frac{2F\cos(\omega t_*)(m_1-m_2)m_1m_2}{m_1+m_2\left(m_2\dot{x}_1(t_*^-)-m_1\dot{x}_2(t_*^-)\right)}\begin{bmatrix} -1 & 1 \\ 1 & -1 \end{bmatrix}, \tag{5}$$

is symplectic. When $m_1 = 1$, $m_2 = 0.9$, $F = 1$, $\omega = 2\pi$, $f = 0.005$, $R = 2$, the two-particle system has a $3T$-periodic solution which linearization is symplectic. Figure 2 presents invariant tori in a neighborhood of this solution. The tori coexist with an attractor consisting of periodic solutions without collisions or impacts.

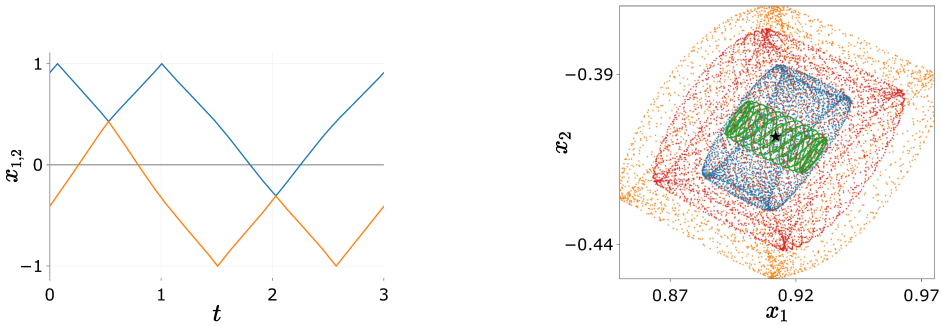

(a) (b)

Figure 2: Panel (a): Time trace of a $3T$-periodic solution of the two-particle system with $m_1 = 1$ (blue), $m_2 = 0.9$ (orange). Panel (b): Projection of the phase portrait of the time T map Φ onto the (x_1, x_2)-plane exhibiting several invariant tori near a period 3 point (star).

References

[1] Shaw S. (1986) On the dynamic response of a system with dry friction, Journal of Sound and Vibration 108, 305–325.

[2] Cone K. and Zadoks R. (1995) A numerical study of an impact oscillator with the addition of dry friction, Journal of Sound and Vibration 188, 659–683.

[3] Babitsky V. I. (1998) Theory of Vibro-Impact Systems and Applications, Springer-Verlag, Berlin Heidelberg.

[4] Bernardo M., Budd C., Champneys A. R., and Kowalczyk P. (2008) Piecewise-smooth dynamical systems: theory and applications, Springer-Verlag London.

Compact weighted residual formulation for periodic solutions of systems undergoing unilateral contact and frictional occurrences

Mathias Legrand[1] and Christophe Pierre[2]
[1]*Department of Mechanical Engineering, McGill University, Montreal, Canada*
[2]*Department of Mechanical Engineering, Stevens Institute of Technology, Hoboken, New Jersey, USA*

Summary. A very compact weighted residual formulation is proposed for the construction of periodic solutions of oscillators subject to unilateral contact and frictional occurrences. The key idea is to express all governing equations as equalities, which can then be satisfied in a weighted residual sense.

Toy system

In order to introduce the proposed formulation, a simple toy system, illustrated in Figure 1, is considered. It is a simple geometrically nonlinear mass-spring system lying on a moving belt of constant linear velocity v. The mass is denoted by m and the stiffness, by k. The length of the spring at rest (in a vertical position when the mass is lying on the belt) is L. The vertical displacement of the mass is $y(t)$ and vertical separation from the belt is possible. The horizontal displacement is $x(t)$. The position at rest is $(x, y) = (0, 0)$. The frictional force acting on the mass is $r_{\mathrm{T}}(t)$ while the unilateral contact

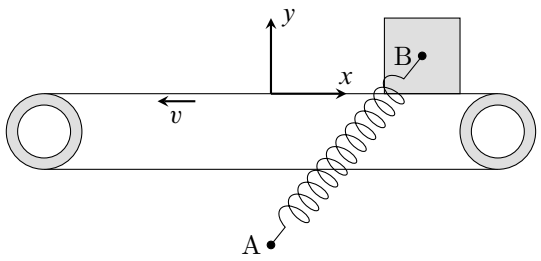

Figure 1: One-dimensional mass-spring moving on a rotating belt. Point A is fixed. The position of point B is $(x(t), y(t))$. The belt is assumed to be infinitely long.

force is $r_{\mathrm{N}}(t)$. The relative tangential velocity between the mass and the belt is $\dot{u}_{\mathrm{T}}(t) = -v + \dot{x}(t)$. In the remainder, time is often dropped for readability purposes.

Signorini unilateral contact and Coulomb's friction conditions expressed as equalities

Given the parametrization of the system of interest, the classical Signorini conditions are expressed as the complementarity conditions

$$r_{\mathrm{N}} \geq 0, \quad y \geq 0, \quad r_{\mathrm{N}} \cdot y = 0 \tag{1}$$

which can be recast into various equivalent nonsmooth equalities, one of which being

$$\forall \rho_{\mathrm{N}} > 0, \quad r_{\mathrm{N}} - \max(r_{\mathrm{N}} - \rho_{\mathrm{N}} y, 0) = 0. \tag{2}$$

Briefly said, the set of points solution to Equation (1) and Equation (2) is the same [1, 2]. Also, with the considered parameterization, Coulomb's friction classically says the following: given a closed contact in the normal direction,

$$\begin{cases} \dot{u}_{\mathrm{T}} = 0 & \Longrightarrow \quad |r_{\mathrm{T}}| \leq \mu r_{\mathrm{N}} \\ \dot{u}_{\mathrm{T}} \neq 0 & \Longrightarrow \quad |r_{\mathrm{T}}| = \mu |r_{\mathrm{N}}| \text{ and } \exists \alpha \geq 0 \,|\, r_{\mathrm{T}} = -\alpha \dot{u}_{\mathrm{T}} \end{cases} \tag{3}$$

where μ is the coefficient of friction. Among others, the above condition can equivalently be recast into the nonsmooth equality [2, 7]

$$\min(|\dot{u}_{\mathrm{T}}|, \mu r_{\mathrm{N}} - |r_{\mathrm{T}}|) = 0 \tag{4}$$

or

$$\forall \rho_{\mathrm{T}} > 0, \quad |\dot{u}_{\mathrm{T}}| - \max(|\dot{u}_{\mathrm{T}}| - \rho_{\mathrm{T}}(\mu r_{\mathrm{N}} - |r_{\mathrm{T}}|), 0) = 0. \tag{5}$$

Newton's impact law

Depending on the context of the investigation, an impact law $\dot{y}^+ = -e\dot{y}^-$ relating the pre- and post-impact velocities, $\dot{y}^-$ and $\dot{y}^+$ respectively, through a coefficient of restitution $e \in [0, 1]$ might be required for the well-posedness of the formulation since Equation (1) alone might not guarantee the uniqueness of the solution [4]. The idea is to test whether a penetration between the bodies in contact has occurred and then enforce the unilateral contact conditions at the velocity level with the above impact law inserted. Altogether, this reads [2]:

$$\begin{cases} y < 0 & \Longrightarrow \quad r_{\mathrm{N}} \geq 0, \quad \dot{y}^+ + e\dot{y}^- \geq 0, \quad r_{\mathrm{N}} \cdot (\dot{y}^+ + e\dot{y}^-) = 0 \\ y \geq 0 & \Longrightarrow \quad r_{\mathrm{N}} = 0 \end{cases} \tag{6}$$

which can be recast into the single equality

$$\forall \rho_{\mathrm{N}}, \quad (\operatorname{sign} y - 1)(r_{\mathrm{N}} - \max(r_{\mathrm{N}} - \rho_{\mathrm{N}}(\dot{y}^{+} + e\dot{y}^{-}), 0) + (\operatorname{sign} y + 1)r_{\mathrm{N}} = 0 \tag{7}$$

with the convention sign $y = 1$ if $y \geq 0$ and sign $y = -1$ otherwise.

Governing equations

Given the geometric nonlinearity induced by the action of the spring on the mass, we introduce the quantity

$$\gamma(x, y) = \frac{\sqrt{x^2 + (L + y)^2} - L}{\sqrt{x^2 + (L + y)^2}}. \tag{8}$$

The two coupled nonlinear and nonsmooth Ordinary Differential Equations

$$m\ddot{x} + k\gamma(x, y)x - r_{\mathrm{T}} = 0 \tag{9a}$$

$$m\ddot{y} + k\gamma(x, y)(y + L) - r_{\mathrm{N}} + mg = 0 \tag{9b}$$

together with either Equation (2) and Equation (4), or Equation (7) and Equation (4), govern the dynamics of the system considered. In Equation (9b), g is the gravity constant. Depending on the level of regularity of the targeted solution, Equation (9) might have to be read in the distributional sense.

Weighted residual formulation

It is suggested to search for periodic solutions by solving the above formulation in a weighted residual sense. All unknowns of the problem are expanded on an appropriate truncated basis of T-periodic functions with N members, commonly the Fourier basis in the Harmonic Balance Method but not necessarily, as follows:

$$x(t) = \sum_k x_k \phi_k(t), \quad y(t) = \sum_k y_k \phi_k(t), \quad r_{\mathrm{N}}(t) = \sum_k N_k \phi_k(t), \quad r_{\mathrm{T}}(t) = \sum_k T_k \phi_k(t). \tag{10}$$

Depending on the smoothness of the selected basis functions, time derivatives might either be obtained by pointwise differentiation in time or expanded on a less smooth basis and related to the differentiated quantity in a weak sense. Concerning Equation (7) which requires access to $\dot{y}^{+}$ and $\dot{y}^{-}$, a Discontinuous Galerkin scheme could be used [6]. If we decide to solve Equation (9), Equation (2) and Equation (4), the weighted residual formulation would take the following form: once the expressions of Equation (10) are inserted in the selected governing equations, find the $4N$ unknowns x_k, y_k, N_k and T_k which satisfy

$$\int_0^T \phi_k(t)(\text{Eq. (9a)})\,\mathrm{d}t = \int_0^T \phi_k(t)(\text{Eq. (9b)})\,\mathrm{d}t = \int_0^T \phi_k(t)(\text{Eq. (2)})\,\mathrm{d}t = \int_0^T \phi_k(t)(\text{Eq. (4)})\,\mathrm{d}t = 0, \quad \forall k. \tag{11}$$

The above integrals can be numerically computed using an appropriate quadrature scheme such as a Riemann sum. The resulting system of nonlinear equations can be also solved using a nonsmooth Newton solver, for instance. The proposed strategy can be seen as a very compact form of the AFT methodology [5] without regularization and shares similarities with the DLFT technique [3] which also relies on the AFT. The rate of convergence of the proposed procedure might depend on the two parameters ρ_{N} and ρ_{T}, which have to be assigned a value in the solvers.

Conclusions

The proposed formulation is very compact and involves simple implementations such as basic integral quadrature schemes and existing nonlinear solvers. Its engineering value lies in its capability to generate coarse approximations without difficulty in contrast to much more advanced time-stepping or event-driven schemes [2]. It can be extended to more elaborate mechanical systems in a straightforward fashion. However, the convergence rate in terms of the number of unknowns is expected to be low and should be investigated with great care.

References

[1] Lu T. and Legrand M. (2021), Nonsmooth Modal Analysis via the Boundary Element Method for One-Dimensional Bar Systems. *Nonlinear Dynamics* 10.1007/s11071-021-06994-z

[2] Acary V. and Brogliato B. (2008), Numerical Methods for Nonsmooth Dynamical Systems: Applications in Mechanics and Electronics, Springer 10.1007/978-3-540-75392-6

[3] Nacivet S., Pierre C., Thouverez F. and and Jézéquel, L. (2003) A dynamic Lagrangian frequency–time method for the vibration of dry-friction-damped systems, *Journal of Sound and Vibration* 10.1016/S0022-460X(02)01447-5

[4] Moreau J.J. (2004), An introduction to Unilateral Dynamics. Novel Approaches in Civil Engineering. *Lecture Notes in Applied and Computational Mechanics* 10.1007/978-3-540-45287-4_1

[5] Cameron T.M. and Griffin J.H. (1989), An Alternating Frequency/Time Domain Method for Calculating the Steady-State Response of Nonlinear Dynamic Systems, *Journal of Applied Mechanics* 10.1115/1.3176036

[6] Schindler T., Rezaei S. Kursawe J. and Acary V. (2015), Half-explicit timestepping schemes on velocity level based on time-discontinuous Galerkin methods, *Computer Methods in Applied Mechanics and Engineering* 10.1016/j.cma.2015.03.001

[7] Xuewen L., Soh A.-K. and Wanji C. (2000), A new nonsmooth model for three-dimensional frictional contact problems, *Computational Mechanics* 10.1007/s004660000202

Dynamic non-smooth fold bifurcations influenced by oscillations and noise

Rachel Kuske*, Chris Budd †,Cody Griffith ‡
*School of Mathematics, Georgia Tech. USA
†Department of Mathematical Sciences, University of Bath, UK
‡University of British Columbia, CA, and 908 Devices, USA

Summary. We contrast the behavior of dynamic bifurcations for smooth and non-smooth fold bifurcations in the presence of oscillatory and noisy forcing. Dynamic bifurcation refers to the state transition or "tipping" that takes place when a parameter slowly varies through a value corresponding to a bifurcation in the static model. Note that the dynamic models correspond to non-autonomous systems with multiple time scales. Through a canoncial model with an underlying static nonsmooth fold bifurcation, we see that the transition is delayed as in the smooth case, depending on the rate of change of the parameter, but the functional form for the non-smooth case is different. We also compare and contrast how oscillatory forcing can shift the tipping or dynamic bifurcation, in both smooth and NS cases. We extend to a higher degree of freedom models with NS fold bifurcations, studying a Stommel model, a two-box ocean model for temperature and salinity. Within this higher dimensional model, we find additional differences for the non-smooth case in the presence of certain types of random forcing.

Contrasts of tipping points in smooth and non-smooth fold bifurcations

We consider a non-autonomous single degree of freedom (DOF) model ,

$$\dot{x} = -\mu + 2|x| - x|x| + A\sin(\Omega t), \quad \dot{\mu} = -\epsilon, \qquad x(0) < 0, \quad \mu(0) > 0, \qquad \epsilon \ll 1, \tag{1}$$

with A and $\Omega = \epsilon^{-\lambda}$ the amplitude and frequency, respectively, of the oscillatory forcing and slowly varying bifurcation parameter μ. For the static system $\epsilon = 0$ there is an underlying non-smooth (NS) fold bifurcation at $\mu = x = 0$ as shown in Fig. 1. Using a series of multiple scale analyses, we obtain approximations for the dynamic bifurcations, often called

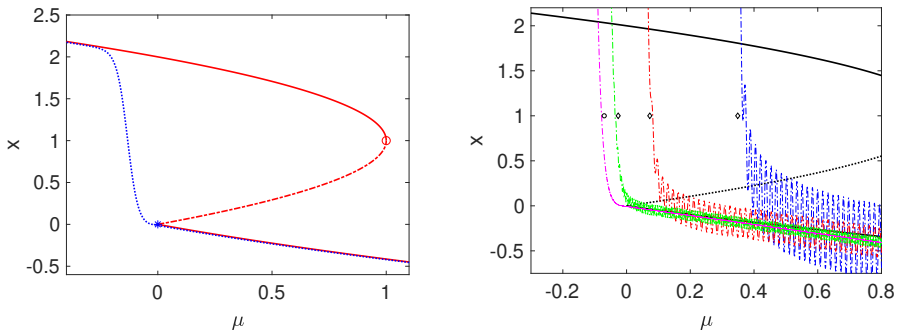

Figure 1: (LEFT) The bifurcation diagram for (1) showing upper and lower equilibrium branches (solid lines) and the unstable middle branch (dash-dotted line). The NS static fold bifurcation is at (0,0) (blue $*$);the smooth fold bifurcation is at (1,1) (red o). The numerical solution (blue dotted line) to (1) is for $A = 0$ and $\epsilon = .05$. (RIGHT). Simulations of (1), superimposed on the static bifurcation curve (black lines), Diamonds: analytical predictions $\mu_{\rm tip}$ for the DB/TP for $\lambda \leq 1$ (simulation in red and green for $A = 2$ and $\lambda = .7, 1$, respectively, and in blue for $A = 5$ and $\lambda = .7$); circle o: analytical prediction of μ_{sv}, (simulation in magenta for $A = 2$, $\lambda = 2$)

.

tipping points (DB/TP), with and without the oscillatory forcing. Here x follows the lower equilibrium branch $x < 0$ as μ decreases. Using the multiple scales expansion $x(t,T) = -\epsilon^{\lambda} A\cos T + \epsilon^{q_1} y_1(t,T) + \ldots \epsilon^{q_2} y_2(t,T) + \ldots$ for $1 \ll \Omega = \epsilon^{-\lambda}$ and $T = \Omega t$, we obtain the DB/TP

$$A \neq 0, \;\; 0 < \lambda \lesssim 1 \qquad \mu_{\rm tip} \;=\; \left(\frac{\epsilon^2}{\Omega}\right)^{1/3} \left(\frac{\pi|A|}{2}\right)^{1/3} \xi_r + \frac{4|A|}{\pi\Omega} \qquad {\rm Ai}(\xi_r) = 0 \text{ for } \xi_r = -2.33811\ldots \tag{2}$$

$$A = 0, \;\; 0 < \lambda \qquad \mu_{\rm sv} \;\sim\; \frac{1}{2}\epsilon\log(\epsilon). \qquad \text{(Ai is the Airy function)} \tag{3}$$

Fig. 2 compares the analytical and numerical results for these DB/TP's. For small frequencies the NS DB/TP is advanced relative to the static $\mu = 0$, while for larger frequencies (larger λ or smaller A/Ω), the DB/TP is positive, with its asymptote at $\mu_{\rm sv}$ corresponding to $A = 0$. Note that $\mu_{\rm tip}$ depends on the ratio A/Ω. Figs. 1 and 2 illustrate advanced DB/TP for larger A/Ω and lagged DB/TP for smaller A/Ω. We contrast these results with the DB/TP for the canoncial smooth dynamic fold bifurcation studied in [1]-[2], $x'(t) = a(\epsilon t) - x^2$, $a = a_0 - \epsilon t$ for $\epsilon \ll 1$. For $A \neq 0$, in both smooth and NS cases, the DB/TP's are the sum of two contributions, one negative contribution which corresponds to a lag due to slowly varying μ, and a second positive contribution corresponding to an advance in tipping due to the oscillations. Thus we have a competition between influences generating advances and lags, with different parametric dependencies. Analogous to the NS case, the DS/TP value of a in the smooth case depends on A/Ω and ϵ, but with a different functional dependency. For example, the asymptote for small A/Ω in the smooth case is $0 > a_{sv} = O(\epsilon^{2/3})$, in contrast to $\mu_{sv} = O(\epsilon\log\epsilon)$. Thus the lag in the DB/TP is larger in the smooth case, as shown Fig. 2 LEFT.

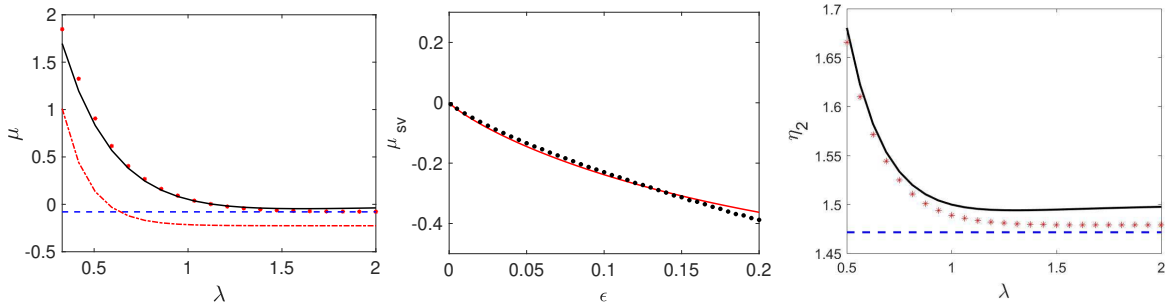

Figure 2: LEFT: For $A = 5$, $\epsilon = .03$. comparison of the critical value $\mu_{\rm tip}$ (black solid line) valid for $\lambda \lesssim 1$ and the limiting $\mu_{\rm sv}$ for larger λ (blue dotted line). Red stars indicate tipping in the numerical solution to (1), corresponding to the value of μ at which x reaches 1. The red dash-dotted line is the analogous results for the smooth fold bifurcation analyzed in [2], for comparison. CENTER: The tipping value for $\mu_{\rm sv}$ approximated by (3) (solid red line) and compared with the numerical result from (1) (black dots) with $A = 0$, taking $x_{\rm tip} = 1$. RIGHT: Same as LEFT, but for (4).

Applications in larger systems

We apply a similar approach in higher DOF models, illustrated via the non-dimensionalized Stommel box model for thermohaline ocean circulation [3],

$$\begin{aligned} \dot{V} &= \eta_1 - \eta_2 + \eta_3(T - V) - T - V|V| + A\sin(\Omega t), \qquad \dot{\eta_2} = -\epsilon \\ \dot{T} &= \eta_1 - T(1 + |V|) + B\sin(\Omega t), \qquad T(0) = T_i, \quad V(0) < 0, \quad \eta_2(0) = \eta_{2i} > \eta_1\eta_3\,. \end{aligned} \tag{4}$$

Here V is the difference between non-dimensional temperature T and salinity S, with underlying static bifurcation structure of V vs. η_2 similar to that of (1) in Fig. 1. Then the equilibrium branches for $V > 0$ ($V < 0$) corresponds to a temperature (salinity)-dominated state. There is slow variation in time for $\epsilon \ll 1$ of the bifurcation parameter η_2 and high frequency oscillations $\Omega \gg \epsilon^{-\lambda}$ for $\lambda > 0$ with amplitudes A and B. Model parameters η_1 and η_3 are positive constants. The varying parameter η_2 is related to the freshwater flux, as also studied in Roberts [4]. Variations in (η_1, η_3) are captured by nonzero A, B, analogous to observed behavior in Huybers [5]. Using the approaches developed for (1), we obtain approximations for the DB/TP $\eta_{2\rm tip}$ as shown in Fig. 2 RIGHT for the NS dynamic bifurcation, capturing the transition from solutions near the salinity-dominated branch for $V < 0$. Note, as in Fig. 2 LEFT, an advanced DB/TP relative to the static bifurcation point $\eta_{2c} \approx 1.5$ occurs for larger values of A/Ω. Lagged DB/TP occurs for smaller A/Ω, with an asymptote to the lag corresponding to slow variation of η_2 and $A = 0$.

Potential influence of coherence resonance in non-smooth dynamic bifurcations

For the model (4) forced by white noise rather than oscillatory forcing, there is the potential for a coherence-resonance (CR)-driven advance of the tipping point. A linear analysis of the salinity-dominated branch for $V < 0$, with static NS bifurcation at $\eta_2 = \eta_{2c}$, shows that the corresponding eigenvalues can be either real or complex. This behavior is in contrast to a smooth fold bifurcation with real eigenvalues of its near-by linearized system, e.g. as is the case for the temperature-dominated branch of (4) for $V > 0$. For the salinity-dominated branch of (4) for $V < 0$, the eigenvalues are typically complex as η_2 approaches η_{2c}, allowing for CR in which noise excites the frequency corresponding to the complex part of the eigenvalues, even if the real part is negative. Using a measure of CR based on the power spectral density of the fluctuations about the attracting salinity-dominated branch, we identify parameter ranges for which this CR produces a large probability of advanced tipping to the temperature-dominated state. (This is also joint work with Ziming Yin, now a co-op at Scotiabank in Toronto, CA.)

Conclusions

Via multiple scale analyses we capture the different parametric dependencies of dynamic bifurcations, i.e. tipping points, in forced systems with smooth and non-smooth (NS) dynamic fold bifurcations. For $O(1)$ forcing amplitude with high frequency oscillations, the advance in the tipping point is larger in the NS case, since the contributions from the lag due to slow variation of parameters is reduced relative to the smooth case. Furthermore, we find that coherence resonance-driven tipping can advance NS fold bifurcations since switching surfaces rather than loss of local attraction to the equilibrium state generates the bifurcation. Then the eigenvalues describing the local behavior near the NS fold bifurcation may be complex, so that the noise can excite frequencies corresponding to the imaginary part of these eigenvalues.

References

[1] R. Haberman, SIAM J. Appl.Math. **37** 1, 69–106 1979.

[2] J. Zhu, Jielin, R. Kuske, T. Erneux, SIAM J. Appl. Dyn. Sys. **14**, 4, 2030–2068, 2015.

[3] H. A. Dijkstra, Nonlinear climate dynamics, Cambridge University Press, 2013.

[4] A. Roberts and R. Saha, Climate Dynamics **48**, 7-8, 2123–2134, 2017,

[5] P. Huybers, Peter and C. Wunsch, Nature **434**, 7032, 491, 2005.

Effect of dry friction on a parametrically excited nonlinear oscillator

Simon Benacchio*, Christophe Giraud-Audine† and Olivier Thomas *
*Arts et Metiers Institute of Technology, LISPEN, HESAM Université, F-59000 Lille, France
†Arts et Metiers Institute of Technology, L2EP, HESAM Université, F-59000 Lille, France

Summary. This study proposes to investigate the effects of dry friction on the behaviour of a parametrically excited nonlinear oscillator using a pendulum as example. A harmonic balance method and time integration simulations are used to respectively compute and validate the solutions of the problem and their stability. The effects of dry friction on the behaviour of the system are discussed.

Context

The parametric resonance phenomenon comes from the excitation of a dynamical system through the modulation of one of its parameter and can be simply described by the Mathieu's equation [1]. This phenomenon has been widely used to enhance the dynamical behaviour of systems for energy harvesting or parametric amplification [2, 3]. Usually it occurs for a forcing frequency different from the resonance of the excited system and results in infinite amplitude of oscillation if no non linearities are present. The latter are thus necessary to stabilize the system motion and obtain a finite amplitude of oscillation. An example of such a system is given by the Mathieu-Duffing's equation. When adding viscous damping, a forcing amplitude threshold depending on the damping coefficient must be overcome to initiate parametric oscillations. Although dry friction is also a common source of damping, few studies deal with this kind of problems [4]. The present study proposes to investigate the effects of dry friction on the behaviour of a parametrically excited nonlinear oscillator. The governing equation is given and the example of the pendulum is used as illustration. A harmonic balance method is used to compute theoretical solutions of the problem. Time integration simulations are compared to these solutions to validate the model and its stability. The effects of dry friction on the behaviour of the pendulum and on its forcing amplitude threshold are discussed.

Theoretical motion of a parametric nonlinear oscillator with dry friction

Governing equation

The Mathieu-Duffing's equation including viscous and dry friction damping terms reads

$$\ddot{\theta} + \mu_1\dot{\theta} + f_0(\dot{\theta}) + (\omega_0^2 - \delta\, 4\Omega^2\cos(2\Omega t))\,\theta - \gamma\,\theta^3 = 0. \tag{1}$$

This equation is the governing equation of a pendulum parametrically excited with a vertical displacement. In this case, θ is the angular displacement of the pendulum and $\dot{\bullet}$ denotes a derivative relative to time t. $\omega_0^2 = g/l$ is the resonance angular frequency of the system with g the gravitational acceleration and l the length of the pendulum. δ and 2Ω are respectively the amplitude and the angular frequency of the forcing. A factor 2 is joined to Ω since the parametric resonance occurs at half of the excitation frequency in the case of the pendulum. The factor $4\Omega^2$ appears due to the double derivative relative to time of the forcing displacement term. The nonlinear coefficient γ comes from the linearisation of the $\sin$ term describing the motion of the pendulum. The viscous damping coefficient is μ_1 and the dry friction term is described by the non-smooth function $f_0(\dot{\theta}) = \mu_0 sign(\dot{\theta})$ if $\dot{\theta} \neq 0$ and $f_0(\dot{\theta}) \in [-\mu_0, \mu_0]$ if $\dot{\theta} = 0$, with μ_0 the dry friction coefficient.

Harmonic balance approach

The harmonic balance method (HBM) is used to find the solutions of Equation (1) using a Fourier series expansion of the angular displacement with only one harmonic :

$$\theta(t) = a(t)\ \cos(\Omega t + \beta(t)) \tag{2}$$

Substituting (2) in (1), considering the expansion of the dry friction function as a one term Fourier series and equating each harmonics in Ω and 3Ω with zero results in a system of four equations named $\mathcal{S}$. Equating all time derivatives of $\mathcal{S}$ with zero and neglecting harmonics higher than the first order, one founds that the amplitude of fixed points can be obtained solving the following equation :

$$\frac{9}{16}\,\gamma^2\,a^6 - \frac{3}{2}\,\gamma(\omega_0^2 - \Omega^2)\,a^4 + \left[(\omega_0^2 - \Omega^2)^2 + \Omega^2\mu_1^2 - 4\Omega^4\delta^2\right]\,a^2 + \frac{8}{\pi}\,\Omega\mu_0\mu_1\,a + \frac{16}{\pi^2}\,\mu_0^2 = 0 \tag{3}$$

The amplitude a is numerically computed to find the non trivial solutions of the pendulum motion. Then, the phase β of the angular displacement is computed such as

$$\tan(2\beta) = \frac{\left(\Omega\mu_1\,a + \frac{4}{\pi}\,\mu_0\right)}{\left(\frac{3}{4}\,\gamma\,a^3 - (\omega_0^2 - \Omega^2)\,a\right)} \tag{4}$$

It is worth mentioning that the trivial solutions $a = 0$ cannot be found with Equation (3) even if these solutions obviously exist according to experiments. The stability of solutions is computed using the method of varying amplitude [5]. The Jacobian $\mathcal{J}$ of the system $\mathcal{S}$ is first calculated. Then, the stability of the solutions is evaluated using the sign of its trace and determinant. Assuming $\mu_1 > 0$, the trace of $\mathcal{J}$ is found to be negative. Thus, the condition for stability is achieved when the determinant of $\mathcal{J}$ is positive.

Time integration approach

Time integration simulations of Equation (1) are used to (i) validate the solutions found using the HBM, (ii) study the trivial solutions of the system when $\mu_0 \neq 0$ and (iii) validate the solution stability computed with the method of varying amplitude. Simulations are computed using the ode45 solver from Matlab (MathWorks, Natick, USA). To avoid numerical issues due to the discontinuities brought by the dry friction term, the switch model proposed in [6] is used. Thus, the dry friction function is not regularized but replaced by a function including a transition phase in addition to the usual stick and slip phases. Backward and forward frequency sweeps are done to obtain the trivial and periodic solutions.

Results

Figure 1 presents solutions of Equation (1) computed with the HBM and time integration simulations. The black dotted line is the backbone curve of the system computed using the HBM. Red lines are the well-known solutions of the parametric pendulum without dry friction whose behaviour is softening. The trivial solution is unstable between the two bifurcation points of the periodic orbits. In this region, the pendulum necessarily jumps on the stable non trivial solution branch when the forcing amplitude is larger than the critical value given by the HBM $\delta_{cr} = \mu_1/2\Omega$. Blue lines are the solutions of the parametric pendulum with dry friction. In this case, non trivial solutions are disconnected from the trivial ones which are always stable according to time integration simulations. According to HBM, the birth of the resulting isola does not occur from a zero amplitude but from a point represented by the blue cross in Figure 1. It is worth mentioning that the HBM does not predict this birth point onto but nearby the backbone curve. The critical forcing amplitude needed to give birth to the isola depends on both the viscous and dry friction coefficient. However, the HBM does not allow the computation of an analytical value for this threshold.

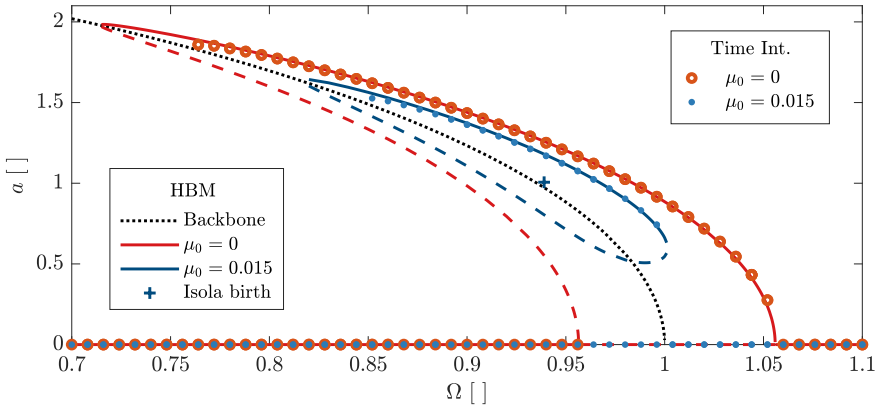

Figure 1: Solutions of Equation (1) computed with the harmonic balance method (lines) and time integration simulations (circle markers) for $\omega_0 = 1$, $\gamma = 1/6$, $\delta = 0.07$, $\mu_1 = 0.1$ and $\mu_0 = 0$ (red) or $\mu_0 = 0.015$ (blue). Plain and dashed lines correspond respectively to stable and unstable solutions. The black dotted line is the conservative solution of the system ($\delta = 0$, $\mu_1 = 0$, $\mu_0 = 0$). The blue cross corresponds to the birth of the isola.

Conclusion and perspectives

A Mathieu-Duffing's equation including a dry friction term was investigated to describe the dynamical behaviour of a parametrically excited oscillator. The example of the pendulum was used to illustrate this problem. Solutions and their stability were respectively computed using a harmonic balance approach and the method of varying amplitude. Results were validated using time integration simulations. The dry friction gave birth to isolated solutions. To further investigate these solutions, the energy principle method detailed in [7] will be used to analytically derive the critical forcing amplitude needed to give birth to the isola. The influence of other parameters like initial conditions on the existence of non trivial solutions will be also discussed.

References

[1] Nayfeh A. H., Balachandran B. (1995) Applied Nonlinear Dynamics: Analytical, Computational, and Experimental Methods. *Wiley, 1 edition*.

[2] Daqaq M. F., Stabler C., Qaroush Y., Seuaciuc-Osòrio T. (2008) Investigation of power harvesting via parametric excitations. Journal of Intelligent Material Systems and Structures.

[3] Thomas O., Mathieu F., Mansfield W., Huang C., Trolier-McKinstry S., Nicu L. (2013) Efficient parametric amplification in micro-resonators with integrated piezoelectric actuation and sensing capabilities. Applied Physics Letters, **102**(16):163504.

[4] Yabuno H., Murakami T., Kawazoe J., Aoshima N. (2004) Suppression of parametric resonance in cantilever beam with a pendulum (Effect of static friction at the supporting point of the pendulum). Journal of Vibration and Acoustics, **126**(1):149-162.

[5] Aghamohammadi M., Sorokin V., Mace B. (2019) On the response attainable in nonlinear parametrically excited systems. Applied Physics Letters, **115**(15):154102.

[6] Leine R.I., van Campen D.H., de Kraker A., van den Steen L. (1998) Stick-slip vibrations induced by alternate friction models. Nonlinear Dynamics, **16**(1):41–54.

[7] Cenedese M., Haller G., (2020) How do conservative backbone curves perturb into forced responses? A Melnikov function analysis. Proceedings of the Royal Society A: Mathematical, Physical and Engineering Sciences, **476**:2234.

Experimental Verification of Stability Theory for a Planar Rigid Body with Two Unilateral Frictional Contacts

Yizhar Or[*], Peter L. Varkonyi[**]

[*]*Faculty of Mechanical Engineering, Technion - Israel Institute of Technolog, Haifa, Israel.*

[**]*Department of Mechanics Materials and Structures, Budapest University of Technology and Economics, H-1111 Budapest, Hungary.*

Summary. Stability of equilibrium states in mechanical systems with multiple unilateral frictional contacts is an important practical requirement, with high relevance for robotic applications. In our previous work, we theoretically analyzed finite-time Lyapunov stability for a minimal model of planar rigid body with two frictional point contacts. Assuming inelastic impacts and Coulomb friction, conditions for stability and instability of an equilibrium configuration have been derived. In this work, we present for the first time an experimental demonstration of this stability theory, using a variable-structure rigid "biped" with frictional footpads on an inclined plane. By changing the biped's center-of-mass location, we attain different equilibrium states, which respond to small perturbations by divergence or convergence, showing remarkable agreement with the predictions of the stability theory. Using high-speed recording of video movies, good quantitative agreement between experiments and numerical simulations is obtained, and limitations of the rigid-body model and inelastic impact assumptions are also studied. The results prove the utility and practical value of our stability theory.

Many robotic systems are based on establishing contacts between bodies, for performing tasks of object manipulation or locomotion. Several characteristic types of contact-based robotic motion exist. In robotic grasping, contacts are typically used to enforce kinematic constraints that immobilize an object with zero relative motion, so contacts are maintained persistent. On the other hand, dynamic tasks such as object juggling and rapid legged locomotion involve intermittent contacts where impacts induce non-smooth transitions in contact states. An intermediate regime uses *quasistatic* manipulation and locomotion tasks with non-prehensile contacts. Such motion often relies on unilateral contacts that are maintained in persistent no-slip state imposed by equilibrating forces that satisfy frictional contact constraints. A common example is quasistatic legged locomotion on rough terrain where gravitational load is resisted by contact forces at the feet's supports.

In the regime of quasistatic motion with unilateral contacts, it is of practical importance to consider *stability* of multi-contact equilibrium states under disturbances caused by model uncertainties, joint coordination inaccuracies, irregular contact surfaces, and more. Common approaches consider robustness of the solution for equilibrium contact forces under disturbances such as localized elastic deformations at contacts or margins of potential energy. A main limitation of these approaches is assuming persistent contacts without accounting for dynamics under small initial perturbations about equilibrium, that do not necessarily maintain contact constraints. This is close in spirit to the well-known concept of *Lyapunov stability* in dynamical systems theory. Analysis of this type of dynamic stability in multi-contact systems is challenging, since any small initial perturbation of displacements and velocities immediately induce response governed by hybrid dynamics involving non-smooth transitions between contact states and impacts. Such systems often involve complicated phenomena such as solutions with *Zeno behavior* and more rarely, *Painlevé paradox* where friction-dominated solution is either indeterminate or inconsistent.

Our recent joint work [1] presented theoretical analysis of finite-time Lyapunov stability for a planar rigid body with two frictional contacts and frictional inelastic impacts. The analysis in [1] reduced the hybrid dynamics of the system in close vicinity of an equilibrium state to a scalar \Poincare map R and scalar magnitude-growth function G, which together encompass the entire response and contact state transitions. Under specific restrictions called *persistent equilibrium*, the work [1] derived theoretical conditions for stability and instability of frictional two-contact equilibria based on properties of the semi-analytic functions R and G, and showed how stability can depend on structural parameters such as friction coefficients and center-of-mass location relative to contact positions.

The goal of this work is to present, for the first time, an experimental demonstration of our stability theory from [1]. Our experimental setup consists of a rigid “biped” with variable structure, which is perturbed from frictional two-contact equilibrium state on an inclined plane. We first present extension of our theoretical analysis in [1] to account for a relaxed notion called *weakly-persistent equilibria* and also derive a simpler stability condition. Both modifications cover cases which are relevant to actual properties of our experimental biped and contact geometry. Upon shifting the biped's variable center-of-mass, our theoretical predictions indicate changes between the two instability mechanisms towards stability. These stability transitions are demonstrated experimentally, and high-speed camera recording enables tracking the biped's motion for quantitative comparison with theoretical simulations, as well as assessing the validity of our rigid-body model assumptions. We find excellent qualitative and good quantitative agreement between the theoretical predictions and experimental measurements, and conclude that our model slightly underestimates stability, where discrepancies are mainly due to added energy dissipation caused by damped elastic vibrations and footpads' compression during impacts. The results demonstrates the utility and practical value of our stability theory. Our present work is based on our recently submitted paper [2].

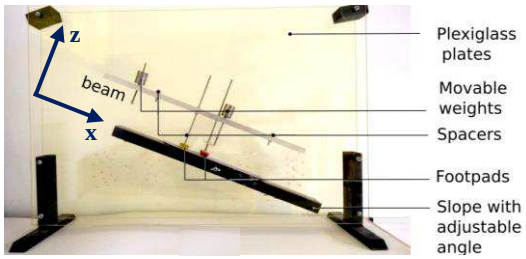

Figure 1: Our experimental setup of a biped on a slope, with variable center-of-mass (COM) and unequal friction on both footpads. The biped is given slight initial perturbation from equilibrium and its response is a sequence of impacts and contact states. Stability and instability can be changed by shifting the biped's COM.

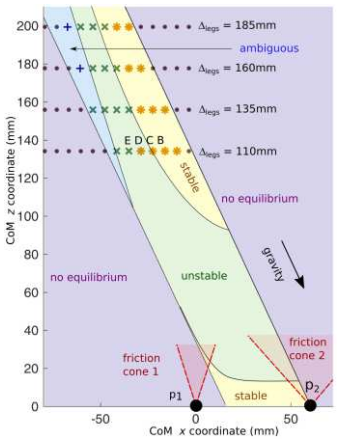

Figure 2: Plot of the biped's COM locations in (x,z) plane, where p1, p2 denote the footpads' contacts. Colored areas denote COM regions where our theoretical analysis predicts stability, instability, ambiguous equilibrium and no equilibrium. The grid of markers denote experimental results:
'●' – no equilibrium
'+' – ambiguous equilibrium
'x' – unstable equilibrium
'*' – stable equilibrium

References

[1] Varkonyi, P. L., & Or, Y. (2017). Lyapunov stability of a rigid body with two frictional contacts. *Nonlinear Dynamics*, *88*(1), 363-393.
[2] Or, Y., & Varkonyi, P. L. (2020). Experimental Verification of Stability Theory for a Planar Rigid Body with Two Unilateral Frictional Contacts, Submitted 2020. *Preprint at arXiv:2008.10323*. Video movie at this LINK.

Monday, July 18, 2022

13:30 - 15:30

MS-20 Wave propagation in Mechanical Systems and Nonlinear Metamaterials

Saint Clair 3B

Chair: Francesco Romeo

13:30 - 13:50
A nonlinear gradient elasticity model for the prediction of seismic waves
DOSTAL Leo, **HOLLM Marten***, METRIKINE Andrei, FĂRĂGĂU Andrei, VAN Dalen Karel
*Institute of Mechanics and Ocean Engineering, Hamburg University of Technology (Eissendorfer Strasse 42, 21073 Hamburg Germany)

13:50 - 14:10
Breather arrest in the damped chains with substantially nonlinear coupling
GENDELMAN Oleg*, VAKAKIS Alexander, STROZZI Matteo, MOJAHED Alireza
*Department of Mechanical Engineering (Technion - Institute of Technology Haifa 32000 Israel Israel)

14:10 - 14:30
Free propagation of nonlinear waves in 1D acoustic metamaterials with inertia amplification
SETTIMI Valeria, **LEPIDI Marco***, BACIGALUPO Andrea
*Department of Civil, Chemical and Environmental Engineering - University of Genoa (Via Montallegro

14:30 - 14:50
Nonlinear dynamics of topological lattices
CHAUNSALI Rajesh*, THEOCHARIS Georgios
*Laboratoire dÁcoustique de lÚniversité du Mans (Laboratoire dÁcoustique de lÚniversité du Mans, LAUM - UMR 6613 CNRS, Le Mans Université, Avenue Olivier Messiaen, 72085 LE MANS France)

A nonlinear gradient elasticity model for the prediction of seismic waves

Leo Dostal*, Marten Hollm*, Andrei V. Metrikine†, Andrei B. Fărăgău† and Karel N. van Dalen†
*Institute of Mechanics and Ocean Engineering, Hamburg University of Technology, Hamburg, Germany
†Faculty of Civil Engineering & Geosciences, TU Delft, Delft, Netherlands

Summary. We present a novel equation of motion for a nonlinear gradient elasticity model. Thereby, higher-order gradient terms are introduced to capture the effect of small-scale soil heterogeneity/micro-structure. Using a newly established finite difference scheme, corresponding solutions including stationary waves are determined. In comparison with a commonly used model for nonlinear seismic waves, which has leading derivatives of second order, the solutions of the novel equations are much smoother. This allows much more accurate numerical computations as well as more realistic predictions of the seismic waves.

Introduction

In order to predict the response of the top soil layers of the earth - the so-called seismic site response- induced by seismic waves, the so-called equivalent linear scheme is used very often. Thereby, soil stiffness and damping are modeled taking a shear modulus and material damping ratio, which are constant in time [1]. However, for high maximum strain levels in the soil layers, the equivalent linear scheme with constant shear modulus and material damping can not adequately represent the behavior of a seismic event over its entire duration, since the strains in the soil layers vary significantly. In order to account for the variation of shear modulus and damping ratio in this case, a nonlinear time domain solution is usually used, e.g. [2].
Actual research in nonlinear modeling for seismic site response is mostly focused on the development of advanced constitutive models, which capture important features of the soil behavior like anisotropy, pore water pressure generation and dilation [3]. In this work, we determine specific solutions including stationary waves in the subsurface, whereby the constitutive behavior is governed by the hyperbolic soil model. Here, the (secant) shear modulus is strain dependent with a non-polynomial nonlinearity. In order to capture the effects of small-scale heterogeneity/ micro-structure, we extend the classical wave equation to a nonlinear gradient elasticity model. This is sometimes also called a higher-order gradient continuum or a micro-structured solid. Compared to the classical continuum, higher-order gradient terms are introduced into the equation of motion, which lead to dispersive effects particularly for shorter waves [4]. These higher-order gradient terms are usually obtained using asymptotic homogenization techniques for periodically inhomogeneous media [4]. Since localized stationary waves exist only because of the balance between dispersive and nonlinear effects, their influence on the behavior of stationary solutions is significant and allows them to propagate without distortion. Since the dispersion prohibits the formation of jumps, physically realizable solutions are obtained.
In this work, the effects of the higher-order gradient terms and the corresponding dispersion are investigated. Thereby, specific solutions of the corresponding equations of motion are presented and compared. It is observed that the classical wave equation contains solutions which have non-physical discontinuities (in the strain) and which vanish in the presence of the higher-order terms.
The structure of this work is as follows: First, we derive the equation of motion of the classical and nonlinear gradient elasticity model, respectively. The derivation is based on Newton's second law and Eringen's general strain-stress relation [5]. Then, an ordinary differential equation is derived, from which stationary solutions for the nonlinear gradient elasticity model are obtained. Afterwards, a numerical scheme for the computation of the derived nonlinear equations of motion in time and space is presented. Using this scheme, solutions of the classical and nonlinear gradient elasticity model are compared. Finally, this work ends with a conclusion.

Model

In this section, a classical and an advanced constitutive model are described in order to capture important features of the soil behavior, respectively. In both cases, the constitutive behavior is governed by the hyperbolic soil model, which results in a strain-dependent shear modulus. As the classical model has non-physical discontinuous solutions, a nonlinear gradient elasticity model is employed.

The classical continuum model

In order to derive the equation of motion, Newton's second law is applied. Let x be the horizontal direction, z the vertical direction and t the time. For transverse waves propagating in the direction of z and considering the one-dimensional situation, it reads [6]

$$\rho \frac{\partial^2 u}{\partial t^2} = \frac{\partial \sigma_{zx}}{\partial z}. \tag{1}$$

Thereby, $u(z,t)$ is the displacement in x, σ_{zx} is the shear stress and ρ is the material density. The corresponding strain can be calculated from the displacement by [6]

$$\varepsilon_{zx} = \frac{1}{2}\frac{\partial u}{\partial z}. \tag{2}$$

In this study, the constitutive behavior is governed by the hyperbolic soil model, which is typically employed for the seismic site response analysis. Here, the strain-dependent shear modulus [7]

$$G(\gamma) = \frac{G_0}{1 + (\gamma/\gamma_{\mathrm{ref}})^{\beta}} \quad \text{with} \quad \gamma = \sqrt{3}|\varepsilon_{zx}| = \frac{\sqrt{3}}{2}\left|\frac{\partial u}{\partial z}\right| \tag{3}$$

is used, whereby γ_{ref} denotes the reference shear strain and $0 < \beta < 1$ is a dimensionless constant. Applying the stress-strain relationship

$$\sigma_{zx} = 2\,G(\gamma)\,\varepsilon_{zx}, \tag{4}$$

Eq. (1) results in

$$\rho\frac{\partial^2 u}{\partial t^2} = \frac{\partial}{\partial z}\left(G(\gamma)\frac{\partial u}{\partial z}\right). \tag{5}$$

This is the wave equation for the classical continuum model.

The nonlinear gradient elasticity model

In order to capture the effects of small-scale soil heterogeneity/micro-structure, the stress strain relationship of Eq. (4) is extended by including higher-order gradient terms. In a nonlinear system, the stress-strain relation can generally be written as [5]

$$\sigma_{zx}(z,t) = \int_{-\infty}^{\infty}\int_{-\infty}^{\infty} g\left(z-\zeta, t-\tau, \gamma(\zeta,\tau)\right)\varepsilon_{zx}(\zeta,\tau)\,\mathrm{d}\zeta\mathrm{d}\tau, \tag{6}$$

whereby the kernel function $g(z,t,\gamma)$ contains the specific nonlocality and history dependence. In order to compute the soil behavior using a partial differential equation instead of an integro-differential equation, the kernel function is taken as a combination of Dirac delta functions $\delta(...)$. This results in [8]

$$g(z-\zeta,t-\tau,\gamma) = 2\big(G(\gamma)\delta(z-\zeta)\delta(t-\tau) - L^2G^{(L)}(\gamma)\delta_{,\zeta\zeta}(z-\zeta)\delta(t-\tau) + T^2G^{(T)}(\gamma)\delta(z-\zeta)\delta_{,\tau\tau}(t-\tau)\big). \tag{7}$$

Thereby, $(...)_{,\zeta\zeta}$ and $(...)_{,\tau\tau}$ denote double partial differentiation with respect to ζ and τ, respectively. Apart from the conventional strain-dependent shear modulus $G(\gamma)$, the kernel function g contains additional strain-dependent elastic moduli $G^{(L)}(\gamma)$ and $G^{(T)}(\gamma)$, respectively. Finally, L and T are time and length scales which specify the nonlocality and history dependence of the medium, respectively.

Without loss of generality, the scales T and L are interrelated in this work by $T^2 = L^2/c_0^2$, whereby $c_0 = \sqrt{G_0/\rho}$ is the shear wave speed corresponding to the small-strain shear modulus G_0 from linear elasticity.

For simplicity, the additional elastic moduli are related to the conventional strain-dependent shear modulus $G(\gamma)$ by

$$G^{(L)}(\gamma) = B_1G(\gamma), \quad G^{(T)}(\gamma) = B_2G(\gamma). \tag{8}$$

Thereby, B_1 and B_2 are dimensionless constants. Inserting Eqs. (2), (6), (7) and (8) into (1) results into

$$\rho\frac{\partial^2 u}{\partial t^2} = \frac{\partial}{\partial z}\left(G(\gamma)\frac{\partial u}{\partial z} - B_1L^2\frac{\partial^2}{\partial z^2}\left(G(\gamma)\frac{\partial u}{\partial z}\right) + B_2\frac{\rho L^2}{G_0}\frac{\partial^2}{\partial t^2}\left(G(\gamma)\frac{\partial u}{\partial z}\right)\right). \tag{9}$$

This is the equation of motion of the nonlinear gradient elasticity model used in this work. A comparison of Eq. (9) with Eq. (5) shows that the effects of small-scale soil heterogeneity/micro-structure are accounted for by the higher-order gradient terms multiplied with B_1 and B_2, respectively.

In this work, the hyperbolic soil model $G(\gamma)$ given in Eq. (3) is also used for the nonlinear gradient elasticity model.

Stationary wave solution

In the following, the influence of the higher-order gradient terms on the behavior of numerical solutions is considered. Thereby, stationary solutions of Eq. (9) are taken considered. These solutions can be determined by assuming that they propagate with constant speed $c \in \mathbb{R}$ through the nonlinear medium while not changing their shape [8]. Applying the transformation $\xi = x - ct$ and assuming stationarity, this results in

$$u_{,tt} = u_{,\xi\xi}c^2, \quad u_{,ztt} = u_{,\xi\xi\xi}c^2, \quad u_{,zt} = -u_{,\xi\xi}c, \quad \frac{\partial}{\partial z} = \frac{\partial}{\partial \xi}. \tag{10}$$

Computing the derivatives of $G(\gamma)u_{,\xi}$ with respect to ξ, we get for $y := u_{,\xi}$ [8]

$$\begin{aligned} y_{,\xi\xi} =& \frac{1}{1-\beta\left(\frac{\sqrt{3}|y|}{2\gamma_{\mathrm{ref}}}\right)^{\beta}\left(1+\left(\frac{\sqrt{3}|y|}{2\gamma_{\mathrm{ref}}}\right)^{\beta}\right)^{-1}}\Bigg\{\frac{\rho c^2\left(1+\left(\frac{\sqrt{3}|y|}{2\gamma_{\mathrm{ref}}}\right)^{\beta}\right)-G_0}{B_2c^2\rho L^2-G_0B_1L^2}y \\ &- \frac{\sqrt{3}\,\mathrm{sgn}(y)}{2\gamma_{\mathrm{ref}}}\Bigg[2\beta^2\left(\frac{\sqrt{3}|y|}{2\gamma_{\mathrm{ref}}}\right)^{2\beta-1}\left(1+\left(\frac{\sqrt{3}|y|}{2\gamma_{\mathrm{ref}}}\right)^{\beta}\right)^{-2} \\ &- (\beta+\beta^2)\left(\frac{\sqrt{3}|y|}{2\gamma_{\mathrm{ref}}}\right)^{\beta-1}\left(1+\left(\frac{\sqrt{3}|y|}{2\gamma_{\mathrm{ref}}}\right)^{\beta}\right)^{-1}\Bigg]y_{,\xi}^2\Bigg\}. \end{aligned} \tag{11}$$

Solving this nonlinear second-order ordinary differential equation, stationary wave solutions of Eq. (9) can be computed.

Numerical scheme for the nonlinear gradient elasticity model

In order to compute the corresponding numerical solutions $u(z,t)$ of Eqn. (5) and (9), a numerical scheme based on finite-difference approximations is used. This scheme has been developed by Dostal et al. [8] and solves partial differential equations of the form

$$\rho\frac{\partial^2 u}{\partial t^2} = \frac{\partial}{\partial z}\left(G\left(\frac{\partial u}{\partial z}\right)\frac{\partial u}{\partial z} - B_1L^2\frac{\partial^2}{\partial z^2}\left(G\left(\frac{\partial u}{\partial z}\right)\frac{\partial u}{\partial z}\right) + B_2\frac{\rho L^2}{G_0}\frac{\partial^2}{\partial t^2}\left(G\left(\frac{\partial u}{\partial z}\right)\frac{\partial u}{\partial z}\right)\right). \tag{12}$$

Thereby, $G\left(\frac{\partial u}{\partial z}\right)$ is an arbitrary function depending on $\frac{\partial u}{\partial z}$. If $G\left(\frac{\partial u}{\partial z}\right)$ is chosen as in Eq. (3), Eq. (12) reduces to Eq. (9). If furthermore B_1 and B_2 are set to zero, Eq. (12) becomes Eq. (5). Since all numerical results presented in the next section are based on the scheme developed in [8], we briefly outline it here.

It is assumed that the analytical solution $u(z,t)$ of Eq. (12) exists in space $z \in [Z_\ell, Z_h]$ and time $t \in [0, \mathbb{T}]$. Therefore, a grid in space

$$Z_\ell = z_0 < z_1 < \cdots < z_M = Z_h, \quad z_i = i\Delta z \;\text{ for } i = 0,\ldots,M,\; \Delta z = \frac{Z_\ell - Z_h}{M}, \tag{13}$$

and time

$$0 = t_0 < t_1 < \cdots < t_N = \mathbb{T}, \quad t_n = n\Delta t \;\text{ for } n = 0,\ldots,N,\; \Delta t = \frac{\mathbb{T}}{N}, \tag{14}$$

is introduced, respectively. Defining

$$h(u_{,z}) := G(u_{,z})\,u_{,z}, \tag{15}$$

Eq. (12) becomes

$$\rho\,u_{,tt} = h_{,z} - B_1L^2h_{,zzz} + B_2\frac{\rho L^2}{G_0}h_{,ttz}. \tag{16}$$

In this way, the structure of the considered partial differential equation is exploited. As will be seen later, this simplifies the calculation of the spatial finite difference approximations.

In order to approximate the derivatives with respect to time, it is assumed that the solution is known at the timepoints t_{n-1} and t_n. Let u_i^n be a grid function, which approximates the analytical solution u at space z_i and time t_n, i. e. $u_i^n \approx u(z_i,t_n)$. Furthermore, let $u_{i,z}^n$ be a grid function approximating $u_{,z}(z_i,t_n)$. Replacing the time derivative with a finite difference approximation, Eq. (12) yields

$$\mathbf{f}(\mathbf{u}^{n+1}) = \mathbf{0} \;\text{ with } \mathbf{u}^{n+1} := \left[u_0^{n+1}, u_1^{n+1}, \ldots, u_M^{n+1}\right]^{\mathrm{T}}, \tag{17}$$

whereby

$$\begin{aligned} f_i(\mathbf{u}^{n+1}) :=& \rho\,\frac{u_i^{n+1}-2u_i^n+u_i^{n-1}}{\Delta t^2} - \frac{h_{,z}(u_{i,z}^{n+1})+2h_{,z}(u_{i,z}^n)+h_{,z}(u_{i,z}^{n-1})}{4} \\ &+ B_1L^2\frac{h_{,zzz}(u_{i,z}^{n+1})+2h_{,zzz}(u_{i,z}^n)+h_{,zzz}(u_{i,z}^{n-1})}{4} - B_2\frac{\rho L^2}{G_0}\frac{h_{,z}(u_{i,z}^{n+1})-2h_{,z}(u_{i,z}^n)+h_{,z}(u_{i,z}^{n-1})}{\Delta t^2}. \end{aligned} \tag{18}$$

A solution of Eq. (18) approximates the corresponding exact solution of Eq. (12) up to an accuracy of $\mathcal{O}(\Delta t^2)$.

Next, the space derivatives $h_{,z}(u_{i,z})$ and $h_{,zzz}(u_{i,z})$ at location $z = z_i$ are approximated. Thereby, the following standard finite differences are used, which have all an accuracy of $\mathcal{O}(\Delta z^2)$:

$$\begin{aligned} u_{i,z} &= \frac{u_{i+1}-u_{i-1}}{2\Delta z} + \mathcal{O}(\Delta z^2), \quad h_{,z}(u_{i,z}) = \frac{h(u_{i+1,z})-h(u_{i-1,z})}{2\Delta z} + \mathcal{O}(\Delta z^2), \\ h_{,zzz}(u_{i,z}) &= \frac{h(u_{i+2,z})-2h(u_{i+1,z})+2h(u_{i-1,z})-h(u_{i-2,z})}{2\Delta z^3} + \mathcal{O}(\Delta z^2). \end{aligned} \tag{19}$$

In order to simplify the notation, the time index n is omitted. If the hyperbolic soil model $G(u_{,z})$ from Eq. (3) is used, we get for $h_{,z}$:

$$\begin{aligned} h_{,z}(u_{i,z}) =& \frac{h(u_{i+1,z}) - h(u_{i-1,z})}{2\Delta z} + \mathcal{O}(\Delta z^2) \\ =& \frac{1}{2\Delta z} \left\{ \frac{G_0}{1 + \left(\frac{\sqrt{3}}{2} \frac{|u_{i+2} - u_i|}{2\Delta z \gamma_{\text{ref}}} \right)^{\beta}} \frac{u_{i+2} - u_i}{2\Delta z} - \frac{G_0}{1 + \left(\frac{\sqrt{3}}{2} \frac{|u_i - u_{i-2}|}{2\Delta z \gamma_{\text{ref}}} \right)^{\beta}} \frac{u_i - u_{i-2}}{2\Delta z} \right\} + \mathcal{O}(\Delta z^2). \end{aligned} \tag{20}$$

The approximation of $h_{,zzz}$ follows analogously.
Now the advantage of the presented numerical scheme can be seen: In Eq. (12), the third-order space derivative of $G(u_{,z})$ has to be computed. However, since the hyperbolic soil model defined in Eq. (3) contains the absolute value function $k(x) = |x|$, the function $G(u_{,z})$ is only one time weakly differentiable. By introducing the function h, the problem of the missing differentiability is circumvented.
With this, the solution $\mathbf{u}^{n+1}$ of $\mathbf{f}(\mathbf{u}^{n+1}) = \mathbf{0}$ can be computed solving a nonlinear system of equations. This can be done iteratively using Newton's method, for example.

Numerical results

In this section, numerical results for the nonlinear Eqs. (5) and (9) are shown. Corresponding results are compared in order to investigate the effects of the higher-order gradient terms. Thereby, the parameters from Table 1 are used. While the values of G_0, ρ, β and γ_{ref} have been chosen to represent soil, the values of B_1 and B_2 are similar to the ones used in [4].

Table 1: Medium parameter values.

G_0 [Pa]	ρ [kg m^{-3}]	β [-]	γ_{ref} [-]	B_1 [-]	B_2 [-]	L [m]
$111.86 \cdot 10^6$	2009.8	0.91	10^{-3}	1	1.78	0.2

Solutions of a Gaussian pulse
First of all, the effects of the higher-order gradient terms are studied for a specific solution, where as initial condition a Gaussian pulse is used:

$$u(z, t = 0) = u_0 \exp\left(-\frac{z^2}{2\sigma^2} \right). \tag{21}$$

Here, the amplitude of the pulse is set to $u_0 = 0.0016\,\text{m}$ and the standard deviation is set to $\sigma = 1\,\text{m}$. In accordance with [2], these values are chosen to obtain a relatively high strain level. The temporal evolution of the numerical solution is computed using the scheme described in the last section, whereby absorbing boundary conditions are applied. Thereby, an additional initial condition u^{-1} at time t_{-1} has to be chosen. In this study, $u^{-1} = u^0$ is used, which results in a solution with no initial velocity.
The resulting solution of Eq. (5) can be seen in Fig. 1. It is observed that the initial pulse divides into two parts, which travel in opposite directions. Furthermore, the numerical solution of the classical model is non-smooth due to the sharp edges (one at the top of the wave and the other at the bottom behind it). This makes the strain discontinuous at those locations, which is not physically admissible. In contrast to this, Fig. 2 shows the corresponding solution of Eq. (9), where the effect of higher-order gradient terms are taken into account. Again, a solution is shown where the initial pulse is divided into two parts. However, the shape of the solution is smoother and does not contain sharp edges. Instead of sharp edges, small oscillations are observed behind the wave, which is consistent with the findings in [4]. This can also be seen in Fig. 3, which shows the corresponding solutions at the end of the simulation time together with the used initial condition. By introducing dispersion, the higher-order gradient terms lead to a solution where sharp edges do not occur and therefore lead to a physically admissible behavior.
Moreover, Fig. 3 shows that after division, both solutions travel with the same speed. Furthermore, a negative displacement is observed at $z = 0\,\text{m}$ after the initial pulse has departed. This could be caused by the combination of the hyperbolic soil model with the Gaussian pulse that has non-zero content at zero wavenumber. However, this shift in negative direction decreases for increasing time. This is shown in Fig. 4, which shows the solution at $z = 0\,\text{m}$ over time.

Stationary solution of the nonlinear gradient elasticity model
Next, the effects of the higher-order gradient terms on the stationary solution of Eq. (9) are investigated. For this, Eq. (11) is computed for the velocity $c = 100\,\text{m/s}$. Since the numerical scheme of the last section needs an additional initial condition u^{-1} at t_{-1}, the corresponding value has to be calculated. As the stationary solution propagates with speed c, the value of u^{-1} is computed by shifting u^0 in space by $c\,t_{-1}$. Since the solution of Eq. (11) is periodic in space, periodic boundary conditions are used to calculate the temporal evolution of the solutions of Eqs. (9) and (5), respectively.
From Eq. (11), the corresponding phase portrait for u_ξ and $u_{\xi\xi}$ can be obtained. In the following, we study solutions where the trajectories approximate the homoclinic orbit. Using the solution of Eq. (11) as initial condition, the resulting

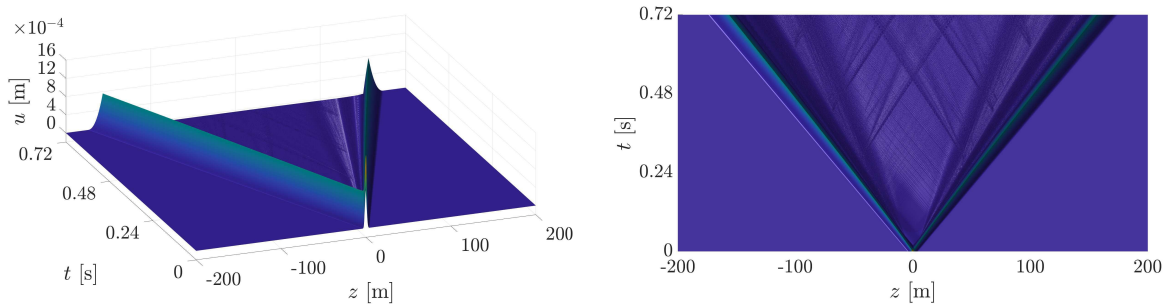

Figure 1: Numerical solution of Eq. (5) for the classical model. Thereby, a Gaussian pulse is chosen as initial condition. The solution is shown from two different perspectives.

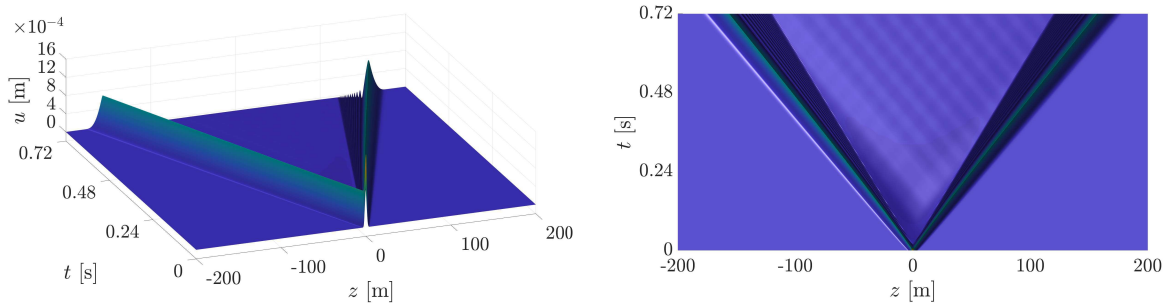

Figure 2: Numerical solution of Eq. (9) for the higher-order elasticity model. Thereby, a Gaussian pulse is chosen as initial condition. The solution is shown from two different perspectives.

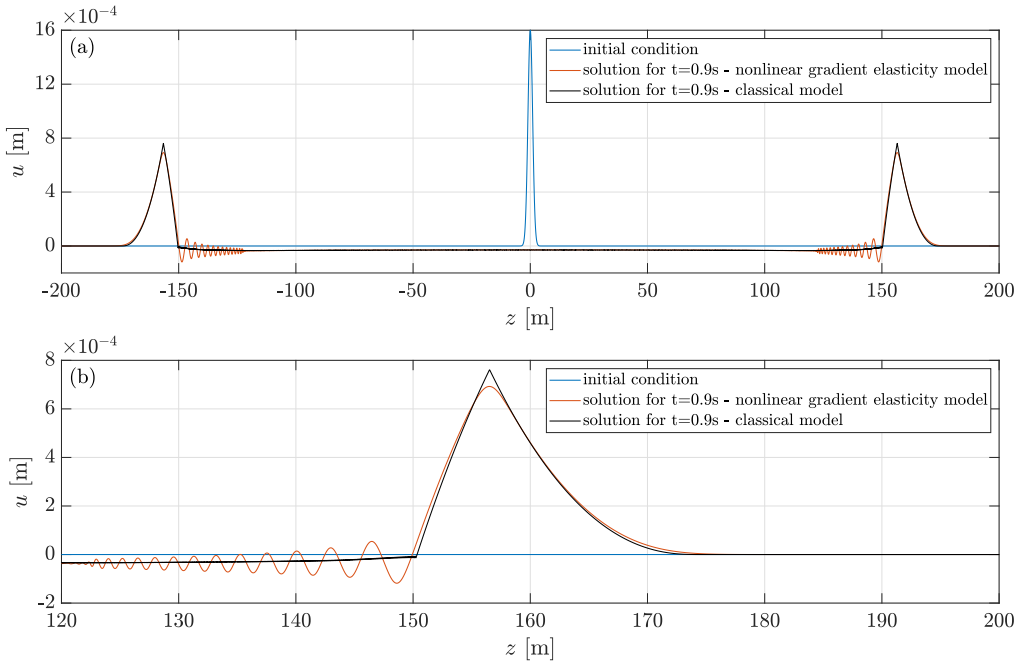

Figure 3: Comparison of the numerical solutions of Eqn. (5) and (9) at the end of the simulation time. In both cases, the Gaussian pulse is used as initial condition. The solution is shown for (a) $z \in [-200\,\mathrm{m},\ 200\,\mathrm{m}]$ and (b) $z \in [120\,\mathrm{m},\ 200\,\mathrm{m}]$, respectively.

solution of Eq. (9) is shown in Fig. 5. It is shown that the solution consists of two plateaus with different heights, which are alternating in space. As the shape of the solution is not changing in time, this is truly a stationary solution.
In order to investigate the effects of the higher-order gradient terms on the stationary solution, Fig. 6 shows the solution of Eq. (5). Thereby, the same initial condition as in Fig. 5 is used. It can be seen that high disturbances are introduced into the temporal evolution of the solution. These disturbances have their spatial origin in the transition area between the two plateaus of the initial condition, where high derivatives occur. They move in the opposite direction to the corresponding stationary solution.
Moreover, Fig. 7 compares the corresponding solutions at the end of the simulation time. It is observed that the higher-order-gradient terms and the disturbance shown in Fig. 6 change the shape of the solution. This shows that the dispersive effects influence the behavior of localized stationary solutions significantly, as they only exist exactly due to the balance

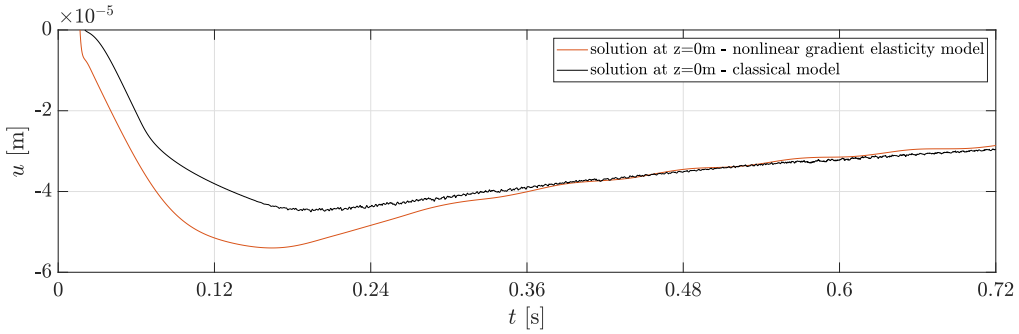

Figure 4: Comparison of the numerical solutions of Eqn. (5) and (9) at $z = 0\,\mathrm{m}$. In both cases, the Gaussian pulse is used as initial condition.

of nonlinear and dispersive effects. Once the dispersive terms are removed, the stationary solution can no longer exist. It has to be noted that oscillations of very small wavelength occur in the solution of Eq. (5). These are arising due to the large values of the derivatives, which lead to numerical inaccuracies. However, these inaccuracies have such a small effect on the solution behavior that they do not destroy the structure of the solution.

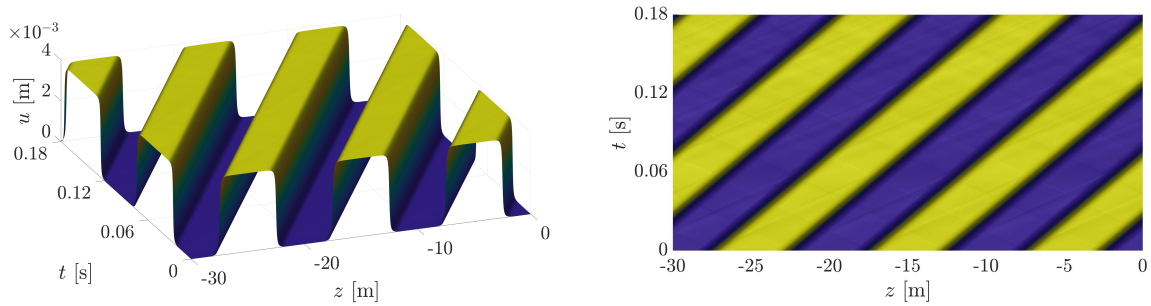

Figure 5: Numerical solution of Eq. (9) for the higher-order elasticity model. Thereby, the stationary solution of Eq. (11) is chosen as initial condition. The solution is shown from two different perspectives.

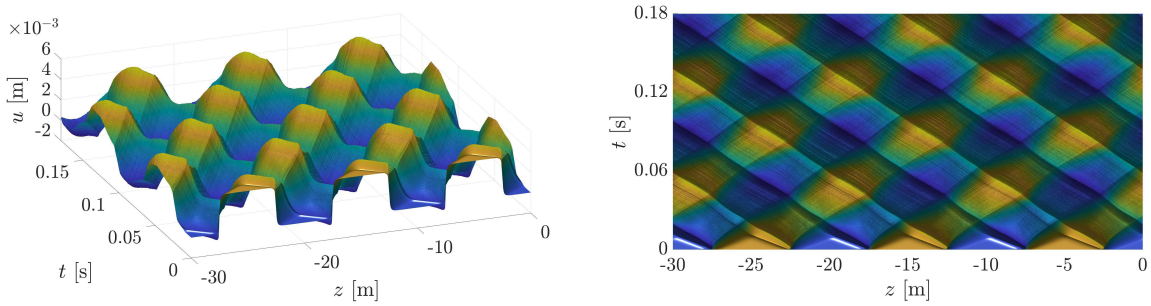

Figure 6: Numerical solution of Eq. (5) for the classical model. Thereby, the stationary solution of Eq. (11) is chosen as initial condition. The solution is shown from two different perspectives.

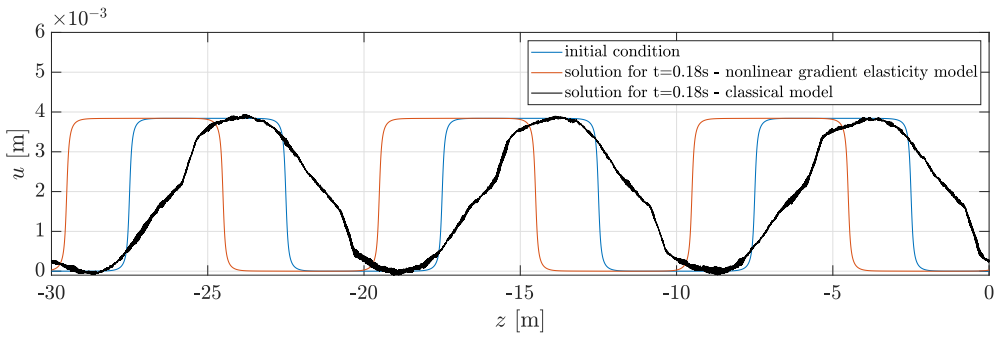

Figure 7: Comparison of the numerical solutions resulting from Eqn. (5) and (9) at the end of the simulation time. In both cases, the stationary solution of Eq. (11) is used as initial condition.

Conclusions

The response of the top layers of the earth induced by seismic waves is investigated. In this study, the constitutive behavior is governed by the hyperbolic soil model, whereby the shear modulus is strain dependent. The effects of small-scale heterogeneity/micro-structure is captured by considering higher-order gradient terms, which introduce dispersive effects. These effects are investigated in this work. For this, the corresponding equations of motion are solved using a numerical scheme, which has been introduced in Dostal et al. [8]. This scheme exploits the structure of the equation of motion and provides an accuracy of $\mathcal{O}(\Delta t^2 + \Delta z^2)$ in time and space.
Having applied this scheme using the Gaussian pulse as initial condition, it is shown that the higher-order gradient terms prohibit the formation of jumps. In this way, they lead to physically realizable solutions.
Moreover, the effects of the higher-order gradient terms are studied for the stationary solution of the equation of motion. Here, it is shown that the dispersive effects influence the behavior of localized stationary solutions significantly, as they only exist exactly due to the balance of nonlinear and dispersive effects. Once the dispersive terms are removed, the stationary solution can no longer exist.
In conclusion, this work shows that the proposed nonlinear gradient elasticity model provides physically realizable solutions. The introduced higher-order gradient terms are necessary and have significant influence on the corresponding solutions.

References

[1] Rodriguez-Marek A., Kruiver P.P., Meijers P., Bommer J.J., Dost B., van Elk J., Doornhof D. (2017) A Regional Site-Response Model for the Groningen Gas Field. *Bull. Seismol. Soc. Am.* **107**:2067–2077.

[2] Régnier J., Bonilla L.-F., Bard P.-Y., Bertrand E., Hollender F., Kawase H., Sicilia D., Arduino P., Amorosi A., Asimaki D., et al. (2016): International Benchmark on Numerical Simulations for 1D, Nonlinear Site Response (PRENOLIN): Verification Phase Based on Canonical Cases. *Bull. Seismol. Soc. Am.* **106**:2112–2135.

[3] Hashash Y.M.A., Phillips C., Groholski D.R. (2010) Recent Advances in Non–Linear Site Response Analysis. In: The 5th International Conference in Recent Advances in Geotechnical Eartqhuake Engineering and Soil Dynamics, San Diego, CA.

[4] Metrikine A. (2006) On causality of the gradient elasticity models. *J. Sound Vib.* **297**:727–742.

[5] Eringen A.C. (2002) Nonlocal Continuum Field Theories. Springer, NY.

[6] Verruijt A. (2009) An Introduction to Soil Dynamics. Vol. 24, Springer, New York

[7] Hardin B. O., Drnevich V. P. (1972) Shear Modulus and Damping in Soils: Measurement and Parameter Effects. *J. Soil Mech* **98**:603–624.

[8] Dostal L., Hollm M., Metrikine A. V., Tsouvalas A., van Dalen, K. N. (2021) Localized stationary seismic waves predicted using a nonlinear gradient elasticity model. *Nonlinear Dyn.* **107**:1107-1125.

Breather arrest in the damped chains with substantially nonlinear coupling

Oleg V. Gendelman*, Matteo Strozzi**, Alireza Mojahed*** and Alexander F. Vakakis***
**Faculty of Mechanical Engineering, Technion Haifa, Israel*
***University of Modena and Reggio Emilia, Italy*
****Faculty of Mechanical Sciences and Engineering, University of Illinois, Urbana-Champaign, USA*

Summary. We explore the breather propagation in a damped oscillatory chain with substantially nonlinear (non-linearizable) nearest-neighbour coupling. It is demonstrated that the combination of the damping and substantially nonlinear coupling leads to rather unusual two-stage pattern of the breather propagation. The first stage occurs at a finite fragment of the chain and is characterized by power-law decay of the breather amplitude. The second stage is featured by extremely small breather amplitudes that decay hyper-exponentially. Thus, one can speak about finite penetration depth of the breather – breather arrest. Specific models considered are the chains of damped linear oscillators with Hertzian or purely cubic nonlinear contact between the nearest neighbours. The effect of the initial excitation and of the viscous damping on the breather penetration depth is explored and approximate scaling relationships between these two parameters are established. These results are then rationalized by considering a simplified model of two damped linear oscillators coupled by strongly nonlinear springs. By using an approximate analytic procedure, we demonstrate that the initial excitation of one of these oscillators results in a finite number of beating cycles in the system. Then, the beating cycle in this system of two coupled oscillators is associated with the passage of the discrete breather between the neighbouring sites in the chain. Somewhat surprisingly, this simplified model reliably predicts the main features of the breather arrest in the chain of oscillators. Generalization for arbitrary coupling function and effect of pre-compression are also discussed.

Phenomenon of the breather arrest

We consider a chain of linear forced-damped osillators coupled by essentially nonlinear springs the model is demonstrated in Figure 1.

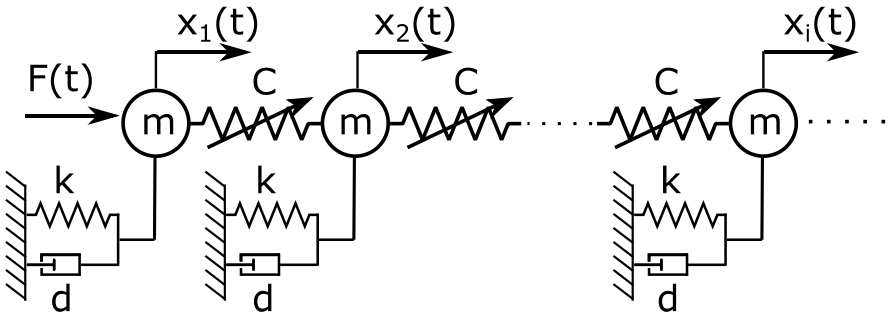

Figure 1. Sketch of the system

The presence of local damping with impulsive forcing inevitably leads to the energy dissipation and therefore decay of the amplitude of the breather propagating along the chain. In the case of linear viscous damping, one intuitively expects that this amplitude decay will be exponential, thus defining characteristic space scale of the decay. However, if the coupling between the neighbours is essentially nonlinear (i.e. non-linearizable), then, due to peculiar interaction between these two factors (essential nonlinearity and damping) one observes an interesting phenomenon of *breather arrest* (BA). The latter is defined as abrupt switch from power-law to hyper-exponential decay of the maximum breather amplitude, leading to a negligibly small amplitude after penetration to *finite* depth in the lattice. Typical dependence of the breather amplitude on the site number (for the case of Hertzian contacts) is presented in Figure 2.

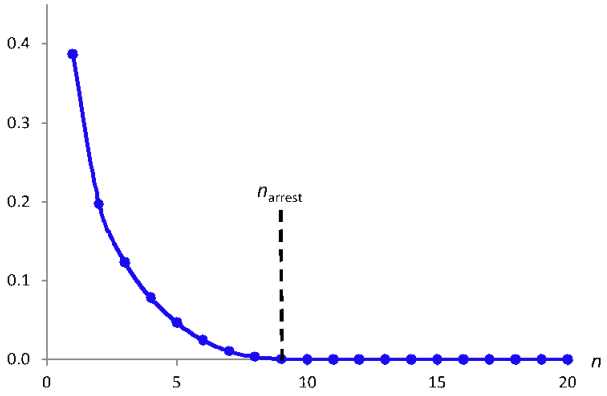

Figure 2. Typical dependence of the breater amplitude on the site.

Numerical simulations demonstrate that the breather penetration depth n_{arrest} scales with initial velocity A and damping coefficient λ according to the approximate relationship:

$$n_{\text{arrest}} \approx A^k \lambda^l \tag{1}$$

In the case of Hertzian contact, one obtains $k = 0.466$ and $l = -0.931$.

Reduced-order model

To assess the BA phenomenon from theoretical viewpoint, and to rationalize the numeric findings, we consider a simplified model that mimics the breather propagation in the chain with strongly nonlinear coupling. This simplification seems to be viable due to extreme localization of the breather in this specific chain. Therefore, it is possible to adopt, in the crudest approximation, that the breather propagation can be understood as a sequence of energy transfers between subsequent particles. Moreover, due to the strong localization, it is possible to assume that each such transfer involves only two neighbouring particles. Thus, the simplified model will consist of two identical oscillators, grounded through pairs of linear springs and viscous dampers, and with essentially nonlinear coupling, as presented in Figure 3.

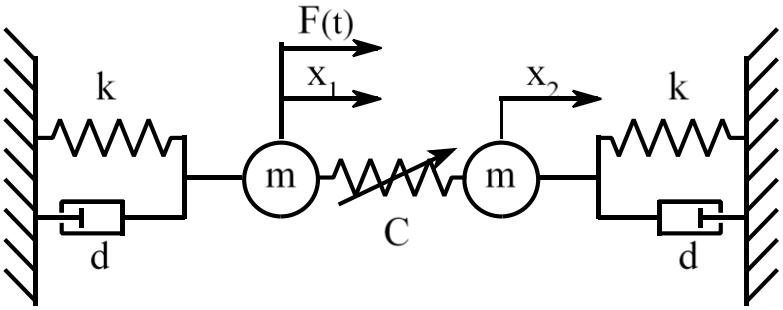

Figure 3. Sketch of the simplified model.

When one of the particles is excited with sufficient amplitude, the beating motion occurs. Each beat is associated with the propagation of the breather by one particle. It is possible to demonstrate that the number of such beats will be finite, due to the strong nonlinearity of the coupling. Then, one can obtain the following estimations for the breather penetration depth, and for the dependence of the breather amplitude on the site number before the arrest:

$$n_{\text{arrest}} \approx \frac{A^{\varepsilon-1}}{\lambda}, \quad A_{\max}(n) \approx A\left(1 - \frac{n}{n_{\text{arrest}}}\right)^{\frac{1}{\varepsilon-1}} \tag{2}$$

Here ε is the power of the substantially nonlinear power-law force. These estimations are in good correspondence with numeric findings. If initial pre-compression exists, the asymptotic evaluations (2) are no more valid, but the two-stage pattern of the breather propagation preserves itself, as demonstrated in Figure 4.

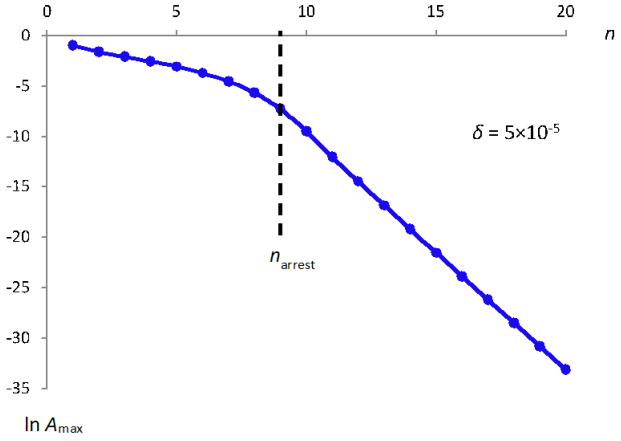

Figure 4 Two-stage breather propagation in granular chain with pre-compression.

These results point on generic character of the observed propagation patterns in damped systems with substantially nonlinear coupling

References

[1] Mojahed, A., Gendelman, O.V. Vakakis, A.F. (2019) Breather arrest, localization, and acoustic non-reciprocity in dissipative nonlinear lattices, *Journal of the Acoustical Society of America*,.**146**, 826-842.

[2] Strozzi M., Gendelman, O.V. (2019) Breather arrest in a chain of damped oscillators with Hertzian contact**,** arXiv:1907.12462

Free propagation of nonlinear waves in 1D acoustic metamaterials with inertia amplification

Valeria Settimi*, Marco Lepidi† and Andrea Bacigalupo ‡

*Department of Structural and Geotechnical Engineering, Sapienza University of Rome, Rome, Italy
†Department of Civil, Chemical and Environmental Engineering, University of Genoa, Genoa, Italy
‡IMT School for Advanced Studies Lucca, Lucca, Italy

Summary. The free propagation of nonlinear harmonic waves in acoustic metamaterials with inertia amplification is investigated. A Lagrangian model is formulated to describe the nonlinear dynamics of a periodic chain of elastically coupled point masses (atoms), realizing a minimal 1D acoustic metamaterial with local inertia-amplifying oscillators. First, the nonlinear equations of motion governing the free undamped oscillations of the tetra-atomic periodic cell are formulated, and the linear dispersion properties governing the small-amplitude range of wave propagation are determined. Second, the harmonically-periodic solutions characterizing the high-amplitude range of wave oscillations are investigated, by employing the method of nonlinear maps. Some non-standard methodological tools are introduced to consistently apply the map approach to the implicit function characterizing the nonlinear difference equations.

Introduction

The band structure of microstructured periodic media has long been attracting the scientific interest of researchers in linear and nonlinear dynamics. In the last years, a renewed attention has been devoted to the parametric and computational design of phononic microstructured materials, targeted at fine-tuning the periodic microstructure to achieve unconventional, superior of functional dispersion properties [1]. In this respect, the pressing technological demand for light-weight materials serving as mechanical low-frequency filters or isolators has favoured the rapid diffusion and success of acoustic metamaterials [2]. Indeed, the free propagation of elastic waves in acoustic metamaterials can be inhibited – even in the absence of dissipation – by the linear mechanism of *local resonance*, which allows the opening, shifting and widening of spectral band gaps by properly tuning the natural frequency of auxiliary periodic oscillators (*resonators*), locally coupled to the cellular microstructure. From the physical viewpoint, low-frequency resonators tend to combine high flexibility with large inertial masses, conflicting with the requirement of material lightness. In order to circumvent this conundrum, proper solutions of inertia amplification can be adopted by introducing panthographic mechanisms, exploiting levered masses coupled in parallel with elastic stiffnesses [3]. In this framework of extreme mechanical solutions, the combination of high microstructural flexibility, pantographically-amplified oscillations and null or minimal dissipation can be the natural scenario for the development of important nonlinear dynamic phenomena.

Lagrangian model of the acoustic metamaterial

A Lagrangian model is formulated to describe the nonlinear dynamics of a periodic chain of undamped oscillators (Figure 1), in which only linear forces of attraction/repulsion are exchanged between any pair of adjacent point masses (*primary atoms*). The atomic chain represents a minimal physical realization of a 1D acoustic metamaterial with inertia-amplifying auxiliary oscillators (*secondary atoms*), rigidly connected to the primary atoms by a panthographic mechanism.

Equations of motion

Collecting the nondimensional displacement variables $u = U_1/L$, $w = (U_3 - U_1)/L$, $u_\ell = U_\ell/L$ and $u_r = U_r/L$ in the vector $\mathbf{u} = (u, w, u_\ell, u_r)$, the exact nonlinear equation governing the motion of the generic cell can be formulated. Expanding in Taylor series around the rest position $\mathbf{u} = \mathbf{0}$ and retaining terms up to the third order, the equation reads

$$\mathbf{M}\ddot{\mathbf{u}} + \mathbf{K}\mathbf{u} + \mathbf{m}_2(\dot{\mathbf{u}}, \dot{\mathbf{u}}) + \mathbf{n}_2(\ddot{\mathbf{u}}, \mathbf{u}) + \mathbf{m}_3(\mathbf{u}, \dot{\mathbf{u}}, \dot{\mathbf{u}}) + \mathbf{n}_3(\ddot{\mathbf{u}}, \mathbf{u}, \mathbf{u}) = \mathbf{0} \tag{1}$$

The quasi-static equilibrium at the cell boundary nodes is instead governed by the linear equation $\mathbf{K}_p\mathbf{u} = \mathbf{f}_p$, where the external forces $\mathbf{f}_p = (f_\ell, f_r)$ can easily be related to the internal stresses $\boldsymbol{\sigma} = (\sigma_\ell, \sigma_r)$. Partitioning the displacement vector $\mathbf{u}$, the inner and outer displacement subvectors read $\mathbf{u}_a = (u, w)$ and $\mathbf{u}_p = (u_\ell, u_r)$, respectively. Collecting all the outer variables in the vector $\mathbf{v} = (u_\ell, u_r, \sigma_\ell, \sigma_r)$, the quasi-static equilibrium equations can be inverted to obtain the static condensation rule $\mathbf{u}_a = \mathbf{S}\mathbf{v}$. After condensation, the nonlinear equations of motion reads

$$\mathbf{M}\ddot{\mathbf{v}} + \mathbf{K}\mathbf{v} + \mathbf{p}_2(\dot{\mathbf{v}}, \dot{\mathbf{v}}) + \mathbf{q}_2(\ddot{\mathbf{v}}, \mathbf{v}) + \mathbf{p}_3(\mathbf{v}, \dot{\mathbf{v}}, \dot{\mathbf{v}}) + \mathbf{q}_3(\ddot{\mathbf{v}}, \mathbf{v}, \mathbf{v}) = \mathbf{0} \tag{2}$$

Focusing the analysis on the only periodic solutions in the nondimensional τ-time domain, the real-valued unknown $\mathbf{v}(\tau)$ can conveniently be expressed in Fourier series (truncated to account for the first harmonic terms)

$$\mathbf{v}(\tau) = \sum_{-\infty}^{\infty} \mathbf{a}_k \, \mathrm{e}^{\imath k\omega\tau} \simeq \mathbf{a}\,\mathrm{e}^{\imath\omega\tau} + \bar{\mathbf{a}}\,\mathrm{e}^{-\imath\omega\tau}, \qquad \text{with} \quad k \in \mathbb{Z} \tag{3}$$

where the Fourier coefficient $\mathbf{a} = (A_\ell, A_r, B_\ell, B_r)$ serves as (unknown) amplitude of the first harmonic component and bar indicates complex conjugate. The nondimensional parameter ω plays the role of circular frequency for the harmonic motion.

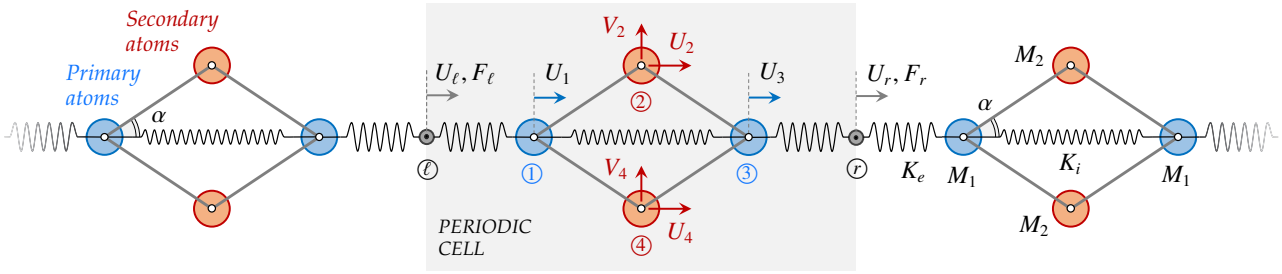

Figure 1: Acoustic metamaterial: (a) tetra-atomic crystal structure, (b) periodic cell of the lagrangian model, (c) mechanical properties.

Nonlinear map approach

The nonlinear equations of motion (2) can be linearized in the small-amplitude oscillation range. Therefore, the linear dispersion functions $\omega(\beta)$ relating the frequency ω to the nondimensional wavenumber β can be determined by applying either the Floquet-Bloch theory [4] or the map approach [5]. The latter technique employs the formal analogy between the wave periodicity (in the β-space) and the Lyapunov stability (in the τ-space) for discrete systems. The map approach can be applied to nonlinear systems governed by explicit equations $\dot{\mathbf{y}} = \mathbf{f}(\mathbf{y})$ to analyze the periodic solutions in the high-amplitude range of wave oscillations [6].

However, the nonlinear equations (2) can be manipulated to achieve only the implicit form $\mathbf{g}(\dot{\mathbf{y}}, \mathbf{y}) = \mathbf{0}$, which may require a different mathematical treatment [7]. Specifically, according to the most general definition of discrete implicit map, $\mathbf{y}_0$ is a p-periodic point of the implicit dynamic system $\boldsymbol{g}(\dot{\mathbf{y}}, \mathbf{y}, \boldsymbol{\alpha}) = \mathbf{0}$ if

$$\begin{cases} \boldsymbol{g}(\mathbf{y}_0, \mathbf{y}_1, \boldsymbol{\alpha}) = \mathbf{0} \\ \boldsymbol{g}(\mathbf{y}_1, \mathbf{y}_2, \boldsymbol{\alpha}) = \mathbf{0} \\ \dots \\ \boldsymbol{g}(\mathbf{y}_{p-2}, \mathbf{y}_{p-1}, \boldsymbol{\alpha}) = \mathbf{0} \\ \boldsymbol{g}(\mathbf{y}_{p-1}, \mathbf{y}_0, \boldsymbol{\alpha}) = \mathbf{0} \end{cases} \tag{4}$$

Therefore, the $\mathbf{y}_0$ stability can be analysed by introducing bifurcation conditions in order to assess the critical values of the parameter set $\boldsymbol{\alpha}$. The periodic points can be searched for the nonlinear system under investigation by setting $\dot{\mathbf{y}} = (A_r, B_r, \bar{A}_r, \bar{B}_r)$ and $\mathbf{y} = (A_\ell, B_\ell, \bar{A}_\ell, \bar{B}_\ell)$ and assuming ω as control parameter in the $\boldsymbol{\alpha}$-set.

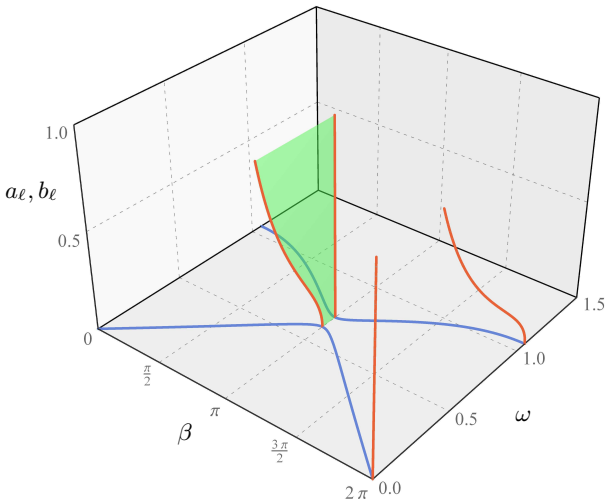

Figure 2: Linear spectrum (blue curves) and amplitude dependent frequency functions (red curves)

Equations (4) can be stated and solved for particular p-cases ($p = 1, 2$), giving solutions $\omega(\mathbf{y}_0, \mathbf{y}_1)$ corresponding to $\beta = 2\pi/p$. Using polar representations $A_\ell = a_\ell\, \mathrm{e}^{\imath\phi}$ and $B_\ell = b_\ell\, \mathrm{e}^{\imath\varphi}$, Figure 2 shows the amplitude-dependent frequency solutions $\omega(a_\ell)$ or $\omega(b_\ell)$, as obtained by setting $\mathbf{y}_1 = \mathbf{y}_0\, \mathrm{e}^{\imath\, 2\pi/p}$. The amplitude-dependent frequency curves have dominant softening behaviour for small amplitudes, as expected for inertial nonlinearities [8], and originate from the linear spectrum for null amplitudes. The softening behaviour tends to enlarge the amplitude-dependent stop bandwidth (green region).

Conclusions

Nonlinear periodic solutions for the free wave propagation have been determined for a 1D acoustic metamaterial waveguide with inertia amplification. The nonlinear mapping approach has been employed, as it applies to discrete implicit maps. Amplitude-dependent frequency functions have been determined for particular oscillation periodicities.

References

[1] Hussein M.I., Leamy M.J., Ruzzene M. (2014) Dynamics of phononic materials and structures: Historical origins, recent progress, and future outlook. *Appl Mech Rev* **66**(4):040802.

[2] Ma G., Sheng P. (2016) Acoustic metamaterials: From local resonances to broad horizons. *Science advances* **2**(2):e1501595.

[3] Yilmaz C. Kikuchi N. (2006) Analysis and design of passive low-pass filter-type vibration isolators considering stiffness and mass limitations. *J Sound Vib* **293**(1-2):171-195.

[4] Bacigalupo A., Lepidi M. (2018) Acoustic wave polarization and energy flow in periodic beam lattice materials. *Int J Solids Struct* **147**:183-203.

[5] Romeo F., Luongo A. (2002) Invariant representation of propagation properties for bi-coupled periodic structures. *J Sound Vib* **257**(5):869-886.

[6] Romeo F., Rega G. (2006) Wave propagation properties in oscillatory chains with cubic nonlinearities via nonlinear map approach. *Chaos Solitons Fractals* **27**(3): 606-617.

[7] Oliveira H.M. (2018) Bifurcation equations for periodic orbits of implicit discrete dynamical systems. *Nonlinear Dynamics* **91**(1):387-402.

[8] Lacarbonara W. (2013) Nonlinear structural mechanics: Theory, dynamical phenomena and modeling. Springer Science & Business Media.

Nonlinear dynamics of topological lattices

Rajesh Chaunsali and Georgios Theocharis
LAUM, CNRS, Le Mans Université, Avenue Olivier Messiaen, 72085 Le Mans, France

Summary. Due to the recent discovery of topological insulators in condensed matter physics, a new notion of topology has emerged in association with the intrinsic wave dispersion of a structure. It has led to several mechanical designs with robust localization of energy in space—potentially offering novel applications in energy harvesting, vibration isolation, and structure health monitoring. The framework of topology fundamentally rests on the linear dynamics of the system. In this work, we present our recent efforts to understand the interplay between nonlinearity and topology in mechanical systems. Our system obeys the dynamics that is governed by a second-order differential equation akin to electronic circuits. In particular, we study one-dimensional nonlinear lattices of both Fermi–Pasta–Ulam–Tsingou and Klein-Gordon types and discuss linear stability of topological states, soliton formation, and nonlinearity-induced topological transition. The findings highlight the effect of nonlinearity on the characteristics of topologically-robust edge states and the role of topology in interpreting purely nonlinear states.

Introduction

It is well-known that a periodic arrangement of structural constituents or properties possesses band gaps, and thus, can filter a range of frequencies from propagating in the medium. Recently, the topological characterization of such systems has enabled researchers to see them in a new light. Two periodic systems showing similar band gaps can still be different on topological grounds. This difference is quantified in terms of the topological invariant calculated from band dispersion. At the physical level, the difference manifests as robust edge/surface states in topologically-nontrivial systems. Such modes are "topologically protected" as small impurities in the system do not affect their presence [1].
The majority of studies on the topological mechanical lattices have so far relied on linear wave dynamics. Some open questions in the area are: What is the effect of nonlinearity on the characteristics of topologically-robust edge states? How can the topological framework be used as a novel tool to interpret purely nonlinear states? Along these lines, in this work, using analytical and numerical tools, we examine three particular aspects of the interplay between topology and nonlinearity in mechanical systems shown next.

Linear stability of topological states

As shown in Fig. 1(a), we take a 1D chain that consists of equal masses and two interconnecting linear springs of stiffness coefficients $1+\gamma$ and $1-\gamma$. Each mass is grounded with a nonlinear spring of cubic nonlinearity, such that the force (F)-deformation(x) profile is $F=\gamma_0 x+\Gamma x^3$, where γ_0 is the linearized ground stiffness and Γ is the parameter for nonlinearity. In the linear limit ($\Gamma=0$), this lattice possesses a band gap due to nonzero γ. Depending on the sign of γ, the system makes a topological transition from a trivial to nontrivial state [2]. Consequently, the topologically-nontrivial system supports a robust edge state with frequency inside the band gap. We examine how the onsite nonlinearity affects the form and stability of such a state. In Figs. 1(b) and 1(c), we show the nonlinear edge states (obtained through the continuation of the linear edge state) and their long-time dynamics for the chain with *softening* ($\Gamma<0$) and *stiffening* ($\Gamma>0$) types of nonlinearity, respectively. We find that the topological edge states are generally unstable due to oscillatory instabilities, leading to the delocalization of energy into the bulk of the chain. However, we find a frequency regime in the case of the *stiffening* nonlinearity that can support linearly stable edge states. This could potentially be useful in confining high-amplitude vibrations at the edges of structures for a long duration.

Moving Dirac soliton excites topological states

In Fig. 1(d), we take another chain similar to previous chain in the linearized limit; however, it has cubic nonlinearity in interconnecting springs. The force (F)-deformation(dx) profile of two alternating springs is $F=(1-\gamma)dx+\Gamma dx^3$ and $F=(1+\gamma)dx+\Gamma dx^3$. Depending on the sign of γ, the system again supports a topological edge state in the linear limit. The frequency of the state lies inside the band gap. Due to nonlinearity, it is possible to find spatially localized solutions that lie in the bulk of the periodic lattice with their frequency inside the band gap. Therefore, for a small band gap ($\gamma << 1$) and nonlinearity ($\Gamma << 1$), we employ the continuum approximation and find Dirac solitons residing inside the band gap. A stationary soliton is shown in Fig. 1(e). We also find a family of moving solitons in the lattice. We demonstrate numerically in Fig. 1(f) that such moving solitons can be used to excite edge states in lattices from far distances without actually placing the vibration source on the edge of the lattice.

Self-induced topological state by nonlinearity management

To achieve a topological transition in a mechanical lattice using nonlinearity, we take a 1D chain that consists of equal masses and two types of nonlinear springs, a *stiffening* and a *softening* spring, periodically alternating along the chain as shown in Fig. 1(g). We choose force (F)-deformation (dx) profiles for two springs as $F=(1-\gamma)dx+\Gamma dx^3$ and $F=(1+\gamma)dx-\Gamma dx^3$. In the linear limit ($\Gamma=0$) the system supports a band gap; however, the system is in a

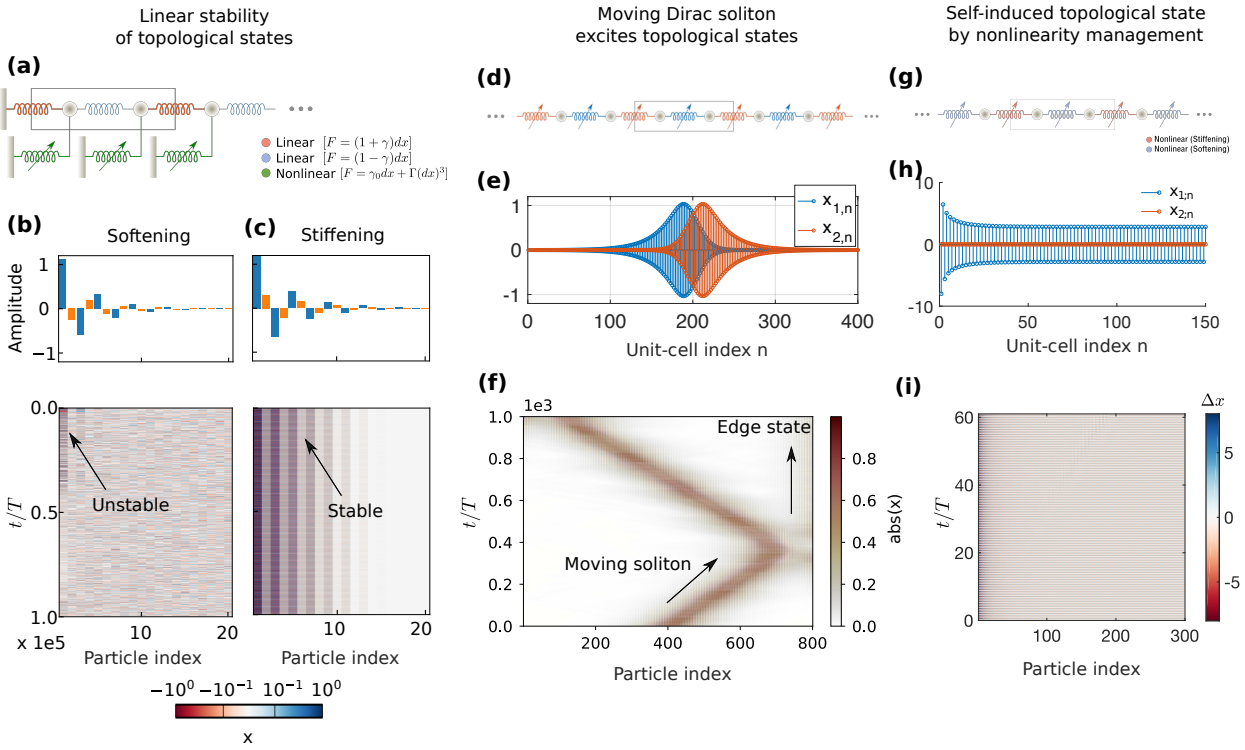

Figure 1: (a) A 1D chain with two linear springs alternating along the length and onsite nonlinearity. (b) One of the nonlinear edge states for *softening* nonlinearity. Below is its spatiotemporal diagram verifying instability. (c) One of the nonlinear edge states for *stiffening* nonlinearity. Below is its spatiotemporal diagram verifying linear stability. (d) A 1D chain with two nonlinear springs alternating along the length. (e) Dirac soliton residing inside the band gap. (f) Spatiotemporal diagram showing a moving Dirac soliton the excites an edge state localized on the right boundary of the lattice. (g) A 1D chain with two types of nonlinear springs (one *stiffening* and another *softening*) alternating along the length. (h) Analytically-obtained edge state in the lattice as a result of the amplitude-dependent topological transition. (i) Spatiotemporal diagram verifying the existence of such a solution in the lattice.

topologically trivial state with no state localized on the edges of the chain. For a system with a small band gap ($\gamma << 1$) and nonlinearity ($\Gamma << 1$), when the amplitude is increased, we witness an effective closure and reopening of the band gap. This leads to an amplitude-dependent topological transition, and we observe the emergence of a self-induced edge state in the system. We show an analytically obtained profile in Fig. 1(h). We note that this has a unique profile different from the ones seen in linear systems. Instead of the amplitude decaying to zero farther away from the edge, we note that it saturates to a nonzero amplitude [3]. We then verify the existence of this solution by performing full numerical simulations for the lattice. We take the nonlinear solution shown in Fig. 1(h) as initial conditions and obtain the spatiotemporal strain diagram in Figs. 1(i). We do not observe any significant scattering for a short time duration, which verifies the existence of the edge state in the system. This study, therefore, highlights novel ways to tailor nonlinearity in mechanical lattices to achieve a topological transition and localize spontaneously some energy at the edges of the system.

Conclusions

In this work, we discuss three different aspects of studying the nonlinear dynamics of topological lattices. First, we find that nonlinearity can generally make a topological edge state linearly unstable. However, depending on the details of nonlinearity, it is possible to find high-amplitude edge states that are linearly stable. Second, nonlinearity makes it possible to achieve spatial localization of energy in defect-free lattices. These solutions, e.g., moving soliton in our case, can be used to excite topological edge states in the lattices from farther distances. And third, an amplitude-dependent topological transition can be achieved by nonlinearity management in mechanical lattices, such that exotic nonlinear states emerge spontaneously on the edges.

References

[1] G. Ma, M. Xiao, and C. T. Chan, "Topological phases in acoustic and mechanical systems," *Nature Reviews Physics 1,* 281, 2019.
[2] R. Chaunsali, E. Kim, A. Thakkar, P. G. Kevrekidis, and J. Yang, "Demonstrating an In Situ Topological Band Transition in Cylindrical Granular Chains," *Physical Review Letters 119 (2),* 024301, 2017.
[3] Y. Hadad, A. B. Khanikaev, and A. Alù, "Self-induced topological transitions and edge states supported by nonlinear staggered potentials," *Phys. Rev. B 93,* 155112, 2016.

Monday, July 18, 2022
16:00 - 18:20

MS-04 Experiments in Nonlinear Dynamics and Control
Rhone 3B

Chair: Emmanuel Rigaud

16:00 - 16:20
Optimal Controller Gain for the Control Based Continuation of a Duffing oscillator
KLEYMAN Gleb, **TATZKO Sebastian***, WALLASCHEK Jörg
*Institute of Dynamics and Vibration Research (An der Universität 1 30823 Garbsen Germany)

16:20 - 16:40
Nonlinear localisation in a cyclic system with unilateral contact
NIEDERGESÄSS Björn*, GROLET Aurelien, HOFFMANN Norbert
*Hamburg University of Technology (Eißendorfer Str. 40 21073 Hamburg Germany)

16:40 - 17:00
Nonlinear modes of cantilever beams at extreme amplitudes: numerical computation and experiments
DEBEURRE Marielle*, GROLET Aurelien, THOMAS Olivier, MATTEI Pierre-Olivier, COCHELIN Bruno
*Arts et Métiers Institute of Technology (8 Boulevard Louis XIV F-59000 Lille France)

17:00 - 17:20
Nonlinear Motions of a Self-adaptive Resonator
SUGIURA Toshihiko*, OCHIAI Koki, LIU Xuefeng, OIKAWA Yuki, PENG Linyu
*Mechanical Engineering, Keio University (3-14-1 Hiyoshi, Kohoku, Yokohama Japan)

17:20 - 17:40
Measuring nonlinear localisation and isolated curve of solutions in a system of two coupled beams
GROLET Aurelien*, THOMAS Olivier, SHAMI Zein Alabidin
*Laboratoire d'Ingénierie des Systèmes Physiques et Numériques (Arts et Métiers - Campus d'Aix-en-Provence2, cours des Arts et Métiers, 13617 AIX EN PROVENCETél.: +33 (0)4 42 93 81 41Laboratoire d'Ingénierie des Systèmes Physiques et numériques (LISPEN EA7515)Arts et Métiers - Campus de Lille8 bd Louis XIV - 59046 Lille CedexTél.: +33 (0)4 42 93 81 41Laboratoire d'Ingénierie des Systèmes Physiques et numériques (LISPEN EA7515)Arts et Métiers - Campus de Cluny (Institut Image de Chalon-sur-Saône)2 rue Thomas Dumorey 71100 CHÂLONS-SUR-SAONETél.: +33 (0)3 85 90 98 60 France)

17:40 - 18:00
Experimental nonlinear dynamic analysis of a machine supporting beam
BRASIL Reyolando*, GARZERI Flavio, BIRCH Robert
*Federal University of ABC (Alameda da Universidade, SN, São Bernardo do Campo, SP Brazil)

Optimal Controller Gain for the Control Based Continuation of a Duffing-Oscillator

Gleb Kleyman, Sebastian Tatzko, Jörg Wallaschek
Institute of Dynamics and Vibration Research, Leibniz University Hannover, Germany

Summary. In the context of control based continuation for the experimental identification of nonlinear dynamic systems a PD-controller is usually exploited to stabilize the unstable branches of so called S-curves. The literature often refers to a simple trial-and-error method in order to determine the controller gains. In this paper the optimal controller gains for a Duffing-oscillator are determined analytically by applying the Harmonic Balance Method (HBM) to obtain a nonlinear algebraic approximation. However, the generalized methodology can be easily extended to any kind of nonlinear dynamic system.

Introduction

Experimental or Control-Based Continuation (CBC) is a promising method for the bifurcation analysis in real life nonlinear experiments. Exploiting the CBC method, it is possible to track a branch of periodic solutions through a fold bifurcation where they become unstable and continue them up to a second bifurcation point where they become stable again. A typical example for such behavior is the frequency response of vibrating structures featuring nonlinear stiffness, [1]. Typically, thin structures tend to behave like this, as they become geometrically nonlinear when excited to vibration amplitudes in the order of their thickness. In particular, it can be shown that the nonlinear restoring force of thin shell elements can be described by quadratic and cubic stiffness terms, [2, 3]. Considering a modal approach, in the more specific case of a transversely loaded hinged-hinged beam, a Duffing-type differential equation can be assumed, [4]. Here, the stiffness term is cubic, but depends on the mode-shape and type of support.
Experimental characterization of nonlinear oscillating systems is a challenging task. There are only few methods that will identify a nonparametric model of the structure, [5]. CBC is one of these methods. The goal of CBC is to estimate the nonlinear frequency response curves (NLFR). Originally, CBC was proposed by [6] as a tool for the bifurcation analysis of a dry-friction oscillator. However, since then the application of CBC has already been experimentally demonstrated on various systems, such as a parameter excited pendulum [7], an electromagnetic and piezoelectric energy harvesting device [8, 9, 10], a nonlinear tuned mass damper (NTMD) [11], a beam with a locally attached nonlinear spring [12], an impact oscillator [13], a Duffing-oscillator, and frictionally coupled beams [14]. There are also several publications that deal with different extensions and improvements compared to the original method. For instance, the adaption of CBC for tracking of backbone-curves [15, 16], increased robustness against measurement noise [17] and the application of FIR-filters to speed up the measurement time [18]. Even the stability of periodic orbits can be assessed during a CBC experiment, as described in [11] and [19].
A main concern in CBC is the applied control strategy. A feedback control is essential to stabilize the unstable periodic orbits of the system in order to trace them through the bifurcation points. Typically, a PD-controller, corresponding to figure 2 is exploited. After finding suitable controller gains, the amplitude $\hat{x}_{\mathrm{ref}}$ of the reference signal is swept (or stepped) and the corresponding force is measured. By means of Newtons method (full CBC), fixed point iteration or an adaptive FIR-filter (simplified CBC), the controller is constrained to be stabilizing but non-invasive with respect to the system dynamics. For the determination of the controller gains, literature often refers to a trial-and-error procedure. However, this can be very time-consuming if at least approximate values are unforeseen. Besides the trial-and-error procedure, in [20], stability maps were created for an impact oscillator by varying the controller gains and evaluating the resulting control error. In that way the optimal settings for this specific experiment were found. Unfortunately, these findings can not be generalized for different types of systems. An application of adaptive control strategies to CBC was presented in [21]. Although the authors approach is formulated for linear systems, they have showed that the method can be successfully applied to nonlinear examples as well. However, the mathematical derivation of the controller equation is very challenging and a generalized proof of concept for nonlinear systems is still pending. This is why we feel like the major control problem is not yet fully solved.
This paper deals with an analytical approximate solution of critical controller gains for a Duffing-type oscillator in a CBC experiment. The Harmonic Balance Method is applied on the closed-loop system in order to determine stabilizing gains of the PD-controller. The results are validated on an experimental single-degree-of-freedom nonlinear oscillator. The concept can be adapted to other systems including the initially mentioned geometrically nonlinear structures. With the developed formula one is capable of predicting the critical controller gains, which can be considered as lower limits, where stabilization is granted. It will be shown, that for polynomial nonlinearities only the polynomial degree and not the coefficients are essential. This makes it very easy to estimate the necessary structural parameters.

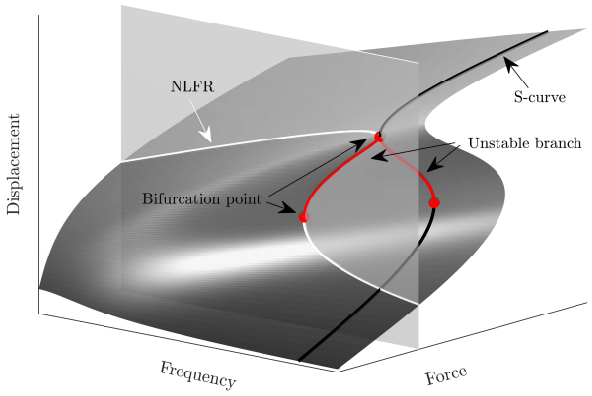

Figure 1: Manifold of a single degree of freedom Duffing-oscillator. White: Nonlinear frequency response curve (NLFR), Black: S-curve, Red lines: Unstable branches, Red dots: Fold bifurcation

Figure 1 shows the displacement amplitude of a stiffening Duffing-oscillator as a three-dimensional manifold plotted versus the excitation frequency and excitation force. The white curve is the nonlinear frequency response (NLFR) of the system. The red dots mark bifurcation points and the red curves are unstable periodic solutions. The black curve can be interpreted as the load-displacement characteristic of the system at a constant excitation frequency. Due to the particular shape, it is referred to as a S-curve in literature. Both types of curves (NLFRs and S-curves) are projections of the same manifold to different parameter spaces. Accordingly, an experimental characterization of such systems can be performed in two different ways: A continuation of the NLFRs varying two parameters at a time (frequency and displacement) like proposed by [20] (full CBC) or tracing the S-curves at constant frequency (simplified CBC). Due to the unique correlation between displacement and forcing amplitude in many systems, the latter approach can be considered as the simpler method. The continuation parameter reduces then to a single variable, which is the displacement amplitude. Either way (full or simplified CBC) a feedback controller is essential to stabilize the unstable periodic orbits.
We will focus on the simplified CBC in this paper. Here, each frequency corresponds to a measurement run and so the control parameters can be adjusted between the runs, if necessary. For a detailed description of the CBC method, please refer to the previously mentioned literature. An application of CBC to the experimental Duffing-oscillator presented within this paper is also found in [14].

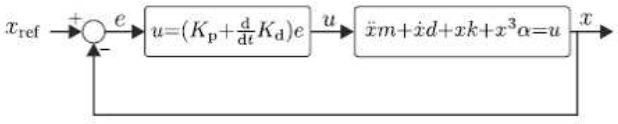

Figure 2: Feedback control loop utilized for control-based continuation.

Condition for a Stabilizing Controller

The equation of motion (EOM) of the forced Duffing-oscillator reads:

$$m\ddot{x} + d\dot{x} + kx + \alpha x^3 = f. \tag{1}$$

Here f is the excitation force and x is the displacement. Harmonically excited at certain frequencies, in open-loop condition, the system features two stable and one unstable periodic solution, as shown in figure 1. The goal is to stabilize the system by a feedback controller such that for a given reference displacement x_{ref} the unstable branch is accessible. A simple PD-controller, corresponding to figure 2, is exploited for this purpose. In closed-loop the excitation force can be expressed in terms of the controller gains (K_{p}, K_{d}) and displacements (x, x_{ref}):

$$f = K_{\mathrm{p}}(x_{\mathrm{ref}} - x) + K_{\mathrm{d}}(\dot{x}_{\mathrm{ref}} - \dot{x}). \tag{2}$$

Inserting equation 2 into 1 the EOM of the feedback-controlled system becomes:

$$m\ddot{x} + (d + K_{\mathrm{d}})\dot{x} + (k + K_{\mathrm{p}})x + \alpha x^3 = K_{\mathrm{p}}x_{\mathrm{ref}} + K_{\mathrm{d}}\dot{x}_{\mathrm{ref}}. \tag{3}$$

The simplified CBC exploits the unique parametrization of S-curves, which many nonlinear systems hold to. Varying x, the S-curves can be traced at constant excitation frequencies. In the closed-loop experiment the displacement is controlled by the reference signal x_{ref}. The excitation force settles automatically according to equation 2. Therefore, in an experiment the amplitude of the reference signal is increased while the resulting force is measured and the S-curves are

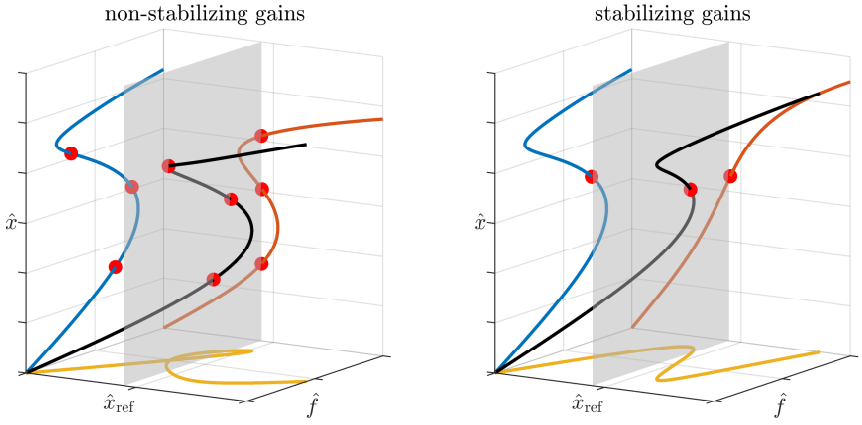

Figure 3: Comparison of the $\hat{x}(\hat{x}_{\mathrm{ref}})-$parametrization for a set of stabilizing and non-stabilizing controller gains (at a constant frequency).

reconstructed from the amplitude values of x and f. In figure 3, the correlations of the amplitudes $\hat{x}$,$\hat{f}$ and $\hat{x}_{\mathrm{ref}}$ for two sets of controller gains are given as 3-dimensional curves. These curves result from the solution of equation 3 under the assumption of harmonic oscillations (Harmonic Balance Method). The gain settings are chosen for a non-stabilizing effect in the left panel and a stabilizing effect in the right panel. The blue, red and yellow curves are projections into different parameter spaces. The blue curves are the already discussed S-curves. S-curves are exploited to characterize the system and therefore this curves must remain independent of the controller settings. Trying to measure the S-curve with inappropriate controller settings can result in cutting of the extreme points (i.e. the bifurcation points), as shown in section Experimental Validation. The red curves map the reference amplitudes $\hat{x}_{\mathrm{ref}}$ to corresponding values of $\hat{x}$. These shapes are parameterized differently for the two sets of controller gains. For stabilizing control, it is desired that the correlation of $\hat{x}_{\mathrm{ref}}$ and $\hat{x}$ becomes unique. This means that for any value of $\hat{x}_{\mathrm{ref}}$ there should be only one corresponding value of $\hat{x}$. This is, what the gray section plane, which runs along a constant value of $\hat{x}_{\mathrm{ref}}$, indicates. If there is only a single solution (operation point), oscillation on the unstable branch of the S-curve can be tuned specifying a certain reference amplitude $\hat{x}_{\mathrm{ref}}$. If there are multiple intersections, the system will automatically settle to a stable solution. From this theoretical considerations, one can claim that the required constraint for a stabilizing control in CBC is the following: *the control gains are optimally set, when the parameterization of $\hat{x}$ and $\hat{x}_{\mathrm{ref}}$ becomes unique*.

Derivation of Optimal Control Gains

In order to find the desired control settings for the Duffing-oscillator, the corresponding $\hat{x}_{\mathrm{ref}}(\hat{x})$-curve is studied analytically. However, the general workflow can be applied to any other nonlinear system, although it may be necessary to extend the principle to a semi-analytical or numerical approach. First, the reference signal is defined to be harmonic and it is assumed that the fundamental harmonic dominates the system response while higher harmonics can be neglected. This approach is known as Harmonic Linearization or Harmonic Balance Method (HBM):

$$\begin{aligned} x \approx \tilde{x} = \hat{x}\sin(\Omega t), \qquad \dot{\tilde{x}} = \Omega\hat{x}\cos(\Omega t), \qquad \ddot{\tilde{x}} = -\Omega^2\hat{x}\sin(\Omega t) \\ x_{\mathrm{ref}} = \hat{x}_{\mathrm{ref,s}}\sin(\Omega t) + \hat{x}_{\mathrm{ref,c}}\cos(\Omega t), \qquad \dot{x}_{\mathrm{ref}} = \Omega\left(\hat{x}_{\mathrm{ref,s}}\cos(\Omega t) - \hat{x}_{\mathrm{ref,c}}\sin(\Omega t)\right). \end{aligned} \tag{4}$$

The varying phase relation between excitation and response is expressed by splitting the reference signal into sine and cosine components but can also be described by complex numbers, [22]. Next, the nonlinear restoring force is approximated in terms of its Fourier series considering the fundamental harmonic Ω:

$$\alpha\tilde{x}^3 = \alpha\hat{x}^3\sin^3(\Omega t) \approx \frac{a_0}{2} + a_1\cos(\Omega t) + b_1\sin(\Omega t), \tag{5}$$

where a_0, a_1 and b_1 are defined as:

$$a_0 = \frac{1}{\pi}\int_{-\pi}^{\pi} f_{\mathrm{nl}}\mathrm{d}\varphi, \qquad a_1 = \frac{1}{\pi}\int_{-\pi}^{\pi} f_{\mathrm{nl}}\cos(\varphi)\mathrm{d}\varphi, \qquad b_1 = \frac{1}{\pi}\int_{-\pi}^{\pi} f_{\mathrm{nl}}\sin(\varphi)\mathrm{d}\varphi \tag{6}$$

With $\varphi = \Omega t$. From eq.6 it follows that in the present example $a_0 = a_1 = 0$. Thus, equation 5 turns into:

$$\alpha\hat{x}^3\sin^3(\Omega t) \approx \alpha\frac{3}{4}\hat{x}^3\sin(\Omega t). \tag{7}$$

Combing equations 3, 4 and 7 gives:

$$\begin{aligned} &\hat{x}\left(-m\Omega^2 + k + K_{\mathrm{p}} + \alpha\frac{3}{4}\hat{x}^2\right)\sin(\Omega t) + \hat{x}\left(d + K_{\mathrm{d}}\right)\Omega\cos(\Omega t) \\ &= \left(K_{\mathrm{p}}\hat{x}_{\mathrm{ref,s}} - \Omega K_{\mathrm{d}}\hat{x}_{\mathrm{ref,c}}\right)\sin(\Omega t) + \left(K_{\mathrm{p}}\hat{x}_{\mathrm{ref,c}} + \Omega K_{\mathrm{d}}\hat{x}_{\mathrm{ref,s}}\right)\cos(\Omega t). \end{aligned} \tag{8}$$

Because sine and cosine are orthogonal to each other, equation 8 can be further split into terms which contain only sine or cosine components:

$$\begin{aligned}\hat{x}_{\mathrm{ref,c}} &= \frac{\Omega}{K_\mathrm{p}}\left((d+K_\mathrm{d})\hat{x} - K_\mathrm{d}\hat{x}_{\mathrm{ref,s}}\right),\\ \hat{x}_{\mathrm{ref,s}} &= \frac{\hat{x}\left(K_\mathrm{d}\Omega^2\left(d+K_\mathrm{d}\right)+K_\mathrm{p}\left(-m\Omega^2+k+K_\mathrm{d}+\alpha\frac{3}{4}\hat{x}^2\right)\right)}{K_\mathrm{d}^2\Omega^2+K_\mathrm{p}^2}.\end{aligned} \tag{9}$$

It can now be solved for the reference amplitude $\hat{x}_\mathrm{ref}$ and the $\hat{x}_\mathrm{ref}(\hat{x})-$curve can be derived as a function of the controller gains:

$$\hat{x}_\mathrm{ref}(K_\mathrm{p},K_\mathrm{d},\hat{x}) = \sqrt{\hat{x}_{\mathrm{ref,c}}^2+\hat{x}_{\mathrm{ref,s}}^2} = \frac{\hat{x}\sqrt{\Omega^2\left(d+K_\mathrm{d}\right)^2+\left(-m\Omega^2+k+K_\mathrm{p}+\alpha\frac{3}{4}\hat{x}^2\right)^2}}{\sqrt{K_\mathrm{d}^2\Omega^2+K_\mathrm{p}^2}}. \tag{10}$$

Equation 10 is visualized in the left panel of figure 4 for a set of non-stabilizing, critical and stabilizing controller gains. In the right panel of figure 4 the gradient of equation 10 for the same gain settings is given. It is obvious that in order to achieve the desired unique parametrization of $\hat{x}_\mathrm{ref}(\hat{x})$, the curve must be monotonous. That means the gradient $\hat{x}'_\mathrm{ref}$ must remain positive for all values of $\hat{x}$. For critical gains the two extreme points of $\hat{x}_\mathrm{ref}(\hat{x})$ (blue curve) merge into a single saddle point (red curve). Here the $\hat{x}_\mathrm{ref}(\hat{x})-$curve has a horizontal tangent, which means the gradient has only a single zero point. This is why, for gains above this values the closed-loop system becomes stable.

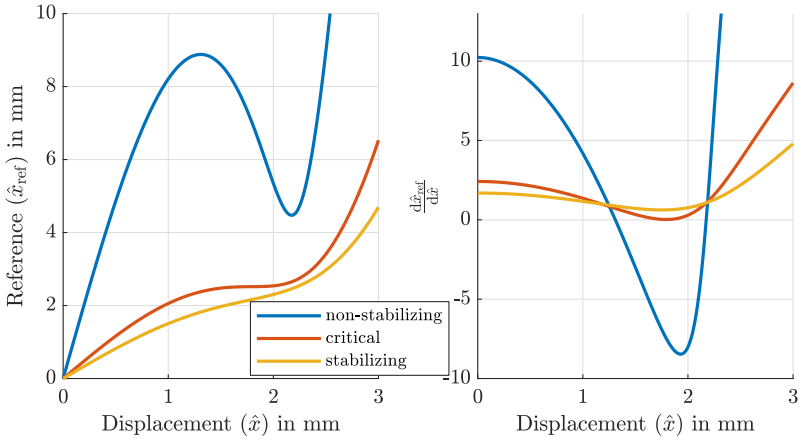

Figure 4: Comparison of the $\hat{x}_\mathrm{ref}(\hat{x})-$curve for a set of stabilizing and non-stabilizing and critical controller gains (at a constant frequency).

First, the special case of a differential controller ($K_\mathrm{p}=0$) is studied. The D-component is sufficient to stabilize most systems featuring nonlinear stiffness. With a differential controller the derivative of equation 10 can be analytically expressed as:

$$\begin{aligned}\hat{x}'_\mathrm{ref} &= \frac{\mathrm{d}\hat{x}_\mathrm{ref}}{\mathrm{d}\hat{x}} = \frac{1}{K_\mathrm{d}\Omega}\left(\gamma+\frac{\gamma'}{2\gamma}\right)\\ \text{where}\quad \gamma &= \sqrt{\Omega^2\left(d+K_\mathrm{d}\right)^2+\left(m\Omega^2-k-\alpha\frac{3}{4}\hat{x}^2\right)^2}\\ \text{and}\quad \gamma' &= \left(\frac{9}{4}\alpha^2\hat{x}^4+3\left(k-\Omega^2m\right)\alpha\hat{x}^2\right)\end{aligned} \tag{11}$$

In order to find the critical value $K_\mathrm{d,crit}$, the gradient $\hat{x}'_\mathrm{ref}$ is set equal to zero, from which follows:

$$2\gamma^2+\gamma'=0. \tag{12}$$

Equation 12 can be rewritten as monic polynomial:

$$\hat{x}^4+\underbrace{\frac{16}{9\alpha}\left(k-\Omega^2m\right)}_{p}\hat{x}^2+\underbrace{\frac{16}{27\alpha^2}\left(\left(d+K_\mathrm{d}\right)^2\Omega^2+\left(k-\Omega^2m\right)^2\right)}_{q}=0. \tag{13}$$

Solutions of equation 13 for $\hat{x}$ are extreme points of $\hat{x}_\mathrm{ref}(\hat{x})$. However, the condition for the critical gain is that the extreme points merge into a saddle point, which means that equation 13 will have only one solution. Substituting $z=\hat{x}^2$

the solution can be expressed as:

$$z = -\frac{p}{2} \pm \sqrt{\frac{1}{4}p^2 - q}. \tag{14}$$

There is only one condition under which equation 14 has zero points at $z = -\frac{p}{2}$:

$$\frac{1}{4}p^2 = q. \tag{15}$$

Solving equation 15 leads to the critical gain $K_{\mathrm{d,crit}}$, which is a function of the oscillation frequency Ω and the mass, damping and stiffness coefficients of the system:

$$K_{\mathrm{d,crit}} = \pm(k - \Omega^2 m)\frac{1}{\sqrt{3}\Omega} - d \tag{16}$$

Note, that although both solutions (negative and positive) are mathematically correct, only the negative is practically relevant. Equation 16 also reveals that the critical gain is independent of the nonlinear coefficient α. That means, it is only necessary to determine the structural parameter of the underlying linear system for optimal controller settings. In most cases this can be easily done performing a linear experimental modal analysis at low level oscillations.
The critical proportional gain $K_{\mathrm{p,crit}}$ can be derived in an analogous way, setting $K_{\mathrm{d}} = 0$ in equation 10. The proportional gain $K_{\mathrm{p,crit}}$ becomes:

$$K_{\mathrm{p,crit}} = \pm\sqrt{3}d\Omega + m\Omega^2 - k. \tag{17}$$

Here, again the solution has mathematically a positive and a negative sign. However, the negative solution is the only valid one. Note, that for $K_{\mathrm{p}} \neq 0$, K_{p} becomes part of the solution z in equation 14, which means increasing K_{p} also increases the displacement amplitude $\hat{x}$ where the saddle point occurs. That means, that the proportional gain alters the general shape of the $\hat{x}_{\mathrm{ref}}(\hat{x})$-parametrization. This fact can be exploited to increase the spatial resolution of the measured curves at some intervals. Although the single proportional-controller has a stabilizing effect in theory, experience shows that in practice this case is rather irrelevant. In real-life applications always a PD-controller should be chosen over a pure P-controller. Without a D-component, the system very slowly approaches a steady state. A PD-controller significantly reduces the settling time.

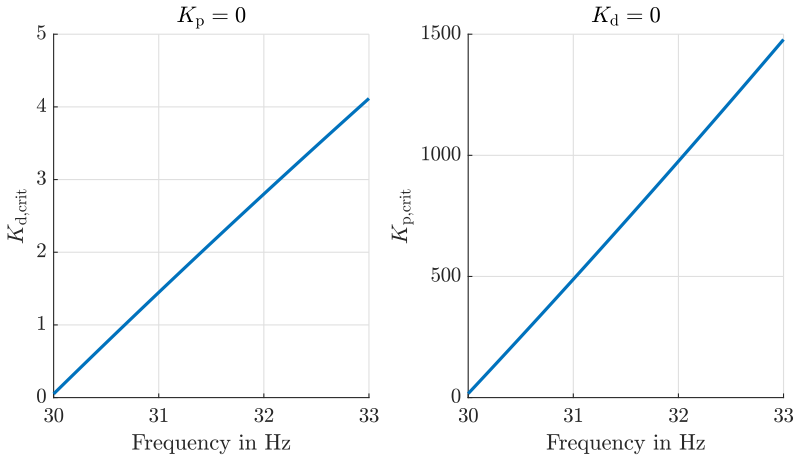

Figure 5: Critical controller gains for different excitation frequencies.

Figure 5 shows the curves corresponding to equations 16 and 17 for the experimental system from section Experimental Validation in the relevant range of frequencies. The linear natural frequency (LNF) of the system is just below 30 Hz. For frequencies higher than this, stabilization is necessary because the NLFR has a significant overhang, see figure 1. It can be seen, that the critical gains increase almost linearly with the frequency starting at the LNF. At 31 Hz the displacement became so high that the upper bifurcation point could not be reached with the used displacement sensor. However, from the equations it is evident, that both values continue to grow for higher frequencies.
It can be seen that the critical P-gain is about two orders of magnitude above the critical D-gain. Accordingly, considering a displacement and a velocity signal with the same signal to noise ratio, the measurement noise is amplified many times more by a stabilizing P-controller than by a pure D-controller. Therefore, in a practical implementation it depends on the measured variable and signal quality, whether the D-component or the P-component should be weighted more, as several combinations will equally stabilize the system. If a PD-controller is employed, the critical gains are reduced because both values contribute to stabilization. This can be mathematically derived performing the calculation from equations 11 to 15 for both, $K_{\mathrm{p}} \neq 0$ and $K_{\mathrm{d}} \neq 0$. The critical differential gain $K_{\mathrm{d,crit}}$ is then a function of the proportional gain K_{p}:

$$K_{\mathrm{d,crit}} = -\frac{1}{\sqrt{3}\Omega}(k + K_{\mathrm{p}}) + \frac{1}{\sqrt{3}}m\Omega - d. \tag{18}$$

m	k	d	α
0.1964 kg	6926 $\frac{\mathrm{N}}{\mathrm{m}}$	0.1046 $\frac{\mathrm{Ns}}{\mathrm{m}}$	$5.27 \cdot 10^7$ $\frac{\mathrm{N}}{\mathrm{m}^3}$

Table 1: Parameter of the Duffing-oscillator.

From equation 18 it can be concluded, that $K_{\mathrm{d,crit}}$ decreases linearly with K_{p} but still increases with Ω. Following equation 18 stability maps can be constructed, compare figure 6. Here, the critical gains from equation 16 and 17 are intersections of the curves with the vertical and horizontal axes. The curves themselves are defined by equation 18. These maps are intended to find proper controller gains for different frequencies. Both components can be weighted as preferred by the user. As long as the values lie above the curves, the feedback-control has the desired stabilizing effect on the system.

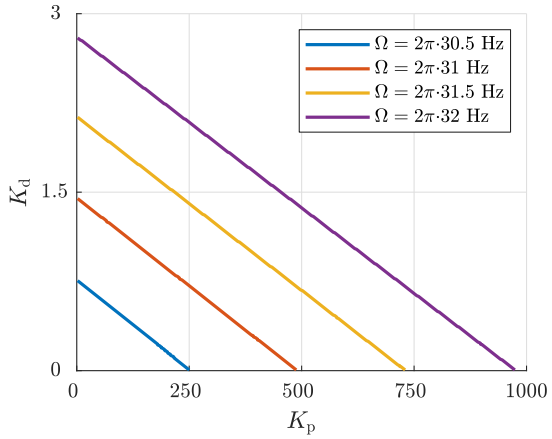

Figure 6: Stability map for the Duffing-oscillator with system parameters from section Experimental Validation. The lines indicate the stability margin for different excitation frequencies.

Experimental Validation

The theoretical considerations are experimentally validated. Hereby, the focus lies on the hypothesis from equation 10, and the resulting critical controller gains according to figures 5 and 6. The experimental setup is a single-degree-of-freedom oscillator, which has already been investigated in [14] and [23]. Figure 7 shows a picture and a schematic representation of the system. The main components are the fixed frame ①, the voice-coil actuator (VCA) ② and the mass ③. The mass is suspended by guitar strings in the middle of the frame. It is excited by the VCA and moves out of the frame plane as illustrated by the schematic view. The VCA is actuated by a power amplifier for electrodynamic shakers made by TIRA. The amplifier supports a current-mode which enables to control the output current directly. The velocity and displacement of the mass is measured at position ④.Due to the geometric nonlinearity between mass displacement and strain of the guitar strings the oscillator exhibits a significant nonlinear stiffness. Following figure 7 the restoring force can be formulated as:

$$F_{\mathrm{k}} = 8k_{\mathrm{s}}\left(1 + \frac{l_{\mathrm{v}} - l_{\mathrm{g}}}{\sqrt{l_{\mathrm{g}}^2 + x^2}}\right). \tag{19}$$

Here k_{s} is the axial stiffness of the strings, l_{v} is the elongation due to the preload force, l_{g} is the free length from mass to corner and x is the displacement. Approximating equation 19 by its truncated Taylor series the nonlinear EOM of the forced system can be written in analogy to equation 1 as:

$$m\ddot{x} + d\dot{x} + \underbrace{8\frac{k_{\mathrm{s}}l_{\mathrm{v}}}{l_{\mathrm{g}}}}_{k}x + \underbrace{4\frac{k_{\mathrm{s}}(l_{\mathrm{g}} - l_{\mathrm{v}})}{l_{\mathrm{g}}^3}}_{\alpha}x^3 = f. \tag{20}$$

It can be seen, that this particular system can be well described by a Duffing-oscillator. In order to find the appropriate model parameters, a two-step procedure was conducted. First, the parameters of the underlying linear system (m, d, k) were determined by sweeping through the resonance frequency at a low level excitation (0.02 N from $29 - 31$ Hz). The frequency response was observed and the modal parameters were extracted, which already correspond to the physical parameters in the case of a single-degree-of-freedom system. The excitation force was reverse calculated from the measured current flowing through the VCA, because both are proportional. In the second step, the system was excited with a significantly larger force of about 0.1 N. Here during the sweep-up the system showed a jump phenomenon. Assuming the EOM from equation 20 is accurate, the nonlinear coefficient α was determined by an optimization algorithm based on Newton's

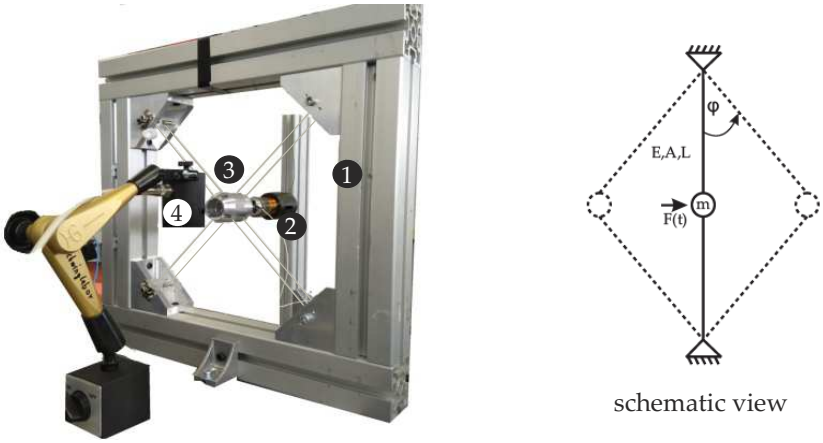

Figure 7: Photograph and schematic view of the Duffing-oscillator.

$\Omega/(2\pi)$	30.3 Hz	30.5 Hz	30.7 Hz
$K_{\mathrm{d,crit}}$	0.47	0.75	1.03

Table 2: Theoretical critical differential gains ($K_{\mathrm{p}} = 0$).

method. For this purpose, the measured time-domain data was matched with a time step simulation until the residuum (difference between the envelopes of both signals) became minimal. As an input signal for the time step integration the actually measured force resp. current signal was used. Figure 8 shows a comparison between the measured velocity and the envelope of the model output after optimization. The estimated system parameters are summarized in table 1. In the following the linear part was used to calculate critical gains corresponding to figures 5 and 6. Three different excitation frequencies were chosen to validate the formulas from equation 10, 16 and 18. The critical differential gains $K_{\mathrm{d,crit}}$ for these frequencies are given in table 2.

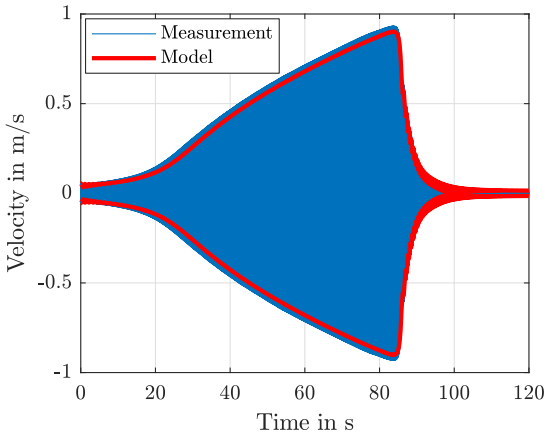

Figure 8: Comparison between measurement and model of the Duffing-oscillator.

After parametric characterization, the CBC procedure was applied to the test-rig. For each CBC run the controller gains were varied around the calculated critical values. The reference amplitude was increased in 0.2 mm steps. First, a pure differential controller was investigated, therefore the P-component was set to zero. In figure 9 the estimated results are shown in comparison with the theoretical curves (black), given by equation 10. On the top panels the $\hat{x}_{\mathrm{ref}}(\hat{x})$-curves are shown for different settings of controller gains and on the bottom panels the corresponding S-curves are plotted. The blue markers indicate values close to the critical gains, see table 2. The red and green markers represent gains below and above the critical values. All measured curves are in good agreement with the theoretical results. Here, especially the red curves illustrate the negative effect of a poorly chosen controller gain. As those curves are not monotonous, at some point the system suddenly transits from one stable solution branch to the other stable solution branch (from Ⓐ to Ⓑ on the upper graph). Therefore, a whole interval of displacement amplitudes is missing on this measurements and the upper bifurcation point is skipped. Similar results were achieved for all three frequencies. The gains with the blue markers are chosen to be close to the critical values. Here, the bifurcation regions are sampled quite well. Best results are achieved for controller gains $30 - 50$ % above the critical values (yellow markers).
The more common case of a PD-controller was also investigated. Therefore, K_{d} was set to a constant value and K_{p} was

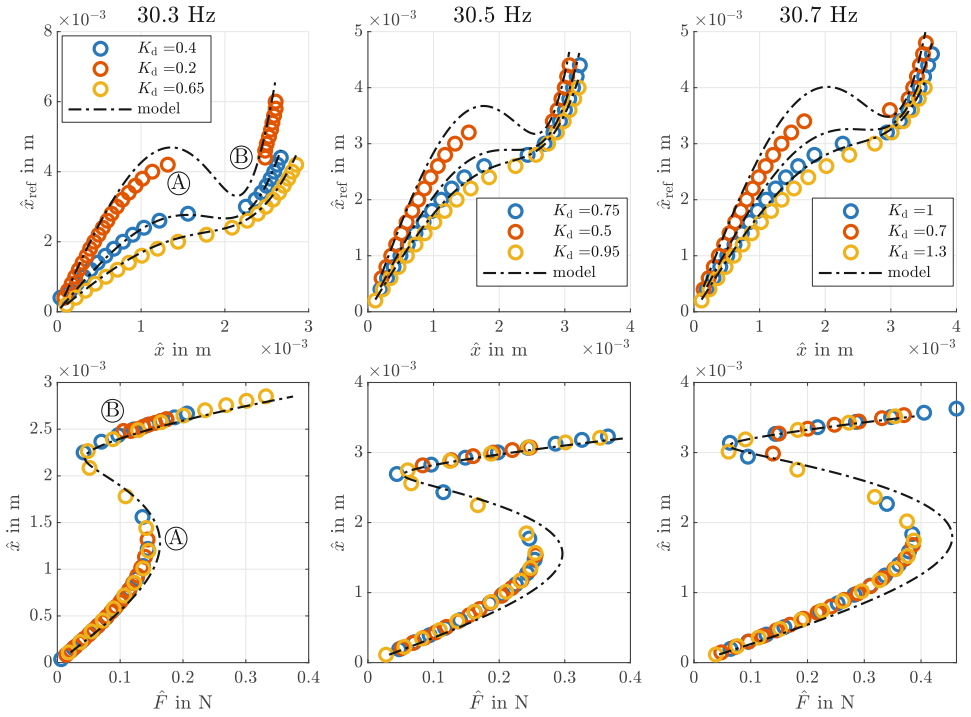

Figure 9: Comparison between measured $\hat{x}_{\mathrm{ref}}(\hat{x})$-curves resp. S-curves and theoretical curves. For all curves applies $K_{\mathrm{p}} = 0$.

varied. The aim of this experiment was to validate the stability map from figure 6. The results for three different settings of K_{d} and totally seven pairs of gain settings are shown in figure 10. The graph on the upper left side shows the distribution of the control gains and the remaining three graphs represent the corresponding S-curves. All curves are captured at 33.3 Hz. The crosses correspond to values close to the theoretical stability margin, which is highlighted as the dotted black line, while circles are values within the instability area. It can be seen, that for all unstable gain settings (circles) the S-curves are not entirely captured. Parts of the unstable branches are skipped. However, for values just above the stability margin the s-curves are sampled well, although $\hat{x}_{\mathrm{ref}}(\hat{x})$ has been incremented by the same step size in all experiments. For $K_{\mathrm{d}} = 0.3$ a third measurement was performed, which is represented by the red stars. Here, the proportional gain was chosen significantly higher than in the other two cases. It appears that featuring a higher P-component, the unstable branch is sampled at a finer spatial resolution. This has been predicted in section already. The reason is that the proportional gain shifts the turning point of the $\hat{x}_{\mathrm{ref}}(\hat{x})-$curve towards higher amplitudes. As a result the $\hat{x}_{\mathrm{ref}}(\hat{x})-$curve is unfolded to a more parabolic shape and so the spacing between two adjacent $\hat{x}-$values becomes smaller, as figure 11 illustrates. The marker style and color in figure 11 correspond to those from figure 10. Depending on the controller setting it is possible to trade of between a finer resolution of the lower stable branch or the unstable and upper branch. For either setting the controller is stabilizing. No significant drop of signal quality by the higher proportional gain ($K_{\mathrm{d}} = 0.3$ and $K_{\mathrm{p}} = 61$ compared to $K_{\mathrm{d}} = 0.3$ and $K_{\mathrm{p}} = 142$) was observed. However, measurement noise could be amplified by higher gains and thus decrease signal quality or even lead to instability of the closed loop system. Therefore, controller gains should not be set too high. Critical gains are good starting points for a manual optimization.

To confirm this, a proportional gain of $K_{\mathrm{p}} = 500$ and a differential gain of $K_{\mathrm{d}} = 1.5$ for the final analysis of the system dynamics was chosen. According to figure 6 this gain settings are stabilizing up to 32 Hz. As at 30.9 Hz the displacement amplitude corresponding to the upper bifurcation point became to large for the sensor, only S-curves from 29.6 Hz to 30.9 Hz in 0.1 Hz are studied in figure 12. As it can be seen, all S-curves have an excellent spatial resolution of the unstable branch. Note, that these are raw results, no filtering or averaging has been applied to the fundamental Fourier coefficients. The scattered measurement data points (black) have been interpolated by cubic splines. This is represented by the gray manifold, similar to figure 1. The red curves in the upper graph of figure 12 are the contour plots of this manifold at specific forcing amplitudes. These NLFR-curves are shown in the bottom graph in detail. Due to the chosen interpolation type they appear noisy, here a higher frequency resolution would have been beneficial. Nevertheless, the NLFR-curves give a better understanding of the system response near resonance, including two stable and one unstable branch, than a sweep test like in figure 8. Conclusively it can be stated, that the theoretical considerations from section Derivation of Optimal Control Gains, led to an analytical formula for the critical gains and enabled a significant speed up of the CBC measurement compared to previous studies, [14]. The time consuming part of finding stabilizing controller gains by trial and error could be omitted and was replaced by an efficient preliminary analysis of the examined system. The Duffing-oscillator approximation for the investigated single-degree-of-freedom system is in good agreement with measurements in terms of $\hat{x}_{\mathrm{ref}}(\hat{x})-$ and S-curves.

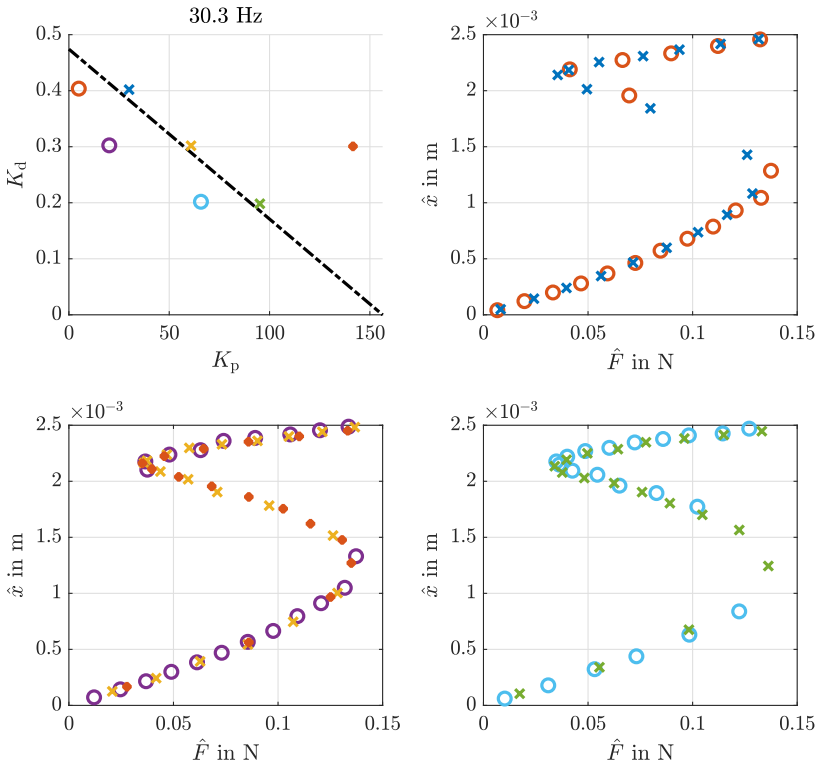

Figure 10: Comparison between controller gains at different locations of the stability map.

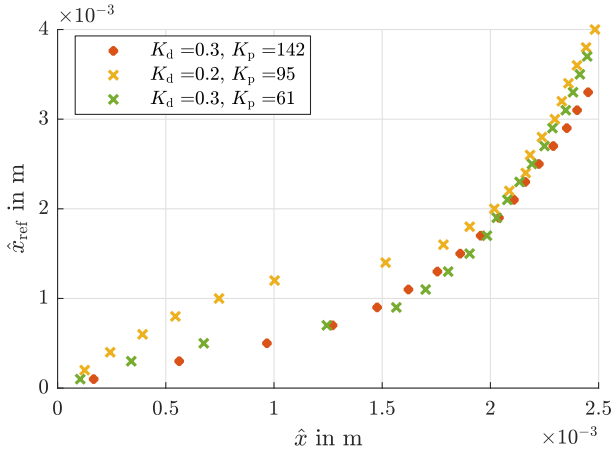

Figure 11: Comparison of different stabilizing controller gains.

Conclusion

In this paper an analytical formula has been derived to find critical controller gains for the stabilizing control of a Duffing-oscillator exploiting a PD-controller. Critical gains are described as the minimum necessary gains to stabilize the unstable periodic orbits of the system. The main application is intended to be the control based continuation of systems that can be approximated by a Duffing-oscillator model. For the formula the structural parameters of the underlying linear system are needed, which can be extracted from experimental modal analysis at low level excitation. The prefactor of the nonlinear cubic term is not required. Although in this paper the derivation has been conducted and validated for the single-degree-of-freedom Duffing-oscillator only, the workflow can be generalized and applied to any nonlinear system. The process incorporates the following steps:

- Find an approximate model for the nonlinear system
- Include controller rule in the equation of motion
- Apply Harmonic Balance to solve for $\hat{x}_\mathrm{ref}(\hat{x})$
- Investigate $\hat{x}_\mathrm{ref}(\hat{x})$ (or its derivative)
- Critical gains are those values which unfold $\hat{x}_\mathrm{ref}(\hat{x})$ so that the curve becomes unique

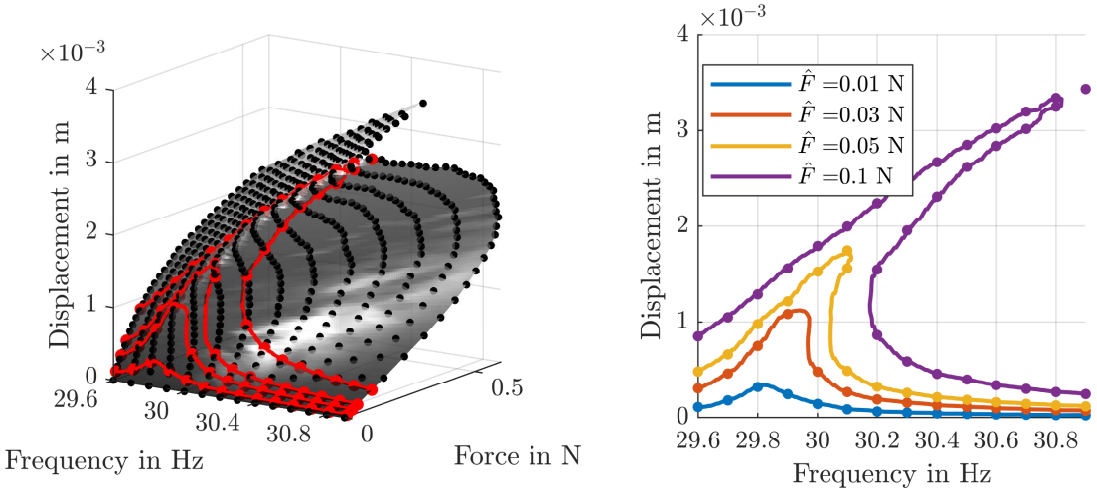

Figure 12: Experimentally determined manifold (left) and reconstructed NLFR-curves (right).

References

[1] A. H. Nayfeh, D. T. Mook, Nonlinear Oscillations, John Wiley & Sons, Inc., 1995.

[2] M. P. Mignolet, A. Przekop, S. A. Rizzi, S. M. Spottswood, A review of indirect/non-intrusive reduced order modeling of nonlinear geometric structures, Journal of Sound and Vibration 332 (10) (2013) 2437–2460. doi:10.1016/j.jsv.2012.10.017.

[3] C. Touze, M. Vidrascu, D. Chapelle, Direct finite element computation of non-linear modal coupling coefficients for reduced-order shell models, Comput Mech 54 (2014) 567–580. doi:10.1007/s00466-014-1006-4.

[4] J. J. Thomsen, Vibrations and Stability, 2nd Edition, Springer-Verlag Berlin Heidelberg, 2003.

[5] J.-P. Noël, G. Kerschen, Nonlinear system identification in structural dynamics: 10 more years of progress, Mechanical Systems and Signal Processing 83 (2017) 2–35.

[6] J. Sieber, B. Krauskopf, Control based bifurcation analysis for experiments, Nonlinear Dyn 51 (2008) 365–377. doi:10.1007/s11071-007-9217-2.

[7] J. Sieber, B. Krauskopf, D. Wagg, S. Neild, A. Gonzalez-Buelga, Control-based continuation of unstable periodic orbits, Journal of Computational and Nonlinear Dynamics 6 (1) (2010). doi:10.1115/1.4002101.

[8] D. Barton, S. Burrow, Numerical continuation in a physical experiment: Investigation of a nonlinear energy harvester, Journal of Computational and Nonlinear Dynamics 6 (2011) 011010. doi:10.1115/1.4002380.

[9] D. Barton, B. Mann, S. Burrow, Control-based continuation for investigating nonlinear experiments, Journal of Vibration and Control 18 (4) (2012) 509–520. doi:10.1177/1077546310384004.

[10] D. Barton, J. Sieber, Systematic experimental exploration of bifurcations with noninvasive control, Phys. Rev. E 87 (2013) 052916. doi:10.1103/PhysRevE.87.052916.

[11] D. Barton, Control-based continuation: Bifurcation and stability analysis for physical experiments, Mechanical Systems and Signal Processing 81 (2017) 54–64. doi:10.1016/j.ymssp.2015.12.039.

[12] L. Renson, A. Shaw, D. Barton, S. Neild, Application of control-based continuation to a nonlinear structure with harmonically coupled modes, Mechanical Systems and Signal Processing 120 (2019) 449–464. doi:10.1016/j.ymssp.2018.10.008.

[13] F. Schilder, E. Bureau, I. F. Santos, J. Thomsen, J. Starke, Experimental bifurcation analysis - continuation for noise-contaminated zero problems, Journal of Sound and Vibration 358 (2015) 251–266. doi:10.1016/j.jsv.2015.08.008.

[14] G. Kleyman, M. Paehr, S. Tatzko, Application of control-based-continuation for characterization of dynamic systems with stiffness and friction nonlinearities, Mechanics Research Communications 106 (2020) 103520. doi:10.1016/j.mechrescom.2020.103520.

[15] L. Renson, A. G. Buelga, D. Barton, S. Neild, Robust identification of backbone curves using control-based continuation, Journal of Sound and Vibration 367 (2016). doi:10.1016/j.jsv.2015.12.035.

[16] L. Renson, D. Barton, S. Neild, Experimental tracking of limit-point bifurcations and backbone curves using control-based continuation, International Journal of Bifurcation and Chaos 27 (2017) 1730002. doi:10.1142/S0218127417300026.

[17] L. Renson, J. Sieber, D. Barton, A. Shaw, S. Neild, Numerical continuation in nonlinear experiments using local gaussian process regression, Nonlinear Dynamics 98 (4) (2019) 2811–2826. doi:10.1007/s11071-019-05118-y.

[18] G. Abeloos, L. Renson, C. Collette, G. Kerschen, Control-based continuation of nonlinear structures using adaptive filtering, in: G. Kerschen, M. Brake, L. Renson (Eds.), Nonlinear Structures & Systems, Volume 1. Conference Proceedings of the Society for Experimental Mechanics Series., Springer, Cham, 2020, pp. 109–112. doi:10.1007/978-3-030-47626-7_17.

[19] E. Bureau, F. Schilder, M. Elmegård, I. Santos, J. Thomsen, J. Starke, Experimental bifurcation analysis of an impact oscillator – determining stability, Journal of Sound and Vibration 333 (21) (2014) 5464–5474. doi:10.1016/j.jsv.2014.05.032.

[20] E. Bureau, F. Schilder, I. Santos, J. Thomsen, J. Starke, Experimental bifurcation analysis of an impact oscillator: Tuning a non-invasive control scheme, Journal of Sound and Vibration 332 (22) (2013) 5883–5897. doi:10.1016/j.jsv.2013.05.033.

[21] Y. Li, H. Dankowicz, Adaptive control designs for control-based continuation in a class of uncertain discrete-time dynamical systems, Journal of Vibration and Control 26 (21-22) (2020) 2092–2109. doi:10.1177/1077546320913377.

[22] S. Tatzko, M. Jahn, On the use of complex numbers in equations of nonlinear structural dynamics, Mechanical Systems and Signal Processing 126 (2019) 626–635. doi:10.1016/j.ymssp.2019.02.041.

[23] S. Mojrzisch, J. Wallaschek, J. Bremer, An experimental method for the phase controlled frequency response measurement of nonlinear vibration systems, in: Proc. Appl. Math. Mech., Vol. 12, 2012, pp. 253–254. doi:10.1002/pamm.201210117.

Nonlinear localisation in a cyclic system with unilateral contact

Björn NIEDERGESÄß*, Aurélien GROLET† and Norbert HOFFMANN *
* *Hamburg University of Technology, Hamburg, Germany*
† *LISPEN, ENSAM Lille, Lille, France*

Summary. The following abstract presents a cyclic structure subjected to unilateral contact in order to investigate nonlinear localisation of vibration. After a brief description of the system, a reduced-order model is derived for numerical analysis. Subsequently, the experimental setup is introduced and the system response to harmonic excitation is depicted. In the nonlinear regime vibration localisation is observed with a high amplitude ratio regarding the beam elements of the structure.

Introduction

Localisation of vibration corresponds to states where the vibration energy is spatially localised to a section of the system so that only this section vibrates in high amplitude. It has been observed in a vast variety of systems either numerically, e.g. for coupled Duffing oscillators [1] and coupled beams [2], or experimentally, e.g. for a microbeam array [3] and a macro mass-spring system [4]. The localisation arises from nonlinear modal interaction, such as 1:1 internal resonances [5]. In this work experimental measurements of localised vibration states are reported in a cyclic structure subjected to unilateral contact.

Presentation of the system and reduced-order model

Presentation of the system

The structure investigated in this paper consists of three clamped-free beams with attached tip masses ordered in a cyclic fashion and coupled through slender connections as depicted in Fig.1. When vibrating in the transverse direction the beams are subjected to unilateral contact enforced at a level between the slender connection and the tip mass. Since the mass of the beams is small compared to the attached tip masses it can be neglected and the system can be regarded as three coupled nonlinear oscillators.

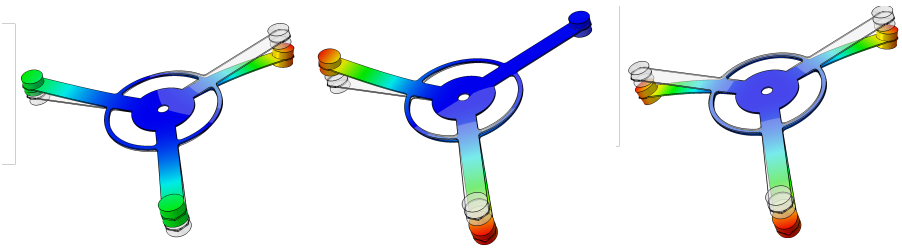

Figure 1: First three linear mode shapes of the considered structure. Note that, due to the symmetry, the first two modes have the same eigen-frequency

Reduced-order model

Based on the FEM mode shapes, a lumped mass model with three degrees of freedom can be derived for numerical analysis. The contact nonlinearity for the i-th oscillator is modeled by a bi-linear force $g(u_i)$: in small amplitude, the beam is not in contact so that the force is zero. When the tip displacement reaches a threshold u_g the effective stiffness increases and tends toward one of a beam with "pinned" boundary condition at the position of the contact. The force can be expressed as a bi-linear function of the tip displacement:

$$g(u_i) = \begin{cases} 0 & \text{if } u_i \leq u_g \\ K(u_i - u_g) & \text{if } u_i \geq u_g, \end{cases} \tag{1}$$

where K is the contact stiffness and u_g is the tip displacement at the moment of contact. In order to find periodic solutions to the equations of motion, the harmonic balance method (HBM) is applied. The solution is searched for a truncated Fourier series and the coefficients are obtained by solving a system of nonlinear algebraic equation. This system will be solved by the asymptotic numeric method (ANM). Both methods (HBM and ANM) are implemented in a common framework in the MANLAB package, along with the stability computation of the periodic solutions [6]. The equations of motion are written in a quadratic form for MANLAB and the required regularisation function g_{reg} of the unilateral contact force is obtained over a hyperbola branch which is defined by the following quadratic equation:

$$g_{reg}[g_{reg} - K(u_i - u_g)] = \epsilon, \tag{2}$$

where a smaller regularisation parameter ϵ indicates a hyperbola closer to the piecewise curve.

Experimental setup and results

Description of the experiment

In the experimental setup the structure depicted in Fig 1 and a contact disk share a common base, which is mounted on two slender plates. The base is excited by a shaker (TIRA TV 51140-M) and vibrates harmonically due to the mode of the supporting plates. Therefor a harmonic excitation signal is fed in the shaker in open loop, processed by an ADwin-Gold control box with a sampling frequency of 4kHz. To measure the response of the system accelerometers are glued to the base, as well as to the three tip masses. When the system is excited close to the first eigenfrequency of the structure the coupled beams start touching the contact disk.

Results

Fig. 2 depicts the measured response of the base and the three tip masses m_i of the structure while excited with a frequency of 11.35 Hz. At this excitation level the structure gets in unilateral contact with the disk which amounts in a disturbance of the harmonic excitation depicted in Panel (a). The nonlinear localisation of the structure is depicted in Panel (b) where the amplitude ratio A_1/A_3 is ~ 9.56 ($A_1/A_2 \sim 7.32$ respectively).

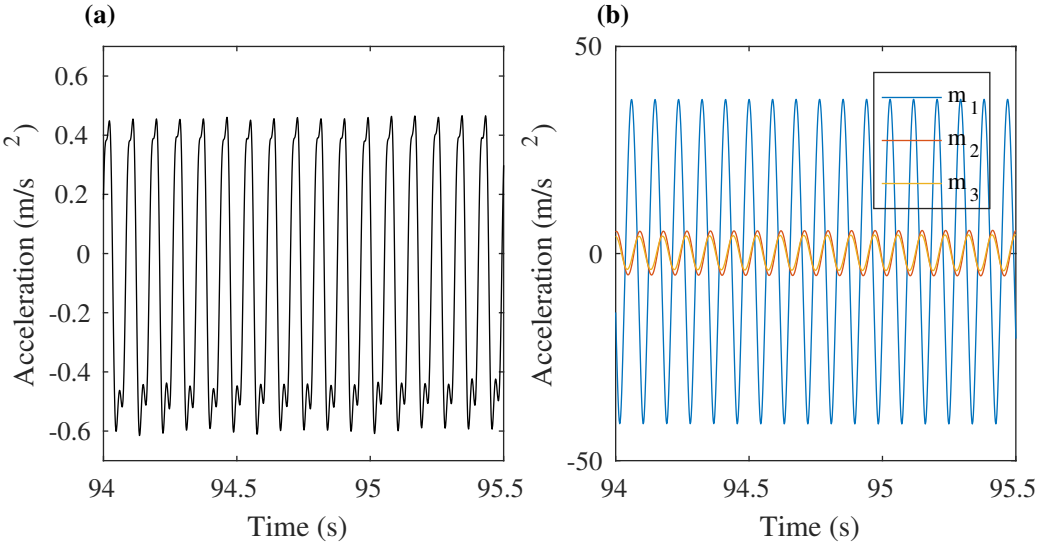

Figure 2: Nonlinear localisation at 11.35Hz : a) Base excitation; b) Response at the tip mass m_i of the structure. m_2 and m_3 vibrate in low amplitude while m_1 vibrates in high amplitude

Conclusions

The abstract considers nonlinear vibrations of a cyclic system subjected to contact nonlinearity. The investigated system can be regarded as a simple qualitative model of more complex structures such as bladed disk in airplane engines. Numerical results based on a reduced-order model indicate that homogeneous solutions can lose their stability to lead to localised states of vibration. The nonlinear localisation is observed in the experimental investigation of the structure.

References

[1] A. Papangelo, F. Fontanela, A. Grolet, M. Ciavarella and N. Hoffmann (2019) Multistability and localization in forced cyclic symmetric structures modelled by weakly-coupled Duffing oscillators. *Journal of Sound and Vibration* **440**:202-211.

[2] M. King and A.F Vakakis (1995) Mode Localization in a System of Coupled Flexible Beams with Geometric Nonlinearities. *Journal of Applied Mathematics and Mechanics* **75**:127-139.

[3] M. Sato, B.E. Hubbard, L.Q. English, A.J. Sievers, B. Ilic, D.A. Czaplewski, H.G. Craighead (2003) Study of intrinsic localized vibrational modes in micromechanical oscillator arrays *Chaos: An Interdisciplinary Journal of Nonlinear Science*. **999**:702-715.

[4] Y. Watanabe, T. Nishida, Y. Doi and N. Sugimoto (2018) Experimental demonstration of excitation and propagation of intrinsic localized modes in a mass–spring chain. *Physics Letters A* 10.1016/j.physleta.2018.04.055.

[5] A.I Manevich and L.I Manevitch, (2005) The Mechanics of Nonlinear Systems with Internal Resonances. *Imperial college press*

[6] B. Cochelin, N. Damil and M. Potier-Ferry (2007) Méthode asymptotique numérique *Hermes Lavoissie*.

Nonlinear modes of cantilever beams at extreme amplitudes: numerical computation and experiments

Marielle Debeurre*, Aurélien Grolet*, Olivier Thomas*, Pierre-Olivier Mattei† and Bruno Cochelin†

*Arts et Metiers Institute of Technology, LISPEN, HESAM Université, F-59000 Lille, France
†Laboratoire de Mécanique et d'Acoustique, École Centrale Marseille, Marseille, France

Summary. Flexible, one-dimensional structures such as slender beams and cables are capable of undergoing highly nonlinear vibrations in extremely large amplitudes. A novel method for computing the behavior and, in particular, the nonlinear modes is here presented based on a geometrically exact finite element beam model that is solved using the continuation software MANLAB. An experimental setup is also described which utilizes a vibration table and Digital Image Correlation to physically observe the extreme amplitude vibration of the flexible cantilever beam.

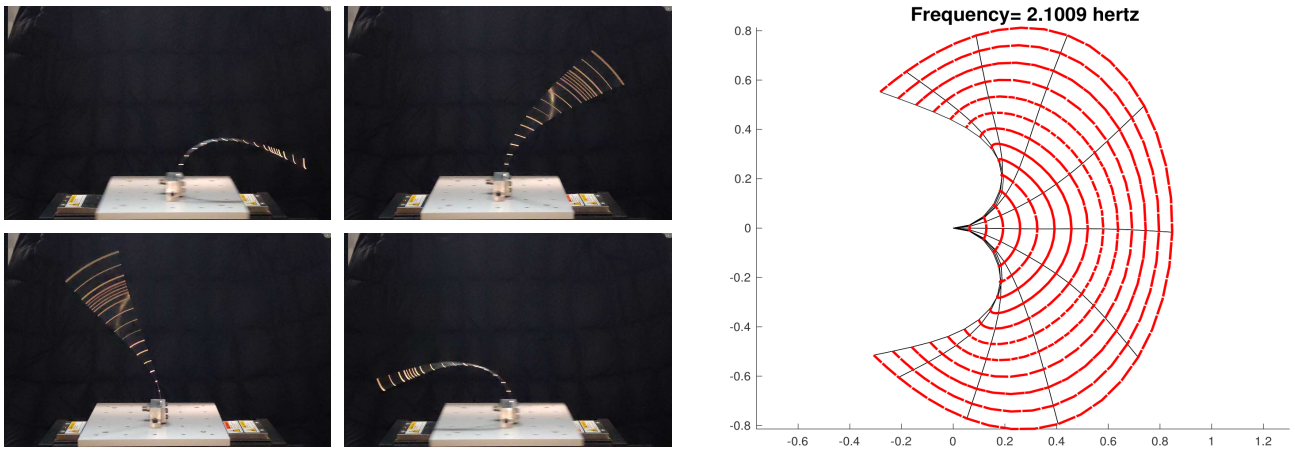

Figure 1 (Left): Four snapshots of preliminary experiments depicting the first nonlinear mode of a cantilever beam in extreme amplitude, achievable due to the bending capabilities of the flexible structure. Figure 1 (Right): Numerical computation of the first nonlinear mode of the cantilever beam, obtained using the path-following continuation solver, MANLAB [2, 3, 4].

Introduction

Although the field of nonlinear dynamics is vast and dense, nonlinear models of highly flexible structures are a subject of continuing research. Wires, cables, rods and hoses are examples of such flexible structures, as their slender, one-dimensional geometry and corresponding mechanical stiffness allow for extreme bending capabilities, especially when resonance conditions are considered. While several methods already exist for the computation of flexible systems, they are often limited, due to either the amount of required computation time or the limited range of applicability. Current strategies for simulation of nonlinear dynamics often utilize direct time integration schemes to solve the equations of motion. While often adequate for many purposes, these strategies can potentially encounter certain limitations, such as in detecting multiple solutions (if present) or bifurcation points. Additionally, further extensions to existing models are needed to capture the behavior of highly nonlinear dynamical systems, such as the present case of extreme amplitude vibration. For this reason, we here propose a custom continuation algorithm for the periodic solution of geometrically exact finite element beam models undergoing extreme amplitude vibrations. Numerical results are then compared with vibration experiments involving slender beam specimens as seen in Fig. 1 (Left).

Numerical model

A geometrically exact finite element discretization is performed for a cantilever beam geometry using Timoshenko-theory beam elements and a total Lagrangian nonlinear formulation [1]. The model is derived from the weak form variational formulation of the equation of motion of a cantilever beam rooted in the principle of virtual work and is traditionally written, for all time t,

$$\mathbf{M}\ddot{\mathbf{q}} + \mathbf{D}\dot{\mathbf{q}} + \mathbf{f_{int}}(\mathbf{q}) = \mathbf{f_{ext}} \tag{1}$$

where $\mathbf{q}$ is a vector of size $3N$ that gathers nodal displacements u_i, w_i and θ_i representing the axial displacement, transverse displacement and cross section rotation of the ith finite element node, respectively, for N nodes: $\mathbf{q} = [u_1 w_1 \theta_1 \dots u_N w_N \theta_N]^T$. $\mathbf{M}$ and $\mathbf{D}$ are the mass and damping matrices, respectively, each of size $3N \times 3N$; $\mathbf{f_{ext}}$ is

the vector of applied external forces and $\mathbf{f_{int}}(\mathbf{q})$ is the nonlinear internal force vector, both of length $3N$, which is a nonlinear function of $\mathbf{q}$ based on the geometrical nonlinearities. The details of the finite element model can be found in Appendix 2 of [1].

Numerical solution

The geometrically exact finite element model described in (1) is then solved numerically using MANLAB, an interactive path-following solver rooted in MATLAB. Given harmonic forcing imposed on the cantilever beam, the resulting motion of the structure is sought periodic. The MANLAB solver employs a unique continuation scheme for periodic solutions, combining the Harmonic Balance Method (HBM) with the Asymptotic Numerical Method (ANM) continuation technique [2]. Traditionally, the principle of the HBM is to decompose a periodic function into a Fourier series truncated to a certain number of harmonics. However, in the present case of a geometrically exact cantilever beam, sine and cosine nonlinearities of the degrees of freedom are involved in the system. To reconcile these nonlinearities and others that may be present in any original system, the solution technique implemented in MANLAB proposes a quadratic recast of the original equation into a new system containing only polynomial nonlinearities of quadratic order or less. Following the quadratic recast, the derivation of the corresponding algebraic system for the Fourier coefficients is rather straightforward [2, 3]. The ANM continuation technique, which uses a pseudo-arc length parameterization, is then applied to yield the path-following solution that is visualized in MANLAB [4].

The combination of HBM and ANM has been shown to be both highly efficient and yet applicable to a broad set of systems containing non-polynomial nonlinearities [3, 4]. Recently, extensions to the method and, therefore, the MANLAB solver, allow for the stability analysis of the various branches of the periodic solution [4]. Using this solver, the computation time for the solution to (1) is greatly reduced and enables a numerical solution for the cantilever structure subject to extreme amplitude vibration (see Fig. 1 (Right)). In the case under study, the nonlinear modes of (1) are computed with periodic solutions of the unforced system, with $\mathbf{f_{ext}} = 0$, as explained in [4].

Experiments

In order to compare with the aforementioned numerical simulations, an experimental strategy has been designed to recreate the extreme amplitude vibrations of flexible specimens using a Long Stroke Shaker vibration table. The experimental strategy here described utilizes a Phase-Locked Loop (PLL) controller, which, for a harmonic excitation $F(t) = F\sin(\Omega t + \phi)$, changes the frequency Ω so that a given phase lag between the phase ϕ of the force signal and that of the system response is induced [5]. Adjustment of the amplitude of excitation with the desired phase lag set to $\pi/2$ provides a robust method for measuring the backbone curve of the system, equivalent to its nonlinear modes. A long and thin stainless steel beam is prepared for the experiments and is fixed at the base to the vibration table to recreate the cantilever condition under investigation. The table vibrates at the selected amplitude F and frequency Ω, thereby exciting the cantilever beam specimen. Preliminary experiments are able to demonstrate the extreme amplitude vibrations using reflective points along the beam (Fig. 1 (Left)). The displacement field along the beam is measured based on differences in the illuminated points through a series of images captured with a rapid motion camera in a technique known as Digital Image Correlation (DIC). The results of the DIC are then compared with numerical results obtained from MANLAB.

Conclusions

In this paper, numerical and experimental extensions to existing strategies for calculation of nonlinear modes of cantilever beams in large amplitude vibrations are presented. A geometrically exact finite element numerical model of the equation of motion is developed and implemented into the MANLAB continuation solver for periodic solutions. The solver is able to describe the motion of highly flexible structures even at extreme amplitudes, which is then compared with experimental results obtained from vibration tests integrating a Phase-Locked Loop for robust calculation of the nonlinear modes. In conclusion, the procedure outlined in this paper presents a novel and efficient method for the calculation and simulation of highly geometrically nonlinear beam structures, even at extreme amplitudes of vibration.

References

[1] O. Thomas, A. Sénéchal, and J. F. Deü. Hardening / softening behavior and reduced order modelling of nonlinear vibrations of rotating cantilever beams. Nonlinear Dynamics, 86(2):129381318, 2016.

[2] Bruno Cochelin, Christophe Vergez. A high order purely frequency-based harmonic balance formulation for continuation of periodic solutions. Journal of Sound and Vibration, Elsevier, 2009, 324 (1-2), pp.243-262.

[3] Sami Karkar, Bruno Cochelin, Christophe Vergez. A high-order, purely frequency based harmonic balance formulation for continuation of periodic solutions: The case of non-polynomial nonlinearities. Journal of Sound and Vibration, Elsevier, 2013, 332 (4), pp.968-977.

[4] Louis Guillot, Arnaud Lazarus, Olivier Thomas, Christophe Vergez, Bruno Cochelin. A purely frequency based Floquet-Hill formulation for the efficient stability computation of periodic solutions of ordinary differential systems. Journal of Computational Physics, Volume 416, 2020, 109477.

[5] V. Denis, M Jossic, C. Giraud-Audine, B. Chomette, A. Renault, O. Thomas. Identication of nonlinear modes using phase-locked-loop experimental continuation and normal form. Mechanical Systems and Signal Processing, Elsevier, 2018, Volume 106, pp.430-452.

Nonlinear Motions of a Self-adaptive Resonator

Toshihiko Sugiura[*], Koki Ochiai[**], Xuefeng Liu[**], Yuki Oikawa[**]and Linyu Peng[*]
[*]*Department of Mechanical Engineering, Keio University, Yokohama, Japan*
[**]*Graduate School of Science and Technology, Keio University, Yokohama, Japan*

Summary. This study reports some experimental results of a beam-slider vibration system which is often called the self-adaptive resonator. It is said to increase the efficient frequency bandwidth of a vibration-based energy harvester. In this study, excitation experiments were carried out focusing on the interaction between the vibrating beam and the slider. The experimental results show that a certain mode of the beam resonates as a result of the slider moving along the beam under excitation at a certain frequency. Some of the results also show the effect of nonlinear modal interactions through the slider movement.

Introduction

A self-adaptive resonator consisting of a beam and a slider was introduced to the field of vibration energy harvesting by Miller[1] as a solution to the problem of narrow resonance frequency range. The proposed system is said to achieve resonance at multiple frequencies, thanks to the slider which, under the condition of excitation, moves along the beam to such a position that the beam will resonate. To discuss the dynamics of the system, we must mention that behaviors of a vibrating beam-slider structure was studied well before it was incorporated to energy harvesting. Recent studies by Lyu[2] report that the adaptive behavior of the system is influenced by the geometrical nonlinearity of the vibrating beam. In this study we conducted some experiments to find out the important factors to explain the motion of the beam and the slider.

Analytical Studies

Governing equations

Figure 1 shows the image of the analytical model. The horizontal position is denoted by x, and the vertical beam displacement at each position is denoted by W. s stands for the position of the slider, which would be a factor that changes the natural frequency and the beam shape. Hence W is a function of time t, x and s, and the equation of the beam and sliders motion can be described as follows[1].

$$\rho A(\ddot{W}+\ddot{W}_O)+EI\frac{d^4W}{dx^4}+\ddot{W}_O+M\left(\ddot{W}+\ddot{W}_O+\ddot{s}\frac{dW}{dx}+2\dot{s}\frac{d\dot{W}}{dx}+\dot{s}^2\frac{d^2W}{dx^2}\right)\delta(x-s)=0 \tag{1}$$

$$M\ddot{s}+M\left[\left(\ddot{W}+\ddot{W}_O+\ddot{s}\frac{dW}{dx}+2\dot{s}\frac{d\dot{W}}{dx}+\dot{s}^2\frac{d^2W}{dx^2}\right)\frac{dW}{dx}\right]_{x=s}=0 \tag{2}$$

M is the slider's mass, W_O is the excitation term, ρ, A, E and I are the density, cross-sectional area, Young's modulus and second moment of inertia of the beam, respectively.

Theory

In early studies, Thomsen[3] assumed that the slider's mass was light compared to the beam, hence neglected the change of the beam shape. This assumption provides a tendency in the slider's motion, that the slider would move toward the antinode of one of the modes which stands out the most. However, experimental studies report that the self-adaptive behaviors ideal to energy harvesting can be observed mostly when the slider's mass is relatively large. This results in not only the change of the beam shape, but also some unnatural motions of the slider, possibly due to linear and nonlinear couplings between the modes or between the beam and the slider.

Before we move on to the experimental study, we must introduce the dependencies of the natural frequency of the first and second mode for a fixed-fixed beam with a fixed additional mass. Figure 2 shows an example of those relationships with a shared horizontal axis indicating the mass position, with the additional mass being slightly heavier than the beam. According to this figure, depending on the position of the slider, the natural frequency ratio of these two modes may become an integer ratio such as 1 to 2, which may cause nonlinear coupling between the modes..

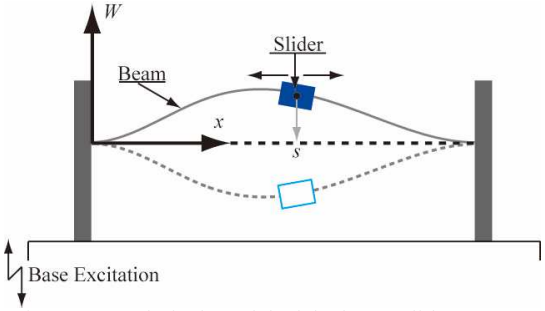

Figure 1: Analytical Model of the beam-slider system.

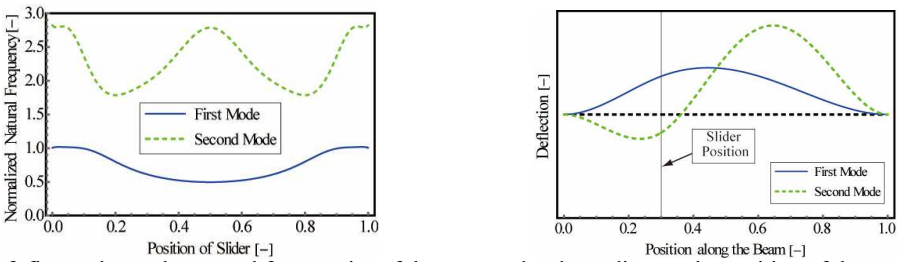

Figure 2: The left figure shows the natural frequencies of the two modes depending on the position of the mass. The right figure shows the corresponding mode shape for a decentered mass.

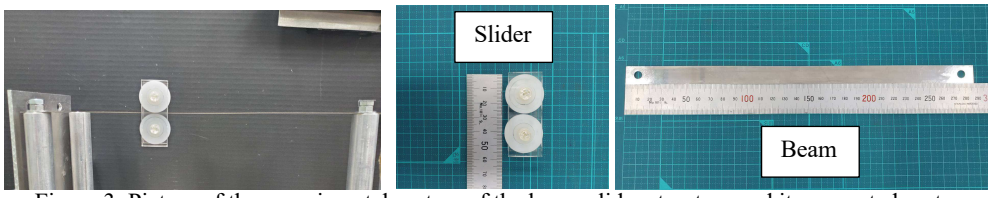

Figure 3: Picture of the experimental system of the beam-slider structure and its separated parts.

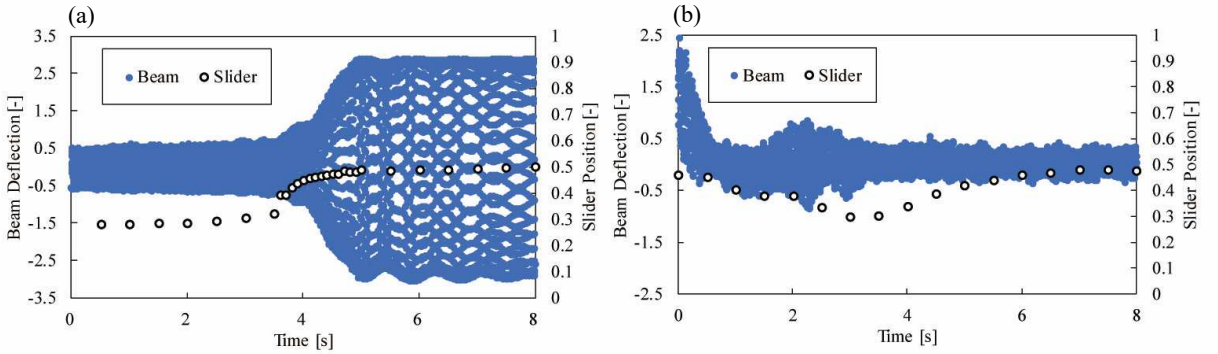

Figure 4: Time histories of slider displacements and beam deflection. The left vertical axis is normalized with the excitation amplitude, while the right vertical axis is normalized with the beam length. The beam deflection was measured at 0.75 according to the right vertical axis. The excitation frequencies were (a)20 Hz and (b)53 Hz while the excitation amplitudes were (a)0.148 mm and (b)0.524 mm.

Experimental Study

Figure 3 shows the parts and the setup of the experimental system. A stainless-steel beam was fixed at both ends to a shaker. In order to make the slider motion as smooth as possible, a pair of plastic bearings were used as the main parts of the slider which interacts with the beam. The gap was small to prevent the slider to rattle or bounce on the beam, but large enough for the slider to move. The slider to beam mass ratio was 1.24, and the first natural frequency of the fixed-fixed beam without the slider was 44 Hz.

Figure 4 shows two of the results obtained by the experiment. (a) is the example of when the system achieved resonance of the first mode. This is caused through the movement of the slider. In the example (b), the slider moved from the center of the beam toward the outer region, then started to move back to the center when it reached a certain position. This motion is difficult to explain when only the second mode with constant mode shape is considered.

Though we have found much more about the beam-slider motion through this experiment, this extended abstract can only provide two examples of the results due to page limitations. Nevertheless, even the two examples alone show that interactions between the vibration modes of the beam are the key to understand the nature of this system.

Conclusion

Experiments were conducted to verify the key aspects to analyze the self-adaptive resonator. The results exhibited the effect of nonlinear modal interactions and therefore theoretical studies ranging to nonlinear analysis of multiple degrees of freedom are essential to truly understand the system.

References

[1] Miller L. M. (2012) Micro-scale Piezoelectric Vibration Energy Harvesting: From Fixed-frequency to Adaptable Frequency Devices. *PhD Thesis*, University of California, Berkeley.

[2] Yu L., Tang L., Xiong L., Yang T., Mace B. R. (2019) A Passive Self-tuning Nonlinear Resonator with Beam-slider Structure. *Proc. SPIE.* **10967**:109670K.

[3] Thomsen J.J. (1996) Vibration Supression by using Self-arranging Mass. *Journal of Sound and Vibration.* **197**(4):403-425

Measuring nonlinear localisation and isolated curve of solutions in a system of two coupled beams

Aurélien GROLET*, Zein A. SHAMI* and Olivier THOMAS *
* *LISPEN, ENSAM Lille, Lille, France*

Summary. This work presents experimental measurement of nonlinear localisation in a system of two coupled beams. In this system, localisation correspond to vibrations states where the symmetry is broken, and where the energy is mainly localised to one of the two beam only, see e.g. [1]. Using a two degrees of freedom reduced order model, one can show that the localised states arise from a 1:1 internal resonance between two particular linear modes [2]. In the case of forced response, for particular conditions, the localised solution can be depicted under the form of an isolated closed curves (isola) in the amplitude-frequency diagram [3]. Experimental measurements showing nonlinear localisation are presented and compared to the numerical solution, showing good agreement.

Presentation of the system

The system considered here consists of a circular plate that has been machined in order to create to parallel beams as indicated on Fig. 1. The body of the circular plate provides a coupling between the beams, and it also restrains the axial displacement of the beams ends, so that non-linearity occurs due to a coupling between axial and transverse motions.
We consider two particular eigen-modes of the structure depicted on Fig. 1. For those modes, the beams vibrate over a first bending mode shape (in phase or out of phase). The structure has been designed such that both modes interact non-linearly to give a localized mode. Indeed, looking at the mid-beam displacement, the modes can be described with the shape $\phi_1 = (1, 1)$ and $\phi_2 = (1, -1)$. Localisation arise due to a modal interaction of the form $q_1(t)\phi_1 + q_2(t)\phi_2$, where q_1 and q_2 are (in-phase) modal amplitudes, leading to a shape of the form $(a_1 + a_2, a_1 - a_2)$, which eventually tends to the localised shape $(1, \epsilon)$ as the amplitude of the first mode a_1 tend to the amplitude of the second mode a_2.

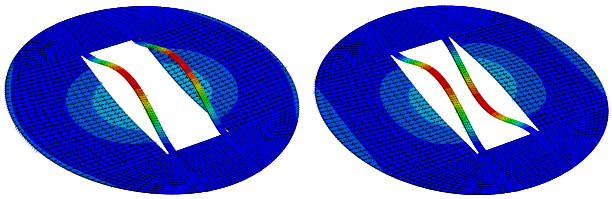

Figure 1: Linear mode shape of interest. Left: in phase mode ($f_1 = 364$ Hz); Right: out-of-phase mode ($f_2 = 367.5$ Hz)

Reduced order model and Numerical solutions

In order to simplify the analysis, a reduced order model is derived using the so called STEP method, particularised to the case of planar structure (see e.g. [4]). Only the two modes of interest are kept in the reduced order model and the reduced set of equation have the following form:

$$\ddot{q}_1 + 2\xi_1\omega_1\dot{q}_1 + \omega_1^2 q_1 + G_1 q_1^3 + C q_1 q_2^2 = f_1 \sin(\Omega t) \tag{1}$$

$$\ddot{q}_2 + 2\xi_2\omega_2\dot{q}_2 + \omega_2^2 q_2 + C q_1^2 q_2 + G_2 q_2^3 = f_2 \sin(\Omega t) \tag{2}$$

where q_i is the modal amplitude of the i-th transverse mode ($i = 1$: in phase mode, $i = 2$ out of phase mode, see Fig.1), ξ_i's are the modal damping ratio, ω_i's are the natural frequencies, f_i's are the the modal forces amplitude and Ω is the excitation frequency. G_1, G_2 and C are the non-linear coefficients obtained through the reduced order model procedure.
Approximated solutions to the system in Eq.(1) are obtained using the Harmonic Balance Method (HBM), coupled with a numerical continuation procedure based on the Asymptotic Numeric Method (ANM) [5].
When the system is forced on the first mode ($f_2 = 0$), if the forcing amplitude is sufficient, it can be observed that the localised solution can be depicted under the form of a closed curve solution in the Amplitude-Frequency diagram (isola), see the left panel of fig.2. When the system is forced on the second mode ($f_1 = 0$), if the amplitude is sufficient, it can be observed that the localised solution stems from the principal resonance curve through a branching point bifurcation, see the right panel of fig.2.

Experimental setup and results

The structure has been machined out of a stainless steel plate using wire cutting. For the experiments, the structure is hanged, which allows to be close to free boundary conditions. The experimental setup is depicted on fig.3.
A magnet and a coil is used to provides excitation to the structure without having an actual physical contact between the structure and the excitation device. To keep the symmetry of the system, another magnet (without coil) is positioned on the opposite side of the plate (see fig.3). The amplitude of the force is controlled by the intensity of the current

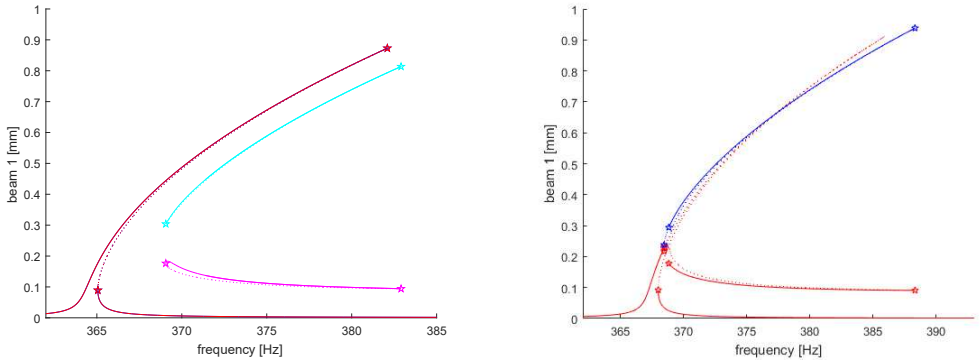

Figure 2: Numerical forced response. Left: force on the first mode, localised states appear as closed curve solution. Right: force on the second mode, localised states arise from the homogeneous (out-of-phase) solution through a branching point bifurcation

sent to the coil, which is monitored using a current clamp. Velocity measurements are carried out using a laser vibrometer.

Example of stepped sine measurements (for a force exciting mainly the second mode) are given on the right panel of fig.3. For low amplitude of forcing, the behaviour of the structure is linear, and both beams vibrates with the same amplitude. When the amplitude increases, the non-linearity starts to be activated and the hardening property of the structure can be observed. Finally, for higher force amplitude, when the displacement amplitude reach a threshold, there is a break of symmetry in the vibration shape of the structure, both beams clearly vibrates with different amplitude. For the highest excitation current (black curve on Fig.3), one can see that the first beam vibrates with an amplitude 7 times greater than the second beam.

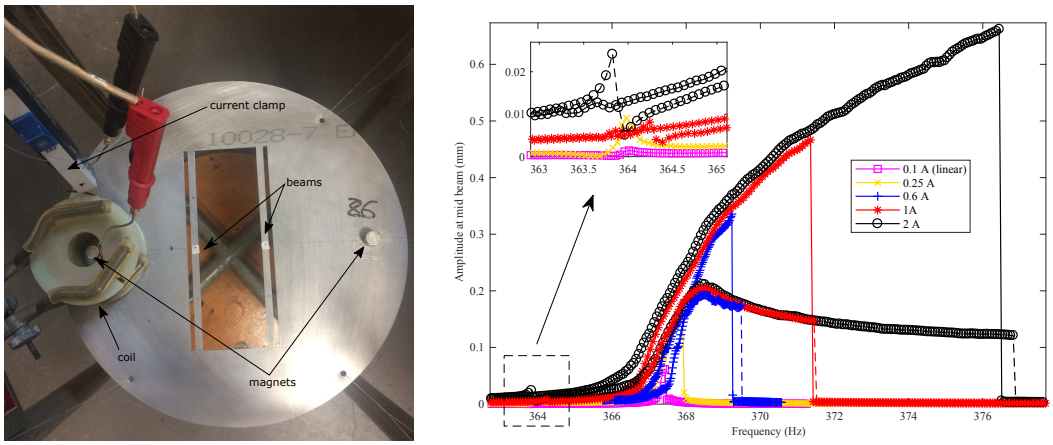

Figure 3: a) Picture of the experimental setup; b) Measurement of localised states when forcing over the second mode (mid-beam amplitude versus frequency of excitation)

Conclusions

This study presents numerical and experimental results about nonlinear localisation in a system of two coupled beams. Experimental measurements using swept sine excitation demonstrate that the localisation can be observed in practice. The numerical and the experimental results agree very well, showing that the reduced order model procedure is able to generate a good representation of the physical system with only a few degrees of freedom.

References

[1] M. King and A.F Vakakis (1995) Mode Localization in a System of Coupled Flexible Beams with Geometric Nonlinearities. *Journal of Applied Mathematics and Mechanics* **75**:127-139.

[2] A.I Manevich and L.I Manevitch, (2005) The Mechanics of Nonlinear Systems with Internal Resonances. *Imperial college press*

[3] A. Grolet, P. Malbos, F. Thouverez (2014)Eigenvalue Method with Symmetry and Vibration Analysis of Cyclic Structures. *Computer Algebra in Scientific Computing. CASC 2014. Lecture Notes in Computer Science* vol 8660. Springer, Cham.

[4] A. Givois, A. Grolet, O. Thomas, and J.F. Deu (2019) On the frequency response computation of geometrically nonlinear flat structures using reduced-order finite element models. *Nonlinear Dynamics* **97**:1747-1781.

[5] B. Cochelin, N. Damil and M. Potier-Ferry (2007) Méthode asymptotique numérique *Hermes Lavoissie*.

Experimental nonlinear dynamic analysis of a machine supporting beam

Reyolando M.L.R.F. Brasil[*], Flávio José Garzeri [**] and Robert Samuel Birch[***]
[*]*CECS, UFABC – Federal University of ABC, São Bernardo do Campo, Brazil*
[**]*Polytechnic School, University of São Paulo, Brazil*
[***]*University of Liverpool, Liverpool, UK*

Summary. We present some new results obtained in experimental nonlinear dynamics analysis of a beam supporting a rotating machine. Two phenomena were detected in our research work. First, the effect of large axial compressive forces on the geometric stiffness of the beam and, consequently, on its free undamped vibration frequencies. The larger these forces are, the smaller the measured frequencies up to a certain point, when strong nonlinearities reverse this trend. Second, the Sommerfeld effect of low power machines getting stuck at resonance and possible occurrence of jump phenomena.

Introduction

We present an experimental study of the effects of geometric nonlinearities on vibrations of rotating machines support structures. Dynamic characteristics of structures depend on their stiffness, damping and mass. The initial stiffness of a structure, computed in its unloaded state, is affected by the applied forces, the so-called geometric stiffness. Compressive forces reduce the stiffness and the frequencies and may lead to buckling, for zero frequencies. In bases of machines excited by the supported equipment, vibrations may affect the structures but, in general, they may generate damage to the suspended equipment and the quality of the production. Although machine support structures are, as a rule, very bulky, little affected by geometric stiffness considerations, the tendency of modern structural engineering, especially in aerospace applications, is towards slender members, due to more efficient materials and powerful analysis tools. Here we study these effects via experimental methods designed to evaluate previous mathematical models. Our model is a metal beam under compression supporting a DC motor. We suppose the original design provided natural frequencies away from the excitation frequency. Nevertheless, the presence of large axial compressive force will reduce the beam stiffness and natural frequencies leading to unexpected, potentially dangerous resonance states. Experimental imperfections led to observation of interesting phenomena not predicted in our previous theoretical and numerical studies. We also observe, as expected, occurrence of the so called Sommerfeld Effect, when underpowered excitation sources get their rotation regime stuck at resonances. Earlier mathematical and numerical work is to be found in [1-3].

Experimental setup

The model beam

Figure 1 displays the experimental setup: a rectangular section steel bar mounted in a calibrated manual hydraulic press intended to apply large axial compressive forces in order to change its geometric stiffness. A small DC electric motor is fixed with PVC fixtures to the beam central section. Unbalanced forces are generated by wooden flywheels with attached small point masses. Several end conditions were studied: embedded ball point, simply cut etc.

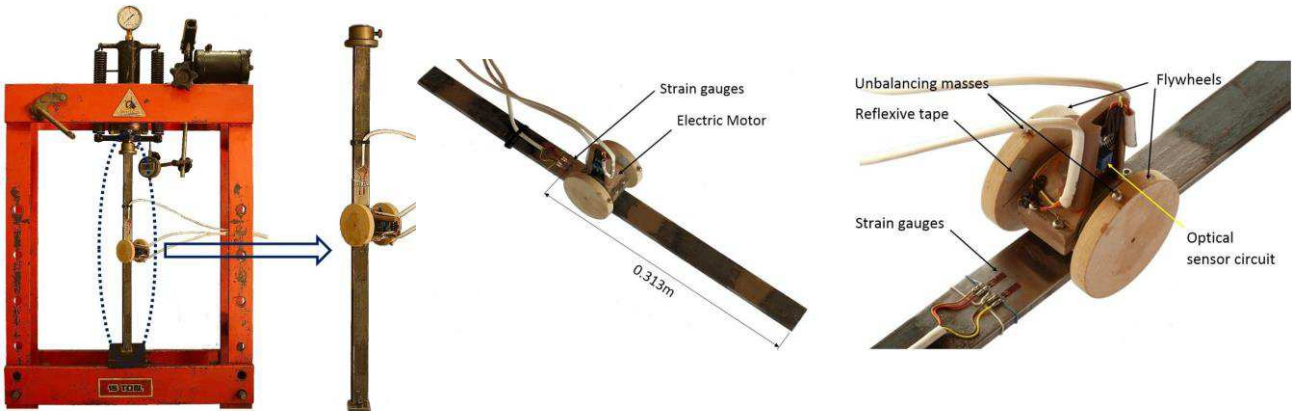

Figure 1: The experimental setup

Instrumentation

Data acquisition was carried out by an 8 channels automatic system coupled to a PC computer, with FFT capabilities. The sensor system comprises: piezoelectric accelerometers to pick up vibrations; strain gauges for strain and bending moments measurement; optical tachometer to access the motor rotation speed; an *ad hoc* designed power control and measurement digital electronic circuit, coupled to a DC supply.

Results and discussion

The effect of large compressive axial forces applied to the beam on the geometric stiffness and 1st free undamped vibration frequency was detected, as displayed in Fig. 2. Frequencies get smaller as the compressive axial force grows, up to a point, where large nonlinearities reverse the trend. Effect of end conditions were also studied and presented in Fig. 2.

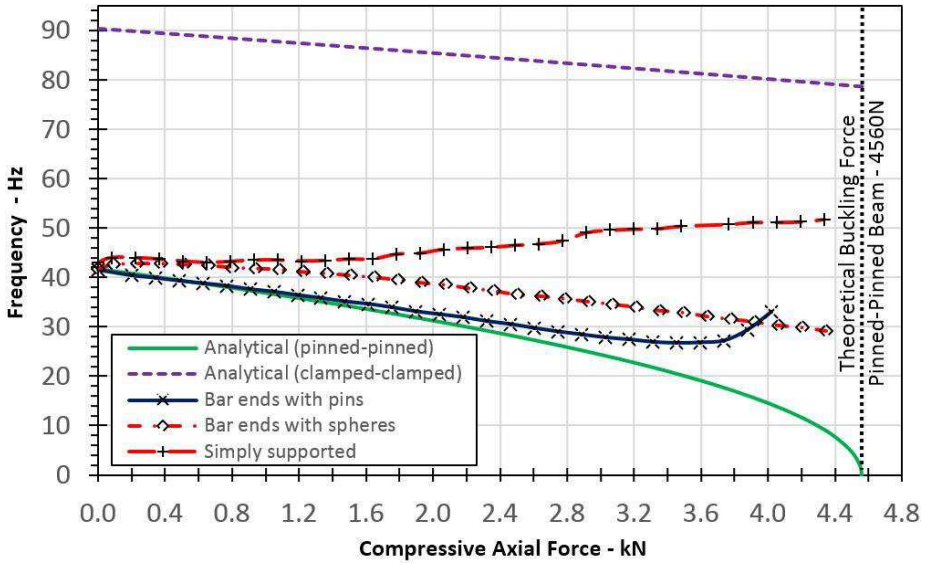

Figure 2: First vibration frequency as function of axial compressive force and end conditions

By controlling the amount of power available to the DC motor, the Sommerfeld effect was also observed, of getting stuck in resonance and occurrence of the jump phenomenon. Figure 3 displays measured forced vibrations accelerations as power is varied linearly from zero through resonance, for a certain value of axial compressive force. Motor angular velocity, measured by the tachometer, is also shown.

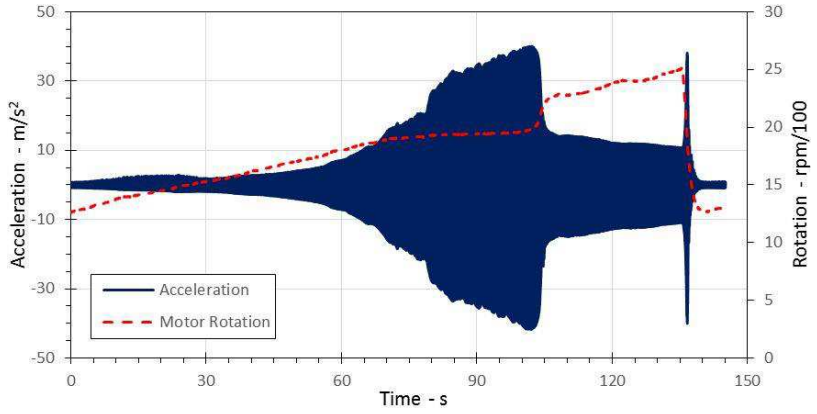

Figure 3: Accelerations and motor rotation speed as power is increased through resonance

Conclusions

An experimental research was carried out on the nonlinear dynamics of a beam supporting a unbalanced rotating machine. The effect of large compressive axial forces upon the geometric stiffness and free undamped vibration frequencies was detected. Further, for underpowered machines, the Sommerfeld effect was also observed, of getting stuck in resonance and occurrence of jump phenomena. Effect of several end conditions was also studied.

We acknowledge support by FAPESP and CNPq, both Brazilian research funding agencies.

References

[1] Balthazar, J.M., Brasil, R.M.L.R.F. et all. (2003) An overview of nonideal vibrations. *Meccanica* **38**, 613-321.

[2] Balthazar, J.M., Brasil, R.M.L.R.F., Garzeri, F.J. (2004) On a nonideal simple portal frame: experimental results. *Applied Mechanics and Materials* **12**, 51-57.

[3] Balthazar, J.M., Brasil, R.M.L.R.F. et all. (2018) An overview of the appearance of the Sommerfeld effect in nonideal systems in macro and MEMS scale. *Nonlinear Dynamics* **91**, 1-12.

Monday, July 18, 2022

16:00 - 18:00

MS-15 Energy Transfer and Harvesting in Nonlinear Systems

Rhone 1

Chair: Lawrence Bergman

16:00 - 16:20
Dynamical analysis of TET in a non-smooth vibro-impact system
LIU Ruofeng, COSTA Dimitri, YURCHENKO Daniil, **KUSKE Rachel***
*Georgia Institute of Technology (Atlanta United States)

16:20 - 16:40
Energy harvesting from vortex induced vibration in MEMS devices using magnetic interaction
NAMBIAR Amal*, PANDEY Manoj
*Amal Nambiar (IIT Madras, Tamil Nadu, India India)

16:40 - 17:00
Frequency-Energy Plot of Unsymmetrical Nonlinear Energy Sink
AL-SHUDEIFAT Mohammad*
*Mohammad A AL-Shudeifat (Khalif Khalifa University United Arab Emirates)

17:00 - 17:20
Escape of two-DOF dynamical system from the potential well
ENGEL Amit*, GENDELMAN Oleg, EZRA Tal, FIDLIN Alexander
*Technion institute of technology (The Technion, Haifa Israel)

Dynamical analysis of TET in a non-smooth vibro-impact system

Ruofeng Liu [1], Dimitri Costa [2], Daniil Yurchenko[3], and Rachel Kuske[2]
[1] *Computational and Applied Math, Rice University, Houston, USA.*
[2] *School of Math, Georgia Tech, Atlanta, USA.*
[3]*IMPEE, Heriot-Watt University, Edinburgh, UK.*

Summary. Applying a novel analysis we study targeted energy transfer (TET) in a non-smooth vibro-impact system (VI), comprising a ball freely moving within a frictionless slot made within a harmonically excited large mass. Both the ball and the mass can move independently between inelastic collisions. The proposed semi-analytical approach allows analyzing TET in the discontinuous piecewise linear systems exactly, in contrast with previous studies via approximations related to a specific state. We obtain parameter ranges for the impact pair to effectively transfer energy to it from the base excited system via a series of impacts.

Problem statement

Targeted energy transfer may be viewed as an extension of a classical linear tuned mass damper (TMD) theory, where a second mass-spring system is added to an original single-degree-of-freedom (SDOF) oscillator to avoid a high-amplitude response near its resonance frequency [1, 2]. The parameters of the resulting two DOF (TDOF) system are selected so achieve a low energy state in the original system, while the added mass-spring subsystem stores the energy of the entire TDOF system. While TMD is a standard approach for vibrational mitigation and energy transfer, used by engineers for over 100 years, it has no direct analogy for nonlinear systems. Without an exact analytical solution for the classical nonlinear TDOF system there is no "obvious" way to choose the systems' parameters for transferring energy from a forced oscillator to a nonlinear energy sink via nonlinear coupling, see [3, 4] and references therein. Analyses are generally based on weakly nonlinear approximations or model reductions. Parametric studies are then limited requiring simulations for explorations of the full nonlinear behavior.

Alternatively, we note that energy transfer in continuous nonlinear systems is a special case of more general nonlinear systems, which can be non-smooth and discontinuous. Considering TET via persistent vibro-impact motion (e.g. as in [5, 6]) we focus on the non-smooth impact pair as in [5, 7], with a small mass ball traveling freely within a slot of length $2b$ made in the large excited mass. The dynamics of the displacements q_1, q_2 of the large and small masses with mass M and m respectively, complemented by the impact conditions at $|q_1 - q_2| = b$, is described by the following equations:

$$M\ddot{q}_1 + c\dot{q}_1 + kq_1 = kE\sin(\omega t + \phi) + c\omega E\cos(\omega t + \phi) \qquad \ddot{q}_2 = 0 \tag{1}$$

$$(\dot{q}_1^+ - \dot{q}_2^+) = -r(\dot{q}_1^- - \dot{q}_2^-) \qquad M\dot{q}_1^+ + m\dot{q}_2^+ = M\dot{q}_1^- + m\dot{q}_2^-, \qquad {}^{-(+)} \text{ before (after) impact} \tag{2}$$

where k is the elastic spring coefficient, E, ω, ϕ are the excitation amplitude, frequency, and initial phase, r is the restitution coefficient, t is the time, the dot indicates derivatives with respect to time. The instantaneous impact conditions (2) capture the two-way energy exchange between the masses, in contrast to the extensive literature on bouncing ball dynamics, where the mass of the ball is typically assumed as negligible [8].

Analytical approach

Within a non-dimensionalized framework, with parameters $\mu = \dfrac{m}{M}$, $A = \dfrac{E}{b}$, $\omega_0 = \sqrt{\dfrac{k}{M}}$, $\Omega = \dfrac{\omega}{\omega_0}$, $\lambda = \dfrac{c}{M\omega_0}$, state variables $x_1 = \dfrac{q_1}{b}$, $x_2 = \dfrac{q_2}{b}$ and rescaled time $\hat{t} = \omega_0 t$, and dropping $\hat{}$'s for the remainder, we integrate the equations of motion (1), and apply the impact conditions (2) when the ball impacts either end of the cavity. This yields the map of the state from the previous impact time t_{k-1} to the next impact time t_k in terms of all system parameters

$$\begin{aligned}
x_{1,k} &= a_1 e^{\frac{-\lambda t_k}{2}}\sin(\gamma t_k) + a_2 e^{\frac{-\lambda t_k}{2}}\cos(\gamma t_k) + b_1\sin(\Omega t_k + \phi) + b_2\cos(\Omega t_k + \phi)\\
\dot{x}_{1,k} &= a_1 e^{\frac{-\lambda t_k}{2}}\left(-\frac{\lambda}{2}\sin(\gamma t_k) + \gamma\cos(\gamma t_k)\right) + a_2 e^{\frac{-\lambda t_k}{2}}\left(-\frac{\lambda}{2}\cos(\gamma t_k) - \gamma\sin(\gamma t_k)\right) + b_1\Omega\cos(\Omega t_k + \phi)\\
&\quad -b_2\Omega\sin(\Omega t_k + \phi),\\
x_{2,k} &= x_{2,k-1} + \left(\frac{1+r}{1+\mu}\dot{x}_{1,k-1} + \frac{\mu - r}{1+\mu}\dot{x}_{2,k-1}\right)\cdot(t_k - t_{k-1})\\
\dot{x}_{2,k} &= \frac{1+r}{1+\mu}\dot{x}_{1,k-1} + \frac{\mu - r}{1+\mu}\dot{x}_{2,k-1}
\end{aligned} \tag{3}$$

Here the conditions are in terms of $x_{j,k}, \dot{x}_{j,k}$ the displacements and velocities at the impact time t_k, corresponding to the end of each sub-interval of continuous motion, so that the superscript $^-$ as in (2) can be dropped without loss of generality. The coefficients a_l,b_l are functions (not given here) of the previous time t_{k-1} and states $\dot{x}_{j,k-1}x_{j,k-1}$. Taking $|x_{1,k-1} - x_{2,k-1}| = 1$ and $|x_{1,k} - x_{2,k}| = -1$ yields the map P_1 for the motion from left to right in the capsule. Similarly

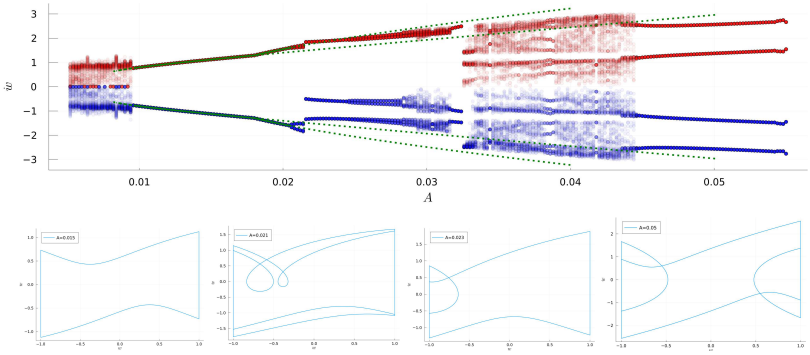

Figure 1: Upper: Bifurcation diagram of relative impact velocity $\dot{w}$ for (red (blue) is left (right) impact obtained numerically) vs. forcing amplitude A; Green solid (dotted) lines are stable (unstable) 1:1 solutions obtained analytically. Lower: Phase planes with $\dot{w}$ vs w at $A = .015, .021, .023$ and $.05$ showing 1:1, 1:1/2T, 2:1, and 2:2 periodic solutions, respectively.

we determine maps for the other motions, e.g. P_2 right to left, and P_3 (P_4) for successive impacts on left (right). Thus it is possible to construct a sequence of maps describing the different periodic motions, whether successive impacts occur on the same or different ends of the slot. We use the notation n:m/pT corresponding to pT-periodic solutions with n (m) impacts on the left (right) of the capsule, given an external forcing with period T on the large mass. Then 1:1 solutions, the simpler case where the ball has alternating impacts on either end of the capsule, are determined from the system (3) given by the composition $P_1 \circ P_2$ together with the periodicity condition. Similarly 2:1 solutions are obtained from the combined equations from the composition $P_3 \circ P_1 \circ P_2$ plus periodicity, and so on for other n:m behaviors. From these compositions plus periodic conditions we obtain the period solution in terms of state vectors $\mathbf{H}_k^* = (\phi_k, \dot{x}_{1,k}, \dot{x}_{2,k}, x_{1,k})$, where the phase shift ϕ_k of the impact is relative to the forcing. Based on these analytical results for the periodic solution, we can also study their linear stability [9], and thus identify analytically both traditional bifurcations such as period doubling and discontinuity-induced bifurcations. The procedure described in this section is also applied to obtain semi-analytical solutions of a soft impact model and are used to analyse the compliant system dynamics.

Comparison of Numerical and Analytical results

Figure 1 shows the numerically obtained bifurcation structure of the relative impact velocity $\dot{w} = \dot{x}_{1k} - \dot{x}_{2k}$ vs. forcing amplitude A, illustrating 1:1, 1:1/2T, 2:1, and 2:2 solutions, as well as chaotic behavior occurring for different A. Stable and unstable 1:1 solutions obtained analytically are shown, indicating good agreement between analytical and numerical results for the stable 1:1 periodic solutions, as well as the regions for instability. From the results we can calculate performance based on energy transfer efficiency, for example, kinetic energy transferred relative to work done by the excitation. This measure (not shown) indicates improved performance via 1:1 type periodic solutions, with some reduced performance at non-smooth bifurcations such as 1:1 to 2:1 transitions.

Conclusions

We study targeted energy transfer in a VI system by expressing the inter-interval dynamics as a sequence of maps. We capture physically-relevant motions via the derived semi-analytical approach that reveal critical parameter dependencies of the dynamics and energy transfer. Developing this approach within the instantaneous (hard) impact condition allows us to generalize to compliant impact conditions.

References

[1] Den Hartog JP (2013) *Mechanical Vibrations*. Courier Dover Pub, New York.

[2] Yurchenko D. (2015) Tuned mass and paramtric pendulum dampers under seismic vibrtions. Encycl. of Earthquake Eng., Springer-Verlag, Berlin.

[3] A. F. Vakakis, O.V. Gendelman, L.A. Bergman, D.M. McFarland, G. Kerschen, and Y.S. Lee, *Nonlinear targeted energy transfer in mechanical and structural systems*. Solid Mechanics and Its Applications book series (SMIA, volume 156), Springer, 2009.

[4] O.V. Gendelman, A. F. Vakakis, Nonlinear energy transfer in dynamical and acoustical systems, *Phil. Trans. Roy. Soc. A:* , 376, 2018.

[5] B. Youssef, R. I. Leine A complete set of design rules for a vibro-impact NES based on a multiple scales approximation of a nonlinear mode *Journal of Sound and Vibration* 501, 2021, 116043.

[6] T. Huang, D. M. McFarland, A. F. Vakakis, O. V. Gendelman, L. A. Bergman, H. Lu, Energy transmission by impact in a system of two discrete oscillators, *Nonlinear Dyn* 100, 135–145, 2020.

[7] T. Li , S. Seguy , A. Berlioz ,Dynamics of cubic and vibro-impact nonlinear energy sink: analytical, numerical, and experimental analysis, *J. Vibr. Acoust.* 138 (3) (2016) .

[8] M di Bernardo, C.J. Budd, A.R. Champneys, and P. Kowalczyk. *Piecewise-smooth dynamical systems: theory and applications*. Applied Mathematical Sciences, Vol. 163, Springer-Verlag, Berlin, 2007.

[9] A. Luo, Period-doubling induced chaotic motion in the LR model of a horizontal impact oscillator, *Chaos, Solitons and Fractals,* 19, 823-839, 2004.

Energy harvesting from vortex induced vibration in MEMS devices using magnetic interaction

Amal Nambiar*, Manoj Pandey†
* *Department of Mechanical Engineering, Indian Institute of Technology Madras, Tamil Nadu, India*
†*Department of Mechanical Engineering, Indian Institute of Technology Madras, Tamil Nadu, India*

Summary. Energy harvesting from the environment is an emerging field and a better alternative to battery-operated systems such as wireless sensors, IoT and lower power electronic devices. Linear energy harvester has maximum power output near its natural frequency, which restricts its operation in narrow bandwidth. To improve the bandwidth and the power output, a pair of magnets with same polarity is used to induce non-linearity in a cantilever beam subjected to vortex induced vibration. This increases the complexity of the problem in FEA softwares as it will be coupled electrical-fluid-mechanical-magnetic problem. Thus, the magnetic force is replaced with nonlinear spring in ABAQUS and the Fluid Structure Interaction is carried out by reducing the complexity to electrical-fluid-mechanical problem. The magnets are placed at a certain distance so that the beam operates as a bistable system. The analysis was carried out for beam with different natural frequencies by changing the tip mass. Using the pair of repulsive magnets, we have found that the energy harvested in non-linear system is higher than the linear energy harvester.
Keywords: Energy harvesting; Fluid Structure Interaction; MEMS; Nonlinear Dynamics; Vortex Induced Vibration

Introduction

With the rapid development of technology in the field of sensors, IoT more emphasis is made on low power based devices. Wireless Sensor Networks(WSNs), IoT applications demand for low-energy wireless nodes typically powered by non-renewable energy storage units(batteries). But the battery have limited lifetime and it is difficult and expensive to replace them. An energy harvester(EH) operated along with a battery could potentially increase the lifetime of the node and eliminate the need to replace the battery. MEMS devices could be easily integrated with the circuit but the process to develop MEMS devices is complex, time consuming and expensive. Thus, FEA simulation allows to analyze or redesign the harvester according to the need. But FEA packages cannot handle complicated coupled problems which are common in non-linear EH. The major problem to analyze a vortex induced vibration based nonlinear EH involving magnets includes the complexity to solve the electrical-fluid-mechanical-magnetic problem. The magnetic force between two cylindrical magnets used in the MEMS cantilever beam is modeled as a nonlinear spring which has the same behavior as the repulsive magnets. The FE model of cantilever nonlinear EH with nonlinear springs is validated with the theoretical model. Application of phase space, bifurcation diagram, Poincaré maps were used to study the nonlinearity effects to enhance the energy harvested.

Analysis

The axial force and lateral forces between two cylindrical magnets [2] is given in Figure 5 (2a). This nonlinear magnetic force is approximated using piecewise linear segments and given as an input in ABAQUS. The beam with nonlinear spring is simulated in ABAQUS with an acceleration of 2 m/s^2(20 Hz) and validated with the theoretical model using equations shown in Figure 5 (1c and 2c)

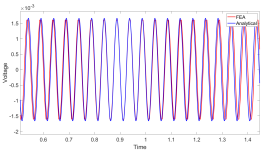

Figure 1: Voltage time history of FEA and theoretical results

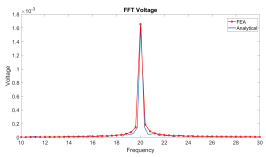

Figure 2: FFT of voltage from theoretical and FE results

Set up

The setup consists of a 2mm cylindrical bluff body and a beam ($5mm \times 0.3mm \times 9\mu m$) which is placed at a distance of 6mm from the center of the bluff body. The magnets(NdFeB N35 grade) have dimension $\phi 0.1 \times 0.1mm$ placed at a distance of $0.4mm$ from each other. Beam is subjected to a uniform input velocity of 2m/s having vortex shedding frequency of 217Hz. The beam operates in a bistable system, for distance less than 0.4mm as shown in Figure 4.

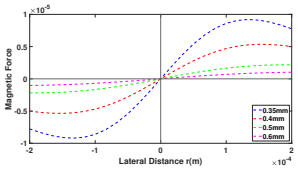

Figure 3: Magnetic force between magnets at different distances

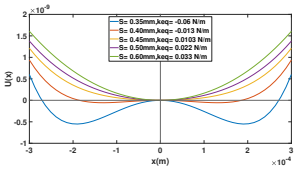

Figure 4: Potential Energy for different magnet distance

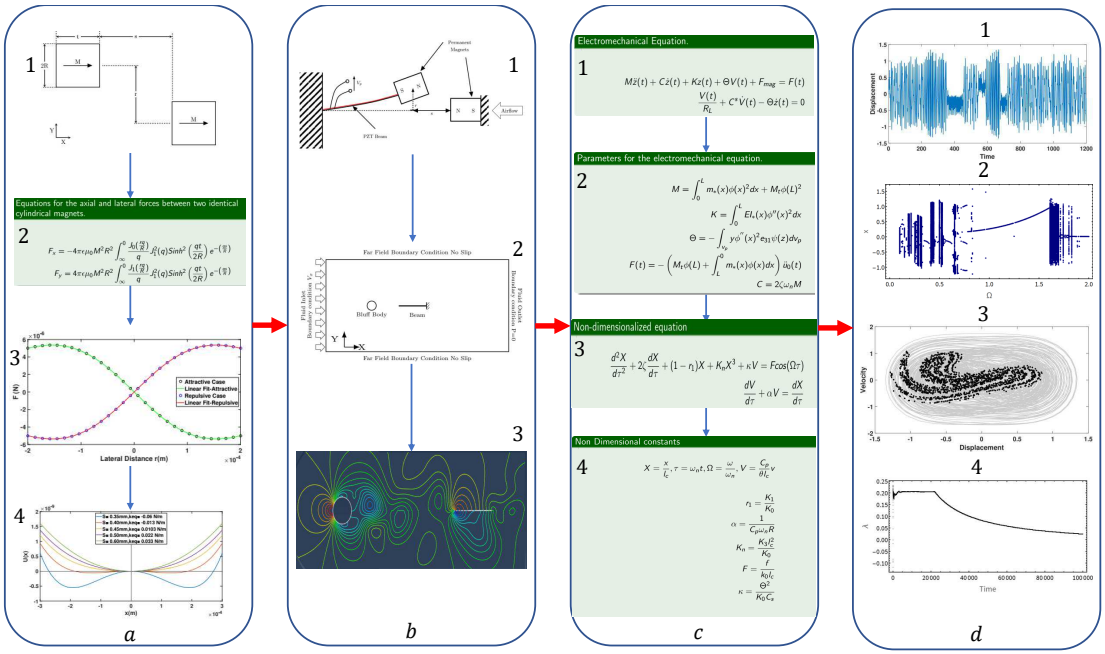

Figure 5: (a) Magnet Design (b) FSI Setup (c) Coupled electromechanical Equation (d) (1) Time history (2) Bifurcation Diagram (3) Phase space (4) Maximum Lyapunov exponents for time series at 131 Hz

The coupled non-dimensionalized equation can be represented as Figure 5 (3c). For beam with natural frequency 131 Hz($\Omega = 1.65$) operates in chaotic range for $\zeta = 0.0275$ as shown in Figure 5 (d)

Discussion

The magnetic force equation was derived with the assumption that the cylindrical magnets are placed axially and there exists uniform magnetization in each magnet. Also, the rotation of the magnet is neglected while simulating magnetic force with nonlinear spring as the rotation of the magnet will be typically below 10° for low base excitation used in energy harvesting applications. Piezoelectric materials are anisotropic by nature. But for our analysis, we have considered both substrate and Piezoelectric material as a linear elastic material model as the strain in the substrate is well below the elastic limit. In HVAC systems airflow is usually unidirectional with operating speeds from 1.8 m/s to 5 m/s. Care must be taken while designing for a bistable system, as adequate forcing is required for the beam to cross the potential barrier.

Conclusion

In this work, we analyzed the nonlinear EH operating as a bistable system using pair of permanent magnets. The bistability causes the beam to cross from one potential to another, thereby increasing velocity and in turn power output. The beam acts as a linear EH when the distance between the magnets is very large. Nonlinear energy harvesters generate more power compared to linear counterparts except at resonance. Beam operating in the chaotic range have higher power output but there is an additional need to design efficient energy harvesting circuit. The system is chaotic for particular values of amplitude, forcing frequency and damping value.

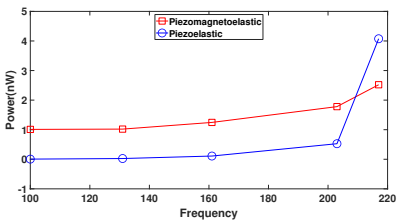

Figure 6: Power ouput of nonlinear and linear harvester

References

[1] Challa V R, Prasad M G, Shi Y and Fisher F T (2008) A vibration energy harvesting device with bidirectional resonance frequency tunability *Smart Mater. Struct.*.[**17**015035]

[2] Deepesh Upadrashta., Yaowen Yang (2015) Finite element modeling of nonlinear piezoelectric energy harvesters with magnetic interaction *Smart Mater. Struct.*[**24**045042]

[3] Erturk A, Hoffmann J and Inman D J(2009) A piezomagnetoelastic structure for broadband vibration energy harvesting *Appl. Phys. Lett.* [**94**254102]

[4] Jackson N(2020) PiezoMEMS Nonlinear Low Acceleration Energy Harvester with an Embedded Permanent Magnet.*Micromachines* [**11**no.5:500]

Frequency-Energy Plot of Unsymmetrical Nonlinear Energy Sink

Mohammad A. AL-Shudeifat
Department of Aerospace Engineering, Khalifa University of Science and Technology, Abu Dhabi, United Arab Emirates

Summary. Studying the nonlinear energy sink (NES) attachment with a linear dynamical oscillator (LO) on the frequency-energy plot (FEP) reveals the underlying nonlinear dynamical behavior of the LO-NES system. In addition, the FEP reveals different kinds of periodic motions on NNMs backbone branches. The unsymmetrical force nonlinear energy sink (UNES) incorporates a cubic stiffness element at one side of its equilibrium position where a weak linear restoring coupling stiffness acts in both directions. The obtained FEP has revealed several unsymmetrical backbones of 1:1 resonance between the UNES and the LO periodic oscillations at different nonlinear frequency levels.

Introduction

The frequency energy plots (FEPs) analysis has a significant impact on revealing the underlying nonlinear dynamics of the structure-NES nonlinear motion. The periodic motion of stiffness-based structure-NES systems have been extensively studied on harmonic NNM backbone curves and their associated branches/tongues of subharmonic and super harmonic periodic motions in the FEPs. The FEPs accompanied with the superimposed wavelet frequency spectrum content have confirmed the existence of different kinds of resonance captures between the primary system and the NES oscillations at the backbones and their associated subharmonic branches and tongues. The resonance captures on the FEPs have explained the rapid and passive targeted energy transfer (TET) from the primary system into the NES attachment [1–5].

UNES Description

The UNES attachment with the LO in [6] is shown in Figure 1 where the UNES mass is coupled with the LO by a cubic stiffness element that acts only to the left-side of the equilibrium position. In addition, the UNES incorporates a weak linear restoring spring that acts in both directions as shown. The physical parameters in [6] are used here for generating the frequency energy plot of the Hamiltonian version of the LO-UNES system (i.e, $\lambda_1 = \lambda_2 = 0$). The other parameters are; LO mass of $M = 1\,\text{kg}$, LO coefficients of stiffness of $k_1 = 1\,\text{N/m}$, NES mass of $m = 0.05\,\text{kg}$, NES coefficients of cubic nonlinear stiffness of $k_{nl} = 1\,\text{N/m}^3$, and the UNES coefficient of weak linear restoring stiffness $k_{res} = 0.03\,\text{N/m}$.

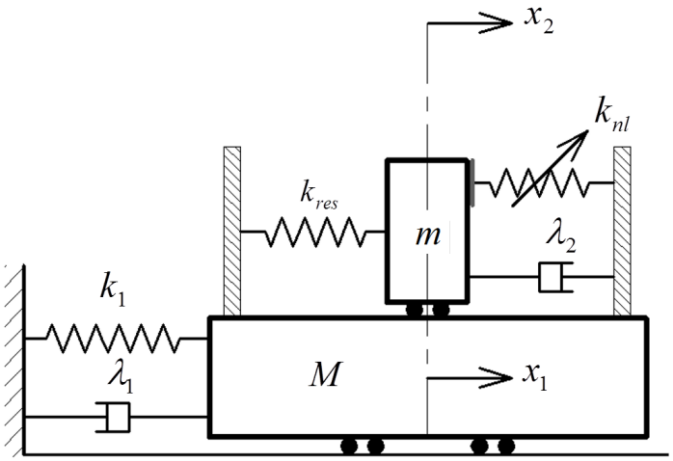

Figure 1: Unsymmetrical NES attachment with a linear oscillator

Frequency Energy Plot of the LO-UNES System

The FEP backbones are generated here by applying the numerical continuation method in [4, 5] with the considered LO-UNES system in Figure 1. The free-response of the Hamiltonian equations of motion of the system is obtained at the given physical parameters in the previous section for zero velocities and nonzero displacements. Therefore, the underlying nonlinear dynamical behaviour due to the influence of the unsymmetrical coupling stiffness force is investigated on the obtained FEP. Accordingly, seven backbone curves (*A1*, *A2*, *B1*, *B2*, *C*, *D* and *E*) are obtained in the FEP as shown in Figure 2. The backbones are named according to the ratio of the frequency content in the oscillation response between the LO and UNES masses. Therefore, $U11\pm$ denotes to an unsymmetrical NNM periodic motion at which the NNM does not pass through the origin in the NNM configuration space where the $+$ and $-$ indices indicate to the in and out of phase periodic motions, respectively. $U11+$branch of the backbone indicates to 1:1 resonance frequency ratio of the in phase periodic motion between the LO and UNES masses. As shown from the FEP, the backbones, *A2*, *B1*, *B2*, and *C*, approach 1, 1/2, 1/3 and 1/4 of the natural frequency of the LO at high energy levels. Unlike other kinds of NESs, all backbones are at 1:1 resonance for different values of the nonlinear frequency.

The NNM, the related periodic time response of the UNES mass and the associated mass of the LO, and the corresponding nonlinear UNES coupling force are plotted for selected data points *a* and *b*, respectively, as shown in Figure 3. For the data point *a*, the NNM does not pass through the origin where this NNM is located at the $U11-$backbone *A1*. Therefore a 1:1 out of phase resonance takes place between the UNES and LO periodic motions. The data point *b* is located $U11-$ backbone *B1*. For this data point, also 1:1 out of phase resonance takes place between the UNES and LO periodic motions. In Figures 3c and 3f, the strong nonlinear effect to the right-side of the equilibrium position of the UNES and the weak linear coupling effect in the left-side are shown.

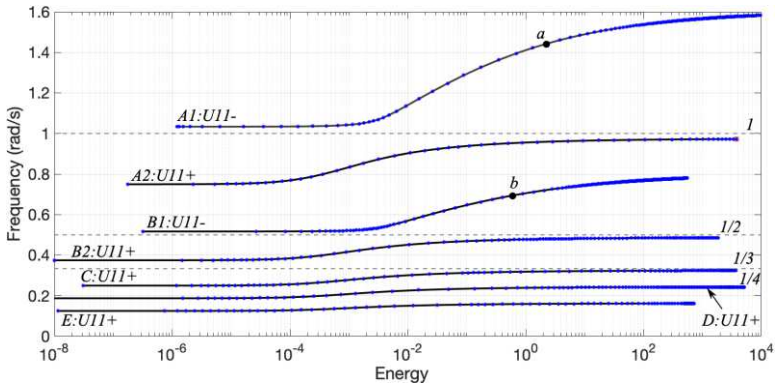

Figure 1: The obtained unsymmetrical backbone curves of the FEP of the LO-UNES system.

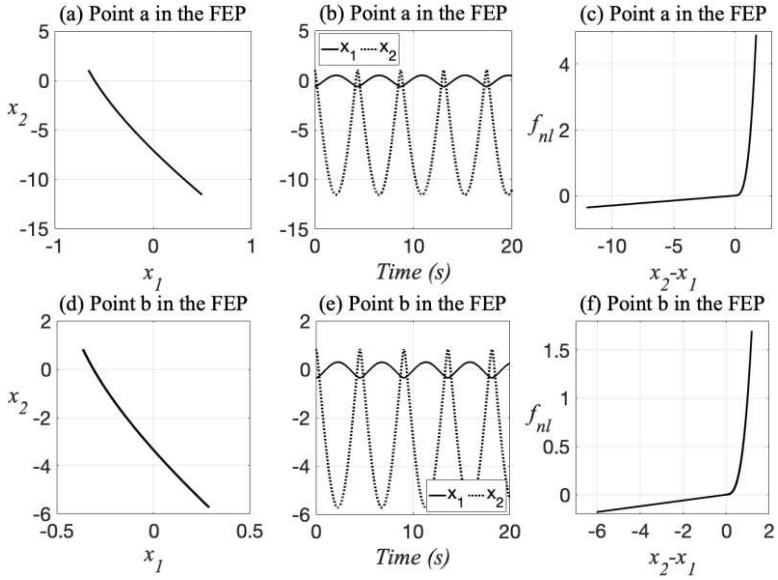

Figure 3: The NNMs in (a) and (d), their corresponding oscillation displacements in (b) and (e), and the corresponding nonlinear coupling forces in (c) and (f) for the data points *a* and *b* in the FEP.

Conclusions

In this study, the frequency energy-dependence of LO-UNES system is studied on the frequency energy plot. The underlying nonlinear dynamical behavior of the LO-UNES is revealed on the FEP. Unlike other existing NESs, the UNES is found to be associated with several backbones of unsymmetrical NNMs of 1:1 in phase and out of phase resonance between the UNES and LO oscillations for wide range of nonlinear frequency levels. The UNES shows a unique capability of functioning at 1:1 resonance at a broadband frequency-energy fashion.

References

[1] Vakakis A.F., Gendelman O.V., Bergman L.A., McFarland D.M., Kerschen G., Lee Y.S. (2008) Nonlinear targeted energy transfer in mechanical and structural systems, Springer Science & Business Media,

[2] Lee Y.S., Kerschen G., Vakakis A.F., Panagopoulos P., Bergman L., McFarland D.M. (2005) Complicated dynamics of a linear oscillator with a light, essentially nonlinear attachment. *Physica D* **204**: 41-69.

[3] Quinn D.D., Gendelman O., Kerschen G., Sapsis T.P., Bergman L.A., Vakakis A.F. (2008) Efficiency of targeted energy transfers in coupled nonlinear oscillators associated with 1:1 resonance captures: Part I. *J. Sound Vib.* **311**: 1228-1248.

[4] Kerschen G., Peeters M., Golinval J-C., Vakakis A.F. (2009) Nonlinear normal modes, Part I: A useful framework for the structural dynamicist. *Mech Syst Signal Process* **23**: 170-194.

[5] Peeters, Maxime, Viguié, Régis, Sérandour, Guillaume, Kerschen, Gaëtan and Golinval, J-C. (2009) Nonlinear normal modes, Part II: Toward a practical computation using numerical continuation techniques. *Mech Syst Signal Process* **23**: pp. 195-216.

[6] Vakakis A.F., Al-Shudeifat M.A., Hasan M.A. (2014). Interactions of propagating waves in a one-dimensional chain of linear oscillators with a strongly nonlinear local attachment. *Meccanica* **49**: 2375-2397

Escape of two-DOF dynamical system from the potential well

A.Engel*, T. Ezra*, O.V.Gendelman*, A.Fidlin**
* *Technion—Israel Institute of Technology, Israel*
** *Karsruhe Institute of Technology*

Summary. The escape of initially excited dynamical system with two degrees of freedom from three different one-dimensional benchmark potential wells is considered. Main challenge is revealing the basic mechanisms that govern the escape in different regions of the parametric space, and constructing appropriate asymptotic approximations for analytic treatment of these mechanisms. In this study numerical and analytical tools are used in order to classify and map the different escape mechanisms for a variety of initial conditions, and to offer the analytic criteria predicting the system's behavior for those cases.

Introduction

Escape from a potential well is a classic problem, relevant in many branches of physics, chemistry and engineering. Among many examples of possible applications, one encounters dynamics of molecules and absorbed particles, celestial mechanics and gravitational collapse [1,2], energy harvesting [3] responses of Josephson junctions [4], various aspects of capture into and escape from the resonance [5], as well as the capsizing of ships [6]. Even more profound, and widely explored manifestation of the escape phenomenon is a dynamic pull-in in microelectromechanical systems (MEMS) [7,8]. In this current study, we will expand the discussion and analyze two DOF systems. For a better understanding of the problem and a more reliable model in our work, three one-dimensional examples of potentials are considered: inverse hyperbolic potential, cubic potential and biquadratic potential. General setting explored in the present work can be presented as two equal particles attached to each other by a spring, and imbedded into the potential well (Fig 1).

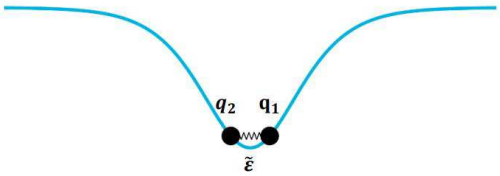

Figure 1: sketch of the general setting

Main challenge is revealing the basic mechanisms that govern the escape in different regions of the parametric space, and constructing appropriate asymptotic approximations for analytic treatment of these mechanisms.

Results

In this study numerical and analytical tools, such as Poincare maps and grid classification, are used in order to classify and map the different escape mechanisms for various initial conditions. Further investigation was performed on two different sets of initial conditions. For the first set of conditions, only one of the particles was excited by a nonzero initial velocity. For the second set of conditions, both particles were excited. For convenience, in this case other coordinates were used: center of mass R and interparticle displacement W. When only W coordinate is excited, one can reveal an additional escape mechanism - dissociation, in which the distance between the particles eventually diverges. In order to investigate the classic escape mechanisms in which both particles escape in the same direction, we add minor disturbance to the center of mass velocity $\dot{R}$.

$$\textit{set I} \quad q_1(0)=q_2(0)=\dot{q}_2(0)=0 \;;\; \dot{q}_1(0)=v_0$$

$$\textit{set II} \quad R(0)=W(0)=0 \;;\; \dot{W}(0)=v_0 \;;\; \dot{R}(0)=0 \;/\; \dot{R}(0)=\delta$$

Variety of analytical and dynamical methods were used to derive the dependence between the minimum energy required for different escape mechanisms of the system and the spring stiffness ε. The resulting relations were validated by the numerical results, as presented in (Fig 2).

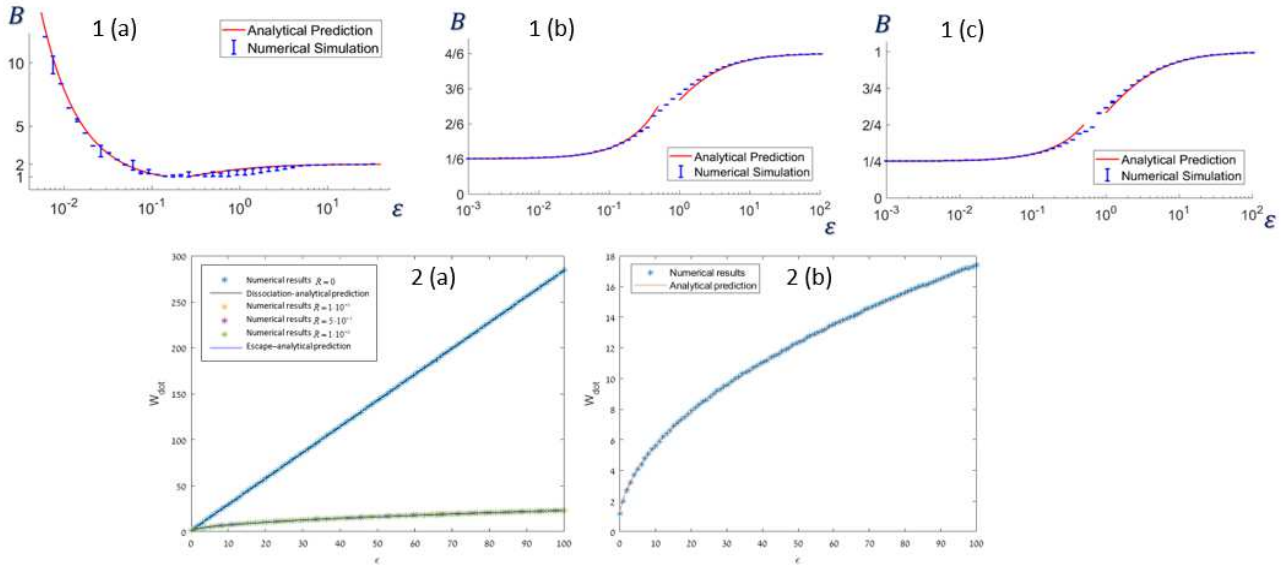

Figure 2: the analytical prediction and numerical results for the different cases (1) set I , minimum energy required to escape as a function of the spring stiffness (a) inverse hyperbolic potential (b) cubic potential (c) biquadratic potential. (2) set II , minimal separation velocity $\dot{W}$ required for each escape mechanism as a function of the spring stiffness (a) biquadratic potential (b) cubic potential

Discussion

For the case of the single particle excitation, a clear distinction between the cases of weak and strong coupling has been revealed. For the small coupling, the escape is achieved when the excited particle has enough energy to pull the remaining particle from the well. For the case of the strong coupling, one can separate the timescale of fast interparticle oscillations; appropriate averaging delivers the modified effective potential for relatively slow evolution of the center of masses. Interestingly, two aforementioned limiting cases faithfully cover almost all space of parameters. To explore the chaotic responses, Lyapunov exponents were calculated, as presented in (Fig 3).

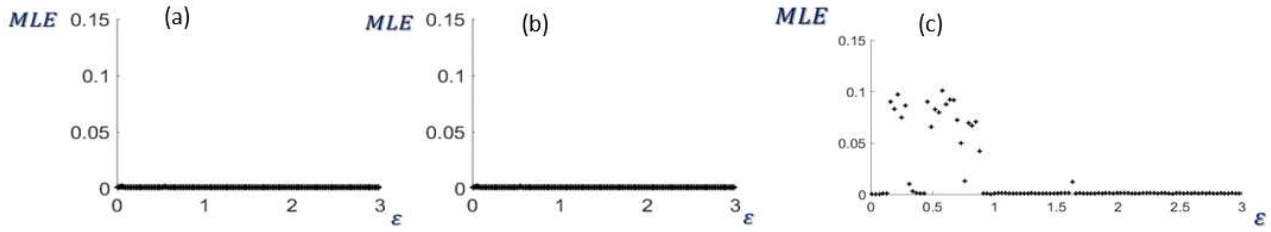

Figure 3: Lyapunov exponents as a function of the spring stiffness (a) Cubic potential (b) Biquadratic potential (c) Hyperbolic potential

Only the inverse hyperbolic potential has shown characteristics of chaotic behavior, mainly for low values of the spring stiffness, while the cubic and biquadratic potentials have not exhibited the chaos-governed escape dynamics. For the other set of initial conditions, a new escape mechanism – dissociation, derived from the symmetry of the initial conditions and the biquadratic potential, was recognized. Along with an additional escape mechanism, related to a parametrically driven acceleration of the center of masses. Those two mechanisms introduced in (Fig 2.2.a)), the dissociation mechanism occurs for higher energy levels while the other is described by lower levels. For those cases no separation of the parameters plane was needed and the same regime described the system for all ranges of the stiffness.

References

[1] Koon, W.S. Lo, M.W., Marsden, J.E., Ross, S.D.: Heteroclinic connections between periodic orbits and resonance transitions in celestial mechanics. Chaos An Interdiscip. J. Nonlinear Sci. 10 427–69 (2000)
[2] Arnold, V.I., Kozlov, V.V., Neishtadt, A.I.: Mathematical Aspects of Classical and Celestial Mechanics. Springer, Berlin (2006)
[3] Junyi Cao, Shengxi Zhou, Wei Wang, and Jing Lin. Influence of potential well depth on nonlinear tristable energy harvesting. APPLIED PHYSICS LETTERS 106, 173903 (2015)
[4] Barone, A., Paterno, G.: Physics and Applications of the Josephson Effect. Wiley, New York (1982)
[5] Quinn, D.D.: Transition to escape in a system of coupled oscillators. Int. J. Non-Linear Mech. 32, 1193–1206 (1997)
[6] Virgin, L.N.: Approximate criterion for capsize based on deterministic dynamics. Dyn. Stab. Syst. 4, 56–70 (1988)
[7] Zhang, W.-M., Yan, H., Peng, Z.-K., Meng, G.: Electrostatic pull-in instability in MEMS/NEMS: a review. Sens. Actuators A Phys. 214, 187–218 (2014)
[8] Younis, M.I., Abdel-Rahman, E.M., Nayfeh, A.: A reducedorder model for electrically actuated microbeam-based MEMS. J. Microelectromech. Syst. 12, 672–680 (2003)

Monday, July 18, 2022
16:00 - 18:20

MS-14 Nonlinear Dynamics for Engineering Design
Rhone 2

Chair: Bogdan Epureanu - Daniele Zulli

16:00 - 16:20
Multiple scale expansion and frequency-response curves of a nonlinear beam model
BABILIO Enrico*, LENCI Stefano, SACCO Elio
*Department of Structures for Engineering and Architecture (DiSt), University of Naples "Federico II" (via Forno Vecchio 36 - 80134, Naples Italy)

16:20 - 16:40
Non-linear dynamics of straight beamswith (orwithout)shape imperfections and very shallow arcs: similarities and differences controlled by boundary conditions
PAULS Vitaly*, LENCI Stefano, SOROKIN Sergey
*Polytechnic University of Marche (60131 Ancona Italy)

16:40 - 17:00
Low Voltage Operation of Vilnius Chaotic Oscillator
PIKUĻINS Dmitrijs*, SERGEJS Tjukovs, IHEANACHO Chukwuma Victor, ALEKSANDRS Ipatovs, GRIZANS Juris
*Institute of Radioelectronics, Riga Technical University (Azenes st. 12, Riga Latvia)

17:00 - 17:20
Nonlinearity in estimating bolt tension from vibrations
BRØNS Marie*, THOMSEN Jon
*Technical University of Denmark [Lyngby] (Anker Engelunds Vej 1, Building 101A, 2800 Kgs. Lyngby Denmark)

17:20 - 17:40
On the reliability of contact models in Vibro-Impact Nonlinear Energy Sinks
LO Feudo Stefania*, JOB Stéphane, CAVALLO Miriam, FRADDOSIO Aguinaldo, PICCIONI Mario Daniele, TAFUNI Alessandro
*Laboratoire QUARTZ (ISAE Supméca - 3 rue Fernand Hainaut - 93400 Saint-Ouen cedex France)

Multiple scale expansion and frequency-response curves of a nonlinear beam model

Enrico Babilio*, Stefano Lenci‡ and Elio Sacco*
*Department of Structures for Engineering and Architecture, University of Naples "Federico II", Naples, Italy
‡Department of Civil and Building Engineering and Architecture, Polytechnic University of Marche, Ancona, Italy

Summary. Slender and highly flexible structures quite often take place in systems designed to meet high to extreme performances. Hence cables, ropes, yarns, hoses and pipelines, which are essential parts of such structures, play a relevant role in practically every engineering field. In mechanical and automotive engineering, large amplitude motions of thin rods can be exploited to design nonlinear vibration absorbers for the reduction of torsional vibrations of drivelines; in assembly and disassembly phases and in system operation, reliable models are needed to predict and analyze the behavior of cables and wiring harnesses, taking also into account effective material properties; accurate structural models of wire ropes are required to study the behavior of rope-ways and cranes on the system level. In aerospace engineering, compact, flexible and slender aerials and booms to be deployed in space are typically used to minimize the room needed to store satellites in launching phases. In textile engineering, complicate interactions among hundreds of yarns have to be controlled to obtain the desired final layout. In biomedical engineering, medical endoscopes characterized by a multilayer structure must be accurately modeled, since they exhibit highly deformed configurations while moving inside narrow curved tubes within the human body. In offshore engineering, floaters, mooring lines, and others structural components of floating wind farms, are subject to structural fatigue and various sources of damping and power cables show complex cross-sectional properties. In civil engineering, estimates of the structural properties from response data coming from non-destructive procedures is critically empowered by a deeper understanding of beam-like structures. However, despite of their ubiquity, slender structures in real operating conditions exhibit responses often too complicated for current modeling tools. In this respect there is a continuous need for reliable models. In this area, this contribution considers a beam model equipped with non-standard constitutive laws and in particular it is aimed at deriving approximate solutions of the equations of motion via asymptotic multiple scale expansion.

Introduction

We consider a geometrically exact beam model deduced by stipulating a relation between one- and three-dimensional formulations for initially straight beams undergoing planar and twist-less deformed states. Using comma notation for derivatives, the equations of motion derived in [1], to which we refer for any further detail, are written as

$$m_0\,u_{,tt} - m_1(\theta_{,t}^2\sin\theta - \theta_{,tt}\cos\theta) + c_0\,u_{,t} + c_1\theta_{,t}\cos\theta = \left(N(1+u_{,x})\sqrt{2\varepsilon+1} - \frac{Tv_{,x}}{\sqrt{2\varepsilon+1}}\right)_{,x} + q_1\,, \tag{1}$$

$$m_0\,v_{,tt} - m_1(\theta_{,t}^2\cos\theta + \theta_{,tt}\sin\theta) + c_0\,v_{,t} - c_1\theta_{,t}\sin\theta = \left(Nv_{,x}\sqrt{2\varepsilon+1} + \frac{T(1+u_{,x})}{\sqrt{2\varepsilon+1}}\right)_{,x} + q_2\,, \tag{2}$$

$$m_1(u_{,tt}\cos\theta - v_{,tt}\sin\theta) + m_2\,\theta_{,tt} + c_1(u_{,t}\cos\theta - v_{,t}\sin\theta) + c_2\,\theta_{,t} = M_{,x} - T\sqrt{2\varepsilon+1} + q_3\,, \tag{3}$$

where $u(x,t)$ and $v(x,t)$ stand for the axial and transverse displacements of the beam axis, $\theta(x,t)$ is the cross-sectional rotation, $N(x,t)$, $T(x,t)$ and $M(x,t)$ are axial, transverse and bending generalized stresses. These are related to the axial strain ε, the shear angle γ and the Lagrangian bending curvature κ, all nonlinear functions of u, v, and θ, by the nonstandard constitutive assumptions

$$N = \frac{\sin^2\gamma}{\sqrt{2\varepsilon+1}}\,K_S + \frac{\varepsilon}{\sqrt{2\varepsilon+1}}\,K_0 + \cos\gamma\left(\frac{3\varepsilon+1}{2\varepsilon+1}\right)\kappa\,K_1 + \frac{1+2\cos^2\gamma}{2\sqrt{2\varepsilon+1}}\kappa^2\,K_2 + \frac{\cos\gamma}{2(2\varepsilon+1)}\kappa^3\,K_3\,, \tag{4}$$

$$T = \sqrt{2\varepsilon+1}\,\frac{\sin 2\gamma}{2}\,K_S - \varepsilon\sin\gamma\,\kappa\,K_1 - \sqrt{2\varepsilon+1}\,\frac{\sin 2\gamma}{2}\,\kappa^2\,K_2 - \frac{\sin\gamma}{2}\kappa^3\,K_3\,, \tag{5}$$

$$M = \varepsilon\sqrt{2\varepsilon+1}\,\cos\gamma\,K_1 + \left(\varepsilon + (2\varepsilon+1)\cos^2\gamma\right)\,\kappa\,K_2 + \frac{3}{2}\sqrt{2\varepsilon+1}\,\cos\gamma\,\kappa^2\,K_3 + \frac{1}{2}\,\kappa^3\,K_4\,. \tag{6}$$

In Eqs. (1-6), the mass, damping and stiffness coefficients are given by

$$m_i = \int_{\mathcal{S}_0}\rho y^i \mathrm{d}A\,,\quad c_i = \int_{\mathcal{S}_0} c y^i \mathrm{d}A\,,\quad K_i = \int_{\mathcal{S}_0}\mathcal{E}\,y^i\,\mathrm{d}A\,,\quad K_S = \int_{\mathcal{S}_0}\mathcal{G}\mathrm{d}A\,, \tag{7}$$

where ρ, c, $\mathcal{E}$ and $\mathcal{G}$ are mechanical parameters and $\mathcal{S}_0$ is the rigid cross section.
Since their introduction, Eqs. (1-3) have been analyzed in some depth [2, 3, 4], mainly through numerical investigations. On the contrary, the present paper, following [5, 6], is focused on analytical developments, based on the method of multiple scales [7]. In particular, to draw the frequency-response curves, the exact partial differential Eqs. (1-3) are analyzed around frequencies corresponding to certain natural bending modes.

Some preliminaries on multiple time scale equations of motion

We introduce three time scales and develop the time and time derivative operator respectively as $t = \tau_0 + \epsilon\tau_1 + \epsilon^2\tau_2$ and $(\cdot)_{,t} = (\cdot)_{,\tau_0} + \epsilon(\cdot)_{,\tau_1} + \epsilon^2(\cdot)_{,\tau_2}$, being $\epsilon \ll 1$ a book-keeping parameter, and assume that the unknowns u, v, and θ in Eqs. (1-3) are small of order ϵ at most and can be expanded, up to the 3rd order, as

$$w_i(x,t) = \epsilon W_{i1}(x;\tau_0,\tau_1,\tau_2) + \epsilon^2 W_{i2}(x;\tau_0,\tau_1,\tau_2) + \epsilon^3 W_{i3}(x;\tau_0,\tau_1,\tau_2)\,, \qquad i = 1,2,3 \tag{8}$$

where w_i are dummy functions such that $u = w_1$, $v = w_2$, $\theta = w_3$, and W_{ij} are unknown functions to be determined.
Based on appropriate choices of the geometric or mechanical properties of the beam, the loads, or even the reference frame, we can accept that some mechanical parameters are zero or negligible for some power of ϵ. In what follows, we assume that c_0 and K_3 are at most of order ϵ^2; m_1, c_1, c_2, K_1 and q_2 are at most ϵ^3; q_1 and q_3 are at most ϵ^4.
We also assume that the loads are periodic functions as

$$q_i(t) = P_i \cos(\Omega_i t) = P_i \cos(\omega_i\tau_0 + \sigma_i\tau_2)\,, \quad i = 1,2,3 \tag{9}$$

i.e., the excitation frequencies are chosen to be close to the corresponding natural frequencies ω_i by means of detuning parameters σ_i, which are assumed to be of order ϵ^2.
Substituting Eq. (8) and corresponding derivatives and Eq. (9) in Eqs. (1-3), taking into account the chosen orders of magnitude of all the coefficients, and collecting terms of like powers of ϵ, we obtain, after some algebra, a perturbation hierarchy as a set of linear differential equations

$$m_0\, W_{1j,\tau_0\tau_0} - K_0\, W_{1j,xx} = \mathcal{P}_{1j}\,, \tag{10}$$

$$m_0\, W_{ij,\tau_0\tau_0} + K_S^{-1}\left(m_0\, m_2\, W_{ij,\tau_0\tau_0} - (m_0\, K_2 + m_2\, K_S)\, W_{ij,xx}\right)_{,\tau_0\tau_0} + K_2\, W_{ij,xxxx} = \mathcal{P}_{ij}\,, \qquad i = 2,3 \tag{11}$$

with the index j, that is the power of ϵ, spanning from 1 to 3.
Notice that terms $\mathcal{P}_{i1}$ vanish, $\mathcal{P}_{i2}$ depend on W_{i1}, and $\mathcal{P}_{i3}$ depend on W_{i1} and W_{i2}. Moreover, because of our assumptions on the orders of magnitude of $q_i(t)$, $\mathcal{P}_{23}$ is the first term in which an external load, namely $q_2(t)$, appears.
Although we consider only three time scales and neglect terms beyond the third order of ϵ in the expansions of unknowns, in multiple-scale approaches any number of scales and any order of ϵ can be considered. Indeed, the corresponding perturbation hierarchy is, at least in principle, simple to manage: starting by solving the first order problem, the right-hand side of second order problem can be computed; then, once second order problem is solved, the third order right-hand side is got, and so on. At any step proper solvability conditions must be met in order to avoid that resonant secular terms appear in the solution. However, typically, algebraic complexity allows to calculate a few terms of the expansion and convergence properties of the expansion remain unknown [8]. We should also point out that the asymptotic expansion introduced in Eqs. (8) for the unknown functions $w_i(x,t)$ gives an accurate representation of them for ϵ approaching zero.
After this brief introduction to the approach, the next step of this study will be to detail about frequency-response curves and time histories, with the aim to compare the behavior of the model we are dealing with to those of other nonlinear beam models available in the scientific literature [9, 10, 11].

Conclusions

The present contribution, which is part of an ongoing research focused on the analysis of a geometrically exact beam model with nonlinear constitutive relationships, reports on preliminaries of a multiple time scale expansion of the equations of motion. The next step, which is still in progress, will focus on approximate time histories, frequency-response curves, and comparison with other nonlinear beam models available in the scientific literature and with results obtained through numerical approaches as finite element or finite difference methods.

References

[1] Babilio E., Lenci S. (2017) On the notion of curvature and its mechanical meaning in a geometrically exact plane beam theory. *Int J Mech Sci*, **128-129**:277–293.

[2] Babilio E., Lenci S. (2017) Consequences of different definitions of bending curvature on nonlinear dynamics of beams. *Procedia Eng*, **199**:1411–1416.

[3] Babilio E., Lenci S. (2018) A simple total-lagrangian finite-element formulation for nonlinear behavior of planar beams. *Proc ASME Des Eng Tech Conf.* DETC2018-85622. Quebec City, Quebec, Canada. August 26–29, 2018.

[4] Babilio E., Lenci S. (2020) On a geometrically exact beam model and its finite element approximation, I. Kovacic, S. Lenci, eds. *IUTAM Symposium on Exploiting Nonlinear Dynamics for Engineering Systems*, IUTAM Bookseries, Springer, **37**, 59–69.

[5] Kloda L., Lenci S., Warminski J. (2018) Nonlinear dynamics of a planar beam-spring system: analytical and numerical approaches. *Nonlinear Dyn*, **94**(3):1721–1738.

[6] Babilio E., Lenci S., Sacco E. (2021) Multiple-scale analysis of a geometrically exact beam model, *25th International Congress of Theoretical and Applied Mechanics*, August 22–27, 2021. Abstract Book, 303–304.

[7] Nayfeh A.H. (2000) *Perturbation methods*. Physics textbook. John Wiley & Sons.

[8] Jakobsen P. (2019) *Topics in applied mathematics and nonlinear waves*. arXiv:1904.07702v1, pages 1–321.

[9] Reissner E. (1972) On one-dimensional finite-strain beam theory: the plane problem. *Z Angew Math Phys*, **23**(5):795–804.

[10] Simo J.C. (1985) A finite strain beam formulation. The three-dimensional dynamic problem. Part I. *Comput Method Appl M*, **49**(1):55–70.

[11] Irschik H., Gerstmayr J. (2011) A continuum-mechanics interpretation of Reissner's non-linear shear-deformable beam theory. *Math Comp Model Dyn*, **17**(1):19–29.

Non-linear dynamics of straight beams with (or without) shape imperfections and very shallow arcs: similarities and differences controlled by boundary conditions

Vitalii Pauls [*], Stefano Lenci [*] and Sergey Sorokin [**]
[*]*Polytechnic University of Marche, Ancona, Italy*
[**]*Aalborg University, Denmark*

Summary. The free and forced vibration problems for slightly curved axially restrained beams are solved in two alternative formulations. The first one is the classical nonlinear model, which accounts for the so-called 'stretching-due-to-bending' effect. In its framework, a slightly curved beam is considered as the straight one with an initial shape imperfection. The second formulation is the standard model of a planar curved beam. Each model describes the interaction between transverse and longitudinal motion of a beam, but in profoundly different manner. Comparison of predictions of these models for small shape imperfections and various boundary conditions is the goal of this paper.

Introduction

Nonlinear vibrations of ideally straight axially restrained hinged beams have been studied in numerous publications with [1-3] being the most recent ones. The canonical model of such a beam implies that an interaction between flexural and axial vibrations occurs due to the essentially non-linear 'stretching-due-to-bending' effect. This coupling mechanism is preserved when a beam acquires arbitrarily small initial shape imperfections. However, vibrations of a slightly curved axially restrained beam can conveniently be modelled within the standard linear theory of planar curved beams, which captures an interaction between flexural and axial vibrations regardless the type of boundary conditions. Furthermore, the nonlinear theory of dynamics of planar curved beams is also well established [4-5]. In this framework, an obvious research question arises:

- What are the validity ranges of the non-linear theory of ideally straight axially restrained beams, the linear theory of curved beams and the non-linear theory of curved beams with respect to the amplitude of initial shape imperfection (initial curvature), vibration amplitudes and boundary conditions?

An attempt to find answer to this question constitutes the subject of the work in progress. Its first preliminary results are presented in what follows.

The model of a curved beam

Our point of departure is the nonlinear model of a circular cylindrical shell [4] adjusted to the plane strain state of deformation. Then two components of displacement (u, w) are considered and the coordinate **s** along the curved axis of a shell's segment (which is now reduced to a beam) is introduced, see Figure 1.

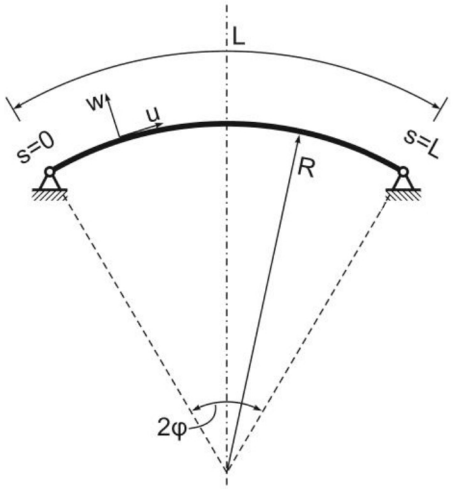

Figure 1: A curved beam with sliding support and force applied

The governing non-linear differential equations obtained by means of the Hamilton's principle are ($\beta \equiv \frac{L}{R}$):

$$-\frac{\rho L^2\left(1-\nu^2\right)}{E}\ddot{u}+u''+\beta w'+\left(w'-\beta u\right)\left(w''-\beta u'\right)+\frac{h^2}{12L^2}\beta\left(\beta u''-w'''\right)$$
$$+\left[u'+\beta w+\frac{1}{2}\left(w'-\beta u\right)^2\right]\left(w'-\beta u\right)\beta=0$$
$$-\frac{\rho L^2\left(1-\nu^2\right)}{E}\ddot{w}-\left[u'+\beta w+\frac{1}{2}\left(w'-\beta u\right)^2\right]\beta+\frac{h^2}{12L^2}\left(\beta u'''-w''''\right)$$
$$+\left[u''+\beta w'+\left(w'-\beta u\right)\left(w''-\beta u'\right)\right]\left(w'-\beta u\right)+\left[u'+\beta w+\frac{1}{2}\left(w'-\beta u\right)^2\right]\left(w''-\beta u'\right)=0$$

The boundary conditions at *s*=0 are $u=w=\beta u'-w''=0$, while the boundary conditions at *s*=1 for the case illustrated in Figure 1 are

$$u'+\beta w+\frac{1}{2}\left(w'-\beta u\right)^2+\frac{h^2}{12L^2}\left(\beta u'-w''\right)\beta+\frac{p\left(1-\nu^2\right)}{Eh}\cos\left(\frac{L}{2R}\right)=0$$
$$\left[u'+\beta w+\frac{1}{2}\left(w'-\beta u\right)^2\right]\left(w'-\beta u\right)+\frac{h^2}{12L^2}\left(\beta u''-w'''\right)+\frac{p\left(1-\nu^2\right)}{Eh}\sin\left(\frac{L}{2R}\right)=0$$
$$\beta u'-w''=0$$

Alternative formulations of boundary conditions at *s*=1 (e.g., sliding support in an absence of the force or full constrain of displacements) are obvious. Likewise, the limit cases of a linear curved beam [4-5] and a nonlinear ideally straight beam [1-3] are readily available from the proposed formulation.

The solution methods and the eigenfrequency analysis

The exact solution of the linear problem of free/forced vibrations of a curved beam is easily obtained regardless the type of boundary conditions. To solve a non-linear problem of vibrations of a curved beam, the canonical method of multiple scales adjusted for the system of partial differential equations is used. The reference solutions of a nonlinear problem of vibrations of an axially restrained beam by the same method are presented in the references [1-3].

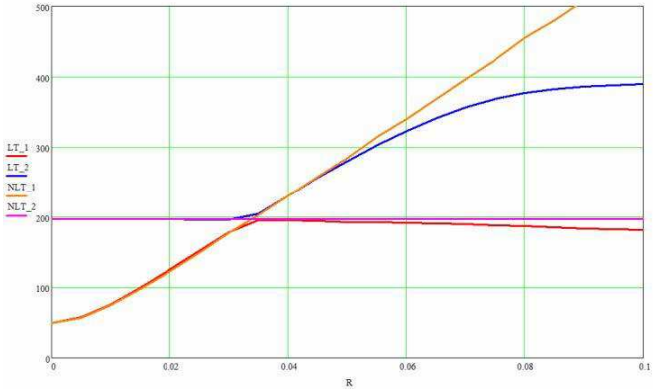

Figure 2: The first and the second eigenfrequency of a curved beam versus curvature parameter

The results of eigenfrequency analysis of an axially restrained hinged beam are presented in Figure 2. The appreciable (exceeding 5%) differences correspond to the amplitude of shape imperfection around 0.06L.

Conclusions

The results obtained so far suggest that the simple linear theory of curved axially restrained beams agrees with the nonlinear theory of straight beams with shape imperfections in a broad range of curvature parameter. Nonlinear vibrations of a curved beam still require careful asymptotic analysis, especially in the case of a vanishingly small curvature.

References

[1] Lenci S, Rega G. (2016) Axial-transversal coupling in the free nonlinear vibrations of Timo- shenko beams with arbitrary slenderness and axial boundary conditions. *Proc R Soc A 472:20160057*
[2] Lenci S., Clementi F. (2018) Axial-transversal coupling in the nonlinear dynamics of a beam with inclined roller *Int. J. Mech. Sci. 144, 490-501*
[3] Lenci S. (2018) Isochronous beams by an inclined roller support *Trans. ASME J. App. Mech. 85 091008*
[4] Pellicano F. (2007) Vibrations of circular cylindrical shells: Theory and experiments *J. Sound and Vibration 303 154-170*
[5] Lacarbonara W. (2013) Nonlinear structural mechanics: theory, dynamical phenomena and modeling Springer NY

Low Voltage Operation of Vilnius Chaotic Oscillator

Dmitrijs Pikulins[*], Sergejs Tjukovs[*], Iheanacho Chukwuma Victor[*],Aleksandrs Ipatovs[*], Juris Grizans[*]

[*]*Institute of Radioelectronics, Riga Technical University, Riga, Latvia*

Summary. The paper is dedicated to the numerical study of nonlinear oscillations exhibited by the Vilnius chaotic generator. The need for practical applicability of the mentioned generator in chaotic communications defined the necessity to study the low-power operation of the circuit, designed initially to be powered from high voltage sources. The bifurcation map and corresponding one-parameter diagrams reveal complex nonlinear dynamics and regions of robust chaotic oscillations.

1. Introduction

The use of chaotic signals generated by various electronic systems has been growing for the last several decades, and it is considered a major candidate for future technologies. Chaotic oscillators have found applications in communications [1]-[3], random number generators [4], chaotic computing [5] and other fields. The main requirements for the practical application of a chaotic oscillator are the circuit's simplicity, the variety of different chaotic modes, and robustness.

The rapid expansion of the Internet of Things (IoT) creates new challenges to electronic circuit design. Numerous applications like environmental sensing and healthcare monitoring impose the need for long-term autonomous operation of electronic modules. In [6], the authors conclude that batteries are the most promising energy source for IoT applications, particularly wireless sensor networks. Energy harvesting techniques suffer from insufficient power levels and often are unpredictable and thus insecure. This, in turn, implies DC voltage levels available to power electronic circuits being in the range of several volts.

Furthermore, industry trends and the natural need for miniaturization of sensor nodes create new challenges in power circuit design. The battery life may determine the useful lifespan of the device in cases where the batteries are not replaceable for any number of reasons. The requirement of long autonomous operation of IoT devices dictates additional restrictions on chaotic generators, including energy efficiency and low power operation.

The current study is dedicated to a comprehensive analysis of the low-voltage operation of the Vilnius chaos oscillator. First presented in 2004 [7], this circuit has been intended to operate from a 20 V source. However, several attempts have been made to adapt this oscillator to IoT applications [3], [8]. Thus, there is a need to study the nonlinear dynamics of the system operated at much lower voltages than it originally was supposed to.

This paper is organized as follows. The second section is devoted to the description of the schematic and analytical model of the Vilnius oscillator. The third section presents the nonlinear analysis of the system dynamics under study at low voltage operation. The last section is devoted to the overall conclusions and suggestions on the applicability of this type of chaotic oscillator.

2. Vilnius Oscillator Schematic and Model

The schematic of the Vilnius chaotic oscillator is depicted in Fig.1. The circuit is easy to implement and modify, as it includes no unique components, just the off-the-shelf operation amplifier, diode, capacitors, inductors and resistors.

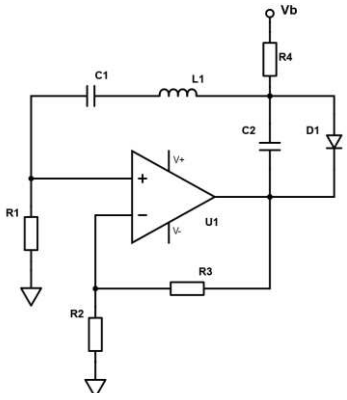

Figure 1: The schematic diagram of the Vilnius oscillator

This oscillator exhibits complex behaviour under specific component parameters despite being relatively simple. The frequency of the waveforms observed in the circuit is determined by reactive components *C1*, *L1*, and *C2*. Thus, it is possible to adapt the scheme for the frequency range of interest. Diode *D1* is the mandatory nonlinear element needed for the chaotic oscillator. It can be a general purpose silicon diode like 1N4148 or Schottky diode. Also, no special

requirements apply for the operational amplifier. A reader can use, for example, an LTspice computer simulation program to get quick insight into the operation of the circuit and to observe typical waveforms. However, even such a brief study reveals that the number of parameters that affect the system's dynamics is too large to adopt a trial and error approach when the robust chaos is of interest. That is why the comprehensive study of nonlinear dynamics using bifurcation diagrams must be performed to identify the regions of chaotic behaviour for further practical implementation of the Vilnius oscillator.

In this study, a system of equations initially developed in [1] is used to describe the dynamics of the system:

$$\frac{dx}{dt} = y \tag{1}$$

$$\frac{dy}{dt} = ay - x - z \tag{2}$$

$$\varepsilon\frac{dz}{dt} = b + y - c(e^z - 1), \tag{3}$$

where $x = \frac{V_{C1}\cdot q}{k_B\cdot T}$; $y = \frac{I_{L1}\cdot q\cdot\sqrt{\frac{L}{C_1}}}{k_B\cdot T}$; $z = \frac{V_{C2}\cdot q}{k_B\cdot T}$; $a = \frac{(k-1)\cdot R_1}{\sqrt{\frac{L}{C_1}}}$; $b = \frac{I_{R4}\cdot q\sqrt{\frac{L}{C_1}}}{k_B\cdot T}$; $c = \frac{I_S\cdot q\cdot\sqrt{\frac{L}{C_1}}}{k_B\cdot T}$; $\varepsilon = \frac{C_2}{C_1}$; $k = 1 + \frac{R_2}{R_1}$; $I_{R4} = \frac{V_b}{R4}$; k_B is Boltzmann's constant; T is the temperature in Kelvins.

The system's parameters of interest are *a*, *b* and *ε*, which could be adjusted by input voltage, variable capacitor C_2 and variable resistors R_1, R_2, R_3, and R_4.

The study of the nonlinear dynamics of the Vilnius oscillator will be provided based on one and two-parameter bifurcation diagrams that allow estimation of the system's mode of operation for various combinations of component values. However, this approach requires obtaining the discrete-time model of the original oscillator. The models could be constructed by application of the Poincare map. In the case of the Vilnius oscillator, *y=0* is selected as the Poincare plane. Thus, the trajectories crossing this plane from one side will define the sampled model and provide the required information on the periodicity of the regimes under study (see Fig.2.).

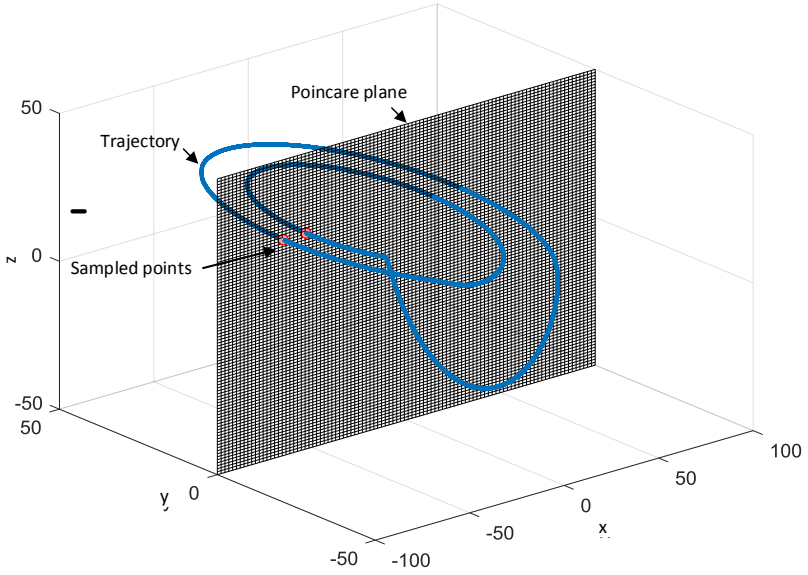

Figure 2. The introduced Poincare plane for obtaining a sampled model of the Vilnius oscillator

All the calculations are made utilizing specially prepared MATLAB scripts, including the solution of the equations with the Runge-Kutta (4,5) method, implemented in the *ode45* function. As the construction of bifurcation diagrams in the wide range of system parameters could be a time-consuming task, the Parallel Computing Toolbox functionality has been intensively utilized to efficiently distribute the computation tasks between all available physical cores of the computer. The results of calculations and the analysis of the obtained diagrams are provided in the next section.

2. Nonlinear Dynamics at Low Voltage Operation

The main goal of the current research is to study the dynamics of the Vilnius oscillator, operating in the voltage range viable for practical applications in wireless sensor networks. Thus, one of the parameters under study is *b*, which is directly connected to the current I_{R4} and voltage V_b. The task is to identify the lowest border of supply voltage at which the system could exhibit robust chaotic oscillations and study the qualitative changes in the dynamics as *b* is varied.

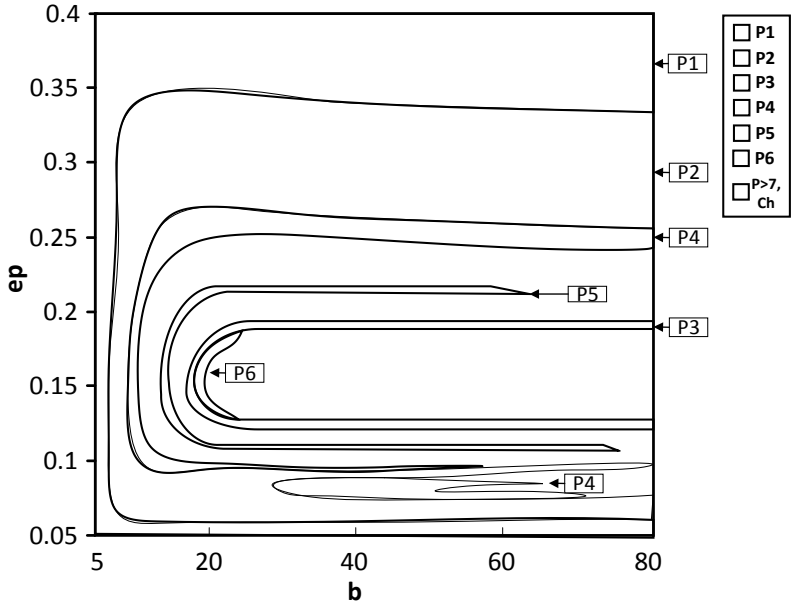

Figure 3: Two parameter bifurcation diagram for a=0.3; b=5-89; ε=0.05-0.4.

The subsequent study of the nonlinear dynamics of the oscillator is based on the construction of a two-parameter bifurcation diagram of the system (bifurcation map) and analysis of the corresponding one-parameter bifurcation diagrams as the cross-sections of the map.

The second parameter, chosen to be varied for the bifurcation map, is ε, physically dependent on the capacitor C_1 and C_2 values. The obtained map for ε=0.05-0.4 and b=5-80 is shown in Fig. 3. Periodic operation modes are depicted up to period-7, and other high-periodic regimes and chaos are shown as white regions.

The bifurcation map demonstrates that for low values of b (defined by input voltage), the system's dynamics are mainly periodic- exhibiting period-1 to period-4 oscillations for all values of ε. From a practical point of view, the system could not be used as the generator of chaotic oscillations for extremely low voltages (defined by b<12). This is also illustrated in Fig.4. The brute-force bifurcation diagram shows the clear transition from P1 to P4 and back to P1 through subsequent period doublings without any signs of chaotic oscillations in the main branches. No coexisting chaotic attractors could be detected either.

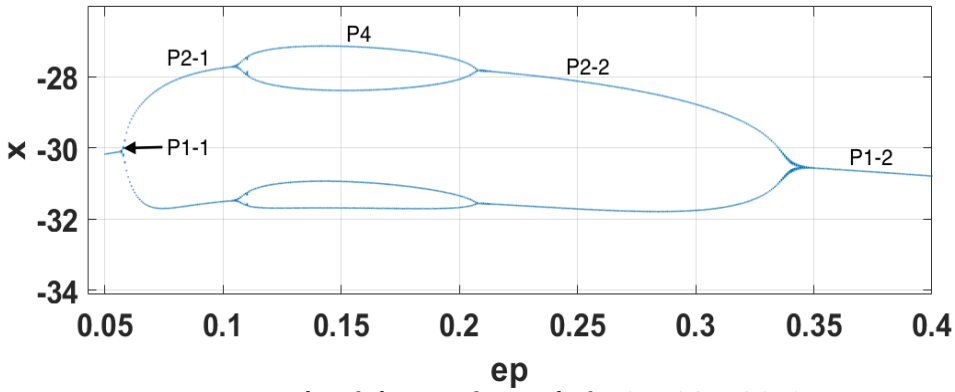

Figure 4: Brute-force bifurcation diagram for b=10; a=0.3; ε=0.05-0.4.

However, there is a definite border (b>12), where the system becomes chaotic for a relatively wide range of ε values. There could be intermittent chaotic dynamics (with various periodic windows) or robust chaos without interrupting periodic modes. Fig. 4 shows classical period-doubling routes to chaos enclosing several intervals of robust chaotic oscillations (RCh1-RCh4). It can be inferred that setting system parameters within the ranges indicated - ε=0.1-0.23 - should guarantee stable chaotic oscillations without the issue of transitioning to some periodic mode due to external noise or fluctuations in the component's values.

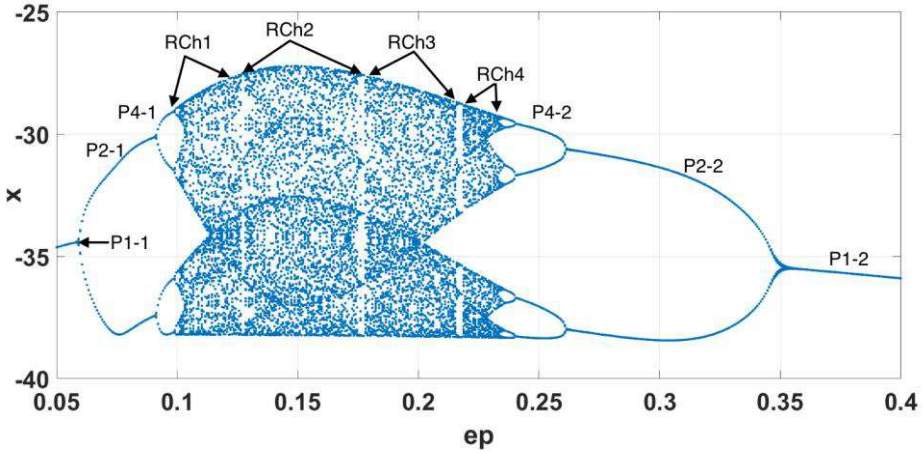

Figure 5: Brute-force bifurcation diagram for b=15; a=0.3; ε=0.05-0.4.

The system's behaviour remains similar for higher values of b, as shown in Fig. 6. However, the amplitude of V_{C1} (variable x) increases. Compared to the previous diagram, the system exhibits a non-smooth transition to chaos from the left side. This phenomenon could be explained by the presence of a diode in the circuit, defining the non-smooth switchings as the voltage rises and a certain threshold is reached. It has been noticed that the systems with non-smooth bifurcations could exhibit robust chaotic oscillations. However, in this case, we still observe some periodic windows in the chaotic regions and the transition to stable periodic regimes as ε reaches 0.24.

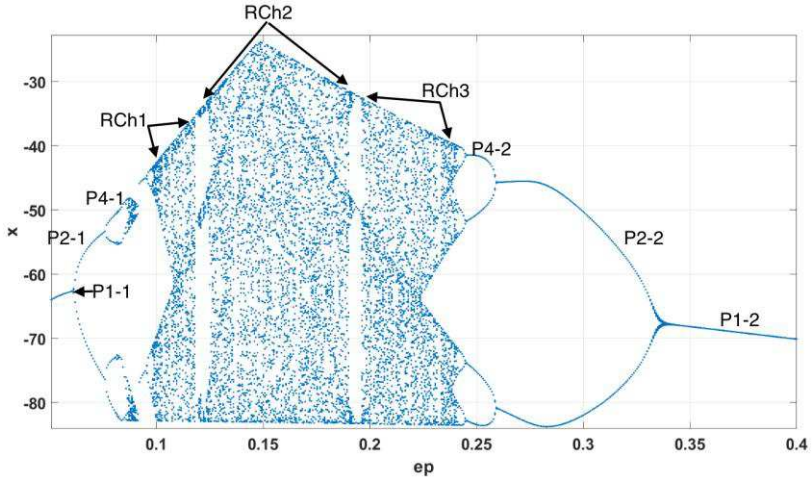

Figure 6: Brute-force bifurcation diagram for b=50; a=0.3; ε=0.05-0.4.

The second part of the investigation is dedicated to constructing the diagrams for fixed values of ε and varying the parameter b. For ε < 0.12, a wide diversity of dynamical patterns could be observed, as b is varied. Fig. 7. shows period doublings, intermittent chaos and wide periodic windows. These regimes could not be relevant for practical applications, as any slight supply voltage variations could cause unpredicted transitions between different modes, compromising the whole system's security. Chaotic attractors observed in the corresponding regions (see Fig.7- Ch) are not dense enough, indicating the insufficient level of diversity required by practical communication systems.

However, the further increase in parameter ε leads to the formation of several robust chaotic regions (see Rch1 and RCh2 in Fig.8.) with acceptable characteristics and durability to parameter changes. But some periodic windows are still present in the defined parameter range (see, e.g. P3 window in Fig.8.). As we are interested in the low-voltage operation of the system, the region of b=12-28 is the most appropriate for the proposed applications.

Setting the ε=0.15 in the middle of the predicted chaotic region in the bifurcation map (see Fig.3), it is possible to obtain the diagram where all periodic windows shrink, and the continuous robust chaotic area is formed. This is demonstrated in Fig.9.

As it could be deduced from Fig.3, the further increase of ε leads to the deterioration of chaotic dynamics and diagrams, similar to those shown in Fig.7 and Fig.8 could be obtained.

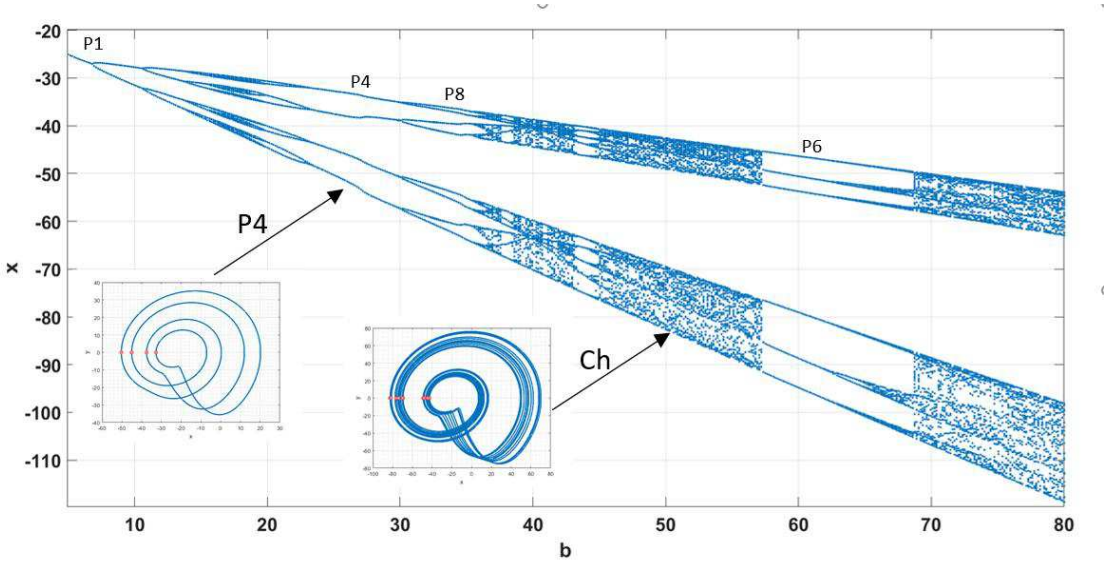

Figure 7: Brute-force bifurcation diagram for a=0.3; ε=0.1; *b*=5-80

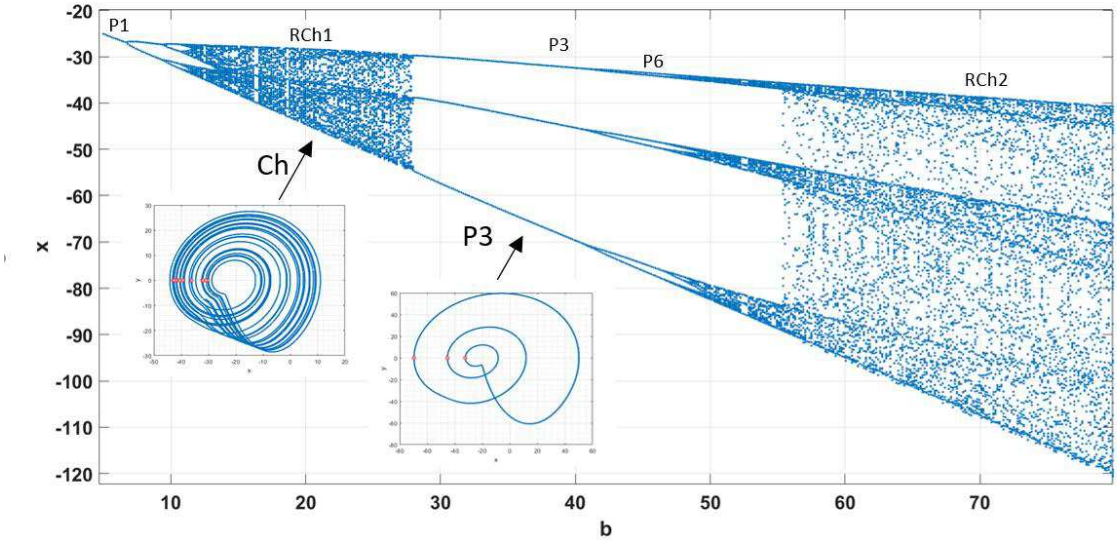

Figure 8: Brute-force bifurcation diagram for a=0.3; ε=0.12; *b*=5-80

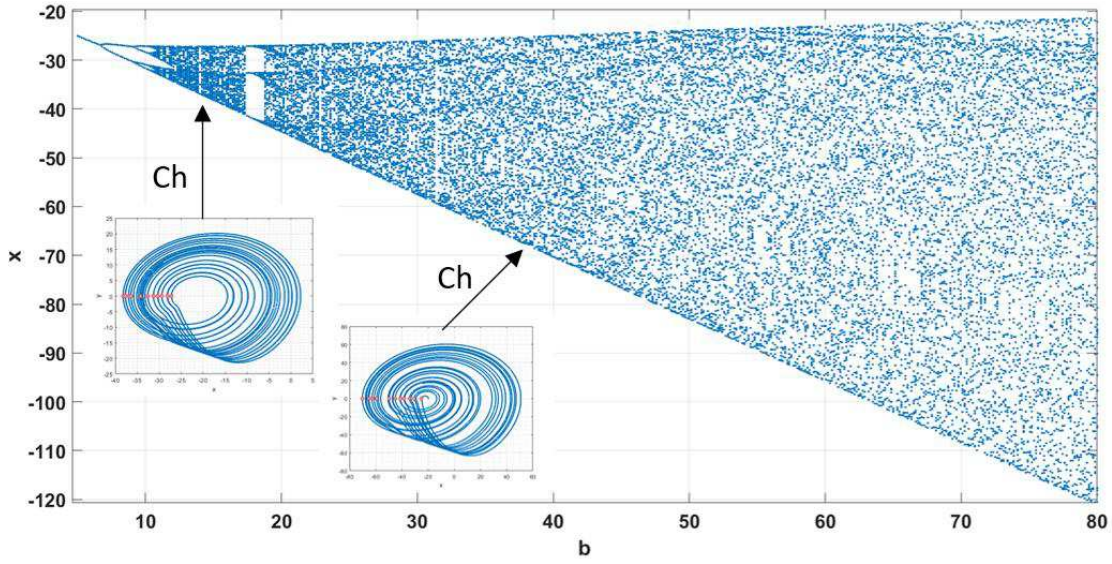

Figure 9: Brute-force bifurcation diagram for a=0.3; ε=0.15; *b*=5-80

3. Conclusions

One of the key parameters defining the applicability of the chaotic oscillators to secure communication systems is energy efficiency (possibility to operate in low-power modes) and robustness (insusceptibility to slight parameter variations and noise). Thus, investigating the dependence of nonlinear dynamics of these kinds of generators on the operation voltage is crucial for practical solutions.

The paper demonstrated the numerical study of possible chaotization scenarios and various nonlinear phenomena observed in the Vilnius chaotic oscillator as system parameters vary. It has been shown that the construction of the bifurcation map allows for the convenient identification of the most appropriate parameter ranges to be used for obtaining robust chaotic modes of operation. The main conclusion is that the Vilnius oscillator could robustly generate chaotic signals required in secure communications, even in low-voltage modes of operation. However, the other systems parameters (e.g. ε) should be fine-tuned to exclude transitions to any periodic regime.

Further study could contain the laboratory experiments allowing the verification of numerical simulations and practical estimation of energy efficiency of the proposed robust chaotic regimes.

Acknowledgement

This work has been supported by the European Regional Development Fund within the Activity 1.1.1.2 "Post-doctoral Research Aid" of the Specific Aid Objective 1.1.1 "To increase the research and innovative capacity of scientific institutions of Latvia and the ability to attract external financing, investing in human resources and infrastructure" of the Operational Programme "Growth and Employment" (No.1.1.1.2/VIAA/4/20/651).

References

[1] Litvinenko, A. and Aboltins, A., 2015. Chaos based linear precoding for OFDM. RTUWO 2015, pp. 13-17.

[2] Litvinenko, A. and Bekeris, E., 2012. Probability distribution of multiple-access interference in chaotic spreading codes based on DS-CDMA communication system. Elektronika Ir Elektrotechnika, 123(7), pp. 87-90.

[3] Babajans, R., Cirjulina, D., Grizans, J., Aboltins, A., Pikulins, D., Zeltins, M. and Litvinenko, A., 2021. Impact of the Chaotic Synchronization's Stability on the Performance of QCPSK Communication System. Electronics, 10(6), 640.

[4] Dantas, W.G., Rodrigues, L.R., Ujevic, S. and Gusso, A., 2020. Using nanoresonators with robust chaos as hardware random number generators. Chaos 30, 043126 (2020).

[5] B. Majumder, S. Hasan, M. Uddin and G. S. Rose, 2018. Chaos computing for mitigating side channel attack. 2018 IEEE International Symposium on Hardware Oriented Security and Trust (HOST), pp. 143-146.

[6] Raj, Abhi, and Dan Steingart. "Power sources for the internet of things." Journal of the Electrochemical Society 165, no. 8 (2018): B3130.

[7] Tamaševičius, A., Mykolaitis, G., Pyragas, V. and Pyragas, K., 2004. A simple chaotic oscillator for educational purposes. European Journal of Physics, 26(1), p.61.

[8] Čirjuļina, D., Pikulins, D., Babajans, R., Anstrangs, D.D., Victor, I.C. and Litvinenko, A., 2020, October. Experimental Study of the Impact of Component Nominal Deviations on the Stability of Vilnius Chaotic Oscillator. In 2020 IEEE Microwave Theory and Techniques in Wireless Communications (MTTW) (Vol. 1, pp. 231-236). IEEE.

Nonlinearity in estimating bolt tension from vibrations

Marie Brøns[*] and Jon Juel Thomsen[*]
[*]*Technical University of Denmark*

Summary. Many technical installations are held together by critical bolted joints. A critical bolted joint can have many appearances, from bolted flanges with many bolts to smaller lap-joints with only a few bolts. *Critical* imply that failure is not accepted, as it would lead to dangerous situations and most likely very costly repairs. Such joints are found in wind turbines, pressurized pipelines, large machinery etc. To ensure safe operation, regular checking and documentation of bolt tension is required, which is both costly and time consuming, and traditional tightening techniques are not very accurate. Recent work has shown potential in estimating bolt tension by using vibrations actively. e.g. by analyzing the vibrational response in a bolt after a hammer impact. Tests of this have been carried out with good results for setups with a single bolt. However, most often a bolted joint consists of multiple bolts holding at least two parts together. The more parts and bolts, the more sources to nonlinear effects from frictional contacts and potential vibrational coupling. In this work, we present the current status of the method with new results from a multi-bolt setup, and raise the question of which potential nonlinear effects need to be considered to apply the method more generally for multi-bolt joints.

Introduction

Traditional tightening methods include torque wrenches and hydraulic tensioners [1]. These cannot estimate the tension, so checking is done by retightening. This can lead to overtightening, which can in turn introduce failure. Furthermore, it is time consuming to retighten all bolts, especially if the retightening revealed that only a few bolts were in fact loose. Newer technologies include bolts with incorporated strain gauge sensors, which is more expensive than traditional bolts and potentially fragile, and ultrasonic transducers [2], which measure bolt elongation. These new advances show that it is definitely of interest to improve both speed, cost and accuracy in estimation of bolt tension. Vibrations could be advantageous to use, as control can then be done without employing heavy equipment and there are direct correlations between tension and bending vibrations. The challenge is to ensure that other mechanism that influence the vibrational response have been investigated, so that a vibrational response of any bolt, in any structure, can be analyzed correctly, thus permitting a robust estimation of tension. To get to that point possible nonlinear effects must be understood.

Bolt tightness indicators based on bending vibrations

A bolt can be considered a beam with rotational and translational linear boundary stiffness springs [3], whose stiffness may increase nonlinearly with tension [3]. As a bolt is tightened the boundary stiffness increases, as well as the tension. In [4] demonstrated that a large number of nonlinear boundary micro springs can effectively behave as a linear spring.
Firstly, a bolt can indeed bend as a beam. This is experimentally investigated in [5] by analyzing measurements from a scanning laser Doppler vibrometer and obtaining actual mode shapes. Furthermore, experimental results for a single bolt show that it is possible to get reproducible results of the first and second transverse natural frequency, increasing first strongly with tension and then linearly, as shows in Figure 1(a) from the small color markers [3,6]. A nonlinear stiffness model adapted from [3] can be fitted to the measurements (dashed lines in Figure 1(a)). The corresponding damping ratio decreases with tension, strongly for low tension, and weakly for high tension [3,6]. Combining the information coming from the bolt tightness indicators can provide an estimate of bolt tension [6,7].

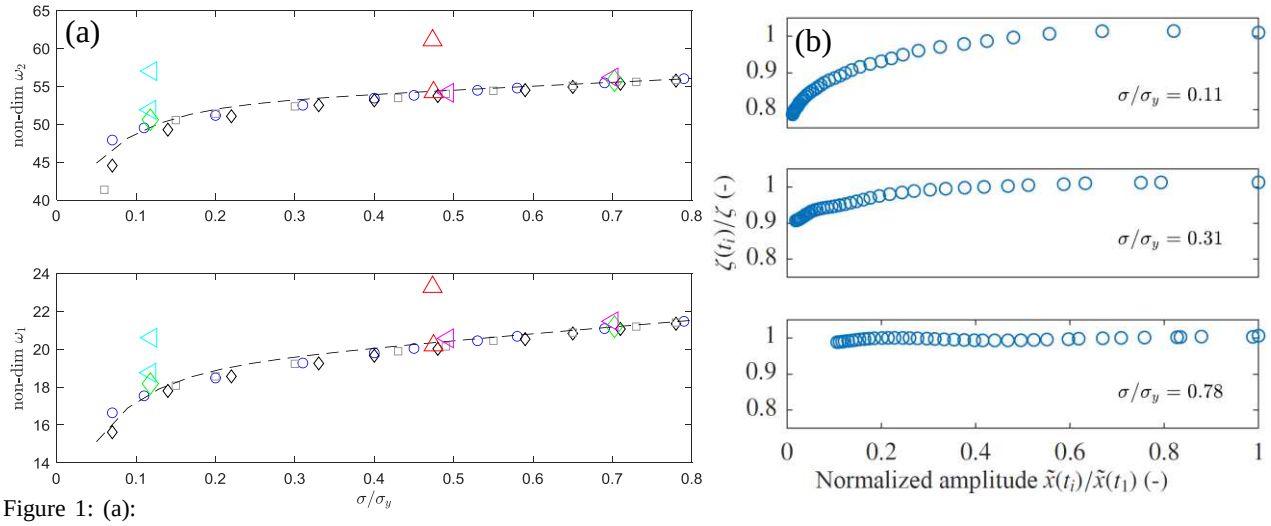

Figure 1: (a): Transverse natural frequency as function of bolt tension: small markers: single bolt experimental data; everything has been taken apart between each color. Large markers: data from a two-bolt setup. Dashed line: theoretical tension-stiffness model adapted from [2]. (b) Time-dependent damping ratio as function of normalized acceleration amplitude.

Nonlinear effects and modal coupling between bolts

Investigations of vibration amplitude dependencies (thus nonlinearity) of the above mentioned bolt tightness indicators, damping ratios and frequency, have revealed to be of significance only under certain circumstances [6]. For practically relevant ranges of excitation level, the transverse natural frequency of a single bolt in a solid cylinder is effectively independent of vibration amplitude [6]. However, the linear damping ratio is not. Figure 1(b) shows the amplitude dependency of the damping ratio (of the first natural frequency) for three levels of tension. It drops for lower tension and smaller amplitude.

Another issue is coupling of vibrations between different planes. A bolt has a symmetric cross section, so there is a possible coupling between the two transverse directions, which appears to be driven by linearly acting imperfection [8]. Another coupling is the nonlinear coupling between transverse and longitudinal vibrations, which can occur in tensioned beams [9]. This nonlinear effect, in combination with imperfections, can allow for exciting transverse vibrations from a longitudinal impact [10].

New experimental results reveal that coupling between two bolts with almost identical tension and boundary stiffness appear to behave as a single coupled system, with co-and anti-phase modes [11]. However, this is only seen for cases where the tension is almost identical, for two bolts with different tension, it appears that interpreting the two bolts as separate entities with separate vibrational response is adequate. This may be the case due to an unknown nonlinear effect: A 1D-beam model of two beams coupled with springs will predict that the anti-phase mode has a higher frequency than the co-phase mode, as pulling in opposite directions will activate the coupling spring and increase boundary stiffness. Experiments show very similar behaviour. Figure 1(a) show also large color markers in pairs; these are measurements from a setup with two bolts and the frequencies are extracted from accelerometer measurements of one of the bolts. For cases with equal tension, there is a jump in frequency, both for first and second mode. However, for two bolts with even slightly different tension, the results are as for two single uncoupled bolts. To be able to fit a 1D-beam model to the measurements of all the cases, it is necessary to change the value of the coupling spring, leading to the question if this can be better explained as a nonlinear vibrational coupling between tension and bending. To investigate this we will introduce a nonlinear coupling spring and compare the results to the linear model.

Conclusions

The first steps in estimation of tension by vibrations have been taken. It is possible to measure natural frequencies and damping ratios in a single bolt and use these as bolt tension indicators. Nonlinearity has been investigated, and shows to be influential only under certain conditions. Tests with multiple bolts show many similarities with results of a single bolt, though under certain conditions coupling can occur, and that coupling can potentially best be modeled as nonlinear. This will be investigated further and updated results will be presented at the conference.

Acknowledgement This work is financially supported by the Danish Council for Independent Research, grant DFF-6111-00385.

References

[1] Bickford, J. H. (2007). *Introduction to the Design and Behavior of Bolted Joints - Non-Gasketed Joints* (Fourth Ed.). CRC Press.
[2] Srinivasan L. (2006) Measurement of Stress in Bolts using Resonant Ultrasound Spectroscopy. MSc thesis, Durham University.
[3] Sah, S. M., Thomsen, J. J., Brøns, M., Fidlin, A., & Tcherniak, D. (2018). Estimating bolt tightness using transverse natural frequencies. *Journal of Sound and Vibration*, 431, 137–149. https://doi.org/10.1016/j.jsv.2018.05.040
[4] Sah, S. M., Thomsen, J. J., and Fidlin, A., 'Estimating bolt tightness from measured vibrations: Effective linearity of nonlinear boundary stiffness', in *Proceedings of the First International Nonlinear Dynamics Conference (NODYCON 2019)*, Feb. 17-20, 2019, Rome, 2.pp.
[5] Brøns, M., Thomsen, J. J., Fidlin, A., Tcherniak, D., Sah, S. M., 'Modal impact testing for estimating bolted joint tightness', in *Proceedings of the International Conference on Noise and Vibration Engineering (ISMA2018)*, Sep. 17-19, 2018, Leuven, Belgium, 8.pp.
[6] M.Brøns, J.J. Thomsen, S.M.Sah, D. Tcherniak, A.Fidlin, Estimating bolt tension from transient vibrations: transient features, nonlieanrity and signal processing, (submitted for journal publication)
[7] Brøns, M., Thomsen, J. J., Sah, S. M., Tcherniak, D., Fidlin, A., 'Analysis of transient vibrations for estimating bolted joint tightness', in *Proceedings of International Modal Analysis Conference - IMAC 2019 (IMAC XXXVII)*, January 28-31, Orlando Florida, USA, 1.pp.
[8] Sah, S. M, Thomsen, J. J., and Tcherniak, D., 'Linearly coupled transverse vibrations of tensioned bolts', (submitted for journal publication)
[9] Sorokin, V. S., Thomsen, J. J., and Brøns, M., 'Coupled longitudinal and transverse vibrations of tensioned Euler-Bernoulli beams with general boundary conditions', (submitted for journal publication)
[10] Sah, S. M., Thomsen, J. J., and Tcherniak, D., 'Transverse vibrations induced by longitudinal excitation in beams with geometrical and loading imperfections', *Journal of Sound and Vibration*, Vol. 444, pp. 152-160, 2019.
[11] Brøns, M., Plaugmann, A., Thomsen, J. J., Fidlin, A., 'Vibration-based bolt tension estimation for multi-bolt joints', in *Proceedings of International Modal Analysis Conference - IMAC 2020*, 4.pp.

On the reliability of contact models in Vibro-Impact Nonlinear Energy Sinks

Stefania Lo Feudo*, Stéphane Job*, M. Cavallo†,*, A. Fraddosio†, M.D. Piccioni†, A. Tafuni†,*
*Laboratoire QUARTZ (EA7393), ISAE-Supméca, 3 Rue Fernand Hainaut, 93400 Saint-Ouen-sur-Seine, France
†Polytechnic University of Bari, 4 Via Edoardo Orabona, 70126 Bari, Italy

Summary. The Vibro-Impact Nonlinear Energy Sinks (VI NES) is a highly nonlinear device employed for dissipating energy of a primary vibrating system. The simplest setup consists of a rigid container enclosing a spherical particle, which slips along the container and impacts against its walls under vibrations. This study assesses the sensibility of the VI NES dynamics to the impact velocity and the contact force estimation.

Introduction

Over the past few years, the use of vibro-impact dampers as vibration absorbers aroused the interest of the research community. Potentially, vibrational energy may be dissipated by the impacts that occur between a particle and one or more rigid barriers linked to a primary structure. Several configurations of vibro-impact systems were proposed, including single-sided VI NES [1, 2], symmetric single-sided VI NES [3] and double-sided VI NES [4, 5].
Refs. [6, 7] verified the efficiency of the VI NES for a primary system subjected to a seismic excitation. The greater part of the vibrational energy is dissipated at the beginning of the ground motion, when the primary structure is highly stressed. Notably, analytical and experimental studies revealed the existence of various dynamical regimes of the VI NES and their effect on the energy dissipation capability [8, 9].
This study focuses on the dynamics of a double-side Vibro-Impact Nonlinear Energy Sink (VI NES) shown in Fig. 1. Since the VI NES performs well in the vicinity of the 1:1 resonance, numerical simulations should be able to calculate as accurately as possible the rebound velocity and instant. We will show the effect of slight delays in the kinetic energy estimation and we will suggest some solutions to improve accuracy of the contact computation.

Instantaneous contact

In the framework of contact mechanics, instantaneous collisions between two rigid bodies lead to a change of direction and velocity depending on the value of the coefficient of restitution (COR) ϵ, which is defined as:

$$\epsilon = \frac{v_1(t_c) - v_2(t_c)}{v_2(0) - v_1(0)}, \tag{1}$$

with $0 \leq \epsilon \leq 1$. $\epsilon = 0$ for perfectly inelastic collisions and $\epsilon = 1$ for perfectly elastic collisions. The COR can be estimated by measuring experimentally the contact duration and the flight time of a bouncing ball [10]. $v_{1,2}(0)$ and $v_{1,2}(t_c)$ are the velocities of the particles before and after the collision, respectively, and t_c the contact duration. When the VI NES is coupled to a primary system for the passive vibration control, the contact duration t_c is generally very small with respect to the dominant time scale and the contact may be approximated as an instantaneous phenomenon. To solve numerically this problem, an event driven scheme may be used. At first, the simulation solves separately the free flight of the particle and the dynamics of the primary system. Then, when the particle collides with a barrier, the particle and primary system initial conditions (IC) are updated with new positions and velocities obtained from the law of conservation of momentum. The numerical integration scheme goes on until the end of the simulation.
Previous studies shown the close link between the VI NES damping capability and its dynamical regime, which ranges from periodic collisions to chaos. Hence, numerical resolution of this non-smooth numerical problem requires very high accuracy in the estimation of the impact velocities. Indeed, a small variation may lead to a huge change in the system

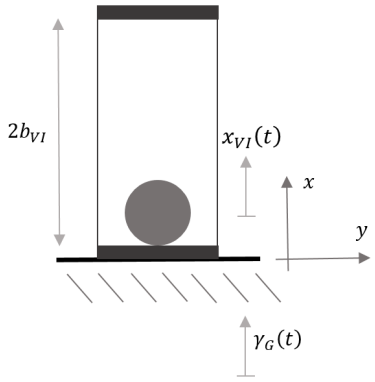

Figure 1: Schematic representation of a VI NES.

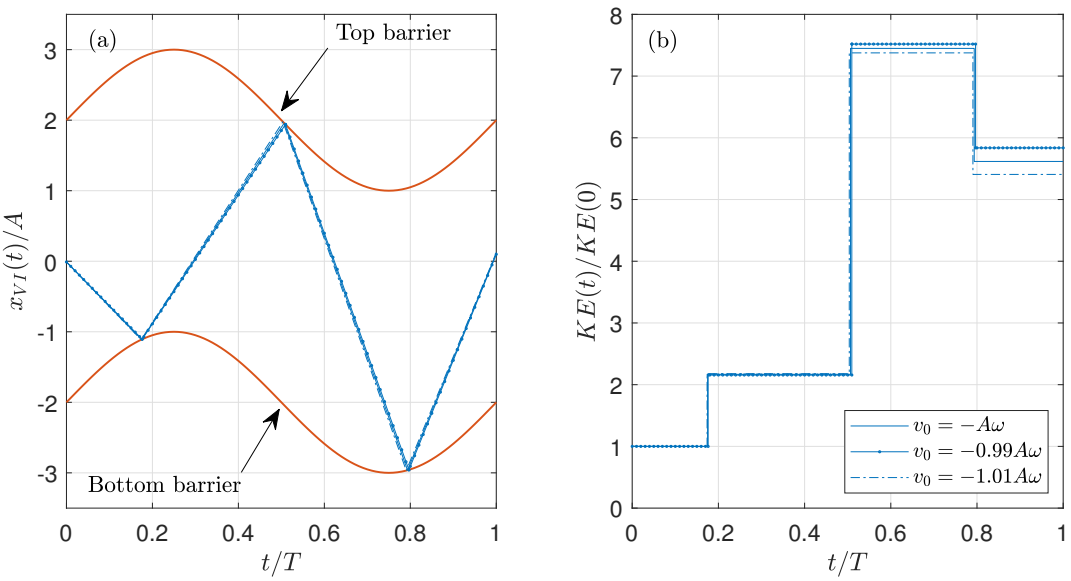

Figure 2: Simulated motion of the VI NES shown in Fig. 1. VI NES is shaken kinematically at $f = 1/T = \omega/2\pi = 100$ Hz with an amplitude $A = 10$ cm (see the red curves). The initial velocity of the particle is $v_0 = -62.8$ m/s. For the sake of clarity, the particle is considered as a point mass interacting with the inner walls of the container. (a) Position and (b) kinetic energy of the particle for $\epsilon = 0.7$ and by varying its initial velocity.

dynamics. As an example, we show in Fig. 2(a-b) the trajectory and the kinetic energy, respectively, of a steel spherical particle impacting against two rigid walls kinematically shaken at $\gamma_G(t) = -A\omega^2 sin(\omega t)$. Here, we implement the instantaneous contact model defined in Eq. 1, such that the contact duration $t_c = 0$ is infinitely small compared to the period of oscillation T and the VI NES dynamics is solved for one period for different initial velocities. As it can be seen, a variation of the order of the 1% of initial velocity leads to a difference of the about the 4% in the kinetic energy after only one period. This bias leads to different energy transfers and thus of energy dissipation. Moreover, this delay can cause an error in the simulation of the system dynamics by falling into one dynamical regime in preference to another.

Conclusions

The capability of a VI NES to damp vibrations of a primary system depends on its dynamical regime. For this reason, much attention must be paid on the numerical computation of the impacts in terms of relative velocity and time. One solution that prevents to increase computational costs, is to enrich the contact model by computing the contact force and using a finite duration continuous interaction potential. Notably, it is possible to demonstrate that the contact duration has a considerable effect on the estimation of the dissipated energy, even for very fast collisions. Another benefit of finite contact modeling is that it allows to evaluate the accelerations and the repulsive forces, which are not provided by the instantaneous contact model.

References

[1] Mohammad A. AL-Shudeifat and Nicholas Wierschem and D. Dane Quinn and Alexander F. Vakakis and Lawrence A. Bergman and Billie F. Spencer (2013) Numerical and experimental investigation of a highly effective single-sided vibro-impact non-linear energy sink for shock mitigation. *International Journal of Non-Linear Mechanics* **52**:96-109.

[2] J. Luo and N. E. Wierschem and S. A. Hubbard and L. A. Fahnestock and D. Dane Quinn and D. Michael McFarland and B. F. Spencer and A. F. Vakakis and L.A. Bergman (2014) Large-scale experimental evaluation and numerical simulation of a system of nonlinear energy sinks for seismic mitigation. *Engineering Structures* **77**:34-48.

[3] W. Li and N.E. Wierschem and X. Li et al. (2020) Numerical study of a symmetric single-sided vibro-impact nonlinear energy sink for rapid response reduction of a cantilever beam. *Nonlinear Dynamics* **100**:951–971.

[4] I Karayannis and A F Vakakis and F Georgiades (2008) Vibro-impact attachments as shock absorbers. *Proceedings of the Institution of Mechanical Engineers, Part C: Journal of Mechanical Engineering Science* **222(10)**:1899-1908.

[5] O.V. Gendelman and A. Alloni (2015) Dynamics of forced system with vibro-impact energy sink. *Journal of Sound and Vibration* **358**:301-314.

[6] F. Nucera and A.F. Vakakis and D. Michael McFarland and L.A. Bergman and G. Kerschen (2007) Targeted energy transfers in vibro-impact oscillators for seismic mitigation. *Nonlinear Dynamics* **50**:651-677.

[7] F. Nucera and D.M. McFarland and L.A. Bergman and A.F. Vakakis (2010) Application of broadband nonlinear targeted energy transfers for seismic mitigation of a shear frame: Computational results. *Journal of Sound and Vibration* **239(15)**:2973-2994.

[8] G. Pennisi and C. Stephan and E. Gourc and G. Michon (2017) Experimental investigation and analytical description of a vibro-impact NES coupled to a single–degree–of–freedom linear oscillator harmonically forced. *Nonlinear Dynamics* **88(3)**:1769-1784.

[9] T. Li and C.H. Lamarque and S. Seguy and A. Berlioz (2018) Chaotic characteristic of a linear oscillator coupled with vibro–impact nonlinear energy sink. *Nonlinear Dynamics* **91(4)**:2319-2330.

[10] M. Nagurka and S. Huang (2004) Mass–Spring–Damper Model of a Bouncing Ball. *Proceedings of the 2004 American Control Conference* **1**:499 - 504.

Monday, July 18, 2022
16:00 - 18:20

MS-03 Computational Methods
Rhone 3A

Chair: Jan Sieber

16:00 - 16:20
A rapid iterative procedure for dynamic integrity assessment
HABIB Giuseppe*
*MTA-BME Lendület Machine Tool Research Group, Department of Applied Mechanics, Budapest University of Technology and Economics (Budapest, Muegyetem rkp. 3. Hungary)

16:20 - 16:40
An Efficient Implementation for the Analysis of Extrema in Dynamical Systems with Delay
AHSAN Zaid*, LI Mingwu, DANKOWICZ Harry, SIEBER Jan
*Department of Mechanical Science and Engineering, University of Illinois at Urbana-Champaign (Urbana,IL United States)

16:40 - 17:00
Non-Conservative Nonlinear Modes Through Energy Resonance
ALCORTA Roberto*, GRENAT Clément, PRABEL Benoit, BAGUET Sébastien
*INSA Lyon, LaMCoS, University of Lyon (69621 Villeurbanne France) - CEA, University of Paris-Saclay (91191 Gif-sur-Yvette France)

17:00 - 17:20
Differential geometric PDE bifurcation problems in pde2path
UECKER Hannes, **MEINERS Alexander***
*Institut für Mathematik (Carl von Ossietzky Universität Oldenburg, Ammerländer Heerstr. 114, D- 26129 Oldenburg Germany)

17:20 - 17:40
Combinatorial models of global dynamics: learning cycling motion from data
BAUER Ulrich, **HIEN David***, JUNGE Oliver, MISCHAIKOW Konstantin, SNIJDERS Max
*Department of Mathematics, Technical University of Munich (Boltzmannstrasse 3 D-85747 Garching Germany)

A novel iterative procedure for rapid dynamic integrity assessment

Giuseppe Habib
Dept. of Applied Mechanics, MTA-BME Lendület Machine Tool Vibration Research Group, Budapest University of Technology and Economics, Budapest, Hungary

Summary. A new algorithm for estimating the robustness of a dynamical system's equilibrium is presented. Unlike standard approaches, the algorithm does not aim to identify the entire basin of attraction of the solution. Instead, it iteratively estimates the so-called local integrity measure, i.e., the radius of the largest hypersphere entirely included in the basin of attraction of a solution and centred in the solution. The procedure completely overlooks intermingled and fractal regions of the basin of attraction, enabling it to provide a meaningful engineering quantity quickly. The algorithm is tested on various mechanical systems. Despite some limitations, it proved to be a viable alternative to more complex and computationally demanding methods, making it a potentially appealing tool for industrial applications.

Introduction

Local stability is one of the most critical properties of a dynamical state. Engineers heavily exploit this concept. Nevertheless, scientists dealing with dynamical systems are aware that, despite its local stability, a system might diverge from its state if subject to a perturbation sufficiently large to make it cross the boundary of its basin of attraction (BOA). However, the definition of a system's BOAs is computationally very demanding. A few methods for the identification of BOAs of dynamical systems exist [1]. Analytical methods are generally based on Lyapunov functions. However, they are not a feasible option for the majority of real applications. The cell mapping method is probably the most efficient numerical technique for BOA estimation [2]. Experimental methods are almost inexistent, except for a few exceptions [3, 4].
The objective of this study is to develop an algorithm for the robustness assessment of equilibrium points. The procedure reduces the computational cost for global stability analysis by identifying the local integrity measure (LIM) [5] only, overlooking fractal and intermingled portions of the BOA, which are hard to identify and practically less relevant.

Methodology

The algorithm is based on a simple framework. Considering a predefined region of the phase space, initially, the maximal value of the LIM is calculated, being equal to the minimal distance between the equilibrium point of interest and the boundary of the region of the phase space considered. Then, a trajectory of the system in the phase space is computed. If the trajectory does not converge to the desired solution, the LIM is estimated as the minimal distance between the equilibrium point of interest and any point of the non-convergent trajectory. The new estimated value of the LIM (an overestimate of the real LIM value) defines a hypersphere in the phase space denominated hypersphere of convergence, limiting the region of interest. If a simulation converges to the desired solution, then the LIM is not reduced in that iteration. Initial conditions of each simulation are chosen as the farthest point from any other already tracked point within the hypersphere of convergence.
In order to automatically classify the computed trajectories, the phase space is divided into cells. A trajectory is classified as converging or non-converging to the desired solution by analyzing the cells in which points of the trajectory lie. To the reduce computational time, if a trajectory reaches a cell already tracked by a previous trajectory, the simulation is interrupted; all cells containing points of the trajectory are classified according to the reached and already tracked cell. A graphical explanation of the classification procedure adopted is illustrated in Fig. 1.

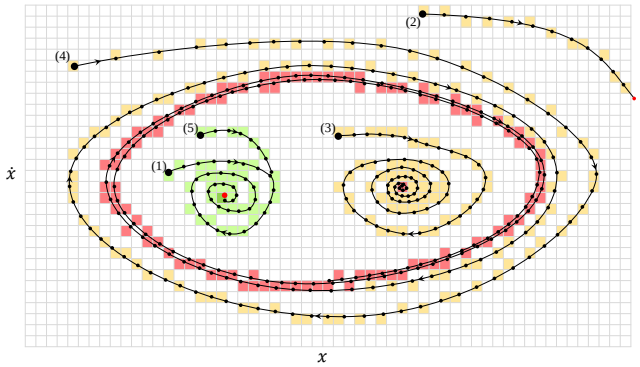

Figure 1: Illustrative examples of trajectory classification. (1) Converging to a known equilibrium; (2) leaving the considered phase space region; (3) converging to an unknown equilibrium; (4) converging to an unknown periodic solution; (5) converging to an already tracked cell.

Results

We implemented the algorithm on systems of various dimensions (up to dimension 8); the analysis illustrated that the algorithm could rapidly and efficiently estimate the LIM value in all cases studied. In particular, the first few iterations already provided a relatively accurate estimate of the real LIM value. The majority of the subsequent simulations converged to the equilibrium of interest, except few ones, which further improved the initial estimate of the LIM. Figure 2a represents the trend of the LIM estimate for the case of a Duffing-van der Pol oscillator with an attached tuned mass damper (4-dimensional system) [6]. The black line in Fig. 2a follows the described path. Light blue lines represent the LIM trend for other repetitions of the algorithm. All curves have a similar tendency. The system under study presents a stable equilibrium point (red cross in Fig. 2b) coexisting with a stable periodic solution (black line in Fig. 2b) for the considered parameter values. We remark that, in Fig. 2b, tracked points are projected on a section of the phase space, which makes it appear that red dots are within the hypersphere of convergence (green dashed line) while they are not.

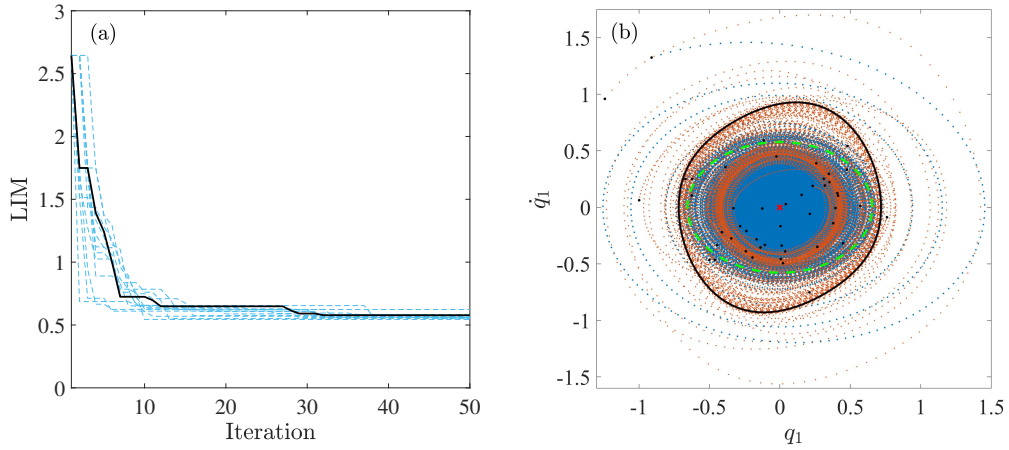

Figure 2: (a) LIM estimated value; (b) projection of the points tracked during the computation; blue and red points: converging and non-converging points, respectively, dashed green line: section of the hypersphere of convergence.

Conclusions

In this study, a new algorithm for estimating the robustness – dynamical integrity – of a stable equilibrium was developed. The algorithm utilizes an approach different from existing numerical methods for global analysis. It does not aim at studying the whole basin of attraction of a solution; instead, it directly tries to estimate the local integrity measure (LIM). From an engineering perspective, this quantity has obvious relevance for the safety of a dynamical system. The obtained results suggest that the proposed algorithm is a viable option for the robustness assessment of an equilibrium point. In particular, thanks to its quickness, it has the potentiality to be utilized in industrial environments, where rapid solutions are generally pursued. Future research developments should aim to make the algorithm utilizable for the robustness estimation of other kinds of solutions, such as periodic motions.

Acknowledgments

The Hungarian National Science Foundation financially supported this research under grant number OTKA 134496.

References

[1] Lenci S., Rega G. (2019) Global nonlinear dynamics for engineering design and system safety. Springer.

[2] Hsu C.S. (1980) A theory of cell-to-cell mapping dynamical systems. *J. Appl. Mech.*, **47**(4):931-939.

[3] Virgin L.N. (2000) Introduction to experimental nonlinear dynamics: a case study in mechanical vibration. Cambridge University Press.

[4] Zakynthinaki M.S., Stirling J.R., CordenteMartínez C.A., Díaz de Durana A.L., Quintana M.S., Romo G.R., Molinuevo J.S. (2010) Modeling the basin of attraction as a two-dimensional manifold from experimental data: applications to balance in humans. *Chaos Interdiscip. J. Nonlinear Sci.*, **20**(1), 013119.

[5] Soliman M.S., Thompson J.M.T. (1989) Integrity measures quantifying the erosion of smooth and fractal basins of attraction. *J. Sound Vib.* **135**(3), 453–475.

[6] Gattulli V., Di Fabio F., Luongo A. (2001) Simple and double Hopf bifurcations in aeroelastic oscillators with tuned mass dampers. *J. Frankl. Inst.* **338**(2–3), 187–201.

An Efficient Implementation for the Analysis of Extrema in Dynamical Systems with Delay

Zaid Ahsan*, Mingwu Li*, Harry Dankowicz* and Jan Sieber†
*Department of Mechanical Science and Engineering, University of Illinois at Urbana-Champaign, Urbana, IL, U.S.A
†College of Engineering, University of Exeter, Exeter, U.K.

Summary. We provide a general framework for optimization along periodic orbits or quasiperiodic invariant tori in dynamical systems with delay. Our recent study [1] developed a methodology for such problems based on the calculus of variations. The formulation presented in [1] did not exploit the typical structure of Jacobians in problems with delay, resulting in high computational costs and difficult-to-generalize algorithms. Here, we reformulate general boundary-value problems for delay equations by decomposing them into ordinary differential equation and algebraic interval coupling conditions. We consider such coupling conditions for various multi-segment boundary-value problems and describe how the necessary optimality conditions along with the corresponding Jacobians may be implemented in the continuation package COCO [2]. Several examples demonstrate the implications to computational efficiency, as well as the ease of problem construction.

Motivating example

Consider the retarded delay-differential equation with periodic forcing

$$\dot{x} = f\left(t, x, g(x,p)(t), p\right) := \begin{pmatrix} -\omega x_2 + x_1\left(t-\alpha\right)\left(1 + r\left(\cos\left(2\pi t/T - 1\right)\right)\right) \\ -\omega x_1 + x_2\left(t-\alpha\right)\left(1 + r\left(\cos\left(2\pi t/T - 1\right)\right)\right) \end{pmatrix}, \tag{1}$$

where $r = \sqrt{x_1^2 + x_2^2}$ and $p = (\alpha, \omega, T)$. Figure 1 shows a family of two-dimensional quasiperiodic invariant tori for this system obtained for fixed delay α and rotation number ρ (ratio of fundamental frequencies). In Fig. 1, the fold point at $\omega \approx 0.44$ separates stable (solid) from unstable (dashed) tori. We may locate the fold and further seek to locate extrema in ω under additional variations in α by considering the set of necessary conditions for stationary values of ω given corresponding dynamic constraints. Specifically, by suitable transformations [1, 2], an equivalent representation for a quasiperiodic invariant torus of (1) on the cylindrical domain $(\varphi, \tau) \in \mathbb{S} \times [0,1]$ (here, $\mathbb{S}$ denotes the unit circle) is in terms of a solution to the differential constraint

$$V_{,\tau}(\varphi,\tau) = Tf\left(T\tau, V(\varphi,\tau), \left[W_{\frac{\alpha}{T}}V\right](\varphi,\tau), p\right) \tag{2}$$

along with the boundary condition

$$V\left(\varphi, 1\right) - V\left(\varphi + 2\pi\rho, 0\right) = 0. \tag{3}$$

Here, the wrapping operator W_a is given by

$$\left[W_a\chi\right](\varphi,\tau) := \chi\left(\varphi - 2\pi j\rho, \tau - a + j\right), \tag{4}$$

where $j \in \mathbb{Z}$ is defined depending on a, φ, τ such that $\tau - a + j \in [0,1)$. This operator captures the dependence of the vector field on a shifted V, consistent with the presence of delay. Let $f_{,2}(\varphi,\tau)$ and $f_{,\omega}(\varphi,\tau)$ denote the partial derivatives of f with respect to its second argument and ω, respectively, evaluated at $\left(T\tau, V(\varphi,\tau), \left[W_{\frac{\alpha}{T}}V\right](\varphi,\tau), p\right)$, let df/dT denote the total derivative of $f\left(T\tau, V(\varphi,\tau), \left[W_{\frac{\alpha}{T}}V\right](\varphi,\tau), p\right)$ with respect to T, and let $h_j(\varphi,\tau)$ denote the partial derivative of f with respect to its third argument evaluated at $\left(T\tau, V, V\left(\varphi - 2\pi j\rho, \tau - \frac{\alpha}{T} + j\right), p\right)$ for $j = 0, 1$. A set of suitably constructed necessary adjoint conditions for stationary values of ω are then given by

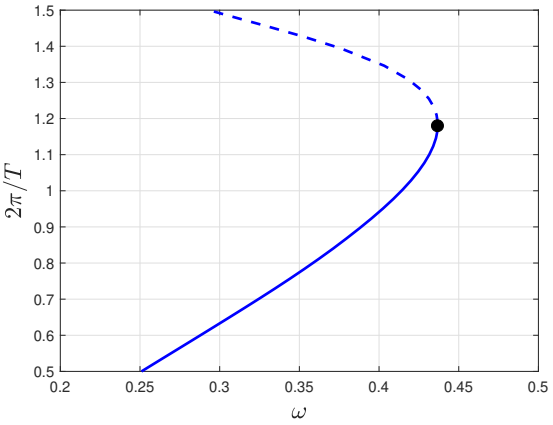

Figure 1: One-dimensional family of quasiperiodic tori [1] obtained with rotation number $\rho \approx 0.6618$ and $\alpha = 1$.

$$-\lambda_{f,\tau}^{\mathrm{T}} - T\lambda_f^{\mathrm{T}} f_{,2} - T\left(W_{-\frac{\alpha}{T}}\lambda_f\right)^{\mathrm{T}} W_{-\frac{\alpha}{T}} h_0 = 0,\ (\varphi,\tau) \in \mathbb{S} \times (0, 1-\alpha/T), \tag{5}$$

$$-\lambda_{f,\tau}^{\mathrm{T}} - T\lambda_f^{\mathrm{T}} f_{,2} - T\left(W_{-\frac{\alpha}{T}}\lambda_f\right)^{\mathrm{T}} W_{-\frac{\alpha}{T}} h_1 = 0\ (\varphi,\tau) \in \mathbb{S} \times (1-\alpha/T, 1), \tag{6}$$

and

$$\lambda_f^{\mathrm{T}}(\varphi,0) + \lambda_{\mathrm{rot}}^{\mathrm{T}}(\varphi - 2\pi\rho) + \lambda_{\mathrm{ph}} V_{,\varphi}^{\star\mathrm{T}}(\varphi) = 0, \qquad \lambda_f^{\mathrm{T}}(\varphi,1) + \lambda_{\mathrm{rot}}^{\mathrm{T}}(\varphi) = 0, \tag{7}$$

$$-\int_0^{2\pi}\int_0^1 \lambda_f^{\mathrm{T}} T f_{,\omega}\,\mathrm{d}\tau\,\mathrm{d}\varphi + \eta_\omega = 0, \qquad -\int_0^{2\pi}\int_0^1 \lambda_f^{\mathrm{T}}\left(f + Tdf/dT\right)\mathrm{d}\tau\,\mathrm{d}\varphi + \eta_T = 0 \tag{8}$$

in terms of the original variables V, ω, and T, a reference function $V^\star$, and a set of Lagrange multipliers λ_f, λ_{rot}, λ_{ph}, η_ω, and η_T, where $\eta_\omega = 1$ and $\eta_T = 0$ at a stationary point. The analysis in [1] demonstrates the successful location of such stationary points (and of the fold in Fig. 1) using a method of successive continuation, first pioneered by Kernévez and Doedel [3].

Software implementation

In the present work, we describe an effort to improve the computational efficiency of the implementation of the continuation problem in the previous section. Specifically, in contrast to the implementation in [1], which involved numerically computed Jacobians and no vectorization of the corresponding discretized problem, we describe an ongoing effort to encode explicit Jacobians in a vectorized form that supports an entire class of continuation problems with delay. These include initial-value problems, multisegment periodic orbits, and quasiperiodic invariant tori, even in the presence of multiple delays. The development platform is COCO, a MATLAB-based software package with an object-oriented construction paradigm that supports building composite problems by coupling instances of simpler problems. As an example, continuation of quasiperiodic invariant tori for a problem without delay was considered in [2] in terms of a multisegment boundary-value problem with all-to-all coupling of segment end points in terms of a suitably formulated Fourier interpolant. This past works motivates the implementation sought in the presence of delay.

Problem decomposition

To illustrate our approach, consider replacing the equation

$$x' = f(\tau, x, g(x,p)(\tau), p) \tag{9}$$

with the decomposition

$$x' = f\left(\tau, x, y, p\right),\ y\left(\tau\right) = g\left(x,p\right)\left(\tau\right) \tag{10}$$

for $\tau \in (0,1)$ in terms of a differential equation and an interval condition. A special case is obtained for $g(x,p)(\tau) := x(\tau - p_1|_{\mathrm{mod}\,[0,1)})$ corresponding to a periodic-orbit problem (omitting the discrete condition of periodicity at $\tau = 0$) with a single discrete delay p_1. In this case, vanishing variations of the Lagrangian

$$L = \int_0^{p_1} \lambda_{\mathrm{int}}^\top(\tau)\left(y(\tau) - x(1+\tau-p_1)\right)\,\mathrm{d}\tau + \int_{p_1}^1 \lambda_{\mathrm{int}}^\top(\tau)\left(y(\tau) - x(\tau-p_1)\right)\,\mathrm{d}\tau \tag{11}$$

with respect to λ_{int} yield the original interval condition, while variations with respect to x yield the contributions $-\lambda_{\mathrm{int}}^\top(\tau+p_1-1)$ and $-\lambda_{\mathrm{int}}^\top(\tau+p_1)$ on $\tau \in (1-p_1,1)$ and $\tau \in (0,1-p_1)$, respectively, to the adjoint differential equations. In general, the proposed decomposition allows us to develop a fully vectorized encoding with explicit Jacobians of a discretization of the differential equation constraint in (10) in terms of a corresponding discretization of x and y, without simultaneously imposing (a discretization of) the interval coupling constraint in (10). It is clear that we may similarly derive a general form of the discretized contributions to the adjoint conditions associated with the differential equation constraint, as well as their Jacobians, without also considering the contributions from the interval coupling constraint. Once these have been encoded in all generality, they may be invoked any number of times in the construction of a multisegment trajectory problem, such as that associated with continuation of quasiperiodic invariant tori. Of course, in a multisegment trajectory problem, the interval coupling conditions typically take a more general form in which y's associated with different segments are expressed in terms of x's associated with multiple other segments. A challenge is the derivation of a general form of the corresponding adjoint conditions, their discretization, and corresponding Jacobians.

Conclusions

A decomposition of the implementation of the necessary conditions for stationary values of an objective function along a constraint manifold defined by a boundary-value problem with delay is proposed in order to support optimization along families of periodic orbits or quasiperiodic invariant tori. The decomposition separates differential constraints from a set of interval conditions by the introduction of additional auxiliary unknowns. The advantage of the proposed decomposition is in the convenience of the implementation, including the vectorization of the discretized constraints and their Jacobians, and its generalization to a number of other problem types, including differential-algebraic problems. We argue that the expense of increasing the number of unknowns is outweighed by the shortened development time for different classes of user-specific optimization problems, per the underlying philosophy of the COCO software development.

References

[1] Ahsan Z., Dankowicz H. and Sieber J. (2019) "Optimization along families of periodic and quasiperiodic orbits in dynamical systems with delay". To appear in *Nonlinear Dynamics*.

[2] Dankowicz H., Schilder F. (2013) Recipes for Continuation. SIAM

[3] Kernévez, J.P., Doedel, E.: "Optimization in bifurcation problems using a continuation method," In *Bifurcation: Analysis, Algorithms, Applications*, Birkhäuser Verlag, Basel, 1987, pp. 153–160.

Non-Conservative Nonlinear Modes Through Energy Resonance

Roberto Alcorta[†], Clément Grenat[†], Benoit Prabel[‡] and Sébastien Baguet [†]
[†]*Univ Lyon, INSA-Lyon, CNRS UMR5259, LaMCoS, France*
[‡]*Université Paris-Saclay, CEA, Service d'Études Mécaniques et Thermiques, 91191, Gif-sur-Yvette, France*

Summary. In this contribution, a method for the numerical computation of nonlinear modes for damped systems is presented. The main idea is to introduce a conservative force term to compensate the non-conservative effects, in such a way that the condition of energy resonance is verified. We describe a systematic approach for the construction of the associated backbone curves and discuss related subjects such as their stability and practical applications.

Introduction

Nonlinear Normal Modes (NNM), which extend the familiar modal analysis to the case of nonlinear mechanical systems, have been a central research topic in dynamics over the past decades. Besides being an interesting theoretical concept, they have been shown to lead to numerous practical applications thanks to their relation to forced resonances, localization, energy transfers and model reduction (see [1] for a review, as well as references therein). Simply stated, the idea behind all methods for the computation of NNMs is to construct an invariant manifold of the conservative equations of motion, either directly or through the continuation of periodic solutions on the manifold [2]. However, modes computed in this fashion do not take into account the presence of non-conservative effects. As a consequence, deviations from the actual backbone curves of the system are to be expected: while they remain small in the case of small proportional damping, they can be considerable when damping is large or when the nonlinear forces involved are fundamentally non-conservative. Hence, just as for the conservative case, efforts have been made to extend the concept of non-conservative modes to nonlinear systems, yielding Non-Conservative Nonlinear Modes (NCNM). Different methodologies for the computation of NCNMs exist, relying on generalizations of the manifold-construction, complex-mode and periodic-motion-continuation techniques. The latter of these, introduced by Krack [3], consists in adding an artificial damping term to compensate for all non-conservative effects and thus achieve periodic motions. This method was applied by Jahn and co-workers [4] to study self-excited vibrations, and in particular to detect limit cycle oscillations. Nevertheless, one of the assumptions of this method is that the non-conservative terms are frequency-independent, which is not the case of, e.g., systems with memory terms. The present contribution introduces a novel, general method for the computation of NCNMs, based on extending the concept of energy resonance from linear modal analysis to the nonlinear case. Upon application of the Harmonic Balance Method (HBM), this leads to the formulation of a conservative equation where the effect of non-conservative terms of any form can be accurately taken into account, and whose solutions correspond to NCNMs.

Energy Resonance

Consider the equations of motion for a system of damped, unforced, nonlinear oscillators. By applying the HBM, they are expressed in the frequency domain with the Fourier coefficients of displacements $\mathbf{X}$ and the fundamental frequency ω as unknowns, giving:

$$\mathbf{R}(\mathbf{X},\omega) = \mathbf{Z}(\omega)\mathbf{X} + \mathbf{F}_{\text{NL}}(\mathbf{X},\omega) = \mathbf{0} \tag{1}$$

where $\mathbf{Z}(\omega) = \omega^2\nabla^2 \otimes \mathbf{M} + \omega\nabla \otimes \mathbf{C} + \mathbf{I} \otimes \mathbf{K}$ is the dynamical stiffness matrix containing inertial, damping and stiffness terms, and $\mathbf{F}_{\text{NL}}(\mathbf{X},\omega)$ represents the Fourier coefficients of all nonlinear forces. Excluding the case of limit cycle oscillations, this equation has no non-trivial solution since it contains non-conservative terms and thus no periodic solutions. If these terms are ignored, a conservative system is obtained, whose solution yields the traditional, undamped nonlinear modes as per Rosenberg's definition:

$$\mathbf{R}_{\text{P}}(\mathbf{X},\omega) = \left[\omega^2\nabla^2 \otimes \mathbf{M} + \mathbf{I} \otimes \mathbf{K}\right]\mathbf{X} + \mathbf{F}_{\text{NL},c}(\mathbf{X},\omega) = \mathbf{0} \tag{2}$$

Drawing a parallel with linear modal analysis, these solutions describe phase resonance. Another possibility, as proposed by Grenat et al. [5], is to compensate the non-conservative terms through the addition of a fictitious conservative force in such a way that the underlying invariant manifold is kept unchanged. This is achieved by considering the condition for energy -rather than phase- resonance, which can be expressed by the scalar equation:

$$\frac{\partial\left(\mathbf{X}^T\mathbf{X}\right)}{\partial\omega} = 0 \tag{3}$$

In this work, we show that Eq. (3) leads to the following conservative system:

$$\mathbf{R}_{\text{E}}(\mathbf{X},\omega) = \left(\omega^2\nabla^2 \otimes \mathbf{M} + \mathbf{I} \otimes \mathbf{K}\right)\mathbf{X} + \mathbf{F}_{\text{NL},c}(\mathbf{X},\omega) - \mathbf{G}_{\text{D}}(\mathbf{X},\omega) = \mathbf{0} \tag{4}$$

where the non-linear terms have been split into a conservative ($\mathbf{F}_{\text{NL},c}$) and a non-conservative part ($\mathbf{F}_{\text{NL},nc}$). The term $\mathbf{G}_{\text{D}}$, for which we have derived an explicit analytical expression, is a function of all non-conservative terms, both linear and

nonlinear. Eq. (4) can be used to compute normal mode solutions regardless of the specific form of the non-conservative terms, under the condition that they are continuous functions of $\mathbf{X}$ and that, as for any autonomous system, a phase equation be appended for closure. Illustrative examples are presented below:

1. Viscous damping

Assuming linear damping of the form: $\mathbf{f}_{\text{nc}}(t) = \mathbf{C}\dot{\mathbf{x}}(t)$:

$$\mathbf{G}_{\text{D}} = \frac{1}{2}\mathbf{I} \otimes \left(\mathbf{M}^{-1}\mathbf{C}\mathbf{C}\right)\mathbf{X} \tag{5}$$

Fig. 1 a) superimposes the frequency response of a Duffing oscillator with high damping to its corresponding NNM and NCNM backbones, for varying excitation levels.

2. Flow-induced added damping

Following [7], forces induced by transverse flow on a flexible cylinder within a rigid array can be modelled by a memory function of the form: $\mathbf{f}_{\text{fe}}(\mathbf{x}, t) = \sum_{k=0}^{N} \mathbf{A}_k \int_0^t e^{-b_k \tau}\mathbf{x}(t-\tau)d\tau$. This leads to added damping terms which are linear in $\mathbf{X}$ but frequency-dependent through the matrices $\mathbf{D}_k(\omega, b_k)$:

$$\mathbf{G}_{\text{D}} = \frac{1}{2}\left\{\sum_{k=0}^{N}\left[\mathbf{I}\otimes\mathbf{M} + b_k\mathbf{D}_k\otimes\mathbf{A}_k\right]^{-1}\left[\mathbf{I}\otimes\mathbf{C} - (\mathbf{D}_k + \omega\nabla^2\mathbf{D}_k^2)\otimes\mathbf{A}_k\right]\left[\mathbf{I}\otimes\mathbf{C} - \mathbf{D}_k\otimes\mathbf{A}_k\right]\right\}\mathbf{X} \tag{6}$$

3. Doubly-clamped viscoelastic beam

Considering a Kelvin-Voigt model [6] to describe the stress-strain relation within the beam, the equations of motion for modal coordinates q_j include non-conservative terms of the form: $\eta q_i q_j \dot{q}_k$ as a result of mid-plane stretching. Fig.1 b) shows the NCNM curves near a 1:5 internal resonance between the first and third bending modes, where considerable deviation from the undamped case is observed for high values of η.

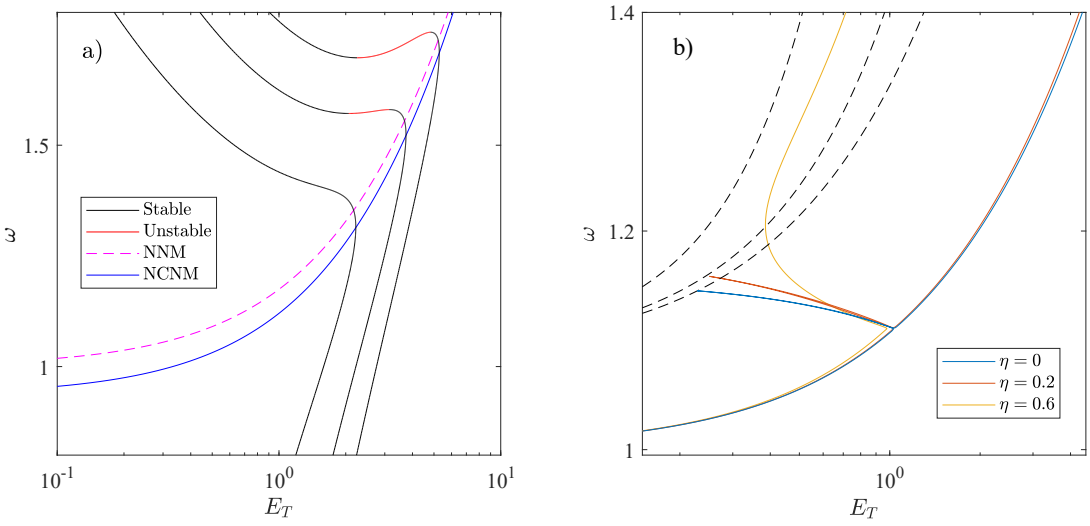

Figure 1: Examples of backbone curves with NCNM formalism. (a) Internal resonance of viscoelastic beam: first (solid) and third (dashed) nonlinear modes for different values of η. (b) Duffing equation with high viscous damping, contrasting NNM and NCNM backbone curves.

Conclusions

In this contribution, we introduced a systematic method for NCNM construction based on the concept of energy resonance. Likewise, its application to diverse mechanical vibration problems was showcased. Further work on this subject includes: bifurcation analysis, a detailed comparison with alternative methods and the experimental targeting of particular nonlinear modes by exploiting the function $\mathbf{G}_{\text{D}}$.

References

[1] Avramov K.V. and Mikhlin Y.V., Appl. Mech. Rev. **65** 2 (2013)
[2] Renson L., Kerschen G. and Cochelin B., J. Sound Vib. **364** (2016)
[3] Krack M., Comput. Struct. **154** (2015)
[4] Jahn M., Stender M., Tatzko S., Hoffmann N., Grolet A. and Wallaschek J., Comput. Struct. **227** (2019)
[5] Grenat C., Baguet S., Dufour R. and Lamarque C-H., Proc. of ASME IDETC/CIE Conference (2018)
[6] Zaitsev S., Shtempluck O., Buks E. and Gottlieb O., Nonlinear Dyn. **67** 1 (2011)
[7] Granger S. and Païdoussis M., J. Fluid Mech. **320** (1996).

Differential geometric PDE bifurcation problems in `pde2path`

Alexander Meiners*, Hannes Uecker†
* *Institut für Mathematik, Universität Oldenburg, D26111 Oldenburg, alexander.meiners@uni-oldenburg.de*
† *Institut für Mathematik, Universität Oldenburg, D26111 Oldenburg, hannes.uecker@uni-oldenburg.de*

Summary. Shape equations, such as the constant mean curvature (CMC) equation or the Helfrich equation, are geometric partial differential equations that arise for example in modeling liquid bridges or red blood cells. Analytical solution of these equations are known only in few situations, and we use numerical continuation to compute solutions and study their parameter dependence. The problems require adaptations of typical PDE numerics because of the quasilinear nature of the equations and the geometrical background. We discuss how some of these issues are treated in the numerical continuation and bifurcation package `pde2path`. To illustrate the implementation, we present some examples of CMC and Helfrich surfaces.

Introduction

Shape equations are differential geometric partial differential equations that typically describe critical points of some energy functional under some constraints. For example, let M be a two dimensional surface (possibly with boundary) immersed in $\mathbb{R}^3$ and parametrized by $\varphi : \Omega \to M$. Then the area functional is

$$\mathrm{area(M)} = \int_M \mathrm{d}S. \tag{1}$$

Now adding a volume constraint one finds that constant mean curvature (CMC) surfaces are critical points, leading to the following boundary value problem: given $V_0 \in \mathbb{R}_+$, find $\varphi : \Omega \to \mathbb{R}^3$ and $H_0 \in \mathbb{R}$ such that

$$H(\varphi) - H_0 = 0, \quad \mathrm{Vol}(\varphi) - V_0 = 0, \quad \varphi|_{\partial\Omega} = \partial M, \tag{2}$$

where H is the mean curvature, $V(\varphi)$ the enclosed volume, and the constant H_0 can for instance be interpretated as a pressure difference when the CMC surfaces model interfaces between fluids.
In general, only a few solutions of (2) and of related (often more complicated) problems are known explicitly, and we have to resort to numerical approximation of solutions. There are various methods for this, see, e.g., [BGN20] for a review of sophisticated methods. Here we follow an approach from [Bru18] and aim to numerically continue solutions of (2) and related problems in parameters, within the framework of the `Matlab` continuation and bifurcation package `pde2path` [Uec21a, Uec21b]. The basic idea is as follows: Let M_0 be a known surface with parametrization $\varphi_0 : \Omega \to \mathbb{R}^3$ satisfying (2) for some V_0 and with mean curvature H_0, and define a new surface via the parametrization $\varphi = \varphi_0 + u\,\nu$, $u : \Omega \to \mathbb{R}$ with suitable boundary conditions, where $\nu : M_0 \to \mathbb{S}^2$ is the unit normal vector of M_0. Then (2) reads

$$F(u, H, V) = \begin{pmatrix} H(\phi) - H \\ V(\phi) - V \end{pmatrix} = 0, \text{ with boundary conditions for } u, \tag{3}$$

which is a quasilinear elliptic equation for u, and after solving (3) we can update $M_0 = M_0 + u\nu$ and repeat. This point of view is also useful analytically, see, e.g., [ES98], and numerically it allows to apply standard predictor–corrector continuation and bifurcation methods to the quasilinear elliptic system (3). In `pde2path`, the (default) discretization of (3) works by the finite element method (FEM), and the associated mesh adaption capatibilities turn out to be very useful to deal with possibly strong deformations of the manifolds M under the continuation.
The method can also be applied to other types of geometric PDEs, also of higher order, for instance fourth order models from mathematical biology, e.g., Willmore and Helfrich functionals for vesicle shapes. In this case, (3) can be rewritten as a system of (2nd order) PDEs for a vector valued (u_1, u_2), and the same ideas apply.

Examples

Simple examples of CMC surfaces with boundaries are spherical caps, for instance the one–parameter CMC family of spherical caps S immersed in $\mathbb{R}^3$ with the boundary $\partial M = \{(x, y, z) \in \mathbb{R}^3 : x^2 + y^2 \le 1, z = 0\}$. These are useful testing problems since a spherical cap with prescribed boundary is uniquely characterized by its volume, and we have an analytical relation between volume and mean curvature, which yields an explicit error analysis. Figure 1 shows a simple continuation of the caps in volume, starting from $H = 0$ (flat disk), and applying some mesh adaptation when under continuation the stretching of the triangles becomes large.
For the spherical caps it is known and intuitively clear that no bifurcations occur along the branch in Fig. 1, cf. [KPP15]. This is different for another classical example, namely liquid bridges [SAR97]. In Fig. 2 we consider CMC surfaces between two unit circles located at $z = \pm 1/2$. For $V = \pi$ we have a straight cylinder with $H_0 = 1/2$, and continuing to larger V we find bifurcations to non–axisymmetric surfaces with 1, 2, ... bulges, with the first bifurcation occuring at $V \approx 5.81$ where the surface meets the planes $z = \pm 1/2$ at the circles tangentially. Here, for efficiency we compute only half the bridges with Neumann boundary conditions in angle, and the algorithm works fast and robustly (including mesh adaptation).

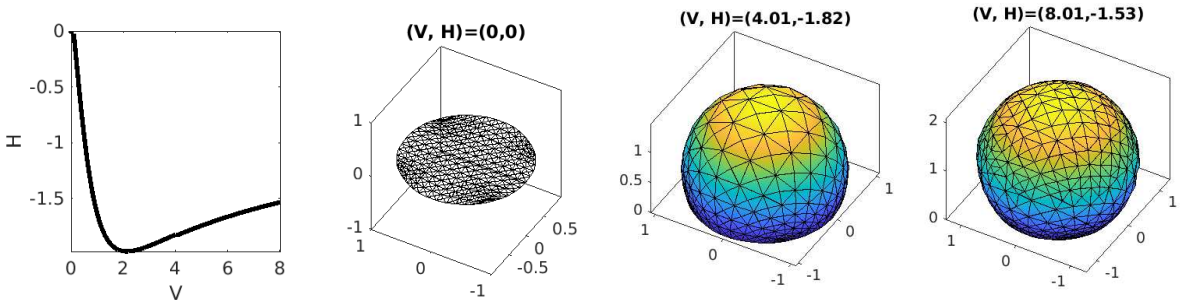

Figure 1: $2H$ over V for the spherical cap example, and sample solutions. At $V = 4.01$ and $V = 8.01$, the colors indicate u in the last step; at $V = 4.01$ we adaptively refine the mesh, see $V = 8.01$.

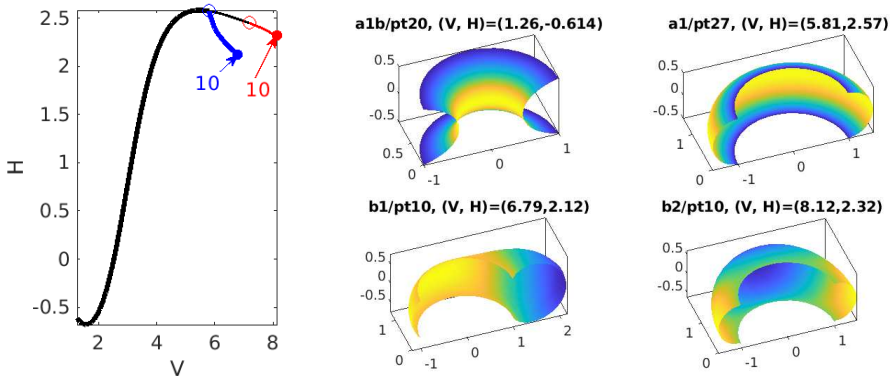

Figure 2: Bifurcation diagram of liquid bridges, and sample solutions. Top row: axisymmetric (black branch), with pt27 near the 1st BP. Bottom: pt10 on blue (left) and red (right) branches. The colors again indicate the last u.

After the above standard examples (also considered in [Bru18]), we consider more complicated problems, including: liquid bridges in different geometries, under gravity and with further terms, bifurcating nodoids [MP02, KPP15] and triply periodic surfaces [KPS18], and time permitting give an outlook on bifurcation results for 4th order equations such as Canham–Helfrich equations for vesicles modeling for instance red blood cells [Sei97].

References

[BGN20] J. Barrett, H. Garcke, and R. Nürnberg. Parametric finite element approximations of curvature-driven interface evolutions. In *Geometric partial differential equations. Part I*, volume 21 of *Handb. Numer. Anal.*, pages 275–423. Elsevier/North-Holland, Amsterdam, [2020] ©2020.

[Bru18] N. D. Brubaker. A continuation method for computing constant mean curvature surfaces with boundary. *SIAM J. Sci. Comput.*, 40(4):A2568–A2583, 2018.

[ES98] J. Escher and G. Simonett. The volume preserving mean curvature flow near spheres. *Proc. Amer. Math. Soc.*, 126(9):2789–2796, 1998.

[KPP15] M. Koiso, B. Palmer, and P. Piccione. Bifurcation and symmetry breaking of nodoids with fixed boundary. *Adv. Calc. Var.*, 8(4):337–370, 2015.

[KPS18] M. Koiso, P. Piccione, and T. Shoda. On bifurcation and local rigidity of triply periodic minimal surfaces in $\mathbb{R}^3$. *Ann. Inst. Fourier (Grenoble)*, 68(6):2743–2778, 2018.

[MP02] R. Mazzeo and Fr. Pacard. Bifurcating nodoids. In *Topology and geometry: commemorating SISTAG*, volume 314 of *Contemp. Math.*, pages 169–186. Amer. Math. Soc., Providence, RI, 2002.

[SAR97] L. Slobozhanin, J. Alexander, and A. Resnick. Bifurcation of the equilibrium states of a weightless liquid bridge. *Phys. Fluids*, 9(7):1893–1905, 1997.

[Sei97] U. Seifert. Configurations of fluid membranes and vesicles. *Advances in Physics*, 46(1):13–137, 1997.

[Uec21a] H. Uecker. *Numerical continuation and bifurcation in Nonlinear PDEs*. SIAM, Philadelphia, PA, 2021.

[Uec21b] H. Uecker. `www.staff.uni-oldenburg.de/hannes.uecker/pde2path`, 2021.

Combinatorial models of global dynamics: learning cycling motion from data

Ulrich Bauer*, David Hien*, Oliver Junge*, Konstantin Mischaikow † and Max Snijders ‡
*Department of Mathematics, Technical University of Munich, Germany
†Department of Mathematics, Rutgers University, Piscataway, NJ, USA
‡Boston Consulting Group

Summary. We describe a computational method for constructing a coarse combinatorial model of a dynamical system in which the macroscopic states are given by elementary cycling motions of the system. Our method is based on tools from topological data analysis and can be applied to time series data. We illustrate the construction by a perturbed double well Hamiltonian as well as the Lorenz system.

Introduction

Conley's fundamental theorem [4] characterizes the global structure of the dynamics of a continuous map on a compact metric space. It states that the space can be decomposed into a (chain) recurrent set and its complement, on which the map behaves gradient-like, i.e. trajectories transit from one recurrent component to another. Around the turn of the century, a computational approach to this theory has been developed [12, 7, 9, 10, 1, 11].
Relatedly, ideas have been put forward in order to characterize the dynamics *within* a transitive component of the chain recurrent set. For example, in [6], certain eigenfunctions of the transfer (or push forward) operator have been used in order to decompose a transitive component into, e.g., *almost invariant* (or metastable) subsets.
The purpose of this note is to outline a computational procedure by which certain *cycling behaviour* of the system can be detected and agglomerated into a coarse model. More precisely, we describe how to detect whether the system exhibits motions along a topological circle in some geometric complex that represents a transitive recurrent component of the system. A key ingredient in this procedure is a construction of circle-valued coordinates on simplicial complexes [5]; its usefulness for analyzing recurrent dynamics was already suggested in [14].
In particular, our technique is applicable if no model is available, but the dynamics is only given in form of a time series of data points $x_k = x(t_k) \in \mathbb{R}^d$, $k = 0, \dots, m$, that are, e.g., sampled from solution curves $x : [0, 1] \to \mathbb{R}^d$ of some differential equation or constructed by a time-delay embedding of scalar measurement data.

The construction

Given a time series $x_0, \dots, x_m$ in $\mathbb{R}^d$, we construct a combinatorial model which captures different types of cycling motion. Our pipeline consists of three main steps: constructing a topological space, finding dynamically relevant coordinates and constructing a combinatorial model.

Discretization of phase space

A first attempt at obtaining a topological space from a time series $x_0, \dots, x_m$ is to construct a Vietoris–Rips complex with base set $X = \{x_0, \dots, x_m\}$. In our setting, this is impractical since the resulting complexes are usually too large to be computationally tractable. In order to circumvent this problem we first quantize our data. For this, choose a radius $r \in \mathbb{R}_{>0}$ and consider the *cubical grid*

$$\mathcal{B} = \mathcal{B}(r) = \left\{ \prod_{\ell=1}^{d} r \left[z_\ell - \tfrac{1}{2}, z_\ell + \tfrac{1}{2} \right) \mid z \in \mathbb{Z}^d \right\}.$$

Since the elements of $\mathcal{B}$ (which we call *cubes* or *boxes*) form a partition of $\mathbb{R}^d$, we can define $Q : \mathbb{R}^d \to \mathcal{B}$ by mapping each point to the unique cube containing the point. Then

$$\mathcal{X} := \{Q(x) \mid x \in X\}$$

is a *cubical* or *box covering* of the point cloud X. For a cube $\xi = \prod_{\ell=1}^{d} r \left[z_\ell - \frac{1}{2}, z_\ell + \frac{1}{2} \right)$ let $z(\xi) = (rz_1, \dots, rz_d)$ be its *center*. We can identify $\mathcal{X}$ with the subset

$$Z := \{z(\xi) \mid \xi \in \mathcal{X}\}$$

of the integer lattice $r\mathbb{Z}^d$. The set Z of box centers is called the *quantization of the point cloud* X. Fig. 1a shows a time series with its cubical cover and the corresponding set of box centers Z.
We then resample the time series such that consecutive points lie in different cubes. For this, set $\tau(0) = 0$ and recursively define

$$\tau(i) = \min\{j > \tau(i-1) \mid Q(x_j) \neq Q(x_{\tau(i-1)})\}$$

The time series $\hat{x}_i = z \circ Q(x_{\tau(i)})$, $i \in [0, T]$ is called the *quantization* of the time series $x_0, \dots, x_m$ at radius r. Here we let T denote the largest finite value of τ and $[k, \ell] := \{k, \dots, \ell\} \subset \mathbb{N}_0$.

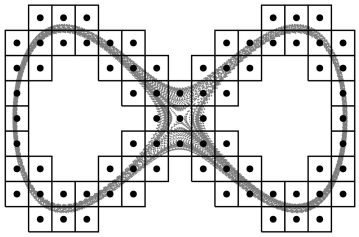

(a) Time series and cubical quantization.

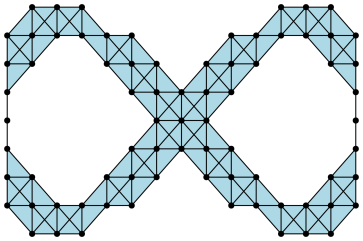

(b) Vietoris–Rips complex

Figure 1: Time series, its quantization and the resulting Vietoris–Rips complex.

Given a set of box centers Z, we construct the Vietoris–Rips complex $\mathcal{K} = \mathrm{VR}(Z, d, \delta)$, where $d(x, y) = \|x - y\|_\infty$ and $\delta = r$ (see the appendix for a definition of the Vietoris–Rips complex). Note that the choice of d and δ allows a point in Z to be connected to all its diagonal neighbors. An example is shown in Fig. 1b.

Coordinates for dynamics

Circular coordinates are the key tool which we use to detect cycling. In the following paragraphs, we review their construction from cohomology, explain how they can be lifted with respect to a time series, and outline how to find elements of $H^1(\mathcal{K}; \mathbb{Z})$ that induce dynamically relevant coordinates. In particuar, we will also define what it means to be cycling with respect to a coordinate.

1. Cohomology and circular coordinates. A circular coordinate, as introduced in [5], is a function $\mathcal{K} \to S^1$ with minimal variation along edges in its homotopy class (in particular, there is no relation to coordinates in the sense of differential geometry). Abstractly, the construction of circular coordinates is motivated by the bijection $H^1(\mathcal{K}; \mathbb{Z}) \cong [\mathcal{K}, S^1]$ where $[\mathcal{K}, S^1]$ denotes the homotopy classes of maps $\mathcal{K} \to S^1$. Explicitly, given a cocycle $\alpha \in Z^1(\mathcal{K}; \mathbb{Z})$, the coordinate $\theta_\alpha : \mathcal{K} \to S^1$ can be constructed by first computing the *harmonic representative* which is given by

$$\operatorname{argmin}\{\|\bar{\alpha}\|^2 \mid \bar{\alpha} = \alpha + d_0\theta, \theta \in C^0(\mathcal{K}; \mathbb{R})\}, \quad \text{where } \|\alpha\|^2 = \sum_{e \in \mathcal{K}^1} \alpha(e)^2,$$

and then using the construction from [5] to obtain a function $\mathcal{K} \to S^1$ which "varies by $\bar{\alpha}(e)$ on each edge e". In this work, the precise construction is not important since we only use the values of this function on the vertices of $\mathcal{K}$ which is given by composing the minimizing θ with the canonical projection $\pi_{S^1} : \mathbb{R} \to S^1 = \mathbb{R}/\mathbb{Z}$. We denote this function by $\theta_\alpha : Z \to S^1$. We remark that θ_α only depends on the cohomology class of α and is unique up to an additive constant on each connected component of $\mathcal{K}$. Examples can be found in Figs. 2 and 3.

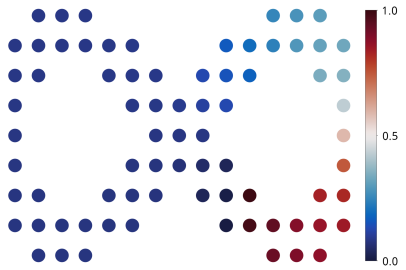

(a) Coordinate θ_α varies around the right hole.

(b) Coordinate θ_β varies around the left hole.

Figure 2: Circular coordinates which capture holes in the complex.

2. Lifted coordinates. Given a quantized time series $\hat{x} : [0, T] \to Z$ and a circular coordinate $\theta : Z \to S^1$ we can form the composite $\theta \circ \hat{x} : [0, T] \to S^1$ which captures the change of the coordinate θ over time. Analogous to continuous maps, we lift this function to a function $\hat{\theta} : [0, T] \to \mathbb{R}$ such that $\pi_{S^1} \circ \hat{\theta} = \theta \circ \hat{x}$: We define the *lifted coordinate* of θ and $\hat{x}$ via $\hat{\theta}(0) = 0$ and

$$\hat{\theta}(t) = \hat{\theta}(t-1) + d_{S^1}(\theta(\hat{x}_t), \theta(\hat{x}_{t-1})), \quad t = 1, \ldots, T,$$

where $d_{S^1}(x, y)$ denotes the signed geodesic distance from y to x on S^1.

For an example, let $\hat{x}$ denote the quantized time setries from Fig. 1a. Fig. 4a shows the first 80 time steps of $\theta_\alpha \circ \hat{x}$, Fig.4b shows the lift $\hat{\theta}$ over the same period of time. One can see from Fig. 4a that the time series does approximately 3.5 turns with respect to the coordinate. The lifted coordinate Fig. 4b captures this directly, as it increases by 3.5.

(a) Coordinate θ_γ varies around both holes.

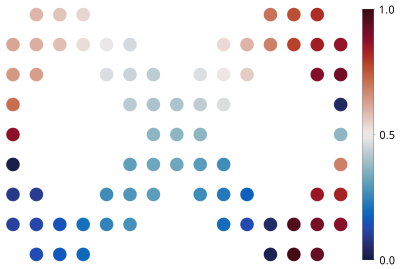

(b) Coordinate θ_δ varies around both holes.

Figure 3: A pair of bad coordinates.

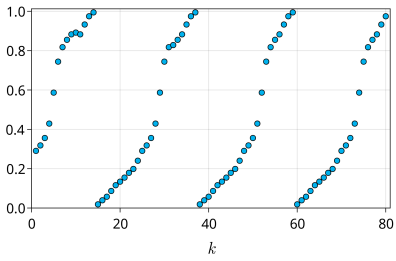

(a) Circular coordinate evaluated along time series.

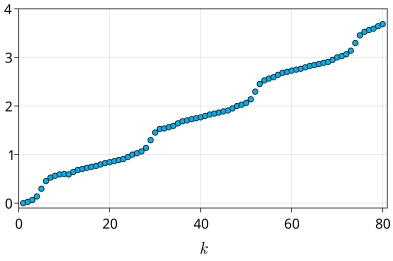

(b) Lifted coordinate.

Figure 4: Circular coordinate and its lift along a time series.

3. Dynamically relevant generators. As described before, every cohomology class in $H^1(\mathcal{K};\mathbb{Z})$ induces a circular coordinate. Some of these coordinates can be used to detected cycling dynamics. For example, the coordinate in Fig. 2a is almost constant on the left side of the complex while it maps the right half of the complex surjectively onto the circle. Therefore, a lift of this coordinate changes significantly if and only if the time series "cycles" around the right hole in the complex. In particular, the coordinate can be used to detect cycling around the right hole. Similarly, the coordinate in Fig. 2b can be used to detect cycling around the left hole. However, not all cohomology classes induce coordinates suitable for detecting cycling dynamics. For example, the coordinates in Figs. 3a and 3b are not suited for detecting cycling dynamics since they vary around both holes.

We now explain how dynamically relevant coordinates can be obtained. Intuitively, we want different coordinates to describe different features of the dynamics. Therefore, large changes in different lifted coordinates should occur at disjoint periods of time. To capture this, we define the *correlation* of two lifted coordinates $\hat{\theta}$ and $\hat{\eta}$ as

$$c(\hat{\theta},\hat{\eta}) = \langle |\Delta\hat{\theta}|, |\Delta\hat{\eta}| \rangle \tag{1}$$

where the i-th entry of the vector $\Delta\hat{\theta}$ is the forward finite difference $\hat{\theta}_{i+1} - \hat{\theta}_i$ and $\langle\cdot,\cdot\rangle$ denotes the standard Euclidean inner product. Since we are interested in describing all possible cycling dynamics in the system, we want to find a correlation minimizing basis. For a basis B of $H^1(\mathcal{K};\mathbb{Z})$ we define its *correlation* as

$$I(B) = \sum_{\substack{\alpha,\alpha'\in B \\ \alpha\neq\alpha'}} c(\hat{\theta}_\alpha, \hat{\theta}_{\alpha'}). \tag{2}$$

As an example, we again consider the time series 1a. From Fig. 4b we know that for the first 80 time steps, the series does 3.5 turns around the right hole. Now consider Fig. 5 where the lifted coordinates for the bases $\{\alpha,\beta\}$ and $\{\gamma,\delta\}$ are plotted for the first 80 time steps. The plots indicate that the lifted coordinates in Fig. 5a have a lower correlation than the ones in Fig. 5b. An explicit computation (for all 1000 time steps) yields the values 0.158 and 12.8, respectively, confirming that the preferred basis has lower correlation.

We now search for a basis with minimal correlation. Assuming $\alpha_1,\ldots,\alpha_n$ is any basis for the free group $H^1(\mathcal{K};\mathbb{Z})$, every basis can be written as $A\alpha_1,\ldots,A\alpha_n$ where $A \in \mathrm{GL}_n(\mathbb{Z})$. In order to find a correlation minimizing basis, we search $\mathrm{GL}_n(\mathbb{Z})$, starting with the identity $A := \mathrm{I}$ and recursively applying basis change operations (sums of rows/columns, multiplication of rows/columns with a unit) to A up to a given depth. Of all these bases we return the one with minimal correlation.

This approach works sufficiently well for simple examples. However, since we are only searching a finite subset of $\mathrm{GL}_n(\mathbb{Z})$ we have no guarantee of actually finding a minimizer. A better algorithm for finding a correlation minimal basis is a topic for future work.

Given a quantized time series and a circular coordinate, cycling dynamics can be inferred from changes in a lift of the coordinate. More precisely, we define a quantized time series $\hat{x}$ to be *cycling along* α if there is an interval $[k,\ell]$ where $\hat{\theta}_\alpha$

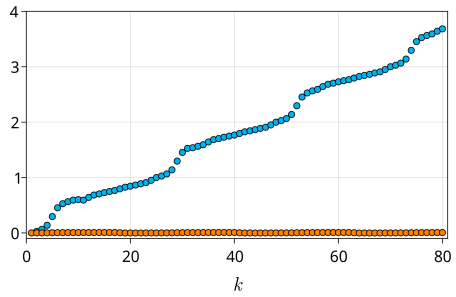

(a) Lift of the coordinates in Fig. 2.

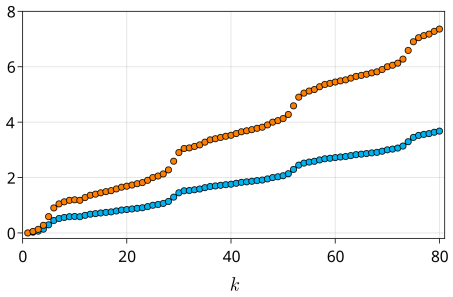

(b) Lift of the coordinates in Fig. 3.

Figure 5: Lifted coordinates for two different bases.

satisfies a *monotonicity criterion* and $|\hat{\theta}_\alpha(\ell) - \hat{\theta}_\alpha(k)| > 1$. The second condition ensures that the time series completes at least one full turn during the segment $[k, \ell]$. The monotonicity criterion we use is the following: Given $\varepsilon > 0$, $\bar{t} \in \mathbb{N}_{>0}$, the lifted coordinate $\hat{\theta} : [0, T] \to \mathbb{R}$ is called $(\varepsilon, \bar{t})$-*increasing along* $[k, \ell]$ if

- $|\theta_\alpha(t + \bar{t}) - \theta_\alpha(t)| > \varepsilon$ for all $t = k, \dots, \ell - \bar{t}$, and
- the sign of $\theta_\alpha(t + \bar{t}) - \theta_\alpha(t)$ is the same for all $t = k, \dots, \ell - \bar{t}$.

For $\bar{t} = 1$, this definition requires $\hat{\theta}_\alpha$ to be monotonic. In practice, it is usually necessary to use $\bar{t} > 1$ due to small back-and-forth movement which decreases the lifted coordinate, or movement orthogonal to the cycling direction which keeps the lifted coordinate constant. Note that the parameters ε and $\bar{t}$ have to be specified by the user; we typically do this by inspecting the lifted coordinates.
We define the subset $E \subset B$ of all *dynamically relevant generators* of a basis B as all $\alpha \in B$ for which the time series is cycling along θ_α. The elements in $B \setminus E$ will be called *spurious* generators.

Macro model for cycling dynamics
We transfer the information on cycling motion back to the cubical covering: A cube ξ in the covering $\mathcal{X}$ is α-*cycling* if the time series is cycling along α on some interval $[k, \ell]$ and there is $j \in [k, \ell]$ such that $\hat{x}_j \in \xi$. For $\xi \in \mathcal{X}$, let $E(\xi) \subset E$ be the set of all dynamically relevant generators α for which ξ is α-cycling.
The cubical covering $\mathcal{X}$ can now be decomposed into equivalence classes: Two cubes are equivalent if they are cycling with respect to the same set of non-spurious generators of $H^1(\mathcal{K}; \mathbb{Z})$:

$$\xi \sim_1 \xi' \iff E(\xi) = E(\xi').$$

We can furthermore distinguish cubes in which the trajectory ceases to be cycling. For this, assume the time series is α-cycling along an interval $[k, \ell]$ which is maximal in the sense that the time series is not α-cycling on any interval which contains $[k, \ell]$. Now let $t \in [k, \ell]$ be the first time step such that $|\hat{\theta}_\alpha(\ell) - \hat{\theta}_\alpha(t)| < 1$. Then the cubes $Q^{-1}(\hat{x}_t), \dots, Q^{-1}(\hat{x}_\ell)$ are precisely those cubes which are hit during the "last full turn" with respect to α in $[k, \ell]$. We call such cubes α-*transient*. For a given cube ξ, we let $E_t(\xi)$ denote the set of all generators which ξ is transient for. As a finer classification of cubes we define

$$\xi \sim_2 \xi' \iff E(\xi) = E(\xi') \text{ and } E_t(\xi) = E_t(\xi').$$

We now classify the cubes in $\mathcal{X}$ according to either of these two equivalence relations and count transitions between the classes. That is, we build the quotient

$$[\mathcal{X}] := \mathcal{X}/\sim = \{[\xi_1]_\sim, \dots, [\xi_T]_\sim\}$$

as well as the transition matrix

$$P(\sim) = (p_{ij}), \quad p_{ij} = \#\{t \in [1, T] \mid \hat{x}_{t-1} \in [\xi_j]_\sim, \hat{x}_t \in [\xi_i]_\sim\}.$$

We now call $(\mathcal{X}/\sim_1, P(\sim_1))$ a macro model, and $(\mathcal{X}/\sim_2, P(\sim_2))$ an extended macro model for the given time series. Figs. 6 and 7 show both macro models for the time series in Fig. 1a.

Experiments

The following results are obtained using our implementation of the pipeline in Section in the programming language Julia [2]. In particular, we use the algorithm in [8] for computing H^1 with integer coefficients.

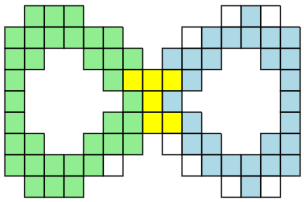

(a) Decomposition.

1157		86	142	α-cyc
	1367	69	6	β-cyc
113	68	134		α-cyc β-cyc
115	6	27		no cycling

(b) Transition matrix.

Figure 6: Macro model for the double well system.

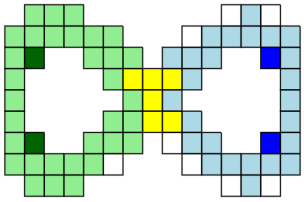

(a) Decomposition.

	10					α-cyc
10	1137			86	142	α-trn
			13			β-cyc
		13	1341	69	6	β-trn
	113		68	134		α-trn β-trn
	115		6	27		no cycling

(b) Transition matrix.

Figure 7: Extended macro model for the double well system.

Perturbed double well

The time series in Fig. 1, which was used to illustrate the constructions in the previous section, was obtained by integrating a stochastically perturbed version of the double well Hamiltonian system

$$dx = f(x)dt + \sigma dB, \tag{3}$$

with $x = (q, p)$, $f(x) = (p, q - q^3)$, $\sigma = (0, 0.025)$ and B denoting Brownian motion. We integrate (3) from the initial value $x = (1, 0.7)$ by the SRIW1 scheme [13] with step size 0.01.

The macro models in Fig. 6 and Fig. 7 were generated using the coordinates in Fig. 2 and the monotonicity criterion "θ is $(0.02, 2)$-increasing". These models are as we would expect for such simple dynamics. The yellow boxes capture the location in phase space where direct transition between loops is possible and the green and blue boxes capture the location where the trajectory cycles around the natural holes.

The Lorenz system

For this example we generated a time series by integrating the Lorenz system with the classical parameters $\sigma = 10$, $\beta = \frac{8}{3}$ and $\rho = 28$ with time step size 0.1 for 1 million time steps using the classical fourth order Runge Kutta method. As starting value, we choose $(0, 10, 0)$, but we discard the first 6000 time steps since they 'close up' the left holes of the complex. This highlights one shortcoming of our current technique which will be addressed in future work.

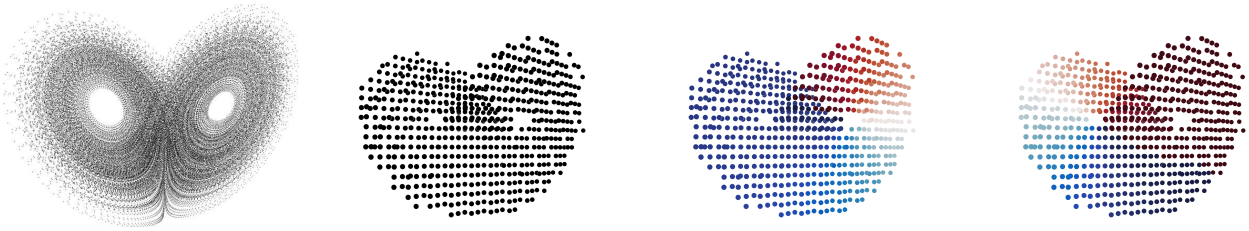

(a) Sampled trajectory. (b) Quantization. (c) Coordinate θ_α. (d) Coordinate θ_β.

Figure 8: Illustration of the pipeline for a trajectory on the Lorenz attractor.

We choose the quantization radius $r = 2.5$ and obtain a Vietoris-Rips complex with two-dimensional first cohomology. We use the monotonicity criterion "θ is $(0.02, 6)$-increasing" for both coordinates. Plots of the time series, the quantized point cloud as well as the coordiantes of the correlation minimizing basis are shown in Fig. 8.

The macro model shown in Fig. 9 nicely captures many important aspects of the dynamics on the Lorenz attractor. We learn that there are (at least) two different types of cycling motion, that each of these occurs in a distinct region in phase space (the blue and green regions), and that these regions intersect (yellow region). We furthermore see that cycling dynamics are present everywhere in the box decomposition since there are no non-cycling boxes.

In the extended macro model (Fig. 10), we see that the cycling regions are subdivided into a cycling set near the center of the wings and a transient set near the outside of the wings. This indicates that all cycling dynamics in the inside of

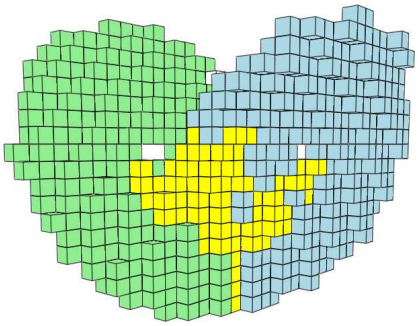

(a) Decomposition.

12060		1042	α-cyc
	12677	901	β-cyc
1043	901	14219	α-cyc β-cyc

(b) Transition matrix.

Figure 9: Macro model for the Lorenz system.

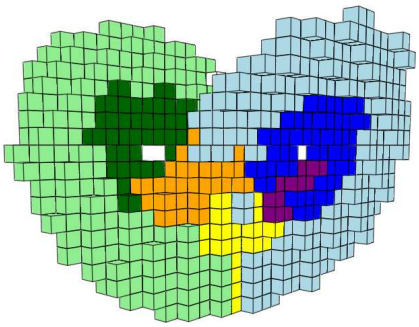

(a) Decomposition.

3046	724			53	305	301	α-cyc
755	7535			37	346		α-trn
		3359	656	128	234	100	β-cyc
		766	7896	30	74	335	β-trn
80	368	9	384	5179	275	904	α-trn β-trn
212	17	229	165	642	3663	5	α-trn β-cyc
336	30	114		1129	36	2386	α-cyc β-trn

(b) Transition matrix.

Figure 10: Extended macro model for the Lorenz system.

the wings eventually moves to the outer regions. The extended model furthermore identifies the regions where direct transitions between cycling dynamics can occur. The purple and yellow regions in Fig. 10a are the only regions where a direct transition from α- to β-cycling dynamics is possible and the orange and yellow regions are the only places that can contain the reverse transition.

Discussion

The techniques described in this paper appear to be a promising novel approach to identifying from time series data regions of phase space in which oscillations occur and locations at which transitions between these oscillations occur. However, a number of distinct questions need to be answered to obtain confidence in applying this technique to complicated higher-dimensional systems, where the results cannot be inspected and modified by visualization. We briefly address those in the following paragraphs.

Construction of the complex. The computation of circle-valued coordinates from data requires the construction of a geometric complex. The approach chosen in this article accomplishes this by constructing a Vietoris–Rips complex from a suitably quantized version of the given time series. In particular, we rely on finding a quantization radius r which is small enough to contain those holes which give rise to dynamically relevant coordinates and large enough to connect the data in a meaningful way. In general, such a radius need not exist. This even happens in the Lorenz system with a trajectory that starts very close to the center of one of the wings.

Finding optimal coordinates. When searching for dynamically relevant coordinates, we encounter the problem of finding a correlation minimizing basis. This poses the natural question of existence and uniqueness of such a basis. In addition, an algorithm is needed to compute this basis or a suitable approximation. Furthermore, even the computation of an arbitrary basis for $H^1(\,\cdot\,;\mathbb{Z})$ is currently not as efficient as we would like. We hope to address this using techniques inspired by those for the computation of (persistent) cohomology with coefficients in a finite field [3].

Identifying cycling motion. In this contribution, cycling motion is identified by analyzing the monotonicity behavior of circular coordinates. While this leads to satisfactory results in the presented examples, we have no general reliable procedure of identifying recurrence. For example, a cycling time series with a bit of back-and-forth movement in every full turn would be difficult to identify using the presented methods.

Appendix: Background

Simplicial complexes. Let V be a finite set. An *(abstract) simplicial complex* with base set V is a subset $\mathcal{K}$ of the power set of V which is closed under the subset relation, i.e. $\sigma \in \mathcal{K}$ implies $\tau \in \mathcal{K}$ for every subset τ of σ. A $\sigma \in \mathcal{K}$ is called a *simplex*, or more precisely a *k-simplex*, where $k = |\sigma| - 1$; the set of k-simplices is denoted by $\mathcal{K}^{(k)}$. In the special cases $k = 0$, 1 or 2 we call σ a vertex, an edge or a triangle, respectively.
Given a finite set $V \subset \mathbb{R}^n$, a metric d on $\mathbb{R}^n$ and a simplex $\sigma \subset V$, the diameter of a simplex is defined as $\operatorname{diam}\sigma = \max_{v,w\in\sigma} d(v,w)$. The simplicial complex $\mathrm{VR}(V,d,r) = \{\sigma \subset V \mid \operatorname{diam}\sigma \leq r\}$ is called the *Vietoris–Rips complex* of V at scale r.

Cochain groups. A *basis* for an abelian group G is a set $(g_i)_{i\in I}$ of elements such that every $g \in G$ can be written uniquely as a finite sum $g = \sum n_j g_j$ with $n_j \in \mathbb{Z}$. An abelian group with a basis is called *free*.
The cochain groups of a simplicial complex are the free abelian groups

$$C^k(\mathcal{K};\mathbb{Z}) = \{\text{functions } \mathcal{K}^{(k)} \to \mathbb{Z}\}$$

where a basis for each group is given by the functions which are 1 on one simplex and 0 on all others.

First Cohomology. Fix a total order on V. We write $[v_0, v_1, \ldots, v_k]$ for a subset $\{v_0, v_1, \ldots, v_k\}$ of V if $v_0 < v_1 < \cdots < v_k$. Clearly, for every $\sigma \in \mathcal{K}$ there are unique $v_0, \ldots, v_k \in V$ such that $\sigma = [v_0, v_1, \ldots, v_k]$.
We define coboundary maps $d_0 : C^0(\mathcal{K};\mathbb{Z}) \to C^1(\mathcal{K};\mathbb{Z})$ and $d_1 : C^1(\mathcal{K};\mathbb{Z}) \to C^2(\mathcal{K};\mathbb{Z})$

$$\begin{aligned}(d_0 f)([v_0,v_1]) &= f(v_1) - f(v_0)\\ (d_1\alpha)([v_0,v_1,v_2]) &= \alpha([v_1,v_2]) - \alpha([v_0,v_2]) + \alpha([v_0,v_1])\end{aligned}$$

Elements in $\ker d_1$ are called *cocycles*, elements in $\operatorname{im} d_0$ *coboundaries*. A calculation shows that $d_1 d_0 = 0$ and therefore $\operatorname{im} d_0 \subset \ker d_1$. We can therefore define the *first cohomology group* as the quotient

$$H^1(\mathcal{K};\mathbb{Z}) = \ker d_1 / \operatorname{im} d_0.$$

It follows from the universal coefficient theorem for cohomology (see section 3.1 of [15]) that $H^1(\mathcal{K};\mathbb{Z})$ is again a free abelian group.

Acknowledgement

The authors thank the DFG for their support via the SFB/TR109 Discretization in Geometry and Dynamics.

References

[1] H. Ban and W. D. Kalies. A computational approach to Conley's decomposition theorem. *J. Comp. Nonl. Dyn.*, 1(4):312–319, 2006.

[2] J. Bezanson, A. Edelman, S. Karpinski, and V. B. Shah. Julia: A Fresh Approach to Numerical Computing. *SIAM Review*, 59: 65–98, 2017.

[3] U. Bauer. Ripser: efficient computation of Vietoris–Rips persistence barcodes. J Appl. and Comput. Topology 5, 391–423 (2021).

[4] C. Conley. *Isolated invariant sets and the Morse index*, volume 38 of *CBMS Regional Conference Series in Mathematics*. American Mathematical Society, Providence, R.I., 1978.

[5] V. de Silva, D. Morozov, and M. Vejdemo-Johansson. Persistent Cohomology and Circular Coordinates. *Discr. Comp. Geom.*, 45(4):737–759, 2009.

[6] M. Dellnitz and O. Junge. On the approximation of complicated dynamical behavior. *SIAM J. Numer. Anal.*, 36(2):491–515, 1999.

[7] M. Dellnitz, O. Junge. Set oriented numerical methods for dynamical systems, B. Fiedler, G. Iooss and N. Kopell (eds.), in: Handbook of Dynamical Systems III: Towards Applications. *World Scientific*, 2002.

[8] S. Harker, K. Mischaikow, M. Mrozek, and V. Nanda. Discrete Morse theoretic algorithms for computing homology of complexes and maps. *Found. Comput. Math.*, 14(1):151–184, 2014.

[9] K. Mischaikow. Topological techniques for efficient rigorous computation in dynamics. *Acta Numer.*, 11:435–477, 2002.

[10] W. D. Kalies, K. Mischaikow, and Vandervorst, R. C. A. M. An algorithmic approach to chain recurrence. *Found. Comput. Math.*, 5(4):409–449, 2005.

[11] K. Mischaikow, M. Mrozek, and F. Weilandt. Discretization strategies for computing Conley indices and Morse decompositions of flows. *J. Comput. Dyn.*, 3(1):1–16, 2016.

[12] G. Osipenko. Construction of attractors and filtrations. In *Conley index theory (Warsaw, 1997)*, volume 47 of *Banach Center Publ.*, pages 173–192. Polish Acad. Sci. Inst. Math., Warsaw, 1999.

[13] A. Rößler. Runge-Kutta methods for the strong approximation of solutions of stochastic differential equations. *SIAM J. Numer. Anal.*, 48(3):922–952, 2010.

[14] P. Skraba, V. de Silva, and M. Vejdemo-Johansson. Topological Analysis of Recurrent Systems. Presented at the NIPS 2012 Workshop on Algebraic Topology and Machine Learning, December 8th, Lake Tahoe, Nevada.

[15] A. Hatcher. Algebraic Topology. Cambridge University Press, Cambridge, 2002

Monday, July 18, 2022

16:00 - 18:20

MS-05 Slow-Fast Systems and Phenomena

Saint Clair 1

Chair: Bernd Krauskopf

16:00 - 16:20
Stability of a driver-vehicle system with steering and throttle control
EDELMANN Johannes*, PLÖCHL Manfred, STEINDL Alois
*TU Wien (Getreidemarkt 9 1060 Wien Austria)

16:20 - 16:40
Nonlinear Oscillations of Acoustic Shock Waves in a Cylindrical Tube
SØRENSEN Mads*, RASMUSSEN Anders, CHRISTIANSEN Peter
*Department of Applied Mathematics and Computer Science, Technical University of Denmark (Richard Petersens Plads, Bldg. 324, DK-2800 Kongens Lyngby Denmark)

16:40 - 17:00
Controlling canard cycles
JARDON Hildeberto*, KUEHN Christian
*Technical University of Munich (Boltzmannstr. 3 85748 Garching bei München, Germany Germany)

17:00 - 17:20
Non-smooth Two Variable Expansions for Separation of Motions In Impact and Impulsively Loaded Oscillators
PILIPCHUK Valery*
*Wayne State University (5050 Anthony Wayne Dr., 2118 Detroit, Michigan 48202 United States)

Stability of a driver-vehicle system with steering and throttle control

Johannes Edelmann*, Manfred Plöchl* and Alois Steindl *
*Institute for Mechanics and Mechatronic, TU Wien, Vienna, Austria

Summary. The stability of a vehicle's driving state depends on the mechanical properties of the vehicle and the road conditions, but to a large amount also on the characteristics of the human driver. The aim of this talk is to study the influence of the driver's reaction on the stability of the steady cornering motion, which for constant control input is asymptotically stable.

Introduction

The stability of a vehicle's driving state depends on the mechanical properties of the vehicle and the road conditions, but to a large amount also on the characteristics of the human driver. The human driver might be replaced by a robot in the case of an automated vehicle. The aim of this talk is to study the influence of the driver's reaction on the stability of the steady motion, which for constant control input is asymptotically stable.
We investigate the loss of stability of a controlled understeering vehicle along a steady-state cornering motion, according to the model described in [1]. To control the trajectory of the vehicle, the human driver is assumed to either adjust the front steering angle δ_F or the driving torque M_R of the rear wheels, according to the deviation of a point P from a reference circle (Fig. 1). If we denote the deviation of the point P from the reference circle by Δr_P and the deviation of the control input $u \in \{\delta_F, M_R\}$ from the stationary value by Δu, the "simplified precision model" [2] takes the form

$$T_M \frac{d\Delta u(t)}{dt} + \Delta u(t) = c_P \Delta r_P(t-\tau) + c_D \frac{d\Delta r_P}{dt}(t-\tau), \tag{1}$$

with human reaction time τ. Delay time T_M, the control gains c_P and c_D depend on the driver's skills and on the handling behaviour of the vehicle. A similar control loop with delay for a vehicle dynamics was investigated in [3].
While frequently used driver models, based on the above modelling approach, are applied for a linear driving regime, a nonlinear design is focussed here. In particular, the brush tyre model, [4] is used for the nonlinear tyre forces at higher lateral accelerations. The driver model is able not only to control the given trajectory with the steering angle, but also with the longitudinal tyre force resulting from the rear wheel drive. This is a skill of a human (expert) driver, but rarely addressed in human driver modelling, but will become in particular important also at automated driving, when individual drive torques may be used to stabilise critical driving manoeuvres in the nonlinear driving regime.

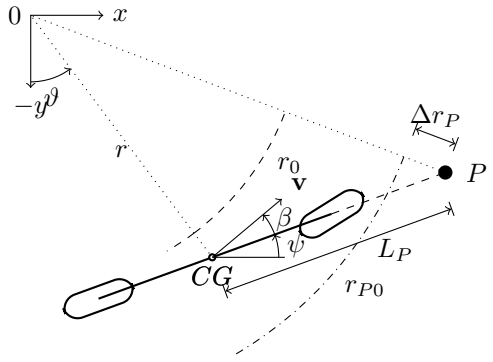

Figure 1: Geometric relations for the driver's preview model: To follow a circle with radius r_0, the driver spots a point P at a distance L_P straight ahead, which should move along a circle with radius r_{P0}.

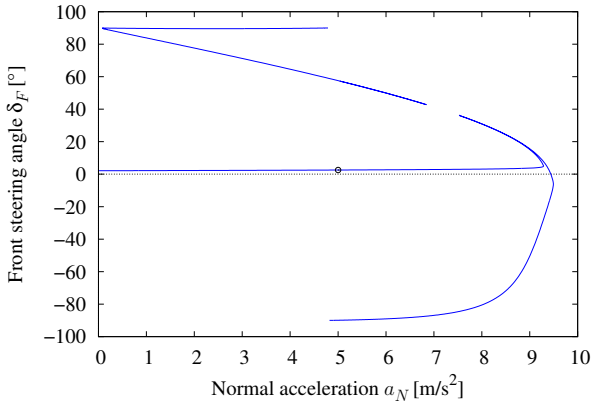

Figure 2: Handling diagram for for the considered vehicle for a steady cornering motion along a circle with radius 80 m. For the considered steady velocity $v = 20$m/s the equilibrium point is asymptotically stable.

Preliminary results

In order to investigate the linear stability of the cornering motion, we choose parameters and control inputs, for which the steady state cornering motion is asymptotically stable. As an example for such a stable motion we select the point indicated in Fig. 2, corresponding to a constant speed $v = 20$m/s. Neglecting the reaction time τ we select control gains, for which the vehicle-driver model is still asymptotically stable. Fixing these parameters, we vary the reaction time τ and determine the critical parameter values, for which a loss of stability due to a Hopf bifurcation occurs.
As can be seen from Figs. 3 and 4, the steering control depends very sensitively on the reaction time for the considered parameter values, whereas the critical reaction time τ_c for pure throttle control is far beyond the usual values.

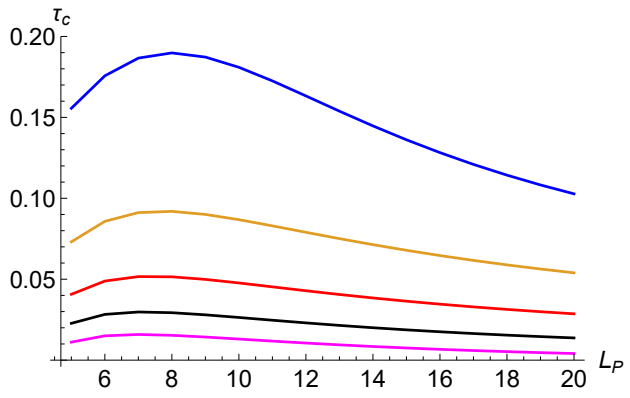

Figure 3: Critical reaction time τ_c for the occurence of a Hopf bifurcation for varying preview length L_P and control gain c_P, varying from 0.1rad/m (blue) to 0.5rad/m (magenta) with fixed value $c_D = 0.02$rad s/m for pure steering control.

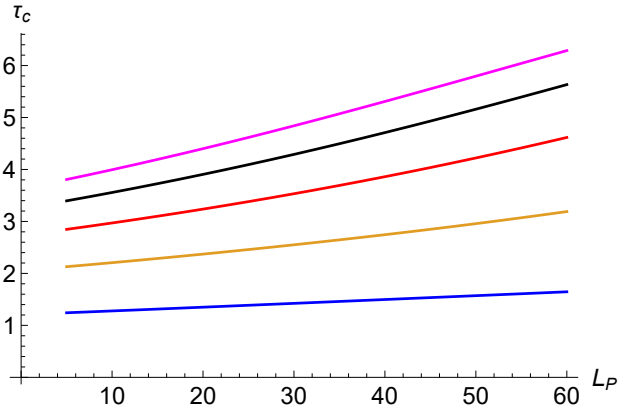

Figure 4: Critical reaction time τ_c for the occurence of a Hopf bifurcation for varying preview length L_P and control gain c_P varying from varying from 2N (blue) to 10N (magenta) with fixed value $c_D = -30$Ns for pure Throttle control.

Further research

We plan to outline realistic estimates for the drivers' control behaviour and explore the resulting driving conditions. Further we will investigate the nonlinear system after loss of stability. In the uncontrolled system considered in [1] we already observed Canard explosions and relaxation oscillations; the feedback control (1) for the drivers' behaviour introduces further time scales into the system dynamics, so we are expecting interesting slow-fast dynamic behaviour of the model.

References

[1] Steindl, A., Edelmann, J., Plöchl, M.: Limit cycles at oversteer vehicle. Nonlinear Dynamics (2019). https://doi.org/10.1007/s11071-019-05081-8

[2] McRuer, D.T.; Graham, B.; Krendel, E.S.; Reisner, W.: Human Pilot Dynamics in Compensatory Systems, AFFDL-TR-65-15, 1965.

[3] Horvath A.; Beda, P.; Takacs, D.: Modelling and stability analysis of a longitudinal wheel dynamics control loop with feedback delay, Vehicle System Dynamics, https://doi.org/10.1080/00423114.2021.1975775.

[4] Pacejka, H.B.: Tire and vehicle dynamics. Butterworth-Heinemann, Oxford (2012)

Nonlinear Oscillations of Acoustic Shock Waves in a Cylindrical Tube

Anders Rønne Rasmussen*, Peter Leth Christiansen†,‡ and Mads Peter Sørensen ‡
*GreenHydrogen, Kolding, Denmark
†Department of Physics, Technical University of Denmark, Kongens Lyngby, Denmark
‡Department of Applied Mathematics and Computer Science, Technical University of Denmark, Kongens Lyngby, Denmark

Summary. We investigate nonlinear and dissipative acoustic waves in a tube driven by a sinusoidal driver at one end and impossing a fixed wall boundary condition at the opposite end. For driving amplitudes close to resonances in the tube, we have found multiple oscillating shock waves in a weakly nonlinear thermoviscous acoustic model. For slow off resonance driving, we observed a nearly linear oscillating ground state superimposed by bursts of oscillating schock waves. The small amplitude nearly harmonic oscillations are slow, whereas the oscillating shock waves exhibit fast propagation back and forth in the tube.

Higher order nonlinear acoustic wave equation

In nonlinear acoustics the wave fields for the flow velocity or pressure will not be simple harmonic waves. Localized shock waves may be generated or acoustic streaming may appear. The resulting flow patterns results from balancing dissipation and nonlinear effects. In the literature oscillating solitons or solitary waves have been studied in a wide range of systems as long Josephson junctions and optical fiber systems. Motivated by these investigations we shall here study oscillating solitary shock waves in a tube driven by a harmonic driver at one end while imposing a fixed wall at the opposite end. We shall asume plane waves in a cylindreical tube of length ℓ.

Mathematical model

A number of model equations for weakly nonlinear acoustic wave propagation have been derived in the literature [1]. Here we use a model for acoustic waves in a Newtonian, viscous and heat conducting gas. Our model is based on the dynamical equations for the fluid motion, continuity, the heat transfer and entropy together with an equation of state. Introducing the velocity potential $\psi = \psi(x,t)$ as function of position x along the tube center axis and at time t, our one dimensional plane wave model in dimensionless variables and coordinates reads [2]

$$\psi_{tt} - \psi_{xx} = \psi_t\psi_{xx} + (\gamma - 2)\psi_{tt}\psi_t + 2\psi_{xt}\psi_x + b\psi_{xxt} \ , \tag{1}$$

where subscripts x and t denote partial derivatives with respect to the space and time variables. The fluid flow velocity $u(x,t)$ is given by the potential through $u = -\psi_x$ and the fluid pressure p is given by $p = \psi_t$. The term $b\psi_{xxt}$ models dissipation and γ equals C_p/C_v with C_p beeing the specific heat at constant pressure and C_v is the specific heat at constant volume.

Boundary conditions

At the left end ($x = 0$) of the tube a sound generator is mounted and at the right end ($x = \ell$) we have a fixed wall. The boundary conditions become

$$u(0,t) = -\psi_x(0,t) = D\sin(\omega t) \quad \text{and} \quad u(\ell,t) = -\psi_x(\ell,t) = 0 \ . \tag{2}$$

The parameter D is the driver amplitude and the driving frequency is denoted by ω. Initially we take a fluid at rest corresponding to $\psi(x,0) = 0$ and $\psi_t(x,0) = 0$. We solve Eq. (1), together with the initial conditions (2), by a semi difference method discretizing to second order in space and integrating in time using a 4-5 order Runge Kutta method. Integration is conducted until steady state has emerged. The following parameters are kept fixed $\ell = 1$, $b = 5 \cdot 10^{-4}$ and $\gamma = 1.4$.

Numerical results

For the driver parameters $D = 0.01$ and $\omega = 2\pi$ the left panel of Fig. 1 shows a three dimensional plot of the fluid velocity field $u(x,t)$ as function of x and t. The driver frequency corresponds to the eigenfrequency of the second harmonic of the linearized model (1). This means we drive the nonlinear equation at a resonance frequency. However, due to damping and the nonlinear terms the emerging steady state solution consists of two oscillating shock waves, travelling forth and back in opposite directions.

The right panel of Fig. 1 shows a plot of the fluid velocity $u(x,t)$ driven at the nonresonant frequency $\omega = 0.1$ and with driver amplitude $D = -0.125$. The simulations reveal the surprizing result that the slowly varying ground state oscillation is superimposed a fast back and forth oscillating shock wave. We observe that during one driver cycle the shock wave oscillations appear for decreasing $u(0,t)$ corresponding to compression of the fluid and disappears for increasing $u(0,t)$ corresponding to decompression.

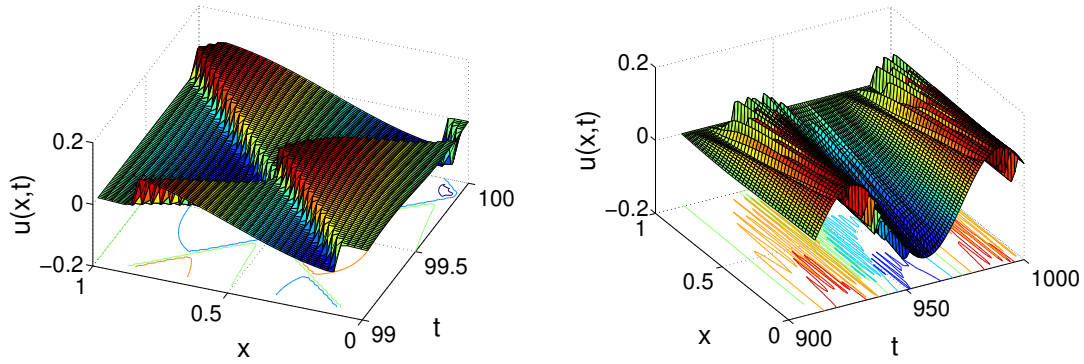

Figure 1: Left: Resonant oscillations of two counter propagating shock waves. Right: Non resonant oscillations superimposed fast travelling shock waves.

Conclusion

Driving nonlinear acoustic plane waves at resonance in a cylindrical tube leads to oscillating shock waves. A driving frequency corresponding to the n'th linear excitation mode in the linearized model of Eq. (1) leads to n oscillating fully nonlinear shocks. However, an upper limit for the number of oscillating shocks is expected given by the width of the shocks and the space available in the tube. For the nonresonant driving case full numerical simulations revealed excitation of a nearly linear ground state superimposed oscillating shock waves in bursts.The shock waves oscillates fast back and forth in comparison to the slow ground state wave oscillation.

Aknowledgement

We acknowledge financial support from Civilingeniør Frederik Leth Christiansen's almennyttige fond.

This work is dedicated to the memory of Yuri B. Gaididei.

References

[1] Jordan P. M. (2016) A survey of weakly-nonlinear acoustic models: 1910-2009. *Mechanics Research Communications* **73**:127-139.

[2] Gaididei Yu. B., Rasmussen A. R., Christiansen P. L. and Sørensen M. P. (2016) Oscillating Nonlinear Acoustic Shock Waves. *Evolution Equations and Control Theory* **5**(3):367-381.

Controlling canard cycles

Hildeberto Jardon-Kojakhmetov*, and Christian Kuehn *
**Zentrum Mathematik, Technische Universität München, Boltzmannstr. 3, 85748 Garching bei München, Germany*

Summary. Canard cycles are periodic orbits that appear as special solutions of fast-slow systems (or singularly perturbed Ordinary Differential Equations). It is well known that canard cycles are difficult to detect, hard to reproduce numerically, and that they are sensible to exponentially small changes in parameters. By combining Geometric Singular Perturbation Theory and state feedback control techniques, we design controllers that stabilize canard cycles of planar fast-slow systems with a folded critical manifold. As an application, we propose a controller that produces stable mixed-mode oscillations in the van der Pol oscillator.

Introduction

Fast-slow systems (also known as singularly perturbed ordinary differential equations are often used to model phenomena occurring in two or more time scales. Examples of these are vast and range from oscillatory patters in biochemistry and neuroscience all the way to stability analysis and control of power networks, among many others. The overall idea behind the analysis of fast-slow systems is to separate the behavior that occurs at each time scale, understand such behavior, and then try to elucidate the corresponding dynamics of the full system. Many approaches have been developed, such as asymptotic methods, numeric and computational tools and geometric techniques, see e.g. [4, 10].

Although the time scale separation approach has been very fruitful, there are some cases in which it does not suffice to completely describe the dynamics of a fast-slow system. The reason is that, for some systems, the fast and the slow dynamics are interrelated in such a way that some complex behavior is only discovered when they are not fully separated. An example of the aforementioned situation are the so-called *canards* [1]. Canards are orbits that, counter-intuitively, stay close for a considerable amount of time to a repelling set of equilibrium points of the fast dynamics. Canards are extremely important in the theory of fast-slow systems, and through them one can explain, for example, the very fast onset of large amplitude oscillations due to small changes of a parameter in neuronal models[3, 9], and the delayed loss of stability due to a slow passage through a singularity [11, 12]. However, due to their very nature, canard orbits are not robust, meaning that small perturbations may drastically change the shape of the orbit.

On the other hand the application of singular perturbation techniques in control theory is far-reaching. Perhaps, as already introduced above, one of the biggest appeals of the theory of fast-slow systems is the time scale separation, which allows the reduction of large systems into lower dimensional ones for which the control design is simpler. Applications range from the control of robots, all the way to industrial biochemical processes, and large power networks [7]. However, as already mentioned, not all fast-slow systems can be analyzed by the convenient time scale separation strategy, and although some efforts from very diverse perspectives have been made, a general theory that includes not only the regulation problem but also the path following and trajectory planning problems is, to date, lacking.

Here we merge techniques of fast-slow dynamical systems with control theory methods to develop controllers that stabilize canard orbits. The idea of controlling canards has already been explored in [2], where an integral feedback controller is designed for the FitzHugh-Nagumo model to steer it towards the so-called "canard regime". In contrast, here we take a more general and geometric approach by considering the canard normal form.

Main results

The formal statements of these results and the corresponding proofs are available in [5].

Consider the fast-slow control problem

$$\begin{aligned} x' &= -y + x^2 + u(x, y, \varepsilon, \alpha) \\ y' &= \varepsilon(x - \alpha), \end{aligned} \tag{1}$$

where $(x, y) \in \mathbb{R}^2$ are the fast and slow variables respectively, $\alpha \in \mathbb{R}$ is a parameter, $0 < \varepsilon \ll 1$ is the perturbation aprameter responsible for the time scale separation, and $u \in \mathbb{R}$ denotes a state-feedback controller.

Our main result is a controller u that renders canard cycles of (1) asymptitically stable as shown in Figure 1.

As an application we consider controlled the van der Pol equation

$$\begin{aligned} x' &= -y + x^2 - \frac{1}{3}x^3 + u \\ y' &= \varepsilon x. \end{aligned} \tag{2}$$

and design a controller that is able to produce in a robust way any type of Mixed-Mode Oscillation (MMO) allowed by the geometry of the critical manifold. An example of such MMO is shown in Figure 2.

Our main techniques of analysis are the blow-up method [6], canard theory [1, 8] and state feedback control design based on Lyapunov stability [13].

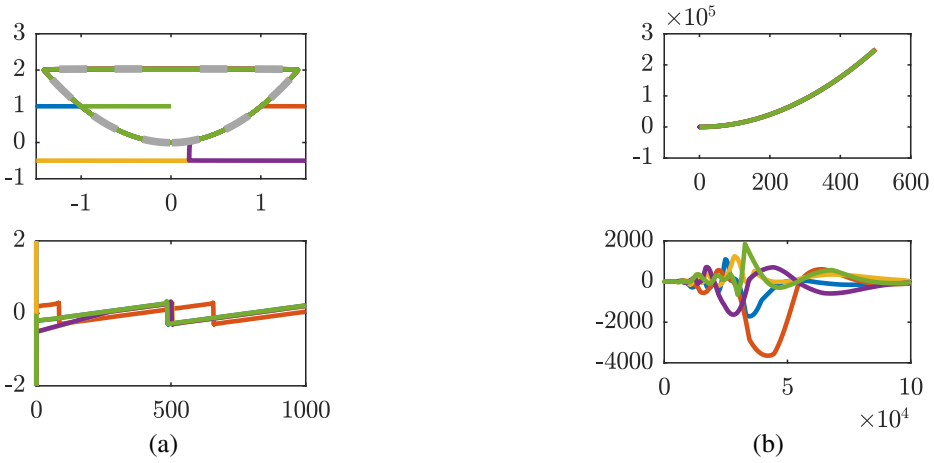

Figure 1: In both columns we show, in the first row the (x, y) phase portrait of the closed-loop system (1) and in the second row the time-series of the corresponding controller. In all these simulations $\varepsilon = 0.01$. (a) The case of bounded canard cycles, where the desired canard cycle to be followed is shown in dashed-grey. (b) The maximal canard case, which is unbounded, and yet can be followed with a bounded controller.

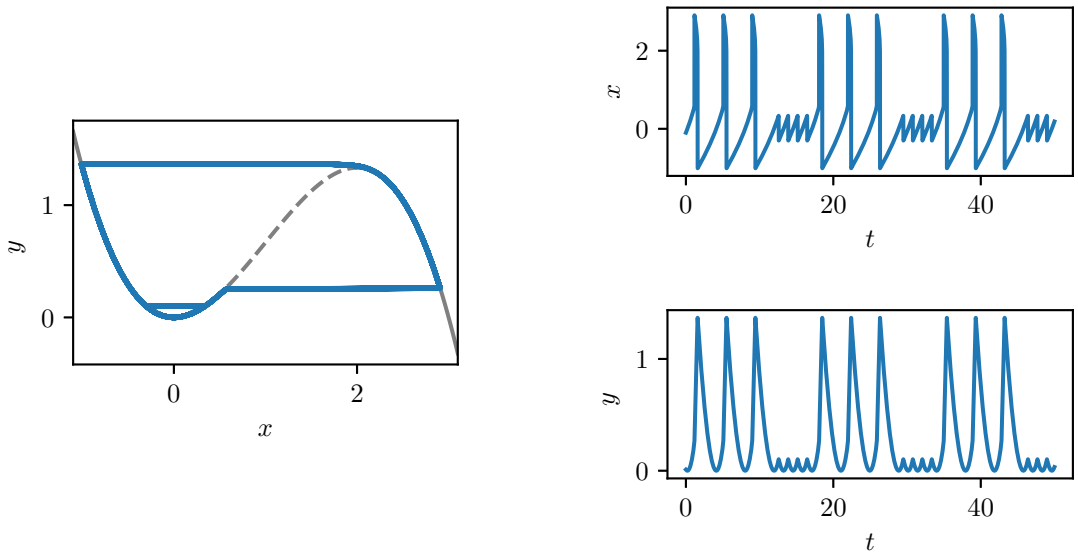

Figure 2: A sample of a Mixed-Mode Oscillation (MMO) with 3 Large Amplitude Oscillations (LAOs) and 4 Small Amplitude Oscillations (SAOs) produced by our controller. Such a controller has as parameters the number of LAOs, the number of SAOs, and the height of the canards.

References

[1] F. Dumortier and R. Roussarie. *Canard cycles and center manifolds*, volume 577. American Mathematical Society, 1996.

[2] J. Durham and J. Moehlis. Feedback control of canards. *Chaos: An Interdisciplinary Journal of Nonlinear Science*, 18(1):015110, 2008.

[3] G. B. Ermentrout and D. H. Terman. *Mathematical foundations of neuroscience*, volume 35. Springer Science & Business Media, 2010.

[4] N. Fenichel. Geometric singular perturbation theory for ordinary differential equations. *Journal of differential equations*, 31(1):53–98, 1979.

[5] H. Jardon-Kojakhmetov and C. Kuehn. Controlling canard cycles. *arXiv preprint arXiv:1911.11861*, 2019.

[6] H. Jardón-Kojakhmetov and C. Kuehn. A survey on the blow-up method for fast-slow systems. *arXiv preprint arXiv:1901.01402*, 2019.

[7] P. Kokotovic, H. K. Khalil, and J. O'Reilly. *Singular perturbation methods in control: analysis and design*, volume 25. SIAM, 1999.

[8] M. Krupa and P. Szmolyan. Extending geometric singular perturbation theory to nonhyperbolic points—fold and canard points in two dimensions. *SIAM journal on mathematical analysis*, 33(2):286–314, 2001.

[9] M. Krupa and P. Szmolyan. Relaxation oscillation and canard explosion. *Journal of Differential Equations*, 174(2):312–368, 2001.

[10] C. Kuehn. *Multiple time scale dynamics*, volume 191. Springer, 2015.

[11] A. I. Neishtadt. On delayed stability loss under dynamical bifurcations I. *Differential Equations*, 23:2060–2067, 1987.

[12] A. I. Neishtadt. On stability loss delay for dynamical bifurcations. *Discrete and Continuous Dynamical Systems. Series S*, 2:897, 2009.

[13] J. J. E. Slotine and W. Li. *Applied nonlinear control*, volume 199. Prentice hall Englewood Cliffs, NJ, 1991.

Non-smooth Two Variable Expansions for Separation of Motions In Impact and Impulsively Loaded Oscillators

Valery Pilipchuk
Wayne State University, Detroit, USA

Summary. Non-smooth two variable expansions for impact and impulsively loaded oscillators are introduced. In particular, the role of fast temporal scale is assigned to the triangle sine wave, whereas amplitude and/or frequency modulations are described in a smooth slow temporal scale. The developed tool allows for derivations of closed form solutions describing non-stationary oscillatory dynamics of systems with cyclical impacts or external impulses. Different illustrating examples of oscillators with amplitude limiters are considered assuming the coefficient of restitution is closed to unity.

Introduction

Nonstationary dynamics of oscillating systems under non-holonomic constraint conditions became of significant interest due to different ideas of using impact oscillators as elements of energy absorbers or harvesters. In contrast to the harmonic oscillator, the basic impact oscillator has no specific natural frequency and therefore can interact with different subsystems in a wide range of spectrum, which is important property for the design of such devices. It is shown in this work that the 'hyperbolic complexification' of the state variables provides the adequate way to describing the effect of energy loss through specific boundary conditions generated by the triangle wave temporal argument. Then analytical algorithms for solving the corresponding boundary value problems are applied. In addition to the possibility of calculations without conditioning the variables at collision times, the suggested type of solutions can be effectively used in different analytical manipulations dictated by the purpose of study due to the closed form of solutions.

Technical details

The present analytical procedure essentially involves a couple of piecewise linear functions admitting also representation in a closed form through elementary functions (Fig.1a)

$$\tau(t)=\frac{2}{\pi}\arcsin\left(\sin\left(\frac{\pi t}{2}\right)\right)=\begin{cases} t & \text{if } -1\le t\le 1\\ 2-t & \text{if } 1<t\le 3\end{cases},\quad \tau\left(t+4\right)\overset{\forall\phi}{=}\tau\left(t\right)$$
$$e(t)=\dot\tau(t)=\operatorname{sgn}\left(\cos\left(\frac{\pi t}{2}\right)\right)=\begin{cases} 1 & \text{if } -1<t<1\\ -1 & \text{if } 1<t<3\end{cases},\quad e\left(t+4\right)\overset{\forall\phi}{=}e\left(t\right) \tag{1}$$

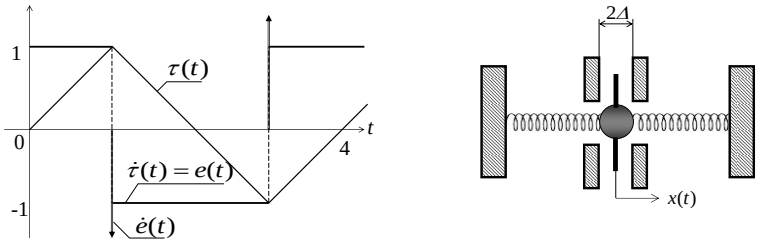

(a) (b)

Figure 1: a) Non-smooth basis, and b) harmonic oscillator with amplitude limiters.

Functions (1) are used in different variations and contents in the literature, see for instance references [1, 2] as relevant to the area. However, normalizations for the amplitudes and periods shown in Fig.1 are essential for the present methodology, in which the rectangular wave $e(t)$ plays the role of a *unipotent* of the so-called *hyperbolic number* due to the property $e^2=1$. Namely any periodic process $x(t)$ of the period $T = 4$ admits representation in the form [3] $x(t)=X(\tau)+Y(\tau)e$. In case of modulated oscillatory motions a slow time η is added as

$$x(t)=X(\tau,\eta)+Y(\tau,\eta)e,\quad e^2=1 \tag{2}$$

where $\tau=\tau(\varphi)$, $e=e(\varphi)$, $\dot\varphi=\omega(\eta)$, $\eta=\varepsilon t$ $(0<\varepsilon<<1)$.

Then the triangle wave τ is considered as a fast temporal scale of the following two variable expansions

$$\begin{aligned} X(\tau,\eta)&=X_0(\tau,\eta)+X_1(\tau,\eta)\varepsilon+X_2(\tau,\eta)\varepsilon^2+O\left(\varepsilon^3\right)\\ Y(\tau,\eta)&=Y_0(\tau,\eta)+Y_1(\tau,\eta)\varepsilon+Y_2(\tau,\eta)\varepsilon^2+O\left(\varepsilon^3\right)\\ \dot\varphi&=\omega(\eta)=\omega_0(\eta)+\omega_1(\eta)\varepsilon+\omega_2(\eta)\varepsilon^2+O\left(\varepsilon^3\right)\end{aligned} \tag{3}$$

Substituting (2-3) into differential equation of motion and using the corresponding condition on velocity at impact times leads to the sequence of boundary value problems for X and Y on the interval of the oscillating time argument $-1\le\tau\le 1$ [4]. Some of the boundary conditions occur as a result of elimination of singularities produced by differentiation of the

basic functions (1), whereas specific boundary condition is imposed by the dissipative interaction with amplitude limiters. *Note that the conventional two variable procedure, which is typically applied to quasi linear vibrating systems, produces the differential equations for slow motions as a result of elimination of secular terms from the expansions [5]. Instead the present analytical algorithm derives the slow time equations from the boundary conditions at* $\tau = \pm 1$. Due to technical complexity of analytical manipulations with series (3) in general form, different adaptations for particular cases at the preliminary stage of derivations can be applied. For instance, free impact vibrations of the model shown in Fig.1b do not have amplitude modulations as long as the energy remains sufficient for reaching the amplitude limiters. In this case, the explicit dependence on η in *X* and *Y* terms of expansions (3) can be ignored as it is done in the example below. The effect of energy loss is completely captured by the slow varying frequency terms.

Example

Free vibrations of the illustrating model, which is shown in Fig. 1b, is described with equations

$$\ddot{x} + \Omega^2 x = 0, \ |x| \le \Delta, \quad \dot{x}(t_i + 0) = -k\dot{x}(t_i - 0), \quad k = 1 - \varepsilon, \quad 0 < \varepsilon \ll 1 \tag{4}$$

This oscillator experiences impulsive reaction forces from the amplitude limiters at collision times. Therefore, assuming that the condition $|x| \le \Delta$ holds, equation (4) is replaced with

$$\ddot{x} + \Omega^2 x = pe'(\varphi), \quad p = p(\eta) = p_0(\eta) + p_1(\eta)\varepsilon + p_2(\eta)\varepsilon^2 + O\left(\varepsilon^3\right) \tag{5}$$

where the slowly varying intensity of impulses $p(\eta)$ is sequentially determined from the boundary conditions obtained by substituting (2) in (5) as

$$\tau = \pm 1: \quad Y = 0, \quad X = \pm\Delta, \quad X'\omega^2 = p \tag{6}$$

The condition on velocity in (4) gives

$$\tau = \pm 1: \quad Y' \mp X' = -(1-\varepsilon)\left(Y' \pm X'\right) \tag{7}$$

As mentioned, conditions (6) eliminate singularities produced by substitution of (2) in (5), whereas conditions (7) require somewhat detailed consideration [4]. Then conducting two steps of the asymptotic procedure gives finally the closed form solution (Fig. 2)

$$x(t) = \Delta\left[\frac{\sin\lambda\tau}{\sin\lambda} - \frac{\varepsilon}{2\Omega}\frac{d\lambda}{d\eta}\left(\frac{\cos\lambda\tau}{\cos\lambda} - \tau\frac{\sin\lambda\tau}{\sin\lambda}\right)e\right] + O(\varepsilon^2)$$
$$\tau = \tau(\varphi), \quad \frac{d\varphi}{dt} = \frac{\Omega}{\lambda}, \quad \frac{d\lambda}{d\eta} = \frac{\Omega}{2}(1+\cos 2\lambda)\left(1 + \frac{\sin 2\lambda}{2\lambda}\right)^{-1} \tag{8}$$

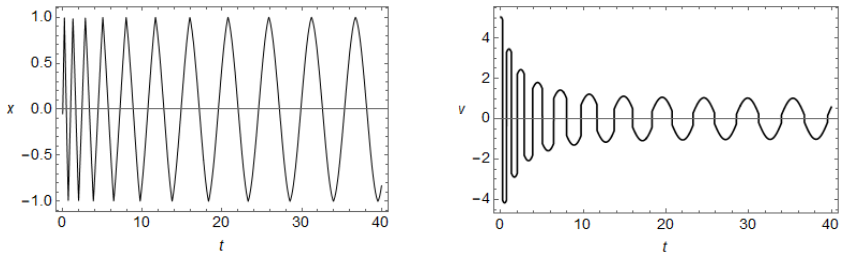

(a) (b)

Figure 2: Time history of the state variables of impact oscillator with energy loss at its boundaries: a) coordinate, and b) velocity showing transition to the so-called 'grazing' regime with near zero impact pulses.

Conclusion

A class of vibrating systems with perfectly stiff amplitude limiters is considered by means of non-smooth time substitutions. The motion is represented as a combination of the oscillating component, which is due to cyclic collisions with the limiters, and a slow decay caused by the energy loss at collision times. A specific modification of the two variable expansions is used, where the non-smooth (triangle wave) temporal argument is viewed as a fast time while the energy decay is described in a slow time scale. As a result, closed-form analytical solutions are obtained that automatically satisfy collision conditions with the energy loss. Three qualitatively different basic types of vibrations are considered to cover periodic, frequency modulated, and amplitude-frequency modulated motions.

References

[1] Zhuravlev, V.F. (1976) Method for Analyzing Vibration-impact Systems by Means of Special Functions. *Izvestiya AN SSSR MTT*, **11**:30--34
[2] Thomsen J.J., Fidlin A. (2008) Near-elastic Vibro-impact Analysis by Discontinuous Transformations and Averaging. *JSV*, **311**: 386-407.
[3] Pilipchuk, V.N. (2001) Impact modes in discrete vibrating systems with bilateral barriers. *Int. J. Nonlinear Mechanics*, **36**:999-1012.
[4] Pilipchuk, V.N. (2015) Closed-form Solutions for Oscillators with Inelastic Impacts. *JSV*, **359**:154-167
[5] Kevorkian J., Cole J. D. (1996) Multiple scale and singular perturbation methods. Springer-Verlag, NY.

Monday, July 18, 2022
16:00 - 18:20

MS-07 Dynamics and Optimization of Multibody Systems
Saint Clair 2

Chair: József Kövecses - Marek Wojtyra

16:00 - 16:20
Coupled Vehicle-Guideway Dynamics Simulations of the Transrapid with Discretized Levitation Magnet Forces
SCHNEIDER Georg[*], SCHMID Patrick, DIGNATH Florian, EBERHARD Peter
[*]Institute of Engineering and Computational Mechanics, University of Stuttgart (Pfaffenwaldring 9, 70569 Stuttgart Germany)

16:20 - 16:40
Joint Reactions Distribution and Uniqueness in Overactuated Multibody Systems
WOJTYRA Marek[*], PĘKAL Marcin
[*]Warsaw University of Technology, Institute of Aeronautics and Applied Mechanics (Nowowiejska 24, 00-665 Warsaw Poland)

16:40 - 17:00
Flight Behaviour of a Two-Line, Four-Point Disk Kite
ROEVEN Luke[*], GUTSCHMIDT Stefanie, ALEXANDER Keith
[*]L Roeven (University of Canterbury, Mechanical Engineering Department New Zealand)

17:00 - 17:20
Identification of Friction Models for MPC-based Control of a Power-Cube Serial Robot
FEHR Joerg, **KARGL Arnim**[*], HANNES Eschmann
[*]Institute of Engineering and Computational Mechanics, University of Stuttgart (Pfaffenwaldring 9, 70569 Stuttgart Germany)

Coupled Vehicle-Guideway Dynamics Simulations of the Transrapid with Discretized Levitation Magnet Forces

Georg Schneider[1], Patrick Schmid[1], Florian Dignath[2], and Peter Eberhard[1]
[1]*Institute of Engineering and Computational Mechanics, University of Stuttgart, Stuttgart, Germany*
[2]*thyssenkrupp Transrapid GmbH, Munich, Germany*

Summary. Magnetic levitation (maglev) is a promising technology for high-speed transportation systems, as shown by the Transrapid line in Shanghai operating successfully for nearly 20 years. Currently, a new high-speed train based on this technology is being developed, driven by China's Ministry of Science and Technology. Magnets are one of the key components of a maglev vehicle's suspension system. Attractive magnet forces ensure the contactless coupling of the vehicle to the guideway. Electromagnets are usually described using finite element (FE) models, electromagnetic circuit models, or simple analytical models for simulation purposes. However, FE magnet models are computationally often overwhelming, especially for transient studies, and thus too slow to use them in large vehicle models for vehicle dynamics simulations. Moreover, the parameterization of FE models often is non-trivial. Therefore, less detailed but fast-computable models are used in such simulations, often providing only a coarse discrete distribution of magnet forces along the vehicle. In this contribution, the coupled vehicle-guideway dynamics is investigated regarding different discretizations of levitation magnet forces. A two-dimensional model of the maglev vehicle Transrapid moving along an infinite elastic guideway is used, considering the heave-pitch motion of the vehicle and the vertical guideway bending. Simulations are performed using either a coarse distribution with two magnet forces per magnet or a fine distribution with twelve magnet forces per magnet, i.e., one magnet force at each magnet pole. It is shown that the simplification of two magnet forces per levitation magnet is valid for vehicle dynamics simulations. The model is parameterized with data from the Transrapid TR08 and uses a self-developed model predictive control (MPC) scheme to control the magnets.

Introduction

In Shanghai, the only commercial high-speed magnetic levitation (maglev) train based on electromagnetic suspension (EMS) technology is in operation at the Shanghai Maglev Transportation (SMT) line between Pudong International Airport and Longyang Road Station. It is operating with a maximum speed of 430 km/h. A new high-speed maglev train with a designed top speed of more than 600 km/h is developed at the Chinese rolling stock manufacturer CRRC Qingdao Sifang Co., Ltd. A prototype of the vehicle has already been presented to the public [1]. In Japan, at the same time the SCMaglev, a high-speed maglev train based on the electrodynamic suspension (EDS) technology using superconducting magnets, is developed [2]. High-speed maglev trains can close the gap between current high-speed railway technology with top speeds of 300 to 350 km/h and aircraft traveling at around 900 km/h. To investigate the dynamic behavior of the coupled system of guideway, vehicle, magnet, and controller, simulations and analyses with suitable models are essential tools in the development process regarding, e.g., the general design or safety and ride comfort aspects.
Magnets are key components of a maglev vehicle's suspension system. Hence, mathematical magnet models sufficiently describing the magnet statics and dynamics are essential for reliably predicting the behavior of a single magnet and eventually of the complete coupled system of vehicle and guideway by means of computer simulations. Depending on the issue to be investigated, the complex electromagnetic field needs to be modeled in different levels of detail. On the one hand, simple magnet models usually neglect effects like magnetic saturation and eddy currents, which become relevant for high loads, failure scenarios, and high velocities. Detailed magnet models taking these effects into account, on the other hand, are often computationally intensive and therefore unsuitable for application in large vehicle models for dynamics simulations. Basically, three ways to simplify physically detailed but computationally intensive magnet models exist. Firstly, simplification by neglecting highly nonlinear physical effects like saturation, see [3], secondly, model reduction procedures still considering these physical effects and at the same time reducing the computational effort, as elaborated in [4], and, thirdly, simplifications concerning the distribution of magnet forces along the vehicle. In literature, various maglev vehicle models are described with different levels of detail regarding the distribution of levitation magnet forces along the vehicle. In [5], a very coarse distribution is applied with four levitation magnet forces per vehicle section in the most complex model variant. The models from [6, 7] use one or two magnet forces per magnet, respectively. In [8], a model of the controlled magnets is presented, providing two magnet forces per magnet, combining both the magnet model and the control law in a PID-T1 system. Another approach is used in [9], where two torques are applied in addition to two forces per magnet. Both are multiplied with position-dependent factors mapping the discrete force application points (FAPs) to the continuous magnet force distribution of the real magnet. A fine distribution with one force per pole is implemented in [3], but the corresponding magnet model is simple with limited valid operational range. In [10], a magnet model with two forces per magnet from [4] is used to analyze the coupled dynamics of a vehicle consisting of three sections with 48 levitation magnet forces in total, moving along an infinite series of elastic guideway elements. While the influence of nonlinear physical effects like saturation and eddy currents has been investigated in detail in [4], the influence of magnet force distribution has not yet been investigated systematically. Therefore, the question arises whether it is a valid simplification in simulations of coupled vehicle-guideway dynamics to summarize the magnet force, which is actually distributed continuously along the magnet, in a single concentrated substitute magnet force per magnet or half magnet, respectively, or if a finer distribution is required with forces acting, e.g., at each pole.

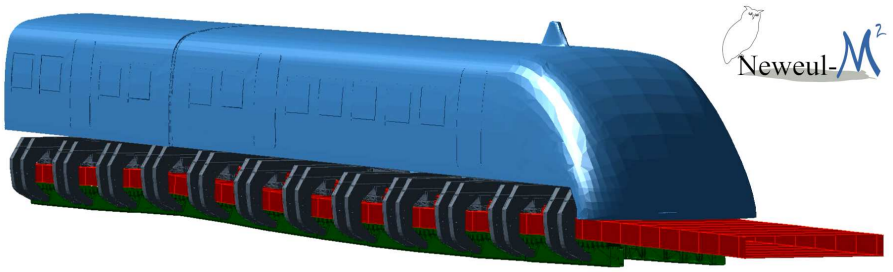

Figure 1: Coupled system of a rigid multibody maglev vehicle and an elastic guideway modeled and visualized with Neweul-M^2.

Simulation Model

In this contribution, the influence of levitation magnet force distribution on the dynamic behavior of the coupled vehicle-guideway system is investigated. A two-dimensional model of a maglev vehicle moving along an infinite elastic guideway based on [10] is used, mapping the heave-pitch motion of the vehicle and the vertical guideway bending. The infinite track is represented by a small number of identical single-span Euler-Bernoulli beams, which are used repeatedly, following the concept of moving system boundaries. The vehicle is modeled as a rigid multibody system with three sections, each one consisting of a car body, levitation chassis, and levitation magnets coupled by air springs and elastomer elements. The mechanical model has 76 degrees of freedom. Figure 1 shows the coupled system modeled and visualized with the in-house multibody simulation toolbox Neweul-M^2 [11]. The vehicle mechanics is parameterized with values from the Transrapid model called TR08, the predecessor of the SMT vehicle running in Shanghai. Parameters representing the first generation of concrete girders at the test facility in northern Germany (TVE) are taken for the guideway elements. The simulation model is basically the one described in [10], therefore, the interested reader is referred to this publication for a complete model description. Nevertheless, to provide a good understanding of the model, its most important aspects are summarized below, as well as the extensions and changes made for the work at hand.

Mechanical Vehicle Model

The vehicle model represents a detailed two-dimensional rigid multibody model of the maglev vehicle Transrapid mapping the heave-pitch motion in the x-z-plane. It represents a longitudinal section of the system. The left and right side of the system, that is the y-direction, are summed up. An overview of the mechanical vehicle components is given in Fig. 2.
The model comprises a rear end section, a mid section, and a front end section. Each section consists of rigid bodies for a car body, four levitation chassis, and seven or eight levitation magnets, respectively. Each section has the length of eight standard levitation magnets, but the magnets are arranged in such a way that a magnet connects the neighboring levitation chassis of two sections. At the front and rear end of the vehicle, bow levitation magnets are installed that are longer and have 14 poles, while standard levitation magnets have twelve poles. Thus, bow levitation magnets have a shifted center of gravity and higher mass and inertia compared to a standard levitation magnet. Each rigid body has two degrees of freedom (DOF): a translational one in z-direction and a rotational one about the y-axis, making up 76 DOF for the complete vehicle.
Stiff elastomer elements connect the car bodies. The support of the car bodies on the levitation chassis is realized by rather soft air springs, also called secondary suspension. The primary suspension, i.e., the connection of levitation magnets and levitation chassis, is realized by stiff elastomer elements again. All elastomer elements and air springs are implemented as linear spring-damper combinations in the model.
Furthermore, the magnets are attracted to the guideway by magnet forces computed by the magnet models described below. For the coupling with the magnet computation, the distances to the guideway reference plane are outputs of the mechanical system for calculating the air gaps, and the magnet forces are inputs to the mechanical system. As shown in Fig. 3, there are two or twelve such inputs and outputs for each standard magnet. For the longer bow magnets, there are

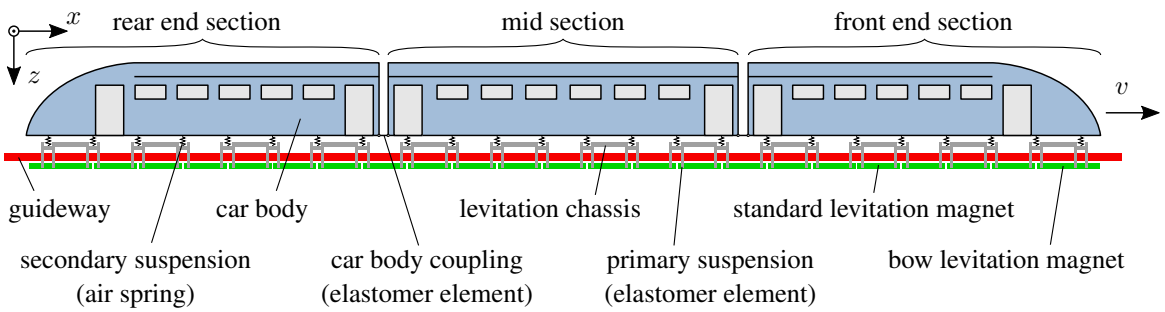

Figure 2: Components of the complete vehicle model on the guideway.

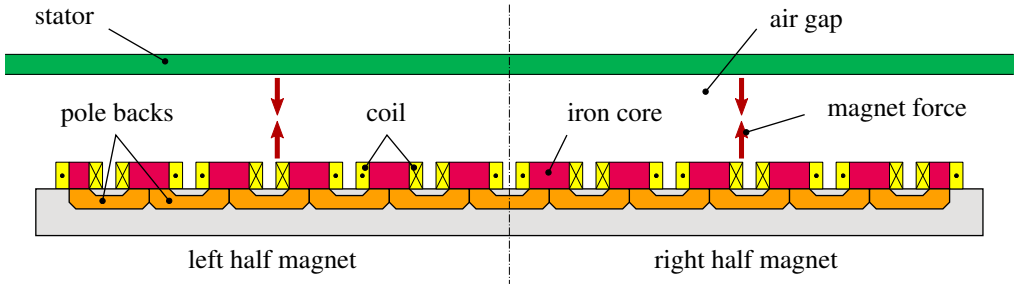

(a) Coarse distribution of magnet forces with one force per half magnet.

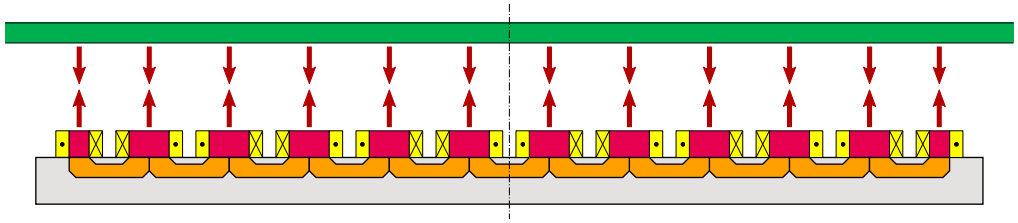

(b) Fine distribution of magnet forces with one force per pole.

Figure 3: Variants of magnet force distributions along a levitation magnet.

either three or fourteen inputs and outputs. Furthermore, the velocities of the poles or FAPs of concentrated substitute forces, respectively, are defined as outputs of the mechanical model. They are necessary to compute the time derivatives of the air gaps at each of the poles or FAPs of concentrated substitute forces, respectively, required by the magnet model to compute the magnet forces.

Mechanical Guideway Model

The track is implemented as a regularly pillared elastic guideway of infinite length. Applying the concept of moving system boundaries as proposed in [12], a small number of identical Euler-Bernoulli beams is used repeatedly, as shown in Fig. 4. In [10], the implementation of this concept to obtain an infinitely long track is described. In short, a guideway element is taken from behind the vehicle as soon as it is no longer required there, its states are reset, and it is placed in front of the vehicle again.

A detailed description of a single guideway element, a simply supported single-span elastic Euler-Bernoulli beam discretized by 24 finite beam elements and reduced to its first three eigenmodes, can be found in [13]. The application of moving magnet forces to the beam by means of equivalent nodal forces and torques at its nodes and the interpolation of nodal coordinates to get the deflections at arbitrary positions between the nodes using Hermite interpolation polynomials is explained there as well.

Compared to the guideway described in [10], additional static guideway disturbances are added to the model for the work at hand. According to the design principles for high-speed maglev systems from the German Federal Railway Authority,

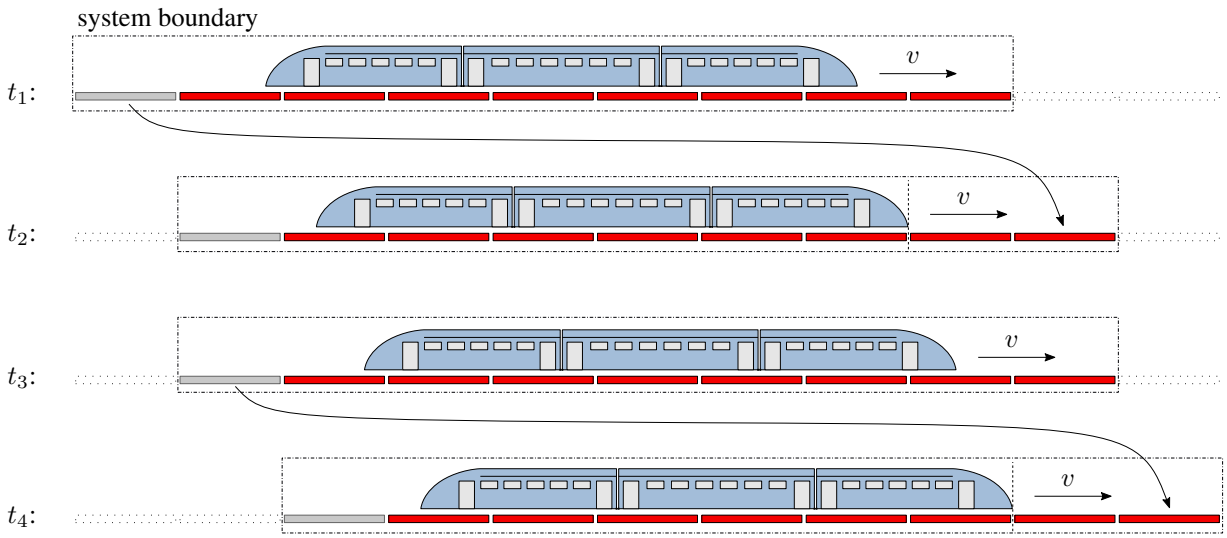

Figure 4: Concept of moving system boundaries: A small number of guideway elements is used repeatedly to realize an infinitely long elastic guideway in an efficient manner.

see [14], different types of guideway irregularities are to be considered. First, there is the bending of the girders when loaded with the vehicle. This effect is taken into account by modeling the guideway elements as elastic Euler-Bernoulli beams. Second, the pillars supporting the girders may have different heights resulting in not perfectly flat positions of the supported girders. And third, for the vertical position of the stator packs mounted to the girders, there are tolerances as well. The last two disturbances are applied to the guideway model in a statistical manner as presented in [15].

Magnet Model

Vehicle and guideway are coupled by the magnet forces of the levitation magnets. With the work at hand, the influence of magnet force distribution on vehicle and guideway dynamics is investigated. Actually, the magnetic field between the poles and the stator is distributed continuously along the magnet. To represent such a continuous distribution with a high degree of detail, a finite element model would be desirable, but this is unsuitable for vehicle dynamics simulations because of the tremendous computation time, enormous parameterization effort, or meshing difficulties. Therefore, the continuous force field must be discretized for computer simulations, and the question arises of how detailed this discretization must be. Therefore, two different discretization approaches are analyzed and compared here: a fine one with one magnet force per pole, and a coarse one with one magnet force per half magnet, i.e., two forces per standard levitation magnet. Both approaches are depicted in Fig. 3.

In [4], a detailed magnet model is presented, considering the physical effects of magnetic reluctances, fringing and leakage flux, magnetic saturation, and eddy currents. It is validated for a standard levitation magnet of the maglev vehicle Transrapid and computes the magnet forces at each of the twelve poles. Additionally, a simplified magnet model is derived from the detailed one based on a reduction technique, providing just one concentrated substitute magnet force per half magnet. Concerning the magnetic and electric properties, it was shown in [4] that the difference with respect to the detailed model is negligible if the air gap is identical at all poles of one magnet. Its computation time is two orders of magnitude faster, making it usable for dynamics simulations of large vehicle models. In the contribution at hand, the influence of magnet force distribution is investigated by applying both magnet models from [4], the detailed magnet model providing one magnet force per pole and the simplified one providing one force per half magnet, to the model of the coupled vehicle-guideway system described above and comparing the results.

Controller

The reciprocal relation of the air gap and the attractive magnet forces – that pull the vehicle to the stator of the guideway from below – leads to an unstable system, which must be actively controlled to allow stable levitation. The air gap must be kept in a safe range to avoid physical contact between the vehicle and the guideway and simultaneously the acceleration has to be reduced to improve ride comfort. Each half magnet has its own gap measurement unit (GMU) and is controlled individually by its own magnet control unit, which provides the voltage for the magnet based on the gap, acceleration, and current measurements. As shown in [10], a self-developed offset-free model predictive control (MPC) scheme from [16] shows a promising performance even for higher speeds than the TR08 was designed for. Therefore, for both levels of detail of magnet force discretization, the magnets are controlled by this MPC controller instead of the actual control algorithm implemented for the TR08.

Coupled System

All subsystems, i.e., vehicle mechanics, guideway mechanics, magnets, and controllers are combined in a Simulink model representing the complete coupled system. The schematic setup of the Simulink model is shown in Fig. 5. For more details

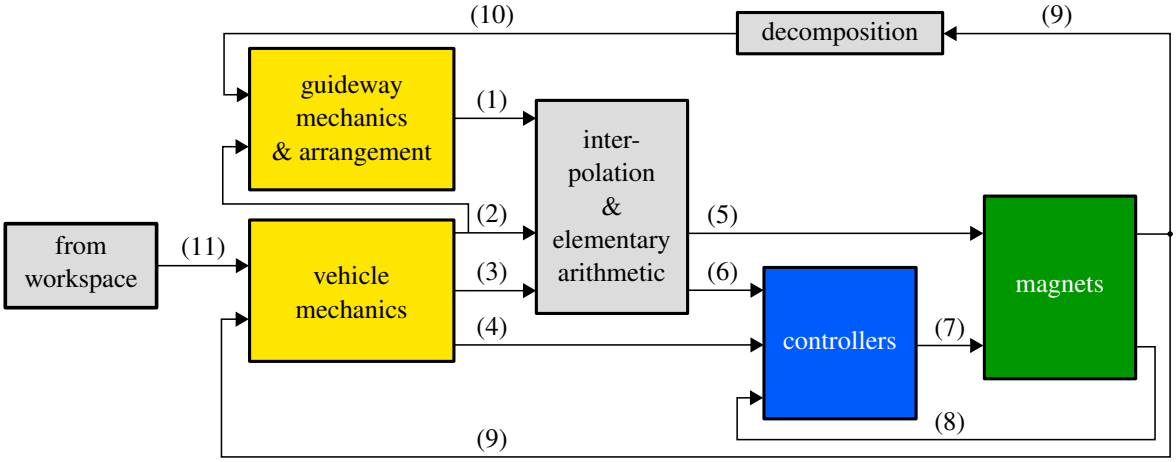

Figure 5: Schematic setup of the coupled model in Simulink. (1) nodal coordinates and velocities of beams, (2) x-positions of magnet forces, (3) magnet z-positions and velocities at magnet FAPs, x-positions of GMUs, magnet z-positions at GMUs, (4) magnet z-accelerations at GMUs, (5) air gaps and air gap velocities at magnet FAPs, (6) air gaps at GMUs, (7) magnet voltages, (8) magnet currents, (9) magnet forces, (10) nodal forces and torques, (11) x-position of front end car body. For more details see [10].

regarding the Simulink model and its signal flow, please refer to [10]. Due to the modular structure of the Simulink model, the individual components can be replaced with little effort. Thus, the simplified magnet model can be replaced easily with the detailed magnet model for the simulations described in the following.

Simulation Results

In the simulated scenario, the vehicle consisting of three sections is traveling on the infinite elastic guideway with a constant speed of 300 km/h. By comparing the two configurations with different force discretization, the necessary degree of detail is determined for vehicle and guideway dynamics analyses.

The simulation results plotted in Figs. 6-10 compare different dynamical quantities for both the detailed and the simplified magnet model. Figure 6 shows various quantities related to the magnet and the controller in the time domain, that is, the air gap s_{GMU} measured at the GMU normalized with the desired air gap s_{des}, the vertical magnet acceleration a_{GMU} measured at the GMU normalized with its maximum a_{max}, the voltage U_{mag} applied to the magnet normalized with the nominal voltage U_{nom}, the current I_{mag} flowing through the magnet normalized with the nominal current I_{nom}, and the magnet force F_{mag} provided by the respective half magnet normalized with the nominal force F_{nom}. Each of them is shown for three positions along the vehicle: at the very rear end, at the center of the mid section, and at the transition from the mid to the front section. An exemplary time range of one second is shown. For the plot of F_{mag}, the forces in the detailed model belonging to the six poles of the respective half magnet are summed up to be compared to the force calculated by the simplified model. In Fig. 7, for the same quantities as in Fig. 6 the relative frequency of occurrence is plotted as bar plot on the left vertical axis together with the corresponding cumulative frequency of occurrence as line plot on the right vertical axis. Figures 8 and 9 show the motion of the levitation chassis and the car body, respectively. That is the vertical translations z_{LC} and z_{CB} and the rotations β_{LC} and β_{CB} about the y-axis. Again, the results obtained with the detailed model are compared to those obtained with the simplified magnet model. For the car body motion, exemplary time ranges of four seconds are plotted. In Fig. 10, the deflection w_{mid} of a single guideway element at mid span is plotted versus the position $x_{\mathrm{MF,front}}$ of the foremost magnet force of the simplified model for both the detailed and the simplified magnet model.

In general, all results are in very good accordance for the simulations with the detailed and the simplified model. For the internal magnet dynamics small differences occur between the detailed model and the simplified model, as revealed by the plots for voltage, current, and magnet force in Figs. 6 and 7. These small differences can be explained by the differences and simplifications made in the simplified model with respect to the detailed model. While it was shown in [4] that the difference is negligible if the air gaps are identical at all poles of one half magnet, the air gaps and their change with time are individually computed here for each magnet pole. By summarizing the magnet forces of a half magnet in a single concentrated substitute magnet force, spatial balancing effects caused by different pole gaps occurring while traveling along an uneven guideway are neglected. However, as can be seen from Figs. 6-10, quantities describing the mechanical vehicle and guideway dynamics like air gap, magnet acceleration, levitation chassis motion, car body motion, and guideway motion are nearly identical for both magnet model variants. For the translation of the levitation chassis z_{LC}, the maximum difference between both model variants is less than 0.43 mm at all three considered positions, corresponding to less than 2.1 % of the maximum absolute amplitude. The mean deviation is below 0.1 mm at each of the three positions. The deviation of the car body translation z_{CB} remains smaller than 0.24 mm for all three sections. This is less than 1.5 % of the maximum absolute amplitude. On average it is even smaller than 0.06 mm for each section. For the guideway deflection at midspan w_{mid}, the difference is less than 0.07 mm between the detailed and the simplified model. That is only 1.2 % of the static guideway deflection when loaded with the vehicle. This means that for the analysis and prediction of vehicle and guideway dynamics, the simplified magnet model is here a sufficiently accurate approximation of the detailed magnet model.

This is a satisfying result, because the simulation time is about a factor of 100 faster with the simplified model than with the detailed model. It takes about 100 hours of real time for 62 seconds of simulation time with the detailed model, while for the same simulation time it takes just about one hour of real time with the simplified model. Additionally, the preprocessing time for creating the mechanical vehicle model takes some extra time if the detailed magnet model is to be used compared to when the simplified model shall be used.

With the results at hand, it can be concluded that a coarse spatial discretization of magnet forces along the maglev vehicle with one magnet force per half magnet is sufficient for vehicle dynamics simulations. Thus, neither finer magnet force discretizations nor FE models for detailed mapping of the magnetic field are necessary for determining the vehicle dynamics. Due to enormous simulation times, such models are unsuitable for application in vehicle dynamics simulations with large vehicle models and multiple magnets. Even with a view to the next few years, simulations with such high computational effort will not be reasonable. Therefore, it is all the more gratifying to see that the simplified model represents the detailed model so well regarding the resulting vehicle and guideway dynamics in a large vehicle model. However, for other simulations such as the elastic deformation of a magnet more complicated and spatially distributed magnet forces are required. As frequently in simulations, the simulation purpose determines the required level of detail in the modeling.

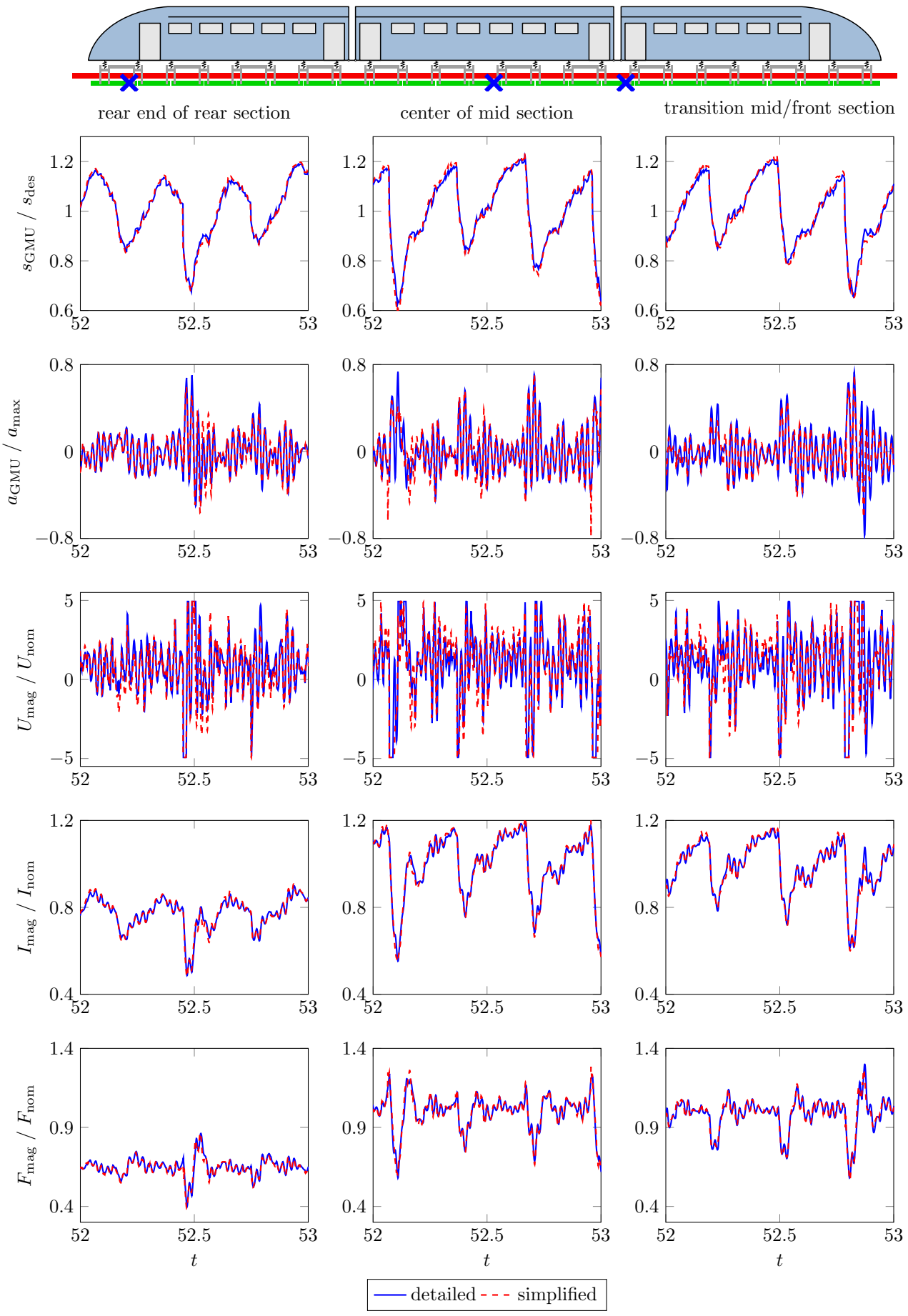

Figure 6: Comparison in the time domain of simulated quantities related to the magnet and the controller obtained with the detailed magnet model and the simplified magnet model at three positions along the vehicle: at the very rear end, at the center of the mid section, and at the transition from the mid to the front section.

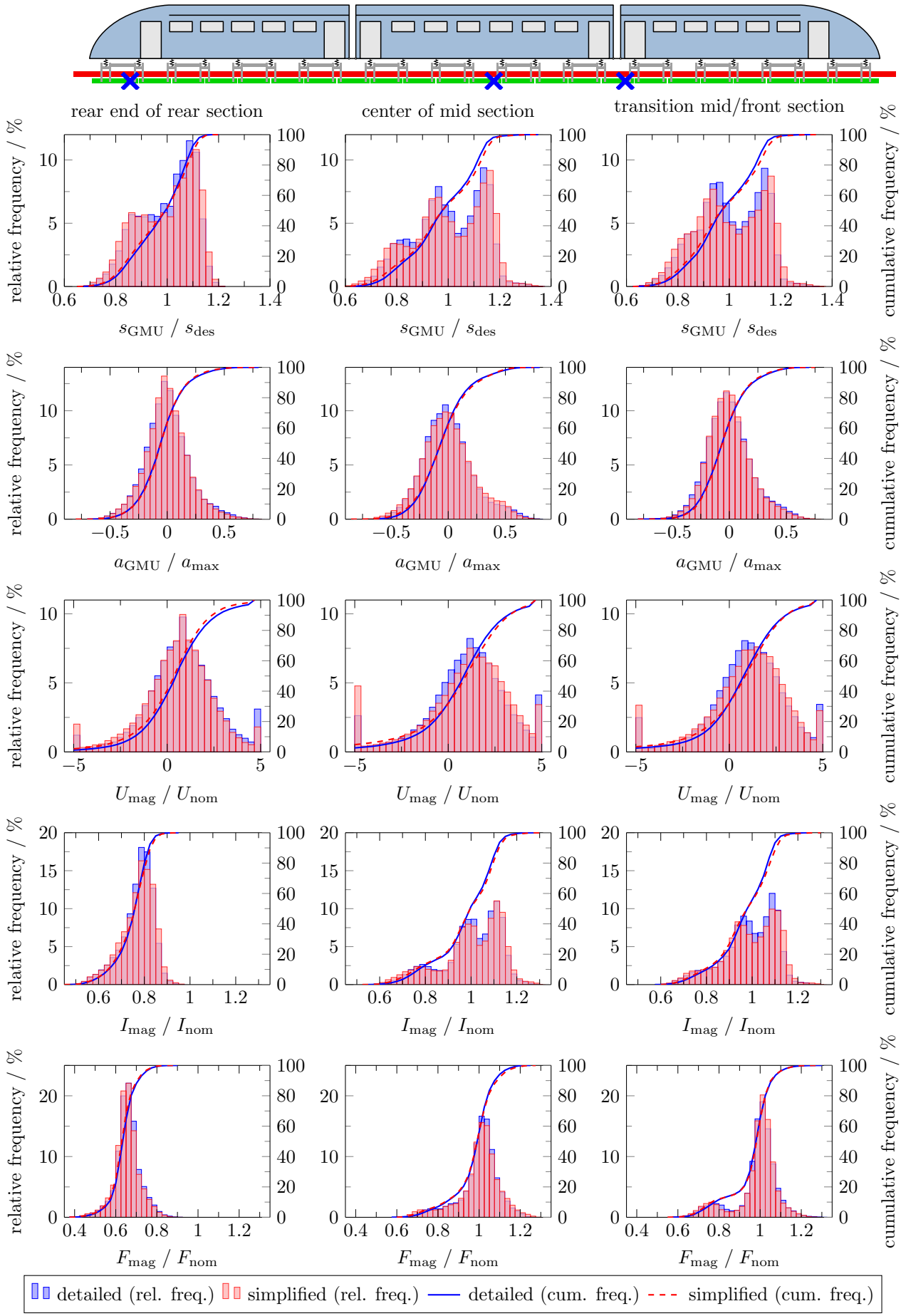

Figure 7: Relative (left vertical axis) and cumulative (right vertical axis) frequency of occurrence of the same quantities and at the same positions along the vehicle as in Fig. 6 obtained with the detailed magnet model and the simplified magnet model.

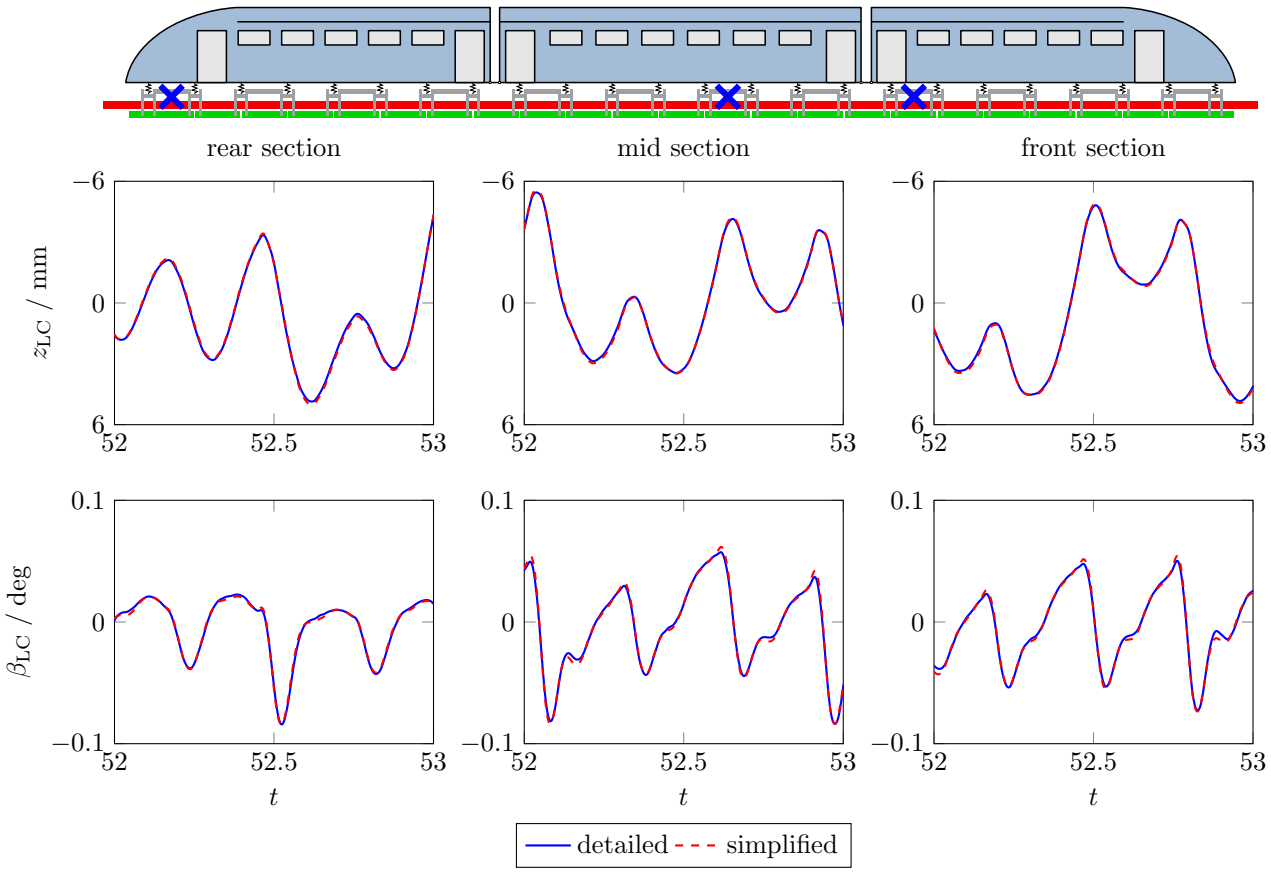

Figure 8: Comparison of simulated translations and rotations of the levitation chassis obtained with the detailed magnet model and the simplified magnet model at three positions along the vehicle: at the very rear end, at the center of the mid section, and at the transition from the mid to the front section.

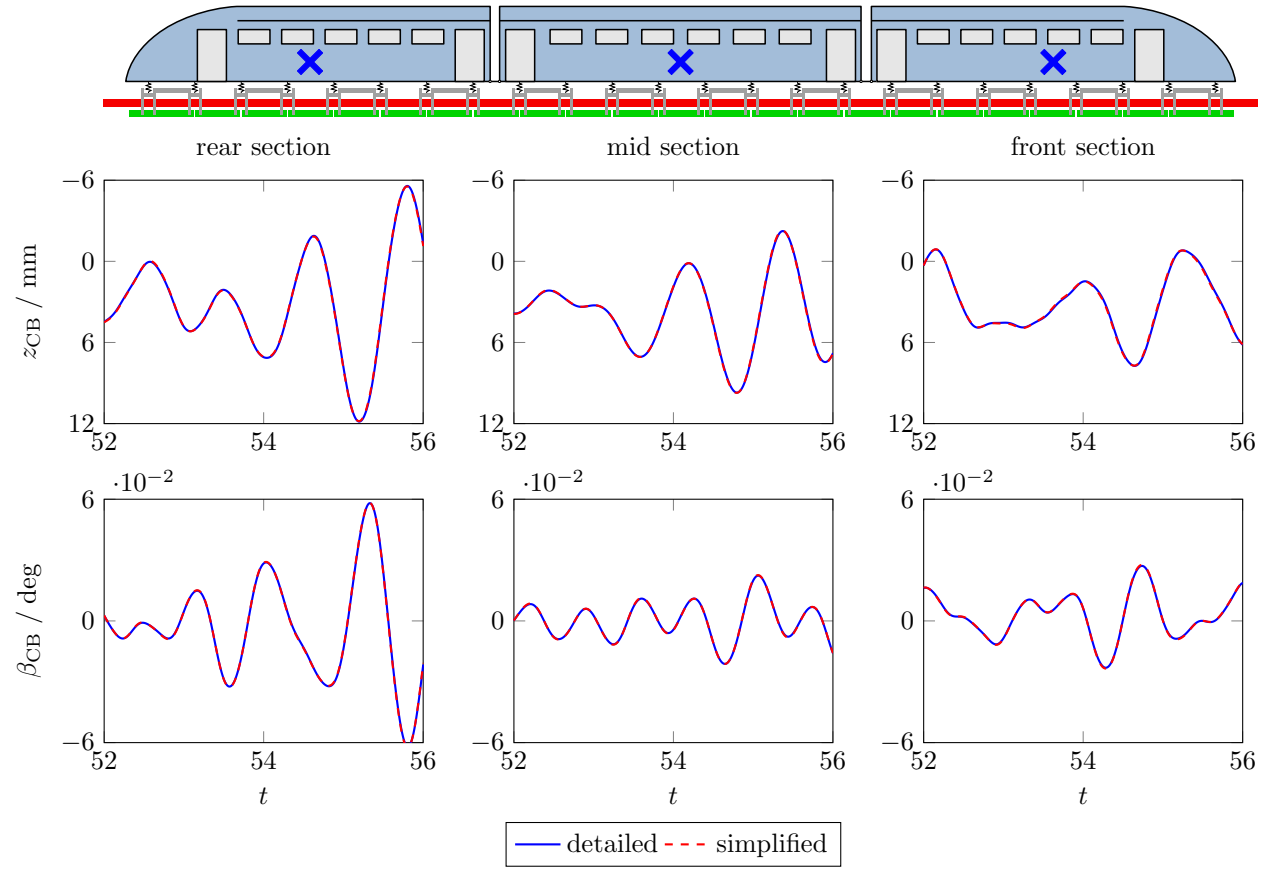

Figure 9: Comparison of simulated translations and rotations of the car bodies of rear, mid, and front section obtained with the detailed magnet model and the simplified magnet model.

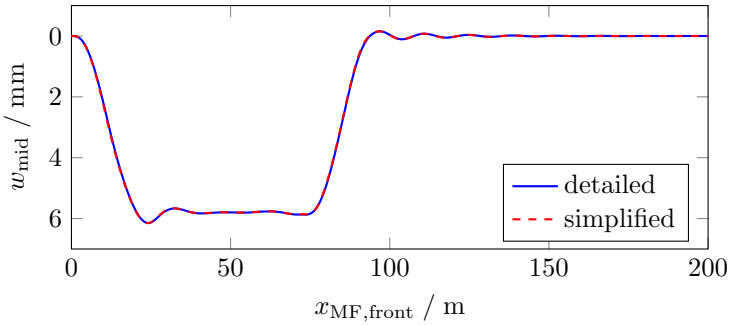

Figure 10: Deflection of a single guideway element at mid span versus position of the foremost simplified magnet force obtained with the detailed magnet model and the simplified magnet model.

Conclusions

This publication investigates the degree of detail of spatial magnet force discretization required for reliable analyses of maglev vehicle and guideway dynamics. Maglev vehicle dynamics simulation models often use fast-computable magnet models providing concentrated substitute magnet forces to approximate the actually continuously distributed magnetic field. However, to the best of the authors' knowledge, no analysis has been published yet showing that this simplification is a valid assumption. Therefore, the novelty of this contribution is the simulative investigation of the high-speed maglev train Transrapid TR08 regarding the influence of different magnet force distributions along the levitation magnets on the behavior of the coupled vehicle-guideway dynamics while the vehicle is traveling along the guideway.
For this purpose, two different magnet force discretizations are compared: a coarse one with one magnet force per half magnet, and a fine one with one magnet force per pole. It is shown that a coarse discretization with a single concentrated substitute magnet force per half magnet is a sufficient approximation when mechanical vehicle and guideway dynamics are in focus and if the magnet model computing this single force provides a sufficiently accurate representation of the magnet dynamics. The used magnet model from [4] proves to fulfill this requirement. There are minor differences in the internal magnet dynamics like voltage or current due to the simplifications of the simplified magnet model providing one force per half magnet with respect to the detailed model providing one force per pole. However, the mechanical vehicle and guideway dynamics turn out to be nearly identical for the simplified and the detailed model.
This is an important and relieving result, because the simplified magnet model providing forces with a coarse discretization has significantly shorter simulation times, about a factor of 100, than the detailed model with a fine discretization. Such detailed magnet models with fine magnet force distributions thus are unsuitable for application in large vehicle models for vehicle dynamics simulations. Instead, the fast-computable simplified magnet model with one force per pole can be used for this purpose, allowing much faster simulations with hardly any loss of quality in the relevant quantities. However, the simplified magnet model has to map the magnet physics sufficiently accurately, of course.

References

[1] XinhuaNet: World's first 600 km/h high-speed maglev train rolls off assembly line. http://www.xinhuanet.com/english/2021-07/20/c_1310072057.htm, accessed December 1, 2021 (2021)

[2] Uno, M.: Chuo Shinkansen project using superconducting maglev system. Japan Railway & Transport Review **68** (2016) 14–25

[3] Wang, Z., Xu, Y., Li, G., Yang, Y., Chen, S., Zhang, X.: Modelling and validation of coupled high-speed maglev train-and-viaduct systems considering support flexibility. Vehicle System Dynamics **57**(2) (2019) 161–191

[4] Schmid, P., Schneider, G., Dignath, F., Liang, X., Eberhard, P.: Static and dynamic modeling of the electromagnets of the maglev vehicle transrapid. IEEE Transactions on Magnetics **57**(2) (2021) 1–15

[5] Ren, S., Romeijn, A., Klap, K.: Dynamic simulation of the maglev vehicle/guideway system. Journal of Bridge Engineering **15**(3) (2010) 269–278

[6] Xia, W., Zeng, J., Dou, F., Long, Z.: Method of combining theoretical calculation with numerical simulation for analyzing effects of parameters on the maglev vehicle-bridge system. IEEE Transactions on Vehicular Technology **70**(3) (2021) 2250–2257

[7] Shen, G., Meisinger, R., Shu, G.: Modelling of a high-speed maglev train with vertical and lateral control. Vehicle System Dynamics **46**(S1) (2008) 643–651

[8] Dignath, F., Schmitz, P., Zheng, Q., Jin, H., Liang, X., Kurzeck, B., Ronde, M.: Fast computable model of the levitation and guidance control for multibody simulation of the Transrapid MAGLEV vehicle. In: 4th International Conference on Railway Technology: Research, Development and Maintenance. Barcelona (September 2018)

[9] Hägele, N., Dignath, F.: Vertical dynamics of the maglev vehicle Transrapid. Multibody System Dynamics **21**(3) (2009) 213–231

[10] Schneider, G., Schmid, P., Dignath, F., Eberhard, P.: Modeling and simulation of a high-speed maglev vehicle on an infinite elastic guideway. In Kövecses, J., Stépán, G., Zelei, A., eds.: Proceedings of the 10th ECCOMAS Thematic Conference on Multibody Dynamics, Budapest University of Technology and Economics (2021) 420–431

[11] Kurz, T., Eberhard, P., Henninger, C., Schiehlen, W.: From Neweul to Neweul-M^2: Symbolical equations of motion for multibody system analysis and synthesis. Multibody System Dynamics **24**(1) (2010) 25–41

[12] Popp, K., Schiehlen, W.: Ground Vehicle Dynamics. Springer, Berlin (2010)

[13] Schneider, G., Liang, X., Dignath, F., Eberhard, P.: Simulation of the maglev train Transrapid traveling on a flexible guideway using the multibody systems approach. In Kecskeméthy, A., Geu Flores, F., eds.: Multibody Dynamics 2019. ECCOMAS 2019. Computational Methods in Applied Sciences. Volume 53. Cham, Springer (2020) 503–510

[14] German Federal Railway Authority: Design principles high-speed maglev system (MSB). Technical report (2007)

[15] Zheng, Q., Dignath, F., Schmid, P., Eberhard, P.: Ride comfort transfer function for the MAGLEV vehicle Transrapid. In: 4th International Conference on Railway Technology: Research, Development and Maintenance. Barcelona (September 2018) Presentation slides available at http://dx.doi.org/10.18419/opus-11268.

[16] Schmid, P., Eberhard, P.: Offset-free nonlinear model predictive control by the example of maglev vehicles. IFAC-PapersOnLine **54**(6) (2021) 83–90

Joint Reactions Distribution and Uniqueness in Overactuated Multibody Systems

Marek Wojtyra* and Marcin Pękal*
*Institute of Aeronautics and Applied Mechanics, Warsaw University of Technology, Warsaw, Poland

Summary. Overactuation is introduced in various mechanisms, especially in parallel kinematic machines. The evident result of overactuation is the non-uniqueness of driving forces required to execute the planned motion. However, in some cases, redundant driving constraints may also affect the uniqueness of joint reactions. In this contribution, the influence of overactuation on the uniqueness of calculated joint reactions is investigated. A procedure for testing the solvability of calculated reactions in the presence of redundant driving constraints is devised. The known numerical methods for constraint reactions uniqueness analysis are adapted to the overactuated case. An example illustrates the investigated problems and demonstrates the proposed analysis methods.

Introduction

Overactuation in multibody systems (MBS) is understood as employing more actuators than required by the number of controlled degrees of freedom of the system. It is introduced due to several reasons, e.g., to eliminate gear backlash or clearances [1], to improve the performance of the system [2], or to reduce torques in joints of the MBS [3]. In the case of parallel kinematics machines, frequently exploited in robotic applications, overactuation may contribute to singularity avoidance [4] or be utilized for obtaining desired torque distribution [5]. Overactuated multibody systems can be treated as a particular case of redundantly constrained systems, where redundancy applies to driving constraints.
Rigid body assumption is commonly utilized in multibody simulations. With this assumption, multibody modeling is less complicated, requires less data, and allows for faster computations. However, in the case of redundantly constrained MBS, this assumption leads to various problems, mainly related to the rank deficiency of the constraint matrix. One of the unwelcome effects is the non-uniqueness of calculated joint reaction forces (or at least some of them). Various methods to handle and analyze overconstrained MBS have been proposed—see, e.g., [6, 7, 8, 9]. Most often, these methods are focused on constraint redundancy introduced by the kinematic structure of the system, whereas overactuation is seldom considered.
In this work, rigid body models of redundantly actuated MBS are analyzed. The research concentrates on the uniqueness of calculated driving forces and joint reaction forces. Methods of uniqueness analysis are developed, and the influence of redundant actuation on joint reaction solvability is pointed out and investigated. An example is provided to exemplify the investigated issues and illustrate the proposed analysis methods.

Outline of the methods and results

Equations of motion of a MBS subjected to geometric and linear nonholonomic constraints can be written as (we assume that absolute coordinates $\mathbf{q}$ are employed to describe the system [10]):

$$\mathbf{M}\ddot{\mathbf{q}} - \mathbf{J}^T\boldsymbol{\lambda} = \mathbf{Q}, \tag{1}$$

where $\mathbf{M}$ is the matrix of inertia, $\boldsymbol{\lambda}$ is the vector of Lagrange multipliers, $\mathbf{Q}$ is the vector of the other generalized forces and velocity-dependent inertial terms.
If no driving constraints are imposed, the constraint matrix is $\mathbf{J}$ defined as:

$$\mathbf{J}^T = \mathbf{J}_K^T = \left[(\boldsymbol{\Phi}_{\mathbf{q}}^K)^T \quad (\boldsymbol{\Psi}^K)^T\right], \tag{2}$$

where $\boldsymbol{\Phi}_{\mathbf{q}}^K$ is the geometric constraints Jacobian and $\boldsymbol{\Psi}^K$ is the linear nonholonomic constraint matrix.
When driving constraints are appended, the constraint matrix becomes:

$$\mathbf{J}^T = \mathbf{J}_{KD}^T = \left[(\boldsymbol{\Phi}_{\mathbf{q}}^K)^T \quad (\boldsymbol{\Psi}^K)^T \quad (\boldsymbol{\Phi}_{\mathbf{q}}^D)^T \quad (\boldsymbol{\Psi}^D)^T\right], \tag{3}$$

where superscript D stands for driving constraints.
The presence of redundant constraints makes the constraint matrix $\mathbf{J}$ rank deficient. The number of redundant constraints is indicated by the magnitude of the matrix $\mathbf{J}$ rank deficiency. As a result of redundant constraints existence, at least some of the joint reaction forces are non-unique. There are some methods that make it possible to determine whether or not the reactions in a specified joint are solvable (e.g., [6, 8]). In the present work, these methods were adapted to analyze systems with driving constraints.
To check if the driving constraints influence the uniqueness of calculated joint reactions, one must first analyze the constraint matrix from Eq. (2) that represents the MBS structure independently from its actuation, and then the complete constraint matrix as of Eq. (3). In this paper, we have proven that **if the driving constraints are non-redundant** (i.e., when the magnitude of matrix $\mathbf{J}$ rank deficiency does not change after introducing driving constraints), then **the solvability of joint reactions remains unchanged**; moreover, the driving forces are unique.

On the other hand, **if the system becomes overactuated** (i.e., the magnitude of rank deficiency increases after the introduction of driving constraints), then: (1) previously non-unique joint reactions remain non-unique, (2) **some of otherwise unique joint reactions may become non-unique**, (3) some (or all) driving forces are non-unique. Note that the methods developed in the present work enable us to determine the solvability of any individual joint reaction before and after the introduction of driving constraints. The crucial point is that the results of the uniqueness analysis obtained for joint reactions alone may differ from those obtained for joint reactions together with redundant driving forces.

Example

The developed analysis methods were used to investigate the uniqueness of joint reactions and driving forces in a redundantly constrained and overactuated mechanism with nonholonomic constraints presented in Fig. 1. Three different actuation variants were analyzed: without driving constraints, with non-redundant driving constraints, and with redundant driving constraints. The results of performed analyses corroborated the findings presented in this contribution.

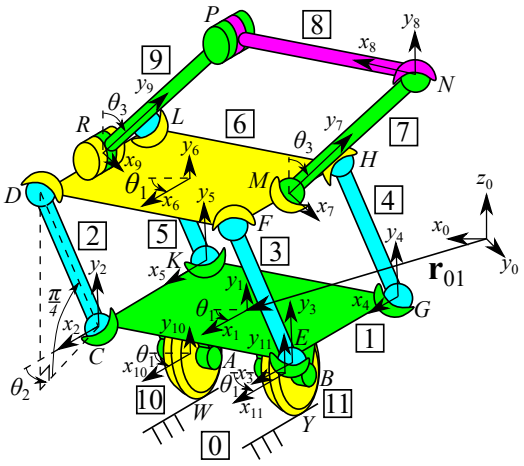

Figure 1: Redundantly constrained and overactuated mechanism with nonholonomic constraints

Conclusions

Overactuation may, in some cases, affect the uniqueness of joint reactions. For the overactuated systems, it is useful to perform a two-stage uniqueness analysis—with and without considering the driving constraints. Such a proceeding enables us to determine the origin of the reaction non-uniqueness of the considered MBS—whether it comes from the system's structure or the redundancy of the driving constraints imposed on the MBS.

Acknowledgements

This work has been supported by the Warsaw University of Technology under a grant awarded by the Scientific Council for Automatic Control, Electronics and Electrical Engineering.

References

[1] Tsai L.-W. (1999) Robot Analysis: The Mechanics of Serial and Parallel Manipulators, Wiley-Interscience.

[2] Wu J., Wang J., Li T., Wang L. (2007) Performance Analysis and Application of a Redundantly Actuated Parallel Manipulator for Milling, J. Intell. Robot. Syst. 50 (2) 163–180.

[3] Ganovski L., Fisette P., Samin J.-C. (2004) Piecewise Overactuation of Parallel Mechanisms Following Singular Trajectories: Modeling, Simulation and Control, Multibody Syst. Dyn. 12 (4) 317–343.

[4] Müller A. (2008) Redundant Actuation of Parallel Manipulators, in: Wu H. (Ed.) Parallel Manipulators towards New Applications, I-Tech Education and Publishing 87-108.

[5] Lorenz M., Corves B., Riedel M. (2014) Kinetostatic Performance Analysis of a Redundantly Driven Parallel Kinematic Manipulator. Proceedings of the ASME 2014 IDTC/CIE Conference, Buffalo, New York, USA. August 17–20, V05BT08A080.

[6] Wojtyra M., Frączek J. (2013) Comparison of selected methods of handling redundant constraints in multibody systems simulations, J. Comput. Nonlin. Dyn. 8 (2): 021007.

[7] González F., Kövecses J. (2013) Use of penalty formulations in dynamic simulation and analysis of redundantly constrained multibody systems, Multibody Syst. Dyn. 29 (1), 57–76.

[8] García de Jalón J., Gutiérrez-López M.D. (2013) Multibody dynamics with redundant constraints and singular mass matrix: existence, uniqueness, and determination of solutions for accelerations and constraint forces, Multibody Syst. Dyn. 30 (3) 311–341.

[9] Wojtyra M., Pękal M., Frączek J. (2020) Utilization of the Moore-Penrose inverse in the modeling of overconstrained mechanisms with frictionless and frictional joints, Mech. Mach. Theory, 153, 103999.

[10] Haug E. J. (1989) Computer aided kinematics and dynamics of mechanical systems, Volume I: Basic methods, Allyn and Bacon.

Flight Behaviour of a Two-Line, Four-Point Disk Kite

Luke Roeven, Stefanie Gutschmidt and Keith Alexander
Department of Mechanical Engineering, University of Canterbury, Christchurch, New Zealand

Summary. Existing work on kite behaviour mainly considers single-line kites and associated dynamics are limited to quasi-static analyses. Mathematical descriptions rely on generalised aerodynamic models which have not been validated experimentally and thus lack being suitable for design optimization purposes. Kites are utilized in both professional sporting activities and potential new energy generation applications. Understanding the dynamics of these kites allows for innovative improvements for such applications. Furthermore, derivations of existing models are typically based on energy methods which are not immediately helpful to inform design optimisation guidelines. In this work we derive the fully non-linear governing dynamic equations of motion for a two-line four-attachment point kite using a four degree of freedom Newton-Euler formulation. We implement an aerodynamic model which has been previously tested and validated (CFD/wind-tunnel) by our group. The analysis considers and focuses on stability regions of selected flight scenario and the maneuverability of the kite for relevant kite design parameters.

Background

A kite is an atypical aerodynamic object and knowledge about its flight dynamics is rare in literature. Over the last decade few articles have been published about two-line kites, even fewer include dynamic analysis [1, 2]. Quasi-static analysis was performed by Dawson [3] to investigate the turning maneuver of a kite. Other existing work has been done on the dynamics of two-line kites by Sánchez et al. [1]. Their work used the Lagrangian formalism to investigate the stability of the kite for different wind speeds and one control parameter, but did not investigate the reason for turning and restorative mechanisms of the kite flight. Research on the topic has recently increased with new applications of kites for energy generation and ship propulsion [4], but the underlying, inherently nonlinear, dynamics is still under-studied. The kite considered in this work consists of two lines, one for each hand (as depicted in new applications) which connect to each side of the kite. These lines, each split to connect to four attachment points on the kite surface, introduce the necessary moments to control the kite. The kite is modelled with circular disks to represent the aerodynamic surfaces as suggested by Stevenson [5] to be able to validate theoretical models with experimental investigation and observation. This is a first approach implementing a validated model; additional, more complex geometries can be introduced in future investigations. The kite system suggests two modes of behaviour: the first representing the stalling behaviour of the kite, the other representing the expected (typical) kite flight. The dynamics of the considered kite shows restorative behaviour along the elevation and pitch variables, but requires attention to control significant changes of the azimuthal angle. In this work we focus on the roll control of a user and its stability regions for a selected set of parameters and ranges.

Model

This kite system is described by five coordinate systems: **global**, **line**, **kite**, and two **disks** (Figure 1). Euler angles are used to define the kinematics of the kite with a 3-2-1 body-fixed rotation [6] resulting in four degrees of freedom, with θ_1 being the elevation of the kite, θ_2 the azimuthal deviation of the kite, θ_3 the pitching of the kite, and θ_4 the yaw of the kite. The nonlinear set of governing state-space equations is of the form

$$\mathbf{A}_{8\times8}\ \dot{\boldsymbol{q}}_{8\times1} = \mathbf{f}_{8\times1}\left(\boldsymbol{M}^L, \boldsymbol{M}^K, \boldsymbol{q}, t\right) \tag{1}$$

$\mathbf{A}_{8\times8}$ represents the inertia matrix, $\mathbf{f}_{8\times1}$ is the forcing vector containing the lift and drag moments as well as the kinematic constraint relations, and $\boldsymbol{q}_{8\times1}$ is defined in Eq. (2a). The moment equations are derived using the **line** and **kite** systems where i denotes the disk number.

$$\boldsymbol{q}_{8\times1} = \left[\theta_1, \ldots, \theta_4, \dot{\theta}_1, \ldots, \dot{\theta}_4\right]^T \quad \text{(a)} \qquad \boldsymbol{M}_{\text{Lift \& Drag}} = \left(\boldsymbol{r}_{\mathrm{C\,P}_i} + \boldsymbol{r}_{\mathrm{O\,C}}\right) \times \boldsymbol{F}_i \quad \text{(b)} \tag{2}$$

$$\boldsymbol{M}^K = \left[\underbrace{\sum_{i=1}^{2} \boldsymbol{r}_{\mathrm{C\,P}_i} \times \boldsymbol{F}_i}_{\text{Lift and Drag}}\right]^K \tag{3}$$

$$\boldsymbol{M}^L = \left[\underbrace{\sum_{i=1}^{2} \boldsymbol{r}_{\mathrm{O\,C}} \times \boldsymbol{F}_i}_{\text{Lift and Drag}} + \underbrace{\boldsymbol{r}_{\mathrm{O\,C}} \times m_k \boldsymbol{g}}_{\text{Weight Force}}\right]^L \tag{4}$$

Parameter values for the centre of pressure and aerodynamic forces are taken from Dawson's work [3]. The kinematic constraint originates from the lines being straight resulting in a limitation of the moment along the roll axis and the magnitude of the pitching angle with respect to the lines.

Analysis & Results

The analysis considers the full set of non-linear equations. The governing equation (1) is solved using a standard numerical integration scheme, Runge-Kutta $\mathcal{O}(4)$. For the stability analysis, the Jacobian of the forcing term was approximated with a central difference formula; its eigenvalues were computed for a selected parameter range of interest.

Figure 2 depicts stability regions of pitch θ_3 and yaw θ_4 angles for a selected azimuthal angle θ_2 of $0°$ and increasing elevation values θ_1 from $0°$ – $90°$. In the order from left to right, the top left figure being $\theta_1 = 0°$ and the bottom right being $\theta_1 = 90°$. Blue zones represent stable solutions, while orange crosses represent unstable solutions, and grey zones represent spurious solutions (e.g. referring to negative line tension or collision with the ground). At $\theta_1 = 0°$ there are two columns of stable solutions, the spurious solution referring to the collision with the ground. As the elevation angle increases the spurious solution disappears and the stable blue region becomes a circle-like zone which migrates from negative to positive θ_3 values. This variation in θ_3 creates a restoring moment which brings the system back to it's elevation equilibrium. However, when the azimuthal angle is varied, the resultant twisting behavior acts to further exacerbate the azimuthal deviation — an unstable equilibrium.

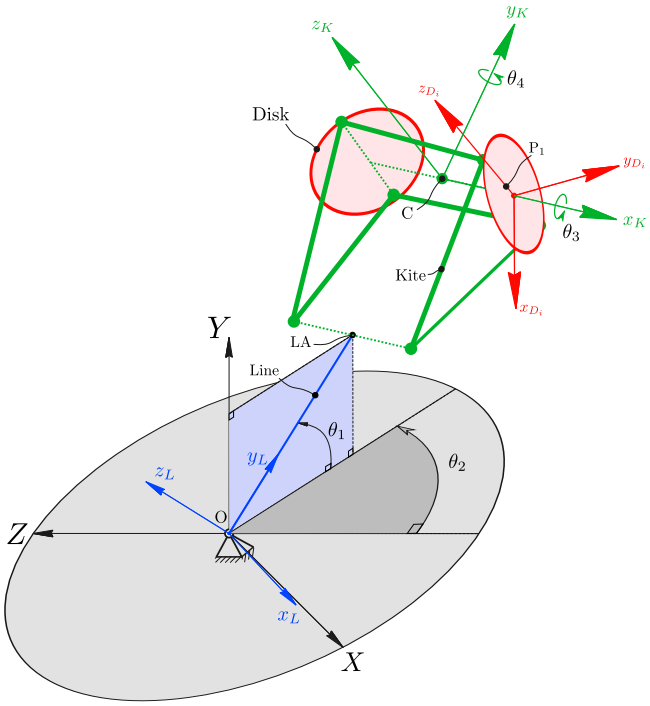

Figure 1: Coordinate systems for the two line kite

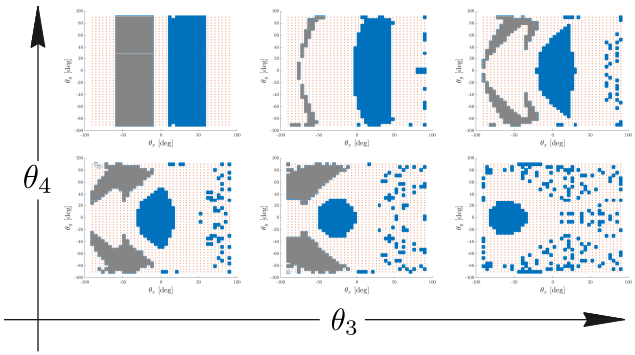

Figure 2: Stability regions of the system as the elevation changes (from left to right — 0,15,30,40,60,90). Blue (filled) → stable, grey (filled) → spurious but stable, orange (cross) → unstable

Conclusion

Kites are being utilised within new applications for energy generation, professional sporting activities, and ship propulsion [4]. Further development of accurate models for these fields will allow for vast and effective design improvements to enhance applications. In this work, a two-line four-attachment point disk kite is modelled using a Newton-Euler formulation. This model utilises validated wind-tunnel data for the aerodynamic forces. The stability of the system is analysed for a specific range of elevation angle values. Results demonstrate how the kite pitches to reach its equilibrium elevation. This technique can be used to optimise multiple design parameters for numerous applications. By observing the stability zones of the kite, the design parameters can be adjusted for specific flight behaviour and characteristics. Additionally, the user control mechanism for operating such kites can be further investigated for better performance.

References

[1] G. Sánchez, M. García-Villalba, and R. Schmehl. Modeling and dynamics of a two-line kite. *Applied Mathematical Modelling*, 47:473–486, 2017.

[2] Han Yan A. Modelling and control of surfing kites for power generation. Master's thesis, Auckland University of Technology, 2017.

[3] Dawson R. Kite turning. Master's thesis, University of Canterbury, 2011.

[4] Nedeleg Bigi, Kostia Roncin, Jean-Baptiste Leroux, and Yves Parlier. Ship towed by kite: Investigation of the dynamic coupling. *Marine Science and Engineering*, 486(8), 2020.

[5] Stevenson J. *Traction Kite Testing and Aerodynamics*. PhD thesis, University of Canterbury, 2003.

[6] Diebel J. Representing attitude: Euler angles, unit quaternions, and rotation vectors. *Matrix*, 58, 01 2006.

Identification of Friction Models for MPC-based Control of a PowerCube Serial Robot

Jörg Fehr*, Arnim Kargl* and Hannes Eschmann*
*Institute of Engineering and Computational Mechanics, University of Stuttgart, Germany

Summary. For model-based control, an accurate and in its complexity suitable representation of the real system is a decisive prerequisite for high and robust control quality. In a structured step-by-step procedure, a model predictive control (MPC) scheme for a Schunk PowerCube robot is derived. Neweul-M^2 provides the necessary nonlinear model in symbolical and numerical form. To handle the heavy online computational burden involved with the derived nonlinear model, a linear time-varying MPC scheme is developed based on linearizing the nonlinear system concerning the desired trajectory and the a priori known corresponding feed-forward controller. To improve the identification of the nonlinear friction models of the joints, a nonlinear regression method and the Sparse Identification of Nonlinear Dynamics (SINDy) are compared with each other concerning robustness, online adaptivity, and necessary preprocessing of the input data. Everything is implemented on a slim, low-cost control system with a standard laptop PC.

Introduction

The use of robots to increase work performance or human-machine interaction for rehabilitation are topics of high topicality. For the performance of robotic manipulators, modeling, control, and sensing play an essential role. Modeling plays an important role in the development process as well as for controlling the robot, e. g., for model-based control concepts like model predictive control (MPC). Model-based control schemes offer many advantages in comparison to individual joint control. The benefits are: (i) operation as a centralized control scheme – the highly nonlinear behavior of such a system is considered; (ii) intuitive parameter tuning – an elaborate and time-consuming parameter tuning necessary for PI or PID-based individual joint control is unnecessary; (iii) constraint considerations - actuator and state limitations are already considered in the control design.

In [1] a model predictive controller (MPC) was derived and implemented for a modular 6-axis Schunk PowerCube robot, see Fig. 4. The general MPC algorithm, see, e. g., [2, 3] is the following: (i) obtain a measurement/estimate of the state; (ii) obtain an optimal input sequence by solving online an open-loop optimal control problem (OCP) over a finite horizon subject to system dynamics and constraints; (iii) apply the first input of the optimal input sequence to the plant/robot; (iv) continue with the first step. Challenges for the application are the highly nonlinear system dynamics as well as the limited computation capacity. Everything should run on a slim low-cost setup, i. e., a standard laptop PC.

These challenges are met by a linear time-variant two-step approach, see Fig. 1. In a first step the nonlinear system dynamics are approximated with a linear time-varying model [4] around the desired trajectory –using an inverse dynamic approach / computed torque approach [5]. In the second step sophisticated techniques for linear MPC are exploited, i. e., the open-source quadratic programming solver qpOASES [6] is used.

The proposed LTV MPC control of the robotic system is able to perform complex trajectories, i. e., motion reversal and zero crossing [1] [1]. Nevertheless, the noticeable difference between calculated feed forward and MPC output, see Fig. 2 along the trajectory implies model inaccuracies. These findings imply that the friction model of the robot's joints still has some weaknesses which limits the performance of the overall control system. Therefore, more effort is needed to identify the friction properties of the joints. Prior to this work, a classical system identification method, i. e., data pre-processing in combination with nonlinear regression, was used to identify the friction properties of a single disassembled module.

Therefore, aim of this work is to evaluate how the large amount of data from different sources, i. e., Artifical Intelligence will facilitate the complex and challenging modeling and system identification of an assembled system – e. g., can the large amount of data be used to identify the effects in the assembled state and/or difference between individual products due to production tolerances.

More specifically, we want to answer the question of whether the Sparse Identification of Nonlinear Dynamics (SINDy) method [7, 8] improve the friction identification. In contrast to black-box AI methods, like Neural Networks or Gaussian Processes – which try to approximate the data by adjusting some weights of a topological system, the SINDy method tries to identify the governing equations from data. It approximates an unknown function $\boldsymbol{f}$ with a library $\boldsymbol{\Theta}(\boldsymbol{X})$ of r potential (nonlinear) terms. The SINDy approach is a parametric approach that, compared to NNs, works without massive amounts of data. The approach allows for on-the-fly model adaptation due to its low computational complexity.

Let us recap the overall goal: "Improve the model-based control performance of a robotic manipulator by improving friction identification using the SINDy approach to identify the governing equation from data." The main features are: (i) the robustness of the approach and (ii) only the friction characteristic is identified – other well-identified or known terms of the system are incorporated as prior knowledge.

In the next section, we describe the model and the methodology in more detail: (i) the robot which serves as an example; (ii) the process control framework; (iii) the derivation of the equation of motion of the rigid multibody system with Neweul-M^2 [9] (iv) the existing friction model, (v) the SINDy concept and (vi) the recording of measurement data. In Section Friction Identification the results of the approach are presented. Finally, in the Conclusion the overall control performance of the system with the improved friction model is discussed.

[1] The complete motion of the manipulator can be seen in the deposited video `https://www.itm.uni-stuttgart.de/en/research/vision-based-control-of-a-powercube-robot/`.

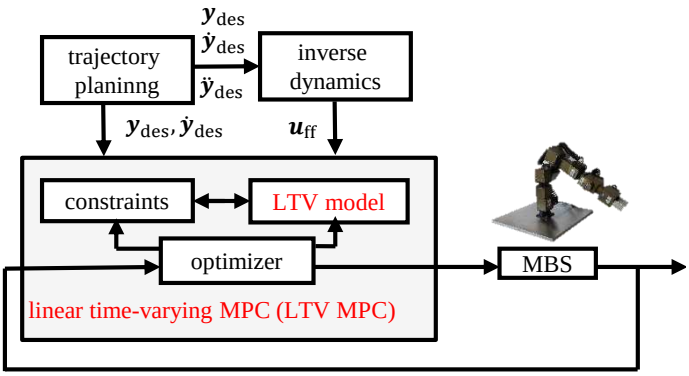

Figure 1: Topologic structure of the two-step control loop with the feed-forward part $\boldsymbol{u}_{\text{ff}}$ and the LTV-MPC part.

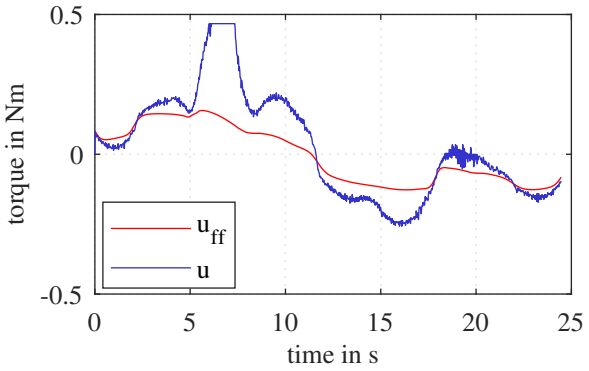

Figure 2: Feed forward torque of the old robot model compared to the MPC output torque applied at joint β during a trajectory with motion reversal.

Model and Methodology

The performance of the SINDy approach is evaluated on a modular 6-axis *Schunk PowerCube Robot*, see Fig. 4. For the considered modular robot a *Process Control Framework* in Matlab Simulink and a *Simulation Model* in Neweul-M^2 is available. We focus on the friction identification of the first three joints of the robot, which are each a rotary unit PR 90 with a Harmonic Drive gear to see the influence of assembly and production differences of the same product. Therefore measurement data is gathered during experiments followed by offline identification of the friction characteristics with nonlinear regression and the proposed *SINDy Framework*, relying on *Sparse Linear Regression*. In the following, we explain the single building blocks for model, *Experimental Measurements* and mathematical methodology.

Schunk PowerCube Robot

The properties of the various links are described in Tab. 1. For the design of the robot a "divide et impera" approach is used. For the first three links the same rotary module (PR 90) is used. The fourth link, is the smaller version(PR 70) within the model series. The fifth and six links of the robot consist of a pan-tilt unit in combination with an anthropomorphic gripper with a spherical wrist, is constructed from the single modules. The robotic manipulator is designed in such a way that the arm has an analytically calculable inverse kinematics.
Each rotary module, consists of a brushless DC-motor which drives a Harmonic Drive gear, which provides torque at each degree of freedom (DOF) based on the defined motor current. The control and power electronics are integrated, and an incremental encoder is used for position and speed evaluation. Furthermore, a brake is incorporated in case of shutdown or power failure.

Process Control Framework

The process control framework is depicted in Fig. 3 , consists of a Microsoft Windows laptop PC with Matlab R2014b and Simulink, including the additional toolboxes Real-Time Windows Target and Simulink Coder. The laptop PC is equipped with an Intel Core i5-3210M CPU (2x2.5 GHz, 8 GB DDR3). The communication between the Simulink model and the hardware is based on an USB-CAN bus interface, which is embedded into Simulink via S-Functions and a communication library from Schunk. A sampling rate of 50 Hz, corresponding to a sampling interval of 20 ms, is used. An external power supply with constant voltage of 24 V in combination with the integrated control and power electronics of modules ensures the necessary torques at the links.
Real-Time Windows Target [10] realizes a real-time engine for Simulink models on a Microsoft Windows PC and offers the capability to run hardware-in-the-loop simulations in real-time. It is a lean solution for rapid prototyping and provides an environment in which a single computer can be used as a host and target computer. Consequently, real-time simulations are executed in Simulink without an external target machine.

Simulation

The robotic manipulator is modeled as rigid multibody system with joint friction. In a first step Neweul-M^2 [9] aids calculating a rigid body model *without friction* with the advantage of generating equations of motion in symbolic and numerical form. A natural choice for generalized coordinates $\boldsymbol{y}$ are the joint coordinates $\boldsymbol{y} = [\beta, \gamma]^{\mathrm{T}}$. Therefore the resulting equation of motion (*without friction*) in minimal form can be denoted as

$$\boldsymbol{M}(\boldsymbol{y})\ddot{\boldsymbol{y}} + \boldsymbol{k}(\boldsymbol{y}, \dot{\boldsymbol{y}}) = \tilde{\boldsymbol{q}}(\boldsymbol{y}, \dot{\boldsymbol{y}}) + \boldsymbol{B}\boldsymbol{u} \tag{1}$$

with the positive definite mass matrix $\boldsymbol{M}$, the vector of generalized Coriolis, centrifugal and gyroscopic forces $\boldsymbol{k}$ and the vector of generalized forces without friction $\tilde{\boldsymbol{q}}$. The system input is the vector $\boldsymbol{u} = [T_2, T_3]^{\mathrm{T}}$ which consists of the applied

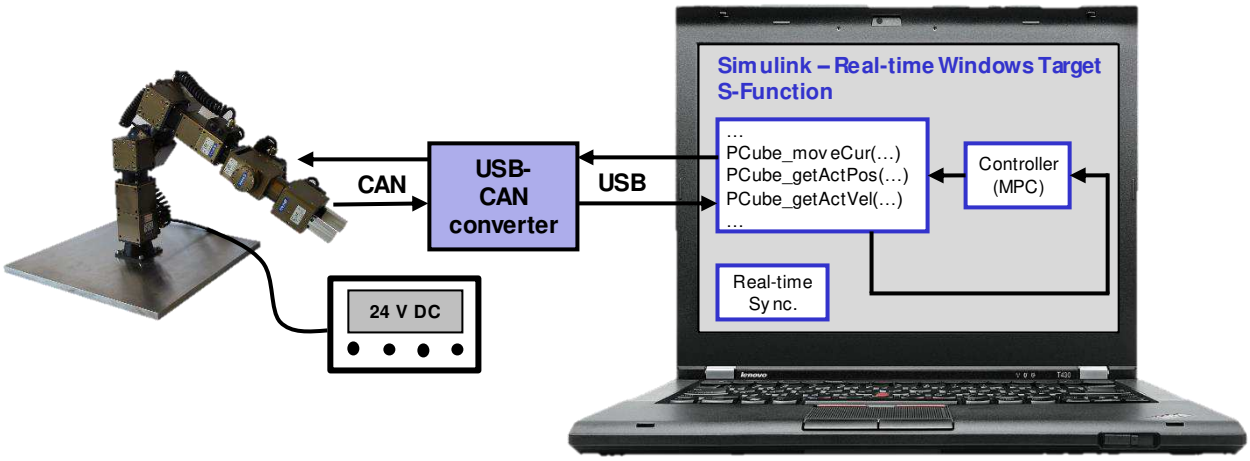

Figure 3: Slim process control framework of the robotic manipulator

motor torque at each joint. Those motor torques are scaled accordingly with gear ratios included in $\boldsymbol{B}$. A linear model $\boldsymbol{u} = K_\mathrm{M}\boldsymbol{i}$ describing the relation between motor torque and motor current is assumed. The motor constant K_M has been identified manually at the hardware. System parameters, such as masses, inertias, link lengths and gear ratios are taken from CAD data and datasheets, supplied by the manufacturers.
In a second step friction torques $\boldsymbol{\tau}(\dot{\boldsymbol{y}})$ are included into the model without friction, resulting in the vector of generalized forces

$$\boldsymbol{q}(\boldsymbol{y}, \dot{\boldsymbol{y}}) = \tilde{\boldsymbol{q}}(\boldsymbol{y}, \dot{\boldsymbol{y}}) - \boldsymbol{\tau}(\dot{\boldsymbol{y}}). \tag{2}$$

For a more intuitive understanding $\boldsymbol{\tau}$ is subtracted from $\tilde{\boldsymbol{q}}$, since positive friction works against the current movement. The equation of motion *with friction* can be gained by substitution of $\tilde{\boldsymbol{q}}$ with $\boldsymbol{q}$ in eq. (1). Joint friction models of the form

$$\tau_i(\dot{y}_i) = a_1\dot{y}_i + a_2\tanh(a_3\dot{y}_i) + a_4\exp(-a_5|\dot{y}_i|)\tanh(3a_3\dot{y}_i), \tag{3}$$

derived in [11] are used in a first application which results in the stated mismatch between feed forward and MPC output. This form of friction model with parameter vector $\boldsymbol{a}$ includes the share of viscous friction corresponding to $a_1\dot{y}_i$, the share of Coulomb friction corresponding to $a_2\tanh(a_3\dot{y}_i)$ as well as the superelevation of the Stribeck curve which is characterized by $a_4\exp(-a_5|\dot{y}_i|)\tanh(3a_3\dot{y}_i)$. The smooth *tanh*-function replaces the *sgn*-function to avoid discontinuities within the model.
Focus lies on identifying more accurate friction models for both joints with either the SINDy method or general nonlinear regression. Therefore data of $\boldsymbol{y}$, $\dot{\boldsymbol{y}}$, $\ddot{\boldsymbol{y}}$ and $\boldsymbol{u}$ has to be collected during experiments or derived after running experiments respectively, such that

$$\boldsymbol{\tau}(\dot{\boldsymbol{y}}) = \tilde{\boldsymbol{q}}(\boldsymbol{y}, \dot{\boldsymbol{y}}) + \boldsymbol{B}\boldsymbol{u} - \boldsymbol{M}(\boldsymbol{y})\ddot{\boldsymbol{y}} - \boldsymbol{k}(\boldsymbol{y}, \dot{\boldsymbol{y}}) \tag{4}$$

can be calculated. Stated methods can then be applied. The resulting values for $\boldsymbol{\tau}$ obviously are dependent on all stated variables $\boldsymbol{y}$, $\dot{\boldsymbol{y}}$, $\ddot{\boldsymbol{y}}$ and $\boldsymbol{u}$. The notation $\boldsymbol{\tau}(\dot{\boldsymbol{y}})$ is chosen due to the assumption that friction effects only depend on joint velocities.

SINDy Concept

The concept of **S**parse **I**dentification of **N**onlinear **Dy**namics (SINDy) founds in the field of applied mathematics. It represents a modern method to gain nonlinear models based on experiment data, a long known challenge in system theory. The main concept behind SINDy can be described as reducing the nonlinear fit to a collection of function candidates to a (sparse) linear regression, which can then be effectively solved with state of the art algorithms, providing robust and efficient solutions.
The SINDy setup consists of a standard representation of a nonlinear system

$$\dot{\boldsymbol{x}} = \boldsymbol{f}(\boldsymbol{x}, \boldsymbol{u}) \tag{5}$$

with state vector $\boldsymbol{x} \in \mathbb{R}^n$, possible input $\boldsymbol{u} \in \mathbb{R}^q$ and the unknown vector field $\boldsymbol{f}$. Starting out simple, assume the state $\boldsymbol{x}$, and its time derivative $\dot{\boldsymbol{x}}$ and the system input $\boldsymbol{u}$ to be known for m unique time instances. The data can then be rearranged into three matrices $\boldsymbol{X}$, $\dot{\boldsymbol{X}}$ and $\boldsymbol{U}$ as follows

$$\boldsymbol{X} = \begin{bmatrix} \boldsymbol{x}^\mathrm{T}(t_1) \\ \boldsymbol{x}^\mathrm{T}(t_2) \\ \vdots \\ \boldsymbol{x}^\mathrm{T}(t_m) \end{bmatrix} \in \mathbb{R}^{m\times n}, \quad \dot{\boldsymbol{X}} = \begin{bmatrix} \dot{\boldsymbol{x}}^\mathrm{T}(t_1) \\ \dot{\boldsymbol{x}}^\mathrm{T}(t_2) \\ \vdots \\ \dot{\boldsymbol{x}}^\mathrm{T}(t_m) \end{bmatrix} \in \mathbb{R}^{m\times n}, \quad \boldsymbol{U} = \begin{bmatrix} \boldsymbol{u}^\mathrm{T}(t_1) \\ \boldsymbol{u}^\mathrm{T}(t_2) \\ \vdots \\ \boldsymbol{u}^\mathrm{T}(t_m) \end{bmatrix} \in \mathbb{R}^{m\times q}. \tag{6}$$

Goal is to approximate the vector field $\boldsymbol{f}$ by a library of r candidate functions $\Theta(\boldsymbol{X}, \boldsymbol{U}) \in \mathbb{R}^{m \times r}$ which are weighed by coefficients $\boldsymbol{\Xi} = [\boldsymbol{\xi}_1, \boldsymbol{\xi}_2, \cdots, \boldsymbol{\xi}_r] \in \mathbb{R}^{n \times r}$ as

$$\dot{\boldsymbol{x}} = \boldsymbol{f}(\boldsymbol{x}, \boldsymbol{u}) \approx \boldsymbol{\Theta}(\boldsymbol{X}, \boldsymbol{U})\boldsymbol{\Xi}, \tag{7}$$

where the columns of the library of candidate functions can contain all kinds of imaginable nonlinear terms. Those can be polynomials in $\boldsymbol{x}$, $\boldsymbol{u}$ or combinations of both or other nonlinear terms like trigonometric functions. Filling this library with appropriate terms requires intuition on how the solution could look and is considered one critical point concerning the success of the SINDy method.
The solution to the linear regression problem introduced in eq. (7) may be calculated with aid of various solvers, e. g., a standard least squares solver

$$\boldsymbol{\xi}_k = \arg\min_{\boldsymbol{w}} \left\| \dot{\boldsymbol{X}}_k - \boldsymbol{\Theta}(\boldsymbol{X}, \boldsymbol{U})\boldsymbol{w} \right\|_2^2. \tag{8}$$

Here $\boldsymbol{\xi}_k$ denotes the k-th column of $\boldsymbol{\Xi}$ while $\dot{\boldsymbol{X}}_k$ denotes the k-th column of $\dot{\boldsymbol{X}}$.
Doing so does result in a reasonable model but at the same time leads to very complex and detailed models with many active function terms. Key feature of the SINDy concept is solving the linear regression problem eq. (7) promoting sparsity within the solution vectors $\boldsymbol{\xi}_k$, which corresponds to the fact that most systems of interest can be described by only a few active terms in $\boldsymbol{f}$. Therefore solution techniques for sparse linear regression are applied to eq. (7). A schematic overview and example for a system with two states is given with Fig. 5.
The overall concept appears to be very flexible regarding to all kinds of dynamical systems. There exists a wide range of extensions which , e. g., allow SINDy to perform in discrete time or even to identify PDEs [7, 12].

The SINDy concept, in general, brings some advantages and some disadvantages compared to other machine learning concepts, e. g., an artificial neural network (NN). Such a NN may be used to describe the unknown vector field $\boldsymbol{f}$, which also gives good results. One general disadvantage of a NN is the training process, which requires large amounts of measureed data to obtain an suitable approximation for $\boldsymbol{f}$. SINDy on the other hand can work with one single short experimental trajectory as in Fig. 2. The SINDy method results in a set of nonlinear differential equations which may even be physically interpretable where a NN just results in some non-interpretable matrix layers. In addition to that, the SINDy results, being differential equations, can be evaluated in their whole domain and possibly even be extrapolated. This is a major advantage over neural networks, which often provide unsatisfying approximation results outside of the domain of the training data. Training data of course, has to cover all important system characteristics for both approaches. Otherwise, some system aspects and properties will be left out in the identified system model.
A crucial drawback of the SINDy concept lies in the function library $\boldsymbol{\Theta}$ and in the fact that only linear combinations of these functions describe the resulting dynamics $\boldsymbol{f}$ of the system. One critical disadvantage of the SINDy concept lies in its function library $\boldsymbol{\Theta}$ and that only linear combinations of those functions can be described in the resulting $\boldsymbol{f}$. Looking at eq. (3), one cannot directly identify a nested term like $a_2 \tanh(a_3 \dot{y}_i)$ with SINDy. Having a look back at eq. (3) one cannot directly identify a term like $a_2 \tanh(a_3 \dot{y}_i)$ with SINDy. The problem is that the parameter a_3 is embedded inside a nonlinear term. We will later avoid this by including multiple terms $\tanh(a_3 \dot{y}_i)$ with different fix parameters a_3 into the library $\boldsymbol{\Theta}$.
The main advantages and problems of the SINDy concept have been briefly touched upon here. In [8], however, a much more detailed comparison of SINDy with artificial neural networks when used in model predictive control can be found.

Sparse Linear Regression

Two algorithms out of the wide variety of sparse linear regression methods were tested and could be applied to the setup. One of them is the so called Least Absolute Shrinkage and Selection Operator (LASSO), which is well known from the

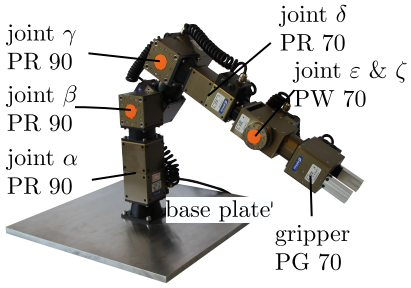

Figure 4: Experimental setup and configuration of the six degrees of freedom Schunk modular manipulator. The control is based on Real-Time Windows Target and Simulink Coder.

Table 1: Technical properties of the Schunk modules.

module name	nom. torque/force	max. velocity
PR 90 (rotary) joint α & β & γ	44.8 Nm	$\omega_{\text{max}} = 25$ rpm
PR 70 (rotary) joint δ	10.0 Nm	$\omega_{\text{max}} = 25$ rpm
PW 70 (pan-tilt) joint ε & ζ	12.0 Nm & 2.0 Nm	$\omega_{\text{max}} = 25$ rpm
PG 70 (gripper)	200 N	$v_{\text{max}} = 82$ mm/s

field of statistics and often used in machine learning applications. The LASSO can be described as ℓ_1 regularized version of the standard least squares linear regression setup and can be written as

$$\boldsymbol{\xi}_k = \arg\min_{\boldsymbol{w}} \left\| \dot{\boldsymbol{X}}_k - \boldsymbol{\Theta}(\boldsymbol{X}, \boldsymbol{U})\boldsymbol{w} \right\|_2^2 + \lambda \left\| \boldsymbol{w} \right\|_1. \tag{9}$$

The parameter $\lambda \geq 0$ adjusts the influence of the penalty term $\|\boldsymbol{w}\|_1$ and therefore determines how sparse the solution vector $\boldsymbol{\xi}_k$ turns out. With $\lambda = 0$ the solution is equal to the standard least squares problem's solution stated in eq. (8).
Another sparsity promoting linear regression approach is given by the Sequential Thresholded Least Squares algorithm (STLS) introduced in [7]. The STLS algorithm is an iterative procedure based on standard least squares solutions and can be described as follows.

- An initial solution $\boldsymbol{\xi}_k^{(0)}$ is calculated as least squares solution with the complete library matrix $\boldsymbol{\Theta}^{(0)} = \boldsymbol{\Theta}(\boldsymbol{X}, \boldsymbol{U})$;
- In each iteration the regression setup reduces by
  - setting entries in $\boldsymbol{\xi}_k^{(r)}$ with absolute value less than a threshold parameter λ to zero;
  - deleting the corresponding columns in $\boldsymbol{\Theta}^{(r)}$, which would then be multiplied by zero, which leads to $\boldsymbol{\Theta}^{(r+1)}$;

  Solving the reduced least squares problem with $\boldsymbol{\Theta}^{(r+1)}$ leads to a new solution vector $\boldsymbol{\xi}_k^{(r+1)}$ which includes the remaining entries of $\boldsymbol{\xi}_k^{(r)}$.
- Iteration ends if no more entries in $\boldsymbol{\xi}_k^{(r)}$ fulfill the threshold condition.

Again, the parameter $\lambda > 0$ determines the sparsity of the solution. One iteration step of the STLS algorithm is illustrated in Fig. 6.
The critical point with both algorithms is choosing an appropriate value for the hyper parameter λ. In practice models for a broad range of parameters λ are calculated which allows finding a good compromise between sparsity of the resulting model and model error along a pareto front. The LASSO combined with k-fold cross validation is able to find this compromise by its own. With the STLS approach as it is described above one has to choose a model by hand. More sparse solutions on the one hand allow for some form of physical interpretation of the result but on the other hand may show a greater model error compared to other more flexible nonlinear regression techniques.

The whole SINDy setup was implemented in Matlab [13]. The STLS algorithm was implemented manually while a LASSO implementation already exists within the Statistics and Machine Learning Toolbox.

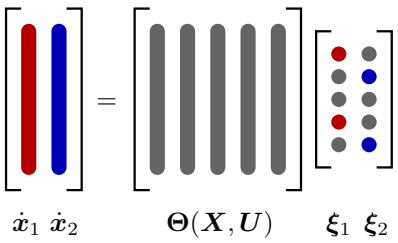

Figure 5: Application of the SINDy concept with sparse linear regression to a system with two states. Grey entries in $\boldsymbol{\xi}_k$ mark entries which are zero.

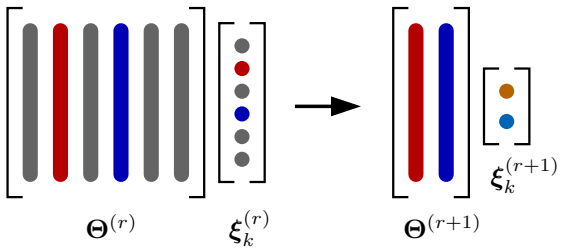

Figure 6: Illustration of the STLS algorithm. Grey entries in $\boldsymbol{\xi}_k^{(r)}$ are set to zero. Corresponding columns in $\boldsymbol{\Theta}^{(r)}$ are removed. $\boldsymbol{\xi}_k^{(r+1)}$ is the new least squares solutions with slightly different entries.

Experimental Measurements

Before taking measurements, a suitable class of trajectories has to be defined used for friction identification. We chose sine-shaped trajectories with variable frequency within this study since they can be constructed relatively easily. Being at least two times continuous differentiable sine trajectories brings smooth acceleration and deceleration, which is crucial for not exceeding joint limitations. Furthermore, differentiation and integration can be done analytically. The sine part of the trajectory can be described as

$$y(t) = \hat{a}\ \sin(\omega(t)t) \tag{10}$$

with a constant amplitude $\hat{a}$. Polynomial acceleration and deceleration phases around the sine trajectory part are needed since the robot starts and ends in a static pose where velocities and accelerations must be zero. Part of such a trajectory can be seen in Fig. 7.
The figure also points out a difficulty with measurement data. The robot's joint positions are measured by absolute angle encoders within each joint, which results in a non-smooth velocity measurement with coarse resolution. Therefore a

suitable differentiation method is needed to calculate joint velocities and accelerations from joint position data. In [8] the use of Total Variation Regularization Differentiation (TVDiff) is recommended. The TVDiff algorithm is introduced in [14]. The paper and Matlab implementations of the algorithm for one- and two-dimensional data, can be found on the author's web page. The idea of TVDiff originates in the Tikhonov regularization where the energy of a signal is minimized according to an energy functional without influencing the signal in a way a low pass filter would do. Variational methods are quite popular in the field of imaging science for efficiently denoising images. TVDiff results for trajectory measurement data are presented in Fig. 7. Figure. 8 demonstrates the advantages of TVDiff over finite differences with a therefore synthesized signal with added white noise. With higher frequencies a slight low pass effect is visible but the results are sufficient for the application with SINDy.

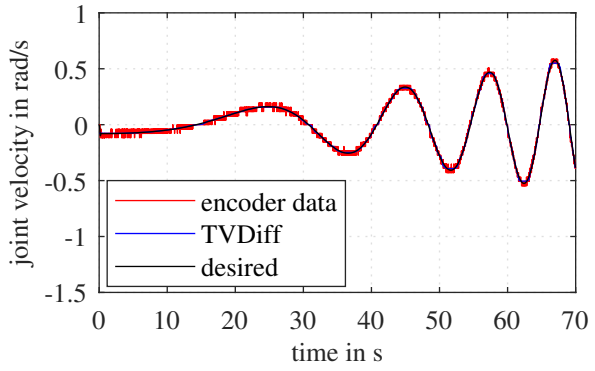

Figure 7: Measured encoder velocity compared with the filtered velocity from position measurements via TVDiff and the desired velocity.

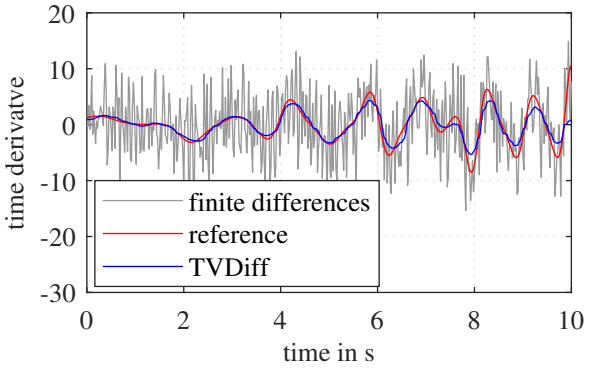

Figure 8: Synthesized example to demonstrate TVDiff advantages over finite differences with comparison to the analytically calculated reference signal.

Friction Identification

With previously described methods almost all infrastructure needed to identify friction models is present. Friction characteristics for robot joints B and C which correspond to the joint coordinates β and γ are displayed in Fig. 9 and Fig. 10. The resulting friction characteristics of both joints, if moved individually, will be dependent on the joint angle. These effects arise from model inaccuracies within the rigid multibody dynamics, e. g., incorrect inertia values or not modeling cables etc. The influence of gravity at non-zero joint angles makes the resulting friction characteristics dependent on the joint angle. This is against the assumption of friction only depending on joint velocity. Therefore for joint B the gained data is preprocessed by selecting data points with $|\beta| < 0.1$ where the influence of gravity is negligible. The filtered data is plotted in Fig. 12. Since many data points remain unused, a different strategy is chosen for joint C. Since it is the upper body of two joints, the influence of gravity can be easily compensated by moving both joints in opposite directions, keeping the upper part of the robot pointing straight upwards. Figure 11 illustrates half of a period of the particular periodic trajectory. Identification with the gravity compensated trajectory leads to the friction characteristics for joint C shown in Fig.10. As stated earlier the SINDy results are compared to a model calculated by nonlinear regression. Eq. 3 therefore functions as template for the nonlinear regression with its parameters a_1 to a_5. The nonlinear regression algorithm used is the `nlinfit` Matlab function which is included in the Statistics and Machine Learning Toolbox as well.

The application of the SINDy concept still requires us to specify a library of function terms. Over time and within many

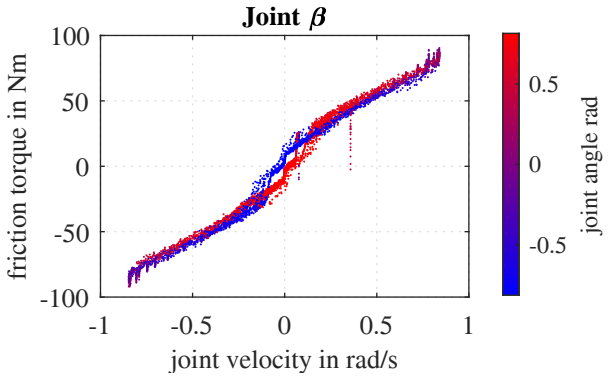

Figure 9: Friction characteristic for joint B measured with a sine trajectory. Only joint B was moved for these measurements.

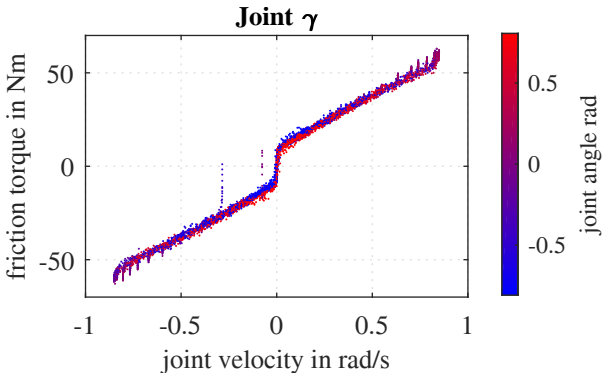

Figure 10: Friction characteristic for joint C measured with a sine trajectory. Joint B and joint C were moved equally in opposite directions to compensate gravity.

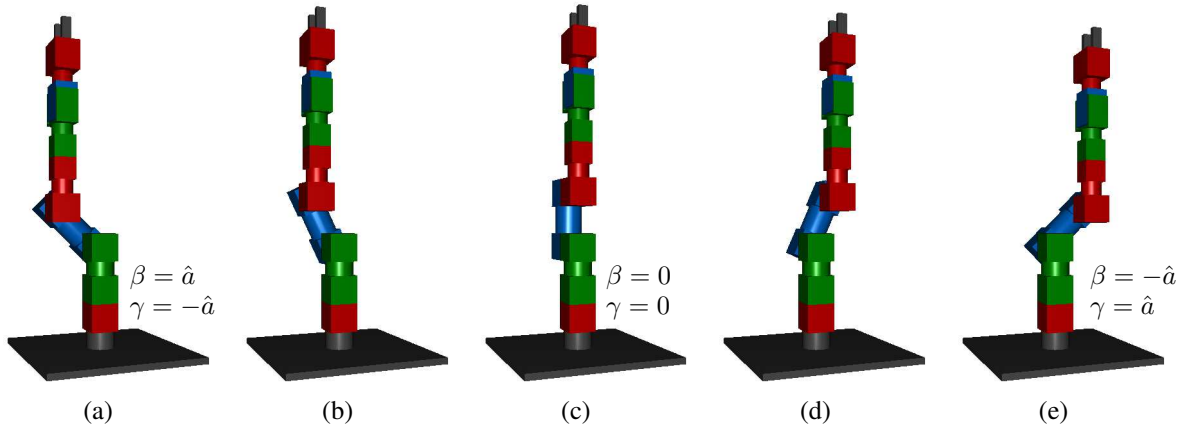

Figure 11: Periodic trajectory for friction identification in joint C. Shown is half a period starting at the left turning point (a), going through the robot's zero position (c) and ending at the right turning point (e). Frames (b) and (d) display intermediate points.

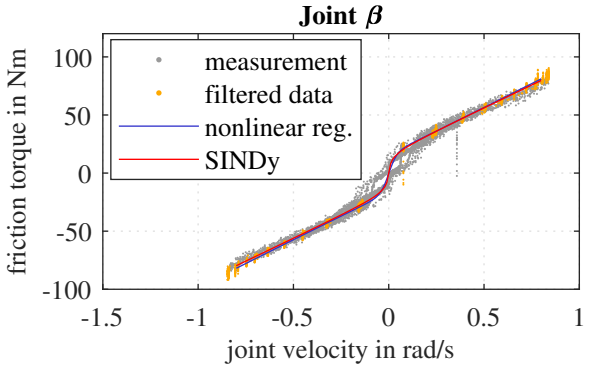

Figure 12: Fitted friction models for joint B after preprocessing measurement data.

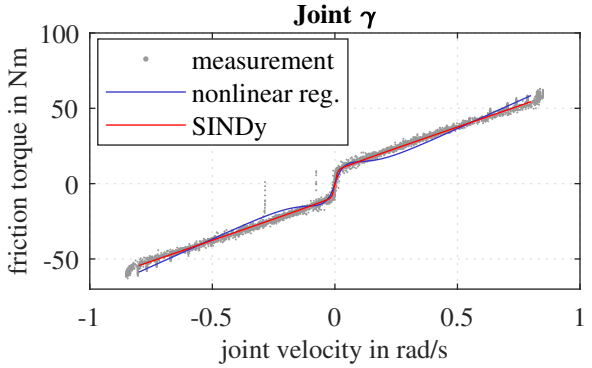

Figure 13: Fitted friction models for joint C. No preprocessing is needed.

experiments the library

$$\boldsymbol{\Theta}(\dot{\boldsymbol{y}}) = \begin{bmatrix} \mathbf{1} & \dot{\boldsymbol{y}} & \operatorname{sgn}(\dot{\boldsymbol{y}}) & \tanh(5\dot{\boldsymbol{y}}) & \tanh(10\dot{\boldsymbol{y}}) & \tanh(20\dot{\boldsymbol{y}}) & \tanh(100\dot{\boldsymbol{y}}) \end{bmatrix} \tag{11}$$

lead to promising results. The library contains functional terms for describing friction characteristics and at the same time, leaves enough options for the sparse linear regression to cancel out function terms. Promoting sparsity without leaving enough options for the algorithm would not lead to the expected results. A finer sampling of the terms $\tanh(a\dot{\boldsymbol{y}})$ was tested but results in high correlations between these functions, ultimately leading to difficulties in sparse linear regression. The library does not contain terms describing the superelevation of the Stribeck curve. This will only be a minor disadvantage since such a superelevation is not noticeable within the measurement data.

Applying SINDy and nonlinear regression to the measurement data together with the earlier discussed preprocessing leads to the the friction models shown in Fig. 12 and Fig. 13. Both regression concepts deliver quite similar results. SINDy outperforms nonlinear regression in the case of joint C, having the ability to choose freely from its function library while the nonlinear regression always has to fit to its function template. While nonlinear regression for the data of joint B would not work properly without preprocessing, the SINDy method would still lead to reasonable results. Although the preprocessed data gives a better friction model and shows that SINDy can even work with a percentage of the available data, making it robust to the amount of available measurement data.

An additional friction identification was performed for link A (corresponding to α) for better comparison of the joint friction characteristics and models. Therefore a linear quadratic regulator was implemented, since there doesn't exist an MPC scheme for the rigid body model with $\boldsymbol{y} = \alpha$. The resulting friction models for link A are displayed in Fig. 14. Again, nonlinear regression as well as the SINDy method perform well, although the measurement data is spread quite heavily. Preprocessing the data is not necessary for either method.

Comparing the newly identified joint friction models to the previously used model from [11] points out two major aspects. At first, friction models differ from joint to joint, although being the same kind of link module (PR90). Secondly, whether the joint friction is identified for an isolated joint or at an assembled robot makes a big difference. Therefore the two newly identified joint friction models differ heavily from the model identified in [11]. While in [11] single isolated joint modules were researched, the additional weight of our robot above joints B and C amplifies friction at the joints' axles. Fig. 15 shows the comparison of the different models. Compared are the SINDy results identified above.

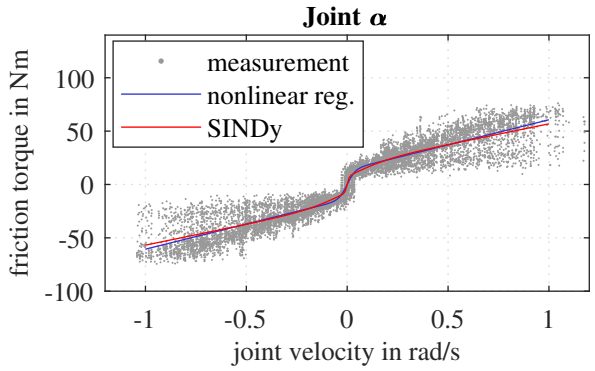

Figure 14: Fitted friction models for joint A. No preprocessing is needed.

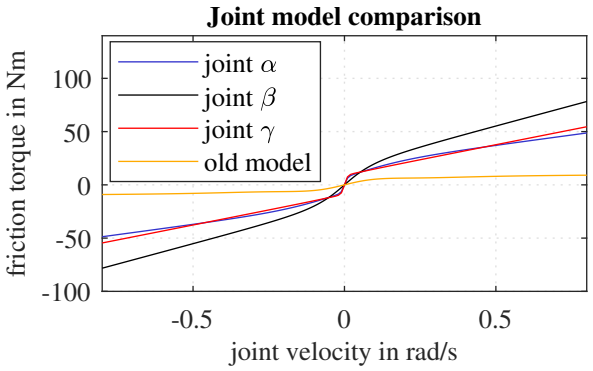

Figure 15: Comparison of the three new joint friction models with the old model from [11]. Visualized are the identified SINDy models.

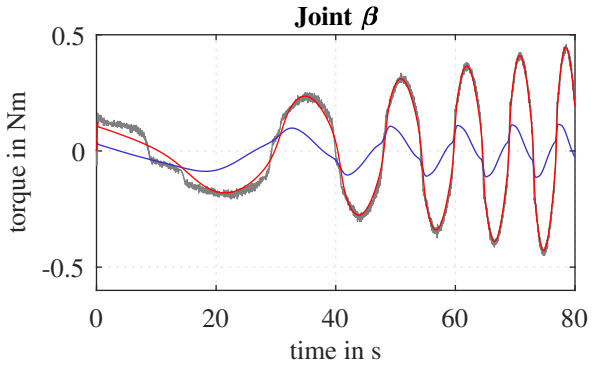

Figure 16: Feed forward torqes of the old and new model compared to the MPC output torque applied at joint β.

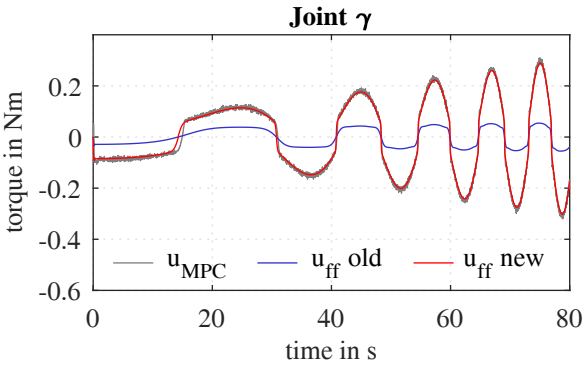

Figure 17: Feed forward torqes of the old and new model compared to the MPC output torque applied at joint γ.

Conclusion

With the methods and results developed throughout this paper, we can finally find the following conclusion. Both, System Identification for Nonlinear Dynamics (SINDy) and nonlinear regression were applied to identify friction models for the relevant joints B and C of the PowerCube robot. Additionally, a friction model for joint A was identified for use with a linear quadratic regulator. The vast improvement of the feed-forward calculations together with the newly identified joint friction models imply a general improvement of the robot model. Although the feed-forward torque almost matches the controller output, slight differences still remain that result from model errors within the rigid body model without friction. However, better trajectory tracking performance, critical for practical usage of the robotic manipulator, could not be improved with the current setup. A first reason lies in using a linearizing MPC approach that does not adequately represent nonlinear system dynamics. Second, the setup underlies limitations in hardware and software. On the hardware side, communication between the robot and the centralized controller in Simulink is limited in speed since the Schunk PowerCube Robot is designed for decentralized joint control schemes such as PID. On the software side, the MPC online optimization cannot be evaluated arbitrarily fast. Both limitations contrast the need for trajectories and linearized dynamics with high resolution in time whenever using LTV MPC.

Further research out of the scope of this publication has shown improvements in trajectory tracking performance with the newly identified friction models when using a truly nonlinear MPC scheme.

When determining the friction, the research has been shown that the friction determination for isolated joint connection modules is not sufficient. Within the robot assembly, the axes of the joints have to bear an additional load, which leads to higher friction.

The SINDy method and its sparse regression algorithms make for a robust and fast method for identifying nonlinear system dynamics. Nonlinear regression in comparison leads to very similar results but needs more computation time due to its nonlinear optimization, making it less capable for real-time applications.

All in all, SINDy's potential to identify parts of unknown system dynamics was successfully presented.

Acknowledgements

Funded by Deutsche Forschungsgemeinschaft (DFG, German Research Foundation) under Germany's Excellence Strategy - EXC 2075 - 390740016. We acknowledge the support by the Stuttgart Center for Simulation Science (SimTech). We thank Patrick Schmid and Georg Schneider for the helpful discussions regarding MPC and the experimental setup.

References

[1] Fehr, J.; Schmid, P.; Schneider, G.; Eberhard, P.: Modeling, Simulation, and Vision-/MPC-based Control of a PowerCube Serial Robot. Applied Sciences, Vol. 10, No. 20, id. 7270, 2020.

[2] Rawlings, J.B.; Mayne, D.Q.: Model Predictive Control: Theory and Design. Madison: Nob Hill Publishing, 2009.

[3] Maciejowski, J.M.: Predictive Control with Constraints. Upper Saddle River: Prentice Hall, 2002.

[4] Schnelle, F.; Eberhard, P.: Real-time Model Predictive Control of a Pendulum. PAMM, Vol. 14, No. 1, pp. 907–908, 2014.

[5] Grotjahn, M.; Heimann, B.: Model-based Feedforward Control in Industrial Robotics. The International Journal of Robotics Research, Vol. 21, No. 1, pp. 45–60, 2002.

[6] Ferreau, H.J.; Kirches, C.; Potschka, A.; Bock, H.G.; Diehl, M.: qpOASES: A Parametric Active-Set Algorithm for Quadratic Programming. Mathematical Programming Computation, Vol. 6, No. 4, pp. 327–363, 2014.

[7] Brunton, S.L.; Proctor, J.L.; Kutz, J.N.: Discovering Governing Equations from Data by Sparse Identification of Nonlinear Dynamical Systems. Proceedings of the National Academy of Sciences, Vol. 113, No. 15, pp. 3932–3937, 2016.

[8] Kaiser, E.; Kutz, J.N.; Brunton, S.L.: Sparse Identification of Nonlinear Dynamics for Model Predictive Control in the Low-data Limit. Proceedings of the Royal Society A: Mathematical, Physical and Engineering Sciences, Vol. 474, No. 2219, p. 20180335, 2018.

[9] Kurz, T.; Eberhard, P.; Henninger, C.; Schiehlen, W.: From Neweul to Neweul-M^2: Symbolical Equations of Motion for Multibody System Analysis and Synthesis. Multibody System Dynamics, Vol. 24, No. 1, pp. 25–41, 2010.

[10] The Mathworks, Inc., Natick, Massachusetts: MATLAB and Real-Time Windows Target R2014b, 2014.

[11] Oberhuber, B.: Ein Beitrag zur modularen Modellierung und Regelung redundanter Robotersysteme (in German). Linz: Trauner, 2013.

[12] Rudy, S.H.; Brunton, S.L.; Proctor, J.L.; Kutz, J.N.: Data-driven Discovery of Partial Differential Equations. Science Advances, Vol. 3, No. 4, id. e1602614, 2017.

[13] MathWorks: Documentation for Matlab, Release 2019b, 2019. Accessed: 2022-03-07, Url: `https://www.mathworks.com/help/releases/R2019b/index.html`.

[14] Chartrand, R.: Numerical Differentiation of Noisy, Nonsmooth Data. ISRN Applied Mathematics, Vol. 2011, id. 164567, 2011.

Monday, July 18, 2022
16:00 - 18:40

MS-10 Non-Smooth Dynamics
Saint Clair 3A

Chair : Remco Leine - Vincent Acary

16:00 - 16:20
Equilibrium of a non-compressible cable subjected to unilateral constraints
BERTRAND Charlélie*, LAMARQUE Claude-Henri, ACARY Vincent, TURE Savadkoohi Alireza
*Laboratoire de Tribologie et Dynamique des Systèmes (3, Rue Maurice Audin, 69518 Vaulx en Velin (CEDEX) France)

16:20 - 16:40
Trajectory Tracking Control for Linear Complementarity Systems with Continuous Solutions
VO Van Nam, **BROGLIATO Bernard***, PRIEUR Christophe
*INRIA Grenoble-Alpes (Inovallée 38334 Montbonnot France)

16:40 - 17:00
Identification and validation of impact models
JONGENEEL Maarten*, WOUW Nathan, SACCON Alessandro
*Eindhoven University of Technology (5612 AZ Eindhoven Netherlands)

17:00 - 17:20
Multiple impacts in granular chains with Kuwabara-Kono dissipation
JAMES Guillaume*, VOROTNIKOV Kirill, BROGLIATO Bernard
*TRIPOP Team (655 avenue de l'Europe, 38334 Saint-Ismier France)

17:20 - 17:40
Non-smooth dynamics modeling of drill-string systems in heterogeneous formations
ARIBOWO Arviandy*, WILDEMANS Roeland, DETOURNAY Emmanuel, VAN De Wouw Nathan
*Eindhoven University of Technology (Den Dolech 2, 5612 AZ, Eindhoven Netherlands)

17:40 - 18:00
Nonlinear granular damping of structures with cavities from additive manufacturing
TATZKO Sebastian*, EHLERS Tobias, KLEYMAN Gleb, LACHMAYER Roland
*Institute of Dynamics and Vibration Research (Appelstraße 11, 30167 Hannover Germany)

18:00 - 18:20
A Nonsmooth Approach for Generating Convex Relaxations of Dynamic Systems
SONG Yingkai*, KHAN Kamil
*Department of Chemical Engineering, McMaster University (1280 Main St W, Hamilton, ON L8S 4L8 Canada)

18:20 - 18:40
Nonsmooth Modal Analysis of Varying Cross-section Bar
LU Tianzheng*, LEGRAND Mathias
*Structural Dynamics and Vibration Laboratory, McGill University (Department of Mechanical Engineering, Room 122, McConnell Engineering Building, McGill University, 817 Sherbrooke St West, Montréal QC H3A 0C3 Canada)

Equilibrium of a non-compressible cable subjected to unilateral constraints

Charlélie Bertrand*, Vincent Acary†, Claude Henri Lamarque* and Alireza Ture Savadkoohi*
* *Univ Lyon, ENTPE, CNRS UMR5513, LTDS, France*
† *Univ Grenoble Alpes, CNRS, Inria, Grenoble INP, France*

Summary. More realistic simulation of complex cable structures shall need the introduction of unilateral constraints to predict the global behavior of a whole structure without neglecting the influence of a realistic boundary condition. Indeed systems like ropeways (or belt drives) may exhibit behaviors that are strongly affected by friction at contacting zones between the cable (or belt material) and support (or pulley). This consideration also opens the gate to the study of the interaction between successive spans. Moreover the numerical simulation of these systems remains delicate due to their geometrical non linearity.

Introduction

Cables are the main features of many light engineering devices among which electric transmission lines, ropeways installation, cable car or lifts. The equilibria of cable system found their root in the sixteenth century. One the first author about the subject might be Leibniz with the two following works on the catenary curve [1, 2]. Far from this historical anecdote, today's engineering design still relies on those works or the parabolic approximation of weighting rope, first introduced by Galileo and made popular by Irvine [3]. From this monograph to current day, the richness of cable behaviours never ceased to be explored. Major studies in modelling and dynamics have been gathered by Rega in his review and work [4]. However, sophisticated boundary condition or constraints never had been deeply investigated for the cable which almost always perfectly hanged between two points and freely hanging. This is the aim of this work.
Impacts, collisions and friction play a key role in the transient regime of vibrating media by producing a high frequency content responses. Beyond the scope of the current application is the case of string music instrument which vibration against an obstacle explain the signal richness [5]. Similar phenomena are expected in a larger problem such as a ropeway and could explain the apparition of large oscillations when a cabin passes along the top of an intermediary pylon. Although cable dynamics have been studied intensively for the three last decades [3, 4, 6] and numerical challenges never ceased to be attacked [7, 8, 9, 10], there are still unanswered questions about different techniques of the Finite Element Method (FEM) [11, 12] applied to a cable which is subjected to nonsmooth constraints despite the existing bibliography about nonsmooth dynamics [13, 14].
Current focus is drawn on the equations for a cable which is subjected to the presence of a circular-shape obstacle and on a FEM associated with this problem. One may refer to the research work done in succession by Bruno et al. [15], Such et al. [16], Impollonia et al. [17] and Crussels-Girona et al. [10] about the equilibrium of a cable subjected to an intermediary pulley as mean of comparison.

System of interest

We are interested in the mechanics of a cable belonging to the Cartesian space $\mathbb{R}^3$ equipped with an orthogonal basis $(\underline{e}_x, \underline{e}_y, \underline{e}_z)$. A cable can be described as a curvilinear domain [6] which cannot resist any torque and compression due to its slenderness and its micro-structure. Each particle of this domain is associated to a unique curvilinear abscissa $S \in [0, L]$ where L stands for the reference length of the cable and a triplet of the Cartesian space:

$$q(S,t) = \begin{bmatrix} x(S,t) \\ y(S,t) \\ z(S,t) \end{bmatrix}. \tag{1}$$

The cable is subjected to external loads collected by $f(S,t) \in \mathbb{R}^2 \to \mathbb{R}^3$. The cable equilibrium is satisfied when tensile forces balance external solicitations and inertial force, which reads:

$$\rho \dot{v}(S,t) = \left(EA(\|q'(S,t)\| - 1) \frac{q'(S,t)}{\|q'(S,t)\|} \right)' + f(S,t) \tag{2}$$

Where $\dot{\bullet}$ and $\bullet'$ stand for derivatives of the variable $\bullet$ with respect to the time and space, respectively. The parameters ρ and EA are respectively the linear density of the cable and the cable rigidity. The velocity of the particle located at S is denoted by $v(S,t)$.
The equations of motion are supplemented by equality and inequality constraints to account for more detailed physics, such as the boundary conditions, the presence of obstacles, impacts or friction. The following constraints are introduced:

$$\text{(Equalities)} \quad a(q(S,t),S,t) = 0 \tag{3}$$

$$\text{(Inequalities)} \quad g(q(S,t),S,t) \geqslant 0 \tag{4}$$

The research of a solution for (2) is then performed in the admissible set $\mathbf{A}_{\text{dm}}$ given by:

$$\mathbf{A}_{\text{dm}} = \left\{ \begin{pmatrix} v(S,t) \\ q(S,t) \end{pmatrix}, \; a\left(q(S,t),S,t\right) = 0, \; g\left(q(S,t),S,t\right) \geqslant 0, \; v \in \mathcal{RCBV}, q \in \mathcal{AC} \right\} \tag{5}$$

where the set of right continuous functions of bounded variations and the set of absolutely continuous functions are denoted by $\mathcal{RCBV}$ and $\mathcal{AC}$.

Finite element procedure

A finite element procedure is derived for the system given by (2)-(5). Following previous work [18], the unconstrained system is written:

$$\mathbf{M}\dot{\mathbf{v}}(t) + \mathbf{C}\mathbf{v}(t) + \mathbf{K}(\mathbf{q}(t))\mathbf{q}(t) - \mathbf{f}(t) = \mathbf{0}, \tag{6}$$

where $\mathbf{v}$ and $\mathbf{q}$ are finite-dimensional vectors collecting the unknowns at nodes. The equality and inequality constraints and their Jacobians are written at each nodes such that :

$$\mathbf{a}(\mathbf{q},t) = \mathbf{0} \quad ; \quad \nabla^{\intercal}\mathbf{a}(t) = \mathbf{A}(t) \tag{7}$$

$$\mathbf{g}(\mathbf{q},t) \geqslant \mathbf{0} \quad ; \quad \nabla^{\intercal}\mathbf{g}(t) = \mathbf{G}(t) \tag{8}$$

The mechanical system at stake can be formulated as a nonlinear complementarity system as follows:

$$\begin{cases} \mathbf{M}\dot{\mathbf{v}}(t) + \mathbf{C}\mathbf{v}(t) + \mathbf{K}(\mathbf{q}(t))\mathbf{q}(t) - \mathbf{f}(t) = \mathbf{A}(t)^{\intercal}\lambda + \mathbf{G}(t)^{\intercal}\mu \\ \dot{\mathbf{q}} = \mathbf{v} \\ \mathbf{a}(\mathbf{q}(t),t) = \mathbf{0} \\ \mathbf{0} \leqslant \mathbf{g}(\mathbf{q}(t),t) \perp \mu \geqslant \mathbf{0} \end{cases} \tag{9}$$

where λ and μ are Lagrange multipliers which can be physically interpreted as reaction forces provided that the Jacobians are normalized.
Let us introduce the following index sets:

$$\mathcal{E} = \{\beta, a^{\beta}(\mathbf{q},t) = 0\}, \qquad \text{(index set of equality constraints)} \tag{10}$$

$$\mathcal{I} = \{\alpha, g^{\alpha}(\mathbf{q},t) \geqslant 0\}, \qquad \text{(index set of inequality constraints)} \tag{11}$$

$$\tag{12}$$

and the following sets:

$$\mathcal{C}(t) = \{\mathbf{q}, \quad \mathbf{a}(\mathbf{q},t) = \mathbf{0}, \quad \mathbf{g}(\mathbf{q},t) \geqslant \mathbf{0}\} \tag{13}$$

$$\mathcal{N}_{\mathcal{C}}(\mathbf{q}) = \left\{ \mathbf{s} \in \mathbb{R}^n,\ \mathbf{s} = -\sum_{\beta\in\mathcal{E}} \lambda^{\beta}\mathbf{A}^{\beta} - \sum_{\alpha\in\mathcal{I}} \mu^{\alpha}\mathbf{G}^{\alpha},\ \mu^{\alpha} \geqslant 0,\ \mu^{\alpha}g^{\alpha}(\mathbf{q}) = 0,\ \alpha \in \mathcal{I} \right\} \tag{14}$$

Time dependencies will be omitted in the following for conciseness. The dynamics given by (9) can be written as an inclusion into the normal cone $\mathcal{N}_{\mathcal{C}}$:

$$\begin{cases} \mathbf{r} = \mathbf{M}\dot{\mathbf{v}} + \mathbf{C}\mathbf{v} + \mathbf{K}(\mathbf{q})\mathbf{q} - \mathbf{f} \\ -\mathbf{r} \in \mathcal{N}_{\mathcal{C}}(\mathbf{q}) \\ \mathbf{q} = \mathbf{q}_0 + \displaystyle\int_0^t \mathbf{v}\ \mathrm{d}t \end{cases} \tag{15}$$

for the smooth phase of the motion. If the motion is nonsmooth, a differential measure equality must be written as:

$$\begin{cases} \mathbf{M}\ \mathrm{d}\mathbf{v} + [\mathbf{C}\mathbf{v} + \mathbf{K}(\mathbf{q})\mathbf{q} - \mathbf{f}]\ \mathrm{d}t = \ \mathrm{d}\mathbf{r} \\ \mathrm{d}\mathbf{q} = \mathbf{v}\ \mathrm{d}t \\ -\ \mathrm{d}\mathbf{r} \in \mathcal{N}_{\mathcal{C}}(\mathbf{q}) \end{cases} \tag{16}$$

where $\mathrm{d}t$ is the Lebesgue measure and $\mathrm{d}\mathbf{r}$ is a reaction force measure. See [14] for details about the decomposition of this measure. This equality means that the reaction force $\mathbf{r}$ tends to pull the system back into the admissible set $\mathcal{C}(t)$. An illustration for this situation is provided in Figure 1. Finally, to favor the use of the Moreau–Jean time–stepping scheme[19, 14], a second order Moreau sweeping process is formulated:

$$\begin{cases} \mathbf{M}\ \mathrm{d}\mathbf{v} + [\mathbf{C}\mathbf{v} + \mathbf{K}(\mathbf{q})\mathbf{q} - \mathbf{f}]\ \mathrm{d}t = \ \mathrm{d}\mathbf{r} \\ \mathrm{d}\mathbf{q} = \mathbf{v}\ \mathrm{d}t \\ -\ \mathrm{d}\mathbf{r} \in \mathcal{N}_{T_{\mathcal{C}}(\mathbf{q})}(\mathbf{v} + e\mathbf{v}^{-}), \end{cases} \tag{17}$$

where e is the coefficient of restitution and $T_{\mathcal{C}}$ the tangent cone to $\mathcal{C}$.
Numerical treatment of this system of equations will be at the heart of the following considerations.

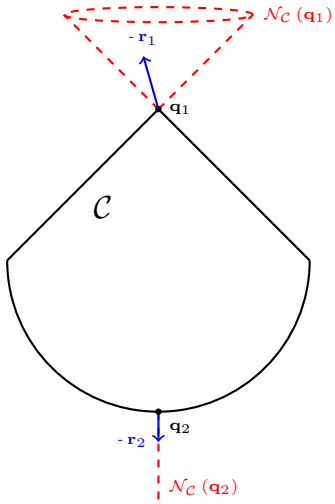

Figure 1: Normal cone and possible reaction forces in $\mathbf{q}_1$ and $\mathbf{q}_2$

Numerical treatment

In the Moreau–Jean time–stepping scheme [19], a θ-method is endowed to approximate integral quantities over a time-step h. For an arbitrary function ζ, it reads:

$$\int_{t_0}^{t_1} \zeta(t)\,\mathrm{d}t \approx h\left[\theta\zeta_1 + (1-\theta)\zeta_0\right] \tag{18}$$

where the subscript $\bullet_0$ (resp. $\bullet_1$) denotes the evaluation of $\bullet$ in t_0 (resp $t_1 = t_0 + h$). In case of the stiffness matrix $\mathbf{K}$, a linearized approximation is endowed as:

$$\mathbf{K}_1(\mathbf{q}_1) \approx \mathbf{K}_0(\mathbf{q}_0) + h\theta\nabla\mathbf{K}_0\mathbf{v}_1 + h(1-\theta)\nabla\mathbf{K}_0\mathbf{v}_0 \tag{19}$$

At last, the constraints are taken fully implicitly in the formulation such that:

$$\int_{t_0}^{t_1} \mathrm{d}\mathbf{r} \approx \mathbf{p}_1 + \mathbf{A}_1{}^\intercal\lambda_1 \tag{20}$$

where p_1 and λ_1 are homogeneous to impulses.
The equality and inequality constraints are considered at the velocity level and are linearized such that it reduces to:

$$\mathbf{A}_0^\beta\mathbf{v}_1^\beta = \mathbf{0}, \beta \in \mathcal{E} \tag{21}$$

$$\bar{g}_1^\alpha = g_0^\alpha + \frac{h}{2}\mathbf{G}_0^\alpha\mathbf{v}_0, \alpha \in \mathcal{I} \tag{22}$$

$$\begin{cases} \text{If } \bar{g}_1^\alpha \leqslant 0, 0 \leqslant \mu_1^\alpha \perp \mathbf{G}_0^\alpha(\mathbf{v}_1 + e\mathbf{v}_0) \geqslant 0 \\ \text{If } \bar{g}_1^\alpha > 0, \mu_1^\alpha = 0 \end{cases}$$

The satisfaction at previous time step is used to get the simplification in (21). Then the equality constraints are reduced to their first-order expand. The whole numerical scheme can be wrapped into the following system:

$$\begin{cases} \widehat{\mathbf{M}}\left(\mathbf{v}_1 - \mathbf{v}_0\right) - \widehat{\mathbf{f}} = \mathbf{p}_1 + \mathbf{A}_0{}^\intercal\lambda_1 \\ \mathbf{A}_0^\beta\mathbf{v}_1^\beta = \mathbf{0}, \beta \in \mathcal{E} \\ \bar{g}_1^\alpha \approx g_0^\alpha + \dfrac{h}{2}\mathbf{G}_0^\alpha\mathbf{v}_0, \alpha \in \mathcal{I} \\ \quad \begin{cases} \text{If } \bar{g}_1^\alpha \leqslant 0, 0 \leqslant \mu_1^\alpha \perp \mathbf{G}_0^\alpha(\mathbf{v}_1 + e\mathbf{v}_0) \geqslant 0 \\ \text{If } \bar{g}_1^\alpha > 0, \mu_1^\alpha = 0 \end{cases} \\ \mathbf{q}_1 = \mathbf{q}_0 + h\theta\mathbf{v}_1 + h(1-\theta)\mathbf{v}_0 \end{cases}$$

where

$$\begin{aligned} \widehat{\mathbf{M}} &= \mathbf{M} + h\theta\mathbf{C} + h^2\theta^2\nabla\mathbf{K}_0 \\ \widehat{\mathbf{f}} &= h\theta\mathbf{f}_1 + h(1-\theta)\mathbf{f}_0 - h\mathbf{C}\mathbf{v}_0 \\ &\quad - h\mathbf{K}_0\mathbf{q}_0 - h^2\theta\nabla\mathbf{K}_0\mathbf{v}_0. \\ \mathbf{p}_1 &= \sum_\alpha \mu_1^\alpha\mathbf{G}_0^{\alpha\intercal} \end{aligned} \tag{23}$$

In order to obtain a mixed linear complementarity problem (MLCP) in a canonical form, the "free" velocity, $\mathbf{v}_f$ is computed for a given $\mathbf{v}_0$ solving the unconstrained system:

$$\mathbf{v}_f = \mathbf{v}_0 + \widehat{\mathbf{M}}^{-1}\widehat{\mathbf{f}} \tag{24}$$

The following iteration is referred as a one step nonsmooth problem (OSNSP) in the literature [14] which aims to obtain the correct impact estimation and the corrected velocity as the solution of:

$$\text{(OSNSP)} \begin{cases} \widehat{\mathbf{M}}\,(\mathbf{v}_1 - \mathbf{v}_f) = \mathbf{p}_1 + \mathbf{A}_0{}^{\intercal}\lambda_1 \\ \mathbf{A}_0\mathbf{v}_1 = \mathbf{0} \\ \mathbf{U}_1^{\alpha} = \mathbf{G}_0^{\alpha}\mathbf{v}_1 \\ \mathbf{p}_1^{\alpha} = \mu_1^{\alpha}\mathbf{G}_0^{\alpha\intercal} \\ \left.\begin{array}{l} \widehat{\mathbf{U}}_1^{\alpha} = \mathbf{U}_1^{\alpha} + e\mathbf{U}_0^{\alpha} \\ 0 \leqslant \mu_1^{\alpha} \perp \widehat{\mathbf{U}}_1^{\alpha} \geqslant 0 \end{array}\right\} \text{for } \alpha \in \mathcal{A}_{\mathbf{ct}} \end{cases} \tag{25}$$

where the active set, $\mathcal{A}_{\mathbf{ct}}$, is, in practice, a prediction of the index set of active constraints which will correspond to a violation of the unilateral constraints :

$$\mathcal{A}_{\mathbf{ct}} = \{\alpha \in \mathcal{I}, \quad \bar{g}_1^{\alpha} \leqslant \mathbf{0}\}, \qquad \text{(index set of active inequality constraints)} \tag{26}$$

The problem (OSNSP) can be written in a canonical mixed linear complementarity problem (MLCP) as:

$$\begin{cases} \begin{bmatrix} \mathbf{A}_0\widehat{\mathbf{M}}^{-1}\mathbf{A}_0{}^{\intercal} & \mathbf{A}_0\widehat{\mathbf{M}}^{-1}\mathbf{G}_0{}^{\intercal} \\ \mathbf{G}_0\widehat{\mathbf{M}}^{-1}\mathbf{A}_0{}^{\intercal} & \mathbf{G}_0\widehat{\mathbf{M}}^{-1}\mathbf{G}_0{}^{\intercal} \end{bmatrix} \begin{bmatrix} \lambda_1 \\ \mu_1 \end{bmatrix} + \begin{bmatrix} \mathbf{A}_0\mathbf{v}_f \\ \mathbf{G}_0\mathbf{v}_f + e\,\mathbf{G}_0\mathbf{v}_0 \end{bmatrix} = \begin{bmatrix} \mathbf{0} \\ \widehat{\mathbf{U}}_1 \end{bmatrix} \\ \\ \mathbf{0} \leqslant \mu_1 \perp \widehat{\mathbf{U}}_1 \geqslant 0 \end{cases} \tag{27}$$

Constrained modes

Although the concept of modes has been thoroughly studied, the idea of a constrained mode is not clear yet. Looking at the mode as a preferential response for the system when solicited, we can extend the research for a periodic response to a system subjected to unilateral and bilateral constraints. Assuming the response will be small around a static equilibrium, the dynamics can be investigated in (9) via introducing a perturbation of the static equilibrium given by:

$$\text{(Static)} \begin{cases} \mathbf{K}(\mathbf{q})\mathbf{q} - \mathbf{f} = \mathbf{A}^{\intercal}\lambda + \displaystyle\sum_{\alpha\in\mathcal{A}_{\mathbf{ct}}} \mu^{\alpha}\mathbf{G}^{\alpha\intercal} \\ \\ \mathbf{a}(\mathbf{q}) = \mathbf{0} \\ \mathbf{0} \leqslant \mathbf{g}(\mathbf{q}) \perp \mu \geqslant \mathbf{0} \end{cases} \tag{28}$$

Considering $\tilde{\mathbf{q}}(t) = \mathbf{q} + \mathbf{d}(t)$, $\tilde{\lambda} = \lambda + \lambda_{\mathbf{d}}$ and $\tilde{\mu} = \mu + \mu_{\mathbf{d}}$ in (9) and expansion around $\mathbf{q}$ combined with (28) yields:

$$\begin{cases} 0 = \mathbf{M}\ddot{\mathbf{d}} + \nabla[\mathbf{K}(\mathbf{q})\mathbf{q} - \mathbf{G}^{\intercal}\mu]\mathbf{d} - \mathbf{A}^{\intercal}\lambda_{\mathbf{d}} - \mathbf{G}^{\intercal}\mu_{\mathbf{d}} \\ 0 = \mathbf{A}\mathbf{d} \\ 0 = \mathbf{G}^{\alpha}\mathbf{d}^{\alpha}, \quad \alpha \in \mathcal{A}_{\mathbf{ct}} \end{cases} \tag{29}$$

From the last two equations, suitable projections into the kernels of $\mathbf{A}$ and $\mathbf{G}$ should be done to obtain an eigenvalue problem. Let us consider $\mathbf{B}_1$ a basis of the kernel of $\mathbf{A}$ (then $\mathbf{B}_1{}^{\intercal}\mathbf{A}^{\intercal} = 0$) and $\mathbf{B}_2$ a basis of the kernel of $\mathbf{G}^{\intercal}\mathbf{B}_1$ (then $\mathbf{B}_2{}^{\intercal}\mathbf{G}^{\intercal}\mathbf{B}_1{}^{\intercal} = 0$). Let us refer to the product $\mathbf{B}_1\mathbf{B}_2$ as $\mathbf{B}$. One can manipulate (29) to obtain a classical evolution problem:

$$0 = \mathbf{B}^{\intercal}\mathbf{M}\mathbf{B}\ddot{\mathbf{d}} + \mathbf{B}^{\intercal}\nabla[\mathbf{K}(\mathbf{q})\mathbf{q} - \mathbf{G}^{\intercal}\mu]\mathbf{B}\mathbf{d} \tag{30}$$

which becomes a classic eigenvalue problem when the assumption of harmonic behavior is made for $\mathbf{d} = \exp(\mathrm{i}\omega t)\mathbf{d}_{\omega}$:

$$0 = \left(\widetilde{\mathbf{K}}(\mathbf{q},\mu) - \omega^2\widetilde{\mathbf{M}}\right)\mathbf{d}_{\omega} \tag{31}$$

with $\mathrm{i}^2 = -1$. This methodology allows to trace linear vibrations around a steady-state. Main assumptions is that oscillations are "small" so that the active set of constraint remains unchanged as proposed by de Veubeke and Géradin [20].

Applications

Constrained mode veering

It is well known that the cable exhibits mode veering for some value of parameter [3, 21]. Here we are interested in the variation of modes for a suspended cable subjected to the presence of an intermediary obstacle of circular shape. That is to say we consider:

$$\mathbf{g}(\mathbf{q}^\alpha)^\alpha = \|\mathbf{q}^\alpha - \mathbf{q}_R\| - R \tag{32}$$

where $\mathbf{q}_R$ and R stand for the circle center and its radius. The obstacle is translated along the $x-$axis as and the frequencies are computed for each equilibrium obtained as illustrated in Figure 4. We see that as one could expect in-plane (IP) modes or out-of-plane (OP) modes are obtained. Veering phenomenon occurs for some obstacle position, creating some possible scenarios of high resonances. We also see that the obtained modes are not single span modes and that an oscillation on the left of the obstacle can be accompanied with oscillation on its right, see Figure 2-3 which is opening the debate for a better physical description of multi-span cable systems.

Constrained dynamics

To account for the time stepping scheme (27) possible applications, we look at the dynamics of cable which only hanged at one end. The cable falls and may hit a vertical wall located at a given position, that is to say:

$$\mathbf{g}(\mathbf{q}) = \mathbf{B}(\mathbf{q} - \mathbf{q}_0) \tag{33}$$

where $\mathbf{B}$ is a diagonal matrix with 1 for arrays $(3j+1, 3j+1)$. Solving the MLCP (27) at each time step allows to compute the dynamics given by (9). Siconos is used to obtain the time response of the system depicted in Figure 5. A cable is falling from an initial catenary position and impacts a wall located on the edge of its initial support.

Conclusion

The global procedure to compute the dynamics of a nonlinear cable subjected to unilateral and bilateral constraints have been presented with several applications. Modes taking into account various types of constraints can be considered and provides interesting features of resonance and dynamical scenarios. The dynamics of an arbitrary system may be computed according to the nonsmooth contact dynamics and open the discussion about the influence of impact on the cable profile and tension.

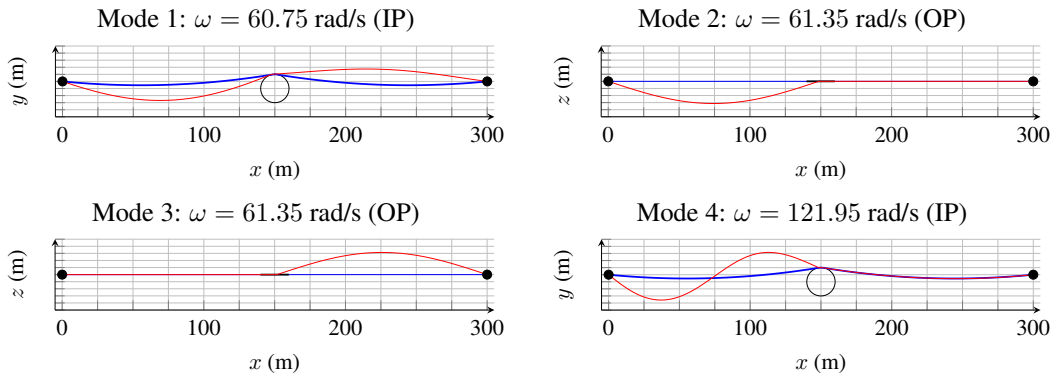

Figure 2: Mode-shapes obtained via FEM for a cable lying on a centred obstacle
Rest position (solid line ——) and perturbed position (solid line ——)
L =301 m ; $\rho = 5.56$ kg/m ; $EA = 1.5$ GPa

References

[1] G.W. Leibniz. The string whose curve is described by bending under its own weight, and the remarkable resources that can be discovered from it by however many proportional means and logarithms. *Acta Eruditorum*, June 1691.

[2] G.W. Leibniz. Solutions to the problem of the catenary, or funicular curve, proposed by M. Jacques Bernoulli. *Acta Eruditorum*, September 1691.

[3] H.M. Irvine. *Cable structures*. Dover, New York, 1992.

[4] G. Rega. "Nonlinear vibrations of suspended cables Part I: Modeling and analysis". *Applied Mechanics Reviews*, 57(6):443, 2004.

[5] C. Issanchou, V. Acary, F. Pérignon, C. Touzé, and J.-L. Le Carrou. Nonsmooth contact dynamics for the numerical simulation of collisions in musical string instruments. *The Journal of the Acoustical Society of America*, 143(5):3195–3205, May 2018.

[6] J.-J. Marigo. *Mécanique des Milieux Continus I*. Paris, École polytechnique, August 2014. Lecture notes, HAL-ID: *cel-01023392*.

[7] C.A. Felippa. Finite element analysis of dimensional cable structures. *Proceedings of the 1st International Conference of Computational Methods in Nonlinear Mechanics; Austin TX*, pages 311–324, 1974.

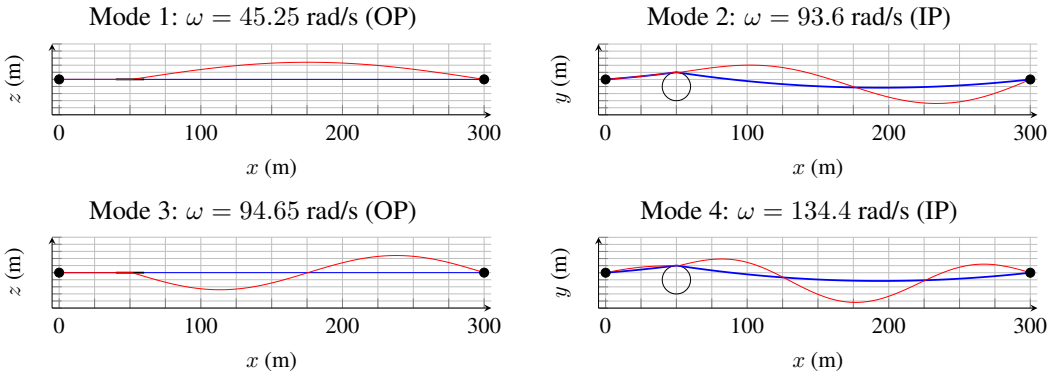

Figure 3: Mode-shapes obtained via FEM for a cable lying on a non-centred obstacle
Rest position (solid line ——) and perturbed position (solid line ——)
L =301 m ; $\rho = 5.56$ kg/m ; $EA = 1.5$ GPa

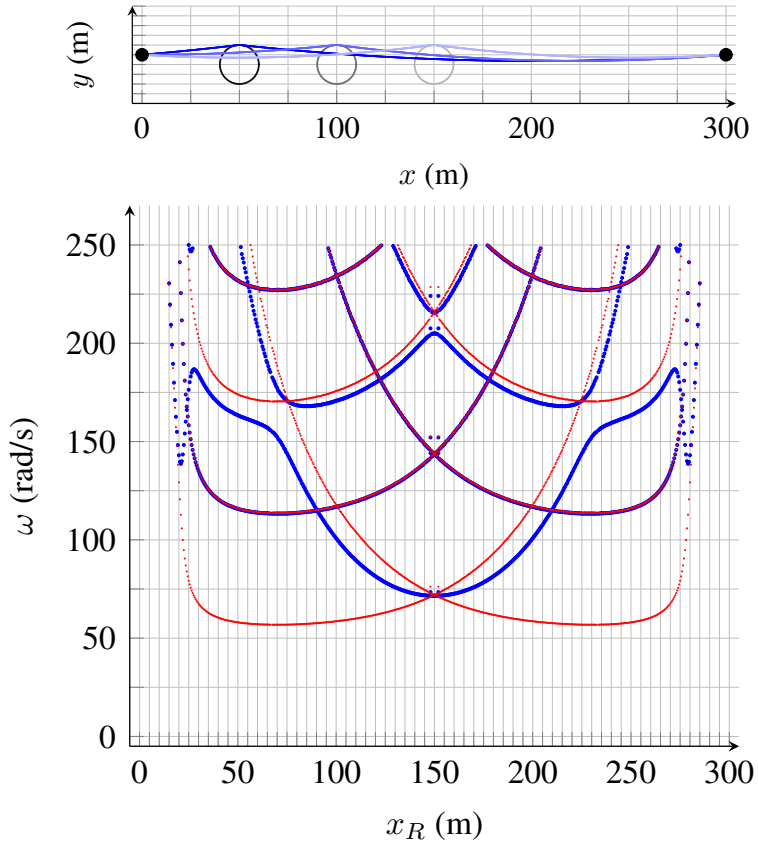

Figure 4: Evolution of the first frequencies for IP-modes (dotted line ·····) and the OP-modes (dotted line ·····) obtained numerically when the obstacle position is varying
L =300.6 m ; $\rho = 5.56$ kg/m ; $EA = 1.5$ GPa

[8] I. Fried. Large deformation static and dynamic finite element analysis of extensible cables. *Computers & Structures*, 15(3):315–319, January 1982.

[9] B.W. Kim, H.G. Sung, S.Y. Hong, and H.J. Jung. Finite Element Nonlinear Analysis for Catenary Structure Considering Elastic Deformation. *Computer Modeling in Engineering & Sciences*, 63(1):29–46, 2010.

[10] M. Crusells-Girona, F.C. Filippou, and R.L. Taylor. A mixed formulation for nonlinear analysis of cable structures. *Computers & Structures*, 186:50–61, July 2017.

[11] O.C. Zienkiewicz and R.L. Taylor. *The finite element method. Vol. 1: The basis*. Butterworth-Heinemann, Oxford, 5. ed., reprinted edition, 2002. OCLC: 249013082.

[12] C. A. Felippa. Nonlinear finite element methods (asen 6107). 2014.

[13] A. Signorini. Sopra alcune questioni di statica dei sistemi continui. *Annali della Scuola Normale Superiore di Pisa - Classe di Scienze*, Ser. 2, 2(2):231–251, 1933.

[14] V. Acary and B. Brogliato. *"Numerical Methods for Nonsmooth Dynamical Systems"*. Springer-Verlag Berlin Heisenberg, 2008.

[15] D. Bruno and A. Leonardi. Nonlinear structural models in cableway transport systems. *Simulation Practice and Theory*, 7(3):207–218, May 1999.

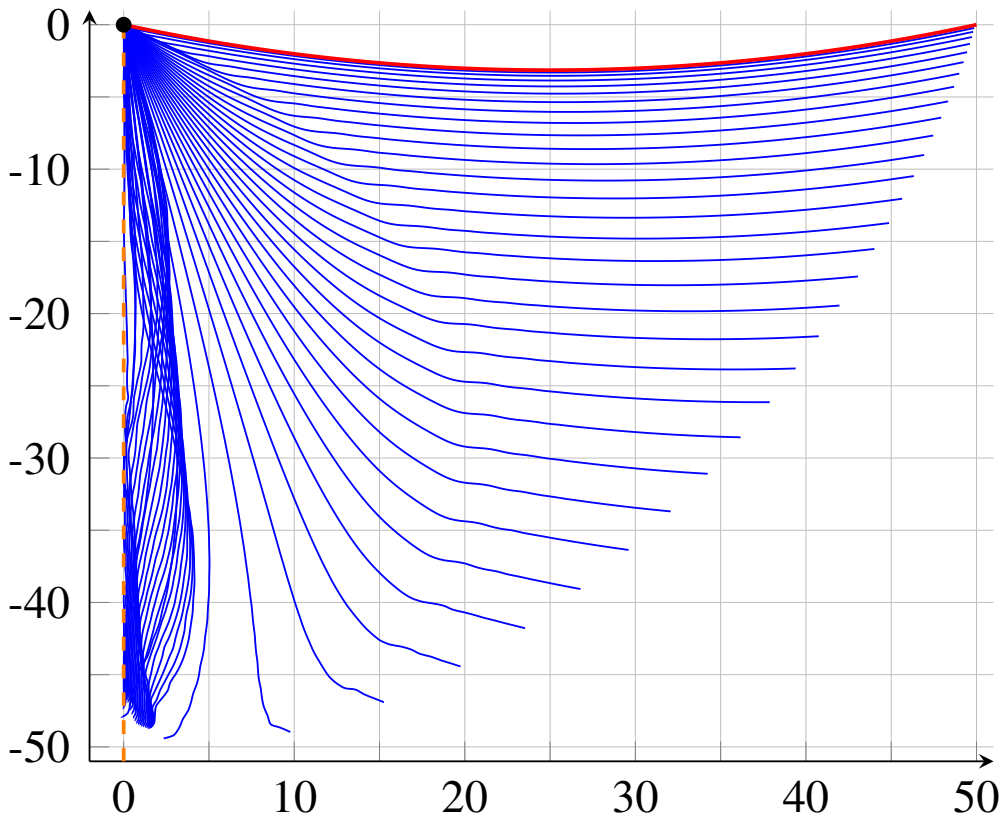

Figure 5: Station of a falling cable (solid line ——) impacting a wall (dashed line - - -) starting from resting catenary (solid line ——) L =50.6 m ; $\rho = 4$ kg/m ; $EA = 1.5$ GPa

[16] M. Such, J. R. Jimenez-Octavio, A. Carnicero, and O. Lopez-Garcia. An approach based on the catenary equation to deal with static analysis of three dimensional cable structures. *Engineering Structures*, 31(9):2162–2170, March 2009.

[17] N. Impollonia, G. Ricciardi, and F. Saitta. Statics of elastic cables under 3D point forces. *International Journal of Solids and Structures*, 48(9):1268–1276, May 2011.

[18] C. Bertrand, V. Acary, C.-H. Lamarque, and A. Ture Savadkoohi. A robust and efficient numerical finite element method for cables. working paper or preprint, January 2020.

[19] M. Jean and J.J. Moreau. Dynamics in the presence of unilateral contacts and dry friction: a numerical approach. In G. Del Pietro and F. Maceri, editors, *Unilateral problems in structural analysis. II*, pages 151–196. CISM 304, Spinger Verlag, 1987.

[20] B. Fraejis de Veubeke, M. Gérardin, and A. Huck. *Structural dynamics*. LTAS, Liège, 1974.

[21] W. Lacarbonara. *The Elastic Cable: From Formulation to Computation*. Springer, 2013.

Trajectory Tracking Control for Linear Complementarity Systems with Continuous Solutions

Van Nam Vo[†], Bernard Brogliato[†] and Christophe Prieur [‡]

[†]*Univ. Grenoble-Alpes, INRIA, Grenoble INP, LJK, 38000 Grenoble, France.*
bernard.brogliato@inria.fr

[‡]*Univ. Grenoble-Alpes, CNRS, Grenoble INP, Gipsa-Lab, 38000 Grenoble, France.*
christophe.prieur@gipsa-lab.fr

Summary. This work concerns the trajectory tracking control for Linear Complementarity Systems (LCS) with continuous solutions. Such systems are strongly nonsmooth and nonlinear. The tracking issue is solved using passivity tools that yield conditions which can be solved with Linear Matrix Inequalities (LMI). Circuits with ideal diodes illustrate the theoretical developments.

1 Introduction

Trajectory tracking is a major problem in Automatic Control. It is well understood for linear time-invariant systems (see [1] and references therein) and some classes of nonsmooth systems [2, 3]. In this study, we study the LCS given by

$$\begin{cases} \dot{x}(t) = Ax(t) + B\lambda(t) + Eu(t), \\ 0 \leq \lambda(t) \perp Cx(t) + D\lambda(t) + Fu(t) \geq 0, \\ x(0) = x_0, \end{cases} \tag{1}$$

where $x(t) \in \mathbb{R}^n, u(t) \in \mathbb{R}^m, \lambda(t) \in \mathbb{R}^p$ with $D = 0, D \succeq 0$, and $D \succ 0$. In case $D \succeq 0$, we restrict to positive semidefinite matrices D of the form $\begin{pmatrix} D_1 & 0 \\ 0 & 0 \end{pmatrix}$, where $D_1 \succ 0$ is square of dimension $q < p$. Our goal is to design the controller u such that $\|x(t) - x_d(t)\| \to 0$ as $t \to \infty$, where x_d is a desired state trajectory. Generally, to find a controller satisfying a given reference is a hard problem. Thus our ambition is only to deal with some sub-classes of problems which we can handle.

1.1 Main Results

Let us first make the following assumptions.

Assumption 1 *There exists a multiplier λ_d such that desired trajectory x_d satisfies*

$$\begin{cases} \dot{x_d}(t) = Ax_d(t) + B\lambda_d(t) + Eu_d(t) \\ 0 \leq \lambda_d(t) \perp Cx_d(t) + D\lambda_d(t) + Fu_d(t) \geq 0, \end{cases}$$

for a given input $u_d \in L^1_{\text{loc}}(\mathbb{R}_+; \mathbb{R}^m)$.

Assumption 2 *There exists a matrix K such that the quadruple $(A + EK, B, C + FK, D)$ is strictly passive.*

Then the following result holds.

Proposition 1 *Suppose that Assumptions 1 and 2 hold. Then the closed-loop system (1) with the state feedback controller*

$$u(t) = K[x(t) - x_d(t)] + u_d(t)$$

has a unique global solution $x(\cdot)$, and $\|x(t) - x_d(t)\| \to 0$ as $t \to +\infty$.

The proof is led with the Lyapunov function $V(z) = z^\top Pz$, $z = x - x_d$, and $P = P^\top \succ 0$ is a solution of the passivity LMI [4, Lemma 3.16, Theorem 4.73]. The controller gain K is calculated by solving the LMI:

$$\begin{pmatrix} QA^\top + AQ + L^\top E^\top + EL + \varepsilon Q & B - QC^\top - L^\top F^\top \\ B^\top - CQ - FL & -(D + D^\top) \end{pmatrix} \preccurlyeq 0. \tag{2}$$

This gives an LMI feasibility problem in the new variables $Q = Q^T \succ 0$ and L. After solving this LMI, the feedback gain K can be recovered from $K = LQ^{-1}$. It may happen that the above LMI has no solutions (see [5, section 2.5.1] for an example). This can be solved by changing the controller structure. Namely, we allow for not only a state feedback, but also that the multiplier $\lambda(t)$ be measurable and part of the controller. In practice the multiplier may be voltages or currents (for circuits) or contact forces (for mechanical systems) and could be measured.

Assumption 3 *There exist matrices K, G such that the quadruple $(A + EK, B + EG, C + FK, D + FG)$ is strictly passive and $D + FG$ is either a zero matrix, or a positive definite matrix, or a matrix in the form $\begin{pmatrix} D_1 & 0 \\ 0 & 0 \end{pmatrix}$ with $D_1 \succ 0$.*

Proposition 2 *Suppose that Assumptions 1 and 3 hold. Then the closed-loop system (1) with the controller*

$$u(t) = K[x(t) - x_d(t)] + G[\lambda(t) - \lambda_d(t)] + u_d(t)$$

has a unique global solution $x(\cdot)$ and $\|x(t) - x_d(t)\| \to 0$ as $t \to +\infty$.

2 Example and Simulations

Let us consider the circuit in Figure 1 with an ideal diode, having the dynamics: $\begin{cases} \dot{x_1}(t) = x_2(t) \\ \dot{x_2}(t) = -\frac{1}{\mathbf{LC}}x_1(t) + \frac{\lambda(t)}{\mathbf{L}} + \frac{u_2(t)}{\mathbf{L}} \\ 0 \leq \lambda(t) \perp \frac{\lambda(t)}{\mathbf{R}} + x_2(t) - \frac{u_1(t)}{\mathbf{R}} \geq 0. \end{cases}$.

From Proposition 1, we get the controller $u^1 = K(x - x_d) + u_d$ with $K = \begin{pmatrix} -1.554224 & -0.261066 \\ -3.228662 & -3.663074 \end{pmatrix}$, and from Proposition 2, the controller $u^2 = K(x - x_d) + G(\lambda - \lambda_d) + u_d$ with $K = \begin{pmatrix} -2.833123 & -1.041382 \\ -4.568759 & -3.291980 \end{pmatrix}, G = \begin{pmatrix} -0.500000 \\ 5.121218 \end{pmatrix}$.

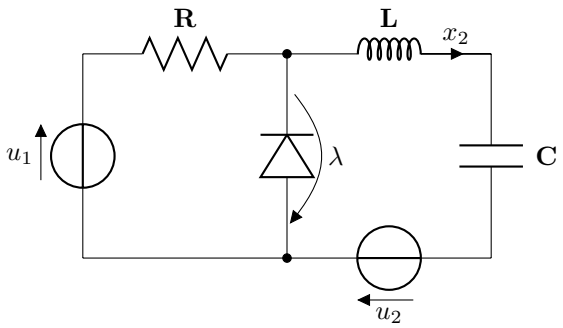

Figure 1: RLCD circuit with two voltage sources.

The matrices are obtained by using YALMIP (https://yalmip.github.io/) with 6-digit accuracy, and using the INRIA code SICONOS (https://nonsmooth.gricad-pages.univ-grenoble-alpes.fr/siconos/index.html) to get the numerical results of this problem. The results are depicted in Figure 2, where x_i^j is the ith component of the closed-loop system's state with controller u^j, and initial conditions $(0.5, 0.5)$.

3 Conclusions

A detailed presentation of this work is made in the report [5] where well-posedness issues are presented, as well as several circuits examples with simulations, and all the codes needed to compute the controller gains (MATLAB, YALMIP and SICONOS).

References

[1] PADULA, F. , NTOGRAMATZIDIS, L., GARONE, E. (2019) MIMO tracking control of LTI systems: A geometric approach. *Systems and Control Letters*, 126, 8-20.

[2] MORARESCU, C. , BROGLIATO, B. (2010) Trajectory tracking control of multiconstraint complementarity Lagrangian systems. *IEEE Transactions on Automatic Control*, 55(6), 1300-1313, June.

[3] VAN DE WOUW, N., LEINE, R.I. (2008) Tracking control for a class of measure differential inclusions. *Proceedings of the 47th IEEE Conference on Decision and Control*, Cancun, Mexico, December 9-11, 2526-2532.

[4] BROGLIATO, B. , LOZANO, R. , MASCHKE, B., EGELAND, O. (2020) Dissipative Systems Analysis and Control. *Springer Nature Switzerland AG*, 3rd Ed.

[5] VO, V.N. (2019) Trajectory Tracking Design for Linear Complementarity Systems with Continuous Solutions. *Matser Thesis, University of Limoges and INRIA Grenoble-Alpes*, available at: https://hal.inria.fr/hal-02267750/document.

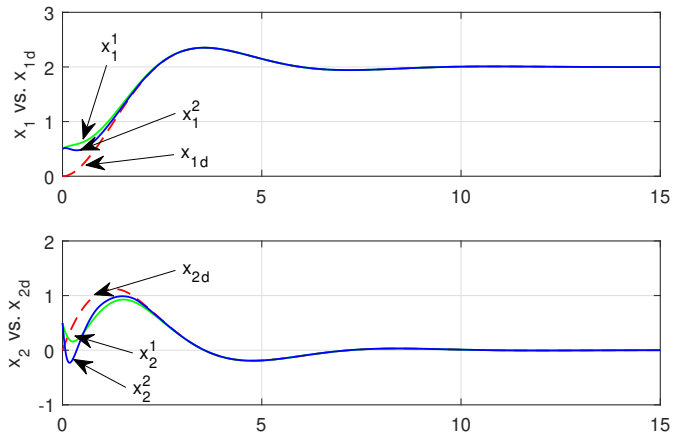

Figure 2: The desired trajectory and the state when using controller u^1 and u^2.

Identification and validation of impact models

Maarten Jongeneel*, Nathan van de Wouw* and Alessandro Saccon *
*Department of Mechanical Engineering, Eindhoven University of Technology (TU/e), The Netherlands

Summary. Predicting the outcome of an impact event is of high importance for proper execution of many robotic tasks. Rigid-body contact models are extensively used in planning and control due to their simplicity and computational efficiency. However, there exists little literature that shows a comparison and verification of these models with real-life experiments, and it is therefore unclear how well these models approximate frictional impact events. In this study, we formulate an identification approach to find the parameters of commonly used contact, friction, and impact models using an experimentally obtained data-set of impact events using a single rigid-body, where the focus lies specifically on spatial frictional impact events. In future work, we will measure, using the identified parameters, the performance of the used models in terms of long-horizon prediction performance by comparing simulated and measured rest poses of a rigid-body tossed on a surface.

Introduction

Many robotic tasks rely on accurate dynamical models of the robot as well as models of the interactions the robot has with its environment or the object it is handling. Detailed understanding of the frictional impact events that occur when dynamic manipulation tasks are executed are important for proper task execution. Quantitative modeling these nonsmooth dynamics related to such stick/slip transitions and impacts events is highly challenging. Various models have been presented in literature and in this study the focus lies on rigid contact models, where the Newton-Euler equations of motion are coupled with ideal unilateral contact constraints (Signorini's contact law), Newton's impact law, and Coulomb's friction law [1, 2]. Newton's and Coulomb's law rely on parameters known as the coefficient of restitution (COR) and coefficient of friction (COF), denoted by e_N and μ, respectively. Identifying these parameters from an experimental data-set requires expertise in both mechanics and optimization, and ultimately gives an approximation of the real physical behavior of the object, as also addressed in [3]. In this study, the goal is to determine to what extent rigid-body dynamics can be used to describe real world physical behavior. More specifically, we focus on a single body impacting a surface and compare measurements with rigid-body simulations to quantify the predictive capacity of these models. The main contribution is that our focus lies on spatial frictional impact events, instead of the planar impact events considered in, for example, [4, 5].

Obtaining impact events from experiments

An experimentally obtained data-set is used to estimate the COR and COF for an uniformly filled carton box impacting a surface, which in our case is the box shown in Figure 1b. Experiments are executed on a robotic setup using a OptiTrack motion capture system to record at 360fps the poses of rigid-objects with sub-millimeter accuracy, see Figure 1a for a picture of the setup. This setup is representing a typical scenario in a logistic application, which sets the context of the project in which the experiments were executed [1]. From the tracking data it is possible to extract the exact configuration of the box and the surface with which the object is impacting and we compute the velocity of the box using a central differencing scheme. Figure 2 shows the twist of the box around a single impact event (happening at the time instance $t = 0$, where the time is normalized around the impact time), where Figure 2a shows the linear velocity component and Figure 2b shows the angular velocity component of the twist. Due to noise in the measurement system, fitted velocities are used to determine the pre-impact velocity (at $t = -1$) and post-impact velocity (at $t = 1$), which will serve as the basis for the identification of the impact map.

Parameter Identification based on post-impact velocity comparison

A total of 129 impact events where collected experimentally, from which we determine the pre- and post-impact velocity of the rigid body, where the pre-impact velocity serves as the input to a model-based simulation. We then let the simulator compute the post-impact velocity of the rigid-body given a certain value for e_N and μ and we compare the simulated post-impact velocity $\tilde{\mathbf{v}}^+$ to the post-impact velocity computed from the measurement data $\mathbf{v}^+$. By performing a grid-based search over the parameter space, we are then able to find the optimum parameters. Mathematically, we define the optimization problem as

$$(\mu^*, e_N^*) = \underset{\mu, e_N, e_T}{\arg\min} \frac{1}{N} \sum_{k=1}^{N} \left(\left\| \text{diag}(\mathbf{w}) \left(\mathbf{v}^+ - \tilde{\mathbf{v}}^+ \right) \right\| \right)_k , \tag{1}$$

$$\text{s.t.} \quad 0 \leq \mu \leq \mu_s, \quad 0 \leq e_N \leq 1, \tag{2}$$

[1]This work was partially supported by the Research Project I.AM. through the European Union H2020 program under GA 871899.

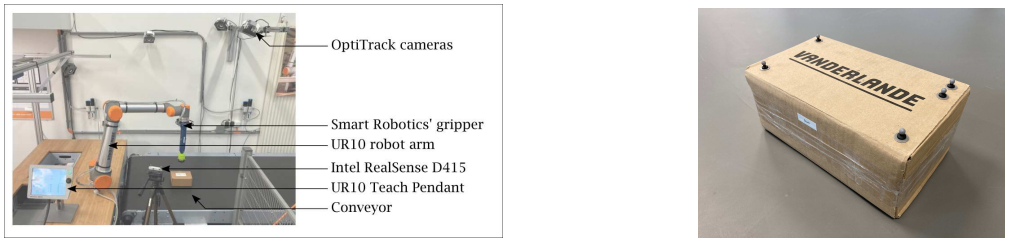

(a) (b)

Figure 1: Experimental setup. Picture of the lab (a) and picture of the carton box (b).

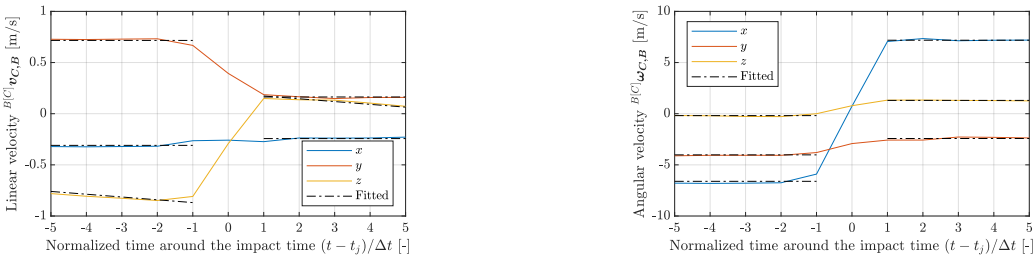

(a) (b)

Figure 2: Linear and angular hybrid velocities obtained from measurements. Fitted hybrid velocities shown as black dotted lines.

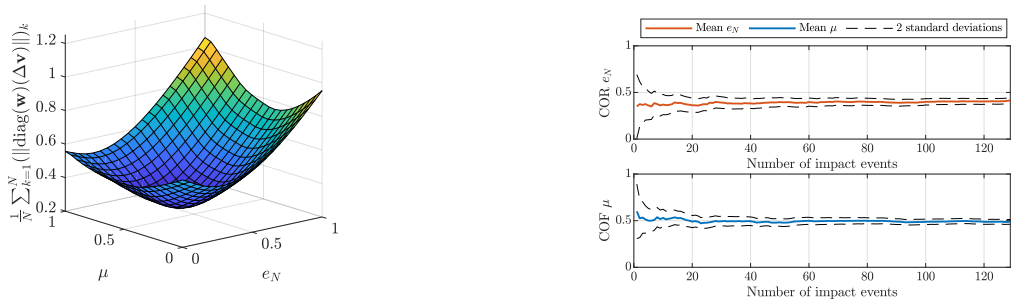

(a) (b)

Figure 3: Sum of computed costs from all 129 combined impact events as obtained for simulations with different parameters (a) and evolution of parameter values for increasing number of impact events (b).

where the simulated post-impact velocity $\tilde{\mathbf{v}}^+$ is a function of the pre-impact pose and velocity and the chosen values for the parameters μ and e_N. Furthermore, in (1), N denotes the total number of impact events and $\mathbf{w}$ is a weighting vector. As a result, the sum of all computed costs can be seen in Figure 3a, while Figure 3b shows the convergence behavior of the values e_N and μ as function of the number of impact events, with the optimum values found as $\mu = 0.48$ and $e_N = 0.38$.

Conclusions

In this study, an experimentally obtained data-set is used for parameter identification of a nonsmooth impact model by comparing post-impact velocities from measurements to those obtained from simulations in a cost function. In future work, the identified parameters will be used for the long-horizon prediction of the objects state and the performance of the nonsmooth models with be measured by comparing simulation results to experimental data.

References

[1] R. Leine and H. Nijmeijer, *Dynamics and bifurcations of non-smooth mechanical systems*, vol. 18 of *Lecture Notes in Applied and Computational Mechanics*. Germany: Springer-Verlag Berlin Heidelberg, 2004.

[2] C. Glocker, *Set-Valued Force Laws: Dynamics of Non-Smooth Systems*, vol. 1. Springer-Verlag Berlin Heidelberg, Jan. 2001.

[3] M. Parmar, M. Halm, and M. Posa, "Fundamental challenges in deep learning for stiff contact dynamics." arXiv:2103.15406, 2021.

[4] N. Fazeli, S. Zapolsky, E. Drumwright, and A. Rodriguez, "Fundamental Limitations in Performance and Interpretability of Common Planar Rigid-Body Contact Models," in *Robotics Research*, (Cham), pp. 555–571, Springer International Publishing, 2020.

[5] N. Fazeli, A. Ajay, and A. Rodriguez, "Long-Horizon Prediction and Uncertainty Propagation with Residual Point Contact Learners," in *2020 IEEE International Conference on Robotics and Automation (ICRA)*, pp. 7898–7904, 2020.

Multiple impacts in granular chains with Kuwabara-Kono dissipation

Guillaume James[†], Kirill Vorotnikov[‡] and Bernard Brogliato [♯]
[†]*Univ. Grenoble-Alpes, Grenoble INP, CNRS, INRIA, LJK, 38000 Grenoble, France. guillaume.james@inria.fr*
[‡]*Sami Shamoon College of Engineering, 84 Jabotinsky St., Ashdod, 77245, Israel. kirilvo@sce.ac.il*
[♯]*Univ. Grenoble-Alpes, INRIA, CNRS, Grenoble INP, Gipsa-Lab, 38000 Grenoble, France. bernard.brogliato@inria.fr*

Summary. We study multiple impacts in a chain of beads using the Kuwabara-Kono (KK) contact model [1], a nonsmooth (not Lipschitz continuous) extension of Hertz contact that accounts for viscoelastic damping. For this purpose, we introduce new numerical schemes which approximate dissipative impacts with good accuracy without including the nonsmooth KK viscoelastic component in the contact force. These schemes are derived using the technique of modified equations, which allows us to construct time-discretizations of the nondissipative Hertz law matching numerical dissipation with KK dissipation at different consistency orders. In addition, analytical approximations of wave profiles are derived using asymptotic expansions, in the limit when the exponent of the contact force becomes close to unity. Numerical tests are performed for the simulation of impacts in Newton's cradle and on alignments of free beads.

1 Introduction

In this work, we introduce a new method for the numerical simulation of granular chains which allows to approximate the KK contact model without explicitly including the nonsmooth viscoelastic term in the contact force, *i.e.*, $\gamma = 0$ in (1):

$$f(\delta) = k\left(\delta_+^\alpha + \gamma \frac{d}{dt}\delta_+^\alpha\right), \tag{1}$$

where $f(\delta)$ is the spring/dashpot contact force, δ is the indentation, and $\alpha = 3/2$ corresponds to the usual KK model [1]. Our approach is based on the technique of modified (or equivalent) equations, in which effects induced by time-discretization (such as numerical dissipation) are analyzed by considering suitable perturbations of the initial differential equation. In addition, analytical approximations of propagating fronts (generated for example by an impacting piston) are obtained using asymptotic expansions, by considering $\alpha - 1$ as a small parameter.

2 KK numerical dissipation

We consider a Newton's cradle, including local attachments consisting of strings or plates. The dynamical equations including local restoring forces, where the attachment of the nth bead is represented by a spring with linear stiffness K_n, are :

$$m_n\ddot{x}_n = -K_n x_n + k_n\delta_{(n-1)+}^{3/2} - k_{n+1}\delta_{n+}^{3/2}, \quad 1 \le n \le N, \tag{2}$$

with $\delta_n = x_n - x_{n+1}$ and $k_1 = k_{N+1} = 0$. In model (2), collisions are assumed nondissipative. Setting $x = (x_1, \ldots, x_N)$, $v = (\dot{x}_1, \ldots, \dot{x}_N)$ and $y = (x, v)$, system (2) can be reformulated as

$$\dot{y} = f(y) = \begin{pmatrix} v \\ g(x) \end{pmatrix}, \tag{3}$$

where the components of $g(x) \in \mathbb{R}^N$ are given by $g_n(x) = \frac{1}{m_n}\left(-K_n x_n + k_n\delta_{(n-1)+}^{3/2} - k_{n+1}\delta_{n+}^{3/2}\right)$. In order to approximate solutions of (10), we introduce the implicit one-step method

$$\begin{aligned}
\frac{X_n^{k+1} - X_n^k}{h} =& \theta V_n^{k+1} + (1-\theta) V_n^k, \\
\frac{V_n^{k+1} - V_n^k}{h} =& \frac{1}{m_n}\left[-(1-\mu) K_n X_n^{k+1} + \theta\left(k_n\left(\Delta_{n-1}^{k+1}\right)_+^{3/2} - k_{n+1}\left(\Delta_n^{k+1}\right)_+^{3/2}\right)\right] \\
&+ \frac{1}{m_n}\left[-\mu K_n X_n^k + (1-\theta)\left(k_n\left(\Delta_{n-1}^k\right)_+^{3/2} - k_{n+1}\left(\Delta_n^k\right)_+^{3/2}\right)\right],
\end{aligned} \tag{4}$$

where $\Delta_n^k = X_n^k - X_{n+1}^k$, h denotes the time step and $Y_k = \left(X_1^k, \ldots, X_N^k, V_1^k, \ldots, V_N^k\right)$ approximates $y(k\,h)$. We consider a modified (or equivalent) equation (see *e.g.*, [3, 4] and references therein) corresponding to the scheme (4) :

$$\dot{Y} = f(Y) + h\,F_1(Y) + O(h^2), \tag{5}$$

where the coefficient F_1 needs to be determined. After some manipulations the modified equation (5) can be rewritten

$$\dot{X}_n = V_n + h\left(\theta - \frac{1}{2}\right) g_n(X) + O(h^2), \tag{6}$$

$$\begin{aligned} m_n\ddot{X}_n + K_n\left(h\left(\theta-\mu\right)\dot{X}_n + X_n\right) =& k_n\left(\Delta_{(n-1)+}^{3/2} + 3\left(\theta-\frac{1}{2}\right)h\Delta_{(n-1)+}^{1/2}\dot{\Delta}_{n-1}\right) \\ &- k_{n+1}\left(\Delta_{n+}^{3/2} + 3\left(\theta-\frac{1}{2}\right)h\Delta_{n+}^{1/2}\dot{\Delta}_{n}\right) + O\left(h^2\right), \end{aligned} \tag{7}$$

with $\Delta_n = X_n - X_{n+1}$, where a KK dissipation term clearly appears. Setting

$$\theta = \frac{1}{2} + \frac{\gamma}{2h} = \mu \tag{8}$$

in (7) and neglecting $O(h^2)$ terms, one recovers the KK model

$$m_n\ddot{X}_n + K_nX_n = k_n\Delta_{(n-1)+}^{3/2} + \frac{3}{2}\gamma k_n\Delta_{(n-1)+}^{1/2}\dot{\Delta}_{n-1} - k_{n+1}\Delta_{n+}^{3/2} - \frac{3}{2}\gamma k_{n+1}\Delta_{n+}^{1/2}\dot{\Delta}_n. \tag{9}$$

This observation leads us to the concept of *tailored numerical dissipation*. In this framework, one discretizes the nondissipative model (2) with the dissipative scheme (4)-(8) in order to approximate the dissipative model (9).

3 Analytical approximations of wave profiles

We consider system (9) with a generalized elastic exponent $\alpha > 1$, without local springs (i.e., $K_n = 0$) and for identical beads, so that m_n and k_n are constant and rescaled to unity :

$$\ddot{X}_n = \Delta_{(n-1)+}^{\alpha} + \alpha\,\gamma\Delta_{(n-1)+}^{\alpha-1}\dot{\Delta}_{n-1} - \Delta_{n+}^{\alpha} - \alpha\gamma\Delta_{n+}^{\alpha-1}\dot{\Delta}_n. \tag{10}$$

We consider the limit case of an infinite chain, assume $\Delta_n \geq 0$ (absence of gaps between beads) and set

$$\Delta_n(t) = \delta\, y(\xi,\tau)^{1/\alpha}, \tag{11}$$

with $\xi = \varepsilon\,(n - c\,t)$, $c = \delta^{(\alpha-1)/2}$, $\tau = \frac{\gamma}{2}\,\varepsilon^2\,c^2\,t$, and $\varepsilon = \frac{\alpha-1}{\alpha\,\gamma\,c}$. The new variable y can be interpreted as a rescaled force variable. Substituting the Ansatz (11) in the dynamical equations (10), and performing an asymptotic expansion with respect to the small parameter ε, one arrives to a logarithmic Burgers equation

$$\partial_\tau y + \partial_\xi\left(y\,\ln y\right) = \partial_\xi^2 y. \tag{12}$$

The expansion is valid for α close enough to unity, and the logarithmic nonlinearity originates from the approximation $(y - y^{1/\alpha})/(1-\frac{1}{\alpha}) \approx y\,\ln y$.
Alternatively, modifying the Ansatz as follows :

$$\Delta_n(t) = \delta\, y(s,\tau)^{1/\alpha}, \tag{13}$$

with $s = 2\sqrt{3}\,\varepsilon\,(n - c\,t)$, $\tau = \sqrt{3}\,\varepsilon^3\,c\,t$, $\varepsilon = (1-\frac{1}{\alpha})^{1/2}$ and c defined as above, one obtains the logarithmic KdV-Burgers equation

$$\partial_\tau y + \partial_s\left(y\,\ln y\right) + \partial_s^3 y = \mu\,\partial_s^2 y, \tag{14}$$

where $\mu = c\,2\sqrt{3}\,\gamma(1-\frac{1}{\alpha})^{-1/2}$. This expansion is valid when $\alpha \to 1^+$ and assuming $\mu = O(1)$, hence γ has to be small. The amplitude equations (12) and (14) both possess stationary front solutions, which can approximate the asymptotic response of a chain impacted by a piston. They are valid in different regimes regarding the amount of contact damping, and the logarithmic KdV-Burgers equation allows to approximate more general underdamped (oscillatory) fronts.
These approximations are tested by performing direct numerical simulations of the KK model. One observes a convergence of the numerical solutions towards analytical profiles when α is close to unity. In addition, the analytical approximations remain meaningful for $\alpha = 3/2$, i.e. rather far from the asymptotic limit where the amplitude equations have been derived.

4 Conclusions

New approaches for the numerical simulation of granular matter *via* the approximation of the Kuwabara-Kono model by suitable numerical dissipation or the derivation of adapted amplitude equations are presented. More details can be found in [2] and [5].

References

[1] Kuwabara G., Kono K. 1987 Restitution coefficient in a collision between two spheres. *Japanese Journal of Applied Physics* **26**, 1230-1233.

[2] James G., Vorotnikov K., Brogliato, B. 2019 Kuwabara-Kono numerical dissipation: a new method to simulate granular matter. To appear in *The IMA Journal of Applied Mathematics.* Available at `https://hal.archives-ouvertes.fr/hal-01878973/document`

[3] Villatoro FR, Ramos JI. 1999 On the method of modified equations. I: Asymptotic analysis of the Euler forward difference method. *Applied Mathematics and Computation* **103**, 111-139.

[4] Hairer E, Lubich C, Wanner G. 2006 *Geometric Numerical Integration: Structure-Preserving Algorithms for Ordinary Differential Equations*, Springer-Verlag Berlin Heidelberg.

[5] James G. 2019 *Continuum limits of the Kuwabara-Kono model*, article in preparation.

Non-smooth dynamics modeling of drill-string systems in heterogeneous formations

Arviandy G. Aribowo*, Roeland Wildemans*, Emmanuel Detournay† and Nathan van de Wouw *,†
*Department of Mechanical Engineering, Eindhoven University of Technology, The Netherlands
†Department of Civil, Environmental and Geo-Engineering, University of Minnesota, U.S.A.

Summary. An extension of the drill-string dynamics model for drilling in heterogeneous rock formations is presented to study the heterogeneity effect on both the axial and torsional dynamics.

Introduction

According to [1], the total loads acting on the Polycrystalline-Diamond-Compact (PDC) bit in rotary drilling systems (see Figure 1-left) are changed abruptly when the bit blades drill into interchangeably harder and softer layers of heterogeneous rock formations. This fast load-change condition due to the formation heterogeneity can affect the dynamic response of the system and therewith the vibrational signature at the bit, which in turn may influence the durability of the PDC bit and drilling efficiency. To this end in this study, the drill-string system model as presented in [2, 3] is extended for vertical drilling scenario in interbedded formations, particularly for the transitional part of the motion of the bit in two heterogeneous layers (see Figure 1-middle). The latter requires a novel bit-rock interaction model of the forces and torques acting on the bit in such transitional phase.

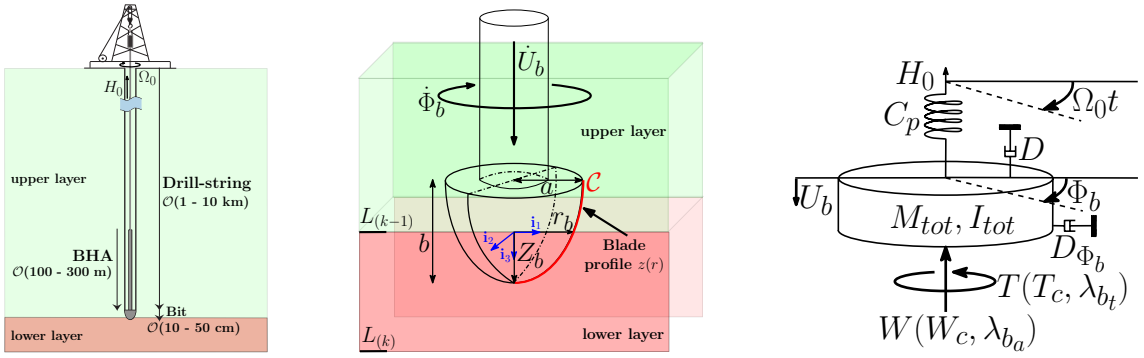

Figure 1: Drilling system schematic for heterogeneous formations (left); the bit transition (middle); model of drill-string system (right).

Dynamic model of drill-string systems in heterogeneous formations

Following the modeling framework in [3] (as depicted in Figure 1-right), the dynamics model of drill-string system incorporating the heterogeneity effect of distinct rock layers is modelled in (scaled) dimensionless form as follows:

$$\mathcal{M}\mathbf{z}'' - \mathcal{H}\left(\tau, \mathbf{z}\,, \mathbf{z}'\,, \mathbf{z}_{\tau_n}\right) = \mathcal{W}\mathcal{L}. \tag{1}$$

Herein, $\mathbf{z}$ is the dimensionless generalized coordinates of the systems and composed by u_b for the axial position of the bit and ϕ_b for the angular position, and all are functions of dimensionless time τ. The matrices in (1) are given by,

$$\mathcal{M} = \begin{bmatrix} 1 & 0 \\ 0 & 1 \end{bmatrix}, \quad \mathbf{z} = \begin{bmatrix} u_b\left(\tau\right) & \phi_b\left(\tau\right) \end{bmatrix}^\top, \quad \mathcal{W} = \begin{bmatrix} \bar{\psi} & 0 \\ 0 & 1 \end{bmatrix}, \quad \mathcal{L} = \begin{bmatrix} \mathcal{L}^{tot}_{k,b_a}\left(\rho_b\right) & \mathcal{L}^{tot}_{k,b_t}\left(\rho_b, \mathcal{L}^{tot}_{k,b_a}\right) \end{bmatrix}^\top, \tag{2}$$

$$\mathcal{H} = \begin{bmatrix} -\gamma {u'}_b \\ \left(-\gamma_\phi {\phi'}_b - \left(\phi_b - \omega_0\,\tau\right)\right) \end{bmatrix} + \begin{bmatrix} -\bar{\psi}\; n\; \delta_n\, \bar{g}^{\varepsilon}_k \left(g^{\varepsilon}_k \left(1 - \eta^l_\zeta\left(\rho_b\right)\right) + \eta^l_\zeta\left(\rho_b\right)\right) \\ -n\,\delta_n\,\bar{g}^{\varepsilon}_k\,\left(g^{\varepsilon}_k\left(1-{\rho_b}^2\right) + {\rho_b}^2\right) \end{bmatrix} + \begin{bmatrix} \bar{\psi}\,\mathcal{W}_a \\ 0 \end{bmatrix}. \tag{3}$$

The number of layers, with each specific thickness, is K (thus the index of each layer is denoted by $k \in \{2, 3, \ldots, K\}$). The single and double prime symbols denote for the time derivatives of $\mathbf{z}$. $\mathbf{z}_{\tau_n}$ stores the delayed coordinates of $\mathbf{z}$ (i.e., $u_b\left(\tau - \tau_n\right)$, $\phi_b\left(\tau - \tau_n\right)$). τ_n is the (state-dependent) time-delay appearing in the rock cutting process. $\mathcal{M}$ is the mass matrix, and n is the number of bit-blades. Furthermore, one of the pivotal elements in the model is the bit-rock interaction that couples the axial and torsional dynamics of the drill-string and has two main components related to cutting and contact. Matrix $\mathcal{H}$ consists of the generalized forces and torques (except from the components related to the wear-flat contact force and frictional torque), i.e., from the stiffness and damping processes, cutting, gravity and the hook-load imposed by the hoisting/top-drive system at the surface. Thus, we have the torsional damping (γ_ϕ), the axial damping (γ), the angular velocity imposed at the surface rotary table (ω_0), and the resultant of the submerged weight of the drill-string and hook-load ($\mathcal{W}_a$). Moreover, the cutting and contact components are extended for encapsulating the rock heterogeneity effect of two distinct horizontal layers in which the bit may be simultaneously drilling. The lithology

parameters influencing these bit force and torque components are the ratio of the intrinsic specific energies between upper and lower layers (g_k^{ε}), the ratio of the frictional coefficients for the contact between upper and lower layers (g_k^{μ}), the ratio of the contact pressures at the bit-rock interface between upper and lower layers (g_k^{σ}), and the ratio between the intrinsic specific energy at the associated layer and its mean values ($\bar{g}_k^{\varepsilon}$). In addition, these bit force and torque components are also affected by the bit parameters related to cutting (η_{ζ}^{l}) and contact (η_{ξ}^{l}), and drill-string design ($\bar{\psi}$). These bit parameters are adapted to the formation layer(s) in which the bit is currently engaged. We use the radius ratio of the bit at the layer boundary (ρ_b as defined in Figure 1-middle) to segregate the portion of the bit engaged in the upper ($(k-1)^{th}$) and lower (k^{th}) layers during the transition. We note that the bit is designed with a particular blade profile ($z(r)$) as a function of its radius r (with maximum radius a). In (3), the depth-of-cut δ_n and the time-delay τ_n are given by,

$$\delta_n = u_b(\tau) - u_b(\tau - \tau_n), \qquad \phi_b(\tau) - \phi_b(\tau - \tau_n) = \frac{2\pi}{n}. \tag{4}$$

Vector $\mathcal{L}$ stores the dimensionless wear-flat contact force ($\mathcal{L}_{k,b_a}^{tot}$) and the associated frictional torque ($\mathcal{L}_{k,b_t}^{tot}$) acting on the bit wear-flats and is affected by the heterogeneity of the layer(s) in which the bit engages (this dependence is indicated by index k). The generalized directions of these forces and torques are contained in matrix $\mathcal{W}$. These forces and torques obey set-valued force laws (reflecting a unilateral contact law in (5) and a Coulomb friction law in (6)) using a proximal-point formulation on velocity level:

$$\mathcal{L}_{k,b_a}^{tot}(\rho_b) = \text{prox}_{\bar{C}_a}\left(\mathcal{L}_{k,b_a}^{tot} - r_1\, u'_b\right), \quad \bar{C}_a = \left\{\mathcal{L}_{k,b_a}^{tot}(\rho_b) \mid -n\, g_{k,\rho_b}^{\sigma}\bar{\mathcal{L}}_{k,b_a} \leqslant \mathcal{L}_{k,b_a}^{tot}(\rho_b) \leqslant 0\right\}, \tag{5}$$

$$\mathcal{L}_{k,b_t}^{tot}(\rho_b, \mathcal{L}_{k,b_a}^{tot}) = \text{prox}_{\bar{C}_t}\left(\mathcal{L}_{k,b_t}^{tot} - r_2\, \phi'_b\right), \quad \bar{C}_t = \left\{\mathcal{L}_{k,b_t}^{tot}(\rho_b) \mid -\beta_{k,\rho_b}\mathcal{L}_{k,b_a}^{tot}(\rho_b) \leqslant \mathcal{L}_{k,b_t}^{tot}(\rho_b) \leqslant \beta_{k,\rho_b}\mathcal{L}_{k,b_a}^{tot}(\rho_b)\right\}. \tag{6}$$

$\bar{\mathcal{L}}_{k,b_a}$ is the nominal contact force for the associated rock layer, while g_{k,ρ_b}^{σ} is the value of g_k^{σ} affected by the bit-geometry at the layer boundary (associated to ρ_b). β_{k,ρ_b} is the bit-design parameter that is also affected by the formation heterogeneity and mainly influences the frictional torque. r_1 and r_2 are some positive arbitrary constants.

Preliminary Simulation Results

The simulation results of the dimensionless model of drill-string system for vertical drilling in heterogeneous formations are shown in Figure 2. Under the influence of the heterogeneity, the torque and weight on bit are fluctuating and not reaching the steady-state limit cycles (associated to the responses in homogeneous rock formulations) while the bit moves in heterogeneous and thin layers, i.e., each layer thickness equal to the bit height. The green area is the soft layer, while the red area is for the hard one. These responses show that in the case of heterogeneous formations, the drill-string dynamics can no longer be described through homogeneous models and the developed heterogeneous model is indeed required.

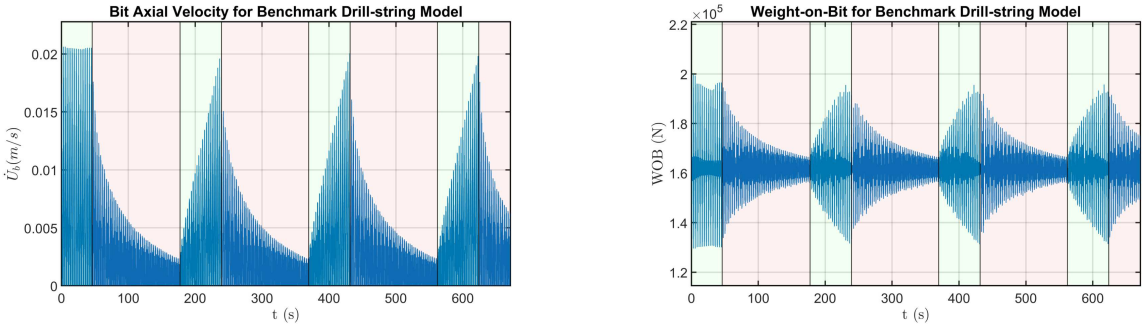

Figure 2: Bit axial velocity/rate-of-penetration in drilling heterogeneous formations (left); weight-on-bit (right).

Conclusion

This abstract presents a drill-string dynamics model with a PDC bit for drilling vertically in the heterogeneous formations with an emphasis on the characterization of the bit-rock interaction during the transition of the bit between two distinct horizontal layers. Next we aim to analyze the drilling efficiency in terms of ROP and to examine the total torsional power losses that can lead to the onset of (torsional) stick slip vibrations in heterogeneous formations.

References

[1] Mensa-Wilmot G., Fear M.J. (2001) The effects of formation hardness, abrasiveness, heterogeneity and hole size on PDC bit performance. *2001 SPE/IADC Drilling Conference, 27 February - 1 March 2001, Amsterdam, Netherlands.*

[2] Detournay E., Richard T., Shepherd M. (2008) Drilling response of drag bits: Theory and experiment. *International Journal of Rock Mechanics and Mining Sciences, Volume 45, Issue 8, pp 1347-1360.*

[3] Wildemans R., Aribowo A.G., Detournay E., van de Wouw N. (2019) Modelling and dynamic analysis of an anti-stall tool in a drilling system including spatial friction. *Nonlinear Dynamics - An International Journal of Nonlinear Dynamics and Chaos in Engineering Systems, Volume 98, Issue 4, pp 2631–2650.*

Nonlinear granular damping of structures with cavities from additive manufacturing

Sebastian Tatzko*, Tobias Ehlers†, Gleb Kleyman* and Roland Lachmayer†
*Institute of Dynamics and Vibration Research, Leibniz University Hannover, Hannover, Germany
†Institute of Product Development, Leibniz University Hannover, Hannover, Germany

Summary. Additively manufactured parts are often created with cavities for weight reduction or other mechanical purposes. These cavities offer the optimal base for granular damping. Unfused raw material particles can be left inside the structure or another granular material can be filled in to increase structural damping. In this paper, a simple mechanical model is developed based on measurements of a basic experiment for granular damping with only a small amount of particles.

Additive manufacturing for lightweight structures

Today, the term additive manufacturing characterizes a multitude of different processes with which almost all materials from metals to plastics to ceramics, glass and concrete can be processed. The potential of additive manufacturing offers new possibilities to realize optimized solutions in the development process. This includes in particular the manufacture of components with a high degree of complexity and shape variance.
The possibility of integrating cavities into components is particularly attractive for lightweight construction. The overall weight is reduced while lattice structures can be added easily to provide the necessary stability. A major drawback of these lightweight integral structures is their susceptibility to vibrations and noise emissions. A common additive manufacturing process for metals is laser powder bed fusion (LPBF). Smallest particles of the raw material are melted with a laser and formed into a structure in layers. A CT-scan of a LPBF-printed beam with unfused material in the cavity is shown in Fig.1a). The raw granular material is removed from the cavities at the end of the manufacturing process. The obvious idea is to leave the unfused granules inside the structure to make use of the granular damping effect [1], [2]. In order to keep the weight low, the raw material can be replaced by another granule with a lower density [3]. The simpler way is to leave only a small part of the granules in the cavity.

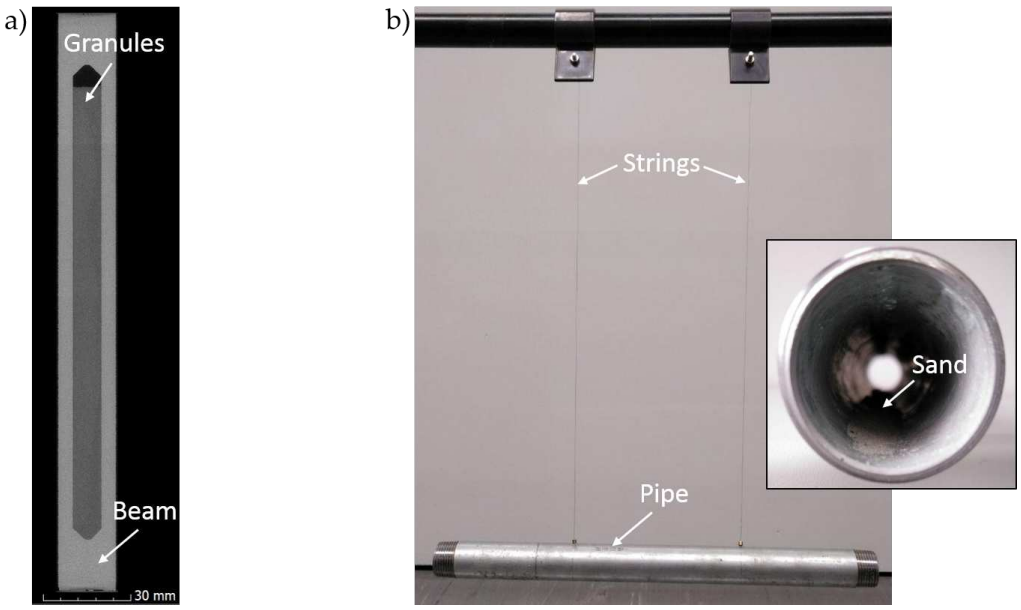

Figure 1: a) Additively manufactured beam with unfused granules in cavity; b) Experimental set up of steel pipe hanging on strings

Fundamental investigations on granular damping

For first investigations on increased damping through a small amount of particles a standard steel pipe is tested with sand as granular medium. Sand can have a strong damping effect on mechanical structures [4]. The pipe hangs freely on strings as shown in Fig.1b). Free decay from impact excitation is recorded with a microphone and then analyzed by applying a short-time Fourier transform (STFT). Fig.2a) shows the results for the unfilled pipe in the frequency range around the first bending mode. Due to a slight asymmetry two close frequencies are recognized. Repeating the measurement with a small amount of sand inside the pipe, see Fig.1b), a strongly increased damping is noticable. After a certain time, the damping effect disappears with a distinct frequency shift., cp. Fig.2b). The structure then vibrates at significantly lower amplitudes with low damping.

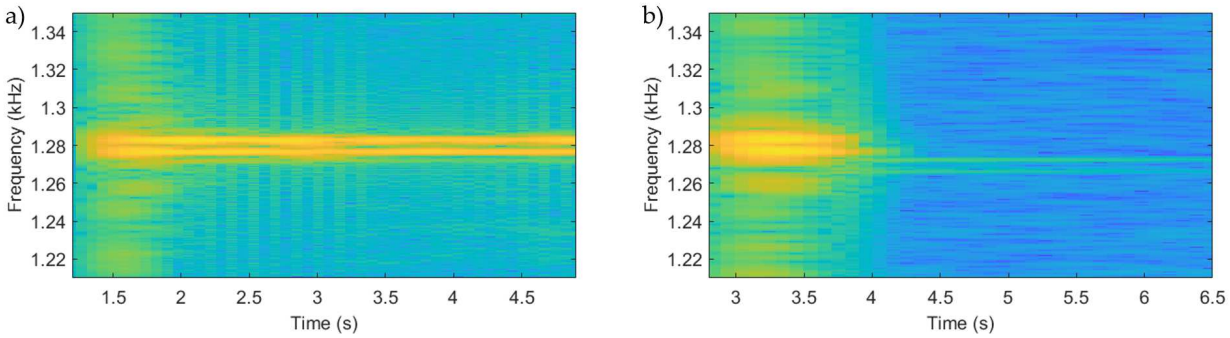

Figure 2: STFT results after impact excitation: a) unfilled pipe ; b) pipe filled with a small amount of sand

Minimal model showing observed phenomena

Motivated by the measurement results, a minimal model is developed to reproduce the observed vibration phenomena. A strongly increased damping with a shift to a lower vibration frequency are approached by the dual mass model shown in Fig.3a). An unbound mass m_2 is connected via Coulomb friction to a single degree of freedom (SDOF) oscillator with mass m_1. The frictional force depends on the relative velocity of the two masses and the factor μF_n. In the case of an impact excitation of the lower mass, it will initially move independently. The upper mass stays at rest due to its inertia and resulting friction forces provide increased vibration damping. After a certain amount of time, the upper mass will move synchronously with the lower mass and practically increase the mass of the SDOF-system. This leads to a sudden reduction of the vibration frequency clearly visible in the spectral analysis result in Fig.3b). Numerical results are obtained by time step integration for which a Matlab/Simulink model of the system is set up. The natural frequency of the system is tuned to match the first bending mode of the pipe. All remaining parameters are manually set in order to obtain a qualitative characteristic close to the measurements. The acoustic measurement results for a single vibration mode could be very well reproduced with the presented minimal model. If it is possible to find a physical interpretation of the model parameters and to identify these parameters from measurements, the minimal model could be used for a simple first approach in granular damping design.

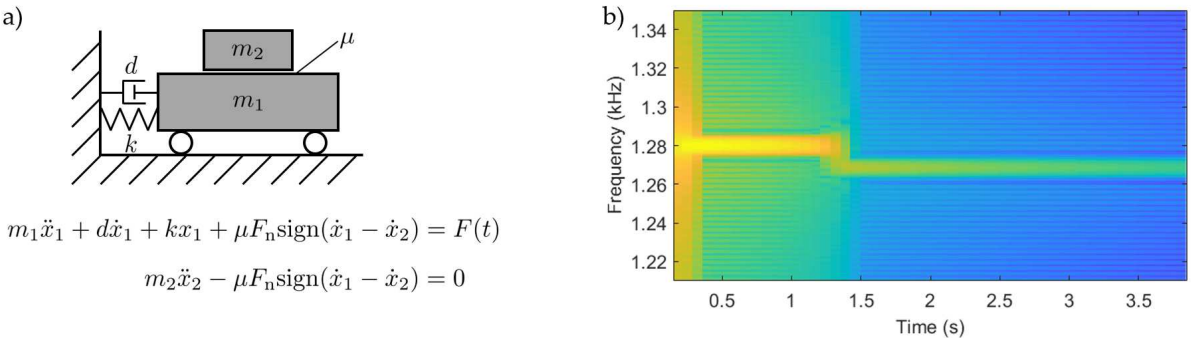

Figure 3: a) Dual mass model and equations of motion; b) STFT result after impact excitation from numerical time integration

Conclusion

Granular damping of structures is a promising and cost-effective method for vibration reduction. Additively manufactured components with cavities of various types open up new possibilities for placing granules. For weight reasons, partially filled cavities are of particular interest. In this work experimental studies are carried out and observed phenomena are modelled using a mechanical oscillator. The model shows the same characteristic as found in measurments and maybe helpful for granular damping design with only a small amount of particles.

References

[1] Scott-Emuakpor, O. et al. (2019) Sustainability Study of Inherent Damping in Additively Manufactured Nickel Alloy. *AIAA Journal Vol. 57*.

[2] Bourinet, J.M., Le Houedec, D. (1999) A dynamic stiffness analysis of damped tubes filled with granular materials *Computers and Structures 73*.

[3] Nayfeh, S. A. et al. (2002) Damping of flexural vibration by coupling to low-density granular materials *Proc. SPIE 4697 Smart Structures and Materials*

[4] Duvigneau, F. et al. (2018) An effective vibration reduction concept for automotive applications based on granular-filled cavities. *Journal of Vibration and Control Vol. 24(1)*.

A Nonsmooth Approach for Generating Convex Relaxations of Dynamic Systems

Yingkai Song and Kamil A. Khan
Department of Chemical Engineering, McMaster University, Hamilton, ON, Canada

Summary. We propose a new approach for generating convex and concave relaxations for the solutions of parametric ordinary differential equations (ODEs), for use in global dynamic optimization and reachability analysis. These relaxations are described as the solutions of an auxiliary nonsmooth ODE system with embedded convex optimization problems. The resulting relaxations are indeed valid relaxations, are convex, and converge rapidly to the original system as the parametric subdomain shrinks. The new approach is compatible with any relaxations for the original right-hand side, and tighter such relaxations will necessarily translate into tighter relaxations for state variables. Especially, if generalized McCormick relaxations are used, the new approach is guaranteed to yield tighter relaxations than a state-of-the-art ODE relaxation approach [1], and thus may reduce the number of iterations for overarching global dynamic optimization. Further implications and examples are discussed.

Background and Motivation

Global dynamic optimization is useful in a wide variety of engineering applications such as parameter estimation, global optimal control, and optimization-based worst-case uncertainty analysis. Compared with stochastic methods for global optimization, deterministic global optimization methods have the advantage that a globally optimal solution is guaranteed to be found within a predefined tolerance in finite computation time. However, current deterministic global dynamic optimization methods based on branch-and-bound [2] can only solve problems of modest size. Thus, improved techniques are sought to extend these methods to problems of practical interest.

One computational bottleneck for global dynamic optimization is generating convex and concave relaxations for state variables with respect to decision variables, termed *state relaxations* [1]. These relaxations are useful for computing lower bounds for the global optimal objective value, which are required in deterministic global optimization algorithms. Moreover, state relaxations could also help construct convex enclosures for the reachable set which is useful in applications involving reachability analysis such as fault detection and robust optimal control. Hence, there is a need in global dynamic optimization to develop efficient and accurate computational tools for generating state relaxations automatically.

State relaxations should have desirable convergence and tightness properties. The relaxations supplied to a branch-and-bound global optimization method must converge rapidly to the underlying model as the decision space is subdivided or else the overall global optimization method will be impeded by cluster effects, in which the method will branch many times on intervals that either contain or are near a global minimum [3]. This notion of rapid convergence has been formalized as *second-order pointwise convergence* [4]. Tighter state relaxations could construct tighter lower bounds for the global optimal objective value, and thus may reduce the overall computational time by reducing the number of required iterations. In reachability analysis, tighter enclosures of the reachable set could reduce the sets' conservatism, which could lead to earlier detection of faults or less conservative control inputs.

New Relaxation Approach

Consider a parametric ODE system of the form

$$\begin{aligned}\dot{\mathbf{x}}(t,\mathbf{p}) &= \mathbf{f}(t,\mathbf{p},\mathbf{x}), \quad \forall t \in (t_0,t_f],\\ \mathbf{x}(t_0,\mathbf{p}) &= \mathbf{x}_0(\mathbf{p}),\end{aligned}$$

where $\mathbf{x}$ denotes dependent state variables and $\mathbf{p}$ denotes system parameters.

We propose a new approach for constructing state relaxations $\mathbf{x}^{cv}(t,\mathbf{p})$ and $\mathbf{x}^{cc}(t,\mathbf{p})$ for states $\mathbf{x}(t,\mathbf{p})$ with respect to $\mathbf{p}$. These relaxations are described as the solutions of an auxiliary ODE system whose right-hand side comprises convex optimization problems with embedded relaxations for $\mathbf{f}$. The auxiliary system is nonsmooth because of the nonsmooth nature of optimal-valued functions. The advantages of this approach are presented as follows. First, if the relaxations for $\mathbf{f}$ have second-order pointwise convergence, then the resulting state relaxations inherit this desirable convergence property which could help avoid cluster effects. Secondly, the new approach is compatible with various relaxations for $\mathbf{f}$, such as αBB relaxations [5] and generalized McCormick relaxations [6], while previously established approaches are typically limited by one particular type of relaxations. Thirdly, tighter relaxations for $\mathbf{f}$ necessarily translate into tighter state relaxations. Thus, it is worthwhile from a dynamic optimization or reachability analysis standpoint to seek tighter relaxation methods for closed-form functions since doing so necessarily translates into superior descriptions of reachable sets for dynamic systems. Especially, if the generalized McCormick relaxations are employed, the new approach necessarily yields tighter state relaxations than a state-of-the-art ODE relaxation approach by Scott and Barton [1], and thus may reduce the number of required iterations for overarching global dynamic optimization.

Proof-of-concept Implementation

Two numerical examples are presented to illustrate the convergence and tightness properties of the new state relaxations. The examples are implemented in MATLAB, using the ODE solver `ode15s` and the local optimization solver `fmincon`.

Example 1

Consider the following parametric ODE system:

$$\dot{x}(t,p) = p(x^2 - 1), \quad x(0,p) \quad = -2,$$

with $t_f = 0.15$ and $-1 \leq p \leq 1$. State relaxations are constructed by the new approach using αBB relaxations of the right-hand side function. Figure 1 shows that the resulting relaxations have second-order pointwise convergence, where X^C denotes the enclosure formed by state relaxations, and P denotes the parametric subdomain.

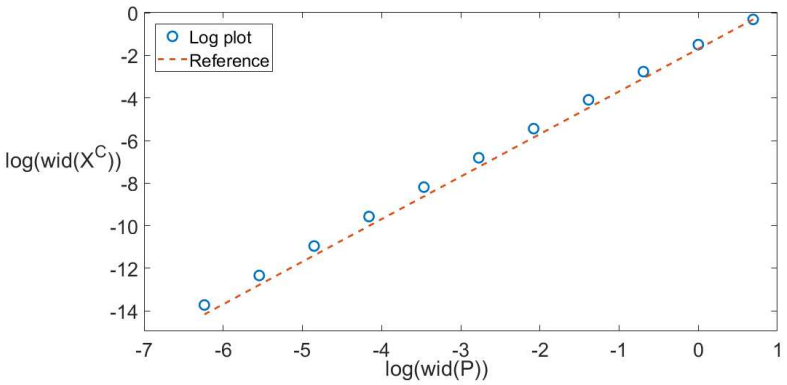

Figure 1: A log-log plot of width of the enclosure formed by state relaxations at $t := t_f$ versus width of the parameter's domain (*circles*) and a reference line with a slope of 2 (*dashed*).

Example 2

The following example is modified from a bioreaction model in [7] by adding more nonlinearities:

$$\dot{x}_1(t,p) = \Big(\frac{1.2x_2}{px_2^2 + x_2 + 7.1} - 0.18\Big)x_1, \qquad x_1(0,p) = 0.82,$$

$$\dot{x}_2(t,p) = 0.36(5.7 - x_2) - \frac{12.636x_2x_1}{px_2^2 + x_2 + 7.1} + \frac{1}{x_1} - x_2^2 + x_1^2x_2, \quad x_2(0,p) = 0.8,$$

with $t_f = 15$ and $0.4 \leq p \leq 0.6$. State relaxations are constructed by the new approach using generalized McCormick relaxations and by the approach of Scott and Barton [1]. Figure 2 shows that the new state relaxations are tighter than Scott–Barton relaxations for this example.

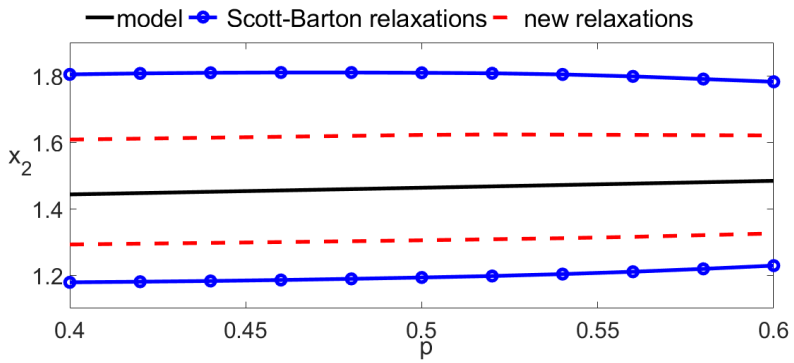

Figure 2: The final state $x_2(t_f, p)$ vs. p (*black-solid*), along with corresponding Scott–Barton relaxations (*blue-circled*) and new relaxations (*red-dashed*), plotted as functions of p at $t := t_f$.

References

[1] Scott J. K., Barton P. I. (2013) Improved relaxations for the parametric solutions of ODEs using differential inequalities. *J. Glob. Optim.* **57**(1): 143-176.

[2] Falk J. E., Soland R. M. (1969) An algorithm for separable nonconvex programming problems. *Manage. Sci.* **15**(9): 550-569.

[3] Wechsung A., Schaber S. D., Barton, P. I. (2014) The cluster problem revisited. *J. Glob. Optim.* **58**(3): 429-438.

[4] Bompadre A., Mitsos, A. (2012) Convergence rate of McCormick relaxations. *J. Glob. Optim.* **52**(1): 1-28.

[5] Adjiman C., Dallwig S., Floudas C., Neumaier A. (1998) A global optimization method αBB, for general twice-differentiable constrained NLPs: I. Theoretical Advances. *Comput. Chem. Eng.* **22**(9): 1137-1158.

[6] Scott J. K., Stuber M. D., Barton P. I. (2011) Generalized McCormick relaxations. *J. Glob. Optim.* **51**(4): 569-606.

[7] Bastin G., Dochain D. (1991) On-line Estimation and Adaptive Control of Bioreactors. Elsevier, Amsterdam.

Nonsmooth Modal Analysis of Varying Cross-section Bar

Tianzheng Lu and Mathias Legrand
Structural Dynamics and Vibration Laboratory, McGill University, Montreal, Québec, Canada

Summary. The nonsmooth modal analysis of a simple one-dimensional bar of constant cross-section has already been successfully performed using a Finite Volume formulation and the Frequency-Domain Boundary Element Method (FD-BEM). Both strategies took advantage of the existence of d'Alembert solution for such problem. The present contribution extends the previous works to a bar of non-constant cross-section for which the d'Alembert solution no longer exists. The proposed scheme combines the finite element method in space to the harmonic balance technique in time. The solution satisfies the unilateral contact condition along with an energy-preserving implicit impact law in a weighted-residual sense. The partial backbone curve of the first mode shows the existence of internal resonances.

Introduction

Within the framework of structural dynamics, modal analysis is a practical tool to predict the occurrence of vibrational resonances, most commonly to prevent them. Various formulations have been proposed in the nonlinear framework where the governing equation contains smooth nonlinear function of the state of system. Nonsmooth modal analysis is one incarnation of nonlinear modal analysis in which the smoothness assumption does not hold, as for instance exhibited in unilaterally-constrained structural dynamics [1, 2]. In this context, a method combining the finite element method (FEM) and harmonic balance method (HBM) is proposed.

System of Interest

The system of interest, in Figure 1, is a one-dimensional bar of finite length L. The displacement field of straight cross-sections is denoted $u(x,t)$ where x is the space coordinate and t is time. The bar is clamped at $x = 0$ (Dirichlet condition) and subject to a unilateral contact condition at $x = L$ (Signorini condition). The cross-section area $A(x)$ is varying along the bar while the mass density ρ and Young's modulus E are constant. Given the initial gap g_0 between the bar at rest and the rigid foundation, the gap function reads $g(t) = g_0 - u(L,t)$. The dynamics of the bar is governed by the Partial Differential Equation

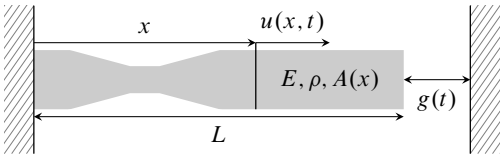

Figure 1: One-dimensional bar system of interest

$$EA_x u_x + EAu_{xx} + \rho A u_{tt} = 0 \tag{1}$$

where $\bullet_\eta$ denotes a partial differentiation with respect to η. Clamping at $x = 0$ reads $u(0,t) = 0$ while unilateral contact at $x = L$ is expressed as

$$-\lambda(t) + \max[\lambda(t) - \alpha g(t), 0] = 0 \tag{2}$$

where $\lambda(t)$ is the contact force and α is a strictly positive real number.

Solution method: Fourier Transform+Finite Elements+Harmonic Balance

The sought families of periodic solutions defining the modal motions are computed through a numerical scheme which assumes that no impact law is explicitly required, in contrast to common practises. First, a Fourier Transform is applied on the unknowns of the problem:

$$\mathcal{F}\{u(x,t)\} = \hat{u}(x,\omega) = \frac{1}{2\pi}\int_{-\infty}^{\infty} u(x,t)\exp(-i\omega t)\mathrm{d}t \quad \text{and} \quad \mathcal{F}\{\lambda(t)\} = \hat{\lambda}(\omega) = \frac{1}{2\pi}\int_{-\infty}^{\infty} \lambda(t)\exp(-i\omega t)\mathrm{d}t. \tag{3}$$

This leads to the two governing equations in the frequency domain

$$EA\hat{u}_{xx} + EA_x\hat{u}_x - \omega^2\rho A\hat{u} = 0 \quad \text{and} \quad -\hat{\lambda}(\omega) + \mathcal{F}\{\max[\lambda(t) - \alpha g(t), 0]\} = 0 \tag{4}$$

where the last term $\mathcal{F}\{\ldots\}$ can unfortunately not be explicitly expressed in terms of $\hat{u}$ and $\hat{\lambda}$. Spatial semi-discretization is applied via the standard FEM with N two-node linear elements and the corresponding $N+1$ nodes. The Dirichlet boundary condition is directly enforced in the discretized weak form of (4) which reads

$$\mathbf{H}(\omega)\hat{\mathbf{u}}(\omega) = \hat{\mathbf{f}}(\omega) \tag{5}$$

with $\mathbf{H}(\omega) = \mathbf{K} - \omega^2\mathbf{M}$ where $\mathbf{K}$ and $\mathbf{M}$ are the classical stiffness and mass matrices. Also, vector $\hat{\mathbf{f}}(\omega) = [0,\ldots,0,\hat{\lambda}(\omega)]^\top$ stores the contact force while vector $\hat{\mathbf{u}}(\omega) = [\hat{u}_0(\omega),\ldots,\hat{u}_{N-1}(\omega),\hat{u}_N(\omega)]^\top$ stores the response nodal displacements, both in the frequency domain. Inverting $\mathbf{H}(\omega)$ yields the relation

$$\hat{u}_N(\omega) = \gamma(\omega)\hat{\lambda}(\omega) \tag{6}$$

where $\gamma(\omega)$ is the last entry of the inverse of $\mathbf{H}(\omega)$. Since periodic solutions are targeted, the time-domain nodal displacements and companion contact force are approximated as

$$\lambda(t) = a_0 + \sum_{k=1}^{M} a_{2k-1} \sin k\Omega t + a_{2k} \cos k\Omega t, \quad u_i(t) = b_{i0} + \sum_{k=1}^{M} b_{i2k-1} \sin k\Omega t + b_{i2k} \cos k\Omega t, \quad i = 1, \ldots, N. \tag{7}$$

Given the form of $\hat{\mathbf{f}}$, the only unknowns of the problem actually are the Fourier coefficients of $u_N(t)$ and $\lambda(t)$, that is the coefficients (a_k, b_{Nk}) for $k = 0, \ldots, 2M$. Accordingly, it is required to establish the corresponding equations to solve for. First, inserting (7) into (6) leads to

$$b_{Nk} = \gamma(k\Omega) a_k, \quad k = 0, \ldots, 2M. \tag{8}$$

Second, noting $\beta(t) \overset{\text{def}}{=} \max(\lambda(t) - \alpha g(t), 0)$ and $T = 2\pi/\Omega$, the HBM version of condition (2) implies

$$a_0 - \frac{1}{T} \int_0^T \beta(t) \mathrm{d}t = 0 \tag{9}$$

along with

$$a_{2k} - \frac{2}{T} \int_0^T \beta(t) \cos k\Omega t \mathrm{d}t = 0 \quad \text{and} \quad a_{2k-1} - \frac{2}{T} \int_0^T \beta(t) \sin k\Omega t \mathrm{d}t = 0, \quad k = 1, \ldots, M \tag{10}$$

where Expressions (7) are first inserted into the above integrals which can then be numerically evaluated using basic quadrature schemes. Continuous families of periodic solutions are built via a classical sequential continuation technique [3, 4] on the frequency parameter Ω, which is thus not treated as an unknown. The resulting system of $4M + 2$ equations (8) to (10) in $4M + 2$ unknowns can be solved using a nonlinear solver. Since autonomous periodic solutions are targeted, it seems justified to say that the classically required energy-preserving impact law is here embedded implicitly in the above integrals. However, we do not have a formal proof of this statement.

Results

The selected cross-section area is $A(x) = 1.5 - x$ with $L = 1$ and the initial gap is $g_0 = 0.001$. The discretization is chosen to be $M = 40$ and $N = 4000$. Results on the first nonsmooth mode are depicted in Figure 2. The backbone

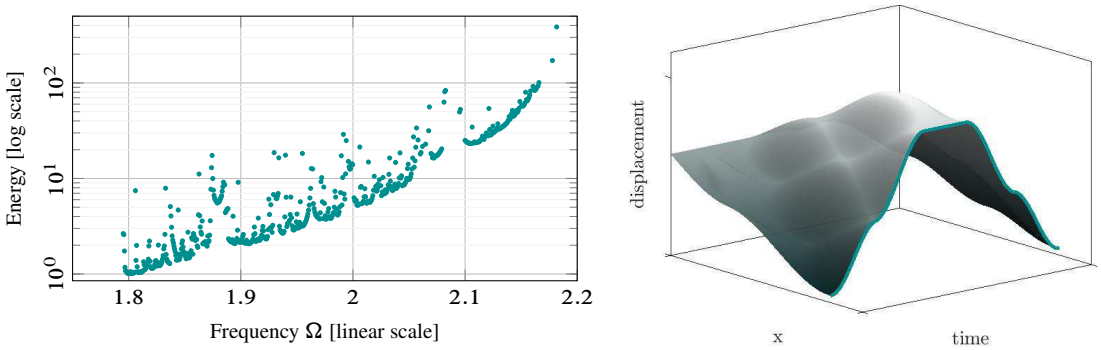

Figure 2: First nonsmooth mode: backbone curve (left) and displacement field at $\Omega = 1.907$ (right).

curve shows the frequency-energy dependency of the modal response and internal resonance mechanisms with higher modes. Unlike the displacement field of the constant cross-section bar which consists of piecewise affine segments, the displacement field found here seems to have smoother functional properties, even with a fine approximation.

Conclusion

A numerical scheme combining FEM and the HBM is proved capable of capturing nonsmooth modes for a one-dimensional varying cross-section bar. The main feature of the proposed scheme is that neither explicit energy-preserving impact laws nor regularization techniques are required at the contact interface even-though classical finite-elements are employed. Instead, the Signorini condition and companion impact law are satisfied in a weighted-residual sense.

References

[1] C. Yoong, A. Thorin and M. Legrand, "Nonsmooth modal analysis of an elastic bar subject to a unilateral contact constraint", *Nonlinear Dynamics*, 2018.

[2] T. Lu and M. Legrand, "Nonsmooth Modal Analysis via the Boundary Element Method for one-dimensional bar systems", *Nonlinear Dynamics*, 2021.

[3] M. Peeters, R. Viguié, G. Serandour, G. Kerschen, and J.-C. Golinval "Nonlinear normal modes, Part II: Toward a practical computation using numerical continuation techniques", *Mechanical Systems and Signal Processing*, 2009.

[4] A. H. Nayfeh and Balachandran, B. *Applied nonlinear dynamics: analytical, computational, and experimental methods*. Wiley, 2008.

Monday, July 18, 2022

16:00 - 18:20

MS-20 Wave propagation in Mechanical Systems and Nonlinear Metamaterials

Saint Clair 3B

Chair: Marco Lepidi

16:00 - 16:20
Theory of harmonic generation in nonlinear elastic waves
KHAJEHTOURIAN Romik, **HUSSEIN Mahmoud***
*University of Colorado Boulder (3775 Discovery Drive, Boulder, CO 80303, USA United States)

16:20 - 16:40
Shocks and solitary waves in series connected discrete Josephson transmission lines
KOGAN Eugene*
*Bar-Ilan University (Department of Physics, Bar-Ilan University, Ramat-Gan 52900 Israel)

16:40 - 17:00
Tunable interface states in locally resonant acoustic chains with inerters
CAJIC Milan*, KARLIČIĆ Danilo, PAUNOVIĆ Stepa, ADHIKARI Sondipon
*Faculty of Science and Engineering, Swansea University (Fabian Way, Crymlyn Burrows, Skewen, Swansea SA1 8EN United Kingdom)

17:00 - 17:20
Nonlinear Wave Disintegration in Phononic Material with Weakly Compressed Rough Contacts
PATIL Ganesh*, MATLACK Kathryn
*Department of Mechanical Science and Engineering, University of Illinois at Urbana Champaign (Sidney Lu Mechanical Engineering Building 1206 W. Green St. MC 244 Urbana, IL 61801 United States)

Theory of harmonic generation in nonlinear elastic waves

Romik Khajehtourian[*], and Mahmoud I. Hussein[**,***]
[*]*Department of Mechanical and Process Engineering, ETH Zurich, Zurich, 8092, Switzerland*
[**]*Ann and H.J. Smead Department of Aerospace Engineering Sciences, University of Colorado Boulder, Boulder, Colorado 80303, USA*
[***]*Department of Physics, University of Colorado Boulder, Boulder, Colorado 80302, USA*

Summary. We present a theory for the dispersion of generated harmonics in a traveling nonlinear wave. The harmonics dispersion relation—derived by the theory—provides direct and exact prediction of the collective harmonics spectrum in the frequency-wavenumber domain, and does so without prior knowledge of the spatial-temporal solution. The new relation is applicable to a family of initial wave functions characterized by an initial amplitude and wavenumber. We demonstrate the theory on nonlinear elastic waves in a homogeneous rod and demonstrate an extension to periodic rods.

Wave motion lies at the heart of many disciplines in the physical sciences and engineering. For example, problems and applications involving light, sound, heat or fluid flow are all likely to involve wave dynamics at some level. In this work, we consider strongly nonlinear wave propagation [1,2] in elastic solids, although the theory presented is in principle applicable to other types of waves such as waves in fluids, gases, and plasma.

We investigate a thick elastic rod admitting longitudinal motion. In the linear limit, this rod is dispersive due to the effect of lateral inertia. The nonlinearity is introduced through either the stress-strain relation and/or the strain-displacement gradient relation. Using a formulation we have developed earlier and demonstrated on thin rods and beams [3], we derive an exact nonlinear dispersion relation for the thick rod. Equation (1) provides the governing nonlinear differential equation considering a linear stress-strain relation and a Green-Lagrange nonlinear relationship between strain and displacement gradient:

$$\partial_{tt}\bar{u} - \partial_{xx}(\alpha\bar{u} + \beta\mathcal{N}(\bar{u}) + \gamma\partial_{tt}\bar{u}), \tag{1}$$

where $\gamma = r^2\nu^2$, r is the polar radius of gyration, and ν is the Poisson's ratio. The Green-Lagrange strain measure is introduced by setting $\alpha = \beta = c^2$ and $\mathcal{N}(\bar{u}) = 3\bar{u}^2/2+\bar{u}^3/2$ where c is the longitudinal speed of sound in the rod. Equation (2) is a statement of the derived nonlinear dispersion relation, and Figure 1 presents it in graphical form with and without accounting for lateral inertia.

$$\omega = c\kappa\sqrt{(2 + 3B\kappa + B^2\kappa^2)/(2 + 2\gamma\kappa^2)}, \tag{2}$$

where ω and κ denote the frequency and wavenumber, respectively, and B represents the wave amplitude.

.

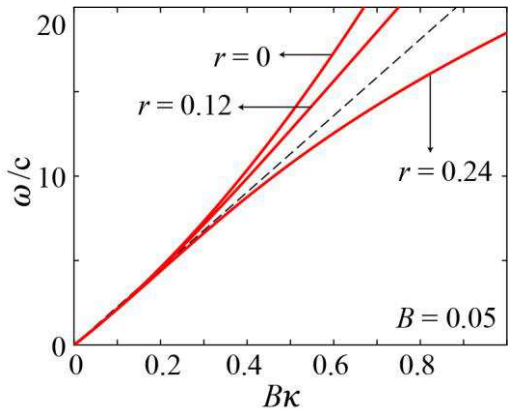

Figure 1. Nonlinear dispersion relation for elastic waves propagating in a thick rod with a radius of gyration r. A non-zero value of r represents the presence of lateral inertial which gives rise to dispersion even when there is no nonlinearity in the system. The wave amplitude is denoted by B. Solid red curves represent dispersion curves for B = 0.05 and dashed black curve represent the linear nondispersive case, i.e., very small value of B.

The derived relation is validated by direct time-domain simulations, examining both instantaneous dispersion (by direct observation) and short-term, pre-breaking dispersion (by Fourier transformations). Figure 2 shows a multi-window overlay of the frequency-wavenumber response obtained by performing a space-time Fourier transform of the

simulation field for a collection of hyperbolic secant signals all with an initial amplitude of $B = 0.025$. Specifically, the contour plot shown is obtained by superimposing the energy spectra of thirty separate simulations for distinct initial wave packets, each following a hyperbolic secant spatial profile and sharing the same amplitude but covering the range of excitation wavenumbers $\kappa_e = 1$ to 30, with increments of 1. What emerges from this exercise is a profile of the fundamental harmonic spanning the various simulations. On the same plot, nonlinear dispersion relation of Eq. (2) is overlaid demonstrating perfect prediction of the simulated nonlinear response [4].

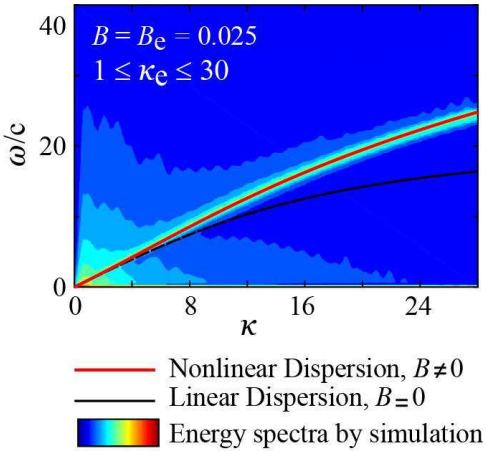

Figure 2. Superposition of harmonics spectra from thirty distinct simulations covering a range of excitation wavenumbers is shown to match perfectly with the general nonlinear dispersion relation of Eq. (2) for the selected value of wave amplitude. Results are for $B = 0.025$ and $r = 0.15$.

The study is then extended to a continuous thin rod with a periodic arrangement of material properties [5]. For this problem we introduce a new method that is based on a standard transfer matrix augmented with a nonlinear enrichment at the constitutive material level. This method yields an approximate band structure that accounts for the finite wave amplitude. Finally, we present an analysis on the condition required for the existence of spatial invariance in the wave profile.

References

[1] Zakharov V.E., Faddeev L.D. (1971) Korteweg-de vries equation: A completely integrable hamiltonian system. *Funct. Anal. Appl.* **5**(4):280–287.
[2] Ablowitz M.J., Kaup D.J., Newell A.C., Segur H. (1974) The inverse scattering transform-fourier analysis for nonlinear problems. *Stud. Appl. Math.* **53**(4):249–315.
[3] Abedinnasab M.H., Hussein M.I. (2013) Wave dispersion under finite deformation. *Wave Motion* **50**:374-388.
[4] Khajehtourian R., Hussein M.I. (2019) Nonlinear dispersion relation predicts harmonic generation in wave motion, arXiv:1905.02523v1.
[5] Hussein M.I., Khajehtourian R. (2018) Nonlinear Bloch waves and balance between hardening and softening dispersion. *Proc. R. Soc. A* **474**:20180173.

Shocks and solitary waves in series connected discrete Josephson transmission lines

Eugene Kogan
Department of Physics, Bar-Ilan University, Ramat-Gan 52900, Israel

Summary. We analytically study the running waves propagation in the discrete Josephson transmission lines (JTL), constructed from Josephson junctions (JJ) and capacitors. Due to the competition between the intrinsic dispersion and the nonlinearity, in the dissipationless JTL there exist running waves in the form of supersonic kinks and solitons. The velocities and the profiles of the kinks and the solitons are found. We also study the effect of dissipation in the system and find that in the presence of the resistors, shunting the JJ and/or in series with the ground capacitors, the only possible stationary running waves are the shock waves, whose velocities and the profiles are also found.

Introduction

The concept that in a nonlinear wave propagation system the various parts of the wave travel with different velocities, and that wave fronts (or tails) can sharpen into shock waves, is deeply imbedded in the classical theory of fluid dynamics [1]. The methods developed in that field can be profitably used to study signal propagation in nonlinear transmission lines [2, 3, 4, 5, 6, 7, 8, 9, 10, 11]. In the early studies of shock waves in transmission lines, the origin of the nonlinearity was due to nonlinear capacitance in the circuit [12, 13, 14].

Interesting and potentially important examples of nonlinear transmission lines are circuits containing Josephson junctions (JJ) [15] - Josephson transmission lines (JTL) [16, 17, 18, 19]. The unique nonlinear properties of JTL allow to construct soliton propagators, microwave oscillators, mixers, detectors, parametric amplifiers, and analog amplifiers [17, 19, 18].

Transmission lines formed by JJ connected in series were studied beginning from 1990s, though much less than transmission lines formed by JJ connected in parallel [20]. However, the former began to attract quite a lot of attention recently [21, 22, 23, 24, 25, 26, 27, 28], especially in connection with possible JTL traveling wave parametric amplification [29, 30, 31].

The interest in studies of discrete nonlinear electrical transmission lines, in particular of lossy nonlinear transmission lines, has started some time ago [32, 33, 34], but it became even more pronounced recently [35, 36, 37]. These studies should be seen in the general context of waves in strongly nonlinear discrete systems [38, 39, 40, 41, 42, 43, 44].

In our previous publication [45] we considered shock waves in the continuous JTL with resistors, studying the influence of those on the shock profile. Now we want to analyse wave propagation in the discrete JTL, both lossless and lossy

The rest of the paper is constructed as follows. In Section we formulate quasi-continuum approximation for the discrete lossless JTL. In Section we show that the problem of a running wave is reduced to an effective mechanical problem, describing motion of a fictitious particle. In Section the velocity and the profile of the kink, and in Section - of the soliton are found from the solution of the effective mechanical problem. In Section we rigorously justify the quasi-continuum approximation for the kinks and solitons in certain limiting cases. In Section we discuss the effect of dissipation on the waves propagation in the discrete JTL. In Section we briefly mention possible applications of the results obtained in the paper and opportunities for their generalization. We conclude in Section . In the Appendix we propose the integral approximation to the discrete equations.

The quasi-continuum approximation

Consider the model of JTL constructed from identical JJ and capacitors, which is shown on Fig. 1. We take as dynamical variables the phase differences (which we for brevity will call just phases) φ_n across the JJ and the charges q_n which have passed through the JJ. The circuit equations are

$$\frac{\hbar}{2e}\frac{d\varphi_n}{dt} = \frac{1}{C}\left(q_{n+1} - 2q_n + q_{n-1}\right) , \tag{1a}$$

$$\frac{dq_n}{dt} = I_c \sin\varphi_n , \tag{1b}$$

where C is the capacitor, and I_c is the critical current of the JJ.

Everywhere in this paper we'll treat $q_n(t)$ ($\varphi_n(t)$) as a function of two continuous variables (z,t), where $z = n\Lambda$, and will make the simplest assumption,

$$q_{n+1} - 2q_n + q_{n-1} = \Lambda^2\frac{\partial^2 q}{\partial z^2} + \frac{\Lambda^4}{12}\frac{\partial^4 q}{\partial z^4} . \tag{2}$$

(To keep in (2) only the first term would be an even simpler assumption, but the effects we'll be talking about are absent in this approximation.) We will call (2) the quasi-continuum approximation and will se later that in certain limiting cases it can be rigorously justified.

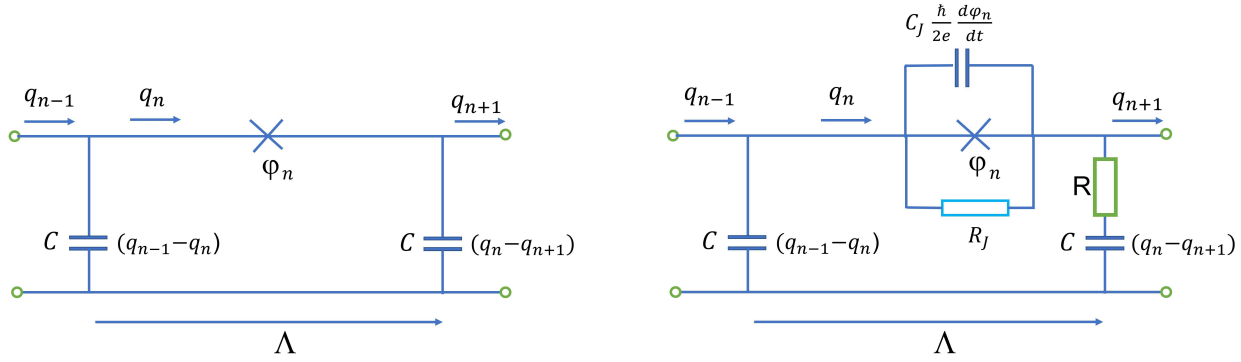

Figure 1: Discrete JTL (left) and discrete JTL with the capacitor and the resistor shunting the JJ and another resistor in series with the ground capacitor (right).

Newtonian equation

The running wave solutions are of the form

$$\varphi(z,t) = \varphi(x)\,, \qquad q(z,t) = q(x)\,, \tag{3}$$

where $x = Ut - z$, and U is the running wave velocity. For such solutions, and after the truncation, Eq. (1) becomes the ordinary differential equation

$$\overline{U}^2 \frac{d\varphi}{dx} = \frac{d\sin\varphi}{dx} + \frac{\Lambda^2}{12}\frac{d^3\sin\varphi}{dx^3}\,; \tag{4}$$

in this paper, for any velocity V, $\overline{V} \equiv V\sqrt{L_J C}/\Lambda$, and $L_J = \hbar/(2eI_c)$. Integrating with respect to x we obtain

$$\frac{\Lambda^2}{12}\frac{d^2\sin\varphi}{dx^2} = -\sin\varphi + \overline{U}^2\varphi + F\,, \tag{5}$$

where F is the constant of integration. Multiplying Eq. (5) by $d\sin\varphi/dx$ and integrating once again we obtain

$$\frac{\Lambda^2}{24}\left(\frac{d\sin\varphi}{dx}\right)^2 + \Pi(\sin\varphi) = E\,, \tag{6}$$

where

$$\Pi(\sin\varphi) = \frac{1}{2}\sin^2\varphi - \overline{U}^2(\varphi\sin\varphi + \cos\varphi) - F\sin\varphi\,, \tag{7}$$

and E is another constant of integration. Equation (6) can be integrated in quadratures in the general case.
We can think about x as time and about $\sin\varphi$ as coordinate of the fictitious particle, thus considering (5) as the Newtonian equation. We are interested in the propagation of the waves characterised by the boundary conditions

$$\lim_{x\to-\infty}\varphi = \varphi_1\,, \qquad \lim_{x\to+\infty}\varphi = \varphi_2\,, \tag{8}$$

Thus the problem of finding the profile of the wave is reduced to studying the motion of the particle which starts from an equilibrium position, and ends in an equilibrium position.
Using the expertise we acquired in mechanics classes, we come to the conclusion that the initial position corresponds to maxima of the "potential energy" $\Pi(\sin\varphi)$, and so does the final position. Either these are two different maxima, or the same maximum. In the latter case the particle returns to the initial position after reflection from a potential wall. (See Figs. 2 (above) and 3.) In the first case the solution describes the kink, in the second - the soliton.
One should compare the running wave velocity with the velocity $u(\varphi_1)$ of propagation along the JTL of small amplitude smooth disturbances of φ on a homogeneous background φ_1 [45]

$$\overline{u}^2(\varphi_1) = \cos\varphi_1 \tag{9}$$

(in this paper we consider only the solutions which lie completely in the sector $(-\pi/2, \pi/2)$.) From the fact that there is a maximum of the "potential energy" at the point φ_1, follows that

$$\left.\frac{d^2\Pi(\varphi)}{d\varphi^2}\right|_{\varphi=\varphi_1} < 0\,. \tag{10}$$

Calculating the derivatives we obtain

$$\overline{U}^2 > \cos\varphi_1\,, \tag{11}$$

that is the running wave is supersonic.

The kinks

In the case of the kink, going in Eq. (5) to the limits $x \to +\infty$ and $x \to -\infty$ we obtain

$$\overline{U}^2 \varphi_1 = \sin\varphi_1 - F \,, \tag{12a}$$

$$\overline{U}^2 \varphi_2 = \sin\varphi_2 - F \,. \tag{12b}$$

Solving (12) relative to $\overline{U}^2$ and F we obtain we obtain

$$\overline{U}^2 = \frac{\sin\varphi_1 - \sin\varphi_2}{\varphi_1 - \varphi_2} \equiv \overline{U}^2_{\text{sh}}(\varphi_1, \varphi_2) \,, \tag{13a}$$

$$F = \frac{\varphi_1 \sin\varphi_2 - \varphi_2 \sin\varphi_1}{\varphi_1 - \varphi_2} \,; \tag{13b}$$

the reason, why we have chosen subscript sh for the velocity in (13a), will become clear in Section .
The result for the kink velocity (13a) is more robust than it looks. In fact, summing up (1a) from far to the left of the kink up to far to the right of the kink we obtain

$$\frac{\hbar}{2e}\frac{d}{dt}\sum_n \varphi_n = \frac{1}{C}\left[(q_{n+1} - q_n)_1 - (q_{n+1} - q_n)_2\right] \,. \tag{14}$$

From the running wave ansatz follows

$$\frac{d}{dt}\sum_n \varphi_n = \frac{U}{\Lambda}\left(\varphi_1 - \varphi_2\right) \,. \tag{15}$$

To deal with the r.h.s. of (14) we need to approximate the finite difference only far away from the kink, where everything changes slowly, and the continuum approximation

$$q_{n+1} - q_n = \Lambda \frac{\partial q}{\partial z} \tag{16}$$

is enough. From (16) and the running wave ansatz follows

$$(q_{n+1} - q_n)_i = \frac{\Lambda}{U}\left(\frac{dq_n}{dt}\right)_i = \frac{\Lambda}{U}\sin\varphi_i \,. \tag{17}$$

Substituting into (14) we recover (13a).
Returning to (13) and taking into account additionally the equality

$$E = \Pi(\sin\varphi_1) = \Pi(\sin\varphi_2) \,, \tag{18}$$

we obtain

$$\varphi_2 \quad = -\varphi_1 \,. \tag{19}$$

Thus the kinks which can propagate in JTL are very special. We also obtain

$$F = 0 \,, \tag{20a}$$

$$\overline{U}^2 = \overline{U}^2_{\text{sh}}(\varphi_1, -\varphi_1) = \frac{\sin\varphi_1}{\varphi_1} \equiv \overline{U}^2_k(\varphi_1) \,. \tag{20b}$$

$$\Pi(\sin\varphi) - E = \frac{1}{2}(\sin\varphi - \sin\varphi_1)^2 - \frac{\sin\varphi_1}{\varphi_1}[\cos\varphi - \cos\varphi_1 - (\varphi_1 - \varphi)\sin\varphi] \,. \tag{20c}$$

Equation (20c) and the results of integration of Eq. (6) for this "potential energy" are graphically presented on Fig. 2 (above).
Consider specifically the limiting case $|\varphi_1| \ll 1$. Expanding the "potential energy" with respect to φ and φ_1 and keeping only the lowest order terms we obtain the approximation to Eq. (6) in the form

$$\Lambda^2 \left(\frac{d\varphi}{dx}\right)^2 = \left(\varphi_1^2 - \varphi^2\right)^2 \,. \tag{21}$$

The solution of Eq. (21) is

$$\varphi(x) = -\varphi_1 \tanh\frac{\varphi_1 x}{\Lambda} \,. \tag{22}$$

Equations (22) coincides with that obtained by Katayama et al. [36]. So does Eq. (20b), being expanded in series with respect to φ_1 and truncated after the first two terms:

$$\overline{U}^2_k(\varphi_1) = 1 - \frac{\varphi_1^2}{6}. \tag{23}$$

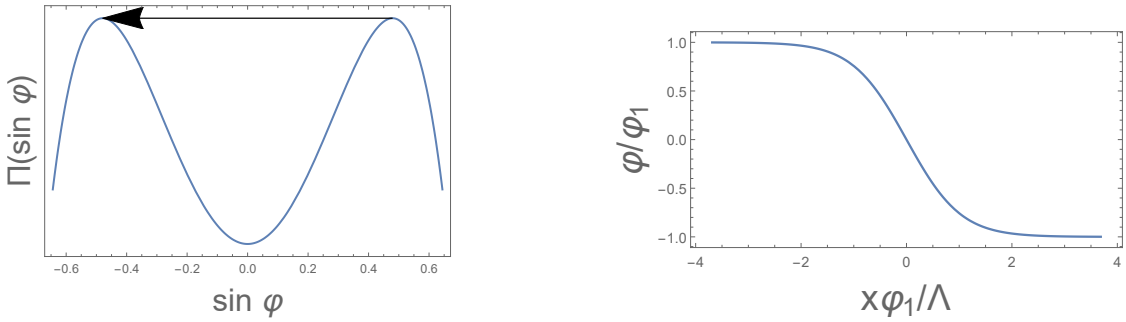

Figure 2: The "potential energy" (20c) (left) and the kink profile calculated with this energy according to Eq. (6) (right). We have chosen $\varphi_1 = .5$.

The solitons

For the soliton $\varphi_2 = \varphi_1$, and two equations of (12) become one equation. As an additional parameter we take the amplitude of the soliton (maximally different from φ_1 value of φ), which we will designate as φ_0. Adding to (12) the equation

$$E = \Pi(\sin\varphi_0) = \Pi(\sin\varphi_1) \tag{24}$$

and solving the obtained system we obtain

$$\overline{U}^2_{sol}(\varphi_1,\varphi_0) = \frac{(\sin\varphi_1 - \sin\varphi_0)^2}{2[\cos\varphi_0 - \cos\varphi_1 - (\varphi_1-\varphi_0)\sin\varphi_0]}\,, \tag{25a}$$

$$\Pi(\sin\varphi) - E = \frac{1}{2}(\sin\varphi_1 - \sin\varphi)^2 - \overline{U}^2_{sol}(\varphi_1,\varphi_0)\,[\cos\varphi - \cos\varphi_1 - (\varphi_1-\varphi)\sin\varphi]\ . \tag{25b}$$

Equation (25b) is graphically presented on Fig. 3 (left).

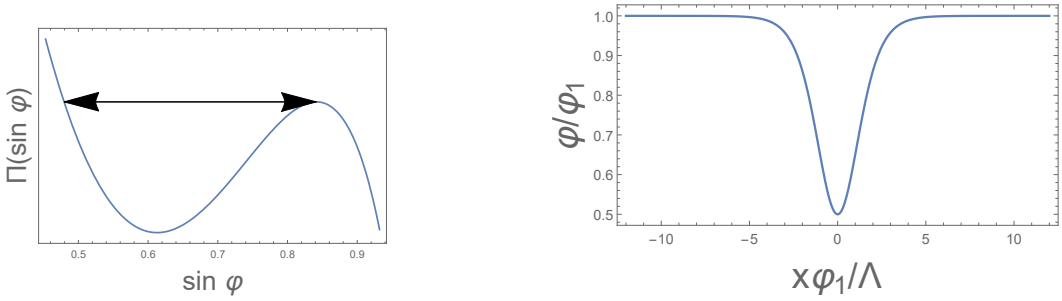

Figure 3: The "potential energy" (25b) (left) and the soliton profile according to Eq. (27) (right)

Considering the limiting case $|\varphi_1|, |\varphi_0| \ll 1$, expanding Eq. (25b) with respect to all the phases and keeping only the lowest order terms we obtain Eq. (6) in the form

$$\Lambda^2\left(\frac{d\varphi}{dx}\right)^2 = (\varphi-\varphi_1)^2(\varphi-\varphi_0)(\varphi+2\varphi_1+\varphi_0)\ . \tag{26}$$

Equation (26) can be integrated in elementary functions

$$\varphi = \varphi_1 - \frac{(4\overline{\varphi}+\Delta\varphi)\Delta\varphi}{4\overline{\varphi}\cosh^2\Phi + \Delta\varphi}\,, \tag{27}$$

where $\Delta\varphi \equiv \varphi_1 - \varphi_0$, $\overline{\varphi} \equiv (\varphi_1+\varphi_0)/2$, $\Phi \equiv \sqrt{(3\varphi_1+\varphi_0)\Delta\varphi}\ x/(2\Lambda)$. Equation (27) is graphically presented on Fig. 3 (right).
In an another limiting case of weak soliton ($\Delta\varphi\cot\varphi_1 \ll 1$), Eq. (6) takes the form

$$\Lambda^2\left(\frac{d\varphi}{dx}\right)^2 = 4\tan\varphi_1\cdot(\varphi-\varphi_1)^2(\varphi-\varphi_0)\ . \tag{28}$$

The solution of Eq. (28) is

$$\varphi = \varphi_1 - \Delta\varphi\,\mathrm{sech}^2\left(\sqrt{\Delta\varphi\tan\varphi_1}x/\Lambda\right)\ . \tag{29}$$

Velocity of the soliton in this approximation is

$$\overline{U}^2_{sol}(\varphi_1,\varphi_0) = \cos\varphi_1 - \frac{\sin\varphi_1}{2}\Delta\varphi. \tag{30}$$

The controlled quasi-continuum approximation

Let us return to Eq. (2). Looking at Eqs. (22) and (27) we realize that in the description of the kinks and solitons with $|\varphi_1| \ll 1$, the expansion parameter is φ_1^2; thus the quasi-continuum approximation (2) can be rigorously justified. However, strictly speaking, truncation of the expansion should be performed in accordance with the truncation of the series expansion of the sine function, and Eq. (4) in the consistent approximation should be written as

$$\overline{U}^2 \frac{d\varphi}{dx} = \frac{d\varphi}{dx} - \frac{1}{6}\frac{d\varphi^3}{dx} + \frac{\Lambda^2}{12}\frac{d^3\varphi}{dx^3} \,. \tag{31}$$

Equation (31) clearly shows the competition between the nonlinearity, described by the second term in the r.h.s. of the equation, and the intrinsic dispersion, caused by the discreteness of the line, described by the third term. Note that (22) is the exact solution of Eq. (31) (with $\overline{U}$ given by (23)).

Looking at Eq. (29) we realize alternatively, that the quasi-continuum approximation can be rigorously justified when it is applied to the description of the solitons with $\tan\varphi_1 \cdot (\varphi_1 - \varphi_0) \ll 1$. The latter quantity is the expansion parameter in the r.h.s. of Eq. (2) in this case. So in the consistent approximation, Eq. (2) should be written as

$$\overline{U}^2 \frac{d\psi}{dx} = \cos\varphi_1 \frac{d\psi}{dx} - \frac{\sin\varphi_1}{2}\frac{d\psi^2}{dx} + \cos\varphi_1 \frac{\Lambda^2}{12}\frac{d^3\psi}{dx^3} \,, \tag{32}$$

where $\psi = \varphi - \varphi_1$. Note that Eq. (29) is the exact solution of Eq. (32) (with $\overline{U}$ given by (30)).

Here we would like to attract the attention of the reader to the following issue. Common wisdom says that the continuum approximation and the small amplitude approximation are independent - there could be a wave with small amplitude, which allows to expand the sine function, but which varies fast in space (wavelength comparable to lattice spacing), so the continuum limit is not justified. And there could be the opposite situation (large amplitude, long wavelength), in which the sine needs to be retained but the continuum limit is allowed.

However, for the kinks and the solitons these approximations are not independent. Parametrically, the length scale of the waves is of the order of the lattice spacing Λ, so, naively, the continuum (or even the quasi-continuum) limit is not justified. What we have shown above, is that for the waves with small amplitude $|\varphi_1|$ $(\tan\varphi_1(\varphi_1 - \varphi_0))$, the length scale is $\Lambda/|\varphi_1|$ $(\Lambda/(\tan\varphi_1(\varphi_1 - \varphi_0)))$, thus justifying the quasi-continuum approximation.

The shocks

Consider JTL with the capacitor and resistor shunting the JJ and another resistor in series with the ground capacitor, shown on Fig. 1 (right). As the result, Eq. (1) changes to

$$\frac{\hbar}{2e}\frac{d\varphi_n}{dt} = \left(\frac{1}{C} + R\frac{\partial}{\partial t}\right)(q_{n+1} - 2q_n + q_{n-1}) \,, \tag{33a}$$

$$\frac{dq_n}{dt} = I_c \sin\varphi_n + \frac{\hbar}{2eR_J}\frac{d\varphi_n}{dt} + C_J\frac{\hbar}{2e}\frac{d^2\varphi_n}{dt^2} \,, \tag{33b}$$

where R is the ohmic resistor in series with the ground capacitor, and C_J and R_J are the capacitor and the ohmic resistor shunting the JJ.

Considering again the running wave solutions we obtain the generalization of Eq. (5)

$$\frac{\Lambda^2}{12}\frac{d^2\sin\varphi}{dx^2} + \left(\frac{C_J}{C} + \frac{R}{R_J}\right)\overline{U}^2\Lambda^2\frac{d^2\varphi}{dx^2} + \left(\frac{R}{Z_J}\cos\varphi + \frac{Z_J}{R_J}\right)\overline{U}\Lambda\frac{d\varphi}{dx} = -\sin\varphi + \overline{U}^2\varphi + F \,, \tag{34}$$

where $Z_J \equiv \sqrt{L_J/C}$ is the characteristic impedance of the JTL, and we discarded the terms with the derivatives higher than of the forth order.

We impose the boundary conditions (8) and try to understand what part of the analysis of Section can be transferred to the present case. The results (12) are determined only by the r.h.s. of Eq. (5), so are (4), following from (12). Since the r.h.s. of Eqs. (5) and (34) are identical, these equations are valid in the present case also. In particular, we obtain

$$\overline{U}^2 = \overline{U}^2_{\rm sh}(\varphi_1, \varphi_2) \,, \tag{35}$$

which explains the subscript we introduced in Eq. (13a).

On the other hand, the resistors, by introducing the effective "friction force", break the "energy" conservation law, which means that the stationary kinks and the solitons we considered previously are no longer possible, however weak the dissipation is. However in the lossy JTL the solutions with $|\varphi_2| \neq |\varphi_1|$ (the shocks) are possible.

The continuum approximation

Looking at Eq. (34) we understand, that when C_J and/or R are large enough, and/or R_j is small enough the first term in the l.h.s. of (34) (the second term in (2)) can be discarded, hence the continuum approximation is valid, and (34) acquires Newtonian form [45]

$$\left(\frac{C_J}{C}+\frac{R}{R_J}\right)\frac{d^2\varphi}{d\tau^2}+\left(\frac{R}{Z_J}\cos\varphi+\frac{Z_J}{R_J}\right)\frac{d\varphi}{d\tau}=-\sin\varphi+\overline{U}^2\varphi+F\,, \tag{36}$$

where we have introduced the dimensionless time $\tau = x/(\overline{U}\Lambda)$. In distinction from case of the kinks and the solitons, now the fictitious particle trajectory connects the "potential energy" maximum with the "potential energy" minimum,
The shocks in the framework of the continuum approximation were studied in our previous publication [45]. In particular, in the simple case when $C_J = 0$, $R = 0$ (when (36) is similar to equation describing the motion of a fluxon in biased long JJ [42]) and for weak shock ($\Delta\varphi \cdot \cot\varphi_1 \ll 1$), where $\Delta\varphi \equiv (\varphi_1 - \varphi_2)/2$, Eq. (36) takes the form

$$\frac{Z_J}{R_J}\frac{d\psi}{d\tau}=\sin\overline{\varphi}\left(\psi^2-\Delta^2\varphi\right)\,, \tag{37}$$

where $\overline{\varphi} \equiv (\varphi_1 + \varphi_0)/2$ and $\psi \equiv \varphi - \overline{\varphi}$. The solution of (37) is

$$\psi=-\Delta\varphi\tanh\left(\frac{R_J}{Z_J}\Delta\varphi\sin\overline{\varphi}\cdot\tau\right)\,. \tag{38}$$

The qualitative analysis

For qualitative analysis of Eq. (34) in the general case, it is better to present it as a system of two first order differential equations

$$\left[\frac{\cos\varphi}{12}+\left(\frac{C_J}{C}+\frac{R}{R_J}\right)\overline{U}^2\right]\Lambda\frac{d\chi}{dx}=\frac{\sin\varphi}{12}\chi^2-\left(\frac{R}{Z_J}\cos\varphi+\frac{Z_J}{R_J}\right)\overline{U}\chi-\sin\varphi+\overline{U}^2\varphi+F\,, \tag{39a}$$

$$\Lambda\frac{d\varphi}{dx}=\chi\,. \tag{39b}$$

Now, one important feature of shocks can be understood immediately. We are talking about the direction of shock propagation. Linearising Eq. (39) in the vicinity of the fixed points $(\chi, \varphi) = (0, \varphi_1)$ and $(\chi, \varphi) = (0, \varphi_2)$ we obtain

$$\Lambda\begin{pmatrix} d\chi/dx \\ d\varphi/dx\end{pmatrix}=\begin{pmatrix} M_i & K_i \\ 1 & 0\end{pmatrix}\begin{pmatrix} \varphi-\varphi_i \\ \chi\end{pmatrix}\,,\quad i=1,2 \tag{40}$$

where

$$K_i=\frac{\overline{U}^2-\cos\varphi_i}{\cos\varphi_i/12+\left(C_J/C+R/R_J\right)\overline{U}^2}\,, \tag{41}$$

and here we are not interested in M_i. From the fact that φ_1 is the unstable fixed point, and φ_2 is the stable fixed point we obtain

$$\cos\varphi_2>\overline{U}^2_{\text{sh}}(\varphi_1,\varphi_2)>\cos\varphi_1\,. \tag{42}$$

The inequalities (42) allow only one direction of shock propagation - from larger $\cos\varphi$ to smaller $\cos\varphi$. Taking into account (9), we can present (42) as

$$\overline{u}^2(\varphi_2)>\overline{U}^2_{\text{sh}}(\varphi_1,\varphi_2)>\overline{u}^2(\varphi_1)\,, \tag{43}$$

thus establishing the connection with the well known in the nonlinear waves theory fact: the shock velocity is lower than the sound velocity in the region behind the shock, but higher than the sound velocity in the region before the shock [1].
Let us write down inequalities (42) explicitly

$$\cos\varphi_2>\frac{\sin\varphi_1-\sin\varphi_2}{\varphi_1-\varphi_2}>\cos\varphi_1\,. \tag{44}$$

We will combine the case we studied up to now, when φ_1 was the phase before the shock and φ_2 - behind the shock, with the opposite case, which corresponds to indices 1 and 2 in (44) being interchanged. The points in the phase space of the shock boundary conditions (φ_1, φ_2), for which neither (44), nor its interchanged version are satisfied, has very simple geometric property. The point (φ_1, φ_2) belongs to that region, if the secant of the curve $\sin\varphi$ between the points φ_1 and φ_2 crosses the curve, like it is shown on Fig. 4 (below). Because $\sin\varphi$ is concave downward for $0 < \varphi < \pi/2$, and concave upward for $-\pi/2 < \varphi < 0$, it never happens if φ_1, φ_2 have the same sign. Hence the shock can exist between

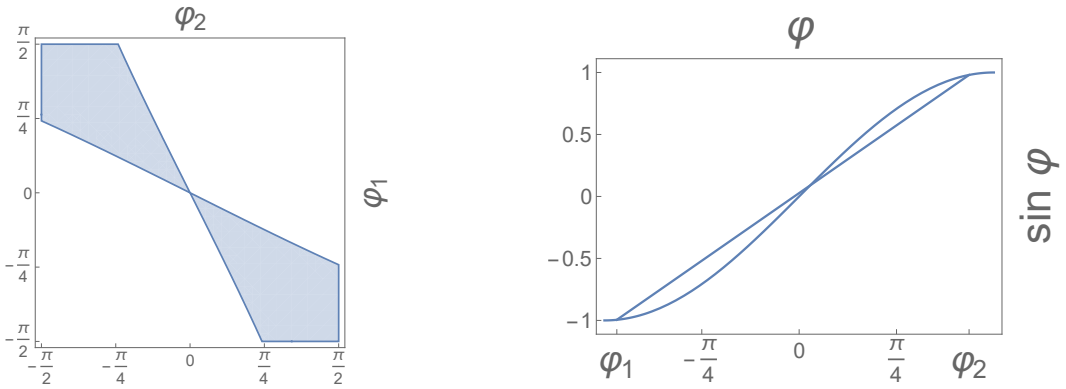

Figure 4: The phase space of the boundary conditions on the ends of the JTL φ_1 and φ_2. The region, which corresponds to the forbidden shock boundary conditions, is shaded (left). The geometric property of the points belonging to the shaded region (right).

any such points. It is not so for φ_1 and φ_2 having opposite signs. We present the phase space of shock boundary conditions on Fig. 4 (above). The forbidden region is shaded.

When the asymptotic phases on the two sides of the JTL belong to the shaded region, probably there exists some intermediate φ_{in} in between, such that the shocks between φ_1 and φ_{in}, and between φ_2 and φ_{in} are allowed. Say, when the phases are φ_1 and $-\varphi_1$, the system can chose the intermediate value $\varphi_{in} = 0$. In this hypothetical case, the shocks move in the opposite directions, and the central part with the phase $\varphi_{in} = 0$ expands with the velocity $2U_{\rm sh}(\varphi_1, 0)$. However, the case of multiple shocks being simultaneously present in the system demands further studies.

The numerical integration

Equation (34) can be easily integrated numerically. For aesthetical reasons let us simplify it by putting $R = 0$ and $C_J = 0$. (Actually, the physical meaning and the relevance of the resistor in series with the ground capacitor is not obvious. We included it because we were able to do it for free. The capacitance of the JJ is certainly physically relevant. Anyhow, when $C_J/C \ll 1$, it can be ignored.) After the simplification and substitution of the results for $\overline{U}$ and F from (4), the equation becomes

$$\frac{\cos\varphi}{12}\Lambda^2\frac{d^2\varphi}{dx^2} = \frac{\sin\varphi}{12}\left(\frac{d\varphi}{dx}\right)^2 - \frac{Z_J}{R_J}\overline{U}\Lambda\frac{d\varphi}{dx} - \frac{(\sin\varphi-\varphi_2)(\varphi_1-\varphi)-(\sin\varphi_1-\sin\varphi)(\varphi-\varphi_2)}{\varphi_1-\varphi_2}\,.$$

The result of the numerical integration are shown on Fig. 5 (compare with Figs. 2 (below) and **??**).

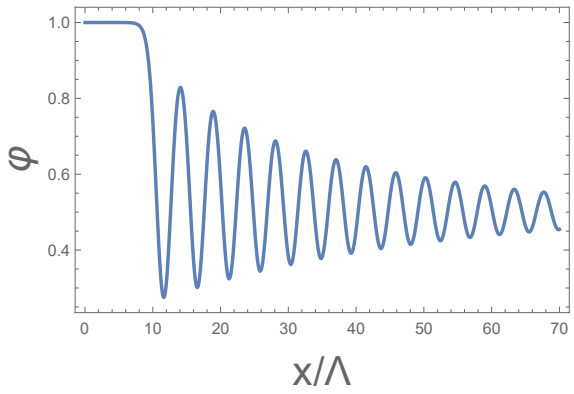

Figure 5: The shock profile according to Eq. (45). We have chosen $\varphi_1 = 1$, $\varphi_2 = .5$, $Z_J/R_J = .005$.

Dissipation is always present in real experiments. And yet we can observe solitary waves (though they are nonstationary, but practically identical to the corresponding stationary solitons at any given moment of time) in case if dissipation is weak enough. Looking at Fig. 5 we realize that weak dissipation does not completely kill solitary waves, it just makes them nonstationary/attenuating. Such solitary waves are observed in numerical calculations and in experiments, as was the case with granular chains [41, 43]. On the other hand, there is a critical rate of dissipation which transforms oscillating stationary shock waves into monotonous [47].

Discussion

Recently, quantum mechanical description of JTL in general and parametric amplification in such lines in particular started to be developed, based on quantisation techniques in terms of discrete mode operators [48], continuous mode

operators [49], a Hamiltonian approach in the Heisenberg and interaction pictures [50], the quantum Langevin method [51], or on partitions a quantum device into compact lumped or quasi-distributed cells [52]. It would be interesting to understand in what way the results of the present paper are changed by quantum mechanics. Particularly interesting looks studying of quantum ripples over a semi-classical shock [53] and fate of quantum shock waves at late times [54]. Closely connected problem of classical and quantum dispersion-free coherent propagation in waveguides and optical fibers was studied recently in Ref. [55].
Finally, we would like to express our hope that the results obtained in the paper are applicable to kinetic inductance based traveling wave parametric amplifiers based on a coplanar waveguide architecture. Onset of shock-waves in such amplifiers is an undesirable phenomenon. Therefore, shock waves in various JTL should be further studied, which was one of motivations of the present work.

Conclusions

We analytically studied the running waves propagation in the discrete Josephson transmission lines (JTL), constructed from Josephson junctions (JJ) and capacitors. Due to the competition between the intrinsic dispersion in the discrete JTL and the nonlinearity, in the dissipationless JTL there exist running waves in the form of supersonic kinks and solitons. The velocities and the profiles of the kinks and the solitons were found. We also studied the effect of dissipation in the system and find that in the presence of the resistors, shunting the JJ and/or in series with the ground capacitors, the only possible stationary running waves are the shock waves, whose velocities and the profiles were also found. We have proposed the integral approximation, which is alternative to the quasi-continuum approximation.

Acknowledgments

The main idea of the present work was born in the discussions with M. Goldstein. We are also grateful to J. Cuevas-Maraver, A. Dikande, M. Inc, P. Kevrikidis, B. A. Malomed, V. Nesterenko, T. H. A. van der Reep, and B. Ya. Shapiro for their comments (some of which were crucial for the completion of the project).

References

[1] G. B. Whitham, *Linear and Nonlinear Waves*, John Wiley & Sons Inc., New York (1999).
[2] D. M. French and B. W. Hoff, IEEE Trans. Plasma Sci. **42**, 3387 (2014).
[3] B. Nouri, M. S. Nakhla, and R. Achar, IEEE Trans. Microw. Theory Techn. **65**, 673 (2017).
[4] L. P. S. Neto, J. O. Rossi, J. J. Barroso, and E. Schamiloglu, IEEE Trans. Plasma Sci. **46**, 3648 (2018).
[5] M. S. Nikoo, S. M.-A. Hashemi, and F. Farzaneh, IEEE Trans. Microw. Theory Techn. **66**, 3234 (2018); **66**, 4757 (2018).
[6] L. C. Silva, J. O. Rossi, E. G. L. Rangel, L. R. Raimundi, and E. Schamiloglu, Int. J. Adv. Eng. Res. Sci. **5**, 121 (2018).
[7] Y. Wang, L.-J. Lang, C. H. Lee, B. Zhang, and Y. D. Chong, Nat. Comm. **10**, 1102 (2019).
[8] E. G. L. Range, J. O. Rossi, J. J. Barroso, F. S. Yamasaki, and E. Schamiloglu, IEEE Trans. Plasma Sci. **47**, 1000 (2019).
[9] A. S. Kyuregyan, Semiconductors **53**, 511 (2019).
[10] N. A. Akem, A. M. Dikande, and B. Z. Essimbi, SN Applied Science **2**, 21 (2020).
[11] A. J. Fairbanks, A. M. Darr, A. L. Garner, IEEE Access **8**, 148606 (2020).
[12] R. Landauer, IBM J. Res. Develop. **4**, 391 (1960).
[13] S. T. Peng and R. Landauer, IBM J. Res. Develop. **17**(1973).
[14] M. I. Rabinovich and D. I. Trubetskov, *Oscillations and Waves*, Kluwer Academic Publishers, Dordrecht / Boston / London (1989).
[15] B. D. Josephson, Phys. Rev. Lett. **1**, 251 (1962).
[16] A. Barone and G. Paterno, *Physics and Applications of the Josephson Effect*, John Wiley & Sons, Inc, New York (1982).
[17] N. F. Pedersen, Solitons in Josephson Transmission lines, in *Solitons*, North-Holland Physics Publishing, Amsterda (1986).
[18] C. Giovanella and M. Tinkham, *Macroscopic Quantum Phenomena and Coherence in Superconducting Networks*, World Scientific, Frascati (1995).
[19] A. M. Kadin, *Introduction to Superconducting Circuits*, Wiley and Sons, New York (1999).
[20] M. Remoissenet, *Waves Called Solitons: Concepts and Experiments*, Springer-Verlag Berlin Heidelberg GmbH (1996).
[21] O. Yaakobi, L. Friedland, C. Macklin, and I. Siddiqi, Phys. Rev. B **87**, 144301 (2013).
[22] K. O'Brien, C. Macklin, I. Siddiqi, and X. Zhang, Phys. Rev. Lett. **113**, 157001 (2014).
[23] C. Macklin, K. O'Brien, D. Hover, M. E. Schwartz, V. Bolkhovsky, X. Zhang, W. D. Oliver, and I. Siddiqi, Science **350**, 307 (2015).
[24] B. A. Kochetov, and A. Fedorov, Phys. Rev. B. **92**, 224304 (2015).
[25] A. B. Zorin, Phys. Rev. Applied **6**, 034006 (2016); Phys. Rev. Applied **12**, 044051 (2019).
[26] D. M. Basko, F. Pfeiffer, P. Adamus, M. Holzmann, and F. W. J. Hekking, Phys. Rev. B **101**, 024518 (2020).
[27] T. Dixon, J. W. Dunstan, G. B. Long, J. M. Williams, Ph. J. Meeson, C. D. Shelly, Phys. Rev. Applied **14**, 034058 (2020)
[28] A. Burshtein, R. Kuzmin, V. E. Manucharyan, and M. Goldstein, Phys. Rev. Lett. **126**, 137701 (2021).
[29] T. C. White et al., Appl. Phys. Lett. **106**, 242601 (2015).
[30] A. Miano and O. A. Mukhanov, IEEE Trans. Appl. Supercond. **29**, 1501706 (2019).
[31] Ch. Liu, Tzu-Chiao Chien, M. Hatridge, D. Pekker, Phys. Rev. A **101**, 042323 (2020).
[32] P. Rosenau, Phys. Lett. A **118**, 222 (1986); Phys. Scripta **34**, 827 (1986).
[33] G. J. Chen and M. R. Beasley, IEEE Trans. Appl. Supercond. **1**, 140 (1991).

[34] H. R. Mohebbi and A. H. Majedi, IEEE Trans. Appl. Supercond. **19**, 891 (2009); IEEE Transactions on Microwave Theory and Techniques **57**, 1865 (2009).

[35] A. Houwe, S. Abbagari, M. Inc, G. Betchewe, S. Y. Doka, K. T. Crepin, and K. S. Nisar, Results in Physics **18**, 103188 (2020).

[36] H. Katayama, N. Hatakenaka, and T. Fujii, Phys. Rev. D **102**, 086018 (2020).

[37] D. L. Sekulic, N. M. Samardzic, Z. Mihajlovic, and M. V. Sataric, Electronics **10**, 2278 (2021).

[38] P. G. Kevrekidis, I. G. Kevrekidis, A. R. Bishop, and E. Titi, Phys. Rev. E, **65**, 046613 (2002).

[39] L. Q. English, F. Palmero, A. J. Sievers, P. G. Kevrekidis, and D. H. Barnak, Phys. Rev. E, **81**, 046605 (2010).

[40] P. G. Kevrikidis, IMA Journal of Applied Mathematics **76**, 389 (2011)

[41] V. Nesterenko, *Dynamics of heterogeneous materials*, Springer Science & Business Media (2013).

[42] B. A. Malomed, *The sine-gordon model: General background, physical motivations, inverse scattering, and solitons*, The Sine-Gordon Model and Its Applications. Springer, Cham, 1-30 (2014).

[43] V. F. Nesterenko, Phil. Trans. R. Soc. A **376**, 20170130 (2018).

[44] B. A. Malomed, *Nonlinearity and discreteness: Solitons in lattices*, Emerging Frontiers in Nonlinear Science. Springer, Cham, 81 (2020).

[45] E. Kogan, Journal of Applied Physics **130**, 013903 (2021).

[46] S. Homma, Prog. Theor. Phys. **76**, 1(1986).

[47] E. B. Herbold and V. F. Nesterenko, Phys. Rev E, **75**, 021304, (2007).

[48] T. H. A. van der Reep, Phys. Rev. A **99**, 063838 (2019).

[49] L Fasolo, A Greco, E Enrico, in *Advances in Condensed-Matter and Materials Physics: Rudimentary Research to Topical Technology*, (ed. J. Thirumalan and S. I. Pokutny), Sceence (2019).

[50] A. Greco, L. Fasolo, A. Meda, L. Callegaro, and E. Enrico, Phys. Rev. B 104, 184517 (2021).

[51] Y. Yuan, M. Haider, J. A. Russer, P. Russer and C. Jirauschek, 2020 XXXIIIrd General Assembly and Scientific Symposium of the International Union of Radio Science, Rome, Italy (2020).

[52] Z. K. Minev, Th. G. McConkey, M. Takita, A. D. Corcoles, and J. M. Gambetta, arXiv:2103.10344 (2021).

[53] E. Bettelheim and L. I. Glazman, Phys. Rev. Lett. **109**, 260602 (2012).

[54] Th. Veness and L. I. Glazman, Phys. Rev. B **100**, 235125 (2019).

[55] A. Mandilara, C. Valagiannopoulos, and V. M. Akulin, Phys. Rev. A **99**, 023849 (2019).

[56] F. G. Tricomi, *Integral equations*, (Mineola, NY: DoverPublications, 1982).

Tunable interface states in locally resonant acoustic chains with inerters

Milan Cajić*,†, Danilo Karličić†, Stepa Paunović† and Sondipon Adhikari ††
*Faculty of Science and Engineering, Swansea University, Swansea, United Kingdom
†Mathematical Institute of the Serbian Academy of Sciences and Arts, Belgrade, Serbia
††James Watt School of Engineering,University of Glasgow, Glasgow, UK

Summary. In this work, we study locally resonant acoustic chains with inerters. Topological properties are investigated on the example of one-dimensional chain with diatomic mass-in-mass unit cells based on the band structure and eigenstate analysis. The existence of interface modes in finite chains is confirmed through natural frequencies and frequency response function analysis. Tuning of interface modes due to introduced inertia amplification effect is observed and investigated in details.

Introduction

The interest for investigation of topologically protected interface states in acoustic and mechanical metamaterials has significantly grown over the past years. Inspired by the phenomena from solid states physics such as the valley and quantum Hall effects, researchers discovered a number of equivalent phenomena in mechanical systems based on acoustic and elastic wave propagation analysis [1]. Since the beginning there was a need to control wave propagation properties in such periodic systems based on approaches that can be divided into two main groups. The first group encompasses active approaches where different external fields such as magnetic or electric field are employed for wave propagation control purposes [2]. The second group encompasses passive or semi-passive strategies that are often based on application of external passive damping devices [3]. Since their discovery, inerters have been widely accepted as efficient vibration attenuation devices [4]. Based on the inertia amplification effect, they are able to reduce the frequency and change properties of periodic structures and other mechanical systems [5]. Here, we apply ideal inerter elements to change the band structure of the locally resonant acoustic chain and at the same time keep the topological properties of the original lattice without inerters.

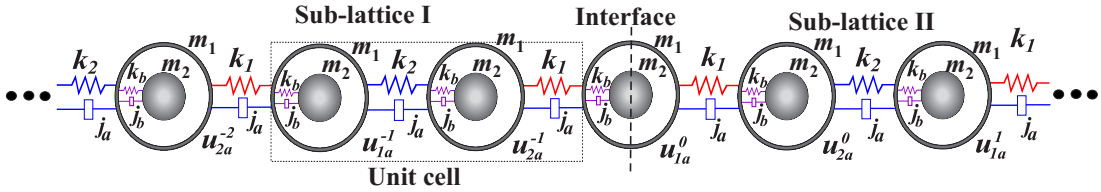

Figure 1: Illustration of one-dimensional locally resonant acoustic chain with interface.

Mathematical model

Let us consider a one-dimensional locally resonant acoustic chain with an interface, for which the equation for the unit cell in the general case can be expressed as

$$\begin{aligned} m_a\ddot{u}^p_{(\zeta)a} + (k_\zeta + k_{\zeta+1})\,u^p_{(\zeta)a} - k_\zeta u^p_{(\zeta-1)a} - k_{\zeta+1}u^p_{(\zeta+1)a} + k_b\left(u^p_{(\zeta)a} - u^p_{(\zeta)b}\right) + \\ j_a\left(2\ddot{u}^p_{(\zeta)a} - \ddot{u}^p_{(\zeta-1)a} - \ddot{u}^p_{(\zeta+1)a}\right) + j_b\left(\ddot{u}^p_{(\zeta)a} - \ddot{u}^p_{(\zeta)b}\right) = 0, \end{aligned} \tag{1}$$

and

$$m_b\ddot{u}^p_{(\zeta)b} + k_b\left(u^p_{(\zeta)b} - u^p_{(\zeta)a}\right) + j_b\left(\ddot{u}^p_{(\zeta)b} - \ddot{u}^p_{(\zeta)a}\right) = 0, \tag{2}$$

where $\zeta = 2, 3, ..., \mathcal{N}-1$, $u_{(\varepsilon)a}$ and $u_{(\varepsilon)b}$, $\varepsilon = 1, 2, ..., \mathcal{N}$ are displacements of outer m_a and inner m_b masses, respectively k_ε, k_b are the springs stiffnesses, while j_a, j_b are the inerter parameters connecting outer and inner masses, respectively. It should be noted that for the adopted notation, the repeating unit cell of the last outer mass is connected to the next unit cell through the spring $k_{\mathcal{N}+1} = k_1$, where equations for the first and the last mass-in-mass sub-systems can be written accordingly. We note that the values of outer and inner masses, inerter parameters and stiffness of inner mass springs are assumed to be the same for different mass-in-mass sub-systems. Size of a unit cell depends on the number of different springs and mass-in-mass sub-units. The system of equations for the one-dimensional finite chain constructed from two sub-lattices connected at interface can be obtained by following the notations given in (Fig.1).

Results and discussion

Topological properties of locally resonant acoustic lattice can be examined through dispersion and eigenstate analysis of a representative unit cell based on the topological invariant called the winding number (here denoted as w) or by using

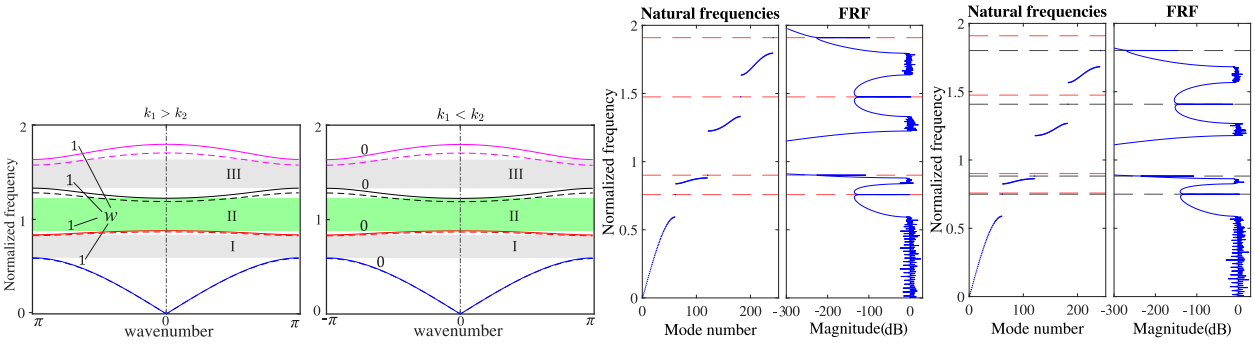

(a) Band structure of a diatomic unit cell (b) Finite chain $k_1 > k_2$ (c) Finite chain inerters $k_1 > k_2$

Figure 2: Band structure, natural frequencies and frequency response function of the one-dimensional locally resonant acoustic chain with diatomic mass-in-mass unit cells.

the the bulk-edge correspondence. Dispersion curves for the representative unit cell can be obtained as a solution of the eigenvalue problem based on Eqs.1 and 2 by considering the stiffnesses $k_1 = k(1+\gamma)$ and $k_2 = k(1-\gamma)$, with k denoting the mean stiffness and γ is the dimensionless parameter. Natural frequencies and frequency response function of the finite chain can be obtained from the corresponding system of equations by considering the $N = 30$ unit cell on each side of the interface. Fig. 2a shows dispersion curves of a diatomic unit cell with (dashed lines) and without (full lines) inerters when $\gamma = 0.5$, $m_2/m_1 = 0.5$, $m_2/m_1 = 0.5$, $k = 10 \times 10^3$[N/m], $k_b = 8 \times 10^3$[N/m] and $j_a = j_b = 0.02$. Four bands and three band gaps can be noticed, where II band gap highlighted in green is of locally resonant origin. By comparing the lattices when $k_1 > k_2$ and $k_1 < k_2$ does not change the band structure but it changes the topology of eigenvectors i.e. the winding number of individual bands change its value from $w = 1$ to $w = 0$. This change physically means that interface modes can appear between the two lattice types. For the finite chain, we can confirm the existence of interface modes within the band gaps by observing its natural frequencies and frequency response function (Figs. 2b and 2c). In the diagram showing the natural frequencies, normalized with respect to the frequency of the local resonator, one can observe four interface modes. The presence of these modes is confirmed in the frequency response function diagram of the outer interface mass. Interface modes that appear inside the band gap II and above the last band are trivial since they will disappear if we change lattice configuration to low stiffness springs ($k_1 < k_2$) at the interface (see Fig. 1). The other two interface modes will remain in both configurations and they are robust and topologically protected. In this case, the effect of inertia amplification on interface states can be seen by comparing the interface mode frequencies of chains with (black dashed lines) and without (red dashed lines) inerters in Fig. 2b. The results reveal the shift of interface mode frequencies to lower values. This effect is especially pronounced at higher frequencies while shifting at lower frequency band gaps is smaller. The similar analysis can be performed for one-dimensional lattices with triatomic mass-in-mass unit cells with and without inerters, where quantized topological invariant winding number can be recovered only in the case when one of the springs connecting the outer masses is different from others.

Conclusions

Recent advances in discovering exotic metamaterials have provided a new insight for understanding the essential processes that create unique wave propagation phenomena and they have initiated a wide range of possible applications in industry and other fields of science. This study is a step forward towards a better understanding of the role of inerters in passive control and tuning of interface modes in locally resonant acoustic chains. Parametric study has demonstrated a significant shifting of interface states when inertia amplification effect is introduced while the topological properties of bands were preserved. This opens new possibilities for application of inerters in more complex lattices or periodic structures capable of generating interface modes.

Acknowledgment

MC and SA acknowledge funding from European Union's Horizon 2020 research and innovation programme under the Marie Skłodowska-Curie grant agreement No. 896942 (METASINK). DK and SP acknowledges the support by the Serbian Ministry of Education, Science and Technological Development through Mathematical Institute of the Serbian Academy of Sciences and Arts.

References

[1] Xin, L., Siyuan, Y., Harry, L., Minghui, L., Yanfeng, C. (2020) Topological mechanical metamaterials: A brief review. *Curr. Opin. Solid State Mater. Sci.* **24**: 100853.

[2] Montgomery, S. M., Wu, S., Kuang, X., Armstrong, C. D., Zemelka, C., Ze, Q., ..., Qi, H. J. (2020) Magneto-mechanical metamaterials with widely tunable mechanical properties and acoustic bandgaps. *Adv. Funct. Mater.* **31**: 2005319.

[3] Lv, X. F., Chuang, K. C., Erturk, A. (2020) Tunable elastic metamaterials using rotatable coupled dual-beam resonators. *J. App. Phys.* **126**: 035107.

[4] Smith M. C. (2020) The inerter: a retrospective. *Annu. Rev. Control Robot. Auton. Syst.* **3**: 361–391.

[5] Cajić, M., Christensen, J., Adhikari, S. (2021) Tuning of topological interface modes in an elastic beam array system with inerters. *Int. J. Mech. Sci.* **205**: 106573.

Nonlinear Wave Disintegration in Phononic Material with Weakly Compressed Rough Contacts

Ganesh U. Patil* and Kathryn H. Matlack *
*Department of Mechanical Science and Engineering, University of Illinois at Urbana-Champaign, Urbana, Illinois, USA

Summary. Phononic media with contact nonlinearity enable unique wave responses, which brings new capabilities in controlling the propagation of mechanical energy both passively and actively. Our previous studies of phononic media with periodic “rough" contacts have demonstrated different wave responses under *zero* or *strong* precompression, however, wave dynamics of these system under *weak* precompression is yet to be understood. Such understanding can help improve the dynamic response of these materials for wave propagation control. Here, we numerically study nonlinear wave propagation through phononic material with rough contacts such that the contacts are weakly compressed and exhibit a strong nonlinear response at high amplitude excitations. Different from uncompressed and strongly compressed media, this system disintegrates the excited waves into constant amplitude compression pulses followed by an oscillatory tail of decaying amplitudes. These two wave profiles are linked through a transition zone in the form of a rarefaction front. Such wave response is attributed to the mechanics of weakly-compressed contact that transmits tension-compression forces at low amplitudes but only compression forces at high amplitudes. We also demonstrate the tunability of the amplitude, speed, and energy of compression pulses via external precompression. Further, owing to the band gap characteristics of the underlying linear phononic media, these materials display spectral filtering of the harmonic waves. Overall, the capability of these materials to transfer information or energy via compression pulses, amplitude-dependent material response, energy transfer from the excitation frequency to other frequency-wavenumber regimes, and tunability through precompression could pave the way for the development of mechanical devices for advanced wave control.

Introduction

Phononic materials are periodic media that allow spatial and temporal control over mechanical waves. Specifically, Bragg scattering [1] and local resonance [2] phenomenon in these materials have enabled band gaps, which are frequencies of strong wave attenuation. These materials also exhibit unprecedented characteristics such as mode conversion [3], Anomalous polarization [3, 4] and wave directionality [5] by virtue of their unit cell geometry. While these studies are within the linear regime, incorporating nonlinearity further enhances dynamic properties in the form of amplitude-dependent response, irreversibility, and frequency conversion (see the review of [6]). All of these exotic properties make nonlinear phononic materials potential candidates for designing engineering materials and devices with advanced functionalities.

A route to achieve nonlinearity within phononic media is via contact interfaces. Phononic media with contact nonlinearity demonstrate excellent flexibility as they can be tuned from linear to a strongly nonlinear regime, through externally applied precompression. When uncompressed, these phononic materials does not support propagation of linear waves, essentially behaving as “sonic vacuum" [7]. On the other hand, high amplitude wave excitations can enable strongly nonlinear wave signatures. This has been demonstrated in granular crystals, which are ordered ensembles of particles (or grains) exhibiting *Hertzian* contact nonlinearity [8] and in continuum phononic materials with *rough* contacts [9]. While the type of contact nonlinearity and modeling of contacting bodies as discrete or continuum reveals interesting differences, the contact-based phononic media, in general, have shown excellent promise in enriching the wave dynamics.

Importantly, the combined effects of periodicity and nonlinearity in contact-based phononic media support different forms of nonlinear waves. For example, uncompressed (strongly nonlinear) granular crystals support the propagation of solitary waves, which are localized traveling waves with a hump-type wave profile propagating with constant speed and amplitude [7, 10]. Depending upon the mass of the striker, the system can support trains of solitary waves as well [11]. On the other hand, strongly compressed (weakly nonlinear) granular crystals support the propagation of harmonic (of oscillatory nature) waves. As a result, the system exhibits amplitude-dependent band diagrams with propagating and attenuation frequency zones [12]. Within a weakly nonlinear regime, granular crystals support energy transfer between frequencies due to harmonic generation [12]. The system can even support discrete breathers [13], which are spatially localized and temporally periodic modes, at band gap frequencies. Damped granular crystals support shock waves that gradually decay in time [14]. Beyond the elastic regime, asymmetric nonlinearity of elastic-plastic Hertzian contacts support the propagation of “signoton", which is a shock wave causing an instantaneous change in the deformation direction [15]. Our recent studies on continuum phononic media with rough contacts reported the emergence of stegotons (a different form of solitary waves with stepwise spatial profile) and acoustic resonances, when uncompressed (i.e. strongly nonlinear interfaces) [9], and frequency conversion from wave self-interactions when strongly compressed (i.e. weakly nonlinear interfaces) [16]. These recent studies further suggest the role of contact nonlinearity in phononic media in enabling unique wave responses with no analog in linear theory.

Despite these studies, nonlinear wave propagation through phononic media with *weakly-compressed rough contacts* is yet to be understood. There are open questions such as (1) how the reported nonlinear responses of these phononic media (acoustic resonances, stegotons and harmonic generation) change when non-zero precompression and high amplitude excitation is involved and (2) whether both strongly and weakly nonlinear wave responses co-exist together. Further, weak precompression may in fact support additional nonlinear responses not possible with uncompressed or strongly

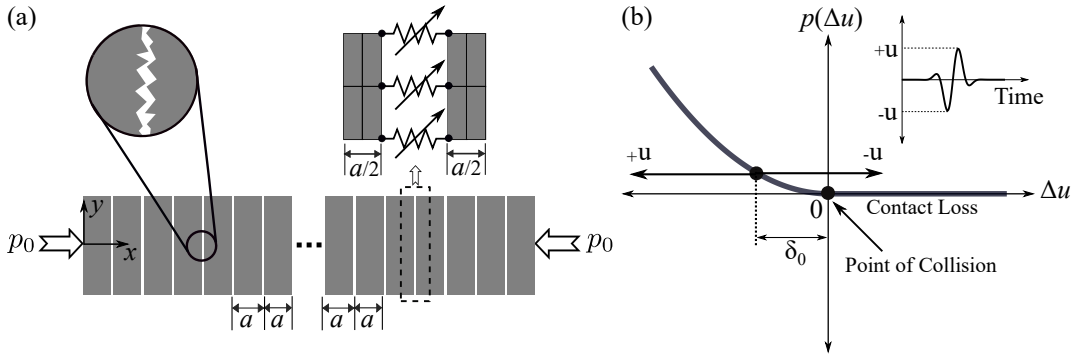

Figure 1: (a) Compressed phononic material with periodic contacts having rough features at the microscale. Schematic of dashed rectangle shows contact modeling as nonlinear springs between elastic layers. (b) Nonlinear contact pressure-gap relationship at rough contacts. The contacts exhibit strongly nonlinear responses as wave displacements, u, are larger than static predeformation, δ_0. Inset is a temporal schematic of the excited wave pulse.

compressed media.

In this paper, we numerically study nonlinear wave propagation through continuum phononic material with weakly compressed rough contacts. We excite wave pulse with amplitude larger than static predeformation to enable strong nonlinearity. We report the evolution of excited waves with propagation distance demonstrating the generation of localized traveling waves and subsequently their separation from low-amplitude harmonic waves. We study the wave response at different center frequency pulses and discuss the frequency-filtering abilities of the phononic material due to its dispersion characteristics. Finally, we also compare the speed and amplitude of generated pulses with the one formed in the uncompressed system, and show the tunability of propagation properties through precompression. The focus of the study is to illustrate nonlinear wave responses achievable in the weakly compressed system, different from uncompressed and strongly compressed configurations.

The paper is organized as follows: First, we describe the phononic material system and corresponding numerical setup. Then, we illustrate the transformation of input waves into waves of different forms due to nonlinearity and dispersion. The tunability of wave propagation is discussed later. Finally, we conclude the paper and provide potential future directions.

Phononic material with weakly compressed rough contacts

The studied phononic material is a one-dimensional system consisting of linear elastic layers of aluminum ($E = 69$ GPa, $\nu = 0.33$, $\rho = 2700$ kg/m^3) of identical length, a, with roughness on either side at the microscale [Fig. 1(a)]. These layers are compressed externally under a precompression, p_0, thus forming a continuum with periodic rough contacts. The layers and contact are assumed to be infinite in the y-direction. The study assumes the wavelength of propagating waves to be three orders of magnitude larger than the rough features of the contacts, allowing contacts to be modeled as nonlinear springs [17]. However, we study wave propagation at wavelengths comparable to layer thickness, thus capturing the effects of continuum layers as well. Due to the inherent feature of contacting bodies, this material does not support any tensile forces during a loss of contact. We assume the roughness on the contacting surface such that the asperities (uneven features on nominal surfaces) are uniformly distributed and that hysteresis associated with their plastic deformation is already removed through multiple loading-unloadings. Under these assumptions, the contacts follow a purely quadratic nonlinear relation between contact pressure, $p(\Delta u)$, and gap, Δu [Fig. 1(b)] [18]. Thus, the contact nonlinearity within our system is as follows:

$$p(\Delta u) = \begin{cases} 0, & \Delta u > 0, \\ \frac{C^2 \Delta u^2}{4}, & \Delta u \leq 0. \end{cases} \tag{1}$$

where $C = 6 \times 10^{10} \sqrt{\text{Pa}}/\text{m}$ [18]. Since $u > \delta_0$ in our analysis (i.e. wave displacement is larger than the predeformation caused by p_0), the dynamics of rough contacts is non-smooth (strongly nonlinear) as contact surfaces can collide and separate [Fig. 1(b)].

To study nonlinear wave propagation through these phononic materials, we construct a finite element (FE) model using COMSOL Multiphysics 5.5a with solid mechanics module based on our previous work [16, 9]. The layers are considered as continua while the contacts are modeled through spring elements with nonlinear characteristics as defined in Eq. 1. The numerical simulation is conducted in two stages: first, the model solves the static problem of external precompression to determine the deformed state of the phononic material and predeformation in the springs. Then, a wave propagation study is conducted through transient analysis. The output of the static analysis is considered as the initial conditions for the wave propagation problem. We model a larger number of unit cells than what we analyze to avoid the effect of end reflections, essentially simulating a phononic material infinite in the positive x-direction. A longitudinal wave pulse [wave schematic in Fig. 1(b)] of amplitude, U, and center frequency, f, with a Gaussian modulation (parameters, $\zeta = 2/f$, $\sigma = 0.5/f$ for Eq. 4 of [9]) was excited from the entire left edge of the FE geometry. Note that the maximum displacement of the

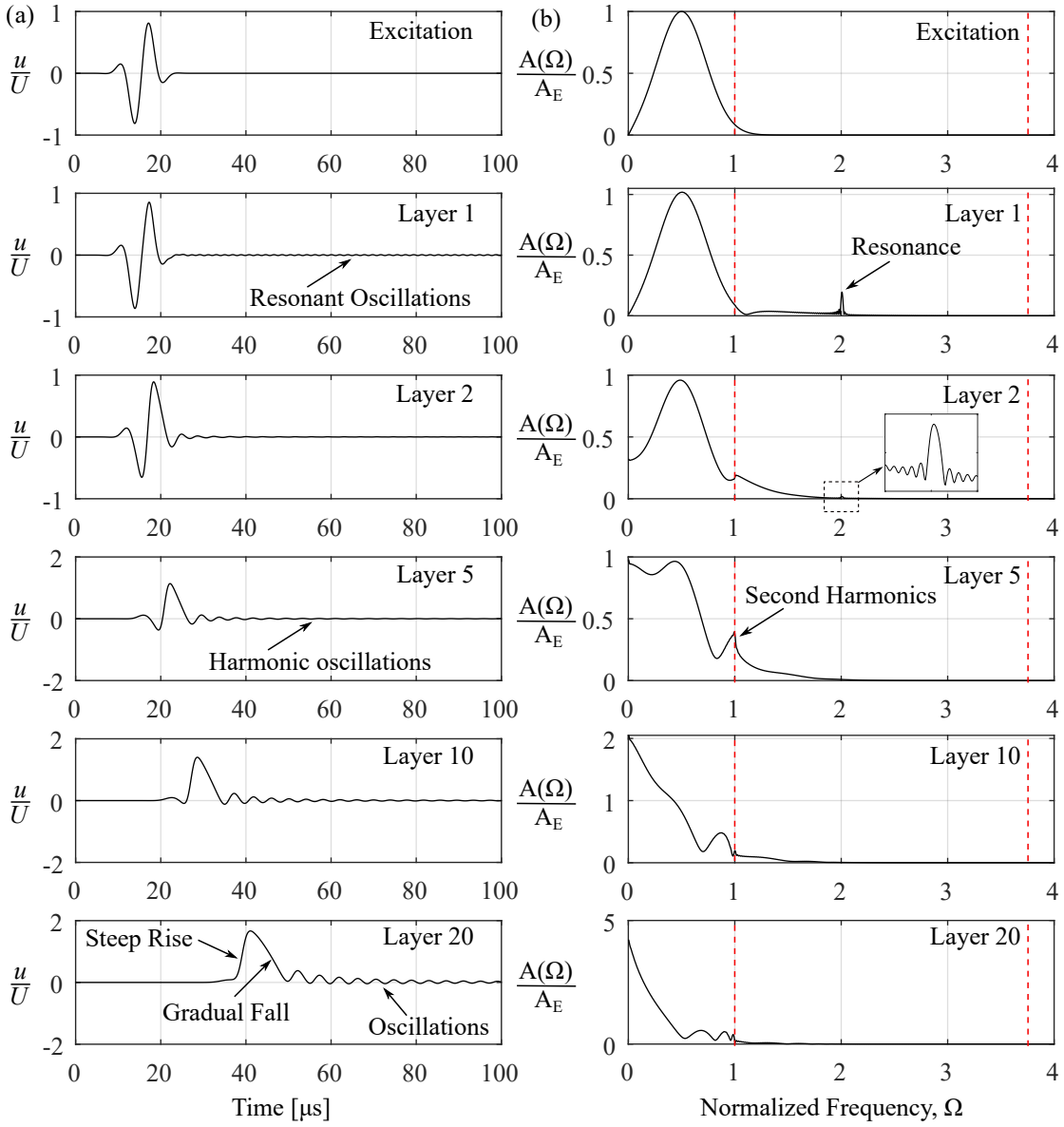

Figure 2: Evolution of input pulse wave with center frequency at $\Omega = 0.5$. (a) Displacement-time profile and (b) frequency content of the propagating wave at multiple locations inside the phononic material. Wave displacements, u, are normalized by pulse excitation amplitude, U, and spectral amplitudes are normalized by spectral excitation amplitude, A_E. The signals are recorded at the center point in the corresponding layers and the layer indices are numbered from the excitation boundary. Red dashed lines are linearized band gap edges.

input pulse [max($|+u|, |-u|$)] is smaller than excitation amplitude, U, due to Gaussian modulation. This specific wave profile corresponds to the typical response of a broadband ultrasonic contact transducer.

Nonlinear wave disintegration

In this section, we study the evolution of the input wave profile in the phononic material with weak external precompression and high amplitude excitation. Specifically, we discuss an example case of $\delta_0/u \approx 0.83$, which allows us to enable strong nonlinearity as well as study the effect of external compression. To inform the selection of frequencies for analysis, we obtained the linearized dispersion of the phononic material [16]. A non-dimensional frequency, Ω, is introduced such that the frequencies are normalized by the lower-edge frequency of the first band gap of the linearized phononic media for the applied p_0 (i.e. band gap starts at $\Omega = 1$). We study two representative cases of input pulse: (1) with center frequency in pass band ($\Omega = 0.5$) and (2) with center frequency at band edge ($\Omega = 1$). The first pulse, consisting of wide band of frequencies within $0 < \Delta\Omega < 1$, was excited to analyze nonlinear wave propagation in a highly dispersive frequency regime of the linearized phononic media. On the other hand, the second pulse, consisting of wide band of frequencies within $0 < \Delta\Omega < 2.5$, was excited to analyze the effect of band gaps on nonlinear wave propagation.

The wave profile changes as the wave propagates through the phononic material [Fig. 2(a)]. Particularly, the input pulse that originally consists of both compression and extension displacement, gradually transforms to a profile which is predominantly in compression only [compare wave profile in layer 1 vs in layer 20 in Fig. 2(a)]. As the wave propagates, the tensile portion of the pulse vanishes with each layer [note gradual reduction in negative displacements from layer 2

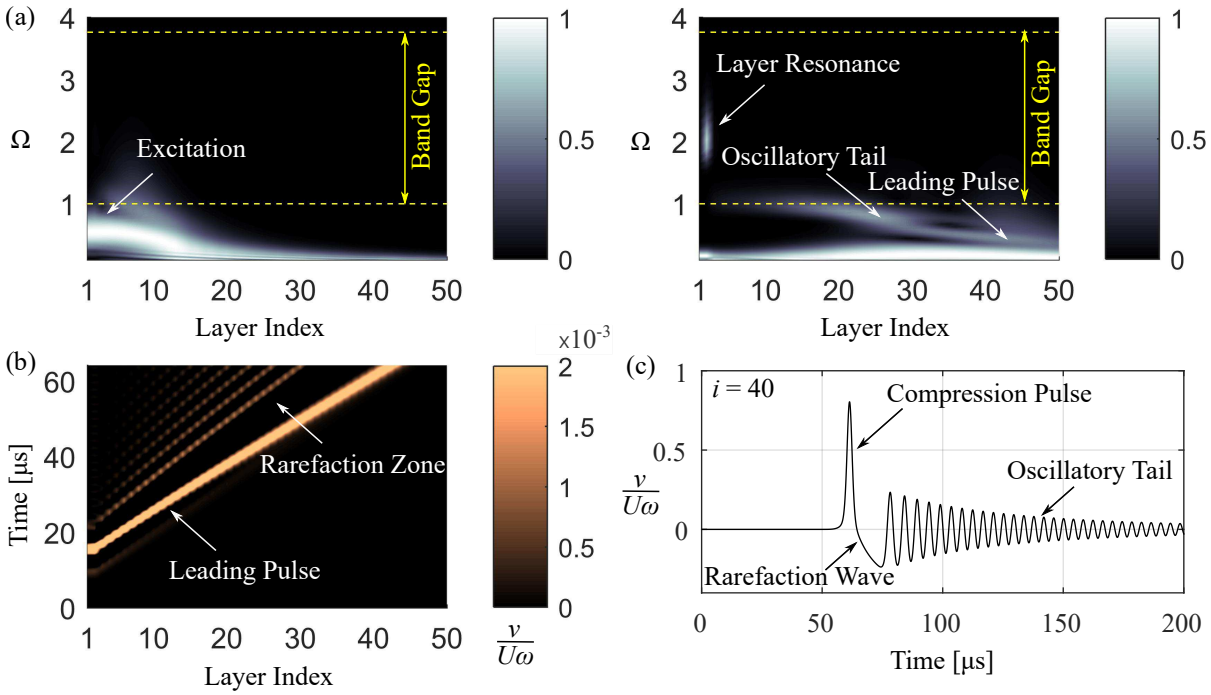

Figure 3: (a) Spatio-spectral and (b) spatio-temporal plots of nonlinear wave propagation for excitation at $\Omega = 0.5$. Spatio-spectral plot (normalized by its maximum value) is shown at an instant when the leading pulse is between the 10th and 20th layer (left) and between the 40th and 50th layer (right). Dashed yellow lines are linearized band gap edges. Layer indices are marked from the excitation boundary. (c) Temporal profile of the disintegrated wave inside the 40th layer. Wave amplitude is denoted in terms of particle velocity, v, normalized by excitation amplitude, U, and angular frequency, ω.

to 20 in Fig. 2(a)]. Moreover, the transmitted compression part is followed by small-amplitude oscillatory waves. The Gaussian input pulse eventually evolves into a waveform that contains three distinct features: (1) a steep increase in profile at the wave front, followed by (2) a gradual amplitude reduction, and (3) an oscillatory tail. This transformation can be understood as follows: The profile of the pulse transmitted across a contact is a combined effect of contact nonlinearity and weak compression. The contacts transmit all compressive forces, whereas only tensile forces that are just enough to counteract the external precompression are transmitted. As a result, once tensile forces exceed external precompression, a contact loss takes place. Therefore, the only harmonic waves supported inside the phononic material are those that contain small amplitude displacements.

This wave evolution also causes frequency conversions, meaning that energy is transferred within the spectral domain. In fact, both strongly and weakly nonlinear effects occur within the phononic material. Specifically, layer 1 resonates at a frequency, $\Omega = 2$ [note resonant oscillations in Fig. 2(a) and a spectral peak in Fig. 2(b) for layer 1]. This resonance corresponds to the mode of the layer under the fixed-forced boundary condition. Note that layer 1 is held fixed at the left end by virtue of excitation profile whereas the right end is a rough contact. This mode is at a frequency slightly higher compared to the first fixed-free mode of the layer, i.e. acoustic resonance given by $\Omega_r = 1.876$ ($\Omega_r = c_0/4a$, where c_0 is the wave speed of the bulk material). This is because, unlike the uncompressed system, the weakly compressed system experiences a non-zero spring force at the contact end, which pushes the mode of the layer to a higher frequency. Even, layer 2 shows a spectral peak at the same frequency [refer inset in Fig. 2(b) for layer 2]. This is surprising since, in an uncompressed system, the second layer from the excitation boundary resonates at a frequency twice the resonance of layer 1 [9]. This is because layer 2 loses its contact with adjacent layers after wave interaction and the contact loss remains in effect due to the lack of external precompression. As a result, layer 2 resonates under free-free boundary conditions. In the current system, however, both layers (1 and 2) are in contact due to external precompression - a state not possible in an uncompressed system. Due to their persistent contact even after the wave-contact interactions, the resonant energy of layer 1 is partly transmitted to layer 2 causing a spectral peak at $\Omega = 2$. In subsequent layers, second harmonics are generated, i.e. $\Omega = 1$ [refer to the spectral peak at Fig. 2(b) for layer 5] - a feature typical of weakly nonlinear systems. These harmonics, however, lie on the band gap edge and beyond. Thus, they do not propagate and therefore their spectral amplitude vanishes at later layers, for example, layers 10 and 20. Frequencies within the pass band propagate while those close to the band gap edge propagate with extremely slow speed. Eventually, the propagating frequency components consist primarily of low frequencies close to 0 Hz, i.e. a localized traveling wave.

One can think of the transformation of the input wave profile and its frequency content as a “disintegration" of the input pulse. Here, we refer to disintegration as a transformation of input pulse into (1) leading pulses of compressive nature, (2) transitioning zone of rarefaction nature, and (3) tails of decaying amplitudes of harmonic nature. This can be seen in terms of the spatial distribution of frequency content [Fig. 3(a)] and temporal dependence of particle velocity [Figs. 3(b) and (c)]. Despite exciting energy in the system around $\Omega = 0.5$, the energy content within phononic material spreads spatially

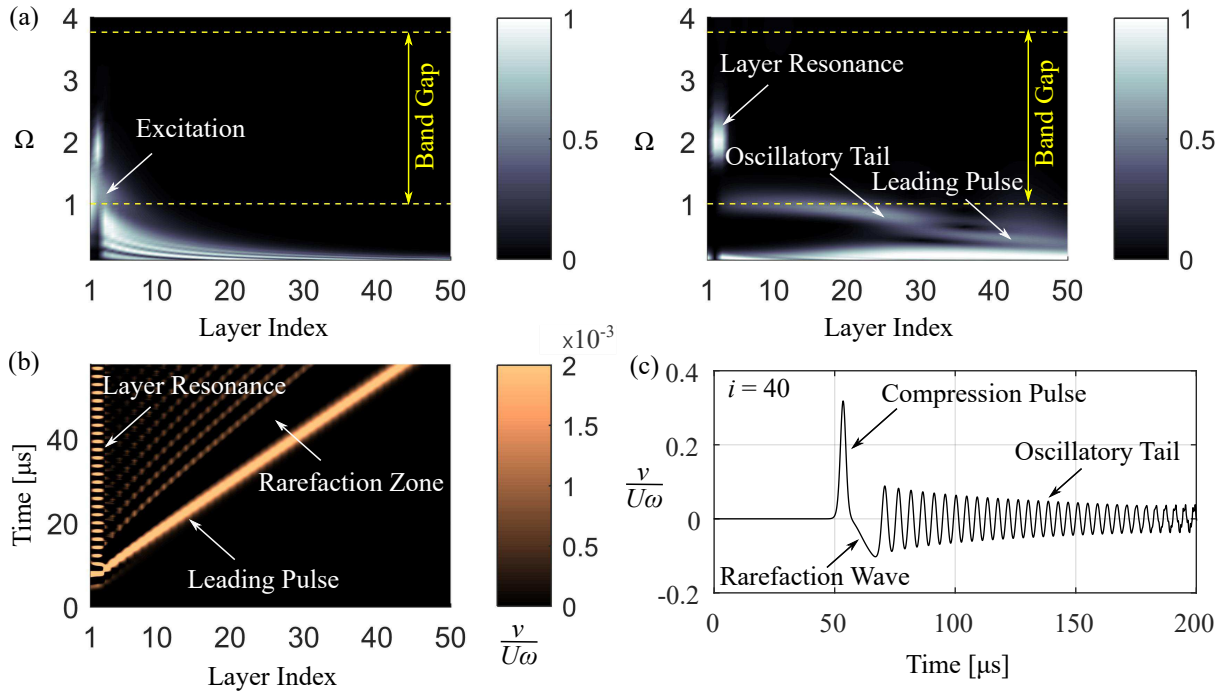

Figure 4: (a) Spatio-spectral and (b) spatio-temporal plots of nonlinear wave propagation for excitation at $\Omega = 1$. Spatio-spectral plot (normalized by its maximum value) is shown at an instant when the leading pulse is between the 1st and 10th layer (left) and between the 40th and 50th layer (right). Dashed yellow lines are linearized band gap edges. Layer indices are marked from the excitation boundary. (c) Temporal profile of the disintegrated wave inside the 40th layer.

due to dispersion while some remains trapped in the form of layer resonances [Fig. 3(a)]. The oscillations correspond to frequencies near the band edge that propagate at a much slower speed. The leading pulse propagates faster than the oscillatory tails and thus overtakes them, causing disintegration, which is clearly visible away from the excitation boundary. The pulse and oscillatory wave profiles are linked through a rarefaction front [Fig. 3(c)]. As a result, the duration over which a rarefaction wave exists in a layer increases with propagation distance [Fig. 3(b)]. This shows that phononic material with contact nonlinearity can support rarefaction waves given non-zero external precompression. Interestingly, similar wave disintegration has been reported in nonlinear metamaterials but with softening-type nonlinearity, i.e. where the exponent of power-law nonlinearity is < 1 [19, 20]. Specifically, these studies reported that an excited compression pulse transforms into a leading rarefaction pulse in tensegrity [19] and origami metamaterials [20].

A similar wave disintegration occurs even in the case when the center frequency of the excited pulse is at the linearized band gap edge, i.e. $\Omega = 1$ (Fig. 4). Importantly, the frequencies $\Omega > 1$ do not propagate through the phononic material, indicating that the band gap exists at these frequencies in this strongly nonlinear regime. In this case, oscillatory tails consist of frequencies within the pass band only. Since the excitation frequency is closer to the resonance frequency of layer 1, there are stronger resonant oscillations of layer 1 compared to when the excitation center frequency is $\Omega = 0.5$ [Compare oscillations at layer index = 1 in Fig. 4(b) and Fig. 3(b)]. The generated compression pulses in these phononic materials are in fact localized traveling waves that propagate with constant speed and amplitude. Due to the hybrid nature of the phononic material, which is continua connected through discrete nonlinearity, these compression pulses are in the form of stegotons showing a step-wise spatial profile [9].

Tunability of compression pulses

In this section, we characterize the dependence of propagation properties of nonlinear waves on external precompression. Specifically, we discuss how external precompression can be used to tune and control the leading compression pulses. The ability to control the speed and amplitude of these pulses can allow greater flexibility and feasibility in utilizing these phononic materials for engineering applications.

By controlling external precompression while keeping the input amplitude the same, we can control the amplitude of the generated compression pulse. The absolute amplitude of these pulses increases with an increase in precompression [Fig. 5(a)]. This is surprising since as precompression increases, the ratio between predeformation and wave amplitude (δ_0/u) increases. As a result, the strength of nonlinearity decreases, which in turn is expected to cause relatively weaker momentum transfer across the contacts. In other words, increasing precompression is expected to generate compression pulses with decreasing amplitudes. However, keeping the same excitation displacement amplitude in the analysis requires larger external work to be done on the system for larger precompressions. This is because the dynamic excitation has to work against the stronger contact forces developed from increased precompressions. Overall, increasing precompression draws more input energy for the same excitation frequency and amplitude, which subsequently generates compression pulses

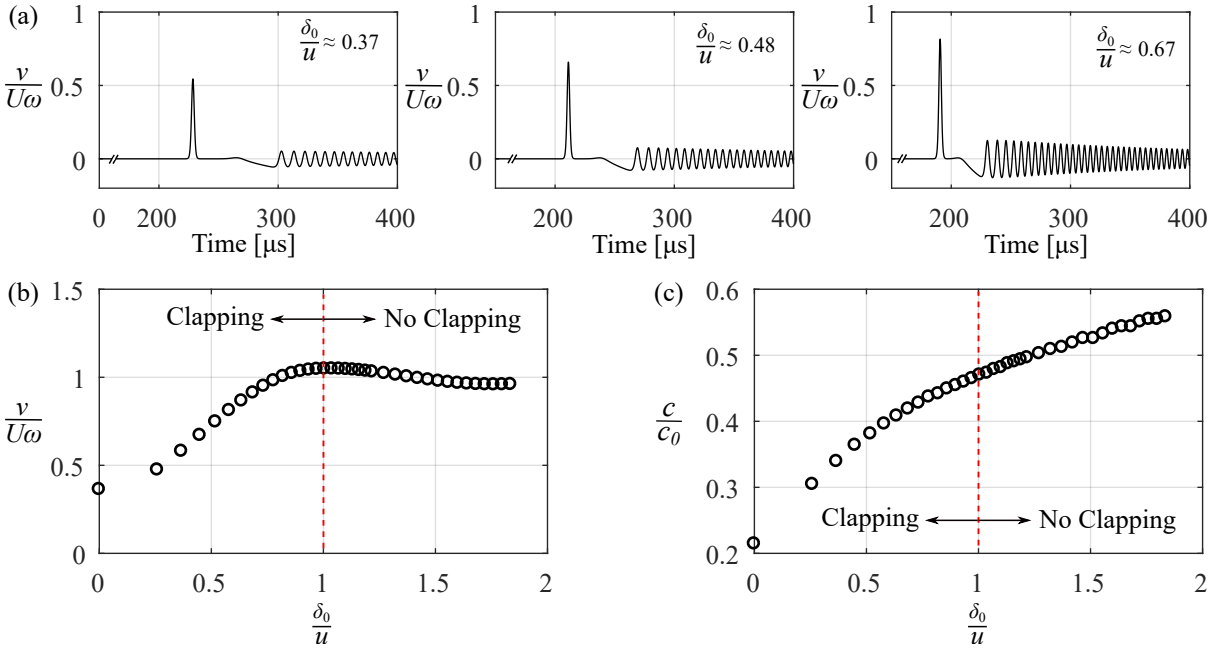

Figure 5: Tunability of nonlinear waves through precompression. (a) Disintegrated wave profile inside the 150th layer for three different precompressions. Dependence of pulse (b) amplitude and (c) wave speed on precompression. Red dashed line is the precompression threshold below which contact clapping occurs.

with larger amplitudes. The rarefaction and harmonic wave amplitudes also increase with compression pulse amplitudes. In other words, stronger precompression supports tensile waves of high amplitudes. Based on these observations, we can conclude that weakly compressed systems exhibit nonlinear wave responses that are a mix of uncompressed and strongly compressed systems, and further allow control over these responses. Specifically, the high amplitude portion of the excitation contributes to strongly nonlinear responses (i.e. compression pulses) as seen in the uncompressed system and low amplitudes contribute to weakly nonlinear responses (i.e. frequency filtering and harmonic waves) as seen in the strongly compressed systems. However, the transition zone from compression pulse to harmonic oscillations is seen only in weakly compressed systems. As waves propagate, compression pulses separate from the rarefaction waves. It is worth noting that the time delay between the compression pulse and rarefaction front can also be controlled through precompression [Fig. 5(a)].

As discussed, the compression pulses are in fact solitary waves as these pulses propagate with constant speed and amplitude. Next, we discuss how the amplitude and speed of these pulses depend on precompression and the threshold value of precompression that can still generate these strongly nonlinear responses. Interestingly, the compression pulses are generated even for the cases where contact clapping is restricted, i.e. when predeformation is larger than the excitation amplitude ($\delta_0/u > 1$) [Fig. 5(b)]. Despite the lack of clapping, this regime is not necessarily weakly nonlinear since excitation amplitudes are not small enough. Note that there exists quadratic nonlinearity between contact force and displacement due to the deformation of rough asperities. This is possibly causing the balance between nonlinearity and dispersion to form a compressive pulse. Further, the amplitude of generated pulses decreases beyond $\delta_0/u > 1$ - a threshold beyond which no clapping is possible. The change in amplitude of compression pulses is less sensitive to $\delta_0/u > 1$ compared to $\delta_0/u < 1$ [note the change in pulse amplitude dependence on precompression before and after the red dashed line in Fig. 5(b)]. The maximum amplitude of the compression pulse is attained at $\delta_0/u = 1$. This is the threshold where clapping is possible and energy added to the system is more than the energy added for $\delta_0/u < 1$.

Contrary, the wave speed of the compression pulses, c, (normalized by bulk wave dilatational wave speed, c_0) increases monotonically with precompression [Fig. 5(c)]. This is consistent with Fig. 5(b) for $\delta_0/u < 1$ since the amplitude and speed of these waves are proportional to each other. We also observe that wave speed changes dramatically for low precompression and depends linearly on precompression at larger values. For $\delta_0/u > 1$, wave speed increases despite a decrease in amplitude. This indicates that the pulses generated beyond $\delta_0/u > 1$ have a different speed-amplitude relationship than solitary waves generated from clapping.

As expected, the fraction of energy carried by the compression pulses as a function of total energy in the system decreases with an increase in precompression (Fig. 6). In fact, the energy carried by the pulses is almost negligible (two orders smaller) for precompressions $u/\delta_0 > 1.5$. This indicates the region of precompression where the phononic material behavior changes into a weakly compressed system.

Conclusions

In this paper, we studied high amplitude nonlinear wave propagation through phononic material with weakly compressed rough contacts. The source of nonlinearity within the material comes from two mechanisms: (1) contact separation and

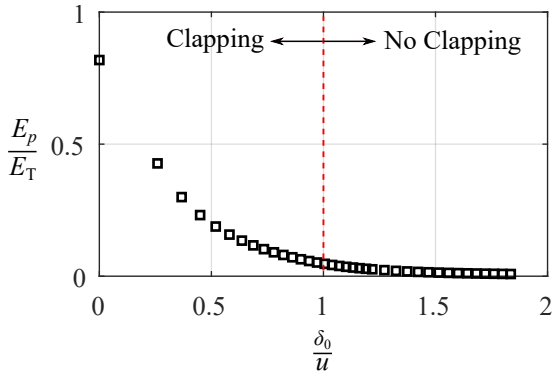

Figure 6: Dependence of the energy carried by the compression pulses (E_p) as a fraction of total energy (E_T) on precompression.

collision at high amplitudes and (2) quadratic contact force-displacement relationship during the contact. Application of non-zero precompression during analysis revealed that both strongly and weakly nonlinear wave responses can coexist. Specifically, the phononic material supports both solitary waves as well as frequency filtering. Importantly, an additional wave signature in the form of wave disintegration is observed in the weakly compressed system. The input pulse breaks down in three different wave forms: (1) a localized traveling wave in the form of compression pulse, (2) a rarefaction wave front, and (3) an oscillatory tail of decaying amplitude. A compression pulse initially leads the wave propagation before separating from other wave forms due to its greater wave speed. Oscillatory tails are associated with the periodic waves at frequencies in the vicinity of band gap and therefore spread spatially. Finally, the propagation properties of the compression pulse, i.e. their amplitude and speed, can be tuned through external precompression.

Contact-based phononic materials would practically require non-zero precompression to keep all surfaces in contact. The results presented in this paper give an idea of how a slight deviation in system parameters dramatically changes the behavior of the phononic material. The effect not only influences the values of propagation parameters but in fact introduces new types of waves. From an application perspective, these weakly compressed phononic materials can be used for developing mechanical sensors and delay switches. Particularly, the rate at which information is carried from one end to the other can be simply controlled in-situ through external precompression. The combined ability of information transfer and frequency filtering could help develop new imaging devices to isolate spurious scattering while transmitting captured data.

While we elucidated wave responses from weak compression, a detailed study of the effects of excitation frequency, pulse bandwidth, and different contact laws is necessary to fully understand the capability of the system. Higher frequency excitation may cause stronger momentum transfer across contacts generating strong compression pulses while different contact laws may dictate the speed-amplitude relationship. Wave excitation with narrow bandwidth may help study higher harmonic generation while wide band excitation could cause wave mixing within input frequencies. These complex behavior may help advance the understanding of how contacts can be exploited to manipulate the propagation of mechanical energy in an unprecedented way.

Acknowledgement

This work was supported by the Army Research Office, USA and was accomplished under Grant Number W911NF-20-1-0250. The views and conclusions contained in this document are those of the authors and should not be interpreted as representing the official policies, either expressed or implied, of the Army Research Office or the U.S. Government. The U.S. Government is authorized to reproduce and distribute reprints for Government purposes notwithstanding any copyright notation herein.

References

[1] M. Sigalas, E. N. Economou, Band structure of elastic waves in two dimensional systems, Solid state communications 86 (3) (1993) 141–143. doi:10.1016/0038-1098(93)90888-T.

[2] Z. Liu, X. Zhang, Y. Mao, Y. Zhu, Z. Yang, C. T. Chan, P. Sheng, Locally resonant sonic materials, science 289 (5485) (2000) 1734–1736. doi:10.1126/science.289.5485.1734.

[3] H. J. Lee, J. R. Lee, S. H. Moon, T. J. Je, E. C. Jeon, K. Kim, Y. Y. Kim, Off-centered Double-slit Metamaterial for Elastic Wave Polarization Anomaly, Scientific Reports 7 (1) (2017) 1–13. doi:10.1038/s41598-017-15746-2.

[4] G. U. Patil, A. B. Shedge, K. H. Matlack, 3D auxetic lattice materials for anomalous elastic wave polarization, Applied Physics Letters 115 (9) (2019) 091902. doi:10.1063/1.5116687.

[5] A. Bayat, S. Gaitanaros, Wave Directionality in Three-Dimensional Periodic Lattices, Journal of Applied Mechanics 85 (1) (2018) 1–17. doi:10.1115/1.4038287.

[6] G. U. Patil, K. H. Matlack, Review of exploiting nonlinearity in phononic material to enable nonlinear wave responses, Acta Mechanica 233 (1) (2022) 1–46. doi:10.1007/s00707-021-03089-z.

[7] V. F. Nesterenko, Propagation of nonlinear compression pulses in granular media, Journal of Applied Mechanics and Technical Physics 24 (5) (1983) 733–743. doi:10.1007/BF00905892.

[8] V. Nesterenko, Dynamics of heterogeneous materials, Springer Science & Business Media, 2013.

[9] G. U. Patil, K. H. Matlack, Strongly nonlinear wave dynamics of continuum phononic material with periodic rough contacts, Physical Review E 105 (2) (2022) 024201. doi:10.1103/PhysRevE.105.024201.

[10] C. Daraio, V. F. Nesterenko, E. B. Herbold, S. Jin, Strongly nonlinear waves in a chain of Teflon beads, Physical Review E 72 (1) (2005) 1–10. doi:10.1103/PhysRevE.72.016603.

[11] M. A. Porter, P. G. Kevrekidis, C. Daraio, Granular crystals: Nonlinear dynamics meets materials engineering, Physics Today 68 (11) (2015) 44–50. doi:10.1063/PT.3.2981.

[12] J. Cabaret, V. Tournat, P. Béquin, Amplitude-dependent phononic processes in a diatomic granular chain in the weakly nonlinear regime, Physical Review E 86 (4) (2012) 1–11. doi:10.1103/PhysRevE.86.041305.

[13] N. Boechler, G. Theocharis, S. Job, P. G. Kevrekidis, M. A. Porter, C. Daraio, Discrete breathers in one-dimensional diatomic granular crystals, Physical Review Letters 104 (24) (2010) 3–7. doi:10.1103/PhysRevLett.104.244302.

[14] E. B. Herbold, V. F. Nesterenko, Shock wave structure in a strongly nonlinear lattice with viscous dissipation, Physical Review E 75 (2) (2007). doi:10.1103/PhysRevE.75.021304.

[15] O. Sadovskaya, V. Sadovskii, Elastoplastic waves in granular materials, Journal of Applied Mechanics and Technical Physics 44 (5) (2003) 741–747.

[16] G. U. Patil, K. H. Matlack, Wave self-interactions in continuum phononic materials with periodic contact nonlinearity, Wave Motion 105 (2021) 102763. doi:10.1016/j.wavemoti.2021.102763.

[17] B. Drinkwater, R. Dwyer-Joyce, P. Cawley, A study of the interaction between ultrasound and a partially contacting solid—solid interface, Proceedings of the Royal Society of London. Series A: Mathematical, Physical and Engineering Sciences 452 (1955) (1996) 2613–2628. doi:10.1098/rspa.1996.0139.

[18] S. Biwa, S. Nakajima, N. Ohno, On the acoustic nonlinearity of solid-solid contact with pressure-dependent interface stiffness, Journal of Applied Mechanics 71 (4) (2004) 508–515. doi:10.1115/1.1767169.

[19] F. Fraternali, G. Carpentieri, A. Amendola, R. E. Skelton, V. F. Nesterenko, Multiscale tunability of solitary wave dynamics in tensegrity metamaterials, Applied Physics Letters 105 (20) (2014). doi:10.1063/1.4902071.

[20] H. Yasuda, C. Chong, E. G. Charalampidis, P. G. Kevrekidis, J. Yang, Formation of rarefaction waves in origami-based metamaterials, Physical Review E 93 (4) (2016) 1–13. doi:10.1103/PhysRevE.93.043004.

Tuesday, July 19, 2022
08:30 - 10:30

MS-21 Nonlinear Dynamics in Acoustics
Saint Clair 2

Chair: Michele Ducceschi

08:30 - 08:50
A Partitioned Finite Element Method (PFEM) for power-preserving discretization of port-Hamiltonian systems (pHs) with polynomial nonlinearity
MATIGNON Denis, CARDOSO-RIBEIRO Flávio Luiz, **LEFÈVRE Laurent***
*Laboratoire de Conception et dÍntégration des Systèmes (50, rue Barthélémy de Laffemas BP54 26902 VALENCE Cedex 09 France France)

08:50 - 09:10
Analytical 1D model of the flow-structure interaction in snoring and sleep apnea
SOARES Filipe*, ANTUNES José, DEBUT Vincent, VERGEZ Christophe, SILVA Fabrice, COCHELIN Bruno
*Instituto Superior Tecnico [Lisboa] (Av. Rovisco Pais, 1 1049-001 Lisboa Portugal)

09:10 - 09:30
Exploiting nonlinear dynamics for manipulation of acoustically levitated particles
BUCHER Izhak*, DOLEV Amit
*Izhak Bucher (Dynamics Laboratory Israel)

09:30 - 09:50
Cristal Baschet: minimal model to predict the emergence of self-sustained oscillations
COUINEAUX Audrey*, GAUTIER François, ABLITZER Frédéric
*Laboratoire d'Acoustique de l'Université du Mans, CNRS UMR 6613, Le Mans, France (Avenue Olivier Messiaen 72085 LE MANS CEDEX 9 France)

A Partitioned Finite Element Method (PFEM) for power-preserving discretization of port-Hamiltonian systems (pHs) with polynomial nonlinearity

Flávio Luiz Cardoso-Ribeiro*, Denis Matignon†, and Laurent Lefèvre‡
*Instituto Tecnológico de Aeronáutica, São José dos Campos, Brazil
†ISAE-SUPAERO - Université de Toulouse, 31055 Toulouse, France
‡Univ. Grenoble Alpes, Grenoble INP, LCIS, Valence, France

Summary. The Partitioned Finite Element Method introduced in [7] provides a structure-preserving discretization for the solution of systems of boundary controlled and observed Partial Differential Equations (PDEs), formulated as distributed-parameter port-Hamiltonian systems (pHs). In particular, the energy balance is preserved at the discrete level. This method, already well-developped for linear systems, is also suitable for nonlinear systems with polynomial nonlinearity, such as the 2D Shallow Water Equations, or the full von-Kármán plate equations.

Port-Hamiltonian systems (pHs)

These are dynamical systems ruled by a Hamiltonian function and conservation laws, together with interaction ports for control $\boldsymbol{u}$ through actuators, and observation or measurements $\boldsymbol{y}$ via sensors; this modelling tool proves very useful for the analysis and control of multiphysics systems: see e.g. [8] for a general presentation. PHs can be finite dimensional (i.e. described by Ordinary Differential Equations (ODEs) with a finite number of d.o.f), or infinite dimensional (i.e. described by Partial Differential Equations PDEs), see [13]. In both cases, all the variables involved in the description do have a clear physical meaning, in contrast with many methods available in the mathematical literature: in particular, anisotropic and heterogeneous media can be accounted for in a very natural way, with no extra complication w.r.t the isotropic and homogeneous cases.

General setting [3]
Let $\mathcal{H}$ the Hamiltonian functional, and (α_1, α_2) the energy variables in the domain Ω. The co-energy variables are defined as the variational derivatives of the Hamiltonian w.r.t. these energy variables: $e_i := \delta_{\alpha_i}\mathcal{H}$. The dynamical system reads:

$$\partial_t \begin{pmatrix}\alpha_1\\ \alpha_2\end{pmatrix} = \begin{bmatrix}0 & -\mathcal{L}^*\\ \mathcal{L} & 0\end{bmatrix}\begin{pmatrix}e_1\\ e_2\end{pmatrix}, \qquad \begin{aligned} u_\partial &= \gamma_0 e_1,\\ y_\partial &= \gamma_\perp e_2,\end{aligned} \tag{1}$$

and the differential operator $\mathcal{L}$ and its adjoint $\mathcal{L}^*$ satisfy the following abstract Green's formula:

$$\langle e_2,\, \mathcal{L}\, e_1\rangle_{L^2(\Omega,\mathbb{A}_2)} - \langle \mathcal{L}^*\, e_2,\, e_1\rangle_{L^2(\Omega,\mathbb{A}_1)} = \langle \gamma_0 e_1,\, \gamma_\perp e_2\rangle_{\partial\Omega}\,. \tag{2}$$

The energy variables $\alpha_i \in L^2(\Omega, \mathbb{A}_i)$, where the sets $\mathbb{A}_i$ are either scalar, vectorial or tensorial quantities. The co-energy variables e_i belong to some appropriate Sobolev spaces, namely: $e_1 \in H^{\mathcal{L}} := \big\{v_1 \in L^2(\Omega, \mathbb{A}_1)|\ \mathcal{L}v_1 \in L^2(\Omega, \mathbb{A}_2)\big\}$, and $e_2 \in H^{\mathcal{L}^*} := \big\{v_2 \in L^2(\Omega, \mathbb{A}_2)|\ \mathcal{L}^*v_2 \in L^2(\Omega, \mathbb{A}_1)\big\}$. Then, the evolution of the Hamiltonian is given by:

$$\frac{d}{dt}\mathcal{H}(\alpha_1(t), \alpha_2(t)) = \langle u_\partial(t),\, y_\partial(t)\rangle_{\partial\Omega}\ , \tag{3}$$

corresponding to a lossless open system, a generalization of a conservative closed system.

Worked-out examples in structural, fluid mechanics and electromagnetism
The practical cases dealt with so far are:

- $\mathcal{L} = \mathrm{div}$ and $\mathcal{L}^* = -\,\mathbf{grad}$, for vectorial and scalar fields in 2D in [12] and [5],
- $\mathcal{L} = \mathrm{Div}$ and $\mathcal{L}^* = -\,\mathrm{Grad}$, for tensorial and vectorial fields in 2D in [1] and [4],
- $\mathcal{L} = \mathbf{curl}$ and $\mathcal{L}^* = \mathbf{curl}$, for vectorial fields in 3D in [9],
- $\mathcal{L} = \mathrm{div}\,\mathrm{Div}$ and $\mathcal{L}^* = \mathrm{Grad}\,\mathbf{grad} = \mathrm{Hess}$ for tensorial and scalar fields in 2D in [2].

In each case, the energy and co-energy variables are defined in accordance with continuum mechanics and physics.

The Partitioned Finite Element Method (PFEM)

This method makes use of the finite element method to open systems of conservation laws, i.e. with collocated boundary controls and observations; it was first introduced in [6], fully detailed in [7], and extended to damped systems in [10].

Principle

The Partitioned Finite Element Method boils down to 3 steps: first provide a weak formulation of the coupled first order system, second perfom an integration by parts on one of the two lines as to highlight the desired boundary control, and third apply a Galerkin procedure by choosing finite element families for each component including the boundary, giving rise to large sparse matrices.

Let us denote the shape functions φ_i^1 for the first variables, φ_j^2 for the second variable and ψ_k for the boundary variables, set the vectors $\Phi_1 := [\varphi_1^1 \cdots \varphi_{N_1}^1]$, $\Phi_2 := [\varphi_1^2 \cdots \varphi_{N_2}^2]$ and $\Psi := [\psi_1 \cdots \psi_{N_\partial}]$, and define the discrete Hamiltonian as $H(\boldsymbol{\alpha}_1, \boldsymbol{\alpha}_2) := \mathcal{H}(\Phi_1\, \boldsymbol{\alpha}_1, \Phi_2\, \boldsymbol{\alpha}_2)$, we end up with the following finite-dimensional port-Hamiltonian system:

$$\begin{aligned} \begin{bmatrix} M_1 & 0 \\ 0 & M_2 \end{bmatrix} \frac{d}{dt} \begin{pmatrix} \boldsymbol{\alpha}_1 \\ \boldsymbol{\alpha}_2 \end{pmatrix} = \begin{bmatrix} 0 & -L^T \\ L & 0 \end{bmatrix} \begin{pmatrix} \boldsymbol{e}_1 \\ \boldsymbol{e}_2 \end{pmatrix} + \begin{bmatrix} 0 \\ B_2 \end{bmatrix} \boldsymbol{u}_\partial, \qquad & M_1 \boldsymbol{e}_1 := \nabla_{\boldsymbol{\alpha}_1} H, \\ & M_2 \boldsymbol{e}_2 := \nabla_{\boldsymbol{\alpha}_2} H, \\ M_\partial\, \boldsymbol{y}_\partial = \begin{bmatrix} 0 & B_2^T \end{bmatrix} \begin{pmatrix} \boldsymbol{e}_1 \\ \boldsymbol{e}_2 \end{pmatrix}. & \end{aligned} \tag{4}$$

The mass matrices M_i of dimension $N_i \times N_i$ are symmetric and positive definite. Matrix L is $N_2 \times N_1$, and the boundary control matrix B_2 is $N_2 \times N_\partial$. Then, mimicking (3), the power balance for open systems is preserved at the discrete level:

$$\frac{d}{dt} H(\boldsymbol{\alpha}_1(t), \boldsymbol{\alpha}_2(t)) = \boldsymbol{u}_\partial^T M_\partial \boldsymbol{y}_\partial\,. \tag{5}$$

Linear examples

When the Hamiltonian is a quadratic and separable functional of the energy variables, the co-energy variables are linear w.r.t. the energy variables, and an explicit closed-form for (4) can be easily obtained, either in terms of $\boldsymbol{\alpha}_i$, or of $\boldsymbol{e}_i$. This strategy has been fully developped and worked out on the anisotropic heterogeneous 2D wave equation in [12], on the Reissner-Mindlin thick plate in [1], on the Kirchhoff-Love thin plate in [2] and also on Maxwell's equations in 3D in [9].

Nonlinear examples

Now the same strategy applies to nonlinear models, keeping the energy and co-energy variables apart. In this case though, the link between the co-energy variable $\boldsymbol{e}_i$ and the energy variables $\boldsymbol{\alpha}_i$ is no more linear and requires some special care. However, in the case of a polynomial nonlinearity, explicit relations can be provided at the discrete level, and more important, these relations can be computed off-line (i.e. an extra application of the FEM does not prove necessary at each time step). This has been worked out on the irrotational 2D Shallow Water in [5] with a nonlinear and non-separable Hamiltonian, on the heat equation with internal energy as Hamiltonian in [11]. The full von-Kármán plate model in [4] is another candidate.

Acknowledgment Part of this work has been performed in the framework of the Collaborative Research DFG and ANR project INFIDHEM n° ANR-16-CE92-0028 (`http://websites.isae.fr/infidhem`).

References

[1] A. BRUGNOLI, D. ALAZARD, V. POMMIER-BUDINGER, AND D. MATIGNON, *Port-Hamiltonian formulation and symplectic discretization of plate models. Part I: Mindlin model for thick plates*, Applied Mathematical Modelling,, 75 (2019), pp. 940–960.

[2] ———, *Port-Hamiltonian formulation and symplectic discretization of plate models. Part II: Kirchhoff model for thin plates*, Applied Mathematical Modelling,, 75 (2019), pp. 961–981.

[3] A. BRUGNOLI, G. HAINE, A. SERHANI, AND X. VASSEUR, *Numerical approximation of port-Hamiltonian systems for hyperbolic or parabolic PDEs with boundary control*. `http://arxiv.org/abs/2007.08326`, 2020.

[4] A. BRUGNOLI AND D. MATIGNON, *A port-Hamiltonian formulation for the full von-Kármán plate model*, in Proc. ENOC, 2021. submitted.

[5] F. L. CARDOSO-RIBEIRO, A. BRUGNOLI, D. MATIGNON, AND L. LEFÈVRE, *Port-Hamiltonian modeling, discretization and feedback control of a circular water tank*, in 2019 IEEE 58th Conference on Decision and Control (CDC), Nice, France, 2019, pp. 6881–6886. invited session.

[6] F. L. CARDOSO-RIBEIRO, D. MATIGNON, AND L. LEFÈVRE, *A structure-preserving partitioned finite element method for the 2d wave equation*, IFAC-PapersOnLine, 51 (2018), pp. 119–124. 6th IFAC Workshop on Lagrangian and Hamiltonian Methods for Nonlinear Control (LHMNC).

[7] ———, *A partitioned finite element method for power-preserving discretiz ation of open systems of conservation laws*, IMA Journal of Mathematical Control and Information, 00 (2020), pp. 1–41. dnaa038.

[8] V. DUINDAM, A. MACCHELLI, S. STRAMIGIOLI, AND H. BRUYNINCKX, *Modeling and Control of Complex Physical Systems: The Port-Hamiltonian Approach*, Springer Berlin Heidelberg, Berlin, Heidelberg, 2009.

[9] G. PAYEN, D. MATIGNON, AND G. HAINE, *Modelling and structure-preserving discretization of Maxwell's equations as port-Hamiltonian system*, in Proc. 21st IFAC World Congress, 2020, pp. 7671–7676. invited session.

[10] A. SERHANI, D. MATIGNON, AND G. HAINE, *A Partitioned Finite Element Method for the Structure-Preserving Discretization of Damped Infinite-Dimensional Port-Hamiltonian Systems with Boundary Control*, in Geometric Science of Information, Nielsen, Frank and Barbaresco, Frédéric, eds., vol. 11712 of Lecture Notes in Computer Science, Springer International Publishing, 2019, pp. 549–558.

[11] ———, *Anisotropic heterogeneous n-D heat equation with boundary control and observation: II. Structure-preserving discretization*, in IFAC-PapersOnLine, vol. 52(7), 2019, pp. 57–62. 3rd IFAC workshop on Thermodynamical Foundation of Mathematical Systems Theory (TFMST).

[12] ———, *Partitioned Finite Element Method for port-Hamiltonian systems with Boundary Damping: Anisotropic Heterogeneous 2D wave equations*, in IFAC-PapersOnLine, vol. 52(2), 2019, pp. 96–101. 3rd IFAC workshop on Control of Systems Governed by Partial Differential Equations (CPDE).

[13] A. J. VAN DER SCHAFT AND B. M. MASCHKE, *Hamiltonian formulation of distributed-parameter systems with boundary energy flow*, Journal of Geometry and Physics, 42 (2002), pp. 166–194.

Analytical 1D model of the flow-structure interaction in snoring

Filipe Soares[*], Jose Antunes[*], Vincent Debut[**], Christophe Vergez[***], Bruno Cochelin[***] and Fabrice Silva[***]

** Instituto Superior Técnico – Centro de Ciências e Tecnologias Nucleares, Lisboa, Portugal*
*** Instituto Politécnico de Castelo Branco – Escola de Artes Aplicadas, Castelo Branco, Portugal*
**** Aix-Marseille Université, CRNS, Centrale Marseille, LMA UMR7031, Marseille, France*

Summary: The most common type of human snoring is characterized by vibrations of the soft-palate, induced by passing air during respiration. Despite being a widespread disorder, its occurrence is poorly understood and, consequently, clinical treatment is often ineffective. This physical system can be characterized, in its essence, by a cantilevered beam subjected to axial flow in a confined passage. These type of fluid-structure interaction systems have been a subject of research for many years, as its fundamental behavior is found in many other practical applications. Most studies are concerned solely with the conditions for linear stability and do not explore the ensuing nonlinear behavior of the system. This is particularly delicate as fluttering beams in confined flows are known to often result in dynamics with intermittent impacts between the beam and the side-walls. Here we present a nonlinear analytical resolution to a simplified 1-D model, based on a modal beam and bulk-flow equations. The model accounts for dissipation through distributed (frictional) and localized head-loss terms. The latter are imposed at the boundary conditions and aims to describe the complex effects occurring outside the domain (turbulence, vortex shedding, etc.). The present analytical resolution leads to a compact system for linear stability analysis, but also to a nonlinear formulation of the fluid-structure interaction. The inclusion of a regularized contact model allows for the computation of the full nonlinear dynamics, including intermittent impacts. Linear stability results are compared to previously published results using 2-D CFD models, and the relative merits of the model are discussed. A series of limit cycles with intermittent impacts between the beam and side-walls are presented to illustrate the nature of the post-instability oscillations. To the authors knowledge, the proposed formulation presents, for the first time, a framework for the comprehensive understanding of the nonlinear dynamics associated with flexible beams in confined axial flow.

Introduction

Recent studies suggest that no less than 30% of the adult population snores habitually. However, due its inherent complexity, the underlying physics and their relation to the type and degree of the disorder remain poorly understood and, consequently, treatment responses are often ineffective [1] [2]. The most common form of snoring is that of palatal snoring, where the vibration of the soft-palate/uvula (see Figure 1-(a)) is induced by the passage of air during respiration. This system can be categorized as a flow induced vibration problem. More specifically, it can be modelled as a flexible cantilever beam in confined axial flow [3] [4].

The static and dynamic instabilities associated with flexible beams/plates subject to axial flow occur also in different contexts from enhanced heat transfer [5], energy harvesting devices [6] or wind musical instruments [7]. The subject has been studied extensively [8], particularly for the case of unconfined flows. In these systems, the typical instability is of the flutter type. In the work of Shoele & Mittal [9], for example, we find some elucidating results regarding the influence of relevant non-dimensional parameters like the fluid-beam mass ratio, the reduced velocity (inverse of Strouhal number) or the confinement ratio (channel height to beam length ratio). Their results show that, at low beam-fluid mass ratios, the instability is of the single-mode flutter type, involving the coupling of the first two in-vacuo beam modes. As mass ratios increase, the initial single-mode flutter ceases to be the principal instability, and successive "mode-transitions" occur, whereby multiple higher-order fluttering modes prevail. This type of instability is commonly referred to as coupled-mode flutter.

More recently, the advances in computational efficiency have enabled the possibility to simulate these fluid-structure interaction (FSI) systems numerically by solving the Navier-Stokes equations in 2D and 3D domains [10]. These FSI models allow a more accurate representation of the physics. However, they also require considerable computational time, which becomes a handicap when analyzing problems whose behavior depends on a wide variety of parameters. For a more thorough parameter mapping, 1D models, based on simplified equations of motion, are not only computationally more efficient but also more tractable, and may provide valuable insights into the core dynamics of the problem.

In the context of simplified approaches, we note the work of Nagakura & Kaneko [11] that have used leakage flow theory to model the linear stability of a cantilever beam in a confined passage. Based on the work by Inada & Hayama [12], they formulate a 1D problem where flow pressure and velocity are taken as cross-sectionally averaged. The confinement is restricted to symmetric channels of constant cross-section, viscous effects are accounted for by a distributed friction term and the energy losses at the trailing edge are encapsulated by a localized head-loss term, imposed at the boundary condition.

By and large, the analytical models developed so far deal solely with the conditions for instability, using linearized equations of motions to study the effect of various parameters on the stability boundaries. Although undeniably a crucial information about the system dynamics, this gives us little insight about the ensuing nonlinear behavior. The

analysis of the nonlinear dynamics might by of valuable interest to various applications, giving information about human snoring, but also working regimes in wind musical instruments or in energy harvesting devices, for example.

In the context of unbounded flows, a number of theoretical and experimental studies can be found, illustrating the array of possible limit cycles arising in this type of systems [13] [14]. However, for instabilities in a confined passage, nonlinear modelling results and experimental observations have demonstrated the regular occurrence of limit cycles with intermittent impacts between the beam and the side walls [15] [16].

In this paper, we deal with a simplified 1D model in the spirit of Nagakura & Kaneko's work [11]. Contrary to their work, we admit channel profiles of any shape. More importantly however, we present an analytical resolution, based on formal solutions of the flow pressure and velocity fields, that leads not only to a compact system for linear stability analysis but also to a fully nonlinear flow formulation. This formulation can be used to explore post-instability regimes at very low computational costs. Additionally, to overcome the previously mentioned limitations, we add the possibility of contact between the flexible beam and the channel walls, enabling the calculation of limit-cycle oscillations (LCO) with, potentially, intermittent impacts.

Model Description

The model presented here deals with the fluid-structure interaction of a flexible beam confined by flow on each upper and lower sides, as illustrated in Figure 1. The formulation presented in the following is generic, in that it can, in principle, be applied to beams with arbitrary boundary conditions. However, in this paper we will deal solely with the particular case of a cantilever beam.

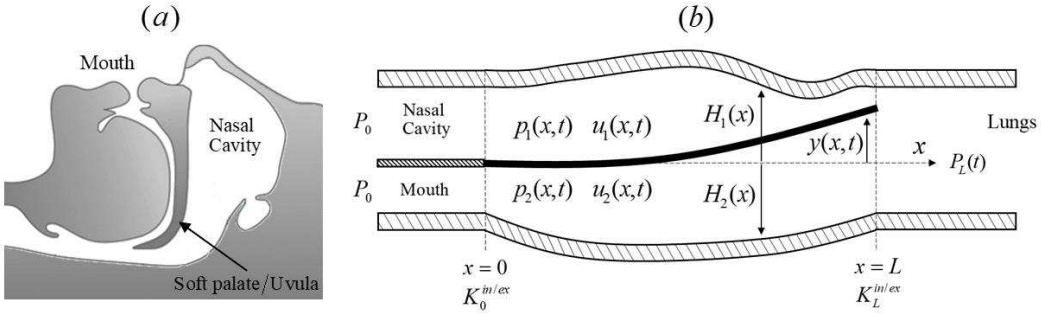

Figure 1 (a) Cross-sectional view of a human upper airway; (b) Schematic representation of the model.

Structural dynamics

The dynamics of a flexible linear beam are defined in terms of N modes, decoupled from the fluid. The modal parameters: modal masses m_n, frequencies ω_n, damping ratios ζ_n and mode shapes $\phi_n(x)$ can be calculated analytically for a beam with uniform cross-section or numerically for beams of any geometry, through either the Euler-Bernoulli or Timoshenko 1D linear beam equations. The beam displacement is developed as

$$y(x,t) = \sum_{n=1}^{N} \phi_n(x) q_n(t) \tag{1}$$

and the beam motion is finally described by the following set of N modal equations

$$m_n \ddot{q}_n(t) + 2m_n \omega_n \zeta_n \dot{q}_n(t) + m_n \omega_n^2 q_n(t) = b \int_0^L \left(p_2(x,t) - p_1(x,t) \right) \phi_n(x) dx \quad , \quad n = 1, 2 \ldots N \tag{2}$$

where b is the beam width and the modal forces are given by the projection of the pressure fields $p_1(x,t)$ and $p_2(x,t)$ (associated with the flow in the upper and lower channels, respectively), unto the beam modes.

Fluid dynamics

To derive the incompressible bulk-flow equations, we first consider small-to-moderate fluctuating channel heights $h_c(x,t)$, defined in terms of the beam motion

$$h_1(x,t) = H_1(x) - y(x,t) \quad ; \quad h_2(x,t) = H_2(x) + y(x,t) \tag{3}$$

where $H_1(x)$ and $H_2(x)$ are the distances from each wall to the position of the beam at rest and the index $c = 1, 2$ corresponds to the upper and lower channels, respectively. Following the derivation by Antunes & Piteau [17], the flow variables are taken as cross-sectionally averaged, $p_c(x,t)$ and $u_c(x,t)$. The continuity and momentum equations of the fluid are given, respectively, for each channel $c = 1, 2$, by

$$\frac{\partial h_c}{\partial t}+\frac{\partial}{\partial x}\left(h_c u_c\right)=0 \quad ; \quad \rho\left[\frac{\partial}{\partial t}\left(h_c u_c\right)+\frac{\partial}{\partial x}\left(h_c u_c^2\right)\right]+h_c\frac{\partial p_c}{\partial x}+\tau_c^w+\tau_c^b=0 \tag{4}$$

where ρ is the fluid's density, τ_c^w and τ_c^b are the shear stresses at the two interfaces (fluid-wall and fluid-beam) in each channel. Following the bulk-flow approach, the tangential stresses will be formulated as a head-loss model, given by

$$\tau_c^{w,b}=\frac{1}{2}\rho u_c\,|u_c|\,f_c^{w,b} \tag{5}$$

where f_c^w and f_c^b are the Fanning friction coefficients for each interface. Additionally, we assume both interfaces have equivalent frictional properties, hence $f_c^w=f_c^b=f$.

Aside from the distributed losses, we include as well singular dissipative effects at the boundaries. These are enforced at the boundary conditions and aim to encapsulate, in a simplified manner, the energy losses (turbulence, vortex shedding, etc.) occurring outside the domain. The second order system (4) is then submitted to the following flow boundary conditions at $x=0$ and $x=L$:

$$p_c(0,t)=P_0(t)-\rho\frac{1}{2}\left(u_c^2(0,t)-u_c(0,t)\left|u_c(0,t)\right|K_0\right) \;\; ; \;\; p_c(L,t)=P_L(t)-\rho\frac{1}{2}\left(u_c^2(L,t)+u_c(L,t)\left|u_c(L,t)\right|K_L\right) \tag{6}$$

where K_0 and K_L are the singular head-loss coefficients at the boundaries; $P_0(t)$ and $P_L(t)$ are the imposed pressures. For the particular case of a cantilevered beam, the head-loss coefficient K_0 is bound to have a minimal effect on the dynamics, as it acts on the clamped end of the beam. For steady inflow (in the positive $x-$direction), it acts simply as a control-valve, limiting the flow energy entering the domain. On the other hand, the turbulent effects expected at the trailing-edge suggest that K_L will probably have a significant effect on the coupling dynamics. Following reference models [11] [18], we will take $K_L=1$ and $K_0=0$, which as shown to provide a reasonable representation in these types of FSI systems.

Nonlinear analytical approach using formal solutions

Integrating the continuity equation (4) with respect to x leads us to a formal solution for the velocity fields in each channel c:

$$u_c(x,t)=\frac{Q_c(t)-\int\dot{h}_c(x,t)dx}{h_c(x,t)} \tag{7}$$

where the "constants" of integration (actually, time domain functions) $Q_c(t)$ represent the global unsteady flow rates (per unit width) in each channel. After replacement of (7) in the momentum equation (4) and again integrating with respect to x, we obtain the formal solution for the pressure field in each channel,

$$p_c(x,t)=\rho\int\left(\begin{array}{c}\dfrac{\int\ddot{h}_c dx}{h_c}-2\dfrac{\dot{h}_c\int\dot{h}_c dx}{h_c^2}+\dfrac{h_c'\left(\int\dot{h}_c dx\right)^2}{h_c^3}-\dfrac{1}{h_c}\dot{Q}_c(t)+2\left(\dfrac{\dot{h}_c}{h_c^2}-\dfrac{h_c'\int\dot{h}_c dx}{h_c^3}\right)Q_c(t)\\ +\dfrac{h_c'}{h_c^3}Q_c(t)^2+f\left(\dfrac{\left(\int\dot{h}_c dx-Q_c(t)\right)\left|\int\dot{h}_c dx-Q_c(t)\right|}{h_c^3}\right)\end{array}\right)dx+S_c(t) \tag{8}$$

where spatial and temporal derivatives are denoted by an upper dash and dot, respectively. The new "constants" of integration $S_c(t)$ describe the pressure at the entrance of the channels $S_c(t)=p_c(0,t)$. From here on, to simplify notation, we define the following auxiliary variables describing the terms in the formal solutions

$$A_c(x,t)=-\frac{\int\dot{h}_c dx}{h_c} \;\; ; \;\; B_c(x,t)=\frac{1}{h_c} \;\; ; \;\; C_c(x,t)=\frac{\int\ddot{h}_c dx}{h_c}-2\frac{\dot{h}_c\int\dot{h}_c dx}{h_c^2}+\frac{\left(\int\dot{h}_c dx\right)^2}{h_c^3}\left(h_c'+f\,\mathrm{sign}\left(\int\dot{h}_c dx-Q_c(t)\right)\right);$$

$$D_c(x,t)=2\left(\frac{\dot{h}_c}{h_c^2}-\frac{\int\dot{h}_c dx}{h_c^3}\left(h_c'+f\,\mathrm{sign}\left(\int\dot{h}_c dx-Q_c(t)\right)\right)\right) \;\; ; \;\; E_c(x,t)=\frac{1}{h_c^3}\left(h_c'+f\,\mathrm{sign}\left(\int\dot{h}_c dx-Q_c(t)\right)\right); \tag{9}$$

To enforce the boundary conditions, we replace the formal solutions (7)-(8) into expressions (6). After some algebra, we obtain two expressions for the constant of integration $S_c(t)$, in terms of $Q_c(t)$, $\dot{Q}_c(t)$ and the beam motion $A_c(x,t)-E_c(x,t)$. At the leading edge ($x=0$) we have simply

$$S_c(t) = P_0 - \rho\frac{1}{2}\left(1+\text{sign}\left(Q_c(t)\right)K_0\right)\left(B_c(0,t)Q_c(t)\right)^2 \tag{10}$$

while at the trailing edge ($x=L$) we get

$$S_c(t) = P_L(t) - \rho\left(\begin{array}{c} -\left(\int B_c(L,t)dx\right)\dot{Q}_c(t) \\ +\left(\int D_c(L,t)dx + A_c(L,t)B_c(L,t)\left[1-\text{sign}\left(A_c(L,t)+B_c(L,t)Q_c(t)\right)K_L\right]\right)Q_c(t) \\ +\left(\int E_c(L,t)dx + \frac{B_c^2(L,t)}{2}\left[1-\text{sign}\left(A_c(L,t)+B_c(L,t)Q_c(t)\right)K_L\right]\right)Q_c^2(t) \\ +\frac{A_c^2(L,t)}{2}\left[1-\text{sign}\left(A_c(L,t)+B_c(L,t)Q_c(t)\right)K_L\right]+\int C_c(L,t)dx \end{array}\right) \tag{11}$$

Then, combining (11) and (10), we are able to remove the constant of integration $S_c(t)$ and obtain two (one for each channel) first-order nonlinear ODEs in terms of the unsteady flow rates $Q_c(t)$,

$$\begin{array}{c} -\left(\int B_c(L,t)dx\right)\dot{Q}_c(t) \\ +\left(\int D_c(L,t)dx + A_c(L,t)B_c(L,t)\left[1-\text{sign}\left(A_c(L,t)+B_c(L,t)Q_c(t)\right)K_L\right]\right)Q_c(t) \\ +\left(\begin{array}{l} \int E_c(L,t)dx - \frac{B_c^2(0,t)}{2}\left(1+\text{sign}\left(Q_c(t)\right)K_0\right) \\ +\frac{B_c^2(L,t)}{2}\left[1-\text{sign}\left(A_c(L,t)+B_c(L,t)Q_c(t)\right)K_L\right] \end{array}\right)Q_c^2(t) \\ +\frac{A_c^2(L,t)}{2}\left[1-\text{sign}\left(A_c(L,t)+B_c(L,t)Q_c(t)\right)K_L\right]+\int C_c(L,t)dx + \frac{P_0(t)-P_L(t)}{\rho} = 0 \end{array} \tag{12}$$

Replacement of the formal solution for the pressure fields (8) into the beam modal equations (2), leads to a set of $2N$ nonlinear ODEs, in terms of the modal displacements $q_n(t)$, modal velocities $r_n(t)=\dot{q}_n(t)$ and the two unsteady flow rates $Q_1(t)$ and $Q_2(t)$. Together with the two flow rate ODEs (12), they form a closed set of first-order nonlinear differential equations describing the 1D fluid-structure model, in the form

$$[\mathbf{A}]\{\dot{\mathbf{x}}\}+[\mathbf{B}]\{\mathbf{x}\}=\{\mathbf{C}\} \tag{13}$$

where $\mathbf{x}=\{r_1(t),\ldots r_N(t),\, q_1(t),\ldots q_N(t),\, Q_1(t),\, Q_2(t)\}$, $[\mathbf{A}]$ and $[\mathbf{B}]$ are (dense) matrices of size $2N+2$, and $\{\mathbf{C}\}$ is a vector containing constant flow terms. Effectively, we are able to discretize our continuous 1D problem into a set of ODEs. However, there are nonlinear terms associated with beam motion (e.g. $\int A_c dx$) which contain modal summations in the denominator. As these terms cannot be simplified analytically, we do not reach "true" time-space separation, in the sense that the formulation does not contain time-independent spatial operators. During time-domain integrations, these terms need to be calculated at each time-step. Despite this fact, the formulation allows for temporal-integrations of the nonlinear system at very modest computational costs.

Results: linear stability and numerical validation

In this paper, for compactness, we have not shown the linearization of the above-mentioned system. It will suffice to say that linearization of the expressions above leads to a closed set of $2N+2$ ODEs (with constant spatial operators), which can then be formulated as an eigenvalue problem, from which we can infer the linear stability of the system under a set of given parameters.

In this section, with the aim of assessing the viability of the 1D simplified modelling approach and validating our results, we compare the linear stability results from our model to reference results. Even though the present modelling approach allows for channels of arbitrary shapes $H_c(x)$, we will consider only symmetric channels of constant section, i.e. $H_1(x)=H_2(x)=H$, on which most literature is based on. For the same reason, we will analyze configurations with flow in the positive direction only.

Following reference studies [9], we will present results in terms of the following non-dimensional parameters

$$U^* = U_0 L\sqrt{\frac{\rho_s e}{EI}} \quad ; \quad M^* = \frac{\rho_f L}{\rho_s e} \quad ; \quad H^* = \frac{H_0}{L} \tag{14}$$

where U^* is a reduced velocity (essentially the inverse of a Strouhal number), M^* is the fluid-beam mass ratio, and H^* is the confinement ratio. In our formulation, $H_0 = H_1(0) + H_2(0)$ and the fluid velocity U_0 is given by the steady component of the inlet velocity, i.e. $U_0 = (\bar{Q}_1 + \bar{Q}_2)/H_0$. Additionally, the Reynolds number Re is accounted implicitly by the Fanning friction coefficient f. To this end, we note the commonly used relation between Reynolds number Re and the friction coefficient f, established based on empirical data of steady flow [19], given by

$$\begin{cases} f = 12\,\mathrm{Re}^{-1} & \text{for} \quad \mathrm{Re} < \mathrm{Re}_0 \quad \text{(laminar)} \\ f = 0.055\,\mathrm{Re}^{-0.25} & \text{for} \quad \mathrm{Re} > \mathrm{Re}_0 \quad \text{(turbulent)} \end{cases} \tag{15}$$

where Re_0 is the Reynolds number separating laminar from turbulent flow ranges, taken here as $\mathrm{Re}_0 = 2500$.

Comparison to results from a 2-D viscous model

Here we compare linear stability results from our simplified model to those obtained by a more realistic 2D viscous model developed recently by Cisoni et al. [20]. In their paper [20], a 2D model is used to solve the nonlinear Navier-Stokes equations in the time-domain, including viscous effects. Several parametric sweeps were carried out to obtain stability curves in the nondimensional $(U^* - M^*)$ plane, for several (H^*, Re) pairings. Figure 2 shows a typical stability map in the $(U^* - M^*)$ plane, calculated with the present model and with the 2-D viscous model. Here, an undamped beam was considered, $\zeta_n = 0$, the confinement ratio was set at $H^* = 1/10$ and the Reynolds number at $\mathrm{Re} = 100$. Note that, in our formulation, the Reynolds number is set implicitly following relation (15), which leads to a friction coefficient $f \approx 0.14$. On the left are the stability boundaries in the $(U^* - M^*)$ plane and on the right the frequencies of the corresponding neutrally stable modes.

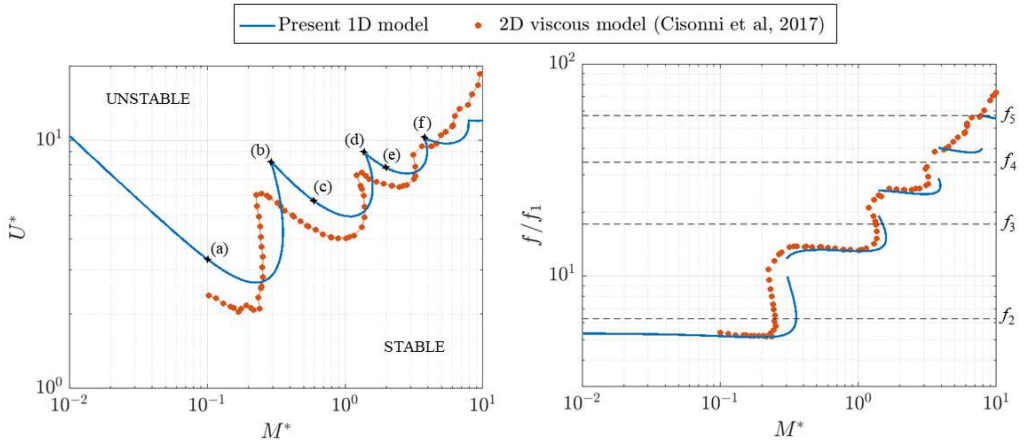

Figure 2 – Stability boundary in the $(U^* M^*)$ *plane (left) and the corresponding frequencies (right) for a system with confinement* $H^* = 1/10$ *and Reynolds number* $\mathrm{Re} = 100$. *The 2-D model results were retrieved from those presented in [20].*

The cascading stability boundary shown in Figure 2 is a typical result of cantilevered structures subject to axial flow, reported in many previous studies, including models which assume inviscid flow (see review in [9]). We note that results from the present model agree qualitatively well with those from the 2D model. Despite some minor quantitative differences, the overall stability behavior of the system is well encapsulated. Namely, the sharp transitions in the stability curves, associated with the well-known mode-switching behavior and illustrated clearly by the abrupt changes in the instability frequency, are well represented. This behavior occurs at increasing mass-ratios, whereby the first unstable mode in the system transitions from lower to higher order, i.e. the main unstable (coupled) mode is dominated by *in-vacuo* beam modes of progressively higher order. To clarify, Figure 3 illustrates the complex mode shapes associated with the various points (a)-(f) indicated in Figure 2. The minor quantitative differences (slight vertical and horizontal shifts in the $M^* - U^*$ plane), are likely explained by the inherent differences in the 1D and 2D modelling approaches, namely, the explicit vs. implicit account of viscous effects or the parabolic vs. constant velocity profiles stemming from explicit/implicit account of boundary layer effects.

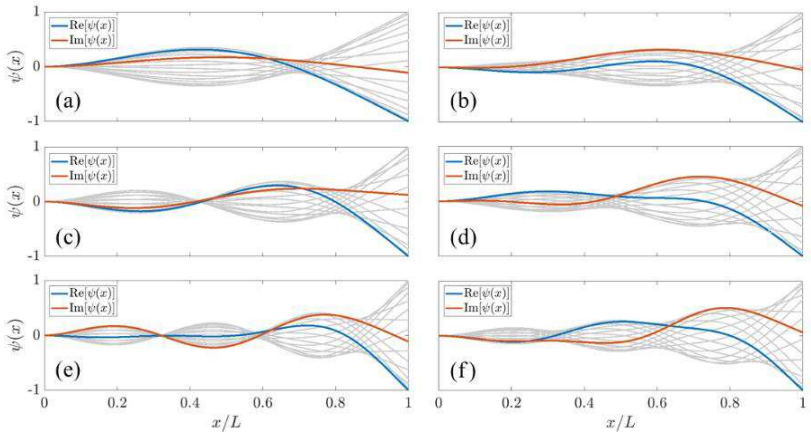

Figure 3 – Complex mode-shapes of the neutrally-stable modes associated with the boundary points (a)-(f) indicated in Figure 2. The real and imaginary parts of the mode shapes are indicated in blue and red, respectively. The grey lines illustrate the actual beam motion associated with the corresponding complex mode shapes.

Results: time-domain integrations and nonlinear dynamics

In this section we aim to explore the nature of the nonlinear regimes associated with a linearly unstable system through numerical time-domain integration. The set of nonlinear ODEs described in above (13) was solved using MATLAB's solver ode15i [21], an implicit scheme with variable time-stepping. Numerical simulations were started with the solutions of the steady configuration $\bar{q}_n$, $\bar{Q}_c$ as initial conditions, and a small perturbation force was applied to all beam modes to induce eventually unstable dynamics.

Stability and impact boundaries

As a first step to characterize the nonlinear behavior of the system, we examine the role of impacts and when they are more likely to occur. To this end, a series of numerical time-domain integrations were performed in the non-dimensional parametric space (U^*, M^*). We considered a symmetric configuration with confinement ratio $H^* = 1/10$, and friction coefficient $f = 0.14$. The simulations were run for several seconds until one of the following scenarios was encountered: (1) oscillations gradually decreased converging to the steady solution (linearly stable dynamics), (2) the oscillations grew until a stable limit cycle was reached, without the occurrence of impacts, or (3) oscillations grew until the beam eventually comes into contact with one of the walls, at which point the simulations were stopped. The difference between the latter two scenarios enabled us to estimate an "impact boundary", that is, a frontier in the (U^*, M^*) plane separating limit cycles with and without impacts. Because contact was not accounted in this first study, the beam was described by only $N = 10$ modes. All modal damping coefficients were set to $\zeta_n = 0.01$. The resulting map is shown in Figure 4.

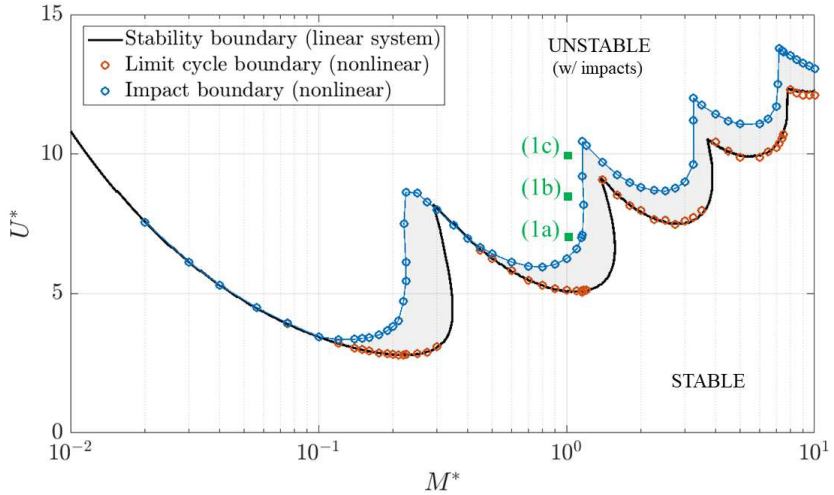

Figure 4 – Stability map of a system with confinement ratio $H^* = 1/10$ and friction coefficient $f = 0.14$, in the (U^*, M^*) plane. The linear stability boundary (black line) is compared to the limit cycle boundary found by the nonlinear simulations (orange circles). The impact boundary (blue line) illustrates the frontier in which unstable dynamics lead to contact between the beam and the confinement walls. The nonlinear limit cycles associated with the points marked (1a-c) will be shown in the following sections.

We see that the stability boundary predicted by the linearized system is coherent with the unstable dynamics observed in the nonlinear simulations. As for the impact boundary, we note that the regions in which limit cycles without impacts occur (grey area) are not extensive. Noticeably, we underline the fact that for small mass ratios (heavy beams or light fluids) these regions simply do not exist and the flutter instability, however weak, inevitably leads to large amplitude beam motions and eventual contact with the side walls. This seems physically plausible as, in these cases, the inertia of heavier beams will tend to outweigh the restoring forces from a light fluid.

Elastic impact model

Numerous experimental (and modelling) observations [3] [4] [14] [16] demonstrate that nonlinear motions of cantilevered plates in confined axial flow regularly present intermittent impacts between the beam and the side-walls. Consequently, previous attempts at modelling limit-cycle oscillations (LCO), eventually encountered limitations in their solutions, at regimes where the motion of the plate is large enough that collisions become inevitable.

In the current bulk-flow formulation, the addition of dynamic impact between the beam and the side walls is not a trivial task. One of the major challenges relates to the fact that the solutions for flow velocity and pressure fields present singularities at the moment of contact, i.e. when the channel height $h_c = 0$. Consequently, classical penalty methods, reliant on "interpenetration", are incompatible with the current flow model. Without dealing with these delicate issues, here we present a pragmatic approach, based on a regularized impact formulation, that allows us to include impacts in a simple manner that is compatible with the flow formulation. Since the fluid equations do not allow for beam penetration, an impact force $F_i(x,t)$ is applied on the beam just before contact, in regions of the beam which have trespassed a small regularization parameter ε (Figure 5). In essence, we allow some flow leakage at the moments of "contact", such that an impact force can be applied to the beam without fully restricting the flow dynamics.

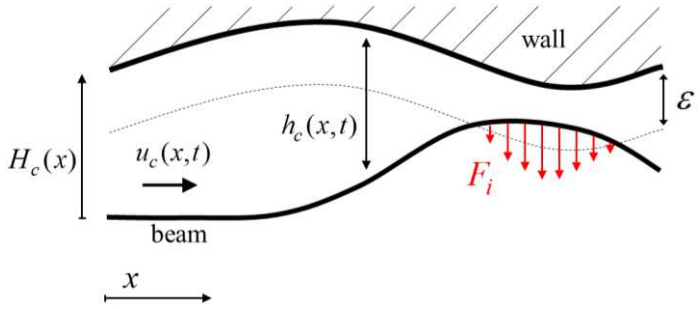

Figure 5 – Illustration of the beam violation right before contact and corresponding impact force.

A simplified version of a classic Hertz model is considered, where the impact force is linearly proportional to a violation parameter $v(x,t)$, describing the penetration distance between the beam a "virtual" wall defined by $H_c(x) - \varepsilon$, as illustrated in Figure 5. Then, the impact force $F_i(x,t)$ is given by

$$F_i(x,t) = \begin{cases} k_i\, v(x,t) & \text{if } v(x,t) > 0 \\ 0 & \text{otherwise} \end{cases} \tag{16}$$

where k_i is an impact stiffness and the violation amplitude is given by $v(x,t) = \varepsilon - h_c(x,t)$. The sign of $F_i(x,t)$ is defined for each channel: $F_i > 0$ for $c = 2$; $F_i < 0$ for $c = 1$.

Illustrative examples of limit-cycle oscillations with intermittent impacts

Here we illustrate a few limit cycles that include intermittent impacts, namely, the solutions for the configurations indicated in Figure 4 by points (1a), (1b) and (1c). These configurations have a constant mass ratio of $M^* = 1$ and various reduced velocities $U^* = [7, \ 8.5, \ 10]$, respectively. For these simulations, a large number of beam modes was considered, $N = 40$, to ensure the impact dynamics are well represented. In the following simulations, the non-dimensional impact stiffness was taken as $k_i^* = k_i / m_1 \omega_1^2 = 10^6$ (normalized by the stiffness of the first beam mode) and the non-dimensional regularization parameter $\varepsilon / H = 10^{-3}$.

Figure 6 shows snapshots of the beam motion and Figure 7 the evolution of the modal velocities $r_n(t)$ and the unsteady flow rates $Q_c(t)$, for the three configurations (1a), (1b) and (1c). Moreover, in Figure 8 we show the phase-portrait of the beam tip, the evolution of the tip displacement $y(L,t)$, the spectra of the tip velocity and RMS-value of the modal displacements $q_n(t)$, for all three configurations. Finally, we show in Figure 9 the impact force applied on the beam throughout the limit cycles. The impact force is expressed as the spatial integral of $F_i(x,t)$, normalized by a reference force $F_0 = m f_1^2 H$, where m is the total mass of the beam and f_1 is the frequency of the first in-vacuo beam mode.

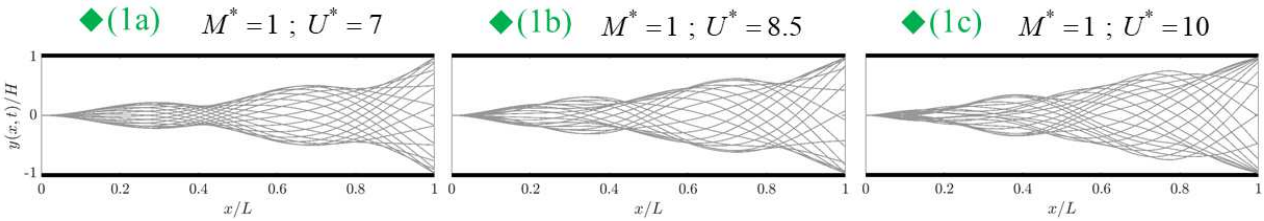

Figure 6 - Snapshots of the beam motion during one cycle for configurations (1a), (1b) and (1c).

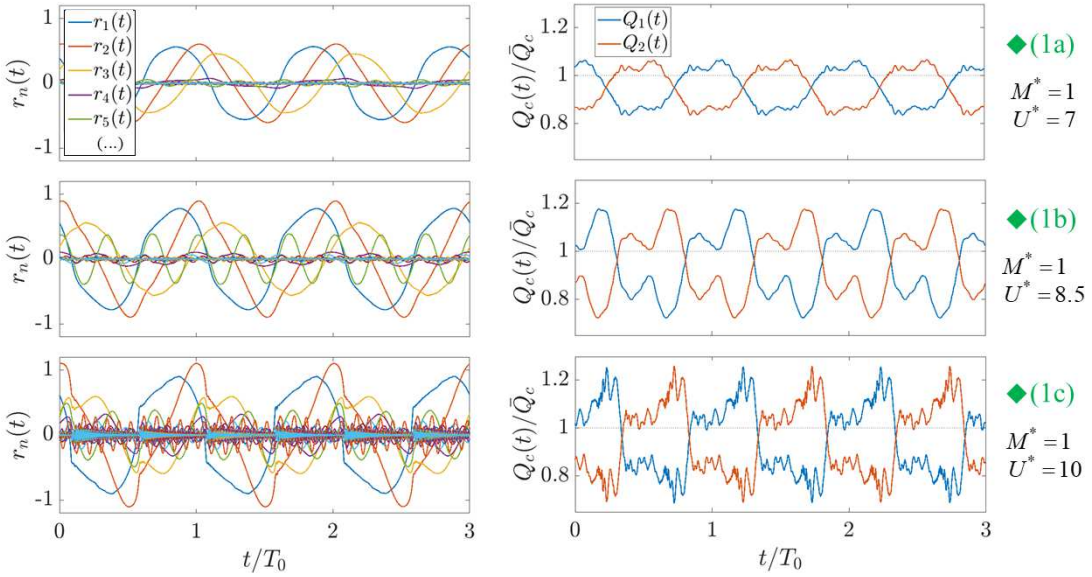

Figure 7 - Temporal evolution of the modal velocities $r_n(t)$ (left) and unsteady flow rates $Q_c(t)$ (right) in the limit cycles associated with configurations (1a), (1b) and (1c). For clarity, time scales are normalized by the fundamental period of the corresponding limit-cycle T_0.

In Figure 6 we notice that, in all cases, intermittent contact occurs solely at the tip of the beam. As the velocity U^* increases (1b-c), impacts become more violent and the beam motion becomes increasingly perturbed, as higher order beam modes are intermittently excited and start playing a more prominent role in the overall beam motion. These effects are also seen by the evolution of the modal velocities shown in Figure 7 and the RMS-values in Figure 8 . When impacts are relatively weak (1a), the tip simply "grazes" the wall and the overall beam motion is not significantly altered compared to the mode shapes estimated by the linear stability analysis.

Similarly, the oscillations of the flow rates become increasingly abrupt in the presence of violent impacts. However, it is interesting to note that sharp changes in the unsteady flow-rate (e.g. bottom-right plot in Figure 7) do not occur at the moments of contact but rather at the moments when the beam motion rapidly shifts from one side of the channel to the other. This effect can be illustrated, for example, by the beam-tip motion shown in Figure 8. Here we notice that as impacts become stronger, the overall contact time also becomes larger, meaning as well that the beam-tip will shift sides more abruptly, hence generating sharp fluctuations in the flow-rates. As expected, flow rates also oscillate around a value slightly lower than their steady component $\bar{Q}_c$. This means that the overall mass transport is reduced by the fluttering beam, compared to a static scenario. This seems physically plausible as, during flutter, some of the energy carried by the flow is transferred to the beam and lost through either structural dissipation or increased flow-dissipation effects.

In Figure 8 we note that the motions become increasingly nonlinear in the presence of stronger impacts. The phase-portrait shows more perturbed motions with larger gradients. Naturally, the spectra of the beam tip show a large number of high order harmonic components, increasing in amplitude as impacts become more violent. It is worth noting that, in limit cycles with very strong impacts (1c), the oscillations are not strictly periodic. Although the low frequency motions are stable, we notice small high frequency perturbations, related to the unsynchronized motion of the intermittently excited higher order beam modes. This behavior is clearly illustrated by the spectra of (1c), where we notice not only an increase in the amplitude of the harmonics, but also a visible presence of noise-like spectral behavior. Nevertheless, these motions might be tentatively classified as perturbed periodic oscillations, rather than aperiodic dynamics.

The impact forces represented in Figure 9 illustrate the fact that, during each beam-wall interaction, the beam tip impacts the wall multiple times. This chattering effect is a typical behavior of systems with impacts in multi-modal structures. In weaker impacts (1a) we notice only a few impacts of decreasing strength while in more violent regimes (1b-c) contact is composed of multiple impacts with stronger associated forces and an overall longer chattering time.

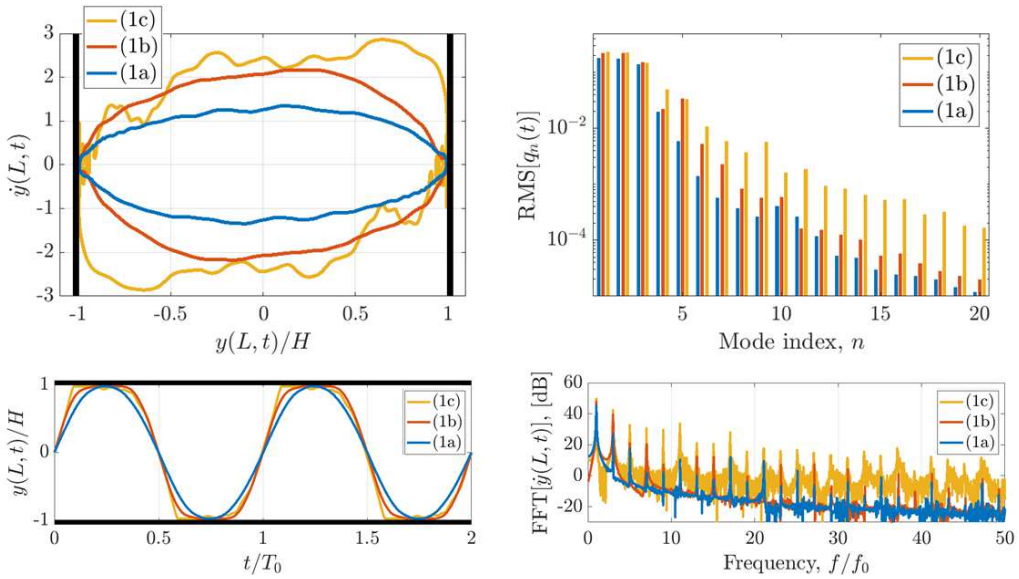

Figure 8 - Phase-portrait of beam tip (top-left); root-mean-square (RMS) value of the modal displacements (top-right); beam tip displacement (bottom-left) and spectra of the tip velocity (bottom-right, for the three configurations (1a), (1b) and (1c). For clarity, time/frequency scales are normalized by the fundamental period/frequency of the corresponding limit-cycle T_0 *and* f_0.

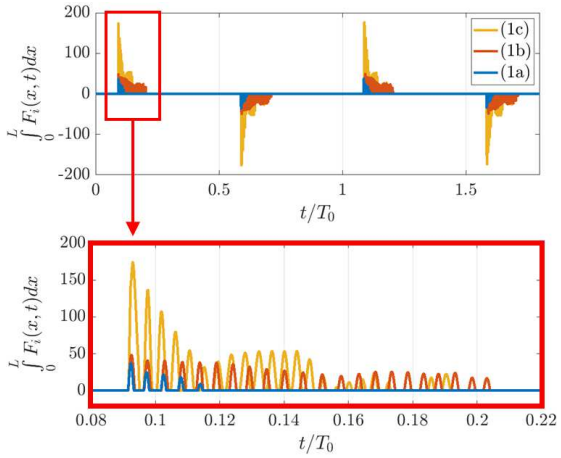

Figure 9 – The evolution of the non-dimensional impact force through the limit-cycles associated with configurations (1a), (1b) and (1c). For clarity, time scales are normalized by the fundamental period of the corresponding limit cycle T_0.

Conclusions

In this paper we have presented a framework for the comprehensive study of the nonlinear dynamics of a flexible beam subject to axial flow in a confined passage. Previous studies have been constrained by either large computational costs associated with 2D CFD models, the lack of a nonlinear flow formulation, and/or by the occurrence of contact between the beam and the side-walls. Here, a 1D model was formulated where the beam is described by its in-vacuo modes and incompressible bulk-flow equations, including distributed and localized head-losses, are used for the flow in both channels. An analytical resolution, based on the formal solutions for the velocity and pressure fields, is developed and leads to a fully nonlinear formulation of the fluid-structure interaction. Moreover, the possibility of contact between the beam and the walls is accounted for by a regularized impact model.

As a preliminary assessment of the potential of the proposed approach, results of linear stability analysis were compared to reference results using more realistic 2D CFD model. Overall, results were positively validated with only minor quantitative differences, at least for relatively narrow passages. Although not shown here, for brevity, it is worth noting that for larger confinement ratios $H/L >\sim 1/5$, we notice larger errors, as expected from the simplifying assumptions made in the bulk-flow approach.

Subsequently, nonlinear time-domain integrations were performed in order to illustrate the dynamical behavior occurring in such systems. Firstly, several simulations were performed to characterize the nonlinear dynamics for different configurations in the (M^*, U^*)-space. This led to a mapping of the nonlinear dynamics, separating the regions where limit cycles with and without impacts occur. Results suggest that, for low mass ratios (heavy beams/light fluids), the initial flutter instability always leads to contact, likely due to the contrast of the inertia of a heavy beam to that of a

light fluid. For moderate-to-large mass ratios, there are regions in the (M^*, U^*)-space where limit cycles without impacts occur, although these are relatively narrow. Secondly, several LCO with intermittent impacts were shown to elucidate the nature of the resulting nonlinear regimes. The lack of experimental data on the ensuing limit-cycles prevents us from a meaningful validation of our results, nevertheless, they seem physically plausible and consistent with experimental observations, at least qualitatively.

To the authors best knowledge, the presented framework allowed, for the first time, the calculations of the post-instability behavior of fluttering beams in confined flow, including vibro-impact dynamics. Future work might deal with the refinement of the impact model, to treat flow contact conditions and include damping. Moreover, bifurcation analysis using methods for the calculation and continuation of periodic solutions can contribute to a more comprehensive understanding of the associated nonlinear dynamics.

References

[1] A. T, V. A and P. O, "Understanding sleep-disordered breathing through mathematical modelling," *Sleep Medical Reviview,* vol. 13, no. 5, pp. 333-343 , 2009.

[2] P. Norton and E. Dunn, "Snoring as a risk factor for disease: an epidemiological survey," 1995.

[3] Y. Aurégan and C. Depollier, "Snoring: Linear Stability Analysis and In-Vitro Experiments," *Journal of Sound and Vibration,* vol. 188, no. 1, pp. 39-54, 1995.

[4] L. Huang, "Mechanical Modeling of Palatal Snoring," *Journal of the Acoustical Society of America,* vol. 97, pp. 3642-3648, 1995.

[5] P. Hidalgo, S. Jha and A. Glezer, "Enhanced heat transfer in air cooled heat sinks using aeroelastically fluttering reeds," *Thermal Investigations of ICs and Systems (THERMINIC),* pp. 1-6, 2015.

[6] S. Sherrit, H. Lee, P. Walkemeyer, T. Winn, L. Tosi and T. Colonius, "Fluid flow nozzle energy harvesters," *Sensors and Smart Structures Technologies for Civil, Mechanical, and Aerospace Systems,* 2015.

[7] F. Avanzini and M. Walstijn, "Modelling the mechanical response of the reed-mouthpiece-lip system of a clarinet. Part 1: a one-dimensional distributed model," *Acta Acustica United with Acustica,* vol. 90, pp. 537-547, 2004.

[8] M. P. Paidoussis, Fluid-Structure Interactions: Slender Structures and Axial Flow, San Diego, California: Academic Press, 2004.

[9] K. Shoele and R. Mittal, "Flutter instability of a thin flexible plate in a channel," *Journal of Fluid Mechanics,* vol. 786, pp. 29-46, 2016.

[10] G. Tetlow and A. Lucey, "Motions of a cantilevered flexible plate in viscous channel flow driven by a constant pressure drop," *Communications in Numerical Methods in Engineering,* 2009.

[11] H. Nagakura and S. Kaneko, "Stability of a cantiliver beam subject to one-dimensional leakage flow," *Proceedings Asia-Pacific Conference '93, Kitakyushiu, Japan,* vol. 1, pp. 352-359, 1993.

[12] F. Inada and S. Hayama, "A Study on the Leakage-Flow-Induced Vibrations. Part 1: Fluid Dynamic Forces and Moments Acting on the Walls of a Narrow Tapered Passage," *Journal of Fluids and Structures,* vol. 4, pp. 395-412, 1990.

[13] Y. Yadykin, V. Tenetov and D. Levin, "The flow induced vibration of a flexible strip hanging vertically in parallel flow. Part 1: temporal aeroelastic instability," *Journal of Fluids and Structures,* vol. 15, pp. 1167-1185, 2001.

[14] S. Alben, "Flag flutter in inviscid channel flow," *Physics of Fluids,* vol. 27, 2015.

[15] X. Wu and S. Kaneko, "Linear and Nonlinear analyses of sheet flutter induced by leakage flow," *Journal of Fluids and Structures,* vol. 20, pp. 927-948, 2005.

[16] K. Fujita, H. Morikazu and A. Shintani, "A consideration on pre- and post-instability of an axisymmetric elastic beam subject to axil leakage flow," *Journal of Fluids and Structures,* vol. 23, pp. 463-478, 2007.

[17] J. Antunes and P. Piteau, "A nonlinear analytical model for the squeeze-film dynamics of parallel plates subject to axial flow," *Journal of Fluids and Structures,* vol. 52, pp. 1491-1504, 2010.

[18] L. P. Tosi and T. Colonious, "Modelling and simulation of a fluttering cantilever in channel flow," *Journal of Fluids and Structures,* 2019.

[19] R. Blevins, Fluid Dynamics, New York, USA: Van Nostrand Reinhold Company, 1984.

[20] J. Cisonni, A. Lucey, N. Elliot and M. Heil, "The stability of a flexible cantilever in viscous channel flow," *Journal of Sound and Vibration,* 2017.

[21] "MATLAB - Numerical Integration and Differential Equations," Mathworks, Inc., 2021. [Online]. Available: https://www.mathworks.com/help/matlab/ref/ode15i.html.

EXPLOITING NONLINEAR DYNAMICS FOR MANIPULATION OF ACOUSTICALLY LEVITATED PARTICLES

Izhak Bucher and Amit Dolev
Mechanical Engineering, Technion, Haifa, Israel

Summary. This paper describes an experimentally verified local and spatial model of a standing waves acoustic levitation system. By tailoring the waveforms fed to an array of ultrasonic transducers, arranged in a dome formation, individual potential-wells' can be created and altered periodically. The waveforms contain a fast part, geared to produce the nonlinear acoustic field and a slow part, tuned to create slow modulation of the local stiffness and principle parametric excitation. The latter can bring about large controlled oscillations of the levitated objects. Presented is a local, nonlinear model describing the dynamics of an individual acoustically levitated particle in a single potential well. And, for the first time, the dynamics of coupled floating particles tied through the weak nonlinear acoustic field, is shown. Nonlinearity of the acoustic field serves several purposes here: (i) It creates the nonlinear field with potential-wells and hence acoustic levitation (ii) It creates large motions and that produce hopping out of potential wells, given a suitably modulated slow excitation.

Introduction

This paper describes a method to perform fast dynamic manipulation of acoustically levitated particles. The results extend high frequency and high intensity acoustic excitation methods to dynamically manipulate standing and traveling wave patterns affecting particles' motion in 3D space in a controlled manner. Sound pressure levels that are generated in standing waves patterns at around 40 kHz can exceed 140db within a restricted area, giving rise to nonlinear acoustic phenomena. Such nonlinear phenomena can hold and mobilize particles of several millimeter in size at 10-80Hz frequencies. State-of-the-art research enables quasi-static motions of levitated particles by affecting the acoustic field and to slowly move their stable locations. The present work shows experiments where parametric excitation is created by modulating the acoustic field such that particles can be made to oscillated within acoustic potential wells. To achieve these goals, high order nonlinear models are generated, and embedded in a fast (1MHz sampling rate) excitation signals. The main uses of acoustic manipulation are in containerless and micro-gravity processing where contamination is a concern, when mild holding forces are sought and when particles and drops are to be mixed or moved in unison.

Described is the model of slow particle motion and its link to the fast (ultrasonic) acoustic excitation. In addition, some fast videos of a working experimental system are analyzed to produce qualitative and quantitative parameters shading light on the physical phenomenon. If viscosity has a small effect compared with the higher order acoustic radiation forces, the analysis of acoustic levitation devices (ALD), usually considers higher terms beyond the linear approximation of the pressure and particle velocity, but viscosity is often neglected in the initial computations.

Acoustic radiation pressure and force – simplified form

To predict nonlinear acoustic phenomenon creating the levitation, the well-known linear acoustic wave equation (2), does not suffice, and higher order terms should be considered [1,2]. Neglecting dissipation and heat related loss [3,4] for simplicity, one can obtain the fundamental nonlinear effect that predicts the stable acoustic potential-wells in space. These field parameters are used, whereas it is assumed that there is no mean flow in the cavity:

$$p = p_0 + p_1 + p_2 + ..., \quad \mathbf{u} = \mathbf{u}_0 + \mathbf{u}_1 + \mathbf{u}_2 + ... = \mathbf{u}_1 + \mathbf{u}_2 + ..., \quad \rho = \rho_0 + \rho_1 + \rho_2 + ... \tag{1}$$

The pressure field comprising the ambient pressure p_0 and high order terms p_1 and p_2, $\mathbf{u}$ is the particle velocity field expended in a similar manner and ρ is the density field comprising the ambient density and higher order terms. In the linear case, the wave equation reduces to

$$\nabla^2 p_1 = \frac{1}{c_0^2}\frac{\partial^2 p_1}{\partial t^2}. \tag{2}$$

In the nonlinear case, the time-averaged acoustic radiation pressure can be calculated from these linear fields [1]:

$$\langle p_2 \rangle = \frac{1}{\rho_0 c_0^2}\langle p_1^2 \rangle - \frac{\rho_0}{2}\langle \mathbf{u}_1 \cdot \mathbf{u}_1 \rangle, \tag{3}$$

whereas c_0 is the sound speed in the medium. The radiation force acting on an object is calculated as:

$$\mathbf{F}_{\text{rad}} = -\int_{S_0} \langle p_2 \rangle \mathbf{n} \mathrm{d}S - \int_{S_0} \rho_0 \langle (\mathbf{n}\cdot\mathbf{u}_1)\mathbf{u}_1 \rangle \mathrm{d}S . \tag{4}$$

whereas S_0 is the object surface while $\mathbf{n}$ represents the surface normal vector. Viscous effects that create oblique and tangent forces [5] are ignored her. For small (i.e., the radius is much smaller than the acoustic wavelength) rigid spheres, the acoustic radiation force is approximated by:

$$\mathbf{F}_{\text{rad}} = -\nabla U, \quad U = 2\pi R^3 \left(\frac{f_1}{3\rho_0 c_0^2}\left\langle \left(p_1^{in}\right)^2 \right\rangle - \frac{f_2 \rho_0}{2}\left\langle \mathbf{u}_1^{in} \cdot \mathbf{u}_1^{in} \right\rangle \right), \; f_1 = 1 - \frac{\rho_0 c_0^2}{\rho_p c_p^2}, \quad f_2 = 2\left(\frac{\rho_p - \rho_0}{2\rho_p + \rho_0} \right). \tag{5}$$

Here, R, ρ_p and c_p are the sphere radius, density and sound speed in the sphere, $\bullet^{in}$ are computed in the absence of the sphere in the field, and U is called Gor'kov potential [6]. It is now possible to define the total potential energy as $U_{\text{tot}} = U + U_{\text{gravity}}$, and levitate objects steadily in the minima of U_{tot}.

Analytical model of a levitated particle subjected to parametric excitation

The dynamics of an acoustically levitated particle is governed by several physical effects: acoustic radiation forces, acoustic streaming, drag force and inertia. To accommodate effects not considered by (5) the following dynamical model for an acoustically levitated particle subjected to PE was developed, were the parameters were estimated experimentally [7].

$$u'' + 2\varepsilon\zeta_1 u' + \varepsilon\zeta_2 u'^2 + \varepsilon^2\zeta_3 u'^3 + \left(1+\varepsilon\gamma\cos(\Omega\tau)\right)\left(u + \varepsilon\kappa_2 u^2 + \varepsilon^2\kappa_3 u^3\right) = \varepsilon\gamma F\cos(\Omega\tau). \quad (6)$$

Equation (6) is dimensionless, where u is the particle position relative to the equilibrium position, ζi are damping coefficients, γ is the parametric excitation (PE) magnitude generated by modulating the voltage provided to the transducer [7], κi are nonlinear stiffness coefficients, Ω is the scaled parametric excitation frequency and F is an external force amplitude. The damping coefficients related terms dissipates energy from the system and can be due to drag, viscosity and acoustic streaming. The paper will include some asymptotic analysis and experimental results.

Contactless particle manipulation via standing wave acoustic levitation - experiments

In standing wave-based levitation, a strong standing wave acoustic field is generated in a confined space, also known as the acoustic cavity. When an object is placed in the cavity it is subjected to an acoustic radiation pressure, the control of this pressure allows manipulation of the object. The ability to control the motion of a floating particles vertically and horizontally is demonstrated by the experimental system depicted in Fig.1.

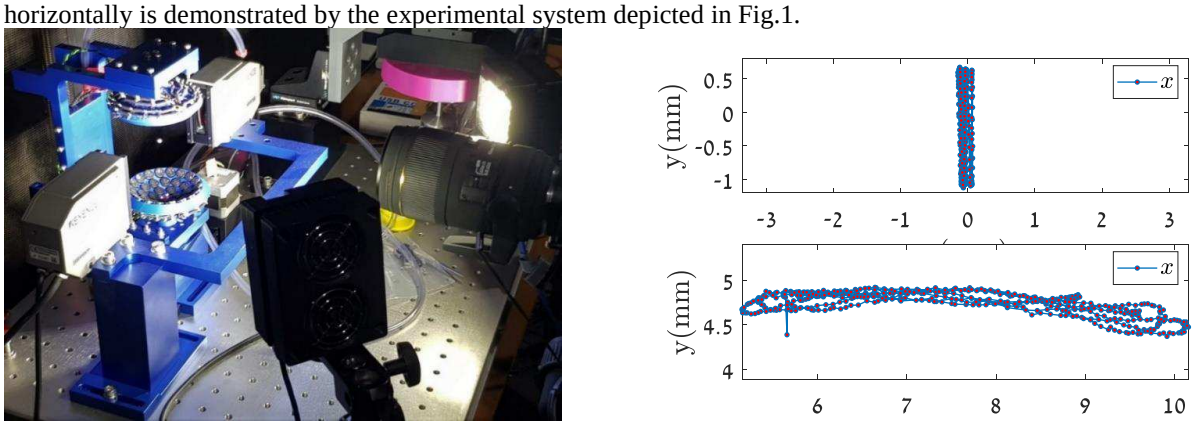

Figure 1. Left: Fast video set-up. Showing single levitated particle and fast Video recording (40,000 fps). Right/top: Fast video particle tracking using (DIC), horizontal oscillations within the potential-well for Ω=16.5 Hz. Right/bottom: vertical oscillation by inducing Ω=31 Hz videos. Links: **horizontal** and **vertical**.)

Another feature not predicted by the Gor'kov's theory is the coupling between levitated particles when the acoustic field is modulated at suitable frequencies as shown below (see also [7]). The frames shown in Figure 2 illustrates that the bottom particle is stationary while the top and 2nd from bottom move in unison. The latter is caused by higher order forces than described by Gor'kov's theory and is one of the proposed topics.

Figure 2. Showing 3 frames from a fast video, spaced about 5 milliseconds apart. Using the experimental system Fig.1. See seconds 7-8 in Link to **VIDEO#1**. For modulating the excitation at 37.83 Hz.

Conclusions

Presented is the analysis and experiments of an acoustic levitation system capable of manipulating levitated particles by means of time varying nonlinear effects. It is shown that previously ignored effects are important for the dynamics of an array of levitated particles. Nonlinear effect are controlled by a model based fast signal processor, showing good agreement with the asymptotic model.

References

[1] M.A.B. Andrade, N. Pérez, J.C. Adamowski, Review of Progress in Acoustic Levitation, Brazilian J. Phys. (2017).
[2] A.D. Pierce, Acoustics, 3rd ed., Springer International Publishing, Cham, 2019. doi:10.1007/978-3-030-11214-1.
[3] M. Hamilton, D. Blackstock, Nonlinear Acoustics: Theory and Applications, 1st ed., academic press, San Diego, 1998.
[4] R.T. Beyer, Nonlinear acoustics, 1974.
[5] S.L. Garrett, Understanding Acoustics, Springer International Publishing, Cham, Switzerland, 2017. doi:10.1007/978-3-319-49978-9.
[6] L.P. Gor'kov, Forces acting on a small particle in an acoustic field within an ideal fluid, Dokl. Akad. Nauk SSSR. 140 (1961) 88–91. http://www.mathnet.ru/eng/dan25473 (accessed November 8, 2018).
[7] A. Dolev, S. Davis, I. Bucher, Noncontact Dynamic Oscillations of Acoustically Levitated Particles by Parametric Excitation, Phys. Rev. Appl. 12 (2019) 034031. doi:10.1103/physrevapplied.12.034031.

Cristal Baschet: minimal model to predict the emergence of self-sustained oscillations

Audrey Couineaux, François Gautier and Frédéric Ablitzer
Laboratoire d'Acoustique de l'Université du Mans, CNRS UMR 6613, Le Mans, France

Context

The Cristal Baschet (Fig. 1a) is a contemporary musical instrument composed of a large number of glass rods arranged in chromatic scale. The sound is produced by rubbing glass rods with wet fingers, which causes the occurrence of stick-slip phenomenon. Each rod is connected to an assembly of threaded shafts, whose mechanical properties determine the pitch of the note. The vibrations are then transmitted to large metal sheets or cones that act as radiating elements. The manufacturing and tuning of the instrument is essentially based on empirical know-how and involves many parameters. Their influence on the sound and playability of the instrument is not clearly understood. One of the problems encountered is the difficulty to produce sounds in the high register of the instrument. In this study, a minimal model of Cristal Baschet is developed to analyze the emergence of self-sustained oscillations by means of linear stability analysis, with the aim of proposing design rules to improve the playability of the instrument.

Model

The minimal model focuses on the interaction between the wet finger and an isolated resonator (Fig. 1b). The resonator consists of a glass rod connected to a threaded shaft. Its dynamic behavior is represented by a set of modes. The modal parameters, which depends on design parameters (geometry, material properties...), can be obtained from a finite element model or from experimental modal analysis of the instrument. To model the occurrence of self-sustained oscillations from the frictional interaction with the finger, the knowledge of mode shapes at the interaction point is sufficient. Two gesture parameters, i.e. parameters that are controlled by the musician, are considered: the velocity of the finger v_f along the rod and the normal force F_N exerted by the finger on the rod. To describe the interaction between the finger and the resonator, the friction law considered in this study assumes that the glass rod perfectly sticks to the finger during sticking phases ($\Delta v = 0$) and that the friction force during sliding phases depends on the relative velocity $\Delta v = \dot{u} - v_f$ between the finger and the glass rod [2]. The sliding friction force is therefore expressed as $F_T = \mu(\Delta v) F_N$ with

$$\mu(\Delta v) = \mu_d + \frac{\mu_s - \mu_d}{1 - \Delta v / v_0} \,, \tag{1}$$

where μ_s is the coefficient of static friction, μ_d the asymptotic coefficient of dynamic friction and v_0 a parameter controlling the shape of the friction curve (Fig. 1c).

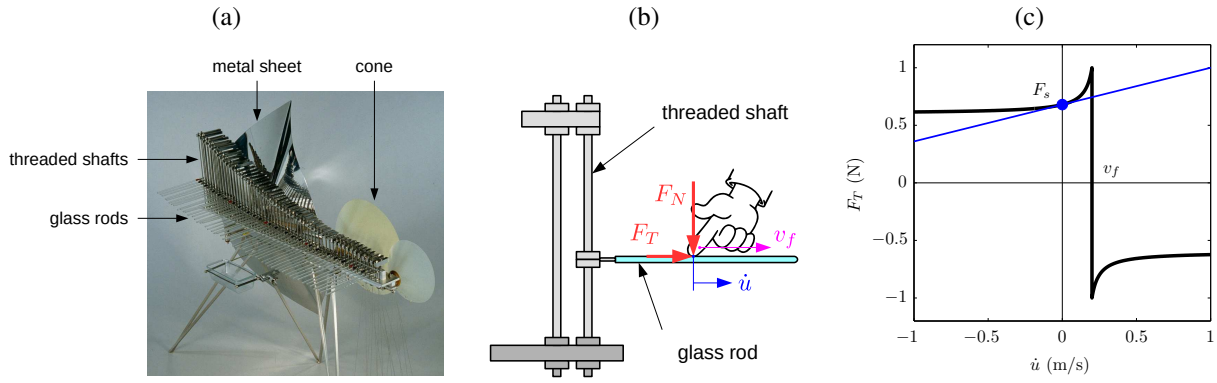

Figure 1: (a) Cristal Baschet (adapted from [1]). (b) Interaction between wet finger and resonator. (c) Friction curve and its linearization around static equilibrium in sliding situation.

Linear stability analysis

As a first step to determine the conditions at which the self-sustained oscillations can occur, the stability of the static solution in a sliding state is examined [3]. For this purpose, it is considered that the glass rod is in static equilibrium (i.e. $\dot{u} = 0$) under the action of a constant friction force F_s resulting from the motion of the finger at constant speed. Assuming small fluctuations of the glass rod velocity around its equilibrium position, a linearization of the friction curve around the static solution is performed to express the corresponding variations in friction force as $F_T \approx F_s + C\dot{u}$, where coefficient C represent the local slope of the friction curve (Fig. 1b). Inserting this linearized expression into the modal equations yields

$$\mathbf{M}\ddot{\mathbf{q}} + \left(\mathbf{C} - C\boldsymbol{\Phi}_f \boldsymbol{\Phi}_f^{\mathrm{T}}\right)\dot{\mathbf{q}} + \mathbf{K}\mathbf{q} = \boldsymbol{\Phi}_f F_s \,, \tag{2}$$

where $\mathbf{M} = \text{diag}(m_n)$, $\mathbf{C} = \text{diag}(2m_n\xi_n\omega_n)$, $\mathbf{K} = \text{diag}(m_n\omega_n^2)$ are the modal mass, damping and stiffness matrices, and $\mathbf{\Phi}_f$ is a column vector containing the value of each mode shape at the location of the finger. Looking for a solution to the homogeneous equation in the form $\mathbf{Q}e^{\lambda t}$, one obtains an eigenvalue problem

$$\left(\lambda^2\mathbf{M} + \lambda\left(\mathbf{C} - C\mathbf{\Phi}_f\mathbf{\Phi}_f^{\mathrm{T}}\right) + \mathbf{K}\right)\mathbf{Q} = \mathbf{0}\,, \tag{3}$$

where each eigenvalue λ characterizes an oscillating component whose amplitude either decreases (if $\mathcal{R}e(\lambda) < 0$) of increases (if $\mathcal{R}e(\lambda) > 0$) over time, corresponding respectively to stability or instability of the static equilibrium. Self-sustained oscillations occurs when the smallest modal damping ratio $\xi_{\mathit{eff}} = -\mathcal{R}e(\lambda)|\lambda|^{-1}$ is negative (Fig. 2). The threshold depends on gesture parameters and friction law (both included in coefficient C) and design parameters (through the value of mode shapes $\mathbf{\Phi}_f$ at the interaction point).

Time-domain simulations

In order to verify the criterion calculated from linear stability analysis, time-domain simulations are performed using an explicit numerical scheme of the form

$$\mathbf{x}(t_{i+1}) = \mathbf{A}\mathbf{x}(t_i) + \mathbf{B}\mathbf{f}(t_i)\,, \tag{4}$$

where $\mathbf{x}$ is a vector containing all modal coordinates and their time derivatives and $\mathbf{f}$ is a vector containing the modal forces. The coefficients in $\mathbf{A}$ and $\mathbf{B}$ are obtained using a piecewise constant approximation of the right-hand side of modal equations. At each time step, the unknown friction force F_T exerted by the finger on the glass rod is obtained by enforcing a sticking or sliding condition. The results of time-domain simulations (Fig. 3) are in agreement with the predictions of linear stability analysis. The amplitude grow rate at various levels of normal force follows the same trend as the evolution of effective modal damping ratio shown in Fig. 2.

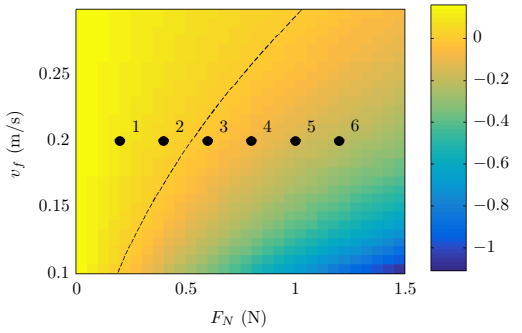

Figure 2: Smallest effective damping ratio ξ_{eff} as a function of the normal force F_N exerted by the finger and its velocity v_f. The dashed line indicates the limit between positive and negative values of the damping ratio, corresponding to stability or instability of the static equilibrium in sliding situation.

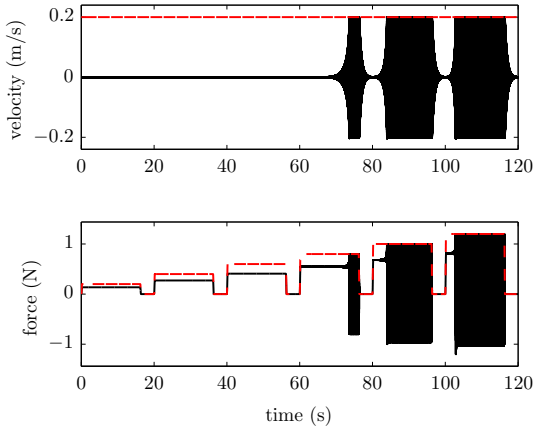

Figure 3: Velocity of the glass rod $\dot{u}$ and friction force F_T obtained from time-domain simulation. The red dashed lines are respectively the finger velocity v_f and the normal force F_N (which also corresponds here to the maximum static friction force since $\mu_s = 1$ in this simulation). The different levels of force correspond to points 1 to 6 in Fig. 2. Although masked by the scale fixed for the velocity, the third level of normal force leads to oscillations with increasing amplitude but low growing rate, not allowing to see the permanent periodic regime.

Conclusion

The minimal model of the Cristal Baschet describes the dependence of the amplitude grow rate of instabilities on the physical parameters: it is shown that the law of friction plays an essential role but its influence depends also on the mode shapes of the resonator at the connection point. These modal parameters are directly adjusted by the instrument maker when he tunes the mobility of these resonators. The model shows that a too low mobility can be responsible for the difficulties in obtaining the sound in the upper register.

References

[1] *Musical Instrument Museums Online (MIMO)* database, `https://mimo-international.com`, Cristal by Bernard Baschet and François Baschet, 1980, inventory number E.983.14.1, Musée de la Musique, Philharmonie de Paris (photo J.M. Anglès).

[2] S. Derler, G.-M. Rotaru, *Stick–slip phenomena in the friction of human skin*, Wear 301(1-2), 324-329, 2013.

[3] V. Debut, J. Antunes, and O. Inacio, *Linear modal stability analysis of bowed-strings*, J. Acoust. Soc. Am. 141(3), 2107–2120, 2017.

Tuesday, July 19, 2022
08:30 - 10:30

MS-04 Experiments in Nonlinear Dynamics and Control
Rhone 3B

Chair: Guilhem Michon

08:30 - 08:50
Parametrically driven morphing of thin piezoelectric surfaces
CARBONI Biagio*, CATARCI Stefano, LACARBONARA Walter
*Department of Structural and Geotechnical Engineering Sapienza University [Rome] (Sapienza Università di Roma, Via Eudossiana 18, 00184 Roma Italy)

08:50 - 09:10
Particle Damping of Floating Oscillating Surge Wave Energy Converters
HAJJ Muhammad*, SHALABY Ahmed, AHMED Alaa, DATLA Raju, MASRI Sami, MI Jia, ZUO Lei
*Civil, Environmental and Ocean Engineering, Stevens Institute of Technology (Hoboken, NJ 07030 United States)

09:10 - 09:30
[no show] Systematic design of particle dampers for low frequency horizontal vibrations
NIKLAS Meyer*, SEIFRIED Robert
*Institute of Mechanics and Ocean Engineering, Hamburg University of Technology (TUHH) (Eißendorfer Straße 42, 21073 Hamburg, Germany Germany)

09:30 - 09:50
Tracing periodic solutions in noise-contaminated experiments
BEREGI Sandor*, BARTON David, REZGUI Djamel, NEILD Simon, SYKORA Henrik
*Faculty of Engineering [Bristol] (University of Bristol, Senate House, Tyndall Avenue, Bristol BS8 1TH, UK United Kingdom)

09:50 - 10:10
Active Vibration Mitigation of High Modal Density of BLUM with Piezoelectric Patches
JAMSHIDI Rasa*, COLLETTE Christophe
*Université de Liège - Faculté des sciences appliquées (Quartier Polytech 1 - Allée de la Découverte, 12 - Sart Tilman - 4000 Liège Belgium)

Parametrically driven morphing of thin piezoelectric surfaces

Biagio Carboni*, Stefano Catarci* and Walter Lacarbonara *
**Dipartimento di Ingegneria Strutturale e Geotecnica, Sapienza University of Rome, Rome, Italy*

Summary. The possibility of exploiting the parametric resonance phenomena to perform morphing of piezoelectric surfaces is here investigated analytically and numerically. The case study consists of a PVDF beam subject to an in-plane pulsating strain applied through voltage variation. The dynamical excitation induces an out-of-plane parametric resonance of the beam which can be driven to excite desired individual modes or combination of them through nonlinear coupling. A nonlinear reduced order model for a piezoelectric thin Euler-Bernoulli beam is developed considering the multi-physics piezo-elastic coupling. The conservation of the electric charge is enforced in 3D while the equations of motion are expressed in 1D using the arclength parametrization along the beam centerline. The analytical treatment is based on the method of multiple scales and allows to obtain the region of the forcing parameters for which the parametric resonance is achieved. The analytical solutions are validated against numerical results provided by the finite element code ABAQUS through which a full 3D nonlinear model is addressed. The analytically obtained transition curves (representing the boundary between resonant and non resonant behavior in the space of forcing parameters) and the frequency response curves are compared to those obtained numerically achieving a good agreement. The voltage thresholds for which the parametric resonances are induced, and the robustness of the responses suggest that the investigated phenomenon is a promising strategy for surface dynamic morphing.

Introduction

A piezoelectric formulation valid rigorously only for parallelepiped-shaped beams is proposed. The model is focused on the parametric resonances induced by a pulsating voltage whose gradient is defined along the thickness [1]. The transition curves defining the forcing parameters for which the beam exhibits a parametric resonance are obtained using the method of multiple scales [2, 3]. The nonlinear equations of motion of the continuous piezoelectric beam are reduced employing a full-basis Galerkin-discretization of the continuous piezoelectric beam [4, 5].
Finally, the closed form asymptotic results are compared with those obtained by the direct integration of the nonlinear dynamic problem performed with the nonlinear finite element software ABAQUS [6]. The results show a good agreement and the simplified hypotheses adopted for the piezoelectric beam model are confirmed. The implemented assumptions could be also used for developing a simplified piezoelectric shell model.

Equations of motion

Consider the 3D Euclidean space with a Cartesian fixed frame (s, y, z) where the position of each point can be defined by a vector $\boldsymbol{x} = s\boldsymbol{e}_1 + y\boldsymbol{e}_2 + z\boldsymbol{e}_3$. The straight beam exhibits a rectangular cross-section of edges b and h and the position of each section along the beam span l, in the reference configuration, is described the vector $\boldsymbol{r}^0 = s\boldsymbol{e}_3$ with $s \in [0, l]$. The local frame in the reference configuration is denoted by $(\boldsymbol{b}_1{}^0, \boldsymbol{b}_2{}^0, \boldsymbol{b}_3{}^0)$. Unit vectors $\boldsymbol{b}_1{}^0$ is collinear with $\boldsymbol{e}_1$ while the pair $(\boldsymbol{b}_2{}^0, \boldsymbol{b}_3{}^0)$ represents a centered and principal frame for the beams cross-section.
The mechanical problem is formulated in the plane $\boldsymbol{e}_1 - \boldsymbol{e}_3$, and the displacement of the central line is denoted by $\boldsymbol{u}(s) = u(s)\boldsymbol{b}_1{}^0 + v(s)\boldsymbol{b}_3{}^0$. The rotation of the beam cross sections is $\boldsymbol{\theta}(s) = \theta(s)\boldsymbol{b}_2{}^0$ where $\boldsymbol{b}_2{}^0$ coincides with e_2. According to Saint-Venant ansatz, stresses and strain states are simplified: $\sigma_{22} = \sigma_{33} = \sigma_{23} = \sigma_{12} = 0$ $\varepsilon_{22} = \varepsilon_{33} = \gamma_{12} = \gamma_{23} = \gamma_{13} = 0$.
On the other hand, it is assumed that the voltage V varies only in the z direction according to the electric boundary conditions to which it is subject. We are interested in the problem in which the top beam surface at $z = h/2$ is connected to ground and presents $V(h/2) = 0$. On the bottom surface a voltage different from zero is assigned, $V(-h/2) = \overline{\Phi}$. Moreover, it is assumed that the potential varies with a quadratic law across the relatively small beam thickness according to

$$V(z,t) = \Phi_0(t) + \Phi_1(t)z + \Phi_2(t)\frac{z^2}{2}. \tag{1}$$

. Imposing the potential boundary conditions given above yields

$$\Phi_1(t) = -\frac{\overline{\Phi}(t)}{h}. \tag{2}$$

The beam axial force and the bending moment can be obtained by integration over the cross-section of the elastic axial tension.
The equations of motion for the nonlinear beam in the current local frame can be written as

$$N' + \frac{\mu}{\nu}M' = \rho A\ddot{u}\cos\theta + \ddot{v}\sin\theta, \tag{3}$$

$$\mu N + (\frac{M'}{\nu})' = -\rho A\ddot{u}\sin\theta + \ddot{v}\cos\theta. \tag{4}$$

where the shear force has been condensed using equation for the balance of the angular momentum, the prime indicates differentiation with respect to s and the overdot with respect to time t. Equation (4) can be condensed considering that the axial force is constant along the beam.

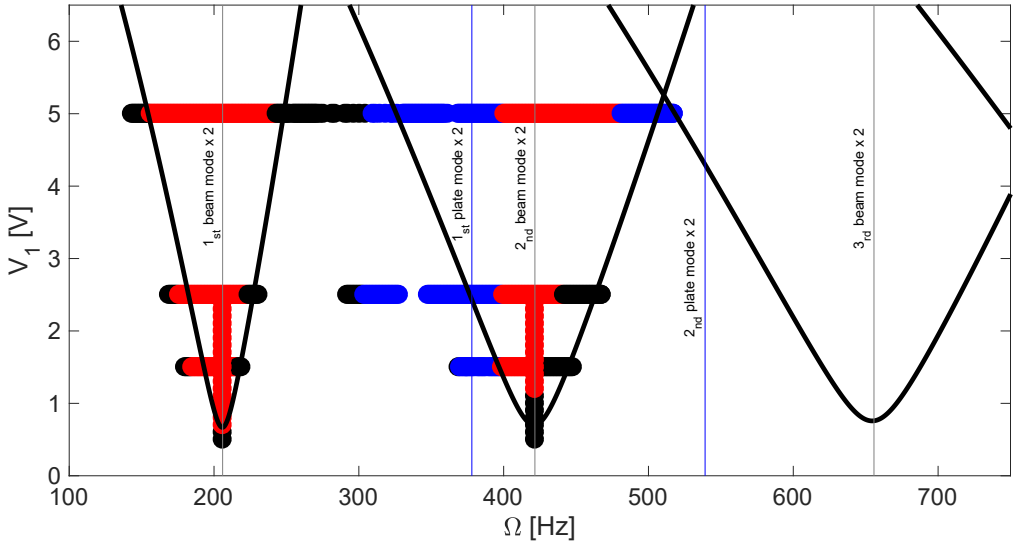

Figure 1: Parametric resonance regions for the PVDF sample where the black solid lines are obtained according to the fifth order solutions for the lowest three beam modes assuming $\zeta = 3\ \%$ and $V_0 = 5$ V; the black and red circles denote nonresonant and resonant responses provided by ABAQUS while the blue circles indicate resonant responses for the plates modes; the gray and blue vertical thin lines are placed at twice the frequencies of the beam-like modes and twice the plate-like frequencies, respectively; the black dashed horizontal lines denote the amplitudes of the AC voltage V_1 for which the ABAQUS simulations were run, namely, $(1.5, 2.5, 5)$ V.

The Method of Multiple Scales

The unknown displacement is expressed as follows

$$v(s,t) = \epsilon v_1(s,t_0,t_2,t_4) + \epsilon^3 v_3(s,t_0,t_2,t_4) + \epsilon^5 v_5(s,t_0,t_2,t_4). \tag{5}$$

and $\Phi_1 = V_0 + \epsilon^2 V_1 \cos\Omega t$ where the forcing frequency is $\Omega = 2\omega + \epsilon^2\sigma$. The parameter σ represents the detuning of the forcing frequency with respect to twice of the frequency of the excited mode. Moreover, the damping ratio is assumed as $\epsilon^2\zeta$. Collecting the terms with the same order of ϵ, the nonlinear equation of motion can be written up to the 5th order and solved asymptotically.

Results

The transition zones identified by ABAQUS are in accordance with the transition curves evaluated with the closed form expression. In fact, the threshold points provided by ABAQUS are very close to the asymptotically obtained curves (see Fig. 1). In particular, the correction obtained with the 5th order frequency response curves (black solid lines) show that the fully numerical and reduced model are in close agreement.

Conclusions

The present paper investigates the parametric resonance conditions induced by a pulsating voltage in a PVDF copolymer beam/plate. The piezoelectric properties of the PVDF film are exploited to induce an initial tensile stress that makes the structure stiffer and increases the natural frequencies. A nonlinear piezoelectric beam model is developed and the transition curves for the lowest three modes are computed using the method of multiple scales. The obtained results are validated via ABAQUS through which the piezoelectric system is addressed within geometrically nonlinear problem formulation.

References

[1] Carboni, B., Catarci, S., Lacarbonara, W. (2022). Parametric resonances of nonlinear piezoelectric beams exploiting in-plane actuation. *Mechanical Systems and Signal Processing*, **163**, 108119.

[2] Nayfeh A.H., Mook D.T. (2008) Nonlinear oscillations. *John Wiley and Sons*.

[3] Lacarbonara W. (2013) Nonlinear structural mechanics: theory, dynamical phenomena and modeling *Springer Science and Business Media*.

[4] Lacarbonara W. (1999) Direct treatment and discretizations of non-linear spatially continuous systems. *Journal of Sound and Vibration* **221(5)**:849–866, .

[5] Arena A., Massimi F., Lacarbonara W. (2020) Dynamic morphing of actuated elastic membranes. In: Kovacic I., Lenci S. (eds) *IUTAM Symposium on Exploiting Nonlinear Dynamics for Engineering Systems*, ENOLIDES, IUTAM Bookseries **37** Springer Cham.

[6] Dassault Systemes Simulia (2013). Abaqus 6.13 userś manual. Dassault Systems, Providence, RI.

Particle Damping of Floating Oscillating Surge Wave Energy Converters

Muhammad Hajj*, Ahmed Shalaby*, Alaa Ahmed*, Raju Datla*, Sami Masri†, Jia Mi‡ and Lei Zuo ‡
*Civil, Environmental and Ocean engineering, Stevens Institute of Technology, Hoboken, NJ, USA
†Civil and Environmental Engineering, University of Southern California, Los Angeles, CA, USA
‡Mechanical Engineering, Virginia Tech, Blacksburg, VA

Summary. Expanding the deployment of oscillating surge wave energy converters to deep waters requires mounting them on submerged platforms close to the water surface. One issue is that large amplitude waves, required for better energy generation, induce large platform motions, particularly in the surge direction. These motions could adversely impact the flap's hydrodynamic performance. We investigate, through an explanatory experimental study, the use of particle damping to control the surge motion of the platform under different wave excitations. The results point to complex nonlinear effects of particle damping and couplings among the different degrees of freedom, which yield differing responses under different excitation parameters.

Introduction

Oscillating surge wave energy converters (OSWEC) are one of the most efficient means for capturing and converting wave energy into a more useful form of energy, e.g., electricity. Because the surge component of ocean wave energy is most prevalent near the water surface, OSWEC wave capture components must be positioned near that surface to realize maximum efficiency. This placement, however, constrains their deployment to shallow water sites. In contrast, mounting the OSWEC onto a submerged platform close to the water surface, as schematically shown in Figure 1, expands the deployment range to deep water locations where there is need to power observation stations, autonomous underwater robots, offshore islands, ships and submarines, among many other blue economy systems and devices.

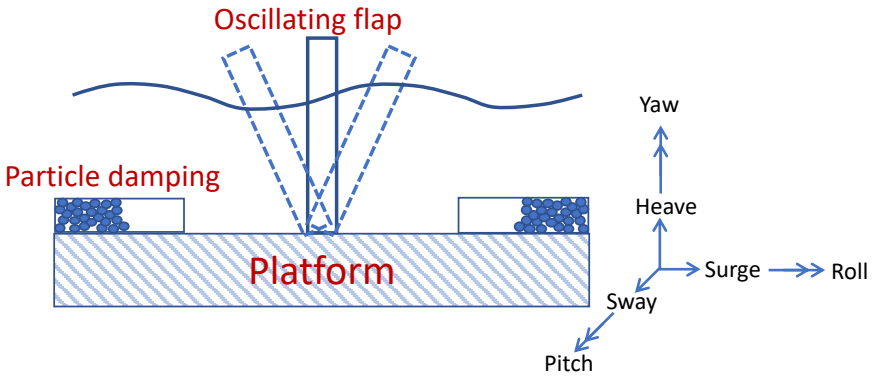

Figure 1: Schematic of oscillating surge wave energy converter mounted on a platform

Although resonance is always desired to achieve large amplitude motions for efficient energy generation, optimal wave energy conversion from a pitching flap-type device may not take place at resonance. Designing the flap to be resonant requires a relatively small added mass, which results in a small wave force. In contrast, designing the flap to attract a large wave force requires a large added mass, which results in a non-resonant device [1]. Clearly, larger wave forces induced by larger wave amplitudes, could be more effective in increasing the power capture than operating at resonance conditions for OSWEC. In the case of a floating oscillating surge wave energy converters (FOSWEC), large wave forces, intended to increase the flap's rotational displacement, could also induce significant platform motions, which may adversely impact the response of the flap oscillator and reduce the level of generated power. Consequently, it is important to control the platform's motion.

One control approach is to introduce passive damping by attaching a set of cylinders or boxes containing particle dampers to the platform, as schematically shown in Figure 1. This robust approach is particularly effective and practical under random excitation [2] and when considering the harsh operational conditions of FOSWEC in high sea states, over a broad range of frequencies defined by irregular wave spectra. Here, we perform experiments in a wave tank to investigate the effectiveness of particle damping in reducing the motion of the platform while increasing the flap's response as desired to enhance the energy generation. The results are used to characterize complex nonlinear effects and nonlinear couplings among the different degrees of freedom.

Experimental Setup

The experiments were performed in the wave tank of the Davidson Laboratory. The tank is 100 m long, 5.4 m wide and 2.1 m deep. The waves are generated by a dry-back, six-paddle, electrically driven, flap type wave-maker capable of generating regular and spectral waves with periods between 2 and 5 seconds and heights up to 0.65 m. Each paddle has

an individual servo-drive with purpose-built digital controller. The tests were performed on a scaled floating oscillating flap mounted on a platform positioned 0.79 m below the water surface. The 1.2 m wide, 0.95 m high and 0.127 m thick oscillating flap (Figure 1) was composed of an aluminum frame filled with foam. Its total mass and mass moment of inertia were respectively 21.5 kg and 5.5 kg.m^2. The flap was hinged to the (1.5 m x 1.17 m) platform, which was built using T-slotted framing rails attached by corner brackets. The platform was held by four strings at the corners that extended underwater and connected to extension springs with loop ends that were firmly held in position by heavy weights on the bottom of the tank. The particle damping system consisted of four 5-cm PVC tubes that were 0.53 m long. These tubes were partially filled with low carbon steel spheres having a diameter of 1.9 cm to yield 18% mass ratio. A displacement sensor was placed on top of the flap frame to measure the relative linear displacement between the flap and the platform. A 3-phase accelerometer and a 3-phase gyroscope IMU were mounted on the platform to measure all rotational and translational accelerations. One wave wire, placed at 5 m upstream of the flap, was used to measure the incident wave height. All data were acquired at the rate of 100 Hz. Tests were conducted for different wave heights and periods.

Particle damping

Figure 2 shows that particle damping yielded a 73% reduction in the platform's surge displacement when the period of the excitation 4.5 cm-wave was set to 4 seconds. This reduction percentage was not, however, consistent. Damping particles did not cause any reduction in the surge displacement when the wave period was set to 4.5 seconds. Furthermore, the platform surge displacement increased by 150% at the lower wave period of 2.85 seconds. Analysis of the pitch and yaw motions showed similar responses, pointing to the complex nonlinear dynamics of particle damping and the coupling between the different degrees of freedom.The impact of reducing the surge motion on the rotational displacement of the flap is deduced from figure 3, which shows that particle damping of the platform's surge motion increased the angular rotation of the flap by about 40%.

In the full paper, we will evaluate and discuss all mechanisms contributing to particle damping of the surge response of the platform. These include collisions between the particles and the container, inelastic particle-to-particle collisions, and frictional losses. These depend on different factors including mass ratio defined as the ratio of the mass of the damping particles to the total mass of the platform and flap; void ratio defined as the ratio of volume not occupied by particles to volume occupied by particles; porosity defined as the ratio of volume not occupied by particles to bulk volume of the particles; clearance defined as the distance particles can travel before impacting the wall, rolling friction; and coefficients of restitution among the particles and with the enclosure. We will also elaborate on the coupling between the different degrees of freedom and energy transfer between the flap and platform motions.

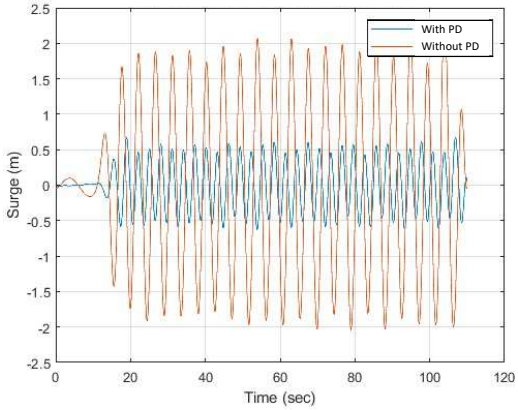

Figure 2: Reduction in surge amplitude induced by particle damping for a wave period of 4 seconds and amplitude of 4.5 cm.

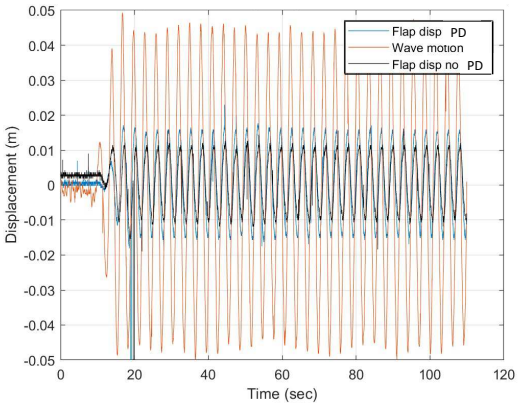

Figure 3: Increase in angular displacement of the flap under particle damping of the platform's surge motion. Wave period 4 seconds.

Conclusions

We tested in a wave tank the use of particle damping to control the surge motion of a near-surface platform supporting an oscillating surge wave energy converter. The data showed effective damping and enhanced flap oscillations under specific excitation conditions, but less effective or even increased motions under other conditions. These observations point to the complex nonlinear features of particle damping.

References

[1] Henry, A., Folley, M., Whittaker, T. (2018) A conceptual model of the hydrodynamics of an oscillating wave surge converter. *Renewable Energy* **118**: 965-972.

[2] Masri, S. F., Ibrahim, A. M. (1973) Response of the impact damper to stationary random excitation. *The Journal of the Acoustical Society of America* **53(1)**: 200-211.

A Design Methods for Particle Dampers in Low Frequency Horizontal Free Vibrations

Niklas Joachim Meyer* and Robert Seifried*
*Institute of Mechanics and Ocean Engineering, Hamburg University of Technology, Hamburg, Germany, www.tuhh.de/mum, n.meyer@tuhh.de, robert.seifried@tuhh.de

Summary. Particle dampers show a huge potential to efficiently damp lightweight structures. However, they suffer from their nonlinear characteristics and the multitude of influence parameters. For horizontal vibrations of low frequency, recently, the rolling attribute of spheres has been used to obtain high energy dissipation rates in driven particle containers. As long as the particle container's acceleration amplitude stays below the gravitational acceleration, this rolling effect of spheres can be used. Hereby, the estimation of the damper's energy dissipation is accurately possible using analytical formulas.
In this paper, a design guideline for a systematic damper design for an underlying structure of low first eigenfrequency under free vibration is presented. To develop this guideline, the analytical expression of the rolling effect of spheres is analyzed in detail. The particle damper is separated into multiple layers with different lengths. Hence, a high damping ratio over a large vibration amplitude range can be obtained. For experimental validation purposes, a simple beam-like structure is utilized. A good agreement between expected and experimental obtained vibration response is achieved for the designed particle dampers.

Introduction

To reduce large vibrations amplitudes of lightweight structures, passive damping techniques are often used. Classical liquid dampers are commonly utilized for these applications. Those dampers are well studied and mathematically easy to describe. However, liquid dampers fail under harsh environmental conditions and do need an anchor point. Thus, for applications where liquid dampers are not suitable, alternative damping technologies are necessary. Hence, *particle dampers* are an alternative, due to their simple and robust design.
Particle damping technology uses containers that are attached to the vibrating structure and are filled with granular material. By structural vibrations, momentum is transferred to the granular material which start to interact with each other. Due to these interactions, energy is dissipated by impacts and frictional phenomena between the particles. Particle dampers show great advantages compared to other damping technologies, as these add only little mass to the primary system [4], are cost-efficient devices, and might be applied to a wide frequency range [2]. Particle dampers can also be applied in harsh environmental conditions [14, 18]. One popular example are spacecraft applications [13]. Despite particle damper's huge potential, their design is still a non-trivial and challenging task. This is because particle motion, also called *motion mode*, and the damper's energy dissipation correlate in a non-trivial way, which is often poorly understood. Identifying these correlations is still part of ongoing research, see e. g. [3, 6, 7, 16, 19, 20, 21].
Especially, for low frequency vibrations, the use of particle dampers is rarely seen so far. For these vibrations, the particle container's acceleration amplitude is mostly below the gravitational acceleration. Hence, particles begin to stick and no relative motion between particles and container is obtained. Thus, only a little amount of energy is dissipated [5]. To face this problem, recently, in [12] the rolling attribute of spheres is studied for horizontal vibrations. It is shown that for low filling ratios, particles begin to slide and roll over the container base instead of sticking. For vibration amplitudes below a certain threshold stroke, which only depends on the filling ratio of the damper, no synchronous particle motion is obtained. This motion is named *scattered state*. The scattered state results in a comparatively low energy dissipation. Increasing the amplitude of the vibration above the threshold stroke, a synchronous particle motion with the container is obtained. The particles start to move as one particle block and collide inelastically with the container walls. This results in high energy dissipation rates and is called *rolling collect-and-collide* motion mode. For both observed motion modes, in [12] analytical equations are derived describing the damper's energy dissipation. These analytical equations are validated by comparison to experimental measurements of a driven particle container.
In this paper, the damper design of [12] is adopted to damp a structure of low first eigenfrequency under free vibration. Therefore, the analytical equations are studied in detail and a simple design guideline is derived. The idea of the design guideline is to separate the particle damper into multiple layers with different lengths. Hence, different vibration amplitudes can be damped efficiently, leading to high damping ratios on a large amplitude range. For validation purposes, a simple beam-like structure is utilized. The base point of the beam is fixed. The particle damper is mounted at the tip of the beam and the damper's velocity is measured using a laser scanning vibrometer. Thus, the system's free response is measured.
This paper is organized as follows: First, in Sect. **Motion Modes** the occurring motion modes for low-intensity horizontal vibrations are introduced. In the following Sect. **Design Guideline**, the particle damper's design guideline is developed. Then, in Sect. **Experimental Validation** the design guideline is applied to design a particle damper for the free vibration attenuation of a simple beam-like structure. Finally, a conclusion is given.

Motion Modes

A motion mode describes the motion of a particle bed inside a harmonic vibrating container of the form $x_\mathrm{c} = X \sin(\Omega\, t)$, with container amplitude X and angular frequency $\Omega = 2\,\pi\, f$. For such a container movement, the corresponding container velocity and acceleration follow to $\dot{x}_\mathrm{c} = V \cos(\Omega\, t)$ and $\ddot{x}_\mathrm{c} = -A \sin(\Omega\, t)$ with $V = X\,\Omega$ and $A = X\,\Omega^2$. For such a container movement, different motion modes of the particle bed can be observed. Various influence parameters affect the occurring motion mode, like excitation intensity and frequency but also gravity, excitation direction, or particle size. The most common motion modes are solid-like, local fluidization, global fluidization, convection, Leidenfrost effect, bouncing collect-and-collide, and buoyancy convection [3, 6, 7, 16, 19, 20, 21].
For horizontal vibrations of low acceleration amplitude, i. e. $A < g$ with g being the gravitational acceleration, two different motion modes can be observed if spherical particles on flat container bases with low filling ratio are used, see [12] for a detailed discussion. An example of such a container is shown in Fig. 4 in form of the later utilized particle damper. The observed motion modes inside this container are called scattered and rolling collect-and-collide and are depicted schematically in Fig. 1. Particle trajectories of these two motion modes, obtained by discrete element simulations, are shown in Fig. 2 [12]. Interestingly, both motion modes only depend on the so-called optimal stroke X_opt, which only depends on the clearance h, i. e. the distance of the particle bed to the opposite container wall as indicated in Fig. 1. Following [12], the optimal stroke is obtained to

$$X_\mathrm{opt} \approx 0.4\, h. \tag{1}$$

To judge about the particle damper's efficiency the effective loss factor $\bar{\eta}$ [6, 11] is used. It is calculated by a scaling of the dissipated energy of the particle damper per radian E_diss with the kinetic energy of the particle system using the mass of the particle bed m_bed, i. e. the mass of all particles, to

$$\bar{\eta} = \frac{E_\mathrm{diss}}{E_\mathrm{kin}} = \frac{E_\mathrm{diss}}{\frac{1}{2}\, m_\mathrm{bed}\, V^2}. \tag{2}$$

Scattered state: The scattered state occurs for container amplitude $X < X_\mathrm{opt}$. This motion mode is similar to the gaslike state observed by Sack [15] under the condition of weightlessness. The particle movement is randomly and chaotic. Hence, in Fig. 1 just a schematic representation of the movement of the particles is shown. Particles are hitting each other and the container walls at random phases. In [12] it is observed that a higher vibration amplitude X leads to more particle collisions while a higher clearance h leads to fewer particle collisions.
The analytical solution of the effective loss factor of the scattered state is shown in Fig. 3 for $X < X_\mathrm{opt}$ being a good approximation to experimental measurements [12]. The effective loss factor starts close to zero for very low container amplitudes, i. e. $X \ll X_\mathrm{opt}$, and increases linearly. At the transition to the rolling collect-and-collide motion mode, i.e. at $X = X_\mathrm{opt}$, the highest value of 0.4 is reached.
Rolling collect-and-collide: The second motion mode observed for low frequency horizontal vibrations is the rolling collect-and-collide one, see also Fig. 1 and Fig. 2. Within this motion mode, i. e. for $X > X_\mathrm{opt}$, the particle bed rolls and slides as one single particle block over the container's base. Thus, the translational and rotational velocities of every single particle are assumed to be identical. First, the particle bed is pushed by the container until the container reaches its maximum velocity, i. e. at $\Omega\, t = n\,\pi$ with $n \in \mathbb{N}$. At this time point the container is positioned at $x_\mathrm{c} = 0$ and its velocity is maximal, i. e. $\dot{x}_\mathrm{c} = \pm V$. As the particle bed is pushed by the container, almost no rotational movement of the particles is seen during this pushing phase, i. e. $\dot{\varphi}_\mathrm{p} = 0$. When the particle container has reached its maximum velocity and starts to decelerate, the particle block leaves the

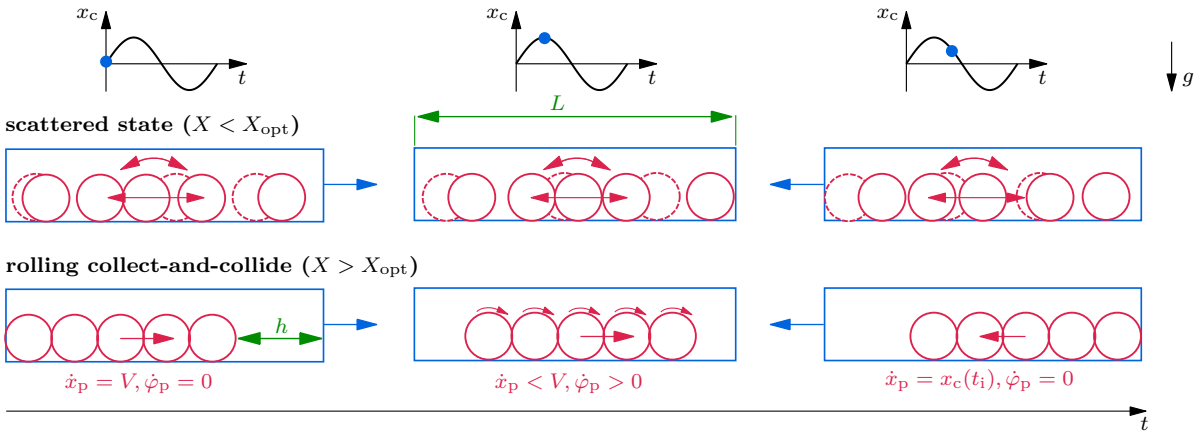

Figure 1: Motion modes at different container strokes for low acceleration amplitudes.
($\dot{x}_\mathrm{c}$: container velocity, $\dot{x}_\mathrm{p}$: particle bed velocity, $\dot{\varphi}_\mathrm{p}$: angular velocity of particles)

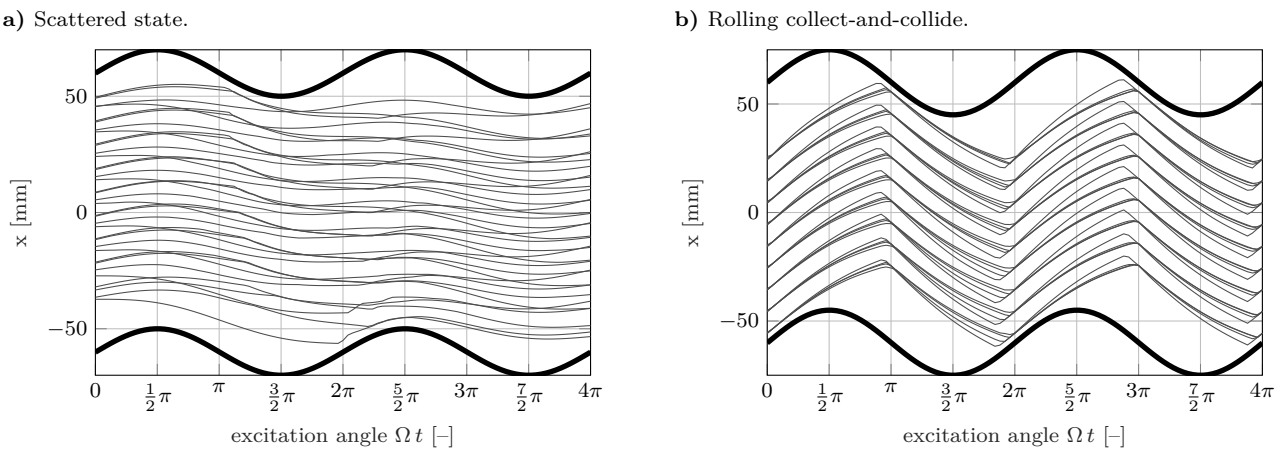

Figure 2: Particles trajectories obtained from DEM simulations for different container strokes [12].

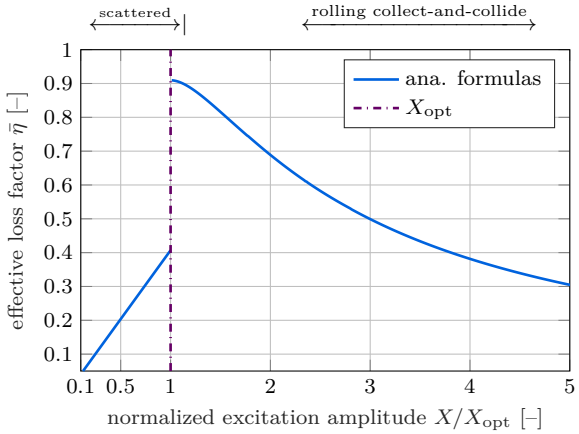

Figure 3: Effective loss factor for scattered and rolling collect-and-collide motion mode [12].

container wall and the single particles start rolling due to friction with the container base. The particle block collides inelastically with the opposite container wall at the impact time point t_{i}. During this impact multiple inter-particle and particle–wall impacts occur. Although, by every single impact, only a small amount of energy is dissipated, in sum a perfectly inelastic collision of the particle bed with the container wall is achieved, i. e. the particle block adopts the velocity of the container [1, 17]. During this inelastic collision, the rotational movement of the particles stops. This sequence is repeated when the particle container moves in the other direction. Hence, in sum, two particle impacts with the container walls occur during one vibration cycle.
The effective loss factor for this motion mode is shown in Fig. 3 for $X > X_{\text{opt}}$. The effective loss factor starts at $X = X_{\text{opt}}$ with its maximum value $\bar{\eta}_{\text{max}} \approx 0.91$ and decreases slowly to higher container amplitudes. This progression of the effective loss factor can be explained by taking the relative velocity between particle bed and container at the impact time point with the container wall into consideration. For very high container amplitudes, i. e. $X \gg X_{\text{opt}}$, the particle bed leaves the container wall with a high velocity. Thus, the particle bed collides after a short period with the opposite container wall, i.e. $\Omega\, t_{\text{i}} \to 0$. Consequently, the relative velocity between particle bed and container at impact is comparatively low, resulting in a low efficiency. When the container amplitude decreases, i. e. is getting closer to X_{opt}, the impact time point increases, and thus the relative velocity at impact increases as well. This leads to a higher damper efficiency. The threshold for this motion mode is at an impact time point of $\Omega\, t_{\text{i}} = \pi$. For this time point, the container is located at $x_{\text{c}} = 0$ but moves in the other direction as the particle block, i. e. $\dot{x}_{\text{c}} = \mp V$. This is the impact time point of maximum relative velocity between particle bed and container and thus of the highest efficiency. For this time point, $X \approx 0.4\, h$ holds. For even lower container strokes, the system switches to the scattered state. This switch happens as for the rolling collect-and-collide motion mode less than two impacts with the container wall per vibration cycle would occur. However, this is a necessary condition of this motion mode.

One should note that the experimental results in [12] are in good agreement with the analytical solutions of the effective loss factor shown in Fig. 3. However, in [12] the testbed to subject the particle container to a sinusoidally motion is set up very precisely. It is obtained that especially a container tilt or a high friction coefficient, significantly lower the effective loss factor.

Design Guideline

To design an appropriate particle damper, at first some general points have to be discussed. At first, it is assumed that the system that should be damped is described by

$$M\ddot{x} + D\dot{x} + Kx = 0, \tag{3}$$

with mass M, structural damping D, stiffness K and particle damper position x. In [8] a detailed description is given, of how to derive this equation of motion for arbitrary structures.
For the damper design, the effective loss factor, see Fig. 3, has to be considered. As the particle damper exhibits much higher effective loss factors during the rolling collect-and-collide motion mode, this motion mode should be realized during the operation of the damper. Likewise, any free vibration of a structure with initial amplitude X_0 will decrease in amplitude over time. Hence, the particle layers should be designed such that $X_0 > X_{\mathrm{opt}}$ holds to ensure an operation within the rolling collect-and-collide motion mode. However, the question arises of how to design the particle layers, i. e. particle mass and clearance h, appropriately.
In the first step, the necessary particle mass needs to be determined. It can be calculated by the desired damping ratio of the structure ζ_{d} and the effective loss factor, see [9]. However, the effective loss factor is not known and changes over time. Experimental measurements, as discussed later, have shown that an appropriate designed particle damper exhibits an effective loss factor of about $\bar{\eta} = 0.5$ on a large amplitude range. So this is a good starting value for design. The particle mass is obtained to

$$m_{\mathrm{bed}} \approx 2\,M\,\frac{\zeta_{\mathrm{d}}}{\bar{\eta}}. \tag{4}$$

Many experimental measurements, see [8], have shown that a separation of the particle container into at least three layers leads to good damping properties. To ensure a high damping over a large vibration amplitude range, the damper layers should be designed such that

$$\frac{X_0}{X_{\mathrm{opt}}} = \{2, 4, 6\}\,, \tag{5}$$

see also Fig. 3. Inserting Eq. (5) into Eq. (1) the clearances of the three damper layers are obtained to

$$h = \left\{\frac{5}{4}, \frac{5}{8}, \frac{5}{12}\right\} \cdot X_0. \tag{6}$$

Hence, starting from an initial vibration amplitude X_0, the effective loss factors are $\bar{\eta}_0 = \{0.69, 0.38, 0.25\}$ and are increasing as the vibration amplitude decreases until the optimal strokes of the individual damper layers are reached. When the optimal stroke of a layer is reached, the particle bed within this layer switches to the scattered state, and the energy dissipation of this layer reduces dramatically. The three optimal strokes are obtained by Eq. (5) to

$$X_{\mathrm{opt}} = \left\{\frac{1}{2}, \frac{1}{4}, \frac{1}{6}\right\} \cdot X_0. \tag{7}$$

Hence, the minimum vibration amplitude of the system will be about $X_{\mathrm{min}} \approx \frac{1}{6}\,X_0$ as for lower vibration amplitudes all three particle layers will be in the scattered state. Hence, only a little amplitude reduction is achieved from that moment. To ensure uniform damping, the particle mass should be distributed evenly over the damper layers. It should be noted that lower vibration amplitudes could be reached if additional damper layers are used with a higher ratio of $X_0/X_{\mathrm{opt}} = 6$. However, for very low vibration amplitudes, the effects of friction or little container tilts are becoming more and more dominant. Hence, additional damping might be hard to realize for very low container amplitudes. See [12] for further details.
To enable the inelastic collision property of the rolling collect-and-collide motion mode, see also Sect. **Motion Modes**, in each particle layer at least three by three particles should be used. To decrease the influence of friction a high particle radius is beneficial. As particle material, steel has been proven to be very durable [9, 12].

Experimental Validation

In the following, the presented design guideline shall be validated experimentally. The used experimental setup is shown in Fig. 4. It consists of a simple beam-like structure with the particle damper mounted at its tip. The elastic length of the steel beam is 512 mm with a rectangular profile of 80 mm × 2 mm and a Young's modulus of $E = 200$ GPa. The base point of the beam-like structure is fixed and the tip consists of an additional mass and the particle container with a total weight of 1270 g. The particle container is made of polyvinyl chloride (PVC) and has a quadratic cross section with an inner edge width and height of 40 mm and a length L of 120 mm in

excitation direction. The container is separated into three horizontal layers with a height of 11 mm each, as shown in Fig. 4-right. Additionally, the length of each layer can be adjusted by separation walls. The container's velocity is measured using a laser scanning vibrometer, the *PSV-500* from POLYTEC, with a sampling frequency of 250 kHz and integrated internally to obtain the output position. The measurement starts at the first zero crossing of the particle container.

For this system, the mass and stiffness for Eq. (3), follow to $M = 1.058\,\mathrm{kg}$ and $K = 143\,\mathrm{N/m}$. The eigenfrequency of the undamped system is $f_0 = \omega_0/(2\pi) = 1.85\,\mathrm{Hz}$. This numerical obtained eigenfrequency is very close to the experimental measured one with only a difference of 0.02 Hz. The structural damping parameter D is obtained from measurements and is with a value of 0.032 kg/s rather small [8, 10]. All three particle layers are filled with 16 steel spheres of 5 mm radius. Hence, a total particle weight of 196 g is used. To verify Eq. (4) for the necessary particle mass, a damping ratio $\zeta = 0.046$ should be measured with this particle setting. An initial amplitude of $X_0 = -63\,\mathrm{mm}$ with clearances according to Eq. (6) are used, i. e. $h \approx \{80, 40, 25\}$ mm. The initial acceleration is $A_0 = 8.5\,\mathrm{m/s^2} < g$. Consequently, the particle bed is in the rolling collect-and-collide motion mode from the very beginning. The three resulting optimal strokes are $X_{\mathrm{opt}} = \{32, 16, 10\}$ mm. Figure 5 shows the trajectory of the system's tip, i. e. the particle damper, and the hull curve of the undamped system. Additionally, the obtained damping ratios are depicted.

During the first vibration cycle, a damping ratio of $\zeta = 0.035$ is achieved, which increases as the container amplitude decreases. The damping ratio stays high with values around $\zeta \approx 0.046$, i. e. the desired damping ratio. Around the three optimal strokes, i. e. at container amplitudes of $X_{\mathrm{c}} = \{32, 16, 10\}$ mm, a kink towards lower damping ratios is seen. This happens as here the corresponding particle layer switches into the scattered state, leading to a reduced energy dissipation. For container amplitudes below 11 mm, only very small damping ratios of about $\zeta \approx 0.02$ are achieved. This container amplitude is close to the theoretical minimum value X_{min} with 10 mm. The low damping ratios are achieved for strokes below 11 mm because all three particle layers are in the scattered state from that moment. In summary, for this system, the design guideline has been proven to be very efficient.

Sensitivity analyses: To prove that the design guideline also works efficiently for other systems, the beam-like structure is modified. The same initial amplitude, the same particle mass and the same clearances are used. For the first modification, an additional mass of 942 g is mounted at the tip. Its total mass is hence $M = 2.0\,\mathrm{kg}$. The new eigenfrequency of this system results in $f_0 = 1.35\,\mathrm{Hz}$. Due to the higher system mass, the achievable damping ratio according to Eq. (4) reduces to $\zeta = 0.025$. The experimental results of the container stroke and damping ratios are shown in Fig. 6. The results show the same qualitative behavior as for Fig. 5, but on a larger time scale, due to the higher system mass. The measured damping ratios are around $\zeta \approx 0.025$. Hence, the design guideline works still efficiently for this system.

For a second modification, a different beam is used. This steel beam has the same length but with a rectangular profile of 80 mm × 3 mm instead of 80 mm × 2 mm. This significantly changes the stiffness to $K = 484\,\mathrm{N/m}$. The system's mass is only a little affected, i. e. $M = 1.108\,\mathrm{kg}$. The system's eigenfrequency follows to $f_0 = 3.33\,\mathrm{Hz}$. Due to the increases eigenfrequency of the system, the acceleration at the initial stroke X_0 increases to $A_0 = 28\,\mathrm{m/s^2} > g$. This causes the system to be in the bouncing collect-and-collide motion mode first [8]. Here, the particles are flying thru the container instead of rolling. Indeed, the optimal stroke is only little affected as it is achieved to $X_{\mathrm{opt}} \approx 0.32\,h$ compared to $X_{\mathrm{opt}} \approx 0.4\,h$. The maximum effective loss factor value is $\bar{\eta}_{\mathrm{max}} \approx 1.27$ compared to $\bar{\eta}_{\mathrm{max}} \approx 0.91$. In Fig. 7 the trajectory of the system's tip and the damping ratios are depicted. Again, the results show similar qualitative behavior as for Fig. 5. Although the theoretical maximum effective loss factor is higher, the damping ratios are very similar compared to Fig. 5. Probably, the container layers hinder the deployment of a purely flying particle state. Indeed, this requires further investigations. Still, the design guideline even works well for container accelerations above the gravitational constant.

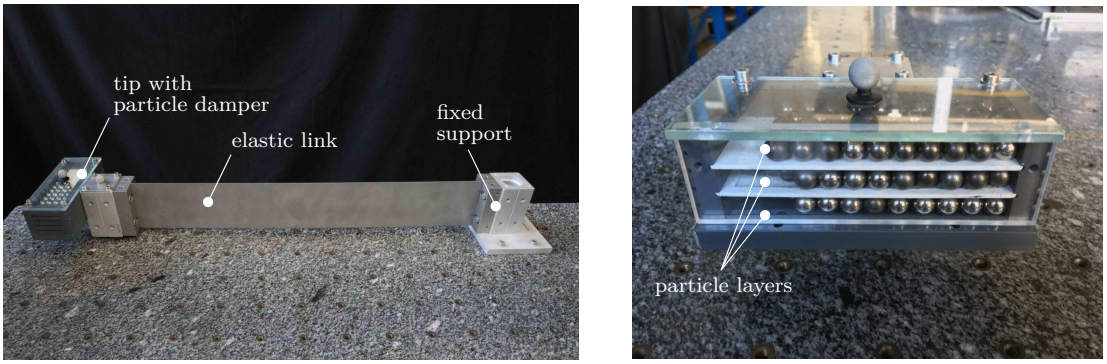

Figure 4: Simple beam-like structure setup with overview (left) and augementation of its tip (right).

a) Trajectory of tip.

b) Damping ratios.

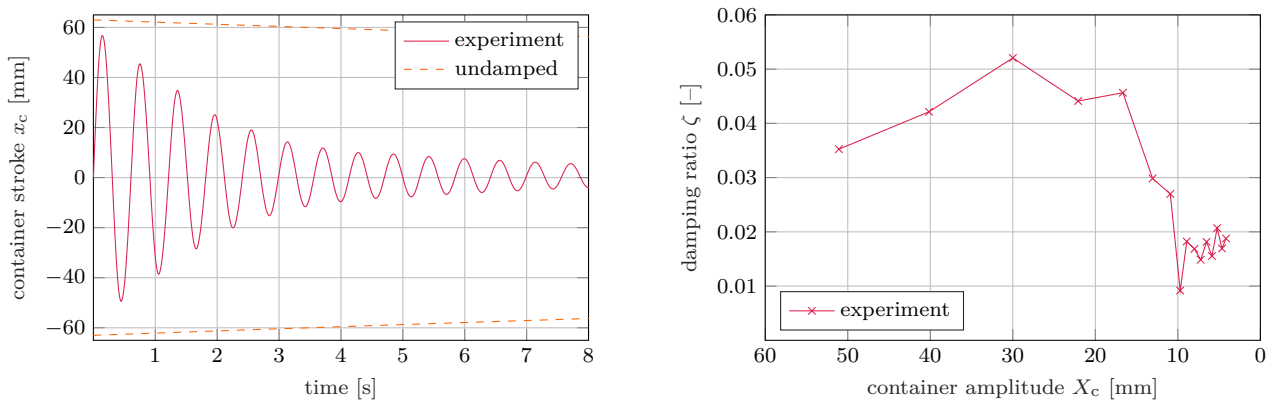

Figure 5: Damped simple beam-like structure with clearances according to Eq. (6) with **a)** trajectory of tip and **b)** damping ratios.

a) Trajectory of tip.

b) Damping ratios.

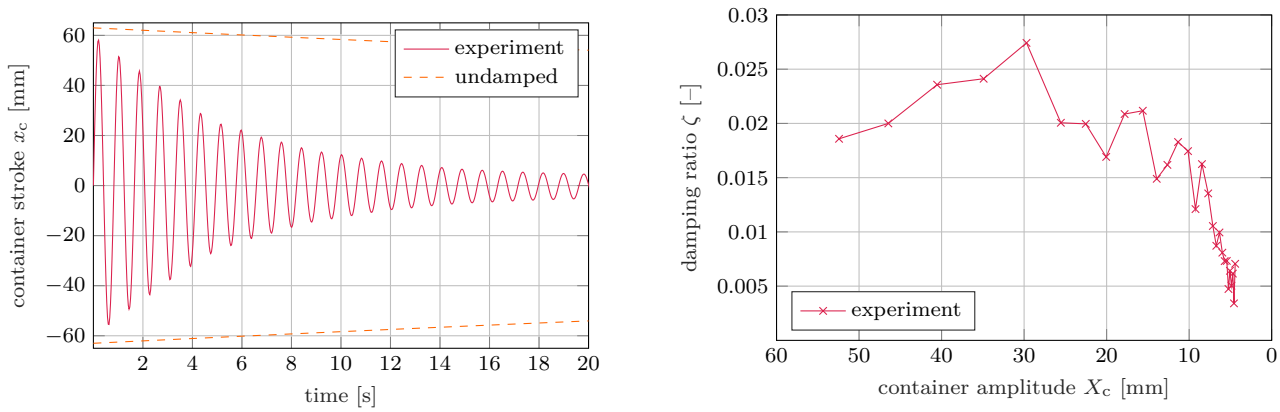

Figure 6: Damped simple beam-like structure with extra mass with **a)** trajectory of tip and **b)** damping ratios.

a) Trajectory of tip.

b) Damping ratios.

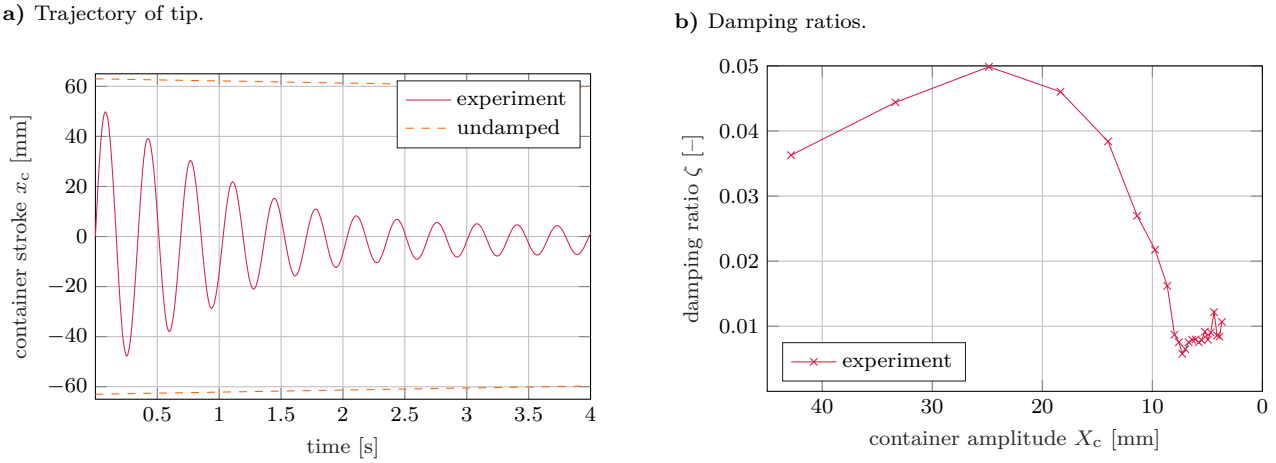

Figure 7: Damped simple beam-like structure with stiffer beam with **a)** trajectory of tip and **b)** damping ratios.

Conclusion

In this paper, a systematic design guideline for the development of layerd particle dampers for low frequency horizontal free vibrations is presented. Hereby, the rolling collect-and-collide motion mode of the particle bed is employed. The particle damper is separated into multiple particle layers and filled with steel spheres. Via the design guideline, the necessary particle mass for the desired damping ratio is determined only based on the structure's mass. A simple analytical equation is given to design the clearances of the different particle layers, i. e. the distances between the particle bed and the opposite container wall.
The efficiency of the design guideline is verified experimentally. A simple beam-like structure is used for this task. The structure is subjected to an initial deflection and the damping ratio of the free vibration is measured. The damping ratios are close to the designed values. Finally, sensitivity analyses are performed by changing either the stiffness of the beam or by adding mass. Either way, the good damping performance is conserved.

Acknowledgements

The authors would like to thank the German Research Foundation (DFG) for the financial support of the project 424825162. The authors would also like to thank Dr.-Ing. Marc-André Pick, Dipl.-Ing. Riza Demir, Dipl.-Ing. Norbert Borngräber-Sander and Wolfgang Brennecke for helping to design and realize the experimental rig.

References

[1] Bannerman, M.N., Kollmer, J.E., Sack, A., Heckel, M., Mueller, P., Pöschel, T.: Movers and shakers: Granular damping in microgravity. Physical Review E **84** (2011). DOI 10.1103/PhysRevE.84.011301

[2] Chen, T., Mao, K., Huang, X., Wang, M.: Dissipation mechanisms of nonobstructive particle damping using discrete element method. Proceedings of SPIE - The International Society for Optical Engineering **4331**, 294–301 (2001). DOI 10.1117/12.432713

[3] Eshuis, P., Weele, K., Meer, D., Lohse, D.: Granular leidenfrost effect: Experiment and theory of floating particle clusters. Physical review letters **95**, 258001 (2006). DOI 10.1103/PhysRevLett.95.258001

[4] Johnson, C.D.: Design of passive damping systems. Journal of Mechanical Design **117**(B), 171–176 (1995). DOI 10.1115/1.2838659

[5] Lu, Z., Wang, D., Masri, S., Lu, X.: An experimental study of vibration control of wind-excited high-rise buildings using particle tuned mass dampers. Smart Structures and Systems **18**, 93–115 (2016). DOI 10.12989/sss.2016.18.1.093

[6] Masmoudi, M., Job, S., Abbes, M.S., Tawfiq, I., Haddar, M.: Experimental and numerical investigations of dissipation mechanisms in particle dampers. Granular Matter **18**(3), 71 (2016). DOI 10.1007/s10035-016-0667-4

[7] Matchett, A.J., Yanagida, T., Okudaira, Y., Kobayashi, S.: Vibrating powder beds: A comparison of experimental and distinct element method simulated data. Powder Technology **107**(1), 13–30 (2000). DOI 10.1016/S0032-5910(99)00080-7

[8] Meyer, N., Schwartz, C., Morlock, M., Seifried, R.: Systematic design of particle dampers for horizontal vibrations with application to a lightweight manipulator. Journal of Sound and Vibration **510**, 116319 (2021). DOI 10.1016/j.jsv.2021.116319

[9] Meyer, N., Seifried, R.: Damping prediction of particle dampers for structures under forced vibration using effective fields. Granular Matter **23**(3), 64 (2021). DOI 10.1007/s10035-021-01128-z

[10] Meyer, N., Seifried, R.: Optimal design of particle dampers for structures with low first eigenfrequency under forced vibration. 7th edition of the International Conference on Particle-based Methods **7** (2021). DOI 10.23967/particles.2021.022

[11] Meyer, N., Seifried, R.: Toward a design methodology for particle dampers by analyzing their energy dissipation. Computational Particle Mechanics **8**(4), 681–699 (2021). DOI 10.1007/s40571-020-00363-0

[12] Meyer, N., Seifried, R.: Energy dissipation in horizontally driven particle dampers of low acceleration intensities. Nonlinear Dynamics (2022). DOI 10.1007/s11071-022-07348-z

[13] Panossian, H.: Structural damping enhancement via non-obstructive particle damping technique. Journal of Vibration and Acoustics **105**(114), 101–105 (1992). DOI 10.1115/1.2930221

[14] Panossian, H.: Non-obstructive particle damping experience and capabilities. Proceedings of SPIE - The International Society for Optical Engineering **4753**, 936–941 (2002). DOI 10.2514/6.2008-2102

[15] Sack, A., Heckel, M., Kollmer, J., Zimber, F., Pöschel, T.: Energy dissipation in driven granular matter in the absence of gravity. Physical review letters **111** (2013). DOI 10.1103/PhysRevLett.111.018001

[16] Saluena, C., Esipov, S.E., Poeschel, T., Simonian, S.S.: Dissipative properties of granular ensembles. Proceedings of SPIE **3327**(1), 23–29 (1998). DOI 10.1117/12.310696

[17] Sanchez, M., Rosenthal, G., Pugnaloni, L.: Universal response of optimal granular damping devices. Journal of Sound and Vibration **331**(20), 4389–4394 (2012). DOI 10.1016/j.jsv.2012.05.001

[18] Simonian, S.S.: Particle beam damper. Proceedings of SPIE - The International Society for Optical Engineering **2445**, 149–160 (1995). DOI 10.1117/12.208884

[19] Wong, C.X., Daniel, M.C., Rongong, J.A.: Energy dissipation prediction of particle dampers. Journal of Sound and Vibration **319**(1-2), 91–118 (2009). DOI 10.1016/j.jsv.2008.06.027

[20] Yin, Z., Su, F., Zhang, H.: Investigation of the energy dissipation of different rheology behaviors in a non-obstructive particle damper. Powder Technology **321** (2017). DOI 10.1016/j.powtec.2017.07.090

[21] Zhang, K., Chen, T., He, L.: Damping behaviors of granular particles in a vertically vibrated closed container. Powder Technology **321**, 173–179 (2017). DOI 10.1016/j.powtec.2017.08.020

Tracing periodic solutions in noise-contaminated experiments

Sandor Beregi, David A. W. Barton, Djamel Rezgui and Simon A. Neild
Faculty of Engineering, University of Bristol, United Kingdom

Summary. In our study, we trace the steady-state solutions of a periodically forced nonlinear oscillator experimentally using control-based continuation. Our investigation is motivated by nonlinear aeroelastic oscillations where the noise load of experiments is often significant due to the unsteady flow in the wake of the vortex-shedding, oscillating bodies. Polluting our experiment with different amount of noise, we evaluate the resilience of the control-based continuation method against random perturbations and assess its capability to retain the response of the underlying deterministic system.

Introduction

Tracing a family of periodic solutions is a long-established area of studying nonlinear systems. For numerical dynamical models, the techniques of bifurcation analysis have become standardised and are available nowadays in several software packages. In experiments however, the steady-state periodic solutions are often traced by performing parameter-sweeps. Although this approach is usually easy to implement it provides limited information from the system as it can capture stable solutions only. Control-based continuation is a technique which implements the ideas of bifurcation analysis in experiments [1]. By applying feedback-control on the system, this method is capable to trace both stable and unstable steady-state periodic oscillations in an experimental setting. To achieve this, a control process is introduced which has to be stabilising and non-invasive, i.e. the steady-state solution of the controlled system is also solution of the open-loop system.
Our study is motivated by examples of aeroelastic oscillations originated in the interaction between inertial, structural and aerodynamic forces. The related vibrations, such as stall flutter of an aerofoil, caused by the periodic detachment and re-attachment of the flow, or the galloping oscillation of blunt elastic structures (e.g. cables) in airflow due to vortex-generation around the body, are substantially nonlinear phenomena. In the literature, several semi-empirical, low-degrees-of-freedom models were developed to investigate these oscillations [2]. Since these models use empirical coefficients there is a great demand for reliable parameter identification methods in this area.

Tracing steady-state solutions in noise-polluted experiments

In experiments, it may be challenging to obtain data which represent the dynamics of the investigated system accurately if the measurements subject to significant noise, as it is often the case with aeroelastic oscillations.
A nonlinear analysis of aeroelastic dynamical models can reveal a rich structure of different steady-state solutions and bifurcations [3, 4]. Nevertheless, in a physical experiment, these oscillations can result in a highly unsteady flow in the wake of the vortex-shedding objects. Thus, one may observe that the magnitude of measurement noise is comparable to the vibration amplitudes. In such conditions, the standard, open-loop parameter-sweeps may not be satisfactory for the characterisation of the system. For instance, in parameter regions with two co-existing stable steady-state solutions, the system may jump repeatedly between the two domains of attraction leading to an incomplete coverage of even the stable solutions [5]. The aim of our study is to demonstrate that tracing the solutions with a control-based method is more resilient against random perturbations than open-loop parameter-sweeps.

Case-study: parameter identification of a forced nonlinear oscillator under noise-load

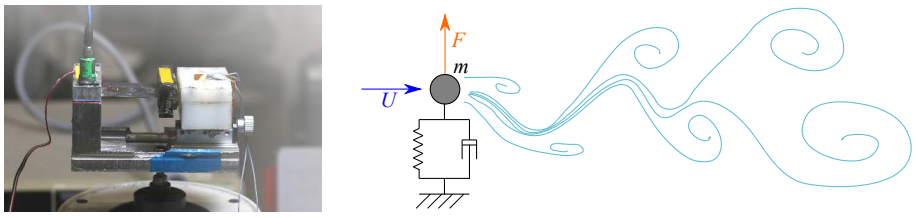

Figure 1: Left panel: The forced nonlinear oscillator. Right panel: The analogous model of vortex-induced vibrations.

To assess the capability of control-based continuation to deal with measurement noise we traced the steady-state solutions of a periodically forced nonlinear oscillator (see Fig. 1). In the experimental rig, the nonlinearity is primarily provided by the magnets mounted to the end of the elastic plate. As the plate vibrates the magnets are passing before the electromagnetic coil resulting in a nonlinear restoring force. The experiment can also be polluted with additional noise by driving current through the coil; thus, measurements can be conducted at different noise-levels.
This experimental setup may be seen as analogous to vortex-induced aeroelastic vibrations. These vibrations are similar to the galloping phenomenon in a sense that they can be originated in the vortex-shedding behind a blunt object as in the case of bridge cables. However, unlike in case of galloping where the frequency of vortex-shedding is equal to the

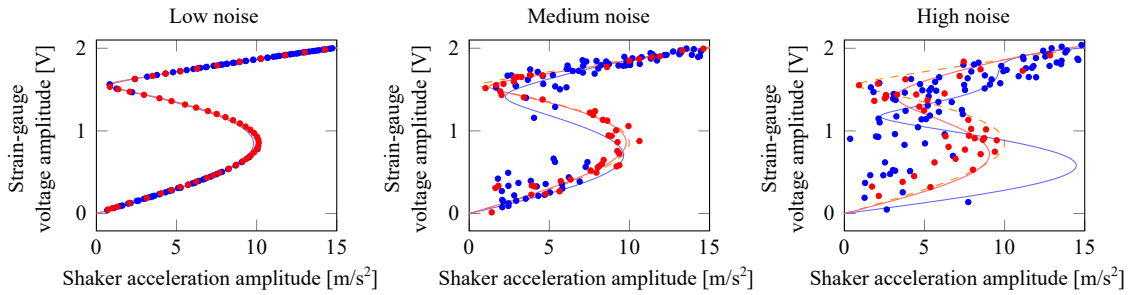

Figure 2: Steady-state response of the periodically forced nonlinear oscillator for different forcing amplitude. The blue markers correspond to amplitude-sweeps, the red ones to control-based continuation, respectively. The blue and red curves indicate the response of the fitted model while the dashed orange curve indicates the low-noise response in the panels corresponding to medium and high noise-levels.

vibration frequency, in case of vortex-induced vibrations, the frequency belonging to vortex-generation depends on the Strouhal number of the flow around the aerofoil [3]. Thus, while galloping is essentially considered as a self-excited vibration, vortex-induced vibrations are often modelled as forced nonlinear systems. One example is the semi-empirical model of Goswami et al. [6] given in the form

$$m\left(\ddot{x} + 2\zeta\omega_{\mathrm{n}}\dot{x} + \omega_{\mathrm{n}}^2 x\right) = F(x, \dot{x}, \ddot{x}, \omega t) \tag{1}$$

where m is the mass of the vibrating object, ω_{n} is the structural natural angular frequency, ζ is Lehr's damping coefficient whereas the aerodynamic force F contains both the nonlinear and the periodic forcing terms.

Robustness against noise

We traced the S-shaped branch of periodic solutions of the experimental rig at different noise levels by performing both open-loop parameter-sweeps and control-based continuation. The acquired data was then used to identify the parameters of a one-degree-of-freedom Duffing-like oscillator with seventh-order nonlinearity. The results of parameter-sweeps and control-based continuation are compared in Fig. 2. At low noise level, the system can be characterised equally well by both methods. If a medium level of noise (around 25 % of the maximum vibration amplitude) parameter-sweeps begin to lose a part of the stable solutions as the jumps from low to high vibration amplitudes occur earlier than the folds in the low-noise solution branch. In the meantime, control-based continuation is still able to retain the original response reasonably well. However, at high noise levels (about 50 % of the maximum vibration amplitude) even the response curve fitted to the data obtained by control-based continuation visibly deviates from the branch corresponding to low noise. Nevertheless, control-based continuation still performs better as parameter-sweeps scarcely capture the bistable parameter region at this level of noise.

Conclusions

Comparing the response curves, acquired at different noise-levels, indicates that control-based continuation is more resilient against noise than open-loop parameter sweeps. Furthermore, having information about the unstable steady-state solutions of the system is clearly advantageous at nonlinear parameter fitting to noisy measurements. Therefore control-based continuation could be effectively used to investigate nonlinear aeroelastic systems experimentally.
Of course, our experimental rig has a relatively simple bifurcation diagram with only one bistable parameter domain and we also have access to the low-noise system. Consequently, if a more complicated structure of bifurcations is expected, based on deterministic theoretical models, the relationship between the measured and theoretical results may be less straightforward. Therefore, it is interesting to investigate what kind of response one can expect to find in a noise-contaminated measurement and how are the results obtained from the experiment related to the underlying deterministic system [7].

References

[1] Renson L., Shaw A.D., Barton D.A.W., Neild S.A., Application of control-based continuation to a nonlinear structure with harmonically coupled modes, *Mechanical Systems and Signal Processing*, Vol. 120, pp. 449-464.

[2] Gabbai R.D., Benaroya H. (2005) An overview of modeling and experiments of vortex-induced vibration of circular cylinders, *Journal of Sound and Vibration*, Vol. 282, pp. 575-616.

[3] Dimitriadis, G. (2017). Introduction to nonlinear aeroelasticity. John Wiley & Sons.

[4] Tartaruga I., Barton D.A.W., Rezgui D., Neild S., (2019) Experimental bifurcation analysis of a wing profile, International Forum on Aeroelasticity and Structural Dynamics, IFASD 2019, 9-13 June 2019, Savannah, Georgia, USA

[5] Barkley D., Kevrekidis I.G., Stuart A.M. Adams J.A. (2006) The Moment Map: Nonlinear Dynamics of Density Evolution via a Few Moments *SIAM J. Applied Dynamical Systems*, Vol. 5. No. 3. pp. 403-434.

[6] Goswami I., Scanlan R.H., Jones N.P. (1993) Vortex-induced vibration of circular cylinders—part 2: new model, *Journal of Sound and Vibration*, Vol. 119, pp. 2288-2302.

[7] Kuehn C., (2012) Deterministic Continuation of Stochastic Metastable Equilibria via Lyapunov Equations and Ellipsoids, *SIAM Journal on Scientific Computing*, Vol 34. No, 3, pp. A1635-A1658

Active Vibration Mitigation of High Modal Density of BLUM with Piezoelectric Patches

Rasa Jamshidi[1,2], Christophe Collette[1,2]

1- BEAMS Department, Universitè Libre de Bruxelles, Belgium

2- Department of Aerospace and Mechanical Engineering, Universitè de Liège, Belgium

Abstract

In this study, active vibration control of bladed drum (BLUM), which has a high modal density, with piezoelectric patches utilizing decentralized controller evaluated experimentally. BLUM has 76 protruding blades, which create 76 modes in a short interval of frequency named as high modal density. High number of modes in a very short frequency range makes mitigating them quite challenging. In this article, 76 collocated pairs of piezoelectric patches are used to damp the vibration of these modes. These modes relate to the displacement of the blades. Therefore, piezoelectric patches are used as sensor to measure the displacement of each blade. Then the collocated actuator piezoelectric patch applies a force in a reverse direction to reduce displacement of the blade, actively. In order to avoid to cause any disturbance for air flow around the blades, the piezoelectric patches are glued in the bottom groove of BLUM where there is no air flow. The blades of BLUM are inclined and in order to increase the performance of the system, the piezoelectric patches are produced in a trapezoidal shape which will increase the control authority of system. 76 Open loops are extracted and an IFF controller is designed to implement in a decentralized manner. 76 pairs of piezoelectric patches are glued on the structure and connected to the connector board. Also, a circuit is designed and produced based on the controller's transfer function to apply on the setup in a decentralized way. The 76 controller boards are connected to the connector board to control the structure's vibration. The structure is excited by the acoustic speakers in the frequency band which the first family mode exists. The structure displacement is measured by a laser vibrometer. The performance index of system shows that in the controlled condition all of 76 modes in the first family mode are damped remarkably.

Keywords: BLUM, Active Vibration Control, Decentralized Controller, Piezoelectric sensor/actuators, Family Mode, High Modal Density.

Tuesday, July 19, 2022

08:30 - 10:30

MS-01 Reduced-Order Modeling and System Identification

Saint Clair 3B

Chair: Majdi Gzal

08:30 - 08:50

Comparison of nonlinear methods for reduced-order modeling of geometrically nonlinear structures

TOUZÉ Cyril*, VIZZACCARO Alessandra, THOMAS Olivier, SALLES Loic, OPRENI Andrea, SHEN Yichang, FRANGI Attilio

*Institute of Mechanical Science and Industrial Applications (Unité de Mécanique, IMSIA 828 Boulevard des Maréchaux 91762 Palaiseau Cedex France)

08:50 - 09:10

Finite elements based reduced order models for geometrically nonlinear and piezoelectric thin structures: validation and three-dimensional effects

THOMAS Olivier*, VIZZACARRO Alessandra, GIVOIS Arthur, GROLET Aurelien, SALLES Loïc, DEÜ Jean-François, TOUZE Cyril

*Laboratoire d'Ingénierie des Systèmes Physiques et Numériques (Arts et Métiers - Campus d'Aix-en-Provence2, cours des Arts et Métiers, 13617 AIX EN PROVENCETél.: +33 (0)4 42 93 81 41Laboratoire d'Ingénierie des Systèmes Physiques et numériques (LISPEN EA7515)Arts et Métiers - Campus de Lille8 bd Louis XIV - 59046 Lille CedexTél.: +33 (0)4 42 93 81 41Laboratoire d'Ingénierie des Systèmes Physiques et numériques (LISPEN EA7515)Arts et Métiers - Campus de Cluny (Institut Image de Chalon-sur-Saône)2 rue Thomas Dumorey 71100 CHÂLONS-SUR-SAONETél.: +33 (0)3 85 90 98 60 France)

09:10 - 09:30

Asymptotic Computation of Invariant Manifolds of large Finite Element structures with Geometric Nonlinearities

VIZZACCARO Alessandra*, OPRENI Andrea, SALLES Loic, FRANGI Attilio, TOUZÉ Cyril

*Department of Mechanical Engineering [Imperial College London] (Imperial College London, London SW7 2AZ United Kingdom) - Faculty of Engineering [Bristol] (University of Bristol, Senate House, Tyndall Avenue, Bristol BS8 1TH, UK United Kingdom)

09:30 - 09:50

Data-driven aerodynamic models for reduced-order aeroelastic simulations

HORVÁTH Dávid András*, LELKES János

*Budapest University of Technology and Economics, Faculty of Mechanical Engineering, Department of Fluid Dynamics (1111 Budapest, Bertalan Lajos Street 4-6. Hungary Hungary)

09:50 - 10:10

Development and Parameter Estimation of a Low Order Model of a Hyperelastic Plate Exhibiting 2:1 Resonant Response

JABER Nizar, **BILAL Nasir***, BAJAJ Anil

*Purdue University (West Lafayette, IN 47907 United States) - School of Mechanical Engineering, Purdue University, West Lafayette, IN 47907, USA (West Lafayette, IN 47907, USA United States)

Comparison of nonlinear methods for reduced-order modeling of geometrically nonlinear structures

Cyril Touzé[*], Alessandra Vizzaccaro[◇], Olivier Thomas[†], Loïc Salles[♯], Andrea Opreni[↬], Yichang Shen[*] and Attilio Frangi[↬]

[*] *IMSIA, ENSTA Paris, CNRS, EDF, CEA, Institut Polytechnique de Paris, Palaiseau, France.*
[◇] *Department of Engineering Mathematics, University of Bristol, United Kingdom.*
[†] *Laboratoire d'Ingénierie des Systèmes Physiques et Numériques, Arts et Métiers, Lille, France.*
[♯] *Skolkovo Institute of Science and Technology, Moscow, Russia.*
[↬] *Department of Civil and Environmental Engineering, Politecnico di Milano, Italy.*

Summary. The aim of this contribution is to review and compare three different methods that have been proposed in order to derive reduced-order models for geometrically nonlinear structures, and relying on a nonlinear technique to better take into account the nonlinearities of the initial problem. The three methods are: implicit condensation, quadratic manifold derived with modal derivatives, and projection onto an invariant manifold, tangent at the origin to the linear eigenspace of the master modes. The methods are briefly reviewed theoretically and then compared with dedicated examples.

Nonlinear techniques for model-order reduction

In the realm of reduction methods for geometrically nonlinear structures, numerous methods have already been proposed in the past, and one can roughly divide the methods according to the fact that they use either a linear or a nonlinear change of coordinates. Among the linear methods, the POD is well-established and has been used for a long time. For the nonlinear techniques, the review paper [1] proposes an overview with applications to finite element (FE) problems.
When referring to vibrating structures discretized by the FE method, mainly three different nonlinear techniques have been proposed in the last years: implicit condensation (IC), quadratic manifold derived with modal derivatives (QM), and the direct parametrisation method for invariant manifolds, giving rise to either graph style or normal style solutions.
The implicit condensation is a non-intrusive method that can be used with any FE code. It relies on applying a series of static loads, having the shape of the selected master modes, to the structure; and retrieving the associated nonlinear displacements [2]. From this set that creates a stress manifold [3], a fitting procedure is derived in order to get the nonlinear restoring force of the master coordinates, which takes implicitely into account the non-resonant coupled modes in a static manner [2, 4].
The quadratic manifold method with modal derivatives have been introduced with the aim of proposing a nonlinear change of coordinates, directly applicable from the FE nodes of a mesh [5]. The main idea is to embed the modal derivatives, earlier defined in order to take into account the amplitude dependence of a mode when the nonlinearities are taken into account, as the quadratic component of the nonlinear mapping. The Galerkin projection is then used to compute the reduced dynamics from the nonlinear mapping.
The invariant manifold approach relies on firm theoretical results from dynamical systems theory. The main idea is to use an invariant manifold that is tangent to the master modes of interest at the origin, in order to obtain a rigorous computation of the amplitude dependence. Whereas the idea has been first introduced by Shaw and Pierre in the 90s [6], later embedded in the normal form theory in order to define nonlinear mappings [7], recent contributions tackled the problem of uniqueness by introducing spectral submanifolds (SSM) [8], as well as using the parametrisation method for invariant manifolds [9] in order to unify the previous derivations in the same settings, allowing one to select either a graph style solution or a normal form approach. However, until recently, the direct application of these methods to FE problems still remained difficult since the derivations assumed the problem expressed in the modal basis as a starting point. Recent contributions overcame this issue, by proposing a direct computation of the reduced dynamics, from the FE nodes to the invariant-based span of the phase space, thanks to dedicated nonlinear mappings, see *e.g.* [10, 11, 12].

Comparisons

Theoretical results

The three reduction methods have been compared in details in the following references [13, 4, 14]. In particular, it has been clearly demonstrated that both IC and QM methods needs a slow/fast assumption in order to propose accurate predictions. By slow/fast separation, it is meant that the eigenfrequencies of the slave modes needs to be larger than those of the master modes. This frequency gap has been estimated in [4, 14] to be around 4, based on the hardening/softening prediction of a single mode reduction. As a matter of fact, this limitation of these two methods comes from their derivation, which is static in nature and neglects important dynamical couplings. In particular, both IC and QM methods are neglecting the velocity dependence in the proposed nonlinear mappings, which then creates important limitations and the need to have this slow/fast separation [4, 14, 1]. As underlined for example in [1], when taking back the velocity dependence in the nonlinear mapping proposed in the QM method, then one recovers the more complete change of coordinates proposed with a direct normal form approach as proposed in [10].

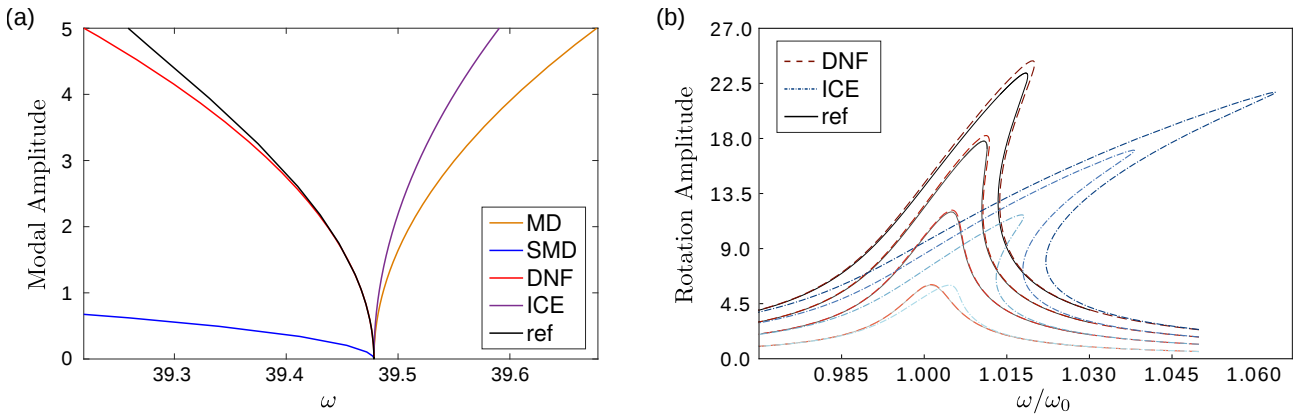

Figure 1: (a) Backbone curves for a linear beam resting on an elastic foundation, comparison between QM methods with either full modal derivatives (MD) or static modal derivatives (SMD), Implicit condensation (ICE), and direct normal form (DNF). Reference solution in black. (b) Comparison between Implicit condensation (IC), direct normal form (DNF) and full-order solution for a MEMS micromirror.

Numerical results

Two different numerical results are reported for the sake of illustration. The first case consists in computing the backbone curve of a linear beam resting on a nonlinear elastic foundation with reduction to a single master mode. The results are shown in Fig. 1(a), highlighting that in such a case, only the solution based on invariant manifold theory is able to correctly reproduce the softening behaviour [15]. The second example is that of a MEMS (Micro Electro Mechanical System) micromirror, discretized with 3D block elements. The mesh has 15 341 nodes.Fig. 1(b) highlights that the IC method overpredicts the hardening behaviour of this structure [16].

References

[1] C. Touzé, A. Vizzaccaro and O. Thomas (2021) Model order reduction methods for geometrically nonlinear structures: a review of nonlinear techniques, *Nonlinear Dynamics*, **105**:1141-1190.

[2] J. J. Hollkamp and R. W. Gordon (2008) Reduced-order models for non-linear response prediction: Implicit condensation and expansion, *J. Sound Vib.*, **318**: 1139-1153.

[3] A. Frangi, and G. Gobat (2019) Reduced order modelling of the non-linear stiffness in MEMS resonators. *Int. J. Non-Linear Mech*, **116**: 211-218.

[4] Y. Shen, N. Béreux, A. Frangi and C. Touzé (2021) Reduced order models for geometrically nonlinear structures: Assessment of implicit condensation in comparison with invariant manifold approach, *Eur. J. Mech. A/Solids*, **86**: 104165.

[5] S. Jain, P. Tiso, J. B. Rutzmoser and D. J. Rixen (2017) A quadratic manifold for model order reduction of nonlinear structural dynamics, *Computers and Structures*, **188**:80-94.

[6] S. W. Shaw, and C. Pierre (1991) Non-linear normal modes and invariant manifolds, *J. Sound Vib.*, **150**:170-173.

[7] C. Touzé, O. Thomas and A. Chaigne (2004) Hardening/softening behaviour in non-linear oscillations of structural systems using non-linear normal modes, *J. Sound. Vib*, **273**(1-2): 77-101.

[8] G. Haller and S. Ponsioen (2016) Nonlinear normal modes and spectral submanifolds: Existence, uniqueness and use in model reduction, *Nonlinear Dynamics*, **86**: 1493-1534.

[9] A. Haro, M. Canadell, J.-L. Figueras, A. Luque, and J. M. Mondelo, J. M. (2016) The Parameterization Method for Invariant Manifolds, Springer-Verlag.

[10] A. Vizzaccaro, Y. Shen, L. Salles, J. Blahos, and C. Touzé (2021) Direct computation of nonlinear mapping via normal form for reduced-order models of finite element nonlinear structures, *Comput. Methods Appl. Mech. Eng.*, **284**: 113957.

[11] A. Vizzaccaro, A. Opreni, L. Salles, A. Frangi, and C. Touzé (2021) High order direct parametrisation of invariant manifolds for model order reduction of finite element structures: application to large amplitude vibrations and uncovering of a folding point, `arXiv:2109.10031`

[12] S. Jain and G. Haller (2021) How to Compute Invariant Manifolds and their Reduced Dynamics in High-Dimensional Finite-Element Models? *Nonlinear Dynamics*, in press.

[13] G. Haller and S. Ponsioen (2017) Exact model reduction by slow/fast decomposition of nonlinear mechanical systems, *Nonlinear Dynamics*, **90**:617-647.

[14] A. Vizzaccaro, L. Salles and C. Touzé (2021) Comparison of nonlinear mappings for reduced-order modelling of vibrating structures: normal form theory and quadratic manifold method with modal derivatives, *Nonlinear Dynamics*, **103**:3335-3370.

[15] Y. Shen, A. Vizzaccaro, N. Kesmia, T. Yu, L. Salles, O. Thomas and C. Touzé (2021) Comparison of reduction methods for finite element geometrically nonlinear beam structures, *Vibration*, **4**(1): 175-204.

[16] A. Opreni, A. Vizzaccaro, A. Frangi and C. Touzé (2021) Model order reduction based on direct normal form: application to large finite element MEMS structures featuring internal resonance, *Nonlinear Dynamics*, **105**: 1237-1272.

Finite elements based reduced order models for geometrically nonlinear and piezoelectric thin structures: validation and three-dimensional effects

O. Thomas*, A. Givois*,†, A. Vizzacaro♭, P. Longobardi♭, A. Grolet*, L. Salles♭,
J.-F. Deü†, Y. Shen♯ and C. Touzé♯
*Laboratoire d'Ingénierie des Systèmes Physiques et Numériques, Arts et Métiers, Lille, France
†Laboratoire de Mécanique des Structures et des Systèmes Couplés, Cnam, Paris, France
♭Department of Mechanical Engineering, Imperial College London, London
♯ IMSIA, Institut of Mechanical Sciences and Industrial Applications, ENSTA Paris, CNRS, EDF,CEA, Institut Polytechnique de Paris, Palaiseau, France.

Summary. This paper presents a general methodology to obtain a reduced order model (ROM) of geometrically nonlinear electro-mechanical structures with piezoelectric transducers. A standard modal reduction is used and the ROM is built using a finite-elements software thanks to a non-intrusive strategy. In this context, this article focuses first on the validation of the proposed reduced order modelling strategy, especially for the piezoelectric part of the ROM, and second to the use of three-dimensional finite elements and associated convergence issues.

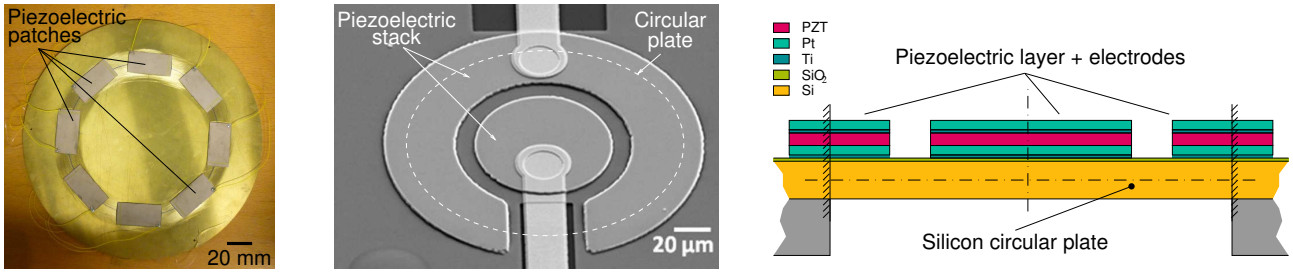

Figure 1: (left) Photograph of two examples of piezoelectric thin structures: a circular plate with eight piezoelectric patches and a micro-plate with two annular piezoelectric patches. (right) cutaway view of the microplate, showing its laminated structure

Geometrical nonlinearities, due to large transverse displacements of thin structures, are encountered in a large range of applications, as long as the thickness of the structure is small corresponding to the other dimensions. On the other hand, the use of piezoelectric materials to actuate or/and sense the vibrations is also widely spread. Applications, among others, range from vibration control [3, 11] to Micro/Nano-Electro Mechanical Systems (M/NEMS) developments, whose purpose can be to master and use the geometrically nonlinear behaviour [12, 14, 10]. This paper focuses on the numerical computation of the frequency response, in the frequency domain, of structures with geometrical nonlinearities and equipped with piezoelectric patches. Recent advances in non-intrusive reduced-order finite element modeling of nonlinear geometric structures offer new perspectives for massive nonlinear prediction in structural computation [7]. An application on piezoelectric nanobridges of such a method has been proposed in [6, 15]. Apart those two references, to the knowledge of the authors, the case of both geometrical nonlinearities and piezoelectric electromechanical coupling has been scarcely considered in the past literature. The purpose of this paper is to fill this gap and to propose a non intrusive method able to efficiently compute the coefficients of a modal reduced order model, taking into account both the geometrical nonlinearities and the direct and converse piezoelectric couplings.

Common architectures of thin structures with piezoelectric layers (see examples on Fig. 1) are often laminated, such as beams with complex cross section [13] and laminated beams/plate structures [2, 4, 1]. When modelling such a structure in a finite-element context, one can consider equivalent single layer theories [9, 6] or simply use three-dimensional finite elements (3DFE). Because in our case some layers of the structure are piezoelectric, in most of the cases, only 3DFE are available in commercial codes. In this article, we will consider both approaches.

We consider an elastic structures with P piezoelectric patches discretized by the finite-elements method. The vector containing the mechanical degrees of freedom is denoted by $\boldsymbol{U}(t)$ and $V^{(p)}$ denotes the voltage across the terminals of the p-th. piezoelectric patch. As shown in [6], considering a modal expansion of $\boldsymbol{U}(t)$ on K modes $(\boldsymbol{\Phi}_k, \omega_k)$ of the structure with all piezoelectric patches short circuited, $\boldsymbol{U}(t) = \sum_{k=1}^{K} \boldsymbol{\Phi}_k q_k(t)$, one obtains the following system of equations for the modal coordinates $q_k(t)$ and the voltages $V^{(p)}$, $\forall\, k = 1, \dots K, p = 1, \dots P$:

$$\begin{cases} \ddot{q}_k + 2\xi_k\omega_k\dot{q}_k + \omega_k^2 q_k + \displaystyle\sum_{i,j=1}^{K} \beta_{ij}^k q_i q_j + \sum_{i,j,l=1}^{K} \gamma_{ijl}^k q_i q_j q_l + \sum_{p=1}^{P} \chi_k^{(p)} V^{(p)} + \sum_{p=1}^{P}\sum_{i=1}^{N} \Theta_{ik}^{(p)} q_i V^{(p)} = F_k, & \text{(1a)} \\ C^{(p)} V^{(p)} - \displaystyle\sum_{k=1}^{K} \chi_k^{(p)} q_k - \sum_{i,j=1}^{K} \frac{1}{2}\Theta_{ij}^{(p)} q_i q_j = Q^{(p)}. & \text{(1b)} \end{cases}$$

In the above equations, three independant groups of term can be identified. First, the geometrical nonlinearities create quadratic and cubic terms in q_k with coefficients β_{ij}^k and γ_{ijlk}^k. Secondly, the piezoelectric linear coupling creates two terms of coefficients $\chi_k^{(p)}$, which correspond to the exchange of energy between the k-th. vibration mode and the p-th. piezoelectric patch. Then, both geometrical nonlinearities and piezoelectric coupling are responsible of additional coupling terms, of coefficient $\Theta_{ij}^{(p)}$, not symmetric because of the $1/2$ factor in the second equation. In addition, $C^{(p)}$ is the electric capacitance of the p-th. patch, F_k is the mechanical forcing and $Q^{(p)}$ is the electric charge contained in one of the electrodes of the p-th. patch.

In this context, this article has several purposes. First, it will be shown that it is possible to extend a particular non intrusive method, the so-called stiffness evaluation procedure (STEP), relying on the static application of prescribed displacements and introduced in [8], to compute the piezoelectric coefficients $\chi_k^{(p)}$ and $\Theta_{ij}^{(p)}$ using a commercial code in a non intrusive way. Then, even if the STEP has been validated in many articles in the past (see [5] and reference therein) to compute the geometrically nonlinear part of the ROM (the quadratic and cubic terms with coefficients β_{ij}^k and γ_{ijlk}^k), it will be shown that using 3DEF is not as straightforward as it could appear at first and that it conducts to strange behaviours of slow convergence as a function of the number K of modes retained in the expansion basis, much slower that in the case of the use of plate or shell two-dimensional finite-elements. Finally, the computation of the coupling coefficients $\chi_k^{(p)}$ and $\Theta_{ij}^{(p)}$ will be validated with comparison to an analytical reference model of a three layers hinged hinged beam with two colloacated piezoelectric patches.

References

[1] C. Ayela, L. Nicu, C. Soyer, É. Cattan, and C. Bergaud. Determination of the d_{31} piezoelectric coefficient of $pbzr_xti_{1-x}o_3$ thin films using multilayer buckled micromembranes. *Journal of Applied Physics*, 100:054908, 2006.

[2] D. Dezest, O. Thomas, F. Mathieu, L. Mazenq, C. Soyer, J. Costecalde, D. Remiens, J.-F. Deü, and L. Nicu. Wafer-scale fabrication of self-actuated piezoelectric nanoelectromechanical resonators based on lead zirconate titanate (pzt). *Journal of Micromechanics and Microengineering*, 25(3):035002, 2015.

[3] J. Ducarne, O. Thomas, and J.-F. Deü. Placement and dimension optimization of shunted piezoelectric patches for vibration reduction. *Journal of Sound and Vibration*, 331(14):3286–3303, 2012.

[4] C. Fuinel, K. Daffé, A. Laborde, O. Thomas, L. Mazenq, L. Nicu, T. Leichlé, and B. Legrand. High-K thin films as dielectric transducers for flexural M/NEMS resonators. In *Proc. of the 29th. IEEE international conference on micro electro mechanical systems (MEMS 2016) conference*, Shanghai, China, January 2016.

[5] A. Givois, A. Grolet, O. Thomas, and J.-F. Deü. On the frequency response computation of geometrically nonlinear flat structures using reduced-order finite element models. *Nonlinear Dynamics*, 97(2):1147–1781, 2019.

[6] A. Lazarus, O. Thomas, and J.-F. Deü. Finite elements reduced order models for nonlinear vibrations of piezoelectric layered beams with applications to NEMS. *Finite Elements in Analysis and Design*, 49(1):35–51, 2012.

[7] M. P. Mignolet, A. Przekop, S. A. Rizzi, and S. M. Spottswood. A review of indirect/non-intrusive reduced order modeling of nonlinear geometric structures. *Journal of Sound and Vibration*, 332(10):2437–2460, 2013.

[8] A. A. Muravyov and S. A. Rizzi. Determination of nonlinear stiffness with application to random vibration of geometrically nonlinear structures. *Computers and Structures*, 81(15):1513–1523, 2003.

[9] J. N. Reddy. *Mechanics of laminated composite plates*. CRC press, 1997.

[10] O. Shoshani, D. Heywood, Y. Yang, T. W. Kenny, and S. W. Shaw. Phase noise reduction in an mems oscillator using a nonlinearly enhanced synchronization domain. *Lournal of Microelectromechanical Systems*, 25(5):870–876, 2016.

[11] O. Thomas, J. Ducarne, and J.-F. Deü. Performance of piezoelectric shunts for vibration reduction. *Smart Materials and Structures*, 21(1):015008, 2012.

[12] O. Thomas, F. Mathieu, W. Mansfield, C. Huang, S. Trolier-McKinstry, and L. Nicu. Efficient parametric amplification in mems with integrated piezoelectric actuation and sensing capabilities. *Applied Physics Letters*, 102(16):163504, 2013.

[13] L. G. Villanueva, R. B. Karabalin, M. H. Matheny, D. Chi, J. E. Sader, and M. L. Roukes. Nonlinearity in nanomechanical cantilevers. *Physical Review B*, 87:024304, 2013.

[14] L. G. Villanueva, E. Kenig, R. B. Karabalin, M. H. Matheny, R. Lifshitz, M. C. Cross, and M. L. Roukes. Surpassing fundamental limits of oscillators using nonlinear resonators. *Physical Review Letters*, 110(17):177208, 2013.

[15] V. Vyas, X. Q. Wang, A. Jain, and M. P. Mignolet. Nonlinear geometric reduced order model for the response of a beam with a piezoelectric actuator. In *Proc. of the 56th AIAA/ASCE/AHS/ASC Structures, Structural Dynamics, and Materials Conference*, Kissimmee, Florida, USA, 2015.

Asymptotic Computation of Invariant Manifolds of large Finite Element structures with Geometric Nonlinearities

Alessandra Vizzaccaro[*,†], Andrea Opreni[‡], Loïc Salles[*,§], Attilio Frangi[‡], and Cyril Touzé[◇]
[*]*Department of Mechanical Engineering, Imperial College London, London, UK*
[†]*Department of Engineering Mathematics, University of Bristol, Bristol, UK*
[‡]*Department of Civil and Environmental Engineering, Politecnico di Milano, Milan, Italy*
[§]*Center for Design, Manufacturing and Materials, Skolkovo Institute of Science and Technology, Moscow, Russia*
[◇]*Institute of Mechanical Sciences and Industrial Applications (IMSIA) ENSTA Paris - CNRS - EDF - CEA - Institut Polytechnique de Paris, Paris, France*

Summary. In this contribution we present a method to directly compute asymptotic expansion of invariant manifolds of large finite element models from physical coordinates and their reduced order dynamics on the manifold. We show the accuracy of the reduction method on selected models, exhibiting large rotations and internal resonances. The results obtained with the reduction compared to full-order harmonic balance simulations show that the proposed methodology can reproduce extremely accurately the dynamics of the original systems with a very low computational cost.

Introduction

Slender structures in large amplitude vibration exhibit geometric nonlinear effects that modify their dynamics. To accurately model structures with complex geometries, large finite element models with a high number of degrees of freedom are often required. Numerically, the geometric nonlinear forces affect all the elements in the structure thus making the simulation of such problems very demanding in terms of computational cost. Reduced order models of geometrically nonlinear structures are then an attractive solution to drastically reduce the size of the problem whilst maintaining the accuracy.
In damped systems, slow invariant manifolds are low-dimensional attractors for the dynamics of high-dimensional nonlinear systems, and therefore represents the ideal candidate for model order reduction. However, their computation was until very recently limited to small system written in modal coordinates [**?**]. Recent developments by the authors [2-4] have proposed the Direct Parametrisation of Invariant Manifolds method (DPIM) to compute invariant manifolds directly in physical coordinates, thus extending the applicability of said model order reduction strategy to large FE structures. A similar work is done in [5].

Direct parametrization of Invariant Manifolds (DPIM)

Mechanical structures in large deformations display geometric nonlinearities in the form of quadratic and cubic restoring forces. When discretised with the finite elements method, the dynamics of such structures can be written as a system of N ordinary differential equations in time, with N the number of degrees of freedom:

$$\mathbf{M}\ddot{\mathbf{U}} + \mathbf{C}\dot{\mathbf{U}} + \mathbf{K}\mathbf{U} + \mathbf{G}(\mathbf{U},\mathbf{U}) + \mathbf{H}(\mathbf{U},\mathbf{U},\mathbf{U}) = \mathbf{0} \tag{1}$$

Invariant manifolds tangent to a given linear *master* subspace of the system are computed as an arbitrary order (o) asymptotic expansion of the physical coordinates $\mathbf{U}$ in terms of the so-called *normal* coordinates $\mathbf{z}$, which are tangent to the linear modal coordinates of the selected *master* mode:

$$\mathbf{U} = \sum_{p=1}^{o} \mathbf{\Psi}^{(p)}(\mathbf{z}) \tag{2}$$

The reduced dynamical model, which represents the dynamics on the computed manifold, is also built as a polynomial function of the normal coordinates in first-order form:

$$\dot{\mathbf{z}} = \sum_{p=1}^{o} \mathbf{f}^{(p)}(\mathbf{z}) \tag{3}$$

The coefficients of the change of coordinates $\mathbf{\Psi}$ and reduced dynamics $\mathbf{f}$ are then found iteratively order by order by assembling a so-called homological equation for each monomial in $\mathbf{z}$, which results in the solution of a series of $N \times N$ linear system of equations.

Numerical Results

Since each homological equation is underdetermined, different styles of parametrisation can be chosen by selecting appropriate resonance conditions, namely the Real Normal Form style (RNF), the Complex Normal Form style (CNF), and the Graph style [3]. The main difference between Normal Form styles and the Graph style is that in the former the manifold is parametrised as an embedding, whereas in the latter it is parametrised as a graph. In most cases, the results provided by each style are very similar but in case the computed manifold presents a folding, the graph style would diverge in

the vicinity of the folding point [6]. Physically, the folding of an invariant manifold can be seen as the point where the nonlinear mode becomes less and less represented by its linear counterpart, at a level such that as the nonlinear modal amplitude continues increasing, then the linear one starts to decrease.
The first nonlinear mode of a cantilever beam is studied here, and it is shown in Fig. 1 that the graph style fails at representing the full system dynamics when the amplitude of oscillations has order of magnitude comparable to the beam length. This failure can be observed both in the non-physical softening effect in the backbone curve and in the divergence of the invariant manifold. On the other hand, both normal form styles can perfectly reproduce the folding in the manifold and the backbone curves obtained with these styles are perfectly overlapped with that obtained from continuation of the full order model, up to very large amplitude oscillations. This exemplifies how powerful the method is in perfectly reproducing the dynamics of a large finite element system with a single oscillator reduced order model.

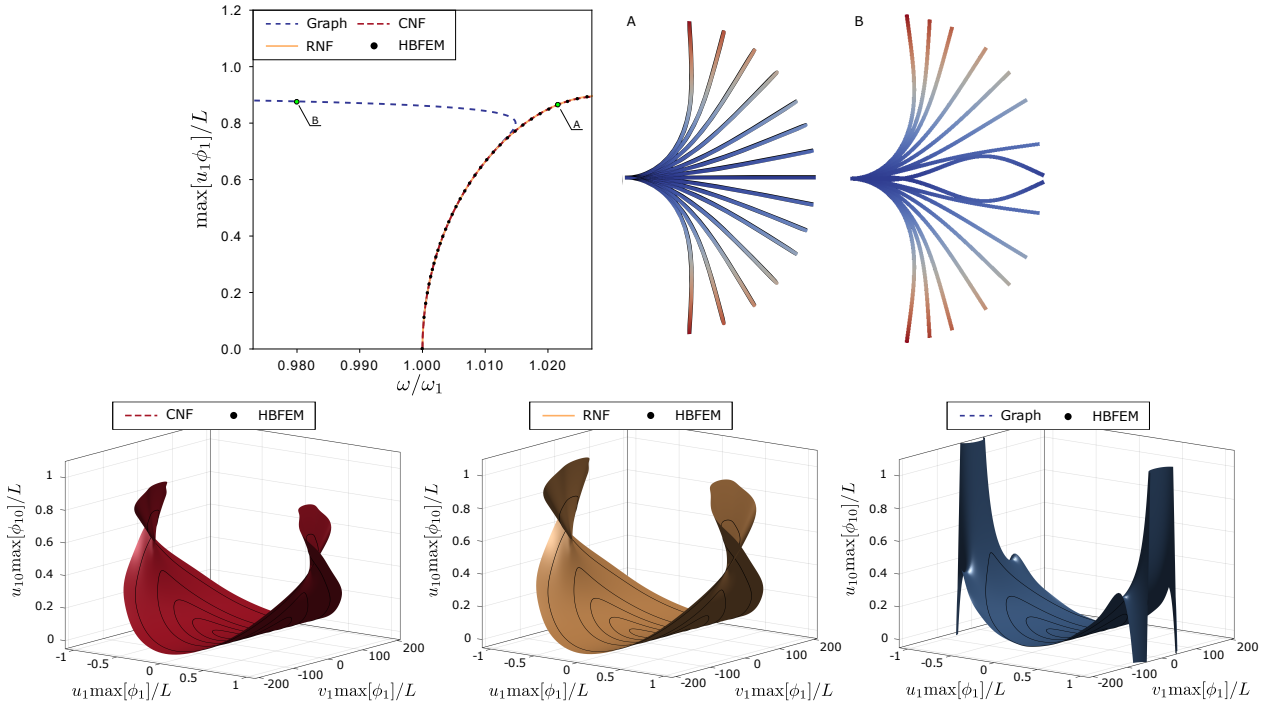

Figure 1: Model reduction of the first nonlinear mode of a cantilever beam up to large amplitude vibration. Backbone curves (top left), reconstruction of reduction at point A and B along the backbone curves (top right), and invariant manifolds (bottom). Three different parametrisation styles are used, and the full order model solution is obtained with harmonic balance method (HBFEM)

Conclusions

Nonlinear modes have become an essential tool for engineers in that they proNonlinear modes have become an essential tool for engineers in that they provide crucial insights on the dynamics of structures. The computation of nonlinear modes and their associated invariant manifolds for model order reduction is of utmost importance for modern industry. In this respect, the extension of nonlinear modes calculations to large scale finite element models is a critical issue that will allow the use of this tool in industrial scale problems. The method proposed here is based on a classical asymptotic expansion of invariant manifolds, but its computation is adapted to the case of FE models with a high number of degrees of freedom. The rigorous mathematical foundation of the method coupled with a thoughtful implementation make it extremely accurate and fast, thus making it the ideal candidate for reduced order modelling of geometrically nonlinear structures in an industrial framework.

References

[1] Touzé C., Vizzaccaro A., Thomas O. (2021) Model order reduction methods for geometrically nonlinear structures: a review of nonlinear techniques. *Nonlinear Dynamics*, **105**, 1237-1272.

[2] Vizzaccaro A., Shen Y., Salles L., Blahoš J., Touzé C., (2021) Direct computation of nonlinear mapping via normal form for reduced-order models of finite element nonlinear structures. *Comput Methods Appl Mech Eng*, **284**, 113957.

[3] Vizzaccaro A., Opreni A., Salles L., Frangi A., Touzé C. (2021, under review) High order direct parametrisation of invariant manifolds for model order reduction of finite element structures: application to large amplitude vibrations and uncovering of a folding point. Submitted to *Nonlinear Dynamics*.

[4] Opreni A., Vizzaccaro A., Frangi A., Touzé C., (2021) Model Order Reduction based on Direct Normal Form: Application to Large FE MEMS Structures Featuring Internal Resonance. *Nonlinear Dynamics*, **105**, 1237-1272.

[5] Jain S., Haller G. (2022, to appear) How to Compute Invariant Manifolds and their Reduced Dynamics in High-Dimensional Finite-Element Models? *Nonlinear Dynamics*, in press.

[6] Ponsioen S., Haller G., (2018) Automated computation of autonomous spectral submanifolds for nonlinear modal analysis. *J Sound Vib*, **420**, 269 – 295.

Data-driven aerodynamic models for reduced-order aeroelastic simulations

Dávid András Horváth, János Lelkes
Budapest University of Technology and Economics, Faculty of Mechanical Engineering, Department of Fluid Dynamics, Budapest, Hungary

Summary. Time-dependent aerodynamic loads of thin elastic structures subjected to airflow can be calculated by numerous methods. Analytical, semi-empirical, reduced-order, and CFD-based models can be utilized to calculate the aerodynamic loads. Calculations of the aerodynamic loads are influenced by nonlinear aerodynamic effects for large deformations of the elastic structure, such as dynamic stall, hysteresis, and vortex formation. In this work, the applicability and accuracy of a data-based identification method for calculating the aerodynamic loads in the time domain are investigated. To create the data-based model, high precision validated CFD simulations were used. The model was constructed using the SINDy (Sparse Identification of Nonlinear Dynamics) algorithm. After the initial data fitting process, the reduced-order aeroelastic simulations with the identified aerodynamic models run up to five magnitudes faster than classical high precision FSI simulations. The most significant advantage of this method is that it can be applied to a large variety of different geometries, and it is also accurate for large deformations and large angles of attack in the nonlinear aerodynamic regime.

Introduction

Obtaining accurate and efficient aerodynamic models has been a fundamental goal of research efforts in aeronautics over the past century [1]. Aerodynamic models are essential for designing aircrafts [2], building large span elastic bridges [3]. Accurate aerodynamic models are used to evaluate static and dynamic aeroelastic stability and develop feedback control laws for aircraft. Closed-form solutions for the attached incompressible unsteady flow problem around a two-dimensional (2D) airfoil exist in both the frequency and time domains [4]. However, these models do not provide acceptable results in the case of rapid oscillations and high angles of attack.
Semi-empirical models such as ONERA and Leishman-Beddoes can be used to approximate the aerodynamic nonlinearity caused by the dynamic stall and flow separation. Lelkes and Kalmár-Nagy modeled the aerodynamic forces for large angles of attack as a piecewise linear function, which was able to capture the phenomenon of dynamic stall [5].
Considering machine learning advancements, developing reduced-order models based on data obtained from measurements or numerical simulations began to gain popularity recently [6]. An overview of data-driven methods in aerospace engineering is given by Brunton et al. [7]. In the work of Pohl et al. [8] the SINDy method is used to derive polynomial models for the lift of an airfoil.
In this paper, the Sparse Identification of Nonlinear Dynamics (SINDy) method [9] is applied to create accurate aerodynamic models of a simple flat plate subjected to airflow using data obtained from CFD (Computational Fluid Dynamics) simulations.

Sparse Identification of Nonlinear Dynamics (SINDy)

In this paper, we use the Sparse Identification of Nonlinear Dynamical systems (SINDy) method, introduced by Brunton et al. [9, 10], and later refined in the work of Champion et al. [11]. An overview of the method and the description of the Python package that is used in our paper is given by Silva et al. [12]. Sparse Identification of Nonlinear Dynamics is a method based on representing the model as a system of possible nonlinear ordinary differential equations, whose right side can be written as a linear combination of some elementary functions [9]. Then a sparsity promoting regression is applied to determine the coefficients, resulting in easily interpretable models with only a few active terms. Physical constraints can be easily incorporated by constraining the regression procedure.
The LASSO and the STLSQ optimization method have been used for the regression. These methods have l_1 and l_2 regularized objective functions, respectively. The STLSQ procedure incorporates an adjustable threshold, any coefficient below this threshold is neglected. Then the regularization is repeated again for some iterations. The norms are defined as

$$l_1(\boldsymbol{x}) = \sum_{i=1}^{n} |x_i|, \tag{1}$$

$$l_2(\boldsymbol{x}) = \sqrt{\sum_{i=1}^{n} (x_i)^2}. \tag{2}$$

Using the formulas (1) and (2), the objective functions for the LASSO and STLSQ optimization procedure are respectively:

$$\frac{1}{2n} ||\boldsymbol{y} - \boldsymbol{X}\,\boldsymbol{w}||_2^2 + \lambda\, ||\boldsymbol{w}||_1\,, \tag{3}$$

$$\frac{1}{2n} ||\boldsymbol{y} - \boldsymbol{X}\,\boldsymbol{w}||_2^2 + \lambda\, ||\boldsymbol{w}||_2^2\,. \tag{4}$$

To determine the hyperparameters, the Optuna [13] package was used. Using this package, a multiobjective optimization was performed with the objectives defined as the error of the integrated model and the number of terms. So-called Pareto-optimal hyperparameter groups were determined. This means that for a given group, there are no other groups, which would result in an improvement over both objectives. This way, multiple models can be chosen, depending on the needs of the given task.

Identified models

The CFD simulations that the models have been trained on were obtained by prescribing a sinusoidal oscillation for the pitch (α) or the plunge (h) motion of the flat plate wing, with a 1m chord length. During the simulations we prescribed the motion in the following form

$$\alpha(t) = \alpha_{amp}\cos(\omega t), \qquad h(t) = h_{amp}\cos(\omega t), \tag{5}$$

where α_{amp} and h_{amp} are the oscillation amplitudes, and ω is the angular frequency of the oscillation.
Data were obtained for three oscillation amplitudes and frequencies of the pitching and plunging motion, resulting in 18 different time series of the aerodynamic lift coefficient. The details of the CFD simulations are described in [14, 15].
Three models were identified, one for each frequency. The frequency was nondimensionalized; the resulting reduced frequency is defined as $k = \frac{\omega b}{U}$, where b is the half chord length, U is the wind velocity, and ω is the angular frequency of the oscillation.
The aerodynamic model equations were created by using the state variables $\alpha, \dot{\alpha}, C_{L_\alpha}, h, \dot{h}, C_{L_h}$. The Reduced-Order Models (ROMs) of the pitch C_{L_α} and the plunge C_{L_h} induced lift coefficients are

$$\dot{C}_{L_\alpha}(\alpha, \dot{\alpha}, C_L; k) = a_1(k)\alpha + a_2(k)\dot{\alpha} + a_3(k)C_{L_\alpha} + a_4(k)\alpha^2 + a_5(k)\alpha\dot{\alpha}\ldots, \tag{6}$$

$$\dot{C}_{L_h}(h, \dot{h}, C_{L_h}; k) = b_1(k)h + b_2(k)\dot{h} + b_3(k)C_{L_h} + b_4(k)h^2 + b_5(k)h\dot{h}\ldots, \tag{7}$$

where a lexicographic ordering was used for the coefficients $a_i(k)$ and $b_i(k)$, which are listed in Table 1 and 2. We assume that the total lift coefficient C_L is the sum of the pitch and the plunge induced lift coefficients, i.e.,

$$C_L = C_{L_\alpha} + C_{L_h}. \tag{8}$$

Reduced frequency	a_1	a_2	a_3	a_{11}	a_{16}	a_{19}	a_{35}	a_{50}
$k = 0.1$	0.213	5.42	0	249	0	0	-665.76	-1.52·10^6
$k = 0.2$	12.2	0	-2.70	0	0	0.799	0	0
$k = 0.5$	4.01	6.32	-1.34	0	-56.5	0.463	0	0

Table 1: The coefficients of the pitch reduced-order model (Eq. (6)).

Reduced frequency	b_1	b_2	b_3	b_9	b_{35}	b_{50}
$k = 0.1$	-0.172	2.874	-0.398	0	0	0
$k = 0.2$	-0.715	2.33	-0.34	0	0	0
$k = 0.5$	-6.47	6.43	-1.6	-0.033	14113	23599

Table 2: The coefficients of the plunge reduced-order model (Eq. (7)).

We determined the Normed Root Mean Squared Error (NRMS) of the aerodynamic models using the formula

$$\text{NRMS}_{C_L} = \frac{1}{C_{Lmax} - C_{Lmin}}\sqrt{\frac{\sum_{i=1}^{N}\left(C_L - \hat{C}_L\right)^2}{N}}, \tag{9}$$

where N is the number of data points, C_L is the CFD simulation data, $\hat{C}_L$, is the predicted value by the ROM simulation, C_{Lmax} is the maximum, while C_{Lmin} is the minimum value of the CFD simulation data. The NRMS for the three pitch and three plunge models can be found in Table 3 and 4, respectively.
For the reduced frequency $k = 0.1$, the lift coefficients from the CFD simulation and the fitted model as the a function of the angle of attack for oscillation amplitudes $\alpha_{amp} \in \{2°, 5°, 10°\}$ are shown in Figure 1.

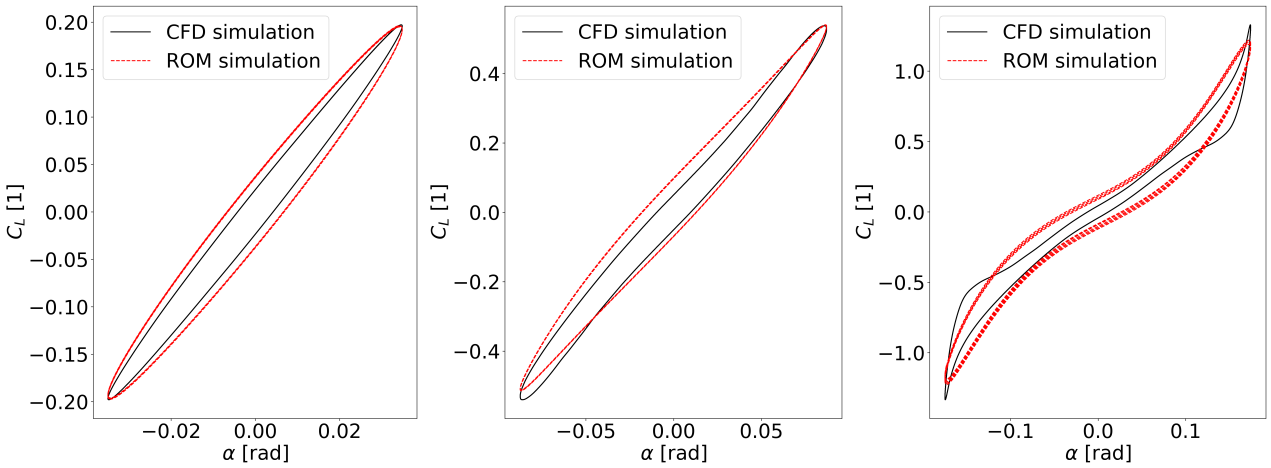

(a) $\alpha_{amp} = 2°$ (b) $\alpha_{amp} = 5°$ (c) $\alpha_{amp} = 10°$

Figure 1: Comparison of the identified ROM with the CFD simulation for $k = 0.1$ and $\alpha_{amp} \in \{2°, 5°, 10°\}$.

Figure 2 illustrates the comparison of the identified ROM with the CFD simulation for $k \in \{0.1, 0.2, 0.5\}$ and $\alpha_{amp} = 10°$. It can be observed that the models provide a very good fit overall, can reproduce the nonlinear behavior associated with the high angle of attack and high-frequency oscillations.

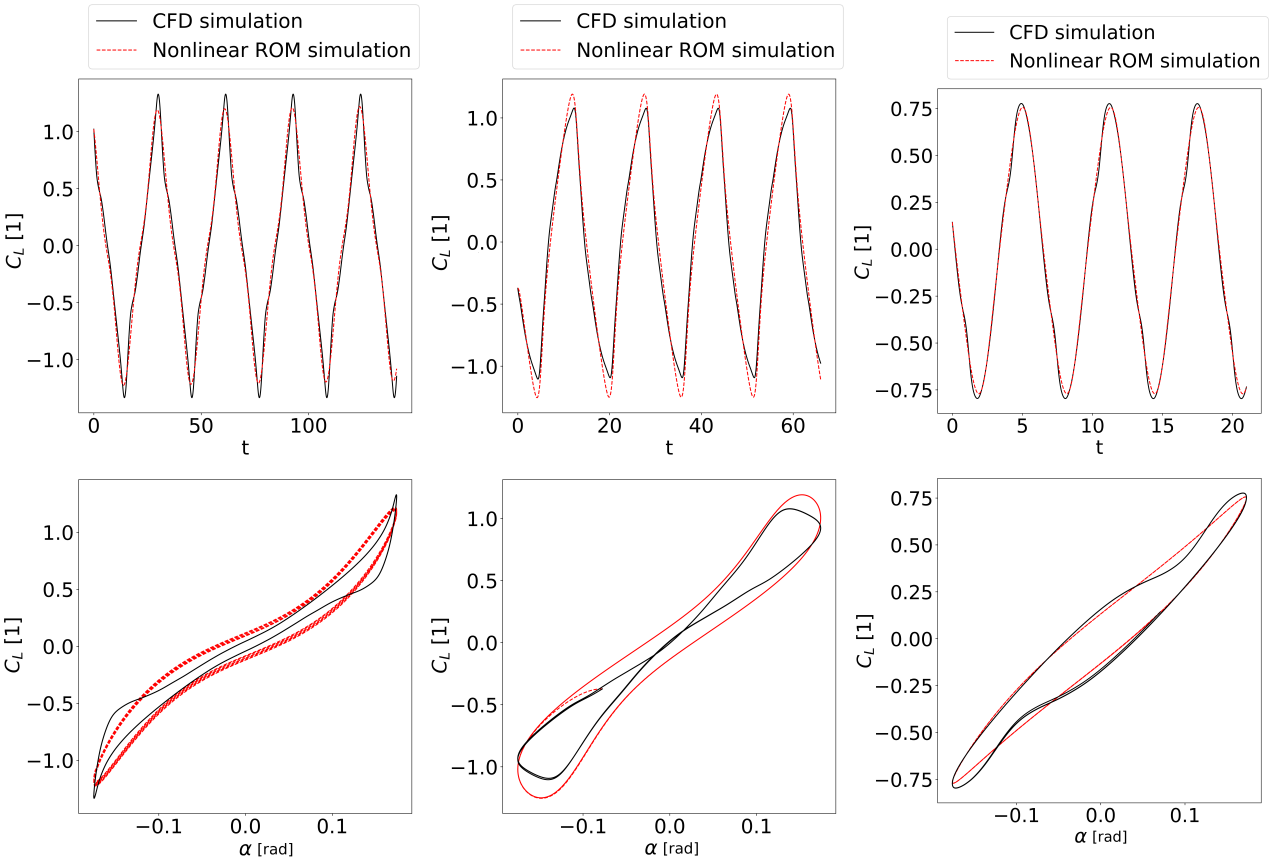

(a) $k = 0.1$ (b) $k = 0.2$ (c) $k = 0.5$

Figure 2: Comparison of the identified ROM with the CFD simulation for $k \in \{0.1, 0.2, 0.5\}$ and $\alpha_{amp} = 10°$.

For the reduced frequency $k = 0.1$, the lift coefficients from the CFD simulation and the fitted model as the a function of the plunge displacement for oscillation amplitudes $h_{amp} \in \{0.02\text{m}, 0.05\text{m}, 0.10\text{m}\}$ are shown in Figure 3. For the low reduced frequency $k = 0.1$, the reduced-order model gives an almost perfect fit.

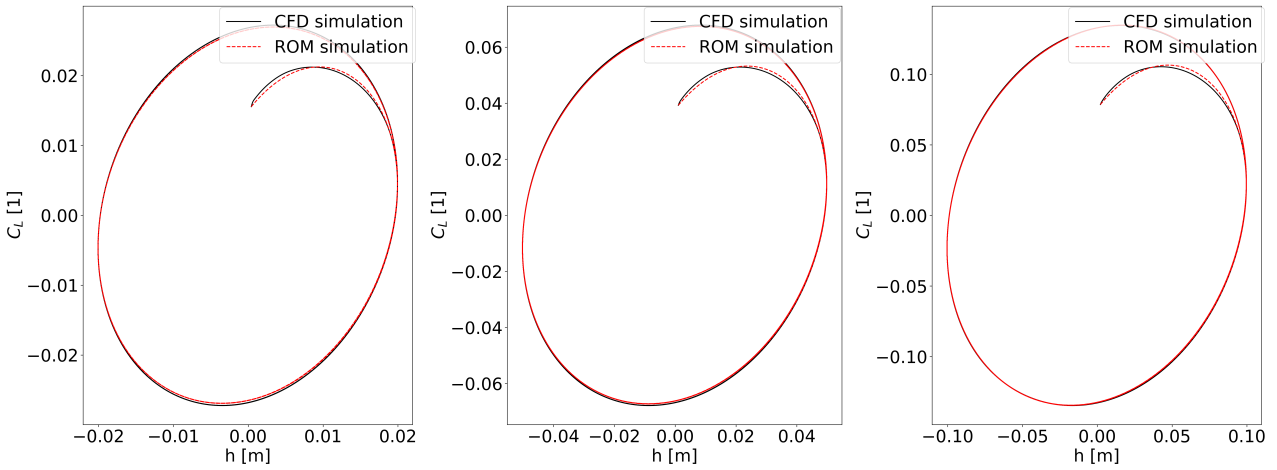

(a) $h_{amp} = 0.02\text{m}$ (b) $h_{amp} = 0.05\text{m}$ (c) $h_{amp} = 0.10\text{m}$

Figure 3: Comparison of the identified ROM with the CFD simulation for $k = 0.1$ and $h_{amp} \in \{0.02\text{m}, 0.05\text{m}, 0.10\text{m}\}$.

Figure 4 illustrates the comparison of the identified ROM with the CFD simulation for $k \in \{0.1, 0.2, 0.5\}$ and plunge amplitudes $h_{amp} = 0.1\text{m}$. It can be observed that the models provide a very good fit overall, can reproduce the nonlinear behavior associated with the high plunge amplitudes and high-frequency oscillations.

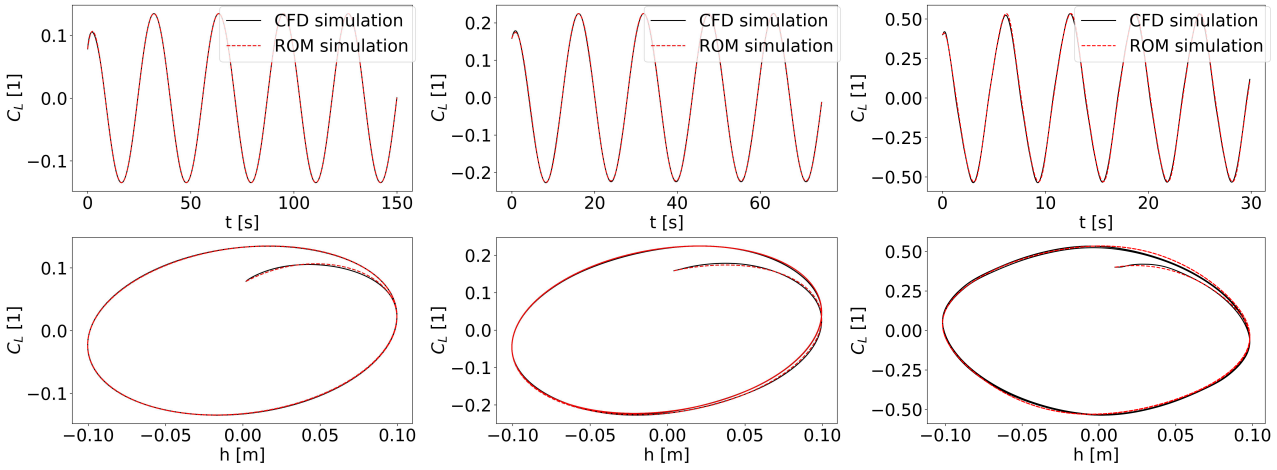

(a) $k = 0.1$ (b) $k = 0.2$ (c) $k = 0.5$

Figure 4: Comparison of the identified ROM with the CFD simulation for $k \in \{0.1, 0.2, 0.5\}$ and $h_{amp} = 0.10\text{m}$.

Oscillation amplitude	Model for $k = 0.1$	Model for $k = 0.2$	Model for $k = 0.5$
2°	2.53%	1.88%	1.66%
5°	2.45%	2.25%	0.94%
10°	3.44%	4.62%	1.61%

Table 3: The NRMS values of the identified aerodynamic models for the pitching motion.

Oscillation amplitude	Model for $k = 0.1$	Model for $k = 0.2$	Model for $k = 0.5$
0.02m	0.46%	0.67%	4.73%
0.05m	0.4%	0.65%	4.13%
0.10m	0.36%	0.65%	0.89%

Table 4: The NRMS values of the identified plunge aerodynamic models.

Performance of the models for coupled pitch and plunge motions

To check the accuracy of the identified models, we have run coupled pitch and plunge motion simulations. We defined the following coupled motion

$$\alpha(t) = \alpha_{amp}\cos(\omega t), \qquad h(t) = h_{amp}\cos(\omega t + \phi), \tag{10}$$

where ϕ is the phase between the motions of the pitch and plunge.
In Figure 5 the comparison is shown between the CFD simulation, and the identified ROM model for $k = 0.1$, $\alpha_{amp} = 10°$, and $h_{amp} = 0.1$m for three different phase shift values. Both the combined pitch-plunge model and also the pitch-only model is shown. It can be observed that the combined model can capture the nonlinear aerodynamic forces for the coupled pitch and plunge motion. Using the combined model, the error in the maximum value of the lift is reduced by up to 87%. The NRMS values of the combined model for the three test cases were under 5%.

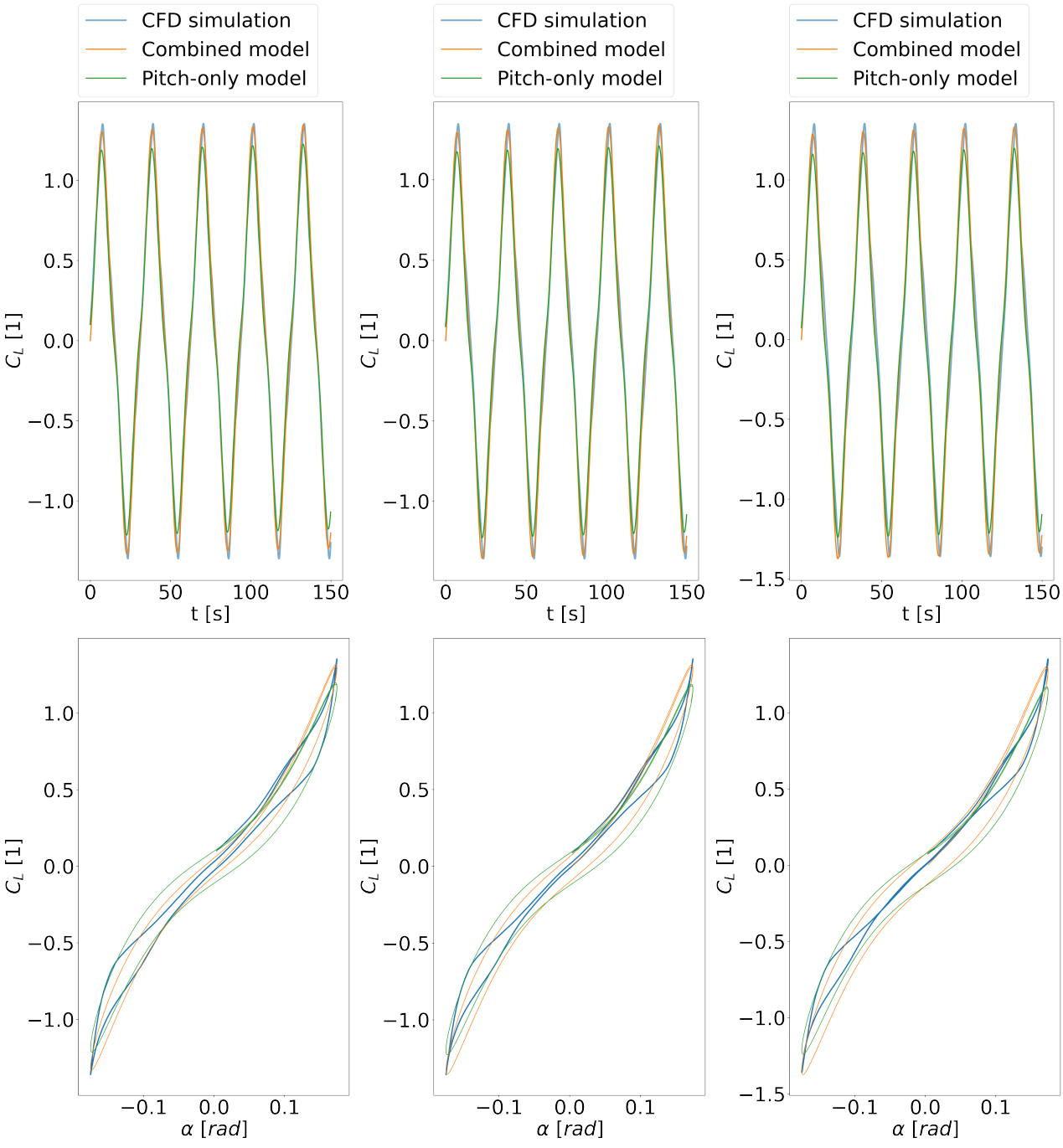

(a) $\phi = 80°$ (b) $\phi = 90°$ (c) $\phi = 100°$

Figure 5: Comparison of the identified ROM with the CFD simulation for $k = 0.1$, $\alpha_{amp} = 10°$, and $h_{amp} = 0.1$m.

Conclusions

The significant problem of creating reduced-order models for aerodynamic loads, valid for large amplitude, and frequency oscillations, was studied. The SINDy method was utilized to extract the governing differential equation of the aerodynamic lift coefficient from CFD data of a flat plate with pitching and plunging motion. This method resulted in easily interpretable, simple models. It was shown that the identified models for one particular frequency show excellent agreement with the CFD simulation data for varying amplitude oscillations. The future goal of this research is to couple the created aerodynamic model to the structural dynamical model of a flexible plate subjected to airflow.

Acknowledgements

The research reported in this paper and carried out at the Budapest University of Technology and Economics has been supported by the ÚNKP-21-3 New National Excellence Program of the Ministry for Innovation and Technology (ITM) of Hungary from the source of the National Research Development and Innovation Fund, and the NRDI Funds (TKP2020 National Challenges Subprogram, Grant No. BME-NCS) based on the charter of bolster issued by the NRDI Office under the auspices of the ITM. The research reported in this paper is part of project no. BME-NVA-02, implemented with the support provided by the ITM of Hungary from the NRDI Fund, financed under the TKP2021 funding scheme. This work has been supported by the Hungarian NRDI Fund under contract NKFI K 137726.

References

[1] Holierhoek, J., De Vaal, J., Van Zuijlen, A., and Bijl, H. (2013). Comparing different dynamic stall models. *Wind Energy*, 16(1):139–158.

[2] Fonzi, N., Brunton, S. L., and Fasel, U. (2020). Data-driven nonlinear aeroelastic models of morphing wings for control. *Proceedings of the Royal Society A*, 476(2239):20200079.

[3] Li, S., Kaiser, E., Laima, S., Li, H., Brunton, S. L., and Kutz, J. N. (2019). Discovering time-varying aerodynamics of a prototype bridge by sparse identification of nonlinear dynamical systems. *Physical Review E*, 100(2):022220.

[4] Boutet, J. and Dimitriadis, G. (2018). Unsteady lifting line theory using the wagner function for the aerodynamic and aeroelastic modeling of 3d wings. *Aerospace*, 5(3):92.

[5] Lelkes, J. and Kalmár-Nagy, T. (2021). Analysis of a piecewise linear aeroelastic system with and without tuned vibration absorber. *Nonlinear Dynamics*, 103(4):2997–3018.

[6] Sun, C., Tian, T., Zhu, X., and Du, Z. (2020). Sparse identification of nonlinear unsteady aerodynamics of the oscillating airfoil. *Proceedings of the Institution of Mechanical Engineers, Part G: Journal of Aerospace Engineering*, 235(7):809–824.

[7] Brunton, S. L., Kutz, J. N., Manohar, K., Aravkin, A. Y., Morgansen, K., Klemisch, J., Goebel, N., Buttrick, J., Poskin, J., Blom-Schieber, A. W., and et al. (2021). Data-driven aerospace engineering: Reframing the industry with machine learning. *AIAA Journal*, page 1–26.

[8] Pohl, J., Semaan, R., and Jones, A. R. (2019). Dynamic lift measurements on an airfoil with periodic flap motion at high reynolds number. *AIAA Scitech 2019 Forum*.

[9] Brunton, S. L., Proctor, J. L., and Kutz, J. N. (2016). Discovering governing equations from data by sparse identification of nonlinear dynamical systems. *Proceedings of the National Academy of Sciences*, 113(15):3932–3937.

[10] Brunton, S. L., Proctor, J. L., and Kutz, J. N. (2016). Sparse identification of nonlinear dynamics with control (sindyc). *IFAC-PapersOnLine*, 49(18):710–715.

[11] Champion, K., Zheng, P., Aravkin, A. Y., Brunton, S. L., and Kutz, J. N. (2020). A unified sparse optimization framework to learn parsimonious physics-informed models from data. *IEEE Access*, 8:169259–169271.

[12] Silva, B. D., Champion, K., Quade, M., Loiseau, J.-C., Kutz, J., and Brunton, S. (2020). Pysindy: A python package for the sparse identification of nonlinear dynamical systems from data. *Journal of Open Source Software*, 5(49):2104.

[13] Akiba, T., Sano, S., Yanase, T., Ohta, T., and Koyama, M. (2019). Optuna. *Proceedings of the 25th ACM SIGKDD International Conference on Knowledge Discovery & Data Mining*.

[14] Lendvai, B. and Lelkes, J. (2021). Aeroelasztikus szárnymodell numerikus vizsgálata: Numerical analysis of aeroelastic wing model. *Nemzetközi Gépészeti Konferencia–OGÉT*, pages 48–51.

[15] Lelkes, J. and Lendvai, B. (2021). Torziós csillapító alkalmazása belebegés megszüntetésére: Application of a torsional absorber for flutter suppression. *Nemzetközi Gépészeti Konferencia–OGÉT*, pages 44–47.

Development and Parameter Estimation of a Low Order Model of a Hyperelastic Plate Exhibiting 2:1 Resonant Response

Nizar Jaber[1], Nasir Bilal[2], and Anil Bajaj[2]
[1]*Department of Mechanical Engineering and the Center for Communication Systems and Sensing, King Fahd University of Petroleum and Minerals, Dhahran, 31261, Saudi Arabia*
[2]*School of Mechanical Engineering, Purdue University, West Lafayette, IN 47907, USA*

Summary. This work presents results of experimental investigation and a low-order model development for resonant complex dynamics of a cantilever macro-plate. The plate is fabricated from a 'hyperelastic' material using 3D printing technology. The geometry of the plate with cut-outs is optimized such that the second linear bending mode frequency ω_{02} is nearly twice the linear first twisting mode frequency ω_{11}. Based on the observed 2:1 resonant response under harmonic excitation near ω_{02}, a low-order 2 DOF dynamic model is developed to simulate the plate response. The unknown model parameters are extracted using Harmonic Balance solutions and curve fitting techniques. A good agreement is observed between the analytical and the experimental results for different excitation levels.

Introduction

Modal coupling and their influence on system response continues to attract much interest and has been the subject of several review papers that study the influence of mode interactions on different structures from the macro to the micro scale and their potential applications [1]. Internal resonance is among the primary nonlinear coupling mechanisms between the different modes of vibration which can be triggered when the ratio between the frequencies of coupled modes is commensurate and the directly excited response amplitude exceeds a certain threshold [1]. Parameter estimation techniques have received significant attention for developing models that can predict the complex dynamics of a structure under loading conditions that are difficult to test experimentally [2]. Most of the prediction techniques rely on error minimizing algorithms that minimize the difference between predictions of the analytical model and the experimental results. Conventionally, one system state is experimentally measured, and the other states are derived using numerical integration or differentiation techniques which amplify noise at low or high frequency. Processing the signal to reduce the high frequency noise might remove the response at higher harmonics and also introduce aliasing in the data [2]. Frequency response approach based on curve fitting eliminates the issues associated with signal processing but requires more theoretical effort and a comprehensive understanding of the system model and the effects of different coefficients on the response [2]. In this work, the plate geometry, Fig. 1a, is designed following the topology optimization procedure described in [3] such that for the cantilever plate, the second bending mode ω_{02} ($71\ Hz$) and the first twisting mode ω_{11} ($35.5\ Hz$) are in 2:1 ratio. The plate is fabricated using 3D printing technology from a hyperelastic material thus incorporating material nonlinearity. To study the plate dynamics, a TIRA shaker is used to actuate the plate at different acceleration levels and a laser Doppler vibrometer is used to record the response.

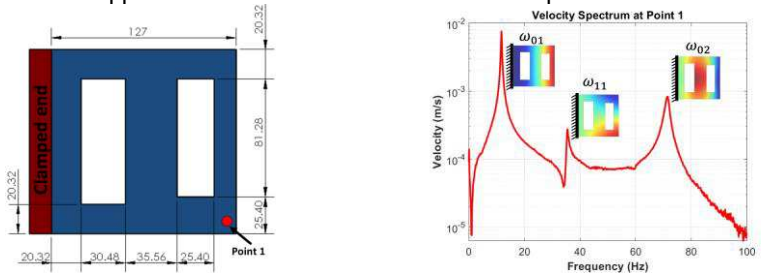

(a) (b)

Figure 1: (a) The dimensions of the optimized plate are in millimeters showing the laser measurements point. Plate thickness = $1.27\ mm$. (b) The FFT of the impulse response showing the first three modes of vibration (insets: Corresponding mode shapes).

Results and discussion

To capture the modal interaction of the two modes in the cantilever plate response, two coupled oscillators described by generalized coordinates $u(t)$ and $v(t)$ are considered. The directly driven mode $u(t)$ is modeled as nonlinear oscillator with linear natural frequency ω_{02} along with cubic $\alpha_c u^3(t)$ and quadratic $\alpha_q u^2(t)$ nonlinear stiffness forces. The experimental data for the directly excited mode shows a nonlinear dependence of the damping on the amplitude of vibration implying that a nonlinear dissipation mechanism needs to be incorporated. Here, a nonlinear damping model compromising of quadratic displacement multiplied by the velocity $u^2(t)\dot{u}(t)$ is assumed. The secondary mode amplitude $v(t)$, the mode only excited due to its coupling with the primary mode, is modeled with a linear oscillator of frequency ω_{11} which equals to half the driven mode frequency ω_{02}, and a nonlinear interaction term. The interaction between the two oscillators is assumed to be nonlinear in the form of $\big(v(t)\big)^2$ acting on the driven oscillator and $u(t)v(t)$ acting on the secondary oscillator. The equations of motion normalized by the modal masses $m_{1,2}$ are then:

$$\ddot{u}(t) + 2\xi_2\omega_{02}\dot{u}(t) + (\omega_{02})^2 u(t) + \alpha_q u^2(t) + \alpha_c u^3(t) + 2\xi_{non}\omega_{02}u^2(t)\dot{u}(t) = \gamma_2\big(v(t)\big)^2 + rA\cos(\Omega t) \quad (1)$$

$$\ddot{v}(t) + 2\zeta_1\omega_{11}\dot{v}(t) + (\omega_{11})^2 v(t) = \gamma_1 u(t)v(t) \quad (2)$$

where ξ_2, ξ_1 are the modal damping ratios acting on the driven and the secondary oscillators, respectively. ξ_{non} is the nonlinear damping coefficient. γ_2, γ_1 are the coupling coefficients between the two modal amplitudes, A is the amplitude

of the base excitation acceleration, and r is the projected modal force acting on the driven oscillator. To extract the unknown parameters, the system of equations are initially numerically integrated for different values of the parameters and the numerical results are compared with experimentally recorded data. Also, the effect of each parameter on the final response is studied which helps in understanding its influence on the system response. Subsequently, the harmonic balance method is used to solve for steady state solutions of Eq. (1) and Eq. (2) in which the response is assumed to have the form of a truncated Fourier series. In the current analysis, two harmonics plus the constant term are utilized. To find the unknown parameters, the parameter extraction procedure is divided into multiple steps. The resonant frequencies values ω_{02} and ω_{11} can be inferred from the impulse response results given in Fig. 1b and are found to be $\omega_{11} = 35.5\ Hz$ and $\omega_{02} = 71\ Hz$. Then, the response in which only the directly excited mode has non-zero response and the internal resonance has not yet activated is considered, see Fig. 2 for the case of 1.65g base excitation. The system of equations assuming zero coupling coefficients, that is, γ_1 and γ_2 are set equal to zero, are solved for different values of the unknown parameters ξ_2, α_q, α_c, ξ_{non}, and r until the simulation results match the experimentally recorded frequency response, as shown in Fig. 2. To extract the coupling coefficients γ_1 and γ_2, the experimental response at 1.75 g, Fig. 3, is considered, and the 2 DOF model in Eq. (1) and Eq. (2) is solved for different sets of coupling coefficients until error is minimized between the harmonic balance results and the experimental response curve. Summary of the all the extracted parameters is given in Table 1. To verify the 2DOF model with the extracted parameter values, Eq. (1) and Eq. (2) are used for higher excitation levels and the simulation results are compared with the corresponding experimental data. As shown in Fig. 4, the harmonic balance results at various excitation levels are in reasonable agreements with the experimental measurements.

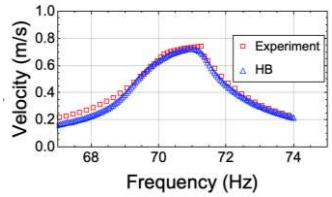

Figure 2: Experimental and harmonic balance frequency response results (HB) for the 1.65 g excitation case.

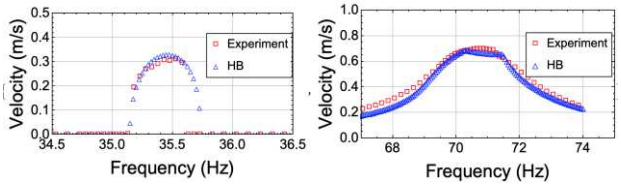

(a) (b)

Figure 3: Experimental and harmonic balance frequency response results (HB) for the 1.75 g excitation case with internal resonance activated. (a) Near ω_{02}. (b) Near ω_{11}.

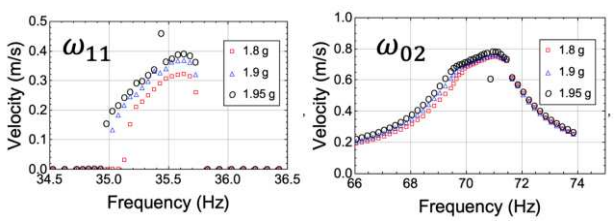

(a)

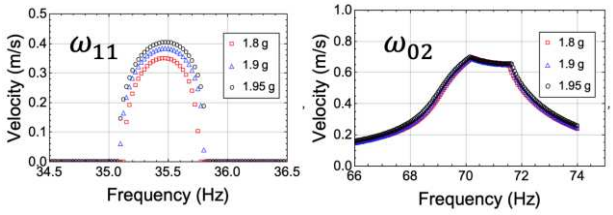

(b)

Fig. 1: Frequency response of the macroplate to a harmonic base excitation at different acceleration levels with internal resonance activated. (a) Experimentally recorded results. (b) Harmonic balance results.

Table 1: Summary of the extracted parameters.

Parameter	ω_{11}	ω_{02}	ξ_2	α_q	α_c	ξ_{non}	r	γ_1	γ_2	ξ_1
Value	35.5	71	2.5×10^{-3}	6×10^{7}	1.54×10^{10}	1.5×10^{4}	0.525	1.45×10^{7}	2.3×10^{6}	0.1

Summary and Conclusions

A two-mode nonlinear model to predict the resonant response of a 3D printed cantilever macroplate to a base excitation is developed. The system is modeled with two nonlinearly coupled oscillators. The plate is designed such that the linear natural frequencies ω_{02} and $\omega_{11}$are in 2:1 frequency ratio. A harmonic balance analysis is used to approximate the response of the coupled oscillators using curve fitting techniques to extract the unknown parameters. The parameter estimation procedure is divided into three steps. In each step, the experimentally recorded results are used to find a subset of the unknown parameters. The final estimated parameters are used to predict the response at higher excitation levels. The analytical model predictions are seen in good agreement with experimental data.

Acknowledgments

This work was support in part by the Alpha P. Jamison Professorship endowment at Purdue University. The authors would like to thank Dr. Astitva Tripathi for his help in designing and fabricating the plate.

References

1. Asadi, K., Yu, J., Cho, H.: Nonlinear couplings and energy transfers in micro- and nano-mechanical resonators: intermodal coupling, internal resonance and synchronization. Philosophical transactions. Series A, Mathematical, physical, and engineering sciences. 376, 20170141 (2018). https://doi.org/10.1098/rsta.2017.0141
2. Malatkar, P., Nayfeh, A.H.: A Parametric Identification Technique for Single-Degree-of-Freedom Weakly Nonlinear Systems with Cubic Nonlinearities. Journal of Vibration and Control. 9, 317–336 (2003). https://doi.org/10.1177/107754603030754
3. Tripathi, A., Bajaj, A.K.: Topology optimization and internal resonances in transverse vibrations of hyperelastic plates. International Journal of Solids and Structures. 81, 311–328 (2016). https://doi.org/https://doi.org/10.1016/j.ijsolstr.2015.11.029

Tuesday, July 19, 2022
08:30 - 10:30

MS-14 Nonlinear Dynamics for Engineering Design
Rhone 2

Chair: Jon Juel Thomsen

08:30 - 08:50
Parametric analysis of a Nonlinear Energy Sink for an unstable dynamic system
TANAYS Rémy*, SANCHES Leonardo, MICHON Guilhem
*Institut Supérieur de lÁéronautique et de lÉspace (ISAE - 10 av. Edouard Belin - BP 54032 - 31055 TOULOUSE Cedex 4 France)

08:50 - 09:10
Parametric and Self-excitation of a Suspension Bridge under Turbulent Wind Flow
DI Nino Simona*, LUONGO Angelo
*Department of Civil, Construction-Architectural and Environmental Engineering, University of L'Aquila (67100 L'Aquila Italy) - International Research Center for the Mathematics & Mechanics of Complex Systems (University of L'Aquila, 67100 L'Aquila Italy)

09:10 - 09:30
Shape Optimization of Curved Mechanical Beams for Zero-Dispersion Point
ROSENBERG Sahar*, SHOSHANI Oriel
*Ben-Gurion University of the Negev (Ben Gurion Blvd, 1, Be'er Sheva 84105, Israel Israel)

09:30 - 09:50
Recent advances on spectral-submanifold-based model reduction: bifurcations and configuration constraints
LI Mingwu*, JAIN Shobhit, HALLER George
*ETH Zürich (Leonhardstrasse 21, 8092, Zürich Switzerland)

09:50 - 10:10
Reduced-Order Modelling of Moore-Greitzer PDEs using Sparse Regression
AYDOGDU Yusuf, **RAVICHANDRAN Thambirajah***, NOVELIA Alyssa, NAMACHCHIVAYA Navaratnam Sri
*Department of Applied Mathematics, University of Waterloo (200 University Avenue West, Waterloo, Ontario N2L 3G1 Canada)

Parametric analysis of a Nonlinear Energy Sink for an unstable dynamic system

Rémy Tanays, Leonardo Sanches and Guilhem Michon
ICA, Université de Toulouse, ISAE-SUPAERO, MINES ALBI, UPS, INSA, CNRS, Toulouse, France

Summary. The theoretical study of the change of steady state regime of an unstable dynamic system coupled to a nonlinear energy sink with the respect of a set of parameters is developed in this paper. This study is carried out by the use of asymptotic methods (multiple scale method mixed with harmonic balance method), it leads to singular perturbed system that is studied with geometric singular perturbation theory. The steady state regime of the dynamic system is linked to the information extracted from the singular perturbed system : the slow flow fixed points and their stability. From this information, analytical conditions are established. These conditions lead to parametric analysis and bifurcation diagrams which are describing the mechanism of steady state regime change. This study will allow to test huge and important set of parameters for a NES rapidly in comparison of numerical or experimental studies.

Introduction

The use of Nonlinear Energy Sink (NES) based on Targeted Energy Transfer is very efficient solutions for passive control. A NES is a device composed of a light mass or inertia compared to the main system, a nonlinear stiffness and a viscous linear damper. NES have been developed for the past ten years and many different technologies are used in order to realize them experimentally. A state of the art is presented in [1] about these technologies such as piece-wise linear, non-smooth, vibro-impact, bistable and magnetic NES.
Among several applications, NES are used to control dynamic instabilities or resonances, e.g.: helicopter ground resonance, friction system (Hultèn's model), airfoil system and systems under periodic excitation.
In order to control unstable or resonant system through nonlinear vibration absorber, a design approach needs to be carried out. The method used for designing a NES consists in predicting the response of the nonlinear system through asymptotic analytical approach. Among different approaches, the complex-averaging method (CX) [2] and the method of the multiple scale combined with the harmonic balance method (MMS-HBM) [3] have been extensively applied. These approaches lead into a singular perturbed set of differential equations of the modulation response amplitude.
This system of equation is later treated by applying the Geometric Singular Perturbation Theory (GSPT) [4] which decompose the complex motion of the system into a fast and a slow dynamic. Such methodology has been recently used to survey the response regimes reached with a NES coupled to a primary system [5]. Based on the best authors knowledge, the GSPT has only been used on the modulation equation obtained with CX-method and this approach has not been further developed for parametric study of the NES's parameters applied on the mitigation of unstable systems.
In this work, the design of NES used to mitigate divergent oscillations of unstable system is carried out. The fast and flow dynamics of the singular perturbed system obtained with the combined MMS-HBM is treated with GSPT. The relation between the critical manifold of the fast dynamics, the nature and position of the fixed points of the slow dynamics and the NES response is evaluated. Finally, an extensive parametric study maps the different regimes of the dynamic system for a large set of NES's parameters and instability severity of the primary system.

Development and Results

The dynamic system considered is a single degree of freedom composed of a mass M, a linear stiffness K and a linear negative damping coefficient C (SDOF in black line) coupled to a NES, composed of a mass m, a nonlinear stiffness k and a linear damping factor c (red line) attached (see Figure 1).

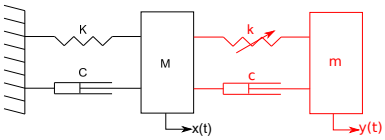

Figure 1: Mechanical model : in black an unstable SDOF, in red a Nonlinear Energy Sink (NES) attached.

By introducing a relative displacement $v = x - y$ between the main system and the NES and the usual parameters such as $\omega^2 = \frac{K}{M}$, $\zeta = \frac{C}{2\omega M}$, $\lambda = \frac{k}{M}$, $r_c = \frac{c}{M}$ and $r_m = \frac{m}{M}$ the equations of motion are obtained :

$$\begin{cases} \ddot{x} + 2\zeta\omega\dot{x} + \omega^2 x + r_c\dot{v} + \lambda v^3 = 0 \\ r_m\ddot{v} - r_m\ddot{x} - r_c\dot{v} - \lambda v^3 = 0 \end{cases} \tag{1}$$

After applying the whole method (MMS-HBM and GSPT) and getting the information from the slow flow (SIM, fixed points, singular folded points, slow flow dynamics and stability) and the fast flow (modulation equation and dynamic fixed point) it is possible to obtain the dynamic of the system represented in Figure 2.
The slow-flow fixed points in red are governing the response of the phase portrait (in black) Figure 2. The cycle is governed mainly by the SIM (in blue), after reaching the first fold point, the system has enough energy to jump on the

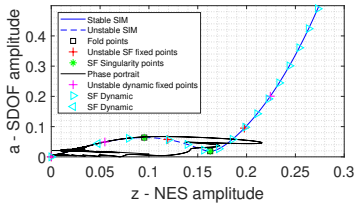

Figure 2: Nonlinear manifold, Slow flow information and Dynamic information with physical parameters $r_m = 4\,\%$, $\alpha = 2\,\%$, $\zeta = -1\,\%$, $\Lambda = 50$.

other stable branch of the Slow Invariant Manifold (SIM). The highest fixed point which is unstable is forcing the system's amplitude to decrease to the second folded point in order to jump back on the first stable branch of the SIM.
From a parametric study, it is possible to understand that the stability (highly linked to the position) of the slow flow fixed points governs the change of steady state response. It is also possible to highlight it by producing a bifurcation diagram (Figure 3a).

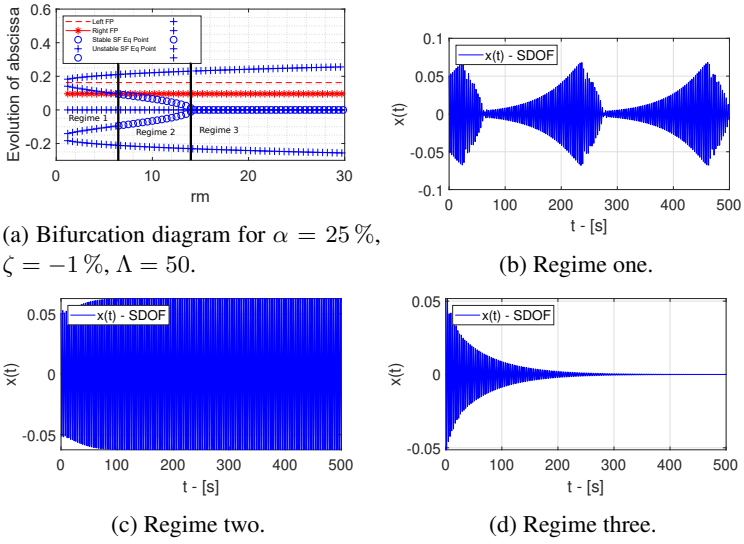

(a) Bifurcation diagram for $\alpha = 25\,\%$, $\zeta = -1\,\%$, $\Lambda = 50$.

(b) Regime one.

(c) Regime two.

(d) Regime three.

Figure 3: Bifurcation mechanism.

Figure 3a shows the mechanism responsible for the steady state regime change. There are three specific areas that will lead to three different regime. The regime one corresponds to a Limit Cycle Oscillations (LCO) with strong or low modulated response (Figure 3b). This regime appears when the intermediate slow flow fixed point is between the two folded singular point of the SIM and unstable. When this fixed point is moving toward the first folded singular point, it becomes stable and then leads to the regime two (Figure 3c). Finally, this point move to the static fixed point (0,0) and leads to the regime three (Figure 3d).

Conclusion

The analytical study of a complex dynamic system composed of an unstable single degree of freedom and a NES through asymptotic methods and singular perturbation method have been addressed. The theoretical result obtained allowed to improve the influence of the NES parameter on the steady state regime of the dynamic system by conducting extensive parametric study and computing bifurcation diagrams. All these results will now be used to design a NES theoretically and reduce the numbers of iterations needed to design a NES that will mitigate the response of an unstable dynamic system.

References

[1] H. Ding, L. Chen. (June 2020) Designs, analysis, and applications of nonlinear energy sinks. *Nonlinear Dynamics* **100(4)** 3061-3107.

[2] E. Gourc, G. Michon, S. Seguy, A. Berlioz. (April 2014) Experimental Investigation and Design Optimization of Targeted Energy Transfer Under Periodic Forcing. *Journal of Vibration and Acoustics* **136(2)** 021021.

[3] A. Luongo, D. Zulli. (November 2012) Dynamic analysis of externally excited NES-controlled systems via a mixed Multiple Scale/Harmonic Balance algorithm. *Nonlinear Dynamics* **70(3)** 2049-2061.

[4] M. Desroches, J.Guckenhemier, B. Krauskopf, C. Kuehn, H.M. Osinga, M. Wechselberger. (January 2012) Mixed-Mode Oscillations with Multiple Time Scales. *SIAM Review* **54(2)** 211-288.

[5] B. Bergeot, S. Bellizzi. (September 2019) Steady-Sate regimes prediction of a multi-degree-of-freedom unstable dynamic system coupled to a set of nonlinear energy sinks. *Mechanical Systems and Signal Processing* **131** 728-750.

Parametric and Self-excitation of a Suspension Bridge under Turbulent Wind Flow

Simona Di Nino[*,**] and Angelo Luongo[*,**]
[*]*International Research Center on Mathematics and Mechanics of Complex Systems, University of L'Aquila, 67100 L'Aquila, Italy*
[**]*Department of Civil, Construction-Architectural and Environmental Engineering, University of L'Aquila, 67100 L'Aquila, Italy*

Summary. In this paper, the analysis of a self-excited suspension bridge under turbulent wind flow is carried out. The stationary wind is responsible for self-excitation, while the turbulent part is responsible for parametric excitations. The simultaneous presence of those excitations is taken into account in a specific resonance condition. The periodic solutions are studied by means of a perturbation method and the effects of the turbulence on the dynamics of the structure are analyzed.

Introduction

Suspension bridges are long, slender flexible structures which are very sensitive to dynamic actions induced by wind, which causes a variety of instability phenomena, related to different kind of excitation. In particular, the aeroelastic instability dealing self-excited vibrations, such as galloping and flutter, is of particular interest, since these phenomena may cause devastating effects, leading to structural collapse like in the famous Tacoma Narrows bridge. The aeroelastic behavior of long-span bridges, and especially the aeroelastic instability, has drawn remarkable attention in the fields of structural engineering and physics. The modern era of bridge aeroelasticity was launched by [1]-[4]. More recently, many linear and nonlinear aeroelastic analysis frameworks for cable-supported bridges were developed, e.g. [5]-[9], to predict the aeroelastic response of bridges under steady and turbulent winds (the most by solving the motion equations by numerical tools).
In this paper, the aeroelastic behavior of a suspension bridge is investigated by a continuous model. A simple analytical model of suspension bridge, subjected to turbulent wind flow, is proposed to analyze the aeroelastic in-plain instability (galloping). The objective is to take into account the possible occurrence of Hopf bifurcations, due to the steady part of the wind, and to analyze modifications on the solutions due to the turbulent part. The main innovative aspect relies in directly attacking the continuous problem by perturbation methods, leading to approximate formulae suitable for preliminary designs.

Model

A standard single-span suspension bridge, made of a main cable, a stiffening girder, uniformly distributed hangers (or suspenders) and two supported towers or pylons, is considered. The main cable is rigidly connected to the support towers, assumed to be rigid. The main cable is assumed to be uniform and elastic, and its bending stiffness is ignored. The structure is subjected to a turbulent wind flow of velocity $U(t)$, blowing orthogonally to the plane of the bridge. A scheme of the model is shown in Fig. 1.

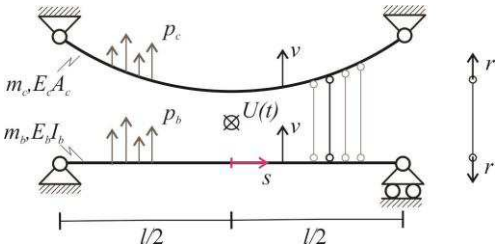

Figure 1: Single-span suspension bridge model.

Linear visco-elastic continuous models of beam and cable are formulated, coupled by vertical suspenders, modeled as uniformly distributed axially rigid links. Both external and internal damping are accounted, this latter according to the Kelvin-Voigt rheological model. The aeroelastic effects of the wind are evaluated via the classical quasi-static theory.

Aerodynamic forces
The aerodynamic load is caused by the wind, which blows orthogonally to the plane of the bridge, with time-dependent velocity $U(t)$. This, triggers in-plane forces, which depend on the structural velocity, as result of the aeroelastic interaction. Only forces on beam are accounted, while force on the cable are neglected. Nonlinear aerodynamic forces are formulated in the framework of the quasi-steady theory (see [10]); by truncating them to the third-order, they read:

$$p^a = -\left(b_1 U(t)\dot{v} + b_3 \frac{1}{U(t)}\dot{v}^3\right) \tag{1}$$

where the coefficients b_i are aerodynamic coefficients depending on the shape of the cylinder cross-section. The wind velocity is decomposed as $U(t) = \bar{u} + u(t)$, where $\bar{u}$ is a constant (average) part, representing the steady component, and $u(t)$ is a periodically time-dependent part, representing the turbulence. By assuming that the turbulent part is small compared to the steady one, the aerodynamic force is expanded is Taylor series.

Equation of motion

The dimensionless motion equations read:

$$\begin{aligned} &\rho^2(1+\eta_b\partial_t)v'''' - (1+\eta_c\partial_t)v'' + \Lambda^2(1+\eta_c\partial_t)\int_{-\frac{1}{2}}^{\frac{1}{2}} v ds + \ddot{v} + \left(c_e + b_1\left(\bar{u}+u(t)\right)\right)\dot{v} + b_3\left(\frac{1}{\bar{u}} - \frac{u(t)}{\bar{u}^2}\right)\dot{v}^3 = 0 \\ &v\left(-\tfrac{1}{2},t\right) = 0 \quad \rho^2(1+\eta_b\partial_t)v''\left(-\tfrac{1}{2},t\right) = 0 \\ &v\left(\tfrac{1}{2},t\right) = 0, \qquad \rho^2(1+\eta_b\partial_t)v''\left(\tfrac{1}{2},t\right) = 0 \end{aligned} \tag{2}$$

The dimensionless parameters Λ^2 and ρ^2 accounts: the first, for the elastic and geometric properties of the cable (known as the Irvine-Caughey cable parameter [11]); the second, for the beam-cable stiffness ratio. The dimensionless terms η_b, η_c and c_e are internal and external damping parameters. The Eqs. (2) are a generalization of the motion equations provided for the first time by Bleich et al. in [12], and recently re-examined by [13], accounting for additional damping and aerodynamic loads. They describe an infinite-dimensional system, parametrically excited by the turbulence. Here the turbulent part is considered harmonic, i.e., $u(t) = \hat{u}\cos(\Omega t)$, where $\hat{u}$ is the amplitude and $\Omega = 2\omega + \sigma$ is the frequency of the parametric excitation, chosen close to the double of the natural frequency ω, with σ a small detuning. Therefore, the condition of principal parametric excitation occurs.

To investigate the behavior of the structure in the nonlinear field, close to the dynamic bifurcation, a nonlinear asymptotic analysis is carried out. The Multiple Scale Method (MSM) is used, by directly attacking the partial differential equations of motion. A bifurcation equation in the amplitude of motion $a(t)$ is obtained, from which periodic oscillations and their stability are analyzed.

Main results

The mains results consist in the stability domains (Fig. 2a) and bifurcation diagrams (Fig. 2b).

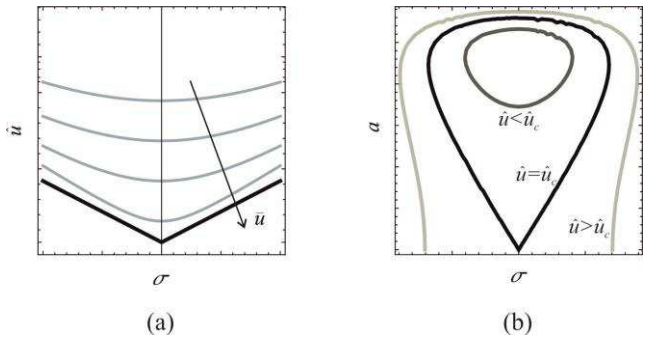

Figure 2: (a) Stability domains; (b) Bifurcation diagrams in presence of turbulent wind.

References

[1] Farquharson F.B. (1952) Aerodynamic stability of suspension bridges, university of Washington experiment station. Bull, 116:1949–54.

[2] Bleich F. (1948) Dynamic instability of truss-stiffened suspension bridges under wind action. In Proc. ASCE, volume 74, pages 1269–1314.

[3] Selberg A. (1963) Aerodynamic effects on suspension bridges. In Int. Conf. Wind Effects on Buildings and Structures, volume 2, pages 462–479.

[4] Scanlan R. H. and Tomo J. (1971) Air foil and bridge deck flutter derivatives. Journal of Soil Mechanics & Foundations Div.

[5] Chen X. and Kareem A. (2003) Aeroelastic analysis of bridges: effects of turbulence and aerodynamic nonlinearities. Journal of Engineering Mechanics 129, 8, pp. 885--895.

[6] Salvatori L. and Borri C. (2007) Frequency-and time-domain methods for the numerical modeling of full-bridge aeroelasticity. Computers & structures 85, 11-14, pp. 675--687.

[7] Arena A. and Lacarbonara W. (2012) Nonlinear parametric modeling of suspension bridges under aeroelastic forces: torsional divergence and flutter. Nonlinear Dynamics 70, 4, pp. 2487--2510.

[8] Wu T., Kareem A., and Ge Y. (2013) Linear and nonlinear aeroelastic analysis frameworks for cable-supported bridges. Nonlinear Dynamics 74, 3, pp. 487--516.

[9] Arena A., Lacarbonara W., and Marzocca P., (2016) Post-critical behavior of suspension bridges under nonlinear aerodynamic loading. Journal of Computational and Nonlinear Dynamics 11, 1, pp. 011005.

[10] Novak M. (1969) Aeroelastic galloping of prismatic bodies. Journal of the Engineering Mechanics Division, 95(1):115–142.

[11] Irvine H. M., & Caughey T. K. (1974) The linear theory of free vibrations of a suspended cable. Proceedings of the Royal Society of London. A. Mathematical and Physical Sciences, 341(1626), 299-315.

[12] Bleich F. (1950) The mathematical theory of vibration in suspension bridges: a contribution to the work of the Advisory Board on the Investigation of Suspension Bridges. US Government Printing Office.

[13] Luco J E. and Turmo J. (2010) Linear vertical vibrations of suspension bridges: A review of continuum models and some new results. Soil Dynamics and Earthquake Engineering, 30(9): 769–781.

Shape Optimization of Curved Mechanical Beams for Zero-Dispersion Point

Sahar Rosenberg* and Oriel Shoshani*
*Ben-Gurion University of the Negev, Be'er-Sheva 84105, Israel

Summary. In this study, we develop an optimization procedure of zero-dispersion point in curved mechanical beams. The zero-dispersion point is associated with a zero-slope in the frequency-amplitude relation of a nonlinear resonator. As an outcome, local to this zero-dispersion point, the nonlinear effect of amplitude-to-frequency noise conversion is eliminated, albeit the large oscillation amplitude. This zero-dispersion point can be used for noise suppression and frequency stabilization of precision clocks and sensitive detectors. The overall goal is to obtain the zero-dispersion point at the highest possible amplitude (for signal-to-noise ratio enhancement) and frequency (for resolution enhancement). To this end, we found the optimal midpoint elevation of the curved beam and optimized its initial bell-shape function using a genetic algorithm to maximize the frequency and energy level of the zero-dispersion point.

Many technological applications use micromechanical beams as a frequency-selective element to attain high RF frequencies. The practical requirement to operate above the noise floor of the device necessitates the need for large-amplitude oscillation (relative to the small size of the micro-beam); these large amplitudes lie deep in the nonlinear range, where there is considerable amplitude-to-frequency (A-f) noise conversion. However, in a specific class of nonlinear resonators, the dependence of oscillation frequency on the energy (or amplitude) may be non-monotonic, generating energy levels where, locally, the frequency is independent of the energy. For example, the oscillation frequency $\omega(E_{\rm tot})$ can exhibit a softening behaviour for low energy levels $E_{\rm tot} < E_{\rm ZD}$, and hardening behaviour for high energy levels $E_{\rm tot} > E_{\rm ZD}$, where in the transition between these two behaviours, there is an extremum of the frequency corresponding to a zero-dispersion (ZD) point $E_{\rm tot} = E_{\rm ZD}$ satisfying the condition $d\omega/dE_{\rm tot}|_{E_{\rm ZD}} = 0$ (Fig. 1, left panel). Hence, small amplitude fluctuations are not translated into frequency fluctuations near this ZD point. Consequently, the ZD point can be used for suppression of frequency noise in both open-loop [1] and closed-loop [2] systems at large vibration amplitudes, which guarantee operation above the noise floor of the device with a large signal-to-noise ratio (SNR).
In this study, we analyze the possibility to generate an optimal ZD point from the well-known and thoroughly explored curved micro-beam [3, 4] (Fig. 1, right panel). In the curved beam, there are inherently hardening and softening nonlinearities, and therefore, we can obtain the ZD point, where these opposing nonlinearities cancel one another and the fluctuations in the amplitude of vibrations do not locally affect the frequency [5].

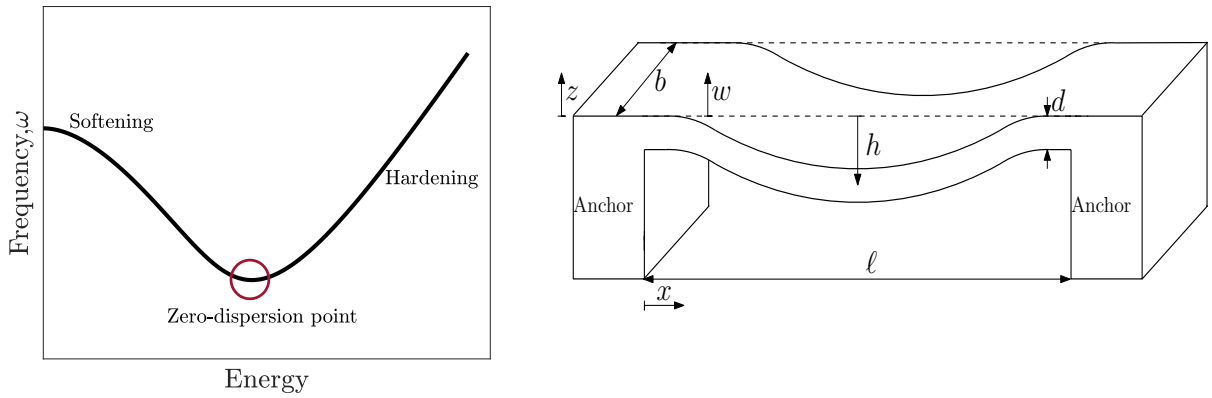

Figure 1: Left panel: The frequency-energy backbone curve of a nonlinear resonator with a zero-dispersion point. At the point of zero-dispersion, $E_{\rm tot} = E_{\rm ZD}$, there is an extremum of the frequency with a zero slope, and hence, the frequency is locally constant. Right panel: Definition sketch of a curved micro-beam. The doubly clamped micro-beam of length ℓ and rectangular cross-section $(b \times d)$ have an initial shape of an inverse bell, which is described by a function $w_0(x)$ and a maximal depth of $h = |w_0(\ell/2)|$.

We consider the conservative transverse vibration of a clamped-clamped shallow arch micro-mechanical beam of an initial shape described by $w_0(x)$ with a maximal height of h, width b, thickness d and length ℓ (Fig. 1, right panel). We wish to obtain a reduced-order nonlinear model for the beam and analyze its dynamics using the Euler-Bernoulli beam model. We assume that the flexural motion of the beam is dominated by its fundamental frequency, and use a single-mode approximation, $w(x,t) = q(t)\phi(x)$, where $\phi(x)$ is the eigenfunction of the fundamental mode that satisfies the doubly clamped beam boundary conditions. We perform a Galerkin projection onto $\phi(x)$ to obtain the following nonlinear ordinary differential equation for the modal coordinate $q(t)$

$$\ddot{q} + \omega_0^2 q + \beta q^2 + \gamma q^3 = 0. \tag{1}$$

For an initially bell-shaped beam with $w_0(x) = h\phi(x)$, the coefficients ω_0^2, β and γ in Eq. (1) are a function of h (the normalized initial elevation of the midpoint of the beam). Moreover, Eq. (1) has an exact analytical solution that describes the strongly nonlinear dynamics of $q(t)$ in terms of elliptic functions [5]. Thus, we can find closed-form expressions for the ZD point $d\omega/dE_{\rm tot}|_{E_{\rm ZD}} = 0$ that yield the energy at the ZD point $E_{\rm ZD}$, and the fundamental frequency at the ZD point $\omega(E_{\rm ZD})$. We note that both $E_{\rm ZD}$ and $\omega(E_{\rm ZD})$ are functions of the coefficients ω_0^2, β and γ, which in turn are functions of h. Therefore, using the initial elevation h as the design parameter, we can optimize these two expressions $E_{\rm ZD} = f(\omega_0^2, \beta, \gamma) = f(h)$ and $\omega_{\rm ZD} = g(E_{\rm ZD}) = g(\omega_0^2, \beta, \gamma) = g(h)$. Specifically, by setting $dE_{\rm ZD}/dh = 0$, we can find the initial elevation h that maximize the energy level of the ZD point, $\max\{E_{\rm ZD}(h)\}$, and by setting $d\omega_{\rm ZD}/dh = 0$ we can find the initial elevation h that maximize the frequency of oscillation at the ZD point, $\max\{\omega_{\rm ZD}(h)\}$. As can be seen form the left panel of Fig. 2, $E_{\rm ZD}$ is an increasing monotonic function of h, and thus, the maximal $E_{\rm ZD}$ is achieved at the maximal initial elevation that is possible $h_{\max}$. In contrast, $\omega_{\rm ZD}$ is not a monotonic function of h (Fig. 2, left panel). Therefore, for given dimensions and properties of the beam, there is a unique optimal frequency (Fig. 2, left panel).
Using the bell-shaped beam $w_0(x) = h\phi(x)$ as an initial shape of the curved beam, we apply a genetic algorithm [6] to find the optimal shape of the curved beam that yields a ZD point at the highest frequency and energy level. The genetic algorithm uses the initial shape of the beam to create a population (group of shape functions) of other solutions in its vicinity. After calculating the objective function $d\omega/dE_{\rm tot}|_{E_{\rm ZD}} = 0$ for each individual (certain shape function) of the population, the algorithm creates the next generation of population using the fittest solutions of the last generation by: (i) selection, where the fittest solutions survive for the next generation, (ii) crossover, where each two solutions are being used to create a new solution, and (iii) mutation, where some of the solutions are changed randomly. For each shape function, we used spectral methods to calculate the coefficients of Eq. (1) and find its ZD point. After 500 generations of a population of 15 individuals, the algorithm converged to an optimal shape function. The ZD point of the new shape function is achieved at energy levels 3 times higher than the initial bell-shaped beam $w_0(x) = h\phi(x)$ and with a frequency of more than 3 times higher (see Fig. 2, right panel).

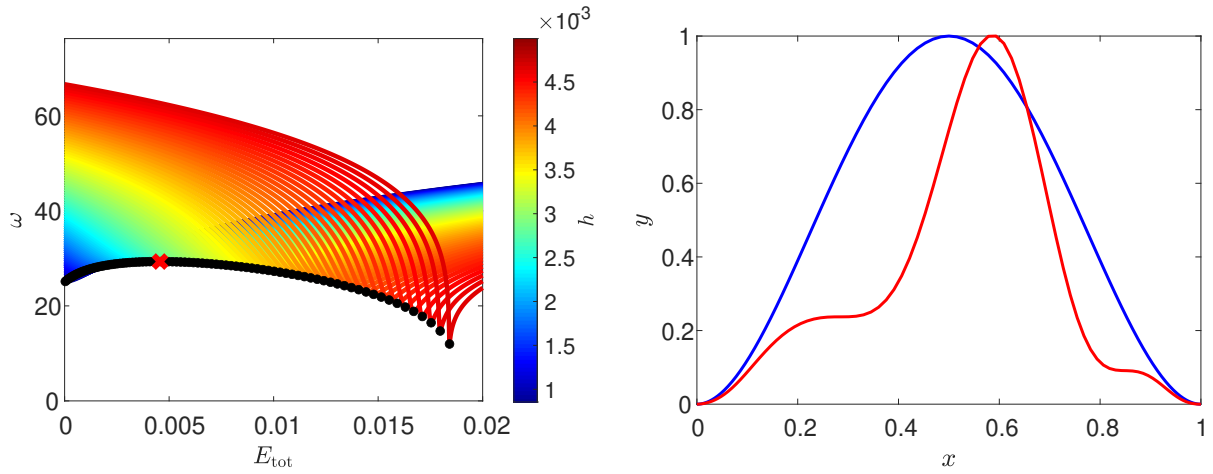

Figure 2: Left panel: The frequency-energy dependency of a bell-shaped beam. The fundamental frequency of oscillation ω is overlaid by the frequency of oscillation at the ZD point $\omega_{\rm ZD}$ (black) as a function of the total energy of the system $E_{\rm tot}$ for different values of initial elevation h. The maximal oscillation frequency at the ZD point, $\max\{\omega_{\rm ZD}(h)\}$, is denoted by the red crossmark on the curve of $\omega_{\rm ZD}$. Right panel: Comparison between the initial bell-shaped function of the beam (in blue) and the optimal shape function after 500 generations of a population of 15 individuals (in red). The frequency and energy of the zero-dispersion point in the optimal shape are threefold higher than in the bell-shaped beam.

References

[1] Dykman, M. I., Mannella, R., McClintock, P. V., Soskin, S. M., Stocks, N. G. (1990). Noise-induced narrowing of peaks in the power spectra of underdamped nonlinear oscillators. Physical Review A, 42(12), 7041.

[2] Miller, N. J., Shaw, S. W., Dykman, M. I. (2021). Suppressing frequency fluctuations of self-sustained vibrations in underdamped nonlinear resonators. Physical Review Applied, 15(1), 014024.

[3] Krylov, S., Ilic, B. R., Schreiber, D., Seretensky, S., Craighead, H. (2008). The pull-in behavior of electrostatically actuated bistable microstructures. Journal of Micromechanics and Microengineering, 18(5), 055026.

[4] Ouakad, H. M., Younis, M. I., Alsaleem, F. M., Miles, R., Cui, W. (2009). The static and dynamic behavior of MEMS arches under electrostatic actuation. In International Design Engineering Technical Conferences and Computers and Information in Engineering Conference (Vol. 49033, pp. 607-616).

[5] Rosenberg, S., Shoshani, O. Zero-dispersion point in curved micro-mechanical beams. Nonlinear Dyn (2021).

[6] Woon, S., Querin, O. Steven, G. Structural application of a shape optimization method based on a genetic algorithm. Struct Multidisc Optim 22, 57–64 (2001).

Recent advances on spectral-submanifold-based model reduction: bifurcations and configuration constraints

Mingwu Li*, Shobhit Jain* and George Haller *
**Institute for Mechanical Systems, ETH Zürich, Switzerland*

Summary. We show how spectral submanifold theory can be used to construct reduced-order models for forced nonlinear systems possibly with internal resonances. We perform continuation of equilibria (or limit cycles) of the reduced-order models to obtain (quasi-) periodic response of the full system and predict their bifurcations. In addition, we show how to construct reduced-order models for constrained mechanical systems using spectral submanifolds. These reduced-order models enable bifurcation analysis and efficient extraction of backbone and forced response curves of high-dimensional mechanical systems with configuration constraints.

Introduction

The analysis of high-dimensional nonlinear mechanical systems has been a significant challenge. The construction of reduced-order models for original high-dimensional systems is then of great importance because they enable efficient nonlinear analysis. Among these constructions, the reduced-order models based on invariant manifolds are prominent for nonlinear systems as they are supported by rigorous theory. In particular, the theory of *spectral submanifolds* (SSM) has laid a solid foundation for constructing mathematically rigorous reduced-order models [1]. Recent developements [2] have enabled the computation of SSMs and their reduced dynamics in physical coordinates. The software implementation of the method has been available in an open-source package, SSMTOOL [3]. In previous studies, the applications have been limited to two-dimensional SSMs. Here, we derive reduced-order models on higher-dimensional SSMs to analyze systems with internal resonances. We integrate continuation package COCO [4] with SSMTOOL to obtain forced response curves and perform bifurcation analysis of internally resonant mechanical systems. We further demonstrate how SSMTOOL can handle mechanical systems with configuration constraints.

Reduced-order model and bifurcation analysis

Reduced-order model

We consider a periodically forced nonlinear mechanical system

$$\boldsymbol{M}\ddot{\boldsymbol{x}} + \boldsymbol{C}\dot{\boldsymbol{x}} + \boldsymbol{K}\boldsymbol{x} + \boldsymbol{f}(\boldsymbol{x}, \dot{\boldsymbol{x}}) = \epsilon \boldsymbol{f}^{\text{ext}}(\Omega t), \tag{1}$$

where $\boldsymbol{x} \in \mathbb{R}^n$ is displacement vector; $\boldsymbol{M}, \boldsymbol{C}, \boldsymbol{K} \in \mathbb{R}^{n\times n}$ are the mass, damping and stiffness matrices; $\boldsymbol{f}(\boldsymbol{x}, \dot{\boldsymbol{x}})$ is a C^r smooth nonlinear function such that $\boldsymbol{f}(\boldsymbol{x}, \dot{\boldsymbol{x}}) \sim \mathcal{O}(|\boldsymbol{x}|^2, |\boldsymbol{x}||\dot{\boldsymbol{x}}|, |\dot{\boldsymbol{x}}|^2)$; and $\epsilon \boldsymbol{f}^{\text{ext}}(\Omega t)$ denotes external harmonic excitation. Let $\boldsymbol{z} = (\boldsymbol{x}, \dot{\boldsymbol{x}})$, the equation of motion (1) can be transformed into a first-order form

$$\boldsymbol{B}\dot{\boldsymbol{z}} = \boldsymbol{A}\boldsymbol{z} + \boldsymbol{F}(\boldsymbol{z}) + \epsilon \boldsymbol{F}^{\text{ext}}(\Omega t), \quad 0 \le \epsilon \ll 1, \tag{2}$$

with appropriate definition of $\boldsymbol{A}, \boldsymbol{B}, \boldsymbol{F}$ and $\boldsymbol{F}^{\text{ext}}$. We assume that $\boldsymbol{z} = \boldsymbol{0}$ is an asymptotically stable fixed point at $\epsilon = 0$. We construct SSM-based reduced-order model for (2) in following steps

1. We determine the master subspace for reduction based on external and internal resonances. Specifically, we first include the modes subject to (near) external resonance with excitation frequency Ω to the master subspace. We further add the modes having internal resonances with the externally resonant modes to the master subspace.

2. We compute the parametrization $\boldsymbol{W}_\epsilon(\boldsymbol{p}, \Omega t)$ of the SSM associated with the master subspace along with its reduced dynamics $\dot{\boldsymbol{p}} = \boldsymbol{R}_\epsilon(\boldsymbol{p}, \Omega t)$, where the parameterization coordinates $\boldsymbol{p}$ are of the same dimension as the that of the master subspace. We express the parametrizations $\boldsymbol{W}_\epsilon(\boldsymbol{p}, \Omega t)$ and $\boldsymbol{R}_\epsilon(\boldsymbol{p}, \Omega t)$ as Taylor series expansion in $\boldsymbol{p}$ and determine the unknown expansion coefficients by balancing polynomials in the invariance equation, as shown in [2].

3. We transform the reduced dynamics $\dot{\boldsymbol{p}} = \boldsymbol{R}_\epsilon(\boldsymbol{p}, \Omega t)$ to factor out the Ωt-dependent terms. In particular, using the transformation $\boldsymbol{p} = \boldsymbol{H}(\Omega t)\boldsymbol{q}$ with an explicit diagonal matrix $\boldsymbol{H}$, we obtain an autonomous reduced-order model

$$\dot{\boldsymbol{q}} = \boldsymbol{h}(\boldsymbol{q}, \Omega, \epsilon). \tag{3}$$

Further details about the above construction can be found in our preprint [5].

Bifurcation analysis

The bifurcation analysis of the full high-dimensional system (2) is simplified to the bifurcation analysis of the reduced-order model (3). This simplification enables the prediction of bifurcations of periodic/quasi-periodic orbits of the full system (2) via the bifurcations of the equilibria/limit cycles of the reduced-order model (3). For instance, we simply identify Hopf bifurcations of equilibria and limit cycles in the reduced system (3) to predict the existence of two-dimensional and three-dimensional quasi-periodic invariant tori in the full system (2) of arbitrary dimension.

We have integrated the continuation package COCO with SSMTOOL to perform such bifurcation analysis. Specifically, we have developed the following three toolboxes within SSMTOOL.

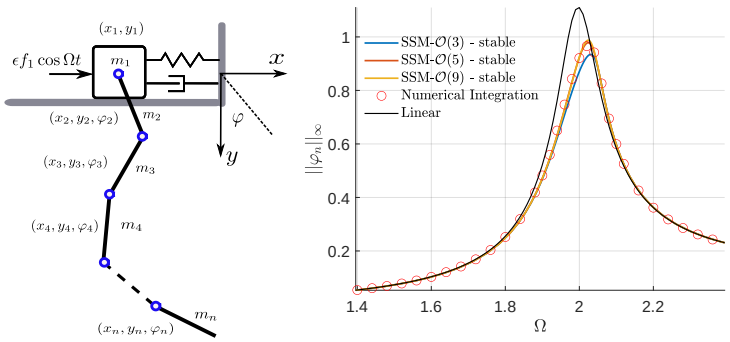

Figure 1: A chain of pendulums (left) with $n = 41$ and the forced response curve of rotation angle of the last pendulum (right).

- `SSM-ep`: continuation of (bifurcated) equilibria of the reduced-order model (3) and the construction of corresponding (bifurcated) periodic orbits of the full system (2);
- `SSM-po`: continuation of (bifurcated) limit cycles of the reduced-order model (3) and the construction of corresponding (bifurcated) two-dimensional quasi-periodic invariant tori of the full system (2);
- `SSM-tor`: continuation of two-dimensional quasi-periodic invariant tori of the reduced-order model (3) and the construction of corresponding three-dimensional quasi-periodic invariant tori of the full system (2).

More details about these toolboxes and their applications to finite-element examples can be found in our preprints [5, 6].

Extension to constrained mechanical systems

Now, we consider a periodically forced nonlinear mechanical system with configuration constraints of the form

$$\boldsymbol{M}\ddot{\boldsymbol{x}} + \boldsymbol{C}\dot{\boldsymbol{x}} + \boldsymbol{K}\boldsymbol{x} + \boldsymbol{f}(\boldsymbol{x}, \dot{\boldsymbol{x}}) + \boldsymbol{G}^\top \boldsymbol{\lambda} = \epsilon \boldsymbol{f}^{\text{ext}}(\Omega t), \quad \boldsymbol{g}(\boldsymbol{q}) = \boldsymbol{0} \tag{4}$$

where $\boldsymbol{x}, \boldsymbol{M}, \boldsymbol{C}, \boldsymbol{K}, \boldsymbol{f}, \epsilon, \boldsymbol{f}^{\text{ext}}$ carry the same definitions as in (1), $\boldsymbol{g} : \mathbb{R}^n \to \mathbb{R}^m$ $(m < n)$ represents configuration constraints, $\boldsymbol{G} = \partial \boldsymbol{g}/\partial \boldsymbol{q}$, and $\boldsymbol{\lambda}$ denotes the Lagrange multipliers corresponding to the configuration constraints.
With $\boldsymbol{z} = (\boldsymbol{x}, \dot{\boldsymbol{x}}, \boldsymbol{\lambda})$, we can again transform (4) into the first-order form (2) with appropriate definition of $\boldsymbol{A}, \boldsymbol{B}, \boldsymbol{F}$ and $\boldsymbol{F}^{\text{ext}}$. We assume $\boldsymbol{g}(\boldsymbol{0}) = \boldsymbol{0}$ such that the origin $\boldsymbol{z} = \boldsymbol{0}$ is still a fixed point of the full system (2). We further assume that $\boldsymbol{G}(\boldsymbol{0})$ is of full rank, i.e., the constraints $\boldsymbol{g}$ are not redundant and the origin is not a singular configuration. As a result, the vector $\boldsymbol{\lambda}$ of the Lagranian multipliers is well-defined. Under these assumptions, the matrix $\boldsymbol{B}$ is singular and the matrix pair $(\boldsymbol{A}, \boldsymbol{B})$ has $3m$ infinite eigenvalues corresponding to the m configuration constraints.
Indeed, the computation of SSM and its associated reduced-order model does not require the invertibility of $\boldsymbol{B}$ matrix [2]. This enables us to use SSMTOOL to construct SSM-based reduced-order model for the full system (4) following the same procedure as in the previous section. Hence, we can again perform bifurcation analysis and obtain backbone and forced response curves of the constrained system (4) directly from the SSM-based reduced-order (3).
As a demonstration, we consider a chain of planar pendulums attached to a harmonically excited oscillator, as shown in Fig. 1. The configuration constraints in this system come from the revolute joints. We extract the forced response curve of the system via a two-dimensional SSM-based reduced-order model. As shown in the right panel of Fig. 1, the forced response curve predicted by this reduced-order model agrees with the one obtained from the numerical time integration of the full system, thereby demonstrating the effectiveness of SSM reduction.

Conclusions

We derived SSM-based reduced-order models for nonlinear systems with internal resonances. Such reduced-order models enable efficient nonlinear analysis of the full systems with arbitrary dimensions. We further extended this analysis to constrained mechanical systems where the equations of motion are in the form of differential-algebraic equations.

References

[1] Haller, G., Ponsioen, S. (2016) Nonlinear normal modes and spectral submanifolds: existence, uniqueness and use in model reduction. *Nonlinear Dyn.* **86(3)**, 1493-1534.

[2] Jain, S., Haller, G. (2021). How to compute invariant manifolds and their reduced dynamics in high-dimensional finite-element models. *Nonlinear Dyn.* https://doi.org/10.1007/s11071-021-06957-4

[3] Jain, S., Thurnher, T., Li, M., Haller, G.: SSMTool 2.1: Computation of invariant manifolds in high-dimensional mechanics problems. https://doi.org/10.5281/ 4156 zenodo.4946625

[4] Schilder, F., Dankowicz, H., Li, M. Continuation Core and Toolboxes (COCO), https://sourceforge.net/projects/cocotools/

[5] Li, M., Jain, S., Haller, G. (2021). Nonlinear analysis of forced mechanical systems with internal resonance using spectral submanifolds–Part I: Periodic response and forced response curve. arXiv preprint arXiv:2106.05162.

[6] Li, M., Haller, G. (2021). Nonlinear analysis of forced mechanical systems with internal resonance using spectral submanifolds–Part II: Bifurcation and quasi-periodic response. arXiv preprint arXiv:2108.08152.

Reduced-Order Modelling of Moore-Greitzer PDEs using Sparse Regression

Yusuf Aydogdu, Thambirajah Ravichandran, Alyssa Novelia and N. Sri Namachchivaya
Department of Applied Mathematics, University of Waterloo, Waterloo, Ontario N2L 3G1, Canada

Summary. This paper develops a data-driven reduced-order model of the viscous Moore-Greitzer (MG) partial differential equations (PDEs) by threading together ideas from dimensionality reduction to sparse regression and compressed sensing. Numerical simulation of the infinite dimensional viscous MG system is reduced into low dimensional data using principal component analysis (PCA) and autoencoder neural networks based dimensionality reduction methods. Based on the observation that MG equations close to bifurcations have a sparse representation (normal forms) with respect to high-dimensional polynomial spaces, we use the Sparse Identification of Nonlinear Dynamics (SINDy) algorithm which uses a collection of all monomials as a sampling matrix and a sparse regression technique to recover a system of two sparse ordinary differential equations (ODEs) with cubic nonlinearities.

Introduction

This paper develops data-driven theory and algorithms to detect and mitigate stall compressor instability. The motivation is to produce a high-fidelity simulation of a jet engine compressor called the digital twin, which has the ability to monitor and diagnose complex systems to improve performance efficiency and utilization. Jet engine compressor models typically integrate a hierarchy of multi-physics and multi-fidelity models which are continually updated with data streams from the sensors. The model used to describe airflow inside the jet engine compressor is the viscous MG equations [12, 22] which consist of a nonlinear partial differential equation (PDE) and two ODEs. There are three types of Hopf bifurcations that can exist in the viscous MG equations corresponding to physical oscillations dominated by the ODE (surge), PDE (rotating stall), or a mixture of both. The objective of this particular work is to use optimization and regression techniques from machine learning to arrive at a lower dimensional description of the PDE from datasets. The success of compressor reduced-order modelling is rooted on accurate representations of the multi-physics and multi-fidelity models.

First, we describe the viscous MG equations, provide an explicit expression for the system's equilibrium, and show that the steady operating axial flow and pressure drifts from the aforementioned equilibrium during PDE bifurcation. Then, we introduce reduced-order modeling (ROM) to significantly alleviate computational costs by projecting the high dimensional state variables onto a low-dimensional subspace. We perform ROM on simulated data from viscous MG equations to construct a set of "good" basis functions. Approximations of bases spanning this subspace are constructed using principal component analysis (PCA) [15, 28] and both linear and nonlinear autoencoder neural networks [26, 27].

It is impossible to effectively "learn" from high dimensional data unless there is some kind of implicit or explicit low dimensional structure. Over the past 10 years, researchers have focused on sparsity as one type of criteria for low-dimensional structure. The inherent sparsity of natural signals is central to the mathematical framework of compressed sensing [5, 6, 9]. The main aim of compressed sensing is to construct a sparse vector from linear measurements of the vector such that the number of observed measurements m is significantly smaller than the dimension n of the original vector and satisfies the "Restricted Isometry Property" (RIP). Intuitively, the existence of a RIP implies that the geometry of sparse vectors is preserved through the measurement matrix, as illustrated in a high dimensional application [23]. These techniques rely heavily on the fact that many dynamical systems can be represented by governing equations that are sparse in the space of all possible functions. The assumption for the low dimensional structure for the MG equations originates from the center manifold theory in dynamical systems [13, 31], where a high dimensional system undergoing Hopf bifurcation can be fully described by projecting the equations onto the subspace of a 2-dimensional center manifold.

Finally, we adapt a recently developed technique called Sparse Identification of Nonlinear Dynamics (SINDy) [4, 7, 8] which has demonstrated the ability to recover governing equations of complex dynamical systems. The methods presented in SINDy approach the problem of automating the discovery of dynamic equations that describe natural systems through the lens of sparsity-promoting regression techniques such as Least Absolute Shrinkage and Selection Operator (LASSO) [29]. To lend insight into this process, the SINDy algorithm was applied to simulated data from various ROM models to recover their respective sparse equations which is then used to reconstruct the original system's dynamics.

Viscous Moore-Greitzer Equations

Model and Analysis

Turbo-jet engine is comprised of 3 parts: axial flow compressor where air gets compressed, the plenum where the air undergoes combustion and rapidly expands, and the turbine where the air is let out (see for example, Figure 1 in [30]). The flow enters from atmospheric pressure at the inlet duct, proceeds through the compressor block where the static pressure is increased, enters the outlet duct, and then exits to atmospheric pressure through the downstream turbine's throttle. The compressor is made out of an entrance duct, an inlet guide vane (IGV), multiple stages of stator-rotor pairs, and an exit duct towards the plenum. A stator is a rotary system with static blades and a rotor comprises of revolving blades.

The following basic assumptions of the MG compressor model [12, 22] are made. The pressure rise across the compressor lags behind the pressure drop delivered by the throttle due to mass storage in the exit duct (or plenum). Across the compressor, the difference between the pressure delivered by the compressor and pressure rise that currently exists across the compressor acts to accelerate the flow rate through the compressor. The flow is assumed to be incompressible and irrotational everywhere except inside the plenum where combustion occurs and rapidly expands the air.

The viscous MG equations for a cylindrical axial flow compressor consist of Laplace's partial differential equation (PDE) for disturbance velocity potential $\tilde{\phi}'(t,\theta,\eta)$

$$\tilde{\phi}'_{\eta\eta} + \tilde{\phi}'_{\theta\theta} = 0. \tag{1}$$

with boundary conditions

$$\psi_c(\Phi(t) + (\tilde{\phi}'_\eta)_0) - \frac{1}{2\pi}\int_0^{2\pi} \psi_c(\Phi(t) + (\tilde{\phi}'_\eta)_0)d\theta - m(\tilde{\phi}'_t)_0 - \frac{1}{a}(\tilde{\phi}'_{t\eta})_0 - \frac{1}{2a}(\tilde{\phi}'_{\eta\theta})_0 - \frac{\nu}{2a}(\tilde{\phi}'_{\eta\theta\theta})_0 = 0 \tag{2}$$

at $\eta = 0$ and $\tilde{\phi}' = 0$ at $\eta = -\infty$ and a pair of ordinary differential equations (ODEs) for annulus average of axial momentum $\Phi(t)$

$$\Psi(t) + \ell_c \frac{d\Phi(t)}{dt} = \frac{1}{2\pi}\int_0^{2\pi} \psi_c(\Phi(t) + (\tilde{\phi}'_\eta)_0)d\theta. \tag{3}$$

and pressure drop from across the compressor $\Psi(t)$

$$\frac{d\Psi(t)}{dt} = \frac{1}{4B^2\ell_c}(\Phi(t) - F_T^{-1}(\Psi(t))). \tag{4}$$

The subscripts of $\tilde{\phi}'$ indicate partial derivatives with respect to time t, angular θ and axial η coordinates of the cylindrical compressor. $(\cdot)_0$ means the quantity is evaluated at the compressor entrance $\eta = 0$. a is the internal compressor lag, $l_c = l_I + l_E + \frac{1}{a}$ is the characteristic compressor length (dimensionless quantity normalized with respect to compressor radius), and B is the plenum to compressor volume ratio [11]. Detailed derivation of the non-viscous model can be found in [11, 12, 22] while the viscous model was developed in [1, 21] and thoroughly derived in [3].

The compressor $\psi_c(\phi)$ and throttle $F_T(\phi)$ characteristic functions that are considered follow [12, 22]

$$\psi_c(\phi) = \psi_{c_0} + H\left[1 + \frac{3}{2}\left(\frac{\phi}{W} - 1\right) - \frac{1}{2}\left(\frac{\phi}{W} - 1\right)^3\right] \tag{5}$$

$$F_T(\phi) = \frac{\phi^2}{\gamma^2}. \tag{6}$$

H and W are the characteristic height and width of the compressor and ψ_{c_0} is a value determined by experiments. Throttle coefficient γ describes the amount of opening - large γ implies a wide open throttle while small γ implies a closed throttle. Equations (1), (2), (3), and (4) can be combined into a compact state-space form $\frac{\partial \mathbf{y}}{\partial t} = \mathbf{A}\mathbf{y} + \mathbf{f}(\mathbf{y})$ following [2]

$$\frac{\partial}{\partial t}\begin{bmatrix} g \\ \Phi \\ \Psi \end{bmatrix} = \begin{bmatrix} K^{-1}\left(\frac{\nu}{2}\frac{\partial^2}{\partial\theta^2} - \frac{1}{2}\frac{\partial}{\partial\theta}\right) & 0 & 0 \\ 0 & 0 & 0 \\ 0 & 0 & 0 \end{bmatrix}\begin{bmatrix} g \\ \Phi \\ \Psi \end{bmatrix} + \begin{bmatrix} aK^{-1}(\psi_c(\Phi+g) - \bar{\psi}_c) \\ \frac{1}{l_c}(\bar{\psi}_c - \Psi) \\ \frac{1}{4B^2 l_c}(\Phi - \gamma\sqrt{\Psi}) \end{bmatrix} \tag{7}$$

by introducing state variable g

$$g(t,\theta) = (\tilde{\phi}'_\eta)_0 = \sum_{n\in Z} |n|\tilde{\phi}'_n(t)e^{in\theta} = \sum_{n\in Z} g_n e^{in\theta}. \tag{8}$$

where

$$\tilde{\phi}'(t,\theta,\eta) = \sum_{n\in Z} \tilde{\tilde{\phi}}'_n(t)e^{|n|\eta + in\theta}, \tag{9}$$

is the solution to (1) and we define

$$\bar{\psi}_c = \frac{1}{2\pi}\int_0^{2\pi} \psi_c(\Phi + g)d\theta. \tag{10}$$

as well as an operator K that acts on $\phi = \sum_{n\in Z}\tilde{\phi}_n e^{in\theta}$ such that

$$K(\phi) = \sum_{n\in Z}\left(1 + \frac{ma}{|n|}\right)\tilde{\phi}_n e^{in\theta}. \tag{11}$$

To inspect the nonlinearities in $\mathbf{f}(\mathbf{y})$, we perform Taylor series' expansion on $\psi_c(\Phi + g)$ up to the third cubic term to expand the integrand of $\bar{\psi}_c$

$$\bar{\psi}_c = \psi_c(\Phi) + \frac{1}{2}\psi''_c(\Phi)\sum_{m,n\in Z}^{m+n=0} g_m g_n + \frac{1}{6}\psi'''_c(\Phi)\sum_{k,m,n\in Z}^{k+m+n=0} g_k g_m g_n. \tag{12}$$

Note that $g(t,\theta)$ has a vanishing average property due to assumptions made to the disturbance flow. Therefore, $\bar{\psi}_c$ is only a function of t and not θ and as a result, $K^{-1}(\bar{\psi}_c) = 0$. The nonlinearity vector $\mathbf{f}(\mathbf{y})$ becomes

$$\mathbf{f}(\mathbf{y}) = \begin{bmatrix} aK^{-1}(\psi_c'(\Phi)g + \frac{1}{2}\psi_c''(\Phi)g^2 + \frac{1}{6}\psi_c'''(\Phi)g^3) \\ \frac{1}{l_c}(\psi_c(\Phi) + \frac{1}{2}\psi_c''(\Phi)\sum_{m,n\in Z}^{m+n=0} g_m g_n + \frac{1}{6}\psi_c'''(\Phi)\sum_{k,m,n\in Z}^{k+m+n=0} g_k g_m g_n - \Psi) \\ \frac{1}{4B^2 l_c}(\Phi - \gamma\sqrt{\Psi}) \end{bmatrix}. \tag{13}$$

The system (7)'s equilibrium consist of $g_e(\theta) = 0$ and $\Psi_e = \psi_c(\Phi_e) = F_T(\Phi_e)$ which means (Φ_e, Ψ_e) lies on the intersection of curves (5) and (6). Φ_e can be solved by finding the root of the polynomial

$$-\frac{H}{2W^3}\Phi_e^3 + \left(\frac{3H}{2W^2} - \frac{1}{\gamma^2}\right)\Phi_e^2 + \psi_{c_0} = 0. \tag{14}$$

(14) has one real root and a pair of imaginary roots, where the real root is

$$\Phi_e = \sqrt[3]{X - Y^3 + \sqrt{X(X-2Y^3)}} + \sqrt[3]{X - Y^3 - \sqrt{X(X-2Y^3)}} - Y \tag{15}$$

and

$$X = \frac{W^3}{H}\psi_{c_0}, \qquad Y = \frac{2W^3}{3H}\left(\frac{1}{\gamma^2} - \frac{3H}{2W^2}\right). \tag{16}$$

For our analysis, γ is the bifurcation parameter to be varied for different kinds of Hopf bifurcation.

The Jacobian of $\mathbf{f}(\mathbf{y})$ at equilibrium is

$$\nabla\mathbf{f}_{\mathbf{y}_e} = \begin{bmatrix} aK^{-1}(\psi_c'(\Phi_e)) & 0 & 0 \\ 0 & \frac{1}{l_c}\psi_c'(\Phi_e) & -\frac{1}{l_c} \\ 0 & \frac{1}{4B^2 l_c} & -\frac{1}{4B^2 l_c}\frac{\gamma^2}{2\Phi_e} \end{bmatrix}. \tag{17}$$

The eigenvalues of $(\mathbf{A} + \nabla\mathbf{f}_{\mathbf{y}_e})$ corresponding to the PDE are

$$\lambda_n = \left(\frac{a|n|}{|n| + am}\right)\left(\psi_c'(\Phi_e) - \frac{\nu}{2a}n^2 - \frac{1}{2a}(in)\right) \tag{18}$$

and the eigenvalues of $(\mathbf{A} + \nabla\mathbf{f}_{\mathbf{y}_e})$ corresponding to the ODEs are

$$\mu_{1,2} = \frac{1}{2l_c}\left[\left(\psi_c'(\Phi_e) - \frac{\gamma}{8B^2\sqrt{\Psi_e}}\right) \pm \sqrt{\left(\psi_c'(\Phi_e) + \frac{\gamma}{8B^2\sqrt{\Psi_e}}\right)^2 - \frac{1}{B^2}}\right]. \tag{19}$$

Hopf bifurcation occurs when a pair of $(\mathbf{A} + \nabla\mathbf{f}_{\mathbf{y}_e})$ eigenvalues' real parts cross the imaginary axis with the derivative of the real parts with respect to γ is not equal to zero. There are three possibilities: surge (ODE bifurcation), stall (PDE bifurcation), and combination (simultaneous ODE and PDE bifurcations).

The critical bifurcation point for surge is $\gamma_{c,surge}$ such that $Re(\mu_{1,2}) = 0$. When $\gamma < \gamma_{c,surge}$, surge occurs. It is difficult to obtain an explicit expression for $\gamma_{c,surge}$ but $\gamma_{c,surge}$ is the solution to

$$\Phi_e(\gamma_{c,surge})\left(2 - \frac{\Phi_e(\gamma_{c,surge})}{W}\right) - \frac{\gamma_{c,surge}^2}{4B^2}\frac{W^2}{3H} = 0. \tag{20}$$

The condition for surge is $\frac{\partial}{\partial\gamma}(Re(\mu_{1,2}))\Big|_{\gamma_{c,surge}} > 0$.

The critical bifurcation point for stall is $\gamma_{c,stall}$ such that $Re(\lambda_1) = 0$. When $\gamma < \gamma_{c,stall}$, stall occurs. Again, it is difficult to obtain an explicit expression for $\gamma_{c,stall}$ but $\gamma_{c,stall}$ is the solution to

$$\Phi_e(\gamma_{c,stall})\left(2 - \frac{\Phi_e(\gamma_{c,stall})}{W}\right) - \frac{\nu W^2}{3aH} = 0. \tag{21}$$

The condition for stall is $\frac{\partial}{\partial\gamma}(Re(\lambda_1))\Big|_{\gamma_{c,stall}} > 0$.

It is possible for the largest PDE eigenvalue pairs and both ODE eigenvalues to simultaneously cross the imaginary axis. This is achieved when $\gamma = \gamma_{c,combo}$ where

$$\psi_c'(\Phi_e(\gamma_{c,combo})) = \frac{\gamma_{c,combo}^2}{8B^2}\frac{1}{\Phi_e(\gamma_{c,combo})} = \frac{\nu}{2a}. \tag{22}$$

For the combination case, it is possible to calculate the expression for the normal form which are the diagonal entries of $(\mathbf{A}+\nabla\mathbf{f}_{\mathbf{y}_e})(\gamma_{c,combo})$

$$\mathbf{D}(\gamma_{c,combo}) = \mathbf{T}^{-1}(\mathbf{A}+\nabla\mathbf{f}_{\mathbf{y}_e})\mathbf{T}(\gamma_{c,combo}) = \operatorname{diag}\left(\begin{bmatrix} (K^{-1}\left(\frac{\nu}{2}(1-n^2)-\frac{1}{2}ni\right) \\ \frac{1}{2l_c}\sqrt{\frac{\nu^2}{a^2}-\frac{1}{B^2}} \\ -\frac{1}{2l_c}\sqrt{\frac{\nu^2}{a^2}-\frac{1}{B^2}} \end{bmatrix}\right). \tag{23}$$

Rotating Stall Simulation Results

The system of equations (7) is integrated using the spectral method. $\theta \in [-\pi, \pi)$ is discretized into 512 equally spaced points, leading to a system of 514 ODEs (512 of which are Fourier coefficients of $g(t,\theta)$) to be numerically integrated using SciPy's `solve_ivp` with $dt = 0.1$. The following parameter values are used in all cases

$$l_c = 8, \quad m = 1.75, \quad a = 1/3.5, \quad \nu = 1, \quad \psi_{c_0} = 1.67H, \quad H = 0.18, \quad W = 0.25. \tag{24}$$

The plenum to compressor volume ratio B and the throttle opening γ are chosen to produce different type of bifurcations, and for the stall case, the simulations results are given below in Figure 1.

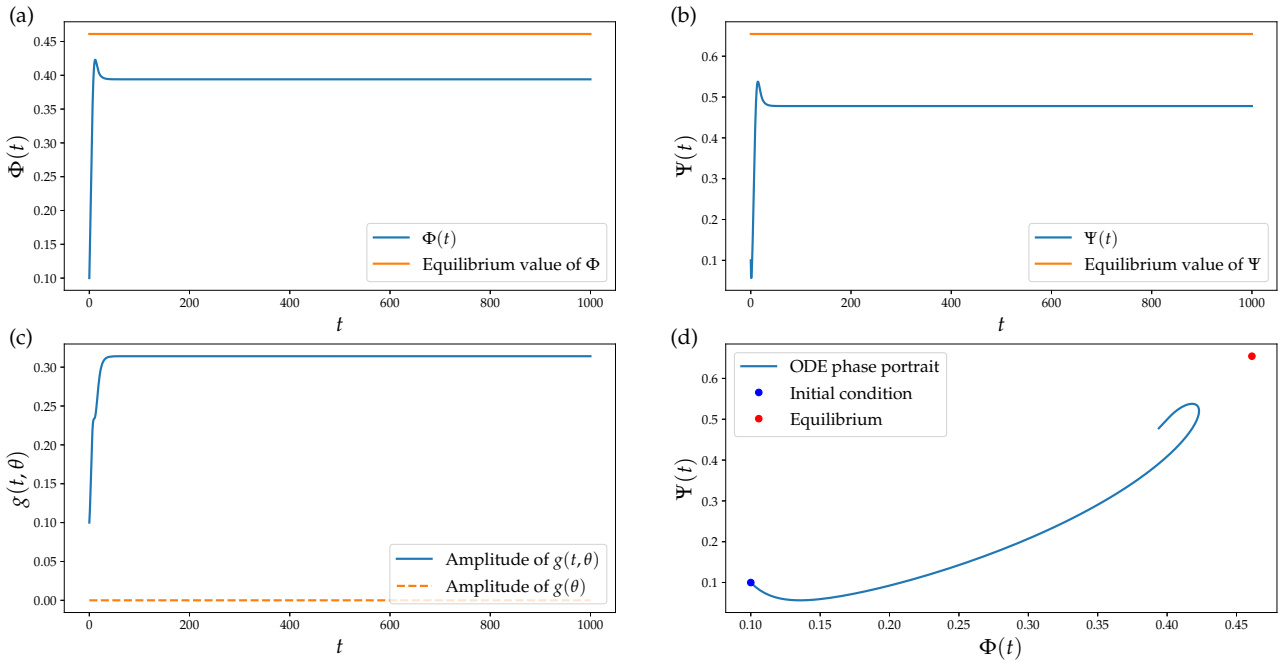

Figure 1: Stall dynamics of viscous Moore-Greitzer equations: (a) $\Phi(t)$ and (b) $\Psi(t)$ do not settle at their stable equilibrium values due to influence from PDE Hopf bifurcation. (c) Amplitude of $g(t,\theta)$ in t settles to a non-zero value during Hopf bifurcation. (d) Phase portrait of ODE states $\Phi(t)$ and $\Psi(t)$ which does not settle at the equilibrium point.

Dimensionality Reduction for Reduced-Order Modelling (ROM)

Principal Component Analysis (PCA)

PCA is also known as proper orthogonal decomposition (POD) in mechanical engineering [15] and discrete Karhunen-Loève expansion in signal processing and information theory [20]. PCA is a method to find principal axes in high dimensional data. These principal axes span the eigenvectors of the covariance matrix of the measurements which are orthonormal to each other such that the individual data along these directions are linearly uncorrelated. PCA can also be used as a dimensionality reduction tool by truncating a measurement's linear combination in its principal axes. Constructing basis functions from data using PCA can be formulated mathematically as a low-rank matrix approximation problem which can be easily computed by using the singular value decomposition (SVD) [10].

Suppose we have N observations of n-dimensional data

$$\mathbf{Y} = [\mathbf{y}_1 \dots \mathbf{y}_N] \tag{25}$$

where $\mathbf{Y} \in \mathbb{R}^{n \times N}$, $\mathbf{y_i} = \mathbf{y}(t_i) \in \mathbb{R}^n$. After centering the data about its empirical mean to get $\mathbf{Y}_0$, define a transformation $\mathbf{W} \in \mathbb{R}^{n \times m}$ where $m < n$ in the context of dimensionality reduction. The lower dimensional data is calculated by

$$\mathbf{X}_0 = \mathbf{W}^T \mathbf{Y}_0. \tag{26}$$

If we use PCA, then the transformation is defined as

$$\mathbf{W} = \mathbf{P}_m = [\mathbf{p}_1 \dots \mathbf{p}_m] \tag{27}$$

where $\mathbf{p}_m$ are the principal axes of $\mathbf{Y}_0$ or the first m eigenvectors of the covariance matrix $\mathbf{Y}_0 \mathbf{Y}_0^T$.

Neural Network Implementation of PCA

An autoencoder is a type of multilayer feedforward neural network that at its simplest form (see Figure 2 without 64-nodes hidden layers) has an input layer with n nodes, followed by a hidden layer with m nodes (where $m < n$), followed by an output layer with n nodes. When the activation functions are chosen to be linear, the input-output relationship is given by

$$\hat{\mathbf{y}} = \mathbf{W}_2(\mathbf{W}_1 \mathbf{y} + \mathbf{b}_1) + \mathbf{b}_2 \tag{28}$$

where $\mathbf{W}_1, \mathbf{W}_2^T \in \mathbb{R}^{m \times n}$ are the encoder and decoder weight matrices, and $\mathbf{b}_1 \in \mathbb{R}^m$, $\mathbf{b}_2 \in \mathbb{R}^n$ are the encoder and decoder bias vectors. Once the optimal $\{\mathbf{W}_1, \mathbf{W}_2, \mathbf{b}_1, \mathbf{b}_2\}$ are found, we can construct an encoder to reduce the input into a reduced-order data $\mathbf{x} \in \mathbb{R}^m$ using $\{\mathbf{W}_1, \mathbf{b}_1\}$ and a decoder to convert the encoded data back to its original dimension using $\{\mathbf{W}_2, \mathbf{b}_2\}$.

Under certain assumptions on the error function landscape, the minimization problem for the autoencoder reduces to

$$\min_{\{\mathbf{W}_2\}} \|\mathbf{Y}_0 - \mathbf{W}_2 \mathbf{W}_2^+ \mathbf{Y}_0\|_F^2. \tag{29}$$

where $\mathbf{W}_2^+$ is the Moore-Penrose inverse/pseudoinverse [25] of $\mathbf{W}_2$. For the case when the columns of $\mathbf{W}_2$ are orthonormal like $\mathbf{P}_m$, then $\mathbf{W}_2^+ = \mathbf{W}_2^T$ will make (29) equal to the reconstruction error of PCA. Therefore, it is clear that $\mathbf{P}_m$ is a solution to the autoencoder optimization problem. The problem is that the product of $\mathbf{P}_m$ with any proper orthogonal matrix $\mathbf{Q} \in \mathbb{R}^{m \times m}$ will be a minimizer $\mathbf{W}_2$, such that there are infinitely many solutions. Coupled with the fact that mini-batch stochastic gradient descent [19] is the go-to optimization algorithm in today's neural network frameworks, there is no guarantee that $\mathbf{W}_2$ converges to the same value when the training procedure is repeated, let alone align itself to $\mathbf{P}_m$. While any $\mathbf{W}_2$ in this space can be used to mimic the input data almost perfectly, this inconsistency is an issue in our problem as we would like to further uncover the underlying structure of the encoded measurements $\mathbf{X} = [\mathbf{x}_1 \dots \mathbf{x}_N]$.

Regularized Linear Autoencoder

An approach to recover the principal axes from autoencoder weights is based on the following hypothesis [26]: the first m left singular vectors of $\mathbf{W}$ is also the first m principal axes of $\mathbf{Y}_0$. This hypothesis can be framed as an autoencoder with a regularizer or penalty to the sum of the Frobenius norms of the encoder weight matrix $\mathbf{W}_1$ and decoder weight matrix $\mathbf{W}_2$

$$\min_{\{\mathbf{W}_1, \mathbf{W}_2\}} \|\mathbf{Y}_0 - \mathbf{W}_2 \mathbf{W}_1 \mathbf{Y}_0\|_F^2 + \lambda(\|\mathbf{W}_1\|_F^2 + \|\mathbf{W}_2\|_F^2). \tag{30}$$

For a large enough λ value, the error surface is guaranteed to be convex with a single global minima which will correspond to the principal axes [17]. Additionally, the minimum values of this loss function is $\mathbf{W}_1^* = \mathbf{W}_2^T$ unlike $\mathbf{W}_1^* = \mathbf{W}_2^+$ in the original approach.

Nonlinear Principal Component Analysis (NLPCA) and Autoencoder

NLPCA was developed to uncover the underlying nonlinear manifold in large dimensional datasets. The neural network architecture we are considering to train our NLPCA autoencoder is shown in Figure 2.

$$\begin{aligned} \mathbf{X} &= \mathbf{W}_2 \tanh(\mathbf{W}_1 \mathbf{Y} + \mathbf{b}_1) + \mathbf{b}_2 \\ \hat{\mathbf{Y}} &= \mathbf{W}_4 \tanh(\mathbf{W}_3 \mathbf{X} + \mathbf{b}_3) + \mathbf{b}_4. \end{aligned} \tag{31}$$

We choose the nonlinear activation function tanh() as in [27] under the justification that a trigonometric function would fit well with the solutions of the MG equations which are spanned by the Fourier basis (8). The NLPCA autoencoder is trained to minimize the loss function of

$$\min_{\{\mathbf{W}_{1,2,3,4}, \mathbf{b}_{1,2,3,4}\}} \|\mathbf{Y} - \hat{\mathbf{Y}}\|_F^2. \tag{32}$$

The resulting $\{\mathbf{W}_{1,2,3,4}\}$ and $\{\mathbf{b}_{1,2,3,4}\}$ are then used to construct an encoder and decoder as per (31).

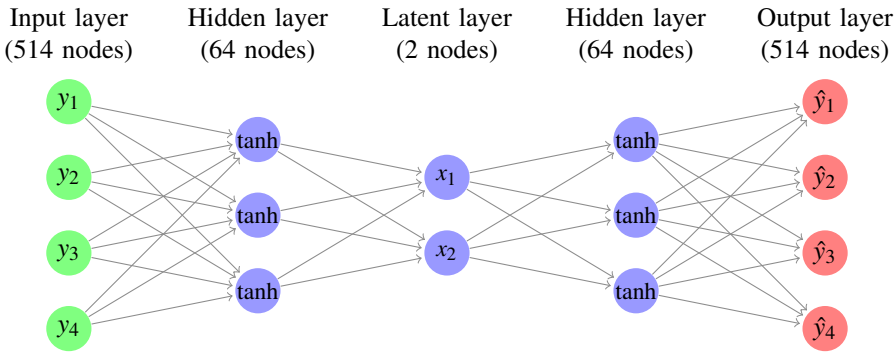

Figure 2: Autoencoder architecture for MG compressor data with tanh() activation function

Sparsity in Reduced-Order Data

Over the past two decades, researchers have focused on sparsity as one type of low-dimensional structure. Given the recent advances in both compressed sensing [6, 9] and sparse regression [29], it has become computationally feasible to extract system dynamics from large multimodal datasets. The term sparse in signal processing context refers to the case where signals (or any type of data, in general) have few non-zero components with respect to the total number of components. It is well known in dynamical systems, the normal forms provide a way of finding a coordinate system in which the dynamical system takes the "simplest" or "minimal" form. The normal forms, which are sparse in the space of homogeneous vector polynomial of certain degree, is calculated by making judicious choices of the solutions to the homological equations [13]. Hence, in the context of our work, close to the bifurcation point, the sparse regression techniques rely heavily on the fact that many dynamical systems can be represented by governing equations that are sparse in the space of all possible functions of a given algebraic structure.

Compressed Sensing

Compressed sensing (CS) is a technique for sampling and reconstructing sparse signals that can be represented by $k << n$ significant coefficients over an n- dimensional basis. The central goal of CS is the recovery of sparse vectors from a small number of linear measurements, which distinguishes CS from other dimensionality reduction techniques. In [9] and [6], the original sparse (k-sparse) signal is projected onto a lower-dimensional subspace via a random projection scheme, called the sampling matrix. More precisely, this broader objective is exemplified by the important special case in which one is interested in finding a vector $S \in \mathbb{R}^n$ using the (noisy) observation or the measurement data

$$Y = \Theta S + \eta, \quad \text{where } \Theta \in \mathbb{R}^{m \times n} \text{ with } k < m < n, \tag{33}$$

is the known sensing or sampling matrix and η is the measurement noise.

In general, this problem cannot be solved uniquely. However, if S is k-sparse i.e., if it has up to k non-zero entries, the theory of CS shows that it is possible to reconstruct S, a k-sparse vector in $\mathbb{R}^n$ uniquely from m linear measurements even when $m << n$, by exploiting the sparsity of S. This can be achieved by finding the sparsest signal consistent with the vector of measurements [9], i.e.

$$\underset{S \in \mathbb{R}^n}{\arg\min} \|S\|_0 \text{ subject to } \|Y - \Theta S\|_2 \leq \varepsilon \tag{34}$$

where $\|S\|_0$ denotes the l_0 norm for S (the number of non-zero entries of S), while ε denotes a parameter that depends on the level of measurement noise η. However, l_0 minimization problem (34) is a non-convex problem which is NP-hard.

Instead of problem (34) we consider its l_1 convex relaxation which may be stated as

$$\underset{S \in \mathbb{R}^n}{\arg\min} \|S\|_1 \text{ subject to } \|Y - \Theta S\|_2 \leq \varepsilon \tag{35}$$

where the l_1 norm (sum of the absolute values of the entries of S) is a convex function. Hence (35) is a convex optimization problem which can accurately approximate the solution to (34) in polynomial time with high probability if measurement matrix Θ is chosen to satisfy a necessary condition called "Restricted Isometry Property" (RIP) [5, 6]. One should note that the l_1 minimization in (35) is closely related to the LASSO problem [29]

$$\underset{S \in \mathbb{R}^n}{\arg\min} \|Y - \Theta S\|_2^2 + \alpha \|S\|_1 \tag{36}$$

where $\alpha \geq 0$ is a regularization parameter. If ε and α in (35) and (36) satisfy some special conditions, the two problems are equivalent; however, characterizing the relationships between ε and α is difficult except for the special case of orthogonal sensing matrices Θ. The practical success of the LASSO can be attributed to the fact that in many cases S is sparse.

Sparse Identification of Dynamical Systems (SINDy)

Sparse identification of nonlinear dynamics (SINDy) [4] is an algorithm for discovering the dynamical equations directly from the data. The problem of model discovery from data can be formulated as a feature selection problem in machine learning. The SINDy algorithm takes m-time measurements of $\mathbf{x} \in \mathbb{R}^n$, $\mathbf{X} = [\mathbf{x}(t_1), \ldots, \mathbf{x}(t_m)]^T \in \mathbb{R}^{m \times n}$ and attempts to discover the structure of a nonlinear differential equation of the form

$$\dot{\mathbf{X}} = \mathbf{f}(\mathbf{X}(t)) \approx \Theta(\mathbf{X})\mathbf{S} \tag{37}$$

where $\Theta(\mathbf{X}) = [\theta_1(\mathbf{X}), \theta_2(\mathbf{X}), ..., \theta_p(\mathbf{X})] \in \mathbb{R}^{m \times p}$ form the dictionary of basis functions, and $\mathbf{S} = [\mathbf{s}_1 \ ... \ \mathbf{s}_k \ ... \ \mathbf{s}_n] \in \mathbb{R}^{p \times n}$ is the matrix of coefficients, where each column $\mathbf{s}_k$ corresponds to an equation with p terms. p is the maximal number of n-multivariate monomials of degree at most d. The majority of $\mathbf{S}$ entries are zero while the remaining non-zero entries identify the active terms contributing to the sparse representation of the dynamics $\mathbf{f}(\mathbf{X})$. To guarantee sparsity, SINDy is reformulated as a LASSO problem

$$\arg\min_{\mathbf{s}_k} \frac{1}{m} \sum_{i=1}^{m} \|\dot{\mathbf{x}}(t_i) - \Theta(\mathbf{x}(t_i))\mathbf{s}_k\|_2^2 + \alpha \|\mathbf{s}_k\|_1 \tag{38}$$

where α is the l_1 regularization coefficient. LASSO is an optimization algorithm that finds a sparse solution for (38) by initializing $\mathbf{s}_k = \mathbf{0}$ and at each iteration, it tries to find an update for $\mathbf{s}_k$ one entry at a time. The coefficient α acts as a threshold such that if the an optimal condition involving α is not satisfied for a particular $\mathbf{s}_k$ entry, the entry is chosen to be equal to zero. Increasing the value of α leads to more zero entries in $\mathbf{s}_k$, resulting in a sparse model.

The dictionary of basis functions for monomial sampling of dynamical system is

$$\Theta(\mathbf{X}) = \begin{bmatrix} | & | & | & | & | \\ \mathbf{1} & \mathbf{X} & \mathbf{X^{P_2}} & \mathbf{X^{P_3}} & \ldots \\ | & | & | & | & | \end{bmatrix}. \tag{39}$$

The dictionary $\Theta(\mathbf{X})$ is constructed by appending candidate nonlinear functions of $\mathbf{X}$ column-wise. Here, higher order polynomials are denoted as $\mathbf{X}^{P_d}$ where d is the order of the polynomial considered. For example, element 1 is a column-vector of ones, element $\mathbf{X}$ is as defined above, element $\mathbf{X}^{P_2}$ is the matrix containing the set of all quadratic polynomial functions of the state vector $\mathbf{x}$, and is constructed as follows:

$$\mathbf{X^{P_2}} = \begin{bmatrix} x_1^2(t_1) & x_1(t_1)x_2(t_1) & \ldots & x_2^2(t_1) & \ldots & x_n^2(t_1) \\ x_1^2(t_2) & x_1(t_2)x_2(t_2) & \ldots & x_2^2(t_2) & \ldots & x_n^2(t_2) \\ \vdots & \vdots & \ddots & \vdots & \ddots & \vdots \\ x_1^2(t_m) & x_1(t_m)x_2(t_m) & \ldots & x_2^m(t_m) & \ldots & x_n^2(t_m) \end{bmatrix}. \tag{40}$$

We interpolate the reduced MG simulation data as a dynamical systems with cubic nonlinearity which is up to $\mathbf{X^{P_3}}$.

ROM Results and Analysis

We run 10 simulations of the viscous MG equations' stall case for $t \in [0, 500]$ with $dt = 0.1$. The initial conditions for $g(t, \theta)$'s amplitude, Φ, and Ψ are drawn from the normal distribution with mean 0.1 and standard deviation 0.05. The first 2000 data points (up to $t = 200$) containing the transient dynamics are discarded. This gives us 10 $\mathbf{Y} \in \mathbb{R}^{3000 \times 514}$ datasets. We perform k-fold cross validation [14] on PCA, regularized autoencoder, and NLPCA autoencoder to find the best ROM parameters to bring down the data dimension to 2. Both autoencoders' training were performed using Adam optimizer [16] with learning rate of 10^{-4} for 10 epochs of 4 mini-batch size for the regularized linear autoencoder and 20 epochs of 4 mini-batch size for the NLPCA autoencoder.

We encode the 10 datasets using the 3 different encoders to obtain 3 versions of 10 $\mathbf{X} \in \mathbb{R}^{3000 \times 2}$. For each group of reduced-order/encoded data, we perform a cubic nonlinearity dynamical system identification using PySINDy [8] paired with LASSO optimizer from Python's `sklearn` package. We train the 3 groups of 10 $\mathbf{X}$ datasets in order to find the best α which hits the sweet spot between sparsity and accuracy using grid search [18]. After finding the best α for each group, we perform another k-fold cross validation to decide on a model that best represent the 10 datasets of each ROM.

The discovered reduced governing equations satisfy the normal form if it is sufficiently described by 4 coefficients μ, ω, b_1, b_2 up to an acceptable numerical tolerance

$$\begin{aligned} \dot{x}_1 &= \mu x_1 - \omega x_2 + b_1(x_1^2 + x_2^2)x_1 - b_2(x_1^2 + x_2^2)x_2 \\ \dot{x}_2 &= \omega x_1 + \mu x_2 + b_2(x_1^2 + x_2^2)x_1 + b_1(x_1^2 + x_2^2)x_2. \end{aligned} \tag{41}$$

However, when the linear operator is semi-simple (as in Hopf bifurcations), the correct identification of a normal form depends critically on the null space of the homological operator [13]. The consequence of this fact is that the nonlinear terms in normal form (41) commutes with the linear term. As shown in [24], a consequence of this property is that, when the equation is normalized to any finite degree, say $k = 3$, and truncated, it will have symmetries that were not present in the original system. More precisely, rewriting the normal form equations (41) at the bifurcation point ($\mu = 0$) as

$$\dot{\mathbf{x}} \quad = \quad A\mathbf{x} + f^*(\mathbf{x}) \quad \mathbf{x} \in \mathbb{R}^2, \tag{42}$$

and letting $\mathbf{x} = \exp(At)\mathbf{y}$, the transformed equations are

$$\dot{\mathbf{y}} \quad = \quad \exp(-At) f^*(\exp(At)\mathbf{y}) \quad \mathbf{y} \in \mathbb{R}^2. \tag{43}$$

Using the commutation property [24] of the normal form f^*,

$$\exp(-At) f^*(\exp(At)\mathbf{y}) = f^*(\mathbf{y}), \quad \forall t \in \mathbb{R},\ \forall \mathbf{y} \in \mathbb{R}^2,$$

the normal form equations in the new variables $\mathbf{y}$ reduce to

$$\dot{\mathbf{y}} \quad = \quad f^*(\mathbf{y}) \quad \mathbf{y} \in \mathbb{R}^2. \tag{44}$$

For post-bifurcation dynamics, the discovered reduced governing equations satisfy the normal form (44) if it is sufficiently described by 2 coefficients (b_1, b_2) up to an acceptable tolerance

$$\begin{aligned} \dot{y}_1 &= b_1(y_1^2 + y_2^2)y_1 - b_2(y_1^2 + y_2^2)y_2 \\ \dot{y}_2 &= b_2(y_1^2 + y_2^2)y_1 + b_1(y_1^2 + y_2^2)y_2. \end{aligned} \tag{45}$$

Hence, MG equations close to a Hopf bifurcation have a sparse representation (45) with respect to high-dimensional polynomial spaces. The practical success and importance of the LASSO can be attributed to correctly identifying the relevant variables when the underlying model is sparse. LASSO algorithm is used in the subsequent sections to recover a system of two sparse ordinary differential equations (ODEs) with cubic nonlinearities.

For the reconstruction, the obtained SINDy equations are integrated using the forward Euler method with a fixed integration time step $dt = 0.1$ to be consistent with the chosen smoothed forward difference differentiation scheme. The global truncation error is then subtracted from the raw numerical integration result to correct the estimate. Lastly, the integrated SINDy data are fed into the decoder of the respective reduction methods to reconstruct the high dimensional time series and compared with the original dataset.

PCA and SINDy

The best SINDy regression is obtained using a LASSO threshold of $\alpha = 0.11$, which outputs a system of two ODEs with 8 coefficients and a R^2 score of 0.9999 on the test data $|||\dot{\mathbf{X}}|||$ as

$$\begin{aligned} \dot{x}_1 &= -0.000144x_1^3 - 0.008137x_1^2x_2 - 0.000144x_1x_2^2 - 0.008136x_2^3 \\ \dot{x}_2 &= 0.008136x_1^3 - 0.000144x_1^2x_2 + 0.008136x_1x_2^2 - 0.000144x_2^3. \end{aligned} \tag{46}$$

The normal form coefficients $(-0.000144, 0.008136)$ are visibly detected. Reconstruction results for a chosen random dataset are shown on the left in Figure 3.

Regularized Linear Autoencoder and SINDy

The best SINDy regression is obtained using a LASSO threshold of $\alpha = 0.30$. The output is a system of two ODEs with 9 coefficients and a R^2 score of 0.9999 on the test data $|||\dot{\mathbf{X}}|||$ and is given as

$$\begin{aligned} \dot{x}_1 &= -0.000440x_2^2 - 0.000145x_1^3 + 0.008138x_1^2x_2 - 0.000143x_1x_2^2 + 0.008138x_2^3 \\ \dot{x}_2 &= -0.008136x_1^3 - 0.000144x_1^2x_2 - 0.008139x_1x_2^2 - 0.000144x_2^3. \end{aligned} \tag{47}$$

The normal form coefficients $(-0.000145, -0.008138)$ are also visibly detected, albeit with wider deviation in values compared to (46) and an additional quadratic term in the first equation. Reconstruction results for a chosen random dataset are shown on the right in Figure 3.

NLPCA Autoencoder and SINDy

The best SINDy regression is obtained using a LASSO threshold of $\alpha = 0.60$. The output is a system of two ODEs with 11 coefficients and a R^2 score of 0.9998 on the test data $|||\dot{\mathbf{X}}|||$ which does not satisfy the normal form. A representative equation (since the outcome is always random) is given as

$$\begin{aligned} \dot{x}_1 &= -0.001031x_2^2 - 0.000091x_1^3 + 0.007704x_1^2x_2 + 0.000429x_1x_2^2 + 0.006863x_2^3 \\ \dot{x}_2 &= -0.001664x_1^2 - 0.000580x_2^2 - 0.007607x_1^3 - 0.000473x_1^2x_2 - 0.007470x_1x_2^2 - 0.000237x_2^3. \end{aligned} \tag{48}$$

Reconstruction results for a chosen random dataset are shown in Figure 4.

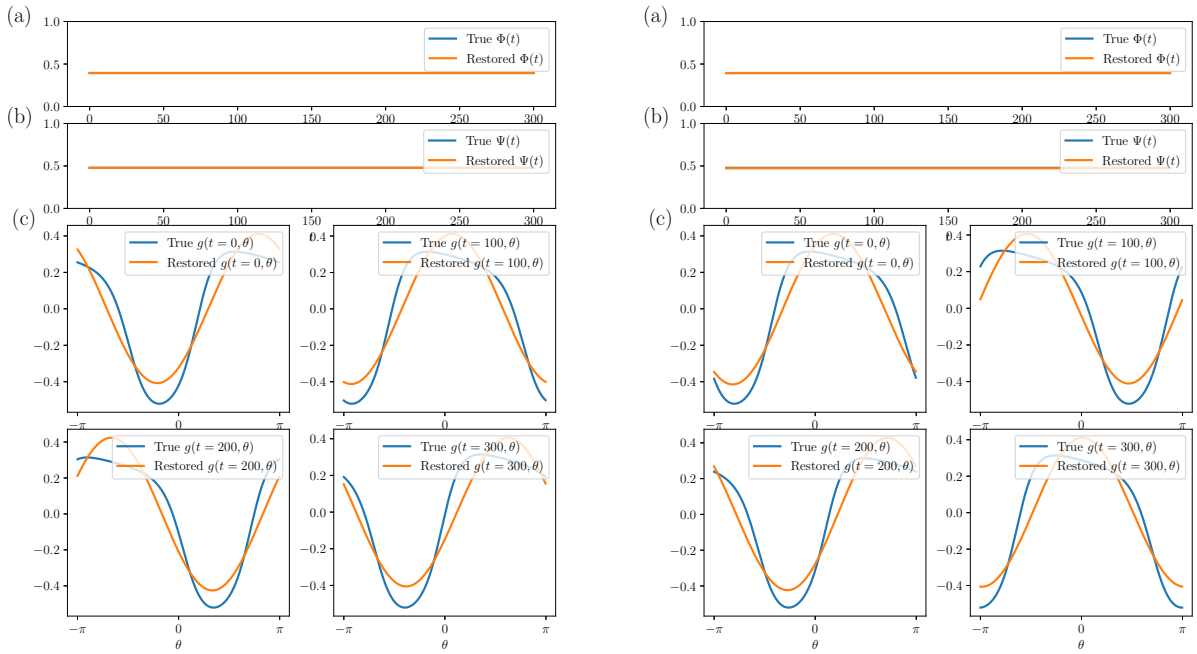

Figure 3: Reconstruction of viscous MG stall dynamics using PCA and SINDy (on the left) and regularized linear autoencoder and SINDy (on the right): (a) $\Phi(t)$, (b) $\Psi(t)$, and (c) $g(t,\theta)$ reconstruction results at $t = 0, 100, 200, 300$

Conclusions

We have showed that it is possible to fully reconstruct the solutions of the viscous MG equations from a system of 2 ODEs up to cubic nonlinearity, constructed from data sets by sparse regression. Additionally, it seems that the only requirement to detect the normal form of the PDE Hopf bifurcation is to have reduced-order data that falls along the first two principle axes, and reconstruction quality is entirely independent of whether normal forms of the underlying PDE is detected or not. The NLPCA autoencoder has to be trained for twice as long (double the number of epochs) compared to the linear autoencoder in order to converge to the local minimum that produces great reconstruction result. Table 1 summarizes our findings for the three chosen dimensionality reduction methods. Our simple approach rooted in physics-based machine learning which involves a priori knowledge of sparsity and the center manifold theory allows us to bypass deep neural network performing synchronized dimensionality reduction and SINDy approach in [7]. It is shown in Table 1 that performing dimensionality reduction and SINDy independently does not result in any significant reconstruction loss. Additionally, it would be interesting to find out if nonlinear principal components would lead us to normal form discovery from a nonlinear autoencoder, and if those components can be found using a simple regularization based approach to ensure the convexity of loss landscape just like its linear counterpart [17].

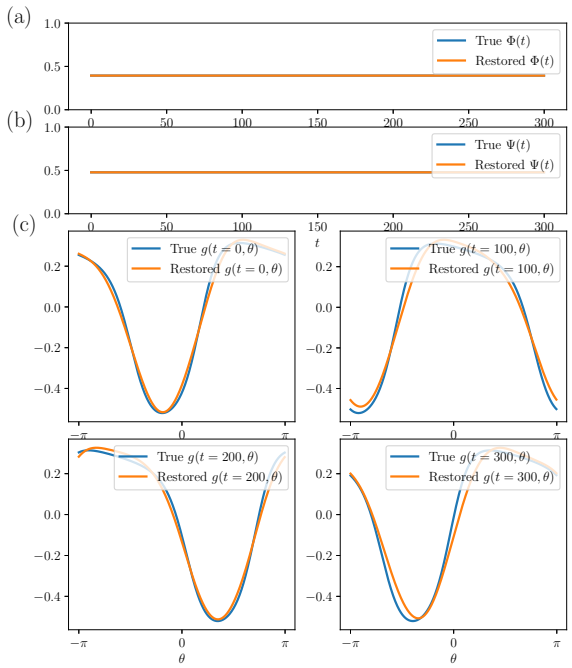

Figure 4: Reconstruction of viscous MG stall dynamics using NLPCA autoencoder and SINDy

	PCA	Linear Autoencoder	NLPCA Autoencoder
Training time	25 s	103 s	283 s
PDE reconstruction R^2 score from training data	0.8973	0.8973	0.9916
PDE reconstruction R^2 score from SINDy equations	0.8950	0.8948	0.9890
Number of RHS terms in reduced equations	8	9	11
Normal form detected	yes	yes	no

Table 1: Summary of viscous MG equations' reconstruction from SINDy models identified from different ROMs.

Acknowledgements: The authors acknowledge partial support for this work from NSERC Discovery grant 50503-10802, TECSIS /Fields-CQAM Lab for Inference and Prediction, and NSERC CRD grant 543433-19. The authors are also grateful to Mr. Yiming Meng his contribution in the viscous MG simulation development.

References

[1] Adomaitis, R. A., Abed, E. H. (1993) Local nonlinear control of stall inception in axial flow compressors. Proc. AIAA 29th Joint Propulsion Conference and Exhibit, 2230.

[2] Birnir, B., Hauksson H. A. (2000) Basic Control for the Viscous Moore–Greitzer Partial Differential Equation. SIAM J. Control Optim., 38(5), 1554-1580.

[3] Birnir, B., Hou, S., Wellander, N. (2007) Derivation of the viscous Moore-Greitzer equation for aeroengine flow. J. Math. Phys., 48(6), 065209-065209.

[4] Brunton, S. L., Proctor, J. L., Kutz, J. N. (2016) Discovering governing equations from data by sparse identification of nonlinear dynamical systems. Proc. Natl. Acad. Sci. U. S. A., 113(15), 3932-3937.

[5] Candés, E.J., Tao, T. (2005) Decoding by linear programming. IEEE Trans. Inf. Theory, 51(12), 4203-4215.

[6] Candés, E. J., Romberg, J. K., Tao, T. (2006) Stable signal recovery from incomplete and inaccurate measurements. Comm. Pure Appl. Math., 59(8), 1207-1223.

[7] Champion K., Lusch B., Kutz J. N., Brunton S. (2019) Data-driven discovery of coordinates and governing equations. Proc. Natl. Acad. Sci. U. S. A., 116(45), 22445-22451.

[8] de Silva, B., Champion, K., Quade, M., Loiseau, J. C., Kutz, J., Brunton, S. (2020) PySINDy: A Python package for the sparse identification of nonlinear dynamical systems from data. J. Open Sources Software, 5(49), 2104.

[9] Donoho D. L. (2006) Compressed sensing. IEEE Trans. Inform. Theory, 52(4), 1289-1306.

[10] Golub, G., Kahan, W. (1964) Calculating the Singular Values and Pseudo-Inverse of a Matrix. J. Soc. Ind. Appl. Math. B, 2(2), 205–224.

[11] Greitzer, E. M. (1976) Surge and rotating stall in axial flow compressors—Part I: Theoretical compression system model. J. Eng. Power, 98(2), 190-198.

[12] Greitzer, E. M., Moore, F. K. (1986) A theory of post-stall transients in axial compression systems: part II—application. Trans. ASME: J. Eng. Gas Turbines Power, 108(2), 231-239.

[13] Guckenheimer, J., Holmes, P. (1983) Nonlinear oscillations, dynamical systems, and bifurcations of vector fields. Springer-Verlag.

[14] Hastie, T., Tibshirani, R., Friedman, J. (2009) The elements of statistical learning: data mining, inference, and prediction. Springer Science & Business Media.

[15] Holmes, P., Lumley, J. L., Berkooz, G., Rowley, C. W. (2012) Turbulence, coherent structures, dynamical systems and symmetry. Cambridge University Press.

[16] Kingma, D.P., Ba, J. (2014) Adam: A Method for Stochastic Optimization. Proc. 3rd Intl. Conf. Learning Representations.

[17] Kunin D., Bloom J., Goeva A., Seed C. (2019) Loss Landscapes of Regularized Linear Autoencoders. Proc. 36th Intl. Conf. Machine Learning, 97, 3560-3569.

[18] Larochelle, H., Erhan, D., Courville, A., Bergstra, J., Bengio, Y. (2007) An empirical evaluation of deep architectures on problems with many factors of variation. Proc. 24th Intl. Conf. Machine Learning, 473-480.

[19] Li, M., Zhang, T., Chen, Y., Smola, A. J. (2014) Efficient mini-batch training for stochastic optimization. Proc. 20th ACM SIGKDD Intl. Conf. Knowledge Discovery and Data Mining, 661-670.

[20] Loève, M. (1978) Probability theory. Vol. II, 4th ed. Graduate Texts in Mathematics 46. Springer-Verlag.

[21] Mezić, I. (1998) A large-scale theory of axial compression system dynamics. Preprint.

[22] Moore, F. K., Greitzer, E. M. (1986) A theory of post-stall transients in axial compression systems: Part I—Development of equations. Trans. ASME: J. Eng. Gas Turbines Power, 108(1), 68-76.

[23] Mukherjee, A., Aydogdu, Y., Ravichandran, T., and Sri Namachchivaya, N. (2022) Stochastic Parameterization Using Compressed Sensing: Application to the Lorenz-96 Atmospheric Model. Tellus A: Dynamic Meteorology and Oceanography, 74(2022), pp.300–317.

[24] Namachchivaya, N. S., Doyle, M. M., Langford, W. F., Evans, N. W. (1994) Normal form for generalized Hopf bifurcation with non-semisimple 1:1 resonance. ZAMP, 45(2), 312-335.

[25] Penrose, R. (1955) A generalized inverse for matrices. Proc. Cambridge Philos. Soc., 51(3), 406–413.

[26] Plaut E. (2018) From Principal Subspaces to Principal Components with Linear Autoencoders. arXiv preprint, 1804.10253.

[27] Scholz M., Vigário R. (2002) Nonlinear PCA: a new hierarchical approach. Proc. ESANN, 439-444.

[28] Sirovich, L. (1987) Turbulence and the dynamics of coherent structures. I. Coherent structures. Q. Appl. Math., 45(3), 561-571.

[29] Tibshirani, R. (1996) Regression shrinkage and selection via the lasso. J. R. Stat. Soc. B, 58(1), 267-288.

[30] Xiao, M. (2008) Quantitative characteristic of rotating stall and surge for Moore–Greitzer PDE model of an axial flow compressor. SIAM J. Appl. Dyn. Syst., 7(1), 39-62.

[31] Xiao, M., Basar, T. (2000) Center manifold of the viscous Moore-Greitzer PDE model. SIAM J. Appl. Math., 61(3), 855–869.

Tuesday, July 19, 2022
08:30 - 10:30

MS-13 Nonlinear Dynamics in Biological Systems
Saint Clair 3A

Chair: Gert Van Der Heijden

08:30 - 08:50
3D FEM Model of Intact Human Middle Ear Compared to Lumped Mass Model and Experimental Results
ZABLOTNI Robert*, RUSINEK Rafal
*Department of Applied Mechanics, Lublin University of Technology, Poland (Nadbystrzycka 36, 20-618 Lublin, Poland Poland)

08:50 - 09:10
Computational model of Deep Brain Stimulation (DBS). Transitions from Healthy to Parkinsonian and DBS treatment.
SPILIOTIS Konstantinos*, STARKE Jens
*Institute of Mathematics, (Ulmenstraße 69, Haus 3 18057 Rostock Germany)

09:10 - 09:30
Cracking Down on Criminals: A Mathematical Model Expoloring Strategies for Curbing Criminal Behaviour
COMISSIONG Donna*, SOOKNANAN Joanna
*The University of the West Indies, St Augustine Campus, Trinidad (Department of Mathematics and Statistics, Faculty of Science and Technology, The University of The West Indies, St Augustine Campus, Trinidad, West Indies. Trinidad and Tobago)

09:30 - 09:50
Equilibrium Bifurcation Analysis of Nonlinear Biochemical Systems using Control-based Continuation and Model Predictive Control
DE Cesare Irene*, MARUCCI Lucia, RENSON Ludovic
*Engineering Mathematics Department [Bristol] (University of Bristol, Senate House, Tyndall Avenue, Bristol BS8 1TH, UK United Kingdom)

09:50 - 10:10
Forced Lotka-Volterra system for bone mechanobiology
SIMONOVIC Julijana*, WOOLLEY Thomas
*Faculty of Mechanical Engineering University of Nis, Serbia (A. Medvedeva 14, 18000 Nis Serbia)

3D FEM Model of Intact Human Middle Ear Compared to Lumped Mass Model and Experimental Results

Robert Zablotni[*], Rafal Rusinek[*]
[*]*Department of Applied Mechanics, Lublin University of Technology, Poland*

Summary. The human body can be considered by micro biomechanical systems and human middle ear is one of the smallest of those systems. In this abstract, finite elements method model and three degrees of freedom lumped mass model of human middle ear is proposed. Moreover in introduction it contains description of intact human middle ear.
Keywords: middle ear; stapes vibration; relaxation; ligaments modelling

Introduction

The human body can be considered as a set of micro biomechanical systems where human middle ear is one of the smallest of those systems. Human ear can be divided into three basic parts sequentially: external ear, middle ear and internal ear. Through auditory canal sonic waves reaches tympanic membrane which sets in motion three bones of a middle ear – the malleus, the incus and the stapes. The stapes transfers waves to the internal ear. Nest in semicircular canals mechanical vibrations are converted into nerve impulses. Over the years, many attempts have been made to create models of the human ear. The first study in this field was published in 1961 by Möller [1] where the first scheme of middle ear mechanism was proposed. Next, a similar model was investigated by Zwislocki [2]. In both publications, authors used an electrical circuit to analyse middle ear system. Currently, the most popular models of human ear are created by means of finite elements method, rarely as lumped mass models. Due to microscopic structure of human middle ear, examinations are extremely difficult. Moreover experimental studies must be carried out on the human temporal bone, therefore the amount of research is limited. For the above reasons, it is necessary to create models of the middle ear and their validation, because the tests carried out on them are limited only by the computing power of computers. Research on human ear models could lead to breakthroughs in the field of laryngology and otolaryngology.

Results and Discussion

The intact human middle ear lumped mass model is presented on Figure 1(a). There are three masses in the model: m_m, m_i and m_s. Each mass corresponds to one of the bones of the human middle ear: m_m – the malleus, m_i – the incus and m_s – the stapes. All masses are connected to each other by springs and dampers that correspond to joints, ligaments and tendons in s human middle ear. In this case presented here, the human middle ear with the Kelvin–Voigt type of viscoelasticity is used for analysing. Parameters as stiffness and damping coefficients of the middle ear used in numerical simulations were taken both from experimental validation and literature. Figure 1 (b) shows meshed Finite Elements Method (FEM) model of the intact human middle ear to compare numerical results. This model was created by Micro CT scanning of the human middle ear. Three bones: the malleus, the incus and the stapes and the eardrum was separated and then they have undergone a scanning procedure. Parts that were obtained were connected in Computer Aided Design (CAD) software. Moreover simplified ligaments and tendons were created in CAD and were connected to the bones. At the end, a simplified cochlea and oval window was made in order to connect the stapedial annular ligament (SAL). Material data for the Finite Elements Model of intact human middle ear was taken from the literature [4].

(a) (b)

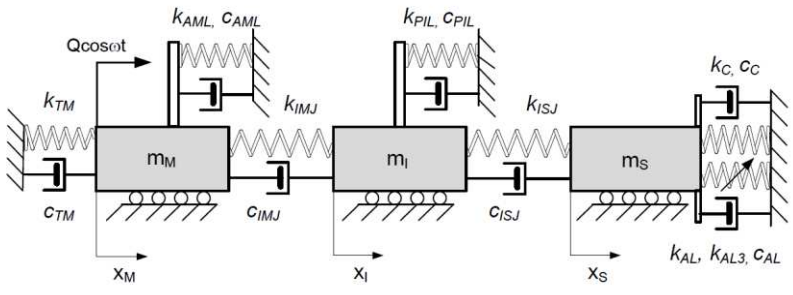

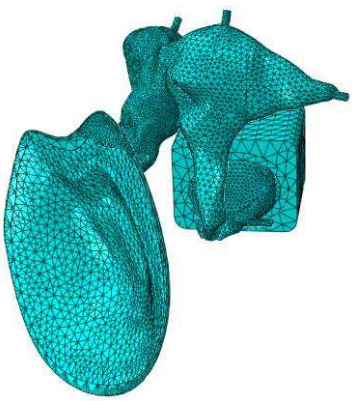

Figure 1: Models of intact human middle ear. (a) 3 degrees of freedom (dof) lumped mass model [3], (b) finite elements method model.

The most demanding aspect of Finite Elements Method modelling was setting the mesh in such a way that the objects do not interpenetrate during the simulation of motion. The next difficulty is determining the time of stabilization for the

system. Another demanding task is to set appropriate boundary conditions of the system which allow proper reproduction of the occurring movements in the middle ear as a result of being forced by an acoustic wave onto the eardrum. The FEM model is compared with the experiment results to assess its correctness .

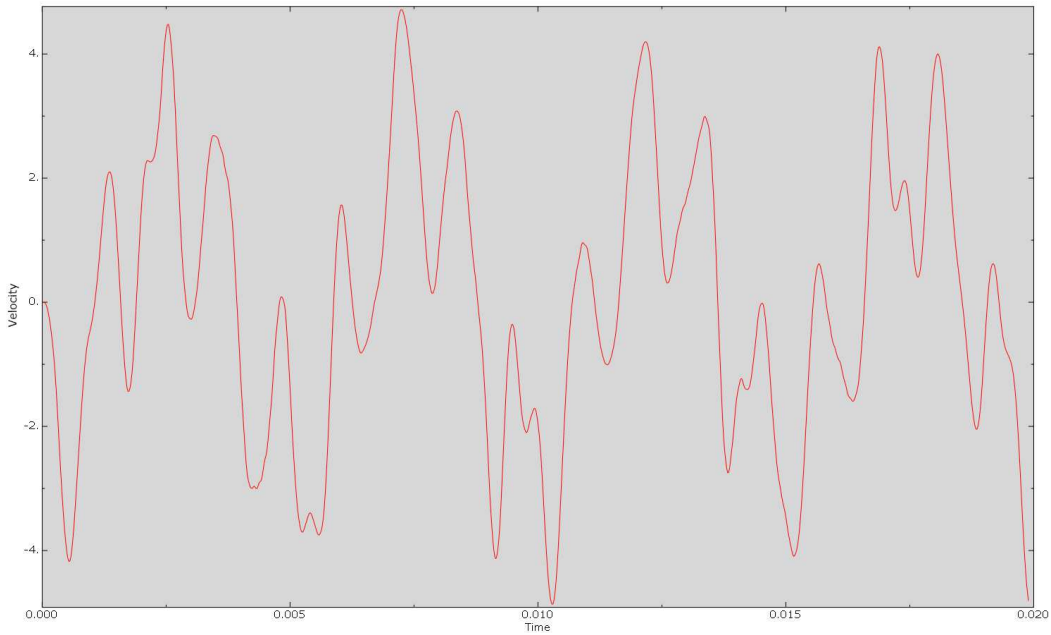

Figure 2:Function of velocity versus time measured on stapes footplate for not-steady state of vibrations in Finite Elements Method model of intact human middle ear for the frequency equal to 200Hz.

In Figure 2, function of velocity versus time for not-steady state of vibrations of human middle ear in FEM model can be observed. For the undefined Rayleigh damping parameters for human middle ear the rumble phenomenon can be observed. By using the appropriate damping parameters velocity of the stapes can be obtained and compared to the experimental data.

Conclusion

A novelty in the Finite Elements Method model is obtaining parts by the Micro CT scanning, which gives an accurate representation of the geometry of the bones of the human middle ear. On the basis of the lumped mass model of intact human middle ear and experimental results, correctness of the FEM model is approved. For the FEM model of the human middle ear, the appropriate material parameters and the Rayleigh's damping parameters allow to shorten the calculation time and obtain results with a similar value to the results obtained experimentally. In the future FEM model will be used to develop model of the middle ear with active implant.

Acknowledgment:

The research was financed in the framework of the project Nonlinear effect in middle ear with active implant, no.2018/29/B/ST 8/01293, funded by the National Science Centre, Poland.

References

[1] Moller A.R. (1961) Network Model of the Middle Ear. *Journal of the Acoustical Society of America* **33**:168–176.
[2] Zwislocki, J. (1962) Analysis of the Middle-Ear Function. Part I: Input Impedance. *Journal of the Acoustical Society of America* **34**:1514–1523.
[3] Rusinek R., Szymanski M., Zablotni R. (2020) Biomechanics of the Human Middle Ear with Viscoelasticity of the Maxwell and the Kelvin–Voigt Type and Relaxation Effect. *Materials* **13(17)**:1-15
[4] Zhou K., Hougang L., Yang J., Zhao Y., Rao Z., Yang S. (2019) Influence of middle ear disorder in round-window stimulation using a finite element human ear model. *Acta of Bioengineering and Biomechanics* **21(1)**:3-12.

Computational model of Deep Brain Stimulation (DBS). Transitions from Healthy to Parkinsonian and DBS treatment.

Konstantinos Spiliotis*, Jens Starke *
*Institute of Mathematics, University of Rostock, D-18057 Rostock, Germany

Summary. The basal ganglia network plays an important role in the movement and emotional control. Changes in the structure and dynamics of the network are closely related to pathological disorders (Parkinson, Dystonia, Depression etc). We developed a large scale biophysical neuronal model in order to study the effect of Deep Brain Stimulation (DBS) in Parkinson and Dystonia. The neural network model consists of 4 major areas of basal ganglia, Globus Pallidus External and Internal (GPE)-(GPI), Subthalamic nucleus (STN) and Thalamus. By changing several model parameters related to the synaptic weights, as well as the frequency of external DBS stimulus, the model switches the dynamics from normal to pathological (Parkinson-Dystonia) to DBS treatment behavior. Combining both, numerical bifurcation analysis and Equation Free Methodology (IEFM), we detect systematically in the parametric space, the dynamical regimes of different dynamics.

Introduction

Deep Brain Stimulation (DBS) consists a revolutionised treatment for movement and mental disorder. After 1997 when the Food and Drug Administration (FDA, USA) approved DBS as a treatment for tremor, the development was rapid including several diseases (Parkinson, Dystonia, Epilepsy) but also mental Disorders (Depression and Obsessive-Compulsive Disorder)[1]. Even in our days then main mechanism behind this treatment remain mysterious. One of the main obstacles is the lack of one coherent framework which joins the different levels-scales of mechanism ranging from microscopic (neurophysiology and genetic variations of the neurons), to macroscopic (i.e. tremor and dyskinesia). An intermediate level, the mesoscopic, is related with dynamics of specific networks of neurons in different nucleus of BG. The dynamics of these networks constitute the bridge of micro and macro behaviour since are affected from the neuron's properties and the emergent patterns which arise define the macroscopic action. In this spirit we propose a computational large-scale biophysical model related to the Parkinson Disease (PD) and DBS treatment. Based on the work presented in [2, 3] we model 4 areas of the Basal Ganglia (BG); the Globus Pallidus External and Internal (GPE-GPI) the Sub-Thalamic Nucleus (STN) and the Thalamus. We show how the variations in the synaptic weights connectivity between the BG areas affects the macroscopic dynamics, switches from normal to PD and how the DBS on the STN acts as a treatment affecting the whole network. In addition, during DBS the model reveals a de-synchronization of the GPI activity which is projected to Thalamus. Combining both, numerical bifurcation analysis and Equation Free Methodology (EFM) [4] and Implicit Equation Free Methodology [5] for multiscale modelling, we detect systematically in the parametric space, the dynamical regimes of different dynamics. Main parameters are the connectivity weights and frequency of DBS.

Description of the Basal Ganglia Network

All BG regions follow the Hodgkin Huxley current balanced formalism. The STN neurons follow the equation [2]

$$C\frac{dV_i}{dt} = -I_{Ca} - I_{Na} - I_K - I_T - I_L - I_{AHP} - I_{GS} - I_{SS} + I_{DBS} \tag{1}$$

where C is the membrane capacity, I_{Ca}, I_{Na}, I_K are the ionic currents, I_L is the leak current, I_{AHP} and I_T are the after hyperpolarized and T currents which are depended on the calcium concentration. The postsynaptic currents $I_{SS} = g_{SS}(V - V_S)\sum_j s_j$ and $I_{GS} = g_{GS}(V - V_G)\sum_j s_j$ correspond to internal STN excitation and inhibition from GPE respectively. The s_i is the activation variable [2, 3] and the summation is taken over the presynaptic neurons. The GPE-GPI neurons follow similar current balance equation

$$C\frac{dV_i}{dt} = I_{app} - I_{Ca} - I_{Na} - I_K - I_T - I_L - I_{AHP} - I_{SG} - I_{GG} \tag{2}$$

where the currents are defined in the same way as the STN [2]. I_{app} represents the input current from the striatum and has the same constant value for all GPE neurons. Finally the Thalamic neurons follows the equation

$$C\frac{dV_i}{dt} = I_L - I_{Ca} - I_{Na} - I_K - I_T - I_L - I_{GiTh} + I_{SM} \tag{3}$$

where the I_{SM} describes the input from sensory motor cortex. The detailed form of the currents and the values of parameters are described in [2].
The STN and GPE areas include N=500 neurons each while the GPi and Thalamus consist of N=200 neuron. For each area we use a small world of network with $k = 10$ and $p = 0.01$[6]. The interconnections between different layers are 1-1 i.e. one STN neuron is adjacent with one GPE neuron and one GPI neuron communicate with one thalamic neuron. A representative image is depicted in Fig.1.

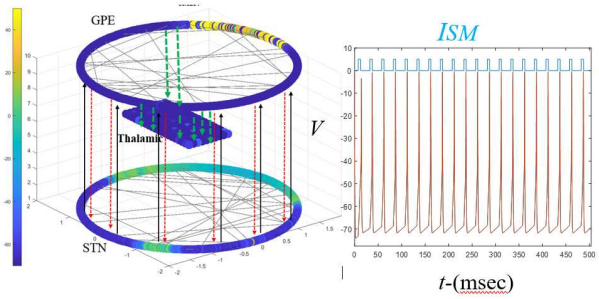

Figure 1: Illustrative image of the whole BG network. Different areas are depicted as small world network. (b) Dynamics of Thalamic neurons under the external input which comes from sensory motor cortex.

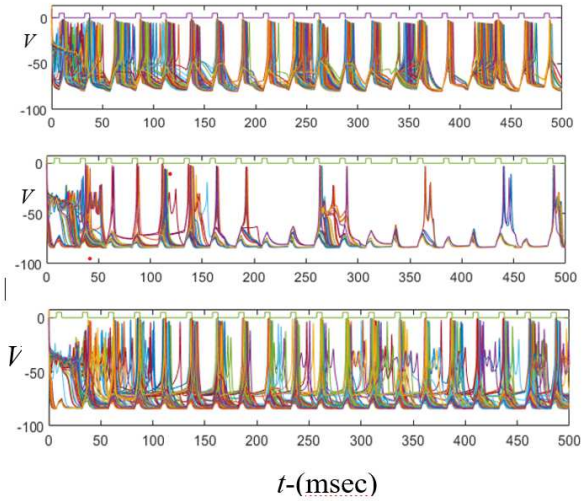

Figure 2: Dynamics of the Thalamics neurons in normal case(first row). During the PD (middle row) and finally under the DBS treatment.

Results

We investigate the dynamics with respect the connectivity weights between the GPI and thalamus. For small value of inhibition g_{GiTh} the thalamic neurons reacts in rights way to external sensory motors inputs see Fig 2. For higher value of g_{GiTh} i.e. higher inhibition, thalamus produces Parkinsonian behaviour: ineffective response to external sensory motor input, while with DBS on and with same connectivity parameters as the PD behaviour, the model shows dynamics close to normal case: The thalamus after transient period, reacts similar (approximately) to healthy normal case see Fig.2. In order to analyse the emergent dynamics we will perform numerical bifurcation analysis, under the Equation Free Methodology [5]. The macroscopic variables are the mean values of the membrane voltage of the four areas.

References

[1] Pycroft L, Stein J., Aziz T. (2018) Deep brain stimulation: An overview of history, methods, and future developments. *Brain and Neuros. Advances* **2**:1-6.

[2] Rubin J., Terman D. (2004) High frequency stimulation of the subthalamic nucleus eliminates pathological thalamic rhythmicity in a computational model. *J Comput Neurosci.* **16**(3):211-235.

[3] Ermentrout B., Terman D.(2012) Neural networks as spatio-temporal pattern-forming systems. Mathematical Foundations of Neuroscience, Vol. 35 Spriner, New York.

[4] Kevrekidis et al. (2003) Equation-free, coarse-grained multiscale computation: Enabling mocroscopic simulators to perform system-level analysis. *Communications in Mathematical Sciences* **1**(4): 715-762.

[5] Marschler C, Sieber J., Berkemer R., Kawamoto A., Starke J. (2014)Implicit Methods for Equation-Free Analysis: Convergence Results and Analysis of Emergent Waves in Microscopic Traffic Models.*SIAM J. Appl. Dyn. Syst.* **13**(3): 1202–1238.

[6] Watts D., Strogatz S. (1998) Collective dynamics of 'small-world' networks. *Nature* **393**: 440.

Cracking Down on Criminals: A Mathematical Model Expoloring Strategies for Curbing Criminal Behaviour

Joanna Sooknanan and Donna M. G. Comissiong
Department of Mathematics and Statistics, The University of the West Indies, St Augustine Campus, Trinidad, West Indies

Summary. Criminal behaviour is a rapidly growing challenge internationally. Policy makers are usually charged with developing strategies to control its spread - while limited by financial constraints. With the use of a model adapted from epidemiology, control strategies in the form of time dependent prevention and treatment efforts to curtail the spread of criminal behaviour may be evaluated. The first control strategy applied encourages potential criminals away from a life of crime while the second strategy targets criminals. We find that a combination of strategies leads to the biggest reduction in the number of criminals and of potential criminals. To be effective, strategies based on single controls require the implementation of more intensive efforts at the start of the control effort.

Extended Abstract

One of the greatest social challenges plaguing many countries nowadays is that of criminal behaviour and its ensuing prevention and reduction. Violent crime can have a negative effect on a countrys economy in a variety of ways. These include reduced economic growth, a decline in tourism, increased emigration in conjunction with a resulting brain drain, a reluctance to invest locally by foreign investors and a general feeling of fear and insecurity by the population. This is compounded when limited resources are available to policy makers. Especially in such instances, whatever measures are used must be cost effective.

An innovative approach to tackling crime that is rapidly gaining popularity is to consider criminal behaviour as an infectious disease and then to use a public health approach to mitigate its spread [1, 2]. This approach may also be used when designing strategies to prevent or disrupt the contagion process, which may then be tested using mathematical models from epidemiology - compartmental models.

Optimal control theory has been implemented to study strategies for the treatment of many diseases including waterborne diseases, HIV, Ebola, Dengue and Pandemic Influenza. In recent times [3], modelling of behaviour using an infectious disease approach has been done for fanatical and violent ideology, violent crime and burglary and gang membership. Our paper deals with the application of optimal control to a dynamic model of criminal behaviour treated as an infectious disease. Our aim is to find the best strategy in terms of combined efforts of prevention and treatment that would minimize the total number of criminals and its cost.

Model Formulation

The population under consideration $N(t)$ consists of people who are "at risk"for engaging in or have engaged in criminal behaviour. N is divided into four disjoint compartments/classes based on status with respect to criminal behavior. These are:

P : Members of the population who are susceptible to criminal behaviour - Potential Criminals.

C : Members of the population who are engaged in criminal behaviour - Criminals.

J : Members of the population who are in prison or in a juvenile delinquency centre.

R : Members of the population who were in an prevention or treatment program and have permanently left life of crime - Recovered people.

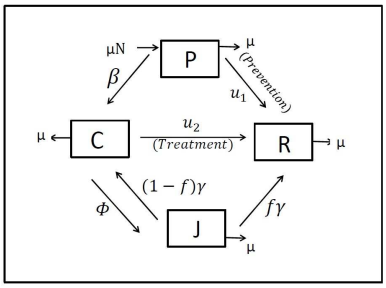

Figure 1: Model Diagram

We consider two separate control programs $u_1(t)$ and $u_2(t)$ applied to the P and C subgroups with the goal of "recovery". These represent programs or strategies which encourage positive behaviour change and include programs designed by the government as well as outreach programs by social service groups, neighbourhood organizations, and the faith community.

The first control strategy $u_1(t)$ is applied to potential criminals P who may become criminals by interaction with criminals C at the rate $\frac{\beta CP}{N}$. However, since a prevention control scheme is applied to the P class, $u_1(t)P$ individuals progress to the recovered class R. Individuals in the criminal class may enter a treatment control program at the rate $u_2(t)$ or go to jail at the rate ϕ. On release from jail, a fraction $(1-f)$ re-join the criminal class and the remainder enters the recovered class at a rate of $f\gamma$ where γ^{-1} represents the time spent in jail. For ease of analysis purposes, we assume a constant size population N with an entry and death rate into the population given by μ. The rate of entry into the system is proportional to the population size and is given by μN. Figure 1 shows the structure of flows within the model which is described by the following set of nonlinear differential equations:

$$P' = \mu N - \frac{\beta CP}{N} - u_1(t)P - \mu P \tag{1}$$

$$C' = \frac{\beta CP}{N} + (1-f)\gamma J - u_2(t)C - \phi C - \mu C \tag{2}$$

$$J' = \phi C - \gamma J - \mu J \tag{3}$$

$$R' = u_1(t)P + u_2(t)C + f\gamma J - \mu R \tag{4}$$

$$N = P + C + J + R \tag{5}$$

Model Analysis – Equilibria and Stability

We study the existence and stability behaviour of the system at its equilibrium points. Two possible equilibrium states are found – the criminal-free equilibrium where the system only consists of potential criminals and the coexistence equilibrium. Coexistence (or endemic) equilibrium points are steady-state solutions where the disease "criminality"persists in the population.

The issue of whether or not a disease can invade a host population and persist or remain endemic involves the introduction of a threshold known as the basic reproductive number R_0. In our model, R_0 represents the average number of potential criminals who are recruited to the criminal class c. If $R_0 < 1$, then the criminal-free equilibrium is locally asymptotically stable. If $R_0 > 1$, then the criminal-free equilibrium is unstable, and the introduction of a criminal will result in an outbreak. In the early stages of a crime outbreak, R_0 is the key quantity of interest, and our goal is to identify mitigation strategies to reduce it below the threshold $R_0 = 1$.

Formulation of the Optimal Control Problem

Our first control strategy ($0 \leq u_1(t) \leq 1$) includes programs and practices that target individuals who have an elevated risk for becoming criminals. The second control strategy ($0 \leq u_2(t) \leq 1$) includes programs to treat criminals. Our goal is to minimize the number of criminals while at the same time minimizing the cost of controls $u_1(t)$, $u_2(t)$ over a time period T given the initial population sizes of all three classes $p(0)$, $c(0)$ and $j(0)$. Thus, we are seeking the optimal control pair $(u_1^*(t), u_2^*(t))$ so that

$$J(u_1^*, u_2^*) = min\left\{J(u_1, u_2) : (u_1, u_2) \in U\right\} \tag{6}$$

where the Lebesgue measurable control set U is defined as

$$U = \{u_1(t), u_2(t) : 0 \leq u_1 \leq 1, 0 \leq u_2 \leq 1, t \in [0, T]\} \tag{7}$$

subject to the model equations.

The objective functional is defined as

$$J(u_1, u_2) = \int_0^T \left[Kc(t) + \frac{B_1}{2}u_1^2 + \frac{B_2}{2}u_2^2\right] dt \tag{8}$$

where B_1 and B_2 are the relative weights attached to the cost or effort required (human effort, material resources, infrastructural resources etc.) to implement each of the control measures. K measures the comparative importance of the criminal burden relative to the control costs. Pontryagin's maximum principle [4] is used to solve this optimal control problem numerically using the backward-forward sweep method [5, 6] with the initial conditions given in [7] and reasonable estimates for the model parameters.

References

[1] Patel D. M., Simon M. A., Taylor R. M., et al. (2013) *Contagion of Violence: Workshop Summary*. National Academies Press.

[2] Slutkin G. (2017) Reducing Violence as the Next Great Public Health Achievement. *Nature Human Behaviour* **1:0025**.

[3] Sooknanan J., Comissiong D. M. G. (2017) When Behaviour Turns Contagious: The Use of Deterministic Epidemiological Models in Modeling Social Contagion Phenomena. *International Journal of Dynamics and Control* **5(4)**:1046-1050.

[4] Pontryagin L. S., Boltyanskii V. T., Gamkrelidze R. V. & Mishcheuko E. F. (1962) The Mathematical Theory of Optimal Processes. Wiley.

[5] Lenhart S., Workman J. T. (2007) Optimal Control Applied to Biological Models. CRC Press.

[6] Rodrigues H. S., Monteiro M. T. T., Torres D. F. M. (2014) Optimal Control and Numerical Software: An Overview *arXiv preprint arXiv:1401.7279*.

[7] Sooknanan J., Bhatt B. S., Comissiong D. M. G. (2012) Life and Death in a Gang - A Mathematical Model of Gang Membership. *Journal of Mathematics Research* **4(4)**:10-27.

Equilibrium Bifurcation Analysis of Nonlinear Biochemical Systems using Control-based Continuation and Model Predictive Control

Irene de Cesare*, Lucia Marucci*,+ and Ludovic Renson †,+
*Engineering Mathematics Department, University of Bristol, UK.
†Department of Mechanical Engineering, Imperial College London, UK.
+ Co-senior and co-corresponding authors; l.renson@imperial.ac.uk; lucia.marucci@bristol.ac.uk

Summary. Control-based continuation (CBC) is a testing method that maps the nonlinear dynamic features of a physical system directly from experiments. The application of CBC has been so far limited to electro-mechanical systems. In this paper, we numerically investigate the application of CBC to a synthetic gene network, the toggle switch. The network's behaviour is simulated using a nonlinear model (with and without noise), and model predictive control (MPC) is exploited to control its dynamics, through the definition of an appropriate control objective function. Our preliminary results show that MPC-based CBC can accurately capture the continuation curve obtained numerically on the full nonlinear model.

Introduction

Mathematical modelling is widely used in System and Synthetic Biology to understand nonlinear biochemical phenomena (e.g. gene expression temporal oscillations), and to design and validate engineered gene circuits. Although widely used, biochemical models can be challenging in both their derivation and associated parameter identification [1, 2]. Parameter and model uncertainty can significantly alter the reliability of model predictions of nonlinear dynamic behaviours.
The application of control-based continuation (CBC) to biological systems, not attempted to date, has the potential to overcome these difficulties, improving the understanding of naturally-occurring nonlinear biochemical dynamics (e.g. oscillations in signalling pathways) and enabling the rapid prototyping of engineered gene regulatory network dynamics. CBC is a non-parametric method that combines feedback control with principles of numerical continuation to map out the dynamic features of a nonlinear physical system directly during experimental tests [3]. The fundamental principles of CBC are well established and the method has been applied to a wide range of non-living (i.e. electro-mechanical) systems [4, 5]. In this contribution, we investigate the use of CBC to detect and track the equilibria of the toggle switch, an engineered genetic circuit [6]. Model-predictive control (MPC), previously exploited to control biological systems [7], is employed to steer the system's dynamics towards steady-state and stabilise unstable responses of the underlying uncontrolled system.

Control-Based Continuation of a synthetic toggle switch's dynamics

We investigate the application of CBC on a toggle switch, one of the first and best characterised synthetic gene network implemented to date in living bacterial cells [6, 8]. The gene network consists of two repressors ($LacI$ and $TetR$) and two inducers (Atc and $IPTG$). Each repressor affects the opposite gene's production, which can be externally tuned through the addiction of chemical inducers. Levels of $LacI$ and $TetR$ can be observed thanks to fluorescent reporters (Figure 1A). The associated deterministic model is mathematically described by a set of four nonlinear differential equations taking into account mRNA transcription and translation of both repressors. For the stochastic scenario, a SDE model for the description of biochemical systems based on pseudo-reactions is considered [9].
We chose Model-Predictive Control (MPC) as control strategy to implement CBC; this method combines state estimation, model prediction and optimization algorithms to find the optimal actuation to apply to a system. At each time step i, the choice of the optimal sequence of N control inputs is based on the minimization of the cost function

$$J_i = \sum_{k=1}^{N} (N-k+1)e(i+k)^2, \tag{1}$$

where the error $e(i+k)$ is defined as the difference between the control target and the prediction of the system's response over N samples. The system response to a particular sequence of control inputs is predicted by integrating in time a linear model of the system. This linear model was identified prior to closed-loop simulations using input-output *in-silico* data and time-domain subspace algorithms. At each time step i, the initial conditions required to initialise simulations are obtained using a Kalman filter that was also derived during the linear identification process. When an optimal sequence of inputs is found, only the actuation for the next time step is applied to the system. This whole optimization process is repeated at each actuation time step i.
Cost function (1) usually includes an additional term to balance tracking performance and control effort. This term is not considered here but replaced by optimization constraints limiting the control action u at time step i to be no more than 30% different from the control action at time step $i-1$.
The inducer $IPTG$ is considered to control the toggle switch's dynamics. IPTG regulates the expression of a fluorescent reporter gene, which is a proxy for the $TetR$ concentration (see Fig. 1A). The controller based on the optimization of Eq. (1) with constraints allows to reach any meaningful value of the $TetR$ concentration. At steady state, the value of the control input ($IPTG$) can be interpreted as the bifurcation parameter [10]. Recording $IPTG$ for a range of target

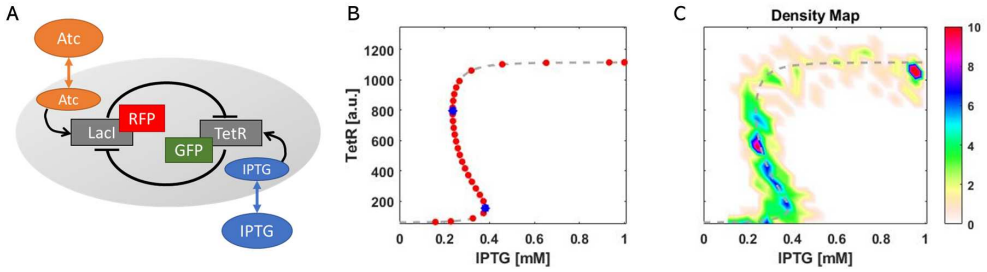

Figure 1: MPC-based CBC of a synthetic toggle switch. A) Schematic representation of the toggle switch, adapted from [6], where RFP and GFP represent the fluorescent proteins binding with $LacI$ and $TetR$. B) CBC results and numerical continuation bifurcation diagram (COCO software) are shown as red points ● and a dotted line (——), respectively; blue points ● design the bifurcation points. $IPTG$ is the inducer, used as bifurcation parameter. C) CBC results on the stochastic model are represented as a density plot: 10 repetitions of the same experiment are run and 300 points are collected.

concentrations, the equilibrium curve of the uncontrolled toggle switch can be traced out. Fig. 1B shows the excellent agreement obtained between bifurcation diagram computed using standard numerical continuation algorithms (dashed line) and CBC results (red dots). Saddle-node bifurcations are highlighted in blue in Fig. 1B. For the stochastic case, multiple simulations are considered and 300 points are collected (Fig. 1C).

Conclusions

This paper investigates the use of CBC for tracking the equilibrium of synthetic gene regulatory networks. Our preliminary *in silico* results demonstrate the feasibility of the approach and the ability of CBC to capture both the stable and unstable behaviours of the original, uncontrolled system. In particular, in the absence of noise, the equilibrium curve measured using CBC perfectly agrees with the one computed using standard numerical continuation. In the stochastic scenario, CBC is still able to uncover the bistable nature of the system as data points qualitative follow the equilibrium curve of the underlying deterministic model. Unstable steady states collected using CBC also prove to be beneficial when estimating model parameters that reproduce bistability. The introduction of CBC to characterise cellular dynamics could benefit both the System and Synthetic Biology communities, providing a valuable tool to explore complex nonlinear dynamics and to gather important information that can eventually enable a more precise prototyping of those dynamics into novel synthetic gene circuits. The application of CBC to biochemical experiments could be done using microfluidics/microscopy platforms for real-time monitoring and control of gene expression in living cells via dynamic modulation of inducer molecules [11].

Acknowledgements

IdC is supported by an EPSRC DTP Scholarship. LM is supported by the Medical Research Council grant MR/N021444/1, by the Engineering and Physical Sciences Research Council grants EP/R041695/1 and EP/S01876X/1, and by the European Union's Horizon 2020 under Grant Agreement No. 766840. LR is funded by a Research Fellowship from the Royal Academy of Engineering (RF1516/15/11).

References

[1] Marucci, L. (2017). Nanog dynamics in mouse embryonic stem cells: results from systems biology approaches. Stem cells international.

[2] Banga J. R.(2008). Optimization in computational systems biology. BMC systems biology.

[3] Sieber, J., Krauskopf, B. (2008). Control based bifurcation analysis for experiments. Nonlinear Dynamics, 51(3), 365-377.

[4] Renson L., Barton D.A., Neild S.A. (2017). Experimental tracking of limit-point bifurcations and backbone curves using control-based continuation. International Journal of Bifurcation and Chaos.

[5] Renson L., Shaw A. D., Barton, D. A. W., Neild, S. A. (2019). Application of control-based continuation to a nonlinear structure with harmonically coupled modes. Mechanical Systems and Signal Processing.

[6] Lugagne J.B., Carrillo S.S., Kirch, M., Köhler, A., Batt, G., & Hersen, P. (2017). Balancing a genetic toggle switch by real-time feedback control and periodic forcing. Nature communications, 8(1), 1671.

[7] Postiglione L.; Napolitano S.; Pedone E.; Rocca D. L.; Aulicino, Francesco; Santorelli, Marco; Tumaini, Barbara; Marucci, Lucia; di Bernardo, Diego. (2018). Regulation of gene expression and signaling pathway activity in mammalian cells by automated microfluidics feedback control. ACS synthetic biology.

[8] Gardner T.S., Cantor C.R., Collins J.J. (2000). Construction of a genetic toggle switch in Escherichia coli. Nature.

[9] Lakatos, E. (2017). Stochastic analysis and control methods for molecular cell biology.

[10] Barton D. A., Sieber J. (2013). Systematic experimental exploration of bifurcations with noninvasive control. Physical Review E, 87(5), 052916.

[11] Menolascina F., Fiore G., Orabona E., De Stefano L., Ferry M., Hasty J., ... & di Bernardo, D. (2014). In-vivo real-time control of protein expression from endogenous and synthetic gene networks. PLoS computational biology, 10(5), e1003625.

Forced Lotka-Volterra System for Bone Mechanobiology

Julijana Simonović[*], Thomas Woolley[**]
[*]*Faculty of Mechanical Engineering University of Niš, Serbia* [**] *Cardiff School of Mathematics, Cardiff University, United Kingdom*

Summary. The architecture and quality of bone tissue in an adult organism predominantly depends on bone cellular organisation and communication processes that are highly driven by external mechanical loading. How physical forces and changes in the mechanical properties of cells and tissues contribute to development, cell differentiation, physiology, and disease, in general, is a major interest of mechanobiology. This paper outlines how mathematical models can help to improve current understanding of bone cellular mechanobiology. Here we introduce an adapted mathematical model for bone remodeling in the form of generalized S-system equations (Lotka-Volterra system) of fifth order that includes periodic received and transduced signal of external loading. Critically, we approach the modelling through both deterministic and stochastic methods, which allow us to consider the intrinsic noisiness of the process.In particular, this model includes osteocytes mechanobiology, which, apart from their biochemical processes and their interactions with other bone remodeling cells, includes external periodic signal transduction and influence that represents a significant advance to the field.

Background and Aims

The bone cell lineages are permanently active in the process of bone remodelling that resorbs old and forms the new content of bone. These activities happen on the daily base with a progression of several micrometres of local bone turnover. The bone architecture and quality depend on many biological, biochemicals, hormonal and physical factors among which external static and dynamic loading play an important role. The bone adaptive mechanobiological processes are governed by the osteoblasts (OBs), osteoclasts (OCs), and osteocytes (OcYs) cells working in concert, all capable of transducing mechanical strain signals into biochemical cues for osteogenesis [1]. However, Osteocytes (OcYs) in particular have been shown in vitro to be the most mechanosensitive bone cell type, demonstrating a higher intrinsic sensitivity to loading than other osteogenic cells. They have also recently been shown to direct osteogenesis in other bone cell types, reinforcing the theory that osteocytes sense mechanical loading in the bone matrix and then orchestrate the adaptive bone remodeling response [2]. Owing to their presence deep within bone matrix, direct experimental observation of osteocytes in vivo has proven extremely challenging. As such, the precise mechanical stimuli, which they experience in vivo, and the mechanisms whereby they sense and transmit these stimuli, remain unknown. Although it is possible to mechanically stimulate bone and quantify the tissue-level changes that occur, it is still extremely challenging to simultaneously delineate the cellular and molecular mechanisms that give rise to these changes. Further, the complexity of the skeletal processes and their interactions with the rest of the body limits the ability of a single biological model to capture all of the relevant biological, biochemical, and biophysical mechanisms of remodelling on all scales simultaneously. Moreover, the parameterization of an established accompanying mathematical model is difficult, given its dependency on the accuracy and availability of data. However, in-silico experiments on established mathematical model reveal important features of nonlinear connections between variables and dependency on parameters of the system. In many cases, the quality of a scientific field depends on how well the mathematical models, developed on the theoretical side, agree with the results of repeatable experiments. Lack of agreement between theoretical mathematical models and experimental measurements often leads to important advances as better theories are developed. With this research, we wish to emphasize the importance, reliability and credibility of mathematical models as a great way of cementing biological intuition. Specifically, they provide causative mechanisms linking inputs and outputs, thereby illuminating underlying assumptions that determine a biological system's dynamics. Finally, they offer a means of predicting new outcomes, as well as highlighting the most sensitive modelled components, resulting in the construction of new experimental hypotheses and more focused experimentation.

Methods and mathematical models

To address the question of how different bone cells interact with each other and the bone microenvironment during remodelling, several cell population models have been proposed in Refs. [3-6]. These types of models are able to monitor changes in cell numbers and bone volume over time and they all modelled the free dynamics of the bone cell system. The formalism of a cell population model can be generalised to be of the form of a S-System of equations of nth order that corresponds to the number of included cellular lineages,

$$\frac{du_i}{dx} = \alpha_i \prod_{j=1}^{2} u_j^{g_{ij}} - \beta_i u_i, i = 1, 2, \dots, n. \qquad (1)$$

If we include OcY, OB, OC and preosteoblastic (pOB) lineages of cells together with a bone mass equation it will be system of 5th order ($n = 5$). System (1) is a homogeneous system of coupled ordinary nonlinear differential equations that is more specifically. In one cycle of targeted remodeling the number of activator cells, both resorbing and forming, is bounded above by approximately 10 OCs and up to 300 OBs, so that in the dynamics of the system (1) the number of OCs drops below one, which occurs frequently. Of course, since we are dealing with exact numbers of cells, such a measurement is unrealistic.

Critically, the problem stems from the direct use of differential equations that assume a modelled population is large enough, for a continuum hypothesis to approximately hold. This hypothesis is obviously invalid at such small population sizes. Thus, for such low numbers of cells it is more correct to produce a discrete interaction model. Specifically, we use a stochastic analogue to simulate the creation and degradation, which encapsulates the noisy features of individual cell division and death [7-9]. From system (1) we are able to extract the stochiometric creation and degradation relations, and present its probabilistic analogue:

$$\emptyset \xrightarrow{\alpha_i u_i u_j} u_i, u_i \xrightarrow{\beta_i} \emptyset, i = 1, 2, \dots, n \text{ and } j \neq i. \qquad (2)$$

Although parameter values exist in the literature they are mainly approximate and are proposed to simplify and justify the model. Further, in all of the literature it is assumed that the γ_{ij} parameters are constant. However, in real bone remodelling processes the γ_{ij} parameters may depend on time and other factors. Unfortunately, these parameters cannot be directly measured and have to be estimated. Based on these recent biological experimental findings we introduce the modification of the model by editing the power low term γ_{31} to time dependent oscillatory function $\gamma_{31}(1 + \sin(\theta t))$, what represent transduced signal of OcY, and inserting the mechanical periodic excitation $A(1 - \cos(\theta t))$ to the responding OcYs.

Results & Discussion

We find that the model can capture the essential autocrine, paracrine and synergistic characteristics of bone cell communication processes in response to the external incentives. Specifically, including oscillatory signals with small delays between received and send a signal by OcY provides the closest matches between mathematical data and biology theory. This can be seen from Fig. 1 where after the period of resorption, the depression of green z line below zero, come the significant changes in the activation of osteoblasts (yellow B line) that results in formation period, the green line above the zero. Comparing with the green line at Fig 1 a) that has no over formation above steady-state value $z_{ss} = 100$. We prove that under the influence of the external periodic signal the local formation of the newly remodelled bone will exceed the amount of resorbed old bone.

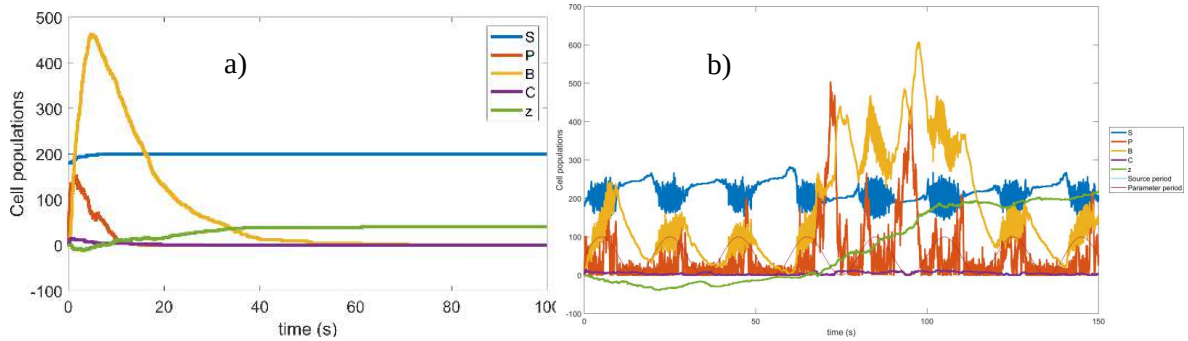

Figure 1: One cycle of bone remodeling: a) free cell communication; b) periodically forced dynamics with external periodic source and parameter γ_{31} out of synchronization by a factor of $\pi/2$, all parameter values are taken from [6] except $k_2 = 0.014$

Conclusions

The results of our research highlighted the importance of the external excitation and mechanotransduction of the signal by the bone cell in the regular bone turnover. The in-silico experiments with forced Lotka-Volterra system of population equations pinpointed the importance of nonlinear deterministic and stochastic analysis in the field of mechanobiology.

References

[1] Giorgi, M., Verbruggen, S. W., & Lacroix, D. (2016). In silico bone mechanobiology: modeling a multifaceted biological system. *Wiley Interdisciplinary Reviews: Systems Biology and Medicine*, *8*(6), 485–505. https://doi.org/10.1002/wsbm.1356;

[2] Bonewald L. Osteocytes: a proposed multifunctional bone cell. J Musculoskelet Neuronal Interact 2002, 2:239.

[3] Simonovic J., (2019), *Simultaneous multi-parametric analysis of bone cell population model*, NODYCON2019 Proceedings, Editors: Prof. B. Balachandran (University of Maryland), Prof. J. Ma (Lanzhou University of Technology), Prof. J.A.T. Machado (Polytechnic Institute of Porto), Prof. G. Stepan (Budapest University of Technology and Economics), and Prof. W. Lacarbonara (Sapienza University of Rome), Springer Conference, *pp.*----, *ISBN*---- accepted for publishing (Dec. 2019)

[4] Pivonka, P., & Komarova, S. V. (2010). Mathematical modeling in bone biology: From intracellular signaling to tissue mechanics. *Bone*, *47*(2), 181–189. https://doi.org/10.1016/j.bone.2010.04.601

[5] Jerez, S. and Chen, B., (2015). Stability analysis of a Komarova type model for the interactions of osteoblast and osteoclast cells during bone remodeling. Math. Biosci., 264, pp.29-37.

[6] Graham, J. M., Ayati, B. P., Holstein, S. A., & Martin, J. A. (2013). The Role of Osteocytes in Targeted Bone Remodeling: A Mathematical Model. *PLoS ONE*, *8*(5), 10–14. https://doi.org/10.1371/journal.pone.0063884

[7] Van Kampen, Nicolaas Godfried. *Stochastic processes in physics and chemistry*. Vol. 1. Elsevier, 1992.

[8] Gillespie, Daniel T. "Stochastic simulation of chemical kinetics." *Annu. Rev. Phys. Chem.* 58 (2007): 35-55.

[9] Schumacher, L. J., Woolley, T. E., & Baker, R. E. (2013). Noise-induced temporal dynamics in Turing systems. *Physical Review E*, *87*(4), 042719.

Tuesday, July 19, 2022

08:30 - 10:30

MS-16 Random Dynamical Systems - Recent Advances and New Directions

Saint Clair 1

Chair: Rachel Kuske

08:50 - 09:10

An efficient method to obtain the response PDF of nonlinear stochastic dynamical systems

SYKORA Henrik, **KUSKE Rachel***, YURCHENKO Daniil

*Georgia Institute of Technology (Atlanta United States)

09:10 - 09:30

Integral feedback in synthetic biology: Negative-equilibrium catastrophe

PLESA Tomislav*, DACK Alex, OULDRIDGE Thomas

*University of Cambridge (Department of Applied Mathematics and Theoretical Physics, University of Cambridge, Wilberforce Road, Cambridge, CB3 0WA, UK United Kingdom)

09:30 - 09:50

Dynamical Analysis of a Multibody Wave Energy Converter excited by Random Waves

HOLLM Marten*, DOSTAL Leo, HÖHNE Joshua, SEIFRIED Robert

*Institute of Mechanics and Ocean Engineering, Hamburg University of Technology (Eissendorfer Strasse 42, 21073 Hamburg Germany)

09:50 - 10:10

Stochastic excitation source modeling for roughness-induced normal vibration at dry sliding conformal contacts under light load

PERRET-LIAUDET Joel*, PONTHUS Nicolas, ZOUABI Chaima, SCHEIBERT Julien

*Laboratoire de Tribologie et Dynamique des Systèmes (Ecole Centrale de Lyon. 36 avenue Guy de Collongue. 69134 ECULLY cedex France)

An efficient method to obtain the response PDF of nonlinear stochastic dynamical systems

Henrik T Sykora*, Rachel Kuske† and Daniil Yurchenko ‡
*Heriot-Watt University, Edinburgh EH14 4AS, United Kingdom
†Georgia Institute of Technology, Atlanta, GA 30332, USA
‡University of Southampton, Southampton SO17 1BJ, United Kingdom

Summary. We present an efficient formulation of the path integration method to approximate the response probability density functions (PDF) of nonlinear stochastic differential systems. We obtain the time-dependent PDF at the next time point by solving the Chapman-Kolmogorov (CK) equation, where we integrate the probability density function (TPDF) of the transition from one state to another (TPDF), for all possible states, weighted by the PDF at the current time. We iteratively evaluate the CK equation via a partitioned formulation of the path integration method: the PDF is represented as an interpolated function, the TPDF from one state to the other is approximated using a numerical scheme, and the integral is evaluated using the Gauss-Legendre quadrature. We record the integration process in a so-called step matrix and transform the evaluation of the CK equation to a matrix-vector multiplication. We demonstrate that this approach increases the performance of the path integration method compared to previously established approaches and analyse the accuracy of different interpolation and time-stepping methods.

Introduction

The probability density function (PDF) is an important tool to investigate the response statistics of dynamical systems subjected to noise excitation. When the dynamical system is represented as a stochastic differential equation (SDE), a commonly used method to determine the response PDF is to solve the corresponding Fokker-Planck or Kolmogorov forward equation. This partial differential equation rarely has an exact analytical solution, and thus in most cases, we have to use a numerical approximation method to solve it. The simplest method to obtain the PDF is through time-domain Mone-Carlo simulations when we numerically integrate the SDE in time and use the realised trajectories to approximate the PDF.

Another method to obtain the PDF of an SDE is the path integration (PI) method. Here we have to solve the Chapman-Kolmogorov (CK) equation, formulated to describe the law of total probability for dynamical systems. The PI method has proven to provide an accurate estimate of the time evolution of the PDF of a dynamical system; however, the CPU time required to compute a PDF is still an issue. The computation time is a critical problem to address if the dimensionality of the state space of the investigated dynamical system is high or when we want to obtain the steady-state PDF for a slowly converging system. In previous formulations of the PI method [1, 2, 3, 4] the CK equation was directly solved in each time step, even in the case of time-invariant or time-periodic systems. There are works [5] that utilise FFT to speed up the time it requires to evaluate the CK equation for each time step; however, the CK equation is still evaluated at each time step.

In this work, we provide a modular approach to solve the CK equation and analyse the effect of different interpolation methods on the accuracy and the performance of the approximation of the PDF delivered by the numerical solution of the CK equation. Furthermore, we transform the process of evaluating the CK equation to a matrix multiplication which significantly speeds up the computation of PDFs of time-invariant and time-periodic systems.

Chapman-Kolmogorov Equation

We consider stochastic differential equations in the form

$$\mathrm{d}\mathbf{x}(t) = \mathbf{f}(\mathbf{x}, t)\mathrm{d}t + \mathbf{g}(\mathbf{x}, t)\mathrm{d}\mathbf{W}_t, \tag{1}$$

where $\mathbf{x} = \begin{bmatrix} x_1 & \dots & x_d \end{bmatrix}^\top$ is the $\mathbb{R}^d$-valued stochastic state variable, $\mathbf{W}_t$ is the $\mathbb{R}$-valued Wiener process (Brownian motion), $\mathbf{f} : \mathbb{R}^d \times [0, T] \mapsto \mathbb{R}^d$, $\mathbf{g} : \mathbb{R}^d \times [0, T] \mapsto \mathbb{R}^d$. We can assume, that the diffusion term $\mathbf{g}$ has only $d - k + 1$ nonzero terms:

$$g_i(\mathbf{x}, t) \equiv 0 \quad \text{for} \quad i < k \leq d. \tag{2}$$

We use the Chapman-Kolmogorov equation to obtain the probability density function $p(\mathbf{x}, t)$ in discrete times t_n and t_{n+1}:

$$p(\mathbf{x}, t_{n+1}) = \int_{\mathbb{R}^d} p(\mathbf{x}, t_{n+1}|\mathbf{x}_0, t_n)p(\mathbf{x}_0, t_n)\mathrm{d}\mathbf{x}_0. \tag{3}$$

As the solution of the Chapman-Kolmogorv equation is not available in an analytical form for a general smooth $\mathbf{f}$ and $\mathbf{g}$, we need to discretise (3) using the path-integration approach. We approximate the transitional probability density function (TPDF) $p(\mathbf{x}, t|\mathbf{x}_0, t_0)$ with the help of a numerical stepping scheme, interpolate the probability density function (PDF) $p(\mathbf{x}, t)$, and evaluate of the integral with the help of the Gauss-Legendre quadrature.

We record the whole calculation process in a step matrix $\mathbf{S}_n$ and substitute the evaluation of the integral (3) with a matrix-vector multiplication:

$$\mathbf{p}_{n+1} = \mathbf{S}_n \mathbf{p}_n. \tag{4}$$

In $\mathbf{p}_n$ we record the interpolation values describing the PDF $p(\mathbf{x}, t)$. In case the SDE in (1) is time-invariant or time-periodic, this approach will lead to a very performant method to solve (3).

Accuracy and Performance

Due to the partitioned formulation of the PI method we are able to separately investigate the effect of the time stepping method used for the approximation of the TPDF $p(\mathbf{x}, t_{n+1}|\mathbf{x}_0, t_n)$ and the interpolation method of the PDF $p(\mathbf{x}, t_n)$ on the accuracy of the approximation. We analyse the different time stepping and interpolation methods through the response PDF of a cubic oscillator:

$$\ddot{x}(t) + 0.3\dot{x}(t) - x(t) + 0.25x(t)^3 = \sqrt{0.075}\,\xi(t). \tag{5}$$

The steady-state PDF $p_{\mathrm{st}}(x, \dot{x})$ of (5) is approximated with the help of the path integration method and is compared with the true solution [6]. To characterise the accuracy of the PI method we use ε_1 that is obtained by integrating the absolute error between the true and approximated steady state PDF $p_{\mathrm{st}}(x, \dot{x})$ for the all the states $x, \dot{x} \in \mathbb{R}$.

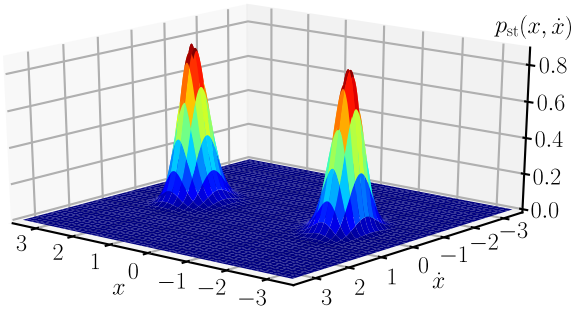

Figure 1: Steady state PDF $p_{\mathrm{st}}(x, \dot{x})$ of the cubic oscillator (5)

.

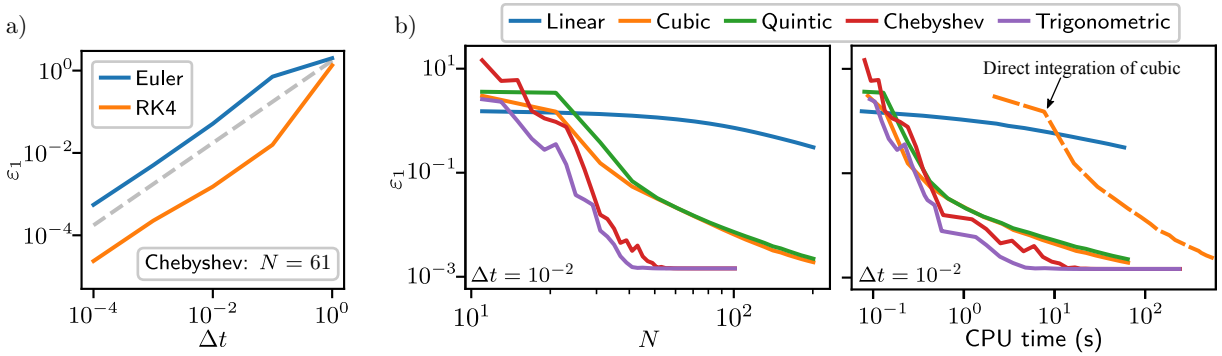

Figure 2: Error ε_1 as a function of (a) time step Δt and (b) number of interpolation nodes N / CPU time of the approximated steady state response PDF $p_{\mathrm{st}}(x, \dot{x})$ of the cubic oscillator (5)

.

We demonstrate that our new formulation allows accurate computation of the PDF of noise-driven nonlinear dynamical systems significantly faster than previous formulations. Additionally, we show that the increased performance of the PI method allows the parametric analysis of a vibro-impact energy harvesting device that is used to harvest energy from noisy ambient vibrations.

References

[1] Naess A., Moe V. (2000) Efficient path integration methods for nonlinear dynamic systems. *Prpbabilistic Engineering Mechanics* **15(2):221–231**

[2] Naess A. (2000) Chaos and nonlinear stochastic dynamics. *Probabilistic Engineering Mechanics***15(1):37–47**

[3] Alevras P., Yurchenko D. (2016) GPU computing for accelerating the numerical Path Integration approach. *Computers & Structures* **171(4):46–53**

[4] Hasnijeh S. G., Naess A., Poursina M., and Karimpour H. (2021) Stochastic dynamical response of a gear pair under filtered noise excitation. *International Journal of Non-Linear Mechanics* **131:103689**

[5] Naess A., Kolnes F. E., Mo E. (2009) Stochastic spur gear dynamics by numerical path integration. *Journal of Sound and Vibration* **302(4–5):936–950**

[6] Caughey T.K. (1971) Nonlinear Theory of Random Vibrations. *Advances in Applied Mechanics* **11:209–253**

Integral feedback in synthetic biology: Negative-equilibrium catastrophe [1]

Tomislav Plesa*, Alex Dack† and Thomas E. Ouldridge†
*Department of Applied Mathematics and Theoretical Physics, University of Cambridge, Wilberforce Road, Cambridge, CB3 0WA, UK
†Department of Bioengineering, Imperial College London, Exhibition Road, London, SW7 2AZ, UK

Summary. A central goal of synthetic biology is the design of molecular controllers that can manipulate the dynamics of intracellular networks in a stable and accurate manner. To address the fact that detailed knowledge about intracellular networks is unavailable, integral-feedback controllers (IFCs) have been put forward for controlling molecular abundances. These controllers can maintain accuracy in spite of the uncertainties in the controlled networks. However, this desirable feature is achieved only if stability is also maintained. In this paper, we show that molecular IFCs can suffer from a hazardous instability called *negative-equilibrium catastrophe* (NEC), whereby all nonnegative equilibria vanish under the action of the controllers, and some of the molecular abundances blow up. We show that NECs place a fundamental limit to design and control of molecular networks.

Extended Abstract

A main objective in synthetic biology is to control living cells [1, 2]. This challenging problem requires addressing a number of complicating factors displayed by intracellular networks:

(N) **Nonlinearity**. Intracellular networks are *bimolecular* (nonlinear), i.e. they include reactions involving two reacting molecules.

(HD) **Higher-dimensionality**. Intracellular networks are *higher-dimensional*, i.e. they contain larger number of coupled molecular species.

(U) **Uncertainty**. The experimental information about the structure, rate coefficients and initial conditions of intracellular networks is *uncertain* (noisy).

To mitigate challenge (U), molecular *integral-feedback controllers* (IFCs) have been put forward, which can maintain accurate control of molecular abundances in spite of some of the uncertainties in the controlled networks [3, 4]. However, this desirable feature is achieved only if stability is also maintained - an important problem which has been predominantly studied when unimolecular and/or lower-dimensional networks are controlled [4, 5, 6, 7]; in contrast, intracellular networks are generally bimolecular and higher-dimensional (challenges (N) and (HD) stated above). To bridge the gap, in this paper we focus on the question of fundamental importance to intracellular control: How do molecular IFCs perform when applied to biochemical networks which are bimolecular, higher-dimensional and uncertain?
We show that at the center of this question are equilibria - stationary solutions of the reaction-rate equations that govern the deterministic dynamics of biochemical networks. In particular, molecular concentrations can reach only equilibria that are nonnegative. In this context, we show that molecular IFCs can destroy all nonnegative equilibria of the controlled system and lead to a control failure; furthermore, this failure can be catastrophic, as some of the molecular abundances can then experience an unbounded increase with time (blow-up) at both deterministic and stochastic (chemical master equation) levels. We call this hazardous phenomenon, involving absence of nonnegative equilibria and blow-up of some of the underlying species abundances, a *negative-equilibrium catastrophe* (NEC), which we outline in Figure 1. In context of electro-mehanical systems, analogous phenomenon is known as integrator windup. We show that unimolecular IFCs do not exist due to a NEC. We then derive a family of bimolecular IFCs that are safeguarded against NECs when uncertain unimolecular networks, with any number of molecular species, are controlled. However, when IFCs are applied on uncertain bimolecular (and hence most intracellular) networks, we show that the problem of preventing NECs generally suffers from the *curse of dimensionality* - the problem becomes intractable as the number of interacting molecular species increases. NECs therefore have broad implications for design and control of molecular networks at both deterministic and stochastic levels.

References

[1] Plesa, T., Dack, A., and Ouldridge, T. E., 2022. Available as https://arxiv.org/abs/2102.10668.

[2] Del Vecchio, D., Dy, A. J., Qian, Y., 2016. *Journal of the Royal Society Interface*, **13**(**120**): 3–43.

[3] Oishi, K., and Klavins, E., 2011. *IET Systems Biology*, Volume 5, Issue 4: 252–260.

[4] Briat, C., Gupta, A., Khammash, M., 2016. *Cell Systems*, **2**(**1**): 15–26.

[5] Aoki, S.K., Lillacci, G., Gupta, A., Baumschlager, A., Schweingruber, D., and Khammash, M., 2019. *Nature*, **570**: 533–537.

[6] Olsman, N., Baetica, A. A., Xiao, F., Leong, Y.P., Doyle, J., and Murray, R., 2019. *Cell Systems*, **9**(**1**): 49–63.

[7] Olsman, N., Xiao, F., Doyle, J., 2019. *ISince*, **14**: 277–291.

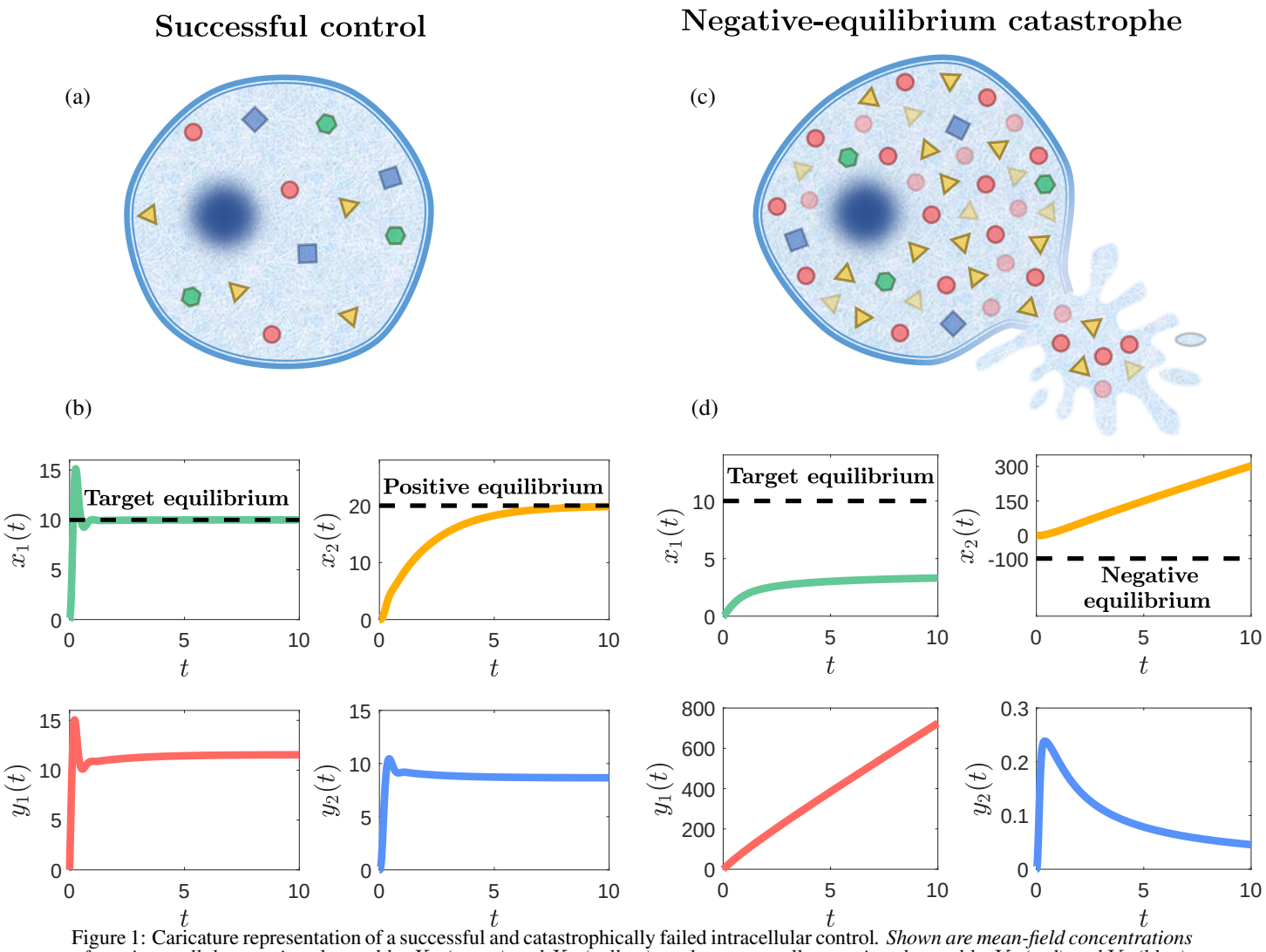

Figure 1: Caricature representation of a successful and catastrophically failed intracellular control. *Shown are mean-field concentrations of two intracellular species, denoted by X_1 (green) and X_2 (yellow), and two controller species, denoted by Y_1 (red) and Y_2 (blue); the goal is to steer the equilibrium of X_1 to a desired set-point.*
Panels (a)–(b) *display a cell successfully controlled with a molecular* IFC. *In particular, panel* (b) *shows that the species X_1 approaches a desired equilibrium, shown as a black dashed line, while the equilibria for the remaining species X_2, Y_1 and Y_2 are positive.*
Panels (c)–(d) *display a cell that has taken lethal damage due to a failure of the* IFC. *In particular, as shown in panel* (d)*, the target equilibrium for X_1 enforces a negative equilibrium for the species X_2. However, since molecular concentrations are nonnegative, this equilibrium cannot be reached and, therefore, control fails. Furthermore, the failure is catastrophic, as concentrations of some of the underlying species (in this example, species X_2 and Y_1) blow up, placing a lethal burden on the cell. Analogous phenomenon occurs at the stochastic level.*

Dynamical Analysis of a Multibody Wave Energy Converter excited by Random Waves

Marten Hollm*, Leo Dostal*, Joshua Höhne* and Robert Seifried*
*Institute of Mechanics and Ocean Engineering, Hamburg University of Technology, Hamburg, Germany

Summary. The dynamics of a novel multibody wave energy converter based on inclined single modules connected to a frame are investigated, on which generators convert the corresponding relative motion into electrical power. Thereby, it is studied under which conditions the inclined individual modules perform the largest relative motions in regular and irregular waves. For this, different setups are analyzed in the presence of wave excitations, which is generated by a random non-white Gaussian stochastic process.

Introduction

Renewable energies play an increasingly important role in modern energy systems. As a consequence, hydropower, solar and wind energy are becoming more and more important. In addition to these well-known examples of renewable energy generation, there is also the possibility to obtain energy from ocean waves. Since wave energy has a high power density compared to wind and solar energy, it is also promising for energy generation [1]. Therefore, several new concepts of wave energy converters (WEC) have been studied in the last years. For example a pendulum energy converter was investigated, whereby its pivot is excited by water waves in such a way that a rotational motion of the pendulum is generated, which can be converted to electrical energy, cf. [2, 3, 4, 5].
This paper deals with the analysis of the dynamical behavior of a multibody WEC, where generators mounted on a frame are each excited by a randomly moving cylindrical floating body (CFB). The CFBs are floating in ocean waves and the energy generation of the generators results in additional damping. Our results consider the case of excitation by a non-white Gaussian random process, which can for example be encountered in real sea states.

Description of the mechanical system

The mechanical system mainly consists of a frame and N CFBs. Figure 1 shows the side view of the structure for the case of $N = 2$ in still water and in the presence of harmonic water waves. In this work, only the motion of the system in the xy-plane with horizontal coordinate x and vertical coordinate y is considered. Each CFB moves along guided rods with corresponding displacement ξ_i in a plane, which is inclined with respect to the frame by the corresponding adjustable inclination angle ε_i, $i \in \{1, \dots, N\}$. The frame can freely move in the xy-plane, whereby the angle of rotation is denoted by β and the horizontal and vertical displacements of the frame are denoted by x_F and y_F, respectively. It is assumed that the frame is in contact with the sea surface and that only the CFBs are excited by water waves. Thereby, the CFBs and the frame are connected by springs and mechanical friction is accounted for by a velocity dependent damping force. Generators convert the relative motion between the CFBs and the frame to electrical energy, leading to an additional electrical damping force.
Let

$$\mathbf{z} = [x_\mathrm{F}, y_\mathrm{F}, \beta, \xi_1, \dots, \xi_N]^\mathrm{T} \tag{1}$$

be the vector of all degrees of freedom of the multi body WEC. Then, the general equation of motion of the mechanical system can be written as

$$\mathbf{M}(\mathbf{z}, t)\ddot{\mathbf{z}} + \mathbf{k}(\mathbf{z}, \dot{\mathbf{z}}, t) = \mathbf{q}(\mathbf{z}, \dot{\mathbf{z}}, t), \tag{2}$$

whereby t is the time, $\mathbf{M}$ is the generalized mass matrix, $\mathbf{k}$ is the vector of Coriolis, centrifugal and gyroscopic forces and $\mathbf{q}$ is the vector of the applied forces.
In order to compute the hydrodynamic forces, the water pressure p must be integrated over the wetted surface of each CFB. Using potential flow theory and Bernoulli's equation of fluid dynamics, the radiation problem as well as the diffraction problem of a moving cylinder has to be solved in order to calculate the hydrodynamic forces [6]. For incoming harmonic water waves with wave amplitude A and wave frequency ω, the corresponding sea surface is given by

$$\eta(x, t) = \mathrm{Re}\{A \exp(\mathrm{i}(\kappa x - \omega t))\} \quad \text{with} \quad \omega^2 = \kappa g \tanh(\kappa H), \tag{3}$$

whereby κ denotes the wave number, g the gravity constant and H the water depth. For this type of water waves, Yeung [7] and Garrett [8] have computed the velocity potential of radiation and diffraction by expressing them as a series of eigenfunctions for the case of a single truncated cylinder. Using this theory, it is assumed that the motion of CFBs does not lead to hydrodynamic forces, which affect other CFBs.

Description of random sea waves

A well-known model of random long-crested sea waves is given by the superposition of harmonic waves with wave frequencies ω and corresponding wave numbers $\kappa(\omega)$. With this, the wave amplitude of each harmonic wave component depends on the underlying sea state, which is given by the corresponding one-sided spectral density $S(\omega)$, cf. [9, 10]. Then, a one dimensional irregular long-crested wave surface can be written as

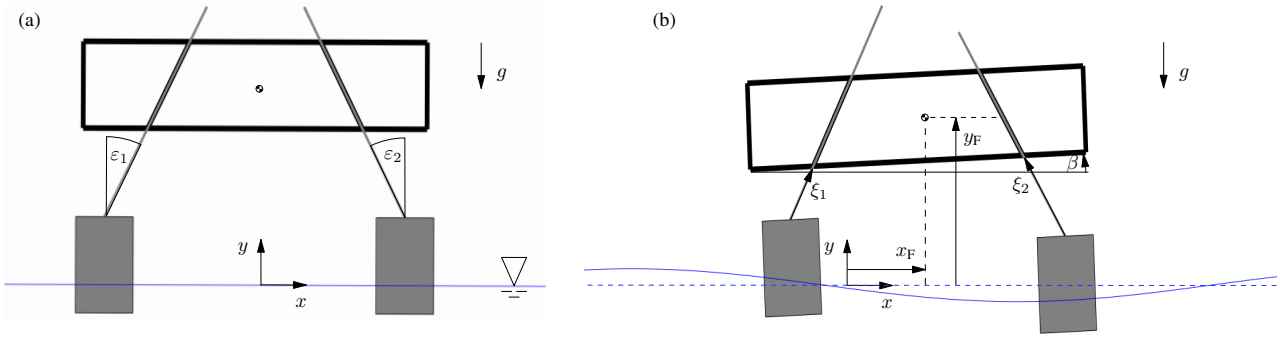

Figure 1: Sketch of the mechanical system in still water position (a) and in the presence of harmonic water waves (b).

$$Z(x,t) = \int_0^\infty \cos\left(\omega t - \kappa(\omega)x + \varepsilon(\omega)\right) \sqrt{2S(\omega)\mathrm{d}\omega}, \tag{4}$$

whereby the integral is not Riemann integral but a summation rule over the frequencies ω. An example for such generated sea waves is shown in Figure 2, where either the space or time is fixed at $x = 0$ or $t = 0$, respectively.
With this developed mechanical model and the study of corresponding numerical results, a detailed analysis is performed showing the influence of design parameters, like the inclination angles ε_i or the number N of CFBs, in order to maximize the harvested energy.

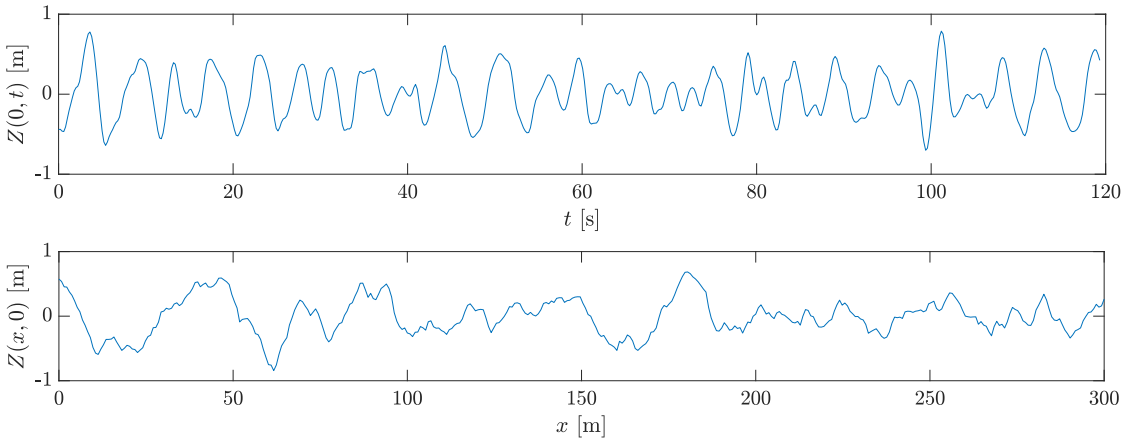

Figure 2: Evolution of a random sea surface in time and space.

References

[1] McCormick M. E. (2013) Ocean wave energy conversion. Courier Corporation.

[2] Vaziri V., Najdecka A., Wiercigroch M. (2014) Experimental control for initiating and maintaining rotation of parametric pendulum. *The European Physical Journal Special Topics*, **223**(4): 795-812.

[3] Yurchenko D., Alevras P. (2018) Parametric pendulum based wave energy converter. *Mechanical Systems and Signal Processing* **99**: 504-515.

[4] Dostal L., Pick M. (2017) Power generation of a pendulum energy converter excited by random loads. In: *Proceedings of the 9th European Nonlinear Oscillations Conference*, Budapest, Hungary.

[5] Dostal L., Korner K., Kreuzer E., Yurchenko D. (2018) Pendulum energy converter excited by random loads. *ZAMM-Journal of Applied Mathematics and Mechanics/Zeitschrift für Angewandte Mathematik und Mechanik* **98**(3): 349-366.

[6] Newman J.N. (2018) Marine Hydrodynamics. The MIT press.

[7] Yeung R. W. (1980) Added mass and damping of a vertical cylinder in finite-depth waters. *Applied Ocean Research* **3**(3): 119–133.

[8] Garrett C. J. R. (1971) Wave forces on a circular dock. *Journal of Fluid Mechanics* **46**(1): 129–139.

[9] Dostal L., Kreuzer E. (2011) Probabilistic approach to large amplitude ship rolling in random seas. *Proceedings of the Institution of Mechanical Engineers, Part C: Journal of Mechanical Engineering Science* **225**: 2464–2476.

[10] Dostal L., Kreuzer E., Sri Namachchivaya N. (2012) Non-standard stochastic averaging of large-amplitude ship rolling in random seas. *Proc. R. Soc. A* **468**, 4146–4173.

Stochastic excitation source modeling for roughness-induced normal vibration at dry sliding conformal contacts under light load

Joël Perret-Liaudet, Nicolas Ponthus, Chaïma Zouabi and Julien Scheibert
Ecole Centrale de Lyon, UMR CNRS 5513, LTDS, France

Summary. This study deals with the roughness-induced normal vibration problem occurring when a rigid rough body slides on a rigid rough surface. To predict this dynamic behaviour, we propose to model the effective random excitation source under the assumption of a very small number of contacts, each affected by a statistically independent stochastic process. Each process is obtained by considering the separation between both topographies when they touch in a single point. Statistical and spectral properties of the vibrational excitation are characterized. On this basis, we demonstrate the relevance of the proposed modelling to reproduce the experimental observations.

Introduction

When a rigid rough body slides on a rigid rough surface, it exhibits random vibrations normal to the nominal contact surfaces. Under light contact pressure, this behaviour is known as roughness-induced vibrations leading to a broadband noise, so-called roughness noise [1]. This problem is a huge nonlinear and stochastic dynamic problem. Indeed, it includes both microscopic and macroscopic scales (roughness versus slider macro-size), short time scales, non-smooth dynamics (loss of contact) and stochastic excitations induced by roughness. Depending on the sliding velocity, recent experimental works about this vibrational problem have clearly shown two main dynamic regimes, observable on the dynamic motion of the slider normal to the surfaces in contact [2,3]. For low sliding velocities, the slider remains very close to the above solid, like a grazing regime, with negligible probability of contact losses. Conversely, for high sliding velocities, the slider jumps above the track with free flights, like a bouncing regime, leading to numerous mechanical shocks between asperities. As an example, these two regimes can be identified on figure 1 which shows the evolution of the slider's free flight time rate Π versus the sliding velocity V. This experiment concerns a stainless steel upper slider in dry contact under its own weight (104 g mass) with a 25x25 mm² apparent surface and a 30 µm RMS roughness. The antagonist stainless steel 25x300 mm² surface is also with a 30 µm RMS roughness. The slider was either pulled or pushed with 20 tests per operating way, which is presented in figure 1 through the uncertainty bars. Further, an example of the vertical acceleration history $\ddot{z}$ of the slider observed in the bouncing regime is shown in figure 2. We can clearly observe long free flights for which $\ddot{z} = g$, and short impacts.

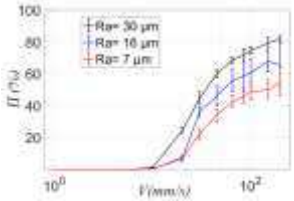

Figure 1: Slider's free flight time rate versus the sliding velocity

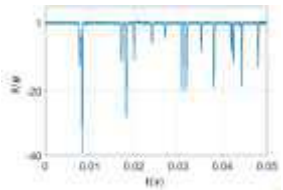

Figure 2: Vertical acceleration in the bouncing regime

The vertical dynamic behavior of the upper slider under its own weight, i.e. submitted to a light normal force, can be heuristically modelled by an equivalent randomly excited bouncing ball system [2,3]. On the basis of this assumption, the transition velocity which separates the two regimes can be predicted by the knowledge of an equivalent random excitation source. This excitation is directly related to the characteristics of the tribological system, defined by the surface topographies, the size of the upper slider, the sliding velocity, and so on. So, being able to model such an excitation constitutes one of the keys to a better knowledge of the nonlinear and stochastic roughness-induced dynamics of sliding bodies. Precisely, the main goal of this paper is to address this question. In particular, we have proceeded to describe the probability density function and the power spectral density of this stochastic excitation as a result of the two sliding conformal rough surfaces in the case of light normal load.

The proposed approach for modelling the excitation source

The excitation source results from interactions between the two rough surfaces in sliding contact. It can be viewed as the normal displacement z_G of the center of mass of the slider $\boldsymbol{G}$. When the applied pressure is very low compared to the material stiffness, one can reasonably assume that the contact is ensured by only three points of contact. Such three-points contact situations are the focus of the present study.

3-points contact modelling and normal displacement of the slider's center of mass

The 3 points in contact necessarily surround the center of mass of the slider. Normal displacements z_j under the points correspond to the separation of the associated antagonist asperities. The schetch in figure 3 represents this scenario. Now, assume that the altitude of each contact, z_j, and also their respective positions (points $\boldsymbol{P}_j$) are known, the vertical motion of the center of mass is given by $z_G = \alpha_{12}z_3 + \alpha_{23}z_1 + \alpha_{31}z_2$, where α_{ij} represents the absolute barycentric coordinates, or area coordinates. Considering isotropic surfaces, the three barycentric coordinates are statistically equivalent. Furthermore, one assumes that displacements z_j and coordinates α_{ij} are independent random variables. So, the displacement of the center of mass behaves like the following random variable $\tilde{z}_G = (z_1 + z_2 + z_3)/3$.

(a) **(b)**

Figure 3: (a) Slider and location of its center of mass $\boldsymbol{G}$, location of each contact point $\boldsymbol{P}_j$, and area coordinates α_{ij}; (b) the equivalent sliding system.

Finally, if we assume that points $\boldsymbol{P}_j$ are sufficiently separated with distances larger than a characteristic topography wavelength to ensure that displacements z_j are independent, and if we assume that the probability density functions $f_{Z_j}(z)$ are almost the same $f_Z(z)$, one obtains the probability density function of $\tilde{z}_G$, i.e. $f_{\tilde{z}_G}(z) = 3(f_Z * f_Z * f_Z)(3z)$. In the same way, one can calculate the power spectral density $S_{\tilde{z}_G\tilde{z}_G}(k)$ as follows $S_{\tilde{z}_G\tilde{z}_G}(k) = S_{ZZ}(k)/3$.

One-point contact modelling

In this frame, we need to characterize the probability density function $f_Z(z)$ and the power spectral density $S_{ZZ}(k)$. It was done in the case of the separation at single-point contact between self-affine topographies. The main results [4] obtained by direct simulations and extreme value theory approach are: (i) the normal motion RMS amplitude is much smaller than that of the equivalent roughness of the two topographies and depends on the ratio of the slider's lateral size over a characteristic wavelength of the topography; (ii) due to the nonlinearity of the sliding contact process, the power spectral density contains wavelengths smaller than the smallest wavelength present in the underlying topographies.

Results and conclusion

In order to validate the proposed scenario, we compared the predicted characteristics of the vertical motion of the center of mass of the slider to the results during grazing regimes obtained through sliding experiments described in the introduction section and direct simulations of the sliding contact.

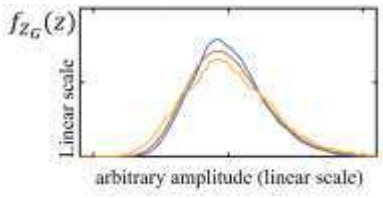

Figure 4: Pdf of the vertical motion of $\boldsymbol{G}$; blue: experimental result; yellow: direct simulation; red: extreme value theory.

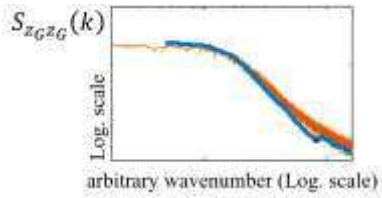

Figure 5: PSD of the vertical motion of $\boldsymbol{G}$; blue: experimental result; yellow: direct simulation; red: analytical.

As we can observe, the statistical properties (see figure 4) as well as the spectral contents (see figure 5) are well captured by the proposed modelling. Within its framework, it was therefore also possible to accurately predict the velocity threshold separating the grazing regime to the bouncing regime. For this, the vertical motion of the slider has been heuristically described with good agreement by the dynamics of an equivalent random bouncing ball system for which the characteristics were given in a previous work [5], including memory effect related to a combination between the sliding velocity and characteristic wavelengths of the equivalent excitation.

To conclude, we have proposed a complete modelling to describe the roughness-induced normal vibration at a dry sliding conformal contacts under light load. Good agreements were obtained with respect to experiments as well as direct simulations. More generally, we provide an improved understanding of roughness-induced vibration problems and a better knowledge of the associated friction and noise.

Acknowledgments

This work was supported by the Ministry of Higher Education, Research and Innovation. It was also supported by Labex Manutech-SISE (ANR-10-LABX-0075) of Université de Lyon within the program Investissements d'Avenir (ANR-11-IDEX-0007) operated by the French National Research Agency. JPL is member of the Labex CeLyA (Acoustic Center at Lyon) of Université de Lyon operated by the Fench National Research Agency (ANR-10-LABX-0060/ANR-11-IDEX-0007).

References

[1] Abdelounis H.B., Le Bot A., Perret-Liaudet J., Zahouani H. (2010) An experimental study on roughness noise of dry rough flat surfaces. *Wear* **268**, 335-345.

[2] Zouabi, C. (2016) Dynamique d'un contact glissant rugueux-rugueux sous faible charge : experiences et modélisation. *PhD Thesis*, ECL.

[3] Ponthus, N. (2019) Contact sec glissant sous faible charge : de la topographie des surfaces à la dyn. des solides et de l'interface. *PhD Thesis*, ECL.

[4] Ponthus N., Scheibert J., Thøgersen K., Malthe-Sørenssen A., Perret-Liaudet J. (2019) Statistics of the separation between sliding rigid rough surfaces: Simulations and extreme value theory approach. *Physical Review E* **99**, 023004.

[5] Zouabi C., Scheibert J., Perret-Liaudet J. (2016) Memory in random boucing ball dynamics. *EPL* **115**, 50006.

Tuesday, July 19, 2022
08:30 - 10:30

MS-03 Computational Methods
Rhone 3A

Chair: Harry Dankowicz

08:30 - 08:50
Analysis of coupled non-linear oscillators by the Asymptotic Numerical Method
CALBRIX Leopold, **GIRAULT Gregory***, CADOU Jean-Marc
*Centre de Recherche - Académie Militaire de Saint-Cyr Coëtquidan (Camp de Saint-Cyr Coëtquidan 56381 Guer Cedex France) - Institut de Recherche Dupuy de Lôme (Rue Saint-Maudé BP 9211656321 LORIENT cedex France)

08:50 - 09:10
Control-based continuation of orbits with complex time profile
SIEBER Jan*, QUINN Courtney
*College of Engineering, University of Exeter (Exeter United Kingdom)

09:10 - 09:30
New MatCont and a numerical bifurcation study of a perception problem in psychophysics
GOVAERTS Willy*, KUZNETSOV Yuri, MEIJER Hil, NEIRYNCK Niels, VAN Wezel Richard
*Department of Applied Mathematics, Computer Science and Statistics, Gent University, Belgium (Krijgslaan 281 - Building S9, 9000 Ghent, Belgium Belgium)

09:30 - 09:50
Finding connecting orbits between saddle periodic orbits as organising centres of complicated dynamics
WONG Nelson, **OSINGA Hinke***, KRAUSKOPF Bernd
*Department of Mathematics, University of Auckland, (The University of Auckland Private Bag 92019 Auckland 1142 New Zealand New Zealand)

ANALYSIS OF COUPLED NON-LINEAR OSCILLATORS BY THE ASYMPTOTIC NUMERICAL METHOD

Léopold Calbrix*, Jean-Marc Cadou*, Grégory Girault*
*Univ Bretagne Sud, CNRS UMR6027, IRDL, France

Summary. This study is based on the theoretical and experimental works of Cadiou et al. [1, 2] who designed a non-linear vibration absorber using an electro-magnetomechanical coupling. The present work limits itself to the pure mechanical response of a 2 degrees-of-freedom oscillator with a cubic non-linear coupling between the Linear Oscillator (LO) and the non-linear energy sink (NES). The numerical analysis is performed using the Harmonic Balance Method (HBM) in association with the Asymptotic Numerical Method (ANM), following the initial idea proposed by Cochelin et al. [3]. This approach offers an understanding of resonance mechanisms of the LO and energy transfers to the NES. Numerical experiments are performed in order to identify influence of the parameter values. Numerical results are also compared to theoretical ones. They confirm the relevancy of the numerical approach which may be retained to the design of a non-linear vibration absorber.

Extended Abstract

Non-linear energy sinks (NES) are known for their efficiency in the vibration mitigation as they do not have to be tuned to the natural frequency of the supporting structure. In this study, a 2 degrees-of-freedon (DOF) model is analysed (Fig.1). It is composed of a Linear Oscillator (LO) non-linearly coupled with the absorber (NES). The LO is defined with its mass m_1, a constant stiffness k_1 and a viscous damping parameter c_1. The absorber is defined through its mass m_2, its viscous damping parameter c_2 and its cubic stiffness k_{2c}. The LO is directly excited by an harmonic force $f(t) = Fcos(\omega t)$. Finally, $x_1(t)$ and $x_2(t)$ denote the LO and NES displacement, respectively. Thus, the problem to be solved reads:

$$\begin{cases} m_1\ddot{x}_1 + c_1\dot{x}_1 + k_1x_1 + c_2(\dot{x}_1 - \dot{x}_2) + k_{2c}(x_1 - x_2)^3 = Fcos(\omega t) \\ m_2\ddot{x}_2 - c_2(\dot{x}_1 - \dot{x}_2) - k_{2c}(x_1 - x_2)^3 = 0 \end{cases}$$

In this study, the problem is solved coupling the Asymptotic Numerical Method (ANM) with the Harmonic Balance Method (HBM). The former is a continuation technique based on Taylor series of the unknowns while the later is a decomposition of unknowns into truncated Fourier series.
In order to efficiently apply the ANM, quadratic recast of equations is a preliminary stage. So, auxiliary variables $y_k = x_k^2$ and velocity variables $v_k = \dot{x}_k$ ($k = 1, 2$) are defined and the non-linear dynamic problem formally reads:

$$\dot{\underline{Y}} = \underline{G}(\underline{Y}, \omega) \text{ with: } \underline{Y} = \{x_1, x_2, v_1, v_2, y_1, y_2\}^\top$$

The HBM is then applied and the unknown $\underline{Y}$ is decomposed into truncated Fourier series with H harmonics:

$$\underline{Y} = \underline{Y}_0 + \sum_{p=1}^{H} \left[\underline{Y}_p^c \cos(p\omega t) + \underline{Y}_p^s \sin(p\omega t)\right]$$

Fourier series are introduced into the non-linear dynamic problem. After balancing terms of the same harmonic index, the components $\underline{Y}_0, \underline{Y}_p^c$ and $\underline{Y}_p^s$ are identified and collected into one single unknown vector $\underline{X}$. Thus, the non-linear problem reads:

$$\underline{R}(\underline{X}, \omega) = \underline{0} \text{ with: } \underline{R}(\underline{X}, \omega) = -\omega\mathbb{M}(\underline{X}) + \mathbb{C} + \mathbb{L}(\underline{X}) + \mathbb{Q}(\underline{X}, \underline{X})$$

where $\mathbb{M}(\underline{X}), \mathbb{C}, \mathbb{L}(\underline{X})$ and $\mathbb{Q}(\underline{X}, \underline{X})$ stand for, respectively, the mass operator, the constant external forcing, the linear operator and the quadratic one. The convenient quadratic expression of the residual $\underline{R}$ allows to solve the problem using the ANM in order to continue solution $\underline{X}$ in respect to the parameter ω. The main advantage of this approach is to compute exactly the associated Jacobian matrix of the residual $\underline{R}$. So, unknowns $\underline{X}$ and ω are sought as truncated series of the path-parameter a:

$$\underline{X} = \sum_{k=1}^{N} a^k \underline{X}_k \quad \text{and} \quad \omega = \sum_{k=1}^{N} a^k \omega_k \quad \text{with} \quad a = \langle X - X_0, X_1 \rangle + (\omega - \omega_0)\omega_1$$

Then, the validity domain of one ANM step is evaluated according to: $a_{\max} = (\epsilon \|\underline{X}_1\| / \|\underline{X}_N\|)^{1/(N-1)}$ and a new continuation step can be performed: $\underline{X}_0^{\text{new}} = \underline{X}(a_{\max})$ and $\omega_0^{\text{new}} = \omega(a_{\max})$. More details can be found, for example, in [4, 5, 6, 7, 8].
This procedure is applied to analyse the dynamic response of the LO and the NES. The response curves are in good agreement with the numerical ones established in [1, 9] for a non-linear vibration absorber without electro-magneto-mechanical coupling (Fig.2).
Additional simulation are performed, for different values of the force F, to identify the appropriate values of the ANM parameters, mainly the number of harmonics H, the truncation order N and the tolerance threshold ϵ (Fig.3).

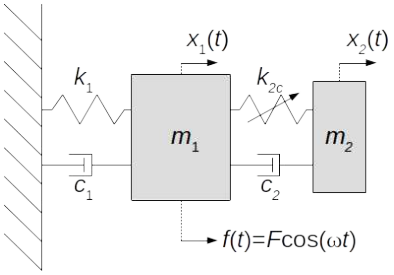

Figure 1: Single-degree-of-freedom oscillator non-linearly coupled with a NES

In particular, continuous solutions are obtained and several dynamic behaviours are highlighted according to the excitation force level F. Bifurcations (Hopf and Neimark-Sacker) are also computed in accordance with theoretical predictions obtained through a combination of the Complexification-Averaging method and the Multiple Scales method [1, 9].
The very first results show the relevancy of the numerical approach which is going to be used in order to study the dynamic behaviour of composite hydrofoil coupled to a NES [10].

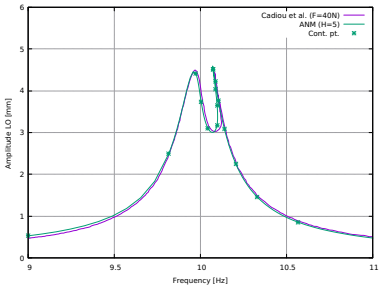

Figure 2: Evolution of the LO amplitude as a function of the frequency for $F = 40$ N with $H = 5$ harmonics. Comparison with result from [1].

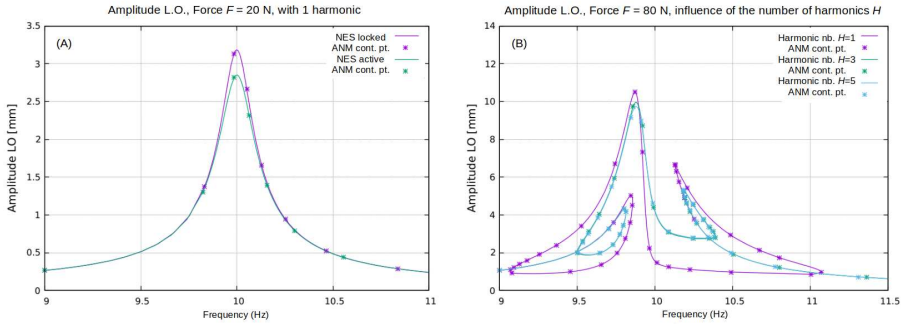

Figure 3: Evolution of the LO amplitude as a function of the frequency. Influence of the parameters on the dynamic behavior: $F = 20$ N with $H = 1$ harmonic (A) ; for $F = 80$ N with $H = 1, 3, 5$ harmonics (B).

References

[1] Cadiou B. (2021) Protection de structures soumises à des sollicitations dynamiques à l'aide d'un absorbeur non-linéaire. *PhD Thesis*, ISAE, Toulouse, France.

[2] Cadiou B., Stephan C., Renoult A., Michon G. (2022) Damping adjustment of a nonlinear vibration absorber using an electro–magnetomechanical coupling. *J. Sound Vib.* **518**:116508.

[3] Cochelin B., Vergez C. (2009) A high order purely frequency-based harmonic balance formulation for continuation of periodic solutions. *J. Sound Vib.* **324**:243-262.

[4] Renson L., Kerschen G., Cochelin B. (2016) Numerical computation of nonlinear normal modes in mechanical engineering. *J. Sound Vib.* **364**:177-206

[5] Guillot L., Vigué P., Vergez C., Cochelin B. (2017) Continuation of quasi-periodic solutions with two-frequency Harmonic Balance Method. *J. Sound Vib.* **394**:434-450

[6] Guillot L., Cochelin B., Vergez C. (2019) A Taylor series-based continuation method for solutions of dynamical systems. *Nonlinear Dyn.* **98**:2827-2845.

[7] Woiwode L., Balaji N.N., Kappauf J., Tubita F., Guillot L., Vergez C., Cochelin B., Grolet A., Krack M. (2020) Comparison of two algorithms for Harmonic Balance and path continuation. *Mech Syst Signal Process* **136**:106503.

[8] Guillot L. (2020) On a quadratic formalism for the continuation of the solutions of dynamical systems and their bifurcations - Applications to reed instruments. *PhD Thesis*, Aix-Marseille Université, Marseille, France.

[9] Stephan C., Pennisi G., Michon G. (2018) Vibrations mitigation based on nonlinear absorbers. *Aerospace Lab* **14**:1-12

[10] Malher A., Doaré O., Touzé C. (2017) Influence of a hysteretic damper on the flutter instability. *J Fluids Struct* **68**:356-369

Control-based continuation of orbits with complex time profile

Jan Sieber*, Courtney Quinn†
*Department of Mathematics, University of Exeter, UK
†CSIRO, Hobart, Austrialia

Summary. We illustrate how unstable trajectories with complex time profiles and large period can be tracked using feedback control-based continuation. The experimental or computational effort is proportional to the period. The approach requires the feedback control to be stabilizing within time of order 1 uniformly along the orbit. The approach is illustrated with a stochastic simulation of a delay model for the Mid-Pleistocene transition of the palaeoclimate ice ages.

Control-based continuation

Control-based continuation applies feedback control to turn a controllable nonlinear dynamical system with inputs and outputs into a system of nonlinear equations, which can then potentially be solved by general-purpose nonlinear solvers or continuation (curve tracking) algorithms; see [2, 6, 7] by Renson, Barton *et al* and Schilder *et al* for detailed descriptions of the methodology. The approach assumes that the user (e.g., experimenter) has implemented a stabilizing feedback control loop. One may assume that the dynamical system follows an ODE of the type

$$\dot{x}(t) = f(t, x(t), \mu, u(t)) \quad \text{where } x(t) \in \mathbb{R}^n \qquad \text{with output} \quad y(t) = g(t, x(t), \mu) \quad \text{where (e.g.) } y(t) \in \mathbb{R}, \tag{1}$$

and μ are system parameters. In the experiments of [2, 6, 7] the dynamical systems were forced oscillators, the output y was a position coordinate and the feedback control was in the form of a PD control, $u(t) = k_p[y(t) - y_\mathrm{r}(t)] + k_d[\dot{y}(t) - \dot{y}_\mathrm{r}(t)]$, with a reference time profile y_r. The control is said to be stabilizing the (for example) T-periodic trajectory $x_*(t)$ (with output $y_*(t) = g(t, x_*(t), \mu)$) of the uncontrolled system $\dot{x} = f(t, x, \mu, 0)$, if for every T-periodic reference $y_\mathrm{r} \approx y_*$ and initial conditions (t, x) close to $(t, x_*(t))$ the controlled system (1) converges to a unique T-periodic limit $y_\mathrm{lim}(t) \approx y_*(t)$. Moreover, the approach requires that the *asymptotic input-output map* $Y : (y_\mathrm{r}, \mu) \mapsto y_\mathrm{lim}$ is continuously differentiable in the space of T-periodic functions. If the stabilization condition is satisfied for the feedback control $y - y_\mathrm{r} \mapsto u$, then one may find the periodic orbit y_* of the uncontrolled system as fixed point of the map Y: $y_\mathrm{r} = Y(y_\mathrm{r}, \mu)$ if and only if $y_\mathrm{r} = y_*$, regardless of the dynamical stability of y_*. This enabled the authors of [1, 2, 5, 6, 7] to track response curves through limit (fold/saddle-node) bifurcations, track fold bifurcations in two parameters, and detect stable and unstable directions of saddle-type orbits in mechanical oscillator experiments.

Solving the nonlinear fixed-point problem $y = Y(y, \mu)$

One difficulty when solving for (or tracking) fixed points of the input-output map Y is that the Jacobian of $Y(y_\mathrm{r}, \mu)$ with respect to its arguments, which Newton iteration-based solvers require, is not known, and can generally be obtained only by performing repeated experiments for small deviations of the inputs, $(y_\mathrm{r} + \delta y_\mathrm{r}, \mu + \delta\mu)$. For mechanical oscillator experiments the periodic orbits are nearly harmonic such that [7] approximated y_r with low-order harmonics: $y_\mathrm{r}(t) \approx P_N[y_\mathrm{r}](t) := \sum_{\ell=-N}^{N} y_\ell b_\ell(t)$, where, in their case, $b_\ell(t) = \cos(\ell\omega t)$ for $\ell \le 0$, $b_\ell(t) = \sin(\ell\omega t)$ for $\ell > 0$, $\omega = 2\pi/T$ and $N \le 10$ typically. Barton, Renson *et al* used a (Newton-)Picard iteration, splitting $y_\mathrm{r} = y_P + y_Q$ with $y_p \in \operatorname{rg} P_1$ and $y_Q \in \operatorname{rg} Q_1$ ($Q_N = I - P_N$). They observed that, for fixed (y_P, μ), the iteration $y_Q \mapsto Q_1 Y(y_p + y_Q, \mu)$ converges to a limit y_Q within measurement accuracy in one or two iterations, defining a map $Y_Q(y_P, \mu)$. This reduced the fixed point problem to the low-dimensional $y_P = P_1 Y(y_p + Y_Q(y_P, \mu), \mu)$ in $\operatorname{rg} P_1$, for which a finite-difference approximation of the Jacobian is feasible.

We generalize this Newton-Picard approach to problems where we expect a severely non-harmonic fixed point y_*, that is, typically problems with large period T. Our illustrating example below considers a forced system with forcing as shown in fig. 1(top-left). The Picard iteration $y_Q \mapsto Q_N Y(y_P + Q_N y_Q, \mu)$ suffers a linear low-frequency instability for increasing periods T and fixed N. This is best illustrated considering the simplest case $\dot{x} = ax - k[y - y_\mathrm{r}]$ with $y = g(x) = x$ and $0 < a < k$ for (1) on an interval $[0, T]$. In this case the map Y is linear and commutes with P_N and Q_N, and the map $y \mapsto Yy$ has unstable eigenvalues corresponding to eigenfunctions of the form $\exp(2\pi\mathrm{i}\ell t/T)$ for all $\ell < T\sqrt{a(2k-a)}/(2\pi) =: m$. Thus, for the Picard iteration $y \mapsto Q_N Y(y_p + y)$ (with fixed y_P) to converge, the projection P_N must be injective on the space spanned by the m lowest harmonic modes. This criterion determines the necessary dimension of the space $\operatorname{rg} P_N$ of variables in which one has to formulate the nonlinear problem for the Newton iteration, which is in general high-dimensional for large periods T:

$$y_P = P_N Y(y_P + Y_Q(y_P, \mu), \mu) \quad \text{for } y_p \in \operatorname{rg} P_N, \text{ where } \dim \operatorname{rg} P_N \sim N \gg 1 \text{ for } T \gg 1, \text{ such that } N \sim T. \tag{2}$$

The problem can be addressed if the control law $y_\mathrm{r} - y \mapsto u$ stabilizes such that perturbations decay on a time horizon h of order 1 uniformly in $[0, T]$ (using the additional arguments in y to indicate initial time and initial condition for state x):

$$|y(t; t_0, x_1) - y(t; t_0, x_2)| \le C \exp(-\gamma(t - t_0))|x_1 - x_2| \tag{3}$$

in (1) for $\gamma > 0$, C of order 1, independent of the period T. In this case perturbations at time t_0 do not have noticeable influence anymore at time $t_0 + h$ (where h is s.t. $C\exp(-\gamma h) \ll 1$). If criterion (3) is satisfied, we may choose for $\operatorname{rg} P_N$,

for example, the space of piecewise constant functions: $[P_N y](t) = T/N \int_{t_{\ell-1}}^{t_\ell} y(s)\mathrm{d}s =: y_\ell$ if $t \in J_\ell = [t_{\ell-1}, t_\ell)$, where $t_\ell = \ell T/N$. The variable for the nonlinear problem (2) is then $(y_1, \ldots, y_N, \mu)$, and (2) poses an equation on each interval J_ℓ. Due to the finite-time decay condition (3), $[\partial/\partial y_\ell] P_N Y|_{J_\nu}$ is small if the distance between ν and ℓ satisfies $|\nu - \ell| > hN/T =: q = O(1)$. Hence the Jacobian $\partial P_N Y/\partial y_P$ has only q non-zero diagonals. This implies that deviations δy_ℓ and δy_ν can be applied simultaneously if $|\ell - \nu| > q$ when determining the finite difference approximation for $\partial P_N Y/\partial y_P$. Consequently, the fixed point problem (2) with a projection P_N chosen such that the Picard iteration is linearly stable on $\mathrm{rg}[I - P_N]$ can be solved with a (computational or experimental) effort that grows linearly in the period T because the number of necessary evaluations of Y is independent of the period T.

Example — quasiperiodically forced delay differential equation (DDE) modelling the Mid-Pleistocene transition
We demonstrate the feasibility for a simple quasiperiodically forced model for palaeoclimate ice ages, modelling the Mid-Pleistocene transition, which is a simplification of a model originally proposed by Saltzman & Maasch, see [3, 4],

$$\mathrm{d}x(t) = \left[-px(t-\tau) + rx(t) - sx(t-\tau)^2 - x(t-\tau)^2 x(t) - aI(t)\right]\mathrm{d}t + \sigma dW_t, \tag{4}$$

for the global ice mass anomaly x over the last 2 million years. Quinn *et al* [3, 4] observed that the forcing by variability of solar insolation $I(t)$, shown in fig. 1(top-left), causes a transition at time t_c from small-amplitude fluctuations around an equilibrium (at $x = -0.5$) to a large-amplitude limit cycle for forcing amplitudes a greater than some critical value a_c ($a_c = 0.1$ for transitions without noise). The time t_c is close to where the Mid-pleistocene transition from rapid to slow ice ages occurrs in data sets. Continuation of the saddle and the attractor for positive a without noise (using DDE-Biftool) shows that the two non-autonomous trajectories pinch at t_c. In the infinite-time limit, saddle and node form a strange non-chaotic attractor at the critical amplitude a_c. We track the saddle for the non-autonomous system (enforcing artificially periodic boundary conditions) as a test case for the control-based continuation of complex time profiles with random disturbances of size σ. Feedback control was trivially applicable by adding it to the solar insolation: $aI(t) + k[y_\mathrm{r} - y]$, where output $y = x$. A typical time profile is shown (in red) in fig. 1(bottom-left), the partial bifurcation diagram is in fig. 1(bottom-right). Note that saddle and node do not form a smooth saddle-node near $a = a_c$ without noise.

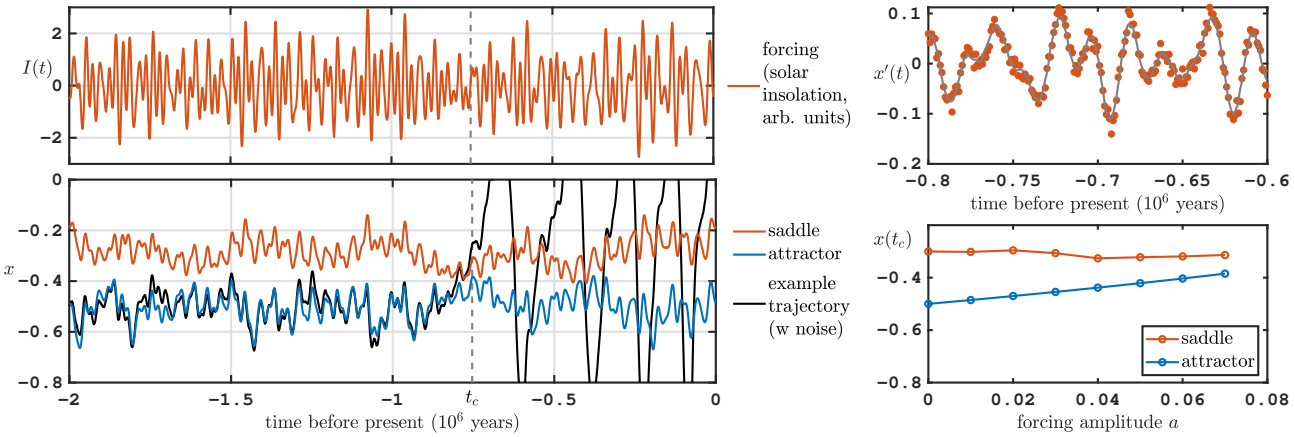

Figure 1: (top-left) Solar insolation $I(t)$ at 65° degree North in the summer [4]; (bottom-left) nonautonomous attractor and saddle, and large-noise ($\sigma = 6 \times 10^{-3}$) trajectory illustrating transition near time t_c, caused by saddle-node pinching; (top-right) approximate $\mathrm{d}x/\mathrm{d}t$ illustrating magnitude of disturbance; (bottom-right) partial bifurcation diagram for value of saddle and attractor at t_c. Parameters as in [3]: $p = 0.95$, $r = s = 0.8$, $\tau = 1.31$, Euler-Maruyama scheme stepsize 0.1, $\sigma = 3 \times 10^{-3}$, $N = 200$, gain $k = 2$.

Potential future experimental test cases are forced mechanical single-degree-of-freedom oscillators with hardening nonlinearity where one may track connecting orbits caused by brief spikes of the forcing amplitude.

References

[1] D.A.W. Barton. Control-based continuation: Bifurcation and stability analysis for physical experiments. *Mechanical Systems and Signal Processing*, 84:54–64, 2017.

[2] D.A.W. Barton, B.P. Mann, and S.G. Burrow. Control-based continuation for investigating nonlinear experiments. *Journal of Vibration and Control*, 18(4):509–520, 2012.

[3] C. Quinn, J. Sieber, and A. S. von der Heydt. Effects of periodic forcing on a paleoclimate delay model. *SIAM Journal on Applied Dynamical Systems*, 18(2):1060–1077, 2019.

[4] C. Quinn, J. Sieber, A. S. von der Heydt, and T. M. Lenton. The mid-pleistocene transition induced by delayed feedback and bistability. *Dynamics and Statistics of the Climate System*, 3(1):dzy005, 2018.

[5] L. Renson, D.A.W. Barton, and S.A. Neild. Experimental tracking of limit-point bifurcations and backbone curves using control-based continuation. *International Journal of Bifurcation and Chaos*, 27(01):1730002, 2017.

[6] L. Renson, J. Sieber, D.A.W. Barton, A.D. Shaw, and S.A. Neild. Numerical continuation in nonlinear experiments using local Gaussian process regression. *Nonlinear Dynamics*, doi: s11071-019-05118-y, aug 2019.

[7] Frank Schilder, Emil Bureau, Ilmar Ferreira Santos, Jon Juel Thomsen, and Jens Starke. Experimental bifurcation analysisâĂŤcontinuation for noise-contaminated zero problems. *Journal of Sound and Vibration*, 358:251–266, 2015.

New MatCont and a numerical bifurcation study of a perception problem in psychophysics

Willy Govaerts*, Yuri A. Kuznetsov†‡, Hil G.E. Meijer ‡, Niels Neirynck* and Richard J.A. van Wezel††

**Department of Applied Mathematics, Computer Science and Statistics, Ghent University, Belgium*

†*Department of Mathematics, Utrecht University, The Netherlands*

‡*Department of Applied Mathematics, Twente University, The Netherlands*

†† *Donders Institute for Brain, Cognition and Behaviour, Radboud University, Nijmegen, The Netherlands*

Summary. We discuss the new GUI environment of the MATLAB software package MatCont for numerical bifurcation studies of continuous dynamical systems. It is built upon the corresponding command line package Cl_MatCont. The package is freely available via sourceforge.net/projects/matcont and offers both interfaces. Mathematically, the functionalities of MatCont with respect to bifurcation techniques are unrivalled. For instance, no other software allows to compute the normal forms of codimension two bifurcations of periodic orbits, or to start curves of codimension one bifurcations of periodic orbits from codimension two equilibrium points. Though widely used, the previous version of MatCont was at the end of its life span of maintainability and the new MatCont gives it a fresh start. It is completely reorganized with a better documentation and an improved data handling with a Data Browser, a Diagram Organizer and a Spreadsheet Viewer. Other new features are the Command Line Interface, the functionality of computing Poincaré maps and many facilities to simplify the use of the software. As an application we discuss a computational model that describes the stabilization of percept choices under intermittent viewing of an ambiguous visual stimulus at long interstimulus intervals. Unlike previous studies we incorporate the time that the stimulus is on (T_{on}) and off (T_{off}) explicitly as bifurcation parameters of the model. We compute the bifurcations of periodic orbits responsible for switching between alternating and repetitive sequences. We show that the region of bistability of repeating and alternating behavior is a wedge in the parameter plane bounded by two curves of limit point bifurcations of periodic orbits and one curve of period-doubling bifurcations.

Introduction

We consider smooth continuous dynamical systems of the form

$$\frac{dx}{dt} \equiv \dot{x} = f(x, \alpha), \quad x \in \mathbb{R}^n,\ \alpha \in \mathbb{R}^m, \tag{1}$$

with state variable x, parameter α and f a sufficiently smooth function (continuous derivatives up to order 5 are needed in some cases). The numerical bifurcation analysis of (1) requires a dedicated software package. For this purpose MATCONT was developed, a MATLAB continuation toolbox available at *http://sourceforge.net/projects/matcont/*. It is a successor package to CONTENT [7] and LINBLF [6].

Bifurcation analysis usually starts with equilibria and periodic orbits (limit cycles). The stable ones can be found by time integration of the system, see the MATCONT manual [4], §6.2 and §7.4. By numerical continuation under variation of a single system parameter one can detect and study the codimension one bifurcations, i.e. limit points and Hopf points for equilibria, limit points of cycles, period-doubling and Neimark-Sacker (torus) bifurcation points for periodic orbits. Further continuation of these codimension one bifurcations under variation of two system parameters leads to the detection and study of codimension two bifurcation points; there are 5 codimension two types of bifurcations of equilibria and 11 types for periodic orbits. MATCONT allows to study all these bifurcations numerically and perform many related tasks, including the study of orbits homoclinic to saddle, homoclinic to saddle-node and heteroclinic orbits. Critical normal form coefficients are computed at bifurcation points. For this we rely on symbolic derivatives or if these are not available, on finite difference approximations. Bifurcation curves are defined by a system of equations consisting of fixed point and bifurcation conditions. The continuation curves can be visualized using the plot capabilities of the GUI; this can be done during and after the continuation. Special windows are provided to help with maintaining systems, diagrams and curves when generating a large amount of data.

Earlier versions of MATCONT and their functionalities were described in [1] and [2]. We will restrict to the new features in the renovated 2019 environment MATCONT7.1 and later versions. From a computer science point of view MATCONT7.1 is a completely new creation. It has a clear separation of computational and control routines to facilitate the maintainability. Its GUI allows a maximal flexibility to reprogram the layout of windows, buttons and input fields on the screen. It contains automatic tests to check if a new MATLAB version produces the same results as the previous version. Error handling of plots is much improved so that malfunctioning of plots (for any reason) does not crash the computations. Unlike the previous versions, it has an external documentation ([8], Ch. 6) and a detailed internal documentation. The internal documentation of a source file is accessed by typing '`doc filename.m`' on the command line; a reference page is then generated based on the comments in the source file.

The core mechanism of the new MATCONT environment is an intermediate layer of routines between CL_MATCONT and the GUI as seen by the user. It is described in [8], Chapter 6; the main elements in this mechanism are the MATLAB

classes *settings, session* and *solution*, cf. the section **Command Line Interface.** This layer also protects against nonsense input in the CL_MATCONT routines.
Important other parts, which can be used semi-autonomously are the generator of the system m-files (*SysGUI.m*), the spreadsheet viewer (*GUISimCurveTable.m* and *GUIContCurveTable.m*) and the GUI subsystems *Data Browser* and *Diagram Organizer*, which are stored in subfolders of the *GUI* folder. The main driver files are `matcont.m`, `GUI/MATCONTGUI.m` and `GUI/Session.m`.
For the practical use of MATCONT it is best to start with the tutorials which are provided with the software; the manual [4] is a good reference to the command line version CL_MATCONT.
To study a system in MATCONT one has to describe it in a *system m-file,* which serves as a handle to the system. MATCONT provides an interface to build such m-files, see the manual [4], §4 or the first tutorial.
The MATCONT panels are described in [8], Ch. 5. The main MATCONT panel is shown in Figure 1. We note in particular the tab line at the top with the six tabs **Select, Type, Window/Output, Compute, Options,** and **Help.**

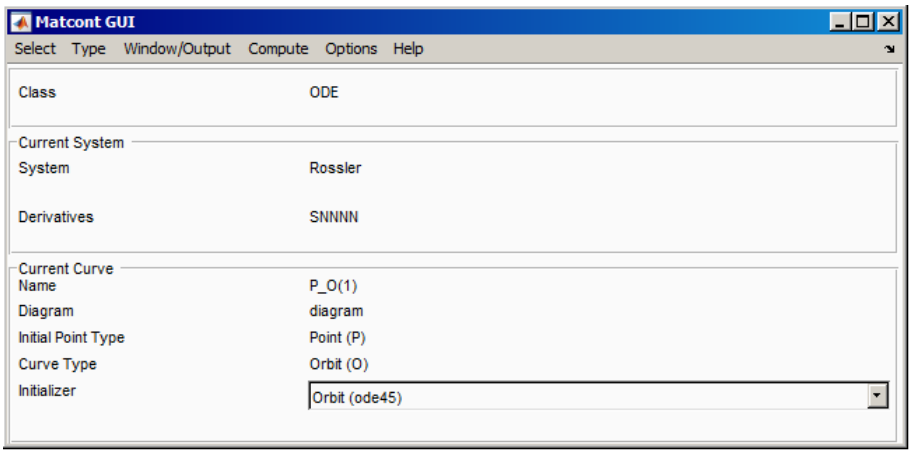

Figure 1: The main MATCONT panel.

Data management in MATCONT

The Diagram Organizer

The database of MATCONT consists of an archive of systems one of which is the *current system*.
A system is internally characterized by a system m-file, a system mat-file and a system directory, all with the name of the system. They are all in the subdirectory **Systems** of MATCONT. When a MATCONT session is closed **(Select|Exit)** then the session information is stored in a file `session.mat` in the **Systems** directory. This allows to restart the MATLAB session at the point where it was stopped.
The m-file is a readable file that contains all defining information on the system; the mat-file contains the same information in a structured way that is accessible to the MATCONT software. Both stay unchanged as long as the system is not changed or deleted.
The directory of each system also contains a file `session.mat` which contains the information that is necessary to restart or reproduce the computations on that system at the stage where it was left, including the position and contents of all windows. However, plots have to be redrawn.
The system directory also has at least one default subdirectory called `diagram`. This and other subdirectories of the system directory are called *diagrams.* Each diagram contains a number of mat-files and each mat-file describes a computed curve with enough information to recompute the curve. Each computed curve contains a number of special points, which includes the first point, the last point, bifurcation points, and zeros of userfunctions but other entities may also be defined as special points. An important example of this is the case of an orbit where a **Select Cycle** object is identified as a special point (for more details see the section **Other New Features**).
Clicking **Select|Organize Diagrams** in the main MATCONT panel opens the Diagram Organizer which allows to move curves from one diagram to another, see Figure 2.

The Spreadsheet Viewer

The Spreadsheet Viewer allows to inspect all stored data of a computed curve. It can be accessed by pressing the **View Curve** button in a Curve window that is opened in the Data Browser. However, it is not possible to load data from the Spreadsheet Viewer for further use in MATCONT.

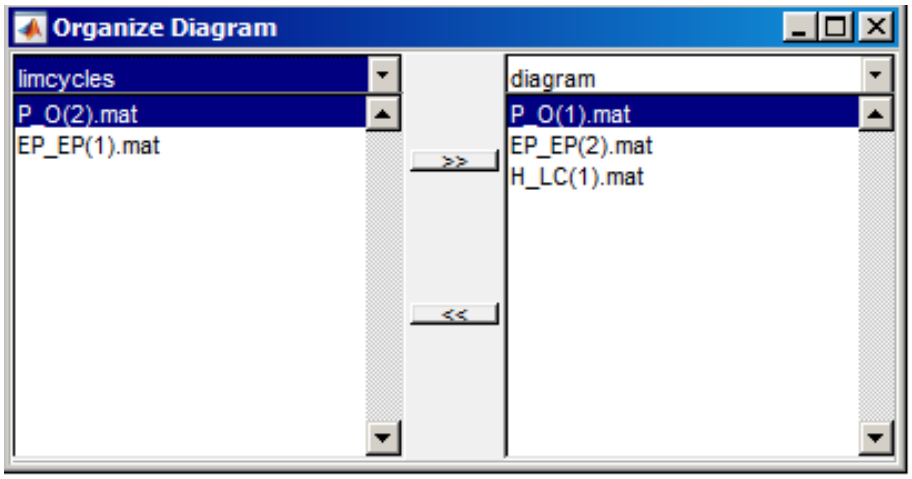

Figure 2: The Diagram Organizer panel.

The Command Line Interface

The Command Line Interface (cli) is a collection of MATLAB commands that allow to use practically all GUI functionalities from the command line in an interactive way.
This has a number of advantages. First, if the number of state variables or parameters is large and provided by an external file, then it is possible to load them as vectors directly into MATCONT. Second, it allows to write a MATLAB script that uses MATCONT in a semi-automatic way, for example to perform a bifurcation analysis for a range of values of parameters which are fixed in each particular bifurcation analysis. Third, it allows to load the raw computed data of a continuation or simulation directly into the Matlab workspace.
In the cli we address directly the intermediate layer of routines. This requires to set one or more of the class variables `settings, session, solution` as global.
To illustrate the use of the cli we introduce the *Rössler* system [10]:

$$\begin{cases} \dot{x} &= -y - z \\ \dot{y} &= x + Ay \\ \dot{z} &= Bx - Cz + xz, \end{cases} \tag{2}$$

where (x, y, z) are the phase variables, and (A, B, C) are the parameters. We introduce it in MATCONT under the name *ROESSLERTest* and let the derivatives of order 1, 2 and 3 be computed symbolically. To perform a time integration we select the initial point type 'Point' and input $x = 1$, $y = 2$, $z = 3$, $A = 0.2$, $B = 0.4$, $C = 0.7$ as initial values. In the **Integrator** window we set the interval to 200. We then turn to the MATLAB command line to inspect the settings:

```
>> global settings
>> settings
settings =
              system: ROESSLERTest
                  IP: Point (P)

        option_pause: At Special Points
      option_archive: 2
       option_output: 1
============================
                time: 0
                co_x: 1
                co_y: 2
                co_z: 3
               coord: [ 1, 2, 3 ]

          parameters: [ 0.2, 0.4, 0.7 ]
                pa_A: 0.2
                pa_B: 0.4
                pa_C: 0.7
============================
            Interval: 200
```

```
       eventfunction: <disabled>
    InitStepSize_sim: <automatic>
     MaxStepSize_sim: <automatic>
        RelTolerance: 0.001
        AbsTolerance: 1e-06
              Refine: 4
         Normcontrol: false

>> settings.co_x
ans =
     1
>> settings.coord
ans =
     1     2     3
```

We can also change some of the settings:

```
>> settings.coord.set([-5 5 10])
>> settings.parameters.set([0 0.4 4.5])
```

In the GUI we can check that these changes are visible in the **Starter** window. There we can also perform the computation. The outcome is stored in the `solution` class. We inspect it in the MATLAB command window:

```
>> global solution
>> solution
solution=
   SimCompSolution with properties:
             t: [1477x1 double]
             y: [1477x3 double]
        method: @ode45
         tspan: [0 200]
       options: [1x1 struct]
         param: [0 0.4000 4.5000]
            tE: []
            yE: []
            iE: []

>> solution.y
ans=
-5.0000 5.0000 10.0000
-5.0763 4.9739  9.5078
...
```

We return to the GUI, select the last point of the computed orbit (use the **View Result** button in the **Control** panel) and declare it to be an equilibrium. By default the Curve Type will now be 'Equilibrium'. We again inspect the `settings`:

```
>> settings
settings =
              system: ROESSLERTest
                  IP: Equilibrium (EP)

============================
        InitStepsize: 0.01
         MinStepsize: 1e-05
         MaxStepsize: 0.1

      MaxNewtonIters: 3
        MaxCorrIters: 10
        MaxTestIters: 10
        VarTolerance: 1e-06
        FunTolerance: 1e-06
       TestTolerance: 1e-05
```

```
               Adapt: 3

        MaxNumPoints: 300
         CheckClosed: 50
============================
                co_x: -0.000335576810360529
                co_y: -0.000180608885605843
                co_z: -3.20127988121691e-05
               coord: [ -0.00033557681, -0.00018060888, -3.2012798e-05 ]

          parameters: [ 0, 0.4, 4.5 ]
                pa_A: 0
                pa_B: 0.4
                pa_C: 4.5
         pa_A_select: false
         pa_B_select: false
         pa_C_select: false

          test_EP_BP: true
           test_EP_H: true
          test_EP_LP: true

         eigenvalues: true
============================
```

We need to select an active parameter in the equilibrium continuation. This can be done via the **Starter** window or via the command line:

```
>> settings.pa_A_select.set(true)
```

We will also restrict the number of computed points to 49. This can be done either via the **Continuer** window or via the command line:

```
>> settings.MaxNumPoints.set(49)
```

We execute the continuation in the GUI. The solution data can be obtained in the MATLAB Command window:

```
>> solution
solution=
ContCurve with properties:

x: [4x49 double]
v: [4x49 double]
s: [3x1 struct]
h: [5x49 double]
f: [3x49 double]

>> size(solution.x)
ans=
     4      49
```

So far all driving steps were executed in the GUI, where they were relegated to the `session` class. In a more advanced use of the cli we can also perform these steps from the command line by declaring the `session` class global. We then add the commands:

```
>> global session
>> session
```

The `session` output recalls the settings and then offers a choice of three buttons, labeled

```
View Computations  View Actions  View Switches
```

Clicking the first button is equivalent to executing the command

```
>> session.select()
```

It provides the numbered list of computations (usually time integrations or continuation runs) that can be selected from the given Initial Point type. They can be selected by clicking, or by typing

```
>> session.select(k)
```

where k is the list number.
Clicking the second button is equivalent to executing the command

```
>> session.compute()
```

It provides a fixed list of options, namely **Forward, Backward,** and **Extend**. The list can be handled as in the previous case.
Clicking the third button is equivalent to executing the command

```
>> session.switches()
```

It provides the list of objects that can be chosen as new Initial Points. The list can be handled as in the previous cases. One can change the type of an initial point from the command-line by using the instruction

```
>> session.changeInitPoint('H')  %force IP type to be 'Hopf (H)'
```

We note that it is always possible to get information about the current system:

```
>> settings.system
ans =
     CLSystem with properties:
name: 'RoesslerTest'
coordinates: {'x'  'y'  'z'}
  parameters: {'A'  'B'  'C'}
dim: 3
time: 't'
handle: @ROESSLERTest
userfunctions: {}
ufdata: []
diagramlocation: 'H:\MatCont7p1\Systems\ROESSLERTest'
derstr: 'SSSNN'
equations: [3x14 char]
```

Event functions and Poincaré maps

A Poincaré section is a (in general, curved) surface in phase space that cuts across the flow of a dynamical system. The Poincaré map transforms the Poincaré section onto itself by relating two consecutive intersection points. Only those intersection points count, which come from the same side of the section. In this way, a Poincaré map turns a continuous-time dynamical system into a discrete-time one. If the Poincaré section is carefully chosen no information is lost concerning the qualitative behaviour of the dynamics. For example, if the system's state is attracted to a limit cycle, one observes dots converging to a fixed point in the Poincaré section as in Figure 5.
When computing an orbit $(t, y(t))$ in MATLAB an event can be defined as going through a zero of a scalar event function $G(t, y)$. If G does not explicitly depend on time in an autonomous dynamical system, this functionality can be used to see the Poincaré map in action. However, one shortcoming of the MATLAB solvers is that they do not interactively report on these events.
In the 6.11 and earlier versions of MATCONT, Poincaré maps were therefore computed by using a specific curve type, called Discrete Orbit (DO). For this type of orbits the ODE solvers were manipulated to use an explicitly implemented approximation strategy to locate the Poincaré intersection points.
In the new GUI, there is no longer a specific curve type. In order to allow for interactive plotting of events, the plot routine monitors sign changes of the values of the event function. Whenever a sign change is observed, the solver is called again on a smaller part of the curve to extract the event. Due to the implementation of this workaround, the list of detected events after computation in rare cases might contain more events than were displayed on an interactive plot.
For the sake of generality MATLAB allows to define vector-valued event functions whereby each component function defines its own event. This is done by setting the Events property to a handle to a function, e.g. `@events` with the syntax `[`value,isterminal,direction] = events(t,y,varargin)
where y is a state vector. The input variable `varargin` is a cell array that contains the values of the parameters. If parameters are explicitly used in the definition of the event function, then `varargin` should be replaced by an explicit list of parameter names.
If there are k event functions then for $i \in \{1, \ldots, k\}$:

- `value(i)` is the value of the $i-$th event function.
- `isterminal(i)` = 1 if the integration is to terminate at a zero of the $i-$th event function and 0 otherwise.
- `direction(i)` = 0 if all zeros of the $i-$th component are to be computed (the default), +1 if only the zeros are needed where the event function increases, and -1 if only the zeros are needed where the event function decreases.

The use of event functions to compute Poincaré maps in CL_MATCONT is discussed in the manual [4]. We now illustrate the GUI implementation by example. We consider again the *Rössler* system (2).
Suppose that we want to compute an orbit and detect two events along it, namely $x = 0.2$ and $y = 0.3$. We need only the events where x, respectively y, are increasing and the integration will not be terminated if an event is detected.
We then define an event function `testEV` as follows:

```
function [value,isterminal,direction]= testEV(t,y,varargin)
value=[y(1)-0.2;y(2)-0.3];
isterminal=zeros(2,1);
direction=ones(2,1);
end
```

The function `testEV.m` is placed in the MATCONT main directory (or anywhere else on the MATCONT path)
We integrate the *Rössler* system from 0 to 100 starting from the point $[-5; 5; 10]$ with parameter values $(0.25, 0.4, 4.5)$ and input the name 'testEV' (without quotes) in the EventFunction field of the **Integrator,** see Figure 3.

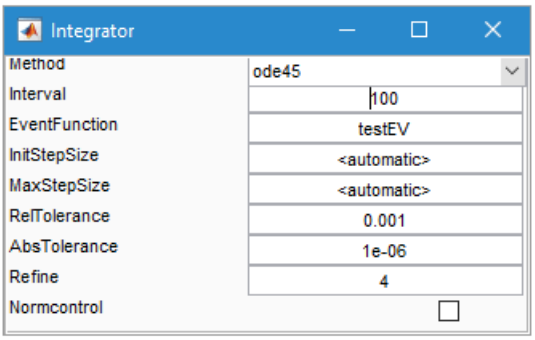

Figure 3: Integrator with an Event function.

We also open a MATCONT **Plot3D** window to display the state variables in the range $\{-9 \leq x \leq 9, -9 \leq y \leq 9, -2 \leq z \leq 11\}$. The 3D output is shown in Figure 4. We note that zeros of the first event function are marked as 'E1', those of the second as 'E2' and so on.
In Figure 5 we show the convergence of the iterates if the Poincaré map to a fixed point in a **Plot2D** window with $\{4.22 \leq x \leq 4.32, 2.3 \leq z \leq 2.8\}$,
The computed output is stored in the mat-file of the computed curve, from where it can be recovered for further use. It can also be sent directly to the MATLAB workspace by pressing the **Export** button in the **Data Browser** window that is opened by pressing the **View Curve** button in the **Control** window after the integration run. In the latter case we get the following output in the MATLAB command window :

```
exported=
  SimCompSolution with properties
         t: [1461x1 double]
 y: [1461x3 double]
  method: @ode45
 tspan: [0 100]
    options: [1x1 struct]
  param: [0.2500 0.4000 4.5000]
    tE: [33x1 double]
 yE: [33x3 double]
 iE: [33x1 double]
```

Here `tE` is the vector of time points where events were discovered, `yE` is the corresponding matrix of state variables and `iE` is a vector of ones and twos which refer to either the first or the second event.
Event points can also be selected as special points in the data browser and by double-clicking on the labels in the plots.

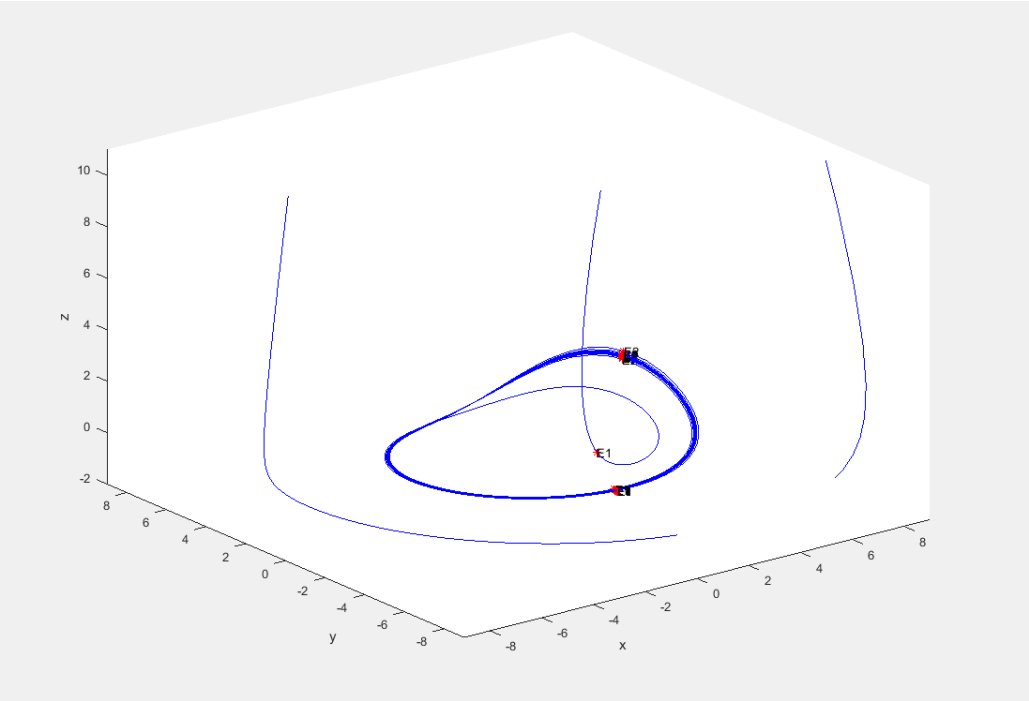

Figure 4: Time integration with event points that converge to fixed points.

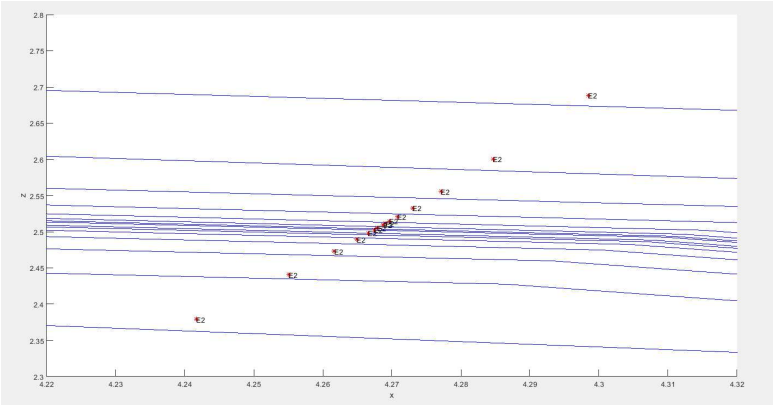

Figure 5: Convergence of the iterates of the Poincaré mapto a fixed point, alternating between points at the bottom left side and the top right side.

Other new features

The new MATCONT has been improved and extended with many new functionalities:

1. The Select Cycle object is presented as a Special Point after each time integration. Selecting it as an initial point opens a subpanel with two fields that allow to choose a convergence criterion and a number of mesh intervals for initializing a curve of periodic orbits that starts from the periodic orbit found by time integration. The number of collocation points is always 4 by default. We note that this requires that the computed orbit covers between one and two periods of the periodic orbit.

2. Graphical 2D and 3D plots are reorganized: only one layout window is presented and nearly everything can be plotted, i.e. many earlier restrictions are lifted.

3. Clicking **Options**|**Plot Properties** in the main panel (Figure 1) opens an edit box panel which allows to assign plot properties (color, linestyle, ...) to each type of computed curve. Defaults are provided for all types of computed curves, which can be overwritten using MATLAB code in the edit boxes. For curves of equilibria and curves of limit cycles, it is possible to differentiate between stable and unstable parts of the curves. Advanced MATLAB users can edit the file *GUICurveModifications.m* to add new differentiations of the plot properties within a curve.

4. Error handling of plots is improved so that plot errors caused by command line interference, or by GUI interference

when computations are suspended, do not crash the computations.

5. Each input field has input restrictions and these are checked to minimize input errors. So for example it will not be possible to input a float or a question mark if a positive integer value is required. Errors are reported in the MATLAB command line. On the other hand, numerical fields can be filled with MATLAB expressions, provided they can be evaluated in the command line. So one can insert $2 * Pi$ instead of its decimal expansion $6.283184...$

6. In continuation plots it is possible to click on a found singular point to obtain information on the curve where it was found, the type of point and the normal form coefficients. By double clicking one selects the point as an initial point for another continuation.

7. The Scroll - key can be used to scroll through MATCONT windows. This functionality had to be implemented separately as MATLAB does not provide this functionality as part of their standard library.

8. Several special keys can be used to control continuation computations, namely: **Escape** to stop, **Space bar** to resume, **Enter** to pause and **Control** to continue (when pressed) or to pause (when released). The use of the **Control** key is new.

Example: Percept switching in the human visual system

Percept switching under the action of an ambiguous visual stimulus is a well-known phenomenon in psychophysics, see e.g. [5, 9]. In [9] the authors discuss a neural explanation of the stabilization of percept choices under intermittent viewing of an ambiguous stimulus. They consider the following system:

$$\begin{cases} X_1' &= (Stim - (1 + A_1)X_1 + \beta A_1 - \gamma S(X_2))/\tau \\ X_2' &= (Stim - (1 + A_2)X_2 + \beta A_2 - \gamma S(X_1))/\tau \\ A_1' &= -A_1 + \alpha S(X_1) \\ A_2' &= -A_2 + \alpha S(X_2) \end{cases} \tag{3}$$

with state variables X_1, X_2, A_1, A_2 and fixed parameters $\alpha = 5$, $\beta = 4/15$, $\gamma = 10/3$, and $\tau = 1/50$. The primary dynamical variables X_1, X_2 are the 'local fields', which correspond to the percept-related components of the membrane potentials of the neurons that encode the two competing percepts, indicated by 1 or 2 respectively. To each primary variable an adaptation variable is associated, called A_1, A_2 respectively. In the local field interpretation these correspond to the (averaged and scaled) gating variables of the neurons. $Stim$ is the amplitude of the stimulus. $S(X_1)$ is a sigmoidal function of X_1, zero for negative values of X_1 and equal to $X1^2/(1 + X1^2)$ for nonnegative values of X_1. $S(X_2)$ is to be interpreted similarly. The precise choice of the sigmoid function does not influence the qualitative behavior of (3).
Line 1 of (3) specifies how X_1 integrates the stimulus with its adaptation variable A_1 and the subtractive cross-inhibition $S(X_2)$. Lines 2 and 4 are dual to Lines 1 and 3.
In [9] the authors consider a 128 by 128 grid of points in a (T_{off}, T_{on}) space. For each point a simulation of (3) is done with the stimulus alternatingly switched off during a time span T_{off} and on during a time span T_{on}. The eventual behavior (after a transient) varies with the choice of T_{off} and T_{on} but also depends on the initial values of the state variables. It includes repeating and alternating patterns and bistability. An important observation is that for fixed T_{on} the behavior can be stabilized by increasing T_{off}, i.e. it leads to a situation where the percept is the same whenever the stimulus switches on (but may still depend on the initial state at the very beginning.)

Modelling of the percept switching system in MATCONT
In MATCONT we approximate the on/off switching by a continuous system with a periodic forcing with period $T_{off}+T_{on}$. This involves the inclusion of T_{off} and T_{on} as new parameters in the system and avoids the need of an enormous number of time integrations, in each of which the resulting stable behaviour can depend upon the initial state values.
Instead we make numerical computations based on the theory of bifurcations of periodic orbits. Boundaries of behavior regions in the (T_{off}, T_{on})-plane are obtained as curves of codimension 1 bifurcations of periodic orbits which meet in codimension 2 points. The periodic forcing is implemented with new independent state variables Y_1, Y_2. More precisely, we consider the following system (in the notation of the MATCONT input field):

```
S1=(X1^2)/(1+X1^2)/(1+exp(-expp*X1))
S2=(X2^2)/(1+X2^2)/(1+exp(-expp*X2))
omega=2*pi/(Ton+Toff)
Stim=1/(1+exp(-expp*(Y1-cos(2*pi*Ton/2/(Ton+Toff)))))
X1'=(Stim-(1+A1)*X1+beta*A1-gamma*S2)/tau
X2'=(Stim-(1+A2)*X2+beta*A2-gamma*S1)/tau
A1'=-A1+alpha*S1
A2'=-A2+alpha*S2
Y1'=-omega*Y2+Y1*(1-Y1^2-Y2^2)
Y2'=omega*Y1+Y2*(1-Y1^2-Y2^2)
```

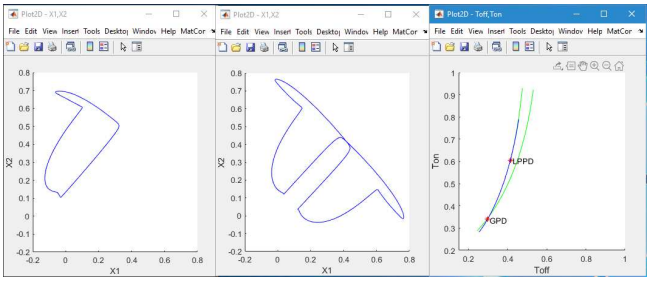

Figure 6: Left: repeating orbit with period $T_{off}+T_{on}$. Middle: alternating orbit with period $2(T_{off}+T_{on})$. Right: wedge of bistability.

with state variables X1, X2, A1, A2, Y1, Y2. The auxiliary variables S1,S2 approximate the sigmoid functions $S(X_1), S(X_2)$, respectively. They help to facilitate the implementation and increase the readability of the MATCONT input. We have also introduced an additional parameter $expp$ to the system, appearing in the equations for $S1$, $S2$ and $Stim$. By increasing its value, the analytical functions for S1 and S2 in the MATCONT system converge to the non-analytical step sigmoid functions that are used in (3). In our computations $expp = 60$. More details are given in [3].
The state variables Y1 and Y2 are decoupled from the other state variables. Their stable behaviour (after a transient) is a periodic orbit of the form $Y1 = \cos(\omega t + P), Y2 = \sin(\omega t + P)$ with a time shift P that depends only on the initial values of Y1,Y2. The period of this orbit is $T_{off} + T_{on}$.
When Y1,Y2 evolve along the unit circle then from the fourth line in the MATCONT system it follows that Stim is alternatingly close to one during a time span T_{on} and close to zero during a time span T_{off}. The stimulus term thus acts as an on/off switch in a periodic forcing of (3).
Fig. 6 (left) shows the (X1,X2) projection of a stable periodic orbit computed by time integration for $T_{off} = 0.6, T_{on} = 0.8$ (after a transient, starting with values of (Y1,Y2) which are not both zero). The time evolution is repeating, i.e. after each on/off cycle we see the same partial trajectory which corresponds to the percept X1 (for a different choice of the initial values of the state variables it can be the percept X2). Fig. 6 (middle) shows the projection of a stable periodic orbit computed by time integration for $T_{off} = 0.2, T_{on} = 0.8$. The time evolution is alternating, i.e. X1 and X2 dominate in turns.
To study the stability regions of repeating and alternating periodic orbits we use the Select Cycle functionality of MATCONT. We start the continuation of limit cycles from the stable limit cycles in Fig. 6 under variation of T_{off}. By using the branch switching functionalities of MATCONT we then construct the bifurcation diagram and find that in (T_{off}, T_{on})–space the stability regions of repeating and alternating orbits overlap in the wedge shown in Fig. 6 (right). The wedge is bounded at the right by a curve (green) of limit points of cycles of alternating periodic orbits. At the left, the boundary consists partly of a curve (green) of limit points of cycles of repeating periodic orbits and a curve (blue) of period-doubling points of repeating periodic orbits. The green and blue curves meet in a fold-flip bifurcation point of cycles denoted by LPPD. The blue curve contains a generalized period-doubling point (GPD) of repeating periodic orbits. The LPPD point is situated at $(0.41416, 0.60659)$, the GPD point at $(0.29837, 0.34146)$.

Conclusion

The MATCONT implementation greatly minimizes the computational work in the study of the perception problem. It confirms and explains the stabilization effect observed in the numerical simulations and allows easy extensions to similar studies with other models or other parameters.

References

[1] Dhooge, A. and Govaerts, W. and Kuznetsov, Yu. A. (2003) MATCONT: A MATLAB package for numerical bifurcation analysis of ODEs. *ACM Trans. Math. Softw.* **29(2)** pp. 141-164. http://doi.acm.org/10.1145/779359.779362.

[2] Dhooge A., Govaerts W., Kuznetsov Yu. A., Meijer, H.G.E., and Sautois, B. (2008) New features of the software MatCont for bifurcation analysis of dynamical systems. *Mathematical and Computer Modelling of Dynamical Systems* **14 (2),** pp. 147-175. https://doi.org/10.1080/13873950701742754

[3] Govaerts W., Kuznetsov Yu. A., Meijer, H.G.E., Neirynck, N. and van Wezel, R., Bistability and stabilization of human visual perception under ambiguous stimulation, *Nonlinear Dynamics, Psychology and Life Sciences*, **25 (3)** pp.297-307.

[4] Govaerts, W. and Kuznetsov, Yu.A. and Meijer, H.G.E. and Al-Hdaibat, B. and De Witte, V. and Dhooge, A. and Mestrom, W. and Neirynck, N. and Riet, A.M. and Sautois, B. (2019) MATCONT:Continuation toolbox for ODEs in Matlab. http://sourceforge.net/projects/matcont/

[5] Gregson, R.A.M. (2004) Transitions between two pictorial attractors. *Nonlinear Dynamics, Psychology and Life Sciences* **8, 41-64.**

[6] Khibnik, A.I. (1990) LINBLF: A program for continuation and bifurcation analysis of equilibria up to codimension three, in: Continuation and Bifurcation: Numerical Techniques and Applications, vol. 313 of NATO Adv. Sci. Inst. Ser. C, Math. Phys. Sci., Dordrecht (eds. Roose, D. and De Dier, B. and Spence, A.) pp.283-296. ISBN = 978-1-4020-6355-8.

[7] Kuznetsov, Yu. A. and Levitin, V.V. (1997) CONTENT: Integrated Environment for analysis of dynamical systems, CWI, Amsterdam.

[8] Neirynck, N. (2019). Advances in numerical bifurcation software: MatCont. *PhD thesis*, Ghent University, Belgium. https://biblio.ugent.be/publication/8615817

[9] Noest A. J., van Ee R., Nijs M. M., and van Wezel R. J. A. (2007) Percept-choice sequences driven by interrupted ambiguous stimuli: A low-level neural model. *Journal of Vision* **7,** pp. 1-14. https://doi.org/10.1167/7.8.10

[10] Roessler, O. (1979) Continuous chaos - four prototype equations, in: Bifurcation Theory and Applications in Scientific Disciplines (eds. Gurel, O. and Roessler, O.), New York Acad. Sci., pp. 376-392.

Finding connecting orbits between saddle periodic orbits as organising centres of complicated dynamics

Nelson Wong*, Hinke M. Osinga* and Bernd Krauskopf*
*Department of Mathematics, University of Auckland, Auckland, New Zealand

Summary. We study heterodimensional cycles between two periodic orbits in a four-dimensional vector field. Such cycles are characterised by a connecting orbit that lies in the intersection of two two-dimensional manifolds; the returning connection is given by a family of connecting orbits in the generic two-dimensional intersection of two three-dimensional manifolds. Heterodimensional cycles are known to organise highly complicated dynamics, which persist under C^1-perturbations of the vector field. There are very few explicit examples known from applications; we study one such example, namely, a vector field model for calcium dynamics in a cell. We employ Lin's method to compute heterodimensional cycles and associated nearby global bifurcations. We present a cycle that is non-orientable and compute its locus in a two-parameter plane. In this way, we explore how it contributes to the organisation of the overall bifurcation structure, which, in turn, elucidates mechanisms behind the generation of C^1-robust chaotic dynamics.

A connecting cycle between two saddle periodic orbits is *heterodimensional* if the periodic orbits have unstable manifolds of different dimensions. Heterodimensional cycles can only exist in vector fields of dimension at least four, and are known to generate highly complicated dynamics [1, 2, 3, 5], including infinitely many periodic and/or homoclinic orbits. Furthermore, if a system has a codimension-one heterodimensional cycle, then every other system in a C^1-neighbourhood about the original system also has a heterodimensional cycle. We are interested in the mechanism behind such C^1-robustness, and study the existence and properties of heterodimensional cycles in an explicit four-dimensional vector field.

Heterodimensional cycles are primarily studied abstractly. In particular, there are very few known examples arising out of applications. We study a model for intracellular calcium oscillations that is known to feature a heterodimensional cycle [7]. The equations are given by

$$\begin{cases} \dot{c} &= v, \\ D_c\,\dot{v} &= s\,v - \left(\alpha + \dfrac{k_f\,c^2}{c^2+\varphi_1^2}\,n\right)\left(\dfrac{\gamma\,(c_t + D_c\,v - s\,c)}{s} - c\right) + k_s\,c - \delta\,(J - k_p\,c), \\ \dot{c_t} &= \delta\,(J - k_p\,c), \\ s\,\dot{n} &= \dfrac{1}{\tau}\left(\dfrac{\varphi_2}{\varphi_2 + c} - n\right). \end{cases} \tag{1}$$

Here, c represents the calcium concentration in the main part of the cell body (the cytosol) and c_t the total calcium concentration inside the cell (including that in an internal calcium store, known as the endoplasmic reticulum or ER); v is the membrane potential; and n is a gating variable that represents the fraction of open channels through which calcium enters the cytosol from the ER. System (1) is written in a moving-frame coordinate system and the differentiation is with respect to the travelling-wave coordinate. We choose the same parameters as in [7] with $s = 9.0$ fixed, and we vary the flux J of calcium entering from outside the cell as our bifurcation parameter; see Table 1.

α	k_s	k_f	k_p	φ_1	φ_2	τ	γ	D_c	δ	s
0.05	20.0	20.0	20.0	2.0	1.0	2.0	5.0	25.0	0.2	9.0

Table 1: Parameter values for the intracellular calcium model (1).

With this explicit model, we can leverage advanced numerical methods to study heterodimensional cycles in a concrete setting. To this end, we set up a two-point boundary value problem (2PBVP) based on Lin's method that represents the (non-robust) connecting orbit. More precisely, we define an orbit segment that starts near a saddle periodic orbit and ends in a three-dimensional cross-section Σ, which we choose to be locally transverse to the flow [6]. We also define a second orbit segment that starts in Σ and ends near another saddle periodic orbit. Here, we fix parameters as in Table 1 and start with $J = 2.957$, which we estimate to be close to the actual bifurcation value. The two orbit segments are restricted such that the difference between their end points in Σ lies in a prescribed *Lin direction*. This 2PBVP can be solved by pseudo-arclength continuation techniques in AUTO [4]. As we vary J, we detect the connecting orbit as a zero of the distance between the end points in Σ. Once the connecting orbit has been found, its locus can be computed by varying two system parameters while keeping the distance at zero.

We find a heterodimensional cycle in system (1) for $J \approx 2.95748$; this cycle is shown in Figure 1 in projection onto (c, v, c_t)-space. Specifically, we show the single connecting orbit Ω_1^{PD} (blue) from the saddle periodic orbit Γ_1 (green) to the saddle periodic orbit Γ_{PD} (green), and the family S of orbits from Γ_{PD} to Γ_1 that forms a two-dimensional surface (red).

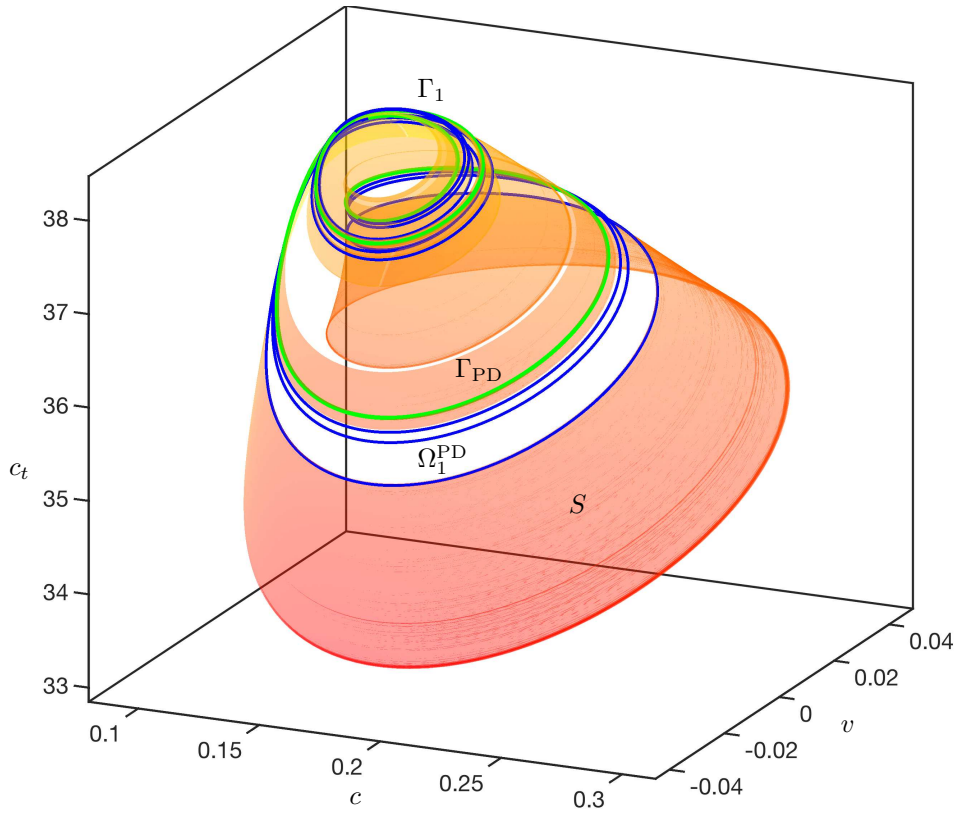

Figure 1: Three-dimensional projection onto (c, v, c_t)-space of the non-orientable heterodimensional cycle in system (1) with $J \approx 2.95748$. Shown are saddle periodic orbits (green) Γ_1 and $\Gamma_{\rm PD}$, the codimension-one connecting orbit $\Omega_1^{\rm PD}$ (blue) from Γ_1 to $\Gamma_{\rm PD}$, and the returning surface S (red) of robust connections.

Importantly, the heterodimensional cycle in Figure 1 is different from the one found in [7]. Its distinguishing feature is that Γ_1 is non-orientable. As we decrease J from near the Hopf bifurcation that creates Γ_1, this periodic orbit undergoes a period-doubling bifurcation, so that it has one negative unstable, one negative stable, and one positive stable Floquet multiplier, with the positive one being associated with the strongest contracting direction. This period-doubling bifurcation is subcritical, and gives rise to a period-doubled orbit that undergoes its own period-doubling bifurcation before merging with $\Gamma_{\rm PD}$ at a fold bifurcation. The periodic orbit $\Gamma_{\rm PD}$ in Figure 1 has one negative stable, one negative unstable, and one positive unstable Floquet multiplier. The closure of S is non-orientable since it is tangent to the weakly stable linear bundle of Γ_1, which is associated with the negative stable Floquet multiplier. The non-orientability complicates the geometry of S: S accumulates onto Γ_1 in a twisting fashion, since the weakly stable linear bundle of Γ_1 locally forms a Möbius band.

Starting from the heterodimensional cycle for $J \approx 2.95748$, we can compute the one-parameter family of this cycle in a two-parameter plane. By studying the bifurcation structure of system (1) locally about this locus, we examine how the parameter plane is organised to give rise to open regions where heterodimensional cycles are found robustly.

References

[1] Bonatti, C., Díaz, L. J., Viana, M. (2005) *Dynamics beyond uniform hyperbolicity: a global geometric and probabilistic perspective*. Springer Verlag, Berlin-Heidelberg.

[2] Bonatti, C., Díaz, L. J. (2008) Robust heterodimensional cycles and C^1-generic consequences. *Journal of the Institute of Mathematics of Jussieu* **7**(3): 469–525.

[3] Díaz, L. J. (1995) Robust nonhyperbolic dynamics and heterodimensional cycles. *Ergodic Theory & Dynamical Systems* **15**: 291–315.

[4] Doedel, E. J., Oldeman, B. E. (2007) AUTO-07P: Continuation and bifurcation software for ordinary differential equations. Department of Computer Science, Concordia University, Montreal, Canada, with major contributions from Champneys, A. R., Dercole, F., Fairgrieve, T. F., Kuznetsov, Yu. A., Paffenroth, R. C., Sandstede, B., Wang, X. J., Zhang, C. H.; available at `http://cmvl.cs.concordia.ca/auto`.

[5] Kostelich, E. J., Kan, I., Grebogi, C., Ott, E., Yorke, J. A. (1997) Unstable dimension variability: a source of nonhyperbolicity in chaotic systems. *Physica D* **109**(1–2): 81–90.

[6] Krauskopf, B., Rieß, T. (2008) A Lin's method approach to finding and continuing heteroclinic connections involving periodic orbits. *Nonlinearity* **21**(8): 1655–1690.

[7] Zhang, W., Krauskopf, B., Kirk, V. (2012) How to find a codimension-one heteroclinic cycle between two periodic orbits. *Discrete and Continuous Dynamical Systems—Series A* **32**(8): 2825–2851.

Tuesday, July 19, 2022
08:30 - 10:30

MS-15 Energy Transfer and Harvesting in Nonlinear Systems
Rhone 1

Chair: Alireza Ture Savadkoohi

08:30 - 08:50
Intense modal energy exchanges in a cantilever beam with a local geometrically nonlinear boundary condition: Simulation and experiment
MOJAHED Alireza, LIU Yang, **BERGMAN Lawrence***, VAKAKIS Alexander
*University of Illinois at Urbana-Champaign (Urbana, IL United States)

08:50 - 09:10
Intermodal targeted energy transfer in a blast-excited 2D linear system with an elliptical hole
VELTMAN Yuval*, GZAL Majdi, GENDELMAN Oleg
*Yuval Veltman (Haifa, Technion, 3200003 Israel)

09:10 - 09:30
Kapitza resistance in basic chain models with isolated defects
PAUL Jithu*, GENDELMAN Oleg
*PhD student (Faculty of Mechanical Engineering, Technion–Israel Institute of Technology Israel)

09:30 - 09:50
Modal interactions in a non-linear mass-in-mass periodic chain
FLOSI Jean*, TURE Savadkoohi Alireza, LAMARQUE Claude-Henri
*École Nationale des Travaux Publics de l'État (3, Rue Maurice Audin, 69518 Vaulx en Velin (CEDEX) France)

09:50 - 10:10
Nonlinear dynamics of a resiliently propped cantilevered beam with a tip mass
TALEBI Bidhendi M. Reza*, PHANI A. Srikantha
*Department of Mechanical Engineering, University of British Columbia, Vancouver, Canada (Department of Mechanical Engineering, 6250 Applied Science Lane, Vancouver, BC, V6T1Z4 Canada)

10:10 - 10:30
Passive control of galloping vibrations by means nonlinear energy sinks
IGNÁCIO Da Silva José Augusto*, SANCHES Leonardo, MARQUES Flávio
*School of Engineering of São Carlos (Av. Trab. São Carlense, 400 - Parque Arnold Schimidt, São Carlos - SP, 13566-590 Brazil)

Intense modal energy exchanges in a cantilever beam with a local geometrically nonlinear boundary condition: Simulation and experiment

Alireza Mojahed[*], Liu Yang[**], Lawrence A. Bergman[***], Alexander F. Vakakis[*]
[*] *Department of Mechanical Science and Engineering, University of Illinois, Urbana, IL, USA*
[**] *State Key Laboratory of Mechanics and Control of Mechanical Structures, Nanjing University of Aeronautics and Astronautics, Nanjing, China*
[***] *Department of Aerospace Engineering, University of Illinois, Urbana, IL, USA*

Summary. The aim of this research is to investigate and determine how a geometrically nonlinear boundary condition, i.e., a strong local nonlinearity, "redistributes" an input energy in the form of an impulsive load, among the modes of vibration of a cantilever beam, thereby increasing its efficacy of energy dissipation. The nonlinear boundary condition is created by grounding the free end of the cantilever beam through a linear spring-damper element at an angle relative to the neutral axis of the beam while at rest. By tracking the time-averaged energy and the effective instantaneous damping ratio of each mode of the beam, we numerically and experimentally show that there are sustained energy exchanges among the modes of vibration of the cantilever beam, the intensity of which depend on the degree of nonlinearity of the boundary condition.

Experimental setup and reduced-order finite-element modeling via system identification

Figures 1a and 1b depict the fully instrumented experimental apparatus consisting of the linear cantilever steel beam with Young's modulus of 192 GPa, density of 7784 kg/m^3, cross-sectional area of 8×44.6 mm^2, length of 1.76 m, and the geometrically nonlinear boundary condition and its corresponding reduced-order model (ROM), respectively. Moreover, figure 1c shows a closeup of the geometrically nonlinear boundary condition, studied in [1], achieved by grounding the free end of the cantilever through a ¼ inch diameter steel rod whose bending stiffness and inherent damping provide the compliance and dissipation of the boundary condition.

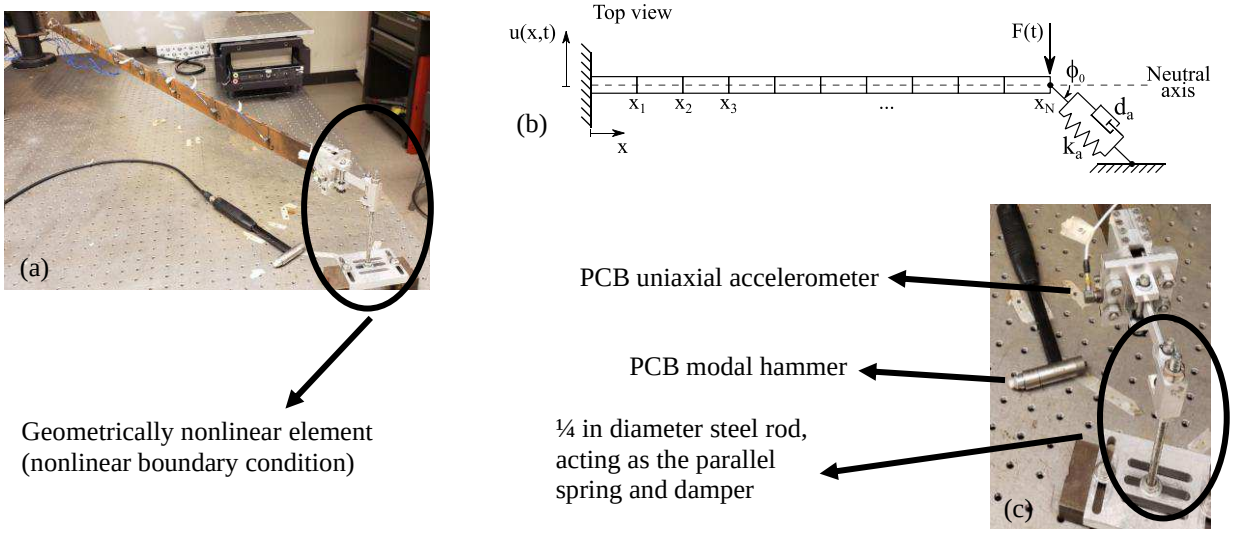

Figure1. Fully instrumented cantilever beam, grounded at its free end through a geometrically nonlinear boundary condition (a), the corresponding reduced-order model (ROM) (b), and zoomed-in view of the geometrically nonlinear boundary condition (c).

In order to create an accurate ROM of the apparatus, we implemented a two-step system identification approach: 1) By applying the Multi-input Multi-output Frequency Domain Identification (MFDID) [2] technique to the response of the cantilever beam, excited by an impulse as shown in figure 1b, we identified the modal parameters, i.e., natural frequencies and modal damping ratios, of the cantilever beam, uncoupled from the nonlinear attachment. 2) Next, we attached the nonlinear element to the fully identified cantilever beam and configured it such that $\phi_0 = 90^\circ$. Then, through time series optimization, we identified the unknown stiffness and damping parameters associated with the nonlinear attachment, k_a and d_a, after which we were able to accurately reproduce the experimentally measured response of the beam by the ROM, the governing equation of which can be expressed as:

$$\mathbf{M\ddot{u}} + \mathbf{C\dot{u}} + \mathbf{Ku} + \mathbf{f}_{\mathrm{nl}} = \mathbf{F(t)}, \qquad \mathbf{u}(0) = \mathbf{0}, \qquad \dot{\mathbf{u}}(0) = \mathbf{0}, \tag{1}$$

where $\mathbf{u} = [u_1, u_2, \dots, u_{\mathrm{N}}]^{\mathrm{T}}$ is the displacement vector corresponding to each node, x_i, $i = 1,2, \dots, \mathrm{N}$ (cf. figure 1b); $\mathbf{M}$, $\mathbf{K}$ are mass and stiffness matrices of the finite element model of the Euler-Bernoulli beam, and $\mathbf{C}$ is the proportional damping matrix of the beam, all obtained from the first step of the identification process. Moreover, $\mathbf{f}_{\mathrm{nl}}$, denotes the nonlinear force vector whose elements, except the N-th, are uniformly zero in time. The N-th element of $\mathbf{f}_{\mathrm{nl}}$, f_b, is expressed as

$$f_b = d_a\left[\frac{(x_{\mathrm{N}} + l_0\sin\phi_0)^2}{(l_0\cos\phi_0)^2 + (x_{\mathrm{N}} + l_0\sin\phi_0)^2}\right]\dot{x}_{\mathrm{N}} + k_a(x_{\mathrm{N}} + l_0\sin\phi_0)\left[1 - \frac{l_0}{\sqrt{(l_0\cos\phi_0)^2 + (x_{\mathrm{N}} + l_0\sin\phi_0)^2}}\right], \tag{2}$$

where l_0 is the natural length of the nonlinear attachment.
It can be shown that the nonlinear force, (2), in the limit of $x_N \ll l_0$ (low energy levels) can be linearized as

$$f_b|_{x_N \ll l_0} = (d_a \sin^2 \phi_0)\dot{x}_N + (k_a \sin^2 \phi_0)x_N. \quad (3)$$

Combining (1)-(3) and assuming low energy, i.e., $x_N \ll l_0$, we can construct the eigenvalue problem

$$\left[-\omega^2 \mathbf{M} + \left(\mathbf{K} + \mathbf{I}.\mathbf{f}_{nl}|_{x_N \ll l_0}\right)\right]\mathbf{u} = \mathbf{0}, \quad (4)$$

where **I** is the identity matrix, and consequently, find the so-called "linearized" modal basis of the system.

Modal energy scattering due to nonlinear boundary conditions

In order to compute the modal response of the nonlinear beam (both the experimental and computational models), we projected each measured response along the beam onto the linearized modal basis of the system. Following this we computed the time-averaged modal energies as described in [3]. By doing so, we can observe not only how much of the total energy of the beam is allocated to each mode, but also follow their variations with time and measure the maximum energy exchange among them for different angles of attachment, ϕ_0.
Finally, we defined a measure of energy exchange among modes by computing and comparing the maximum fluctuation in the percentage of each of the instantaneous modal energies, which corresponds to the maximum percentage of energy being exchanged among the modes. Figure 2 shows the energy exchange measure for the first two modes, for both the experimental system and the ROM.

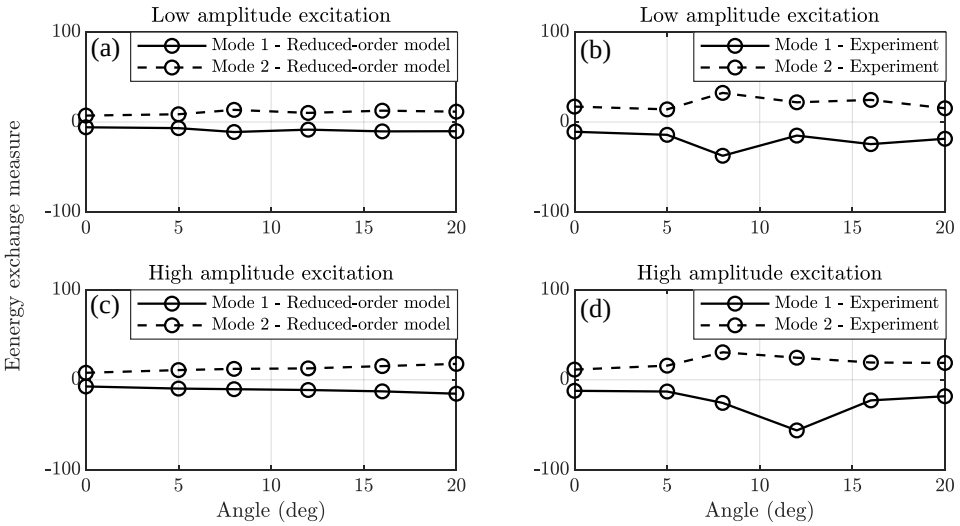

Figure 2. Energy exchange measures of the first two modes as a function of ϕ_0, computed from the ROM (a) and the experiment (b), for a low intensity impulse; (c) and (d) show similar graphs for a high intensity impulse.

Figure 2, especially the energy exchange measures computed from the experimental results, shows that, for a certain range of angle of inclination, $8^\circ < \phi_0 < 12^\circ$, the percentage of energy exchanged between modes 1 and 2, is maximized. This effect is achieved not only due to energy tunability of the nonlinearity but also due mainly to the existence of the angle of inclination, ϕ_0, which can be tuned to directly affect the degree of nonlinearity of the boundary condition.

Conclusions

In this research we investigated the effects of a strong local geometric nonlinearity on the modal interactions that occurred in a cantilever beam whose free end was grounded through a geometrically nonlinear element, which consisted of a linear spring-damper element at an angle, ϕ_0, relative to the neutral axis of the beam while at rest. After building an experimental apparatus, we created a reduced-order finite element model for the experiment and updated its parameters by implementing frequency domain and time domain system identification techniques. Next, we projected the response of the nonlinear beam onto the modal space obtained from the updated computational model, and calculated the amount of energy in each of the projected modes. We recorded the maximum energy exchange among the projected modes for different values of ϕ_0 and showed that by tuning this parameter properly it is possible to achieve the maximum amount of energy exchange from the low-frequency modes to high-frequency modes, thereby increasing the dissipation capabilities of the system.

References

[1] Mojahed, Alireza, et al. (2018) Strong geometric softening–hardening nonlinearities in an oscillator composed of linear stiffness and damping elements. *International Journal of Non-Linear Mechanics* **107**:94-111.

[2] Kim, Saang Bum, B. F. Spencer Jr, and Chung-Bang Yun. (2005) Frequency domain identification of multi-input, multi-output systems considering physical relationships between measured variables. *Journal of Engineering Mechanics* **131.5**:461-472.

[3] AL-Shudeifat, Mohammad A., Alexander F. Vakakis, and Lawrence A. Bergman. (2016) Shock mitigation by means of low- to high-frequency nonlinear targeted energy transfers in a large-scale structure. *Journal of Computational and Nonlinear Dynamics* **11.2**: 021006.

Intermodal targeted energy transfer in a blast-excited 2D linear system with an elliptical hole

Yuval Veltman, Majdi Gzal and Oleg V. Gendelman
Faculty of Mechanical Engineering, Technion – Israel Institute of Technology, Haifa, Israel

Summary. This work explores the implementation of the intermodal targeted energy transfer (IMTET) concept for passive mitigation of a 2D linear oscillator subjected to blast excitation in its weak direction. The considered model contains 3 degrees-of-freedom, namely, two directions of translation (i.e., horizontal and transversal), and rotational direction. The passive mitigation here is achieved by inducing extreme, fast time scale energy transfers from weak structural mode (characterized by lower-frequency and large amplitude) which was initially excited by the blast excitation to strong structural modes (i.e., higher-frequency ones with a small amplitudes). These targeted (directed) energy transfers are governed by a non-resonant nonlinear dynamical mechanism induced by vibro-impacts between the main structure and a rigid barrier which constrained the structure to move within an elliptical hole. By redistributing the blast energy from low- to high-frequency structural modes the amplitude of the overall structural response is reduced in an extremely fast time scale, and the intrinsic dissipative modal capacity of the structure itself is better utilized. Additional blast energy dissipation is achieved by inelastic vibro-impacts.

Introduction

Passive mitigation of engineering structures subjected to extreme loads is of considerable interest in real life applications for preventing structural damage and human loss. Several linear and nonlinear absorbers have been investigated in the literature for this purpose [1,2]. Recently, a new concept was introduced [3] for blast mitigation through intermodal targeted energy transfer (IMTET) mechanism which based on irreversible nonlinear non-resonance energy scattering that passively transfers a significant portion of the blast energy from low-frequency structural modes (in particular, the fundamental mode) to high-frequency modes of the structure. Such passive IMTET was achieved by introducing local strong nonlinearities, in the form of vibro-impacts. The IMTET concept was first implemented on a benchmark blast-excited two-degree of freedom (DOF) linear system by introducing to the system a single impact clearance [3]. Then, an extension of IMTET mechanism in multi-DOF systems was conducted in [4], in which a computationally study to explore the concept of IMTET to mitigate the effect of blast loading on a nine-story steel structure was performed.
Here in this study, the IMTET concept will be extended to two-dimensional structures, with the rationale of channeling energy from "weak" to "strong" direction, thus utilizing much more effectively the intrinsic dissipative capacity of the structure itself.

Model description and governing equations

Here we consider a 3DOF oscillator with two directions of translation (i.e., horizontal and transversal) and one of rotational direction. The oscillator consists of a mass m with moment of inertia I moving on both horizontal and vertical directions. The mass is connected to two linear dampers with coefficients c_1 and c_2, and a torsional dumper with coefficient γ. Two linear springs with stiffness $k_1$and k_2 and a torsional spring with stiffness k_3 are attached to the mass as well. The mass movement is constrained by a rigid element, in center of an elliptical hole going throw the mass, with width $2a$ and height $2b$, and rotated by an angle α, as shown in Figure 1.

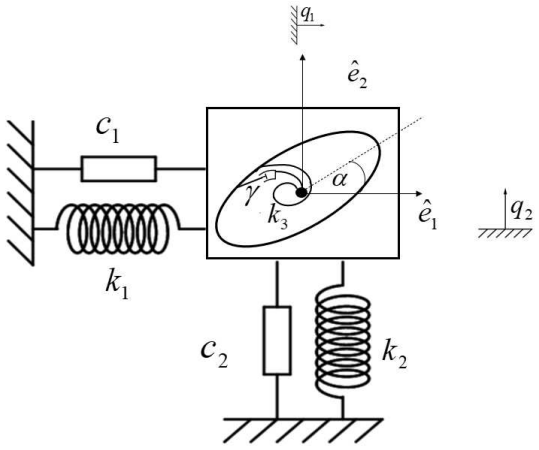

Figure 1: Schematic of the considered system

Let q_1 and q_2 denote the horizontal and the transversal displacements, respectively, the equations of motion between the impacts are given by:

$$m\frac{\partial^2 q_1}{\partial t^2} + c_1\frac{\partial q_1}{\partial t} + k_1 q_1 = 0 \qquad (1)$$

$$m\frac{\partial^2 q_2}{\partial t^2} + c_2\frac{\partial q_2}{\partial t} + k_2 q_2 = 0$$
$$I\frac{\partial^2 \theta}{\partial t^2} + \gamma\frac{\partial \theta}{\partial t} + k_3\theta = 0$$

When the rigid element location satisfies the equation of the ellipse in respect to the center of mass, collision happens and the mass changes its velocity instantaneously according to the Newtonian impact law. The collision is defined using coefficient of restitution and coefficient of friction and take under consideration angular impulse. After numerically solving the equations of motion we can explore the efficiency of the mechanism. The simulation parameters are chosen with respect to a real steel beam with rectangular cross section. We have simulated the system for different coefficients of restitution, namely, $r = 0.6{,}1$ and compared the results with the linear case, i.e., without the constraint, for an equal initial condition of impact. To explore the efficiency here we the normalized energy η as the ratio between the instantaneous energy $E(t)$ and the initial energy $E(0)$:

$$\eta(t) = \frac{E(t)}{E(0)} \qquad (2)$$

We define the characteristic damping time of the system τ as $\ln(\eta(\tau)) = -1$, in other words, it is the time in which the energy drops by a factor of 1/e of its initial value in a time inverse to the damping coefficient.

Results

As a preliminary results, the horizontal and transversal responses subject to initial conditions that excite only the horizontal direction are shown in Figure 2(left). It is clear that when the vibro-impacts occur, the modes interact immediately, and a substantial amount of energy is transferred from the horizontal to the transversal mode. The latter is characterized by a substantially higher modal dissipative capacity. Thus, an enhancement of the damping properties of the system is realized through utilization of the intrinsic modal structure and excitation of the higher-frequency transversal mode. Figure 2(right) shows the logarithm of the normalized energy as a function of time for the following three cases: linear, nonlinear with purely elastic impacts, and nonlinear with inelastic impacts. It can be seen that the presence of the impacts in the system leads to a significant decrease in the characteristic damping time, even when purely elastic impacts are considered.

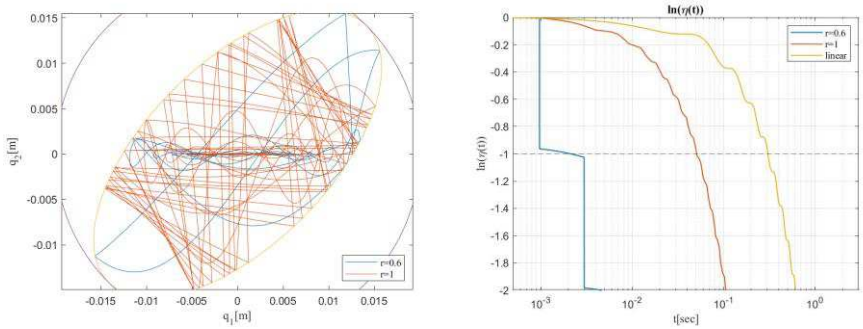

Figure 2: The center of mass trajectory in the $q_1 q_2$ plane (left); The instantaneous energy of the system (right)

Conclusions

In this work, the non-resonance nonlinear mechanism for efficient and rapid low- to high-frequency energy scattering, which is referred to as intermodal targeted energy transfer—IMTET, is implemented for passive mitigation of a 2D linear oscillator subjected to blast excitation in its weak direction. The numerical exploration revealed that channeling the blast energy, within the modal space, from low- to high-frequency structural modes enables an extremely fast mitigation of the overall structural response, and a drastic reduction of the characteristic damping time in the benchmark system.
Such observations open up an entirely new domain of research on constructive utilization of different directions for possible displacement of the structure, in particular channeling energy from "weak" to "strong" direction by means of the IMTET.

References

[1] Soong TT, Dargush GF (1997). Passive Energy Dissipation Systems in Structural Engineering. John Wiley & Sons: Chichester,West Sussex, England.

[2] Vakakis, A.F., Gendelman, O.V., Bergman, L.A., McFarland, D.M., Kerschen, G., Lee, Y.S. (2008) Nonlinear Targeted Energy Transfer in Mechanical and Structural Systems. Solid Mechanics and Its Applications. Springer, Dordrecht.

[3] M. Gzal, B. Fang, A.F. Vakakis, L.A. Bergman, O.V. Gendelman (2020) Rapid non-resonant intermodal targeted energy transfer (IMTET) caused by vibro-impact nonlinearity. Nonlinear Dyn, **101**, pp. 2087-2106.

[4] Majdi Gzal, Alexander F. Vakakis, Lawrence A. Bergman, Oleg V. Gendelman (2021) Extreme intermodal energy transfers through vibro-impacts for highly effective and rapid blast mitigation. Communications in Nonlinear Science and Numerical Simulation, Volume **103**.

Kapitza resistance in basic chain models with isolated defects

Jithu Paul[*] and O. V. Gendelman[*]
[*]*Faculty of Mechanical Engineering, Technion–Israel Institute of Technology, Haifa, Israel*

Summary. Kapitza resistance due to isolated defect is explored numerically in benchmark chain models (linear, β-FPU, rotator and Frenkel-Kontorova). Kapitza resistance is found independent on chain length and temperature in linear model, but dependent on thermostat characteristics. In β-FPU model, the anomaly as in the heat conductivity continues, Kapitza resistance vanishes with the chain length and depend on temperature and thermostat. In Rotator and Frenkel-Kontorova models, which are characterized by normal heat conductivity, Kapitza resistance also shows convergence with chain length and independent on thermostat. Except for the linear model, the findings are similar to the heat conductivity characteristics in the respective models.

Kapitza resistance/Interfacial thermal resistance is defined as the ratio of discontinuity in the temperature gradient at the material interface to the heat flux flowing across the interface. It was first observed by Kapitza, in the junction between liquid helium II and a solid, during his experiments on superfluidity. Although numerous theoretical works have been devoted to explain Kapitza resistance, the two widely known models are Acoustic Mismatch Model (AMM) which is defined for very low temperatures and Diffuse Mismatch Model (DMM) which is defined for very high temperatures. Majority of the analytical, numerical works were based on AMM. The heat management problem, especially in nanoscale devices, involves the bulk conduction as well as the interfacial heat conduction. In this regard, Kapitza resistance and heat conductivity are two sides of a coin. We have well-known results for one-dimensional heat conduction problem and the studies divide models based on convergence and divergence of heat conductivity in the thermodynamic limit. But the behavior of Kapitza resistance in these models is less understood. More than just a theoretical concept, the divergence of heat conductivity is already established by experimental studies [1] for quasi-one-dimensional systems. Since interfacial thermal resistance is also a crucial factor that deciding the heat transport, the current study can shed light into thermal management problems in nano-scale devices. The present study conducted for Kapitza resistance behavior in basic benchmark models: linear, β-FPU, rotator and Frenkel-Kontorova. We choose isolated defect (isotopic defect/coupling defect) to create the interfacial boundary and to avoid the complications of the non-reciprocity.

We follow two numerical approaches: first, a semi-analytical method for linear model, which is based on the famous Rieder-Lebowitz-Lieb (RLL) method [2]; second, molecular dynamics simulations. In all cases, the non-equilibrium heat transport is established by connecting the chain to Langevin thermostats at both ends. In RLL method, the basic idea is to numerically solve the necessary and sufficient condition for the stationary state of a harmonic crystal from the generalized Liouville equation. In molecular dynamics simulations, we follow numerically the time evolution of the Hamiltonian with discrete time interval. We use Verlet algorithm to solve the equations of motion using homemade FORTRAN-95 codes. The results obtained for linear, β-FPU, rotator and Frenkel-Kontorova models are very-briefly discussed below.

It is well-known that in linear model, phonon does not exchange energy between modes and the phonon spectra is totally dependent on thermostat characteristics. We observed the heat flux and the temperature drop at the interface scales with the temperature and the Kapitza resistance is independent on chain length and temperature. We know heat conductivity was diverging with chain length in linear model. But we cannot say Kapitza resistance is normal for linear model because the Kapitza resistance is totally dependent on the thermostat since nothing in the chain can influence the phonons. Another observation for the linear model (more or less similar in other models also) is Kapitza resistance shows diverging behavior with the strength of the isolated defect when the strength goes to infinity.

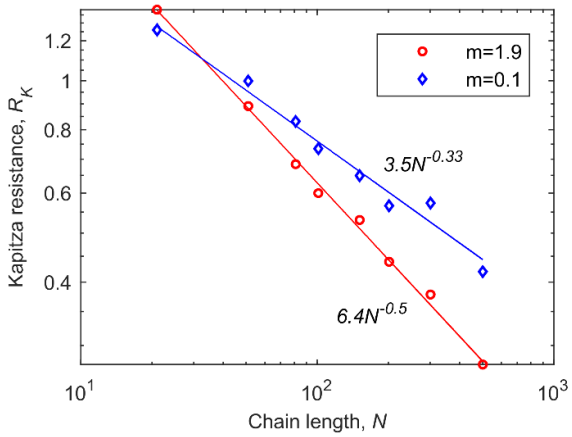

Figure 1: Power law decrease of the Kapitza resistance with the chain length for the chain with β-FPU interaction.

Heat transport in β-FPU model is always a puzzling problem since the observation of absence of thermalization by Fermi-Pasta-Ulam. Heat conductivity shows divergence with an exponent close to $1/3$ [3]. The anomaly continues in the case of Kapitza resistance which demands normalization of heat flux. Although the exponent dependent on the defect strength, still it is closer to $-1/3$ (Figure 1). The Kapitza resistance decreases with increase in temperature, which shows the temperature

affects the phonon scattering process at the interface. As in the linear model, Kapitza resistance here also dependent on thermostat.

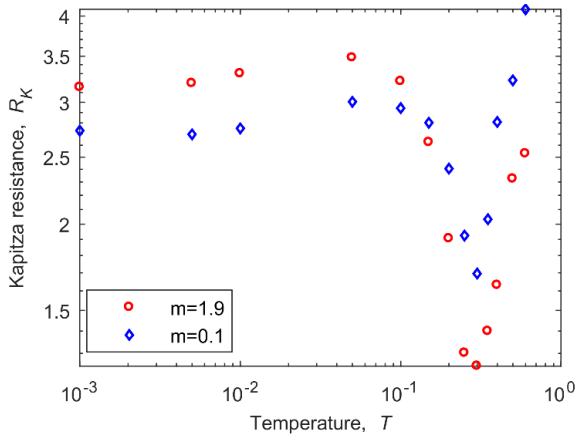

Figure 2: Temperature dependence of the Kapitza resistance in the chain of rotators.

Rotator model are well-known for momentum conserving models which obey convergence of thermal conductivity [4]. Kapitza resistance showed normal behavior here, that is, converges in the thermodynamic limit and independent thermostat characteristics at a temperature above the rotobreathers can get excited. The strong nonlinearity allows the system to forget about the thermostat characteristics and the phonon locking by the rotobreathers allows the normal diffusion. The activation of rotobreathers and its effect on the Kapitza resistance can be observed as a dip in the Kapitza resistance-temperature plot (Figure 2).

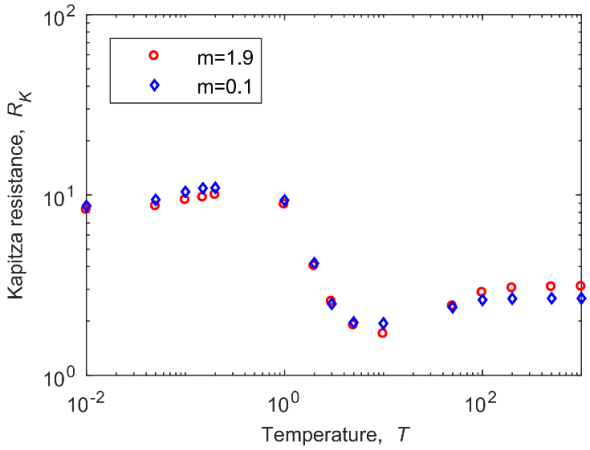

Figure 3: Dependence of the Kapitza resistance on the chain average temperature in the Frenkel-Kontorova model.

Coming to the Frenkel-Kontorova model, Kapitza resistance is normal and independent of thermostat characteristics at intermediate temperatures (Figure 3). We know the similar observation for heat conductivity since activation of topological kinks only happens at intermediate temperature range [5]. The linear characteristics at very low temperatures happens due to the weak nonlinearity and at high temperatures the chain detaches from the substrate.
In conclusion, linear model showed Kapitza resistance that is independent of chain size (contrary to heat conductivity) and temperature, but dependent on thermostat. The addition of cubic linearity makes the Kapitza resistance anomalous, that is, dependent on thermostat and chain length in the thermodynamic limit (need of normalized heat flux). Rotator and Frenkel-Kontorova models showed normal Kapitza resistance. In all the nonlinear models Kapitza resistance decreases, immediately after the very low temperature regime (linear regime) which needed to be investigated further.

References

[1] C.W.Chang, D.Okawa, H. Garcia, A. Majumdar and A. Zettl, Phys. Rev. Lett. **101**, 075903 (2008).
[2] Z. Rieder, J. L. Lebowitz, and E. Lieb, Journal of Mathematical Physics **8**, 1073 (1967).
[3] S. Lepri, R. Livi, and A. Politi, EPL **43**, 271 (1998).
[4] O. V. Gendelman and A. V. Savin, Phys. Rev. Lett. **84**, 2381 (2000).
[5] A. V. Savin and O. V. Gendelman, Phys. Rev. E **67**, 041205 (2003)

Modal interactions in a non-linear mass-in-mass periodic chain

Jean Flosi[†], Alireza Ture Savadkoohi[†] and Claude Henri Lamarque[†]
[†]*Univ Lyon, ENTPE, CNRS UMR5513, LTDS, France*

Summary. The multiple-scale dynamics of a forced periodic chain composed of 2 degree of freedom mass-in-mass cells with cubic non-linearity is studied. A continuous approach leads to dispersion equations and allows to define the modal decomposition of continuous physical coordinates of the system. Because of the system nonlinearity, a $1:3$ internal resonance is considered. The continuous model is projected on these two modes in order to study associated energy exchanges. Fast and slow dynamics leads to detection of slows invariant manifolds (SIM) and frequency responses of the chain.

Considered model of the chain

Meta-materials are developed to present unusual non natural responses against external or internal actions. In the vibro-acoustics domain, mass-in-mass systems are an example of meta-materials [1, 2]. We are considering the system presented in Fig.1: a L-periodic chain composed of mass-in-mass cells linearly linked two by two. Each cell is composed of a principal mass m_1 linked non-linearly to its inner mass m_2.

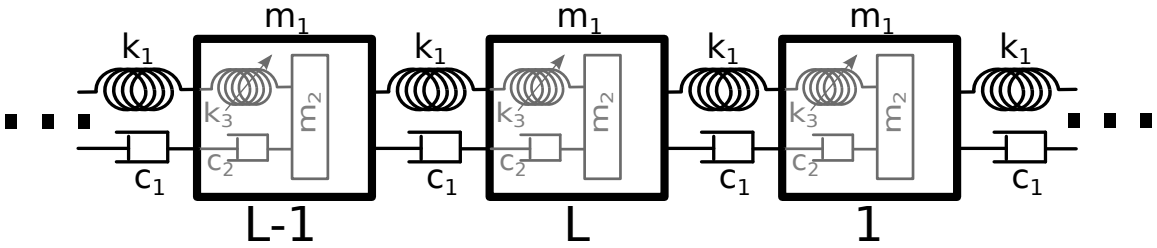

Figure 1: Scheme of the L-periodic chain composed by cubic nonlinear mass-in-mass cells

Governing equations are:

$$\begin{cases} m_1\dfrac{d^2u_1}{dt^2}+k_1(2u_1-u_L-u_2)+k_3(u_1-v_1)^3+c_1(2\dfrac{du_1}{dt}-\dfrac{du_L}{dt}-\dfrac{du_2}{dt}) \\ +c_2(\dfrac{du_1}{dt}-\dfrac{dv_1}{dt})=F_1\sin(\Omega t) \\ \\ m_1\dfrac{d^2u_j}{dt^2}+k_1(2u_j-u_{j-1}-u_{j+1})+k_3(u_j-v_j)^3+c_1(2\dfrac{du_j}{dt}-\dfrac{du_{j-1}}{dt}-\dfrac{du_{j+1}}{dt}) \\ +c_2(\dfrac{du_j}{dt}-\dfrac{dv_j}{dt})=F_j\sin(\Omega t) \text{ for } j\in[2,...,L-1] \\ \\ m_1\dfrac{d^2u_L}{dt^2}+k_1(2u_L-u_{L-1}-u_1)+k_3(u_L-v_L)^3+c_1(2\dfrac{du_L}{dt}-\dfrac{du_{L-1}}{dt}-\dfrac{du_1}{dt}) \\ +c_2(\dfrac{du_L}{dt}-\dfrac{dv_L}{dt})=F_L\sin(\Omega t) \\ \\ m_2\dfrac{d^2v_j}{dt^2}+k_3(v_j-u_j)^3+c_2(\dfrac{dv_j}{dt}-\dfrac{du_j}{dt})=0 \text{ for } j\in[1,...,L] \end{cases} \tag{1}$$

The periodicity leads to following boundary conditions:

$$\begin{cases} u_j(t)=u_{L+j}(t) \\ \dfrac{du_j(t)}{dt}=\dfrac{du_{L+j}(t)}{dt} \end{cases} \text{ pour } j\in[1,...,L] \tag{2}$$

Continuous approach

X is the initial spatial variable and the distance of two adjacent cells at rest is Δx. We introduce the continuous normalized space variable $x=\dfrac{X}{\Delta x}$ and new continuous functions:

$$\begin{cases} u(x,\tau)=u(x=j-1,\tau), x\in[0,L], j=\{1,...,L+1\} \\ v(x,\tau)=v(x=j-1,\tau), x\in[0,L], j=\{1,...,L+1\} \end{cases} \tag{3}$$

We use the new continuous coordinates:

$$\begin{cases} U(x,t)=u(x,t) \\ V(x,t)=u(x,t)-v(x,t) \end{cases} \tag{4}$$

and applying change of variables $\tau = \omega t = \sqrt{\frac{k_1}{m_1}}t$, $\varepsilon\Lambda = \frac{k_3}{k_1}$, $\varepsilon\chi_1 = \frac{c_1}{\sqrt{k_1 m_1}}$, $\varepsilon\chi_2 = \frac{c_2}{\sqrt{k_1 m_1}}$, $\varepsilon f_j = \frac{F_j}{k_1}$ and $\mu = \frac{\Omega}{\omega}$, continuous expression of system 1 is:

$$\begin{cases} \dfrac{\partial^2 U}{\partial \tau^2}(x,\tau) - \dfrac{\partial^2 U}{\partial x^2}(x,\tau) + \varepsilon\Lambda V^3(x,\tau) - \varepsilon\chi_1 \dfrac{\partial}{\partial\tau}\dfrac{\partial^2}{\partial x^2}U(x,\tau) + \varepsilon\chi_2 \dfrac{\partial}{\partial\tau}V(x,\tau) \\ = \varepsilon f(x)\sin(\mu\tau) \\ \\ \dfrac{d^2(U-V)}{d\tau^2}(x,\tau) - \Lambda V^3(x,\tau) - \chi_2 \dfrac{\partial V}{\partial\tau}(x,\tau) = 0 \end{cases} \tag{5}$$

The study of the linearized system leads to the dispersion equation of the system. We consider a $1:3$ internal resonance and we define:

$$\begin{cases} U(x,\tau) = p_1(\tau)\cos(\omega_1 x + \Theta_1) + p_3(\tau)\cos(\omega_3 x + \Theta_3) \\ V(x,\tau) = q_1(\tau)\cos(\omega_1 x + \Theta_1) + q_3(\tau)\cos(\omega_3 x + \Theta_3) \end{cases} \qquad \omega_k = \frac{2k\pi}{L}, k \in [1,\ldots,L] \tag{6}$$

Fast and slow dynamics study

In order to detect the different dynamics of the system, multiple scale method [3] is applied. Modal projection allows to obtain different set of governing equations from the continuous Eq.5 and asymptotic responses of the system are considered [4]. Detection of fast dynamics [5] leads to the determination of the two SIMs associated to projected system on the first and third mode. Example of SIM obtain from projection on first mode is plotted in Fig.2 from two different angles, where N_1 stands for associated amplitude of the outer mass for first mode and M_1 and M_3 stand for associated amplitudes of the inner mass for first and third modes respectively. Analytical SIM is plotted in blue while numerical integration using Runge Kutta is plotted in red. Slow dynamics study at the order ε^1 allows to determine singular and

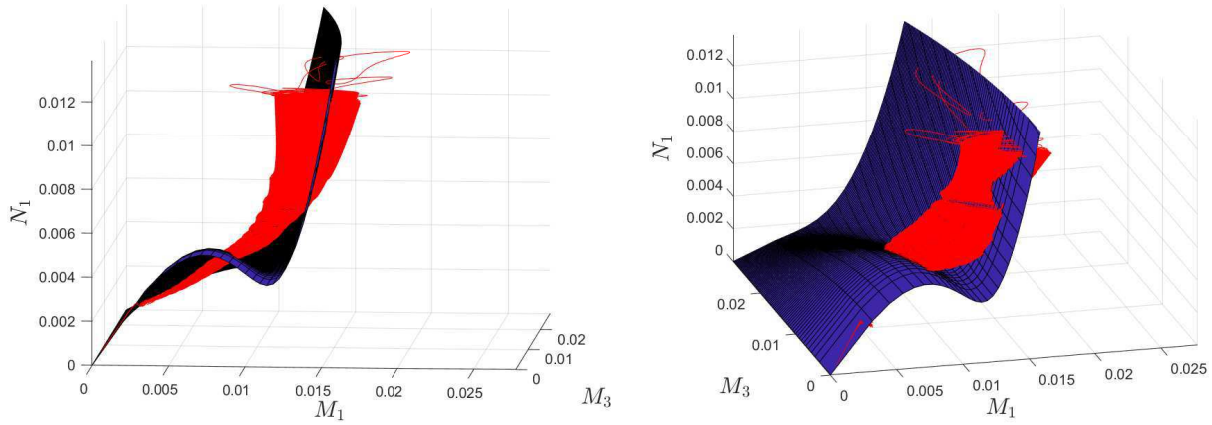

Figure 2: Multiangle representation of the SIM obtained after projection on first mode for free system with initial deformation.

equilibrium points. These points lead to the prediction of periodic and quasi-periodic behaviors. Study can be generalized for the $1:k$ resonance.

References

[1] Cveticanin, L. (2018) Influence of nonlinear subunits on the resonance frequency band gaps of acoustic metamaterial,Nonlinear Dynamics 93.

[2] Wang, X. (2014) Dynamic behaviour of a metamaterial system with negative mass and modulus, International Journal of Solids and Structures 51.

[3] Nayfeh, A.H. and Mook, D.T. (1979) Nonlinear Oscillations,

[4] Manevitch, L. (2001) The Description of Localized Normal Modes in a Chain of Nonlinear Coupled Oscillators Using Complex Variables, Nonlinear Dynamics 25.

[5] Charlemagne, S.,Ture Savadkoohi, A. and Lamarque, C. H. (2018) Dynamics of a linear system coupled to a chain of light nonlinear oscillators analyzed through a continuous approximation, Physica D: Nonlinear Phenomena.

Nonlinear dynamics of a resiliently propped cantilevered beam with a tip mass

M. Reza Talebi Bidhendi*, A. Srikantha Phani*
*Department of Mechanical Engineering, University of British Columbia, Vancouver, Canada

Summary. A practical friction control application in railway industry lead us to consider a cantilever beam with a tip mass and a spring support– a problem least studied in the literature from nonlinear dynamics perspective. We study the harmonically forced nonlinear dynamic response of this prototypical system using a reduced two degree of freedom model and compare its bifurcation characteristics, computed by AUTO, with that of the full system. The tip spring couples the first two flexural modes through a length dependent kinematic nonlinearity and brings their frequency ratio to nearly 2:1. We find (a) the reduced order model is adequate to understand the first bifurcation (pitchfork) and the subsequent Hopf bifurcation and (b) The threshold force for the nonlinear response grows with the initial length of the spring.

Problem statement

Cantilevered beam with tip mass is a canonical problem extensively studied under the tip excitation and under the base excitation [1]. Nonetheless, the present problem of an end excited cantilevered beam with a tip mass mounted on an external elastic support has not received attention, and we are led to it through a friction control application in railways [2, 3]. Similar situations can arise in the vibration energy harvesting, vibration mitigation, and sensing mechanisms [4]. Restoring force due to the elastic support has been shown to produce nonlinear terms of kinematic origin in the governing differential equations (DEs) [5, 6]. A similar situation arises in our problem, sketched in Fig.1(a). A long steel beam with a diameter of 4 mm and length of 254 mm is loaded by an aluminum tip mass ($70\times50\times20$ mm^3) and a rigid rod of density of 7800 kg/m^3 and diameter of 4 mm and length of 40 mm. The external support at tip ($k_{ext} = 1000\ N/m$) with an initial length (L) imposes a two-to-one ratio between the first vertical (f_1) and the lateral (f_2) natural frequencies of the structure, $f_1 \approx 2f_2$. The linear modal parameters of the structure (damping ratio(ζ), stiffness(k), natural frequency (f)) without the addition of the external support are obtained using a finite element model as $k_1 = 317.98\ N/m, \zeta_1 = 0.097, f_1 = 6.12\ Hz, k_2 = 362.58\ N/m, \zeta_2 = 0.129, f_2 = 6.59\ Hz$. Indices one and two refer to the vertical and the lateral directions, respectively. After the attachment of the elastic support to the structure, the vertical linear natural frequency becomes $f_1 = 12.46\ Hz$ while the other linear modal parameters do not change. Using the linear modal properties of the structure, a minimal model as shown in Fig.1(b) can be identified, with the governing equations:

$$\ddot{\tilde{y}} + 2\zeta_1\omega_1\dot{\tilde{y}} + \omega_1^2\tilde{y} + \frac{k_{ext}(1+\tilde{y})}{m_1}(1 - \frac{1}{\sqrt{(1+\tilde{y})^2+\tilde{x}^2}}) = \frac{F}{m_1 L}cos(\Omega t) \tag{1}$$

$$\ddot{\tilde{x}} + 2\zeta_2\omega_2\dot{\tilde{x}} + \omega_2^2\tilde{x} + \frac{k_{ext}\tilde{x}}{m_2}(1 - \frac{1}{\sqrt{(1+\tilde{y})^2+\tilde{x}^2}}) = 0 \tag{2}$$

where $\tilde{y} = y/L$, $\tilde{x} = x/L$, $\omega_i = \sqrt{k_i/m_i}$; $m_i, i = 1, 2$ are the masses; F is the excitation amplitude, and Ω is the excitation frequency. The above equations are solved numerically for non-zero initial conditions, and compared with the full-scale multi-body dynamics model in ADAMS software which accounts for all the modes of the structure, i.e, no modal truncation.

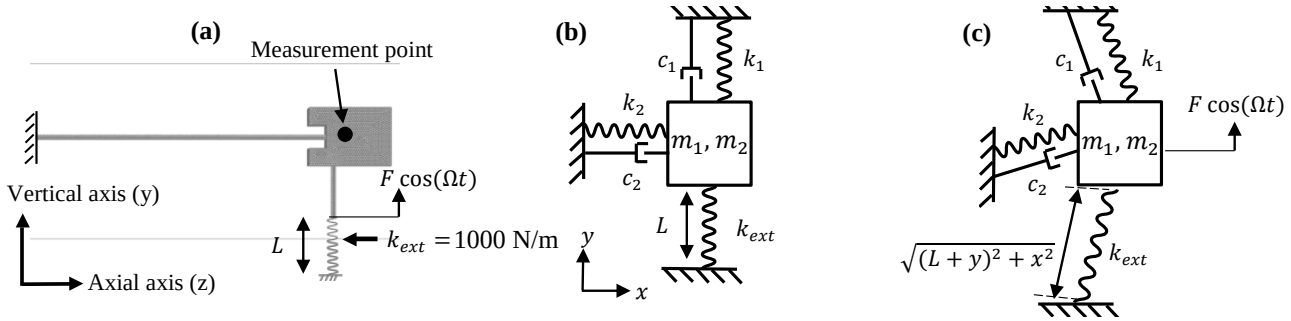

Figure 1: (a) Model of end excited cantilevered beam with tip mass mounted on the elastic support. (b) A minimal two-DOF model of the structure: $c_i = 4\pi\zeta_i m_i f_i$. (c) Deformed structure under the vertical excitation force. Note that the first vertical and lateral modes have almost the same natural frequencies ($f_1 \approx f_2$) without the external spring. The external support introduces kinematic nonlinearities and imposes 2:1 internal resonance in the structure ($f_1 \approx 2f_2$) . Note that x and y are the lateral and the vertical axis, respectively.

Results

Force-response curves are calculated by fixing the excitation frequency (Ω) and increasing the excitation amplitude (F), and vice versa [7]. When the excitation frequency is close to the first vertical natural frequency, $\Omega \approx 2\pi f_1$, the first lateral mode is excited through a 2:1 resonance (pitchfork bifurcation) as shown in Fig.2(a). The vertical displacement decreases initially, in Fig.2(b), and then increases. A further increase in F will produce a Hopf bifurcation leading to the aperiodic response of the structure, see the dotted line in Fig.2(a). Fixing the excitation amplitude and sweeping the excitation frequency, Fig.2(d) and Fig.2(e), we can observe that there is a frequency interval over which the lateral mode is activated. Internal resonance property is evident through the frequency splitting in Fig.2(f). The sensitivity of the force threshold to the initial length of the external spring is shown in Fig.2(c), where we observe that the force amplitude divided by the length remains constant, for the two lengths shown. Note that Fig.2(c) is a magnified version of Fig.2(a) near the onset of first bifurcation. We note that while the reduced order model is adequate for $L = 0.5\ mm$, discrepancies exist for $L = 2.5\ mm$, indicating the limit of the reduced model.

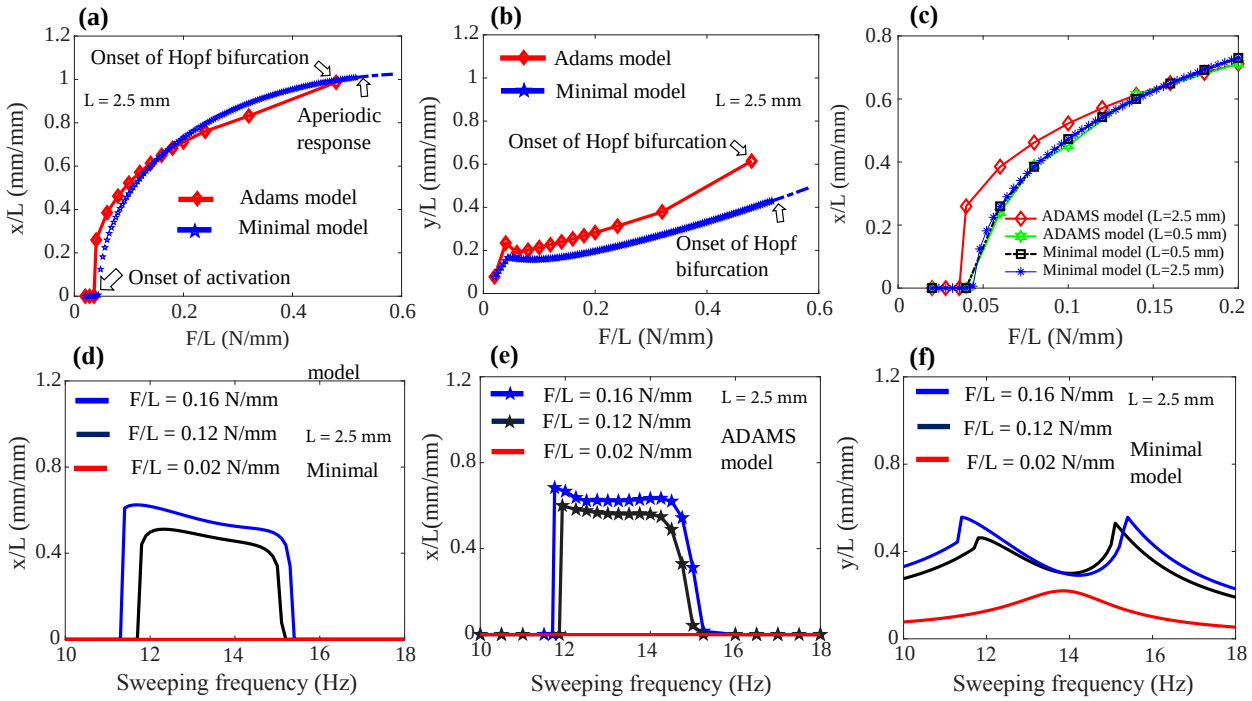

Figure 2: (a) Force-response curve of the lateral response with $\Omega = 2\pi \times 12Hz$. (b) Force-response curve of the vertical response with $\Omega = 2\pi \times 12Hz$. (c) Sensitivity of the force threshold to the initial length of the external spring. (d) Lateral response of the minimal model due to the different excitation levels and frequencies. (e) Lateral response of the Adams model for the different excitation levels and frequencies. (f) Vertical response of the minimal model due to the different excitation levels and frequencies.

Conclusions

The elastically propped cantilever beam with a tip mass, subjected to harmonic excitation, shows pitchfork and Hopf bifurcations when the forcing amplitude is increased at a fixed frequency, and vice versa. The 2:1 internal resonance between two flexural modes with displacements in mutually orthogonal planes are superficially similar to Froude oscillations of a ship, but without saturation since we retain all nonlinear terms here, albeit in the first two modes in our reduced model. We find (a) the reduced order model is adequate to understand the first bifurcation (pitchfork) and the subsequent Hopf bifurcation and (b) initial length of the spring acts as a design tuning parameter to activate the first lateral mode.

References

[1] Meesala, V.C., Hajj, M.R.(2019) Parameter sensitivity of cantilever beam with tip mass to parametric excitation. *Nonlinear Dyn* **95(4)**:3375-3384. *Nonlinear Dyn* **95(4)**:3375-3384

[2] Sharma, C.P., Phani, A.S.(2015) Stability analysis of on-board friction modifier systems at the wheel–rail interface. *J. Vib. Acoust* **137(5)**:051007

[3] Talebi Bidhendi, M.R.(2018) An experimental study of nonlinear oscillations in railroad friction control systems (T). University of British Columbia. Retrieved from https://open.library.ubc.ca/collections/ubctheses/24/items/1.0371958

[4] Harne, R.L., Wang, K.W.(2017) Harnessing bistable structural dynamics for vibration control, energy harvesting and sensing. *Wiley*

[5] Mojahed, A., Moore, K., Bergman, L.A. and Vakakis, A.F.(2018) Strong geometric softening–hardening nonlinearities in an oscillator composed of linear stiffness and damping elements. *Int.J.Non-Linear Mech*, **107**:94-111.

[6] Yang, T.L., Rosenberg, R.M.(1968) On forced vibrations of a particle in the plane. *Int.J.Non-Linear Mech* **3(1)**:47-63

[7] Nayfeh, A.H., Balachandran, B.(1989) Modal interactions in dynamical and structural systems. *Appl.Mech.Rev* **42(11S)**:175-201

Passive control of galloping vibrations by means nonlinear energy sinks

José Augusto Ignácio da Silva[†], Leonardo Sanches[*] and Flávio Donizeti Marques [†]
[†] *School of Engineering of São Carlos, University of São Paulo, Brazil*
[*] *Univesité de Toulose, Institut Clement Ader - ISAE - Supaero, France*

Summary. The present paper aims to analyze the passive control of a structure subject to aeroelastic galloping by using nonlinear energy sinks (NES). A lumped parameter model is adopted, and a steady approach to the aerodynamic loads is considered. A pure cubic stiffness NES is placed inside the prismatic structure. A mathematical model is established, and the Method of Multiple Scales (MMS) is used to build analytical solutions. Bifurcation diagrams can be drawn with these solutions, which allows characterizing the suppression regimes induced by the absorber. The use of coupled NES seems reasonable to passively control the nonlinear aeroelastic galloping.

Introduction

The galloping phenomenon comprises one of several engineering problems ruled by flow-induced vibrations. This phenomenon is essentially nonlinear and characterized by a self-excited mechanism. Limit cycle oscillations (LCO) take place from a particular flow speed, highlighting the galloping bifurcation. These motions can present very large amplitude, leading to fatigue and failure of structural components [1]. In this way, the present paper aims to investigate the application of NES to passive control galloping vibrations. NES consists of a dynamic vibration absorber with nonlinear characteristics that works according with the Target Energy Transfer (TET) theory [2]. In particular to this work, a pure cubic NES stiffness is considered and placed inside a prismatic body subjected to galloping excitation. A steady and nonlinear approach to the aerodynamic loads is considered [1]. Asymptotic analysis is carried out using MMS. The built analytical solutions allow accessing the amplitude and stability of the system's motion with efficiency. Bifurcation diagrams can be generated with these solutions, and the suppression regimes induced by NES can be characterized.

Mathematical Modeling and Asymptotic Analysis with MMS

The model assumes a rigid square prism with mass m, height h, and is supported by a suspension with linear stiffness k and viscous damper coefficient c. An NES is embedded inside of the structure to promote a passive control effect, which consists of an oscillator with a small mass m_n linked to the prism by a pure cubic spring (k_n), and a linear viscous damper (c_n). The motion of prism and NES masses are accounted for by the $y(t)$ and $y_n(t)$ degrees of freedom in the y-direction. Figure 1 presents an illustration of a system immersed in airflow with velocity U aligned to the x-direction, promoting the motion only in the y-direction.

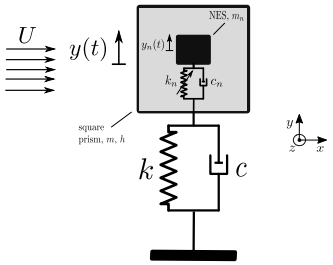

Figure 1: Sprung prism coupled with NES to passive control of the galloping phenomenon.

The governing system's equations of motion are given by:

$$\begin{cases} (1-\epsilon\hat{\mu}_n)\eta''(\tau)+\eta(\tau)=\epsilon\hat{n}\left[\mathcal{A}_1\eta'(\tau)-\mathcal{A}_3{\eta'}^3(\tau)\right]-\epsilon\hat{\lambda}_n\upsilon'(t)-\epsilon\hat{\gamma}_n\upsilon^3(\tau) \\ \epsilon\hat{\mu}_n\upsilon''(\tau)+\hat{\lambda}_n\upsilon'(\tau)+\epsilon\hat{\gamma}_n\upsilon^3(\tau)=\epsilon\hat{\mu}_n\eta''(\tau) \end{cases}. \tag{1}$$

with $\tau=\omega_n t$, $()'=d()/d\tau$, $()''=d^2()/d\tau^2$, $\eta(\tau)=y(\tau)/h$, $\omega_n=\sqrt{k/m}$, $\upsilon(\tau)=(y(\tau)-y_n(\tau))/h$, $\mu_n=m_n/m$, $\gamma_n=k_n h^2/(m\omega_n^2)$, $\lambda_n=c_n/(m\omega_n)$, $n=\rho h^2/(2m)$, $V=U/(\omega_n h)$, $\mathcal{A}_1=VC_f^l-2\zeta/n$, $\mathcal{A}_3=C_f^c/V$, $\zeta=c/(2m\omega_n)$, and $\hat{()}=()/\epsilon$.

The MMS assumes the following expansion of the generalized coordinates, $\eta(\tau)=\eta_0(\tau_0,\tau_1)+\epsilon\eta_1(\tau_0,\tau_1)$ and $\upsilon(\tau)=\upsilon_0(\tau_0,\tau_1)+\epsilon\upsilon_1(\tau_0,\tau_1)$ [3]. Replacing this result in Eq. (1), and collecting the common terms with ϵ^0 and ϵ, two set of equations are obtained. The set ϵ^0 comprises only the equivalent linear undamped motion of the prism, and its solution can be written by $\eta_0(\tau_0,\tau_1)=C(\tau_1)e^{j\tau_0}+[c.c.]$, where $C(\tau_1)$ is the prism complex-slowly amplitude, $j=\sqrt{-1}$ is the imaginary unity and $[c.c.]$ refeers to the complex conjugate. Similarly, the NES motion is assumed to be $\upsilon_0(\tau_0,\tau_1)=B(\tau_1)e^{j\tau_0}+[c.c.]$, with $B(\tau_1)$ being the NES complex-slowly amplitude [3]. The ϵ-order problem can be solved by using the previous expressions, and considering $C=(1/2)ae^{j\alpha}$, $B(\tau_1)=(1/2)be^{j\beta}$. Thence, NES motion results in:

$$X_a=\theta_1 X_b+\theta_2 X_b^2+\theta_3 X_b^3 \tag{2}$$

where $X_a = a^2$, $X_b = b^2$, $\theta_1 = 1 + \hat{\lambda}_n^2/\hat{\mu}_n^2$, $\theta_2 = -\frac{3}{2}(\hat{\gamma}_n/\hat{\mu}_n)$, and $\theta_3 = \frac{9}{16}(\hat{\gamma}_n^2/\hat{\mu}_n^2)$. Equation (2) defines the Slow Invariant Manifold (SIM) structure, two folding points can be characterized, and a maximum NES critical damping can be defined by $\lambda_{n_{crit}} = (\sqrt{3}/3)\mu_n$ (i.e., $\lambda_n \leq \lambda_{n_{crit}}$) [3]. Similarly, the equation that describes the prism motion can be combined with Eq. (2), and for the steady state condition the equilibrium points can be calculated by solving the following polynomial equation:

$$X_b^5 + \Gamma_1 X_b^4 + \Gamma_2 X_b^3 + \Gamma_3 X_b^2 + \Gamma_4 X_b + \Gamma_5 = 0, \tag{3}$$

with $\Gamma_1 = \frac{2\theta_2}{\theta_3}$, $\Gamma_2 = \frac{2\theta_1}{\theta_3} + \frac{\theta_2^2}{\theta_3^2}$, $\Gamma_3 = \frac{2\theta_1\theta_2}{\theta_3^2} + \frac{\psi_1}{\psi_2\theta_3}$, $\Gamma_4 = \frac{\theta_1^2}{\theta_3^2} + \frac{\theta_2\psi_1}{\theta_3^2\psi_2}$, $\Gamma_5 = \frac{(\theta_1\psi_1 - 1)}{\psi_2\theta_3^2}$, $\psi_1 = \frac{\hat{n}\mathcal{A}_1}{\hat{\lambda}_n}$ and $\psi_2 = -\frac{3\hat{n}\mathcal{A}_3}{4\hat{\lambda}_n}$. Considering the airspeed with parameter, bifurcations diagrams can be draft based on the solutions of Eqs. (2), (3), allowing to access both amplitude and stability of the motions. These diagrams are essential to characterize the suppression regime responses induced by NES and yours boundaries.

Results and Discussions

The system under study was analyzed considering the following parameters: $n = 4.3\times10^{-4}$, $\zeta = 1.96\times10^{-3}$, $C_f^l = 2.69$, and $C_f^c = 168$ [1]. To validate the analytical approach, time integration results were obtained using the fourth-order Runge-Kutta method with a time step of a 10^{-2} seconds. For each simulated case, an arbitrary initial condition is used to find the steady state motions.

Figure 2(a) compares analytical and numerical bifurcations (♦, ×, ■) of the system considering $\mu_n = 0.05$, $\gamma_n = 1.5$ and $\lambda_n = 0.03\lambda_{n_{crit}}$, where a good agreement between the results is observed. Furthermore, a new bifurcation behavior is induced in the structure by its dynamic interaction with the NES. Unstable branches take place, and news response regimes are detected along the non-linear galloping boundary. The characterization of these suppression regimes is depicted in Figure 2(b). The first one, referred to as CR, comprises a complete suppression of phenomenon. The second regime (PS) occurs when partial suppression is observed through stable LCOs with small amplitudes. The third regime (SMR) is distinguished by competing two different response regimes driven by the initial condition. When small perturbations are imposed, the system exhibits strongly modulated responses (SMR) [2] with lower amplitudes. In contrast, for higher levels, the system jumps to LCOs with larger amplitudes (WS), which results in a weak suppression performance. The upper unstable branch depicts the basin of attraction that delimits these two different behaviors.

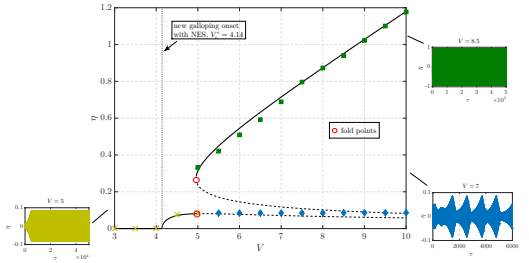

(a) ——— stable with NES, - - - unstable with NES, ♦ SMR, × small amplitude LCO, ■ high amplitude LCO.

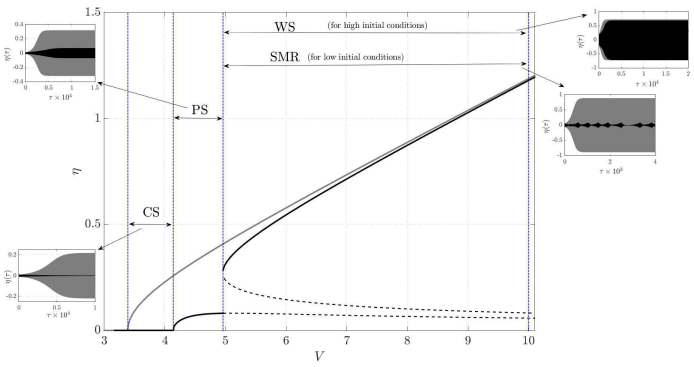

(b) ——— stable with NES, - - - unstable with NES, ——— without NES.

Figure 2: (a) Validation of MMS-based bifurcation analysis of the system, (b) Characterization of suppression regimes.

Conclusions

The paper investigated the application of an NES with pure cubic stiffness to the passive control of the nonlinear aeroelastic galloping. A benchmark lumped parameter model is used, and the aerodynamic loads are calculated through a nonlinear steady approach. Analytical treatments are carried out based on the MMS, and the solutions are numerically validated. Results comprise a study of the impact of the NES inclusion to the structure and the influence on the nonlinear response in post-galloping with NES. Suppression regimes are characterized based on the bifurcation diagrams in the function of responses induced by NES. To use this type of vibration absorber seems reasonable to control the galloping phenomenon. Further investigation will comprehensively analyze the effect of NES parameters on the boundaries of suppression regimes induced by it and establish the relationship between these regimes and the TET phenomenon.

References

[1] Paidoussis M. P., Price S. J., de Langre E. (2011) Fluid-Structure Interactions. Cambridge University Press, NY.

[2] Vakakis, A.F., Gendelman, O. (2001) Energy pumping in nonlinear mechanical oscillators: part II—resonance capture. *J. Appl. Mech.* 68(1), 42–48.

[3] Luongo A., Zulli D. (2014) Aeroelastic instability analysis of NES-controlled systems via a mixed multiple scale/harmonic balance method. *Journal of Vibration and Control*, 20(13),1985-1998.

Tuesday, July 19, 2022
08:30 - 10:30

MS-09 Nonlinear Dynamics in Engineering Systems
Auditorium Lumiere

Chair: Francesco Pellicano - Yury Vetyukov

08:30 - 08:50
Controlling orbits in nonlinear vibration energy harvesters dynamics
SAINT-MARTIN Camille*, MOREL Adrien, CHARLEUX Ludovic, ROUX Émile, BADEL Adrien
*Laboratoire SYstèmes et Matériaux pour la MEcatronique (Maison de la mécatronique 7, chemin de Bellevue 74940 Annecy-le-Vieux France)

08:50 - 09:10
Degradation at transition zones in railway tracks: 1-D and 2-D model comparison
FĂRĂGĂU Andrei*, METRIKINE Andrei, VAN Dalen Karel
*Faculty of Civil Engineering and Geosciences, Delft University of Technology (Stevinweg 1, 2628 CN, Delft Netherlands)

09:10 - 09:30
Dynamic response assessment of impact meta-dampers
CHONDROGIANNIS Kyriakos Alexandros*, DERTIMANIS Vasilis, MASRI Sami, CHATZI Eleni
*Institute of Structural Engineering [ETH Zürich] (Stefano-Franscini-Platz 5, 8093 Zürich Switzerland)

09:30 - 09:50
Dynamics of Piecewise Linear Mathieu Equation with Non-Zero Offset
K R Jayaprakash, **STAROSVETSKY Yuli***
*Department of Mechanical Engineering [Haifa] (Technion - Institute of Technology Haifa 32000 Israel Israel)

09:50 - 10:10
Estimation of downhole and bit-rock interaction parameters in real-time using an adaptive observer for drilling processes
KANDALA Shanti Swaroop*, SHOR Roman
*Postdoctoral Associate (Department of Chemical and Petroleum Engineering, University of Calgary, Calgary, Alberta Canada)

10:10 - 10:30
Analysis of an hydraulic switching converter with analog hysteresis feedback control
ZAGAR Philipp*, SCHEIDL Rudolf
*Johannes Kepler University Linz, Institute of Machine Design and Hydraulic Drives (Altenbergerstr 69, 4040 Linz Austria)

Controlling orbits in nonlinear vibration energy harvesters dynamics

Camille Saint-Martin*, Adrien Morel*, Ludovic Charleux*, Emile Roux* and Adrien Badel*
*Univ Savoie Mont Blanc, SYMME, F-74000, Annecy, France

Summary. Nonlinear mechanical resonators combined with piezoelectric transducers are widely used in vibration energy harvesting applications for their broadband behavior. Such nonlinear vibration energy harvesters may exhibit various orbits for a given excitation, each of them being associated with a given harvested power. Thus, in order to optimize the harvested power, it is crucial to find ways to jump from low power orbits to high power orbits, and to remain on them as long as possible. In this paper, we present a mathematical framework to test and study how effective is a given orbit jump strategy. Starting from the analytical model of a Duffing-type nonlinear mechanical energy harvester, we describe some of its dynamics, and we introduce a command function that can be used to impact the dynamics of the harvester. Thereafter, we will test and evaluate a set of command functions based on sinusoidal current injection.

Introduction

Vibrations are ubiquitous in nature and their energy can be scavenged via vibration energy harvesters (VEH) to replace batteries in low power electronic systems [1]. Nonlinear VEH have attracted the energy harvesting community because of their frequency behaviors that allow to harvest a relatively large power even if the vibration frequency shifts away from the harvester resonant frequency (for review, see e.g. [2]). However, such nonlinear VEH exhibit complex dynamical behaviors. Indeed, for a given excitation, they can oscillate on several orbits, often very different [3]. It is then necessary to find ways to stay in higher energy orbits to maximize the harvested power. For instance, [4] and [5] proposed to dynamically modify the buckling level of the VEH. [6] and [7] proposed to implement such orbit jump with a perturbation of the electrical load or with electrical impulses, respectively. While there are many existing orbit jump strategies in the literature [4, 5, 6, 7], there is a lack of mathematical framework that would allow their comparison in a unified way. In this paper, we introduce the nonlinear VEH model with an additional command function that allows to test and evaluate electrically-induced orbit jump strategies. The proposed modeling framework will allow to evaluate orbit jump strategies based on two major criteria: their potential for orbit jump and their energy consumption.

Electromechanical dynamics nonlinear vibration energy harvesters

A vibration energy harvester usually involves 3 sub-systems: a mechanical resonator, an electronic energy extraction circuit and a storage unit. In this study, we focus on the Duffing-type resonator and the influence of the extraction circuit on its dynamical behavior. A complete scheme of the system is given in Fig.1(a). The resonator consists of buckled steel beams on which a proof mass M is fixed. A piezoelectric transducer is used for mechanical-to-electrical energy conversion. It has a force factor α and a blocked capacitance C_p. The piezoelectric element is connected to the extraction circuit drawing an electrical current i. The piezoelectric voltage is noted v. The harvested power corresponds to the one collected in the electronic extraction circuit connected to the piezoelectric element.

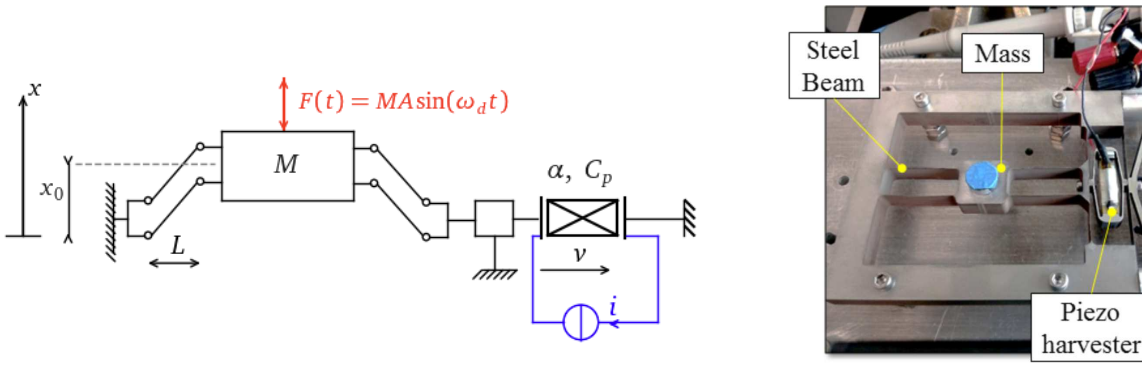

(a) (b)

Figure 1: (a) Schematic of the vibration energy harvester (b). Experimental prototype of a Duffing-type VEH [8].

The electromechanical dynamics of this nonlinear VEH can be modeled as follows:

$$\begin{cases} \ddot{x} = -\dfrac{\omega_0^2}{2}\left(\dfrac{x^2}{x_0^2} - 1\right)x - \dfrac{\omega_0}{Q}\dot{x} - 2\dfrac{\alpha}{ML}xv + A\sin(2\pi f_d t) \\ \dot{v} = 2\dfrac{\alpha}{LC_p}x\dot{x} - \dfrac{1}{C_p}i \end{cases} \tag{1}$$

where x is the position of the mass M. The resonator presents two stable positions at $x = \pm x_0$ (each corresponding to a

local minimum of the elastic potential energy and associated with a potential well). From the linearized behavior obtained from small oscillations around $x \approx x_0$, a natural angular frequency ω_0 and a mechanical quality factor $Q > 0$ can be found. The resonator is submitted to a sinusoidal ambient acceleration of amplitude A and frequency f_d. The nonlinear ordinary differential equations (1) were numerically solved for different vibration frequency values f_d and from different initial states $\boldsymbol{X}(0) = \begin{pmatrix} x^0 & \dot{x}^0 & v^0 \end{pmatrix}^\top$. Each simulation was performed until convergence to a periodic or a chaotic regime. The orbits were deduced and classified by type (periodic or chaotic) and, when periodic, by their harmonic or subharmonic order. These subharmonic orbits correspond to the case where the mass oscillates at a frequency which is a submultiple of the vibration frequency. An orbit is high when the mass oscillates around the two stable equilibrium positions. On the other hand, an orbit is low when the mass oscillates around one of the two stable equilibrium positions. In this paper, we take the following notations: H1H (resp. H1L) for a first order high (resp. low) harmonic and SH5H (resp. SH5L) for a fifth order high (resp. low) subharmonic. In the case where the electronic circuit is a simple resistor $R = 7.8$ kΩ, the current is given by $i = v/R$. The average harvested power corresponds to the power dissipated in the resistor and can be computed by calculating the mean value of $v.i = v^2/R$.

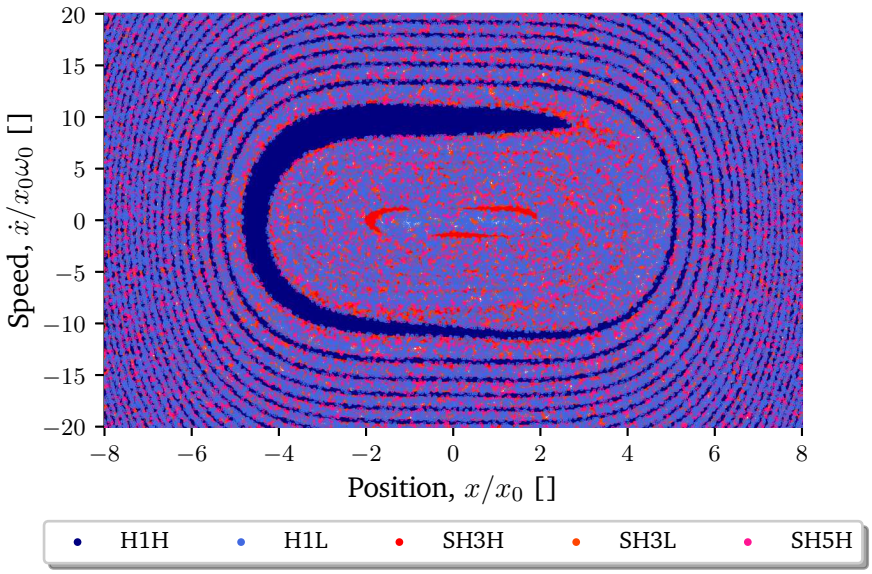

Figure 2: Basins of attraction for $f_d = 50$ Hz with a grid of 400 000 starting points [9].

The basins of attraction of the bistable (for $f_d = 50$ Hz) are shown in Fig.2. As seen in Fig.2, for a given vibration frequency and for some initial conditions, one can start on a low energy orbit. For example, at $f_d = 50$ Hz the system can start on H1L, SH3L, SH5H, SH3H or H1H (best case), and when the system stabilizes on H1L it is interesting to perturb the system by means of an orbit jump strategy in order to converge to a highest orbit (SH3L, SH5H, SH3H or H1H). In Fig.3, we can observe that multiple orbits of various powers coexist for a given vibration frequency. The longer one stays on highest power orbits, the better the performance. The goal of our study is to define a command function i_u that enables to jump from low power orbits to high power orbits. [1]

Dynamics adjustment by current injection

One way to induce such orbit jump is to dynamically modify one of the state-variable of the electromechanical system (i.e., x, $\dot{x}$ or v). From a practical point of view, it is much easier to implement a change of v than a change of x or $\dot{x}$, thanks to an adaptive electrical circuit. To modify the piezoelectric voltage v and to avoid any voltage discontinuities, we add an injection current i_u to the load current i_L. In this case, the total current flowing in the piezoelectric material i is given by $i = i_L - i_u$. We then end up with an optimal control problem where the output to control is the orbit and the command function is the injected current $i_u : t \mapsto \mathbb{R}$ which is assumed to be a continuous piecewise function.

[1] In this analysis the jump from chaotic orbits (present around 25 Hz, see Fig.3) will not be discussed.

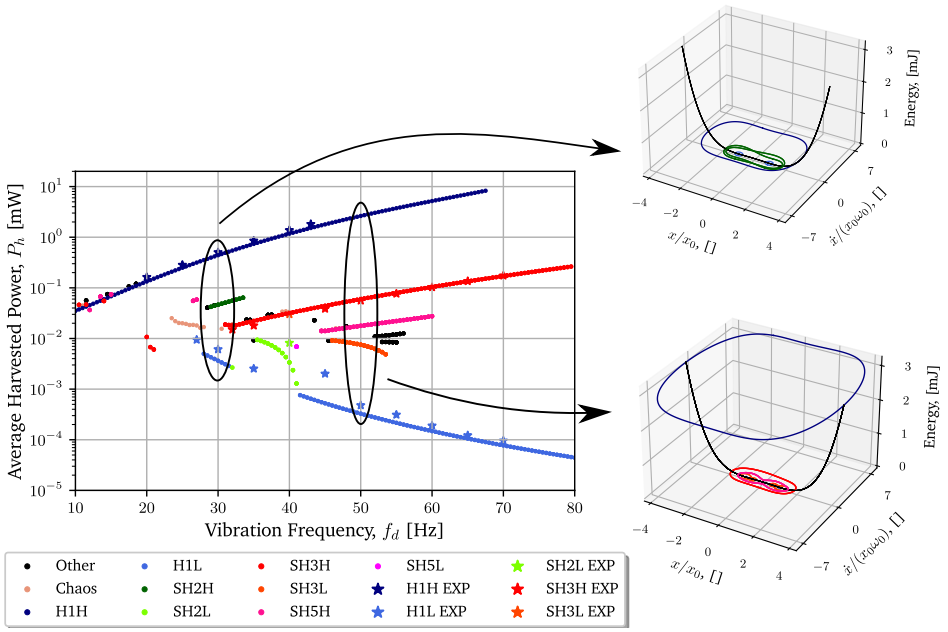

Figure 3: Simulated average harvested power as a function of the vibration frequency f_d for the different existing orbits [9].

$$\begin{cases} \ddot{x} = -\dfrac{\omega_0^2}{2}\left(\dfrac{x^2}{x_0^2}-1\right)x - \dfrac{\omega_0}{Q}\dot{x} - 2\dfrac{\alpha}{ML}xv + A\sin(2\pi f_d t) \\ \dot{v} = 2\dfrac{\alpha}{LC_p}x\dot{x} - \dfrac{1}{C_p}i_{\mathrm{L}} + \dfrac{1}{C_p}i_u \\ \dot{E} = \dfrac{2\alpha}{L}x\dot{x}v - C_p v\dot{v} = v.i = v.i_{\mathrm{L}} - v.i_u \\ \boldsymbol{X}(0) = \begin{pmatrix} x^0 & \dot{x}^0 & v^0 \end{pmatrix}^\top \end{cases} \tag{2}$$

Where E is the total harvested energy. The instantaneous harvested power $\dot{E}$ can be calculated from the power consumption of the load $v.i_{\mathrm{L}} \geq 0$ minus the injected power $v.i_u$. If we control the injected current function i_u, we can change the trajectory $t \mapsto \boldsymbol{X}(t)$ by punctually modifying the piezoelectric voltage v. Starting from this mathematical framework, the next section will present the analysis and evaluation of electrically-induced orbit jump strategies.

Results and discussion

We define a command function that consists in injecting a sinusoidal current at a certain time t_0. This injected current presents an amplitude I_e, a phase shift ψ_e with respect to the ambient excitation and an angular frequency ω_e. Moreover, the current is injected for a duration Δt, such as the orbit jump stops at $t_0 + \Delta t$. Since the excitation of the system is harmonic, we define dimensionless parameters k_{t_0} and $k_{\Delta t}$ as follows: $k_{t_0} = t_0/T_d$ and $k_{\Delta t} = \Delta t/T_d$. Therefore, there are five influence orbit jump parameters $(k_{t_0}, k_{\Delta t}, I_e, \psi_e, \omega_e)$ to study.

$$i_u(t) = \begin{cases} I_e \sin(\omega_e t + \psi_e), & \text{for } t/T_d \in [k_{t_0}, k_{t_0} + k_{\Delta t}] \\ 0, & \text{otherwise} \end{cases} \tag{3}$$

To analyze the effectiveness of this orbit jump technique consisting in the injection of current (3), we start on a low energy orbit. Thereafter, we simulate different combinations of $(k_{t_0}, k_{\Delta t}, I_e, \psi_e, \omega_e)$ and analyze their influence on the dynamics of the harvester. Figure 4 presents an example of the orbit jump strategy for $f_d = 50$ Hz with arbitrary parameter values $(k_{t_0}, k_{\Delta t}, I_e, \psi_e, \omega_e) = (0.35, 2.5, 0.18, 1.6\pi, 2\omega_d)$. Figure 4(a) shows the corresponding injected current waveform (3) during the first few periods and after 1 000 periods. At the beginning of the simulation, the system oscillates on the lowest existing orbit (H1L) during 5 vibration periods T_d. For $t = (5 + k_{t_0})T_d = 5.35T_d$, the orbit jump strategy using the injected current described in Fig.4(a) is applied for a duration of $\Delta t = 2.5T_d$. Fig.4(b,c) show that there is no transient and the VEH converges almost directly to the H1H steady state (green and red curves). This convergence is similar to the one obtained with a buckling level modification (see [4, 5]).

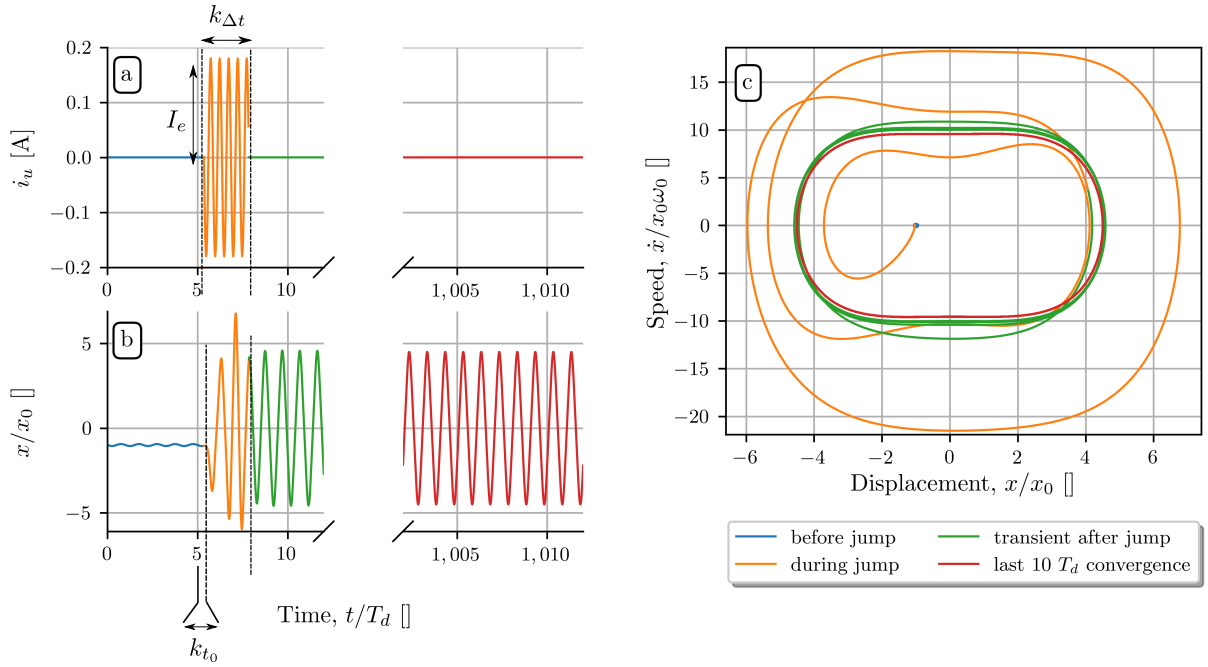

Figure 4: (a) Sinusoidal injected current (3) as a function of time with parameter values $(k_{t_0}, k_{\Delta t}, I_e, \psi_e, \omega_e) = (0.35, 2.5, 0.18, 1.6\pi, 2\omega_d)$, (b) displacement as a function of time for $f_d = 50$ Hz before (H1L in blue), during (in orange) and after (in green and red) the orbit jump. (c) Trajectory in the dimensionless phase plane $(x/x_0, \dot{x}/x_0\omega_0)$.

The invested energy during the orbit jump E_{inv} (4) consists in the integral of the instantaneous harvested power subtracted from the instantaneous injected power over the jump duration. (5) computes total injected energy during the orbit jump, considering both the current flowing in the piezoelectric material and the current flowing in the load R.

$$E_{\text{inv}} = \int_{t_0}^{t_0+\Delta t} \left[v(t).i_u(t) - v(t).i_L(t)\right] dt \tag{4}$$

$$E_{\text{inj}} = \int_{t_0}^{t_0+\Delta t} v(t).i_u(t)dt = E_{\text{inv}} + \int_{t_0}^{t_0+\Delta t} v(t).i_L(t)dt \tag{5}$$

Thereafter, an evolutionary algorithm inspired from natural selecting process [10, 11] is used for investigating optimal orbit jump parameters $(k_{t_0}, k_{\Delta t}, I_e, \psi_e, \omega_e)$ that belong to $[0,1] \times [0,50] \times [0,0.2] \times [0,2\pi] \times [0,4\omega_0]$ where $\omega_0 = 121$ rad.s^{-1}. Using the glossary of evolutionary strategies, the *population* is an orbit jump parameters (*individuals*) collection, the *fitness* corresponds to the objective function value that is the total injected energy (5) under the constraint that individuals have converged to the targeted orbit (of higher energy than the initial orbit). The best 10% of individuals are selected for the next generation and the classic operations of crossing (single point crossover) and mutation are applied. By means of evolutionary strategy, optimum orbit jump parameters values are obtained at 50 Hz: $(k_{t_0}^{\text{opt}}, k_{\Delta t}^{\text{opt}}, I_e^{\text{opt}}, \psi_e^{\text{opt}}, \omega_e^{\text{opt}}) = (0.80, 2.08, 0.04, 2.49, 415.34)$.

Running simulations with identical initial condition $\boldsymbol{X}(0)$ that belongs to the basin of attraction of the H1L at 50 Hz and taking $(k_{t_0}, k_{\Delta t}, I_e, \psi_e, \omega_e)$ in $\{k_{t_0}^{\text{opt}}\} \times \{k_{\Delta t}^{\text{opt}}\} \times [0, 0.2] \times [0, 2\pi] \times \{\omega_e^{\text{opt}}\}$ gives Fig.5 scatter plot $(\psi_e/2\pi, I_e)$. Note that, if the injected current amplitude I_e is almost zero, the injection of current is too low and the system remains stuck on the initial orbit H1L (light blue area in the bottom of Fig.5). To jump from H1L to SH3H (resp. H1H), it is necessary to consider the parameter values that are associated with red (resp. dark blue) areas in Fig.5 (for example, area in the upper right (resp. in the middle left)). Arrows in Fig.5 give examples of parameters combinations (materialized by stars) assuring jump from H1L to H1H, SH3H and SH3L, respectively. Generally, the injected current amplitude increases with the energy level of the targeted orbit. For example, in order to reach H1H when starting from H1L, the value of I_e needs to be higher than those to reach SH3L or SH5H.

Figure 6 presents this optimal orbit jump solution parameters obtained by using the aforementioned algorithm. Figure 6(a) shows that the injected current is applied on a relatively short instant. Note that the injection of current is stopped when the VEH is in the neighbourhood of the basin of attraction of H1H.

For each initial orbit, optimum orbit jump parameters that allow to reach the highest energy orbit are found by means of aforementioned algorithm. Table 1 gives invested energy values associated with optimal orbit jump parameters for jumping from a given initial orbit to a given targeted orbit for $f_d = 47$ Hz. For example, invested energy required to jump from H1L to H1H is 2.54 mJ. Table 1 underlines, for some frequencies, the interest of jumping in "k-times" ($k > 1$, integer), i.e., in k low cost jumps. As a matter of example, for jumping from H1L to H1H, one might imagine jumping from H1L to SH3L, to SH5H, to SH3H, then to H1H. The sum of the invested energies associated to each step is equal to 1.79 mJ, which is lower than the invested energy for jumping directly from H1L to H1H (2.54 mJ).

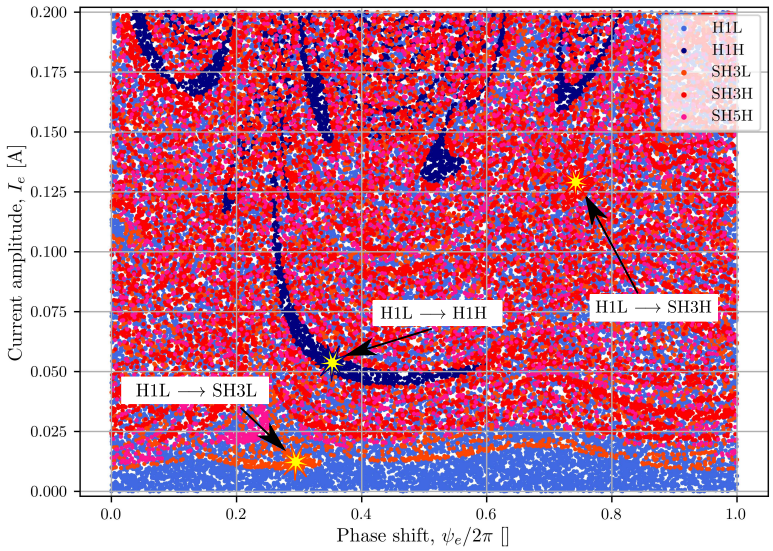

Figure 5: Map $(k_{t_0}^{\text{opt}}, k_{\Delta t}^{\text{opt}}, I_e, \psi_e/2\pi, \omega_e^{\text{opt}})$ starting from H1L for $f_d = 50$ Hz. Arrows from left to right illustrate candidate values for $(\psi_e/2\pi, I_e)$ in order to jump from H1L to SH3L, from H1L to H1H or H1L to SH3H. The map has been computed with 50 000 quintuplets $(k_{t_0}^{\text{opt}}, k_{\Delta t}^{\text{opt}}, I_e, \psi_e, \omega_e^{\text{opt}})$ where $(I_e, \psi_e) \in [0, 0.2] \times [0, 2\pi]$.

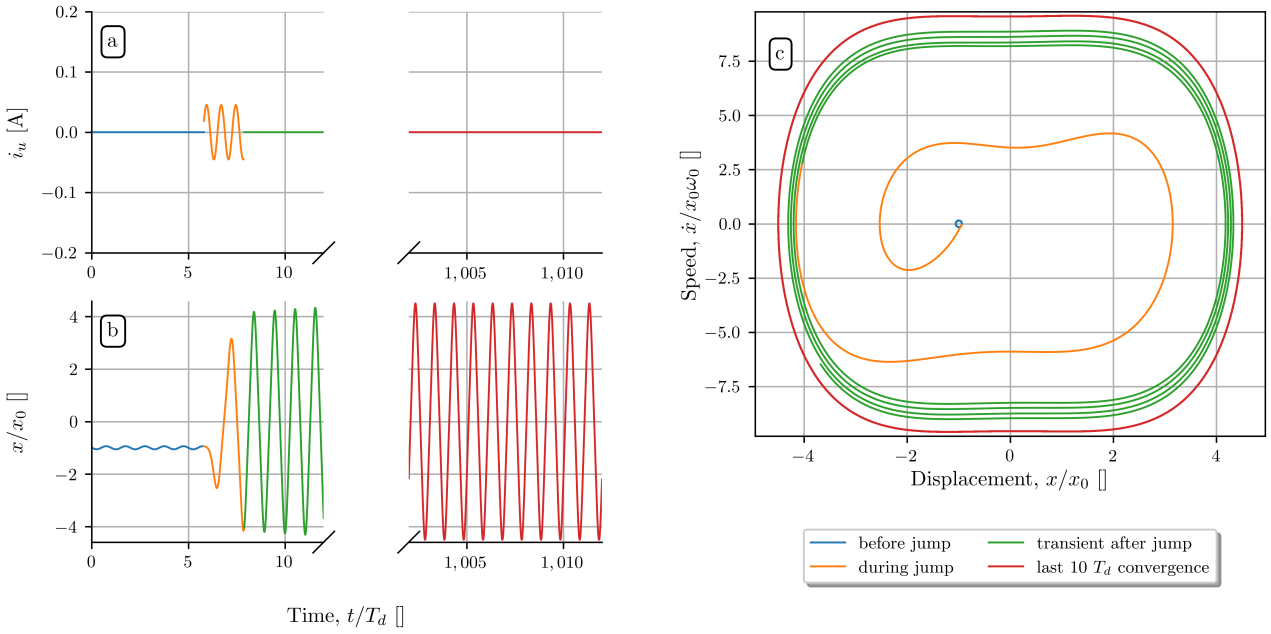

Figure 6: (a) Sinusoidal injected current (3) as a function of time with optimal parameter values $(k_{t_0}^{\text{opt}}, k_{\Delta t}^{\text{opt}}, I_e^{\text{opt}}, \psi_e^{\text{opt}}, \omega_e^{\text{opt}}) = (0.80, 2.08, 0.04, 2.49, 415.34)$. (b) Displacement as a function of time for $f_d = 50$ Hz before (H1L in blue), during (in orange) and after (in green and red) the optimized orbit jump. (c) Trajectory in the dimensionless phase plane $(x/x_0, \dot{x}/x_0\omega_0)$.

Figure 7 shows the optimal invested energy required to jump from the lowest existing orbit to H1H (resp. SH3H) as a function of the vibration frequency. Note that there are few values of the invested energy required for jumping on the two targeted orbits (H1H and SH3H) for vibration frequencies below 25 Hz because there is almost only H1H in this vibration frequency range. Figure 7 shows that the invested energy increases with the vibration frequency[2]. Moreover, this orbit jump strategy makes it possible to reach H1H from the lowest existing orbit until its cutoff frequency at 67 Hz. Note that, the optimal amplitude I_e^{opt} necessarily increases with the vibration frequency and the energy level of the targeted orbit.

[2]Indeed, the displacement of H1H becomes larger with the vibration frequency, which explains why the energy gap between H1H and H1L becomes wider [9].

Initial orbit \ Targeted orbit	SH3L	SH5H	SH3H	H1H
H1L	5.10^{-3}	1.10^{-2}	$3.7.10^{-2}$	2.54
SH3L	0	7.10^{-3}	$1.8.10^{-2}$	2.06
SH5H	/	0	3.10^{-2}	2.08
SH3H	/	/	0	1.75

Table 1: Optimal invested energy (4) (mJ) required to jump from an initial orbit (left column) to a targeted orbit (top row) for $f_d = 47$ Hz. Invested energy values for jumping from H1L to H1H with 4 intermediates jumps are colored in red while the invested energy for jumping from H1L to H1H in one time is colored in blue.

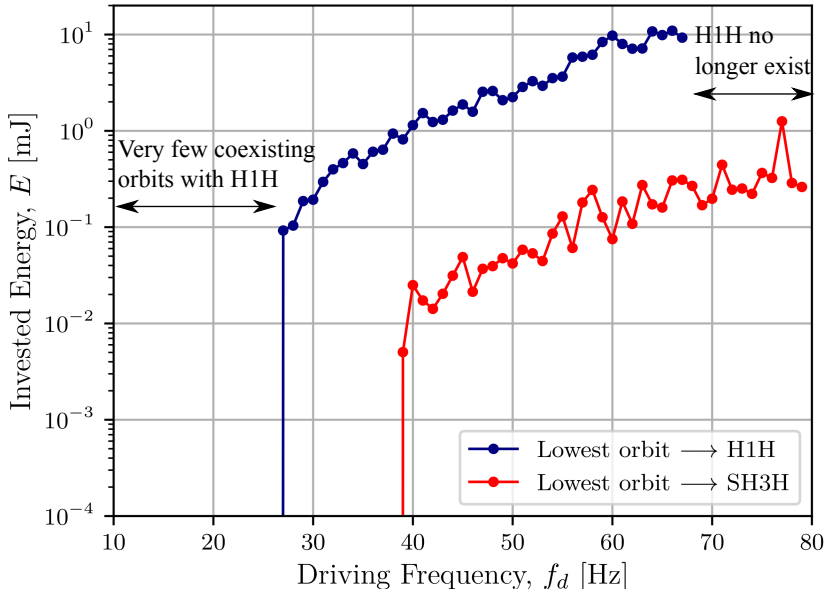

Figure 7: Evolution of the optimal invested energy required to jump from the lowest existing orbit to H1H (in blue) and those to jump from the lowest existing orbit to SH3H (in red) as a function of the vibration frequency.

Conclusion

In the present paper, we proposed a mathematical framework in order to analyze and evaluate electrically-induced orbit jump strategies. From this framework, we studied an orbit jump approach based on a sinudoidal injected current. By means of an evolutionary algorithm, the optimal set of parameters of this orbit jump approach has been determined. Among results of this analysis is that the optimal injection current that minimizes the injected energy is relatively short and stopped when the VEH is in the neighbourhood of the basin of attraction of the targeted orbit. Another insights is that, for some frequencies, the injected current consumes less energy to jump from a low energy orbit to a high energy orbit with multiple small jumps instead of a single large jump. In the future, the proposed framework could be used to find the optimal orbit jump strategy with a generic current waveform with many additional degrees of freedom.

Acknowledgements

This project has received funding from the European Union's Horizon 2020 research and innovation program under grant agreement No 862289.

References

[1] Sezer N., Koç M., (2021) A comprehensive review on the state-of-the-art of piezoelectric energy harvesting. *Nano Energy* https://doi.org/10.1016/j.nanoen.2020.105567

[2] Jia Y., (2020) Review of nonlinear vibration energy harvesting: Duffing, bistability, parametric, stochastic and others, *Journal of Intelligent Material Systems and Structures* https://doi.org/10.1177/1045389X20905989

[3] Lansbury A.N., Thompson J. M. T., Stewart H. B., (1992) BASIN EROSION IN THE TWIN-WELL DUFFING OSCILLATOR. *International Journal of Bifurcation and Chaos* https://doi.org/10.1142/S0218127492000677

[4] Huguet T., Lallart M., Badel A., (2019) Orbit jump in bistable energy harvesters through buckling level modification. *Mechanical Systems and Signal Processing*, **128**:202–215 https://doi.org/10.1016/j.ymssp.2019.03.051

[5] Huang Y., Liu W., Yuan Y., Zhan Z., (2020) High-energy orbit attainment of a nonlinear beam generator by adjusting the bukling level. *Sensors and Actuators A: Physical*, **312**:112164 https://doi.org/10.1016/j.sna.2020.112164

[6] Wang J., Liao W.-H., (2019) Attaining the high-energy orbit of nonlinear energy harvesters by load perturbation. *Energy Conversion and Management* https://doi.org/10.1016/j.enconman.2019.03.075

[7] Udani J. P., Arrieta A. F., (2017) Sustaining high-energy orbits of bi-stable energy harvesters by attractor selection. *Applied Physics Letters 111* https://doi.org/10.1063/1.5000500

[8] Huguet T., (2018). Vers une meilleure exploitation des dispositifs de récupération d'énergie vibratoire bistables : Analyse et utilisation de comportements originaux pour améliorer la bande passante. Ph.D. thesis. https://tel.archives-ouvertes.fr/tel-01957377

[9] Saint-Martin C., Morel A., Charleux L., Roux E., Benhemou A., Badel A., (2022). Power expectation as a unified metric for the evaluation of vibration energy harvesters. *Mechanical Systems and Signal Processing*. https://doi.org/10.1016/j.ymssp.2022.109482

[10] Sivanandam S., Deepa S., (2008). Genetic Algorithms. In: Introduction to Genetic Algorithms. *Springer*. https://doi.org/10.1007/978-3-540-73190-0_2

[11] Konak A., Coit D. W., Smith A. E., (2006). Multi-objective optimization using genetic algorithms: A tutorial. *Reliability Engineering & System Safety*, https://doi.org/10.1016/j.ress.2005.11.018

Degradation at transition zones in railway tracks: 1-D and 2-D model comparison

Andrei B. Fărăgău*, Andrei V. Metrikine*, Karel N. van Dalen*
*Faculty of Civil Engineering and Geosciences, Delft University of Technology, Delft, the Netherlands

Summary. Transition zones in railway tracks are areas with considerable variation of track properties (i.e., foundation stiffness) encountered near structures such as bridges. Due to strong amplification of the railway track's response, transition zones are prone to rapid degradation. To study this degradation, researchers and engineers have developed models ranging from simple 1-D models (e.g., beam on Winkler foundation) to complex 3-D models with accurate geometry and material behaviour. This study compares a 1-D model to a 2-D one with the aim of assessing if the degradation patterns predicted by the more simplistic model are accurate. We choose a very simple geometry for the 2-D model such that the comparison is restricted to (mainly) the influence of the soil layer (present in the 2-D model) on the predicted degradation at transition zones; incorporating the soil layer makes the response of the supporting structure frequency and wavenumber dependent as well as non-local, characteristics which are not usually incorporated in 1-D models. Preliminary results show that the degradation predicted by the 1-D model is significantly larger than the one in the 2-D model.

Introduction

Transition zones in railway tracks are areas with significant variation of track properties (e.g., stiffness, mass, etc.) encountered near man-made structures such as bridges, tunnels or culverts. These zones require more frequent maintenance than the regular parts of the railway track, leading to high costs and reduced availability of the track. A substantial part of the maintenance performed in transition zones is concerned with restoring the vertical position of the track, which changes over time due to soil and ballast settlement.

To understand the settlement mechanisms at transition zones, researchers have developed a multitude of computational models. They range from 1-D models (e.g., beam on Winkler foundation) to 3-D finite element models (FEM) models with accurate geometry of the real scenario. For predictive purposes, the models with more accurate geometry are preferred; these predictive models are important and show reasonable agreement to measurements, especially due to their accurate geometry representation and material behaviour. However, their complexity makes it difficult to investigate specific mechanisms due to the multitude of phenomena simultaneously at play. That is why, for research focusing on individual mechanisms, the simpler models (e.g., 1-D models) are preferred. Nonetheless, the simplistic models may overlook important features that can render their results incorrect.

This study compares two such models, namely a 1-D and a 2-D model, in terms of degradation (after one load passage) with the purpose of judging if the results obtained with the simplified model are trustworthy. The 1-D model is composed of a beam on nonlinear and inhomogeneous Kelvin foundation and is described in [1] while the 2-D model consists of an infinite beam and a viscoelastic-continuum layer (i.e., soil) connected through a layer of nonlinear and inhomogeneous springs and dashpots (Figure 1). The layer of springs-dashpots represents the effective contribution of all components between the rail and soil (i.e., railpads, ballast and sub-ballast). In both models, the nonlinearity and inhomogeneity are located in the layer of springs-dashpots; the nonlinear behaviour of the springs models the compaction of ballast (Figure 1), while the inhomogeneity represents the transition zone. The 2-D model has a simple geometry such that the comparison is restricted to (mainly) the influence of the soil layer on the results; incorporating the soil layer makes the response of the supporting structure frequency and wavenumber dependent as well as non-local, characteristics which are not usually incorporated in 1-D models.

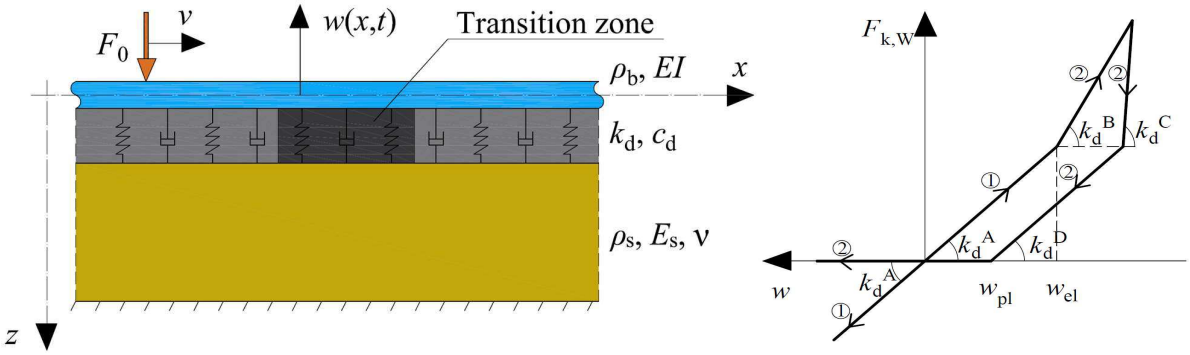

Figure 1: Model schematics: an infinite beam and an elastic-continuum layer connected through a layer of nonlinear and inhomogeneous springs and dashpots, acted upon by a moving constant load (left panel); Piecewise-linear constitutive law of the ballast (right panel).

Tuning the 1-D model

To compare the two models, the parameters of the 1-D model need to be tuned to the ones of the 2-D model. The tuning is performed for the steady-state response in each of the domains (open track and stiff zone) individually. Advanced algorithms have been developed to make the response of the 1-D model match well that of 2D/3D models (see [2]). However, this study aims to investigate if most of the models used in literature, which do not use a complex tuning technique, can predict a correct degradation pattern. Therefore, the tuning is done in a more standard manner. Firstly, the static track stiffness is matched in the two models. Secondly, the mass of the rail in the 1-D model is chosen such that the critical velocities are matched in the two models. Finally, the damping in the 1-D model is chosen based on engineering judgement; nonetheless, the damping in the 1-D model has been varied and for reasonable values it does not significantly affect the results.

Preliminary results

Figure 2 presents the degradation predicted by the two models after one load passage. For the 2-D model, there are two cases presented depending on how the nonlinear constitutive model is defined. Firstly, case A considers that the degradation is governed by the differential displacement between the beam and the top surface of the soil since the nonlinear constitutive model is only for ballast; this represents a realistic case. Secondly, case B assumes the degradation to be governed by the displacement of the beam only; this case is not representative of reality and is considered just for comparison reasons.

Preliminary results show that the degradation in the 1-D model is significantly higher than in the 2-D model (case A). The main reason is that the degradation in the 1-D model is based on the displacement of the beam, while in the 2-D model the degradation is dictated by the differential displacement between the beam and the top surface of the soil. Since the soil is considerably softer than the ballast, the differential settlement between the beam and the top surface of soil is small, leading to reduced degradation. When imposing the degradation to be dictated by the displacement of the beam only (case B), the degradation predicted by the two models becomes comparable in magnitude, although still larger in the 1-D model. This shows that the large difference in degradation (1-D vs 2-D case A) is caused by the springs in the 1-D model being fixed at the bottom while in the 2-D model (case A) the springs lay on a compliant medium.

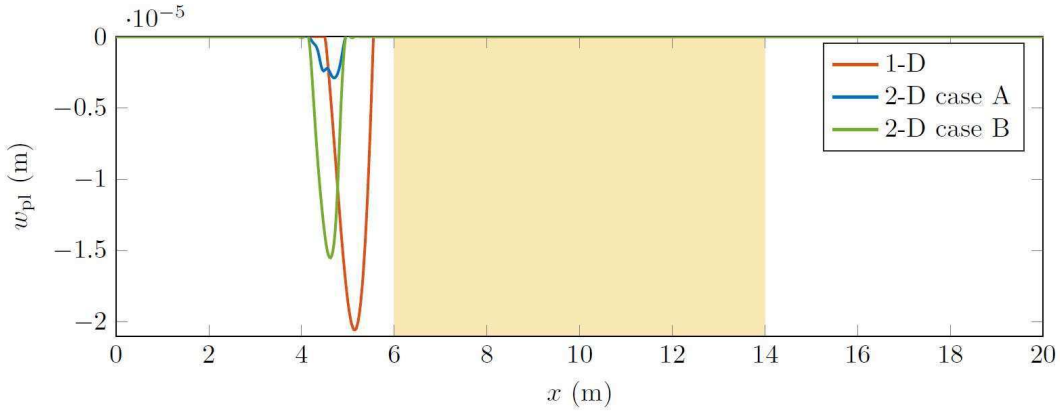

Figure 2: Degradation predicted by the two models after 1 load passage for a load velocity of 85% the critical velocity; the location of the transition zone is marked by the yellow background.

Conclusions

This study compares two models (1-D and 2-D) representative of railway tracks at transition zones, in terms of the predicted ballast degradation with the purpose of judging if the results obtained with the simplified model are trustworthy. Preliminary results show that the degradation after one load passage predicted by the 1-D model is significantly larger than the one in the 2-D model. This is mainly caused by the springs in the 1-D model being fixed at the bottom while in the 2-D model the springs lay on a compliant medium. The shortcoming of the simplified model considered here could be overcome by adopting a model with two beams connected by the nonlinear and inhomogeneous springs (representative for ballast compaction) and resting on Kelvin foundation. Finally, simplified models (beam on elastic foundation) potentially overestimate the predicted degradation at transition zones.

References

[1] Fărăgău, A.B., Keijdener, C., de Oliveira Barbosa, J.M., Metrikine, A.V., van Dalen, K.N. (2021) Transition radiation in a nonlinear and infinite one-dimensional structure: a comparison of solution methods. *Nonlinear Dyn.* **103**, 1365–1391.

[2] Rodrigues, A., Dimitrovová, Z. (2021) Applicability of a Three-Layer Model for the Dynamic Analysis of Ballasted Railway Tracks. *Vibration.* **4**, 151-174.

Dynamic Response Assessment of Impact Meta-Dampers

Kyriakos Alexandros I. Chondrogiannis[*], Vasilis K. Dertimanis[*], Sami F. Masri[**] and Eleni N. Chatzi[*]
[*]*Institute of Structural Engineering, ETH Zurich, Stefano-Franscini-Platz 5, 8093 Zurich, Switzerland*
[**]*Viterbi School of Engineering, University of Southern California, University Park, Los Angeles, CA 90089, USA*

Summary. Recently, the concept of metamaterials, initially studied for electromagnetic applications has gained interest within a civil engineering context [1, 3]. It has been shown that periodic arrangement of resonators, referred to as unit cells, can provide beneficial properties in vibration absorption, within a specific range of frequencies, the so-called bandgap. In order to take advantage of the full potential these unique structures can offer, a wider breadth of the bandgap is pursued, while additionally shifting the lower bound to lower frequencies renders metamaterials appealing for civil engineering applications. One promising solution to this requirement is the use of nonlinear resonators, which form part of the metamaterial configuration. In the current work, periodic structures consisting of impact damper resonators are investigated, thus introducing a highly nonlinear behaviour. The performance of a single impact damper has already been investigated [4] and its dynamic response has been proven to be advantageous for vibration attenuation. Further exploiting this phenomenon, the current study is extended to multiple degree of freedom (MDOF) systems, which are investigated both numerically and analytically. The MDOF systems occur as concatenation of a finite number of impact damper unit cells. Several characteristics of the proposed configuration are explored as variable parameters for optimization purposes. For the assessment of the system's efficiency, different metrics are being studied, including the frequency response function and the total energy loss as a result of the metastructure contribution. The results confirm the potential of utilization of the metamaterial concept, building on impact phenomena, for vibration attenuation.

Introduction

A significant concern in large-scale civil structures lies in response under dynamic loading, e.g. earthquakes. For this reason, the research community has been constantly working on designing systems, which are able to ensure structural safety, by minimizing the effects of the excitation on the structure. Recently, a novel idea has begun to draw attention in civil engineering applications, building on the concept of metamaterials or metastructures. These are structures characterized by extraordinary filtering properties, attained as a result of diversified mechanisms, such as their microscopic geometry, periodic arrangement, etc [5]. When the frequency of the incoming excitation lies within the constructed filter limits, the propagation of motion is arrested, thus forming a "bandgap". The challenge that arises, however, lies in the range of the bandgap as well as in the proper adjustment of the lower frequency threshold, which is essential in many engineering applications. In the current work, strong nonlinearities, in the form of impacts, are introduced, in order to address this challenge. Nonlinear attachments to the primary system are generally termed as nonlinear energy sinks (NES). There is extended research and literature in the field of NES, as for reference in the work of Vakakis et al. [4], which also investigates impact dampers as a nonlinear attachment from the non-smooth events point of view. Moreover, in the work of Ibrahim et al [2], analytical approximations of the dynamic behaviour of impacts are provided. Important is the contribution of Masri and colleagues on impact dampers, regarding their general motion [6], their stability analysis [7], as well as their dynamic response to random excitation [8]. Furthermore, the concept of impact dampers is closely associated with particle dampers. In fact, a lattice of several impact dampers can be considered to be a single particle damper. A detailed investigation on the latter, under random excitation, is provided in the work of Lu et al. [9].

Meta-impactor

The idea of the meta-impactor is inspired by the beneficial effect that a single impact damper can have on a structure, under dynamic loading [4]. The attempt is to protect a specific mass with the metamaterial configuration. The concept of the current work is based on the consecutive arrangement of impact damper unit cells (Figure 1). The unit cells consist of a rigid container, containing a laterally unconstrained mass, free to impact on the respective bounds. Furthermore, the resonators are connected elastically to each other, as well as to the protected mass on one end, and to a fixed support on the other. In the current study, the response of the system is investigated under input of a harmonic force F.

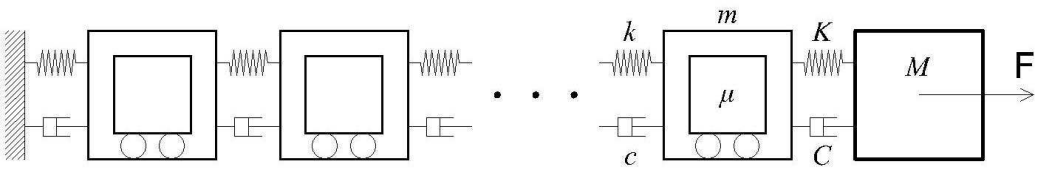

Figure 1: Metamaterial lattice configuration

Analysis

The response of the system is studied both numerically and analytically. As for the first part, every impact is analyzed as a non-smooth event, while the equations of motion are affected by a discontinuity. This approach provides results, which are directly linked to the specified parameters of each system (mass, stiffness, damping, etc.) and are restricted to discrete combinations of those parameters. Multiple analyses with varying parameters are carried out for optimization purposes, an example of which is shown in Figure 2. In order to better assess the behaviour of the metamaterial, an analytic parametric approach is pursued. For this reason, the non-smooth interaction between the container and the inner mass is approximated by a continuous highly-nonlinear function. In this setting, the analysis can be carried out parametrically, taking into consideration the variability of the system's characteristics.

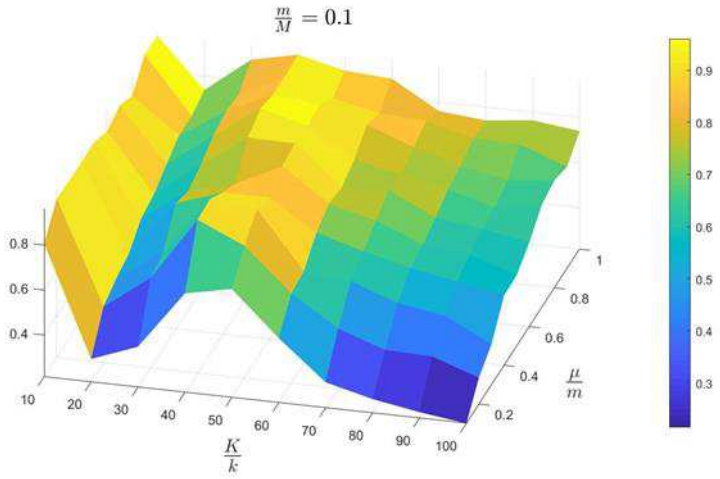

Figure 2: Percentage of energy absorption of the total input energy at 1 Hz for a 2 unit cell lattice and varying masses/stiffness ratios

Conclusions

The purpose of this study is to evaluate the performance of metamaterial lattices, consisting of impact damper unit cells, for vibration mitigation. The assessment of the performance is determined, depending on the frequency response function of the system, as well as on the calculation of the total energy absorption. Furthermore, the results of the numerical and analytical procedures are compared, revealing consistency of the analytical approximation. This is particularly helpful for further simulations and subsequent analyses of the resulting dynamics. The concept of metamaterials is proven effective, given a proper design and optimization process, and is suited for shielding of structures from vibrations.

References

[1] Dertimanis, V.K., Antoniadis I.A., Chatzi E.N. (2016). Feasibility analysis on the attenuation of strong ground motions using finite periodic lattices of mass-in-mass barriers, Journal of Engineering Mechanics, 142(9), 10.1061/(ASCE)EM.1943-7889.0001120, 04016060.
[2] Ibrahim, R.A. (2009). Vibro-Impact dynamics: Modelling, Mapping and Applications, Springer, Berlin, Germany, 2009.
[3] Palermo, A., Krödel, S., Matlack, K.H., Zaccherini, R., Dertimanis, V.K., Chatzi, E.N., Marzani, A. and Daraio, C., Hybridization of Guided Surface Acoustic Modes in Unconsolidated Granular Media by a Resonant Metasurface, Physical Review Applied, 9, 054026 – Published 17 May 2018, https://doi.org/10.1103/PhysRevApplied.9.054026.
[4] Vakakis, A.F., Gendelman, O.V., Bergman, L.A., McFarland, D.M., Kerschen, G. and Lee, Y.S., (2008). Nonlinear Targeted Energy Transfer in Mechanical and Structural Systems, Vol. I & II, Springer, New York.
[5] Cui, T. J., Smith, D. R. and Liu, R. (2010). Metamaterials, Springer, New York.
[6] Masri, S.F. (1970). General Motion of Impact Dampers, The Journal of the Acoustical Society of America, 47, 229- 237.
[7] Masri, S.F. (1968). Stability Boundaries of the Impact Damper, Journal of Applied Mechanics, 35(2), 416-417.
[8] Masri, S.F. and Ibrahim, A.M. (1973). Response of the Impact Damper to Random Excitation, The Journal of the Acoustical Society of America, 53(1), 200-211.
[9] Lu, Z., Masri, S.F. and Lu, X. (2011). Studies of the performance of particle dampers attached to a two-degree-of-freedom system under random excitation. Journal of Vibration and Control. 17. 1454-1471. 10.1177/1077546310370687.

Dynamics of Piecewise Linear Mathieu Equation with Non-Zero Offset

K. R. Jayaprakash [*] and Yuli Starosvetsky [**]
[*] *Discipline of Mechanical Engineering, Indian Institute of Technology Gandhinagar, Gujarat, India*
[**] *Faculty of Mechanical Engineering, Israel Institute of Technology-Technion, Haifa, Israel*

Summary. The current work considers a piecewise linear Mathieu equation with the point of asymmetry being non-zero. The considered oscillator is essentially nonlinear and the primary objective of this study is to explore the regions of instabilities as a function of the excitation amplitude, frequency and interestingly the initial energy imposed on the oscillator. In this study we invoke energy-angle variables and the method of averaging to analytically describe the interesting energy dependent instability zones. We explore the instability zones in the vicinity of $1:1$ parametric resonance. We show that the derived analytical model provides a fairly good first order approximation to the unstable regions emerging in the vicinity of $1:1$ resonances and it is expected that the analytical method described is applicable to higher order resonances as well.

Introduction

Many computational and analytical attempts have been devoted to understanding of the complex dynamics of a 1DOF piecewise linear oscillator (PWLO) model subject to various types of excitations such as external and parametric forcing. Shaw and Holmes [1] have analysed semi-analytically the harmonically forced PWLO for the periodic orbits and their bifurcations. This study has been followed by Thompson et. al [2] who analysed numerically the subharmonic resonances, bifurcations and chaotic regimes of forced PWLO. Natsiavas [3] has considered the forced response of PWLO with bi-linear damping and successfully derived the relatively simple, semi-analytic solution for n-periodic orbits and analysed their stability. Using a similar approach, author has analysed the n-periodic response including stability analysis of PWLO incorporating the Van-der-Pol type damping [4]. Other works by Natsiavas et al. [5, 6] present the parametric excitation of piecewise linear oscillator as a typical model of gear backlash and asymmetric stiffness. A computational study by Chatterjee et al. [7] was performed on the model proposed by Natsiavas et al. [5] exploring the regions of instability. The current study dwells on the analytical description of these instability regions using asymptotic analysis. The resulting modulation equation provides a first order approximation of these instability boundaries in this class of systems and the approximations obtained by the considered method are found to be good in the case of sufficiently low excitation level.

Model and Analysis

Let us consider a piecewise linear (PWL) oscillator with a non-zero offset ($a > 0$) subject to a parametric excitation,

$$\ddot{q} + f(q) + \varepsilon P \cos(\Omega_e t) q = 0 \tag{1a}$$

$$f(q) = \begin{cases} q, q < a \\ \delta^2 q + (1-\delta^2)a, q \geq a \end{cases} \tag{1b}$$

The above equation is scaled such that the stiffness coefficient is unity for $q < a$, whereas the corresponding coefficient is $\delta \geq 1$ for $q \geq a$. In what follows δ will be referred to as the 'asymmetry parameter' and a as the 'offset parameter'. In fact, Eq. (1) or its different variants have been previously considered in several theoretical works for the two important limiting cases.

Unlike the linear Mathieu equation, its PWL counterpart with a non-zero offset, possesses the energy dependent parametric instability zones. To illustrate this fact, we plot the energy ($E(t)$) corresponding to Eq. (1) assuming the parametric excitation in the vicinity of $1:1$ resonance with the fixed level of excitation amplitude (P) and frequency for the two different initial energy levels ($E(0)$). As is clear from the results of Figure 1, formation of unbounded response strongly depends on initial energy. The main objective of the present study is to characterize analytically these energy dependent instability zones. This is done by reformulating the system in terms of the action (I) - angle (θ) (A-A) variables ($q(I,\theta)$), transforming to energy (E)-angle variables ($q(E,\theta)$) and averaging in the vicinity of ($1:n$) resonance. Subsequent analysis of the averaged equations reveals the formation of quite interesting, energy dependent instability regions for a general resonance condition ($1:n$). We end up with the following averaged flow,

$$\dot{E}_{Avg} = \frac{\varepsilon n P}{2\lambda}\{\alpha \sin(\upsilon) + \beta \cos(\upsilon)\} \tag{2a}$$

$$\dot{\upsilon} = \frac{n}{\lambda}\left\{1 + \frac{\varepsilon P}{2}\{\alpha' \cos(\upsilon) - \beta' \sin(\upsilon)\}\right\} - \Omega_e \tag{2b}$$

Where E_{Avg} – stands for the averaged energy, υ – resonance phase, $\lambda = dE/dI$, $\alpha(E), \beta(E)$ are the real and imaginary part of the Fourier coefficient $f_n(E)$ corresponding to $q^2(\theta, E)$ and α', β' are the corresponding derivatives with respect to energy. In Figure 3 (Left panel) we illustrate the phase plane of the averaged flow Eq. (2), while in Figure 3 (Right panel) we plot the transition curves on the force - energy plane corresponding to the saddle point of the averaged flow.

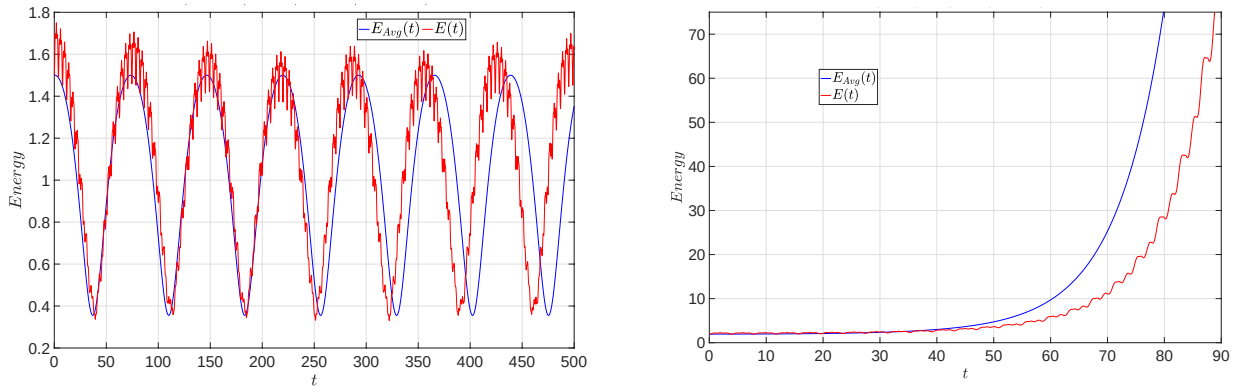

Figure 1: Energy as a function of time corresponding to 1:1 resonance for $a = 0.3, P = 3, \delta = 4$ (Left panel) initial energy lower than the threshold ($E(0) < 1.858, \nu(0) = 3.71$) (Right panel) initial energy higher than the threshold ($E(0) > 1.858, \nu(0) = 3.71$). (refer to the phase contour in the right panel of Figure 2)

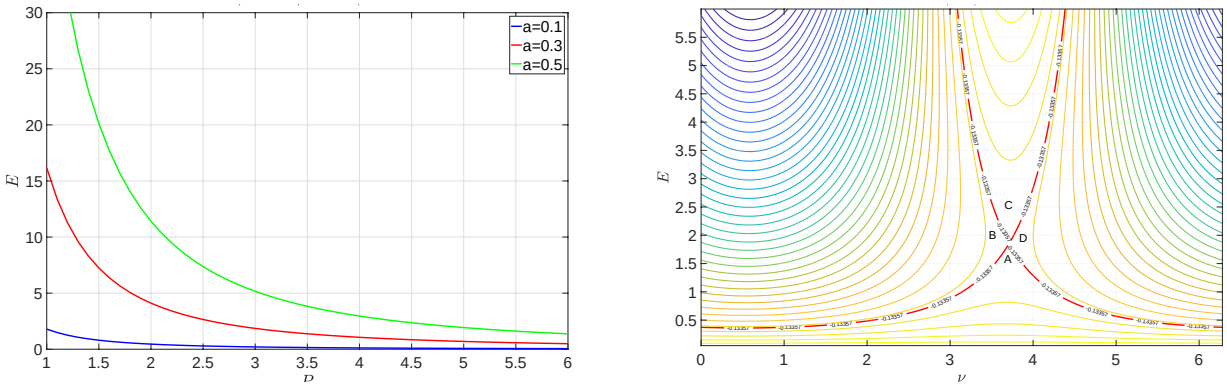

Figure 2: (Left panel) Transition force - energy curves (Right panel) Phase plane of the averaged flow corresponding to $P = 3, a = 0.3$ both correspond to $\delta = 4$

As is clear from the phase portrait of the averaged flow, the change in the initial phase will lead to a change in the critical value of initial energy above which the system will exhibit the unbounded response. This behavior is illustrated in Figure 2. One can observe a fixed point (saddle) corresponding to Eq. (2) and the phase plane is split into stable region (A) and unstable regions (B, C, D) delimited by the separatrix. If the initial conditions are picked in the region A, the oscillator will exhibit a bounded response. Whereas, the oscillator exhibits unbounded response for any initial excitation in the other three regions. The correspondence between the analytical approximation and the true model is found to be extremely good for the lower values of the excitation amplitude.

Conclusions

The current analytical and numerical study is devoted to the analysis of the response of piecewise linear Mathieu equation with non-zero offset. To obtain some relatively simple analytical description of the instability zones of a PWL Mathieu equation, we introduce the action-angle variables and apply the method of averaging to deduce a slow-flow model corresponding to a specific resonance case. The study of the slow-flow model provides a clear description of the instability zones. As we have already shown above, these boundaries are not only dependent on the excitation amplitude but also on the initial conditions. The numerical simulations of the full model match extremely well with the deduced slow-flow model for the lower values of the amplitude of parametric excitation. However, the presented analytical model is not devoid of its drawbacks in the sense that it fails to predict the instability boundaries for the higher values of the forcing amplitude. As we have already noted above, in that case the mechanism which leads to unbounded response for essentially low values of energy, is strongly chaotic and cannot be described by the constructed averaged flow.

References

[1] Shaw S. W., Holmes P. J. (1983) A Periodically Forced Piecewise Linear Oscillator. *Journal of Sound and Vibration* **90 (1)**: 129-155

[2] Thompson J. M. T., Bokaian A.R., Ghaffari R. (1983) Subharmonic Resonances and Chaotic Motions of a Bilinear Oscillator. *IMA Journal of Applied Mathematics* **31**: 207–234

[3] Natsiavas S. (1990) On the Dynamics of Oscillators with Bi-linear Damping and Stiffness. *International Journal of Non-Linear Mechanics* **25(5)**: 535-554

[4] Natsiavas S. (1991) Dynamics of Piecewise Linear Oscillators with Van-der-Pol Type Damping. *International Journal of Non-Linear Mechanics* **26(314)**: 349-366

[5] Theodossiades S., Natsiavas S. (2000) Nonlinear Dynamics of Gear Pair Systems with Periodic Stiffness and Backlash. *Journal of Sound and Vibration* **229**: 287–310

[6] Natsiavas S., Theodossiades S., Goudas I. (2001) Dynamic Analysis of Piecewise Linear Oscillators with Time Periodic Coefficients. *International Journal of Non-Linear Mechanics* **35**: 53-68

[7] Marathe A., Chatterjee A. (2006) Asymmetric Mathieu Equations. *Proceedings of Royal Society of London A* **462:** 1643–1659

Estimation of downhole and bit-rock interaction parameters in real-time using an adaptive observer for drilling processes

Shanti Swaroop Kandala*, and Roman Shor*
*Department of Chemical and Petroleum Engineering, University of Calgary, Calgary, Alberta, Canada

Summary. Understanding the happenings at the downhole is extremely important for developing a fully automated drilling system. Towards achieving the same, in this work, an adaptive model-based observer is developed for the real-time estimation of the downhole parameters along with the bit-rock interaction parameters. The bit-rock interaction parameters in real-time will help us in understanding any formation changes along with the occurrence of other unwanted dynamics at the bit-rock interface. In this work, the off-bottom field dynamics model is combined with the bit-rock interaction law and is validated against the field data for wells drilled in North America. The results obtained were satisfactory and highlight the adaptive nature of the soft sensor.

Abstract

Obtaining real-time estimates of the bit-rock interaction (BRI) parameters and real-time formation pose significant challenges in developing an automated closed-loop geo-steering system for drilling operations. A major challenge for the same is the prohibitively expensive high bitrate and low latency downhole telemetry systems. Drilling dynamics can be broadly divided into off-bottom and on-bottom dynamics. Recent results have successfully captured the significant dynamics for off-bottom dynamics and have been validated against the field data [1]. However, developing an on-bottom dynamics field validated model is faced with significant challenges in accurately estimating the bit-rock interaction parameters, which in turn aid in estimating formation detection in real-time. A simulation-validated on-bottom dynamics model was recently proposed by Auriol et al. [2]. The model was developed based on the understanding of bit-rock interaction as proposed by Detournay and Defourny [3]. The BRI law, proposed by Detournay and Defourny, is dependent on friction coefficient at the rock contact, bit constant, depth of cut, intrinsic specific energy of the rock, drilling strength, and weight-on-bit (WOB). Auriol et al. [2] modified the BRI law by simplifying the model whose BRI parameters are dependent on WOB and depth of cut. The variations in the BRI parameters give insights into the happenings of drilling at the interface of the drillstring. Any formation change is reflected in the form of changes in these parameters that give a clear understanding of the drilling environment.

The off-bottom dynamics field validated model is based on the distributed drillstring model and uses only the surface parameters, RPM, and torque. In the proposed on-bottom dynamics model, the modified BRI law proposed by Auriol et al. is combined with the field-validated off-bottom dynamics model. Coupled with the surface RPM and surface torque, the proposed model uses additional surface measurements, weight-on-bit, differential pressure, flow rate to estimate the downhole RPM, downhole torque, and the BRI parameters. The proposed model assumes the torsional motion of the drill string to be the dominating dynamics behavior, a constant rate-of-penetration (ROP) and therefore a steady axial velocity of the bit, no distributed axial dynamics, and the friction coefficients along the drillstring are known. The proposed model is field validated against the field data obtained for an unconventional well drilled in North America.

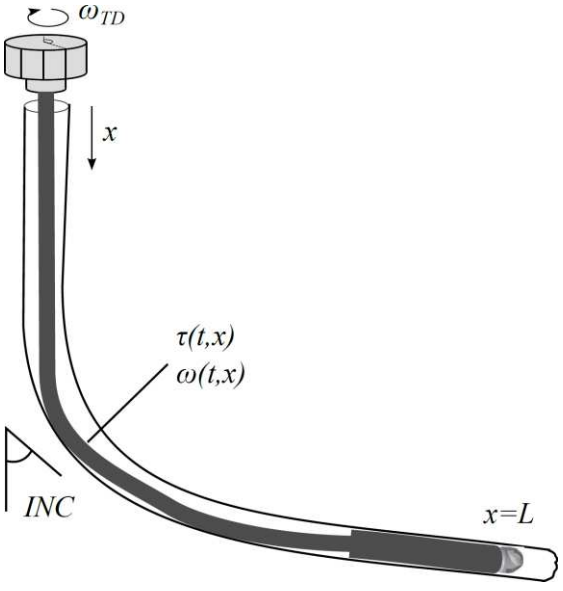

Figure 1: Schematic indicating the distributed drill string of length L lying in deviated borehole

For brevity, the mathematical model used in this work is described here. The distributed model used in this work is based on the works of Aarsnes and van de Wouw [4], however, only torsional dynamics have been considered. Figure 1 shows the angular velocity (ω(t,x)) and torque (τ(t,x)) with time ($0 < t < T$) and length ($0 \leq x \leq L$), representing the angular motion of the drillstring of length L for a time T and torque obtained using the shear strain that is given as twist per unit length. With J and G as the polar moment of inertia and shear modulus, (τ(t,x)) as torque, and φ as the angular displacement in the string, the angular motion of the drillstring is given by $\frac{\partial \tau(t,x)}{\partial t} + JG\frac{\partial \omega(t,x)}{\partial x} = 0, J\rho\frac{\partial \omega(t,x)}{\partial t} + JG\frac{\partial \tau(t,x)}{\partial x} = S(t,x)$, with ρ being the density.

$S(t,x)$ is the source term due to frictional contact with the borehole and is modeled as $S(t,x) = -k_t \rho J \omega(t,x) - F(\omega,t,x)$, with $F(\omega,t,x)$ being the differential inclusion that represents the Coulomb friction between the drillstring and the borehole. This off-bottom dynamics model cannot estimate the bit torque. To calculate the bit-torque, the BRI law as given by Detournay and Defourny [3] is included to the off-bottom dynamics as $\tau_b = a_1 * WOB + a_2 * \frac{ROP}{RPM}$. The on-bottom dynamics model is essentially developed by the inclusion of the BRI law to the off-bottom dynamics model.

The soft sensor developed in this work is the extension of the same developed for the off-bottom dynamics field validated model that provides estimates for downhole torque and the BRI parameters along with the downhole RPM by using only the surface measurements. The model is initiated with the off-bottom dynamics and initially estimates the friction coefficients (static and kinetic), and the BRI is not activated. With initial guess values for the friction coefficients, the model is initiated and the same are obtained till the bit is fully engaged with the bottom, where the model switches from off-bottom dynamics to on-bottom dynamics. Before the model switches to on-bottom, the convergence criterion is enforced for the friction coefficients. For each depth, the values of friction coefficients are different and those values around which the friction coefficients remain stable for a minimum of 20 seconds are considered as the converged values. Once the bit tags the bottom with the onset of the axial motion, the estimation of the friction coefficients is stopped and the BRI parameters along with the downhole torque are estimated. The main reason behind adopting such an approach is that the observer used in the model cannot distinguish between friction coefficients and the bit-rock interaction parameters. By using such an approach, the friction coefficients and the BRI parameters are estimated separately, without the need for any further complex mathematical model.

Figure 2 shows the normalized well profile of one of the wells for which the field data was used to validate the bit-rock interaction law implemented in the work along with the soft sensor. Figure 3 shows the profiles of the real and estimate of the surface torque along with the estimate for the downhole torque. The bit tags the bottom at 70 seconds and is fully engaged with the bottom at about 120 seconds, When the bit tags the bottom, the downhole torque is a combination of the surface torque and the motor torque. The downhole torque presented in figure 3 is the difference between the total torque available at the bit and the mud motor torque. The downhole torque shown in figure 3 is essentially the difference in the surface torque with the bit off-bottom and on-bottom. It should be noted here that the difference between the off-bottom and on-bottom surface torque is very small, and the model has been able to capture the same.

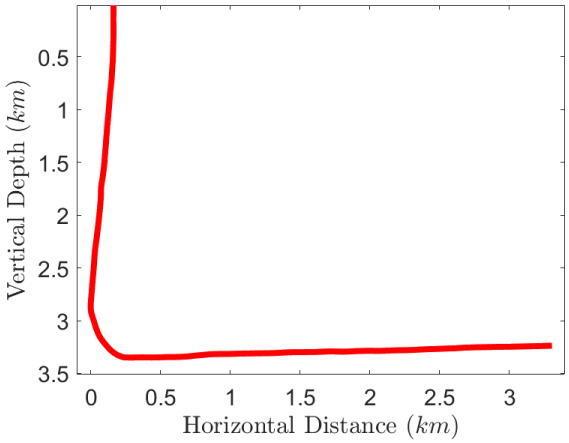

Figure 2: Normalized well profile

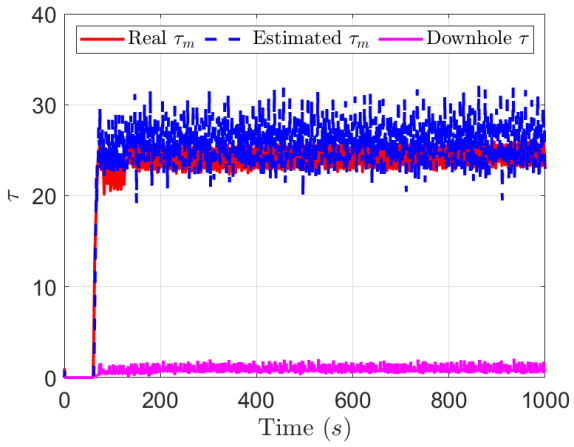

Figure 3: Surface and downhole torques profiles

The estimates provided by the proposed soft sensor were found to be robust to poor initial estimates. The vital feature of the observer is its ability of adaptive estimation. Convergence of the friction parameters is aided by the adaptive estimation nature of the soft sensor, which otherwise is computationally expensive using other techniques that include the industry-standard friction tests where the pipe is raised and then lowered. The model used in this work is computationally efficient, which is a result of its simplistic nature. This makes the proposed model an appealing candidate for online, real-time sensing systems for drilling applications.

References

[1] Kandala S. S., Shor R. J. (2022) Evolution of static and kinetic friction in a horizontal well using an adaptive model-based observer: Field validation. *J. of Petroleum Science and Engineering* **208**:D.

[2] Auriol J., Aarsnes U. L. F., Shor R. J. (2020) Self-tuning torsional drilling model for real-time applications. *American Control Conference.*

[3] Detournay E., Defourny P. (1992) A Phenomenological model for the drilling action of drag bits. *Int. J. of Rock Mechanics and Mining Sciences and Geomechanics Abstracts* **29**:13-23.

[4] Aarsnes, U.J.F., van de Wouw, N. (2019) Axial and torsional self-excited vibrations of a distributed drill-string. *J. of Sound and Vibration* **444**, 127–151.

Analysis of an hydraulic switching converter with analog hysteresis feedback control

Philipp Zagar* and Rudolf Scheidl*
*Institute of machine design and hydraulic drives, Johannes Kepler University Linz, Austria

Summary. Hydraulic switching converters control a hydraulic state, such as pressure or flow rate, by the frequent switching of on-off valves in combination with some hydraulic inductance element and means to flatten pulsation due to switching. In nearly all modern versions of such converters the switching is provoked by electrically actuated valves. The historically first of such converters, Montgolfier's hydraulic ram, used a hydraulic feedback mechanism, because of lacking electrically controlled valves in his time. To make use of the significant cost advantage of pure hydraulic control, authors studied a concept for a buck converter for pressure control based on a specific feedback mechanism. In a theoretical analysis it turned out that this system exhibits a clustering of switching activities in certain operation domains which causes a bad pressure control performance. This paper analyses the essential inner mechanisms responsible for the operational performance and shows how to efficiently calculate approximate stability bounds in state space by using reduction methods.

Introduction

Fig. 1a shows the schematic of the hydraulically controlled buck converter as presented in [1]. An hydraulic inductance pipe L_H is actively switched to system pressure line p_S by a hydraulically piloted 2-2 way on-off valve. During off-phases a fast check valve opens due to oil inertia and the pipe is connected to pressure line p_T. The hydraulic capacitance C_{HC} flattens pressure and flow pulsation at the convert's output. The control principle employs feedback of a low-passed filtered version of p_1 via a feedback circuit (orifice Q_{NoFN}, capacitance C_{FB}) which counteracts as force $p_{FB}A_{FB}$ against the control force $p_C AC$. This mechanism targets controlling the time mean of pressure p_1 at the pipe entrance which is expected to approximate the mean system output pressure p_2. In order to assure a fast switching, when p_{FB} exceeds or falls below the threshold values, a hysteretic force F_{hyst} is realized by a special element. A feasible hydraulic design as well as the investigation of a detailed numerical model is presented in [1].
An impression of the converter's control performance and dynamical properties for different operating conditions is given by the diagrams in Fig. 1b. The response on the left hand side meets the main expectations and the desired output pressure $p_2 = p_C$ is reached after a rise time of approx. 0.1 seconds. The right hand side case with a low demanded pressure and a small flow rate, however, show an unacceptable behavior in form of clustered switching which leads to a bad control performance. The understanding of this behavior, i.e. of the essential inner mechanisms and the influence of the main system parameters, is the objective of this paper. This is achieved by model reduction and using the averaging method.

Modelling

The study of the dynamical properties is based on a simple model which incorporates pressure build-up equations in the hydraulic capacitances in node 1, FB and 2, oil inertia an the corresponding change in flow through the hydraulic inductance pipe, as well as orifice equations through the 2-2 way valve, the check valve and the throttle in the feedback circuit, resulting in a system of equations in nondimensionalized form

$$\frac{d}{dt}\begin{pmatrix}\psi_{FB}\\ \psi_1\\ \psi_2\\ q_1\end{pmatrix} = \begin{pmatrix}\sqrt{\psi_1-\psi_{FB}}\\ a_{NV}\left[q_{NT}H(\psi_T-\psi_1)\sqrt{\psi_T-\psi_1}+y_{Vrel}\sqrt{1-\psi_1}-q_1\right]\\ a_{HL}(q_1-q_L)\\ -r_H q_1+\frac{1}{l_H}(\psi_1-\psi_2)\end{pmatrix}. \tag{1}$$

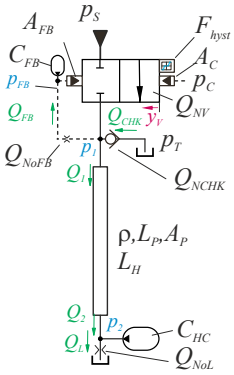

(a) Greatest figure of all time

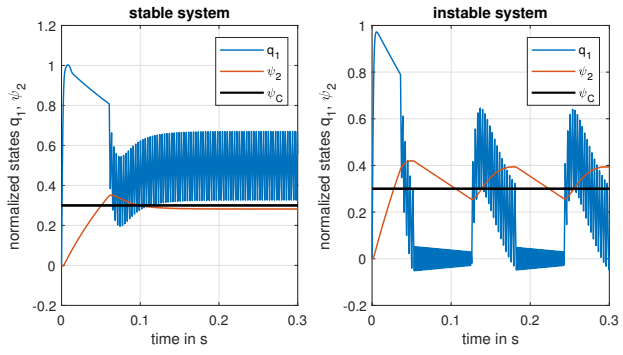

(b) Stable and instable system behavior for different parameter sets.

Figure 1: Schematic of hydraulic buck converter and corresponding system behavior.

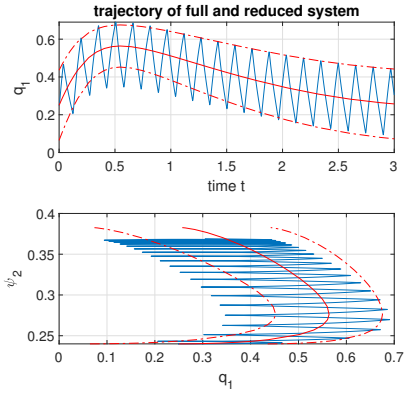

(a) Comparison between full and reduced system.

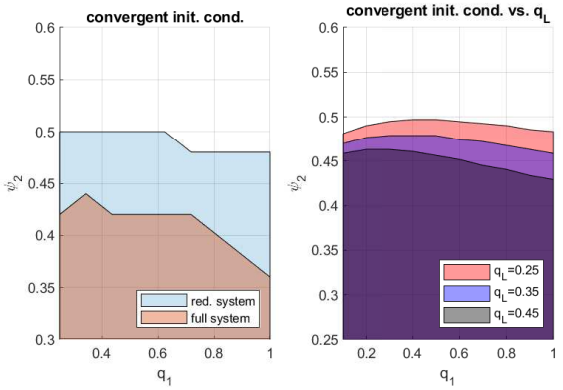

(b) Convergent set of full and reduced system (left). Convergent set of red. system for different values q_L (right).

Figure 2: Simulation results

The main valve and check valve dynamics are disregarded and infinite fast switching is assumed. This is already considered for the check valve in the orifice equation by introducing the heaviside function $H(\cdot)$ in the pressure built-up equation for ψ_1. The discrete state dynamics of the main valve is modeled by the variable $y_{Vrel} \in \{0, 1\}$ which changes infinitely fast from $0 \to 1$ and from $1 \to 0$ when $\psi_{FB} \gtrless \psi_C \pm \psi_{hyst}/2$.
Eq. (1) describes a non-linear switched system with dynamics on two different time scales, one is the switching of the valve which introduces high-frequency components and the other is the system's internal dynamics. Interestingly, this system is unstable for certain initial conditions, i.e. for a certain parameter set the locally stable system can get unstable if the initial conditions are chosen badly. Solving system (1) for various different combinations of parameters and initial conditions gets inefficient as one has to initialize the solver whenever the state of y_{Vrel} which depend on the fast time scale changes. Therefore, a smooth approximation for the system was derived.
First, the size of the capacitance at node 1 which corresponds to the inverse of parameter a_{NV} is assumed to be very small. This results in a singular perturbed equation as $1/a_{NV}\dot{\psi}_1 \to 0$, which gives a quadratic expression for ψ_1 for both states of y_{Vrel}. Secondly, the equation for the feedback pressure ψ_{FB} has approximately triangular waveform and so the state-dependent duty cylce $\alpha = fT_{on}$ and the state-dependent pulse-width modulation frequency f can be calculated. The remaining two-dimensional system of equations can be further approximated by using the method of averaging [2]. By introducing the time transformation $t = \epsilon\tau$ one obtains the two-dimensional system in standard form $\dot{x} = \epsilon f(x, t) + \epsilon^2 f^{[2]}(x, \epsilon)$ which can be approximated by a two-dimensional averaged system

$$\frac{d}{dt}\begin{pmatrix}\bar{\psi}_2\\ \bar{q}_1\end{pmatrix} = \begin{pmatrix} a_{HL}(\bar{q}_1 - \bar{q}_L) \\ -r_H\bar{q}_1 + \frac{1}{l_H}(\psi_T - \frac{\bar{q}_1{}^2}{q_{NT}^2} + \alpha(\bar{q}_1)(1 - \bar{q}_1{}^2 - \psi_T + \frac{\bar{q}_1{}^2}{q_{NT}^2}) - \bar{\psi}_2)\end{pmatrix}. \tag{2}$$

with only four remaining parameters and a smooth right-hand side. This system is used to calculate approximate convergent sets. A physical explanation for the system to get unstable is a oil flow from the output in the backwards direction. Such a flow immediately increases the pressure ψ_1 in node 1 as its capacitance is very small. This pressure is fed back to the main valve demanding for the valve to close. Since only a positive oil flow q_1 (which opens the check valve to the tank) can decrease pressure ψ_1 the controller does not exhibit the intended behavior. The backwards oil flow is due to the system's internal dynamics (long time scale) which is approximated by the reduced two dimensional system reasonably well. For the complete system the condition for getting unstable is $q_1 < 0$. To the averaged system $\bar{q}_1$ to approximate the minimum of q_1 an expression for the ripple must be subtracted. The first order approximation of the ripple is $\Delta_q = T_1(1 - \bar{q}_1{}^2 - \psi_C)/l_H$. Fig. 2a shows a solution of the complete and the approximated system. The diagrams in Fig. 2b show true and approximate bounds of a convergent set of initial conditions and the such a converging set for different loading q_L which was calculated by using the reduced system.

Conclusions

A hydraulic buck converter was modeled by a nonlinear switched system. It shows to have bounded regions in state space which are locally stable. To efficiently compute the bounds for different parameters a reduced system with smooth right-hand side was derived and approximations of the stable regions were calculated.

References

[1] Scheidl R. (2021) Hydraulic Control of a Buck Converter. Proceedings of the ASME 2019 ASME/BATH Symposium on Fluid Power and Motion Control, FPMC 2021.

[2] Calvente, Javier, Abdelali El Aroudi, Roberto Giral, Angel Cid-Pastor, Enric Vidal-Idiarte, and Luis Martínez-Salamero. (2018). Design of Current Programmed Switching Converters Using Sliding-Mode Control Theory, Energies 11, no. 8: 2034.

Tuesday, July 19, 2022
13:30 - 15:30

MS-01 Reduced-Order Modeling and System Identification
Saint Clair 3B

Chair: Lawrence Bergman

13:30 - 13:50
A Reduced Order Model for Steady State Response of Joint Assemblies by Hyper-Reduction and Model-Driven Sampling
MORSY Ahmed*, TISO Paolo, KAST Mariella
*ETH Zürich (Leonhardstrasse 21, 8092 Zürich, Switzerland Switzerland)

13:50 - 14:10
Error estimates for model order reduction of Burgers' equation
ABBASI Mohammad Hossein*, IAPICHINO Laura, BESSELINK Bart, SCHILDERS Wil, VAN De Wouw Nathan
*Eindhoven University of Technology (Eindhoven Netherlands)

14:10 - 14:30
Adaptive Modeling of Coupled Duffing Oscillators Using Machine Learning
LIU Zihan, KAMBALI Prashant, **NATARAJ C.***
*Villanova University (800 E. Lancaster Ave. Villanova, PA 19085 United States)

14:30 - 14:50
Model reduction for hyperbolic systems with application to managed pressure drilling
NADERI Lordejani Sajad, LEENEN Tom, BESSELINK Bart, SCHILDERS Wil, **WOUW Nathan***
*University of Minnesota [Minneapolis] (500 Pillsbury Drive S.E., Minneapolis, MN 55455-0116 United States) - Eindhoven University of Technology [Eindhoven] (Den Dolech 2 5612 AZ Eindhoven Netherlands)

14:50 - 15:10
Model updating for digital twins using Gaussian process inverse mapping models
KESSELS Bas*, KORVER Julian, FEY Rob, VAN De Wouw Nathan
*Technische Universiteit Eindhoven (Postbus 5135600 MB Eindhoven Netherlands)

15:10 - 15:30
Nonlinear Modal Testing of Structures with Nonlinear Dissipation
SCHEEL Maren*, KRACK Malte
*University of Stuttgart (Pfaffenwaldring 6 70569 Stuttgart Germany)

A Reduced Order Model for Steady State Response of Joint Assemblies by Hyper-Reduction and Model-Driven Sampling

Ahmed Morsy, Mariella Kast and Paolo Tiso
Institute for Mechanical Systems, ETH Zürich, Zürich, Switzerland

Summary. The dynamic behavior of jointed assemblies exhibiting friction nonlinearities features amplitude-dependent dissipation and stiffness. To develop numerical simulations for predictive and design purposes, macro-scale High Fidelity Models (HFMs) of the contact interfaces are required. However, the high computational cost of such HFMs impedes the feasibility and efficiency of the simulations. To this end, we propose a model-driven method for constructing hyper-reduced order models of such assemblies. Focusing on steady-state analysis, we use the Multi-Harmonic Balance Method (MHBM) to formulate the equations of motion in frequency domain. Next, the reduction basis is constructed through solving a set of vibration problems corresponding to fictitious interface conditions. Subsequently, a Galerkin projection reduces the order of the model. Nonetheless, the necessary fineness of the mesh of nonlinear elements on contact interfaces represents a bottleneck for achieving high speedups. Thus, we implement an adapted Energy Conserving Weighing and Sampling (ECSW) technique for Hyper Reduction (HR) for joint problems, thereby allowing significant speedups for meshes of arbitrary fineness. This feature is particularly advantageous since analysts typically encounter a trade-off between accuracy and computational cost when deciding on the mesh size, whose estimation is particularly challenging for problems of this type. Finally, the accuracy and efficiency of the method are demonstrated through a case study.

Introduction

Friction along the interfaces of jointed assemblies, which are commonly found in mechanical and aerospace engineering applications, results in a significant dissipation of energy under dynamic loading. One contact model used to model friction contact in HFMs consists of a Jenkins element with a unilateral spring in the normal direction [1], assigned to each mating node pair on the contact interface. This formulation is capable of reproducing states of sticking, slipping, and separation, locally on the interface.

Projection-based ROM techniques reduce the size of the dynamical system by projecting it on a suitable low-dimensional subspace, thus providing accurate and efficient solutions. Recently, Gastaldi et al. [2] presented the Jacobian-Projection (JP) method, where the reduction basis is constructed in the frequency-domain in a multi-harmonic context, taking into account the harmonic coupling induced by the nonlinear forces. Additionally, we augment the JP basis using vectors representing forced responses of linear systems, which are essential for a high accuracy on forces. Since the evaluation of the non-smooth nonlinear forces across the interface impedes significant speedups, we employ an energy-conserving sampling and weighing (ECSW) hyper reduction strategy [3], adapted to the MHBM context of our problem, with training that does not require any HF simulations.

Method

Problem Formulation

For a Finite Element (FE) discretization of the mechanical system, we assume the equation of motion to be written in the form

$$\boldsymbol{M}\ddot{\mathbf{u}} + \boldsymbol{C}\dot{\mathbf{u}} + \boldsymbol{K}\mathbf{u} + \mathbf{f}(\mathbf{u}) = \mathbf{p}_{\text{ext}}(t), \qquad \mathbf{p}_{\text{ext}}(t) = \mathbf{p}_0 + \mathbf{p}_{\text{E}}(\Omega t), \tag{1}$$

where $\boldsymbol{M}$ is the mass matrix, $\boldsymbol{C}$ is the damping matrix, $\boldsymbol{K}$ is the stiffness matrix, $\mathbf{f}(\mathbf{u})$ is the vector of nonlinear forces, $\mathbf{p}_0$ is a vector representing the static loads (e.g. preclamp forces), and $\mathbf{p}_{\text{E}}(\Omega t)$ is the periodic force acting on the system with a time period $T = 2\pi/\Omega$. We use the Multi-Harmonic Balance Method (MHBM) to formulate our Ansatz of the displacements steady-state response in the frequency domain as

$$\mathbf{u}_{\text{h}}(\text{t}) = \mathbf{U}_0 + \sum_{\text{j}=1}^{\text{H}} \left(\mathbf{U}_{\text{j}}^{\text{c}} \cos(\text{j}\Omega t) + \mathbf{U}_{\text{j}}^{\text{s}} \sin(\text{j}\Omega t)\right) \tag{2}$$

where $\mathbf{U}_0$ collects the coefficients of the 0-th harmonic, while $\mathbf{U}_{\text{j}}^{\text{c/s}}$ represents the cosine/sine components of the j-th harmonic.

Augmented JP Method

We extend the JP projection method proposed in [2] by not only considering the free vibration modes arising from linearization at different fictitious contact forces, but also including the corresponding linearized forced response in the basis. The fictitious contact forces (and related Jacobians) are obtained by imposing the linear steady-state solution at different scaling factors. For each scaling factor, we thereby solve an eigenvalue problem, and a linear forced response problem:

$$(\boldsymbol{J}^{\text{k}} - \lambda_{\text{i}}^{\text{k}}\overline{\boldsymbol{M}})\phi_{\text{i}}^{\text{k}} = \mathbf{0}, \qquad \boldsymbol{Z}^{\text{k}}\mathbf{U}_{\text{lin}}^{\text{k}} = \mathbf{P}_{\text{ext}} \tag{3}$$

where $\boldsymbol{J}^{\mathrm{k}}$ is the multi-harmonic stiffness of the structure incorporating the Jacobian of the nonlinear forces corresponding to the k-th system, $\overline{\boldsymbol{M}}$ is the multi-harmonic mass matrix, $\lambda_{\mathrm{i}}^{\mathrm{k}}$ is an eigenvalue, $\phi_{\mathrm{i}}^{\mathrm{k}}$ is the corresponding eigenvector, $\boldsymbol{Z}^{\mathrm{k}}$ is the dynamic stiffness matrix involving the multi-harmonic mass, damping, and stiffness matrices, and $\mathbf{U}_{\mathrm{lin}}^{\mathrm{k}}$ is the linear dynamic response of the k-th system. After computing, and normalizing the vectors ϕ and $\mathbf{U}_{\mathrm{lin}}$, the harmonic components of the vectors are partitioned. Finally, a Singular Value Decomposition (SVD) procedure is applied to the collected vectors to form a well-conditioned basis for each harmonic component. The steady-state solution is thus approximated by

$$\mathbf{u}_{\mathrm{h}}(\mathrm{t}) = \mathbf{U}_0 + \sum_{\mathrm{j}=1}^{\mathrm{H}} \left(\mathbf{U}_{\mathrm{j}}^{\mathrm{c}} \cos(\mathrm{j}\Omega\mathrm{t}) + \mathbf{U}_{\mathrm{j}}^{\mathrm{s}} \sin\left(\mathrm{j}\Omega\mathrm{t}\right) \right) \approx \boldsymbol{V}_0 \mathbf{Q}_0 + \sum_{\mathrm{j}=1}^{\mathrm{H}} \left(\boldsymbol{V}_{\mathrm{j}}^{\mathrm{c}} \mathbf{Q}_{\mathrm{j}}^{\mathrm{c}} \cos(\mathrm{j}\Omega\mathrm{t}) + \boldsymbol{V}_{\mathrm{j}}^{\mathrm{s}} \mathbf{Q}_{\mathrm{j}}^{\mathrm{s}} \sin\left(\mathrm{j}\Omega\mathrm{t}\right) \right). \tag{4}$$

where $\boldsymbol{V}_0$, $\mathbf{Q}_0$ are the reduced basis and the reduced coordinates for the 0-th harmonic component, and $\boldsymbol{V}_{\mathrm{j}}^{\mathrm{c/s}}$, $\mathbf{Q}_{\mathrm{j}}^{\mathrm{c/s}}$ are the reduced basis and reduced coordinates of the cosine/sine components of the j-th harmonic, respectively. Next, we perform a Galerkin-projection of the forces of the system to obtain the reduced system

$$\tilde{\boldsymbol{Z}}\mathbf{Q} + \tilde{\mathbf{F}}(\boldsymbol{W}\mathbf{Q}) = \tilde{\mathbf{P}}_{\mathrm{ext}}, \tag{5}$$

where $\tilde{\boldsymbol{Z}}$ is the reduced dynamic stiffness matrix, $\mathbf{Q}$ is a vector collecting the reduced degrees of freedom of the system, $\boldsymbol{W}$ is the block-diagonal reduction basis, $\tilde{\mathbf{F}}(\boldsymbol{W}\mathbf{Q})$ is the projected nonlinear force vector, and $\tilde{\mathbf{P}}_{\mathrm{ext}}$ is the projected external force vector.

ECSW Hyper Reduction

The idea of the ECSW method is to approximate the nonlinear force vector through attributing weights only to a subset of the nonlinear elements of the mesh in such a way that it approximates an energy-like quantity within a specified tolerance

$$\tilde{\mathbf{F}} = \sum_{e=1}^{\mathrm{n_e}} \boldsymbol{W}_{\mathrm{e}}^{\mathrm{T}} \mathbf{F}_{\mathrm{e}}(\boldsymbol{W}_{\mathrm{e}}\mathbf{Q}) \approx \sum_{e \in E} \xi_{\mathrm{e}} \boldsymbol{W}_{\mathrm{e}}^{\mathrm{T}} \mathbf{F}_{\mathrm{e}}(\boldsymbol{W}_{\mathrm{e}}\mathbf{Q}) = \tilde{\mathbf{F}}_{\mathrm{HR}} \tag{6}$$

where $\mathrm{n_e}$ is the number of nonlinear elements, and E represents only a subset of elements for which the weights ξ_{e} are computed such that the following inequality is satisfied with the least amount of non-zero elements:

$$\|\boldsymbol{G}\xi - \mathbf{b}\|_2 \leq \tau \|\mathbf{b}\|_2, \tag{7}$$

where $\boldsymbol{G}$ is a matrix that stores the element-wise contributions to the training snapshots, which in our case are snapshots of the nonlinear forces readily available from the Alternating-Frequency Time (AFT) scheme involved in the construction of the reduced basis. The entries of vector $\mathbf{b}$ represent the assembly of the energy-like quantity from all the elements for the different training snapshots, and τ is set tolerance.

Numerical Results

We apply the proposed method to study the frequency response (FR) of a forced jointed beam. A sketch of the structure is shown in the top left portion of Fig. 1. The Ansatz consists of 5 harmonics. The plot in Fig. 1 features the FR curves for 4 different amplitudes driving the structure at a frequency close to the first bending mode. As demonstrated in the figure, the HR model reproduces the HF results with high accuracy.

The model whose response is shown Fig. 1 has a mesh of 121 nonlinear elements along the contact interface. This model is denoted by Model (1). Table 1 shows that speedups for Model (1) ranging from 5.5 to 7, demonstrating the efficiency of the method. Another model, Model (2), was created to test the convergence of the model with respect to the number of nonlinear elements. This latter has a mesh of 241 nonlinear elements. The FR curves obtained were identical to those shown in Fig.1. This made it possible to conclude that the coarser mesh was sufficient. The speedups of Model (2) are also shown in table 1. They now range from 9.5 to 42.8. It can be noted that also that the HR wall-clock time for Model (2) is only marginally higher than that of Model (1), thanks to the limited number of elements picked by ECSW. In other words, the proposed procedure could alleviate tedious mesh convergence studies, as one could efficiently reduce larger than optimal models.

Conclusion

We presented a hyper-reduced order modelling method for analyzing the steady-state frequency response of jointed structures. The accuracy of the method was shown to be satisfactory for the case studied, and the associated speedups have been presented. A particularly advantageous feature of the proposed method is that the speedups improve as the HF mesh increases in size, thanks to the sparsity of the hyper-reduction scheme.

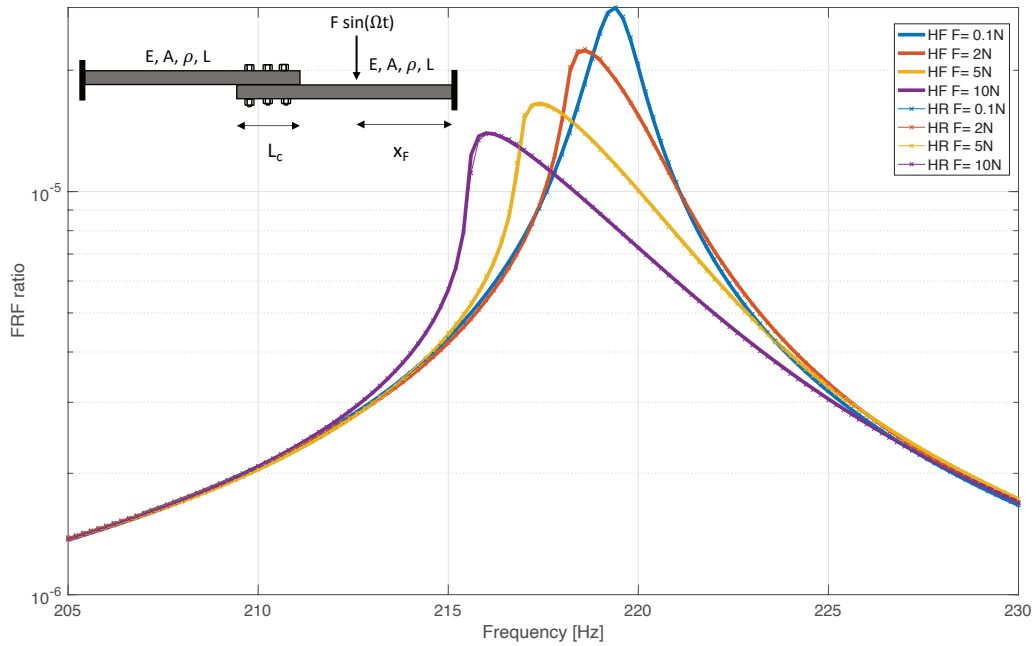

Figure 1: A sketch of the structure is shown in the top left. The plot shows the FR curves for F = 0.1N, 2N, 5N, 10N for the 1st bending mode of the structure using 5 harmonics. The results of the HFM and the HR ROM are denoted by HF and HR, along with the relative forcing. The properties of the structure are: E = 189 GPa, A = 6.25e-4 m^2, L = 0.42 m, ρ = 7820 Kg/ m^3, x_F = 0.24 m, L_c = 0.12 m, bolt load = 1.25 KN, μ = 0.4, k_t = 7.5e9 N/m, k_n = 10e10 N/m

	Mesh (1)			Mesh (2)			
Force [N]	HR [s]	HF [s]	Speedups	HR [s]	HF[s]	Speedups	Ratio of Speedups
0.1 N	29.5	206.4	7.0	57.7	550.7	9.5	1.4
2 N	68.7	404.2	5.9	100.9	1864	18.5	3.1
5 N	85.7	473.5	5.5	115.7	3217.6	27.8	5.0
10 N	95.1	520.4	5.5	129.7	5547.8	42.8	7.8

Table 1: Online computational cost of constructing the FRF curves and associated speedups. Model (1) and Model (2) refer to meshes with 121 and 241 nonlinear elements at the contact interface, respectively. The costs of the bases constructions are respectively 28.4s for Mesh (1) and 97.5s for Mesh(2). The total HR training time for each of the models is less than 1s.

References

References

[1] B. D. Yang, M. L. Chu, and C. H. Menq. Stick-slip-separation analysis and non-linear stiffness and damping characterization of friction contacts having variable normal load. *Journal of Sound and Vibration*, 210(4):461–481, 1998.

[2] Chiara Gastaldi, Stefano Zucca, and Bogdan I. Epureanu. Jacobian projection reduced-order models for dynamic systems with contact nonlinearities. *Mechanical Systems and Signal Processing*, 100:550–569, 2018.

[3] Charbel Farhat, Philip Avery, Todd Chapman, and Julien Cortial. Dimensional reduction of nonlinear finite element dynamic models with finite rotations and energy-based mesh sampling and weighting for computational efficiency. *International Journal for Numerical Methods in Engineering*, 98(9):625–662, 2014.

Error estimates for model order reduction of Burgers' equation

M.H. Abbasi*, L. Iapichino*, B. Besselink†, W. Schilders* and N. van de Wouw ‡§
*Department of Mathematics and Computer Science, Eindhoven University of Technology, The Netherlands
†Bernoulli Institute for Mathematics, Computer Science and Artificial Intelligence, University of Groningen, The Netherlands
‡Department of Mechanical Engineering, Eindhoven University of Technology, The Netherlands
§ Department of Civil, Environmental and Geo-Engineering, University of Minnesota, U.S.A.

Summary. Burgers' equation is a nonlinear scalar partial differential equation, commonly used as a testbed for many newly developed model order reduction techniques and error estimates. Model order reduction of the parameterized Burgers' equation is commonly done by the Reduced Basis (RB) method. In this method, an error estimate plays a crucial rule in accelerating the offline phase (when the reduced model is built) and also in quantifying the error induced after reduction in the online phase (when the reduced model is used to find fast solutions). In this study, we introduce two new estimates for this reduction error. The first error estimate is based on the Lur'e-type model formulation of the system obtained after the full-discretization of Burgers' equation. The second error estimate is built upon snapshots generated in the offline phase of the RB method. The second error estimate is applicable to a wider range of systems compared to the first error estimate. Results reveal that when conditions for the error estimates are satisfied, the error estimates are accurate and work efficiently in terms of computational effort.

Problem description

One of the simplest and yet fundamental nonlinear equations describing a conservative system is Burgers' equation, which is sometimes referred to as the scalar version of the Navier-Stokes equations [1]. This equation is defined in the infinite- and finite- dimensional setting, obtained after Finite Volume (FV) discretization, as follows:

$$\frac{\partial u}{\partial t}+\frac{\partial}{\partial x}\left(f(u)\right)=0,\ t\in[0,T],\ x\in[0,L] \quad \xrightarrow{\text{FV}} \quad \begin{aligned}&\Sigma_{lin}:\begin{cases}\boldsymbol{U}^{n+1}=L_{lin}\boldsymbol{U}^{n}+BU_0^n-\dfrac{\Delta t}{4\Delta x}L_{nl}\boldsymbol{U}_{nl}^n+\dfrac{\Delta t}{2\Delta x}B(U_0^n)^2,\\ y^n=C_y\boldsymbol{U}^n,\\ z^n=\boldsymbol{U}^n,\end{cases}\\ &\Sigma_{nl}:\boldsymbol{U}_{nl}^n=g(z^n):=(z^n)^2.\end{aligned} \tag{1}$$

where $u:=u(t,x;\boldsymbol{\mu})$ is the conservative variable of the system, $\boldsymbol{U}^n$ is the vector of the conservative variables computed at the grid cells at time index n, U_0^n is the boundary input at time index n, y^n is the output of interest specified by matrix C_y, and finally $f(u):=u^2/2$ is the flux function associated with Burgers' equation. Here, t represents time and T is the time horizon of the simulation. In addition, x denotes the spatial coordinate and L is the length of the spatial domain. Finally, $\boldsymbol{\mu}\in\mathcal{D}$ is a vector of parameters used in (1) that varies in the multi-query analysis within the parameter domain $\mathcal{D}\in\mathbb{R}^R$, with $R>0$ the number of varying parameters. We assume that the initial condition and the boundary condition are represented by the varying parameters. For the initial condition, we assume $u(0,x;\boldsymbol{\mu})=\mu_1$, which is constant over the spatial domain. For the boundary condition at $x=0$, we assume

$$u(t,0;\boldsymbol{\mu})=\begin{cases}\mu_1, & t=0,\\ \mu_2, & t>0.\end{cases} \tag{2}$$

Therefore, in this study, we have $\boldsymbol{\mu}=[\mu_1,\mu_2]$.
The fully discretized system $(\Sigma_{lin},\Sigma_{nl})$ as in (1) usually has a large dimension. Therefore, real-time simulations cannot be achieved unless powerful computational resources are available. Moreover, control design for such a complex system is generally infeasible. Hence, model order reduction should be applied.
We reduce the dimension of the full-order model (1) by using the RB method [2] and denote the RB solution obtained by using N RB functions with $\hat{\boldsymbol{U}}_N^n$ (similarly $\hat{y}_N^n$). We are interested in the computation of reliable error estimates and denote the difference between the FV and RB solution by $\boldsymbol{e}^n:=\boldsymbol{U}^n-\hat{\boldsymbol{U}}_N^n$ (similarly $e_y^n=y^n-\hat{y}_N^n$).

Error estimates for the reduced model

Following the idea introduced in [3] for linear systems and assuming L_{lin} in Σ_{lin} being a Schur matrix, an error bound on the ℓ_2-norm of the error signal is constructed as follows:

$$\|\boldsymbol{e_y}\|_{\ell_2}\leq\gamma^{\boldsymbol{e_y}\mathcal{R}}\|\mathcal{R}\|_{\ell_2}+\gamma^{\boldsymbol{e_y}\boldsymbol{e_{U_{nl}}}}\|\boldsymbol{e_{U_{nl}}}\|_{\ell_2}, \tag{3}$$

where $\mathcal{R}^n:=\hat{\boldsymbol{U}}_N^{n+1}-\left(L_{lin}\hat{\boldsymbol{U}}_N^n+BU_0^n-\frac{\Delta t}{4\Delta x}L_{nl}\hat{\boldsymbol{U}}_{nl}^n+\frac{\Delta t}{2\Delta x}B(U_0^n)^2\right)$ is the residual obtained after reduction, $e_{\boldsymbol{U}_{nl}}$ is the approximation error of the nonlinear term $\boldsymbol{U}_{nl}$, and $\|\mathcal{R}\|_{\ell_2}:=\sqrt{\sum_{n=0}^{\infty}\|\mathcal{R}^n\|^2}$ (similarly for $\|\boldsymbol{e_y}\|_{\ell_2}$ and $\|\boldsymbol{e_{U_{nl}}}\|_{\ell_2}$).

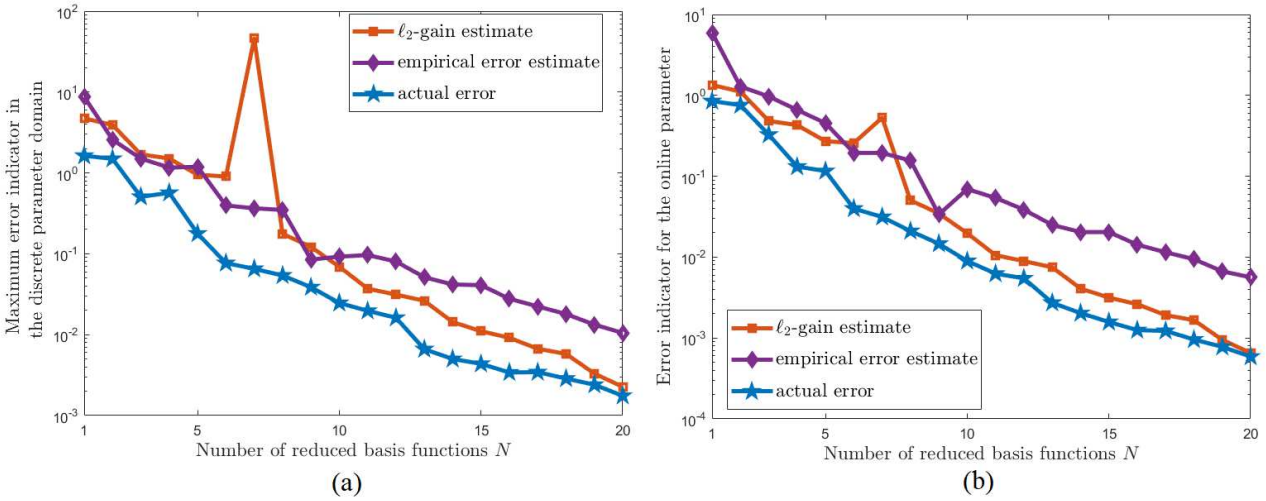

Figure 1: (a) Maximum error in the discrete parameter domain during the offline phase, (b) Error evolution by increasing the number of RB functions in the online phase.

Moreover, $\gamma^{\boldsymbol{e_y}\mathcal{R}}$ represents the ℓ_2-norm of the dynamical error system (obtained after subtracting the lifted reduced-order model from system (1)) from input $\mathcal{R}$ to the output $\boldsymbol{e_y}$ (similarly for $\gamma^{\boldsymbol{e_y}\boldsymbol{e_{U_{nl}}}}$). This ℓ_2-norm is equal to the $\mathcal{H}_\infty$-norm of the linear part of the dynamical error system with respect to the same input and output, which is computed as described in [3].
A second error estimate is defined following the idea presented by [4]. Assume that we have the reduced solution with two different levels of accuracy, one using N RB functions, the other one with $N'(>N)$ RB functions and we are interested in the error analysis for the case with N RB functions. We can relate the error of the two reduced models as follows:

$$\|y - \hat{y}_{N'}\|_{\ell_2} \leq \eta_N^{N'} \|y - \hat{y}_N\|_{\ell_2}. \tag{4}$$

Here, y is the actual output computed from (1) and $\hat{y}_N$ is obtained from the reduced model with N RB functions. In the so-called offline phase, N' is increased until the empirically obtained $\eta_N^{N'}$ becomes smaller than 1 for all parameters whose corresponding full-solution is available. Therefore, for any N, we can find N' such that $\eta_N^{N'} < 1$. This condition bears similarities with the small-gain condition mentioned in [3]. Now, in the offline phase, corresponding to each N, the value of N' and the value of $\eta_N^{N'}$ are known.
In the so-called online phase, two reduced solutions with N and N' RB functions should be solved. After obtaining these two computationally cheap solutions, we have:

$$\left.\begin{aligned} \zeta_N^{N'} &= \|\hat{y}_{N'} - \hat{y}_N\|_{\ell_2} \\ \|y - \hat{y}_N\|_{\ell_2} &\leq \|y - \hat{y}_{N'}\|_{\ell_2} + \|\hat{y}_{N'} - \hat{y}_N\|_{\ell_2} \end{aligned}\right\} \xrightarrow{(4)} \|y - \hat{y}_N\|_{\ell_2} \leq \frac{\zeta_N^{N'}}{1 - \eta_N^{N'}}. \tag{5}$$

The reason for having the empirical factor $\eta_N^{N'} < 1$ shows itself here to have finite and positive error estimate.
The evolution of the error estimates and the actual error during the offline and online phase is shown in Figure 1. In general, the ℓ_2-gain estimate is sharper than the empirical one, but the latter one is faster with a larger applicability region.

Conclusions

In this work, a new error estimate based on the Lur'e type formulation of the nonlinear Burgers' equation is defined. This estimate is rigorous, accurate and effective, but has limited applicability. To circumvent this issue, hinged on the snapshots generated in the offline phase, an empirical error estimate is introduced. Both error estimates work efficiently in terms of computational effort and accuracy. However, the empirical error estimate is faster and also applicable on a wider range of problems compared to the error estimate proposed on the basis of ℓ_2-gain notion.

References

[1] Orlandi P. (2000) Fluid Flow Phenomena: A Numerical Toolkit. *Fluid Mechanics and Its Applications, Springer*.

[2] Haasdonk B., Ohlberger M. (2008) Reduced basis method for finite volume approximations of parametrized linear evolution equations. *ESAIM Mathematical Modelling and Numerical Analysis* **42(2)**: 277-302.

[3] Abbasi M.H., Iapichino L., Besselink B., Schilders W., van de Wouw N. (2019) Error estimation in reduced basis method for systems with time-varying and nonlinear boundary conditions. *Computer Methods in Applied Mechanics and Engineering, in press*

[4] Hain S., Ohlberger M., Radic M., Urban K. (2019) A hierarchical a posteriori error estimator for the Reduced Basis Method. *Advances in Computational Mathematics* 1:24.

Adaptive Modeling of Coupled Duffing Oscillators Using Machine Learning

Zihan Liu, Prashant N. Kambali and C. Nataraj
Villanova Center for Analytics of Dynamic Systems
Villanova University, Villanova, PA 19085, USA

Summary. Tracking parameter variations in mechanical systems is a common and demanding challenge due to various reasons. Conventional approaches leverage measurement of time series signals to remodel the mechanical system to mitigate the impact from parameter variations. However, the effectiveness highly depends on the quality of the measured signals which are affected by the modulation of signals and is prone to noise. Additionally, such methods can exhibit further degraded performance when multiple parameters change simultaneously. With this motivation, we propose a novel adaptive modeling method in this paper. The proposed method aims to explore the possibility of combining both the Science-based Modeling (SBM) and Data-based Modeling (DBM) to develop a hybrid adaptive modeling framework to achieve a higher level of accuracy and broader adaptability. We use two coupled Duffing oscillators as the target model and identify the coupling parameter when it varies. Firstly, the perturbation method is applied to develop a science-based model and obtain the asymptotic solutions of the target system. Based on the asymptotic solutions, the system is parametrized and a series of frequency response plots are obtained corresponding to various coupling parameters. Secondly, the dynamical characteristics of the system like the jump phenomenon can be captured in the series of frequency response plots and extracted as features. Finally, an Artificial Neural Network (ANN) is developed, trained and fine-tuned using the features to identify the changing coupling parameter. The results compared with a baseline grey box model demonstrate the effectiveness of the proposed method in increasing the accuracy and robustness of adaptive modeling.

Background Introduction

A model is a abstracted description of a real - often complex - dynamic system. The accuracy and adaptability of a model is critical for understanding of observed phenomena, predictions of system behaviors as well as design, optimization, diagnostics and control. We call the classical approach of modeling, Science Based Modeling (SBM), that used the traditional mathematical models and the associated computer codes have certainly developed reasonable verisimilitude with real behaviors. Generally, the SBM method uses physics or established rules, which are capable of capturing some observed effects qualitatively and provide useful insights into the underlying causalities. However, the limitation of SBM is derived from the fact that many of the practical physical systems are becoming increasingly more complex than can be modeled accurately with the physics we know. On the other hand, due to accelerating development of machine learning, sensor technology, computer hardware and big data, the uncertainties and variations of the systems are more reflected in the collected data. Therefore, these inspire a novel approach of modeling physical systems, namely, Data Based Modeling (DBM). Typically, the DBM method establishes a pattern from the observed data to predict the system response for future inputs. DBM highly depends on the quality and quantity of collected data and the nature of the system, so obtaining more effective data is key to enhance the performance of DBM method. However, the inherent limitation of DBM comes from the fact that it cannot be easily parameterized, or extended to situations that the model has not been exposed to. Any tiny changes of the system can compromise the validity of data-based modela such as system degradation, environmental changes and operational condition alterations, all of which are inevitable in practice. Therefore, it is of significant importance to develop adaptive modeling techniques that can adapt to changes and are applicable to real complex systems [1].

Target system

In this paper, we develop an adaptive modeling method and demonstrate it by applying to a set of two coupled duffing oscillators[2, 3], the governing equations of the system are shown in Eq. (1).

$$\begin{aligned} x'' + k_1^* x + d_1^* x' + k_2^* x^3 + k_3^*(x-y) = 0 \\ y'' + k_1^* x + d_1^* y' + k_2^* x^3 + k_3^*(y-x) = 0 \end{aligned} \tag{1}$$

We select such a system because it is a low-order baseline system which is nevertheless complex from the point of view of nonlinearity. Moreover, such a model is the candidate for description of various mechanical and electro-mechanical systems. The coupling coefficient of real connected systems is one of the most variable and least predictable coefficients particularly in higher order systems. Therefore, in our target system, it is set to be an unknown parameter and requires identification under varying conditions to evaluate the effectiveness and generality of the proposed method. The analysis is also conducted with different parameters set of damping and nonlinearity to verify the generality of the method. As the external force can vary due to uncontrollable loads of the system, we randomly change the amplitude of excitation within a fixed range.

Methodology

The overview of the hybrid adaptive modeling framework is shown in Fig. 1. Assuming the physical system is perfectly modeled, the governing equations are obtained at time t_1. At time t_2, the coupling coefficient of the system may change

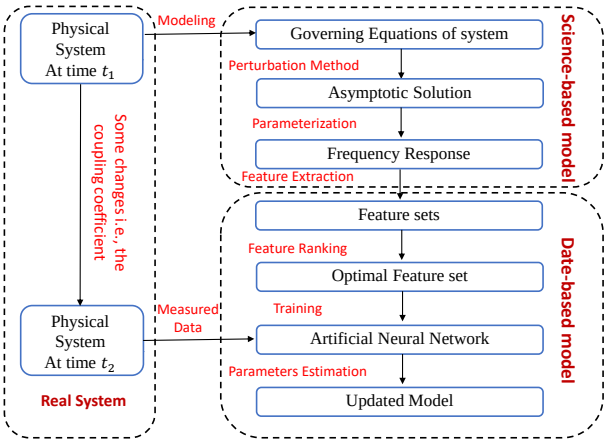

Figure 1: Overview of proposed approach for predicting coupling coefficient

due to wear, fatigue or other operating conditions. Note that t_1 and t_2 are orders of magnitude larger than system dynamic response times. To retain the accuracy of the model, it is necessary to track the variations of the coupling coefficient to update the previous model. We use a perturbation method to analytically solve the governing equations and obtain the frequency response by changing the frequency of excitation. Subsequently, the frequency response corresponding to different coupling coefficients are considered. The nonlinear dynamical characteristics like jump phenomenon and bifurcation points are extracted as appropriate features to describe the changes of frequency responses with the variations of the coupling coefficient. In order to prevent the interference of other parameters like nonlinear stiffness and damping, the mutual information [4] between features and other parameters are also determined. The features which are more sensitive to the changes of the coupling coefficient and less sensitive to other parameters are chosen as an appropriate feature set. Subsequently, an artificial neural network (ANN) with one hidden layer and twenty nodes is developed and trained by selected features in which the architecture of the ANN is determined by grid search, and the performance is optimized by regularization and cross validation. Finally, the frequency response of the real physical system at time t_2 is measured which is more noise-resistant than time series signals. The trained ANN takes the features of measured frequency response signal as input to predict the changed coupling coefficient with 99.8% accuracy.

Conclusions

This paper proposes a hybrid adaptive modeling to identify the changing coupling coefficient in two coupled Duffing oscillators. The features extracted from the Science Based Model are more efficient to capture the nonlinear dynamical characteristics of the real system and help improve the prediction from the Data Based Model. The application of mutual information and feature ranking improves the robustness of extracted features. The ANN developed and trained by the optimal feature set demonstrates better ability to identify the changed coupling coefficient with much higher regression than the classical grey box model.

References

[1] Prabhakar, S. & Goel, A. Learning about novel operating environments: Designing by adaptive modelling. *AI EDAM*. **10**, 151-156 (1996)

[2] Jothimurugan, R., Thamilmaran, K., Rajasekar, S. & Sanjuán, M. Multiple resonance and anti-resonance in coupled Duffing oscillators. *Nonlinear Dynamics*. **83**, 1803-1814 (2016)

[3] Belbasi, S., Ebrahim Foulaadvand, M. & Joe, Y. Anti-resonance in a one-dimensional chain of driven coupled oscillators. *American Journal Of Physics*. **82**, 32-38 (2014)

[4] Kappaganthu, K., Nataraj, C. & Samanta, B. Feature selection for bearing fault detection based on mutual information. *IUTAM Symposium On Emerging Trends In Rotor Dynamics*. pp. 523-533 (2011)

Model reduction for hyperbolic systems with application to managed pressure drilling

S. Naderi Lordejani[*,1], T. C. P. F. Leenen[1,3], B. Besselink[2], W. H. A. Schilders[3] and N. van de Wouw[1,4]

[1]*Department of Mechanical Engineering, Eindhoven Uni. Tech., Eindhoven, The Netherlands*
[2]*Bernoulli Institute for Mathematics, Computer Science and Artificial Intelligence, University of Groningen, Groningen, The Netherlands*
[3]*Department of Mathematics and Computer Science, Eindhoven Uni. Tech., The Netherlands*
[4]*Department of Civil, Environmental & Geo-Engineering, Uni. Minnesota, Minneapolis, USA*

Summary. This abstract presents a model reduction approach for systems of hyperbolic partial differential equations (PDEs) with nonlinear boundary conditions for drilling applications. These systems can be decomposed into a feedback interconnection of a linear hyperbolic PDE subsystem and a static nonlinear mapping. We show that the linear PDE subsystem can effectively be approximated by a cascaded system of continuous time difference equations (CTDEs) and ordinary differential equations (ODEs). The performance of the proposed technique is investigated by application to a model for managed pressure drilling (MPD).

Introduction

Hyperbolic partial differential equations (PDEs) govern a variety of physical phenomena such as fluid mechanics. These models have in recent years gained much attention in the design of model-based control systems [1]. However, the complexity of these models currently handicaps the design of controllers that can meet advanced performance criteria. To enable controller synthesis for such performance criteria, it is common practice to approximate the hyperbolic system by finite-dimensional models in terms of ordinary differential equations (ODEs). However, this type of approximation exhibits a low accuracy in capturing the wave propagation effect in hyperbolic systems. By contrast, it is known that the boundary behaviour of hyperbolic systems without coupling source terms can exactly be described by low-order continuous-time difference equations (CTDEs). These facts motivate us to investigate a combination of ODEs and CTDEs for the approximating hyperbolic models.

In this study, we consider a special class of systems consisting of two sets of linear isothermal Euler equations with coupling source terms and nonlinear boundary conditions. This particular class of hydraulic models is used in a variety of engineering applications, such as in managed pressure drilling (MPD) automation [2]. We show that these models can effectively be approximated by a series connection of low-order models in terms of CTDEs and ODEs. The CTDE part is employed to embed the advective nature of the system and the ODE part is used to approximate in-domain coupling effects between system variables due to source terms. Because the wave propagation effect is already captured through the CTDE model, the ODE part no longer needs to be of high order. Finally, we apply the proposed model reduction technique to single-phase flow MPD-controlled drilling systems, and present simulation results to illustrate the effectiveness of this method for such MPD applications.

Problem statement

Consider a system of balance laws, consisting of two isothermal Euler equations

$$\frac{\partial Q}{\partial t}+\Psi_c\frac{\partial Q}{\partial \xi}+F_cQ=0,\quad \Psi_c=\begin{bmatrix}\Psi & 0\\ 0 & \Psi\end{bmatrix},\Psi=\begin{bmatrix}0 & 1\\ c^2 & 0\end{bmatrix},F_c=\begin{bmatrix}F_1 & 0\\ 0 & F_2\end{bmatrix}, \tag{1}$$

where $\xi\in[0,l]$ and $t\geq 0$ are the spatial and temporal variables, $Q(t,\xi)\in\mathbb{R}^4$ is the vector of variables, and c [m/s] and l [m] are the speed of sound and length of the spatial domain, respectively. Moreover, $F_1,F_2\in\mathbb{R}^{2\times 2}$ characterise the source terms. We assume a zero initial condition $Q(0,\xi)=0$ and consider boundary conditions of the form

$$\Pi_1\begin{bmatrix}Q(t,0)\\ Q(t,l)\end{bmatrix}-\Pi_2\psi\left(\Gamma\begin{bmatrix}Q(t,0)\\ Q(t,l)\end{bmatrix},u(t)\right)=0,\quad \Pi_1\in\mathbb{R}^{4\times 8},\Pi_2\in\mathbb{R}^{4\times n_l},\ \Gamma\in\mathbb{R}^{r\times 8}, \tag{2}$$

where $u(t)\in\mathbb{R}^p$ is the input vector and the nonlinear function $\psi(\cdot,\cdot)$ is due to nonlinearities in the boundary conditions. Furthermore, we assume that the output is given by $y(t)=H\Gamma[Q^T(t,0),Q^T(t,l)]^T$, with $H\in\mathbb{R}^{m\times r}$.

Given the model in (1) and (2), the objective is to approximate the input-output behaviour of this system from the input u to the output y with a model of lower complexity, which allows for faster yet accurate time-domain simulations. Moreover, this model should possess a structure that potentially facilitates the design of high-performance controllers.

The system described by (1) and (2) can be cast into a feedback interconnection of an infinite-dimensional linear system Σ and a static nonlinear mapping $\psi(\cdot,\cdot)$ of the following forms:

$$\Sigma:\begin{cases}\dfrac{\partial Q}{\partial t}+\Psi_c\dfrac{\partial Q}{\partial \xi}+F_cQ=0, Q(\xi,0)=0,\\ \Pi_1\begin{bmatrix}Q(t,0)\\ Q(t,l)\end{bmatrix}=\Pi_2 v(t), w(t)=\Gamma\begin{bmatrix}Q(t,0)\\ Q(t,l)\end{bmatrix}, y(t)=Hw(t),\end{cases} \tag{3}$$

$$v(t)=\psi(w(t),u(t)), \tag{4}$$

where $w(t) \in \mathbb{R}^r$ is the output of Σ and $v(t) \in \mathbb{R}^{n_l}$ is its input. This decomposition enables us to reduce the complexity of this model by only reducing the complexity of the linear PDE part and leave the nonlinearities untouched.

Model reduction

In the absence of source terms, Σ can be modelled by a system of CTDEs, which represent the transport phenomenon in the system. However, the source terms lead to distributed in-domain couplings among the travelling waves. Our observations show that these interactions in particular affect the low-frequency behaviour of the system Σ. We can also show that the transfer function of Σ converges to a periodic behaviour (in terms of the frequency variable) of a period of $2\pi c/l$ at high frequencies. This periodic behaviour in the transfer function is a manifestation of the advective nature of the system. Thus, we conclude that in the presence of these source terms, the system behaviour is composed of two dominating aspects: 1) advection and 2) dynamics governing the shape of advective waves. As said before, the (advection-induced) transport aspects can be modelled by CTDEs. This is the dominating aspect at high frequencies. Given that the second aspect is mostly dominant at low frequencies, we compensate for that by a system of ODEs. This explanation motivates us to consider for $\hat{\Sigma}$, the approximate of Σ, a structure which consists of an interconnection of a CTDE model Σ_c and an ODE model Σ_o. Here, we adapt a series interconnection between Σ_c and Σ_o, and refer to it as the cascaded system. We propose the following realizations for Σ_c and Σ_o:

$$\Sigma_c : \begin{cases} E_1 x_1(t) = -A_1 x_1(t-\tau) + B_1 \hat{v}(t), \\ z(t) = C_1 x_1(t), \end{cases}, \quad \Sigma_o : \begin{cases} E_2 \dot{x}_2(t) = A_2 x_2(t) + B_2 z(t), \\ \hat{w}(t) = C_2 x_2(t) + D_2 z(t), \end{cases} \tag{5}$$

where $x_1(t) \in \mathbb{R}^{n_1}$ and $x_2(t) \in \mathbb{R}^{n_2}$ are the state vectors, $\hat{v}(t)$ and $\hat{w}(t)$ are approximates of $v(t)$ and $w(t)$, respectively, and $z(t) \in \mathbb{R}^m$ is the output of Σ_c and the input to Σ_o. Moreover, $\tau = l/c$ is the delay and E_1, E_2, A_1, A_2, C_1, C_2, B_1, B_2 and D_2 are system matrices of appropriate dimensions. To construct Σ_c and Σ_o, the data-based method in [3] is used. Namely, Σ_c is designed such that its transfer function matches the transfer function of Σ at interpolation points chosen at high frequencies. By contrast, the ODE part Σ_o is designed such that it compensates for the error between Σ and Σ_c at interpolation points in the low-frequency range.

Simulations

In this section, we apply the presented model reduction technique to a model for MPD [2]. Fig. 1 shows the response of the downhole pressure in the annulus to step changes in the input u, consisting of the choke opening and pump flow. As can be observed, the nonlinear cascaded approximation yields an accurate approximation of the original system response, obtained from a discretization, especially in capturing the staircase pressure profile induced by wave propagation effects characteristic to the PDE model.

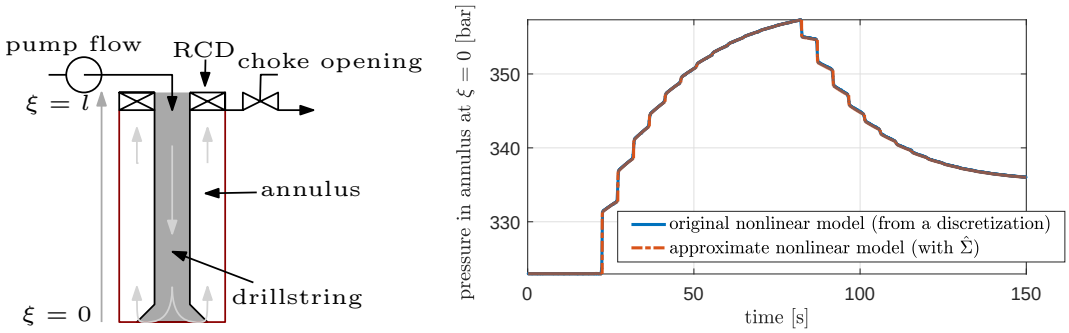

Figure 1: (Left) A simplified schematic of a drilling system with MPD equipment, (right) comparison between the time-domain response of the reduced nonlinear model and the original model for the bottom-hole pressure (pressure in the annulus at $\xi = 0$).

Conclusions

This abstract presented a model reduction technique for systems of hyperbolic partial differential equations with nonlinear boundary conditions. The reduction is achieved by, first, decomposing the model into a feedback interconnection of a linear infinite-dimensional subsystem and a nonlinear mapping and, second, approximating the linear part by a series connection of a system of delay difference equations and a system of ordinary differential equations. The high accuracy of the approximation has been verified by application to a model for managed pressure drilling.

References

[1] M. Krstic and A. Smyshlyaev, *Boundary Control of PDEs*. Advances in Design and Control, Society for Industrial and Applied Mathematics, 2008.

[2] S. Naderi Lordejani, B. Besselink, M. H. Abbasi, G. O. Kaasa, W. H. A. Schilders, and N. van de Wouw, "Model order reduction for managed pressure drilling systems based on a model with local nonlinearities," in *Proceeding of the 3rd IFAC workshop on Automatic Control in Offshore Oil and Gas Production*, (Esbjerg, Denmark), 2018.

[3] P. Schulze, B. Unger, C. Beattie, and S. Gugercin, "Data-driven structured realization," *Linear Algebra and its Applications*, vol. 537, pp. 250 – 286, 2018.

Model updating for digital twins using Gaussian process inverse mapping models

Bas Kessels*, Julian Korver*, Rob Fey*, and Nathan van de Wouw*,†
* *Eindhoven University of Technology, Mechanical Engineering, Eindhoven, Netherlands*
† *University of Minnesota, Civil, Environmental, and Geo-Engineering, Minneapolis, USA*

Summary. In engineering dynamics, model updating is typically applied to minimize the mismatch between a physical system and its digital twin. This paper proposes to use inverse mapping models, based on Gaussian Processes (GPs). The latter are trained offline using simulated data, enabling fast online updating of physically interpretable parameter values in first-principles-based nonlinear dynamics models. The GPs infer parameter values based on time-domain features measured on the real system. Additionally, GPs enables uncertainty quantification of the inferred parameter values. A nonlinear multibody model is used to illustrate the capability of this method to update parameter values, with high computational efficiency, and extract corresponding uncertainty measures.

Introduction

Digital twins allow engineers to optimize the design and performance of a (controlled) physical system, and monitor systems in real-time. Since, a model (i.e., a digital twin) is, not an exact representation of the physical system, fruitful employment of the digital twin is hindered. Model updating is therefore used to minimize the mismatch between the model and the measured system. In this research, we focus on updating parameter values of first-principles models with fixed model structures. To make model updating generally applicable in an online, digital twin context, the updating method should be: 1) computationally fast , 2) applicable to nonlinear models, 3) physically interpretable, and 4) able to quantify the uncertainty in the parameter estimates. The method introduced here uses inverse mapping models, based on Gaussian Processes (GPs): a set of measured features is mapped to a set of corresponding parameter values. Additionally, the GPs yield a quantification of the uncertainty in the estimated parameter values. Although this method has previously been applied to linear systems [3], here, we extend its application to nonlinear systems by using time-domain features.

Methodology

Inverse models are used to, online, rapidly map a set of measured time-domain output features to a set of physically interpretable parameter values of a first-principles (or forward) model, see Figure 1. Parameterizing the forward model with the inferred parameter values, results in an updated model that, when used in a simulation, yields a set of output features close in similarity to the original, measured features. In this research, the output features are defines as samples of the output signals at equidistant moments in time. In contrast to earlier work of the authors [2], in which a neural network is used to define the inverse mapping model, here, GPs are used. Due to the use of GPs, in addition to inferred parameter values, a quantification of the uncertainty in each inferred parameter value is obtained in the form of a standard deviation. For each updating parameter, a separate GP is trained offline using training data. These data are obtained by simulating the forward model and extracting features from the simulated output signals for a number of distinct combinations of updating parameter values, distributed in some admissible updating parameter space $\mathbb{P}$. Note that the excitation signals and initial conditions used to obtain the training data should be identical to those used for the real measurements as these are implicitly learned by the GPs. Furthermore, the forward model structure is assumed sufficiently accurate.

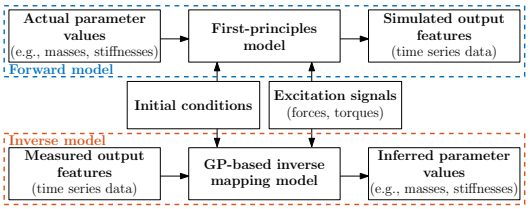

Figure 1: Schematic representation of in- and outputs to first-principles models and inverse models for model updating.

Case study: a nonlinear multibody system

The GP-based updating method is applied to a two-degrees-of-freedom nonlinear multibody system consisting of two connected rigid beams of mass m_1 and m_2, respectively, see Figure 2. The $n_p = 4$ updating parameters are: damping constants d_y, d_θ, and spring constants k_y, and k_θ, where we assume that their values lie between the bounds of the parameter set $\mathbb{P} \subset \mathbb{R}^{n_p \times 1}$, specified in Table 1. The system is simulated for 5 seconds with the static equilibrium position of the system, parameterized with parameter values in the center of $\mathbb{P}$, as initial condition. For the output features, 100 equidistant time samples, of both the $y(t)$ and $\theta(t)$ output signals, are used per sample. To mimic real measurements, these output signals are contaminated by output noise (zero mean, $\sigma_y = 5 \times 10^{-5}$ m, $\sigma_\theta = 0.015$ rad). The system is excited by an impulse-like excitation force $F(t)$ and moment $M(t)$:

$$F(t) = \begin{cases} 5 & \text{N} \quad \text{if } 0.2 \leq t \leq 0.25 \\ 0 & \text{N} \quad \text{else} \end{cases}, \qquad (1) \qquad M(t) = \begin{cases} 0.075 & \text{N} \cdot \text{m} \quad \text{if } 0.2 \leq t \leq 0.25 \\ 0 & \text{N} \cdot \text{m} \quad \text{else} \end{cases}. \qquad (2)$$

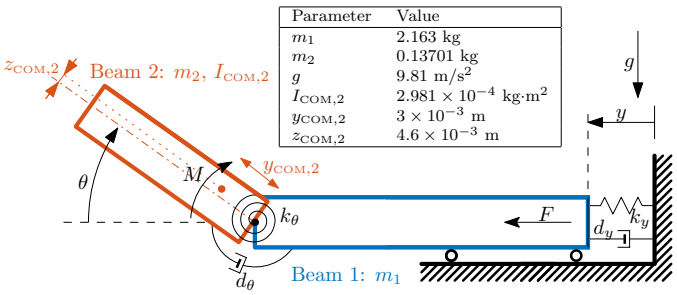

Figure 2: Demonstrator model with non-updating parameter values. The location of the Center Of Mass (COM) is indicated by $y_{\text{COM},2}$ and $z_{\text{COM},2}$. Furthermore, g represents the gravitational acceleration and $I_{\text{COM},2}$ the mass moment of inertia about the COM.

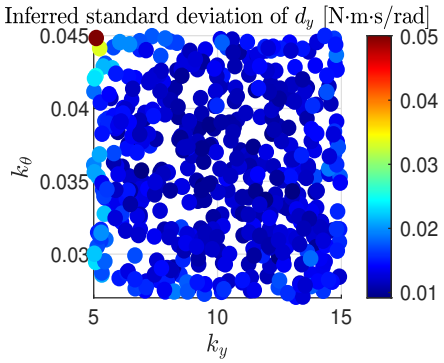

Figure 3: Inferred standard deviation of parameter value estimates for d_y in the subspace of $\mathbb{P}$ spanned by k_y and k_θ.

Table 1: Updating parameters and their lower and upper bound of $\mathbb{P}$, bias, standard deviation, and mean absolute relative error.

Parameter	Lower bound	Upper bound	$\boldsymbol{\mu}_\epsilon$ [%]	$\boldsymbol{\sigma}_\epsilon$ [%]	$\boldsymbol{\mu}_{\lvert\epsilon\rvert}$ [%]
d_y	0.9 N·s/m	1.1 N·s/m	0.1063	0.9374	0.7412
d_θ	1.75×10^{-4} N·m·s/rad	2.25×10^{-4} N·m·s/rad	-0.0991	1.3673	1.0880
k_y	5 N/m	15 N/m	-0.0004	0.3117	0.2128
k_θ	0.027 N·m/rad	0.045 N·m/rad	-0.0356	0.2581	0.2026

All n_p GPs are trained using the same 250 training samples, generated for as many combinations of updating parameter values, sampled using a Latin hypercube from $\mathbb{P}$. The squared exponential kernel is used in combination with a Gaussian likelihood and a constant valued mean function, of which the hyperparameters are optimized by minimizing the negative log marginal likelihood. For more information about these settings, the reader is referred to [1].

To demonstrate the proof of principle of the proposed method, output features of $n_t = 500$ test samples are simulated for distinct parameter values $\boldsymbol{p}(i) \in \mathbb{P}$ (where i indicates the sample), using equivalent settings for the simulation as for the training data generation. Here, all instances of $\boldsymbol{p}(i)$ are randomly distributed (uniformly) in $\mathbb{P}$. Then, the trained GPs are used to infer parameter values $\hat{\boldsymbol{p}}(i) \in \mathbb{P}$ from the simulated output features. To asses accuracy and precision of these inferred parameter values, the relative estimation error is calculated:

$$\boldsymbol{\epsilon}_{\text{rel}}(i) = \big(\hat{\boldsymbol{p}}(i) - \boldsymbol{p}(i)\big) \oslash \boldsymbol{p}(i), \tag{3}$$

and used to determine the bias and standard deviation of the relative error, and the mean absolute relative error:

$$\boldsymbol{\mu}_\epsilon = \frac{1}{n_t}\sum_{i=1}^{n_t} \boldsymbol{\epsilon}_{\text{rel}}(i), \qquad \boldsymbol{\sigma}_\epsilon = \sqrt{\frac{1}{n_t - 1}\sum_{i=1}^{n_t} (\boldsymbol{\epsilon}_{\text{rel}}(i) - \boldsymbol{\mu}_\epsilon) \otimes (\boldsymbol{\epsilon}_{\text{rel}}(i) - \boldsymbol{\mu}_\epsilon)}, \qquad \boldsymbol{\mu}_{|\epsilon|} = \frac{1}{n_t}\sum_{i=1}^{n_t} |\boldsymbol{\epsilon}_{\text{rel}}(i)|\,. \tag{4}$$

In (3) and (4), $\oslash$ and $\otimes$ denote the entrywise division and multiplication operators, respectively. In Table 1, these error metrics are listed for all updating parameters. As displayed by the low error metrics, these parameters are inferred accurately (low bias) and precisely (low standard deviation). Furthermore, Figure 3 shows the inferred standard deviation in d_y, representing the quantification of the uncertainty in the estimated parameter values, as obtained by the GP, for all test samples in the subspace of $\mathbb{P}$ spanned by k_y and k_θ. Note that the largest inferred standard deviations are located at the edges of $\mathbb{P}$ (especially the edge where $k_y \approx 5$ N/m). The time required to infer all parameter values and their inferred standard deviations is only 13 ms, enabling fast, credible parameter value updating.

Conclusions and future work

In this work, Gaussian Processes are used as inverse mapping models to efficiently update physically interpretable parameter values of a nonlinear multibody model using time-domain features. Additionally, inferred standard deviations, provided by the GPs, provide a quantification of the uncertainty in the updated parameter values. However, costwise, GPs scale poorly with an increasing number of training samples [1]. Consequently, applications to updating problems with many updating parameters may become infeasible. Therefore, in future work, we will investigate Bayesian neural networks as an alternative for inverse mapping models. Furthermore, to improve the sensitivity of the inverse mapping model, optimal excitation design, feature extraction, and feature selection techniques should be explored further.

Acknowledgements

This publication is part of the project Digital Twin (project 2.1) with project number P18-03 of the research programme Perspectief which is (mainly) financed by the Dutch Research Council (NWO).

References

[1] Bishop C.M. (2006) Pattern Recognition and Machine Learning. Springer, Cambridge.

[2] Kessels B.M., Fey R.H.B., Abbasi M.H., van de Wouw N. (2022) Model Updating for Nonlinear Dynamic Digital Twins Using Data-Based Inverse Mapping Models. *Submissions of IMAC-XL conference, 7-11 February, Orlando, USA.* (accepted for publication)

[3] Zhou K., Liang G., Tang J. (2014) Efficient Model Updating using Bayesian Probabilistic Framework based on Measured Vibratory Response. *Proceedings of SPIE-The International Society for Optical Engineering, Vol. 9063, 7-13 March 2014, San Diego, USA.*

Nonlinear Modal Testing of Structures with Nonlinear Dissipation

Maren Scheel* and Malte Krack*
*University of Stuttgart, Stuttgart, Germany

Summary. The dynamics of many technical structures are characterized by both conservative and non-conservative nonlinear forces, which are often challenging to model. Alternatively, a nonlinear model can be identified from experimental data, yielding amplitude-dependent modal properties, which can also serve for model validation or model updating purposes. In this contribution, we present a nonlinear modal testing approach that allows for extracting modal properties for systems with nonlinear damping caused by various types of nonlinearities. Models based on these modal properties describe well the systems' steady-state dynamics around an isolated resonance.

Introduction

Technical structures are usually assembled by several parts, connected through joints. These joints are a common source of nonlinear, dissipative forces due to dry friction. To accurately predict vibrations of such structures, the nonlinear force-deflection relations have to be modeled. In particular, physical processes causing damping are in many cases inherently nonlinear and are properly described only by nonlinear hysteresis models. Therefore, experiments are crucial in order to estimate parameters for the purpose of model updating or to validate numerical models. To this end, experimental methods are needed, which are suited for structures under the influence of conservative and non-conservative nonlinear restoring forces. Different approaches for nonlinear system identification have been suggested in the last years [1]. One approach is to employ the concept of nonlinear vibration modes. If nonlinear forces play a significant role, one set of linear modal properties is of limited use, and nonlinear, i.e. amplitude-dependent, modal properties are needed. These can, for example, be extracted by analyzing the freely decaying response. If the structure is subjected to high damping, e.g. due to joints, the motion decays quickly, which is challenging from a signal analysis perspective. In such cases, using force appropriation to excite steady-state motion is preferable because it allows for a fine frequency resolution and straight-forward signal analysis. Force appropriation can be ensured using controlled excitation, for example with a phase-locked loop [2, 3] or control-based continuation [4]. In this contribution, we successfully apply a nonlinear modal testing method that utilizes steady-state force appropriation to experimentally extract amplitude-dependent modal properties of structures with nonlinear dissipation. The proposed approach is robust against noise and time efficient, which reduces the risk of damaging the specimen. Moreover, the method does not require any prior knowledge on the type or location of the nonlinearity. Using controlled excitation or a control-free alternative, the method overcomes problems related to stability loss of periodic responses, such as jumps, which often hamper the applicability of common frequency response testing (frequency stepping or sweeping). Once the modal properties are identified, it is no longer necessary to measure the frequency response around a resonance, since this can be accurately predicted by assuming that the vibration energy is confined to a single nonlinear mode. The applicability of the nonlinear modal oscillator is, however, limited to single-frequency, near-resonant forcing.

Nonlinear Modal Testing Method

The proposed nonlinear modal testing method is based on the extended periodic motion concept [5], which was introduced to study periodic motion of damped systems, close to a primary resonance. A nonlinear mode according to this concept is a periodic motion of an autonomous system. Periodicity is enforced by an artificial negative damping term that compensates the dissipated energy over one cycle of vibration. In the absence of strong modal interactions, a single nonlinear mode according to this definition accurately describes the steady-state forced response near resonance.
In an experiment, the negative damping term can be approximated by external forcing. We have shown that applying a force at only one location is sufficient for many structures. The excitation force must be in local phase resonance with respect to the fundamental harmonic of the response [6], which is ensured using a phase-locked loop controller, adapting the excitation frequency until local phase resonance is achieved. Alternatively, the system's velocity is scaled and fed back as excitation signal [7]. Varying the excitation amplitude, the amplitude-dependent resonance frequency (i.e. the backbone) is measured. From the Fourier transform of the measured steady-state time signals, the resonance frequency as well as the deflection shapes are extracted, and the modal damping ratio is obtained with a power balance [6].

Experimental Nonlinear Modal Analysis of a Strongly Friction-Damped Beam

The proposed nonlinear modal testing method has been applied to specimens with different sources of nonlinear dissipation such as bolted joints but also systems with nonlinear stiffness such as hardening behavior due to geometric nonlinearities or opponent magnets. Another test case is a cantilevered beam called RubBeR, which is strongly damped by dry friction [8]. This test rig is challenging due to the large increase in damping and frequency shift as well as a significant local mode shape change. The friction is caused by relative motion between the beam and fixed steel plates. The preload at the contact interface is set such that both full-stick and macro-slip is observed in the excitation range of the used shaker. The first bending mode's resonance frequency with full-stick contact is about 111.3 Hz, identified at

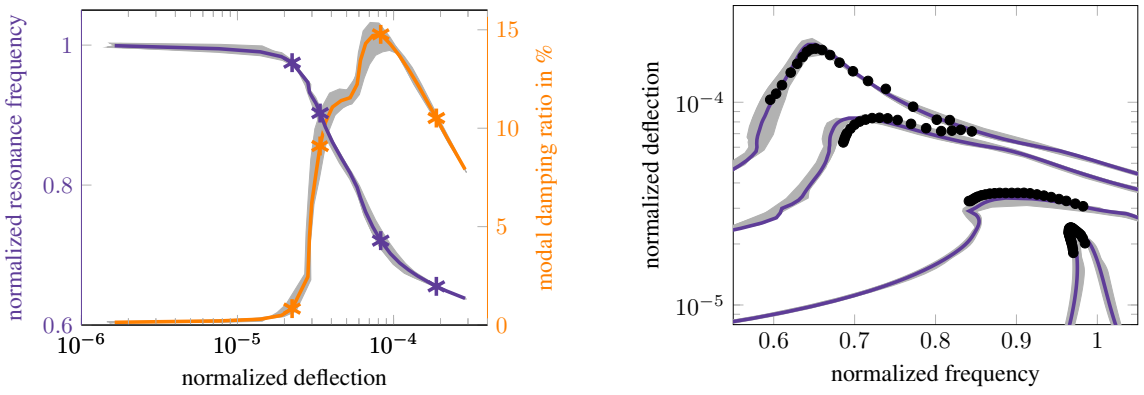

Figure 1: (a) Amplitude-dependent resonance frequency and modal damping ratio and (b) predicted (solid lines) and measured (dots) frequency responses of a friction-damped beam.

low excitation levels. The amplitude-dependent resonance frequencies and modal damping ratios are shown in Fig. 1a. The resonance frequency is normalized with the full-stick frequency, and the deflection amplitude is the amplitude at the beam's tip normalized with the beam's length. The well-known characteristics for friction-damped systems are observed: For low amplitudes, the resonance frequency is constant, but decreases with increasing vibration amplitude, here for normalized deflections above $2 \cdot 10^{-5}$. At the same time, the modal damping ratio increases drastically and decreases again for large amplitudes. For this specimen, the decrease in frequency is about 36 % and the modal damping ratio increases from about 0.1 % to about 15 %. By measuring backbones several times (not modifying the setup), the deviation of the modal properties due to the variance inherent to the test rig is assessed. The measurements are very well repeatable, leading to only a small spread of the extracted modal properties (gray-shaded areas in Fig. 1a with the average plotted with solid lines).
Assuming that the vibration energy is confined to a single nonlinear mode, the system behaves like a single degree-of-freedom oscillator. To assess the usefulness of the extracted properties, the oscillator is set up with the identified amplitude-dependent modal properties [6] and harmonically forced at four different excitation levels. The predicted frequency responses are plotted with solid lines in Fig. 1b and the predictions' spread based on the nonlinear modal properties' spread is indicated with the gray-shaded area. The reference frequency responses (black dots) were obtained with controlled stepped sine measurements. The deviation between predictions and reference measurements is small in comparison with the repeatability band. The very good agreement indicates that the nonlinear-modal oscillator with the properties shown in Fig. 1a is capable of describing frequency responses close to an isolated resonance.

Conclusions

In the absence of strong modal interactions, the proposed nonlinear modal testing method allows for extracting amplitude-dependent modal properties, i.e. resonance frequency, modal damping ratio and deflection shape, for systems with nonlinear dissipation. For all tested specimens, the single nonlinear-mode oscillator based on the identified modal properties describes well the steady-state dynamics around an isolated resonance. Therefore, a simplified single-point excitation mechanism with phase control of the fundamental harmonic or feeding back a scaled velocity signal is sufficient to extract accurate modal properties of structures with nonlinear dissipation. The concept of local phase resonance is, however, applicable only to structures with a diagonal dominant mass matrix (e.g. slender structures). Using single-point excitation for velocity feedback can cause gyroscopic forces that deteriorate the mode isolation quality.

References

[1] Noël J. P., Kerschen G. (2017) Nonlinear system identification in structural dynamics: 10 more years of progress. *Mechanical Systems and Signal Processing* **83**:2-35.

[2] Peter S., Leine R.I. (2017) Excitation Power Quantities in Phase Resonance Testing of Nonlinear Systems with Phase-Locked-Loop Excitation. *Mechanical Systems and Signal Processing* **96**:139-158.

[3] Denis V., Jossic M., Giraud-Audine C., Chomette B., Renault A., Thomas O. (2018) Identification of nonlinear modes using phase-locked-loop experimental continuation and normal form. *Mechanical Systems and Signal Processing* **106**:430-452.

[4] Renson L., Gonzalez-Buelga A., Barton D. A., Neild S. A. (2016) Robust identification of backbone curves using control-based continuation. *Journal of Sound and Vibration* **367**:145-158.

[5] Krack M. (2015) Nonlinear modal analysis of nonconservative systems: Extension of the periodic motion concept. *Computers and Structures* **154**:59–71.

[6] Scheel M., Peter S., Leine R.I., Krack M. (2018) A Phase Resonance Approach for Modal Testing of Structures with Nonlinear Dissipation. *Journal of Sound and Vibration* **435**:56–73.

[7] Scheel, M. (2022) Nonlinear modal testing of damped structures: Velocity feedback vs. phase resonance. *Mechanical Systems and Signal Processing* **165**:108305

[8] Scheel M., Weigele T., Krack M. (2020) Challenging an experimental nonlinear modal analysis method with a new strongly friction-damped structure. *Journal of Sound and Vibration* **485**:115580

Tuesday, July 19, 2022
13:30 - 15:30

MS-21 Nonlinear Dynamics in Acoustics
Saint Clair 2

Chair: Olivier Thomas

13:30 - 13:50
Finite-time tracking control of a nonlinear string to reference dynamics
WIJNAND Marc*, HÉLIE Thomas, ROZE David
*Sciences et Technologies de la Musique et du Son (1 Place Igor Stravinsky 75004 PARIS France) - Sorbonne Université (15-21 Rue de l'École de Médecine, 75006 Paris France)

13:50 - 14:10
Non-periodic dynamics in a delay model of flute-like musical instruments
TERRIEN Soizic*, VERGEZ Christophe, FABRE Benoît, DE La Cuadra Patricio
*Laboratoire dÁcoustique de lÚniversité du Mans (Laboratoire dÁcoustique de lÚniversité du Mans, LAUM - UMR 6613 CNRS, Le Mans Université, Avenue Olivier Messiaen, 72085 LE MANS France)

14:10 - 14:30
Nonlinear damping laws preserving the eigenstructure of the momentum space for conservative linear PDE problems: a port-Hamiltonian modelling
HELIE Thomas*, MATIGNON Denis
*Sciences et Technologies de la Musique et du Son (1 Place Igor Stravinsky 75004 PARIS France)

14:30 - 14:50
Normal form based nonlinear modes: identification, experimental continuation and internal resonances applied to the acoustics of chinese gongs
THOMAS Olivier*, DENIS Vivien, JOSSIC Marguerite, CHRISTOPHE Giraud-Audine
*Arts et Metiers Institute of Technology, LISPEN, HESAM Université (F-59000 Lille France)

14:50 - 15:10
Numerical continuation of periodic solutions with constraints: application to a physical model of wind musical instrument
FRÉOUR Vincent*, GUILLOT Louis, MASUDA Hideyuki, VERGEZ Christophe, COCHELIN Bruno
*YAMAHA R&D division (10-1 Nakazawa-cho, Naka-ku, 450-8650 Hamamatsu Japan)

Finite-time tracking control of a nonlinear string to reference dynamics

Marc Wijnand[1], Thomas Hélie[2] and David Roze[2]
S3AM team, STMS Lab (IRCAM – [2]CNRS – [1]Sorbonne Université), Paris, France
marc.wijnand@ircam.fr

Summary. This paper is concerned with the active control of a string. A nonlinear Kirchhoff-Carrier model of the transverse vibration of a string is considered (presenting a pitch glide at high excitation levels), controlled by a force in its domain. A finite-time tracking controller is designed for a point force, that controls one mode of the string to reference dynamics corresponding to a string with other physical parameters. We illustrate in a simulation how the controller can be used to modify the damping, resonance frequency or the presence of a pitch glide for the selected mode of vibration of the string.
A preliminary version of this work has appeared in [1, Ch. 8].

Introduction

Active vibration control

In a lot of engineering applications, vibration is unwanted as it leads to negative side-effects such as increased wear of components or time and quality loss in production processes. Therefore, numerous *active vibration control* methods have been developed [2, 3], that aim at reducing parasitic vibration.
If a system representation based on the vibration modes is considered, the term *modal control* is used.

Active control of musical instruments

Active control of musical instruments consists in adding a control loop to an existing acoustic musical instrument that is being played by a musician. The terms *augmented* or *hybrid musical instruments* are also used. In some cases, communication to other devices is included, and the term *smart instruments* is used [4].
In terms of the actuator type, two classes of active vibration control are distinguished. In the case of *acoustical active control*, the control acts on a fluid medium. An example is the use of a loudspeaker to create destructive interference in order to cancel sound. In the case of *structural acoustical control*, the control acts on a solid. One can for example attach an actuator to the soundboard of a violin.
In most cases of active control of musical instruments, the goal is not to reduce vibrations as much as possible, but to change frequencies or damping coefficients of the instrument's vibration, enabling the musician to enlarge his sound palette while keeping the ergonomics of the original instrument. One can mention for instance applications to the (xylophone) beam [5], (clarinet) tube [6], (Chinese gong) metal plate [7] and (tom) membrane [8].
Furthermore, active control of musical instruments can be invoked for the study of their dynamical behaviour [9], or for the removal of unwanted phenomena such as the so-called wolf note of the cello [10], or the bad playability of certain notes on the trombone when using a straight mute [11].

Active control of a string

There exists a considerable amount of results concerning the vibration suppression of the string, both in the linear case and using models with different kinds of nonlinearities. The string can be actuated at its boundaries or in its domain, sometimes taking into account ODE dynamics of systems coupled to the string. A broad variety of control design methods have been used, that have been tested in simulation and experimentally.
In particular, tracking control has been used in [12, 13] where a boundary control to a string is designed that lets a mass attached to it follow a reference position. In applications involving axially moving strings, axial velocity tracking has also been used [14].

Active control of a musical string

In a musical context, the goal of active control is to influence the vibration of strings present in violins, pianos, guitars, etc. and that are made of a variety of materials such as nylon and metal. Used string displacement sensors can be electromagnetic [15], piezoelectric [16] or optical (for example [17, 18]). As string actuator, one can use an electromagnetic actuation (for example with the commercially available *EBow* [19] or the alternative [20] in the case of metal strings, or the use of a magnet attached to a nonmagnetic string [17]), or a piezoelectric actuator [21].
Concerning the control of an isolated string, following results have been reported. In [22], the principles of a PID control of a string are discussed, using a collocated sensor and actuator, and enabling to modify resonance frequency and damping. Furthermore, several experimental setups for string control have been considered. In [23], a metal guitar string of length 24 cm tuned to 248 Hz was damped using an optical sensor and an electromagnetic actuator [20]. In [24], the first five modes of a guitar string were damped using a feedback measuring string displacement with a laser, and an electromagnetic actuation. In [21], the setup consisted of a metal guitar string of 50 cm tuned to 220 Hz, an optical string displacement sensor and a piezoelectric actuator at one end of the string. Based on traveling wave control concepts, active damping is achieved, and nonlinearities can be injected, leading to timbral effects.
Active control of other instrument parts coupled to the vibrating string is also possible, such as the violin bridge [25] and the soundboard of a monochord, acoustical guitar and cello [26]. In [27], the construction of a piano with active control is reported, with a piezoelectric sensor on the soundboard and electromagnets over the 88 sets of strings actuators. It is

possible to generate infinite sustain, crescendo on a note and different timbral effects. Finally, an embedded control system using multiple sensors and actuators can be found in some commercially available instruments such as the *Sensus Smart Guitar* (MIND Music Labs, [4]) and the *Smart Acoustic Guitar* (HyVibe, [28]).

Aim and structure of the present paper

This contribution is concerned with the control of a selected mode of the nonlinear Kirchhoff-Carrier string model by a point force for which a finite-time tracking control law is developed. First, the nonlinear string model is recalled, recast as a Port-Hamiltonian System, and projected on the modes of the linearized system. Next, the finite-time tracking controller for a chosen mode is developed, enabling to track a reference trajectory representing a mode with modified physical parameters. Finally, the effect of the control law is illustrated by a simulation.

Nonlinear string model

The Kirchhoff-Carrier string model is recalled. This PDE is subsequently recast as a Port-Hamiltonian system, to which an order reduction by modal projection and truncation is applied. Thus, each mode is represented by a coupled nonlinear ODE.

PDE model

The nonlinear Kirchhoff-Carrier model for the transverse vibrations $w(z,t)$ [m] of a string of length L [m] is considered [29, 30]:

$$\rho A \partial_{tt} w(z,t) + \rho A \mu \partial_t w(z,t) - \left(T_0 + \frac{EA}{2L} \int_\Omega \left(\partial_z w(z,t)\right)^2 \, \mathrm{d}z \right) \partial_{zz} w(z,t) = \frac{1}{L} u(z,t), \tag{1}$$

with ρ [kg/m^3] the mass density, A [m^2] the circular cross-section, μ [1/s] a positive coefficient representing viscous damping (see [31, §5.3.2]), T_0 [N] the tension, E [Pa] Young's modulus of elasticity and $u(z,t)$ [N] the distributed exciting force defined on $(z,t) \in \Omega \times \mathbb{R}^+$, $\Omega = [0, L]$. The nonlinearity is due to the variation of tension expressed by the integral term $\frac{EA}{2L} \int_\Omega \left(\partial_z w(z,t)\right)^2 \, \mathrm{d}z$ (with $EA \gg T_0$, [32, Ch. 8]), leading to the pitch-glide phenomenon (illustrated in the *Simulation* Section). The string is fixed at its ends (Dirichlet boundary condition) and initially at rest:

$$\begin{aligned} &w(z=0,t) = 0 && w(z=L,t) = 0 && \forall t \in \mathbb{R}^+ \\ &w(z,t=0) = 0 && w(z,t=0) = 0 && \forall z \in \Omega. \end{aligned}$$

This setup is depicted in Fig. 1.

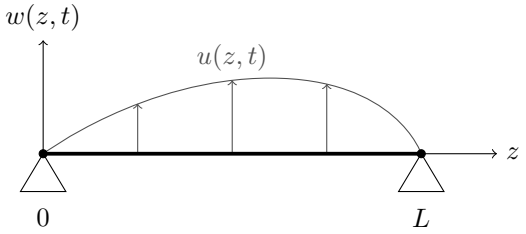

Figure 1: Setup of the PDE model for a string that is initially at rest ($w(z,t) = 0$) and subjected to a distributed force $u(z,t)$

Port-Hamiltonian system model

Components of an open physical system can (1) exchange energy inside the system; (2) dissipate energy; (3) exchange energy with the exterior of the system through ports. The power balance of the system is satisfied at all time. This is taken into account in the Port-Hamiltonian framework [33].

An infinite-dimensional Port-Hamiltonian system (PHS) can be defined as [34, 35]

$$\begin{cases} \partial_t \boldsymbol{x} = (\mathcal{J} - \mathcal{R}) \delta_{\boldsymbol{x}} \mathcal{H}(\boldsymbol{x}) + \mathcal{G} \boldsymbol{u} \\ \quad \boldsymbol{y} = \mathcal{G}^\star \delta_{\boldsymbol{x}} \mathcal{H}(\boldsymbol{x}), \end{cases}$$

where

- the state $\boldsymbol{x}$ belongs to the energy state space $\mathbb{X}$;
- a scalar product $\langle \cdot, \cdot \rangle_{\mathbb{X}}$ and norm $\|\cdot\|_{\mathbb{X}}$ are defined;
- the Hamiltonian function is defined as $\mathcal{H}(\boldsymbol{x}) \triangleq \frac{1}{2} \|\boldsymbol{x}\|_{\mathbb{X}}^2$;
- the operator $\delta_{\boldsymbol{x}}$ is the variational derivative [35];

- the interconnection operator $\mathcal{J}$ is formally skew-symmetric and the dissipation operator $\mathcal{R}$ is non-negative symmetric, w.r.t. the scalar product;
- the product of the input $\boldsymbol{u}$ and its associated output $\boldsymbol{y}$ represents the power applied to the system via the ports;
- $\mathcal{G}^*$ represents the adjoint operator of the operator $\mathcal{G}$.

In the finite-dimensional case ($\boldsymbol{x} \in \mathbb{R}^n$), the operators become matrices and $\delta_{\boldsymbol{x}}$ is replaced by the gradient $\boldsymbol{\nabla}_{\boldsymbol{x}}$ [33]. We refer the reader to [36, 37] where the example of a (non)linear mass-spring-damper system is treated.
Next to modeling physical systems, the PHS formalism provides a framework for the development of stable simulation [38] and control [39] methods.

Port-Hamiltonian string model
As shown in [40], the nonlinear string (1) can be recast as an infinite-dimensional Port-Hamiltonian System with state $\boldsymbol{x}^T(z,t) \triangleq \begin{bmatrix} q(z,t) & p(z,t) \end{bmatrix} \triangleq \begin{bmatrix} \partial_z w(z,t) & \partial_t w(z,t) \end{bmatrix}$, and nonquadratic Hamiltonian function [32, Ch. 8]

$$\mathcal{H}(\boldsymbol{x}(z,t)) = \frac{\rho A}{2} \int_\Omega p^2(z,t)\,\mathrm{d}z + \frac{1}{2}\left[T_0 + \frac{EA}{4L}\int_\Omega q^2(z,t)\,\mathrm{d}z\right]\int_\Omega q^2(z,t)\,\mathrm{d}z, \tag{2}$$

leading to the following infinite-dimensional PHS formulation:

$$\begin{cases} \dfrac{\mathrm{d}}{\mathrm{d}t}\begin{bmatrix} q \\ p \end{bmatrix} = \left(\begin{bmatrix} 0 & \frac{1}{\rho A}\partial_z \\ \frac{1}{\rho A}\partial_z & 0 \end{bmatrix} - \begin{bmatrix} 0 & 0 \\ 0 & \frac{1}{\rho A}\mu \end{bmatrix}\right)\begin{bmatrix} \delta_q \mathcal{H} \\ \delta_p \mathcal{H} \end{bmatrix} + \begin{bmatrix} 0 \\ \frac{1}{\rho A L} \end{bmatrix} u \\ \qquad y = \begin{bmatrix} 0 & \frac{1}{\rho A L} \end{bmatrix}\begin{bmatrix} \delta_q \mathcal{H} \\ \delta_p \mathcal{H} \end{bmatrix}, \end{cases} \tag{3}$$

with the variational derivative of the Hamiltonian function (2) equal to

$$\delta_{\boldsymbol{x}}\mathcal{H}(\boldsymbol{x}(z,t)) = \begin{bmatrix} \delta_q \mathcal{H}(\boldsymbol{x}(z,t)) \\ \delta_p \mathcal{H}(\boldsymbol{x}(z,t)) \end{bmatrix} = \begin{bmatrix} \left(T_0 + \frac{EA}{2L}\int_0^L q^2(z,t)\,\mathrm{d}z\right) q(z,t) \\ \rho A\, p(z,t) \end{bmatrix}.$$

The input $u(z,t)$ being the force applied to the string, and the output $y(z,t) = (1/L)\partial_t w(z,t)$ with $\partial_t w(z,t)$ the transverse velocity, the expression $\int_\Omega u(z,t)y(z,t)\,\mathrm{d}z$ [W] represents the instantaneous external power transferred to the string.

Modal projection and order reduction
The infinite-dimensional PHS model (3) is projected on the N first eigenmodes of the linear string (Eq. (1) without the term $\frac{EA}{2L}\int_\Omega (\partial_z w(z,t))^2\,\mathrm{d}z$), that are given by $e_n(z) = \sqrt{\frac{2}{L}}\sin\left(\frac{n\pi}{L}z\right), n > 0$ (Fig. 2):

$$w(z,t) \approx \sum_{n=1}^{N} e_n(z) W_n(t).$$

Figure 2: First 6 eigenmodes $e_n(z)$ of the linear string of length L. The nodes (stationary points) are indicated by dots.

Then, defining

$$\boldsymbol{x}(z,t) = \begin{bmatrix} \frac{\mathrm{d}}{\mathrm{d}z}e_1(z) \dots \frac{\mathrm{d}}{\mathrm{d}z}e_N(z) & \boldsymbol{O}_{1\times N} \\ \boldsymbol{O}_{1\times N} & e_1(z)\dots e_N(z) \end{bmatrix}\begin{bmatrix} \boldsymbol{W}(t) \\ \frac{\mathrm{d}}{\mathrm{d}t}\boldsymbol{W}(t) \end{bmatrix} = \boldsymbol{\Phi}^\intercal(z)\boldsymbol{X}(t), \tag{4}$$

the Hamiltonian function $\mathcal{H}(\boldsymbol{x}(z,t)) = \frac{1}{2}\int_0^1 \boldsymbol{x}^\intercal(z,t)\mathcal{M}(z,t)\boldsymbol{x}(z,t)\,\mathrm{d}z$ (2) becomes

$$H(\boldsymbol{X}(t)) = \frac{1}{2}\int_0^1 \boldsymbol{X}^\intercal(t)\boldsymbol{\Phi}(z)\mathcal{M}(z,t)\boldsymbol{\Phi}^\intercal(z)\boldsymbol{X}(t)\,\mathrm{d}z = \frac{1}{2}\boldsymbol{X}^\intercal(t)\boldsymbol{M}_N(t)\boldsymbol{X}(t),$$

with

$$\boldsymbol{M}_N(t) = \begin{bmatrix} \boldsymbol{D}_N^2\left(T_0 + \frac{EA}{4L}\boldsymbol{X}^\intercal(t)\boldsymbol{N}_N\boldsymbol{X}(t)\right) & \boldsymbol{O}_{N\times N} \\ \boldsymbol{O}_{N\times N} & \rho A \boldsymbol{I}_{N\times N} \end{bmatrix}, \quad \boldsymbol{N}_N = \begin{bmatrix} \boldsymbol{D}_N^2 & \boldsymbol{O}_{N\times N} \\ \boldsymbol{O}_{N\times N} & \boldsymbol{O}_{N\times N} \end{bmatrix}, \quad \boldsymbol{D}_N^2 = \frac{\pi^2}{L^2}\mathrm{diag}(1, 2^2, \dots, N^2).$$

Next, premultiplying the first equation of the PHS (3) by $\boldsymbol{\Phi}(z)$, integrating it w.r.t. $z \in \Omega$, substituting (4) and using the localized controller setup (7) that will be defined below, one obtains following finite-dimensional PHS:

$$\begin{cases} \dfrac{\mathrm{d}}{\mathrm{d}t}\boldsymbol{X}(t) = \left(\dfrac{1}{\rho A}\begin{bmatrix}\boldsymbol{O}_{N\times N} & \boldsymbol{I}_{N\times N}\\ -\boldsymbol{I}_{N\times N} & \boldsymbol{O}_{N\times N}\end{bmatrix} - \dfrac{\mu}{\rho A}\begin{bmatrix}\boldsymbol{O}_{N\times N} & \boldsymbol{O}_{N\times N}\\ \boldsymbol{O}_{N\times N} & \boldsymbol{I}_{N\times N}\end{bmatrix}\right)\begin{bmatrix}\boldsymbol{D}_N^2(T_0 + \frac{EA}{2L}\boldsymbol{X}^\intercal(t)\boldsymbol{N}_N\boldsymbol{X}(t)) & \boldsymbol{O}_{N\times N}\\ \boldsymbol{O}_{N\times N} & \rho A\boldsymbol{I}_{N\times N}\end{bmatrix}\boldsymbol{X}(t)\\ \qquad\qquad + \dfrac{1}{\rho AL}\begin{bmatrix}\boldsymbol{O}_{N\times 1}\\ \varphi_1\\ \vdots\\ \varphi_N\end{bmatrix}U(t)\\ y(z,t) = \begin{bmatrix}0 & \frac{1}{L}\end{bmatrix}\boldsymbol{\Phi}^\intercal(z)\boldsymbol{X}(t), \end{cases} \tag{5}$$

with $\varphi_n \triangleq e_n(\ell)$, and ℓ and $U(t)$ will be defined by (7).
The $(N+n)^{\text{th}}$ line of the dynamics for $\boldsymbol{X}(t)$ gives

$$\ddot{W}_n(t) = -\frac{1}{\rho A}n^2\frac{\pi^2}{L^2}\left(T_0 + \frac{EA}{2L}\Sigma(t)\right)W_n(t) - \mu\dot{W}_n(t) + \frac{\varphi_n}{\rho AL}U(t), \tag{6}$$

where

$$\Sigma(t) \triangleq \sum_{n=1}^{N} n^2\frac{\pi^2}{L^2}W_n^2(t).$$

Each mode n is a nonlinear oscillator with a coupling to the other modes due to the term $\Sigma(t)$, and that is controlled by $U(t)$.

Finite-time tracking control

Hypotheses concerning the control layout are made and the control goal is stated. Then, an existing finite-time control law is applied to obtain the tracking controller that will control one mode of the nonlinear string (5) to chosen reference dynamics.

Controller setup

Following hypotheses are made.

1. *(Point force)* We use a single actuator that is able to deliver a localized force $U(t)$ [N]:

$$u(z,t) \triangleq \delta(z-\ell)U(t), \tag{7}$$

with $\delta(z-\ell)$ the Dirac delta distribution that activates the control law $U(t)$ at the position $z = \ell$ (cf. Fig. 3).

Furthermore, we suppose here that the application of a force at $z = \ell$ does not modify the eigenmodes $e_n(z)$. Then, one can write

$$u(z,t) = \sum_{n=1}^{N}\langle u(z,t), e_n(z)\rangle \cdot e_n(z) = \sum_{n=1}^{N} e_n(\ell)U(t)\cdot e_n(z) \triangleq \sum_{n=1}^{N}\varphi_n U(t)\cdot e_n(z).$$

Because of this hypothesis, the force $\varphi_n U(t)$ is applied to each mode n. Therefore, only one mode can be controlled at a time.

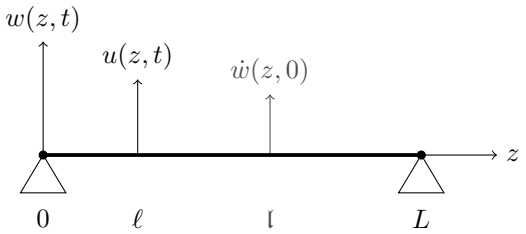

Figure 3: String that is initially at rest, subjected to a point force at $z = \ell$, and with an initial velocity applied at $z = \iota$ (see *Simulation*)

2. *(Known state)* It is supposed that the entire state $\boldsymbol{X}(t)$ of the projected PHS model (5) is known from the measured system output[1] $\boldsymbol{y}_{\text{meas}}(z,t)$, possibly after using an observer.

[1] In general, the measured output $\boldsymbol{y}_{\text{meas}}(z,t)$ differs from the PHS output $\boldsymbol{y}(z,t)$ defined as the conjugated variables with respect to the system input variables $\boldsymbol{u}(z,t)$, in the sense that $\int_\Omega \boldsymbol{u}(z,t)\boldsymbol{y}(z,t)\,\mathrm{d}z$ represents the instantaneous power applied to the PHS.

Control goal

A system $\{\mathcal{S}\}$ described by (5) represents the dynamics of the first N modes of the nonlinear string with physical parameters (ρ, T_0, μ, E). Following Hypothesis 1, our goal is to construct a controller $\{\mathcal{C}\}$ that lets one mode of the real system $\{\mathcal{S}\}$ track the dynamics of a virtual reference system $\{\mathcal{S}^*\}$ with desired physical parameters $(\rho^*, T_0^*, \mu^*, E^*)$, for an excitation by the same initial conditions (Fig. 4). To this means, a finite-time tracking controller will be designed.

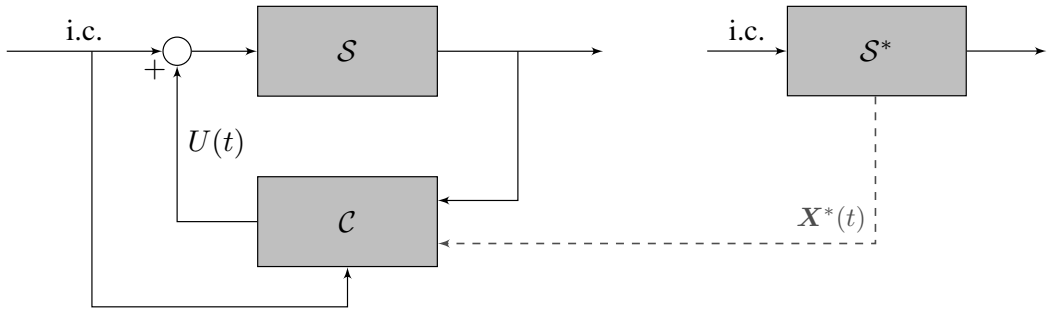

(a) Closed loop system $\{\mathcal{S}\&\mathcal{C}\}$ (b) Desired system dynamics $\{\mathcal{S}^*\}$

Figure 4: Tracking control layout (i.c.: initial conditions). The dashed arrow represents the reference trajectory $\boldsymbol{X}^*(t)$ corresponding to the reference system $\{\mathcal{S}^*\}$ that is in reality simulated inside the controller $\{\mathcal{C}\}$.

Finite-time control

Finite-time control [41] is a nonlinear control method enabling to reach an equilibrium point in a finite time. This finite settling time is a stronger property than in the case of asymptotic or exponential control. Finite-time control has useful properties for time-constraint and robust control [42].
Finite-time stability of an ODE with state $\boldsymbol{x}(t) \in \mathbb{R}^n$ is defined as follows.

Definition 1 (Finite-time stability [42]) *Let $\dot{\boldsymbol{x}} = \boldsymbol{F}(\boldsymbol{x})$ represent a closed-loop system, with $\boldsymbol{F}(\boldsymbol{x})$ continuous and $\boldsymbol{F}(\boldsymbol{0}) = \boldsymbol{0}$. Let $\boldsymbol{\Psi}^t(\boldsymbol{x}_0)$ be the time evolution of the state for a given initial state $\boldsymbol{x}_0$.*
The origin is a finite-time stable *equilibrium if there exists an open neighborhood $U \subset \mathbb{R}^n$ of the origin, where following statements hold:*

1. ***Finite-time convergence.*** *There exists a settling-time function $T : U\backslash\{0\} \to \mathbb{R}_{\geq 0}$ such that for each $\boldsymbol{x}_0 \in U\backslash\{0\}$, the evolution $\boldsymbol{\Psi}^t(\boldsymbol{x}_0)$ is defined and unique on $t \in [0, T(\boldsymbol{x}_0)[$ and $\lim_{t \to T(\boldsymbol{x}_0)} \boldsymbol{\Psi}^t(\boldsymbol{x}_0) = 0$.*
2. ***Lyapunov stability.*** *There exists a monotonically increasing function $\delta(\cdot)$, $\delta(0) = 0$, such that for each $\boldsymbol{x}_0 \in U$, $\|\boldsymbol{\Psi}^t(\boldsymbol{x}_0)\| \leq \delta(\|\boldsymbol{x}_0\|)$ for each $t \geq 0$.*

Furthermore, if $U = \mathbb{R}^n$, the origin is globally finite-time stable.

Several finite-time control laws have been designed for different kinds of ODE systems. They necessarily are non Lipschitz continuous at the equilibrium point [41]. For ODE systems of dimension $n = 2$, following law can be used.

Lemma 1 (Finite-time stabilisation of the double integrator [43]) *The origin of the double integrator*

$$\begin{cases} \dot{z}_1(t) = z_2(t) \\ \dot{z}_2(t) = v(t) \end{cases} \tag{8}$$

is finite-time stable for the control law

$$v(t) = -\kappa_1 \lfloor z_1(t) \rceil^{\frac{\alpha}{2-\alpha}} - \kappa_2 \lfloor z_2(t) \rceil^{\alpha},$$

where $\kappa_1, \kappa_2 > 0$, $\alpha \in]0, 1[$ and $\lfloor z \rceil^{\alpha} \triangleq \operatorname{sign}(x)|x|^{\alpha}$.

No explicit expression for the dependence of the settling-time on the control parameters $(\kappa_1, \kappa_2, \alpha)$ is known. Therefore, these parameters have to be tuned numerically. We refer the reader to [37] for an application of this law to a (non)linear mass-spring-damper system.

Finite-time tracking control applied to the nonlinear string

A finite-time tracking controller is developed for a chosen mode $M \in [\![1, \ldots, N]\!]$ by imposing the dynamics of (8) to the error

$$e(t) \triangleq W_M(t) - W_M^*(t)$$

between the real modal displacement $W_M(t)$ and the reference modal displacement $W_M^*(t)$ of mode M. A finite-time stabilization of

$$W_M(t) \to W_M^*(t), \quad \dot{W}_M(t) \to \dot{W}_M^*(t)$$

is thus obtained for the error dynamics

$$\frac{\mathrm{d}}{\mathrm{d}t}\begin{bmatrix} e(t) \\ \dot{e}(t) \end{bmatrix} = \begin{bmatrix} \dot{e}(t) \\ -\kappa_1 \lfloor e(t) \rceil^{\frac{\alpha}{2-\alpha}} - \kappa_2 \lfloor \dot{e}(t) \rceil^{\alpha} \end{bmatrix}. \tag{9}$$

After substituting the expression (6) for the real ($W_M(t)$) and desired ($W_M^*(t)$) oscillators, one solves (9) for the control law $U(t)$, which corresponds to

$$\begin{aligned} U(t) = \frac{1}{\varphi_M}\Big[& -\rho A L \left(\kappa_1 \lfloor W_M - W_M^* \rceil^{\frac{\alpha}{2-\alpha}} + \kappa_2 \left\lfloor \dot{W}_M - \dot{W}_M^* \right\rceil^{\alpha}\right) \\ & + M^2 \frac{\pi^2}{L}\left(T_0 W_M - \frac{\rho}{\rho^*} T_0^* W_M^* + \frac{A}{2L}\left(E\Sigma W_M - \frac{\rho}{\rho^*} E^*\Sigma^* W_M^*\right)\right) + \rho A L\left(\mu \dot{W}_M - \mu^* \dot{W}_M^*\right)\Big]. \end{aligned} \tag{10}$$

Applying this finite-time tracking control law to the system $\mathcal{S}$ will control its Mth mode to the Mth mode of the reference system $\mathcal{S}^\star$. As previously mentioned, because of Hypothesis 1, we do not have additional degrees of freedom to act on the other modes $n \neq M$.
The design of the control parameters $(\kappa_1, \kappa_2 > 0, \alpha \in]0,1[)$ present in the tracking controller has to ensure that it has faster dynamics than the dynamics of the nonlinear string (by Tikhonov's theorem, see for instance [44, Theorem A.11]). Their values have to be assessed by a simulation, that is presented in the next session.

Simulation

A system $\{\mathcal{S}\}$ is considered, with physical parameters from [45, Table 1] representing a steel string with fundamental frequency $f = \frac{1}{2L}\sqrt{\frac{T_0}{\rho A}} = 55\,\text{Hz}$:

$$L = 1{,}8\,\text{m}, \qquad A = \pi \cdot (1{,}5\,\text{mm})^2, \qquad \rho = 7800\,\frac{\text{kg}}{\text{m}^3}, \qquad E = 2 \cdot 10^{11}\,\text{Pa}, \qquad \mu = 3\,\frac{1}{\text{s}}, \qquad T_0 = 2161\,\text{N}.$$

The string is excited by an initial velocity localized at $z = \mathfrak{l}$ (Fig. 3):

$$\dot{w}(z,0) = V_0\left[\frac{\text{m}}{\text{s}}\right] \cdot \delta(z - \mathfrak{l}),$$

whose projection on mode $e_n(z)$ yields the initial conditions $\dot{W}_n(0) = V_0\sqrt{\frac{2}{L}}\sin\left(\frac{n\pi}{L}\mathfrak{l}\right)$, $n \in [\![1, \ldots, N]\!]$.
The controlled system $\{\mathcal{S}\&\mathcal{C}\}$ using control law (10) is simulated for two cases:

① a reference system $\{\mathcal{S}^*\}$ where the parameters (T_0, ρ, μ) of the linearized string model are modified for the mode $M = 2$, leading to a change in frequency and damping,

② a reference system $\{\mathcal{S}^*\}$ where the parameter E of the nonlinear string model is modified for the mode $M = 1$, leading to a modification of the pitch-glide effect.

The simulations are performed using the backwards Euler method [46] with time step $\delta t = 10^{-5}\,\text{s}$, using $N = 10$ modes and initial conditions with $V_0 = 50\,\frac{\text{m}}{\text{s}}$. Excitation location $\mathfrak{l}$ and control location ℓ will be set in function of the shape of the chosen controlled mode M (cf. Fig. 2, and [22, §II.C]).

Example ①: frequency and damping modification

Modifying the tension T_0 and/or mass density ρ, one can change the frequency of the Mth mode: $f_M^* = \frac{M}{2L}\sqrt{\frac{T_0^*}{\rho^* A}}$, whereas modifying the damping coefficient μ enables to damp the string quicker (active damping) or less quick (infinite sustain).
We consider the case where the string is excited at $\mathfrak{l} = \frac{1}{4}L$ and controlled at $\ell = \frac{3}{4}L$. The mode $M = 2$ is controlled to a reference trajectory with $T_0^* = 1.12T_0$ and $\rho^* = 0.88\rho$ (corresponding to $f_2^* = 124$ Hz $> f_2 = 110$ Hz), $\mu^* = 1.5\mu$ (increased damping), $E^* = E$ (no pitch-glide modification). Control parameters $\kappa_i = 0.5 \cdot 10^{11}$ and $\alpha = 0.95$ were used. A tracking of the reference signal $W_2^*(t)$ is achieved by $W_2(t)$ under the action of the control law $U(t)$ (Fig. 5). The spectral content of the second mode (Fig. 7) confirms that its frequency was increased to f_2^*, and that the signal is damped more quickly.
One can observe the effects of the control law $U(t)$ on the other modes $n \neq 2$, such as the appearance of low-amplitude harmonics in the higher-order modes, that cannot be influenced in the current control setup. Furthermore, we note that the 4th mode is not excited by the initial conditions nor by the control law $U(t)$, as both are located at a node of this mode ($\dot{W}_4(0) = 0, \varphi_4 = 0$; cf. Fig. 2).

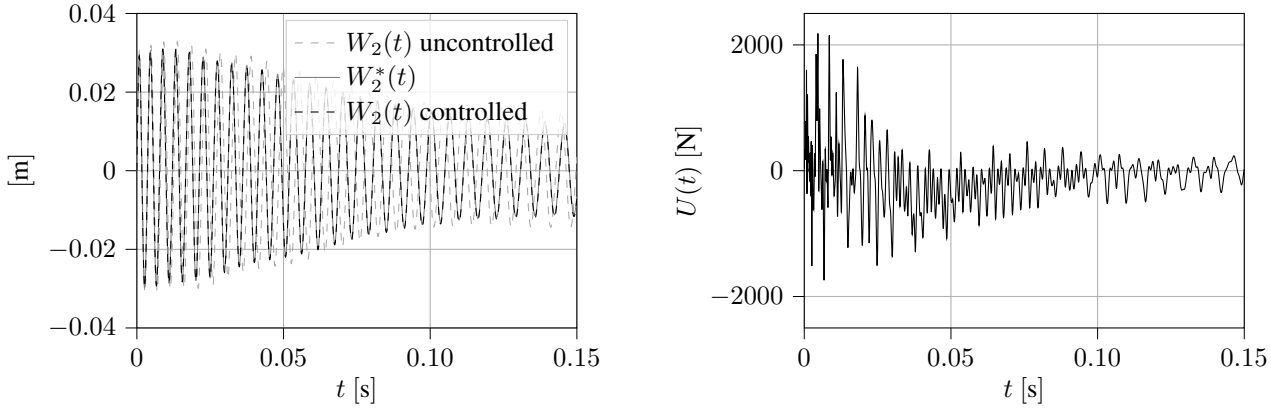

(a) Controlled mode 2

(b) Control law

Figure 5: Example ①: controlled mode 2 and control law

Example ②: pitch-glide attenuation

A pitch glide is the nonlinear phenomenon where the frequency increases with increasing amplitude of the transverse vibration $w(z,t)$ of the string, because of the tension modulation expressed by the term

$$\frac{EA}{2L}\int_\Omega (\partial_z w(z,t))^2 \,\mathrm{d}z$$

in (1). This phenomenon was visible in Example ① (Fig. 7).

In this second example, we consider the case where the string is excited at $\mathfrak{l} = 0.4L$ and controlled at $\ell = 0.5L$. The mode $M = 1$ is controlled to a reference trajectory with $T_0^* = T_0$ and $\rho^* = \rho$ (no frequency modification), $\mu^* = \mu$ (no damping modification) and $E^* = 0.3E$ (pitch-glide attenuation[2]). Control parameters $\kappa_i = 1 \cdot 10^{10}$ and $\alpha = 0.95$ were used.

A tracking of the reference signal $W_1^*(t)$ is achieved by $W_1(t)$ under the action of the control law $U(t)$ (Fig. 6). The spectral content of the first mode (Fig. 8) confirms that the pitch-glide phenomenon is attenuated.

Again, one can observe the effects of the control law $U(t)$ on the other modes $n \neq 1$, that cannot be influenced in the current control setup. In particular, the pitch-glide effect is increased for the second mode (and higher modes, although their amplitude is smaller), and harmonics appear in the higher-order modes.

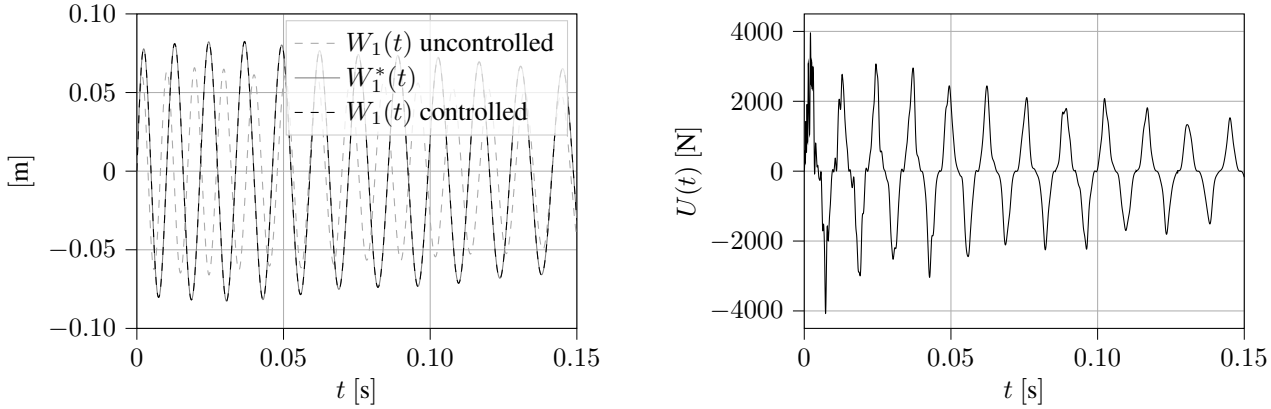

(a) Controlled mode 1

(b) Control law

Figure 6: Example ②: controlled mode 1 and control law

Conclusions and perspectives

A tracking controller was designed, that is able to modify physical model parameters of a chosen mode of a truncated modal model of a nonlinear Kirchhoff-Carrier string taking into account the pitch-glide phenomenon. Two use cases were illustrated in simulation, where frequency, damping and the pitch glide-phenomenon were modified, and the effect on the other modes was observed.

Future works include the consideration of a more realistic sensor and actuator setup taking into account their placement [22, §II.C] and the development of an observer in order to reconstruct the state. Furthermore, robustness of the controller against measurement noise or bad parameter estimation can be assessed.

[2] A reference stiffness of $E^* = 0$ would correspond to a pitch-glide removal, but requires unrealistic force levels of 30 kN for $U(t)$. This control goal was used in the preliminary simulation shown in [1, §8.4]. An analysis of the required control power as in [22, Appendix B] is not performed here.

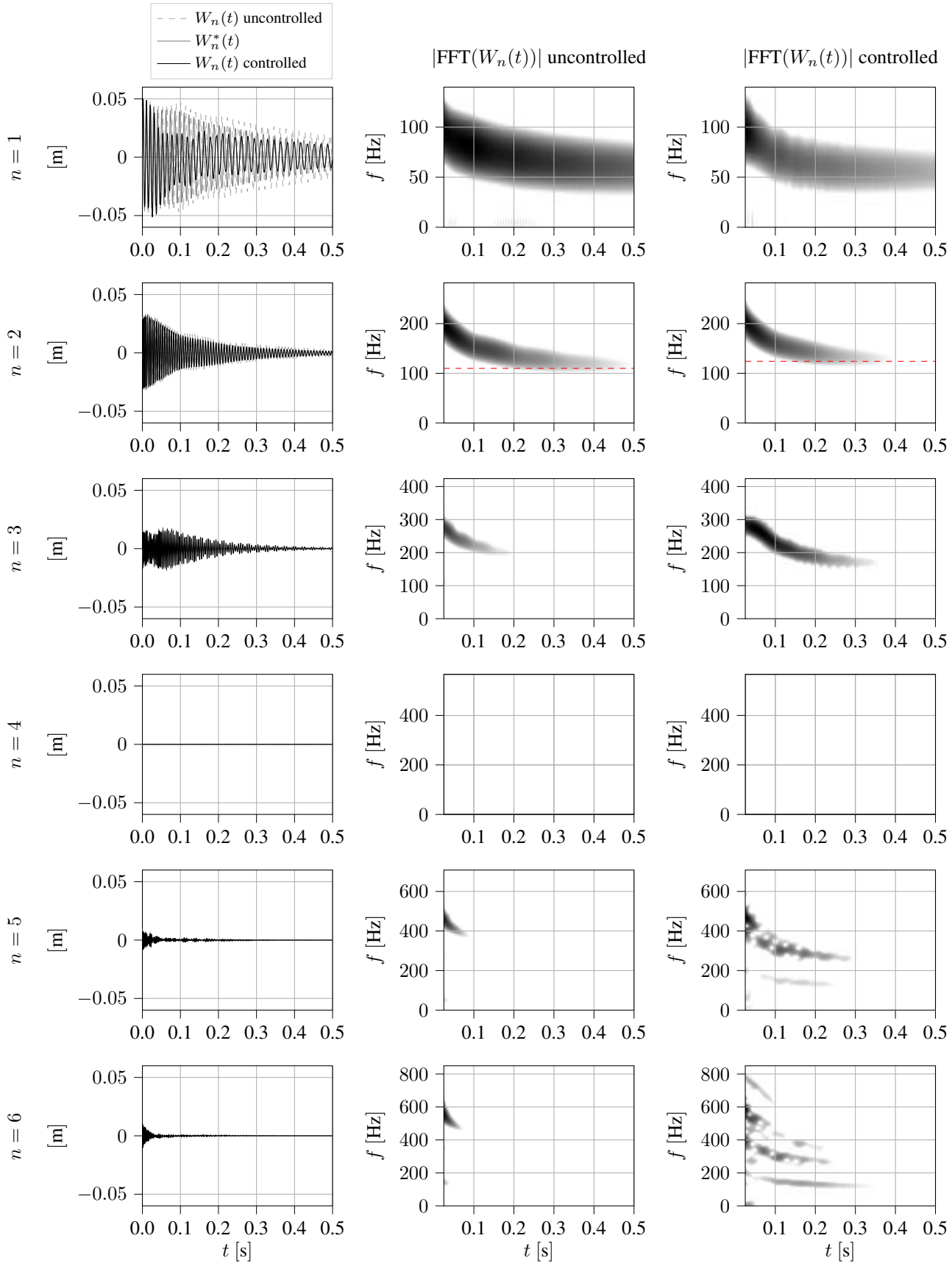

Figure 7: Example ①: time evolution and spectral content of the first 6 modes. The FFT is calculated using a Hann window and the same logarithmic color scale is used for the (un)controlled cases of a given mode. Red dashed lines indicate the asymptotic values of the frequencies (corresponding to the linearized string model) for mode 2 in the (un)controlled cases.

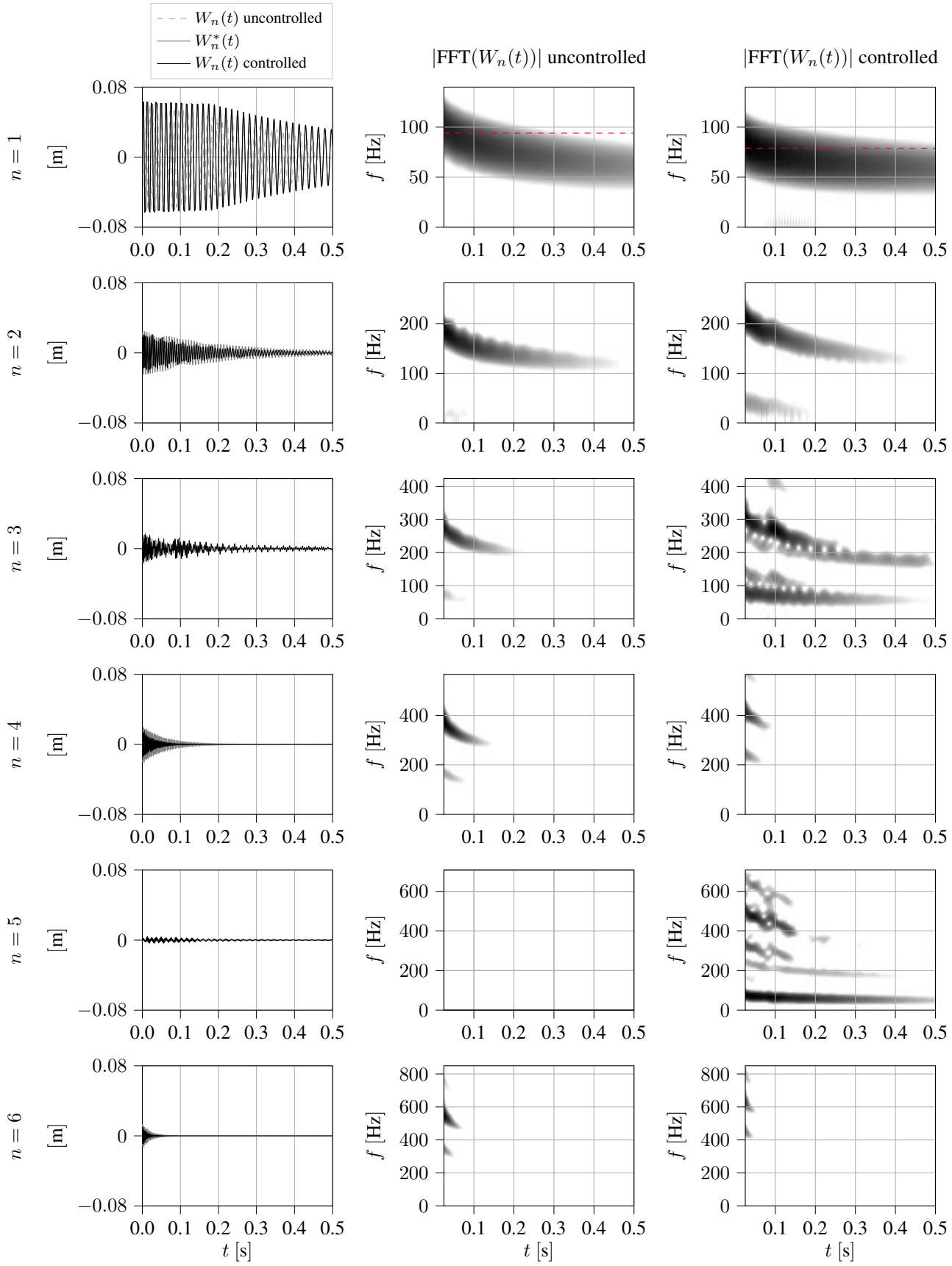

Figure 8: Example ②: time evolution and spectral content of the first 6 modes. The FFT is calculated using a Hann window and the same logarithmic color scale is used for the (un)controlled cases of a given mode. Red dashed lines indicate the starting frequencies of the pitch glide for mode 1 in the (un)controlled cases.

Acknowledgments

The authors thank the support of ANR project Finite4SoS (ANR 15 CE23 0007) and ANR-DFG project Infidhem (ANR 16 CE92 0028).

References

[1] Wijnand, M. (2021). *Contrôle en temps fini de systèmes vibratoires hybrides couplant équations aux dérivées partielles et équations aux dérivées ordinaires : les cas du tom et du câble pesant*. PhD thesis, Sorbonne Université, Paris, France.

[2] Elliott, S. J. and Nelson, P. A. (1993). Active noise control. *IEEE signal processing magazine*, 10(4):12–35.

[3] Fuller, C. C., Elliott, S., and Nelson, P. A. (1996). *Active control of vibration*. Academic Press.

[4] Turchet, L., McPherson, A., and Fischione, C. (2016). Smart instruments: towards an ecosystem of interoperable devices connecting performers and audiences. In *Proceedings of the Sound and Music Computing Conference*, pages 498–505.

[5] Boutin, H., Besnainou, C., and Polack, J.-D. (2015). Modifying the resonances of a xylophone bar using active control. *Acta Acustica united with Acustica*, 101(2):408–420.

[6] Meurisse, T., Mamou-Mani, A., Benacchio, S., Chomette, B., Finel, V., Sharp, D. B., and Caussé, R. (2015). Experimental Demonstration of the Modification of the Resonances of a Simplified Self-Sustained Wind Instrument Through Modal Active Control. *Acta Acustica united with Acustica*, 101(3):581–593.

[7] Jossic, M., Mamou-Mani, A., Chomette, B., Roze, D., Ollivier, F., and Josserand, C. (2017). Modal active control of Chinese gongs. *The Journal of the Acoustical Society of America*, 141(6):4567–4578.

[8] Wijnand, M., d'Andréa-Novel, B., Hélie, T., and Roze, D. (2020). Active control of the axisymmetric vibration modes of a tom-tom drum using a modal-based observer-regulator. In *EAA e-Forum Acusticum*.

[9] Benacchio, S., Mamou-Mani, A., Chomette, B., and Finel, V. (2016). Active control and sound synthesis–two different ways to investigate the influence of the modal parameters of a guitar on its sound. *The Journal of the Acoustical Society of America*, 139(3):1411–1419.

[10] Neubauer, P., Tschesche, J., Bös, J., Melz, T., and Hanselka, H. (2018). An active-system approach for eliminating the wolf note on a cello. *The Journal of the Acoustical Society of America*, 143(5):2965–2974.

[11] Meurisse, T., Mamou-Mani, A., Caussé, R., Sluchin, B., and Sharp, D. B. (2015). An active mute for the trombone. *The Journal of the Acoustical Society of America*, 138(6):3539–3548.

[12] Mounier, H., Rudolph, J., Fliess, M., and Rouchon, P. (1998). Tracking control of a vibrating string with an interior mass viewed as delay system. *ESAIM: Control, Optimisation and Calculus of Variations*, 3:315–321.

[13] Rudolph, J. and Woittennek, F. (2010). Flatness-based control without prediction: example of a vibrating string. *PAMM*, 10(1):629–630.

[14] Zhang, F., Nagarkatti, S. P., Costic, B., Dawson, D. M., and Rahn, C. D. (1999). Velocity Tracking Control of an Axially Accelerating String and Actuator System. In *Proceedings of the 38th IEEE Conference on Decision and Control (Cat. No. 99CH36304)*, volume 5, pages 4325–4330. IEEE.

[15] Paiva, R. C., Pakarinen, J., and Välimäki, V. (2012). Acoustics and modeling of pickups. *Journal of the Audio Engineering Society*, 60(10):768–782.

[16] Freed, A. and Isvan, O. (2000). Musical Applications of New, Multi-axis Guitar String Sensors. In *26th International Computer Music Conference*.

[17] Weinreich, G. and Caussé, R. (1986). Digital and analog bows: hybrid mechanical-electrical systems. In *ICASSP'86. IEEE International Conference on Acoustics, Speech, and Signal Processing*, volume 11, pages 1297–1299. IEEE.

[18] Leroy, N., Fléty, E., and Bevilacqua, F. (2006). Reflective Optical Pickup For Violin. In *International Conference on New Interfaces for Musical Expression (NIME06)*.

[19] Heet, G. S. (1978). String instrument vibration initiator and sustainer. US Patent 4,075,921.

[20] Berdahl, E., Backer, S., and Smith III, J. O. (2005). If I had a Hammer: Design and Theory of an Electromagnetically-prepared Piano. In *Proceedings of the International Computer Music Conference*.

[21] Donovan, L. (2018). *Travelling Wave Control of Stringed Musical Instruments*. PhD thesis, Queen Mary University of London.

[22] Berdahl, E., Smith III, J. O., and Niemeyer, G. (2012). Feedback control of acoustic musical instruments: Collocated control using physical analogs. *The Journal of the Acoustical Society of America*, 131(1):963–973.

[23] Berdahl, E., Smith III, J. O., and Freed, A. (2006). Active damping of a vibrating string. In *2006 International Symposium on Active Control of Sound and Vibration*.

[24] Cheekati, B. and Bhikkaji, B. (2013). A negative imaginary approach to the actuation of a guitar string. *Mechatronics*, 23(8):997–1004.

[25] Boutin, H. and Besnainou, C. (2008). Physical parameters of the violin bridge changed by active control. In *Acoustics'08, Paris*, pages 7247–7252.

[26] Benacchio, S. (2014). *Contrôle actif modal appliqué aux instruments de musique à cordes*. PhD thesis, Université Pierre et Marie Curie – Paris VI.

[27] McPherson, A. (2010). The Magnetic Resonator Piano: Electronic Augmentation of an Acoustic Grand Piano. *Journal of New Music Research*, 39(3):189–202.

[28] HyVibe (2017). Smart Acoustic Guitar, Paris. `https://www.hyvibeguitar.com/`.

[29] Kirchhoff, G. (1876). *Vorlesungen über mathematische Physik: Mechanik*. B. G. Teubner, Leipzig.

[30] Carrier, G. F. (1945). On the non-linear vibration problem of the elastic string. *Quarterly of applied mathematics*, 3(2):157–165.

[31] Chaigne, A. and Kergomard, J. (2016). *Acoustics of musical instruments*. Springer.

[32] Bilbao, S. (2009). *Numerical sound synthesis: finite difference schemes and simulation in musical acoustics*. John Wiley & Sons.

[33] Maschke, B. M. and van der Schaft, A. J. (1992). Port-controlled Hamiltonian systems: modelling origins and systemtheoretic properties. *IFAC Proc. Volumes*, 25(13):359–365.

[34] Curtain, R. F. and Zwart, H. (1995). *An Introduction to Infinite-Dimensional Linear Systems Theory*. Springer.

[35] Villegas, J. A. (2007). *A Port-Hamiltonian Approach to Distributed Parameter Systems*. PhD thesis, University of Twente.

[36] Lopes, N., Hélie, T., and Falaize, A. (2015). Explicit second-order accurate method for the passive guaranteed simulation of port-Hamiltonian systems. *IFAC-PapersOnLine*, 48(13):223–228.

[37] Wijnand, M., d'Andréa-Novel, B., Hélie, T., and Roze, D. (2018). Contrôle des vibrations d'un oscillateur passif : stabilisation en temps fini et par remodelage d'énergie. In *Congrès Français d'Acoustique*.

[38] Falaize, A. and Hélie, T. (2016). Passive Guaranteed Simulation of Analog Audio Circuits: A Port-Hamiltonian Approach. *Applied Sciences*, 6(10):273.

[39] Ortega, R., van der Schaft, A., Maschke, B., and Escobar, G. (2002). Interconnection and damping assignment passivity-based control of port-controlled Hamiltonian systems. *Automatica*, 38(4):585–596.

[40] Hélie, T. and Roze, D. (2016). Corde non linéaire amortie : formulation hamiltonienne à ports, réduction d'ordre exacte et simulation à passivité garantie. In *13ème Congrès Français d'Acoustique*.

[41] Haimo, V. T. (1986). Finite time controllers. *SIAM Journal on Control and Optimization*, 24(4):760–770.

[42] Bhat, S. P. and Bernstein, D. S. (2000). Finite-time stability of continuous autonomous systems. *SIAM Journal on Control and Optimization*, 38(3):751–766.

[43] Bernuau, E., Perruquetti, W., Efimov, D., and Moulay, E. (2015). Robust finite-time output feedback stabilisation of the double integrator. *International Journal of Control*, 88(3):451–460.

[44] Canudas de Wit, C., Siciliano, B., and Bastin, G. (1996). *Theory of Robot Control*. Springer-Verlag.

[45] Hélie, T. and Roze, D. (2008). Sound synthesis of a nonlinear string using Volterra series. *Journal of Sound and Vibration*, 314(1-2):275–306.

[46] Moré, J. J., Garbow, B. S., and Hillstrom, K. E. (1980). User guide for MINPACK-1. Technical report, Argonne National Laboratory.

Non-periodic dynamics in a delay model of flute-like musical instruments

Soizic Terrien*, Christophe Vergez†, Benoît Fabre‡ and Patricio de la Cuadra**
* *Laboratoire d'Acoustique de l'Université du Mans, CNRS UMR 6613, Le Mans, France*
† *Aix Marseille Univ, CNRS, Centrale Marseille, LMA UMR7031, Marseille, France*
‡ *Sorbonne Université, UMR 7190, LAM-Institut d'Alembert, Paris, France*
** *Escuela de Ingeneria-Instituto de Musica, Pontificia Universidad Catolica de Chile, Santiago, Chili*

Summary. We investigate the emergence of quasiperiodic sound regimes in a model of flute-like musical instruments. The model itself is a system of delay differential equations of neutral type (NDDEs). We employ advanced numerical continuation methods to compute bifurcation diagrams in the space of relevant playing and making parameters. Our results show the role played by the detuning between the instrument resonance frequencies in the emergence of quasiperiodic regimes.

Self-sustained musical instruments are complex nonlinear dynamical systems and show a wealth of dynamical regimes. This includes equilibrium solutions where no sound is produced and periodic oscillations which most often correspond to the notes produced by the instrument, but also non-periodic oscillation regimes [1]. The exisence and stability of these different sound regimes depend sensitively on making parameters which are fixed by the instrument maker and on playing parameters which are continuously tuned by experienced players. In the context of western classical music, non-periodic sound regimes are most of the time avoided and can be considered as a defect of the musical instrument or as a lack of control from the musician. On the other hand, some non periodic sounds, often referred to as *multiphonics*, are often played on purpose in jazz, contemporary or traditional music. Flute-like instruments in particular, show a diversity of non-periodic sound regimes (see Figure 1). This includes *multiphonic sounds* played on purpose in transverse flutes and recorders, *rolling notes* which instrument makers try to avoid, modulated regimes due to wall vibrations [2], but also, *e.g.*, *sonidos rajados*, a highly-modulated sound produced by traditional pan-like flutes from Central Chile [3]. Here we consider a model of flute-like musical instrument, and investigate the physical mechanism responsible for the emergence of non-periodic regimes.

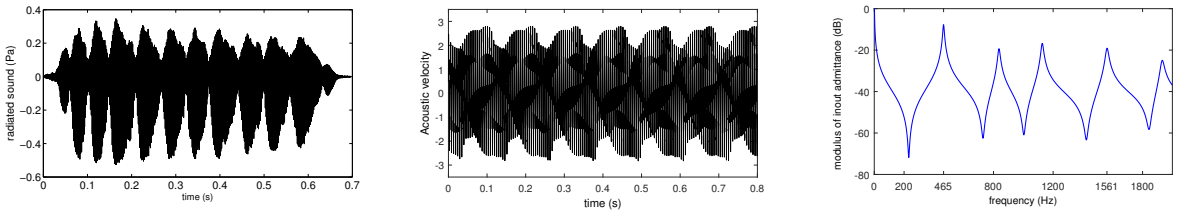

Figure 1: Left: Non periodic sound played by a traditional chilean pan-like flute. Middle: Non periodic simulated sound obtained using the NDDE model of a recorder. Right: Modulus of the input admittance of an alto recorder, for the fingering used to play the note B flat. The admittance is modelled as a sum of 6 resonant modes.

In flute-like musical instruments such as transverse flutes, recorders, quenas and organ pipes, the sound production results from the coupling between an intrinsically unstable air jet blown by the musician and an acoustic resonator which is composed of the air column contained in the pipe of the instrument [4]. Depending on the instrument, the pipe can include several tone holes: different *fingerings*, corresponding to different combinations of open and closed tone holes, are used by the musician to change the properties of the acoustical resonator, including its resonance frequencies and damping factors. More precisely, the air pressure in the musician mouth results in the emergence of an air jet at the output of a channel which is a part of the instrument (for recorders) or formed by the musicians lips (in transverse flutes, pan-like flutes ...). This air jet is intrinsically unstable and oscillates around a sharp edge called *labium*. This oscillation results in an alternate flow injection inside and outside the instrument pipe, which constitutes a dipolar pressure source for the acoustic resonator. The acoustic waves thus created propagate in the acoustic resonator and perturb back the air jet at the channel exit. This perturbation is amplified while convected along the jet, and sustains the air jet oscillation and, as such, the sound production. Importantly, the convection time of the perturbation along the air jet introduces a delay τ in the system, whose value is directly related to the pressure P_m in the musician's mouth, which is one of the main control parameter. Overall, flute-like instruments are modelled by a system of $2n$ delay differential equations of neutral type (NDDE), with n the number of acoustic modes taken into account to model the resonator, as shown in Figure 1 (right).

We focus here on the theoretical investigation of this model, and use advanced numerical methods to perform a bifurcation analysis. Because delay differential equations (DDEs) have an infinite dimensional phase space, they are more complicated to solve numerically than ordinary differential equations (ODEs). In particular, specific numerical methods have to

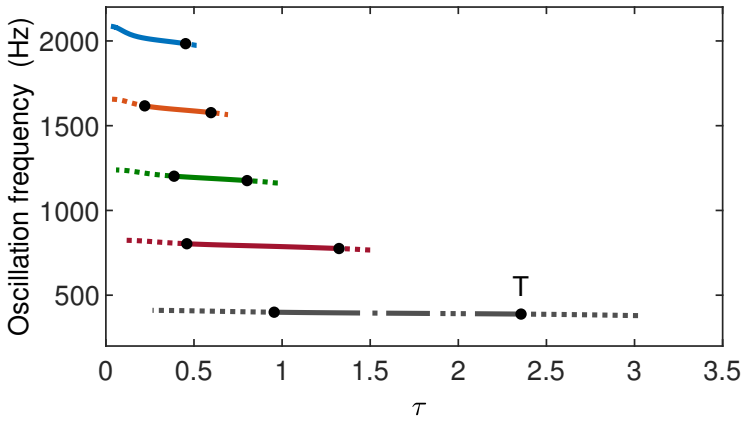

Figure 2: Bifurcation diagram of the NDDE flute model, showing the frequency along branches of stable (solid lines) and unstable (dotted lines) periodic solutions, with respect to the delay τ. Black dots correspond to torus bifurcation points T, where a periodic solution changes stability, with two complex conjugate Floquet multipliers crossing the unit circle.

be considered for the calculation and continuation of their solutions. We use here the continuation toolbox DDE-Biftool [5, 6]. This allows for the calculation and continuation of equilibrium solutions, periodic solutions and their respective bifurcations in system of DDEs. More precisely, a collocation method is used to compute periodic solutions. This is coupled to a predictor-corrector algorithm to continue the branches of solutions with respect to a parameter of interest of the physical model. Here, these numerical methods have been adapted so that the same calculations are possible for NDDEs [7, 8].

The bifurcation analysis of the NDDE model of flute-like instruments shows that multiple branches of periodic solutions emerge in Hopf bifurcations when the main control parameter P_m increases, which corresponds to a decreasing value of the delay τ (see Figure 2). From a musical point of view, the different branches of periodic solutions correspond to the different *registers* of the instruments, that is to say to periodic regimes associated with the different acoustic modes of the resonator. These periodic regimes have oscillation (*playing*) frequencies close to the resonance frequencies of the instrument, and can be interpreted as the different notes played by a musician for a given fingering. The stability analysis of these periodic solution show that they destabilise through torus bifurcations when the mouth pressure P_m increases further (*i.e.* when τ decreases). These bifurcations can lead to stable quasiperiodic oscillations. We investigate further the emergence of quasiperiodic regimes by performing the numerical continuation of curves of torus bifurcation in the (P_m, ξ)-plane. Here, ξ is an inharmonicity parameter, which models the detuning between the different acoustic resonant modes. The obtained bifurcation set demonstrates the major role played by the resonator inharmonicity on the existence and stability of quasiperiodic regimes.

Overall, our results provide a better understanding of the physical mechanism responsible for the emergence of non periodic sound regimes in flute-like musical instruments. They strongly suggest that experimentally-observed modulated sound regimes can be interpreted as quasiperiodic oscillations on a stable torus, resulting from the loss of stability of one of the *registers* of the instrument. The bifurcation analysis unveils the major role played by the inharmonicity of the acoustic resonator in this process. This paves the way towards a better experimental control of non-periodic sound regimes, which instrument makers and musicians either try to avoid or to enhance depending on the musical and cultural context.

References

[1] Backus J. (1978) Multiphonic tones in the woodwind instruments. *J. Acous. Soc. Am.* **63**:591-599.

[2] Gautier F., Nief G., Gilbert J. and Dalmont J.P. (2012) Vibro-acoustics of organ pipes – Revisiting the Miller experiment (L). *J. Acous. Soc. Am.* **131**:737-738.

[3] Wright H.A.K. and Campbell D.M. (1998) Analysis of the sound of chilean pifilca flutes. *The Galpin Society Journal* **51**:51-63.

[4] Fabre B. and Hirschberg A. (2000) Physical modeling of flue instruments: A review of lumped models. *Acta Acustica united with Acustica* **86**:599-610.

[5] Engelborghs K., Luzyanina T. and Roose D. (2002) Numerical bifurcation analysis of delay differential equations using DDE-BIFTOOL. *ACM Transactions on Mathematical Software* **28**:1–21.

[6] Sieber J., Engelborghs K., Luzyanina T., Samaey G. and Roose D. (2014) DDE-BIFTOOL Manual-Bifurcation analysis of delay differential equations. *arXiv preprint arXiv:1406.7144*.

[7] Barton D.A.W., Krauskopf B. and Wilson R.E. (2006) Collocation schemes for periodic solutions of neutral delay differential equations. *J. Difference Equations and Applications* **12**:1087–1101.

[8] Terrien S., Vergez C., Fabre B. and Barton D.A.W. (2014) Calculation of the steady-state oscillations of a flute model using the orthogonal collocation method *Acta Acustica united with Acustica* **100**:690-704.

Nonlinear damping laws preserving the eigenstructure of the momentum space for conservative linear PDE problems: a port-Hamiltonian modelling

Thomas Hélie*, Denis Matignon†
*S3AM team, Laboratory of Science and Technology of Music and Sound, IRCAM-CNRS-SU, Paris, France
†University of Toulouse, ISAE-Supaéro, Toulouse, France

Summary. Application to morphing in sound synthesis with the mutation of damping material properties leads us to introduce a class of nonlinear damping models operating on the momentum equation of the Hamiltonian formulation of a conservative mechanical PDE; the modal decomposition of the original linear vibrating structure is useful to analyze the preserved geometric features.

Initial conservative mechanical problem

We consider *linear conservative mechanical* systems, the solutions of which admit an eigen-decomposition. Typically, they can be finite-dimensional (mass-stiff) ODE systems, or infinite-dimensional continuous problems on a *bounded space domain* with *homogeneous boundary conditions*, governed either by the PDE (1) or by Hamiltonian descriptions (2a-2b).

PDE description

The models under consideration have the form

$$M(z)\ddot{w}(z,t) + \mathcal{K}(z)w(z,t) = f(z,t) \;\text{ for all }\; (z,t) \in \Omega \times \mathbb{R}_+, \tag{1}$$

with zero initial conditions, where z and t denote the space and time variables, Ω a bounded space domain, w a displacement, f an external force, M a mass matrix and $\mathcal{K}$ a structured differential stiffness operator. Technically, we assume that $M(z)$ is a symmetric uniformly positive definite matrix ($M \in L^\infty(\Omega, S_n^+)$, $\varepsilon\,\mathrm{Id} \le M(z) \le \|M\|_{L^\infty}\,\mathrm{Id}$), that $\mathcal{K}(z)$ is a symmetric positive differential operator such that $M^{-1}\mathcal{K}$ defines a self-adjoint operator on a Hilbert space $\mathbb{H}$. In practice, $\mathcal{K}$ can be a spatial operator with classical (e.g. Dirichlet or Neumann) homogeneous boundary conditions (see example).

Hamiltonian description

We also assume that this model admits a Hamiltonian description (including the excitation). The mechanical state $X = [q,p]^\intercal$ is composed of a configuration variable $q(z,t) := \mathcal{J}_{qp}(z)\,w(z,t)$ (that typically encodes a geometrical deformation) and the momentum $p(z,t) := M(z)\,\dot{w}(z,t)$. The Hamiltonian is $H\big(X=[q,p]^\intercal\big) = \frac{1}{2}\int_\Omega \big(p(z)^\intercal L_p(z) p(z) + q(z)^\intercal L_q(z) q(z)\big)\,\mathrm{d}z$ with $L_p := M^{-1}$ and L_q symmetric and uniformly positive, so that its variational derivative is $\delta_X H(X) = \mathcal{L}X$ with $\mathcal{L} := \mathrm{diag}(L_q, L_p)$. The governing equation is

$$\partial_t X = \mathcal{J}\,\delta_X H(X) + \begin{bmatrix}0\\1\end{bmatrix} f \qquad \text{with } \mathcal{J}(z) = \begin{bmatrix} 0 & \mathcal{J}_{qp}(z) \\ -\mathcal{J}_{qp}^*(z) & 0 \end{bmatrix}, \tag{2a}$$

$$v = [0,1]\,\delta_X H(X), \tag{2b}$$

where $\mathcal{J} = -\mathcal{J}^*$ is skew-symmetric ($\mathcal{J}_{pq} = -\mathcal{J}_{qp}^*$). The observation equation (2b) produces the power-conjugated variable v of excitation f, and this system is power-balanced: $\mathrm{d}H(X(\cdot,t))/\mathrm{d}t$ is the sum of the external power $\langle f(\cdot,t), v(\cdot,t)\rangle$ supplied in Ω and that incoming through boundaries (zero for the homogeneous conditions assumed in this paper) [2]. Equation (2a) relates the efforts $e = [e_q, e_p]^\intercal := \delta_X H = [L_q\,q, L_p\,p]^\intercal)$ to the flows $f = [f_q, f_p]^\intercal := \partial_t X = [\dot{q}, \dot{p}]^\intercal$. Note that its interpretation on the displacement variable reads

$$f_q = \mathcal{J}_{qp} e_p \quad \longrightarrow \quad (\mathcal{J}_{qp}\,\dot{w}) = \mathcal{J}_{qp}\,\dot{w} \qquad \text{(kinematic concordance equation)} \tag{3}$$

$$f_p = -\mathcal{J}_{qp}^* e_q + f \quad \longrightarrow \quad (M\,\ddot{w}) = -\mathcal{J}_{qp}^* L_q \mathcal{J}_{qp} w + f \qquad \text{(momentum balance)} \tag{4}$$

and $v = \dot{w}$ (output), so that the momentum balance corresponds to (1) with the meaningful factorization $\mathcal{K} = \mathcal{J}_{qp}^* L_q \mathcal{J}_{qp}$.

Example of a rectangular membrane

Consider a 2D membrane ($z = (x,y) \in \Omega = (0,X)\times(0,Y)$) with transverse displacement w [m], surface mass density $M(z) = \rho(z) > 0$ [Kg/m^2], tension tensor $T_{2\times2}(z)$ [N/m] and with fixed boundaries so that $\mathcal{K}(z) = -\mathrm{div}\Big(T_{2\times2}(z)\vec{\mathrm{grad}}\Big)$ is defined on $\mathcal{D} = \{w \in H^2(\Omega) \text{ s.t. } w|_{\partial\Omega} = 0\}$ in (1).
For a homogeneous membrane with constant parameters $\rho(z) = \rho_0$ and $T_{2\times2}(z) = T_0 I_2$, both operators $\mathcal{K}(z) = -T_0\Delta$ and $M(z)^{-1}\mathcal{K}(z) = -(T_0/\rho_0)\Delta$ involve the standard Laplacian $\Delta := \mathrm{div}\,(\vec{\mathrm{grad}}) = \partial_x^2 + \partial_y^2$ defined on domain $\mathcal{D}$.
In this simple case, $M^{-1}\mathcal{K}$ is a Riesz-spectral operator. Its point spectrum is composed of positive eigenvalues ω_{mn}^2 with $\omega_{mn} = \sqrt{\frac{T_0}{\rho_0}}\sqrt{(\frac{m\pi}{X})^2 + (\frac{n\pi}{Y})^2}$ for integers $m,n \ge 1$. These eigenvalues ω_{mn}^2 are associated with the eigenfunctions $e_{mn}(x,y) = \frac{2}{\sqrt{XY}}\sin(\frac{m\pi x}{X})\sin(\frac{n\pi y}{Y})$, which are orthonormal in $\mathbb{H} = L^2(\Omega)$. The dynamics $w_{mn}(t) := \langle w(\cdot,t), e_{mn}\rangle_{\mathbb{H}}$ carried by each modal space function e_{mn} is governed by (1) projected on e_{mn} ($\ddot{w}_{mn} + \omega_{mn}^2 w_{mn} = \langle f, e_{mn}\rangle_{\mathbb{H}}$). Each ODE is associated with two poles $\lambda_{mn}^\pm = \pm i\omega_{mn}$ (roots of the characteristic polynomials $\mathcal{P}_{mn}(\lambda) = \lambda^2 + \omega_{mn}^2$).

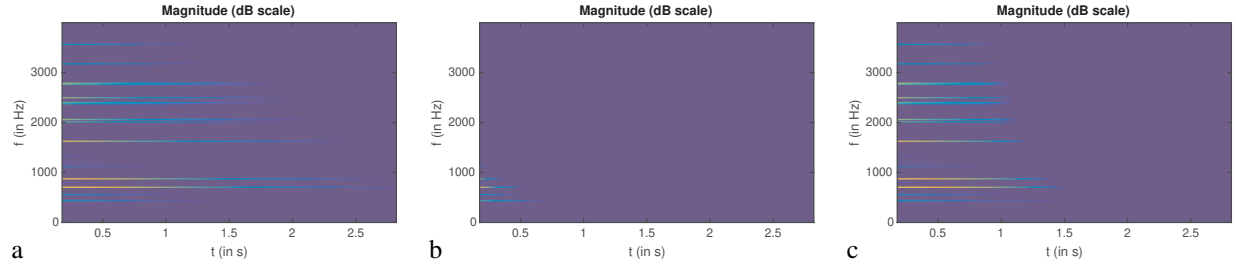

Figure 1: Spectrograms of signals produced for: (a,b) linear damping for two sets of parameters; (c) a nonlinear damping with behaviour "a" at high energies and "b" at low energies.

A natural Hamiltonian description is obtained by introducing the strain[1] $\vec{q} := \vec{\text{grad}}\, w$ (meaning that $\mathcal{J}_{qp} := \vec{\text{grad}}$ and $\mathcal{J}_{qp}^* = -\text{div}$)), the surface momentum $p := \rho_0 \partial_t w$ and the Hamiltonian weighted by $L_p = 1/\rho_0$ and $L_q = T_0\, I_2$. Matrix $\mathcal{J}$ is then given by $\mathcal{J}(z) := \begin{bmatrix} 0 & \mathcal{J}_{qp}(z) \\ -\mathcal{J}_{qp}^*(z) & 0 \end{bmatrix} = \begin{bmatrix} 0 & \vec{\text{grad}} \\ \text{div} & 0 \end{bmatrix}$, and $\mathcal{J}\delta_X H = \mathcal{J}\mathcal{L} = \begin{bmatrix} 0 & \frac{1}{\rho_0}\vec{\text{grad}} \\ T_0 \text{div} & 0 \end{bmatrix}$ is a Riesz-spectral operator with eigenvalues $\lambda_{mn}^{\pm} = \pm i\omega_{mn}$ and eigenfunctions $E_{mn}^{\pm} := [\vec{q}_{mn} := \vec{\text{grad}}\, e_{mn}, p_{mn}^{\pm} := \rho_0 \lambda_{mn}^{\pm} e_{mn}]^\intercal$. We now look for damping that preserves the kinematics (3) and the eigenstructure of the p-subspace (modes e_{mn}).

Structured damping class: linear and nonlinear models

Modifying the governing equation (2a) as $\partial_t X = (\mathcal{J} - \mathcal{R})\, \delta_X H + [0,1]^\intercal f$ introduces some dissipation in the system if $\mathcal{R}(z) = \mathcal{R}(z)^*$ is symmetric positive.
In this paper, inspired by [1] and following previous work in [3, 4], we first propose the linear damping class built on the parameters and the structure of the initial conservative system thanks to a polynomial function $\mathbb{P}$ with positive coefficients:

$$\mathcal{L}\mathcal{R} = \Sigma\, \mathbb{P}\big((\mathcal{L}\mathcal{J})^*\, (\mathcal{L}\mathcal{J}) \big) \;\text{ with } \Sigma = \begin{bmatrix} 0_{qq} & 0_{qp} \\ 0_{pq} & I_{pp} \end{bmatrix}. \tag{5}$$

Theorem: equation (5) defines a damping class that : (i) preserves the kinematics concordance equation (3) of the original problem, between $\partial_t \vec{q}$ and $\delta_p H$; (ii) preserves the eigenstructure of the p-subspace.
The element of the proof are the positivity of operators $(\mathcal{L}\mathcal{J})^*(\mathcal{L}\mathcal{J})$ and of the coefficients of $\mathbb{P}$ for the dissipation, the selection matrix Σ that operates property (i), and the powers of $(\mathcal{L}\mathcal{J})^*(\mathcal{L}\mathcal{J})$ generated by the polynomial $\mathbb{P}$ for (ii). $\diamond$

Secondly, we generalize the previous class from linear to *nonlinear* dynamics, by making the positive coefficients of the polynomial $\mathbb{P}$ depend on the state $X(t)$ and using the new damping operator $\mathcal{R}\big(X(t)\big)$ instead of $\mathcal{R}$: indeed, passivity and properties (i-ii) still stem from the genuine structure (5).

Simulation for the homogeneous membrane

Three simulations of a membrane (see spectrograms of $\partial_t w$ in figure 1a-c) are performed for three damping polynomials $\mathbb{P}_{a,b,c}$ of the operator $(\mathcal{L}\mathcal{J})^*(\mathcal{L}\mathcal{J}) = \frac{T_0}{\rho_0}\,\text{diag}(-\vec{\text{grad}}\,\text{div}, -\Delta)$: $\mathbb{P}_a$ of degree 0 (fluid damping) with constant coefficient; (b) $\mathbb{P}_b$ of degree 1 (fluid and structural damping) with constant coefficients; (c) an interpolation $\mathbb{P}_c = f(e)\mathbb{P}_a + (1-f(e))\mathbb{P}_b$ for e.g. the interpolation function $f(e) = \tanh\sqrt{e/e_0}$ driven by the energy signal $e(t) = H(X(t))$. As a result the damping locally behaves like (a) for energies $e \gg e_0$, like (b) for $e \ll e_0$ (including the sound extinction), building a physically-morphed sound in-between that can be interpreted as complex or mutating materials.

Conclusion

The port-Hamiltonian setting proves useful to analyze morphing strategies applied to sound synthesis, since the geometry of the underlying physics can be fully preserved during the transformation involving nonlinear damping models, which are easily parameterized using polynomials.

References

[1] Caughey, T.K. and O'Kelly, M.E.J. (1965). Classical normal modes in damped linear dynamic systems. ASME, *J. Applied Mechanics*, 583-588.

[2] van der Schaft, A.J. and Maschke, B.M. (2002) Hamiltonian formulation of distributed-parameter systems with boundary energy flow. *Journal of Geometry and Physics*, **42-(1-2)**:166-194.

[3] Matignon, D. and Hélie, T. (2013). A class of damping models preserving eigenspaces for linear conservative port-Hamiltonian systems. *European Journal of Control*, **19-6**:486-494.

[4] Hélie, T. and Matignon, D. (2015). Nonlinear damping models for linear conservative mechanical systems with preserved eigenspaces: a port-Hamiltonian formulation. *IFAC-PapersOnLine*, **48-13**:200–205.

[1] we use $\vec{q}$ to mark the 2D vector on the configuration variable.

Normal form based nonlinear modes: identification, experimental continuation and internal resonances applied to the acoustics of chinese gongs

O. Thomas*, V. Denis†, M. Jossic♯, C. Giraud-Audine♭
*Arts et Métiers Institute of Technology, LISPEN, HESAM Université, Lille, France
†Laboratoire de Mécanique Gabriel Lamé, INSA Val-de-Loire, France,
♯Musée de la Musique, Paris, France,
♭Arts et Métiers Institute of Technology, L2EP, HESAM Université, Lille, France,

Summary. This article presents several topics related to the use of nonlinear modes and normal forms to analyse and model the vibratory response of geometrically nonlinear structures. It is first shown that the normal form theory provides a mathematically rigorous and clear framework to exhibit the mathematical form of very reduced order models. Then, this theory is applied to model the nonlinear vibrations of chinese opera gongs, that exhibits particular frequency glides in normal playing conditions, under an impulse forcing at center. It is shown that at low amplitude, a single Duffing like oscillator is sufficient to precisely explain this behaviour, due to the hardening/softening behaviour of the fundamental axisymmetric vibration mode. At larger amplitude, mode coupling are experimentally observed, well recovered by a reduced order model reduced to a few nonlinear modes involved in a 1:2:2 internal resonance.

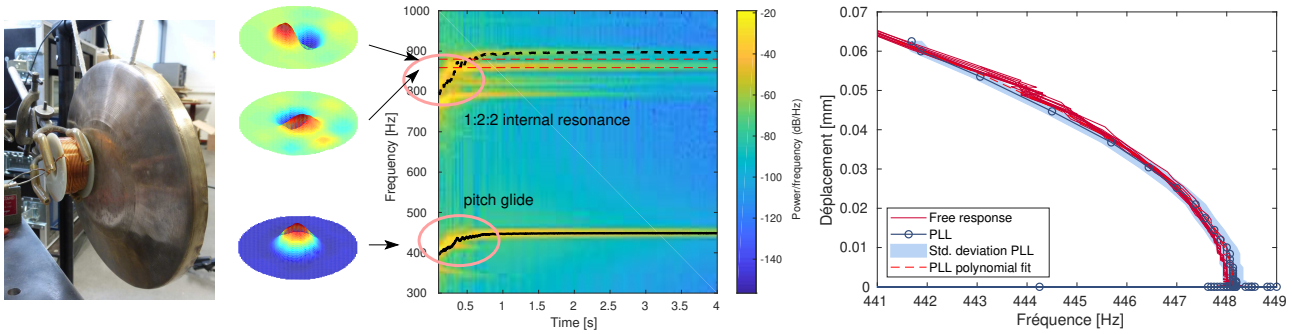

Figure 1: (left) Photograph of a chinese opera gong and the coil magnet driving system used for experimental identification; (middle) spectrogram of the acceleration signal after a mallet strike, measured by an accelerometer glued on the gong; (right) backbone curves of the fundamental nonlinear mode obtained from the free vibration regime after a mallet strike and from an experimental continuation with a phase locked loop.

Chinese opera gongs take the form of an axisymmetric thin shell, such the one shown in Fig. 1(left). When the gong is hit with a mallet at its center, a very characteristic pitch glide can be heared. This can be related to a change of the instantaneous frequency of vibrations, that can be seen on the vibration spectrogram of Fig. 1(middle) around the natural frequency of the fundamental axisymmetric mode. Then, the same spectrogram also shows that the second harmonics of the vibration signals mixes with a couple of higher modes with companion asymmetric mode shapes. In this article, we show that those two features (the pitch glide and the mode interaction) can be quantitatively recovered by reduced order models, that take the form of a few coupled nonlinear oscillators, justified by the normal form theory applied to a generic nonlinear modal model of the system.

Nonlinear modes and normal form

We consider an elastic structure whose displacement $w(\boldsymbol{x},t)$ at time t and position $\boldsymbol{x}$ is expanded on a family of N eigenmodes of the linearized and undamped model:

$$w(\boldsymbol{x},t)=\sum_{k=1}^{N}\Phi_k(\boldsymbol{x})q_k(t), \tag{1}$$

where $(\omega_k,\Phi_k(\boldsymbol{x}))$ are the k-th natural angular frequency and mode shape. In free undamped vibrations, the modal coordinates $q_k(t)$ satisfy the following set of coupled nonlinear equations, for all $k=1,\dots N$:

$$\ddot{q}_k+\omega_k^2q_k+\sum_{i,j=1}^{N}\beta_{ij}^kq_iq_j+\sum_{i,j,l=1}^{N}\gamma_{ijl}^kq_iq_jq_k=0, \tag{2}$$

where β_{ij}^k and γ_{ijl}^k are nonlinear coefficients stemming from the geometrical nonlinearities. Using normal forms, as introduced in [9], a nonlinear polynomial change of coordinate is introduced, leading to replace model (2) by a new one, function of the new (normal) coordinates $u_k(t)$. This new dynamical system has an important property: it involves only resonant nonlinear terms. This property enables a rigorous and straightforward truncation strategy, divided in two cases.

If there are no internal resonance relation between the oscillations frequencies, the resonant terms are only of cubic order and they do not break the invariance of the oscillators. Consequently, a motion on a single oscillator (the i-th.) is possible and takes the form:

$$u_k = 0 \ \ \forall k \neq i, \quad \ddot{u}_i + \omega_i^2 u_i + \Gamma_1 u_i^3 + \Gamma_2 u_i \dot{u}_i^2 = 0, \tag{3}$$

where (Γ_1, Γ_2) are two coefficients depending on the nonlinear coefficients β_{ij}^k and γ_{ijl}^k, that take into account the influence of all linear modes. This particular motion, linked to its invariance property, defines a nonlinear mode, whose dynamics is governed by the single oscillator (3). The values of Γ_1 and Γ_2 defines the hardening or softening feature of the nonlinear mode [9, 8].

If there is an internal resonance between some modes, the corresponding oscillators have to be kept in the dynamics and are coupled by particular nonlinear terms. There form can be easily deduced from the internal resonance relation. For instance, in the case of a 1:2 internal resonance between modes 1 and 2, there natural frequencies verify the relation $\omega_2 \simeq 2\omega_1$ and the normal form reduced order model is:

$$u_k = 0, \ \ \forall k \neq 1, 2, \quad \left\{ \begin{array}{l} \ddot{u_1} + \omega_1^2 u_1 + \alpha_1 u_1 u_2 = 0, \\ \ddot{u_2} + \omega_2^2 u_2 + \alpha_2 u_1^2 = 0, \end{array} \right. \tag{4}$$

where (α_1, α_2) are the coefficients of the two quadratic resonant terms [6].

If the damping is small, it's influence on the invariant manifolds geometry can be neglected and a modal viscous damping terms of the form $2\xi_k \omega_k \dot{u}_k$, with $\xi_k \ll 1$, can be added in the above models with no loss of accuracy.

Identification

If an accurate model is at hand, the values of the coefficients of the normal forms (3), (4) can be obtained from the ones of the modal model (2) using the formula of [9] or directly from a finite-element model [5]. Another strategy is to rely on experiments to identify those coefficients. At low amplitude and without internal resonance, we can show that the influence of coefficients (Γ_1, Γ_2) on the dynamics can be embedded into a single cubic coefficient, whose sign governs the hardening / softening behaviour of the nonlinear mode. As shown in [1, 3], this coefficient can be efficiently estimated with an experimental backbone curve, that can be measured by experimental continuation based on a Phase-Locked Loop (PLL). As a consequence, it is here proven that an accurate reduced order model for this low amplitude single nonlinear mode motion is a classical Duffing oscillator. This identification procedure can be extended to measure more complex dynamics, such those involving 1:1 internal resonance [2]. In the case of the internal resonance of Eq. (4), coefficients (α_1, α_2) can be estimated by experimental forced responses, as explained in [7, 4].

Acoustics of a chinese gong

The above method can be applied to chinese opera gongs, in order to investigate and explain their particular sound. Considering first their pitch glide, it is possible to extract from a free response in normal playing conditions the relation between the instantaneous frequency of oscillations as a function of the amplitude. It can be shown that it matches exactly the experimental backbone curve (Fig. 1(right)), leading to the conclusion that the characteristic pitch glide of the Chinese opera gongs is an acoustic manifestation of the hardening / softening behaviour of their fundamental nonlinear mode, whose frequency changes as a function of the amplitude because of the geometrical nonlinearities. Then, using a model of the form (4) with an additional cubic term, the 1:2:2 internal resonance of Fig. 1(middle) can also be recovered by proper estimation of coefficients (α_1, α_2).

References

[1] V. Denis, M. Jossic, C. Giraud-Audine, B. Chomette, A. Renault, and O. Thomas. Identification of nonlinear modes using phase-locked-loop experimental continuation and normal form. *Mechanical Systems and Signal Processing*, 106:430–452, 2018.

[2] A. Givois, J.-J. Tan, C. Touzé, and O. Thomas. Backbone curves of coupled cubic oscillators in one-to-one internal resonance: bifurcation scenario, measurements and parameter identification. *Meccanica*, 55:581–503, 2020.

[3] M. Jossic, B. Chomette, V. Denis, O. Thomas, A. Mamou-Mani, and D. Roze. Effects of internal resonances in the pitch glide of chinese gongs. *The Journal of the Acoustical Society of America*, 144(1):431–442, 2018.

[4] M. Monteil, O. Thomas, and C. Touzé. Identification of mode couplings in nonlinear vibrations of the steelpan. *Applied Acoustics*, 89:1–15, 2015.

[5] Y. Shen, N. Kesmia, C. Touzé, A. Vizzaccaro, L. Salles, and O. Thomas. Predicting the type of nonlinearity of shallow spherical shells: comparison of direct normal form with modal derivatives. In *Proceedings of NODYCON 2021*, Roma, Italy, February 2021.

[6] O. Thomas, C. Touzé, and A. Chaigne. Non-linear vibrations of free-edge thin spherical shells: modal interaction rules and 1:1:2 internal resonance. *International Journal of Solids and Structures*, 42(11-12):3339–3373, 2005.

[7] O. Thomas, C. Touzé, and É. Luminais. Non-linear vibrations of free-edge thin spherical shells: experiments on a 1:1:2 internal resonance. *Nonlinear Dynamics*, 49(1-2):259–284, 2007.

[8] C. Touzé and O. Thomas. Non-linear behaviour of free-edge shallow spherical shells: effect of the geometry. *International Journal of non-linear Mechanics*, 41(5):678–692, 2006.

[9] C. Touzé, O. Thomas, and A. Chaigne. Hardening/softening behaviour in non-linear oscillations of structural systems using non-linear normal modes. *Journal of Sound Vibration*, 273(1-2):77–101, 2004.

Numerical continuation of periodic solutions with constraints: application to a physical model of wind musical instrument

Vincent Fréour*, Louis Guillot†, Hideyuki Masuda*, Christophe Vergez† and Bruno Cochelin†
*YAMAHA R&D division, 10-1 Nakazawa-cho, Naka-ku, 450-8650 Hamamatsu, Japan
†Aix Marseille Univ., CNRS, Centrale Marseille, LMA UMR7031, 4 impasse Nikola Tesla, 13013 Marseille, France

Summary. Numerical continuation using the Asymptotic Numerical Method (ANM), together with he Harmonic Balance Method (HBM), allows to follow the periodic solutions of non-linear dynamical systems such as physical models of wind instruments. This has been successfully applied to practical problems such as the categorization of musical instruments from the calculated bifurcation diagrams [2]. Nevertheless, one problem often encountered concerns the uncertainty on some parameters of the model, the values of which are set arbitrarily because too difficult to measure experimentally. In this work we propose a novel approach where constraints based on experimental measurements are added to the system, as well as the uncertain parameters of the model relaxed. This approach allows the continuation of the periodic solution with constraints to be performed, together with the calculation of the variation of the relaxed parameters along the solution branch. A successful application of this technique to a physical model of a trumpet is presented in this paper.

Physical model of the {player-trumpet} system and continuation

We consider a one-dimensional lip model, coupled to the resonator impedance described by a series of complex modes similar to what is proposed in [2]. The coupling between the mechanical oscillator and the acoustic resonator is achieved by a stationary Bernoulli flow equation, considering turbulent mixing in the mouthpiece with no pressure recovery. The mechanical and acoustic equations are given in system 1, where y is the vertical lip position (y_0 is the lip position at rest), ω_l, Q_l, μ_l and b the lip mechanical parameters, s_k and C_k with $k \in [1, N]$ the modal parameters of the N resonances of the acoustic impedance of the instrument, Z_c the characteristic impedance, u the volume flow, p the downstream pressure at the input of the instrument (in the mouthpiece), and p_0 the upstream (mouth) static pressure.

$$\begin{cases} \ddot{y}(t) + \frac{\omega_l}{Q_l}\dot{y}(t) + {\omega_l}^2(y(t) - y_0) = \frac{1}{\mu_l}(p_0 - p(t)) \\ \dot{p}_k(t) = Z_c C_k u(t) + s_k p_k(t), \forall k \in [1, N] \end{cases} \tag{1}$$

with $p(t) = 2\sum_{k=1}^{N} \Re(p_k(t))$ and $u = \sqrt{\frac{2|p_0 - p|}{\rho}} b \cdot sign(p_0 - p) \cdot \theta(y)$, where $\theta(y) = \frac{|y|+y}{2}$, b is the lip width and ρ is the air density.

The case of a negative opening of the lips is managed by introducing the function $\theta(y)$ which enforces $u = 0$ if $y < 0$. The modal parameters of the N modes of the impedance are extracted from the measured input impedance using the high resolution method ESPRIT [3]. In this model, the values of the lip parameters are critical but particularly difficult to set, as it is extremely difficult to evaluate them experimentally.
We choose to work with the Asymptotic Numerical Method (ANM) implemented in the software MANLAB [4]. This method is based on the expansion of the solutions under the form of truncated Taylor series, providing analytical formulations of the branch of solution. Recently, this method has been associated to the Harmonic Balance Method (HBM) for the search of periodic solutions of oscillating systems [5].
One requirement of MANLAB relies on the recast of nonlinearities of the model into, at most, quadratic nonlinearities. The complete quadratic dimensionless model can be found in [2].

Continuation with constraints

Two constraints are introduced as follows:

$$\|\tilde{p}\|_{L2} = S\gamma + I, \tag{2}$$

where $\gamma = p_0/P_M$ is the dimensionless mouth pressure with $P_M = \mu_l {\omega_l}^2 y_0$, S and I are constant values, and $\|\tilde{p}\|_{L2} = 2\left\|\sum_{k=1}^{N} \Re(\tilde{p}_k)\right\|_{L2}$.
The second constraint simply writes as follows:

$$f_0 = F, \tag{3}$$

where F is a constant value.
Adding two equations to the system requires two parameters of the model to be relaxed, that is two unknowns to be introduced. We choose to relax Q_L and $\zeta = Z_c b y_0 \sqrt{\frac{2}{\rho P_M}}$ (ζ can be seen as an "embouchure" parameter). This requires to recast the system of equations in order to preserve the quadratic property of the model.

Results and conclusions

Figure 1 shows the result of continuation with constraints applied to the physical model described in previous section. In the bottom plot, the evolution of $\|\tilde{p}\|_{L2}$ with respect to γ measured on a trumpet player during a slow crescendo-decrescendo maneuver is represented in red. A linear fit of the red curve is applied, which gives S and I (Eq. 2) and defines the constraint on $\|\tilde{p}\|_{L2}$. The constraint on f_0 is such as it remains constant and equal to the value at the initial calculation point (about the playing frequency of a Bb4).

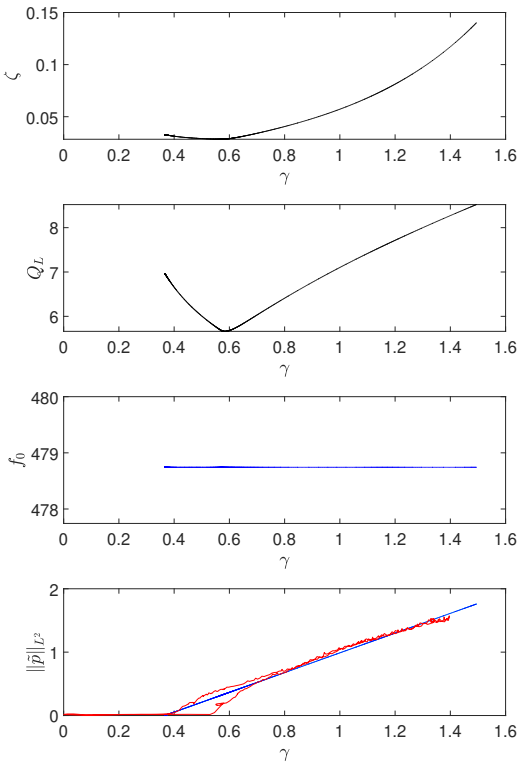

Figure 1: Results from continuation with constraints. Evolution of ζ, Q_L, f_0 and $\|\tilde{p}\|_{L2}$ with respect to the dimensionless mouth pressure γ. In red is the evolution of $\|\tilde{p}\|_{L2}$ with respect of γ measured on trumpet player during a slow crescendo-decrescendo maneuver.

It can be seen that the two constraints are well respected: f_0 is constant with respect to γ, and $\|\tilde{p}\|_{L2}$ evolves linearly with respect to γ (the solution branches, in blue, are superimposed with the target constraint on Fig. 1 bottom plots). The stability of the branch was computed and the branch was found stable across the whole range of γ. The variations of ζ and Q_L are represented on the two top plots. Significant variations of these two variables are observed, showing the importance of adapting these parameters in order to match the constraints.
These results highlight the ability of the ANM to calculate the evolution of some parameters of the model while applying some mathematical constraints to the output of the continuation calculation. By defining these constraints from experimental data, this approach can be seen as an inversion method, allowing to retrieve the parameter values of the model necessary to achieve a given performance (playing a crescendo-decrescendo at completely constant playing frequency).
This method then shows great perspectives for the parametrisation of physical models of brass instruments, as well as for objective comparison of brass instruments.

References

[1] Velut, L. (2016) Contrôle par le musicien des régimes d'oscillation des instruments de la famille des cuivres. PhD thesis, Université de Provence Aix-MarseilleI I, Marseille, France.

[2] Fréour, V, Guillot, L., Masuda, H., Usa, S., Tominaga, E., Tohgi, Y., Vergez, C., and Cochelin, B. (2020) Numerical continuation of a physical model of brass instruments: Application to trumpet comparisons. *J. Acoust. SOc. Am.*, **148 (2)**:748-758.

[3] Roy, R., and Kailath, T., (1989) Esprit: Estimation of signal parameters via rotational invariance techniques. *IEE Trans. Acoust. Speech, Signal Process.*, **37 (7)**:984-995.

[4] MANLAB web site, http://manlab.lma.cnrs-mrs.fr/

[5] Cochelin, B., and Vergez, V., (2009) A high order purely frequency-based harmonic balance formulation for continuation of periodic solutions *Journal of Sound and Vibration.*, **324**:243-262.

Tuesday, July 19, 2022
13:30 - 15:30

MS-13 Nonlinear Dynamics in Biological Systems
Saint Clair 3A

Chair: Gert Van Der Heijden

13:30 - 13:50
Musical tonality and nonlinear dynamics
BUKS Eyal*
*Technion (Haifa, Israel Israel)

13:50 - 14:10
Theoretical considerations of the mechanics of whisker sensors
STAROSTIN Eugene*, VAN Der Heijden Gert, GOSS Victor
*London South Bank University (103 Borough Road,London SE1 0AA United Kingdom)

14:10 - 14:30
Influence of mass on horizontal forced oscillations in oscillatory model of a young tree with branches
JOVANOVIC George*, HEDRIH Andjelka
*Mathematical Institute of Serbian Academy of Sciences and Arts (Kneza Mihaila 36, 11 000 Belgrade Serbia)

14:30 - 14:50
Influence of vaccination and social distancing on epidemic prevention
BATISTELA Cristiane*
*Escola Politecnica da Universidade de Sao Paulo [Sao Paulo] (Av. Prof. Luciano Gualberto, 380 - Butantã, São Paulo - SP, 05508-010 Brazil)

14:50 - 15:10
Dynamics of a Self-Propelled Soft Capsule Moving in the Small Intestine
TIAN Jiyuan, WANG Zepeng, **LIU Yang***, PRASAD Shyam
*University of Exeter (North Park Road, Exeter United Kingdom)

Musical tonality and nonlinear dynamics

Eyal Buks*
*Andrew and Erna Viterbi Department of Electrical Engineering, Technion, Haifa 32000 Israel

Summary. The current study is motivated by some observations of highly nonlinear dynamical effects in biological auditory systems. We examine the hypothesis that one of the underlying mechanisms responsible for the observed nonlinearity is self-excited oscillation (SEO). According to this hypothesis the detection and processing of input audio signals by biological auditory systems is performed by coupling the input signal with an internal element undergoing SEO. Under appropriate conditions such coupling may result in synchronization between the input signal and the SEO. In this talk I will present some supporting evidence for this hypothesis by showing that some well-known phenomena in musical tonality can be explained by the Hopf model of SEO and the Arnold model of synchronization. Moreover, some mathematical properties of these models are employed as guidelines for the construction of some modulations that can be applied to a given musical composition. The construction of some intriguing patterns of musical harmony is demonstrated by applying these modulations to known musical pieces [1].

References

[1] https://buks.net.technion.ac.il/MuH/

Theoretical considerations of the mechanics of whisker sensors

Eugene L. Starostin*†, Gert H. M. van der Heijden† and Victor G. A. Goss*
*School of Engineering, London South Bank University, 103 Borough Rd, London SE1 0AA, UK
†Department of Civil, Environmental and Geomatic Engineering, University College London, Gower St, London WC1E 6BT, UK

Summary. Employing elastic rod theory we study the question which forces and moments measured at the base of a mammal's whisker (tactile sensor) allow for the prediction of the location in 3D space of the point at which the whisker makes contact with an object. We show that, in the case of non-tip contact, the minimum number of independent forces or moments is three but that conserved quantities of the rod equilibrium equations prevent certain triples from giving a unique solution. The existence of these conserved quantities depends on the shape and material properties of the whisker. For tapered or intrinsically curved whiskers there is no obstruction to the prediction of the contact point. Our results explain recent numerical observations in the literature and offer guidance for the design of robotic tactile sensory devices.

Introduction

Mammal whiskers (vibrissae) allow terrestrial animals to obtain information about geometrical and mechanical properties of the environment [1]. Animal whiskers are thin flexible rods grown out of follicles and consist of dead cells; there are no sensors along the length of a whisker. Sensing therefore relies on the detection by mechanoreceptors at the whisker base of forces and moments induced by contact with an external object and transmitted through the elastic medium. Knowledge of how whiskers perform their sensory functions is of interest to engineers designing artificial tactile sensors [2]. To use such artificial whiskers in robotics, it is essential to be able to determine the location, with respect to a reference frame, of the point along the whisker shaft at which contact with an object occurs.

If three forces and three moments (in three independent spatial directions) are measured at the (fixed) whisker base, then a suitable mechanical model of the whisker (e.g., a 1D continuum elastic rod or beam model [3]) allows the entire configuration of the whisker, and hence the contact point, to be determined. These six measurements, however, require an expensive six-axis load cell. It is natural, therefore, to ask whether fewer measurements would suffice to uniquely predict the location of the contact point.

Past studies of this contact problem have mainly focussed on the planar case, where the contact point is specified by two coordinates [4]. Whisker configurations, especially those with intrinsic curvature, may generally be non-planar. The whisker contact problem was numerically studied in 3D in [5]. All 20 possible combinations of triples of base forces and moments were analysed, however no theoretical explanation of the results was given.. Here we show that the difference in the predictive ability of triples of forces and moments is mainly caused by the existence of conserved quantities, which arise for whiskers with certain geometrical profiles (curvature, taper, etc.).

Boundary conditions and conserved quantities

The solution of an nth-order ODE, $du/ds = f(u)$, $u \in \mathbb{R}^n$, $s \in [a, b]$, involves n integration constants. In physical problems a unique solution is then usually obtained by imposing n boundary conditions at $s = a$ and/or $s = b$ to fix those integration constants. For a linear ODE it is a rigorous result that a unique solution is obtained if the n boundary conditions are linearly independent. For a nonlinear ODE (or nonlinear boundary conditions) the result is only true locally (i.e., near a given solution) and only 'generically', i.e., away from branching points (bifurcations) for special values of any parameters in the equations or values imposed at the boundary. (In the special case that all boundary conditions are specified at one end, i.e., for an initial-value problem, a unique solution is guaranteed also for a nonlinear ODE.)

A conserved quantity (first integral) of the ODE is a function of the dependent variables u_i ($i = 1, ..., n$) whose value is constant along solutions of the equation. The presence of such quantities may put constraints on the specification of boundary conditions [6]. For instance, in the simple case that one of the variables itself, say u_k, is a conserved quantity and we choose the boundary condition $u_k(a) = c$, then $u_k(b) = d$ is not a proper boundary condition at the other end: if c and d were unequal there would obviously be no solution, while if c and d were equal there might be infinitely many solutions (depending on the other boundary conditions). In either case the BVP is said to be ill-posed. Another, independent, boundary condition needs to be imposed instead to obtain a locally unique solution (i.e., a solution with no infinitesimally close solutions). It is not always a priori clear that a given ODE has one or several conserved quantities and well-posedness of a nonlinear BVP is generally not straightforward.

Conserved quantities can be viewed as continuous symmetry properties of the ODE. A more obvious example of continuous symmetry is rotational symmetry of the equations, in which case for a well-posed BVP one has to impose boundary conditions that break the symmetry, thereby picking out one of the continuous family of solutions. Besides continuous symmetry a BVP may also have discrete symmetry, for instance, reflection symmetry, in which case the BVP has multiple *isolated* solutions. Each of these will generally be locally unique and the BVP is considered well-posed, with the solution being *globally* non-unique. 'Modes' (i.e., eigenfunctions) in eigenvalue problems, which also occur as isolated solutions, are other examples of globally non-unique solutions. Conserved quantities do not necessarily distinguish between such solutions.

Equilibrium equations for an elastic whisker

We model the whisker-object contact problem by formulating a two-point boundary-value problem using Kirchhoff rod theory [3]. Let $Oxyz$ be an orthogonal laboratory frame fixed at the base of the whisker (Fig. 1). The whisker is taken to be inextensible and unshearable and to have length L. Its centreline is denoted by $\mathbf{r}(s) = (x(s), y(s), z(s))$, where $s \in [0, L]$ is arclength along the whisker, $s = 0$ corresponding to the base O and $s = L$ corresponding to the tip. Under the above assumptions we can introduce an orthonormal material frame $\{\mathbf{d}_1, \mathbf{d}_2, \mathbf{d}_3\}$ with $\mathbf{d}_1$ tangent to the centreline $\mathbf{r}$, i.e., $\mathbf{r}' = \mathbf{d}_1$, and $\mathbf{d}_2$ and $\mathbf{d}_3$ directed along principal axes of the whisker's cross-section (here and in the following a prime denotes differentiation with respect to s). By orthonormality of the material frame there exists a vector $\boldsymbol{\Omega}$ such that $\mathbf{d}_i' = \boldsymbol{\Omega} \times \mathbf{d}_i \qquad (i = 1, 2, 3)$. The components of this vector in the material frame, $(\omega_1, \omega_2, \omega_3) =: \boldsymbol{\omega}$, $\omega_i = \boldsymbol{\Omega} \cdot \mathbf{d}_i$, are the strains of the theory, i.e., the curvatures ω_2 and ω_3, about $\mathbf{d}_2$ and $\mathbf{d}_3$, and the twist ω_1, about $\mathbf{d}_1$ [3].

The force and moment balance equations for the whisker are

$$\mathbf{F}' + \boldsymbol{\omega} \times \mathbf{F} = \mathbf{0}, \quad \mathbf{M}' + \boldsymbol{\omega} \times \mathbf{M} + \mathbf{i} \times \mathbf{F} = \mathbf{0}, \tag{1}$$

where $\mathbf{F} = (F_1, F_2, F_3)$ and $\mathbf{M} = (M_1, M_2, M_3)$ are triples of force and moment components in the material frame and $\mathbf{i} = (1, 0, 0)$. We assume the linear constitutive relations: $M_1 = C(s)\omega_1, \quad M_2 = B(s)\omega_2, \quad M_3 = B(s)(\omega_3 - \omega_{30}(s))$. Here, $B(s)$ and $C(s)$ are the bending and torsional stiffnesses, resp. They are not constant in the particular case of a tapered rod. The undeformed shape of the whisker is assumed planar but may be curved with intrinsic curvature $\omega_{30}(s)$.

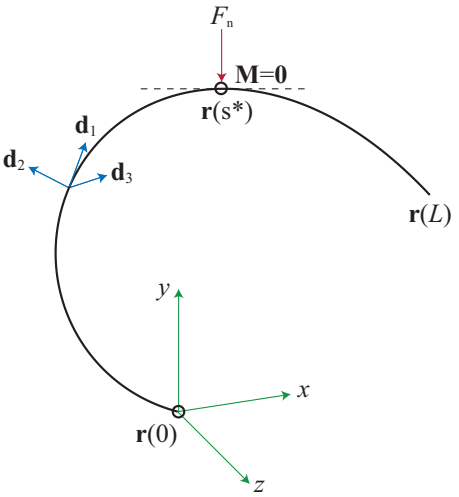

Figure 1: Coordinate systems for a whisker in point contact with an object at $s = s^*$. For frictionless contact the contact force F_n is normal to the whisker.

Eqs. (1) imply, respectively, that $\mathbf{F} \cdot \mathbf{F}$ and $\mathbf{F} \cdot \mathbf{M}$ are constant. If $\omega_{30} \equiv 0$, then $M_1 = \text{const}$. The Hamiltonian $H = M_1^2/(2C) + (M_2^2 + M_3^2)/(2B) + M_3\omega_{30} + F_1$ is conserved provided B, C and ω_{30} are constant, i.e. the rod is translationally symmetric in the arclength s [6].

Table 1: Triples $\mathbf{P}$ of measurements that give rise to an **ill-posed** BVP with non-isolated solutions, for various intrinsic shapes of the rod (* stands for any of the other quantities).

rod	cylindrical	tapered
straight ($\omega_{30} = 0$)	$(M_1, *, *)$ $(\alpha, \beta, *)$	
	(F_1, M_2, M_3) $(F_1, M_n, *)$	
curved ($\omega_{30} \neq 0$)	-	-

We assume the whisker to be fixed in both position and orientation at the base ($s = 0$). At the contact point ($s = s^\star \leq L$) a normal contact force will act from the surface of the object onto the whisker for a frictionless single-point contact. We therefore consider the following boundary conditions: $\mathbf{r}(0) = \mathbf{0}, \mathbf{d}_i(0) = \mathbf{d}_{i,0}, \mathbf{P}(0) = \mathbf{P}_0, F_1(s^\star) = 0, \mathbf{M}(s^\star) = \mathbf{0}$, where $\mathbf{P} = (P_1, P_2, P_3)$ is the vector of base measurements consisting of three components chosen from the six force and moment components. We also introduce polar representations of the force and moment in the whisker [5]. Thus we write $F_2 = F_n \cos\alpha$, $F_3 = F_n \sin\alpha$, $M_2 = M_n \cos\beta$, $M_3 = M_n \sin\beta$. Here $F_n = \sqrt{F_2^2 + F_3^2}$ and $M_n = \sqrt{M_2^2 + M_3^2}$ are the magnitudes of the normal force and moment components, while α and β are the angles these components make with the material axes.

We note that three base measurements are sufficient for the well-posedness of the tactile sensing BVP. We analyse how this well-posedness depends on the precise choice of measured components P_i.

Summary of results

The results of our analysis are summarised in Table 1, where those combinations of force/moment measurements are listed that are **not appropriate** in the design of an effective set of sensors at the base of a robotic whisker. A tapered whisker may here be interpreted as any whisker whose B or C is not constant.

References

[1] Evans M. H., Loft M. S. E., Campagner D. and Petersen R. S. (2019) Sensing the Environment with Whiskers. Oxford Research Encyclopedia, Neuroscience (oxfordre.com/neuroscience), subject: Sensory Systems.

[2] Pipe T. and Pearson M. J. (2016) Whiskered Robots. Scholarpedia of Touch, Scholarpedia.

[3] Love A. E. H. (1927) A Treatise on the Mathematical Theory of Elasticity. Cambridge University Press.

[4] Solomon J. H. and Hartmann M. J. Z. (2011) Radial distance determination in the rat vibrissal system and the effects of Weber's law. *Philosophical Transactions of the Royal Society B: Biological Sciences*, **366**(1581):3049–3057.

[5] Huet L. A., Rudnicki J. W. and Hartmann M. J. Z. (2017) Tactile sensing with whiskers of various shapes: Determining the three-dimensional location of object contact based on mechanical signals at the whisker base. *Soft Robotics*, **4**(2):88–102.

[6] Dichmann D. J., Li, Y. and Maddocks, J. H. (1996) In: Mathematical Approaches to Biomolecular Structure and Dynamics, volume 82 of IMA Volumes in Mathematics and its Applications, chapter Hamiltonian formulations and symmetries in rod mechanics, pages 71 – 113. The Institute for Mathematics and Its Applications.

Influence of mass on horizontal forced oscillations in oscillatory model of a young tree with branches

Andjelka N. Hedrih [*], Djordje Jovanovic [*]

[*] *Mathematical Institute of Serbian Academy of Sciences and Arts (MI SANU) Belgrade, Serbia*

Summary. In this paper we analysed the influence of mass on amplitudes of horizontal forced oscillations in previously developed model of complex oscillatory system that resembles corymb type of inflorescence. For describing oscillatory behavior of this system under external force influence deflection coefficients were used. The analysis was done for the case of single frequency external excitation for two different values of circular frequencies. For the value 10/s for the external force circular frequency we obtained nonlinear correlation between amplitudes and masses.

Introduction

Plants and trees oscillate under the influence of wind. This is particularly important for young seedlings that can be damaged before the plant is fully rooted in the ground. Oscillations of tree stem of living trees can be studied through different approaches [1, 2], where it is possible to measure the natural frequencies of trees [3]. Type and structure of wood structure (material properties of the system that could be considered as complex oscillatory system) and characteristics of wind (an external force) may contribute to the damage of a tree and cause it to crack or fall. Mechanical stability of trees is thus a very important problem [4]. Young tree seedlings are of particular interest in urban area exposed to the wind. Recently we developed the model of a complex oscillatory systems that was inspired by corymb type of inflorescence [5]. We use this model (Fig1) to study the influence of mass of tree branches on amplitudes of horizontal forced oscillations at the certain points of the tree stem.

Description of the model

The system could be assumed as ideally elastic system consisting of material particles on rigid massless rods with length ℓ_i with the angle β_i to light elastic console with length ℓ. Length of the console corresponds to the tree stem, and length of the massless rods to the tree branches. Material particles at the end of the massless rods correspond to the mass of the branch. The approximations of this system are: connections between rigid massless rods and elastic console are rigid, oscillations of console and system are small, tilts of tangent to elastic axis of banded console are very small and negligible, tilts of console cross-section during console banding according to x and y axis of cross section are very small and negligible. Masses of material particles are equal. System oscillates in horizontal and vertical plane. Bending stiffness of the elastic console is equal in horizontal and vertical plane. For describing oscillatory behavior of this system influence coefficients of deflection were used. Displacement influence coefficients were determined on the basis of equations of elastic line of console load with unit force and unit momentum. Forced oscillations of the system can be described by two independent subsystems of ordinary differential equations in vertical and horizontal plane. Each subsystem of ordinary differential equations consists of four coupled ordinary differential equations of second order in the following form:

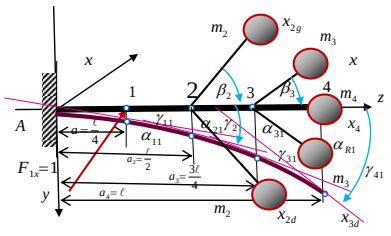

Figure 1. Complex oscillatory systems that can be used for studding oscillations of tree with branches. (Taken from ref [1].

Table 1. Resonant values of oscillations of the console for different masses of single material points (branches)

Resonant values Ωy(1/s)	1kg	1.3kg	1.6kg	1.9kg	2.2kg	2.5kg	2.8kg
R1	5.924	5.196	4.724	4.325	4.028	3.771	3.556
R2	3.435	3.013	2.681	2.427	2.301	2.158	1.559
R3	8.074	7.049	6.383	5.837	5.425	5.113	4.837

For oscillations in horizontal plane:

$$x_i = \alpha_{i1}F_{01x}\sin\Omega_x t + \alpha_{i2}\left(-2m_2\ddot{x}_2\right)+\alpha_{i3}\left(-2m_3\ddot{x}_3\right)+\alpha_{i4}\left(-m_4\ddot{x}_4\right)+ \\ +\delta_{i2}\left(-2m_2\ddot{x}_2\ell_2\sin\beta_2\right)+\delta_{i3}\left(-2m_3\ddot{x}_3\ell_3\sin\beta_3\right) \qquad i=1\ldots4 \qquad (1)$$

Where α_{ik} and δ_{ik} are influence coefficients of deflection on cross section "i" under unit force $F_{k=1}$ and under unit

momentum. $M_{k=1}$ respectively, on section 'k'. For calculating the influence coefficients of deflection the bending stiffness of the elastic console is needed and is equal to: $B_x = B_y = EI_x = EI_y = E\frac{r^4\pi}{4}$ where $I_x = I_y = \frac{r^4\pi}{4}$ is the axial moment of inertia of the surface of the cross-sectional area for the corresponding central axis passing through the center of the circle. E is Young's module of elasticity, r is half a diameter of the console.

We analyze influence of mass of tree branches on amplitudes of horizontal forced oscillations at the certain points of the tree stem. Numerical analysis was done for the following data: E=10,7x10^{9}Pa, r=0,015m, $\ell_2 = \ell_3 = 0.55m$, $\ell = 1.5m$, $\beta_2 = \pi/4$ $\beta_3 = \pi/6$; $\Omega_y = 5/s$ and for $\Omega_y = 10/s$, for different masses (from 1-3kg with step 0.3).

Results

Dependences of amplitudes of masses of material particles on their ends (branches) for two values of circular frequency of external force are shown on Fig.2. Graphs were obtained by calculating all the values numerically using Python programming language. Library numpy was used for determinant calculation, while matplotlib was used for graph plotting. In the Table 1. tree resonant values are shown for each mass value for which characteristic local minimum and maximum of amplitudes in certain point of the complex oscillatory model are obtained when circular frequency of the external force is $\Omega_y = 10/s$.

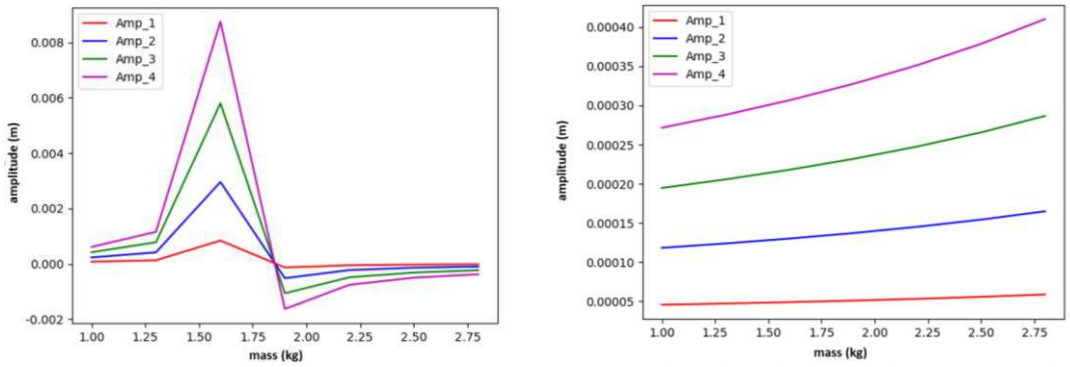

A B

Figure 2. A. Amplitudes of oscillations of four different points for different masses of material particles for $\Omega_y = 10/s$. B. Amplitudes of oscillations of four different points for different masses of material particles for $\Omega_y = 5/s$.

Conclusions

We analysed influence of mass on amplitudes of horizontal oscillations of a complex oscillatory model of young three with branches under external force with circular frequency of $\Omega_y = 5/s$ and $\Omega_y = 10/s$. When circular frequency of the external force is 5/s, which is around resonant frequencies for most of the selected masses we obtained constantly increasing amplitudes of forced horizontal oscillations of our complex oscillator. For the case when circular frequency of the external force is 10/s, amplitudes of forced horizontal oscillations of our complex oscillator have nonlinear character showing local maximum and minimums. Maximum amplitude for the chosen data systems is for mass 1.6 kg per branch. Absolute minimum of the amplitude is for mass 2.8 kg per branch. Specific combination of the parameters of the system and circular frequency of the external force determine the maximum amplitude of forced oscillations and it has a nonlinear character.

Acknowledgements: Parts of this research is supported by the Ministry of Sciences and Technology of Republic of Serbia through Mathematical Institute SASA, Belgrade Grant ON174001 "Dynamics of hybrid systems with complex structures, Mechanics of materials."Authors would like to thank to prof. Katica (Stevanovic) Hedrih for useful consultations and suggestions.

References

[1] Kovacic I, Dragi Radomirovic, Zukovic M, Benka P, Nikolic M. (2018) Characterisation of tree vibrations based on the model of orthogonal oscillations. ScieNtiFic REPORTs 8:8558.

[2] Brüchert F, Speck O, and Spat H-H. (2003) Oscillations of plants' stems and their damping: theory and experimentation. Phil. Trans. R. Soc. Lond. B 358, 1487–1492.

[3] Baker C.J. (1997). Measurements of the natural frequencies of trees. J. Exp. Bot, 48, 310:1125-1132.

[4] James K.R., Haritos N., and Ades P. K. (2006). Mechanical stability of trees under dynamic loads. Am. J. Botany 93(10): 1522–1530.

[5] Hedrih A, Atanasovska I and Jovanovic Dj. (2019). Inflorescence inspired complex oscillatory systems. In Booklet of Abstracts of Symposium "Nonlinear Dynamics –Scientific work of Prof. Dr Katica (Stevanović) Hedrih", Mathematical Institute of the Serbian Academy of Sciences and Arts, Belgrade, 04.-06. September 2019, Editors: Ivana Atanasovska, Anđelka Hedrih, Milan Cajić, Mathematical Institute of the Serbian Academy of Sciences and Arts, Belgrade (Sven, Niš), pp. 117-118.

Influence of vaccination and social distancing on epidemic prevention

Cristiane M. Batistela*, Marien M. Ramos†, Manuel A. M. Cabrera† and José R. C. Piqueira ‡
*Automation and Control Laboratory, São Paulo University, Control Engineering Departament, São Paulo, Brazil.
†Automation and Control Laboratory, São Paulo University, Control Engineering Departament, São Paulo, Brazil.
‡Automation and Control Laboratory, São Paulo University, Control Engineering Departament, São Paulo, Brazil.

Summary. To analyse the effect of vaccination strategies and the reinfection or temporary acquired immunity of individuals in a population with virus presence as well the social distancing, a variation of the SIR (Susceptible-Infected-Removable) model is proposed. The calculation of the equilibrium points for the stability analysis of the system is performed. Two equilibrium points were found, one disease-free and the other endemic, for which the existence conditions are discussed. The stability of the points was analysed and the results were verified through simulations varying the parameters of vaccination, reinfection and social distancing.

Introduction

Due to technological advances, which used to take time to get from one place to another, today it travels in a matter of hours, facilitating the risk of the appearance of a new virus quickly turning into a pandemic. The interest in studying the modeling of infectious diseases lies in understanding the mechanisms of transmission and thus being able to establish prevention policies. Mathematical modelling is useful to show the dynamics of disease spread and indicate which parameters are relevant to guide control strategies.
One of the ways to study the spread of a disease is to establish models composed of a set of formal mathematical symbols to relate population groups, dividing them into compartments, giving rise to compartmental models [1, 2]. These models are an approximation of the real relationships existing in the object of study [3, 4]. For this matter, differential equations are used that establish dynamic relationships between their states depending on the rate of infection, social isolation, mortality, recovery, and vaccination rate [5].
These models contributed to the study of Covid-19 [6]. A disease that quickly became a serious pandemic, claiming the lives of millions of people around the world [7]. The present work aims to analyse the influence of the vaccination rate, as well as the influence of its effectiveness in reducing the spread of the virus.
For this, it is proposed a modification in the Susceptible - Infected - Removed (SIR) compartment model proposed by Kermack and McKendrick in 1927 [8, 9, 10]. In this new model, social distancing, the effect of the vaccine [11, 12], and its effectiveness in coordinated actions are considered. We want to study the influence of varying the effectiveness of vaccination on the endemic balance [13, 14, 15], as well as the effort needed to ensure its stability.
In addition, it is intended to evaluate the influence of the model parameters on the basic reproduction number of the infection (R_0). Which measures the infectivity of a pathogen in an environment in which no one has acquired immunity to it. With this parameter indicate the effective reproduction number (R_e), exposed to the real conditions of disease evolution and relating to the influence of variations in efficacy on vaccination strategies. The objective of the article is to study the effects of vaccination to prevent the spread of epidemics, to determine the minimum effort of the vaccine as well as the effect of reinfection in the disease control process.

Models Descriptions

The proposed model is a modification of the original SIR model proposed by Kermack and Mckendrick [8, 9, 10]. In this model, the susceptible population S is infected at a rate when it comes in contact with an infected individual from I. The effect of social distancing measures in the susceptible individuals is introduced by the parameter θ, and the subject to the condition $0 < \theta < 1$ and ω is the group to which vaccination is given.
The compartment I represents the infectious population in the incubation phase prior to the onset of symptoms and this population can be asymptomatic or symptomatic. The total population is considered constant, the mortality rate is equal for members of all classes, μ is the mortality and birth rate assumed to be equal, β is the recovery rate, and δ is the reinfection rate, as shown in figure 1.
The model assumes the following hypotheses:

- Fixed population;
- The ways to stop being susceptible is if a person becomes infected, if he is immunized by vaccination or by the mortality rate;
- When the person recovers, they receive permanent immunity;
- The probability of infection is not affected by age, sex or social status;

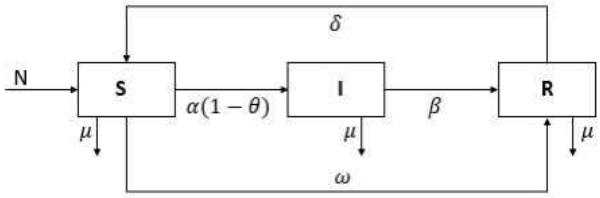

Figure 1: SIR model with vaccine influence, social isolation and reinfection rate.

- The birth and death rate are part of the considerations;
- All births fall into the susceptible class;
- The mortality rate is the same for all compartments and mortality is assumed to be equal to the birth rate.
- The reinfection rate demonstrates the possibility that the individual will be susceptible again.

The model assumes the following notations:
S(t) Number of susceptible individuals at time (t); I(t) Number of infected individuals at time (t); R(t) Number of individuals recovered at time (t); α probability of a susceptible individual becoming infected; β: probability of an infected recovering; θ: social isolation rate; ω vaccination rate of the susceptible; μ mortality rate; δ reinfection rate; N the death is equal for members of all three classes, and it is assumed that the birth and death rates are equal so that the total population is stationary.

Equations
Considering these elements, the model can be described as:

$$\begin{cases} \dot{S} &= \mu N - \frac{\alpha(1-\theta)S(t)I(t)}{N} - \omega S(t) - \mu S(t) + \delta R(t); \\ \dot{I} &= \frac{\alpha(1-\theta)S(t)I(t)}{N} - \beta I(t) - \mu I(t); \\ \dot{R} &= \beta I(t) + \omega S(t) - \mu R(t) - \delta R(t). \end{cases} \tag{1}$$

With constant populations:

$$\dot{S} + \dot{I} + \dot{R} = 0. \tag{2}$$

consequently:

$$S(t) + I(t) + R(t) = N. \tag{3}$$

Taking into account the population density:

$$s = \frac{S}{N}; i = \frac{I}{N}; r = \frac{R}{N}. \tag{4}$$

By substituting (4) in (1):

$$\begin{cases} \dot{s} &= \mu - \alpha(1-\theta)si - \omega s - \mu s + \delta r; \\ \dot{i} &= \alpha(1-\theta)si - \beta i - \mu i; \\ \dot{r} &= \beta i + \omega s - \mu r - \delta r; \end{cases} \tag{5}$$

with the initial conditions $s(0) \geq 0$, $i(0) \geq 0$ and $r(0) \geq 0$.
Here μ is the recruitment and natural death rate, α is the effective contact rate between susceptible and infected individuals, ω is the rate of vaccination, θ is the social isolation and δ is the reinfection rate. All the parameters are positive and for θ the restriction considered $0 < \theta < 1$.

Disease-free and endemic equilibrium points
To investigate the influence of the introduction of feedback from the recovered individuals with no immunity, the equilibrium points from (5) must be determined and their stability must be discussed.
For the proposed model, there are two equilibrium points: one endemic and the other free from infection.
Disease-free equilibrium point:

- P_1 (s^*,i^*,r^*) = $(\frac{\mu+\delta}{\omega+\mu+\delta}, 0, \frac{\omega}{\omega+\mu+\delta})$;

Endemic equilibrium point:

- P_2 (s^*,i^*,r^*) such as:
- s^* = ($\frac{\beta+\mu}{\alpha(1-\theta)}$);
- i^* =($\frac{\mu(\mu+\delta)(\alpha(1-\theta))+\delta\omega(\beta+\mu)-(\beta+\mu)(\omega+\mu)(\mu+\delta)}{(\alpha(1-\theta))\mu(\beta+\mu+\delta)}$);
- r^* = ($\frac{\beta}{\mu+\delta}i^* + \frac{\omega(\beta+\mu)}{(\mu+\delta)(\alpha(1-\theta}$);

Consequently, the existence condition for the endemic equilibrium P_2 is given by

$$\mu(\mu+\delta)(\alpha(1-\theta)) + \delta\omega(\beta+\mu) > (\beta+\mu)(\omega+\mu)(\mu+\delta). \tag{6}$$

and obtain:

$$\omega < \mu\left(\frac{\alpha(1-\theta)}{(\beta+\mu)} - 1\right) \tag{7}$$

From the analysis of the endemic point, it can be seen that to guarantee its existence, it is necessary to respect the condition 7. Analyzing this point, the minimum vaccination effort necessary to reach the point free of infection can be concluded.

Stability analysis
In order to analyse the local stability of the system, the jacobian of the model is calculated at the equilibrium points.

$$J = \begin{bmatrix} -\alpha(1-\theta)i^* - \omega - \mu & -\alpha(1-\theta)s^* & \delta \\ \alpha(1-\theta)i^* & \alpha(1-\theta)s^* - \beta - \mu & 0 \\ \omega & \beta & -\delta - \mu \end{bmatrix}.$$

Analyzing the Jacobian at point P_1:

$$J_{P1} = \begin{bmatrix} -\omega - \mu & -\alpha(1-\theta)s^* & 0 \\ 0 & \alpha(1-\theta)s^* - \beta - \mu & 0 \\ \omega & \beta & -\mu \end{bmatrix}.$$

Using the mathematical tool Matlab 2015, the eigenvalues of the resulting Jacobian matrix are calculated, in order to analyze the stability of the equilibrium point.
Eigenvalues P_1:
$\lambda_1 = -\mu$;
$\lambda_2 = -\omega - \mu - \delta$;
$\lambda_3 = \alpha(1-\theta)s^* - \beta - \mu$.
The stability analysis for model figure 1 presents the disease free equilibrium point and, considering the existence condition, the eigenvalues are given by: $\lambda_1 = -\mu$, $\lambda_2 = -\omega - \mu - \delta$ and $\lambda_3 = \alpha(1-\theta)s^* - \beta - \mu$. The third eigenvalue indicates that if ($s^* < \frac{\beta+\mu}{\alpha(1-\theta)}$) the system is asymptotically stable and if ($s^* > \frac{\beta+\mu}{\alpha(1-\theta)}$) the system becomes unstable indicating a bifurcation in the parameter space.
substituting the variable s^* for the expression calculated at the disease-free equilibrium point, we obtain:

$$\omega > \frac{(\mu+\delta)(\alpha(1-\theta))}{\beta+\mu} - \mu - \delta, \tag{8}$$

from 8 we can conclude the minimum necessary effort of the vaccination strategy to eradicate the epidemic.

Numerical experiments

In order to clarify the stability results obtained analytically for points P_1 and P_2, a series of numerical experiments were carried out.
From the analysis of point P_1 the bifurcation condition 8 is obtained for which the system can behave in a stable or unstable way. To show this behaviour, simulations were performed by varying the values of the system parameters. Figure 2, figure 3 show that for any initial condition, point P_1 it's stable if $\omega > \frac{(\mu+\delta)(\alpha(1-\theta))}{\beta+\mu} - \mu - \delta$.
On the other hand, when the condition $\omega < \frac{(\mu+\delta)(\alpha(1-\theta))}{\beta+\mu} - \mu - \delta$ is set, the system always reaches stability at the endemic point P_2 , behaviour that is shown in figures 5, 6 and 7.
Figure 4 shows that starting from an initial condition (S,I,R)=(0.9, 0.12, 0.08), close to the equilibrium point P_1, and with parameter values $\alpha = 0.6, \beta = 0.6, \theta = 0.1, \delta = 0.2, \mu = 0.01$ and $\omega = 0.3$. guaranteeing the stability condition, the P_1 point is reached.
Figure 5 shows that starting from an initial condition (S,I,R)=(0.3, 0.7, 0.0), far to the equilibrium point P_1, and with parameter values $\alpha = 0.6, \beta = 0.6, \theta = 0.1, \delta = 0.2, \mu = 0.01$ and $\omega = 0.3$. guaranteeing the stability condition, the P_1 point is reached.

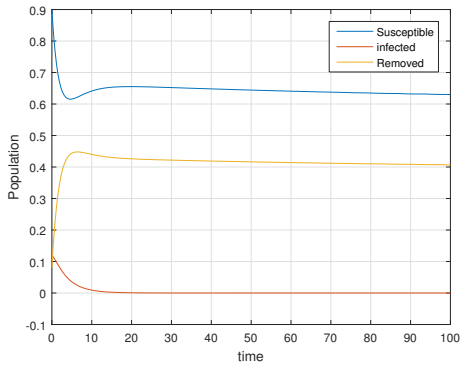

Figure 2: disease free point.

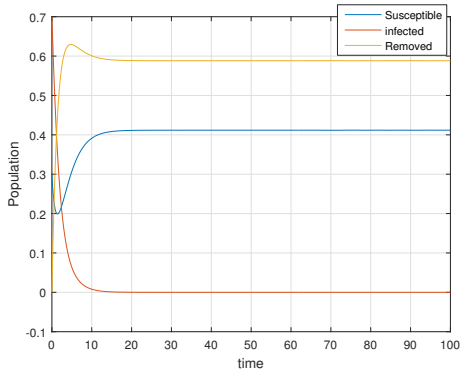

Figure 3: disease free point.

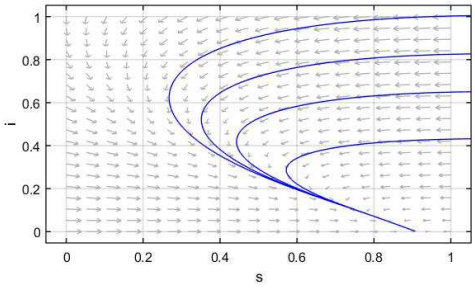

Figure 4: disease free point phase.

In the figure 6 shows the phase diagram of the system with the combination of parameters so that the existence of a disease-free equilibrium point is guaranteed. Each trajectory represents a possible initial condition of the system variables (Susceptible and Infected) and their evolution over time until reaching the equilibrium point. The arrows indicate the direction of movement of the trajectories.

Figure 7 shows that starting from an initial condition (S,I,R)=(0.3, 0.7, 0.0), close to the equilibrium point P_2, and with parameter values $\alpha = 0.9, \beta = 0.3, \theta = 0.1, \delta = 0.2, \mu = 0.3$ and $\omega = 0.1$. guaranteeing the stability condition, the P_2 point is reached.

Figure 8 shows that starting from an initial condition (S,I,R)=(0.8, 0.2, 0.0), far from the equilibrium point P_2, and with parameter values $\alpha = 0.9, \beta = 0.3, \theta = 0.1, \delta = 0.2, \mu = 0.3$ and $\omega = 0.1$. guaranteeing the stability condition, the P_2 point is reached.

In the figure 9 shows the phase diagram of the system with the combination of parameters so that the existence of a endemic equilibrium point is guaranteed. Each trajectory represents a possible initial condition of the system variables (Susceptible and Infected) and their evolution over time until reaching the equilibrium point. The arrows indicate the

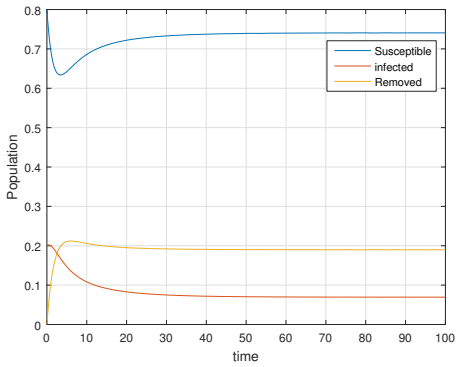

Figure 5: Endemic point

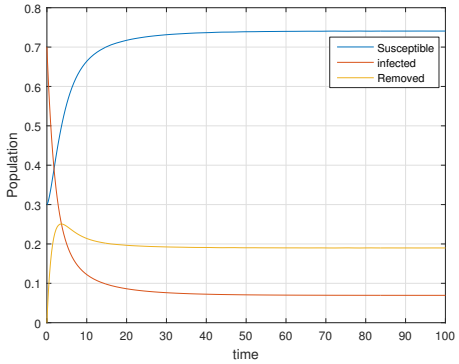

Figure 6: Endemic point

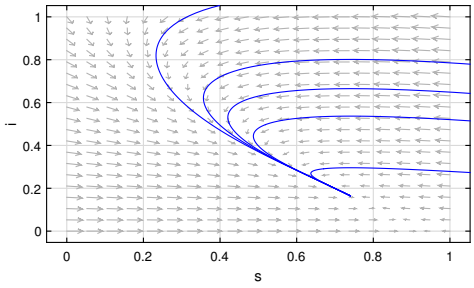

Figure 7: Endemic point phase

direction of movement of the trajectories.
The proposed model is intended to show that in a population where the disease has a temporary immunity character, there is a minimum vaccination effort necessary to eradicate the disease. This result can be verified through variations in the change in the parameters of vaccination, reinfection and social distancing.
In order for the disease-free point to be reached, a minimum vaccination effort given by the equation 8. If the vaccination strategy does not follow this regime, the disease will remain in the population indicating endemic characteristics.

Conclusion

This paper presented a modification of the Susceptible-Infected-Removed (SIR) compartmental model proposed by Kermack and McKendrick in 1927. The social distance, the effect of the vaccine, and its effectiveness in coordinated actions were considered. In addition, the influence of variation in vaccination efficacy on the endemic equilibrium, and the effort required to ensure its stability, were studied.

From the analytical and numerical results, it can be said that the model has two equilibrium points, one endemic and the other disease-free, the existence of each being given by a bifurcation condition that depends on the probability of infection, the social distance and the recovery and infection rates. From there it is possible to find the minimum effort necessary to prevent the epidemic from occurring.
As shown above the existence of the endemic or disease-free point depends on the value of the existence condition. The higher the vaccination and social distancing, the faster the disease-free point will be reached.

References

[1] Abelló Ugalde, I. A., Guinovart Díaz, R., and Morales Lezca, W. (2021). El modelo SIR básico y políticas antiepidémicas de salud pública para la COVID-19 en Cuba. Revista Cubana de Salud Pública, 46, e2597.

[2] Febles Gámez, E. (2020). Las matemáticas que hay detrás de las epidemias mundiales.

[3] Salas, M. A. (2009). Diseños experimentales en modelos compartimentales con observaciones correladas (Doctoral dissertation, Universidad de Castilla-La Mancha).

[4] Hernández, J. X. V. (2007). Modelos matemáticos en epidemiologıa: enfoques y alcances.

[5] Batistela, C. M., Cabrera, M. A., Ramos, M. M., Dieguez, G. M., and Piqueira, J. R. Influência da imunidade temporária na dinâmica de propagação do COVID-19 e sua relação com o isolamento social e imunização.

[6] González-Fuenzalida, F., and González-Cohens, F. (2021). Epidemias en la actualidad: de cómo los modelos matemáticos y estadísticos permiten entenderlas, aún a profesionales adversos a ellos. Revista médica de Chile, 149(3), 422-432.

[7] Strickland, J. C., Reed, D. D., Hursh, S. R., Schwartz, L. P., Foster, R. N., Gelino, B. W., ... and Johnson, M. W. (2021). Integrating Operant and Cognitive Behavioral Economics to Inform Infectious Disease Response: Prevention, Testing, and Vaccination in the COVID-19 Pandemic. medRxiv

[8] Kermack, W.O. and McKendrick, A.G. (1927). A contribution to the mathematical theory of epidemics. Proceedings of the Royal Society of London. Series A, Containing papers of a mathematical and physical character, 115(772), 700-721.

[9] Kermack, W.O. and McKendrick, A.G. (1932).Contributions to the mathematical theory of epidemics. ii.the problem of endemicity. Proceedings of the Royal Society of London. Series A, containing papers of a mathematical and physical character, 138(834), 55-83.

[10] Kermack, W.O. and McKendrick, A.G. (1933). Contributions to the mathematical theory of epidemics. iii.further studies of the problem of endemicity. Proceedings of the Royal Society of London. Series A, Containing Papers of a Mathematical and Physical Character, 141(843), 94-122.

[11] Moschin, S. (2020). Modelli epidemiologici compartimentali: modello SIR e possibili estensioni.

[12] Macchia-de Sánchez, C. L., and Villalba-Vizcaíno, V. T. Vacunación contra COVID-19 y embarazo Vaccination against COVID-19 and pregnancy.

[13] Kwok, K. O., Li, K. K., Wei, W. I., Tang, A., Wong, S. Y. S., and Lee, S. S. (2021). Influenza vaccine uptake, COVID-19 vaccination intention and vaccine hesitancy among nurses: A survey. International journal of nursing studies, 114, 103854.

[14] Moore, S., Hill, E. M., Tildesley, M. J., Dyson, L., and Keeling, M. J. (2021). Vaccination and non-pharmaceutical interventions for COVID-19: a mathematical modelling study. The Lancet Infectious Diseases, 21(6), 793-802.

[15] Paltiel, A. D., Schwartz, J. L., Zheng, A., and Walensky, R. P. (2021). Clinical Outcomes Of A COVID-19 Vaccine: Implementation Over Efficacy: Study examines how definitions and thresholds of vaccine efficacy, coupled with different levels of implementation effectiveness and background epidemic severity, translate into outcomes. Health Affairs, 40(1), 42-52

Dynamics of a self-propelled soft capsule moving in the small intestine

Jiyuan Tian*, Zepeng Wang*, Yang Liu* and Shyam Prasad†
*College of Engineering, Mathematics and Physical Sciences, University of Exeter, Exeter, UK
†Endoscopy Unit, Royal Devon and Exeter NHS Foundation Trust, Exeter, UK

Summary. In this work, we study the dynamics of a vibro-impact soft capsule self-propelling in the small intestine for capsule endoscopy through finite element modelling. Soft coating by using the super-soft silicone rubber was used to reduce the potential damage induced by the rigid capsule on the intestine. Our studies indicate that the dynamics of the capsule becomes complex due to the capsule-intestine interaction, and the coating's elastic modulus and thickness may affect the performance of the capsule significantly. Therefore, a proper selection of these coating parameters is vital for capsule design.

Introduction

The small intestine, an anatomical site previously considered inaccessible to clinicians due to its small diameter and lengthy size, is the part of the gastrointestinal tract between the stomach and the colon as illustrated in Fig. 1(a). Since its introduction into clinical practice twenty years ago, capsule endoscopy [1] has become established as the primary modality for examining the surface lining of the small intestine. However, its reliance on peristalsis for passage through the intestine leads to significant limitations [2], in particular due to the unpredictable and variable locomotion speed. Significant abnormalities, e.g., small-bowel bleeding, may be missed, due to intermittent high transit speeds that lead to incomplete visualisation of the intestinal surface. Furthermore, each case produces up to 100,000 still images, from which video footage is generated, taking 30-90 minutes for the clinician to examine in its entirety. The current procedure is considered both time-consuming and burdensome for clinicians.

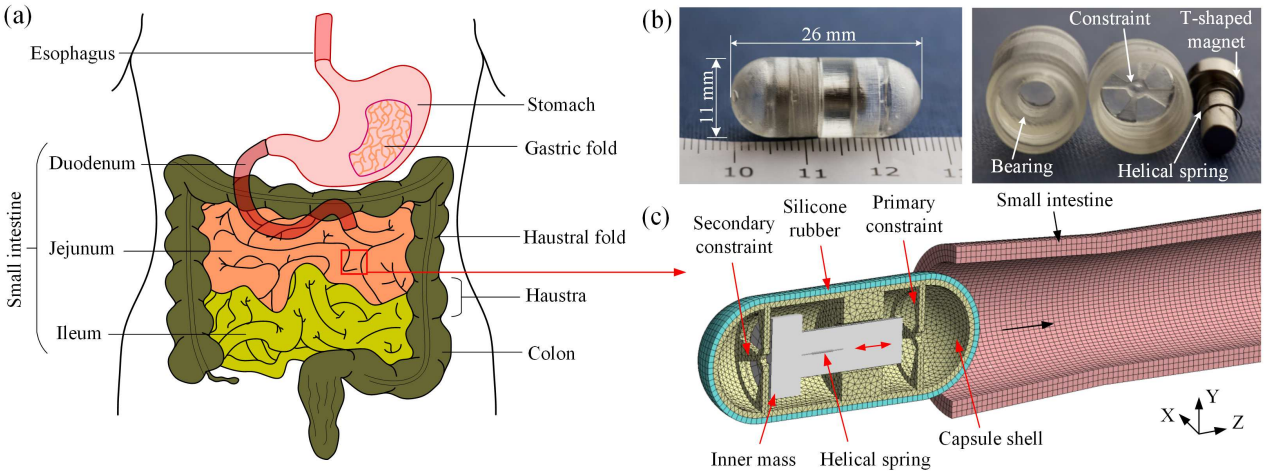

Figure 1: (a) Anatomy of the gastrointestinal tract, (b) external and internal views of the rigid capsule prototype [3] and (c) cross-sectional view of the finite element model, where the coated capsule consists of an inner mass (T-shaped magnet) vibrating and impacting with the primary and the secondary constraints under external magnetic excitation and the interaction of a helical spring.

Building a reliable propulsive mechanism in a capsule (with 26 mm in length and 11 mm diameter) for active endoscopy is a challenging task. Different propulsion methods were proposed in the past few decades for small-intestine diagnosis. The purpose of this work is to study the dynamics of a soft capsule self-propelled in the small intestine through finite element (FE) modelling. The self-propelled capsule developed in the Applied Dynamics and Control Lab at the University of Exeter [3] as shown in Fig. 1(b) can progress either forward or backward driven by its internal vibrations and impacts. Previous FE investigation [4, 5] has focused on studying the capsule-intestine interaction by using a rigid capsule made of polyethylene. However, to reduce the potential damage caused by the rigid shell on the intestine and optimise the capsule's movement, super-soft silicone rubber was used to coat the capsule shell. In this work, we explored the complex dynamics of the coated capsule moving in the lumen of the small intestine as presented in Fig. 1(c) under different coating parameters, such as the coating's elastic modulus and thickness.

Finite element model

FE modelling of the capsule-intestine contact was carried out by using ANSYS WORKBENCH with the consideration of material parameter configuration, geometry, contact settings, meshing, constraints and loads. As can be seen from Fig. 1(c), the polyethylene capsule shell was costed by the super-soft silicone rubber uniformly, and the diameter of the coated capsule was kept as 11 mm. The inner mass made by a T-shaped magnet can move forward and backward under the excitation of an external square-wave magnetic field. The frequency, amplitude and duty cycle ratio of the magnetic

field were the control parameters to be tested, and the capsule was driven within a small intestine with an inner diameter of 10 mm. If the interaction force between the inner mass and the capsule is greater than the intestinal friction, the capsule will move either forward or backward. In the present work, we studied the influence of capsule coating's elastic modulus and thickness on its dynamics and progression speed and compare them with the original capsule without any coating.

Numerical results

Capsule's progression and phase trajectories under different elastic moduli of the coating obtained from the FE model are presented in Fig. 2. Based on our simulation, the capsule has an average speed of 14 mm/s when the elastic modulus of the coating is 8 psi, and the average speed is 21 mm/s when the coating is increased to 10 psi. As the elastic modulus increases to 12, 14 and 16 psi, the capsule oscillates at its original position only without any progression. According to our observation, this was due to the fact that the intestine moved together with the capsule, so no relative movement was generated between the capsule and the intestine. When the capsule has no coating, the average speed of the capsule is 18 mm/s. As can be seen from the phase portraits in Fig. 2, the capsule has periodic motions for all the cases. However, the capsule cannot repeat the exact periodic motion, which is due to the asymmetric capsule-intestine interaction.

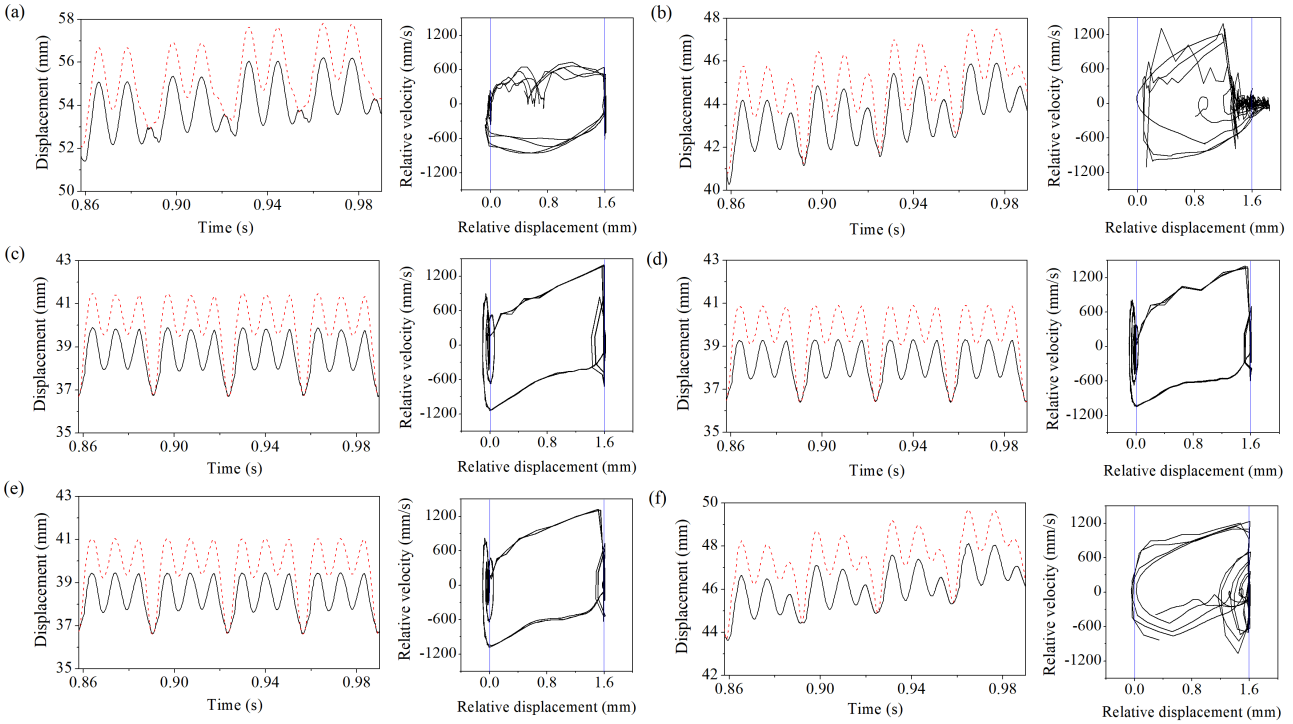

Figure 2: Time histories of displacements of the capsule (black solid lines) and the inner mass (red dashed lines) and their corresponding phase trajectories (relative displacement versus velocity between the inner mass and the capsule) obtained for the elastic moduli of the coating at (a) 8 psi, (b) 10 psi, (c) 12 psi, (d) 14 psi, (e) 16 psi and (f) no coating. The inner mass was driven by a square-wave excitation with the frequency of 30 Hz, the amplitude of 0.3 N and the duty cycle of 80%. Left and right vertical blue lines on the phase portraits indicate the impact boundaries for the secondary and the primary constraints, respectively.

Conclusions

To conclude, the coating of the capsule has a significant influence on the nonlinear motion of the capsule. With a proper selection of elastic modulus and thickness of the coating, an optimum progression of the capsule can be achieved. Our further studies indicate that a harder coating may lead to a greater capsule-intestine contact pressure, while a thicker coating can reduce the contact pressure which can minimise the damage induced by the capsule on the intestine.

References

[1] Iddan, G., Meron, G., Glukhovsky, A., Swain P. (2000) Wireless Capsule Endoscopy. *Nature* **405**:417-418.

[2] Ciuti, G., Menciassi, A., Dario, P. (2011) Capsule Endoscopy: from Current Achievements to Open Challenges. *IEEE Rev. Biomed. Eng.* **4**:59-72.

[3] Liu, Y., Páez Chávez, J., Zhang, J., Tian, J., Guo, B., Prasad, S. (2020) The Vibro-Impact Capsule System in Millimetre Scale: Numerical Optimisation and Experimental Verification. *Meccanica* **55**:1885–1902.

[4] Guo, B., Liu, Y., Prasad, S. (2019) Modelling of Capsule–Intestine Contact for a Self-Propelled Capsule Robot via Experimental and Numerical Investigation. *Nonlinear Dyn.* **98**:3155-3167.

[5] Guo, B., Ley, E., Tian, J., Zhang, J., Liu, Y., Prasad, S. (2020) Experimental and Numerical Studies of Intestinal Frictions for Propulsive Force Optimisation of a Vibro-Impact Capsule System. *Nonlinear Dyn.* **101**:65-83.

[6] Yan, Y., Liu, Y., Manfredi, L., Prasad, S. (2019) Modelling of a vibro-impact self-propelled capsule in the small intestine. *Nonlinear Dyn.* **96**:123-144.

Tuesday, July 19, 2022

13:30 - 15:30

MS-08 Nonlinear Phenomena in Mechanical and Structural Systems

Rhone 3B

Chair: Jerzy Warminski

13:30 - 13:50

Application of proportional ?ghost? damping for sliding or yielding structures in time history dynamic analyses

BOUDY Bastien*, MOUSSALLAM Nadim, BIDET Jean-Paul

*Framatome (10 rue Juliette recamier 69006 Lyon France)

13:50 - 14:10

Basins of attraction for the model of rotating hub with two pendulums

SZMIT Zofia*, ANDONOVSKI Nemanja, STEFANO Lenci, WARMINSKI Jerzy

*Department of Applied Mechanics, Faculty of Mechanical Engineering, Lublin University of Technology (36 Nadbystrzycka St. 20-618 Lublin Poland)

14:10 - 14:30

Bifurcation Elimination in Rotor Gas Bearing Systems Applying Numerical Continuation with Embedded Design Optimization Scheme

PAPAFRAGKOS Panagiotis*, GAVALAS Ioannis, RAPTOPOULOS Ioannis, CHASALEVRIS Athanasios

*National Technical University of Athens [Athens] (Zografou Campus - 9, Iroon Polytechniou str - 15780 Zografou, Athens Greece)

14:30 - 14:50

Why does the tippedisk invert? Theory and experiments

SAILER Simon*, LEINE Remco

*Institute for Nonlinear Mechanics, University of Stuttgart (Pfaffenwaldring 9 70569 Stuttgart Germany)

14:50 - 15:10

Effect of Nonlinear Electromechanical Coupling in Implanted Middle Ear

RAFAL Rusinek*

*Lublin University of Technology (Nadbystrzycka 36, Lublin Poland)

Application of proportional "ghost" damping for sliding or yielding structures in time history dynamic analyses

Bastien Boudy[*], Nadim Moussallam [**] and Jean-Paul Bidet [***]
[*]*Engineer, Framatome Mechanical Engineering department, France*
[**]*Expert Engineer in Dynamic Analysis, Framatome Mechanical Engineering department, France*
[***]*Deputy Manager of Structural Analysis Section, Framatome Mechanical Engineering department, France*

Extended abstract

When studying the response of a structure to a dynamic excitation, the modelling of energy dissipation has always been a challenge to the engineers. Different methodologies were set up for different kinds of problems. These include the modelling of friction forces, hysteretic behavior and restitution coefficients for non-linear structures. For linear structures, modelled with finite elements, the general practice is to use either viscous equivalent modal damping or viscous proportional "Rayleigh" damping.

Content overview

The first part of the paper gives a quick overview of the most usual representations of energy dissipation in dynamic analyses, with a particular focus on the use of a proportional Rayleigh damping and its drawbacks when applied to a linear but not linearly supported structure. The second part describes the "ghost" damping methodology set in place to overcome those drawbacks. The third part presents tests case basis on which the "ghost" damping was checked, including simple examples representative of a handling crane, a fuel rack and a seismically isolated building.

PART 1: Representation of energy dissipation in usual engineering practices

Values for modal damping are found in numerous seismic design codes around the world and they constitute the energy dissipation modelling basis for most applications in the industry (see references [1], [2], [3],and [5]). It has become common practice to try to apply these modal damping values to dynamic problems that are not solved on a modal basis. To do so with a finite element model, the most widely applied method consists in building a viscous damping matrix [C] as a linear combination of the mass matrix [M] and the stiffness matrix [K], α and β being referred to as the Rayleigh coefficients. This method is referred to as the Rayleigh method, after the work of Baron Rayleigh in the 1870s (see [6] in the references). It is possible to create a [C] matrix that produces a required given modal damping value, although for only two structural modes at most.

For the case of linear structures, with a non linear supporting system, which will be the main focus of this paper, an unwanted effect of using a Rayleigh damping, even only on the linear part of the model, is that it produces damping forces that will spuriously limit, and ultimately stop the motion of the structure relative to its support basis. Indeed, the α[M] part of the Rayleigh damping matrix is predominantly diagonal. These diagonal terms, when multiplied by the velocity vector, produce damping forces proportional to the velocity of each node relative to the calculation referential, as illustrated by equation (1) for a two mass system, with a single degree of freedom for each node (U_X is the displacement of node X relative to the calculation referential, M_X the mass attached to this node).

$$\left\{F_{\alpha_damping}\right\} = \alpha \begin{bmatrix} M_1 & 0 \\ 0 & M_2 \end{bmatrix} \begin{Bmatrix} \dot{U}_1 \\ \dot{U}_2 \end{Bmatrix} = \begin{Bmatrix} \alpha M_1 \dot{U}_1 \\ \alpha M_2 \dot{U}_2 \end{Bmatrix} \qquad (1)$$

Any rigid body motion of this two mass system relative to the calculation referential gives rise to non intended resisting damping forces. This phenomenon will be referred to as the "spurious damping of rigid body motions" in this paper.

On the other hand, the β[K] part of the Rayleigh damping produces forces that are only proportional to the relative velocities between nodes connected by an element. As an example, if a spring of stiffness K_1 connects the two masses of the simple system described earlier, the resulting damping forces are illustrated by equation (2).

$$\left\{F_{\beta_damping}\right\} = \beta \begin{bmatrix} K_1 & -K_1 \\ -K_1 & K_1 \end{bmatrix} \begin{Bmatrix} \dot{U}_1 \\ \dot{U}_2 \end{Bmatrix} = \begin{Bmatrix} \beta K_1 (\dot{U}_1 - \dot{U}_2) \\ \beta K_1 (\dot{U}_2 - \dot{U}_1) \end{Bmatrix} \qquad (2)$$

These forces do represent dissipation of energy because of structural deformation, which is generally the objective assigned to Rayleigh damping.

The inadequacy of using the α[M] part of the Rayleigh damping is known and some references can be found in regulatory documentations such as [1] and [2]. As a consequence, cautious engineers will only use the β[K] part and therefore loose the ability to properly damp the lower frequency modes of the structures. Such approach invariably results in overly conservative estimations of the structural responses.

PART 2: Description of the 'GHOST" damping methodology

The so-called "ghost" damping methodology has been specifically developed for the case of linear structures on a non linear support. Its objective is to overcome the two drawbacks of the Rayleigh proportional damping method identified in Part 1: controlled modal damping value on only two modes and spurious damping of rigid body motions. In the case of non linearly supported linear systems, the non linear support is generally explicitly modelled and is itself a source of energy dissipation, through friction coefficients (case of a handling crane) or modelling of a hysteretic material behaviour (case of a seismically isolated building). The linear part is modelled by linear stiffness and mass matrices, [K] and [M], which remain constant throughout the calculations.

The "ghost" methodology aims at producing damping forces on the linear structure which are only proportional to the structure deformation velocities. This is what happens with the usual Rayleigh damping for purely linear systems. To achieve this goal, the rigid body motion of the linear part of the model is subtracted from its overall movement when constructing the damping forces vectors. The form of these desired damping forces is illustrated in equation (3) for the two-masses-one-stiffness system described earlier.

$$\left\{F_{\alpha_damping}\right\} = \begin{Bmatrix} \alpha M_1 (\dot{U}_1 - \dot{U}_{g1}) \\ \alpha M_2 (\dot{U}_2 - \dot{U}_{g2}) \end{Bmatrix} \text{ and } \left\{F_{\beta_damping}\right\} = \begin{Bmatrix} \beta K_1 (\dot{U}_1 - \dot{U}_2) \\ \beta K_1 (\dot{U}_2 - \dot{U}_1) \end{Bmatrix} \qquad (3)$$

The β[K] part is of the same nature as the proportional Rayleigh damping β[K] matrix. The α [M] part results in forces proportional to the node velocity minus the rigid body motion velocity at the node location. In this equation, U_{gX} represents the displacement of node X due only to the rigid body motion.

PART 3: Tests cases basis for the "GHOST" damping methodology

Tests cases will be developed in the full article.

Acknowledgment

This work was developed within the SINAPS@ project. It benefited from the French state funding managed by the National Research Agency under program RNSR Future Investments bearing reference No. ANR-11-RSNR-0022-04.

Conclusions

Two drawbacks of using a classic proportional Rayleigh damping methodology in the dynamic analysis of non-linearly supported linear structures were highlighted: spurious damping of rigid body motions and under-damping of some major modes located in between the first and the last mode frequencies of interest. These drawbacks are known and the cautious engineer will usually make conservative assumptions to avoid the first one. The present paper describes a methodology to suppress the spurious damping of rigid body motion by using a "ghost" structure within a FE model and generate damping forces proportional to the actual structure velocities relative to its "ghost". At the same time, different Rayleigh coefficients are used for different directions, in order to bring the equivalent modal damping values of the linear part of the model closer to the targets in each direction, often defined in the codes.

References

[1] ASME, (2004), "Boiler & pressure vessel code", Section III, Division I, Appendix N, USA
[2] ASN Guide 2/01, (2006) "Considering the risk of an earthquake when designing civil engineering structures of nuclear installations, excluding long term storage of radioactive waste", Appendix I, France
[3] IAEA Safety reports series n°28, (2003), "Seismic evaluation of existing nuclear power plants".
[4] Moussallam, N., Vlaski, V. (2011). "Respective role of the vertical and horizontal components of an earthquake excitation for the determination of floor response spectra of a base isolated nuclear structure – Application to Gen IV reactors." Transactions, SMiRT 21, New Delhi, India.
[5] RG 1.61, (1973), "Damping values for seismic design of nuclear power plants", US NRC, USA.
[6] Strutt, J. W., Baron Rayleigh, (1877), "The theory of sound", Volume I, Chapter V, Cambridge, United Kingdom.

Basins of attraction for the model of rotating hub with two pendulums

Zofia Szmit*, Nemanja Andonovski †, Stefano Lenci† and Jerzy Warmiński*
*Department of Applied Mechanics, Faculty of Mechanical Engineering, Lublin University of Technology, Lublin, Poland
†Department of Civil and Building Engineering and Architecture, Polytechnic University of Marche, Ancona, Italy

Summary. The goal of this paper is to study nonlinear dynamics of the system consisting of two pendulums attached to a hub rotating in the horizontal plane. Equations of motion are derived from Lagrange equations of the second kind. Next, the equations are transformed to the system of six first-order ordinary differential equations. Based on the set of first-order differential equations of motion basins of attraction are calculated. Moreover, the synchronisation phenomenon is studied in case of symmetric and nonsymmetric pendulums.

Introduction

Rotating structures have many applications in mechanical and aerospace engineering, like for example arms of industrial robots, wind turbines, helicopter rotors and jet engines. Additionally, pendulums are very well known as a dampers for instance in high buildings and helicopter rotor dampers. There are many publications, which are concentrated on pendulums, like a paper about a model consisting of chains of nonlinear coupled pendulums subjected to harmonic excitations [1]. Authors studied nonlinear dynamics and synchronisation phenomenon for that theoretical model, they examined an influence of initial conditions as well as an influence of horizontal excitation on motion of the chain system. Most of the paper about dynamics of pendulums are focused on pendulums rotating only in a vertical plane, while a different approach is presented in [2]. Authors presented numerical results for a model of a hub with pendulums rotating in the horizontal plane, they proved that the model is strongly nonlinear and even chaotic motion may appear. Authors linearised the problem and solved such equations analytically for small oscillations. Whereas, analysis of basin of attraction are very useful, specially in case of strongly nonlinear systems. They consist regions of all the initial conditions that converge to associated attractors forward in time. Analyzing the basins of attraction we can inspect the impact of initial conditions on the global behaviour of a dynamical system [3].
The aim of this paper is to study the dynamics and synchronisation phenomenon in a system composed of a rotating hub with two pendulums. Basins of attractions are calculated to study excited vibrations of the system. Additionally, the synchronisation phenomenon in a case of symmetric and nonsymmetric system and bifurcation scenario is study as well.

Model and equations of motion

The analyzed model consists of the two pendulums attached to a rigid hub rotating in the horizontal plane. Mathematical pendulums are connected to the hub by joints treated as a flapping hinge with nonlinear Duffing's type spring and a linear viscous damper.

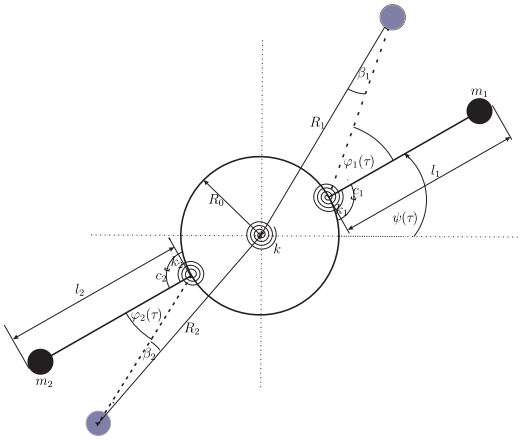

Figure 1: Model of the hub with two pendulums rotating in the horizontal plane; top view

The hub is described by radius R_0 and mass moment of inertia J_0, while m_j and l_j are mass and length of the pendulums, c_j is a viscous damping coefficient and k_j, k_j^*, k and k^* are the nonlinear spring coefficients, where $j = 1, 2$. Two types of nonlinear springs, first type in the hinges and second type spring connecting the hub with background are used in the model. Additionally we assume that, the hub may oscillate or rotate in the horizontal plane, while pendulums may oscillate and also rotate around the hinge in their relative motion. The gravity force does not influence the dynamics of the system, because of the hub rotation in a horizontal plane. Motion of the hub is represented by angle of rotation ψ, while variables φ_j are a coordinates of relative motion of the pendulum with respect to the hub.

The differential equations of motion are derived on the basis of Lagrange equations of the second kind and written in the dimensionless form as shown below:

$$\begin{aligned}
&(1+\gamma_1+\gamma_2)\,\ddot{\psi}+\zeta_h\dot{\psi}+2\frac{\gamma_1}{\delta_1}\dot{\delta}_1\dot{\psi}+2\frac{\gamma_2}{\delta_2}\dot{\delta}_2\dot{\psi}+\frac{\gamma_1}{\delta_1}\cos\beta_1\ddot{\varphi}_1+\frac{\gamma_2}{\delta_2}\cos\beta_2\ddot{\varphi}_2\\
&+\frac{\gamma_1}{\delta_1^2}\cos\beta_1\dot{\delta}_1\dot{\varphi}_1+\frac{\gamma_2}{\delta_2^2}\cos\beta_2\dot{\delta}_2\dot{\varphi}_2+\frac{\gamma_1}{\delta_1}\frac{d}{d\tau}\left(\cos\beta_1\right)\dot{\varphi}_1+\frac{\gamma_2}{\delta_2}\frac{d}{d\tau}\left(\cos\beta_2\right)\dot{\varphi}_2+\kappa_h\psi+\kappa_h\psi^3=\mu\\
&\ddot{\varphi}_1+\delta_1\cos\beta_1\ddot{\psi}+\delta_1\frac{d}{d\tau}\left(\cos\beta_1\right)\dot{\psi}+\cos\beta_1\dot{\delta}_1\dot{\psi}-\delta_1\frac{d\delta_1}{d\varphi_1}\dot{\psi}^2\\
&-\cos\beta_1\dot{\delta}_1\dot{\psi}-\delta_1\frac{d}{d\tau}\left(\cos\beta_1\right)\dot{\psi}+\zeta_1\dot{\varphi}_1+\omega_{01}^2\varphi_1+\kappa_1\omega_{01}^2\varphi_1^3=0\\
&\ddot{\varphi}_2+\delta_2\cos\beta_2\ddot{\psi}+\delta_2\frac{d}{d\tau}\left(\cos\beta_2\right)\dot{\psi}+\cos\beta_2\dot{\delta}_2\dot{\psi}-\delta_2\frac{d\delta_2}{d\varphi_2}\dot{\psi}^2\\
&-\cos\beta_2\dot{\delta}_2\dot{\psi}-\delta_2\frac{d}{d\tau}\left(\cos\beta_2\right)\dot{\psi}+\zeta_2\dot{\varphi}_2+\omega_{02}^2\varphi_2+\kappa_2\omega_{02}^2\varphi_2^3=0,
\end{aligned}\tag{1}$$

where μ is external harmonic torque supplied to the hub, defined as: $\mu=\rho\cos(\omega\tau)$. The equations of motion (1) are strongly nonlinear and coupled by inertia and nonlinear geometric terms. First equation describes the motion of the hub, while two other equations represent the motion of each pendulum.

Results

The set of equations have been transformed to the system of six first-order ordinary differential equations and the following relations have been introduced: $\psi=y_o,\dot{\psi}=y_1,\varphi_1=y_2,\dot{\varphi}_1=y_3,\varphi_2=y_4$ and $\dot{\varphi}_2=y_5$. In the numerical calculation it is assumed that the pendulum No. 1 is slightly shorter then second pendulum. Firstly, the resonance curves and trajectories of the system attractors are computed. Next, basins of attraction are obtained, which is very time consuming numerical procedure.

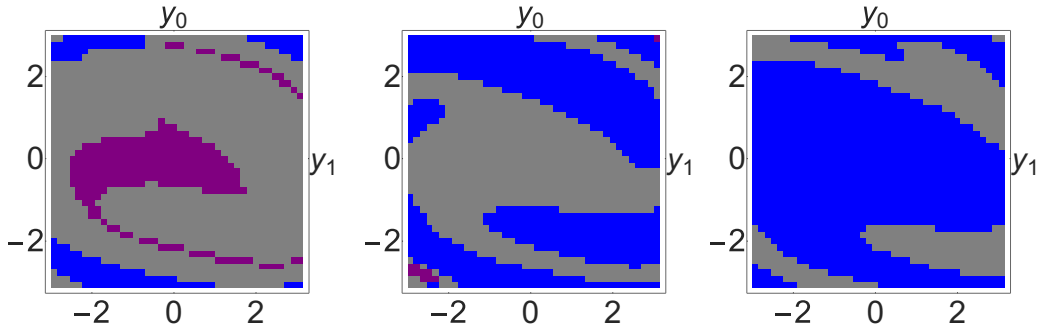

Figure 2: Basin cross-section of the hub, segment with $y_{2-5}=0.075$ for the excitation frequency a) $\omega=1.4$, b) $\omega=1.5$ and c) $\omega=1.6$

In Fig. 2 we are able to see basin cross-section for the hub, where initial states of pendulums are close to zero. For the frequency $\omega=1.4$ the gray basin takes most of the area, for higher values of ω the blue basin increases significantly. Furthermore, results on Fig. 2 shows that the motion of the hub in most of the cases converge to gray and blue attractors, while purple attractor has impact motion of pendulums. Blue, purple and gray attractors are corresponding to periodic motion.

Final remarks

The strongly nonlinear model of the hub rotating in the horizontal plane with two pendulums is studied. The resonance curves and trajectories of the system attractors are computed as well as basins of attraction. The obtained results give us more accurate understanding of the dynamics of the analyzed model.

Acknowledgment

This work is financially supported by grant FNM 30/IM/2019.

References

[1] Marcheggiani, L., Chacon, R., Lenci, S. (2014) On the Synchronization of Chains of Nonlinear Pendula Connected by Linear Springs.*The European Physical Journal - Special Topics* **223**:729-756.

[2] Warminski, J., Szmit, Z., Latalski J. (2014) Nonlinear dynamics and synchronisation of pendula attached to a rotating hub.*The European Physical Journal - Special Topics* **223**:827-847.

[3] Hsu, C.S. (1987) Cell-to-Cell Mapping: A Method of Global Analysis for Nonlinear Systems.*Springer-Verlag*

Bifurcation Elimination in Rotor Gas Bearing Systems Applying Numerical Continuation with Embedded Design Optimization Scheme

Panagiotis Papafragkos, Ioannis Gavalas, Ioannis Raptopoulos and Athanasios Chasalevris
School of Mechanical Engineering, National Technical University of Athens, Athens, Greece

Abstract

High speed rotor systems mounted on gas foil bearings present bifurcations which change the quality of stability, and may compromise the operability of rotating systems, or increase noise level when response amplitude drastically increases. The paper identifies the dissipating work in the gas film to be the source of self-excited motions driving the rotor whirling close to bearing's surface. The energy flow among the components of the system is evaluated for various design sets of bump foil properties, rotor stiffness and unbalance magnitude. The paper presents a methodology to retain the dissipating work at positive values during the periodic limit cycle motions caused by unbalance. An optimization technique is embedded in the pseudo arc length continuation of limit cycles, those evaluated (when exist) utilizing an orthogonal collocation method. The optimization scheme considers the bump foil stiffness and damping as the variables for which bifurcations do not appear in a certain speed range. It is found that Neimark-Sacker bifurcations, which trigger large limit cycle motions, do not exist in the unbalanced rotors when bump foil properties follow the optimization pattern. Period doubling bifurcations are possible to occur, without driving the rotor in high response amplitude. Different design sets of rotor stiffness and unbalance magnitude are investigated for the efficiency of the method to eliminate bifurcations. The quality of the optimization pattern allows optimization in real time, and bearing properties shift values during operation, eliminating bifurcations and allowing operation in higher speed margins.

Introduction

Gas Foil Bearings (GFBs) are part of a promising oil-free technology in modern high-speed rotating machinery, distinguished for their reliability, simplicity, and environmentally friendly characteristics. Relying on a thin gas film building up an aerodynamic, load-carrying lubrication wedge, such bearings are self-acting and do not require any external pressurization. Most notably, due to the absence of solid-to-solid contact between the airborne rotor journal and the bearing sleeve, excessively low wear and power loss can be achieved. Several types of GFBs have been introduced in the past, with the most common and efficient being the bump type foil bearing. The major difference detected in comparison with the conventional oil bearings is the presence of a thin gas film as a lubricant, which results to building up an aerodynamic, load-carrying lubrication wedge and eliminates the need for external pressurization [1-4].

During the last few decades, the potential of GFBs has been widely confirmed by a great number of successful applications in air cycle machines of commercial aircraft [5]. Lately, in particular as a result of insurmountable speed, temperature, and weight limitations of conventional rolling-element bearings, novel concepts of oil-free turbochargers [6], oil-free rotorcraft propulsion engines [7], and micro gas turbines [8] are gaining increasing interest. Gas foil bearings have been successfully used in high-speed turbomachines, and they present a remarkable reliability. As the stiffness of the foils is much smaller than that of the fluid film, the foil bearings can adapt to various working conditions through foil deformations. Owing to these advantages, foil bearings are identified as a potential alternative for oil bearings. If properly designed and operated, foil bearings would incur very slight wear and have a long service life [7].

The design of a GFB is a multi-physical problem, and the research work on GFBs follows generically scientific objectives which have to couple each other at most times; these are mainly a) the material development (super alloys) for use in the GFB components [3], b) the fluid-structure interaction including the aerodynamic lubrication problem (compressible flow) and the structural problem predicting the bump foil structure dynamic properties and dynamic behaviour [9-12], c) the nonlinear dynamics of simple or complex rotors mounted on GFBs [13-19], d) the development of alternative GFB configurations including also adjustable configurations and control schemes [20].

Nonlinear dynamics of rotor-GFB systems, and its study with tools like continuation methods, is relatively new object. Continuation methods have been applied on the nonlinear dynamics of rotor systems on oil bearings of several types [21,22], and recently in GFB rotor systems as well [23]. Bifurcations of Hopf type have been investigated at both bearing types (with oil and gas) [24]. The strongly nonlinear aerodynamic forces render a variety of motions and stability quality in the system, including periodic, quasi periodic and chaotic motions. Further to that, the system has the potential of totally different motions even at the same operating speed, according to initial conditions and operating parameters, such unbalance magnitude. Dynamic systems present stable and unstable solution branches and respective bifurcation sets, and this is the case in rotor-GFB systems too. Nonlinear dynamics of rotor-GFB systems were mostly used to correlate the quality of response of the system with advances in top/bump foil structure simulation, or alternative models in the aerodynamic simulation.

Further to the aerodynamic modelling and, the bump type foil modelling has been investigated during the last decades as its properties are directly correlated to the aerodynamic performance of the bearing. Heshmat et al. [1] introduced the so-called simple elastic foundation model, consisting of linear elastic uncoupled springs. No viscous damping was taken

into account until Peng and Carpino [9] and Ku and Heshmat [26] took into consideration the top-to-bump foil and bump-to-housing Coulomb friction damping. Later on, Peng and Carpino [27] introduced a 2D foil model structure characterized by linear stiffness and damping coefficients, while considering the elastic behaviour of the bump foil. Alternative approaches have been published by Lez et al. [25] and other researchers [23], where the foil bumps and their interaction are modelled by multi-degree freedom systems. Baum et al. [12] introduced another foil structure, consisting of rigid, massless, beam-like elements with one finite dimension in axial direction and no coupling of the elements in the circumferential one, where each bump foil is modelled by a non-linear spring and a linear damper.

This paper aims to the insight of the local instability mechanisms, which trigger bifurcations, and drive the response of the system far from its elastic response (self-excited vibrations), usually close to the bearing clearance in journal positions and the rotor-stator clearance along the rotor. In this paper, it is found that the dissipating energy in the gas film should be directly correlated to the first (at lower speed) bifurcation detected in such a system, this being a Neimark-Sacker bifurcation in the unbalanced system, at most cases, or a period-doubling (flip) bifurcation in some others. Specifically, this paper benefits from the well-known lemma that self-excited motions are triggered when negative damping is included in the system; similar notification was made in [28] for rotors on oil bearings, under linear harmonic analysis. The energy flow is evaluated in this system for various design sets and this is used to an optimization scheme to avoid bifurcations in a certain speed range. The paper is organized as follows:
The dynamic system of consisting of an elastic Jeffcott rotor mounted on two GFBs is composed for the autonomous and the non-autonomous case. The composition of the system renders a set of ordinary differential equations of 1st order (ODE set). The aerodynamic lubrication model and the bump foil structural model follow existing literature [12,14]. The authors program the pseudo arc length continuation method [29-31] with embedded orthogonal collocation method to provide the potential periodic solutions of the ODE set with unbalance excitation.

Moreover, the quality of motions developed in such system is discussed evaluating the bifurcation sets, the time-frequency decomposition of the response and Floquet multipliers, for some design scenarios and at a certain speed range. The energy flow is evaluated in the system during the respective periodic motions, with primary interest on the dissipative work of gas forces. An optimization scheme of successive polls for the two GFB design variables is implemented from the literature [32] and retains the dissipative work in the gas film positive in the respective speed range; Neimark-Sacker bifurcations are found to be eliminated in the respective speed range. However, period doubling bifurcations still exist at some cases, without these to drive the response at high amplitudes though. Different rotor stiffness and unbalance magnitude are considered in the results. The paper concludes that maximizing the dissipative work in the gas film does not trigger self-excited motions of the system, in a certain operating speed range, approximately two times wider than the respective without optimization of the GFB properties.

Modelling and Formulation of the Nonlinear Dynamic System

The physical model of the flexible rotor and of the gas foil bearings is presented in Fig. 1 where the symmetric rotor model considers the well-known Jeffcott rotor. The analytical dynamic model includes 4 DoFs for the rotor (due to symmetry), and the unique parameter of rotor design included in the model is the rotor's lateral stiffness $\bar{k}_s$. The gas foil bearing model [2] considers linear spring and damping properties in the bump foil in the radial direction, and the key parameters of the gas bearing design consider the bump foil compliance $\bar{\alpha}_f$, and the pump foil damping coefficient c_f as a function of the loss factor η.

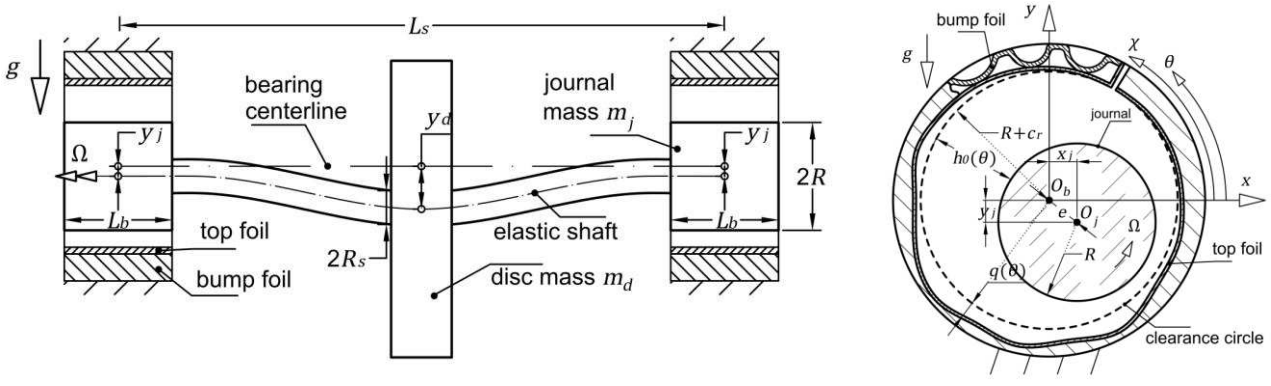

(a) (b)

Figure 1: a) representation of an elastic Jeffcott rotor model with two journal masses at its ends, mounted on two gas-foil bearings; b) representation of the gas foil bearing configuration

Analytical model of the gas bearing

The assumptions introduced in the elastoaerodynamic lubrication problem are: a) isothermal gas film, b) laminar flow of the gas, c) no-slip boundary conditions, d) continuum flow, e) negligible fluid inertia, f) ideal isothermal gas law $(p/\rho = \text{constant})$, g) negligible entrance and exit effects, and h) negligible curvature $(R \approx R + c_r)$. The Reynolds

equation for compressible gas flow under these assumptions is given in Eq. (1) [12], and it is an implicit function of time and of journal and top foil kinematics.

$$\frac{\partial}{\partial \bar{x}}\left(\bar{p}\bar{h}^3\frac{\partial \bar{p}}{\partial \bar{x}}\right)+\kappa^2\frac{\partial}{\partial \bar{z}}\left(\bar{p}\bar{h}^3\frac{\partial \bar{p}}{\partial \bar{z}}\right)=\bar{\Omega}\frac{\partial}{\partial \bar{x}}\left(\bar{p}\bar{h}\right)+2\frac{\partial}{\partial \tau}\left(\bar{p}\bar{h}\right) \tag{1}$$

Analytical solution for Eq. (1) cannot be defined; a common approach to evaluate the pressure distribution is the FDM. The pressure domain is converted into a grid of $i=1,\ldots,N_X+1$ and $j=1,\ldots,N_Z+1$ points, where i and j are the indexes in the circumferential and axial direction respectively, see Fig. 3a.

The Reynolds equation is first rewritten defining the first time derivative of the pressure in Eq. (2a) and after some math in Eq. (2b). Then, the discrete Reynolds equation is defined in the grid points expressing the partial derivatives with finite differences.

$$\frac{\partial}{\partial \tau}\left(\bar{p}\bar{h}\right)=\frac{1}{2}\frac{\partial}{\partial \bar{x}}\left(\bar{p}\bar{h}^3\frac{\partial \bar{p}}{\partial \bar{x}}\right)+\frac{\kappa^2}{2}\frac{\partial}{\partial \bar{z}}\left(\bar{p}\bar{h}^3\frac{\partial \bar{p}}{\partial \bar{z}}\right)-\frac{\bar{\Omega}}{2}\frac{\partial}{\partial \bar{x}}\left(\bar{p}\bar{h}\right) \tag{2a}$$

$$\dot{\bar{p}}=\frac{1}{2\bar{h}}\frac{\partial}{\partial \bar{x}}\left(\bar{p}\bar{h}^3\frac{\partial \bar{p}}{\partial \bar{x}}\right)+\frac{\kappa^2}{2\bar{h}}\frac{\partial}{\partial \bar{z}}\left(\bar{p}\bar{h}^3\frac{\partial \bar{p}}{\partial \bar{z}}\right)-\frac{\bar{\Omega}}{2\bar{h}}\frac{\partial}{\partial \bar{x}}\left(\bar{p}\bar{h}\right)-\frac{\bar{p}\dot{\bar{h}}}{\bar{h}} \tag{2b}$$

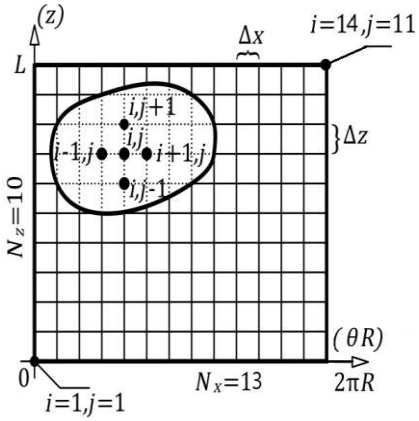

Figure 2a: Finite difference grid $N_x \times N_z$ used for the evaluation of pressure distribution

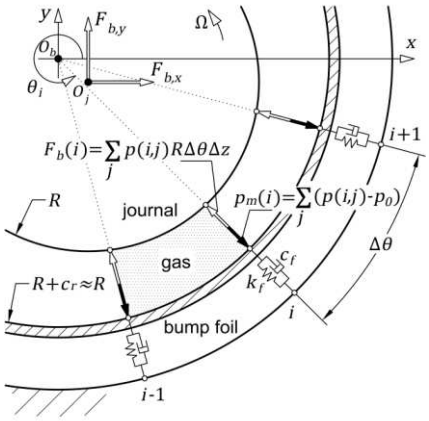

Figure 2b: Definition of the mean pressure p_m applied over bearing length L_b, and of gas force F_b with respective indexes.

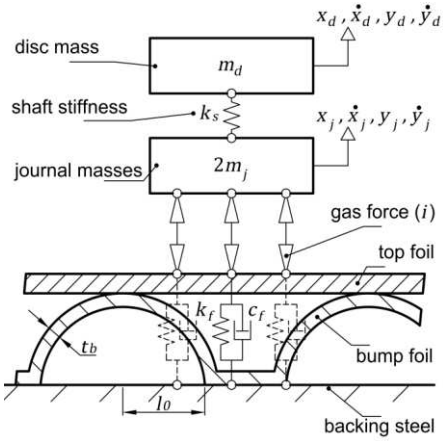

Figure 2c: Representation of the physical model; bump foil is modelled by linear springs and dampers.

The dimensionless parameters of gas pressure $\bar{p}$, gas film thickness $\bar{h}$, spatial coordinates (circumferential and axial respectively) θ and $\bar{z}$, time τ, rotating speed $\bar{\Omega}$, and ratio $\kappa = R/L_b$ are included in the elastoaerodynamic lubrication problem of Eq. (1). The gas film thickness function is defined in Eq. (3) for the continuous and the discrete pressure domain (finite difference grid) where $\bar{q}=\bar{q}(\theta)$ (or $\bar{q}_i=\bar{q}(\theta_i)$ in the discrete pressure domain) is the foil deformation in radial direction, see also Fig. 2a and Fig. 3b.

$$\bar{h}=1-\bar{x}_j\cos\theta-\bar{y}_j\sin\theta+\bar{q}, \qquad \bar{h}_i=1-\bar{x}_j\cos\theta_i-\bar{y}_j\sin\theta_i+\bar{q}_i \tag{3}$$

Boundary and initial conditions of the problem are defined in continue. Ambient pressure is assumed at the starting and ending angle of the foil (periodic boundary condition) in Eq. (4), in the continuous and the discrete pressure domain respectively.

$$\bar{p}(\tau,\theta_0,\bar{z})=\bar{p}(\tau,\theta_0+2\pi,\bar{z})=1, \qquad \bar{p}_{1,j}=\bar{p}_{N_X+1,j}=1 \tag{4}$$

Taking into account the symmetry of the lubrication problem, instead of assuming the gas pressure equal to the ambient p_o at the axial ends, $\bar{p}(\bar{z}=0)=\bar{p}(\bar{z}=1)=1$, the boundary condition can be written in Eq. (5) (for the continuous and the discrete pressure domain). In this way the lubrication problem is solved in the half domain, reducing the evaluation cost severely.

$$\left.\frac{\partial \bar{p}}{\partial \bar{z}}\right|_{\bar{z}=1/2}=0, \qquad \frac{\bar{p}_{i,N_Z/2}-\bar{p}_{i,N_Z/2-1}}{\Delta\bar{z}}=0 \tag{5}$$

Last, the initial conditions for the dimensionless form of the problem are defined in Eq. (6) (in the continuous and the discrete pressure domain).

$$\bar{p}\left(\tau=0,\theta,\bar{z}\right)=1,\ \overset{\langle t_0\rangle}{\bar{p}}_{i,j}=1 \text{ and } \bar{q}\left(\tau=0,\theta\right)=0,\quad \overset{\langle t_0\rangle}{\bar{q}}_{i}=0 \tag{6}$$

After evaluating gas pressure $\bar{p}$ (as $\bar{p}_{i,j}$), the nonlinear gas forces are determined in Eq. (7), where $\Delta\bar{x} = 2\pi / N_X$ and $\Delta\bar{z} = 1 / N_Z$.

$$\bar{F}_{B,X} = -\int_0^{2\pi}\int_0^1 \left(\bar{p}-1\right)\cos\theta d\bar{z}d\theta = -\sum_{i=2}^{N_X}\sum_{j=2}^{N_Z}\left(\left(\bar{p}_{i,j}-1\right)\cos\theta_i\Delta\bar{x}\Delta\bar{z}\right) \tag{7a}$$

$$\bar{F}_{B,Y} = -\int_0^{2\pi}\int_0^1 \left(\bar{p}-1\right)\sin\theta d\bar{z}d\theta = -\sum_{i=2}^{N_X}\sum_{j=2}^{N_Z}\left(\left(\bar{p}_{i,j}-1\right)\sin\theta_i\Delta\bar{x}\Delta\bar{z}\right) \tag{7b}$$

In this way the aerodynamic problem renders $N_X \cdot N_Z$ ODEs of 1st order with respect to the time derivative of the point pressure in Eq. (8)

$$\dot{\bar{\mathbf{p}}} = \left\{\dot{\bar{p}}_{i,j}\right\} = \mathbf{f}_B\left(\bar{\mathbf{p}},\bar{\mathbf{x}},\dot{\bar{\mathbf{x}}},\bar{\mathbf{q}},\dot{\bar{\mathbf{q}}}\right) \tag{8}$$

The vectors $\bar{\mathbf{x}}$ and $\bar{\mathbf{q}}$ may be perceived as $\bar{\mathbf{x}} = \left\{x_j \quad y_j \quad x_d \quad y_d\right\}^{\mathrm{T}}$ representing the journal motion (coupled to the disc motion through the rotor's equations of motion) and $\bar{\mathbf{q}} = \left\{\bar{q}_1 \quad \bar{q}_1 \quad \dots \quad \bar{q}_{N_X}\right\}^{\mathrm{T}}$ representing the foil motion (coupled to the journal motion through the Reynolds equation due to the gas film thickness function).

It is important to mention that it is quite common that sub-ambient pressure arises in GFBs. The sub-ambient pressure can cause the top foil to separate from the bumps into a position in which the pressure on both sides of the pad is equalized. Heshmat et al. [1] introduced a set of boundary conditions accounting for this separation effect. More specifically, a simple Gümbel boundary condition is imposed, meaning that sub-ambient pressures are discarded when integrating the pressure in Eq. (7) to obtain the bearing force components $\bar{F}_{B,X}$, $\bar{F}_{B,Y}$ essentially leaving the sub-ambient regions ineffective. In terms of numerical calculations, the assumption made by Heshmat [1] can be simply explained as following: in case fluid pressure p is lower than the ambient p_0, then the former should be considered equal to p_0 and the foil deformation at these points will be zero $\left(\bar{q}_i = 0 \text{ for } \bar{p}_i < 1\right)$.

The simplified model for the bump foil structure is depicted at Fig. 2b. The structure consists of $N_X - 2$ linear massless elements of stiffness $\bar{k}_f$ (compliance $\bar{\alpha}_f = 1/\bar{k}_f$) and damping $\bar{c}_f$. The springs and dampers mount the corresponding $N_X - 1$ top foil stripes of area $\Delta x \cdot L_b$ (or dimensionless area $\Delta\bar{x}\cdot 1$), see Fig. 3b. The top foil of the bearing is not covering a complete cylinder; a single gap can be found at $\theta = \theta_0$, see Fig. 2a, where the top foil is clamped to the bearing housing. Therefore, the moving top foil stripes are $N_X - 1$, see Fig. 3b. The top foil stripes are assumed to remain parallel to the bearing longitudinal axis during their lateral motion, therefore no axial coordinate is required for the top foil motion. The geometry of the foil structure and its properties, shown in Figs. 2a and 3b, render the dimensionless compliance $\bar{\alpha}_f = 2p_0\left(l_0/t_b\right)^3\left(1-\nu^2\right)s_0/\left(c_r E\right)$ [14]. The motion of each of the top foil stripe is excited by the mean gas pressure $\bar{p}_{m,i}$ acting on the top of it, creating the gas force $\bar{F}_B(i)$, see Figs. 2b and 3b. The mean gas pressure $\bar{p}_{m,i}$ is defined in Eq. (9) (in the continuous and discrete pressure domain respectively), for dimensional and dimensionless form.

$$p_m(\theta) = \frac{1}{L_b}\int_0^{L_b} p(\theta)dz, \quad p_{m,i} = \frac{1}{L_b}\sum_{j=2}^{N_Z}\left(p_{i,j}\Delta z\right), \qquad \bar{p}_{m,i} = \frac{1}{1}\sum_{j=2}^{N_Z}\left(\bar{p}_{i,j}\Delta\bar{z}\right) = \frac{1}{N_Z}\sum_{j=2}^{N_Z}\left(\bar{p}_{i,j}\right) \tag{9}$$

The foil stiffness and damping coefficient are given as $\bar{k}_f = 1/\bar{\alpha}_f$ and $\bar{c}_f = \eta\bar{k}_f$ for foil motion synchronous to the excitation. The $N_X - 1$ ODEs that describe the radial displacement $\bar{q}_i$ of the stripe i are defined in Eq. (10).

$$\bar{c}_f\dot{\bar{q}}_i + \bar{k}_f\bar{q}_i = \bar{p}_{m,i}, \qquad i = 2,3,...,N_X \tag{10}$$

The ODEs in Eq. (10) may be written as in Eq. (11) to be used in continue.

$$\dot{\bar{\mathbf{q}}} = \left\{\dot{\bar{q}}_i\right\} = \mathbf{f}_F\left(\bar{\mathbf{q}},\bar{\mathbf{p}},\bar{\mathbf{x}},\dot{\bar{\mathbf{x}}}\right) \tag{11}$$

Analytical model of the flexible rotor

The equations of motion for the Jeffcott rotor shown in Fig. 1 are defined in Eq. (12) for the journal and the disc, in the two main directions, horizontal and vertical.

$$\ddot{\bar{x}}_j = \frac{m_d}{2m_j}\bar{k}_s\left(\bar{x}_d - \bar{x}_j\right) + \xi \cdot \bar{F}_{B,X}\,, \qquad \ddot{\bar{y}}_j = \frac{m_d}{2m_j}\bar{k}_s\left(\bar{y}_d - \bar{y}_j\right) + \xi \cdot \bar{F}_{B,Y} - \sigma \tag{12a}$$

$$\ddot{\bar{x}}_d = -\bar{k}_s\left(\bar{x}_d - \bar{x}_j\right) + \bar{F}_{U,X}\,, \qquad \ddot{\bar{y}}_d = -\bar{k}_s\left(\bar{y}_d - \bar{y}_j\right) + \bar{F}_{U,Y} - \sigma \tag{12b}$$

The ODEs in Eq. (12) may be written in Eq. (13), in the state space representation, to be used in continue.

$$\dot{\bar{\mathbf{x}}} = \mathbf{f}_R\left(\bar{\mathbf{p}}, \bar{\mathbf{x}}, \dot{\bar{\mathbf{x}}}, \bar{\mathbf{q}}, \dot{\bar{\mathbf{q}}}\right) \tag{13}$$

In Eq. (12) $\bar{k}_s$ is the dimensionless shaft stiffness coefficient, and ξ, σ are dimensionless parameters defined in Eq. (14).

$$\xi = \frac{36\mu^2 L R^5}{m_j p_0 {c_r}^5}, \qquad \sigma = \frac{36\mu^2 R^2 g}{{p_0}^2 {c_r}^5} \tag{14}$$

In addition, in Eq. (12), $\bar{F}_{U,X}$ and $\bar{F}_{U,Y}$ are the dimensionless unbalance forces defined in Eq. (15a) for constant rotating speed $\bar{\Omega}$, and in Eq. (15b) for linearly varying rotating speed $\bar{\Omega} = \bar{a} \cdot \tau$ with constant acceleration $\bar{a}$.

$$\bar{F}_{U,X} = \varepsilon \cdot \bar{\Omega}^2 \cos\bar{\varphi}_r\,, \qquad \bar{F}_{U,Y} = \varepsilon \cdot \bar{\Omega}^2 \sin\bar{\varphi}_r\,, \qquad \bar{\varphi}_r = \bar{\Omega}\tau \tag{15a}$$

$$\bar{F}_{U,X} = \varepsilon\left(\bar{\Omega}^2 \cos\bar{\varphi}_r + \bar{a}\sin\bar{\varphi}_r\right), \qquad \bar{F}_{U,Y} = \varepsilon\left(\bar{\Omega}^2 \sin\bar{\varphi}_r - \bar{a}\cos\bar{\varphi}_r\right), \qquad \bar{\varphi}_r = \bar{a}\tau^2/2 \tag{15b}$$

Dimensionless unbalance eccentricity $\varepsilon = e_u / c_r$ follows in this paper the ISO unbalance grades (G-grades) for low, medium, and high unbalance as G1, G2.5 and G6.3 correspondingly. The unbalance located in the disc is of magnitude $u = \left(m_d + 2m_j\right)e_u$ at each case, and the corresponding eccentricity e_u is given by Eq. (16), where the service speed of the system is selected at $\Omega_r = 2500\,\text{rad/s}$.

$$e_u[\text{mm}] = \frac{G}{\Omega_r[\text{rad/s}]}, \qquad G = 1,\ 2.5,\ 6.3 \tag{16}$$

Composition and solution of the dynamic system

Eqs. (8), (11), and (13) compose a coupled ODE set which is composed by the discretized Reynolds equation in the $\mathbf{f}_B$ equations, the foil motion in $\mathbf{f}_F$ equations, and the rotor motion in $\mathbf{f}_R$ equations. The coupled nonlinear ODE set is defined in Eq. (17) expressing a non-autonomous dynamic system which will be studied with respect to the bifurcation parameter $\bar{\Omega}$. The ODE set is characterized as non-autonomous due to the explicit time presence in the equations of unbalance forces, see Eq. (15). The state vector $\bar{\mathbf{s}}$ and the respective functions $\mathbf{f}$ are defined in Eq. (18).

$$\dot{\bar{\mathbf{s}}} = \mathbf{f}\left(\bar{\mathbf{s}}, \bar{\Omega}, \tau\right) \tag{17}$$

$$\bar{\mathbf{s}} = \left\{\bar{\mathbf{p}} \quad \bar{\mathbf{q}} \quad \bar{\mathbf{x}}\right\}^{\mathrm{T}},\ \mathbf{f} = \left\{\mathbf{f}_B \quad \mathbf{f}_F \quad \mathbf{f}_R\right\}^{\mathrm{T}} \tag{18}$$

The total number of equations in Eq. (17) (size of vector function $\mathbf{f}$) is $N = \left(N_X \cdot N_Z\right) + \left(N_X - 1\right) + 8$ with the first term coming from the pressure equations, the second term coming from the foil equations, and the third term from the rotor equations in state space.

The ODE set in Eq. (17) renders the time response of the physical system when time integration is applied [32]. The system is numerically stiff and special algorithms are applied in time integration [32]. Furthermore, the Reynolds equation can be reduced in size applying an order reduction method [12], improving the computational cost. The time integration can handle both cases of unbalance equations, for constant rotating speed or for run-up, see Eq. (15).

An orthogonal collocation method [30] is applied for the computation of limit cycle motions produced by the ODE set in Eq. (17) at a constant $\bar{\Omega}$; Eqs. (15a) apply for unbalance forces at this case. Numerical continuation of limit cycles has been programmed by the authors according to pseudo arc length continuation method [29,33] with embedded collocation scheme [30]. The formulation of the method is defined also in Appendix A1. As the collocation method cannot handle non-autonomous ODE systems, Eq. (17) has to be converted to autonomous. This is achieved by coupling the ODE set of Eq. (17) with a two DoF oscillator, see Eq. (19), whose unique solution is a harmonic motion of frequency $\bar{\Omega}$, see Eq. (20) [30].

$$\dot{\bar{s}}_{N+1} = f_{N+1} = \bar{s}_{N+1} + \bar{\Omega}\cdot\bar{s}_{N+2} - \bar{s}_{N+1}\cdot\left(\bar{s}_{N+1}^2 + \bar{s}_{N+2}^2\right) \tag{19a}$$

$$\dot{\bar{s}}_{N+2} = f_{N+2} = -\bar{\Omega}\cdot\bar{s}_{N+1} + \bar{s}_{N+2} - \bar{s}_{N+2}\cdot\left(\bar{s}_{N+1}^2 + \bar{s}_{N+2}^2\right) \tag{19b}$$

$$\bar{s}_{N+1} = \cos\left(\bar{\Omega}\tau\right), \quad \bar{s}_{N+2} = \sin\left(\bar{\Omega}\tau\right) \tag{20}$$

The size of the final autonomous ODE set is $N+2$ and is defined in Eq. (21) with the unbalance forces to be defined at constant rotating speed, in Eq. (22).

$$\dot{\tilde{\bar{\mathbf{s}}}} = \tilde{\mathbf{f}}\left(\tilde{\bar{\mathbf{s}}}, \bar{\Omega}\right) \tag{21a}$$

$$\tilde{\bar{\mathbf{s}}} = \left\{\bar{\mathbf{s}}^{\mathrm{T}} \quad \bar{s}_{N+1} \quad \bar{s}_{N+2}\right\}^{\mathrm{T}}, \quad \tilde{\mathbf{f}} = \left\{\mathbf{f}^{\mathrm{T}} \quad f_{N+1} \quad f_{N+2}\right\}^{\mathrm{T}} \tag{21b}$$

$$\bar{F}_{U,X} = \varepsilon \cdot \bar{\Omega}^2 \bar{s}_{N+1}, \qquad \bar{F}_{U,Y} = \varepsilon \cdot \bar{\Omega}^2 \bar{s}_{N+2} \tag{22}$$

Results and Discussion

The dynamic system defined in Eq. (19) in autonomous and in Eq. (20) in non-autonomous version is investigated on its potential to develop a variety of bifurcation sets with respect to the key design parameters, namely rotor stiffness $\bar{k}_s$, foil compliance $\bar{a}_f$, foil loss factor η, and unbalance magnitude u. In this paper, the key design parameters are defined within specific intervals, composing the case studies which are presented in continue. The design parameters follow a variation of "low", "reference", and "high". This is interpreted to the rotor stiffness values $\bar{k}_s = 0.3,1,3$ (flexible to rigid rotor), foil compliance values $\bar{a}_f = 0.01,0.1,1$ (stiff to flexible foil), foil loss factor $\eta = 0.005, 0.05, 0.5$ (low to high foil damping), and unbalance magnitude $u(G1), u(G2.5), u(G6.3)$ (low to high unbalance). A reference system is defined with the design parameters to be $\bar{k}_s = 1$, $\bar{a}_f = 0.1$, $\eta = 0.05$, and $u(G6.3)$.

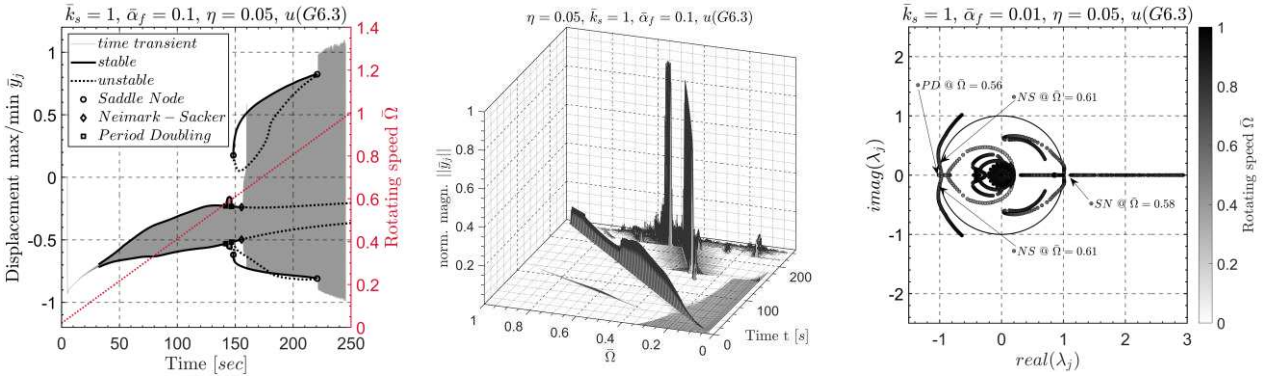

(a) (b) (c)

Figure 3: Reference system of $\bar{k}_s = 1$, $\bar{a}_f = 0.1$, $\eta = 0.05$, and $u(G6.3)$ a) Transient response and continuation of limit cycles during run-up b) STFT of the response time history c) Floquet multipliers of the corresponding limit cycles

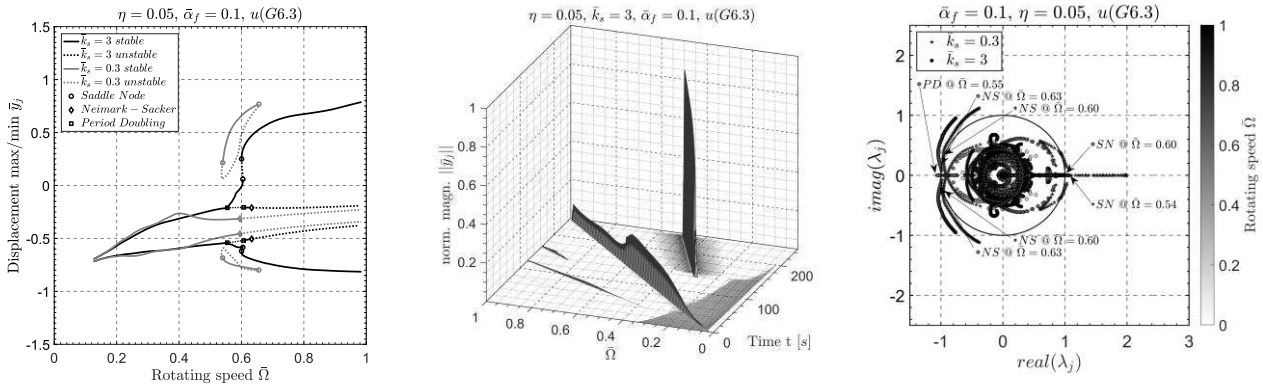

(a) (b) (c)

Figure 4: System of $\bar{k}_s^-, \bar{k}_s^+, \bar{a}_f = 0.1, \eta = 0.05, u = (G6.3)$ a) Continuation of limit cycles, b) STFT of the response time history $\bar{k}_s^+$, c) Floquet multipliers of the corresponding limit cycles.

In Fig. 3a the time history of the journal motion in the vertical plane is presented together with the maximum and minimum values of the limit cycle at each rotating speed. It has to be clarified that the rotating speed is retained constant when limit cycles are evaluated, and the unbalance forces are applied with different formulas in the ODE system in the transient run-up and in the ODE system for constant rotating speed. A reference bifurcation set is established in Fig. 3a with PD, SN, and NS bifurcations to be presented. The frequency content of the time history

obtained during the run-up is depicted in Fig. 3b where time-frequency decomposition is applied. The Floquet multipliers in Fig. 3c provide information regarding the quality of bifurcations mentioned above. In Fig. 4 considers systems of different rotor stiffness, and two cases are presented in Fig. 4a for $\bar{k}_s^{+} = 3$ and $\bar{k}_s^{-} = 0.3$. One may notice the difference compared to the reference case. Period doubling bifurcation is not noticed in this case.

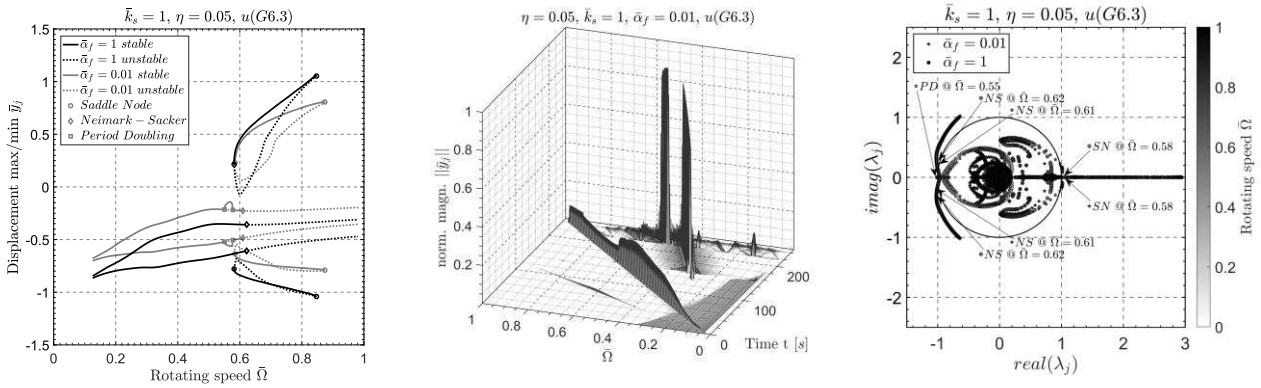

(a) (b) (c)

Figure 5: System of $\bar{k}_s = 1$, $\bar{a}_f{}^{-}, \bar{a}_f{}^{+}$, $\eta = 0.05$, $u = (G6.3)$. a) Continuation of limit cycles, b) STFT of the response time history for $\bar{a}_f{}^{+}$, c) Floquet multipliers of the corresponding limit cycles.

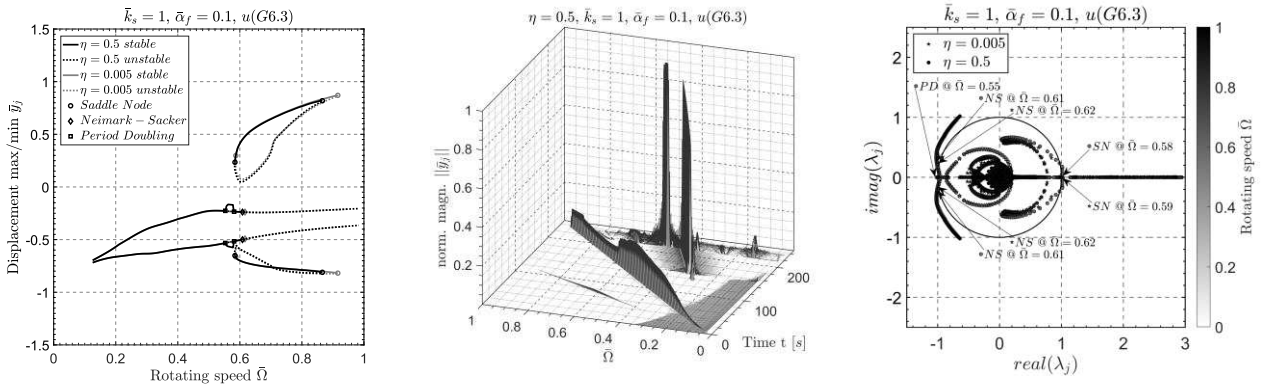

(a) (b) (c)

Figure 6: System of $\bar{k}_s = 1$, $\bar{a}_f = 0.1$, η^{-}, η^{+}, $u(G6.3)$. a) Continuation of limit cycles, b) STFT of the response time history for η^{+}, c) Floquet multipliers of the corresponding limit cycles for η^{+}.

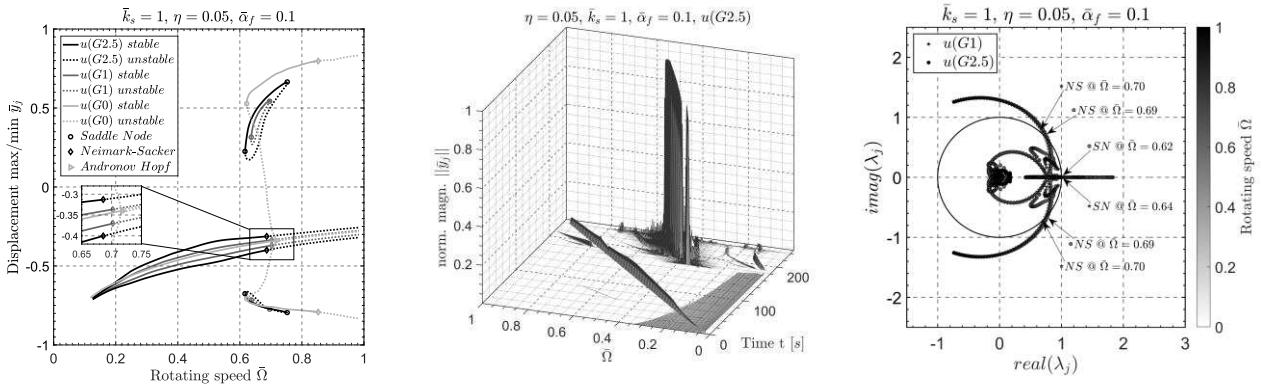

Figure 7: System of $\bar{k}_s = 1$, $\bar{a}_f = 0.1$, $\eta = 0.05$. a) Continuation of limit cycles, b) STFT of the response time history, c) trajectory, Poincare map, and FFT at $\bar{\Omega} = 0.97$, d) Floquet multipliers of the corresponding limit cycles.

In Fig. 5, systems of different foil compliance are considered, and two cases are presented in Fig. 5a, for $\bar{a}_f{}^{+} = 1$ (flexible foil) and $\bar{a}_f{}^{-} = 0.01$ (rigid foil). One may notice the different bifurcation sets compared to the reference case, and the previous case. The type of bifurcations are same to this at the reference case, but the speed in which they appear is different.

In Fig. 6, systems of different foil damping are considered, and two cases are presented in Fig. 6a, for $\eta^{+}=0.5$ (high foil damping) and $\eta^{-}=0.005$ (low foil damping). The influence of foil damping in the bifurcation set is not severe, compared to the reference design (see Fig. 3).

In Fig. 7, systems of different unbalance are considered. It is worth noticing that the autonomous system of $u(G0)$ loses local stability of fixed point equilibria through an Andronov-Hopf bifurcation, at similar speed where the unbalanced systems lose local stability through NS bifurcations. Further to that, in the unbalanced systems, the higher the unbalance is, the lower the speed of NS bifurcations is. Stable limit cycles close to radial clearance occur with higher amplitude in the balanced system, than in the unbalanced systems. In the balanced system the limit cycles of amplitude close to radial clearance will lose stability through a NS bifurcation at high speeds.

Energy flow and optimization for bifurcation elimination

The work of the bearing forces is evaluated in Eq. (23a), the work of the bump foil forces is evaluated in Eq. (23b), and the work of unbalance forces in evaluated in Eq. (23c).

$$W_B = 2\sum_{i=1}^{N_t}\left(F_{B,X}(i)\cdot\delta x_j(i)+F_{B,Y}(i)\cdot\delta y_j(i)\right)=W_{cb}+\underbrace{W_{kb}}_{=0} \tag{23a}$$

$$W_f = 2\sum_{i=1}^{N_t}\left(\sum_{j=1}^{N_s}F_{f,j}(i)\cdot\delta q_j(i)\right)=W_{cf}+\underbrace{W_{kf}}_{=0}\ ,\quad W_{fu}=\sum_{i=1}^{N_t}\left(F_{U,X}(i)\cdot\delta x_d(i)+F_{U,Y}(i)\cdot\delta y_d(i)\right) \tag{23b,c}$$

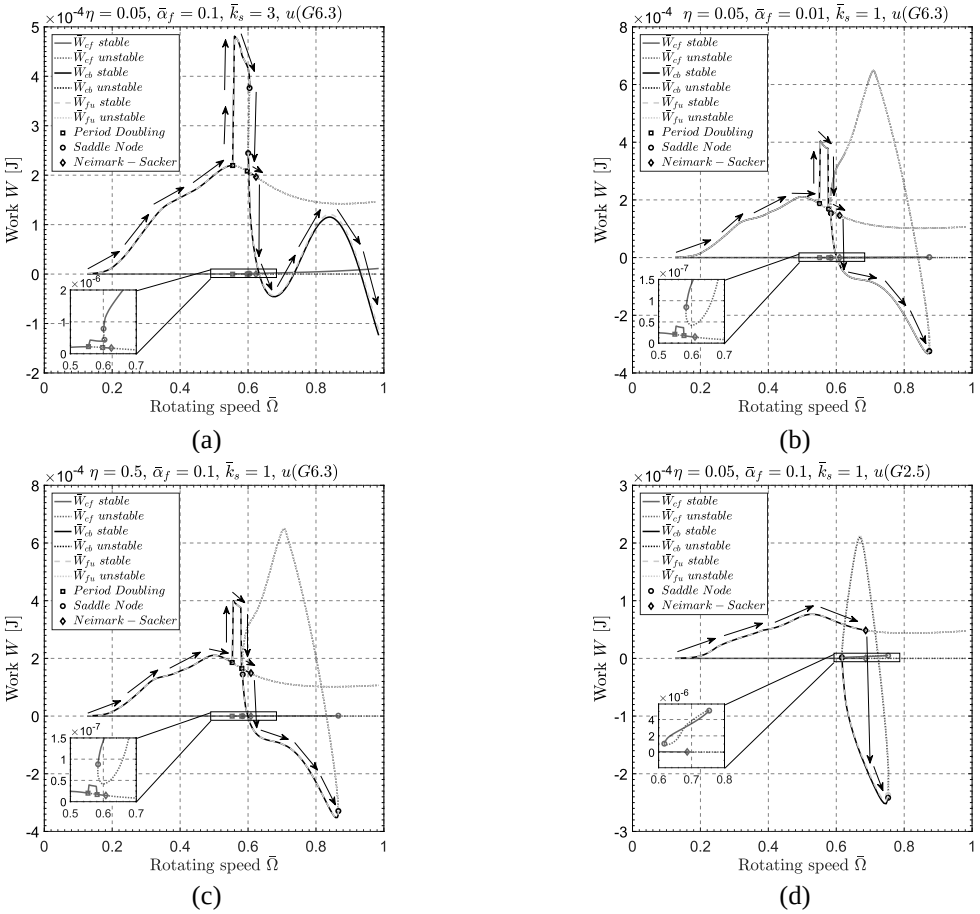

Figure 8: Evaluation of energy flow at the respective limit cycles for a) $\bar{k}_s=3$, $\bar{\alpha}_f=0.1$, $\eta=0.05$, $u(G6.3)$ b) $\bar{k}_s=1$, $\bar{\alpha}_f=0.01$, $\eta=0.05$, $u(G6.3)$, c) $\bar{k}_s=1$, $\bar{\alpha}_f=0.1$, $\eta=0.5$, $u(G6.3)$, and d) $\bar{k}_s=1$, $\bar{\alpha}_f=0.1$, $\eta=0.05$, $u(G2.5)$.

In Figs. 8a-d, both stable and unstable limit cycles are considered with the respective notation. At all cases, it is found that Neimark-Sacker bifurcations are triggered simultaneously to the reverse (from positive values to negative) of the dissipating work in the gas film W_{cb}, meaning that energy is not dissipated in the gas film (when $W_{cb}<0$) and self-excitation takes place. The respective limit cycles for the cases in Fig. 8 can be found in the previous Section. In Figs. 8a-d, the arrows depict the path that would be followed during the run-up of the system (time integration).

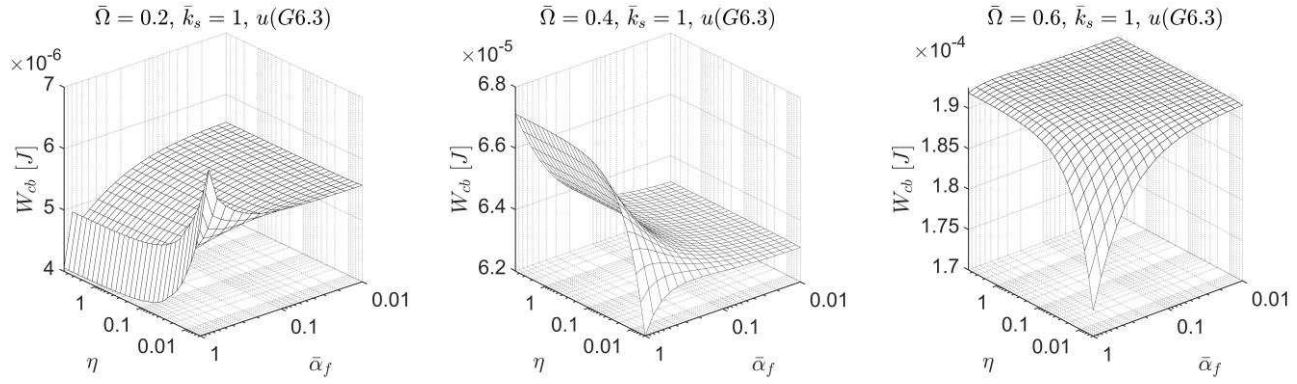

(a) (b) (c)

Figure 9: Dissipated energy in the gas film in one limit cycle for various values of foil compliance $\bar{a}_f$ and foil loss factor η, at a) $\bar{\Omega} = 0.2$, b) $\bar{\Omega} = 0.4$, c) $\bar{\Omega} = 0.6$

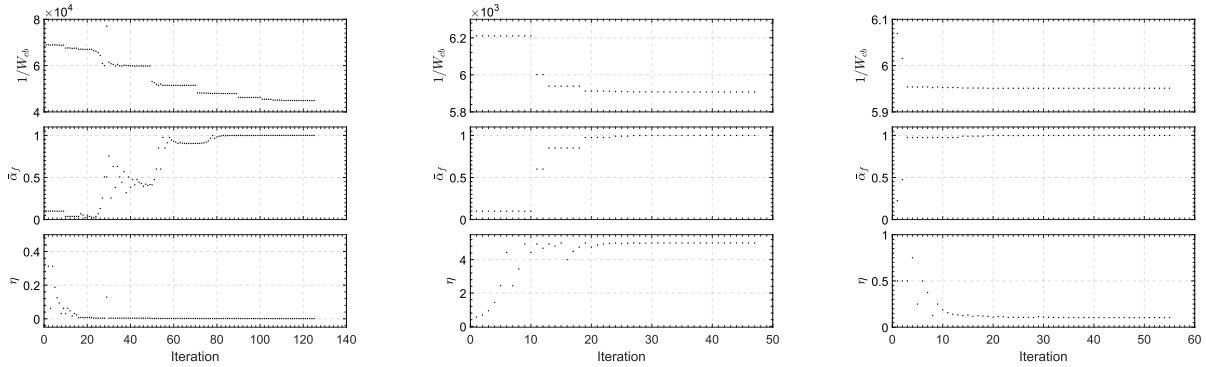

(a) (b) (c)

Figure 10: Optimization of the dissipated energy in the gas film of the reference system with $\bar{k}_s = 1$ and $u(G6.3)$ with respect to the foil compliance $\bar{a}_f$ and the foil loss factor η, at a) $\bar{\Omega} = 0.2$, b) $\bar{\Omega} = 0.4$, c) $\bar{\Omega} = 0.6$.

The optimization requires the minimization of an objective function OBJ, which is defined as the inverse of dissipated energy in the gas film, $OBJ = 1/W_{cb}$. Starting from random input values for foil compliance $\bar{a}_f$ and foil loss factor η, the optimization pattern renders after some iterations the values of $\bar{a}_f$ and η that maximize W_{cb} at every speed $\bar{\Omega}$. The limit cycle is plotted in Figs. 11 and 12 with the respective values $\bar{a}_f$ and η at each speed, for various design cases. Different rotor stiffness is considered in Fig. 11, and different unbalance magnitude applies in Fig. 12; the efficiency of the methodology to suppress bifurcations at a desired speed range is depicted. The operating speed range is limited by the limit values for the foil compliance $\bar{a}_f$ and the foil loss factor η, here defined as $0.01 \le \bar{a}_f \le 2$ and $0.0005 \le \eta \le 10$. These values may be considered differently according to the design limitations in each application of the rotating system. Considering the bifurcations sets evaluated in Section 3.2 for various designs, Figs. 15 and 16 depict elimination of bifurcations in approximately double speed range. It is also worth noticing that the bifurcation-free speed range is limited by a secondary Hopf (Neimark-Sacker) bifurcation at all cases of design.

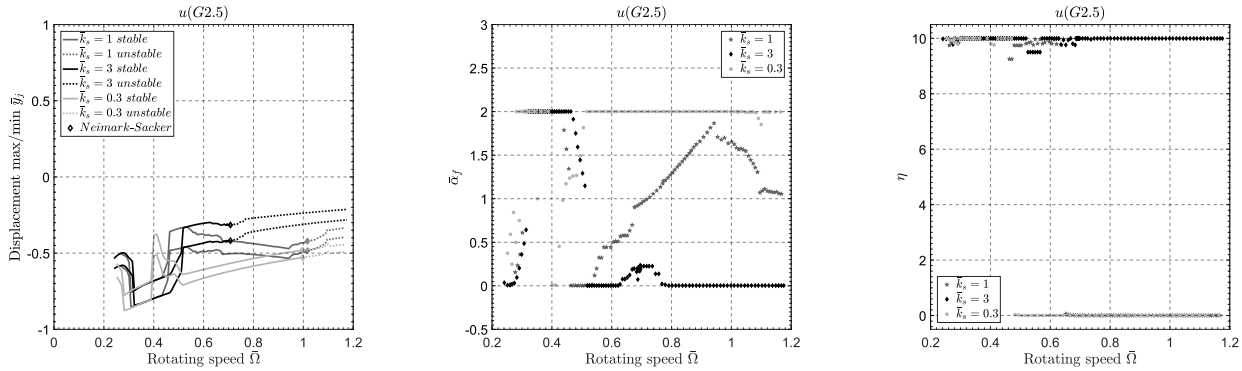

(a) (b) (c)

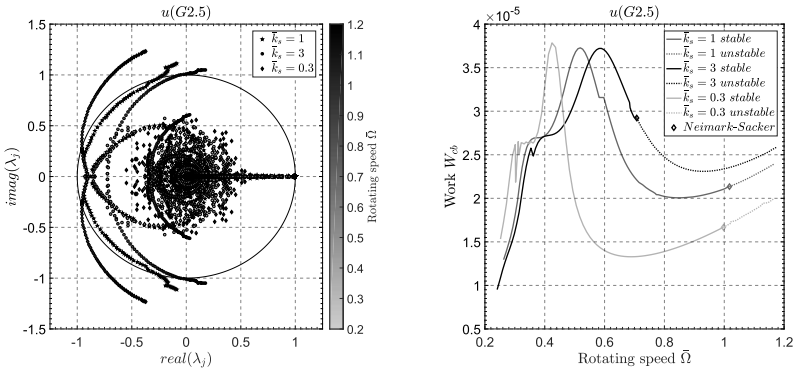

(d) (e)

Figure 11: Elimination of bifurcations at a speed range for the system of $u(G2.5)$ and $\bar{k}_s = 0.1$, $\bar{k}_s = 1$, $\bar{k}_s = 3$ a) journal motion limit cycles and corresponding values for b) compliance $\bar{a}_f$,c) loss factor η ,d) Floquet multipliers e) dissipating work in the gas film

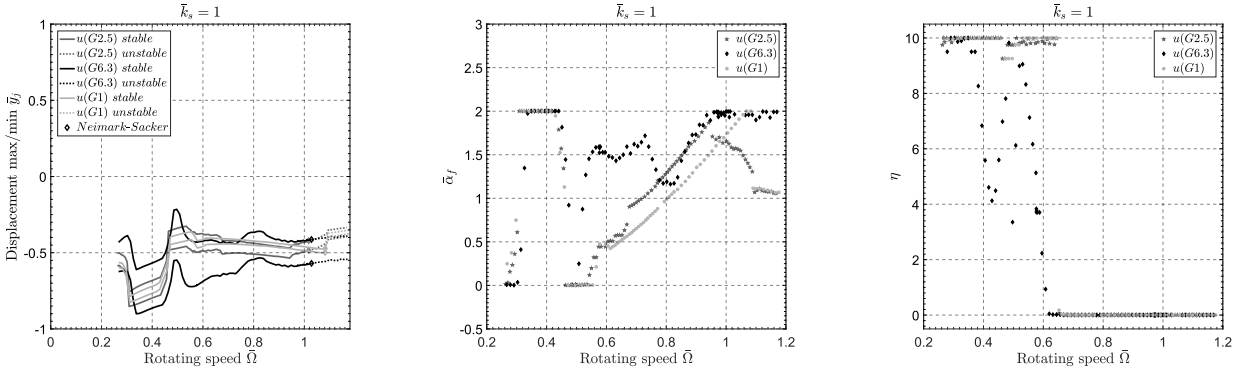

(a) (b) (c)

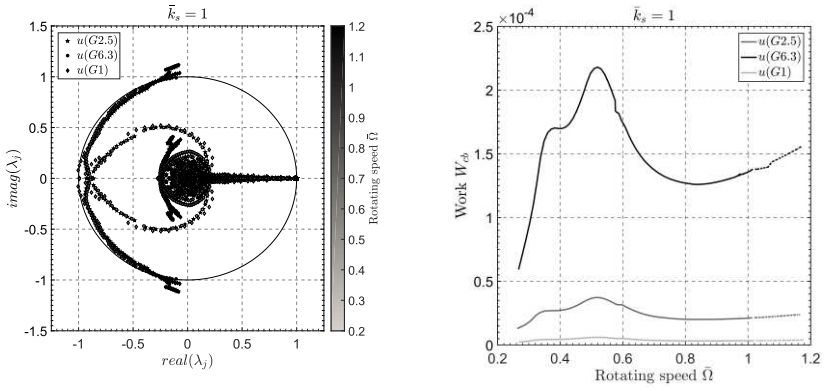

(d) (e)

Figure 12: Elimination of bifurcations at a speed range for the system of $\bar{k}_s = 1$ and $u(G1)$, $u(G2.5)$, $u(G6.3)$ a) journal motion limit cycles, and corresponding values for b) compliance $\bar{a}_f$ c) loss factor η ,d) Floquet multipliers e) dissipating work in the gas film

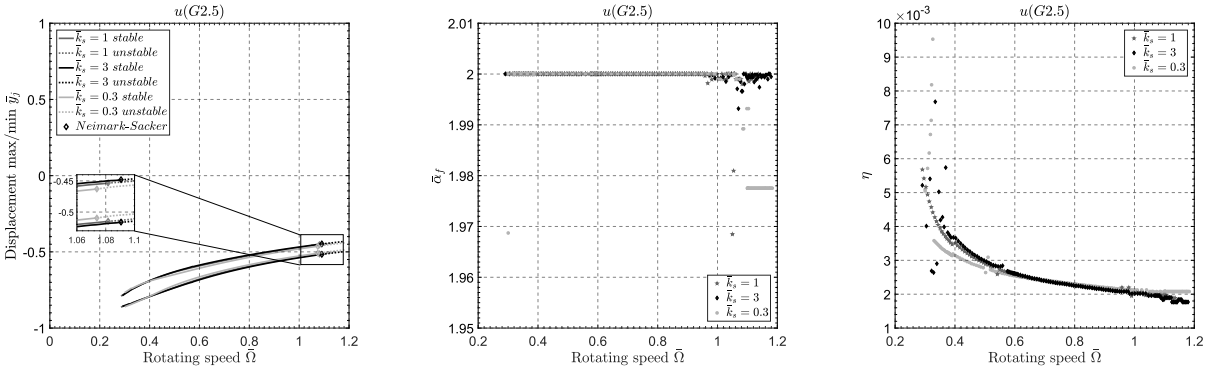

(a) (b) (c)

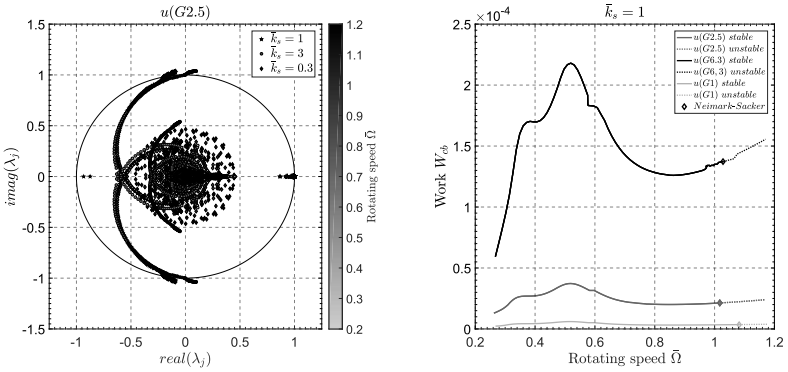

(d) (e)

Figure 13: Elimination of bifurcations at a speed range for the system of $u(G2.5)$ and $\bar{k}_s = 0.1$, $\bar{k}_s = 1$, $\bar{k}_s = 3$ a) journal motion limit cycles, and corresponding values for b) compliance $\bar{a}_f$,c) loss factor η d) Floquet multipliers e) dissipating work in the gas film

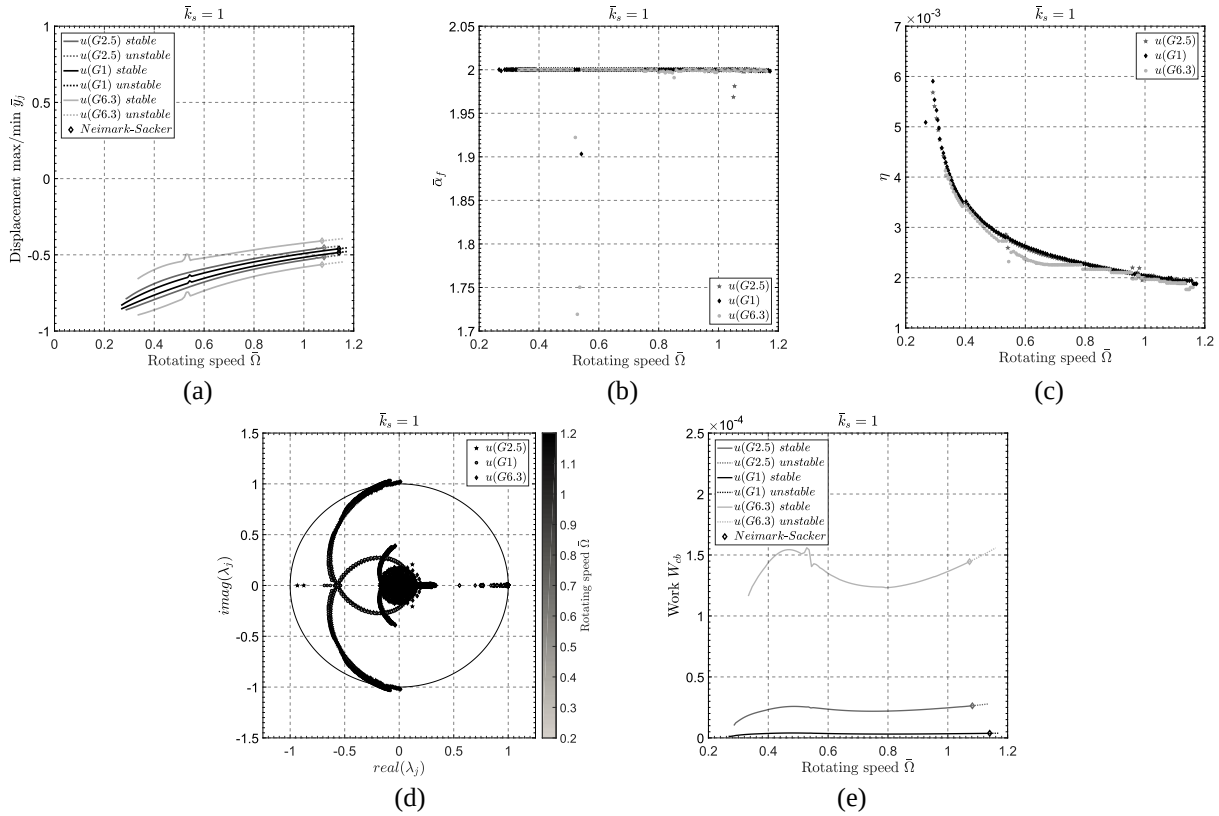

(a) (b) (c)

(d) (e)

Figure 14: Elimination of bifurcations at a speed range for the system of $\bar{k}_s = 1$ and $u(G1)$, $u(G2.5)$, $u(G6.3)$ a) journal motion limit cycles, corresponding values for b) compliance $\bar{a}_f$,c) loss factor η ,d) Floquet multipliers e) dissipating work in the gas film

An alternative objective function was investigated, in Figs. 13 and 14, on the potential to extend the operating speed range without bifurcation, at higher speeds. At each limit cycle $\underset{\sim}{\overset{i}{\mathbf{s}}}$, the highest magnitude of the Floquet multipliers was defined as objective function, $OBJ = \max\left(\left|\mu_j\right|\right)$, neglecting the one existing always at the unity circle, point $(+1,0)$. In this way, all Floquet multipliers are retained inside the unity circle, $\left|\mu_j\right| < 1$. The evaluation time of limit cycles was lower at this case, as the computation of dissipative work is not required. However, the applicability in a real system is questioned as it not of the authors' knowledge whether Floquet multipliers can be evaluated in real time. However, different index for stability is investigated by the authors though operational modal analysis.

Conclusions

The bifurcation set of a rotating shaft on gas foil bearings is presented in this paper for various design cases of rotor stiffness and gas bearing properties, in a certain range of rotating speed which acts as the bifurcation parameter. The periodic limit cycle motions are evaluated applying a pseudo arc length continuation method with embedded orthogonal collocation. The work of the non-conservative and nonlinear damping force of the gas film is evaluated at each limit cycle motion, even when unstable, as the collocation method allows for this possibility. The dissipative work of the gas

film forces is found to be correlated to the self-exciting mechanism which triggers bifurcations of the solution branches for elastic unbalance response (stable motion). The loss of this local stability (through Neimark-Sacker bifurcation) occurs simultaneously with the reversal in the energy flow in the gas film, meaning that the dissipative work changes sign when the NS bifurcation takes place. At each limit cycle, an optimization pattern utilizing successive polls is applied to maximize the dissipated work in the gas film, defining the values for bump foil stiffness and damping, and thus avoid bifurcations according to the previous notation. The optimization pattern reveals that bifurcations are avoided when reducing the foil stiffness, doubling the operating speed range without bifurcations to take place. The procedure is repeated for several design scenarios of rotor stiffness and unbalance magnitude, and similar efficiency is noticed regarding bifurcation elimination. Research on design solutions to implement the change of foil damping and stiffness in a real system belongs to ongoing work.

Acknowledgments

The authors would like to thank *Alexander von Humboldt Foundation* for the funding of this work.

References

[1] Heshmat, H., Walowit, J., Pinkus, O.: Analysis of gas lubricated foil journal bearings. ASME J. Lubr. Technol 105(4), 647 (1983). https://doi.org/10.1115/1.3254697
[2] Agrawal, G.L.: Foil air/gas bearing technology-an overview, In: ASME 1997 International Gas Turbine and Aeroengine Congress and Exhibition, ASME Digital Collection, pp. 1–11(1997). https://doi.org/10.1115/97-GT-347
[3] DellaCorte, C.: Oil-Free shaft support system rotordynamics: Past, present and future challenges and opportunities. Mech. Syst. Signal Process. 29, 67–76 (2012). https://doi.org/10.1016/j.ymssp.2011.07.024
[4] Samanta, P., Murmu, N., Khonsari, M: The evolution of foil bearing technology. Trib. Int. 135, 305–323 https://doi.org/10.1016/j.triboint.2019.03.021
[5] Howard, S. A.; Bruckner, R. J.; DellaCorte, C.: Radil, K. C. Gas foil bearing technology advancements for closed Brayton cycle turbines. Tech. Rep. NASA TM-214470, National Aeronautics and Space Administration, United States of America (2007). https://doi.org/10.1063/1.2437506
[6] Howard, S. A.: Rotordynamics and design methods of an oil-free turbocharger. Tech. Rep. NASA CR-208689, National Aeronautics and Space Administration, United States of America (1999). https://doi.org/10.1080/10402009908982205
[7] Howard, S. A.; Bruckner, R. J.; Radil, K. C. Advancements toward oil-free rotorcraft propulsion. Tech. Rep. NASA TM-216094, US (2010)
[8] Vleugels, P., Waumans, T., Peirs, J., Al-Bender, F., Reynaerts, D.: High-speed bearings for micro gas turbines: Stability analysis of foil bearings. J. Micromech. Microeng. 16(9), S282 (2006). https://doi.org/10.1088/0960-1317/16/9/S16
[9] Peng, J.P., Carpino, M.: Calculation of stiffness and damping coefficients for elastically supported gas foil bearings. J. Tribol. 115(1), 20–27 (1993). https://doi.org/10.1115/1. 2920982
[10] San Andrés, L., Kim, T.H.: Forced nonlinear response of gas foil bearing supported rotors. Tribol. Int. 41(8), 704– 715 (2008). https://doi.org/10.1016/j.triboint.2007.12.009
[11] Leister, T., Baum, C., Seemann, W. Computational Analysis of Foil Air Journal Bearings Using a Runtime-Efficient Segmented Foil Model. ASME Journal of Fluids Engineering. 140(2) 021115 (2018). https://doi.org/10.1115/1.4037985
[12] Baum, C., Hetzler, H., Schröders, S., Leister, T., Seemann, W. A computationally efficient nonlinear foil air bearing model for fully coupled, transient rotor dynamic investigations. Tribol. Int. 153, 106434 (2020). https://doi.org/10.1016/j.triboint.2020.106434
[13] Pham, H., Bonello, P.: Efficient techniques for the computation of the nonlinear dynamics of a foil-air bearing rotor system, In: ASME Turbo Expo 2013: Turbine Technical Conference and Exposition, ASME Digital Collection, V07BT30A011 (2013). https://doi.org/10.1115/GT2013-94389
[14] Bhore, S.P., Darpe, A.K.: Nonlinear dynamics of flexible rotor supported on the gas foil journal bearings. J. Sound Vib. 332(20), 5135–5150 (2013). https://doi.org/10.1016/j.jsv.2013.04.023
[15] Larsen, J.S., Santos, I.F.: On the nonlinear steady-state response of rigid rotors supported by air foil bearings-theory and experiments. J. Sound Vib. 346, 284–297 (2015). https://doi.org/10.1016/j.jsv.2015.02.017
[16] Larsen, J.S., Santos, I.F., von Osmanski, S.: Stability of rigid rotors supported by air foil bearings: Comparison of two fundamental approaches. J. Sound Vib. 381, 179–191 (2016). https://doi.org/10.1016/j.jsv.2016.06.022
[17] Leister, T., Baum, C., Seemann, W.: On the Importance of Frictional Energy Dissipation in the Prevention of Undesirable Self-Excited Vibrations in Gas Foil Bearing Rotor Systems. Technische Mechanik 37, 2-5, 280 – 290 (2017). https://doi.org/10.24352/UB.OVGU-2017-104
[18] Hoffmann, R., Pronobis, T., Liebich, R.: Non-linear stability analysis of a modified gas foil bearing structure, In: Proceedings of the 9th IFToMM International Conference on Rotor Dynamics, Springer, pp. 1259–1276 (2015). https://doi.org/10.1007/978-3-319-06590-8_103
[19] von Osmanski, S., Larsen, J.S., Santos, I.F.: Multi-domain stability and modal analysis applied to gas foil bearings: Three approaches. J. Sound Vib. 472, 115174 (2020). https://doi.org/10.1016/j.jsv.2020.115174
[20] Feng, K., Cao, Y., Yu, K., Guan, H., Wu, Y., Guo, Z.: Characterization of a controllable stiffness foil bearing with shape memory alloy springs. Tribology International 136, 360-371 (2019). https://doi.org/10.1016/j.triboint.2019.03.068
[21] Anastasopoulos, L., Chasalevris, A.: Bifurcations of Limit Cycles in Rotating Shafts Mounted On Partial Arc and Lemon Bore Journal Bearings in Elastic Pedestals. ASME Journal of Computational and Nonlinear Dynamics (2022). https://doi.org/10.1115/1.4053593
[22] Gavalas, I., Chasalevris, A.: Nonlinear Dynamics of Turbine generator Shaft Trains: Evaluation of Bifurcation Sets Applying Numerical Continuation. ASME Journal of Engineering for Gas Turbine and Power. Accepted for publication (2022)
[23] Leister, T.: Dynamics of Rotors on Refrigerant Lubricated Gas Foil Bearings, Ph.D. Thesis, Karlsruhe Institute of Technology, Germany (2021)
[24] Chasalevris, A.: Stability and Hopf bifurcations in rotor-bearing-foundation systems of turbines and generators. Tribology International 145, 106154 (2020). https://doi.org/10.1016/j.triboint.2019.106154
[25] Le Lez, S., Arghir, M., Frene, J.: A new bump-type foil bearing structure analytical model. Journal of Engineering for Gas Turbines and Power 129(4), 1047–1057 (2007). https://doi.org/10.1115/1.2747638
[26] Ku, C. P., Heshmat, H.: Compliant foil bearing structural stiffness analysis: Part I-Theoretical model including strip and variable bump foil geometry. Journal of Tribology 114(2), 394–400 (1992). https://doi.org/10.1115/1.2920898
[27] Peng, J.P., Carpino, M.: Finite element approach to the prediction of foil bearing rotor dynamic coefficients. Journal of Tribology 119(1), 85–90 (1997). https://doi.org/10.1115/1.2832484
[28] Chen, W.J.: Energy analysis to the design of rotor bearing systems. ASME J. Eng. Gas Turb. and Power. 119(2), 411–417 (1997). https://doi.org/10.1115/1.2815590
[29] Doedel, E.J., Keller, H.B., Kernevez, J.P.: Numerical analysis and control of bifurcation problems (II): Bifurcation in infinite dimensions. International Journal of Bifurcation and Chaos 1(3), 745-772 (1991). https://doi.org/10.1142/S0218127491000555
[30] Doedel, E.J.: Lecture Notes on Numerical Analysis of Nonlinear Equations, Department of Computer Science, Concordia University, Montreal
[31] Nayfeh, A.H., Balachandran, B.: Applied nonlinear dynamics. J. Wiley & Sons (1995). https://doi.org/10.1002/9783527617548
[32] Shampine, L.F., Reichelt, M.W.: The MATLAB ODE Suite. SIAM J. Sci. Comput. 18(1), 1–22 (1997). https://doi.org/10.1137/S1064827594276424
[33] Meijer, H., Dercole, F., Olderman, B.: Numerical bifurcation analysis. Encyclopedia of Complexity and Systems Science, R. A. Meyers Ed., Springer New York, 6329-6352 (2009). https://doi.org/10.1007/978-0-387-30440-3_373

Why does the tippedisk invert? Theory and experiments

Simon Sailer and Remco I. Leine
Institute for Nonlinear Mechanics, University of Stuttgart, Stuttgart, Germany

Summary. The *Tippedisk* is a mechanical-mathematical archetype for a peculiar friction-induced inversion phenomenon that occurs when the disk is spun rapidly about an in-plane axis, with the center of gravity rising counterintuitively as the orientation of the disk inverts. To qualitatively understand the dynamical behavior of the tippedisk, a nonlinear analysis is performed leading to a singularly perturbed structure of the system equations. Application of singular perturbation theory implies the study of the long-term behavior on a two-dimensional slow manifold, which finally allows to qualitatively explain the non-intuitive inversion behavior. Due to the technical simplicity of the system, the pronounced nonlinear behavior can be easily compared with real experiments.

Introduction

In the scientific research community, there are various gyroscopic systems which are interacting with a frictional support, such as Euler's disk [1], the rattleback [2], the tippetop [3], and the nonlinear dynamics of rolling basketballs [4]. Because of their technical simplicity, these systems lead to low-dimensional system equations that are ideally suited for the application of nonlinear dynamics theory. The tippetop [5, 6], as well as the related dynamics of spinning eggs [7], correspond to a subclass of gyroscopic systems, which show a counterintuitive rise of the center of gravity (COG), caused by friction-induced instability phenomena. This behavior is counterintuitive since the potential energy increases with the height of the center of gravity, which can be observed directly by eye. The decrease in kinetic energy, on the other hand, can not be detected without measurement because the change in spinning speed is relatively small. The tippedisk, being basically a rigid eccentric disk, was introduced in [9] as a new mechanical-mathematical archetype for a peculiar friction-induced inversion phenomenon that exhibits inversion behavior when rotated rapidly about an in-plane axis, see Fig. 1. The mechanical model derived in [9] forms the basis for the following analysis and was reduced in [10], accompanied by a local stability analysis. We aim to conduct an in-depth stability analysis for the tippedisk

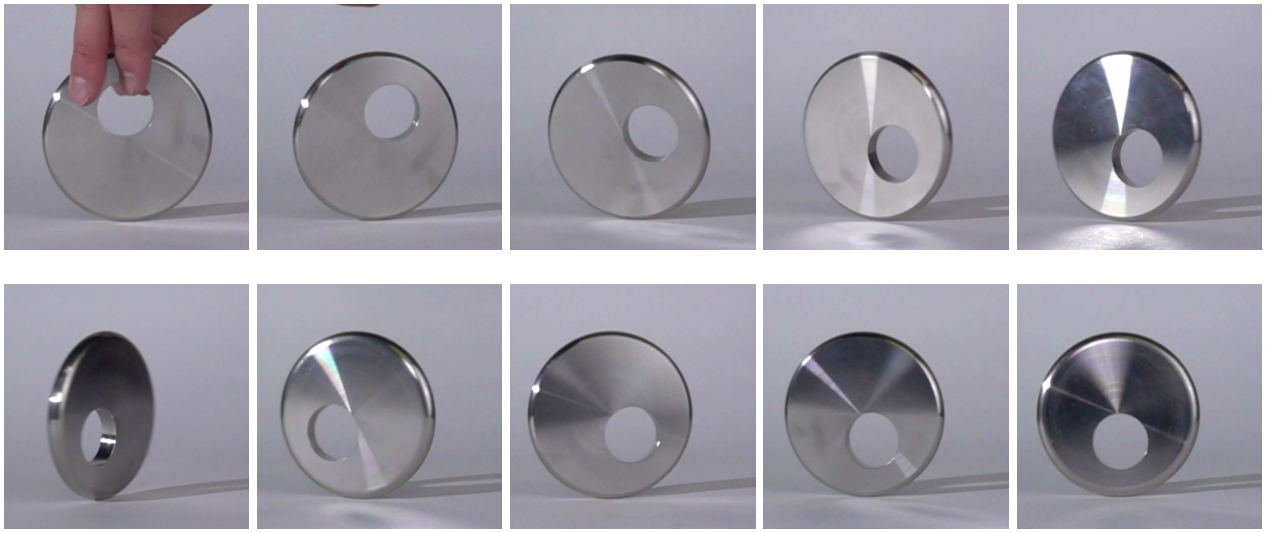

Figure 1: Tippedisk: stroboscopic sequence of the inversion phenomenon.

in order to qualitatively understand the global behavior. In an experimental setup, the qualitative dynamics of the mathematical model can be compared with the dynamic behavior of the real system.

Mechanical model

In [10] a minimal mechanical model was derived, which is able to describe the inversion phenomenon of the tippedisk. The mechanical system consists of an infinitely thin unbalanced disk, with mass m, radius r and eccentricity e. The simplest way to design such a disk, where the COG and the geometric center G do not coincide, is to take a homogeneous disk and to drill a hole (remove mass) at an arbitrary point, which does not coincide with the geometric center G of the disk. As the tippedisk does not detach during inversion, the unilateral constraint at the contact point C can be equivalently replaced by a bilateral one. In Figure 2, the mechanical model is shown.

The body-fixed B-frame is attached to the disk, such that $\mathbf{e}_z^B$ lies perpendicular to the surface of the disk. The $\mathbf{e}_x^B$-vector is defined as the normalized vector of $\mathbf{r}_{GS}$, which points from the geometric center G to the center of gravity S. To describe the contact point C, we introduce the grinding G-frame, in which $\mathbf{r}_{GC} = -r\,\mathbf{e}_y^G$ holds. The comparison with a quaternion based model implies that Euler angles α, β and γ, in common z-x-z-convention, are sufficient to describe the inversion phenomenon of the disk, see [9]. The angle α corresponds to the spinning angle, which describes the rotation around a vertical $\mathbf{e}_z^I$-axis. The inclination of the disk is measured by the inclination angle β, while γ describes the rolling angle of the disk.

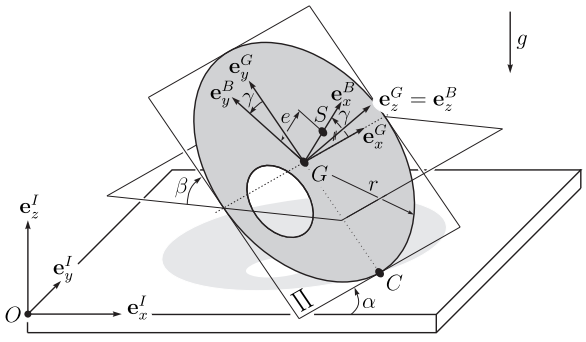

Figure 2: Mechanical model: tippedisk

Dimensions

The dimensions of the considered specimen can be found in Fig. 3 and Table 1. In the previous works [9, 10, 11], the inertial properties were approximated by an assumed density and simplified geometry. In order to ensure better comparability between simulation and experiment, a more exact calculation of the mass and inertia properties is performed here. Therefore, the mass $m = 0.425\,\mathrm{kg}$ of the considered specimen was measured directly on a calibrated scale.

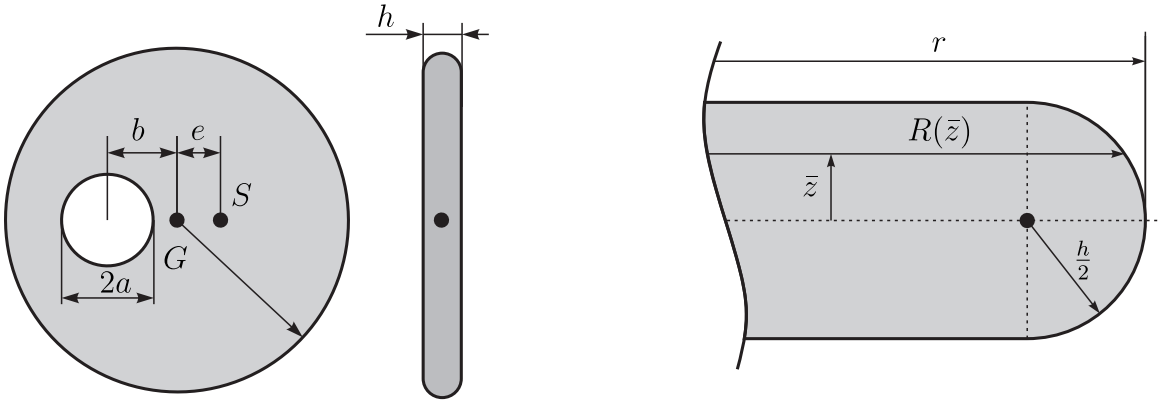

Figure 3: Geometry of the tippedisk

Table 1: Dimensions of the tippedisk

Property	Parameter	Magnitude	Unit
Disk radius	r	0.045	m
Hole radius	a	0.015	m
Distance	b	0.02	m
Disk height	h	0.01	m
Volume	V	$5.359 \cdot 10^{-5}$	m^3

Table 2: Mass properties of the tippedisk

Property	Parameter	Magnitude	Unit
Mass	m	0.425	kg
Density	ρ	7930	$\mathrm{kg/m}^3$
Eccentricity	e	$2.64 \cdot 10^{-3}$	m
${}_B\mathbf{\Theta}_G(1,1)$	A	$0.233 \cdot 10^{-3}$	$\mathrm{kg\ m}^2$
${}_B\mathbf{\Theta}_G(2,2)$	B	$0.211 \cdot 10^{-3}$	$\mathrm{kg\ m}^2$
${}_B\mathbf{\Theta}_G(3,3)$	C	$0.437 \cdot 10^{-3}$	$\mathrm{kg\ m}^2$

In Fig. 3 it is shown that the radius

$$R(\bar{z}) = r - \frac{h}{2} + \sqrt{\left(\frac{h}{2}\right)^2 - \bar{z}^2} \tag{1}$$

of the rounding depends on the $\bar{z}$ coordinate. Under consideration of this rounded edge, the volume yields a triple integral

$$V = \pi h(r^2 - a^2) - \int_0^{2\pi} \int_{-\frac{h}{2}}^{+\frac{h}{2}} \int_{R(\bar{z})}^{r} \bar{r}\,\mathrm{d}\bar{r}\mathrm{d}z\mathrm{d}\varphi \tag{2}$$

and, after a little algebra, the corresponding solution for the total volume V of the disk is given as

$$V = \pi h(r^2 - a^2) + \pi \left(\frac{h}{2}\right)^2 \left[\left(\frac{5}{3} - \frac{\pi}{2}\right) h + (\pi - 4)r\right] = 5.359 \cdot 10^{-5}\,\mathrm{m}^3. \tag{3}$$

Assuming a homogeneous material, the specific mass density is equal to the relation $\rho = \frac{m}{V}$ of weighed mass m and calculated total volume V, yielding $\rho = 7930\frac{\text{kg}}{\text{m}^3}$. With this density ρ and the dimensions of the unbalanced disk, the inertia properties are calculated with sufficient accuracy using the commercial CAD software 'SolidWorks' and are listed in Table 2.

Singularly perturbed equations of motion

In [10] a reduction of the full model equations was derived to reduce the dimension of the state-space. It turned out that the horizontal position of the COG can be neglected during the inversion process. The spinning speed $\Omega = \dot{\alpha}$ changes only slightly and therefore can be set approximately constant, which allows to introduce the spinning speed Ω as bifurcation parameter.
Defining the new minimal coordinates $\mathbf{z} = [\beta,\ \gamma]^{\mathrm{T}}$ and the scalar[1] minimal velocity $\mathbf{v} = \dot{\beta}$, the dynamic behavior under longitudinal rolling of the disk is completely described by the system of equations

$$\begin{aligned} \dot{\mathbf{z}} &= \mathbf{B}(\mathbf{z})\mathbf{v} + \boldsymbol{\beta}(\mathbf{z}) \\ \mathbf{M}(\mathbf{z})\dot{\mathbf{v}} - \mathbf{h}(\mathbf{z},\mathbf{v}) &= -\frac{\mu m g}{\varepsilon}\mathbf{w}_y\gamma_y, \end{aligned} \tag{4}$$

with $\mathbf{B}(\mathbf{z}) = [1,\ 0]^{\mathrm{T}}$ and $\boldsymbol{\beta}(\mathbf{z}) = [0,\ -\Omega\cos\beta]^{\mathrm{T}}$ defining the kinematics. The mass matrix $\mathbf{M}$ and the vector of gyroscopic and gravitational forces $\mathbf{h}$ are given as

$$\mathbf{M} = A\cos^2\gamma + \bar{B}\sin^2\gamma + m(r + e\sin\gamma)^2\cos^2\beta, \tag{5}$$

and

$$\begin{aligned} \mathbf{h} = &+(A\cos^2\gamma + \bar{B}\sin^2\gamma)\Omega^2\sin\beta\cos\beta \\ &- 2(A - \bar{B})\Omega\dot{\beta}\cos\beta\sin\gamma\cos\gamma \\ &+ m(r + e\sin\gamma)^2\dot{\beta}^2\sin\beta\cos\beta \\ &+ me(r + e\sin\gamma)\Omega^2\sin\beta\cos^3\beta\sin\gamma \\ &- me(r + e\sin\gamma)(3\sin^2\beta - 2)\Omega\dot{\beta}\cos\beta\cos\gamma \\ &- mg(r + e\sin\gamma)\cos\beta, \end{aligned} \tag{6}$$

where the auxiliary variable $\bar{B} := B - me^2$ has been used. The right-hand side contains the generalized force direction

$$\mathbf{w}_y = (r + e\sin\gamma)\sin\beta, \tag{7}$$

and the lateral sliding velocity

$$\gamma_y = (r + e\sin\gamma)\dot{\beta}\sin\beta - e\Omega\sin^2\beta\cos\gamma. \tag{8}$$

The friction and smoothing coefficients are assumed to be $\mu = 0.3$ and $\varepsilon = 0.1\frac{\text{m}}{\text{s}}$. A more detailed derivation of the reduced equations of motion can be found in [10].

According to [11], the dynamics of the tippedisk must be considered on two different timescales, as Eq. 4 yields a singularly perturbed structure. Introducing the slow variables $\mathbf{x} = [\beta,\ \gamma]^{\mathrm{T}}$ and the fast variable $\mathbf{y} = \eta = \dot{\beta}$, we obtain the singularly perturbed dynamical system

$$\begin{aligned} \dot{\mathbf{x}} &= \mathbf{f}(\mathbf{x},\mathbf{y}) \\ \varepsilon\,\dot{\mathbf{y}} &= \mathbf{g}(\mathbf{x},\mathbf{y};\varepsilon) = \mathbf{g}_0(\mathbf{x},\mathbf{y}) + \mathbf{g}_1(\mathbf{x},\mathbf{y})\,\varepsilon, \end{aligned} \tag{9}$$

with

$$\mathbf{f}(\mathbf{x},\mathbf{y}) = \begin{bmatrix} \eta \\ -\Omega\cos\beta \end{bmatrix} \in \mathbb{R}^2, \tag{10}$$

$$\mathbf{g}_0(\mathbf{x},\mathbf{y}) = -\mathbf{M}^{-1}\mu m g\,\mathbf{w}_y(\mathbf{x})\gamma_y(\mathbf{x},\mathbf{y}) \in \mathbb{R}, \tag{11}$$

and

$$\mathbf{g}_1(\mathbf{x},\mathbf{y}) = \mathbf{M}^{-1}\mathbf{h}(\mathbf{x},\mathbf{y}) \in \mathbb{R}, \tag{12}$$

by normalizing and pre-multiplying Eq. (4) with the 'small' smoothing coefficient $\varepsilon > 0$ of the friction law, cf. [12]. The fast subsystem is then given as

$$\varepsilon\,\dot{\mathbf{y}} = \mathbf{g}(\mathbf{x},\mathbf{y};\varepsilon) = \mathbf{g}_0(\mathbf{x},\mathbf{y}) + \mathbf{g}_1(\mathbf{x},\mathbf{y})\,\varepsilon. \tag{13}$$

[1] Although the minimal velocity is scalar, we stick to vector notation and write $\mathbf{v}$ to keep the singularly perturbed equations of motion in a general, mechanical structure.

For $\varepsilon = 0$, the fast dynamics degenerates to the algebraic equation $\mathbf{g}_0(\mathbf{x}, \mathbf{y}) = 0$, which, according to Eq (11), states that the relative velocity $\gamma_y(\mathbf{x}, \mathbf{y})$ vanishes, i.e., the contact point of the tippedisk is in a state of pure rolling. Since the relative lateral sliding velocity $\gamma_y(\mathbf{x}, \mathbf{y})$ depends linearly on the fast variable $\eta = \dot{\beta}$, the critical manifold exists globally since the Jacobian $\frac{\partial \mathbf{g}_0}{\partial \mathbf{y}}\big|_{\mathbf{x},\mathbf{y}}$ is invertible. The corresponding critical manifold $\mathcal{M}_c$ is given as

$$\mathcal{M}_c := \left\{ (\mathbf{x}, \mathbf{y}) \in \mathbb{R}^3 |\ \mathbf{y} = \mathbf{h}_c(\mathbf{x}) = \frac{e \sin\beta \cos\gamma}{(r + e\sin\gamma)} \Omega \ , \mathbf{x} \in \mathbb{R}^2 \right\}, \tag{14}$$

being the zero order approximation of the slow manifold, which is given up to orders $\mathcal{O}(\varepsilon^2)$ as

$$\mathcal{M}_s := \left\{ (\mathbf{x}, \mathbf{y}) \in \mathbb{R}^3 |\ \mathbf{y} = \frac{e \sin\beta \cos\gamma}{(r + e\sin\gamma)} \Omega + \mathbf{h}_1(\mathbf{x})\varepsilon + \mathcal{O}(\varepsilon^2) \ , \mathbf{x} \in \mathbb{R}^2 \right\}, \tag{15}$$

with

$$\mathbf{h}_1(\mathbf{x}) = \frac{\partial \mathbf{g}}{\partial \mathbf{y}}\bigg|^{-1}_{\mathbf{x},\mathbf{h}_c} \left[\frac{\partial \mathbf{h}_c}{\partial \mathbf{x}}\bigg|_{\mathbf{x}} \mathbf{f}(\mathbf{x}, \mathbf{h}_c) - \mathbf{g}_1(\mathbf{x}, \mathbf{h}_c) \right]. \tag{16}$$

The stability of the slow manifold, characterized by the distance dynamics

$$\mathbf{d}' = \frac{\partial \mathbf{g}_0}{\partial \mathbf{y}}\bigg|_{\mathbf{x},\mathbf{h}_c} \mathbf{d}, \tag{17}$$

is asymptotically stable, since the Jacobian

$$\frac{\partial \mathbf{g}_0}{\partial \mathbf{y}}\bigg|_{\mathbf{x},\mathbf{h}_c} = -\mathbf{M}^{-1} \mu m g \, (r + e\sin\gamma)^2 \sin^2\beta \tag{18}$$

is strictly negative for all $\beta \in (0, +\pi)$, i.e., in a basin of attraction the orbits are attracted by the invariant manifold $\mathcal{M}_s$. Therefore, the asymptotic behavior of attracted solutions is governed by the reduced two-dimensional system

$$\begin{aligned} &\mathbf{h}_s(\mathbf{x}) \approx \mathbf{h}_c(\mathbf{x}) + \varepsilon \mathbf{h}_1(\mathbf{x}) \\ &\dot{\mathbf{x}} = \mathbf{f}\left(\mathbf{x}, \mathbf{h}_s(\mathbf{x})\right), \end{aligned} \tag{19}$$

neglecting orders $\mathcal{O}(\varepsilon^2)$.

Qualitative dynamics of the tippedisk

According to the simplification of the systems equations, performed in [10], and the singularly perturbed structure, discussed in [11], the qualitative dynamics of the tippedisk can be analyzed in the β-γ-space. Within this representation, we must first characterize the stationary spinning states of the disk, namely 'non-inverted' and 'inverted' spinning. Figure. 4 shows the two possible stationary spinning solutions of the tippedisk.

With respect to the chosen parametrization of the disk, the non-inverted stationary spinning corresponds to the point $(\beta = +\frac{\pi}{2}, \gamma = -\frac{\pi}{2})$. Inverted spinning is characterized by $(\beta = +\frac{\pi}{2}, \gamma = +\frac{\pi}{2})$. Due to trigonometric ambiguity, both stationary spinning solutions occur with 2π periodicity in the rolling angle γ, i.e., the point $(\beta = \frac{\pi}{2}, \gamma = +\frac{3\pi}{2})$ can be also identified as non-inverted spinning equilibrium. During the inversion, the disk remains almost in a vertical plane, so the inclination can be restricted to the interval $\beta \in [\frac{\pi}{3}, \frac{3\pi}{4}]$.

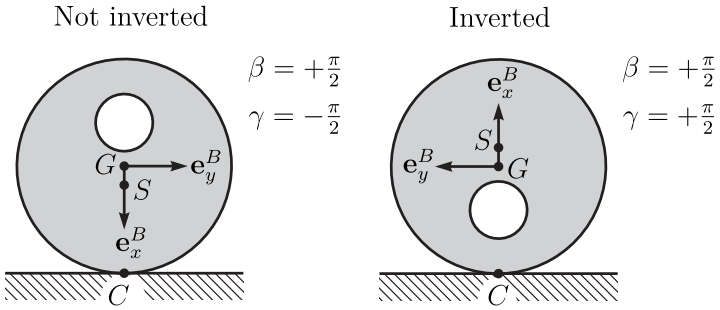

Figure 4: Stationary spinning solutions of the tippedisk

According to the linear stability analysis of [10], the equilibrium corresponding to 'non-inverted spinning' is unstable for any spinning speed Ω. The stability of 'inverted spinning' solutions is characterized by a supercritical Hopf-bifurcation at the critical spinning speed Ω_{crit}, being approximately given in closed-form as

$$\Omega_{\text{crit}} = \sqrt{\frac{(r+e)^2}{r} \frac{mg}{B - me^2}} = 30.21 \, \frac{\text{rad}}{\text{s}}. \tag{20}$$

At slow spinning speeds $\Omega < \Omega_{\text{crit}}$, the inverted spinning of the disk is unstable, and stable at supercritical spinning velocities $\Omega > \Omega_{\text{crit}}$. Following [11], the dynamical behavior on the slow manifold $\mathcal{M}_s$ is shown in

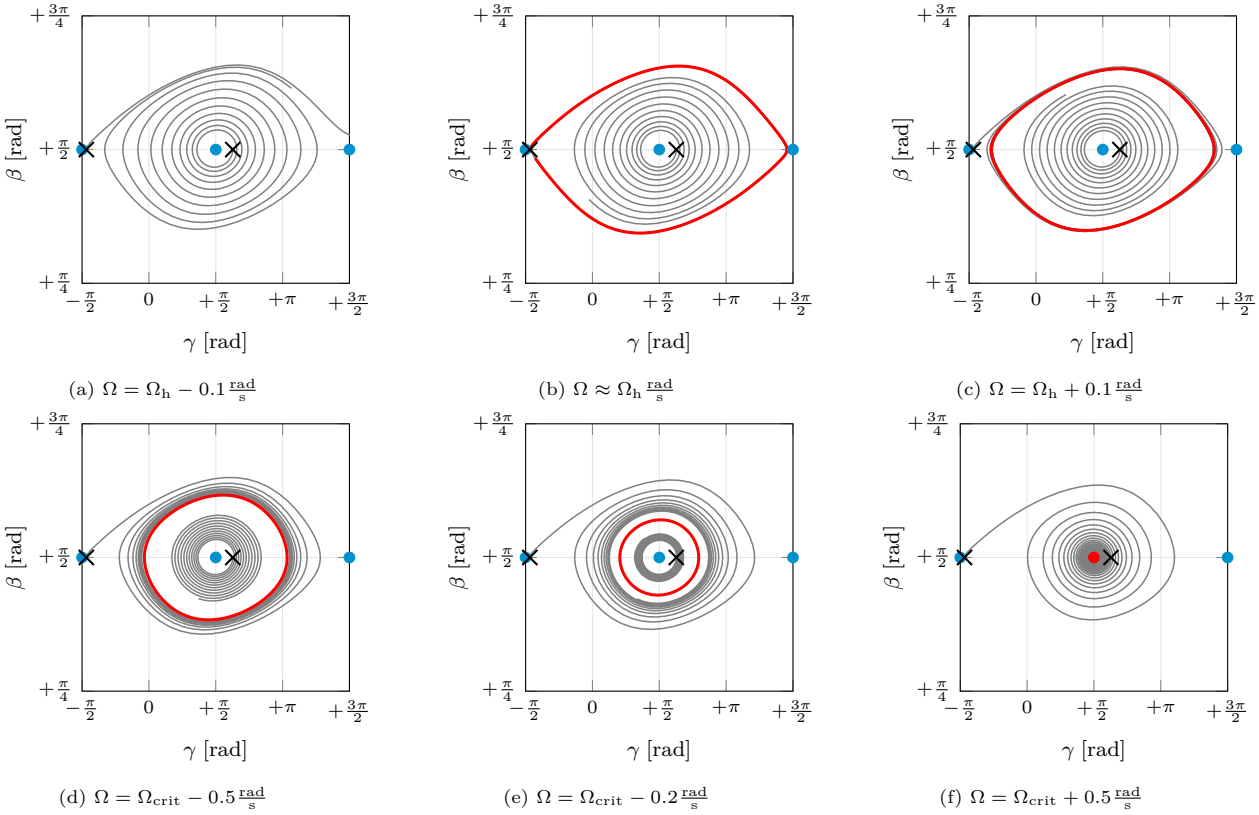

(a) $\Omega = \Omega_\mathrm{h} - 0.1\,\frac{\mathrm{rad}}{\mathrm{s}}$ (b) $\Omega \approx \Omega_\mathrm{h}\,\frac{\mathrm{rad}}{\mathrm{s}}$ (c) $\Omega = \Omega_\mathrm{h} + 0.1\,\frac{\mathrm{rad}}{\mathrm{s}}$

(d) $\Omega = \Omega_\mathrm{crit} - 0.5\,\frac{\mathrm{rad}}{\mathrm{s}}$ (e) $\Omega = \Omega_\mathrm{crit} - 0.2\,\frac{\mathrm{rad}}{\mathrm{s}}$ (f) $\Omega = \Omega_\mathrm{crit} + 0.5\,\frac{\mathrm{rad}}{\mathrm{s}}$

Figure 5: Qualitative dynamics in (β,γ)-plane: Solutions which are depicted in gray are initialized at the corresponding black cross and are obtained by time integration over the time span $\Delta t = 10\,\mathrm{s}$. Stable periodic solutions (red) originate from numerical shooting.

Fig. 5, using the corrected mass and inertia properties from Table-2. To study the dynamical behavior, we assume that the angular velocity $\dot{\alpha} = \Omega$ is constant, which identifies the bifurcation parameter Ω and leads to a foliation of the state-space. The evolution of solutions for different spinning speeds Ω are shown in β-γ-space, Fig. 5. Two unstable 'non-inverted spinning' configurations correspond to the points $(\beta = \frac{\pi}{2}, \gamma = -\frac{\pi}{2})$ and $(\beta = \frac{\pi}{2}, \gamma = \frac{3\pi}{2})$ and are shown in light blue. The inverted configuration is characterized by the dot at $(\beta = \frac{\pi}{2}, \gamma = \frac{\pi}{2})$. Unstable inverted spinning is indicated by a blue dot, stable inverted spinning by a red dot. At time $t_0 = 0\,\mathrm{s}$, two solutions are initialized at the black crosses at $\mathbf{x}_0^1 = (\beta = \frac{\pi}{2}, \gamma = -\frac{\pi}{2} + 0.1)$ and $\mathbf{x}_0^2 = (\beta = \frac{\pi}{2}, \gamma = \frac{\pi}{2} + 0.4)$ for each subfigure. The resulting trajectories are shown as gray curves. For $\Omega < \Omega_\mathrm{h}$, solutions are repelled by the inverted spinning equilibrium (Fig. 5a). At $\Omega_\mathrm{h} \approx 29.3\frac{\mathrm{rad}}{\mathrm{s}}$, a periodic solution (with period time $T = \infty$) arises connecting two non-inverted stationary spinning solutions (Fig. 5b). This connection can be interpreted as two heteroclinic connections because two different equilibrium points $(\beta = \frac{\pi}{2}, \gamma = -\frac{\pi}{2})$ and $(\beta = \frac{\pi}{2}, \gamma = \frac{3\pi}{2})$ are connected. From a physical point of view, this connection can also be called a homoclinic, since both connected points describe inverted spinning. If the spinning speed is increased but still subcritical, i.e., $\Omega_\mathrm{h} < \Omega < \Omega_\mathrm{crit}$ holds, solutions are attracted by a stable periodic orbit that shrinks with increasing spinning velocity Ω (Figs. 5c-5e). Due to the supercritical Hopf-bifurcation, the periodic solution vanishes at Ω_crit. For supercritical spinning speeds, i.e., $\Omega > \Omega_\mathrm{crit}$, the inverted spinning equilibrium is stable (shown as red dot), so that the solutions converge asymptotically to the inverted spinning configuration (Fig. 5f), which qualitatively explains the inversion phenomenon.

Experiments

In order to verify the validity of the qualitative dynamics of the tippedisk, presented in [11], preliminary experiments were performed. This was done with the help of an object tracking system that combines the measurements of six high-speed cameras, each of which records the movement of the disk from a different angle and at 500 frames per second. Figure 6a, shows a post-processed image of one high-speed camera with different marker frames. In Figs. 6b and 6c, the spinning angle α and the projection of the state onto the β-γ-plane are shown for four different runs, each starting with a different initial spinning velocity Ω_i^* and all initialized near non-inverted spinning motion. With time, the spinning speed Ω, which is the time derivative of the spinning angle α, gradually decreases due to dissipation caused by frictional forces. The black and the dark gray trajectories belong to very fast spinning speeds and quickly settle near the inverted spinning motion. The gray trajectory is at an intermediate initial spinning speed Ω_3^* and is reminiscent of the periodic limit cycle

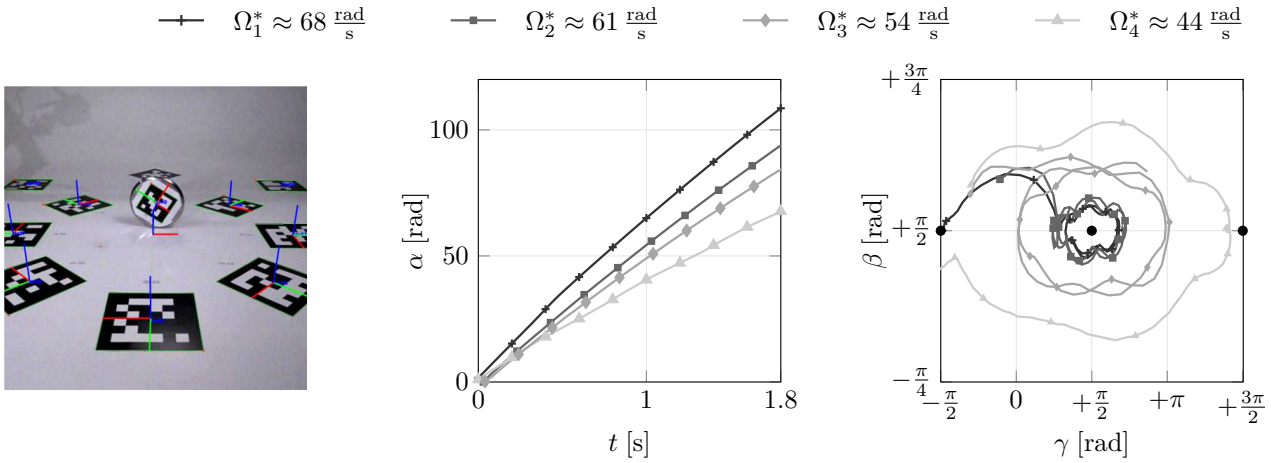

(a) Example of one processed high-speed video.

(b) Experimental obtained evolution of the spinning angle α

(c) Experimental obtained dynamics projected into the β-γ-space

Figure 6: Experiments of the tippedisk. All solutions are starting in the neighborhood of non-inverted stationary spinning at different initial spinning speeds.

between heteroclinic and Hopf bifurcation. Finally, the light gray trajectory appears to be qualitatively close to the heteroclinic connection. The measurements seem to agree with the qualitative behavior of the reduced model derived in [11]. Comparing the spinning speeds, the initial rotational velocity Ω_i^* does not match the magnitude of the bifurcation parameter Ω of the reduced model, with similar qualitative inversion behavior. This discrepancy seems to be due to the decrease in angular velocity and needs to be analyzed in future research.

Conclusions

In this work, the dynamic analysis of the tippedisk was studied based on a minimal mechanical model that contains the relevant effects and is able to describe the inversion phenomenon of the tippedisk. Consideration of the singularly perturbed structure allows the dynamics to be reduced to a two-dimensional system, so that the origin of the inversion phenomenon can be studied in the corresponding reduced system. An in-depth analysis suggests a bifurcation scenario in which a heteroclinic bifurcation accompanied by the emergence of an attractive periodic solution is followed by a supercritical Hopf bifurcation in which this periodic solution disappears. Closed-form expressions approximately characterize the associated critical spinning velocity Ω_{crit}. When the corresponding bifurcation point is crossed, the inverted configuration becomes stable and subsequently attracts almost all solutions. Preliminary experiments shown in Fig. 6 support the results of the qualitative analysis from [11] of the reduced model derived in [10]. By studying the mechanical system at all model levels and in conjunction with experimental observations, the nonlinear behavior of the tippedisk can finally be understood and the magic behind the phenomenon of inversion revealed.
Therefore, the tippedisk forms a wonderful archetype system for friction-induced instabilities, linking analytical and nonlinear dynamics with applied mechanics and allowing the comparison of the qualitative behavior of a mechanical model with experiments on a real specimen.

References

[1] Leine R.I. (2009) Experimental and theoretical investigation of the energy dissipation of a rolling disk during its final stage of motion. *Arch Appl Mech* **79**:1063-1082.

[2] Borisov A.V., Mamaev I.S. (2003) Strange attractors in rattleback dynamics. Physics-Uspekhi **46**:393–403.

[3] Bou-Rabee N.M., Marsden J.E., Romero L.A. (2004) Tippe Top inversion as a dissipation-induced instability. *SIAM J. Appl. Dyn. Syst.* **3**, 352-377.

[4] Antali M., Havas V., Hogan S.J., Stepan G. (2021) Nonlinear dynamics of a basketball rolling around the rim. *Nonlinear Dyn.* **104**, 3013-3037.

[5] Magnus K. (1971) Kreisel. Springer, Berlin; Heidelberg; New York.

[6] Cohen R.J. (1977) The tippe top revisited; *American Journal of Physics* **45**:12-17.

[7] Moffatt K., Shimomura Y. (2002) Classical dynamics: Spinning eggs — a paradox resolved. *Nature* **416**:385–386.

[8] Leine R.I., Glocker Ch. (2003) A set-valued force law for spatial Coulomb–Contensou friction. *Eur. J. Mech. A/Solids*, **22**:193-216.

[9] Sailer S., Eugster S.R., Leine R.I. (2020) The Tippedisk: a Tippetop Without Rotational Symmetry. *Regul. Chaot. Dyn.* **6**:553–580.

[10] Sailer S., Leine R.I. (2021) Model reduction of the tippedisk: a path to the full analysis. *Nonlinear Dyn.* **105**:1955–1975.

[11] Sailer S., Leine R.I. (2021) Singularly perturbed dynamics of the tippedisk. *Proc. R. Soc. A.* **477**.

[12] Shchepakina E., Sobolev V., Mortell M.P. (2014) Singular Perturbations. Springer International Publishing.

Effect of Nonlinear Electromechanical Coupling in Implanted Middle Ear

Rafal Rusinek*, Krzysztof Kecik*, Andrzej Mitura*
*Department of Applied Mechanics, Lublin University of Technology, Poland

Summary. The nonlinear electromechanical coupling between the middle ear structure and the implantable hearing device is analysed in order to explain combined dynamics of human middle ear, body of an implant and electric circuit that powers the implant. Numerical simulations of a lumped mass model shows harmonic, subharmonic and even chaotic vibrations for chosen range of excitation frequency.
Keywords: middle ear implant; implantable middle ear hearing device; electromechanical coupling

Introduction

Probably more than one third of people over 65 years of age suffer from clinically significant hearing deficits. Only a mild to moderate hearing loss can be improved by conventional hearing aids. Patients with hearing loss of approximately 50 to 90 dB may receive greater benefit from other, more technologically advanced devices such as implantable middle ear hearing devices (IMEHDs shown in Figure 1a). IMEHDs can be used for both conductive and sensorineural hearing loss, therefore they are becoming more and more popular nowadays. A typical IMEHD consists of three parts: a microphone, a signal processor and a floating mass transducer (FMT) [1,2,3]. The literature of the subject usually reports clinical studies on the application of IMEHDs in various medical cases. The effect of mass loading the ossicles with a FMT, an influence of different coupler types and various techniques of FMT implantation are investigated. However, widespread clinical research does not go together with theoretical investigation. Undoubtedly, there is a lack of biomechanical model that could explain the behaviour of the human middle ear with an implant and especially an influence on mechanical part of the system on electrical circuit and vice versa. Therefore here, a nonlinear electromechanical coupling between the middle ear structure and the IMEHD is analysed.

Results and Discussion

The model of implanted middle ear (Figure 1b) consists of three masses that represent the malleus (m_M), the incus (m_I) and the stapes (m_S). The masses are connected to each other and to the temporal bone by the joints (IMJ – the incudo-malleal joint, ISJ – the incudostapedial joint) and ligaments (AML – the anterior malleal ligament, PIL – the posterior incudal ligament, AL – the annular ligament). Damping and stiffness properties of the elements are denoted as c and k, respectively, including the cochlea (c_c and k_c), and the tympanic membrane (c_{TM}, k_{TM}). The stapes is excited by the FMT consisting of a magnet (M_m) suspended in a metal case (M_c) with dashpots (c_m) and springs (km). The magnet is moved by electromagnetic field generated by an electrical circuit with resistance R and conductance L supplied by a voltage source $U(t)$. E_{EM} denotes the electromotive force that generates an electro dynamic force (P) acting in the mechanical subsystem. The FMT is fixed to the incus long process with a clip whose linear damping and stiffness coefficients are denoted as c_{CLIP}, k_{CLIP}. The electromechanical coupling is described as α.

(a) (b)

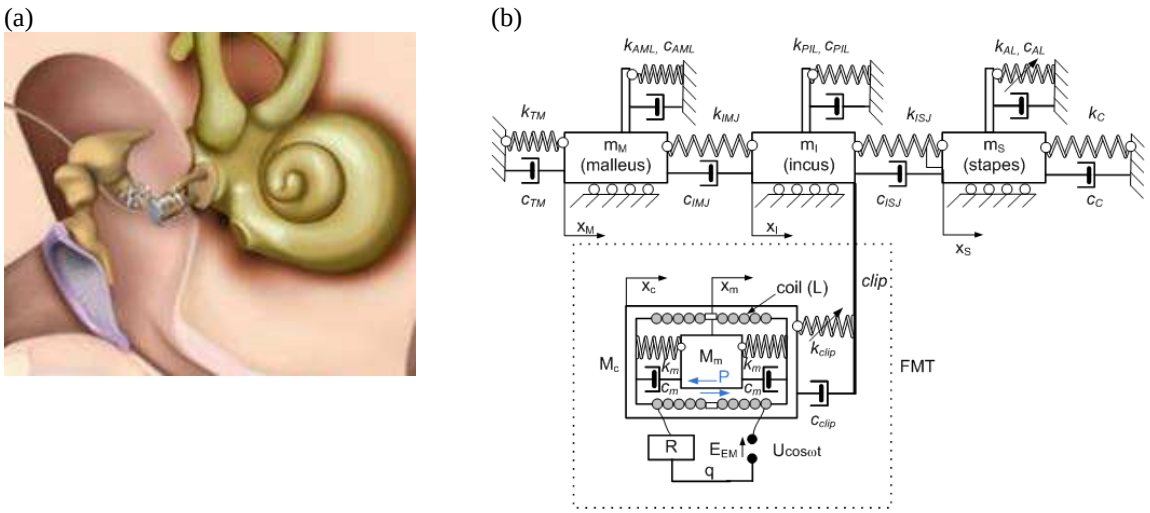

Figure 1: Schematic view of the middle ear with a floating mass transducer (a), lumped mass model of implanted middle ear (b).

Then, the governing differential equations of the IME are as follows

$$
\begin{aligned}
&\ddot{x}_M m_M + \tilde{k}_{11} x_M + \tilde{k}_{12} x_I + \tilde{c}_{11} \dot{x}_M + \tilde{c}_{12} \dot{x}_I = 0 \\
&\ddot{x}_I m_I + \tilde{k}_{21} x_M + \tilde{k}_{22} x_I + \tilde{k}_{23} x_S + \tilde{k}_{24} x_c + \tilde{\beta}_{24} (x_I - x_c)^2 + \tilde{\gamma}_{24} (x_I - x_c)^3 + \tilde{c}_{21} \dot{x}_M + \tilde{c}_{22} \dot{x}_I + \tilde{c}_{23} \dot{x}_S + \tilde{c}_{24} \dot{x}_c = 0 \\
&\ddot{x}_S m_S + \tilde{k}_{32} x_I + \tilde{k}_{33} x_S + \tilde{c}_{32} \dot{x}_I + \tilde{c}_{33} \dot{x}_S + \tilde{\gamma}_3 x_S^3 = 0 \\
&\ddot{x}_c m_c + \tilde{k}_{42} x_I + \tilde{k}_{44} x_c + \tilde{k}_{45} x_m + \tilde{c}_{42} \dot{x}_I + \tilde{c}_{44} \dot{x}_c + \tilde{c}_{45} \dot{x}_m - \tilde{\beta}_{24} (x_I - x_c)^2 - \tilde{\gamma}_{24} (x_I - x_c)^3 - \tilde{\beta}_{45} (x_c - x_m)^2 + \tilde{\gamma}_{45} (x_c - x_m)^3 = \alpha \dot{q} \\
&\ddot{x}_m m_m + \tilde{k}_{54} x_c + \tilde{k}_{55} x_m + \tilde{c}_{54} \dot{x}_c + \tilde{c}_{55} \dot{x}_m + \tilde{\beta}_{45} (x_c - x_m)^2 - \tilde{\gamma}_{45} (x_c - x_m)^3 = -\alpha \dot{q} \\
&L\ddot{q} + R\dot{q} + \alpha(\dot{x}_c - \dot{x}_m) = U_0 \cos(\omega t)
\end{aligned}
\tag{1}
$$

where

$$
\alpha = \alpha_0 - \alpha_1 (x_c - x_m)^2 \quad or \quad \alpha = \alpha_0 e^{-n\left|(x_c - x_m + d)\right|} \sin[w(x_c - x_m + d)] \tag{2}
$$

(a) (b)

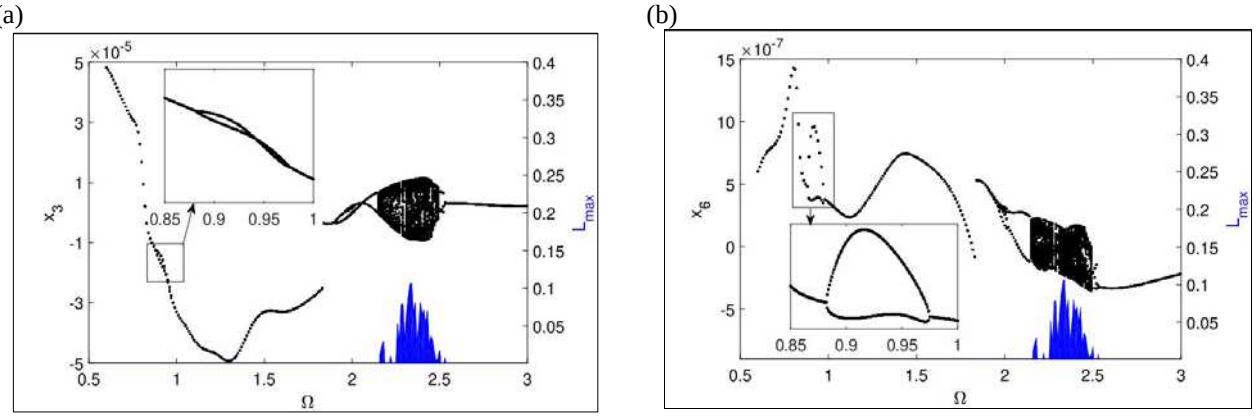

Figure 2: Bifurcation diagrams of stapes motion (a), magnet motion (b) with positive value of maximal Lyapunov exponent (blue).

The results of numerical simulation are presented in Figure 2 as bifurcation diagrams, where Figure 2a presents stapes motion while Figure 2b – motion of the magnet. Both, the stapes and the magnet exhibit regular and chaotic vibrations depending on excitation frequency.

Concluding Remarks

Electromechanical coupling between the electrical circuit and the mechanical part of the implanted middle ear strongly influences system dynamics causing harmonic, subharmonic and even chaotic vibrations for chosen range of excitation frequency.

Acknowledgment:

The research was financed in the framework of the project Nonlinear effect in middle ear with active implant, no.2018/29/B/ST 8/01293, funded by the National Science Centre, Poland.

References

[1] Bankaitis A.U., Fredrickson J.M. (2002) Otologics middle ear transducer (met) implantable hearing device: rationale, technology, and design strategies, *Trends Amplif*. **6** (2) 53–60..
[2] Beleites T, Neudert M., Bornitz M., Zahnert T. (2014) Sound transfer of active middle ear implants, *Otolaryngol. Clin. North Am.* **47** (6) 859–891.
[3] Maw J. (2019) The vibrant soundbridge, *Otolaryngol. Clin. North Am.* **52** (2) 285–295.

Tuesday, July 19, 2022

13:30 - 15:30

MS-16 Random Dynamical Systems - Recent Advances and New Directions

Saint Clair 1

Chair: Rachel Kuske

13:30 - 13:50
Multiplicative Road Models with Bounded Realizations Applied in Non-Linear Vehicle Road Dynamics
WEDIG Walter*
*Karlsruher Institut für Technologie (P.O.box 3640, 76021 Karlsruhe Germany)

13:50 - 14:10
Multiscale analysis for traveling-pulse solutions to the stochastic FitzHugh-Nagumo equations
EICHINGER Katharina, **GNANN Manuel***, KUEHN Christian
*Delft Institute of Applied Mathematics (PO Box 5031 2600 GA Delft The Netherlands Netherlands)

14:10 - 14:30
Nonlinear and stochastic dynamics in a forced vibro-impact energy harvester
KUSKE Rachel*, YURCHENKO Daniil, SERDUKOVA Larissa
*Georgia Institute of Technology (Atlanta United States)

14:30 - 14:50
Probabilistic response of a vibration energy harvester for realistic torsional vibrations
ALEVRAS Panagiotis*, GUNN Ben, THEODOSSIADES Stephanos
*Department of Mechanical Engineering, School of Engineering, University of Birmingham (Birmingham United Kingdom)

14:50 - 15:10
Simulation of Road Surfaces Profiles by a Stochastic Parametrical Model
AMS Alfons*
*TU Freiberg (Lampadiusstr. 6, 09599 Freiberg Germany)

Multiplicative Road Models with Bounded Realizations Applied in Non-Linear Vehicle Road Dynamics

Walter V. Wedig*
*KIT-Karlsruher Institut für Technologie, Karlsruhe, Germany

Summary. Multiplicative road models generate stationary vehicle excitations which are distributed similar to Gaussian processes but bounded in any given range by means of suitable nonlinearities. For increasing multiplicative noise, the nonlinear process becomes uniformly distributed and change to sinusoidal distributions for growing noise intensities. Both, the multiplicative and sinusoidal roads, are applied to excite quarter car models with one degree of freedom in order to work out the dynamical behavior and stability of vehicle road systems and to discuss them in comparison with classical ground excitations by means of Gaussian models or harmonic wave roads.

1. Introduction to vehicle road dynamics

To introduce basics of vehicle road dynamics, Figure 1 shows the model of a quarter vehicle model [1-6] rolling with constant speed v on a wavy road with level z and frequency $\Omega > 0$ measurable by means of wave length $L = 2\pi/\Omega$. The wavy road defined in Eq. (2), initiates vertical vehicle vibrations y described by the equation (1) of motion

$$\ddot{y} + 2D\omega_1(\dot{y} - \dot{z}) + \omega_1^2(y - z) = 0\,, \qquad , \tag{1}$$

$$z(s) = \mathrm{Z}\cos(\Omega s)\,, \qquad s = \mathrm{v}t, \tag{2}$$

where $\omega_1$is the natural frequency of the vehicle and D denotes its damping, given by $\omega_1^2 = c/m$ and $2D\omega_1 = b/m$, respectively. In Eq. (2), Z is the road amplitude and s the longitudinal coordinate $s = \mathrm{v}t$ when the vehicle drives with constant speed v. In the stationary case, Eqs (1) and (2) lead to the amplitude ratio Y/Z of response and excitation

$$(Y/Z)^2 = \frac{1+(2D\nu)^2}{(1-\nu^2)^2+(2D\nu)^2}\,, \qquad \nu = \mathrm{v}\,\Omega/\omega_1\,. \tag{3}$$

In Figure 2, the amplitude ratio Y/Z is plotted versus the related frequency speed $\nu = \mathrm{v}\Omega/\omega_1$ for the two damping values $D = 0.1$ and $D = 0.2$. Both curves are drawn in red color. They start in $\nu = 0$ with the ratio $Y/Z = 1$ and end in $\nu = \infty$ with $Y/Z = 0$. They become maximal near the resonance for $\nu = 1$. In Figure 2, λ is the image variable of the vehicle velocity in the range $0 \le \lambda \le 2$ with two different scales: $\lambda = \nu$ in the left half and $\lambda = 2 - 1/\nu$ in the right one. This scaling [6] has the advantage that the amplitude ratio can be drawn for all velocities $0 \le \nu < \infty$.

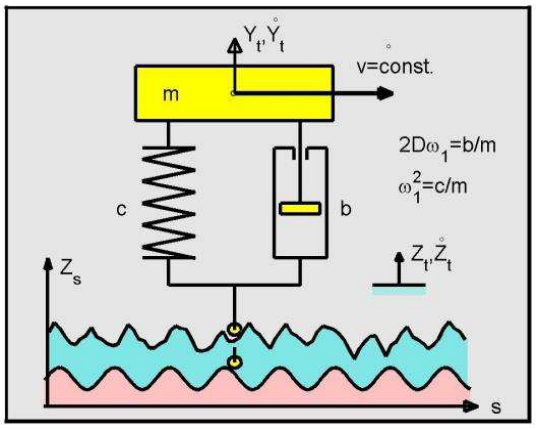

Figure 1: Quarter car model rolling with constant speed v on sinusoidal (orange) or random (cyan) wave roads

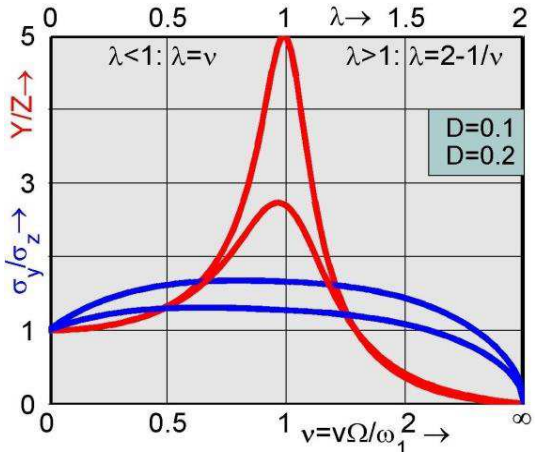

Figure. 2: Standard deviation (blue) and amplitude (red) ratio of response and excitation versus vehicle speed

Stochastic road models [7-12] are assumed to be normally distributed with zero mean and standard deviation σ_z. They are modeled e.g. by means of the linear first order system under white noise

$$dZ_t = -\mathrm{v}\Omega Z_t dt + \sigma\sqrt{\mathrm{v}}dW_t\,, \qquad E(dW_t^2) = dt\,, \tag{4}$$

where $\mathrm{v} > 0$ is the vehicle velocity and σ denotes the intensity of noise realized by the Wiener increment dW_t. The application of the noise spectrum $S_w(\omega) = 1$ and the Fourier transforms leads to the road spectrum

$$S_z(\omega) = \frac{\mathrm{v}\sigma^2}{\omega^2 + (\mathrm{v}\Omega)^2}\,, \qquad \sigma_z^2 = \frac{1}{2\pi}\int_{-\infty}^{+\infty} S_z(\omega)d\omega = \frac{\sigma^2}{2\Omega}\,. \tag{5}$$

The road spectrum is integrated over all frequencies ω to obtain the variance σ_z^2, noted in Eq. (5). The same method can be applied to Eq. (1) to obtain the vehicle spectrum $S_y(\omega)$ which is integrated in order to get the associated standard deviation ratio

$$(\sigma_y/\sigma_z)^2 = \frac{2D+(1+4D^2)\nu}{2D(1+2D\nu+\nu^2)}\ , \qquad \nu = \mathrm{v}\Omega/\omega_1. \tag{6}$$

In Eq. (6), the time frequency $\mathrm{v}\Omega$ represents the corner frequency of the road spectrum $S_z(\omega)$ in Eq. (5). Now, it takes the role of the middle frequency of the wavy road surface in Eq. (2). In Figure 2, the standard deviation ratio of vehicle response and road excitation, calculated in Eq. (6), is plotted for the same two damping values, as before. Therewith, the result obtained in Eq. (6) can be directly compared with the amplitude ratio in Eq. (3). Obviously, resonance magnifications are much stronger in the harmonic case in comparison with random roads when the vehicle is driving near the resonance velocity $\nu = 1$. Outside of the resonant speed range, however, the magnification is inverted, completely. In the over-critical speed range, the amplification of the standard deviation ratio is more than double as big in comparison with the harmonic case when the vehicle is driving e.g. with $\nu = 2$.

2. Extensions to multiplicative road models

The linear first order road model, determined by the spectrum (5), is extended to multiplicative road models of second order which are introduced by means of the two non-linear stochastic differential (Itô) equations [13, 14]

$$dZ_t = \mathrm{v}\Omega U_t dt, \qquad V_t^2 = 1-(Z_t/z_0)^2-(U_t/u_0)^2, \tag{7}$$

$$dU_t = -\mathrm{v}\Omega(2\delta U_t + Z_t)dt + V_t\sigma\sqrt{\mathrm{v}}dW_t\,, \qquad E\left(dW_t^2\right) = dt, \tag{8}$$

where $\mathrm{v} > 0$ denotes the vehicle velocity and σ gives the intensity of white noise dW_t/dt. The parameter Ω is the middle road frequency and δ determines the bandwidth of the two processes Z_t and U_t of the road level and slope, respectively. The non-linear process V_t introduces process limitations by the values z_0 and u_0 which are freely selectable. For infinitely growing values $z_0, u_0 \to \infty$, Eqn. (7) and (8) become linear and their stationary solutions are normally distributed. For finite values $|z_0|, |u_0| < \infty$, the stationary processes are limited by the ellipse $(z/z_0)^2 + (u/u_0)^2 = 1$. In the symmetric case that $z_0 = u_0 = r_0$, the limitation is a circle. When the stationary solutions take vanishing values, multiplicative noise becomes additive with $V_t = 1$ and the system has the strongest possible driving. When the solutions are on the ellipse, noise is excluded by $V_t = 0$ and the system possesses the strongest possible decay behavior.

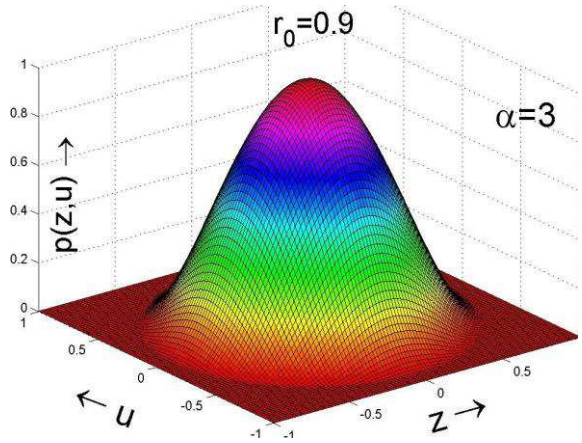

Figure 3: Two-dimensional distribution of level and slope with the limitation $z_0 = u_0 = 0.9$ and the exponent $\alpha = 3$

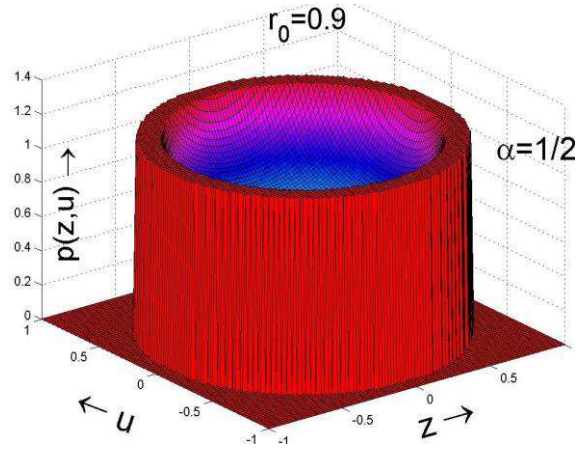

Figure. 4: Singular two-dimensional density of road level and slope for the same limitations and exponent $\alpha = 1/2$

The density distribution $p(z,u,t)$ of the road processes is determined by means of the Fokker-Planck equation [15]

$$\frac{\partial p}{\partial t} = \frac{\partial}{\partial u}[\mathrm{v}\Omega(2\delta u + z)p] - \frac{\partial}{\partial z}[\mathrm{v}\Omega u p] + \frac{1}{2}\sigma^2\mathrm{v}\frac{\partial^2}{\partial \mathrm{u}^2}\left\{\left[1-\left(\frac{\mathrm{z}}{\mathrm{z}_0}\right)^2-\left(\frac{\mathrm{u}}{\mathrm{u}_0}\right)^2\right]\mathrm{p}\right\}. \tag{9}$$

In the stationary case, the density $p(z,u)$ is independent on time and satisfies the stationary Fokker-Planck equation

$$0 = 2\delta\left(p + u\frac{\partial p}{\partial u}\right) + z\frac{\partial p}{\partial u} - u\frac{\partial p}{\partial z} + \frac{\sigma^2}{2\Omega}\frac{\partial^2}{\partial u^2}\left\{\left[1-\left(\frac{\mathrm{z}}{\mathrm{z}_0}\right)^2-\left(\frac{\mathrm{u}}{\mathrm{u}_0}\right)^2\right]\mathrm{p}\right\}. \tag{10}$$

Note that the velocity v is dropped out in Eq. (10) because of $\partial p/\partial t = 0$; i.e. the statistical configuration of the road is independent on velocity and can be applied for all speeds. In the symmetric case $z_0 = u_0 = r_0$,.Eq. (10) is solved by

$$p(z,u) = C\left[1-(z/r_0)^2-(u/r_0)^2\right]^{\alpha-1}, \qquad \alpha = r_0^2 2\delta\Omega/\sigma^2 > 0, \tag{11}$$

where C is the integration constant of normalization. The two-dimensional density, noted in Eq. (11), can be integrated for $\alpha > 0$. This coincides with the stability condition $\delta > 0$ of the linear oscillator for $z_0, u_0 \to \infty$. For $\alpha = 1$, the density $p(z,u)$ in Eq. (11) is uniformly distributed. For $\alpha = 2$, it is parabolic. For $\alpha = 3$, the density $p(z,u)$ possesses a forth order shape as shown in Figure 3 for the limitation $r_0 = 0.9$. In this case, the two-dimensional density is zero on

the limitation circle with a vanishing gradient. The two-dimensional density in Eq. (11) becomes singular for $0 < \alpha < 1$. In Figure 4, the density is plotted e.g. for $\alpha = 1/2$. In this case, $p(z,u)$ coincides with the stationary density of the sinusoidal road surface, noted in Eq. (2).

3. Vehicle dynamics with multiplicative road models

The application of Itô's calculus to the multiplicative road model of Eqn. (7) and (8), leads to the three increments

$$d(Z_t^2) = 2\mathrm{v}\Omega Z_t U_t dt, \quad V_t^2 = 1 - (Z_t/z_0)^2 - (U_t/u_0)^2,$$
$$d(Z_t U_t) = \mathrm{v}\Omega(U_t^2 - 2\delta Z_t U_t - Z_t^2)dt + Z_t V_t \sigma\sqrt{\mathrm{v}}\, dW_t,$$
$$d(U_t^2) = -2\mathrm{v}\Omega\left(2\delta U_t^2 + Z_t U_t\right)dt + V_t^2\sigma^2\mathrm{v}dt + V_t\sigma\sqrt{\mathrm{v}}\, dW_t,$$

in which the expectation operator can be applied to obtain the associated moment's equations. In the stationary case, the first equation and the second one lead to $E(Z_t U_t) = 0$ and $E(U_t^2) = E(Z_t^2)$, respectively. Taking into account that $E(V_t dW_t)$ is vanishing and $E(V_t^2)$ follows from Eq. (7), the third equation gives the stationary square mean

$$E(Z_t^2) = E(U_t^2) = \frac{1}{1/z_0^2 + 1/u_0^2 + 4\delta\Omega/\sigma^2}\,. \tag{12}$$

The result in Eq. (12) coincides with the square means of the linear road model under white noise obtained for the limiting case $z_0, u_0 \to \infty$. Note that the above square mean equations are linear although the state equations (7) and (8) are non-linear. Both is possible because of the specially adapted non-linearity in Eq. (7).

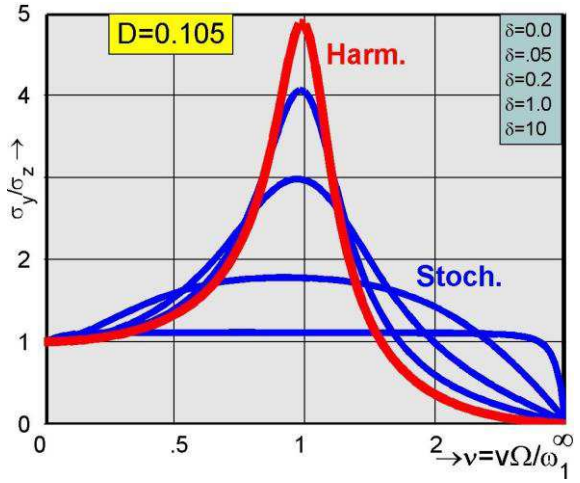

Figure 5: Standard deviation ratio of response and excitation for the road bandwidth $\delta = 0$ (Harm.) and $\delta > 0$ (Stoch.)

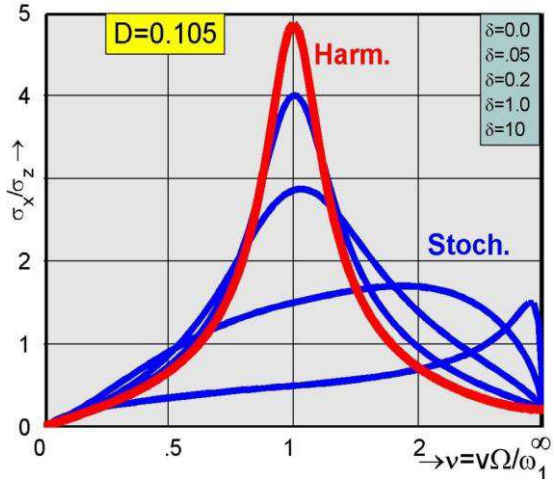

Figure.6: Standard deviation of the vertical vibration velocity versus the related vehicle speed for the damping $D = 0.105$

The multiplicative road model is applied to the quarter vehicle, shown in Figure 1. The introduction of the coordinate $\dot{y} = \omega_1 x$ of the vertical vibration velocity into equation (1) of motion leads to the associated first order system

$$dY_t = \omega_1 X_t dt, \qquad dX_t = -\left[2D\left(\omega_1 X_t - \dot{Z}_t\right) + \omega_1(Y_t - Z_t)\right]dt \tag{13}$$

where the time derivative $\dot{Z}_t$ is given by the increment $dZ_t = \mathrm{v}\Omega U_t dt$ in Eq. (7). The stationary co-variances of all excitation processes Z_t, U_t times all response processes Y_t, X_t are calculable by means of the matrix equation

$$\begin{bmatrix} 0 & -1 & -\nu & 0 \\ 1 & 2D & 0 & -\nu \\ \nu & 0 & 2\delta\nu & -1 \\ 0 & \nu & 1 & 2(D+\delta\nu) \end{bmatrix} \begin{bmatrix} E(Z_t Y_t) \\ E(Z_t X_t) \\ E(U_t Y_t) \\ E(U_t X_t) \end{bmatrix} = \begin{bmatrix} 0 \\ E(Z_t^2) \\ 0 \\ 2D\nu E(U_t^2) \end{bmatrix}, \tag{14}$$

where the square means of the road excitation are already calculated in Eq. (12). Note that the co-variance matrix in Eq. (14) is skew-symmetric. Hence, the co-variance matrix is positive definite. Its determinant Δ is calculated to

$$\Delta = (\nu^2 - 1)^2 + 4\nu(D + \delta\nu)(\delta + D\nu). \tag{15}$$

Subsequently, the stationary moment's equations of the vehicle processes are set up and solved, as follows:

$$E(Y_t^2)/E(Z_t^2) = [1 + 4\nu(D + \delta\nu)(\delta + D\nu) + \delta\nu^3/D\,]/\Delta, \tag{16}$$
$$E(X_1^2)/E(Z_t^2) = \nu^2[1 + 4D\nu(\delta + D\nu) + \delta\nu/D]/\Delta\,. \tag{17}$$

In Figure 5 and 6, the square roots of the square mean ratios in Eq. (16) and (17) are plotted versus the related vehicle speed for the damping $D = 0.105$ and five different bandwidth values δ of the road excitation. For vanishing bandwidth $\delta = 0$, the result in Eqn.(16) coincide with the amplitude ratio (3) of a vehicle rolling on wavy roads with harmonic contour surface. The same holds for Eq. (17). For growing bandwidth δ, the resonance peaks in both amplitude-velocity

diagrams are reduced in comparison with the harmonic case. However, the standard deviations (blue) become bigger than the amplitude (red) ratios when the vehicle is driving sufficiently outside the resonance velocity. For higher vehicle speeds e.g. $\nu = 2$, the magnification by stochastic excitations becomes even stronger in comparison with the harmonic case. For very slow and very high speeds, the standard deviation ratios are independent on the bandwidth of the road frequencies and coincide with the results of harmonic road excitation. For the special case of white noise with infinitely increasing bandwidth, Eq. (16) gives $\sigma_y/\sigma_z = 1$ for all vehicle speeds $\nu < \infty$ and $\sigma_y/\sigma_z = 0$ for $\nu = \infty$.

4. Non-stationary models of vehicle speed fluctuations

In Figure 1, the wavy road is modeled by the sinusoidal form $z(t)$. This model is extended to its stochastic version

$$Z_t = \cos\phi_t, \qquad d\phi_t = \Omega\mathrm{v}dt + \sigma dW_t, \tag{18a,b}$$

where $\Omega\mathrm{v}$ is the time frequency given by the road frequency Ω times the vehicle velocity v which is perturbed by white noise $\sigma\dot{W}_t$ of intensity σ, when speed fluctuations through driving moment and air resistance are measurable and taken into account in a purely kinematic modeling. The application of Itô's calculus to the road process Z_t leads to

$$dZ_t = -(\Omega\mathrm{v}dt + \sigma dW_t)\sin\phi_t - (\sigma^2/2)\cos\phi_t dt\,.$$

The stochastic road model (18a,b) is applied to Eq. (1) of the vehicle road system in the slightly modified form

$$\ddot{Y}_t + 2D\omega_1\dot{Y}_t + \omega_1^2 Y_t = \mu\left(2D\omega_1\dot{Z}_t + \omega_1^2 Z_t\right), \tag{19}$$

where μ is the amplitude of the road excitation. Note that sinusoidal excitations like $z(t) = \cos\omega t$ are non-stationary with the mean value $m_z = (\omega T)^{-1}\sin\omega T$ which converge to the stationary zero value with linearly growing time T. In order to eliminate this non-stationary behavior, amplitudes A_t, B_t, G_t, H_t are introduced into Eq. (19) by means of Eqn. (20a) and (21a). The application of Itô's calculus leads to the transformed equations, as follows:

$$Y_t = A_t\cos\phi_t + B_t\sin\phi_t\,, \qquad dA_t = (\sigma^2 A_t/2 - \Omega\mathrm{v}B_t + \omega_1 G_t)dt - \sigma B_t dW_t, \tag{20a,b}$$

$$\dot{Y}_t/\omega_1 = G_t\cos\phi_t + H_t\sin\phi_t, \quad dB_t = (\sigma^2 B_t/2 + \Omega\mathrm{v}A_t + \omega_1 H_t)dt + \sigma A_t dW_t, \tag{21a,b}$$

$$dG_t = [-\omega_1 A_t - \Omega\mathrm{v}H_t + (\sigma^2/2 - 2D\omega_1)G_t - \mu(\omega_1 - D\sigma^2)]dt - \sigma H_t dW_t, \tag{22}$$

$$dH_t = [-\omega_1 B_t + \Omega\mathrm{v}G_t + (\sigma^2/2 - 2D\omega_1)H_t - 2D\mu\Omega\mathrm{v}]dt + \sigma(G_t - 2D\mu)dW_t. \tag{23}$$

Numerical integrations of the transformed equations (20b), (21b), (22) and (23) are performed by means of the Maruyana scheme with the time step size $\Delta\tau = \omega_1\Delta t = 10^{-3}$ for $N = 2\cdot 10^7$ samples. The Wiener increments [16] are approximated by $\Delta W_n = N_n\sqrt{\Delta t}$ where the numbers N_n are normally distributed with zero mean and unit mean square $E(N_n^2) = 1$. Associated parameters are chosen by $D = 0.1$, $\mu = 1$ and $\sigma = 0.2\sqrt{\omega_1}$. In Figure 7, simulation results of the displacement means $E(A_t)$ and $E(B_t)$ as well as the density distributions $p(a)$ and $p(b)$ are plotted versus the related speed $\Omega\mathrm{v}/\omega_1$.The density $p(a)$ is marked by blue colour and $p(b)$ is green. Both densities show the resonance effect when the vehicle drives with velocity $\nu = 1$. For further growing speed, the densities of both displacement processes are concentrated around the zero axes. This represents the self-centering effect, already known in rotor dynamics. For $\sigma = 0$, the density distributions $p(a)$ and $p(b)$ degenerate to delta needles around the means values $E(A_t)$ and $E(B_t)$.

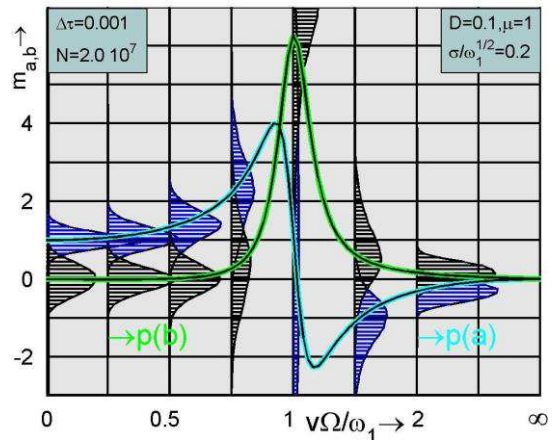

Figure.7: Mean amplitudes and densities of A_t and B_t versus frequency speed related to natural car frequency

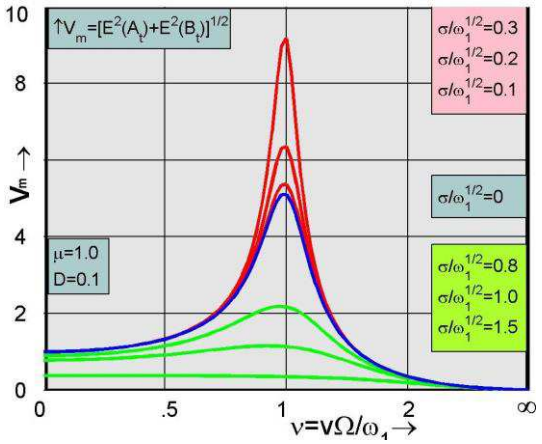

Figure 8: Resonance diagram for growing noise intensity: the resonance is first increased and then decreases again.

The application of the expectation operator $E(\cdot)$ to Eqn. (20b), (21b), (22) and (23) leads to the matrix equation

$$\begin{bmatrix} \sigma^2/2 & -\Omega\mathrm{v} & \omega_1 & 0 \\ \Omega\mathrm{v} & \sigma^2/2 & 0 & \omega_1 \\ -\omega_1 & 0 & \sigma^2/2 - 2D\omega_1 & -\Omega\mathrm{v} \\ 0 & -\omega_1 & \Omega\mathrm{v} & \sigma^2/2 - 2D\omega_1 \end{bmatrix} \begin{bmatrix} E(A_t) \\ E(B_t) \\ E(G_t) \\ E(H_t) \end{bmatrix} = \mu \begin{bmatrix} 0 \\ 0 \\ \omega_1 - D\sigma^2 \\ 2D\Omega\mathrm{v} \end{bmatrix}, \tag{24}$$

by which the stationary mean values of all amplitude processes are calculable. In Figure 8, the resultant mean amplitude $V_m = [E^2(A_t) + E^2(B_t)]^{1/2}$ of both displacement means $E(A_t)$ and $E(B_t)$ is plotted versus the related velocity for vanishing noise (blue) and for growing noise intensity (red). The latter leads to stable mean amplitude with resonance magnifications up to a critical noise intensity where the resonance peak is reduced (green), again. In this case, the mean amplitude mean becomes unstable. This stability behavior follows from the diagonal term $\Delta = (\sigma^2/2 - 2D\omega_1)\,\sigma^2/2$ in Eq. (24) which is negative for weak noise intensities and become positive for growing noise. More details are obtained when the almost sure stability [17] of the amplitudes in Eqs. (20b), (21b). (22) and (23) is investigated. Stability in mean is investigated by means of the eigen-values [17] of the mean amplitudes matrix in Eq. (24).

5. Resonance reduction and induction by means of filtered noise

It is interesting how the resonance behavior of the amplitude processes is changing when the velocity perturbation by white noise $\sigma \dot{W}_t$ in Eq. (18b) is replaced by the more realistic perturbation of filtered noise $\omega_g \Psi_t$, as follows:

$$\dot{Y}_t = \omega_1 X_t\,, \qquad \dot{\Phi}_t = \Omega\mathrm{v} + \omega_g \Psi_t\,, \quad d\Psi_t = -\omega_g \Psi_t dt + \sigma dW_t, \tag{25 a,b,c}$$

$$\dot{X}_t = -\omega_1(2DX_t + Y_t) + \mu[\omega_1 \cos\Phi_t - 2D(\Omega\mathrm{v} + \omega_g \Psi_t)\sin\Phi_t]. \tag{26}$$

The stationary filtered noise in Eq. (25c) is normally distributed with zero mean and mean square $\sigma_\psi^2 = \sigma^2/(2\omega_g)$. The application of the amplitude processes (20a) and (21a) to the vehicle equations (25a) and (26) leads to

$$d\vec{V}_t = (A\vec{V}_t + \omega_g B \Psi_t \vec{V}_t)dt + \mu(\vec{x} - 2D\omega_g \Psi_t \vec{y})dt, \tag{26}$$

where the vector $\vec{V}_t = (A_t, B_t, G_t, H_t)'$ of the four amplitudes are determined by the matrices A and B as follows:

$$A = \begin{bmatrix} 0 & -\Omega\mathrm{v} & \omega_1 & 0 \\ \Omega\mathrm{v} & 0 & 0 & \omega_1 \\ -\omega_1 & 0 & -2D\omega_1 & -\Omega\mathrm{v} \\ 0 & -\omega_1 & \Omega\mathrm{v} & -2D\omega_1 \end{bmatrix}, \qquad B = \begin{bmatrix} 0 & -1 & 0 & 0 \\ 1 & 0 & 0 & 0 \\ 0 & 0 & 0 & -1 \\ 0 & 0 & 1 & 0 \end{bmatrix}$$

$$\vec{V}_t = (A_t, B_t, G_t, H_t)', \qquad \vec{x} = (0,0,\omega_1, -2D\Omega\mathrm{v})', \qquad \vec{y} = (0,0,0,1)'.$$

The vectors $\vec{x}$ and $\vec{y}$, noted above, determine the inhomogeneous part in Eq. (26). Note that in Eq. (26) there is a non-linear term in form of $\Psi_t \vec{V}_t$ with a product of state processes. The product possesses the increment

$$d(\Psi_t \vec{V}_t) = [A\Psi_t \vec{V}_t + \omega_g B \Psi_t^2 \vec{V}_t + \mu(\Psi_t \vec{x} - 2D\omega_g \Psi_t^2 \vec{y}) - \omega_g \Psi_t \vec{V}_t]dt + \vec{V}_t \sigma dW_t, \tag{27}$$

which couples the system vector $\vec{V}_t$ to higher potencies of the perturbation Ψ_t. This coupling effect is approximately removed in the stationary moments equations of Eqn. (26, 27) by means of the Gaussian closure, as follows:

$$AE(\vec{V}_t) + \omega_g B E(\Psi_t \vec{V}_t) = -\mu \vec{x}\,, \qquad E(\Psi_t^2 \vec{V}_t) = E(\Psi_t^2) E(\vec{V}_t), \tag{28a,b}$$

$$\omega_g \sigma_\psi^2 B E(\vec{V}_t) + (A - \omega_g I) E(\Psi_t \vec{V}_t) = \mu 2D\omega_g \sigma_\psi^2\, \vec{y}\,, \qquad E(\Psi_t^2) = \sigma^2/(2\omega_g). \tag{29a,b}$$

In Eq. (29a), I denotes the unit matrix. Note that in Eq. (29a) the expectation of the product $\Psi_t^2 \vec{V}_t$ is approximately replaced by the product of both mean values. Numerical evaluations of Eqn. (28a) and (29a) are shown in Figure 9 where the mean amplitude V_m is plotted versus the vehicle velocity v for $D = 0.1$, $\mu = 1$ and the noise intensities $\sigma = 0.2\sqrt{\omega_1}$ (green) and $\sigma = 0.5$ (blue). For $\omega_g = 0$, the green and blue lines coincide with the deterministic case of vanishing perturbations. For growing bandwidth of the perturbation, the resonance peak is reduced. The resonance reduction becomes stronger for increasing noise intensities σ and for increasing low-pass frequency ω_g. This effect is physically explainable by the fact that high frequencies are filtered out and only low frequencies are retained in the perturbation. However, low velocity frequencies vΩ are not contributing to resonance effects.

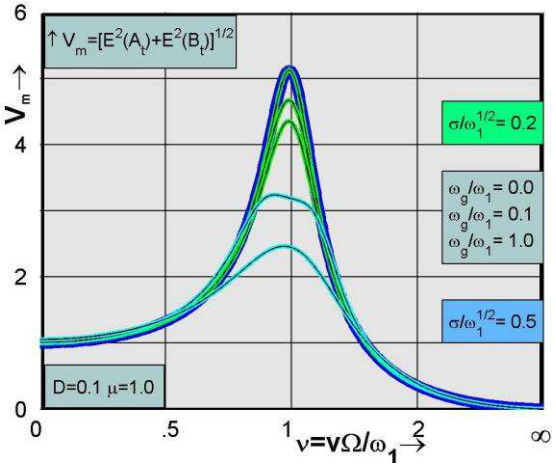

Figure.9: Resonance reduction in the mean amplitudes V_m for growing noise intensity and perturbation bandwidth

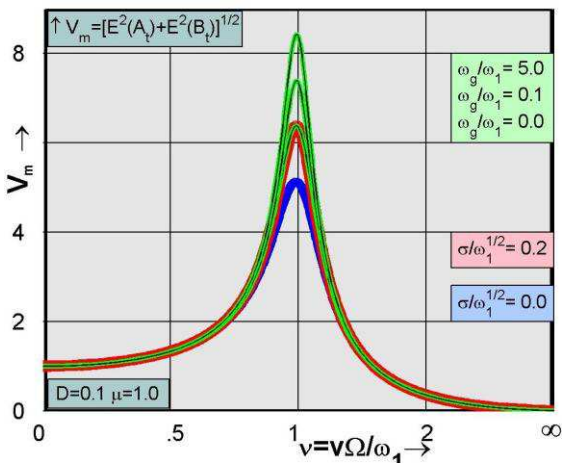

Figure 10: Resonance induction from blue to red line via growing noise intensity and perturbation bandwidth (green)

The resonance reduction is completely inverted when instead of low-pass noise one applies the high-pass perturbation

$$Z_t = \cos\phi_t, \qquad \dot{\Phi}_t = \Omega\mathrm{v} + \dot{\Psi}_t\,, \quad d\Psi_t = -\omega_g\Psi_t dt + \sigma dW_t, \tag{30abc}$$

where white noise $\sigma\dot{W}_t$ in Eq. (18b) is now replaced by $\dot{\Psi}_t$ in Eq. (30b). Consequently, perturbations with low frequencies are filtered out. High frequency parts are retained. The introduction of Eqn. (30) into Eq. (19) leads to

$$dY_t = \omega_1 X_t dt, \qquad d\phi_t = (\Omega v - \omega_g\Psi_t)dt + \sigma dW_t\,, \qquad d\Psi_t = -\omega_g\Psi_t dt + \sigma dW_t, \tag{31a,b,c}$$

$$dX_t = -\omega_1(2DX_t + Y_t)dt + \mu\big[(\omega_1 - D\sigma^2)\cos\phi_t + (\omega_g\Psi_t - \Omega\mathrm{v})\sin\phi_t\big]dt - \mu 2D\sigma\sin\phi_t dW_t\,. \tag{32}$$

The application of the amplitude processes (20a) and (21a) to Eqn. (31) and (32) leads to the vector equation

$$d\vec{V}_t = \big(A\vec{V}_t - \omega_g B\Psi_t\vec{V}_t\big)dt + \mu\big(\vec{x} + 2D\omega_g\Psi_t\vec{y}\big)dt + \big(B\vec{V} - 2D\mu\vec{y}\big)\sigma dW_t \tag{33}$$

where the vector $\vec{V}_t$ contains the four amplitude processes. The matrix A and the vectors $\vec{x}$ are given by

$$A = \begin{bmatrix} \sigma^2/2 & -\Omega\mathrm{v} & \omega_1 & 0 \\ \Omega\mathrm{v} & \sigma^2/2 & 0 & \omega_1 \\ -\omega_1 & 0 & \sigma^2/2 - 2D\omega_1 & -\Omega\mathrm{v} \\ 0 & -\omega_1 & \Omega\mathrm{v} & \sigma^2/2 - 2D\omega_1 \end{bmatrix}, \qquad \vec{x} = \begin{bmatrix} 0 \\ 0 \\ \omega_1 - 2D\,\sigma^2/2 \\ -2D\Omega\mathrm{v} \end{bmatrix}, \qquad .$$

where B and $\vec{y}$ are already noted in the last section. The non-linear term $\Psi_t\vec{V}_t$ in Eq. (33) possesses the increment

$$d(\Psi_t\vec{V}_t) = \big[A\Psi_t\vec{V}_t + \omega_g B\Psi_t^2\vec{V}_t + \mu(\Psi_t\vec{x} - 2D\omega_g\Psi_t^2\vec{y}) - \omega_g\Psi_t\vec{V}_t\big]dt + \vec{V}_t\sigma dW_t \tag{34}$$

in which the system vector $\vec{V}_t$ is coupled to higher potencies of the perturbation Ψ_t. This coupling is approximately removed by means of the Gaussian closure, noted in Eq. (35b). In the stationary case, the insertion of the Gaussian closure condition into Eq. (34) leads to the linear moments equations

$$AE(\vec{V}_t) - \omega_g BE\big(\Psi_t\vec{V}_t\big) = -\mu\vec{x}\,, \qquad E(\Psi_t^2\vec{V}_t) = E(\Psi_t^2)E\big(\vec{V}_t\big), \tag{35a,b}$$

$$BE\big(\vec{V}_t\big)\sigma^2/2 + \big(A - \omega_g I\big)E\big(\Psi_t\vec{V}_t\big) = \mu 2D\vec{y}\sigma^2/2\,, \qquad E(\Psi_t^2) = \sigma^2/\big(2\omega_g\big). \tag{36a,b}$$

where I is the unit matrix. Numerical evaluations of Eqs. (35a) and (36a) are shown in Figure 10 where the mean amplitude V_m is plotted versus the related vehicle velocity v for $D = 0.1$ and $\mu = 1$. The blue line stands for $\sigma = 0$ of vanishing noise perturbations. For $\sigma = 0.5\sqrt{\omega_1}$ and $\omega_g/\omega_1 = 0$, one obtains the red line overlaid by the green one in coincidence with the white noise case shown in Figure 8. For $\omega_g/\omega_1 = 0.1$ and $\omega_g/\omega_1 = 5$ of growing perturbation bandwidth, there is a further increasing of the resonance peak. This resonance induction is probably explained by the destabilizing effect of harmonic parameter excitations when for $\Omega\mathrm{v} = 2\omega_1$the perturbation frequency coincides with the double eigen-frequency of the oscillator.

6. Lyapunov exponents and rotation numbers in vehicle dynamics

Vehicle vibrations which are described by rotating coordinates are physically existent if they are almost sure stable or asymptotically stable with probability one. In the unstable case, the separation into rotating processes is not possible and the vehicle equations must be retransformed back to their original equations in non-rotating coordinates. The stability in mean and the almost sure stability [17] of the vehicle vibrations in rotating coordinates is investigated by means of a projection on hyper-spheres and application of the multiplicative ergodic theorem of Osceledets [18]. For these purposes, Eqn. (20b), (21b), (22) and (23) are reduced with $\mu = 0$ to the homogenous form and transformed by means of the two-dimensional system of polar coordinates (P_t, Γ_t) and (Q_t, θ_t), which leads to the stability equations

$$\begin{aligned} A_t = P_t\cos\Gamma_t\text{:} &\qquad dP_t = [\omega_1\cos(\Theta_t - \Gamma_t)\,Q_t + \sigma^2 P_t]dt, \\ B_t = P_t\sin\Gamma_t\text{:} &\qquad d\Gamma_t = [\omega_1\sin(\Theta_t - \Gamma_t)\tfrac{Q_t}{P_t} + \Omega\mathrm{v}]dt + \sigma dW_t, \\ G_t = Q_t\cos\Theta_t\text{:} &\qquad dQ_t = [-\omega_1\cos(\Theta_t - \Gamma_t)\,P_t + (\sigma^2 - 2D\omega_1)Q_t]dt, \\ H_t = Q_t\sin\Theta_t\text{:} &\qquad d\Theta_t = [\omega_1\sin(\Theta_t - \Gamma_t)\tfrac{P_t}{Q_t} + \Omega\mathrm{v}]dt + \sigma dW_t. \end{aligned}$$

The above equations project the displacements (A_t, B_t) and the velocities (G_t, H_t) on two circles with radii (P_t, Q_t) and angles (Γ_t, Θ_t). A second application of polar coordinates by means of Eqs. (37a) and (38a) eliminates the two radii (P_t, Q_t) and projects the entire motion on hyper-sphere with one radius R_t and three angles determined by

$$P_t = R_t\cos\Psi_t\text{:} \qquad dR_t = [\sigma^2 - D\omega_1(1 - \cos 2\Psi_t)]R_t dt, \tag{37}$$

$$Q_t = R_t\sin\Psi_t\text{:} \qquad d\Psi_t = -\omega_1(D\sin 2\Psi_t + \cos\Delta_t)dt, \tag{38}$$

$$\Delta_t = \theta_t - \Gamma_t\text{:} \qquad d\Delta_t = \omega_1\sin\Delta_t(\cot\Psi_t - \tan\Psi_t)dt, \tag{39}$$

$$\Sigma_t = \theta_t + \Gamma_t\text{:} \qquad d\Sigma_t = \omega_1\sin\Delta_t(\cot\Psi_t + \tan\Psi_t)dt + 2\omega_e dt + 2\sigma dW_t, \tag{40}$$

where difference and sum angle (Δ_t, Σ_t) are additionally introduced by means of Eqn. (39a) and (40a). Eq. (37) is integrated by means of variable separation and leads to the top Lyapunov exponent

$$\lambda_{top} = \lim_{t\to\infty}\frac{1}{t}\ln(R_t/R_0) = \sigma^2 - D\omega_1\left(1 - \lim_{t\to\infty}\frac{1}{t}\int_0^t\cos 2\Psi_\tau d\tau\right). \tag{41}$$

If the top Lyapunov exponent is negative, the stationary solutions of Eqn. (20b), (21b), (22) and (23) are asymptotically stable with probability one or almost surely stable. For $\lambda_{top} > 0$, the solutions are unstable and grow, exponentially.

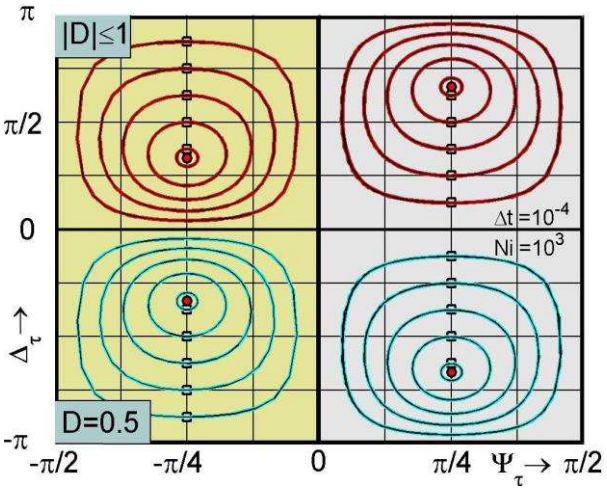

Fig. 11: Limit cycles of projection angles Δ_τ and Ψ_t around red centers for under-critical damping $D \leq 1$

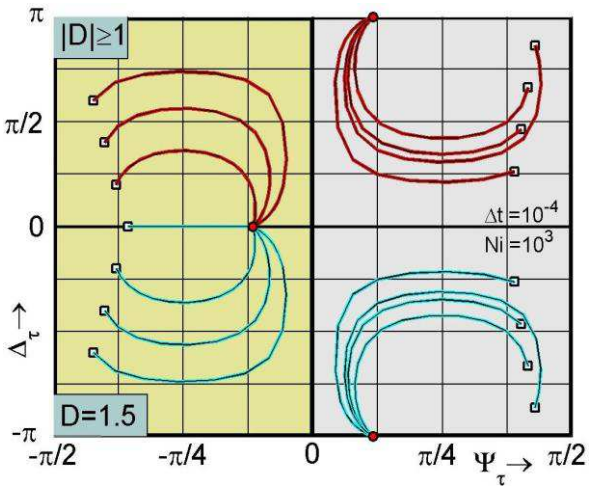

Fig. 12: Transient projection angles and their ending in singular fix-points for over-critical damping $D \geq 1$

According to Eq. (41), the top Lyapunov exponent is determined by the noise intensity, the system damping and the time average of the cosine of the stability angle Ψ_t, which is coupled with the difference angle Δ_t. Both angles are determined by Eqn. (38b) and (39b) which are non-linear, noise-free and decoupled from the sum angle Σ_t in Eq.(40b) where additive noise is still active. In Figure 11 and 12, Eqn. (38b) and (39b) are numerically evaluated for the under- and overcritical damping $D = 0.5$ and $D = 1.5$ on the left and right side, respectively. The angle solutions are 2π −periodic in Δ and π −periodic with respect to Ψ. For $D \leq 1$, Figure 11 shows stationary limit cycles of both angles $(\Lambda_\tau, \Psi_\tau)$. They are calculable without any transient time behavior for arbitrary initial values applying an Euler scheme e.g. with the scan rate $\Delta_\tau = \omega_1 \Delta t = 0.001$. All limit cycles in Figure 11 are symmetric with respect to $\Psi = \pm\pi/4$. Because of this symmetry the time average in Eq. (41) can also be obtained by the four stationary fix-points $\Psi = \pm\pi/4$ and $\cos\Delta = \pm D$ which represent the center of the limit cycles marked by red circles. The insertion of these center values into Eq. (41) leads to one top Lyapunov exponent and two rotation numbers, as follows:

$$\lambda_{top} = \sigma^2 - D\omega_1 \quad \text{and} \quad \rho_{\Gamma,\theta} = \Omega\mathrm{v} \pm \omega_1\sqrt{1 - D^2} \qquad \text{for } D \leq 1. \tag{42}$$

The rotation numbers are time averages of rotating angle processes, applied to the angles increments $d\Gamma_t$ and $d\Theta_t$. They are calculated by the stationary values $(\sin\Delta)^2 = 1 - D^2$ and $Q/P = \tan\Psi = \pm 1$. In Figure 12, Eqn. (38b) and (39b) are evaluated for the overcritical damping $D = 1.5$ where instead of limit cycles transient solutions are obtained. Starting with any initial values, both angles $(\Lambda_\tau, \Psi_\tau)$ move to the stationary fix-points $\Delta = 0, \pm\pi$ and $\sin 2\Psi = \pm 1/D$. The insertion of these stationary angle values leads to two Lyapunov exponents and one rotation number

$$\lambda_{1,2} = \sigma^2 - \omega_1\left(D \mp \sqrt{D^2 - 1}\right) \quad \text{and} \quad \rho_{\Gamma,\theta} = \Omega\mathrm{v} \qquad \text{for } D \geq 1. \tag{43}$$

where the fix-points solutions are inserted into the ergodic integrals of Lyapunov exponent and rotation number.

In Figure 13, the rotation numbers are plotted versus the frequency speed $\Omega\mathrm{v}$ for the natural frequency $\omega_1 = 1$ and three damping values. For $D = 0$, one obtains two straight lines with positive slopes marked by thick red color. For $D = 0.9$, both rotation numbers are drawn in green and coincide in yellow for $D = 1$. Associated rotation numbers with negative slopes are obtained for negative speed frequencies. In Figure 14, the stability map is obtained by plotting the related critical noise intensity σ_{cr}^2/ω_1 versus the vehicle damping. With $\lambda_{top} = 0$, the stability boundaries are

$$\sigma_{cr}^2/\omega_1 = D \qquad \text{for} \quad D \leq 1,$$
$$\sigma_{cr}^2/\omega_1 = D - \sqrt{D^2 - 1} \qquad \text{for} \quad D \geq 1.$$

In Figure 14, the stability region is marked by green color. Inside the green region, the stationary solutions of Eqn. (20b), (21b), (22) and (23) are asymptotically stable with probability one or almost surely stable. Over the green region, the solutions are unstable. Obviously, one needs linearly increasing to stabilize the system for growing noise. However, this effect holds up to $D = 1$, only. Overcritical damping is less effective since growing damping stabilizes weak noise perturbations, only. For $D \to \infty$, vehicle and road are rigidly coupled. Hence, stabilization is no longer possible. For an extended stability investigation, the above polar coordinate system (P_t, Γ_t) and (Q_t, θ_t) is applied to Eq.(24). For $\mu = 0$, this leads to the same stability equations for the angles (Γ_t, θ_t) and radii (P_t, Q_t) except that σ^2 in the radii equations is replaced by $\sigma^2/2$ when because of $E(dW_t) = 0$ there is noise in Eq. (24). Therewith, the radius equation (37) reads as

$$dR_t = [\sigma^2/2 - D\omega_1(1 - \cos 2\Psi_t)]R_t dt. \tag{44}$$

As already shown before, the Lypaunov exponents of the mean value solutions are calculated to

$$\lambda_{m,} = \sigma^2/2 - D\omega_1, \qquad \text{for} \qquad D \leq 1,$$
$$\lambda_{m,} = \sigma^2/2^2 - \omega_1\left(D \mp \sqrt{D^2 - 1}\right), \qquad \text{for} \quad \text{for } D \geq 1.$$

The rotation numbers of the mean value solutions remain unchanged. In Figure 12, the stability boundaries of the mean

value solutions are plotted in Figure 14, marked by blue lines. Note that stability and rotation behavior of the mean value solutions can also investigated by means of the four eigen-values of Eq. (24) where the real and imaginary parts take the role of Lyapunov exponents and rotation numbers, respectively. Correspondingly, one finds one real part and four imaginary parts for $D \leq 1$. In the overcritical case $D \geq 1$, the eigen-values of Eq. (24) lead to two real parts and two imaginary parts. According to [19], the stability behavior can also be investigated by means of the p-th mean behavior in order to get the almost sure stability for $p = 0$ and the stability in mean for $p = 1$. In [21], one finds approximations of stability boundaries of second order systems for all exponents $p \geq 0$.

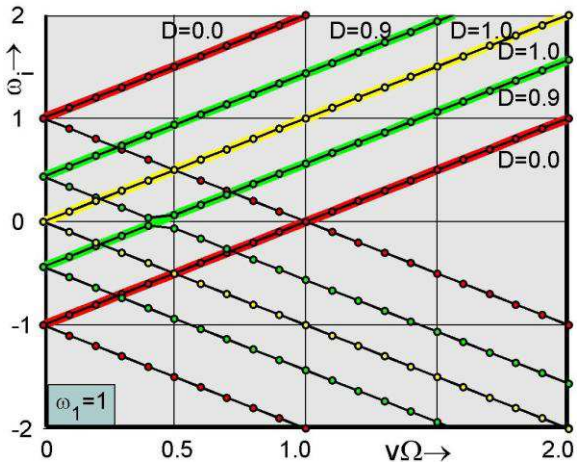

Fig. 13: Four rotation numbers depending on speed frequency for the damping values $D = 0, 0.9$ and 1.0

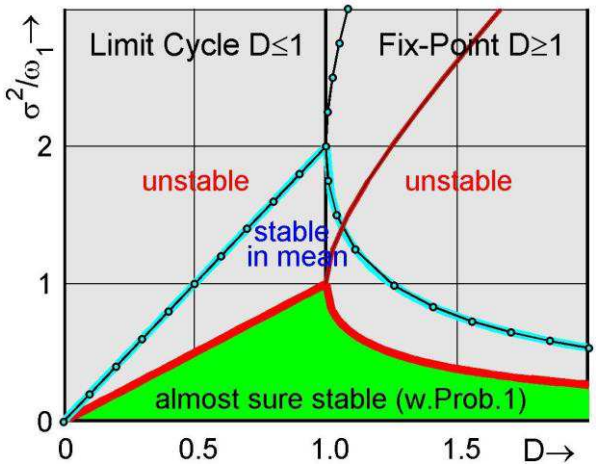

Fig. 14: Boundaries for almost sure stability and stability in mean plotted against system damping

7. Conclusions

There are two multiplicative road models which include the limiting case of deterministic harmonic roads. The first one is obtained by non-linear filter equations driven by white noise. Their stationary solutions are similar to Gaussian but bounded with vanishing mean and standard deviation which coincides with the deterministic behavior in the limiting case of vanishing excitation bandwidth $\delta = 0$. Because of specially adapted non-linearity, the mean square equations calculated by means of Itô's calculus are linear. The second model applies sinusoidals where the excitation frequency is perturbed by white noise of intensity σ. Inversely to the first model, standard deviations are zero and mean values coincide with the deterministic harmonic behavior passing to the limit case $\sigma = 0$ of vanishing noise perturbation. New results are found for more realistic perturbations by means of filtered noise. For low-pass filtered perturbations, the resonance peak is reduced. However, it is increased applying white noise perturbations. This resonance induction is even stronger when instead of white noise high-pass filtered perturbations are applied.

References

[1] Wedig, W.V.: Dynamics of Cars Driving on Stochastic Roads, In: Spanos & Deodatis (Eds), Rotterdam, Millpress, 647-654, 2003.
[2] Wedig, W.V.: Digital Simulation of Road-Vehicle Systems. Prob. Engineering Mechanics, 27, pp. 82-87. 2012.
[3] Wedig, W V.: Velocity Turbulences in Stochastic Road-Vehicle Dynamics, Proc. of the 15th Intern. Prob. Workshop, Dresden 2017, TUDpress, 1-13.
[4] Popp, K. and Schiehlen, W.O.: Fahrdynamik, Teubner, 1993.
[5] Rill,G.: Road Vehicle Dynamics: Fundamentals and Modeling, CRC Press, Boca Raton FL, 2012.
[6] Klotter, K.: Kinetik der Schwinger, Hütte, Theoretische Grundlagen, 4. Abschnitt Schwingungen, w. Ernst & Sohn, Berlin, 571-584, 1955
[7] Doods, C.J. and Robson, D.J.: The Description of Road Surface Roughness, Journal Sound and Vibration, 31, 175-183, 1973
[8] Sobczyk, K., MacVean, D.B. and Robson, J.D. :Response to Profile-Imposed Excitation with Randomly Varying Transversal Velocity, Journal . . Sound and Vibration, 52, 1, pp. 37-49, 1977.
[9] Braun, O. Untersuchungen von Fahrbahnunebenheiten und Anwendungen der Ergebnisse, Diss. Universität Hannover,1969.
[10] Wedig, W.V.: Simulation of Road-Vehicle Systems, Probabilistic Engineering Mechanics, 27, 82-87, 2012.
[11] Wedig, W.V. Jump Phenomena in Road-Vehicle Dynamics, Int. Journal of Dynamics and Control, 4, 21-28, 2016
[12] Wedig, W.V. New Resonances and Velocity Jumps in Nonlinear Road-Vehicle Dynamics, in: Proceedings of IUTAM Symposium on Analytical . Methods in Nonlinear Dynamics, P. Hagedorn (ed.), 2015, Procedia IUTAM, Elsevier, 1-9. 2016 (available online at www.sciencedirect.com).
[13] Arnold, L.: Stochastic Differential Equations. New York, Wiley, 1974.
[14] Itô, K.: On stochastic differential equations, American Math. Society 4, 1-51, 1951.
[15] Bunke, H.: Gewöhnliche Differentialgleichungen mit zufälligen Parametern, Akademie, Berlin, 1972.
[16] Kloeden, P. and Platen, P E.: Numerical Solution of Stochastic Differential Equations: A Review, Heidelberg, Springer, 1995.
[17] Wedig, W.V.: Lyapunov Exponents and Rotation Numbers in Rotor and Vehicle Dynamics, Procedia Engineering, 199, 875-881, 2017.
[18] Oseledets. V. I. :A multiplicative ergodic theorem: Lyapunov characteristic numbers for dynamical systems. Trans. Moscow Math. Soc. 19, (1968), 197–231.
[19] Arnold, L.: Random dynamical systems. Springer Verlag, 2003.
[20] Wedig, W.V.: Lyapunov exponent of stochastic systems and related bifurcation problems. In:Stochastic Structural Dynamics–Progress in Theo . Theory and Applications, eds. Ariaratnam, Schueller, & Elishakoff, Elsevier Applied Science, 315-327, 1988.

Multiscale analysis for traveling-pulse solutions to the stochastic FitzHugh-Nagumo equations

Katharina Eichinger*, Manuel V. Gnann† and Christian Kuehn‡
*CEREMADE, Université Paris Dauphine, PSL, Pl. de Lattre Tassigny, 75775 Paris Cedex 16, France and INRIA-Paris, MOKAPLAN, 2 Rue Simone IFF, 75012 Paris, France
†Delft Institute of Applied Mathematics, Faculty of Electrical Engineering, Mathematics and Computer Science, Delft University of Technology, Mekelweg 4, 2628 CD Delft, Netherlands
‡Center for Mathematics, Technical University of Munich, Boltzmannstr. 3, 85747 Garching near Munich, Germany

Summary. We consider the stochastic FitzHugh-Nagumo equations, whose deterministic equivalent allows for fast and stable traveling-pulse solutions. In this talk, we investigate the stability of fast pulses in case of additive noise and derive a multiscale decomposition for small stochastic forcing. Our method is based on adapting the wave velocity by solving a stochastic ordinary differential equation and tracking perturbations of the wave meeting a stochastic partial differential equation coupled to an ordinary differential equation. Previous works have focused on applying this method to scalar equations, such as the stochastic Nagumo equation, which carry a self-adjoint structure. This structure is lost in case of the FitzHugh-Nagumo system and the linearization does not generate an analytic semigroup. We show that this problem can be overcome by making use of Riesz spectral projections in a certain way. This provides a relevant generalization as our approach appears to be applicable also to general stochastic nerve-axon equations, the stochastic periodically-forced NLS equation, or systems of stochastic reaction-diffusion equations with spectrum parallel to the imaginary axis.

The talk and the following presentation are based on and adapted from [4], respectively.

The stochastic FitzHugh-Nagumo equations

Consider the *stochastic FitzHugh-Nagumo equations* driven by additive noise

$$\mathrm{d}u(t,x) = \left(\nu\partial_x^2 u(t,x) + f(u(t,x)) - v(t,x)\right)\mathrm{d}t + \sigma\,\mathrm{d}W(t,x) \quad \text{for} \quad (t,x)\in\mathbb{R}_+\times\mathbb{R}, \tag{1a}$$

$$\mathrm{d}v(t,x) = \varepsilon\left(u(t,x) - \gamma v(t,x)\right)\mathrm{d}t \quad \text{for} \quad (t,x)\in\mathbb{R}_+\times\mathbb{R}, \tag{1b}$$

in which the *electric potential* u and the *gating variable* v are functions of time t and position x on a neural axon. Here, $\nu\partial_x^2 u$ determines the spatial diffusion on the axon with $\nu > 0$ and the reaction term $f(u)$ is nonlinear and typically reads $f(u) = \chi(u)\,u\,(1-u)\,(u-a)$ with $0 < a < 1$ and a suitable cut off χ. The term $\sigma\,\mathrm{d}W$ is additive noise, with W denoting an infinite-dimensional Wiener process taking values in a suitable Hilbert space H. The parameter $\varepsilon > 0$ determines the coupling strength of the electric potential u to the gating variable v and will be assumed to be sufficiently small. The parameter $\gamma > 0$ is a decay constant of the gating variable v.

Traveling-pulse solutions and their stability

The deterministic variant of (1) with $\sigma = 0$ allows for traveling-pulse solutions of the form $u(t,x) = \hat{u}(\xi)$ and $v(t,x) = \hat{v}(\xi)$, where $\xi = x + st$ and $s\in\mathbb{R}$ is the pulse's velocity. The vectorial function $\left(\hat{u}, \frac{\mathrm{d}\hat{u}}{\mathrm{d}\xi}, \hat{v}\right)$ is a nontrivial homoclinic orbit of a three-dimensional continuous and autonomous dynamical system

$$\tfrac{\mathrm{d}\hat{u}}{\mathrm{d}\xi} = \hat{u}', \quad \tfrac{\mathrm{d}\hat{u}'}{\mathrm{d}\xi} = \frac{1}{\nu}\left(s\hat{u}' - f\left(\hat{u}\right) + \hat{v}\right), \quad \tfrac{\mathrm{d}\hat{v}}{\mathrm{d}\xi} = \frac{\varepsilon}{s}\left(\hat{u} - \gamma\hat{v}\right) \quad \text{for} \quad \xi\in\mathbb{R}. \tag{2}$$

Existence of nontrivial pulses with $(\hat{u},\hat{v})^{\mathrm{t}} \to (0,0)^{\mathrm{t}}$ as $\xi\to\pm\infty$ is ensured if $\gamma \geq 0$ is sufficiently small [11]. Indeed, a singular perturbation argument around $\varepsilon = 0$ and $s = 0$ yields existence of a *slow pulse* with wave speed $s \approx 0$, which by Sturm-Liouville theorey turns out to be unstable. Nonetheless, there is also a *fast pulse*, in what follows denoted by $(\hat{u},\hat{v})$, corresponding to much higher wave speeds $s = s(f,\varepsilon)$, constructed in [1, 2] employing the method of isolating blocks of the fast and slow subsystems [3]. Using an Evans function analysis, stability of the fast pulse in the space of bounded uniformly continuous functions was first proved in [7]. Stability in $L^2(\mathbb{R};\mathbb{R}^2)$ and $H^1(\mathbb{R};\mathbb{R}^2)$ was proved in [5, 12, 13].

Our approach for computing the velocity correction

We investigate the following decomposition

$$u(t,x) = \hat{u}\left(x + st + \varphi(t)\right) + u_\varphi(t,x), \qquad v(t,x) = \hat{v}\left(x + st + \varphi(t)\right) + v_\varphi(t,x) \tag{3}$$

of solutions to (1), in which the function $\varphi(t)$ is a random correction to the pulse's position, and $u_\varphi(t,x)$ and $v_\varphi(t,x)$ denote lower-order fluctuations that are uniquely defined through (3) for any $\varphi = \varphi(t)$. Ideally, we would like to choose φ to minimize the distance in the direction of the traveling wave between the solution $X := (u,v)^{\mathrm{t}}$ of the FitzHugh-Nagumo SPDEs (1) and the suitably translated traveling wave $\hat{X} = (\hat{u},\hat{v})^{\mathrm{t}}$, i.e.,

$$\varphi(t) \in \operatorname{argmin}_{\varphi\in\mathbb{R}} \left\| \Pi^0_{st+\varphi}\left(X(t,\cdot) - \hat{X}(\cdot + st + \varphi)\right)\right\|_H^2, \quad \text{with} \quad X := \begin{pmatrix} u \\ v \end{pmatrix}, \quad \hat{X} := \begin{pmatrix} \hat{u} \\ \hat{v} \end{pmatrix}, \tag{4}$$

where $\|\cdot\|_H$ is the H-norm in the spatial variable and $\Pi^0_{st+\varphi}$ is a suitable projection onto the pulse such that $\Pi^0_{st+\varphi}\frac{\mathrm{d}\hat{X}}{\mathrm{d}\xi}(\cdot + st + \varphi) = \frac{\mathrm{d}\hat{X}}{\mathrm{d}\xi}(\cdot + st + \varphi)$. However, as problem (4) is not necessarily convex, uniqueness of a minimizer is not certain. Following [8] and replacing (4) by the weaker condition for a critical point of finding $\varphi = \varphi(t)$, we may impose

$$0 = \left(\Pi^0_{st+\varphi}\left(X(t,\cdot) - \hat{X}(\cdot + st + \varphi)\right), \frac{\mathrm{d}\hat{X}}{\mathrm{d}\xi}(\cdot + st + \varphi)\right)_H, \tag{5}$$

where $(\cdot,\cdot)_H$ is the inner product of H. This approach has been employed in [6] for more general classes of SPDE systems, but the results only hold up to the first stopping time when the local minimum becomes a saddle point. Here, we follow [8], i.e., $\varphi(t)$ is approximated by a process $\varphi^m(t)$ fulfilling the random ordinary differential equation

$$\frac{\mathrm{d}\varphi^m}{\mathrm{d}t}(t) = m\left(\Pi^0_{st+\varphi^m(t)}\left(X(t,\cdot) - \hat{X}(\cdot + st + \varphi^m(t))\right), \frac{\mathrm{d}\hat{X}}{\mathrm{d}\xi}(\cdot + st + \varphi^m(t))\right)_H \tag{6}$$

for given initial data and a sufficiently large relaxation parameter $m > 0$.

Results

We obtain the following results:

1. We establish existence and uniqueness of solutions to (1) using the variational approach for equations with locally monotone coefficients [9, 10].
2. We give a short proof of deterministic stability in $L^2(\mathbb{R};\mathbb{R}^2)$ of the fast pulse $\hat{X} = (\hat{u},\hat{v})^{\mathrm{t}}$, which simplifies the presentations in [5, 12, 13].
3. We derive an SODE defining the correction of the wave's velocity. The leading-order part of this SODE contains a linear damping term due to the relaxation method of the frame and additive stochastic fluctuations obtained from projecting the infinite-dimensional noise onto a translate of $\frac{\mathrm{d}\hat{X}}{\mathrm{d}\xi}$.
4. We prove a multiscale expansion
$$X(t,\cdot) = \hat{X}(\cdot + st + \sigma\varphi^m_0(t)) + \sigma X^m_0(t,\cdot) + o(\sigma), \tag{7}$$
where $(\sigma\varphi^m_0, \sigma X^m_0)$ solves the scaled linearized evolution of (φ^m, X^m).
5. We consider the limit $m \to \infty$ of immediate relaxation. Here, we prove that
   - the multiscale expansion (7) remains satisfied as $m \to \infty$,
   - as $\sigma \searrow 0$ the first exit time where the multiscale decomposition cannot be guaranteed to hold anymore converges to the entire time interval,
   - by employing deterministic stability, the second moment $\mathbb{E}\,\|X^\infty_0(t,\cdot)\|^2_H$ of fluctuations transverse to the traveling pulse mode after correcting the wave velocity stays bounded,
   - the second moment $\mathbb{E}\left\|X(t,\cdot) - \hat{X}(\cdot + st)\right\|^2_H$ of fluctuations transverse to the traveling wave mode without correcting the wave velocity asymptotically can grow linearly in time.

We conclude by discussing generalizations of our work, such as the application to other (systems of) SPDEs with spectrum parallel to the imaginary axis or the stability of more complicated patterns.

References

[1] G. A. Carpenter. *Traveling-wave solutions of nerve impulse equations*. ProQuest LLC, Ann Arbor, MI, 1974. Thesis (Ph.D.)–The University of Wisconsin - Madison.

[2] C. C. Conley. On traveling wave solutions of nonlinear diffusion equations. In *Dynamical systems, theory and applications (Rencontres, Battelle Res. Inst., Seattle, Wash., 1974)*, pages 498–510. Lecture Notes in Phys., Vol. 38. Springer, Berlin, 1975.

[3] C. C. Conley and R. Easton. Isolated invariant sets and isolating blocks. *Trans. Amer. Math. Soc.*, 158:35–61, 1971.

[4] K. Eichinger, M. V. Gnann, and C. Kuehn. Multiscale analysis for traveling-pulse solutions to the stochastic fitzhugh-nagumo equations. *arXiv:2002.07234 (to appear in Ann. Appl. Probab.)*, 2021.

[5] A. Ghazaryan, Y. Latushkin, and S. Schecter. Stability of traveling waves for degenerate systems of reaction diffusion equations. *Indiana Uni. Math. J.*, 60(2):443–471, 2011.

[6] J. Inglis and J. MacLaurin. A general framework for stochastic traveling waves and patterns, with application to neural field equations. *SIAM J. Appl. Dyn. Syst.*, 15(1):195–234, 2016.

[7] C. K. R. T. Jones. Stability of the travelling wave solution of the FitzHugh-Nagumo system. *Trans. Amer. Math. Soc.*, 286(2):431–469, 1984.

[8] J. Krüger and W. Stannat. A multiscale-analysis of stochastic bistable reaction-diffusion equations. *Nonlinear Anal.*, 162:197–223, 2017.

[9] W. Liu and M. Röckner. SPDE in Hilbert space with locally monotone coefficients. *J. Funct. Anal.*, 259(11):2902–2922, 2010.

[10] W. Liu and M. Röckner. *Stochastic partial differential equations: an introduction*. Universitext. Springer, Cham, 2015.

[11] C. Rocsoreanu, A. Georgescu, and N. Giurgiteanu. *The FitzHugh-Nagumo Model - Bifurcation and Dynamics*. Kluwer, 2000.

[12] J. Rottmann-Matthes. *Computation and Stability of Patterns in Hyperbolic-Parabolic Systems*. PhD thesis, Bielefeld University, Bielefeld, Germany, 2010.

[13] V. Yurov. *Stability estimates for semigroups and partly parabolic reaction diffusion equations*. PhD thesis, University of Missouri, Columbia, USA, 2013.

Nonlinear and stochastic dynamics in a forced vibro-impact energy harvester

Daniil Yurchenko*, Larissa Serdukova† and Rachel Kuske †
* *Department of Mechanical Engineering, Heriot-Watt, Edinburgh UK*
† *School of Mathematics, Georgia Tech, Atlanta, GA, USA*

Summary. Vibro-impact (VI) energy harvesting (EH) systems represent a class of highly nonlinear (non-smooth) systems with impact-type component interactions. A recently proposed VI-EH device, comprises a main mass, subjected to an external excitation, and a smaller mass within, traveling freely in a slot in between two dielectric elastomer (DE) membranes, deforming them at impact. As a highly flexible polymer with high dielectric permittivity and nonlinear responses properties, DE has desirable properties given its chemical composition, response to excitation, superior energy density and suitability for low frequency applications. In order to predict the specific performance of the VI-EH device, we develop a new (semi)-analytical approach for analysis of nonlinear stochastic dynamics in non-autonomous non-smooth impacting systems. This methodology relies on capturing the bifurcation structure and its influence on output energy, providing insight into the role of dynamics in energy harvesting efficiency and in the optimal design of the device. The analysis also reveals a generic mechanism and energy transfer phenomenon in nonlinear impacting systems.

Complex dynamics of the vibro-impact energy harvester (VI-EH)

The proposed VI-EH device is a vibro-impacting mechanical system, consisting of a cylinder of length s and mass M, an inner ball with mass m ($M \gg m$) moving within the cylinder between impacts with dielectric elastomer (DE) membranes at both ends of the cylinder. The system is inclined with an angle of β and forced with a harmonic excitation $F(\omega t + \phi)$ along the direction of its axis. We neglect friction between the ball and the cylinder, and track the relative position $Z = X - x$, for X the non-dimensionalized displacement of the cylinder center and x the location of the ball. The equation of motion and impact condition for the kth impact at time $t = t_k$ are

$$\ddot{Z} = f(t) + \bar{g}, \quad f(t) = F(\omega t + \varphi), \qquad \dot{Z}_k^+ = -r\dot{Z}_k^-, \;\; Z_k = \pm\frac{d}{2}, \quad Z_k = Z(t_k). \tag{1}$$

Here $\bar{g} = -Mg\sin\beta/\|F\|$, where g is gravity, and $\|F\|$ the norm of F. The impact condition is applied on the bottom (top) ∂B (∂T) membrane of the VI-EH device at $(x - X) = \pm d/2$ for $d = \frac{s}{x_c}$, with $\dot{Z}^{\pm}$ the non-dimensionalised relative velocity of the ball before (-) (after (+)) impact and r the restitution coefficient. The parameter d captures the influence of length, amplitude of excitation, and frequency via the factor $x_c = \frac{\|\hat{F}\|\pi^2}{M\omega^2}$. Integrating (1) between impacts for $t \in (t_{k-1}, t_k)$ yields

$$\dot{Z}(t) = -r\dot{Z}_{k-1}^- + \bar{g}(t - t_{k-1}) + F_1(t) - F_1(t_{k-1}), \;\; F_1(t) = \int f(t)dt, \tag{2}$$

and integrating (2) we get the analogous equation for $Z(t)$. At the kth impact, the maps for $\dot{Z}_k^-$ and Z_k^- are obtained by taking $t = t_k$ in (2) and the similar equation for Z, with $Z_k = \pm d/2$ at impact. Combining these maps we get all possible motions of the ball, $P_1 : \partial B \mapsto \partial T$, $P_2 : \partial T \mapsto \partial B$, $P_3 : \partial B \mapsto \partial B$, $P_4 : \partial T \mapsto \partial T$.

Using P_j together with the impact conditions and F periodic, we first study periodic motions of an inclined VI-EH, such as those shown in the phase planes of Fig. 1 (Left). The nonlinear analysis provides the bifurcation and stability conditions for different types of behavior within a non-dimensionalized framework, allowing us to capture the results in terms of dependence on parameters d, r, and β, and excitation, also considered in [1] for $\beta = 0$. For an incline $\beta \neq 0$, gravity naturally contributes to the asymmetric state and different nonlinear behaviors. We find transitions and stability for two families of periodic solutions. The first has a 1:1 ratio of impacts on ∂T to ∂B per excitation period, obtained by alternating P_1 and P_2. The analysis shows that these 1:1 behaviors are characterized by the triples $(\dot{Z}_k, \phi_k, \Delta t_k)$. Here ϕ_k is the phase difference between the impact and a trough (or peak) of F, and $\Delta t_k = t_{k+1} - t_k$. A second family has a 1:n ratio of impacts on ∂T and ∂B. These follow from grazing bifurcations and are composed of P_3, P_1, P_2. In Fig. 1 (Middle) we show these families in terms of $\dot{Z}_k$ from numerics for a range of d. Analytical solutions reproduce these branches in [2]. As shown in Fig. 1 (Left and Middle) for decreasing d, there are periodic doublings of the 1:1 family ($d > d_{\text{graz}} \approx .2$, d_{graz} corresponding to a grazing bifurcation), until the grazing bifurcation leads to the 1:2 ratio of impacts ($d < .2$). Following an impact on δB, non-monotonic behavior of the relative velocity $\dot{Z}$ appears as a loop in the phase plane trajectory after $\dot{Z}$ crosses 0 on the trajectory away from $Z = \pm d/2$. For d_{graz} we have $\dot{Z}_{k+1} = Z_{k+1} = 0$, corresponding to a transition to P_3 before P_2, yielding a 1:2 solution.

Energy is harvested via impacts with the DE membranes, with $U_{\text{imp}}^{(i)}$ the voltage at the ith impact obtained from geometrical parameters of the membrane and $\dot{Z}_i$ [4]. The harvested voltage $U_{imp} - U_{in}$ is shown in Fig. 1 (Middle), for U_{in} a constant input voltage applied to the membranes, and d decreases with increasing amplitude of forcing $\|F\|$. Note that grazing bifurcations and 1:2 periodic solutions correspond to low velocity impacts, yielding an abrupt loss of average energy output per impact.

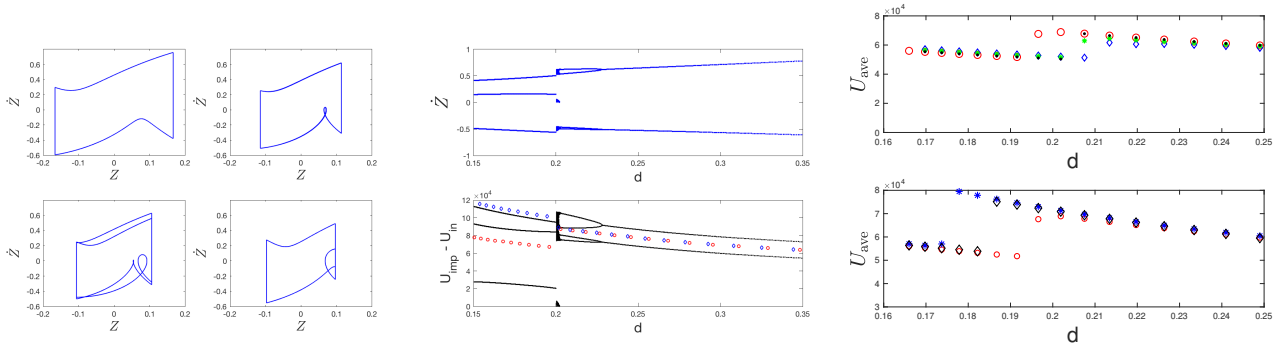

Figure 1: (Left). Limit cycles in the phase plane for Z,$\dot{Z}$ with different sequences of impacts in the VI-EH model (1) for decreasing d; all but lower right with 1:1 ratio per period of forcing, lower right is 2:1. Middle Upper: Impact velocity $\dot{Z}_k$ vs. d; Lower: Corresponding output voltage (black), red (blue) for average output per impact (unit time); Right: Average energy output per impact. Red circles for small constant β and no feedback; Upper: blue for larger β, symmetrically distributed, green and black for asymmetric distribution of β with small mean. Lower: blue and black for different levels of feedback.

Influence of randomness

The analytical results provided by the nonlinear maps reveal potential sensitivities to certain parameters for the different states, indicating conditions under which stochastic effects influence transitions. For example, the dependency of grazing bifurcations on ϕ_k suggests that stochastic fluctuations in the phase can benefit energy output by disrupting low velocity impacts. We derive stochastic nonlinear maps describing probabilistic transitions between states, thus capturing both detrimental and beneficial effects of random fluctuations on the energy output.

The stochastic variations of the maps P_j are derived from the physical model, depending on the stochastic source and transition of interest. Such variations were found in [3], which considered stochastic versions of the Nordmark map for compliant impacts near grazing. The phase plane analysis in [2] motivates a simple efficient formulation to study the behavior near the underlying period doubling bifurcations, based on considering separately the stochastic versions of P_1 and P_2 to capture the dilation of trajectories in $\dot{Z}_k$ on P_2. A similar dilation of ϕ_k on P_1 indicates a complementary approach, that capitalizes on the sensitivity to $\phi_k \ll 1$, as already suggested from the nonlinear expressions of $\sin\phi_k$ in the triple $(\dot{Z}_k, \phi_k, \Delta t_k)$ for the 1:1 families [2]. To capture the influence of parameter uncertainties, we break P_j into submaps, between key points corresponding to $\dot{Z} = 0$, $Z = \pm d/2$, and $\ddot{Z} = 0$, all important features in the approach to grazing shown in Fig 1 (Left).

We find that certain noise in ϕ, relaxing rapidly to fluctuations about its mean, yields an averaging effect that generates an effective reduction in the forcing amplitude. Then the attracting 1:1 periodic behavior is sustained over a larger range of d. Specifically, for smaller d, the 1:2 behavior is displaced, as is the corresponding lower average energy output per impact.

Fig. 1 (Right) shows the influence of other noise and asymmetries on $U_{\rm ave}$ vs. d. Certain random fluctuations in β advance $d_{\rm graz}$ to larger values, even counter-intuitively for asymmetric distributions of β with a small average $\overline{\beta} \ll 1$. If there is a non-negligible tail probability for $\beta = O(1)$ (green and black markers in Fig. 1 (Right upper)), the average energy output is closer to that obtained for random $\beta = O(1)$ (blue diamonds) than for smaller deterministic β (red circles), suggesting that even for short transient periods of $\beta = O(1)$, the system remains in the 1:2 behavior over a longer time period. Also, feedback of the capsule motion at a lagged time leads to an effective phase shift in the forcing, potentially avoiding repeated ∂B impacts for $\phi_k \ll 1$ (blue and black markers in Fig. 1 Right lower) and shifting reduced $U_{\rm ave}$ to smaller d. There are a number of ways to model this effect, including randomness to capture lack of precise feedback. The newly derived stochastic maps near the critical transitions related to 1:1 and 1:2 periodic solutions explain how noise influences transitions between different levels of energy output.

Conclusions

Semi-analytical nonlinear analyses of a novel model for vibro-impact energy harvesting (VI-EH) captures parametric and excitation dependencies of the output voltage. The results point to parameter ranges and scenarios where noise and asymmetries can be either detrimental or beneficial for the energy output. Via novel stochastic analyses and computations, we reveal the sensitivities of the system to random fluctuations and asymmetries. These indicate analysis-based design features for the VI-EH device.

References

[1] A. Luo, *Journal of Vibration and Acoustics*, 124, 420-426, (2002).

[2] L. Serdukova, R. Kuske, and D. Yurchenko, *Nonlinear Dynamics* (to appear). https://doi.org/10.1007/s11071-019-05289-8.

[3] D.J.W. Simpson and R. Kuske, *J. Vibration and Control,* 24, 407-426, 2016.

[4] D. Yurchenko, D. V. Val, Z. H. Lai, G. Gu, and G. Thomson, *Smart Mater. Struct.,* 26, 105001, 2017.

Probabilistic response of a vibration energy harvester for realistic torsional vibrations

Panagiotis Alevras[*], Ben Gunn[**] and Stephanos Theodossiades[**]
[*]*Department of Mechanical Engineering, School of Engineering, University of Birmingham, Birmingham, UK*
[**]*Wolfson School of Mechanical, Electrical and Manufacturing Engineering, Loughborough University, Loughborough, UK*

Summary. A nonlinear vibration energy harvester for converting energy from the torsional oscillations of an automotive powertrain is considered under random engine running speeds. Engine data recorded form several real-life routes are used to describe the spectral properties of the powertrain vibrations, and particularly their frequency distribution in city and highway driving cycles. Joint response Probability Density Functions of the stochastic coupled electromechanical oscillator are calculated with a numerical Path Integration approach. The impact of noise on the mean power output is assessed by comparing the resulting random power output statistics with deterministic expressions based on the mean engine speed.

Introduction

Vibration energy harvesting is a recent concept that involves scavenging energy from ambient mechanical vibrations and converting it to useful electricity to power small electronic devices, such as sensors and wireless data transmitters [1]. These systems are designed such that mechanical power take-off is optimised, and this is usually achieved by establishing high-amplitude response to the exciting vibrations of the host system, such as resonant linear response or broadband high energy response in the case of nonlinear harvesters [2]. However, vibrations in structures and machines are usually the result of complex interactions between nonlinearly coupled components, exhibiting a diverse interaction with system modes and the inherent randomness of environmental forces. This is particularly pertinent to automotive vibrations whereby linear and torsional vibrations of the powertrain components are subject to a multi-factor dependence on environmental conditions, road surface conditions, driving behaviour, route and mode of driving (city/highway). As a result, harvesters are essentially required to capture energy from vibrations that cannot be adequately described by conventional deterministic approaches.
Recently, a concept for harvesting energy from the torsional vibrations of a propulsion shaft has been introduced [3]. In this paper, a stochastic framework for calculating this device's mean harvested power is presented. Randomness of the powertrain vibrations frequency is modelled by exploiting the direct link of the dominant vibration frequency to the engine speed and the engine architecture. Transient and steady-state driving scenarios are considered through a statistical analysis of engine speeds recorded in real-life driving scenarios. Expressions of the spectral distributions of the input vibrations are then used within an advanced computational framework to accurately calculate joint Probability Density Functions (PDF) of the harvester's mechanical and electrical generalised variables.

Problem Formulation

Consider a rotational vibration energy harvester as the one shown in Figure 1(a). This concept has been recently introduced for harvesting energy from the torsional vibrations of propulsion shafts [3]. The system has been designed to harvest energy from torsional vibrations rather than the main shaft speed, thereby minimising the impact of the device on the main transmission of power with potentially favourable reduction of the shaft speed fluctuations. The reader is referred to [3] for a detailed description of the device and the ensuing analysis that leads to the following equations of motion:

$$\begin{aligned} J\ddot{\phi} + c_m\dot{\phi} + k_1\phi + k_3\phi^3 - \widehat{\Theta}I &= J\ddot{a} \\ L\dot{I} + (R_{load} + R_{int})I + \widehat{\Theta}\dot{\phi} &= 0 \end{aligned} \tag{1}$$

where $\ddot{a}$ denotes the shaft vibrations which act as base excitation to the rotational harvester with inertia J, mechanical damping c_m and potential energy $U(\phi) = k_1\phi^2/2 + k_3\phi^4/4$. The electrical properties are denoted by L – inductance, R_{load} – load resistance, R_{int} – coil resistance and $\widehat{\Theta}$ – electromagnetic coupling. Dominant vibration frequencies in rotary applications are linked with orders of the main rotation speed. In 2-cylinder, 2-stroke IC engines for example, powertrain vibrations are dominated by the 2nd engine order. However, as it is shown in Figure 1(b), the engine speed that determines the dominant vibration frequency is a randomly varying quantity (see Figure 1(d)). This data has been recorded in a real driving cycle down the route shown in Figure 1(c). Therefore, the exciting base vibrations can take the following form to consider random modulations of the excitation's phase:

$$\begin{aligned} \ddot{a} &= A\cos(q) \\ \dot{q} &= v + \sigma\zeta(t) \end{aligned} \tag{2}$$

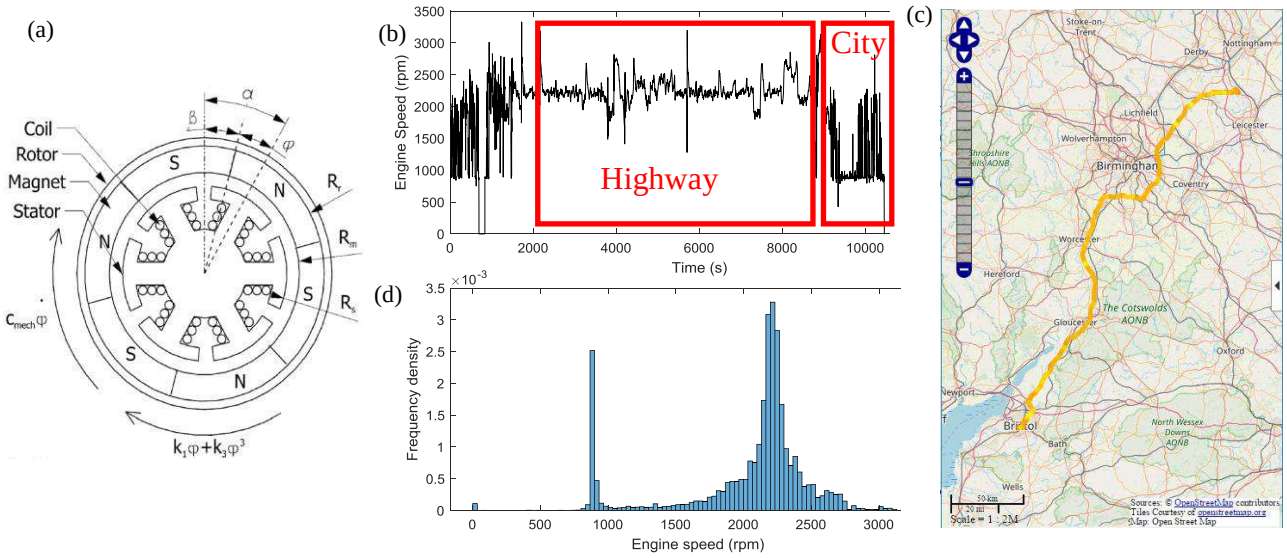

Figure 1: (a) sketch of the rotational vibration energy harvester; (b) engine speed during mixed drive cycle; (c) route map of displayed data; (d) distribution of engine speed in mixed cycle.

where $\zeta(t)$ is a Gaussian delta-correlated white noise process with $\langle \zeta(t)\zeta(t+\tau)\rangle = 2\pi D\delta(\tau)$. Note that randomness is only considered in the phase of the vibrations since the vibration amplitude can be considered to be slow-varying. More explicit representation of the speed's spectral properties can be used by colouring the white noise process with higher order linear filters.

Path Integration

The joint response PDF of the stochastic system described by Eqs (1) and (2) is computed by means of a numerical Path Integration (PI) technique. The response PDF contains probabilistic information for the harvester's kinematic and electrical variables, allowing accurate calculation of the electrical power output probability distribution. This method is based on an iterative approach for calculating in short time steps the response PDF, which at time t can be expressed from the PDF at $t' = t - \Delta t$ exploiting the Markov property of the solution vector and the total probability law [4]:

$$p(\mathbf{z}, q, t) = \int_{state\ space} p(\mathbf{z}, q, t|\mathbf{z}', q', t')p(\mathbf{z}', q', t')dzdq \tag{3}$$

where $p(\mathbf{z}, q, t|\mathbf{z}', q', t')$ is the transition probability density function (TPD) and $\mathbf{z}$ is the system's state vector. The short time propagation TPD is Gaussian distribution and thus, the TPD may be written as [4]:

$$p(\mathbf{z}, q, t|\mathbf{z}', q', t') = \delta[\mathbf{z} - \mathbf{z}' - \mathbf{r}(\mathbf{z}', q', \Delta t)] \frac{1}{\sqrt{2\pi D\Delta t}} \exp\left\{-\frac{[q - q' - r_4(\mathbf{z}', q', \Delta t)]^2}{2D\Delta t}\right\} \tag{4}$$

where δ is the Dirac delta function and $\mathbf{r}(z', q', \Delta t)$, $i = 1,2,3,\ldots$ are 4th order Runge-Kutta increments of $\mathbf{z}$ and q. Iterative application of Eqs (3) and (4) lead to the computation of the joint response PDF, whereby standard rules are applied to compute the marginal PDF of the current and the electrical power.

Discussion

Preliminary calculations have shown that randomness has a significant impact on the mean power output compared with using the average engine speed in deterministic models. This is particularly important for vibrations in the frequency range in-between the deterministic saddle-node bifurcations, where multiple attractors co-exist. Early results indicate that randomness particularly affects the establishment of high energy solution branches as the solution approaches the jump-down bifurcations. This is due to the shrinking area of the deterministic basin of attraction which makes the high-amplitude desired solution more sensitive to random fluctuations. Further analysis using the described procedure will reveal the full impact of randomness on the harvested electrical power.

References

[1] Stephen N. G. (2206) On energy harvesting from ambient vibration. *J. Sound Vib.* **293** 409–425.
[2] Alevras P., Theodossiades S., Rahnejat H. (2018) On the dynamics of a nonlinear energy harvester with multiple resonant zones. Nonlin Dyn **92**(3) 1271-1286.

[3] Gunn B. E., Theodossiades S., Rothberg S. J. (2019) A Nonlinear Concept of Electromagnetic Energy Harvester for Rotational Applications. *J. Vib. Acoust.* **141**(3): 031005 (13 pages).
[4] Yurchenko D., Naess A., Alevras P. (2013) Pendulum's rotational motion governed by a stochastic Mathieu equation. *Probabilist. Eng. Mech.* **31** 12-18.

Simulation of Road Surfaces Profiles by a Stochastic Parametrical Model

Alfons Ams
Institute of Mechanics and Fluiddynamics
Technical University of Freiberg, Freiberg, Germany

Summary. Road irregularities have an important influence on the dynamic behavior of vehicles. Knowledge of their characteristics and magnitude is essential for the design of the vehicle. The problem of interest is the simulation of road surfaces profiles because modern test facilities and computer simulations of vehicle dynamics needs driving excitations. An import issue is the power spectral densities and the approximation by analytical formulas. In the paper a stochastic parametrical nonlinear model of first order with bounded amplitudes will be discussed. Some analytical and numerical results will be shown.

Road Surface Profiles

The road surface profiles are defined by ISO8608 Mechanical vibration – Road surface profiles – Reporting of measured data [1]. Figure 1 shows an example of a measured road.

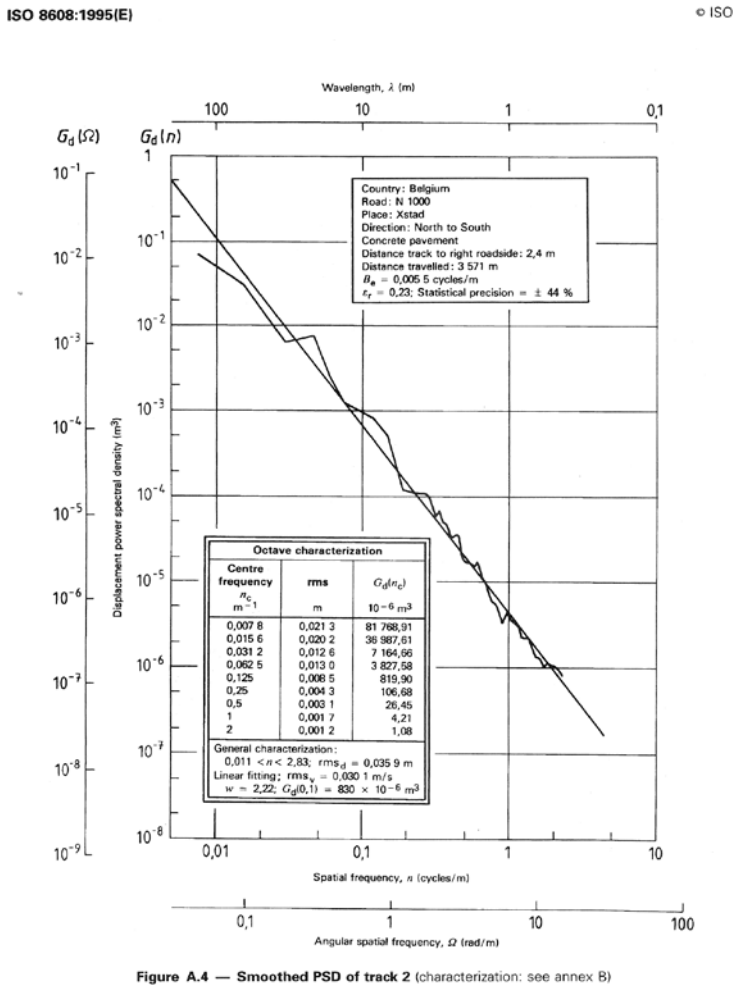

Figure A.4 — Smoothed PSD of track 2 (characterization: see annex B)

Figure 1: Measured road surface profile [1]

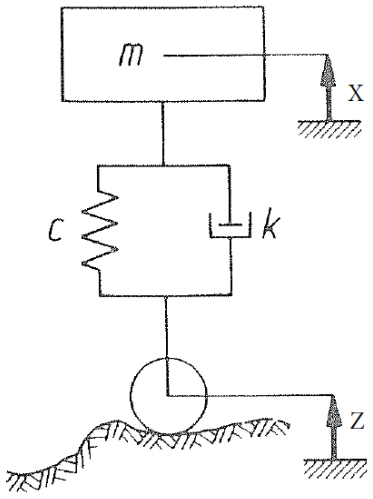

Figure 2: A quarter car (1 DOF) with road surface profile Z_t

Stochastic Parametrical Model

The stochastic parametrical nonlinear model of first order

$$\dot{Z}_t = \left(\frac{1}{2}\sigma^2 - \omega_0\right) Z_t + \sqrt{Z_0^2 - Z_t^2}\,\sigma \dot{W}_t$$

with σ intensity of white noise, Z_0 the maximum amplitude, ω_0 the corner frequency and W_t the Wiener process with the mean value $\mathrm{E}\{dW_t\} = 0$ and the variance $E\{dW_t^2\} = dt$. The stochastic differential equation (Ito) is

$$\mathrm{d}Z_t = -\omega_0 Z_t \mathrm{dt} + \sqrt{Z_0^2 - Z_t^2}\,\sigma dW_\mathrm{t} \qquad |Z_t| \leq Z_0$$

The Fokker Planck equation of the probability density function is

$$\frac{\partial \mathrm{p}}{\partial \mathrm{t}} - \omega_0 \frac{\partial}{\partial z}\,[zp] - \frac{\sigma^2}{2}\,\frac{\partial^2}{\partial z^2}\,[(Z_0^2 - z^2)p] = 0$$

The stationary solution of the density function can be calculated to

$$\mathrm{p(z)} = C\,(Z_0^2 - z^2)^{\left(-1+\omega_0/\sigma^2\right)} \qquad \sigma^2 < \omega_0$$

The constant C fulfilled the normalization condition $\int_{-Z_0}^{+Z_0} p(z)dz = 1$. The auto correlation function of the stationary process Z_t is

$$R_z(\tau) = \sigma_z^2\, e^{-\omega_0|\tau|}$$

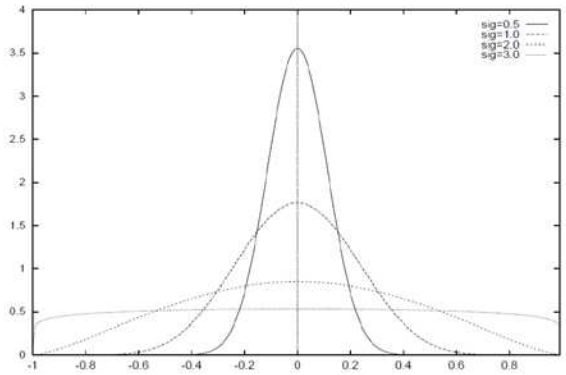

Figure 3: Stationary density distributions p(z) with $\omega_0 = 10,\ Z_0 = 1$ and different σ

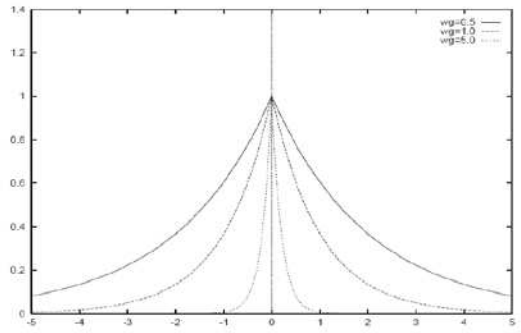

Figure 4: Auto correlation function $R_z(\tau)$ with $\sigma_z = 1$ and different ω_0

A numerical realization of the stationary process Z_t with the parameters $\omega_0 = 10,\ Z_0 = 1, \sigma = 0.5$ and $N = 10^6$ time steps shows figure 3.

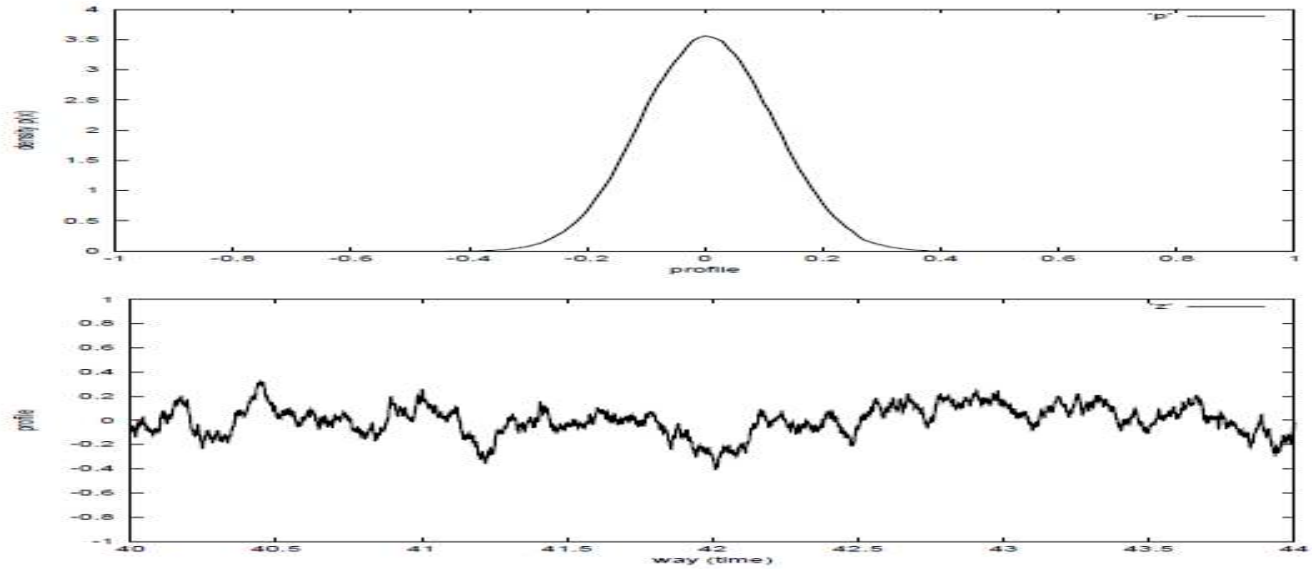

Figure 3: Numerical realization of the stationary process Z_t ($\omega_0 = 10,\ Z_0 = 1, \sigma = 0.5, N = 10^6$)

References

[1] ISO 8608:1995(E), Mechanical vibration - Road surface profiles - Reporting of measured data.
[2] Wedig W.: Dynamics of Cars Driving on Stochastic Roads, In: Spanos P., Deodatis G. (Eds), CSM-4., Rotterdam, Millpress, p. 647 - 654, 2003.
[3] Doods C. J., Robson J. D.: The Description of Road Surface Roughness, Journal Sound and Vibration, 31, p. 175 - 183, 1973.
[4] Arnold L.: *Stochastic Differential Equations*. New York, Wiley, 1974

Tuesday, July 19, 2022
13:30 - 15:30

MS-12 Micro- and Nano-Electro-Mechanical Systems
Rhone 3A

Chair: S. Krylov

13:30 - 13:50
Electrostatic nonlinear trimming of ring-based MEMS coriolis vibrating gyroscopes
ARIFIN Davin*, MCWILLIAM Stewart
*University of Nottingham (University Park, Nottingham NG7 2RD United Kingdom)

13:50 - 14:10
Broadband parametric amplification for nonlinear micro ring gyroscopes
BARAKAT Ahmed A.*, HAGEDORN Peter
*Dynamics and Vibrations Group, Technical University of Darmstadt (Dolivostr. 15, Darmstadt. Germany) - Graduate School of Computational Engineering, Technical University of Darmstadt (Dolivostr. 15, Darmstadt. Germany) - Design and Engineering Dept., Ain Shams University (ElSarayat St. 1, Abbaseyya, Cairo Egypt)

14:10 - 14:30
Chaos in a non-linear non-buckled microresonator
DEFOORT Martial*, RUFER Libor, BASROUR Skandar
*Techniques of Informatics and Microelectronics for integrated systems Architecture (46 Av Félix Viallet 38031 GRENOBLE CEDEX 1 France)

Electrostatic Nonlinear Trimming of Ring-Based MEMS Coriolis Vibrating Gyroscopes

Davin J. Arifin, Stewart McWilliam
Faculty of Engineering, University of Nottingham, UK

Summary. The effects of electrostatic nonlinearity on rate measuring performance of a capacitive MEMS Coriolis Vibrating Gyroscope (CVG) with an imperfect sensing element are investigated. The electrostatic nonlinearity is a result of large amplitude vibration of the ring, which modifies the capacitive forcing and induces self-induced parametric amplification. A cubic-order nonlinear mathematical model is used to describe the electrostatic nonlinearity and expressions are developed for the scale factor and bias. It is shown that parametric pumping induces an amplification range that enhances rate sensitivity and electrostatic non-linearity has potential to negate the effects of imperfection.

Model Description

For MEMS rate-measuring CVG's having a ring resonator [1] the dominant source of nonlinearity is electrostatics due to capacitive actuation and sensing of ring displacements. The dynamics of the sense mode used to detect rate is significantly affected by self-induced parametric amplification [1, 2] when the vibration amplitude is large and the modal properties modulate at twice its vibration frequency. In the small amplitude regime imperfections degrade the scale factor and bias [3]. The potential for nonlinearity to negate or reverse these effects is presented here.

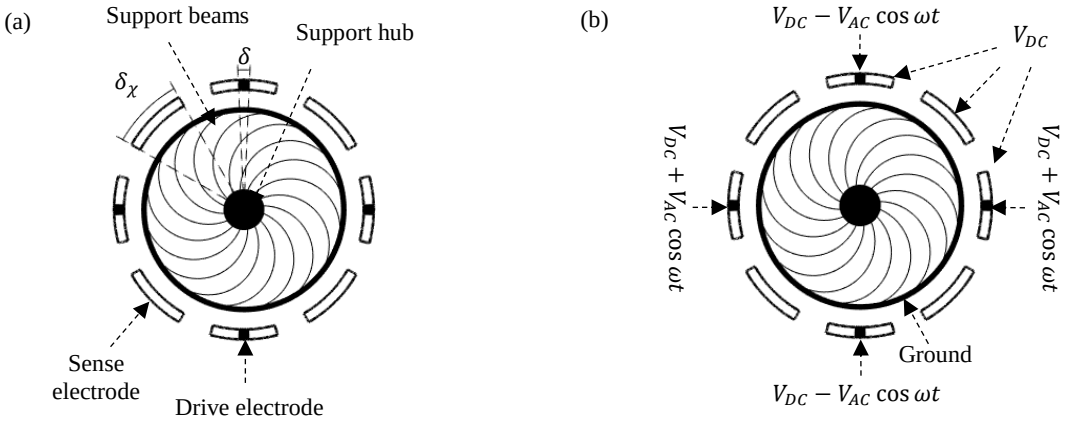

Figure 1: (a) Schematic general layout; (b) voltage profile applied by individual electrodes

Figures 1(a) and 1(b) show the ring element, capacitive electrodes and support structure for a typical device together with the voltages applied across electrode gaps. Voltage V_{AC} drives the ring into its 2θ flexural primary mode. Voltage V_{DC} is primarily responsible for electrostatic nonlinearity. A cubic-order nonlinear model is used to describe the dynamics of the primary (drive) and secondary (sense) modes. Assuming the applied angular rate is much smaller than the natural frequency, $V_{AC} \ll V_{DC}$, and the ring is thin and midsurface-inextensional, the equation of motion for the sense mode is:

$$\ddot{Y} + \frac{\omega_0}{Q}\dot{Y} + Y\left[{\omega_0}^2(1 - \mu_\omega \cos 4\theta_\omega) + \kappa\frac{X^2}{{g_0}^2}\right] = -\frac{8}{5}\dot{X}\Omega - {\omega_0}^2\mu_\omega \sin 4\theta_\omega\, X \qquad (1)$$

X, Y are modal coordinates describing the drive and sense modes respectively; ω_0 is the undamped natural frequency and Q is the Q factor for the perfect ring. In practice, $Y \ll X$ so nonlinear terms in Y have been neglected. κ is the nonlinear elastic coupling strength from the drive mode to the sense mode and results in amplitude-dependent resonance. μ_ω is an imperfection parameter and Ω is the applied angular rate. The sense mode is subjected to: i) Coriolis forcing proportional to $\dot{X}\Omega$; ii) imperfection-induced quadrature force proportional to μ_ω; and iii) parametric excitation arising from nonlinear elastic coupling κ. The drive mode modulates the stiffness of the sense mode at approximately twice its effective vibration frequency. The amplitude and phase of the sense mode oscillation are obtained using the averaging method and the scale factor S^C and bias Ω_0^C are found to be:

$$S^C = -\frac{\frac{8}{5}x{\omega_X}^2\left(\frac{\omega_0}{Q}\right)}{{\omega_X}^2\left(\frac{\omega_0}{Q}\right)^2 + \left({\Delta_\omega}^2 + \xi_y\right)\left({\Delta_\omega}^2 - \xi_y\right)} \qquad \Omega_0^C = -\frac{{\omega_0}^2\mu_\omega \sin 4\theta_\omega\left({\Delta_\omega}^2 + \xi_y\right)}{\frac{8}{5}{\omega_X}^2\left(\frac{\omega_0}{Q}\right)} \qquad (2,3)$$

Here ${\Delta_\omega}^2 = 2{\omega_0}^2\mu_\omega \cos 4\theta_\omega + \frac{x^2}{4{g_0}^2}(3\gamma - 2\kappa)$ is the frequency detuning parameter and $\xi_y = \kappa\frac{x^2}{4{g_0}^2}$ is the pumping strength, where γ is the modal Duffing coefficient and x is the drive amplitude. $\kappa, \gamma < 0$ characterize the nonlinear modal stiffnesses and $|\kappa| \leq |\gamma|$, where $|\kappa| = |\gamma|$ when $\delta_\chi = 45°$. For small-amplitude operation, $\xi_y = 0$ and ${\Delta_\omega}^2 \propto \mu_\omega$.

Nonlinearity causes amplitude-dependent frequency detuning and parametric pumping and both interact with the imperfection to modify the scale factor and bias at large amplitude.

Scale factor and bias

The scale factor for an ideal, linear CVG behaves linearly with drive amplitude x and inversely with bandwidth, so a high Q factor is desirable. In (2) the $(\Delta_\omega{}^2 + \xi_y)(\Delta_\omega{}^2 - \xi_y)$ term plays a key role in the nonlinear modification of the scale factor when the amplitude-dependent frequency detuning parameter and parametric pumping strength interact i.e.:

i. $(\Delta_\omega{}^2 + \xi_y)(\Delta_\omega{}^2 - \xi_y) > 0$ - nonlinearity interacts constructively with imperfection, reducing the scale factor.
ii. $(\Delta_\omega{}^2 + \xi_y)(\Delta_\omega{}^2 - \xi_y) = 0$ -nonlinearity negates imperfection effectively trimming the device.
iii. $(\Delta_\omega{}^2 + \xi_y)(\Delta_\omega{}^2 - \xi_y) < 0$ -nonlinear amplification occurs as the effective bandwidth is reduced.

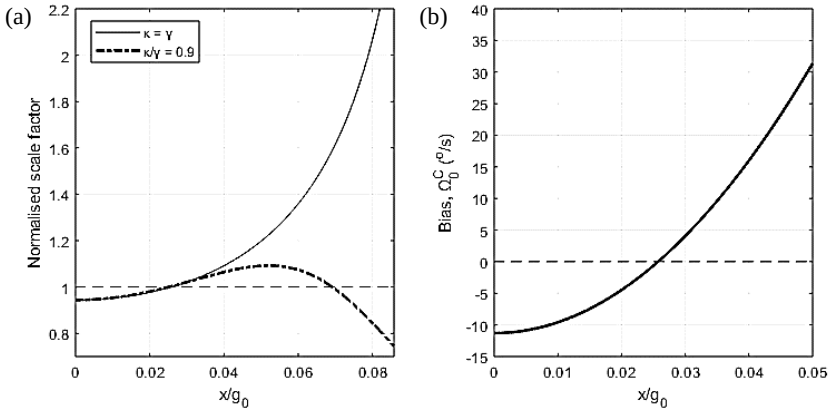

Figure 2: Variation of (a) S^C normalized relative to the trimmed, linear case for continuous ($\kappa = \gamma$) and discontinuous ($|\kappa| < |\gamma|$) biasing electrodes, and (b) Ω_0^C with the gap-normalised drive amplitude

When $(\Delta_\omega{}^2 + \xi_y)(\Delta_\omega{}^2 - \xi_y) < 0$ the result is a pure nonlinear effect, because without parametric pumping the imperfection always acts to reduce the scale factor. Figure 2 shows that nonlinear amplification occurs for a range of drive amplitudes. A consequence of this is that the imperfect device has an enhanced scale factor compared to a linear, trimmed device. This amplification range is defined by $-|\xi_y| < \Delta_\omega{}^2 < |\xi_y|$ and the amplification increases as the pumping strength ξ_y increases. The upper bound of this range grows without bound when $\gamma = \kappa$ because the variation of $(\Delta_\omega{}^2 + \xi_y)(\Delta_\omega{}^2 - \xi_y)$ with drive amplitude is monotonic in this case, so nonlinear trimming only occurs at the lower bound when the parametric pumping negates the effects of frequency detuning, i.e. $\Delta_\omega{}^2 = -\xi_y$. In practice higher order nonlinearities play a role in limiting the vibration amplitude. On the other hand, if the difference between γ and κ is large such that $|\kappa| \ll |\gamma|$, which corresponds to the case when the biasing electrode span is small, the upper and lower bounds approach each other and the amplification range reduces. The lower bound of this range when $\Delta_\omega{}^2 = -\xi_y$ also plays a role in nullifying the bias. Figure 2(b) indicates that the bias is increasingly sensitive to the operational drive amplitude as the amplitude increases. The bias variation is monotonic, either increasing or decreasing, and nonlinear trimming of the device to nullify the bias is only possible if the amplitude dependent frequency detuning is negated by the parametric pumping, i.e. $\Delta_\omega{}^2$ and ξ_y have opposite signs. As electrostatic nonlinearity is softening, this can only occur when the drive excitation is applied at an angular position close to the maximum frequency axis, i.e. $\mu_\omega \cos 4\theta_\omega > 0$.

Conclusions

Electrostatic nonlinearity in ring-based MEMS CVGs interacts with ring imperfections due to self-induced parametric pumping and amplitude-dependent frequency detuning of the modes. These nonlinear effects have potential to negate performance degradation caused by imperfection, effectively trimming the device, but can enhance sensitivity in particular drive amplitude ranges. The lower bound of the amplification range effectively nullifies the bias in the specific case where the frequency detuning is negated by parametric pumping. The performance enhancement offered by electrostatic nonlinearity for imperfect devices is most significant when the cubic-order modal stiffnesses are balanced.

References

[1] P. M. Polunin and S. W. Shaw, "Self-induced parametric amplification in ring resonating gyroscopes," *International Journal of Non-Linear Mechanics*, vol. 94, pp. 300-308, 2017/09/01/ 2017.
[2] S. H. Nitzan *et al.*, "Self-induced parametric amplification arising from nonlinear elastic coupling in a micromechanical resonating disk gyroscope," (in eng), *Scientific reports*, vol. 5, p. 9036, Mar 12 2015.
[3] C. Acar and A. Shkel, *MEMS Vibratory Gyroscopes-Structural Approaches to Improve Robustness*, 1 ed. Springer US, 2009.

Broadband parametric amplification for nonlinear micro ring gyroscopes

Ahmed A.Barakat*†‡, Peter Hagedorn*
*Dynamics and Vibrations Group, fnb, TU Darmstadt, Darmstadt, Germany
†Graduate School of Computational Engineering, TU Darmstadt, Darmstadt, Germany
‡Design and Production Engineering Dept., Ain Shams University, Cairo, Egypt

Summary. Parametric amplifiers have been well known in the electronic industry as well as in micro electromechanical systems (MEMS). However, they are typically confined to amplify the signals of these systems at primary or secondary resonance frequencies. Parametric amplification can nonetheless be extended to be broadband under certain conditions and system parameters. To the best of the authors' knowledge, this is not yet applied in microsystems, although being highly promising especially for the industry of micro sensors and transducers. On the other hand, in the industry of rate gyroscopes, the micro-ring gyroscope is being developed for over a decade in order to reach the accuracy level of tactical or inertial grade gyroscopes, while maintaining relatively low production costs of MEMS. For that sake, parametric amplification was studied for micro-ring gyroscopes with different excitation methods. However, the idea of having "global" amplification was not yet applied. For this reason, this contribution aims at presenting a parametric excitation method for nonlinearly modeled micro-ring gyroscopes which can provide "global" improvement in the amplification and the performance for a broadband frequency spectrum.

Introduction

Parametric resonances have long benn studied since the 1831 by Faraday. They were up to this date in practice the only useful phenomenon acquired through parametric excitation, i.e. through having a time-varying coefficient in the system's partial differential equation (PDE). The common practice, at least in the microsystems industry, did not make use so far from an important observation by Cesari in 1939. He found in at least two degree-of-freedom (DOF) systems, that an asynchronous parametric excitation can lead to "global" phenomena across the whole frequency spectrum [1]. This will be explained in the next section.

On the other hand, researchers aim at improving micro gyroscopes to attain the tactical grade level (0.1 deg/h bias stability), seeking the level of inertial grade (<0.01 deg/h) afterwards. For micro gyroscopes, nonlinear resonances were used in the literature to overcome asymmetries due to fabrication, as they allow energy transfer between vibration modes [2], thus improving sensitivity. Moreover, parametric resonances proved to "squeeze" mechanical and electrical noises [3], which contribute in improving the Angle Random Walk (ARW) and bias stability. Also by operating in the nonlinear regime, parametric excitations were found to provide much higher amplification, however, this was not adequately theoretically investigated till recently [4]. To this end, this work aims at extending the authors' investigation of the global effects induced by phase-shifted parametric excitations in linearly modeled micro-ring gyroscopes [5] to the nonlinear case.

Global effects

The previously mentioned global effects are discussed here for a linear system. In the current practice of paramteric excitation mechanisms, instability or amplification were exhibited at the primary resonance frequency equal to double the natural frequency, i.e. $\Omega = 2\omega_i$, or at the countably infinite secondary frequencies $\frac{\omega_i \pm \omega_j}{n}$, where $i = 1, 2,\ j = 1, 2,\ n \epsilon \mathbb{N}$. But by applying the theory of Cesari we could get an amplification and/or instability at every excitation frequency, hence, that is named as a "global" effect. One such consequence can be driving the system in a state of "total instability", i.e. at every frequency. Having said that, it may seem as bad news to engineering applications, however, for a system that behaves nonlinearly this could be translated to having higher amplitude, gain or amplification at a non-trivial stable stationary solution. This can be achieved by having phase-shifted off-diagonal time periodic functions in the parametric excitation matrix $\boldsymbol{C}(t)$. This effect can be simply illustrated for a two DOF system

$$\ddot{\boldsymbol{q}} + (\boldsymbol{D} + \boldsymbol{G})\dot{\boldsymbol{q}} + (\boldsymbol{K} + \boldsymbol{C}(t))\boldsymbol{q} = \boldsymbol{0}, \tag{1}$$

where $\boldsymbol{D}, \boldsymbol{G}, \boldsymbol{K}$ and $\boldsymbol{C}(t)$ are the damping, gyroscopic, stiffness and parametric excitation matrices, respectively. The resulting phenomenon can be illustrated in Fig.1. The figure shows a global destabilization of the system in absence of other excitation mechanisms, explained by having a positive eigenvalue at all frequencies except for *anti-resonances*.

Modeling of the nonlinear micro ring gyroscope

As shown in Fig. 2, the micro ring gyroscope is modeled as an elastic inextensible ring totally surrounded by curved electrodes, each at an angle $\bar{\theta}_k$. The ring was found to exhibit two degenerate modes at the first vibration frequency, the antinodes for the first mode and second modes are at angles $\bar{\theta}_k = (\frac{n\pi}{2}), (\frac{n\pi}{2} + \frac{\pi}{4})$ respectively. For modeling the ring's elastic dynamics we follow Natsiavas [7] by considering only flexural vibrations in thin rings. The elastic and electrostatic potential energy, U_d and U_e respectively, are then found to be

$$U_d = \frac{EI}{2R^3} \int_0^{2\pi} \left[u + \frac{\partial^2 u}{\partial \theta^2} + \frac{1}{2R} \left(\frac{\partial u}{\partial \theta} \right)^2 \right]^2 d\theta, \qquad U_e \simeq \frac{-\epsilon_0 b R}{2d} \sum_{n=0}^{4} \int_0^{2\pi} (V_{DC} + V_{AC})^2 \frac{u^n}{d^n} d\theta,$$

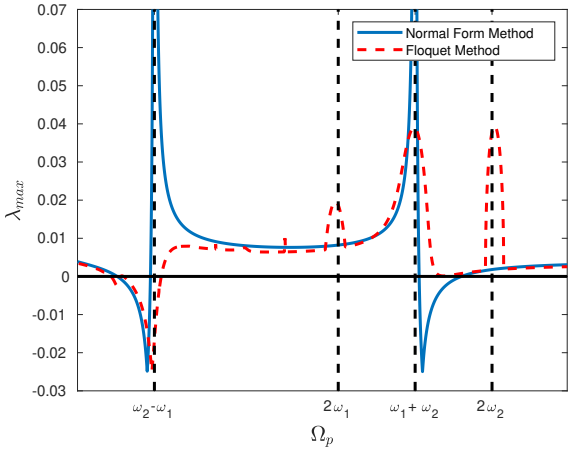

Figure 1: Global destabilization of a 2 DOF system

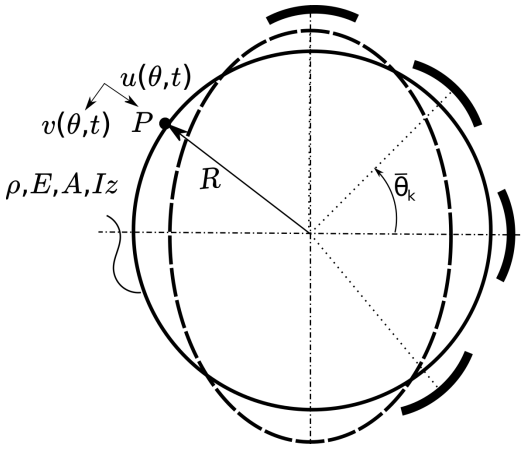

Figure 2: A sketch of the micro ring gyroscope

where R is the mean radius, u and v are the radial and circumferential displacements of a point on the centroidal axis respectively (s. Fig. 2), ϵ_0 is the electric constant, b, h are the ring's thickness and width respectively, d is the initial gap between each electrode and the ring's body, and V_{DC}, V_{AC} are the direct and alternating voltages respectively applied on the electrodes. On the other hand, the kinetic energy for the ring in a rotating frame will be

$$T = \frac{\rho bh}{2} \int_0^{d\pi} [u, v]^T . [u, v]^T R d\theta.$$

Applying the *ansatz* proposed by Natsiavas but for only two vibration modes, $u(\theta, t) = A(t)\cos(2\theta) + B(t)\sin(2\theta) - \frac{9}{16R}\left[A^2(t) + B^2(t)\right]$, and considering the alternating voltage to be distributed approximately according to $V_{AC}(\theta, t) = V_{AC}(t)\cos(2\theta)$, we get two nonlinear ordinary differential equations in $A(t)$ and $B(t)$ representing the system dynamics for the drive (primary) and sense (secondary) modes respectively.

Normal form transformation

However, since the resulting equations of motions are highly nonlinear, an analytical method is required to develop a better understanding of the gyroscope's dynamics. Different perturbation methods are widely used to analyze those systems, but we prefer here to use the normal form method, since it proved to have comparatively better accuracy for highly nonlinear systems involving parametric excitation. An approximate analytical solution is therefore derived, through which the highest eigenvalue could be calculated in terms of system's and excitation parameters, this was used as an indication for system stability. This can be seen in Fig. 1, in which the normal form method was used to simulate the eigenvalues of the system in (1) for all but resonant frequencies, complying with the numerical results calculated by the Floquet method. Two main findings are specially important; firstly the system is destabilized for approximately the whole frequency spectrum, that is specially important in tuning the exciation frequency. Since this would overcome the problem of the loss of sensitivity by mistuning. And secondly, this can give a new method of controlling the gyroscope's response through frequency control. This method will then be applied on the already derived equations of motion, and thereby the effect of the parametric excitation on the nonlinear micro gyroscope will be illustrated, in a similar way to what is explained for the linear system in (1).

Conclusions

This work contributes to understanding the observed nonlinear behavior of the micro-ring gyroscopes, since its nonlinear model was not sufficiently discussed in the literature [4]. Moreover, we propose a novel excitation method in the field of micro sensors, which offers an unprecedented flexibility in tuning as well as amplifying the micro ring gyroscope. This is believed to contribute to the development of current MEMS gyroscopes towards achieving an inertial grade accuracy.

References

[1] Cesari, Lamberto. 1939. "Sulla Stabilità Delle Soluzioni Delle Equazioni Differenziali Lineari." Annali Della Scuola Normale Superiore Di Pisa-Classe Di Scienze 8 (2): 131-48.

[2] Oropeza-Ramos, Laura A., Christopher B. Burgner, and Kimberly L. Turner. 2009. "Robust Micro-Rate Sensor Actuated by Parametric Resonance." Sensors and Actuators, A: Physical 152 (1): 80-87.

[3] Prakash, Gyan, Arvind Raman, Jeffrey Rhoads, and Ronald G. Reifenberger. 2012. "Parametric Noise Squeezing and Parametric Resonance of Microcantilevers in Air and Liquid Environments." Review of Scientific Instruments 83 (6): 065109.

[4] Polunin, Pavel M., and Steven W. Shaw. 2017. "Self-Induced Parametric Amplification in Ring Resonating Gyroscopes." International Journal of Non-Linear Mechanics 94 (September): 300-308.

[5] Barakat, A., R. Lima, R. Sampaio and P. Hagedorn. 2020. "Bimodal parametric excitation of a micro-ring gyroscope". PAMM 20 (1).(*in print*)

[6] Yoon, Sungjin, Usung Park, Jaewook Rhim, and Sang Sik Yang. 2015. "Tactical Grade MEMS Vibrating Ring Gyroscope with High Shock Reliability." Microelectronic Engineering 142 (July): 22-29.

[7] S. Natsiavas, "Dynamics and stability of non-linear free vibration of thin rotating rings," Int. J. Non. Linear. Mech., vol. 29, no. 1, pp. 31-48, Jan. 1994.

Chaos in a non-linear non-buckled microresonator

Martial Defoort, Libor Rufer and Skandar Basrour
Univ. Grenoble Alpes, CNRS, Grenoble INP, TIMA, Grenoble 38000 France

Summary. Chaos is a phenomenon describing the complex dynamics of many systems, from the evolution of the weather to the dynamics of cosmic entities. Since a few decades, generating chaos from a physical system has triggered a lot of research, especially in the optical domain. In the mechanical domain, chaos generation has been investigated mainly with buckled structures. These bistable systems enter in a chaotic regime upon the application of a strong enough alternative force. However, in the micromechanical domain, buckling a structure is demanding and typically requires a large voltage, incompatible with available technology. In this paper, we describe a new way of generating chaos from a Micro Electro-Mechanical System (MEMS) using the dynamical bistability of a nonlinear system, activated by a modulated signal within the resonance of the system. We measured the generated chaos experimentally with a microresonator, and characterized it with Poincaré sections and Lyapunov exponent measurements. In our case, the chaos generation does not need any specific requirement, and it is readily applicable in many structures, opening a new path for MEMS-based chaos generators.

Introduction

For half-a-century, chaos has triggered a lot of research around the world, both for fundamental and applied research. Chaos is characterized mainly by a non-periodic regime whose evolution is extremely sensitive to initial conditions. However, it is a deterministic system: an absolute knowledge of these initial conditions would enable to fully describe the system evolution, without the need to introduce any form of randomness. In practice, the knowledge of the initial conditions is limited by the precision of the measurement, such that the long-term prediction of the evolution of a chaotic system diverges, giving the illusion of a random system. This property is at the core of many researches, such as fluid mixing [1] or noiseless sensing [2].
Since the discovery of chaos synchronization [3], a tremendous amount of work has been dedicated to physical chaos generation, using either electronic [4] or optical [5] approaches. However, in the mechanical domain, chaos generation has mainly been limited to theoretical studies [6]–[8] since its experimental implementation is usually too complex, especially in micromechanical systems. Indeed, a common way to generate chaos consists in the realization of a bistable system, which is usually obtained by buckling the structure. However, the force required to perform the necessary buckling is typically generated through an electrostatic coupling, with an applied voltage ranging from a few tens to hundreds of volts [9], [10]. In this paper, we present an original way of generating chaos with a nonlinear non-buckled MEMS structure, requiring low voltages.

Methodology and results

We performed our experiment using a thin disk of radius of 400 µm and thickness of 10 µm. Using a piezoelectric transduction, the device is driven by applying a voltage between the bottom and the outer top electrode, and the mechanical displacement is then measured through the inner top electrode (Fig. 1 a). For small displacements, the device being in a linear regime, the amplitude varies proportionally with the driving force. The structure has a resonant frequency of 71.5 kHz and a quality factor of 1100 at low pressure (≈ 1 mbar). By increasing the driving force beyond the regime of small displacements, the MEMS will gradually enter in a nonlinear regime, mainly due to a cubic nonlinearity known as the Duffing nonlinearity. In this regime, for a positive nonlinearity, the shape of the resonance line bends towards higher frequencies, creating a hysteresis. In this frame, the resonator experiences a dynamical bistable regime similar to the one induced by buckling (Fig. 1 b).

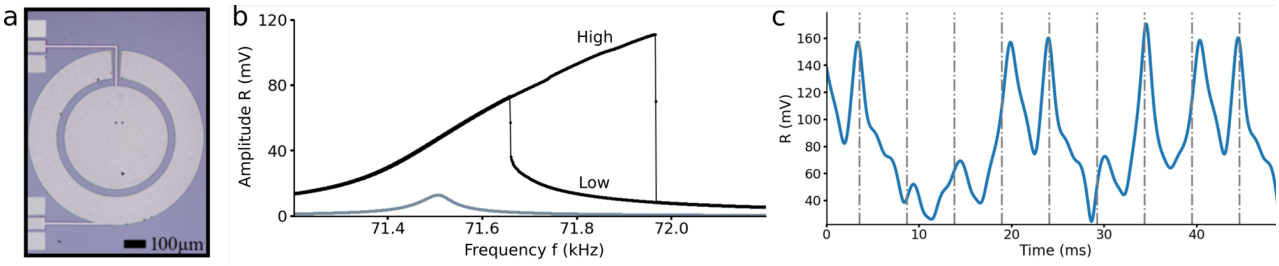

Figure 1: Dynamically bistable chaos. a) The microphotograph of the MEMS showing the outer and inner electrodes (the common bottom electrode covers the opposite side). **b)** At low amplitudes (grey), the MEMS response is linear, but as the drive amplitude increases, its resonance bends to form a hysteresis (black) with two available states (low and high amplitude) for a large frequency range. **c)** Applying a modulation on the driving signal, the system switches between the two states, and at a high enough modulation frequency the system's response displays a chaotic pattern. Grey dashed lines highlight the periodicity of the applied modulation, demonstrating no correlated periodicity in the output signal.

By driving the structure with an amplitude-modulated signal within its hysteresis, the system switches from one to the other state, namely high and low amplitude, and at a sufficiently high modulation frequency this switching becomes

erratic and the MEMS response exhibits a chaotic signal (Fig. 1 c). In our case, we used a modulation frequency of three times the bandwidth of the system, corresponding to 195 Hz.
Because of both non-periodic and non-reproducible features, specific tools are used to study the chaotic regime. In order to characterize the complexity of a chaotic regime, a common approach consists in a stroboscopic analysis of the generated signal, called the Poincaré section. This is performed by sampling a temporal signal at regular intervals defined by the modulation frequency (grey dashed lines in Fig. 1 c) and plotting the results in the phase space (Fig. 2 a). The generated Poincaré section presents the structure of the non-periodic chaos, extracting order from the apparent noise of the signal. Although a chaotic signal is unique, its Poincaré section represents a reproducible signature testifying the complexity of the generated chaos.

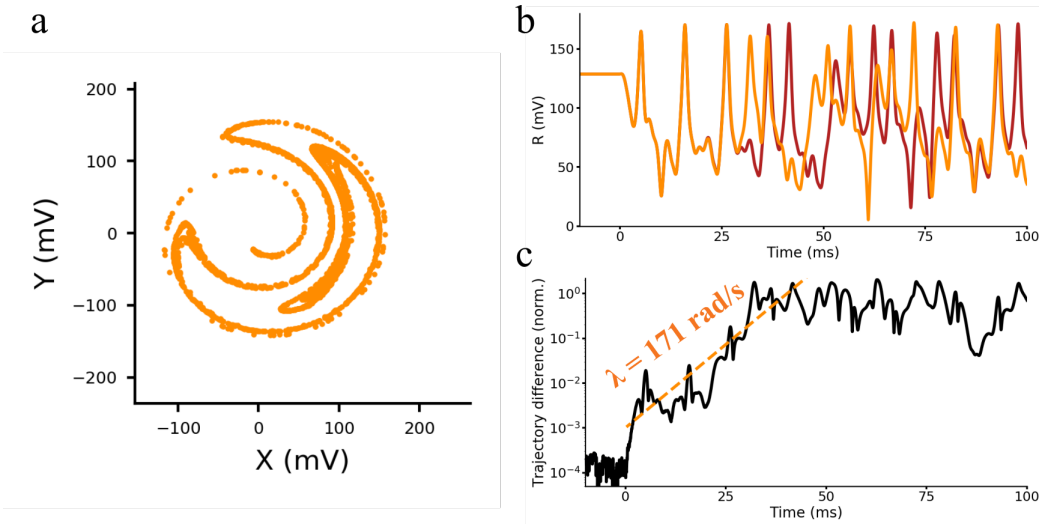

Figure 2: Poincaré section and Lyapunov exponent measurement. The chaotic signals are generated at a modulation frequency of 195 Hz with a driving voltage of 1 V. **a)** By sampling the chaotic signal every 1/195 second, a specific signature emerges from the chaos, forming a Poincaré section. **b)** In the chaotic regime, two measurements (orange and red) with extremely close initial conditions will tend to diverge in the chaotic regime (starting at the time $t = 0$). **c)** From the difference between the two trajectories, the Lyapunov exponent is extracted using an exponential fit.

Another interesting property of chaos lies in how sensitive to the initial conditions the system is. This property is characterized by the Lyapunov exponent, which describes how two initially close trajectories of the same system converge or diverge after some time. For a positive Lyapunov exponent, the trajectories diverge, which is the main property of chaotic systems, and its absolute value characterizes how fast the divergence is: it describes the memory of the system. The precision with which the Lyapunov exponent can be experimentally measured directly depends on how precisely the system can be set at similar initial conditions, ultimately limited by the noise of the system. In our case we were able to get initial conditions as close as 100 ppm, enabling to fit correctly the Lyapunov exponent, which we find to be 171 rad/s for our system (Fig. 2 b, c).

Conclusion

We demonstrated a new technique for MEMS-based chaos generation, using the dynamical bistability of the nonlinear system combined with an amplitude modulated driving force. We characterized the generated chaos with Poincaré sections and Lyapunov exponent measurements, giving information about the complexity and the memory of the system, essential to understand the behavior of the chaotic system.

References

[1] J. M. Ottino *et al.*, « Microfluidic systems for chemical kinetics that rely on chaotic mixing in droplets », *Philos. Trans. R. Soc. Lond. Ser. Math. Phys. Eng. Sci.* (2004).
[2] Guanyu Wang *et al.*, « The application of chaotic oscillators to weak signal detection », *IEEE Trans. Ind. Electron.* (1999).
[3] L. M. Pecora and T. L. Carroll, « Synchronization in chaotic systems », *Phys. Rev. Lett.* (1990).
[4] L. O. Chua *et al.*, « A universal circuit for studying and generating chaos. I. Routes to chaos », *IEEE Trans. Circuits Syst. Fundam. Theory Appl.* (1993).
[5] A. Argyris *et al.*, « Chaos-based communications at high bit rates using commercial fibre-optic links », *Nature* (2005).
[6] E. Maani Miandoab *et al.*, « Chaos prediction in MEMS-NEMS resonators », *Int. J. Eng. Sci.* (2014).
[7] M. S. Siewe and U. H. Hegazy, « Homoclinic bifurcation and chaos control in MEMS resonators », *Appl. Math. Model.* (2011).
[8] W. G. Dantas and A. Gusso, « Analysis of the Chaotic Dynamics of MEMS/NEMS Doubly Clamped Beam Resonators with Two-Sided Electrodes », *Int. J. Bifurc. Chaos* (2018).
[9] Y. C. Wang *et al.*, « Chaos in MEMS, parameter estimation and its potential application », *IEEE Trans. Circuits Syst. Fundam. Theory Appl.* (1998).
[10] J. Barceló *et al.*, « Chaotic Signal Generation in the MHz Range with a Monolithic CMOS-MEMS Microbeam Resonator », *IEEE 32nd International Conference on Micro Electro Mechanical Systems (MEMS)*, 2019.

Tuesday, July 19, 2022

13:30 - 15:30

MS-14 Nonlinear Dynamics for Engineering Design

Rhone 2

Chair: Guilherme Franzini

13:30 - 13:50
Revisiting The Nonlinear Free Vibrations of Hanging Cables - The Use of a Direct Approach on The Partial Differential Equations of Motion
VERNIZZI Guilherme, **LENCI Stefano***, FRANZINI Guilherme
*Università Politecnica delle Marche [Ancona] (Piazza Roma 22, 60121 Ancona Italy)

13:50 - 14:10
The effect of temperature on thermo-elastic plate response: FE and reduced model
DONEVA Simona*, WARMINSKI Jerzy, MANOACH Emil
*Institute of Mechanics, Bulgarian Academy of Sciences (Bulgaria, Sofia, 1040 1 "15 Noemvri" Str. Bulgaria) - Department of Applied Mechanics, Lublin University of Technology (Nadbystrzycka 36, 20-618 Lublin Poland)

14:10 - 14:30
The effect of the fibre orientation on the geometrically non-linear vibrations of tow placed composite plates with real clamped boundaries
RIBEIRO Pedro*, ANTUNES Ana Margarida, AKHAVAN Hamed, DIAS Rodrigues José
*Faculdade de Engenharia da Universidade do Porto (Rua Dr. Roberto Frias, s/n 4200-465 Porto Portugal)

14:30 - 14:50
The Effects of Screen Curvature On The Transient Dynamics Of Automotive Windscreen Wipers
GRAHAM Bradley*, MAVROS Georgios, KNOWLES James
*Loughborough University (Loughborough University, Ashby Road, LE11 3TU UK United Kingdom)

14:50 - 15:10
Using Spectral Submanifolds for Forced Response Prediction in Nonlinear Finite Element Models: Direct and Nonintrusive methods
JAIN Shobhit, **CENEDESE Mattia***, HALLER George
*ETH Zürich (Leonhardstrasse 21, 8092, Zürich Switzerland)

Revisiting The Nonlinear Free Vibrations of Hanging Cables – The Use of a Direct Approach on The Partial Differential Equations of Motion

Guilherme Jorge Vernizzi* †, Sefano Lenci† and Guilherme Rosa Franzini *
*Offshore Mechanics Laboratory - LMO, Escola Politécnica, University of São Paulo, Brazil
†Università Politecnica delle Marche, Ancona, Italy

Summary. In this paper the nonlinear free vibrations of a hanging cable are investigated. The analysis is carried out by applying the method of multiple scales directly on the planar equations of motion for a cable with arbitrary sag and inclination. The only simplification used is that the static strain is small. The methodology allows to obtain results regarding the corrections in modal shape and variations of frequency as function of the initial amplitude. The obtained results show that the hard/softening behaviour that this kind of structure can undergo is in qualitative agreement with previous works.

Introduction

The use of hanging cables as structural elements is commonly found in several engineering application. This type of use can be found in transmission lines, bridges, offshore oil exploration activities, among others. These structures exhibit a rich dynamics, being under extensive efforts in research practice. In order to better understand the dynamic behaviour of these structures, the study of the free vibrations is a problem of interest. This study provides the behaviour of the natural frequencies and modes depending on the structural properties, both from linear and nonlinear perspectives.
The linear modes for a horizontal hanging cable with small sag were deeply investigated in [1], making an analytical study regarding modal properties and the cross-over phenomenon. Following, in [2], the linear modal properties are obtained for inclined taut strings. The results show the mode hybridization and the veering phenomenon that occurs in the inclined configuration. In [3], the linear modes for an arbitrarily sagged inclined cable are obtained. The latter considers an inextensible cable causing modal hybridization to be missed, which can be an important drawback in some problems.
In [4] nonlinear modes are obtained for a vertical beam under tension, with the vertical cable as a particular case. The nonlinear modal properties of a horizontal cable are investigated in [5], using the method of multiple scales (MMS) on a discrete model obtained with the Galerkin method. In [6], the nonlinear modes for an inclined cable with small sag are obtained directly from the partial differential equations (PDEs), disregarding the axial dynamics.
To the best of the authors' knowledge, the investigation of the nonlinear free vibrations of an arbitrary inclined sagged cable with a direct analytical approach on the PDEs is not reported in the literature. One important motivation for this kind of investigation can be found in [7], were it is stated and shown with examples that model discretization using the Galerkin method may furnish wrong qualitative behaviour for the system under study due to obtaining the wrong sign in some coefficients. The major contribution of the present work is then the investigation of nonlinear free vibrations of hanging cables with arbitrary sag and inclination using the MMS directly applied to the PDEs.

Mathematical model

The model herein considered is that of a hanging elastic cable, immersed in fluid, with axial stiffness EA, immersed weight γ_s and axial and transversal masses per unit length m and m_t respectively. The difference between directions is kept in order to allow to include added mass effects. The cable is hanging between two fixed supports with an horizontal distance d and a vertical distance h. It is also considered that the tension $T_e\,(s)$ and the angle with the horizontal direction $\theta\,(s)$ in the static configuration are known, with s being the arclength in the static configuration. Being u and v the axial and transversal displacements with respect to the static configuration, the equations of motion obtained from the balance laws for a cable element (see [8] for example) are given as:

$$T_e'\,(\cos\gamma - 1) - T_e\,(\theta' + \gamma')\sin\gamma + T_d'\cos\gamma - T_d\,(\theta' + \gamma')\sin\gamma = m\ddot{u} \tag{1}$$

$$T_e'\sin\gamma - T_e\theta' + T_e\,(\theta' + \gamma')\cos\gamma + T_d'\sin\gamma + T_d\,(\theta' + \gamma')\cos\gamma = m_t\ddot{v} \tag{2}$$

In the equations the static equilibrium is already substituted. T_d stands for the dynamic tension variation, γ is the dynamic variation of θ, u is the displacement in the tangential direction and v is the displacement in the transversal direction. Primes denote differentiation with respect to s while dots represent differentiation with respect to time. Now, the hypothesis of small static strain is used, which allows to write for the strain $\varepsilon = \varepsilon_s + \varepsilon_d$, with the subscripts denoting the static and dynamic parts. With that, it is possible to simply write $T_d = EA\varepsilon_d$. Finally, from differential geometry, the compatibility conditions are obtained, namely $\sin\gamma = (u\theta' + v')\,/\,(1+\varepsilon_d)$, $\cos\gamma = (1 + u' - v'\theta')\,/\,(1+\varepsilon_d)$ and $\varepsilon_d = \sqrt{1 + 2\left(u' - v\theta' + uv'\theta' - u'v\theta' + \left(u'^2 + v'^2 + (u\theta')^2 + (v\theta')^2\right)/2\right)} - 1$. The MMS is then applied considering three terms in the expansion for u and v, alongside with three time scales. The development is not reported for the sake of the size of the extended abstract.

Application example

In order to show the functionality of the methodology, some backbone curves for three different cables are obtained. The data for the material properties are obtained from a typical steel catenary riser. The common properties for the three cases are $EA = 2314$MN, $m = 108$kg/m, $m_t = 141.24$kg/m, $\gamma_s = 727$N/m and structural diameter $D = 0.2032$m. For the horizontal cable, $d = 1500$m and $h = 0$m. For the almost vertical cable, $d = 1$m and $h = 1800$m. Finally for the inclined cable, $d = 1500$m and $h = 1800$m. In all the cases the natural length of the cable was taken as the one obtained from an inextensible catenary configuration. The horizontal component of the tension is $T_h = 680550$N for the horizontal and the inclined cable, while is taken as 680N for the vertical one. The backbone curves showing the vibration frequency ω with respect to the natural linear frequency ω_0 as a function of the amplitude A_0 are presented in Fig. 1. It is possible to see

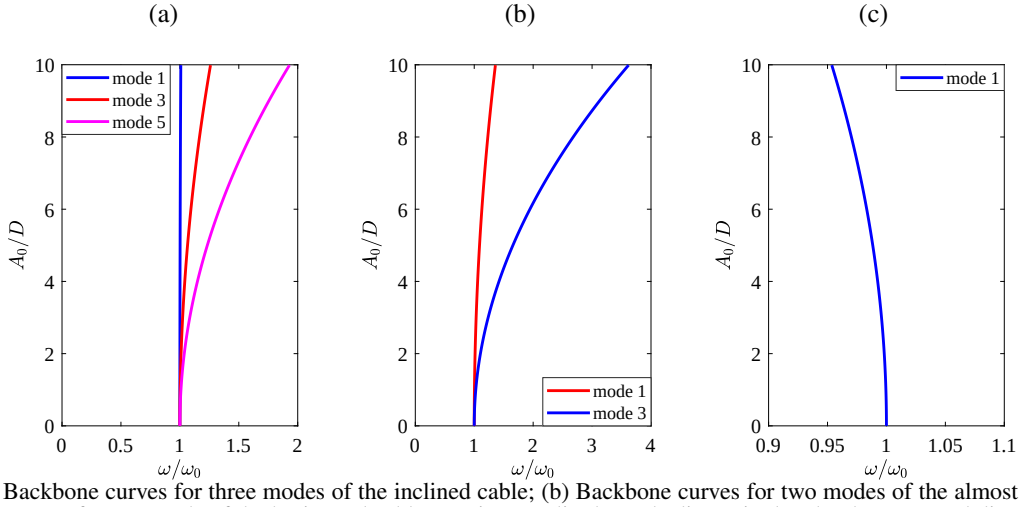

Figure 1: (a) Backbone curves for three modes of the inclined cable; (b) Backbone curves for two modes of the almost vertical cable; (c) Backbone curves for one mode of the horizontal cable. Motion amplitude made dimensionless by the structural diameter.

that both hardening and softening behaviours are obtained, as well as the more intense hardening when going from the chosen inclined model to the almost vertical one. Further examples and analysis of the results are left to the full paper. For the sake of comparison of the qualitative behaviour, the softening behaviour for the horizontal configuration is obtained in [5] while the terms of the fourth order in the expansion are not noticeable. The almost vertical configuration can be compared to the results in [6]. Finally, examples of hardening in inclined cables can be seen in [9].

Conclusions

From the nonlinear equations of motion for a hanging cable, with the small static strain as only simplification hypothesis, nonlinear solutions for the free vibrations were obtained with the method of multiple scales applied directly to the PDEs of motion. The results presented show that the methodology is capable of reproducing some known qualitative results for the dependency of the frequency of vibration with the amplitude of vibration. Further results and comparisons are planned for the full paper and the presentation.

Acknowledgements

The first author acknowledges the São Paulo Research Foundation (FAPESP) for research grants n. 2016/25457-1 and 2017/16578-2, the latter a financial support to his internship at Università Politecnica delle Marche.

References

[1] Irvine H.M., Caughey T.K. (1974) The linear theory of Free vibrations of a suspended cable. Proc R Soc Lond A Math Phys Sci 341:299-317.

[2] Triantafyllou M.S. (1984) The dynamics of taut inclined cables. Q J Mech Appl Math 37:421-440.

[3] Pesce C.P., Fujarra A.L.C., Simos A.N., Tannuri E.A. (1999) Analytical and closed form solutions for deep water riser-like eigenvalue problem. In: Proceedings of the Ninth (9th) International Offshore and Polar Engineering Conference, Brest, France, 1999. 255-264.

[4] Mazzilli C.E.N., Lenci S., Demeio L. (2014) Non-linear free vibrations of tensioned vertical risers. In: ENOC Proceedings of the 8th European Nonlinear Dynamics Conference, Vienna, Austria, 2014.

[5] Luongo A., Rega G., Vestroni F. (1984) Planar non-linear free vibrations of an elastic cable. Int J Non Linear Mech 19:39-52.

[6] Vernizzi G.J., Franzini G.R., Pesce C.P. (2020) Non-linear Free Vibrations of a Hanging Cable with Small Sag. In: Kovacic I., Lenci S. (eds) IUTAM Symposium on Exploiting Nonlinear Dynamics for Engineering Systems. ENOLIDES 2018. IUTAM Bookseries, vol 37. Springer, Cham.

[7] Troger H., Steindl A. (1991) Nonlinear stability and bifurcation theory. An introduction for engineers and applied scientists. Springer-Verlag Wien, NY.

[8] O'Reilly O.M. (2017) Modeling nonlinear problems in the mechanics of strings and rods, the role of the balance laws. Springer International Publishing.

[9] Srinil N., Rega G. (2007) Two-to-one resonant multi-modal dynamics of horizontal/inclined cables. Part II: internal resonance activation, reduced-order models and nonlinear normal modes. Nonlinear Dyn 48:253-274.

The effect of temperature on thermo-elastic plate response: FE and reduced model

Simona Doneva[*,**], Jerzy Warminski [*] and Emil Manoach[**]
[*]*Department of Applied Mechanics, Lublin University of Technology, Lublin, Poland*
[**]*Institute of Mechanics, Bulgarian Academy of Sciences, Sofia, Bulgaria*

Summary. In the present work a thermo-elastic model of a circular plate is analyzed. Nonlinear oscillations of a heated plate subjected to dynamic loading are studied. A model of the plate is based on the geometrically nonlinear Mindlin plate theory. Two different approaches are used to study the problem: a pure numerical study by the finite element method (FEM) and an analytical study based on the harmonic balance method applied to the reduced model taking into account the first vibration mode. The influence of the loading and the elevated temperature on dynamic behaviour is studied for buckling and post buckling states.

Introduction

The plates are used in many technological areas. Being fundamental structural elements often the plates are subjected to mechanical and thermal loadings which lead to intensive large amplitude vibrations. The temperature can change the reaction of mechanical structures and in some cases, close to critical points, even a small temperature variation may give unexpected change in the system response. The case when the studied problem of thermally induced vibrations or vibrations produced by coupled mechanical and thermal loads is nonlinear its detailed investigation is specially important. Detailed analysis of local and global nonlinear dynamics of plates for various thermal and mechanical loads are conducted in [1,2].

In this work we analyze the effect of thermal loading on the nonlinear vibrations of a circular plate according to the extended Mindlin plate theory taking into account the geometrically nonlinearities due to the large displacements. FEM is used to study the response of the plate in the time domain. A reduced model based on the Galerkin ortogonalization method is the second approach to study the problem. By harmonic balance method the response of the plate is studied in the frequency domain. The resonance curves are determined from the analytically obtained modulation equations. Stability of the solution is studied in details.

Physical method

A circular plate with radius *R* and thickness *h* vibrating asymmetrically due to a harmonic mechanical loading is taken into consideration. It is accepted that the plate gets an elevated temperature instantly and the temperature is distributed uniformly along the plate surface and thickness. Based on extended Mindlin plate theory, and accepting that the inertia term in mid-plane can be neglected, the equations of the plate vibration are:

$$Ah\left[\frac{\partial^2 u}{\partial r^2}+\frac{\partial w}{\partial r}\frac{\partial^2 w}{\partial r^2}+\frac{1}{r}\frac{\partial u}{\partial r}-\frac{u}{r^2}+\frac{1}{2r}(1-\nu)\left(\frac{\partial w}{\partial r}\right)^2\right]=0$$

$$D\left[\frac{\partial^2 \psi}{\partial r^2}+\frac{1}{r}\frac{\partial \psi}{\partial r}-\frac{\psi}{r^2}\right]-k^2Gh\left(\frac{\partial w}{\partial r}+\psi\right)-c_2\frac{\partial \psi}{\partial t}-\frac{\rho h^3}{12}\frac{\partial^2 \psi}{\partial t^2}=0$$

$$k^2Gh\left(\frac{\partial^2 w}{\partial r^2}+\frac{1}{r}\frac{\partial w}{\partial r}+\frac{\partial \psi}{\partial r}+\frac{\psi}{r}\right)+Ah\left[\frac{\partial u}{\partial r}+\frac{1}{2}\left(\frac{\partial w}{\partial r}\right)^2+\frac{\nu}{r}u-\frac{1+\nu}{h}\alpha_T\Delta T\right]\left(\frac{\partial^2 w}{\partial r^2}+\frac{1}{r}\frac{\partial w}{\partial r}\right)+$$

$$Ah\left[\frac{\partial^2 u}{\partial r^2}+\frac{\nu}{r}\frac{\partial u}{\partial r}-\frac{\nu}{r^2}u+\frac{\partial w}{\partial r}\frac{\partial^2 w}{\partial r^2}\right].\left(\frac{\partial w}{\partial r}\right)+c_1\frac{\partial w}{\partial t}-\rho h\frac{\partial^2 w}{\partial t^2}=-p(r,t)$$

Where *u* and *w* are in-plane and transversal displacements, ψ is the angular rotation, c_1 and c_2 are damping coefficients, ρ is the density, υ is Poison's ratio, E is the Young modulus, T is the temperature and

$$A=\frac{E}{1-\nu^2},\ D=Ah^3/12$$

The boundary conditions for a clamped, in-plane fixed plate are:

$$u(0,t)=u(R,t)=w(R,t)=0,\psi(R,t)=0$$

The model of the plate represented by PDE is reduced to the ODE by the Galerkin method based on the modes projection and taking into account excitation, distributed according to the first mode shape. For the first mode reduction we obtain just one nonlinear differential equation:

$$\ddot{q}_1+2\xi_1\omega_1\dot{q}_1+\omega_1^2q_1+F_{NL1}q_1^3+F_{NT1}\Delta Tq_1=F_{NP1}\sin\omega t$$

Here F_{NL1}, F_{NT1} and F_{NP1} are constants obtained numerically, ω_1 is the first natural frequency and ξ_1 is a damping coefficient. Applying harmonic balance method, after some algebraic manipulations we obtained a cubic algebraic equation:

$$-16P^2+9z^3\gamma^2+z^2(24\lambda T\gamma+24\alpha\gamma-24\gamma\omega^2)+z(16\lambda^2T^2+32\lambda T\alpha+16\alpha^2$$
$$-32\lambda T\omega^2-32\alpha\omega^2+16\beta^2\omega^2+16\omega^4)=0$$

which is solved analytically.

FEM and numerical results

Using the FE program ANSYS Mechanical APDL the plate is discretized by a quad mapped mesh with 2700 elements and 2884 nodes. Four nodes finite element SHELL 181 is used. The response of the plate is studied for different values of the loading, excitation frequencies and different temperatures. Generally, the elevated temperatures lead to enlarging of the amplitude of vibrations. At Fig. 1 we show time history diagrams of response of the plate centre for 4 different temperatures. It is clear seen that at ΔT=30 and ΔT=40 the plate buckles and continues to vibrate around a new equilibrium state.

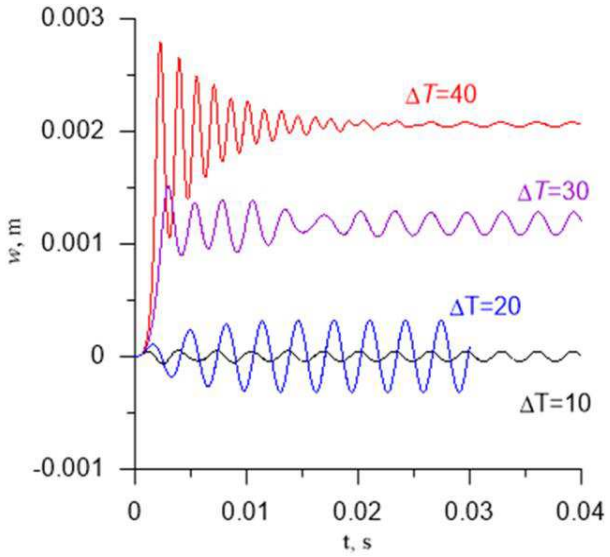

Fig. 1: Time history diagrams of the plate centre of the plate subjected to harmonic loading with p=1500 N/m^2 and ωe=312.5 Hz.
Black colour – ΔT=10; Blue colour – ΔT= 20;
Purple colour – ΔT= 30 , Red colour – ΔT=40.

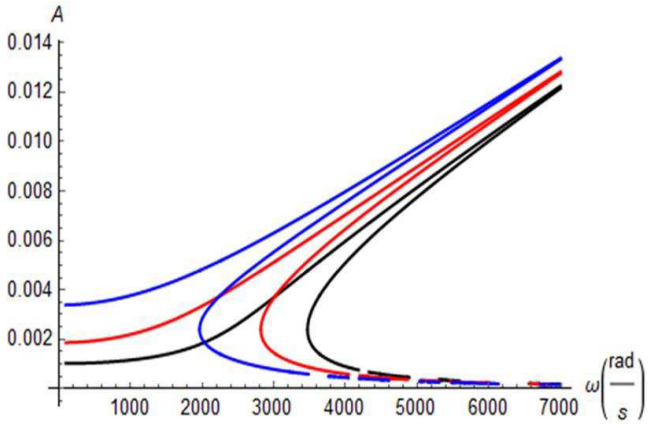

Fig. 2: Resonance curves by HBM for ΔT = 20 (black), ΔT = 30 (red) and ΔT = 40 (blue).

HBM solution

The algebraic equation obtained by HBM is solved for different values of the loading parameters and the temperature. An example for such solutions are the resonance curves shown in Fig. 2. The hardening behaviour of the resonance curves are clearly expressed due to the large deflections. The elevated temperature increases the amplitudes and changes the resonance curve in the direction of lower frequencies. It is seen that multiple and unstable solutions can occur.

Conclusions

Geometrically nonlinear thermo-elastic vibration of a Mindlin circular plate is studied by two different methods. In the first approach by FEM is demonstrated that the elevated temperature can change dramatically the response of the plate and could provoke the plate to complex response, including buckling and bifurcations. The second approach allows to obtain easily the resonance curves and to study the influence of the loading parameters and the elevated temperature on the behaviour of the plate. The computations based on the first mode reduction show the stiffening effect of the resonance curve.

References

[1] Settimi,V., .Saetta, E., Rega, G. Local and global nonlinear dynamics of thermomechanically coupled composite plates in passive thermal regime, Nonlinear Dynamics (2018) 93: 167 doi: 10.1007/s11071-017-3648-1

[2] Amabili M., Carra S, Thermal effects on geometrically nonlinear vibrations of rectangular plates with fixed edges, Journal of Sound and Vibration 321, 2, 936-954 (2009)

The effect of the fibre orientation on the geometrically non-linear vibrations of tow placed composite plates with real clamped boundaries

Pedro Ribeiro[*], Ana Margarida Antunes[*,**,1], Hamed Akhavan[*,**] and José Dias Rodrigues[*]
[*]*DEMec, Faculdade de Engenharia da Universidade do Porto, Porto, Portugal*
[**]*INEGI, Porto, Portugal*

Summary. Curvilinear reinforcement fibres can, within limits, be used to tailor the stiffness of composite laminated plates so that they have specific dynamic properties. The dynamic response of a plate to external forces is strongly affected both by boundary conditions and by the stiffness of the plate near the boundaries. Using a combination of experimental and numerical analyses, this work intends to analyse how the stiffness of the boundaries and the stiffness of tow placed composite plates near the boundaries interact to influence the geometrically non-linear response to harmonic external forces.

Introduction

The application of curvilinear reinforcement fibres in laminated composite plates leads to a variation of the stiffness within the plate domain, allowing designers to tailor the plate so that it meets specific demands more efficiently. Hence, there has been a considerable amount of research on this type of laminated plates [1]. The stiffness of the plate near the boundaries and its relation with the boundary conditions themselves have a major influence on the dynamic response. Classical boundary conditions, i.e., combinations of free, hinged or clamped edges, are typically considered by researchers. However, in practice it is not possible to exactly implement classical boundary conditions, with the clamped edge case particularly difficult to approach [2]. A more realistic representation of "real clamps" is achieved by considering elastically restrained edges [3].
This work intends to analyse how the non-linear response is affected by changes of the fibre path near the plate's edges, when the latter are elastically restrained. For that purpose, a physical/mathematical model, which considers that the edges are supported on translational and rotational springs, is developed. The values of the stiffness of the boundary springs are adjusted so that the theoretical linear modes of vibration approach experimentally identified ones [4].

Mathematical model

An equivalent single-layer type formulation, based on Kirchhoff's hypothesis, but accounting for geometrical non-linear terms in the Von Kármán sense, is adopted. Components *u*, *v* and *w* (respectively in directions *x*, *y* and *z*) of the middle-plane displacements are written as series with products of shape functions by generalized coordinates and the principle of virtual work is applied. Apart from new stiffness terms due to the elastically restrained edges, the equations of motion are similar to the ones given in [5].

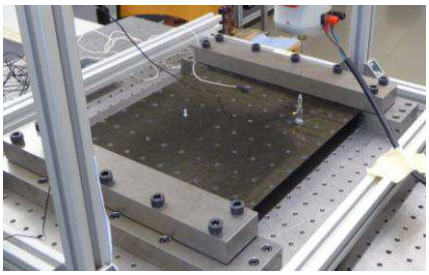

(a)

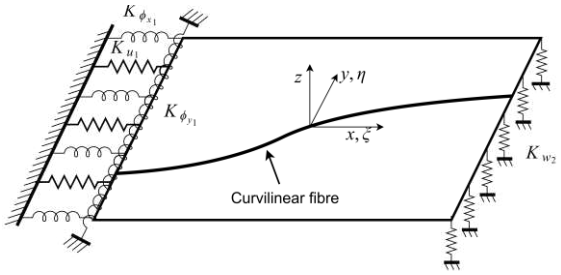

(b)

Figure 1: Experimental set-up (a) and schematic representation of a plate supported by distributed springs (b); only some springs are depicted.

In the laboratory, the plate is fixed only on two opposite edges using stiff steel blocks, as shown in Figure 1 (a). The corresponding model with translational and torsional distributed springs is shown in Figure 1 (b), where some distributed springs are drawn on the left-hand side and one on the right-hand side, for the sake of clarity. K_{u_i} and K_{w_i} represent the values of the stiffness per unit length of translational springs along the *x* and *z* axes, respectively; $K_{\phi_{x_i}}$ and $K_{\phi_{y_i}}$ represent the torsional stiffness per unit length of springs that rotate, respectively, about the *x* and the *y* axes. Index *i* is equal to 1 if ξ=-1 and equal to 2 if ξ=1. Displacement at the boundaries is small, so it is still reasonable to assume that these stiffness coefficients are constant, even though this work is in the geometrically non-linear regime.

The virtual works done by the distributed forces and moments due to the various boundary springs are

$$\delta W_{K_u} = -\int_{-1}^{1} K_{u_1} u(-1,\eta,t)\,\delta u(-1,\eta)\frac{b}{2}\mathrm{d}\eta - \int_{-1}^{1} K_{u_2} u(1,\eta,t)\,\delta u(1,\eta)\frac{b}{2}\mathrm{d}\eta \quad (1)$$

$$\delta W_{K_w} = -\int_{-1}^{1} K_{w_1} w(-1,\eta,t)\,\delta w(-1,\eta)\frac{b}{2}\mathrm{d}\eta - \int_{-1}^{1} K_{w_2} w(1,\eta,t)\,\delta w(1,\eta)\frac{b}{2}\mathrm{d}\eta \quad (2)$$

[1] Now at *Vestas Design Centre Porto*, Portugal

$$\delta W_{K_{\phi_y}} = -\int_{-1}^{1} K_{\phi_{y1}} w_{,x}(-1,\eta,t)\delta w_{,x}(-1,\eta)\frac{b}{2}\mathrm{d}\eta - \int_{-1}^{1} K_{\phi_{y2}} w_{,x}(1,\eta,t)\delta w_{,x}(1,\eta)\frac{b}{2}\mathrm{d}\eta \quad (3)$$

$$\delta W_{K_{\phi_y}} = -\int_{-1}^{1} K_{\phi_{x1}} w_{,y}(-1,\eta,t)\delta w_{,y}(-1,\eta)\frac{b}{2}\mathrm{d}\eta - \int_{-1}^{1} K_{\phi_{x2}} w_{,y}(1,\eta,t)\delta w_{,y}(1,\eta)\frac{b}{2}\mathrm{d}\eta \quad (4)$$

The ordinary differential equations of motion are obtained by applying the principle of virtual work and have the following form [5]

$$\mathbf{M}\ddot{\mathbf{q}}_w(t) + \mathbf{C}\dot{\mathbf{q}}_w(t) + \mathbf{K}\mathbf{q}_w(t) + \mathbf{K}_{nl}(\mathbf{q}_w(t))\mathbf{q}_w(t) = \mathbf{p}_w(t) \quad (5)$$

where **M** is the mass matrix, **C** a matrix due to viscous damping, **K** a constant stiffness matrix and $\mathbf{K}_{n\lambda}(\mathbf{q}_w(t))$ a stiffness matrix that represents non-linear effects. Most of the terms due to the elastic supports are explicitly given in [4], they alter stiffness matrix **K**; the remaining matrices are given in [5]. Vector $\mathbf{q}_w(t)$ contains the transverse generalised coordinates; $\mathbf{p}_w(t)$ is the vector of generalised transverse external forces. Although we are accounting for in-plane displacements at the boundaries, these are still extremely small and so is the in-plane inertia. Hence, the latter is neglected and, consequently, the non-linearities of the set of equations of motion (5) are of the cubic type.

Sample results and closure

Several frequency response functions were measured (Figure 2) and employed to obtain natural modes of vibration in the linear regime [4]. With this data, the stiffnesses of the boundary springs were adjusted, resulting in models that provide modal data that is reasonably similar to the experimentally obtained results [4]. As an example, Table 1 shows that the linear natural frequencies of vibration computed by the model with elastic supports ($\omega_i^{Springs}$) are much closer to the experimental ones ($\omega_i^{experimental}$) than the frequencies computed using a model that adopts theoretical, exact, clamped boundary conditions (ω_i^{CFCF}).

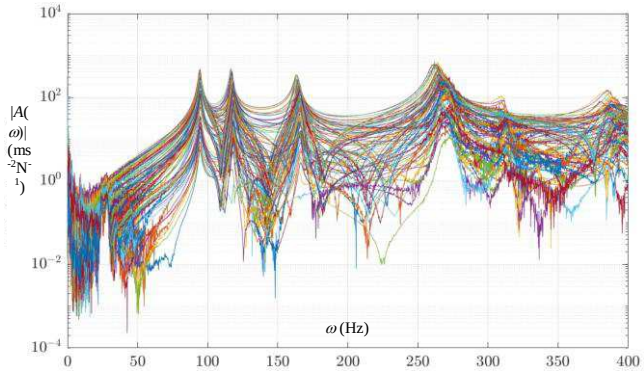

Figure 2: Frequency response functions from measurements on the plate represented on Figure 1 (a).

Table 1. Experimental and theoretical natural frequencies (in Hz).

Mode number	1	2	3	4	5	6	7
$\omega_i^{experimental}$	95.13	117.6	165.0	258.0	275.8	307.3	361.6
$\omega_i^{Springs}$	97.35	116.1	175.7	277.5	286.3	321.6	405.4
ω_i^{CFCF}	136.7	153.1	211.7	315.7	379.9	403.0	486.1

Harmonic excitations are applied and the non-linear response is computed using the harmonic balance and continuation methods [5]. Simulations are carried out for diverse fibre paths. The dynamic response is analysed, with particular attention paid to the combined influence of the elasticity of the supports and of the plate's stiffness near the boundaries.

Acknowledgement

This research is carried out in the framework of project Nº 030348, POCI-01-0145-FEDER-030348, "Laminated composite panels reinforced with carbon nanotubes and curvilinear carbon fibres for enhanced vibration and flutter characteristics", funded by FEDER, through *Programa Operacional Competitividade e Internacionalização* – COMPETE 2020, and by National Funds (PIDDAC), through FCT/MCTES.

References

[1] Ribeiro P., Akhavan H., Teter A., Warminski J. (2014) A review on the mechanical behaviour of curvilinear fibre composite laminated panels. *J Compos Mater* **48**:2761-77.
[2] Ewins D.J. (2000) Modal Testing: Theory, Practice and Application. Research Studies, Baldock.
[3] Szilard R. (1973) Theory and Analysis of Plates: classical and numerical methods. Prentice-Hall.
[4] Antunes A. M. (2019) Modes of Vibration of Hybrid Variable Stiffness Composite Laminated Plates: modelling, experimental verification and analysis. *MSc dissertation*. Faculdade de Engenharia da Universidade do Porto, Porto.
[5] Ribeiro P., Stoykov S. (2015) Forced periodic vibrations of cylindrical shells in laminated composites with curvilinear fibres. *Comp Struct* **131**:462-478.

The Effects of Screen Curvature On The Transient Dynamics Of Automotive Windscreen Wipers

Bradley Graham*, James Knowles* and Georgios Mavros*
*Aeronautical & Automotive Engineering Department Loughborough University, UK

Summary. In this paper we study the effects of automotive windscreen curvature on the transient dynamics of a wiper blade. To do this we utilise a finite element (FE) model to obtain contact force distributions for multiple screen curvatures in a single axis. The distributions obtained are directly integrated into a multiple connected mass-spring-damper (MSD) system to analyse the transient dynamics.

Introduction

The primary function of windscreen wipers is to remove water and debris from the windscreen, ensuring the driver has a clear view of the road ahead. The successful operation of windscreen wipers is therefore imperative for the vehicle occupants' safety. Predicting wiper performance at the design stage is important to ensure their safe operation: whilst the purpose of windscreen wipers is simple, the non-linear contact and sliding mechanisms which govern the operation are complex. Because of these complexities, a lot of preliminary design decisions are based on empirical data rather than predictive models. This can present constraints of unknown necessity on other aspects of a vehicle's design (e.g. windscreen curvature). There is hence a need to develop physics-based models of wiper performance that can be used as evaluative tools early in the design stage.

Approach

This work presents an analysis of the impact that the contact distribution has on the transient dynamics of a windscreen wiper blade. We consider the curvature of the screen in a single axis, the y axis. For the purpose of our model we maintain the geometry of the wiper blade used in the FE model. Initially we take a commercially available screen, of curvature G for analysis. We subsequently establish a mathematical expression of the screen to adjust the curvature to $\frac{1}{3}G$ and $\frac{5}{3}G$. We utilise multiple connected mass spring damper systems to represent the full length of the blade, and to allow for direct integration of the distributions computed via a finite element (FE) model. A continuously differentiable Stribeck curve[1] which features six constants is used to capture the transient friction characteristics of the blade. The Stribeck curve is modified to agree with a recognised range of fiction coefficients, $0.1 - 0.6$, associated to wet friction[2]. Additionally, we use experimental values for both the stiffness, K, and damping, C, which were presented by Shigeki Okura and Tohru Sekiguchi[3]. For our study we consider a discretisation that corresponds to a real-life discretisation distance of $2mm$ on a $600mm$ wiper blade, providing much greater resolution than currently offered by experimental measures.

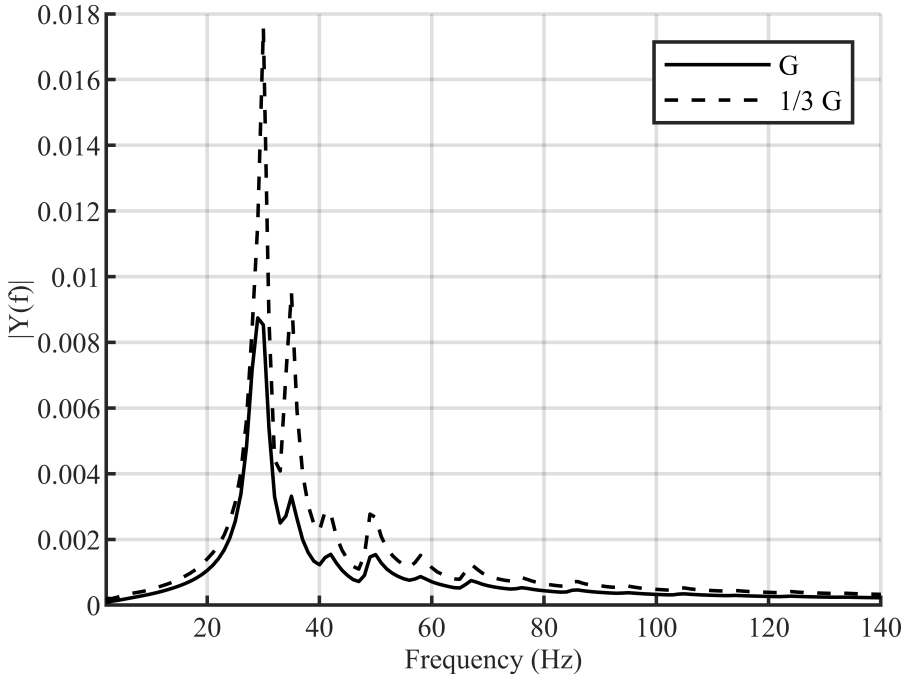

Figure 1: Fourier Decomposition of Transient Dynamics Associated to Nominal Screen Curvature G and $\frac{1}{3}G$

Figure 1 shows the Fourier decomposition of the transient dynamics data for a nominal curvature, G and $\frac{1}{3}G$. In the nominal case, we find a peak in the amplitude of frequency at $30Hz$. Additionally, there are a number of underlying beats with a greater frequency than the peak, but significantly lower amplitude. When considering the a reduced curvature case, we find that the peak frequency remains constant at $30Hz$, but has a much greater amplitude. The underlying beats that were visible in the nominal case are also present in the reduced curvature case. As with the peak frequency, the amplitude of the beat frequencies also increase. However, the increase in amplitude, decreases as we consider higher frequencies. Additionally we find that a uniform distribution does not yield a more desirable dynamic response than the current contact distributions that feature on flat style wiper blades, but in fact a screen of greater curvature can yield reduced amplitudes of the frequencies observed. Throughout our study we observe a dominant peak frequency, $30Hz$, such a frequency is associated to a chatter response of wiper blades[4].

Conclusions

The non-linear complexities and current reliance on empirical data associated to windscreen wipers necessitate the development of models and analyses such as presented above. The work presented shows how small design decisions such as the curvature of a windscreen, can dramatically affect wiper system performance, and shows how some small design changes can aid in the functional operation of windscreen wipers. These results show the importance of understanding the effects that screen curvature has on not only the transient dynamics but also the frequency response of the blade, providing insight into improving wiper quality.

References

[1] Makkar, C., Dixon, W.E., Sawyer, W.G. and Hu, G., 2005, July. *A new continuously differentiable friction model for control systems design.* In Proceedings, 2005 IEEE/ASME International Conference on Advanced Intelligent Mechatronics. (pp. 600-605). IEEE.

[2] Robert Bosch. *Automotive Handbook.* 8th ed. Plochingen: Bosch, 2011.

[3] Okura, Shigeki, Tohru Sekiguchi, and Takio Oya. *Dynamic analysis of blade reversal behavior in a windshield wiper system*. SAE transactions (2000): 183-192.

[4] Awang, I. M., et al. *Modeling and simulation of automotive wiper noise and vibration using finite element method.* EVALUATION OF AN AUTOMOTIVE WIPER NOISE AND VIBRATION CHARACTERISTICS USING NUMERICAL APPROACH (2009): 13.

Using Spectral Submanifolds for Forced Response Prediction in Nonlinear Finite Element Models: Direct and Nonintrusive methods

Shobhit Jain*, Mattia Cenedese* and George Haller *
*Institute for Mechanical Systems, ETH Zürich, Switzerland

Summary. Finite element models of realistic nonlinear structures are characterized by very high dimensionality that renders simulations of the full system infeasible. Exact model reduction aims to achieve a drastic reduction of the full system's variables in a mathematically justifiable fashion. Specifically, Spectral Submanifolds have recently been shown to result in exact reduced-order models for periodically and quasiperiodically forced, nonlinear mechanical systems. In this work, we demonstrate recent advances towards the computation of SSMs that enable the treatment of realistic finite-element models using direct as well as non-intrusive/data-driven methods.

Background

The prediction of a steady-state response to an externally applied dynamic load is of special significance in engineering applications. Mechanical structures are usually characterized by light damping which results in exceedingly long integration times before a steady state is reached. Despite the broad availability of dedicated software packages [2, 3], the computation and continuation of the steady-state in response to periodic forcing remains a serious computational challenge for full-scale nonlinear finite element models.

Direct computation of SSMs

We consider finite-element discretized system of second-order ordinary differential equations for the generalized displacement $\mathbf{x}(t) \in \mathbb{R}^n$ given as

$$\mathbf{M}\ddot{\mathbf{x}} + \mathbf{C}\dot{\mathbf{x}} + \mathbf{K}\mathbf{x} + \mathbf{f}(\mathbf{x}, \dot{\mathbf{x}}) = \epsilon \mathbf{f}^{\text{ext}}(\Omega t), \tag{1}$$

where $\mathbf{M}, \mathbf{C}, \mathbf{K} \in \mathbb{R}^{n \times n}$ are the mass, stiffness and damping matrices; $\mathbf{f}(\mathbf{x}, \dot{\mathbf{x}}) \in \mathbb{R}^n$ is the purely nonlinear internal force; $\mathbf{f}^{ext}(\Omega t) \in \mathbb{R}^n$ denotes the external forcing, which is periodic in t with frequency Ω; and $0 < \epsilon \ll 1$ is a scalar forcing amplitude parameter.

The recent theory of Spectral Submanifolds (SSM) [1] has laid the foundation for a rigorous model reduction of such nonlinear systems, leading to reliable steady-state response predictions within feasible computation times. Further developments [4] have enabled the computation of SSMs and their reduced dynamics by solving the associated invariance equations directly in physical coordinates using only the eigenvectors associated to the master modal subspace. The software implementation of the method has been available in an open-source package, `SSMTool` [5], making direct SSM computations scalable to realistic, nonlinear finite-element models.

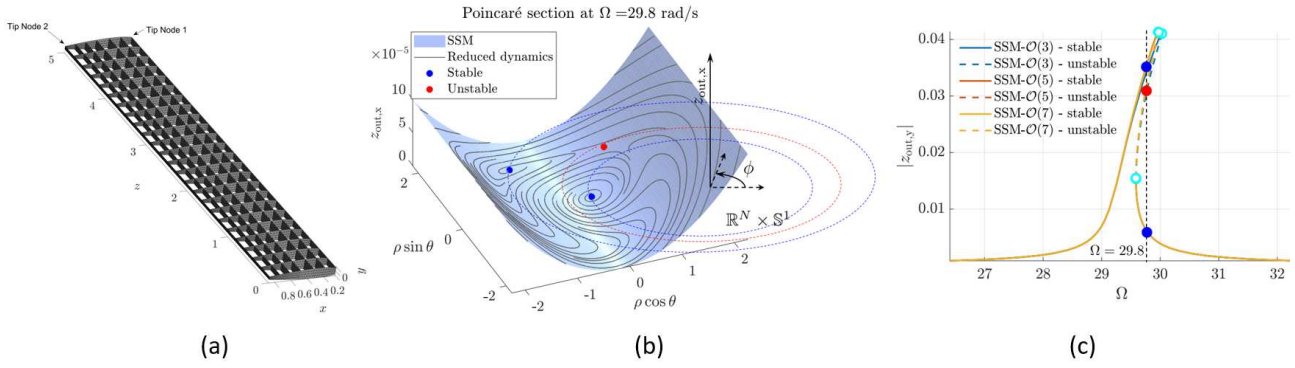

Figure 1: (a) The finite-element mesh of a geometrically nonlinear aircraft wing (illustrated after removing the skin panels) with n =133,290 degrees of freedom. The wing is cantilevered at the $z = 0$ plane (see ref. [6] for model details.) (b) Poincaré section of the non-autonomous SSM computed around the first mode for the near-resonant forcing frequency $\Omega = 29.8$ rad/s. (c) Forced response curves obtained using local SSM computations at $\mathcal{O}(3), \mathcal{O}(5)$ and $\mathcal{O}(7)$ that converge towards a hardening response. (see ref. [4] for computational details.)

In this contribution, we demonstrate applications of SSMs towards the extraction of *forced response curves* (FRC) directly from finite element models. For instance, Figure 1a shows the finite element mesh of a geometrically nonlinear aircraft wing structure containing 133,920 degrees of freedom. We extract the forced response of this model around its first natural frequency by analyzing the reduced dynamics on the two-dimensional SSM associated to the first mode, as shown in Figure 1b. The hyperbolic fixed points of the reduced dynamics on this SSM in polar-coordinates (ρ, θ) directly provide us the stable (blue) and unstable (red) periodic orbits on the FRC for different values of forcing frequency Ω (see Figure 1c.) We refer to ref. [4] for further details.

Nonintrusive computation of SSMs

As commercial finite element software seldom provide intrusive access to the nonlinearity $\mathbf{f}$ of system (1), the direct SSM computation procedure discussed above has limited applicability for the users of commercial codes. At the same time, however, recent advances [7, 8] towards data-driven computation of SSMs and their reduced dynamics have paved the way for nonintrusive applications of SSM theory.

To this end, we construct data-driven, nonlinear reduced-order models on SSMs using the open-source package `SSMLearn` [9]. We base this construction on unforced decaying trajectory data obtained from black-box finite-element simulations. We also take advantage of the knowledge of the master modes associated to the underlying SSM, which is readily available from commercial finite element software and aids computations. Thanks to the rigorous theory backing SSMs, our reduced-order models, which are trained on a minimal number of *unforced* simulation trajectories, are capable of accurately predicting the forced response of the full nonlinear mechanical systems.

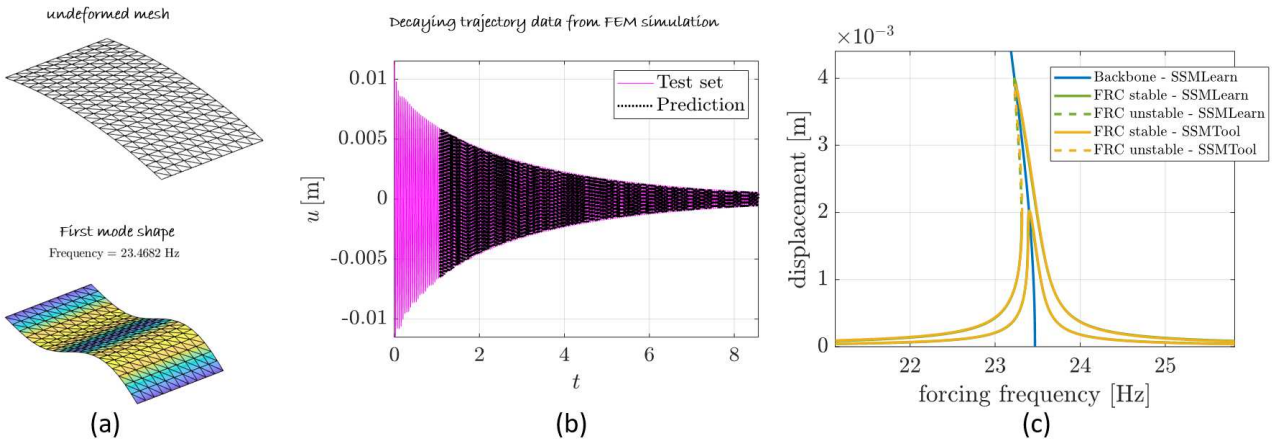

Figure 2: (a) The finite element mesh and the first mode shape of a shallow curved rectangular arch which is simply-supported on opposite ends. (b) Decaying trajectory data of the unforced system (c) Forced response predictions obtain from the data-driven reduced-order model trained on unforced trajectory data via `SSMLearn` agree with the analytic predictions based on direct SSM computations via `SSMTool`.

As an illustration, we consider a finite element model of a geometrically nonlinear shell structure [4] with 1,320 degrees of freedom, as shown in Figure 2b. Assuming linear viscous damping, we simulate two trajectories decaying from initial deflections given to the structure in the shape of the first vibration mode scaled by two different magnitudes. We use truncated simulation data from one of these trajectories to learn the slowest two-dimensional SSM and its nonlinear reduced dynamics up to an a priori determined accuracy. The second trajectory, which is unseen for the training procedure, is then used for testing the prediction of our data-driven model, as shown in Figure 2b.

Finally, we observe that our data-driven model is capable of predicting the forced response of the full system around the first natural frequency as shown in Figure 2c. Here, we obtain agreement with the analytic predictions of the reduced-order model on the same SSM when computed directly [4] via `SSMTool`.

References

[1] Haller, G., & Ponsioen, S. (2016). Nonlinear normal modes and spectral submanifolds: existence, uniqueness and use in model reduction. Nonlinear Dynamics, 86(3), 1493–1534.

[2] Dankowicz, H., Schilder, F. (2013). Recipes for Continuation, SIAM. ISBN 978-1-611972-56-6.

[3] Krack, M., & Gross, J. (2019). Harmonic Balance for Nonlinear Vibration Problems. Springer Cham. ISBN 978-3-030-14022-9 https://doi.org/10.1007/978-3-030-14023-6

[4] Jain, S. & Haller, G. (2021). How to compute invariant manifolds and their reduced dynamics in high-dimensional finite element models. Nonlinear Dynamics, https://doi.org/10.1007/s11071-021-06957-4

[5] Jain, S., Thurnher, T., Li, M., Haller, G. (2021). SSMTool: Computation of invariant manifolds in high-dimensional mechanics problems. Zenodo: https://doi.org/10.5281/zenodo.4614201

[6] Jain, S., Tiso, P., Rutzmoser, J. B., & Rixen, D. J. (2017). A quadratic manifold for model order reduction of nonlinear structural dynamics. Computers & Structures, 188, 80âĂŞ94. https://doi.org/10.1016/J.COMPSTRUC.2017.04.005

[7] Cenedese, M., Axas, J., Bäuerlein, B., Avila, K. & Haller, G. (2021). Data-driven modeling and prediction of non-linearizable dynamics via spectral submanifolds, submitted.

[8] Cenedese, M., Axas, J., Yang, H., Eriten, M. and Haller, G. (2021). Data-driven nonlinear model reduction to spectral submanifolds in mechanical systems. Preprint arXiv:2110.01929

[9] Cenedese, M., Axas, J & Haller, G. (2021). SSMLearn: Data-driven reduced order models for nonlinear dynamical systems. To be released.

Tuesday, July 19, 2022
13:30 - 15:30

MS-15 Energy Transfer and Harvesting in Nonlinear Systems
Rhone 1

Chair: Baptiste Bergeot

13:30 - 13:50
Nonlinear Dynamics of a Ring-based Vibratory Energy Harvester
ASOKANTHAN Samuel, **GEBREL Ibrahim***, WANG Ligang
*The University of Western Ontario (London, ON N6A 5B9 Canada)

13:50 - 14:10
Non-smooth nonlinearities as restoring forces in a mass-in-mass cell
DA Silveira Zanin Camila*, TURE Savadkoohi Alireza, BAGUET Sébastien, DUFOUR Régis
*Univ Lyon, ENTPE, LTDS UMR CNRS 5513 (3 Rue Maurice Audin, 69518 Vaulx-en-Velin France)

14:10 - 14:30
Noise control via exploiting nonlinear interactions
GOURDON Emmanuel*, TURE Savadkoohi Alireza, LAMARQUE Claude-Henri
*Laboratoire de Tribologie et Dynamique des Systèmes (3, Rue Maurice Audin, 69518 Vaulx en Velin (CEDEX) France)

14:30 - 14:50
On the determination of high energy output operation ranges of a piezoelectric bistable energy harvesting system by parallel computing
GRÄBNER Nils*, LENTZ Lukas, VON Wagner Utz
*Technische Universität Berlin, Chair of Mechatronics and Machine Dynamics (Einsteinufer 5-8, 10587 Berlin Germany)

14:50 - 15:10
Targeted energy transfer between a linear oscillator and a time-dependent nonlinear systems
LABETOULLE Aurélie*, GOURDON Emmanuel, TURE Savadkoohi Alireza
*École Nationale des Travaux Publics de l'État (3, Rue Maurice Audin, 69518 Vaulx en Velin (CEDEX) France)

Nonlinear Dynamics of a Ring-based Vibratory Energy Harvester

Ibrahim F. Gebrel[*], Liganag Wang [**] and Samuel F. Asokanthan[*]
[*] *Dept. of Mech. and Matls. Engineering, The University of Western Ontario, London, ON N6A5B9, Canada*
[**] *Dept. of Mathematica, Harbin University, Harbin, Heilongjiang 150001,China*

Summary. This paper is concerned with nonlinear dynamic analysis and design of a novel ring-based Bi-stable energy harvesting device that is considered as an alternative to the beam and tube models used thus far. The Mathematical model for the ring structure to generate nonlinear harvester model as well as the nonlinear magnetic force that acts on the ring structure is formulated. The highly sensitive ring second flexural mode when combined with the nonlinear harvester model as well as nonlinear external magnetic force results in an ideal combination that yields increased frequency range. Numerical predictions of nonlinear dynamic response characteristics when the system is subjected to ambient harmonic excitation have been performed for the purposes of gaining an insight into the dynamics and power generation of this new class of harvesters.

Concept and Modeling

In this paper, the nonlinear governing equations of flexural motion of vibrating thin circular rings are developed for the purposes of investigating the nonlinear dynamic behavior of ring harvester. Galerkin's procedure is used to discretize the nonlinear equations for numerical response predictions. Gebrel et al [1] have presented the first study of a novel ring-based mono-stable energy harvesting device employing a linear system model subjected to ambient as well as nonlinear magnetic forces. The geometry and parameters used in the present study have been described in detail in [1].The general equations of motion that govern the transverse and circumferential motions are derived via Hamilton's principle, as described in [2]. In the present study, models using various configurations for the magnets are examined so that efficient bi-stable energy harvesting systems utilizing the sensitive second mode of a ring structure may be realized in practice. A schematic diagram of the magnetic configurations system is shown in Figure 1. In order to represent the oscillatory nonlinear magnetic force that acts on the ring structure, a novel design and analysis of a theoretical model formulation is employed. This analysis is restricted to mono-stable/bi-stable configurations that depend on the nonlinear terms. Magnets B and C are considered identical and their distance from magnet A is designated as d as shown in Figure 1.

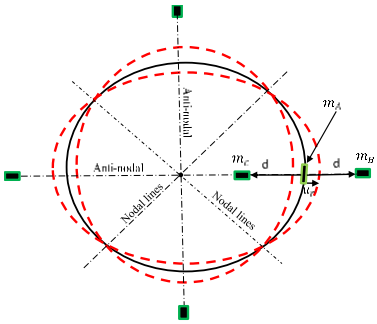

Figure 1: A schematic of ring and magnet configurations

The present study focuses on bi-stable energy-harvesting based on ring structure using the primary and secondary co-ordinates. System equations (1) and (2) have been employed together with equation (3) that represents the output power generation. The final nonlinear equations of motion that govern the nonlinear dynamic behavior of ring harvester employing the second flexural mode with nonlinear magnetic force as well as harmonic ambient excitation are derived as

$$\left[\rho h\pi + 2\rho h\pi\left(\frac{n\gamma}{2r}\right)^2 A_n^2\right]\ddot{A_n} + 2\rho h\pi\left(\frac{n\gamma}{2r}\right)^2 A_n B_n \ddot{B_n} + 2\zeta\omega_0\dot{A_n} + \left[\frac{EI}{br^4}(n^2-1)n^2 + k_r\right]\pi A_n +$$

$$\left[\frac{EA}{br^2} + k_r\right]\left(\frac{n\gamma}{2r}\right)^2 [A_n^2 + B_n^2]\pi A_n + 2\rho h\pi\left(\frac{n\gamma}{2r}\right)^2 \left[\dot{A}_n^2 + \dot{B}_n^2\right]A_n - \gamma_1 \underline{I} = f_{Nm1}(A_n, B_n, \theta_i) + f_e \quad (1)$$

$$\left[\rho h\pi + 2\rho h\pi\left(\frac{n\gamma}{2r}\right)^2 B_n^2\right]\ddot{B_n} + 2\rho h\pi\left(\frac{n\gamma}{2r}\right)^2 A_n B_n \ddot{A_n} + 2\zeta\omega_0\dot{B_n} + \left[\frac{EI}{br^4}(n^2-1)n^2 + k_r\right]\pi B_n +$$

$$\left[\frac{EA}{br^2} + k_r\right]\left(\frac{n\gamma}{2r}\right)^2 [A_n^2 + B_n^2]\pi B_n + 2\rho h\pi\left(\frac{n\gamma}{2r}\right)^2 \left[\dot{A}_n^2 + \dot{B}_n^2\right]B_n = 0 \quad (2)$$

$$L\dot{\underline{I}} + \check{R}\,\underline{I} + \gamma_1 \dot{A_n} = 0\,. \quad (3)$$

The parameters A_n and B_n represent the displacement of the ring in the transverse primary and the secondary directions, E is the Young's modulus, I denotes area moment of inertia for the ring cross-section , ρ is the mass density, and EI denotes flexural rigidity. The quantification of the nonlinear terms are governed by the parameter γ . Also, A is the cross

sectional area of ring, b the axial thickness of ring, h the radial thickness, r the mean radius of the ring, ζ the mechanical damping ratio while ω_0 and n, respectively, represent the natural frequency and the number of modes. Oscillatory external nonlinear magnetic force magnitude is represented by $f_{Nm}(A_n, B_n, \theta_i)$, while the area moment of inertia of the ring cross section about its neutral axis is expressed as $I = bh^3/12$. The harmonic excitation to be received from the ambient vibratory energy sources is represented by $f_e = fcos(\omega t)$, where ω is the excitation frequency, and f is the excitation amplitude. The positions of magnets on the system correspond to θ_i, $i = 1,2,3,4$. Induced electrical current is denoted by $\underline{I}$, L is the inductance of the coil, and $\check{R}$ represents the load resistance, while γ_1 denotes the transducer constant [3]. The expressions for the nonlinear magnetic force that affects the system at four positions are derived in the primary co-ordinate A_n as

$$f_{Nm1}(A_n, B_n, \theta_i) = \frac{\mu_0}{2\pi} M_A M_B V_A V_B \sum_{i=1}^{4} (\cos(n\theta_i) - \frac{n\gamma}{2r} A_n) * \left[\frac{3}{\left(d - A_n \cos(n\theta_i) - B_n \sin(n\theta_i) + \frac{n\gamma}{4r}[A_n^2 + B_n^2]\right)^4} - \frac{3}{\left(d + A_n \cos(n\theta_i) + B_n \sin(n\theta_i) - \frac{n\gamma}{4r}[A_n^2 + B_n^2]\right)^4} \right], \quad (4)$$

where M_A, M_B are the magnetization, V_A, V_B represent the volume of the source magnet, and d is the distance between magnets.

Results and Discussion

In the present study, a nonlinear model which includes a complex nonlinear inertia/stiffness terms as well as a nonlinear magnetic force as depicted in equations (1) and (2) have been employed. For the purposes of predicting the nonlinear response characteristic of the bi-stable ring harvester, equations (1) and (2) have been solved numerically. The system parameters are chosen based on the available experimental set up that has been used to investigate the system natural frequency in the previous study [1]. The details regarding the electrical subsystem have been described in detail in ref [1]. Figure 2(a) shows the phase-plane trajectory for bi-stable behavior depicted via two-well potential when the harvester is under ambient excitation and excitation frequency of $60\,rad/sec$. The nonlinearities seem to be evident from the plot, hence suggesting the behavior of the bi-stable configuration for the harvester due to nonlinearities of the system as well as nonlinear magnetic force. Furthermore, nonlinearity can be seen in the Poincare' map results as shown in Figure 2(b), where the map appear as a cloud of unorganized points in the phase plane in Figure 2(a) due to the influence of nonlinear terms. Figure 2(c) shows the bifurcation diagram of the response current under various excitation levels. The excitation level ranging from $0 - 20\ m/s^2$ has been considered for this study. It may be inferred from this Figure that the bi-stable harvester undergoes alternating periodic and chaotic responses with the increase of the excitation level, which demonstrates a strong nonlinear behavior.

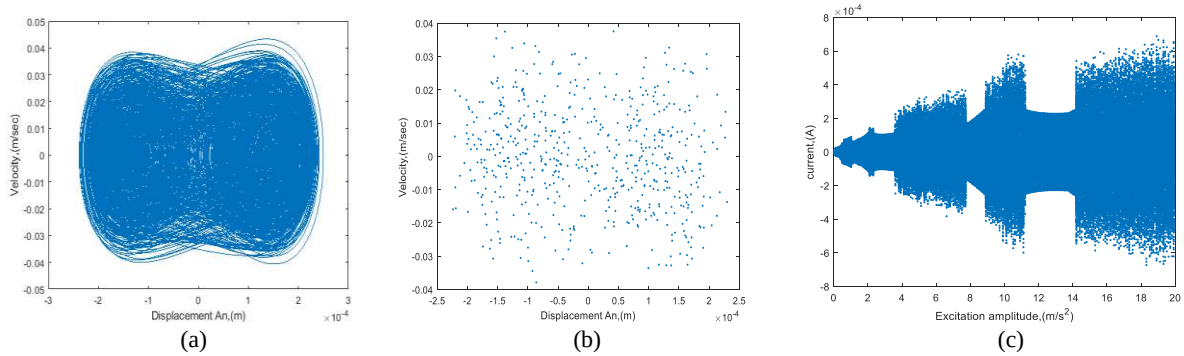

(a) (b) (c)

Figure 2: (a) Two well-potential bi-stable harvester, (b) Poincare' map for bi-stable harvester, and (c) Bifurcation diagram of response versus excitation amplitude for bi-stable harvester.

Conclusions

The main objective of this paper is to present the feasibility as well as nonlinear dynamic characteristics of a ring-based vibratory bi-stable energy harvester. When compared with the corresponding mono-stable harvester, an increased frequency range have been demonstrated. The dynamics of this class of harvester has been examined via dynamic response, Poincare map as well as bifurcation plots. The results provide confidence in employing the inherent bi-stability behavior available in this class of energy harvesters for energy production, in practice.

References

[1] Gebrel, I.F.; Wang, L.; Asokanthan, S. F. (2019) Dynamic Analysis and Design of a Novel Ring-Based Vibratory Energy Harvester. *Vibration*, 2,271-284; DOI: 10.3390/vibration2030017.

[2] Asokanthan, S.F.; Cho, J. (2006) Dynamic Stability of Ring – Based Angular Rate Sensors. *Journal of Sound and Vibration*, 295(3-5), 571-583; DOI:10.1016/j.jsv.2006.01.028.

[3] Mann, B.P.; Owens, B.A.; (2010) Investigations of a Nonlinear Energy Harvester with a Bi-stable Potential Well. Journal of Sound and Vibration 2010, 329(9), 1215-1226; DOI:10.1016/j.jsv.2009.11.034.

Non-smooth nonlinearities as restoring forces in a mass-in-mass cell

Camila da Silveira Zanin[†‡], Alireza Ture Savadkoohi[†], Sébastien Baguet [‡] and Régis Dufour [‡]
[†]*Univ Lyon, ENTPE, CNRS, LTDS, UMR5513, 69518 Vaulx-en-Velin Cedex, France*
[‡]*Univ Lyon, INSA Lyon, CNRS, LaMCoS, UMR5259, 69621 Villeurbanne, France*

Summary. The energy exchanges between particles of a mass-in-mass cell with nonlinear restoring forcing function are studied. Two types of non-smooth compound nonlinearities are considered as restoring forcing function acting on the inner mass. The governing equations of the system are treated analytically with the time multiple scale method in order to find the slow invariant manifold (SIM) as well as singular and equilibrium points of the system. Finally, quasi-analytical system responses are confronted with numerical ones obtained by direct time integration. Interestingly, the SIM of the system possesses several unstable zones and the frequency response curves exhibit isolated solutions.

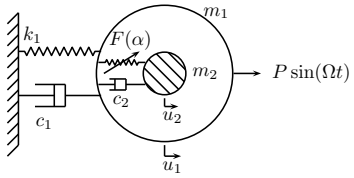

Figure 1: Model of the mass-in-mass cell.

.

The studied system is represented in Fig. 1. It is composed of an outer mass, m_1, grounded by a constant stiffness k_1 and a damping coefficient c_1. The outer mass is coupled to an inner mass, m_2, with a damping coefficient c_2 and a nonlinear restoring force $F(\alpha)$ which depends on the relative displacement of the two masses. The general governing equations of a 2-dof meta-cell systems are similar to a main system coupled with an attached nonlinear absorber [1].

$$\begin{cases} m_1\ddot{u}_1 + k_1 u_1 + c_1\dot{u}_1 + F(u_1 - u_2) + c_2(\dot{u}_1 - \dot{u}_2) = P\sin(\Omega t) \\ m_2\ddot{u}_2 + F(u_2 - u_1) + c_2(\dot{u}_2 - \dot{u}_1) = 0 \end{cases} \tag{1}$$

Two types of non-smooth compound nonlinearities are considered for $F(\alpha)$, which are plotted in Fig. 2:

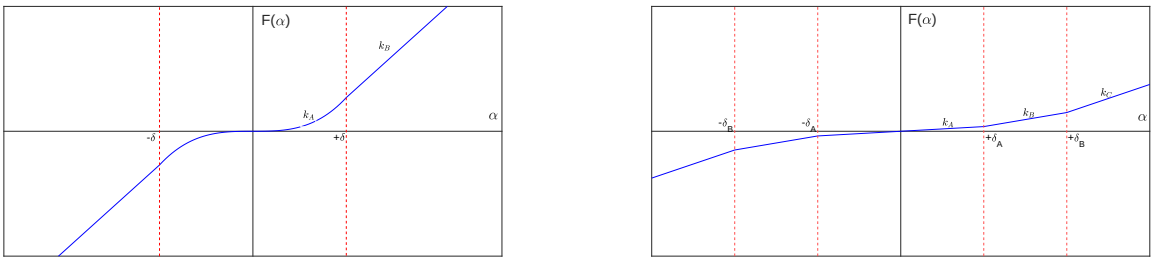

(a) (b)

Figure 2: Considered nonlinearities for the restoring force $F(\alpha)$: a) Pure cubic and linear; b) Piece-wise linear.

A nondimensionalized time $\tau = \sqrt{\frac{k_1}{m_1}}t$ and the coordinates of relative displacement and the center of masses of two oscillators are introduced to the system variables. After this, the complex variables of Manevitch [2] are applied. A Galerkin method based on truncated Fourier series, involving the first harmonics of the system, is employed and a time multiple scales method [3] is carried out in order to find the SIM and the dynamical characteristic points of the system [1]. In more details, the SIM is detected at fast time scale, while the equilibrium and singular points are detected at slow time scale, leading to prediction of periodic and non-periodic regimes [4].

For a given set of system parameters, two SIMs of the system corresponding to the restoring forcing functions of Figs. 2a and 2b are illustrated in Figs. 3a and 3b, respectively. In these plots, N_1 and N_2 represent the amplitudes of the center of mass and of the relative displacement of the two oscillators, respectively. These figures are accompanied by free responses obtained by direct numerical time integration of Eq. 1 without external excitation. In both figures, it is seen that, starting

from the initial condition, the system follows the SIM and it bifurcates twice before going to the rest position (expected position for free responses of the damped system).

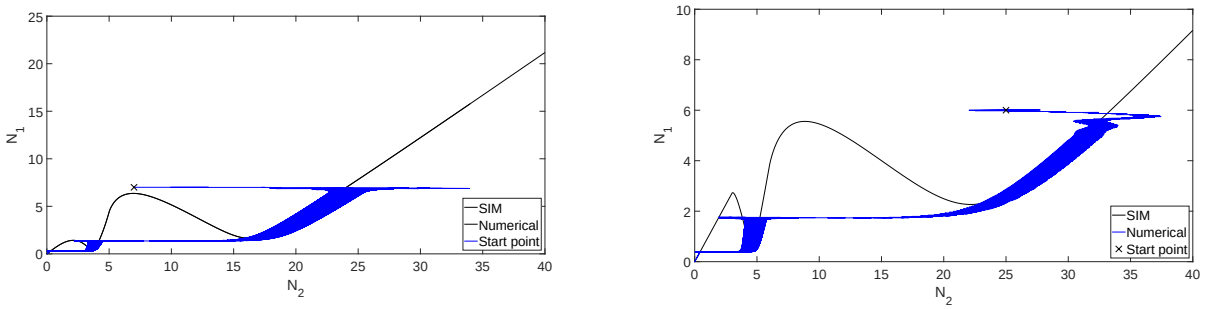

(a) (b)

Figure 3: SIM and corresponding numerical free responses: a) System with the nonlinearity of Fig. 2a and initial conditions $(w, v, \dot{w}, \dot{v}) = (7, 7, 0, 0)$; a) System with the nonlinearity of Fig. 2b and initial conditions $(w, v, \dot{w}, \dot{v}) = (6, 25, 0, 0)$.

Furthermore, the equilibrium points can be determined for sweeping de-tuning parameter σ. This parameter represents a sweep of the frequency of excitation around the frequency of the outer mass (the system is studied around a $1:1$ resonance). Thus, frequency responses curves can be obtained for a given forcing amplitude, which permits identifying the position of all equilibrium points and predict the amplitude levels of the cell. As an exemple, Fig. 4 shows the frequency response curve of the system corresponding to the nonlinearity of Fig. 2a for a given forcing amplitude. In this figure, the equilibrium points located in the unstable zones of the SIM are in green colour.

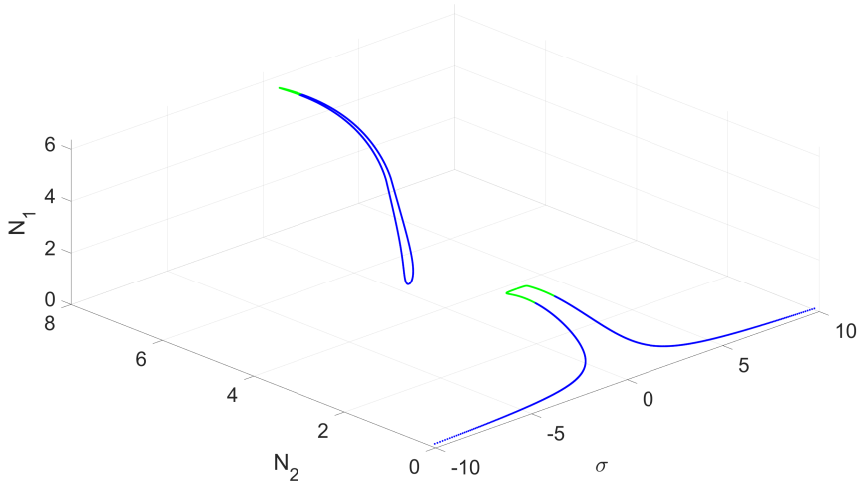

Figure 4: Detected equilibrium points of the system with respect to the de-tuning parameter σ for the system with restoring forcing function of Fig. 2a. σ is a de-tuning parameter representing a sweep of the frequency of excitation around the frequency of the outer mass (the system is studied around a $1:1$ resonance).

The developments presented here provide design tools for tuning the non-smooth nonlinearities of the inner mass in order to control the system, which presents different leves of energy reduction, acting like a gearbox. As a perspective, these theoretical results will be compared with a designed experimental test setup.

References

[1] Vakakis A. F. (2008) Nonlinear targeted energy transfer in mechanical and structural systems. *Nonlinear Targeted Energy Transfer in Mechanical and Structural Systems* **156**.

[2] Manevitch L. I. (2001) The description of localized normal modes in a chain of nonlinear coupled oscillators using complex variables. *Nonlinear Dynamics* **25**:95-109.

[3] Nayfeh A., Mook D. I. (1979) Nonlinear Oscillations. John Wiley and Sons, New York.

[4] Ture Savadkoohi A., Lamarque C.-H., Weiss M., Vaurigaud B., Charlemagne S. (2016) Analysis of the 1:1 resonant energy exchanges between coupled oscillators with rheologies. *Nonlinear Dynamics* **84**:2145-2159.

Noise control via exploiting nonlinear interactions

Emmanuel Gourdon*, Alireza Ture Savadkoohi* and Claude-Henri Lamarque*
*Univ Lyon, ENTPE, CNRS UMR5513, LTDS, France

Summary. Nonlinear behaviours of acoustical resonators, such as Helmholtz resonators in nonlinear regimes [1] or electroacoustic absorbers [2], are used to obtain targeted energy transfer [3] from an acoustical mode to the resonators. It is shown that the noise control is carried out via nonlinear interactions between acoustical mode and the absorbers leading to periodic or modulated regimes.

Nonlinear noise control

Let us consider an acoustical resonator which is composed of a cavity (container of the air) and the orifice (the neck). If the length of the neck is smaller than the wavelength, then the overall system can be modelled as a mass-spring oscillator where the lumped mass is in fact the encased mass of the air in the orifice while the air inside the cavity acts as the spring. With analogy of mechanical engineering, we are interested to create a nonlinear restoring forcing function which can be coupled to an acoustical mode for creation of acoustical energy tunnelling between the mode and the resonator with nonlinear responses.

Nonlinear behaviours of the acoustical resonator

Figure 1 depicts different geometries of the neck of the resonator: The classical straight neck (H_1) of the acoustical resonator is tailored in a linear (H_2) and quadratic manner (H_3). Table 1 summarises dimensions of each configuration while the length of the cavity for all case is 25 mm. The resonators are coupled to the Kundt tube [4] and the system is excited by different sinusoidal forces while the pressures inside the cavity during the resonance are measured. All resonators show three regimes categorizing as linear, almost linear and nonlinear. Moreover, it is seen that tailoring the geometry of the neck accelerates reaching to the nonlinear domain. The actual limitation of current study is that even via tailoring the system, it reaches to the nonlinear domain at high sound pressure levels, around 125-130 dB. There are ongoing works to reduce this pressure level so that the proposed system can be applied for buildings.

	H_1	H_2	H_3
l	8.5	8.5	8.5
r_0	1.5	1.5	1.7
r_1	1.5	2	3.25

Table 1: Characteristics of different configurations of necks (mm). l stands for the length of the neck.

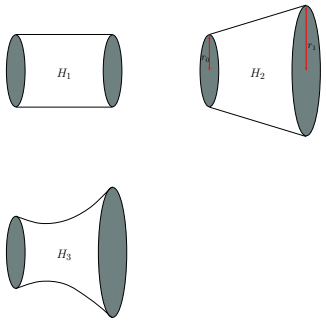

Figure 1: Considered geometries for the neck of the resonator.

The governing equation of the acoustical resonator can be represented by following equation (see for example [5]):

$$\frac{\mathrm{d}^2x}{\mathrm{d}t^2} + \sigma\frac{\mathrm{d}x}{\mathrm{d}t}\left|\frac{\mathrm{d}x}{\mathrm{d}t}\right| + \delta\frac{\mathrm{d}x}{\mathrm{d}t} + \left(x - \alpha x^2 + \beta x^3\right) = -p \tag{1}$$

Equation 1 shows that the system possesses linear and nonlinear damping terms together with the linear, quadratic and cubic (until third order developments) restoring forcing function. This system has been studied in detail by Alamo Vargas et al. [1] for different excitation terms p showing that it can present softening and hardening behaviours. The idea is to couple this resonator with nonlinear responses (or other resonators such as electroacoustic absorbers with similar behaviours) to an acoustical mode for nonlinear noise control. The next section discusses about noise control via proposed system.

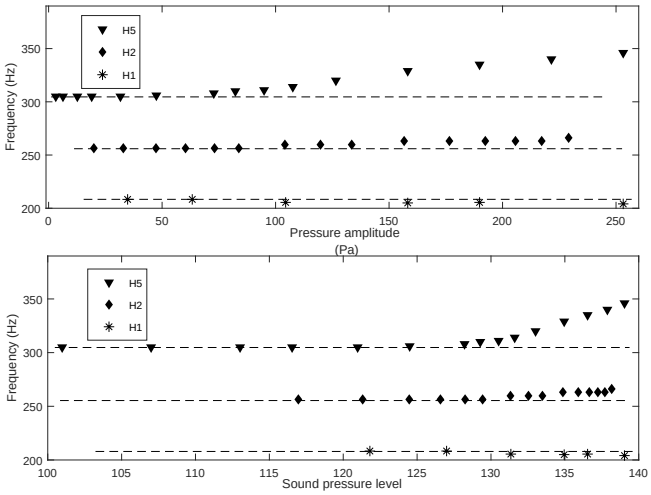

Figure 2: Variations of resonant frequency versus pressure amplitude (Pa) and sound pressure level (dB) inside the cavity.

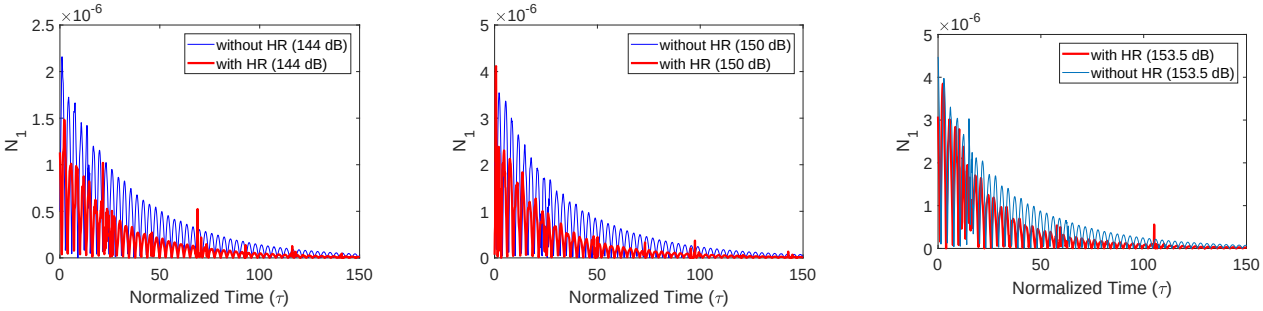

Figure 3: Free vibration responses at the middle of the tube for different excitation amplitudes. These amplitudes create pressures of 144 dB, 150dB and 153.5dB at the bottom of the cavity of the resonator [6]. N_1 stands for the amplitude of the acoustical mode.

Passive noise control: coupling an acoustical mode to the resonator with nonlinear response

The explained resonator in previous section is coupled to a tube via a coupling box [6]. The first acoustical mode of tube with the frequency of 378.6Hz has been generated. For creation of the free vibration, several sinusoidal signals with the frequency of 378.6Hz are sent, then stopped and measurements are registered. Experimental results are collected in Fig. 3. It is seen that the resonator is capable of controlling the acoustical mode. Moreover, the control process is carried out in two global phases: the first part is via nonlinear interactions between oscillators and second part which is similar to the energy reduction by classical damped systems. Analytical developments are also carried out showing that the system can be attracted by periodic [7] or modulated [8] regimes. Results are collected in [6].

Conclusions

It is shown that via changing the geometry of the classical resonator, the emergence of the nonlinear behaviours of the resonator will be accelerated. Moreover, via coupling this resonator to an acoustical mode, it is possible to create a noise control via exploiting nonlinear interactions between oscillators. There is an ongoing work which deals with creation of nonlinearities via electric circuits for acceleration of noise control.

References

[1] Alamo Vargas V., Gourdon E. Ture Savadkoohi (2018) Nonlinear softening and hardening behavior in Helmholtz resonators for nonlinear regimes. *Nonlinear Dynamics* **91**: 217-231.

[2] Bitar D. Gourdon E., Lamarque C.-H., Collet M. (2019) Shunt loudspeaker using nonlinear energy sink. *Journal of Sound and Vibration* **456**: 254-271.

[3] Vakakis A.F., Gendelman O.V., Bergman L.A., McFarland D.M., Kerschen G., Lee Y.S. (2009) Nonlinear Targeted Energy Transfer in Mechanical and Structural Systems I & II. Springer Netherlands.

[4] Gourdon E., Ture Savadkoohi A., Cauvin B. (2019) Effects of shape of the neck of classical acoustical resonators on the sound absorption quality for large amplitudes: experimental results. *Building Acoustics*, under review.

[5] Yu G. K., Zheng Y. D., Shen Y. (2019) Nonlinear Amplitude-Frequency Response of a Helmholtz Resonator. *Journal of Vibration and Acoustics* **133**: 024502.

[6] Gourdon E., Ture Savadkoohi A., Alamo Vargas V. (2018) Targeted Energy Transfer From One Acoustical Mode to an Helmholtz Resonator With Nonlinear Behavior. *Journal of Vibration and Acoustics* **140**: 061005.

[7] Ture Savadkoohi A., Lamarque C.-H., Weiss M., Vaurigaud B., Charlemagne S. (2016) Analysis of the 1:1 resonant energy exchanges between coupled oscillators with rheologies. *Nonlinear Dynamics* **2016**: 2145-2159.

[8] Starosvetsky Y., Gendelman O. (2018) Strongly Modulated Response in Forced 2D of Oscillatory System With Essential Mass and Potential Asymmetry. *Physica D* **237**: 1719-1733.

On the determination of high energy output operation ranges of a piezoelectric bistable energy harvesting system by parallel computing

Nils Gräbner*, Lukas Lentz* and Utz von Wagner*
*Technische Universität Berlin, Chair of Mechatronics and Machine Dynamics

Summary. Nonlinearities in energy harvesting (EH) systems are introduced by intention to broaden the range of operation parameters with high energy output. Nevertheless, as multiple solutions occur due to these nonlinearities, the determination of optimal operation conditions is a challenging task. A method based on parallel computing with numerical time integration is presented to determine these optimal operational parameters in the case of a bistable piezoelectric energy harvesting system under harmonic excitation, where excitation frequency and excitation amplitude are considered. Therefore the basins of attraction are taken into account to get a measure for the occurrence of multiple solutions.

Introduction

Bistable systems have the potential for efficient EH, due to their ability to undergo so called interwell solutions with large displacements around both stable equilibrium positions and therefore high energy output in a wide range of excitation frequencies [1]. The challenge is that also intrawell solutions, i.e. solutions with small displacements around one stable equilibrium or chaotic solutions may coexist for the same parameter set. Which one of these solutions occurs is determined by the initial conditions which are in a real world EH application neither known nor controllable. To find parameter sets with likely high energy output, the probability of each solution is determined in the following. Therefore, the model of a bistable EH system first introduced by Erturk [2] in 2009 and extensively analyzed in [3] is used. It contains one mechanical degree of freedom with a cubic nonlinearity and a coupling with an electric circuit. It is given by the nondimensional equations

$$x''(\tau) + dx'(\tau) + \frac{1}{2}(-x(\tau) + x(\tau)^3) + \theta_1 U(\tau) = f\cos(\eta\tau), \tag{1}$$

$$-\frac{\Theta_2}{c_\mathrm{p}}x'(\tau) + U'(\tau) + \frac{1}{Rc_\mathrm{p}}U(\tau) = 0, \tag{2}$$

where f (normalized excitation amplitude) and η (normalized excitation frequency) are considered as the operational parameters in the following. The state variable x, depending on the normalized time τ, is proportional to the displacement of a beam, which is discretized in space by the first eigenfunction. U characterizes the voltage at the piezos. The numeric values for the dimensionless parameters are given by $d = 0.01$, $\Theta_1 = 0.13$, $\Theta_2/c_\mathrm{p} = 0.24$, $1/Rc_\mathrm{p} = 0.55$ and $R = 1$. For more detailed information see [3]. The goal is to determine harmonic excitations given by η and f, for wich the system has a high probabilty to undergo interwell solutions.

General behavior of the bistable magnetoelastic energy harvesting system

Figure 1a shows the steady state solutions and their basins of attraction of the EH system in the case $f = 0.1$ and $\eta = 0.5$. The results are computed by numerical time integration using the standard Runge-Kutta method (RK4).

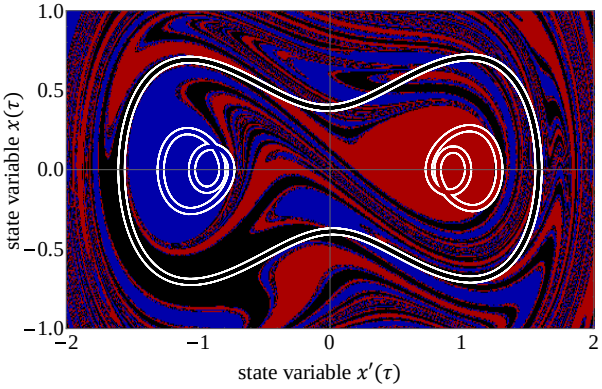

Figure 1a: Phase trajectories of intrawell solution around negative equilibrium position (blue), intrawell around positive equilibrium position (red) and interwell solution (black). The red, blue and black areas indicate initial conditions resulting in the respective solution, i.e. basins of attraction.

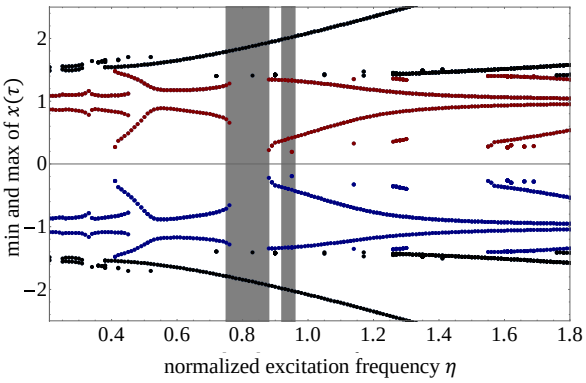

Figure 1b: Maximal and minimal values of the displacement for each stationary solution as funtion of the normalized excitation frequency η for $f = 0.1$.

The type of the solution is classified by its color, where black indicates an interwell solution and blue and red describe intrawell solutions around negative and positive equilibrium positions respectivly. In figure 1b all stationary solutions for a fixed excitation amplitude of $f = 0.1$ are shown with respect to the normalized excitation frequency η between 0.2 and 1.8. Each solution is represented by its maximum and minimum value of the state variable x. The same color code as before is applied with the addition that the gray areas indicate that there also chaotic solutions occur. It is noticeable, that for every η, where an interwell solution exists, also intrawell or chaotic solutions coexist. At this point it is so far unknown which of the coexisting solutions is most likely to occur in a real world application and therefore it is difficult to determine an operational parameter range were the energy output of the EH system is high.

Determination of high energy output operational parameter ranges

To identify operation ranges with high energy output it must be considered that each solution occurs with a different probability depending on the probability of the corresponding initial conditions, if multiple asymptotically stable solutions coexist. Therefore the coresponding basin of attraction must be taken into account. When the basin of attraction is known, it is possible to predict which solution will occur for each set of initial conditions. However, in a real world EH application the initial conditions are unknown. In this paper the probability density function $p(x_0, x_0')$ of the initial conditions is assumed as the addition of two normal distributions around both equilibrium position with a standard deviation of 0.3. If $p(x_0, x_0')$ is known, the probability P of a specific solution is

$$P = \int_{-\infty}^{\infty} \int_{-\infty}^{\infty} p(x_0, x_0')\, b(x_0, x_0') \mathrm{d}x_0 \mathrm{d}x_0',$$

where $b(x_0, x_0')$ is an indicator function which is 1 if the specific initial conditions (x_0, x_0') are in the basin of attraction of the considered solution and 0 otherwise. To determine $b(x_0, x_0')$ using numerical integration the investigated area is limited and discretized. In our case x_0 is considered between -2.0 and 2.0 and x_0' between -1.0 and 1.0. The step size in both directions is $d = 0.008$. To compute a discretized version of the function $b(x_0, x_0')$ a numerical time integration with every possible combination of x_{0_i} and x_{0_k}' must be performed. The integration time for each integration must be long enough that the steady state solution is reached. By comparing each steady state solution with the specific one, $b(x_{0_i}, x_{0_k}')$ can be set for all investigated initial conditions. Finally the probability of the specific solution can be determined by

$$P = \sum_{i=1}^{500} \sum_{k=1}^{250} p(x_{0_i}, x_{0_k}')\, b(x_{0_i}, x_{0_k}') d^2.$$

The results are shown in Figure 2a which is an extension of figure 1b since it additionally contains the information about the probability of each solution. The probability is visualized by the intensity of each color. For instance the interwell solution is visualized by different gray shades where white indicates a probability of 0.0 and black a probability of 1.0. It can be seen that for η in a range from 0.6 to 0.7 (green box) the probability that the system shows a high energy interwell solution is large. Hence this indicates that for a given f, η should preferably be in this area for high energy output. To achieve these results it is necessary to carry out a large number of numerical time integrations, since for each considered η (160 different values) it is required to compute the individual basin of attraction, which is generally time consuming ($500 \cdot 250 \cdot 160 = 20{,}000{,}000$ integrations). This can only be done by using a computing technique on a graphics processing unit. Therefore the time integration method (RK4) is implemented as a CUDA kernal by using the PYTHON package NUMBA. By reducing the resolution of the computed basins of attraction from $d = 0.008$ to $d = 0.08$ this approach also enables to consider further parameter variations, for example different excitation amplitudes. A corresponding result is shown in Figure 2b where the probability of the interwell solution is visualized over the normalized excitation frequency and the normalized excitation amplitude. The information in this Figure clearly demonstrates the optimal operational range of the parameters η and f for which the probability is large, that we have a high energy output.

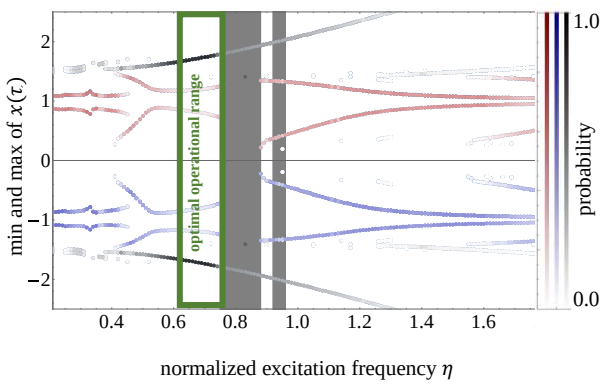

Figure 2a: Absolute maximal and absolute minimal value of x for each stationary solution with respect to η for $f = 0.1$. The opacity of each color indicates the probability of each specific solution.

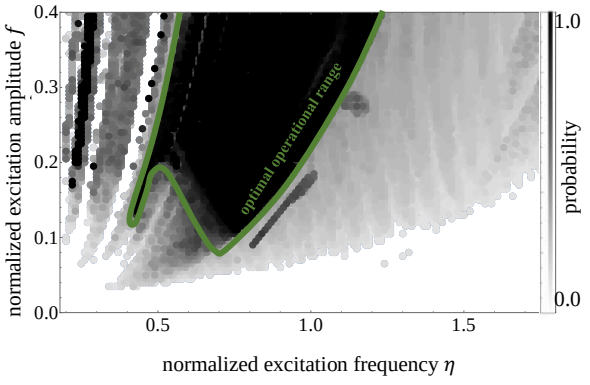

Figure 2b: Apperance probability of the interwell solution with respect to η and f. Dark black indicates a high probability for the interwell solution. Therefore dark areas indicate beneficial operation values for η and f.

References

[1] HARNE, R. L.; WANG, K. W. "A review of the recent research on vibration energy harvesting via bistable systems." Smart materials and structures, 2013, 22. Jg., Nr. 2, S. 023001.

[2] ERTURK, A.; HOFFMANN, J.; INMAN, D. J. "A piezomagnetoelastic structure for broadband vibration energy harvesting." Applied Physics Letters, 2009, 94. Jg., Nr. 25, S. 254102.

[3] LENTZ, L. "On the modelling and analysis of a bistable energy-harvesting system", Doctoral Thesis, 2019, Technische Universität Berlin.

Targeted energy transfer between a linear oscillator and a time-dependent nonlinear systems

Aurélie Labetoulle*, Emmanuel Gourdon* and Alireza Ture Savadkoohi*
*Univ Lyon, ENTPE, CNRS UMR5513, LTDS, France

Summary. Targeted energy transfer between two weakly and linearly coupled oscillators is studied. One of oscillators possesses time-dependent damping and nonlinear restoring forcing terms. Thanks to the detection of different system dynamics, its phase-dependent characteristics are clarified leading to having finer vision about energy channelling between such oscillators. The developments prepare design tools for tuning parameters of the time-dependent oscillator leading to the design of energy channelling between two oscillators.

We would like to design the targeted energy transfer [1] between a linear and a time-dependent nonlinear oscillator. Our considered system is composed by a linear oscillator weakly coupled to an absorber with a time-dependent cubic rigidity [2] and damping (see Fig. 1). The considered system can correspond to an acoustical mode which is linearly coupled to an adaptative acoustical resonator in nonlinear domains.The studying of such resonators with fixed parameters have been already articulated in [3, 4, 5] for membrane and Helmholtz resonators and has been programed for a loudspeaker in [6].

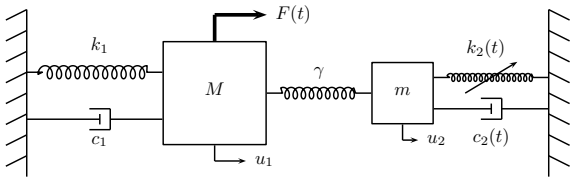

Figure 1: System with time-dependent cubic rigidity and damping

To study the behaviour of this system around a $1:1$ resonance, we consider the nondimensioned governing equations. Then, to have the envelope of the response of the system we introduce the complex variables of Manevitch [7]. To detect the different dynamics of the system, the multiple scales method [8] is used. Hence, we introduce fast and slow time scales. We keep only the first harmonics of the system via truncating other harmonics.

From the study of the fast dynamics of the system we can define the equation of the slow invariant manifold (SIM) which corresponds to the energy of the first linear oscillator (N_1) as functions of that of the absorber (N_2) and also the phase (δ_2). Moreover, we can detect the local extrema of the SIM. Introducing the perturbation in the complex variables of Manevitch, the unstable zone of the SIM can be clarified.

From the study of the slow dynamics of the system, we are able to define the equilibrium, singular points and the backbone curve of the system. These developments permit to predict different possible periodic or non-periodic regimes as functions of excitation amplitude and frequency.

For the system with time dependent rigidity and damping, we represent in Fig. 2 the SIM with its unstable zone accompanied by results obtained from direct numerical integration of the governing equations of the system without external excitation but under initial conditions. We notice that the SIM depends on three parameters: the energy of the linear oscillator (N_1), the energy of the nonlinear oscillator (N_2) and its phase (δ_2) contrary to the case with constant parameters where the SIM only depends on N_1 and N_2. Moreover we can observe in the Fig. 2b that the numerical integration follows the SIM and therefore the analytical predictions. The Fig. 3 represents different views of the equilibrium points of this system and the unstable zone of the SIM. We observe that, there are two branches: a main branch (i) and an isola (ii).

Depending of progress of the work, some experimental results will be probably presented.

References

[1] Vakakis A. F., Gendelman O. V., Bergman L. A., McFarland D.M., Kerschen G. and Lee Y.S. (2008). Nonlinear targeted energy transfer in mechanical and structural systems. *Springer, Dordrecht*.

[2] Labetoulle A., Ture Savadkoohi A. and Gourdon E. (2021). Detection of different dynamics of two coupled oscillators including a time-dependent cubic nonlinearity. *Acta Mechanica*, doi: 10.1007/s00707-021-03119-w.

[3] Bellet R., Cochelin B., Herzog P., Mattei P.-O. (2010). Experimental study of targeted energy transfer from an acoustic system to a nonlinear membrane absorber. *Journal of Sound and Vibration* **329(14)**:2768-2791.

[4] Alamo Vargas V., Gourdon E. and Ture Savadkoohi A. (2018). Nonlinear softening and hardening behavior in Helmholtz resonators for nonlinear regimes. *Nonlinear Dynamics* **91(1)**:217-231.

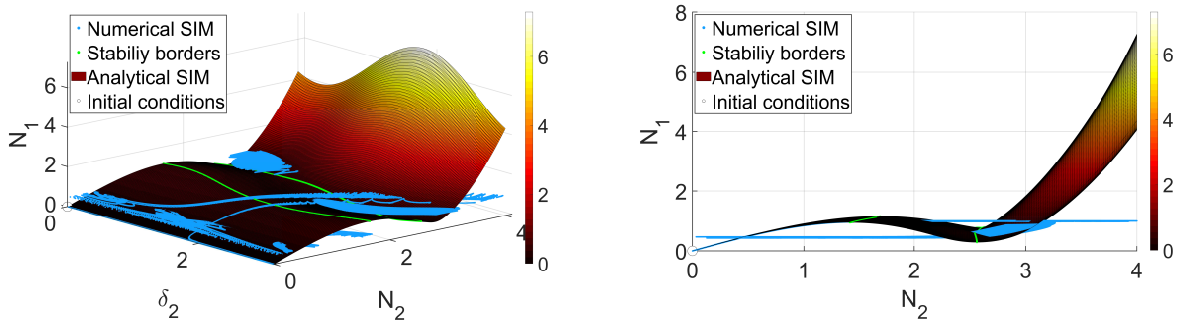

Figure 2: The SIM of the system with its unstable zone (green line) and numerical results (blue line). a) Three-dimensional view (δ_2, N_2, N_1); b) Two-dimensional view (N_2,N_1).

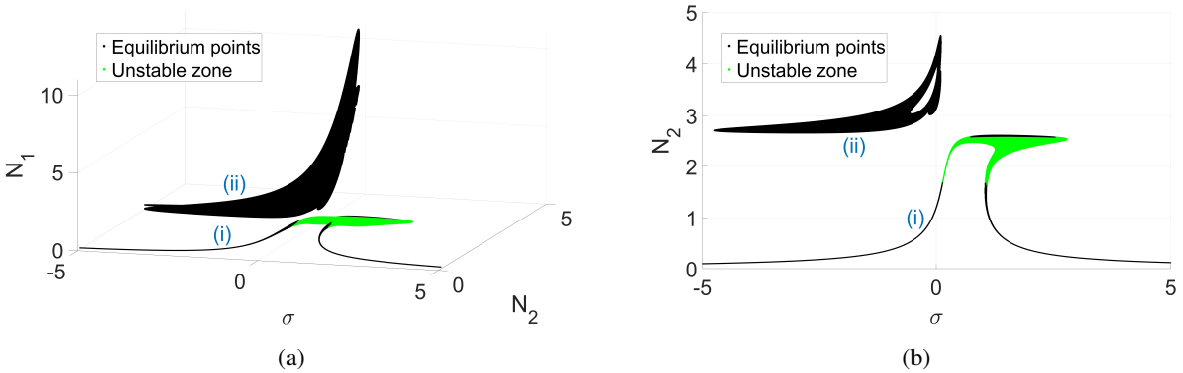

Figure 3: Different views of collected equilibrium points. σ is the de-tuning of the frequency of excitation for analyzing system behaviours around a $1:1$ resonance. a) (σ, N_2, N_1); b) (σ, N_2). The equilibrium points located in unstable zone of the SIM are represented in green.

[5] Gourdon E., Ture Savadkoohi A. and Alamo Vargas V. (2018). Targeted energy transfer from one acoustical mode to an Helmholtz resonator with nonlinear behavior. *Journal of Vibration and Acoustics* **140(6)**:061005 (8).

[6] Morell M., De Bono E., Collet M., Gourdon E., Ture Savadkoohi A. Innovative electroacoustic resonator control enforcing non-linear dynamics at low excitation levels. *SPIE, Smart Structures + Nondestructive Evaluation*, 6-10 March 2022, Long Beach, California, US.

[7] Manevitch L. I. (2001) The Description of Localized Normal Modes in a Chain of Nonlinear Coupled Oscillators Using Complex Variables. *Nonlinear Dynamics* **25**:95-109.

[8] A. H. Nayfeh and D.T. Mook (1995) Nonlinear oscillations. *Wiley classics library*.

Tuesday, July 19, 2022

13:30 - 15:30

MS-09 Nonlinear Dynamics in Engineering Systems

Auditorium Lumiere

Chair: Gabor Stepan - Ekaterina Pavlovskaia

13:30 - 13:50
Learning-based Model Matching for Fault Detection and Isolation of Nonlinear Systems
GHANIPOOR Farhad[*], MURGUIA Carlos, MOHAJERIN Esfahani Peyman, VAN De Wouw Nathan
[*]Department of Mechanical Engineering, Eindhoven University of Technology (Eindhoven Netherlands)

13:50 - 14:10
Subcritical Hopf bifurcation in the dynamics of a pressure relief valve
KÁDÁR Fanni[*], STEPAN Gabor
[*]Department of Applied Mechanics, Budapest University of Technology and Economics (1111 Budapest, Műegyetem rkp. 5. Hungary)

14:10 - 14:30
Multi-mode approximation of VIVs in vertical and horizontal flexible risers
KURUSHINA Victoria, **PAVLOVSKAIA Ekaterina**[*]
[*]University of Aberdeen (Centre for Applied Dynamics Research, University of Aberdeen, King's College, Aberdeen, AB24 3UE, United Kingdom United Kingdom)

14:30 - 14:50
Nonlinear dynamic analysis of a nonlocal nanobeam resting on fractional visco-Pasternak foundation by using the incremental harmonic balance method
NESIC Nikola[*], CAJIC Milan, KARLICIC Danilo, JOVIC Srdjan
[*]University of Priština, Faculty of Technical Sciences (38220 Kosovska Mitrovica, Kneza Milosa 7, Serbia Serbia)

14:50 - 15:10
Nonlinear Vibrations of Long Slender Continua Coupled with Discrete Inertia Elements Moving Vertically in a Tall Structure
KACZMARCZYK Stefan[*]
[*]University of Northampton (University Drive Northampton NN1 5PH United Kingdom)

Learning-based Model Matching for Fault Detection and Isolation of Nonlinear Systems

Farhad Ghanipoor*, Carlos Murguia*, Peyman Mohajerin Esfahani†, and Nathan van de Wouw*
* *Department of Mechanical Engineering, Eindhoven University of Technology, Eindhoven, The Netherlands*
† *Delft Center for Systems and Control, Delft University of Technology, Delft, The Netherlands*

Summary. This abstract presents a method for fault detection and isolation (FDI) in nonlinear uncertain systems. The proposed method has two stages: first, an offline training of a static map to capture the unstructured uncertainty; second, an online fault detection, isolation, and estimation scheme. A nonlinear mechanical benchmark system is used to illustrate the performance of the scheme.

Introduction

The reliable functioning of high-tech systems can only be achieved through predictive maintenance, for which techniques for fault detection (is a fault occurring?) and fault isolation (what is the fault source?) are essential prerequisites [1]. We aim to develop a hybrid (physics-learning) fault detection and isolation (FDI) scheme that provides superior monitoring performance by leveraging cutting-edge machine learning (ML) algorithms and first-principles physics-based models. This abstract is organized as follows. First, the problem formulation is elaborated. Then, the proposed methodology is briefly presented. Next, the proposed method is evaluated by a benchmark FDI problem using simulation results. Finally, concluding remarks are discussed.

Problem Formulation

Consider a nonlinear dynamical system of the form:

$$\begin{cases} \dot{x}(t) = g(x(t), u(t)) + \eta(x(t), u(t)) + \omega(t) + \phi(x(t), u(t), t), \\ y(t) = x(t) + \nu(t), \end{cases} \tag{1}$$

where $t \in \mathbb{R}^+$, $x \in \mathbb{R}^{n_x}$, $y \in \mathbb{R}^{n_x}$, $u \in \mathbb{R}^{n_u}$ are time, state, measured output, and known input vectors, respectively, and $n_x, n_u \in \mathbb{N}$. Function $g : \mathbb{R}^{n_x} \times \mathbb{R}^{n_u} \mapsto \mathbb{R}^{n_x}$ is a known nonlinear function. Function $\eta : \mathbb{R}^{n_x} \times \mathbb{R}^{n_u} \mapsto \mathbb{R}^{n_x}$ represents unknown model uncertainty. Functions $\omega, \nu : \mathbb{R}^+ \mapsto \mathbb{R}^{n_x}$ are unknown disturbances, and function $\phi : \mathbb{R}^{n_x} \times \mathbb{R}^{n_u} \times \mathbb{R}^+ \mapsto \mathbb{R}^{n_x}$ is the unknown process fault.

Methodology

The proposed methodology has two stages: 1. offline uncertainty learning, and 2. online FDI scheme (see Fig. 1). First, in the offline learning stage, a static map for unstructured uncertainty is trained on the basis of the healthy system input and output data (i.e., for the system with $\phi = 0$). We use a supervised method (i.e., linear regression in this abstract) to find the static map from system input and output to uncertainty in the training phase. Labeled data for the supervised learning of the model uncertainty is obtained using the known part of the system dynamics and healthy system input and output historical data. Then, in the online stage, we estimate the fault by matching the faulty model and the approximately known model of the healthy system (which is constituted by a physics-based model and the trained uncertainty model). Based on the estimated fault signal, the fault can be detected and isolated using the CUSUM-based procedure [3] as a change detection method.

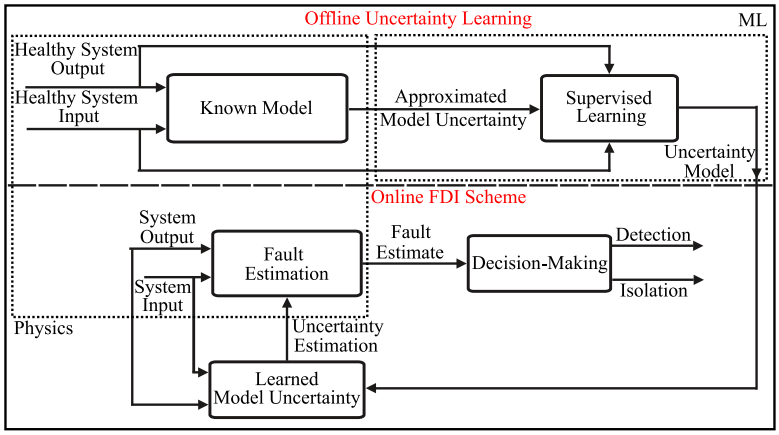

Figure 1: Offline uncertainty learning and online FDI scheme block diagrams.

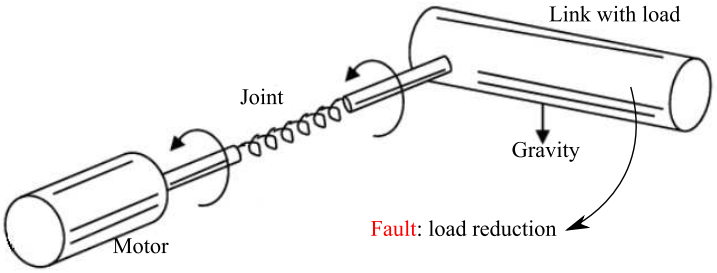

Figure 2: The nonlinear benchmark schematic.

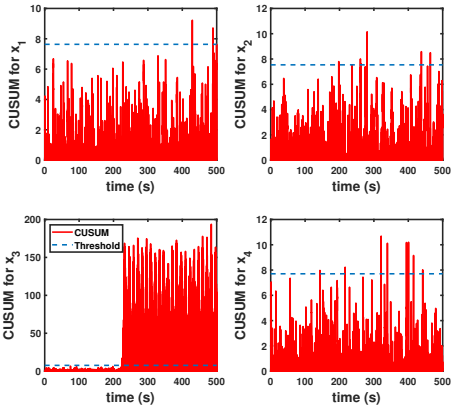

Figure 3: The CUSUM sequences and the thresholds.

Simulation Results

In what follows, the methodology is applied to a nonlinear benchmark system (a single-link robotic arm with a revolute elastic joint, see schematic in Fig. 2) [2]. This system has the structure introduced in (1) and four states, $x(t) = [x_1(t), x_2(t), x_3(t), x_4(t)]^T$. In the simulation, a fault is induced in the third equation of the right-hand side of (1). The fault, which reduces the link mass, occurs abruptly at 225 seconds. The CUSUM-based thresholds and sequences for each state are depicted in Fig. 3. The CUSUM sequence is a cumulative sum of the estimated fault, which is compared to the CUSUM threshold for fault detection. It is clear from the left-down plot of the figure that the fault can be detected by the proposed method since the CUSUM sequence exceeds the threshold after the fault occurrence. Furthermore, to indicate the capability of the proposed method, it is compared with a linear conventional observer-based FDI method to detect a small fault (Fig. 4). This small fault is the same as the previous fault. However, its magnitude is one-fifth of the previous one. It can be seen in the figure, unlike the proposed method, the linear method cannot detect the fault due to ignoring the nonlinearity and uncertainty.

Conclusions

The proposed methodology for FDI of nonlinear systems has improved fault detectability compared to conventional methods in the presence of nonlinearity and uncertainty for the benchmark system.

Acknowledgment

This publication is part of the project Digital Twin project 4.3 with project number P18-03 of the research programme Perspectief which is (mainly) financed by the Dutch Research Council (NWO).

References

[1] Ding, S. X. (2008). Model-based fault diagnosis techniques: design schemes, algorithms, and tools. Springer Science & Business Media.

[2] Keliris, C., Polycarpou, M. M., & Parisini, T. (2016). An integrated learning and filtering approach for fault diagnosis of a class of nonlinear dynamical systems. IEEE transactions on neural networks and learning systems, 28(4), 988-1004.

[3] Murguia, C., & Ruths, J. (2016). Cusum and chi-squared attack detection of compromised sensors. In 2016 IEEE Conference on Control Applications (CCA) (pp. 474-480).

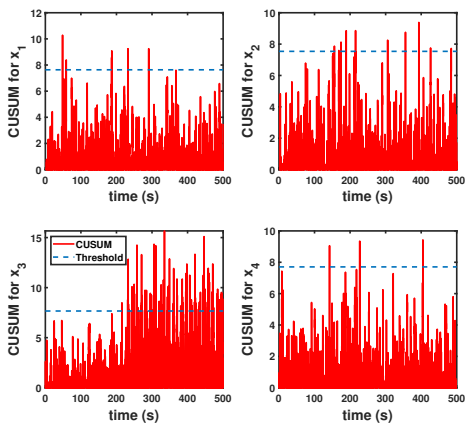

(a) The proposed method.

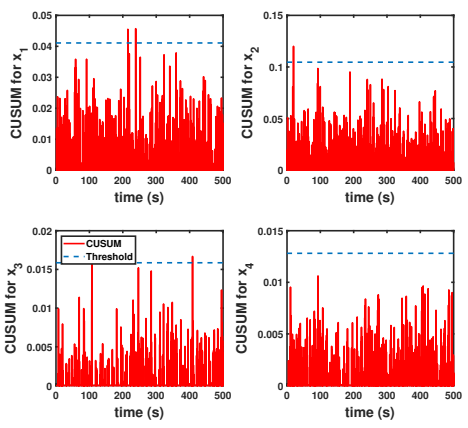

(b) The linear observer.

Figure 4: The CUSUM sequence for the small fault and the thresholds.

Subcritical Hopf bifurcation in the dynamics of a pressure relief valve

Fanni Kádár[†] and Gabor Stepan[†]
[†]*Department of Applied Mechanics , Budapest University of Technology and Economics, Budapest, Hungary*

Summary. The direct spring operated pressure relief valves are prone to harmful vibrations, which endanger the protected system under pressure. The studied mathematical model describes a system consisting of a vessel and of a pressure relief valve mounted on the vessel. The mathematical model with the state variables of valve lift, valve disk velocity and vessel pressure shows strong asymmetric nonlinearities. Our adapted numerical simulation is appropriate to produce bifurcation diagrams with the bifurcation parameter of the inlet flow rate, and also to draw the phase portrait. At the certain range of parameter combinations the equilibrium state loses the stability through subcritical Hopf bifurcation. In the case of dense parameter sweep in the phase space an unstable limit cycle appears between the trajectories. This unstable limit cycle can be calculated analytically by executing the Hopf bifurcation calculation. In comparison with the numerical unstable limit cycle, we studied the effect of the asymmetry of the nonlinearties on the analytically calculated unstable limit cycle. Global bifurcation diagram is constructed to trace the dynamical behaviour of the system 'outside' the unstable limit cycle, which includes impacts with the valve seat.

Introduction

The mathematical model of the direct spring operated pressure relief valve (see Fig. 1a) can be derived from the Newtonian equation of the valve disk and from the mass balance equation of the vessel [1]:

$$y_1' = y_2\,, \tag{1}$$
$$y_2' = -\kappa y_2 - (y_1 + \delta) + y_3\,, \tag{2}$$
$$y_3' = \beta\,(q - \sqrt{y_3}y_1)\,, \tag{3}$$

where the dimensionless coordinates $y_{1,2,3}$ represent the valve lift, the valve disk velocity and the overpressure in the vessel, respectively. The dimensionless parameters are the inlet flow rate q, the damping coefficient κ, the opening pressure δ, and stiffness β of the fluid, which are obtained from the physical parameters in Fig. 1a according to the following formulas:

$$q = \frac{Q_{\text{in}}}{\frac{Ap_0}{k} D\pi C_d \sqrt{\frac{2p_0}{\rho}}}\,, \quad \kappa = \frac{b}{m}\sqrt{\frac{m}{k}}\,, \quad \delta = \frac{kx_0}{Ap_0} = \frac{p_{\text{open}}}{p_0}\,, \quad \beta = \sqrt{\frac{m}{k}}\frac{E}{V}\frac{AD\pi}{k}\sqrt{\frac{2p_0}{\rho}}\,.$$

During operation, only the flow rate q can change, which is chosen as bifurcation parameter. The volume V of the vessel is inversely proportional to the β, and it has an essential influence on the stability of the equilibrium state and also on the type of stability loss. Figure 2a shows a stability diagram of the equilibrium in the plane of the parameters q and β. It can be seen that the system is stable for small and large β values. We study the loss of stability at $\beta = 10$, which belongs to the small vessel volume. For this data the bifurcation diagram is shown in Figure 2b. The analytically calculated and numerically checked critical flow rate value at the Hopf bifurcation is $q_{\text{cr}} = 5.930$.

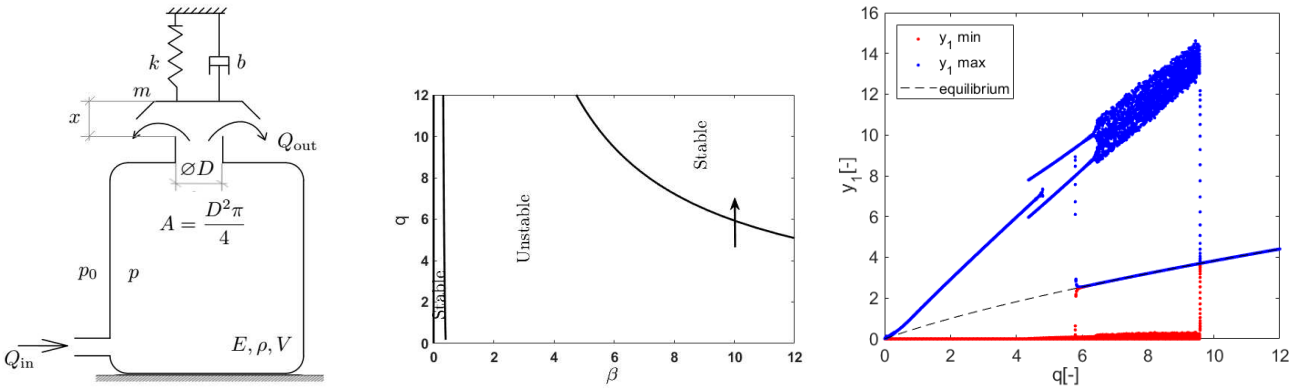

(a) Mechanical model (b) Stability chart for $\kappa = 0.7\,, \delta = 3$ (c) Bifurcation diagram for $\beta = 10$

Figure 1: Modelling, stability and bifurcations of the pressure relief valve

Nonlinear analysis

The 3rd degree approximation of the system (1-3) around the equilibrium y_{10}, y_{20}, y_{30} has the form:

$$\begin{bmatrix}\xi_1'\\ \xi_2'\\ \xi_3'\end{bmatrix} = \begin{bmatrix}0 & 1 & 0\\ -1 & -\kappa & 1\\ -\beta\sqrt{y_{30}} & 0 & -\beta\frac{y_{10}}{2\sqrt{y_{30}}},\end{bmatrix}\begin{bmatrix}\xi_1\\ \xi_2\\ \xi_3\end{bmatrix} + \begin{bmatrix}0\\ 0\\ \beta\left(-\frac{1}{2\sqrt{y_{30}}}\xi_1\xi_3 + \frac{y_{10}}{8\sqrt{y_{30}^3}}\xi_3^2 + \frac{1}{8\sqrt{y_{30}^3}}\xi_1\xi_3^2 - \frac{y_{10}}{16\sqrt{y_{30}^5}}\xi_3^3\right)\end{bmatrix} \tag{4}$$

At the bifurcation point, the linear part has the eigenvalues $\lambda_{1,2} = \pm i\omega, \lambda_3 := \lambda \in \Re^-$. Since the nonlinearity is strongly asymmetric, there are 2nd degree terms in Eq. (4). Consequently, the system has to be reduced to the centre manifold that is approximated by 2nd degree terms, too. The centre manifold can be calculated in the eigenbasis of coordinates (u_1, u_2, u_3), and it is tangent to the plane spanned by the complex conjugate eigenvectors. The lengthy algebraic calculation involves also the Near Identity transformation:

$$\begin{bmatrix}u_1\\ u_2\end{bmatrix} = \mathbf{I}\begin{bmatrix}v_1\\ v_2\end{bmatrix} + \begin{bmatrix}\sum_{j+k=\{2,3\}}\varphi_{jk}(\mu)v_1^j v_2^k\\ \sum_{j+k=\{2,3\}}\psi_{jk}(\mu)v_1^j v_2^k\end{bmatrix}, \tag{5}$$

which leads to the 3rd order normal form for (v_1, v_2). This way, we obtain the Poincare-Lyapunov constant $\Delta = 0.028 > 0$, which refers to subcritical Hopf bifurcation. The emerging unstable limit cycle has the amplitude:

$$r = \sqrt{-\frac{\text{Re}\lambda_{1,2}'\big|_{q=q_{\text{cr}}}}{\Delta}(q - q_{\text{cr}})}, \tag{6}$$

where the root tendency $\text{Re}\lambda_{1,2}' = -0.046 < 0$ can be calculated from the characteristic equation by implicit derivation with respect to the bifurcation parameter q. Through a polar coordinate transformation $v_1 = r\cos(\omega\tau), v_2 = r\sin(\omega\tau)$. Transforming back only the linear part of Eq. (5) to the original phase space makes the calculation easier, and has a sufficient result for symmetric systems [2], but Fig. 2b shows with dashed red line how this treatment effects the location of the limit cycle for this strongly asymmetric case. The limit cycle can fit better to the numeric unstable limit cycle when the 2nd degree terms are transformed back, too. After the polar coordinate transformation, the second degree terms result in constant and $\sin(2\omega\tau), \cos(2\omega\tau)$ terms multiplied by r^2. If the linear system is shifted with this constant only, then the unstable limit cycle is shown by red continuous line in Fig. 2b. The trace of the unstable limit cycle fits best by transforming back also the 2nd degree terms, which is represented with red dots in Fig. 2b.

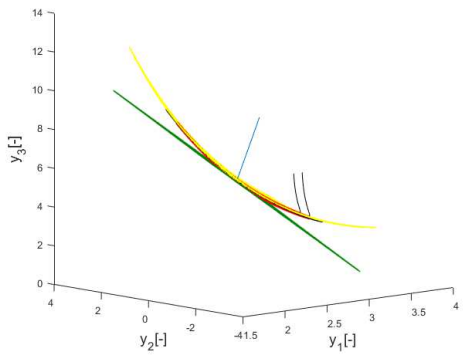

(a) Centre manifold (yellow), tangent plane (green), two numerical trajectories (black), analytical limit cycle (red)

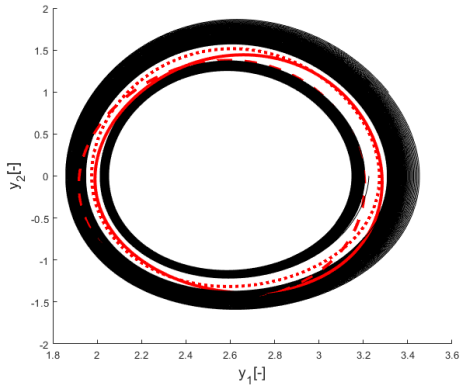

(b) A stable and an unstable numerical trajectories (black) embracing the unstable limit cycle (white) and analytical limit cycles with 3 different approximations (red)

Figure 2: Numerical and analytical results presented in the phase space of pressure relief valve

The global dynamics of the system 'outside' the unstable limit cycle is determined by the impacts of the valve disk and the seat. This is characterized by the numerical bifurcation diagram in Fig. 1c, which fits perfectly to the analytically predicted unstable limit cycle.

References

[1] Licskó G., Champneys A., Hős Cs. (2009) Nonlinear Analysis of a Single Stage Pressure Relief Valve. *IAENG International Journal of Applied Mathematics* **39**:4.

[2] Stepan G. (1991) Chaotic Motion of Wheels. *Vehicle System Dynamics* **20(6)** pp. 341-351.

Multi-mode approximation of VIVs in vertical and horizontal flexible risers

Victoria Kurushina[*,†] and Ekaterina Pavlovskaia[‡]
[*]*Centre for Perspective Research and Innovative Development, Industrial University of Tyumen, Tyumen, 625000, Russia*
[†]*School of Engineering, Newcastle University, Newcastle, NE1 7RU, United Kingdom*
[‡]*Centre for Applied Dynamics Research, University of Aberdeen, King's College, Aberdeen, AB24 3UE, United Kingdom*

Summary. In this study, oscillations of a vertical flexible structure with pinned-pinned ends in uniform flow are modelled and compared with the responses of a horizontal structure. Wake oscillator approach is adopted to simulate vortex-induced forces in the in-line and cross-flow directions and multi-mode approximation of the structural response is developed. Differences in the observed multi-mode lock-in behaviour and hysteretic responses for vertical and horizontal configurations are discussed for the case previously considered in experiments [1].

Introduction

Wake oscillator method allows simplifying calculations of the fluid forces acting on the slender structure vibrating in the fluid flow so that complex phenomenon of vortex-induced vibrations (VIVs) for a variety of structures and case parameters could be investigated with limited computational efforts. In the current study, analysis of vertical pipe vibrations is performed based on the previous investigations of a flexible structure in 1D [2] for the wake oscillators presented in [3].

Flexible riser model

Initially in straight configuration, flexible structure with pinned-pinned ends is considered vibrating in uniform current in 2 dimensions, accounting for the in-line and cross-flow displacements that varies along the length, L. The pipe is modelled as an Euler–Bernoulli beam whereas external fluid forces are described using nonlinear wake oscillator equations. Here, the Krenk-Nielsen oscillator [4] with the frequency doubling coefficients is selected to predict the drag force fluctuations based on the study [3] where the effect of phenomenological oscillators on the performance of the flexible riser model for the horizontal configuration were considered. The obtained coupled system of nonlinear partial differential equations is simplified employing Galerkin–type discretisation to create reduced order model. The resulting ordinary differential equations are solved numerically providing multi-mode approximations of the structure displacements and non-dimensional fluid force coefficients. The obtained model is applicable for both horizontal and vertical configurations and can be written in non-dimensional form for *i*th mode as:

$$\begin{aligned}
\ddot{X}_i &+ 2a\Omega_R\dot{X}_i + \omega_{ni}^2 X_i = \frac{W_w}{Lm_*\omega_0^2}\sum_{n=1}^{N} X_n\Phi_{ni} + \frac{a\Omega_R^2}{i\pi^2 St}(1-\cos(i\pi)) + \frac{b\Omega_R^2}{4\pi St}w_i - b\Omega_R\sum_{n=1}^{N}\sum_{m=1}^{N} w_n\dot{X}_m\Pi_{nmi} \\
&+ \frac{c\Omega_R}{2}\sum_{n=1}^{N}\sum_{m=1}^{N} q_n\dot{Y}_m\Pi_{nmi} + 2\pi aSt\sum_{n=1}^{N}\sum_{m=1}^{N}\dot{X}_n\dot{X}_m\Pi_{nmi} + \pi aSt\sum_{n=1}^{N}\sum_{m=1}^{N}\dot{Y}_n\dot{Y}_m\Pi_{nmi}, \\
\ddot{Y}_i &+ a\Omega_R\dot{Y}_i + \omega_{ni}^2 Y_i = \frac{W_w}{Lm_*\omega_0^2}\sum_{n=1}^{N} Y_n\Phi_{ni} - \frac{b}{2}\Omega_R\sum_{n=1}^{N}\sum_{m=1}^{N} w_n\dot{Y}_m\Pi_{nmi} + \\
&+ \frac{c}{4\pi St}\Omega_R^2 q_i - c\Omega_R\sum_{n=1}^{N}\sum_{m=1}^{N} q_n\dot{X}_m\Pi_{nmi} + 2\pi aSt\sum_{n=1}^{N}\sum_{m=1}^{N}\dot{X}_n\dot{Y}_m\Pi_{nmi}, \\
\ddot{w}_i &- 2\varepsilon_{x1}\Omega_R\dot{w}_i + 2\varepsilon_{x2}\Omega_R\sum_{n=1}^{N}\sum_{m=1}^{N}\sum_{l=1}^{N}\left(\dot{w}_n w_m w_l\Psi_{nmli}\right) + 2\frac{\varepsilon_{x3}}{\Omega_R}\sum_{n=1}^{N}\sum_{m=1}^{N}\sum_{l=1}^{N}\left(\dot{w}_n\dot{w}_m\dot{w}_l\Psi_{nmli}\right) + 4\Omega_R^2 w_i = A_x\ddot{X}_i, \\
\ddot{q}_i &- \varepsilon_y\Omega_R\dot{q}_i + \varepsilon_y\Omega_R\sum_{n=1}^{N}\sum_{m=1}^{N}\sum_{l=1}^{N}\left(\dot{q}_n q_m q_l\Psi_{nmli}\right) + \Omega_R^2 q_i = A_y\ddot{Y}_i,
\end{aligned}$$

where X_i and Y_i are in-line and cross-flow displacements multipliers, w_i and q_i are wake coefficients multipliers, Ω_R is vortex shedding frequency, St is Strouhal number, $\varepsilon_{x1}, \varepsilon_{x2}, \varepsilon_{x3}, \varepsilon_y$ are dimensionless wake oscillator damping coefficients, A_x, A_y are empirical coupling coefficients, Φ_{ni}, Π_{nmi} and Ψ_{nmli} are dimensionless coefficients obtained during the discretisation procedure due to the mode interaction, a, b, c are dimensionless coefficients depending on the initial drag, fluctuating drag and lift coefficients respectively, N is total number of modes considered, ω_{ni} is the *i*th natural frequency, ω_0 is reference frequency, m_* is mass per unit length (including structural mass and fluid added mass), W_w is weight of structure per unit length. Then the displacements and wake coefficients are calculated as

$$X(\zeta,\tau) = \sum_{n=1}^{N} X_n(\tau)\widetilde{X}_n(\zeta); \quad Y(\zeta,\tau) = \sum_{n=1}^{N} Y_n(\tau)\widetilde{Y}_n(\zeta); \quad w(\zeta,\tau) = \sum_{n=1}^{N} w_n(\tau)\widetilde{w}_n(\zeta); \quad q(\zeta,\tau) = \sum_{n=1}^{N} q_n(\tau)\widetilde{q}_n(\zeta).$$

where τ is non-dimensional time and the sinusoidal functions $\widetilde{X}_n(\zeta), \widetilde{Y}_n(\zeta), \widetilde{w}_n(\zeta), \widetilde{q}_n(\zeta)$ depending on the location along the beam $\zeta = \frac{z}{L}$ are used. Here, z is the longitudinal coordinate, and $z = 0$ indicates the bottom for the vertical configuration.

For our analysis, the configuration of the riser was selected to match the case experimentally investigated in [1] where a flexible tube with internal fluid with the weight of 2.97 N/m, length of 2.92 m, diameter of 0.018 m, and applied tension of 147 N was considered in the Reynolds number range from around 1780 to 14800. The other relevant parameters were the mass ratio of 1.17 and damping ratio of 0.025.

Results

Comparison of the lock-in curves calculated for in-line and cross-flow displacement amplitudes for the independent velocity points and under decreasing and increasing flow velocity is performed in this study for the horizontal and vertical risers, as illustrated in Figs 1a and 1b. Hysteretic behaviour is observed in the valleys between the lock-in peaks. The co-existing solutions obtained with decreasing and increasing velocities indicate significant differences in the displacement magnitudes. Figures 1c and 1d demonstrate displacement amplitudes of three co-existing solutions along the riser length for a chosen value of the reduced velocity of $U_R = 10.48$. Analysis of the obtained responses reveal a different number of modes observed in the in-line and cross-flow directions. An apparent asymmetry towards higher amplitudes in the response of the vertical structure is noticeable below $\zeta = 0.50$.

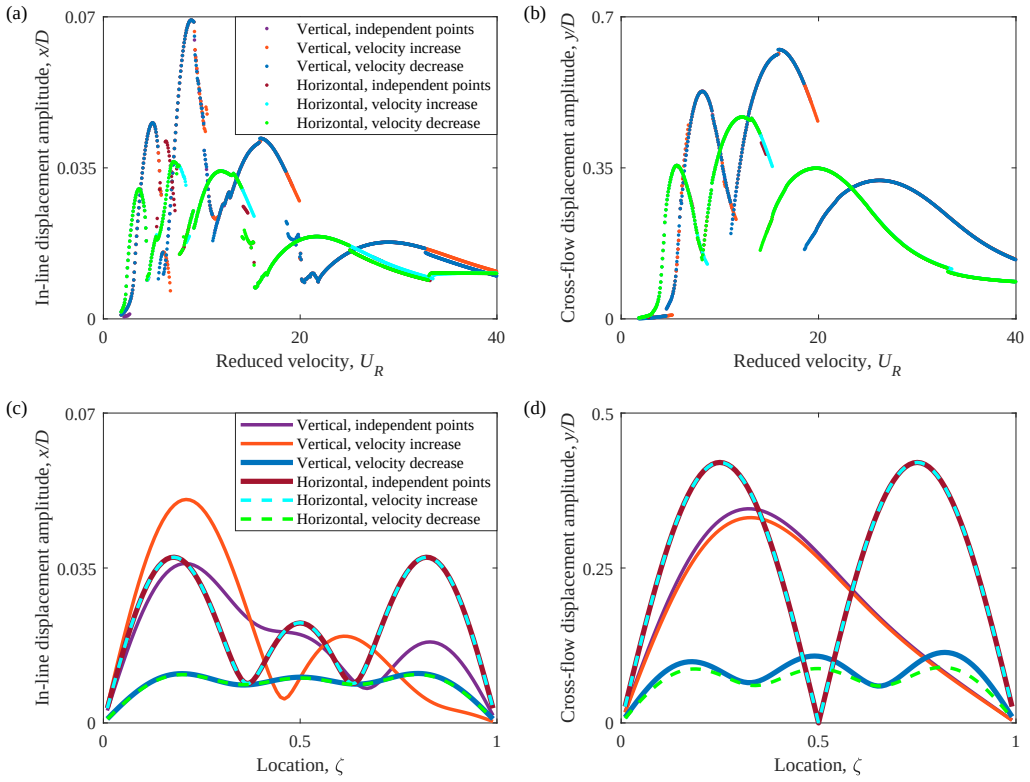

Figure 1: Dynamics of a vertical and horizontal flexible riser for the range of reduced velocity predicted by the 3 mode approximation: (a) in-line and (b) cross-flow displacement multi-mode lock-in at $\zeta = 0.25$; (c) in-line and (d) cross-flow displacement amplitude variation along the riser length at the reduced velocity of $U_R = 10.48$.

Conclusions

This study investigates the differences in the predicted behaviour of a flexible structure in uniform flow for vertical and horizontal configurations under increasing and decreasing flow velocity, and also in the limited case, when the structure starts oscillating from zero initial conditions for each flow velocity. Vertical model shows the higher amplitudes of displacement from the initial position than the horizontal structure in general. Vertical structure also demonstrates a large asymmetry of the response, a more notable contribution of the nearby modes at the nodal points and a slight delay in the peak occurrence in the reduced velocity range, compared to the horizontally positioned one.

References

[1] Sanaati B., Kato N. (2012) A study on the effects of axial stiffness and pre-tension on VIV dynamics of a flexible cylinder in uniform cross-flow. *Applied Ocean Research* **37**:198-210.

[2] Pavlovskaia E., Keber M., Postnikov A., Reddington K., Wiercigroch M. (2016) Multi-modes approach to modelling of vortex-induced vibration. *International Journal of Non-Linear Mechanics* **80**: 40-51.

[3] Kurushina V., Pavlovskaia E., Wiercigroch M. (2020) Modelling of flexible structure VIV in a uniform flow. *International Journal of Engineering Science* **150**: 103211.

[4] Krenk S., Nielsen, S.R.K. (1999) Energy balanced double oscillator model for vortex-induced vibrations. *Journal of Engineering Mechanics* **125(3)**:263-271.

Nonlinear Dynamic Analysis of a Nonlocal Nanobeam Resting on Fractional Visco-Pasternak Foundation by Using the Incremental Harmonic Balance Method

Nikola Nešić[*], Milan Cajić[**], Danilo Karličić[***] and Srdjan Jović[*]
[*]*University of Priština, Faculty of Technical Sciences, 38220 Kosovska Mitrovica, Kneza Milosa 7, Serbia*
[**]*Mathematical Institute of the Serbian Academy of Sciences and Arts, Belgrade, Serbia*
[***] *College of Engineering, Swansea University, Fabian Way, Crymlyn Burrows, Swansea SA1 8EN, UK*

Summary. This paper investigates the dynamic behaviour of a geometrically nonlinear nanobeam resting on the fractional visco-Pasternak foundation and subjected to dynamic axial and transverse loads. The fractional-order governing equation of the system is derived and then discretized by using the single-mode Galerkin discretization. Corresponding forced Mathieu-Duffing equation is solved by using the incremental harmonic balance (IHB) method for the strong nonlinear case. Methodology and results are validated against the solution via multiple scales method for the weakly nonlinear case. A parametric study is performed for order two and three superharmonic resonance conditions and for primary resonance case. The results demonstrated a significant influence of fractional-order and damping parameter of the visco-Pasternak foundation as well as the nonlocal parameter and external excitation load on frequency response of the system.

Introduction

A special class of beam models is so-called nonlocal beams, where the nonlocal elasticity constitutive equation is employed to consider the small-scale effects [1]. Such nonlocal beams are usually referred to in the literature as nanobeams due to the nano-scale dimensions of structures. The incremental harmonic balance method is used to study nonlinear dynamic behaviour of beam structures by many authors, e.g. see [2]. The main advantage of harmonic balance techniques is that they can be employed to find the periodic solutions of strongly nonlinear systems without introducing a small parameter like in perturbation techniques [3]. Shen et al. [4] investigated the Mathieu-Duffing oscillator by the incremental harmonic balance (IHB) method and determined the stability of the periodic solution using the Floquet theory. Later, this method was extended to study the nonlinear Duffing [5] and forced Mathieu-Duffing type [6] fractional-order differential equations, where the fractional derivative term was approximated through the Galerkin procedure. This study aims to employ the incremental harmonic balance techniques to study the frequency response of a nanobeam system resting on the fractional visco-Pasternak type foundation. Pasternak elastic foundation model is usually used for materials which besides normal deflection contain shearing distortion. It should be noted that, under certain assumptions, a nonlocal beam model could represent nanostructures such as carbon nanotubes. In that case, boundary conditions to analyze the free or forced vibration of a nanobeam structure can be prescribed based on the end conditions in a carbon nanotube i.e. a number of layers of fixed atoms in the lattice (e.g. see [7]). If only one layer of atoms is fixed at both ends of carbon nanotube, we can use simply supported (S-S) boundary conditions in the mechanical model, and if several layers of atoms are fixed, we can use boundary conditions of clamped-clamped (C-C) nanobeam. The single-mode Galerkin method is used to discretize the governing equation and obtain the nonlinear response for the fractional-order forced Mathieu-Duffing equation. The results are verified by the comparison of amplitude-frequency curves from the multiple scales and incremental harmonic balance methods obtained for the superharmonic resonance conditions of order two and three and a primary resonance case.

Problem definition

The governing equation for the forced vibration of a nanobeam resting on the fractional visco-Pasternak foundation is derived based on the model presented in Fig.1. Following parameters are used: L is the length of the nanobeam, ρ is the density, A is the cross-sectional area of homogenous nanobeam, $\bar{\delta}$ and $\bar{G}_p$ are the coefficients of the fractional visco-Pasternak foundation, D^{α} is the operator of the Caputo fractional-order derivative, $\bar{F}_0$ is the amplitude of static load while $\bar{F}_1$ is the amplitude of the dynamic force of the frequency Ω_1.

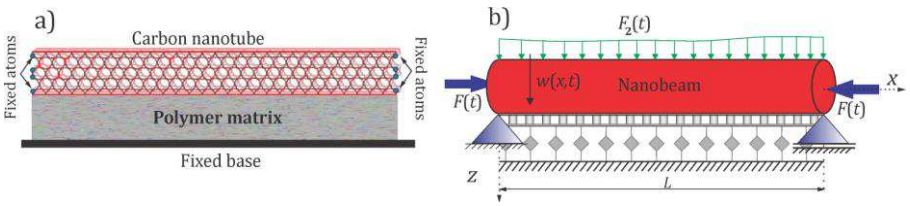

Figure 1: Nanobeam on fractional visco-Pasternak foundation a) physical and b) mechanical model

Based on the Euler-Bernoulli beam theory and von Kármán nonlinear deformation, nonlocal constitutive equation and the Newton's second law for the elementary part of the nanobeam, the following nonlinear fractional-order partial differential equation of motion of the nanobeam resting on the fractional visco-Pasternak foundation can be derived

$$\rho A\frac{\partial^2 w}{\partial t^2}+\ D^{\alpha}w\,\bar{\delta}+\ D^{\alpha}\left(\frac{\partial^2 w}{\partial x^2}\right)\bar{G}_p+(\bar{F}_0+\bar{F}_1\cos\Omega_1 t)\frac{\partial^2 w}{\partial x^2}$$
$$-\frac{EA}{2L}\frac{\partial^2 w}{\partial x^2}\int_0^L\frac{1}{2}\left(\frac{\partial w}{\partial x}\right)^2 dx+EI\frac{\partial^4 w}{\partial x^4}-\mu\left[\rho A\frac{\partial^4 w}{\partial t^2\partial x^2}+\ D^{\alpha}\frac{\partial^2 w}{\partial x^2}\bar{\delta}+\ D^{\alpha}\left(\frac{\partial^4 w}{\partial x^4}\right)\bar{G}_p\right.$$
$$\left.+(\bar{F}_0+\bar{F}_1\cos\Omega_1 t)\frac{\partial^4 w}{\partial x^4}-\frac{EA}{2L}\frac{\partial^4 w}{\partial x^4}\int_0^L\frac{1}{2}\left(\frac{\partial w}{\partial x}\right)^2 dx\right]=\bar{F}_2\cos\Omega_2 t\ . \qquad (1)$$

Solution procedures

The partial differential equation (1) is nondimensionalized and after introducing a new time scale $\bar{\tau}=\bar{\Omega}\tau$ and we assume the solution of nondimensional version of Eq.(1) as $\bar{w}(\bar{x},\tau)=\phi(\bar{x})q(\tau)$, nonlinear fractional-order forced Mathieu-Duffing equation is obtained in the following form

$$\bar{\Omega}^2 q''+\varepsilon\gamma_{12}\bar{\Omega}^{\alpha}D_{\bar{\tau}}^{\alpha}q+(\omega_n^2-\varepsilon\gamma_3 F_1\cos\bar{\tau})q+\varepsilon\gamma_4 q^3=\tilde{f}\cos\bar{\tau}, \qquad (2)$$

For some initial guess q_0 of the steady-state modal amplitude, a neighbouring state of motion can be expressed in the form $q=q_0+\Delta q,\ \bar{\Omega}=\bar{\Omega}_0+\Delta\bar{\Omega}$, where q_0 and Δq can be represented as sums of trigonometric functions and corresponding weighting coefficients. Based on Galerkin procedure as described in papers [5, 6], Eq. (2) is discretised and Newton-Rapson method is applied to solve for increments of amplitude when $\Delta\bar{\Omega}=0$.

Numerical results

Here, we show the numerical results obtained by the presented incremental harmonic balance (IHB) method for finding the frequency response of the system. We verify the results by comparing the steady-state frequency responses for the superharmonic resonance case $2\bar{\Omega}\approx\omega_n$ obtained by the IHB and the multiple scales method (MS), as given in Fig. 2a. Influence of the fractional-order derivative parameter for weak nonlinearity and the nonlocal parameter for strong nonlinearity on the amplitude-frequency responses are given in Fig. 2b and Fig. 2c, respectively.

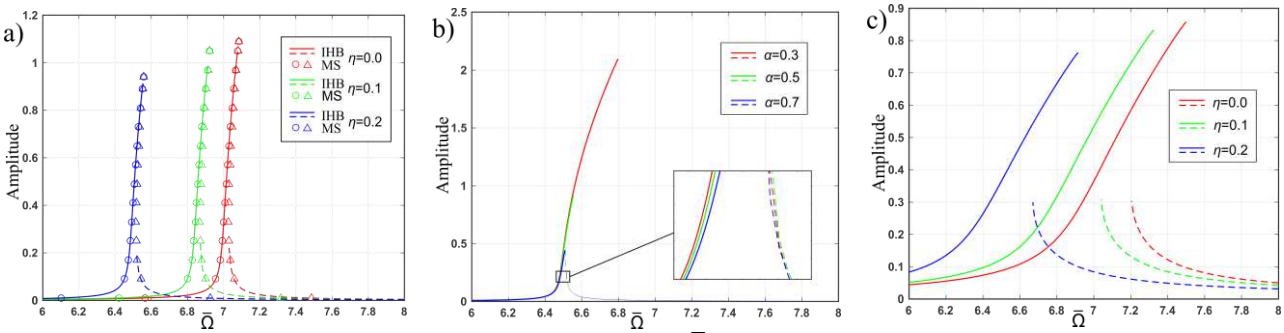

Figure 2: Frequency response for the superharmonic resonance case $2\bar{\Omega}\approx\omega_n$: a) weak nonlinearity, changes of nonlocal parameter, IHB vs MS, b) weak nonlinearity, changes of order of fractional derivative, c) strong nonlinearity, changes of nonlocal parameter.

Conclusions

From the validation study, it is revealed that the incremental harmonic balance method is in good agreement with the multiple scales analysis for the weakly nonlinear case. The advantage of the incremental harmonic balance method lies in the fact that it does not require the introduction of small parameter and thus strong nonlinearity cases can be observed. It has been demonstrated that introduction of the incremental harmonic balance method in the analysis of nonlocal structures can possibly lead to more reliable analysis of strongly nonlinear nano-scale systems.

References

[1] Reddy, J. N. (2007). Nonlocal theories for bending, buckling and vibration of beams. *Int J Eng Sci* **45.2-8**:288-307.
[2] Sze, K. Y., Chen, S. A., & Huang, J. L. (2005). The incremental harmonic balance method for nonlinear vibration of axially moving beams. *J Sound Vibr* **281.3-5**:611-626.
[3] Niu, J., Shen, Y., Yang, S., & Li, S. (2018). Higher-order approximate steady-state solutions for strongly nonlinear systems by the improved incremental harmonic balance method. *J Vibr Control* **24.16**:3744-3757.
[4] Shen, J. H., Lin, K. C., Chen, S. H., & Sze, K. Y. (2008). Bifurcation and route-to-chaos analyses for Mathieu–Duffing oscillator by the incremental harmonic balance method. *Nonlin Dyn* **52.4**:403-414.
[5] Shen, Y. J., Wen, S. F., Li, X. H., Yang, S. P., & Xing, H. J. (2016). Dynamical analysis of fractional-order nonlinear oscillator by incremental harmonic balance method. *Nonlin Dyn* **85.3**:1457-1467.
[6] Wen, S. F., Shen, Y. J., Wang, X. N., Yang, S. P., & Xing, H. J. (2016). Dynamical analysis of strongly nonlinear fractional-order Mathieu-Duffing equation. *Chaos* **26.8**:084309.
[7] Ansari, R., & Sahmani, S. (2012). Small scale effect on vibrational response of single-walled carbon nanotubes with different boundary conditions based on nonlocal beam models. *Comm Nonlin Sci Num Sim* **17.4**:1965-1979.

Nonlinear Vibrations of Long Slender Continua Coupled with Discrete Inertia Elements Moving Vertically in a Tall Structure

Stefan Kaczmarczyk*
*Engineering Dept, Faculty of Arts, Science and Technology, University of Northampton, Northampton, UK

Summary. A nonlinear mathematical model of axially moving long slender continua coupled with discrete inertia elements deployed in a tall structure is developed. In engineering applications such a system represents a vertical transportation system (high-rise lift/elevator). The longitudinal motion of the discrete masses that represent the car, counterweight and compensating sheave assembly are constrained by a a nonlinear damping device. Numerical simulation techniques are then used to predict a range of complex dynamic interactions and resonance phenomena which in turn informs the development of vibration control strategies.

Introduction

Tall buildings and structures are subjected to sway motions of large amplitude and low frequency due to resonance conditions induced by wind loads and long-period seismic excitations [1,2]. These sources of excitation affect the performance of vertical transportation systems (VTS; high-rise lift/elevator systems) deployed in buildings [3]. The fundamental natural frequencies of tall buildings fall within the frequency range of the wind and seismic excitations and the sway motions form a base motion excitation mechanism which acts upon the components of VTS [4]. Particularly affected are long slender continua (LSC) such as suspension ropes, compensating and travelling cables. The lengths of these elements vary when the VTS moves vertically within the host structure. The lateral motions of the LSC are coupled with the vertical motions of discrete masess installed in the hoisway, such as the car, counterweight of the compensating sheave assembly (CSA).
Complex resonance interactions arise in the system when the frequency of the base excitation is tuned to one (or more) natural frequencies of the system.Substantial research efforts has been devoted to the issue of mitigating the effects of the dynamic responses that might occur. In the first instance the masses and geometry of the system can be adjusted to change the resonance frequencies to shift the resonance regions. However, in most cases the structural constraints and design limitations do not leave much space for the changes to be effective. Active vibration control strateges involving boundary lateral motions and/or longitudinal motions (such as active stiffness control [4]) can be considered to mitigate the effects of resonances. However, these approaches involve the application of expensive and sophisticated actuator control algorithms and often passive methods are preferred to be used. For example, the industrial practice to mitigate the effects of dynamic interactions in a high-rise elevator system involves the application of a hydraulic tie-down device attached at the CSA. The damping force is then a nonlinear function of the CSA's velocity. The aim of this study is to develop a numerical simulation model to predict and to analyse the nonlinear vibrational interactions in the system under resonance conditions. The characteristics of the damping device can then be optimised and adjusted to minimize the effects of adverse dynamic responses of the system.

Nonlinear dynamics model

Figure 1 shows a VTS system mounted within a vertical cantilever host structure subject to ground motions $s_r(t)$, $r = 1,2$ in the in-plane and out-of-plane directions, respectively. The structure undergoes bending elastic deformations with the in-plane and out-of-plane displacements at the top end ($z = z_0$) denoted as $w_{r0}(t)$, respectively. The fundamental modal responses of the structure can be defined by the following equation

$$\ddot{W}_r(t) + 2\zeta_r\omega_r\dot{W}_r(t) + \omega_r^2 W_r(t) = -\frac{\ddot{s}_r(t)}{m_r}\int_0^{Z_0} m_s(z)\,\Psi_r(z)\,dz \tag{1}$$

where $r = 1,2$ and W_r represent the modal coordinates. The natural frequencies of the structure are denoted as ω_r, ζ_r represent the modal damping ratios, $\Psi_r(z)$ are the eigenfunctions (mode shape functions) of the structure. In this formulation $0 \le z \le z_0$, $m_s(z)$ is the linear mass density of the structure and $m_r = \int_0^{z_0} m_s(z)\Psi_r^2(z)\,dz$. The deflections at the top of the structure are then be determined as $w_{r0} = \Psi_r(Z_0)W_r(t)$, $r = 1,2$. The equations of motion of the LSC treated as continua with small bending stiffness are given as

$$\begin{aligned} &m_i\overline{v}_{itt} + E_iJ_i\overline{v}_{ixxxx} - \left\{T_i - m_i\left[V^2 + (g - a_i)x_i\right] + E_iA_ie_i\right\}\overline{v}_{ixx} + m_ig\overline{v}_{ix} + 2m_iV\overline{v}_{ixt} = F_i^v\left[t, L_i(t)\right],\ i = 1,\ldots 4,\\ &m_i\overline{w}_{itt} + E_iJ_i\overline{w}_{ixxxx} - \left\{T_i - m_i\left[V^2 + (g - a_i)x_i\right] + E_iA_ie_i\right\}\overline{w}_{ixx} + m_ig\overline{w}_{ix} + 2m_iV\overline{w}_{ixt} = F_i^w\left[t, L_i(t)\right],\ i = 1,\ldots 4. \end{aligned} \tag{2}$$

The response of discrete masses are desribed by following equations

$$\begin{aligned} &M_1\ddot{q}_1 - E_1A_1e_1 + E_2A_2e_3 = 0; M_2\ddot{q}_2 - E_1A_1e_4 + E_2A_2e_2 = 0,\\ &M_3\ddot{q}_3 + E_1A_1e_1 + E_1A_1e_4 + c_3\left|\dot{q}_3\right|^{\alpha-1}\dot{q}_3 = 0;\ I_3\ddot{\theta}_3 - RE_1A_1e_1 + RE_1A_1e_4 = 0 \end{aligned} \tag{3}$$

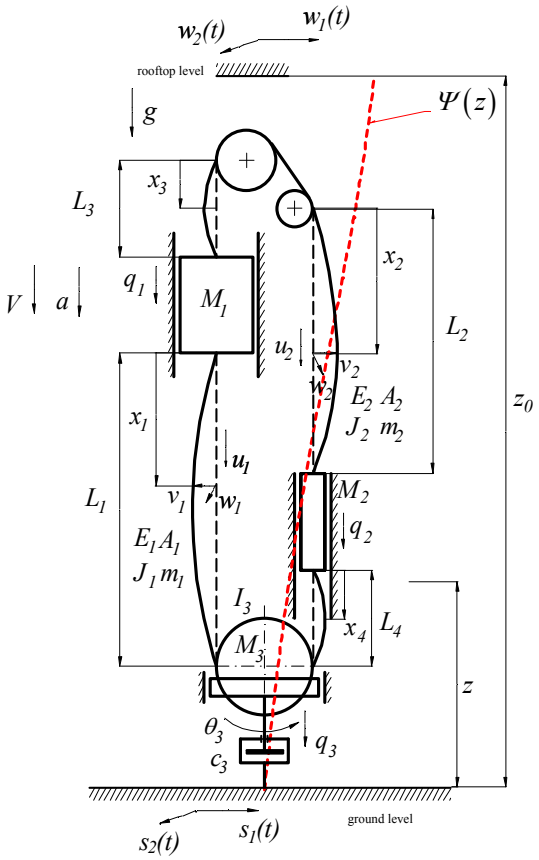

Figure 1: Greatest figure of all time

where $\bar{v}_i(x_i,t), \bar{w}_i(x_i,t)$, i = 1,2,…, 4, represent the dynamic displacements of the LSC, F_i^v, F_i^w are the excitation terms, E_1, A_1, J_1, m_1 and E_2, A_2, J_2, m_2 are the modulus elasticity, cross-sectional effective area, second moment of area, and mass per unit length of the compensating ropes and the suspension ropes, respectively. The compensating ropes are of length L_1 at the car side and the suspension ropes are of length L_2 at the counterweight side, respectively. The length of the suspension rope at the car side and the compensating rope at the counterweight side are denoted as L_3 and L_4, respectively. The lengths of suspension ropes and compensating cables are time-varying so that $L_i = L_i(t)$, $i = 1,\ldots,4$. The masses and dynamic displacements of the car, counterweight and the compensating sheave assembly are represented by M_1, M_2 and M_3, q_1, q_2 and q_3, respectively. The speed and acceleration/ deceleration of the car are denoted by V and a, respectively, and T_i, denote the rope quasi-static tensions. In this model the quantities e_i are the quasi-static axial strains in the LSC system. The kinematic constraint equation to be used in equations (2-3) is expressed as $\Upsilon \equiv 2q_3 - u_1(L_1,t) - u_4(L_4,t) = 0$.

Results and conclusions

The model is solved numerically and the results demonstrate the resonance behaviour of the system. The resonance frequencies of the LSC componets can be shifted / changed by the use of different masses of the CSA. The frequencies of the suspension ropes depend on the mass of the car (and the corresponding mass of the counterweight) as well as on the car loading conditions. The characteristics of the hydraulic tie-down / damping device can be optimised and adjusted to minimize the effects of adverse dynamic interactions taking place in the system. It should be noted that the nature of the dynamic conditions present in high-rise building systems is such that small changes of the natural frequencies of the structure might result in large changes of the resonance conditions that arise in the installation.

References

[1] Kijewski-Correa, T., Pirinia, D. 2007 Dynamic behavior of tall buildings under wind: insights from full-scale monitoring, *The Structural Design of Tall and Special Buildings*, **16**, pp. 471-486.

[2] Saito, T. 2016 Response of high-rise buildings under long period earthquake ground motions, *International Journal of Structural and Civil Engineering Research*, **5**(4), pp. 308-314.

[3] Sánchez Crespo, R., Kaczmarczyk, S., Picton, P., Su, H. 2018 Modelling and simulation of a stationary high-rise elevator system to predict the dynamic interactions between its components**,** *International Journal of Mechanical Sciences.* **137**, pp. 24-45.

[4] Kaczmarczyk, S., Picton, P. 2013 The prediction of nonlinear responses and active stiffness control of moving slender continua subjected to dynamic loadings in a vertical host structure, *International Journal of Acoustics and Vibration,* **18**(1), pp. 39-44.

Tuesday, July 19, 2022
16:00 - 18:20

MS-01 Reduced-Order Modeling and System Identification
Saint Clair 3B

Chair: Majdi Gzal

16:00 - 16:20
On reduced-order models for resonant nonlinear dynamics: Galerkin truncation, nonlinear normal mode, and dominant spectrum decomposition
GUO Tieding, **REGA Giuseppe***
*Sapienza University of Rome (Rome 00197 Italy)

16:20 - 16:40
Reduced-order model based on cyclic symmetric properties to tackle nonlinear mistuned cyclic structures
QUAEGEBEUR Samuel*, CHOUVION Benjamin, THOUVEREZ Fabrice, BERTHE Loïc
*Safran Helicopter Engines (Safran Helicopter Engines, 64511 Bordes France) - Laboratoire de Tribologie et Dynamique des Systèmes (36 Avenue Guy de Collongue, 69134 Ecully Cedex France)

16:40 - 17:00
Non-intrusive reduced-order modeling of the drift flux model using a residual recurrent neural network
ABBASI Mohammad Hossein*, IAPICHINO Laura, SCHILDERS Wil, VAN De Wouw Nathan
*Eindhoven University of Technology (Eindhoven Netherlands)

17:00 - 17:20
Reduced-order Modeling from Experimental Data via Spectral Submanifolds
CENEDESE Mattia*, AXÅS Joar, HALLER George
*ETH Zürich (Leonhardstrasse 21, 8092, Zürich Switzerland)

17:20 - 17:40
Stable and Fast Identification of Continuous-Time Lur'e-Type Systems
SHAKIB Mohammad Fahim*, POGROMSKY Alexander, PAVLOV Alexey, WOUW Nathan
*Eindhoven University of Technology [Eindhoven] (Den Dolech 2 5612 AZ Eindhoven Netherlands)

On reduced-order models for resonant nonlinear dynamics: Galerkin truncation, nonlinear normal mode, and dominant spectrum decomposition

Tieding Guo[*], Giuseppe Rega[**]
[*]*College of Civil Engineering, Hunan University, Changsha, China*
[**] *Dipartimento di Ingegneria Strutturale e Geotecnica, Sapienza University of Rome, Rome, Italy*

Summary. It is well-known that perturbation analysis of reduced-order models (ROMs) of nonlinear structures produced by classical Galerkin truncation (using single or finite linear modes) might lead to erroneous results. At least three different approaches were proposed for resolving this issue in the literature, besides increasing retained modes (thus obtaining not a minimal ROM), namely, perturbation by directly attacking the continuous partial differential equations (PDEs), rectified Galerkin truncation, and nonlinear normal modes. The latter two give their ROMs but the first does not, although all the three lead to notably improved nonlinear responses. The three should be equivalent to each other in the sense of improved characterization of structure's nonlinearity, although at first glance they are quite different in their formulations. Our key observation is that the underlying essential similarity of the three resolutions is that the structure's dominant nonlinearity effects are always well captured *before* mode truncations (in distinct and subtle manners). Inspired by this similarity, we propose a new reduced-order modelling approach based upon dominant spectrum decomposition idea, with also comparisons of the above three existing methods being discussed. Explicitly, the key dominant dynamic patterns/features (indicated by their associated spectrum) inherent with nonlinear structures are captured before mode truncation. These dynamic patterns include not only the directly excited structural modes (always retained in classical Galerkin truncation), but also those dominant passive patterns which are slaved to the quadratic nonlinearity, sub-(super) harmonic excitations, or hard non-zero boundary conditions.

Basic formulation

Three typical one-dimensional scenarios in weakly nonlinear dynamics are discussed [1, 2], explicitly
(a) Hard sub-(super) harmonic excitation problem denoted by

$$\ddot{w}(x,t)+L[w]=F(x)\cos\Omega t+\varepsilon N_3[w]-2\varepsilon\mu\dot{w} \tag{1}$$

with boundary conditions $w(0,t)=w(1,t)=0$. Here $L[\cdot]$, $N_3[\cdot]$ are the structure's linear and geometric cubic-nonlinear operators, $F\sim O(1)$, $\Omega=3\omega_m+\varepsilon\sigma$ are the amplitude and frequency of a hard sub-harmonic external excitation, with ε being a small parameter for proper perturbation analysis, and σ a detuning parameter.

(b) Quadratic (and cubic) nonlinearity problem governed by

$$\ddot{w}(x,t)+L[w]=N_2[w]+N_3[w]+F\cos\Omega t-2\mu\dot{w} \tag{2}$$

with $w(0,t)=w(1,t)=0$. Here $w(x,t)\sim O(\varepsilon)$ is the structure's displacement, and $L[\bullet]$, $N_2[\bullet]$, and $N_3[\bullet]$ are the linear, quadratic and cubic (spatial) operators, respectively. $F\sim O(\varepsilon^3)$ is the excitation, with $\Omega=\omega_m+\varepsilon^2\sigma$.

(c) Hard sub-(super) harmonic moving boundary problem represented by

$$\ddot{w}(x,t)+L[w]=\varepsilon N_3(w,t)-2\varepsilon\mu\dot{w},\quad w(0,t)=0,\ w(1,t)=s(t)=S_0\cos\Omega t \tag{3}$$

where the boundary motion $s(t)=S_0\cos\Omega t$ is a hard sub-harmonic kinematic excitation with $S_0\sim O(1)$, $\Omega=3\omega_m+\varepsilon\sigma$. Here S_0, Ω are amplitude and frequency of boundary motion, respectively.

For the three problems above we point out that, essentially, one single structural mode, i.e., the m-th mode $(\omega_m,\ \phi_m)$, is directly excited and will thus survive in the corresponding ROMs in the absence of internal resonance, meaning that it is possible to use a single-mode Galerkin truncation like $w(x,t)\approx\phi_m q_m(t)$ for Eqs. (1) and (2) and $w(x,t)\approx\phi_m q_m(t)+\psi_0(x)s(t)$ for Eq.(3), where a shape function $\psi_0(x)$ is introduced for satisfying the non-zero boundary motion $s(t)$, with $\psi_0(0)=0,\ \psi_0(1)=1$. However, it turns out that the induced perturbation results do not agree with the direct perturbation outcomes (regarded as the most accurate), indicating that the single-mode truncation is incorrect and that more structural modes should be retained in the Galerkin truncation.

Error source analysis

Our observation is that, although only the m-th structural mode is directly excited, there are possibly other passive dominant dynamic patterns which should be captured. For example, if only the m-th mode is retained in the low-order Galerkin-reduced model, all the following response components, i.e., q_j, $j\neq m$, will be completely neglected [1, 2]

$$q_1=B_1e^{i\omega_1T_0}+\hat{c}_1e^{i\Omega T_0}+cc.,\quad q_2=B_2e^{i\omega_2T_0}+\hat{c}_2e^{i\Omega T_0}+cc.,\cdots q_j=B_je^{i\omega_iT_0}+\hat{c}_je^{i\Omega T_0}+cc.,\cdots \tag{4}$$

The key subtle point is that, although the free structural modal amplitudes $B_j\to0,\ j\neq m$ will vanish eventually (not being directly or indirectly excited), certain forced components $p_j=\hat{c}_je^{i\Omega T_0}+cc.,\ j\neq m$ might be non-trivial (say, be

of comparable amount with respect to the retained components q_m and p_m). These non-trivial forced components $p_j = \hat{c}_j e^{i\Omega T_0} + cc.$ are exactly what we meant by dominant passive dynamic patterns besides the retained (ω_m, ϕ_m), which could be caused by hard secondary excitations, quadratic nonlinearity and hard boundary motion. Explicitly,

$$F\cos\Omega t \text{ for Eq.(1)}, \quad N_2[\phi_m,\phi_m]q_m^2 \text{ for Eq.(2)}, \quad -\left(-\Omega^2 I + L\right)\psi_0(x)S_0\cos\Omega t \text{ for Eq.(3)} \tag{5}$$

are the (non-secular) sources inducing non-trivial passive dynamic patterns, and should be fully captured. If single-mode truncation is used, only the *m*-th projected component of the terms in Eq.(5) will be considered. This is the error source ensuing from the perturbation analysis when using single-mode based ROMs.

Dominant spectrum decomposition and minimal ROMs [2]

We propose the following single-mode truncation corrected by the dominant spectral decomposition, i.e.,

$$w(x,t) = \phi_m(x)\cdot q_m(t) + \sum \Phi_{\Omega_i}(x)\cdot p_{\Omega_i}(t) \tag{6}$$

where $\left(\phi_m,\ q_m \sim e^{i\omega_m t}\right)$ is the directly excited structural mode, and $\left(\Phi_{\Omega_i},\ p_{\Omega_i} \sim e^{i\Omega_i t}\right)$ are the *i*-th forced components or passive dynamic patterns due to various sources denoted by Eq.(5) above, with $\{\Omega_1,\Omega_2,\cdots\}$ being the set of frequencies of these dynamic patterns, entering explicitly the low-order equation of motion as

$$\left(\partial^2/\partial t^2 + L\right)\sum \Phi_{\Omega_i}(x)\cdot p_{\Omega_i}(t) = \text{source terms in Eq.(5)} \tag{7}$$

Therefore, using Eqs. (6) and (7), we derive the new ROMs of the nonlinear structure denoted by

$$\left(\partial^2/\partial t^2 + L\right)\phi_m q_m(t) = \underbrace{0}_{\text{source terms in Eq.(5) eliminated}} + \varepsilon \mathrm{RT}\left[\phi_m, q_m, \Phi_{\Omega_i}, p_{\Omega_i}\right] + \mathrm{NST} \tag{8}$$

Perturbation analysis using ROMs in Eq.(8) agrees with the direct perturbations, as illustrated in Fig.1 below for the moving boundary problem in Eq.(3), where κ_{S2} is one key parameter of the modulation equations. Here RT and NST are short for resonant and non-secular terms, respectively. Note that discrete-1 uses $w(x,t) \approx \phi_m q_m(t) + \psi_0(x)s(t)$, with partially projected passive dynamic pattern captured, while discrete-2 uses $w(x,t) = \phi_m q_m(t) + \psi_0 s(t) + \Phi_\Omega(x)\, p_\Omega(t)$ with passive dynamic patterns fully captured, where $s(t) = p_\Omega(t)$, $\psi_0 + \Phi_\Omega = \Lambda_{B1}\left[g_\Omega(x,\xi)\right]$ and g_Ω is the steady Green's function [1,2]. Results will also be discussed by comparing with those based upon rectified Galerkin method [3] and nonlinear normal modes (NNMs) [4].

Note that the dominant spectrum decomposition technique above can be essentially used for reduced-order modelling of more general (strong/weak) nonlinear systems, if passive dynamic patterns can be explicitly obtained (numerical simulations might be employed for detections), although in this presentation we focus on approximate analytical passive patterns which can be derived in a perturbation formulation.

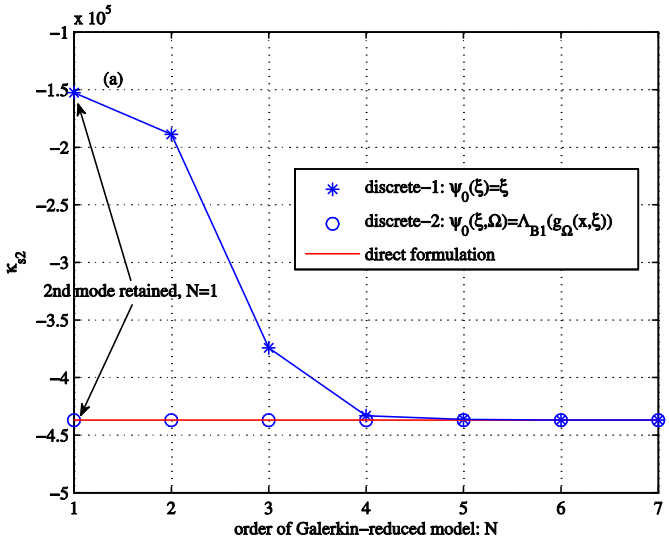

Fig.1 Convergence of modulation parameters in the modulation equations for the moving boundary problem [1]

References

[1] T.D Guo, G. Rega (2019), On direct and discretized perturbation formulations revisited for nonlinear structures' moving boundary problem, European Journal of Mechanics-A/Solids, submitted

[2] T.D Guo, G. Rega, H.J Kang (2019), Perturbation analysis using structure's Galerkin-truncated model: error source, physics interpretation, and a general correction procedure, Nonlinear Dynamics, submitted

[3] A. H Nayfeh (1998), Reduced-order models of weakly nonlinear spatially continuous systems, Nonlinear Dynamics, 15:105-125

[4] C. Touzé, M. Amabili, M O. Thomas (2008), Reduced-order models for large-amplitude vibrations of shells including in-plane inertia, Computer Methods in Applied Mechanics and Engineering, 197: 2030-2045

Reduced-order model based on cyclic symmetric properties to tackle nonlinear mistuned cyclic structures

Samuel Quaegebeur[*,†], Benjamin Chouvion[*], Fabrice Thouverez[*] and Loïc Berthe[†]
[*] *Ecole Centrale de Lyon, LTDS UMR 5513, 69130, Ecully, France*
[†] *Safran Helicopter Engines, 64511, Bordes, France*

Summary. This paper deals with cyclic systems, such as for instance turboengines, in the presence of random mistuning and geometrical nonlinearities. A new methodology based on cyclic components is proposed to create a nonlinear reduced-order model. It is applied on a simplified bladed-disk with a cubic nonlinearity for both tuned and mistuned cases. Internal resonances in which several modes of a system exchange energy are recovered. A comparison of the amplification factor due to mistuning between the linear and nonlinear structures is given.

1 Introduction

This paper studies the dynamics of cyclic structures such as turboengines. For perfectly tuned linear systems, Valid and Ohayon [1] proved that their model could be written in terms of cyclic components. As underlined in [2, 3], the full system of equations, controlling the dynamics of the structure, can thus be split into multiples much smaller cyclic systems. The modes associated with these cyclic components, also called nodal diameters, form a modal basis of the equations of motion. The thorough review given by Mitra and Epureanu [4] presents the properties of cyclic structures and underlines two ongoing problematics for such systems: the nonlinear and the mistuning effects.
In this paper, geometrical nonlinearities are investigated. As the bypath ratio of turboengines is getting larger, effects due to large deformation are getting more pronounced in recent practical applications. Such nonlinearities couple the different nodal diameters of the system. Consequently the size of the cyclic system becomes equal to the onde of the full system and applying cyclic symmetric properties loses its advantages. However combining the specific cyclic geometry of the structure and nonlinear effects reveals some interesting complex phenomena. These have been widely studied by the scientific community. Vakakis [5] studied the nonlinear characteristics (similar modes, localization, energy transfer) of a simplified tuned cyclic structure and compared his result with experimental ones [6]. Georgiades et al. [7] studied modal interactions occuring in cyclic structures. Sarrouy et al. [8] proposed a methodology to determine the multiple periodic solutions of a tuned cyclic structure. Internal resonances [9], transfer of energy from one mode to another, were investigated in these papers. More recently Grolet et al. [10] and Fontanela et al. [11] studied the phenomenon of dark solitons in cyclic structures. All of these papers solved the full system of equation which is time-consuming. Recently, we propose in [12] a methodology to determine which nodal diameter gets coupled in a tuned cyclic structure. This allows to decrease significantly the size of the problem and to express the nonlinearity in the cyclic domain. With this strategy, employing the cyclic symmetry property gets again more computationally interesting.
Random mistuning corresponds to the presence of small imperfection in the cyclic structure, due to manufacturing tolerances for instance. This theoretically breaks the cyclic symmetry property and the entire system must be solved to capture exactly the whole dynamics. In terms of modal properties, the mistuning leads to a split of frequencies of the degenerated modes as explained in [4, 5]. Methodologies [13, 14] that use cyclic symmetric properties have been developed to reduce the size of the linear system of equations. They assume that the motion of the system is mostly controlled by the tuned modes. In a series of papers, Bladh et al. [15, 16, 17] proposed a new methodology to create a reduced-order model (ROM) in order to perform many simulations for multiple random mistuning patterns. This probability study has provided an amplification factor curve with respect to the level of mistuning. This amplification factor is defined as the ratio of the maximal displacement of the mistuned structure over the tuned one. Such analysis is time-consuming, even for linear problems, but the concept of amplification factor is extremely interesting for engines manufacturers. Studies [18] have shown that intentional mistuning patterns (large and controlled difference between the sectors) reduce the impact of random mistuning on the response amplitude and thus allow a better prediction of the system dynamics.
In this paper, both random mistuning and geometrical nonlinearity are considered. The objective is to present a new methodology to create non-linear ROMs that can be used to predict amplification factor of nonlinear mistuned structures. Section 2 presents how mistuning and nonlinearities can be taken into account in a cyclic formulation. Section 3 details the new ROM methodology that is based on these cyclic components. The simplified bladed-disk (blisk) used as test-case will be presented in Section 4. Finally, a probability approach will then be conducted in Section 5 to determine the amplification factor for the linear and nonlinear blisk systems.

2 Cyclic symmetry formulation

This section first recalls the cyclic symmetric properties of a linear system before introducing nonlinearities and mistuning.

2.1 Linear cyclic symmetric systems

Let consider a cyclic structure composed of N identical sectors (tuned system), such as the one illustrated in Figure 1. The dynamics of the entire structure is described with the equation:

$$\mathbf{M}\ddot{\mathbf{u}} + \mathbf{C}\dot{\mathbf{u}} + \mathbf{K}\mathbf{u} = \mathbf{f}_{\text{ext}}, \tag{1}$$

where $\mathbf{M}$, $\mathbf{C}$ and $\mathbf{K}$ represent the mass, damping and stiffness matrices. The vectors $\mathbf{u}$ and $\mathbf{f}_{\text{ext}}$ denote the displacement and the external forces associated with the entire structure. As detailed in [3, 12] the cyclic symmetry property only requires to model a single sector (whose mass, damping and stiffness matrices will be noted $\mathbf{M}_0$, $\mathbf{C}_0$ and $\mathbf{K}_0$). Applying the spectral Fourier matrix $\mathbf{F}$ (normalized by a factor $\sqrt{N}$) and the matrix $(\mathbf{B}_k)_{k\in[\![0,K]\!]}$ (where $K = \frac{N}{2}$ if N is even and $\frac{N-1}{2}$ otherwise) which relates to a phase change function of the nodal diameter considered between the left and right boundaries of a sector, one obtains the following decoupled equation of motion in the cyclic domain for each nodal diameter k,

$$\tilde{\mathbf{M}}_k\ddot{\tilde{\mathbf{u}}}_k + \tilde{\mathbf{C}}_k\dot{\tilde{\mathbf{u}}}_k + \tilde{\mathbf{K}}_k\tilde{\mathbf{u}}_k = \tilde{\mathbf{f}}_k, \tag{2}$$

where $\tilde{\mathbf{M}}_k = \bar{\mathbf{B}}_k^T\bar{\mathbf{F}}\mathbf{M}_0\mathbf{F}\mathbf{B}_k$ and similarly for the damping and stiffness matrices. The operators $.^T$ and $\bar{.}$ denote respectively the tranpose of a vector or matrix and the complex conjugate. The vectors $\tilde{\mathbf{u}}_k$ and $\tilde{\mathbf{f}}_k$ represent the cyclic component of the displacement and the external forces associated with the nodal diameter k. The initial problem (Equation (1)) contains $N \times N_{\text{dof}}$ unknowns (with N_{dof} the number of degrees of freedom of one sector). It is transformed into N independent problems with N_{dof} unknowns each (corresponding to Equation (2) applied $\forall k \in [\![0, K]\!]$).

In turboengines application, one stage of blisk usually gets excited by another stage. This creates an excitation force with specific properties: in most cases the excitation either follows a traveling or a standing wave pattern. The associated wave number of the excitation force will be noted h_{ex} [19]. As a consequence, Equation (2) needs only to be solved for this specific nodal diameter h_{ex} as the remaining nodal diameters are not excited and therefore do not respond.

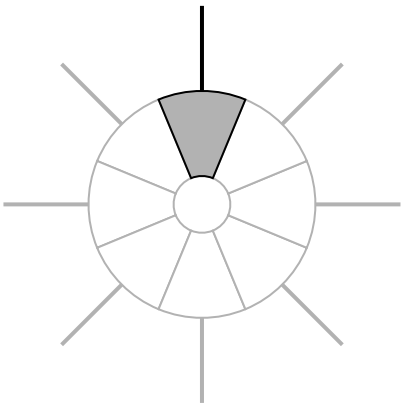

Figure 1: General cyclic structure. The cyclic symmetry property requires to model only a single sector such as the one illustrated in grey color.

2.2 Nonlinear cyclic symmetric systems

In the presence of internal nonlinearities (the cyclic boundaries are assumed to be free of nonlinear forces), the system (2) gets coupled from the nonlinear terms and needs to be solved for all k simultaneously. The equation of motion in the cyclic domain becomes:

$$\tilde{\mathbf{M}}_k\ddot{\tilde{\mathbf{u}}}_k + \tilde{\mathbf{C}}_k\dot{\tilde{\mathbf{u}}}_k + \tilde{\mathbf{K}}_k\tilde{\mathbf{u}}_k + \tilde{\mathbf{f}}_{\text{nl},k}\left(\tilde{\mathbf{u}}\right) = \tilde{\mathbf{f}}_k, \qquad \forall k \in [\![0, K]\!], \tag{3}$$

where $\tilde{\mathbf{f}}_{\text{nl},k}\left(\tilde{\mathbf{u}}\right)$ are the cyclic nonlinear forces for the $k-$th nodal diameter. Those are function of the displacement written here in terms of cyclic components such that $\tilde{\mathbf{u}} = \left[\tilde{\mathbf{u}}_0^T, ..., \tilde{\mathbf{u}}_K^T\right]^T$. The components $\tilde{\mathbf{u}}_k$ for the degenerated diameters ($k \in [\![1, K-1]\!]$ if N is even and $k \in [\![1, K]\!]$ if N is odd) are complex values. The nonlinear terms couple a priori all nodal diameters. Therefore the system (3) has the same size as (1).

In some of our recent work [12], we showed how to identify which nodal diameter get coupled for a given excitation when the structure exhibits polynomial nonlinearities. Applying this methodology reduces the system (3) to the following

$$\tilde{\mathbf{M}}_k\ddot{\tilde{\mathbf{u}}}_k+\tilde{\mathbf{C}}_k\dot{\tilde{\mathbf{u}}}_k+\tilde{\mathbf{K}}_k\tilde{\mathbf{u}}_k+\tilde{\mathbf{f}}_{\mathrm{nl},k}\left(\tilde{\mathbf{u}}\right)=\tilde{\mathbf{f}}_k,\qquad\forall k\in\left(k_m\right),\tag{4}$$

where k_m is a reduced set of the interacting nodal diameters found by the methodology explained in [12]. In practice the nonlinear term $\tilde{\mathbf{f}}_{\mathrm{nl},k}$ can be either obtained by calculating the nonlinear forces in the physical domain (function of the displacement and using Fourier transforms back and forth) or by computing them directly in the cyclic domain (see the method proposed in [12]).

2.3 Nonlinear mistuned cyclic symmetric systems

Only random mistuning (small variations between sectors) is considered in this work. Stiffness variations are assumed but the method can be easily extended for mass or damping mistuning. Consider the cyclic system illustrated in Figure 1 and assume that each sector shows a slight variation in its stiffness matrix such that, for a sector j, its stiffness is defined with

$$\mathbf{K}_j=\mathbf{K}_0+\Delta\mathbf{K}_j,\tag{5}$$

where $\Delta\mathbf{K}_j$ denotes the mistuned part of sector j. In order to get the general equation of motion in the cyclic domain, one applies the same cyclic symmetric procedure (the same projections) as explained above despite the fact that the sectors are not necessarily all identical. The system of equations becomes

$$\tilde{\mathbf{M}}_k\ddot{\tilde{\mathbf{u}}}_k+\tilde{\mathbf{C}}_k\dot{\tilde{\mathbf{u}}}_k+\tilde{\mathbf{K}}_k\tilde{\mathbf{u}}_k+\Delta\tilde{\mathbf{K}}_{k,a}\tilde{\mathbf{u}}+\Delta\tilde{\mathbf{K}}_{k,b}\bar{\tilde{\mathbf{u}}}+\tilde{\mathbf{f}}_{\mathrm{nl},k}\left(\tilde{\mathbf{u}}\right)=\tilde{\mathbf{f}}_{\mathrm{ext},k},\qquad\forall k\in[\![0,K]\!],\tag{6}$$

When applying the Fourier matrix, the physical mistuned matrix gets split into $\Delta\tilde{\mathbf{K}}_a$ and $\Delta\tilde{\mathbf{K}}_b$. They are respectively multiplied by $\tilde{\mathbf{u}}$ and its complex conjugate.. In (6), $\Delta\tilde{\mathbf{K}}_{k,a}$ and $\Delta\tilde{\mathbf{K}}_{k,b}$ represent these mistuned parts impacting the $k-$th nodal diameter. The construction of these matrices follows standard linear algebra from the cyclic symmetric properties and are not detailed here for brevity. As highlightened in (6), the mistuning effect also creates coupling between the cyclic components (the whole $\tilde{\mathbf{u}}$ vector is present) and thus the system must be solved for all nodal diameters simultaneously.
For better readibility, the different equations (6) for all k are concatenated using block diagonal matrices and it gives

$$\tilde{\mathbf{M}}\ddot{\tilde{\mathbf{u}}}+\tilde{\mathbf{C}}\dot{\tilde{\mathbf{u}}}+\tilde{\mathbf{K}}\tilde{\mathbf{u}}+\Delta\tilde{\mathbf{K}}_a\tilde{\mathbf{u}}+\Delta\tilde{\mathbf{K}}_b\bar{\tilde{\mathbf{u}}}+\tilde{\mathbf{f}}_{\mathrm{nl}}\left(\tilde{\mathbf{u}}\right)=\tilde{\mathbf{f}}_{\mathrm{ext}}\tag{7}$$

The purpose of the new methodology presented in this study is to compute a nonlinear reduced-order model (ROM) of system (7).

3 Methodology to create a nonlinear ROM

The following methodology is based on the theory of normal nonlinear mode (NNM) developed by Rosenberg [21] and the synthesis procedure of Szemplinsky [22].

3.1 Evaluation of the NNMs

The first step of the proposed ROM creation is to compute the NNMs associated with the $k-$th cyclic component of the underlying perfect cyclic symmetric system. They are defined as the solutions of the following autonomous and conservative system associated with (4) in which only the nodal diameter k is taken into account in the nonlinear term (the system is thus decoupled),

$$\tilde{\mathbf{M}}_k\ddot{\tilde{\mathbf{u}}}_k+\tilde{\mathbf{K}}_k\tilde{\mathbf{u}}_k+\tilde{\mathbf{f}}_{\mathrm{nl},k}\left(\tilde{\mathbf{u}}_k\right)=\mathbf{0}.\tag{8}$$

The NNMs are computed with the Harmonic Balance Method (HBM) with a pseudo arc-length procedure [20]. The solution of (8) is supposed periodic of fundamental frequency ω and sought as

$$\tilde{\mathbf{u}}_k=\sum_{n=-N_h}^{N_h}\tilde{\mathbf{c}}_{k,n}\mathrm{e}^{\mathrm{i}n\omega t}.\tag{9}$$

where N_h is the maximum number of harmonics retained and $\tilde{\mathbf{c}}_{k,n}$ are the harmonics coefficients of the $k-$nodal diameter. For a degenerated diameter, each harmonic coefficient is independent as $\tilde{\mathbf{u}}_k$ is a complex vector; however for non-degenerated diameters, one has $\tilde{\mathbf{c}}_{n,k}=\bar{\tilde{\mathbf{c}}}_{n,-k}$ and thus a real vector is obtained. Substituting (9) in (8) and projecting the system on the exponential basis with the scalar product,

$$\langle f,g\rangle=\frac{1}{T}\int_0^T f\left(t\right)\bar{g}\left(t\right)\mathrm{d}t,\tag{10}$$

one retrieves the HBM system of equations to solve with $\tilde{\mathbf{c}}_{k,n}$ and ω as unknowns. The nonlinear forces are evaluated with the Alternating Frequency Time (AFT) procedure [23]. In practice, for an intialization on mode i, we only retrieve for each nodal diameter the harmonics coefficients -1 and 1: $\tilde{\mathbf{c}}_{i,k,\pm1}$. These are then normalized by a control coordinate and are used to form the vector denoted later $\boldsymbol{\phi}^{\mathrm{nl}}_{i,\pm1}$, which provides the shape of the displacement for all DOFs parametrized by the control coordinate.

3.2 Synthesis procedure

The second step is to build a nonlinear reduction basis. The solution of (7) is sought after in the form of (11) for each nodal diameter (index k). The cyclic displacement of each of these nodal diameters is defined with multiple nonlinear modes (index i up to I) whose calculation is explained in Section 3.1, supplemented by multiple linear modes (index m up to M).

$$\begin{aligned}\tilde{\mathbf{u}}_k \quad = \quad & \sum_{i=1}^{I}\left[\boldsymbol{\phi}^{\mathrm{nl}}_{i,1}\left(\left|\boldsymbol{\alpha}^{\mathrm{nl}}_{i,n>0}\right|\right)\left(\sum_{n=1}^{N_h}\alpha^{\mathrm{nl}}_{i,n}\mathrm{e}^{\mathrm{i}n\omega t}\right)+\boldsymbol{\phi}^{\mathrm{nl}}_{i,-1}\left(\left|\boldsymbol{\alpha}^{\mathrm{nl}}_{i,n<0}\right|\right)\left(\sum_{n=-1}^{-N_h}\alpha^{\mathrm{nl}}_{i,n}\mathrm{e}^{\mathrm{i}n\omega t}\right)\right] \\ & +\sum_{m=1}^{M}\left[\boldsymbol{\phi}^{\mathrm{lin}}_{m}\left(\alpha^{\mathrm{lin}}_{m,1}\mathrm{e}^{\mathrm{i}\omega t}+\alpha^{\mathrm{lin}}_{m,-1}\mathrm{e}^{-\mathrm{i}\omega t}\right)\right] \qquad\qquad \forall k\in[\![0,K]\!].\end{aligned} \tag{11}$$

The generalized coordinates associated with the NNMs are approximated with a Fourier expansion (of order N_h) whose coefficients are $\alpha^{\mathrm{nl}}_{i,n}$. As explained in [21], $\boldsymbol{\phi}^{\mathrm{nl}}_{i,\pm1}\left(\left|\boldsymbol{\alpha}^{\mathrm{nl}}_{i}\right|\right)$ depends on the amplitude of the generalized coordinates and is thus evaluated via an interpolation process at every solver iteration. Linear modes can also be added to the synthesis procedure if necessary and those are represented by mode shapes $\boldsymbol{\phi}^{\mathrm{lin}}_{m}$ and generalized coordinates $\alpha^{\mathrm{lin}}_{m,1}$ and $\alpha^{\mathrm{lin}}_{m,-1}$. Equation (11) is the synthesis associated with a degenerated nodal diameter: each NNM is split into two parts (the positive and negative harmonic coefficients) to respect the eigenvalue multiplicity. For a non-degenerated diameter, the cyclic component is only controlled with its positive harmonic (its negative counterpart is its complex conjugate). Mathematically the reduction (11) can also be written as

$$\tilde{\mathbf{u}}_k=\sum_{n=-N_h}^{N_h}\tilde{\mathbf{c}}_{k,n}\mathrm{e}^{\mathrm{i}n\omega t}, \qquad \forall k\in[\![0,K]\!], \tag{12}$$

where the harmonic coefficients are sought after as

$$\begin{pmatrix}\tilde{\mathbf{c}}_{-N_h}\\ \vdots\\ \tilde{\mathbf{c}}_{n}\\ \vdots\\ \tilde{\mathbf{c}}_{N_h}\end{pmatrix}=\underbrace{\begin{pmatrix}\boldsymbol{\phi}^{\mathrm{nl}}\left(\left|\boldsymbol{\alpha}^{\mathrm{nl}}\right|\right) & \boldsymbol{\phi}^{\mathrm{lin}}\end{pmatrix}}_{\boldsymbol{\Phi}}\underbrace{\begin{pmatrix}\boldsymbol{\alpha}^{\mathrm{nl}}\\ \boldsymbol{\alpha}^{\mathrm{lin}}_{1}\\ \boldsymbol{\alpha}^{\mathrm{lin}}_{-1}\end{pmatrix}}_{\boldsymbol{\alpha}}, \tag{13}$$

where $\tilde{\mathbf{c}}_n=[\tilde{\mathbf{c}}_{0,n},...,\tilde{\mathbf{c}}_{K,n}]^T$ gathers the $n-$th harmonic coefficients of all nodal diameters and $\boldsymbol{\alpha}^{\mathrm{nl}}$ is the concatenation of $\left(\boldsymbol{\alpha}^{\mathrm{nl}}_{i,n}\right)_{(i,n)\in[\![1,I]\!]\times[\![-N_h,Nh]\!]}$. Similarly, the unknowns $\boldsymbol{\alpha}^{\mathrm{lin}}_{\pm1}$ contains the generalized coordinates for the different linear modes. The matrix $\boldsymbol{\Phi}$ is created by combining appropriately the different basis: the NNMs and the linear modes. The solution (12) is substituted in (7) and the system is then projected in the exponential basis (see Equation (10)). This gives:

$$\begin{pmatrix}\tilde{\mathbf{Z}}_{-N_h} & \cdots & 0\\ \vdots & \ddots & \vdots\\ 0 & \cdots & \tilde{\mathbf{Z}}_{N_h}\end{pmatrix}\begin{pmatrix}\tilde{\mathbf{c}}_{-N_h}\\ \vdots\\ \tilde{\mathbf{c}}_{N_h}\end{pmatrix}+\begin{pmatrix}0 & \cdots & \Delta\tilde{\mathbf{K}}_b\\ \vdots & \iddots & \vdots\\ \Delta\tilde{\mathbf{K}}_b & \cdots & 0\end{pmatrix}\begin{pmatrix}\tilde{\bar{\mathbf{c}}}_{-Nh}\\ \vdots\\ \tilde{\bar{\mathbf{c}}}_{N_h}\end{pmatrix}+\begin{pmatrix}\tilde{\mathbf{c}}_{\mathbf{f}_{\mathrm{nl},-N_h}}\\ \vdots\\ \tilde{\mathbf{c}}_{\mathbf{f}_{\mathrm{nl},N_h}}\end{pmatrix}=\begin{pmatrix}\tilde{\mathbf{c}}_{\mathbf{f}_{\mathrm{ext},-N_h}}\\ \vdots\\ \tilde{\mathbf{c}}_{\mathbf{f}_{\mathrm{ext},N_h}}\end{pmatrix} \tag{14}$$

where $\tilde{\mathbf{Z}}_n=(\mathrm{i}n\omega)\tilde{\mathbf{M}}+(\mathrm{i}n\omega)\tilde{\mathbf{C}}+\tilde{\mathbf{K}}+\Delta\tilde{\mathbf{K}}_a$ is the dynamical rigidity matrix associated with the harmonic $n\in[\![-N_h,N_h]\!]$. The vectors $\tilde{\mathbf{c}}_{\mathbf{f}_{\mathrm{nl},n}}$ and $\tilde{\mathbf{c}}_{\mathbf{f}_{\mathrm{ext},n}}$ gather the $n-$th harmonic coefficients of all nodal diameters for the nonlinear and external forces. The nonlinear forces are evaluated with the same procedure as the one explained in Section 3.1. The harmonic coefficients in (14) are then substituted by (13). Finally, the last stage of the ROM creation is premultiplying this equation by $\boldsymbol{\Phi}^T$,

$$\left(\bar{\boldsymbol{\Phi}}^T\tilde{\mathbf{Z}}\boldsymbol{\Phi}\right)\boldsymbol{\alpha}+\left(\bar{\boldsymbol{\Phi}}^T\left(\mathbf{J}_{1+2N_h}\otimes\Delta\tilde{\mathbf{K}}_b\right)\bar{\boldsymbol{\Phi}}\right)\bar{\boldsymbol{\alpha}}+\bar{\boldsymbol{\Phi}}^T\tilde{\mathbf{c}}_{\mathbf{f}_{\mathrm{nl}}}=\bar{\boldsymbol{\Phi}}^T\tilde{\mathbf{c}}_{\mathbf{f}_{\mathrm{ext}}}, \tag{15}$$

where $\tilde{\mathbf{Z}}$ is a block diagonal matrix containing $\left(\tilde{\mathbf{Z}}_n\right)_{n\in[\![-N_h,N_h]\!]}$. The vectors $\boldsymbol{\alpha}$, $\tilde{\mathbf{c}}_{f_{\mathrm{nl}}}$ and $\tilde{\mathbf{c}}_{f_{\mathrm{ext}}}$ are vertically concatenated. The matrix $\mathbf{J}_{1+2N_h}$ is the exchange matrix ($\mathbf{J}_{1+2N_h,i,j}=\delta_{2N_h+2-i,j}$).
To couple the different modes, the nonlinear forces (term $\tilde{\mathbf{c}}_{\mathbf{f}_{\mathrm{nl}}}$) are evaluated with the AFT procedure while solving (15).

Even though the notation suggests that the same expansion is performed for each nodal diameter, the new methodology can be adjusted and each nodal diameter written with different modal basis and harmonic expansion.
This formulation is different from the synthesis proposed by Krack et al. [24] for the following reasons: the reduced Equation (15) uses cyclic components, a multi-harmonic expansion and a reevaluation of the nonlinear forces (once with the NNM evaluation and once with the synthesis stage).
In practice, the unknowns of system (15), $\boldsymbol{\alpha}$, are solved with a Newton-Raphson solver. For better efficiency, the semi-analytical jacobian of this system is provided to the solver. The work of Joannin et al. [25] provides insights on how to compute the jacobian in a similar problem.

3.3 Choice of nodal diameters and modes

The methodology proposed is efficient if the user chooses wisely the NNMs to compute, the linear modes and the HBM expansion order. As explained in Section 2, turboengines are usually excited by a specific excitation force with a given wave number h_{ex}. Moreover only random mistuning is accounted in this paper which induces an assumed slight variation around the tuned response of the system.
As a consequence, only NNMs of the nodal diameters that interact in the tuned system (see [12]) are evaluated. In the case of a mistuned structure, corrections are made possible by taking into account the linear modes of the remaining nodal diameters.
The selection of which modes to compute depends on the probability of the appearance of internal resonances and thus on the spectral repartition of the natural frequencies of the system.

4 Application for a tuned and a mistuned blisks

The purpose of this Section is to validate the methodology explained in Section 3. The reference solution used for validation is the HBM employed on the full system with $N_h = 3$ harmonics. Comparison of computation time between the reference solution and the ROM procedure is provided in Section 4.4.

4.1 Simplified model and ROM creation

The proposed methodology is tested on a simplified blisk composed of $N = 24$ sectors, one of which is illustrated in Figure 2. A cubic nonlinearity is applied at the tip of the blade to model symmetric large displacement. This test case was already used in [12] to study a perfectly tuned structure. The mass, damping and stiffness values can be found in Tables 1 and 2 of the aforementioned article. Figure 3 represents the natural frequencies of the underlying linear tuned system. In the remaining of the article, an external force with $h_{ex} = 3$ is applied and is set to excite the first mode of the nodal diameter 3 of the system. Based on [12], we know that the third and ninth nodal diameters will be coupled. Moreover, Figure 3 allows to see that the first and third modes of the nodal diameter 3 are almost commensurable, and similarly for the first and second modes of the ninth nodal diameter. As a consequence 1:3 internal resonances may occur. The NNMs computed will therefore be those associated with these 4 natural frequencies (depicted by red circles in Figure 3). In the rest of this section, the reduction basis used is composed of these 4 NNMs, expanded with the HBM up to $N_h = 3$, associated with more or less linear modes depending on the situation.

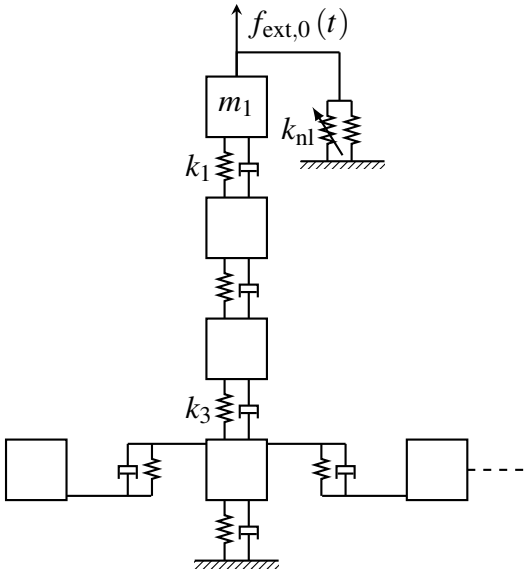

Figure 2: Description of the simplified blisk.

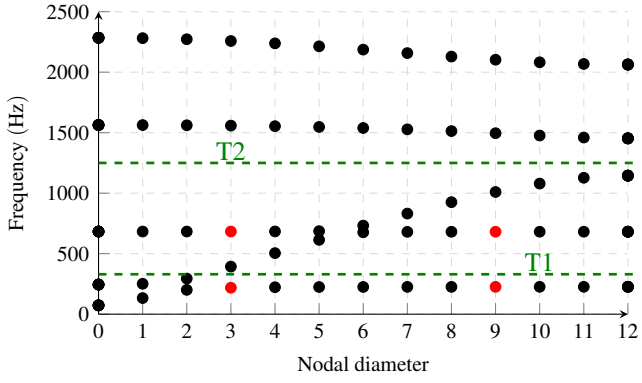

Figure 3: Natural frequencies for each nodal diameter.

The tuned system is first studied in Section 4.2. Section 4.3 focuses on mistuning and a random mistuning pattern is introduced on top of the spring stiffness values k_1 and k_3, see Figure 2. The new stiffnesses are defined as

$$k_{m,i} = k_i\,(1+\varepsilon\xi_i)\,, \qquad i \in \{1,3\} \tag{16}$$

where $k_{m,i}$ is the mistuned stiffness value used instead of k_i ($i = 1$ ou 3). The parameters ε and ξ_i are the mistuning parameters: ε controls the level of mistuning ($\varepsilon \in [0,1]$) and ξ_i is a random value taken from an uniform law in $[-0.1, 0.1]$. Table 1 provides the random mistuning pattern used in this section.

Sectors	S1	S2	S3	S4	S5	S6	S7	S8
ξ_1 (in%)	0.0094	−8.8	−9.2	0.43	6.4	4.4	3.2	9.5
ξ_3 (in%)	−0.583	3.6	−8.6	−8	6.4	−7	0.37	3
	S9	S10	S11	S12	S13	S14	S15	S16
	6	−1.4	−8.3	−6.5	6.6	−8.8	0.54	3.1
	−0.92	6.5	−7.3	−2.2	6.1	−2	−1.7	2.6
	S17	S18	S19	S20	S21	S22	S23	S24
	−4.2	−9.7	−6.7	−2.6	−0.21	−9	−8.9	−4.6
	−1.4	9.7	−7.9	−6	−3.2	8.4	4.8	−1.5

Table 1: Numerical values used for ξ.

For each simulation, a bifurcation analysis [26] and branch switching algorithms [27] are performed. Solving (15) provides the generalized coordinates which can then be employed to recover the displacement of the entire structure. In the following section, the results illustrated are the displacement amplitude of the mass m_1 for the third and ninth nodal diameters. Those are noted respectively $\tilde{u}_3$ and $\tilde{u}_9$.

4.2 Results for the tuned structure

First the ROM procedure is validated for the tuned model. The external force is applied on mass m_1, and is defined as:

$$\tilde{f}_{\text{ext},3} = 25\left(\mathrm{e}^{-\mathrm{i}\omega t} + \mathrm{e}^{\mathrm{i}\omega t}\right). \tag{17}$$

This high amplitude force was chosen to exhibit multiple nonlinear phenomena for the tuned case and thus to verify the accuracy of the ROM for these complex situations.

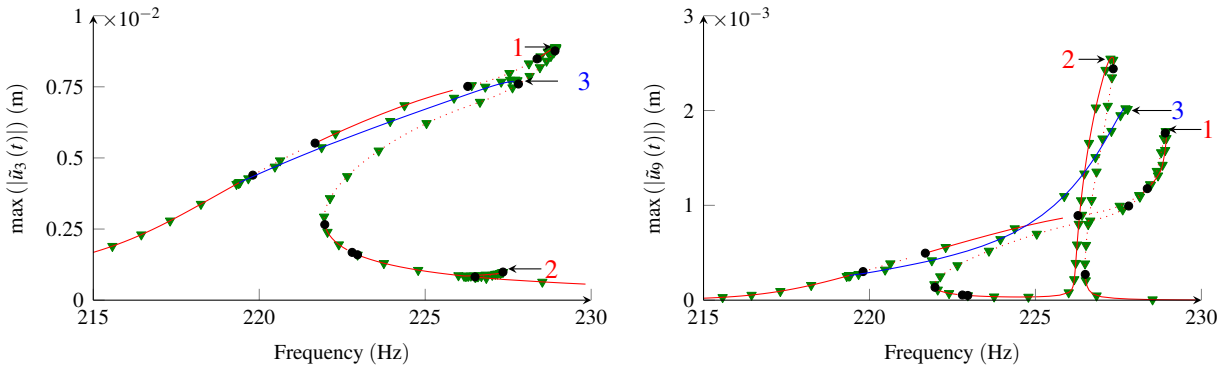

Figure 4: Frequency forced response for the tuned system. (▾): reference solution; (—): ROM solution for the stable main branch; (····): ROM solution for the unstable main branch; (—): ROM solution for the bifurcated branch; (●): bifurcation points.

The results obtained with the ROM procedure and the reference solution are provided in Figure 4. Two branches are represented: the main branch of solution and a bifurcated branch initiated from a symmetry-breaking bifurcation (only the stable part of this branch is represented in Figure 4). The ROM solution perfectly matches the reference solution with a huge computational time saving as detailed in Table 2. Multiple internal resonances are obtained in Figure 4. They are highlightened by arrows and number and the harmonics coefficients of the response at these points are represented in Figure 5. For the peak numbered 1, on the main branch, $\tilde{u}_3$ mainly responds with its first harmonic (see Figure 5a); however $\tilde{u}_9$ responds both on its first and third harmonics. It shows that a 1:1 and 1:3 internal resonances have taken place. For the peak numbered 2, still located on the main branch, the amplitude of $\tilde{u}_9$ is higher than $\tilde{u}_3$ (see Figure 5b) and is mainly due to

its first harmonic. An 1:1 internal resonance is occuring. Notice that for both of these peaks, the solution has a standing wave form similar to the external force (because $\tilde{c}_{k,n} = -\bar{\tilde{c}}_{k,-n}$). For the peak numbered 3 located on the bifurcated branch, the solution has a forward traveling wave shape (because $\tilde{c}_{k,n<0} \neq 0$ and $\tilde{c}_{k,n>0} = 0$). Moreover Figure 5c shows a 1:3 internal resonance.

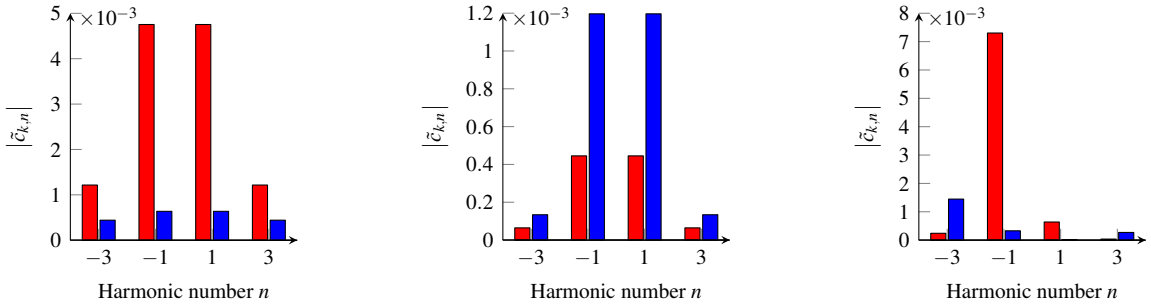

(a) Peak 1 (main branch). (b) Peak 2 (main branch). (c) Peak 3 (bifurcated branch).

Figure 5: Amplitude of the harmonics coefficients of the response at the three peaks mentioned in Figure 4. (—): $\tilde{c}_{3,n}$; (—): $\tilde{c}_{9,n}$. The second harmonic is not represented as it is exactly equal to 0.

The same model was used in [12] with a different reduction procedure and similar results were obtained. Overall, this example has shown that the proposed ROM is perfectly able to recover complex phenomena such as internal resonances and branch switching for a tuned system.

4.3 Results for the mistuned structure

The random mistuning pattern given in Table 1 is now introduced in the system. Three values of ε are studied: 0.01, 0.1 and 1, corresponding respectively to a deviation of 0.1%, 1% and 10% between the tuned and mistuned systems. A traveling wave excitation is applied on m_1 such that

$$\tilde{f}_{\text{ext},3} = 2.5\text{e}^{-\text{i}\omega t}. \tag{18}$$

This force is 10 times smaller than the standing wave force used for the tuned case and its amplitude is more typical of turboengines applications.

For $\varepsilon = 0.01$ and $\varepsilon = 0.1$, the nonlinear basis is supplemented with all the linear modes below the threshold 1 of Figure 3 (represented by the dashed green line T1) that are used to take into account the other nodal diameters. For $\varepsilon = 1$, the system is largely mistuned (10% deviation) and the first three modes of each nodal diameter are included in the reduction basis (represented by the dashed green line T2 in Figure 3). For this system, all nodal diameters are coupled and respond; however only the third and ninth nodal diameters will be represented as they control the main dynamics. The stability of the response was not studied as the main purpose of the article is to validate the accuracy of the ROM with respect to the reference solution.

Figure 6 represents the forced response for the three values of ε. For these different configurations, no bifurcated branch was obtained. As ε increases, the amplitude of $\tilde{u}_3$ and $\tilde{u}_9$ decreases. The energy initially contained in these two nodal diameters is gradually transfered to the rest of the nodal diameters due to the mistuning effect. Moreover, we can observe the appearance of multiple linear resonances for the third and ninth nodal diameters. This is expected as frequency splitting occurs [28]. The new methodology perfectly matches the result of the reference solution.

In mistuned systems, detecting internal resonances is an arduous task as all nodal diameters are expected to respond. Figure 7 represents the harmonic coefficients of $\tilde{u}_3$ and $\tilde{u}_9$ for the peaks represented in Figure 6. For peak 1 of Figure 6a ($\varepsilon = 0.01$), the solution shows a traveling shape and the third harmonic of $\tilde{u}_9$ is dominant. It gives evidence to a 1:3 internal resonance (see Figures 7a). Similar results are obtained for peak 3 of Figure 6b ($\varepsilon = 0.1$) as shown in Figures 7b. The peaks 2 and 4 for the $\varepsilon = 0.01$ and $\varepsilon = 0.1$ are associated with a standing wave solution as depicted in Figures 7d and 7e for instance. For both peaks of Figure 6c ($\varepsilon = 1$), the solution has a standing wave shape and only the first harmonic responds for $\tilde{u}_3$ and $\tilde{u}_9$.

Obtaining a standing wave solution, even though the excitation is defined with a traveling form, was expected for mistuned system [28]. However Figure 7 presents an interesting trend: as ε increases, the internal resonances progressively disappear. Studying succesively Figure 7a, 7b and 7c (increase of ε), one can observe that the amplitude of the third harmonic of $\tilde{u}_9$ diminishes in aid of the first harmonic. As a consequence, it is expected that large mistuning would remove internal resonances. In order to make a definitive statement, further studies should be conducted but these are beyond the scope of this paper

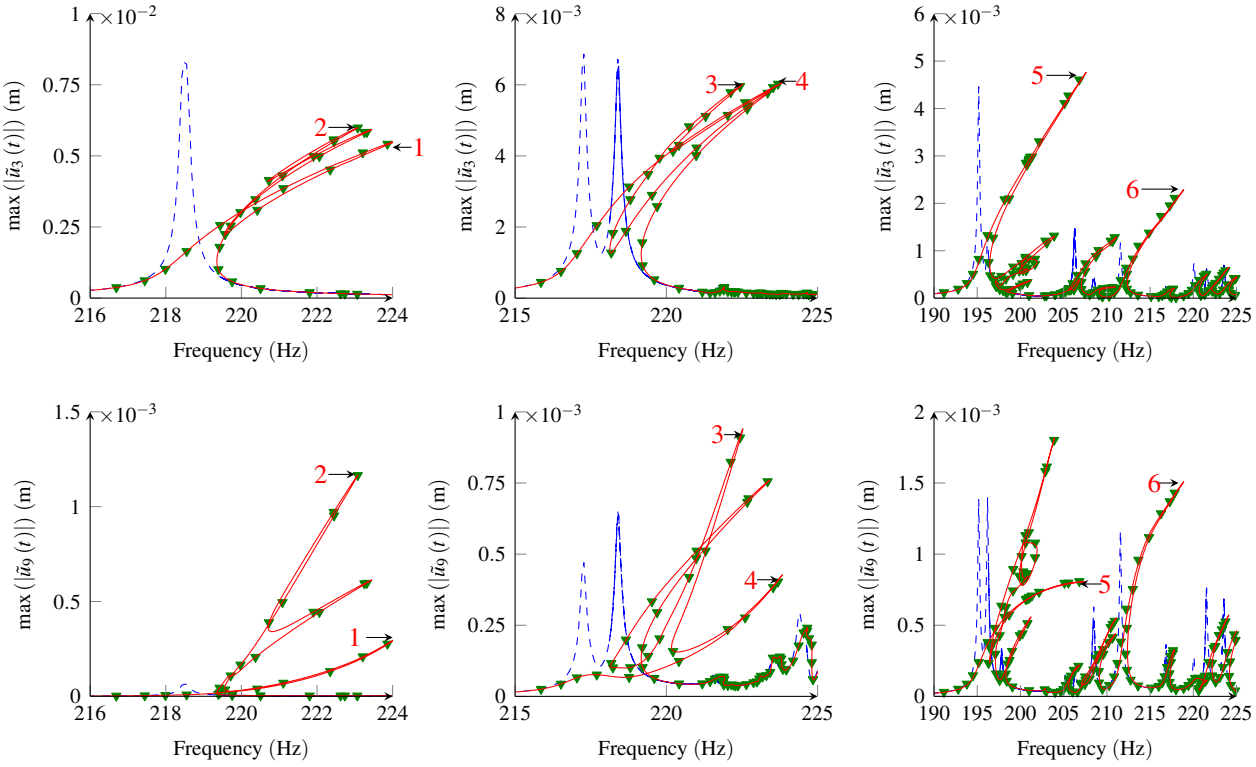

(a) $\varepsilon = 0.01$. (b) $\varepsilon = 0.1$. (c) $\varepsilon = 1$

Figure 6: Frequency response function for different levels of mistuning. (- -): linear response; the rest of the legend matches the one of Figure 4.

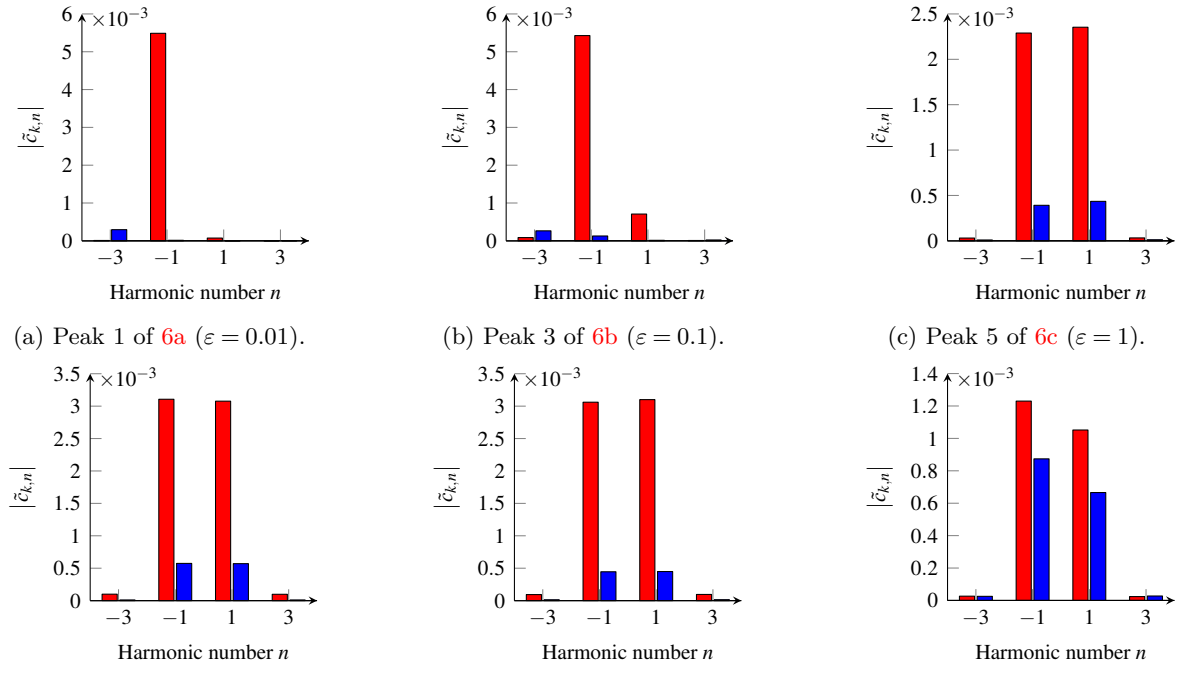

(a) Peak 1 of 6a ($\varepsilon = 0.01$). (b) Peak 3 of 6b ($\varepsilon = 0.1$). (c) Peak 5 of 6c ($\varepsilon = 1$).

(d) Peak 2 of 6a ($\varepsilon = 0.01$). (e) Peak 4 of 6b ($\varepsilon = 0.1$). (f) peak 6 of 6c ($\varepsilon = 1$).

Figure 7: Harmonics content for the response on the six peaks of Figure 6. The legend matches the one of Figure 5.

4.4 Computation time comparison

For both tuned and mistuned systems, the proposed ROM has shown great accuracy and enables to recover complex nonlinear phenomena. Table 2 compares the computation time between the ROM and the reference solutions.

Test case	Method	Number of unknowns	Computation time (min)
Tuned system	Reference	720	24
	ROM	48	3
Mistuned system ($\varepsilon = 0.01$)	Reference	720	59
	ROM	108	24
Mistuned system ($\varepsilon = 0.1$)	Reference	720	145
	ROM	108	43
Mistuned system ($\varepsilon = 1$)	Reference	720	202
	ROM	186	81

Table 2: Computation time for the different test cases and methodologies. The simulations were run on a standard computer with Intel Core i7 2.30GHz 8Go.

The computation time of the new methodology is greatly reduced compared to the reference solution (2 to 8 times faster). The computation time of the NNMs is not taken into account in Table 2 as it is negligible (below 20 s and needs to be computed only once for all simulations).

5 Amplification factor

When considering mistuned systems, turboengineers are used to study the maximal amplitude of the (physical) displacement obtained over all sectors. The amplification factor (AF) is defined as the ratio between this maximum amplitude and the amplitude of the (single) peak obtained in a perfectly tuned system. This is illustrated in Figure 8 for the linear case. We propose a similar definition in the presence of nonlinearity, see Figure 9. Both of these Figures are obtained on the test case of Figure 2 with a 2.5 N traveling wave excitation and $h_{ex} = 3$. The mistuning pattern is the one presented in Table 1 with $\varepsilon = 0.1$.

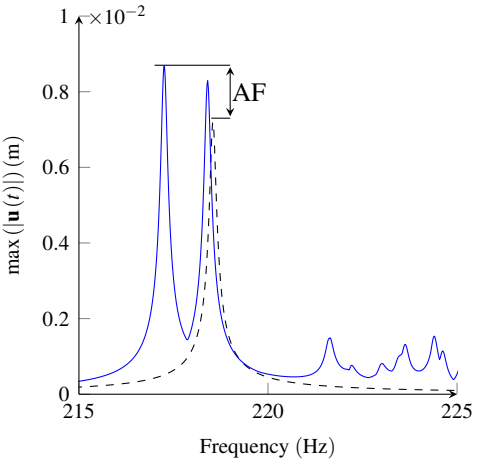

Figure 8: Tuned (- -) and mistuned (—) linear frequency forced responses.

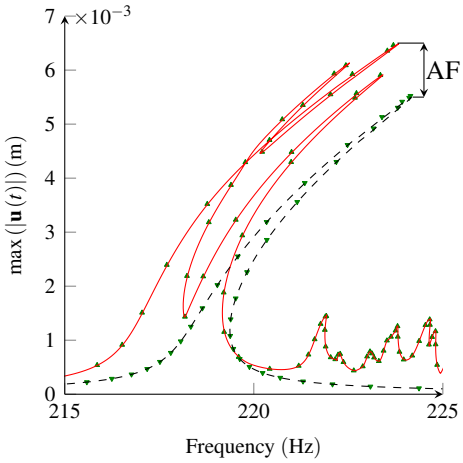

Figure 9: Tuned (- -) (respectively (▼)) and mistuned (—) (respectively (▲)) nonlinear frequency forced responses obtained with the ROM (respectively the reference solution).

The amplification factor relates to the amplification of the response due to the mistuning. In practice, one must generate a large number of random mistuning patterns to determine the overall behaviour of the AF. Extended studies have performed such tasks [17, 29] for linear systems. For instance, to determine accurately the 95th AF threshold (corresponding to 95% of mistuned blisks below this AF), one way is to launch a Monte Carlo simulation with a large number of samples. The simulation consists in randomly picking a large number of mistuning patterns (for a given law), and sweep the excitation frequency for each of them to determine the associated maximal amplitude. If one wants to reach a given accuracy, then the larger the AF-threshold, the

more simulations must be run. These calculations are time-consuming but it was shown, for instance in [17], that the distribution of the AF law was a three-parameter Weibull law, and this allows to reduce greatly the number of simulations needed. In the following, we have used a Weibull law reconstructed with only 50 simulations.
We have run these simulations for a 2.5 N traveling force and $h_{ex} = 3$. The mistuning definition follows Equation (16) with $\varepsilon = 1$ and ξ is taken within an uniform law with 15 different standard deviations (from 1% to 15% with a step of 1%). Figure 10a represents the AF with respect to the standard deviation for the linear system. Figure 10b provides the same information for the nonlinear system. For both of these Figures, the 95th, 50th and 5th percentiles (percentage of systems below the threshold) are represented. The maximum AF is obtained for $\varepsilon_{\max} \approx 3\%$ for the linear system and $\varepsilon_{\max} \approx 9\%$ for the nonlinear one. The value of the maximum AF is close to 1.9 for the linear system and 1.8 for the nonlinear one. Beyond this value of $\varepsilon_{\max}$, the AF decreases. This behaviour has already been observed, in [29] for instance. The ROM solution matches well the reference solution with a significant computational time saving: the trend is correctly captured and errors are below 7% for a high level of mistuning.
Notice that the results were obtained with a specific excitation force. While Figure 10a remains valid for other levels of excitation (at h_{ex} fixed), the nonlinear results of Figure 10b are expected to vary. For a complete map of the influence of the mistuning, one must run these computations for all values of h_{ex} as well as for different force amplitudes.

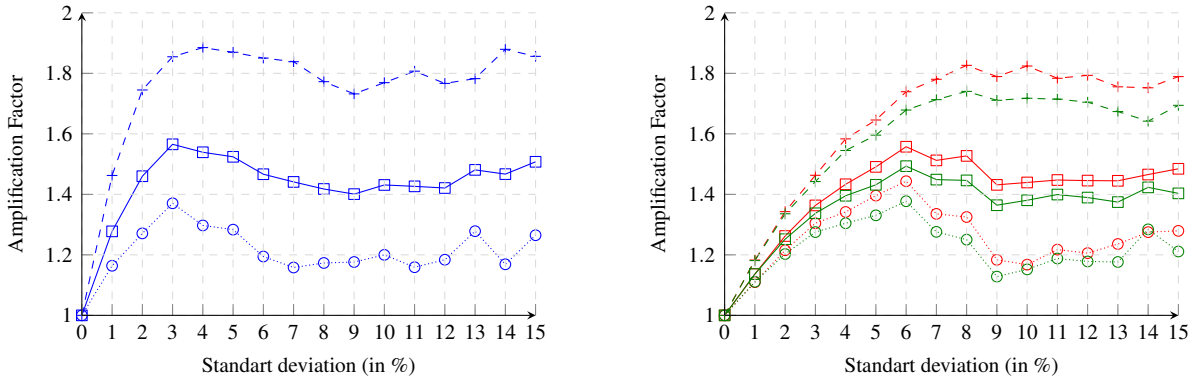

(a) Linear Solution.

(b) Nonlinear solution for the ROM/reference procedures.

Figure 10: Amplification factor with respect to the deviation of the random mistuned pattern. (-+):95th percentile; (-⊟-): 50th percentile; (··o··): 5th percentile. The blue, red and green colors denote respectively the linear case, the ROM and the reference solutions for the nonlinear case.

6 Conclusion

This paper presented a new reduced-order model methodology based on the computation of cyclic normal nonlinear modes. It is able to handle randomly mistuned cyclic structures while exhibiting complex nonlinear behaviour such as internal resonances. The method has been validated for a simplified blisk and has shown great accuracy while reducing significantly the computation time.
A probabilist study was conducted to study the impact of both the nonlinearity and the mistuning on the amplification factor of the system. For both linear and nonlinear systems, mistuning may lead to an amplification of 90% in the response. This maximum is however reached for different values of standard deviation. For both systems a plateau is reached after a relatively large value of standard deviation.
This new methodology is expected to be applicable and efficient for finite-element models of engineered structures. It thus offers probabilist opportunities which, at this date, could not be achieved. However, applying the same procedure to intentional mistuned structures (large discrepancies between the blades) is expected to be less efficient because the system is no longer close to its tuned counterpart.

Acknowledgements

The authors would like to acknowledge the financial support of Safran Helicopter Engines.

References

[1] Valid R. and Ohayon R. 1985 Théorie et calcul statique et dynamique des structures à symétries cycliques. *La Recherche aérospatiale*

[2] MacNeal, R. H. 1973 NASTRAN cyclic symmetry capability.

[3] Thomas, D. L. 1979 Dynamics of rotationally periodic structures *International Journal for Numerical Methods in Engineering*

[4] Mitra, M. and Epureanu, B.I. 2019 Dynamic Modeling and Projection-Based Reduction Methods for Bladed Disks With Nonlinear Frictional and Intermittent Contact Interfaces *ASME, Applied Mechanics Reviews*

[5] Vakakis, A. F. 1992 Dynamics of a nonlinear periodic structure with cyclic symmetry *Acta Mechanica*

[6] Tobias, S. A. and Arnold, R. N. 1957 The Influence of Dynamical Imperfection on the Vibration of Rotating Disks *Proceedings of the Institution of Mechanical Engineers*

[7] Georgiades F. and Peeters M. and Kerschen G. and Golinval J. C. and Ruzzene M. 2009 Modal Analysis of a Nonlinear Periodic Structure with Cyclic Symmetry. *AIAA Journal*

[8] Sarrouy, E. and Grolet, A. and Thouverez, F. 2011 Global and bifurcation analysis of a structure with cyclic symmetry *International Journal of Non-Linear Mechanics*

[9] Nayfeh, Ali H. and Mook, Dean T. 2008 Nonlinear Oscillations *John Wiley & Sons*

[10] Tobias, S. and Grolet, A. and Hoffmann, N. and Thouverez, F. and Schwingshackl, C. 2016 Travelling and standing envelope solitons in discrete non-linear cyclic structures *Mechanical Systems and Signal Processing*

[11] Fontanela, F. and Grolet, A. and Salles, L. and Chabchoub, A. and Hoffmann, N. 2018 Dark solitons, modulation instability and breathers in a chain of weakly nonlinear oscillators with cyclic symmetry *Journal of Sound and Vibration*

[12] Quaegebeur S. and Chouvion B. and Thouverez F. et al. 2020 Energy transfer between nodal diameters of cyclic symmetric structures exhibiting polynomial nonlinearities: Cyclic condition and analysis. *Mechanical Systems and Signal Processing*

[13] Yang, M.-T. and Griffin, J. H. 1999 A Reduced Order Model of Mistuning Using a Subset of Nominal System Modes *American Society of Mechanical Engineers*

[14] Feiner, D. M. and Griffin, J. H. 2002 A Fundamental Model of Mistuning for a Single Family of Modes *American Society of Mechanical Engineers*

[15] Bladh, R. and Castanier, M. P. and Pierre, C. 2001 Component-Mode-Based Reduced Order Modeling Techniques for Mistuned Bladed Disks Part I: Theoretical Models *American Society of Mechanical Engineers*

[16] Bladh, R. and Castanier, M. P. and Pierre, C. 2001 Component-Mode-Based Reduced Order Modeling Techniques for Mistuned Bladed Disks Part II: Applications *Journal of Engineering for Gas Turbines and Power*

[17] Bladh, R. and Castanier, M. P. and Pierre, C. 2002 Dynamic Response Predictions for a Mistuned Industrial Turbomachinery Rotor Using Reduced-Order Modeling *Journal of Engineering for Gas Turbines and Power*

[18] Castanier, M.P. and Pierre, C. 2002 Using Intentional Mistuning in the Design of Turbomachinery Rotors *AIAA Journal*

[19] Grolet, A. and Thouverez, F. 2012 Free and forced vibration analysis of a nonlinear system with cyclic symmetry: Application to a simplified model *Journal of Sound and Vibration*

[20] Kerschen, G. and Peeters, M. and Golinval, J. C. and Vakakis, A. F. 2009 Nonlinear normal modes, Part I: A useful framework for the structural dynamicist *Mechanical Systems and Signal Processing*

[21] Rosenberg, R. M. 1962 The Normal Modes of Nonlinear n-Degree-of-Freedom Systems *Journal of Applied Mechanics*

[22] Szemplińska-Stupnicka, W. 1979 The modified single mode method in the investigations of the resonant vibrations of non-linear systems *Journal of Sound and Vibration*

[23] Cameron, T. M. and Griffin, J. H. 1989 An Alternating Frequency/Time Domain Method for Calculating the Steady-State Response of Nonlinear Dynamic Systems *Journal of Applied Mechanics*

[24] Krack M.,and Panning-von Scheidt L. and Wallaschek J. 2013 A method for nonlinear modal analysis and synthesis: Application to harmonically forced and self-excited mechanical systems. *Journal of Sound and Vibration*

[25] Joannin, C. and Chouvion, B. and Thouverez, F. and Ousty, JP and Mbaye, M. 2017 A nonlinear component mode synthesis method for the computation of steady-state vibrations in non-conservative systems *Mechanical Systems and Signal Processing*

[26] Seydel, R. 2010 Practical Bifurcation and Stability Analysis *Springer-Verlag*

[27] Xie, L. and Baguet, S. and Prabel, B. and Dufour, R 2017 Bifurcation tracking by Harmonic Balance Method for performance tuning of nonlinear dynamical systems *Mechanical Systems and Signal Processing*

[28] Joannin, C. and Chouvion, B. and Thouverez, F. and Mbaye, M. and Ousty, J.-P. 2015 Nonlinear Modal Analysis of Mistuned Periodic Structures Subjected to Dry Friction *Journal of Engineering for Gas Turbines and Power*

[29] Castanier, M.P. and Pierre, C. 2006 Modeling and analysis of mistuned bladed disk vibration: Status and emerging directions *AIAA Journal*

Non-intrusive reduced-order modeling of the drift flux model using a residual recurrent neural network

M.H. Abbasi*, L. Iapichino*, W. Schilders* and N. van de Wouw ††
*Department of Mathematics and Computer Science, Eindhoven University of Technology, The Netherlands
†Department of Mechanical Engineering, Eindhoven University of Technology, The Netherlands
† Department of Civil, Environmental and Geo-Engineering, University of Minnesota, U.S.A.

Summary. Projection-based Model Order Reduction (MOR) aims at reducing the computational cost associated with the solution of large-scale dynamical systems to be used in many-query settings such as optimization and control. For nonlinear systems, significant cost reduction is only possible through an additional approximation of the nonlinear terms to reduce the computational effort of the Reduced-Order Model (ROM). These hyper-reduction techniques often lead to instability when the nonlinear terms are not approximated with a high accuracy. Increasing the accuracy of the nonlinearity approximation increases the complexity of the ROM and will question the original motivation behind MOR to obtain a faster simulator and a system with lower number of states for controller design. In this study, a non-intrusive (data-based without the need for the physical model) Reduced Basis (RB) method is proposed for a highly nonlinear model, called the Drift Flux Model (DFM), to simulate multi-phase flow inside a pipe. A set of RB functions are extracted from a collection of high-fidelity solutions by changing the input signals of the system via a Proper Orthogonal Decomposition (POD). The solution of the ROM is obtained through a linear combination of these RB functions with coefficients obtained by a Residual Recurrent Neural Network (RRNN). The RRNN approximates the map between the input signals and the increment of projection coefficients of the high-fidelity solution onto the reduced space. The generation of the RB functions and the training of the RRNN are performed during the offline phase, while the RB solution of a new input signal can be recovered via the outputs of the RRNN in the online phase. The proposed method decouples the offline and the online phases, and provides fast and reliable solutions of the original DFM.

Problem description

One of the widely accepted models to simulate multi-phase flow is the DFM [1], a highly nonlinear set of conservation laws described as below:

$$\begin{cases} \dfrac{\partial}{\partial t}(\alpha_l\rho_l) + \dfrac{\partial}{\partial x}(\alpha_l\rho_l v_l) = 0, \\ \dfrac{\partial}{\partial t}(\alpha_g\rho_g) + \dfrac{\partial}{\partial x}(\alpha_g\rho_g v_g) = 0, \\ \dfrac{\partial}{\partial t}(\alpha_l\rho_l v_l + \alpha_g\rho_g v_g) + \dfrac{\partial}{\partial x}(\alpha_l\rho_l v_l^2 + \alpha_g\rho_g v_g^2 + p) = F + G, \end{cases} \quad t \in [0,T], x \in [0,L], \quad \begin{cases} 1 = \alpha_l + \alpha_g, \\ v_g = K(\alpha_l v_l + \alpha_g v_g) + S, \\ p = (\rho - \rho_0)c_l^2 + p_0, \\ p = \rho_g c_g^2, \end{cases} \tag{1}$$

where $\alpha_i(t,x), \rho_i(t,x), v_i(t,x), p(t,x)$ represent volume fraction, density and velocity of phase i and the common pressure, respectively. The subscript $i \in \{l, g\}$ denotes the liquid and gas phase with c_i the sound velocity in the medium of phase i, K and S two constants implying the flow regime and p_0 and ρ_0 the reference pressure and density. Here, t represents time and T is the time horizon of the simulation. In addition, x denotes the spatial coordinate and L is the length of the spatial domain. Finally, $F(t,x)$ and $G(t,x)$, respectively, denote the frictional and gravitational terms, which add extra nonlinearity to (1).

Highly nonlinear finite-volume schemes are developed to solve (1) [1], rendering the discretized system of equations even more complex. Therefore, real-time simulations cannot be achieved unless powerful computational resources are available. Moreover, control design for such a complex system is generally infeasible. Hence, MOR should be applied.

Reduced-order model

Intrusive (projection-based) MOR of (1) leads to an unstable system unless the nonlinear parts are approximated with a high accuracy. To circumvent this issue, a non-intrusive (data-based) MOR is applied in this study, which in addition resolves the need to access the physical model and enables the use of highly nonlinear and accurate finite-volume schemes. The algorithm introduced in [3] is used here together with an RRNN structure as shown in Figure 1. The variables W and b are, respectively, the weight coefficients and the bias values of each node in the hidden layer, to be specified during the training. It is well-known that recurrent neural networks trained on the residual values (variation of states over each time step) have a higher capability in approximating dynamical systems [4].

The RRNN structure takes the input signals of the system and gives the temporal variation of the coefficients of the RB functions as an output. Since we are dealing with a dynamical system, the coefficients of the RB functions in the previous time step are also fed as an input to the RRNN.

Results

In the simulations for the RRNN, we have used one hidden layer consisting of 20 nodes with one time-step delay ($0:1$ in the delay layer means both $u(t)$ and $u(t-1)$ are considered as the training inputs). The delay in the recurrent structure

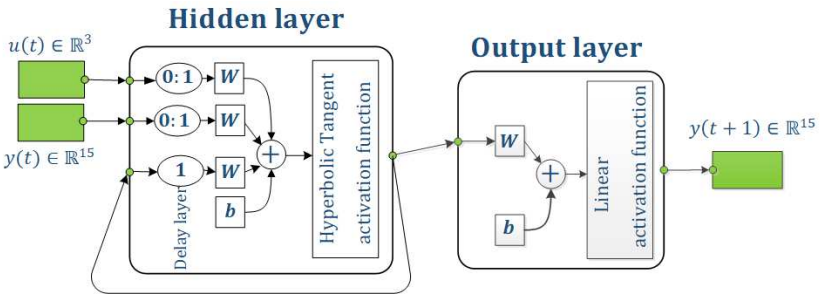

Figure 1: The nonlinear autoregressive network with exogenous inputs combined with RRNN.

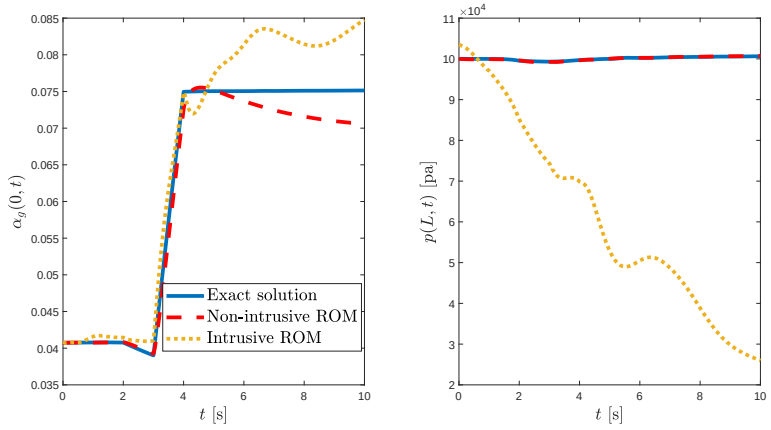

Figure 2: Comparison of the approximation of $\alpha_g(0,t)$ and $p(L,t)$.

is also set to one. The inputs to the system ($u(t)$ in Figure 1) are liquid and gas mass flow rates at the left boundary and the valve opening at the right boundary (3 inputs in total, $u(t) \in \mathbb{R}^3$). We have considered three independent variables α_g, v_l and p in (1) and assigned 5 RB functions for each (15 outputs in total, $y(t) \in \mathbb{R}^{15}$). To train the RRNN, five different samples of inputs $u(t)$ are fed into the structure and the coefficients of the hidden layer (W and b) are regulated to minimize the mean-squared error between the RRNN outputs and the temporal variations of the coefficients of the RB functions obtained after applying POD to the snapshots.

To test the RRNN generalization, a new input is provided for the network and the comparison of the state variables has been performed. The evolution of the state variables α_g at the inlet of the computational domain and the pressure p at the outlet of the computational domain is shown in Figure 2 for the actual solution, the intrusive and the non-intrusive ROMs. The intrusive method gives unbounded and unstable solution over time although the nonlinear terms are approximated by 10 collateral basis functions using the Empirical Interpolation Method [5]; two times more accurate than the linear terms. On the other hand, the non-intrusive one gives reasonably accurate results and is much faster than the full-order model. The speedup (obtained by dividing the CPU time of solving the full-order model to the CPU time of solving the ROM) for the non-intrusive method is 71.1 while for the intrusive one is only 2.05. To increase the accuracy in approximating the gas volume fraction, the number of the RB functions should be increased; however, as the approximation of pressure is of higher importance, we are satisfied with the performance of the non-intrusive ROM.

Conclusions

In this work, a non-intrusive MOR is applied to the DFM to reduce its corresponding computational time. Contrary to the projection-based MOR that develops an unstable system, the non-intrusive method provides an accurate and a stable reduced-order system, which is solved much faster compared to the original model.

References

[1] Abbasi M.H., Naderi Lordejani S., Velmurugan N., Berg C., Iapichino L., Schilders W., van de Wouw N. (2019) A Godunov-type Scheme for the drift flux model with variable cross section. *Journal of Petroleum Science and Engineering* **179**: 796–813.

[2] Haasdonk B., Ohlberger M. (2008) Reduced basis method for finite volume approximations of parametrized linear evolution equations. *ESAIM Mathematical Modelling and Numerical Analysis* **42(2)**: 277-302.

[3] Wang Q., Hesthaven J.S., Ray D. (2019) Non-intrusive reduced order modeling of unsteady flows using artificial neural networks with application to a combustion problem. *Journal of Computational Physics* **384**: 289-307.

[4] Pawar A.,Rahman S.M., Vaddireddy H., San O., Rasheed A., Vedula P. (2019) A deep learning enabler for nonintrusive reduced order modeling of fluid flows. *Physics of Fluids* **31**: in press.

[5] Barrault M., Maday Y., Nguyen N.C., Patera A.T. (2004) An empirical interpolation method: application to efficient reduced-basis discretization of partial differential equations. *Comptes Rendus Mathematique* **339(9)**:667-672.

Reduced-order Modeling from Experimental Data via Spectral Submanifolds

Mattia Cenedese, Joar Axås and George Haller
Institute for Mechanical Systems, ETH Zürich, Switzerland

Summary. Reduced-order modeling is among the leading theoretical and computational challenges for data concerning nonlinear systems in mechanics, ranging from structures and fluid flows, to their interaction and other multi-physics problems. Data-driven model reduction methods are well-established for linear dynamical systems, while available approaches for nonlinear systems often reveal to be sensitive in the identified parameters, and to be limited in prediction capabilities. With this contribution, we present an approach based on the theory of spectral submanifolds, which captures explicit nonlinear models from data. Without specific assumptions on the type of observables or the kind of measurements, our method identifies nonlinear models that exhibit the footprint of geometric nonlinearities or nonlinear damping in the observed dynamics. Our reduced-order models, which are trained on decaying vibrations data, are also capable to accurately predict forced-responses of the nonlinear dynamical system. We show the performances of our algorithm on measurement data of oscillations in structural or fluid dynamics.

Introduction

In the context of data-driven reduced order modeling, the most common approaches in the literature are Principal Orthogonal Decompositions (POD) followed by Galerkin projections [1] or Dynamic Mode Decomposition (DMD) [2]. The former method, however, needs the knowledge of the governing equations of motion to retrieve the reduced dynamics, while DMD is purely data-driven, but it cannot capture essentially nonlinear (or *non-linearizable*) dynamics [3], as, for example, transitions between equilibrium states or nonlinear frequency responses of structural vibrations. Available approaches from machine learning tend to not be robust or easy to handle for extrapolation or prediction [4]. In this contribution, we present an approach based on the recent theory of spectral submanifolds (SSMs) [5] that can extract reduced-order models from generic observables capitalizing on normal forms.

Results and discussion

Our method is a two-step procedure, whose details are described in [7]. After having embedded the data in a suitable observable space (either by using Whitney or Takens-type embedding, depending on available measurements), we perform data-driven dimensionality reduction by modeling the SSM geometry. Our reduced coordinates are the projection to the modal subspace tangent to the SSM at the equilibrium, and the nonlinearities are described via polynomials. From these arbitrary coordinates, we then seek the reduced dynamics in normal form by minimizing the conjugacy error among data, and, for oscillatory problems, the general normal form related to m linearized modes of the system reads

$$\begin{aligned}\dot{\rho}_j &= -\alpha_j(\boldsymbol{\rho},\boldsymbol{\theta})\rho_j,\\ \dot{\theta}_j &= \omega_j(\boldsymbol{\rho},\boldsymbol{\theta}),\end{aligned} \qquad j=1,2,...,m, \quad m\geq 1, \quad \boldsymbol{\rho}=(\rho_1,\rho_2,...\rho_m), \quad \boldsymbol{\theta}=(\theta_1,\theta_2,...\theta_m). \tag{1}$$

The maps α_j and ω_j are the nonlinear continuations of linearized frequency and damping, identifying how dissipation and frequency change with respect to the normal form modal amplitudes $\boldsymbol{\rho}$ and eventually phases $\boldsymbol{\theta}$, whose latter dependence is only showing up in internally resonant systems. We also remark that our modeling approach when related to multiple non-resonant modes do not assume the modes to be uncoupled. We use (1) to study the dynamics and make predictions for eventual forced responses, and afterwards, using the SSM geometry, we can trace back normal form amplitudes to physical observed quantities. To show the performance of our method in capturing the nonlinear behavior in systems with different physics, we consider an example in fluid-structure interaction and one featuring structural vibrations.

We first consider the liquid sloshing example from [6, 7] depicted in Fig. 1(a), where measurements are carried out via a laser system and the excitation is provided by moving the platform onto which the tank sits. We set our observable to be horizontal position of the water center of mass and we focus on the slowest system mode. We train our SSM-based model from the resonance decay data shown in Fig. 1(b) using cubic nonlinearities, showing already good accuracy in reconstructing test trajectories. The model identifies the nonlinear backbone curves, characterizing damping $\alpha(\rho)$ and frequency $\omega(\rho)$, and is then used to compute frequency responses, which follows the reduced dynamics

$$\dot{\rho} = -\alpha_0\rho - \beta\rho^3 + f\sin(\psi), \qquad \dot{\psi} = \omega_0 + \gamma\rho^2 - \Omega + \frac{f}{\rho}\cos(\psi), \tag{2}$$

where Ω is the forcing frequency, f the forcing amplitude and $\psi=\theta-\Omega t$ the phase lag. Forced periodic solutions can be sought in closed form from eq. (2). In Fig. 1(c), we show these forced responses, where the dots are experimental measurements for different forcing frequency and forcing amplitude values, while solid lines are predictions from (2), after proper calibration for finding the normal form forcing amplitude f. Even tough our model has been trained only on unforced data, it exhibits great accuracy in predicting forced responses (thanks to our detailed modeling of softening and of nonlinear damping), also for amplitudes being higher with respect to those of training data.

Another example is the two-beam system of Fig. 1(d). The first two modes of this assembly feature a $1:2$ internal resonance and system nonlinearities are due to weak frictional contact happening at the joint between the inner beam and

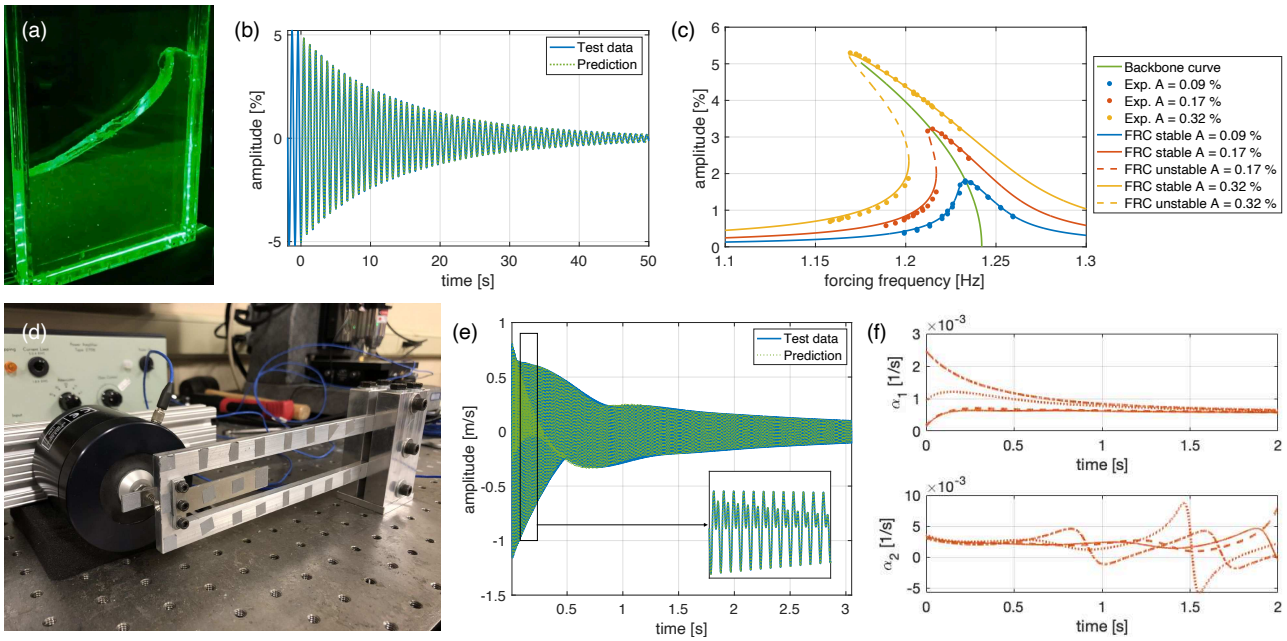

Figure 1: (a) Photo of measurements of liquid sloshing in a tank. (b) Decaying oscillations released from resonant quadrature forcing with model predictions. The amplitude is the horizontal displacement of the center of mass of the water inside the tank, expressed in percentage after normalization with respect to the tank width. (c) Analytical Forced Response Curves (FRCs), the damped backbone curve (blue solid line) and experimental measurements for different forcing amplitudes and frequencies. (d) Picture of the resonant tester structure. (e) Decaying resonant oscillations excited via hammer impact of the inner beam along with model predictions. The amplitude is the velocity of the inner beam tip. (f) Nonlinear damping trends for the slow α_1 and fast α_2 modes along some decaying trajectories.

the external one, which is clamped to the ground on the other side. Decaying vibrations are excited using hammer impacts on different locations of the inner beam and our observable is the inner tip velocity measured via laser scanner vibrometry. Due to internal resonance, transients show two dominant frequencies, cf. Fig. 1(e), as they very quickly converge to the slow four-dimensional SSM, i.e., related to the two slow system modes. In this case, our method automatically detects the internal resonance from data and it identifies a cubic order model with the specific form

$$\begin{aligned}
\dot{\rho}_1 &= -\alpha_{0,1}\rho_1 - \beta_{11}\rho_1^3 - \beta_{12}\rho_2^2\rho_1 - \rho_1\rho_2\left(\sigma_{11}\cos\psi - \sigma_{12}\sin\psi\right), \\
\dot{\rho}_2 &= -\alpha_{0,2}\rho_2 - \beta_{21}\rho_1^2\rho_2 - \beta_{22}\rho_2^3 - \rho_1^2\left(\sigma_{21}\cos\psi + \sigma_{22}\sin\psi\right), \\
\rho_1\dot{\theta}_1 &= +\omega_{0,1}\rho_1 + \gamma_{11}\rho_1^3 + \gamma_{12}\rho_2^2\rho_1 + \rho_1\rho_2\left(\sigma_{11}\sin\psi + \sigma_{12}\cos\psi\right), \\
\rho_2\dot{\theta}_2 &= +\omega_{0,2} + \gamma_{21}\rho_1^2\rho_2 + \gamma_{22}\rho_2^3 + \rho_1^2\left(\sigma_{22}\cos\psi - \sigma_{21}\sin\psi\right),
\end{aligned} \tag{3}$$

where $\psi = \theta_2 - 2\theta_1$ is the internal phase shift. Our data-driven model is able to reconstruct trajectories test with an average $1.2\ \%$ error, as in the example of Fig. 1(e). In particular, the damping of the fast mode undergoes consistent variation as shown in Fig. 1(f), becoming also negative for some times, since the fast mode tries to absorb energy from the slow mode. Additional details of this example are reported in [8].

Our data-driven approach is implemented on the open-source MATLAB® package `SSMLearn`, which is to be released soon. Other than the source code, the repository contains the data sets discussed in this contribution and the live-scripts with their analysis, and also additional worked examples.

References

[1] Lu, K., Jin, Y., Chen, Y., Yang, Y., Hou, L., Zhang, Z., Li, Z. and Fu, C. (2019) Review for order reduction based on proper orthogonal decomposition and outlooks of applications in mechanical systems. *Mech Syst Signal Process*, **123**:264-297.

[2] Schimd, P.J. (2010) Dynamic mode decomposition of numerical and experimental data. *J. of Fluid Mech.* **656**:5-28.

[3] Page, J., Kerswell, R.R. (2019) Koopman mode expansions between simple invariant solutions. *J. of Fluid Mech.* **879**:1-27.

[4] Brunton, S.L., Proctor, J.L., Kutz, J.N. (2016) Discovering governing equations from data by sparse identification of nonlinear dynamical systems. *PNAS* **113**(15):3932-3937.

[5] Haller, G., Ponsioen, S. (2016) Nonlinear normal modes and spectral submanifolds: existence, uniqueness and use in model reduction. *Nonlinear Dyn.* **86**(3):1493-1534.

[6] Bäuerlein, B., Avila, K. (2021) Phase lag predicts nonlinear response maxima in liquid-sloshing experiments. *J. of Fluid Mech.* **925**:A22.

[7] Cenedese, M., Axås, J., Bäuerlein, B., Avila, K., Haller, G. (2021) Data-driven modeling and prediction of non-linearizable dynamics via spectral submanifolds, *submitted*.

[8] Cenedese, M., Axås, J., Yang, H., Eriten, M., Haller, G. (2021) Data-driven nonlinear model reduction to spectral submanifolds in mechanical systems, *arXiv:2110.01929*.

Stable and Fast Identification of Continuous-Time Lur'e-Type Systems

Fahim Shakib[*], Alexander Pogromsky[*], Alexey Pavlov[†] and Nathan van de Wouw[*,‡]
[*]*Dept. of Mechanical Engineering, Eindhoven, Univ. of Tech., the Netherlands*
[†]*Dept. of Geoscience and Petroleum, NTNU, Trondheim, Norway*
[‡] *Dept. of Civil, Environmental, and Geo- Engineering, Univ. of Minnesota, USA*

Summary. This abstract proposes an approach for parametric system identification for a class of continuous-time Lur'e-type systems. To overcome the computational drawbacks of numerical forward integration, the Mixed-Time-Frequency (MTF) algorithm is used to compute model responses in a fast way. These model responses are required to evaluate the cost function, which quantifies the mismatch between the measured and simulated steady-state output response. Furthermore, we show that the gradient of the cost function with respect to the model parameters can also be computed using the MTF algorithm. Hence, the MTF algorithm facilitates efficient use of global and local optimization methods to minimize the cost function, which yields the identified parameter set. Finally, by enforcing the identified model to be inside the set of convergent models, we certify a stability property of the identified model, which allows for safe generalization to other inputs than those used to train the model. The proposed approach is successfully applied in mechanical ventilation, where parameters of a first-principle model are identified. This case study highlights the benefits of the proposed approach.

Identification Problem

A practically relevant class of nonlinear systems is the class of Lur'e-type systems, see Figure 1. In such systems, the linear time-invariant (LTI) dynamics are captured in an LTI block and all the nonlinearities are captured in a static nonlinear block placed in the feedback loop. We consider the problem of parametric identification of so-called continuous-time *convergent* Lur'e-type systems. Convergent systems are systems that, for any bounded input, have a unique, globally asymptotically stable (GAS) steady-state solution that is bounded on the whole time axis [3]. For the class of Lur'e-type system, sufficient conditions for exponential convergence exist [5]. Our goal is to find parameters of the Lur'e type system that ensures the closest fit between the steady-state model response and the measured steady-state output response, while also ensuring that the identified model is convergent. We consider the case where both the input $w(t)$ and output $z(t)$ are scalar. The feedback signals $y(t)$ and $u(t)$ are considered *not measured*.
A property of convergent systems is that for T-periodic input $w(t)$, the steady-state output $z(t)$ is also T-periodic, facilitating the use of only steady-state data for the purpose of identification. The considered cost function, measuring the squared identification error, is given by

$$J(\theta) = \frac{1}{N}\sum_{k=0}^{N-1} \epsilon(t_k,\theta)^2 := \frac{1}{N}\sum_{k=0}^{N-1} \left(z_{simulated}(t_k,\theta) - z_{measured}(t_k)\right)^2 \tag{1}$$

with θ being the model parameter vector, parameterizing the LTI system matrices and the nonlinearity in Figure 1, N the number of samples in one period, t_k the sampling times (uniformly spaced) and $z_{simulated}(t,\theta)$, $z_{measured}(t)$, the simulated and measured steady-state response, respectively. Next, we define Θ as the set of parameters θ which renders the considered Lur'e-type model convergent. The objective is to minimize $J(\theta)$ in (1) while ensuring convergence by guaranteeing $\theta \in \Theta$. We consider the state dimension to be known and the model parametrization to be given by the user. The identification problem can now be formulated as follows:

$$\hat{\theta} = \arg\min_{\theta\in\Theta} J(\theta). \tag{2}$$

Cost Function Minimization

The constrained optimization problem (2) is solved in a two-step fashion. In the first step, initial parameter estimates are obtained. If the model is derived from first-principle modeling, then the user could provide initial parameter estimates based on physical insights. Otherwise, the best linear approximation [4] can be used, which yields a *linear* initial model in a fast way. Alternatively, any global parameter search algorithm [1] can be used, which results in a full *nonlinear* initial model, however, at the expense of computational time.
In the second step, a gradient-based search is used to optimize all parameters of the full nonlinear model. In order to evaluate the cost function (1), computation of the model response is required. Doing this using numerical forward

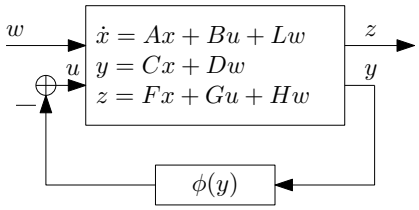

Figure 1: Considered Lur'e-type system.

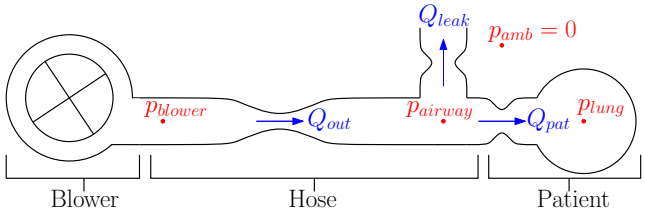

Figure 2: Experimental setup of mechanical ventilation.

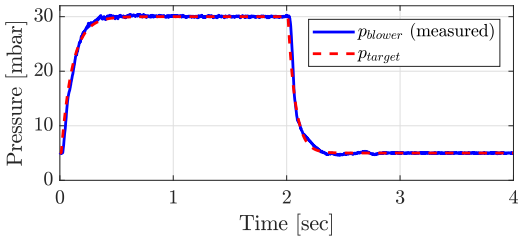

Figure 3: Realistic breathing pattern.

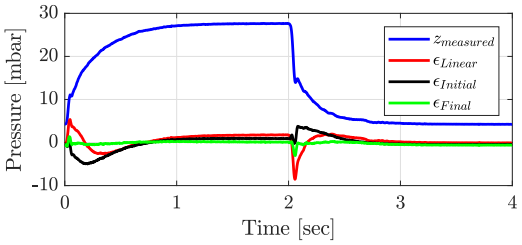

Figure 4: Measured response and remaining errors as defined in (1).

integration is a computationally expensive task. Therefore, for the class of convergent Lur'e-type systems, [3] developed the so-called Mixed-Time-Frequency (MTF) algorithm. This algorithm computes iteratively the response of the LTI block in frequency-domain and the response of the static nonlinearity in time-domain, which are both computationally efficient steps. It can be shown that for convergent Lur'e-type systems, this iterative computational approach is guaranteed to converge, ensuring the accurate and fast computation of the 'true' steady-state model response.
Besides the steady-state model response, also the gradient of the cost function (1) with respect to the model parameters is required in any gradient-based optimization approach to minimize the cost function in (1). One of our main contributions of this work is to show that this gradient can be obtained by simulation of a *parameter sensitivity system*, which is again a *convergent* Lur'e-type system. Hence, again the MTF algorithm can be used as a means of fast and accurate computation of the output response of this sensitivity system to obtain the gradient of the cost function. Using well-established optimization routines [2], the constrained optimization problem (2) can then be solved in a fast way by exploiting the computational benefits of the MTF algorithm.

Experimental Case Study in Mechanical Ventilation

The proposed approach is applied to find the parameters of a first-principles model of the mechanical ventilation setup schematically depicted in Figure 2. Mechanical ventilation is used in intensive care units to assist or stimulate respiration of patients who are unable to breathe on their own. The blower realizes the pressure p_{blower} by an internal control-loop which tracks the target breathing cycle p_{target}, both depicted in Figure 3. The measured pressure p_{blower} is considered as the input of the system. Air flows through a hose into the lungs of the patient, where at the patient-side of the hose the airway pressure p_{airway} is measured and considered as the output of the system. Also an intentional leakage component with known characteristics is present in order to refresh the air to the patient. Using first-principles modeling, a Lur'e-type model characterized by five parameters can be derived. The static nonlinearity in the model stems from the nonlinear pressure-flow characteristic of the hose, being characterized by a linear and quadratic resistance. Rather than using humans in these experiments, the ASL5000 breathing simulator is used, which simulates the lung behavior of patients, being characterized by a resistance and compliance parameter. The fifth parameter is the resistance of the leakage component, which is known by means of calibration. The case where the patient is fully sedated is considered, which implies no breathing activity from the patient.
A one minute experiment is performed where 15 periods of the 4 seconds periodic input depicted in Figure 3 are applied to the system. The average of the last 12 periods of p_{blower} and p_{airway} are used as *steady-state* input and output data, respectively, for the purpose of identification. Such a short experiment time is of crucial importance in this application as time is extremely costly in such medical settings. Parameters of an 'average' patient model are used to initialize a gradient-based exterior-point optimization algorithm to minimize the cost function in (1).
The measured steady-state output p_{airway} is depicted in Figure 4, together with the error obtained by the initial model $\epsilon_{Initial}$ (this is a model with *average* patient-hose parameters) and the model obtained after the gradient-based search ϵ_{Final}. For comparison, also the error of an identified *linear* model (using subspace techniques) is plotted in Figure 4. In this figure, the benefits of identifying a nonlinear model are clearly visible as it yields a much smaller error than the initial and linear model. This is also confirmed by the yielded cost (1), which is 2.55 for the initial model, 2.40 for the linear model and 0.17 for the final model. Furthermore, as we performed *parametric* system identification, the parameters of the model represent physical quantities that reveal important medical information on the patient and medical ventilation equipment, which are useful for medical personnel. To illustrate the computationally efficiency, a total of 1530 model responses were computed in *only* 13 seconds in the gradient-based search. The obtained model is guaranteed to exhibit the *convergence* property, which is highly instrumental for prediction purposes in controller design in mechanical ventilation.

References

[1] Marco Locatelli and Fabio Schoen. *Global optimization: theory, algorithms, and applications*, volume 15. Siam, 2013.

[2] Panos Y Papalambros and Douglass J Wilde. *Principles of optimal design: modeling and computation*. Cambridge university press, 2000.

[3] A Pavlov and Nathan van de Wouw. Fast computation of frequency response functions for a class of nonlinear systems. In *Proc. of 47th IEEE conf. on Decision and Control*, pages 1180–1186, 2008.

[4] Rik Pintelon and Johan Schoukens. *System identification: a frequency domain approach*. John Wiley & Sons, 2012.

[5] VA Yakubovich. Matrix inequalities method in stability theory for nonlinear control systems: I. absolute stability of forced vibrations. *Automation and remote control*, 7:905–917, 1964.

Tuesday, July 19, 2022
16:00 - 18:20

MS-10 Non-Smooth Dynamics
Saint Clair 3A

Chair: Vincent Acary - Remco Leine

16:00 - 16:20
Nonsmooth dynamics of slip and stick with a finite-sized contact area
VARKONYI Peter*, ANTALI Mate
*Budapest University of Technology and Economics (H-1111 Budapest Muegyetem rkp 3 Hungary)

16:20 - 16:40
Nonsmooth Modal Analysis of a Rectangular Plate in Unilateral Contact
URMAN David*, LEGRAND Mathias
*Structural Dynamics and Vibration Laboratory, McGill University (Room 122, McConnell Engineering Building, McGill University, 817 Sherbrooke St West, Montréal QC H3A Canada)

16:40 - 17:00
Numerical Methods for Nonsmooth DAEs
ROCCA Alexandre*, ACARY Vincent, BROGLIATO Bernard
*INRIA Grenoble-Alpes (Inovallée 38334 Montbonnot France)

17:00 - 17:20
Simulation of a Hall Flowmeter Funnel with a novel non-smooth numerical procedure for granular media
PROFIZI Paul, **CHARLES Alexandre***
*Université de Technologie de Troyes (12 rue Marie CurieCS 4206010004 TROYES CEDEX France) - Safran Tech (Rue des Jeunes Bois, Châteaufort, 78114 Magny-les-Hameaux France)

17:20 - 17:40
Tangencies in the phase space of mechanical systems with spatial Coulomb friction
ANTALI Mate*
*Budapest University of Technology and Economics (H-1111 Budapest, Muegyetem rkp. 3. Hungary)

17:40 - 18:00
The hidden bridge between continuous and discontinuous worlds and why period 2 may imply chaos
AVRUTIN Viktor*, JEFFREY Mike
*IST, University of Stuttgart (Pfaffenwaldring 9, 70569 Stuttgart Germany)

18:00 - 18:20
Non-smooth Reduced Interface Models for Co-simulation of Mechanical Systems
RAOOFIAN Ali, **KÖVECSES József***, TEICHMANN Marek
*Department of Mechanical Engineering, McGill University (817 Sherbrooke St. West, Montreal, QC H3A 0C3 Canada)

Nonsmooth dynamics of slip and stick with a finite-sized contact area

Péter L. Várkonyi*, Máté Antali†
*Department of Mechanics, Materials, and Structures, Budapest University of Technology and Economics, Budapest, Hungary
† Department of Applied Mechanics, Budapest University of Technology and Economics, Budapest, Hungary

Summary. Dry friction laws like the Coulomb law and many of its extensions predict forces that are discontinuous functions of slip velocity. In state space, this discontinuity occurs along discontinuity manifolds corresponding to sticking of the physical contacts. Previous works studied the dynamics induced by these models when the discontinuity manifold is codimension-one (Coulomb law in 2 dimensions) or codimension-two (Coulomb friction in 3 dimensions). Here we investigate the dynamics in more general contact models, which leads to higher codimension discontinuity manifolds. In particular, we analyse in details the Coulomb-Contensou friction model describing the friction forces and torques at a finite-sized contact area. Among others we show that the direction of slip velocity as well as the ratio between the spinning angular velocity and the slip velocity have predictable values at each transition between slip and stick.

Dynamics induced by discontinuous friction models

If completely rigid bodies are assumed with a single-point contact, the Coulomb friction law describes the friction force as a nonsmooth function of slip velocity. Namely,

$$\vec{\lambda}_f = -\mu\lambda_n \frac{\vec{s}}{|\vec{s}|}, \tag{1}$$

where $\lambda_n > 0$ is the normal force between the surfaces, $\vec{\lambda}_f$ is the tangential (friction) force, $\vec{s}$ is the relative velocity between the surfaces at the contact point, and μ is the friction coefficient. This model involves a discontinuity when $|\vec{s}| = 0$. In the case of planar (two-dimensional) friction problems with Coulomb friction, the discontinuity occurs along a codimension-1 manifold in phase space [1]. Such systems belong to the class of Filippov systems, for which a well-established theory describes when and how systems converge to discontinuity manifold and how they continue to evolve after that point.

When a planar model involves several point contacts, each of them induces a codimension-1 disconinuity manifold. These manifolds may intersect giving rise to secondary discontinuity manifolds of higher codimension, and a hierarchical system of discontinuities. The theory of Filippov systems was extended to such systems in [2] and [3].

A qualitatively different scenario occurs in the case of spatial (three-dimensional) friction problems. In that case, the Coulomb law gives rise to a discontinuity along an isolated codimension-2 manifold where both components of the slip velocity $\vec{s}$ vanish simultaneously. This lead to the recent introduction of the concept of *extended Filippov systems*, and the development of theory describing how systems behave in the neighbourhood of such discontinuities [4]. Among others, special features of slip-stick transitions, and the conditions of persistent stick motion were developed.

The Coulomb friction law requires refinement and extension where the stiffness of the contacting bodies is not large enough. Then, the local normal deformations have to be considered which creates a finite contact area. The Coulomb friction can be applied *locally* between the tangential and normal force distributions. By integration over the contact area, the resultant friction force $\vec{\lambda}_f$ and the friction torque τ_f can be computed with respect to a reference point of the contact area. This calculation can be found in the literature by using appropriate series expansion and closed form analytical approximations [5, 6]. It was found that the relative *slipping velocity* $\vec{s}$ and the *spinning angular velocity* ω are coupled in the tangential force $\vec{\lambda}_f$ and the drilling torque τ_f. According to those result in the literature, a simple phenomenological approximation of the friction law can be given as

$$\vec{\lambda}_f = -\mu_\lambda\lambda_n \frac{\vec{s}}{\sqrt{|\vec{s}|^2 + (c_\omega\omega)^2}}, \tag{2}$$

$$\tau_f = -\mu_\tau\lambda_n \frac{c_\omega\omega}{\sqrt{|\vec{s}|^2 + (c_\omega\omega)^2}}. \tag{3}$$

In (2)-(3), μ_λ, μ_τ are dimensionless coefficients proportional to the friction coefficient μ, and the model parameter c_ω characterises the interaction between the translational and rotational friction effects. As a limit case for very large local stiffness of the bodies, the contact area becomes a contact point, and these parameters are assumed to tend to $\mu_\lambda \to \mu$, $\mu_\tau \to 0$ and $c_\omega \to 0$. In this limit case, (2) leads to the Coulomb friction law (1) with a codimension-2 discontinuity. However, for a finite contact stiffness, the model has a discontinuity when $|\vec{s}| = 0$ and $\omega = 0$ at the same time. It means a codimension-3 discontinuity, but friction models including coupling between rolling and slipping (see e.g. [7]) are expected to initiate discontinuity manifolds up to the codimension-5 case. Currently there is no theory describing this class of non-smooth dynamical systems.

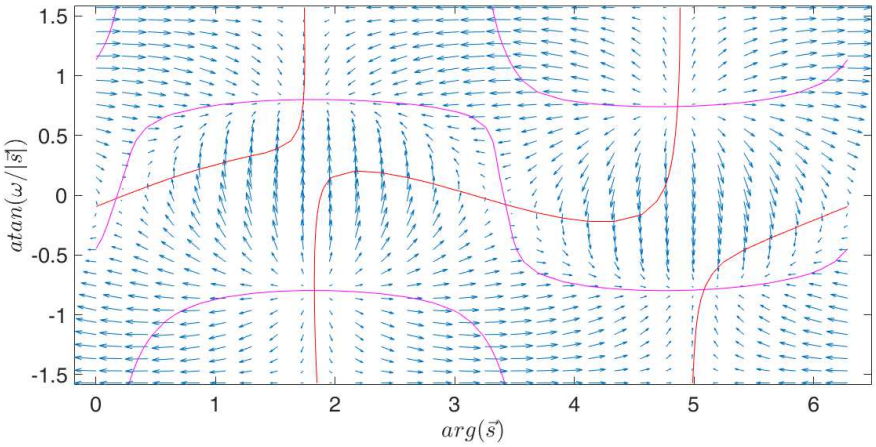

Figure 1: A projection of the 2-sphere with an example of the vector field representing fast dynamics of a slipping contact in the presence of the friction model (2)-(3). The curves represent nullclines of the dynamics. The field has 6 fixed points at the intersections of the nullclines.

Vector fields with higher codimension discontinuities

The recent theory of *extended Filippov systems* [4] addresses dynamics of a system with state variables $\vec{x}$ in the neighborhood of a codimension-2 discontinuity manifold of state space that occurs at $\vec{u}(\vec{x}) = 0$ for some $\vec{u}(\vec{x}) \in \mathbb{R}^2$. The theory is based on the observation, that the variable $\vec{u}$ can be replaced by polar variables $r = |\vec{u}|$, and $\phi = \arg(\vec{u})$ (i.e. the angle of $\vec{u}$). Then, for $r << 1$, ϕ evolves on a faster time-scale than r. The theory of smooth slow-fast dynamical systems offers an efficient tool to analyze the emerging dynamics. In most cases, ϕ rapidly converges to fixed points, and the slow dynamics of r is evaluated at those points.
Here, we apply the same technique to systems where a codimension n discontinuity occurs at $\vec{u} = 0$, $\vec{u} \in \mathbb{R}^n$. We again decompose $\vec{u}$ to a slow variable $r \in \mathbb{R}$ and fast variables $\vec{\phi} \in \mathbb{S}^{n-1}$ over the $n-1$ sphere. In many cases, the fast dynamics converges to fixed points, where the one-dimensional slow dynamics can be analyzed easily.

Application to the dynamics of finite-sized contacts

Consider a rigid multi-body system with smooth behavior except for one single finite-sized contact area with dry friction. The state variable $\vec{x}$ consists of the generalized coordinates $\vec{q}$ and their time derivatives $\dot{\vec{q}}$. The equations of motion and kinematic constraints enable one to develop equations for the dynamics of the slip velocity $\vec{s}$ and angular velocity of slip ω in the following form:

$$\dot{\vec{u}} := \begin{bmatrix} \dot{\vec{s}} \\ \dot{\omega} \end{bmatrix} = \mathbf{M}^{-1}(q) \begin{bmatrix} \vec{\lambda}_f \\ \tau_f \end{bmatrix} + \vec{b}(q, \dot{q}) \tag{4}$$

Here $\vec{b}$ is the acceleration in the absence of frictional forces and $\mathbf{M}$ is a 'local mass matrix' associated with the reference point of the contact region. One can combine this equation with a friction model like (2)-(3). Then, replacement of $\vec{u}$ by the variables r and $\vec{\phi}$ as described above uncovers intriguing fast dynamics over the 2-sphere when $r << 1$ (Fig. 1). It appears that the limit sets of the fast dynamics are two to six fixed points. The slow dynamics is either convergence to or divergence from $r = 0$ (i.e. stick) at each of the fixed points. This observation implies that slip-stick and stick-slip transitions always occur through non-trivial combinations of rotational and translational motion at the contact surface. The analysis also hints at the possibility of ambiguous cases where persistence of stick is undecidable within the scope of rigid body theory.

References

[1] Di Bernardo M. et al. (2008) Piecewise-smooth Dynamical Systems. Springer, London.

[2] Dieci L., Lopez L. (2011) Sliding motion on discontinuity surfaces of high codimension. A construction for selecting a Filippov vector field *Numer. Math.* **117**:779-811.

[3] Jeffrey M. R. (2015) Dynamics at a switching intersection: hierarchy, isonomy, and multiple sliding *J. Appl. Dyn. Syst.* **13**(3):1082-1105.

[4] Antali M., Stepan G. (2018) Sliding and crossing dynamics in extended Filippov systems *J. Appl. Dyn. Syst.* **17**(1):823-858.

[5] Leine R.I., Glocker C. (2003) A set-valued force law for spatial Coulomb-Contensou friction *Eur. J. Mech. A - Solid* **22**:193-216.

[6] Kudra G., Awrejcewicz J. (2011) Tangens hyperbolicus approximations of the spatial model of friction coupled with rolling resistance *Int. J. Bifurcat. Chaos* **21**(10):2905-2917.

[7] Beregi S., Takacs D. (2019) Analysis of the tyre-road interaction with a non-smooth delayed contact model *Multibody Syst Dyn* **45**(2):185-201.

Nonsmooth Modal Analysis of a Rectangular Plate in Unilateral Contact

David Urman and Mathias Legrand
Department of Mechanical Engineering, McGill University, Montreal, Canada

Summary. A scheme for the nonsmooth modal analysis of a rectangular plate in frictionless unilateral contact with a rigid foundation is demonstrated. Application of nonsmooth modal analysis requires finding periodic solutions to the Signorini problem. To this end, the nodal boundary method in the framework of the finite element method is used. It allows to approximate the solution through a system of nonsmooth ordinary differential equations in the internal displacements of the plate. The resulting system exhibits chattering-free periodic solutions numerically found via the harmonic balance method. Sequential continuation is used for detection of nonsmooth modes.

Introduction

Nonsmooth modal analysis (NMA) refers to the application of nonlinear modal analysis on structures for which the dynamics is governed by nonsmooth equations [7]. In the present work, the subject of analysis is a rectangular plate, with in-plane displacements, in unilateral contact with a rigid obstacle expressed via the usual Signorini complementarity conditions [1]. In essence, NMA requires the detection of families of periodic motions to the autonomous system [5, 7, 9]. Generally, NMA requires use of numerical techniques since closed-form solutions to the Signorini problem do not generally exist [7, 9]. In [9], the wave finite element method (WFEM) was used for NMA of the bar and has proven to provide accurate result for the case of the uniform-area bar. However, extension of this methodology to two-dimensional systems has failed due to high numerical energy dissipation effectively annihilating periodic solutions [9]. The finite element method (FEM) has also been commonly used to solve the Signorini problem numerically [3]. In the FEM framework, there exist several numerical schemes for treatment of the Signorini conditions. However, those were not used for NMA for various reasons. For example, schemes utilizing a fully elastic Newtonian impact law exhibit non-physical chattering [3, 7] while the penalty [3] and Nitsche [2] methods do not exactly enforce impenetrability with the obstacle in the discrete setting. The mass redistribution method (MRM) [4], while allowing for energy conservation and elimination of chattering, requires solving a constrained optimization problem in many variables to form the reduced mass matrix. However, the *Nodal Boundary Method* (NBM) eliminates chattering by reducing the mass and stiffness matrices via a series of linear operations on the mass matrix's rows and columns [8]. The ordinary differential equations (ODEs) resulting from NBM exhibit periodic solutions which can be found via the harmonic balance method (HBM) [8]. Continuous families of periodic solutions are then found via sequential continuation along different periods of the motion [5].

Boundary Value Problem for Periodic Motions with Unilateral Contact

Within the framework of two-dimensional in-plane elasticity, we investigate the problem of a thin and isotropic plate prone to unilateral contact with a rigid foundation. The equation governing the motion of the plate reads

$$\rho\bar{\mathbf{u}}_{tt}(\mathbf{x},t) - \mathbf{div}(\boldsymbol{\sigma}(\bar{\mathbf{u}}(\mathbf{x},t))) = \mathbf{0}, \quad (\mathbf{x},t) \in \Omega \times [0,\infty) \tag{1}$$

where $\bar{\mathbf{u}}(\mathbf{x},t) : \mathbb{R}^2 \times \mathbb{R}^+ \to \mathbb{R}$ and ρ describe the displacement field and density, respectively. The stress tensor $\boldsymbol{\sigma}(\bar{\mathbf{u}}(\mathbf{x},t))$ is related to the displacements via a classical plane-stress assumption. Other than the classic Neumann and Dirichlet boundary conditions, a portion Γ_{C} of the plate's boundary is prone to the unilateral contact conditions

$$0 \leq g_0 - \bar{\mathbf{u}}(\mathbf{x},t)\cdot\mathbf{n}, \quad \sigma_n \leq 0, \quad (g_0 - \bar{\mathbf{u}}(\mathbf{x},t)\cdot\mathbf{n})\sigma_n(\bar{\mathbf{u}}(\mathbf{x},t)) = 0, \quad \mathbf{x} \in \Gamma_{\mathrm{C}} \tag{2}$$

where g_0 defines the distance between the non-deformed boundary and the rigid obstacle. The contact pressure is captured by $\sigma_n(\bar{\mathbf{u}}(\mathbf{x},t)) = \mathbf{n}^\top\boldsymbol{\sigma}(\bar{\mathbf{u}}(\mathbf{x},t))\mathbf{n}$ where $\mathbf{n}$ is the outward normal to the contact boundary. For NMA, we search for solutions of period T such that $\bar{\mathbf{u}}(\mathbf{x},0) = \bar{\mathbf{u}}(\mathbf{x},T)$ and $\bar{\mathbf{u}}_t(\mathbf{x},0) = \bar{\mathbf{u}}_t(\mathbf{x},T)$.

Nodal Boundary Method

The NBM applies on the FEM formulation of the Signorini problem, stated in Equations (1) and (2), which takes the form

$$\mathbf{M}\ddot{\mathbf{u}}(t) + \mathbf{K}\mathbf{u}(t) = \mathbf{G}^\top\boldsymbol{\lambda}(t) \tag{3}$$

$$\boldsymbol{\lambda}(t) + \mathbf{max}(\mathbf{0}, g\mathbf{1} - \mathbf{u}_{\mathrm{C}}(t) - \boldsymbol{\lambda}(t)) = \mathbf{0} \tag{4}$$

where $\mathbf{u}(t) \in \mathbb{R}^N$ constitute the N nodal displacements approximating the displacement field $\bar{\mathbf{u}}(\mathbf{x},t) \approx \mathbf{P}(\mathbf{x})\mathbf{u}(t)$ with $\mathbf{P}(\mathbf{x})$ denoting piecewise-Lagrangian shape functions. In the NBM, we distinguish between nodal displacements $\mathbf{u}_{\mathrm{C}}(t)$ on Γ_{C} and the remainder of the nodal displacements $\mathbf{u}_{\mathrm{O}}(t)$ such that $\mathbf{u}(t) = (\mathbf{u}_{\mathrm{O}}(t)\ \mathbf{u}_{\mathrm{C}}(t))^\top$. It is well known that formulation (3) and (4) form an ill-posed problem due to the existence of infinitely many values for $\boldsymbol{\lambda}$ at the moment of contact [1]. In the NBM, we attempt to resolve this ill-posedness by assigning $\boldsymbol{\lambda}$ a relationship with $\mathbf{u}(t)$ via the FEM

approximation of the boundary integral on Γ_C:

$$\mathbf{G}^T\boldsymbol{\lambda} \leftarrow \int_{\Gamma_C} \mathbf{P}^\top(\mathbf{x})\sigma_n(\mathbf{P}(\mathbf{x})\mathbf{u}(t))\mathrm{d}\mathbf{x} = \mathbf{G}^\top(\mathbf{N}_C\mathbf{u}_C(t) + \mathbf{N}_O\mathbf{u}_O(t)) \tag{5}$$

where $\mathbf{N}_C$ and $\mathbf{N}_O$ are constant matrices. Substitution of (5) into (4) results in an LCP in $\mathbf{u}_C(t)$ admitting a unique solution for given $\mathbf{u}_O(t)$ and g. This unique solution consists of piecewise constant matrix $\mathbf{A}(\mathbf{u}_O(t), g)$ and vector $\mathbf{d}(\mathbf{u}_O(t), g)$ such that $\mathbf{u}_C(t) = \mathbf{A}(\mathbf{u}_O(t), g)\mathbf{u}_O(t) + g\mathbf{d}(\mathbf{u}_O(t), g)$. The values of $\mathbf{A}$ and $\mathbf{d}$ can be found numerically by solving the LCP. From this expression, we construct the NBM approximation of the displacement which always satisfies (4) and (5) along with the FEM approximation of the Signorini conditions

$$\bar{\mathbf{u}}(\mathbf{x}, t) \approx \mathbf{P}(\mathbf{x})(\mathbf{A}^*(\mathbf{u}_O, g)\mathbf{u}_O(t) + \mathbf{d}^*(\mathbf{u}_O, g)), \quad \mathbf{A}^*(\mathbf{u}_O, g) = \begin{bmatrix} \mathbf{I} \\ \mathbf{A}(\mathbf{u}_O, g) \end{bmatrix}, \quad \mathbf{d}^*(\mathbf{u}_O, g) = \begin{bmatrix} \mathbf{0} \\ \mathbf{d}(\mathbf{u}_O, g) \end{bmatrix}. \tag{6}$$

In the FEM framework, substitution of approximation (6) into (3) yields the system of ODEs

$$(\mathbf{A}^*(\mathbf{u}_O, g))^\top(\mathbf{M}\mathbf{A}^*(\mathbf{u}_O, g)\ddot{\mathbf{u}}_O(t) + \mathbf{K}\mathbf{A}^*(\mathbf{u}_O, g)\mathbf{u}_O(t) + \mathbf{K}\mathbf{d}^*(\mathbf{u}_O, g)) = \mathbf{0} \tag{7}$$

which are nonsmooth ODEs (due to $\mathbf{A}^*$ and $\mathbf{d}^*$) in $\mathbf{u}_O(t)$. Periodic solutions of the ODE can be found via the HBM [8]. Then, sequential continuation is used to determine families of periodic solutions of the plate in unilateral contact, in a similar fashion to [5].

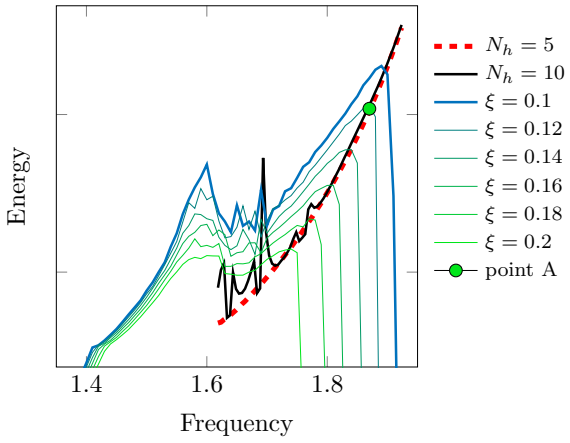

Figure 1: Forced response of the plate for various damping coefficients ξ and backbone curves generated via NBM-HBM with varying number of harmonics N_h.

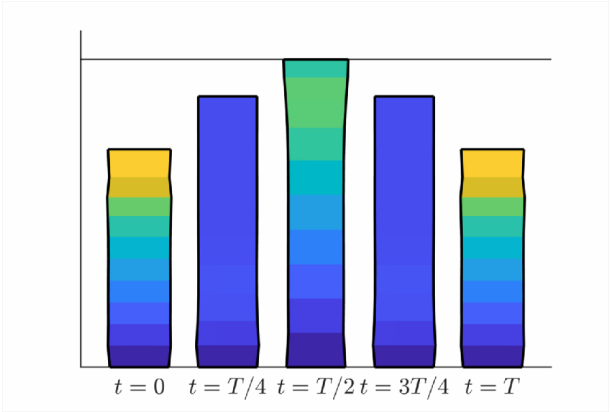

Figure 2: Solution at point A in Figure 1 at different times fractions of the period $T = 2\pi/1.87$. Color gradient represents $||\mathbf{u}(\mathbf{x}, t)||_2$

Conclusions

Under the NBM's formulation of the Signorini problem, NMA of the plate was conducted successfully. Indeed, this formulation may apply to more intricate structures prone to unilateral contact. Therefore, future work shall include expanding the NBM formulation to practical engineering cases. Also, comparison of NBM against Nitsche method for purposes of NMA is considered. While Nitsche applies the Signorini conditions in a weak sense, the NBM does so in a strong sense and it is of interest to compare the rates of convergence of both methods to the true solution.

References

[1] Brogliato B. (1999) Nonsmooth Mechanics, Models, Dynamics and Control. Springer

[2] Chouly F., Fabre M., Hild P., Mlika R., Pousin J. and Renard Y. (2017) An Overview of Recent Results on Nitsche's Method for Contact Problems. Geometrically Unfitted Finite Element Methods and Applications. *Lecture Notes in Computational Science and Engineering*, **121**:93-141

[3] Doyen D., Ern A. and Piperno S. (2011) Time-Integration Schemes for the Finite Element Dynamic Signorini Problem, *SIAM Journal of Scientific Computing*, **33**(1):223-249

[4] Khenous H.B., Laborde P. and Renard Y. (2008) Mass redistribution method for finite element contact problems in elastodynamics, *European Journal of Mechanics-A/Solids*, **27**(5):918-932

[5] Lu, T. and Legrand, M. (2021) Nonsmooth Modal Analysis via the Boundary Element Method for One-Dimensional Bar Systems. *Nonlinear Dynamics*

[6] Moreau J.J. (2004) An introduction to Unilateral Dynamics. Novel Approaches in Civil Engineering. *Lecture Notes in Applied and Computational Mechanics*, **14**:1-46

[7] Thorin A. and Legrand M. (2018) Nonsmooth modal analysis: From the discrete to the continuous settings. Advanced Topics in Nonsmooth Dynamics: Transactions of the European Network for Nonsmooth Dynamics, 191-234. Springer.

[8] Urman D. and Legrand M. (2021) Nodal-Boundary Finite-Element Method for the Signorini Problem in Two Dimensions. *IDETC-CIE 2021 International Design Engineering Technical Conferences & Computers and Information in Engineering Conferences*, Virtual, Online

[9] Yoong C. (2018) Nonsmooth Modal Analysis of a Finite Elastic Bar subject to a Unilateral Contact Constraint. PhD thesis, McGill University.

Numerical Methods for Nonsmooth DAEs

Alexandre Rocca*, Vincent Acary* and Bernard Brogliato*
**University Grenoble-Alpes, Inria, CNRS, Grenoble INP, LJK, 3800 Grenoble, France (e-mail: firstname.surname@inria.fr)*

Summary. In this work, we will discuss the various approaches to simulate hybrid differential algebraic equations (hybrid DAEs), i.e., dynamical systems with some algebraic constraints switching with respect to the state variables. Then, we will present our recent work on the simulation of such hybrid DAE through a reformulation as DAEs with non-smooth constraints. Finally, we show on some examples that numerical methods for non-smooth dynamical systems can be extended for the simulation of these non-smooth DAEs.

Hybrid DAEs are an increasing share of the simulated hybrid systems. They can be found in a large panel of engineering domains such as, but not limited to, chemical process engineering [15], electronics [1], for a long time in mechanical systems [4], and in numerous cyber-physical systems. In most of these domains, engineers rely on model-based design language such as Modelica [8] to define their dynamics in a piecewise manner using conditional statements. The resulting dynamical systems are of the form:

$$\begin{cases} \dot{\mathbf{x}}(t) = \mathbf{f}(\mathbf{x}(t), \mathbf{z}(t)) \\ \quad 0 = \mathbf{g}_i(\mathbf{x}(t), \mathbf{z}(t)) \\ \qquad , \forall (\mathbf{x}(t), \mathbf{z}(t)) \in \mathcal{X}_i. \end{cases} \tag{1}$$

The variables $\mathbf{x}$, $\mathbf{z}$ are the differential and algebraic variables, respectively. The sets $\mathcal{X}_i = \{(\mathbf{x}, \mathbf{z}) \in \mathbb{R}^{n_1+n_2=n} \mid \mathbf{h}_i(\mathbf{x}, \mathbf{z}) > 0\}$ define a partition of $\mathbb{R}^n$ such that: $\bigcup_i \overline{\mathcal{X}}_i = \mathbb{R}^n$, $\mathrm{int}(\mathcal{X}_i) \neq \emptyset$, for all i. In addition, let assume that $i \neq j$, $\partial\mathcal{X}_i \cap \partial\mathcal{X}_j = \emptyset$. Indeed, the definitions of the dynamics on the border of a partition are, in general, ambiguous.

Related Works

It is first worth to mention that some works, such as [14], have taken the approach of relaxing the non-smoothness inherent to the hybrid DAE using smooth versions of a step function such as the sigmoid function, Hill function, or the hyperbolic tangent. If these works enable a direct application of known numerical methods for non-linear DAEs, they, in general, worsen the numerical simulation efficiency due to the high stiffness, but also the numerical stability because of bad conditioning inherent to stiff systems. This was for example noted for the simulation of electronic systems with diodes [1].

Another approach, taken by V. Merhmann et al. [7, 11], is to use numerical methods defined for hybrid DAE structured as hybrid automata. Their implementation relies on event based numerical methods and explicit transition functions to correctly re-initialise the system after switching. It is noteworthy that they detect and simulate in some particular case sliding modes in a similar fashion to Filipov sliding motion [6] for ODEs. In particular, this concept of continuous solutions for hybrid DAE as been formalised and studied by I.V Matrosov [9, 10] in an unrelated work. The work of A. Benveniste et al. [3] uses non-standard analysis to construct well-defined transitions from one mode to another in the context of hybrid DAE even in presence of varying index. In particular, this work pairs well with [11] as the definition by the user of the DAE initialisation at switching is not needed anymore. It is also worth to mention the work of S. Trenn [16] that defines the solutions of hybrid DAE with exogenous switching. In particular, he introduces the notion of distributional solutions which can also be used to efficiently solve inconsistent initial conditions.

Outside of the hybrid automata approach, the hybrid DAE have also been studied as non-smooth dynamical systems. For example, differential variational inequalities (DVI) form a class of non-smooth DAEs which are studied in [12]. In particular, they give well-posedness results, and some numerical methods are analysed, for DVI with a structure similar to index-1 DAEs. K. Camlibel et al. [5] extend results of well-posedness of differential inclusions to differential algebraic inclusions with maximal monotone operators. In additions, they study the well-posedness of non-smooth linear DAEs with some passivity properties.

Analysis of Non-smooth DAEs

In a previous work [13], we proposed to relax the switching algebraic equations $\mathbf{g}_i(\mathbf{x}, \mathbf{z}) = 0$ from (1) by filling-in the graph of the constraints. This is achieved by using step-functions $\mathrm{s}^+(\cdot)$ in a similar fashion to [2] in order to build a generalised constraint.

$$\mathbf{g}(\mathbf{x}, \mathbf{z}) = \sum_i \left(\prod_{j \neq i} (1 - \mathrm{s}^+(\mathbf{h}_j(\mathbf{x}, \mathbf{z}))) \right) \mathrm{s}^+(\mathbf{h}_i(\mathbf{x}, \mathbf{z})) \mathbf{g}_i(\mathbf{x}, \mathbf{z}) = 0\,. \tag{2}$$

The actual definition of $\mathbf{g}(\mathbf{x}, \mathbf{z})$ will depend of the choice of the step-function definition when $h_j(\mathbf{x}, \mathbf{z}) = 0$. Then, we studied the effect of such relaxation in (3), a particular 2-dimensional example (see Figure 1), and we have shown that the constraint (2) is relaxed as a generalised equation, whose well-posedness can be studied. We show that the system with

the generalised constraint (2) presents continuous sliding solutions that are not exhibited by the methods of [11] and [9].

$$\begin{cases} \dot{x}_1(t) = 1 + \mathrm{B}_1 z(t) \\ \dot{x}_2(t) = \mathrm{B}_2 z(t) \\ \quad 0 \in \ \mathrm{sign}(x_1(t)) + |x_1(t))| - x_2(t)\,. \end{cases} \tag{3}$$

Then, by studying the well-posedness of the implicit Euler numerical discretization of this example (4), we conjecture an extension of the implicit Euler numerical scheme for simulation of such non-smooth DAEs. This improved Euler numerical scheme has proven to yield good results on our example (see convergence results on Fig. 2).

$$\begin{aligned} p^*_{k+1} := \min_{\mathbf{x}_{k+1},\mathbf{z}_{k+1},\boldsymbol{\lambda}_{k+1}} \quad & \|\mathbf{x}_{k+1} - \mathbf{x}_k\|\,, \\ \text{s.t} \quad & x_{1,k+1} - x_{1,k} = h(1 + \mathrm{B}_1 z_{k+1}) \\ & x_{2,k+1} - x_{2,k} = h\mathrm{B}_2 z_{k+1} \\ & 0 \in \ \mathrm{sign}(x_{1,k+1}) + |x_{1,k+1}| - x_{2,k+1}\,, \end{aligned} \tag{4}$$

In this work, we will extend this analysis the more general class of hybrid DAEs that can be formulated as mixed linear complementarity systems. Indeed, in [13], we have seen the constraint (2) can be expressed as mixed linear complementary problems. We show that such representation can be used for the numerical simulation of a wide variety of systems involving hybrid DAEs. We provide both a study of implicit Euler discretization, and numerical simulations of concrete case studies implemented with SICONOS a toolbox for the simulation of non-smooth dynamical systems.

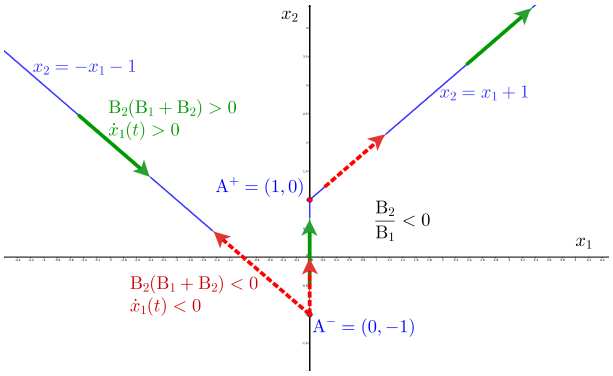

Figure 1: In red and green, we show two possible solutions of the example studied in [13].

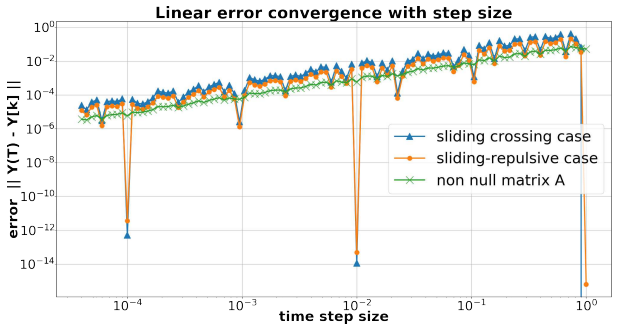

Figure 2: Linear convergence of implicit Euler extension for various cases of the example studied in [13].

References

[1] ACARY, V., BONNEFON, O., AND BROGLIATO, B. *Nonsmooth modeling and simulation for switched circuits*, vol. 69. Springer Science & Business Media, 2010.

[2] ACARY, V., DE JONG, H., AND BROGLIATO, B. Numerical simulation of piecewise-linear models of gene regulatory networks using complementarity systems. *Physica D: Nonlinear Phenomena 269* (2014), 103–119.

[3] BENVENISTE, A., CAILLAUD, B., ELMQVIST, H., GHORBAL, K., OTTER, M., AND POUZET, M. Structural analysis of multi-mode dae systems. In *Proceedings of the 20th International Conference on Hybrid Systems: Computation and Control* (2017), ACM, pp. 253–263.

[4] BROGLIATO, B. Nonsmooth mechanics: Models, dynamics and control, third edition. *Communications and Control Engineering* (2016).

[5] CAMLIBEL, K., IANNELLI, L., TANWANI, A., AND TRENN, S. Differential-algebraic inclusions with maximal monotone operators. In *IEEE 55th Conference on Decision and Control (CDC)* (2016), IEEE, pp. 610–615.

[6] FILIPPOV, A. F. Differential equations with discontinuous right-hand side. *Matematicheskii sbornik 93*, 1 (1960), 99–128.

[7] HAMANN, P., AND MEHRMANN, V. Numerical solution of hybrid systems of differential-algebraic equations. *Computer Methods in Applied Mechanics and Engineering 197*, 6-8 (2008), 693–705.

[8] HENNINGSSON, E., OLSSON, H., AND VANFRETTI, L. Dae solvers for large-scale hybrid models. In *Proceedings of the 13th International Modelica Conference, Regensburg, Germany, March 4–6, 2019* (2019), no. 157, Linköping University Electronic Press.

[9] MATROSOV, I. V. Existence of solutions of the algebro-differential equations. *Automation and Remote Control 67*, 9 (2006), 1408–1415.

[10] MATROSOV, I. V. On right-hand uniqueness of solutions to nondegenerated algebro-differential equations with discontinuances. *Automation and Remote Control 68*, 1 (2007), 9–17.

[11] MEHRMANN, V., AND WUNDERLICH, L. Hybrid systems of differential-algebraic equations–analysis and numerical solution. *Journal of Process Control 19*, 8 (2009), 1218–1228.

[12] PANG, J.-S., AND STEWART, D. E. Differential variational inequalities. *Mathematical Programming 113*, 2 (2008), 345–424.

[13] ROCCA, A., ACARY, V., AND BROGLIATO, B. Index-2 hybrid DAE: a case study with well-posedness and numerical analysis. Research report, Inria - Research Centre Grenoble – Rhône-Alpes, Nov. 2019, https://hal.inria.fr/hal-02381489.

[14] SOUZA, D. F. D. S., VIEIRA, R. C., AND BISCAIA JR, E. C. Strategies for numerical integration of discontinuous dae models. In *Computer Aided Chemical Engineering*, vol. 20. Elsevier, 2005, pp. 151–156.

[15] STECHLINSKI, P., PATRASCU, M., AND BARTON, P. I. Nonsmooth differential-algebraic equations in chemical engineering. *Computers & Chemical Engineering 114* (2018), 52–68.

[16] TRENN, S. Switched differential algebraic equations. In *Dynamics and Control of Switched Electronic Systems*. Springer, 2012, pp. 189–216.

Simulation of a Hall Flowmeter Funnel with a novel non-smooth numerical procedure for granular media

Paul Profizi* and Alexandre Charles*†
*Safran Tech, Modeling & Simulation, Rue des Jeunes Bois, Châteaufort, 78114 Magny-Les-Hameaux, France
†Université de Technologie de Troyes, 12 rue Marie Curie, CS 42060 10004 Troyes CEDEX

Summary. Previous work proposed a new NSCD procedure fixing convergence issues for small dynamical systems. We demonstrate here the resulting improved implicit solver efficiency compared to the existing Jean-Moreau scheme, when applied to large systems such as granular media.

Introduction

The Discrete Element Method [Cunedall and Strack, 1979] has emerged from rock mechanics problems and is now applied to many other engineering problems. Besides DEM, the lesser known NonSmooth Contact Dynamics procedure [Jean, 1999] offers an alternative procedure for this type of problems. This latter scheme, essentially a stable backward Euler scheme in time, is mathematically more sounded [Moreau, 1999]. However, Alart and Renouf [Alart and Renouf, 2018] point out that the procedure is still hampered by non- or slow-convergence pathologies linked with its incremental solver. In a previous work [Charles et al., 2018], a new NSCD procedure was set up to fix convergence issues in small (dof) dynamical systems simulations. Since one cannot expect this convergence to be granted for larger systems, the procedure is applied to granular media simulation and shows a great improvement in solver efficiency for these problems compared to Jean-Moreau.

Numerical procedure

Differences and common points with respect to the original Jean-Moreau NSCD scheme are shown in Table 1. Both are Backward Euler schemes with a midpoint update rule. However, at step 5, Jean and Moreau solve at the same time impact and dry friction whereas we solve first the frictionless impact and only then friction in a staggered way. Jean and Moreau's way conveys a very direct implementation but challenges the convergence of the Nonlinear Gauss Seidel. This leads to drift-off in the simulation due to the necessary cut-off in convergence search after a given (high) number of iterations is reached. Jean notes that "The method has proven in applications to behave nicely as soon as the time step is small enough and the friction coefficient is lying in the range allowed" [Moreau, 1999, Jean, 1999]. One can object the subsequent error being only controlled by refining the time step, this somehow cancels the advantage of using an NSCD method versus a DEM. The presented procedure instead conveys a more intricated implementation and the necessity at step 3 to infer, from Coulomb law, a dry friction constitutive law in terms of Lagrange's generalized forces. We show next that the current method does however scale well and the gain is worth the pain in the case of a Hall Flowmeter Funnel simulation.

Step	Jean Moreau	current procedure
1	Evaluation of midpoint approximants	
2	Contact detection	
3	a. Normals and tangents **in euclidian space**	a. Normals and tangents **in Lagrange's generalized forces space** b. Inference of a dry friction law on the Lagrange's generalized forces [Charles and Ballard, 2014]
4	Contactless equation of dynamics and contactfree predictor	
5	a. Coulomb and standard inelastic shock laws resolution with a Nonlinear Gauss Seidel (max 3000 iterations)	a. Standard inelastic shock law resolution (NLGS, max 1500 iterations) b. Inferred friction law resolution (NLGS, max 1500 iterations)
6	Actualization of final velocities and positions	

Table 1: Comparison of the Jean Moreau and the current NSCD procedure

2D Simulation of a Hall Flowmeter Funnel

The increase in efficiency for solving the contact conditions using the novel procedure is illustrated with the simulation of the flow of a granular medium under gravity through a funnel, inspired by the Hall Flowmeter Funnel. In Figure 1 the initial state of the simulation is shown, along with the state of the granular medium at two subsequent moments during the flow. This case was chosen due to the compacting phase the granular medium has to go through and the resulting multiple self-equilibrated contact force networks usually causing convergence issues.

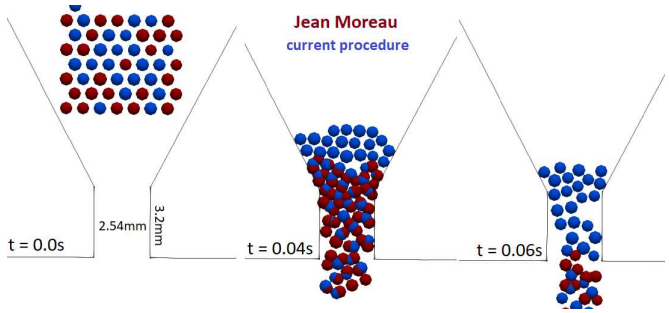

Figure 1: Illustration of the 2D Hall Flowmeter funnel with evolution of the granular medium configuration with time for the same 50 particles (the radii following a normal distribution of average $0.3mm$ and a deviation of 5%) for both procedures and here with a time step of $1e^{-4}s$. The difference in behaviour due to higher interpenetrations for Jean Moreau is clearly visible.

The simulation is run using both procedures for a total simulated time of $0.1s$. The results in terms of CPU time and cumulative penetration error when varying the time step are given in Figure 2. The penetration error is the sum of particle interpenetrations as well as residual penetration of particles in obstacles.

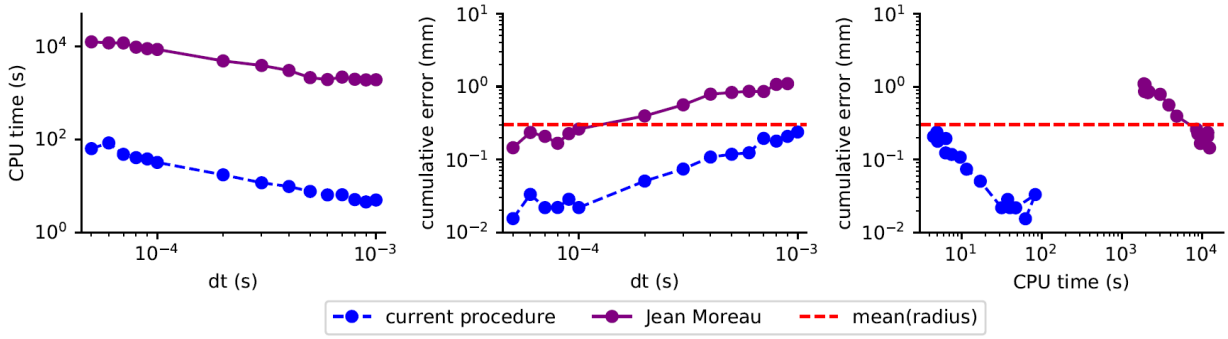

Figure 2: Influence of time step on CPU time and cumulative error for both procedures in the case depicted in Figure 1.

The source for this difference in computational efficiency can be traced to the time spent iterating during the solving of the contact conditions as depicted in Figure 3. One clearly sees the NLGS of the Jean-Moreau procedure maxing out its (unusually high) number of allowed iterations while the novel approach, thanks to its preconditioning and reformulation of the problem, converges very quickly (in less than 100 iterations) even though it has to go through two NLGS.

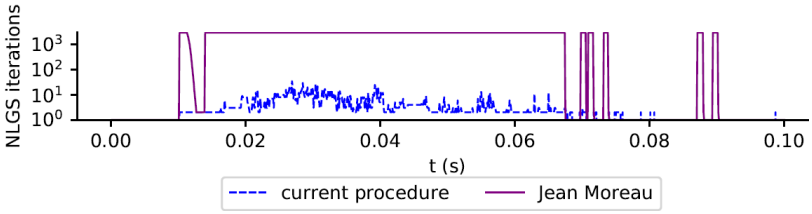

Figure 3: Total NLGS iterations for contact resolution at each time step in the case depicted in Figure 1.

Take aways

In the presentation, a novel nonsmooth procedure, until then limited to small archetypal problems, is upscaled to the case of granular media. The final outcome is a swift integration in time (3 orders of magnitude faster than the typical JM NSCD for an equivalent penetration error). The procedure is also illustrated on a selective laser melting powder bed spreading.

References

[Alart and Renouf, 2018] Alart, P. and Renouf, M. (2018). On inconsistency in frictional granular systems. *Comp. Part. Mech.*, 5:161âĂŞ174.

[Charles and Ballard, 2014] Charles, A. and Ballard, P. (2014). *ENOC 2014 - Proceedings of 8th European Nonlinear Dynamics Conference*, chapter A formulation of the dynamics of multibody systems with unilateral constraints and friction in the configuration space. Institute of Mechanics and Mechatronics, Vienna University of Technology.

[Charles et al., 2018] Charles, A., Casenave, F., and Glocker, C. (2018). A catching-up algorithm for multibody dynamics with impacts and dry friction. *Computer Methods in Applied Mechanics and Engineering*, 334:208 – 237.

[Cunedall and Strack, 1979] Cunedall, P. and Strack, O. (1979). A discrete numerical model for granular assemblies. *Geotechnique*, 29(1):74–65.

[Jean, 1999] Jean, M. (1999). The non-smooth contact dynamics method. *Computer Methods in Applied Mechanics and Engineering*, 177:235–257.

[Moreau, 1999] Moreau, J.-J. (1999). Numerical aspects of sweeping process. *Computer Methods in Applied Mechanics and Engineering*, 177:329–349.

Tangencies in the phase space of mechanical systems with spatial Coulomb friction

Mate Antali
Department of Applied Mechanics, Budapest University of Technology and Ec., Budapest, Hungary

Summary. When modelling dry friction between rigid bodies, the Coulomb friction law leads to discontinuity surfaces in the phase space of the resulting dynamical system. This discontinuity is a codimension-1 subspace in the case of a planar (two-dimensional) contact and it is a codimension-2 subspace in the case of a spatial (three-dimensional) contact. The qualitative mathematical description of the trajectories is well-established in the literature for the former case, and some results has been recently added to the latter topic by the author. In this work, the tangency points are analysed, which points divide the discontinuity surface to 'sliding regions' and 'crossing regions'. These regions coincide to the existence or non-existence of rolling-sticking solutions, thus, tangencies as boundary points are strongly related to these physical phenomena. The qualitative analysis of tangencies at codimension-2 discontinuities are carried out by analytical methods and the results are demonstrated on mechanical problems with spatial Coulomb friction.

Tangencies in piecewise smooth vector fields

The mathematical concepts are presented in the simplest geometrical case in the phase space, but the formulation can easily modified for more general situations. Consider a dynamical system in the form $\dot{x} = F(x)$, where $x = (x_1, \dots x_m) \in \mathbb{R}^m$. We assume that the vector field F is smooth on $\mathbb{R}^m$ except in a *discontinuity set* $\Sigma = \{x : x_1 = 0\}$. We call F a *piecewise smooth* vector field according to the two smooth regions $x_1 > 0$ and $x_1 < 0$. The set Σ has $m-1$ dimensions, thus, we call it a codimension-1 discontinuity. Consider the normal vector $n = (1, 0, \dots 0)$ of Σ at a chosen point $\tilde{x} \in \Sigma$. If the limits

$$\lim_{\varepsilon \to 0^+} F(\tilde{x} + \varepsilon n) = F^+(\tilde{x}), \qquad \lim_{\varepsilon \to 0^+} F(\tilde{x} - \varepsilon n) = F^-(\tilde{x}), \tag{1}$$

exist and $F^+(\tilde{x}) \neq F^-(\tilde{x})$ for all $\tilde{x} \in \Sigma$ then F is called a *Filippov-system*. In the vicinity of the discontinuity set, two generic types of behaviour occur according to the first components F_1^+ and F_1^- of the limit vectors. The case $F_1^+ \cdot F_1^- > 0$ is called *crossing*, where the trajectories of F can be continued through the discontinuity. The case $F_1^+ \cdot F_1^- < 0$ is called *sliding*. In this case, the so-called *sliding dynamics* can be defined inside Σ by using the convex set generated by F^+ and F^- (for the details, see [1] or [2]).

The boundary between these two cases is when $F_1^+ = 0$ or $F_1^- = 0$, which is called a *tangency point* or simply a *tangency*, because the vector field is tangent to the discontinuity set from either side. Tangencies separate the crossing and sliding regions of the discontinuity set. Tangencies often considered as singularities of the phase space; the analysis of these points gives qualitative information about the local behaviour of the vector field. The simplest tangencies are called *invisible fold* and *visible fold* (see Figure 1), more complicated cases can be found in the literature (see [3] and Chapter 6 of [4]).

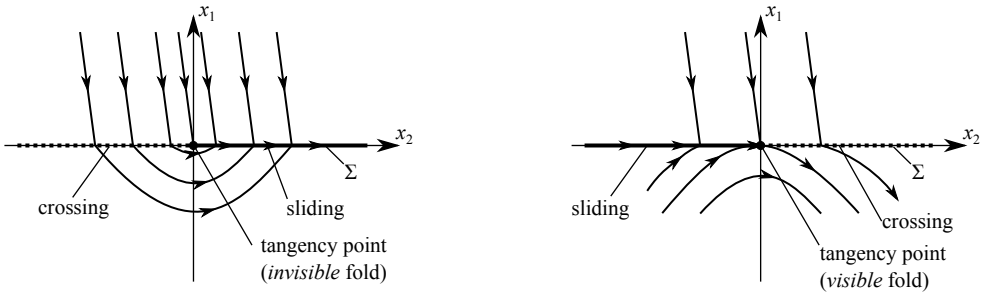

Figure 1: Two basic types of tangencies in piecewise smooth systems. Left panel: invisible fold. The term 'invisible' expresses that although the vector field is tangent to the discontinuity set Σ, we can find no finite trajectory which is tangent to Σ. Right panel: visible fold. The term 'visible' expresses that there exists a trajectory which just touches Σ at the tangency point.

Analysis of tangencies at codimension-2 discontinuities

Let us now turn to the systems with codimension-2 discontinuities. Consider a system $\dot{x} = F(x)$ in the case when F is smooth everwhere except in the set $\Sigma = \{x : x_1 = x_2 = 0\}$. That is, Σ is now a codimension-2 discontinuity. Then, the continuously many normal directions to Σ can be parametrised by an angle ϕ as $n(\phi) = (\cos\phi, \sin\phi, 0, \dots 0)$. We assume that for all $\tilde{x} \in \Sigma$, the limit

$$\lim_{\varepsilon \to 0^+} F(\tilde{x} + \varepsilon n(\phi)) = F^*(\tilde{x}, \phi) \tag{2}$$

exist for all angles $\phi \in [0, 2\pi)$. Then, we can call the vector field as an extended Filippov system. In such systems, the sliding and crossing regions can be defined by transforming to polar coordinates and using the concept of limit directions

[5]. We can define the concept of tangency points directly by requiring that the vector field is *tangent* to the discontinuity if both components F_1^* and F_2^* of the limit vector vanish in the normal plane to Σ. That is, we call $\tilde{x}$ a tangency point if there exists a direction $\phi_1 \in [0, 2\pi]$ such that $F_1^*(\tilde{x}, \phi_1) = 0$ and $F_2^*(\tilde{x}, \phi_1) = 0$.
In this work, the tangencies can be analysed by similar tools those of the tangencies of codimension-1 discontinuities. However, these methods should be adjusted to the specialities of the codimension-2 discontinuity set. The vector field can be transformed to a truncated series form and by analytical tools, the local structure of the trajectories can be determined. The singularity conditions of the different types of the tangencies are investigated. Moreover, regularization is applied at the discontinuity, which provides a further insight into the problem.

Tangencies and mechanical problems with Coulomb friction

When Coulomb friction is assumed between rigid bodies, the two-dimensional contact problem usually leads to a piecewise smooth system where $x_1 = u$ is the relative velocity at the contact point. Then, the static (*sticking* or *rolling*) contact state corresponds to the sliding dynamics inside the discontinuity set while the *slipping* state occurs outside the discontinuity. The sliding region coincides with the region where the rolling/sticking state is permitted by the friction model. Similarly, the crossing region coincides to the region where the sticking state is not available due to slipping. It can be shown [6] that in the case of spatial Coulomb friction with a codimension-2 discontinuity, the same coincidence appears between these mathematical objects of the phase space and the mechanical phenomena.
In both the planar and spatial cases, the tangencies are located at the boundary where the rolling/sticking motion becomes realizable. Therefore, the local analysis of the vector field at the tangencies can be applied to explore the behaviour of bodies at the limit of slipping.

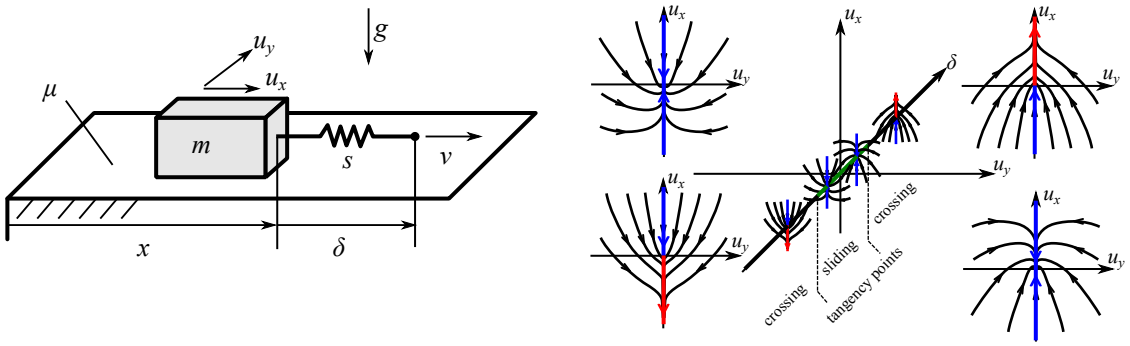

Figure 2: A three-dimensional mechanical model containing tangencies as important singularities at the boundary of slipping and sticking. Left panel: the sketch of the model. A block is pulled on a rough surface with a spring. The mass of the block is m, the stiffness of the spring is s, the friction coefficient on the surface is μ, and the end of the spring is pulled with a constant velocity v. The state space of the block can be described by $x = (u_x, u_y, \delta)$ where u_x and u_y are the components of the slipping velocity of the block and δ denotes the deformation of the spring. Right: the sketch of the phase space of the system with the projection of some typical trajectories onto the normal plane of the discontinuity. The blue and red half-lines denote the attracting and repelling limit directions, respectively.

The results are demonstrated on mechanical examples. For example, consider Figure 2, where we can see a block pulled by a spring on a rough surface. Analysis of the phase phase shows that there are two tangency points and one of them are a visible fold, the another is an invisible fold. It can be shown that although trajectories can reach the sliding region of the discontinuity, the only way to leave it is going through the *visible fold tangency*, that is, any solution containing sticking must go through the tangency point. In more complicated problems with a higher dimension of the phase space, the tangency point form boundary surfaces in the discontinuity. These surfaces behave as separatrices between the qualitatively different branches of solutions.

References

[1] Di Bernardo M. et al. (2008) Piecewise-smooth Dynamical Systems. Springer, London.

[2] Leine R., Nijmeijer H. (2004) Dynamics and Bifurcations of Non-Smooth Mechanical Systems. Springer, Berlin Heidelberg.

[3] Kristiansen K.U., Hogan S.J. (2019) On the interpretation of the piecewise smooth visible-invisible two-fold singularity in $\mathbb{R}^3$ using regularization and blowup *Journal of Nonlinear Science* **29**(2):723-787.

[4] Jeffrey M.R. (2019) Hidden Dynamics – The Mathematics of Switches, Decisions and Other Discontinuous Behaviour. Springer Nature, Switzerland.

[5] Antali M., Stepan G. (2018) Sliding and crossing dynamics in extended Filippov systems *J. Appl. Dyn. Syst.* **17**(1):823-858.

[6] Antali M., Stepan G. (2019) Nonsmooth analysis of three-dimensional slipping and rolling in the presence of dry friction *Nonlinear Dynamics* **97**(3):1799-1817.

The hidden bridge between continuous and discontinuous worlds and why period 2 may imply chaos

Viktor Avrutin*, Mike Jeffrey†
*Institute for Systems Theory and Automatic Control, University of Stuttgart, Germany
†Department of Engineering Mathematics, University of Bristol, Ada Lovelace Building, Bristol UK

Summary. We report a recently developed approach for the investigation of discontinuous maps. Using so-called hidden orbits, we demonstrate that several aspects of the dynamics well-known for continuous maps can also be transferred to discontinuous maps. Moreover, hidden orbits help us to understand the dynamics of maps with steep branches, which are known to be hard to investigate otherwise.

Motivation

Discontinuous maps appear naturally in many areas of nonlinear dynamics. In some situations, they act as approximate models of systems where the rules governing the dynamic behaviour undergo a fast (but continuous) change at some borders in the state space. In other situations, the change of the rules at the boundaries is in fact discontinuous.
It is well known that many properties of discontinuous maps differ quite significantly from the corresponding properties of continuous ones. For example, it is easy to show that the famious rule "period three implies chaos" applies to continuous maps and does not apply to their discontinuous counterparts where a 3-cycle may exist alone. Similarly, bifurcation diagrams one can observe in continuous maps are well organized: for instance, the branches corresponding to stable solutions appearing at (smooth or non-smooth) fold and flip bifurcations are typically connected via branches corresponding to unstable solutions which appear at the same bifurcations and determine the basin boundaries of coexisting attractors. In discontinuous maps, such unstable branches may be missing, the stable solutions may appear at border collision bifurcations "as if from nowhere", and the basins may be separated not only by unstable orbits but also by the discontinuities and their preimages. Chaotic attractors in continuous maps are always cyclic, while in discontinuous maps they may be acyclic as well. Because of these – and many other – differences, it is indeed hard to believe that the two worlds can be unified, i.e., that it is possible to develop an approach dealing with discontinuous maps in such a way that several properties of continuous maps are restored as far as possible.

Approach

A novel approach for the investigation of discontinuous maps has been recently suggested in [1]. The key idea of the approach is to extend the definition of a discontinuous map in such a way that at the discontinuities, the function is considered to be *set-valued* (in particular, for 1D maps, *interval-valued*). It is worth emphasizing that following this approach, the orbits of the map remain single-valued. An orbit visiting a discontinuity is mapped to a point belonging to the corresponding set; if an orbit visits the discontinuity again, it may be mapped to the same or to a different point. Accordingly, in addition to all orbits existing in the original discontinuous map, every time an orbit of such an extended map (referred to as a map with vertical branches) visits a discontinuity, an infinite number of forward orbits (so-called *hidden orbits*) is created. By construction, a *hidden orbit* is an orbit including points inside the discontinuities, and if a hidden orbit $\{x_n \mid n = 1, 2, \dots\}$ satisfies $x_{n+p} = x_n$ for all n, the orbit forms a *hidden cycle* of period p. Clearly, each hidden cycle is repelling and can easily be computed, as its points are given by preimages of the corresponding discontinuity.

Results

There are several different application areas for the proposed approach.

- When dealing with all kinds of discontinuous maps, the corresponding maps with vertical branches simplify the bifurcation analysis by adding to the bifurcation diagrams the "missing" unstable branches given by hidden cycles. In this way, by the bifurcation structures in discontinuous maps can be described in terms well-known for continuous maps: for example, the border collision bifurcations at which a cycle appears "as if from nowhere" turn into the usual border collision flip and fold bifurcations [2]. Hidden orbits unify also the treatment of basin boundaries: if in a discontinuous map these boundaries are given by a discontinuity and its preimages, in a corresponding map with vertical branches there is a (repelling) hidden cycle at the basin boundary, similarly to continuous maps.

- A discontinuous map may act as a model of a system with a very fast but continuous switching process. In such cases, a more detailed modeling leads to maps with steep branches which are quite hard to deal with (from the numerical point of view, but also because the laws governing the fast switching process are not always known). Here, a map with vertical branches provides an approximation for dynamics involving steep branches. Clearly, a cycle including points on a steep branch is strongly repelling and hard to find numerically. By contrast, to calculate a corresponding hidden cycle is a simple task, as it is given by a sequence of preimages of the discontinuity.

- By definition, a map with vertical branches is discontinuous but connected. Several fundamental theorems have been proven for continuous maps and do not apply to discontinuous ones. However, one may ask whether the requirement for continuity of the function may be relaxed and whether the connectedness would be sufficient as well. This is the case for the Sharkovsky theorem (which implies, in particular, the well-known rule "period three implies chaos"): this theorem can be proven not only for continuous but also for maps with vertical branches [3]. In this way, hidden cycles restore the Sharkovsky ordering, providing all cycles which are missing in the usual discontinuous map (without vertical branches). On the other hand, if one can prove that a hidden cycle of a certain period does not exist in a map with vertical branches, then a non-hidden cycle of this period must exist in the corresponding discontinuous map.

- A striking property of hidden orbits is that the existence of two distinct hidden cycles implies that a countable number of other hidden cycles and an uncountable number of hidden aperiodic orbits exist as well. Although all these orbits may be located at a final number of points in the state space (the points of discontinuities and their preimages), their union can be seen as a hidden chaotic repeller. It is worth noting that under perturbation of a map with a vertical branch to a map with a steep branch, this chaotic repeller persists, becoming non-hidden.

  In the simplest case, the existence of a hidden fixed point and a hidden 2-cycle implies the existence of hidden cycles of all periods, which can be interpreted as an unexpected form of the well-known rule, namely "periods one and two imply chaos" [4].

References

[1] M. Jeffrey and S. Webber. The hidden unstable orbits of maps with gaps. Proc. R. Soc. A, 476(2234):20190473, 2020

[2] V. Avrutin and M. Jeffrey. Bifurcations of hidden orbits in discontinuous maps. Nonlinearity 34:6140-6172, 2021

[3] P. Glendinning and M. Jeffrey. Hidden dynamics for piecewise smooth maps. Nonlinearity 34:3184-3198, 2021

[4] M. Jeffrey and V. Avrutin. Period 2 implies chaos in steep or nonsmooth maps. Nonlinearity (submitted 2021)

Non-smooth Reduced Interface Models for Co-simulation of Mechanical Systems

Ali Raoofian*, József Kövecses* and Marek Teichmann †
*Department of Mechanical Engineering and Centre for Intelligent Machines, McGill University, 817 Sherbrooke St. West, Montreal, QC H3A 0C3, Canada
†CM Labs Simulations, 645 Wellington, Montreal, QC H3C 1T2, Canada

Summary. In a co-simulation setup, an entire system is divided into multiple subsystems modelled separately which may be simulated with different solvers and time scales suited to the subsystems. These subsystems are then interfaced and coupled in order to simulate the whole system. For interactive rates, the non-iterative coupling schemes are used which are prone to instability. This problem can become more challenging when non-smoothness is introduced into the modelling. In this work, an efficient model-based coupling approach is introduced which is able to account for contact state transmissions between the communication points, resulting in more stable and accurate results compared to other coupling methods. To further clarify the advantages of the proposed approach, an illustrative example is also presented.

Introduction

Co-simulation is generally used to simulate systems consisted of different sub-systems with different nature; like multi-body systems interacting with hydraulics, electronics or even other mechanical sub-systems which are modelled with different phenomena. The main challenges for modelling such complex systems are related to the interfacing of these sub-system components. One challenge will raise when contact interactions are included in the modelling which introduces non-smoothness to the dynamics and increases the complexity of the model. Contact interactions which are also known as unilateral constraints, transform the underlying dynamics problem by adding inequalities into the dynamic formulation and turn it to a linear or a non-linear complementarity problem. In real-time applications, efficiency of the simulation is also a requirement, where we are usually interested in non-iterative co-simulation because there is not enough time to go back in time and resolve for a time step. Stability is a key element in non-iterative co-simulation which is related to the size of the macro time step. To make a co-simulation more stable, we can estimate the subsystem variables between the communication points and couple the subsystems. One promising way to estimate these variables is to use model-based coupling in which the mechanical system is reduced into an interface model that emulates the dynamics of the mechanical system at the interface. However, there still exist some aspects in model-based co-simulation which can be further improved.
In this work, we are looking at non-smooth interface models. The idea is that to add some information about the unilateral contacts of the full model in the interface model. This information would help us to estimate contact state changes during macro time step using an interface model. As will be illustrated, this will enable us to successfully simulate some dynamic behaviours which cannot be captured otherwise.

Dynamic formulation of the interface model

Consider a multibody system subjected to unilateral and bilateral constraints where friction is also neglected. In a general form, the dynamic equations of a multibody system can be written in the impulse-momentum level as

$$\hat{\mathbf{M}}\mathbf{v}^+ + h\hat{\mathbf{c}} = \mathbf{M}\mathbf{v} + h\mathbf{f}_\mathrm{a} + h(\mathbf{A}_\mathrm{i}^\mathrm{T}\boldsymbol{\lambda}_\mathrm{i}^+ + \mathbf{A}_\mathrm{b}^\mathrm{T}\boldsymbol{\lambda}_\mathrm{b}^+ + \mathbf{A}_\mathrm{u}^\mathrm{T}\boldsymbol{\lambda}_\mathrm{u}^+) \tag{1}$$

where the contents of the *modified mass matrix* $\hat{\mathbf{M}}$, and *modified Coriolis and centrifugal terms* $\hat{\mathbf{c}}$ are determined with the time discretization method used [1]. $\mathbf{q} = \mathbf{q}(t_\mathrm{k})$ and $\mathbf{v} = \mathbf{v}(t_\mathrm{k})$ are the generalized coordinate and velocity of the system which are related by the transformation $\dot{\mathbf{q}} = \mathbf{N}\mathbf{v}$ and are known at the instant t_k. Moreover, $\mathbf{f}_\mathrm{a}$ and $\boldsymbol{\lambda}_\mathrm{i}$ are the applied and interface forces and $\mathbf{A}_\mathrm{i}$ is the corresponding interface Jacobian matrix. Similarly, $\boldsymbol{\lambda}_\mathrm{b}$ and $\boldsymbol{\lambda}_\mathrm{u}$ are the bilateral and unilateral constraint forces and their corresponding Jacobian matrices are $\mathbf{A}_\mathrm{b}$ and $\mathbf{A}_\mathrm{u}$. Then, considering a time step of size h, its configuration, velocity and unknown constraint forces in the next time-step are shown with $+$ sign. The constraint and the interface velocity arrays are related to the generalized velocity array $\mathbf{v}$ as $\mathbf{w}_\mathrm{j} = \mathbf{A}_\mathrm{j}\mathbf{v}$ $(\mathrm{j} \equiv \mathrm{i}, \mathrm{b}, \mathrm{u})$, which can be discretized through time using the first-order Taylor series expansion as

$$\mathbf{w}_\mathrm{j}^+ = \mathbf{A}_\mathrm{j}\mathbf{v}^+ + h\dot{\mathbf{A}}_\mathrm{j}\mathbf{v} \tag{2}$$

Knowing that $\mathbf{w}_\mathrm{b} = \mathbf{0}$, Eqs. (1) and (2) can be cast into a single matrix form which alongside the complementarity condition of the unilateral constraints will form a *Mixed Linear Complementarity Problem* (MLCP) as,

$$\begin{cases} \begin{bmatrix} \hat{\mathbf{M}} & -\mathbf{A}_\mathrm{b}^\mathrm{T} & -\mathbf{A}_\mathrm{u}^\mathrm{T} & -\mathbf{A}_\mathrm{i}^\mathrm{T} \\ \mathbf{A}_\mathrm{b} & \mathbf{0} & \mathbf{0} & \mathbf{0} \\ \mathbf{A}_\mathrm{u} & \mathbf{0} & \mathbf{0} & \mathbf{0} \\ \mathbf{A}_\mathrm{i} & \mathbf{0} & \mathbf{0} & \mathbf{0} \end{bmatrix} \begin{bmatrix} \mathbf{v}^+ \\ h\boldsymbol{\lambda}_\mathrm{b}^+ \\ h\boldsymbol{\lambda}_\mathrm{u}^+ \\ h\boldsymbol{\lambda}_\mathrm{i}^+ \end{bmatrix} + \begin{bmatrix} h(\hat{\mathbf{c}} - \mathbf{f}_\mathrm{a}) - \mathbf{M}\mathbf{v} \\ h\dot{\mathbf{A}}_\mathrm{b}\mathbf{v} \\ h\dot{\mathbf{A}}_\mathrm{u}\mathbf{v} \\ h\dot{\mathbf{A}}_\mathrm{i}\mathbf{v} \end{bmatrix} = \begin{bmatrix} \mathbf{0} \\ \mathbf{0} \\ \mathbf{w}_\mathrm{u}^+ \\ \mathbf{w}_\mathrm{i}^+ \end{bmatrix} \\ \\ \mathbf{0} \le \mathbf{w}_\mathrm{u}^+ \perp \boldsymbol{\lambda}_\mathrm{u}^+ \ge \mathbf{0} \end{cases} \tag{3}$$

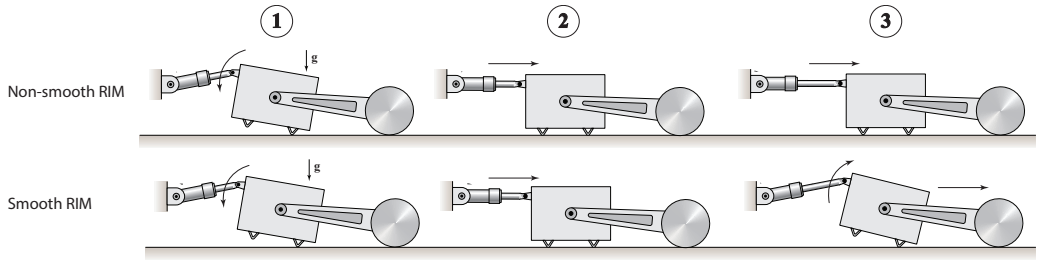

Figure 1: The manoeuvre sequence of the multibody system using smooth and non-smooth RIMs.

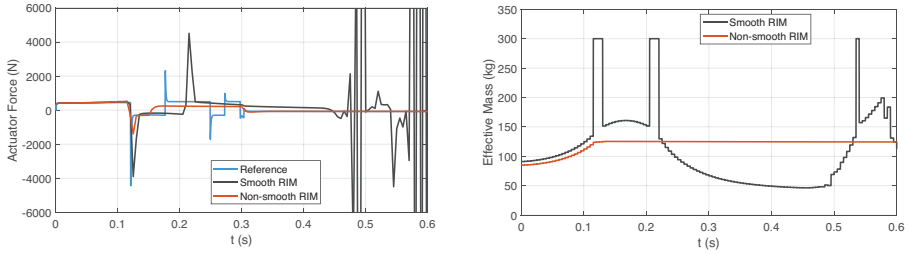

Figure 2: Actuator force (left) and effective mass of the reduced model (right).

The final goal is to obtain a reduced interface model that represents dynamics of the mechanical system associated with interface degrees of freedom parameterized by $\mathbf{w}_\mathrm{i}$. From the first and second rows in Eq. (3), the generalized velocities $\mathbf{v}^+$ and bilateral constraint impulse $h\boldsymbol{\lambda}_\mathrm{b}^+$ can be determined and be substituted into the third and forth rows. Then, the MLCP in Eq. (3) can be rewritten as

$$\begin{cases} \begin{bmatrix} \mathbf{H}_{\mathrm{uu}} & \mathbf{H}_{\mathrm{ui}} \\ \mathbf{H}_{\mathrm{ui}}^{\mathrm{T}} & \mathbf{H}_{\mathrm{ii}} \end{bmatrix} \begin{bmatrix} h\boldsymbol{\lambda}_\mathrm{u}^+ \\ h\boldsymbol{\lambda}_\mathrm{i}^+ \end{bmatrix} + \begin{bmatrix} \mathbf{b}_\mathrm{u} \\ \mathbf{b}_\mathrm{i} \end{bmatrix} = \begin{bmatrix} \mathbf{w}_\mathrm{u}^+ \\ \mathbf{w}_\mathrm{i}^+ \end{bmatrix} \\ \mathbf{0} \leq \mathbf{w}_\mathrm{u}^+ \perp \boldsymbol{\lambda}_\mathrm{u}^+ \geq \mathbf{0} \end{cases} \tag{4}$$

Eq. (4) is the *reduced interface model* (RIM) of non-smooth multibody systems which includes the complementarity condition and is able to capture the contact state transformation between the communication points. This reduced model may be referred to as *non-smooth RIM*. The advantages of this formulation will be demonstrated in the next section through numerical simulation.

Example and discussion

A planar model of a hydraulically actuated box with two bottom wedges connected to a disc through a revolute joint was used to illustrate the efficiency of the proposed RIM in a co-simulation setup. The hydraulic actuator is the first subsystem and set of the box and the disc are regarded as the second subsystem. Also, the box and the disc are allowed to slide without friction. In the manoeuvre shown in the Fig. 1, the box is initially a bit rotated around the right wedge. Then, the box will be pushed forward by the actuator under the effect of gravity. According to the reference solution (co-simulation using *zero order hold* setup with macro step size of $h = 0.2$ ms), as the multibody setup moves forward, the box rotates counterclockwise so that bot of its wedges touches the ground and the system continues to move forward horizontally. However, when the *smooth RIM* method introduced in [2] is used for model-based co-simulation, the contact points of the box are treated as bilateral constraints during the macro step which makes the system over-constrained when both wedges touch the ground. This can be also seen in Fig. 2 where the effective mass of the reduced model is depicted and, at the instances that both wedges are in contact with the ground, the effective mass shows a sudden rise in value due to the over-constraining. The over-constraining and the resulting high effective mass values will store excessive pressure in the hydraulic actuator and makes the system unstable so that in some instances, the box jumps off the ground and the whole simulation becomes unstable. The sudden rise in actuator force is also depicted in Fig. 2. However, by employing the proposed method, the contact detachment is taken into account in the reduced model and as it is evident from Fig. 2, the behaviour captured by the non-smooth RIM is similar to the reference solution. It should be mentioned that both model-based simulations were simulated with $h = 5$ ms.

References

[1] Acary V., Brogliato B. (2008) Numerical Methods for Nonsmooth Dynamical Systems: Applications in Mechanics and Electronics. Springer Science and Business Media, Springer, Berlin.

[2] Peiret A., Gonzalez F., Kovecses J., Teichmann M. (2020) Co-Simulation of Multibody Systems With Contact Using Reduced Interface Models. *J. Comput. Nonlinear Dynam* **15(4)**:041001.

Tuesday, July 19, 2022

16:00 - 18:00

MS-07 Dynamics and Optimization of Multibody Systems

Saint Clair 2

Chair:Régis Dufour

16:00 - 16:20
[visio] Three-Link Snake Robot with a Single Control Input
DOSAEV Marat*, KLIMINA Liubov, SELYUTSKIY Yury
*Institute of Mechanics, Lomonosov Moscow State University (119192, 1 Michurinskiy pr-t, Moscow, Russia Russia)

16:20 - 16:40
[visio] Feedback Control for a Body Carrying a Chain of Oscillators
OVSEEVICH Alexander*, ANANIEVSKI Igor
*Ishlinsky Institute for Problems in Mechanics RAS (Prospekt Vernadskogo, 101-1, Moscow 119526 Russia)

16:40 - 17:00
[visio] Swing Oscillations Generated by Sitting Human
FORMALSKII Alexander*, KLIMINA Liubov, JENKINS Alejandro
*Institute of Mechanics, Lomonosov Moscow State University (119192 Moscow, Michurinskiy prosp., 1 Russia)

17:00 - 17:20
[visio] Dynamics of Interacting Populations in a Bounded Domain: Control and Estimation under Nonlinearity and Uncertainty
FILIPPOVA Tatiana*
*Krasovskii Institute of Mathematics and Mechanics, UB RAS, Ural Federal University (16 S.Kovalevskaya Str., Ekaterinburg 620990 Russia)

17:20 - 17:40
Controlled motion of two interacting particles on a rough inclined plane
BOLOTNIK Nikolay*, FIGURINA Tatiana, BOGOSLAVSKII Ivan
*institute for Problems in Mechanics [Moscow] (Prospekt Vernadskogo, 101-1, Moscow 119526 Russia Russia)

17:40 - 18:00
Reorientation of a rigid body by means of an auxiliary mass
CHERNOUSKO Felix*
*Institute for Problems in Mechanics [Moscow] (Prospekt Vernadskogo, 101-1, Moscow 119526 Russia Russia)

Three-Link Snake Robot with a Single Control Input

Marat Dosaev, Liubov Klimina and Yury Selyutskiy
Institute of Mechanics, Lomonosov Moscow State University, Moscow, Russia

Summary. A three-link snake robot is proposed controlled by an internal flywheel installed at the first link. There are spiral springs installed in joints between links. These springs are non-deformed when angles between the links are zero. The robot performs plane-parallel motion over a rough surface. Each link contacts with the surface at a single point. Anisotropic dry friction acts at the contact points. The friction coefficient corresponding to the direction along the link direction is much smaller than that corresponding to the direction transversal to the link. The control torque is applied to the internal flywheel. Parameters of the mechanism and coefficients of the control law are adjusted to ensure irreversible propulsion of the robot along a prescribed direction.

Introduction

Snake robots can be used for works in aggressive areas. Such devices are widely discussed in the literature, and various schemes of construction and control are proposed for them, e.g. [1, 2]. Most of the research in this field assumes that there are motors which control angles between links in each joint. In the current work, we show that the presence of such motors is not necessary to obtain a snake-like motion of a link mechanism. We suppose that the only control applied to the system is associated with the rotation of a single inner flywheel installed at the leading link. Similar approach to the control of a three-link mechanism is applied in [3] for a swimming robot.

Description of the system, statement of the problem

The robot consists of three links AB, BD, DE located in OXY plane and connected to each other by cylindrical joints B and D (fig. 1). Spiral springs with the stiffness c are installed in joints. These springs are non-deformed when all links make a single straight line. The inner flywheel with the shaft A, the mass m_0, and the central moment of inertia J_0 is installed at the first link. The point A is the center of mass of the first link; this link has the mass $(m_1 - m_0)$ and the central moment of inertia J_1. Masses m_2 and m_3 of the links BD and DE are concentrated in the points C and E, respectively. The current position of the robot is described by coordinates x, y of the point A and angles φ_i, $i = 1,2,3$ between links and OX axis. The angle of orientation of the inner flywheel is a cyclic coordinate; ω_0 is the absolute angular speed of the flywheel.

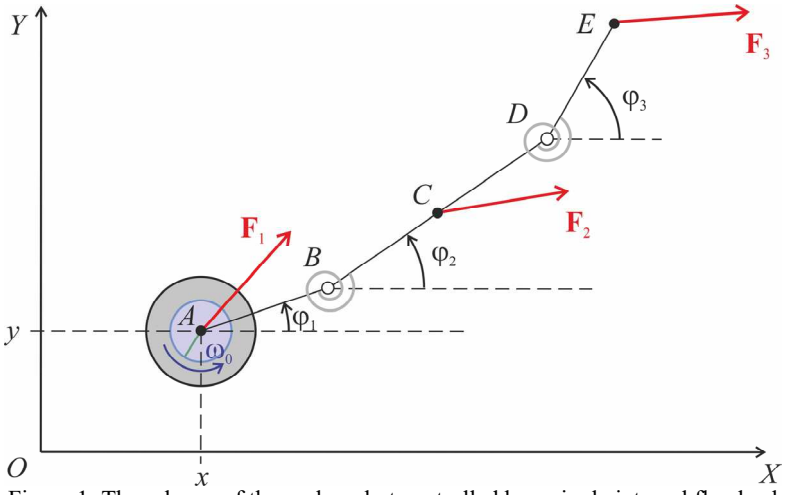

Figure 1: The scheme of the snake robot controlled by a single internal flywheel

Each link contacts the supporting plane in a single point: A, C, E. Anisotropic dry friction $\mathbf{F}_i$ is applied at each contact point; the corresponding friction model is taken from [4]. The friction coefficient $\mu_{i\xi}$ corresponding to the motion along the link is much smaller than $\mu_{i\eta}$ corresponding to the motion in the transversal direction. $V_{i\xi}, V_{i\eta}$ are projections of the speed $\mathbf{V}_i$ of the contact point on the axis directed along the link and the axis orthogonal to it. The following relation holds:

$$\begin{pmatrix} F_{i\xi} \\ F_{i\eta} \end{pmatrix} = -\begin{pmatrix} \mu_{i\xi} & 0 \\ 0 & \mu_{i\eta} \end{pmatrix} \begin{pmatrix} V_{i\xi} \\ V_{i\eta} \end{pmatrix} \frac{m_i g}{V_i}.$$

The single control torque U is applied to the shaft of the flywheel. It is limited in the absolute value by the constant $U_{\max}$. The goal of the control is to ensure the existence of an attracting self-sustained irreversible mode of propulsion of the robot opposite to OX axis. This means that the projection V_x of the velocity $\mathbf{V}$ of the center of mass on OX shouldn't change sign and the average value of projection V_y of $\mathbf{V}$ on OY should be zero.

Methods and main results

Equations of motion are derived basing the Lagrange formalism. Generalized forces are associated with dry friction forces, corresponding generalized torques Q_i, and the control torque U applied to the flywheel:

$$\frac{d}{dt}\left(\frac{dK}{d\dot{x}}\right)=F_{1x}+F_{2x}+F_{3x},\quad \frac{d}{dt}\left(\frac{dK}{d\dot{y}}\right)=F_{1y}+F_{2y}+F_{3y},\quad \frac{d}{dt}\left(\frac{dK}{d\dot{\varphi}_i}\right)-\frac{dK}{d\varphi_i}+\frac{dP}{d\varphi_i}=Q_i\quad (i=1,2,3),\quad \frac{d}{dt}\left(\frac{dK}{d\omega_0}\right)=U;$$

$$F_{ix}=F_{i\xi}\cos\varphi_i-F_{i\eta}\sin\varphi_i,\quad F_{iy}=F_{i\xi}\sin\varphi_i+F_{i\eta}\cos\varphi_i\quad (i=1,2,3);$$

$$Q_1=r(F_{2y}+F_{3y})\cos\varphi_1-r(F_{2x}+F_{3x})\sin\varphi_1,\quad Q_2=r(F_{2y}+2F_{3y})\cos\varphi_2-r(F_{2x}+2F_{3x})\sin\varphi_2,\quad Q_3=r(F_{3y}\cos\varphi_3-F_{3x}\sin\varphi_3).$$

Here K and P are kinetic and potential energies, respectively. The control torque U is as follows:

$$U=\begin{cases}U_p, & |U_p|\le U_{\max},\\ \operatorname{signum}(U_p)\cdot U_{\max}, & |U_p|>U_{\max},\end{cases}\qquad U_p=-\left(a_0\operatorname{signum}\left(\sin(2\pi w_0 t)\right)-k_0 y-k_1\varphi_1\right).$$

The first term of the U_p represents a periodic excitation aimed to ensure oscillations of the inner flywheel. The other two terms are required to ensure zero average shift of links from the axis OX during the self-sustained propulsion.

Analysis of motion equation was performed by direct numerical integration with different geometrical and mass parameters, coefficients of the control law and initial component $\dot{x}(0)$ of the velocity of the point A. Initial values of other variables were zero. The total mass of the system was supposed to be equal to 0.5 kg, moments of inertia: $J_0=0.0005$ kgm^2, $J_1=0.002$ kgm^2. Lengths of links were not varied: AB=BC=CD=DE=0.05 m. The maximum value of the control torque was fixed: $U_{\max}$=0.1 N. Friction coefficients were fixed: $\mu_{i\xi}=0.03$, $\mu_{i\eta}=0.9$ $(i=1,2,3)$.

Parameter continuation was used to find the set of parameters providing higher speed of motion at the program mode.

It was shown that an attracting regime of irreversible propulsion exists in a rather wide range of parameters. In particular, high speed of propulsion is achieved for the following set: $m_1=m_3=0.2$ kg, $m_2=0.1$ kg, $c=0.15$ kgm^{2}s^{-2}, $a_0=0.1$ Nm, $w_0=1.2$ s^{-1}, $k_0=-0.1$ N, $k_1=0.1$ Nm. The transition process with initial value $\dot{x}(0)=0.1$ m/s is shown in the fig. 2: initially robot was pushed in the direction opposite to the target direction; at first, the center of mass decelerates, then it starts accelerating and reaches the attracting self-sustained motion in the prescribed direction, i.e. against OX. At the attracting regime, the x-component V_x of the speed of the center of mass is always negative. Thus, the motion is irreversible. The average value $\langle V_x\rangle$ of the component V_x is about -0.37 m/s, and the average value of V_y is zero.

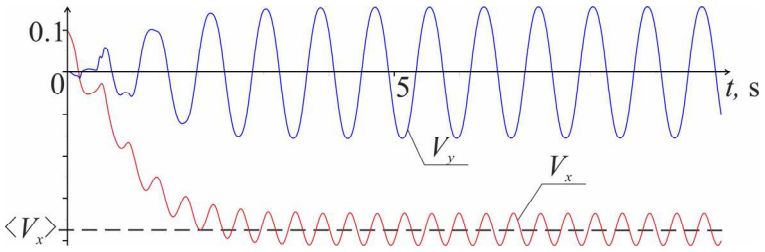

Figure 2: Components of the speed of the center of mass during the transition to the program mode (an example)

The control ensures transition of the system to the program regime of motion from a wide range of initial conditions. The program motion is irreversible with respect to the axis OX. It should be noticed, that the presence of springs in joints as well as the anisotropy of friction are necessary conditions for the existence of the desired irreversible mode of propulsion of the proposed robotic scheme.

Conclusions

A new scheme of the snake robot is proposed without any control inputs applied in inter-link joints. The only control is the torque applied to the inner flywheel installed at the first link. The robot performs a plane-parallel motion over a rough surface. An anisotropic dry friction acts in the points of contact between the robot and the supporting surface. The parameters of the construction and coefficients of the control law are adjusted to ensure existence of attracting propulsion mode of motion that is irreversible with respect to the preferable direction of propulsion.

This works is supported by Russian Science Foundation (project No.22-21-00303).

References

[1] Transeth A. A., Pettersen K. Y., Liljebäck P. (2009) A Survey on Snake Robot Modeling and Locomotion. *Robotica*. **27**(7): 999-1015.
[2] Chernousko F. L. (2018) Locomotion of multibody robotic systems: dynamics and optimization. *Theoretical and Applied Mechanics*. **45**(1):17-33.
[3] Pollard B., Tallapragada P. (2019) Passive Appendages Improve the Maneuverability of Fishlike Robots. *IEEE/ASME Transactions on Mechatronics*. **24**(4):1586-1596.
[4] Zmitrowicz A. (1989) Mathematical descriptions of anisotropic friction. *Int. J. Solids and Structures*. **25**(8):837-862.

Feedback Control for a Body Carrying a Chain of Oscillators

Igor Ananievski and Alexander Ovseevich
Ishlinsky Institute for Problems in Mechanics RAS
Prospekt Vernadskogo, 101-1, Moscow 119526 Russia

Summary. We study steering of a linear chain of point masses connected via springs to the equilibrium, by means of a bounded force applied to the first mass in the chain. In other words, we design an explicit feedback control that bring the system to a given terminal rest state in a finite time. Thus, we prove the complete controllability of the system, and describe explicitly the feedback control proposed. Then, we show its robustness with respect to unknown disturbances.

The chain of n oscillators: Problem statement

We consider a control problem for a system representing a solid body carrying a chain of n linear oscillators modelled by point masses connected via springs (Fig. 1). The whole system moves along a horizontal line under the action of a control force and an external disturbance applied to the carrying body.

Figure 1: A body carrying the chain of oscillators

Equations of motion have the form

$$\begin{aligned} &m_0\ddot{x}_0 = -k_1x_0 + k_1x_1 + u + v \\ &m_i\ddot{x}_i = k_ix_{i-1} - (k_i + k_{i+1})x_i + k_{i+1}x_{i+1}, \quad i = 1, \dots, n-1 \\ &m_n\ddot{x}_n = -k_nx_{n-1} + k_nx_n \end{aligned} \tag{1}$$

Here, we have the controllable mass m_0, which is subject to control u, and disturbances v. Each mass $m_i, i = 0, \dots, n$ has coordinate x_i, and the Hooke law $F_i = k_i(x_i - x_{i-1})$ gives the force from mass m_{i-1} to m_i.
Assuming $x = (x_0, x_1, \dots, x_n)$, we can write (1) in the Cauchy normal form

$$\dot{x} = A_1x + \frac{1}{m_0}b(u + v)$$

where A and b are the block matrices

$$A_1 = \begin{pmatrix} 0 & I \\ A_0 & 0 \end{pmatrix}, \quad b = \begin{pmatrix} 0 \\ e \end{pmatrix}$$

$$A_0 = \begin{pmatrix} -\frac{k_1}{m_0} & \frac{k_1}{m_0} & 0 & \dots & 0 \\ \frac{k_1}{m_1} & -\frac{k_1+k_2}{m_1} & \frac{k_2}{m_1} & \ddots & \vdots \\ 0 & \ddots & \ddots & \ddots & 0 \\ \vdots & \ddots & \frac{k_{n-1}}{m_{n-1}} & -\frac{k_{n-1}+k_n}{m_{n-1}} & \frac{k_n}{m_{n-1}} \\ 0 & \dots & 0 & \frac{k_n}{m_n} & -\frac{k_n}{m_n} \end{pmatrix}, \; e = \begin{pmatrix} 1 \\ 0 \\ \vdots \\ 0 \end{pmatrix}$$

and I is the unit matrix.
We assume that we know the current values $x_0, \dot{x}_0, x_1$, while the other coordinates are not directly observable. Therefore, a measured output is

$$y = Dx, \quad D = \begin{pmatrix} 1 & 0 & 0 & 0 & \dots 0 \\ 0 & 1 & 0 & 0 & \dots 0 \\ 0 & 0 & 1 & 0 & \dots 0 \end{pmatrix}$$

Theorem 1 *Pair (A_1, b) is controllable and the pair (A_1, D) is observable.*

Thus, we can in principle bring the system under consideration to any given state, at least if the disturbances are absent.

Control of canonical systems

The control problem stated can be reduced [1, 2] to the control problem for canonical system

$$\dot{z} = Az + B(u + v) \tag{2}$$

where

$$A = \begin{pmatrix} 0 & 0 & 0 & \dots & 0 \\ -1 & 0 & 0 & \dots & 0 \\ 0 & -2 & 0 & \ddots & \vdots \\ \vdots & \ddots & \ddots & \ddots & 0 \\ 0 & \dots & 0 & -2N-1 & 0 \end{pmatrix}, \quad B = \begin{pmatrix} 1 \\ 0 \\ \vdots \\ 0 \end{pmatrix}, \quad z, B \in \mathbf{R}^{2N+2} \tag{3}$$

We use matrices

$$q_{ij} = \int_0^1 x^{i+j-2}(1-x)dx = \frac{1}{(i+j)(i+j-1)}, \quad i,j = 1,\dots,2N+2$$
$$Q = q^{-1}, \quad C = -\frac{1}{2}B^T Q, \quad \delta(T) = \mathrm{diag}\{T^{-1}, T^{-2}, \dots, T^{-2N-2}\}$$

Note, that for the scalar control system (2),(3) the matrix C is a row-vector $C = (C_1, \dots, C_{2N+2})$. This allows to define the canonical feedback control by

$$u(z) = C\delta(T(z))z$$

which takes the form

$$u(z) = \frac{C_1}{T(z)}z_1 + \frac{C_2}{T^2(z)}z_2 + \dots + \frac{C_{2N+2}}{T^{2N+2}(z)}z_{2N+2} \tag{4}$$

in the scalar control case. The function $T(z)$ is found from the equation

$$\langle Q\delta(T)z, \delta(T)z\rangle = 1 \tag{5}$$

Theorem 2 *(see [2])*

A) Equation (5) define positive $T = T(z)$ uniquely.

B) The control (4) is bounded: $|u| \le \frac{1}{2}\sqrt{N(N+1)}$.

C) If there are no disturbances, the control (4) brings state z to 0 in time $T(z)$.

Theorem 3 *If disturbances v satisfy*

$$|v| \le c < \frac{1}{2\sqrt{N(N+1)}}$$

the derivative of T satisfies inequality

$$\dot{T} \le -\sigma, \ \sigma > 0$$

and control (4) brings state z to 0 in a finite time $T = O(T(z))$.

Acknowledgment

This work was supported by the Russian Science Foundation, project no. 21-11-00151.

References

[1] Brunovsky P. (1970) *Kibernetika* (6), 176-188.

[2] Ovseevich A. (2015) A Local Feedback Control Bringing a Linear System to Equilibrium *JOTA* 165, 532-544.

Swing Oscillations Generated by Sitting Human

Alexander Formalskii [*], Alejandro Jenkins [**] and Liubov Klimina[*]
[*]*Institute of Mechanics, Lomonosov Moscow State University, Moscow, Russia*
[**]*Universidad de Costa Rica, San José, Costa Rica*

Summary. Oscillations pumped by the human sitting on the swing are modeled. The model is represented by a three-link mechanism. Control torques are applied in the knee- and hip- joints. The control strategy is proposed that allows generation and maintaining of oscillations with large amplitude and also rotation around the suspension point. Control torques are designed as autonomous feedbacks depending on the angle and the angular speed of rotation of the swing. Numerical simulation is performed. The anthropomorphism of the proposed control is illustrated.

Introduction

Pumping of a swing is systematically discussed in the literature as a classical example of forced oscillations. This paper deals with the case of pumping a rigid swing by a sitting person. The paper provides the following novel results: it is shown that the anthropomorphic strategy of pumping is quasi-optimal one, the control strategy is proposed that can pump the swing to stationary rotation (not only to oscillations), the numerical simulation is performed for the three-link model of the system while usually only oscillations of a double-link model are discussed (see, for example, [1-5]).

Statement of the Problem

Three-link planar hinge mechanism models a human pumping a swing (see Fig. 1a). Link *VP* models a body, link *PK* – both thighs, and *KF* – both shins. Link *PK* is rigidly joined to the rod that corresponds to the swing. The rod is pivotally joined to the suspension point *O* that is the axis of rotation of the swing. The viscous friction torque with coefficient *c* acts at this axis. The angle of rotation of the swing is denoted as φ. One inter-link hinge *K* models two knee-joints, second hinge *P* – two hip-joints. Two limited control torques are applied at these two inter-link joints *K* and *P*. Thus, the system has three degrees of freedom, but only two control torques are applied. So, this system is under-actuated one. Angles α in joint *K* and β in joint *P* can be changed in limits $\alpha_{\min} \le \alpha \le \alpha_{\max}$ and $\beta_{\min} \le \beta \le \beta_{\max}$. Here $\alpha_{\min/\max}$, $\beta_{\min/\max}$ are given constants. The limitation upon these angles is modeled via relatively strong single-side spiral springs in joints *K* and *P* which practically ensures that angles α and β do not leave the prescribed domain. These springs model ligaments and tendons.

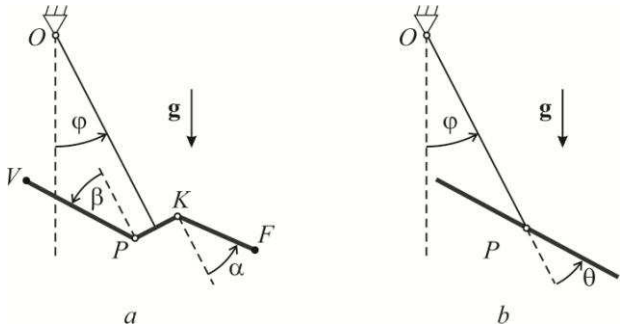

Figure 1: The schemes of the three-link and simplified double-link mechanisms

The goal of the control is to pump the swing as fast as possible and to the largest amplitude taking into account the restrictions imposed on the control. In this paper, the solution that is "close to optimal" is proposed.

Design of the control and simulation

As a preliminary step the quasi-optimal control is designed for the simplified double-link model in which a human is substituted by a single rigid body (see Fig. 1b) and the limited angle θ is a control input. This control strategy is represented by a relay-type function $\theta^*(\varphi, \dot{\varphi})$ that ensures pumping the swing to the large amplitude oscillations or even to stationary rotations (depending on parameters $\theta_{\min/\max}$ and friction coefficient *c* in the suspension joint):

$$\theta^*(\varphi,\dot{\varphi}) = \begin{cases} \theta_{\max}, & \text{if} \quad \dot{\varphi}\cos\varphi \ge 0, \\ \theta_{\min}, & \text{if} \quad \dot{\varphi}\cos\varphi < 0. \end{cases}$$

Function $\theta^*(\varphi,\dot{\varphi})$ is used as the program function in the initial problem for the three-link mechanism (with $\theta_{min/max}$ equal to $\alpha_{min/max}$ or $\beta_{min/max}$ correspondingly). Control torques are designed as combinations of linear feedbacks with respect to the differences between the current and program angles and their derivatives. Efficiency of this control strategy is illustrated by numerical simulation with parameters of the model similar to parameters of the human. This simulation shows that if friction coefficient c is rather large, then oscillations of the swing tend to a stationary oscillatory mode corresponding to a cycle in the configuration space (see Fig. 2). But if friction coefficient c is sufficiently small, then the swing is pumped to a stationary rotation corresponding to the cycle in the space $(\varphi \bmod 2\pi, \alpha, \beta)$. These cycles are attracting ones.

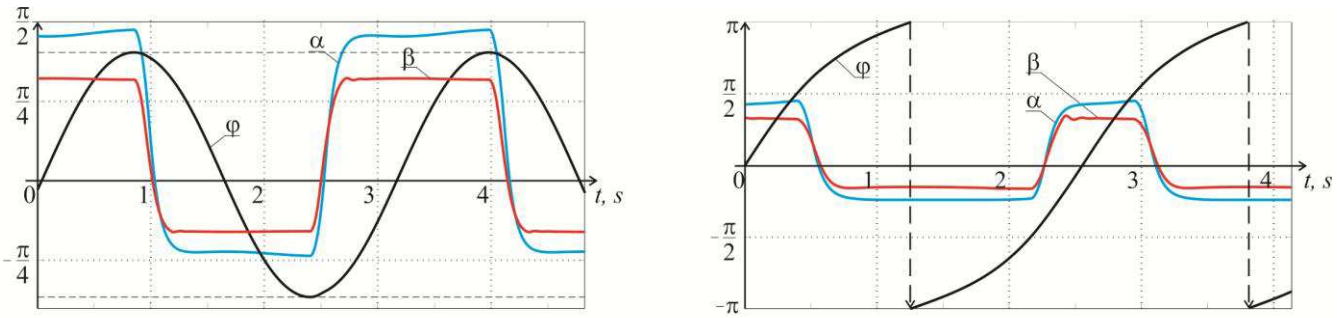

a) the case of a large viscous friction coefficient (stationary oscillations)

b) the case of a small viscous friction coefficient (stationary rotations)

Figure 2: Illustration of stationary oscillations and rotations of the swing

Conclusion

The designed control allows maintaining oscillations in wide range of amplitudes as well as rotational motion with a constant period depending on the restrictions upon angles α, β and on the viscous friction coefficient c.

References

[1] Case W.B., Swanson M.A. (1990) The pumping of a swing from the seated position. *American J. of Physics* **58**(5): 463-467.
[2] Wirkus S., Rand R., Ruina A. (1998) How to pump a swing. *The College Mathematics J.* **29**(4): 266-275.
[3] Roura P., González J. A. (2010) Towards a more realistic description of swing pumping due to the exchange of angular momentum. *European J. of Physics* **31**(5): 1195.
[4] Linge S.O. (2012) An assessment of swinger techniques for the playground swing oscillatory motion. *Computer methods in biomechanics and biomedical engineering* **15**(10): 1103-1109.
[5] Nikolov S., Zaharieva D. (2017) Dynamics of swing oscillatory motion in Hamiltonian formalism. *Mechanics, Transport, Communications* **15**(3): VII-7-VII-12.

Dynamics of Interacting Populations in a Bounded Domain: Control and Estimation under Nonlinearity and Uncertainty

Tatiana F. Filippova
Department of Optimal Control, Krasovskii Institute of Mathematics and Mechanics,
Ural Branch of Russian Academy of Sciences,
Ural Federal University, Ekaterinburg, Russian Federation

Summary. The nonlinear control systems of Lotka - Volterra type which describe the dynamics of the interaction of predators and their preys are studied. It is assumed that the initial states of the system are not known precisely but belong to a given ellipsoid in the state space and there is no additional information (for example, probabilistic, statistical, etc.) on unknown values. We find the external ellipsoidal estimates of corresponding reachable sets for control systems under study. The considered models may describe the behavior of competing firms, population growth, environmental change, development of individual industries, etc. The results of modeling based on proposed methods are included to illustrate the main proposed ideas and presented estimation algorithms.

Introduction

The problem of state estimation for control systems under conditions of nonlinearity and uncertainty is studied. The case is investigated here when the probabilistic data of noise and possible errors is not available, and only some restriction on unknown parameters and functions are given. Models of this kind may be found in many applied problems including physics, economics, biology, ecology, etc. As one of the important and key idea to study such problems we use the so-called set-membership approach which was developed earlier [1, 2, 3, 4] to deal with a whole set of feasible parameters, consistent with the model structure, for systems with bounded uncertainty, with special types of measurements characterization etc.
The solutions of such classes of control and estimation problems with set-membership uncertainty are based on the construction and on the analysis of the corresponding reachable sets or their analogs. In this paper we study the procedures of upper estimating reachable sets for nonlinear control systems of Lotka-Volterra type. We use here the ideas and results of state estimation theory developed for nonlinear control systems which have a special quadratic dynamical structure [5, 6, 7, 8] and several new schemes of the problem solution are developed here. We prove here theoretical results and formulate related numerical algorithms for constructing external ellipsoidal estimates of reachable sets for nonlinear uncertain control systems of the studied type. Numerical examples and results of related simulations are included to illustrate the basic ideas and results.

Problem statement

The paper deals with the problems of control and state estimation for a dynamical control system

$$\dot{x}(t) = A(t)x(t) + f(x(t)) + G(t)u(t), \;\; x \in R^n, \;\; t_0 \leq t \leq T, \tag{1}$$

with unknown but bounded initial state

$$x(t_0) = x_0, \;\; x_0 \in X_0, \;\; X_0 \subset R^n, \tag{2}$$

and with control constraint

$$u(t) \in U, \;\; U \subset R^m, \;\; \text{for a.e. } t \in [t_0, T]. \tag{3}$$

Here matrices $A(t)$ and $G(t)$ (of dimensions $n \times n$ and $n \times m$, respectively) are assumed to be continuous on $t \in [t_0, T]$, X_0 and U are compact and convex. The nonlinear n-vector function $f(x)$ in (1) is assumed to be of quadratic type

$$f(x) = (f_1(x), \ldots, f_n(x)), \;\; f_i(x) = x' B_i x, \; i = 1, \ldots, n, \tag{4}$$

where B_i $(i = 1, \ldots, n)$ are constant $n \times n$ - matrices.
In previous studies [5, 6, 7, 8], it was taken as the main assumption that matrices B_i in (1)–(4) are positive definite; this additional condition simplified the analysis of nonlinearity in studying the structure and the properties of reachable sets of the control system (1)–(4).
As a particular kind of the above control problem we consider here the following Lotka-Volterra system which describes the classical ecological predator-prey (or parasite-host) model with additional control functions:

$$\left\{ \begin{array}{rcl} \dot{x_1}(t) & = & ax_1 - bx_1x_2 + u_1, \\ \dot{x_2}(t) & = & -cx_2 + dx_1x_2 + u_2, \end{array} \right. \qquad x(t_0) = x_0, \;\; t_0 \leq t \leq T. \tag{5}$$

Here we assume that numbers $a, b, c, d > 0$ are given and initial vectors x_0 are unknown but bounded, that is we have the inclusion $x_0 \in X_0$, where X_0 is a given compact subset of R^2. This assumption may be interpreted for example in such

a way that we do not know exactly the initial states (or amounts) of predators and prey. We assume also that controls $u(t)$ in (3)-(5) are taken measurable in Lebesgue on $[t_0, T]$, also the inclusion is true

$$u(t) \in U, \quad \text{a.e. } t \in [t_0, T], \tag{6}$$

where $U \in compR^2$. The choice of a control can influence, in particular, the rate of change in amounts of predators and prey.

Basing on results of ellipsoidal calculus [1, 4] and estimation schemes described in [5, 6, 8] we present here the modified state estimation approaches which use the special structure of nonlinearity of studied control system (1)–(6) and combine advantages of estimating tools mentioned above. Numerical simulation schemes together with modeling examples are also included.

Main results

Note first that we have in the system (5)-(6) a bit more simple situation than in general case of the system (1)-(4), namely we have the equality $f(x)' = x_1 x_2 \cdot (-b, d)$. The idea used here in the analysis of reachable sets of the system (5)–(6) is based on the following transformion of the system (1)–(4) to the new one which will include only positive definite quadratic forms, this case is more convinient for the analysis and for further numerical modeling. So we consider the following modified control system

$$\begin{gathered} \dot{z} = A^* z + f_\varepsilon^{(1)}(z) \cdot d^{(1)} + f_\varepsilon^{(2)}(z) \cdot d^{(2)} + w(t), \\ z_0 \in \mathcal{Z}_0, \quad w \in \mathcal{W}, \quad t_0 \le t \le T, \end{gathered} \tag{7}$$

with

$$A^* = \begin{pmatrix} A & -C \\ -C & A \end{pmatrix}$$

and with functions $f_\varepsilon^{(1)}(z)$ and $f_\varepsilon^{(2)}(z)$ being the positive definite quadratic forms with matrices $B_\varepsilon^{(1)} = diag\{1, \varepsilon^2\}$ and $B_\varepsilon^{(2)} = diag\{\varepsilon^2, 1\}$, respectively.

We can find now the external ellipsoidal estimates of reachable set $Z(t)$ of the system (7) applying for this purpose results of [7]. The case of the presence of a state constraint on the dynamics of the dynamical system is considered separately; here, the possibility of applying the procedure for removing restrictions using the results of [2] is discussed.

We formulate also a numerical discrete-time algorithms of ellipsoidal estimating the reachable sets of the studied uncertain system. Examples and numerical simulation results related to procedures of set-valued approximations of trajectory tubes and reachable sets are also presented.

Conclusions

The paper deals with the problems of control and state estimation for a dynamical control system with unknown but bounded initial state. The solution to the differential control system is studied through the techniques of trajectory tubes of the theory of differential inclusions. The estimation approach uses the special nonlinear structure of the Lotka-Volterra system. Examples and numerical results related to state estimation procedures of reachable sets are presented.

The research was supported by the Russian Foundation for Basic Researches (RFBR) under Project 18-01-00544a.

References

[1] Kurzhanski A. B., Valyi I. (1997) Ellipsoidal Calculus for Estimation and Control. Birkhauser, Boston.

[2] Kurzhanski A. B., Filippova T. F. (1993) On the Theory of Trajectory Tubes – a Mathematical Formalism for Uncertain Dynamics, Viability and Control. *Advances in Nonlinear Dynamics and Control: a Report from Russia, Progress in Systems and Control Theory, (ed. A.B. Kurzhanski)*, Birkhauser, Boston. V. 17:122-188.

[3] Schweppe F. (1973) Uncertain Dynamic Systems. Prentice-Hall, Englewood Cliffs, New Jersey.

[4] Chernousko F. L. (1994) State Estimation for Dynamic Systems. CRC Press, Boca Raton.

[5] Filippova T. F. (2014) Asymptotic Behavior of the Ellipsoidal Estimates of Reachable Sets of Nonlinear Control Systems with Uncertainty. *Proc. of the 8th European Nonlinear Dynamics Conference (ENOC 2014)*. Vienna, Austria, July 6-11, 2014, H. Ecker, A. Steindl and S. Jakubek (Eds.), Institute of Mechanics and Mechatronics, TU-Vienna, Austria. CD-ROM volume (ISBN: 978-3-200-03433-4). Paper-ID 149. Vienna, 2014.

[6] Filippova T. F. (2017) Differential Equations of Ellipsoidal State Estimates for Bilinear-Quadratic Control Systems under Uncertainty. *J. Chaotic Modeling and Simulation (CMSIM)*, **1**:85–93, 2017.

[7] Filippova, T. F. (2017). Ellipsoidal estimates of reachable sets for control systems with nonlinear terms. *IFAC-PapersOnLine: 20th World Congress of the International Federation of Automatic Control (IFAC-2017), Toulouse, France, July 9-14, 2017: proceedings*, **50(1)**:15925–15930.

[8] Filippova T.F. (2019) Description of Dynamics of Ellipsoidal Estimates of Reachable Sets of Nonlinear Control Systems with Bilinear Uncertainty. *Lecture Notes in Computer Science. 2019. Vol. 11189 (Nikolov G., Kolkovska N., Georgiev K. (eds) Numerical Methods and Applications, NMA 2018)*. Springer, Cham, 97–105.

Controlled motion of two interacting particles on a rough inclined plane

Ivan Bogoslavskii*, Nikolay Bolotnik * and Tatiana Figurina *
**Institute for Problems in Mechanics of the Russian Academy of Sciences, Moscow, Russia*

Summary. Two interacting particles on a rough inclined plane are considered. Coulomb's friction acts between the particles and the underlying surface. The system is controlled by the force of interaction of the particles. It is assumed that the parameters of the system are such that one of the bodies can be moved upward along a line of maximum slope provided that the other body is resting. The controllability of the system between two arbitrary states of rest is investigated. The system is proved to be controllable if the particles do not lie on a common line of maximum slope at the initial instant. A control algorithm that alternates quasistatic and fast modes of motion is constructed.

Statement of the problem

Consider a system of two particles on an inclined plane Π (Fig. 1a). Let m and M denote the masses of the particles ($m < M$), k the coefficient of Coulomb's friction between the particles and the underlying plane, γ the inclination angle of the plane, g acceleration due to gravity, $\mathbf{F}$ the interaction force applied by particle M to particle m. We assume that for $\mathbf{F} = 0$, both particles can stay at rest and that particle m can be moved from the state of rest by the force $\mathbf{F}$ upward along the line of maximum slope, while particle M does not move:

$$kM\cos\gamma \geq (M+m)\sin\gamma + km\cos\gamma. \tag{1}$$

Let the system under consideration be at rest at the initial instant. The aim of our study is to find out whether the system can be driven from the initial state to any other state of rest on the plane. For the horizontal plane ($\gamma = 0$), this is impossible. We are interested in the controllability of the system in principle. For this reason, we do not impose any constrains on the magnitude of the control force, allow instantaneous change in the positions of the particles, and assume that the particles may move through one another. If the particles at the initial instant rest on the common line of maximum slope, they cannot quit this line, and this case will not be considered. We will show that the system can be driven between

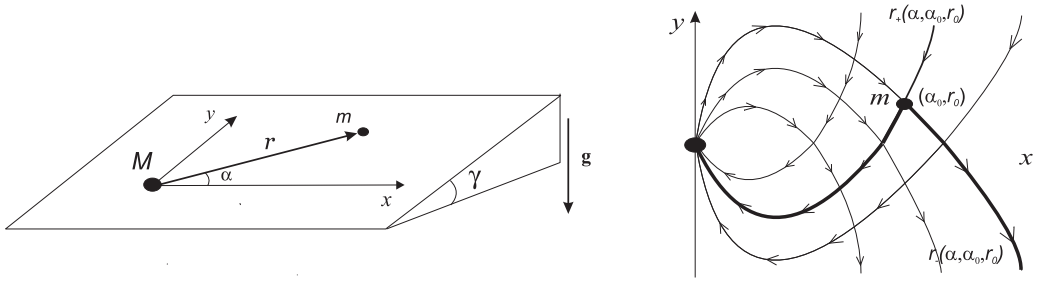

Figure 1: a) Two-particle system on an inclined plane, b) Quasistaic trajectories of particle m

the initial and terminal states by combining two types of motions: quasistatic motions and fast motions. The quasistatic motion is a slow motion that can be regarded as a continuous sequence of equilibria, while for fast motion we admit an instantaneous change in the positions of the particles.

Quasistatic motions

Inequality (1) implies that in quasistatic motions, only particle m moves, while particle M is at rest. Denote by L_M the line of maximum slope passing through the point M. Introduce in plane Π the coordinate frame Mxy (Fig. 1a). The axis y lies on line L_M and is directed upward. The trajectories of the quasistatic motion of particle m are defined by the equation

$$\frac{dr}{d\alpha} = \pm\frac{r\sqrt{1-a^2\cos^2\alpha}}{a\cos\alpha}, \quad a = \frac{\tan\gamma}{k}, \tag{2}$$

where r and α are the polar coordinates of particle m in plane Π related to the pole M and the polar axis Mx. When moving quasistatically, particle m cannot intersect line L_M; therefore we assume $\alpha \in (-\pi/2,\, \pi/2)$. Sign minus on the right-hand side in Eq. (2) corresponds to the repulsive motion when the interaction force $\mathbf{F}$ applied to particle m acts from M toward m, while sign plus corresponds to the attractive motion. Equation (2) has a closed-form solution in terms of elementary functions. Denote by $r_\pm(\alpha, \alpha_0, r_0)$ the solution of Eq.(2) subject to the initial conditions $r(\alpha_0) = r_0$. The function r_+ (r_-) monotonically increases (decreases) as α increases in the interval $(-\pi/2, \pi/2)$. The functions r_+ and r_- have the following properties:

$$\lim_{\alpha\to\pi/2} r_-(\alpha) = 0, \qquad \lim_{\alpha\to-\pi/2} r_-(\alpha) = \infty, \qquad \lim_{\alpha\to-\pi/2} r_-(\alpha)\cos\alpha = \infty. \tag{3}$$

$$\lim_{\alpha\to\pi/2} r_+(\alpha) = \infty, \quad \lim_{\alpha\to-\pi/2} r_+(\alpha) = 0, \quad \lim_{\alpha\to\pi/2} r_+(\alpha)\cos\alpha = \infty. \tag{4}$$

$$r_-(\alpha, \alpha_0, r_0) = r_+(-\alpha, -\alpha_0, r_0). \tag{5}$$

According to the properties of Eqs. (3)–(5), the trajectories of the quasistatic motion of particle m on plane Π have the shape shown in Fig. 1b. For each point $(\alpha_0,\, r_0)$ on the plane, one can indicate an area (attainable area) to each point of which particle m can be driven quasistatically. This area is bounded by the curves $r_\pm(\alpha, \alpha_0, r_0)$ (thick lines in Fig. 1b). One can drive particle m to any internal point (α_1, r_1) of the attainable area using one switching between the repulsive and attractive motions; the particle moves first along the curve $r_-(\alpha, \alpha_0, r_0)$ or $r_+(\alpha, \alpha_0, r_0)$ and then, respectively, along the curve $r_+(\alpha, \alpha_1, r_1)$ or $r_-(\alpha, \alpha_1, r_1)$. In particular, using one switching, one can get quasistatically to the point $(\alpha_0 - \delta\alpha,\, r_0)$, $\delta\alpha \ll 1$, from the point $(\alpha_0,\, r_0)$. Then, similarly, using one switching, one can get to the point $(\alpha_0 - 2\delta\alpha,\, r_0)$ from the point $(\alpha_0 - \delta\alpha,\, r_0)$, and so on. By letting $\delta\alpha \to 0$, we obtain that the trajectory of particle m can be made arbitrarily close to the circular arc of radius r_0; the angle α monotonically decreases, approaching but not reaching a value of $-\pi/2$. Therefore, particle m can be driven from the point $(\alpha_0,\, r_0)$ quasistatically along a trajectory arbitrarily close to the circular arc $r = r_0$, $\alpha \in (-\pi/2, \alpha_0]$, with monotonically decreasing angle α. We will call such a motion the quasistatic motion along a circumference.

All the aforesaid remains valid for the quasistatic motion for $\alpha \in (\pi/2,\, 3\pi/2)$. In this case, the repulsive and attractive trajectories will be symmetric about the My-axis to the respective trajectories for $\alpha \in (-\pi/2,\, \pi/2)$; particle m can be driven along a circumference, with α monotonically approaching but not reaching a value of $3\pi/2$.

Fast motions. An algorithm for driving the system to the terminal state

By fast motions we understand the motions that drive the system between different states of rest in an infinitesimal time. The force of interaction between the particles for such motions is much larger than the external friction forces; therefore, the system's center of mass and the line that connects the particles are fixed. We allow the particles in the fast motion to pass through one another, changing as a result the direction of the vector $\overrightarrow{Mm}$ to the opposite one. By means of the fast motion, we can move particle M to any position on the initial line Mm.

By alternating fast and quasistatic motions one can move particle m to any position on the plane, with particle M remaining arbitrarily close to its initial position. We will show this for the case where the initial and terminal positions of particle m belong to different half-planes with respect to line L_M. We assume for definiteness that $\alpha \in (\pi/2, 3\pi/2)$ for the initial positions and $\alpha \in (-\pi/2, \pi/2)$ for the terminal position. We will show first that particle m can be brought onto a semicircumference of an arbitrarily small radius on the right half-plane, i.e., to any position $(\alpha^*,\, r^*)$ such that $r^* = \varepsilon$, $\varepsilon \ll 1$, and $\alpha^* \in (-\pi/2, \pi/2)$, while the change in the position of particle M is small. To this end we at the first stage move quasistatically particle m toward particle M until the distance r between the particles becomes $r = \varepsilon$. If at this instant the angle α does not satisfy the inequality $|\alpha - 3\pi/2| \le |\pi/2 - \alpha^*|$, we move particle m along a circumference until this inequality holds. After this, we perform the fast motion as a result of which particles m and M change their positions on the line Mm to the positions that are symmetric about the center of mass. The change in the position of particle M at this stage is small (the distance moved by this particle is less than ε), while the distance between the particles does not change. At the final stage, particle m moves quasistatically clockwise (with the angle α monotonically decreasing) until the angle α becomes equal to the desired value α^*. Thus we proved the possibility for particle m to be driven to an arbitrary point of a circumference of small radius on the right half-plane. Taking into account the fact that the quasistatic repulsive and attractive trajectories that go out from all points $(\alpha^*,\, r^*)$, $\alpha^* \in (-\pi/2, \pi/2)$, $r^* = \varepsilon$, sweep the entire right half-plane, we conclude that particle m can be driven quasistatically into any position on the right half-plane. Somewhat simplifying, we can regard the algorithm presented above as driving particle m onto particle M followed by the motion of particle m along an arbitrary trajectory of quasiatatic repulsion that goes out from the origin.

In conclusion, we describe an algorithm that drives the system to the desired terminal state. We will confine ourselves to the case where the terminal positions of the particles do not lie on the common line of maximum slope. At the first stage, by alternating fast and quasistatic motions as was described above, we bring the system to a position in which the line that connects the particles passes through the terminal position of particle M. Then by means of fast motion we move particle M to its terminal position. Finally, by using the algorithm described above, we move particle m to the desired terminal state; at this stage, the change in the position of particle M is arbitrarily small.

Conclusions

It is proved that if at the initial instant the particles do not lie on the common line of maximum slope, the system can be driven into an arbitrarily small neighborhood of any terminal position on an inclined rough plane by combining quasiastatic and fast motions. A system of two interacting particles is a simple model of limbless worm-like crawlers. This biomimetic principle of motion can be used for mobile microrobots. It is important that when on a horizontal plane, a two-particle locomotion system that is in a state of rest at the initial time instant can move only along a line that connects the initial positions of the particles, whereas on an inclined plane, the system can be driven to any terminal position.

Reorientation of a rigid body by means of an auxiliary mass

Felix Chernousko*
**Institute for Problems in Mechanics, Russian Academy of Sciences, Moscow, Russia*

Summary. Possible control of the space orientation for a rigid body by means of an auxiliary movable point mass is considered. The motion of the point mass is proposed that provides the prescribed change of the body orientation.

Introduction

Control of the space orientation of a rigid body can be implemented by means of an auxiliary internal mass that is equipped with an actuator and can move relative to the body. Two-dimensional motions of such systems in the absence of external forces are analyzed in [1, 2, 3] where time-optimal controls are obtained. Three-dimensional motions are considered in [4]. In the paper, a simple control is proposed which provides , in the absence of external forces, the prescribed change of the rigid body orientation by means of an internal movable mass.

Basic equation

We consider a mechanical system consisting of a rigid body *P* of mass *M* and a particle *Q* of mass *m* (Fig. 1). Denote by *C* the center of mass of body *P* and by *O* the center of mass of system *P*+*Q*. Suppose that external forces are negligible and system *P*+*Q* is at rest at the initial time moment $t = 0$. Then its center of mass *O* is at rest for all *t*, whereas the momentum of system *P*+*Q* and its angular momentum stay constant and equal to zero. The following equation is derived from these conservation laws [1, 3, 4]:

$$\mathbf{J} \cdot \boldsymbol{\omega} + \mu M \mathbf{r} \times (\boldsymbol{\omega} \times \mathbf{r} + \mathbf{v}) = 0, \quad \mu = m/(M + m), \tag{1}$$

where $\mathbf{J}$ is the tensor of inertia of body *P* relative to its center of mass *C*, $\boldsymbol{\omega}$ is the angular velocity of body *P*, $\mathbf{r} = CQ$ is the position vector of point mass *Q* relative to *C*, and $\mathbf{v}$ is the velocity of point *Q* relative to body *P*.

Reorientation

Let us introduce the Cartesian coordinate system $Cx_1x_2x_3$ connected with body *P*, its axes Cx_i being principal central axes of inertia of body *P*, $i = 1, 2, 3$. Suppose that body *P* should be transferred from its initial state of rest to the prescribed terminal state of rest by means of an auxiliary particle *Q*. We assume that the initial and terminal positions of particle *Q* coincide with the center of mass *C* of body *P*. Hence, the required motion is the change of the orientation of body *P*.

This motion can be implemented by means of three successive plane turns of body *P* about its three principal central axes of inertia Cx_i, $i = 1, 2, 3$. For the rotation about axis Cx_i, body *P* must turn by a given angle $\Delta\varphi_i$ while the movable mass *Q* must start and finish its motion at point *C*. Both body *P* and particle *Q* should be at rest at the beginning and the end of this motion. Therefore, to design the required three-dimensional re-orientation, it is sufficient to construct such

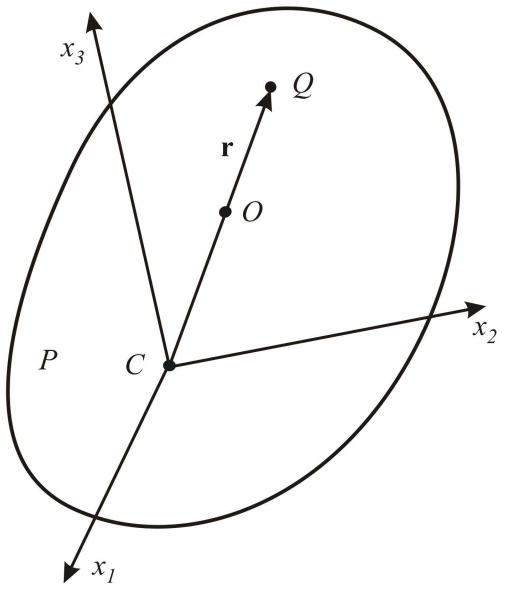

Figure 1: Mechanical system

plane motion of particle *Q*, with $\mathbf{r} = \mathbf{v} = 0$ at the beginning and the end of motion, that provides the required rotation of body *P*.

Plane motion

Without loss of generality, let us consider rotation of body *P* about axis Ox_3. Point *Q* will move in plane Cx_1x_2, its trajectory begins and ends at point *C*. Time-optimal trajectories of point *Q* found in [1, 3] for small μ, are circular arcs. Following this example, we will seek the trajectory of point *Q* as a circle with radius *R* passing through point *C*. Its center *S* can be chosen arbitrarily in plane Cx_1x_2.
Denote by *I* the moment of inertia of body *P* about axis Cx_3 and by φ the angle of rotation of the body about this axis. Then the vectorial equation (1) is reduced to the following equation

$$\dot{\varphi} = -\frac{\mu M R^2(1-\cos\psi)}{I + 2\mu M R^2(1-\cos\psi)}\dot{\psi}, \tag{2}$$

where ψ is the angle between radii *SC* and *SQ*; this angle defines the position of point *Q* along its circular trajectory. By integrating equation (2), we obtain

$$\varphi(t) = \frac{1}{a}\text{Arctan}(a\tan\frac{\psi}{2}) - \frac{\psi}{2}, \tag{3}$$

where

$$a = (1 + 4\mu M R^2 I^{-1})^{1/2}. \tag{4}$$

According to equation (3), the angle φ of rotation of body *P* about axis Cx_3 depends only on angle ψ, i.e., on the position of particle *Q* on its circular trajectory. When point mass *Q* makes the full rotation along its trajectory ($\psi = 2\pi$), body *P* turns by angle

$$\Delta\varphi = \pi(a^{-1} - 1), \quad -\pi < \Delta\varphi < 0.$$

To turn body *P* by an arbitrary angle, mass *Q* can make several (*n*) revolutions along its circular trajectory. Hence, the total angle of rotation $\Delta\varphi$ of body *P* can be estimated as follows

$$|\Delta\varphi| = \pi n(a-1)/a. \tag{5}$$

Using formulas (4) and (5), we obtain the expression for the radius *R* of the circular trajectory of point mass *Q*:

$$R = \frac{[I\alpha(1-\alpha/2)]^{1/2}}{(2\mu M)^{1/2}(1-\alpha)}, \quad \alpha = \frac{|\Delta\varphi|}{\pi n}. \tag{6}$$

To turn body *P* about axis Cx_3 by angle $\Delta\varphi$, particle *Q* should move in plane Cx_1x_2 along a circular trajectory of radius *R* given by (6). The center of the trajectory and the time history of motion $\psi(t)$ can be arbitrary.
This trajectory must pass through the center of mass *C* of body *P*, and the velocity of particle *Q* at point *C* must be zero. To decrease the domain of motion for particle *Q*, we can, according to equation (6), increase the number of revolutions *n*. The circular motions of particle *Q* relative to body *P* can be accomplished by means of rotating wheels.

Conclusions

Possible motions of an auxiliary point mass relative to a rigid body are described which provide an arbitrary prescribed reorientation of the body in space in the absence of external forces.

Acknowledgements. The work is supported by Russian Science Foundation (Grant 18-11-00307).

References

[1] Chernousko F.L. (2018) Optimal control of the motion of a two-mass system. *Doklady Mathematics* **97**:295-299.

[2] Shmatkov A.M. (2018) Time-optimal rotation of a body by displacement of a mass point. *Doklady Physics* **63**:337-341.

[3] Chernousko F.L. (2019) Optimal two-dimensional motions of a body controlled by a moving internal mass. *Multibody System Dynamics* **46**:381-398.

[4] Naumov N.Y., Chernousko F.L. (2019) Reorientation of a rigid body controlled by a movable internal mass. *Journal of Computer and Systems Sciences International* **58**(2):252-259.

Tuesday, July 19, 2022
16:00 - 18:20

MS-05 Slow-Fast Systems and Phenomena
Saint Clair 1

Chair: Oleg Gendelman

16:00 - 16:20
Phase resetting as a two-point boundary value problem
KRAUSKOPF Bernd, **LANGFIELD Peter***, OSINGA Hinke M.
*IHU Lyric, INRIA Bordeaux (Pessac-Bordeaux France)

16:20 - 16:40
Resonant nonlinear triad interactions of acoustic–gravity waves
KADRI Usama*
*School of Mathematics, Cardiff University (Abacws, Senghennydd Road, Cathays, Cardiff, Wales, UK, CF24 4AG United Kingdom)

16:40 - 17:00
Multi-scale and multi-pathways: How the ULF waves hoard electrons into precipitation
VAINCHTEIN Dmitri*, ZHANG Xiaojia, ARTEMYEV Anton
*Nyheim Plasma Institute, Drexel University (C. & J. Nyheim Plasma Institute 200 Federal St., Suite 500 Camden, NJ 08103 United States)

17:00 - 17:20
Slow-fast dynamics in vibratory pile driving: field tests and numerical modelling
TSETAS Athanasios*, TSOUVALAS Apostolos, METRIKINE Andrei
*Faculty of Civil Engineering and Geosciences, Delft University of Technology (Stevinweg 1, 2628 CN, Delft Netherlands)

17:20 - 17:40
On the Escape of a Resonantly Excited Couple of Colliding Particles from a Potential Well under Bi-harmonic Excitation
GENDA Attila*, FIDLIN Alexander, GENDELMAN Oleg
*Institute of Engineering Mechanics, Karlsruhe Institute of Technology (Kaiserstraße 10, 76131, Karlsruhe Germany)

Phase resetting as a two-point boundary value problem

Bernd Krauskopf*, Peter Langfield** and Hinke M. Osinga*
*Department of Mathematics, University of Auckland, New Zealand
**Inria Bordeaux–Sud-Ouest, Talence, France and IHU Liryc, Electrophysiology and Heart Modeling Institute, Fondation Bordeaux Université, Pessac-Bordeaux, France

Summary. Phase resetting is used in experiments with the aim to classify and characterise different neurons by their responses to perturbations away from a periodic bursting pattern. The same approach can also be applied numerically to a mathematical model. Resetting is closely related to the concept of isochrons of a periodic orbit, which are the submanifolds in its basin of attraction of all points that converge to this periodic orbit with a specific phase. Until recently, such numerical phase resets were performed in an ad-hoc fashion, and the development of suitable computational techniques was only started in the last decade or so. We present an approach based on the continuation of solutions to a two-point boundary value problem that directly evaluates the phase associated with the isochron that the perturbed point is located on. We illustrate this method with the FitzHugh–Nagumo model and investigate how the resetting behaviour is affected by phase sensitivity in the system.

In certain physiological experiments, a perturbation is applied to an oscillator, and one is interested in how the dynamics relaxes back to its regular rhythm [3, 12]. The resulting phase-shift is known as a phase reset, and recorded in terms of a *phase response curve* (PRC) or *amplitude response curve* (ARC); these are obtained by varying the phase at which the reset is applied, or by varying the amplitude of the reset when applied at a fixed given phase, respectively. Phase resets give insight into the underlying dynamics of biological oscillator, such as circadian clocks, yeast cells, and the cell cycle [12].

Mathematically, the oscillator is an attracting periodic orbit. Points on the periodic orbit have a relative phase, and any point in the basin of attraction can similarly be assigned an asymptotic (or latent) phase, defined as the phase with which the point converges to the periodic orbit [11]. The set of all points with the same asymptotic phase forms a manifold, called an isochron, and the family of isochrons foliates the basin of attraction [5]. Theoretically, a PRC or ARC can be computed by determining the phases of the isochrons that are associated with the reset points. In practice, this idea has proved to be rather challenging. Traditionally, ad-hoc model simulation has been applied [2, 4, 11]. Recently, more accurate techniques have been developed for the computation of isochrons, which are amenable for isochrons of systems that exhibit strong or even extreme phase sensitivity in possibly large regions of phase space; see [8] and references therein. Consequently, there are now also much better algorithms for the computation of PRCs, ARCs, and other resetting curves [6, 9].

Our method [10] computes one-dimensional isochrons of planar systems by pseudo-arclength continuation of solutions to a suitable boundary value problem (BVP). It has the advantage that it can generate very accurate approximations of isochrons globally, over a very large part of phase space. We adapt this method here so that we can generate PRCs or ARCs also with a BVP approach; we use the package AUTO [1] throughout to obtain solution families of the respective BVPs. The BVP that defines a phase reset consists of four orbit segments that are related via boundary conditions. Each orbit segment is a solution to the vector field given in the form

$$\tfrac{d}{ds}\mathbf{u} = T\,\mathbf{f}(\mathbf{u}),$$

where $\mathbf{f} : \mathbb{R}^2 \to \mathbb{R}^2$ defines the original vector field and time is rescaled to time s measured in units T of total integration time of the respective orbit segment. Hence, T is treated as a parameter.

The first two orbit segments define the periodic orbit $\Gamma := \{\mathbf{u}(s) \in \mathbb{R}^2 \mid 0 \le s \le 1\}$, with period T_Γ, and its associated vector bundle $\mathbf{v} := \{\mathbf{v}(s) \in \mathbb{R}^2 \mid 0 \le s \le 1\}$ of the stable Floquet multiplier of Γ; each vector $\mathbf{v}(s)$ is tangent to the isochron associated with the point $\gamma_\vartheta \in \Gamma$ such that $\gamma_\vartheta = \mathbf{u}(s)$. For both orbit segments, the parameter T is set to the period T_Γ of Γ. Instead of imposing a phase condition—which would be necessary if one wants to continue Γ in a parameter—we allow the head point $\mathbf{u}(0) = \mathbf{u}(1)$ on Γ to vary; in other words, $\mathbf{u}(0)$ is not necessarily equal to the point $\gamma_0 \in \Gamma$ with phase 0. We keep track of the phase that corresponds to a shifted head point $\mathbf{u}(0)$ by way of a third orbit segment $\mathbf{w} := \{\mathbf{w}(s) \in \mathbb{R}^2 \mid 0 \le s \le 1\}$ that starts at $\mathbf{w}(0) = \mathbf{u}(0)$ and ends at $\mathbf{w}(1) = \gamma_0$. For numerical reasons, the end condition for $\mathbf{w}$ is relaxed so that $\mathbf{w}(1)$ is allowed to differ from γ_0 in the direction of its (linearised) isochron. The total integration time for $\mathbf{w}$ is measured in fractions of T_Γ, that is, we set $T = \nu\, T_\Gamma$ for this orbit segment. The fourth and final orbit segment defines the orbit segment $\mathbf{p} := \{\mathbf{p}(s) \in \mathbb{R}^2 \mid 0 \le s \le 1\}$ of a reset point $\mathbf{p}(0)$ converging back to Γ. Its total integration time is an integer multiple of T_Γ and its end point is $\mathbf{p}(1) = \mathbf{u}(0) + \eta\,\mathbf{v}(0)$, for some small parameter $0 < \eta \ll 1$; here, $\mathbf{v}(0)$ has length 1.

The PRC is then found by continuation in ν as the variation in phase $\varphi = 1 - \nu$, while $\mathbf{p}(0)$ traces the path of a shifted periodic orbit; the ARC is defined similarly by setting $\mathbf{p}(0) = \gamma_\vartheta + A\,\mathbf{d}$ and varying the reset amplitude A, where $\mathbf{d}$ is a reset direction.

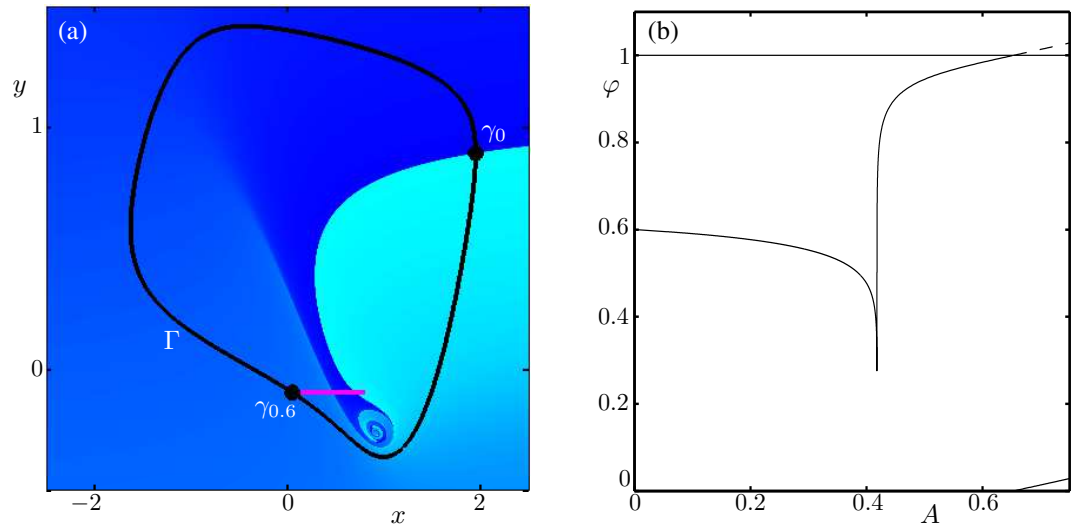

Figure 1: Phase-resetting for the FitzHugh–Nagumo system (1) where a reset is applied in the direction $\mathbf{d} = (1, 0)^t$ from the point $\gamma_{0.6} \in \Gamma$ with varying amplitude $A \in [0, 0.75]$. Panel (a) shows Γ with its isochrons plotted on a colour gradient from cyan at phase 0 to dark blue at phase 1; the purple curve indicates the A-dependent reset. Panel (b) shows the resulting phase $\varphi = 1 - \nu$ versus A.

As an example, we consider the two-dimensional FitzHugh–Nagumo system, which is the iconic polynomial model for which Winfree found that it exhibits extreme phase sensitivity due to its slow-fast nature [12]. The model is given as

$$\left\{ \begin{array}{rcl} \dot{x} &=& c\,\left(y + x - \frac{1}{3}\,x^3 + z\right), \\ \dot{y} &=& -\frac{1}{c}\,\left(x + a - b\,y\right), \end{array} \right. \tag{1}$$

where we fix $z = -0.4$, $a = 0.7$, and $b = 0.8$ as in [12], but set $c = 2.5$. For these parameter values, there exists an attracting periodic orbit Γ with period $T_\Gamma \approx 10.71$. We define the point with zero phase as the point $\gamma_0 \in \Gamma$ that has a maximum with respect to the x-coordinate; this point is $\gamma_0 \approx (1.94,\, 0.89)$.

Figure 1(a) shows Γ together with its isochrons; the isochron associated with γ_0 is coloured cyan and the other isochrons are similarly coloured on a colour gradient from cyan to dark blue. We apply a reset to the point $\gamma_{0.6}$ that lies on Γ at time $0.6\,T_\Gamma$ further along from γ_0. The reset is in the horizontal direction $\mathbf{d} = (1, 0)^t$, and we vary its amplitude A in the interval $[0, 75]$; see the purple line in Figure 1. Hence, $\gamma_{0.6}$ is reset to the point $\gamma_{0.6} + A\,\mathbf{d}$ and we compute the ARC as the corresponding A-dependent asymptotic phase $\varphi = 1 - \nu$ of the reset point $\gamma_{0.6} + A\,\mathbf{d}$.

Figure 1(b) shows the computed ARC as φ against A. Note that the A-parametrised line of reset points passes through a region with extreme phase sensitivity [7]. Consequently, the ARC becomes near vertical in this region, which lies approximately at $A = 0.42$. Our numerical continuation set-up has no trouble traversing such a phase-sensitive region and the ARC can be obtained reliably and efficiently even if it has a near-vertical derivative; note also the discontinuity at $A \approx 0.67$, where φ jumps from 1 to 0.

References

[1] Doedel, E. J., Oldeman, B. E. (2007) Auto-07P: Continuation and bifurcation software for ordinary differential equations. With major contributions from Champneys, A. R., Dercole, F., Fairgrieve, T. F., Kuznetsov, Yu. A., Paffenroth, R. C., Sandstede, B., Wang, X. J., Zhang, C. H.; available at `http://cmvl.cs.concordia.ca/auto`.

[2] Ermentrout, B. (1996) Type I membranes, phase resetting curves, and synchrony. *Neural Computation* **8**(5): 979–1001.

[3] Ermentrout, G. B., Terman, D. H. (2010) *Mathematical Foundations of Neuroscience*. Springer-Verlag, New York.

[4] Glass, L., Winfree, A. T. (1984) Discontinuities in phase-resetting experiments. *American Journal of Physiology-Regulatory, Integrative and Comparative Physiology* **246**(2): R251–R258.

[5] Guckenheimer, J. (1975) Isochrons and phaseless sets. *Journal of Mathematical Biology*. **1**(3): 259–273.

[6] Guillamon, A., Huguet, G. (2009) A computational and geometric approach to phase resetting curves and surfaces. *SIAM Journal on Applied Dynamical Systems* **8**(3): 1005–1042.

[7] Langfield, P., Krauskopf, B. Osinga, H. M. (2014) Solving Winfree's puzzle: the isochrons in the FitzHugh–Nagumo model. *Chaos* **24**(1): 013131.

[8] Langfield, P., Krauskopf, B. Osinga, H. M. (2015) Forward-time and backward-time isochrons and their interactions. *SIAM Journal on Applied Dynamical Systems* **14**(3): 1418–1453.

[9] Mauroy, A., Rhoads, B., Moehlis, J., Mezić, I. (2014) Global isochrons and phase sensitivity of bursting neurons. *SIAM Journal on Applied Dynamical Systems* **13**(1): 306–338.

[10] Osinga, H. M., Moehlis, J. (2010) Continuation-based computation of global isochrons. *SIAM Journal on Applied Dynamical Systems* **9**(4): 1201–1228.

[11] Winfree, A. T. (1974) Patterns of phase compromise in biological cycles. *Journal of Mathematical Biology* **1**(1): 73–93.

[12] Winfree, A. T. (2001) *The Geometry of Biological Time*. 2nd ed., Springer-Verlag, New York.

Resonant nonlinear triad interactions of acoustic–gravity waves

Usama Kadri
School of Mathematics, Cardiff University, Cardiff CF24 4AG, UK

Summary. Acoustic waves, such as underwater sounds generated by earth-plate movements, and gravity waves, such as surface ocean waves, are two types of waves that are thought to share very little in common. However, recently it has been shown theoretically that acoustic–gravity waves can interact and share energy. Such interaction could explain natural phenomena such as microseisms (faint earth tremor), but also has many implications from tsunami mitigation and energy harnessing, to creating new measurement techniques that can be applied in invasive medical operations. In this talk I will present a review on nonlinear interaction of acoustic–gravity waves, theory and applications.

Background

Acoustic (compression) waves and free-surface (gravity) waves are virtually decoupled for two main reasons. Firstly, the speed of sound in water far exceeds the maximum phase speed of gravity waves. Secondly, the mode shape with depth is oscillatory for acoustic modes, and exponentially decaying for gravity waves. Nevertheless, it has been argued theoretically that these two types of wave motion could exchange energy via resonant triad nonlinear interactions [1, 2, 3, 4, 5]. There are two cases of interest this review talk focuses on: (I) two gravity waves interacting with an acoustic mode of a comparable frequency (almost double) [1, 2, 3]; and (II) two acoustic modes interact with a gravity wave of a comparable lengthscale [4, 5]. In the first case, the theory suggests that for a perfectly tuned triad almost all energy initially stored in the gravity waves can transfer into the generated acoustic mode, whereas for wavepackets a maximum of 40% energy transfer can be obtained [2]. This has implications at the ocean scale where interacting surface gravity waves can generate microseism (faint earth tremor) deep at the ocean floor [6, 7]. Not less interestingly is the particular solution where two gravity waves of identical frequency generate a standing acoustic mode [8]. Such setting might explain a physical phenomenon known as time reversal [9, 10]. The same solution might explain the evolution of Faraday waves [8, 11] that find various applications in physics. In the second case, the interaction of two acoustic modes with one gravity wave has implications on underwater communication [4], wave energy harnessing, or more ambitiously tsunami mitigation [5].

Amplitude evolution equations

We consider the propagation of surface-gravity waves interacting with acoustic wave disturbances in water of constant depth over a rigid bottom. The equation governing the velocity potential in the fluid interior is obtained by combining continuity with the unsteady Bernoulli equation, i.e cubic nonlinear wave equation. The boundary conditions are the standard higher order kinematic and dynamic conditions, at the surface; and the no-penetration condition at the bottom. In the first case, resonance is possible among two surface -gravity waves and a single acoustic mode. The conditions for resonance comprise an interplay of the frequencies $\sigma_+ + \sigma_- = \omega$, and wavenumbers $k_+ + k_- = \kappa$, where $\sigma_\pm$ and $k_\pm$ represent the two gravity waves, which combined form the acoustic mode represented by ω and κ. To derive the evolution equations we employ multiple-scale analysis, which yields

$$\frac{\partial A}{\partial t} + c_1 \nabla A + c_2 \nabla^2 A \propto S_+ S_-, \qquad \frac{\partial S_\pm}{\partial \tau} \propto A S_\mp^* + [\text{cubic terms}] \tag{1}$$

where A and $S_\pm$ are the amplitudes of the acoustic and two gravity waves, t is the interaction timescale, ∇ is the gradient (∂_x, ∂_y), and c_1 and c_2 are constants. The derived evolution equations allow quantifying the parameters (i.e. frequency, wavelength, and amplitude) needed to finely tune the interaction, which controls the energy exchange. Following a similar approach we derive the amplitude evolution equations for two acoustic modes interacting with a gravity wave. Now, the conditions for resonance become $\omega_+ + \omega_- = \sigma$, and wavenumbers $\kappa_+ + \kappa_- = k$ and the evolution equations are fundamentally different. The following are some examples that will be discussed.

Example 1: Faraday Waves

This case is analogous to a surface gravity disturbance (Gaussian) of frequency ω over a fluid layer that is subject to a continuous vertical oscillation, e.g. due to underwater tremor, at double the frequency. The interaction excites subharmonic standing field of Faraday-type waves of frequency 2ω, as shown in the figure 1 (from [11]).

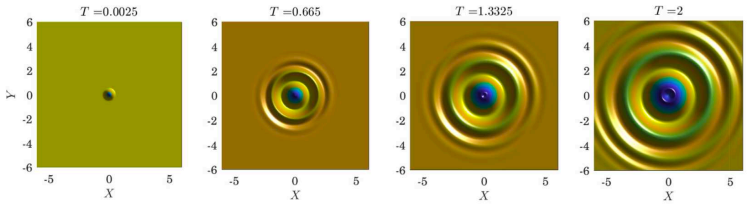

Figure 1: Evolution of Faraday-type waves from a gravity disturbance interacting with a long-crested acoustic mode [11].

Example 2: Time-Reversal

A mathematical model for the evolution of a time-reversed gravity wave packet from a nonlinear resonant triad perspective is derived [8]. Here the sudden appearance of an acoustic mode is analogous to a sudden vertical oscillation of the liquid film, which resonates with the original surface-gravity wave packet causing the generation of an oppositely propagating (time-reversed) surface-gravity wave of an almost identical shape, see figure 2

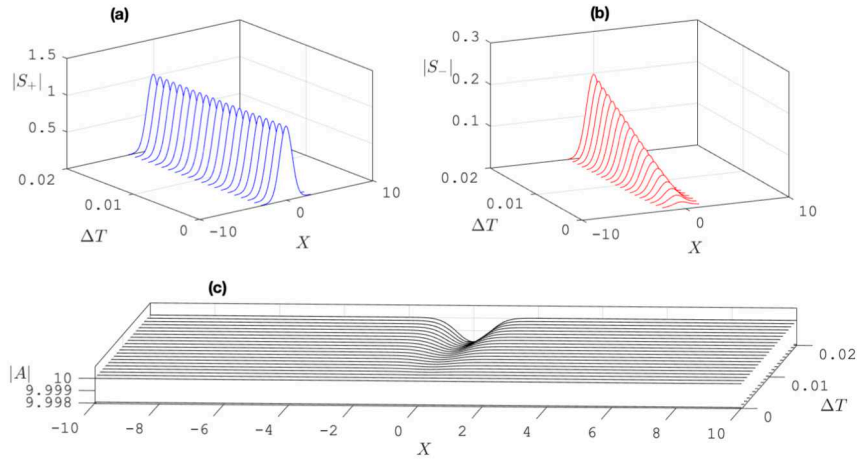

Figure 2: Amplitude evolution of time reversal triad: (a) original disturbance; (b) time reversed disturbance; (c) sudden acoustic mode.

Example 3: Tsunami Mitigation

A tsunami interaction nonlinearly with two acoustic modes. The tsunami envelope is redistributed behind over a larger space and its amplitude is reduced, see figure 3.

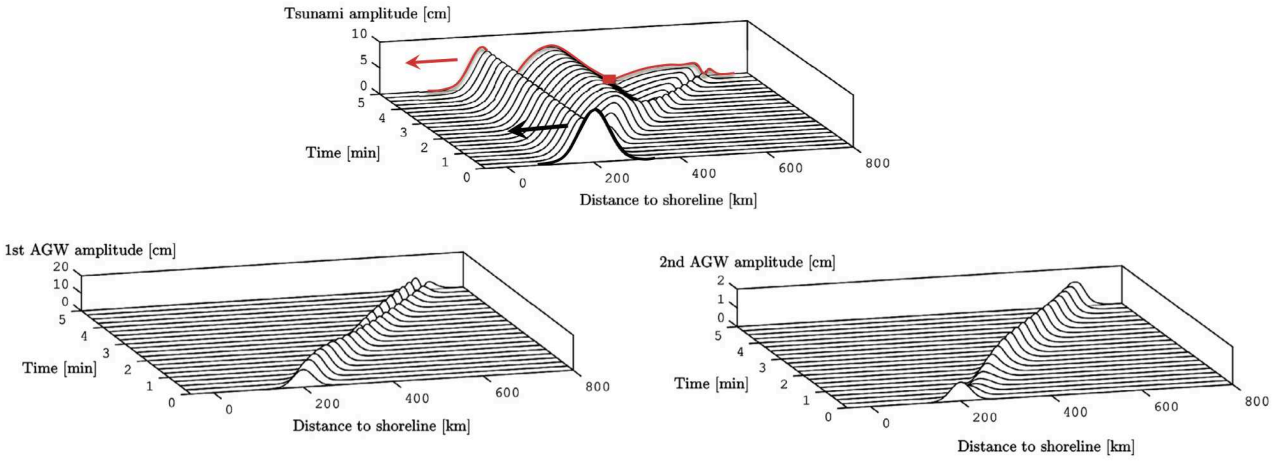

Figure 3: Amplitude evolution. A tsunami propagates from right to left (top), exchanges energy with two acoustic waves (middle and bottom), that propagate from left to right, [5].

References

[1] U. Kadri, M. Stiassnie, 2013. J. Fluid Mech. 735, R6, doi:10.1017/jfm.2013.539.

[2] U. Kadri, T.R. Akylas, 2016. J. Fluid Mech. 788, R1 doi:10.1017/jfm.2015.721.

[3] X. Yang, F. Dias, S. Liao, 2018. J. Fluid Mech. 849:111–35.

[4] U. Kadri, 2016. Eur. J. Mech. B/Fluid, 55(1), 157-161, doi:10.1016/j.euromechflu.2015.09.008.

[5] U. Kadri, 2017. Heliyon 3(1), pp. e00234, doi:10.1016/j.heliyon.2017.e00234

[6] M.S. Longuet-Higgins, 1950. Philos. Trans. R. Soc. London A, 243(857), 1-35.

[7] S. Kedar, M.S. Longuet-Higgins, F. Webb, N. Graham, R. Clayton, C. Jones, 2008. Proc. R. Soc. A, 464, 777–793.

[8] U. Kadri, 2019. Fluids 4 (2), 91.

[9] A. Przadka, S. Feat, P. Petitjeans, V. Pagneux, A. Maurel, M. Fink, 2012. Phys. Rev. Lett. 2012, 109, 064501.

[10] M. Fink, E. Fort 2017. Eur. Phys. J. Spec. Top. 226, 14771486.

[11] U. Kadri, Z. Wang, 2021. Commum Nonlinear Sci Numer Simul 93, 105514.

Multi-scale and multi-pathways: How the ULF waves hoard electrons into precipitation

Dmitri Vainchtein*, Xiaojia Zhang†, and Anton Artemyev†
*Nyheim Plasma Institute, Drexel University, Philadelphia, USA
†University of California, Los Angeles, USA

Summary. The nonlinear resonant electron scattering by whistler-mode chorus waves is one of the main drivers of the electron precipitation into the Earth's atmosphere. However, the electron precipitation shows signs of modulation by much slower ultra-low-frequency (ULF) waves, that cannot be in resonance with electrons. In this presentation we use the Hamiltonian frameworks for slow-fast systems to consider two-pronged impact of the ULF waves on the electrons' dynamics: First, ULF waves modulate the whistler waves; and second, ULF waves directly affect electron distribution functions. We implement THEMIS observations of ULF waves and modulated whistler waves to perform numerical simulations of electron dynamics. We show how the quasi-linear and nonlinear regimes of electron scattering by whistlers interchange within one ULF period and how this interplay of the two regimes affect the electron scattering (precipitation) rates.

Ultra-low-frequency (ULF) and whistler waves in the Earth magnetosphere

Ultra-low-frequency (ULF, 0.001–1 Hz) perturbations are generated at the magnetopause and propagate into the inner magnetosphere, and effectively modulate whistler waves. Close to the magnetopause, VLF wave bursts have the same periodicity as the ULF perturbations. Our results demonstrate that almost the entire outer magnetosphere (from the geostationary orbit to most elliptical orbits), including the outer radiation belts, is significantly influenced by ULF perturbations excited by magnetopause dynamic responses to the solar wind. Space observations show that ULF wave modulate not only whistler intensity, but also pitch-angle distributions of electrons. ULF waves propagate with velocities much smaller than electron thermal velocity. Therefore the interaction of ULF waves with electrons is non-resonant (in this proposal we do not consider the azimuthal resonances effective mostly for relativistic electrons). This interaction causes quasi-periodic changes of characteristic pitch-angle of distribution functions. We use conservation of the electron adiabatic invariants (the magnetic moment and the second adiabatic invariant) to describe the evolution of electron distributions. We will fit spacecraft measurements of electron distributions in the 1-100 keV energy range, and rewrite this fitted distribution in terms of adiabatic invariants. With ULF magnetic field included in calculation of invariants, we compute electron distribution for several time moments within one ULF wave period.

The nonlinear wave-particle interaction

Consider a relativistic electron interacting with a whistler wave propagating at an arbitrary angle θ relative to the background magnetic field. In the absence of the resonance overlapping, which is the most typical situation in the inner magnetosphere, the corresponding Hamiltonian is

$$H = m_e c^2 \gamma + \frac{eB_w}{k_\parallel \gamma} \sum_{n=0,\pm 1,..} h^{(n)} \sin\left(\phi + n\psi\right), \quad \gamma = \sqrt{1 + \frac{p_\parallel^2}{m_e^2 c^2} + \frac{2\mu\Omega_{ce}}{m_e c^2}} \tag{1}$$

In (1), n is a harmonic number, function $h^{(n)}(\mu, \theta, s, p_\parallel)$ defines the effective wave amplitude for a particular harmonic [1], $(s, p_\parallel)$ are field-aligned coordinate and momentum, (ψ, μ) are gyrophase and magnetic moment ($\mu = p_\perp^2/2m_e\Omega_{ce}$), $\Omega_{ce} = \Omega_{ce}(s)$ is an electron gyrofrequency, ϕ, $k_\parallel(s)$, and $\omega(t)$ are a wave phase, field-aligned wave vector component, and wave frequency. Particle energy $E \approx H - m_e c^2 = m_e c^2(\gamma - 1)$, magnetic moment $\mu = \mu(\gamma, \alpha)$ is defined by γ and particle equatorial pitch-angle α. Wave amplitude B_w is much smaller than a typical particle energy ($eB_w/k \ll E$).
Dynamics of particles governed by Eq.(1) includes nonlinear resonant scattering and trapping, citeOmura, Artemyev. Nonlinear scattering occurs at almost every resonant interaction and produces changes of the electron energy and pitch-angle, $\Delta^S E$ and $\Delta^S \alpha$, see Fig. 1(a,b). Such changes cause a drift in the energy/pitch-angle space, directed towards relatively small values of E and α. This drift cannot be described by the quasi-linear diffusion. Not every resonant particle is scattered, though, but some of them are trapped. Particle trapping (such as the one occurring at about $t = 90$ in Fig. 1(a,b)) results in significant changes of the energy and pitch-angle, $\Delta^P E$, $\Delta^P \alpha$. Such changes are much stronger than any individual change due to scattering, but the number of particles trapped at a single resonance crossing is much smaller than the number of scattered particles. The relative amount of resonant particles (with a given energy and pitch-angle) being trapped during a given resonant interaction is called *probability of trapping*.

Probabilistic approach: a single wave

Consider a 2D space (E, α) with a discretization (i, j), i.e., the electron distribution function $f(E, \alpha)$ is defined as $f_{ij} = f(E_i, \alpha_j)$. We can introduce the quantity $s_{mn}^{kl}(W)$ as a probability of a particle to move from the state (E_k, α_l) to the state (E_m, α_n) due to a single scattering with a given wave. The letter W indicates all the relevant wave's characteristics, most importantly the amplitude, the frequency, and the angle of the wave propagation. For each concrete wave, one can

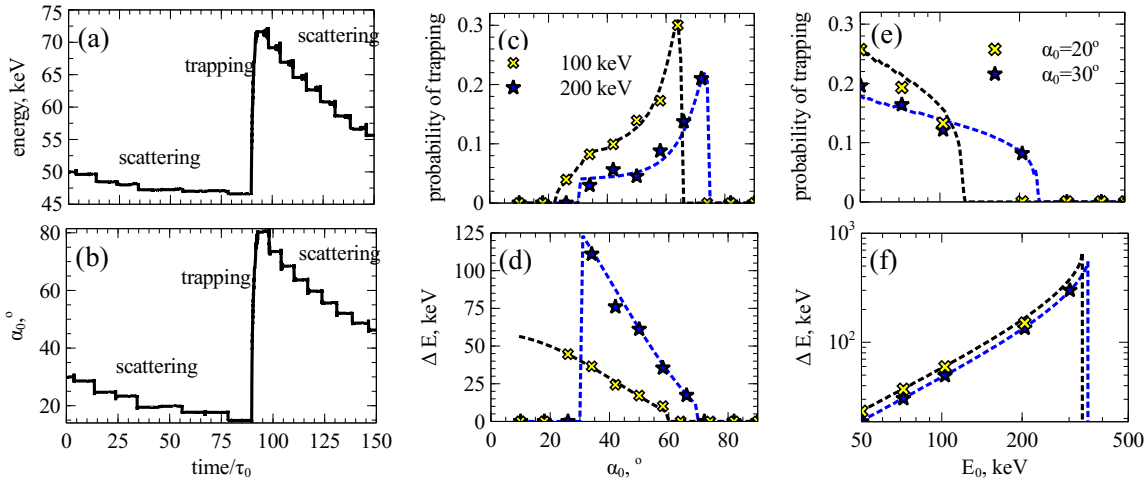

Figure 1: (a,b) A fragment of a 100 keV electron trajectory: electron energy (panel (a)) and pitch-angle (panel (b)). This fragment includes several scattering and one trapping. Time is normalized by a typical bounce period $\tau_0 = LR_E/c \sim 1/7$s (R_E is the Earth radius). (c-f) Main characteristics of electron trapping by oblique (c,d) and parallel (e, f) waves. Analytic results (curves) are shown together with test particle simulations (symbols): energy change in trapping $\Delta^P E$ and the probability of trapping for various initial energy E_0 and pitch-angle α_0 .

view all $s^{kl}_{mn}(W)$ as the elements of a big 4D matrix, that defines the phase space transport due to scattering. Similarly, we can introduce the probability for trapping in the same way as we did for scattering: $p^{kl}_{mn}(W)$ is a probability of a particle to move from the state (E_k, α_l) to the state (E_m, α_n) due to a single trapping into resonance with a given wave. Almost all of the matrix elements are zero. Thus we arrive at

$$\frac{\partial f_{ij}}{\partial t} = -\frac{2}{\tau_{ij}} f_{ij} + \sum_{kl} R^{kl}_{ij}(W) f_{kl}; \quad R^{kl}_{ij}(W) = \frac{N_{kl}}{\tau_{kl}} \left(s^{kl}_{ij}(W) + p^{kl}_{ij}(W) \right) \tag{2}$$

where each $\tau_{ij} = \tau(E_i, \alpha_j)$ is the bounce period. Elements of $R^{kl}_{ij}(W)$ depend on wave characteristics. There is a noticeable difference between $s^{kl}_{mn}(W)$ and $p^{kl}_{mn}(W)$: while the non-zero elements of $s^{kl}_{mn}(W)$ correspond to nearby cells (around $k = m, l = n$), the elements of $p^{kl}_{mn}(W)$ are somewhat removed from there. Note that Eq. (2) is linear with respect to the distribution function f_{ij}, and nonlinear with respect to properties of the wave, W. The nonlinearity is included in the array $R^{kl}_{ij}(W)$.

Multiple waves

For an ensemble of waves, let $\rho(W)$ define the statistical weight of a certain set of parameters, $\rho(W)$ describes statistics of the wave amplitude B_w and frequency ω). The distribution $\rho(W)$ is normalized so that $\int \rho(W) dW = T_{int}/T_{tot}$ where T_{tot} is the total duration of spacecraft measurements and T_{int} is a cumulative duration of observations of intense waves. Normalized $\rho(W)$ gives a

$$\frac{\partial f_{ij}}{\partial t} = -\frac{n_{ij}}{\tau_{ij}} \frac{T_{int}}{T_{tot}} f_{ij} + \sum_{kl} \left(\int_W R^{kl}_{ij}(W) \rho(W) dW \right) f_{kl} = -\frac{n_{ij}}{\tau_{ij}} \frac{T_{int}}{T_{tot}} f_{ij} + \sum_{kl} \langle R^{kl}_{ij} \rangle f_{kl} \tag{3}$$

where $\langle R^{kl}_{ij} \rangle = \int_W R^{kl}_{ij}(W) \rho(W) dW$. For a given state (E_i, α_j), $\langle R^{kl}_{ij} \rangle$ contains two groups of nonzero elements in the (E, α) space. The elements located near the "target" cell describe the efficiency of scattering, which, for the first cyclotron resonance, results in energy/pitch-angle decrease. The elements related to trapping are located relatively far from the "target" and they correspond to energy/pitch-angle increase.

Conclusions

The objective of the current research was to describe how the ULF waves impact the dynamics of electrons in the Earth magnetosphere: directly through the non-resonant interaction, and indirectly through modulating the whistler waves, that do have the non-linear resonance interaction with electrons. The research was supported in part by the NASA award 80NSSC19K0266.

References

[1] Tao, X., Bortnik, J., (2010). Nonlinear interactions between relativistic radiation belt electrons and oblique whistler mode waves. *Nonlinear Processes in Geophysics* **17**:599–604.

[2] Artemyev, A. V. et al., (2014). Electron scattering and nonlinear trapping by oblique whistler waves: The critical wave intensity for nonlinear effects. *Physics of Plasmas* **21**:102903.

[3] Nunn, D., Omura, Y., (2015). A computational and theoretical investigation of nonlinear waveparticle interactions in oblique whistlers. *J. Geophys. Res.* **120**:2890–2911.

Slow-fast dynamics in vibratory pile driving: field tests and numerical modelling

Athanasios Tsetas*, Apostolos Tsouvalas* and Andrei V. Metrikine *
*Faculty Of Civil Engineering and Geosciences, Delft University of Technology, The Netherlands

Summary. This paper presents a study of vibration-based pile driving methods on the basis of field data and numerical modelling. Based on field data from an extensive field test campaign and existing results found in the relevant literature, the vibratory pile installation is shown to constitute a slow-fast dynamical process. Moreover, a three-dimensional numerical model for the analysis of vibratory pile driving is presented, comprised by a thin cylindrical shell (pile), a linear elastic layered half-space (soil) and a frictional interface. Based on the latter numerical model, the relevant experimental findings are discussed and compared in order to shed light into the complex pile-soil behavior during vibratory driving and the emergence of slow-fast pile motion.

Extended abstract

Presently, over 80% of the offshore wind turbines (OWTs) in Europe are founded on monopiles [1]. These foundations are most commonly installed by impact hammer, albeit this method poses a source of noise pollution, harmful to marine life, and can compromise the structural integrity and fatigue life of a monopile [2]. To this end, environmentally friendly alternatives are investigated for offshore monopile installation, such as vibratory methods. The standard axial vibratory pile driving is used onshore for decades, with advantageous features such as high installation speed and low axial pile loading. However, in the offshore industry the use of the vibratory driving technique is limited, due to the lack of field data and knowledge gaps related to the complex pile-soil behaviour during installation and the post-installation effects.
To further the potential of vibration-based methods a new technology – the Gentle Driving of Piles (GDP) – has been proposed by TU Delft [3]. The GDP method is based on simultaneous application of low-frequency/axial and high-frequency/torsional vibrations at the pile head and aims to improve installation performance and reduce underwater noise emissions. Medium-scale field tests have been performed at Maasvlakte II site, at the port of Rotterdam (see Fig. 1), in which different pile installation methods were investigated, with a focus on the classical vibratory and GDP methods.

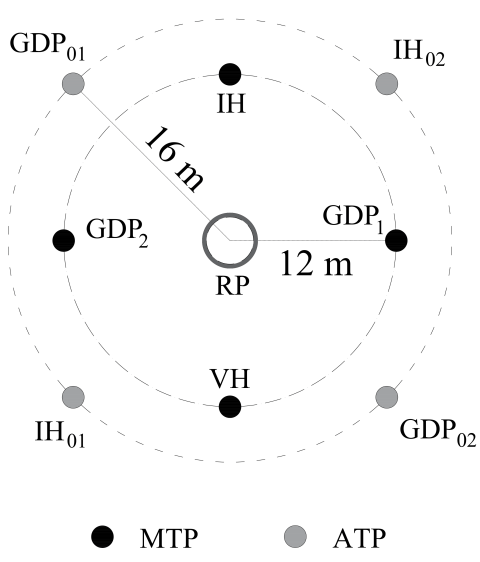

(a)

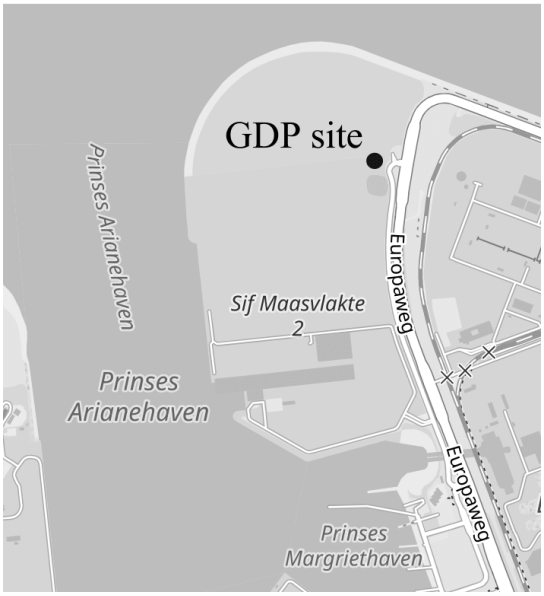

(b)

Figure 1: (a) Test pile layout and (b) GDP test site.

In this paper, the vibratory and GDP installation methods are studied and the emergence of pile penetration into the soil medium as a slow-fast dynamical process is presented. In principle, the pile is forced by the combination of a periodic excitation at the pile top and the self-weight of the pile and the vibratory device. The resulting motion can be distinguished into a slow motion of the rigid body type and a fast motion characterized by the fundamental driving frequency and its super-harmonics. The main findings of the installation tests and the comparison of the two methods are discussed. Furthermore, a three-dimensional model for the analysis of pile installation for the considered methods is presented. Specifically, the pile is modelled as a thin cylindrical shell, according to the Love-Timoshenko theory [4], in order to properly capture the pile motion. The soil continuum is modelled as an elastic layered half-space, by means of the thin layer method (TLM), augmented with perfectly matched layers (PMLs) [5]. Finally, a frictional interface is used to couple the pile-soil system and permit pile slip. The numerical solution of the presented model is based on the alternating frequency-time harmonic balance method, in order to address the problem with a computationally fast approach.

In the topic of vibratory pile driving two classes of models are employed, i.e. the engineering-oriented one-dimensional models and the advanced research-oriented three-dimensional models. The former describe in a simplistic manner the non-linear pile-soil interaction during driving, neglecting effects such as the non-local and frequency dependent soil-reaction. The latter models -although more rigorous- rely on a multitude of parameters for the soil constitutive model, which cannot be customarily obtained by *in situ* measurements. Therefore, their use in engineering practice remains unfeasible, especially considering their excessive computational cost. The model presented in this work aims to bridge the gap between the two classes, by employing a more physically sound soil reaction with reduced semi-empirical soil parameters, while retaining the computational efficiency required for use in engineering practice. To that end, the predictions of the developed model are validated with the field data; the latter is of great essence for the GDP method, which cannot be analysed by other existing numerical models.

Figure 2: Installation test of a pile driven by the GDP method.

References

[1] Ramírez, L., Fraile, D. and Brindley, G. (2021). Offshore wind in europe: Key trends and statistics 2020. *WindEurope*.

[2] Tsouvalas, A. (2020). Underwater noise emission due to offshore pile installation: A review. *Energies*, **13**(12), 3037.

[3] Metrikine, A.V., Tsouvalas, A., Segeren, M.L., Elkadi, A.S., Tehrani, F.S., Gómez, S.S., Atkinson, R., Pisanó, F., Kementzetzidis, E., Tsetas, A., Molenkamp, T., van Beek, K. and de Vries, P. (2020) GDP: A new technology for Gentle Driving of (mono)Piles. In *Proceedings of the 4th International Symposium on Frontiers in Offshore Geotechnics, Austin, TX, USA* (pp. 16-19).

[4] Timoshenko, S. P., and Woinowsky-Krieger, S. (1959). Theory of plates and shells. McGraw-hill.

[5] de Oliveira Barbosa, J. M., Park, J., and Kausel, E. (2012). Perfectly matched layers in the thin layer method. *Computer methods in applied mechanics and engineering*, **217**, 262-274.

On the Escape of a Resonantly Excited Couple of Colliding Particles from a Potential Well under Bi-harmonic Excitation

Attila Genda * , Alexander Fidlin* and Oleg Gendelman **
*Institute of Engineering Mechanics, Karlsruhe Institute of Technology, Karlsruhe, Germany
**Mechanical Engineering, Technion – Israel Institute of Technology, Haifa, Israel

Summary. Escape dynamics of a damped two-particle system with internal collisions in a truncated quadratic potential well under biharmonic excitation is investigated. It is assumed that the excitation frequencies are tuned to the $2l$-fold values of the modal natural frequency of the relative motion and to the modal frequency of the center of mass on the bottom of the potential well. Although the escape is an essentially non-stationary process, the critical forcing amplitude strongly depends on the stationary amplitudes of the relative vibrations within the two particles. The characteristic escape curve for the critical force moves up with the increasing relative vibrations.

Introduction

Escape from a potential well is an important topic in non-linear dynamics. The problem arises in various fields of physics and engineering [1]-[5].
A broad spectrum of physical phenomena from the dynamics of molecules to celestial mechanics has been studied in the literature, discussing topics such as energy harvesting [6], the physics of Josephson junctions [7], transient resonance dynamics of oscillatory systems [8, 9] or such phenomena as capsizing of ships [3, 10]. A further example for an escape related topic is the dynamic pull-in in microelectromechanical systems (MEMS) [11]-[16].
First, in 1940, Kramer started to investigate the forced escape phenomenon regarding the thermal activation of chemical reactions [17, 18]. Despite of much research which has taken place in the last 80 years, important unsolved problems still exist regarding the escape process [19].
In the case of constant forcing, escape might occur as a consequence of the slow variation of the system parameters which leads to subsequent bifurcations of the steady-state regimes of the response [2, 11, 12]. Thompson investigates extensively the mechanisms leading to escape in a cubic model potential. His numerical results describe the phenomenon of escape along a broad scale of the excitation frequency of the harmonic forcing. It reveals the chaotic processes leading to escape near the critical forcing amplitude curve. Using Melnikov's method [32] a good approximation can be given for the numerical location of a part of the critical force curve.
Different modeling approaches can be found in the literature to give analytic criteria for the escape. In the paper of Virgin, [3] harmonically forced and damped particles are investigated in three different model potentials, where the steady state response of the particle's motion is used to obtain the partly empirically corrected analytic criterion. The author assumes a harmonic response with an additional bias to correct asymmetries of the potential.
Technically relevant potential wells in general exhibit a monotonically decreasing stiffness when moving away from the center of the potential well. This is necessary to flatten out the profile of the potential, otherwise its depth could not be finite.
In the paper [3] some model potential wells are also investigated numerically. The numerical results show a sharp minimum of the critical forcing amplitude depicted along the forcing frequency. This sharp minimum takes smaller values than the linearized eigenfrequency of the potential well. Papers [14, 15] investigating the problem of dynamic pull-in in MEMS devices also come to similar results regarding the shape of the critical forcing curve.
In the papers [20, 21] investigating the safe basins of attraction for various dynamical systems similar patterns for the sharp minimum were found. This let's the reader formulate a hypothesis about the above mentioned feature of the critical forcing curve as an inherent property of the escape phenomena. In the papers [22, 25] for different potentials this hypothesis was investigated using harmonic forcing.
The above two papers investigate the escape dynamics of the harmonically forced bodies assuming 1:1 resonance. The applied method is able to take into account the transient dynamics of the system, which can be described by the slow flow on the resonance manifold. Varying the initial conditions (IC) allows the identification of two different escape mechanisms. The simpler to describe maximum mechanism (MM) corresponds to the case when the oscillation amplitude reaches the escape threshold as a consequence of the excitation. In this case, exciting with the critical force results in an amplitude value that just reaches the escape threshold. The other mechanism is the so called saddle mechanism (SM). It is different from the previous mechanism, because the amplitude of the vibration stays quite small even if the forcing amplitude is almost critical. When the critical forcing amplitude is reached, the vibration amplitude starts to increase abruptly and escape takes place. At the lowest point of the critical force curve both mechanisms can be observed at the same time. The approach resembles the research done in [23, 24] describing transient phenomena in coupled oscillator systems with the use of limiting phase trajectories (LPT).
In paper [28] a system of a pair of strongly coupled particles in a truncated quadratic potential well with a bi-harmonic excitation, consisting of a high and a low frequency component, was investigated. The paper introduced a new method to model the effect of the high-frequency excitation using an effective force field which was derived by convolution of the original force field and the probability density function of the fast movement around the center of mass of the two particles.

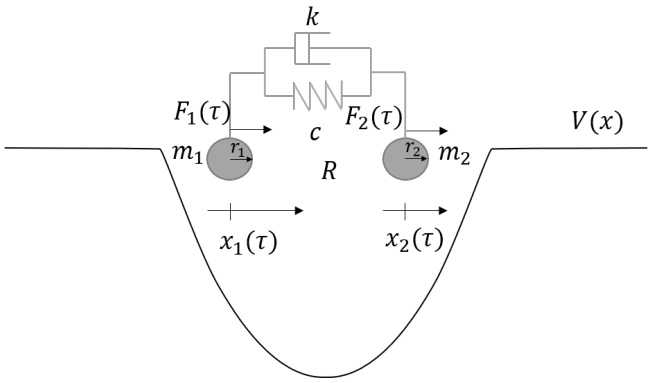

Figure 1: The setting of the collision problem in a potential well with harmonic force excitation.

The multi-body problem was simplified that way to a single body problem for which standard techniques could be applied. The research also showed that the high-frequency excitation has a stabilizing effect on the escape behavior with the used model potential, for which, being the model of a linear oscillator, a single particle has a critical forcing amplitude tending to 0 at the the resonance frequency. In the case of two bodies, however, the minimal value of the critical force curve is greater than 0 and it is shifted to a lower frequency than the linearized eigenfrequency of the potential.
In the present paper, the model presented in [28] is modified such that the particles, although they are still considered as point masses, are not able to penetrate each other, but an almost elastic collision, with the coefficient of restitution R takes place every time they get in touch with each other, i.e. the distance between them is $\Delta := r_1 + r_2$.
First, the mathematical model of the problem is introduced. Then, after bringing the equations into an appropriate form using a coordinate transformation, the first step of the model reduction based on the so called 'unfolding transformation' is described. With the use of this result, the further reduction of the model takes place in the next section, which is based on a probabilistic type of averaging, that leads to a single particle problem in a modified, effective potential. In the section 'Numerical results and discussion' the reduced model is compared to the original problem by direct numerical integration using parameter values spanned by a grid on the excitation frequency – force amplitude plane, highlighting the stabilizing effect of the high-frequency excitation. The findings of the paper are summarized in the 'Conclusions' section.

Description of the model

Let us consider the following problem setting depicted in Fig. 1.
The coupled pair of particles with masses m_1 and m_2 is excited harmonically in a one-dimensional quadratic potential well. The linear spring between the particles has the stiffness $k \gg 1$ and the linear damper is described by the damping coefficient c of $\mathcal{O}(1)$. The potential well is defined individually for both of the particles by $V_1(x) = m_1 V(x)$ and $V_2(x) = m_2 V(x)$, respectively, where m_1 and m_2 are of $\mathcal{O}(1)$. Poly-harmonic forces, given by $F_1(t)$ and $F_2(t)$, respectively, can act on both of the bodies. The particles cannot penetrate through each other and hence collide every time they are at a distance $\Delta := r_1 + r_2$ from each other. The collision is nearly elastic, which means the coefficient of restitution is close to one, i.e. $R \approx 1$.
The differential equations describing the motion of the system are given by

$$\begin{bmatrix} m_1 & 0 \\ 0 & m_2 \end{bmatrix} \begin{bmatrix} \ddot{x}_1 \\ \ddot{x}_2 \end{bmatrix} + \begin{bmatrix} c & -c \\ -c & c \end{bmatrix} \begin{bmatrix} \dot{x}_1 \\ \dot{x}_2 \end{bmatrix} + \begin{bmatrix} k & -k \\ -k & k \end{bmatrix} \begin{bmatrix} x_1 \\ x_2 \end{bmatrix} + \begin{bmatrix} m_1 V'(x_1) \\ m_2 V'(x_2) \end{bmatrix} = \begin{bmatrix} F_1(\tau) \\ F_2(\tau) \end{bmatrix} \qquad \text{if } x_1 + \Delta < x_2, \tag{1}$$

$$x_{1+} = x_{1-}, \qquad x_{2+} = x_{2-}, \qquad \text{if } x_1 + \Delta = x_2, \tag{2}$$

$$\dot{x}_{1+} = \frac{R m_2(\dot{x}_{2-} - \dot{x}_{1-}) + m_1 \dot{x}_{1-} + m_2 \dot{x}_{2-}}{m_1 + m_2}, \qquad \dot{x}_{2+} = \frac{R m_1(\dot{x}_{1-} - \dot{x}_{2-}) + m_1 \dot{x}_{1-} + m_2 \dot{x}_{2-}}{m_1 + m_2}, \tag{3}$$

where V is defined as

$$V(x) = \begin{cases} \frac{1}{2}x^2 - \frac{1}{2} & |x| \le 1, \\ 0 & |x| > 1, \end{cases} \tag{4}$$

The excitation force can be chosen in general as

$$F_j(\tau) = \sum_{i=1}^{p} A_{ji} \sin(\Omega_{ji}\tau + \beta_{ji}), \qquad \text{with } j \in 1, 2 \text{ and } p \in \mathbb{N}^+. \tag{5}$$

In order to be able to excite the center of the mass in the potential well and the relative vibrations within the particles simultaneously, the excitation in the current investigation is chosen to be

$$F_1(\tau) = F_{11}\sin(\Omega_{11}\tau + \beta_{11}) + F_{12}\sin(\Omega_{12}\tau + \beta_{12}), \tag{6}$$
$$F_2(\tau) = 0. \tag{7}$$

The coordinates x_1 and x_2 can be linearly transformed to the new coordinates

$$y_1 := \frac{m_1 x_1 + m_2 x_2}{m_1 + m_2}, \qquad y_2 := x_2 - x_1, \tag{8}$$

thus, y_1 describes the movement of the particle's center of mass and y_2 gives the distance between the particles. By having collisions, y_2 can never be smaller than Δ. The inverse of the coordinate transformation is substituted back into Eq. (1), which leads to

$$\begin{aligned}
&\ddot{y}_1 + \mu V'(y_1 - (1-\mu)y_2) + (1-\mu)V'(y_1 + \mu y_2) \\
&\quad = \frac{1}{m_1 + m_2}\left(F_{11}\sin(\Omega_{11}\tau + \beta_{11}) + F_{12}\sin(\Omega_{12}\tau + \beta_{12})\right) \qquad \text{if } y_2 > \Delta, &(9)\\
&y_{1+} = y_{1-}, \qquad \dot{y}_{1+} = \dot{y}_{1-}, \qquad \text{if } y_2 = \Delta, &(10)\\
&\ddot{y}_2 + \frac{c}{m}\dot{y}_2 + \frac{k}{m}y_2 + \underbrace{V'(y_1 + \mu y_2) - V'(y_1 - (1-\mu)y_2)}_{\text{small coupling term of } \mathcal{O}(1) \text{ since } \frac{k}{m} \gg V'(x)} \\
&\quad = -\frac{F_{11}}{m_1}\sin(\Omega_{11}\tau + \beta_{11}) - \frac{F_{12}}{m_1}\sin(\Omega_{12}\tau + \beta_{12}) \qquad \text{if } y_2 > \Delta, &(11)\\
&y_{2+} = y_{2-}, \qquad \dot{y}_{2+} = -R\dot{y}_{2-}, \qquad \text{if } y_2 = \Delta, &(12)
\end{aligned}$$

with

$$\frac{1}{m} := \frac{1}{m_1} + \frac{1}{m_2}, \qquad \mu := \frac{m_1}{m_1 + m_2}. \tag{13}$$

Eq. (11) is coupled to Eq. (9) only through a small term, which, if both terms of the sum are evaluated inside of the potential, is equal to y_2 and if both terms are evaluated outside of the potential, is equal to 0. Otherwise, the small coupling term is not independent of y_1 anymore, but still, even in this case the force of the potential is very small compared to the force of the spring. In addition, the case, when both particles are in the potential well, is the most dominant one, thus the small coupling term can be approximated by y_2 very well. By doing so, Eq. (11) becomes linear and can be solved easily.

$$\begin{aligned}
&\ddot{y}_2 + \frac{c}{m}\dot{y}_2 + \left(\frac{k}{m} + 1\right)y_2 = -\frac{F_{11}}{m_1}\sin(\Omega_{11}\tau + \beta_{11}) - \frac{F_{12}}{m_1}\sin(\Omega_{12}\tau + \beta_{12}) \qquad \text{if } y_2 > \Delta, &(14)\\
&y_{2+} = y_{2-}, \qquad \dot{y}_{2+} = R\dot{y}_{2-}, \qquad \text{if } y_2 = \Delta, &(15)
\end{aligned}$$

Since the damping coefficient, $\frac{c}{m}$ in the investigated case is not small, the homogeneous solution will decay in relatively short time and the relevant part of the solution becomes the particular solution [29]-[30]. The frequency of the resonance peak in the motion of y_2 without collision would be

$$\Omega_{02} = \sqrt{\frac{k}{m} + 1 - \frac{c^2}{2m^2}}, \tag{16}$$

but the collisions have a significant effect on the high frequency vibration, which has to be discussed first in order to be able to determine the vibration amplitude and so the probability density function (PDF) of the high-frequency oscillations. In the current investigation we are interested in the escape behavior of the two-particle system with large inner vibrations under a low-frequency and small force amplitude excitation. To get large vibrations in the relative motion of the particles the appropriate excitation frequencies should be found.

The resonance frequency of the particle's center of mass in the potential well is not influenced by the collisions. When both particles are in the potential well, Eq. (9) simplifies to

$$\ddot{y}_1 + y_1 = \frac{1}{m_1 + m_2}\left(F_{11}\sin(\Omega_{11}\tau + \beta_{11}) + F_{12}\sin(\Omega_{12}\tau + \beta_{12})\right), \tag{17}$$

which means that the linearized eigenfrequency of y_1 is $\Omega_{01} = 1$.

In the next section the focus is set on the description of the vibration amplitude of the relative movement depending on the choice of the excitation frequency.

The first step of the model reduction: resonance of the colliding particles under high-frequency excitation

The analysis of the resonance frequencies of Eq. (14) is already performed by *Fidlin* in chapter 3.5 of [31]. In the present section of this paper the content of the book is repeated mostly, however, due to a printing error in the book, a somewhat different result is obtained in the end.

In order to be able to apply the results from the book, a preliminary step is needed. With a coordinate transformation it has to be ensured that the term y_2 in Eq. (14) has the coefficient 1.

Introducing the new, dimensionless time $t = \omega_0 \tau$, with $\omega_0 = \sqrt{\frac{k}{m} + 1}$ the time derivatives can be rewritten as follows

$$\dot{y}_2 = \frac{\mathrm{d}y_2}{\mathrm{d}\tau} = \omega_0 \frac{\mathrm{d}y_2}{\mathrm{d}t} = \omega_0 y_2', \tag{18}$$

$$\ddot{y}_2 = \frac{\mathrm{d}^2 y_2}{\mathrm{d}\tau^2} = \omega_0^2 \frac{\mathrm{d}^2 y_2}{\mathrm{d}t^2} = \omega_0^2 y_2'', \tag{19}$$

where the time derivative with respect to the dimensionless time is indicated by a prime ('). Rewriting Eq. (14) in the dimensionless time yields

$$y_2'' + \frac{c}{\omega_0 m} y_2' + y_2 = \underbrace{-\frac{F_{11}}{m_1 \omega_0^2} \sin\left(\frac{\Omega_{11}}{\omega_0} t + \beta_{11}\right)}_{\text{Negligible}} - \frac{F_{12}}{m_1 \omega_0^2} \sin\left(\frac{\Omega_{12}}{\omega_0} t + \beta_{12}\right). \tag{20}$$

Given that Ω_{11} is chosen to be in the nearby of $\Omega_{01} = 1$, the effect of the first term on y_2 is negligibly small. Defining the following parameters

$$\beta := \frac{c}{\omega_0 m}, \qquad \varepsilon := \frac{F_{12}}{m_1 \omega_0^2}, \qquad \omega := \frac{\Omega_{12}}{\omega_0}, \tag{21}$$

we can rewrite Eq. (20) can be rewritten as follows

$$y_2'' + \beta y_2' + y_2 = -\varepsilon \sin(\omega t + \beta_{12}) \qquad \text{if } y_2 > \Delta, \tag{22}$$

$$y_{2+} = y_{2-}, \qquad y_{2+}' = -R y_{2-}'. \quad \text{if } y_2 = \Delta. \tag{23}$$

Using the so called 'unfolding transformation'

$$y_2 = |z| + \Delta, \tag{24}$$

Eq. (22) can be written as

$$z'' + \beta z' + z = (-\Delta - \varepsilon \sin(\omega t + \beta_{12}))\ \mathrm{sgn} z \qquad \text{if } z \neq 0, \tag{25}$$

$$z_+' - z_-' = -(1 - R) z_- \qquad \text{if } z = 0. \tag{26}$$

Using the Van der Pol transformation with

$$z = A \sin\varphi, \qquad z' = A \cos\varphi. \tag{27}$$

and a newly defined, uniformly rotating phase

$$\psi = \omega t + \beta_{12}, \tag{28}$$

Eq. (25) can be transformed to

$$A' = -\beta A \cos^2\varphi + (-\Delta - \varepsilon \sin\psi) \cos\varphi\ \mathrm{sgn} \sin\varphi \qquad \text{if } \varphi \neq n\pi,$$

$$A_+ - A_- = -(1 - R) A_- \qquad \text{if } \varphi = n\pi, \tag{29}$$

$$\varphi' = 1 + \beta \sin\varphi \cos\varphi + \frac{\Delta + \varepsilon \sin\psi}{A} |\sin\varphi|, \tag{30}$$

$$\psi' = \omega. \tag{31}$$

With the usual definition of the *resonant surface* and *resonant solutions* as also defined in [31], we focus on the parameter values of ω for which the averaged right hand side becomes discontinuous, as in the vicinity of those values, large amplitude responses may occur. 'Dangerous' terms are

$$< \sin\psi \cos\varphi\ \mathrm{sgn} \sin\varphi > = \frac{1}{2\pi} \int_0^{2\pi} \sin(\omega t + \gamma) \cos t\ \mathrm{sgn} \sin t \mathrm{d}t, \tag{32}$$

$$< \sin\psi |\sin\varphi| > = \frac{1}{2\pi} \int_0^{2\pi} \sin(\omega t + \gamma) |\sin t| \mathrm{d}t, \tag{33}$$

$$\gamma = \psi_0 - \varphi_0, \tag{34}$$

which expression can have values different from zero for values $\omega_l = 2l$, $l = 1, 2, 3...$ Then, by introducing

$$\delta = \frac{\omega}{2l} - 1, \qquad \theta = \varphi - \frac{\psi}{2l}, \tag{35}$$

Eq. (29) can be rewritten as

$$A' = -\beta A \cos^2\varphi - \Delta\cos(\varphi)\mathrm{sgn}(\sin\varphi) - \varepsilon \sin\big(2l(\varphi-\theta)\big)\cos\varphi\,\mathrm{sgn}(\sin\varphi) \qquad \text{if } \varphi \neq n\pi, \tag{36}$$

$$A_+ - A_- = -(1-R)A_- \qquad \text{if } \varphi = n\pi, \tag{37}$$

$$\theta' = -\delta + \beta\sin\varphi\cos\varphi + \frac{\Delta + \varepsilon\sin\big(2l(\varphi-\theta)\big)}{A}|\sin\varphi|, \tag{38}$$

$$\varphi' = 1 + \beta\sin\varphi\cos\varphi + \frac{\Delta + \varepsilon\sin\big(2l(\varphi-\theta)\big)}{A}|\sin\varphi|. \tag{39}$$

Taking small values for δ, the discontinuous averaging procedure can be performed. Using the notations of [31], the four integrals to be evaluated are

$$J_1 = \frac{1}{2\pi}\int_0^{2\pi} \sin(2l\varphi)|\sin\varphi|\mathrm{d}\varphi = \frac{1}{\pi}\int_0^{\pi} \sin(2l\varphi)\sin\varphi\mathrm{d}\varphi = 0, \tag{40}$$

$$J_2 = \frac{1}{2\pi}\int_0^{2\pi} \cos(2l\varphi)|\sin\varphi|\mathrm{d}\varphi = -\frac{2}{\pi(4l^2-1)}, \tag{41}$$

$$J_3 = \frac{1}{2\pi}\int_0^{2\pi} \sin(2l\varphi)\cos\varphi\,\mathrm{sgn}\sin\varphi\mathrm{d}\varphi = \frac{4l}{\pi(4l^2-1)}, \tag{42}$$

$$J_4 = \frac{1}{2\pi}\int_0^{2\pi} \cos(2l\varphi)\cos\varphi\,\mathrm{sgn}\sin\varphi\mathrm{d}\varphi = 0. \tag{43}$$

Using the above results and averaging yields the following differential equations

$$A' = -\left(\frac{1}{2}\beta + \frac{1-R}{\pi}\right)A - \frac{4l\varepsilon}{\pi(4l^2-1)}\cos 2l\theta, \tag{44}$$

$$\theta' = -\delta + \frac{2\Delta}{\pi A} + \frac{2\varepsilon}{\pi(4l^2-1)}\frac{\sin(2l\theta)}{A}. \tag{45}$$

Eq. (44) differs from Eq. (3.95) in [31] by the additional factor 3 in the denominator, which is a printing error. Setting the left hand side to 0, the stationary solution, A_* and θ_* can be obtained.

$$\frac{\frac{1}{2}\beta + \frac{1-R}{\pi}}{2l}A_* = -\frac{2\varepsilon}{\pi(4l^2-1)}\cos 2l\theta*, \tag{46}$$

$$\delta A_* - \frac{2\Delta}{\pi} = \frac{2\varepsilon}{\pi(4l^2-1)}\sin 2l\theta_*. \tag{47}$$

Eliminating θ_* and introducing

$$\beta_l = \frac{\frac{1}{2}\beta + \frac{1-R}{\pi}}{2l}, \qquad \varepsilon_l = \frac{\varepsilon}{4l^2-1}, \tag{48}$$

one obtains

$$\beta_l^2 A_*^2 + \left(\delta A_* - \frac{2\Delta}{\pi}\right)^2 = \frac{4\varepsilon_l^2}{\pi^2}. \tag{49}$$

Its solution for A is then

$$A_{1,2} = \frac{2}{\pi}\frac{\delta\Delta \pm \sqrt{\varepsilon_l^2(\beta_l^2+\delta^2) - \Delta^2\beta_l^2}}{\beta_l^2+\delta^2}. \tag{50}$$

Only the root with the plus sign is a stable solution (see proof in [31]) therefore the stationary amplitude is

$$A_* = \frac{2}{\pi}\frac{\delta\Delta + \sqrt{\varepsilon_l^2(\beta_l^2+\delta^2) - \Delta^2\beta_l^2}}{\beta_l^2+\delta^2}. \tag{51}$$

For fixed Δ, β_l and ε_l but for varying δ the maximal value of A_* can be found by setting

$$\left.\frac{\partial A_*}{\partial\delta}\right|_{\delta_{\max}} \stackrel{!}{=} 0, \tag{52}$$

which leads to

$$\delta_{\max} = \frac{\Delta\beta_l}{\varepsilon_l}. \tag{53}$$

Inserted in Eq. (51) the biggest amplitude value estimated by the analytic approach is

$$A_{*,\max} = \frac{\varepsilon_l}{\beta_l}, \tag{54}$$

independent from Δ, i.e. for every feasible choice of Δ the maximal amplitude is the same for some $\delta_{\max}$.
Now we can write the solution

$$z(t) = A_* \sin\left(\frac{\omega t}{2l} + \varphi_0\right) \tag{55}$$

for some φ_0, thus

$$y_2(t) = A_* \left|\sin\left(\frac{\omega t}{2l} + \varphi_0\right)\right| + \Delta. \tag{56}$$

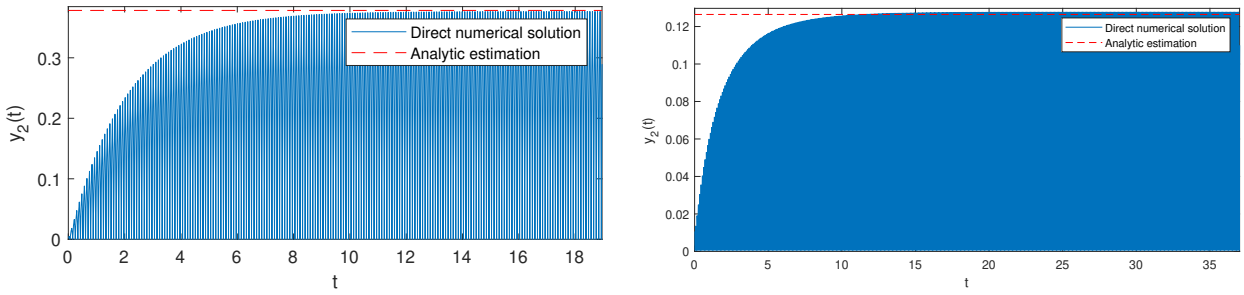

(a) $m_1 = 1$, $m_2 = 5$, $\Omega_{12} = 61.988$ ($l = 1$) and $\Delta = 0$.

(b) $m_1 = 2$, $m_2 = 1$, $\Omega_{12} = 138.71$ ($l = 2$) and $\Delta = 0.0006$.

Figure 2: Comparison of the numerical solution for y_2 with the theoretically estimated stationary amplitude for $c = 0.5$, $k = 800$, $F_{12} = 15$. The theoretical model can predict the stationary amplitude very accurately.

The second step of the model reduction: calculating the effective slow potential using the probabilistic description of the high-frequency oscillations

Given the amplitude of y_2, the PDF of the high-frequency oscillations around the common center of mass, y_1 can be determined as

$$\begin{bmatrix} z_1 \\ z_2 \end{bmatrix} = \begin{bmatrix} x_1 - y_1 \\ x_2 - y_1 \end{bmatrix} = \begin{bmatrix} y_1 - \frac{m_2}{m_1+m_2} y_2 - y_1 \\ y_1 + \frac{m_1}{m_1+m_2} y_2 - y_1 \end{bmatrix} = \begin{bmatrix} -\frac{m_2}{m_1+m_2} y_2 \\ \frac{m_1}{m_1+m_2} y_2 \end{bmatrix}. \tag{57}$$

As it can be expected, the movement is not symmetric around y_1, unless the masses are equal. In general the PDFs of the individual particles, $\rho_i(x)$ are given by arcsine distributions cut in the middle as depicted in Fig 3. To write the probability density function of z_1 and z_2, first, we define

$$A_{1*} = (1-\mu)A_*, \qquad A_{2*} = \mu A_*, \qquad \Delta_1 = (1-\mu)\Delta, \qquad \Delta_2 = \mu\Delta, \tag{58}$$

thus

$$z_1 = -A_{1*}\left|\sin\left(\frac{\omega t}{2l} + \varphi_0\right)\right| - \Delta_1, \qquad z_2 = A_{2*}\left|\sin\left(\frac{\omega t}{2l} + \varphi_0\right)\right| + \Delta_2. \tag{59}$$

In general the probability density function (PDF), $\rho(x)$ of a function, $f(t)$, which is strictly monotonically increasing and continuously differentiable on the interval (a, b) is given by

$$\rho(x) = \frac{1}{f'[f^{-1}(x)]} \cdot \frac{1}{b-a} \qquad \text{for } f(a) < x < f(b). \tag{60}$$

If the function, $f(t)$ is strictly monotonically decreasing, its PDF is just the negative of the above expression. Thus in the special case of

$$f(t) = A_{i*}\sin(\Omega t + \beta) + \Delta_i \tag{61}$$

we have

$$\rho(x) = \frac{1}{\Omega\sqrt{A_{i*}^2 - (x-\Delta_i)^2}} \frac{1}{b-a}, \tag{62}$$

where a and b are such, that the function increases monotonically between them. Since $f(t)$ is periodic, it suffices to determine the PDF of one period, which in the case of z_1 and z_2 can be done by splitting the period into a monotonically increasing and monotonically decreasing part. As the two parts obviously has the same PDF in this case, it is enough to determine the PDF of the monotonically decreasing part for z_1 and the monotonically increasing part for z_2, that we achieve by choosing

$$a = -\frac{2l\varphi_0}{\omega}, \qquad b = \frac{2l\left(\frac{\pi}{2} - \varphi_0\right)}{\omega}, \qquad \Omega = \frac{\omega}{2l}, \tag{63}$$

then we can write

$$\rho_1(x) = \begin{cases} \frac{2}{\pi\sqrt{A_{1*}^2 - (x+\Delta_1)^2}} & \text{for } -A_{1*} - \Delta_1 < x < -\Delta_1, \\ 0 & \text{otherwise,} \end{cases} \tag{64}$$

$$\rho_2(x) = \begin{cases} \frac{2}{\pi\sqrt{A_{2*}^2 - (x-\Delta_2)^2}} & \text{for } \Delta_2 < x < A_{2*} + \Delta_2. \\ 0 & \text{otherwise.} \end{cases} \tag{65}$$

The PDF of the particle system, $\rho(x)$ is obtained finally by the weighted sum of the individual probability density functions

$$\rho(x) = \mu\rho_1(x) + (1-\mu)\rho_2(x). \tag{66}$$

A numeric example is given in Fig. 3.

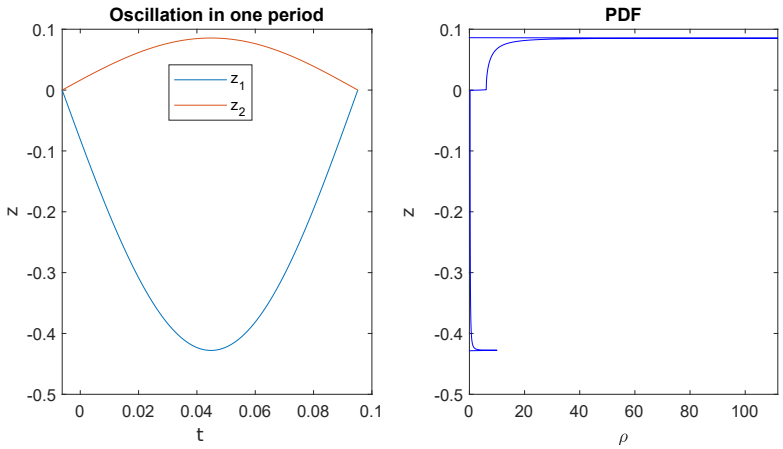

Figure 3: One period of the high-frequency oscillation and the corresponding PDF with masses $m_1 = 1$ and $m_2 = 5$.

Effective potential by convolution

Eq. (9) can be rewritten now as follows

$$\ddot{y}_1 + \mu V'(y_1 + z_1) + (1-\mu)V'(y_1 + z_2) = \frac{1}{m_1 + m_2}\left(F_{11}\sin(\Omega_{11}\tau + \beta_{11}) + F_{12}\sin(\Omega_{12}\tau + \beta_{12})\right). \tag{67}$$

The arguments of $V'(\cdot)$ oscillates with a high frequency around y_1, instead of calculating the exact values for every moment, a kind of averaging is used to obtain an effective potential $\tilde{V}$. As during a period of the high frequency vibration z_i the change of y_1 is small, we can get the averaged force at y_1 by calculating the total force on the particle density cloud at y_1 having the PDF $\rho_1(x)$ and $\rho_2(x)$. The latter operation can be performed, as for any continuously distributed volume in a force field, by the following integral transformation

$$\tilde{V}'(y_1) = \int_{-\infty}^{\infty} V'(x)\rho(x - y_1)\mathrm{d}x. \tag{68}$$

In our special case the integral can be evaluated analytically. First we define the positions

$$d_1 = -1 - \Delta_2 - A_{2*}, \qquad d_2 = -1 - \Delta_2, \qquad d_3 = -1 + \Delta_1, \qquad d_4 = -1 + \Delta_1 + A_{1*}, \tag{69}$$

$$d_5 = 1 - \Delta_2 - A_{2*}, \qquad d_6 = 1 - \Delta_2, \qquad d_7 = 1 + \Delta_1, \qquad d_8 = 1 + \Delta_1 + A_{1*}. \tag{70}$$

In the following, we will only consider the case, when $\Delta + A_* < 2$, so that we can guarantee that $d_1 \dots d_9$ are in ascending order. With the help of the above positions we can define the domains

$$D_1 = \{x \in \mathbb{R} | x \leq d_1\}, \tag{71}$$
$$D_i = \{x \in \mathbb{R} | d_{i-1} \leq x < d_i\} \qquad \text{for } i = 2 \dots 8, \tag{72}$$
$$D_9 = \{x \in \mathbb{R} | d_8 \leq x\}. \tag{73}$$

Thus, the effective force field can be written as

$$\tilde{V}'(y_1) = \begin{cases} 0 & x \in D_1, \\ (1-\mu)\left(y_1 + \Delta_2 + \frac{2}{\pi}\left(\sqrt{A_{2*}^2 - (1+\Delta_2+y_1)^2} - (y_1+\Delta_2)\arcsin\left(-\frac{1+\Delta_2+y_1}{A_{2*}}\right)\right)\right) & x \in D_2, \\ (1-\mu)\left(y_1 + \Delta_2 + \frac{2}{\pi}A_{2*}\right) & x \in D_3, \\ \mu\left(\frac{2}{\pi}\left(\sqrt{A_{1*}^2 - (\Delta_1 - 1 - y_1)^2} + (\Delta_1 - y_1)\arcsin\left(\frac{\Delta_1 - 1 - y_1}{A_1}\right) - A_{1*}\right)\right) + (1-\mu)\left(y_1 + \Delta_2 + \frac{2}{\pi}A_{2*}\right) & x \in D_4, \\ y_1 & x \in D_5, \\ \mu\left(y_1 - \Delta_1 - \frac{2}{\pi}A_{1*}\right) + (1-\mu)\left(\frac{2}{\pi}\left(A_{2*} - \sqrt{A_{2*}^2 - (1-\Delta_2-y_1)^2} + (\Delta_2+y_1)\arcsin\left(\frac{1-\Delta_2-y_1}{A_{2*}}\right)\right)\right) & x \in D_6, \\ \mu\left(y_1 - \Delta_1 - \frac{2}{\pi}A_{1*}\right) & x \in D_7, \\ \mu\left(-\frac{2}{\pi}\left(\sqrt{A_1^2 - (1+\Delta_1-y_1)^2} + (\Delta_1 - y_1)\arcsin\left(\frac{1+\Delta_1-y_1}{A_{1*}}\right)\right) - \Delta_1 + y_1\right) & x \in D_8, \\ 0 & x \in D_9. \end{cases} \tag{74}$$

Through integration the effective potential can be determined as well. As the potential can be shifted arbitrarily by a constant, we set the condition $\tilde{V}(-\infty) \stackrel{!}{=} 0$. However, the analytic expression for $\tilde{V}(y_1)$ is very complex, so we dispense with giving an exact formula here.
Please note, that Eq. (74) is valid for arbitrary values of Δ, however, in practical cases Δ is limited to $\mathcal{O}(\varepsilon)$, thus the intervals D_3 and D_7 do not have a significant role.
In Fig. 4 a graphical example is represented for a certain parameter choice (cf. the caption of Fig. 4).

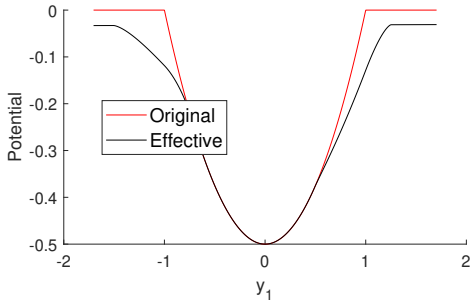

(a) Potential–$\tilde{V}(y_1)$

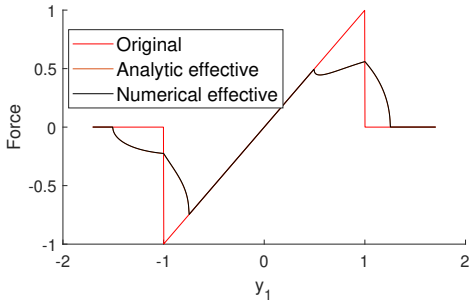

(b) Force–$\tilde{V}'(y_1)$

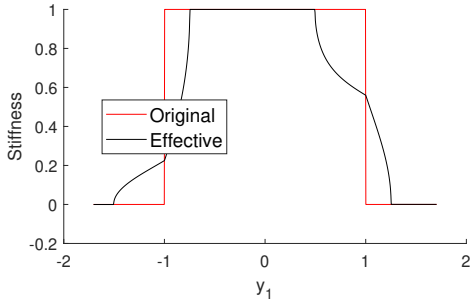

(c) Stiffness–$\frac{\tilde{V}'(y_1)}{y_1}$

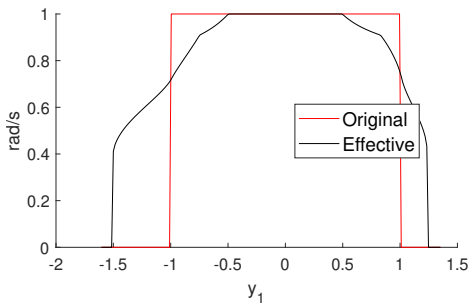

(d) Eigenfrequency–$\omega(y_1)$

Figure 4: Non-linear force field and some other derived quantities generated by $m_1 = 2$, $m_2 = 1$, $c = 0.5$, $k = 800$, $F_{12} = 30$, $\Omega_{12} = 69.335$ ($l = 1$), $\Delta = 0.0006$.

A very important effect, due to the asymmetric integration kernel, is the asymmetry of the effective force field. Therefore all the other quantities derived from it, are asymmetric as well. Moreover, the potential energy on the right boundary of the potential is also different from the potential energy on the left hand side of the potential, which might lead to an asymmetric escape behavior. The probabilities of escaping to the right might differ from the probability of escaping to the left. The further the ratio $\frac{m_1}{m_2}$ is from 1, the greater is the asymmetry, which leads to vibrations with a symmetry center different from 0.

Numerical results and discussion

A good way to determine the goodness of the order reduction method applied above is to depict the escaping/non-escaping points on the low excitation frequency–low excitation force plane. In Fig. 5 such a comparison can be seen. It is important to note, that the sharp minimum (Ω_C, F_C), observed by many authors in the literature, can be determined more or less. However, in Fig. 5 on the right from the minimum, i.e. for $\Omega_{11} > \Omega_C$ there is not really a frequency dependent critical forcing value, above which escape happens for whatever forcing amplitude. Instead the transition from no-escape into escape happens through a fractal-like boundary and there exist even separated non-escaping 'islands' in the 'see' of escaping $\Omega_{11} - F_{11}$ parameter combinations. Such a time evolution is shown in Fig. 6. The remarkable feature of the model reduction is, that even these non-escaping islands of the parameter combinations remain preserved. When the non-linear part of the effective force gets smaller (cf. 5b), we can observe a less chaotic behavior around the critical force values. Moreover, it is also obvious that the minimally needed force amplitude moves up, as the non-linearity of the effective force field increases, due to the increasing amplitude of the relative motion. This simple fact explains also, why the escaping region in the $\Omega_{11} - F_{11}$ plane moves closer to the point $(1, 0)$, when the relative motion is excited with a higher resonant frequency but unchanged force amplitude. Eq. (54) and Eq. (48) show the simple relationship between the excitation frequency and the amplitude of the caused resonant motion that shows a decreasing amplitude with increasing value for l.

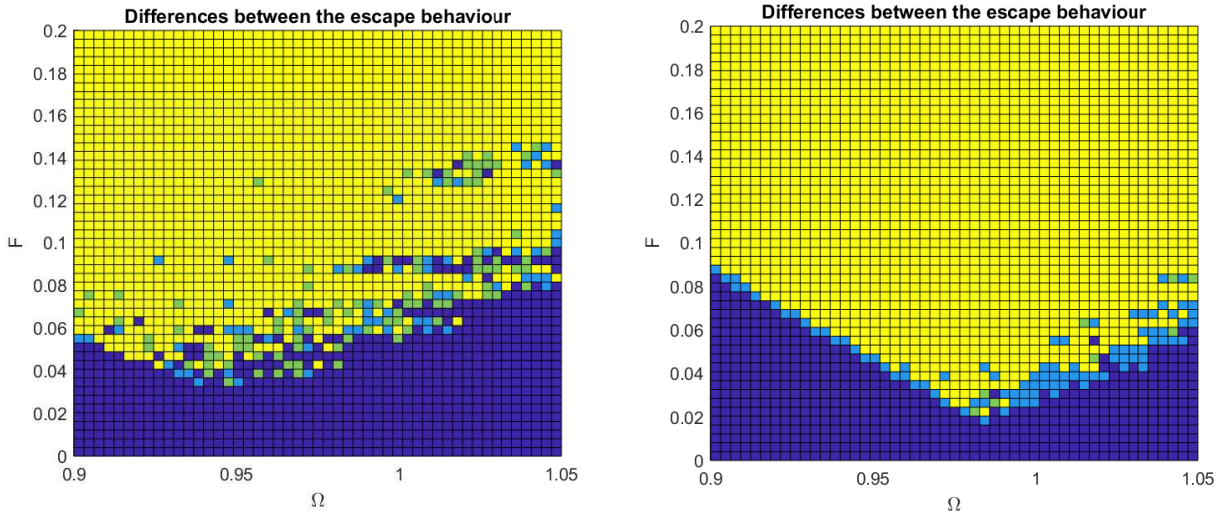

(a) First resonant frequency is excited, $\Omega_{12} = 69.34$ ($l = 1$).

(b) Second resonant frequency is excited, $\Omega_{12} = 138.67$ ($l = 2$).

Figure 5: Comparison of the reduced model to the original one with parameter values $m_1 = 2$, $m_2 = 1$, $c = 0.5$, $k = 800$, $F_{12} = 30$, and $\Delta = 0.0006$. Dark blue dots mean no escape for both models, bright blue is escape in the simplified model, but no escape in the original model, green is no escape in the simplified model, but escape in the original one. Yellow stands for escape in both models. $F := \frac{F_{11}}{m_1+m_2}$.

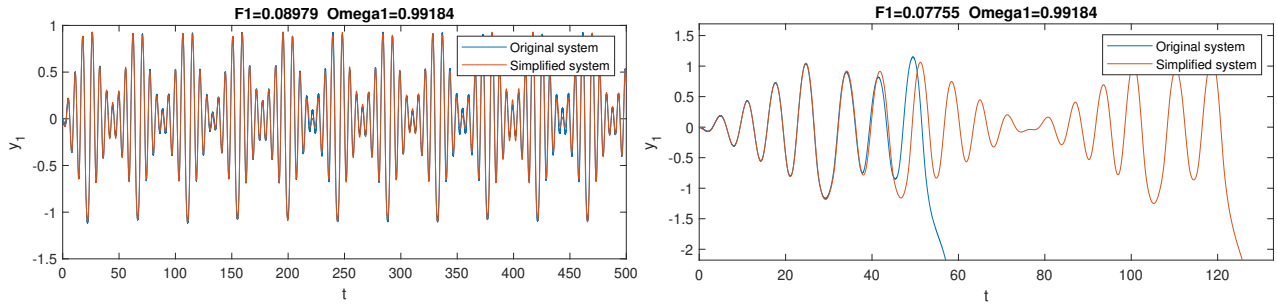

(a) No-escape-island: $\Omega_{11} = 0.9918$, $\frac{F_{11}}{m_1+m_2} = 0.0898$

(b) Below the island: $\Omega_{11} = 0.9918$, $\frac{F_{11}}{m_1+m_2} = 0.0775$

Figure 6: $m_1 = 2$, $m_2 = 1$, $c = 0.5$, $k = 800$, $F_{12} = 30$, $\Omega_{12} = 69.335$ ($l = 1$) and $\Delta = 0.0006$.

Conclusions

In the present work escape of a strongly coupled, colliding pair of particles from a potential well under bi-harmonic excitation was investigated. Through a coordinate transformation from the physical coordinates of the particles into the coordinates of the common center of mass and into the distance of the particles the motion could be decomposed into a

slow and into a fast variable. After determining the oscillation amplitudes of the fast motion with the use of the so called 'unfolding transformation', a certain type of averaging, appropriate to use also with piece-wisely defined functions being based on the probability density function of the fast motion, was performed. The resulting formulas for the effective force-field are fully analytic, thus a huge reduction in the simulation time can be achieved (5 hours vs 4 minutes in the example shown). It turns out, that even such properties of the system remain well conserved, as for example the location of the non-escaping islands on the low excitation frequency–low forcing amplitude ($\Omega_{11} - F_{11}$) plane. Although in the current work escape was investigated in a truncated quadratic potential well, the application of the PDF based averaging method is straightforward for several different potentials as well.

Many questions may remain open in the Reader regarding the further analysis of the escape behavior of a colliding pair of coupled particles. What happens if the resonant frequencies of the relative motion are of the same magnitude as the eigenfrequency of the bottom of the potential well? How do the initial conditions of the particles influence the escape behavior? How to proceed in case of poly-harmonic excitation? What if the collision of the particles is a random process? What happens when there are more than two colliding particles?

The authors of this paper hope, that many of the readers will feel motivated to find answers to these and many other different questions arising when studying the thrilling topic of escape from a potential well.

References

[1] Landau, L.D., Lifshitz, E.M.: Mechanics, 3rd edn. Butterworth, Herrmann (1976)

[2] Thompson, J.M.T.: Chaotic phenomena triggering the escape from a potential well. In: Szemplinska-Stupnicka, W., Troger, H. (eds.) Engineering Applications of Dynamics of Chaos, CISM Courses and Lectures, vol. 139, pp. 279–309. Springer, Brelin (1991)

[3] Lawrence N. Virgin, Raymond H. Plaut, Ching-Chuan Cheng, Prediction of escape from a potential well under harmonic excitation, International Journal of Non-Linear Mechanics, Volume 27, Issue 3, 1992, Pages 357-365, ISSN 0020-7462, https://doi.org/10.1016/0020-7462(92)90005-R.

[4] Virgin, L.N.: Approximate criterion for capsize based on deterministic dynamics. Dyn. Stab. Syst. 4, 56–70 (1989)

[5] Sanjuan, M.A.F.: The effect of nonlinear damping on the universal escape oscillator. Int. J. Bifurc. Chaos 9, 735–744 (1999)

[6] Mann, B.P.: Energy criterion for potential well escapes in a bistable magnetic pendulum. J. Sound Vib. 323, 864–876 (2009)

[7] Barone, A., Paterno, G.: Physics and Applications of the Josephson Effect. Wiley, New York (1982)

[8] Arnold, V.I., Kozlov, V.V., Neishtadt, A.I.: Mathematical Aspects of Classical and Celestial Mechanics. Springer, Berlin (2006)

[9] Quinn, D.D.: Transition to escape in a system of coupled oscillators. Int. J. Non-Linear Mech. 32, 1193–1206 (1997)

[10] Belenky, V.L., Sevastianov, N.B.: Stability and Safety of Ships—Risk of Capsizing. The Society of Naval Architects and Marine Engineers, Jersey City (2007)

[11] Elata, D., Bamberger, H.: On the Dynamic Pull-In of Electrostatic Actuators with Multiple Degrees of Freedom and Multiple Voltage Sources. Journal of Microelectromechanical Systems 15, 131–140 (2006)

[12] Leus, V., Elata, D.: On the dynamic response of electrostatic MEMS switches. J. Microelectromech. Syst. 17, 236–243 (2008)

[13] Younis, M.I., Abdel-Rahman, E.M., Nayfeh, A.: A reducedorder model for electrically actuated microbeam-based MEMS. J. Microelectromech. Syst. 12, 672–680 (2003)

[14] Alsaleem, F.M., Younis, M.I., Ruzziconi, L.: An experimental and theoretical investigation of dynamic pull-in in MEMS resonators actuated electrostatically. J. Microelectromech. Syst. 19, 794–806 (2010)

[15] Ruzziconi, L., Younis, M.I., Lenci, S.: An electrically actuated imperfect microbeam: dynamical integrity for interpreting and predicting the device response. Meccanica 48, 1761–1775 (2013)

[16] Zhang, W.-M., Yan, H., Peng, Z.-K., Meng, G.: Electrostatic pull-in instability in MEMS/NEMS: a review. Sens. Actuators A Phys. 214, 187–218 (2014)

[17] Kramers, H.A.: Brownian motion in a field of force and the diffusion model of chemical reactions. Physica (Utrecht) 7, 284–304 (1940)

[18] Fleming, G.R., Hanggi, P.: Activated Barrier Crossing. World Scientific, Singapore (1993)

[19] Talkner, P., Hanggi, P. (eds.): New Trends in Kramers' Reaction Rate Theory. Springer, Berlin (1995)

[20] Rega, G., Lenci, S.: Dynamical integrity and control of nonlinear mechanical oscillators. J. Vib. Control 14, 159–179 (2008)

[21] Diego Orlando, Paulo B. Gonçalves, Stefano Lenci, Giuseppe Rega, Influence of the mechanics of escape on the instability of von Mises truss and its control, Procedia Engineering, Volume 199, 2017, Pages 778-783, ISSN 1877-7058, https://doi.org/10.1016/j.proeng.2017.09.048.

[22] Gendelman, O.V. Escape of a harmonically forced particle from an infinite-range potential well: a transient resonance. Nonlinear Dyn 93, 79–88 (2018). https://doi.org/10.1007/s11071-017-3801-x

[23] Manevitch, L.I.: New approach to beating phenomenon in coupled nonlinear oscillatory chains. Arch. Appl. Mech. 77, 301–312 (2007)

[24] Manevitch, L.I., Gendelman, O.V.: Tractable Modes in Solid Mechanics. Springer, Berlin (2011)

[25] Gendelman, O.V., Karmi, G. Basic mechanisms of escape of a harmonically forced classical particle from a potential well. Nonlinear Dyn 98, 2775–2792 (2019). https://doi.org/10.1007/s11071-019-04985-9

[26] V.M. Volosov, B.I. Morgunov, Method of Averaging in the Theory of nonlinear Oscillating Systems, Moscow State University, Moscow, 1971 (in Russian).

[27] M Balachandra, PR Sethna, A generalization of the method of averaging for systems with two time scales. Archive for Rational Mechanics and Analysis, 1975 – Springer, https://link.springer.com/content/pdf/10.1007/BF00280744.pdf

[28] Genda, A., Fidlin, A. & Gendelman, O. On the escape of a resonantly excited couple of particles from a potential well. Nonlinear Dyn (2021). https://doi.org/10.1007/s11071-021-06312-7

[29] Alexander Fidlin, Olga Drozdetskaya, On the Averaging in Strongly Damped Systems: The General Approach and its Application to Asymptotic Analysis of the Sommerfeld Effect, Procedia IUTAM, Volume 19, 2016, Pages 43-52, ISSN 2210-9838, https://doi.org/10.1016/j.piutam.2016.03.008.

[30] Fidlin A, Thomsen J.J. Non-trivial effects of high-frequency excitation for strongly damped mechanical systems. Int. J. of Non-Linear Mechanics 2008; 43: 569 – 578.

[31] A. Fidlin, Nonlinear Oscillations in Mechanical Engineering, 1st edn. Springer-Verlag Berlin Heidelberg, 2006, ISBN 978-3-540-28116-0, DOI 10.1007/3-540-28116-9

[32] Guckenheimer, J. and Holmes, P. I983 Nonlinear oscillations, dynamical systems, and bifurcations of vector fields. New York: Springer-Verlag.

Tuesday, July 19, 2022
16:00 - 18:20

MS-08 Nonlinear Phenomena in Mechanical and Structural Systems
Rhone 3B

Chair: Oded Gottlieb

16:00 - 16:20
Coupled Thermoelastic Large Amplitude Vibrations of Bi-Material Beams
MANOACH Emil*, DONEVA Simona, WARMINSKI Jerzy
*Institute of Mechanics, Bulgarian Academy of Sciences (Acad. G. Bonchev Street, block 4 Institute of Mechanics Bulgaria)

16:20 - 16:40
Couplings and nonlinearities modelling in drillstring dynamics
MANIN Lionel, **MAHJOUB Mohamed***, DUFOUR Régis, ANDRIANOELY Marie-Ange, TRAN Quang Thinh, NGUYEN Khac Long, MENAND Stephane
*Helmerich & Payne - DrillScan (26 rue Emile Decorps, Villeurbanne France)

16:40 - 17:00
Escape Dynamics of a Parametrically Excited Particle from an Infinite Range Potential
K R Jayaprakash*, GENDELMAN Oleg
*Indian Institute of Technology Gandhinagar (Palaj, IIT Gandhinagar, Gandhinagar-382355, Gujarat India)

17:00 - 17:20
Explanation of the Locomotion of a Rigid Body along a Vibrating Nonlinear Beam
MÜLLER Florian*, VAKAKIS Alexander, KRACK Malte
*Universität Stuttgart [Stuttgart] (Keplerstraße 7, 70174 Stuttgart Germany)

17:20 - 17:40
Harmonic Balance Method for the stationary response of continuous systems with nonlinear hysteretic damping under harmonic excitation
ZHANG Jiangyi, FĂRĂGĂU Andrei, VAN Der Esch Anton, METRIKINE Andrei, **VAN Dalen Karel***
*Faculty of Civil Engineering and Geosciences, Delft University of Technology (Stevinweg 1, 2628 CN, Delft Netherlands)

17:40 - 18:00
Harmonic balance-based crack size estimation in an ultrasonic fatigue specimen
KISER Shawn*, GUSKOV Mikhail, REBILLAT Marc, RANC Nicolas
*Procédés et Ingénierie en Mécanique et Matériaux [Paris] (151 Boulevard de l'Hôpital, 75013 Paris France)

18:00 - 18:20
Influence of friction damping on frequency lock-in in cyclic structure
BYRTUS Miroslav*, DYK Stepan
*University of West Bohemia [Plzeň] (Univerzitní 2732/8, 306 14 Plzeň 3 Czech Republic)

Coupled Thermoelastic Large Amplitude Vibrations of Bi-Material Beams

Emil Manoach[*], Simona Doneva [**] and Jerzy Warminski[***]
[*]*Institute of Mechancs, Bulgarian Academy of Sciences, Sofia, Bulgaria*
[**] *Institute of Mechancs, Bulgarian Academy of Sciences, Sofia, Bulgaria and Lublin University of Technology, Nadbystrzycka 36, 20-618 Lublin, Poland*
[***] *Lublin University of Technology, Nadbystrzycka 36, 20-618 Lublin, Poland*

Summary. The goal of this work is to develop a theoretical and numerical models of the coupled and uncoupled vibration of bi-material beams subjected the combined action of mechanical and thermal loads. The geometrically nonlinear version of the Timoshenko beam theory is used to describe the theoretical model of the problem. Starting from the geometrical, constitutive and equilibrium equations of each layer the governing equations of the bi-material beam are derived. The beam is subjected to heat flux and periodic mechanical loading. The influence of the elevated temperature or the heat propagation along the beam length and thickness on the response of the beam was studied.

Introduction

Among the most popular composite structures the bi-material structures and especially the bi-material beams are frequently used in different braches in industry. The growing interest to mechanical behavior of the bi-material beam can be connected with different MEMS (see, for example https://istegim2019.sciencesconf.org/285421). The thermoelastic behaviour of such beams is a subject of interest because of their applicability as well as because of the complex behaviour of the structures due to the different elastic and thermal properties of the layers.
Generally, the most of the studies of the dynamic response of the thermally loaded beam consider that the structure gets elevated temperature instantly, and the heat propagation is not included in the model.
The goal of the present work is to derive the equations of the geometrically non-linear vibration of a bi-material beam with non-symmetric layers according to the Timoshenko beam theory. Based on these equations it is aimed to study the coupled and uncoupled geometrically nonlinear vibrations of the beam as well as the vibration of the beam at constant elevated temperature. The influence of the coupled terms in the governing equations and the new terms counting the non-uniform layers are specially studied for different material properties and different thermal loadings. The speed of the propagation of the temperature along the different layers is also analyzed. The reduced model created on the base of Galerkin approach allows analysis of the beam response in the frequency and time domains and an estimation of the stability of the solution, as well. Three dimensional finite element model of the bi-material beam is created in order to verify the results.

Theoretical model

A beam with length l, width b and thickness h is considered. The beam consists of two layers made of different materials (Material 1 and Material 2) with thickness h_1 and h_2 ($h=h_1+h_2$). The geometrical scheme of the beam is shown in Fig. 1.

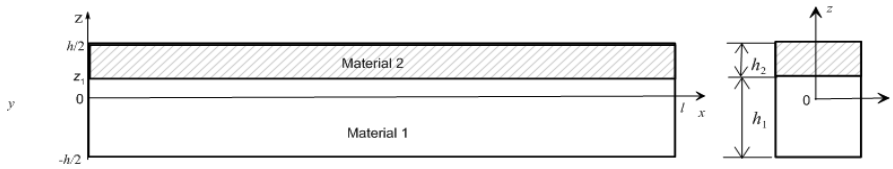

Fig. 1 The geometrical scheme of the beam model

The equations describing the coupled problem of the temperature propagation and the beam vibrations as a result of the action of a heat flow and of mechanical load with intensity $p(x,t)$ are:

$$\frac{c_p^{(i)}}{\lambda_T^{(i)}}\frac{\partial T}{\partial t}=\frac{\partial^2 T}{\partial x^2}+\frac{\partial^2 T}{\partial z^2}-\frac{\alpha_T^{(i)}E^{(i)}T_0}{\lambda_T^{(i)}}\frac{\partial \varepsilon^{(i)}}{\partial t},\quad i=1,2$$

$$\frac{\partial N}{\partial x}-c_1^{(i)}\frac{\partial u}{\partial t}-\rho^{(i)}bh^{(i)}\frac{\partial^2 u}{\partial t^2}=0,\ -\frac{\partial M}{\partial x}+Q-c_2^{(i)}\frac{\partial \psi}{\partial t}-\rho^{(i)}I^{(i)}\frac{\partial^2 \psi}{\partial t^2}=0,$$

$$\frac{\partial Q}{\partial x}+N\left(\frac{\partial^2 w}{\partial x^2}\right)+\frac{\partial N}{\partial x}\frac{\partial w}{\partial x}-c_1^{(i)}\frac{\partial w}{\partial x}-\rho F\frac{\partial^2 w}{\partial t^2}=-p(x,t)$$

where $I^{(i)}$ is the inertia moment of ith layer, $\rho^{(i)}$ is the density of the ith material $T(x,z,t)$ is current temperature, T_0 is the initial constant temperature, $\lambda_T^{(i)}$ is the thermal conductivity of ith material and $c_p^{(i)}$ is the heat capacity per unit volume,

$\alpha_T^{(i)}$ is the coefficient of the thermal expansion , $E^{(i)}$ is the Young's modulus of the ith layer, $c_1^{(i)}$ and $c_2^{(i)}$ are damping coefficients, $w(x,t)$ is the transverse displacement, $\psi(x,t)$ is the rotation angle and

$$\varepsilon^{(i)} = -z\frac{\partial \psi}{\partial x} + \alpha_T^{(i)}\left(T - T_0\right) + \frac{\partial u}{\partial x} + \frac{1}{2}\left(\frac{\partial w}{\partial x}\right)^2$$

After integrations along each layer thickness the generalized stresses *N*, *M* and *Q* are expressed by the displacements and then the governing equations of the bi-material beam are derived.
In comparison with the classical Timoshenko beam equations, additional nonlinear terms appear in the equations describing the longitudinal displacements, transverse displacements and the angular rotations.

Numerical approach

The equation for the heat propagation is discretized with respect to the space variables (*x* and *z*) by the finite difference method. The partial differential equations for the beam vibration are transformed to a system of coupled nonlinear ordinary differential equations by the Galerkin approach using the expansion of the generalized displacement vector in a series of the product of the normal modes of the linear Timoshenko beam and time dependent coefficients. The algorithm for the solution of the problem is based on the successive solution of the equations for the mechanical vibrations of the beam and for the heat transfer. The algorithm is similar to the one described in [1].

Numerical examples

Two cases of the problem have been studied: (i) beam at elevated temperature and (ii) beam subjected to a heat impact. The influence of the elevated temperature applied together with periodic loading on the beam is studied in time and frequency domain.
In the case of the heat impact the propagation of the temperature along the beam layers and specially at the interface layer is studied. It is shown that in the case of short and intensive heat pulses the beam can buckle (Fig. 2). The influence of the nonlinear terms appeared due to the different properties of the materials is estimated.
In some cases, the coupled terms may influence the temperature propagation as can be seen in Fig. 3.

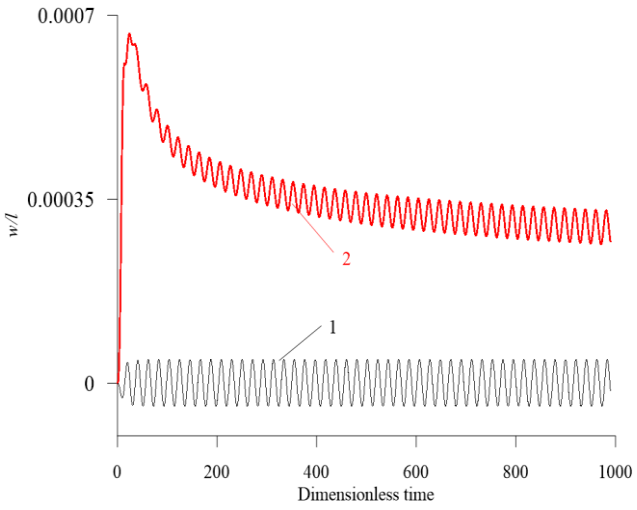

Fig. 2. Time history of the response of the beam subjected to thermal and harmonic loading with 1- no heating; 2-heat impact with duration $\bar{t}_0$ =30 (dimensionless time) and q_0=9000 W/m^2.

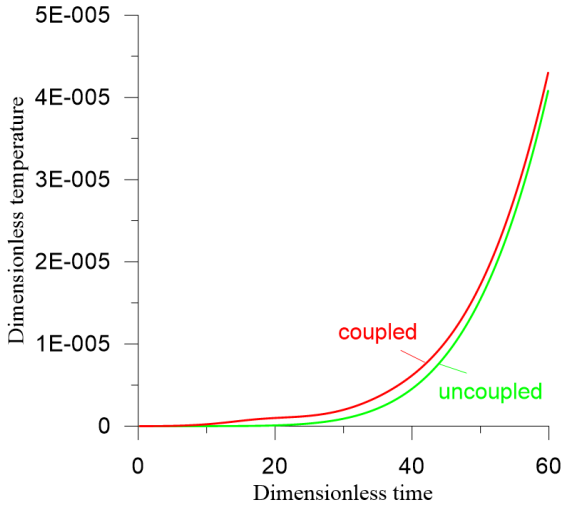

Fig. 3. Variation of the temperature at the beam center at 6th interface layer of the beam cross-section.

Conclusions

A theoretical model of the dynamic behaviour of Timoshenko beam is developed. The model includes a full coupling of the mechanical and thermal fields i.e. the thermal field influences the beam motion and the beam motion influence the heat propagation. The dynamic behavior of the beam is studied in the case of coupled, uncoupled vibration, as well as the case of elevated constant temperature. 3D finite element model of the problem and a reduced model are used and the results obtained by both models are compared.

References

[1] Manoach E, Ribeiro, P. (2004) . Coupled, thermoelastic, large amplitude vibrations of Timoshenko beams. Int. J. Mechanical Sciences, 46, 1589-1606 .

Couplings and nonlinearities modelling in drillstring dynamics

L. Manin†*, M. Mahjoub**, R. Dufour*, M-A. Andrianoely*, Q T. Tran*, K. L. Nguyen**, S. Menand**,
*Univ Lyon, INSA-Lyon, CNRS UMR5259, LaMCoS, France
**Helmerich & Payne - DrillScan, 26 Rue Emile Decorps 69100 Villeurbanne, France
mohamed.mahjoub@hpinc.com

Summary. The drillstring dynamics is a complicated nonlinear rotordynamics problem. The slender drillstring is immersed in a 3D well in the presence of mud, drillstring-well contacts, fluid-structure interactions, bending-torsion-axial vibrations. The induced vibration problems increase the energy loss and cause failures. In order to understand and predict better the vibrations phenomena a Finite Element model is proposed. The simulation results are compared to field data.
Keywords: Nonlinear rotordynamics, drillstring, fluid-structure interaction, rotor-stator contact, contact models

Drillstring description

In rotary drilling which addresses today more and more geothermal application, drillstring is a very slender rotor immersed in a well with a 3D trajectory, Fig. 1. The drillstring, driven by an electrical motor within a 0-180 rpm range, is an assembly of pipes 9 to 10 m long confined in tension in a 3D curvilinear well of several kilometers. Towards the drill bit, over 100 to 200 meters long, the drill collars have a larger outer diameter to ensure the Weight On Bit (WOB) on the rock and then constitute the Bottom Hole Assembly (BHA). Stabilizers act as bearings to maintain the drill collar concentric with the well and permit directional drilling. The drill collar is kept in compression with, at its upper end, the tension-compression neutral point. The mud, i.e. the drilling fluid, circulates downward inside the drill-pipes and upward in the pipe-well annular space. The role of the mud is to clean out rock debris and calories, to lubricate the numerous drillstring – bore hole contacts.

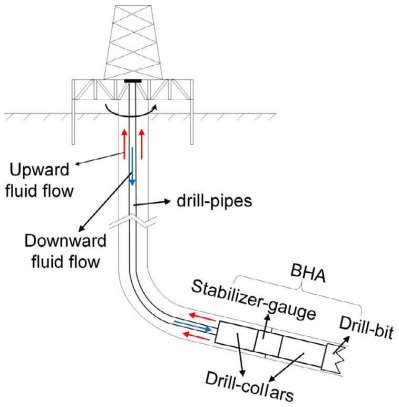

Fig. 1. Sketch of the drillstring immersed in the well

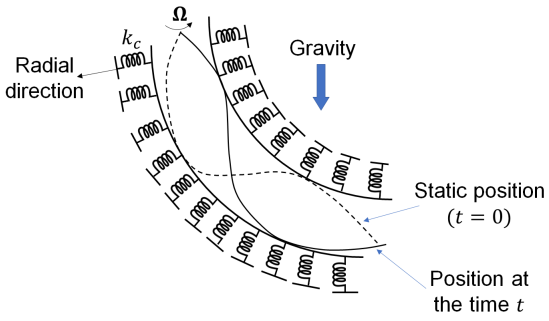

Fig. 2. Configuration of nonlinear response computation

Nonlinear phenomena

Solicited by mud pulses, mass unbalances, pipe-well interactions and friction, motor and resistant torques as well as the axial forces of the various drill-bit shapes, the drill string has a dynamic behavior governed by equations of motion involving in particular the fluid-structure coupling, the nonlinearities of contact, and the axial-bending-torsion couplings. The drillstring is therefore a complex dynamic system because it is non conservative, gyroscopic, with parametric excitations, and necessarily non-linear. Thus, it is expected in the different portions of the drill string, nonstationary behaviors, stick-slip motion, tool-bit bouncing, forward and backward, periodic, quasi-periodic, and chaotic whirls. This set of phenomena induces, in particular, energy loss, failures. Consequently, the Rate of Penetration (ROP) decreases while the Non-Productive Time (NPT) increases.

Coupled and nonlinear proposed model

Facing these technical issues requires to understand as well as possible the drillstring behavior with the implementation of a specific nonlinear rotordynamics model in order to predict in fine the forced dynamics response, the total amount of friction torques, and the drill pipe stresses. The proposed model is based on the Finite Element method using Timoshenko beam elements with 6 degrees of freedom per node. At the beginning of the computational process, the FE mesh of the drillstring is vertical and its positioning on the 3D-well neutral line is computed without any external load, combining the Newton-Raphson technique with a co-rotational formulation. The obtained path serves for starting the Newton-Raphson iterative method for calculating the drillstring quasi-static equilibrium position inside the well by considering: the drillstring pre-loading induced by the 3D-well, the gravity, the buoyancy, the nonlinear well end-stops, the inner and annular fluids, the static stress-stiffening due to the Weight-on-Bit (WOB), and the torque on-Bit (TOB). The drillstring-well contacts are modeled with contact stiffness and damping which are smoothed by using the arctan function. From this quasi-static equilibrium, assuming that the contacts remain permanent and linear, a classical modal analysis is carried out and a Campbell diagram is plotted by employing specific criteria that tracks the mode shapes and

classifies them. In the case of the nonlinear response, the contacts are free to become unilateral, see Fig. 2. Finally, the dynamic response of the complete FE model in the time domain is governed by the following set of nonlinear equations:

$$\boldsymbol{M}\ddot{\boldsymbol{\delta}} + \boldsymbol{C}\dot{\boldsymbol{\delta}} + \boldsymbol{K}\boldsymbol{\delta} = \boldsymbol{F}(t, \boldsymbol{\delta}, \dot{\boldsymbol{\delta}})$$

$$\boldsymbol{M} = \boldsymbol{M}_{\mathrm{a}} + \boldsymbol{M}_{\mathrm{fe}} + \boldsymbol{M}_{\mathrm{fi}}$$

$$\boldsymbol{C} = \Omega(\boldsymbol{C}_{\mathrm{ac}}^{\boldsymbol{T}} - \boldsymbol{C}_{\mathrm{ac}}) + \boldsymbol{C}_{\mathrm{ad}} + \boldsymbol{C}_{\mathrm{fe}}(\Omega) \qquad \boldsymbol{C}_{\boldsymbol{ad}} = c_M \boldsymbol{M}_{\boldsymbol{a}} + c_K(\boldsymbol{K}_a + \boldsymbol{K}_{\mathrm{gpa}} + \boldsymbol{K}_{\mathrm{gpo}}(\boldsymbol{\delta}_{\mathrm{s}}))$$

$$\boldsymbol{K} = \boldsymbol{K}_{\mathrm{pa}} + \boldsymbol{K}_{\mathrm{gpo}}(\boldsymbol{\delta}_{\boldsymbol{s}}) + \boldsymbol{C}_{\mathrm{ac}}^{\boldsymbol{T}}\dot{\Omega} \qquad \boldsymbol{K}_{\mathrm{pa}} = \boldsymbol{K}_{\mathrm{a}} + \boldsymbol{K}_{\mathrm{gpa}} + \boldsymbol{K}_{\mathrm{fe}}$$

$$\boldsymbol{F} = \boldsymbol{F}_{\mathrm{s}} + \boldsymbol{F}_{\mathrm{u}}(t) + \boldsymbol{F}_{\mathrm{c}}\left(\boldsymbol{\delta}, \dot{\boldsymbol{\delta}}, \boldsymbol{\Omega}, \mathrm{ROP}\right) - \boldsymbol{F}_{\boldsymbol{\theta_z}}\dot{\Omega} + \boldsymbol{R}_{\mathrm{ipa}}$$

$\boldsymbol{M_a}$, $\boldsymbol{M_{fi}}$,	Mass matrices of the drillstring and of the inner mud
$\boldsymbol{M_{fe}}$, $\boldsymbol{C_{fe}}$, $\boldsymbol{K_{fe}}$,	Mass matrices of the annular mud
$\boldsymbol{C_{ac}}$, $\boldsymbol{C_{ad}}$,	Matrices of gyroscopic effect and of Rayleigh damping (coeff c_M, c_K)
$\boldsymbol{F_{\theta_z}\dot{\Omega}}$,	Torque vector
$\boldsymbol{F_c}$, $\boldsymbol{F_u}$,	Contact load and mass unbalance force vectors
$\boldsymbol{R_{ipa}}$,	Vector of the static pre-loading

The dynamic response is computed using a RK4 scheme with an adaptative time step. A reduced model based on the Craig and Bampton technique is also available. The simulations are carried out on a field unconventional well with downhole measurements. Figure 3 presents the full-spectral analysis of the orbits all along the drillstring abscissa while Fig. 4 compares predicted and measured lateral accelerations.

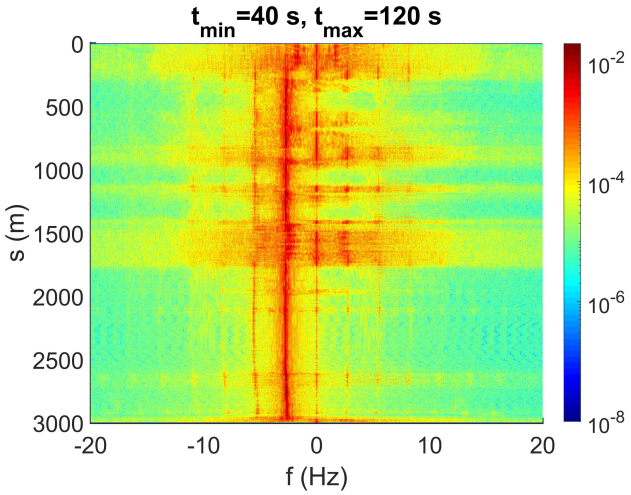

Fig. 3. Full spectrum analysis all along the drillstring.

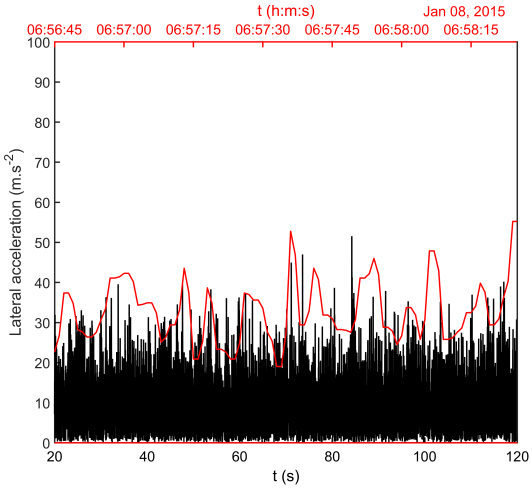

Fig. 4. Measured (red) and predicted (black) radial acceleration at a downhole sensor

Acknowledgment

The authors are indebted to the *Agence Nationale de la Recherche* for its financial support given to this research. In the framework of the LaBCoM-SME program of ANR 15-LCV4-0010-01, this research is conducted by DrilLab, a joint laboratory founded by DrillScan and INSA Lyon – LaMCoS.

† Our friend and colleague Lionel Manin passed away in May 2021. May his memory be honored and his dynamic management of DrilLab acknowledged.

References

Ritto T. G. , Soize C , Sampaio R . Non-linear dynamics of a drill-string with uncertain model of the bit - rock interaction. Int J Non-Linear Mech 2009; 44: 865–76.

Nguyen, K.-L., Tran, Q.-T., Andrianoely, M.-A. et al. 2020. Nonlinear rotordynamics of a drillstring in curved wells: Models and numerical techniques. Int. J. Mech. Sci, 166: 105225, doi:10.1016/j.ijmecsci.2019.105225.

Nguyen, K.-L., Tran, Q.-T., Andrianoely, M.-A. et al. 2019. Campbell Diagram Computation. J. Vib and Acoust., ASME, 141(4): 041009, doi:10.1115/1.4042933.

Tran, Q.-T., Nguyen, K.-L., Manin, L. et al. 2019. Nonlinear dynamics of directional drilling with fluid and borehole interactions. J. Sound and Vib., 462: 114924, doi:10.1016/j.jsv.2019.114924.

Duran C., Manin L., Andrianoely M.-A., Bordegaray C., Battle F., Dufour R., Effect of rotor-stator contact on the mass unbalance response, in: 9th IFToMM International Conference on Rotor Dynamics, Proceedings, vol. 21, 2014, pp. 1965–1975. Milano, IT, Sepp. 2225, 2014.

Wilson, J. K. and Heisig, G. 2015. Nonlinear Drillstring-Dynamics Modeling of Induced Vibrations in Unconventional Horizontals. *SPE Drilling & Completion* 30 (3). SPE-173049-PA. https://doi.org/10.2118/173049-PA.

Yan Y., Wiercigroch M., Dynamics of rotary drilling with non-uniformly distributed blades. Int J Mech Sci 2019; 160:270–81.

Escape Dynamics of a Parametrically Excited Particle from an Infinite Range Potential

K. R. Jayaprakash [*], Oleg Gendelman[**]
[*]*Discipline of Mechanical Engineering, Indian Institute of Technology Gandhinagar, Gujarat, India*
[**]*Faculty of Mechanical Engineering, Technion-Israel Institute of Technology, Haifa, Israel*

Summary. The current papers dwells on the classical problem of escape from a potential well. The considered potential well in this study is infinite range, with one global minimum and reaching maximum asymptotically at infinity. The particle is parametrically excited and we consider the threshold of escape of this particle from the bottom of the well. The analytical study is based on invoking the canonical action-angle variables and the averaged dynamics on a resonance manifold.

Introduction

The oscillatory behavior of a dynamical system is governed by the potential to which the system is subjected to. In order to study the dynamics of the system close to the center (local minimum in a conservative system), one could linearize the system and add the nonlinear terms as weak perturbations. However, such quasilinear dynamical systems seldom model the behavior away from the center. For example, the classical case of escape dynamics of a forced particle from a potential well can hardly be analytically studied using a weakly nonlinear model, since problem of escape is essentially a transient phenomenon. Such problem are plenty in the domain of applied physics and engineering and have been quite extensively studied [1]. From an engineering perspective, the dynamical behavior of capsizing of sea vessels is provided by Virgin [2], whereas the dynamic pull-in and the escape dynamics thereof in MEMS devices were reported by Younis et al. [3], studies by Virgin et al. [4] considers escape from a well under harmonic excitation, while Mann [5] considers an energy-based criterion for escape from the double well of a magnetic pendulum. Recent studies by Gendelman et al. [6, 7] invoke the canonical action-angle (AA) variables and averaging [8] to study the escape. Current study is based on the framework of AA variables.

As such, an analytical prediction of the particle escape from the potential well becomes quite relevant. We consider an undamped particle oscillating in an infinite-range potential. The minimum of the well is Lyapunov stable and the fixed point persists even with the application of parametric excitation. However, the excitation can render the fixed point unstable, but may not necessarily lead to escape. In contrast, for certain parameter range (excitation frequency and amplitude) one can observe escape (ref. Fig. 1) of the particle. The objective herein is to numerically and analytically study the parameter range of amplitude and frequency that leads to escape and the route thereof. The escape is characterized by breaching of the separatrix (connecting the two fixed points at $(\pm\infty, 0)$) as shown in Fig. 1.

Mathematical modeling and analysis

Consider the dynamics of a parametrically excited (amplitude ε and frequency Ω) particle in an infinite-range potential

$$\ddot{q} + \frac{\partial V(q,t)}{\partial q} = 0;\ V(q,t) = -\frac{\{1 + \varepsilon \sin(\Omega t)\}}{2\cosh^2(q)} \tag{1}$$

We are interested in the transition values of (Ω, ε) that would render a particle situated close to the bottom (but not exactly at the bottom) of the well to escape. To this end, we introduce the AA (I, θ) variables and the canonical transformation resulting in $p = p(I,\theta), q = q(I,\theta)$. The perturbed Hamiltonian in AA variables is

$$\mathcal{H}(I,\theta,t) = \mathcal{H}_0(I) - \varepsilon \sin(\Omega t)\{1 + C^2 \sin^2(\theta)\}^{-1}/2 \tag{2}$$

Where $\mathcal{H}_0(I) = -(1-I)^2/2\,, C = \sqrt{2I - I^2}/(1-I)$ and $I = 0$ corresponds to the bottom of the well. Since $q(I,\theta)$ is 2π periodic, the perturbation term in Eq. 2 can be expanded in Fourier series. We consider $2:1$ resonance and thereby introduce slow phase variable $\vartheta = 2\theta - \Omega t$. On averaging the slow-flow equation corresponding to the evolution of AA variables over the fast phase variables, we have the averaged $(I \mapsto J, \vartheta \mapsto \psi)$ slow-flow equations in the form,

$$\begin{aligned} \dot{J} &= -\varepsilon J\{1 + (J-2)^{-1}\}\cos(\psi) \\ \dot{\psi} &= 2(1-J) + \varepsilon\{1 - 2(J-2)^{-2}\}\sin(\psi) - \Omega \end{aligned} \tag{3}$$

The fixed points of the slow-flow equations are readily calculable to be (i) $J = 0, \sin(\psi) = 2\,(\Omega - 2)/\varepsilon$, (ii) $J = 1, \sin(\psi) = -(\Omega/\varepsilon)$ (iii) $\psi = \pi/2\,, 3\pi/2\,, \{2(1-J) - \Omega\}(J^2 - 4J + 4) \pm \varepsilon(J^2 - 4J + 2) = 0$ respectively. The fixed point at $\psi = \pi/2\,, J > 0$ is a center and $\psi = 3\pi/2\,, J > 0$ is a saddle for $\Omega < 2$. For a specific value of $\Omega < 2$, with an increase in the excitation amplitude, the saddle goes through a pitchfork bifurcation and there is emergence of two additional fixed points (i). Upon bifurcation, fixed point at $\psi = 3\pi/2\,, J < 0$ is a center, but not of much significance. The bifurcations would become apparent by investigating the integral of motion of the averaged system given by

$$\mathcal{M}(J,\psi) = -(1-J)^2 + \varepsilon J(J-1)(J-2)^{-1}\sin(\psi) - J\Omega \tag{4}$$

The bifurcation point corresponds to the threshold of the excitation amplitude resulting in escape. The locus of these points is shown in Fig. 2 as red curves (LB_{avg}, RB_{avg}) emanating from $\Omega = 2$. Incidentally, these curves also correspond to the instability boundary of the Mathieu equation $\ddot{x} + x\{1 + \varepsilon \sin(\Omega t)\} = 0$, resulting from the linearization of Eq. 1 about (0,0). The escape threshold for the exact system (Eq. 1) is indicated as LB_{ex}, RB_{ex}. As observable, there is the close match of the LB_{avg} and LB_{ex}. However, the right boundary shows a very distinct transition wherein the averaged system predicts a much lower escape threshold in comparison to the actual dynamical system (Eq.

1). It is noted that along the boundary predicted by the averaged system, the center corresponding to the bottom of the potential well bifurcates to a saddle. This is evidenced by the Poincare maps of Fig. 3 ($\Omega = 1.8$). In fact, along LB_{ex}, the creation of this saddle leads to the particle escape. In contrast, in the regions other than LB_{ex}, the creation of the saddle (along LB_{avg}, RB_{avg}) leads to chaotic motion albeit bounded. On further increase in the excitation amplitude, the tori are broken and the particle escapes. This behavior is observable in the Poincare maps of Fig. 4 ($\Omega = 1.9$). The minimum force amplitude required for the escape corresponds to a frequency $\Omega < 2$ ($\Omega \cong 1.85$) and is owing to the fact that Eq. 1 exhibits softening nonlinearity.

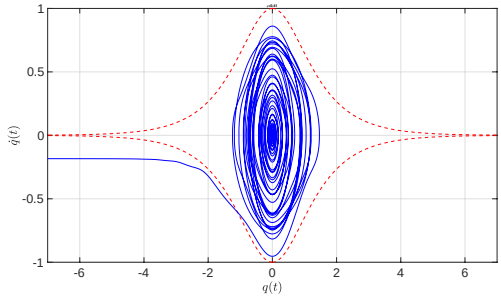

Figure 1: Particle escape from the bottom $(q(0) = 10^{-6}, \dot{q}(0) = 0$ of the potential well for ε=0.41,Ω=1.8. (Broken red curves correspond to the separatrix)

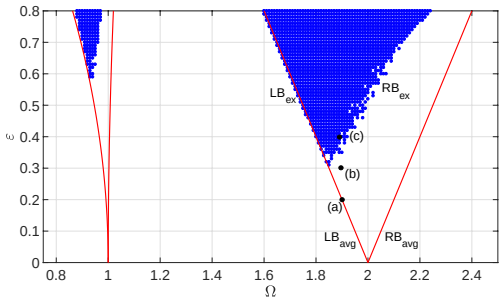

Figure 2: Escape threshold. Blue shaded region (num. simulation of Eq. 1) corresponds to particle escape (for $t \leq 6000$). The red lines emanating from $\Omega = 2$ correspond to the point of bifurcation corresponding to Eq. 3 and those emanating from $\Omega = 1$ correspond to the Mathieu equation described above

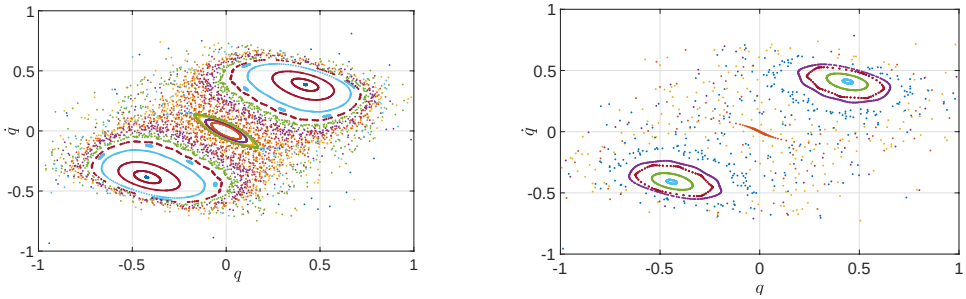

Figure 3: Poincare maps corresponding to $\Omega = 1.8$ (left panel) $\varepsilon = 0.3$ (right panel) $\varepsilon = 0.39$

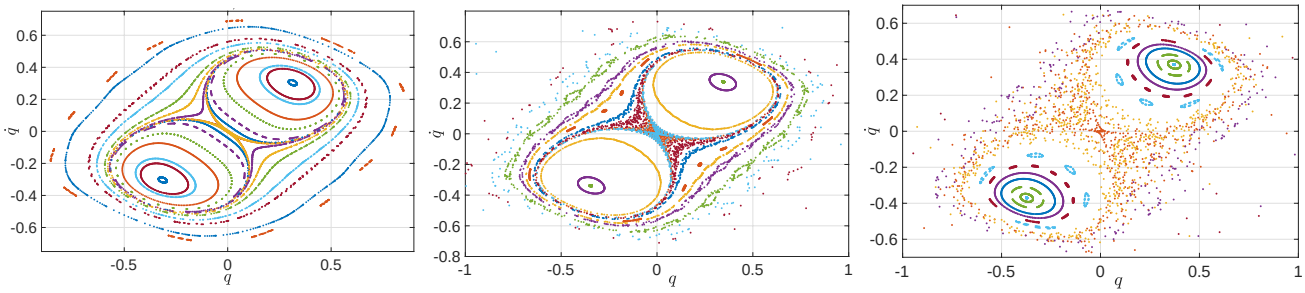

Figure 4: Poincare maps corresponding to $\Omega = 1.9$ (a) $\varepsilon = 0.2$, (b) $\varepsilon = 0.3$, (c) $\varepsilon = 0.4$ (a-c refers to the points indicated in Fig. 2)

Conclusions

The current study considers the escape dynamics of a parametrically excited particle (located close to the bottom of the well) from an infinite-range potential. We invoke the AA variables and study the dynamics of the system on the resonance manifold and predict the threshold for escape as a function of frequency. For certain (Ω, ε), the bifurcation of the bottom of the well to a saddle leads to the escape, whereas for other parametric range, the escape is through a chaotic route as evidenced by the Poincare maps and the slow-flow model fails to predict the escape in this case.

References

[1] Thompson J. M. T. (1989) Chaotic Phenomena Triggering the escape from a Potential Well. *Proceedings of Royal Society London A* **421**:195-225
[2] Virgin L. N. (1989) Approximate Criterion for Capsize based on Deterministic Dynamics. *Dynamics and Stability of Systems* **4(1)**: 55-70
[3] Alsaleem F. M., Younis M. I., Ruzziconi L. (2010) An Experimental and Theoretical Investigation of Dynamic Pull-in in MEMS Resonators Actuated Electrostatically. *Journal of Microelectromechanical Systems* **19(4)**: 794-806
[4] Virgin L. N., Plaut R. H., Cheng C. C. (1992) Prediction of Escape from a Potential Well Under Harmonic Excitation. *International Journal of Non-linear Mechanics* **72(3)**: 357-365
[5] Mann B. P. (2009) Energy Criterion for Potential Well Escapes in a Bistable Magnetic Pendulum. *Journal of Sound and Vibration* **323**: 864-876
[6] Gendelman O. V. (2018) Escape of a Harmonically Forced Particle from an Infinite-range Potential Well: A Transient Resonance. *Nonlinear Dynamics* **93**: 79-88
[7] Gendelman O. V., Karmi G. (2019) Basic Mechanisms of Escape of a Harmonically Forced Classical Particle From a Potential Well. *Nonlinear Dynamics* https://doi.org/10.1007/s11071-019-04985-9
[8] Lichtenberg A. J., Lieberman M. A. (1992) Regular and Chaotic Dynamics. Springer-Verlag, NY

Explanation of the Locomotion of a Rigid Body along a Vibrating Nonlinear Beam

Florian Müller*, Alexander F. Vakakis‡ and Malte Krack*
*University of Stuttgart, Germany
‡University of Illinois at Urbana-Champaign, USA

Summary. Several independent research groups have investigated the self-adaptive behavior of a clamped-clamped beam with attached slider. Under harmonic base excitation the slider passively moves to a certain position on the beam, going along with a significant increase of amplitude. We are the first to fully explain this complex process theoretically by means of a model reproducing the behavior. Moreover, we show that the slider's movement takes places on a slower time scale compared to the beam's vibration. Exploiting this temporal separability, we explain the different mechanisms yielding transport towards or away from beam's center.

Introduction

A harmonically forced clamped-clamped beam with a slider free to move axially on the beam has been experimentally investigated by different groups [1, 2, 5]. After initially small vibrations, the slider moved to a certain position, where vibration amplitude increased significantly. After this process, the amplitude and the final slider position, which is in many cases away from the antinode at beam's center, were maintained in steady state. In case the slider is initially placed close enough to the beam's center, it moves towards clamping first and turns back towards center at some point. The turning point is accompanied with a jump to higher vibration level and the movement back goes along with a further increase of amplitude [1]. In [1, 2], beside experimental results, models were presented, assuming that the slider is constrained to the beam in the vertical direction. Simulation results exhibit a slider movement towards the beam's center going along with an increase of amplitude. However, a movement towards clamping, a jump of amplitude and a steady state slider position away from center couldn't be reproduced. In [3, 4], we present a model accounting for a gap between slider and beam, which gives rise to unilateral and frictional contact interactions and consider also the beam's stiffening geometric nonlinearity. This model has the capability to reproduce all features of the self-adaptive process. In [5] we present an experimental validation of this model, yielding excellent agreement of measurements and simulation. In the present contribution we demonstrate that the beam's vibration and the slider's movement take place on well separated time scales and exploit this separability to study the different mechanisms producing locomotion of the slider systematically.

Separable timescales of vibration and slider movement

The considered specification of the self-adaptive beam-slider system corresponds to the beryllium-copper beam described in [1]. A schematic of the model is depicted in Fig. 1a. The beam is modeled according to Euler-Bernoulli theory, where the deformation is approximated by the lowest frequency bending mode and the stiffening geometric nonlinearity due to the fixed ends is considered. To model unilateral and dry frictional contact interactions between beam and slider, the Signorini and Coulomb laws combined with Newton's impact law are used. The resulting set-valued force laws are solved numerically applying Moreau's time stepping scheme. The contact model and simulation procedure are adopted from [3]. A simulation of a successful self-adaptive process is depicted in Fig. 1b in terms of the vibration's amplitude as a function of the resulting slider position (dashed black). While vibration amplitude is initially small, the slider moves towards clamping. At $\tilde{s}/L \approx 0.24$, the slider turns and the amplitude jumps to a higher level. After this, the slider moves back towards center, while the amplitude increases further. During the whole process, the global horizontal movement of the slider is slow compared to the beam's vibration [4]. To prove the independence of these time scales, we study the steady state response depending on the relative slider position. In order not to affect the slider's dynamics by an additional constraint, we let the slider's horizontal displacement s free, but consider the given relative slider position $\tilde{s}$ always when evaluating the contact kinematics during the simulation. This essentially yields a model where the beam is moved with the slider horizontally [5]. For each relative slider position we numerically integrate until steady state, increase the relative slider position by a small $\Delta\tilde{s}$ and again integrate until steady state, starting from the final state of the previous point. The results for increasing and decreasing $\tilde{s}$ exhibit a high and a low amplitude branch, see Fig. 1b (green and orange lines). This behavior can be explained by the beam's stiffening nonlinearity [4]. Clearly, the response of the system with free slider follows the low amplitude branch first, jumps, and follows the high amplitude branch then. The steady state model enables us to evaluate also the slider's absolute horizontal displacement s. In Fig. 1c we illustrate the steady state absolute slider velocity by means of slider's displacement per beam length and evaluation periods. In the range of $\tilde{s}$ which is relevant for the self-adaptive process, the steady state slider velocity corresponding to the low (high) amplitude branch points towards clamping (beam's center). This is in qualitative and good quantitative agreement with the self-adaptive process. Also on the fast time scale of vibration, the steady state model coincides very well with the system with free slider (time histories not shown for brevity). Alltogether, this proves the separability of the different time scales [6].

Vibration induced locomotion towards center or clamping

We now want to explain, why the slider is transported towards clamping (beam's center) during the low (high) amplitude phase. To this end, we study the periodically dominated vibrations obtained by the steady state model exemplary

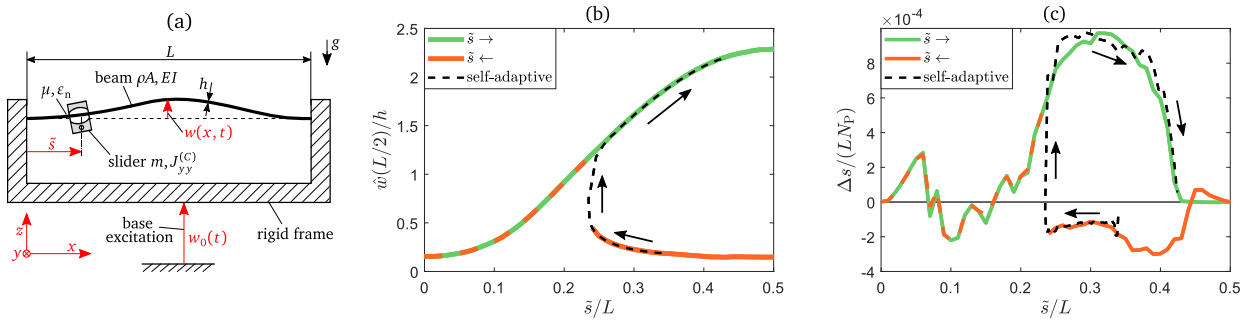

Figure 1: (a) Two dimensional model of self-adaptive system. (b) Vibrational amplitude versus relative slider position. (c) Averaged normalized slider velocity versus relative slider position. [6]

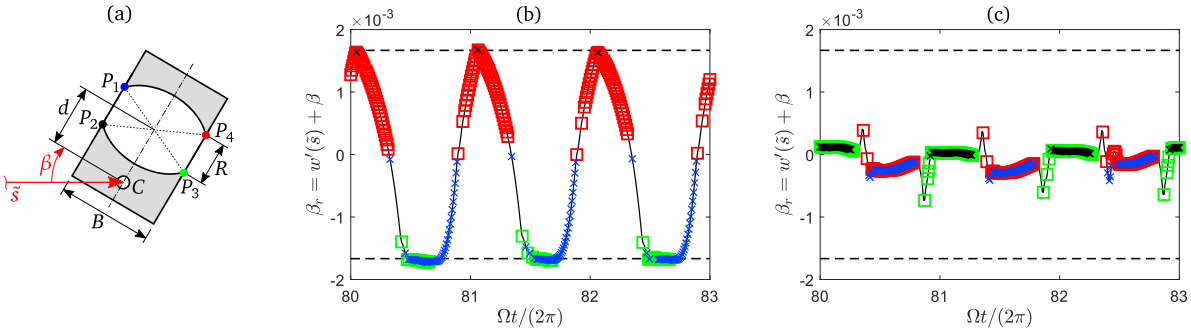

Figure 2: (a) Slider detail. (b) Relative slider rotation (steady state model, $\tilde{s} = 0.3$, low vibration level). (c) Relative slider rotation (steady state model, $\tilde{s} = 0.3$, high vibration level). Markers indicate active contacts, where the colors match with P_1 through P_4 in (a). [6]

at $\tilde{s}/L \approx 0.3$. We start with the simple explanation for the high amplitude phase. Here, the beam's elastic deformation is close to a monoharmonic oscillation which is approximately in phase with the excitation and big compared to the clearance between slider and beam. During almost one half of an excitation cycle, both upper contact points are in contact. During the other half of the cycle, both lower points are in contact, see Fig. 2c. Therefore the system behaves like a beam with vertically constrained but horizontally movable body. For this simplified system, the inertia force acting on the slider has a horizontal component stemming from the beam's slope, which can be approximated $m\ddot{s} = -m\left[\ddot{w}(s) + \ddot{w}_0\right] w'(s)$. This force points always to center. In case of a very small [3, 4] or no [2] gap, the slider moves to center also for low amplitude level. Instead of that, successful adaptation is obtained in case the clearance is chosen in the order of magnitude of the vibration level corresponding to the low amplitude branch, which allows for a complex limit cycle, see Fig. 2b. This limit cycle contains states of maximum and minimum possible relative rotation between slider and beam. The crucial transportation of the slider's center of mass C towards clamping is obtained during rolling on the upper contacts P_1 and P_4 from minimum to maximum possible rotation [6].

Conclusions

The beam's vibration and slider's movement take place on well separated time scales, which can be shown by using a steady state model with prescribed relative slider position. Studying the periodically dominated steady state responses corresponding to the different phases of the self-adaptive process explains the slider's locomotion. Further work could focus on optimization of the system and application as energy harvester or vibration absorber.

References

[1] Miller, L. M. et al. (2013) Experimental passive self-tuning behavior of a beam resonator with sliding proof mass. *Journal of Sound and Vibration* **332**(26): 7142–7152.

[2] Yu, L. et al. (2019) A passive self-tuning nonlinear resonator with beam-slider structure. *Active and Passive Smart Structures and Integrated Systems XII, SPIE*

[3] Krack, M. et al. (2017) Toward understanding the self-adaptive dynamics of a harmonically forced beam with a sliding mass. *Archive of Applied Mechanics* **87**(4):699-720

[4] Müller, F., Krack, M. (2020) Explanation of the self-adaptive dynamics of a harmonically forced beam with a sliding mass. *Archive of Applied Mechanics* **90**(7):1569–1582

[5] Müller, F. et al. (2022) Experimental validation of a model for a self-adaptive beam-slider system. *In preparation*

[6] Müller, F. et al. (2022) On the locomotion of a rigid body along a nonlinear vibrating beam yielding self-adaptive behavior. *In preparation*

Harmonic Balance Method for the stationary response of continuous systems with nonlinear hysteretic damping under harmonic excitation

Jiangyi Zhang[*], Andrei B. Fărăgău[**], Anton van der Esch[***], Andrei V. Metrikine[**], Karel N. van Dalen[**]

[*]*College of Underwater Acoustic Engineering, Harbin Engineering University, China*

[**]*Faculty of Civil Engineering and Geosciences, Delft University of Technology, Delft, the Netherlands*

[***]*Department of Built Environment, Eindhoven University of Technology, Eindhoven, the Netherlands*

Summary. Under harmonic excitation, soil exhibits softening behaviour that can be captured through the so-called hyperbolic soil model. The response of systems with such a material model can elegantly be obtained using the classical Harmonic Balance Method (HBM). Soil also exhibits nonlinear hysteretic damping under harmonic excitation, feature which is not incorporated in the hyperbolic soil model. The response of a system that includes also the nonlinear hysteretic damping cannot be obtained using the classical HBM. This work demonstrates the application of an advanced HBM (more specifically, alternating frequency-time HBM) for finite and infinite systems that exhibit softening behaviour and nonlinear hysteretic damping. The purpose of this model is to, in the future, investigate the influence of the nonlinear hysteretic damping on the response of such systems, as opposed to linear viscous or hysteretic damping that is usually adopted. To conclude, we show that the advanced HBM is an effective tool for revealing fundamental characteristics of continuous systems with softening behaviour and nonlinear hysteretic damping whose stationary responses consist of either standing or propagating waves.

Introduction

The Harmonic Balance Method (HBM) is often applied to compute the stationary response of nonlinear *discrete* systems to harmonic loading. It is known to be very efficient as it does not require the simulation of the transient response before reaching the stationary regime, and it can efficiently yield frequency-response curves.

The HBM has been applied to nonlinear *continuous* systems too, but in many cases the nonlinearity is discrete and thus localized at one or multiple points; both finite [1] and infinite [2,3] models have been considered. Furthermore, Chronopoulos [4] presents the general framework for the application of the HBM to an infinite composite structure having distributed but still localized nonlinearity; however, the considered numerical example still only deals with a discrete nonlinear spring connecting two linear parts of the structure. To fill this gap, one of the authors' previous works [5] presents the application of the HBM to continuous systems with distributed nonlinearity, where both finite and semi-infinite systems are considered.

In the previous work [5], the material damping is assumed to be linear. However, soil (among other materials) exhibits nonlinear and hysteretic damping under cyclic loading. For systems with such a material model, the stress-strain relation consists of loading and unloading branches that are different from each other. As the transition points (in the stress-strain relation) from loading to unloading are response dependent and, therefore, not known a priori, the classical HBM, being a purely frequency-based method, cannot be applied. Instead, a so-called alternating frequency-time HBM can be used. Furthermore, the material behaviour described by the so-called Masing model, well-known in soil mechanics, is used to introduce the strain dependence of the shear modulus as well as the nonlinear hysteretic damping, which obviously leads to nonlinearity of non-polynomial type.

To demonstrate the application of this advanced HBM, three canonical problems are investigated (like those in [5]). More specifically, one finite-size system and two semi-infinite systems are considered, and all of them are subject to harmonic excitation at a boundary. The three systems and their stationary responses can be described as follows (see also Figure 1):

a) a 1-D nonlinear layer with a free surface and rigid base: standing shear waves
b) a 1-D nonlinear half-space with a rigid base: vertically propagating shear waves
c) a 2-D axially symmetric nonlinear medium of infinite extent with a circular cavity: radially propagating compressional waves

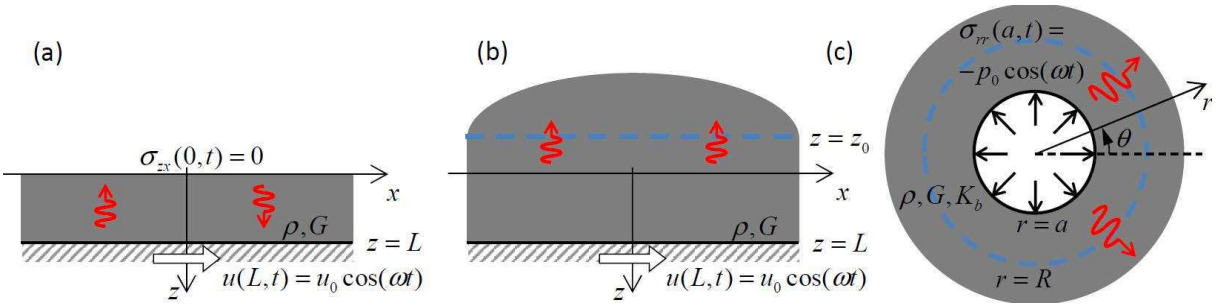

Figure 1: The three different systems (a, b, c) considered in this study. The blue line indicates the fictitious surface beyond which the behavior is linear.

Solution method

The methodology of the alternating frequency-time HBM is as follows. Firstly, an initial guess of the system's response is made based on which the transition points from loading to unloading can be determined. Then, these transition points are assumed to be fixed (not anymore response dependent) and the resulting nonlinear system can then be solved using the classical HBM. This leads to a different response than the initial guess and different transition points from loading to unloading. This process is then repeated until the response has converged. The iterations are performed using a slightly more sophisticated form of the Newton-Raphson method (so-called Levenberg-Marquardt method), which is used to circumvent a potentially singular Jacobian matrix.

As for the spatial discretization, a basic lumping method is used to derive a lattice that mimics the behaviour of the continuous systems (a, b, and c). Additionally, to accommodate the semi-infinite extent of systems b and c, it is possible to identify a fictitious surface beyond which the behaviour is essentially linear (due to the amplitude decay of the waves propagating away from the source). The region beyond that surface is therefore replaced by an exact frequency-dependent non-reflective boundary condition that is applied at the fictitious surface, so that only a finite domain needs to be discretized in the application of the advanced HBM.

Results and conclusion

In Figure 1, we present the response of the system with an expanding cavity (c). The softening behaviour can be observed by the larger amplitude of vibration compared to the linear system. The third harmonic can also be clearly observed, although its amplitude is significantly smaller than the one of the fundamental harmonic; this characteristic has also been observed in [5]. Additionally, it can be seen that the induced nonlinearity is significant from the more than 60% reduction in shear modulus at the cavity surface. Finally, the stress-strain relation follows the Masing model, and it shows that the advanced HBM is capable of handling systems with non-smooth transition in properties.

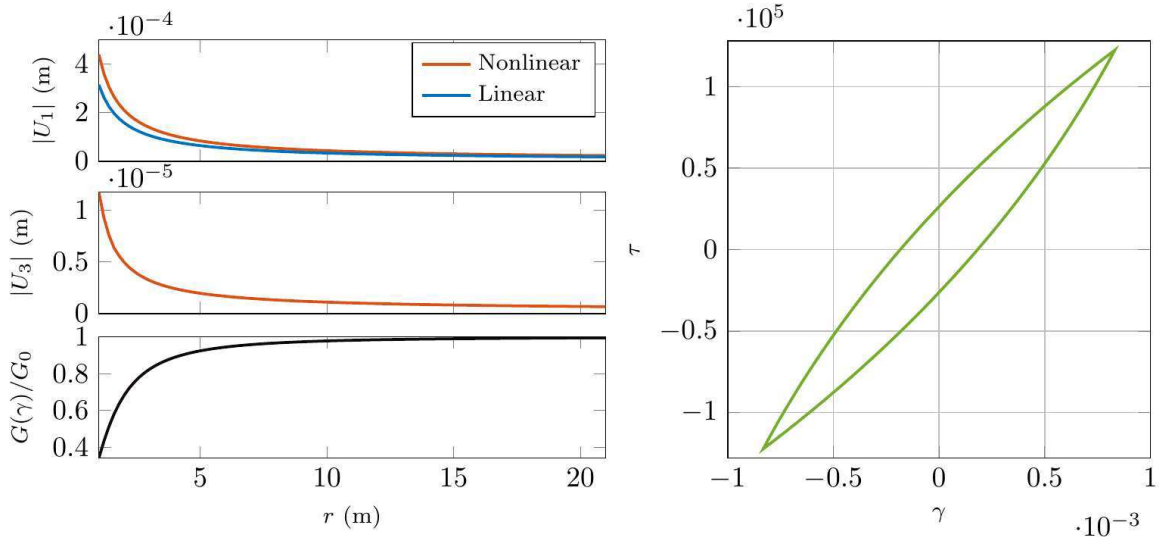

Figure 2: The response of system (c); the amplitude of the first and third harmonics (top and middle panels), the normalized shear modulus (bottom panel), and the stress-strain relation evaluated at the cavity surface (right panel).

To conclude, the advanced HBM is an effective tool for revealing fundamental characteristics of nonlinear continuous systems of finite and semi-infinite dimension that have nonlinear hysteretic damping and whose stationary responses consist of, respectively, standing and propagating waves. The considered systems have applications in earthquake and geotechnical engineering, among others, but the presented methodology is generic.

References

[1] B. Chouvion, Vibration analysis of beam structures with localized nonlinearities by a wave approach, Journal of Sound and Vibration 439, 2019, 344-361.

[2] X. Fang, J. Wen, D. Yu, G. Huang, and J. Yin, Wave propagation in a nonlinear acoustic metamaterial beam considering third harmonic generation, New Journal of Physics 20, 2018, 123028.

[3] B. Lombard and J. Piraux, Propagation of compressional elastic waves through a 1-D medium with contact nonlinearities. In: Leger A., Deschamps M. (eds) Ultrasonic Wave Propagation in Non Homogeneous Media, Springer Proceedings in Physics, 2009, 128, Springer, Berlin, Heidelberg.

[4] D. Chronopoulos, Calculation of guided wave interaction with nonlinearities and generation of harmonics in composite structures through a wave finite element method, Composite Structures 186, 2018, 375-384.

[5] J. Zhang, E. Sulollari, A. B. Fărăgău, F. Pisanò, P. van der Male, M. Martinelli, A. V. Metrikine, K. N. van Dalen, Harmonic balance method for the stationary response of infinite and semi-infinite nonlinear dissipative continua: Three canonical problems, Nonlinear Dynamics of Discrete and Continuous Systems, Springer, 2020, 255-274.

Harmonic balance-based crack size estimation in an ultrasonic fatigue specimen

Shawn L. Kiser*, Mikhail Guskov*, Marc Rebillat*, and Nicolas Ranc*
*PIMM, Arts et Métiers Institute of Technology, CNRS, Cnam, HESAM University, 151 boulevard de l'Hopital, 75013 Paris, France

Summary. Closing-opening cracks during ultrasonic fatigue tests are suspected to generate nonlinearities in the vibration signal. Due to the periodicity of the ultrasonic transducer and choice of non-smooth stiffness nonlinearity, the Harmonic Balance method is utilized to simulate the resulting 1DOF dynamic model. The energy that transferred from the fundamental harmonic to higher harmonics is represented as a harmonic amplitude ratio parameter and is utilized to inverse model a nonlinear crack parameter for an experimental signal. A feature of this dynamic model allows for the addition of nonlinear effects that evolve with the fatigue specimen's life.

Introduction

During ultrasonic fatigue tests, the evolving spectrum of a vibration signal is suspected to contain essential information about the nature of fatigue damage, such as crack initiation time and actual size. Traditionally, the properties studied from this information are the second harmonic, the eigenmodes, or the extremely small variations of resonance frequency. These vibration properties are affected by micro-plasticity and by the formation of cracks which can therefore be used to detect micro-structural changes [1, 2].
The approach proposed here consists of modeling the dynamical response of the standing wave of the system. A key feature of a cyclically closing-opening crack is an instantaneous, nonlinear, and very local change of stiffness of the system. This nonlinearity leads to a nonlinear dynamic response of the system and, as a consequence, manifestation of higher-harmonic generation in the vibration response. A closing-opening crack's restoration force is typically modeled by an asymmetric piecewise linear or bilinear stiffness [3]. Thus the goal of this study is to inverse model a nonlinear crack parameter γ using the Harmonic Balance method (HBM) [4] to obtain a nonlinear dynamic response of the system. Ideally, this can allow for real-time crack initiation and possibly size evolution monitoring.

Harmonic Balance dynamic modeling

During ultrasonic fatigue testing, seen in fig. 1(a), repeatedly transmitted ultrasonic waves at a resonant or anti-resonant frequency form a longitudinal standing wave in the fatigue specimen [1]. The undamaged fatigue specimen can be schematized as an equivalent 2 degree-of-freedom (DOF) lumped mass-spring oscillator. The oscillator's total mass $2m$ and stiffness k are tuned to resonate at the specimen's first longitudinal mode. The phase difference between the excitation and vibration is minimized by a phase-locked loop (PLL) within the converter. A longitudinal standing wave is produced with peaks at specimen's extremities, i.e., the oscillator's masses. This phenomenon has two consequences: First, the power required from the converter can be minimized. Second, the specimen's motion allows for a half specimen representation, or 1DOF system, that is dynamically modeled with respect to the specimen's elongation, i.e., a mass-spring excited by base motion at an anti-resonance frequency $\omega_{\text{anti}} = \sqrt{2}\omega_{\text{res}}$ with $\omega_{\text{res}} = \omega_0\sqrt{1-\zeta^2}$ [5], where $\omega_0 = \sqrt{k/m}$.

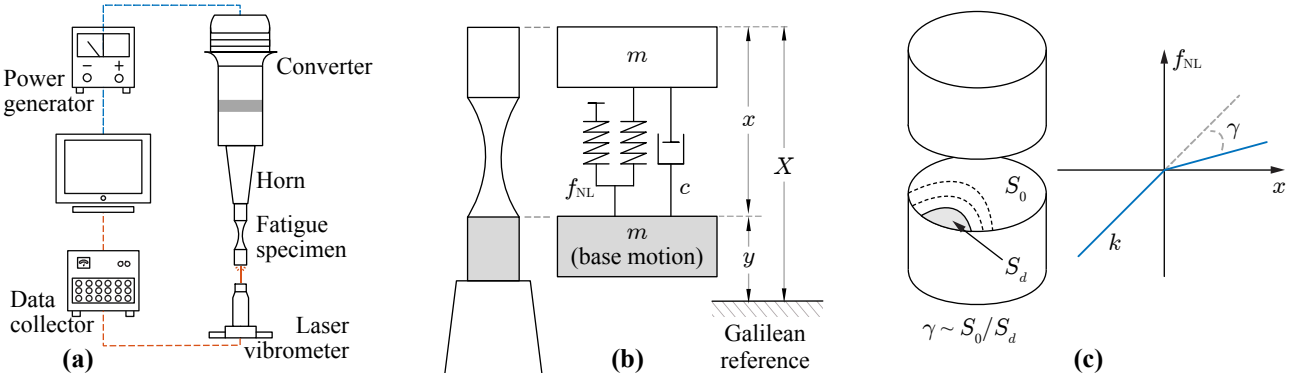

Figure 1: (a) Schematic of ultrasonic fatigue test experimental setup, (b) fatigue specimen model with absolute displacement of mass X and Galilean reference displacement for mass x and base y, and (c) concept of crack nonlinearity parameter $\gamma \sim S_d/S_0$ with plot of the bilinear stiffness restoration force f_{NL}

The 1DOF system has the equation of motion:

$$m\ddot{X} = F, \quad \text{with} \quad F = -c\dot{x} - f_{\text{NL}} = -c\dot{x} - k(1-\gamma H)x, \tag{1}$$

where m, X, F, represents the upper mass, the absolute displacement of the system, and the force transmitted to the upper mass through the central part of the specimen respectively. The fatigue specimen is forced at the base, with displacement y, seen in fig. 1(b). The force F is obtained by splitting X into the relative displacement of the fatigue specimen free-end x and base (lower mass) motion y. When the exerted force on the mass is due to base excitation, eq. (1) becomes:

$$m\ddot{x} + c\dot{x} + k(1-\gamma H)x, = -m\ddot{y}, \tag{2}$$

with γ suspected to be correlated to the crack area ratio (see fig. 1(c)) and H represents the Heaviside function evaluated for values of x. It is assumed that the base moves harmonically with the amplitude of the base's motion U, and the frequency of the base's motion, ω_b, such that $y(t) = U\cos(\omega_b t)$. Eq. (2) is solved via HBM, yielding a finite Fourier decomposition for x, with j harmonics:

$$x \approx \mathrm{Re}\left(\sum A_j e^{ij\omega_{\text{anti}}t}\right). \tag{3}$$

Since the standing wave is distorted as it passes through the crack nonlinearity, energy is transferred from the fundamental harmonic to the higher harmonics. Thus, a harmonic amplitude ratio α is defined at the anti-resonant frequency ω_{anti} as:

$$\alpha_n = \frac{A_n(\omega_{\text{anti}})}{A_1(\omega_{\text{anti}})}, \quad \text{for } n > 1, \tag{4}$$

where peak amplitudes A_1 and A_n correspond to the fundamental and n^{th} higher harmonics, respectively. This anti-resonant frequency is assumed to be the frequency of the base's motion.

Experimental details and results

A short-time Fourier transform (STFT) algorithm [6] is utilized to extract the first five harmonics and the anti-resonant frequency from the down-sampled velocity vibration signal, seen in fig. 2(a). Consequently, $\alpha_2', \ldots, \alpha_5'$ is calculated using the relation in eq. (4) with $(\,\cdot\,)'$ representing an experimentally determined parameter. The dynamic model, seen in eq. (2) , is computed via HBM for $1\text{e}{-4} < \gamma < 2\text{e}{-1}$ and the corresponding $\alpha_2, \ldots, \alpha_5$ are extracted. The dynamic model's γ, α relationship are curve fitted with first-order power equations. Experimental $\alpha_2', \ldots, \alpha_5'$ are found with their respective curve fits, seen in fig. 2(b). Under modeling assumptions, γ' at the zeroth cycle is undamaged. Thus, fig. 2(c) shows the evolution of damage parameters $\gamma_2', \ldots, \gamma_5'$. The second and third harmonics are seen to follow similar paths until 8e5 cycles in which they diverge exponentially. At cycles nearing fatigue, the third, fourth, and fifth harmonics rapidly grow, with the fifth harmonic the quickest. Despite γ' not equal throughout the evolution, the order of magnitude is consistent between the different harmonics. The authors estimate that there is a magnitude factor of approximately 1e2 that would lead to a measurement of crack size evolution if $\gamma S_0 = S_d$.

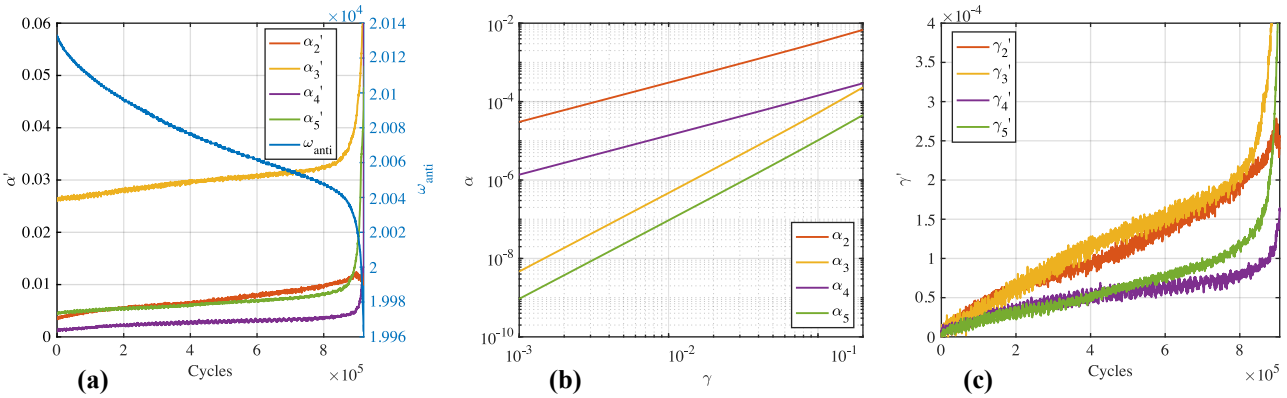

Figure 2: (a) Experimental α' (left axis) and experimental ω_{anti} (right axis) versus cycles, (b) HBM simulated γ versus α first-order power equations fits, and (c) experimental γ' versus cycles

Conclusions

The nonlinear crack parameter γ was calibrated with a bilinear stiffness dynamic model. α is computed with HBM for multiple harmonics and compared with experimental γ's versus cycles. Bilinear stiffness can qualitatively describe nonlinear behaviors for the second and third harmonics for cycles before approximately 8e5, but other nonlinearities are influencing higher harmonics and at cycles nearing failure. The form of eq. (3) allows for additional non-linearities to dynamically model the fatigue behavior of higher harmonics in conjunction with bilinear stiffness.

References

[1] Kumar A., Adharapurapu R.R., Jones J.W., Pollock T.M. (2011) In situ damage assessment in a cast magnesium alloy during very high cycle fatigue. *Scripta Mater* **64**:65-68.

[2] Heinz S., Balle F., Wagner G., Eifler D. (2013) Analysis of fatigue properties and failure mechanisms of Ti6Al4V in the very high cycle fatigue regime using ultrasonic technology and 3D laser scanning vibrometry. *Ultrasonics* **53**:1433-1440.

[3] Broda D., Staszewski W.J., Martowicz A., Uhl T., Silberschmidt V.V. (2014) Modelling of nonlinear crack-wave interactions for damage detection based on ultrasound – A review. *J Sound Vib* **333**:1097-1118.

[4] Sarrouy E., Sinou J.-J. (2011) Non-linear periodic and quasi-periodic vibrations in mechanical systems – on the use of the harmonic balance methods. In: Advances in Vibration Analysis Research. InTech.

[5] Inman D.J. (2014) Base excitation, in: Engineering Vibration. Pearson.

[6] Allen, J.B., Rabiner, L.R., (1977) A unified approach to short-time Fourier analysis and synthesis. *P IEEE* **65**:1558-1564.

Influence of friction damping on frequency lock-in in cyclic structure

Miroslav Byrtus* and Štěpán Dyk *
**Department of Mechanics, University of West Bohemia, Pilsen, Czech Republic*

Summary. The paper deals with modelling and investigation of lock-in phenomena in bladed cyclic structure which is further influenced by friction damping couplings. The investifation is focused on how the friction can affect the unstable behaviour during frequency lock-in regimes.

Introduction

The fliud-structure interaction (FSI) phenomenon arises when an elastic structure interacts with the embracing fliud flow. A particular case of FSI in which an alternate shedding of vortices forms the vibration of the structure is Vortex-Induced Vibration (VIV). The natural vortex shedding frequency is dependent on the velocity of the flow. The vortex sheddding exerts a periodic unsteady force on the body. As the vortex shedding frequency approaches the the natural frequency of the body, the two frequencies lock-in for a small range of the velocity flow [2]. Experimental characterization of lock-in is performed in [1].
The FSI plays significant role in modern aerofoils and turbine blades which are designed for higher efficiencies and higher power under higher operational temperatures and flow rates. Higher operational safety and economical demands force the designers to be more precise during phase of design with respect to operational condition laying out of the area with loss of stability [3, 4, 5]. The fluid-induced forces create an aero-elastic couplings between the aerofoils and the fluid flow. Moreover, in the case of periodical structures (gas or steam turbine blades in bladed disks) the aero-elastic coupling influences not only the single blade but the adjacent blades as well. There are many experimental works investigating experimentally the conditions of instability origin, e.g. [7, 8]. The paper deals with the modelling and dynamical analysis of a periodic blade system influenced by VIV and friction-damping in inter-blade couplings.

Cyclic structure of blade profiles influenced by VIV

Further, it is assumed the cyclic structure formed by a bladed disk has N_B blades which are created by identical airfoil profiles. Each blade is modelled by the approach presented in the previous section, i.e. it comprises two degrees of freedom (bending and torsion) and moreover these two motion are mutually coupled by so called bending-torsion coupling, see [6]. Usually, in steam turbine applications, the bladed disks are equipped with different kinds of shrouding, which causes that the system of blades mounted on a rotating disk become more stiff, especially with respect to axial flow direction.
The time-varying vortex force due to the alternating sheddin of vortices in the wake causing the VIV is modeled by the van der Pol equation. The van der Pol model has two significant properties: i) self-sustained stable limit cycle oscillation and ii) the lock-in with the frequency of external forcing [2].
In Fig. 1, the blade cascade of a bladed disk is depicted in a plane view. The axis of rotational symmetry designates the axis of rotor symmetry which is the bladed disk attached to. Further, it is assumed that the flow direction is parallel with the blade chords. The shrouding is supposed to be mounted at tips of the blades and it is modelled by means of two lumped springs representing bending k_{shb} and torsional k_{sht} stiffness of each shrouding section between two adjacent blades.

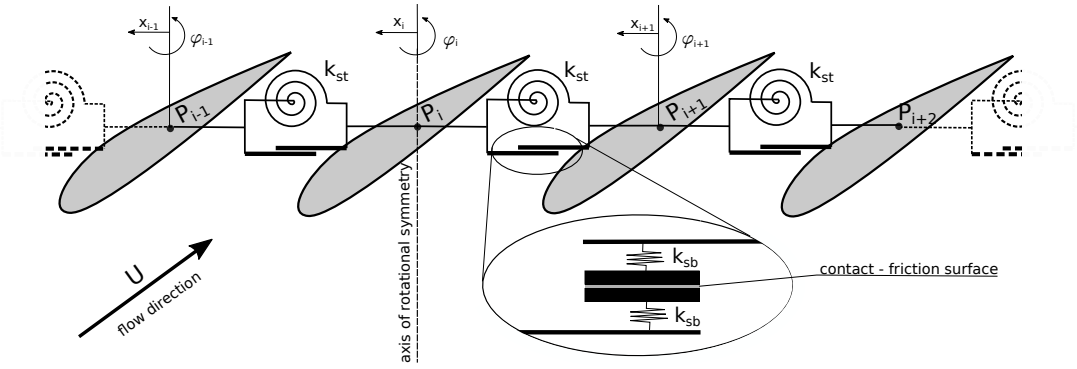

Figure 1: Bladed cascade section with contact-friction shrouding coupling modelling.

The derivation of the linearized mathematical model of a bladed disk with the influence VIV is based on the methodology presented in [2]. Here, it is extended for a cyclic structure and completed by the influence of interblade damping-friction forces which are incopororated in shrouding coupling. It can be advantageously written in matrix form

$$\mathbf{M}_{BD}\ddot{\mathbf{q}}_{BD} + \mathbf{C}_{BD}\dot{\mathbf{q}}_{BD} + \mathbf{K}_{BD}\mathbf{q}_{BD} = \mathbf{f}_{BD}^{E} + \mathbf{f}_{BD}^{FC}, \tag{1}$$

where $\mathbf{M}_{BD}$, $\mathbf{C}_{BD}$ and $\mathbf{K}_{BD}$ are rectangular of order $3N_B$ mass, damping and stiffness matrices of a complex bladed disk model. Right hand side of (1) contains force vectors of friction coupling $\mathbf{f}_{BD}^{FC}$. Vector of generalized coordinates is of following form $\mathbf{q}_{BD} = [\ldots, x_i, \varphi_i, q_i, \ldots]^T \in \mathbb{R}^{3N_B}$, where index $i = 1, \ldots, N_B$ designates the particular blade. The coordinate q_i is governed by van der Pol equation which is used for the wake dynamics.

Lock-in in the cyclic structure

The figures below show multiple frequency lock-in reagarding different mode shapes of the structure (left). Real parts of the eigen values witness of the stability. It is clear that when the frequency lock-in happens, the system exhibit can unstable vibration.

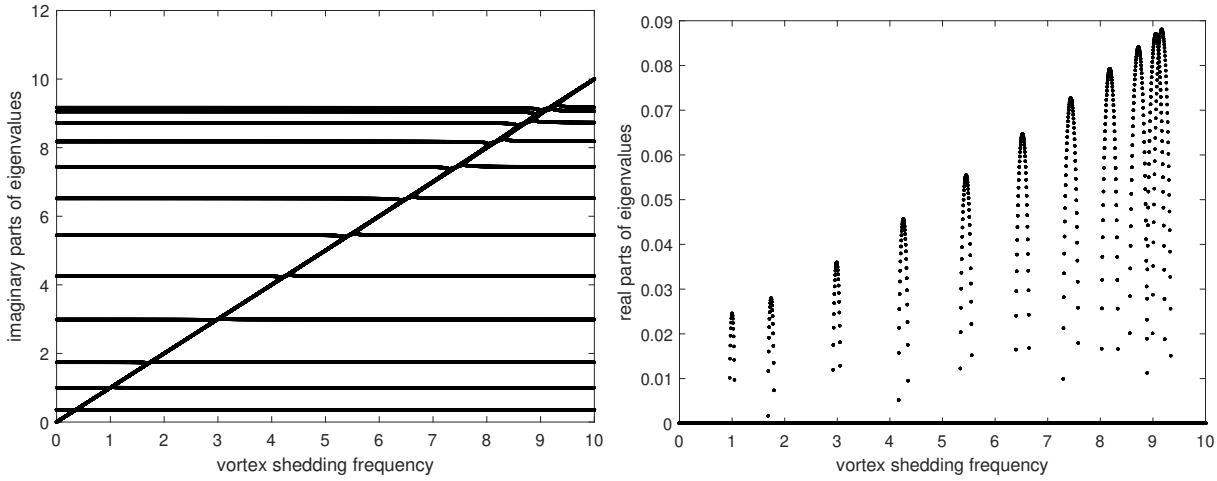

Figure 2: Frequency lock-in areas and stability charts for cyclic structure created of identical air-foil profile connected by shrouding.

Conclusions

The paper presents phenomenological model of vortex-induced vibration in a cyclic structure which is formed by blade profiles. The attention is paid on the investigation of lock-in phenomenon using linearized model, which will further completed by nonlinear friction terms based on LuGre friction model. There is obvious in the presented results, that the system losses its stability during the lock-in phases. The future aim is to propose suitable damping mechanism which is based on friction dampers and complete the analyses with experimental data.

Acknowledgement: This work was supported by the GA CR project No. 20-26779S "Study of dynamic stall flutter instabilities and their consequences in turbomachinery application using mathematical, numerical and experimental methods".

References

[1] Giannini O., Sestieri A. (2016) Experimental characterization of veering crossing and lock-in in simple mechanical systems, *Mechanical Systems and Signal Processing* **72-73**:846-864.

[2] Hoskoti L., Dinesh A.A., Ajay M. (2020) Frequency lock-in during nonlinear vibration of an airfoil coupled with van der Pol Oscillator, *Journal of Fluids and Structures* **92**:102776.

[3] Fung Y.C. (1993) An Introduction to the theory of aeroelasticity, Dover Publications, Inc.

[4] Hodges D.H., Pierce G.A. (2002) Introduction to structural dynamics and aeroelasticity, Cambridge University Press.

[5] Tondl A., Ruijgrok T., Verhulst F., Nebergoj R. (2000) Autoparametric Resonance in Mechanical Systems, Cambridge University Press.

[6] Hayat K. et al. (2016) Flutter performance of bend-twist coupled large-scale wind turbine blades, *Journal of Sound and Vibration* **370**:149-162.

[7] Ertveldt J., Lataire J., Pintelon R., Vanlanduit S. (2012) *Flutter speed prediction based on frequency-domain identification of a time-varying system*, Proceedings of ISMA2012-USD2012, 3013-3024.

[8] Hobeck J.D., Inman D.J. (2016) *Dual cantilever flutter: Experimentally validated lumped parameter modeling and numerical characterization*, Journal of Fluid and Structures **61**:324-338.

[9] Byrtus M., Hajzman M., Dupal J., Polach P. (2016) *Dynamic phenomena of a blade system with aero-elastic coupling*, Proceedings of ISMA2016-USD2016, 3013-3024.

[10] di Bernardo M., Budd C.J., Champneys A.R., Kowalczyk P. (2008) Picewise-smooth dynamical systems (Theory and Applications), Springer-Verlag London Limited.

Tuesday, July 19, 2022
16:00 - 18:20

MS-06 Fractional Derivatives
Rhone 3A

Chair: Pierre Melchior

16:00 - 16:20
A new dynamical attractive and repulsive fractional potential for UAV in 3D dynamical environment
MELCHIOR Pierre*, RUIZ Kendric, VICTOR Stephane, CHAUMETTE Serge
*Université de Bordeaux / Bordeaux INP (IMS - UMR 5218 CNRS Université de Bordeaux 351 cours de la Libération, Bât. A31 33405 TALENCE cedex France)

16:20 - 16:40
Time-domain Wave Propagation in Rigid Porous Media using Equivalent Fluid Model with a Quadratic Nonlinearity.
MOUFID Ilyes*, MATIGNON Denis, RONCEN Rémi, PIOT Estelle
*ONERA / DMPE, Université de Toulouse [Toulouse] (F-31055 Toulouse France)

16:40 - 17:00
Influence of fractional viscoelastic connecting layers on the response of a beam-mass array exposed to motion of supports
PAUNOVIĆ Stepa*, CAJIC Milan, KARLICIC Danilo
*Mathematical Institute of the Serbian Academy of Sciences and Arts, Serbia (Kneza Mihaila 36, Belgrade Serbia)

17:00 - 17:20
Free and forced modes of fractional-type torsional oscillations of complex rod
(STEVANOVIÉ) Hedrih Katica, **HEDRIH Andjelka***
*Mathematical Institute of Serbian Academy of Sciences and Arts (Kneza Mihaila 36, 11 000 Belgrade Serbia)

A new dynamical attractive and repulsive fractional potential for UAV in 3D dynamical environment

Kendric Ruiz* †, Stéphane Victor*, Pierre Melchior* and Serge Chaumette †
*Université de Bordeaux, CNRS, IMS UMR 5218 , Bordeaux INP/Enseirb-Matmeca – 351 cours de la Libération, 33405 Talence cedex, France
(email: firstname.lastname@ims-bordeaux.fr †Université de Bordeaux, CNRS, Labri UMR 5800 , Bordeaux INP/Enseirb-Matmeca – 351 cours de la Libération, 33405 Talence cedex, France
(email: firstname.lastname@labri.fr)

Summary. In recent years, applications for drones have multiplied, from surveillance, exploration, rescue and transport applications. UAVs are more and more autonomous, therefore real-time trajectory planning is necessary and can be achieved with potential fields. A quick study is proposed to better scale attractive and repulsive forces which has always been problematic when dealing with artificial potential fields. The purpose of this article is to develop a new dynamical fractional potential attractive and repulsive field usable in a dynamical 3D environment by taking into account the obstacle dynamics (position and speed) and theirs dangerousness. This makes it possible to avoid the obstacle in a more robust way, both from a safety point of view and from a trajectory optimization point of view. The potential fields are based on the relative position and speed of the drone in relation to the target for the attractive potential field or to the obstacle for the repulsive one.

Introduction

Path planning is used to find a suitable path between two points (mostly provided by the GPS) while avoiding obstacles in the environment. These obstacles can be dynamical or static. The notion of danger is therefore necessary to avoid a type of obstacle in the most harmonious way. Research on potential field methods has been extensively studied [1, 2, 3, 4, 5]. However, most methods are generally adapted for a static environment or do not take into account the type of obstacle (see e.g. [6, 7]). [8] have improved work on artificial potential fields by taking into account the obstacle dynamics. In this sense, [9] and [10] have interpreted the attractive field as a control loop ensuring stability degree robustness of the trajectory towards mass variations of the ego-vehicle and disturbances by taking into account the position and speed of the target as defined by [8] (see Fig. 1). Also, a novel interpretation of robust control is proposed in [5] for autonomous vehicle. The objective of this article is to present a new potential attractive and repulsive field adapted to a dynamical 3D environment that ensures the robustness of the trajectory. Potential fields are well adapted for drone applications because its holonomic model can be identified by a point mass. The potential field method allows this mass to be taken into account for both attractive and repulsive. The concept of danger will also be taken into account, the obstacles will be considered as known and the method makes it possible to avoid the obstacle with a softer trajectory according to the obstacle type, in other words, its dangerousness (pedestrian, buildings, bicycle, car etc.). In Ge & Cui, no distinction is proposed to differentiate the dangerousness of obstacles (it is safer to go nearer a wall than a human). Therefore, Weyl repulsive potential definition has introduced a fractional degree to distinguish obstacles with their dangerousness. By gaining on differentiating obstacle danger, the dynamical behaviors of obstacle has been lost. Therefore, the paper proposes a new definition of attractive and repulsive field that takes into account both dangerousness and dynamics of the obstacles. Moreover, it is often difficult to scale the attractive and repulsive potential forces. A methodology is proposed to efficiently scale them.
A fractional attractive force is presented in section 2. Section 3 presents a new dynamical fractional repulsive force. To finally conclude in section 4.

Fractional Attractive Force

In [10], the [8] method has been reinterpreted as a control loop, see Figure 1.
This virtual attractive force is defined by:

$$F_{att} = \alpha_p \left(\boldsymbol{p}_{tar} - \boldsymbol{p}_{ego} \right) + \alpha_v \left(\boldsymbol{v}_{tar} - \boldsymbol{v}_{ego} \right) \tag{1}$$

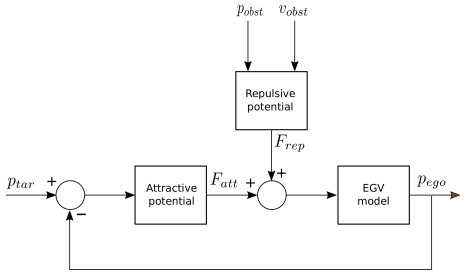

Figure 1: Dynamical interpretation of Ge and Cui attractive and repulsive forces

where $\boldsymbol{p}_{tar}$ and $\boldsymbol{p}_{ego}$ respectively are the real-time positions of the target and the ego-vehicle (EGV). $\boldsymbol{v}_{tar}$ and $\boldsymbol{v}_{ego}$ respectively are the real-time speeds of the target and the ego-vehicle. α_p and α_v are positive constants that define a lead-phase controller.
Introducing the error $e(t) = \boldsymbol{p}_{tar} - \boldsymbol{p}_{ego}$, and considering the fractional derivating of the velocity, it then comes:

$$F_{att} = \alpha_p e(t) + \alpha_v \frac{d^n e(t)}{dt^n}, \tag{2}$$

where $\boldsymbol{a}_{tar}$ and $\boldsymbol{a}_{ego}$ respectively are the real-time acceleration of the target and the ego-vehicle and m_{ego} is the mass of the ego-vehicle.
Under zero initial conditions, the Laplace transform of relation (2) gives:

$$F_{att}(s) = \left(\alpha_p + \alpha_v s^n\right) E(s), \tag{3}$$

where $E(s)$ is the transform Laplace of $e(t)$.

Fractional Repulsive Force

Ge & Cui potential field definition depends both on the distance ρ between the EGV and the obstacle, and their relative velocities v_{RO}. Weyl potential field solely depends on the distance while distinguishing obstacle dangerousness with order n. Therefore, it is proposed to differentiate the obstacle dangerousness by keeping the order n in the Weyl repulsive field definition, and by adding distance and relative speed to add reactivity to the obstacle. The new fractional repulsive potential becomes:

$$U_{rep}\left(\boldsymbol{p}, \boldsymbol{v}\right) = \frac{\left(\rho_s\left(\boldsymbol{p}, \boldsymbol{p}_{obs}\right) - \rho_m\left(\boldsymbol{v}_{RO}\right)\right)^{n-2} - \rho_{max}^{n-2}}{\rho_{min}^{n-2} - \rho_{max}^{n-2}}, \tag{4}$$

from where one draws the following repulsive forces:

$$F_{repv} = \eta \frac{(n-2)\left(\rho_s\left(\boldsymbol{p}, \boldsymbol{p}_{obs}\right) - \rho_m\left(\boldsymbol{v}_{RO}\right)\right)^{n-3} \boldsymbol{v}_{RO}}{\rho_s\left(\boldsymbol{p}, \boldsymbol{p}_{obs}\right) a_{max}\left(\rho_{min}^{n-2} - \rho_{max}^{n-2}\right)} \boldsymbol{v}_{RO\perp} \boldsymbol{n}_{RO\perp} \tag{5}$$

and

$$F_{repp} = \eta \frac{(n-2)\left(\rho_s\left(\boldsymbol{p}, \boldsymbol{p}_{obs}\right) - \rho_m\left(\boldsymbol{v}_{RO}\right)\right)^{n-3} \left(1 + \frac{\boldsymbol{v}_{RO}}{a_{max}}\right)}{\left(\rho_{min}^{n-2} - \rho_{max}^{n-2}\right)} \boldsymbol{n}_{RO}. \tag{6}$$

Now, the repulsive potential field function takes into account an order n to manage obstacle avoidance according to its dangerousness and the obstacle speed to operate in a dynamical environment.

Conclusion

In trajectory planning, artificial potential fields provide good results for trajectory planning in dynamical environments. It remains essential for real-time application and allows a good reactivity of the EGV. The Ge & Cui force allows taking into account the velocity of obstacles but it is not robust to a change in mass. The Weyl potential force associates a degree of danger with an obstacle. A new dynamical fractional attractive and repulsive field is presented allying both advantages and guarantees robustness due to mass variations. This method takes into account the obstacle dynamical aspects such as positions and speeds, and associates dangerousness to a fractional order. The fractional regulator in an attractive form, which allows robustness in terms of EGV mass variations.

References

[1] Khatib, O. (1985). Real-time obstacle avoidance for manipulators and mobile robots. In Proceedings. 1985 IEEE International Conference on Robotics and Automation, volume 2, 500–505.

[2] Hwang, Y.K. and Ahuja, N. (1992). A potential field approach to path planning. IEEE Transactions on Robotics and Automation, 8(1), 23–32.

[3] Krogh, B. and Thorpe, C. (1986). Integrated path planning and dynamic steering control for autonomous vehicles. In Proceedings. 1986 IEEE International Conference on Robotics and Automation, volume 3, 1664–1669

[4] Sfeir, J., Saad, M., and Saliah-Hassane, H. (2011). An improved artificial potential field approach to real-time mobile robot path planning in an unknown environment. In 2011 IEEE International Symposium on Robotic and Sensors Environments (ROSE), 208–213.

[5] Receveur, J., Victor, S., and Melchior, P. (2019). New interpretation of fractional potential fields for robust path planning. Fractional Calculus & applied analysis, 22(1), 113–127.

[6] Li, G., Tong, S., Cong, F., Yamashita, A., and Asama, H. (2015). Improved artificial potential field-based simultaneous forward search method for robot path planning in complex environment. In 2015 IEEE/SICE International Symposium on System Integration (SII), 760–765.

[7] Mac, T.T., Copot, C., Hernandez, A., and De Keyser, R. (2016). Improved potential field method for unknown obstacle avoidance using uav in indoor environment. In 2016 IEEE 14th International Symposium on Applied Machine Intelligence and Informatics (SAMI), 345–350.

[8] Ge, S. and Cui, Y. (2002). Dynamic motion planning for mobile robots using potential field method. Autonomous Robots, 13(3), 207–222.

[9] Poty, A., Melchior, P., and Oustaloup, A. (2004). Dynamic path planning for mobile robots using fractional potential field. In First International Symposium on Control, Communications and Signal Processing, 2004., 557–561.

[10] Metoui, B., Melchior, P., Najar, S., Abdelkrim, M.N., and Oustaloup, A. (2009). Robust path planning for dynamic environment based on fractional attractive force. In 2009 6th International MultiConference on Systems, Signals and Devices, 1–8.

Time-domain Wave Propagation in Rigid Porous Media using Equivalent Fluid Model with a Quadratic Nonlinearity

Ilyes Moufid*, Denis Matignon†, Rémi Roncen*, and Estelle Piot*
*ONERA / DMPE - Université de Toulouse, F-31055 Toulouse, France
†ISAE-SUPAERO - Université de Toulouse, F-31055 Toulouse, France

Summary. The acoustic properties of rigid porous media can be described by the equivalent fluid model (EFM) in the frequency domain, involving complex-valued functions. These physical quantities can be irrational, which leads to fractional derivatives in the time domain. Besides, this model is built with a constant flow resistivity, which is known to grow linearly with the flow velocity in the Forchheimer regime. Hence, a correction on the EFM is made according to the Darcy-Forchheimer law, leading to a more general model with an additional nonlinear term. Here, an approach is presented to formulate the EFM equations with the Forchheimer's correction in the time domain, where the fractional derivatives described by causal convolution are approximated by additional differential equations. It results in a nonlinear system on which an energy-based analysis is performed to ensure its stability under suitable conditions.

Nonlinear equivalent fluid model equations

When the material can be assumed rigid, acoustic wave propagation in porous media can be well represented by:

$$\begin{cases} \rho_0\alpha_\infty\,\partial_t\mathbf{u} + \boldsymbol{\nabla} p + M\,\mathbf{u} + N\,(g\star\partial_t\mathbf{u}) \;=\; -F_\xi\,|\mathbf{u}|\mathbf{u}\;, & \text{(1a)}\\ \chi_0\,\partial_t p + \boldsymbol{\nabla}\cdot\mathbf{u} + (\gamma-1)N'\,(h\star\partial_t p) \;=\; 0\;, & \text{(1b)}\end{cases}$$

where ρ_0 is the ambient fluid density, α_∞ the high frequency limit of the material dynamic tortuosity, χ_0 the ambient fluid adiabatic compressibility, and γ the heat capacity ratio; $\mathbf{u}$ and p are the particle velocity and pressure, respectively. Factor M is defined through Darcy's law. The two terms involving the kernel functions g and h and the convolution operator $\star$ account for viscous and thermal losses in the porous medium. Definitions of M, N, N', g and h are based on the dynamic tortuosity α and the dynamic compressibility β, for which complex-valued analytical models exist, such as the JCAPL model [1], presented below with the same parameters:

$$\hat{\alpha}(s) = \alpha_\infty\left[1+\frac{M}{s}+N\frac{\sqrt{1+\dfrac{s}{L}}-1}{s}\right], \quad (2) \qquad \hat{\beta}(s) = \gamma-(\gamma-1)\left[1+\frac{M'}{s}+N'\frac{\sqrt{1+\dfrac{s}{L'}}-1}{s}\right]^{-1}, \quad (3)$$

where $\hat{f}$ denotes the Laplace transform of f, s is the Laplace variable and all the coefficients are defined from physical quantities, detailed in [1]. Lastly, an additional nonlinear term to the initial EFM is taken into account in the right-hand side of (1a), representing the inertial effects induced by high amplitude waves travelling in the material. It comes from the nonlinear Fochheimer equation [2] where the multiplying factor F_ξ depends on the Forchheimer nonlinearity parameter ξ, computed in experimental studies [3, 4] by considering a linear relation between the total flow resistivity σ and the velocity amplitude:

$$\sigma = \sigma_0\,(1+\xi\phi|\boldsymbol{u}|)\;, \tag{4}$$

where ϕ is the porosity and σ_0 is the static flow resistivity. This relation is known as Forchheimer's correction.

Nonlinear equivalent fluid model with additional differential equations

In order to build an efficient numerical scheme for (1), a reformulation of the equations is performed using the additional differential equations (ADE) method [5]. The irrational functions $\hat{g}$ and $\hat{h}$ are first approximated by rational functions $\hat{G}$ and $\hat{H}$, written as multipole models and parameterized by a set of real or complex conjugate weights and poles:

$$\hat{G}(s) = \sum_{k=1}^{K}\frac{r_k}{s-s_k}\;, \quad (5) \qquad \hat{H}(s) = \sum_{k=1}^{K'}\frac{r'_k}{s-s'_k}\;. \quad (6)$$

All the parameters r_k, r'_k, s_k and s'_k are here assumed to be real and can be computed using different available methods [6, 7, 8]. Then, using (5) and (6) in system (1) written in the Laplace domain, leads to the following system:

$$\begin{cases} \rho_0\alpha_\infty\,s\,\hat{\mathbf{u}} + \boldsymbol{\nabla}\hat{p} + M\,\hat{\mathbf{u}} + N\displaystyle\sum_{k=1}^{K}\left(r_k+\frac{r_k s_k}{s-s_k}\right)\hat{\mathbf{u}} = -F_\xi\widehat{|\mathbf{u}|\mathbf{u}}\;,\\ \chi_0\,s\,\hat{p} + \boldsymbol{\nabla}\cdot\hat{\mathbf{u}} + (\gamma-1)N'\displaystyle\sum_{k=1}^{K'}\left(r'_k+\frac{r'_k s'_k}{s-s'_k}\right)\hat{p} = 0\;. \end{cases} \tag{7}$$

In order to express the discrete equivalent in the time domain, the inverse Laplace transform is applied, leading to a new set of equations with causal convolutions which are computed by introducing additional variables as follows:

$$\boldsymbol{\varphi_k}(t) = (e_{s_k}\star\mathbf{u})(t)\;, \quad (8) \qquad \psi_k(t) = (e_{s'_k}\star p)(t)\;, \quad (9)$$

where $e_x : t\to e^{xt}\mathrm{H}(t)$ and H is the Heaviside function.

Each of these additional variables is solution to a first-order ordinary differential equation and can be computed with a standard time-integration scheme. Finally, the global system of equations in the time domain reads:

$$\begin{cases} \rho_0\alpha_\infty\,\partial_t\mathbf{u} + \boldsymbol{\nabla} p + \left(M + N\sum_{k=1}^{K} r_k\right)\mathbf{u} + N\sum_{k=1}^{K} r_k s_k \boldsymbol{\varphi_k} \;=\; -F_\xi|\mathbf{u}|\mathbf{u}\;, \\ \chi_0\,\partial_t p + \boldsymbol{\nabla}\cdot\mathbf{u} + (\gamma-1)\left(N'\sum_{k=1}^{K'} r'_k\right)p + (\gamma-1)\,N'\sum_{k=1}^{K'} r'_k s'_k \psi_k \;=\; 0 \quad , \\ \partial_t\boldsymbol{\varphi_k} = s_k\boldsymbol{\varphi_k} + \mathbf{u} \qquad\qquad (\forall k\in[1,K])\;, \\ \partial_t\psi_k = s'_k\psi_k + p \qquad\qquad (\forall k\in[1,K'])\;. \end{cases} \tag{10}$$

Note that in (10), there are no spatial derivatives in the ADE. Hence, when the system is discretized with a numerical scheme based on fluxes, these fluxes depend on the velocity and pressure variables, but not on the additional variables. Consequently, the problem to solve at each mesh interface does not grow with the number of additional variables.

Stability analysis

Hereafter, a stability analysis of system (10) is performed thanks to the energy functional defined below:

$$\mathcal{E}(t) := \frac{1}{2}\left(\rho_0\alpha_\infty\int_\Omega \|\mathbf{u}\|^2\;\mathrm{d}x - N\sum_{k=1}^{K} r_k s_k\int_\Omega \|\boldsymbol{\varphi_k}\|^2\;\mathrm{d}x\right) + \frac{1}{2}\left(\chi_0\int_\Omega p^2\,\mathrm{d}x - (\gamma-1)\,N'\sum_{k=1}^{K'} r'_k s'_k\int_\Omega \psi_k^2\,\mathrm{d}x\right), \tag{11}$$

the derivative of which is

$$\begin{aligned} \frac{\mathrm{d}\mathcal{E}}{\mathrm{d}t}(t) = \;& -M\int_\Omega \|\mathbf{u}\|^2\;\mathrm{d}x \;-\; F_\xi\int_\Omega |\mathbf{u}|\,\|\mathbf{u}\|^2\;\mathrm{d}x \;-\; N\sum_{k=1}^{K} r_k\int_\Omega \|\partial_t\boldsymbol{\varphi_k}\|^2\;\mathrm{d}x \\ & -\;(\gamma-1)\,N'\sum_{k=1}^{K'} r'_k\int_\Omega (\partial_t\psi_k)^2\;\mathrm{d}x \;-\; \int_{\partial\Omega}(p\,\mathbf{u})\cdot\mathbf{n}\,\mathrm{d}\sigma\;. \end{aligned} \tag{12}$$

From (11) and (12), combined with the fact that ρ_0, α_∞, χ_0 and $(\gamma-1)$ are necessarily positive for porous media, as well as the parameters M, N, N', F_ξ, we impose the following sufficient conditions to ensure stability:

$(\mathbf{C_1})$ the weights $(r_k, r'_k)_k$ are positive, $(\mathbf{C_2})$ the poles $(s_k, s'_k)_k$ are negative.

When both these conditions are met, $\mathcal{E}$ is a positive-definite functional, which is decreasing in time without external contributions at the boundary $\partial\Omega$ of the domain Ω.

Conclusion

This work formulates the nonlinear EFM equations for porous media in the time domain, with the diffusive part of the complex-valued functions α and β described by a set of weights and poles. In addition, a proof of stability is given under conditions on the sign of these, conditions satisfied by the JCAPL model for a realistic range of physical parameters. A numerical study will be carried out in order to check the theoretical results and to investigate the effects of nonlinearity.

Acknowledgment This research has been financially supported by ONERA and by ISAE-SUPAERO, through the EUR TSAE under grant ANR-17-EURE-0005.

References

[1] Allard J.F., Atalla N. (2009) Propagation of Sound in Porous Media: Modelling Sound Absorbing Materials. 2nd ed. *John Wiley & Sons, Ltd*.

[2] Cimolin F., Discacciati M. (2013) Navier-Stokes/Forchheimer models for filtration through porous media. *Applied Numerical Mathematics* **72**:205-224.

[3] Umnova O., Attenborough K., Standley E., Cummings A. (2003) Behavior of rigid-porous layers at high levels of continuous acoustic excitation: Theory and experiment. *The Journal of the Acoustical Society of America* **114.3**:1346-1356.

[4] Turno D., Umnova O. (2013) Influence of Forchheimer's nonlinearity and transient effects on pulse propagation in air saturated rigid granular materials. *The Journal of the Acoustical Society of America* **134.6**:4763-4774.

[5] Dragna D., Pineau P., Blanc-Benon P. (2015) A generalized recursive convolution method for time-domain propagation in porous media. *The Journal of the Acoustical Society of America* **138.2**:1030-1042.

[6] Horoshenkov K.V., Attenborough K., Chandler-Wilde S.N. (1998) Padé approximants for the acoustical properties of rigid frame porous media with pore size distributions. *The Journal of the Acoustical Society of America* **104.3**:1198-1209.

[7] Gustavsen B., Semlyen A. (1999) Rational approximation of frequency domain responses by vector fitting. *IEEE Transactions on power delivery* **14.3**:1052-1061.

[8] Monteghetti F., Matignon D., Piot E. (2020) Time-local discretization of fractional and related diffusive operators using Gaussian quadrature with applications. *Applied Numerical Mathematics* **155**:73-92.

Influence of fractional viscoelastic connecting layers on the response of a beam-mass array exposed to motion of supports

Stepa Paunović*, Milan Cajić*, Danilo Karličić†
*Mathematical Institute of the Serbian Academy of Sciences and Arts, Belgrade, Serbia
†College of Engineering, Swansea University, United Kingdom

Summary. Herein the dynamic response of a system of fractional viscoelastic beams embedded in fractional viscoelastic medium and excited by motion of their supports is analysed, and the influence of properties of the connecting medium, modelled as a set of connecting layers, on the system behaviour is investigated. First, the approximate solution to the problem is obtained through the use of the Galerkin discretisation, impulse response method, Fourier transform and Residue theory, and then it is applied to analyse, both qualitatively and quantitatively, the influence of fractional-order derivative model parameters on the dynamic properties of beam arrays.

Introduction

There are many possible mechanical and engineering applications of systems of cantilever beams connected into an array and excited by motion of their supports, particularly for vibration attenuation and energy harvesting purposes [1]. One type of such systems, where cantilever beams are embedded in fractional viscoelastic medium, which is modelled by a set of light viscoelastic layers, and placed inside a moving container, is the subject of this study, and it is schematically depicted in Fig. 1. Dynamics of beam arrays with elastic and viscoelastic properties has already been investigated, e.g. [2]. There has also been some research regarding the fractional-order derivative viscoelastic systems (e.g. [3]), but these solutions are applicable only for rational derivative orders. Freundlich [4] recently presented the exact solution for the dynamic response of a single cantilever with a tip mass under transverse motion of the support, while the beam material was modelled with damping of an arbitrary order of fractional derivative. In our recent study, we have obtained an approximate solution to the problem of vibration of a system of fractional viscoelastic cantilevers, connected by a fractional viscoelastic layers and excited by transverse motion of the support, where the fractional derivatives of arbitrary order were used. In the herein presented paper, this solution procedure is briefly described, and then it is applied to analyse the previously mentioned array of connected cantilevers confined in a transversally moving container, schematically presented in Fig. 1, in order to determine the influence of the connecting layers' material properties on the dynamic response of the system.

Mathematical model and the approximate solution to the considered problem

A system of N_b fractional viscoelastic Euler-Bernoulli cantilever beams embedded in fractional viscoelastic medium and confined inside a transversally moving container, as presented in Fig. 1, is analysed. Each beam is of length L and carries $N_{m(k)}$ concentrated masses $m_{(k)_p}$ attached at $x_{m(k)} \in (0, L),\ p = 1, 2, \ldots, N_{m(k)},\ k = 1, 2, \ldots N_b$. Beams can have mutually different mass density ρ_k, cross sectional area A_k, moment of inertia I_k and relaxed elasticity modulus E_k, but they have the same fractional derivative order α and retardation time τ_1. The medium is modelled as a set of connecting layers, with prolonged compliance coefficient κ, fractional derivative order β and retardation time τ_2 being the same throughout the system. Here we will use only the left Riemann-Liouville fractional derivative of order γ as defined in [5], here denoted by $D^\gamma(\bullet) \equiv (\bullet)^{(\gamma)}$, $\gamma \in (0, 1)$. The container moves transversally, following an arbitrary function $w_s(t)$.

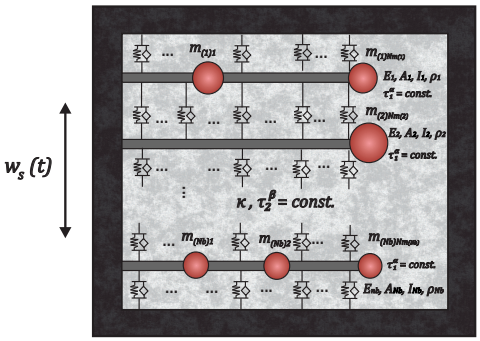

Figure 1: Schematic representation of the considered mechanical system

For the k-th beam of the system ($k = 1, 2, \ldots, N_b$), the equation of motion for transverse beam displacements $w_{(k)}(x, t)$ and the corresponding boundary conditions (BCs), noting that $w_{(0)} = w_{(N_b+1)} \equiv w_s$, can be formulated as

$$E_k I_k (1 + \tau_1^\alpha D^\alpha) w_{(k)}'''' + \left(\rho_k A_k + \sum_{p=1}^{N_{m(k)}} m_{(k)p} \delta(x - a_{(k)p}) \right) \ddot{w}_{(k)} - \kappa(1 + \tau_2^\beta D^\beta)(w_{(k+1)} + w_{(k-1)}) + \\ + 2\kappa(1 + \tau_2^\beta D^\beta) w_{(k)} = 0\ ; \qquad \text{BCs}: \quad w_{(k)}(0, t) = w_s(t), \quad w'_{(k)}(0, t) = w''_{(k)}(L, t) = w'''_{(k)}(L, t) = 0 \tag{1}$$

The solution procedure and the influence of the connecting layer properties

In order to homogenise the BCs, the absolute displacements are decomposed into the rigid body motion part and the displacements relative to the supported beam end - $w_{(k)}(x,t) = w_s(t) + v_{(k)}(x,t)$. Then, the relative displacements are approximated by the Galerkin weighted residual method as $v_{(k)}(x,t) \approx \sum_{i=1}^{n} \phi_{(k)i}(x) q_{(k)i}(t)\,, \quad k = 1, 2, \ldots, N_b$, with the bare beam mode shapes used as the trial functions and the weighting functions. This leads to a system $n \times N_b$ coupled fractional-order differential equations which can be expressed in matrix form as

$$\mathbf{K}\mathbf{q} + \mathbf{C}_\alpha \mathbf{q}^{(\alpha)} + \mathbf{C}_\beta \mathbf{q}^{(\beta)} + \mathbf{M}\ddot{\mathbf{q}} = \mathbf{Q} \tag{2}$$

where $\mathbf{K}$, $\mathbf{C}_\alpha$, $\mathbf{C}_\beta$ and $\mathbf{M}$ are the stiffness matrix, beam material damping matrix, connecting layer damping matrix and mass matrix of the whole system, respectively, and $\mathbf{q}$ and $\mathbf{Q}$ are the vector of the yet undetermined time functions and the vector of the inertial forces in the whole system. The unknown time functions $\mathbf{q}^{\mathrm{T}} = \{\mathbf{q}_1, \mathbf{q}_1, \ldots, \mathbf{q}_{N_b}\} = \{q_{(1)_1}, q_{(1)_2}, \ldots, q_{(1)_n}, q_{(2)_1}, \ldots, q_{(N)_n}\}$ will be determined by first finding the system impulse response $\mathbf{g}$, where $\mathbf{g}$ is the vector of $n \times N_b$ corresponding Green functions $G_i(t),\ i = 1, 2, \ldots, n \times N_b$.

The impulse response is determined by taking the Fourier transform of the system and then using the equivalent elastic system to obtain the decoupled system of equations, assuming relatively small damping. This leads to (almost) diagonalised system matrices, i.e. a system of $n \times N_b$ decoupled polynomial algebraic equations with fractional exponents:

$$s_r^2 + C_{\alpha rr}^d s_r^\alpha + C_{\beta rr}^d s_r^\beta + \omega_r^2 = 0\,, \qquad r = 1, 2, \ldots, n \times N_b \tag{3}$$

where $s = \imath\omega$, with $\omega_r^2 = K_{rr}^d / M_{rr}^d$ being the r-th undamped system frequency, and $C_{\alpha rr}^d$, $C_{\beta rr}^d$, K_{rr}^d, M_{rr}^d are the r-th diagonal elements of the corresponding diagonalised matrices. After finding the roots of each of these equations, the inverse Fourier transform is applied with the use of the Residue theory, and the Green functions are again coupled to obtain the impulse response of the original system. Once the impulse response is determined, the sought time functions are obtained by taking the convolution with the inertial forces of the system $q_i(t) = \int_0^t G_i(t-\tau) Q_i(\tau) d\tau\,,\ i = 1, 2, \ldots, n \times N_b$, thus providing the complete (approximate) solution to the considered problem. The influence of the connecting layer material properties was investigated on a system of $N_b = 3$ cantilever beams with $N_{m(1)} = 2$, $N_{m(2)} = 1$, $N_{m(3)} = 3$ equidistantly attached masses of half of each beam's weight. Geometrical and material properties of each beam were adopted the same as in [4], with $\tau_1 = 0.001s,\ \alpha = 0.8$. The container was set to follow the motion function $w_s(t) = w_0 \sin \omega_s t^2$, with $w_0 = 1mm,\ \omega_s = 10s^{-1}$. The parameters τ_2, β and κ were varied, and their influence on the relative displacements of the free end of the first beam in the array are presented in Fig. 2.

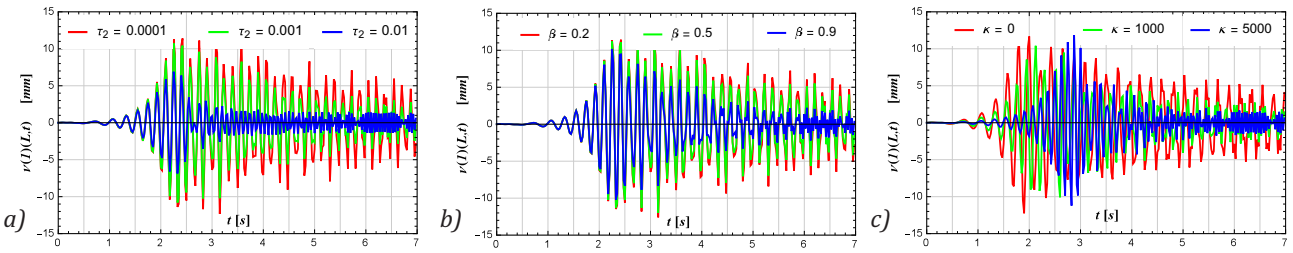

Figure 2: Influence of the connecting layer properties on the dynamic response of the system

Conclusions

It can be seen that the connecting layer greatly affects system behaviour. An increase in retardation time τ_2 and order of fractional derivative β of the connecting layer leads to a more rapid vibration attenuation, as shown in Fig. 2a) and b), respectively, while an increase in the layer's relaxed compliance coefficient leads not only to an increase in damping, but in the fundamental system frequency as well, which causes the resonant state shift observed in Fig. 2c).

Acknowledgment

This research was supported by the Serbian Ministry of Education, Science and Technological Development (project 174001). D.K. was supported by the Marie Skłodowska -Curie Actions - European Commission: 799201-METACTIVE.

References

[1] Meruane, V., Pichara, K. (2016) A broadband vibration-based energy harvester using an array of piezoelectric beams connected by springs. *Shock and Vibration* **Article ID 9614842**:1-13.

[2] Kelly, S. G., Nicely, C. (2015) Free Vibrations of a series of beams connected by viscoelastic layers. *Adv. in Acoust. and Vib.* **Article ID 976841**:1-8.

[3] Sorrentino, S. and Fasana, A. (2007) Finite element analysis of vibrating linear systems with fractional derivative viscoelastic models. *Jnl. of Sound and Vib.* **299**:839-853.

[4] Freundlich, J. (2019) Transient vibrations of a fractional Kelvin-Voigt viscoelastic cantilever beam with a tip mass and subjected to a base excitation. *Jnl. of Sound and Vib.* **438**:99-115.

[5] Rossikhin, Y., Shitikova, M. (2010) Application of fractional calculus for dynamic problems of solid mechanics: novel trends and recent results. *Applied Mechanics Reviews.* **63**:010801.

Free and forced modes of fractional-type torsional oscillations of a complex rod

Katica (Stevanović) Hedrih*,**, Andjelka Hedrih*

*Department of Mechanics,Mathematical Institute of Serbian Academy of Sciences and Arts, (MI SANU), Belgrade, Serbia,

**Faculty of Mechanical Engineering, University of Niš, Serbia

Summary. In this paper we study torsional oscillations of a complex rod made of material with viscoelastic properties. Free and forced modes of fractional-type torsional oscillations of a discrete system of a complex rod are described by a system of differential fractional order equations for a special case. The kinetic energy, deformation work, and generalized energy dissipation function of a fractional type system are identified for a special case. It has been shown that in the general case of such fractional type systems, with torsional oscillations, there are no independent modes, and that the system behaves as a nonlinear system.

Model of torsional oscillations of a complex rod

Figure 1 represents a model of a complex rod which is considered as a fractional-type discrete complex system. It consists of a discrete complex structure composed of light rigid rods of negligible mass, length ℓ_k, $k=1,2,3,4$ that bear material points m_k, $k=1,2,3,4$, at their free ends, and are rigidly connected to the main rod at an angle β_k, $k=1,2,3,4$ at the other end. The rods are in pairs symmetrically arranged and rigidly joined in the sections of the main rod 1,2,3 and 4 at distances $\frac{\ell}{4}$, $\frac{\ell}{2}$, $\frac{3\ell}{4}$ and ℓ, measured from the left fixed end of the main rod, and where ℓ is the length of the main rod. In the cross-section, at distance $\frac{\ell}{4}$ from left end of the main rod, a one-frequency momentum $\mathsf{M}_{z,1}=\mathsf{M}_{z,01}\sin(\Omega_1 t+\varphi_1)$, with amplitude $\mathsf{M}_{z,01}$, frequencies Ω_1 and φ_1 phase is applied.

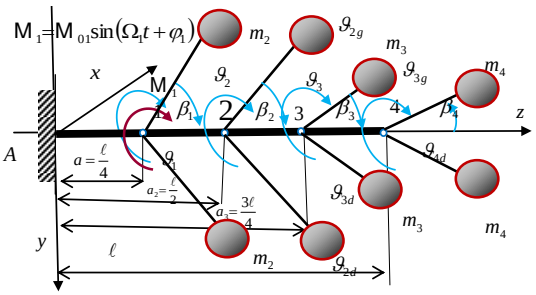

Figure 1. Model of a complex rod. This complex system which is considered as discrete system which torsional non-linear oscillations can be described using fractional derivatives.

For a case of an ideally elastic material, a segment rigidity of a torsion rod is equivalent to the rigidity of a torsion spring c_t and is determined by a constitutive relation of the torsion momentum-torsion angle, M_1 and ϑ. The rigidity of a torsion spring c_t is defined as $c_t=\frac{GI_0}{\ell}$ where G is the modulus of sliding of the rod's material, and $\mathbf{I}_0$ is the polar moment of the cross-sectional area of the main rod [1.2]. **Assumptions of the model:** all masses are equal and all angles are equal and the indentations are of equal lengths. The system is homogeneous. Materials of which beam and rods are made have viscoelastic properties and the constitutive relation of the moment M_1 of torsion of the angle ϑ, of torsion of the beam segment can be written in the form:

$$\mathsf{M}_t=-\left(c_t\vartheta+c_{t\alpha}\mathsf{D}_t^{\alpha}[\vartheta]\right) \tag{1}$$

where $c_{t\alpha}$ is the stiffness of the fractional type of dissipative properties of the torsion deformation of the beam segment considered as a torsion spring, and $\mathsf{D}_t^{\alpha}[\bullet]$ is a differential operator of the fractional order in the following form (see References [3-6]):

$$\mathsf{D}_t^{\alpha}[\vartheta(t)]=\frac{d^{\alpha}\vartheta(t)}{dt^{\alpha}}=\vartheta^{(\alpha)}(t)=\frac{1}{\Gamma(1-\alpha)}\frac{d}{dt}\int_0^t\frac{\vartheta(\tau)}{(t-\tau)^{\alpha}}d\tau,\ \alpha\in(0.1),t\in(0.b) \tag{2}$$

where α is a rational number between 0 and 1, determined experimentally and $\Gamma(1-\alpha)$ is the Gamma function.

The kinetic energy, deformation work, and generalized energy dissipation function of the fractional type system

Free and forced modes of fractional-type torsional oscillations of a discrete system of a complex rod are described by a system of differential fractional order equations for a special case. The system of the fractional order differential equations can be written in matrix form:

$$\mathbf{A}\{\ddot{\vartheta}_k\}+\mathbf{C}\{\vartheta_k\}+\mathbf{C}_\alpha\{\mathsf{D}_t^\alpha[\vartheta_k]\}=0 \tag{3}$$

where $\mathbf{A}$ is the matrix of coefficients of inertia, $\mathbf{C}$ is the matrix of coefficients of elasticity and $\mathbf{C}_\alpha$ is a matrix of coefficients of the system of fractional properties. If the relation $c_{t,\alpha,k}=\kappa_\alpha c_{t,k}$, $k=1,2,3,4$ is valid, then $\mathbf{C}_\alpha=\kappa_\alpha\mathbf{C}$ and, in that case, the system belongs to a special class of fractional type systems in which main modes of fractional type are independent. In this case, we can apply a procedure for transformation of the generalized coordinates into the main coordinates like for the corresponding linear system.

Expressions for kinetic energy $\mathbf{E}_k$, deformation work $\mathbf{A}_{def}$ of the torsional deformed system, and the generalized function Φ_w [5,6] of fractional-type dissipation of the system energy are

$$\mathbf{E}_k=\frac{1}{2}\sum_{k=1}^{k=4}\mathbf{J}_{z,k}\dot{\vartheta}_k^2=\sum_{k=1}^{k=4}m_k(\ell_k\sin\beta_k)^2\dot{\vartheta}_k^2, \tag{4}$$

$$\mathbf{A}_{def}=\mathbf{E}_p=c_{t,1}\vartheta_1^2+\frac{1}{2}c_{t,2}(\vartheta_2-\vartheta_1)^2+\frac{1}{2}c_{t,3}(\vartheta_3-\vartheta_2)^2+\frac{1}{2}c_{t,4}(\vartheta_4-\vartheta_3)^2 \tag{5}$$

$$\Phi_w=\frac{1}{2}c_{t,\alpha,1}(\mathsf{D}_t^\alpha[\vartheta_1])^2+\frac{1}{2}c_{t,\alpha,2}(\mathsf{D}_t^\alpha[\vartheta_2-\vartheta_1])^2+\frac{1}{2}c_{t,\alpha,3}(\mathsf{D}_t^\alpha[\vartheta_3-\vartheta_2])^2+\frac{1}{4}c_{t,\alpha,4}(\mathsf{D}_t^\alpha[\vartheta_4-\vartheta_3])^2 \tag{6}$$

To obtain a system of fractional order differential equations that describe the torsional oscillations of the observed discrete complex structure, Lagrange differential equations of the second order were used.

Independent fractional order differential equations for describing free main fractional type modes are in the following form:

$$\ddot{\xi}_s+\omega_s^2\xi_s+\kappa_\alpha\omega_s^2\mathsf{D}_t^\alpha[\xi_s]=0,\ s=1,2,3,4 \tag{7}$$

and for describing forced main fractional type modes:

$$\ddot{\xi}_s+\omega_s^2\xi_s+\kappa_\alpha\omega_s^2\mathsf{D}_t^\alpha[\xi_s]=h_s\sin(\Omega_1 t+\varphi_1),\ s=1,2,3,4 \tag{8}$$

where ξ_s are main coordinates, ω_s are eigen frequencies of a fractional order system, κ_α is the constant of proportionality. When $c_{t,\alpha,k}\neq\kappa_\alpha c_{t,k}$ and $\mathbf{C}_\alpha\neq\kappa_\alpha\mathbf{C}$, the fractional-type modes are coupled and the system behaves in a non-linear way, and there is an interaction between fractional-type modes.

Conclusions

Torsional oscillations of a complex rod with viscoelastic properties are analyzed. The main idea applied in the paper is that the segment rigidity of the described torsion rod is equivalent to the rigidity of a torsion spring. The kinetic energy, deformation work, and generalized energy dissipation function of the fractional type system are identified. Free and forced main fractional type modes are defined. It has been shown that in the general case of such fractional type systems with torsional oscillations, there are no independent modes, and that the system behaves as a nonlinear system. When system belongs to an after-mentioned special class of fractional type systems, main modes of fractional type are independent.

Acknowledgement. Parts of this research were supported by the Ministry of Education, Sciences and Technology of Republic Serbia trough Mathematical Institute Serbian Academy of Sciences and Arts, Belgrade.

References

[1] Rašković, D., *Theory of Oscillations,* Naučna knjiga, Beograd, 1965, p. 503. (in Serbian)
[2] Rašković, D., *Steinght of Materials,* Naučna knjiga, Beograd, 1977, p. 426. (in Serbian).
[3] Bačlić, B.S., Atanacković, T. (2000) Stability and creep of a fractional derivative order viscoelastic Rod. *Bulletin T, CXXI de L'Academie Serbe des Sciences st de Arts* -Class des Sciences Mathematques et Naturelles Sciences, No. 25, 115-131.
[4] Hedrih (Stevanović) K. (2011) Analytical mechanics of fractional order discrete system vibrations. Chap in Monograph. *Advances in nonlinear sciences* Vol. 3, JANN, Belgrade, pp. 101-148. ISSN: 978-86-905633-3-3.
[5] Hedrih (Stevanović) K. (2014) Generalized function of fractional order dissipation of system energy and extended Lagrange differential equation in matrix form, Dedicated to 86th Anniversary of Radu Miron's Birth. *Tensor* Vol. 75, No. 1. pp. 35-51. Tensor Society (Tokyo), c/o Kawaguchi Inst. of Math. Soc. Japan. ISSN 0040-3604.
[6] Hedrih (Stevanović), K.R., Machado J.M. T. (2015) Discrete fractional order system vibrations. *International Journal Non-Linear Mechanics* Vol 73, pp. 2–11.

Tuesday, July 19, 2022

16:00 - 18:20

MS-14 Nonlinear Dynamics for Engineering Design

Rhone 2

Chair: Carlos Mazzilli

16:00 - 16:20

Dissipation Effects in Mechanical Systems

BUDAI Csaba, **KÖVECSES József***, STEPAN Gabor

*Department of Mechanical Engineering and Centre for Intelligent Machines, McGill University (817 Sherbrooke Street West, Montréal (Québec) Canada H3A 0G4 Canada)

16:20 - 16:40

Dynamic stability of tuned vibration absorbers allowing a rotational mobility

MAHE Vincent*, RENAULT Alexandre, GROLET Aurelien, THOMAS Olivier, MAHÉ Hervé

*Valeo Transmissions, Centre d'Étude des Produits Nouveaux (Espace Industriel Nord, Route de Poulainville, 80009 Amiens Cedex 1 France) - Laboratoire d'Ingénierie des Systèmes Physiques et Numériques (Arts et Métiers - Campus d'Aix-en-Provence2, cours des Arts et Métiers, 13617 AIX EN PROVENCETél.: +33 (0)4 42 93 81 41Laboratoire d'Ingénierie des Systèmes Physiques et numériques (LISPEN EA7515)Arts et Métiers - Campus de Lille8 bd Louis XIV - 59046 Lille CedexTél.: +33 (0)4 42 93 81 41Laboratoire d'Ingénierie des Systèmes Physiques et numériques (LISPEN EA7515)Arts et Métiers - Campus de Cluny (Institut Image de Chalon-sur-Saône)2 rue Thomas Dumorey 71100 CHÂLONS-SUR-SAONETél.: +33 (0)3 85 90 98 60 France)

16:40 - 17:00

Analytical Criterion of Multimodal Snap-through Flutter of Thin-walled Panels

PILIPCHUK Valery*

*Wayne State University (5050 Anthony Wayne Dr., 2118 Detroit, Michigan 48202 United States)

17:00 - 17:20

Forced vibration analysis of non-linear Euler-Bernoulli beam using Efficient Path Following Method

MOUSAVI Seyed Mojtaba*, JELVEH Meisam, SADR Mohammad Homayoune, TOHIDI Hadi

*Amirkabir University of Technology (424 Hafez Ave, Tehran, Iran, 15875-4413 Iran)

Dissipation Effects in Mechanical Systems

Csaba Budai*, József Kövecses† and Gábor Stépán‡
*Department of Mechatronics, Optics and Mechanical Engineering Informatics, Budapest University of Technology and Economics, Budapest, Hungary
†Department of Mechanical Engineering and Centre for Intelligent Machines, McGill University, Montréal, Québec, Canada
‡Department of Applied Mechanics, Budapest University of Technology and Economics, Budapest, Hungary

Summary. Dissipation is part of every physical system. This paper looks at a possible classification of such effects based on the dynamic response characteristics. It highlights some interesting non-trivial characteristics that particularly enter when a system otherwise unstable is stabilized by dissipative effects. These response properties can have various useful applications, and they can contribute to determining the dominant dissipation sources in mechatronic systems.

Introduction

Mechanical system models generally include forces that arise from fundamental physical phenomena [2]. Dissipative effects represent one of such basic classes of forces. The dissipative mechanisms at the micro-scale usually lead to some resultant effective representations at the macro-scale, which are commonly used in dynamic system models. These generally appear in two fundamental forms: one is when the damping/dissipative force model is directly proportional with the velocity, i.e., viscous and structural damping models, and the second group is when the dissipative force model depends on the sign of the velocity but not necessarily the magnitude, i.e., friction models [3].

Dynamic model

The mathematical models for these can be written considering one degree-of-freedom canonical models as

$$m\ddot{q} + b\dot{q} + kq + c\,\mathrm{sgn}\,(\dot{q}) = f, \tag{1}$$

where q represents the generalized coordinate parametrizing the single degree-of-freedom as a function of time, m is the related to the generalized mass/inertia, k is the stiffness, and b is the viscous/structural damping coefficient. The magnitude of the friction force is denoted by c, and f represents the other forces acting on the system.
If mechanical systems without dissipation are considered then one possible classification can be based on their stability. The behaviour of a mechanical system model with purely inertia and stiffness terms is always stable by the Lyapunov sense. These inertia and stiffness terms represent the physical system elements and generally derive from the Lagrangian of the system. However, this usually represent only one part of the physical system.
The other forces that can enter in f determine in general whether the overall system is stable or not. Instability can result from various effects that can be introduced by these forces. Several of the major effects include some form of time delay. One important group of applications is virtual environments where f include discrete-time computer generated representation of virtual interaction forces.
Based on Eq. (1), the two limit cases are considered where either only viscous/structural damping, $b\dot{q}(t)$ term, or friction-based dissipation, $c\,\mathrm{sgn}\,(\dot{q}(t))$ term, exists. As an illustration, these are shown for the case where f vanishes and when f represents a virtual stiffness with formula $f(t) = -k_\mathrm{p} q(t_j)$, where k_p is the virtual stiffness coefficient, and $q(t_j)$ represents the sampled position in every jth sampling instant, i.e., $t_j = jt_\mathrm{s}$ with $j \in \mathbb{Z}$, and t_s denotes the sampling time. With the reduced number of free parameters, Eq. (1) is rewritten

$$\ddot{q}(t) + 2\zeta\omega_\mathrm{n}\dot{q}(t) + \omega_\mathrm{n}^2 q(t) + \sigma\omega_\mathrm{n}^2\,\mathrm{sgn}\,(\dot{q}(t)) = -\tfrac{k_\mathrm{p}}{m} q(t_j), \quad t \in [t_j, t_j + t_\mathrm{s})\,, \tag{2}$$

where the natural angular frequency $\omega_\mathrm{n} = \sqrt{k/m}$, the damping ratio $\zeta = b/(2m\omega_\mathrm{n})$, and $\sigma = c/k$. In order to obtain a more compact model, the dimensionless time $T = \omega_\mathrm{n} t$ is also introduced. Thus, the dimensionless sampling instant is $T_j = j\omega_\mathrm{n} t_\mathrm{s} = j\tau$. Based on these, the equation of motion can be given as

$$q''(T) + 2\zeta q'(T) + q(T) + \sigma\,\mathrm{sgn}\,(q'(T)) = -p\,q(T_j), \quad T \in [T_j, T_j + \tau)\,, \tag{3}$$

where $p = k_\mathrm{p}/k$, and prime denotes the differentiation with respect to the dimensionless time.

Dissipation analysis

The first case of f results in a stable system, while the second case produces a system that can be unstable without dissipation, and adding dissipative effects can stabilize the system. In the case of only viscous/structural damping the response properties are well-known; it generally shows exponential decay type characteristics. In the case of unforced and in the case of applied virtual stiffness, the vibration characteristics are presented in Fig. 1a and Fig. 1b, respectively.

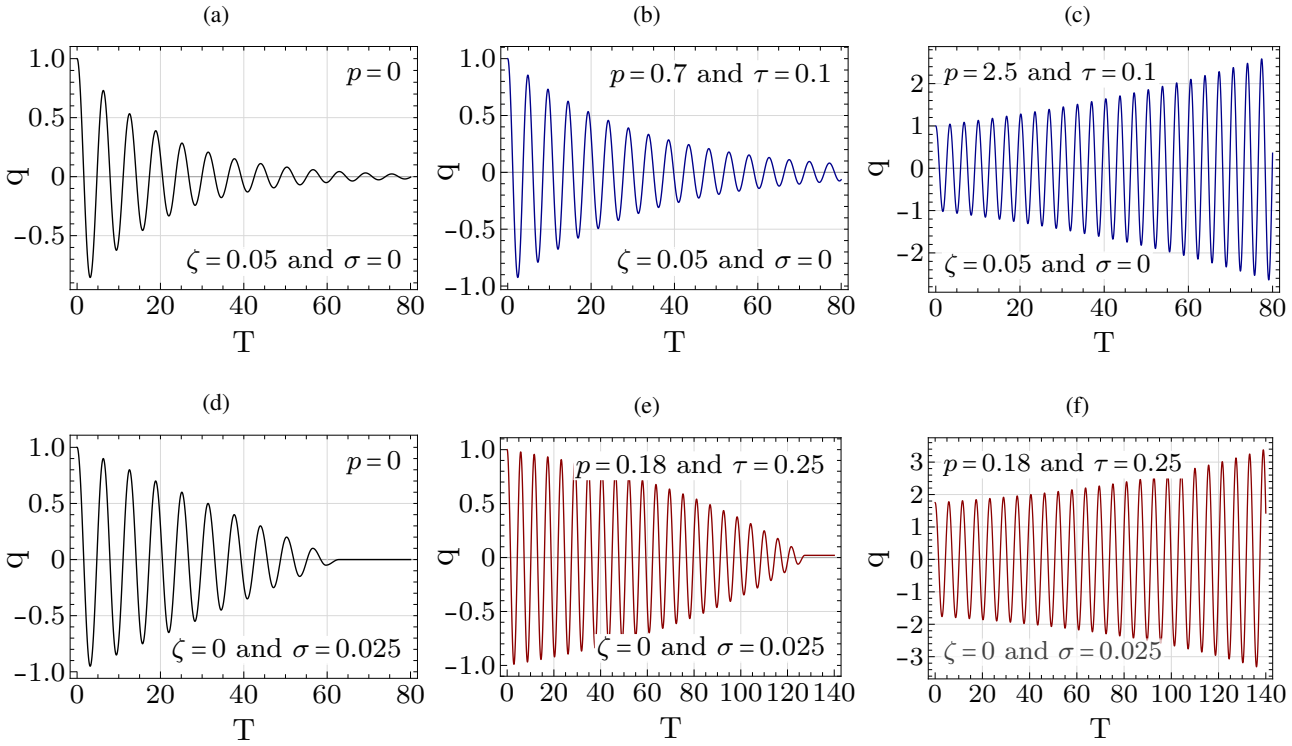

Figure 1: Fundamental vibration shapes due to the effect of different kind of dissipation phenomena

It can be also observed that the effect of sampling results in an effective negative viscous damping; thus with increasing virtual stiffness coefficient the effect of dissipation decreases, and there may be loss of stability, as it is shown in Fig. 1c. However, for the second case where only friction-based dissipative effects exist, the response characteristics are much less trivial.

There is a difference between the behaviours of a stable system and a dissipation-stabilized system. In the case when f vanishes, linear decaying amplitude exists, while in case of the additional virtual stiffness, the so-called concave amplitude decay [1] can be observed. These behaviours are shown in Fig. 1d and Fig. 1e, respectively. Due to the presence of friction-based dissipation, the system become sensitive to the initial conditions resulted in an unstable limit cycle. The resulted in unstable motion is presented in Fig. 1f.

It is noted that the behaviours of such concave decaying characteristics in various systems when generating discrete-time virtual interaction forces were experimentally observed [1]. Such observations can generally indicate that Coulomb friction may act as dominant dissipative and stabilizing effect for these cases.

Conclusions

In this paper, the vibration decay characteristics of mechanical systems were investigated by considering either viscous/structural damping or dry friction as the primary source of dissipation. The fundamental vibration shapes were presented for the unforced case, and for that case when the acting force represents virtual stiffness. It was highlighted that the influence of different physical dissipation resulted in some non-trivial vibration decaying characteristics that particularly enter when a system otherwise unstable is stabilized by dissipative effects.

Acknowledgement

The research reported in this paper was supported by the National Research, Development and Innovation Fund of Hungary under Grant No. PD 128398, and by TUDFO/51757/2019-ITM, Thematic Excellence Program. The work was also supported by the Higher Education Excellence Program of the Ministry of Human Capacities of Hungary (BME FIKP-MI/FM), and by the Natural Sciences and Engineering Research Council of Canada (NSERC).

References

[1] C. Budai, L. L. Kovács, J. Kövecses, and G. Stépán. Effect of dry friction on vibrations of sampled-data mechatronic systems. *Nonlinear Dynamics*, 88(1):349–361, 2017.

[2] D. J. Inman. *Engineering Vibration*. Pearson, 4th edition, 2014.

[3] E. Pennestrí, V. Rossi, P. Salvini, and P.P. Valentini. Review and comparison of dry friction force models. *Nonlinear Dynamics*, 83:1785–1801, 2016.

Dynamic stability of tuned vibration absorbers allowing a rotational mobility

V. Mahé[♯,♭], A. Renault[♭], A. Grolet[♯], O. Thomas[♭] and H. Mahé[♭]
[♯]*Arts et Métiers Institute of Technology, LISPEN, HESAM Université, 8 bd. Louis XIV 59046 Lille, France*
[♭]*Valeo Transmissions, Centre d'Étude des Produits Nouveaux Espace Industriel Nord, Route de Poulainville, 80009 Amiens Cedex 1, France*

Summary. Rotating machines are often subject to fluctuating torques, leading to vibrations of the rotor and finally to premature fatigue and noise pollution. These vibrations can be reduced using tuned vibration absorbers (TVA). These passive devices are made of several masses oscillating along a given trajectory relative to the rotor. Previous studies showed that the dynamics of these devices is subject to instabilities. In this paper, the dynamic stability of a new class of TVA is investigated. The particularity of this new class is that the TVA now admits a significant rotation motion relative to the rotor, in addition to the traditional translation motion. Efficiency of such devices is optimal for a perfect synchronous motion of oscillating masses. However, due to non linearities, masses unisson can be broken for the benefit of energy localization on a given absorber, leading to a loss of mitigation performances. To assess the stability of such devices, a dynamical model based on an analytic perturbation method is established. The aim of this model is to predict analytically localisation and jumps of the response. The validity of the model is confirmed through a comparison with a numerical resolution of the system's dynamics.

Presentation of the system

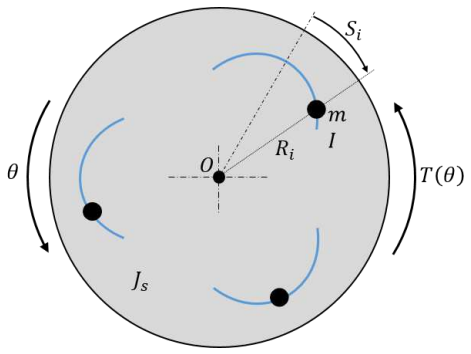

Figure 1: Scheme of the system studied for $N = 3$ absorbers

The system considered in this study consist of a rotor (or support plate) of inertia J_s rotating about its center O with a mean velocity Ω with respect to the galilean frame. Its angular position is written θ. On this rotor are articulated N identical absorbers of mass m and inertia I. These absorbers are located along their trajectory through the curvilinear abscissa S_i. The distance from point O to the mass center of the ith absorber is written $R_i(S_i)$, $i = 1, \dots N$. The shape of the trajectory is controled through this function. In addition to the translation motion along the trajectory, the rotation of the absorbers about their mass center with respect to the rotor frame is considered in this study, and denoted by $\alpha_i(S_i)$. A mechanical device enables to prescribe it as a function of S_i. We choose R_i (respectively α_i) to be a symmetric (respectively antisymmetric) function as it is the case in practice due to design issues. Finally, this system is subject to an external tork $T(\theta)$. In this framework, the equations of the system take the form:

$$\boldsymbol{M}(\boldsymbol{q})\ddot{\boldsymbol{q}} + \boldsymbol{f_{in}}(\boldsymbol{q}, \dot{\boldsymbol{q}}) + \boldsymbol{C}\dot{\boldsymbol{q}} + \boldsymbol{f_{int}}(\boldsymbol{q}) = \boldsymbol{F}\cos(n_e\theta)\,, \tag{1}$$

where $\boldsymbol{q} = [\theta, ..., S_i, ...]^T$ is the vector of unknowns (T denotes the transpose). $\boldsymbol{M}(\boldsymbol{q})$ is the mass matrix and depends on $\boldsymbol{q}$. $\boldsymbol{C}$ is the damping matrix. $\boldsymbol{f_{in}}(\boldsymbol{q}, \dot{\boldsymbol{q}})$ is the inertial forces vector, including Coriolis terms, and depends on $\boldsymbol{q}$ and $\dot{\boldsymbol{q}}$. $\boldsymbol{f_{int}}(\boldsymbol{q})$ is the internal forces vector and depends on $\boldsymbol{q}$. The external forces vector is $\boldsymbol{F} = [T_1, ..., 0, ...]^T$ where T_1 is the amplitude of the fundamental harmonic of the external torque. Finally, n_e is the excitation order and it can be regarded as a proportionality coefficient between the excitation frequency and the mean rotation speed.
Performing a linear study of this system, one can find that the $N+1$ eigenfrequencies can be written $\omega_0 < \omega_1 < \omega_2$ where ω_1 is of multiplicity $N-1$ and is also the natural frequency of the absorbers uncoupled from the rotor. The corresponding eigenmodes read $\phi_0 = [1, 0, \dots, 0]^T$, $\phi_2 = [-a, 1, \dots, 1]^T, a > 0$. ϕ_0 is a rigid body mode for which the absorbers are not excited and ϕ_2 is a mode for which absorbers are in-phase and in phase opposition with respect to the rotor. The mode shapes corresponding to the $N-1$ degenerated modes of eigenfrequency ω_1 all have a zero first component so that this mode is not excited by the external torque. For instance, for $N = 2$, $\phi_1 = [0, 1, -1]^T$: the absorbers are out of phase.

Non-linear study

In practice, the absorbers create an antiresonance of the rotor at frequency ω_1, which is thus the chosen operating point of the system [1]. In the following, a non-linear study of the steady-state response of the system is carried out in the vicinity of this operating point and we are interested in the response of the absorbers. An analytical model representing the dynamical behaviour of the system is developped. Following [2], the first step to build the model is to perform a change of the independent variable from t to θ and a scaling of the parameters. Then, to continue the study, we choose in this work to use the multiple scale method [3]. This approach leads to the obtention of a system of the form

$$\begin{cases} D_1 A_i = f_1(A_i, A_j, \varphi_i, \varphi_j) \\ D_1 \varphi_i = f_2(A_i, A_j, \varphi_i, \varphi_j) \end{cases} \tag{2}$$

where D_1 represents the derivative with respect to the slow time, and A_i and φ_i are the amplitude and phase of the first harmonic of the scaled i^{th} absorber's response. On the one hand, using the fact that the stable response of the absorbers is governed by the in-phase mode, one can solve (2) to get the unisson response of the absorbers. On the other hand, the stability of (2) can be assessed through the computation of the determinant of its jacobian [4]. This leads to the obtention of two bifurcation curves. The intersection of these curves with the absorbers' response indicates a stability change towards either a non-synchronous response of the absorbers (i.e. the absorbers stop moving in unisson) or an unstable periodic response (this leads to jumps phenomena).

Results and introduction of the design space

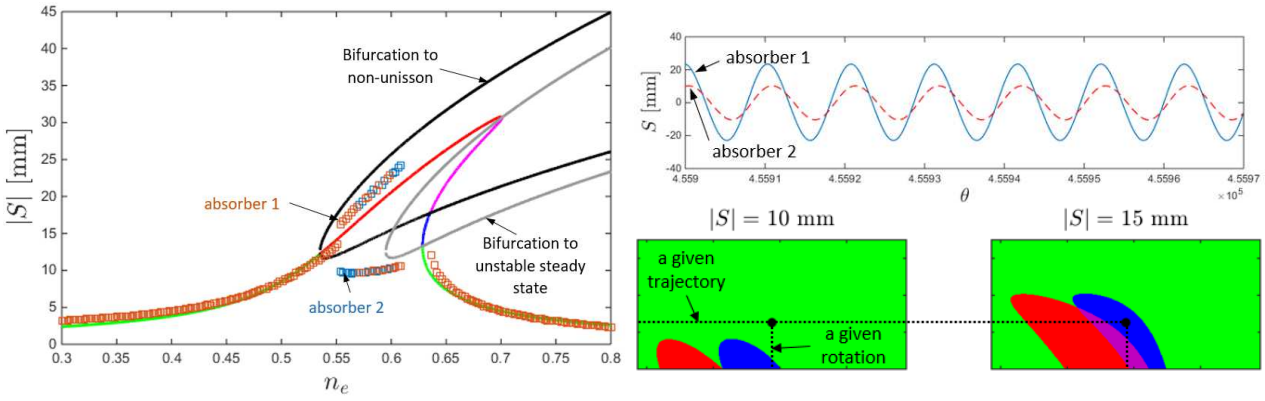

Figure 2: Left hand side: Analytic and numerical comparison of the absorbers' order response. Squares are numerical results. Top right hand side: Time signal of a non-unisson motion of the absorbers. Bottom right hand side: maps of designs representing their associated stability. The black dot corresponds to a given design (i.e. a given trajectory and a given rotation function). A color code indicates the stability of the response. Green: stable; red: unisson unstable; blue: steady state unstable; purple: unisson and steady state unstable

We choose here to apply the above study on a system of $N = 2$ absorbers. Fig.2 presents the response of the absorbers as a function of the excitation order, which has the meaning of a driving frequency. In this case, ω_1 corresponds to $n_e = 0.5$ and the resonance to ω_2. The numerical results are obtained through time integrations of the equations of motion using a Runge-Kutta algorithm. Like what was observed in the case of absorbers with a pure translation motion [5], results show that the system looses its stability through a pitchfork bifurcation in favor of a non-synchronous response. The model allows to accurately predict the bifurcation point, which is theoretically located at the intersction of the black curve (limit of unisson unstability region) and the unisson response. The time signal shown in Fig.2 clearly shows the difference in amplitude and in phase of the response of the non-synchronous response of the absorbers.
For a given excitation order and absorbers' amplitude, one can use the analytical model to assess the stability of several designs of TVA simultaneously. Designs can be defined by their associated trajectory and rotation functions, so that the result takes the form of 2D maps as it is shown on Fig.2. The black dot represented on these maps is fixed, as it is a given design. We can see that depending on the absorbers' amplitude of motion, this design goes through different stability states. These maps can be very efficient to determine whether a given design is prone to desynchronisation and/or jumps.

Conclusions

This study presents analytical and numerical results about non-linear localisation and jumps in a TVA. This work generalises previous studies to TVA with absorbers admitting a rotation about their mass center. The analytical and numerical results agree very well, showing that the model developped is able to give a good representation of the physical system. The design space has been introduced, allowing a quick assessment of the efficiency of TVA designs.

References

[1] A. Renault, O. Thomas, H. Mahé (2018) Numerical antiresonance continuation of structural systems. *Mechanical Systems and Signal Processing* **116**:963-984.

[2] A. Alsuwaiyan and S. Shaw (2002) Performance and dynamic stability of general-path centrifugal pendulum vibration absorbers. *Journal of Sound and Vibration* **252**:791-815.

[3] A. Nayfeh (2000) Perturbation methods. *WILEY*.

[4] J. Issa and S. Shaw (2015) Synchronous and non-synchronous responses of systems with multiple identical nonlinear vibration absorbers. *Journal of Sound and Vibration* **348**:105-125.

[5] A. Grolet, A. Renault and O. Thomas (2017) Energy localisation in periodic structures: application to centrifugal pendulum vibration absorbers. *ISROMAC 2017, Maui, Hawaii*.

Analytical Criterion of Multimodal Snap-through Flutter of Thin-walled Panels

Valery Pilipchuk
Wayne State University, Detroit, USA

Summary. Condition, under which thin-walled shallow panels can develop cyclical snap through dynamics due to airflow loads, is derived in the explicit analytical form. The methodology is based on the asymptotic of a perfectly flexible structure whose continuous manifold of equilibrium positions in the multidimensional space of configurations serves as a family of generating solutions. It is shown that supercritical airflows can cause global trajectories near such manifolds associated with a two-way snap through between the original and inverted positions of the panel.

Introduction

The term 'flutter' may cover quite different situations involving different mathematical tools of analyses [1]. The focus of the present study is flow induced dynamics with essentially nonlinear snap-through effects. Complexity of such type of problems is due to a multimodal strongly nonlinear structural behavior accompanied by a strong spatial coupling between the modes. The adapted elastic model of a shallow cylindrical panel ignores the longitudinal inertia term while taking into account the influence of membrane forces on the bending deformation as the only cause of geometrical nonlinearity [2, 3]. Assuming the presence of some initial imperfection and thus existence of multiple equilibrium positions, we define a snap-through flutter as the global panel dynamics with a cyclical self-sustained snap-through effect caused by the non-conservative aerodynamic load. Note that preserving the symmetric configuration during the snap-through motion would typically require a significant compression of the panel surface. As a result, any path through the least potential barrier must involve certain modal transitions avoiding significant tension-compression deformations that requires multimodal considerations. On one hand, this essentially complicates the analysis by increasing the problem dimension. However, on the other hand, increasing the dimension reveals a simple enough analytical estimate for the generating trajectory due to the asymptotic of a perfectly flexible panel. This represents a core of the approach, which assumes a global linearization near the manifold of a perfectly flexible panel [5, 6].

Technical details

Let us consider the elastic panel in a gas flow as schematically shown in Fig.1. The problem is reduced to the two-dimensional provided that the panel is subjected to a cylindrical bending. The panel thickness h is small compared to the amplitude of initial imperfection α, which itself is small compared to the span of the panel l. The outer surface of the panel interacts with the gas flow whose unperturbed velocity U is directed along the x-axis as shown in Fig.1.

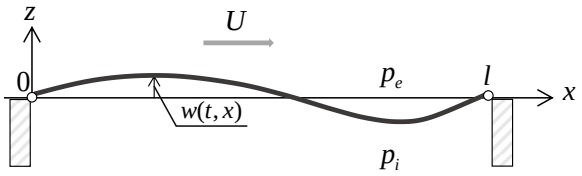

Figure 1: Aeroelastic model of a shallow panel in gas flow under the 'external' p_e and 'internal' p_i pressure loads.

The Lagrangian function of the panel is obtained based on the assumptions [2] as

$$L=\frac{1}{2}\rho h\int_0^l\left(\frac{\partial w}{\partial t}\right)^2 dx-V[w],\quad V[w]=\frac{Ehl}{2\left(1-\nu^2\right)}e[w]^2+\frac{Eh^3}{24\left(1-\nu^2\right)}\int_0^l\left(-\frac{\partial^2 w}{\partial x^2}+\frac{\partial^2 w_0}{\partial x^2}\right)^2 dx \tag{1}$$

$$e[w]=\frac{1}{2l}\int_0^l\left[\left(\frac{\partial w}{\partial x}\right)^2-\left(\frac{\partial w_0}{\partial x}\right)^2\right]dx \tag{2}$$

where $e[w]$ is the longitudinal strain, $V[w]$ is the potential energy of elastic deformations, and $w_0=w_0(x)$ is the shape of initial imperfection. Also, the variation of work done by the static pressure drop and nonconservative aerodynamic loads is given by

$$\delta A=\int_0^l f_z\delta w dx,\quad f_z(t,x)=\Delta p-2\gamma\rho h\frac{\partial w}{\partial t}-\rho_\infty cU\frac{\partial w}{\partial x},\quad \Delta p=p_i-p_e \tag{3}$$

where the aerodynamic load corresponds to a linearized equation of the so-called piston theory; see an overview in [4]. The manifold of zero-strain configurations is defined as

$$M_f=\{w: e[w]=0\} \tag{4}$$

Then the linearization of the differential equation of motion near the manifold (4) is conducted with a continual version of transformation [5, 6] in the form

$$w=\tilde{w}+\varepsilon n\zeta,\quad n=\nabla_{\tilde{w}}e[\tilde{w}]/\left\|\nabla_{\tilde{w}}e[\tilde{w}]\right\|,\quad \varepsilon^2=\left(h/\alpha\right)^2/12\ll 1 \tag{5}$$

where, $\nabla_{\tilde{w}}$ is the so-called variational derivative, which is taken at the arbitrary "point" $\tilde{w} \in M_f$, and the symbol $\|\ldots\|$ denotes the Euclidian distance in the functional space of the panel configurations, therefore *n* (5) is a unit vector, which is always perpendicular to the manifold.

Two-mode illustration

Transformation (5) admits a clear visualization (Fig.2) after the following two-mode approximation of the panel' shape

$$w(t,x) = \alpha\left(q_1(t)\sin\frac{\pi x}{l} + q_2(t)\sin\frac{2\pi x}{l}\right), \quad w_0(x) = \alpha\sin\frac{\pi x}{l} \tag{6}$$

Note that expansion (6) provides an exact discretization of the corresponding free panel. However, it becomes just an approximation due to the presence of first derivative $\partial w/\partial x$ in the loading function.

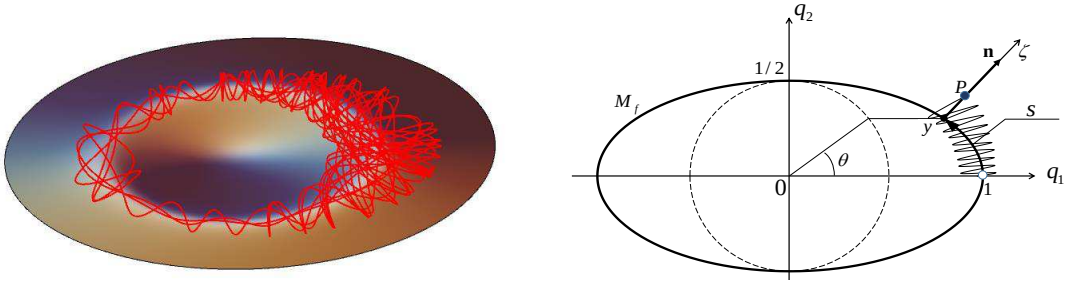

(a) (b)

Figure 2: a) Two-mode snap-through trajectory around the potential hill of tension-compression deformations in the neighborhood of zero-strain manifold (4) M_f, and b) the local normal coordinate ζ near an arbitrary point $y(\theta)$ of the manifold M_f.

Fig. 2a shows a typical shape of the potential energy $V = V(q_1, q_2)$ with a sample trajectory of a free panel, which is averagely resembles the shape of elliptic zero-strain curve shown in Fig2b, including its generalized coordinate θ describing the tangential motion, and the coordinate ζ describing the fast normal component associated with tension-compression.

Result

Fig.2b justifies the averaging procedure with respect to the fast normal motion component compared to the slow tangential motion. This finally gives an asymptotic one-degree-of-freedom effectively conservative system for the tangential motion

$$\frac{d}{dt}\left[\frac{1+3\sin^2\theta}{4}\left(\frac{d\theta}{dt}\right)^2 + \varepsilon^2 V_{eff}(\theta, Q)\right] = O(\varepsilon^4), \quad V_{eff}(\theta, Q) = \frac{4}{3}Q\theta + (10+6\cos\theta)\sin^2\left(\frac{\theta}{2}\right) \tag{7}$$

Analyzing equation $\partial V_{eff}/\partial\theta = 0$ gives the critical number *Q* above which this equation has no real roots:

$$Q_* = \frac{2cl^3\rho_\infty U_*}{\pi^4 D} = \frac{1}{8}\sqrt{\frac{1}{2}\left(827 + 73\sqrt{73}\right)} \tag{8}$$

If $Q > Q_*$ then system (7) has no equilibrium points and as a result will continue to rotate around the ellipse.

Conclusion

It is shown that a strong enough airflow can result in global dynamic trajectories near such manifolds associated with two-way snap through between the original and inverted positions of the panel. The effective tangential to the manifold forces created by the airflow, dissipation, static pressure drop, and structural elasticity adequately determine conditions for qualitatively different dynamic regimes. In particular, it is shown that a strong enough airflow can result in global dynamic trajectories near such manifolds associated with a two-way snap through between the original and inverted positions of the panel. It must be noted that the developed approach is applicable to other problems with different types of loading as well as analyses of free vibrations accompanied by large amplitudes with or without snap through events.

References

[1] Dowell H. (2014) A Modern Course in Aeroelasticity: Solid Mechanics and Its Applications. Springer International Publishing.
[2] Kauderer H. (1958) *Nichtlineare Mechanik*. Berlin, Springer
[3] Bolotin V., Grishko A., Kounadis A., Gantes C., Roberts J. (1998) Influence of Initial Conditions on the Postcritical Behavior of a Nonlinear Aeroelastic System. *Nonlinear Dynamics* **15**, 63-81.
[4] Amabili M. (2008) *Nonlinear Vibrations and Stability of Shells and Plates*. Cambridge University Press.
[5] Pilipchuk V. (1986) Method of Investigating Nonlinear Dynamics Problems of Rectangular Plates with Initial Imperfections. *Soviet Appl. Mech*. **22**, 162-168.
[6] Nagaev R. F., Pilipchuk V.N. (1989) Nonlinear Dynamics of a Conservative System that Degenerates to a System with a Singular Set. *PMM* **53**(2), 190-195.

Forced vibration analysis of non-linear Euler-Bernoulli beam using Efficient Path Following Method

Seyed Mojtaba Mousavi*, Meisam Jelveh*, Mohammad Homayoune Sadr † and Hadi Tohidi‡
* *PhD candidate, Department of Aerospace Engineering, Amirkabir University of Technology, Iran*
†*Assistance Professor, Department of Aerospace Engineering,Amirkabir University of Technology*
‡*Automotive Engineering Researcher, Safety and Restraint System Department, GÜNSEL Electric Vehicles (NEU Ltd.), Turkish Republic of Northern Cyprus*

Summary. This study focuses on the nonlinear response of dynamical systems due to harmonic force excitation using numerical continuation methods. Nonlinear Normal Modes (NNMs) is a powerful tool for studying behavior of nonlinear vibrational systems. Pseudo arc length continuation method is a very powerful method which is capable to handle strongly nonlinear systems by calculate the NNMs. Several methods are available to compute NNMs. Recently reviewed articles mention the computational cost of the pseudo arc length continuation method that limits its application. Based on assumption presented in other references and eliminate a mathematical construction, in this research used an updating formula to reduce the computational cost of pseudo arc length continuation algorithm. This modified method is called Efficient Path-Following Method (EPFM). In order, forced response of a single degree of freedom duffing system is computed using EPFM method. It seen that this method has decreased computational time considerably up to 70%. The results are in very good conformance to those obtained in other references which shows the accuracy the method. To study the ability of EPFM to handle continues systems, a nonlinear Euler-Bernoulli beam is considered and stable and unstable branches of the solution are computed. It observed that as the nonlinearity of the system gets stronger the updating formula becomes more effective.

Introduction

The structural engineers have utilized modern engineering knowledge to modelling the complex dynamic behavior of structure. For example, rotorcraft, turbomachines, airplanes, bridges, marine platforms, and robotic complex arm have become lighter, this way provide the possibility of operating at higher rates and velocities. Obviously, these On the other hand it could be led to non-linear response of structural systems. The structural response is affected by the nonlinearity. It may also cause complex resonance phenomena. Which makes it impossible to predict system behavior. *Rauscher* and *Mikhlin* develop a definition for modal analysis in nonlinear systems and naming it as "Nonlinear Normal Mode (NNM)". Shaw and Pierre modified the concept of NNM for the class of weakly nonlinear systems. Today, One of the well-known tool to provide a solution of nonlinear dynamical systems is NNMs.[1, 2] Namely, The movement of a system during internal resonance described using NNMs. also nonlinear vibration absorbers designing [2], also providing reduce order model of a nonlinear dynamic system to show system frequency changes and system deformation during free or forced vibration in nonlinear structures [3]. Also it applications include micromechanical oscillators and energy harvesting. Along with analytical methods such as harmonics, multiple scales and other methods for calculating the periodic responses of nonlinear dynamical systems, there are many numerical methods that are preferred because of their less complexity and less mathematical operators. There are many numerical algorithms for computing periodic solution families in nonlinear systems [4, 5].
One of the powerful methods in computation of periodic solution are neumerical continuation methods. *Kerschen* by combination of Shooting method and Pseudo Arc length with continuation presented a High-performance algorithm to calculate the nonlinear normal modes which are defined as periodic solutions of the nonlinear system [3, 6]. Michael W. Sracic in 2010 try to extend the Peeters algorithm to a system with cubic nonlinearity under the harmonic forced excitation [7]. Renson in 2016 has published an reviewed article [8] and studied the various methods for computation of nonlinear normal modes [numerical computation of NNM]. They mention that the "continuation method is a very powerful method for computation of periodic solutions however the computational cost has limited its application to large scale systems".
This paper presents the numerical continuation method modification to speed up the periodic solutions computations. The assumptions and basis of the modified algorithm based on [6, 7], changes made include integrating an updating formula in the algorithm and elimination of phase equation to decrease the computational time of the algorithm. To speed up the process of calculating the periodic solutions we eliminate the phase equation that presented by peeters, and using updating formula presented in [9]. The presented algorithm is called Efficient Path Following Method (EPFM)(Figure 1.f). Numerical experiments show that EPFM is approximately 60-70 percent faster. The theoretical foundations and the algorithm are presented first. Then, a one D.o.F.system and a nonlinear Euler-Bernoulli beam would be studied.

Theory and Algorithm

Governing equation of motion of a N-D.o.F system under harmonic force takes the following form in state space:

$$\dot{\mathbf{z}} = \mathbf{g}\left(\mathbf{z}(\mathbf{z}_0, t, T), t, T\right) = \begin{pmatrix} \dot{\mathbf{x}} \\ -\mathbf{M}^{-1}\left(\mathbf{C}\dot{\mathbf{x}} + \mathbf{K}\mathbf{x} + \mathbf{f}_{nl} - \mathbf{F}_e\right) \end{pmatrix} \tag{1}$$

Where $\mathbf{M}$, $\mathbf{K}$, and $\mathbf{C}$ are the mass matrix, stiffness matrix and the damping coefficient matrix, respectively, $\mathbf{f}_{nl}$ is the vector

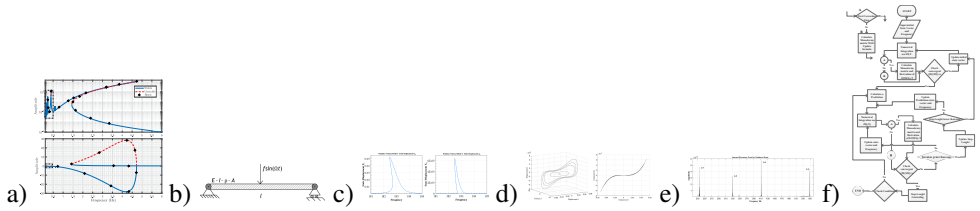

Figure 1: Results figures

of stored nonlinear force and $\mathbf{F}_e$ is the external harmonic force. $\mathbf{z} = [\mathbf{x}\,\dot{\mathbf{x}}]^T_{2N\times 1}$, t is independent variable of time and T is the period of oscillation s. The response of the system to the initial conditions of $\dot{\mathbf{z}}(t=0) = \mathbf{z}_0 = [\mathbf{x}_0\dot{\mathbf{x}}_0]^T$ is represented as $\mathbf{z}(t) = \mathbf{z}(\mathbf{z}_0, t, T)$ to indicate the dependence of the system's response to the initial conditions,$\mathbf{z}(\mathbf{z}_0, t=0) = \mathbf{z}_0$.
To compute periodic solution integrated Eq.(1) over time interval $[0, T]$. We need to look for the following conditions.

$$\mathbf{H}(\mathbf{z}_0, t, T) \equiv \mathbf{z}_T(\mathbf{z}_0, t, T) - \mathbf{z}_0 \approx 0 \tag{2}$$

Using Newton-Raphson algorithm process try to find periodic condition by expansion of the Eq.(2) as follows:

$$\left.\frac{\partial \mathbf{H}}{\partial \mathbf{z}_0}\right|_{(T,\mathbf{z}_0)} \Delta\mathbf{z}_0 + \left.\frac{\partial \mathbf{H}}{\partial T}\right|_{(T,\mathbf{z}_0)} \Delta T = -H(\mathbf{z}_0, t=T, T) \tag{3}$$

To calculate the periodic response, the equation (3) must be established. The partial derivatives of the equation (3) is calculated based on the procedure given in [7].
The only difference is the calculation of the first derivative which is calculated in the first iteration. Monodromy matrix ($\frac{\partial \mathbf{H}}{\partial \mathbf{z}_0}$) calculated by sensitivity analysis, then in the next iterations, updating formula given in [9] is used to calculate it. the updating formula defined as follows:

$$\left.\frac{\partial \mathbf{H}}{\partial \mathbf{z}_0}\right|^{k+1} = \left.\frac{\partial \mathbf{H}}{\partial \mathbf{z}_0}\right|^{k} + \mathbf{H}^{k+1}\frac{\left(\Delta\mathbf{z}_0^k\right)^T}{|\Delta\mathbf{z}_0|} \tag{4}$$

Results

Considering a system with one degree of freedom governed by Duffing equation presented in [7]. The results show that for force amplitude equal 0.1, EPFM was %52 faster than [7] and for amplitude equal 1.0, EPFM faster about %70, that result show in Figure 1.a. Also a nonlinear Euler-Bernoulli (Figure 1.b) analysed, Figure 1.c depict the periodic solutions compute by EPFM method and Figure 1.d show two dimensional manifold of 1st NNM. EPFM also captured superharmonic and subharmonic peaks as well Figure1.e. in this case EPFM is faster about %60 too.

Conclusions

An effective method is introduced in this study to compute periodic response of nonlinear systems under harmonic excitation. The method is called Efficient Path Following Method (EPFM). The algorithm is a combination of single shooting method and pseudo arc length continuation. The difference between EPFM and other algorithms is that, it uses an updating formula to compute jacobian matrix in correction step. that EPFM also reduces one of the equations in shooting method to speed up computation of periodic responses.
By analyzing the results and computational time, it is concluded that the EPFM is a very effective method for computation of periodic response of nonlinear systems and as the D.o.Fs of the system increase and the nonlinearity of the system gets stronger, this method gets more effective.

References

[1] McConnell KG and Varoto PS (1995) *Vibration testing: theory and practice*. John Wiley & Sons.

[2] Vakakis AF, Gendelman OV, Bergman LA, McFarland DM, Kerschen G and Lee YS (2008) *Nonlinear targeted energy transfer in mechanical and structural systems*, volume 156. Springer Science & Business Media.

[3] Kerschen G, Peeters M, Golinval JC and Vakakis AF (2009) Nonlinear normal modes, part i: A useful framework for the structural dynamicist. *Mechanical Systems and Signal Processing* 23(1): 170–194.

[4] Govaerts WJ (2000) *Numerical methods for bifurcations of dynamical equilibria*, volume 66. Siam.

[5] Seydel R (2009) *Practical bifurcation and stability analysis*, volume 5. Springer Science & Business Media.

[6] Peeters M, Viguié R, Sérandour G, Kerschen G and Golinval JC (2009) Nonlinear normal modes, part ii: Toward a practical computation using numerical continuation techniques. *Mechanical systems and signal processing* 23(1): 195–216.

[7] Sracic MW and Allen MS (2011) Numerical continuation of periodic orbits for harmonically forced nonlinear systems. In: *Civil Engineering Topics, Volume 4*. Springer, pp. 51–69.

[8] Renson L, Kerschen G and Cochelin B (2016) Numerical computation of nonlinear normal modes in mechanical engineering. *Journal of Sound and Vibration* 364: 177–206.

[9] Jelveh M (2015) *Analysis of Nonlinear dynamic systems using nonlinear normal modes*. PhD Thesis, Amirkabir University of Technology.

Tuesday, July 19, 2022
16:00 - 18:20

MS-15 Energy Transfer and Harvesting in Nonlinear Systems
Rhone 1

Chair: Anton Krivtsov - Emmanuel Gourdon

16:00 - 16:20
Passive suppression of axial-flow-induced vibrations of a cantilevered pipe discharging fluid using non-linear vibration absorbers
SCHWENCK Franco Maciel Vitor*, FRANZINI Guilherme, KHEIRI Mojtaba
*Escola Politecnica da Universidade de Sao Paulo [Sao Paulo] (Av. Prof. Luciano Gualberto, 380 - Butantã, São Paulo - SP, 05508-010 Brazil)

16:20 - 16:40
Passive Nonlinear Energy Sink for Pathological Tremor Reduction
GEBAI Sarah*, TURE Savadkoohi Alireza, LAMARQUE Claude-Henri
*École Nationale des Travaux publics de l'État (3 Rue Maurice Audin, 69120 Vaulx-en-Velin France)

16:40 - 17:00
Resonance Capture Cascade in Nonlinear Piezoelectric Shunt
DEKEMELE Kevin*, VAN Torre Patrick, LOCCUFIER Mia
*Ghent University (Technology park 125 Belgium)

17:00 - 17:20
Single mode control of overhead transmission line conductor with a nonlinear absorber
LEROUX Matthieu*, TURE Savadkoohi Alireza, LANGLOIS Sébastien
*École Nationale des Travaux Publics de l'État (3, Rue Maurice Audin, 69518 Vaulx en Velin (CEDEX) France) - Université de Sherbrooke, Faculté de Génie, Département de Génie Civil et de Génie du Bâtiment (Université de Sherbrooke, Québec, J1K 2R1 Canada)

17:20 - 17:40
Theoretical description of thermal transient grating experiment: dynamical and kinetic approaches.
SOKOLOV Aleksei*, BORISENKOV Bogdan, WOLFGANG Müller, KRIVTSOV Anton
*Technische Universität Berlin (Straße des 17. Juni 135 10623 Berlin Germany)

17:40 - 18:00
The Oscillating Frequencies and Energy Harvesting of a Piezoelectric Bimorph with Various Tail Structures in Different Hydraulic Flow Rate
CHEN Huai-Pu*, HUANG Yu-Hsi, LIN Hoang-Yan
*Department of Electrical Engineering, National Taiwan University (No.1, Sec.4, Roosevelt Rd., Taipei Taiwan)

Passive suppression of axial-flow-induced vibrations of a cantilevered pipe discharging fluid using non-linear vibration absorbers

Vitor Schwenck Franco Maciel[†], Mojtaba Kheiri[‡] and Guilherme Rosa Franzini[†]
[†]*Offshore Mechanics Laboratory, Escola Politécnica, University of São Paulo, Brazil*
[‡]*Fluid-Structure Interactions & Aeroelasticity Laboratory, Concordia University, Canada*

Summary. The present work addresses passive suppression of vibrations induced by internal axial flow in a cantilevered flexible pipe discharging fluid. The suppressor utilized is a rotative non-linear vibration absorber (NVA) composed of a mass connected to the extremity of a rigid bar hinged to the main structure by means of a dashpot. Numerical results from the mathematical model show that the NVA is able to bound the pipe structural response even in the supercritical flow regime.

Introduction

Today, the problem of a cantilevered pipe conveying fluid is considered as a classical problem in the study of the dynamics and stability of structures because of its simplicity and potential for displaying a wide range of complex dynamics. This problem belongs to a broader class of open dynamical systems with axial momentum transportation, and several studies, such as [1] and [2], have been made on the extension of Euler-Lagrange's equations and Hamilton's principle for such systems. Pipes conveying fluid, in their myriad of applications, such as heat exchangers and risers are susceptible to flow-induced instabilities and vibrations which in turn can lead to fatigue failure, excessive noise and leaks.

Non-linear vibration absorbers (NVAs) have been studied in the last decades as alternatives to linear suppressors, such as the tuned mass damper (TMD), for passive suppression of oscillations. Even though the literature on the use of NVAs for suppressing axial-flow-induced vibrations is recent, studies have shown that they are capable of adapting and effectively operating even if the load is broadbanded due to an energy transferring concept called Targeted Energy Transfer (TET), as documented in [3] and [4].

This paper focuses on the use of a particular class of suppressors, called rotative NVA, with the objective of suppressing axial-flow-induced vibrations of cantilevered pipes discharging fluid. Such a suppressor is composed of a point mass connected to the extremity of a rigid bar which, in turn, is hinged to the pipe via a dashpot. In [3], the authors discuss passive suppression of internal-flow-induced oscillations of a pinned-pinned pipe using a different type of NVA. To the best of the authors' knowledge, the use of a rotative NVA for suppressing axial-flow-induced vibrations of pipes conveying fluid has not been previously addressed and is the main novelty of the present work.

Mathematical model

Consider a flexible pipe discharging fluid as shown in Fig. 1a. The pipe has the length L, the diameter D, the bending stiffness EI and the mass per unit length m. The fluid has the mass per unit length M and flows at a constant velocity U. At a point $\bar{x}$ along the pipe length, the NVA is placed and constrained to rotate in the (y,z)-plane. The device has the mass m_n, the radius r and the damping constant c. The pipe transverse displacement is represented by $w(x,t)$ while the angular displacement of the NVA is $\theta(t)$. It is assumed that the pipe is inextensible and that the flow is incompressible and has a uniform profile in the pipe (i.e. the plug flow model). By using the extended Hamilton's principle found in [5], the dimensional equations of motion can be found and are made dimensionless using the following quantities:

$$\tau = \left(\frac{EI}{m+M}\right)^{1/2}\frac{t}{L^2},\ \ \xi = \frac{x}{L} = \frac{s}{L},\ \ \eta = \frac{z}{L} = \frac{w}{L},\ \ \gamma = \frac{(m+M)gL^3}{EI},\ \ \hat{\delta}(\xi-\bar{\xi}) = L\delta(x-\bar{x}),$$
$$\hat{c} = \frac{cL^2}{m_n\left(\frac{EI}{m+M}\right)^{1/2}r^2},\ \ u = \left(\frac{M}{EI}\right)^{1/2}UL,\ \ \hat{m}_n = \frac{m_n}{(m+M)L},\ \ \beta = \frac{M}{(m+M)},\ \ \hat{L} = \frac{L}{D},\ \ \hat{r} = \frac{r}{D}, \tag{1}$$

where s is the curvilinear coordinate along the pipe length, and δ is the Dirac Delta function. The resulting dimensionless partial differential equation is then discretized using Galerkin's method, with the adoption of the first five mode shapes of a cantilevered Euler-Bernoulli beam, i.e., $\eta(\xi,\tau) \cong \sum_{n=1}^{5} A_n(\tau)\psi_n(\xi)$, where ψ_n are the mode shapes and A_n are the corresponding generalized coordinates. Using the notation $(\,)' = \partial/\partial\xi$ and $\dot{(\,)} = \partial/\partial\tau$, the final system of six coupled second-order ordinary differential equations is obtained in the form of equations (2) and (3), for $k = 1, ..., 5$.

Results

Consider three different systems: system 1 is the unaltered (or plain) pipe, system 2 is composed of the pipe and a lumped mass rigidly attached to the pipe at different spanwise locations and, finally, system 3 is the one with the NVA. System 2 allows for investigations into the effect of the placement of the stationary lumped mass on the critical flow velocity – "static" effect – via Lyapunov's Indirect Method. On the other hand, system 3 allows for investigations into the capability of the device to mitigate vibrations of the main structure due to its motion with respect to the pipe, which locally dissipates energy in the associated dashpot (TET mechanism). Here, passive suppression is achieved by a "dynamical" effect.

$$\left(\sum_{n=1}^{5}\int_0^1 \psi_k\psi_n d\xi + \hat{m}_n\sum_{n=1}^{5}\int_0^1 \hat{\delta}(\xi-\bar{\xi})\psi_k\psi_n d\xi\right)\ddot{A}_n + \left(2\beta^{\frac{1}{2}}u\sum_{n=1}^{5}\int_0^1 \psi_k\psi_n' d\xi\right)\dot{A}_n +$$
$$+\left(\sum_{n=1}^{5}\int_0^1 \psi_k\psi_n'''' d\xi + u^2\sum_{n=1}^{5}\int_0^1 \psi_k\psi_n'' d\xi - \gamma\sum_{n=1}^{5}\int_0^1 (1-\xi)\psi_k\psi_n'' d\xi + \gamma\sum_{n=1}^{5}\int_0^1 \psi_k\psi_n' d\xi\right)A_n -$$
$$-\frac{\hat{r}}{\hat{L}}\hat{m}_n(\ddot{\theta}\sin\theta + \dot{\theta}^2\cos\theta)\int_0^1 \hat{\delta}(\xi-\bar{\xi})\psi_k d\xi = 0, \tag{2}$$

$$\ddot{\theta} - \frac{\hat{L}}{\hat{r}}\sin\theta\sum_{n=1}^{5}\ddot{A}_n\psi_n(\bar{\xi}) + \hat{c}\dot{\theta} = 0. \tag{3}$$

Throughout this extended abstract, we assume $\beta = 0.20$ and $\gamma = 10$. An example of the analysis on the "static" effect of the device is given in Fig. 1b, which shows the variation of u_{cl}/u_c (u_c and u_{cl} being the critical flow velocities for systems 1 and 2, respectively) as a function of the lumped mass value and its location. As seen, counter-intuitively, the lumped mass has a destabilizing effect with the exception of the region approximately defined by $\bar{\xi} \in [0.35, 0.65]$ and $\hat{m}_n \in [0.025, 0.2]$, in which the critical flow velocity ratio u_{cl}/u_c increases as $\hat{m}_n$ is increased. For system 3, the "dynamical" effect is then evaluated through a numerical integration of the equations of motion at $u = u_{cl}$, which leads to unbounded responses of system 2. Considering $A_1(0) = 0.1$ and $\theta(0) = 0.1$ as the non-trivial initial conditions, Fig. 3c presents the time-history of the displacement at the free end of the pipe, i.e. $\eta(\xi = 1, \tau)$, the associated amplitude spectrum and the angular response of the NVA, $\theta(\tau)$, for the case in which the suppressor is placed at $\bar{\xi} = 0.5$ and is characterized by $\hat{m}_n = 0.01$, $\hat{c} = 0.2$ and $\hat{r} = 0.6$. Both time series are shown within $\tau \in [2000, 4000]$ range. Note that the response is bounded, even though for a supercritical internal flow velocity for system 2.

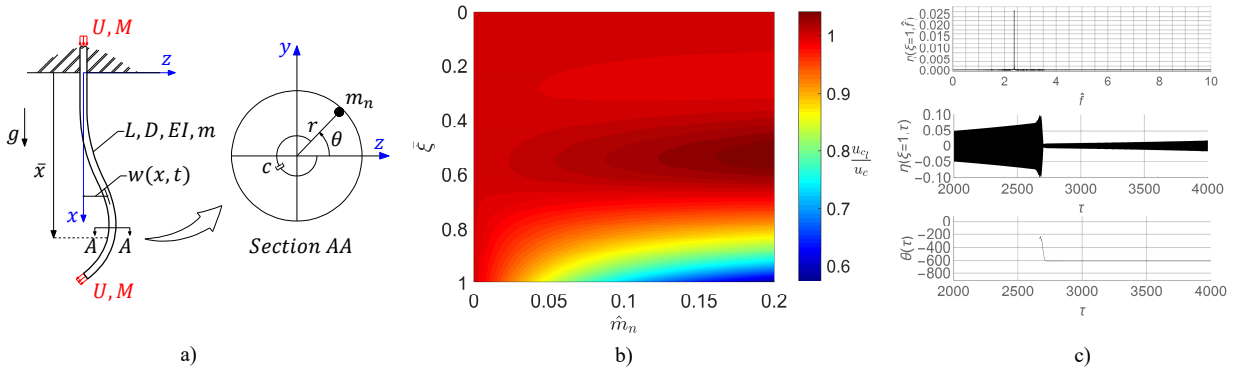

Figure 1: a) Schematic drawing of the system, b) (u_{cl}/u_c) as a function of $(\hat{m}_n; \bar{\xi})$ - System 2, c) Example of response - System 3.

From Fig. 3c, a strongly modulated response composed of two intermittent regimes can be observed. The first regime is characterized by a growth in the pipe response, while the device oscillates around the positions that are aligned with the pipe motion, i.e. where $\cos\theta = \pm 1$. Then, when the energy reaches a certain threshold, the NVA rotates with practically the same frequency as the oscillation frequency, that is $\hat{f} = 2.37$. Hence, we may conclude that the observed passive suppression is associated with a $1:1$ resonance.

Conclusions

A rotative NVA was utilized to successfully mitigate vibrations of a cantilevered flexible pipe discharging fluid. Both the "static" and "dynamical" effects were examined. While the former showed to have an important role in the stability of the system (i.e., the critical internal flow velocity), the latter was responsible for bounding the dynamical response due to energy dissipation. More numerical results along with a more comprehensive analysis of the static and dynamic effects will be presented in the full-length paper.

Acknowledgements

The authors acknowledge FAPESP for the grants 19/27855-2 and 2021/04434-1 and CNPq for the grants 305945/2020-3 and 161955/2021-5.

References

[1] Benjamin T.B., and Batchelor, G. K. (1962) Dynamics of a system of articulated pipes conveying fluid - I.Theory. *Proceedings of the Royal Society of London. Series A. Mathematical and Physical Sciences* **457-486**

[2] Casetta L. and Pesce C.P. (2013) The generalized Hamilton's principle for a non-material volume. *Acta Mechanica* **919–924**

[3] Yang T., Liu T., Tang Y., Hou S., and Lv X. (2018) Enhanced targeted energy transfer for adaptive vibration suppression of pipes conveying fluid. *Nonlinear Dynamics* **1937-1944**

[4] Lee Y.S. et al. (2008) Passive non-linear targeted energy transfer and its applications to vibration absorption: a review. *Journal of Multi-Body Dynamics*

[5] Païdoussis M.P. (2014) Fluid-Structure Interactions and Axial Flow. Volume 1, 2nd Edition, *Elsevier Science*

Passive Nonlinear Energy Sink for Pathological Tremor Reduction

Sarah Gebai, Alireza Ture Savadkoohi and Claude Henri Lamarque
LTDS UMR CNRS 5513, École Nationale des Travaux publics de l'État

Summary. Medications used to reduce the pathological tremor causes severe side effects which affects the life quality of the patients. A mechanical solution using nonlinear passive controllers is suggested to reduce the tremor. A light weight non-smooth nonlinear energy sink (NES) attached to the forearm of a modeled upper limb system was able to reduce the angular motions, of different parts of the upper limbs, after a short period of time.

Introduction

Tremor is an involuntary oscillatory movement of a body part triggered by alternating simultaneous antagonistic muscles contractions. It is associated with neurological disorders which lead to pathological tremor, like the Parkinson and essential tremors. Neurologically disordered patients suffer from a frustrating involuntary tremor which prevents the patients from achieving their daily life tasks and can cause social isolation. There is still no cure for the pathological tremor, and the effect of the used medication and surgical treatments are temporary. In addition, the treatments can cause severe side effects specially in case of non-responsiveness or medication failure.
Research interest was recently shifted to find a mechanical solution for reducing the vibration tremor energy at the upper limbs of the patient. The mechanical absorber is suggested to counter-act the tremor and to compensate the failure of the muscles in performing accurate motor movements. A passive controller, using a non-smooth nonlinear energy sink (NES) [1], is suggested in this paper to reduce the involuntary tremor of a modeled upper limb system.

Modeled system

The upper limbs of the human is modeled dynamically to reflect the tremulous motion. The response of the system is used to design the physical parameters of the nonlinear vibration absorber placed at the forearm segment. The performance of the suggested controller is examined by comparing the response of the system before and after the addition of the NES.

Upper limbs

The upper limb is modeled as a two degrees-of-freedom (DOF) system oscillating in the vertical plane as shown in shown in Figure 1. The upper limbs can be modeled as two rigid links, the upper-arm as one segment, and the forearm and hand together as a separated segment [2]. The links are represented as massless rods of length (l) with a concentrated mass (m) placed at the position of the centroid (r), where the indices 1 and 2 refer to the upper arm and forearm, respectively. The modeled system allows the flexion-extension planar motion at the shoulder and elbow joints, where θ_1 and θ_2 are the angular displacement responses at these joints, respectively.
The musculoskeletal modeling of the upper limb is reached by the addition of the shoulder, elbow and Biceps brachii muscles to the skeletal system. The passive elements of the muscles are the stiffness (k) and damper (c), such that the indices 1, 2 and 3 corresponds to the shoulder, elbow and Bicesps brachii. The upper limb system is excited the active torques generated by the muscles. The signals of the muscles can be measured by the Electromyography (EMG), which can be used to detect the operational frequency of the muscle, and the amplitude of the signal at this frequency. The inertial measurement unit (IMU) can be used to determine the acceleration and angular velocity ranges, which needs to be reached by the responses of the modeled upper limb system.

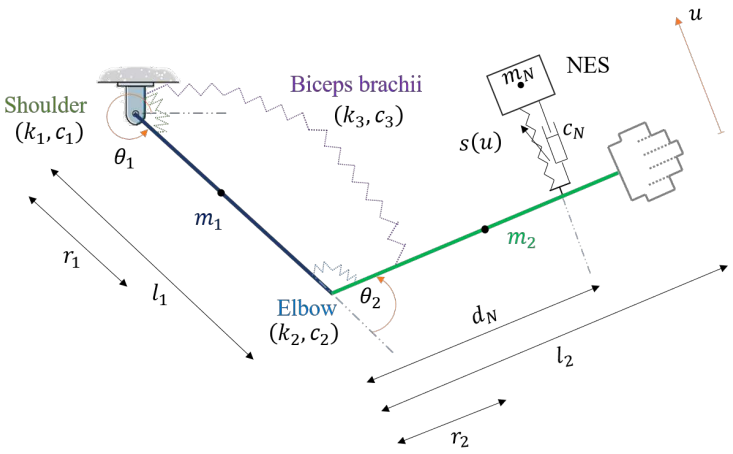

Figure 1: Dynamical modeling of the upper limb in the vertical plane with a NES

Nonlinear absorber

The well modeled upper limb system leads to an accurate design of the NES parameters. The NES has a light weight mass (m_N), placed at the forearm segment at a distance (d_N) away from the elbow joint. The displacement response of the NES (u) is acting in the vertical place, in a direction perpendicular to the forearm segment. The NES oscillating in this direction, is designed to absorb the flexion-extension angular displacement of the upper limbs during its oscillation in the vertical plane. A non-smooth piece-wise linear function is chosen for the NES since it can create, a better controllability effects, when attached to a system affected by the gravitational field, than the cubic restoring function [3]. The piece-wise linear function is characterized by the stiffness of the NES (k_N) and the clearance ($2d$).The damping of the NES is c_N.

Complexification of the system

The nonlinear equation representing the motion of the global system (upper limbs with NES) is derived using Euler-Lagrange formula. The equations are linearized using Taylor series multivariable linearization method in terms of θ_1 and θ_2, while preserving the nonlinearity of the NES (u).
The complex variables of Manevitch [4], are applied to the partially linearized equations of motion transformed to the modal coordinates. The multiple scale method [5] is used to treat the system at different timescales, low timescale $\tau_0 = t$ and fast timescale $\tau_j = \epsilon^j t$, such that t is the time, $\epsilon = \frac{m_1}{m_N}$ and $j = \{1, 2\}$. The averaged equation is obtained by applying a truncated Fourier series (constant terms and first harmonics) [6] to the equations transformed to the modal coordinates.

Results and discussion

The response of the system is analyzed in different time scales. The slow invariant manifold (SIM) and characteristic points of the system are obtained from the analytical study. The numerical response of the system shows to follow the SIM obtained analytically. The parameters of the NES are designed such that resonance occurs at the fundamental frequency of the main system. Figure 2 shows the angular displacement response at the shoulder and elbow joints before and after the addition of the NES, for different m_N. The controllability response of the NES is faster when its mass is higher. The NES of 20.7 g reduces the response of the system after 180 s. The mass of the NES can still be increased to obtain a faster performance.

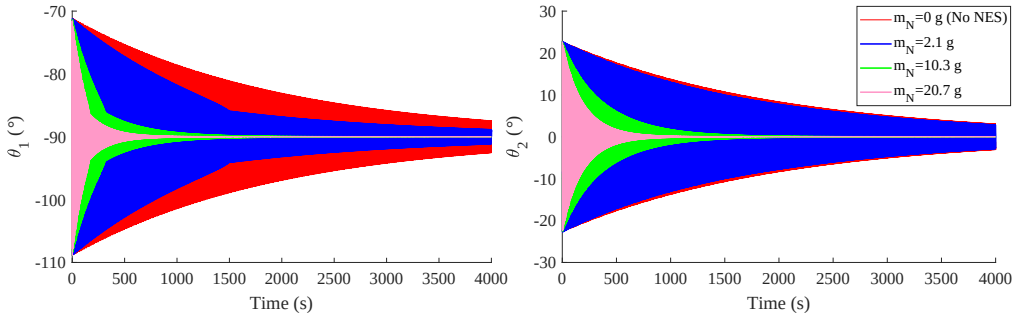

Figure 2: Angular displacement signals at the shoulder and elbow joints simulated numerically with and without NES for different m_N

Conclusions

The NES with piece-wise linear function is effective in reducing the involuntary tremor gravitational energy transmitted to the upper limbs due to the muscles contraction. The NES can be designed in the form of a non-invasive device to help people with pathological tremor.

Acknowledgement

The authors would like to thank CNRS for supporting this work in the framework of the "programme de prématuration du CNRS".

References

[1] Vakakis A., Gendelman O., Bergman L., McFarland D., Kerschen G., Lee Y. (2008) Nonlinear Targeted Energy Transfer in Mechanical and Structural Systems. Solid Mechanics and Its Applications, Springer, NL.

[2] Jackson K.M., Joseph J.T., Wyard S.J. (1978) A mathematical model of arm swing during human locomotion. *J. Biomech* **11**(6):277-289.

[3] Hurel, G., Ture Savadkoohi A., Lamarque, C.-H. (2019) Nonlinear vibratory energy exchanges between a two-degree-of-freedom pendulum and a nonlinear absorber. *J. Eng. Mech* **145**(8):04019058.

[4] Manevitch L.I. (2001) The description of localized normal modes in a chain of nonlinear coupled oscillators using complex variables. *Nonlinear Dyn* **25**(1):95-109.

[5] Nayfeh A.H., Mook D.T. (1979) Nonlinear oscillations. Wiley, NY.

[6] True Savadkoohi A., Lamarque C.-H., Weiss M., Vaurigaud B., Charlemagne S. (2016) Analysis of the 1:1 resonant energy exchanges between coupled oscillators with rheologies. Nonlinear Dynamics, **86**(4):2145-2159.

Resonance Capture Cascade in Nonlinear Piezoelectric Shunt

Kevin Dekemele*, Patrick Van Torre** and Mia Loccufier*
*Departement of Electromechanical, Systems and Metal Engineering, Ghent University, Belgium
**Departement of Information Technology, Ghent University, Belgium

Summary. Nonlinear energy sinks (NESs) serve to transfer and absorb vibration energy of a mechanical system. They are locally attachted to the system and consist of a light mass, a damper and a nonlinear stiffness. Compared to linear dynamic vibration absorbers (DVA), NESs mitigate vibrations over a wider frequency band. If the mechanical system is subjected to a shock load, a NES is able to dissipate the energy of each mode separately and sequentially, from high to low frequency. This unique feature is called resonance capture cascade (RCC). When piezoelectric (PE) patches are bonded with the vibrating mechanical system, it can serve as an electrical DVA, provided a suitable shunt circuit is attached over the PE electrodes. In literature, several nonlinear shunts have been proposed and implemented. While the increased robustness has been discussed, there has been no attempt thus far to design an electrical NES specifically for resonance capture cascade. In this abstract the RCC capabilities of a mechanical NES as well as an electrical NES is shown.

Introduction

Machines are made lighter and more compact, civil structures become higher and slender. Consequently, more flexible mechanical systems are created which are susceptible to unacceptable vibration levels. To protect these mechanical systems, an auxiliary structure is attached, called a dynamic vibration absorber. It typically consists of a linear mass-spring-damper system. The linear DVA is able to mitigate a single frequency really well. However, it does so only in a narrow frequency band and as such, if the mechanical system has shifting vibration frequencies or multi-modal vibrations, the linear DVA fails to mitigate the vibrations down to an acceptable level. To increase the bandwidth of the DVA, a nonlinear energy (NES) sink has been proposed in literature [1]. The NES has a nonlinear connecting spring which typically has a cubic spring characteristic.

Resonance Capture Cascade with Mechanical NES

If a mechanical system is shock loaded, a free vibration ensues, consisting of several vibration modes. While a linear DVA is not able to decay all modes efficiently, a NES can engage in resonance capture cascade (RCC). During RCC, the NES mitigates the vibration modes sequentially, from high to low frequency [1]. More recently, the author of the current abstract [2] presented a thorough study of RCC and tuning of the NES to increase the speed of RCC. To introduce RCC, a mechanical system with 2 vibration modes is equipped with a NES, Figure 1a. The NES has the following dynamics:

$$m_{na}\ddot{x}_{na} + c_{na}(\dot{x}_{na} - \dot{x}_1) + k_{na}(x_{na} - x_1)^3 + k_{lin}(x_{na} - x_1) = 0 \tag{1}$$

with m_{na} the NES' mass, c_{na} the NES' damping, k_{na} the NES' nonlinear stiffness and k_{lin} the NES' linear stiffness. The bottom mass of the mechanical system is subjected to an initial speed of $\dot{x}_1(0) = 1$. The RCC is seen in the NES vibrations, Figure 1c, with the shifting vibration frequency best seen on its wavelet transform Figure 1d. At first, the NES vibrates with the frequency of the second mode. Then, after about 25 s, the NES shifts its frequency to the first vibration mode. After about 120 s, the NES is barely moving. The vibration in the mechanical system, Figure 1e are mitigated over the 120 s where the NES is active, with the second mode decaying first, and then the first mode. A small amount of residual energy is left after RCC.

Resonance Capture Cascade with Electrical NES as Piezo Electric Shunt

By bonding piezoelectric (PE) material to a vibrating mechanical system, the vibration energy can be transferred to electrical energy. Similar vibration mitigation performance as with mechanical DVAs can be achieved by shunting the electrodes of the PE with a suitable circuits. Because of the similar dynamical equations in mechanical and electrical domain, a NES shunt was proposed in [3]. However, no attempt thus far has been made to achieve RCC. The dynamics of a NES is highly similar to the nonlinear shunt:

$$L\ddot{q} + R\dot{q} + \frac{1}{C_3}q^3 + \frac{1}{C_1}q + V = 0 \tag{2}$$

with V the voltage over the PE electrodes, generated by the vibrations, and $q = \int I dt$ the charge. A numerical investigation now shows that RCC occurs in the electrical NES. The vibrating mechanical systems are two cantilever beams with tip masses, connected at the tip with a spring, Figure 1c. The proposed mechanical system has two dominant modes and is easy to construct experimentally. The PE patch is shunted with a NES. The electrical vibrations in the current are shown on Figure 1f and Figure 1g . The behavior is identical to the mechanical NES. The second mode is mitigated first, followed by the first mode. This can be seen as well in the tip displacement of the beam, Figure 1h.

Conclusions

Resonance capture cascade (RCC) is the unique feature of nonlinear energy sinks (NESs) that can be exploited to mitigate transient multi-modal vibrations. During RCC, vibration modes of a vibrating mechanical system are sequentially mitigated, from high to low frequency. This feature is associated with mechanical NES. In this abstract is is shown that this unique feature of the NES is also possible in shunted piezoelectric patches.

References

[1] A. F. Vakakis, O. V. Gendelman, L. A. Bergman, D. M. McFarland, G. Kerschen, and Y. S. Lee. *Nonlinear targeted energy transfer in mechanical and structural systems*, volume 156. Springer Science & Business Media, 2008.

[2] K. Dekemele, R. De Keyser, and M Loccufier. Performance measures for targeted energy transfer and resonance capture cascading in nonlinear energy sinks. *Nonlinear Dynamics*, 93(2):259–284, 2018.

[3] B. Zhou, F. Thouverez, and D. Lenoir. Essentially nonlinear piezoelectric shunt circuits applied to mistuned bladed disks. *Journal of Sound and Vibration*, 333(9):2520–2542, 2014.

[4] `https://www.piceramic.com/en/products/piezoceramic-actuators/patch-transducers/p-876-duraact-patch-transducer-101790/`.

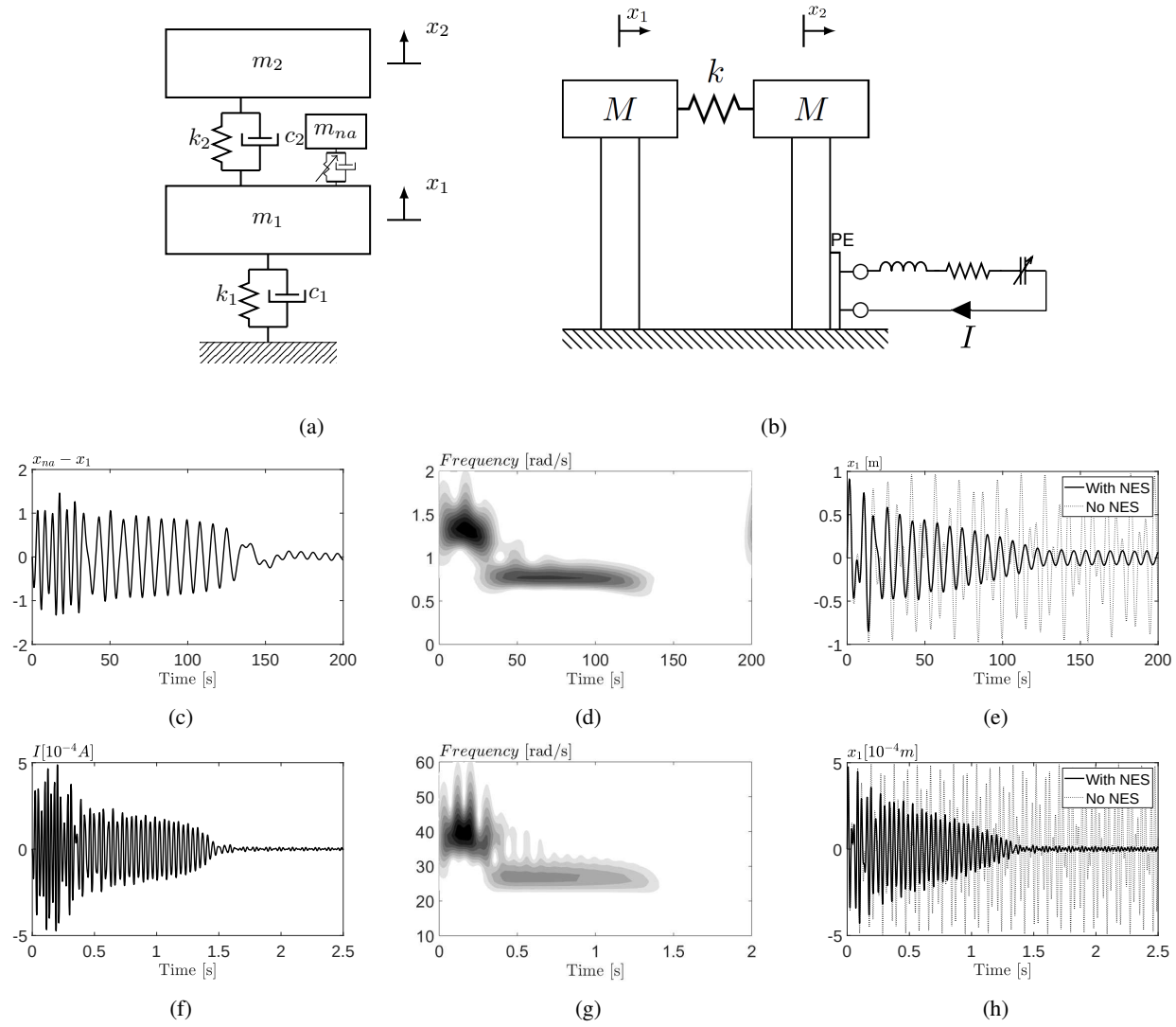

Figure 1: Mechanical system (a) with $c_1 = c_1 = k_{lin} = 0$, $m_1 = k_1 = 1$, $k_2 = m_2 = 0.2$, $m_{na} = 0.05$, $l_{na} = 0.07$ and $c_{na} = 0.02$. Mechanical system (b) consisting of two aluminum cantilever beams of 170 mm length, 35 mm width and 2 mm thick, tip masses $M = 0.033$ kg and connecting spring $k = 550$. The shunt consist of $L = 250$ H, $R = 5000$ Ω, $C_3 = 0.25$ μF^3 and $C_1 = -50$ nF. The bonded PE patch the DURA-ACT P-876.A15 of PI [4]. The mechanical NES vibrations (c) and its wavelet transform (d). On (e), the vibrations of the first mass of (a) and on (h) the vibrations of the tip of the first cantilever beam of (b).

Single mode control of overhead transmission line conductor with a nonlinear absorber

Matthieu Leroux[*,†], Alireza Ture Savadkoohi[*] and Sébastien Langlois[†]
[*]*Univ Lyon, ENTPE, CNRS UMR5513, LTDS, France*
[†]*Département de Génie Civil et de Génie du bâtiment, Université de Sherbrooke, Sherbrooke, Canada*

Summary. The possibility of controlling of oscillations of overhead transmission lines by a nonlinear absorber is studied. We consider a linear beam with elastic boundaries conditions in displacement and rotation under harmonic excitations. After complexification of the system variables, we study the system at different time scales. The fast time scale provides the SIM (Slow invariant Manifold). Then, a stability study of the SIM is performed. Studying the slow time scale leads to detection of equilibrium and singular points of the system. Finally, we compare the analytical results with numérical solution obtained with the finite element method (FEM)(Code_Aster).

Introduction

Galloping of overhead transmission lines brings large amplitude at low frequency oscillations [1]. This phenomenon occurs when there is an aerodynamic instability on iced conductors [1]. Since the 1930s several researchers work on a better understanding of this phenomenon and to predict the amplitude of oscillation depending on the wind parameters [2]. Some devices have been designed to mitigate the amplitude of oscillations caused by galloping. Torsion pendulum have been designed to reduce galloping vibrations [3]. Interphase spacers have been developped to avoid shot circuits and collisions between conductors [4]. On the other hand, there are some nonlinear dampers that can reduce aeolian vibration like Hydro-Quebec damper [6]. However, galloping mitigation with a nonlinear energy sink (NES) [5] have not been stydied yet. The NES has a small mass in comparison with the primary system and the two systems are coupled by a nonlinearity [7]. Hence, the main objective of this study is the behaviour of a cable coupled with a NES. We will locally modelise the cable with a linear beam with elastic boundary conditions in displacement and rotation. We conduct an analytical study of the system at different time scales. Complexification method of Manevitch [8] is used to understand the asymptotic behaviour of the system. We will validate the analytical results by comparison with the numerical solution obtained from the finite element method (FEM) Code_Aster.

Linear beam with elastic boundary conditions coupled to a NES

We consider the system of a beam with elastic boundary conditions coupled with a nonlinear oscillator. We can see on figure 1a the boundary conditions in translation k_0, k_L and rotation k_{R0}, k_{RL}. The nonlinear oscillator is coupled to the beam at the distance l_n from the extreme left part of the beam. One can see on figure 1b the restoring forcing function of the non-smooth NES. Only one modal coordinate of the beam wil be taken into account, for instance the coordinate of the first mode. The system is under external sinusoidal excitations $F_1(t)$, $F_2(t)$. We will consider the vertical displacement of the beam $v(x,t)$ and the vertical displacement of the oscillator $u(t)$. The effects of gravity are neglected.

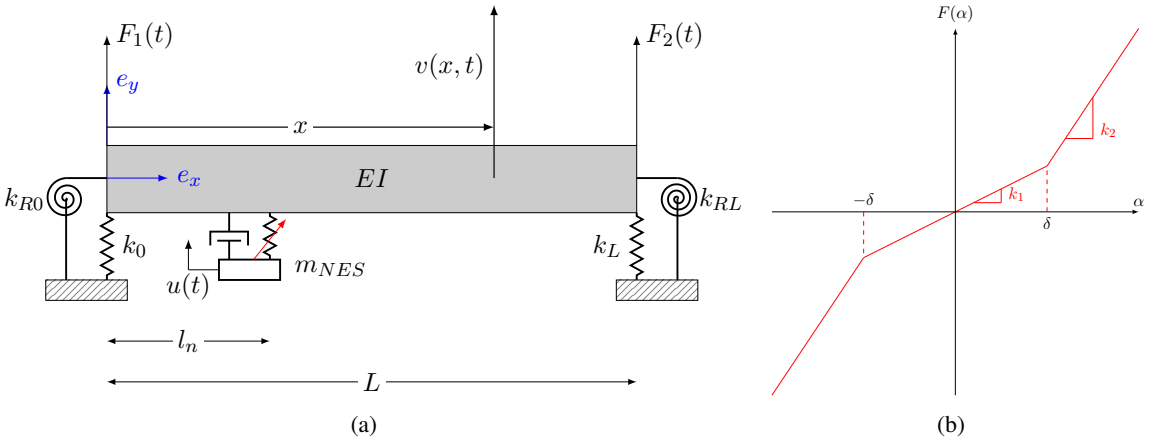

Figure 1: a) Linear beam with elastic boundary conditions coupled to a NES; b) non-smooth NES restoring forcing function.

The system behaviour around a 1:1 resonance is studied. We project the governing equations of the system on the first mode. The variables of Manevitch are introduced to study the enveloppe response of the system [8]. Different time scales are introduced and the system behaviour at each time scale is detected. By studying the dynamics at fast time scale we obtain the slow invariant manifold (SIM) [9]. One can see on figure 2 the SIM curve for cubic and non-smooth NES.
Then, we study the dynamics at a slow time scale and we obtain the equilibrium points depending on the excitation parameters namely, frequency and the amplitude [10]. On figure 3 one can see the equilibrium point depending on σ the normalised excitation frequency.

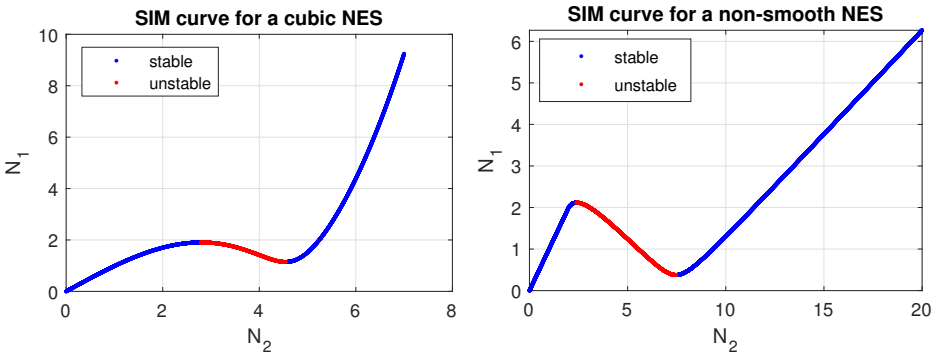

(a) (b)

Figure 2: The SIM of the system for a) cubic NES; b) non-smooth NES, N_1 and N_2 stand for energies related to the mode and the NES, respectively.

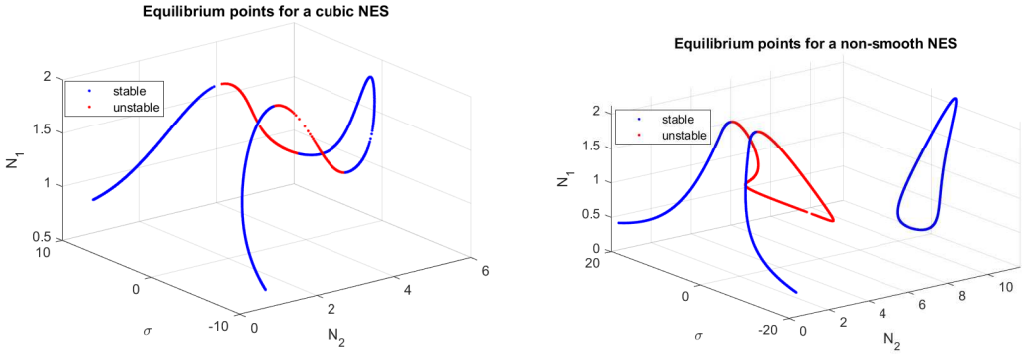

(a) (b)

Figure 3: Equilibrium points in three dimensions (N_2,σ,N_1) for a) cubic NES; b) non-smooth NES, σ is the detuning parameter from studying the behaviour around a 1:1 resonance.

Finally, we can validate our theorical results with numerical integration with RK4 method and compare with FEM solution obtained with Code_Aster. The FEM enables to detect system response for a given σ and to compare its enveloppe with the analytical prediction. The developpements provide design tools for tuning parameters of the NES.

References

[1] P. Van Dyke, D. Havard, and A. Laneville (2008) Effect of Ice and Snow on the Dynamics of Transmission Line Conductors, Atmospheric Icing of Power Networks, Springer Netherlands.

[2] J. P. D. Hartog. (1932) Transmission line vibration due to sleet. *Transactions of the American Institute of Electrical Engineers* **51**:1074-1076.

[3] D. G. Havard, J. C. Pohlman. (1984) Five years field trials of detuning pendulums for galloping control. *IEEE Transactions on Power Apparatus and Systems* **PAS-103** 318-327.

[4] A. Edwards, R. Ko. (1979) Interphase spacers for controlling galloping of overhead conductors. *IEEE Symposium on Mechanical Oscillations of Overhead Conductors* 101-109.

[5] A. F. Vakakis, O. V. Gendelman, L. A. Bergman, D. M. McFarland, G. Kerschen, and Y. S. Lee. (2008) Nonlinear targeted energy transfer in mechanical and structural systems. *Springer Science & Business Media* **56**.

[6] S. Langlois, F. Legeron. (2014) Prediction of Aeolian Vibration on Transmission-Line Conductors Using a Nonlinear Time History Model-Part I : Damper Model. *IEEE Transactions on Power Delivery* **29**:1168-1175.

[7] Y. S. Lee, A. F. Vakakis, L. A. Bergman, D. M. McFarland, G. Kerschen, F. Nucera, S. Tsakirtzis, P. N. Panagopoulos. (2008) Passive non-linear targeted energy transfer and its applications to vibration absorption : A review. *Proceedings of the Institution of Mechanical Engineers, Part K: Journal of Multi-body Dynamics* **222**:77-134.

[8] V. V. Smirnov, L. I. Manevitch. (2020) Complex envelope variable approximation in nonlinear dynamics. *Russian Journal of Nonlinear Dynamics* **16**:491-515.

[9] L.I. Manevitch, O.V. Gendelman. (2011) Tractable Models of Solid Mechanics, Foundations of Engineering Mechanics, Springer Berlin Heidelberg.

[10] A. Ture Savadkoohi, C.-H. Lamarque, M. Weiss, B. Vaurigaud, and S. Charlemagne. (2016) Analysis of the 1 :1 resonant energy exchanges between coupled oscillators with rheologies. *Nonlinear dynamics* **86**:2145-2159.

Theoretical description of thermal transient grating experiment: dynamical and kinetic approaches.

Aleksei Sokolov*, Bogdan S. Borisenkov†, Wolfgang H. Müller*, and Anton M. Krivtsov †
*Technical University of Berlin, Berlin, Germany
† Peter the Great St.Petersburg Polytechnic University, St.Petersburg, Russia

Summary. Thermal grating technique is a promising method for direct measurement of transient anomalous heat conduction. This work analyses approaches for theoretical description of this experiment. Kinetic and dynamical approaches to problem of initial sinusoidal perturbation are found to be handful. Behavior of amplitude decay calculated from these models plays a role of a signature of heat conduction regime. Decay of amplitude is analyzed using analytical, and molecular dynamics approaches. A comparison with available literature is presented.

Experimental studies confirm that in in ultrapure materials heat can propagate ballistically (non-diffusively), which leads to the phenomenon of thermal superconductivity [1, 2, 3, 4] . This fact opens up broad perspectives for the practical applications of ultrapure crystals for design of new materials with unique properties and devices constructed with use of these materials [4].

The difficulty in study of ballistic thermal processes in real materials lies in the fact that it occurs at very high speeds (speed of sound in crystals, e.g., >10 km/s for graphene [5]). Moreover, since the process is fundamentally different from Fourier's law, it lacks the thermal conductivity coefficient as a material parameter. However, even when the Fourier's law does not hold, in an experimental setting and molecular dynamic simulations when a steady non-equilibrium temperature gradient is applied to the specimen, it turns out that it is convenient to use the mathematical formulation of Fourier's law and to observe the size dependence of thermal conductivity as a signature of anomalous regimes [6, 7, 8, 9]. Thus, experimental methods, which have now already become a standard, have been developed to determine the thermal conductivity coefficient from Fourier's law [10]. These methods, however, cannot describe transient processes. A promising alternative of steady methods is the thermal grating technique which is a direct measurement of transient anomalous heat conduction [11].

In this work we focus on the theoretical description of transient thermal grating experiment [11]. In this experiment a sinusoidal periodic temperature excitation is created on a surface of the sample. Thus, a two dimensional heat transport occurs. Since the sinusoidal initial profile is excited along one axis, the heat transport remains quasi one dimensional. Let us consider initial temperature distribution as a periodic harmonic function along the spatial coordinate x.

$$T(x,0) = e^{iqx}, \tag{1}$$

where $q = \frac{2\pi}{L}$ is a wavenumber, L is the period of initial excitation. Let us assume that the evolution of this excitation remains periodic in space and has the form

$$T(x,t) = A_1(t)e^{iqx}, \tag{2}$$

where $A_1(t)$ is the amplitude which depends on time t.

The solution for function $A(t)$ can be found using different approaches and methods. Let us first consider the model where the heat transport is modeled using the particles – heat carriers which are called phonons [12]. Probability density function $f(x,y,t,u,v)$ describing distribution of these particles is goverened by the Boltzmann transport equation

$$\frac{\partial f}{\partial t} + u\frac{\partial f}{\partial x} + v\frac{\partial f}{\partial y} = f^{scat}, \tag{3}$$

where f^{scat} is the function describing scattering between the particles. Let us for simplicity first consider the case when $f^{scat} = 0$, i.e., when the particles propagate without scaterring – ballistically. In the one dimensional case the equation then takes the form

$$\frac{\partial f}{\partial t} + u\frac{\partial f}{\partial x} = 0, \tag{4}$$

and f is not deendent of y: $f = f(x,t,u,v)$. Let us consider isotropic "grey" medium, i.e., medium where all the particles propagate in all directions with the same absolute velocity. Let us suppose that the distribution function corresponds to Eqs. (1), (2) and has the form

$$f(x,0,u,v) = f^0(u,v)e^{iqx}, \quad f(x,t,u,v) = A_2(t)f^0(u,v)e^{iqx}. \tag{5}$$

Substitution of this anzatz (5) into (4) yeilds a linear diferential equation for A_2

$$\frac{\partial A_2}{\partial t} + iquA_2 = 0, \tag{6}$$

and solving the this equation yeilds

$$A_2(t) = e^{-iqut}. \tag{7}$$

Thus the solution for f has the form $f(x,u,v,t) = f_0(u,v)e^{i(qx-qut)}$. Initial distribution over velocities for a case of grey medium, i.e., all the particles has constant absolute velocities and uniformly distributed random directions, may be written in the form

$$f_0(u,v) = \frac{1}{\pi}\delta(u^2+v^2-c^2), \tag{8}$$

where c is the absolute velocity of particles, and the factor $1/\pi$ arises from normalizing condition $\int\int f_0(u,v)\mathrm{d}u\mathrm{d}v = 1$. Density of particles given in a chosen point of space in time $\rho(x,t)$ is found by integration over all velocities

$$\rho(x,t) = \frac{1}{\pi}\int_{-\infty}^{\infty}\int_{-\infty}^{\infty}\delta(u^2+v^2-c^2)e^{i(qx-qut)}\mathrm{d}u\mathrm{d}v. \tag{9}$$

We are interested in the decay of the amplitude and not in the spatial dependency e^{iqx}. From (9) it is seen that amplitude is described by

$$A_3(t) = \frac{1}{\pi}\int_{-\infty}^{\infty}\int_{-\infty}^{\infty}\delta(u^2+v^2-c^2)e^{-iqut}\mathrm{d}u\mathrm{d}v. \tag{10}$$

Change of variables to the polar coordinates in integration in (10) $u = r\sin\theta$, $v = r\cos\theta$, $\mathrm{d}u\mathrm{d}v = r\mathrm{d}r\mathrm{d}\theta$ yeilds

$$A_3(t) = \frac{1}{\pi}\int_0^{2\pi}\int_0^{\infty}\delta(r^2-c^2)e^{-iqrt\cos\theta}r\mathrm{d}r\mathrm{d}\theta = \frac{1}{2\pi}\int_0^{2\pi}e^{-iqct\cos\theta}\mathrm{d}\theta = J_0(cqt), \tag{11}$$

where J_0 is a Bessel function of the first kind. Molecular dynamical simulation performed to check analytical prediction, Eq. (11). Simulation results confirm analytical predictions.
We would like to note that Bessel function has a power decay of amplitude $\sim 1/\sqrt(t)$, thus, obtained result contradicts with results obtained from the dynamical approach in [13] and solution of BTE from the kinetic approach [14]. The study of this discrepancy is a direction for further research.

References

[1] Chih-Wei Chang, David Okawa, Henry Garcia, Arunava Majumdar, and Alex Zettl. Breakdown of fouriers law in nanotube thermal conductors. *Physical review letters*, 101(7):075903, 2008.

[2] Zhaohui Wang, Jeffrey A Carter, Alexei Lagutchev, Yee Kan Koh, Nak-Hyun Seong, David G Cahill, and Dana D Dlott. Ultrafast flash thermal conductance of molecular chains. *science*, 317(5839):787–790, 2007.

[3] Tzu-Kan Hsiao, Bor-Woei Huang, Hsu-Kai Chang, Sz-Chian Liou, Ming-Wen Chu, Si-Chen Lee, Chih-Wei Chang, et al. Micron-scale ballistic thermal conduction and suppressed thermal conductivity in heterogeneously interfaced nanowires. *Physical Review B*, 91(3):035406, 2015.

[4] Li Shi, Chris Dames, Jennifer R Lukes, Pramod Reddy, John Duda, David G Cahill, Jaeho Lee, Amy Marconnet, Kenneth E Goodson, Je-Hyeong Bahk, et al. Evaluating broader impacts of nanoscale thermal transport research. *Nanoscale and Microscale Thermophysical Engineering*, 19(2):127–165, 2015.

[5] S.V. Dmitriev, J.A. Baimova, A.V. Savin, and Y.S. Kivshar. Ultimate strength, ripples, sound velocities, and density of phonon states of strained graphene. *Computational Materials Science*, 53(1):194–203, 2012.

[6] S. Lepri, R. Livi, and A. Politi. Thermal conduction in classical low-dimensional lattices. *Physics reports*, 377(1):1–80, 2003.

[7] A. Dhar, A. Kundu, and A. Kundu. Anomalous heat transport in one dimensional systems: a description using non-local fractional-type diffusion equation. *Frontiers in Physics*, 7:159, 2019.

[8] R. Saito, M. Mizuno, and M.S. Dresselhaus. Ballistic and diffusive thermal conductivity of graphene. *Physical Review Applied*, 9(2):024017, 2018.

[9] K. Saito and A. Dhar. Heat conduction in a three dimensional anharmonic crystal. *Physical review letters*, 104(4):040601, 2010.

[10] S. Volz. *Microscale and nanoscale heat transfer*, volume 107 of *Topics in Applied Physics*. Springer-Verlag Berlin Heidelberg, 2007.

[11] Samuel Huberman, Ryan A Duncan, Ke Chen, Bai Song, Vazrik Chiloyan, Zhiwei Ding, Alexei A Maznev, Gang Chen, and Keith A Nelson. Observation of second sound in graphite at temperatures above 100 k. *Science*, 364(6438):375–379, 2019.

[12] John M Ziman. *Electrons and phonons: the theory of transport phenomena in solids*. Oxford university press, 2001.

[13] Vitaly A Kuzkin and Anton M Krivtsov. Fast and slow thermal processes in harmonic scalar lattices. *Journal of Physics: Condensed Matter*, 29(50):505401, 2017.

[14] Kimberlee C Collins, Alexei A Maznev, Zhiting Tian, Keivan Esfarjani, Keith A Nelson, and Gang Chen. Non-diffusive relaxation of a transient thermal grating analyzed with the boltzmann transport equation. *Journal of Applied Physics*, 114(10):104302, 2013.

The Oscillating Frequencies and Energy Harvesting of a Piezoelectric Bimorph with Various Tail Structures in Different Hydraulic Flow Rate

Huai-Pu Chen[*], Yu-Hsi Huang[**], and Hoang-Yan Lin*
[*]*Department of Electrical Engineering, National Taiwan University, Taipei, Taiwan*
[**]*Department of Mechanical Engineering, National Taiwan University, Taipei, Taiwan*

Summary.
The piezoelectric bimorph (PZT) was adopted as an energy harvester for a newly underwater application basing on the combination of piezoelectricity and flow induced vibration. The shape of piezoelectric energy harvester was optimized through the theoretical simulation code, ANSYS. Then, the energy harvesters with seven different types of tail fins were tested in flow field experiments with a large hydraulic recirculating flume from 0.6 to 5.37 m/sec. We discover there are two main regions of oscillating frequencies for PZT and the spectrum modes depend on three swing modes for this underwater energy harvester. The amount of power generation does not only positively correlate with the increase of flow rate, but also depend on the oscillating frequencies of PZT. When it produces an obvious and unique oscillating frequency, there is a larger amount of power it can get.

Abstract

Piezoelectric Materials are recently adopted as energy harvesters besides sensors or switches. Especially there is recently a new energy harvesting concept proposed to convert hydraulic kinetic energy into useable electrical energy with piezoelectric bimorph. This concept is based on the combination of piezoelectricity and flow induced vibration. In the research, we propose an innovative fixation method, hyperplastic adhesive, resolved fracture and waterproof for piezoelectric component (PZT-brass-PZT). And we also conduct a thorough theoretical simulation and a full-scale flow field experiments to optimize the energy harvester and analyze the relevance between power generation and oscillating frequencies of piezoelectric energy harvester from hydraulic flow rate 0.6 to 5.37 m/sec.
The designed energy harvester includes three structures, the bluff body, the piezoelectric material and the tail fin. A three-dimensional simulation code, ANSYS, based on the finite element numerical calculation was used to simulate dynamic state of fluid field through the bluff body with/without a tail fin to identify the optimal shape to be “the triangle prism with a tail fin” (Figure 1).
Then, the energy harvesters with seven different types of tail fins were tested in flow field experiments with a large hydraulic recirculating flume (Figure 2). A giant venturi tube was customized to increases the hydraulic flow rate 9 folds from 0.6 to 5.37 m/sec which was the highest record in Taiwan on piezoelectric energy harvesting researches. In addition, a customized micro-power rectifier and counter module was applied to accurately evaluate on the electromechanical transferring energy.
From the flow field experiments, based on fluid characteristic the hydraulic flow rate 0.6 to 5.37 m/sec can be separated into three regions - Low Flow Rate Region(below 3.1m/sec), Transition Region(3.1 ~ 4.2m/sec) and High Flow Rate Region(above 4.2m/sec). We discover there are two main regions of oscillating frequencies for PZT and the spectrum modes depend on three swing modes. The ratio of magnitude under the two frequency regions changes with flow rate (Figure 3). This means, the energy harvester can measure the real-time flow rate by PZT plate oscillating frequencies. Another discovery is that the amount of power generation does not only positively correlate with the increase of flow rate, but also depend on the oscillating frequencies of PZT. When it produces an obvious and unique oscillating frequency, there is a larger amount of power it can get (Figure 4).

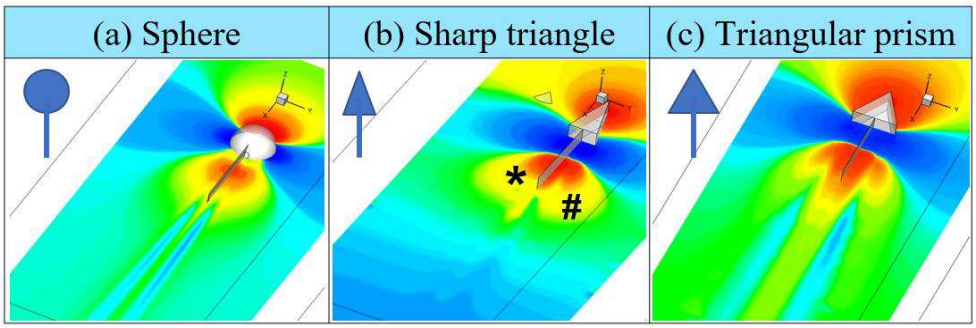

Figure 1. How bluff body shapes change the dynamic analysis of the flow field.

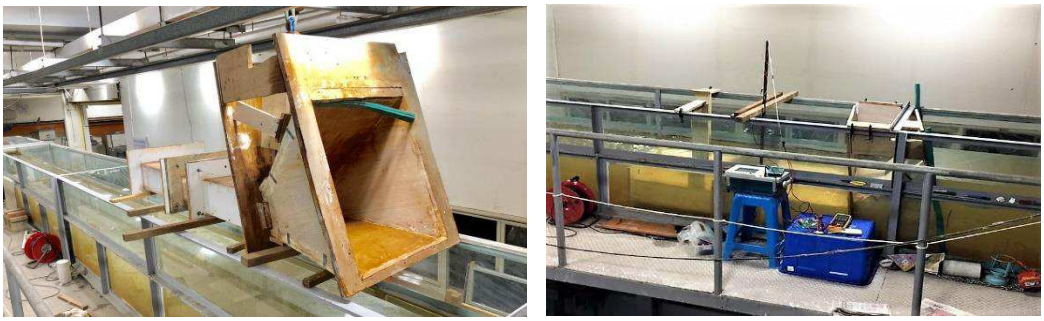

Figure 2. Flow field experimental equipment (a) Giant venturi tube, (b) Recirculating flume with giant venture

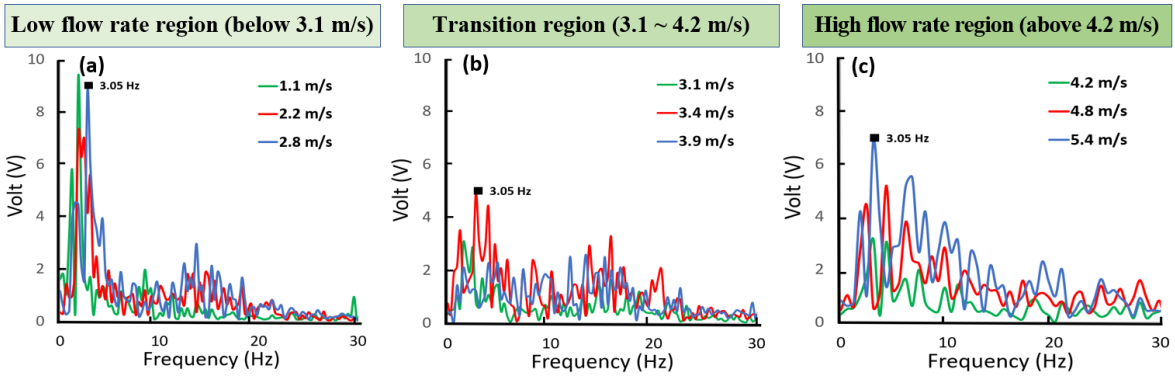

Figure 3. Oscillating frequencies in various flow rates with different system models. (a)Swing oscillation frequencies in Low Flow Rate Region. The smooth flow field produces an obvious and unique oscillating frequency. (b)Swing oscillation frequencies in Transition Region. The flow field starts to produce voids, it becomes unstable and complicated, and the oscillation frequency range becomes more irregular. (c)Swing oscillation frequencies in High Flow Rate Region. There are slug voids. The oscillating frequency resembles that of the low flow rate region, but the range in oscillation frequency from 4 - 15 Hz is significantly larger.

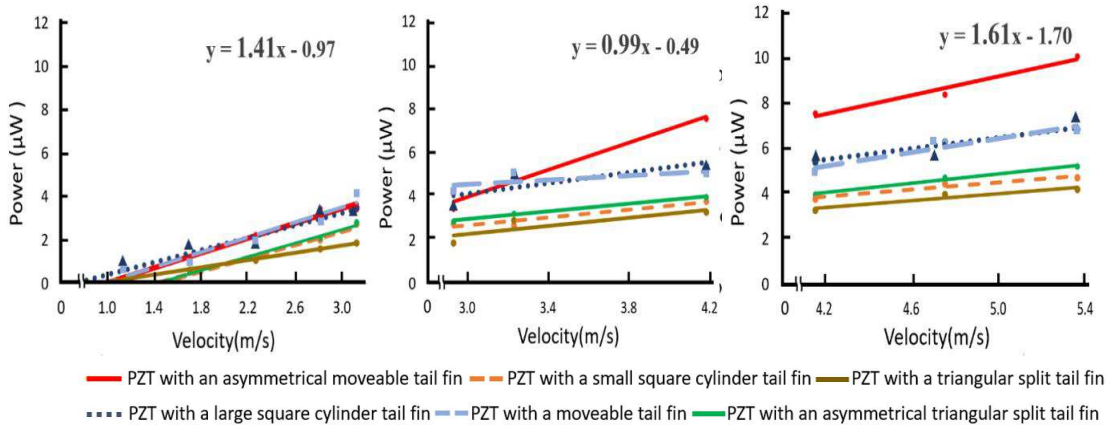

Figure 4. Comparison of power generation with different tail fin structure designs.

References

[1] Michael W. Shafer. (2013) Testing of vibrational energy harvesting on flying birds. Proc. of ASME Conference on Smart Materials, Adaptive Structures and Intelligent Systems, Sept. 16-18, Snowbird, UT, No. 3063.

[2] Huidong Li, (2016) An Energy Harvesting Underwater Acoustic Transmitter for Aquatic Animals. Scientific Reports, DOI:10.1038/srep33804.

[3] Weiken Chin, (2017) Enhancement of Energy Harvesting Performance by a Coupled Bluff Splitter Body and PVEH Plate through Vortex Induced Vibration near Resonance, Applied Sciences, vol. 7, 921.

[4] Xinyu An, (2017) Design and CFD Simulations of a Vortex-Induced Piezoelectric Energy Converter (VIPEC) for Underwater Environment, Renew. Sustain. Energy, 70, 193–214.

Tuesday, July 19, 2022
16:00 - 18:20

MS-09 Nonlinear Dynamics in Engineering Systems
Auditorium Lumiere

Chair: A. Steindl - S. Kaczmarczyk

16:00 - 16:20
Influence of gear topology discontinuities on the nonlinear dynamic response of a gear train subjected to multiharmonic parametric excitation
MELOT Adrien*, BENAICHA Youness, PERRET-LIAUDET Joël, RIGAUD Emmanuel
*Laboratoire de Tribologie et Dynamique des Systèmes (36 Avenue Guy de Collongue, 69134 Ecully Cedex France)

16:20 - 16:40
Experimental investigation of Circular Cylindrical Shell with non newtonian fluid
ZIPPO Antonio*, PELLICANO Francesco, IARRICCIO Giovanni
*Università degli Studi di Modena e Reggio Emilia, Dipartimento di Ingegneria Enzo Ferrari, Centre InterMech - MO.RE. (Via Pietro Vivarelli 10, 41125 - Modena Italy)

16:40 - 17:00
Reconfigurable Feedback Control of a Flexible Structure with a Nonstationary Backlash via a Digital-Twin Framework
VERED Yoav*, ELLIOTT Stephen
*Institute of Sound and Vibration Research, University of Southampton (University Rd, Highfield, Southampton SO17 1BJ United Kingdom)

17:00 - 17:20
Stochastic Response of Hopf Adaptive Frequency Oscillator
LI Xiaofu, SHOUGAT Md Raf E Ul, FENDLEY Casey, DEAN Robert, **BEAL Aubrey***, PERKINS Edmon
*University of Alabama in Huntsville (301 Sparkman Drive, Huntsville, AL 35899 United States)

Influence of gear topology discontinuities on the nonlinear dynamic response of a gear train subjected to multiharmonic parametric excitation

Adrien Mélot*, Youness Benaicha* and Joel Perret-Liaudet* and Emmanuel Rigaud*
*Laboratoire de Tribologie et Dynamique des Systèmes, UMR CNRS 5513, Ecole Centrale de Lyon, 36 avenue Guy de Collongue, 69134 Ecully Cedex, France

Summary. This work investigates the influence of holed gear blanks on the nonlinear dynamic behaviour of a flexible gear train. The system is excited by a multiharmonic internal excitation, namely a time-varying mesh stiffness and the static transmission error. This presentation will summarise the numerical procedure that has been developed to study such systems. A reference configuration without holes is used to give insight into the underlying dynamics and to highlight the effects of holed gear blanks. A thorough parametric study then addresses the robustness of the forced response curves and bifurcation structure to changes in gear blank topology.

Introduction

Weight reduction is a recurring concern in the design of modern mechanical systems. One of the most widespread solution to design lightweight gears is to resort to adding holes in the gear blanks. An accurate prediction of the dynamic behaviour of gears remains challenging due to the functional backlash, necessary to allow for assembly and operation, which can lead to contact loss and a strongly nonlinear response [1]. We herein propose an algorithm based on the harmonic balance method to investigate the dynamics of such systems. The proposed approach is able to take into account the internal excitation associated to geared systems. This excitation consists of the static transmission error (STE), whose origin lies in the teeth deflection under load, manufacturing defects and potential tooth profile modifications, and the time-varying mesh stiffness expressed as the derivative of the transmitted load relative to the STE [2].

Dynamic model

The proposed dynamic model [3] considers a reverse spur gear pair (same number of teeth on the input and ouput gears) modelled as lumped inertias and masses denoted I_1 and m_1 for the input gear and I_2 and m_2 for the output gear. Because both gears have the same number of teeth the shafts rotate at a fundamental frequency Ω. The shafts are modelled by torsional stiffnesses K_1 and K_2 and are supported by bearings of stiffness K_b. The input and ouput are modelled by two lumped inertias I_{in} and I_{out}, respectively. The gears are connected by a nonlinear element consisting of a time-varying

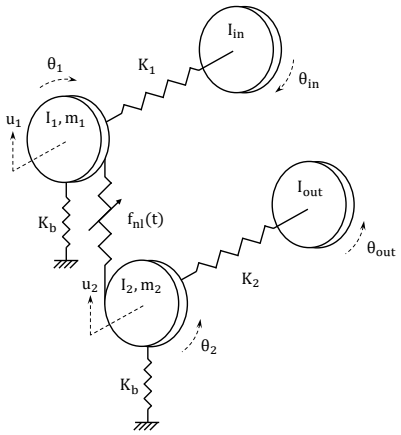

Figure 1: Dynamic model of the flexible transmission considered in this study.

piecewise linear stiffness. It includes the backlash *2b* and the static transmission error as a gap function $g(t)$:

$$\mathbf{f}_{nl}(\mathbf{q}) = \mathbf{G}k_m(t)\left(\mathbf{G}^T\mathbf{q} - g(t)\right)\mathcal{H}\left(\mathbf{G}^T\mathbf{q} - g(t)\right) + \mathbf{G}k_m(t)\left(\mathbf{G}^T\mathbf{q} + g(t)\right)\mathcal{H}\left(-\mathbf{G}^T\mathbf{q} - g(t)\right) \tag{1}$$

Here, $\mathcal{H}$ is the Heaviside step function and $\mathbf{G}$ is a 6×1 column vector allowing for the projection of the displacements in the global reference frame on the line of action. The gap function $g(t)$ is expressed as

$$g(t) = b + q_s(t) - \frac{F_s}{k_m(t)} \tag{2}$$

where $q_s(t)$ is the static transmission error, $k_m(t)$ the mesh stiffness and F_s corresponds to the transmitted load. There exists a number of methods to compute the static transmission error. However this work considers gears with holes which warrants the use of a multibody analysis.

Numerical methods

Due to the functional backlash, the equations of motions of the above described systems are strongly nonlinear. The harmonic balance offers an efficient framework to compute the nonlinear response in the frequency domain. The equation of motion takes the general form

$$[\mathbf{M}]\,\ddot{\mathbf{q}} + [\mathbf{C}]\,\dot{\mathbf{q}} + [\mathbf{K}]\,\mathbf{q} + \mathbf{f}_{nl}(\mathbf{q}, \dot{\mathbf{q}}) = \mathbf{f}_{ex} \tag{3}$$

where $\mathbf{q}$ contains the generalised displacement of each DoF and $[\mathbf{M}]$, $[\mathbf{C}]$, $[\mathbf{K}]$ are respectively the mass, damping and stiffness matrices. $\mathbf{f}_{ex}$ is the vector of external periodic forcing and $\mathbf{f}_{nl}$ the vector of nonlinear forces, i.e. the mesh force caused by contact, or lack thereof, between gear teeth. The terms in equation (3) are thus expanded as truncated Fourier series. More specifically, the generalised displacements are expressed as

$$\mathbf{q} \approx \sum_{k=0}^{H} \mathbf{a}_k cos(k\Omega t) + \mathbf{b}_k sin(k\Omega t) = [\mathbf{T} \otimes [I_n]]\tilde{\mathbf{q}} \tag{4}$$

where $\mathbf{T}$ contains the harmonic base functions up to the truncation order H, $\otimes$ is the Kronecker tensor product, $[\mathbf{I}_n]$ the identity matrix of size n and $\tilde{\mathbf{q}}$ is the vector in which the Fourier coefficients are stored. The nonlinear forces are treated by the well-known alternating frequency/time procedure [4]. An arc-length continuation method is coupled with the HBM to build the frequency response curves. Hill's method [5] is used to assess the stability of the computed points and a number of test functions are defined to locate smooth [6, 7] and grazing bifurcations.

Numerical example

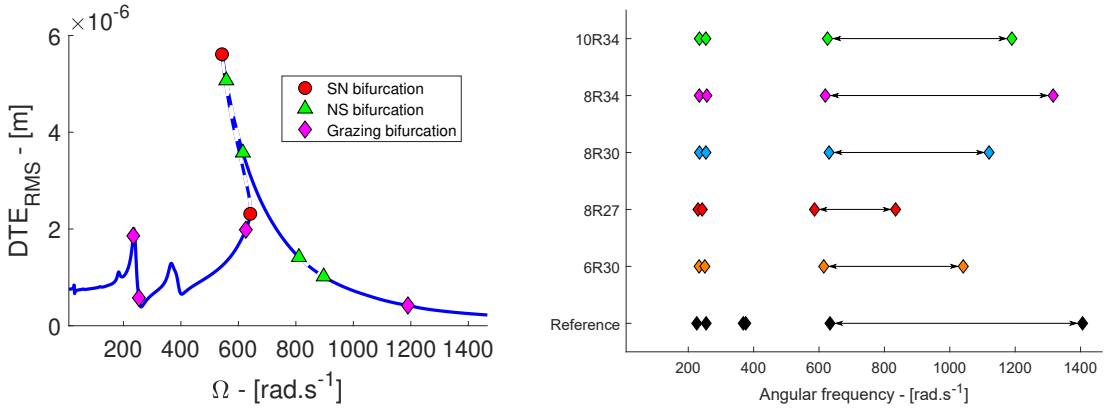

(a) (b)

Figure 2: Forced response curve (a) and grazing bifurcation diagram (b). Dashed lines indicate unstable regions and solid lines indicate stable regions. Saddle-node, Neimark-Sacker and grazing bifurcations are represented with circle, triangle and diamond markers, respectively.

Conclusion

A numerical methodology has been developed to study the influence of gear topology discontinuities on the dynamics of geared systems. Results show that holes have a beneficial effect in curtailing the frequency range where the system exhibits vibro-impacts, both at low and high torques.

References

[1] Rigaud E., Perret-Liaudet J. (2020) Investigation of gear rattle noise including visualization of vibro-impact regimes. Journal of Sound and Vibration 467, 115026.

[2] Garambois, P., Donnard G., Rigaud E., Perret-Liaudet J. (2017) Multiphysics coupling between periodic gear mesh excitation and input/output fluctuating torques: Application to a roots vacuum pump. Journal of Sound and Vibration 405:158 - 174.

[3] Nevzat Özgüven H., Houser D.R. (1988) Mathematical models used in gear dynamics—A review. Journal of Sound and Vibration 121(3):383-411.

[4] Cameron T. M., Griffin J.H. (1989) An Alternating Frequency/Time Domain Method for Calculating the Steady-State Response of Nonlinear Dynamic Systems. Journal of Applied Mechanics, American Society of Mechanical Engineers.

[5] Peletan L., Baguet S., Torkhani M., Jacquet-Richardet G. (2013) A comparison of stability computational methods for periodic solution of nonlinear problems with application to rotordynamics. Nonlinear Dynamics 72(3):671-682.

[6] Govaerts W. (2000) Numerical bifurcation analysis for odes. Journal of Computational and Applied Mathematics 125:5 –68.

[7] Govaerts W., Sijnave B. (1999) Matrix manifolds and the jordan structure of the bialternate matrix product. Linear Algebra and its Applications 292:245–266.

Experimental investigation of Circular Cylindrical Shell with non newtonian fluid

Antonio Zippo*, Giovanni Iarriccio* and Francesco Pellicano*
* *Università degli Studi di Modena e Reggio Emilia, Dipartimento di Ingegneria Enzo Ferrari, Centre InterMech - MO.RE.*

Summary. In the presented study the nonlinear vibrations of a fluid-filled circular cylindrical shell under base excitation is investigated. A PET thin shell with an aluminium top mass is harmonically excited through an electrodynamic shaker in the neighbourhood of the natural frequency of the first axisymmetric mode. The dilatant fluid is composed of a cornstarch-water mixture with 60% cornstarch and 40% water of total weight. The preliminary results show a strong non-linear response due to the coupling between the fluid and structure and the shaker-structure interaction that leads to a very interesting dynamic response of the system.

Introduction

The behaviour of thin-walled structure dynamics is always of high attention from the scientific community due to the extensive number of applications that can be found in engineering from macro to nanoscales (propellant tanks, micro-electro-mechanical systems, nanotubes, etc.).
In literature, it is possible to find several references where the response of thin-walled structures subjected to external forcing has been analyzed in presence of fluid-structure interaction [1-3], extreme temperature conditions [4-5] or interaction with electrodynamic shakers [6]. With the purpose of analyzing the response of the shell in presence of multiple interactions, an experimental study on the nonlinear vibrations of a fluid-filled cylindrical shell carrying a top mass has been carried out: the test setup is described, and preliminary results of the bifurcation analysis are presented.

Experimental setup and tests procedure

The specimen is a polymeric circular cylindrical shell, see Figure 1: an aluminum cylindrical mass is glued on the shell top edge; conversely, the bottom edge of the shell is clamped to a shaking table.
The following sensors have been adopted: three triaxial accelerometers placed on the top mass at 120°, a monoaxial accelerometer at the base of the shell, a laser vibrometer to measure the lateral velocity on the mid-height of the shell.
The test article has been excited in the axial direction through a harmonic load, with a step-sweep controlled output, the voltage signal sent to the shaker amplifier is closed-loop controlled; to avoid interaction between the control system and the specimen under study, no controls have been used for controlling the shaker base motion.
The harmonic forcing load consists of a stepped-sine sweep of frequency band 100-500 Hz with a step of 2.5 Hz. All the tests have been performed with the shell full filled with quiescent fluid.

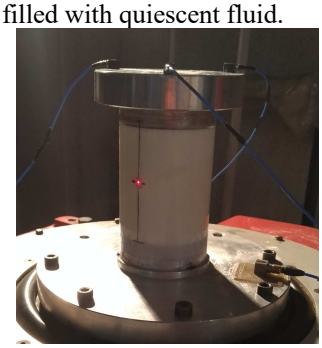

Figure 1: fluid-filled polymeric circular cylindrical shell with a top mass

Preliminary results

In this section, a short overview of the preliminary results, obtained from the postprocessing of the experimental data, is shown. In figure 2 the amplitude frequency diagrams shown a transfer of energy to the lateral motion at increasing of the excitation. The bifurcation diagram of the radial velocity (figure 3a) and top acceleration (figure 3 b) of the downwards test at 0.48 Volt and the bifurcation diagram of the radial velocity (figure 3c) of the upwards test at 0.34 Volt shows clearly that the dynamic scenario of the shell is strongly nonlinear.

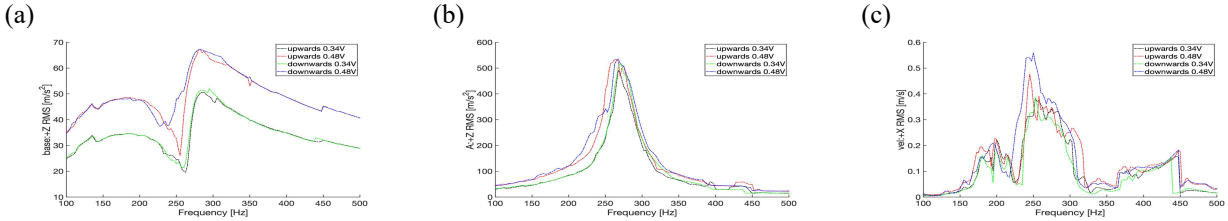

Figure 2: amplitude frequency diagram of (a) base acceleration (b) top acceleration (c)lateral velocity

This remark is confirmed by the Poincaré maps of the vertical acceleration of the top mass and the radial velocity of the shell: a 4-period subharmonic (Figure 3d) to chaotic states at 250Hz(Figure 3e) confirmed by the time history of the velocity (figure 3f) , and in the case of upwards at 0.34 Volt a period-doubling with amplitude modulation at 292.5 Hz: Poincarè maps (figure 3g) and spectrum of lateral velocity normalized respect to the forcing frequency at 292.5Hz (figure 3h) has been observed in the experimental analysis.

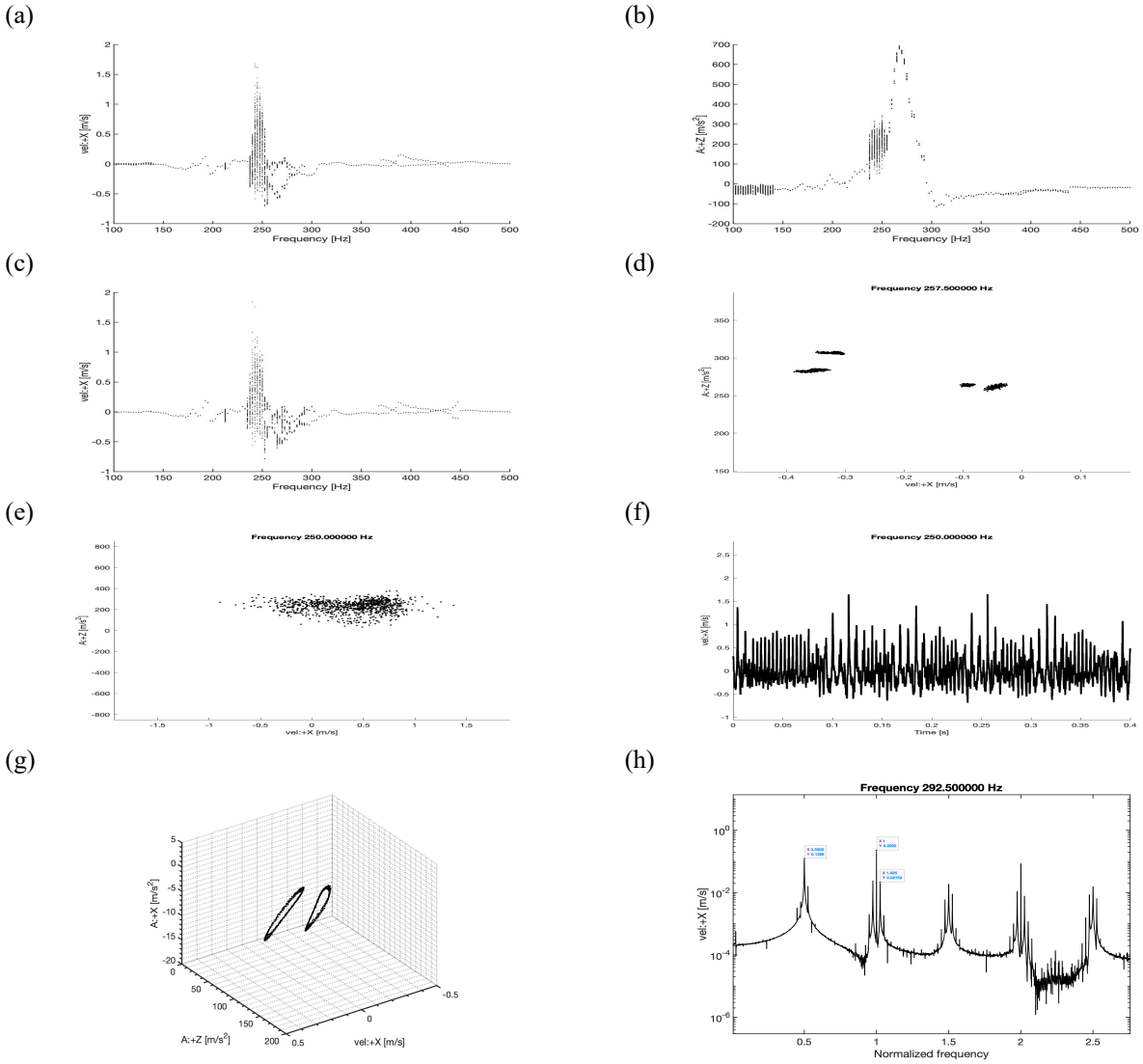

Figure 3: Bifurcation diagram and Poincaré maps of the fluid-filled shell response: experimental bifurcation diagram of the lateral velocity (a), top mass acceleration in axial direction (b) downwards 0.48V and lateral velocity upwards case at 0.34 V(c) , 4-period subharmonic response (d), chaotic motion: Poincaré maps(e) and time history (f), period-doubling with amplitude modulation: Poincarè maps (g) and spectrum of lateral velocity (h)

References

[1] Chiba, N., Tani, J., Yamaki, N., (1987) Dynamic stability of liquid-filled cylindrical shells under vertical excitation, part I: experimental results. *Earthquake Engineering and Structural Dynamics* **15**:23-26.

[2] Sivak, V. F., Telalov, A. I., (1991) Experimental investigation of vibrations of a cylindrical shell in contact with a liquid. *Soviet Applied Mechanics* **27**:484-488.

[3] Amabili, M., Pellicano, F., Païdoussis, M. P., (1998) Nonlinear vibrations of simply supported, circular cylindrical shells, coupled to quiescent fluid. *Journal of Fluid and Structure* **12**:883-918.

[4] Zippo, A., Barbieri, M., Iarriccio, G., Pellicano, F., Nonlinear vibrations of circular cylindrical shells with thermal effects: an experimental study(2020) Nonlinear Dynamics, 99 (1), pp. 373-391. DOI: 10.1007/s11071-018-04753-1

[5] Zippo, A., Barbieri, M., Pellicano, F., Temperature gradient effect on dynamic properties of a polymeric circular cylindrical shell (2019) Composite Structures, 216, pp. 301-314, DOI: 10.1016/j.compstruct.2019.02.098

[6] Pellicano, F., (2011) Dynamic instability of circular cylindrical shell carrying a top mass under base excitation: experiments and theory. *International Journal of Solids and Structures* **48**:408-427.

Reconfigurable Feedback Control of a Flexible Structure with a Nonstationary Backlash via a Digital-Twin Framework

Yoav Vered* and Stephen J. Elliott *
*Institute of Sound and Vibration Research, University of Southampton, Southampton, United Kingdom

Summary. The following work portrays a method to adaptively reconfigure a nonlinear controller to ensure the asymptotical stability of a position control mechanism that exhibits nonlinear and nonstationary backlash. The presented approach utilises a remote-based digital twin to perform the reconfiguration. Thus, the digital controller can be implemented locally using simple hardware. At the same time, the reconfiguration process takes place on a remote server that uses the acquired signal and dynamical models to perform simulations and calculations at a high rate. The proposed approach is demonstrated based on a numerical simulation of a three degrees-of-freedom structure coupled to an electrical DC motor via a lead screw. The lead screw exhibit backlashes whose characteristic width grows during the normal operation of the mechanism. Such system loses their closed-loop stability when the backlash becomes large. A nonlinear dead zone is used to restabilise the closed-loop system. The dead zone parameter is tuned based on a digital twin to ensure the closed-loop asymptotical stability and to avoid over-conservative design. Finally, the successful use of the proposed methodology is presented based on the simulation results.

Introduction

When a feedback-controlled mechanical system characteristic changes over time, the original design of the controller can lead to instabilities [1]. Wear and tear lead to such changes by introducing, for example, a nonlinear backlash. Although backlash is present in most mechanical position control systems [2], its effect on the linear feedback law is frequently neglected. However, even when the backlash is considered when formulating the identification and control problem [2, 3], its characteristics are usually modelled as a time-invariant. However, these time-invariant models are not applicable when wear and tear processes occur [4], in which case the characteristics of the backlash change over time.
To account for the time dependence of the backlash, an adaptive controller [3] can be used. However, the downside of doing so is that the controller's structure is complex, and its implementation is not straightforward. Therefore, in this work, a PID controller [5] is considered, with the addition of a dead zone to overcome the limit cycles introduced by the backlash and maintain minimal control effort minimal in the backlash gap [3]. The dead zone parameter is estimated asynchronously using a remotely-based digital twin [6] to monitor the changing backlash.
The core purpose of the digital twin is to create a fusion between physical and data-based models. Most research on digital twins is concerned with utilising them for decision-making and structural health monitoring, with only a few remarks on the use of digital twins in control, using classical ideas like controller scheduling [7]. This is in contrast to the past developments in digital signal processing, which have led to a more profound understanding of advanced control methodologies [8, 9]. Therefore, this work tries to pave the way and demonstrate the capabilities of incorporating digital twins into system control by employing the digital twin as an asynchronous estimator, resulting in a simple structure of the digital controller. This idea is not, by any means, a demonstration of the full capabilities of digital twins but only acts as a stepping stone towards a fuller understanding of digital twins' potential use in feedback control.

Control problem formulation

PID Feedback controllers are widely used for position control of flexible structures [5]. The schematics of a position controller of a flexible mechanism are presented in Figure 1(a). The mechanism is composed of 3 lumped masses con-

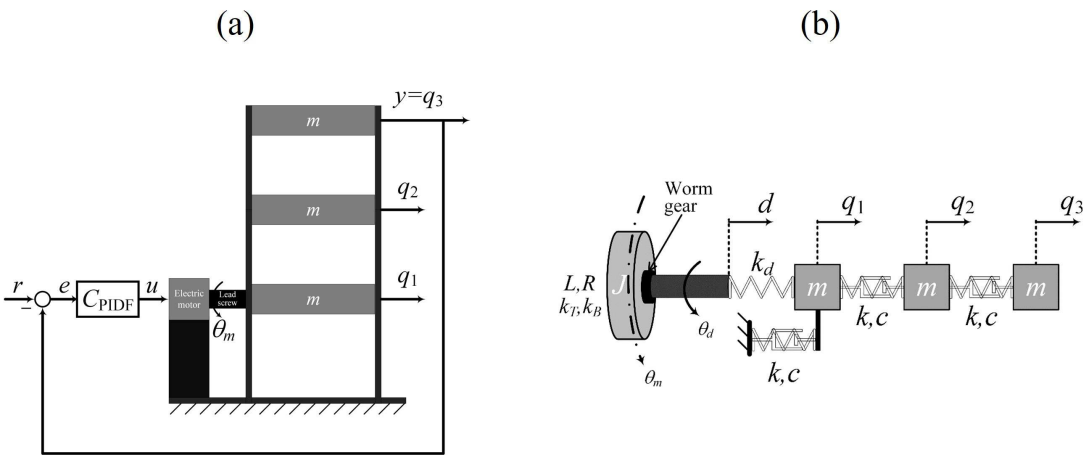

Figure 1: The position control system models. (a) – Schematic of the feedback position control. (b) – Lumped elements model.

nected via flexible beams. An electrical motor that is connected via a lead screw to the bottom mass is used to drive the system. The system's lumped model shown in Figure 1(b) is used for the numerical simulation. In the lumped model of Figure 1(b), L and R denote the electrical motor's inductance and resistance, respectively, J its lumped inertia, k_B and k_T are the torque and back-emf motor's constants, θ_m the angular position, and ω_m the angular velocity.
The motor is connected to the lower mass via a lead screw, whose angle is denoted as θ_d, and its end position, d, is related to its angular position via

$$d = p\theta_d, \tag{1}$$

where p denotes the lead screw's pitch. The lead screw elasticity is modelled using a linear spring k_d, which in the following simulation is assumed to be infinitely rigid. m, k, and c denote the lumped mass of each platform and the connecting beams' elasticity and dissipation, which are assumed to be linear. Finally, q_i $i = 1, 2, 3$, denote the horizontal position of each platform. The physical values used throughout the paper are given in Table 1.

Table 1: Physical properties and values used in the numerical simulation of the three DOF with the DC electrical motor

Symbol	Value, units	Symbol	Value, units	Symbol	Value, units
m	5.2, kg	J	$5 \cdot 10^{-6}$, $\mathrm{kg \cdot m^2}$	p	$10^{-3}/2\pi$, m/rad
k	10^4, N/m	L	10^{-3}, H	k_T	0.8, (N·m)/A
c	36.9, N/(m·s)	R	12, Ohm	k_B	0.1, V/(m/s)

Linear models and controller
Assuming that the inertial loading of the structure is negligible compared to the motor's torque, a single direction coupling model can be used to represent the motor and platform dynamics. The motor's input-output relation under these assumptions can be written as

$$\theta_m = \frac{1}{s}\frac{k_T}{JLs^2 + JRs + k_B k_T}u, \tag{2}$$

where u denotes the input voltage to the motor. The top platform and the lead screw positions are related via:

$$q_3 = \frac{c^2 s^2 + 2cks + k^2}{m^2 s^4 + 3cms^3 + (c^2 + 3km)s^2 + 2cks + k^2}d. \tag{3}$$

When the lead screw backlash is neglected, i.e., $\theta_d = \theta_m$, the static relation of Eq. (1) can be used to couple the two systems' dynamics.
To control the motion and position of the top platform such that it follows a stepwise constant reference signal, r, a feedback PID controller of the following form

$$C_{PID}(s) = K_p + K_i\frac{1}{s} + K_d\frac{s}{T_f s + 1}, \tag{4}$$

is introduced, where K_p, K_i, and K_d are the proportional, integral, and differential gains, respectively, and T_f is the differential filter time constant. Such that the motor's input voltage u is obtained from the tracking error $e = r - q_3$ as

$$u = C_{PID}(s)e. \tag{5}$$

The PID was designed to achieve a zero steady-state error, a bandwidth frequency of 10 rad/s, and a minimum phase margin of 10 deg.

Nonlinear backlash model
Since the positioning mechanism is based on a lead screw, it might exhibit backlash in practice, mainly as it wears. A simple model for backlash, which is a nonlinear dynamic element, is by introducing a dynamic dead zone of known width whenever the velocity changes sign [3].
The following nonlinear model can be used to relate the motor and lead screw angular velocities:

$$\omega_d = \begin{cases} \omega_m & (\mathrm{sign}(\omega_m) > 0 \text{ and } \theta_m - \theta_d \geq \theta_b/2) \text{ or } (\mathrm{sign}(\omega_m) < 0 \text{ and } \theta_m - \theta_d \leq -\theta_b/2) \\ 0 & \text{Otherwise} \end{cases}, \tag{6}$$

where θ_b denotes the backlash gap angle.
A time-invariant backlash model, with a constant backlash gap angle θ_b, is readily available with many simulation software. However, since the backlash gap angle is time-varying here, a separate procedure for the state transition was used, based on the model of Eq. (6). To illustrate its response, Figure 2 shows the output of the backlash model for a gap angle of $\theta_b = 40$ degrees, and for an amplitude changing sinusoidal input of the following form:

$$\theta_m(t) = (1 + t/10)\sin(2\pi t).$$

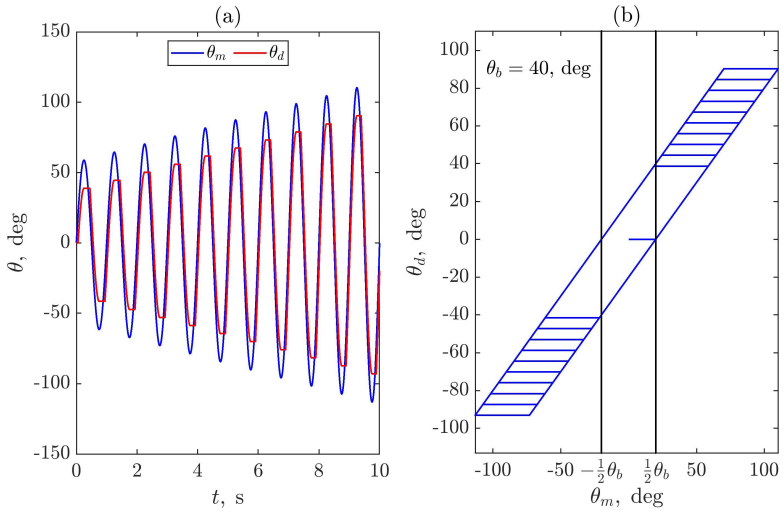

Figure 2: Simulation results for the backlash model for an amplitude-modulated sinusoidal input.

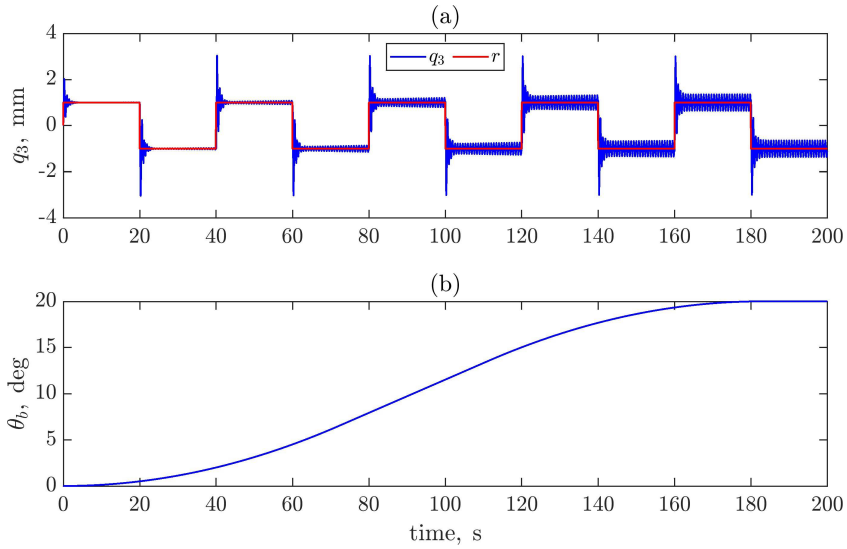

Figure 3: Simulation results for the linear controller with a nonstationary backlash.

The lost motion between θ_m and θ_d can be seen in Figure 2(a), which shows their two waveforms, whereas the nonlinear characteristics of the backlash are more transparent in Figure 2(b), which plot one against the other.
The simulation results of the feedback position control mechanism with a predetermine backlash's gap angle profile are shown in Figure 3. When the width is small, the position control is applied successfully to the system, and the top mass position does converge to the required reference position. However, a limit cycle is observed when the width becomes more significant, and the system can no longer be considered asymptotically stable.

Switched dead zone controller

A dead zone of a prechosen width is incorporated into the controller to capture and maintain the backlash's effect and restabilise the system [3]. The controller input-output relation can now be read as:

$$u_{dz} = \begin{cases} C_{PID}(s)e_{dz} & |e| > \varepsilon_{dz} \\ 0 & \text{Otherwise} \end{cases}, \tag{7}$$

where

$$e_{dz} = \begin{cases} e & |e| > \varepsilon_{dz} \\ 0 & \text{Otherwise} \end{cases}, \tag{8}$$

and the dead zone tolerance, ε_{dz}, is given by:

$$\varepsilon_{dz} = p\hat{\theta}_b, \tag{9}$$

$\hat{\theta}_b$ being the backlash gap angle estimation.

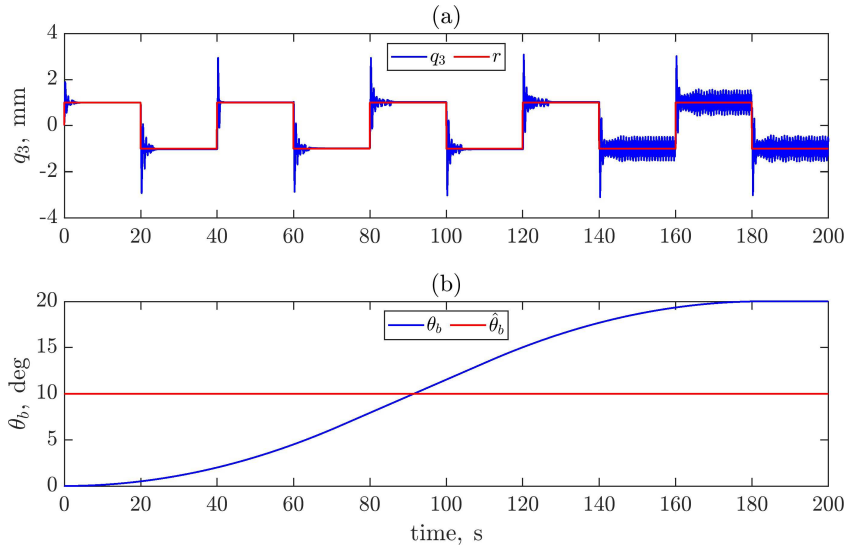

Figure 4: Simulation results for the dead zone controller with a nonstationary backlash and a constant backlash gap angle estimation.

If the controller's dead zone width is tuned too conservatively, i.e., $\hat{\theta}_b$ is chosen large, a significant bias is introduced between the required and actual position. Moreover, no force is applied to the structure inside the dead zone, and its response decays similarly to its initial condition response. Thus, the desired damping levels of the designed controller are lost, and the settling time can become significantly longer.

A second simulation was carried out using the same backlash's width profile with the dead zone switched controller. In the simulation, the backlash gap angle estimator was chosen as the mean value, i.e., $\hat{\theta}_b = 10$ deg. The simulation's results are shown in Figure 4. It is clear that the system again loses stability when the real backlash's gap angle is significantly larger than the modelled one. Moreover, when the actual backlash's gap angle is smaller, the settling time does get longer as anticipated. An estimation of the backlash is proposed to ensure the closed-loop stability and reduce the amount of conservative used for choosing the dead zone width. The backlash's gap angle estimation is done via a remote digital twin to avoid overflowing the controller and to enable, in the future, the use of more sophisticated estimation and designing methods.

Digital twin reconfigurable controller

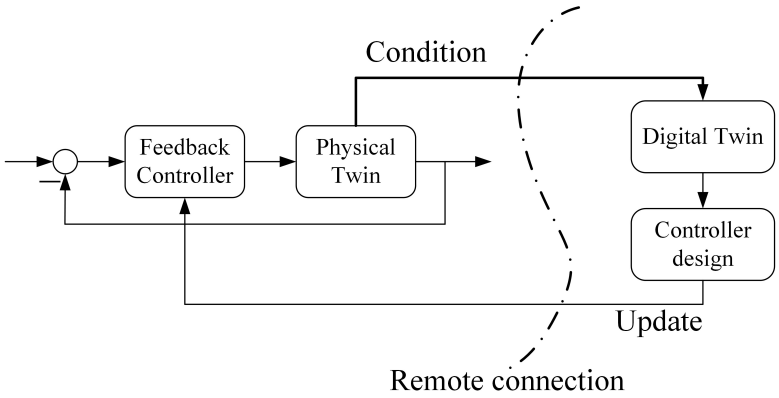

Figure 5: Schematics of the digital twin based reconfigurable controller.

The digital twin is a modern concept in engineering. At its core, the digital twin aims to create a fusion between meaningful physical models of a system, combined with measured data collected from different sensors throughout the physical system's operation [6]. The digital twin as a concept has so far been used during several stages of a product's life-cycle: designing, manufacturing, and condition monitoring. However, the use of a digital twin is not as common in control theory [7], specifically motion control. Although many systems for which digital twins are considered, like wind turbines and aircraft [6], depend on motion controllers for their smooth operation. The idea put forward in this work is to use a simple model of a digit twin to monitor the backlash's width and reconfigure the dead zone feedback controller. The block diagram of Figure 5 represents the physical system (physical twin and feedback controller) on the left-hand side and the simulated system (digital twin and controller design) on the right-hand side. The main difference between the use of a digital twin framework and adaptive control [1, 8], is the asynchronous nature of the communication and the ability to

use highly detailed simulations. Therefore, ensuring that the digital feedback controller will operate properly, where the states' and controller's estimation and reconfiguration occur on a remote server.

Backlash gap angle estimation

It is assumed that the control signal, u, and the top platform position, q_3, are measured and are sent to the digital twin asynchronous. After each data transmission, the digital twin can be used to simulate the internal signals of the feedback system. It is desired to estimate both the output and input of the backlash and compare them to estimate the backlash angle. The input of the backlash, the motor's angle, is estimated using the measured control signal, which is fed to the discretised dynamical model of Eq. (2), assuming a zero-order hold and an ideal sampler. The output of the backlash, the lead screw's angle, is estimated using the measured top platform position and a digital-based delayed inverse of the dynamical model of Eq. (3). An impulse invariant discretisation algorithm is used [9] to ensure that the sampled system remains minimum phase, up to the addition of zeros at the origin. Then the inverse filter of the sampled system can be calculated. A discrete modelling delay of N samples is added to the sampled system inverse filter to ensure causality. The minimal value of N required for causality is equal to the pole excess of the sampled system. Since N step delay is added to the backlash output, a similar delay is added to the digital-sampled motor's dynamics. The estimators of the motor and lead screw's angles, $\hat{\theta}_m$ and $\hat{\theta}_d$, are thus the output of the following two sampled time linear systems:

$$\hat{\theta}_m = z^{-N}\hat{G}_1(z)u, \tag{10}$$

$$\hat{\theta}_d = z^{-N}\hat{G}_2^{-1}(z)y, \tag{11}$$

where $\hat{G}_1(z)$ and $\hat{G}_2(z)$ are the discretised dynamical model of Eq. (2) and Eq. (3), respectively.
To estimate the backlash angle, θ_b, the difference between the angles is calculated. It follows from the backlash definition that if $\omega_d \neq 0$, then $\theta_m - \theta_d = \Delta\theta_{\pm}$, where the plus or minus are chosen based on the sign of ω_m. Therefore, it follows that

$$\theta_b = \Delta\theta_+ - \Delta\theta_-, \tag{12}$$

Equation (12) is accurate up to measurement and estimation errors. Therefore, a threshold is used for the lead screw's angular velocity criteria to overcome these errors. In addition, based on the previous simulation of Figure 4, it seems safer to use a slight overestimation of the backlash gap angle. Consequently, the estimated values which correspond to the angular velocity threshold are rounded up to the nearest scaled-integer degree, and the mean is taken as the estimator. If degree units are used, then the estimator is:

$$\hat{\theta}_b = \frac{1}{N_{\Delta\theta_+}} \sum_{t_s \in t_+} \lceil \Delta\theta_+ \rceil_{l/2} - \frac{1}{N_{\Delta\theta_-}} \sum_{t_s \in t_-} \lfloor \Delta\theta_- \rfloor_{l/2}, \tag{13}$$

where t_+ represents the sampling times when $\omega_d \neq 0$ and $\omega_m > 0$, similarly, t_- represents the sampling times when $\omega_d \neq 0$ and $\omega_m < 0$, $N_{\Delta\theta_+}$ and $N_{\Delta\theta_-}$ denote the number of elements in each time subset, and the ceil l and floor l operators are defined as:

$$\lceil x \rceil_l := l \cdot \text{ceil}(x/l) \ , \lfloor x \rfloor_l := l \cdot \text{floor}(x/l). \tag{14}$$

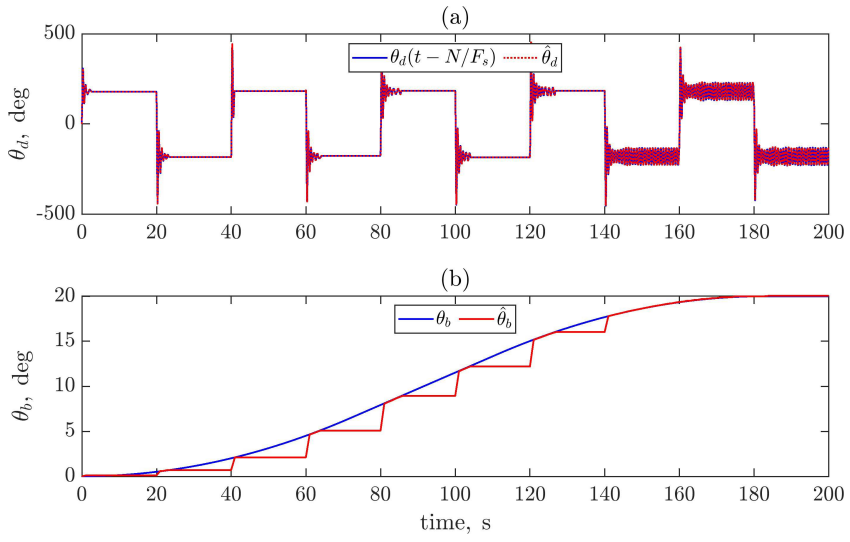

Figure 6: Post-processing identification of the time-varying backlash angle.

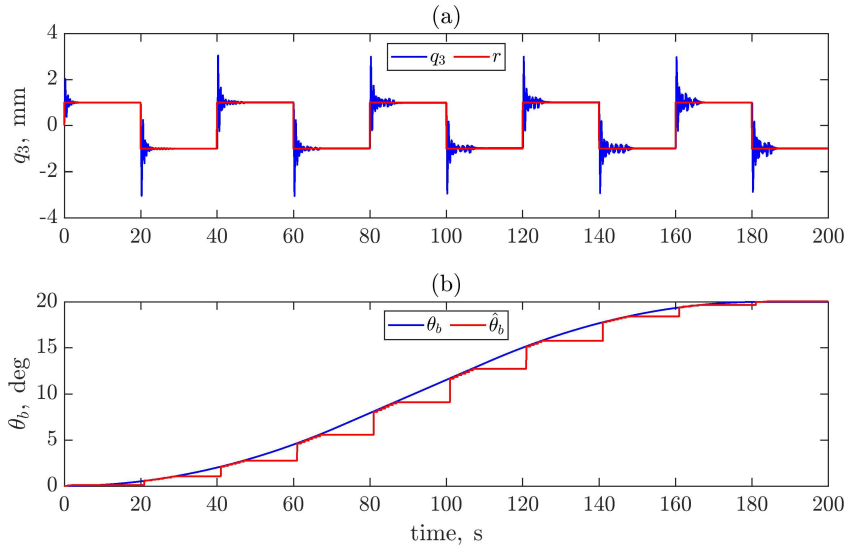

Figure 7: Simulation results for the digital twin reconfigurable controller with a nonstationary backlash.

To check the estimation algorithm and help tune the angular velocity threshold, the simulation data in Figure 4 was post-processed. A 5000 Hz sampling frequency was used, the angular velocity threshold was set to $\varepsilon_b = 0.1$ rad/s, the number of discrete delays added to the digital sampled inverse system $N = 2$, and the rounding factor was chosen as $l = 1/10$. Figure 6(a) shows the command and output signals, and Figure 6(b) shows the actual and estimated backlash angles obtained using the proposed estimation algorithm. When the input to the digital sampled inverse system is constant (The top mass is at rest following a step change), the estimated lead screw's angle matches the measured one. However, if the input is not constant, a small phase and gain delay are present. This is due to the dynamics of the inverse filter. Consequently, the actual and estimated angles differ whenever the lead screw angular velocity is nonzero. However, as seen in Figure 6(b), the estimation algorithm successfully identifies the backlash angle, even though the two angles differ slightly. The results of Figure 6 were obtained based on noncausal signal post-processing, so the backlash angle estimation has no delay. In the following subsection, the real-time use of a digital twin is simulated, including this processing delay, to include its effects in restabilising the system.

Real-time simulation

A third simulation was carried out based on the block diagram of Figure 5, the dead zone PID controller, and the backlash estimation method. The backlash gap angle estimator was initialised to be zero. To account for the communication delay between the physical and digital twin, a 1-second delay was added.
Figure 7 shows the results of the digital twin reconfigurable dead zone controller. Note that unlike the previous simulation results (Figure 4), the reconfigurable controller now restabilises the nonlinear feedback system at all times. Even though a bias in the final position of each step is present, the worst bias is under 2% of the required reference amplitude. The lead screw's angle estimation procedure yields a sufficiently accurate estimation for stable control, and the delay due to the data transfer does not significantly affect the estimation and control. These results show that the backlash's estimation is accurate and that the closed-loop system remains stable throughout the entire manoeuvre.

Conclusions

This paper puts forward the idea of utilising a digital twin to estimate the nonstationary characteristics of a nonlinear mechanism and, in turn, reconfigure a feedback controller to stabilise the system. The advantage of using a digital twin over classical adaptive control is using asynchronous communication and utilising the server's high computation power. Doing so ensures that the digital controller will operate without introducing additional delays or overflows. Moreover, elaborate models can be used for the inverse estimation problems associated with the signal estimation procedure. Finally, the numerical simulation results are an indication of future possibilities. Mainly, by employing the digital twin, evolved nonlinear mechanisms characteristic can be identified, and a simulation-based design of a reconfigurable controller.

References

[1] Åström K.J., Wittenmark B. (2013) Adaptive control, Courier Corporation.

[2] Vörös J. (2010) Modeling and identification of systems with backlash. *Automatica*, 46(2), 369-374.

[3] Nordin M., Gutman, P.O. (2002) Controlling mechanical systems with backlash—a survey. *Automatica*, 38(10), 1633-1649.

[4] Villwock S., Pacas M. (2008) Time-domain identification method for detecting mechanical backlash in electrical drives. *IEEE Trans. Ind. Electron.*, 56(2), 568-573.

[5] Åström K.J., Murray R.M. (2010) Feedback Systems. Princeton university press.

[6] Wagg D.J., Worden K., Barthorpe R.J., Gardner P. (2020) Digital twins: state-of-the-art and future directions for modeling and simulation in engineering dynamics applications. *ASCE-ASME J Risk and Uncert in Engrg Sys Part B Mech Engrg*, 6(3).

[7] Dal Borgo M., Gardner P., Zhu Y., Wagg D.J., Au S.K., Elliott, S.J. (2020) On the development of a digital twin for the active vibration control of a three-storey structure. *ISMA-USD 2020 Proceedings*.

[8] Elliott, S.J. (2000) Signal processing for active control. Elsevier.

[9] Åström K.J., Wittenmark B. (2013) Computer-controlled systems: theory and design, Courier Corporation.

Stochastic Response of Hopf Adaptive Frequency Oscillator

XiaoFu Li*, Md Raf E Ul Shougat*, Casey Fendley†, Robert Dean†, Aubrey Beal‡, Edmon Perkins*
*Dept. of Mechanical & Aerospace Eng., North Carolina State University, Raleigh, NC, USA
†Dept. of Electrical & Computer Eng., Auburn University, Auburn, AL, USA
‡Dept. of Electrical & Computer Eng., University of Alabama in Huntsville, Huntsville, AL, USA

Summary. Although not studied extensively, adaptive frequency oscillators (AFOs) could have many useful applications. AFOs possess the capability of synchronizing their oscillating frequency with their input frequency. Here, the noise-influenced dynamics of the Hopf Adaptive Frequency Oscillator (HAFO) are analyzed in a probabilistic manner. By adding a stochastic forcing term to the ordinary differential equations (ODEs), the resulting stochastic differential equations (SDEs) are integrated using the Euler-Maruyama (EM) method to obtain direct numerical solutions and the probabilistic dynamics of the oscillator. Additionally, a hardware circuit realization of the HAFO is fabricated, and the experimental results and the simulation results are compared. Efforts are made to quantify the working capability of the oscillator, which is limited by nonideal electrical components. The influence of noise on the HAFO circuit will also be investigated and compared with the results obtained through the Euler-Maruyama simulations.

Hopf Adaptive Frequency Oscillator

The Hopf Adaptive Frequency Oscillator is capable of synchronizing its oscillating frequency to an oscillatory input signal. The HAFO with the capability of learning the frequency of any rhythmic inputs are widely used for robotic locomotion control, by using the HAFOs as central pattern generators to tune the walking patterns in a cooperative way [1, 2]. The HAFO is an augmented form of the Hopf oscillator [3], which has an additional state related to the frequency:

$$\begin{aligned} \frac{dx}{dt} &= (\mu - r^2)x - \omega y + kF(t) \\ \frac{dy}{dt} &= (\mu - r^2)y + \omega x \\ \frac{d\omega}{dt} &= -sgn(y)kF(t) \end{aligned} \tag{1}$$

where $r = \sqrt{x^2 + y^2}$, k is the amplitude of the deterministic forcing function, μ is a constant related to the limit cycle amplitude, and $F(t)$ is a sinusoidal forcing function. The first two equations are the typical version of the Hopf oscillator, while the $\frac{d\omega}{dt}$ equation allows frequency adaptation. The learning process is embedded into the dynamical system, and there are not any pre- or post-processing procedures needed to accomplish the frequency synchronization. This behavior may be observed in Fig. 1.

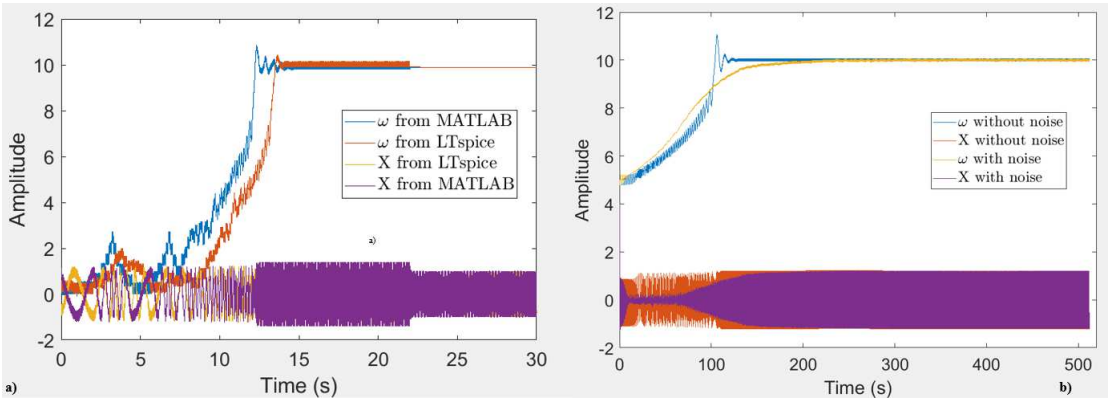

Figure 1: a) MATLAB simulation and LTspice simulation of eqs. 1. The sinusoidal forcing causes the HAFO to adapt. After the forcing is set to zero at t = 22 s, the HAFO "remembers" the input frequency. Additionally, the x output from both simulations overlaps with each other when the frequency adaptation is accomplished. b) MATLAB simulation of eqs. 2 by the Euler-Maruyama method. The noise amplitude is 10% of the amplitude of the sinusoidal forcing function. With the addition of noise, the frequency adaptation takes a longer time, but there is no overshoot. The x output from both cases overlaps with each other after the transient response.

Influence of Noise

Previously, the stochastic response of the HAFO was approximated by using a Fokker-Plank formulation [4]. As noise can change the dynamic stability of nonlinear systems [5, 6], it is important to further explore the effects of noise on the HAFO. To consider the effects of noise on the HAFO, the sinusoidal function, $F(t)$, is replaced with $\hat{F}(t) + \frac{\sigma}{k}\dot{W}(t)$. Here, $\hat{F}(t)$ is a sinusoidal function, $\dot{W}(t)$ is white Gaussian noise, and σ is the amplitude of the noise. Making this replacement, the stochastic differential equations are:

$$\begin{aligned} \frac{dx}{dt} &= (\mu - r^2)x - \omega y + k\hat{F}(t) + \sigma\dot{W}(t) \\ \frac{dy}{dt} &= (\mu - r^2)y + \omega x \\ \frac{d\omega}{dt} &= -sgn(y)k\hat{F}(t) - sgn(y)\sigma\dot{W}(t) \end{aligned} \tag{2}$$

This set of SDEs can then be simulated using the Euler-Maruyama method, depicted in Fig. 1.

Circuit Realization

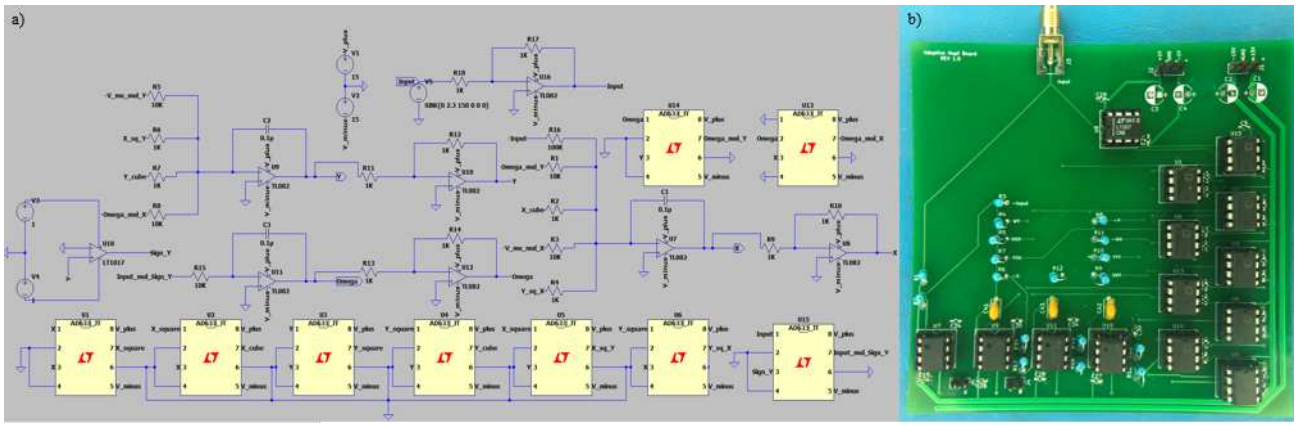

Figure 2: a) The circuit diagram in LTspice. b) A printed circuit board (PCB) of the HAFO.

The circuit design (Fig. 2) was inspired from [7], which presents an electronic implementation of the Lorenz chaotic oscillator for radar applications. To make the hardware circuit easier to implement, the original set of equations is modified, as in [8]:

$$\begin{aligned} \frac{dx}{dt} &= (\mu - r^2)x - \omega y + kF(t) \\ \frac{dy}{dt} &= (\mu - r^2)y + \omega x \\ \frac{d\omega}{dt} &= -\frac{y}{\sqrt{x^2+y^2}}kF(t) \end{aligned} \tag{3}$$

The modification of eqs. 1 does not change the frequency adaptation property. However, it does affect the length of the transient response and the error (the difference between the steady-state frequency of the oscillator and the frequency of the input signal). In Fig. 3, a comparison between the experimental circuit and the LTspice simulation is shown. Filtering was performed on the experimental data in MATLAB. Nonideal electronic components cause discrepancies between the experimental circuit and the simulated circuit. The voltages reported in the figure must be converted to find the frequency in Hertz.

Conclusions

AFOs could prove to have useful properties for mechatronics. To gain better understanding of their dynamics, numerical simulations of the deterministic and stochastic system are pursued, while a PCB implementation provides experimental insight. In Fig. 3, the experimental frequency was recorded with an oscilloscope, and LTspice was used to simulate the HAFO circuit. The variation between the experimental results and the numerical results is lower than 5%. The modeling of the HAFO on the hardware circuit achieved by the PCB is practical and inexpensive. Further work will be pursued to determine their efficacy as analog controllers.

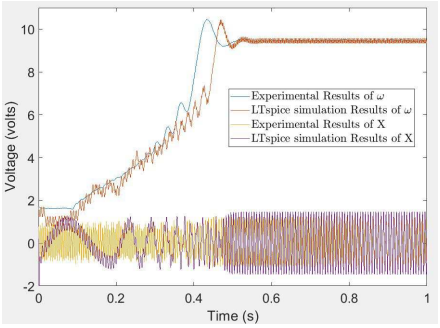

Figure 3: Comparison between the experiment and simulation.

References

[1] X. Xiong, F. Wörgötter, and P. Manoonpong, "Adaptive and energy efficient walking in a hexapod robot under neuromechanical control and sensorimotor learning," *IEEE transactions on cybernetics*, vol. 46, no. 11, pp. 2521–2534, 2015.

[2] M. Thor and P. Manoonpong, "A fast online frequency adaptation mechanism for cpg-based robot motion control," *IEEE Robotics and Automation Letters*, vol. 4, no. 4, pp. 3324–3331, 2019.

[3] L. Righetti, J. Buchli, and A. J. Ijspeert, "Dynamic hebbian learning in adaptive frequency oscillators," *Physica D: Nonlinear Phenomena*, vol. 216, no. 2, pp. 269–281, 2006.

[4] J. Buchli, L. Righetti, and A. J. Ijspeert, "Frequency analysis with coupled nonlinear oscillators," *Physica D: Nonlinear Phenomena*, vol. 237, no. 13, pp. 1705–1718, 2008.

[5] E. Perkins and T. Fitzgerald, "Continuation method on cumulant neglect equations," *Journal of Computational and Nonlinear Dynamics*, vol. 13, no. 9, p. 090913, 2018.

[6] E. Perkins and B. Balachandran, "Noise-influenced dynamics of a vertically excited pendulum," in *ASME 2013 International Design Engineering Technical Conferences and Computers and Information in Engineering Conference*, American Society of Mechanical Engineers Digital Collection, 2013.

[7] C. S. Pappu, B. C. Flores, P. S. Debroux, and J. E. Boehm, "An electronic implementation of lorenz chaotic oscillator synchronization for bistatic radar applications," *IEEE Transactions on Aerospace and Electronic Systems*, vol. 53, no. 4, pp. 2001–2013, 2017.

[8] A. Ahmadi, E. Mangieri, K. Maharatna, S. Dasmahapatra, and M. Zwolinski, "On the vlsi implementation of adaptive-frequency hopf oscillator," *IEEE Transactions on Circuits and Systems I: Regular Papers*, vol. 58, no. 5, pp. 1076–1088, 2010.

Wednesday, July 20, 2022

08:30 - 10:30

MS-22 Special session dedicated to L.I. Manevitch

Saint Clair 1

O. Gendelman, I. Andrianov, Y Mikhlin

08:30 - 08:50
Unified perspectives on nonlinear model reduction
REGA Giuseppe*, GUO Tieding
*Sapienza University of Rome (Rome 00197 Italy)

08:50 - 09:10
A General Bayesian Nonlinear Estimation Method Using Resampled Smooth Particle Hydrodynamics Solutions of the Fokker-Planck Equation
DUFFY Michael, CHUNG Soon-Jo, **BERGMAN Lawrence***
*University of Illinois at Urbana-Champaign (Aerospace Engineering, 104 South Wright St., Urbana, Illinois United States)

09:10 - 09:30
Coupled nonlinear oscillators: closed form solutions
STEFANO Lenci*
*Department of Civil and Building Engineering, and Architecture [Ancona] (via Brecce Bianche, 60131 Ancona Italy)

09:30 - 09:50
Phase - locked breathers in the damped driven granular chains
KOVALEVA Margarita, **STAROSVETSKY Yuli***
*Technion - Israel Institute of Technology [Haifa] (Technion City, Haifa 3200003 Israel)

09:50 - 10:10
Nonlinear Phenomena in Shells with Random Excitation
PELLICANO Francesco*, ZIPPO Antonio, IARRICCIO Giovanni
*Università degli Studi di Modena e Reggio Emilia, Dipartimento di Ingegneria Enzo Ferrari, Centre InterMech - MO.RE. (V. P. Vivarelli 10 41125 Modena ITALY Italy)

10:10 - 10:30
Intermodal targeted energy transfer (IMTET) concept in seismically excited model of twenty-story steel structure
GZAL Majdi, CARRION Juan, AL-SHUDEIFAT Mohammed, SPENCER Bill, VAKAKIS Alexander, BERGMAN Lawrence, **GENDELMAN Oleg***
*Department of Mechanical Engineering [Haifa] (Technion - Institute of Technology Haifa 32000 Israel Israel) - Technion - Israel Institute of Technology, Faculty of Mechanical Engineering, (Technion City, Haifa, 32000 Israel)

Unified perspectives on nonlinear model reduction

Tieding Guo[*], Giuseppe Rega[**]
[*]*College of Civil and Architecture Engineering, Guangxi University, Nanning, China*
[**] *Dipartimento di Ingegneria Strutturale e Geotecnica, Sapienza University of Rome, Rome, Italy*

Summary. The past decade has witnessed renewed interests to nonlinear model reduction and many differently motivated techniques are proposed, including nonlinear normal modes (NNMs), direct multi-scale method (dMSM, full-basis), normal form (NF), sub-spectral manifolds (SSMs), quadratic manifolds (QM, using a mode derivative concept), low-order elimination technique (LOE). There is indeed demand for unified perspectives on the whole nonlinear model reduction matter, aiming at a better understanding of subtle connections among all these reduction methods.

In this talk, the recent low-order elimination (LOE) technique using a passive pattern concept will be first discussed, and then used to outline some unified perspectives on nonlinear model reduction, which are developed based upon two different basic problems, i.e., truncation order and truncation degree. The former refers to the common reduced dimension or number of dominant modes, while the latter refers to truncation degree of polynomials employed to approximate invariant manifold/transformation/passive pattern.

An explicit theoretical correspondence among these reduction methods will be detailed, placing in particular NNMs/dMSM/NF/LOE within a unified framework in the sense of refined finite mode truncation, which justifies various claims/observations in literature that all these refined reduction methods correct the routine/flat Galerkin (say, single-mode) truncated model.

Another unified perspective is built by focusing on various reduced-order models (ROMs) of general quadratic/cubic nonlinear structures, produced by different reduction methods with two-, three-, and four-degree truncations. It turns out that all the truncations produce valid and equivalent, but seemingly different, ROMs. Through translating invariant manifolds and nonlinear transformation terminology into low-order elimination language using passive patterns, we frame various reduction approaches within the same formulation and finally give a unified elucidation of distinct reduction methods in the sense of truncation degree.

Model truncation issues

We take a quadratic/cubic nonlinear structure as an archetypical model

$$\partial^2 w/\partial t^2 + L[w] = N_2[w] + N_3[w] + \cdots \tag{1}$$

with boundary conditions $B_0[w] = B_1[w] = 0$. Here $w(x,t)$ is the displacement, $L[\cdot]$, $N_2[\cdot]$ and $N_3[\cdot]$ are the structure's linear, quadratic and cubic spatial operators, respectively. Using single-mode truncation (*m*-th mode is assumed to dominate asymptotic dynamics), we deduce routine Galerkin model for model (1)

$$\ddot{q}_m + \omega_m^2 q_m = \langle \phi_m, N_2[\phi_m, \phi_m] \rangle q_m^2 + \langle \phi_m, N_3[\phi_m, \phi_m, \phi_m] \rangle q_m^3 + \cdots \tag{2}$$

where $\langle \phi_i, \phi_j \rangle = \delta_{ij}$, $\langle \phi_i, L[\phi_j] \rangle = \omega_i^2 \delta_{ij}$, with ω_i and ϕ_i being *i*-th modal frequency and shape. However it is often criticized due to completely neglecting non-essential modes $q_l, l \neq m$, which leads to possible error predictions.

Truncation order problem: refined finite mode truncation

(1) The *NNMs* method introduces the following invariant manifolds

$$q_l = g_l(q_m, \dot{q}_m) \sim O(q_m^2, \dot{q}_m^2), \quad \dot{q}_l = h_l(q_m, \dot{q}_m) \sim O(q_m^2, \dot{q}_m^2), \quad l \neq m \tag{3}$$

to enslave the non-essential modes ($l \neq m$) to the dominant one, satisfying manifold equations (say, up to second order)

$$\frac{\partial g_l}{\partial q_m}\dot{q}_m + \frac{\partial g_l}{\partial \dot{q}_m}\left(-\omega_m^2 q_m\right) = h_l, \quad \frac{\partial h_l}{\partial q_m}\dot{q}_m + \frac{\partial h_l}{\partial \dot{q}_m}\left(-\omega_m^2 q_m\right) = -\omega_l^2 g_l + \langle \phi_l, N_2[\phi_m, \phi_m] \rangle q_m^2 \tag{4}$$

(2) The *full-basis or direct perturbation* method designs a 'ladder-type' expansion scheme like

$$O(\varepsilon): \quad D_0^2 q_{m1} + \omega_m^2 q_{m1} = 0, \quad O(q_{l1}) \ll O(q_{m1}), \quad l \neq m \tag{5}$$

$$O(\varepsilon^2): \quad D_0^2 q_{m2} + \omega_m^2 q_{m2} = \langle \phi_m, N_2[\phi_m, \phi_m] \rangle q_{m1}^2, D_0^2 q_{l2} + \omega_l^2 q_{l2} = \langle \phi_l, N_2[\phi_m, \phi_m] \rangle q_{m1}^2, \quad l \neq m \tag{6}$$

to dynamically condense the non-essential modes ($l \neq m$) to the dominant one $q_m, \dot{q}_m$ (satisfying Eq.(6) at $O(\varepsilon^2)$)

$$q_{l2} = \frac{\langle \phi_l, N_2[\phi_m, \phi_m] \rangle}{0^2 + \omega_l^2}\left(\frac{q_m^2}{2} + \frac{\dot{q}_m^2}{2\omega_m^2}\right) + \frac{\langle \phi_l, N_2[\phi_m, \phi_m] \rangle}{-4\omega_m^2 + \omega_l^2}\left(\frac{q_m^2}{2} - \frac{\dot{q}_m^2}{2\omega_m^2}\right), \quad l \neq m \tag{7}$$

(3) The (*simplified*) *normal form* method introduces the following nonlinear near-identity transformations

$$q_l = p_l + \hat{G}_l(p_m, \dot{p}_m), \quad \dot{q}_l = \dot{p}_l + \hat{H}_l(p_m, \dot{p}_m), \quad l = 1, 2 \cdots \tag{8}$$

to reformulate the original full-basis discretized Galerkin model as

$$\begin{aligned} \ddot{p}_l + \omega_l^2 p_l &= 0 + 2\langle \phi_l, N_2[\phi_m, \phi_m] \rangle p_m \hat{G}_m \\ &+ \sum_{j=1, j\neq m}^{\infty} \langle \phi_l, N_2[\phi_j, \phi_m] + N_2[\phi_m, \phi_j] \rangle \hat{G}_j p_m + \langle \phi_l, N_3[\phi_m, \phi_m, \phi_m] \rangle p_m^3 \end{aligned} \tag{9}$$

satisfying the simplified homological equations (say, up to second order)

$$\nabla_Y \hat{M}_l\left[\Lambda_m\right]Y-\left[\Lambda_l\right]\hat{M}_l=\left[0,\left\langle\phi_l,N_2\left[\phi_m,\phi_m\right]\right\rangle p_m^2\right]^T,\ \hat{M}_l\triangleq\left[\hat{G}_l,\hat{H}_l\right],Y=\left[p_m,\dot{p}_m\right]^T,\ \nabla_Y\triangleq\left[\partial/\partial p_m,\ \partial/\partial\dot{p}_m\right] \quad (10)$$

(4) The *low-order elimination* technique [1] designs a new displacement decomposition augmented by passive patterns

$$w(x,t)=\phi_m(x)q_m(t)+\sum\Phi_{\Omega_k}(x)P_{\Omega_k}(t) \quad (11)$$

where $\left(\phi_m,q_m\sim e^{\mathrm{i}\omega_m t}\right)$ is the dominant mode and $\left(\Phi_{\Omega_k},P_{\Omega_k}\sim e^{\mathrm{i}\Omega_k t}\right)$ is the *k*-th passive pattern produced by low-order quadratic source terms, with $\Omega_p\triangleq\left\{0,2\omega_m\right\}$, satisfying

$$\sum_{\Omega_k\in\{0,2\omega_m\}}\left(-\Omega_k^2 I+L\right)\Phi_{\Omega_k}(x)P_{\Omega_k}(t)=N_2\left[\phi_m,\phi_m\right]q_m^2,\ \ B_0\left[\Phi_{\Omega_k}\right]=B_1\left[\Phi_{\Omega_k}\right]=0 \quad (12)$$

$$P_0(t)=q_m^2/2+\dot{q}_m^2/\left(2\omega_m^2\right),\qquad P_{2\omega_m}(t)=q_m^2/2-\dot{q}_m^2/\left(2\omega_m^2\right) \quad (13)$$

leading to so-called low-order elimination in the reference model

$$\left(\frac{\partial^2}{\partial t^2}+L\right)\phi_m q_m=\boxed{0}+\sum_{\Omega_k\in\Omega_p}\left(N_2\left[\phi_m,\Phi_{\Omega_k}\right]+N_2\left[\Phi_{\Omega_k},\phi_m\right]\right)q_m p_{\Omega_k}+N_3\left[\phi_m,\phi_m,\phi_m\right]q_m^3+\cdots \quad (14)$$

Quite interestingly, the four distinctly motivated reduction methods above are equivalent to each other, and a theoretical correspondence can be established [2].

Truncation degree problem

Due to the correspondence/equivalence above, the truncation degree problem in nonlinear model reduction is developed in the low-order elimination formulation using passive patterns. We consider full/non-full truncations of degree two

$$w(x,t)=\phi_m q_m+\Phi_0 P_0+\Phi_{2\omega_m}P_{2\omega_m}+\cdots,\qquad w(x,t)=\phi_m q_m+\overline{\Phi}_0 P_0+\overline{\Phi}_{2\omega_m}P_{2\omega_m}+\cdots \quad (15)$$

and also full/non-full truncations of degree three

$$\begin{aligned}
w(x,t)&=\phi_m q_m+\Phi_0 P_0+\Phi_{2\omega_m}P_{2\omega_m}+\Phi_{\omega_m}P_{\omega_m}+\Phi_{3\omega_m}P_{3\omega_m}+\cdots\\
w(x,t)&=\phi_m q_m+\Phi_0 P_0+\Phi_{2\omega_m}P_{2\omega_m}+\overline{\Phi}_{\omega_m}P_{\omega_m}+\overline{\Phi}_{3\omega_m}P_{3\omega_m}+\cdots\\
w(x,t)&=\phi_m q_m+\overline{\Phi}_0 P_0+\overline{\Phi}_{2\omega_m}P_{2\omega_m}+\hat{\Phi}_{\omega_m}P_{\omega_m}+\hat{\Phi}_{3\omega_m}P_{3\omega_m}+\cdots
\end{aligned} \quad (16)$$

Note non-full truncation means the pattern shape functions $\overline{\Phi}_{\Omega_k}$ and $\hat{\Phi}_{\Omega_k}$ are incomplete with master components being skipped. It turns out that the NNMs method (invariant manifolds) can always be regarded as a non-full truncation (thus non-full elimination) technique, while the existing normal form method can be regarded as either a non-full three-degree truncation, or a full two-degree truncation with further third order simplification. Interestingly, for quadratic/cubic structures, all the reduction methods, either degree two or three, full or non-full, lead to equivalent third-order ROMs. Furthermore, in degenerate case, a four-degree truncation will be required [3].

The two unified perspectives on nonlinear model reduction are further illustrated in Fig.1 and the numerical results are obtained by applying the reduction methods above to a nonlinear foundation beam example.

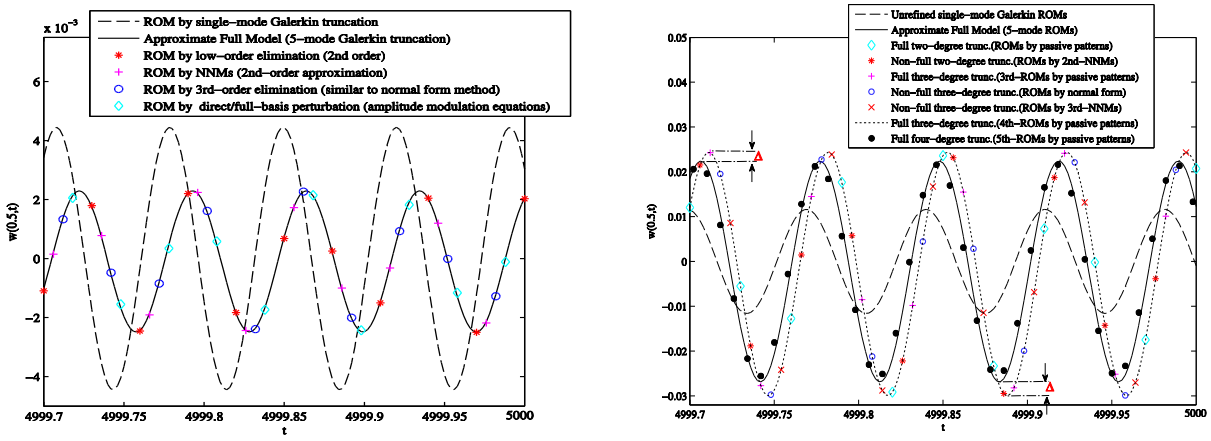

(a) (b)

Fig.1 Unified perspectives and numerical illustrations: (a) truncation order problem [2]; (b) truncation degree problem (degenerate dynamics) [3]

References

[1] T.D Guo and G. Rega, Reduced-order modelling of nonlinear structures: A low-order elimination technique using passive patterns, submitted, 2021

[2] T.D Guo and G. Rega, On model reduction techniques of nonlinear structures: Theoretical correspondence and refined finite mode truncation, preprint, 2022

[3] T.D Guo, G. Rega, H.J, Kang, On the minimal degree of truncation for nonlinear model reduction: A low-order elimination perspective, preprint, 2022

A General Bayesian Nonlinear Estimation Method Using Resampled Smooth Particle Hydrodynamics Solutions of the Fokker-Planck Equation

Michael Duffy*, Soon-Jo Chung** and Lawrence Bergman***
*Dept. of Aerospace Engineering, University of Illinois, Urbana, IL, USA
Current employer: Raytheon Missiles and Defense Co., Tucson, AZ, USA
** Div. of Eng'g and Applied Science, California Institute of Technology, Pasadena, CA, USA
*** Dept. of Aerospace Engineering, University of Illinois, Urbana, IL, USA

Summary. The state estimation problem for noisy nonlinear systems remains a difficult problem, particularly as the dimension of the state space grows large. This presentation will consist of a brief introduction to the problem as a diffusion process and its solution employing smooth particle hydrodynamics (SPH) to advance the estimator through the state space in time. Performance comparisons between the current algorithm, the particle filter, and the extended Kalman filter for Duffing systems of two and four dimensions will be presented.

Introduction

The effectiveness of a nonlinear estimator in a noisy environment depends on many factors, one being the accuracy with which it can predict the state dynamics of the underlying dynamical system between measurements. It is well known that a memoryless nonlinear dynamical system driven by additive and/or multiplicative Gaussian white noise can be represented by a system of D nonlinear stochastic differential equations of the Ito form, where D is the number of system states. The Bayesian optimal prior can be obtained by solving the corresponding Fokker-Planck Equation (FPE), governing the evolution of the transition probability density function of the system response over the state space [1]. The FPE is a degenerate, linear, elliptic-parabolic partial differential equation having D spatial dimensions, plus time, on an infinite spatial domain, for $t \geq 0$. To date, for the nonstationary (transient) problem, analytical solutions exist only for the scalar case, $D = 1$, the exception being the linear system subject to additive noise for which the analytical solution can be found for arbitrary D. Thus, although computational solutions of the nonstationary FPE for nonlinear systems of dimension $D = 3$ have been tractable since the mid-1980s, solution remains problematic for realistic systems with $D > 3$ due to scaling issues caused by the well-known "curse of dimensionality," and it remains extraordinarily difficult and costly to achieve accurate solutions to higher dimensional problems over the entire state space [2,3].
This presentation is a summary of our recent work addressing a general nonlinear filter based on solving the nonstationary FPE in $\mathbf{R}^D$ using Smooth Particle Hydrodynamics (SPH) at lower resolution which, for the limited number of four-dimensional systems studied, appears to result in reasonably accurate state estimation results. The filter is enabled by an efficient heuristic resampling scheme of the SPH solution, also briefly discussed. The resulting FPE-SPH filter appears able to replicate the accuracy of both the well-known, simulation-based Particle Filter (PF) and linearization-based Extended Kalman Filter (EKF) for lower dimensional systems, while being more robust than the EKF, at least for the several higher-dimensional systems examined [4].
In the limited time available, a short exposition of the underlying theory will be given, followed by a comparison of results obtained for two-dimensional and four-dimensional Duffing oscillators.

Background

Consider a system of stochastic differential equations of the form

$$d\mathbf{x} = \mathbf{f}(\mathbf{x},t)dt + \mathbf{g}(\mathbf{x},t)d\mathbf{W}(t) \tag{1}$$

$$\mathbf{y} = \mathbf{h}(\mathbf{x},t) + \mathbf{v}(t) \tag{2}$$

where $\mathbf{x},\mathbf{f} \in \mathbb{R}^D$, $\mathbf{g} \in \mathbb{R}^{D\times D_N}$, and $\mathbf{w} \in \mathbb{R}^{D_N}$, subjected to zero mean Gaussian white noise that defines a Wiener process $d\mathbf{W}(t) = \sqrt{t}\mathbf{w}$, $E[\mathbf{w}(t)] = 0$, $E[\mathbf{w}(t)\mathbf{w}^{\mathrm{T}}(t+\tau)] = \mathbf{Q}\delta(\tau)$. Also, $\mathbf{y}$ is a state measurement process, where $\mathbf{y},\mathbf{h} \in \mathbb{R}^{D_0}$ and $\mathbf{v} \in \mathbb{R}^{D_0}$ is a nonzero mean Gaussian white noise, and $E[\mathbf{v}(t)] = 0$, $E[\mathbf{v}(t)\mathbf{v}^{\mathrm{T}}(t+\tau)] = \mathbf{R}\delta(\tau)$. There exists a corresponding Fokker-Planck-Kolmogorov equation which defines the evolution in time of the transition probability density function of the system states, which takes the form

$$\frac{dp}{dt} = -\sum_{i=1}^{D}\frac{\partial}{\partial x_i}(D_i^{(1)}p) + \frac{1}{2}\sum_{i=1}^{D}\sum_{j=1}^{D}(D_{ij}^{(2)}p) \tag{3}$$

subject to

$$p(\mathbf{x},0 \mid \mathbf{x}_0) = \prod_{i=1}^{D}\delta(x_i - x_{i0}) \tag{4}$$

where $D_i^{(1)}$ and $D_{ij}^{(2)}$ are the deviate moments derived from eq. (1).

Results and Conclusions

For systems with simpler dynamics, the FPE-SPH, PF and EKF filters perform very similarly when properly parameterized. Differences emerge for systems such as the Duffing where the double-well potential of the PDF can result in rapid changes in an individual transient trajectory. In an estimation context sufficient process noise, measurement noise, and/or time between update steps can result in extreme EKF divergence. The PF and FPE-SPH filters on the other hand are robust against these sudden switches, which can be seen in the single run history below in Figure 1 and 25 run NEES in Figure 2.

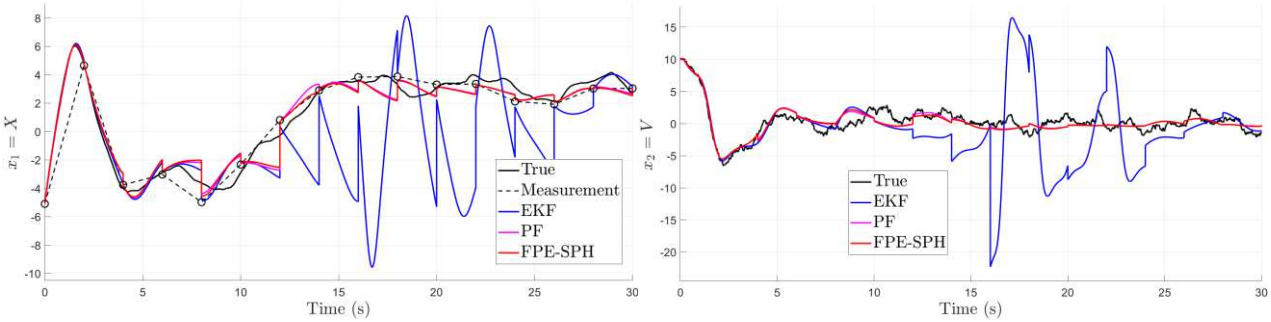

Figure 1: Example 2D Duffing estimated state histories (position, velocity) demonstrating EKF divergence.

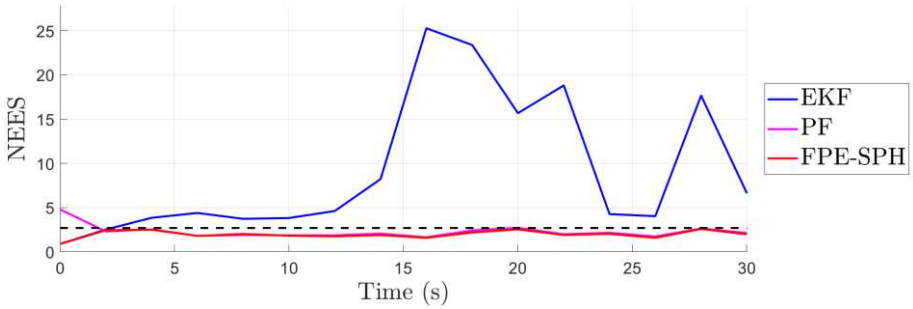

Figure 2: 2D Duffing NEES (25 Monte-Carlo runs, different initial conditions, common seeds between filters)

Robustness of the FPE-SPH filter extends up to four-state systems where one of the oscillators possesses a Duffing term. The system parameters simulated are not severe enough to result in EKF divergence as with the two state Duffing, but the results confirm that the FPE-SPH Filter is an accurate estimator in higher dimensional systems. The RMS error is shown in Figure 3.

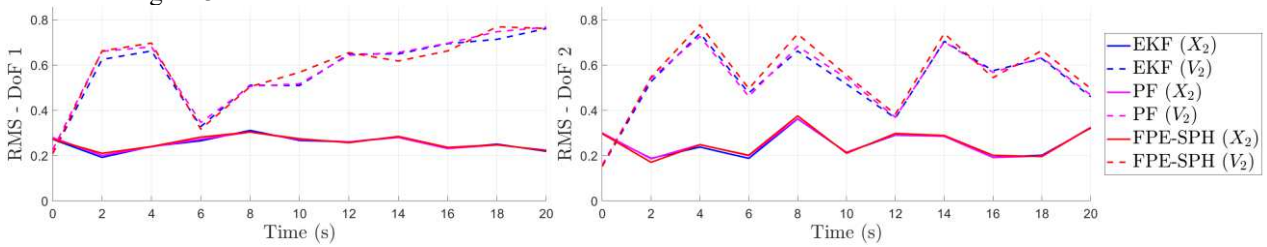

Figure 3: RMS Errors for 4D Nonlinear System, separated by degree of freedom (10 runs)

The FPE-SPH filter can accomplish this with only 5,000 particles using conservative runtime acceleration parameters compared to the PF's 100,000. Improvements to the underlying algorithm to better handle higher dimensional behavior and more aggressive parameterization to further prioritize run time might allow for further scaling to tackle systems with more than four states. Please refer to the references for information about the algorithms employed.

References

[1] Duffy, M. (2019) Efficient Solution of the Fokker-Planck Equation Via Smooth Particle Hydrodynamics for Nonlinear Estimation. *PhD Thesis*, University of Illinois at Urbana-Champaign.

[2] Spencer, B.F. Jr., Bergman, L.A. (1993) On the Numerical Solution of the Fokker-Planck Equation for Nonlinear Stochastic Systems. *Nonlinear Dynamics*, **4**(4), 357-372.

[3] Wojtkiewicz, S.F., Bergman, L.A., Spencer, B.F. Jr., Johnson, E.A. (2001) Numerical Solution of the Four-Dimensional Nonstationary Fokker-Planck Equation. In: Narayanan, S., Iyengar, R.N. (eds), IUTAM Symposium on Nonlinearity and Stochastic Structural Dynamics. *Solid Mechanics and its Applications*, **85**, Springer, Dordrecht.

[4] Duffy, M., Chung, S-J., Bergman, L. (2022) A General Bayesian Nonlinear Estimation Method using Resampled Smooth Particle Hydrodynamics Solutions of the Underlying Fokker-Planck Equation." *International Journal of Nonlinear Mechanics* (special issue dedicated to Professor L. Manevitch), in review.

Coupled nonlinear oscillators: closed form solutions

Stefano Lenci*
*Department of Civil and Building Engineering and Architecture, Polytechnic University of Marche, Ancona, Italy

Summary. The mathematical solution of a system of two coupled Duffing oscillators is obtained in closed form by extending to this 2 DOF system a technique previously used for 1 DOF systems. A parametric investigation is proposed to illustrate the usefulness of the exact solution to detect the main dynamical phenomena, in particular those related to the modal coupling which is the main characteristic of this archetypal system.

Introduction

A two Degrees of Freedom (DOF) nonlinear oscillator is an archetypal system that allow to detect, in a simple way, the modal coupling in nonlinear mechanical systems. It permits focusing on the main phenomena, without unessential mathematical developments that sometimes hide the main physical characteristics of interest. Furthermore, it is obtained when a two-mode reduced order model of any, even infinite dimensional, system is considered. It is the natural evolution of the study of simple 1 DOF archetypal systems, like Duffing, Helmholtz, van der Pool, etc., that have been largely studied in the past.
Although it looks a simple model, it is not yet fully investigated, even if several studies have been devoted to modal coupling of different, specific, engineering systems. Furthermore, all previous works used numerical simulations or approximated analytical methods, notably the multiple time scale method.
In this work, which is based on [1] and take advantage from the ideas of [2-4], we consider an exact, closed form, solution for a system of two Duffing oscillators, linearly and nonlinearly coupled. This permits a full parametric investigation and detection of "all" dynamical outcomes due to coupling.

Governing equations and solution

A system of two Duffing linearly and nonlinearly coupled oscillators is governed by the equations

$$\begin{aligned} M_x\ddot{x} + D_x\dot{x} + K_x x + K_{3x}x^3 + D_{xy}(\dot{x}-\dot{y}) + K_{xy}(x-y) + K_{3xy}(x-y)^3 = G_x(t), \\ M_y\ddot{y} + D_y\dot{y} + K_y y + K_{3y}y^3 + D_{xy}(\dot{y}-\dot{x}) + K_{xy}(y-x) + K_{3xy}(y-x)^3 = G_y(t), \end{aligned} \tag{1}$$

where M_i are the masses, D_i the damping coefficients, K_i the linear stiffnesses, K_{3i} the nonlinear stiffnesses and $G_i(t)$ the external forces. To obtain the closed form solution, the excitations are assumed to be in the form

$$\begin{aligned} G_x(t) = D_x\dot{x} + D_{xy}(\dot{x}-\dot{y}) + K_{xy}(x-y) + K_{3xy}(x-y)^3 - S_x x - S_{3x}x^3, \\ G_y(t) = D_y\dot{y} + D_{xy}(\dot{y}-\dot{x}) + K_{xy}(y-x) + K_{3xy}(y-x)^3 - S_y y - S_{3y}y^3, \end{aligned} \tag{2}$$

where S_x, S_{3x}, S_y, S_{3y} are parameters that can be chosen freely. Inserting (2) in (1) yields

$$\ddot{x} + (\omega_x^2 + W_x)x + (k_x + C_x)x^3 = 0, \quad \ddot{y} + (\omega_y^2 + W_y)y + (k_y + C_y)y^3 = 0, \tag{3}$$

where

$$\omega_x^2 = \frac{K_x}{M_x}, \;\; W_x = \frac{S_x}{M_x}, \;\; k_x = \frac{K_{3x}}{M_x}, \;\; C_x = \frac{S_{3x}}{M_x}, \;\; \omega_y^2 = \frac{K_y}{M_y}, \;\; W_y = \frac{S_y}{M_y}, \;\; k_y = \frac{K_{3y}}{M_y}, \;\; C_y = \frac{S_{3y}}{M_y}. \tag{4}$$

Equations (3) are two uncoupled Duffing equations, for which the closed form solutions are

$$x(t) = A_x cn(a_x t, b_x), \;\; y(t) = A_y cn(a_y t, b_y), \tag{5}$$

where

$$\begin{aligned} a_x^2 = (\omega_x^2 + W_x) + (k_x + C_x)A_x^2, \;\; b_x^2 = \frac{(k_x + C_x)A_x^2}{2a_x^2}, \\ a_y^2 = (\omega_y^2 + W_y) + (k_y + C_y)A_y^2, \;\; b_y^2 = \frac{(k_y x + C_y)A_y^2}{2a_y^2}. \end{aligned} \tag{6}$$

and where "cn" is the Jacobian elliptic function. $x(t)$ and $y(t)$ are periodic with period

$$T_x = \frac{4K(b_x)}{a_x}, \;\; T_y = \frac{4K(b_y)}{a_y}. \tag{7}$$

The solutions of interest are those for which $T_x = T_y (= T)$, i.e. both $x(t)$ and $y(t)$ oscillate with the same period (but not with the same amplitudes A_x and A_y). Actually, this is an equation linking A_x and A_y (e.g. $A_y(A_x)$), once all the other parameters are known. Then, from (7) one gets the period of the excitation $T_x = T(A_x)$ and $T_y = T(A_y)$. Inverting these expressions one obtains the frequency response curves $A_x(T)$ and $A_y(T)$. Further details, including how to determine its stability, can be found in [1].
An advantage of the proposed method is that it is possible to use the free parameters S_x, S_{3x}, S_y, S_{3y} to shape the excitation and to have it as close as possible to a desired target, still keeping the closed form expressions for the *nonlinear* oscillations.

An example

To shortly illustrate the previous findings we consider

$$\omega_x = 2.5,\ \ W_x = -4.5,\ \ k_x = 2,\ \ C_x = 0,\ \ \omega_y = 2.5,\ \ W_y = 0,\ \ k_y = -1,\ \ C_y = 0,$$
$$M_x = 1,\ \ M_y = 2,\ \ D_x = 0.01,\ \ D_{xy} = 0.02,\ \ D_x = 0.03,\ \ K_{xy} = 0.5,\ \ K_{3xy} = 0.4, \qquad (8)$$

which corresponds to the perfect internal resonance ($\omega_x = \omega_y$) with the x mode hardening and the y mode softening. The solution of $T_x = T_y$ is reported in Fig. 1. For $A_x = 1$ one obtains $A_y = 1.9731$ and $T = 3.5009$. The corresponding excitations $G_x(t)$ and $G_y(t)$ and solutions $x(t)$ and $y(t)$ are illustrated in Fig. 2. In Fig. 3 it is shown how choosing $W_x = -4.47979443$, $C_x = 0.036619325$, $W_y = 0.14970754$, $C_y = 0.024427757$ allows to strongly reduce $G_y(t)$, by leaving practically unchanged $G_x(t)$. This is an example of shaping the excitation, which can be improved by using optimization algorithms. Much more results, including frequency response curves, are reported in [1].

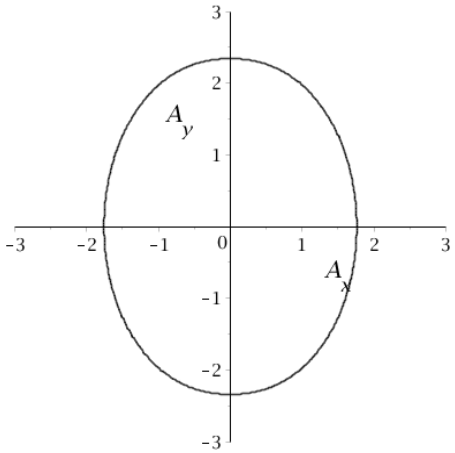

Figure 1: The solution $A_y(A_x)$ for the parameter (8).

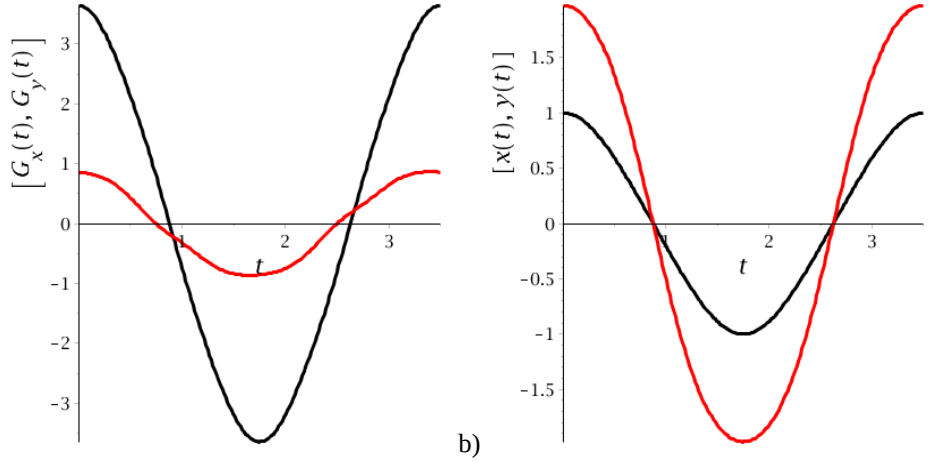

Figure 2: a) $G_x(t)$ (black) and $G_y(t)$ (red); b) $x(t)$ (black) and $y(t)$ (red). $A_x = 1$ and parameters (8).

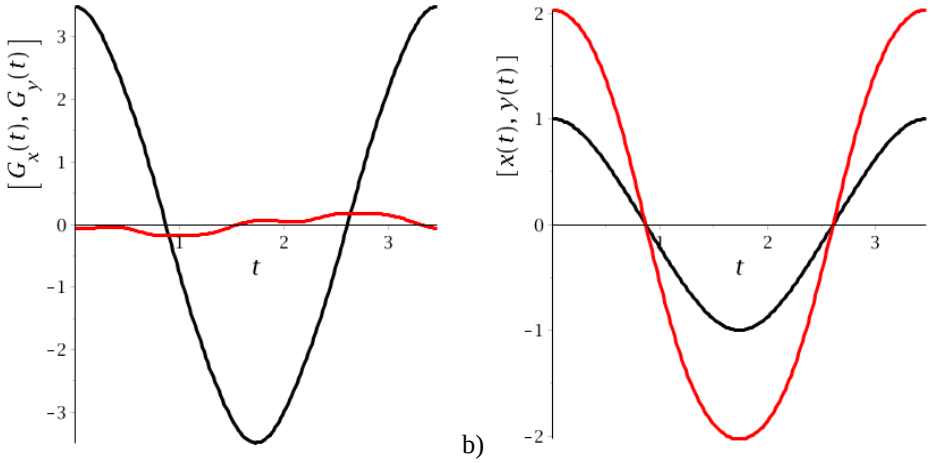

Figure 3: As Fig. 2, but with $W_x = -4.47979443$, $C_x = 0.036619325$, $W_y = 0.14970754$, $C_y = 0.024427757$.

References

[1] Lenci S. (2022) Exact solutions for coupled Duffing oscillators. *Mech. Sys. Sign. Proc.* **165**: 108299.
[2] Hsu C.S (1960) On the application of elliptic functions in nonlinear forced oscillations. *Quat. Appl. Math.* **17**, 352-356.
[3] Vakakis A.F., Blanchard A. (2018) Exact steady states of the periodically forced and damped Duffing oscillator. *J. Sound Vib.* **413**:57-65.
[4] Kovacic I. (2018), Externally excited undamped and damped linear and nonlinear oscillators: Exact solutions and tuning to a desired exact form of the response. *Int. J. Non-Linear Mech.* **102**:72-81.

Phase - locked breathers in the damped driven granular chains

Margarita Kovaleva[*], Yuli Starosvetsky[**]
[*]*N.N. Semenov Federal Center for Chemical Physics, Russian Academy of Sciences, Moscow, Russia*
[**]*Faculty of Mechanical Engineering, Technion Israel Institute of Technology, Haifa, Israel*

Summary. Over the past few decades, dynamics of one-dimensional (1D) granular lattices has become a subject of immense theoretical and experimental research. In the present talk we will discuss the fundamental problem of nonlinear wave propagation in the damped-driven, granular lattice mounted on a linear elastic foundation which assumes the general type of strongly nonlinear, inter-site potential and subject to an external harmonic forcing in the form of a traveling wave. In the present work we will focus on the analysis of moving breather solution forming in the damped-driven chain.

Introduction

Of late, a special type of localized excitations forming in granular medium has become a subject of immense theoretical and experimental research. This special type of solutions is manifested by a spatial energy localization and time periodicity which are usually referred to in the literature as intrinsically localized modes (ILM) or Discrete Breathers (DB). To the best of authors knowledge the first theoretical study of the dynamics of localized modes in compressed granular chains has been reported in [1]. In fact as it was shown in this study, these localized modes are formed due to the presence of the mass defects. The first experimental study of the formation of long-lived, DB solutions in granular medium has been performed on the compressed, di-atomic granular crystal [2]. This groundbreaking experimental study of DBs has been followed by a systematic theoretical analysis of existence and stability of these spatially localized solutions [3]. All the DB solutions reported in [2-3] correspond to the bright breather solutions emerging in the di-atomic, essentially compressed granular chains. Additional theoretical and experimental study of compressed, mono-atomic granular crystal [4], have demonstrated the existence of dark breather solutions in these chains. These special nonlinear waves have also been reported in theoretical and experimental study of the damped, driven, compressed granular crystals [5]. In fact all the DB solutions existing in granular configurations reported in [2-5] have been considered solely for the pre-compressed state of granular medium. Therefore, when considering the uncompressed state of granular chains, one may wonder whether these spatially localized and time periodic nonlinear wave solutions exist. As a matter of fact, existence of discrete breathers in the un-loaded granular crystals, has been reported at first for one-dimensional, uncompressed granular chain subject to a linear on-site potential and an inter-particle Hertzian interaction [6]. In the same study, formation of static and traveling DBs has been demonstrated numerically. Passing to a small amplitude limit, authors derived the reduced model which has been coined a name of discrete p-Schrodinger (DpS) equation. This model can be regarded as a slow flow model, which approximates the slow (amplitude and phase) modulation of the low amplitude regimes of the original granular setup.

Model

Present study has been motivated by the earlier work by James et al. [8] who derived the analytical approximation for the moving breather supported by the DpS chain. In the present work we consider the DpS chain, subject to the external forcing and dry friction. As it has been shown by James the slow modulation of low amplitude oscillatory solutions can be efficiently described by the discrete p-Schrodinger equation which can be derived through the common multi-scale procedure [6-7]. Following same idea we consider p-Schrodinger equation with forcing and dry friction terms:

$$\frac{d\varphi_k}{dt_1}=\frac{i\sigma}{2}\varphi_k-\lambda\frac{\varphi_k}{|\varphi_k|}+\frac{iF}{2}e^{ik\gamma}+i\mu\left(\varphi_k-\varphi_{k-1}\right)\left|\varphi_k-\varphi_{k-1}\right|^m+i\mu\left(\varphi_k-\varphi_{k+1}\right)\left|\varphi_k-\varphi_{k+1}\right|^m \tag{1}$$

Asymptotic expansion

Assuming the following asymptotic scaling of forcing, damping and the power of non-linearity,

$$m=\nu^2,\ F=\tilde{F}\nu^2,\lambda=\tilde{\lambda}\nu^2,\varphi_n=(-1)^n\rho_n e^{i\gamma n} \tag{2}$$

we proceed with the multiple-scale expansion,

$$\rho_n=\phi\left(\xi,\tau\right),\ \xi=\nu\left(n-c_q\tau_1\right),\ \tau=\nu^2\tau_1\,. \tag{3}$$

Log – NLS equation

Proceeding to the multiple-scale technique we end up with the damped-driven Log – NLS equation

$$\phi_\tau=-\lambda\frac{\phi}{|\phi|}+\frac{iF}{2}+\frac{3i\beta\cos\gamma}{8}\phi_{\xi\xi}+\frac{3i\beta\Omega^2}{8}\phi\ln\left|\Omega\phi\right|,\quad \Omega=\sqrt{\left(2+2\cos\gamma\right)} \tag{4}$$

Seeking for the stationary (in terms of the super-slow time scale) traveling soliton solution we obtain the following second order ODE.

$$\phi_{\xi\xi\xi} + \frac{8i\lambda}{3\beta\cos\gamma}\frac{\phi}{|\phi|} + \frac{8F}{6\beta\cos\gamma} + \frac{\Omega^2}{\cos\gamma}\phi\ln|\Omega\phi| = 0 \tag{5}$$

Assuming the phase-locked solution (strictly locked phase $\phi = R(\xi)e^{i\vartheta}$, $R, \vartheta \in \mathrm{Re}$, $\vartheta - const$) the complex ODE equation is split into the real and imaginary part:

$$R_{\xi\xi\xi} = -\frac{8F}{6\beta\cos\gamma}\cos(\vartheta) - \frac{\Omega^2}{\cos\gamma}R\ln|\Omega R|; \tag{6a}$$

$$-\frac{8\lambda}{3\beta\cos\gamma} + \frac{4F}{3\beta\cos\gamma}\sin\vartheta = 0. \tag{6b}$$

The real part is the second order ODE which depicts the evolution of the amplitude, while the second imaginary part is an algebraic equation which defines the stationary phase of the breather solution:

$$\sin\vartheta = \frac{2\lambda}{F};\ \cos\vartheta = \pm\sqrt{1-\left(\frac{2\lambda}{F}\right)^2} \tag{7}$$

It can be easily inferred from the imaginary part we have two solutions which emerge through the typical saddle – node bifurcation. To illustrate better the dynamics of two distinct breather solutions on both branches we illustrate the following phase portraits.

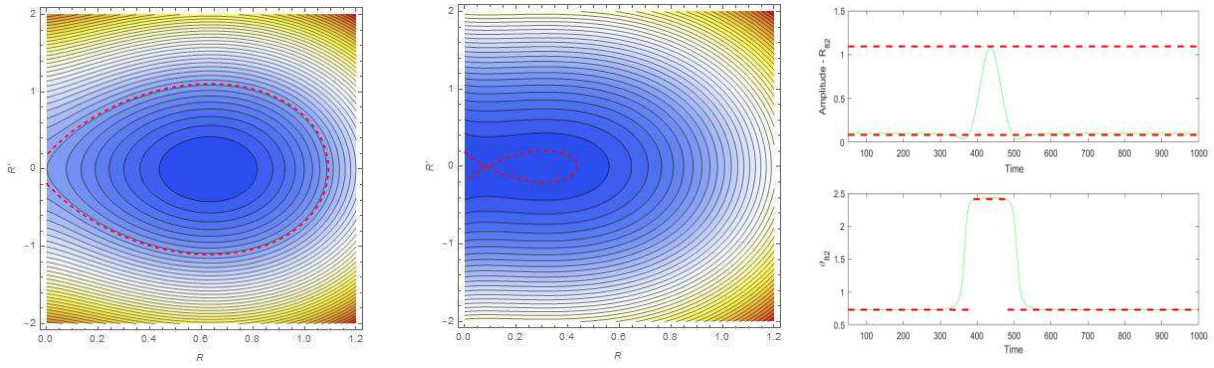

a) b) c)

Figure 1: Phase planes of the two branches of the equation (a) First branch (b) Second branch (c) Time histories of the response of the DpS chain (Amplitude – upper panel, phase – lower panel), red-dashed lines stand for the phase locked approximation

Clearly the homoclinic orbit of the phase plane shown in the right panel corresponds to the phase locked solitons solution. However, this solution could not be reproduced in the extensive numerical simulations. We conjecture that this solution is unstable. Interestingly enough there exists an additional, phase locked, soliton solution which can be approximated using both phase planes. This solution emanates from the saddle of the right phase plane (Figure 1b) (to the left of the saddle) and continues along the unstable manifold of the saddle up to the point of zero amplitude. When reaching this point there is a jump to the second branch which means that the solution changes phase. Further evolution of the trajectory on the second branch is denoted with the red, dashed line on the left phase plane (Figure 1a). When it reaches again the point of zero amplitude there is a subsequent jump to the first branch and then it gradually converges to a saddle of the first branch along the stable manifold. Here we would like to emphasize that the proposed solution is just an approximation as there is no immediate jump in the phase for the true system solution. This can be clearly seen from the results of Figure 2 where the jump from the vicinity of one phase to the second one, occurs in the fast time scale. Using our analytical model and in particular the analysis of the phase plains, we predict the amplitude, the background and the speed of the traveling soliton. As for the phase of this solution we can clearly see the fast evolution of the phase in the true DpS from one state (first branch) to another (second branch). Obviously enough this transient evolution of the phase from one state to another cannot be captured by our phase locked approximation.

Conclusions

New family of traveling solitons in the forced-damped DpS chain has been observed. The original approach of the analysis of the breathers in the conservative system developed by James [8], allowed us to predict the possibility of formation of phase locked DB in the damped-driven DpS. These solutions can be depicted on the phase plane in the Log-NLS limit.

Acknowledgements

MK is thankful to the grant supported by Russian Foundation for Basic Research project no. 18-03-00716. YS acknowledges the financial support of Israeli Science Foundation, Grant No. 1079/16

References

[1] G. Theocharis,M. Kavousanakis, P.G. Kevrekidis, C. Daraio, M.A. Porter, I.G. Kevrekidis, Localized breathing modes in granular crystals with defects, Phys. Rev. E. 80, 066601 (2009).
[2] N. Boechler, G. Theocharis, S. Job, P.G. Kevrekidis, M.A. Porter, C. Daraio, Discrete Breathers in One-Dimensional Diatomic Granular Crystals, Phys. Rev. Lett. 104, 244302 (2010).
[3] G. Theocharis, N. Boechler, P.G. Kevrekidis, S. Job, M.A. Porter, C. Daraio, Intrinsic energy localization through discrete gap breathers in one-dimensional diatomic granular crystals, Phys. Rev. E. 82, 056604 (2010).
[4] C. Chong, P.G. Kevrekidis, G. Theocharis, C. Daraio, Dark breathers in granular crystals, Phys. Rev. E., 87, 042202 (2013).
[5] C. Chong, F. Li, J. Yang, M. O. Williams, I. G. Kevrekidis, P. G. Kevrekidis, C. Daraio, Damped-driven granular chains: An ideal playground for dark breathers and multibreathers, Phys. Rev. E., 89, 032924 (2014).
[6] G. James, Nonlinear waves in Newton's cradle and the discrete p-Schrdinger equation, Math. Models Meth. Appl. Sci. 21, 2335-2377 (2011).
[7] James G., Kevrekidis P.G., Cuevas J., Breathers in oscillator chains with Hertzian interactions, Phys. D 251, 39 (2013)
[8] James G., Traveling breathers and solitary waves in strongly non-linear lattices, Philosophical Transactions A 376 (2018) https://doi.org/10.1098/rsta.2017.0138

Nonlinear Phenomena in Shells with Random Excitation

Francesco Pellicano[*,**], Antonio Zippo [*,**], Giovanni Iarriccio[*]
[*]*Dipartimento di Ingegneria Enzo Ferrari, University of Modena and Reggio Emilia, Modena, Italy*
[**] *Centre InterMech - MO.RE., University of Modena and Reggio Emilia, Modena, Italy*

Summary. The nonlinear dynamics of a thin circular cylindrical shell subjected to thermal gradients and random excitation is experimentally investigated. The combination of broadband random loading and thermal conditions both at different homogenous temperature and with thermal gradients across the shell thickness. The phenomenon of synchronization is observed at particular thermal and loading conditions: a severe transfer of energy from a broadband excitation to an almost subharmonic out of band response is experimentally observed.

Introduction

In several applications like aerospace automotive and civil engineering the role of thin-walled structures have a key function, for example, bodywork panels, fuselage or aircraft and satellite panels together with storage tower.
A crucial factor in thin walled structures is the performance under random forcing whose dynamics, characterized by strong nonlinearity can give rise to unexpected complex phenomena that cannot be predicted by the traditional engineering tools and theories.
It is well known that chain of non-linear oscillators under intense periodic forcing could exhibit a "mode-locking" phenomenon that synchronizes the exciting load with the response. A similar phenomenon, which is much less investigated, can happen when a nonlinear system is excited with a broadband random forcing [1], for example when internal resonances are present; in such cases it has been proven the possibility of entrainment of regular harmonic responses by the system. This phenomenon is said “synchronization” of non-linear oscillators subjected to random forcing [2,7], it has been partly investigated proving the unusual phenomenon of conveying the random spectral energy to specific frequencies, determining remarkable vibration amplitudes.
In recent research published on Ref. [4, 5] it is proved that the effect of temperature greatly influences the instability regions and the vibration levels, moreover, it was pointed out that high environmental temperature leads to a more complex dynamics.
In the present work an experimental investigation of the synchronization phenomenon is carried out. A circular cylindrical shell made of polymeric material is considered; the shell is mounted on a shaking table, the shell axis is vertical, the bottom is clamped to the table, the top is closed with a rigid disk. The shaking table provides a base motion in the direction of the shell axis. The temperature is controlled inside and outside the shell. Several random excitation level and types are considered (different frequency bands) as well as several internal and internal temperatures.

Experimental setup and results

The experimental test consists of a specimen mounted on an electrodynamic shaker coupled with a climate chamber and monitored by accelerometers, laser vibrometer and a telemeter. The specimen is a thin cylindrical shell made of Polyethylene terephthalate (P.E.T.), a thermoplastic polymer, a top mass, made of aluminum alloy, is glued with special epoxy glue, resistant to high temperature, on the top of the specimen. The bottom of the shell is clamped to the fixture through a shaft collar that guarantees a uniform connection to the vibration table adapter (VTA), i.e. a clamped-clamped boundary condition is guaranteed on the bottom and the top.
Figure 1 shows the experimental setup including the control system, the shaker and the climate chamber. Inside the shell, a cartridge heater is mounted and is used to adjust the temperature inside the shell and to obtain the desired thermal gradient across the shell wall, see Figure 2; a mirror periscope has been used to allow the laser beam measuring the lateral vibration of the shell. An accelerometer located on the base of fixture, for control purposes, three triaxial accelerometers are located equally spaced on the top disk.
A random controlled broadband base excitation is applied at the base through the electrodynamic shaker. Each test is carried out at different bandwidth and different overall RMS.
The forcing is a band limited random (900-1500 Hz), see figure 3, with a 28°C thermal gradient from 48°C in the inner surface and 20°C in the outer surface, the Power Spectral Density is shown. In figure 3a the pink box identifies the electrical flat spectrum of the random signal provided to the shaker and controlled by the electronic controller, no out of band electric power is provided out of band. On the base the spectral energy is uniform in the band (900-1500 Hz) which is controlled; there is an energy transfer to superharmonics, where evident spikes are present; such spikes are due to the shaker-shell nonlinear interaction; therefore, the base motion contains a strong deterministic component (harmonic). On the top disk a clear deterministic (subharmonic) response takes place in correspondence of the first axisymmetric mode of the shell (467Hz) and, similarly to the base spectrum, high frequency out of band spikes are present.
The novelty of the present paper consists in the experimental evidence of the synchronization phenomenon: when the nonlinear system is excited with random forcing a strong transfer of energy to specific harmonics can take place. It is worthwhile to point out that the phenomenon appears only for certain environmental and forcing conditions.

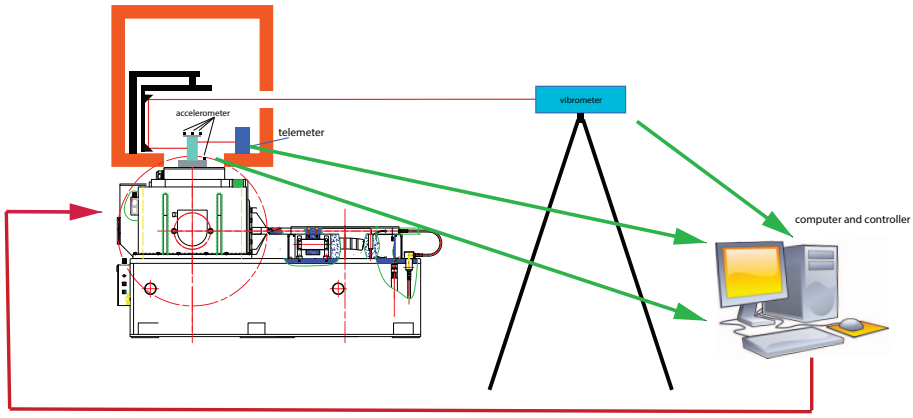

Figure 1: schematic view of experimental setup

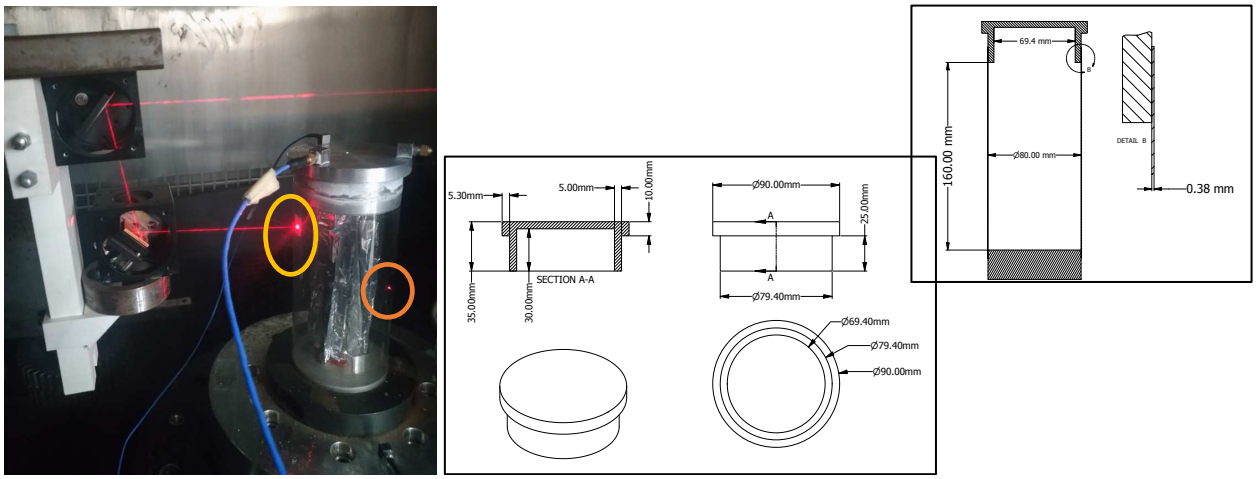

Figure 2: specimen, internal heater cartridge, vibrometer spot light (yellow circle) and telemeter spot light (orange circle)

a) b)

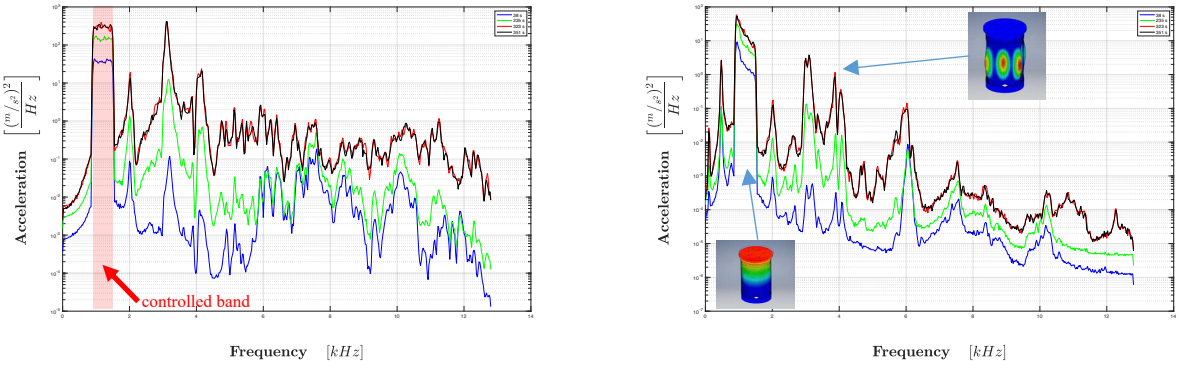

Figure 3: PSD of VTA a) base excitation and b) top shell vertical response

References

[1] Ibrahim R. A. and Roberts J. W. (1976) Broad Band Random Excitation of a two-degree-of-freedom autoparametric coupling. J. *of Sound and Vibration* **44(3)**:335-348.

[2] Jensen, R.V. (1998) Synchronization of randomly driven nonlinear oscillators. *Physical Review E - Statistical Physics, Plasmas, Fluids, and Related Interdisciplinary Topics*, **58 (6)**:R6907-R6910.

[3] Jensen, R.V. (2002) Synchronization of driven nonlinear oscillators. *American Journal of Physics*, **70(6)**:607-619.

[4] Zippo, A., Iarriccio, G., Pellicano, F., (2021) Synchronicity Phenomena in Circular Cylindrical Shells Under Random Excitation, *Advanced Structured Materials*, **157**:127-157. DOI: 10.1007/978-3-030-75890-5_8

[5] Zippo, A., Barbieri, M., Iarriccio, G., Pellicano F., (2019) Nonlinear vibrations of circular cylindrical shells with thermal effects: an experimental study. Nonlinear Dynamics, **99**:373–391.

Intermodal targeted energy transfer (IMTET) concept in seismically excited model of twenty-story steel structure

Majdi Gzal[1], Juan E. Carrion[2], M.A. Al-Shudeifat[3], B.F. Spencer Jr[4], Alexander F. Vakakis[5], Lawrence A. Bergman[6] and Oleg V. Gendelman[1]

[1]*Department of Mechanical Engineering, Technion –Israel Institute of Technology, Haifa, Israel*
[2]*Department of Civil Engineering, Universidad de Cuenca, Cuenca, Ecuador*
[3]*Department of Aerospace Engineering, Khalifa University, Abu Dhabi, UAE*
[4]*Department of Civil and Environmental Engineering, University of Illinois, Urbana, USA*
[5]*Department of Mechanical Science and Engineering, University of Illinois, Urbana, USA*
[6]*Department of Aerospace Engineering, University of Illinois, Urbana, USA*

Summary. This study investigates the intermodal targeted energy transfer (IMTET) concept for passive mitigation of a model of large-scale twenty-story steel structure subjected to seismic excitation. This is achieved by introducing strategically placed, local strong nonlinearities, in the form of vibro-impacts of the floors of the building with a relatively light, yet stiff, auxiliary core structure. These impacts rapidly, robustly and irreversibly redistribute the input seismic energy within the modal space of the structure through extremely rapid IMTET from low-to-high frequency structural modes, yielding drastically enhanced mitigation of unprecedented effectiveness, right from the very first cycle of the structural response. Moreover, when optimized, this new concept can be realized fully passively, without the need to adding any mass to the building, and with minimal increase in the resulting floor accelerations and local stresses. Therefore, the IMTET methodology for seismic mitigation has the potential to be truly transformative in the field of hazard mitigation of civil infrastructure.

Introduction

The dynamical responses of structures subjected to extreme loads (such as blast, earthquakes, shock) poses a significant challenge and has attracted great interest among researchers and engineers [1]. One of most important issues here is rather limited suppression achieved for the first few (but most intensive and dangerous) cycles of the structural response to the excitation. Consequently, many new and innovative structural protection fully passive concepts have been proposed, developed, and even implemented, being classified as linear, and nonlinear passive mitigation strategies [1, 2]. Specifically, load mitigation based on irreversible (directed) passive nonlinear vibration energy transfers, known as targeted energy transfers (TETs) has been widely explored for passive vibration control and energy harvesting purposes. This approach is based on transferring energy from a directly excited primary structure to a set of secondary strongly nonlinear structures (referred to as nonlinear energy sinks – NESs), where it is localized and locally dissipated without scattering back to the primary structure [2]. The dynamical mechanisms governing such TET mechanism are isolated or multiple (i.e., cascades of) transient resonance captures. However, such resonant energy transfers to the NESs are achieved through relatively slow modulations of the structural modal amplitudes, which, for some applications involving extreme loads, e.g., blast or seismic excitations, prove not to be fast enough.
Recent studies [3, 4], however, has shown that nonlinear resonance is not the only fundamental mechanism for achieving TET, since it can also be realized through a non-resonant fast scale mechanism involving non-smooth effects. This has been employed to explore the concept of intermodal targeted energy transfer (IMTET) to mitigate the effect of blast loading on a nine-story steel structure [4]. In this study, we explore the implementation of the IMTET strategy for seismic passive protection of tall buildings (in particular, twenty-story) subject to strong earthquakes.

Model description

The primary structure considered here is the benchmark 20-story steel building designed by Brandow & Johnston Associates for the SAC Phase II Steel Project, and its geometrical and physical properties are given in details in [5]. To achieve seismic mitigation using the IMTET concept, a flexible internal core structure is introduced, with distributed clearances with respect to the floors of the primary twenty-story building, as shown in Figure 1.

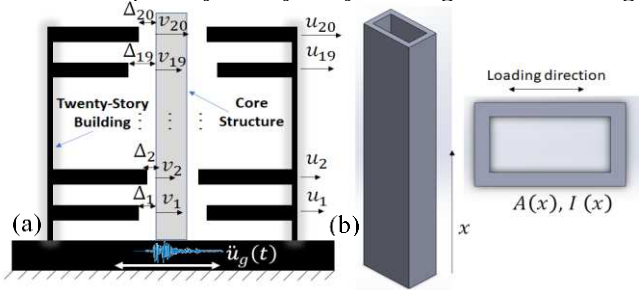

Figure 1: Seismically excited 20-story primary building with internal flexible core structure: Schematic of (a) the integrated building-core, and (b) the flexible core structure

Denoting by $\boldsymbol{M}$, $\boldsymbol{K}$, $\boldsymbol{C}$, and $\boldsymbol{M_{cs}}$, $\boldsymbol{K_{cs}}$ and $\boldsymbol{C_{cs}}$, the mass, stiffness and damping matrices of the primary building and the core structure, respectively, the equations of motion are given by:

$$\begin{aligned} \boldsymbol{M}\ddot{\boldsymbol{u}} + \boldsymbol{C}\dot{\boldsymbol{u}} + \boldsymbol{K}\boldsymbol{u} - \boldsymbol{f}^{NL}(\dot{\boldsymbol{u}}, \boldsymbol{u}, \dot{\boldsymbol{v}}, \boldsymbol{v}, \Delta) &= -\boldsymbol{M}\boldsymbol{\Gamma}\ddot{u}_g \\ \boldsymbol{M}_{\boldsymbol{cs}}\ddot{\boldsymbol{v}} + \boldsymbol{C}_{\boldsymbol{cs}}\dot{\boldsymbol{v}} + \boldsymbol{K}_{\boldsymbol{cs}}\boldsymbol{v} + \boldsymbol{f}^{NL}(\dot{\boldsymbol{u}}, \boldsymbol{u}, \dot{\boldsymbol{v}}, \boldsymbol{v}, \Delta) &= -\boldsymbol{M}_{\boldsymbol{cs}}\boldsymbol{\Gamma}\ddot{u}_g \end{aligned} \quad (1)$$

where $\ddot{u}_g$ is ground acceleration, $\boldsymbol{u}$ and $\boldsymbol{v}$ the displacement vectors of the building floors and core contact points, respectively, $\boldsymbol{\Gamma}$ the influence vector for base motion, and Δ the vector of clearance gaps. Uniaxial seismic excitation is assumed, along the weak direction of the primary building (Figure 1(a)). The vector $\boldsymbol{f}^{NL}(\dot{\boldsymbol{u}}, \boldsymbol{u}, \dot{\boldsymbol{v}}, \boldsymbol{v}, \Delta)$ contains the inelastic Hertzian contact interactions, and its jth element is given by:

$$\boldsymbol{f}_j^{NL}(\dot{\boldsymbol{u}}, \boldsymbol{u}, \dot{\boldsymbol{v}}, \boldsymbol{v}, \Delta) = k_c \left[\left[v_j - u_j - \Delta_j \right]_+^{\frac{3}{2}} - \left[u_j - v_j - \Delta_j \right]_+^{\frac{3}{2}} \right] \left(1 + \frac{3(1-r)}{2\left(\dot{u}_j^- - \dot{v}_j^-\right)} \left(\dot{u}_j - \dot{v}_j \right) \right) \quad (2)$$

where $k_c = \frac{2E\sqrt{R}}{3(1-\nu^2)}$ is a stiffness coefficient (Hunt and Crossley, 1975), assuming that the impact is between a semi-sphere of radius R on the core structure and a contact point on a flat plane on the primary building, with the contacting bodies having the same Young's modulus E and Poisson's ratio ν. Also, $\dot{u}_j^-$ and $\dot{v}_j^-$ are the contact velocities of the jth floor just before the impact, and r is a restitution coefficient. The subscript $(+)$ indicates that only non-negative values of the arguments in the brackets should be taken into account, with zero values being assigned otherwise.

Preliminary results

The computational results provide a preliminary demonstration of the effectiveness of IMTET for rapid seismic mitigation of the primary building response subjected to Kobe (1995) ground motion. Figure 2(left) shows an extremely rapid attenuation of the overall structural response, compared to the linear case of no core (i.e., infinite gaps). The governing nonlinear mechanism responsible for the drastic enhancement in seismic mitigation is shown in Figure 2(right), where the percentage of input seismic energy eventually dissipated by the inherent (modal) dissipation of each of the ten leading structural modes of the primary building (with no core) is depicted. Indeed, compared to the linear case of no core – where the energy dissipation is dominated by the fundamental structural mode in the case of optimized clearance gaps the seven leading modes participate in energy dissipation. Hence, there is a noteworthy, rapid, and irreversible nonlinear targeted energy transfer (or IMTET) from the low structural modes to the higher ones, causing rapid reduction of the structural response.

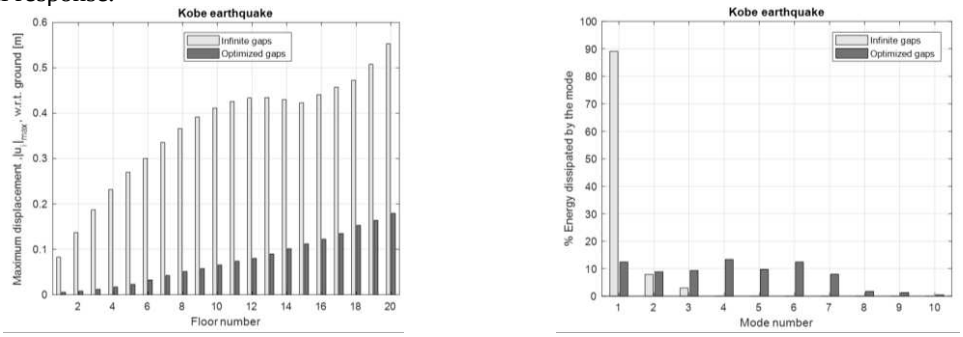

Figure 2: Primary building with optimized core and no core subject to the Kobe earthquake: Maximum floor displacement (left); Input seismic energy (%) dissipated by the inherent damping of the leading modes of the primary building (right)

Conclusions

In this work, a radically new concept for seismic mitigation of civil infrastructure is discussed, based on extremely rapid nonlinear scattering of seismic energy from low-to-high frequency modes of a building through strong local nonlinearities, which is referred to as intermodal targeted energy transfer (IMTET). The results show that the overall level of system vibration is reduced not by adding extra dissipative elements but rather by redistributing energy from lower to higher frequencies where the vibration amplitudes decrease. Moreover, the dissipative capacity of the system itself is radically enhanced since a much larger set of vibration modes (especially high-frequency ones) participate in the response, which can greatly enhance the rate of energy dissipation. Hence, IMTET provides a new approach to passive energy management.

References

[1] Housner, G.W., Bergman, L.A., Caughey, T.K., Chassiakos, A.G., Claus, R.O., Masri S.F., Skelton, R.E., Soong, T.T., Spencer, B.F., Yao, J.T.P. (1997) Structural control: Past, present, and future. *J. Eng. Mech.* **123** (9), 897–971.

[2] Vakakis, A.F., Gendelman, O.V., Bergman, L.A., McFarland, D.M., Kerschen, G., Lee, Y.S. (2008) Nonlinear Targeted Energy Transfer in Mechanical and Structural Systems. Solid Mechanics and Its Applications. Springer, Dordrecht.

[3] M. Gzal, B. Fang, A.F. Vakakis, L.A. Bergman, O.V. Gendelman (2020) Rapid non-resonant intermodal targeted energy transfer (IMTET) caused by vibro-impact nonlinearity. *Nonlinear Dyn*, **101**, pp. 2087-2106.

[4] Majdi Gzal, Alexander F. Vakakis, Lawrence A. Bergman, Oleg V. Gendelman (2021) Extreme intermodal energy transfers through vibro-impacts for highly effective and rapid blast mitigation. Communications in Nonlinear Science and Numerical Simulation, Volume **103**.

[5] Spencer, B.F., Jr., Christenson, R.E. and Dyke, S.J. (1999) Next Generation Benchmark Control Problems for Seismically Excited Buildings. *Proc., 2nd World Conf. on Structural Control*, Vol.**2**, pp.1135–1360.

Wednesday, July 20, 2022

08:30 - 10:30

MS-16 Random Dynamical Systems - Recent Advances and New Directions

Rhone 2

Chair: Subramanian Ramakrishnan

08:30 - 08:50
[no show] Non-linear dynamic stability of mono-symmetric thin walled beams under random excitation
TAYEBI Sajad*
*Sajad H Tayebi (133,Babataher Avenue,Tehranno,Tehran Iran)

08:50 - 09:10
StochasticDelayDiffEq.jl - An Integrator Interface for Stochastic Delay Differential Equations in Julia
SYKORA Henrik, RACKAUCKAS Christopher, WIDMANN David, **BACHRATHY Daniel***
*MTA-BME Lendület Machine Tool Research Group, Department of Applied Mechanics, Budapest University of Technology and Economics (Budapest, Muegyetem rkp. 3. Hungary)

09:10 - 09:30
The Effects of Measurement Noise on Vehicle Motion Control with Delayed State Feedback
VÖRÖS Illés*, TAKÁCS Dénes
*Budapest University of Technology and Economics (Budapest, Muegyetem rkp. 3, 1111 Hungary)

09:30 - 09:50
The Relevance of Spectral Submanifolds and Slow Manifolds for Randomly Excited Mechanical Systems
BREUNUNG Thomas*, KOGELBAUER Florian, HALLER George
*Eidgenössische Technische Hochschule Zürich (Leonhardstrasse 21 8092 Zürich Switzerland)

09:50 - 10:10
The hysteretic dynamics of a harmonically excited snap-through oscillator in the presence of additive noise excitations
CHAWLA Rohit, **ROUNAK Aasifa***, PAKRASHI Vikram
*Aasifa Rounak (218A, School of Mechanical and Materials Engineering, University College Dublin, Belfield Ireland)

Non-linear dynamic stability of mono-symmetric thin walled beams under random excitation

Sajad Haji Tayebi*
*Department of Civil Engineering, Imam Khomeinie International University, Qazvin, Iran

Summary. The focus of my presentation is to study the non-linear dynamic stability of a viscoelastic thin walled beam with cross section having one axis of symmetry and subjected to a dynamical axial compressive load P(t) (generally eccentric).The equations of motion is derived and the method of stochastic averaging is used to decoupled the governing equations into Itô equations. For small damping and weak stochastic fluctuation, the expressions are derived for the moment Lyapunov exponent.

Introduction

Thin walled beams are widely used in construction, aircraft, ship building, etc. Also, with the increasing use of materials, there exists the need for analyzing viscoelastic structures under dynamic loading. Therefore, there are lots of works in both deterministic and stochastic domains. The general theory of thin walled beams was investigated by Vlasov [1] and the dynamic instability of elastic system was explained by Bolotin [2]. Stratonovich formulated the method of stochastic averaging [3] and it mathematically proved by Khasminskii [4]. There are the overwhelming number of papers in the literature. The modern theory of stochastic dynamic stability is founded on Lyapunov exponents and moment Lyapunov exponents [5]. Also for distinguishing among the different cases of resonances, the method of multiple scales is used.

Formulation

The flexural-torsional vibration of a thin walled beam with mono-symmetric I-section is presented in Fig.1. In the present article, the boundary condition is considered as both ends simply supported.

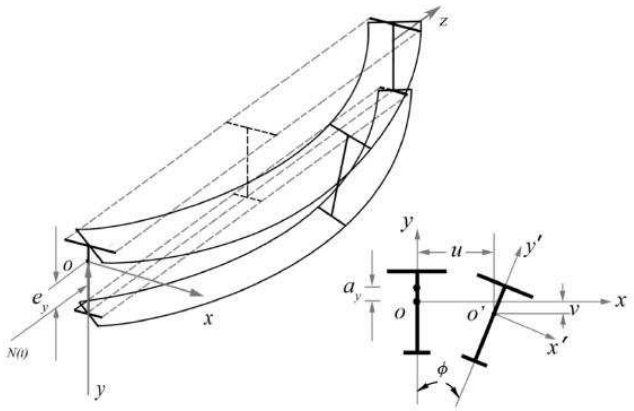

Figure 1

The equations of motion is defined as [1]. In these equations, we can see inertia components Δq, ΔM, ΔN which are nonlinearly related to the principal displacements u and ϕ. By locating a mass on the movable end [2] and adding the viscous damping and also replacing the elastic modulus by the Voltera operators E(1-H) [5], the governing partial differential equations become:

$$
\begin{aligned}
&E\left(1-\mathrm{H}\right)J_y\left(\frac{\partial^4}{\partial z^4}u(z,t)\right)+P(t)\left(\frac{\partial^2}{\partial z^2}u(z,t)\right)+P(t)\left(a_y-e_y\right)\left(\frac{\partial^2}{\partial z^2}\phi(z,t)\right)+m\left(\frac{\partial^2}{\partial t^2}u(z,t)\right)\\
&\quad+\mathrm{D}_u\left(\frac{\partial}{\partial t}u(z,t)\right)+m\,a_y\left(\frac{\partial^2}{\partial t^2}\phi(z,t)\right)\\
&+\left(\frac{\partial^2}{\partial z^2}\Delta M(z,t)\right)\phi(z,t)+2\left(\frac{\partial}{\partial z}\Delta M(z,t)\right)\left(\frac{\partial}{\partial z}\phi(z,t)\right)+\Delta M(z,t)\left(\frac{\partial^2}{\partial z^2}\phi(z,t)\right)+\left(\frac{\partial}{\partial z}\Delta N(z,\right.\\
&\quad\left.t)\right)\left(\frac{\partial}{\partial z}u(z,t)+a_y\left(\frac{\partial}{\partial z}\phi(z,t)\right)\right)\\
&+\Delta N(z,t)\left(\frac{\partial^2}{\partial z^2}u(z,t)+a_y\left(\frac{\partial^2}{\partial z^2}\phi(z,t)\right)\right)=0
\end{aligned}
\tag{1}
$$

$$P(t)\left(a_y\text{-}e_y\right)\left(\frac{\partial^2}{\partial z^2}u(z,t)\right)+E\left(1-\mathrm{H}\right)J_\omega\left(\frac{\partial^4}{\partial z^4}\phi(z,t)\right)\left[P(t)\left(r^2+2\beta_y e_y\right)-T\left(1-\mathrm{H}\right)J_d\right]\left(\frac{\partial^2}{\partial z^2}\phi(z,t)\right)+m r^2\left(\frac{\partial^2}{\partial t^2}\phi(z,t)\right)+m a_y\left(\frac{\partial^2}{\partial t^2}u(z,t)\right)+\mathrm{D}_\phi\left(\frac{\partial}{\partial t}\phi(z,t)\right)+\left(\frac{\partial}{\partial z}\Delta N(z,t)\right)\left[r^2\left(\frac{\partial}{\partial z}\phi(z,t)\right)+a_y\left(\frac{\partial}{\partial z}u(z,t)\right)\right]+\Delta N(z,t)\left[r^2\left(\frac{\partial^2}{\partial z^2}\phi(z,t)\right)+a_y\left(\frac{\partial^2}{\partial z^2}u(z,t)\right)\right]+\Delta M(z,t)\left(\frac{\partial^2}{\partial z^2}u(z,t)\right)-2\beta_y\left(\left(\frac{\partial}{\partial z}\Delta M(z,t)\right)\left(\frac{\partial}{\partial z}\phi(z,t)\right)+\Delta M(z,t)\left(\frac{\partial^2}{\partial z^2}\phi(z,t)\right)\right)-\Delta q(z,t)\,a_y\,\phi(z,t)=0$$

(2)

With the aid of the Galerkin method, (1) and (2) can be converted into two ordinary differential equations. To show that damping, viscoelasticity and excitation are small, a parameter $0 < \varepsilon << 1$ is introduced. The axial thrust P(t) is assumed to be a stationary stochastic process.

Stochastic averaging

To apply the averaging method, one should consider first the unperturbed system which can be solved by the method of operators. The solutions are:

$$u_1 = a_1\cos\left(\omega_1 t+\phi_1\right)+a_2\cos\left(\omega_2 t+\phi_2\right),\ u_2=\alpha_1 a_1\cos\left(\omega_1 t+\phi_1\right)+\alpha_2 a_2\cos\left(\omega_2 t+\phi_2\right)$$

(3)

The method of variation of parameters is applied to determine the solutions of the perturbed system. Here, in the present article, because of the nonlinearities, there is a difference in the applying of this method with the other papers.

By averaging the responses over one period, we can expect to obtain accurate results. This may be done by applying the method of stochastic averaging. Through the method of stochastic averaging, the system can be approximated by Itô stochastic differential equations.

Moment Lyapunov exponents

To have a complete picture of dynamic stability, it is important to investigate both the moment and almost-sure stability which is the topic of the present work.

However, the stability of the *p*th moment of the solution of system is governed by the *p*th moment Lyapunov exponent defined by:

$$\Lambda(p)=\lim_{t\to\infty}\frac{1}{t}\log E\left[\,\|\boldsymbol{u}\|^{\,p}\right]$$

(4)

If the Λ is negative, the *p*th moment is asymptotically stable; otherwise, it is unstable [5]. One can obtain the largest Lyapunov exponent (5) through its relation with moment Lyapunov exponents (6).

$$\lambda=\lim_{t\to\infty}\frac{1}{t}\log\|\boldsymbol{u}\|$$

(5)

$$\lambda_{\max}=\Lambda'(0)=\lim_{p\to 0}\frac{\Lambda(p)}{p}$$

(6)

In this article, I use the moment Lyapunov exponents for analyzing the dynamic stability of system.

References

[1] Vlasov V. (1963) Thin-walled elastic beams. Jerusalem: Israel Program for Scientific Translations.

[2] Bolotin V. V. (1964) The dynamic stability of elastic systems. San Francisco, Amsterdam: Holden-Day.

[3] Stratonovich R. L. (1963) Topics in the Theory of Random Noise. Gordon and Breach Science Publishers, Inc, New York.

[4] Khasminskii R. Z. (1966) A limit theorem for the solutions of differential equations with random right-hand sides. *Theory of Probability and Its Applications* **11(3)**:390-406. English translation

[5] Xie W. C. (2006) Dynamic Stability of Structures. Cambridge University Press, Cambridge.

StochasticDelayDiffEq.jl - An Integrator Interface for Stochastic Delay Differential Equations in Julia

Henrik T Sykora*, Christopher V. Rackauckas †, David Widmann ‡ and Dániel Bachrathy*
*MTA-BME Lendület Machine Tool Research Group, Department of Applied Mechanics, Budapest University of Technology and Economics, Budapest, Hungary
†Department of Mathematics, Massachusetts Institute of Technology, Cambridge MA, USA
‡Department of Information Technology, Centre for Interdisciplinary Mathematics, Uppsala University, Uppsala, Sweden

Summary. In this work an efficient tool is presented to numerically solve stochastic delay differential equations by transforming them to stochastic differential equations. This approach allows the use of methods originally implemented for stochastic differential equations, while algorithms specialized to delay problems can be also be included. The convergence and stability of the numerous solver methods are investigated through Monte-Carlo simulations for different case studies.

Introduction

In scientific computing to analyze the behavior of dynamical systems a widely used approach is to numerically integrate the corresponding differential equation (DE). For a large number of problem classes (e.g., ordinary DEs (ODEs), delay DEs (DDEs), stochastic ODEs (SODEs or SDEs)), there is a wide range of official integrator solutions to choose from, both open-source and commercial [8]. However, for stochastic delay DEs (SDDEs) there exists no such solver, despite that there are algorithms already introduced since the late 90's [1, 5, 3] along with proof of convergence for SDDEs with point delays.
The goal of this work is to introduce a feature rich and "easy-to-use" open source tool to solve stochastic delay differential equations. These features include but are not limited to parallelized Monte-Carlo calculations, use of arbitrary precision numbers or the automatic differentiation of the solution w.r.t. to the parameters of the SDDE. This solver is available as a Julia package under the name of StochasticDelayDiffEq.jl and is part of the DifferentialEquations.jl [7] ecosystem.

Stochastic Delay Differential Equations as SODEs

Consider the Itô stochastic delay differential equation (SDDE)

$$\mathrm{d}x(t) = f(x(t), x_t, t)\mathrm{d}t + g(x(t), x_t, t)\mathrm{d}W(t), \qquad x(\theta) = \varphi(\theta),\ -\tau \le \theta \le 0, \tag{1}$$

where $f, g : \mathbb{R}^d \times C([-\tau, 0), \mathbb{R}^d) \times \mathbb{R} \to \mathbb{R}^d$ are smooth functions, $x_t(\theta) = x(t+\theta) \in \mathbb{R}^d, \theta \in [-\tau, 0)$ defines the state at time t (segment of the solution), $W(t)$ is an $\mathcal{F}_t$-measureable standard Wiener process and the initial state $\varphi : [-\tau, 0] \to \mathbb{R}^d$ is sufficiently nice and $\mathcal{F}_0$ measureable. Note that the present state $x(t)$ is separated from the solution segment x_t and this study is restricted to systems with J number of point delays, namely $0 < \tau_1 < \tau_2 < \ldots < \tau_J := \tau$, since distributed delays can be approximated as point delays using e.g. shifted Dirac delta distributions [4] or via Clenshaw-Curtis quadrature [9].
Since all values of the interval x_t are available at time t, the SDDE (1) can be rewritten as a SODE:

$$\mathrm{d}x(t) = \hat{f}(x(t), t)\mathrm{d}t + \hat{g}(x(t), t)\mathrm{d}W(t). \tag{2}$$

The transformation is performed by dynamically embedding the initial φ and current x_t states into the functions $\hat{f}$ and $\hat{g}$ as a time dependent inhomogenity, namely

$$\hat{f}(x(t), t) = f(x(t), \phi_t, t), \qquad \hat{g}(x(t), t) = g(x(t), \phi_t, t), \tag{3}$$

where

$$\phi_t(\theta) = \begin{cases} \varphi(t+\theta) & t+\theta \le 0 \\ x(t+\theta) & t+\theta > 0 \end{cases}. \tag{4}$$

This representation is similar to the method of steps [2], however it allows uninterrupted integration (with discontinuity handling) and the utilization of the solver algorithms and features of the already existing SODE ecosystem from *StochasticDiffEq.jl* [6].

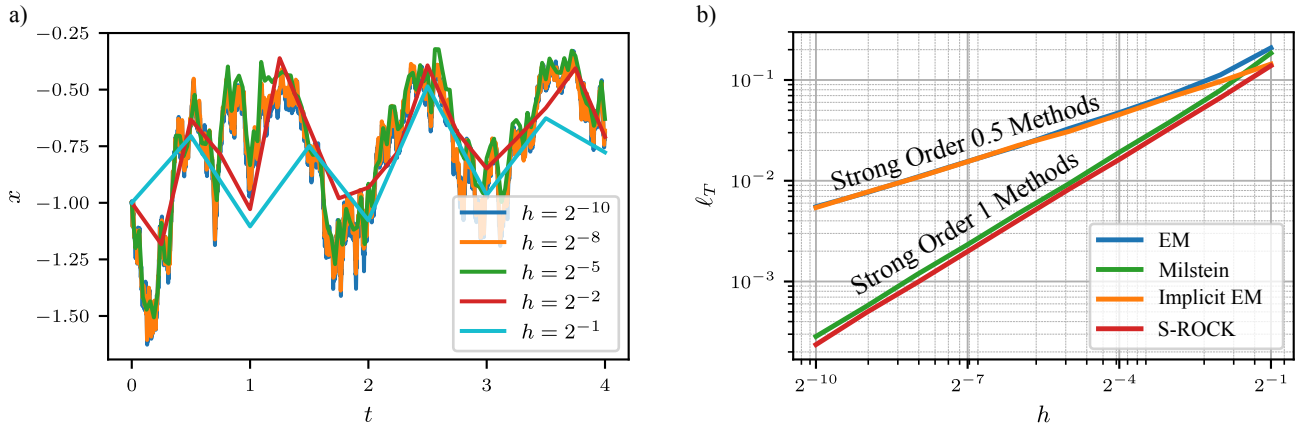

Figure 1: Demonstration of the convergence of multiple methods for $f(x(t), x(t-1), t) = x(t) - \sin(x(t-1))$, $g(x(t), x(t-1), t) = \sin(x(t))$ and $\varphi(t) = t - 1$. The sample trajectories in a) are calculated with the Euler-Maruyama method using multiple time resolutions h, and with delay $\tau = 1$, while the trajectories are integrated up to time $T = 4$. For the convergence plots in b) the ℓ_T measure is used, defined in Eq. (7).

Convergence tests

As an example, if the general SDDE (1) has a single point delay it can be rewritten in the form

$$\mathrm{d}x(t) = f(x(t), x(t-\tau), t)\mathrm{d}t + g(x(t), x(t-\tau), t)\mathrm{d}W(t). \tag{5}$$

If the Euler-Maruyama method is chosen from the package as the integrator algorithm with time step $h = \tau/N_h$, where $N_h \in \mathbb{N}^+$, the approximation of the value $x_{n+1} \approx x(t_{n+1} = (n+1)\,h)$ inherently reduces to:

$$x_{n+1} = x_n + f(x_n, x_{n-N_h}, t_n)\,h + g(x_n, x_{n-N_h}, t_n)\,\xi_n\,\sqrt{h}, \qquad \xi_n \sim \mathcal{N}(0,1), \tag{6}$$

which is shown to be convergent to the solution of (5) in [1]. The presented solver package can help to show the strong and weak convergence of other methods from the *StochasticDiffEq.jl* as well as newly created methods for SDDEs. Some examples are shown in Fig. 1, where numerical Monte-Carlo experiments were used to approximate the convergence of the solution at the final time point T by studying

$$\ell_T(h) = \mathbb{E}\big(\big\|x^h(T) - x^{h_{\mathrm{ref}}}(T)\big\|_2\big), \tag{7}$$

where x^h is the solution of the SDDE (1) approximated with time resolution h and $h_{\mathrm{ref}} = 2^{-15}$ is the reference time resolution.

Acknowledgement

This work was supported by the Hungarian Scientific Research Fund (OTKA FK-124462), by the Hungarian Ministry of Human Capacities (NTP-NFTÖ-19-B-0127) and by the Higher Education Excellence Program of the Ministry of Human Capacities in the frame of Artificial intelligence research area of Budapest University of Technology and Economics (BME FIKP-MI).

References

[1] Baker C.T.H., Buckwar E. (1999), Introduction to the Numerical Analysis of Stochastic Delay Differential Equations, MCCM, Numerical Analysis Technical Report, Manchester University, ISSSN 1360–1725

[2] Bellman R. (1961), On the computational solution of differential-difference equations, J. Math. Anal. Appl. 2, 108-110.

[3] Cao W., Zhang Z., Karniadakis G.E. (2015), Numerical Methods for Stochastic Delay Differential Equations Via the Wong-Zakai Approximation, SIAM Journal on Scientific Computing, 37(1), pp. A295–A318

[4] Insperger T., Stépán G. (2011) Semi-Discretization for Time-Delay Systems. Springer, NY.

[5] Kloeden P.E., Shardlow T. (2012), The Milstein Scheme for Stochastic Delay Differential Equations Without Using Anticipative Calculus, Stochastic Analysis and Applications, 30(2), pp. 181–202

[6] Rackauckas C., Nie Q., (2016). Adaptive Methods for Stochastic Differential Equations via Natural Embeddings and Rejection Sampling with Memory. Discrete and Continuous Dynamical Systems — Series B, 22(7), pp. 2731–2761.

[7] Rackauckas, C., Nie, Q., (2017). DifferentialEquations.jl — A Performant and Feature-Rich Ecosystem for Solving Differential Equations in Julia. Journal of Open Research Software. 5(1), p.15.

[8] Rackauckas C.V. (2018), A Comparison Between Differential Equation Solver Suites In MATLAB, R, Julia, Python, C, Mathematica, Maple, and Fortran. The Winnower 6:e153459.98975.

[9] Lloyd N. T. (2000) Spectral Methods in MATLAB. SIAM.

The Effects of Measurement Noise on Vehicle Motion Control with Delayed State Feedback

Illés Vörös* and Dénes Takács*,†
*Department of Applied Mechanics, Budapest University of Technology and Economics, Budapest, Hungary
†MTA-BME Research Group on Dynamics of Machines and Vehicles

Summary. The stability properties of the single track vehicle model with proportional, delayed feedback control are investigated in the presence of measurement noise. The moment stability and the stationary behavior of the resulting stochastic system is analyzed using the stochastic semi-discretization method and numerical simulations are conducted to verify the results.

Introduction

The stabilization of path following is a fundamental element of numerous autonomous driving functions from lane keeping to self-driving. The focus of this work is to investigate the effects of measurement noise in the feedback loop of a path following controller with time delay, leading to a system of stochastic delay differential equations (SDDE's).
A number of important results have been developed over the years for the analysis of such systems. The moment stability of the solution in the linear case was presented in [1]. In [2], an approximate Fokker-Planck equation was introduced for the stationary solutions of nonlinear SDDE's with small delays. The stability of linear control systems with time delay was investigated in [3] using the Lyapunov exponent approach. The Taylor expansion of the control force was used in [4] and [5] to investigate the control of stochastic time delay systems in the linear and the non-linear case, respectively.
In this paper, the stochastic semi-discretization method [6] is used in order to determine the second moment of the stationary solution of a path following controller with time delay and measurement noise. Due to the so-called autonomous stochastic resonance phenomenon, the effects of the noise excitation may be amplified close to the stability boundaries, leading to an exceedingly large variance of the system response even if the control gains are selected from the stable parameter domain. The stochastic semi-discretization method generates a mapping of the discretized second moment, which can be used to assess the stability properties and the steady state solution of the second moment dynamics. As a result, specific regions of the control gains can be established within the stable domains that correspond to a given maximum allowable variance of the solution.
The rest of the paper is organized as follows: the mathematical model of the closed-loop system is introduced first. The second moment of the stationary solution is analyzed along the stable domain of control parameters with the help of the stochastic semi-discretization method and the results are verified by numerical simulations of the linear system. Next, the effects of a cutoff frequency in the measurement noise are investigated, then numerical simulations are also performed on the non-linear system by applying filtered white noise.

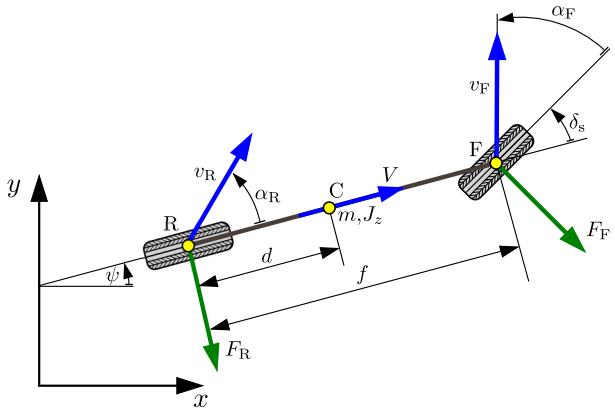

Figure 1: The single track vehicle model

Vehicle model

The mechanical model of our analysis is based on the single track vehicle model (see Fig. 1) with linear tire characteristics, according to [7]. Linearizing the system around the rectilinear motion along the x axis leads to the linear system $\dot{\mathbf{x}}(t) = \mathbf{A}\mathbf{x}(t) + \mathbf{B}\delta_\mathrm{s}(t)$, where the state vector $\mathbf{x} = \begin{bmatrix} y & \psi & \sigma_1 & \sigma_2 \end{bmatrix}^\mathrm{T}$ includes the lateral position, yaw angle, lateral velocity

Table 1: Parameter values used for stability maps and simulations

f (m)	d (m)	m (kg)	J_z (kgm^2)	C_F (N/rad)	C_R (N/rad)	V (m/s)	τ (s)	σ_y (m)	σ_ψ (rad)
2.7	1.35	1430	2500	45000	45000	20	0.5	0.1	0.005

and yaw rate of the vehicle, respectively. The steering angle is denoted by δ_s, while the system and input matrices are

$$\mathbf{A} = \begin{bmatrix} 0 & V & 1 & 0 \\ 0 & 0 & 0 & 1 \\ 0 & 0 & A_{33} & A_{34} \\ 0 & 0 & A_{43} & A_{44} \end{bmatrix} \quad \text{and} \quad \mathbf{B} = \begin{bmatrix} 0 \\ 0 \\ B_3 \\ B_4 \end{bmatrix} \tag{1}$$

with the elements

$$\begin{gathered} A_{33} = -\frac{B_3}{V} - \frac{C_\mathrm{R}(J_z + md^2)}{mVJ_z}\,, \quad A_{34} = -B_3\frac{f}{V} - V\,, \quad B_3 = \frac{C_\mathrm{F}(J_z + md(d-f))}{mJ_z}\,, \\ A_{43} = -\frac{B_4}{V} + \frac{C_\mathrm{R}d}{VJ_z}\,, \quad A_{44} = -B_4\frac{f}{V}\,, \quad B_4 = \frac{C_\mathrm{F}(f-d)}{J_z}\,. \end{gathered} \tag{2}$$

The vehicle parameters include the mass m, the yaw moment of inertia J_z (with respect to the center of gravity), the wheelbase f, and the distance d between the rear axle and the center of gravity. V denotes the longitudinal speed of the vehicle (assumed to be constant), and the tire cornering stiffnesses are denoted by C_F (front axle) and C_R (rear axle). The control goal is to reach stable rectilinear motion along the x axis, therefore the steering angle is generated by the delayed feedback of the vehicle's lateral position y and its yaw angle ψ: $\delta_\mathrm{s}(t) = \mathbf{K}\mathbf{x}(t-\tau) = -P_y y(t-\tau) - P_\psi \psi(t-\tau)$, where $\mathbf{K} = \begin{bmatrix} -P_y & -P_\psi & 0 & 0 \end{bmatrix}$ includes the control gains. The time delay τ consists of sensor and communication delays, processing times, as well as the dynamics of the steering mechanism.

In order to represent measurement noise in the control loop, the above model is extended by adding an additive noise component to the feedback signal of both y and ψ. This may include effects from environmental noise or the slight jumps in the estimation results of the lane detection system in each frame in case of a vision-based solution. The noise is modeled as a one-dimensional Langevin force excitation Γ_t [9], with the intensities σ_y and σ_ψ collected in $\mathbf{D}_\mathrm{m} = \begin{bmatrix} \sigma_y & \sigma_\psi & 0 & 0 \end{bmatrix}^\mathrm{T}$. Overall, the resulting linear, stochastic, time delay system can be written as

$$\dot{\mathbf{x}}(t) = \mathbf{A}\mathbf{x}(t) + \mathbf{B}\mathbf{K}\mathbf{x}(t-\tau) + \boldsymbol{\sigma}\Gamma_t\,, \quad \text{where} \quad \boldsymbol{\sigma} = \mathbf{B}\mathbf{K}\mathbf{D}_\mathrm{m}\,. \tag{3}$$

Since the Langevin force excitation Γ_t is defined such that its integration leads to the Wiener process W_t [9], Eq. (3) can be rewritten into the incremental form

$$\mathrm{d}\mathbf{x}(t) = \left(\mathbf{A}\mathbf{x}(t) + \mathbf{B}\mathbf{K}\mathbf{x}(t-\tau)\right)\mathrm{d}t + \boldsymbol{\sigma}\mathrm{d}W_t\,. \tag{4}$$

Stability analysis

The system may lose its stability in two ways: at $P_y = 0$, a static loss of stability occurs, which corresponds to a real characteristic root crossing the imaginary axis. At the rest of the stability boundaries, a complex conjugate pair of roots moves to the right half-plane, leading to an oscillatory loss of stability. The analytical derivation of these stability boundaries for the deterministic system using the D-subdivision method is detailed in [7].

In order to investigate the stability properties of the stochastic delay differential equation (4), the stochastic mapping $\mathbf{y}_{n+1} = \mathbf{F}\mathbf{y}_n + \mathbf{g}$ is defined by discretizing the system with respect to the delayed term [6, 8]. The size of $\mathbf{y}_n$ depends on the resolution of the discretization; $\mathbf{F}$ is based on the deterministic part of Eq. (4) ($\mathbf{A}$ and $\mathbf{BK}$), and $\mathbf{g}$ is calculated from $\boldsymbol{\sigma}$. For the exact definition of the above mapping, the reader is referred to [6].

The stability of the mean dynamics is determined by $\mathbf{F}$ (leading to the results presented in [7]), while the second moment stability is analyzed according to [6]. Note that first moment stability is required for the stability of the second moment process, therefore it is sufficient to check only the latter. Moreover, since there is no multiplicative noise term in our model, stability analysis of the first and second moment dynamics leads to the same results. In other words, the introduction of additive sensor noise does not influence the stability boundaries of the system. However, due to the autonomous stochastic resonance effect, the steady-state second moment values may start to increase near the stability boundaries. This means that even though the control gains are chosen from the stable parameter domain, the variance of the steady state solution may become unacceptably large.

In order to check this, the first order stochastic semi-discretization method was applied with the help of the corresponding Julia package [6]. A discretization step of 0.05 s was used and the vehicle parameters were selected according to Table 1. The effect of autonomous stochastic resonance is illustrated in Fig. 2 (a), where the steady state second moment of y (denoted by $M_{\mathrm{st},y}$) is plotted along the stable parameter domain of the control gains. The sections of the stability map were chosen according to the control gains that lead to the most highly damped response of the deterministic system ($P_y = 0.00077\ \mathrm{m}^{-1}$, $P_\psi = 0.0805$).

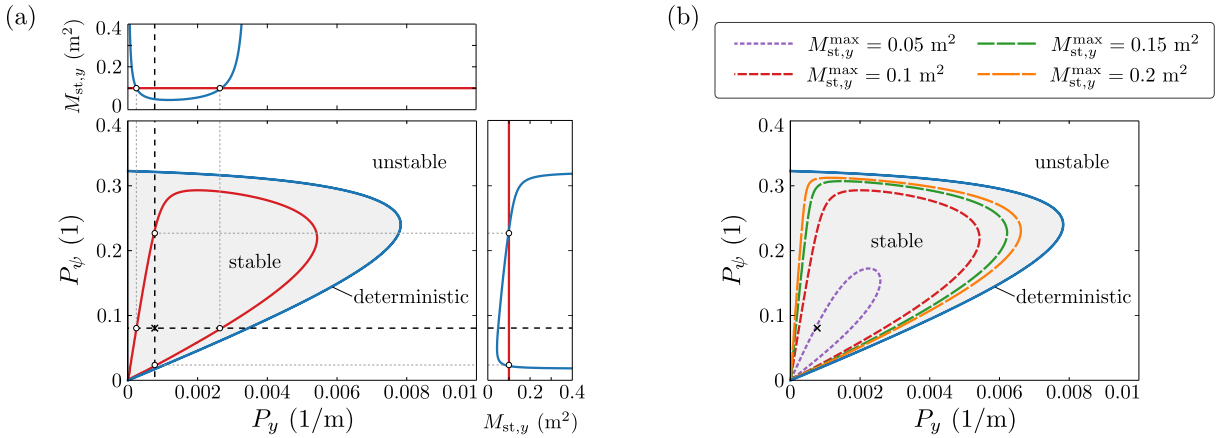

Figure 2: (a) The effect of sensor noise on the steady state second moment of y; (b) regions of the stability map corresponding to different limits on $M_{\mathrm{st},y}$; the deterministic optimum is denoted with a cross

Figure 2 (b) shows a practical stability map that demonstrates how the usable domain of control parameters shrinks if we want to limit the steady state second moment of y. Notice that the minimum of $M_{\mathrm{st},y}$ does not fall into the deterministic optimum (that is based on the eigenvalues of $\mathbf{F}$). Instead, it depends on the values of σ_y and σ_ψ, and the amplification due to the control gains.

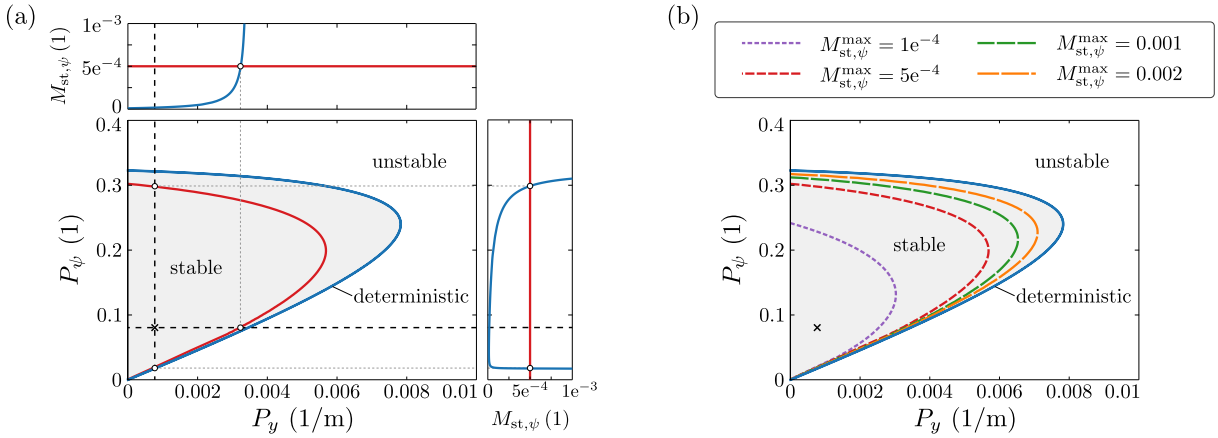

Figure 3: (a) The effect of sensor noise on the steady state second moment of ψ; (b) regions of the stability map corresponding to different limits on $M_{\mathrm{st},\psi}$; the deterministic optimum is denoted with a cross

Figure 3 shows similar practical stability maps with regards to the steady state second moment of the yaw angle ψ. Note the different shape of the contour lines compared to those in Fig. 2. As P_y is decreased, the vehicle takes much longer to reach the equilibrium (in terms of mean dynamics), since the position error is very weakly compensated (at $P_y = 0$, a static loss of stability occurs, where the vehicle path diverges). This also means that the steering action does not suppress the stochastic jumps around the equilibrium as effectively once the steady state is reached, leading to an increase in $M_{\mathrm{st},y}$ (as seen in Fig. 2 (a)). On the other hand, the control action related to ψ is not affected as P_y is decreased, which explains why there is no increase in $M_{\mathrm{st},\psi}$ in Fig. 3 (a) (note that $M_{\mathrm{st},\psi}$ does not reach zero at $P_y = 0$). Another effect to keep in mind, however, is that decreasing the gains not only decreases the control action, but it also suppresses the noise amplitude that appears in δ_{s}. Therefore decreasing the control gains directly leads to decreased noise gains, which means that the second moments are generally lower near the origin of the stability maps (unless of course stochastic resonance effects appear due to the proximity of a stability boundary).

In order to verify the results, 1000 Monte-Carlo simulation runs were conducted using the Euler-Maruyama method [10]. The control gains were chosen according to the deterministic optimum, and an initial condition of $y(t \leq 0) = 3\,\mathrm{m}$ was used (while the rest of the initial state values were set to zero), representing a lane change manoeuvre. The simulations were run for 100 seconds, with a time step of $0.005\,\mathrm{s}$. In order to calculate the stationary second moment, the first 30 seconds of the simulations were cut to ensure proper decay of the transients. There is good accordance between the numerically determined stationary second moment and the result of the stochastic semi-discretization method (see the first two columns of Table 2). This is also illustrated in Fig. 4, where the square root of the stationary second moment according to the semi-discretization method (shown in red) matches the sample standard deviation of the Monte-Carlo runs (shown in blue; note that the expected value of the stationary solution is zero).

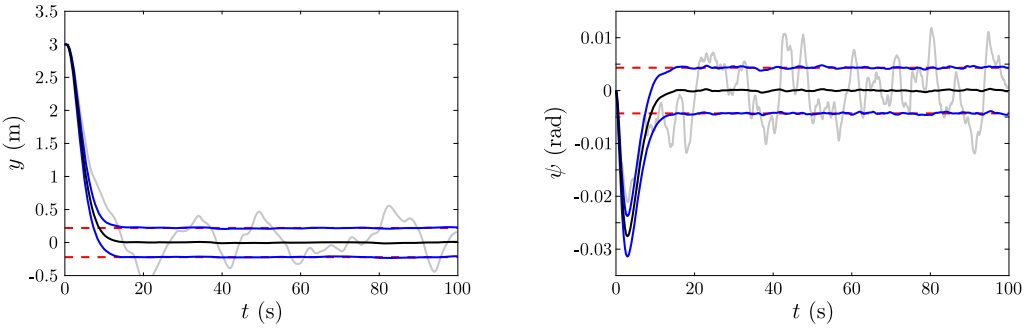

Figure 4: Simulation results of 1000 Monte-Carlo runs of the linear system. Black lines show the sample mean and blue lines denote the standard deviations of the samples. An arbitrarily chosen single realization is shown in light gray, while the red dashed lines represent the square root of the stationary second moments calculated using stochastic semi-discretization.

Table 2: Stationary second moment values determined using different methods

	Stochastic SD	Linear simulation	Non-linear simulation
$M_{\mathrm{st},y}\,(\mathrm{m}^2)$	0.04867	0.04783	0.04896
$M_{\mathrm{st},\psi}\,(\mathrm{rad}^2)$	1.8642e-5	1.8553e-5	1.8741e-5

Colored noise, simulation of the nonlinear system

A possible extension of the previously detailed model is the use of colored noise in the form of a first order Markov process [11]. This approach incorporates a cutoff frequency ω_c to limit the bandwidth of measurement noise due to e.g. digitization. The noise processes corresponding to the feedback signal of y and ψ are

$$\dot{w}_y = -\frac{1}{T_y} w_y + \sigma_y^\mathrm{c} \Gamma_t \,, \qquad \dot{w}_\psi = -\frac{1}{T_\psi} w_\psi + \sigma_\psi^\mathrm{c} \Gamma_t \,, \tag{5}$$

where w_i ($i \in \{y, \psi\}$) denote the state of the noise process and the time constants T_i determine the correlation time of the noise and the corresponding cutoff frequency ($\omega_\mathrm{c} = 1/T_i$). This time constant is assumed to be equal for both measurement signals.
As opposed to the previous section, the Langevin force excitation Γ_t is now used to generate the colored noise process, instead of directly acting on the feedback signal. Its intensity σ_i^c is chosen such that the energy content of the colored noise process (at low frequency levels) matches the corresponding white noise process used in the previous section, leading to

$$\left(\sigma_i^\mathrm{c}\right)^2 = \frac{\sigma_i^2}{T_i^2} \,, \qquad i \in \{y, \psi\} \,. \tag{6}$$

Using the above noise processes, the closed-loop system is of the form

$$\dot{\mathbf{x}}(t) = \mathbf{A}\mathbf{x}(t) + \mathbf{B}\mathbf{K}\left(\mathbf{x}(t-\tau) + \mathbf{D}\begin{bmatrix} w_y \\ w_\psi \end{bmatrix}\right) \,, \qquad \mathbf{D} = \begin{bmatrix} 1 & 0 & 0 & 0 \\ 0 & 1 & 0 & 0 \end{bmatrix}^\mathrm{T} \,. \tag{7}$$

Combining Eq. (5) and Eq. (7), the system can be turned to a similar form as Eq. (3)

$$\dot{\mathbf{X}}(t) = \left[\begin{array}{c|cc} \mathbf{A} & \multicolumn{2}{c}{\mathbf{BKD}} \\ \hline \mathbf{0}_{2,4} & -1/T_y & 0 \\ & 0 & -1/T_\psi \end{array}\right] \mathbf{X}(t) + \left[\begin{array}{c|c} \mathbf{BK} & \mathbf{0}_{4,2} \\ \hline \mathbf{0}_{2,4} & \mathbf{0}_{2,2} \end{array}\right] \mathbf{X}(t-\tau) + \left[\begin{array}{cc} \mathbf{0}_{4,2} & \\ \hline \sigma_y^\mathrm{c} & 0 \\ 0 & \sigma_\psi^\mathrm{c} \end{array}\right] \Gamma_t \tag{8}$$

using the augmented state vector

$$\mathbf{X} = \begin{bmatrix} y & \psi & \sigma_1 & \sigma_2 & w_y & w_\psi \end{bmatrix}^\mathrm{T} \,. \tag{9}$$

$\mathbf{0}_{i,j}$ represents the zero matrix of size $i \times j$.
The stability maps in Fig. 5 demonstrate how the cutoff frequency of the measurement noise affects the previously shown robust stability maps. At the boundary of dynamic loss of stability (the so-called D-curve), a complex conjugate pair of characteristic roots crosses the imaginary axis at $\mathrm{i}\omega$. The value of ω continuously increases along the stability boundary from $\omega = 0$ at the origin to approximately $\omega = 2$ rad/s where the D-curve crosses the vertical axis slightly above $P_\psi = 0.3$. The line style of the deterministic boundary in Fig. 5 shows the relation between the selected cutoff frequency and the system dynamics. The section of the stability boundary where the imaginary part of the corresponding characteristic roots is below the cutoff frequency is shown in blue, while the sections plotted in dashed gray are above ω_c.

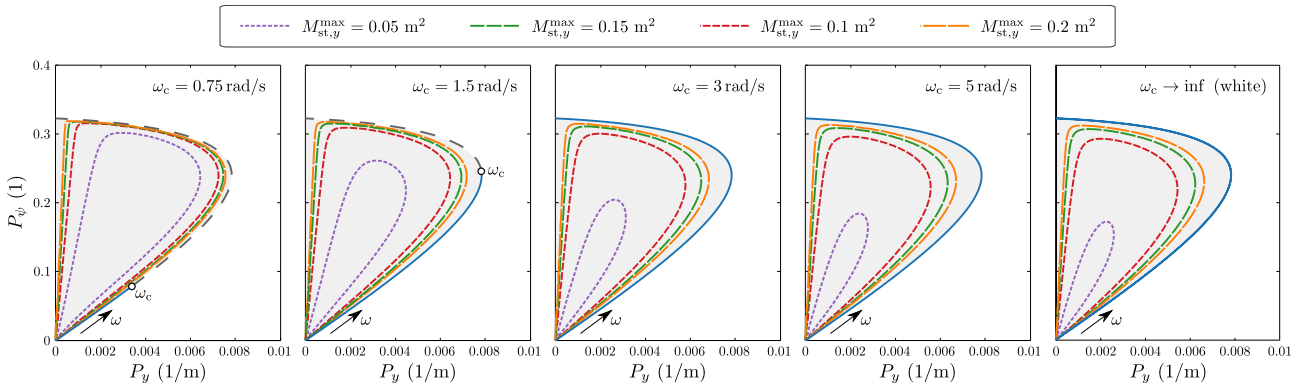

Figure 5: Robust stability maps in terms of the steady state second moment of y while increasing the cutoff frequency of the sensor noise (ω_c). The styling of the deterministic boundary shows the relation between the frequency component ω of the critical characteristic roots at the boundary and the cutoff frequency ω_c (blue: $\omega < \omega_c$, gray dashed: $\omega > \omega_c$).

It can be seen that as long as only a small section of the stability boundary (and therefore the corresponding dynamics) is excited, the stochastic resonance effect is not very strong, the stationary second moment of y remains small throughout the majority of the stable parameter domain, and there is not much difference between the deterministic and the robust stability boundaries. However, as the cutoff frequency is increased, the stochastic excitation has a stronger effect on the dynamics, and the contour lines of $M_{\mathrm{st},y}$ start tending towards those shown for white noise excitation. Since the vehicle model acts as a low-pass filter with relatively slow dynamics, the colored sensor noise also has to have a very low cutoff frequency in order to show a meaningful difference in terms of the steady-state dynamics of the system compared to a white noise excitation. Therefore there is not much benefit in taking into account the cutoff frequency of the sensor noise in most practical cases, where ω_c is typically at least 10 Hz.

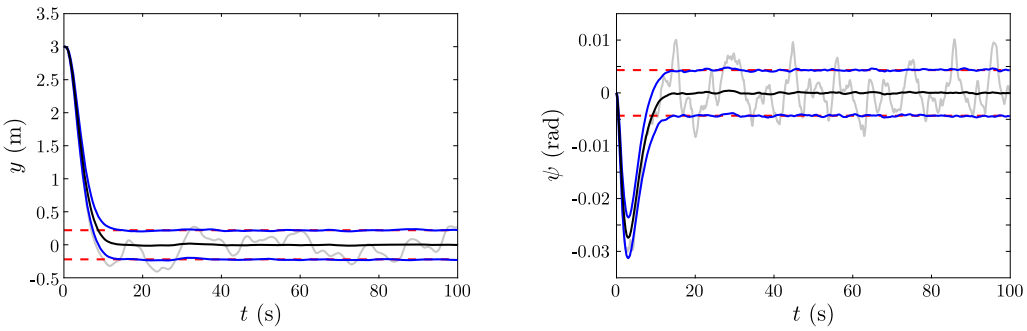

Figure 6: Simulation results of 1000 Monte-Carlo runs of the non-linear system. Black lines show the sample mean and blue lines denote the standard deviations of the samples. An arbitrarily chosen single realization is shown in light gray, while the red dashed lines represent the square root of the stationary second moments calculated using stochastic semi-discretization.

On the other hand, a possible advantage of modeling the additive sensor noise as a first order Markov process is that this approach allows the numerical simulation of the non-linear system too (the non-linear system equations can be found in [7]). In spite of feeding back the measurement noise through non-linear functions, the overall system remains driven by an additive, white noise source, which is easy to handle mathematically.
The results in Fig. 6 and Table 2 show that there is minimal difference in the observed stationary second moments between performing simulations on the linear and the non-linear system. This is mainly due to the fact that only geometrical non-linearities are considered, which do not have a strong effect in the performed lane change manoeuvre, especially once the steady state is reached. Even though there is constant steering action due to the stochastic effects, the steering and side-slip angles all remain small enough that the system stays well within the linear regime. Nevertheless, this still provides a useful example of simulating a non-linear system with direct feedback of measurement noise.

Conclusion

The stability and steady-state dynamics of a path tracking controller were investigated in the presence of time delay and measurement noise. It was shown how the choice of control parameters influences the steady-state dynamics. Due to the autonomous stochastic resonance effect, it is possible to choose control gains from the linearly stable parameter domain that still lead to unacceptably large variance in the steady-state solution. The included robust stability maps aim to provide guidelines about which regions of the stable domain should be avoided for this reason. The results determined using the stochastic semi-discretization method were verified by numerical simulations. The simulation of the non-linear stochastic system was achieved by using filtered white noise. A possible extension of the present study is to also consider the effects of road excitation as another noise source in the system.

Acknowledgment This research was partly supported by the National Research, Development and Innovation Office under grant no. NKFI-128422 and by the Higher Education Excellence Program of the Ministry of Human Capacities in the frame of Artificial intelligence research area of Budapest University of Technology and Economics (BME FIKP-MI). The authors would like to thank Henrik Sykora for his valuable comments.

References

[1] Mackey M. C., Nechaeva I. G. (1995) Solution moment stability in stochastic differential delay equations. *Physical Review E* **52**(4):3366-3376.

[2] Guillouzic S., L'Heureux I., Longtin A. (1999) Small delay approximation of stochastic delay differential equations. *Physical Review E* **59**(4):3970-3982.

[3] Grigoriu M. (1997) Control of time delay linear systems with Gaussian white noise. *Probabilistic Engineering Mechanics* **12**(2):89-96.

[4] Di Paola M., Pirrotta A. (2001) Time delay induced effects on control of linear systems under random excitation. *Probabilistic Engineering Mechanics* **16**(1):43-51.

[5] Bilello C., Di Paola M., Pirrotta A. (2002) Time delay induced effects on control of non-linear systems under random excitation. *Meccanica* **37**(1-2):207-220.

[6] Sykora H. T., Bachrathy D., Stépán G. (2019) Stochastic semi-discretization for linear stochastic delay differential equations. *International Journal for Numerical Methods in Engineering* **119**(9):879-898.

[7] Vörös I., Várszegi B., Takács D. (2019) Lane Keeping Control Using Finite Spectrum Assignment with Modeling Errors. *ASME 2019 Dynamic Systems and Control Conference* DSCC2019-8960.

[8] Insperger T., Stépán G. (2011) Semi-discretization for time-delay systems: stability and engineering applications. Springer Science & Business Media, New York.

[9] Øksendal B. (2003) Stochastic differential equations. Springer, Berlin, Germany.

[10] Higham D. J. (2001) An algorithmic introduction to numerical simulation of stochastic differential equations. *SIAM review* **43**(3):525-546.

[11] Maybeck P. S. (1982) Stochastic models, estimation, and control. Academic Press, New York.

The Relevance of Spectral Submanifolds and Slow Manifolds for Randomly Excited Mechanical Systems

Thomas Breunung*, Florian Kogelbauer† and George Haller*
* *Institute for Mechanical Systems, ETH Zürich, Zürich, Switzerland*
† *Mathematics for Advanced Materials-OIL, AIST-Tohoku University, Sendai 980-8577, Japan*

Summary. Invariant manifolds, such as nonlinear normal modes, spectral submanifolds and normally hyperbolic invariant manifolds are the key to understand the dynamical behavior of nonlinear mechanical systems and serve as natural candidates for model-order reduction. While numerous related invariant manifold results are available for unforced and periodically forced nonlinear mechanical systems, the case of random external forcing has not been studied from this perspective. Here, we clarify the role of deterministic invariant manifolds in the case of small white noise excitation and demonstrate our results on explicit mechanical systems.

Introduction

To account for parameter uncertainty, unmodeled degrees of freedom or unknown disturbances in realistic engineering structures, the use of statistical methods is unavoidable [1]. Gaussian white noise is commonly considered to account for such random perturbations. Whether the deterministic invariant manifolds, such as nonlinear normal modes, spectral submanifolds or normally hyperbolic invariant manifolds, are of relevance under uncertainties or random external excitation has, however, remained unclear.

Various definitions of nonlinear normal modes have been proposed in the literature (cf. [2] for a review) and multiple computational algorithms for the unforced or periodically forced nonlinear mechanical systems have been developed [3]. Recently, Haller and Ponsioen [4] identified the smoothest nonlinear continuation of a spectral subspace of the linearization as spectral submanifold (SSM). While spectral submanifolds have proven valuable for model-order reduction, the related computational tools assume a completely deterministic nature of the system. This assumption, however, does not generally hold for structures which are subject to parameter uncertainties and external (unmodeled) disturbances.

Counterparts to deterministic dynamical features, such as normally hyperbolic invariant manifolds or stable/center manifolds of fixed points, for randomly perturbed mechanical systems are intricate to establish mathematically. Berglund and Gentz [5] assume an idealized slow-fast decomposition in the deterministic system, while the stable and center manifolds established in [6] generally depend on the realization of the random process. Therefore, each realization results in a different reduced-order model, which is computational costly and limits relevance of the reduced-order model significantly.

In contrast, the probability density function (PDF) is independent of the realization. In the case of Gaussian white noise excitation, the time evolution of the probability density is governed by the Fokker-Planck equation [7]. Explicit solutions of the Fokker-Planck equation, however, are only available in specific cases, and approximate numerical methods discretizing the Fokker-Planck equation or Monte Carlo simulations are computationally expensive [8].

Recently, Haller et al. [9] derived tools to identify material diffusion barriers, including material surfaces that extremize the diffusive transport of the PDF in the phase space. By the definition of these barriers, the transport of the PDF across them is purely driven the by small stochastic perturbations of the otherwise deterministic system. Specifically, *perfect barriers* block the transport at leading order completely and thereby demarcate regions of the phase space that trajectories generally not penetrate. Similarly, ridges of the diffusion barrier strength (*DBS*) highlight surfaces with strong diffusive transport, i.e., regions where trajectories accumulate. Both identifiers (perfect barriers and DBS) can be computed from purely deterministic quantities associated with the dynamical system and hence computationally expensive numerical methods such as Monte-Carlo approximations can be avoided.

Set-up

In this talk, we apply the methods from [9] for diffusive transport in fluids to mechanical systems excited by Gaussian white noise with small intensity. Specifically, we consider N-degree-of-freedom mechanical systems of the form

$$\mathbf{M}\ddot{\mathbf{q}} + \mathbf{C}\dot{\mathbf{q}} + \mathbf{K}\mathbf{q} + \mathbf{S}(\mathbf{q}) = \sqrt{\nu}\mathbf{f}(\mathbf{q})d\mathbf{W}, \qquad \mathbf{q} \in \mathbb{R}^N, \tag{1}$$

where $\mathbf{M}$, $\mathbf{C}$ and $\mathbf{K}$ are the mass, damping and stiffness matrices. The geometric nonlinearity $\mathbf{S}(\mathbf{q})$ is a nonlinear function of the position, such that $\mathbf{S}(\mathbf{q}) = \mathcal{O}(|\mathbf{q}|^2)$. The vector $d\mathbf{W}$ collects M independent one-dimensional Brownian motions and the matrix $\mathbf{f}(\mathbf{q}) \in \mathbb{R}^{N\times M}$ prescribes their directions. Since $\mathbf{f}$ can depend on the coordinates $\mathbf{q}$ (cf. eq. (1)), our formulation also covers parametric random excitations.

After transforming system (1) into first order, we introduce the probability density function $\rho(\mathbf{q}, \dot{\mathbf{q}}, t)$ depending on the phase space location and time, both of which are suppressed in our notation for simplicity. The time evolution of ρ is then governed by the classic Fokker-Planck equation [7], which can be recast in the advection-diffusion form

$$\frac{D\rho}{Dt} = \frac{\nu}{2}\nabla\cdot\big(\nabla\cdot\mathbf{f}(\mathbf{q})\mathbf{f}^\top(\mathbf{q})\big) + k\rho. \tag{2}$$

The constant k in equation (2) depends on the damping $\mathbf{C}$ and $D\rho/Dt = \partial\rho/\partial t + \mathbf{v}\cdot\nabla\rho$ denotes the material derivative. The results of Haller et al. [9] on transport barriers can be applied to equations of the form (2). These results yield

invaraint manifolds of an associated, deterministic barrier equation. The manifolds obtained in this fashion are barriers to the diffusive transport of the PDF of the original mechanical system (1).

Results

We numerically investigate whether distinguished transport extremizers align with known deterministic slow manifolds or fast stable manifold of stable fixed points. More specifically, we investigate the modified Shaw-Pierre example [10]

$$\begin{bmatrix} m_1 & 0 \\ 0 & m_2 \end{bmatrix} \ddot{\mathbf{q}} + \begin{bmatrix} c_1 + c_2 & -c_2 \\ -c_2 & c_1 + c_2 \end{bmatrix} \dot{\mathbf{q}} + \begin{bmatrix} k_1 + k_2 & -k_2 \\ -k_2 & k_1 + k_2 \end{bmatrix} \mathbf{q} + \begin{bmatrix} \kappa q_1^3 \\ 0 \end{bmatrix} = \sqrt{\nu} \begin{bmatrix} 0 \\ 1 \end{bmatrix} dw, \tag{3}$$

where the intensity ν is a small parameter ($\nu \ll 1$) and dw indicates Gaussian white noise. Further, we investigate the classical Duffing oscillator [11]

$$q + cq + kq + \kappa q^3 = \sqrt{\nu}\, dw. \tag{4}$$

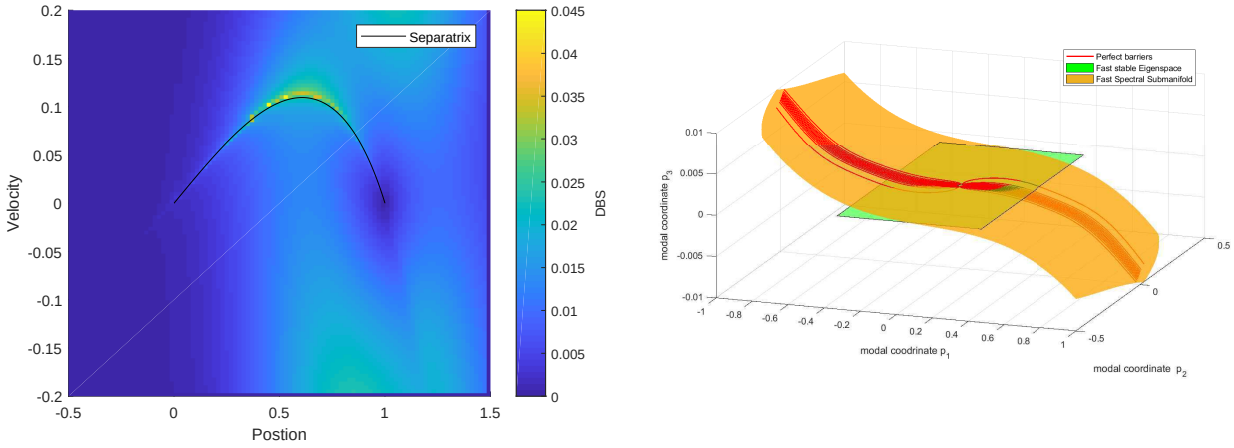

(a) Duffing oscillator (4)

(b) Shaw-Pierre example (3).

Figure 1: Diagnostics from [9] applied to the Shaw-Pierre Example (3) and Duffing oscillator (4).

For systems (3) and (4), we plot the diagnostics for transport barriers from [9] in Fig. 1. In the case of the stochastically forced Duffing oscillator (4) the slow manifold connecting the saddle type fixed point at the origin with the stable node at $q = 1$ is successfully identified as a DBS ridge (cf. Fig. 1a). For the Shaw-Pierre example (3), the fast stable submanifold is successfully identified as a perfect barrier for the stochastically excited nonlinear system (cf. Fig. 1b).

Conclusion

We demonstrate that the methods developed in [9] link classic deterministic normally hyperbolic manifolds or stable submanifolds of nonlinear mechanical systems to the stochastic dynamics arising under small random perturbations to the deterministic system. Our analysis is based on purely deterministic quantities and thereby avoids computationally expensive methods, such as Monte-Carlo approximations.

References

[1] Lutes, L.D. and Sarkani, S. (2004) Random vibrations: analysis of structural and mechanical systems. Butterworth-Heinemann.

[2] Kerschen, G., Peeters, M., Golinval, J.C. and Vakakis, A.F. (2009) Nonlinear normal modes, Part I: A useful framework for the structural dynamicist. *Mechanical Systems and Signal Processing* **23**(1):170-194.

[3] Renson, L., Kerschen, G. and Cochelin, B. (2016) Numerical computation of nonlinear normal modes in mechanical engineering. *J. of Sound and Vib.* **364**:177-206.

[4] Haller, G. and Ponsioen, S. (2016) Nonlinear normal modes and spectral submanifolds: existence, uniqueness and use in model reduction. *Nonlinear Dyn.* **86**(3):1493-1534.

[5] Berglund, N. and Gentz, B. (2003) Geometric singular perturbation theory for stochastic differential equations. *J. of Diff. Eq.* **191**(1):1-54.

[6] Arnold, L. (1995) Random dynamical systems. Springer, Berlin, Heidelberg.

[7] Risken, H. (1996) The Fokker-Planck Equation. Springer, Berlin, Heidelberg.

[8] Soize, C. (1994) The Fokker-Planck equation for stochastic dynamical systems and its explicit steady state solutions (Vol. 17). World Scientific.

[9] Haller, G., Karrasch, D. and Kogelbauer, F. (2019) Barriers to the Transport of Diffusive Scalars in Compressible Flows. *SIAM J. of Appl. Dyn. Sys.* **19**(1):85-123.

[10] Shaw, S.W. and Pierre, C. (1993) Normal modes for non-linear vibratory systems. *J. of Sound and Vib.*, **164**(1):85-124.

[11] Guckenheimer, J. and Holmes, P. (2002) Nonlinear oscillations, dynamical systems, and bifurcations of vector fields. Springer, New York.

The hysteretic dynamics of a harmonically excited snap-through oscillator in the presence of additive noise excitations

Rohit Chawla, Aasifa Rounak and Vikram Pakrashi
UCD Centre for Mechanics, Dynamical Systems and Risk Laboratory, School of Mechanical and Materials Engineering, University College Dublin, Ireland
SFI MaREI Centre, University College Dublin, Ireland
UCD Energy Institute, University College Dublin, Ireland

Summary. The noisy dynamics of the system called the smooth and discontinuous (SD) oscillator in its frequency domain is studied. The nonlinearity is smooth (continuous) or nonsmooth (discontinuous) depending on the value of the smoothness parameter α. It was observed that the hysteretic region decreases with a higher correlation in noise. Furthermore, an increase in the smoothness parameter in the presence of noise also has the effect of reducing the hysteretic region.

Introduction

The study of discontinuous nonlinear systems subjected to stochastic excitations using non-smooth transformations, approximate analytical methods, numeric-analytical methods and numerical methods are few [1]. Most of these studies were carried out with the assumption of noise being uncorrelated in nature. However, white noise is a mathematical abstraction and the noise occurring in real physical systems often has a finite bandwidth. Furthermore, the problem is more involved in the vicinity of a bifurcation as the presence of a subcritical bifurcation in a deterministic dynamical system leads to the formation of a pair of stable solutions separated by an unstable branch, thus creating a hysteretic loop when a forward and a backward bifurcation is carried out. The dynamics follows a particular bifurcation branch until the critical value of a control parameter is reached, followed by a sudden transition to another branch. However, if the integration is carried out using the varying the same control parameter in the reverse manner, the critical transition occurs at a different value. Noise has the potential to influence these critical parameters [2]. The dependence of the size of the hysteresis loop on the intensity and correlatedness of noise is thus important to demarcate the stability regime of the dynamical system. The complexity of the problem is increased when there is an interplay of nonsmoothness in the dynamical system. To decipher the underlying dynamics of such noise-induced transitions, an archetypal snap-through truss oscillator has been considered. The dynamics of the system can be considered to be smooth or non-smooth depending on the smoothing parameter α in the problem. The non-dimensionalized equations of motion of this system are given by Eq. 1. In the smooth regime, the system is observed to bear significant resemblance to the Duffing oscillator, exhibiting the standard dynamics governed by the hyperbolic structure associated with the double well. At the discontinuous limit however, the dynamics diverges substantially. The loss of local hyperbolicity leads to a jump in the velocity flow when crossing from one well to another. The system has coexisting attractors in the presence of damping and external excitations.

$$\ddot{x} + 2\zeta\dot{x} + x\left(1 - \frac{1}{\sqrt{x^2+\alpha^2}}\right) = f_0 \cos\omega t + n\lambda(t), \tag{1}$$

where ζ is the damping coefficient, f_0 is the amplitude of forcing and ω is the corresponding forcing frequency. $\lambda(t)$ depicts the Ornstein Uhlenbeck noise and n denotes its intensity.

Results and discussions

The results of direct numerical simulations using forward integration has been shown in Fig. 1. It can be observed that in the presence of noise, the upper branch near $\simeq \omega = 0.8$ is continued for a larger magnitude of frequency before there is a transition to the lower amplitude branch. The transition is depicted by a saddle-node bifurcation of limit cycles, leading to the creation of a stable and and unstable branch of bifurcations [4]. It is also observed that the lower amplitude branch has a marked increase in the observed maximum amplitude of oscillations post the saddle-node bifurcation. Thereafter, the effect of correlatedness in noise on the transition to the lower branch is studied. The intensity of noise, mean and variance are kept constant at 0.5,0 and 0.1 and the mean reverting speed is varied, here denoted by θ. The system is assumed to be ergodic and the maximum amplitude is computed with one simulation from an ensemble of realizations where a long time history of 10^3 cycles is considered. It was observed that the transition occurred for a lower magnitude of frequency when the mean reversion speed of the Ornstein Uhlenbeck process was higher *i.e.* higher correlatedness in noise led to a proponent of transition to the lower amplitude branch when a forward numerical integration is carried out; see Fig. 2.

Furthermore, the effect of varying the smoothing parameter in the SD oscillator on the transition to the lower branch is studied. Fig. 3. is a depiction of the variation of nonlinear restoring force as a function of α. It can be observed that the restoring force becomes stiff as α decreases and is discontinuous at $\alpha = 0$ [3]. Fig. 4 depicts the variation in the control parameter leading to the occurrence of the nonsmooth saddle-node bifurcation. As α decreases, the bifurcation is delayed to a higher parameter of ω. Also, a corresponding increase in the maximum amplitude of the response has been observed post occurrence of the bifurcation. For the simulations, the intensity of noise n is kept constant at 0.5 and the process parameters of the Ornstein Uhlenbeck process are $0, 0.5, 0.3$ respectively. The step size of integration is fixed at 0.001.

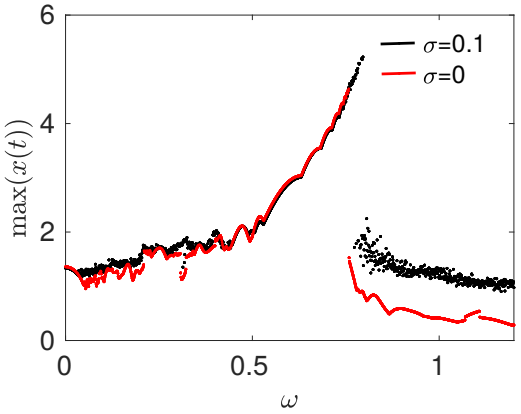

Figure 1: The frequency response of the SD oscillator for $\alpha = 1.1, f_0 = 0.25, \zeta = 0.0141$ using numerical integration with stochastic Runge-Kutta method when $\sigma = 0, 0.1$.

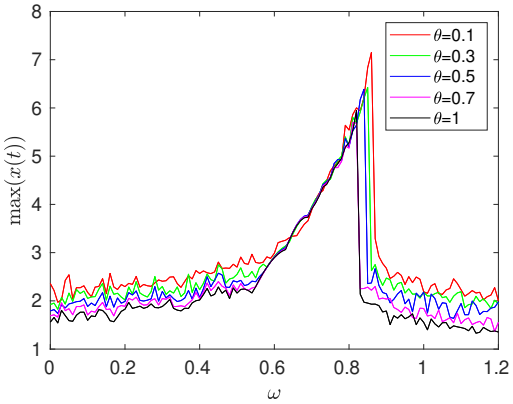

Figure 2: The frequency response of the SD oscillator with Stochastic Runge-Kutta method with different correlated noises.

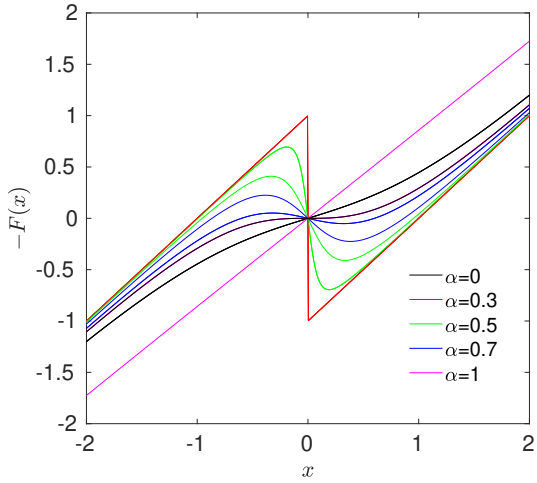

Figure 3: Nonlinear restoring force for different values of α.

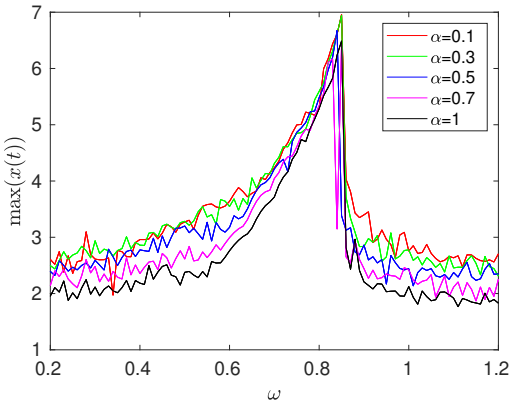

Figure 4: The frequency response of the SD oscillator with Stochastic Runge-Kutta method with different values of the smoothing parameter α.

A systematic semi-analytical and numerical approach to determine the effect of additive noise on the region of co-existence of attractors in a SD oscillator is currently under investigation. The noise is appended to the harmonic excitation in the system. The effect of the degree of nonlinearity given by α, the intensity of noise n, correlatedness of noise $\lambda(t)$, damping ζ are explored.

References

[1] Narayanan, S., Kumar, P. (2021). Dynamics of Nonlinear Oscillators with Discontinuous Nonlinearities Subjected to Harmonic and Stochastic Excitations. Journal of The Institution of Engineers (India): Series C, 102(6), 1321-1363.

[2] Butkovskii, O. Y., Kravtsov, Y. A., Surovyatkina, E. D. (1997). Use of hysteresis in bifurcation systems to measure noise. Technical Physics, 42(9), 1099-1101.

[3] Cao, Q., Wiercigroch, M., Pavlovskaia, E. E., Grebogi, C., Thompson, J. M. T. (2006). Archetypal oscillator for smooth and discontinuous dynamics. Physical Review E, 74(4), 046218.

[4] Santhosh, B., Narayanan, S., Padmanabhan, C. (2016). Discontinuity induced bifurcations in nonlinear systems. Procedia IUTAM, 19, 219-227.

Wednesday, July 20, 2022
08:30 - 10:30

MS-21 Nonlinear Dynamics in Acoustics
Saint Clair 2

Chair: Cyril Touzé

08:30 - 08:50
Passive control of flexural beam vibrations using nonlinear absorbers combined with an Acoustic Black Hole
LI Haiqin, **TOUZÉ Cyril***, PELAT Adrien, GAUTIER François
*Institut des Sciences de la mécanique et Applications industrielles (828 bd des maréchaux 91762 Palaiseau cedex Franceanciennement LAMSID UMR 8193 France)

08:50 - 09:10
Resonant Triads of Acoustic-Gravity Waves in Shallow Water
RICKETTS Evan*, KADRI Usama
*School of Engineering, Cardiff University (Queen's Buildings, 14-17 The Parade, Cardiff CF24 3AA United Kingdom)

09:10 - 09:30
Study of the behaviour of the trombone using bifurcation diagrams
MATTÉOLI Rémi*, GILBERT Joël, MAUGEAIS Sylvain, VERGEZ Christophe, DALMONT Jean-Pierre
*LAUM, Laboratoire d'Acoustique de l'Université du Mans (Avenue Olivier Messiaen, 72085 Le Mans France)

09:30 - 09:50
Fast Explicit Algorithms for Hamiltonian Numerical Integration
BILBAO Stefan*, DUCCESCHI Michele
*Acoustics and Audio Group, University of Edinburgh (Room 2.10, Alison House, 12 Nicolson Sq., Edinburgh, EH8 1DR United Kingdom)

09:50 - 10:10
Real-time simulation of the struck piano string with geometrically exact nonlinearity via a scalar quadratic energy method
DUCCESCHI Michele*, BILBAO Stefan, WEBB Craig
*Dept of Engineering, University of Bologna (Viale Risorgimento 2, 40136, Bologna, Italy Italy)

Passive control of flexural beam vibrations using nonlinear absorbers combined with an Acoustic Black Hole

Haiqin Li*†, Cyril Touzé*, Adrien Pelat† and François Gautier†
* *IMSIA, Institut of Mechanical Sciences and Industrial Applications, ENSTA Paris, CNRS, EDF, CEA, Institut Polytechnique de Paris, Palaiseau, France.*
† *LAUM, Laboratoire d'Acoustique de l'Université du Mans, Le Mans, France*

Summary. Acoustic Black Hole (ABH) is a new passive technique for vibration damping of thin-walled strutures such as beams and plates. It consists of a local decrease in the thickness profile, associated to the deposit of a thin viscoelastic coating in the thinnest region. One of the common feature for this technique is that it is very efficient in the high frequency range, but it is less optimal in the low frequency range. To overcome this limitation,we propose to investigate the benefit brought by different types of nonlinear dampers into the system. The effect of a Tuned Mass Damper (TMD), a Nonlinear Energy Sink, and a Bistable Nonlinear Energy Sink are respectively considered and compared. The dynamics of these systems are numerically solved using a modal approach with an energy conserving scheme. Then, by defining some frequency indicators, the low frequency performance of each aforementioned strategy is characterized. It is demonstrated that, if appropriately designed, all the proposed methods can effectively reduce the low frequency resonance peaks in the ABH structure, and hence improve the average performance of an ABH.

Introduction

The Acoustic Black Hole (ABH) effect has become an increasingly popular technique for passive noise and vibration control. Its one dimensional implementation (i.e its implementation in a beam structure) consists of a local decrease of the thickness according to a power law profile associated to the adding of a thin viscoelastic damping layer in the tapered area [1]. Existing theoretical, numerical and experimental papers show that Acoustic Black Holes induce significant localization of the bending waves, and have a strong damping effect in the middle and high frequency ranges [1]. Some design rules based on the analysis of the wave scattering induced by an ABH termination have been proposed [2] to achieve high modal damping coefficients, the underlying mechanism being interpreted using the critical coupling concept [3]. However, a significant limitation of the ABH effect leads in the fact that it is effective in the mid-high frequency range. A cut-on frequency has been defined [4], for representing the critical frequency threshold below which the ABH loses its efficiency. To overcome this issue, the idea of associating the ABH effect with some other nonlinear effects has emerged: geometrical non linearities due to vibrations with large amplitudes have been exploited [5], as well as strong nonlinearities induced by vibro-impacts [6].
In this paper, the interest of adding three different types of vibration absorbers to a beam ABH termination are tested in order to meet the requirement of a broadband passive energy mitigation. A classical tuned mass damper (TMD) is first considered, which consists of a linear device that has been proven to be a very reliable passive mitigation strategy in a large number of contexts [7, 8]. It could be awaited that once a TMD is attached to an ABH beam and tuned to one of its resonant modes below the cut-on frequency, where the ABH effect is ineffective, the peak response reduced [9], and the average perfomance of the ABH could hence be improved.
Considering the known major drawback that TMD is only effective in a narrow frequency band, a more broadband nonlinear vibration absorber consisting of an NES with cubic nonlinearity [10] is also proposed. Unlike a linear system, a unique nonlinear phenomenon called targeted energy transfer [11] could be observed for effective broadband vibration mitigation [12, 13]. A third proposition of absorber consists of a recently studied Bistable Nonlinear Energy Sink (BNES), for which the targeted energy transfer can be activated with a lower energy barrier [15, 16].
The purpose of this paper is thus to use the aforementioned three types absorbers in order to improve the performance of the ABH below its cut-on frequency, and to compare their performances. The numerical modeling of all the considered systems will be formulated in Section 2. Section 3 is mainly devoted to the numerical results, the performance of each methods will be discussed, before the conclusion given in section 4.

Equations of motion

Let us consider an ABH beam coupled to a single vibration absorber consisting in an elementary 1-DOF oscillator (see Fig. 1). The absorber is located at $x = x_c$. Its mass m is assumed to be small compared to that of the beam. It is characterized by its linear stiffness k_l, its cubic nonlinear stiffness k_n, and its damping coefficient 2σ. Considering such parameters, the three different types of absorbers can be modeled by varying k_l and k_n. More precisely, a linear TMD [7, 8] is obtained by setting $k_l > 0, k_n = 0$; while the classical NES [11] with cubic nonlinearity corresponds to the arrangement of $k_l = 0, k_n > 0$. Finally, the case of a BNES [15, 16] can be obtained for $k_l < 0, k_n > 0$.
The ABH beam is supposed to have a constant thickness h_0 in the region $x \in [0, x_{abh}]$. An ABH profile is assumed in the right hand region $x \in [x_{abh}, L]$: The thickness $h_b(x)$ is decreasing with respect to the variable x, in the form of the

power-law function

$$h_b(x) = \begin{cases} h_0, & \text{for } x \in [0, x_{abh}] \\ h_0 \left(\dfrac{x - x_{end}}{x_{abh} - x_{end}} \right)^2, & \text{for } x \in [x_{abh}, L] \end{cases} \tag{1}$$

The cross-section of the ABH beam is assumed to be rectangular and with width b, such that the cross-section area $A(x)$ and the inertia moment $I(x)$ writes respectively $A(x) = bh_b(x)$ and $I(x) = bh_b(x)^3/12$. Finally, a viscoelastic layer is added in the ABH region in consideration of ensuring the damping for a practical ABH with an inevitable truncation thickness h_t.

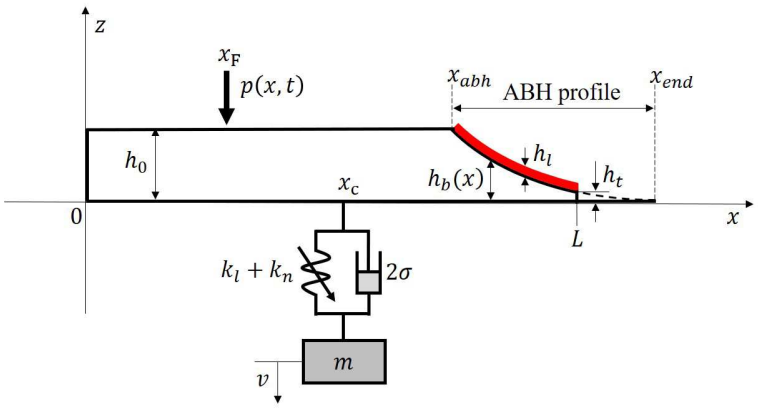

Figure 1: The layout of the considered system consists of an ABH beam coupled to a lightweight oscillator located at x_c. A thin damping layer (red) of thickness h_l is added along the ABH profile.

Let $u(x,t)$ be the transverse displacement of the beam, and $v(t)$ the motion of the absorber. The governing equation for the system can then be written as

$$\rho(x)A(x)\frac{\partial^2 u}{\partial t^2} + \frac{\partial^2}{\partial x^2}\left(D(x)\frac{\partial^2 u}{\partial x^2}\right) + f\delta(x - x_c) = p\delta(x - x_F), \tag{2a}$$

$$m\ddot{v} = f, \tag{2b}$$

$$f = k_l w + k_n w^3 + 2\sigma\dot{w}, \tag{2c}$$

$$w = u\left(x_c,\ t\right) - v, \tag{2d}$$

where $\rho(x)$ is the material density of the beam, and $D(x) = E(x)I(x)$ is the bending stiffness, $p = p(x,t)$ stands for the pointwise external force induced at the position $x = x_F$. The force $f = f(x,t)$ is the restoring force of the oscillator written in form of the relative motion $w = u\left(x_c,\ t\right) - v$. The mass ratio ϵ defined by $\epsilon = m/m_{beam}$ is supposed to be small (m is the mass of the absorber and m_{beam} is the total mass of the beam). As for the boundary conditions, the beam is considered to be clamped at $x = 0$ and free at $x = L$.

The damping induced by the viscoelastic layer is modelled with the Ross-Kerwin-Ungar method [2], in which a complex bending stiffness $D^*(x)$ is introduced and can be expressed as,

$$D^*\left(x\right) = \begin{cases} E_b I_b(x)\left(1 + j\eta_b\right), & \forall x \in [0, x_{abh}], \\ E_b I_b(x)\left[\left(1 + j\eta_b\right) + \dfrac{E_l}{E_b}\left(\dfrac{h_l}{h_b(x)}\right)^3\left(1 + j\eta_l\right) + \right. & \\ \left. \dfrac{3\left(1 + \frac{h_l}{h_b(x)}\right)^2 \frac{E_l h_l}{E_b h_b(x)}\left(1 - \eta_b\eta_l + j\left(\eta_b + \eta_l\right)\right)}{1 + \frac{E_l h_l}{E_b h_b(x)}\left(1 + j\eta_l\right)}\right], & \forall x \in [x_{abh}, L], \end{cases} \tag{3}$$

where j is the imaginary unit, E_b, I_b, and η_b stand respectively for the bending stiffness, the Young's modulus, the moment of inertia and the loss factor of the beam alone, while E_l and η_l are the Young's modulus and the loss factor of the viscoelastic layer. In addition, a modification on the thickness $h(x) = h_b(x) + h_l$ and material density $\rho(x) = \left(\rho_b h_b + \rho_l h_l\right)/h$ at the ABH area are also performed due to the added mass of the damping layer.

A modal approach, whose implementation details are given in [6], is applied to numerically solve the problem described in 2 in the time domain. A special emphasize on the added new dof introduced by the nonlinear damper will be further explained here. First of all, the beam displacement is written as $u(x,t) = \sum_{k=1}^{N_m} \phi_k(x) q_k(t)$, where $q_k(t)$ is the modal

coordinate associated to mode $\phi_k(x)$, and N_m is the number of modes kept in the expansion. Introducing the modal expansion into (2), and projecting the dynamics onto each mode yields :

$$\ddot{q}_k + 2\xi_k\omega_k\dot{q}_k + \omega_k^2 q_k = p\phi_k\left(x_F\right) - f\phi_k\left(x_c\right), \tag{4a}$$

$$m\ddot{v} = f, \tag{4b}$$

$$f = k_l w + k_n w^3 + 2\sigma\dot{w}, \tag{4c}$$

$$w = \sum_{k=1}^{N_m} q_k\phi_k\left(x_c\right) - v, \tag{4d}$$

where ω_k and ξ_k are respectively the eigenfrequency and the the modal damping ratio associated to each mode k. Hence, the original problem with PDE is transferred to a set of ODEs with time variables only. Before solving Eqs. (4), a eigenvalue problem should be solved to determine $\phi_k\left(x\right)$, ω_k, and ξ_k for each mode. Such eigenvalue problem is written from Eq. (2a), considering that $f = p = 0$. A finite difference method with a non-uniform grid is applied to discretize the variable thickness of the ABH beam. All the complete details are given in [2]. They are skipped here for conciseness. Once the eigenvalue problem solved, the last step of the numerical model consists in the time integration of Eqs. (4). It is done using the exact energy conserving numerical scheme developed in [17].

Let $t_n = n\Delta t$, with n the step index and Δt the time step. The specific feature of the numerical integrator developed in [17] is to use the modal approach for the linear part, whereas the contact force are computed in the physical space. To that purpose, the relationship between the modal space and the physical space needs to be explicited. We introduce $\mathbf{S}_F = \left[\phi_1\left(x_F\right),\ \phi_2\left(x_F\right),\ \cdots,\ \phi_{N_m}\left(x_F\right)\right]$, as the modal matrix containing the first N_m beam modes at x_F , and $\mathbf{S}_c = \left[\phi_1\left(x_c\right),\ \phi_2\left(x_c\right),\ \cdots,\ \phi_{N_m}\left(x_c\right)\right]$ the modal matrix at point x_c. The relationship with the modal expansion allows one to write $u\left(x_c, n\Delta t\right) = \mathbf{S}_c\mathbf{q}$, and $u\left(x_F, n\Delta t\right) = \mathbf{S}_F\mathbf{q}$. With these definitions, Eqs. (4) can then be written at each time step n as:

$$\mathbf{q}^{n+1} = \mathbf{C}\mathbf{q}^n - \tilde{\mathbf{C}}\mathbf{q}^{n-1} + \Delta t^2\left(\mathbf{S}_F^T p^n - \mathbf{S}_c^T f^n\right), \tag{5a}$$

$$m\delta_{t.}v^n = f^n, \tag{5b}$$

$$f^n = k_l w^n + k_n (w^n)^2 \mu_{t.} w^n + 2\sigma\delta_{t.}w^n, \tag{5c}$$

$$w^n = \mathbf{S}_c\mathbf{q}^{\mathbf{n}} - v^n. \tag{5d}$$

where p^n and f^n are respectively the external and restoring forces at time step n. The matrices $\mathbf{C}$ and $\tilde{\mathbf{C}}$ are two diagonal matrices whose expressions could be found in [17], $\delta_{t.}$ is a centred time difference reading $\delta_{t.}w^n = \left(w^{n+1} - w^{n-1}\right)/2\Delta t$, and $\mu_{t.}$ is an averaging operator: $\mu_{t.}w^n = \left(w^{n+1} + w^{n-1}\right)/2$. The advantage of this particular choice stems from the consideration of ensuring the energy conserving properties and avoid numerical dispersion. It should be noted that before the numerical analysis, a convergence study should first be performed on the sampling frequency $F_s = 1/\Delta t$ and the number of modes N_m, in order to appropriately select the numerical parameters. It was demonstrated that an arrangement with $N_m = 20$ and $F_s = 16$kHz is sufficiently enough for obtaining accurate results in our studies.

Nonlinear dampers attached to a uniform beam

The first results and comparisons of the three selected methods (TMD, NES and BNES) have been first tested numerically on a simply supported uniform beam. goal is here to suppress one targeted single resonance of the beam using each of the three selected methods. Fig. 2 provides two simulation results: 1/ the optimization of the nonlinear cubic stiffness k_c and the location x_c of a NES is performed using the energy dissipation E_{diss} cost function (see Fig. 2(a)). 2/ The performance of the system subjected to a harmonic excitation at the circular frequency ω_F in the vicinity of the fundamental frequency of the beam ω_1 is illustrated in Fig. 2(b).

It can be seen that with a appropriate design, each strategy, either a TMD, a NES, or a BNES can effectively suppress the resonance peak of the beam which confirms their efficiency. For the next step, the three methods will then be applied to the ABH beam in order to improve the low frequency performance, with comparisons and optimizations for each of the three mentioned method.

Nonlinear dampers attached to an ABH beam

Parameters of the ABH beam and linear performance

The geometrical and material parameters for the selected ABH beam used in our simulations are listed in Table 1. These choices are related to the experimental beam used in the previous works in[2]. The first line in Table 1 defines also a uniform beam of constant thickness, which will be used subsequently as reference in order to draw out comparisons.

The driving mobility defined as the ratio between the velocity spectrum and the input force spectrum at x_F, is compared in Fig. 3 between the reference (naked) beam and the ABH beam. It could be found that the ABH effect is particularly noticeable on the high-frequency part of the mobility. The cut-on frequency of the ABH effect is evaluated at $f_c = 500$ Hz,

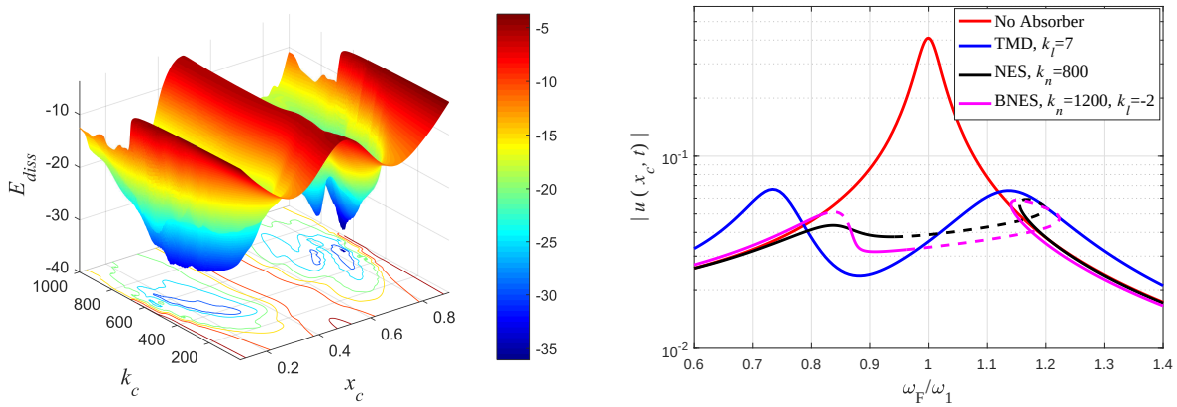

(a) (b)

Figure 2: (a): Dissipated Energy E_{diss} of a NES having a purely nonlinear cubic stiffness k_c and located at x_c. (b): Frequency response of the beam under a harmonic excitation in the vicinity of the first resonance frequency ω_1. Comparisons among the optimized TMD, NES and BNES configurations, with the same damping $\sigma = 0.1$. $|u(x_c,t)|$ refers to the beam displacement at the attached point, the dashed lines indicate that the periodic solution is unstable.

Beam parameters	ABH profile	viscoelastic layer
L=80cm	x_{abh}=71cm	h_l=400μm
h_0=4mm	x_{end}=80.685cm	E_l=10Mpa
b=2cm	h_t=20μm	ρ_l=1000 kg $\cdot$ m^3
E_b=70Gpa		η_l=160%
ρ_b=2700kg $\cdot$ m^3		
η_b=0.2%		

Table 1: Geometrical and material parameters selected for the studied ABH beam.

above which excellent damping properties in the ABH beam with strong attenuation of the sharp resonance peaks (more than 20dB) could be observed. However, at the frequency range below 500Hz, sharp resonance peaks still exist, the ABH almost has no effect. Therefore, in the next sections, our goal will be to improve the damping properties of the ABH effect in the frequency range $[0, 500]$ Hz, by associating the ABH with a special vibration absorber: TMD, NES or BNES.

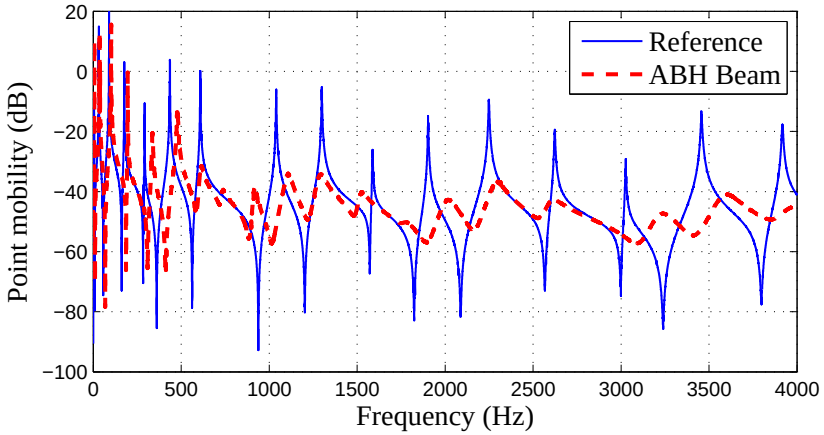

Figure 3: Comparison of the driving mobilities of the ABH and the uniform beam given in Table 1. Excitation and measurement point are fixed at $x_F = 24$ cm. The excitation is a white noise excitation on $[0, 5000]$ Hz, with amplitude 1 N.

Effect of vibration absorbers on ABH beam

To investigate in the effect of the adding vibration absorber on the performance of the ABH beam, a white noise excitation in the frequency band $[0, 500]$ Hz is considered. Four different cases including the ABH beam without damper (the reference case), the ABH with an attached TMD, the ABH coupled to a NES with pure cubic stiffness, the ABH coupled to a BNES with both cubic stiffness and negative linear stiffness, are then discussed and compared. Fig. 4 shows the output velocity spectrum at the excitation point for each case. Clearly enough, each method could be able to reduce the resonant responses in the targeted low frequency range, while for this typical simulation, the performance is significant for the first 4 modes but less important for the others. More precisely, for mode 2, a 15-25dB reduction could be observed,

and for mode 3, this reduction is around 10-20dB. Thus, by using a linear or nonlinear absorber, the average performance of the ABH beam at the low frequency range is considerably improved. On the other hand, the spectra above the 500Hz indicate that while not significant, the nonlinearity of the NES and BNES brings some transfer of the energy from the low frequency to the high frequency, whereas the TMD shows a linear behaviour without such energy transfer.

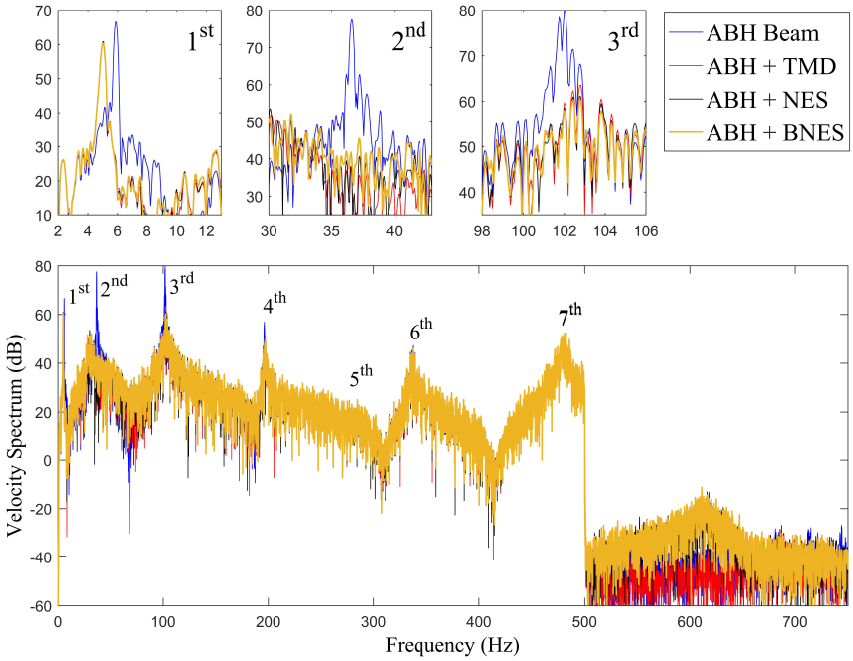

Figure 4: Reduction of the resonance peaks of an ABH beam by using a TMD with $k_l = 800$ N/m, a NES with $k_n = 3 \times 10^9$ N/m^3, and a BNES with $k_l = -300$ N/m, $k_n = 3 \times 10^9$ N/m^3. For all cases, $\sigma = 0.5\text{N} \cdot \text{s/m}$, $x_c = 0.72$ m. The beam is excited with a white noise of $[0, 500]$ Hz, with an amplitude $A = 5$ N and a location $x_F = 0.24$ m. The dynamics are simulated up to 10s.

A performance indicator is proposed for a more quantitative comparison :

$$I = 10\log_{10}\left(\frac{\int_{f_0}^{f_{end}} V_c^2 \,\mathrm{d}f}{\int_{f_0}^{f_{end}} V_{ref}^2 \,\mathrm{d}f}\right), \tag{6}$$

where V stands for the power spectrum of velocity at the exciting point, with subscript c or ref referring respectively to the current case and the reference case (*i.e.* the ABH beam without attachment). This indicator allows one to assess the improvements brought by each method over an arbitrary frequency band $[f_0, f_{end}]$. Having in mind the purpose that we want to compare the performances of the three vibration absorbers in the low frequency range below the cut-on freuqency of the ABH, some useful indicators can thus be defined in Tab. 2. Here, I_{ω_1} to I_{ω_3} are the indicators quantifying the reduction in the vicinity of each eigenfrequencies ω_1 to ω_3, while I_{ave} provides an evaluation for the average performance at the low frequency band $[0,\ 500]$ Hz of the ABH beam.

Indicators	I_{ω_1}	I_{ω_2}	I_{ω_3}	I_{ave}
$\omega_i/2\pi$ (Hz)	5.9	36.7	101.9	/
$[f_0,\ f_{end}]$ (Hz)	[0, 15]	[30, 45]	[95, 110]	[0, 500]

Table 2: Frequency bands used for defining the performance indicators

The performance indicators for all the cases considered in Fig. 4 are reported in Fig. 5. Considering the fact that the chosen excitation signal is random, a single simulation result may not give an accurate value for the indicators, hence a average values over 20 random selections for each indicator I_{ω_1} to I_{ave}, together with the standard variations is depicted in Fig. 5. One can see that the variations brought by the randomness of the excitation is significant. For I_{ω_1}, a worst fluctuation at around $\pm$6dB is observed. At the higher frequencies , the indicators are less prone to variations. As a result, there finally exists a variation at around $\pm$1.5dB for the average performance I_{ave}. Thus, a single simulation is not sufficient enough to provide accurate values for each indicator. A Monte Carlo method for obtaining convergence results has then been performed. It is shown that, by make the average value of at least 5 times of simulation samples, I_{ave} can be converged to to a very small variation of less than 0.2dB. In this paper hereafter, for each case, we will repeat 10 times each simulation, and we will take the average value for computing the indicators.

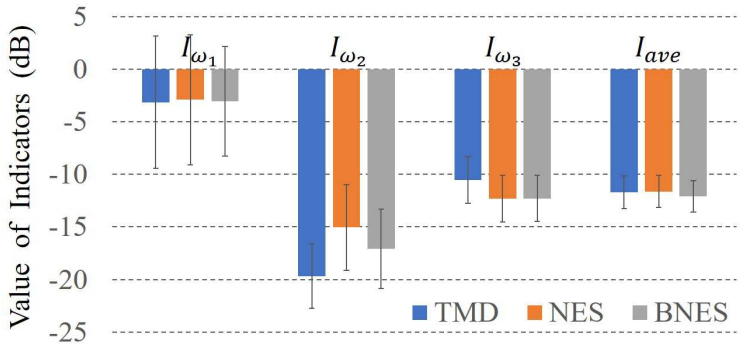

Figure 5: Histograms of indicators I_{ω_1} to I_{ave} calculated for the four cases given in Fig. 4. Average values and standard deviation are computed from 20 randomly generated white noise excitations with amplitude 5N and frequency band $[0, 500]$Hz.

It should be emphasized that the parameters associated to each method are randomly selected, hence their performances are not really optimized currently but discussed thanks to the help of the indicators. It allows to propose some guidelines for an optimal design.

Tuning the vibration absorbers: parametric study

This section is devoted to the parametric tuning and the optimization of the different vibration absorbers. The interested parameters are the linear and nonlinear stiffnesses k_l and k_n, the damping coefficient σ, and the location x_c. For all the simulations, the external force is a white noise excitation limited to the low frequency band $[0, 500]$Hz, with amplitude $A = 5$N and location $x_F = 0.24$m.

Since the linear and nonlinear stiffnesses play an important role in the energy transfer between the ABH and the vibration damper, their effects are first investigated. Fixing x_c=0.72m, σ=0.5Ns/m, and $\epsilon = 0.1$ and varying k_l and k_n, the values of different indicators are depicted in Fig. 6 for the three vibration absorbers.

As the linear stiffness k_l in the TMD increases, I_{ω_1}, I_{ω_2}, I_{ω_3}, and I_{ave} show a similar trend, with different minimum values for each indicator (see Fig. 6(a)). For example, I_{ω_1} meets its optimal value of $I_{\omega_1} = -15$dB for $k_l = 20$N/m, showing that the best reduction is obtained for the resonance peak of the first mode. For I_{ω_2} and I_{ω_3}, the optimal stiffnesses are $k_l = 500$N/m and $k_l = 5000$N/m, respectively. Each optimal stiffness is just consistent with the eigenfrequency of the correspond mode, which is also the key rule in the classical frequency tuning of TMD. Nevertheless, the combined effects reported by the average indicator I_{ave} show that a global minimum can be found for k_l around 1000N/m.

For the case of an attached NES, trends similar to the TMD case can be observed (see Fig. 6(b)). The optimal performance for the reduction of the resonance peaks of modes 1-3 could be found respectively for $k_n = 10^7 \mathrm{N/m^3}$, $k_n = 10^9 \mathrm{N/m^3}$, and $k_n = 3 \times 10^{10} \mathrm{N/m^3}$, with indicators respectively equal to I_{ω_1}=-15dB, I_{ω_2}=-23dB, I_{ω_3}=-20dB. Besides, for the average performance, $k_n = 2 \times 10^9 \mathrm{N/m^3}$ gives the optimal tuning.

In Fig. 6(c-d), the effect of the negative stiffness k_l shows quite different trends for different values of k_n. For a relatively small value of $k_n = 10^6 \mathrm{N/m^3}$, the effect of varying k_l is important. The optimal performance can be easily observed for each single mode 1-3 as $k_l = -10 \mathrm{N/m}$, $k_l = -300 \mathrm{N/m}$, and $k_l = -2000 \mathrm{N/m}$ respectively, and the optimal average performance is obtained within $k_l \in [300, 500]$ N/m. However, for higher values of k_n, for example $k_n = 2 \times 10^9 \mathrm{N/m^3}$ (see Fig. 6(d)), where the nonlinear stiffness has been tuned to the optimal value found for the pure cubic NES, the effect of k_l become much less noticeable: varying k_l does not bring an evident improvement and the indicators remain stable on a wide range of k_l. In this case, the dynamical behaviour is dominated by the nonlinear stiffness. Consequently, the effect of having a (now small) linear negative stiffness is negligible and the dynamics of the damping mechanism is dominated by that of a classical NES with targeted energy transfer. Finally, as testified by the abrupt increase of I_{ave} for $k_l < -1000$, one can remark that when the negative linear stiffness becomes too large, the performance is largely reduced.

The influence of the damping σ on the performance of each vibration damper is depicted in Fig. 7. In each case, as damping increases, the performance improves at first and then decreases, hence for effective vibration suppression, neither too large nor to small value of damping is appropriate. This conclusion could be explained by the fact that when the damping is too small, the absorber might be insufficient to damp out the energy, while an inappropriately too large value on the other hand reduces also the relative motion the energy transfer between the beam and the absorber becomes more difficult. As a result, a damping coefficient of $\sigma = 3 \ \mathrm{N \cdot s/m}$ could be selected for the best suppression. Note the difference among the absorbers, one can conclude that at low damping level, NES and BNES generally show a much better behaviour than the TMD due to their strong nonlinearity. However, the difference becomes less significant when the damping increases up to $\sigma = 1 \ \mathrm{N \cdot s/m}$, since overdamped motions make it more difficult for the NES and BNES to activate their nonlinearity and take advantage of it.

Varying the location of the vibration absorbers on the ABH beam, the performance indicator I_{ω_2} of mode 2 as a function of x_c is depicted in Fig. 8(a), for each of the three tested configurations: TMD, NES and BNES. Interestingly, a direct link between on the value of I_{ω_2} and the corresponding mode shape function is observed, whatever the absorber is mounted on the ABH beam. This point is verified by the fact that the absolute value of the mode function $|\phi_2(x)|$, when multiplied

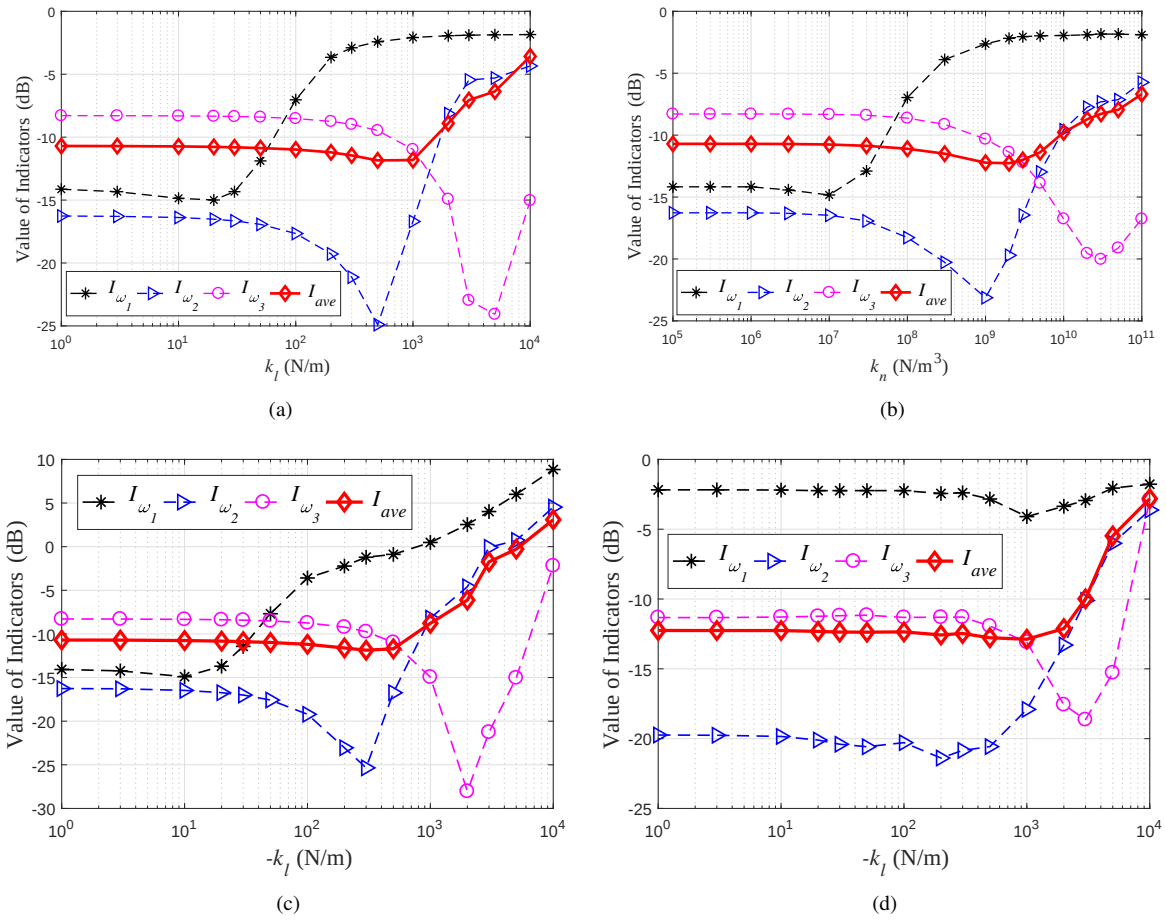

Figure 6: Variations of indicators I_{ω_1}, I_{ω_2}, I_{ω_3}, and I_{ave} as functions of the linear and nonlinear stiffnesses: (a) TMD, indicators as function of linear stiffness k_l (b) NES, indicators as function of the nonlinear stiffness k_n, (c) BNES, indicators as function of the negative stiffness $-k_l$, with nonlinear stiffness fixed as $k_n = 10^6$ N/m^3, (d) BNES, indicators as function of the negative stiffness $-k_l$, with $k_n = 2 \times 10^9$ N/m^3.

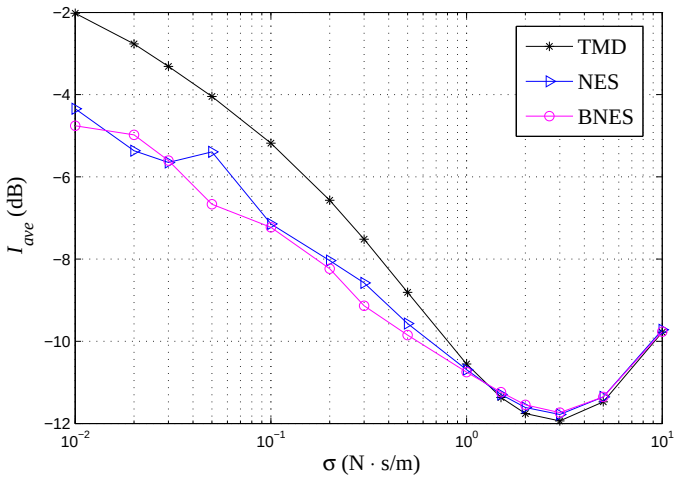

Figure 7: Effect of the damping coefficient σ on the indicator I_{ave}. The TMD Stiffness is $k_l = 500$N/m, the NES Stiffness $k_n = 2 \times 10^9$N/m^3, and the BNES Stiffnesses are $k_n = 2 \times 10^9$N/m^3, $k_l = -300$N/m. For all the absorbers, the mass ratio is ϵ=0.1

by a certain coefficient, is well fitted with the variation of the indicator I_{ω_2}. Hence, as an direct conclusion, in order to obtain an optimal reduction of a given mode, the linear or nonlinear dampers should be located at a local maximum of the given mode described by the shape function.

Considering the combined effects of the low frequency modes involved below the cut-on frequency, the value of average performance indicator I_{ave} exhibits the variation depicted in Fig. 8(b). For all the absorbers, the optimal location lies clearly in the ABH termination (gray area) of the beam, where most of the vibration is localized. However, for practical considerations, one should keep in mind also that in this ABH area, the thickness of the ABH severely decrease from

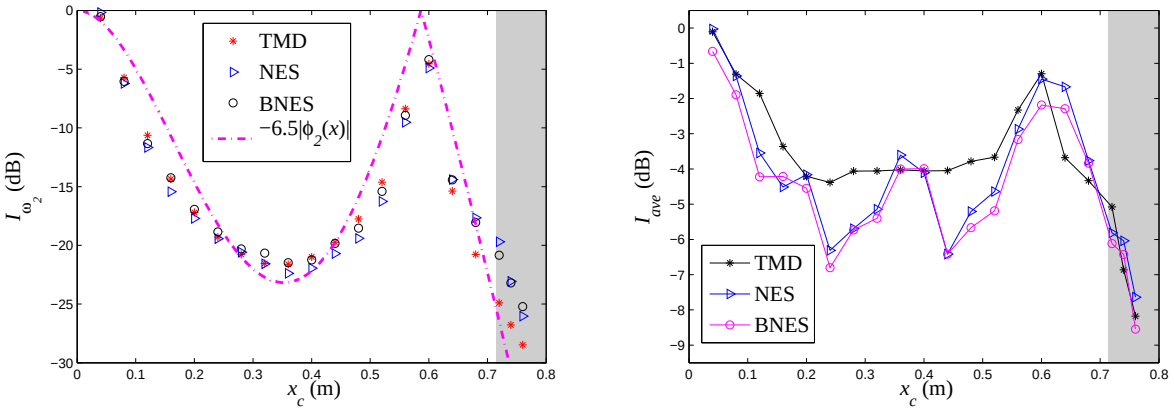

(a) (b)

Figure 8: Effect of the position x_c of the absorbers on the values of the performance indicators. TMD stiffness is $k_l = 500$N/m, NES stiffness $k_n = 2 \times 10^9 \mathrm{N/m}^3$, and BNES stiffnesses are $k_n = 2 \times 10^9 \mathrm{N/m}^3$ and $k_l = -300$N/m, (a): value of I_{ω_2}, (d): value of I_{ave}. The damping for each vibration damper is selected as $\sigma = 0.5\mathrm{N \cdot s/m}$ for (a) and $\sigma = 0.05\mathrm{N \cdot s/m}$ for (b). The gray area refers to the ABH profile.

$x = 0.71$m in the selected design. Consequently, for practical reasons it does not appear as desirable to set a damper in this region of small thickness where the beam is weaker. On the region on constant thickness, there are also two optimal positions clearly observed for the NES and BNES, at $x_c = 0.24$m and $x_c = 0.44$m. While the TMD shows a quite flat plateau at a wider range $x \in [0.2, 0.55]$m, and is not able to produce averaged improved performance below -4dB. This important difference also shows that the nonlinear absorbers are more sensitive to the location as compared to the TMD.

Robustness to the forcing amplitude

The last parameter to be studied is the forcing amplitude. Indeed, as it is expected, the influence of this parameter is crucial for the cases of a NES ad a BNES. It is well known that unlike a linear system, a nonlinear system has quite different performance at different energy levels, hence a NES or BNES that is optimally designed at one energy level might loses its effectiveness at another energy level, and vice versa. On the other hand, for a NES, an energy barrier exists for activating targeted energy transfer, making the NES generally not able for effective vibration suppression in too small vibration amplitudes, while a BNES is known to have a smaller energy barrier. Thus the effect of forcing amplitude becomes to be of special significance for evaluating the performance of these vibration absorbers.

For forcing amplitude A increases from 0.01 to 100N, the variations of I_{ω_2} and I_{ave} are shown in Fig. 9. The performances of TMD (black), NES (blue) and BNES (red) are then compared for two different values of parameters, where the solid lines refers to the case where the optimal parameters in each strategy, while the dashed lines show how they behave in a weak damping case with internal damping $\sigma = 0.05$. Indeed, it has appeared interesting to show this case since the optimal damping value is very large and probably difficult to implement in a practical situation.

Major differences could be found for the three absorbers on the effect of forcing amplitude. As it can be expected, the TMD is always independent to the amplitude: the indicator at all excitation level remains the same. On the other hand, the performances of the NES or the BNES are highly relevant to the amplitude, in Fig. 9(a), a energy barrier at 0.1N could be observed for the NES. Below this barrier, the performance of I_{ω_2} is weak and it starts to increase to meet an optimal performance around 2.5N. The performance is deteriorated at very large amplitudes. Similar conclusion is also evidenced for the average performance I_{ave} in Fig. 9(b). When adding a negative stiffness in the NES, representing a BNES, the performance at the low amplitude level that limited by the energy barrier is improved. Finally, at very high excitation level, the performance of NES and BNES are similar, and both ineffective.

In a summary all these results show that all the proposed solutions, if appropriately designed and tuned, are able to achieve a clear broadband vibration mitigation.

Conclusion

Aiming at improving the low frequency performance of a beam equipped with an ABH termination three different types of vibration absorbers (TMD, NES and BNES) have been proposed and simulated numerically. The main results confirm that all the proposed vibration absorbers, despite being linear or nonlinear, once appropriately designed, could be effective to reduce the low frequency resonance peaks in the ABH beam with a reduction at more than 10dB.

The parametric effect in each method is also discussed. The values of the stiffnesses (linear and non-linear) play the most important role for the performance of each absorber and it should be carefully designed according to different applications. On the other hand, at weak damping level, NES and BNES outperform the TMD, but for large values of the damping, they behaves linearly and all the three absorbers exhibit similar performances. The investigation on the location illustrates that whatever the absorber is, its optimal performance for a single resonance modes lies in the local maximum of the targeted

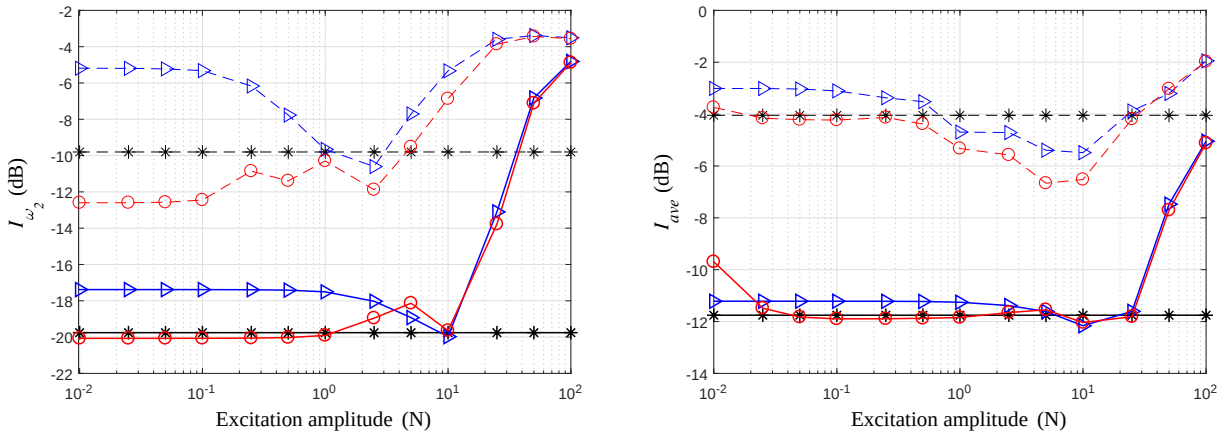

Figure 9: Robustness of the performance indicators according to the forcing amplitude, (a): value of I_{ω_2}, (b): value of I_{ave}. Solid line: computation with the optimal parameters, dashed line: comparison in the weak damping case. dashed black: TMD with $k_l = 500$N/m and weak damping $\sigma = 0.05\text{N} \cdot \text{s/m}$; solid black: TMD with optimized parameters $\sigma = 2\text{N} \cdot \text{s/m}$ and $k_l = 500$N/m; dashed blue: NES with $k_n = 2 \times 10^9 N/m^3$ and weak damping $\sigma = 0.05\text{N} \cdot \text{s/m}$; solid blue: NES with optimized parameters $\sigma = 2\text{N} \cdot \text{s/m}$ and $k_n = 2 \times 10^9 N/m^3$; dashed red: BNES with $k_n = 2 \times 10^9 N/m^3$, $k_l = -300$N/m, and weak damping $\sigma = 0.05\text{N} \cdot \text{s/m}$; solid red: BNES with optimized parameters $\sigma = 2\text{N} \cdot \text{s/m}$, $k_l = -300$N/m, and $k_n = 2 \times 10^9 N/m^3$;

mode function.

A Robustness study to the forcing amplitude demonstrates that while a TMD with linear behavior is always independent on the vibration level, the NES and BNES could be strongly dependent on the forcing amplitude. A NES is generally effective only at a moderate excitation level, and its performance is deteriorated at low and high amplitude levels. Hence for a robustness point of view, a TMD is better than the NES. Using a BNES improves a lot the performance at low amplitude level, but the performance at high amplitude level stays also ineffective.

References

[1] V.V. Krylov, F.J.B.S. Tilman, Acoustic 'black holes' for flexural waves as effective vibration dampers, Journal of Sound and Vibration, 2004, **274**(3-5): 605-619.

[2] V. Denis, A. Pelat, F. Gautier, B. Elie, Modal overlap factor of a beam with an acoustic black hole termination, Journal of Sound and Vibration, 2014, **333**, 2475-2488.

[3] J. Leng, V. Romero-García, A. Pelat, R. Picó, J-P. Groby, F. Gautier, Interpretation of the Acoustic Black Hole effect based on the concept of critical coupling, Journal of Sound and Vibration, 115199, 2020.

[4] O. Aklouche, A. Pelat, S. Maugeais, F. Gautier, Scattering of flexural waves by a pit of quadratic profile inserted in an infinite thin plate, Journal of Sound and Vibration, 2016, **375**, 38-52.

[5] V. Denis, A. Pelat, C. Touzé, F. Gautier. Improvement of the acoustic black hole effect by using energy transfer due to geometric nonlinearity, International Journal of Non-Linear Mechanics,2017, **94**:134-145.

[6] H. Li , C. Touzé, A. Pelat, F. Gautier and X. Kong, A vibro-impact acoustic black hole for passive damping of flexural beam vibrations, Journal of Sound and Vibration, 2019, **450**, 28-46.

[7] J. D. Hartog, Mechanical Vibrations, McGraw-Hill, New-York, 1934.

[8] C. Lee, Y. Chen, L. Chung, Y. Wang, Optimal design theories and applications of tuned mass dampers, Engineering Structures, 2006, **28**(1): 43-53.

[9] S. Krenk and J. Høgsberg, Tuned mass absorber on a flexible structure. Journal of Sound and Vibration, 2014, **333**(6): 1577-1595.

[10] M. Parseh, M. Dardel and M. H. Ghasemi, Performance comparison of nonlinear energy sink and linear tuned mass damper in steady-state dynamics of a linear beam, Nonlinear Dynamics, 2015, **81**(4): 1-22.

[11] Y. S. Lee, A. F. Vakakis, L. A. Bergman, L.A., D. M. McFarland, G. Kerschen, F. Nucera, S. Tsakirtzis and P. N. Panagopoulos, Passive non-linear targeted energy transfer and its applications to vibration absorption: a review. Proceedings of the Institution of Mechanical Engineers, Part K, Journal of Multi-body Dynamics, 2008, **222**(2): 322-329.

[12] O. V. Gendelman, Y. Starosvetsky, and M. Feldman, Attractors of harmonically forced linear oscillator with attached nonlinear energy sink , part I: description of response regimes, Nonlinear Dynamics, 2008, **51**(1-2): 31-46.

[13] O. V. Gendelman, Y. Starosvetsky and M. Feldman, Attractors of harmonically forced linear oscillator with attached non- linear energy sink, part II: optimization of a nonlinear vibration absorber, Nonlinear Dynamics, 2008, **51**(1-2): 47-57.

[14] F. Georgiades and A. F. Vakakis, Dynamics of a linear beam with an attached local nonlinear energy sink, Communications in Nonlinear Science and Numerical Simulation, 2007, **12**(5), 643-651.

[15] G. Habib and F. Romeo, The tuned bistable nonlinear energy sink. Nonlinear Dynamics, 2017, **89**(1):179-196.

[16] D. Qiu, T. Li, S. Seguy, and M. Paredes, Efficient targeted energy transfer of bistable nonlinear energy sink: application to optimal design. Nonlinear Dynamics, 2018, **92**(2):443-461.

[17] C. Issanchou, S. Bilbao, J.L. Le Carrou, C. Touzé, and O. Doaré. A modal-based approach to the nonlinear vibration of strings against a unilateral obstacle: Simulations and experiments in the pointwise case. Journal of Sound and Vibration, 2017, **393**:229-251.

Resonant Triads of Acoustic-Gravity Waves in Shallow Water

Evan Ricketts* and Usama Kadri†
*School of Engineering, Cardiff University, Cardiff, CF24 3AA, UK
†School of Mathematics, Cardiff University, Cardiff, CF24 4AG, UK

Summary. We consider the interaction of wave disturbances for shallow water of uniform depth. When we allow for compressibility effects in the linear theory, acoustic waves are assumed to be decoupled from free-surface gravity waves due to their disparity in propagation. However, it is possible to have energy exchange between acoustic and gravity wave modes given a non-linear interaction through a resonating triad. In this study, we analyse the case of a single gravity wave and two counter propagating acoustic modes which are of comparable length scales, but differing temporal scales. We derive amplitude evolution equations to describe the cyclic exchange of energy they exhibit through asymptotic methods, and implement them numerically to gain insight into the energy exchange of the triad with respect to the steepness of the waves. We find that the interaction allows a periodic exchange of energy in the triad where the steepness parameter is proportional to the a magnitude and inversely proportional to the period.

Introduction

In classical water-wave theory, the effects of compressibility are ignored, which stems from the idea that acoustic waves are essentially decoupled from free-surface waves. This assumption can be rationalised for the linear theory due to the speed of sound in water exceeding that of the maximum phase speed of surface waves, thus giving rise to differing spatial and/or temporal scales in the acoustic modes, and a somewhat decoupled system. However, when considering the non-linearity of the two types of waves, this assumption may not be as well justified. In a seminal paper by Longuet-Higgins [1], it has been shown that quadratic interactions of surface gravity waves can excite compression modes when we consider water of finite depth. It was argued that the formulation of oceanic microseisms could be due to such nonlinear coupling. Through studying quadratic interactions of two counter propagating wave trains of the same frequency, the behaviour was not in keeping with the classical theory, due to a non-decaying pressure component. Accounting for compressibility gave rise to resonance in the second order when an acoustic mode had double the frequency of the surface wave. Thus, the effects of compressibility must be considered to allow for this non-decaying component.
In this work we consider a non-linear coupling of acoustic and gravity waves in water of finite depth, and their interaction through a resonating triad. In recent years, numerical evidence has been presented that the resonant behaviour seen in Longeut-Higgins (1950) is a particular example of a resonant triad for two surface waves travelling in opposing directions and a propagating acoustic wave mode[2]. Also shown was that the amplitude of the free acoustic-gravity wave which was generated at resonance, or near-resonance conditions, was significantly larger than that of the bound acoustic-gravity wave, being generated far from resonance conditions. It was argued that the resonating triad amplitudes should be governed by a system of ordinary differential equations, and evolve in time, being governed by amplitude evolution equations of the same form as that of a standard resonant triad, see [3]. Following this, asymptotic theory was developed for resonant triad interactions concerning acoustic-gravity waves, taking waves of comparable temporal but differing spatial scales[4]. As Kadri and Stiassnie (2013)[2] suggested, it was shown that there is a resonance interaction between a given triad of two opposing gravity waves and a long-crested acoustic wave. Due to the interaction time scale being longer than that of a standard resonant triad, cubic terms were needed to display the wave self-interaction. What followed later was the derivation of evolution equations through asymptotic methods for both the acoustic wave and both gravity waves[4].
In the following we proceed with a similar approach as Kadri and Akylas, (2016)[4], but consider a triad of two counter-propagating acoustic modes, and a single gravity wave. In light of this, we consider differing temporal, but comparable spatial scales of the acoustic-gravity modes, and use multiple scale analysis to derive the evolution equations for the given amplitudes of the waves. Section 2 details the formulation of the the problem, deriving the governing equations and finding the dispersion relations through linearisation. Section 3 discusses the resonance conditions and the cyclic exchange of energy. Section 4 derivation for the evolution equations for a normal mode wave form, and Section 5 presents a numerical solution to the problem with results and conclusions on the interaction and its corresponding energy exchange.

Preliminaries

We look at the propagation of surface and acoustic wave disturbances in water of a constant depth h with a rigid bottom ($z = -h$), accounting for the effects of compressibility and gravity. In this setting we consider water as an inviscid barotropic fluid such that the density ρ of the fluid is solely a function of its pressure p, the motion of such fluid to be irrotational, and the speed of sound $c = (dp/d\rho)^{1/2}$ to be constant. An important parameter μ, defined as

$$\mu^2 = \frac{gh}{c^2}, \tag{1}$$

for g the gravitational acceleration, controls the effects of compressibility relative to gravity. Generally we can say that $\mu \ll 1$ due to the fact that the speed of sound in water, $c = 1.5 \times 10^3\,\mathrm{m\,s^{-1}}$, and would surpass the maximal phase velocity of gravity waves $(gh)^{1/2}$.

The following analysis is focused on nonlinear interactions of a single gravity wave mode with two acoustic wave modes, all of similar spatial but differing temporal scales. The temporal disparity arises from the frequency of the gravity wave being much smaller than that of the acoustic waves. To interpret μ, we can take $\tau_{ac} \sim h/c \implies \tau_{gr} \sim (\lambda/g)^{1/2}$, where τ_{ac} is the acoustic time scale and τ_{gr} the gravity time scale. If we take the scales to be comparable, this implies that $\tau_{ac} \sim \mu\tau_{gr}$, where μ can be thought of as the ratio of temporal scales. Thus, to introduce non-dimensional variables, we can take the time scale and length scale as $(h/g)^{1/2}$ and h respectively.
Due to the assumption of an irrotational fluid, the problem can be formulated in terms of a velocity potential $\phi(x, z, t)$ such that we have a velocity field $\boldsymbol{u} = \boldsymbol{\nabla}\phi$. The governing equation for $\phi(x, z, t)$ within the fluid interior is determined by combining continuity with the unsteady Bernoulli equation[1, 4], such that $\phi(x, z, t)$ satisfies

$$\frac{1}{\mu^2}(\phi_{xx} + \phi_{zz}) - \phi_{tt} - \phi_z - |\boldsymbol{\nabla}\phi|_t^2 - \frac{1}{2}(\phi_x|\boldsymbol{\nabla}\phi|_x^2 + \phi_z|\boldsymbol{\nabla}\phi|_x^z) = 0. \tag{2}$$

The standard kinematic and dynamic conditions are applicable at the free surface $z = \eta(x, t)$, and it is sufficient to satisfy these conditions up to third order in the perturbations for the weakly nonlinear analysis that is to follow. Once the two free-surface conditions have been expanded about $z = 0$, η can be expressed in terms of ϕ at the desired order. Thus, it is possible to obtain the boundary condition for ϕ on $z = 0$ [4]

$$\begin{aligned}\phi_{tt} + \phi_z + |\boldsymbol{\nabla}\phi|_t^2 - (\phi_t(\phi_{tt} + \phi_z))_z + \frac{1}{2}\boldsymbol{u}\cdot\boldsymbol{\nabla}(|\boldsymbol{\nabla}\phi|^2) - (\phi_t|\boldsymbol{\nabla}\phi|_t^2)_z \\ -\frac{1}{2}\{(\phi_{tt} + \phi_z)(|\boldsymbol{\nabla}\phi|^2 - \phi_t^2)\}_z = 0 \text{ for } (z = 0)\end{aligned} \tag{3}$$

At the rigid bottom, the standard no penetration condition is derived

$$\phi_z = 0 \qquad (z = -1) \tag{4}$$

We now analyse the linear problem which is responsible for the disparity in temporal scales. We can drop the nonlinear terms in (2), (3) and (4) and assume ϕ as

$$\phi = f(z)\exp\left(\frac{1}{2}\mu^2 z\right)\exp\left(\mathrm{i}\,(kx - \sigma t)\right) \tag{5}$$

being the normal mode form, and seek wave modes propagating along x with wave number and frequency k and σ respectively. By substituting (5) into (2), (3) and (4), the boundary-value problem for the vertical profile $f(z)$ becomes

$$\begin{aligned}\frac{\mathrm{d}^2\hat{f}}{\mathrm{d}z^2} + \Omega^2 f = 0, \text{ for } (-1 < z < 0) \\ -\omega^2\hat{f} + \mu^2\frac{\mathrm{d}\hat{f}}{\mathrm{d}z} + \frac{1}{2}\mu^4\hat{f} = 0, \text{ for } (z = 0) \\ \frac{\mathrm{d}\hat{f}}{\mathrm{d}z} + \frac{1}{2}\mu^2\hat{f} = 0, \text{ for } (z = -1)\end{aligned} \tag{6}$$

where $\Omega^2 = \omega^2 - k^2 - \frac{\mu^4}{4}$ and $\omega = \mu\sigma$. As $\mu \ll 1$, we assume the solution of this system to be oscillatory, giving us the solution

$$\hat{f} = \cos\Omega(z + 1) - \frac{\mu^2}{2\Omega}\sin\Omega(z + 1). \tag{7}$$

The dispersion relation for the gravity mode can be obtained in the standard way by substitution of the solution (7) into the boundary condition, specifically at $z = 0$, such that

$$\sigma^2 = \lambda\tanh\lambda \tag{8}$$

where ignoring compressibility gives $k = \lambda$. To find a similar relation for the acoustic mode, we first notice that $\Omega^2 > 0$, implying that we can take $\Omega = \sqrt{\omega^2 - k^2} + O(\mu^4)$. Thus, by substituting our general solution back into the boundary condition at $z = 0$ as well as our expression for Ω, we have the acoustic dispersion relation

$$\omega^2 = \omega_n^2 + k^2 + \frac{\omega_n^2 - k^2}{\omega_n^2 + k^2}\mu^2 + O(\mu^4), \tag{9}$$

where $\omega_n = (n + \frac{1}{2})\pi$.

Resonance Conditions

It has been seen numerically that if we allow for the influence of compressibility, two gravity waves can interact resonantly with an acoustic-gravity wave [2, 4]. In this study, we consider if the same holds true for two counter propagating acoustic modes (k_+, ω_+) and (k_-, ω_-), and a single gravity mode $(k, \mu\sigma)$. In order for these to form a resonant triad, they must satisfy the prescribed resonance conditions

$$\text{(i)} \quad k_+ + k_- = k \quad \text{and} \quad \text{(ii)} \quad \omega_+ - \omega_- = \mu\sigma. \tag{10}$$

as well as the appropriate dispersion relations (8), (9). Hence, we investigate said triads in the limit as $\mu \ll 1$.
If we define

$$\text{(I)} \quad \omega_\pm = \tilde{\omega} \pm \frac{\mu\sigma}{2} \quad \text{and} \quad \text{(II)} \quad k_\pm = \frac{k}{2} \tag{11}$$

then by (I) and our acoustic dispersion relation (9),

$$\begin{aligned} \tilde{\omega}^2 \pm \mu\sigma\tilde{\omega} + \frac{\mu^2\sigma^2}{4} &= \omega_n^2 + k_\pm^2 + \frac{\omega_n^2 - k_\pm^2}{\omega_n^2 + k_\pm^2}\mu^2 + O(\mu^4) \\ \implies k_\pm^2 &= \tilde{\omega}^2 - \omega_n^2 \pm \mu\sigma\tilde{\omega} + O(\mu^2). \end{aligned} \tag{12}$$

Thus, if these conditions are satisfied along with the given dispersion relations, then the gravity mode can form a resonant triad with two counter-propagating acoustic waves for the given conditions. Under these conditions, we expect interactions between the resonant triad to results in a somewhat cyclic exchange of energy between the participants. As is seen in [4], due to having disparity in the temporal scales, the interaction time scale and the amplitude evolution equations will vary compared with the standard theory on resonance interactions.

Amplitude Evolution Equations

We look to derive the amplitude equations for our resonant triad. The two acoustic modes of complex amplitudes $A_\pm$ with frequencies $\omega_\pm$ interact with a single gravity mode of amplitude S and frequency $\mu\sigma$ such that $A_+ = \mathrm{e}^{\mathrm{i}(k_+x - \omega_+ t)}$, $A_- = \mathrm{e}^{\mathrm{i}(k_- x - \omega_- t)}$, and $S = \mathrm{e}^{\mathrm{i}(kx - \mu\sigma t)}$. Thus, under appropriate assumptions, the expanded velocity potential can be seen as

$$\begin{aligned} \varphi =& \epsilon\{A_+(X,T)\cos\omega_n(z+1)\mathrm{e}^{\mathrm{i}(k_+x-\omega_+t)} + c.c.\} \\ &+\epsilon\{A_-(X,T)\cos\omega_n(z+1)\mathrm{e}^{\mathrm{i}(k_-x+\omega_-t)} + c.c.\} \\ &+\epsilon\{S(X,T)\cosh\lambda(z+1)\mathrm{e}^{\mathrm{i}(kx-\epsilon^{\frac{1}{2}}\sigma t)} + c.c.\} \quad + \quad . \quad . \quad . \end{aligned} \tag{13}$$

where $X = \epsilon x$, $\lambda^2 = k^2 - \mu^2\sigma^2$ and $c.c$ is the complex conjugate. The amplitudes depend on the "slow" time $T = \epsilon t$, where the wave steepness $0 < \epsilon \ll 1$ is related to μ as $\mu = \epsilon^{\frac{1}{2}}$. We begin by substituting (13) into our governing equations (2) through (4), and collect terms based on those which are proportional to $\mathrm{e}^{\mathrm{i}(kx-\mu\sigma t)}$ and $\mathrm{e}^{\mathrm{i}(k_+x-\omega_+t)}$. By doing this, we are left with terms which contribute towards resonance in the form of a reduced boundary-value problem. We then formulate a solvability condition based on this, whereby the amplitude evolution equations will follow. We start with the gravity mode by collecting terms which are proportional to $\mathrm{e}^{\mathrm{i}(kx-\mu\sigma t)}$, and impose a correction to (13) of leading order $O(\epsilon^{\frac{5}{2}})$ of the form

$$\epsilon^{\frac{5}{2}}\Big\{F(X,z,T)\exp\Big\{\mathrm{i}(kx - \epsilon^{\frac{1}{2}}\sigma t)\Big\} + c.c\Big\}, \tag{14}$$

such that F satisfies the boundary-value problem

$$\begin{aligned} \epsilon^{\frac{5}{2}}F_{zz} - k^2\epsilon^{\frac{5}{2}}F = R_1 \text{ for } (-1 < z < 0) \\ \epsilon^{\frac{5}{2}}F_z = R_2 \text{ for } (z = 0) \\ F_z = 0 \text{ for } (z = -1) \end{aligned} \tag{15}$$

where

$$\begin{aligned} R_1 =& -2\mathrm{i}\epsilon k\frac{\partial S}{\partial X}\cosh\lambda(z+1) - 2\mathrm{i}\epsilon^{\frac{5}{2}}\sigma\frac{\partial S}{\partial T}\cosh\lambda(z+1) - \epsilon^2\sigma^2 S\cosh\lambda(z+1) + \epsilon\lambda S\sinh\lambda(z+1) \\ &+ 2\mathrm{i}\epsilon^{\frac{5}{2}}k_+k_-\sigma A_+A_-\cos^2\omega_n(z+1) - 2\mathrm{i}\epsilon^{\frac{5}{2}}\omega_n^2\sigma A_+A_-\sin^2\omega_n(z+1) \\ R_2 =& \ 2\mathrm{i}\epsilon^{\frac{5}{2}}\sigma\frac{\partial S}{\partial T}\cosh\lambda + \epsilon^2\sigma^2 S\cosh\lambda - \epsilon\lambda S\sinh\lambda + 2\mathrm{i}\epsilon^{\frac{5}{2}}\omega_n^2\sigma A_+A_- \end{aligned} \tag{16}$$

The solution to the corresponding homogeneous system is $\cosh kz$, so we must be able to employ a certain solvability condition for the in-homogeneous problem (15). Here, we multiply both sides of the field equation by $\cosh kz$ and integrate over the whole domain $-1 < z < 0$, such that

$$kR_2 + R_1\Big|_{z=-1}\sinh k = k\int_{-1}^{0} R_1\cosh kz\,\mathrm{d}z. \tag{17}$$

Finally, we obtain the evolution equation for the gravity mode by substituting our expressions for R_1 and R_2 into the solvability condition (17), resulting in

$$\frac{\partial S}{\partial T} - \frac{k}{\epsilon^{\frac{3}{2}}}\Big(\frac{\sigma}{\lambda^2-\sigma^2}\Big)\frac{\partial S}{\partial X} = -\frac{\sigma S}{2\mathrm{i}\epsilon^{\frac{3}{2}}}\Big\{\epsilon\sigma^2 - \frac{\lambda^2}{\lambda^2-\sigma^2}\Big\} + \frac{A_+A_-}{\lambda\cosh\lambda-\sinh\lambda}\Big\{\Psi + (\sinh\lambda - k)\omega_n^2 - \frac{k^2}{4}\sinh\lambda\Big\} \quad (18)$$

where $\Psi = \frac{k^4+2k^2\omega_n^2}{4k^2+16\omega_n^2} - \frac{2\omega_n^4}{2k^2+8\omega_n^2}$. Similarly, we employ a correction of

$$\epsilon^2\big\{F(X,z,T)\exp\{\mathrm{i}(k_\pm x - \omega_\pm t)\} + c.c.\big\} \quad (19)$$

so that for leading order of $O(\epsilon^2)$, we are left with acoustic-gravity interaction and cubic acoustic self interaction terms. Here, the solution to the homogeneous system is $\cos\omega_n(z+1)$, and we can formulate the solvability condition in a similar way as above. After multiplication by the homogeneous solution, and integrating over the domain, we arrive at the condition

$$-\frac{\omega_n}{\omega_\pm^2}R_4(-1)^n = \int_{-1}^{0} R_3\cos\omega_n(z+1)\,\mathrm{d}z \quad (20)$$

where

$$\begin{aligned} R_3 =& -2\mathrm{i}\epsilon k_\pm\frac{\partial A_\pm}{\partial X}\cos\omega_n(z+1) - 2\mathrm{i}\epsilon^2\omega_\pm\frac{\partial A_\pm}{\partial T}\cos\omega_n(z+1) - \epsilon\omega_n A_\pm\sin\omega_n(z+1)\\ &+ 2\mathrm{i}\epsilon^2 k_\mp k\omega_\pm A_\mp S\cos\omega_n(z+1)\cosh\lambda(z+1)\\ &+ 2\mathrm{i}\epsilon^2\omega_n\omega_\pm\lambda A_\mp S\sin\omega_n(z+1)\sinh\lambda(z+1) = 0,\\ R_4 =& \epsilon\omega_n A_\pm(-1)^n - 2\mathrm{i}\epsilon^2\omega_n\omega_\pm\lambda A_\mp S(-1)^n\sinh\lambda = 0. \end{aligned} \quad (21)$$

Again, we compute the necessary integrals and rearrange to give us the acoustic evolution equation

$$\frac{\partial A_\pm}{\partial T} + \frac{k_\pm}{\epsilon\omega_\pm}\frac{\partial A_\pm}{\partial X} = \frac{\omega_\pm^2 - 2\omega_n^2}{2\mathrm{i}\epsilon\omega_\pm^3}A_\pm - 2\sinh\lambda\Phi A_\mp S \quad (22)$$

where

$$\Phi = \frac{4\omega_n^4\lambda + \omega_n^2\lambda^3 - \omega_\pm^2\omega_n^2\lambda}{8\omega_\pm^2\omega_n^2 + 2\omega_\pm^2\lambda^2} - \frac{3\lambda^3 - 8\omega_n^2\lambda}{32\omega_n^2 - 8\lambda^2}, \quad (23)$$

Simulation and Discussion

As we now have our evolution equations, we want to gain a qualitative understanding of the interaction they convey, and whether there is periodic exchange of energy. The equations derived were solved numerically in MATLAB by an explicit Runge–Kutta method. By making use of the acoustic and gravity dispersion relations, we are able to define the variables needed in the solution process. We can then run the analyses for various initial conditions and see the temporal evolution of the triad interaction. We note that all waves are assumed to be of Gaussian form.

Figures 1 and 2 show the interaction where we assume no spatial influences. It can be seen quite clearly in figure 1 how the generation of the gravity wave plays out, and the cyclic exchange of energy, where the change in amplitude is periodic. There is an overall increase and decrease in the amplitude of the acoustic modes which is sinusoidal. The gravity wave quickly grows and decays, transferring its energy back and forth between the two acoustic modes. Similarly in figure 2, when all waves begin with amplitude of 1, we can see how the energy is shared amongst the triad. When the amplitude of the gravity wave is high, the energy has been transferred, so that of the acoustic is lower, and vice versa. In both cases, the acoustic waves mirror each other and as such the temporal evolution has been given for a single acoustic mode.

The variable ϵ is pivotal to the way the interaction plays out. It represents the steepness of the waves, so taking ϵ higher will result in greater energy transfer to the gravity wave. In the case of of figure 1, $\epsilon \sim 0.3$, which is why the maximum amplitude of the generated gravity wave does not grow above 0.15, whereas, when taking a larger epsilon in the case of figure 2, the maximum amplitude grows above 1.

We now want to analyse the energy exchange in terms of the value of the steepness, ϵ. We again look at the case where the gravity wave is generated, relating to the initial conditions $S(0) = 0$ and $A_\pm(0) = 1$. It is justifiable to take the two acoustic modes as equal for simplicity. The other parameters such as σ and $\omega_\pm$ are prescribed by the overall set up of the problem and are related through the acoustic and gravity dispersion relations as before. Under these initial conditions, we have the conservation law

$$\int_{-\infty}^{\infty}(|S|^2 + 2|A|^2)\,\mathrm{d}X = 2\int_{-\infty}^{\infty}|S_0|^2\,\mathrm{d}X \quad (24)$$

where the initial condition $S_0 \to 0$ as $X \to \pm\infty$. In our computation we took the initial condition $S_0 = \exp\{-X^2\}$, the Gaussian wave packet. Then we can see from (24) that

$$E(T) = \frac{1}{\sqrt{2\pi}}\int_{-\infty}^{\infty}|S|^2\,\mathrm{d}X \quad (25)$$

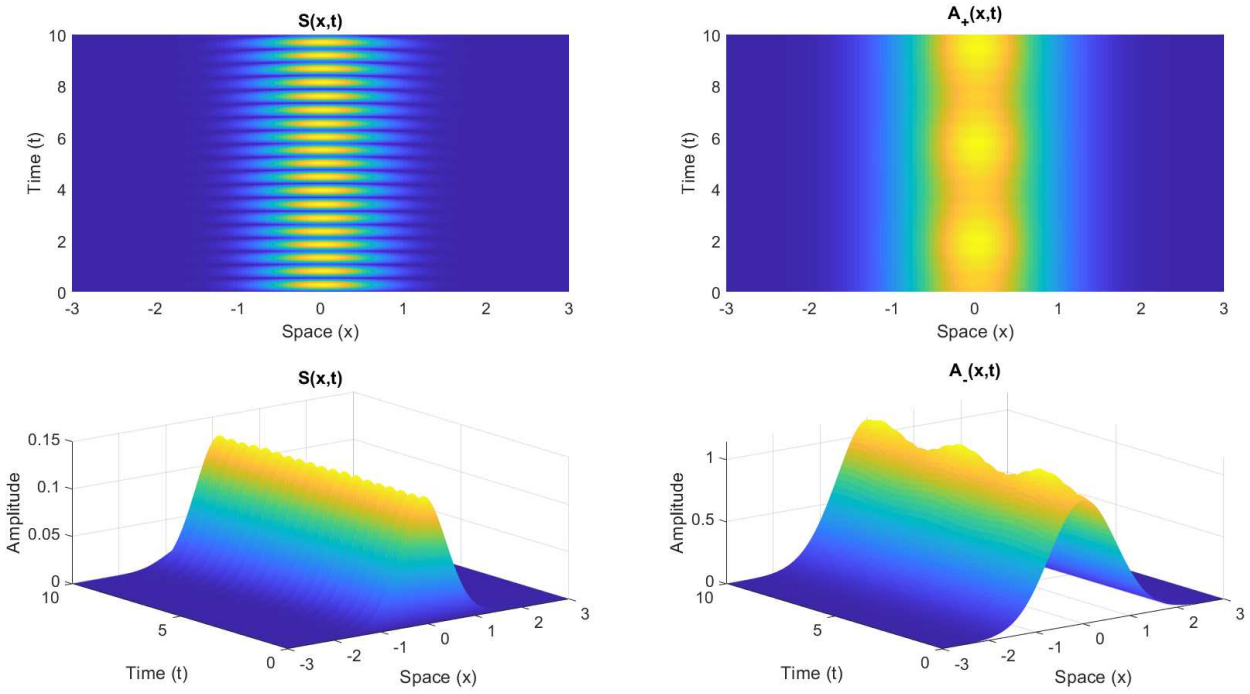

Figure 1: Generation of gravity wave with no spatial influences

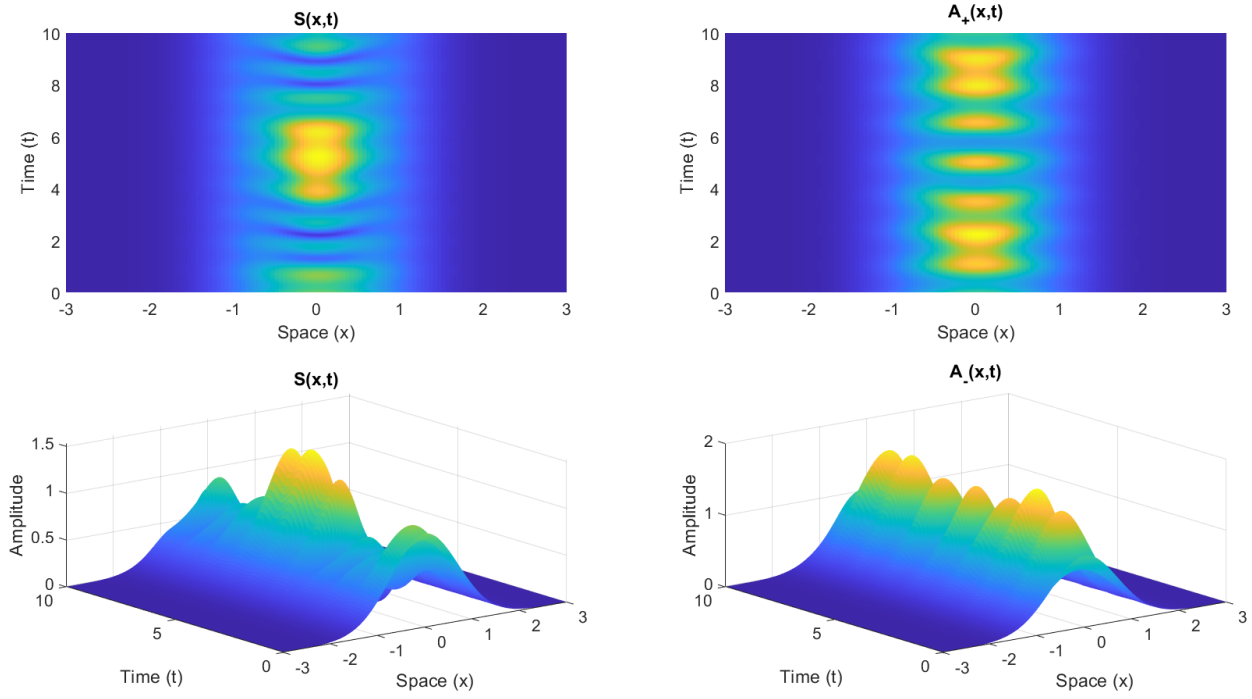

Figure 2: Interaction when all waves begin with amplitude 1 for non-spatial dependencies

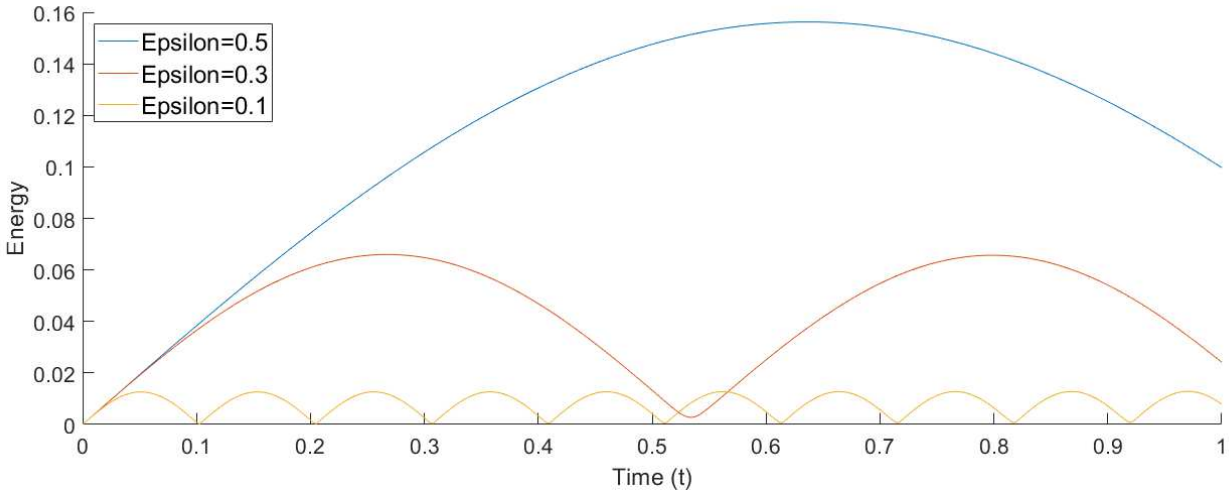

Figure 3: Transfer of energy to the gravity mode over time for varying small ϵ

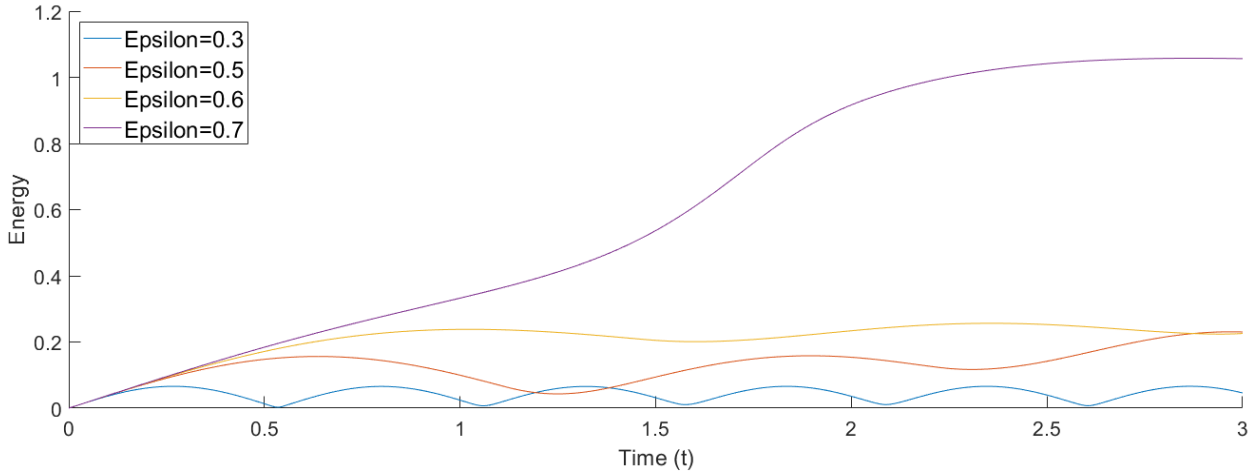

Figure 4: Transfer of energy for increasing ϵ

is the energy of the gravity wave generated. Implementing (25) numerically, we observe how increasing ϵ results in a larger amount of energy transferred to the generated gravity mode over time as shown in figure 3. Here, we used the outlined conditions above, and took small values of ϵ. As $\epsilon \to 0$, the amount of energy transferred becomes smaller, but much more frequent in its exchange, as indicated by $\epsilon = 0.1$ compared with $\epsilon = 0.5$. The periodic behaviour of curves is representative of the energy transfer between the acoustic modes and the generated gravity wave.
It is also worth analysing the rate and magnitude of energy exchange as $\epsilon \to 1$, which is shown in figure 4. As ϵ increases, we begin to have infinite periodicity occurring, where the value of the energy plateaus. This is due to our assumptions upon ϵ, mainly being that it can not be $O(1)$. So as we approach the value of 1, our resonance condition breaks down, and less energy is able to be exchanged back to the acoustic mode from the gravity wave.

Conclusion

We have derived spatial and temporal evolution equations in the case of a resonant triad of acoustic-gravity waves, and using these, have been able to analyse the energy exchange between them. Similarly to what was observed in Kadri and Akylas (2016), triad interaction of this nature differs from a standard resonant triad due to the disparity of temporal scales for the given waves. Through the presented asymptotic analysis and numerical implementation, the cyclic exchange of energy expected in a conventional resonant triad is observed, resulting from cubic self-interaction terms that were preserved when taking certain leading order. These terms directly impact the amplitude-dependent change in gravity wave frequency and the exchange of energy from surface to acoustic waves.
Similarly, the importance of the steepness parameter ϵ has been highlighted, heavily changing the interaction and effecting the cyclic exchange of energy. As the steepness increases we see larger periodicity with more energy being exchanged in each cycle. Further analysis should be conducted to investigate its effects for alternative initial conditions. Here, the generation of a single gravity wave was observed, but this choice was arbitrary. Further to this, the relationship between the interaction time and amplitudal growth would be worth investigating, as we would then have a wider picture of how

the given interaction occurs. If we were able to analyse this interaction time, and find its relationship with the amount of energy transferred, then we would have much more control over the given interaction.

References

[1] Longeut-Higgins, M. S. (1950), A Theory of the Origin of Microseisms. *Philosophical Transactions of the Royal Society of London. A*, **243**:1-35.

[2] Kadri, U. and Stiassnie, M. (2013), Generation of an acoustic-gravity wave by two gravity waves, and their subsequent mutual interaction. *Journal of Fluid Mechanics*, **735**.

[3] Bretherton, F. P. (1964), Resonant interactions between waves. The case of discrete oscillations. *Journal of Fluid Mechanics*, **20**:457-479.

[4] Kadri, U. and Akylas, T. R. (2016), On resonant triad interactions of acoustic-gravity waves. *Journal of Fluid Mechanics*, **788**:R1.

[5] Kadri, U. (2016), Triad resonance between a surface-gravity wave and two high frequency hydro-acoustic waves. *European Journal of Mechanics - B/Fluids*, **55(1)**:157-161

Study of the behaviour of the trombone using bifurcation diagrams

Rémi Mattéoli*, Joël Gilbert*, Sylvain Maugeais†, Christophe Vergez‡ and Jean-Pierre Dalmont*
*Laboratoire d'Acoustique de l'Université du Mans, UMR CNRS 6613, France
†Laboratoire Manceau de Mathématiques, Le Mans Université, France
‡Aix Marseille Univ, CNRS, Centrale Marseille, LMA, UMR 7031, France

Abstract

In this study, an acoustic resonator – a bass trombone – with multiple resonances coupled to an exciter – the player's lips – with one resonance is modelled by a multidimensional dynamical system, and studied using the continuation and bifurcation software AUTO [1]. Bifurcation diagrams are explored with respect to the blowing pressure, with focus on the minimal blowing pressure giving stable periodic regime.

Brass instruments can be described thanks to both linear and nonlinear mechanisms: a localised nonlinear element (the lips' valve effect) excites a passive linear acoustic multimode element (the musical instrument, usually characterised by its input impedance in the frequency domain); the latter acoustic resonator in turn exerts a retroaction on the former mechanical resonator. Such musical instruments are self-sustained oscillators: they generate an oscillating acoustic pressure (the note played) from a static overpressure in the player's mouth (the blowing pressure).

A brass instrument having N acoustic modes and M mechanical modes can be mathematically modelled as an autonomous nonlinear dynamical system of dimension $2(N+M)$ [2, 3]. On the one hand, the corresponding acoustic input impedance of the resonator is defined in the Fourier domain by the ratio between the pressure and the volume flow at the input of the instrument :

$$P(\omega) = Z(\omega)U(\omega) \tag{1}$$

with ω the angular frequency. The modulus of Z is shown figure 1 for a bass trombone. Since AUTO requires equations to be expressed in the time domain, a modal decomposition is performed on the measured input impedance of a bass trombone in order to obtain an analytical form for $Z(\omega)$, thus allowing equation (1) to be expressed in the time domain by taking its inverse Fourier transform.

On the other hand, the nonlinear behaviour of the lips can be modelled by the relation between the volume flow $u(t)$ and the acoustic pressure $p(t)$:

$$u(t) = wh(t)\,\Theta(h)\,\mathrm{sgn}\,(p_m - p(t))\sqrt{\frac{2\,|p_m - p(t)|}{\rho}} \tag{2}$$

with w and $h(t)$ the width and the height of the lips' aperture respectively, p_m the mouth pressure, and ρ the air density. The Heaviside distribution Θ accounts for the fact that lips cannot interpenetrate: as soon as the lips touch ($h = 0$), the volume flow is forced to zero. The sign function sgn accounts for the possibility of having an airflow going from the instrument into the player's mouth, in the absence of experimental evidence to the contrary.

Eventually, $h(t)$ can be linked to $p(t)$ to close the system by the following equation, which accounts for the resonance of the lips :

$$\ddot{h} + \frac{\omega_l}{Q_l}\dot{h} + \omega_l^2\,(h - h_0) = \frac{p_m - p}{\mu} \tag{3}$$

with ω_l and Q_l being respectively the frequency resonance and the quality factor of the lips, and μ the lips' mass per unit area.

In this study, the input impedance of the brass instrument addressed – a bass trombone – will be described by $N = 12$ acoustic modes, and the exciter – the player's lips – will be assumed to have only one mechanical mode ($M = 1$), resulting in a 26-dimensional dynamical system. It is worth noting that this minimal brass model does not account for the « brassy » sound produced by a trombone, which requires a nonlinear description of sound propagation in the instrument to be addressed.

The behaviour of the instrument can be first studied close to its static equilibrium using the Linear Stability Analysis (LSA), so as to determine if oscillatory regimes (corresponding to the instrument producing a sound) could potentially arise from destabilised equilibrium eigenvalues of the linearised system. Such an approach has already been carried out in [4], especially to characterise the ease of playing of a brass instrument. Indeed, the latter can be related as a first approximation to the linear threshold pressure (figure 2a), since the lower the threshold pressure, the lower the physical effort the player has to make to play a note.

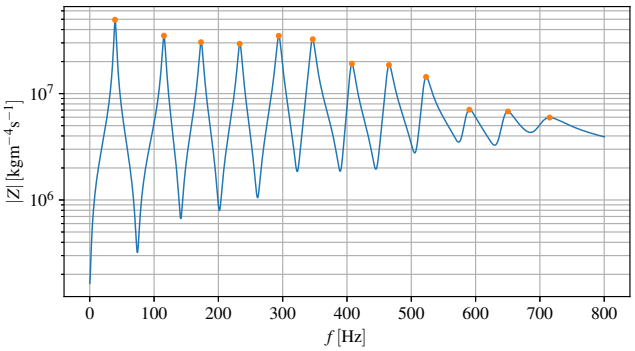

Figure 1: Modulus of the input impedance of a bass trombone vs. frequency. 12 resonances (orange dots) can be seen, corresponding to $N = 12$ acoustic modes.

for $n > 5$, thus implying $p_{\text{thresh}}^{\text{osc}} = p_{\text{thresh}}^{\text{lin}}$ for these.

The ease of playing is then assessed in more depth through the study of the dynamic behaviour of the instrument, using the continuation and bifurcation software AUTO [1] as in [5] or using an alternative continuation method (Manlab) as in [6], thanks to which bifurcation diagrams are explored with respect to the blowing pressure for instance. The oscillation threshold pressure can then be infered from such a diagram (figure 2b). It is worth noticing that the oscillation threshold pressure is not necessarily equal to the linear threshold pressure, as it is the case on figure 2b. It then results in an actual threshold pressure lower than the linear threshold pressure given by the LSA (figure 2c), hence the need to take into account the dynamic behaviour of the system. Also, the nth regimes are all direct Hopf bifurcations

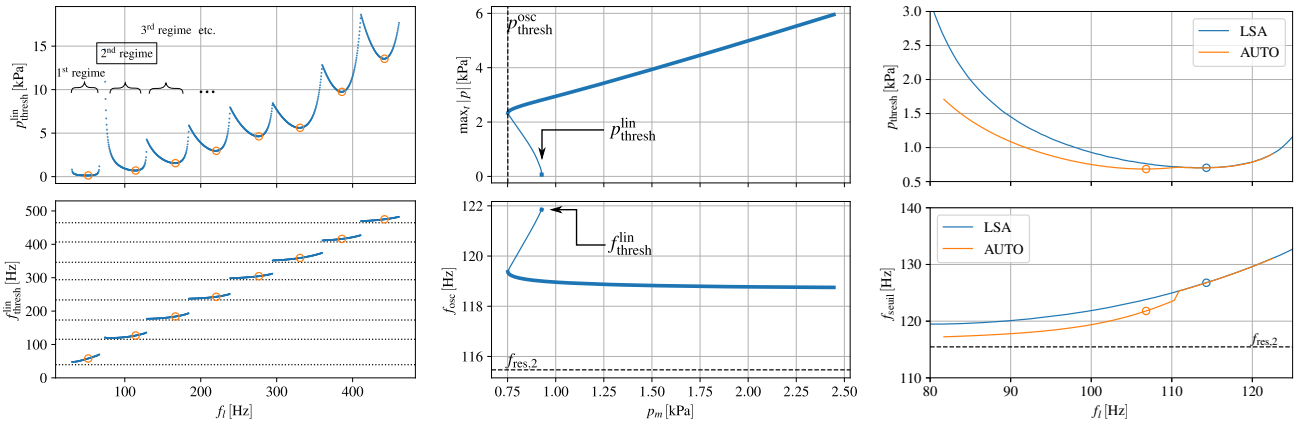

(a) LSA of a bass trombone

(b) Bifurcation diagram (2nd regime of a bass trombone; $f_l = 100\,\text{Hz}$)

(c) Superposition of p_{thresh} given by the LSA and AUTO (2nd regime of a bass trombone; $f_l \in [80\,\text{Hz}, 125\,\text{Hz}]$)

Figure 2: Linear Stability Analysis (left), bifurcation diagrams (middle), and comparison of threshold pressure values given by the LSA and AUTO (right), corresponding to the case of the input impedance of a bass trombone shown figure 1. Left: top and bottom plots represent respectively the linear threshold pressure and frequency vs. the lip frequency. The orange circles identify the value of f_l corresponding to a local minimum of the curve (easiest note to obtain), and dotted lines represent the resonance frequencies of the input impedance for comparison. Middle: Top and bottom plots represent respectively the maximum amplitude of the periodic oscillation branches and the frequency of the corresponding periodic solutions vs. the blowing pressure. Right: top and bottom plots represent respectively the threshold pressures and frequencies given by the LSA and AUTO vs. the lip frequency. As for figure 2a, the circles identify the value of f_l corresponding to a local minimum of a curve.

In the present study, the effects of the inclusion of the instrument's dynamic behaviour on the minimum threshold pressure is focused on, so as to enrich the results given by the Linear Stability Analysis.

References

1. *Auto-07p/Auto-07p* AUTO-07P, May 16, 2020. `https://github.com/auto-07p/auto-07p`.
2. Chaigne, A. & Kergomard, J. *Acoustics of musical instruments* Originally published in France as: Acoustique des instruments de musique. Second edition. Paris : Éditions Belin, 2013. 844 pp. ISBN: 978-1-4939-3677-9 (ASA Press : Springer, New York, New York, 2016).
3. Campbell, M., Gilbert, J. & Myers, A. *The Science of Brass Instruments* ISBN: 978-3-030-55684-6 (Springer-Verlag, 2021).
4. Velut, L., Vergez, C., Gilbert, J. & Djahanbani, M. How Well Can Linear Stability Analysis Predict the Behavior of an Outward Valve Brass Instrument Model ? *Acta Acustica united with Acustica* **103,** 132–148. `https://hal.archives-ouvertes.fr/hal-01245846` (2017).
5. Gilbert, J., Maugeais, S. & Vergez, C. Minimal Blowing Pressure Allowing Periodic Oscillations in a Simplied Reed Musical Instrument Model: Bouasse-Benade Prescription Assessed through Numerical Continuation. *Acta Acustica.* `https://hal.archives-ouvertes.fr/hal-02994219` (2020).
6. Fréour, V. *et al.* Numerical Continuation of a Physical Model of Brass Instruments: Application to Trumpet Comparisons. *The Journal of the Acoustical Society of America* **148,** 748–758. ISSN: 0001-4966. `https://asa.scitation.org/doi/10.1121/10.0001603` (Aug. 1, 2020).

Fast Explicit Algorithms for Hamiltonian Numerical Integration

Stefan Bilbao* and Michele Ducceschi†
*Acoustics and Audio Group, University of Edinburgh, Edinburgh UK
†Department of Industrial Engineering, University of Bologna, Bologna, Italy

Summary. Numerical integration methods for Hamiltonian systems are of importance across many disciplines, including musical acoustics, where many systems of interest are very nearly lossless. Of particular interest are methods possessing a conserved pseudoenergy. Though most such methods have an implicit character, an explicit method was proposed recently by Marazzato et al. The proposed method relies on a continuous integration which must be performed exactly in order for the conservation property to hold—as a result, it holds only approximately under numerical quadrature. Here, we show an explicit scheme for Hamiltonian integration, with a different choice of pseudoenergy, which is exactly conserved. Most importantly, a fast implementation is possible through the use of structured matrix inversion, and in particular Sherman Morrison inversion of the rank 1 perturbation of a matrix. Applications to the cases of fully nonlinear string vibration, and to the Föppl-von Kármán system describing large amplitude plate vibration are illustrated. Computation times are on par with the simplest non-conservative methods, such as Störmer integration.

Introduction

Numerical integration methods that preserve an invariant energy-like quantity (or pseudoenergy) form part of the larger family of geometric numerical integration methods [1]. In a recent article [2], an explicit method for Hamiltonian integration was presented, incorporating a conserved pseudo-energy. The method relies, however, on a continuous integration, meaning that pseudoenergy is only preserved approximately due to discretisation error.

New methods, relying on potential energy quadratisation are suitable for systems under more restrictive conditions (non-negativity of the potential energy) [3]. In this paper, it will be shown that such methods can be made fully explicit through structured matrix inversion techniques, and in particular, Sherman Morrison inversion for matrices under a rank-1 perturbation. This allows for extremely efficient numerical solution, while maintaining pseudo-energy conservation to machine accuracy. In particular, no full linear system solutions are required to advance the solution, in contrast with what has been presented for other methods based on quadratization [3]. Numerical stability is ensured, through the enforced non-negativity of the numerical energy.

Two examples, that of fully nonlinear string vibration, and the nonlinear vibration of a thin plate according to the Föpplvon Kármán system are presented, illustrating good numerical behaviour, and acceleration relative to other energy conserving designs. In a companion paper [4], the realistic case of piano string vibration will be broached in detail, as well as the very important topic of the possibility of the shift in the potential energy of the system in order to improve convergence rates.

Hamiltonian Systems and Quadratisation

Consider a Hamiltonian $H(\mathbf{p}, \mathbf{q})$ of the form:

$$H\left(\mathbf{p}, \mathbf{q}\right) = \tfrac{1}{2}\mathbf{p}^T\mathbf{M}^{-1}\mathbf{p} + V\left(\mathbf{q}\right) \tag{1}$$

Here, $\mathbf{p}\left(t\right)$ and $\mathbf{q}\left(t\right)$ are $N \times 1$ vectors and functions of time $t \geq 0$. $\mathbf{M} > 0$ is a constant symmetric $N \times N$ mass matrix (for simplicity constrained here to be diagonal). $\mathbf{p}$ and $\mathbf{q}$ have the interpretation of generalized momentum and position, respectively. Hamilton's equations [5] follow as

$$\mathbf{M}\dot{\mathbf{q}} - \mathbf{p} = \mathbf{0} \qquad \dot{\mathbf{p}} + \nabla V = \mathbf{0} \tag{2}$$

Here, ∇ is the gradient with respect to $\mathbf{q}$, and dots indicate time differentiation. Equations (2) require initialisation through $\mathbf{p}(0) = \mathbf{p}_0$ and $\mathbf{q}(0) = \mathbf{q}_0$.

Under the constraint that $V \geq 0$, one may write, using $\psi = \sqrt{2V}$,

$$H\left(\mathbf{p}, \mathbf{q}\right) = \tfrac{1}{2}\mathbf{p}^T\mathbf{M}^{-1}\mathbf{p} + \tfrac{1}{2}\psi^2 \tag{3}$$

Now, Hamilton's equations may be written as

$$\mathbf{M}\dot{\mathbf{q}} - \mathbf{p} = \mathbf{0} \qquad \dot{\mathbf{p}} + \psi\mathbf{g} = \mathbf{0} \qquad \dot{\psi} = \mathbf{g}^T\dot{\mathbf{q}} \tag{4}$$

where the intermediate variable $\mathbf{g} \triangleq \nabla\psi$ has been introduced. Such a quadratisation of the potential energy has appeared recently in the context of port-Hamiltonian methods [6, 7], and in finite difference schemes modeling collisions [8] and for string vibration under nonlinear conditions [9], and in other areas such as the modeling of binary fluids [10].

Notice that the form of the Hamiltonian in (1) is not the most general available, and thus some restrictions are placed on the range of applications in this paper. First, the energy is quadratic in the momentum $\mathbf{p}$, and thus the resulting dynamics are linear in $\mathbf{p}$—a very common choice across many application areas in structural vibration. Second, the potential energy V is constrained to be non-negative—a condition also common in structural vibration, but violated in other systems, such as the N-body problem under a gravitational potential. The numerical stability property of the methods presented in this paper hinges on these two restrictions.

A Pseudo-energy Conserving Explicit Fast Algorithm

Consider now a time-interleaved scheme for the dynamical system in (4):

$$\mathbf{q}^{n+1} = \mathbf{q}^n + k\mathbf{M}^{-1}\mathbf{p}^{n+\frac{1}{2}} \qquad \mathbf{p}^{n+\frac{1}{2}} = \mathbf{p}^{n-\frac{1}{2}} - \frac{k}{2}\left(\psi^{n+\frac{1}{2}} + \psi^{n-\frac{1}{2}}\right)\mathbf{g}^n \qquad \psi^{n+\frac{1}{2}} = \psi^{n-\frac{1}{2}} + \frac{1}{2}\left(\mathbf{g}^n\right)^T\left(\mathbf{q}^{n+1} - \mathbf{q}^{n-1}\right) \tag{5}$$

It is defined for discrete time sequences $\mathbf{q}^n$, $\mathbf{p}^{n+\frac{1}{2}}$ and $\psi^{n+\frac{1}{2}}$, for integer n, representing approximations at times $t = nk$ to $\mathbf{q}(t)$ and at times $t = \left(n+\frac{1}{2}\right)k$ to $\mathbf{p}(t)$ and $\psi(t)$. Here, k is the time step. $\mathbf{g}^n$ may be calculated explicitly by evaluating the analytic gradient of ψ at $\mathbf{q}^n$. The scheme (5) conserves the following pseudoenergy:

$$H^{n+\frac{1}{2}} = \frac{1}{2}\left(\mathbf{p}^{n+\frac{1}{2}}\right)^T\mathbf{M}^{-1}\mathbf{p}^{n+\frac{1}{2}} + \frac{1}{2}\left(\psi^{n+\frac{1}{2}}\right)^2 = \text{constant} \tag{6}$$

and thus $H^{n+\frac{1}{2}} = H$ is a constant for all n. It is non-negative, implying unconditional stability, as well as bounds on $\mathbf{p}^{n+\frac{1}{2}}$ for all n. In particular, (6) above implies that

$$\|\mathbf{p}^{n+\frac{1}{2}}\| \leq \sqrt{\frac{2H}{\lambda_{\max}(\mathbf{M})}} \tag{7}$$

where $\lambda_{\max}(\mathbf{M})$ is the maximum eigenvalue of $\mathbf{M}$, and $\|\mathbf{p}^{n+\frac{1}{2}}\|$ is the L_2 norm of $\mathbf{p}^{n+\frac{1}{2}}$.

Fast Update

At first glance, the updates (5) appear to be implicit, thus requiring an iterative solver at each time step. This is not the case, however. Given $\mathbf{q}^n$, $\mathbf{q}^{n-1}$ and $\psi^{n-\frac{1}{2}}$ (as well as $\mathbf{g}^n$, determined directly from $\mathbf{q}^n$), they may be consolidated into an update of the form

$$\mathbf{A}^n\mathbf{q}^{n+1} = \mathbf{b}^n \qquad \mathbf{A}^n = \mathbf{M} + \frac{k^2}{4}\mathbf{g}^n\left(\mathbf{g}^n\right)^T \qquad \mathbf{b}^n = 2\mathbf{M}\mathbf{q}^n - k^2\mathbf{g}^n\psi^{n-\frac{1}{2}} - \left(\mathbf{M} - \frac{k^2}{4}\mathbf{g}^n\left(\mathbf{g}^n\right)^T\right)\mathbf{q}^{n-1} \tag{8}$$

This update, which does not require iterative solvers, can be simplified by exploiting the structure of $\mathbf{A}^n$, which is a rank one perturbation of a matrix with an easily computed explicit inverse ($\mathbf{M}$). Using the Sherman-Morrison formula [11],

$$\left(\mathbf{A}^n\right)^{-1} = \mathbf{M}^{-1} - \frac{k^2}{4}\frac{\mathbf{M}^{-1}\mathbf{g}^n\left(\mathbf{g}^n\right)^T\mathbf{M}^{-1}}{1 + \frac{k^2}{4}\left(\mathbf{g}^n\right)^T\mathbf{M}^{-1}\mathbf{g}^n} \tag{9}$$

For diagonal $\mathbf{M}$ a linear system solution requires $O(N)$ operations (and for full $\mathbf{M}$, a linear system involving $\mathbf{M}^{-1}$ must be solved, which is the same as in the case of other algorithms presented [2]).

Example: Nonlinear String Vibration

As a nontrivial example of interest in musical acoustics, consider the case of fully nonlinear string vibration including longitudinal/transverse coupling [12]. This system has been dealt with by various authors, leading to energy-conserving methods relying on nonlinear iterative solvers [13], quadratised methods requiring full linear system solution [9] as well as in the recent article by Marazzato et al. [2]. It may be written as the following (nondimensional) coupled system of PDEs:

$$\partial_t^2 u = \partial_x\left(\partial\mathcal{V}/\partial w_u\right) \quad \partial_t^2 v = \partial_x\left(\partial\mathcal{V}/\partial w_v\right) \qquad w_u = \partial_x u \quad w_v = \partial_x v \tag{10}$$

Here, $u(x,t)$ and $v(x,t)$ are the longitudinal and transverse displacement of a string, defined for $x \in [0,1]$, and $t \geq 0$. ∂_t and ∂_x represent partial differentiation with respect to x and t, respectively.

The potential energy density $\mathcal{V}$ is defined by

$$\mathcal{V}(w_u, w_v) = \frac{1}{2}\left(w_u^2 + w_v^2\right) - \alpha\left(\sqrt{(1+w_u)^2 + w_v^2} - 1 - w_u\right) \tag{11}$$

The complete Hamiltonian for the system is

$$H = \int_0^L \tfrac{1}{2}\left(\partial_t u\right)^2 + \tfrac{1}{2}\left(\partial_t v\right)^2 + \mathcal{V} dx \tag{12}$$

After semidiscretisation (using, e.g., basic finite difference operators to approximate spatial differentiation), a Hamiltonian ODE system of the form of (1) results. Simulation results are presented in Figure 1, under initial conditions of increasing amplitude, and illustrating pseudo-energy conservation to machine accuracy. Calculation time is comparable to that of basic explicit methods (such as, e.g., Störmer). For more details regarding the particular application to the problem of nonlinear string vibration, the reader is referred to the companion paper [4]. A key aspect not discussed here is the possibility of adding an offset, or gauge to the potential energy, which can have a significant ameliorating effect on convergence rates in the resulting numerical implementation. See [4].

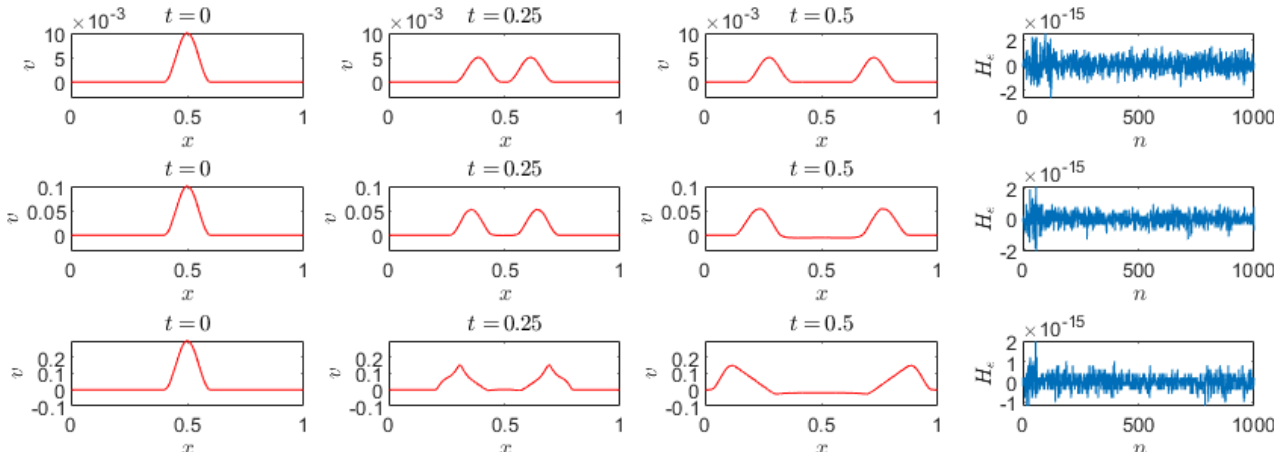

Figure 1: Wave propagation for a pseudo-energy conserving scheme for the nonlinear string system, as defined in (10), with $\alpha = 0.8$, and $k = 10^{-4}$. The string is initialised with zero initial velocity conditions, and with $u = 0$, and with v set to raised cosine distributions of increasing amplitude (top: 0.01, middle: 0.1, bottom; 0.3). At right, the relative energy variation $H_e^n = \left(H^{n+1/2} - H^{n-1/2}\right)/H^{1/2}$ is plotted as a function of time step n, showing energy conservation to machine accuracy (approximately 10^{-15}).

Split Forms and Numerical Methods

In some cases, it can be useful to split the potential energy $V(\mathbf{q})$ as

$$V(\mathbf{q}) = V_0(\mathbf{q}) + V'(\mathbf{q}) \qquad \text{where} \qquad V_0(\mathbf{q}) = \tfrac{1}{2}\mathbf{q}^T\mathbf{K}\mathbf{q} \quad \text{and} \quad V'(\mathbf{q}) \geq 0 \tag{13}$$

for some positive definite matrix $\mathbf{K} > 0$. While the underlying dynamics are unchanged under such a splitting, it becomes possible to apply different numerical integration techniques to different parts of the problem. In particular, V_0, a quadratic form, may encapsulate the underlying linear dynamics of a particular system, and V' additional effects due to a nonlinear mechanism.

Under the constraint that $V' \geq 0$, one may write, using $\psi = \sqrt{2V'}$,

$$H\left(\mathbf{p}, \mathbf{q}\right) = \tfrac{1}{2}\mathbf{p}^T\mathbf{M}^{-1}\mathbf{p} + \tfrac{1}{2}\mathbf{q}^T\mathbf{K}\mathbf{q} + \tfrac{1}{2}\psi^2 \tag{14}$$

Hamilton's equations may be written as

$$\mathbf{M}\dot{\mathbf{q}} - \mathbf{p} = \mathbf{0} \qquad \dot{\mathbf{p}} + \mathbf{K}\mathbf{q} + \psi\mathbf{g} = \mathbf{0} \qquad \dot{\psi} = \mathbf{g}^T\dot{\mathbf{q}} \tag{15}$$

where $\mathbf{g} = \nabla\psi$ as before.

Numerical Scheme

Consider the following time-interleaved scheme:

$$\mathbf{q}^{n+1} = \mathbf{q}^n + k\mathbf{M}^{-1}\mathbf{p}^{n+\frac{1}{2}} \qquad \mathbf{p}^{n+\frac{1}{2}} = \mathbf{p}^{n-\frac{1}{2}} - k\mathbf{K}\mathbf{q}^n - \tfrac{k}{2}\left(\psi^{n+\frac{1}{2}} + \psi^{n-\frac{1}{2}}\right)\mathbf{g}^n \qquad \psi^{n+\frac{1}{2}} = \psi^{n-\frac{1}{2}} + \tfrac{1}{2}\left(\mathbf{g}^n\right)^T\left(\mathbf{q}^{n+1} - \mathbf{q}^{n-1}\right) \tag{16}$$

The update follows, from the extension of (8), as

$$\mathbf{A}^n\mathbf{q}^{n+1} = \mathbf{b}^n \qquad \mathbf{A}^n = \mathbf{M} + \frac{k^2}{4}\mathbf{g}^n\left(\mathbf{g}^n\right)^T \qquad \mathbf{b}^n = (2\mathbf{M} - k^2\mathbf{K})\mathbf{q}^n - k^2\mathbf{g}^n\psi^{n-\frac{1}{2}} - \left(\mathbf{M} - \frac{k^2}{4}\mathbf{g}^n\left(\mathbf{g}^n\right)^T\right)\mathbf{q}^{n-1} \tag{17}$$

and again, a fast implementation is possible using Sherman Morrison, through the explicit inversion of $\mathbf{A}^n$.

This scheme now possesses the conserved numerical energy:

$$H^{n+\frac{1}{2}} = \tfrac{1}{2}\left(\mathbf{p}^{n+\frac{1}{2}}\right)^T\mathbf{M}^{-1}\mathbf{p}^{n+\frac{1}{2}} + \tfrac{1}{2}(\mathbf{q}^{n+1})^T\mathbf{K}\mathbf{q}^n + \tfrac{1}{2}\left(\psi^{n+\frac{1}{2}}\right)^2 = \text{constant} \tag{18}$$

This expression, though conserved, is of indefinite sign, due to the second term. However, this term may be bounded as

$$\tfrac{1}{2}(\mathbf{q}^{n+1})^T\mathbf{K}\mathbf{q}^n \geq -\tfrac{1}{8}(\mathbf{q}^{n+1} - \mathbf{q}^n)^T\mathbf{K}(\mathbf{q}^{n+1} - \mathbf{q}^n) = -\tfrac{k^2}{8}\left(\mathbf{p}^{n+\frac{1}{2}}\right)^T\mathbf{M}^{-1}\mathbf{K}\mathbf{M}^{-1}\mathbf{p}^{n+\frac{1}{2}} \tag{19}$$

and thus

$$H^{n+\frac{1}{2}} \geq \tfrac{1}{2}\left(\mathbf{p}^{n+\frac{1}{2}}\right)^T(\mathbf{M}^{-1} - \tfrac{k^2}{4}\mathbf{M}^{-1}\mathbf{K}\mathbf{M}^{-1})\mathbf{p}^{n+\frac{1}{2}} + \tfrac{1}{2}\left(\psi^{n+\frac{1}{2}}\right)^2 \tag{20}$$

A condition for non-negativity then follows as

$$k \leq \frac{2}{\lambda_{\max}\left(\mathbf{M}^{-\frac{1}{2}}\mathbf{K}\mathbf{M}^{-\frac{1}{2}}\right)} \tag{21}$$

where $\mathbf{M}^{\frac{1}{2}}$ is the positive matrix square root of the diagonal matrix $\mathbf{M}$. (If $\mathbf{M}$ is not diagonal, but still positive definite, then the condition above may be generalized to include the unique trangular factors of $\mathbf{M}$.) This serves as a numerical stability condition for scheme (16). Notice that the scheme is now conditionally stable, but the stability condition depends only on the linear dynamics, and is independent of the nonlinearity. This scheme is distinct from (5), which is unconditionally stable. Indeed, beyond these two choices a family of conservative conditionally stable methods is available, depending on how the splitting of the potential energy V is carried out.

Example: The Föppl-von Kármán Equations

Consider a flat, thin plate, of thickness ξ in m, and of material characterised by Young's modulus E, in Pa, density ρ, in kg$\cdot$ m^{-3}, and Poisson's ratio ν. The plate is assumed defined over a region $(x, y) \in \mathcal{D} \in \mathbb{R}^2$, and has displacement $u(x, y, t)$. High amplitude vibration of the plate is described by the The Föppl-von Kármán equations:

$$\rho\xi\Delta\partial_t^2 u = -D\Delta\Delta u + \mathcal{L}(u, F) \qquad \frac{2}{E\xi}\Delta\Delta F = -\mathcal{L}(u, u) \tag{22}$$

Here, $D = E\xi^3/12(1-\nu^2)$ is the flexural rigidity for the plate, and $F(x, y, t)$ is the Airy stress function, Δ is the two-dimensional Laplacian operator $\Delta = \partial_x^2 + \partial_y^2$, where ∂_x and ∂_y represent partial differentiation with respect to x and y, respectively. $\Delta\Delta$ is the biharmonic operator. The special bilinear operator $\mathcal{L}$ is defined by

$$\mathcal{L}(f, g) = \partial_x^2 f\partial_y^2 g + \partial_y^2 f\partial_x^2 g - 2\partial_x\partial_y f\partial_x\partial_y g \tag{23}$$

Two initial conditions, $u(x, y, 0)$ and $\partial_t u|_{x,y,t=0}$ are required; in this paper, boundary conditions are chosen to be simply supported over the boundary $\partial\mathcal{D}$ of $\mathcal{D}$ [14].

The Hamiltonian for this system is given by

$$H = \iint_{\mathcal{D}} \frac{\rho\xi}{2}(\partial_t\xi)^2 + \frac{D}{2}(\Delta u)^2 + \frac{1}{2E\xi}(\Delta F)^2 d\sigma \tag{24}$$

(Note that this particular form of the Hamiltonian is not the most general, but holds under simply supported conditions. It must be augmented by an additional term in the case of, e.g., free edge conditions.)

Semidiscretization

Consider the simple case of a square plate defined over $(x, y) \in [0, L]^2$, for some plate side length L. Assume also that the displacement $u(x, y, t)$ is approximated over a grid with a grid function $u_{l,m}(t)$ such that

$$u_{l,m}(t) \approxeq u(x = lh, y = mh, t) \qquad l, m = 1, \ldots, M-1 \tag{25}$$

Here, h is the grid spacing, and is chosen such that $h = L/M$, for some integer M. Simply supprted conditions are assumed here, so that $u_{l,m}(t) = 0$ for $l, m = 0, M$.

There are many approaches to spatial discretization; the simplest is to make use of basic difference operators of the form:

$$\delta_{x\pm} u_{l,m} = \pm \tfrac{1}{h} \left(u_{l\pm 1,m} - u_{l,m} \right) \qquad \delta_{y\pm} u_{l,m} = \pm \tfrac{1}{h} \left(u_{1,m\pm 1} - u_{l,m} \right) \tag{26}$$

which are forward and backward approximations to the spatial derivatives ∂_x and ∂_y, respectively. (Note that the time dependence of $u_{l,m}$ has been suppressed above.) Approximations to the Laplacian and biharmonic operator follow as

$$\delta_\Delta = \delta_{x+}\delta_{x-} + \delta_{y+}\delta_{y-} \qquad \delta_{\Delta\Delta} = \delta_\Delta \delta_\Delta \tag{27}$$

A discrete approximation ℓ to the bilinear operator $\mathcal{L}$ may be written, for two grid functions $f_{l,m}$, $g_{l,m}$, as

$$\begin{aligned} \ell(f,g) \quad = \quad & \delta_{x+}\delta_{x-} f \delta_{y+}\delta_{y-} g + \delta_{y+}\delta_{y-} f \delta_{x+}\delta_{x-} g \\ & - \tfrac{1}{2}\delta_{x+}\delta_{y+} f \delta_{x+}\delta_{y+} g - \tfrac{1}{2}\delta_{x+}\delta_{y-} f \delta_{x+}\delta_{y-} g - \tfrac{1}{2}\delta_{x-}\delta_{y+} f \delta_{x-}\delta_{y+} g - \tfrac{1}{2}\delta_{x-}\delta_{y-} f \delta_{x-}\delta_{y-} g \end{aligned} \tag{28}$$

A centered second order accurate approximation to (22) follows as

$$\rho\xi \ddot{u}_{l,m} = -D\delta_{\Delta\Delta} u_{l,m} + \ell(u, F) = 0 \qquad \frac{2}{E\xi}\delta_{\Delta\Delta} F_{l,m} = -\ell(u,u) \tag{29}$$

It is useful, at this stage, to introduce consolidated vector representations $\mathbf{u}(t)$ and $\mathbf{F}(t)$ of $u_{l,m}(t))$ and $F_{l,m}(t)$; both are $(M-1)^2 \times 1$ column vectors (grid points at the plate edges have been removed here, due to the use of simply supported boundary conditions). All of the difference operators δ above may be replaced by matrix equivalents $\mathbf{D}$. In particular, $\mathbf{D}_{x-}$, $\mathbf{D}_{y-}$ are of dimensions $M(M-1) \times (M-1)^2$, $\mathbf{D}_{x+}$, $\mathbf{D}_{y+}$ are of dimensions $(M-1)^2 \times M(M-1)$, and $\mathbf{D}_\Delta$ and $\mathbf{D}_{\Delta\Delta}$ are of dimensions $(M-1)^2 \times (M-1)^2$. In this case, simply supported boundary conditions have been taken into account—all matrices are sparse, with $O(M^2)$ nonzero entries.
In this case, (29) can be rewritten as

$$\rho\xi \ddot{\mathbf{u}} = -D\mathbf{D}_{\Delta\Delta}\mathbf{u} + \ell(\mathbf{u}, \mathbf{F}) = \mathbf{0} \qquad \frac{2}{E\xi}\mathbf{D}_{\Delta\Delta}\mathbf{F} = -\ell(\mathbf{u},\mathbf{u}) \tag{30}$$

To arrive at a first order form (15) in terms of momentum $\mathbf{p} = \mathbf{M}\dot{\mathbf{u}}$ and displacement $\mathbf{q} = \mathbf{u}$, with associated Hamiltonian (14) and energy splitting (13), one may use

$$\mathbf{M} = \rho\xi h^2 \mathbf{I}_{(M-1)^2} \qquad \mathbf{K} = Dh^2 \mathbf{D}_{\Delta\Delta} \qquad V' = \frac{h^2}{2E\xi} |\mathbf{D}_\Delta \mathbf{F}|^2 \tag{31}$$

where here, $\mathbf{I}_{(M-1)^2}$ is the identity matrix of size $(M-1)^2 \times (M-1)^2$.

Fully Discrete Schemes

The most basic scheme for the Föppl-von Kármán system follows from a centered difference approximation to the semi-discrete system of ODEs (30). Introducing the discrete-time vectors $\mathbf{u}^n$ and $\mathbf{F}^n$, approximating $\mathbf{u}(t)$ and $\mathbf{F}(t)$ at $t = nk$, for integer n and a time step k, the Störmer scheme results as

$$\frac{\rho\xi}{k^2}\left(\mathbf{u}^{n+1} - 2\mathbf{u}^n + \mathbf{u}^{n-1}\right) = -D\mathbf{D}_{\Delta\Delta}\mathbf{u}^n + \ell(\mathbf{u}^n, \mathbf{F}^n) = \mathbf{0} \qquad \frac{2}{E\xi}\mathbf{D}_{\Delta\Delta}\mathbf{F}^n = -\ell(\mathbf{u}^n, \mathbf{u}^n) \tag{32}$$

This scheme is simple, but stability is highly dependent on both the choice of time step and on the initial conditions—in general, this scheme will become unstable as the size of the initial condition is increased. The first equation represents the update, and is fully explicit. The second requires the solution of a linear system involving the matrix $\mathbf{D}_{\Delta\Delta}$. As this is of a known form, a Cholesky factorisation may be computed prior to entering the runtime loop, greatly accelerating calculation. This scheme will be referred to as Scheme I subsequently here.

A family of energy-conserving and provably numerically stable schemes has been presented in previous work [15, 14]. Though too elaborate to present in detail here, in its most general form, the update equation is of the form

$$\mathbf{A}^n \mathbf{u}^{n+1} = \mathbf{b}^n \tag{33}$$

where, as in (32), $\mathbf{u}^n$ is the plate displacement in vector form. Here, $\mathbf{A}^n$ and $\mathbf{b}^n$ are a matrix/vector pair which in general are dependent on $\mathbf{u}^n$ and $\mathbf{u}^{n-1}$; Although no iterative solvers are required, and thus existence/uniqueness are guaranteed, the linear system to be solved must be constructed anew at each time step, in contrast with (32), and thus compute times are much longer. This scheme will be referred to as Scheme II subsequently here.

Finally, one may employ he fast conservative scheme, as given in (16), and under the choices given in (31). This scheme will be referred to as Scheme III subsequently here. In this case, the scheme is stable under the condition (21) which reduces, in this case, to the following condition on the grid spacing h in terms of the time step k:

$$h \geq h_{\min} = 2\sqrt{k}\left(D/\rho\xi\right)^{\frac{1}{4}} \tag{34}$$

Table 1: Timing comparison: Schemes I, II and III for the Föppl-von Kármán System. Run times for 1 s output are given, with time steps k as indicated.

Scheme	$k = 10^{-3}$	$k = 5 \times 10^{-4}$	$k = 10^{-4}$	$k = 5 \times 10^{-5}$	$k = 10^{-5}$
I: Störmer-Verlet	0.032	0.142	0.344	6.04	25.24
II: Energy conserving	0.149	0.636	8.92	327.8	1742.8
III: Fast energy conserving	0.055	0.290	0.593	7.76	31.36

Numerical Results: Föppl-von Kármán Equations

As an example, consider a square plate of side length $L = 0.5$ m, of thickness $\xi = 0.002$ m, and made of steel, with $E = 2 \times 10^{11}$ Pa, $\rho = 7850$ kg$\cdot$ m^{-3}, and $\nu = 0.3$. Simply supported boundary conditions are assumed, and the plate is assumed initialised in the lowest linear mode shape, and with zero transverse velocity, so that

$$u(x, y, 0) = a\xi \sin(\pi x/L) \sin(\pi y/L) \qquad \partial_t u|_{x,y,t=0} = 0 \tag{35}$$

for some non-dimensional amplitude a. See Figure 2, illustrating plate displacement u_{o} at the plate center as a function of time, as well as the relative numerical energy variation H_e, defined as

$$H_e^{n+\frac{1}{2}} = \frac{H^{n+\frac{1}{2}} - H^{\frac{1}{2}}}{H^{\frac{1}{2}}} \tag{36}$$

The time step is chosen as $k = 10^{-4}$ s. In all cases, the relative energy variation is on the order of machine accuracy in double precision floating point arithmetic. See also figure 3, illustrating convergence of computed waveforms to trusted high accuracy solutions generated using the standard Scheme I (Störmer) with a very small time step.

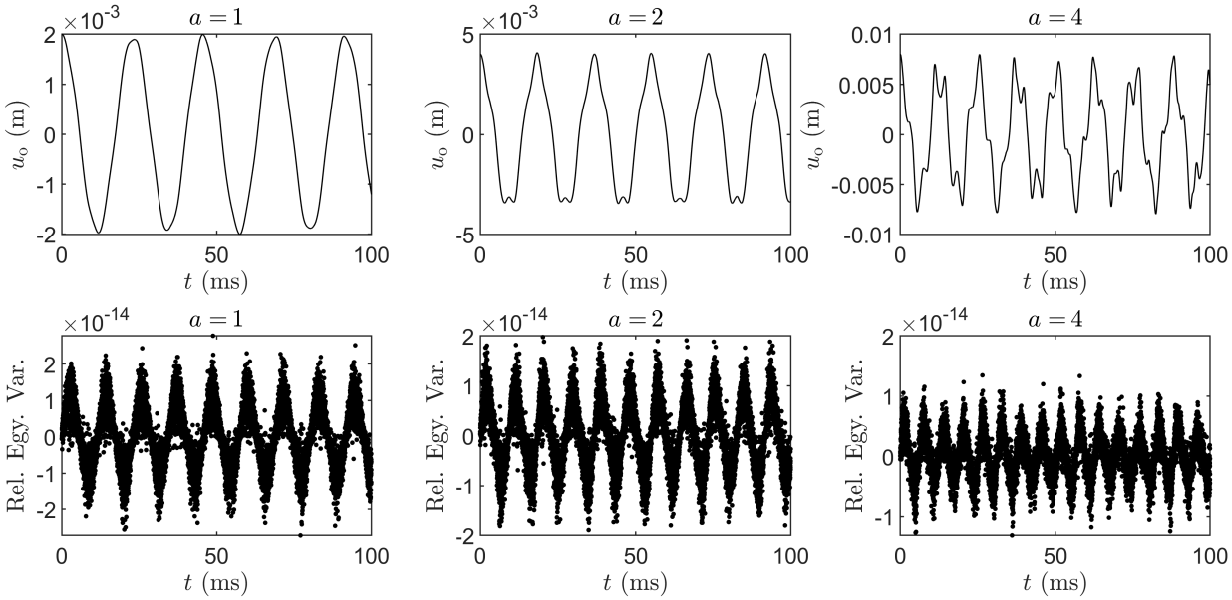

Figure 2: Top row: plate displacement at the plate center, as a function of time, for different initial condition amplitudes $a = 1$, $a = 2$ and $a = 4$. Bottom row: relative numerical energy variation H_e, as defined in (36).

In Table 1 timings per second output are given, for the plate with parameters as described above, and using different time steps k as indicated. All computations were performed in Matlab on a Lenovo P50 laptop on a Xeon E3. Timings are given for the basic Störmer method (Scheme I), the stable energy conserving method as given in [15] (Scheme II) and the new stable energy conserving method presented here (Scheme III). As is clearly evident, the new method performs nearly on par with Störmer, in cases where Störmer is stable—recall that this scheme has obscure stability properties that are highly dependent on on the initialisation. These results were computed with initial condition (35) with $a = 4$; at higher amplitudes, Störmer exhibits instability at larger time steps.

Concluding Remarks

A fully explicit method for Hamiltonian numerical integration has been presented here, with a pseudo-energy conservation property leading to unconditional numerical stability—it is different in character from other explicit methods presented

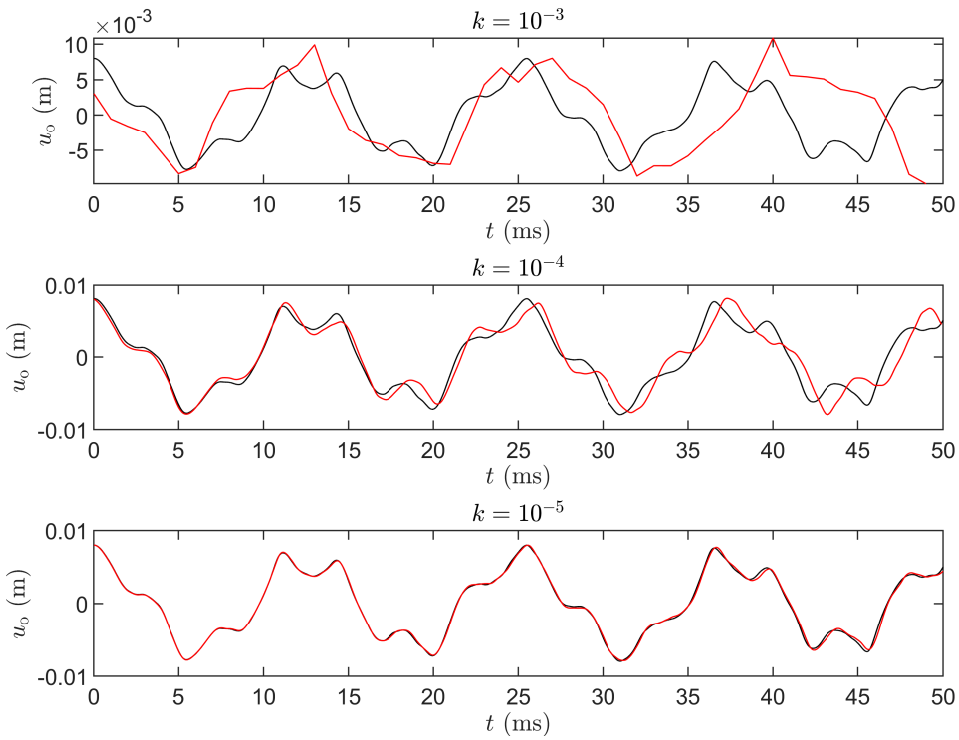

Figure 3: Computed waveforms at the plate center, using scheme III (in red) at different choices of time step k as indicated. Here, a high initial condition amplitude of $a = 4$ is chosen. For reference, a high accuracy solution is computed using Scheme I (Störmer) using a small time step of $k = 10^{-6}$ s, and is shown in black.

recently, in that an additional update is required for the root-potential energy, which is treated as a new independent variable. An extension to the case of split potential forms is also presented, useful in arriving at conditionally stable numerical methods.

The fully explicit character of the eventual update follows from the exploitation of matrix structure, and leads to large increases in computational speed relative to other provably stable energy conserving methods. The method on the whole is nearly as efficient as the simplest explicit schemes for Hamiltonian integration.

Acknowledgments

This work was supported by the European Research Council (ERC), under grant 2020-StG-950084-NEMUS.

References

[1] E. Hairer, C. Lubich, and G. Wanner, *Geometric Numerical Integration*, Springer Series in Computational Mathematics, 2006.

[2] F. Marazzato, A. Ern, C. Mariotti, and L. Monasse, "An explicit pseudo-energy conserving time-integration scheme for Hamiltonian dynamics," *Comp. Methods Appl. Mech. Eng.*, vol. 347, pp. 906–927, 2019.

[3] J. Shen, J. Xu, and J. Yang, "The scalar auxiliary variable (sav) approach for gradient flows," *J. Comput. Phys.*, vol. 353, pp. 407–416, 2018.

[4] M. Ducceschi, S. Bilbao, and Craig J. Webb, "Real-time simulation of the struck piano string with geometrically exact nonlinearity via a scalar quadratic energy method," in *Proceedings of the European Nonlinear Dynamics Conference*, Lyon, France, July 2022.

[5] H. Goldstein, C. Poole, and J. Safko, *Classical Mechanics*, Pearson, 2001.

[6] N. Lopes, T. Hélie, and A. Falaize, "Explicit second-order accurate method for the passive guaranteed simulation of port-hamiltonian systems," in *Proc. 5th IFAC 2015*, Lyon, France, July 2015.

[7] A. Falaize, *Modélisation, simulation, génération de code et correction de systèmes multi-physiques audios: Approche par réseau de composants et formulation Hamiltonienne À Ports*, Ph.D. thesis, Université Pierre et Marie Curie, Paris, July 2016.

[8] M. Ducceschi and S. Bilbao, "Non-iterative solvers for nonlinear problems: the case of collisions," in *Proc. DAFX*, Birmingham, UK, 2019.

[9] M. Ducceschi and S. Bilbao, "Non-iterative, conservative schemes for geometrically exact nonlinear string vibration," in *Proc. ICA*, Aachen, Germany, September 2019.

[10] X. Yang, "Linear and unconditionally energy stable schemes for the binary fluid-surfactant phase field model," *Comp. Methods Appl. Mech. Eng.*, vol. 318, pp. 1005–1029, 2017.

[11] J. Sherman and W. Morrison, "Adjustment of an inverse matrix corresponding to a change in one element of a given matrix," *Annals of Mathematical Statistics*, vol. 21, no. 1, pp. 124–127, 1950.

[12] P. Morse and U. Ingard, *Theoretical Acoustics*, Princeton University Press, Princeton, New Jersey, 1968.

[13] J. Chabassier and P. Joly, "Energy preserving schemes for nonlinear Hamiltonian systems of wave equations: Application to the vibrating piano string," *Comp. Methods Appl. Mech. Eng.*, vol. 199, no. 45, pp. 2779–2795, 2010.

[14] S. Bilbao, *Numerical Sound Synthesis*, John Wiley and Sons, Chichester, UK, 2009.

[15] S. Bilbao, "A family of conservative finite difference schemes for the dynamical von Kármán plate equations," *Numerical Methods for Partial Differential Equations*, vol. 24, no. 1, pp. 193–216, 2008.

Real-time simulation of the struck piano string with geometrically exact nonlinearity via a scalar quadratic energy method

Michele Ducceschi*, Stefan Bilbao† and Craig J. Webb‡
*Dipartimento di Ingegneria Industriale, University of Bologna, Italy
†Acoustics and Audio Group, University of Edinburgh, UK
‡ Physical Audio Ltd, London, UK

Summary. This work addresses the problem of the struck piano string. This system is highly nonlinear, and a sound representation of the energy balance is therefore necessary in any time stepping routine used in simulation, in order to preserve stability. Many algorithms have been developed in previous works. Among them, some present fully-implicit discretisations, which are only approachable using iterative root finders such as Newton-Raphson. Others are linearly-implicit, but not quite suited for real-time rendering. Here, a novel approach is presented, based on the idea of energy quadratisation. It will be shown that, when the nonlinearities are consolidated into a scalar auxiliary state function, the time stepping scheme presents a fast inversion formula. A C++ implementation of the proposed scheme yields indeed compute times below real-time, for typical strings.

Introduction

The dynamics of musical strings is often assumed to be linear. However, many perceptual phenomena cannot be explained by linear theory alone, and inclusion of nonlinearities results therefore necessary [1]. This is certainly true for the piano, where the appearance of "phantom partials" in the output spectra is often explained in terms of the nonlinear coupling between the transverse and the longitudinal waves. Furthermore, the intermittent hammer-string interaction cannot be modelled linearly [2]. At the simulation level, a sound representation of the energy balance of the hammer-string system is necessary to preserve stability of the underlying time stepping scheme, and this can be accomplished via fully-implicit discretisations [3, 4]. The finite element method, in particular, is preeminent here, see e.g. [5, 6], where the conservation of a non-negative numerical energy allows to derive a stability condition involving the mesh size and the time step. Since these methods are fully-implicit, they require the solution of a large nonlinear algebraic system at each time step, for which existence and uniqueness of the solution must be proven, and which are only approachable using iterative routines such as Newton-Raphson. Further complications arise in the choice of the tolerance thresholds and maximum number of iterations of the routine [7, 8].
In recent years, a new class of schemes has emerged, based on the idea of "quadratisation": when the nonlinear potential energy is non-negative, it can be written as the square of an auxiliary function. This leads to schemes for which the update is computable as the solution of a linear system, thus sidestepping the machinery of iterative root finders. Besides the obvious computational advantage, existence and uniqueness of the computed solution are proven by inspection of the update matrix alone. These methods have appeared in various guises, including applications in Port-Hamiltonian systems [9, 10, 4, 11], nonlinear parabolic phase-field models [12, 13, 14], and others. This latter class of methods is often referred to as "Invariant Energy Quadratisation" (IEQ) method, in that the auxiliary state function is treated as an independent grid function to be solved for. This method has been applied successfully to the geometrically exact nonlinear string [15, 16]. In this work, a different kind of quadratisation is proposed, where the auxiliary state function is not treated as a distributed state variable, but as a scalar one. This idea shares some similarities with the "Scalar Auxiliary Variable" (SAV) approach [17], but it also exploits the form of the update matrix to yield an extremely efficient algorithm. The application of this method to Hamiltonian system is the subject of a companion paper [18]; here, the example of the struck string is considered in detail. First, the problem is semi-discretised in space, resulting in a system of nonlinearly coupled ordinary differential equations in time. Then, all the nonlinear components (i.e. the geometric nonlinearity of the string, and the hammer-string nonlinear potential) are consolidated into a single, scalar state function. Then, it shown that the update matrix is in the form of a rank-1 perturbation of a diagonal matrix, and thus invertible efficiently using the Sherman-Morrison formula [19]. A computational test is then performed, showing that a sound implementation of this method in C++ yields speedups of the order of 10^2, compared to Matlab implementations of previously available methods. In particular, compute times for typical piano strings are below real-time. The introduction of a shift constant in the nonlinear potential energy is also illustrated, aiding convergence of the quadratised numerical scheme.

A Continuous Struck String Model

Piano strings are known to vibrate in a nonlinear regime as a consequence of the large strains originating during motion [1, 20]. The striking mechanism is also nonlinear, due to the intermittent contact between the string and the hammer

[2, 21]. A suitable mathematical model incorporating these effects may be given as follows:

$$(\rho A\partial_t^2 - \mathcal{L}_u)u(x,t) = \partial_x\left(\frac{\partial\phi_s}{\partial(\partial_x u)}\right) + \delta(x-x_c)\frac{d\phi_c}{d\eta}, \tag{1a}$$

$$(\rho A\partial_t^2 - \mathcal{L}_v)v(x,t) = \partial_x\left(\frac{\partial\phi_s}{\partial(\partial_x v)}\right), \tag{1b}$$

$$M_h\frac{d^2U(t)}{dt^2} = -\frac{d\phi_c}{d\eta}, \tag{1c}$$

$$\eta(t) = U(t) - \int_0^L \delta(x-x_c)u(x,t)\,\mathrm{d}x. \tag{1d}$$

Above, constants appear as: ρ, the string's volume density; A the area of the string's cross section; M_h, the mass of the hammer. The notation ∂_s^p denotes the p-th partial derivative with respect to s. $u = u(x,t) : [0,L]\times\mathbb{R}_0^+ \to \mathbb{R}$ is the transverse displacement of the string, and $v = v(x,t) : [0,L]\times\mathbb{R}_0^+ \to \mathbb{R}$ is the longitudinal displacement, where L is the string length; $\mathcal{L}_u$, $\mathcal{L}_v$ are linear differential operators (to be specified shortly) including the tension, stiffness and loss components for the two displacements; $\phi_s : \phi_s(\partial_x u, \partial_x v) : \mathbb{R}\times\mathbb{R} \to \mathbb{R}_0^+$ is the nonlinear potential density due to the string's large stretching; $\phi_c : \phi_c(\eta) : \mathbb{R} \to \mathbb{R}_0^+$ is the collision potential modelling the hammer-string interaction; $U = U(t) : \mathbb{R}_0^+ \to \mathbb{R}$ is the hammer's displacement; $\eta = \eta(t) : \mathbb{R}_0^+ \to \mathbb{R}$ defines the compression of the hammer felt, expressed as the difference between the hammer and string displacements at the contact point x_c.
The linear operators $\mathcal{L}_u$, $\mathcal{L}_v$ are given as:

$$\mathcal{L}_u = T_0\partial_x^2 - EI\partial_x^4 - 2\rho A(\sigma_0 - \sigma_1\partial_x^2)\partial_t; \quad \mathcal{L}_v = T_0\partial_x^2 - 2\rho A\sigma_l\partial_t. \tag{2}$$

$\mathcal{L}_u$ includes tension and stiffness terms, the latter borrowed from the Euler-Bernoulli beam theory (this is largely sufficient for musical strings, see e.g. [22, 23]). T_0 is the applied tension, E is Young's modulus, I is the area moment of inertia. Losses in the transverse direction are modelled via the terms proportional to the coefficients $(\sigma_0,\, \sigma_1) \geq 0$, yielding a quadratic loss profile in the frequency domain. Inclusion of more refined loss profiles, such as the one proposed by Cuesta and Vallette [24], is possible, but this will be neglected here for simplicity. $\mathcal{L}_v$ includes a tension term, and a simple loss model proportional to $\sigma_l \geq 0$.
The forms of the potentials are given here as:

$$\phi_s(\partial_x u, \partial_x v) = \frac{EA - T_0}{2}\left(\sqrt{(1+\partial_x v)^2 + (\partial_x u)^2} - 1\right)^2, \quad \phi_c(\eta) = \frac{B}{\alpha+1}[\eta]_+^{\alpha+1}. \tag{3}$$

Here, B is the stiffness coefficient of the hammer felt, $\alpha \geq 1$ is an exponent: these values can be determined experimentally [25]. The notation $[\cdot]_+$ stands for "positive part", that is $[\eta]_+ \triangleq 0.5(\eta + |\eta|)$. Note that $\phi_c = 0$ whenever $\eta \leq 0$, that is, the collision model is one-sided, and note that this model is consistent only when the hammer strikes from below. Note as well that $\phi_s \geq 0$ when $EA \geq T_0$, a condition that is always verified for musical strings. In view of the numerical application shown below, it is convenient to lump the nonlinear potentials into one single scalar function ϕ, as

$$\phi(\partial_x u, \partial_x v, \eta) = \int_0^L \phi_s(\partial_x u, \partial_x v)\,\mathrm{d}x + \phi_c(\eta) + \frac{p_0}{2}, \tag{4}$$

where $p_0 \geq 0$ is a constant shifting the zero-point of the potential, but not affecting the equations of motion. This constant will prove useful in the numerical scheme presented below.
Equation (1c) must be completed by two initial conditions, setting the hammer in motion. These can be given as $U_0 \triangleq U(t=0)$ and $V_0 \triangleq dU/dt(t=0)$. Furthermore, the string's boundary conditions are given as: $u(0,t) = u(L,t) = \partial_x^2 u(0,t) = \partial_x^2 u(L,t) = v(0,t) = v(L,t) = 0$. These define an energy conserving set of boundary conditions; in particular, the string is simply-supported transversely and fixed longitudinally. Under such conditions, system (1) is energy-passive. A proof may be obtained by taking an l_2 inner product (i.e. an integral over the domain) of (1a) with $\partial_t u$, of (1b) with $\partial_t v$, and a product of (1c) with dU/dt, and summing the three equations. After suitable integrations by parts [16], one gets the following energy balance

$$\frac{dH}{dt} = -2\rho A\left(\int_0^L \left(\sigma_0(\partial_t u)^2 + \sigma_l(\partial_t v)^2 + \sigma_1(\partial_t\partial_x u)^2\right)\,\mathrm{d}x\right) \leq 0, \tag{5}$$

where the energy is

$$H(t) = \int_0^L \left(\frac{\rho A}{2}\left((\partial_t u)^2 + (\partial_t v)^2\right) + \frac{T_0}{2}\left((\partial_x u)^2 + (\partial_x v)^2\right) + \frac{EI}{2}(\partial_x^2 u)^2\right)\,\mathrm{d}x + \frac{M_h(dU/dt)^2}{2} + \phi \geq 0 \tag{6}$$

Equation (5) represents the energy balance of the hammer-string, encoding passivity (i.e. the total energy is positive, and decays over time).

Semi-discretisation

System (1) may be semi-discretised in a number of ways, yielding a system of coupled nonlinear ordinary differential equations in time. Here, a finite difference approach will be adopted, but the numerical method described below applies equally to any other suitable semi-discrete problem, obtained for instance via Galerkin-type methods (modal methods, finite elements, etc.). For the finite difference method, the continuous domain of length L is divided into segments of length h, the grid spacing. Let the total number of subintervals be M, that is, the grid is composed of $M+1$ grid points, including the boundary points. Then, the continuous displacements $u(x,t)$, $v(x,t)$ are approximated by grid functions $\mathbf{u}(t)$, $\mathbf{v}(t)$, which may be taken as column vectors of length $M-1$: here, the end points need not be stored or updated, since the boundary conditions are of fixed type. Difference matrices are now introduced, starting from the definition of the backward difference matrix acting on the column vector $\mathbf{u}$:

$$\mathbf{D}^- \mathbf{u} = \frac{1}{h}([\mathbf{u}^\intercal, 0] - [0, \mathbf{u}^\intercal]). \tag{7}$$

Note that this is a rectangular matrix of size $M \times M-1$. From this, one may define the forward difference matrix, the Laplace operator and the biharmonic operator, as

$$\mathbf{D}^+ = -(\mathbf{D}^-)^\intercal, \quad \mathbf{D}^2 = \mathbf{D}^+\mathbf{D}^-, \quad \mathbf{D}^4 = (\mathbf{D}^2)^2, \tag{8}$$

and note that these matrices are consistent with the prescribed boundary conditions in the transverse and longitudinal directions. Note as well that the Laplace and biharmonic operators are of size $M-1 \times M-1$. Owing to these definitions, semi-discretisation of the linear operators $\mathcal{L}_u$, $\mathcal{L}_v$ in (2) is obtained as

$$\mathfrak{l}_u = T_0\mathbf{D}^2 - EI\mathbf{D}^4 - 2\rho A(\sigma_0 - \sigma_1\mathbf{D}^2)\frac{d}{dt}; \quad \mathfrak{l}_v = T_0\mathbf{D}^2 - 2\rho A\sigma_l\frac{d}{dt}. \tag{9}$$

The Dirac delta function is here approximated using a linear Lagrange interpolant, that is, via the column vector $\mathbf{J}$ of length $M-1$. This is an all-zero vector, except at the grid points $m_c \triangleq \text{floor}(x_c/h)$ and m_c+1, for which

$$J_{m_c} = (1-\alpha)/h, \; J_{m_c+1} = \alpha/h, \quad \text{where } \alpha = x_c/h - m_c. \tag{10}$$

Using this definition, a semi-discrete version of (1d) is obtained as:

$$\eta(t) = U(t) - h\,\mathbf{J}^\intercal\,\mathbf{u}(t). \tag{11}$$

Note that the letter η is used here in a different fashion than in (1d) (in this section, the semi-discrete definition (11) is adopted). It is now convenient to define two interleaved grid functions, $\mathbf{q}$ and $\mathbf{r}$, which are column vectors of length M defined as:

$$\mathbf{q} = \mathbf{D}^-\mathbf{u}, \quad \mathbf{r} = \mathbf{D}^-\mathbf{v}. \tag{12}$$

Owing to these, a semi-discrete version of the nonlinear potential ϕ in (4) is obtained as:

$$\Phi = h\sum_{i=1}^{M}\Phi_s^i(q_i, r_i) + \Phi_c(\eta) + \frac{p_0}{2}; \text{ where } \Phi_s^i = \frac{EA - T_0}{2}\left(\sqrt{(1+r_i)^2 + q_i^2} - 1\right)^2, \; \Phi_c = \frac{B}{\alpha+1}[\eta]_+^{\alpha+1}. \tag{13}$$

Note that here $\Phi = \Phi(\mathbf{q}, \mathbf{r}, \eta) : \mathbb{R}^M \times \mathbb{R}^M \times \mathbb{R} \to \mathbb{R}_0^+$, and it will be necessary to compute partial derivatives according to $\mathbf{q}, \mathbf{r}, \eta$. These are denoted as

$$(\nabla_{\mathbf{q}}\Phi)_i \triangleq \frac{\partial\Phi_s^i}{\partial q_i}, \quad (\nabla_{\mathbf{r}}\Phi)_i \triangleq \frac{\partial\Phi_s^i}{\partial r_i}, \quad (\nabla_\eta\Phi) \triangleq \frac{d\Phi_c}{d\eta}, \quad i = 1, ..., M. \tag{14}$$

The chain rule gives

$$\frac{d\Phi}{dt} = (\nabla_{\mathbf{q}}\Phi)^\intercal\frac{d\mathbf{q}}{dt} + (\nabla_{\mathbf{r}}\Phi)^\intercal\frac{d\mathbf{r}}{dt} + (\nabla_\eta\Phi)\frac{d\eta}{dt} = \underbrace{[-\left(\mathbf{D}^+\nabla_{\mathbf{q}}\Phi\right)^\intercal - h\nabla_\eta\Phi\mathbf{J}^\intercal, -\left(\mathbf{D}^+\nabla_{\mathbf{r}}\Phi\right)^\intercal, \nabla_\eta\Phi]}_{\mathbf{g}_\Phi^\intercal}\frac{d\mathbf{w}}{dt}, \tag{15}$$

where $\mathbf{w} \triangleq [\mathbf{u}^\intercal, \mathbf{v}^\intercal, U]^\intercal$ is the state vector, lumping the longitudinal and transverse string grid functions, and the hammer's displacement. Note that the second equality in (15) is obtained using the transposition property of the forward and backward difference matrices in (8), and the definition of η in (11). Owing to these definitions, the semi-discrete equations can be written in compact form, as:

$$\mathbf{M}\frac{d^2\mathbf{w}(t)}{dt^2} + \mathbf{C}\frac{d\mathbf{w}(t)}{dt} + \mathbf{K}\mathbf{w}(t) = -\mathbf{S}\,\mathbf{g}_\Phi, \tag{16}$$

where $\mathbf{M} \triangleq \text{diag}([\rho A\mathbf{I}, \rho A\mathbf{I}, M_h])$, $\mathbf{K} \triangleq \text{diag}([-T_0\mathbf{D}^2+EI\mathbf{D}^4, -T_0\mathbf{D}^2, 0])$, $\mathbf{C} \triangleq \text{diag}([2\rho A(\sigma_0\mathbf{I}-\sigma_1\mathbf{D}^2), 2\rho A\sigma_l\mathbf{I}, 0])$, $\mathbf{S} \triangleq \text{diag}([\mathbf{I}/h, \mathbf{I}/h, 1])$. Here, the operator "diag" produces a block-diagonal matrix, with blocks given as components separated by commas. The matrix $\mathbf{I}$ is here the $M-1 \times M-1$ identity matrix.
In (16), the left-hand side includes all the linear components (the mass, stiffness and loss matrices), and the nonlinearities are now lumped in the vector $\mathbf{g}_\Phi$ as defined in (15). From here, it is now easy to see that system (16) is energy-passive: it is sufficient to multiply both sides of the equation on the left by $\left(\mathbf{S}^{-1}\frac{d\mathbf{w}}{dt}\right)^\intercal$. This gives

$$\frac{d\mathfrak{h}}{dt} = -\frac{d\mathbf{w}^\intercal}{dt}\tilde{\mathbf{C}}\frac{d\mathbf{w}}{dt} \leq 0, \text{ with } \mathfrak{h} = \frac{1}{2}\frac{d\mathbf{w}^\intercal}{dt}\tilde{\mathbf{M}}\frac{d\mathbf{w}}{dt} + \frac{1}{2}\mathbf{w}^\intercal\tilde{\mathbf{K}}\mathbf{w} + \Phi \geq 0, \tag{17}$$

where the "tilde" notation indicates the rescaled matrices $\tilde{\mathbf{M}} = \mathbf{S}^{-1}\mathbf{M}$, $\tilde{\mathbf{K}} = \mathbf{S}^{-1}\mathbf{K}$, $\tilde{\mathbf{C}} = \mathbf{S}^{-1}\mathbf{C}$ (the scaling by the factor h is needed here to restore units of Joules in the transverse and longitudinal string components). Note that the "tilde" matrices are all non-negative, hence the inequalities in (17) ensue.

Quadratisation

The expression for the semi-discrete energy $\mathfrak{h}$ in (17) includes a linear part, given by the sum of quadratic forms corresponding to the kinetic and linear potential energy components, plus the nonlinear potential Φ. It results therefore convenient to "quadratise" the nonlinear potential via the transformation

$$\Psi = \sqrt{2\Phi}, \tag{18}$$

for the function $\Psi = \Psi(\mathbf{q}, \mathbf{r}, \eta) : \mathbb{R}^M \times \mathbb{R}^M \times \mathbb{R} \to \mathbb{R}_0^+$. This transformation is always well-defined since Φ is non-negative. This transformation yields a semi-discrete system entirely equivalent to (16), but expressed in terms of Ψ as:

$$\mathbf{M}\frac{d^2\mathbf{w}(t)}{dt^2} + \mathbf{C}\frac{d\mathbf{w}(t)}{dt} + \mathbf{K}\mathbf{w}(t) = -\Psi(t)\mathbf{S}\,\mathbf{g}_\Psi, \tag{19}$$

where

$$\mathbf{g}_\Psi = [-\left(\mathbf{D}^+\nabla_\mathbf{q}\Psi\right)^\intercal - h\nabla_\eta\Psi\mathbf{J}^\intercal, -\left(\mathbf{D}^+\nabla_\mathbf{r}\Psi\right)^\intercal, \nabla_\eta\Psi], \tag{20}$$

and note that the partial derivatives of Ψ are easily obtained from (14), since e.g. $\nabla_\mathbf{q}\Psi = \nabla_\mathbf{q}\Phi/\Psi$. Division by Ψ in the expression of the partial derivatives may be ill defined when the shift constant p_0 in (13) is set to zero, and it will therefore be necessary to shift the potential energy by a finite amount. Application of the chain rule gives

$$\frac{d\Psi}{dt} = \mathbf{g}_\Psi^\intercal\frac{d\mathbf{w}}{dt}. \tag{21}$$

The energy balance now reads:

$$\frac{d\mathfrak{h}}{dt} = -\frac{d\mathbf{w}^\intercal}{dt}\tilde{\mathbf{C}}\frac{d\mathbf{w}}{dt} \leq 0, \text{ where } \mathfrak{h} = \frac{1}{2}\frac{d\mathbf{w}^\intercal}{dt}\tilde{\mathbf{M}}\frac{d\mathbf{w}}{dt} + \frac{1}{2}\mathbf{w}^\intercal\tilde{\mathbf{K}}\mathbf{w} + \frac{\Psi^2}{2} \geq 0, \tag{22}$$

and the expression for the energy only contains quadratic terms. Note that the nonlinear energy components are now lumped in the single scalar function Ψ. The "quadratised" expression for the nonlinear energy is convenient since it can be exploited in a time-stepping integrator yielding a non-negative nonlinear numerical energy, as detailed below. Note that this type of quadratisation is fundamentally different from the one proposed in [15, 16], in that here the auxiliary state function is a scalar, and not a distributed quantity. Applications of this method to Hamiltonian systems are presented in the companion paper [18].

Time Stepping Procedure

(19) defines a system of nonlinearly coupled ordinary differential equations in time. Integration is now performed using finite differences. To that end, the continuous state vector $\mathbf{w}(t)$ is approximated at the time $t_n = kn$ by a vector time series $\mathbf{w}^n$, where $n \in \mathbb{N}$ is the time index, and $k = 1/f_s$ is the time step, defined as the multiplicative inverse of the sample rate f_s. The basic operators in discrete time are the identity and shift operators, defined as:

$$1\mathbf{w}^n = \mathbf{w}^n, \quad e_+\mathbf{w}^n = \mathbf{w}^{n+1}, \quad e_-\mathbf{w}^n = \mathbf{w}^{n-1}. \tag{23}$$

From these, the time difference operators can be defined as:

$$\delta_+ = \frac{e_+ - 1}{k}, \ \delta_- = \frac{1 - e_-}{k}, \ \delta_\cdot = \frac{e_+ - e_-}{2k}. \tag{24}$$

These are the forward, backward and centred operators respectively. The second-difference operator is obtained by combining the the operators above:

$$\delta_2 = \delta_+\delta_- \,. \tag{25}$$

Finally, averaging operators can be written as:

$$\mu_+ = \frac{e_+ + 1}{2},\ \mu_- = \frac{1 + e_-}{2},\ \mu_\cdot = \frac{e_+ + e_-}{2}. \tag{26}$$

The auxiliary state function is discretised on an interleaved time grid, so that $\Psi(t) \to \Psi^{n-1/2}$. The definitions of the difference operators are formally unchanged when applied to an interleaved time series, so that e.g. $\delta_+ \Psi^{n-1/2} = (\Psi^{n+1/2} - \Psi^{n-1/2})/k$, etc. Note that $\Psi^{n-1/2}$ will be treated here as an *independent* scalar time series, to be updated at each time step. To that end, it is necessary to discretise (19) along with the time derivative of Ψ in (21). One possible such discretisation is given here as

$$\mathbf{M}\,\delta_2 \mathbf{w}^n + \mathbf{C}\,\delta_- \mathbf{w}^n + \mathbf{K}\,\mathbf{w}^n = -\mu_+ \Psi^{n-1/2}\,\mathbf{S}\,\mathbf{g}_\Psi^n, \quad \delta_+ \Psi^{n-1/2} = (\mathbf{g}_\Psi^n)^\intercal \delta_\cdot \mathbf{w}^n. \tag{27}$$

This defines a three-step scheme, in which the updates $\mathbf{w}^{n+1}$, $\Psi^{n+1/2}$ are obtained from the previous state values $\mathbf{w}^n, \mathbf{w}^{n-1}$, $\Psi^{n-1/2}$. Note as well that $\mathbf{g}_\Psi^n$ is known, and computed from (20) at the time step n, using the analytic expressions for the derivatives of the continuous function Ψ.
System (27) is completed by initial conditions on $\mathbf{w}$ and Ψ. At the initial time $n = 0$, it is assumed that the string is at rest, with the hammer moving according the initial conditions given above. The time series Ψ must be initialised accordingly, using definition (18) and the expression of Φ from (13). Thus

$$\mathbf{w}^0 = [\mathbf{0}^\intercal, \mathbf{0}^\intercal, U_0]^\intercal, \quad \mathbf{w}^1 = [\mathbf{0}^\intercal, \mathbf{0}^\intercal, kV_0 + U_0]^\intercal, \quad \Psi^{1/2} = \sqrt{p_0}. \tag{28}$$

Scheme (27) is energy-conserving. A proof is obtained by multiplying on left by $(\mathbf{S}^{-1}\delta_\cdot \mathbf{w}^n)^\intercal$, and using various identities (not shown here for brevity; see e.g. [20]). One gets

$$\delta_+ \mathfrak{h}^{n-1/2} = -(\delta_\cdot \mathbf{w}^n)^\intercal\, \tilde{\mathbf{C}}\, \delta_\cdot \mathbf{w}^n \leq 0, \tag{29}$$

where

$$\mathfrak{h}^{n-1/2} = \frac{1}{2}(\delta_+ \mathbf{w}^n)^\intercal \left(\tilde{\mathbf{M}} - \frac{k}{2}\tilde{\mathbf{C}}\right) \delta_+ \mathbf{w}^n + \frac{1}{2}(\mathbf{w}^n)^\intercal\, \tilde{\mathbf{K}}\, e_- \mathbf{w}^n + \frac{(\Psi^{n-1/2})^2}{2}. \tag{30}$$

This expresses the fully-discrete energy balance. It is worth noting that the expression for the fully discrete energy (30) is not positive semi-definite in all cases (as opposed to the semi-discrete energy in (22), which is always non-negative). However, conditions on non-negativity can be obtained by inspection of the linear part alone, since the nonlinear energy is here clearly non-negative, and expressed via the square of Ψ. It is possible to show (see e.g. [20, 16]) that, when the loss coefficients are small (as is the case for all musical strings), a sufficient condition for the non-negativity of the total discrete energy is

$$h \geq \sqrt{E/\rho}\, k. \tag{31}$$

When this condition is enforced, the discrete energy is non-negative, and hence stability of the time stepping scheme follows. Note that (31) is the CFL condition associated with the longitudinal motion, and it is expressed as a lower bound on h: this is much larger than the natural bound for the transverse waves (which is of the order of $\sqrt{T_0/\rho A}\, k$ for thin strings). Thus, enforcing condition (31) has consequences in the choice of the sample rate f_s, which has to be chosen much larger than typical audio rates (such as e.g. 44.1 kHz) to get enough resolution within the audio band.
Note as well that in (27) the operator δ_- was used to approximate the time derivative of the losses. This formally produces a first-order convergent scheme in time. However, it also allows for a fast update, as detailed below. Since losses are small, and since the time step k has to be chosen in the $10^{-5} - 10^{-6}$ range, this approximation does not introduce significant errors compared to a second-order accurate discretisation of the same derivative.

Scheme Update

Scheme (27) yields an efficient update equation. To show this, first use the identity $\mu_+ = (k/2)\delta_+ + 1$ in order to express the right-hand side of the first equation in (27) in terms of $\delta_\cdot \mathbf{w}^n$ from the second equation. Then, one rearranges the terms to get

$$\left(\frac{\mathbf{M}}{k^2} + \frac{1}{4}\mathbf{S}\,\mathbf{g}_\Psi^n\,(\mathbf{g}_\Psi^n)^\intercal\right)\mathbf{w}^{n+1} = \left(\frac{2\mathbf{M}}{k^2} - \frac{\mathbf{C}}{k} - \mathbf{K}\right)\mathbf{w}^n + \left(-\frac{\mathbf{M}}{k^2} + \frac{\mathbf{C}}{k} + \frac{1}{4}\mathbf{S}\,\mathbf{g}_\Psi^n\,(\mathbf{g}_\Psi^n)^\intercal\right)\mathbf{w}^{n-1} - \Psi^{n-1/2}\mathbf{S}\,\mathbf{g}_\Psi^n, \tag{32}$$

and note that the update matrix is now composed of the diagonal matrix $\mathbf{M}/k^2$ plus the rank-1 perturbation $\frac{1}{4}\mathbf{S}\,\mathbf{g}_\Psi^n\,(\mathbf{g}_\Psi^n)^\intercal$. This is invertible in $O(M)$ operations using the Sherman-Morrison formula [19, 18]. Once $\mathbf{w}^{n+1}$ is known, one may compute $\Psi^{n+1/2}$ using the second equation in (27).

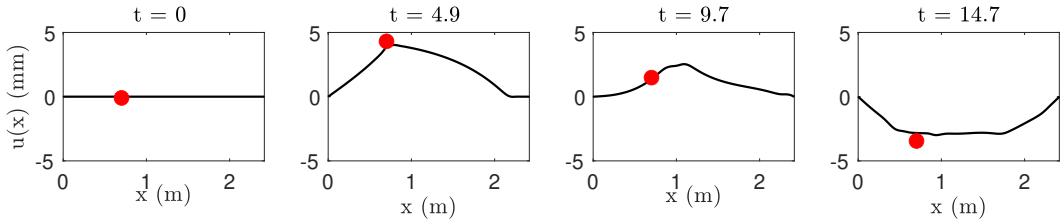

Figure 1: Snapshots of the hammer-string interaction. Here, the hammer and the string parameters are taken from [25], for the C2 string. The hammer initial velocity is 2 m/s. The sample rate used is $12 \cdot 48000$ Hz, resulting in a state size $2M - 1 = 547$ components. The times indicated are in ms.

Numerical Experiments

Scheme (27) is now tested in a number of numerical experiments. Figure 1 shows snapshots of the hammer-string dynamics, for the C2 piano string (the string and hammer parameters are taken from [25]). As expected, the hammer strikes the string intermittently. Here, the string's largest displacement is of the order of 4 mm, large enough to entail nonlinear effects.

The energetic behaviour of scheme (27) is checked in Figure 2, where the same C2 string is simulated in the absence of losses (that is, the matrix $\mathbf{C}$ is the zero matrix here). The discrete energy (30) is indeed conserved, with the error in the range of 10^{-14}. Note that here the kinetic energy includes that of the string and the hammer; the linear potential energy includes the string's alone, and the nonlinear energy includes the contributions of both the string's large displacement and the hammer-string collision. Note that the shift constant p_0 was set to a finite amount, to avoid division by zero in the computation of the derivatives of Ψ.

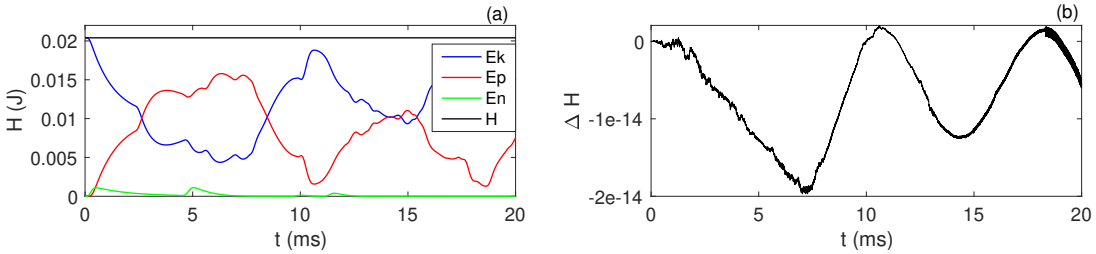

Figure 2: (a) Energy components and (b) energy error for the same case as Figure 1. In (a), E_k is the kinetic energy (comprising the string and the hammer), E_p is the linear potential energy of the string, E_n is the nonlinear potential energy including the string's nonlinear energy and the hammer-string collision potential, H is the total energy. In (b), ΔH is defined as $1 - \mathfrak{h}^{n-1/2}/\mathfrak{h}^{1/2}$, where the expression for the discrete energy $\mathfrak{h}$ is as per (30). In this simulation, the shift constant p_0 is set to 10^{-15}.

A quick convergence test is presented in Figure 3. Here, the time domain solutions at one output point are plotted, for a number of sample rate values. As mentioned above, significant oversampling factors are needed, compared to audio rate, since the number of grid points is now set according to bound (31), yielding a large grid spacing compared to typical wavelengths in the transverse direction. For high enough sample rates (OF $\gtrsim 12$), the computed solutions are very close, but discrepancies are evident for low-sampled waveforms. Various tests were run (not shown here), indicating that an oversampling factor of at least 12 is usually required for good resolution within the audio band. Some audio files are available on the companion webpage[1].

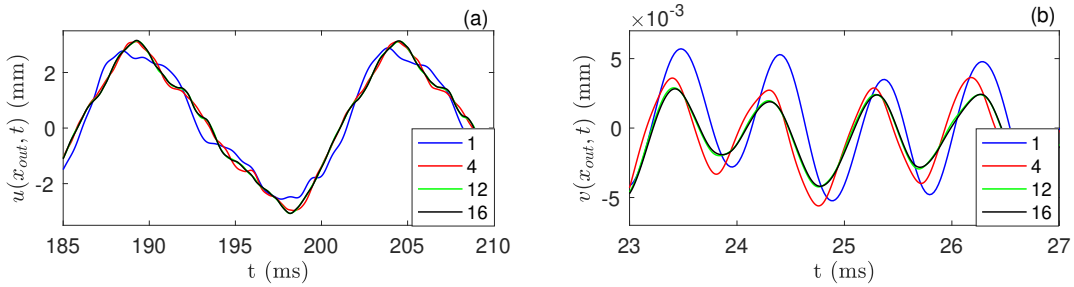

Figure 3: Convergence test under various oversampling factors for a base sample rate $f_{s0} = 48$ kHz, indicated in the legend. (a): transverse displacement. (b): longitudinal displacement. Here $x_{out} = 0.32L$, and the string's parameters are the same as in Figure 1.

Figure 4 presents the output spectra of the longitudinal displacement under three different hammer initial velocities. Note the change in brightness as the velocity increases, as well as the appearance of phantom partials.

[1] `https://mdphys.org/ENOC_2022.html`

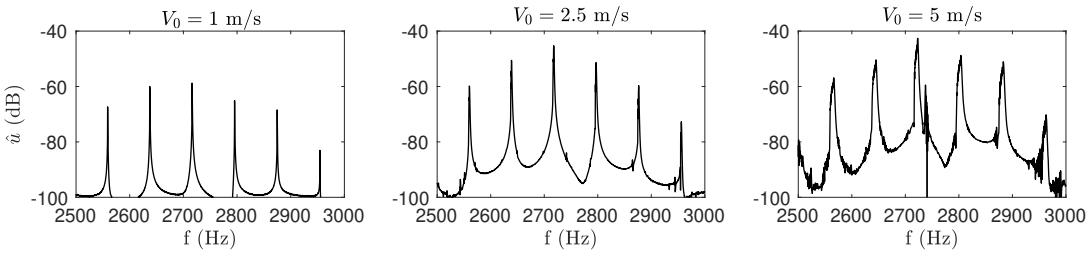

Figure 4: Output spectra for the D2 string, with initial hammer velocities as indicated. Output is extracted at $x_{out} = 0.32L$

Table 1 presents a computational testing comparing various schemes, and implementations. Two schemes, called `ICA_IT` and `ICA_NIT`, are taken from [15]. `ICA_IT` is a finite difference iterative scheme, obtained via a fully-implicit conservative discretisation of the gradient in a fashion similar to that used in many works, see e.g. [3, 4, 5, 26]; `ICA_NIT` is a non-iterative finite difference scheme obtained via quadratisation, in a fashion similar to the scheme presented here, but where the nonlinear auxiliary variable Ψ is approximated via a *grid function*, and not as a single scalar variable as here (that is, it is not possible to update `ICA_NIT` using the fast Sherman-Morrison formula, though the scheme's update is in a form of a linear system). `LU_NIT`, presented in [16], is also a non-iterative scheme, where the transverse waves are simulated using finite differences, and the longitudinal waves are approximated using a modal approach. The system is again in "quadratised" form, and a block LUD decomposition is adopted to compute the update. All these schemes were coded in Matlab. Finally, `SM_MTL` and `SM_C++` present the compute times for the fast Sherman-Morrison formula

OF	M	M_{long}	`ICA_IT`	`ICA_NIT`	`LU_NIT`	`SM_MTL`	`SM_C++`
1	10	2	14.6	8.73	7.59	14.1	0.008
2	21	4	24.7	19.8	16.1	16.4	0.029
4	42	7	53.4	41.4	22.5	19.1	0.108
8	85	14	145	102	87.0	26.6	0.362
12	128	21	267	191	173	37.8	0.756
16	170	28	453	324	279	58.3	1.15

Table 1: Compute time / real time ratios, using various schemes and implementations, for the D3 piano string from [25]. Here, `ICA_IT` and `ICA_NIT` are, respectively, the finite difference iterative and non-iterative schemes presented in [15]; `LU_NIT` is the non-iterative mixed finite difference-modal method described in [16] (where the transverse displacement is approximated using finite differences, and the longitudinal displacement using a modal approach); `SM_MTL` is the Sherman-Morrison implementation presented here, using Matlab; `SM_C++` is the same scheme implemented in C++. In the table, OF indicates the oversampling factor for a base sample rate $f_{s0} = 48$ kHz. M is the number of grid points; M_{long} is the number of longitudinal modes used in `LU_NIT`. In this test, for simplicity, the hammer was not considered, and the string was initialised in its first mode of vibration in the transverse direction, i.e. $u_0(x) = 0.01 \sin(\pi x/L)$. The size of the state vector, for all schemes, is then $2M - 2$, with the exception of `LU_NIT` for which the size is $M - 1 + M_{long}$. Below-real-time simulations are highlighted. All simulations were run on a 2016 Macbook Pro, equipped with a 2.9 GHz Intel i7 processor. Matlab simulations were run in MatlabR2020.

given here, using both Matlab and C++ implementations. A few aspects are worth commenting. First, note that the rate of growth of the compute times for the two `SM` schemes is much lower than for the other schemes, since, as remarked previously, the Sherman-Morrison formula is solvable in $O(M)$ operations. Second, note how the C++ implementation yields considerable speedups compared to Matlab. Here, all the matrix operations were "unrolled", avoiding the need for sparse matrix libraries. Update (32) is remarkably fast, yielding under-real-time compute times for systems with over 250 nonlinearly coupled degrees-of-freedom. Compared to typical fully-implicit discretisations, such as `ICA_IT` coded in Matlab, `SM_C++` is about 350 times faster at OF = 12.

Concluding Remarks

The piano string was modelled using a nonlinear, geometrically exact model, and including the hammer-string interaction. The model was first discretised in space using the finite difference method, and then "quadratised" via a scalar auxiliary state function. The resulting system was then integrated in time. It was shown that the update matrix lends itself to a fast inversion via the Sherman-Morrison formula. A C++ implementation of the proposed scheme was given, yielding speedups of a few orders of magnitude compared to Matlab realisations of previously available schemes. In particular, real-time simulations of typical piano strings are now available. The proposed schemes are part of a larger class of schemes of recent development, based on the idea of quadratisation.

Acknowledgments

This work was supported by the European Research Council (ERC), under grant 2020-StG-950084-NEMUS.

References

[1] P. Morse and U. Ingard. *Theoretical Acoustics*. Princeton University Press, Princeton, NJ, USA, 1968.

[2] S. Bilbao, A. Torin, and V. Chatziioannou. Numerical modeling of collisions in musical instruments. *Acta Acust United with Acust*, 101:155–173, 2015.

[3] T. Itoh and K. Abe. Hamiltonian-conserving discrete canonical equations based on variational difference quotients. *J. Comput. Phys.*, 76(1):85–102, 1988.

[4] A. Falaize and T. Hélie. Passive Guaranteed Simulation of Analog Audio Circuits: A Port-Hamiltonian Approach. *Appl Sci*, 6:273–273, 2016.

[5] J. Chabassier and P. Joly. Energy preserving schemes for nonlinear Hamiltonian systems of wave equations: Application to the vibrating piano string. *Comput Method Appl Mech*, 199(45):2779–2795, 2010.

[6] J. Chabassier. *Modélisation et simulation numérique d'un piano par modèles physiques. (Modeling and simulation of a piano by physical modelling.)*. PhD thesis, Ecole Polytechnique X, Paris, 2012.

[7] F. Fontana and E. Bozzo. Newton–Raphson solution of nonlinear delay-free loop filter networks. *IEEE/ACM Trans. Audio, Speech, Lang. Process.*, 27(10):1590–1600, 2019.

[8] V. Chatziioannou, S. Schmutzhard, and S. Bilbao. On iterative solutions for numerical collision models. In *Proc Int Conf On Digital Audio Effects (DAFx-17)*, Edinburgh, UK, September 2017.

[9] N. Lopes, T. Hélie, and A. Falaize. Explicit second-order accurate method for the passive guaranteed simulation of port-hamiltonian systems. In *Proc 5th IFAC 2015*, Lyon, France, July 2015.

[10] A. Falaize. *Modélisation, simulation, génération de code et correction de systèmes multi-physiques audios: Approche par réseau de composants et formulation Hamiltonienne À Ports. (Modeling, Simulation, code generation and correction of multiphysics audio systems: Component network approach and Port-Hamiltonian formulation)*. PhD thesis, Université Pierre et Marie Curie, Paris, July 2016.

[11] N. Lopes. *Approche passive pour la modélisation, la simulation et l'étude d'un banc de test robotisé pour les instruments de type cuivre. (Passive approach for modelling, simulation and study of a robotic test bench for brass instruments.)*. PhD thesis, Université Pierre et Marie Curie, Paris, July 2016.

[12] X. Yang. Linear, first and second-order, unconditionally energy stable numerical schemes for the phase field model of homopolymer blends. *J Comput Phys*, 327:294–316, 2016.

[13] X. Yang. Linear and unconditionally energy stable schemes for the binary fluid-surfactant phase field model. *Comp Methods Appl Mech Eng*, 318:1005–1029, 2017.

[14] J. Zhao, Q. Wang, and X. Yang. Numerical approximations for a phase field dendritic crystal growth model based on the invariant energy quadratization approach. *Int J Numer Meth Eng*, 110(3):279–300, 2017.

[15] M. Ducceschi and S. Bilbao. Non-iterative, conservative schemes for geometrically exact nonlinear string vibration. In *Proc Int Conf Acoust (ICA 2019)*, Aachen, Germany, September 2019.

[16] M. Ducceschi and S. Bilbao. Simulation of the geometrically exact nonlinear string via energy quadratisation. *J Sound Vib*, 2022 (in press).

[17] J. Shen, J. Xu, and J. Yang. The scalar auxiliary variable (sav) approach for gradient flows. *J. Comput. Phys.*, 353:407–416, 2018.

[18] S. Bilbao and M. Ducceschi. Fast explicit algorithms for hamiltonian numerical integration. In *Proceedings of the European Nonlinear Dynamics Conference*, Lyon, France, July 2022.

[19] J. Sherman and W. J. Morrison. Adjustment of an inverse matrix corresponding to a change in one element of a given matrix. *Ann Math Stat*, 21:124–127, 1950.

[20] S. Bilbao. *Numerical Sound Synthesis: Finite Difference Schemes and Simulation in Musical Acoustics*. Wiley, Chichester, UK, 2009.

[21] M. Ducceschi, S. Bilbao, S. Willemsen, and S. Serafin. Linearly-implicit schemes for collisions in musical acoustics based on energy quadratisation. *J. Acoust. Soc. Am.*, 149(5):3502–3516, 2021.

[22] M. Ducceschi and S. Bilbao. Linear stiff string vibrations in musical acoustics: Assessment and comparison of models. *J Acoust Soc Am*, 140(4):2445–2454, 2016.

[23] M. Ducceschi and S. Bilbao. Conservative finite difference time domain schemes for the prestressed Timoshenko, shear and Euler-Bernoulli beam equations. *Wave Motion*, 89:142 – 165, 2019.

[24] C. Valette and C. Cuesta. *Mécanique de la corde vibrante*. Hermès, Paris, 1993.

[25] J. Chabassier and M. Duruflé. Physical parameters for piano modeling. Technical report, 2012. Available at `https://hal.inria.fr/hal-00688679v1/document`.

[26] V. Chatziioannou and M. van Walstijn. Energy conserving schemes for the simulation of musical instrument contact dynamics. *J Sound Vib*, 339:262–279, 2015.

Wednesday, July 20, 2022

08:30 - 10:30

MS-08 Nonlinear Phenomena in Mechanical and Structural Systems

Rhone 3B

Chair: Jaroslaw Latalski

08:30 - 08:50
Influence of the base motion on the dry-whip onset of an on-board rotor-journal bearing system
BRIEND Yvon*, CHATELET Eric, DUFOUR Régis, ANDRIANOELY Marie-Ange, LEGRAND Franck, BAUDIN Sophie
*Univ Lyon, INSA-Lyon, CNRS UMR5259, LaMCoS, F-69621, France (20 Avenue Albert Einstein France)

08:50 - 09:10
Investigation of bifurcations in a nonlinear rotor system using numerical continuation
AKAY Mehmet*, SHAW Alexander, FRISWELL Michael
*Swansea University (Swansea University Bay Campus Fabian Way Crymlyn Burrows Swansea SA1 8EN Wales, UK United Kingdom)

09:10 - 09:30
Investigation of energy dissipation based on shock and friction to suppress critical self-excited vibrations in drilling systems
KULKE Vincent, OSTERMEYER Georg-Peter, **HOHL Andreas***
*Baker Hughes (Baker-Hughes-Straße 1, 29221 Celle Germany)

09:30 - 09:50
Model order reduction for geometrically nonlinear beams featuring internal resonance and centrifugal effect
MARTIN Adrien*, OPRENI Andrea, VIZZACCARO Alessandra, SALLES Loic, FRANGI Attilio, TOUZÉ Cyril
*Institute of Mechanical Science and Industrial Applications (Unité de Mécanique, IMSIA 828 Boulevard des Maréchaux 91762 Palaiseau Cedex France)

09:50 - 10:10
Modeling and Simulations of the Nonlinear Dynamics of Carbon Nanotube Based Resonator Assuming Nonlocal Strain and Velocity Gradient Theories
OUAKAD Hassen*, SEDIGHI Hamid
*SULTAN QABOOS UNIVERSIY (Al Khoudh, MUSCAT, OMA Oman)

10:10 - 10:30
Modelling and dynamics of smart composite box beam with nonlinear constitutive behaviour of active elements
LATALSKI Jaroslaw*, WARMINSKI Jerzy
*Department of Applied Mechanics, Lublin University of Technology (Nadbystrzycka 36, 20-618 Lublin Poland)

Influence of the base motion on the dry-whip onset of an on-board rotor-journal bearing system

Yvon Briend[*], Eric Chatelet [*], Régis Dufour[*], Marie-Ange Andrianoely[*], Franck Legrand and Sophie Baudin[**]

[*]*Univ Lyon, INSA-Lyon, CNRS UMR5259, LaMCoS, F-69621, France*

[**]*Avnir Engineering, F-69621, France*

Summary: In this paper, the special class of on-board rotor undergoing rotor-stator contact is under investigation. In particular, a well-known and harmful contact instability, the dry-whip phenomenon, is addressed. The aim of the paper is to present original experiments evidencing this instability being triggered by a multi-axial shock translation from the rigid rotor base. Moreover, the influence of the base motion parameters, such as the shock amplitudes, directions and time instants, on the onset of dry-whip is investigated both numerically and experimentally.

Introduction

On-board rotors represent a very special class of rotors, which are subject to motions of their base that may induce high vibration levels. In practice, they can be encountered in a large variety of industrial fields such as energy, transports, defense, etc. In this context, these systems have recently raised a particular interest as highlighted by the literature [1-2]. Due to the base motions, contact is likely to occur between rotating and non-rotating parts. In some cases, these contacts can lead to harmful dynamic instabilities, such as the dry-whip phenomenon, threatening the structural integrity of the mechanical systems. The latter is characterized by a sudden change in the whirl that leads to backward whirl owing to the tangential friction contact forces, which causes high displacement amplitudes and frequencies. It can be triggered by a mass unbalance only or in combination with an external disturbance [3] such as a hammer impact or a base motion.
The evidencing of the dry-whip phenomenon as caused by base motion is relatively recent [4]. The aim of this paper is to emphasize the experimental and numerical outcomes of [4]. Moreover, the conditions of onset of the instability depending on the base motion parameters are investigated in more details.

Experimental and numerical investigations

The on-board rotor test rig (two disks mounted on a slender shaft) used in this context is modelled with Timoshenko beam elements and its mesh is sketched in Figure 1. It is equipped with two short fluid film bearings at Nodes 6 and 23 and with multiple contact rings. The ring at Node 15 is intended to be the first one to experience rotor-stator contacts and to be responsible for the dry-whip occurrence while the others are stator bores used rather for safety requirements.

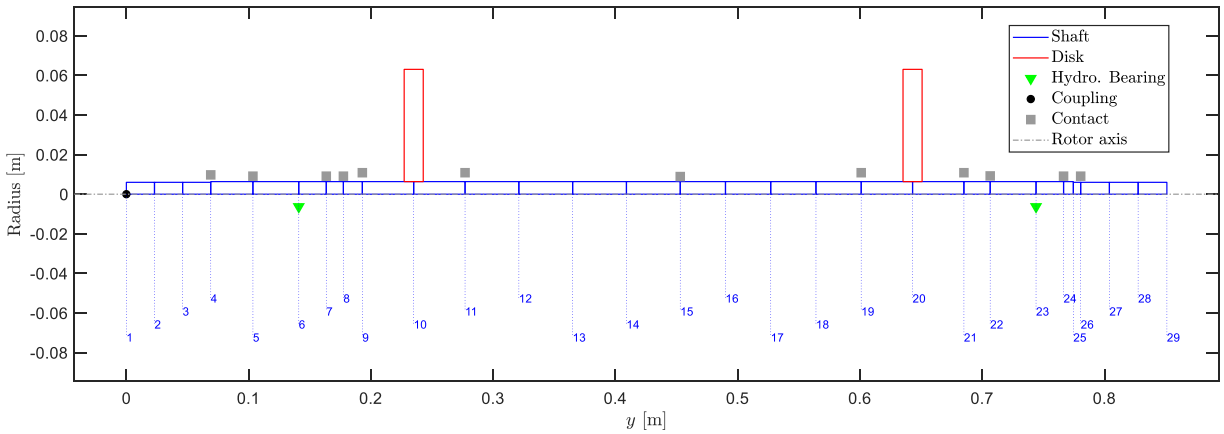

Figure 1: FE mesh of the on-board rotor-bearing system mounted on finite-length journal bearings and equipped with multiple contact rings

In a first study case, the rotor rotates at a fixed speed of rotation of 1700 rpm and two mass unbalances of 2.37 10^{-3} kg with a 57.0 10^{-3} m gyration radius are screwed on each disk at 0° and 20°. After reaching the steady-state response, a multi-axial base motion composed of two synchronous transverse shocks (pre- and post- 10 ms pulse of 15 m/s²) is imposed suddenly and briefly in order to trigger the dry-whip. The measured response in terms of the full spectrogram of the Node 16 transverse displacements is shown in Figure 2. The whirl transition from forward at ~28 Hz (1700 rpm) to backward at ~-170 Hz is clearly identified when the shock is performed near t=2.55 s. Meanwhile, critical vibration levels are also highlighted, until t=~6 s where the instability suddenly vanished because of the motor-shaft coupling failure and the damping effects.

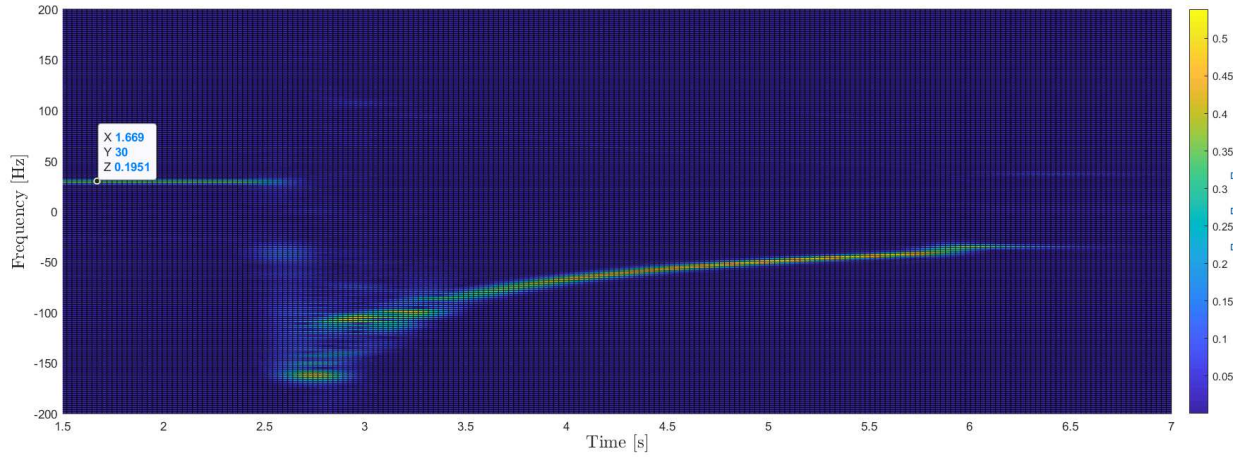

Figure 2: Full spectrogram of the measured Node 16 orbit of the test rig subject to mass unbalance and to pre- and –post pulse from the base

Then, the instant of the shock is varied numerically in order to impact the contact ring at different rotation angles and to assess if this may favor or inhibit the dry-whip triggering. To this aim, ten values of time instants, equally distributed between 0° and 360° (0° and 360° corresponding to t=2.55 s and t=2.55s + *T*, respectively, with *T* the mass unbalance period), are performed. The results are presented in Figure 3. It is noticed that for all instants, the dry-whip is triggered, however, it is more delayed and many rebounds are found for instants near 216°. This result can be assigned to the variation of the angle of contact and to the radial velocity of impact that change with the shock instant.

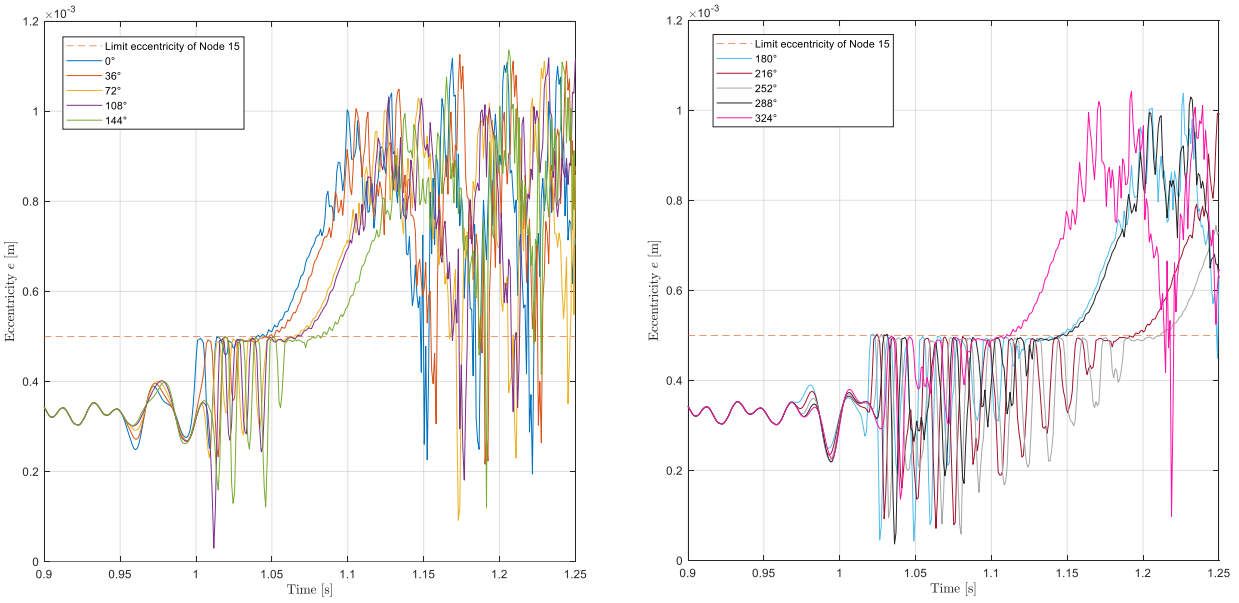

(a) (b)

Figure 3: Numerical eccentricities of Node 16 of the test rig subject to mass unbalance and to a base transverse shock translation at t=0,95s with different time instants equivalent to (a) [0°-144°] and to (b) [180°-324°]

Acknowledgments

The authors are indebted to the French National Research Agency (Funder ID: 10.13039/501100001665) (ANR) for its financial support within the framework of the LaBCoM-SME AdViTAM, ANR-16-LCV1-0006 and Equipex PHARE 10-EQPX-0043.

References

[1] Soni, T., Dutt, J. K., & Das, A. S. (2019). Parametric stability analysis of active magnetic bearing supported rotor system with a novel control law subject to periodic base motion. *IEEE Transactions on Industrial Electronics*, *67*(2), 1160-1170.

[2] Su, Y., Gu, Y., Keogh, P. S., Yu, S., & Ren, G. (2021). Nonlinear dynamic simulation and parametric analysis of a rotor-AMB-TDB system experiencing strong base shock excitations. *Mechanism and Machine Theory*, *155*, 104071.

[3] Jiang, J. Determination of the global responses characteristics of a piecewise smooth dynamical system with contact. *Nonlinear Dyn* **57,** 351–361 (2009)

[4] Briend, Y., Chatelet, E., Dufour, R., Andrianoely, M. A., Legrand, F., Sousa Jr, M. S., Steffen Jr, V. and Baudin, S. (2021). Dry-whip phenomenon in on-board rotordynamics: Modeling and experimentation. *Journal of Sound and Vibration*, *513*, 116398.

Investigation of bifurcations in a nonlinear rotor system using numerical continuation

Mehmet S Akay*, Alexander D Shaw*, Michael I Friswell*
*College of Engineering, Swansea University, Swansea, United Kingdom

Summary. Nonlinearities in rotating systems have been seen to cause a wide variety of rich phenomena, however the understanding of these phenomena has been limited because numerical approaches typically rely on 'brute force' time simulation, which are inefficient due to issues of step size and settling time, cannot locate unstable solution families and may miss key responses if the correct initial conditions are not used. This work uses numerical continuation to explore the responses of such systems in a more systematic way. A simple isotropic rotor system with a smooth nonlinearity is studied, and the rotating frame is used to obtain periodic solutions. Asynchronous responses with oscillating amplitude are seen to initiate at certain drive speeds due to internal resonance, in a manner similar to that observed for non-smooth rotor stator contact systems in previous literature. These responses are isolated, in the sense that they will only meet the more trivial synchronous responses in the limit of zero damping and out of balance forcing. In addition to increasing our understanding of the responses of these systems, the work establishes the potential of numerical continuation as a tool to systematically explore the responses of nonlinear rotor systems.

Introduction

Nonlinear dynamic system's response can show bifurcations with small changes in its parameters. Therefore, systematically locating these bifurcation points is vital. Rotating machinery makes this more challenging with gyroscopic coupling that ties the whirl frequencies to the rotor speed. As a result, the internal resonance phenomenon can occur in a large range of operating rotor speeds, resulting in the bouncing orbits involving rotor-stator contact. The contacting interaction can be defined in various ways in the literature, ranging from rigid impact [1] to soft penalty contact [2].
For the solution of nonlinear problems within rotordynamics field, time simulations [3] and analytical and semi-analytical approaches based on harmonic balance method [4] have been used, aside from experimental investigations. However, this work uses the numerical continuation method applied directly to the systems of ODE, as a contrast to Refs. [5], due to its advantages over time simulations in computational cost and over algebraic methods in setup simplicity.
The analysed system is a 2-dof overhung rotor with isotropic cubic nonlinearity, shown in Figure 1 in the dimensional form. The equation of motion is nondimensionalised and transformed into the autonomous rotating coordinate frame equations given in Eq. (1).

$$U'' + \left(-\hat{\Omega}J\left(\hat{I}_p - 2\right) + 2\zeta\right)U' + \left(\hat{\Omega}^2\left(\hat{I}_p - 1\right) + 1 + 2\zeta\hat{\Omega}J\right)U + \gamma\hat{r}^2U = \hat{m}\hat{e}\hat{\Omega}^2\begin{Bmatrix}1\\0\end{Bmatrix}, \qquad J = \begin{bmatrix}0 & -1\\ 1 & 0\end{bmatrix} \tag{1}$$

where hat indicates the nondimensional form, $U = [\hat{u}, \hat{v}]$ is the rotating coordinate vector with coordinates $\hat{u}$ and $\hat{v}$, $\hat{\Omega}$ is the rotor speed, $\hat{I}_p$ is polar moment of inertia, ζ is damping ratio, J is a skew symmetric matrix, γ is the cubic stiffness, $\hat{r}$ is the distance of disk geometric centre to the stationary equilibrium, $\hat{m}$ is the disk mass, $\hat{e}$ is the eccentricity of the disk, $(.)'$ is the derivative with respect to time, all in nondimensional forms.
The main focus of this work is on asynchronous periodic orbits that are caused by internal resonance, and we address similarities and differences to the case of contacting nonlinearity. The solutions found are validated with time simulation. AUTO open-source ODE numerical continuation software and MATLAB ode45 explicit integrator were used in the study.

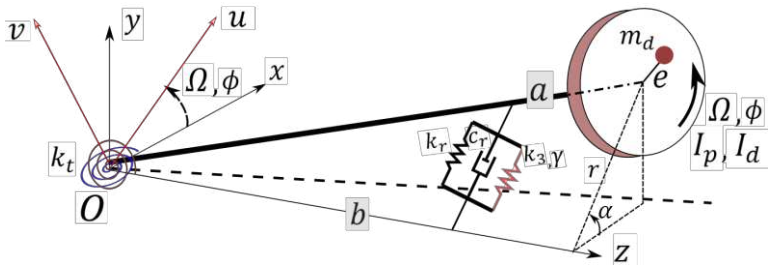

Figure 1: The 2-dof overhung rotor system with isotropic cubic stiffness.

Results

The bifurcation diagram resulting from the numerical continuation procedure is plotted in Figure 1(a). In this plot, the responses of the system with different damping levels are given together to see the effect of damping. The solution includes the synchronous response, which is skewed highly towards right due to stiffening, and asynchronous response that has two distinct sets of solution families, named here as double- and single-loop solution families after their apparent shapes in Figures 1(b) and 1(c). These orbits are periodic due to being viewed in the rotating frame (otherwise quasi-periodic in the stationary frame). Figures 1(d) and 1(e) show close-ups of asynchronous response to the synchronous solution. The double-loop and single-loop solutions were linked to the internal resonance conditions 3:1 and 2:1 in the rotating coordinates, respectively, by comparing them to the Campbell diagram with signed frequencies. These clearly show the closeness of the periodic responses to the stationary ones in the case of very low damping, ζ=1e-5. The periodic solutions were shown to be present only below a certain damping value that is peculiar to the solution family. This limit

was found to be 0.0116 for double-loop solutions and 0.082 for single-loop solutions, as illustrated in Figure 2.

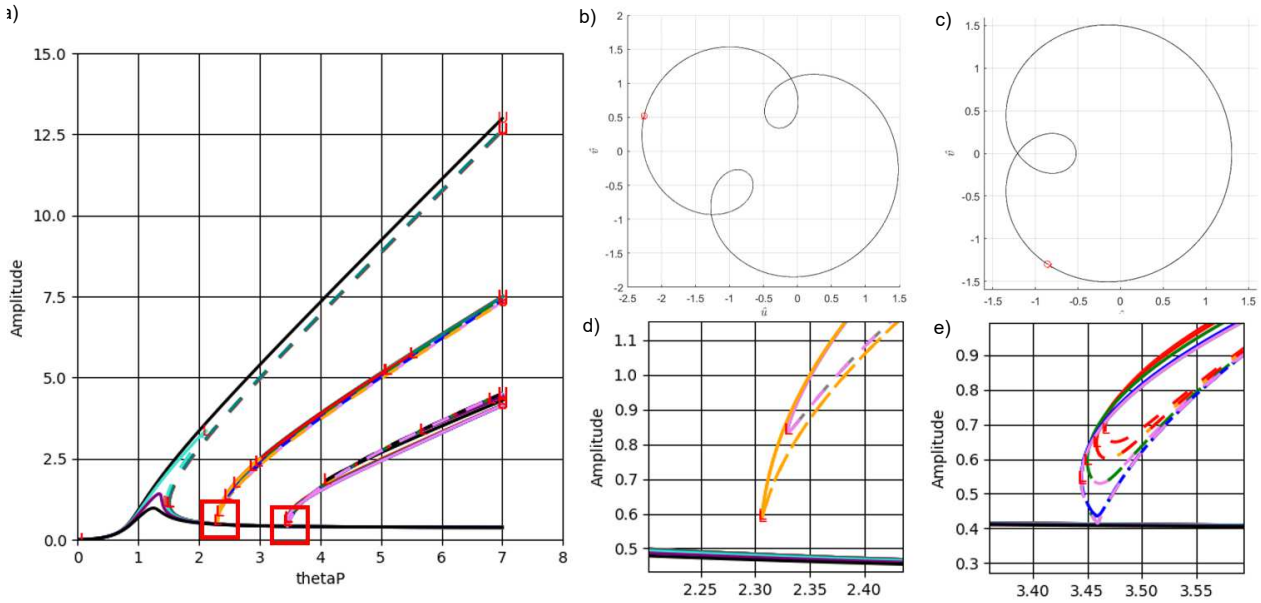

Figure 1: a) Continuation results as bifurcation diagram, b-c) double- and single-loop periodic orbits in rotating frame, d-e) and their low damping tips' close-up. Red "L" signs locate the folds of the solution families. Dashed lines show unstable solutions.

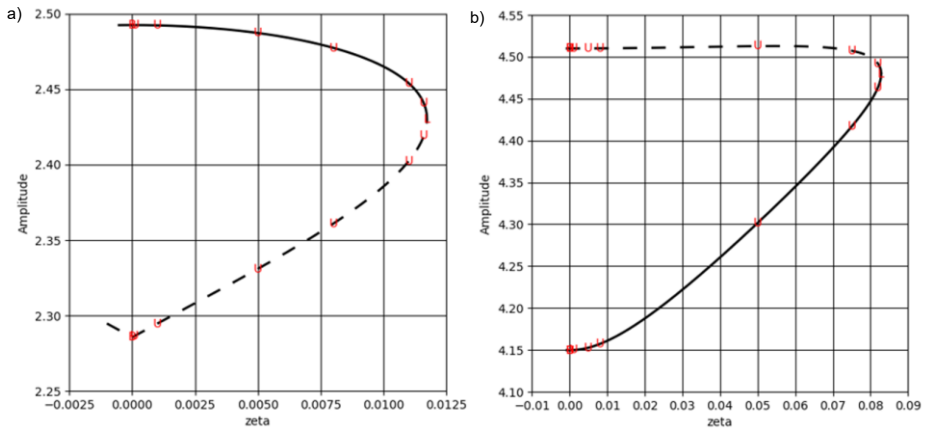

Figure 2: Damping limits for a) double- and b) single sloop solution families were 0.0116 and 0.082, respectively. The "U" signs locate the orbits corresponding to the sampled damping values. Dashed lines show unstable solutions.

Conclusions

The softer extreme of rotor-stator contact interaction was investigated by replacing the contact with a cubic stiffness nonlinearity. Direct application of continuation on the equations of motion was easy to setup and the solution procedure can be validated with time simulations easily. The following conclusions were drawn. The previously reported intermittent contact patterns for the models of hard impact and compliant snubber rings can also be observed in the case of the geometric nonlinearity of cubic stiffness. The level of damping changes the region where periodic motions was expected. Higher damping can cause the periodic solutions to disappear from the bifurcation diagrams. However, for low damping there is a limit to the growth of the periodic orbit region towards the lower rotor speeds; for very low values of damping (e.g. ζ=1e-4 and 1e-5) the periodic solution family approaches the synchronous solutions. It might be inferred that the gap closes asymptotically as ζ and the oscillation amplitude approach zero. This indicates that this region requires very little disturbance for synchronous solutions to jump to the periodic orbits.

References

[1] K. Mora, A. R. Champneys, A. D. Shaw, and M. I. Friswell, "Explanation of the onset of bouncing cycles in isotropic rotor dynamics; a grazing bifurcation analysis," *Proc. R. Soc. A Math. Phys. Eng. Sci.*, vol. 476, no. 2237, 2020, doi: 10.1098/rspa.2019.0549.

[2] G. Von Groll and D. J. Ewins, "The harmonic balance method with arc-length continuation in rotor/stator contact problems," *J. Sound Vib.*, vol. 241, no. 2, pp. 223–233, 2001, doi: 10.1006/jsvi.2000.3298.

[3] E. Chipato, A. D. Shaw, and M. I. Friswell, "Frictional effects on the nonlinear dynamics of an overhung rotor," *Commun. Nonlinear Sci. Numer. Simul.*, vol. 78, 2019, doi: 10.1016/j.cnsns.2019.104875.

[4] A. D. Shaw, A. R. Champneys, and M. I. Friswell, "Normal form analysis of bouncing cycles in isotropic rotor stator contact problems," *Int. J. Mech. Sci.*, vol. 155, no. March 2018, pp. 83–97, 2019, doi: 10.1016/j.ijmecsci.2019.02.035.

[5] L. Peletan, S. Baguet, M. Torkhani, and G. Jacquet-Richardet, "Quasi-periodic harmonic balance method for rubbing self-induced vibrations in rotor–stator dynamics," *Nonlinear Dyn.*, vol. 78, no. 4, pp. 2501–2515, 2014, doi: 10.1007/s11071-014-1606-8.

Investigation of energy dissipation based on shock and friction to suppress critical self-excited vibrations in drilling systems

Vincent Kulke[*], Georg-Peter Ostermeyer[*] and Andreas Hohl[**]
[*] Institute of Dynamics and Vibrations, Department of Mechanical Engineering, TU Braunschweig
[**]Baker Hughes, Celle, Germany

Summary. In this article, a passive damper based on energy dissipation through shocks and dry friction (shock-friction damper) is investigated with regard to its effectiveness for damping self-excited torsional vibrations similar to those occurring in deep drilling. A minimal model based on a modally reduced complex finite element model of a drill string and a lumped mass representing the inertia of the forcedly connected damper is introduced for an effective and precise investigation of the dynamic motion and damping effect. Particular focus is on the energy flow within the dynamic system and on the change of the dissipation process in the friction contact. The resulting damping effect is compared with the self-excitation due to the bit-rock interaction in the drilling system. Parameters of the considered mode as well as parameters of the damper are examined regarding the damping effect. The shock-friction damper is compared to conventional friction dampers.

Introduction

In downhole drilling systems, various types of vibration occur that can reduce drilling performance and result in premature failure of components [1]. Especially in hard and dense formations, high-frequency torsional oscillations (HFTO) occur in the range of 50 to 500 Hz. These oscillations are self-excited torsional vibrations of higher-order modes that can lead to critical torsional loads. Downhole measurement data show that the self-excitation can be described by a torque characteristic at the bit that decreases with the rotary speed. In [2], an analytical criterion based on a modal transformation is introduced to determine modes that are prone to self-excitation by linearizing the torque characteristic at the mean rotary speed of the drillstring. Increasing the damping of a system is a well-known approach to reduce self-excited vibration amplitudes. Tondl investigated the effect of tuned mass dampers and dry friction [3] on self-excited vibrations. Different types of friction contacts and friction dampers for various fields of engineering were investigated and classified [4]. For example, a friction damper is analyzed in [5] designed for railway wheels consisting of an inertia mass and a friction contact. In drilling systems, the effectiveness of inertia-based dampers is limited due to the small design space in the bottom-hole assembly (BHA) that is naturally limited by the drilled borehole size [6]. This reality necessitates investigation and optimization of the nonlinear forces characteristics between the inertia-mass to dampen the structure effectively. Similar efforts and analysis for nonlinear attachments show a significant effect on the energy output of a dynamic system [7].

Modeling of a passive shock-friction damper

To investigate drillstring vibrations, a finite element model of an entire drillstring using the angular deviations $\boldsymbol{x}$ from the operating point (constant angular speed and twist) with $\boldsymbol{M}\ddot{\boldsymbol{x}} + \boldsymbol{C}\dot{\boldsymbol{x}} + \boldsymbol{K}\boldsymbol{x} = \boldsymbol{f}$ is used. Herein, $\boldsymbol{M}, \boldsymbol{C}$ and $\boldsymbol{K}$ are the mass, damping and stiffness matrices and $\boldsymbol{f}$ an external force vector. The critical torsional modes are determined by a modal analysis and stability considerations. Following the modal transformation, the physical degrees of freedom $\boldsymbol{x}$ are expressed by $\boldsymbol{x} = \boldsymbol{\Phi}\boldsymbol{q}$ with the mass-normalized modal matrix $\boldsymbol{\Phi}$ and the modal degrees of freedom $\boldsymbol{q}$.
To perform an efficient and accurate investigation of the damping effect and dynamic behavior of the nonlinear shock-friction damper regarding critical self-excited drill string vibrations, the complex drilling system is reduced. Downhole measurement data show that mostly one critical mode dominates the dynamic motion of the entire drillstring when HFTO occurs. Resulting in a modal single-degree-of-freedom system $\ddot{q} + 2D_i\omega_{0,i}\dot{q} + \omega_{0,i}^2 q = \sum_{j=1}^{n} \varphi_{i,j} M_j$ where $\omega_{0,i}$ and D_i are the natural frequency and modal damping of the *i*-th mode ($D_i < 0$ for the self-excited HFTO-mode), M_j is an external torque that acts at the *j*-th node and $\varphi_{i,j}$ is the mass-normalized modal amplitude of the i-th mode at the j-th node. This minimal model can be extended to any damping force characteristic to determine its influence on the critical mode. The equation of motion

$$\begin{pmatrix} 1 & 0 \\ 0 & J \end{pmatrix}\begin{pmatrix} \ddot{q} \\ \ddot{x} \end{pmatrix} + \begin{pmatrix} 2D_i\omega_i & 0 \\ 0 & 0 \end{pmatrix}\begin{pmatrix} \dot{q} \\ \dot{x} \end{pmatrix} + \begin{pmatrix} \omega_i^2 & 0 \\ 0 & 0 \end{pmatrix}\begin{pmatrix} q \\ x \end{pmatrix} = \begin{pmatrix} -\varphi_{i,j} M\left(\varphi_{i,j}\dot{q} - \dot{x}\right) \\ M\left(\varphi_{i,j}\dot{q} - \dot{x}\right) \end{pmatrix} \tag{1}$$

describes a critical mode connected by a torque to an inertia mass.
The torque between the inertia mass and the structure (Equation 2) consists of a friction contact with a normal force F_N, a coefficient of friction μ, a friction radius r and an elastic backlash with a stiffness c and a width S.

$$M\left(\varphi_{i,j}\dot{q} - \dot{x}\right) = \begin{cases} F_\mathrm{N}\mu r\ \mathrm{sgn}\left(\varphi_{i,j}\dot{q} - \dot{x}\right), & \left|\varphi_{i,j}q - x\right| < S \\ F_\mathrm{N}\mu r\ \mathrm{sgn}\left(\varphi_{i,j}\dot{q} - \dot{x}\right) + c\left(\left|\varphi_{i,j}q - x\right| - S\right)\mathrm{sgn}\left(\varphi_{i,j}q - x\right), & \left|\varphi_{i,j}q - x\right| \geq S \end{cases} \tag{2}$$

The relative angular speed $v_\mathrm{rel} = \varphi_{i,j}\dot{q} - \dot{x}$ and the relative angular displacement $x_\mathrm{rel} = \varphi_{i,j}q - x$ between the damper and the structure are composed of the modal and physical degree of freedom.

Investigation of vibration response and energy flow

To investigate the influence of the nonlinear shock-friction damper on the structure and the energy flow within the system time domain, simulations are used. Figure 2 (left) shows the motion of the structure and the damper. For small amplitudes, sticking occurs in the friction contact. No relative movement between the structure and the damper takes place. Due to the self-excitation ($D_i < 0$), energy periodically flows into the system (Figure 2, right), resulting in an increase of the amplitude in the sticking phase. At a certain amplitude, the inertial torque of the damper is greater than the friction torque $J\ddot{x} > F_N \mu r$, resulting in sliding regimes and energy dissipation in the friction contact. When the dissipated energy in the friction contact is not sufficient to stabilize the system, the amplitude increases further, resulting in an increased relative displacement and thus in shocks between the damper and the structure.

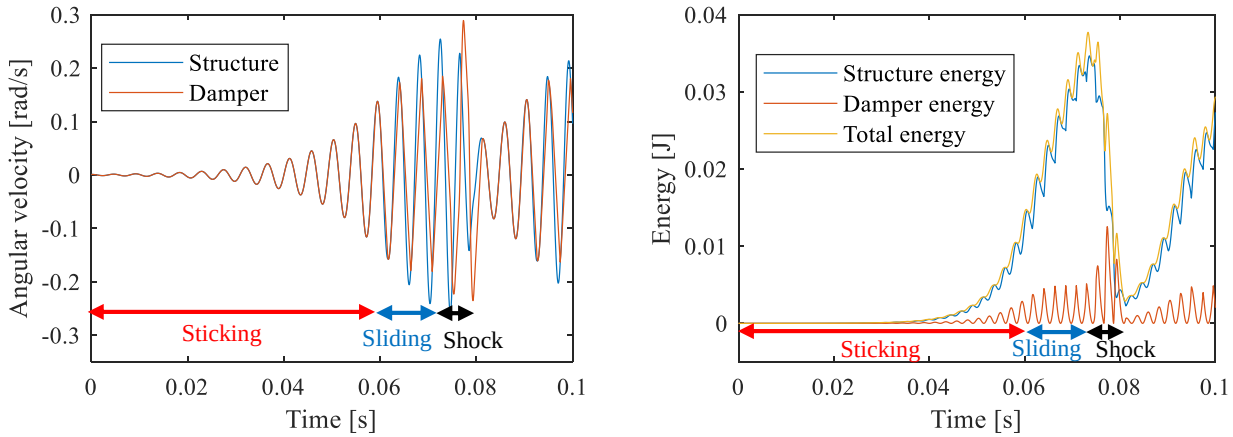

Figure 2: (left) Time response of the damper and the structure, (right) Energy flow within the system

These shocks, which do not occur in a conventional friction damper, lead to an energy transfer between the damper and the structure. Figure 2 (right) shows that while a shock occurs the energy is dissipated in the self-excited structure while the total energy remains almost constant and the energy of the damper increases. This leads to two positive effects on the stability and energy output of the system. The energy transfer reduces the energy of the structure, resulting in a reduced amplitude and thus lower energy input due to self-excitation. Secondly, the energy transfer to the damper increases the relative speed between the damper and the structure, dissipating the energy in the friction contact. Analyses with several modes show similar effects regarding the energy distribution, leading to an improved effectiveness in adjusted parameter ranges.

Parameter influences

Analyzing various parameters show that an increase of the inertia of the damper or the mass normalized modal amplitude at the position of the friction contact results in an increased damping. This is similar to the conventional friction damper without backlash, for which an analytical solution $D_{\max} = \frac{2}{\pi^2} \varphi_{i,j}^2 J$ is found by harmonic linearization [6]. In contrast to the conventional friction damper, the provided damping depends on the backlash width, the friction torque and the natural frequency. A reference for the influence of these parameters is given by the amplitude at which relative displacement occurs $\hat{q} = \frac{F_N \mu r}{\varphi_{i,j} J \omega_{0,j}^2}$. If this amplitude is significantly smaller compared to the backlash width, the damper acts like a conventional friction damper. If the amplitude is much higher, the damping effect is reduced due to limited movement.

Conclusions

This paper examines a combined friction and shock damper for its suitability to reduce self-excited torsional vibrations in downhole drilling systems. The combination of friction and backlash results in passive shocks, causing energy transfer between the self-excited structure and the damper that positively influences the energy output. Compared to a conventional friction damper without backlash, an increase in the damping effect is achieved by adjusting the normal force and backlash width with regard to the vibration frequency.

References

[1] Reckmann H., Jogi P., Kpetehoto F., Chandrasekaran S., Macpherson J. (2010) MWD Failure Rates Due to Drilling Dynamics. IADC/SPE
[2] Hohl A., Tergeist M., Oueslati H., Jain J., Herbig C., Ostermeyer G.-P., Reckmann H. (2015) Derivation and experimental validation of an analytical criterion for the identification of self-excited modes in drilling systems. Journal of Sound and Vibration 342, 290-302
[3] Tondl A. (1976) Quenching of self-excited vibration: effect of dry friction. Journal of Sound and Vibration 45(2), 285-294
[4] Popp K., Panning L., Sextro W. (2003) Vibration Damping by Friction Forces: Theory and Applications. Journal of Vibration and Control 9, 419-448
[5] López I., Busturia J., Nijmeijer H. (2004) Energy dissipation of a friction damper. Journal of Sound and Vibration 278, 539-561
[6] Kulke V., Ostermeyer G.-P., Tergeist M., Hohl A. (2019) Semi-analytical approach for derivation of an equivalent modal friction-damping ratio and its application in a self-excited drilling system. ASME/IMECE International Mechanical Engineering Congress and Exposition, Salt Lake City
[7] Vakakis A.F., Gendelman O.V., Bergman L.A., McFarland D.M., Kerschen G., Lee Y.S. (2009) Nonlinear Targeted Energy Transfer in Mechanical and Structural Systems. Springer Netherlands, Dordrecht

Model order reduction for geometrically nonlinear beams featuring internal resonance and centrifugal effect

Adrien Martin[1], Andrea Opreni[2], Alessandra Vizzaccaro[3], Loïc Salles[4], Attilio Frangi[2], Cyril Touzé[1]

[1]*IMSIA, ENSTA Paris, CNRS, EDF, CEA, Institut Polytechnique de Paris, Palaiseau, France.*
[2]*Department of Civil and Environmental Engineering, Politecnico di Milano, Milano, Italy.*
[3]*Department of Engineering Mathematics, University of Bristol, Bristol, England.*
[4]*Center for Design, Manufacturing and Materials, Skolkovo Institute of Science and Technology, Moscow, Russia.*

Summary. The direct parametrisation of invariant manifold is used for model order reduction of large amplitude vibrations of clamped-clamped and rotating cantilever beams. A particular emphasis is set on the computation of the backbone curve in case of internal resonance. For the clamped beam, the 1:5 resonance between first and third mode occuring at large amplitude, is reproduced with the model. For the rotating cantilever, a Campbell diagram is first used to detect the appearance of a 1:5 resonance, which is then computed with the reduction method.

Introduction

The study of slenders structures is becoming a prominent issue in several industries as the mass gain becomes crucial. For instance, in the aeronautic industry, the development of more efficient engines by the use of ever larger fan is targeted. This leads to the design of large fan blades, i.e. more than 1 meter long. In order to compensate the dimension of the blade, ligther and softer materials are used, such as composite materials. The combination of the slenderness of the blade with the softeness of the material may induce large displacements of the structure when it is submitted to a dynamical loading. It is then important to predict such behaviours, which can lead to specific phenomena like mode coupling and internal resonances, and to the premature failure of the structure.
Model order reduction methods are often used to compute more easily the nonlinear dynamics of such structures [6]. For application to finite element (FE) problems, important steps have been made recently with the possibility of computing directly nonlinear mappings to go from the physical space to the reduced subspace where the dynamics is governed by a very small number of master modes. The Direct Normal Form (DNF) has been proposed in [4], elaborated on a third-order development based on previous works in modal space [5]. An arbitrary order expansion, fully relying on the parametrisation method of invariant manifolds [3], has also been proposed in [7].
In this contribution, the direct parametrisation of invariant manifold is applied to two different test cases featuring internal resonances. In the case of the clamped beam, it is known that a 1:5 internal resonance exists between the 1st and 3rd flexural modes [8]. Concerning the rotating cantilever beam, the internal resonance condition may appear with the rotation and the stiffening of the structure. We will thus show the appearance of a 1:5 internal resonance between the 2nd and the 4th flexural modes, and compute its backbone with the reduction method.

Reduction method with the direct parametrisation

The Direct Parametrisation of Invariant Manifold (DPIM) is very briefly recalled here, relying on the developments shown in [7], and adapted in order to handle the effect brought by centrifugal force for a rotating system. The general equations of motion writes, using standard notations:

$$\mathbf{M}\ddot{\mathbf{x}} + [\mathbf{K} + \mathbf{N}]\mathbf{x} + \mathbf{g}(\mathbf{x}, \mathbf{x}) + \mathbf{h}(\mathbf{x}, \mathbf{x}, \mathbf{x}) = \mathbf{f}_\Omega, \tag{1}$$

with $\mathbf{N}$ the spin softening matrix, $\mathbf{f}_\Omega$ the centrifugal effects, and where the Coriolis forces have not been taken into account [2], in contrary to geometric nonlinear terms expressed via $\mathbf{g}$ and $\mathbf{h}$. These equations can be rewritten around the static equilibrium position $\mathbf{x}_0$, depending on the rotation speed, by introducing $\mathbf{x} = \mathbf{x}_0 + \mathbf{u}$, leading to:

$$\mathbf{M}\ddot{\mathbf{u}} + \mathbf{K}_\mathrm{t}\mathbf{u} + \mathbf{g}(\mathbf{u}, \mathbf{u}) + 3\mathbf{h}(\mathbf{x}_0, \mathbf{u}, \mathbf{u}) + \mathbf{h}(\mathbf{u}, \mathbf{u}, \mathbf{u}) = \mathbf{0} \tag{2}$$

with $\mathbf{K}_\mathrm{t} = \mathbf{K} + \mathbf{N} + 2\mathbf{g}(\mathbf{x}_0, \mathbf{I}) + 3\mathbf{h}(\mathbf{x}_0, \mathbf{x}_0, \mathbf{I})$ the tangent stiffness matrix.
The direct parametrisation method introduces a nonlinear mapping between the original coordinates (displacement $\mathbf{u}$ and velocity $\mathbf{v}$), and a new, *normal coordinate* $\mathbf{z}$, which describes the motion on invariant manifold associated to the selected linear master modes, as $\mathbf{u} = \boldsymbol{\Psi}(\mathbf{z})$ and $\mathbf{v} = \boldsymbol{\Upsilon}(\mathbf{z})$, where $\boldsymbol{\Psi}$ and $\boldsymbol{\Upsilon}$ are unknowns to be determined. The reduced dynamics is also searched under the form $\dot{\mathbf{z}} = \mathbf{f}(\mathbf{z})$. All unknowns are expanded via polynomial expressions at arbitrary order, and solved for, by plugging the expansions in the invariance equation [7]. At each order p, the homological equation gathers the unknowns, which depends only on previous orders, while the first-order term leads to the known modal problem.
Importantly, different styles of solutions exist. Finally, the reduced dynamics, which contains very few equations, can be solved with numerical continuation. The results shown in the next section used MATCONT [1] for this step.

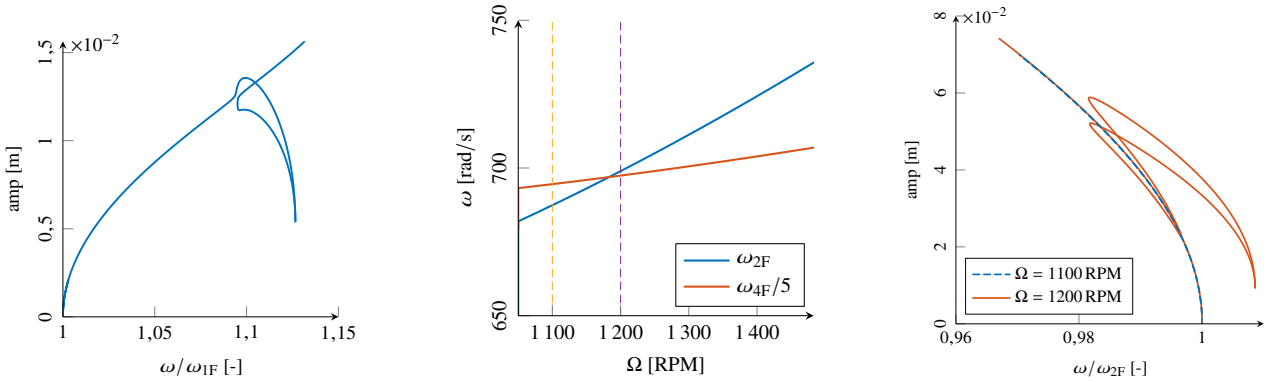

(a) backbone curve of the clamped beam

(b) Campbell diagram of the rotating beam

(c) backbone curves of the rotating beam

Figure 1: Internal resonances of the beam with 2 boundary conditions : clamped and rotating cantilever

Application case : nonlinear beam

The DPIM is applied here on a beam with dimensions $1\,\mathrm{m}$-$2\,\mathrm{cm}$-$3\,\mathrm{cm}$. The space is discretised with 27-nodes hexaedral elements with 50 elements in the length and 2×2 in the cross-section.
The first configuration considered is the clamped one. The backbone curve of the first mode is searched for, since it is known that at relatively large amplitudes, it meets a nonlinear internal resonance relationship with the 3rd flexural mode (their linear frequency ratio being $\omega_{3\mathrm{F}} = 5.36\,\omega_{1\mathrm{F}}$). Since a 1:5 resonance is at hand, the parametrisation is developed up to order five, using a complex normal form style. The backbone curve is shown in figure 1a, and is found to very well reproduce the tongue of internal resonance (see *e.g.* [8] for a reference, full-order solution).
The other configuration is the rotating cantilever beam. For this, we consider the 2nd and the 4th flexural modes. In this case, the internal resonance does not appear without rotation, even though the relation is $\omega_{4\mathrm{F}} = 5.45\,\omega_{2\mathrm{F}}$. As it is visible on the Campbell diagram on figure 1b, the 2 modes cross at a rotation speed around $1180\,\mathrm{RPM}$. In fig. 1c two backbone curves are shown, computed with the reduced order model method. Before the crossing, for a rotational speed of $1100\,\mathrm{RPM}$, the backbone shows a classical softening behaviour without internal resonance (blue dashed curve in fig. 1c). On the other hand, for $\Omega = 1200\,\mathrm{RPM}$, the backbone shows a clear tongue of internal resonance (orange curve in fig. 1c), highlighting that the 1:5 internal resonance is excited and revealed by the model.

Conclusion

The DPIM [7] has been applied to compute the reduced order model solution of a beam where 2 modes interact in an internal resonance with 2 different boundary conditions. The interesting case is the rotating beam where a condition for the internal resonance to occur has been found on the rotation speed. The method allows to predict those specific behaviors with a very small computation time. Those results need full order model resolution to be compared with, which will be achieved in the near future.

References

[1] A. Dhooge, W. Govaerts, Y. A. Kuznetsov, H. G. E. Meijer, and B. Sautois. New features of the software matcont for bifurcation analysis of dynamical systems. *Mathematical and Computer Modelling of Dynamical Systems*, 14(2):147–175, 2008. doi:10.1080/13873950701742754.

[2] T. Gmür. *Dynamique des Structures : Analyse modale numérique des systèmes mécaniques*. EPFL Press, 2012.

[3] A. Haro, M. Canadell, J.-L. Figueras, A. Luque, and J.-M. Mondelo. *The parameterization method for invariant manifolds. From rigorous results to effective computations*. Springer, Switzerland, 2016. doi:10.1007/978-3-319-29662-3.

[4] S. Jain and G. Haller. How to compute invariant manifolds and their reduced dynamics in high-dimensional finite-element models. *Nonlinear Dynamics*, 2021. doi:10.1007/s11071-021-06957-4.

[5] C. Touzé. *Normal form theory and nonlinear normal modes: Theoretical settings and applications*, pages 75–160. Springer Vienna, Vienna, 2014. doi:10.1007/978-3-7091-1791-0_3.

[6] C. Touzé, A. Vizzaccaro, and O. Thomas. Model order reduction methods for geometrically nonlinear structures: a review of nonlinear techniques. *Nonlinear Dynamics*, 105:1141–1190, 2021. doi:10.1007/s11071-021-06693-9.

[7] A. Vizzaccaro, A. Opreni, L. Salles, A. Frangi, and C. Touzé. High order direct parametrisation of invariant manifolds for model order reduction of finite element structures: application to large amplitude vibrations and uncovering of a folding point, 2021. arXiv:2109.10031.

[8] A. Vizzaccaro, Y. Shen, L. Salles, J. Blahoš, and C. Touzé. Direct computation of nonlinear mapping via normal form for reduced-order models of finite element nonlinear structures. *Computer Methods in Applied Mechanics and Engineering*, 384:113957, 2021. doi:10.1016/j.cma.2021.113957.

Modeling and Simulations of the Nonlinear Dynamics of Carbon Nanotube Based Resonator Assuming Nonlocal Strain and Velocity Gradient Theories

Hassen M. OUAKAD*, Hamid M. Sedighi **

*Department of Mechanical & Industrial Engineering, Sultan Qaboos University, Engineering College, PO-Box 33, AlKhoudh, 123, Muscat, OMAN, Corresponding Author Email: houakad@squ.edu.om

**Mechanical Engineering Department, Faculty of Engineering, Shahid Chamran University of Ahvaz, Ahvaz, IRAN

Summary. In this work, the mutual influence of the nonlocal behavior superimposed to the size effects on the dynamics of electrically actuated single walled carbon nanotube based resonator are examined. In this regards, two nonlinear models to capture the nano-structure nonlocal size effects are considered: the strain and the velocity gradients theories. A reduced-order model based on the Differential-Quadrature Method (DQM) to discretize the governing nonlinear equation of motion and acquire a discretized-parameter nonlinear model of the system is investigated. Both model results show that non-local as well size effects should not be neglected since they somehow improve the prediction of corresponding dynamic amplitudes and most importantly the critical resonant frequencies of such nano-resonators.

Introduction

Thanks to their amazing electro-mechanical features, carbon nanotubes (CNTs) and their respective compounds have shown potential applications in numerous electronic devices, energy storage, smart materials and composites, sensors and actuators and etc... Consequently, a lot of researchers and scientists worldwide [1-5] have been attracted to investigate their interesting physio-mechanical properties by introducing non-classical models. Several non-classical continuum theories have been presented and developed to pave the way for precisely extracting the size-dependent behavior of CNTs for future applications. To cite few, nonlocal theories [1] and strain gradient elasticity theory [2] are very useful to account for the nanoscale characteristics of nanostructures. In nonlocal theories, it is assumed that the stress at a specific point is a function of the strains of that point and its neighborhood as well [3]. It is demonstrated that the nonlocal theories only consider the inter-atomic long-range force [4] and the gradient elasticity theory exclusively takes into account the higher-order microstructure deformation mechanism [5]. From another point of view, the gradient elasticity theory captures the hardening behavior of nanoscale structure and, on the contrary, can only model the softening behavior of nanostructures like CNTs [4]. Therefore, in order to predict two different behaviors simultaneously and combine both possible features in nanoscale structures, it is convenient to merge two theories to bring into account two distinct properties at the same time. The key motivation behind this research work is to conduct a comprehensive study to account for the nonlocality of the stress in nanostructures incorporating the complete gradient elastic analysis of structures, that is to say, the strain and velocity gradients are included in the generalized governing equations.

Problem formulation

The investigated CNT-based resonator, Fig.1, is triggered by its lower substrate with an assumed initial gap width *d*. The CNT will be assumed as a cylindrical beam shape of radius $\tilde{R}$, and length *L*. The area moment of inertia of $I=\pi\tilde{R}^4/4$ and a resultant cross-sectional area $A=\pi\tilde{R}^2$. It also has a Young's modulus *E*=1 *TPa* and a density ρ=1.35 g/cm^3 [6].

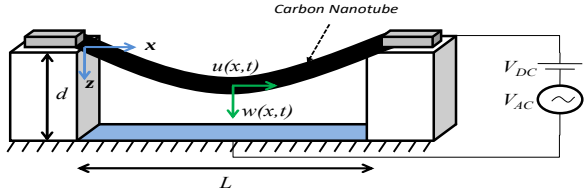

Figure 1: 3D drawing of an electrostatically actuated SWCNT based resonator.

Through considering the nonlocal effects of higher-order strain gradients $\varepsilon_{ij,k}$, in which the index *k* after the comma denotes the differentiation with respect to x_k, the extended Eringen's model gets the following expression for the internal potential energy as [7,8]:

$$U_0\left(\varepsilon_{ij},\varepsilon'_{ij},\alpha_0;\varepsilon_{ij,m},\varepsilon'_{ij,m},\alpha_1\right)=\frac{1}{2}\varepsilon_{ij}C_{ijkl}\int_V\alpha_0\left(\left|x-x'\right|,e_0a\right)\varepsilon'_{kl}dV+\frac{l_s^2}{2}\varepsilon_{ij,m}C_{ijkl}\int_V\alpha_1\left(\left|x-x'\right|,e_1a\right)\varepsilon'_{kl,m}dV=\frac{1}{2}\int_V\left(\sigma_{ij}\varepsilon_{ij}+\sigma^{(1)}_{ijm}\varepsilon_{ij,m}\right)dV \qquad (1)$$

where e_0a and e_1a represent the influence of the inter atomic long range force and l_s stands for the strain gradient length parameter. In the framework of an Euler-Bernoulli beam theory and taking into consideration the so-called von-Karman nonlinearity, the relation for the strain-displacement of the beam (to the first order) can be written as $\varepsilon_{xx}=u_{,x}+w_{,x}{}^2/2-zw_{,xx}$. Employing the Hamilton's principle, the following normalized nonlinear governing equations of a fixed-fixed CNT resonator based on the nonlocal strain and velocity gradient theories [4]:

$$\left(1-\mu_s\frac{\partial^2}{\partial x^2}\right)\frac{\partial^4 w}{\partial x^4}+\left(1-\mu_0\frac{\partial^2}{\partial x^2}\right)\left(\frac{\partial^2 w}{\partial t^2}+\alpha_d\frac{\partial w}{\partial t}-\alpha_r\frac{\partial^4 w}{\partial x^2\partial t^2}-\alpha_s\left(\int_0^1\left(\frac{\partial w}{\partial x}\right)^2dx\right)\frac{\partial^2 w}{\partial x^2}\right)=\alpha_e\Gamma(w)+\mu_k\left(2\frac{\partial^4 w}{\partial x^2\partial t^2}-\alpha_r\frac{\partial^6 w}{\partial x^4\partial t^2}\right); \qquad (2)$$

where μ_k is the velocity gradient kinetic internal length scale and:

$$\alpha_s = \frac{Ad^2}{2I},\ \alpha_e = \frac{\pi\varepsilon_0 L^4}{EId^2},\ \alpha_r = \frac{I}{AL^2},\ \alpha_d = \tilde{c}\frac{L^4}{EI},\ \mu_0 = \left(\frac{ea}{L}\right)^2,\ \mu_s = \left(\frac{l_s}{L}\right)^2,\ \mu_k = \left(\frac{l_k}{L}\right)^2,\ \text{and}\ R = \frac{\tilde{R}}{d}, \tag{3}$$

Spatial Discretization using the Differential Quadrature Method

In order to numerically solve the nonlinear governing equation (14), we suggest to implement the Differential Quadrature Method (DQM) superimposed to the Finite-Difference Method (FDM). For the accuracy of the numerical results, the subsequent lattice distribution is assumed as $x_i = 1/2[1-\cos((i-1)\pi/(n-1))],\quad i = 1,2,...n$ [9]. Therefore, for a normalized space variable x in the interval (0,1) and defining n discretization points in the space domain, the pth-sequence derivative of w at point $x = x_i$ is written as $\partial^p w/\partial x^p\big|_{x=x_i} = \sum_{j=1}^{n} D_{ij}^{(p)} w_j$. The weighting coefficient matrix of the first sequence derivative is defined as $D_{ij}^{(p=1)} = \prod_{k=1,k\neq i}^{n}(x_i - x_k)/(x_i - x_j)\prod_{k=1,k\neq j}^{n}(x_j - x_k),\ i,j = 1,2,...,n,\ i \neq j$

Nonlinear Dynamic Analysis: Results and Discussion

As a case study, the parameters of the studied SWCNT are considered as: d=100 nm, L=3000nm and $\tilde{R}$ =30 nm. In this work 19 discretization points is used in the DQM to get the converged results. The variation of the steady-state maximum deflection $W_{\max}$ versus the forcing AC frequency **Ω** is outlined in Fig. 2 for different values of the nonlocal parameter μ_0. As can be seen, when V_{DC}= 1 volt, an increase of the nonlocal parameter resulted in decreasing the maximum dynamic amplitude of the CNT. Furthermore, when considering the nonlocality effect, a softening-like behavior of the CNT is been replaced by a hardening type behavior. Figure 3 displays the frequency response of CNT for different values of the strain gradient parameter μ_s. It is evident that the maximum amplitude of the system is increased by increasing the value of DC voltage and the bandwidth expansion is increased as the DC excitation voltage increases. Figure 4 shows the frequency-response curves for three different values of velocity gradient parameter μ_k. As can be observed, the maximum dynamic deflection of the structure is considerably amplified by increasing the velocity gradient parameter and consequently the bandwidth expansion increases as the velocity gradient parameter increases.

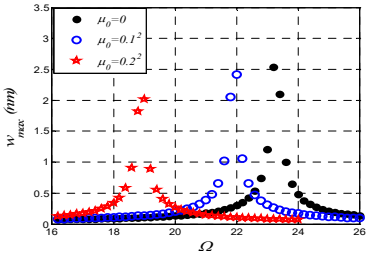

Figure 2: Dynamic response for three different nonlocal parameters for for V_{DC}= 1 *Volt*, V_{AC}= 1 *Volt*.

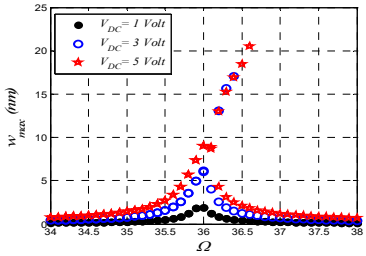

Figure 3: Dynamic response for three different values of the DC voltage for μ_s= 0.1^2.

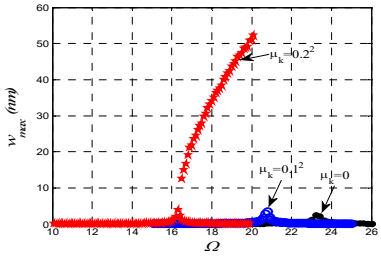

Figure 4: Dynamic response for three different velocity gradient parameters (a) VDC= 1 Volt, VAC= 1 Volt.

Conclusion

In this numerical investigation, the nonlinear dynamics of an electrically actuated doubly-clamped single-walled carbon nanotube resonator is carried out. A nonlinear Euler-Bernoulli beam model incorporating both the nonlocal and strain/velocity gradient theories is implemented. The derived nonlinear governing equation is discretized through a Differential Quadrature Method (DQM). The acquired results in this work demonstrated the fact that neglecting the nonlocal as well as the size effects imposed considerable errors in the estimation of the dynamic response of SWCNT and consequently in determining accurately its dynamical parameters such as: its resonant deflection (approx. 10-20% error) its fundamental resonant frequency (approx.15-20% error).

References

[1] Eringen A.C. (2002) Nonlocal Continuum Field Theories (first-ed), Springer-Verlag New York.
[2] Lam D.C., Yang F., Chong A.M., Wang J., Tong P. (2003) Experiments and theory in strain gradient elasticity. *J. Mech. Phys. Solids.* **51**, 1477-1508.
[3] Picu C.R. (2002) The Peierls stress in non-local elasticity. *J. Mech. Phys. Solids.* **50**, 717–735.
[4] Ouakad H.M., El-Borgi S., Mousavi S.M., Friswell M.I. (2018) Static and dynamic response of CNT nanobeam using nonlocal strain and velocity gradient theory. *Appl. Math. Model.* **62**, 207-222.
[5] Zhu L., Li L. (2017) Closed form solution for a nonlocal strain gradient rod in tension. *Int. J. Engg. Sci.* **119**, 16-28.
[6] Yu M.F. (2004) Fundamental mechanical properties of carbon nanotubes: current understanding and the related experimental studies. *J. Engg. Mater. Tech.* **126**, 271-278.
[7] Eringen A.C. (1983) On differential equations of nonlocal elasticity and solutions of screw dislocation and surface waves. *J. Appl. Phys.* **54**, 4703-4710.
[8] Mindlin R.D. (1964) Micro-structure in linear elasticity, *Arch. Ration. Mech. Anal.* **16**(1), 51-78.
[9] Tomasiello S. (1998) Differential Quadrature Method: Application to Initial-Boundary-Value Problems, *J. Sound Vib.* **218**, 573-585.

Modelling and dynamics of smart composite box beam with nonlinear constitutive behaviour of active elements

Jarosław Latalski*, Jerzy Warmiński*

*Department of Applied Mechanics, Faculty of Mechanical Engineering, Lublin University of Technology, Lublin, Poland

Summary. The presented research discusses the mathematical modelling of composite thin-walled beams with embedded active elements made of piezoceramic materials. The the analysis the nonlinear relations in piezoceramics with respect to electric field (electrostrictive effect) is considered to properly capture the behaviour of the transducer in near-resonant conditions. Moreover, the importance of disregarding/accounting for the magnetic effects is highlighted. In the adopted model of the piezoceramic actuation the bending load to the hosting composite beam is achieved by means of d_{31} piezoelectric effect. The governing equations of the system are derived using Hamilton's principle for a beam undergoing complex deformation involving transverse and in-plane shearable bending, torsion and axial deformations. The obtained system of partial differential equations is transformed into a set of ordinary ones by the Galerkin discretization method. The results of performed numerical studies show the importance of non-linear terms for accurate prediction of systems dynamic properties; in particular one can observe the softening phenomenon near the resonance zone due to the nonlinear characteristics of the PZT layers and electrostrictive effect.

Over recent 10-20 years smart composite elements have received a considerable attention due to their potential for designing adaptive structures that are both light in weight and possess adaptive capabilities. Due to their unique properties like e.g. high strength-to-weight ratio and high structural damping the composite based smart structures are very competitive for many designs. In particular active transducers based on piezoelectric/piezoceramic materials have found numerous applications ranging from astronautics and aerospace technology to the automotive industry and civil engineering. Typical examples might be spacecraft antennas, helicopter rotor blades, wind turbines, multi-stable morphing shells, bridge elements etc.

Modelling of smart composite structures

The physics involved in piezoelectric theory can be regarded as a coupling between Maxwell's equations of electromagnetism and elastic stress equations of motion. The coupling takes place through the piezoelectric constitutive equations providing the relationships between the tensors of stress and strain and the vectors of electric field and electric flux density.

The system of Maxwell's equations in vector form is written as

$$\begin{aligned} \nabla \cdot \mathbf{D} &= \rho_e \\ \nabla \cdot \mathbf{B} &= 0 \\ \nabla \times \mathbf{E} &= \dot{\mathbf{B}} \\ \tfrac{1}{\mu}(\nabla \times \mathbf{B}) &= i_b + \dot{\mathbf{D}} \end{aligned} \tag{1}$$

where $\mathbf{D}$ is the electric flux density vector, also known as the electric displacement vector, ρ_e is the charge density, $\mathbf{B}$ is the magnetic induction, $\mathbf{E}$ is the electric field intensity vector and μ is the magnetic permeability constant. The over dots represent differentiation with time t.

In the literature there are mainly three approaches to deal with electromagnetic effects when modelling the behaviour of piezoelectric domain [1]:

- electrostatic approach when all magnetic effects ale completely ignored. This involves $\mathbf{B} = \dot{\mathbf{D}} = \rho_e = i_b = 0$. Therefore the system of Maxwell's equations is reduced to $\nabla \cdot \mathbf{D} = 0$ and $\nabla \times \mathbf{E} = 0 \Rightarrow \mathbf{E} = -\nabla\phi$. This approach is the simplest one and simultaneously the most common one even when studying dynamics of smart structures. This is due to the fact that the electric potential ϕ is directly available,
- quasi-static approach that rules out some but not all the magnetic effects. Typically $\rho_e = i_b = 0$ but D and B are time-dependent. Thus, the $(1)_2$ implies that there exists a magnetic potential vector $\mathbf{A}$ such that $B = \nabla \times \mathbf{A}$. Therefore, the electric potential is related to electric field and changes in magnetic potential: $\mathbf{E} = -\nabla\phi - \dot{\mathbf{A}}$,
- fully dynamic when $\mathbf{A}$ and $\dot{\mathbf{A}}$ are left in the analysis. Depending on the type of material, body charge density ρ_e and body current density i_b can also be non-zero.

The well known physically linear relationships between the tensors of stress and strain and the vectors of electric field and electric displacement for piezoelectric materials are applicable to a particular case where nonlinear effects are negligible [2, 3]. However, numerous theoretical and experimental studies suggest the piezoceramics can exhibit nonlinear constitutive properties resulting from high electric fields, near resonant operation regimes or stress-strain hysteresis [4, 5, 6, 7, 8].

To properly capture these phenomena authors postulate to enhance the classical piezoelectric constitutive formulation by adopting the higher-order relations with respect to electric field [9]

$$\begin{aligned} \boldsymbol{\sigma} &= \mathbf{C}\boldsymbol{\varepsilon} - \mathbf{e}\mathbf{E} - \hat{\mathbf{b}}\,\mathrm{sgn}(E_3)\mathbf{E}^2 \\ \mathbf{D} &= \mathbf{e}\boldsymbol{\varepsilon} + \boldsymbol{\xi}\mathbf{E} + \boldsymbol{\chi}\mathrm{sgn}(E_3)\mathbf{E}^2 \end{aligned} \tag{2}$$

In the above relations $\mathbf{C}$ stands for the second order piezoceramic elasticity tensor at constant electric field, $\mathbf{e}$ is the tensor of piezoelectric coefficients, $\boldsymbol{\xi}$ is second order permittivity tensor, $\hat{\mathbf{b}}$ is effective electrostrictive constants tensor, $\boldsymbol{\chi}$ is third order electric susceptibility tensor. Moreover, the variables $\boldsymbol{\sigma}$ and $\boldsymbol{\varepsilon}$ stand for stress and strain tensors, respectively.

The submitted research is a continuation of former author's studies on dynamics of smart composite thin-walled beams [10, 11]. In the former one an electromechanical coupled theory is used to develop the equations of motion of a rotating thin-walled beam with surface bonded/embedded piezoelectric transducers. In the mathematical model of the hybrid structure, the non-classical effects like material anisotropy, rotary inertia and transverse shear deformation as well as an arbitrary beam pitch angle and hub mass moment of inertia are incorporated. It has been shown this approach results in an additional equation of motion for the hub sub-system and significantly enhances the generality of the formulation. Comparing to the purely mechanical model with simplified approach, the proposed electromechanical one introduces additional stiffness-type couplings between individual degrees of freedom of the system. In the following paper [11] the dynamics of layered composite piezo-beam with lamination scheme exhibiting the circumferentially uniform stiffness properties of the cross section has been presented. Moreover, the two-way coupling interaction involving the spatial distribution of electric field in the piezoceramic domain has been discussed.

Acknowledgements

The work is financially supported by grant 2016/23/B/ST8/01865 from the National Science Centre, Poland.

References

[1] Tiersten H.F. (1969) Linear Piezoelectric Plate Vibrations. Plenum Press, New York, USA.

[2] Gaudenzi P.: (2009) Smart Structures: Physical Behaviour, Mathematical Modelling and Applications. John Wiley & Sons, Ltd., Chichester, United Kingdom.

[3] Leo D.J. (2007) Engineering Analysis of Smart Material Systems. John Wiley & Sons, Inc., Hoboken, USA.

[4] Fan J., Stoll W.A., Lynch S.C. (1999) Nonlinear constitutive behaviour of soft and hard PZT: experiments and modeling. *Acta Mater* **47**(17):4415-4425.

[5] Hall D.A. (2001) Review: Nonlinearity in piezoelectric ceramics. *J Mater Sci* **36**(19):4575–4601.

[6] Arafa A., Baz A. (2004) On the nonlinear behaviour of piezoelectric actuators. *J Vib Control* **10**:387-398.

[7] Birman V. (2005) *Physically nonlinear behaviour of piezoelectric actuators subject to high electric fields*. US Army Research Office Report 45137.1-EG-II.

[8] Sohrabi A.M., Muliana A.H. (2015) Nonlinear and time dependent behaviors of piezoelectric materials and structures. *Int J Mech Sci* **94-95**:1–9.

[9] Joshi S.P. (1999) Non-linear constitutive relations for piezoceramic materials. *Smart Struct* **1**:80–83.

[10] Latalski J. (2016) Modelling of a rotating active thin-walled composite beam system subjected to high electric fields. In: Naumenko, K., Assmus, M., (eds) Advanced Methods of Continuum Mechanics for Materials and Structures, vol. 60 of Advanced Structural Materials. Springer, Singapore

[11] Latalski J., Warminski J. (2019) Nonlinear vibrations of a rotating thin-walled composite piezo-beam with circumferentially uniform stiffness (CUS). *Nonlinear Dynam* (in-press) doi: 10.1007/s11071-019-05175-3.

Wednesday, July 20, 2022
08:30 - 10:30

MS-03 Computational Methods
Rhone 3A

Chair: Harry Dankowicz

08:30 - 08:50
Phase resonance of an oscillator with polynomial stiffness
VOLVERT Martin*, KERSCHEN Gaëtan
*Aerospace and Mechanical Engineering Department [Liège] (1, Chemin des Chevreuils Sart Tilman 4000 Liège Belgium)

08:50 - 09:10
Parallel Harmonic Balance Method: towards very large scale systems
SALLES Loic*, BLAHOS Jiri, VIZZACARRO Alessandra, EL Haddad Fadi
*Department of Mechanical Engineering [Imperial College London] (Imperial College London, London SW7 2AZ United Kingdom)

09:10 - 09:30
Tracking basin boundaries with Clustered Simple Cell Mapping method
GYEBRÓSZKI Gergely*, CSERNÁK Gábor
*MTA-BME Research Group on Dynamics of Machines and Vehicles (H-1111, Budapest, Műegyetem rkp 3. Hungary)

09:30 - 09:50
Asymptotic-preserving and hybrid finite-volume/Monte-Carlo methods for kinetic equations in the plasma edge of a fusion reactor
SAMAEY Giovanni*
*KU Leuven, Departement of Computer Science (Celestijnenlaan 200A, 3001 Heverlee Belgium)

Phase resonance of an oscillator with polynomial stiffness

Martin Volvert and Gaëtan Kerschen
Space Structures and Systems Laboratory, Aerospace and Mechanical Engineering Department, University of Liège, Quartier Polytech 1 (B52/3), Allée de la Découverte 9, Liege, B-4000, Belgium

Summary. This paper extends the linear concept of phase resonance, which occurs when the damping forces counterbalance exactly the external forces, to oscillators with polynomial stiffness. To this end, a first-order averaging technique is applied to a one degree-of-freedom oscillator with arbitrary polynomial stiffness. We show that phase resonance exists in the vicinity of amplitude resonance and is associated with a phase resonance of $\pi/2$.

Introduction

Modal analysis has been, and continues to be, the dominant dynamical method used in structural design. The goal of modal analysis is to find the vibration modes, resonance frequencies and damping ratios of the considered system [1]. One key assumption of modal analysis is linearity.
In linear theory, the resonant behavior of dynamical systems can be characterized either the amplitude or phase resonance. Amplitude resonance corresponds to a relative maximum in the frequency response function whereas phase resonance is associated with quadrature between the displacement and the external forcing. At phase resonance, the external forcing cancels exactly the damping force with the result that the resonance frequency coincides with the natural frequency of the linear system. The difference between the two resonances remains small for weakly damped systems.
However, real-world structures are intrinsically nonlinear because they may feature advanced materials, friction and contact [2]. In this context, the present study proposes to extend the concept of phase resonance to oscillators with arbitrary polynomial stiffness. To do so, a first-order averaging technique is applied to a one degree-of-freedom oscillator and we show that phase resonance exists in the vicinity of amplitude resonance for a phase lag of $\pi/2$.

Oscillator with polynomial stiffness

The governing equation of motion of a harmonically-forced oscillator with arbitrary polynomial stiffness is

$$m\ddot{x}(t) + c\dot{x}(t) + kx(t) + \sum_{d=2}^{n} k_d x^d(t) = f\sin\omega t \tag{1}$$

where m, c, k and k_d represent the mass, damping, linear and nonlinear stiffness coefficients, respectively. f is the forcing amplitude whereas ω is the excitation frequency of period T. The natural frequency of the undamped, linearized system is $\omega_0 = \sqrt{\frac{k}{m}}$. Through mass normalization, Equation (1) can be recast into:

$$\ddot{x}(t) + 2\bar{\zeta}\,\omega_0\,\dot{x}(t) + \omega_0^2 x(t) + \sum_{d=2}^{\infty} \alpha_d x^d(t) = \bar{\gamma}\sin\omega t \tag{2}$$

where $\bar{\zeta} = \frac{c}{2\sqrt{km}}$, $\alpha_d = k_d/m$ and $\bar{\gamma} = f/m$.

An averaging technique

We consider a weakly nonlinear oscillator of the form:

$$\ddot{x}(t) + \omega_0^2 x(t) = \varepsilon f(x(t), \dot{x}(t)) \tag{3}$$

When $\varepsilon = 0$, the periodic solution of (3) is written as:

$$x(t) = u\cos\omega_0 t - v\sin\omega_0 t \tag{4}$$

where u and v are constants. When $\varepsilon \neq 0$, we seek a solution of frequency ω such that $\omega^2 - {\omega_0}^2 = \varepsilon\,\Omega$. The solution is expressed as in Equation (4) but with time-dependent u and v:

$$x(t) = u(t)\cos\omega t - v(t)\sin\omega t \tag{5}$$

We impose that the velocity should have the same form as in the case $\varepsilon = 0$, *i.e.*,

$$\dot{x}(t) = -u(t)\,\omega\sin\omega t - v(t)\,\omega\cos\omega t \tag{6}$$

Equation (6) holds if:

$$\dot{u}(t)\cos\omega t - \dot{v}(t)\sin\omega t = 0 \tag{7}$$

Differentiating Equation (6) and replacing $\ddot{x}(t)$ and $x(t)$ in Equation (3) yields:

$$\dot{u}(t)\,\omega\sin\omega\,t+\dot{v}(t)\,\omega\cos\omega\,t=-\varepsilon\left[f(x(t),\dot{x}(t))+\Omega\,x(t)\right] \tag{8}$$

Finally, taking into account Equations (7) and (8) and solving for $\dot{u}$ and $\dot{v}$, a system of first-order equations is obtained:

$$\begin{cases}\dot{u}=-\frac{\varepsilon}{\omega}\left[f(x(t),\dot{x}(t))+\Omega\,x(t)\right]\sin\omega\,t\\ \dot{v}=-\frac{\varepsilon}{\omega}\left[f(x(t),\dot{x}(t))+\Omega\,x(t)\right]\cos\omega\,t\end{cases} \tag{9}$$

This system has a suitable form to apply first-order averaging, which is performed herein using the Krylov-Bogolyubov technique [3, 4], which consists in integrating these equations over one period of time T, during which u and v are considered to be constants:

$$\begin{cases}\dot{u}=-\frac{\varepsilon}{\omega}\frac{1}{T}\int_0^T\left[f(x(t),\dot{x}(t))+\Omega\,x(t)\right]\sin\omega\,t\,\mathrm{d}t\\ \dot{v}=-\frac{\varepsilon}{\omega}\frac{1}{T}\int_0^T\left[f(x(t),\dot{x}(t))+\Omega\,x(t)\right]\cos\omega\,t\,\mathrm{d}t\end{cases} \tag{10}$$

Or alternatively, if we consider $\omega\,t=\theta$:

$$\begin{cases}\dot{u}=-\frac{\varepsilon}{\omega}\frac{1}{2\pi}\int_0^{2\pi}\left[f(x(\theta),\dot{x}(\theta))+\Omega\,x(\theta)\right]\sin\theta\,\mathrm{d}\theta\\ \dot{v}=-\frac{\varepsilon}{\omega}\frac{1}{2\pi}\int_0^{2\pi}\left[f(x(\theta),\dot{x}(\theta))+\Omega\,x(\theta)\right]\cos\theta\,\mathrm{d}\theta\end{cases} \tag{11}$$

Finally, $x(t)$ is often represented using the polar coordinates r and ϕ such that $x(t)=r(t)\sin\left(\omega\,t-\phi(t)\right)$ with $r=\sqrt{u^2+v^2}$ and $\phi=\mathrm{atan2}(-u,-v)$, where $u=-r\sin\phi$ and $v=-r\cos\phi$. Furthermore, we can express the time derivatives of r and ϕ as:

$$\begin{cases}\dot{r}=\frac{\partial r}{\partial u}\dot{u}+\frac{\partial r}{\partial v}\dot{v}=\frac{u}{r}\dot{u}+\frac{v}{r}\dot{v}\\ \dot{\phi}=\frac{\partial\phi}{\partial u}\dot{u}+\frac{\partial\phi}{\partial v}\dot{v}=\frac{v}{r^2}\dot{u}-\frac{u}{r^2}\dot{v}\end{cases} \tag{12}$$

For conciseness, the time dependence for u, v, r and ϕ is dropped in the remainder of this chapter.

First-order averaging of an oscillator with polynomial stiffness

Scaling of the equation of motion

Considering Equation (2), we scale the system such that $\bar{\zeta}=\varepsilon\zeta$, $\bar{\alpha_d}=\varepsilon\alpha_d$ and $\bar{\gamma}=\varepsilon\gamma$, with ζ, α, $\gamma=\mathcal{O}(1)$, we obtain a weakly nonlinear oscillator:

$$\ddot{x}(t)+\omega_0^2x(t)=\varepsilon\left(\gamma\sin\omega t-2\zeta\,\omega_0\,\dot{x}(t)-\sum_{d=2}^{\infty}\alpha_d x^d(t)\right) \tag{13}$$

Assuming a forcing frequency in the vicinity of the natural frequency of the linear system, i.e., $\omega^2-{\omega_0}^2=\varepsilon\Omega$, we can apply an averaging technique and the displacement as explained in Section . This consists in solving:

$$\begin{cases}\dot{u}=-\frac{\varepsilon}{\omega}\frac{1}{2\pi}\int_0^{2\pi}\left[\left(\gamma\sin\theta-2\zeta\,\omega_0\,\dot{x}(\theta)-\sum_{d=2}^{\infty}\alpha_d x^d(\theta)\right)+\Omega\,x(\theta)\right]\sin\theta\,\mathrm{d}\theta\\ \dot{v}=-\frac{\varepsilon}{\omega}\frac{1}{2\pi}\int_0^{2\pi}\left[\left(\gamma\sin\theta-2\zeta\,\omega_0\,\dot{x}(\theta)-\sum_{d=2}^{\infty}\alpha_d x^d(\theta)\right)+\Omega\,x(\theta)\right]\cos\theta\,\mathrm{d}\theta\end{cases} \tag{14}$$

For clarity, the different terms are analysed separately, *i.e.*, the forcing, damping, frequency and stiffness terms. Furthermore, to solve these integrals, we make use of the fact that:

$$\int_0^{2\pi}\cos^a\theta\sin^b\theta\,\mathrm{d}\theta=\frac{1}{2}\left[(-1)^a+1\right]\left[(-1)^b+1\right]\frac{\Gamma\left(\frac{a}{2}+\frac{1}{2}\right)\Gamma\left(\frac{b}{2}+\frac{1}{2}\right)}{\Gamma\left(\frac{a}{2}+\frac{b}{2}+\frac{1}{2}\right)} \tag{15}$$

which is always equal to 0 if either a or b is odd. Therefore, we can write:

$$\frac{1}{2\pi}\int_0^{2\pi}\cos^{2n}\theta\sin^{2m}\theta\,\mathrm{d}\theta=\frac{1}{\pi}\frac{\Gamma\left(n+\frac{1}{2}\right)\Gamma\left(m+\frac{1}{2}\right)}{\Gamma\left(n+m+\frac{1}{2}\right)} \tag{16}$$

where Γ is the *Gamma* function.

Forcing term

For $\dot{u}$ and $\dot{v}$, we have respectively:

$$\frac{1}{2\pi}\int_0^{2\pi}\gamma\sin^2\theta\,\mathrm{d}\theta=\frac{\gamma}{2} \tag{17}$$

and

$$\frac{1}{2\pi}\int_0^{2\pi}\gamma\cos\theta\sin\theta\,\mathrm{d}\theta=0 \tag{18}$$

Damping term
For $\dot{u}$ and $\dot{v}$, we have respectively:

$$-\frac{1}{2\pi}\int_0^{2\pi} 2\zeta\,\omega_0\left(-u\,\omega\sin^2\theta - v\,\omega\cos\theta\sin\theta\right)\,\mathrm{d}\theta = \zeta\,\omega_0\,\omega\,u \tag{19}$$

and

$$-\frac{1}{2\pi}\int_0^{2\pi} 2\zeta\,\omega_0\left(-u\,\omega\cos\theta\sin\theta - v\,\omega\cos^2\theta\right)\,\mathrm{d}\theta = \zeta\,\omega_0\,\omega\,v \tag{20}$$

Frequency term
For $\dot{u}$ and $\dot{v}$, we have respectively:

$$\frac{1}{2\pi}\int_0^{2\pi} \Omega\left(u\cos\theta\sin\theta - v\sin^2\theta\right)\,\mathrm{d}\theta = -\frac{\Omega\,v}{2} \tag{21}$$

and

$$\frac{1}{2\pi}\int_0^{2\pi} \Omega\left(u\cos^2\theta - v\cos\theta\sin\theta\right)\,\mathrm{d}\theta = \frac{\Omega\,u}{2} \tag{22}$$

Polynomial stiffness terms
For $\dot{u}$ and $\dot{v}$, we need to solve respectively:

$$-\sum_{d=2}^{\infty}\frac{1}{2\pi}\int_0^{2\pi}\alpha_d\left(u\cos\theta - v\sin\theta\right)^d\sin\theta\,\mathrm{d}\theta \tag{23}$$

and

$$-\sum_{d=2}^{\infty}\frac{1}{2\pi}\int_0^{2\pi}\alpha_d\left(u\cos\theta - v\sin\theta\right)^d\cos\theta\,\mathrm{d}\theta \tag{24}$$

To do so, we need to expand the polynomial term using the binomial expansion:

$$(u\cos\theta - v\sin\theta)^d = \sum_{p=0}^{d}\binom{d}{p}(u\cos\phi)^{d-p}(-v\sin\theta)^p \tag{25}$$

which thus gives for $\dot{u}$ and $\dot{v}$, respectively:

$$-\sum_{d=2}^{\infty}\alpha_d\sum_{p=0}^{d}\binom{d}{p}u^{d-p}(-v)^p\frac{1}{2\pi}\int_0^{2\pi}\cos^{d-p}\theta\sin^{p+1}\theta\,\mathrm{d}\theta \tag{26}$$

and

$$-\sum_{d=2}^{\infty}\alpha_d\sum_{p=0}^{d}\binom{d}{p}u^{d-p}(-v)^p\frac{1}{2\pi}\int_0^{2\pi}\cos^{d-p+1}\theta\sin^{p}\theta\,\mathrm{d}\theta \tag{27}$$

The result of the integrals depends on the parity of the exponents of the sine and cosine terms and the different possibilities are studied hereafter.

Case 1: d and p are odd.
In this case, we set $d = 2i+1$ and $p = 2j+1$. For $\dot{u}$ we have:

$$\sum_{i=1}^{\infty}\alpha_{2i+1}\sum_{j=0}^{i}\binom{2i+1}{2j+1}u^{2(i-j)}v^{2j+1}\frac{1}{2\pi}\int_0^{2\pi}\cos^{2(i-j)}\theta\sin^{2(j+1)}\theta\,\mathrm{d}\theta \neq 0 \tag{28}$$

for which the result depends on the values of i and j. For $\dot{v}$, we have:

$$\sum_{i=1}^{\infty}\alpha_{2i+1}\sum_{j=0}^{i}\binom{2i+1}{2j+1}u^{2(i-j)}v^{2j+1}\frac{1}{2\pi}\int_0^{2\pi}\cos^{2(i-j)+1}\theta\sin^{2j+1}\theta\,\mathrm{d}\theta = 0 \tag{29}$$

since both exponents are odd.

Case 2: d is odd and p is even.
In this case, we set $d = 2i + 1$ and $p = 2j$. For $\dot{u}$ we have:

$$-\sum_{i=1}^{\infty}\alpha_{2i+1}\sum_{j=0}^{i}\binom{2i+1}{2j}u^{2(i-j)}v^{2j}\frac{1}{2\pi}\int_0^{2\pi}\cos^{2(i-j)+1}\theta\sin^{2j+1}\theta\,\mathrm{d}\theta = 0 \tag{30}$$

since both exponents are odd. For $\dot{v}$, we have:

$$-\sum_{i=1}^{\infty}\alpha_{2i+1}\sum_{j=0}^{i}\binom{2i+1}{2j}u^{2(i-j)+1}v^{2j}\frac{1}{2\pi}\int_0^{2\pi}\cos^{2(i-j+1)}\theta\sin^{2j}\theta\,\mathrm{d}\theta \neq 0 \tag{31}$$

for which the result depends on the values of i and j.

Case 3: d and p are even.
In this case, we set $d = 2i$ and $p = 2j$. For $\dot{u}$ we have:

$$-\sum_{i=0}^{\infty}\alpha_{2i}\sum_{j=0}^{i}\binom{2i}{2j}u^{2(i-j)}v^{2j}\frac{1}{2\pi}\int_0^{2\pi}\cos^{2(i-j)}\theta\sin^{2j+1}\theta\,\mathrm{d}\theta = 0 \tag{32}$$

since one of the exponents is odd. For $\dot{v}$, we have:

$$-\sum_{i=0}^{\infty}\alpha_{2i}\sum_{j=0}^{i}\binom{2i}{2j+1}u^{2(i-j)}v^{2j}\frac{1}{2\pi}\int_0^{2\pi}\cos^{2(i-j)+1}\theta\sin^{2j}\theta\,\mathrm{d}\theta = 0 \tag{33}$$

since one of the exponents is odd.

Case 4: d is even and p is odd.
In this case, we set $d = 2i$ and $p = 2j + 1$. For $\dot{u}$ we have:

$$\sum_{i=0}^{\infty}\alpha_{2i}\sum_{j=0}^{i}\binom{2i}{2j+1}u^{2(i-j)-1}v^{2j+1}\frac{1}{2\pi}\int_0^{2\pi}\cos^{2(i-j)-1}\theta\sin^{2(j+1)}\theta\,\mathrm{d}\theta = 0 \tag{34}$$

since one of the exponents is odd. For $\dot{v}$, we have:

$$\sum_{i=0}^{\infty}\alpha_{2i}\sum_{j=0}^{i}\binom{2i}{2j+1}u^{2(i-j)-1}v^{2j+1}\frac{1}{2\pi}\int_0^{2\pi}\cos^{2(i-j)}\theta\sin^{2j+1}\theta\,\mathrm{d}\theta = 0 \tag{35}$$

since one of the exponents is odd.

Summary:
Therefore, we end up with:

$$\sum_{i=1}^{\infty}\alpha_{2i+1}\sum_{j=0}^{i}\binom{2i+1}{2j+1}u^{2(i-j)}v^{2j+1}\frac{1}{2\pi}\int_0^{2\pi}\cos^{2(i-j)}\theta\sin^{2(j+1)}\theta\,\mathrm{d}\theta \tag{36}$$

and

$$-\sum_{i=1}^{\infty}\alpha_{2i+1}\sum_{j=0}^{i}\binom{2i+1}{2j}u^{2(i-j)+1}v^{2j}\frac{1}{2\pi}\int_0^{2\pi}\cos^{2(i-j+1)}\theta\sin^{2j}\theta\,\mathrm{d}\theta \tag{37}$$

for $\dot{u}$ and $\dot{v}$, respectively. We thus observe that the stiffness of even orders do not participate in the motion around the primary resonance at first order.

Averaged solution around the primary resonance
The average solution for $\dot{u}$ is therefore:

$$\dot{u} = -\frac{\varepsilon}{\omega}\left(\frac{\gamma}{2} + \zeta\,\omega_0\,\omega\,u - \frac{\Omega\,v}{2} + \sum_{i=1}^{\infty}\alpha_{2i+1}\sum_{j=0}^{i}\binom{2i+1}{2j+1}u^{2(i-j)}v^{2j+1}\frac{1}{2\pi}\int_0^{2\pi}\cos^{2(i-j)}\theta\sin^{2(j+1)}\theta\,\mathrm{d}\theta\right) \tag{38}$$

and for $\dot{v}$:

$$\dot{v} = -\frac{\varepsilon}{\omega}\left(\zeta\,\omega_0\,\omega\,v + \frac{\Omega\,u}{2} - \sum_{i=1}^{\infty}\alpha_{2i+1}\sum_{j=0}^{i}\binom{2i+1}{2j}u^{2(i-j)+1}v^{2j}\frac{1}{2\pi}\int_0^{2\pi}\cos^{2(i-j+1)}\theta\sin^{2j}\theta\,\mathrm{d}\theta\right) \tag{39}$$

Those equations can be gathered in order to get $\dot{r}$ and $\dot{\phi}$ using the relations from Equation 12. However, this leads to complex expressions and it is interesting to see if the effect of the polynomial stiffness can be simplified.

Solution for $\dot{r}$

First, for $\dot{r}$, it is possible to show that when we use the relation: $u\dot{u} + v\dot{v}$, then we have for the polynomial stiffness terms:

$$\begin{aligned}\sum_{i=1}^{\infty}\alpha_{2i+1}\sum_{j=0}^{i}\binom{2i+1}{2j+1}u^{2(i-j)+1}v^{2j+1}\frac{1}{2\pi}\int_0^{2\pi}\cos^{2(i-j)}\theta\sin^{2(j+1)}\theta\,\mathrm{d}\theta \\ -\sum_{i=1}^{\infty}\alpha_{2i+1}\sum_{j=0}^{i}\binom{2i+1}{2j}u^{2(i-j)+1}v^{2j+1}\frac{1}{2\pi}\int_0^{2\pi}\cos^{2(i-j+1)}\theta\sin^{2j}\theta\,\mathrm{d}\theta = 0\end{aligned} \tag{40}$$

Taking out the constant terms, we end up with:

$$\sum_{j=0}^{i}\frac{u^{2(i-j)+1}v^{2j+1}}{2\pi}\left(\binom{2i+1}{2j+1}\int_0^{2\pi}\cos^{2(i-j)}\theta\sin^{2(j+1)}\theta\,\mathrm{d}\theta - \binom{2i+1}{2j}\int_0^{2\pi}\cos^{2(i-j+1)}\theta\sin^{2j}\theta\,\mathrm{d}\theta\right) = 0 \tag{41}$$

and therefore, we need to prove that

$$\binom{2i+1}{2j+1}\int_0^{2\pi}\cos\theta^{2(i-j)}\sin^{2(j+1)}\theta\,\mathrm{d}\theta - \binom{2i+1}{2j}\int_0^{2\pi}\cos\theta^{2(i-j+1)}\sin^{2j}\theta\,\mathrm{d}\theta = 0 \tag{42}$$

in order to show that Equation (40) is valid.

The first step is to use the results of the integrals from Equation (16) and rewrite Equation (42) as:

$$\frac{2}{\Gamma(i+2)}\left(\binom{2i+1}{2j+1}\Gamma(i-j+\frac{1}{2})\Gamma(j+1+\frac{1}{2}) - \binom{2i+1}{2j}\Gamma(i+1-j+\frac{1}{2})\Gamma(j+\frac{1}{2})\right) \tag{43}$$

After that, we can make use of the following property of the *Gamma* function:

$$\Gamma(n+\frac{1}{2}) = \binom{n-\frac{1}{2}}{n}n!\sqrt{\pi} \tag{44}$$

for non-negative integer values of n, as well as the following binomial coefficient property:

$$\binom{n}{k} = \frac{n-k+1}{k}\binom{n}{k-1} \tag{45}$$

to rewrite Equation (43) as

$$\frac{2\pi}{\Gamma(i+2)}(i-j)!j!\binom{i-j-\frac{1}{2}}{i-j}\binom{j-\frac{1}{2}}{j}\binom{2i+1}{2j}\left(\frac{2i-2j+1}{2j+1}(j+\frac{1}{2}) - (i-j+\frac{1}{2})\right) = 0 \tag{46}$$

which proves the relation from Equation (40).

Finally, we can write for $\dot{r}$:

$$\dot{r} = -\frac{\varepsilon}{\omega r}\left(\zeta\,\omega_0\,\omega\,r^2 - \frac{\gamma}{2}r\sin\phi\right) \tag{47}$$

Solution for $\dot{\phi}$

In the case of $\dot{\phi}$, we need to use the relation $v\dot{u} - u\dot{v}$ and therefore, the terms related to the polynomial stiffness can be written as:

$$\begin{aligned}\sum_{i=1}^{\infty}\alpha_{2i+1}\sum_{j=0}^{i}\binom{2i+1}{2j+1}u^{2(i-j)+1}v^{2(j+1)}\frac{1}{2\pi}\int_0^{2\pi}\cos^{2(i-j)}\theta\sin^{2(j+1)}\theta\,\mathrm{d}\theta \\ +\sum_{i=1}^{\infty}\alpha_{2i+1}\sum_{j=0}^{i}\binom{2i+1}{2j}u^{2(i-j+1)}v^{2j+1}\frac{1}{2\pi}\int_0^{2\pi}\cos^{2(i-j+1)}\theta\sin^{2j}\theta\,\mathrm{d}\theta\end{aligned} \tag{48}$$

which can be simplified and written under the form:

$$\sum_{i=1}^{\infty}\alpha_{2i+1}C\sum_{j=0}^{i+1}\binom{i+1}{j}u^{2(i+1-j)}v^{2j} = \sum_{i=1}^{\infty}\alpha_{2i+1}C(u^2+v^2)^{i+1} = \sum_{i=1}^{\infty}\alpha_{2i+1}Cr^{2(i+1)} \tag{49}$$

where C is a constant to be determined. To demonstrate this, we need to show that:

$$\begin{aligned}\sum_{j=0}^{i}\frac{1}{2\pi}\left(\binom{2i+1}{2j+1}u^{2(i-j)}v^{2(j+1)}\int_0^{2\pi}\cos^{2(i-j)}\theta\sin^{2(j+1)}\theta\,\mathrm{d}\theta + \binom{2i+1}{2j}u^{2(i-j+1)}v^{2j}\int_0^{2\pi}\cos^{2(i-j+1)}\theta\sin^{2j}\theta\,\mathrm{d}\theta\right) \\ = C\sum_{j=0}^{i+1}\binom{i+1}{j}u^{2(i+1-j)}v^{2j}\end{aligned} \tag{50}$$

First, we rearrange the left hand side of Equation (51) such that:

$$\begin{aligned}
&\binom{2i+1}{0} u^{2(i+1)} \frac{1}{2\pi} \int_0^{2\pi} \cos^{2(i+1)} \theta \, \mathrm{d}\theta \\
&+ \binom{2i+1}{1} u^{2i} v^2 \frac{1}{2\pi} \int_0^{2\pi} \cos^{2i} \theta \sin^2 \theta \, \mathrm{d}\theta + \binom{2i+1}{2} u^{2i} v^2 \frac{1}{2\pi} \int_0^{2\pi} \cos^{2i} \theta \sin^2 \theta \, \mathrm{d}\theta \\
&+ \dots \\
&+ \binom{2i+1}{2k-1} u^{2(i+1-k)} v^{2(k)} \frac{1}{2\pi} \int_0^{2\pi} \cos^{2(i+1-k)} \theta \sin^{2k} \theta \, \mathrm{d}\theta + \binom{2i+1}{2j} u^{2(i+1-k)} v^{2k} \frac{1}{2\pi} \int_0^{2\pi} \cos^{2(i+1-k)} \theta \sin^{2k} \theta \, \mathrm{d}\theta \\
&+ \dots \\
&\binom{2i+1}{2i+1} v^{2(i+1)} \frac{1}{2\pi} \int_0^{2\pi} \sin^{2(i+1)} \theta \, \mathrm{d}\theta
\end{aligned} \tag{51}$$

Or simply:

$$\begin{aligned}
&\binom{2i+1}{0} u^{2(i+1)} \frac{1}{2\pi} \int_0^{2\pi} \cos^{2(i+1)} \theta \, \mathrm{d}\theta \\
&+ \sum_{j=1}^{i} \left(\binom{2i+1}{2j-1} + \binom{2i+1}{2j} \right) u^{2(i+1-j)} v^{2j} \frac{1}{2\pi} \int_0^{2\pi} \cos^{2(i+1-j)} \theta \sin^{2j} \theta \, \mathrm{d}\theta \\
&\binom{2i+1}{2i+1} v^{2(i+1)} \frac{1}{2\pi} \int_0^{2\pi} \sin^{2(i+1)} \theta \, \mathrm{d}\theta
\end{aligned} \tag{52}$$

Which can be further simplified by making use of the fact that first:

$$\binom{2i+1}{2j-1} + \binom{2i+1}{2j} = \binom{2(i+1)}{2j} \tag{53}$$

and second:

$$\binom{2i+1}{0} = \binom{2i+1}{2i+1} = 1 = \binom{2(i+1)}{0} = \binom{2(i+1)}{2(i+1)} \tag{54}$$

which leads to

$$\sum_{j=0}^{i+1} \binom{2(i+1)}{2j} u^{2(i+1-j)} v^{2j} \frac{1}{2\pi} \int_0^{2\pi} \cos^{2(i+1-j)} \theta \sin^{2j} \theta \, \mathrm{d}\theta \tag{55}$$

The final step consists in showing that:

$$\binom{2(i+1)}{2j} \frac{1}{2\pi} \int_0^{2\pi} \cos^{2(i+1-j)} \theta \sin^{2j} \theta \, \mathrm{d}\theta = C \binom{i+1}{j} \tag{56}$$

To do so, we make use of the fact that a binomial coefficient can be written using the *Gamma* function:

$$\binom{n}{k} = \frac{\Gamma(n+1)}{\Gamma(k+1)\Gamma(n-k+1)} \tag{57}$$

Furthermore, using the results from Equation (16), we can write the left hand side of Equation (56) as:

$$\frac{1}{\pi} \frac{\Gamma(2z_1)}{\Gamma(2z_3)\Gamma(2z_2)} \frac{\Gamma(z_2)\Gamma(z_3)}{\Gamma(z_1 + \frac{1}{2})} \tag{58}$$

where $z_1 = i + 1 + \frac{1}{2}$, $z_2 = i + 1 - j + \frac{1}{2}$ and $z_3 = k + \frac{1}{2}$. Using the Legendre duplication formula:

$$\Gamma(z)\Gamma(z + \frac{1}{2}) = 2^{1-2z} \sqrt{\pi} \Gamma(2z) \tag{59}$$

it is possible to rewrite Equation (58) as:

$$\frac{\Gamma(2i+3)}{2^{2(i+1)}\Gamma^2(i+2)} \binom{i+1}{j} = C_i \binom{i+1}{j} \tag{60}$$

where $C_i = \frac{\Gamma(2i+3)}{2^{2(i+1)}\Gamma^2(i+2)}$ is a constant that only depends on i. Therefore, we can indeed rewrite Equation (48) as Equation (49). Finally, we can write for $\dot{\phi}$:

$$\dot{\phi} = -\frac{\varepsilon}{\omega \, r^2} \left(\sum_{i=1}^{\infty} \alpha_{2i+1} C_i r^{2(i+1)} - \frac{\Omega}{2} r^2 - \frac{\gamma}{2} r \cos \phi \right) \tag{61}$$

Solution at steady-state

Since we are interested in solutions at steady-state, we have $\dot{r} = \dot{\phi} = 0$ and therefore

$$\begin{cases} r = \frac{\gamma}{2\zeta\,\omega_0\,\omega}\sin\phi \\ \sum_{i=1}^{\infty}\alpha_{2i+1}C_i r^{2i+1} - \frac{\Omega}{2}r = \frac{\gamma}{2}\cos\phi \end{cases} \tag{62}$$

where the first relation shows that the amplitude r does not directly depend on the nonlinear stiffness coefficients α_d. This relation also confirms that even order stiffness do not participate in the motion around the primary resonance.

Amplitude and phase resonances

Amplitude resonance occurs when both $\frac{\partial r}{\partial\,\omega}$ and $\frac{\partial r}{\partial\phi}$ are equal to 0. From Equation (62), we obtain:

$$\begin{cases} \frac{\partial r}{\partial\phi} = \frac{\gamma}{2\zeta\,\omega_0\,\omega}\left(\cos\phi - \frac{\sin\phi}{\omega}\frac{\partial\,\omega}{\partial\phi}\right) = 0 \\ \frac{\partial r}{\partial\,\omega} = \frac{\gamma}{2\zeta\,\omega_0\,\omega}\left(\cos\phi\frac{\partial\phi}{\partial\,\omega} - \frac{\sin\phi}{\omega}\right) = 0 \end{cases} \tag{63}$$

where

$$\frac{\partial\phi}{\partial\,\omega} = -\frac{2}{\gamma\sin\phi}\left(\sum_{i=1}^{\infty}\alpha_{2i+1}C_i(2i+1)r^{2i}\frac{\partial r}{\partial\,\omega} - \frac{1}{2}\left(\frac{2\,\omega}{\varepsilon}r + \frac{\omega^2 - {\omega_0}^2}{\varepsilon}\frac{\partial r}{\partial\,\omega}\right)\right) \tag{64}$$

Eventually, we have

$$\frac{\partial r}{\partial\,\omega} = \frac{\gamma^2\sin^2\phi\,(\omega - \varepsilon\zeta\,\omega_0\tan\phi)}{\left(2({\omega_0}^2 - \omega^2)\zeta\,\omega_0\,\omega + \varepsilon\left(2\gamma^2\zeta^2\,{\omega_0}^2\,\omega^2\cos\phi + \sum_{i=1}^{\infty}\alpha_{2i+1}C_i(2i+1)\frac{(\gamma\sin\phi)^{2i+1}}{(2\zeta\,\omega_0\,\omega)^{2i-1}}\right)\right)} = 0 \tag{65}$$

This relation is verified when:

$$\tan\phi_a = \frac{\omega_a}{\varepsilon\zeta\,\omega_0} \tag{66}$$

Since we consider a small damping ratio $\bar{\zeta} = \varepsilon\zeta$, the phase lag ϕ_a at amplitude resonance is very close to $\frac{\pi}{2}$.
On the other hand, phase resonance for linear and nonlinear systems occurs when the external forcing counterbalances exactly the damping forces [5]. From the first equation in Equation (62), we see that this happens when the phase lag is $\pi/2$. Phase resonance thus occurs in the immediate vicinity of amplitude resonance.

Numerical validation on a Helmholtz-Duffing oscillator

The previous results are applied to a Helmholtz-Duffing oscillator governed by the following equation:

$$\ddot{x}(t) + 2\bar{\zeta}\,\omega_0\,\dot{x}(t) + \omega_0^2 x(t) + \bar{\beta}x^2(t) + \bar{\alpha}x^3(t) = \bar{\gamma}\sin\omega t \tag{67}$$

According to Equation 62, first-order averaging around the primary resonance gives

$$\begin{cases} r = \frac{\gamma}{2\zeta\,\omega_0\,\omega}\sin\phi \\ \frac{3\alpha}{8}r^3 - \frac{\Omega}{2}r = \frac{\gamma}{2}\cos\phi \end{cases} \tag{68}$$

Setting $\bar{\beta} = 0.05$ N/(kg m^2), $\bar{\alpha} = 0.05$ N/(kg m^3) and $\bar{\zeta} = 0.005$, the numerical solution using a harmonic balance continuation procedures with 8 harmonics is compared to the analytical solution from Equation (68) in Figure 1. The two methods give very similar results around the primary resonance. In addition to that, the phase resonance points, which correspond to a phase lag of $\frac{\pi}{2}$ for the first harmonic component of the solution, is also plotted and both techniques show that it is indeed in the vicinity of the amplitude resonance.

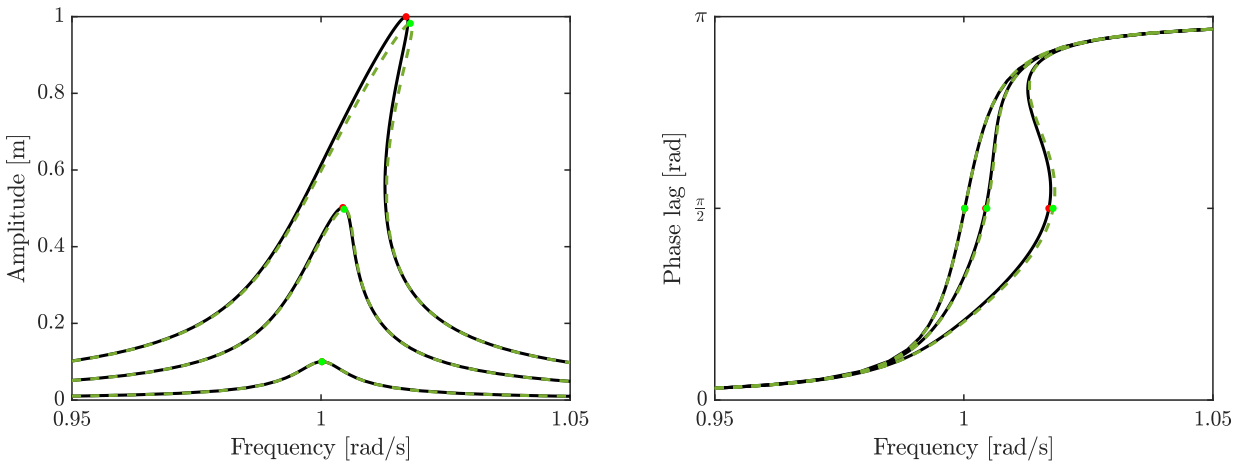

(a) (b)

Figure 1: Nonlinear frequency responses (Numerical: black, analytical: green) around the primary resonance of the Helmholtz-Duffing oscillator for forcing amplitudes $\bar{\gamma}$ of 0.001N, 0.005N and 0.01N: (a) amplitude and (b) phase lag. The red (numerical) and green (analytical) dots correspond to a phase lag of $\frac{\pi}{2}$.

Conclusion

A first-order averaging technique was applied around the primary resonance of an oscillator with arbitrary polynomial stiffness. The results show that phase resonance associated with a phase lag of $\frac{\pi}{2}$ exists in the immediate neighborhood of amplitude resonance in the case of weak damping. These results are in agreement with those of Peeters et al. [5] and Haller et al. [6].

References

[1] D. J Ewins. *Modal testing : theory, practice, and application*. Baldock, Hertfordshire, England ; Philadelphia, PA : Research Studies Press, 2nd edition, 2000.

[2] Gaëtan Kerschen, Keith Worden, Alexander F. Vakakis, and Jean-Claude Golinval. Past, present and future of nonlinear system identification in structural dynamics. *Mechanical Systems and Signal Processing*, 20(3):505 – 592, 2006.

[3] N.M. Krylov and N.N. Bogolyubov. *Introduction to non-linear mechanics*. Princeton University Press, 1947.

[4] Ali H. Nayfeh. *Perturbation methods*. John Wiley & Sons, New York, 1973.

[5] M. Peeters, G. Kerschen, and J.C. Golinval. Dynamic testing of nonlinear vibrating structures using nonlinear normal modes. *Journal of Sound and Vibration*, 330:486–509, 2011.

[6] M. Cedenese and G. Haller. How do conservative backbone curves perturb into forced responses? a melnikov function analysis. *Proceedings of the Royal Society A*, 476:20190494, 2020.

Parallel Harmonic Balance Method: towards very large scale systems

Loïc Salles*, Jiri Blahos*, Alessandra Vizzacarro* and Fadi El Haddad*
* *Departmanent of Mechanical Engineering, Imperial College, London, UK*

Summary. This paper presents a parallel implementation of harmonic balance method coupled with continuation method. The different elements for a parallel implementation are introduced. The obtained software permits to accurately solve problem that has never been studied in this manner before. The results obtained with the proposed approach gives hints for creating accurate reduced order modelling.

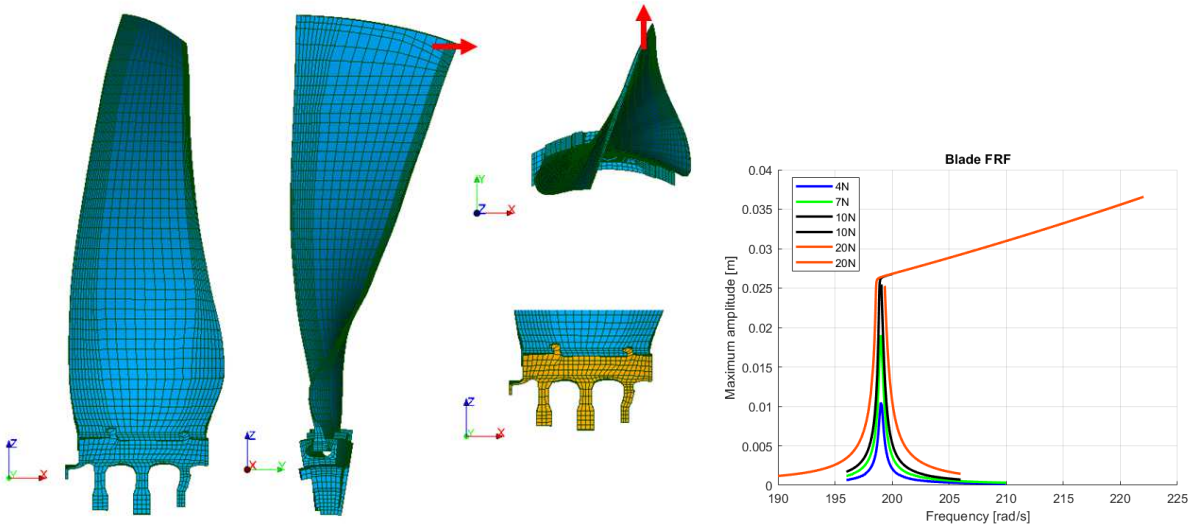

Figure 1: Fan blade with nonlinear frequency response

High-cycle fatigue caused by large resonance stresses remains one of the most common causes of turbine blade failures. Nonlinear vibration can have an important effect on the high cycle fatigue of components. Harmonic Balance Method is an efficient technique to model the nonlinear vibration of turbomachinery components. Efficient software have been developped for the last two decades but are still limited to reduced size system [5, 4, **?**].

We propose in this work to present the element to develop continuation method based on harmonic balance method for large scale system. We will explore in the paper two types of common nonlinearities: localized (contact with friction) and non-locolized (large deformation). The equation of motion and its transformation to nonlinear algeabric system will be introduced. We proposed an original implementation [6] that allows to easily treat any type of problem: frequency response, nonlinear modal analysis or limite cycle oscillation. We will then how any type of localized nonlinearities can be treated using harmonic balance method and alternating frequency time procedure [3]. We will present how the computation of nonlinear forces can be parallelised using both OPENMP and MPI programming language.

In a second part the paper focus on the non-localized nonlinearities and their implementation in the Finite Element framework. A C++ code has been developped and solves the nonlinear HBM problem in parallel, using MPI. A 3rd party software package is used to load and distribute a mesh. Standard finite element scheme is then used to assemble the sparse system matrices (mass, stiffness, damping) in parallel using CSR format. Nonlinearities are added using the alternating frequency time (AFT) procedure. Frequency domain dofs are organised in a way that keeps them on the same MPI rank as their corresponding mesh nodes to minimise necessary communication. To solve the nonlinear HBM problem the Newton-Raphson iterative algorithm is used. For the underlying linear problem, we used a 3rd party software package based on parallel sparse implementation of the LU decomposition [1]. The code results have been verified against previous results presented in the scientific literature. The code has been tested on multi-million degree of freedom problems. A decent speed-up was obtained for number of MPIs up to approx. 100 MPI ranks.

Several numerical results on academic problems (cantilever beam and clamped-clamped beam) will illustrate the proposed method and gives hint for creating reduced order model. It will be shown that care has to be taken when creating reduced order model for structure in large deformation.

The paper will finish with recommendation about future work needed to develop more scalable continuation methods for nonlinear vibration analysis.

References

[1] Amestoy P.R., Duff I.S., L'Excellent, J-Y. Koster J. (2001) A fully asynchronous multifrontal solver using distributed dynamic scheduling *SIAM J. on Matrix Analysis and Applications* **23**:15-41

[2] Guillot L., Cochelin B., Vergez C. (2019) A Taylor series-based continuation method for solutions of dynamical systems *Nonlinear Dynamics* **98**:2827-2845

[3] Krack M., Gross Johann (2019) Harmonic Balance for Nonlinear Vibration Problems Springer, Cham

[4] Nacivet S., Pierre C., Thouverez F., Jézéquel L. (2003) A dynamic Lagrangian frequency–time method for the vibration of dry-friction-damped systems *Journal of Sound and Vibration* **265**:201-2019

[5] Petrov, E.P. and Ewins, D.J. (2004) State-of-the-art dynamic analysis for non-linear gas turbine structures *Proceedings of the Institution of Mechanical Engineers, Part G: Journal of Aerospace Engineering* **218**:199-211

[6] Salles L., Vizzaccaro A., Sun Y. (2019) Seventh International Conference on NONLINEAR VIBRATIONS, LOCALIZATION AND ENERGY TRANSFER, Marseille, France

Tracking basin boundaries with Clustered Simple Cell Mapping method

Gergely Gyebrószki[†] and Gábor Csernák[†]
[†]*MTA-BME Research Group on Dynamics of Machines and Vehicles, H-1111, Budapest, Műegyetem rkp 3.*

Summary. The Simple Cell Mapping (SCM) method [3] is a simple and effective algorithm to analyse the (discretized) state space of dynamical systems. A state space region is divided into cells and an image cell (where the dynamics lead to) is determined for each cell. SCM is able to find chaotic attractors and – depending on the cell resolution – repellers, and their basin of attraction. Chaotic structures are usually represented by a periodic cell group with high period, while basins of attraction are composed of transient cell sequences leading to periodic groups.
Previously, we have improved the SCM method with the ability to extend its underlying state space region and join the new state space region to the previous SCM solution. This method is called Clustered Simple Cell Mapping (CSCM) [2]. We show that CSCM can be a valuable tool for automatically exploring the state space or tracking certain features – for example the basin of attraction of an attractor or the closure of a chaotic repeller, especially in the case, where the underlying system can exhibit crisis bifurcations. An example is shown using the well-known Ikeda-map [4].

Clustered Simple Cell Mapping

Simple Cell Mapping (SCM) is a great tool to quickly analyse the state space of dynamical systems. An initial state space region is discretized into cells, for each cell a single image cell is determined, usually by following a trajectory from the center point of each cell for a given time step, or by applying the map corresponding to discrete systems. The SCM method then classifies cells as either periodic cells (belonging to a periodic group) or transient cells (leading to one of the periodic groups within the state space, or the region outside – the sink cell). Chaotic attractors or repellers are usually represented by a periodic cell group with high periodicity.
There are several extensions for the SCM method, some of them exploits certain properties of a class of dynamical systems: eg. discontinuous systems [5], or Filippov systems [1]. In [2] we have introduced the Clustered Simple Cell Mapping (CSCM) method, another extension aiming to adaptively extend the analysed state space region in a computationally effective manner. Clustered SCM is able to join an additional state space region to the so called *cluster* of SCMs, and update the solution by re-using the existing cell classification in the initial SCM region.
The concept is illustrated in Fig. 1: the left region is the initial SCM solution containing a periodic group (denoted by dark grey ■) and a set of transient cells leading to it (gray colour ■). The right state space region is added to the cluster of SCMs: this allows the discovery of transient cells leading to a previously classified periodic group (green ■), a new periodic group (at the boundary of the two regions) and non-trivial transients in the initial SCM's region (denoted by orange ■).
Clustered Simple Cell Mapping allows the continuation of SCM solutions towards state space structures (e.g. basins of attraction) that get clipped by the initial choice of state space region.

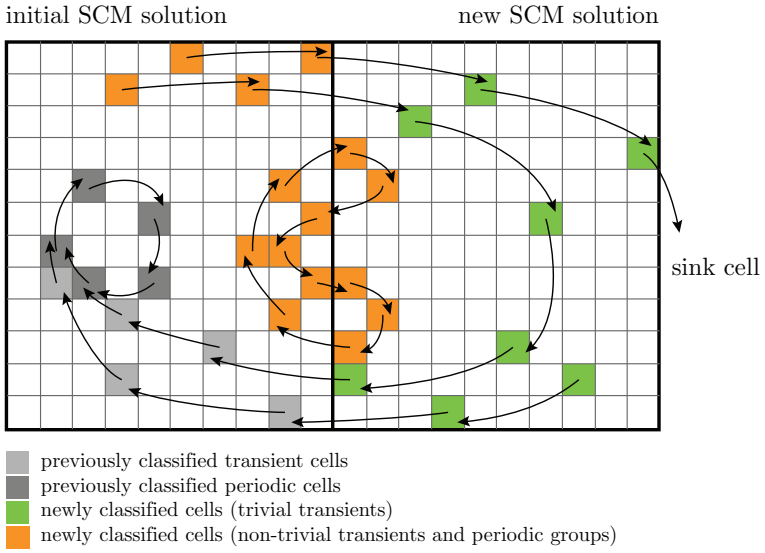

Figure 1: The concept of the Clustered Simple Cell Mapping (CSCM) method.

The Ikeda-map

The Ikeda-map [4] is originated from a model of light going around across a nonlinear optical resonator. Depending on its parameters it can have fixed points, chaotic attractors or a repeller in its state space and can exhibit crisis bifurcations.

$$\begin{aligned} x_{n+1} &= 1 + u\,(x_n\,\cos(t_n) - y_n\,\sin(t_n)) \\ y_{n+1} &= u\,(x_n\,\sin(t_n) + y_n\,\cos(t_n)), \end{aligned} \tag{1}$$

where u is a parameter and:

$$t_n = 0.4 - \frac{6}{1 + x_n^2 + y_n^2}. \tag{2}$$

An application example

We show an example of state-space exploration by using the CSCM method in the case of the Ikeda-map defined by Eq. (1). The starting region (denoted by 1 in Fig. 2) is a 6×6 square at $(0, 0)$ in the (x, y) plane, where a chaotic repeller resides. Note, that the repeller can only be found by SCM if the cell resolution is sufficiently coarse, to artificially *stabilize* it. The adaptive state-space extension algorithm adds another 8 square-shaped state space region to the cluster, by following the basin of attraction along the four main directions. This is shown on Fig. 2, where the successive state-space regions are numbered. After the initial exploration procedure, the cluster is made convex by adding regions 10 to 12. As the last state space region is included – where a fixed point resides – the SCM algorithm is able to classify its basin of attraction as well (denoted by shades from green to blue based on step numbers needed to reach the fixed point).

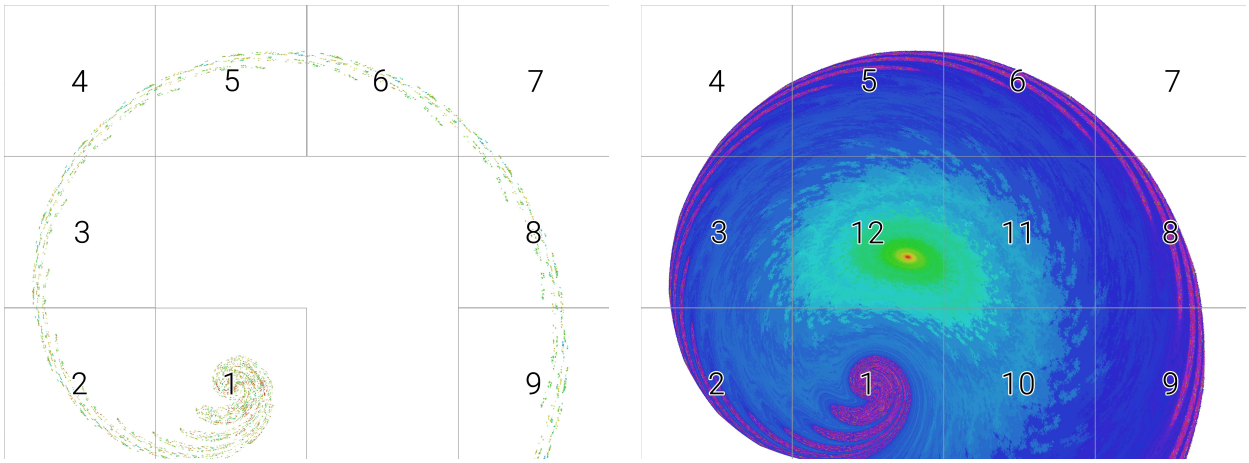

Figure 2: A CSCM cluster consisting of 9 SCM solutions (*left*) and 12 SCM solutions (*right*) of the Ikeda-map with $u = 0.96$. The state space region consists of squares with side lengths of 6.0. The first region's center is at $(0, 0)$. The whole cluster spans from $(x_0, y_0) = (-9, -3)$ to $(x_1, y_1) = (15, 15)$.

Conclusions

Clustered Simple Cell Mapping is a method allowing the successive expansion of the state space region corresponding to an SCM solution of a dynamical system. This allows quick and computationally effective exploration of the state space in case of crisis bifurcations (where certain state space features *explode*), or tracking basins of attraction as shown in Fig. 2. Since existing SCM solutions are re-used when the cluster is expanded, CSCM allows interactive or real-time applications.

Acknowledgements

The research reported in this paper and carried out at BME has been supported by the Hungarian National Research, Development and Innovation (NRDI) Office under Grant No. NKFI-128422.

References

[1] Erazo, C., Homer, M.E., Piiroinen, P.T., Di Bernardo, M. (2017). Dynamic cell mapping algorithm for computing basins of attraction in planar filippov systems. International Journal of Bifurcation and Chaos **27**(12), 1730041

[2] Gyebrószki, G., Csernák, G. (2017). Clustered simple cell mapping: An extension to the simple cell mapping method. Communications in Nonlinear Science and Numerical Simulation **42**, 607–622

[3] Hsu, C.: Cell-to-Cell Mapping: A Method of Global Analysis for Nonlinear Systems, *Applied Mathematical Sciences*, vol. 64. Springer, Singapore (1987)

[4] Ikeda, K., Daido, H., Akimoto, O. (1980). Optical turbulence: Chaotic behavior of transmitted light from a ring cavity. Phys. Rev. Lett. **45**, 709–712

[5] de Kraker, B., van der Spek, J.A.W., van Campen, D.H.: Extensions of cell mapping for discontinuous systems. In: M. Wiercigroch, B. de Kraker (eds.) Applied Nonlinear Dynamics and Chaos of Mechanical Systems with Discontinuities, chap. 4, pp. 61–102. World Scientific (2000)

Asymptotic-preserving and hybrid finite-volume/Monte-Carlo methods for kinetic equations in the plasma edge of a fusion reactor

Giovanni Samaey*, Bert Mortier*, Emil Løvbak*, Niels Horsten‡ and Martine Baelmans‡
*Department of Computer Science, Celestijnenlaan 200A, B-3001 Leuven, Belgium
‡Department of Mechanical Engineering, Celestijnenlaan 300A, B-3001 Leuven, Belgium

Summary. Nuclear fusion reactor design crucially depends on numerical simulation. The plasma can usually be modeled using fluid equations (for mass, momentum and energy). However, the reactor also contains neutral (non-charged) particles (which are important in its operation), of which both the position and velocity distribution is important. This leads to a Boltzmann-type transport equation that needs to be discretised with a Monte Carlo method. In high-collisional regimes, the Monte Carlo simulation describing the evolution of neutral particles becomes prohibitively expensive, because each individual collision needs to be tracked. In this talk, we look into several strategies to overcome this computational bottleneck.

Introduction

Numerical simulations of the plasma edge play a key role in the divertor design of nuclear fusion reactors [1]. The divertor needs to handle large power loads and is essential for the power and particle exhaust in a reactor. Two types of particles are modeled in plasma edge models: the plasma, consisting of charged particles (ions and electrons), and the neutral particles. The plasma can usually be described with a Navier-Stokes-like fluid model, discretized in space with a finite volume (FV) method. For the neutrals, however, a more microscopic, kinetic description is necessary, in which the particle distribution is modeled in a position-velocity phase space. Due to the additional dimensions in velocity space, FV simulation of the kinetic equations is computationally prohibitive. Therefore, one turns to Monte Carlo (MC) simulation.
Plasma and neutral particles interact through collisions, which can be charge exchange (an ion and neutral particle collide and exchange charge) or ionization (a neutral particle becomes a plasma particle). Due to these interactions, the plasma and neutral models need to be coupled, leading, for instance, to the B2-EIRENE code [2]. During charge-exchange collisions, momentum and energy are transferred between plasma and neutrals. During ionization, also mass is exchanged. Additionally, neutrals arise from the plasma due to surface and volumetric recombination of ions and electrons. Because of the different nature of the two types of discretizations (MC and FV), the two codes cannot be solved simultaneously, and an iterative procedure is needed. One thus simulates the neutral particles against a fixed plasma "background" and estimates the source terms (mass, momentum and energy) for the plasma equations. One then solves the plasma equations with these estimated sources. This procedure is repeated until no more corrections are required.
Although B2-EIRENE is used worldwide for the analysis of experimental tokamaks and for the design of ITER, computation time is a serious bottleneck. One reason is the number of collisions neutral particles undergo in a realistic setting. Large reactors suitable for electricity generation typically operate in a so-called detached regime. In this regime, one aims at an increased interaction of the neutrals with the ions, especially by means of charge-exchange collisions. The goal is to create a kind of neutral "cushion" that prevents the ions to flow immediately to the divertor targets. While this regime is advantageous to avoid a direct interaction between the plasma and the divertor (and thus lengthens the lifetime of the reactor), this has a detrimental effect on the computational cost of the MC simulation, since each individual collision needs to be tracked.
In this presentation, we overview a number of approaches that can alleviate the computational burden associated with the high-collisional regime.

Kinetic-diffusion Monte Carlo methods

One option is to avoid simulating each invididual collision. In the limit of infinite collision rate, the law of large numbers dictates the approach of an advection-diffusion like particle behaviour, in which the accumulated effect of an infinite amount of collisions is aggregated in a Brownian motion (diffusion). To maintain accuracy and remove exploding simulation costs in high-collisional regimes, one can define hybridized particles that exhibit both kinetic behaviour and diffusive behaviour depending on the local collisionality [3]. Features of the method are maintaining an asymptotically correct distribution and a correct mean, variance, and correlation for all values of the collisionality.

Multilevel Monte Carlo methods

An alternative approach is to reduce the number of Monte Carlo particles that needs to be simulated via an appropriate variance reduction technique. One very appealing option is the multilevel Monte Carlo method[5]. Asymptotic-preserving schemes as defined above result in an additional time discretization error, possibly resulting in an unacceptably large bias for larger time steps. To remove this bias, we can define a multilevel Monte Carlo scheme that reduces this bias by combining estimates using a hierarchy of different time step sizes. The multilevel Monte Carlo method relies heavily on the construction of correlated trajectories on two subsequent levels. We demonstrate how to correlate trajectories using different time steps. We also present a strategy for selecting the levels in the multilevel scheme. This approach signifi-

cantly reduces the computation required to perform accurate simulations of the considered kinetic equations, compared to classical Monte Carlo approaches.

Hybrid finite-volume Monte Carlo methods

Finally, one can also reduce the variance of the simulation by using an approximate fluid model for the neutral particles, discretized with a finite volume methods. This deterministic simulation can be used as a control variate, allowing the Monte Carlo simulation to focus on solely the deviation of the kinetic model with respect to the approximate fluid model.

References

[1] Kukushkin A.S., Pacher H.D., Kotov V., Pacher G.W., and Reiter D. (2011) Finalizing the ITER divertor design: the key role of SOLPS modeling *Fusion Eng. Des.* **86**:2865-2873.

[2] Reiter D., Baelmans M., and Börner, P. (2005) The EIRENE and B2-EIRENE codes, *Fusion Sci. Technol.* **47**:172-186.

[3] Mortier B., Samaey G., Baelmans M. (2019) Kinetic-diffusion asymptotic-preserving Monte Carlo algorithms for plasma edge neutral simulation. *Contributions to Plasma Physics*, in press.

[4] Horsten N., Samaey G., Baelmans M. (2019) Hybrid fluid-kinetic model for neutral particles in the plasma edge. *Nuclear Materials and Energy* **18**:201-207.

[5] Løvbak E., Samaey G., Vandewalle S. (2019) A multilevel Monte Carlo method for asymptotic-preserving particle schemes. Submitted. `https://arxiv.org/abs/1907.04610`.

Wednesday, July 20, 2022

08:30 - 10:30

MS-18 Control and Synchronization in Nonlinear Systems

Rhone 1

Chair: A. Pavlov, B. Brogliato

08:30 - 08:50

A Hybrid Position Feedback Controlled Bistable Metamaterial Concept

SIMSEK Mehmet, SCHIENI Rick, BURLION Laurent, **BILGEN Onur***

*Rutgers University (Department of Mechanical and Aerospace Engineering 98 Brett Rd Piscataway, NJ 08854 United States)

08:50 - 09:10

Effect of Topology upon Relay Synchronization in Multilayer Neuronal Networks

DRAUSCHKE Fenja*, OMELCHENKO Iryna, SAWICKI Jakub, SCHÖLL Eckehard

*Institut für Theoretische Physik, Technische Universität Berlin (Hardenbergstr. 36, 10623 Berlin Germany)

09:10 - 09:30

Adaptive control for compensation of non-linear hose characteristics in mechanical ventilation

REINDERS Joey*, HUNNEKENS Bram, OOMEN Tom, VAN De Wouw Nathan

*Demcon Advanced Mechatronics (Best Netherlands) - Eindhoven University of Technology [Eindhoven] (Eindhoven Netherlands)

09:30 - 09:50

An Input-Output Approach Towards Synchronization Under Communication Constraints

THOMAS Jijju*, STEUR Erik, HETEL Laurentiu, FITER Christophe, RICHARD Jean-Pierre, VAN De Wouw Nathan

*Department of Mechanical Engineering, Eindhoven University of Technology (Department of Mechanical Engineering, Eindhoven University of Technology, The Netherlands Netherlands) - Ecole Centrale de Lille, CRIStAL UMR CNRS 9189 (Ecole Centrale de Lille/Université de Lille, CRIStAL UMR CNRS 9189, 59650 Villeneuve d'Ascq, France France) - Inria Lille (Inria Lille, Villeneuve d'Ascq, France France)

09:50 - 10:10

Constrained input modulation for impulse-based motion control

RUDERMAN Michael*

*University of Agder (Postboks 422, 4604 Kristiansand Norway)

A Hybrid Position Feedback Controlled Bistable Metamaterial Concept

Mehmet Simsek,[*] Rick Schieni,[**] Laurent Burlion,[**] and Onur Bilgen[**]
[*] *Koç University, Sariyer, Istanbul, Turkey*
[**] *Rutgers University, Piscataway, NJ, 08854, USA*

Summary. The hybrid position feedback controller, proposed previously by the authors, is a control technique for bistable systems and it is based on the well-known positive-position-feedback controller. This controller is an unstable-then-stable position feedback controller, which is a second-order single-degree-of-freedom system in nature. The hybrid controller takes advantage of the resonant mode of a bistable system about one equilibrium position, destabilizes the system, and dynamically induces snap-through between the two equilibria. In this paper, a new multi degree of freedom metamaterial concept that utilizes the hybrid position feedback controller is introduced. An arbitrary number of bistable "segments" or "material elements" are attached to each other in a serial (or parallel) manner to generate a "distributed" bistable structure – also referred to as a metamaterial. Due to the simplicity of the hybrid controller, the physical implementation of proposed approach can be realized using simple circuit elements distributed in the material domain. This new metamaterial inherits the multiple bistable positions that its building blocks have; hence, the metamaterial becomes multi-stable. It can hold multiple positions without consuming power and has the capability of achieving many shapes. The proposed metamaterial concept can be used in various applications: locomotion in bioinspired systems, undulatory motion, morphing aerodynamic surfaces, wave guiding, and vibration attenuation. The concept can also be used in energy harvesting to enable maximum power extraction for a given vibratory input.

Introduction

Bistable structures are useful in many applications such as morphing aerodynamic surfaces, vibration energy harvesters, robotic actuators and mechanisms, and for locomotion of bioinspired systems where energy may be severely limited. A bistable system has two stable configurations and one unstable equilibrium.

The dynamics of bistable structures have been studied by various researchers [1-9]. The control of bistable structures using piezoelectric actuators has received significant attention in the last two decades. Shultz et al. [10] demonstrated one directional snap-through of a bistable plate using a piezoelectric actuator with static excitation. Arrieta et al. [11-13] studied the dynamic properties of bistable structures and achieved only one-directional snap-through. Later, Arrieta et al. [14] and Bilgen et al. [15] introduced resonant control with a surface bonded piezoelectric device. Zarepoor et al. [16] demonstrated the energy characteristic of a Duffing-Holmes (D-H) type bistable structure under dynamic forcing. Simsek et al. [17, 18] demonstrated an automated method for bidirectional state transfer on a wing-like cross-ply bistable plate using the hybrid control strategy and a piezocomposite actuator. Simsek et al. [19] demonstrated the prevention of chaotic behavior for Duffing-Holmes oscillator by applying the Hybrid Position Feedback (HPF) controller, which consists of the Negative Position Feedback (NPF) and Positive Position Feedback (PPF) controllers. Simsek et al. [20] analyzed the stability and response types of Duffing-Holmes oscillator with the HPF controller. Simsek et al. [21] demonstrated a piezoelectric-material induced monotonic snap-through without possibility of triggering cross-well oscillations or chaotic response. Crosswell oscillations are undesirable, as only one state is desirable (and nominal) for various applications. To this end, a hybrid position feedback (HPF) controller shows superior performance in terms of control, stability, and performance both theoretically and experimentally. In that work, the application of the HPF controller to a bistable unsymmetric cross-ply composite plate with surface-bonded piezoelectric actuators was presented.

Metamaterials or metastructures have engineered functionality that conventional materials or structures do not exhibit naturally. They have a broad range of applications from electromagnetics, acoustics, energy harvesting to vibration control. The assembly of HPF controlled bistable elements can be used to create a metamaterial or a metastructure. A system consisting of individual bistable units can form a desired configuration. Each individual element can be either at one state or the other which eventually forms a multi-stable metastructure. The proposed design can be implemented either using mechanical components such as mass-, damper- and spring-like elements, or it can be realized using circuit elements such as inductor-, resistor-, and capacitor-like elements.

The paper is organized as follows. First, the HPF control scheme is discussed. Next, the metamaterial concept is introduced. Then, the preliminary numerical simulation results are presented.

Hybrid Position Feedback Control

The hybrid position feedback controller was previously proposed by the authors to enable stable and monotonic cross-well transition of bistable (or multi-stable) structures [17, 18]. The controller is designed based on the dynamics of the stable equilibrium positions of a bistable structure around which it exhibits linear behavior for small perturbations. The control method first achieves system destabilization to make the structure move away from its current stable equilibrium position, and subsequently stabilize the system to the other (target) stable equilibrium position. The proposed hybrid control scheme employs the well-known PPF controller, and its modified version, the NPF controller. The PPF controller is a second order damped system (filter) that creates approximately 180° phase difference between input and output of the system in a certain gain range [22], which enables the system to dissipate energy through the controller. The NPF controller is a modified version of a PPF controller, here used to create a destabilizer by exploiting the phase

characteristics. As a destabilizer, the NPF controller, is expected to provide kinetic energy to the system until it reaches the desired threshold position (i.e. the unstable equilibrium.) Ref. [23] proposed and compared different switching methods for the HPF controller, and presented an analysis of the control effort and settling time.
The control diagram of the HPF controller is represented in Figure 1. In this diagram, the parameters of the NPF and PPF controllers are the same given by the block G. The reference signal $r(s)$ is considered as zero since system is in stabilizer and destabilizer mode. The authors have also investigated the system where the NPF and PPF controller parameters are individually selected and tuned.

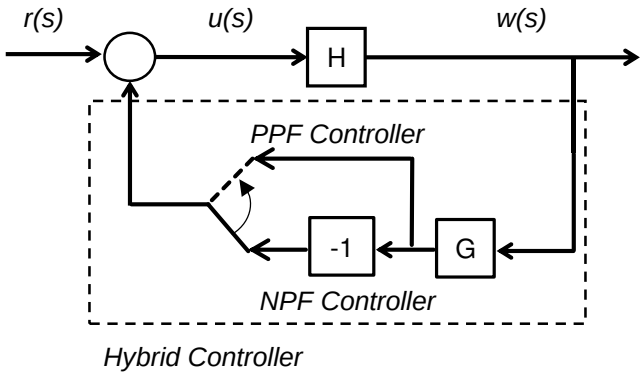

Figure 1: The block diagram for the hybrid position feedback controller.

First, the so-called NPF mode is used to start the cross-well transfer by making the PPF controller intentionally unstable. When the feedback gain is -1, the system is destabilized, and the apparent dynamic stiffness of the system becomes negative. The controller induces an oscillatory response with increasing amplitude. When the system position reaches a threshold value at the unstable equilibrium, the feedback gain is changed to +1. This leads to a stable controlled (i.e. decaying) system response with decreasing amplitude. Figure 3 illustrates the cross-well motion of an example bistable system with the hybrid controller. In the figure, the stable states of the bistable structure are labeled as S1 and S2. The current position and the unstable equilibrium position are represented by w and w_{u0} respectively.

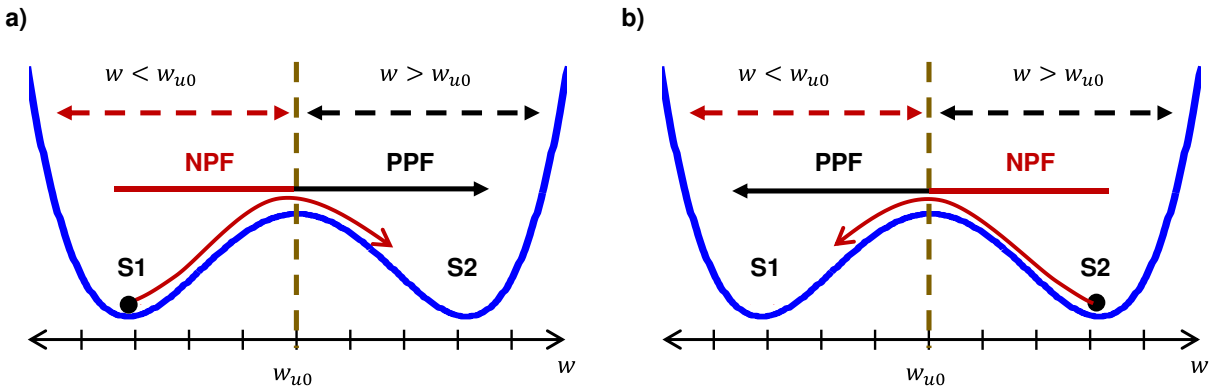

Figure 2: Illustration of state transfer a) from state 1 to state 2, and b) from state 2 to state 1.

For the state transfer from state 1 to 2, the structure is destabilized around equilibrium position S1 by using the NPF mode of the HPF controller. Due to the destabilization, the structure starts an increasing amplitude oscillation around the first equilibrium position. Once the amplitude reaches the unstable equilibrium, the structure snaps towards the second stable equilibrium position S2. The crossover is detected by an internal logic and the controller mode is switched to the PPF mode to attenuate the response around the target state of 2.
Figure 3 depicts the mechanical representation of the D-H system and HPF controller. In the system k_1 , c and k_{nl1} are linear stiffness, damping constant and cubic stiffness of system, respectively. k_c and c_c are the stiffness and damping parameter of HPF controller.

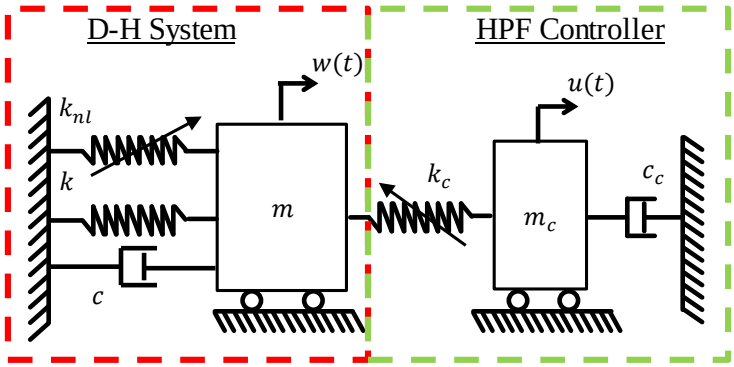

Figure 3: Mechanical model of the bistable Duffing-Holmes system with the hybrid position feedback controller.

The coupled system equations become:

$$\ddot{w} + 2\zeta\omega_n \dot{w} - {\omega_n}^2 w + \frac{k_{nl}}{m} w^3 = g_n {\omega_n}^2 u \tag{1}$$

$$\ddot{u} + 2\zeta_f \omega_f \dot{u} + {\omega_f}^2 u = g_f {\omega_f}^2 w \tag{2}$$

where ω_n *and* ζ represent natural frequency and damping ratio of the underlying linear system respectively, and g_n is the structure input gain. Here, it is noted that the actual value of input gain $g_n {\omega_n}^2$ is not constant in a physical implementation as the voltage/strain level changes [24, 25]. In this paper an effective g_n value previously determined from experiments is utilized [26]. The controller parameters ζ_f and ω_f correspond to damping ratio and natural frequency of the controller, respectively. The control gain is denoted as g_f and it is simply a proportional amplification of the feedback signal.

The complete system response depends on controller frequency, damping and gain, and depends on the system damping constant and other system parameters. The coupled system can yield three response types, namely, "intra-well," "single cross-well," and "multiple cross-well" types of responses. The "intra-well" response corresponds a response that will not reach to the threshold limit, while "single cross-well" response crosses the threshold limit once, and "multiple cross-well" response crosses twice or more.

The Metamaterial Concept and Mathematical Representations

In this paper, two different mechanical representations are considered. They are series and parallel configurations. The series configuration represents a cantilevered beam, and the parallel configuration represents an elastic foundation. Both of these configurations have different utilities in actual implementation.

Series Configuration

The so-called series configuration is presented in Figure 4. In this approach, the metamaterial concept is realized by connecting one bistable unit to next one with linear and cubic stiffnesses, and a viscous damper. A dedicated HPF controller is attached to each DOF. The series configuration represents a beam-like structure; however, with a multi-stable characteristic as opposed a "natural" monostable characteristic.

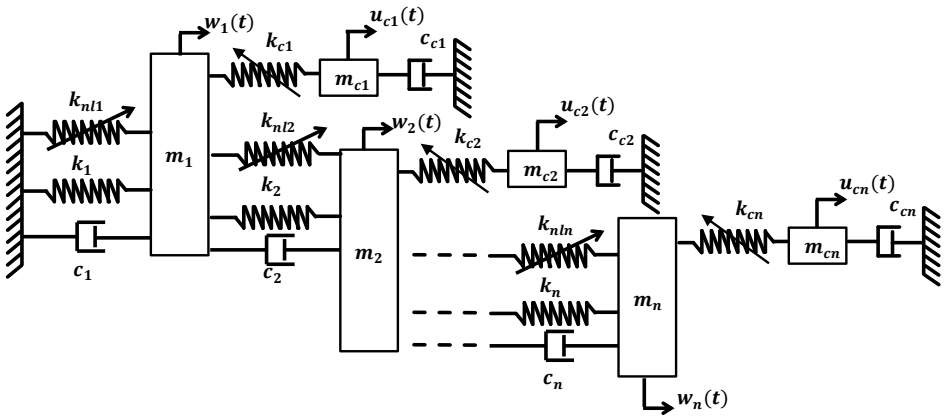

Figure 4: Mechanical model of the MDOF cascade bistable Duffing-Holmes system with the hybrid controller in series configuration.

The nonlinear coupling between the masses produces complex dynamics and a capability for the system to adopt various static or dynamic shapes. The proposed metamaterial concept is realized by adding multiple bistable oscillators in series. Figure 5 shows a representative model of cantilever beam with bistable elements connected in series.

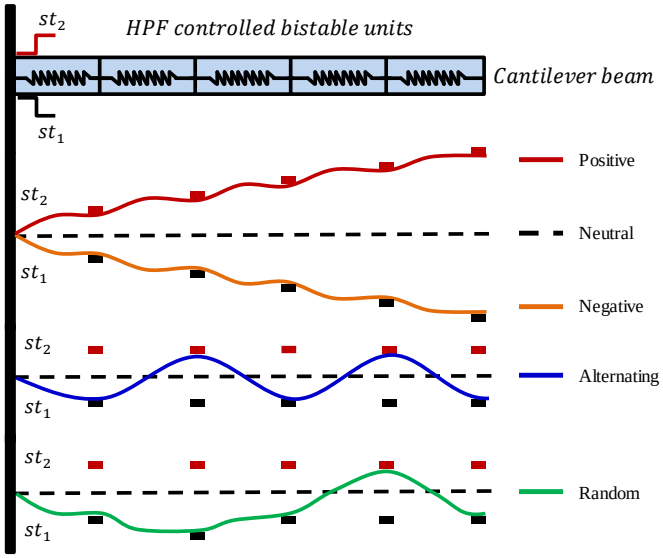

Figure 5: An illustration of a beam like metastructure with multiple bistable elements connected in series.

Parallel Configuration

Figure 5 shows an alternative, so-called parallel, configuration in which each DOFs is connected to the ground with a linear and cubic stiffness, and a viscous damper. In addition, a linear stiffness is used to connect the DOFs to each other. A dedicated HPF controller is attached to each DOF.

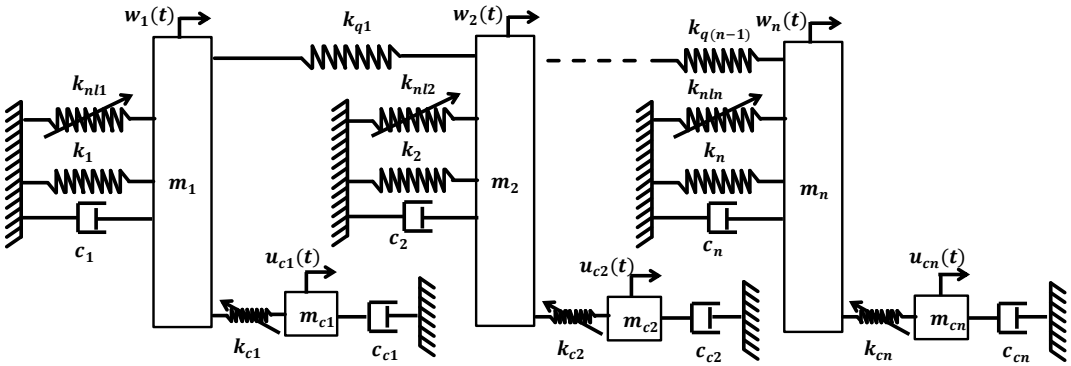

Figure 6: Mechanical model of the MDOF cascade bistable Duffing-Holmes system with the hybrid controller in parallel configuration.

This configuration reduces the coupling effect between the DOFs which minimizes the effort required to snap from one stable equilibrium while maintaining the connection between the DOFs. The proposed metamaterial concept is realized by adding multiple bistable oscillators in parallel. Figure 7 shows a representative model of a plate with bistable elastic foundation.

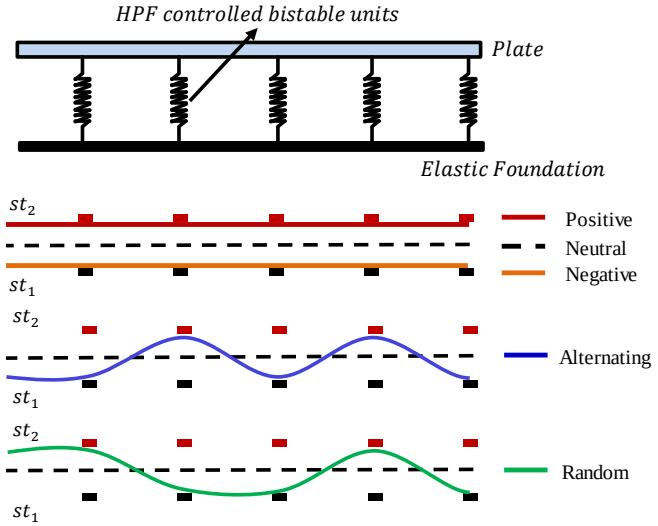

Figure 7: An illustration of a plate like metastructure with multiple bistable elements connected in parallel.

Simulation Results and Feasibility Analysis

Both the series and parallel configurations are examined through numerical integration. The dynamic response of the system is obtained using Dormand-Prince numerical integration method.

Series Configuration

The dynamic response of the series configuration is studied. Figure 8 presents the mechanical model of the 2DOF cascade bistable Duffing-Holmes system with the hybrid controller.

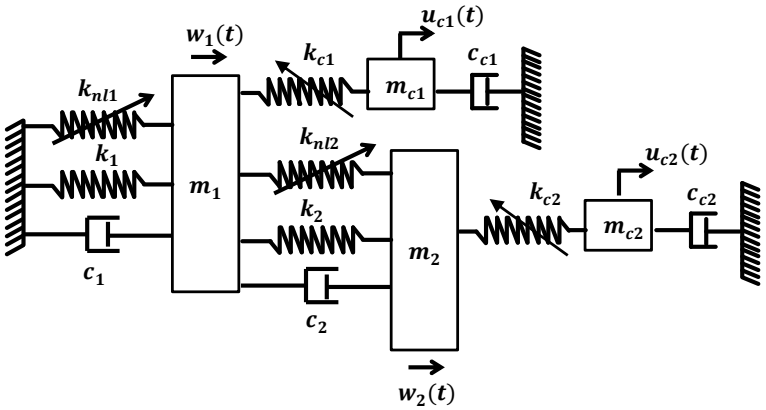

Figure 8: Mechanical model of the 2DOF cascade bistable Duffing-Holmes system with the hybrid controller in series configuration.

The governing equation for the series configuration is written as follows assuming unit mass for each DOF,

$$\ddot{w}_1 + 2\zeta_{s1}\omega_{s1}\,\dot{w}_1 - \omega_{s1}^2 w_1 + k_{nl1}w_1^3 - k_{nl2}(w_2 - w_1)^3 - \mathrm{k_2 w_2} - \mathrm{c_2}\dot{w}_2 = \omega_{s1}^2\, u_{c1} \tag{3}$$

$$\ddot{u}_{c1} + 2\zeta_{c1}\omega_{c1}\,\dot{u}_{c1} + \omega_{c1}^2 u_{c1} = g_{f1}\omega_{c1}^2\, w_1 \tag{4}$$

$$\ddot{w}_2 + 2\zeta_{s2}\omega_{s2}\,\dot{w}_2 - \omega_{s2}^2 w_2 + k_{nl2}(w_2 - w_1)^3 - \mathrm{k_2 w_1} - \mathrm{c_2}\dot{w}_1 = \omega_{s2}^2\, u_{c2} \tag{5}$$

$$\ddot{u}_{c2} + 2\zeta_{c2}\omega_{c2}\,\dot{u}_{c2} + \omega_{c2}^2 u_{c2} = g_{f2}\omega_{c2}^2\, w_2 \tag{6}$$

where $\omega_{s1}, \omega_{c1}, \omega_{s2}, \omega_{c2}$ *and* $\zeta_{s1}, \zeta_{c1}, \zeta_{s2}, \zeta_{c2}$ represent frequencies and damping ratios of the system and controllers, g_{f1} and g_{f2} is the controller gains for each DOF. $k_{nl1}$and k_{nl2} are cubic stiffness terms for the first and second DOFs, respectively. k_2 and c_2 are stiffness and damping terms representing linear coupling between the masses.
The dynamic response of the series configuration is presented in Figure 9. The HPF authority for two different scenarios is tested for weakly coupled 2DOF system. In the first scenario, HPF switches the first and second DOFs forward. In the second scenario, the HPF moves both DOFs backward from one state to another.

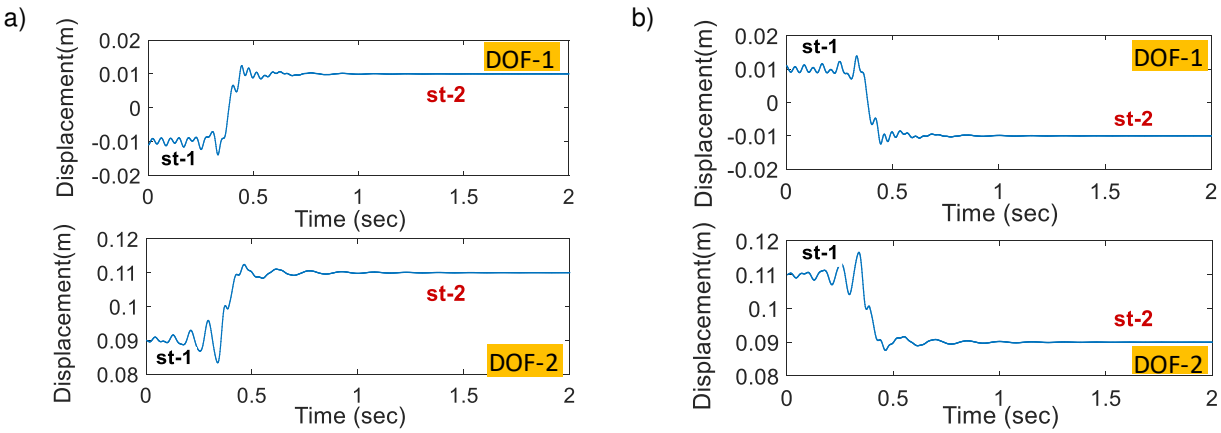

Figure 9: Example time response for the series 2DOF cascade bistable Duffing-Holmes system with the hybrid controller: a) DOF-1 st1->st2 and DOF-2 st1->st2, b) DOF-1 st2->st1 and DOF-2 st2->st1.

A parametric analysis is carried out to determine the controller parameters that satisfy the desired switch properties for different cases. The proposed schematic for series configuration can be realized when two DOFs achieve forward, backward, converse state transfer. In the analysis, two controller parameters $\zeta_{_\mathrm{npf}}$ and $g_{_\mathrm{npf}}$ are chosen since they have the major effect on switching behavior. In the analyses, the $\zeta_{_\mathrm{npf}}$ and $g_{_\mathrm{npf}}$ are equal for the two DOFs – they are swept

through a range to determine the optimum values that satisfy the desired switching behaviors. Figure 10 presents a parametric analysis for the series configuration.

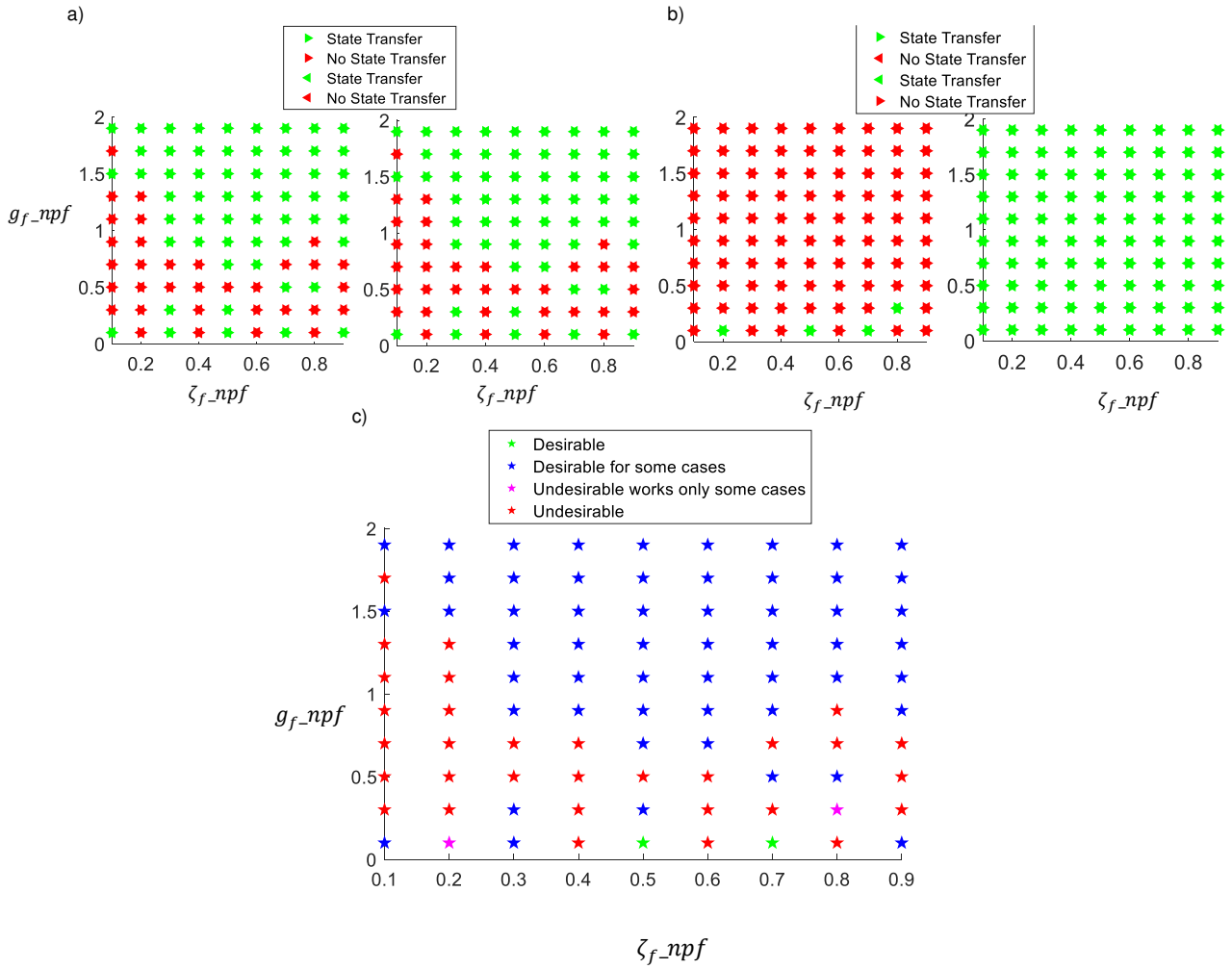

Figure 10: Parametric analysis for the series 2DOF cascade bistable Duffing-Holmes system with the hybrid controller a) Forward (DOF-1 and DOF-2: st1->st2) and Backward (DOF-1 and DOF-2: st2->st1) state transfer case, b) Converse State transfer case (DOF-1: st1->st2 and DOF-2: st2->st1, vice versa), c) all cases together.

Figure 10a presents a forward and backward state transfer behavior with respect to the controller parameters. The triangle pointing left or right shows the configuration of controller. The green and red colors indicate that initial configuration is desirable (i.e., intended state transfer) and undesirable (i.e., no state transfer), respectively. Figure 10b demonstrates the analysis carried out for converse state transfer where DOF-1 is set to achieve state transfer from state 1 to state 2 while DOF-2 is set to achieve state transfer from state 2 to state 1. Also, vice-versa case simulation is presented in this figure. Figure 10c demonstrates the behavior of controller for all cases mentioned above. The green color indicates the controller parameters that achieve successful state transfer for all scenarios. Figure 11 shows the time responses for desired configuration.

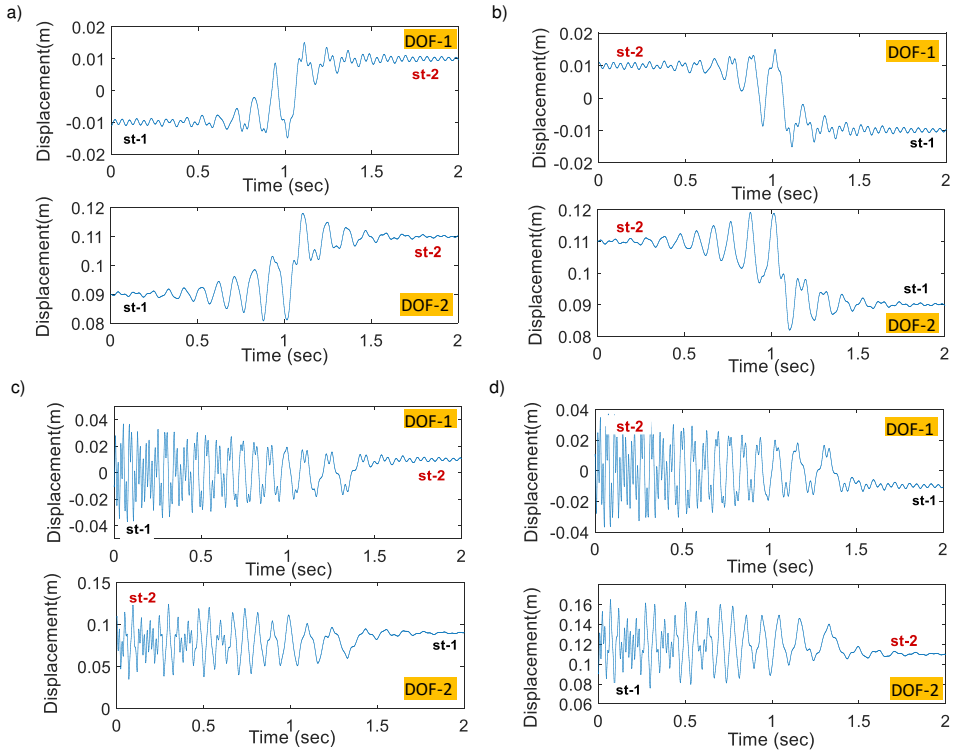

Figure 11: Time response for the parameters $\zeta_{f_{npf}} = 0.5$ *and* $g_{f_{npf}} = 0.1$ that achieves all scenarios of series configuration.

Parallel Configuration

The dynamic response of the parallel configuration is studied. Figure 12 presents the mechanical model of the 2DOF cascade bistable Duffing-Holmes system with the hybrid controller.

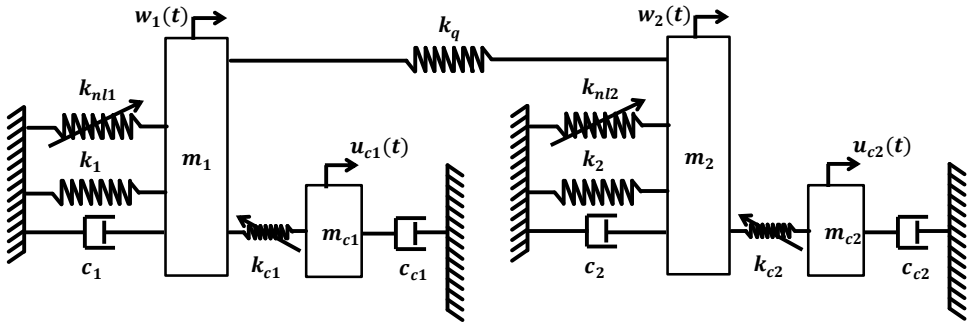

Figure 12: Mechanical model of the 2DOF cascade bistable Duffing-Holmes system with the hybrid controller in parallel configuration.

The governing equation for parallel configuration is written as follows assuming unit mass for each DOF,

$$\ddot{w}_1 + 2\zeta_{s1}\omega_{s1}\,\dot{w}_1 - \omega_{s1}^2 w_1 + k_{nl1}w_1^3 - k_q(w_2 - w_1) = \omega_{s1}^2\,u_{c1} \tag{7}$$

$$\ddot{u}_{c1} + 2\zeta_{c1}\omega_{c1}\,\dot{u}_{c1} + \omega_{c1}^2 u_{c1} = g_{f1}\omega_{c1}^2\,w_1 \tag{8}$$

$$\ddot{w}_2 + 2\zeta_{s2}\omega_{s2}\,\dot{w}_2 - \omega_{s2}^2 w_2 + k_{nl2}w_2^3 + k_q(w_2 - w_1) = \omega_{s2}^2\,u_{c2} \tag{9}$$

$$\ddot{u}_{c2} + 2\zeta_{c2}\omega_{c2}\,\dot{u}_{c2} + \omega_{c2}^2 u_{c2} = g_{f2}\omega_{c2}^2\,w_2 \tag{10}$$

where $\omega_{s1}, \omega_{c1}, \omega_{s2}, \omega_{c2}$ *and* $\zeta_{s1}, \zeta_{c1}, \zeta_{s2}, \zeta_{c2}$ represent frequencies and damping ratios of the system and controllers, g_{f1} and g_{f2} is the controller gains for each DOF. $k_{nl1}$and k_{nl2} are cubic stiffness terms for the first and second DOFs, respectively.

The dynamic response of the parallel configuration is presented in Figure 13. The control authority for four different scenarios is tested for a weakly coupled 2DOF system. In the first and second scenario, the HPF keeps the first DOF at the first state while switching the second DOF forward and backward from one state to another. In the third and fourth scenario, the first DOF is attracted to the second state while the second DOF switches forward and backward between the states.

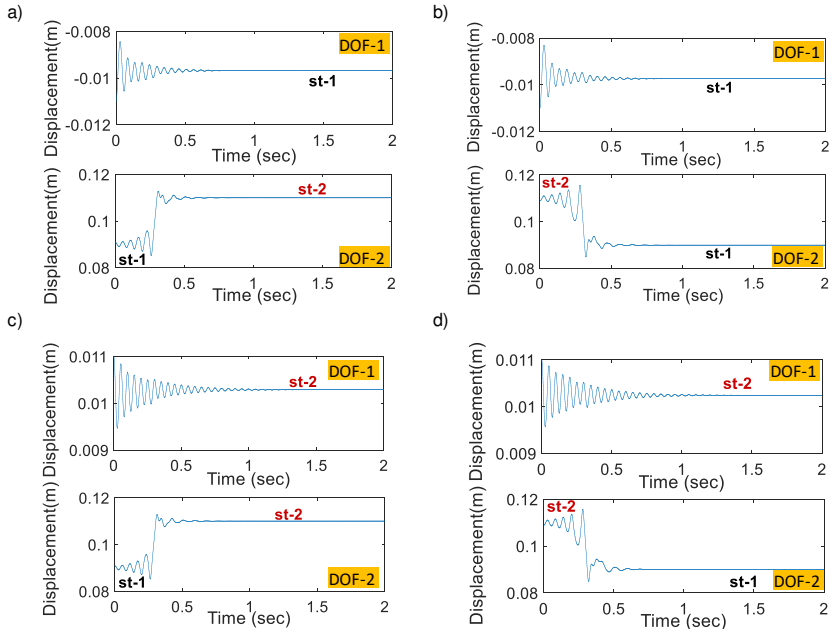

Figure 13: Example time response for the parallel 2DOF cascade bistable Duffing-Holmes system with the hybrid controller: a) DOF-1@st1 and DOF-2 st1->st2, b) DOF-1@st1 and DOF-2 st2->st1, c) DOF-1@st2 and DOF-2 st1->st2 and d) DOF-1@st2 and DOF-2 st2->st1.

A parametric analysis is carried out to determine the controller parameters that satisfy the desired switch properties for different cases. The proposed schematic for parallel configuration can be realized when two DOFs achieve forward, backward, converse state transfer. In the analysis, two controller parameters $\zeta_{_npf}$ and $g_{_npf}$ are chosen since they have the major effect on switching behavior. In the analyses, the $\zeta_{_npf}$ and $g_{_npf}$ are equal for both DOFs – they are swept through a range to determine the optimum values that satisfy the desired switching behaviors. Figure 14 presents a parametric analysis for the parallel configuration.

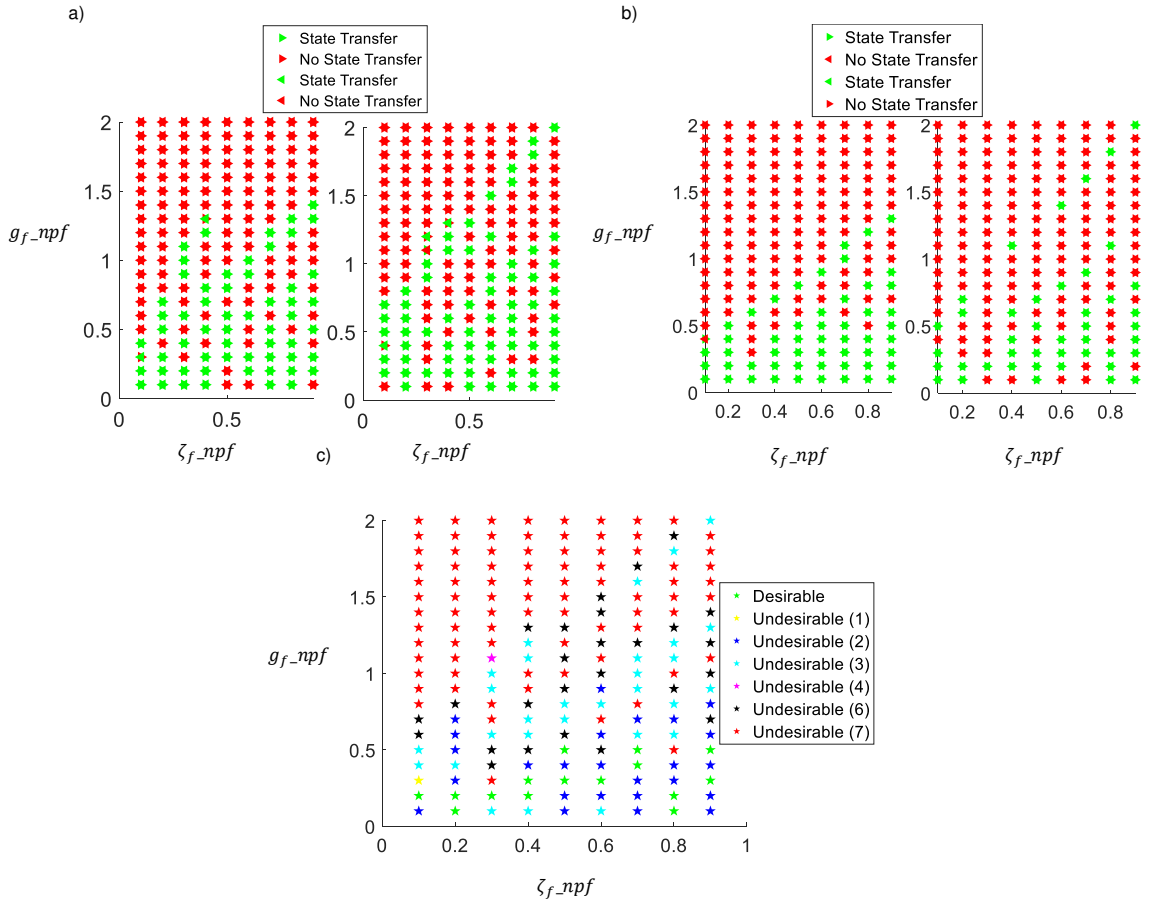

Figure 14: Parametric analysis for the series 2DOF cascade bistable Duffing-Holmes system with the hybrid controller a) Forward (DOF-1 and DOF-2: st1->st2) and Backward (DOF-1 and DOF-2: st2->st1) state transfer case, b) Converse State transfer case (DOF-1: st1->st2 and DOF-2: st2->st1, vice versa), c) all cases together.

Figure 14a presents a forward and backward state transfer behavior with respect controller parameters. The triangle pointing left or right shows the configuration of controller. The green and red colors indicate that initial configuration successful and unsuccessful, respectively, as described previously. Figure 14b demonstrates the analysis carried out for converse state transfer where DOF-1 is set to achieve state transfer from state 1 to state 2 while DOF-2 is set to achieve state transfer from state 2 to state 1. Also, vice-versa case simulation is presented in this figure. Figure 14c demonstrates the behavior of controller for all cases mentioned above. The green color indicates the controller parameters that achieve convergence to the desired state for all scenarios. The other colors in the figure are undesirable with the number of unsatisfied case indicated in the legend. Figure 15 shows the time responses for desired configuration.

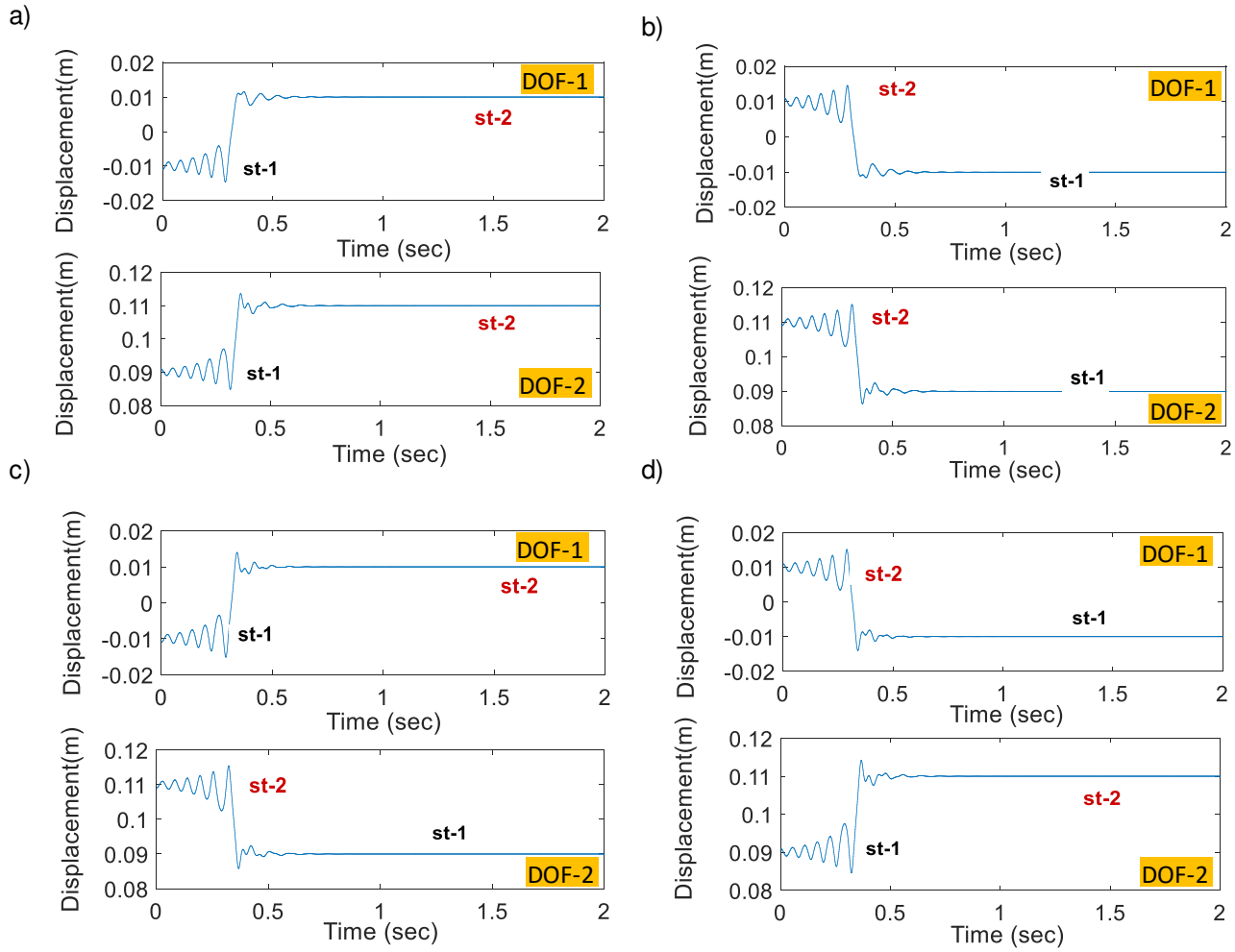

Figure 15: Time response for the parameters $\zeta_{f_{npf}} = 0.5$ *and* $g_{f_{npf}} = 0.3$ that achieves all scenarios of parallel configuration.

Conclusions

A multi degree of freedom metamaterial concept that utilizes the hybrid position feedback controller is introduced. An arbitrary number of bistable "segments" or "material elements" are attached to each other in a serial or parallel manner to generate a "distributed" bistable structure. The initial results, derived for 2DOF systems, show the merit of the proposed concept which can be applied to many applications. Due to the simplicity of the hybrid controller, the physical implementation of the proposed approach can be realized using simple circuit elements distributed in the material domain. The proposed metamaterial concept can be used in various applications: locomotion in bioinspired systems, undulatory motion, morphing aerodynamic surfaces, wave guiding, and vibration attenuation. The concept can also be used in energy harvesting to enable maximum power extraction for a given vibratory input.

References

[1] A. F. Arrieta, S. A. Neild, and D. J. Wagg, "On the cross-well dynamics of a bi-stable composite plate," *Journal of Sound and Vibration*, vol. 330, no. 14, pp. 3424-3441, 2011.

[2] M. Follador, A. T. Conn, B. Mazzolai, and J. Rossiter, "Active-elastic bistable minimum energy structures," *Applied Physics Letters*, vol. 105, no. 14, p. 141903, 2014.

[3] K. Murphy, L. Virgin, and S. Rizzi, "Experimental snap-through boundaries for acoustically excited, thermally buckled plates," *Experimental mechanics*, vol. 36, no. 4, pp. 312-317, 1996.

[4] M. T. Petralia and R. J. Wood, "Fabrication and analysis of dielectric-elastomer minimum-energy structures for highly-deformable soft robotic systems," in *2010 IEEE/RSJ International Conference on Intelligent Robots and Systems*, 2010: IEEE, pp. 2357-2363.

[5] H. Stewart, J. Thompson, Y. Ueda, and A. Lansbury, "Optimal escape from potential wells-patterns of regular and chaotic bifurcation," *Physica D: Nonlinear Phenomena*, vol. 85, no. 1-2, pp. 259-295, 1995.

[6] J. Thompson, "Loss of engineering integrity due to the erosion of absolute and transient basin boundaries," in *Nonlinear Dynamics in Engineering Systems*: Springer, 1990, pp. 313-320.

[7] J. Thompson, S. Bishop, and L. Leung, "Fractal basins and chaotic bifurcations prior to escape from a potential well," *Physics Letters A*, vol. 121, no. 3, pp. 116-120, 1987.

[8] J. M. T. Thompson, "Chaotic phenomena triggering the escape from a potential well," *Proceedings of the Royal Society of London. A. Mathematical and Physical Sciences*, vol. 421, no. 1861, pp. 195-225, 1989.

[9] J. A. Wright, "Safe basins for a nonlinear oscillator with ramped forcing," *Proceedings of the Royal Society A: Mathematical, Physical and Engineering Sciences*, vol. 472, no. 2194, p. 20160190, 2016.

[10] M. R. Schultz, M. W. Hyer, R. B. Williams, W. K. Wilkie, and D. J. Inman, "Snap-through of unsymmetric laminates using piezocomposite actuators," *Composites science and technology*, vol. 66, no. 14, pp. 2442-2448, 2006.

[11] A. Arrieta, D. Wagg, and S. Neild, "Dynamic snap-through for morphing of bi-stable composite plates," *Journal of Intelligent Material Systems and Structures*, vol. 22, no. 2, pp. 103-112, 2011.

[12] A. F. Arrieta, O. Bilgen, M. I. Friswell, and P. Ermanni, "Modelling and configuration control of wing-shaped bi-stable piezoelectric composites under aerodynamic loads," *Aerospace Science and Technology*, vol. 29, no. 1, pp. 453-461, 2013.

[13] A. F. Arrieta, O. Bilgen, M. I. Friswell, and P. Hagedorn, "Passive load alleviation bi-stable morphing concept," *AIP Advances*, vol. 2, no. 3, p. 032118, 2012.

[14] A. F. Arrieta, O. Bilgen, M. I. Friswell, and P. Hagedorn, "Morphing dynamic control for bi-stable composites," in *22nd International Conference on Adaptive Structures and Technologies (ICAST), Corfu, Greece*, 2011, pp. 10-12.

[15] O. Bilgen, A. F. Arrieta, M. I. Friswell, and P. Hagedorn, "Dynamic control of a bistable wing under aerodynamic loading," *Smart materials and structures*, vol. 22, no. 2, p. 025020, 2013.

[16] M. Zarepoor and O. Bilgen, "Constrained-energy cross-well actuation of bistable structures," *AIAA journal*, vol. 54, no. 9, pp. 2905-2908, 2016.

[17] M. R. Simsek and O. Bilgen, "Hybrid position feedback controller for inducing cross-well motion of bistable structures," *AIAA journal*, vol. 54, no. 12, pp. 4011-4021, 2016.

[18] M. R. Simsek and O. Bilgen, "A Hybrid Position Feedback Controller for Inducing Cross-Well Motion of Bistable Structures," in *24th AIAA/AHS Adaptive Structures Conference*.

[19] M. R. Simsek and O. Bilgen, "Non-Chaotic Cross-Well State Transfer of Duffing-Holmes Type Bistable Systems," in *Smart Materials, Adaptive Structures and Intelligent Systems*, 2017, vol. 58264: American Society of Mechanical Engineers, p. V002T04A007.

[20] M. R. Simsek and O. Bilgen, "The Duffing-Holmes oscillator with hybrid position feedback controller: Stability and response analysis," in *Smart Materials, Adaptive Structures and Intelligent Systems*, 2018, vol. 51944: American Society of Mechanical Engineers, p. V001T04A012.

[21] M. R. Simsek and O. Bilgen, "The Duffing-Holmes Oscillator Under Hybrid Position Feedback Controller: Response Type and Basin of Attraction Analyses," *International Journal of Structural Stability and Dynamics*, vol. 20, no. 09, p. 2050101, 2020.

[22] M. R. Simsek, *A hybrid position feedback controller for bistable structures*. Old Dominion University, 2016.

[23] R. Schieni, M. Simsek, T. Cunis, O. Bilgen, and L. Burlion, "Control of Bistable Structures Using a Modified Hybrid Position Feedback Controller," in *AIAA SCITECH 2022 Forum*, 2022, p. 0922.

[24] O. Bilgen, Y. Wang, and D. J. Inman, "Electromechanical comparison of cantilevered beams with multifunctional piezoceramic devices," *Mechanical Systems and Signal Processing*, vol. 27, pp. 763-777, 2012.

[25] E. F. Crawley and E. H. Anderson, "Detailed models of piezoceramic actuation of beams," *Journal of Intelligent Material Systems and Structures*, vol. 1, no. 1, pp. 4-25, 1990.

[26] O. Bilgen, M. R. Simsek, and A. F. Arrieta, "Minimum energy cross-well actuation of bistable piezocomposite unsymmetric cross-ply plates," in *ICAST2014: 25th International Conference on Adaptive Structures and Technologies*, 2014: Delft Univ. of Technology Delft, The Netherlands, pp. 6-8.

Effect of Topology upon Relay Synchronization in Multilayer Neuronal Networks

Fenja Drauschke*, Iryna Omelchenko*, Jakub Sawicki*, and Eckehard Schöll*
*Institut für Theoretische Physik, Technische Universität Berlin, Germany

Summary. Relay synchronization is a dynamical phenomenon occurring in complex networks when remote parts of the network synchronize due to their interaction via a relay. This phenomenon can be observed in lasers, electronic circuits, biological systems. We investigate relay synchronization scenarios in a three-layer network and elaborate the effect of inhomogeneous network topology of the individual layers.

Complex networks are currently of great interest, since they allow to model various types of real-world systems, such as social networks, economical, biological, financial, transportation systems, as well as neural activity in the brain [1]. In many cases the network can be divided into several similar parts, called layers, where interaction inside the layers and between the layers can be qualitatively different [2]. Multiplex networks are a special class of such multilayer structures, where each layer consists of the same number of nodes and only one-to-one interaction between the corresponding nodes of neighbouring layers are allowed [3].

Relay (or remote) synchronization between layers which are not directly connected is an intriguing phenomenon, which has some similarities with relay synchronization of chaotic lasers [4]. In neuroscience various scenarios have been uncovered where specific brain areas act as a functional relay between other brain regions, having a strong influence on signal propagation, brain functionality, and dysfunctions [5, 6], as well as visual processing [7].

We examine relay synchronization in a three-layer neuronal network, where the dynamics of individual nodes is governed by the FitzHugh-Nagumo system, widely used to describe spiking dynamics of neurons. In the simplest configuration, the individual layers have a nonlocal ring topology, where each node interacts with its neighbours within some fixed coupling range. In such a network, we observe relay synchronization when spatio-temporal patterns of the two outer layers synchronize, but the middle layer which transfers the signal, performs different dynamics. Later on, we replace regular links with random shortcuts, which results in the formation of a small-world topology inside the layers. With the irregular topology in the layers we uncover dynamical scenarios of relay synchronization. In the focus of our study are chimera states- patterns of coexisting coherent and incoherent domains [8, 9, 10, 11], which can be observed in isolated layers of the network [12].

Our model is described by the following system of differential equations:

$$\dot{\mathbf{x}}_i^m = \mathbf{F}(\mathbf{x}_i^m(t)) + \frac{\sigma_m}{L_i^m}\sum_{j=1}^{N}\mathbf{G}_{ij}^m\mathbf{H}(\mathbf{x}_j^m(t)-\mathbf{x}_i^m(t)) + \sigma_{ml}\sum_{l=1}^{3}\mathbf{H}(\mathbf{x}_i^l(t)-\mathbf{x}_i^m(t)), \tag{1}$$

where $i = 1, ..., N$ numbers the nodes inside each layer, $m = 1, 2, 3$ labels the layer, $\mathbf{x} = (x, y)^T$ is a state variable, and the local dynamics is described by the FitzHugh-Nagumo system $\mathbf{F}(x, y) = \left(\frac{1}{\varepsilon}(x - \frac{x^3}{3} - y), x + a\right)^T$. The adjacency matrices $\mathbf{G}^m$ define the topology of each layer, and L_i^m is the number of links belonging to the ith node of the mth layer. σ_m is the strength of the couplings inside the layers, and σ_{ml} the strength of the couplings between the layers. The matrix $\mathbf{H}$ defines the interaction scheme between the two-dimensional individual systems. Usually, we allow not only direct, but also cross coupling between the variables x and y. Fig. 1 shows schematically the structure of the three-layer network, where each layer has a nonlocal coupling topology, the outer layers are shown in grey, and the middle relay layer is shown in red. As a measure for synchronization between the layers we employ the global synchronization error:

$$E^{ij} = \lim_{t\to\infty}\frac{1}{NT}\int_0^T\sum_{k=1}^{N}||\mathbf{x}_k^j(t)-\mathbf{x}_k^i(t)||dt, \tag{2}$$

which takes values close to 0 when the patterns in the layers $m = i, j$ are synchronized. When coherent and incoherent domains coexist spatially in each layer, we observe nontrivial synchronization scenarios, where the coherent domains of

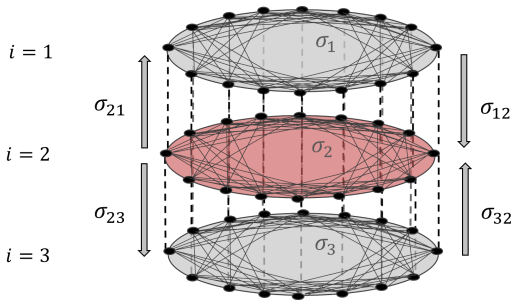

Figure 1: Schematic structure of a three-layer network

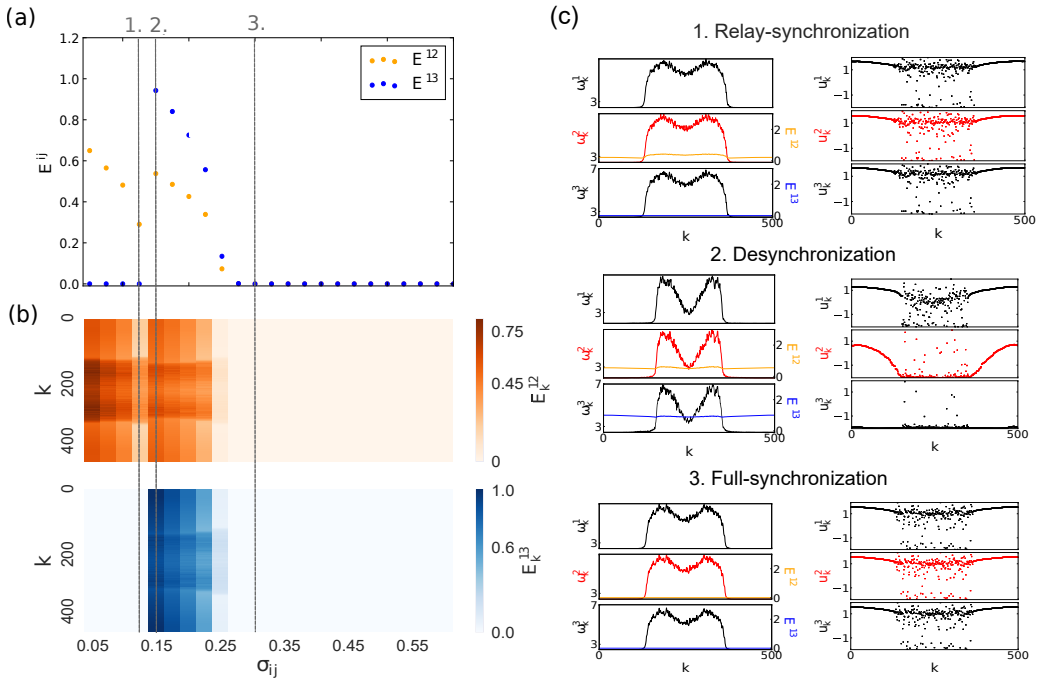

Figure 2: Scenario of synchronization transitions depending on the inter-layer coupling strength σ_{ij}. (a) Global synchronization error; (b) local synchronization error; (c) mean phase velocity profiles and inter-layer synchronization errors (left column) and snapshots (right column) for three values of σ_{ij} marked by vertical lines in (a), (b).

the patterns synchronize while the incoherent domains perform different dynamics. To distinguish this special kind of partial synchronization, we introduce the local synchronization error

$$E_k^{ij} = \lim_{t\to\infty} \frac{1}{T} \int_0^T ||\mathbf{x}_k^j(t) - \mathbf{x}_k^i(t)||dt. \tag{3}$$

When the topology of the layers in the network is regular, we observe complete relay synchronization of chimera patterns in the outer layers, as well as partial relay synchronization, where only the coherent domains of patterns synchronize [13]. If we change the topology of the outer layers by replacing the regular links with random shortcuts, we find the scenarios shown in Fig. 2. Here the global and local inter-layer synchronization errors for increasing coupling strength between the layers, and examples of snapshots of chimera states and their mean phase velocities are depicted. We analyze the role of the system parameters and uncover parameter regions where full and partial relay synchronization occurs. Our results may be useful for understanding remote synchronization in brain networks.

References

[1] S. H. Strogatz, Nature **410**, 268 (2001).

[2] S. Boccaletti, G. Bianconi, R. Criado, C. I. del Genio, J. Gómez-Gardeñes, M. Romance, I. Sendiña Nadal, Z. Wang, and M. Zanin, Phys. Rep. **544**, 1 (2014).

[3] M. Kivelä, A. Arenas, M. Barthélemy, J. P. Gleeson, Y. Moreno, and M. A. Porter, J. Complex Networks **2**, 203 (2014).

[4] M. C. Soriano, J. García-Ojalvo, C. R. Mirasso, and I. Fischer, Rev. Mod. Phys. **85**, 421 (2013).

[5] P. Roelfsema, A. Engel, P. König, and W. Singer, Nature **385**, 157 (1997).

[6] D. S. Soteropoulos and S. N. Baker, J. Neurophysiol. **95**, 1194 (2006).

[7] X. Wang, V. Vaingankar, C. S. Sanchez, F. T. Sommer, and J. A. Hirsch, Nat. Neurosci. **14**, 224 (2011).

[8] Y. Kuramoto and D. Battogtokh, Nonlin. Phen. in Complex Sys. **5**, 380 (2002).

[9] D. M. Abrams and S. H. Strogatz, Phys. Rev. Lett. **93**, 174102 (2004).

[10] M. J. Panaggio and D. M. Abrams, Nonlinearity **28**, R67 (2015).

[11] E. Schöll, Eur. Phys. J. Spec. Top. **225**, 891 (2016).

[12] I. Omelchenko, O. E. Omel'chenko, P. Hövel, and E. Schöll, Phys. Rev. Lett. **110**, 224101 (2013).

[13] J. Sawicki, I. Omelchenko, A. Zakharova, and E. Schöll, Phys. Rev. E **98**, 062224 (2018).

Adaptive control for compensation of non-linear hose characteristics in mechanical ventilation

Joey Reinders*†, Bram Hunnekens*, Tom Oomen †, and Nathan van de Wouw†‡
*DEMCON Advanced Mechatronics, Best, The Netherlands
†Eindhoven University of Technology, Department of Mechanical Engineering, Eindhoven, The Netherlands
‡University of Minnesota, Department of Civil, Environmental and Geo- Engineering, Minneapolis, MN, USA

Summary. Mechanical ventilators are medical devices used to assist patients to breathe. The aim of this paper is to develop a control approach that compensates the pressure drop over the hose that connects the ventilator to the patient. In [1], a similar strategy is considered assuming a linear system model, which is valid in a small operating range. To achieve the desired performance in the entire operating range, the quadratic nature of the resistance of an actual hose is considered in this paper. Using a quadratic hose model and a recursive least-squares estimator, the control law proposed in [1] is significantly improved. Through an experimental case study, a significant gain in pressure tracking performance is shown.

Background

Mechanical ventilation is commonly used in Intensive Care Units (ICUs) to save lives of patients who are unable to breathe by themselves. To assist these patients a mechanical ventilator is used. A schematic overview of a mechanical ventilator, with a single-hose setup, and a patient is depicted in Figure 1.
In this paper, the ventilation setup as depicted in Figure 1 and Pressure Controlled Ventilation (PCV) of sedated patients is considered. In PCV, the goal is to ensure that the pressure near the patients airway, i.e., p_{aw}, follows a reference as shown in Figure 2. This reference has two different pressure levels to ensure that air flows in and out of the lungs. Therewith, inspiration and expiration of the patient are supported. In practice, damage to the lung tissue should be prevented, e.g., by overshoot in pressure. Therefore, the pressure tracking performance should be accurate.

Previous work and open challenges

The control goal is to ensure that the airway pressure p_{aw}, see Figure 1, tracks the target pressure p_{target}. This is achieved by controlling the blower outlet pressure p_{out}. The airway pressure near the patient's mouth is defined as $p_{aw} = p_{out} - \Delta p$, with Δp the pressure drop over the hose. In [1], a novel adaptive control law is proposed that compensates for this pressure drop. A block scheme of this control law is shown in Figure 3. During ventilation, a linear hose resistance, i.e., $\hat{R}_{lin}$, is estimated using a recursive least-squares estimator. This estimate in combination with the measured flow is used to compute an estimate of the pressure drop over the hose, i.e., $\Delta\hat{p} = \hat{R}_{lin}Q_{out}$. Then, $\Delta\hat{p}$ is used to increase the blower outlet pressure, i.e., $p_{out} = p_{target} + \Delta\hat{p}$. Theoretically, this results in perfect tracking, independent of the patient, leak, or hose parameters, for time-varying target pressures.
Although the results in [1] are promising for use-cases with relatively small flow variations, in an experimental case study it is observed that for large flows performance deteriorates. This is caused by the typically non-linear hose characteristics, see Figure 4. This figure shows that the linear model 1 is an accurate representation of the hose resistance for the low flow regime. However, for large flow variations the linear models show a significant deviation from the measured values. It is clearly shown that a quadratic hose model is a better representation of the measured hose characteristics. This quadratic hose model is defined as follows:

$$\Delta p = R_{lin}Q_{out} + R_{quad}Q_{out}|Q_{out}|, \tag{1}$$

where R_{lin} and R_{quad} are unknown. Combining this non-linear hose resistance model with a linear model for the patient lung dynamics results in a non-linear dynamical model of the patient-hose system. The exact model is omitted for brevity. In the following sections, it is shown how the quadratic hose parameters are estimated online and, subsequently included in the control law to accurately compensate for the pressured drop over the hose and therewith improve performance.

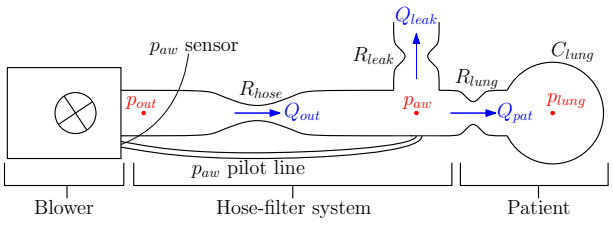

Figure 1: Schematic representation of the blower-hose-patient system of the considered ventilation system.

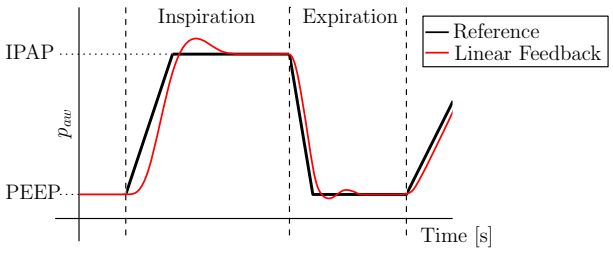

Figure 2: Airway pressure (p_{aw}) during one breathing cycle of pressure controlled ventilation.

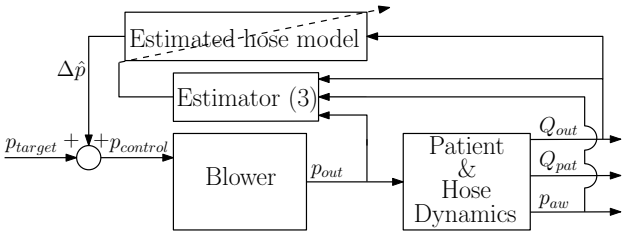

Figure 3: Block diagram of the considered control approach.

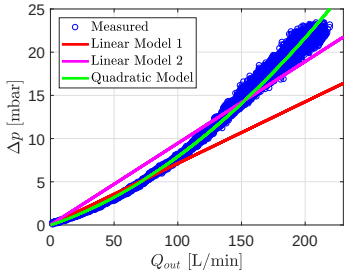

Figure 4: Quadratic characteristics of a typical hose system.

Proposed control strategy

In this paper, the following quadratic-hose model is included in the control law depicted in Figure 3:

$$\Delta\hat{p} = \hat{R}_{lin}Q_{out} + \hat{R}_{quad}Q_{out}|Q_{out}|. \tag{2}$$

To complete the adaptive control law an estimator is used to obtain estimates $\hat{R}_{lin}$ and $\hat{R}_{quad}$ of the two hose parameters. These parameters are obtained using a Recursive Least Squares (RLS) estimator with exponential forgetting factor, see [2]. The considered estimator dynamics are given by:

$$\dot{\hat{\theta}}(t) = P(t)\frac{\Delta p(t) - \hat{\theta}(t)\phi_0(t)}{m^2}\phi_0(t), \text{ and } \dot{P}(t) = \beta P(t) - P(t)\frac{\phi_0(t)\phi_0^T(t)}{m^2}P(t), \tag{3}$$

where $\hat{\theta}(t) = \begin{bmatrix}\hat{R}_{lin}(t)\\ \hat{R}_{quad}(t)\end{bmatrix}$, $\Delta p(t) = p_{out}(t) - p_{aw}(t)$, $P(t) = \begin{bmatrix}P_{11}(t) & P_{12}(t)\\ P_{21}(t) & P_{22}(t)\end{bmatrix}$, $\phi_0(t) = \begin{bmatrix}Q_{out}(t)\\ Q_{out}(t)|Q_{out}(t)|\end{bmatrix}$, m is the scalar normalization parameter, and β is the scalar exponential forgetting factor.

Experimental results

The overall approach is implemented on an experimental ventilation setup, schematically depicted in Figure 1, and the obtained results are shown in Figures 5a and 5b. In Figure 5a, it is clearly seen that the tracking performance upon convergence is improved significantly. Furthermore, Figure 5b shows that the oscillations in the estimates are reduced. Concluding, performance is significantly increased by compensating for the non-linear hose characteristics.

Conclusions

This paper clearly shows that extending the adaptive control strategy in [1] with a non-linear (quadratic) hose model can significantly improve pressure tracking performance. This means that pressure support of mechanically ventilated patients can be improved by compensating for the non-linear hose characteristics.

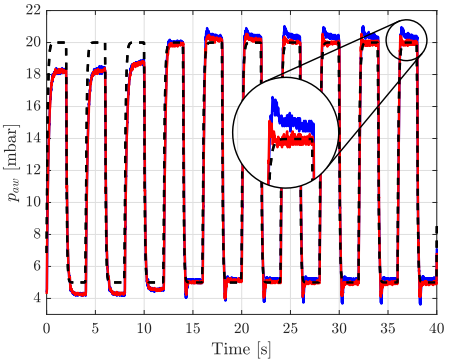

(a) Resulting airway pressure of the controller in [1] and the controller of this paper.

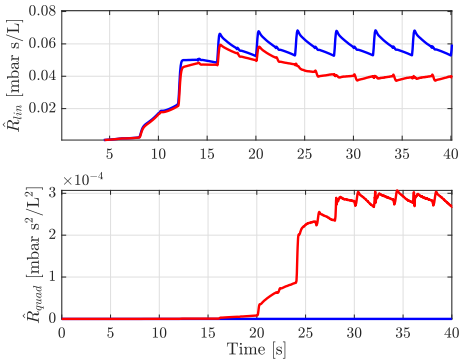

(b) Resistance estimates of (1), using the controller in [1] and the controller of this paper.

Figure 5: Experimental results showing the tracking performance and estimated parameters of the controller proposed in [1] (——) and the controller proposed in this paper (——). Clearly showing improved tracking of the reference pressure (▪ ▪ ▪) by including the non-linear hose characteristics.

References

[1] J. Reinders, F. Heck, B. Hunnekens, T. Oomen, and N. van de Wouw, "Online hose calibration for pressure control in mechanical ventilation" *In Proceedings of the American Control Conference, Philadelphia, USA*, pp. 5414-5419, 2019.

[2] P.A. Ioannou and J. Sun, "Robust Adaptive Control". Upper Saddle River, NJ: Prentice-Hall, 1996.

An Input-Output Approach Towards Synchronization Under Communication Constraints

Jijju Thomas[*,†,‡], Erik Steur[*], Laurentiu Hetel[†], Christophe Fiter[†], Jean-Pierre Richard[†,‡], Nathan van de Wouw[*,⋆]

[*]*Department of Mechanical Engineering, Eindhoven University of Technology, The Netherlands*
[†]*Ecole Centrale de Lille/Université de Lille, CRIStAL UMR CNRS 9189, 59650 Villeneuve d'Ascq, France*
[‡]*Inria Lille, Villeneuve d'Ascq, France*
[⋆]*Department of Civil, Environmental and Geo-Engineering, University of Minnesota, Minneapolis, MN 55455 USA.*

Summary. This work presents a novel approach towards synchronization analysis of nonlinear systems, diffusively coupled via a networked communication channel. The system under consideration is a two-agent nonlinear system, under the constraint that information is transmitted between the two systems using an aperiodic communication strategy. The system setting is remodelled as the feedback-interconnection of a continuous-time system, and an operator that captures the perturbations introduced by communication constraints. By studying the properties of the remodelled system, i.e., the feedback-interconnection, in the framework of Dissipativity Theory, we provide a novel stability criterion that guarantees exponential synchronization.

Introduction

In many natural and practical circumstances, the phenomenon of synchronization has caught the attention of researchers and scientists from various fields. Typical examples include flashing fireflies, firing neurons, etc. In control theory, synchronization is a topic of interest in areas such as master-slave synchronization of nonlinear systems [Nijmeijer and Mareels, 1997]. In practical applications such as cooperative control of multi-agent systems [Olfati-Saber et al., 2007], synchronization can be analyzed with a control theoretic approach for networks of nonlinear systems [Pogromsky et al., 2002]. In such contexts, synchronization problems become more complex due to uncertainties introduced via the networked communication channel. For example, delays introduced in the network increase the complexity of synchronization problems [Steur and Nijmeijer, 2011]. In addition to delays, individual systems could be connected via sampled-data coupling.

In recent years, master-slave synchronization problems of linear sampled-data systems have been studied, and different approaches have been proposed to study the relation between sampling period, coupling strength, and synchronization [Hua et al., 2015]. In existing results, it is typically considered that individual systems have the same sampling frequency. However, in practical scenarios, individual systems usually transmit information at different frequencies over a network, depending upon the communication channel, data traffic, etc. In this work, we consider a bidirectionally coupled, sampled-data, two-agent nonlinear system, wherein individual systems transmit information over a networked communication channel, at possibly different, aperiodic frequencies.

Problem Statement

We consider a two-agent interconnected system as shown in Figure 1a, wherein the dynamics of individual sub-system Σ_i, $i = 1, 2$, is of relative degree one, and is given by

$$\begin{aligned} \dot{x}_i(t) &= f(x_i(t)) + Bu_i(t), \\ y_i(t) &= Cx_i(t), \quad i = 1, 2, \end{aligned} \tag{1}$$

where $x_i \in \mathbb{R}^n$, $u_i, y_i \in \mathbb{R}^m$ are the state, input, and output, respectively. The function $f\colon \mathbb{R}^n \mapsto \mathbb{R}^n$ is a sufficiently smooth vector field, and B and C are matrices with appropriate dimensions, with $CB =: b \in \mathbb{R}^{m\times m}$, b being positive definite and without loss of generality, diagonal. The ith output is transmitted to the jth sub-system only at instants given by the sequence $s^i_{k+1} = s^i_k + h^i_k, h^i_k \in [\underline{h}_i, \bar{h}_i], k \in \mathbb{N}, i = 1, 2$. Without loss of generality, we consider $s^i_0 = 0$, $i = 1, 2$.

Assumption 1: The ith sub-system has access to local output information at time instants $t = s^j_k, j \neq i, k \in \mathbb{N}$.

The aforementioned assumption reflects a practical scenario wherein individual systems can be sampled locally at a high frequency, but data transmission over a networked communication channel occurs at a lower frequency, depending on network induced constraints or requirements. Exploiting this assumption, we have that $\Sigma_i, i = 1, 2$, has access to local information at instants $s^j_k, j \neq i$. Consequently, the synchronizing coupling is designed as

$$\begin{aligned} u_1(t) &= -\sigma(y_1(s^2_k) - y_2(s^2_k)), \forall t \in [s^2_k, s^2_{k+1}), \\ u_2(t) &= -\sigma(y_2(s^1_k) - y_1(s^1_k)), \forall t \in [s^1_k, s^1_{k+1}), \end{aligned} \tag{2}$$

where $\sigma \in \mathbb{R}_+$ is the constant coupling strength. Since $CB > 0$, there exists a coordinate transformation so that the ith sub-system dynamics are given by

$$\Sigma_i : \begin{cases} \dot{z}_i(t) &= q(z_i(t), y_i(t)), \\ \dot{y}_i(t) &= a(z_i(t), y_i(t)) + bu_i(t), i = 1, 2, \end{cases} \tag{3}$$

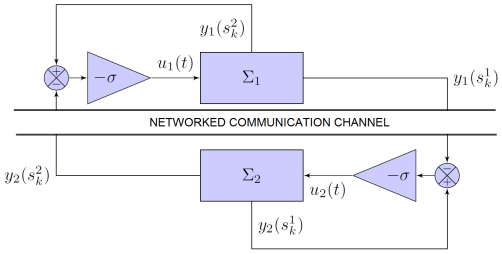

(a) Bidirectionally coupled systems Σ_1 and Σ_2 under asynchronous sampled-data transmission.

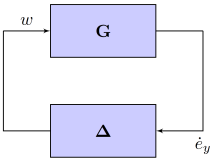

(b) System shown in Figure 1a represented as a feedback-interconnection.

Figure 1: (a) Systems Σ_1 and Σ_2 coupled via a networked communication channel and, (b) an equivalent feedback-interconnection representation.

where $z_i \in \mathbb{R}^{n-m}$, $u_i, y_i \in \mathbb{R}^m$, $q\colon \mathbb{R}^{n-m} \times \mathbb{R}^m \mapsto \mathbb{R}^{n-m}$, and $a\colon \mathbb{R}^{n-m} \times \mathbb{R}^m \mapsto \mathbb{R}^m$.

Assumption 2: The solution of the closed-loop system (3), (2) is ultimately bounded.

Definition 1: The bidirectionally coupled system given by (3), (2) is said to synchronize if $\lim_{t\to\infty} \|e(t)\| \to 0$, where $e(t) = \begin{bmatrix} e_y^T(t) & e_z^T(t) \end{bmatrix}^T$, and $e_y(t) = y_1(t) - y_2(t)$, $e_z(t) = z_1(t) - z_2(t)$, for any initial conditions $(z_1(0), y_1(0))$ and $(z_2(0), y_2(0))$.

Assumption 3: (Demidovich Condition [Pavlov et al., 2005]) There exists a positive definite matrix $P \in \mathbb{R}^{(n-m)\times(n-m)}$, such that the internal state dynamics given by $\dot{z}_i(t) = q(z_i(t), y_i(t))$, $i = 1, 2$, satisfies

$$P\frac{\partial q}{\partial z_i}(z_i, y_i) + \frac{\partial q^T}{\partial z_i}(z_i, y_i)P \leq -\delta I_{n-m}, P = P^T > 0, \delta > 0. \tag{4}$$

In this work, we provide conditions that guarantee exponential synchronization of the coupled system (3), (2).

Main Result

The system (3), (2) shown in Figure 1a is remodelled such that the effects introduced due to aperiodic sampling are decoupled from the continuous-time network, as shown in Figure 1b. In Figure 1b, the operator $\mathbf{G}$ represents the dynamics of the system (1) in the absence of sampling, i.e., $\mathbf{G}$ represents a 'continuous-time' version of the system (3), (2). Additionally, the operator $\mathbf{\Delta}$ captures the error induced in the system due to asynchronous sampling. Consequently, the feedback-interconnection shown in Figure 1b represents the bidirectionally coupled, sampled-data system configuration shown in Figure 1a, by considering the effects of sampling as a perturbation to the continuous-time system operator $\mathbf{G}$. By studying the properties of the feedback-interconnection $\mathbf{G} - \mathbf{\Delta}$, we provide conditions that guarantee exponential stability of the error dynamics $e(t)$, i.e., exponential synchronization of the system (3), (2). We adapt the result provided in [Omran et al., 2016], wherein a dissipativity based framework was employed to prove asymptotic stability of nonlinear systems with aperiodic sampled-data control. The properties of operator $\mathbf{\Delta}$ are characterized by a function $\mathcal{S}$ that satisfies

$$\int_0^t \mathcal{S}(\theta, e_y(\theta), \phi\{y_1(\theta), y_2(\theta), z_1(\theta), z_2(\theta)\}, w(\theta))d\theta \leq 0, \forall t \geq 0, \tag{5}$$

where

$$\begin{aligned}\mathcal{S}(t, e_y(t), \phi\{y_1(t), y_2(t), z_1(t), z_2(t)\}, w(t)) \\ := w^T(t)Rw(t) - \gamma^2(\phi(y_1(t), y_2(t), z_1(t), z_2(t)) - 2b\sigma e_y(t) + b\sigma w(t))^T R(\phi(y_1(t), y_2(t), z_1(t), z_2(t)) \\ -2b\sigma e_y(t) + b\sigma w(t)),\end{aligned} \tag{6}$$

with $\gamma^2 = \frac{4(\bar{h}_1^2+\bar{h}_2^2)}{\pi^2}$, $w(t) = (\mathbf{\Delta}\dot{e}_y)(t)$, and $\phi(y_1(t), y_2(t), z_1(t), z_2(t)) = a(z_1(t), y_1(t)) - a(z_2(t), y_2(t))$. For a positive definite storage function V, if the condition

$$\dot{V}(e(t)) + \alpha V(e(t)) \leq e^{-\alpha t}\mathcal{S}(t, e_y(t), \phi\{y_1(t), y_2(t), z_1(t), z_2(t)\}, w(t)), \forall t \geq 0, \alpha > 0, \tag{7}$$

holds, then the system setting given by (3), (2), synchronizes exponentially with a decay rate of at least $\alpha/2$.

References

[Hua et al., 2015] Hua, C., Ge, C., and Guan, X. (2015). Synchronization of chaotic Lur'e systems with time delays using sampled-data control. *IEEE Transactions on Neural Networks and Learning Systems*, 26(6):1214–1221.

[Nijmeijer and Mareels, 1997] Nijmeijer, H. and Mareels, I. M. Y. (1997). An observer looks at synchronization. *IEEE Transactions on Circuits and Systems I: Fundamental Theory and Applications*, 44(10):882–890.

[Olfati-Saber et al., 2007] Olfati-Saber, R., Fax, J. A., and Murray, R. M. (2007). Consensus and cooperation in networked multi-agent systems. *Proceedings of the IEEE*, 95(1):215–233.

[Omran et al., 2016] Omran, H., Hetel, L., Petreczky, M., Richard, J.-P., and Lamnabhi-Lagarrigue, F. (2016). Stability analysis of some classes of input-affine nonlinear systems with aperiodic sampled-data control. *Automatica*, 70:266 – 274.

[Pavlov et al., 2005] Pavlov, A., van de Wouw, N., and Nijmeijer, H. (2005). *Convergent Systems: Analysis and Synthesis*, pages 131–146. Springer Berlin Heidelberg, Berlin, Heidelberg.

[Pogromsky et al., 2002] Pogromsky, A., Santoboni, G., and Nijmeijer, H. (2002). Partial synchronization: from symmetry towards stability. *Physica D: Nonlinear Phenomena*, 172(1):65 – 87.

[Steur and Nijmeijer, 2011] Steur, E. and Nijmeijer, H. (2011). Synchronization in networks of diffusively time-delay coupled (semi-)passive systems. *IEEE Transactions on Circuits and Systems I: Regular Papers*, 58(6):1358–1371.

Constrained input modulation for impulse-based motion control

Michael Ruderman
Department of Engineering sciences, University of Agder, 4604, Norway

Summary. We revisit the impulse-based motion control, introduced in [9], from a viewpoint when the control signal is constrained by the actuator limits. We demonstrate how the impulsive control [9] is modulated for the weighted input impulses, and what the consequences it has for the control performance. In addition, the state transients as a jumping map are discussed, when the amplitude-bounded (modulated) impulses can no longer guarantee the asymptotic convergence, and the stable limit cycles can appear instead.

Introduction

Hybrid control systems (see for example [6, 7] and references therein) allow for both continuous and discrete dynamics, while the discrete control actions may appear in form of the continuously or event- or state-depended switching of the bounded control value or, alternatively, in form of the discrete impulses with finite energy content. Intensive research on the possibly uniform and generalized description of the hybrid dynamical systems and, especially, on their stability analysis and stabilization was performed already one and half decades ago. Here we exemplary refer to the several available seminal (correspondingly tutorial) works like [4], and special issues like introduced in [1].
Impulsive dynamics (see e.g. [3] for basics) appear quite often in evolution of the natural processes, where some short-term perturbations (or generally stimuli) act instantaneously in the form of impulses and, thus, give rise to instantaneous jumps of the thereby affected dynamic states. A classical academic example is the bouncing ball (see for example in [4]), while in engineering, the various vibro-impact [3] systems can be found, for example, in the mechanical play-pairs also known as backlash [10]. When it comes to impulsive control actions, then the input impulse, or impulsive force cf. [3],

$$p_0 = \lim_{\Delta t \to 0} \int_{t_0}^{t_0+\Delta t} u(\tau) d\tau \tag{1}$$

at the controlling instant t_0 is, to say, scaling the Dirac measure δ_{t_0}, so that the impulsive control effort $u = p_0\,\delta_{t_0}$ cannot be a function of time. Analysis of such control systems may require to properly denote and handle the impulsive differential equations (see e.g. [5]). At the same time, introduction of a supplementary jump (or jumping) map (cf. the unified modeling framework provided in [2]) of the state transitions at all $t = t_0$ enables the further use of conventional system notations for all $t \neq t_0$ by means of e.g. ODEs or, correspondingly, state-space equations. In applications, one cannot expect that the impulse magnitude will keep a well-specified control action $u(\cdot)$ always below some finite actuator constraint. Therefore, once the input signal is inherently bounded $|u(\cdot)| < U$ by some positive system constant U, an impulsive control cannot be directly implemented, no matter which particular control strategy is lying behind.
Hybrid impulsive motion control, addressed in this work, was introduced in [9] while some preliminary formulation, including an experimental case study, was demonstrated before in [11]. The impulsive control was proposed for systems of the second order with uncertain upper-bounded damping, while the state axes represent the guard conditions that trigger a dedicated impulsive control action as soon as one of the both is crossed. One can notice that other impulsive controls were also proposed formerly in [8] and [12], for the mechanical systems with friction. In either approach, however, an impulsive action occurs first when a motion trajectory falls on the position axis, which implies several zero velocity (and subsequent re-acceleration) phases before it converges to the origin. In the following, we will briefly summarize the impulse-based control [9], for convenience of the reader, and then address the impulse modulation for bounded inputs.

Impulse-based motion control

The impulse-based motion control [9] is given by

$$m\ddot{x} + d\dot{x} + kx = \underbrace{-\alpha \operatorname{sign}(\dot{x}) \frac{\mathrm{d}}{\mathrm{d}x} \operatorname{sign}(x) - \beta \operatorname{sign}(x) \frac{\mathrm{d}}{\mathrm{d}\dot{x}} \operatorname{sign}(\dot{x})}_{\equiv u}, \tag{2}$$

where the continuous system dynamics is shaped by the inertial mass $m > 0$ and uncertain (or in the worst case unknown) stiffness and damping constants $k, d > 0$, respectively. Note that the upper-bound of the damping coefficient $d < D$ needs to be known. The discrete control value u is parameterized by $\alpha, \beta > 0$ and is acting only when the motion trajectory crosses one of the state axes, i.e. at $(0, \dot{x}_0)$ or $(x_0, 0)$. This provides a disjoint jump set $\mathcal{D} = \dot{X}_0 \cup X_0 = \{(x, \dot{x}) \in \mathbb{R}^2 \,|\, x = 0 \cup \dot{x} = 0\}$ and makes both control actions (on the right-hand side of (2)) respectively disjunctive and, therefore, simultaneously appearing only in zero equilibrium $(x, \dot{x}) = \mathbf{0}$, while $\operatorname{sign}(0) = 0$ is defined. The proposed control system (2) is well fitting into the autonomous-impulse hybrid systems framework [2] and, thus, can be fully described by $\dot{\mathbf{x}} = f(\mathbf{x})$ if $\mathbf{x} \in \mathcal{C}$ and $\mathbf{x}^+ \in J(\mathbf{x})$ if $\mathbf{x} \in \mathcal{D}$, where the flow and jump maps are f and J, respectively. The belonging flow and jump sets are disjoint so that $\mathcal{C} = \mathbb{R}^2 \backslash \mathcal{D}$. The parametric conditions for the gains are $0.5m|\dot{x}_0| \leq \alpha < m|\dot{x}_0|$ and $\beta = 0.5|x_0|D$, while a state value during last crossing of the orthogonal axis is denoted by the subindex zero, i.e. x_0 and $\dot{x}_0$ correspondingly. For further details on and analysis of the impulse-based motion control we refer to [9].

Modulation of bounded control input

The impulsive control action in (2) requires a control effort $|u| = 2\alpha\delta(\dot{x}_0) \vee 2\beta\delta(x_0)$, where $\delta(\cdot)$ is the Dirac delta function, cf. with eq. (1). Recall that the Dirac delta function can be seen as distributional derivative of the sign-function, weighted by factor 2, and can then be defined and constrained to satisfy the identity as follows:

$$\delta(y) = \begin{cases} \infty, & \text{if } y = 0, \\ 0, & \text{if } y \neq 0; \end{cases} \qquad \int_{-\infty}^{\infty} \delta(y)\mathrm{d}y = 1; \qquad \delta(y_0) = \lim_{\Delta t \to 0} p_{\Delta t}(t_0). \tag{3}$$

Note that the last expression is (3) relates the Dirac delta function to the square pulse p of duration Δt and amplitude $(\Delta t)^{-1}$, cf. with an impulsive force in (1). Since the square pulse has unity 'strength' (or 'weight'), it is evident that for a constrained actuator (with $\max u = U$) the pulse duration $T \equiv \Delta t$ is required to be $T = 2(\alpha \vee \beta)U^{-1}$. That leads to an inevitable modulation of the discrete (impulsive) control as $u \mapsto u[x_0, \dot{x}_0](t_0 \leq t \leq t_0 + T)$. In order to analyze the impact of such control modification on the convergence performance of (2), cf. [9], one needs to evaluate

$$\mathbf{x}^+ = \exp\big(A(t_0 + T)\big)\,\mathbf{x}_0(t_0) \mp \int_{t_0}^{t_0+T} \exp\big(A(t - \tau)\big)\,B\,U d\tau, \tag{4}$$

which provides inhomogeneous (particular) solutions for $\mathbf{x}_0 = [0, \dot{x}_0]^T \vee [x_0, 0]^T$ at the time instant t_0 of the control pulse. Here $A \in \mathbb{R}^{2\times 2}$ and $B \in \mathbb{R}^{2\times 1}$ are the associated system matrix and input distribution vector resulting from the left-hand side of (2). Note that the sign before the integral in (4) changes depending on the quadrants in which the trajectory undergoes zero-crossing. The "$-$" sign captures either $x = 0$ crossing from the II-nd to the I-st quadrant or $\dot{x} = 0$ crossing from the I-st to the IV-th quadrant. And the $+$ sign appears for the corresponding zero-crossings from the IV-th to the III-rd or from the III-rd to the II-nd quadrant. For an asymptotic convergence of the state trajectory towards zero equilibrium, driven by a sequence of the control impulses $u(t_{0,n})$ with $n = 1, \ldots, N$ where $N \to \infty$, it is sufficient to demonstrate constant decrease of Euclidean norm of the state vector after each executed pulse, i.e. $\|\mathbf{x}^+\|_2 < \|\mathbf{x}_0\|_2$.
A symbolic solution of (4) is computable, yet cumbersome, so that solely several numerical observations are shown and discussed below. For the sake of simplicity, no linear damping is assumed, i.e. $d = D = 0$, so that the left-hand side of (2) represents a harmonic oscillator for the assigned $m = 0.1$ and $k = 10$. The initial values are assigned to be $[x, \dot{x}](t = 0) = [-0.001, 0.1]$, and the forward Euler solver with $\Delta t = 0.0001$ sec is used. The difference between the

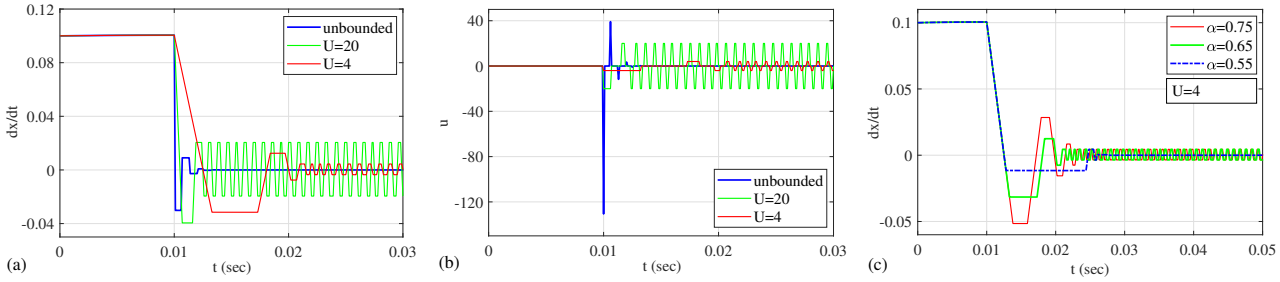

converging unbounded control and that U-bounded, which runs into stable limit cycles, is demonstrated in the diagrams (a) and (b). An avoidance of limits cycles and, thereupon, further convergence towards zero equilibrium is demonstrated in the diagram (c) with variation of the α-parameter. A more detailed analysis of the parametric conditions of the occurrence or escape of the limit cycles calls for an explicit solution of (4), equally as for periodic solutions with impulses at $t_{0,n}$.

References

[1] P.J. Antsaklis. Special issue on hybrid systems: theory and applications a brief introduction to the theory and applications of hybrid systems. *Proceedings of the IEEE*, 88(7), 2000.

[2] M.S. Branicky, V.S. Borkar, and S.K. Mitter. A unified framework for hybrid control: model and optimal control theory. *IEEE Transactions on Automatic Control*, 43(1), 1998.

[3] B. Brogliato. *Nonsmooth Mechanics: Models, Dynamics and Control*. Springer, 2016.

[4] R. Goebel, R.G. Sanfelice, and A.R. Teel. Hybrid dynamical systems. *IEEE Control Systems Magazine*, 29(2), 2009.

[5] S. Leela, F.A. McRae, and S. Sivasundaram. Controllability of impulsive differential equations. *J. of Math. Anal. and Appl.*, 177(1):24–30, 1993.

[6] D. Liberzon. *Switching in systems and control*. Springer, 2003.

[7] J. Lunze and F. Lamnabhi-Lagarrigue. *Handbook of hybrid systems control: theory, tools, applications*. Cambridge University Press, 2009.

[8] Y. Orlov, R. Santiesteban, and L.T. Aguilar. Impulsive control of a mechanical oscillator with friction. In *American Control Conference*, 2009.

[9] M. Ruderman. Impulse-based hybrid motion control. In *IEEE Annual Conference of the Industrial Electronics Society*, 2017.

[10] M. Ruderman. On stiffness and damping of vibro-impact dynamics of backlash. In *IEEE International Symposium on Industrial Electronics*, 2021.

[11] M. Ruderman and M. Iwasaki. Impulse-based discrete feedback control of motion with damping uncertainties. In *IEEE Annual Conference of the Industrial Electronics Society*, 2014.

[12] N. Van de Wouw and R.I. Leine. Impulsive control of mechanical motion systems with uncertain friction. In *IEEE 50th Conference on Decision and Control and European Control Conference*, 2011.

Wednesday, July 20, 2022
08:30 - 10:30

MS-09 Nonlinear Dynamics in Engineering Systems
Auditorium Lumiere

Chair: Robert Parker - Daniel Johnston

08:30 - 08:50
The FutureForge manipulator and an approximate analytical solution algorithm for its nonlinear dynamics
JOHNSTON Daniel*, CARTMELL Matthew, WYNNE Bradley, PAKRASHI Vikram, KOVACIC Ivana
*University of Strathclyde (16 Richmond St Glasgow G1 1XQ, Glasgow, Scotland United Kingdom)

08:50 - 09:10
Towards a simple calibration of a scour-depth sensor
BELMOKHTAR Mohamed*, SCHMIDT Franziska, CHEVALIER Christophe, TURE Savadkoohi Alireza, LAMARQUE Claude-Henri
*Laboratoire expérimentation et modélisation pour le génie civil et urbain (14-20 Boulevard Newton, 77420 Champs-sur-Marne France)

09:10 - 09:30
Transient deformation of a beam travelling on a moving rough surface
VETYUKOV Yury*, SCHEIDL Jakob
*Technische Universität Wien (Technische Universität Wien (TUW), Institute of Mechanics and Mechatronics, Getreidemarkt 9, 1060 Vienna Austria)

09:30 - 09:50
Influence of Gyroscopic Effects on Nonlinear Dynamics of High-Speed Planetary Gears Having an Elastic Ring
WANG Chenxin, **PARKER Robert***
*University of Utah (201 Presidents Cir, Salt Lake City, UT 84112 United States)

09:50 - 10:10
Prediction of Limit Cycles of Lateral Oscillations in Drilling Processes: Numerical Analysis and Experimental Validation
HEYSER Dennis*, SCHWEIZER Bernhard, VOLZ Marcel, ABELE Eberhard
*Institute of Applied Dynamics (Technische Universität Darmstadt L1|01 Otto-Berndt-Straße 2 D-64287 Darmstadt Germany)

The FutureForge Manipulator and an Approximate Analytical Solution Algorithm for its Nonlinear Dynamics

Daniel Johnston*, Matthew Cartmell*, Bradley Wynne*, Vikram Pakrashi**, and Ivana Kovacic***

**Department of Mechanical and Aerospace Engineering, University of Strathclyde, Glasgow, Scotland*

***UCD Centre for Mechanics, Dynamical Systems and Risk Laboratory, School of Mechanical and Materials Engineering, University College Dublin, Dublin, Ireland*

****CEVAS, Faculty of Technical Sciences, University of Novi Sad, Serbia*

Abstract. This paper examines a linearisation algorithm developed for the nonlinear dynamics of the *FutureForge* manipulator - part of a state-of-the-art forging platform being built in Glasgow, Scotland. Building on previous work, the authors investigate means of obtaining approximate analytical solutions for the highly nonlinear system with a view to developing a practical control system in future work. This is done by a combination of algebraic approximation methods, a practical understanding of the machine's operating characteristics, as well as the application of a perturbation method. The devised method is verified by comparing the resulting approximate analytical solutions with numerical solutions to the nonlinear problem.

Keywords: Linearisation, Industrial Manipulators

1 Introduction

This work follows on from a previous piece of work involving many of the same authors [1]. Previously, the authors examined the design of a large-scale industrial manipulator for the *FutureForge* project commissioned by the Advanced Forming Research Centre (AFRC) in Glasgow, Scotland. The manipulator's intended purpose is to handle metallic workpieces through their treatment in a 2,000-tonne hydraulic press: carrying them to and from the press, positioning them in the press appropriately, and ensuring their precise placement throughout these movements. Since this earlier work's publication, the manipulator has been successfully installed at the AFRC and a working control system has been implemented by Clansman Dynamics Ltd. The work we describe in this paper contributes to the development of a digital twin of the manipulator that will be used to train operators in a virtual reality environment.

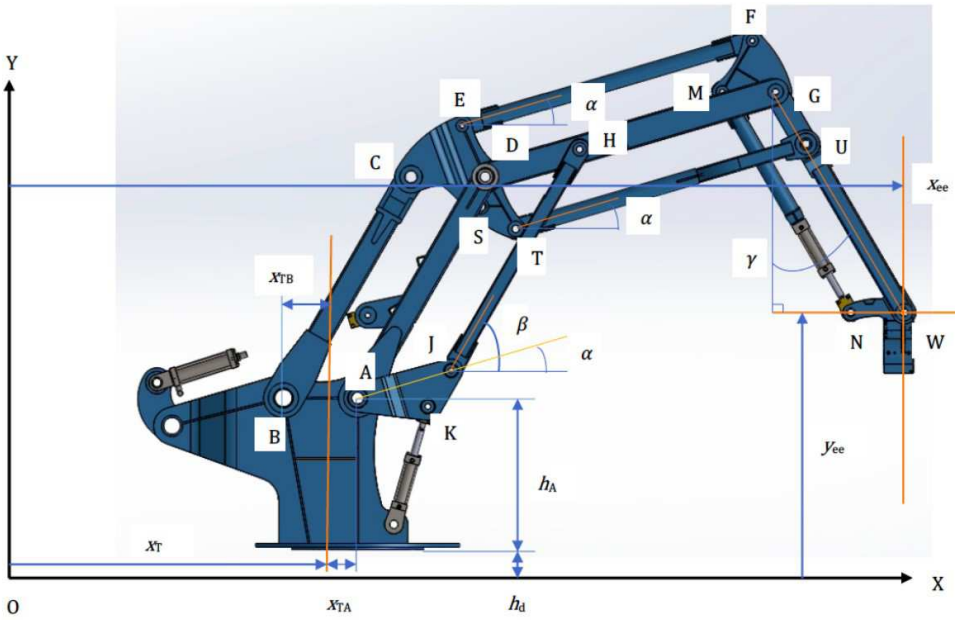

Figure 1: A schematic diagram of the *FutureForge* manipulator, depicting its configuration in its 2D planar workspace. This image previously appeared in the preceding work by Cartmell *et al.* [1].

Interestingly, the manipulator we are considering is rather unique in the field of industrial robotics. At first glance, it appears to be a serial system since the end-effector's position is governed by the positioning of three – apparently sequential – parallelogram linkages. Definitionally, serial manipulators are open kinematic chains of links, and, in many industrial examples, the motion of their end-effectors is actuated by revolute or prismatic actuators located at the joints between links

[2]. For configurations such as this, many powerful techniques have been developed to the end of solving the dynamics and kinematics involved. Such methods include Meldrum, Rodriguez, and Franklin's recursive approach to matrix inversion [3] and Saha's approach to decomposition of the inertia matrix [4]. Furthermore, several control approaches are based on this type of configuration also. These include Gazit and Widrow's "Back Propagation Through Links" method [5]; Ouyang and Zhang's virtual velocity-based method [6]; and, Talebpour and Namvar's application of adaptive control to serial manipulators in the context of satellite testing [7]. However, this manipulator may not be regarded as serial. Instead, the end-effector's position is driven by two actuators at its base. Therefore, the *FutureForge* manipulator might be thought of as a hybrid between a serial and a parallel manipulator. To be clear what we mean by this: the end-effector's position, in the planar workspace, is the result of a series of parallelogram configurations, these individually being closed-chain mechanisms; and, the configurations of each parallelogram are dictated by the parallelograms preceding them. We consider the linkage ordering as flowing from base to end-effector. In this way, the manipulator benefits from having a large workspace relative to its size and footprint [8]. Additionally, the parallelogram structure of the linkages allows it to carry heavier workpieces with greater accuracy [9]. The trade-off in realising these benefits is that the resulting system is significantly more complex to model analytically.

1.1 Summary and Influence of Previous Work

In the work preceding this [1], the authors discussed how the manipulator was intended to operate. Due to its novel design, actuating the hydraulics connected to link AD moves the end-effector purely horizontally. Similarly, the hydraulic actuator connected to point K causes vertical motion in the end-effector. One significant point to note, however, is that this "vertical actuation" does involve some variance in the end-effector's horizontal position such that its path is somewhat curved due to physical constraints of the mechanism. The authors derived the governing dynamics of the manipulator via Lagrangian mechanics and were able to solve this model numerically.

The model that resulted is expressed as a system of two governing equations: one for actuation of the cylinder connected at K (the "vertical case"); and, one for actuation of the cylinder connected to AD (the "horizontal case"). The generalised coordinates in the equations are the angles controlled by these two actuating cylinders: $\alpha(t)$, for the vertical actuation angle; and, $\beta(t)$, for the horizontal actuation angle. Thus, later in this present work when we refer to the "vertical actuation problem", we simply mean the ODE which is derived from the Lagrange equation

$$\frac{d}{dt}\left(\frac{\partial L}{\partial \alpha'(t)}\right) - \frac{\partial L}{\partial \alpha} = Q_v \tag{1}$$

where Q_v is the generalised force applied through this cylinder at K. Similarly, the "horizontal actuation problem" refers to the ODE resulting from

$$\frac{d}{dt}\left(\frac{\partial L}{\partial \beta'(t)}\right) - \frac{\partial L}{\partial \beta} = Q_h \tag{2}$$

in which Q_h is the generalised force applied through the cylinder connected to AD. Note that, in the above equations and throughout this paper, we use the prime notation to denote differentiation with respect to time, staying consistent with the previous work mentioned, thus $\alpha' = \frac{d}{dt}\alpha(t)$, and $\beta' = \frac{d}{dt}\beta(t)$.

The ODEs that result from these two applications of Lagrange's equation are highly nonlinear and exhibit coupling between the two actuation coordinates $\alpha(t)$ and $\beta(t)$. Moreover, they are incredibly cumbersome to manage analytically to the point of being intractable - the curious reader is referred to Eqs (44) and (79) in [1]. As such, the present work was begun to attempt a linearisation strategy which could yield approximate analytical solutions to the underlying dynamics. The resulting linearised model will then be used in a control system for the manipulator – to be implemented in a virtual reality (VR) model of the manipulator. Since the manipulator's operation will always be controlled by a human operator, it is the role of this mathematical model and control system to replicate effectively the physical behaviour of the manipulator as accurately as possible where the physical machine must be capable of submillimetre accuracy in end-effector placement.

At the end of the previous work, we outlined a means of simplifying these aforementioned equations. Firstly, the two governing equations are simplified by collecting their terms into the following groups (and arranging them in this order in Eqs (3) and (4)): linear and nonlinear inertia, linear and quadratic damping, nonlinear restoring force, and excitation. Applying these groupings, we simplify the equations considerably. For the vertical actuation problem, the resulting form of the governing equation is

$$a_1\alpha'' + a_2\cos(2\alpha)\alpha'' + a_3\alpha' + a_4\sin(2\alpha)(\alpha')^2 + a_5\cos(\alpha) + a_6\sin(\alpha) = Q_v, \tag{3}$$

and the horizontal actuation problem is

$$b_1\beta'' + b_2\cos(2\beta)\beta'' + b_3\beta' + b_4\sin(2\beta)(\beta')^2 + b_5\cos(\alpha) + b_6\sin(\beta) = Q_h, \tag{4}$$

where the design specifications of the manipulator contribute to the constant a-terms in Eq (3) and b-terms in Eq (4). These specifications detail the individual component masses, lengths, and mass moments of inertia. From this point, the previous work introduced a small perturbation parameter, ε, into the governing dynamics via these constant terms. A development of this small parameter's introduction is elaborated on in Section 2.1. Then, we continue through Sections 2.2-2.4 to describe the linearisation process we have adopted. Finally, we discuss our results and conclusions in Sections 3 and 4 respectively.

2 Linearisation of the Governing Equations

2.1 Introduction of the Small Parameter

In the original governing equations, Eqs (3) and (4), the constant a and b-terms are functions of the design specifications of the manipulator: component lengths, masses, mass moments of inertia, and geometric offsets. By computing these specifications to find the numerical values of all a and b-terms, we can compare their magnitudes to introduce a small parameter, ε. This parameter is introduced to constants deemed significantly smaller than others. By this, we mean terms which are at least 100-times smaller than the largest constant in the same equation. Based on this approach, for Eq (3) we find that

$$a_2 = \varepsilon\overline{a}_2, \quad a_3 = \xi_{jf} + \varepsilon\xi_{af}, \quad a_4 = \varepsilon\overline{a}_4, \quad \text{and} \quad a_6 = \varepsilon\overline{a}_6. \tag{5}$$

Additionally, for Eq (4) we find

$$b_2 = \varepsilon\overline{b}_2, \quad b_3 = \varepsilon\xi_{jf} + \varepsilon^2\xi_{af}, \quad b_4 = \varepsilon\overline{b}_4, \quad \text{and} \quad b_6 = \varepsilon\overline{b}_6. \tag{6}$$

In the previous work by Cartmell *et al.*, the linear damping was manually introduced into the governing equations to account for both the viscous joint friction and aerodynamic drag in a single "lumped"-parameter [1]. Now notice that we have also expanded the definition of these linear damping coefficients a_3 and b_3. These expanded definitions split the two sources of drag so that they may be treated independently and can contribute to the $O(\varepsilon^0)$ and $O(\varepsilon^1)$ perturbation equations more appropriately. Notice the key difference between the substitutions in (5) and (6) is that the linear damping coefficient contributes to a higher order of perturbation equation for the horizontal problem than in the vertical problem. This is consistent with our strategy for introducing ε, however, it may be desirable to electively allow linear damping to contribute to the generating, $O(\varepsilon^0)$, problem for the horizontal actuation problem.

2.2 Transcendental-Algebraic Conversion

Referred to as the "TAC", the transcendental-algebraic conversion step is intended to pave the way for the substitution of asymptotic expansions of α and β. In this step, each transcendental term is replaced with an algebraic approximation derived via appropriate Taylor Series expansions. For the vertical actuation problem, we compute Taylor Series expansions of $\cos(2\alpha)$, $\sin(2\alpha)$, $\cos(\alpha)$, and $\sin(\alpha)$. The centres of these expansions are at $\alpha = 0$ radians, the centre of the operational range of α, to benefit from the expansions' accuracy in both the positive and negative α directions. A MATLAB algorithm has been constructed to determine the minimum order of approximation required to ensure a maximum error of 0.1% in these approximations versus their respective target functions. Based on discussions with our industrial collaborators (the AFRC), this error requirement may be tightened or relaxed. Regardless, the method progresses in an identical fashion. The same approach is implemented for the horizontal problem, this time with the expansions centred at $\beta = \frac{\pi}{2}$ radians, the centre of the operational range of β.

To study the errors introduced by this step, we compute the numerical solutions of Eqs (3) and (4) and compare them to the numerical solutions of the approximated equations given by the TAC step. The impact of this approximation can be seen in each of the cases examined in Section 3 and is referred to in the included graphs as "Num (post-TAC)". Given $\alpha \in [-0.305, 0.305]$ radians and $\beta \in [\frac{\pi}{3}, \frac{2\pi}{3}]$ radians, the errors depicted in Figures 2-17 are very small indeed. Nonetheless, given how these errors grow with time, the orders of approximations may require further considerations if very long durations of manoeuvres are to be simulated

2.3 Exploitation of the Excitation Function

Until this point, the excitations applied to the vertical and horizontal cases were defined as constants, Q_v and Q_h respectively. Here we define them as nonlinear functions of both the relevant actuation angle and time. This approach is not dissimilar to Hsu's exploitation of strategically tuned excitation functions, according to the brief description in Hsu's work in [10]).

For the manipulator to resist falling under its own weight, part of the total excitation must go towards balancing the gravitational restoring force. This component of the excitation is denoted by $R_v(\alpha)$ and $R_h(\beta)$ for the vertical and

horizontal problems respectively. However, for there then to be motion, there must also be an excitation beyond this gravity-balancing component. We represent this with a time dependent component in the two cases as $F_v(t)$ and $F_h(t)$ respectively. Thus, the revised definitions of the excitations are

$$Q_v = R_v(\alpha) + F_v(t) \tag{7}$$

for the vertical problem, and

$$Q_h = R_h(\beta) + F_h(t) \tag{8}$$

for the horizontal problem. Note that, to carry out its intended role, $R_v(\alpha)$ must equal the vertical restoring force.

$$R_v(\alpha) = a_5 \cos(\alpha) + a_6 \sin(\alpha) \tag{9}$$

The same is similarly true for the horizontal equivalent, $R_h(\beta)$, and the restoring force in the horizontal problem. Therefore, these two components of the excitations will balance any occurrence of the restoring forces throughout the perturbation equations, not just in the generating problem. This is also true for the horizontal case. Additionally, the time-dependent excitations, $F_v(t)$ and $F_h(t)$, will only contribute to the generating solutions. Note that other authors have previously adopted methods that involve assuming the absence of a gravitational restoring force [11]. In this section, we have provided a justification for this from an operational standpoint, rather than simply stating it as an *a priori* assumption.

2.4 Extraction of the Perturbation Equations from the Simplified Model

With the governing equations now suitably prepared, we can introduce one final pair of substitutions, the asymptotic approximations of $\alpha(t)$ and $\beta(t)$

$$\alpha(t;\varepsilon) \approx \alpha_0(t) + \varepsilon\alpha_1(t) \tag{10}$$

$$\beta(t;\varepsilon) \approx \beta_0(t) + \varepsilon\beta_1(t). \tag{11}$$

Substituting these into the revised governing equations and collecting the $O(\varepsilon^0)$ and $O(\varepsilon^1)$ terms, we find the following equations:

$$a_{0,2,1}\alpha_0'' + a_{0,1,1}\alpha_0' = a_{0,0,1}F_v \tag{12}$$

$$\begin{aligned} a_{1,2,1}\alpha_1'' + a_{1,1,1}\alpha_1' =& \left(a_{1,0,1} + a_{1,0,2}\alpha_0^2\right)\alpha_0'' \\ & - a_{1,0,3}\alpha_0' + \left(a_{1,0,4}\alpha_0 + a_{1,0,5}\alpha_0^3\right)\left(\alpha_0'\right)^2 \end{aligned} \tag{13}$$

$$b_{0,2,1}\beta_0'' = b_{0,0,1}F_h \tag{14}$$

$$\begin{aligned} b_{1,2,1}\beta_1'' =& \left(b_{1,0,1} + b_{1,0,2}\beta_0 + b_{1,0,3}\beta_0^2\right)\beta_0'' \\ & + b_{1,0,4}\beta_0' + \left(b_{1,0,5} + b_{1,0,6}\beta_0 + b_{1,0,7}\beta_0^2 + b_{1,0,8}\beta_0^3\right)\left(\beta_0'\right)^2. \end{aligned} \tag{15}$$

Eqs (12) and (14) are the generating problems for the vertical and horizontal cases respectively. Similarly, Eqs (13) and (15) are the $O(\varepsilon^1)$ dynamics of the vertical and horizontal cases. Note the subscripts utilised for the a and b constants in Eqs (12) to (15). These are used to usefully identify components of the solution and to identify their origin in the problem. This method of encoding the constants' origins and occurrences is inspired by [12] but is distinct from this approach as our work is significantly more limited although serving our purpose adequately. The three numbers used have different functions: the first refers to the ε-order of the problem that the constant first appears in; the second refers to the order of derivative multiplying the constant; and, the third is a simple counter. For example, the constant $a_{0,2,1}$ (i.e., with the subscripts 0, 2, and 1) is found in the $O(\varepsilon^0)$ problem, is the coefficient of the 2nd derivative of the dependent variable, and is the 1st coefficient with these previous two designators. By contrast, the constant $b_{1,0,5}$ is the 5th constant to occur in the $O(\varepsilon^1)$ horizontal problem on the right-hand side of the equation. Note this feature of the "0"-designator in our notation: since we have removed all occurrences of the gravitational restoring force from all levels of the manipulator's dynamics, the "0"-designator is not reserved for the coefficients of the dependent variables and can be freely used for terms arranged on the right-hand sides of Eqs (12)-(15).

As was mentioned briefly previously, a key difference between the horizontal and vertical problems is the relative insignificance of linear damping in the former. The result of this is seen in comparing the two generating problems. For the sake of illustration, we continue this paper with the assumption that linear damping should not contribute to the horizontal problem at the $O(\varepsilon^0)$ level. If this assumption needed to be changed, then the solution process for the horizontal case precisely follows the algorithm of the vertical case. From this point, the solution of the linearised system is relatively simple to compute analytically. As intended, both $O(\varepsilon^0)$ problems may be solved independently of their $O(\varepsilon^1)$ counterparts.

3 Results

To inspect the quality of our proposed linearisation algorithm, we compare the approximate analytical (AA) solutions to the numerical solutions of the governing equations at three points in the process. These three points for finding numerical solutions are: before any linearisation takes place, Eqs (3) and (4); immediately after the TAC step is undertaken; and, once the governing problems are stated as perturbation equations. We undertake four cases to examine, these are detailed in Table 1. Cases 1 and 2 consider relatively slow motions of the end-effector; while, Cases 3 and 4 consider faster, more abrupt motions. At the time of writing, we are seeking data from our industrial collaborators that describes manoeuvres undertaken in physical testing of the machine. When this becomes available, we will compare the model against this. However, for now we are only concerned with the efficacy of the linearisation process.

Case	ε	**Initial Conditions**				**Vertical Actuation**		**Horizontal Actuation**	
		$\alpha(0)$ (rad)	$\alpha'(0)$ (rad/s)	$\beta(0)$ (rad)	$\beta'(0)$ (rad/s)	F_v (kN)	t_v (s)	F_h (kN)	t_h (s)
1	0.001	-0.3054	0	1.0472	0	3	3	5	3
2	0.001	0.3054	0	2.0944	0	-3	3	-5	3
3	0.001	-0.3054	0	1.0472	0	30	1	50	1
4	0.001	0.3054	0	2.094	0	-30	1	-50	1

Table 1: Cases examined to test the suitability of the linearisation algorithm in the absence of physical test data.

Using the kinematic equations of the earlier work [1], we can inspect the impact of the errors found on the accuracy of the end-effector's placement. Using the expressions for the end-effector's Cartesian position, we can see that changes of over $1.8{\times}10^{-4}$ radians in β result in the end-effector motion exceeding 1mm. Given our previously stated intent that the control system we will go on to implement should be accurate on a sub-millimetre scale, we can acknowledge that the absolute error in β should be less than this value. For α, the equivalent condition on the error is found as $\pm 3{\times}10^{-4}$ radians. This is also why the initial positions in Table 1 are rounded to 4 decimal places (since 0.0001 is less than either the α or β tolerance stated).

3.1 Case 1

In Case 1, we see the following approximations of the vertical actuation problem arise from our linearisation process. Note that the numerical values included in the equations listed in the following equation, and the rest of Section 3, are rounded to 5 significant figures since this is consistent with the initial conditions.

$$\begin{aligned}\alpha(t) \approx &-88.573 - 1.1043\times10^{-8}e^{-0.1699t} + 6.0005\times10^{-8}e^{-0.13595t} - 1.1744\times10^{-7}e^{-0.10196t}\\ &+ 3.5945\times10^{-7}e^{-0.067974t} + 88.2694e^{-0.033987t} - 0.0017626e^{-0.033987t} + 3.0000t\\ &- 1.8765\times10^{-9}te^{-0.13595t} + 8.7830\times10^{-9}te^{-0.10196t} - 5.7442\times10^{-9}te^{-0.067974t}\\ &- 3.0007\times10^{-5}te^{-0.033987t} - 1.9186\times10^{-9}t^2 - 1.2755\times10^{-10}t^2e^{-0.10196t}\\ &+ 5.7531\times10^{-10}t^2e^{-0.067974t} - 7.6792\times10^{-10}t^2e^{-0.033987t}\\ &+ 1.7371\times10^{-11}t^3 - 4.3351\times10^{-12}t^3e^{-0.067974t} + 8.7297\times10^{-12}t^3e^{-0.033987t}\\ &- 7.3669\times10^{-14}t^4 - 1.4734\times10^{-13}t^4e^{-0.033987t}\end{aligned} \tag{16}$$

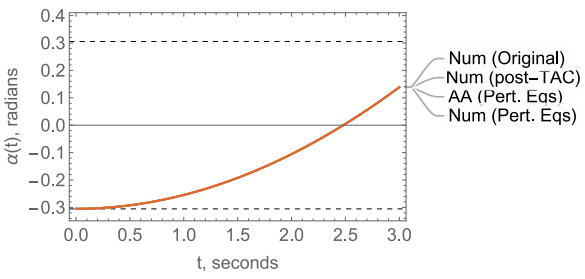

Figure 2: Approximate solutions of the vertical problem for Case 1. Note the operational limits of α marked at ± 0.3054.

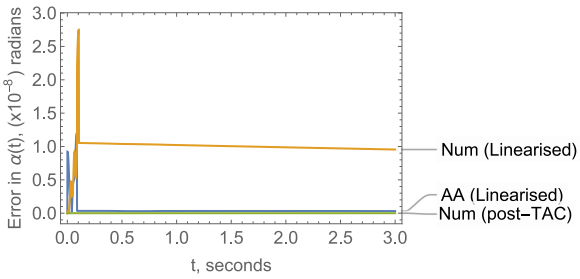

Figure 3: The absolute error for each approximation in Fig 2 versus "Num (Original)" as a reference.

As can be seen, with a cursory glance at Fig 2, as well as in Fig 3, the approximate analytical solution and two numerical solutions are extremely close to the numerical solution of the original problem. The reason for the numerical solution of the linearised problem, "Num (Linearised)", having a slightly larger error versus the target solution is simply that the

numerical method used naturally introduces numerical errors where the analytical method does not.

For the horizontal actuation problem, we initially see another very close resemblance between the four illustrated solutions in Fig 4. Note that the approximate analytical solution for this is given by

$$\begin{aligned}\beta(t) \approx & 1.0472 + 0.040710t^2 - 2.5948 \times 10^{-4}t^3 - 2.1092 \times 10^{-4}t^4 \\ & + 3.7226 \times 10^{-6}t^6 + 9.6805 \times 10^{-8}t^8 - 1.6916 \times 10^{-9}t^{10}.\end{aligned} \tag{17}$$

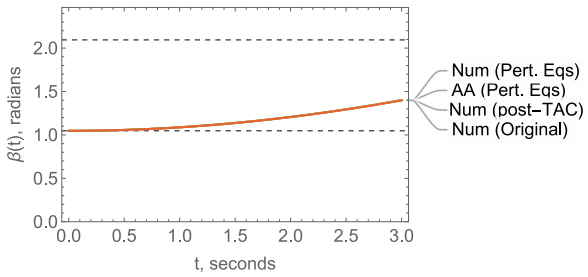

Figure 4: Approximate solutions of the horizontal problem for Case 1. Note the operational limits of β at $\frac{\pi}{3}$ and $\frac{2\pi}{3}$.

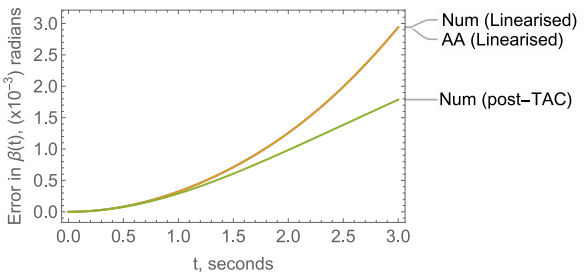

Figure 5: The absolute error for each approximation in Fig 4 versus "Num (Original)" as a reference.

However, under closer inspection, we see that the absolute error in each of these is significantly higher than in the vertical problem. There are two factors that contribute to this reduced accuracy through the linearisation process. The first, most significant, of these is the order of Taylor Series approximation used in the TAC step. This will have a significant impact on the horizontal actuation problem since the operational range of β is significantly larger. The second of these reasons is the lack of linear damping included in the generating problem. Although these two factors clearly contribute to reduced accuracy of the model, only a comparison with physical testing data will rule whether they are acceptable trade-offs or not. If they are found to be unacceptable, we can simply increase the approximation order at the TAC stage or be sure to include linear damping in the generating dynamics.

3.2 Case 2

Similarly to Case 1, we see greater accuracy in the vertical actuation problem than in the horizontal problem although the latter may still be satisfactorily accurate. The vertical approximate analytical solution for this is simply the solution for Case 1 multiplied by (-1). Whereas, that of the horizontal actuation problem is

$$\begin{aligned}\beta(t) \approx & 2.09440 - 0.040710t^2 + 2.5949 \times 10^{-4}t^3 + 2.1092 \times 10^{-4}t^4 \\ & - 3.7226 \times 10^{-6}t^6 - 9.6805 \times 10^{-8}t^8 + 1.6916 \times 10^{-9}t^{10}\end{aligned} \tag{18}$$

where we note that $\beta(0)$ is simply the new initial condition and all other terms are the negatives of those in Case 1.

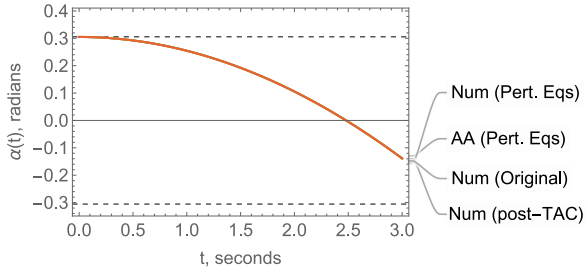

Figure 6: Approximate solutions of the vertical problem for Case 2. Note the operational limits of α marked at ± 0.305.

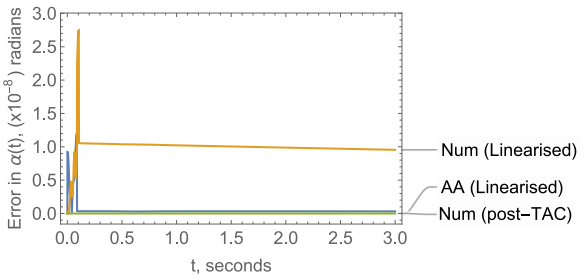

Figure 7: The absolute error for each approximation in Fig 6 versus "Num (Original)" as a reference.

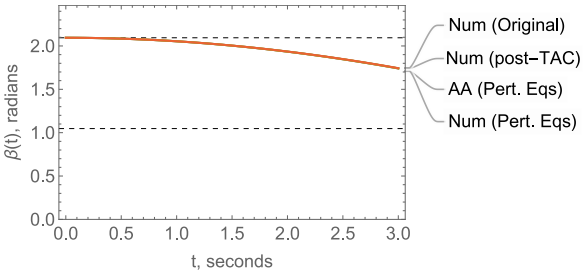

Figure 8: Approximate solutions of the horizontal problem for Case 2. Note the operational limits of β at $\frac{\pi}{3}$ and $\frac{2\pi}{3}$.

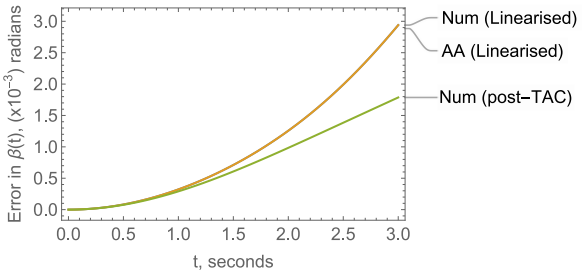

Figure 9: The absolute error for each approximation in Fig 8 versus "Num (Original)" as a reference.

3.3 Case 3

Case 3, as previously stated, is intended to be a more aggressive version of Case 1. What we are interested in here is how the approximations behave with a reduced duration of manoeuvre and with higher driving forces. The approximate analytical solution for the vertical actuation problem is as follows.

$$\begin{aligned}\alpha(t) \approx &-883.29 - 0.0011043e^{-0.16993t} + 0.0059833e^{-0.13595t} - 0.011665e^{-0.10196t} \\ &+ 0.035894e^{-0.067974t} + 882.69e^{-0.033987t} + 0.26223e^{-0.033987t} \\ &+ 30.012t - 1.8765\times10^{-4}te^{-0.13595t} + 8.7596\times10^{-4}te^{-0.10196t} - 5.6412\times10^{-4}te^{-0.067974t} \\ &- 0.0010491te^{-0.033987t} \\ &- 1.9138\times10^{-4}t^2 - 1.2755\times10^{-5}t^2e^{-0.10196t} + 5.7412\times10^{-5}t^2e^{-0.067974t} \\ &- 7.6558\times10^{-5}t^2e^{-0.033987t} \\ &+ 1.7344\times10^{-6}t^3 - 4.3351\times10^{-7}t^3e^{-0.067974t} + 8.6763\times10^{-7}t^3e^{-0.033987t} \\ &- 7.3669\times10^{-9}t^4 - 1.4734\times10^{-8}t^4e^{-0.033987t}\end{aligned} \tag{19}$$

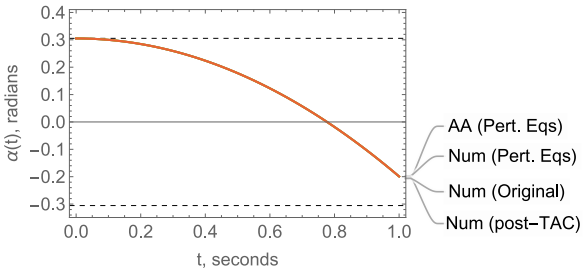

Figure 10: Approximate solutions of the vertical problem for Case 3. Note the operational limits of α marked at ±0.305.

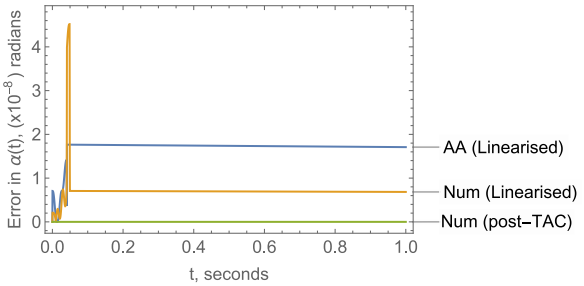

Figure 11: The absolute error for each approximation in Fig 10 versus "Num (Original)".

We see, for the vertical problem, that the resulting errors are all extremely small as in previous results. Note that the only difference in this case is that the numerical solution of the fully linearised problem is now lower than the approximate analytical solution. The errors depicted here are so low, however, that we are not concerned with this subtle change.

Interestingly, the horizontal results are very similar to those of Case 1 too. This reinforces the idea that these errors can be reduced by a higher-order approximation in the TAC step – since the accuracy of this step is dependent on the physical range, in β, of the manoeuvre rather than on its duration directly. The analytical approximation for this is found to be as follows.

$$\begin{aligned}\beta(t) \approx &1.0472 + 0.40710t^2 - 0.0025948t^3 - 0.021092t^4 \\ &+ 0.0037226t^6 + 9.6805\times10^{-4}t^8 - 1.6916\times10^{-4}t^{10}\end{aligned} \tag{20}$$

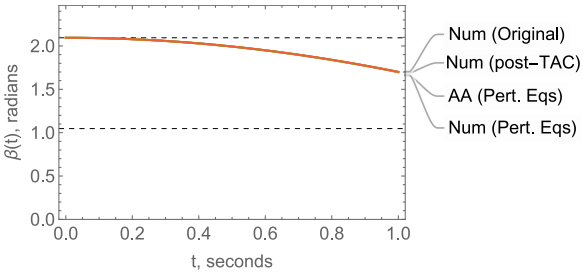

Figure 12: Approximate solutions of the horizontal problem for Case 3. Note the operational limits of β at $\frac{\pi}{3}$ and $\frac{2\pi}{3}$.

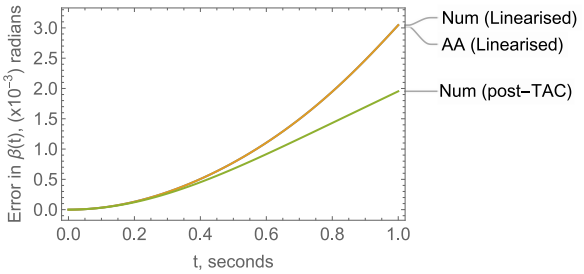

Figure 13: The absolute error for each approximation in Fig 12 versus "Num (Original)".

3.4 Case 4

For Case 4, both vertical and horizontal actuation problems give very similar results to Case 3. The approximate analytical solution for the vertical actuation problem for Case 4 is equal to that of Case 3 multiplied by (-1); whereas, the horizontal problem is

$$\begin{aligned}\beta(t) \approx & 2.0944 - 0.40710t^2 + 0.0025948t^3 + 0.021092t^4 \\ & - 0.0037226t^6 - 9.6805 \times 10^{-4}t^8 + 1.6916 \times 10^{-4}t^{10}\end{aligned} \tag{21}$$

where the constant term is the value of the initial β-condition for Case 4 and the rest of the approximation is identical to that of Case 3 multiplied by (-1).

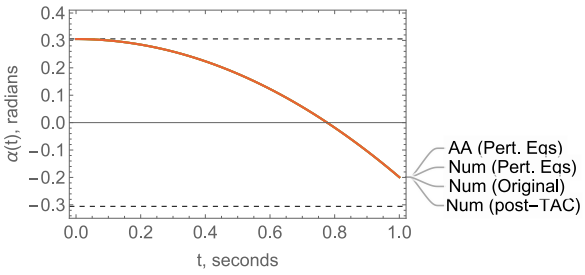

Figure 14: Approximate solutions of the vertical problem for Case 4. Note the operational limits of α at ± 0.305.

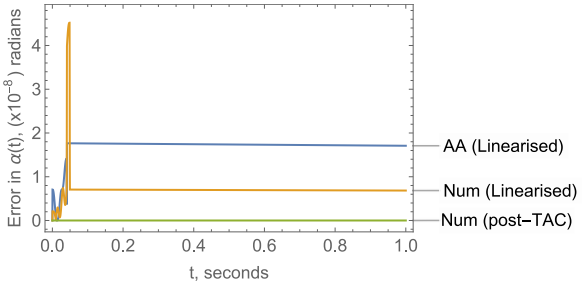

Figure 15: The absolute error for each approximation in Fig 14 versus "Num (Original)".

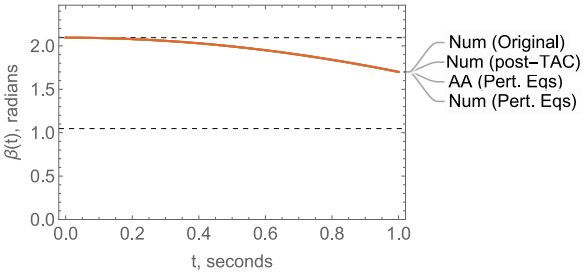

Figure 16: Approximate solutions of the horizontal problem for Case 4. Note the operational limits of β at $\frac{\pi}{3}$ and $\frac{2\pi}{3}$.

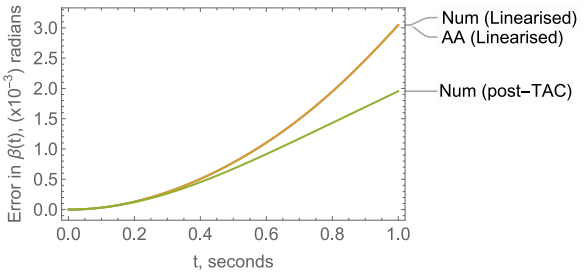

Figure 17: The absolute error for each approximation in Fig 16 versus "Num (Original)".

From the graphs illustrating the absolute errors in the horizontal problems for Cases 1 and 2, all errors are less than the β tolerance value (1.8×10^{-4} radians) up to 0.7 seconds. And, for Cases 3 and 4, all errors are less than this value up to 0.25 seconds. Through all of the examined cases, the error in α is below 5×10^{-5} radians throughout the time domains - well within the previously stated tolerance of 3×10^{-4} radians. These observations can be used to show that that the linearisation algorithm supports the requirement of submillimetre accuracy in end-effector placement – particularly given the sharp, abrupt motions involved in manoeuvring a workpiece through the active forge.

4 Conclusion and Comments for Continuing Work

In this work, we have presented an algorithm for the linearisation of the governing dynamics of a large-scale industrial manipulator. The manipulator - as part of the *FutureForge* project commissioned by the AFRC - has a unique design that rules-out many established techniques which are designed around serial or parallel manipulators. Previous work led to the derivation of the nonlinear governing equations we have considered, and continuing collaboration with our industrial partners will see the presented algorithm undergo further fine-tuning. The presented algorithm sees a small perturbation parameter, ε, introduced to the governing dynamics via the relative magnitude of the constant coefficients. Then, the transcendental terms are approximated via algebraic expressions using appropriately ordered Taylor Series expansions. Observations about the machine's practical operations are then made to remove the restoring forces from consideration at all levels of the resulting perturbation problems. We then inspected the results achieved by comparing our approximate analytical solutions against numerical solutions to the original, nonlinear governing dynamics. By comparison with these numerical solutions, we also illustrated the errors introduced at the TAC stage and at the conclusion of the linearisation process. We found that the approximate analytical solutions for the vertical actuation problem are well-within the acceptable range of accuracy for the context of our work. The errors found in the horizontal actuation problem are notably larger, but these may still be acceptable pending comparison with physical test data from our industrial collaborators. In the instance that they are above the acceptable limits of error, we have noted suitable courses of action in Section 3.

Going forward, we are actively seeking to compare our simulations against the physical test data gathered by our industrial collaborators. In parallel with this, we are in the process of designing a suitable, robust control system for implementation in the digital twin model of this manipulator.

Acknowledgements. We wish to acknowledge the work of Clansman Dynamics Ltd (based in East Kilbride, Scotland) in constructing the *FutureForge* manipulator on behalf of the AFRC and for providing the necessary design specifications so that we could carry out our own work. We also acknowledge the funding contribution provided by Clansman Dynamics Ltd to the PhD studentship of D. Johnston. Additionally, V. Pakrashi would like to acknowledge Science Foundation Ireland Centre I-FORM.

References

[1] M. Cartmell, I. Gordon, D. Johnston, S. Liang, L. McIntosh, and B. Wynne, *Modelling the dynamics of a large-scale industrial manipulator for precision control*, Advanced Problems in Mechanics, Russian Academy of Sciences, 2021 [in print].

[2] Y. Chen, G. Leitmann, and J. Chen, "Robust control for rigid serial manipulators: A general setting," in *American Control Conference*, vol. 2, IEEE, 1998, 912–916 vol.2, ISBN: 0743-1619. DOI: 10.1109/ACC.1998.703540.

[3] D. Meldrum, G. Rodriguez, and G. Franklin, "An order (n) recursive inversion of the jacobian for an n-link serial manipulator," in *IEEE International Conference on Robotics and Automation*, vol. 2, IEEE Comput. Soc. Press, 1991, pp. 1175–1180. DOI: 10.1109/ROBOT.1991.131768.

[4] S. Saha, "A decomposition of the manipulator inertia matrix," *IEEE Transactions on Robotics and Automation*, vol. 13, no. 2, pp. 301–304, 1997, ISSN: 1042-296X. DOI: 10.1109/70.563652.

[5] R. Gazit and B. Widrow, "Backpropagation through links: A new approach to kinematic control of serial manipulators," in *Tenth International Symposium on Intelligent Control*, IEEE, 1995, pp. 99–104, ISBN: 2158-9860. DOI: 10.1109/ISIC.1995.525044.

[6] F. Ouyang and T. Zhang, "Virtual velocity vector-based offline collision-free path planning of industrial robotic manipulator," *International journal of advanced robotic systems*, vol. 12, no. 9, p. 129, 2015, ISSN: 1729-8806 1729-8814. DOI: 10.5772/60127.

[7] M. Talebpour and M. Namvar, "Zero-gravity emulation of satellites in present of uncalibrated sensors and model uncertainties," in *2009 IEEE Control Applications, (CCA) Intelligent Control, (ISIC)*, IEEE, 2009, pp. 1063–1068, ISBN: 1085-1992. DOI: 10.1109/CCA.2009.5280698.

[8] S. Ajwad, J. Iqbal, M. Ullah, and A. Mehmood, "A systematic review of current and emergent manipulator control approaches," *Frontiers of Mechanical Engineering*, vol. 10, no. 2, pp. 198–210, 2015, ISSN: 2095-0241. DOI: 10.1007/s11465-015-0335-0.

[9] Y. Patel and P. George, "Parallel manipulators applications - a survey," *Modern Mechanical Engineering*, vol. 2, pp. 57–64, 2012. DOI: 10.4236/mme.2012.23008.

[10] I. Kovacic, *Nonlinear Oscillations*, 1st ed. Springer, Cham, 2020, pp. X, 273. DOI: 10.1007/978-3-030-53172-0.

[11] K. Lee and G. Chirikjian, "A new perspective on o(n) mass-matrix inversion for serial revolute manipulators," in *2005 IEEE International Conference on Robotics and Automation*, vol. 2005, IEEE, 2005, pp. 4722–4726, ISBN: 1050-4729. DOI: 10.1109/ROBOT.2005.1570849.

[12] N. Motazedi, M. Cartmell, and J. Rongong, "Extending the functionality of a symbolic computational dynamic solver by using a novel term-tracking method," *Proceedings of the Institution of Mechanical Engineers, Part C: Journal of Mechanical Engineering Science*, vol. 232, no. 19, pp. 3439–3452, 2017, ISSN: 0954-4062. DOI: 10.1177/0954406217737104.

Towards a simple calibration of a scour-depth sensor

Mohamed Belmokhtar*, Franziska Schmidt *, Christophe Chevalier *, Alireza Ture Savadkoohi† and Claude Henri Lamarque †

* *Univ Paris Est, IFSTTAR, Champs-sur-Marne, France*

† *Univ Lyon, ENTPE, LTDS, CNRS UMR 5513, France*

Summary. This extended abstract presents an innovative method for scour monitoring, based on the dynamic response of a bridge pile embedded in the riverbed. Apart from the mechanical and physical characteristics of the pile itself, soil-structure interaction (SSI) affects the dynamical behaviour of the system. This may result in a sensibility of the eigenfrequencies of the pile to soil conditions. As a consequence, analytical and numerical developments are carried out for an Euler-Bernoulli beam model (representing the pile), which is embedded in a Pasternak soil (springs with a shear layer) for SSI. Using Hamilton's Principle and endowing the non-linear boundary conditions, system frequencies are derived by seeking for non-trivial roots of the characteristic equation of the system.

Introduction

A majority of bridge collapses are due to hydraulic risks [1], among which scour. Today, several scour monitoring techniques exist [2], as for example:

- Water depth-measuring devices,
- Analyzing changes in dynamic behavior of structural elements (bridge pier or instrumented rod).

In this study, we will consider both technologies in order to characterize scour.

Evaluation of natural frequencies of the system

Let us consider an Euler-Bernoulli Beam partially embedded in a Pasternak-modelled Soil [3] (see Fig. 1): Hamilton's principle with specific boundary conditions leads us to a non-linear formulation. In fact, because of the external environment change, the formulation makes us deal with non-linear boundary conditions, in particular at the end of the pile in the soil.
In our investigation, we treat the general nonlinear problem in two sets of linear problems with two constitutive dynamical equations:

- An equation for the free part of the beam $x < 0$:

$$EI\frac{\partial v^4}{\partial^4 x}(x,t) + \rho A\frac{\partial v^2}{\partial^2 t}(x,t) = 0,$$

- and an equation for the embedded part of the beam $x > 0$:

$$EI\frac{\partial v^4}{\partial^4 x}(x,t) - g\frac{\partial v^2}{\partial^2 x}(x,t) + kv(x,t) + \rho A\frac{\partial v^2}{\partial^2 t}(x,t) = 0.$$

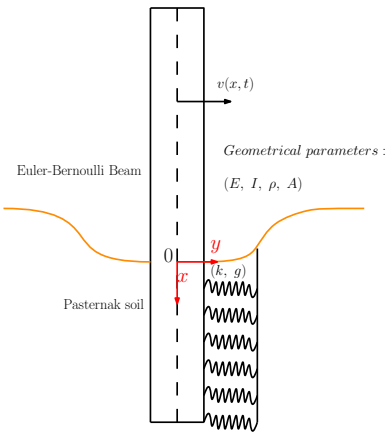

Figure 1: Mathematical model of the considered sysetm.

In our study, we focus on the modal analysis of the structure. Then, using modal projection and by solving equation of eigenfrequencies numerically (Newton method), the response of frequency as a function of scour depth is plotted. This response is also compared with finite difference method. The first step of our investigation permits us to see that reaching to correct numerical results can be elaborating for being sure that the system is not attracted by another root. Even if it converges, this method may be long.

Equivalent cantilevered beam of the system

The straightforward method of the previous section is costly. When we plot the natural frequency as a function of scour-depth (Fig. 2), variations are similar to a behaviour of cantilevered beam of a given length. This observation results in the development of the concept of added free length "ϵ" in the cantilevered beam (see Fig. 3): an equivalent length can be defined.
This means that we can include a modification of the length, adding "ϵ", to have the same frequency.

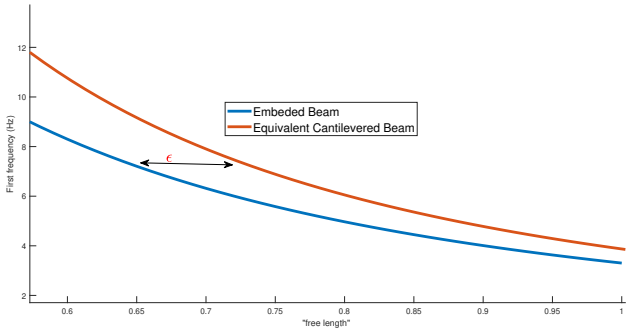

Figure 2: Variation of the first frequency with the normalized free length

The next step in our investigation is to introduce analytically this equivalent length to fix the same eigenfrequencies for the scour-depth sensor of a given length: this equivalent length can be obtained as a result of an asymptotic approach of the non-trivial function of which natural frequencies are solutions. The precision of this method depends on the depth of foundation and a coefficient which is linked to the SSI.

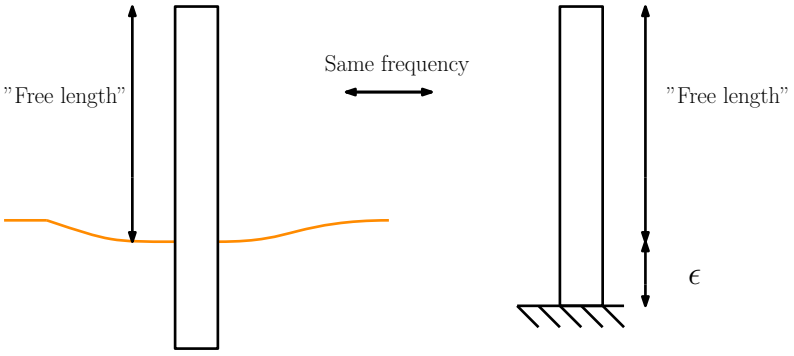

Figure 3: Equivalent cantilevered beam

Conclusions

Comparison between our analytical and numerical model and experimental results [4] are carried out to obtain the validation of the equivalent length as parameters of an inverse problem. It is shown that for deep foundations where the flexural rigidity of the beam is higher than the soil rigidity, the analytical model matches with the experimental results: depth sensor measures accurately the progression of scour depth. In the other case, non-linearities can no longer be treated with this method: the soil reaction itself has a nonlinear behavior.

References

[1] Wardhana K. and Hadipriono F. C. (2003) Analysis of recent bridge failures in the United States. *J. of Performance of Constructed Facilities* **3**:(17)

[2] Prendergast L. J. and Gavin K.(2014) A review of bridge scour monitoring techniques. *J. of Rock Mechanics and Geotechnical Engineering* **138-149**:(2)

[3] Pasternak P. L. (1954) On a new method of analysis of an elastic foundation by means of two constants. *osudarstvennoe Izdatelstvo Literaturi po Stroitelstvu I Arkhitekture*, URSS.

[4] Boujia N. (2018) Vulnérabilité des ouvrages d'art au risque d'affouillement des fondations. *Phd Thesis* Univ. Paris-Est.

Transient deformation of a beam travelling on a moving rough surface

Yury Vetyukov* and Jakob Scheidl*
*Institute of Mechanics and Mechatronics, TU Wien, Vienna, Austria

Summary. In this paper we study the quasi-static deformation of a beam pressed against a moving rough surface by the field of gravity. While the beam is transported in the axial direction together with the travelling foundation, it deforms and slides in the lateral direction because of the misaligned linear bearings at the boundaries of the control domain. Considering small deflections and a geometrically linear beam model, we present a numerical approach to analyse the time evolution of the deformed state of the beam. Analytical solutions are obtained for several specific cases of the boundary conditions and validated against the numerical results.

Introduction

Lateral deformation of axially moving slender structures with frictional contact is usually undesired in technical applications such as rolling mills [1] or transport belts [2, 3]. The highly nonlinear frictional response encountered in these problems induces dynamical behaviour even at slow quasi-static motion, when inertial effects are negligible. Numerical simulation tools, created to investigate the mechanics or to develop a model-based controller design, rely on the mathematical models of moving contact of deformable bodies at non-material kinematic description. Simplified semi-analytical approaches allow, however, to better understand the nature of the arising phenomena and to validate the complicated numerical schemes. Thus, an analytical study of the motion of an endless beam, transported by a moving rough surface across a control domain, has been presented in [4]. The beam is forced to enter the control domain and to leave it through a pair of linear bearings, which are laterally misaligned relative to each other. The analysis shows, that, as long as the misalignment is small and the maximal friction force is sufficiently large, the stationary deformed configuration of the beam becomes self-similar with infinitely many segments of sliding friction in alternating directions.
It should be noted, that the time evolution of the deformation of the beam on a rough foundation because of the bending moment on a free end has been thoroughly analysed earlier in [5], where the appearance of self-similar solutions was demonstrated as well. A similar formulation with thermally induced bending moments and self-similar deformation pattern studied in [6] relates to the cool down of railway rails after hot rolling. Nevertheless, the presently considered moving contact problem with transport conditions is a novel formulation, described by a different mathematical model.

Problem formulation

In the present paper we extend the results of [4] by investigating the transient deformation of the beam owing to a given law of the lateral motion of the bearing at the entry to the control domain. The model problem is depicted in Fig. 1. The linear bearings, which constrain the motion of the beam at the boundaries, are considered as prismatic joints, such that the deflection w takes on given values and the slope vanishes there, $w' = 0$. The joint at the entry moves in lateral direction over time t according to a given law $w_0(t)$. Under the condition of perfect adhesion, the beam would be transported along the axial coordinate x with the velocity v of the travelling foundation and its deformed shape would become

$$w(x,t) = w_0(t - x/v). \tag{1}$$

However, the boundary conditions at the exit prismatic joint and the bending stiffness of the beam trigger sliding, thus creating a system with a non-trivial dynamic behaviour.
In the geometrically linear setting, small lateral deflections do not affect the axial velocity of a particle of the beam, which thus always coincides with the transport speed $\dot{x} = v$. The lateral component of the velocity of a particle

$$\dot{w}(x,t) = \partial_t w + v w' \tag{2}$$

comprises the local (Eulerian) time derivative $\partial_t w$, computed at a given axial position $x = \mathrm{const}$, and a convective term featuring the derivative with the spatial coordinate $w' = \partial_x w$. The relative velocity $\dot{w}$ between the particle and the foundation determines the Coulomb's dry friction force q according to

$$\dot{w} > 0 : \; q = -q_0, \quad \dot{w} = 0 : \; -q_0 < q < q_0, \quad \dot{w} < 0 : \; q = q_0 \tag{3}$$

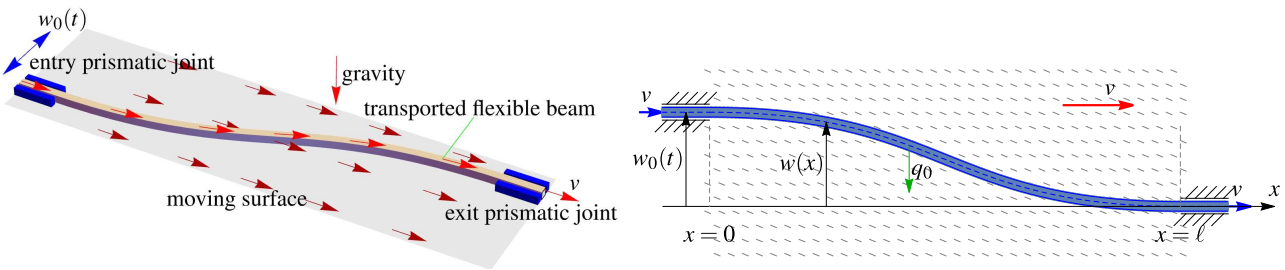

Figure 1: Flexible beam transported across a control domain by a moving rough surface: 3D perspective and view from above

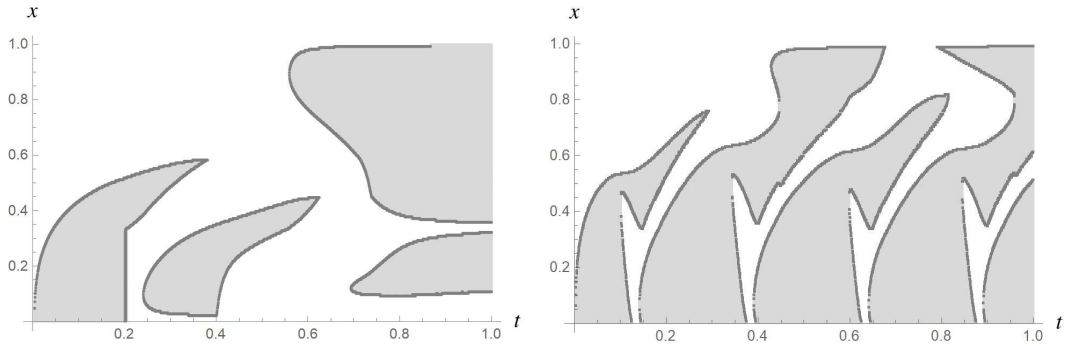

Figure 2: Time evolution of the segments of sliding (gray areas), parameters: $a = 1$, $q_0 = 1$, $v = 1$, unit length of the control domain; left: linear growth with $\bar{w}_0 = 1/300$ and $t_0 = 0.2$; right: harmonic excitation at the entry with $w_0 = \sin(4\pi t)/300$

with q_0 being the sliding friction force, which bounds the static friction force. Now we demand that the beam is in static equilibrium at all times:

$$aw'''' = q \tag{4}$$

with a denoting the bending stiffness of the beam. Complemented with specific boundary conditions, the equations determine the time evolution of the zones of stick and sliding friction as well as the motion of the beam.

Discussion of the solution strategies

The main difficulty in obtaining the solution in terms of $w(x,t)$ and $q(x,t)$ is that the nonlinear equations cannot be resolved for the time derivative $\partial_t w$, which would otherwise facilitate the direct time integration of the evolution law. A regularization with a small inertial term and second-order time derivative would prohibit an analytical solution and require a computationally costly numerical time integration with small time steps. The above outlined quasi-static problem may be tackled numerically in a very efficient manner using the non-material finite element formulation with the transport condition for the deflection field as discussed in [4].
While the stationary solution with $\partial_t w = 0$ in case of constant deflections at the boundaries of the control domain is extensively analysed in [4], the present study focuses on the transient behaviour in response to two distinct cases of the imposed deflection at the entry $w_0(t)$:

- Linear growth followed by constant deflection:

$$w_0 = \begin{cases} \bar{w}_0 t/t_0, & t < t_0 \\ \bar{w}_0, & t \geq t_0 \end{cases} \tag{5}$$

  Sliding is inevitable during the growth stage $t < t_0$, as the boundary condition $w' = 0$ at $x = 0$ contradicts the full adhesion solution (1). One expects, that a "wave" of the length vt_0 shall be transported by the travelling foundation until it reaches the exit prismatic joint. However, a more complicated process with reverse sliding is suggested by numerical analysis at higher values of the amplitude $\bar{w}_0$, see left part of Fig. 2. The stationary solution with alternating segments of sliding friction and a self-similar deformed configuration establishes over time during the subsequent transient stage.

- Harmonic excitation:

$$w_0 = \bar{w}_0 \sin \omega t. \tag{6}$$

  As long as the amplitude $\bar{w}_0$ is small, sliding shall again take place only in the vicinity of the entry point. The length of the segment of sliding shall change in time according to a complicated law, which can approximately be established in an analytical solution. Numerical analysis suggests, however, that higher values of $\bar{w}_0$ result into more segments of sliding near the entry point, see right part of Fig. 2. Finding an estimate for the critical value of the amplitude, at which the solution changes qualitatively, is a challenging mathematical task.

References

[1] Vetyukov, Y., Gruber, P.G., Krommer, M., Gerstmayr, J., Gafur, I. and Winter, G. (2017) Mixed Eulerian–Lagrangian description in materials processing: deformation of a metal sheet in a rolling mill. *Int. J. Numer. Methods Eng.* **109**(10):1371-1390.

[2] Scheidl, J., Vetyukov, Y., Schmidrathner, C., Schulmeister, K. and Proschek, M (2021) Mixed Eulerian-Lagrangian shell model for lateral run-off in a steel belt drive and its experimental validation. *Int. J. Mech. Sci.* **204**:106572.

[3] Schmidrathner, C., Vetyukov, Y. and Scheidl, J. (2021) Non-material finite element rod model for the lateral run-off in a two-pulley belt drive *Z. Angew. Math. Mech.*:e202100135.

[4] Vetyukov, Y. (2021) Endless elastic beam travelling on a moving rough surface with zones of stick and sliding. *Nonlinear Dyn.* **104**:3309-3321.

[5] Stupkiewicz, S., Mróz, Z. (1994) Elastic beam on a rigid frictional foundation under monotonic and cyclic loading. *Int. J. Solids Struct.* **31**(24):3419-3442.

[6] Nikitin, L.V., Fischer, F.D., Oberaigner, E.R., Rammerstorfer, F.G., Seitzberger, M. and Mogilevsky, R.I. (1996) On the frictional behaviour of thermally loaded beams resting on a plane. *Int. J. Mech. Sci.* **38**(11):1219-1229.

Influence of Gyroscopic Effects on Nonlinear Dynamics of High-Speed Planetary Gears Having an Elastic Ring

Chenxin Wang and Robert G. Parker
Department of Mechanical Engineering, University of Utah, Salt Lake City, UT 84112, USA

Summary. Numerical simulations show that gyroscopic effects can significantly influence the nonlinear dynamics (resonances and parametric instabilities) of planetary gears having a deformable ring at high speed. Analytical solutions at resonances and parametric instabilities that include the gyroscopic effects are derived and used to explain the numerical results.

Introduction

Vibrations of planetary gears arise primarily from periodically changing sun-planet and ring-planet tooth mesh excitation as the gears rotate. A resonance occurs when a harmonic L of the mesh frequency Ω_m approaches a natural frequency ω_q (i.e., $L\Omega_\mathrm{m} \approx \omega_q$). A parametric instability occurs when $L\Omega_\mathrm{m} \approx \omega_p + \omega_q$, where ω_p and ω_q can be the same. Near resonances or parametric instabilities, vibrations can become large enough that nonlinear tooth separation occurs. The ring has substantial elastic deformation when it is designed to be thin for weight saving. Gyroscopic (i.e., Coriolis) effects become significant for high-speed systems, but their influence on the nonlinear dynamics of planetary gears having an elastic ring are not yet known.

This work derives closed-form solutions for the nonlinear dynamics of planetary gears with a deformable ring using the model in [1]. The model includes speed-dependent gyroscopic and centripetal effects. The tooth mesh excitation is modeled as time-varying stiffnesses that include tooth separation nonlinearity. Numerical integration of the dynamic model shows the significant impact of gyroscopic effects on the resonances and parametric instabilities at high speed.

Numerical results

Fig. 1 shows the RMS of dynamic ring-planet mesh deflection from numerical integration of a planetary gear system having a deformable ring without (black dashed line) and with (green dotted line) gyroscopic effects. The differences highlight the significant influence of gyroscopic effects. One resonance ($\Omega_\mathrm{m} \approx \omega_4$) and one parametric instability ($\Omega_\mathrm{m} \approx \omega_1 + \omega_2$) are present for the system without gyroscopic effects. When gyroscopic effects are included, an additional resonance at $\Omega_\mathrm{m} \approx \omega_3$ occurs. For the resonance $\Omega_\mathrm{m} \approx \omega_4$, the peak amplitude decreases and the peak resonant frequency shifts to the right with inclusion of gyroscopic effects. The parametric instability $\Omega_\mathrm{m} \approx \omega_1 + \omega_2$ is absent for the system with gyroscopic effects.

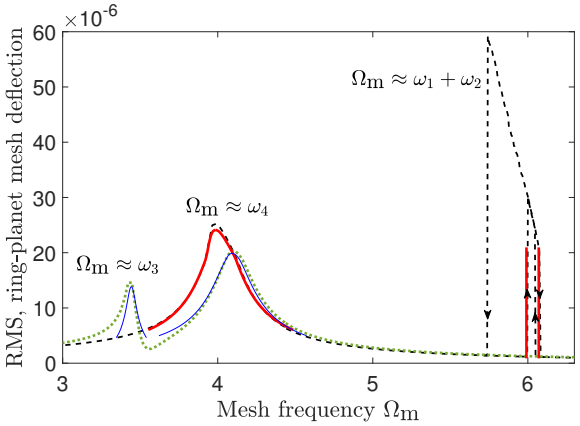

Figure 1: RMS (mean removed) values of dimensionless ring-planet mesh deflection from numerical integration of a planetary gear system having a deformable ring without (black dashed line) and with (green dotted line) gyroscopic effects over a range of dimensionless mesh frequencies. These RMS results are identical for every planet. The arrows indicate results from increasing and decreasing speed simulations. The thick (red) and thin (blue) solid lines are the analytical results from Eq. (1) for the two resonances $\Omega_\mathrm{m} \approx \omega_3$ and $\Omega_\mathrm{m} \approx \omega_4$ and Eq. (3) for the one parametric instability $\Omega_\mathrm{m} \approx \omega_1 + \omega_2$ for the system without and with gyroscopic effects.

Analytical explanation

Resonances

The amplitude-frequency relation for a resonance $L\Omega_\mathrm{m} \approx \omega_q$ (whether the system is gyroscopic or not) is derived as

$$\Omega_\mathrm{m} = \frac{\omega_q}{L} + \frac{\omega_q}{La_q}\left(2R_1 + R_2 a_q \pm \sqrt{4|R_3|^2 - (\nu_q a_q)^2}\right), \tag{1a}$$

$$R_3 = N\left(k_{\mathrm{s}1}^{(L)}\bar{\Delta}_{\mathrm{s}1}^{[q]}\Delta_{\mathrm{s},0} + k_{\mathrm{r}1}^{(L)}\bar{\Delta}_{\mathrm{r}1}^{[q]}\Delta_{\mathrm{r},0}\right), \tag{1b}$$

where a_q is the real-valued amplitude of the resonant mode, ν_q is the modal damping ratio, R_1 and R_2 are real-valued terms associated with tooth contact loss, N is the number of planets, $k_{j1}^{(L)}$ for $j = \text{s, r}$ are the L-th harmonic coefficients (complex-valued) of the first sun-planet and ring-planet mesh stiffness variations, $\Delta_{j,0}$ are the static sun-planet and ring-planet mesh deflections (real-valued and identical for every planet) due to the applied torque, $\Delta_{j1}^{[q]}$ are the first sun-planet and ring-planet modal mesh deflections (complex-valued), and the overbar denotes complex conjugate. Vanishing of the square root term in Eq. (1a) gives the peak resonant amplitude

$$a_{q,\text{p}} = 2|R_3|/\nu_q. \tag{2}$$

Eqs. (1b) and (2) explain why the resonance $\Omega_\text{m} \approx \omega_3$ does not occur for the system without gyroscopic effects but occurs for the system with them (Fig. 1). In the absence of gyroscopic effects, mode 3 is a mode where the modal sun-planet and ring-planet mesh deflections vanish (i.e., $\Delta_{sn}^{[3]} = \Delta_{rn}^{[3]} = 0$ for $n = 1, 2, \ldots, N$) [2], such that the R_3 for this mode and the peak amplitude $a_{3,\text{p}}$ in Eq. (2) vanish. When gyroscopic effects are included, mode 3 becomes a mode with nonzero $\Delta_{sn}^{[3]}$ and $\Delta_{rn}^{[3]}$ [3]. This leads to nonzero R_3 in Eq. (1b) and nonzero $a_{3,\text{p}}$ in Eq. (2) and therefore the occurrence of the resonance $\Omega_\text{m} \approx \omega_3$ for the system with gyroscopic effects in Fig. 1.

Eq. (1) shows that gyroscopic effects shift the resonant frequencies by changing the natural frequencies. The ω_4 increases when gyroscopic effects are included, so the resonant frequency for $\Omega_\text{m} \approx \omega_4$ shifts to the right. This prediction matches the numerical results in Fig. 1.

Eqs. (1b) and (2) reveal that gyroscopic effects affect the peak amplitudes of resonances by changing vibration mode quantities. Gyroscopic effects change the modal mesh deflections $\Delta_{sn}^{[4]}$ and $\Delta_{rn}^{[4]}$. At high speed, this change is significant. This alters the values of R_3 in Eq. (1b). R_3 changes significantly for mode 4, which affects the associated peak amplitude $a_{4,\text{p}}$. As shown in Fig. 1, the analytical predictions capture this effect.

Parametric instabilities

The boundaries of the range of mesh frequencies for a parametric instability $L\Omega_\text{m} \approx \omega_p + \omega_q$ to occur are derived as

$$\Omega_\text{m}^{\{L,p,q\}} = \frac{(\omega_p + \omega_q)}{L} \pm \frac{\nu_p\omega_p + \nu_q\omega_q}{L}\sqrt{|D_{pq}^{(L)}|^2/(\nu_p\nu_q) - 1}, \tag{3a}$$

$$D_{pq}^{(L)} = N(k_{\text{r1}}^{(L)}\bar{\Delta}_{\text{r1}}^{[p]}\bar{\Delta}_{\text{r1}}^{[q]} + k_{\text{s1}}^{(L)}\bar{\Delta}_{\text{s1}}^{[p]}\bar{\Delta}_{\text{s1}}^{[q]}). \tag{3b}$$

Eq. (3a) gives that a parametric instability is eliminated by damping when

$$|D_{pq}^{(L)}| < \sqrt{\nu_p\nu_q}. \tag{4}$$

Eqs. (3) and (4) apply to both non-gyroscopic and gyroscopic planetary gears having a deformable ring.

Eqs. (3b) and (4) show that gyroscopic effects change the occurrence of a parametric instability by changing modal mesh deflections. The parametric instability $\Omega_\text{m} \approx \omega_1 + \omega_2$ for the system without gyroscopic effects has $|D_{1,2}^{(1)}| = 0.0211 > \sqrt{\nu_1\nu_2} = 0.02$. Therefore, this parametric instability is present in Fig. 1. When gyroscopic effects are included, the modal mesh deflections $\Delta_{j1}^{[1]}$ and $\Delta_{j1}^{[2]}$ for $j = \text{s, r}$ change so that $|D_{1,2}^{(1)}|$ decreases (see Eq. (3b)). This leads to $|D_{1,2}^{(1)}| = 0.0172 < \sqrt{\nu_1\nu_2} = 0.02$. The parametric instability $\Omega_\text{m} \approx \omega_1 + \omega_2$ is absent in Fig. 1 in the presence of gyroscopic effects.

Conclusions

Gyroscopic effects alter the occurrence of resonances, shift resonant frequencies, and change resonant amplitudes associated with nonlinear behavior induced by contact loss. These influences are significant for high-speed planetary gears having an elastic ring. A closed-form amplitude-frequency relation derived for the resonances of planetary gears without and with gyroscopic effects reveal how these effects change the resonant behavior by their influence on the natural frequencies and vibration modes. For example, changes of modal mesh deflections of a resonant mode can change the resonant amplitude and, sometimes, change whether a resonance occurs or not.

The influence of gyroscopic effects on parametric instabilities of planetary gears having an elastic ring is similarly substantial. The analytical results reveal that gyroscopic effects change the occurrence/absence of parametric instabilities and the mesh frequency range where a given instability occurs. These effects arise principally from changes to the modal mesh deflections of the participating modes.

References

[1] Wang C., Parker R.G. (2020) Dynamic modeling and mesh phasing-based spectral analysis of quasi-static deformations of spinning planetary gears with a deformable ring. *Mechanical Systems and Signal Processing* **136**:106497.

[2] Wu X., Parker R.G. (2008) Modal properties of planetary gears with an elastic continuum ring gear. *Journal of Applied Mechanics, Transactions ASME* **75**:0310141–03101412.

[3] Wang C., Parker R.G. (2021) Modal properties and parametrically excited vibrations of spinning epicyclic/planetary gears with a deformable ring. *Journal of Sound and Vibration* **494**:115828.

Prediction of Limit Cycles of Lateral Oscillations in Drilling Processes: Numerical Analysis and Experimental Validation

Dennis Heyser[*], Bernhard Schweizer [*], Marcel Volz[**] and Eberhard Abele[**]
[*]*Institute of Applied Dynamics, Technical University of Darmstadt, Darmstadt, Germany*
[**] *Institute of Production Management, Technology and Machine Tools, Technical University of Darmstadt, Darmstadt, Germany*

Summary. Several experimental investigations have shown that drilling processes are likely to develop limit cycles at approximately integer multiples of the tool rotation frequency. As a consequence, the whirling oscillations generate N-lobed holes. In literature, linear models are presented to explain the onset of the instability and to analyze the exponential growth or decay of this whirling phenomenon. However, to predict the orbit of the limit cycles, more involved models are required, which take the relevant nonlinearities into account [1,2,3]. This work deals with a nonlinear drilling model. The cutting forces involve the so-called regenerative effect, which leads to a delay differential equation (DDE). Nonlinear rubbing effects, which occur at the contact under the cutting edge, are considered. Also, the contact at the bore hole wall is taken into account and its stabilizing effect on the drilling process is shown. The presented drilling model is able to predict the bore hole shape as well as the circularity of a real drilling process with high accuracy. The model can be used to optimize the drilling parameters and the shape of the tool in order to improve real drilling processes.

Motivation

Basically, two phenomena are distinguished in cutting tool vibrations: (i) Chatter which appears approximately at the tools torsion natural frequency and (ii) lateral oscillations at odd multiples of the tool rotation frequency.
Currently, often two machining steps are necessary to create bore holes with high precision: Drilling and finishing afterwards, for example by reaming, to reach the required accuracy.
To analyze and clearly understand the physical effects occurring in drilling processes and to optimize these processes (i.e. reducing the amplitudes of the lateral oscillations by optimization of the tool shape and cutting parameters), a nonlinear two degree of freedom model is applied in the current work. The model yields a system of coupled delay differential equations, which is solved numerically.

Physical Model

The drilling model includes the mass, structural damping and stiffness of the tool as well as external forces due to the contact with the workpiece. The external forces consist of the cutting force, the rubbing force and the contact force at the bore hole wall.
The cutting force is assumed to be proportional to the uncut chip area and obtained experimentally similar to an experimental setup introduced by *Bayly et al.* [1]. Since the uncut chip area depends on the current position of the tool and the position at the previous cutting-edge passage, a time delay is generated in the differential equations.
Rubbing occurs due to material compression under the cutting edge. *Chiou* and *Liang* [4] suggested a linear rubbing force model for turning processes. Their approach is extended to a nonlinear model and adapted to oblique cutting, which leads to a dependence on the feed rate, cutting velocity, current tool vibrations and tool wear.
Previous experimental investigations by *Volz et al.* [3] have shown a strong correlation between the land width of the tool, which supports it against the bore hole surface, and the amplitude of the lateral oscillations. Therefore, a model for the wall contact is introduced. On one hand, this contact model takes elastic effects into account. On the other hand, a nonlinear damper - similar to the rubbing force model - is integrated, which incorporates the energy dissipation in the contact.

Experimental Investigations

The cutting force model is based on experimental data. The drilling tests were conducted in aluminum alloy (AlSi7Mg0.3) using a 10 mm diameter sold carbide twisted drill with four lands, a TiAlN top coating and a ZrN deck layer. Since the uncut chip area increases linearly with the feed rate, cutting force tests with different feed rates were performed. The measured cutting forces are plotted over the corresponding uncut chip areas and the slope of this plot yields the approximately linear relation of the change in force per change in uncut chip area. In the numerical simulations, this slope is used as proportionality factor to calculate the cutting force on cutting lip segments with the aid of the current and the delayed tool position.

Simulation

The DDE is discretized with an implicit integration scheme, namely with a variable-step size, variable-order BDF solver. In order to handle the time delay, the following strategy has been applied.
The simulation time is split into equal intervals, where the interval length corresponds to the time delay. In each interval the simulation results (displacements and velocities) from the previous interval are known and used to take the delay part in the equations of motion into account, which may then be interpreted as an external time function. The problem is

the initialization of the simulation, because the initial conditions must be known as a function of time over one delay period. Therefore, the simulation is firstly started with the trivial solution of the DDE. In a second step, a rectangular-shaped external force is applied in order to initialize the lateral vibrations.

Results and Conclusions

In the simulations, the contact stiffness parameters used in the bore hole wall contact model as well as for the rubbing force model are adopted from a turning test presented by *Chiou* and *Liang* [4]; the parameters have been slightly modified and adapted to fit the drilling process. The feed rate, cutting velocity and pre-hole diameter are varied and the damping is increased successively to describe the behavior of chip flow and coolant water in the drilling process. The damping has no significant influence on the amplitude of the appearing limit cycles, but on the frequency of the oscillation and therefore on the bore hole shape.
A comparison between a simulation and measurements is depicted in *Figure 1*. In this case, the ratio between the limit cycle frequency and the tool rotational frequency is approximately three. A transformation from the tool tip movement to the outer cutting edges represent the emerging bore hole contour as a three-lobed hole. The shape and magnitude of the simulated bore holes (blue) show a high accordance with the experimental results (red) with respect to the circularity. For a better visualization, the plot is stretched by the factor 41 around the gauss circle of the simulated data (black solid line). The drilling experiments have been carried out with a pre-hole diameter of 4 mm. Note that the circularity is defined as radial distance between the outermost (outer blue dashed line) and innermost (inner blue dashed line) circles.

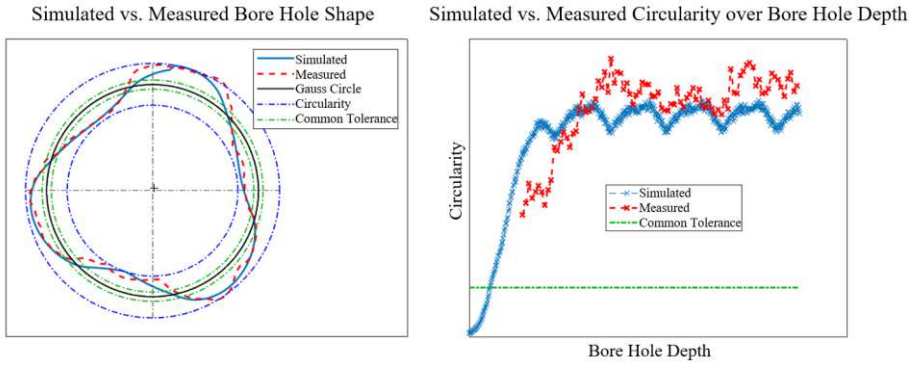

Figure 1: Left: Simulated (blue) vs. measured (red) bore hole shape at a specific bore hole depth. Right: Simulated (blue) vs. measured (red) circularity over bore hole depth and a common tolerance for drilling processes (green).

Summarizing: The presented drilling model is able to predict the circularity of drilling processes with a special consideration of lateral oscillations of the drilling tool tip. Within the validation of the implemented model, a high agreement of the results from the simulation with those from the machining tests could be achieved.
In a following step, a great range of parameter studies, including the cutting parameters and the shape of the tool, can be conducted with the numerical model to identify the most important parameters for improving the drilling process. Possibly the process can be optimized to reach a specified tolerance without an additional reaming step.

References

[1] Bayly, P.V.; Lamar, M.T.; Calvert, S.G. : *Low-Frequency Regenerative Vibration and the Formation of Lobed Holes in Drilling. Journal of Manufacturing Science and Engineering*, **2002**, Vol. 124, pp. 275–285.
[2] Altintas, Y.; Ahmadi, K. : *Stability of Lateral, Torsional and Axial Vibrations in Drilling. International Journal of Machine Tools & Manufacture*, **2013**, Vol. 68, pp. 63–74.
[3] Volz, M.; Abele, E.; Weigold, M. : *Lateral Vibrations in Deep Hole Drilling due to Land Width Variation. Journal of Manufacturing and Materials Processing*, **2020**, pp. 28.
[4] Chiou, R.Y.; Liang, S.Y. : *Chatter Stability of a Slender Cutting Tool in Turning with Tool Wear Effect. International Journal of Machine Tools & Manufacture*, **1998**, Vol. 38, pp. 315–327.

Wednesday, July 20, 2022
08:30 - 10:30

MS-17 Time-periodic systems
Saint Clair 3A

Chair:Thomas Pumhoessel

08:30 - 08:50
A Koopman View on the Harmonic Balance and Hill Method
BAYER Fabia*, LEINE Remco
*Institute for Nonlinear Mechanics, University of Stuttgart (Institut für nichtlineare Mechanik Pfaffenwaldring 9 70569 Stuttgart Germany)

08:50 - 09:10
An extreme time-periodic oscillator
ANZOLEAGA Grandi Alvaro*, PROTIÈRE Suzie, LAZARUS Arnaud
*Institut Jean Le Rond dÁlembert (Boite 162 4 place Jussieu 75005 Paris France)

09:10 - 09:30
Asymptotic description of the wear process in dry-running reciprocating compressors
JURISITS Richard*, KAUFMANN Andreas, KORNFELD Matthias, ANTRETTER Thomas
*University of Applied Sciences Vienna (Vienna Austria)

09:30 - 09:50
Attractor Targeting by Dual-frequency Driving
HEGEDŰS Ferenc, **KRÄHLING Péter***, MARCEL Aron, LAUTERBORN Werner, METTIN Robert, PARLITZ Ulrich
*Budapest University of Technology and Economics, Department of Hydrodynamic Systems (H-1111, Budapest, Műegyetem rkp. 3., D building Hungary)

09:50 - 10:10
[no show] Broadband Stabilization with Combined Anti-Resonances
KRAUS Zacharias*, BARAKAT Ahmed, HAGEDORN Peter
*Dynamics and Vibrations Group, Technical University of Darmstadt (Dolivostraße 15, 64293 Darmstadt Germany)

A Koopman View on the Harmonic Balance and Hill Method

Fabia Bayer* and Remco I. Leine*
*Institute for Nonlinear Mechanics, University of Stuttgart, Germany

Summary. The Koopman operator provides a way to approximate the dynamics of a nonlinear system by a linear time-invariant system of higher order. In this paper, we aim to study nonlinear time-periodic systems and propose a specific choice of Koopman basis functions combining the Taylor and Fourier bases. This basis allows to recover all equations necessary to perform the Harmonic Balance Method as well as the Hill analysis directly from the linear lifted dynamics. The Mathieu equation and a more general Hill equation are used to exemplify these findings.

Introduction

In the recent years, the Koopman framework and especially its data-driven counterpart, the Extended Dynamic Mode Decomposition, have gained immense popularity [10, 3, 11, 7, 2]. This is due to its auspicious promise: Global representation of a nonlinear system by a linear operator. To this end, in the Koopman framework, the dynamical system is defined through the propagation of functions on the state space, also called observables, over time. While the corresponding operator is linear in its argument, the considered function spaces are usually infinite-dimensional. Therefore, in practice, a linear approximation is considered which is restricted to a finite-dimensional space spanned by a finite number of predefined basis functions. It is well-known that the approximation quality of this restriction strongly depends on the choice of basis functions.
Classically, the Koopman framework is applied to time-autonomous systems $\dot{\mathbf{x}} = \mathbf{f}(\mathbf{x})$ and the approximate linear dynamics obtained by the Koopman lift then takes the form $\dot{\mathbf{z}} = \mathbf{A}\mathbf{z}$. The incorporation of a time-dependent input $\mathbf{v}(t)$ into the dynamics, i.e. $\dot{\mathbf{x}} = \mathbf{f}(\mathbf{x}, \mathbf{v}(t))$ or simply $\dot{\mathbf{x}} = \mathbf{f}(\mathbf{x}, t)$, generally poses problems in the Koopman framework as the system can only be approximated by a linear time-variant system $\dot{\mathbf{z}} = \mathbf{A}\mathbf{z} + \mathbf{B}\mathbf{u}(t)$ if products of state and input are neglected.
In this paper we focus on nonautonomous systems for which the input is time-periodic, i.e. $\mathbf{v}(t) = \mathbf{v}(t+T)$. In particular, we propose a specific choice of observable functions which contains observables depending both on state and time. We demonstrate that this representation contains all frequency information of the system up to some chosen frequency order $N_{\mathbf{u}}$. This means that this basis is a good choice for a Koopman lift, as it retains structural information.
After a short overview about Koopman theory, the specific periodic basis is introduced together with a matching inner product. It is demonstrated how all equations necessary for the Harmonic Balance Method as well as the Hill method follow from the Koopman lift in these specific observables. This means that the (approximate) stability information for the system is retained in the Koopman lift. The findings are illustrated using two variants of the Hill equation.

Koopman theory overview

Consider a nonautonomous time-periodic finite-dimensional dynamical system governed by $\dot{\mathbf{x}} = \mathbf{f}(\mathbf{x}, t)$, where $t \in \mathbb{R}$ is the time, $\mathbf{x}(t) \in \mathcal{X} \subseteq \mathbb{R}^n$ is the state trajectory starting at $\mathbf{x}(t_0) = \mathbf{x}_0$ and $\mathbf{f} : \mathcal{X} \times \mathbb{R} \to \mathcal{X}$ is a smooth vector field which is T-periodic in t. The family of maps $\boldsymbol{\phi}_t(\mathbf{x}_0, t_0) = \mathbf{x}(t)$ characterizes the flow of the system and assigns to each (initial) configuration $(\mathbf{x}_0, t_0)$ the resulting state after time t has passed.
The Koopman framework [10] considers output functions $g(\mathbf{x}, t)$, also called observables. Any spaces of functions over the complex or real numbers are permitted in the general Koopman framework. In this work, we consider in particular the space $\mathcal{F}$ of complex-valued functions $g : \mathcal{X} \times \mathbb{R} \to \mathbb{C}$ which are real analytic on $\mathcal{X}$ and T-periodic in the last argument t.
Given any function g, it may be of interest how its function values evolve along the trajectories of the system. For instance, in the Lyapunov framework, it is desired that function values of a Lyapunov candidate decrease over time for any starting point. The operator $K^t : \mathcal{F} \to \mathcal{F}; g \mapsto g \circ \phi_t$ performs this shift along the trajectory for arbitrary functions g from the considered function space. The family of all these operators for any t is called the Koopman semigroup of operators.
It is easy to see that for suitable $\mathcal{F}$, this Koopman semigroup contains all information about the system without explicitly knowing the vector field $\mathbf{f}$ or the flow $\boldsymbol{\phi}_t$. In particular, if $\mathcal{F}$ is chosen such that the identity function id is contained in the vector space, then the flow can be recovered easily by simply evaluating $K^t(\mathrm{id})$. As a trivial counterexample, consider the one-dimensional vector space of constant functions. Any constant function will not change while being evaluated along an arbitrary trajectory of $\mathbf{x}$. Therefore, in this case, the Koopman operator semigroup is well-defined, albeit trivial. No information about the underlying system is retained. This example shows that an appropriate choice of function space is a crucial part of the Koopman framework.
Under the aforementioned assumptions for the particular function space $\mathcal{F}$ and the vector field $\mathbf{f}$, there also exists the operator $L : \mathcal{F} \to \mathcal{F}, g \mapsto \dot{g}$ mapping an observable g to its total time derivative $\dot{g}$ with

$$\dot{g}(\mathbf{x}, t) = \frac{\partial g(\mathbf{x}, t)}{\partial \mathbf{x}} \mathbf{f}(\mathbf{x}, t) + \frac{\partial g(\mathbf{x}, t)}{\partial t} \,. \tag{1}$$

This operator is called the infinitesimal Koopman generator. Again, for suitable $\mathcal{F}$, this representation alone is a sufficient way to describe the behavior of the dynamical system. In particular, if $\mathrm{id} \in \mathcal{F}$, the vector field $\mathbf{f}$ is easily recovered.
In addition, the Koopman generator and the Koopman semigroup of operators are linear in the argument g, even if the governing differential equation is nonlinear. This comes at the cost of dealing with a mapping on an (infinite-dimensional) function space instead of the (finite-dimensional) state space.

On a finite-dimensional subspace $\mathcal{F}_{\hat{N}} \subset \mathcal{F}$ spanned by $\hat{N}$ linearly independent basis functions $\{\psi_l\}_{l=1}^{\hat{N}}$, any projection $\Pi_{\hat{N}} : \mathcal{F} \to \mathcal{F}_{\hat{N}}$ defines a finite-dimensional approximation $\hat{L} : \mathcal{F}_{\hat{N}} \to \mathcal{F}_{\hat{N}}$ of L on $\mathcal{F}_{\hat{N}}$ by $L_{\hat{N}} := \Pi_{\hat{N}} L$. The approximation process and the subsequent approximation error are visualized in Figure 1. As the subspace $\mathcal{F}_{\hat{N}}$ generally is not closed w.r.t. L, the result of Lg must be projected back to $\mathcal{F}_{\hat{N}}$, introducing some approximation error. Again, the choice of basis functions for $\mathcal{F}_{\hat{N}}$ is crucial. Since $\mathcal{F}_{\hat{N}}$ is finite-dimensional, elements of $\mathcal{F}_{\hat{N}}$ can be represented by a

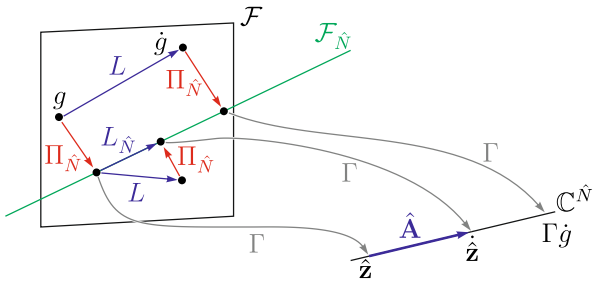

Figure 1: Schematic drawing of the infinitesimal Koopman generator L, its finite-dimensional approximation $L_{\hat{N}}$ and the matrix representation $\hat{\mathbf{A}}$.

column vector of coefficients $\hat{\mathbf{z}} \in \mathbb{C}^{\hat{N}}$. In Figure 1, this is visualized by the map $\Gamma : \mathcal{F}_{\hat{N}} \to \mathbb{C}^{\hat{N}}$. This map can be extended to observables $g \in \mathcal{F} \setminus \mathcal{F}_{\hat{N}}$. In this case, the resulting vector $\hat{\mathbf{z}}$ represents $\Pi_{\hat{N}} g$, which is the projection of g onto $\mathcal{F}_{\hat{N}}$.
The matrix representation of $L_{\hat{N}}$ is $\hat{\mathbf{A}} \in \mathbb{C}^{\hat{N} \times \hat{N}}$ with $\Gamma L_{\hat{N}} g = \hat{\mathbf{A}} \Gamma g$. This matrix also defines a linear time-invariant autonomous differential equation, namely

$$\dot{\hat{\mathbf{z}}} = \hat{\mathbf{A}} \hat{\mathbf{z}} \,. \tag{2}$$

This linear system is called the Koopman lift and describes the dynamics represented in $L_{\hat{N}}$, i.e. it is a finite-dimensional linear approximation of the original system dynamics. The Koopman lift matrix $\hat{\mathbf{A}}$ can be derived from the original nonlinear dynamics manually by using a column vector $\mathbf{\Psi} := \left(\psi_1, \ldots, \psi_{\hat{N}}\right)^{\mathrm{T}}$ of the basis functions of $\mathcal{F}_{\hat{N}}$, computing $\frac{\mathrm{d}\mathbf{\Psi}}{\mathrm{d}t}$ and identifying terms linear in elements of $\mathbf{\Psi}$ after applying the projection $\Pi_{\hat{N}}$. If this projection is orthonormal, the matrix entry $\hat{\mathbf{A}}_{i,j}$ at i-th row and j-th column is given by $\hat{\mathbf{A}}_{i,j} = \left\langle \frac{\mathrm{d}\psi_i}{\mathrm{d}t}, \psi_j \right\rangle$, where $\langle ., . \rangle$ denotes the corresponding inner product.

Koopman lift for time-periodic systems

For smooth autonomous systems in the Koopman framework, it is customary to consider as basis functions a finite set of monomials $\psi_{\boldsymbol{\beta}}(\mathbf{x}) = \mathbf{x}^{\boldsymbol{\beta}}$, where $\boldsymbol{\beta} \in \mathbb{N}^n$ is a multi-index and standard multi-index calculation rules (see, for example, [14, p. 319]) apply. As time-periodic functions are considered in the presented case, we propose in this paper to include as basis functions combinations of polynomial terms as well as Fourier terms of the correct base frequency, i.e. basis functions of the form $\psi_{\boldsymbol{\beta},k} := \mathbf{x}^{\boldsymbol{\beta}} e^{ik\omega t}$, where $\omega = \frac{2\pi}{T}$. The functions $\{\psi_{\boldsymbol{\beta},k} | k \in \mathbb{Z}, \boldsymbol{\beta} \in \mathbb{N}^n\}$ are an orthonormal system within the initially considered vector space $\mathcal{F}$ w.r.t. the inner product

$$\langle g, h \rangle := \int_0^T \left(\frac{1}{(\boldsymbol{\beta}!)^2} \sum_{\boldsymbol{\beta} \in \mathbb{N}^n} \frac{\partial^{\boldsymbol{\beta}} g}{\partial \mathbf{x}^{\boldsymbol{\beta}}}\bigg|_{0,t} \frac{\partial^{\boldsymbol{\beta}} \bar{h}}{\partial \mathbf{x}^{\boldsymbol{\beta}}}\bigg|_{0,t} \right) \mathrm{d}t \,. \tag{3}$$

By slight abuse of notation, the inner product is extended to vector-valued functions $\mathbf{g} \in \mathcal{F}^l$, $\mathbf{h} \in \mathcal{F}^m$ element-wise via

$$\langle \mathbf{g}, \mathbf{h} \rangle := \begin{pmatrix} \langle g_1, h_1 \rangle & \ldots & \langle g_1, h_m \rangle \\ \vdots & \ddots & \vdots \\ \langle g_l, h_1 \rangle & \ldots & \langle g_l, h_m \rangle \end{pmatrix} \,. \tag{4}$$

Let $N_{\boldsymbol{\beta}}, N_{\mathbf{z}}, N_{\mathbf{u}} \in \mathbb{N}$ be integers which describe the assumed maximum polynomial order of the state and maximum frequency order of the state and input, respectively. Let $\{\boldsymbol{\beta}_l\}_{l=1}^{N_{\boldsymbol{\beta}}}$ be a set of multi-indices with $\mathbf{0} \notin \{\boldsymbol{\beta}_l\}_{l=1}^{N_{\boldsymbol{\beta}}}$. For the

sake of brevity, define $N = N_{\boldsymbol{\beta}}(2N_{\mathbf{z}} + 1)$. Consider now the specific finite-dimensional subspace $\mathcal{F}_N \subset \mathcal{F}$ spanned by $\boldsymbol{\Psi} = (\boldsymbol{\Psi}_{\mathbf{z}}^{\mathrm{T}}, \mathbf{u}^{\mathrm{T}})^{\mathrm{T}}$ with

$$\boldsymbol{\Psi}_{\mathbf{z}}(\mathbf{x}, t) := (\mathbf{x}^{\boldsymbol{\beta}_1} e^{i\omega N_{\mathbf{z}} t}, \dots, \mathbf{x}^{\boldsymbol{\beta}_1} e^{0}, \dots, \mathbf{x}^{\boldsymbol{\beta}_1} e^{-i\omega N_{\mathbf{z}} t}, \mathbf{x}^{\boldsymbol{\beta}_2} e^{i\omega N_{\mathbf{z}} t}, \dots, \mathbf{x}^{\boldsymbol{\beta}_{N_{\boldsymbol{\beta}}}} e^{-i\omega N_{\mathbf{z}} t})^{\mathrm{T}} \tag{5}$$

$$\mathbf{u}(t) := (e^{-i\omega N_{\mathbf{u}} t}, \dots, e^{0}, \dots, e^{i\omega N_{\mathbf{u}} t})^{\mathrm{T}} . \tag{6}$$

It is reasonable to include the state $\mathbf{x}$ itself in the basis such that there is a selector matrix $\mathbf{C}_{\mathbf{z}} \in \mathbb{R}^{n \times N}$ containing some rows of the identity matrix with $\mathbf{C}_{\mathbf{z}} \boldsymbol{\Psi}_{\mathbf{z}}(\mathbf{x}, t) = \mathbf{x}$. There exist other options to recover $\mathbf{x}$ if $\mathbf{C}_{\mathbf{z}}$ is allowed to be time-dependent. However, for the considerations of this paper, choosing $\mathbf{C}_{\mathbf{z}}$ to be constant is sufficient. Using the projection defined by the inner product (3), the Koopman lift approximation of the nonlinear system with respect to the basis $\boldsymbol{\Psi}$ is governed by

$$\dot{\hat{\mathbf{z}}} := \begin{pmatrix} \dot{\mathbf{z}} \\ \dot{\mathbf{u}} \end{pmatrix} = \langle \dot{\boldsymbol{\Psi}}, \boldsymbol{\Psi} \rangle \hat{\mathbf{z}} = \begin{pmatrix} \langle \dot{\boldsymbol{\Psi}}_{\mathbf{z}}, \boldsymbol{\Psi}_{\mathbf{z}} \rangle & \langle \dot{\boldsymbol{\Psi}}_{\mathbf{z}}, \mathbf{u} \rangle \\ \langle \dot{\mathbf{u}}, \boldsymbol{\Psi}_{\mathbf{z}} \rangle & \langle \dot{\mathbf{u}}, \mathbf{u} \rangle \end{pmatrix} \begin{pmatrix} \mathbf{z} \\ \mathbf{u} \end{pmatrix} =: \begin{pmatrix} \mathbf{A} & \mathbf{B} \\ * & * \end{pmatrix} \begin{pmatrix} \mathbf{z} \\ \mathbf{u} \end{pmatrix} , \tag{7}$$

where $\mathbf{A} \in \mathbb{C}^{N \times N}$ and $\mathbf{B} \in \mathbb{C}^{N \times (2N_{\mathbf{u}}+1)}$ are constant matrices. The dynamics of $\mathbf{u}$ is approximated by the lower rows of the large matrix in (7). Since $\mathbf{u}$ is state-independent and its time history in (6) is known a priori, the lower rows of (7) are superfluous and the original nonlinear system is approximated by the LTI system $\dot{\mathbf{z}} = \mathbf{A}\mathbf{z} + \mathbf{B}\mathbf{u}$.

Koopman-based Harmonic Balance Method

In the standard Harmonic Balance Method (HBM), a periodic solution is approximated by its Fourier expansion up to order $N_{\mathbf{u}}$ with unknown parameters via

$$\mathbf{x}_p(t) = \sum_{k=-N_{\mathbf{u}}}^{N_{\mathbf{u}}} \mathbf{p}_k e^{ik\omega t} =: \mathbf{P}_{\mathrm{hb}} \mathbf{u} \tag{8}$$

with $\mathbf{u}$ as in (6) and $\mathbf{P}_{\mathrm{hb}} = (\mathbf{p}_{-N_{\mathbf{u}}}, \dots, \mathbf{p}_{N_{\mathbf{u}}})$. The coefficients $\mathbf{p}_k$ are then determined by equating the Fourier expansions of $\frac{\mathrm{d}\mathbf{x}_p}{\mathrm{d}t}$ from the definition (8) and $\mathbf{f}(\mathbf{x}_p, t)$ for every order up to $N_{\mathbf{u}}$. With $(2N_{\mathbf{u}} + 1)$ frequencies considered in total, this results in a system of $n(2N_{\mathbf{u}} + 1)$ equations for the coefficients in $\mathbf{P}_{\mathrm{hb}}$. While the left-hand side of the equation as well as linear components of $\mathbf{f}$ are easy to handle, the nonlinear components can usually not be expressed analytically. The individual equations for each order are thus usually determined and simultaneously solved using the fast Fourier transform with an alternating frequency and time (AFT) scheme for nonlinear components of $\mathbf{f}$ [4]. However, the equations for each order can also be isolated by projecting onto the corresponding basis function from the collection in $\mathbf{u}$ through the inner product (3). Hence, the HBM approximates a periodic solution by solving the $2N_{\mathbf{u}} + 1$ equations collected in

$$\langle \frac{\mathrm{d}\mathbf{x}_p}{\mathrm{d}t}, \mathbf{u} \rangle = \langle \mathbf{f}(\mathbf{x}_p(\cdot), \cdot), \mathbf{u} \rangle . \tag{9}$$

With this notation, it is remarked that the numerically cumbersome task of calculating the Fourier coefficients of the nonlinear components of $\mathbf{f}$ is hidden in the definition of the inner product.

For Koopman-based HBM, again, a periodic orbit with unknown coefficients as in (8) is assumed. Now, the dynamics of a perturbation around this periodic orbit is regarded, i.e. the shifted system with state $\mathbf{y} = \mathbf{x} - \mathbf{x}_p$ is considered. Analogously to the original system, the shifted system can be lifted using the methodology as introduced above. This Koopman lift is of the form (7), with the $\mathbf{A}$ and $\mathbf{B}$ matrices depending on the parameters $\mathbf{p}_k$. Now evaluating only those rows of $\mathbf{z}$ which directly approximate the state $\mathbf{y} \approx \mathbf{C}_{\mathbf{z}}\mathbf{z}$ and using the linearity of the infinitesimal Koopman generator yields

$$\dot{\mathbf{y}}(t) \approx \mathbf{C}_{\mathbf{z}}\dot{\mathbf{z}}(t) = \mathbf{C}_{\mathbf{z}}\mathbf{A}\mathbf{z}(t) + \mathbf{C}_{\mathbf{z}}\mathbf{B}\mathbf{u}(t) = \mathbf{C}_{\mathbf{z}}\mathbf{A}\mathbf{z}(t) + \langle \mathbf{f} - \frac{\mathrm{d}\mathbf{x}_p}{\mathrm{d}t}, \mathbf{u} \rangle \mathbf{u}(t) . \tag{10}$$

As $\mathbf{z} = 0$ implies $\mathbf{y} = 0$ and thus $\mathbf{x} = \mathbf{x}_p$, we have to require that $\dot{\mathbf{y}} = 0$ in this case. As the rows of $\mathbf{u}$ are linearly independent, it follows from (10) that all entries of the inner product, or equivalently of the matrix $\mathbf{B}$, must then be zero. Thus, by comparing (9) and (10), the HBM equations are exactly given by $\mathbf{C}_{\mathbf{z}}\mathbf{B} = \mathbf{0}$ for the Koopman lift as introduced.

Stability Analysis

When a periodic orbit $\mathbf{x}_p$ is found (via HBM or otherwise), the next interesting question is that of its stability properties; that is, whether trajectories that start sufficiently close to the periodic orbit will approach it, stay close to it or tend away from it with increasing time. To evaluate the stability properties, the dynamics of a perturbation $\mathbf{y} = \mathbf{x} - \mathbf{x}_p$ from the periodic solution is considered. Substitution of this definition into the original system yields

$$\dot{\mathbf{y}} = \mathbf{f}(\mathbf{x}_p + \mathbf{y}) - \dot{\mathbf{x}}_p := \mathbf{J}(t)\mathbf{y} + \mathcal{O}(\|\mathbf{y}\|^2) , \tag{11}$$

where $\mathbf{J}(t) = \frac{\partial \mathbf{f}}{\partial \mathbf{x}}\big|_{t,\mathbf{x}_p(t)}$ is the system Jacobian. This system has an equilibrium at zero, which corresponds to the periodic orbit of the original system, and the stability analysis of the periodic orbit reduces to the stability analysis of this equilibrium. To make qualitative (stability/instability) statements around the origin, it is usually sufficient to discard higher-order terms and only regard the linearized time-varying perturbation equation $\dot{\mathbf{y}} = \mathbf{J}(t)\mathbf{y}$. This will be the convention for the remainder of this paper unless stated otherwise.
The fundamental solution matrix $\mathbf{\Phi}(t)$ is the solution to the variational equation

$$\dot{\mathbf{\Phi}}(t) = \mathbf{J}(t)\mathbf{\Phi}(t)\,; \qquad \mathbf{\Phi}(0) = \mathbf{I} \tag{12}$$

and any state can be obtained via $\mathbf{y}(t) = \mathbf{\Phi}(t)\mathbf{y}_0$. In particular, the fundamental solution matrix $\mathbf{\Phi}(T) := \mathbf{\Phi}_T$ is called the monodromy matrix of the system and its eigenvalues $\{\lambda_k\}_{k=1}^n$ are called Floquet multipliers [15]. The Poincaré map $\mathbf{y}_{k+1} = \mathbf{\Phi}_T\mathbf{y}_k$ provides snapshots for the evolution of the perturbation $\mathbf{y}$, spaced at a time distance of T. Therefore, stability analysis of the linear time-periodic system reduces to stability analysis of the Poincaré map. Hence, if all Floquet multipliers are of magnitude strictly less than one, the equilibrium of the LTV system and thus the periodic solution of the original system are stable; if at least one eigenvalue has a magnitude strictly larger than one, they are unstable.
Alternatively to the Floquet multipliers, the stability properties of a time-periodic linear system can be characterized by the Floquet exponents. In the linear system as above there exist n solutions $\mathbf{y}_k(t) = \mathbf{p}_k(t)e^{\alpha_k t}$, where $\mathbf{p}_k$ is T-periodic [15]. Hence, stability is characterized by the real parts of the Floquet exponents $\{\alpha_k\}_{k=1}^n$. If at least one Floquet exponent lies in the open right half plane, i.e. if at least one real part is larger than zero, the equilibrium is unstable. These Floquet exponents are not uniquely defined. It is easy to see that if $\mathbf{p}_k(t), \alpha_k$ generate a solution $\mathbf{y}_k(t)$, the same solution is generated by $\tilde{\alpha}_k = \alpha_k + il\omega$ and $\tilde{\mathbf{p}}_k(t) = \mathbf{p}_k(t)e^{-il\omega t}$ with $l \in \mathbb{Z}$. Hence, in total, there are infinitely many valid Floquet exponents, which can be categorized into n distinct groups. As all entries of one group have the same real part, it is sufficient for stability analysis to know any one entry from each of the n groups.

Hill method

When a periodic orbit is determined using the purely time-domain-based shooting method, the monodromy matrix is a direct byproduct of the continuation method [13]. In this case, the numerically obtained monodromy matrix can be evaluated directly to obtain the Floquet multipliers and their stability information.
When the Harmonic Balance Method is computed in the standard way, however, stability information about the identified limit cycle is unclear without further investigation. The Hill method offers a frequency-domain-based way to approximate the Floquet exponents of the linearized perturbation equation.
The Floquet exponents are eigenvalues of the infinite Hill matrix $\mathbf{H}_\infty$ [8], which is constructed from the Fourier coefficients of $\mathbf{J}(t) = \sum_{k=-\infty}^{\infty} \mathbf{J}_k e^{i\omega k t}$ and reads as

$$\mathbf{H}_\infty = \begin{pmatrix} \ddots & \vdots & \vdots & \vdots & \iddots \\ \dots & \mathbf{J}_0 + i\omega\mathbf{I} & \mathbf{J}_{-1} & \mathbf{J}_{-2} & \dots \\ \dots & \mathbf{J}_1 & \mathbf{J}_0 & \mathbf{J}_{-1} & \dots \\ \dots & \mathbf{J}_2 & \mathbf{J}_1 & \mathbf{J}_0 - i\omega\mathbf{I} & \dots \\ \iddots & \vdots & \vdots & \vdots & \ddots \end{pmatrix}. \tag{13}$$

This infinite-dimensional eigenproblem has infinitely many discrete eigenvalues. They correspond identically to the Floquet exponents $\tilde{\alpha}$ for all $l \in \mathbb{Z}$ as introduced above and can be sorted into n groups, where the entries of each group differ by multiples of $i\omega$ [12]. However, in practice, only the eigenvalues of a finite-dimensional matrix approximation of $\mathbf{H}_\infty$ can be computed numerically. The matrix

$$\mathbf{H} = \begin{pmatrix} \mathbf{J}_0 + iN\omega\mathbf{I} & \mathbf{J}_{-1} & \dots & \mathbf{J}_{-2N} \\ \mathbf{J}_1 & \mathbf{J}_0 + i(N-1)\omega\mathbf{I} & \dots & \mathbf{J}_{-2N+1} \\ \vdots & \vdots & \ddots & \vdots \\ \mathbf{J}_{2N} & \mathbf{J}_{2N-1} & \dots & \mathbf{J}_0 - iN\omega\mathbf{I} \end{pmatrix} \tag{14}$$

of size $N \times N$ (recall $N = n(2N_\mathbf{u} + 1)$) consists of the N most centered rows and columns of $\mathbf{H}_\infty$ and approximates the original infinite-dimensional matrix. In the absence of truncation error, the eigenvalues of $\mathbf{H}$ are some subset of the eigenvalues of $\mathbf{H}_\infty$, i.e. the Floquet exponents. Due to the inevitable error which generally comes with truncation, however, this does not quite hold. The N eigenvalues of $\mathbf{H}$ will be called Floquet exponent candidates below.
The matrix $\mathbf{H}$ has a block Toeplitz structure and for sufficiently large $N_\mathbf{u}$, the bands near the diagonal dominate as the Fourier coefficients of $\mathbf{J}$ tend to zero for $N_\mathbf{u}$ large enough. Loosely speaking, this means that some eigenvalues affiliated most with the central rows of $\mathbf{H}$ are less impacted by the truncation and provide a better approximation to the Floquet exponents than others. The search for a selection criterion which determines the best approximation to the Floquet exponents from the Floquet candidates has received much attention in the literature [5, 16, 8, 12].
For sufficiently large $N_\mathbf{u}$, it is proven that the candidates with lowest imaginary part in modulus converge to the true Floquet exponents [16]. An alternative criterion selects those candidates whose eigenvectors are most symmetric [8, 6], as

they should correspond most to the middle rows of the block Toeplitz matrix $\mathbf{H}$. Even though there currently is no formal convergence proof for this symmetry-based sorting method, numerical results indicate faster convergence than with the aforementioned eigenvalue criterion [1].
For both these criteria, all eigenpairs of the large matrix have to be computed first and then most of them are discarded. As the cost of solving an eigenvalue problem is of the order $\mathcal{O}(N^3)$, the computational cost of the approach is usually dominated by determining the eigendecomposition of a large matrix.

Koopman-based Hill method
Consider again the lifted perturbation dynamics (10) around a periodic solution. As explained above, for a periodic solution, the matrix $\mathbf{B}$ should vanish and the autonomous system $\dot{\mathbf{z}} = \mathbf{A}\mathbf{z}$ remains. After the coefficients $\mathbf{p}_k$ of the periodic solution are substituted into $\mathbf{A}$, it is a matrix with purely numerical entries. Let $\mathbf{C}_\mathrm{H}$ denote the real selection matrix sorting all terms in $\mathbf{\Psi_z}$ which are linear in $\mathbf{x}$ such that

$$\mathbf{C}_\mathrm{H}\mathbf{\Psi_z}(\mathbf{y},t) = \left(\mathbf{y}^\mathrm{T}e^{iN\omega t}, \mathbf{y}^\mathrm{T}e^{i(N-1)\omega t}, \dots, \mathbf{y}^\mathrm{T}e^{-iN\omega t}\right)^\mathrm{T} . \tag{15}$$

Entries in $\mathbf{C}_\mathrm{H}\mathbf{\Psi_z}$ are of the form $\mathbf{y}e^{-ik\omega t}$ and are sorted by ascending k ranging from $-N$ to N. Note that $\frac{\partial(\mathbf{C_H\Psi_z})}{\partial t} = \mathbf{\Omega C_H \Psi_z}$ with $\mathbf{\Omega} = \mathrm{diag}\,(iN\omega, i(N-1)\omega, \dots, -iN\omega)$. The matrix $\mathbf{C}_\mathrm{H}\mathbf{A}\mathbf{C}_\mathrm{H}^\mathrm{T}$ can be rearranged using the definition (7). After block-wise differentiation of $\mathbf{C}_\mathrm{H}\mathbf{\Psi_z}$, the Jacobian $\mathbf{J}$ is expressed by its Fourier expansion. Finally, after identifying terms corresponding to $(\mathbf{C}_\mathrm{H}\mathbf{\Psi_z})$ in the first argument of the inner product, it follows that

$$\mathbf{C}_\mathrm{H}\mathbf{A}\mathbf{C}_\mathrm{H}^\mathrm{T} = \left\langle \frac{\mathrm{d}\,(\mathbf{C}_\mathrm{H}\mathbf{\Psi_z})}{\mathrm{d}t}\mathbf{C}_\mathrm{H}^\mathrm{T}, \mathbf{\Psi_z} \right\rangle = \left\langle \left(\frac{\partial \mathbf{C}_\mathrm{H}\mathbf{\Psi_z}}{\partial \mathbf{y}}\mathbf{J}\mathbf{y} + \frac{\partial \mathbf{C}_\mathrm{H}\mathbf{\Psi_z}}{\partial t} \right), \mathbf{C}_\mathrm{H}\mathbf{\Psi_z} \right\rangle = \mathbf{H} . \tag{16}$$

Thus, all stability information obtained for a time-periodic system by the Hill method is also contained in the Koopman lift of the system. In particular, if $\mathbf{\Psi_z}$ only contains terms that are linear in $\mathbf{x}$ and not of higher polynomial orders, then $\mathbf{C_H}$ is quadratic and orthogonal. This makes (16) a similarity transform and it can be concluded that the eigenvalues of $\mathbf{A}$ are identical to those of $\mathbf{H}$, i.e. the Floquet candidates.

Examples

Two variants of the Hill equation $\ddot{x} + g(t)x = 0$ with $g(x)$ being 2π-periodic are used to exemplify and illustrate the properties discussed above. First, the Koopman lift for the scalar Mathieu equation with $g(t) = a + 2b\cos(2\omega t)$ is provided explicitly for the lowest possible $N_\mathbf{u}$ as an example for the structure both in the $\mathbf{A}$ and the $\mathbf{B}$ matrix. The stability properties of the Mathieu equation are then investigated using both a HBM variant and the Floquet exponents retrieved from the Koopman lift. Finally, a more complicated expression for g is analyzed to illustrate the impact of the choice of $N_\mathbf{u}$.

Mathieu equation
As an example, consider the scalar Mathieu equation $\ddot{x} + (a + 2b\cos(2t))x = 0$. In the (a,b)-space, regions of stability and instability are separated by branches of nontrivial periodic solutions [9], which are visualized in a so-called Ince-Strutt diagram.
For treatment in the Koopman framework, the system is brought to first-order form with $\mathbf{x} = (x, \dot{x})^\mathrm{T}$. The first-order dynamics is then of the form

$$\dot{\mathbf{x}} = \mathbf{J}(t)\mathbf{x} = \begin{pmatrix} 0 & 1 \\ -a - 2b\cos(2t) & 0 \end{pmatrix}\mathbf{x} = \left[\begin{pmatrix} 0 & 1 \\ -a & 0 \end{pmatrix} + \begin{pmatrix} 0 & 0 \\ -b & 0 \end{pmatrix}\left(e^{i\omega t} + e^{-i\omega t}\right) \right]\mathbf{x} . \tag{17}$$

The Fourier decomposition of $\mathbf{J}(t)$ can be read directly from (17). Assume a periodic solution $\mathbf{x}_p = \mathbf{x} - \mathbf{P}_\mathrm{hb}\mathbf{u}$ with $\mathbf{u}$ as in (6) and $\mathbf{P}_\mathrm{hb}$ collecting the $\mathbf{p}_k$ from HBM column-wise. Choose a vector of basis observables $\mathbf{\Psi_z}$ which only contains terms linear in $\mathbf{x}$. For readability of the result, assume that $\mathbf{\Psi_z}$ is already sorted as in (15). Hence, in this case, $\mathbf{C}_\mathrm{H}$ is the identity matrix. The selection matrix $\mathbf{C_z}$ is of the form

$$\mathbf{C_z} = \begin{pmatrix} 0 & \dots & 0 & 1 & 0 & 0 & \dots & 0 \\ 0 & \dots & 0 & 0 & 1 & 0 & \dots & 0 \end{pmatrix} \tag{18}$$

with a 2×2 identity matrix in the middle, surrounded by blocks of zeros with $2N_\mathbf{u}$ columns each. Performing the Koopman lift (7) on $\mathbf{y} = \mathbf{x} - \mathbf{x}_p$ yields for $N_\mathbf{u} = 1$ the linear time-invariant system

$$\dot{\mathbf{y}} \approx \mathbf{C_z}(\mathbf{A}\mathbf{z} + \mathbf{B}\mathbf{u}) = \mathbf{C_z}\begin{pmatrix} i\omega & 1 & 0 & 0 & 0 & 0 \\ -a & i\omega & 0 & 0 & -b & 0 \\ 0 & 0 & 0 & 1 & 0 & 0 \\ 0 & 0 & -a & 0 & 0 & 0 \\ 0 & 0 & 0 & 0 & -i\omega & 1 \\ -b & 0 & 0 & 0 & -a & -i\omega \end{pmatrix}\mathbf{z} + \left[\mathbf{A}_{3:4}\begin{pmatrix} \mathbf{p}_{-1} \\ \mathbf{p}_0 \\ \mathbf{p}_1 \end{pmatrix} \; \mathbf{A}_{5:6}\begin{pmatrix} \mathbf{p}_{-1} \\ \mathbf{p}_0 \\ \mathbf{p}_1 \end{pmatrix} \; \mathbf{A}_{1:2}\begin{pmatrix} \mathbf{p}_{-1} \\ \mathbf{p}_0 \\ \mathbf{p}_1 \end{pmatrix} \right]\mathbf{u}, \tag{19}$$

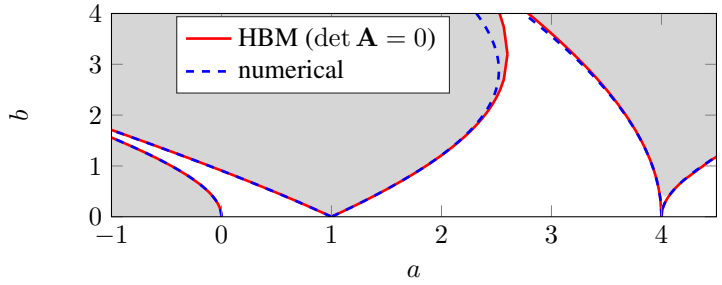

Figure 2: Ince-Strutt diagram for the Mathieu equation. Stable (unstable) regions determined by Koopman-based Hill method of order 4 in white (gray). Transition curves, i.e. parameter combinations which admit nontrivial periodic solutions, determined by Koopman-based HBM (solid red) and numerically using a shooting procedure (dashed blue).

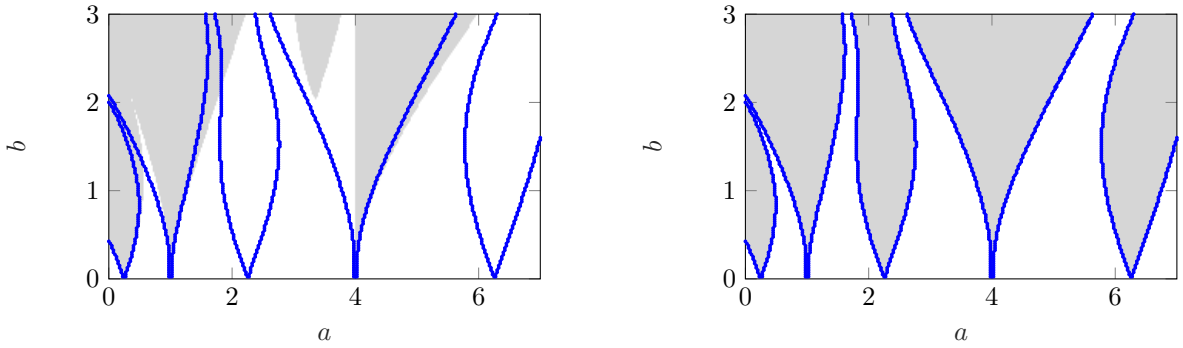

(a) $N_{\mathbf{u}} = 2$ (b) $N_{\mathbf{u}} = 10$

Figure 3: Stability charts for the more complicated Hill's equation (20). Stable (unstable) regions determined by Koopman-based Hill method in white (gray). Transition curves determined by direct numerical integration of the variational equation (12) in blue.

where $\mathbf{A}_{i:j}$ denotes the i-th to j-th rows of $\mathbf{A}$. Hence, all rows of $\mathbf{A}$ reoccur in $\mathbf{C_z B}$. The entries in $\mathbf{A}$ do not depend on $\mathbf{p}_k$ in this special case. This is because the original dynamics of the Mathieu equation is linear in the state. As the linear time-varying system has an equilibrium at $\mathbf{x} = \mathbf{0}$, the HBM equations coded in $\mathbf{C_z B}$ are a homogeneous linear equation system for the parameters $\mathbf{p}_k$. The system only has nontrivial periodic solutions on the stability boundary curves. If the dynamical system has a nontrivial periodic solution, then the linear equation system resulting from HBM must have one as well. This means that the determinant of this linear equation system, or equivalently that of $\mathbf{A}$, must vanish. This is an approximate algebraic condition for the transition curves which separate stable and unstable regions in the Ince-Strutt diagram based on the HBM using the Koopman lift of the system.
In the $\mathbf{A}$ matrix, the 2×2 block Toeplitz structure of (14) is clearly visible. With the Hill method, this can also be used to approximate the stability regions using the Floquet candidates found as eigenvalues of $\mathbf{A}$. Here, the eigenvalues of $\mathbf{A}$ with lowest imaginary part in modulus were used as Floquet exponent approximations. For the case $N_{\mathbf{u}} = 4$, the stability regions and transition curves found by the Koopman-based HBM and Koopman-based Hill method are pictured in Figure 2. In the white regions, the two eigenvalues of $\mathbf{A}$ with imaginary part closest to zero both have a real part of zero, while in the gray regions, one has a real part larger than zero and the other has a real part smaller than zero. A comparison with numerically obtained transition curves using a shooting procedure based on [9] shows good approximation quality for the first instability tongues already for small $N_{\mathbf{u}}$.
Below, we consider the more complicated Hill's equation

$$g(t) = a + b(\sin(t) + \sin(8t) + \cos(5t) + \cos(3t)) \; . \tag{20}$$

In contrast to the previous Mathieu equation, higher frequencies are part of the dynamics. This means that the matrix $\mathbf{A}$ of the Koopman lift (or, equivalently, the $\mathbf{H}$ matrix of the Hill method) exhibits a diagonal band structure only if $N_{\mathbf{u}}$ is chosen larger than before. Additionally, block symmetry in $\mathbf{A}$ is lost. As expected it is visible in Figures 3a and 3b that low orders of $N_{\mathbf{u}}$ are now not sufficient to capture the dynamics. Higher orders of $N_{\mathbf{u}}$, however, do capture the stability regions accurately.

Conclusion

In the Koopman framework, the choice of observables plays a crucial role for the accuracy of the final finite-dimensional Koopman lift. In this work, the connection between a specific choice of Koopman observables based on Taylor as well

as Fourier monomials and established frequency domain tools for the analysis of time-periodic nonlinear systems is highlighted. This connection motivates the use of this type of observables in a Koopman-based setting and provides some legitimization. In further research, this connection could be utilized to carry over structural insights from the original nonlinear system into its frequency representation.

References

[1] B. Bentvelsen and A. Lazarus. Modal and stability analysis of structures in periodic elastic states: application to the Ziegler column. *Nonlinear Dynamics*, 91(2):1349–1370, 2018.

[2] D. Bruder, X. Fu, R. B. Gillespie, C. D. Remy, and R. Vasudevan. Data-driven control of soft robots using Koopman operator theory. *IEEE Transactions on Robotics*, 37(3):948–961, 2021.

[3] M. Budišić, R. Mohr, and I. Mezić. Applied Koopmanism. *Chaos: An Interdisciplinary Journal of Nonlinear Science*, 22(4):047510, 2012.

[4] T. M. Cameron and J. H. Griffin. An alternating frequency/time domain method for calculating the steady-state response of nonlinear dynamic systems. *J. Appl. Mech*, 56(1):149–154, 1989.

[5] T. Detroux, L. Renson, L. Masset, and G. Kerschen. The harmonic balance method for bifurcation analysis of large-scale nonlinear mechanical systems. *Computer Methods in Applied Mechanics and Engineering*, 296:18–38, 2015.

[6] L. Guillot, A. Lazarus, O. Thomas, C. Vergez, and B. Cochelin. A purely frequency based Floquet-Hill formulation for the efficient stability computation of periodic solutions of ordinary differential systems. *Journal of Computational Physics*, 416:109477, 2020.

[7] M. Korda and I. Mezić. On convergence of extended dynamic mode decomposition to the Koopman operator. *Journal of Nonlinear Science*, 28(2):687–710, 2018.

[8] A. Lazarus and O. Thomas. A harmonic-based method for computing the stability of periodic solutions of dynamical systems. *Comptes Rendus Mécanique*, 338(9):510–517, 2010.

[9] R. I. Leine. Non-smooth stability analysis of the parametrically excited impact oscillator. *International Journal of Non-Linear Mechanics*, 47(9):1020–1032, 2012.

[10] A. Mauroy, Y. Susuki, and I. Mezić. Introduction to the Koopman operator in dynamical systems and control theory. In *The Koopman Operator in Systems and Control. Concepts, Methodologies and Applications*, pages 3–33. Cham: Springer, 2020.

[11] I. Mezic. On applications of the spectral theory of the Koopman operator in dynamical systems and control theory. In *54th IEEE Conference on Decision and Control, CDC 2015, Osaka, Japan, December 15-18, 2015*, pages 7034–7041. IEEE, 2015.

[12] G. Moore. Floquet theory as a computational tool. *SIAM Journal on Numerical Analysis*, 42(6):2522–2568, 2005.

[13] M. Peeters, R. Viguié, G. Sérandour, G. Kerschen, and J.-C. Golinval. Nonlinear normal modes, Part II: Toward a practical computation using numerical continuation techniques. *Mechanical Systems and Signal Processing*, 23(1):195–216, 2009.

[14] M. Reed and B. Simon. *Functional Analysis*. Number 1 in Methods of Modern Mathematical Physics. Academic Press, revised and enlarged edition, 1980.

[15] G. Teschl. *Ordinary Differential Equations and Dynamical Systems*. Number 140 in Graduate Studies in Mathematics. American Mathematical Society, Providence, Rhode Island, 2012.

[16] J. Zhou, T. Hagiwara, and M. Araki. Spectral characteristics and eigenvalues computation of the harmonic state operators in continuous-time periodic systems. *Systems & Control Letters*, 53(2):141–155, 2004.

An extreme time-periodic oscillator.

Alvaro Anzoleaga Grandi*, Suzie Protière* and Arnaud Lazarus*
* *Institut Jean Le Rond ∂' Alembert, CNRS UMR7190, Sorbonne Université Paris, France*

Summary. Parametric instabilities are dynamical instabilities possibly arising when the mechanical state of a structure is periodically modulated in time. It is sometimes seen as a phenomenon to avoid for example with sailing ships (parametric rolling) but it can also be exploited to study vibrating fluids (Faraday waves [1]) or Nano-Electro- Mechanical Systems [2]. One well-known limitation in fully exploiting classic parametric instabilities based on small periodic modulation of a mechanical state is that inherent friction forces rapidly cancel sub harmonic parametric resonances. To overcome this drawback, we propose to "extremely" modulate the mechanical state of the system in order to enhance parametric instabilities and therefore allow for new promising dynamic functionalities. This original way of enhancing and controlling parametric instabilities is illustrated here through the numerical and experimental implementation of an electromagnetic pendulum. We find that it is possible to greatly enhance the number of sub harmonic instability regions and also that the width of these regions can be controlled.

Keywords : Parametric instabilities, structural vibrations, experimental vibrations, Meissner Equation, Floquet theory.

Experimental system under study

Our goal is to periodically vary a mechanical system between two very different states in order to enhance parametric instabilities, even in the presence of classic internal friction forces. For illustrative purposes, we set up in the lab the proof of concept shown in Fig.1a). The experiment consists of a magnetic pendulum that is symmetrically placed between two attracting electromagnets. When the electromagnets are off, the system is a simple pendulum characterized by a natural frequency $\omega_0 \approx 9$ rad/s as illustrated in the experimental plot of Fig.1c). When turning the electromagnets on through an electrical current I, the state of the pendulum can be drastically modified. In our example of Fig.1, when the control parameter I is slightly below I_{max}, our system is naturally oscillating with a slower natural frequency. Above $I = I_{max}$, our system is no more oscillating but diverging: attracted to the right or left electromagnet depending on the imperfections in our experiment. This mechanical system is therefore a simple first realization of what we coined an *extreme parametric oscillator*: with a single parameter, in this case I, we are drastically and easily changing the state of our system. In classical parametric oscillators, this extreme modulation is hardly reachable because the geometrical mechanical modulation parameters that come into play (the length of the pendulum or the effective gravity for example) are not easily varied on such scales [1][2].

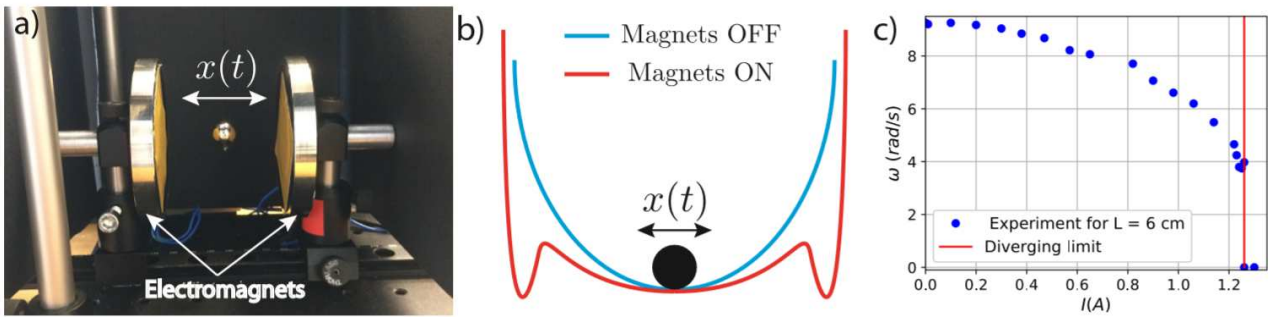

Figure 1: The electromagnetic parametric oscillator under study. a) A pendulum whose mass is made of steel, is symmetrically placed between two identical attracting electromagnets that are periodically turned on (red energy states in b)) and off (blue energy states in b)). b) Simplified "Particle in a time-varying potential well" model. c) Evolution of the natural frequency of the pendulum for various value of the electrical current I in the two electromagnets when the laters are separated by $L = 6$ cm. Below $I < I_{max}$, the pendulum is naturally oscillating if perturbed. Eventually, for I close to the diverging limit I_{max} , the natural frequency goes down. Above I_{max} the mass is no more oscillating but diverging.

To investigate the dynamic behavior of our extreme parametric oscillator, we periodically turn the electromagnets on or off with a period T, in a square wave fashion making the system modulate bewteen two states (see Fig.2a)). Fig.2b) represents the experimental stability diagram of the pendulum in the modulation parameter space (T, I). For some (T, I), the system is dynamically stable (blue triangles), i.e. the pendulum is slightly vibrating (because of small imperfections) but stays close to the trivial vertical state. The crosses indicate the modulation parameters for which the mass was parametrically unstable, i.e. dynamically impacting the electromagnets. The color legend indicates the number of cycles the pendulum is doing in the emerging nonlinear vibrational regime. Modes with an integer number of M represent T-periodic unstable regions when the other M numbers represent $2T$ unstable regions. At relative low modulation amplitude, $I < 1$ A, the pendulum is often stable, except eventually for the first or second parametric instability regions. For "extreme" modulation amplitude such as $I \approx I_{max}$, it is possible to trigger highly sub-harmonic instability regions, here up to the 58th instability region ($M = 29$) when the current record demonstrated in a micro electromechanical device is found to be the 28th instability region [2].

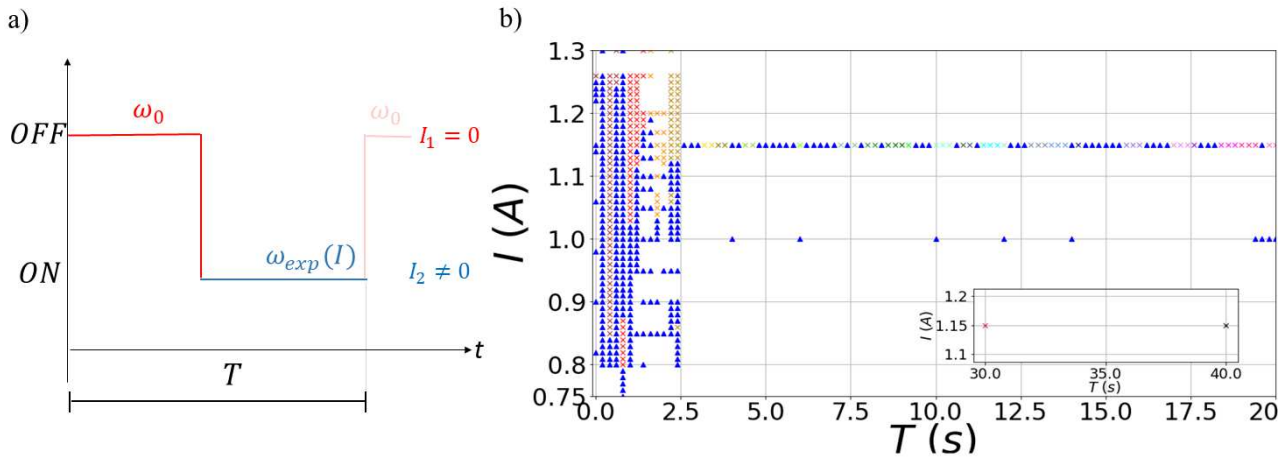

Figure 2: a) The electromagnets are turned on and off in a square wave fashion with period T. The amplitude of modulation is the electrical current I when the electromagnets are on. b) Experimental stability chart of the pendulum in the modulation parameter space (T, I). Blue triangles represent stable states where the mass stays close to the middle of the electromagnets. Crosses represent unstable states where the pendulum dynamically diverges and eventually impact the electromagnets.

Model of an extreme time-periodic oscillator

The aforementioned experimental mechanical system can be seen as a non-damped pendulum that oscillates periodically between a natural frequency ω_0 and ω_{exp} following a square wave function. Based on the theoretical study of the Meissner equation[3] a linear theoretical model for the stability of the vertical pendum can be obtained:

$$\ddot{\theta}(\tau) + \left(\alpha^2 + \beta^2 sgn(cos(\tau))\right)\theta(\tau) = 0 \tag{1}$$

with α^2 and β^2 two dimensionless parameters. Fig.3 represents the stability of Fig.2b) represented in the analytical space (α^2, β^2). With this experimental setup we are able to observe extreme periodic instability for the first time (large values for α^2 and β^2). For small values of α^2 and β^2 the model represents correctly the evolution of the experimental system. The alternation between stable and unstable analytical regions shows a good agreement with those found experimentally. In conclusion it is possible to trigger extreme parametric oscillations experimentally and to develop a corresponding linear theoretical model. This new approach could be promising for very large-band energy harvesting devices.

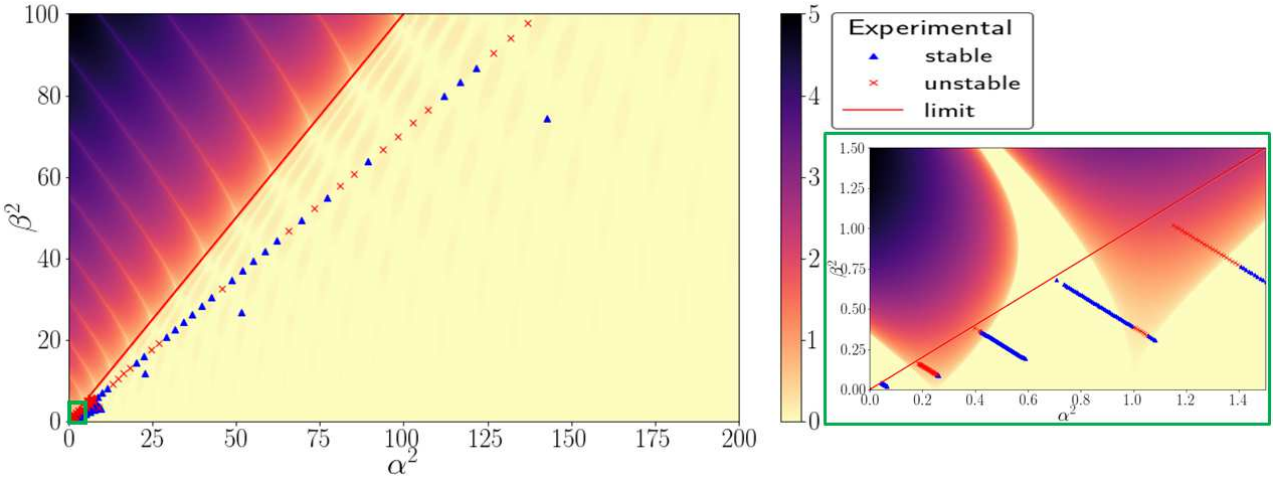

Figure 3: Analytical stability chart with experimental results presenting several instability regions. The numerical results represent the evolution of the real part of the Floquet exponent of equation (1) [4]. If it is equal to zero than the movement of the system is stable. Values larger than zero mean the solution of the system increases exponentially so the system is unstable. The blue triangles correspond to the experimental stable states and the red crosses correspond to the unstable ones. The red curve ($\alpha^2 = \beta^2$) represents the limit between systems that are naturally stable and systems naturally unstable (over the limit).

References

[1] S. Douady (1990) Experimental study of the Faraday instability *J. Fluid Mech* ,Vol 221, pp383-409.

[2] Y. Jia, S. Du and A.A. Seshia (2016) Twenty-Eight Orders of Parametric Resonance in a Microelectromechanical Device for Multi-band Vibration Energy Harvesting. *Scientific Reports* Vol 6, 30167.

[3] Chikara Sato (2015) Correction of Stability Curves in Hill-Meissner's Equation. *International Centre for Mechanical Sciences* Vol 562.

[4] Sébastien Neukirch, Arnaud Lazarus and Corrado Maurini (2015) Stablility of discretized nonlinear elastic systems. *International Centre for Mechanical Sciences* Vol 562.

Asymptotic description of the wear process in dry-running reciprocating compressors

Richard Jurisits*, Andreas Kaufmann†, Matthias Kornfeld† and Thomas Antretter‡
*University of Applied Sciences Vienna, Vienna, Austria
†HOERBIGER Wien GmbH, Vienna, Austria
‡Institute of Mechanics, Montanuniversitaet Leoben, Leoben, Austria

Summary. The dynamics of sealing elements within a reciprocating compressor is considered in a 2D model as described in [1]. Linear elastic effects of the sealing ring, periodically changing gas pressure loads driven by the external piston movement and dry wear at the moving contact surface between the ring and the piston rod are explicitly included. Two governing equations for the dynamical quantities of interest are specified, together with three small, non-dimensional parameters characterizing the problem. Following [3], an asymptotic analysis is sketched, involving two time scales, where rapid changes due to the compression cycle as well as slow changes due to wear are considered.

Introduction

We consider the dynamics of sealing elements typically used in industrial reciprocating compressors or pumps. So called packing elements seal the higher gas pressure in the compression chamber against the lower ambient pressure. These elements consist of one or more packing rings held in so called cups within a packing housing. The ring seals the gas pressure dropping from P_1 on the cylinder side to P_2 on the crank side by being pressed against the facing side of the cup on the right and to the moving rod below, see Figure 1, taken from [1]. Depending on the sealing efficiency, there is an (undesired) gas flow from left to right.

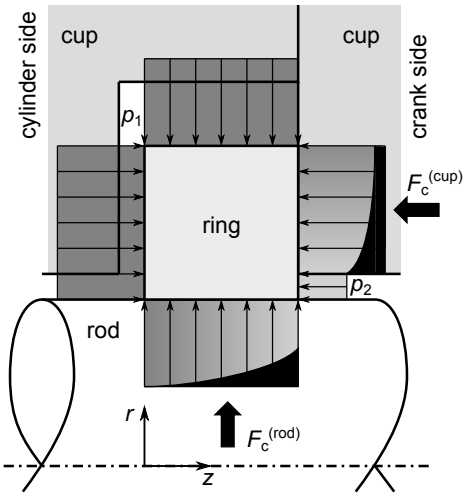

Figure 1: Gas pressure and contact forces acting on a sealing ring, taken from [1].

The rod is connected to a piston in the compression chamber and moves periodically in horizontal direction, driven externally by a motor running at a fixed frequency, creating a desired delivery pressure. This gives rise to a periodically changing pressure P_1 in the cup. Due to the dynamic contact between ring and rod, the process is subject to dry wear leading to material loss on the inner side of the ring.

Problem formulation and model

We completely adapt the analytical axisymmetric 2D model for the sealing ring from [1], see Figure 1. The ring material is described by Hooke's law and is assumed to be in a state of plane strain. Stresses and strains are functions of the radial coordinate r only. The contact force from the rod is uniformly distributed in (axial) z-direction, giving rise to a contact pressure P_c, and a ring wear that does not depend on z. In contrast to [1], we assume a periodically changing pressure P_1 on the upper side of the ring and a periodically moving rod on the lower side. Gas pressure effects over the contact surface, friction forces and inertial effects are ignored. Depending upon the contact pressure P_c, ring material is worn away over a large time compared to the compression period length. Archard's wear law is used to describe the wear process, where the long term wear rate and the course of the contact pressure P_c are the quantitites of interest.
Due to the wear process the inner radius $R^{(i)}$ of the ring grows, and so does the displacement $u^{(i)}$ in radial direction as to fulfill the contact condition $R^{(i)} + u^{(i)} = D/2$ with D being the rod diameter. Combined with Archard's law, a governing equation for $R^{(i)}$ as a function of time may be derived, where the gas pressure P_1 is acting as an external excitation.

Asymptotic description

Writing down the equations in non-dimensional form, one can identify two small, non-dimensional parameters governing the problem:

$$\varepsilon := \frac{KV_0P_D}{(D/2)\omega}, \quad \delta := \frac{P_D}{E}. \tag{1}$$

K is the wear coefficient from Archard's law, V_0 is a reference velocity (amplitude) of the rod movement, the discharge pressure P_D is serving as a reference pressure, ω is the angular frequency of the piston movement, and E is Young's modulus of the ring material.According to [1], for practical cases the relationship $\varepsilon = \mathcal{O}(\delta)$ is valid, i.e. ε being much smaller than δ.
Asymptotic investigations of the problem were already performed in [3], where the parameter ε (though defined slightly different) was identified. In [3], a somewhat idealized physical situation was investigated and analyzed by the method of multiple scales.
Introducing the non-dimensional quantity $\rho := R^{(o)}/R^{(i)}$ being the quotient of the constant outer ring radius $R^{(o)}$ to the time-dependent inner ring radius $R^{(i)}$, the following governing equation may be derived:

$$\frac{\mathrm{d}\rho}{\mathrm{d}t} = -\varepsilon \frac{\dot{p}_1 p_c \rho}{1 + \delta\, r_o \frac{\rho}{1-\rho^2}(p_c - p_1)}. \tag{2}$$

Here t is the dimensionless time, p_1 is the dimensionless gas pressure, p_c the dimensionless contact pressure, and r_o the dimensionless outer ring radius. The gas pressure in equation (2) may be considered as a given periodic excitation function with the (constant) frequency of the piston movement. Equation (2) is supplemented by a non-linear, algebraic equation resulting from the contact condition between ring and rod, involving the dynamical quantities ρ and p_c. Thereby, the quantity ρ is directly related to the wear rate.
The parameter δ expresses the relative size of the involved gas pressures compared to the material stiffness of the ring, being of the order of 10^{-2} in practical situations. The much smaller parameter ε characterizes the wear process taking place on a much slower timescale compared to the dynamics arising from the compression cycle. We address to tackle the problem by performing a coupled asymptotic expansion of the equations with respect to ε and δ, taking into account that $\varepsilon = \mathcal{O}(\delta)$. In in analogy to [3], we introduce two timescales t and εt to seek for a solution within a multiple scales analysis.

Summary and conclusions

We considered the dynamics of a sealing element within a reciprocating compressor, being subject to dry wear on the moving contact between sealing ring and piston rod. Based upon previous works [1]-[3], we have specified two governing equations for the dynamical quantities ρ (a dimensionless inverse inner ring radius) and the dimensionless contact pressure p_c. These quantities are affected by rapid changes due to the piston movement and slow changes due to the wear process. A small parameter ε distinguishes between the two time scales and may serve as an asymptotic parameter for a calculation of perturbations to solve the governing equations.

References

[1] A. Kaufmann, T. Lindner-Silwester, T. Antretter (2018) Modeling Dry Wear of Piston Rod Sealing Elements of Reciprocating Compressors Considering Gas Pressure Drop Across the Dynamic Sealing Surface. *J. Tribol.* **140(4)**:042201.

[2] Fritz, B. (2019) Development of a comprehensive cylinder lubrication model for reciprocating piston compressors to minimise oil consumption. *PhD Thesis*, Faculty of Mechanical and Industrial Engineering, University of Technology Vienna.

[3] A. Kaufmann, M. Kornfeld (HOERBIGER Wien GmbH), T. Antretter (Montanuniversitaet Leoben), A novel concept for the efficient analysis of high cycle dry wear using asymptotic expansion, unpublished manuscript

Attractor Targeting by Dual-frequency Driving

Ferenc Hegedűs*, Péter Krähling*, Marcel Aron†, Werner Lauterborn‡, Robert Mettin‡ and Ulrich Parlitz†

*Department of Hydrodynamic Systems, Faculty of Mechanical Engineering, Budapest University of Technology and Economics, Budapest, Hungary

†Research Group Biomedical Physics, Max Planck Institute for Dynamics and Self-Organization and Institut für Dynamik komplexer Systeme, Georg-August-Universität Göttingen, Göttingen, Germany

‡Drittes Physikalisches Institut, Georg-August-Universität Göttingen, Göttingen, Germany

Summary. A control technique to continuously drive a non-linear, harmonically excited oscillator between different kinds of periodic orbits is presented. The basis of the method is a temporary dual-frequency driving of the system. Results show that two periodic orbits existing at two different frequency values (single frequency driving) having arbitrary periodicity can be smoothly transformed into each other. The method is a proper tuning of the excitation amplitudes of a dual-frequency driving combining the two corresponding frequencies. The requirements are the suitable choice of the frequency pair and the matching of the torsion numbers of the bounding bifurcation points of the periodic orbits.

Introduction

In non-linear systems, multiple domains of periodic attractors might exist in a given parameter space [1]. These domains can overlap each other meaning that at their union, the system is even multi-stable [2]. The different stable solutions usually represent different system performances; for instance, a chemical reactor can have different chemical yield. Thus, it is important to be able to drive a system onto a desired stable state in its parameter space. The main aim of this study is to propose a technique that is suitable to smoothly drive a system from one periodic domain to another.

The method works for harmonically driven non-linear oscillators in the parameter plane of its driving amplitude A_1 and frequency ω_1. The technique is based on the addition of a second harmonic component to the driving with amplitude A_2 and frequency ω_2. With a proper tuning of the driving amplitudes, a periodic attractor exists at ω_1 with $A_2 = 0$ can be smoothly transformed onto another periodic orbit exists at ω_2 with $A_1 = 0$. That is, the beginning and the end of the transformation is a single frequency driven system, and the intermediate states have dual-frequency driving. Throughout the rest of the paper, the requirements of the transformation possibilities are discussed in general; and an example is presented based on the Keller–Miksis equation that is a second order ordinary differential equation describing the radial pulsation of a single spherical bubble [3].

The control technique

For simplicity, let us consider dual-frequency driven second order non-linear oscillators written as

$$\dot{x}_1 = f(x_1, x_2), \tag{1}$$

$$\dot{x}_2 = g(x_1, x_2) + A_1 \cos \omega_1 t + A_2 \cos \omega_2 t. \tag{2}$$

Assume that at fixed frequency ω_1, there is a domain (section) of periodic solution with period p_1 in the A_1 parameter line (the amplitude of the second component is $A_2 = 0$). Similarly, assume that there is another segment of periodic solution with period p_2 in the A_2 parameter line ($A_1 = 0$) at frequency value ω_2 different from ω_1. Both periodic segments are bounded by bifurcation points having torsion numbers q [4]. The schematic draw in Fig. 1A demonstrates such an example in the parameter plane of the excitation amplitudes A_1 and A_2. There are two requirements for the existence of a set of solutions that connects the two segments of these periodic orbits (blue and red lines in Fig. 1A). Without a detailed derivation, the first condition is that the ratio of the periods and ratio of the employed frequencies must be equal:

$$\frac{p_1}{p_2} = \frac{\omega_1}{\omega_2}. \tag{3}$$

It must be stressed that periods of the obits p_1 and p_2 are defined according to the period of the single frequency excitation $T_1 = 2\pi/\omega_1$ and $T_2 = 2\pi/\omega_2$, respectively. If the condition given by Eq. (3) holds, the periods of the two kinds of orbits presented in Fig. 1A by the blue and red lines become equal via employing the period of the dual-frequency driving T as a global Poincaré section. In this case, codimension-2 bifurcation curves might exists that connect the bifurcation point pairs (q_{11}, q_{21}) and (q_{12}, q_{22}) (see the black curves in Fig. 1A). For such an existence, the connected torsion numbers must be equal representing topologically the same local flow of the vector field along the black codimension-2 curves:

$$q_{11} = q_{21}, \tag{4}$$

$$q_{12} = q_{22}. \tag{5}$$

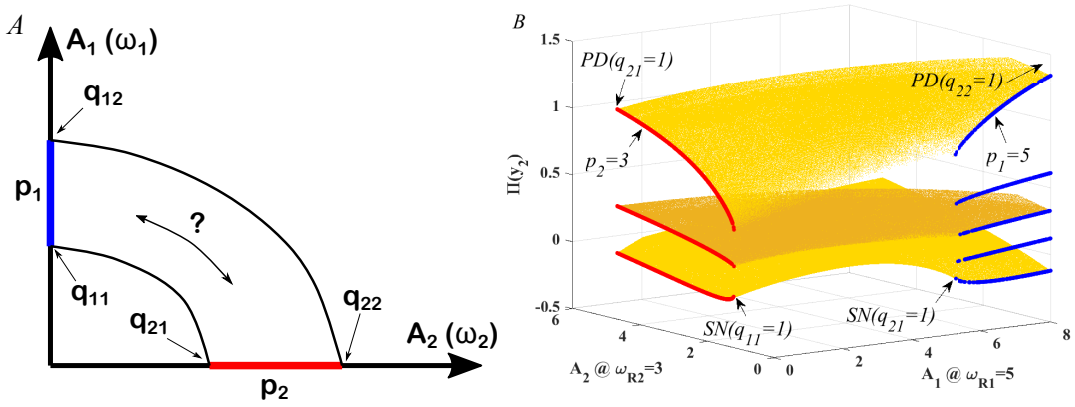

Figure 1: Panel A: Schematic draw of the transformation possibility between two periodic orbits with arbitrary periodicity in the parameter plane of the amplitudes of the dual-frequency driving. Panel B: Transformation between period-3 and period-5 orbits through the yellow surfaces. The employed model is the dual-frequency driven Keller–Miksis equation being a second order ordinary differential equation.

The control technique is demonstrated in Fig. 1B employing the Keller–Miksis equation being a second order non-linear oscillator. For the details of the equation, the reader is referred to the review paper [3]. The frequency combination used is $\omega_{R1} = \omega_1/\omega_0 = 5$ and $\omega_{R2} = \omega_2/\omega_0 = 3$, where ω_0 is the linear resonance frequency of the system. The periods of the orbits studied are $p_1 = 5$ and $p_2 = 3$. Thus, the condition given by Eq. (3) holds. In this figure, the saddle-node and the period doubling bifurcation points are marked by SN and PD respectively. Their torsion numbers are all equal: $q_{11} = q_{12} = q_{21} = q_{22} = 1$ fulfilling also the second requirement defined via Eqs. (4)-(5). The periodic orbits corresponding to the single frequency driving are highlighted by the blue (period-5 at $\omega_{R1} = 5$) and red (period-3 at $\omega_{R2} = 3$) curves. The yellow surfaces represent a set of periodic orbits connecting the period-3 and the period-5 orbits. Therefore, with a proper tuning of the amplitudes A_1 and A_2 of the dual-frequency driving, the system can be smoothly transformed between the period-3 orbits lying on the red curves and the period-5 attractors represented by the blue curves. Observe that the dual-frequency driving is temporary and that the initial and final state of the transformation relate to single frequency driving with different frequencies. It must be emphasized that with a different choice of frequency pairs, transformation can be achieved between other pairs of periodic orbits.

Conclusions

The main significance of the proposed control technique is that a given system can be driven to a desired periodic solution in excitation-amplitude–frequency-parameter plane. The advantage of the method is that direct attractor selection is possible meaning that the final state of the trajectory is not incidental (as in case of many control of multistability techniques). The disadvantage is that a detailed knowledge of the bifurcation structure of the periodic orbits is required to control the system confidently. It is worth mentioning that the technique is first identified in the previous paper of the authors [5]; however, only for a specific pair of periodic orbits and a generalisation was not discussed.

Acknowledgement

This paper was supported by the Alexander von Humboldt Foundation, by the János Bolyai Research Scholarship of the Hungarian Academy of Sciences, and by the Higher Education Excellence Program of the Ministry of Human Capacities in the frame of Water science & Disaster Prevention research area of Budapest University of Technology and Economics (BME FIKP-VÍZ).

References

[1] Hegedűs F., Kalmár C. (2018) Dynamic stabilization of an asymmetric nonlinear bubble oscillator. *Nonlinear Dyn.* **94**:307-324.

[2] Pisarchik A. N., Feudel U. (2014) Control of multistability. *Phys. Rep.* **540**:167-218.

[3] Lauterborn W., Kurz T. (2010) Physics of bubble oscillations. *Rep. Prog. Phys.* **73**:106501.

[4] Parlitz U., Lauterborn W. (1986) Resonances and torsion numbers of driven dissipative nonlinear oscillators. *Z. Naturforsch. A* **41**:605-614.

[5] Hegedűs F., Lauterborn W., Parlitz U., Mettin R. (2018) Non-feedback technique to directly control multistability in nonlinear oscillators by dual-frequency driving. *Nonlinear Dyn.* **94**:273-293.

Broadband Stabilization with Combined Anti-Resonances

Zacharias Kraus*, Ahmed A. Barakat* and Peter Hagedorn*
*Dynamics and Vibrations Group, Technical University of Darmstadt, Darmstadt, Germany

Summary. The study of anti-resonances in parametrically excited systems in the recent years was focused mainly on bimodal systems. Assuming it to be strictly a bimodal coupling phenomenon, anti-resonances in systems with multiple degrees of freedom (DoF) were seen as a generalization without added effects. Recent findings, however, hint at an interesting behavior when multiple anti-resonances arise in close vicinity of each other. In the present contribution, these effects will be discussed and assessed with perturbational methods, aiming at understanding the underlying phenomenon, which is expected to be advantageous especially in enhancing the robustness and intensity of vibration mitigation.

Introduction

Ever since the discovery of anti-resonance by Tondl [8], further research by Schmieg [7], until recent investigations conducted by Dohnal [1, 2] and finally comprehensive semi-analytical describtion by Karev [3, 4, 5], anti resonance was interpreted as coupling between two modes. However, recent findings suggest that multiple anti-resonances can not be viewed in isolation in all cases. Following [6], Lyapunov characteristic exponents (LCEs) are used to gain insight into the system's behavior. Floquet theory is applied to the parametrically excited system with excitation period time T, resulting in Floquet multipliers ρ_i, from which the LCEs λ_i can be derived by

$$\lambda_i = \frac{1}{T} \ln |\rho_i|. \tag{1}$$

Numerical Observations

In [6], it was shown that in systems with multiple degrees of freedom (MDoF), under the right conditions anti-resonances may appear at multiple excitation frequencies Ω. This is illustrated in Fig. 1, using the system introduced in [2, 9] and studied further in [6] as an example. The anti-resonances are approximately at the combination frequencies $\Omega = \Sigma_{21} = \omega_1 + \omega_2$ and $\Sigma_{32} = \omega_3 + \omega_2$.

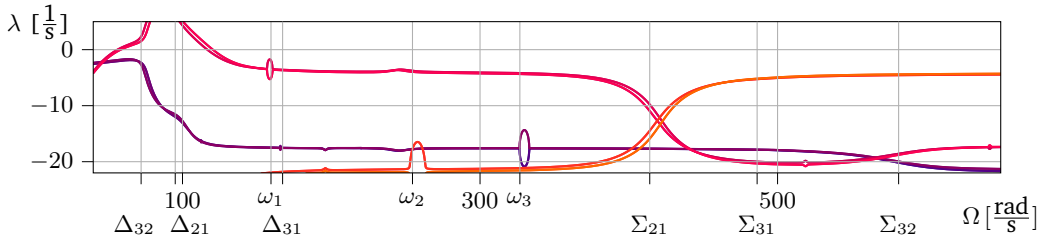

Figure 1: LCEs λ_i of example system [6] over excitation frequency Ω for $\kappa = 1$, $\varepsilon_p = 0.15$. Two sepearte anti-resonances are visible.

The numerical results obtained by applying Floquet theory indicate that for a certain amplitude ε_p of parametric excitation, while having asymmetrically skewed excitation terms by a factor κ in a MDoF (see (2)), a minimum of the largest of the LCEs involved in anti-resonances $\max(\lambda_i)$ can be achieved. This leads to the anti-resonances laying on top of each other, as visible in Fig. 2.

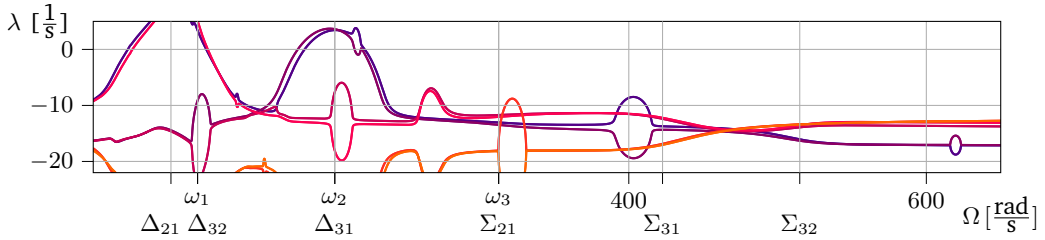

Figure 2: LCEs λ_i of example system [6] over excitation frequency Ω for $\kappa = 0.729$, $\varepsilon_p = 0.158$. Two anti-resonances occur at the same frequency.

The exact relation between the values of all LCEs λ_i and the equivalent damping of the system is yet to be fully understood. Thus, numerical simulation of the system's amplitudes after an initial displacement is used to clarify the effects of the

two combined anti-resonances shown in Fig. 2. Fig. 3 shows the summed squares of amplitudes of all DoF of the example system. With the dashed line indicating the reference time at which the unexcited system's amplitudes become negligibly small, it is apparent that a stabilizing effect is not only caused around the frequency of anti-resonances but for all frequencies apart from resonances.

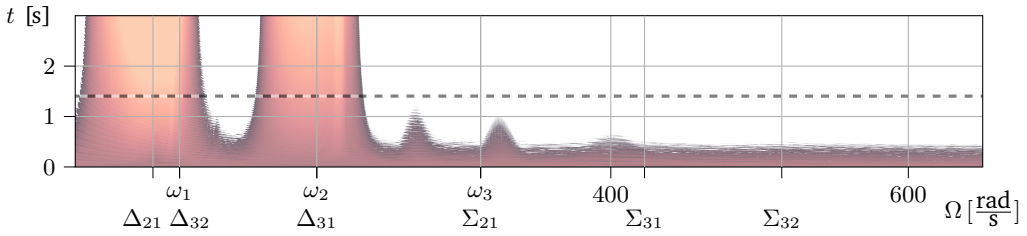

Figure 3: Summed squares of amplitudes in all DoF after initial pertubation recorded over time t and with respect to the parametric excitation frequency Ω. Reference time where unexcited system reaches negligible small amplitudes shown with dashed line (- - -). Lighter shade means larger amplitudes.

Perturbation analysis

In order to get a better insight into the observed phenomenon, the system is to be analyzed analytically. As a first step, the system model is reduced for the sake of generalizing the studied system, which leads to a three-dimensional equation of motion

$$\begin{aligned}\ddot{\underline{u}} + \varepsilon \begin{pmatrix} \mu_1 & 0 & \mu_{13} \\ 0 & \mu_2 & 0 \\ \mu_{13} & 0 & \mu_3 \end{pmatrix} \dot{\underline{u}} + \left[\begin{pmatrix} \omega_1^2 & 0 & 0 \\ 0 & \omega_2^2 & 0 \\ 0 & 0 & \omega_3^2 \end{pmatrix} + \dots \right. \\ \left. \dots + (1-\kappa) \begin{pmatrix} 0 & k_{12} & k_{13} \\ k_{21} & 0 & k_{23} \\ k_{31} & k_{32} & 0 \end{pmatrix} + \left[\begin{pmatrix} 0 & f_{12} & f_{13} \\ f_{21} & 0 & f_{23} \\ f_{31} & f_{32} & 0 \end{pmatrix} - \kappa \begin{pmatrix} 0 & f_{21} & f_{31} \\ f_{12} & 0 & f_{32} \\ f_{13} & f_{23} & 0 \end{pmatrix} \right] \varepsilon_p \cos(\Omega t) \right] \underline{u} = 0,\end{aligned} \tag{2}$$

with the displacement $\underline{u}$, damping μ_i, eigenfrequencies of the undamped unexcited system ω_i^2, off-diagonal stiffness terms k_{ij}, parametric excitation coefficients f_{ij} and frequency Ω, small parameter ε, amplitude of parametric excitation $\varepsilon_p = \mathcal{O}(\varepsilon)$ and asymmetry parameter κ.

The findings are to be analyzed using multiple scales. For this purpose, the displacement $\underline{u}$ and asymmetry parameter κ are perturbated, described by a power series with respect to the small parameter ε:

$$\begin{aligned}\underline{u} &= \underline{u}_0 + \varepsilon \underline{u}_1 + \varepsilon^2 \underline{u}_2 + \mathcal{O}(\varepsilon^3), \\ \kappa &= 1 + \varepsilon\kappa_1 + \varepsilon^2\kappa_2 + \mathcal{O}(\varepsilon^3).\end{aligned} \tag{3}$$

The ongoing study aims then at using the outcomes of the multiple scales analysis in understanding the reason behind the stabilizing effect of coinciding anti-resonances at approximately all excitation frequencies. In this way, a generalization of this phenomenon can be achieved for a 3 DoF system and, moreover, extended to generic MDoF systems. Such an effect could be a powerful tool in mitigating vibrations in industrial applications.

References

[1] Dohnal, F., Verhulst, F. (2008) Averaging in vibration suppression by parametric stiffness excitation. *Nonlinear Dynamics* **54(3)**:231-248

[2] Dohnal, F., Chasalevris, A. (2015) Inducing modal interaction during run-up of a magnetically supported rotor. *13th Intl. Conference Dyn. Sys. Theory and Applications DSTA*

[3] Karev, A., Hagedorn, P. (2019) Global stability effects of parametric excitation. *J. Vibration and Control* **448**:34-52.

[4] Karev A., Hagedorn P. (2020) Simultaneous Resonance and Anti-Resonance in Dynamical Systems Under Asynchronous Parametric Excitation. *J. Comput. Nonlinear Dyn.* **15**

[5] Karev A. (2021) Asynchronous Parametric Excitation in Dynamical Systems. *PhD thesis*, TU Darmstadt, Darmstadt.

[6] Kraus Z., Karev A., Hagedorn P., Dohnal F. (2021) Enhancing vibration mitigation in a jeffcott rotor with active magnet bearings through parameteric excitation. *Nonlinear Dyn.*

[7] Schmieg H. (1976) Kombinationsresonanz bei Systemen mit allgemeiner harmonischer Erregermatrix (Combination resonance in systems with general harmonic excitation matrix). *PhD thesis*, University of Karlsruhe, Karlsruhe

[8] Tondl A. (2008) To the problem of self-excited vibration suppression. *Engineering Mech.* **15(4)**:297-307

[9] Zhang X. (2003) Aktive Regel- und Kompensationsstrategien für magnetgelagerte Mehrfreiheitsgrad-Rotoren. (Active control and compensation strategies for multi-degree-of-freedom rotors with magnetic bearings). *PhD thesis*, GCA-Verlag, Herdecke

Wednesday, July 20, 2022
08:30 - 10:30

MS-19 Fluid-Structure Interaction
Saint Clair 3B

Chair: Oded Gottlieb

08:30 - 08:50
Bifurcations of an Optically Excited Achiral Nano-Ellipsoid in a Stationary Fluid
BERGHAUS Tomer*, MILOH Touvia, SEPYAN Gregory, GOTTLIEB Oded
*Tel Aviv University (Tel Aviv Israel)

08:50 - 09:10
VSIV Experimental Analysis of a Catenary Riser Model in the Modal Space
SALLES Rafael, **PESCE Celso***
*Escola Politécnica, University of São Paulo (Av. Prof. Mello Moraes 2231 05508-030 São Paulo, SP Brazil)

09:10 - 09:30
Dynamics and stability of a planar three-link swimmer with passive visco-elastic joint in Ideal fluid
TOVI Elon*, OR Yizhar
*Faculty of Mechanical Engineering, Technion - Israel Institute of Technology (Haifa, Technion City Israel)

09:30 - 09:50
Effect of Piezoelectric Coupling on Dynamical Transitions of a Flexible Beam in Viscous Flow
CHATTERJEE Rajanya*, SHAH Chhote, GUPTA Sayan, SARKAR Sunetra
*Department of Applied Mechanics, Indian Institute of Technology Madras (IIT Madras, Chennai, Tamilnadu, India. Pin-600036 India)

09:50 - 10:10
Cantilevered Extensible Pipes Conveying Fluid: a Consistent Reduced-Order Modeling via the Extended Hamilton's Principle for Nonmaterial Volumes
TOMIN Daniel, ORSINO Renato, **PESCE Celso***
*Escola Politécnica, University of São Paulo (Av. Prof. Mello Moraes 2231 05508-030 São Paulo, SP Brazil)

Bifurcations of an Optically Excited Achiral Nano-Ellipsoid in a Stationary Fluid

Tomer Berghaus*, Touvia Miloh *, Gregory Ya Slepyan**, Oded Gottlieb***
*School of Mechanical Engineering, Tel Aviv University, Israel
**School of Electrical Engineering, Tel Aviv University, Israel
***Faculty of Mechanical Engineering, Technion - Israel Institute of Technology, Israel.

Summary. We derive and investigate a system of equations describing the three-dimensional dynamics of a prolate and oblate achiral ellipsoidal particle subjected to a linearly polarized, electromagnetic excitation. A half-wave plate rotates the polarization direction of the transmitted light by an angle Ω and the linearly polarized electric field induces a dipole moment in the particle that depends on the product of the polarizability tensor and the electric field. To minimize energy, the induced dipole moment tends to align with the field yielding an optical torque. The basic assumption in the development of the equations of motion was that the given ellipsoid rotates around its center of mass with negligible inertia due low Reynolds number. The nanoscale dimensions of the given particle enable problem formulation in the Rayleigh regime which yields a set of three nonlinear equations for the angular velocities in terms of Euler angles. Transformation of the equations of motion to an autonomous dynamical system enabled a linear stability analysis of multiple coexisting equilibria corresponding to stable and unstable periodic orbits in the lab frame. A set of Hopf bifurcations in the autonomous system revealed existence of nonstationary quasiperiodic and chaotic motions in the lab frame governed by three nondimensional parameters.

Introduction

The advent of the laser sparked numerous research areas and one of these has been and manipulation of matter by light. In 1986 Ashkin and co-workers showed that a single tightly focused beam could be used to hold, in three dimensions, a microscopic particle near beam focus, which is now known as optical tweezers. The potential uses of contact free control of microscopic and nanoparticles has maintained high scientific interest for more than three decades. Major advances in the field have been coupled with technological innovations such as dynamic control using holographic optical tweezers, engineering of beam shapes and ultraprecise tracking techniques. Optical trapping at the micro [1] and nano [2] scales is well documented in several reviews. We note that the dynamics of tri-axial ellipsoids in shear flow reveal existence of periodic [3], quasiperiodic [4] and chaotic [5] solutions. However, to date ellipsoids immersed in a fluid and excited by a modulated optical field, have been shown to be periodic or quasiperiodic [6]. Thus, our aim in this work, is to provide a sptio-temporal physical model of the rotational dynamics of a triaxial nano-ellipsoid (Fig.1 left), to validate the existence of periodic and quasiperiodic rotations documented for long cylindrical achiral nanorods [7] and to determine existence of nonstationary chaotic rotations. We consider an achiral ellipsoidal particle with principal axes $(\mathbf{a},\mathbf{b},\mathbf{c})$ and permittivity $(\boldsymbol{\varepsilon_2})$ suspended in a liquid of permittivity $(\boldsymbol{\varepsilon_1})$. A rotating frame of reference is attached to the particles mass center where the Eulerian angles $(\boldsymbol{\theta},\boldsymbol{\phi},\boldsymbol{\psi})$ correspond to pitch, yaw and roll (Fig.1 left). The ellipsoid is nonmagnetic so the relative magnetic permeability can be considered as a unity.

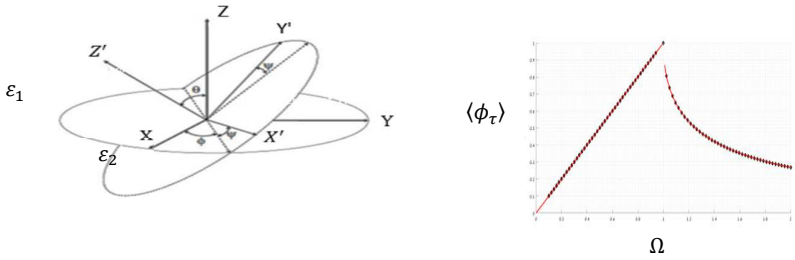

Fig.1: Definition sketch of a nanoscale ellipsoid (left) and the bifurcation diagram for a spheroidal particle (right).

A linearly polarized impinging electric field goes through a half-waveplate that rotates the polarization direction. This exciting electric field induces a dipole moment that depends on the product of the polarizability tensor and the electric field. To minimize energy, the induced dipole moment tends to align with the field yielding an optical torque. The basic assumption in the development of the equations was that the given particle is trapped, i.e., not subjected to gradient force and rotates around its center of mass. Since the dimensions of the ellipsoid are significantly small compared to the wavelength of the exciting field, the phase is considered constant over the particle. Moreover, since the half wave plate rotates at an angular frequency which is much slower than the angular optical frequency the total torque is averaged over one optical cycle. Under the assumption of low Reynolds number, inertial terms are neglected [8], which means that the angular drag is equal to the total optical torque on the particle. For example, it has been shown that for planar rotational dynamics of dielectric nanorod, close to a critical frequency, the optical torque is a factor of much higher than the corresponding rotation due to Brownian motion during a given time interval [6]. Furthermore, we note that the bifurcation structure of a nano-spheroid (a>b=c) includes periodic rotations (Fig.1 right-$\Omega < 1$) or quasiperiodic motions (Fig.1 right-$\Omega > 1$) which have been demonstrated experimentally for a long cylinder [6].

Results

The non-dimensional equations governing the motion were constructed in the theoretical framework of Newtonian rigid body dynamics yielding a third-order autonomous system controlled by nondimensional parameters that depend on the particle material properties, and the angular drag coefficients (α, β) and an additional parameter that depends on the slow half wave plate rational frequency and the electric field magnitude (Ω). An investigation of the nonlinear dynamical response of ellipsoidal particles, with varying dimension and material properties, was carried out using linearization methodology yielding an eigenvalue problem. The analysis reveals a diverse local bifurcation structure (Fig.2 left) that includes coexisting bi-stable equilibria and a narrow range of limit cycle oscillations (Fig.2 right) due to subcritical Hopf threshold (depicted by the red line in Fig.2 left).

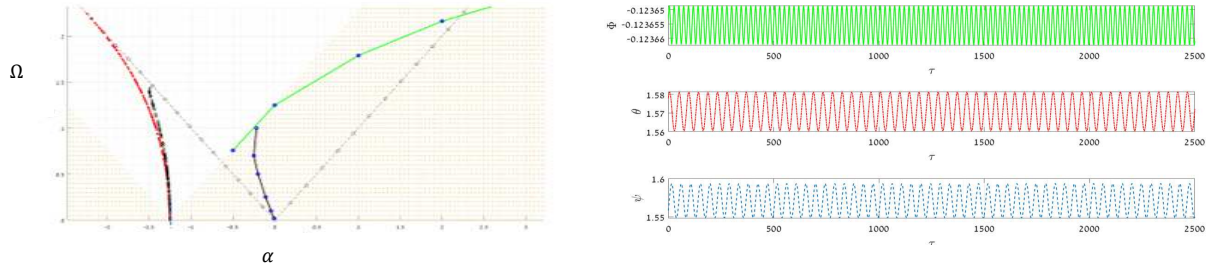

Fig.2: Stability map for a gold nano-ellipsoid with exciting frequency Ω as a function of a material parametre α (left) and time histories of limit cycle oscillations in the Eulerian frame where $\Phi=\phi-\Omega\tau$(right).

Discussion

The classification of different solutions is portrayed in the Cartesian physical state space (Figs. 3,4). It is shown that equilibrium in the Euler angle autonomous system corresponds to a periodic solution in Cartesian space, whereas a periodic solution corresponds to a quasiperiodic Cartesian state space (Fig.3 blue triangles). Furthermore, nonstationary chaotic solutions were found between two secondary bifurcation thresholds (Fig.3 red squares). Moreover, additional quasiperiodic solutions were found for $\Omega > 1$ for which no equilibrium is reached in the Eulerian state space. It is noteworthy that the limiting case of a nano-spheroid is governed by a single non-dimensional parameter (Ω) and its bifurcation structure at steady state (Fig.1 right) does not include chaotic rotations. We note possible excitation with two frequencies may yield a region of chaotic interactions for incommensurate frequency ratios.

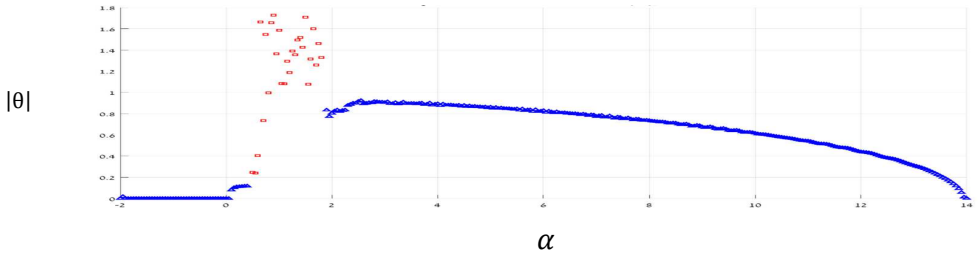

Fig. 3: Bifurcation diagram for a hybrid nano-ellipsoid where $\Omega = 0.5, \beta = 1$.

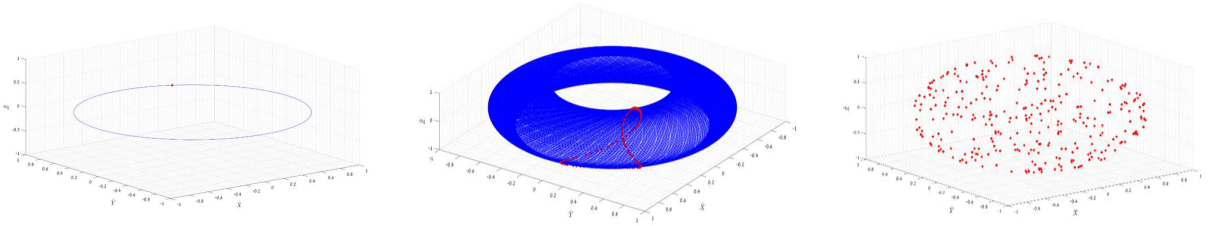

Fig.4: Poincare' maps overlaid on the lab frame physical state space (Z(X,Y)) of periodic (left) and quasiperiodic (center) solutions. Poincare' map of a chaotic solution (right).

References

[1] Grier D. (2003) A Revolution in optical manipulation, Nature**, 424**, 810.
[2] Ishihara H. (2021) Optical manipulation of nanoscale materials by linear and nonlinear resonant optical responses, Adv. Phys. **6**:1,1885991.
[3] Jeffery, G. B. (1922) The motion of ellipsoidal particles immersed in a viscous fluid, Proc. R. Soc. Lond. A, **102**, 161-179.
[4] Hinch, E. J., Leal, L. G. (1979) Rotation of small non-axisymmetric particles in a simple shear flow, J. Fluid Mech. **92**, 591-608.
[5] Yarin A.L., Gottlieb O., Roisman I. V (1997) Chaotic rotation of triaxial ellipsoids in simple shear flow, J. Fluid Mech.,**340**, 83-100.
[6] Shelton W.A., Bonin K.D. and Walker T.G. (2005) Nonlinear motion of optically torqued nanorods, Phys. Rev. E, **71**, 036204.
[7] Liang Z., Fan D. (2018) Visible light–gated reconfigurable rotary actuation of electric nanomotors, Science Advances, **4**: 0981.
[8] Miloh T. (2019) Light-induced thermoosmosis about conducting ellipsoidal nanoparticles, Proc. R Soc. Lond. A: **475**, 2223.

VSIV Experimental Analysis of a Catenary Riser Model in the Modal Space

Rafael Salles, Celso P. Pesce
Offshore Mechanics Laboratory, Escola Politécnica, University of São Paulo, Brazil

Summary. Vortex Self-Induced Vibration (VSIV) is a highly nonlinear fluid-structure interaction that can occur in catenary risers when there is an imposed motion at the structure hang-off point. The fluid-structure coupling shows persistent response, *i.e.* there is no lateral vibration mitigation after a post-critical in-plane induced oscillatory flow. The present study aims at analyzing multi-modal response of a small-scale catenary riser model using Garlerkin's decomposition. The frequency ratio parameter, as the one used in linear oscillator resonance analysis, shows to be a strong control parameter altogether with the modal Keulegan-Carpenter number.

Vortex Self-Induced Vibration (VSIV) phenomenon

The Vortex Self-Induced Vibration (VSIV) belongs to the class of Flow Induced Vibration (FIV) phenomena in fluid-structure nonlinear dynamics study field. Generally, the VSIV occurs always on slender flexible structures, as risers and umbilical cables, that are launched in catenary-like configuration, so that an imposed movement at their top end, as those caused by gravitational waves, causes an oscillating movement at their configuration plane (henceforth called in-plane movement). As a result of such in-plane oscillations, vortex shedding is established and it induces lift forces that causes out of plane oscillating vibrations.

Some intermittent vibrations were firstly reported in experimental tests conducted within large-scale models of steel catenary risers (SCR) in Grant et al. [1], which later were further exploited by Le Cunff et al. [2] in their experimental campaigns with small scale SCR model. Initially, Le Cunff et al. [2] described the VSIV as Heave Induced Lateral Motion (HILM) and later experimental campaigns conducted by Fernandes et al. [3] broadened the scope of HILM renaming the phenomenon as VSIV. Fernandes et al. [3] also points out that the VSIV were observed in real riser structures of Petrobras P18 platform.

Over the last decade, the VSIV was observed and reported in small scale SCR models, as in Rateiro et al. [4] and Pesce et al. [5], in which multi-modal out of plane responses occurs due to in-plane movement caused by harmonic vertical displacements imposed at the top. Their experimental campaign shown that the structure dynamic response is highly nonlinear, coupling VSIV with internal resonance phenomenon and even parametric instabilities amid the multi-modal responses. VSIV was also reported in some recent papers Fu et al. [6].

The VSIV presents some idiosyncratic features: the synchronization amid in-plane and out-of plane oscillating movements is persistent, not occurring the structural and fluid oscillators decoupling as when the VIV reaches the post-critical regime; several lateral amplitude response peaks are observable and they are related to the cycle number control parameter, $N = f_b/f_n$ (f_b is the out of plane response frequency and f_n, the in-plane one), which always assumes integer values; the cycle number N values depends on the Keulegan-Carpenter number (KC), assuming larger values as the KC increases; and a jump phenomenon that decreases the N value as the in-plane movement velocity increases.

As a result of all features aforementioned, the out-of-plane response never fades away and can assume fairly large values of the structure diameter, $\mathcal{O}(D)$. Besides, the VSIV bares a close similarity to the responses observed in rigid cylinder subjected to oscillating flow, as shown in classical results obtained by Sarpkaya and Rabaji [7] and Sumer and Fredsøe [8]. This similarity is pointed out in several of VSIV idiosyncratic features, specially when regarding KC and N as strong control parameters to the cylinder persistent lateral response, which later in the present study will be complemented by the frequency ratio, $f^\star = f_b/f_N$ (f_N is the natural frequency of the considered out of plane mode).

VSIV acting upon a small scale flexible cylinder model experimental response: modal approach

Experimental set-up

The small-scale flexible cylinder experimental model used in the present analysis is the same one already thoroughly discussed in Rateiro et al. [4] and Pesce et al. [5]; see Figure 1a. The experimental tests were conducted at the Institute for Technological Research (IPT) towing tank and the 3D model Cartesian displacement response was directly measured using underwater optical target tracking cameras; see [4]–[5]. The estimated measurement precision isof the order $\mathcal{O}(1mm)$; see Salles and Pesce [9]. In addition the effective traction at hang-off point is also obtained using a load cell; Figure 1b.

Considering the displacement results at local reference frames comprised of the tangent and normal versors, $\vec{t}$ and $\vec{n}$, respectively, which spans the catenary plane and the orthogonal binormal versor, $\vec{b}$, Figure 1c shows the multi-modal binormal dynamic response, due to the in-plane movement caused by the hang-off imposed motion. Particularly, in this selected case, the second out of plane mode shows up as the dominant response mode.

Galerkin's decompostion and VSIV modal response

Galerkin's decomposition acts as a spacial filter, grouping the nonlinear dynamic responses into a small number of modal series. The chosen modal basis was determined using a discrete beam model and a finite element solver. Considering the dominant in-plane modal series as an input for the multi-modal response out-of-plane, it is possible to broaden the concept of the Keulegan-Carpenter parameter, considering it as a modal value.

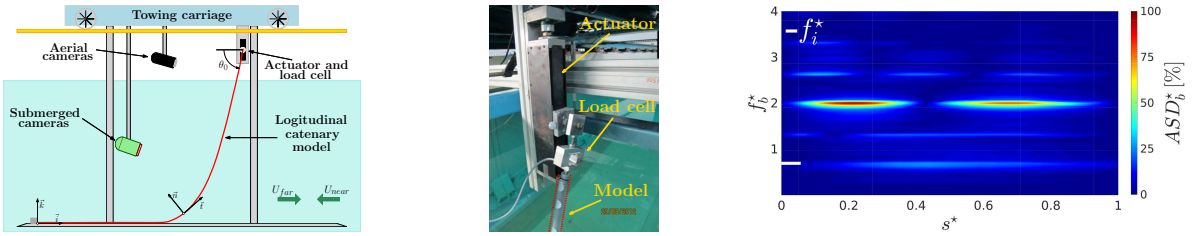

(a) (b) (c)

Figure 1: Flexible cylinder tests subjected to imposed movement at the top: a) experimental set-up; b) as-built model hang-off, displaying the actuator and a load cell; c) lateral amplitude spectrum of a selected case frequency response, showing multi-modal response, particularly with dominant second out of plane mode.

The frequency ratio amid dominant frequency response in-plane and the natural frequencies out-of-plane shows to be a strong control parameter, recovering a classical result of linear oscillators resonance response. The present study aims at analyzing the relation observed within all lateral modal peak-to-peak displacement, $2A_b^{(k)\star}$ for all in-plane modal frequency ratios; see illustrative results in Figures 2a–b. By working on the modal-space, grouping the results into small ranges of modal-KC numbers, strongly similar modal responses are revealed, enlarging the analysis contained in [2]–[6], made in the configuration space, and broading Sumer's & Fredsøe's [8] experimental results, obtained with a rigid cylinder mounted on linear springs in a given direction and forced to oscillate in the orthogonal direction. During the conference and in a full paper yet to come, much more results will be shown and discussed, as synchronisms, internal resonances and maps of typical orbits in the modal space.

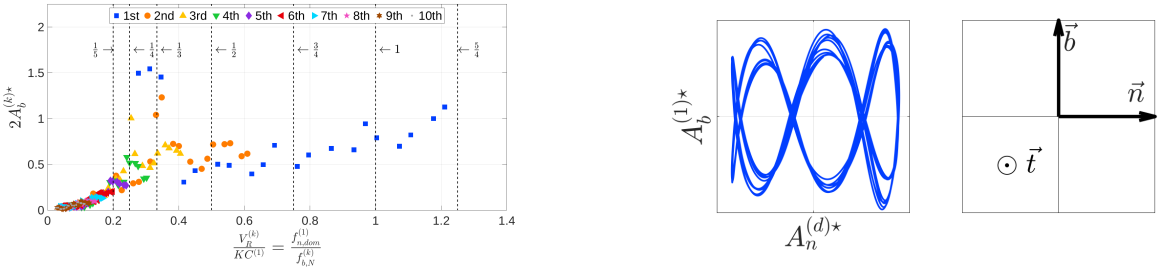

(a) (b)

Figure 2: Modal space VSIV results for $30.2 \leq KC^{(d)} \leq 34$: a) Peak lateral modal displacement (each lateral mode is depicted as a different colored marker) as a function of frequency ratio parameter considering the first in-plane mode; b) Modal orbit of selected out-of-plane mode against dominat in-plane modal response.

Acknowledgments

This study was financed in part by the Coordenação de Aperfeiçoamento de Pessoal de Nível Superior - Brasil (CAPES) Finance Code 001 and by the CNPq research grant n. 308220/2018-3. The authors also acknowledges IPT for the use of the towing tank facility and Petrobras for having supported the experimental campaign. Special thanks to Prof. Gustavo Assi, for encouragement and discussions, and FAPESP for supporting the Conference attendance, Grant 2022/04072-5.

References

[1] Grant, R. G. and Litton, R. W. and Mamidipudi, P. (1999) Highly Compliant Rigid (HCR) Riser Model Tests and Analysis. Proc. Annual Offshore Tech. Conf. **2**.

[2] Le Cunff, C. and Biolley, F. and Damy, G. (2005) Experimental and Numerical Study of Heave-Induced Lateral Motion (HILM). OMAE **3**:757-765.

[3] Fernandes, A.C. and Mirzaeisefat, S. and Cascão, L.V. (2014) Fundamental behavior of Vortex Self Induced Vibration (VSIV). J. Applied Ocean Research **47**:183-191.

[4] Rateiro, F. and Gonçalves, R. T. and Pesce, C. P. and Fujarra, A. L. C. and Franzini, G. R. and Mendes, P. (2013) A Model Scale Experimental Investigation on Vortex-Self Induced Vibrations (VSIV) of Catenary Risers. Proc. OMAE **7**:183-191.

[5] Pesce, C. P. and Franzini, G. R. and Fujarra, A. L. C. and Gonçalves, R. T. and Salles, R. and Mendes, P. (2017) Further experimental investigations on vortex selfinduced vibrations (VSIV) with a small-scale catenary riser model. Proc. OMAE **2**.

[6] Fu, S. and Wang, J. and Baarholm, R. and Wu, J. and Larsen, C. M. (2014) Features of Vortex-Induced Vibration in Oscillatory Flow. JOMAE **136**:011801.

[7] Sarpkaya, T. and Rajabi, F. (1979) Dynamic Response Of Piles To Vortex Shedding In Oscillating Flows. Proc. Annual Offshore Tech. Conf. **1979-May**:2523-2528.

[8] Sumer, B. M. and Fredsøe, J. (1988) Transverse Vibrations of an Elastically Mounted Cylinder Exposed to an Oscillating Flow. JOMAE **1988-11**:387.

[9] Salles, R. and Pesce, C. P. (2017) Experimental Assessments of the Added Mass of Flexible Cylinders in Water: The Role of Modal Shape Representation. Lectures Notes in Mech. Engi.: Proc. of 2017 DINAME **PartF6**:215-235.

Dynamics and stability of a planar three-link swimmer with passive visco-elastic joint in Ideal fluid

Elon Tovi*, Yizhar Or *
*Faculty of Mechanical Engineering, Technion - Israel Institute of Technology, Haifa, Israel.

Summary. We study the nonlinear dynamics of a three-link swimmer model in ideal fluid, where inertial forces due to added mass are dominating while viscous drag forces are negligible. We consider an underactuated swimmer where one joint is periodically actuated while the other joint is passive and viscoelastic, with torsional spring and damper. The swimmer's motion depends significantly on the amplitude and frequency of the actuated joint angle. Optimal frequency is found where the swimmer's net displacement per cycle is maximized, under symmetric periodic oscillations of the passive joint. In addition, upon crossing critical values of amplitude and frequency, the system undergoes a bifurcation where the symmetric solution loses stability and asymmetric solutions evolve, for which the swimmer moves along an arc. We analyze these phenomena using numerical simulations and analytical methods of *Floquet* theory and *Hill's determinant*. The results demonstrate the important role of *parametric excitation* on stability of motion for flexible underactuated locomotion.

Introduction

Autonomous swimming robots have a promising potential for various applications such as surveillance and protection in marine environment, search and rescue missions, and maintenance operations within pipe systems of complex infrastructures [1], [2]. A common model assumes ideal fluid [3], [4], where the viscosity is negligible and the swimmer-fluid interaction is induced by reactive forces that represent added mass effect. Our previous work [4] used this model to study multi-link swimmers under kinematic input prescribing all joint angles, numerically, analytically and experimentally (Figure 1b). Inspired by biological swimmers in nature that utilize body flexibility, the recent work [5] studied a modified model of planar three-link swimmer having one passive viscoelastic joint (torsional spring + damper) and one actuated joint with oscillating angle $\theta_2(t) = \varepsilon \cos(\omega t)$, see Figure 1a. Unlike [4], in the semi-passive model [5] the excitation frequency ω and amplitude ε of the active joint have a significant effect on the response of the passive elastic joint and the resulting motion.

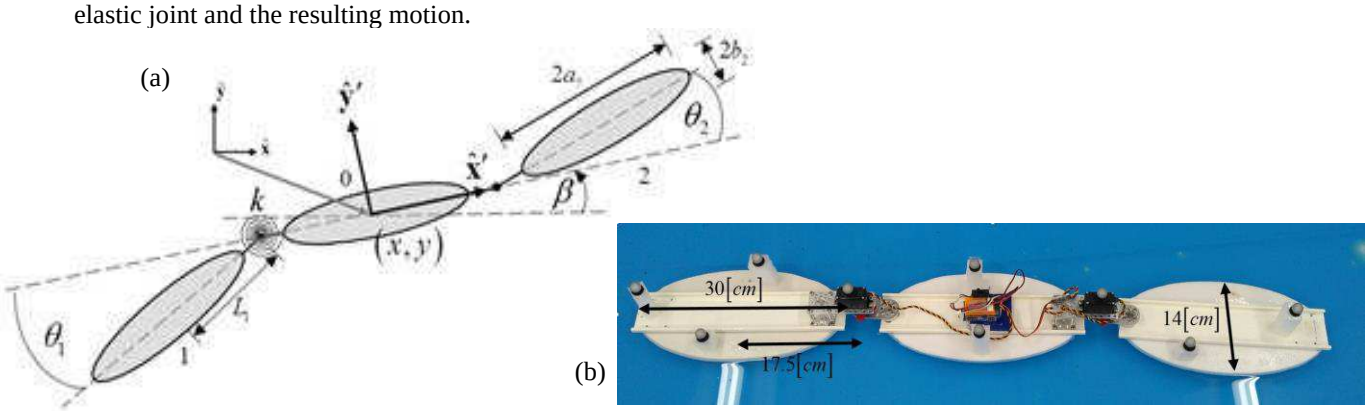

Figure 1: **(a).** Swimmer model – (x, y) are the position of the body-fixed reference frame origin. β is the rotation angle of the body-fixed reference frame. a_i and b_i are the major and minor radii of the elliptic links. θ_i are the relative angles between links. **(b).** Our previous experimental robotic swimmer with two actuated joint angles [4]

Results

In this work, we revisit the model in [5] and study its nonlinear dynamics and stability, both numerically and analytically. Numerical simulations of the system's nonlinear dynamics result in symmetric periodic motion, in which the passive joint angle $\theta_1(t)$ is oscillating symmetrically about zero while the swimmer's net motion is translation along a straight line (Figure 2, blue curves). For a fixed amplitude ε, An optimal frequency ω is found where the net displacement per cycle is maximized (Figure 3, top left). Analyzing stability of periodic solutions reveals a bifurcation point depending on input's amplitude and frequency, where the symmetric periodic solution loses stability and a pair of stable asymmetric solutions evolve, which involve oscillations of $\theta_1(t)$ about nonzero mean angle, resulting in net rotation such that the swimmer moves along an arc (Figure 2, red curves). Asymptotic analysis of the symmetric solution under small-angle assumption $\varepsilon \ll 1$ enables obtaining explicit expressions for the optimal frequency and displacement. Analyzing small variations about the symmetric periodic solution gives a Hill-type equation (linear time-periodic 2nd- order ODE) whose stability can be approximated using truncated Hill's determinant [6]. We obtain analytic conditions for the stability transitions depending on input's amplitude and frequency, which agree with the numerical simulations (Figure 4). Finally, we conduct additional numerical simulations in order to analyze added effects of nonzero initial momentum, drag forces, and tension spring mechanism at the passive joint.

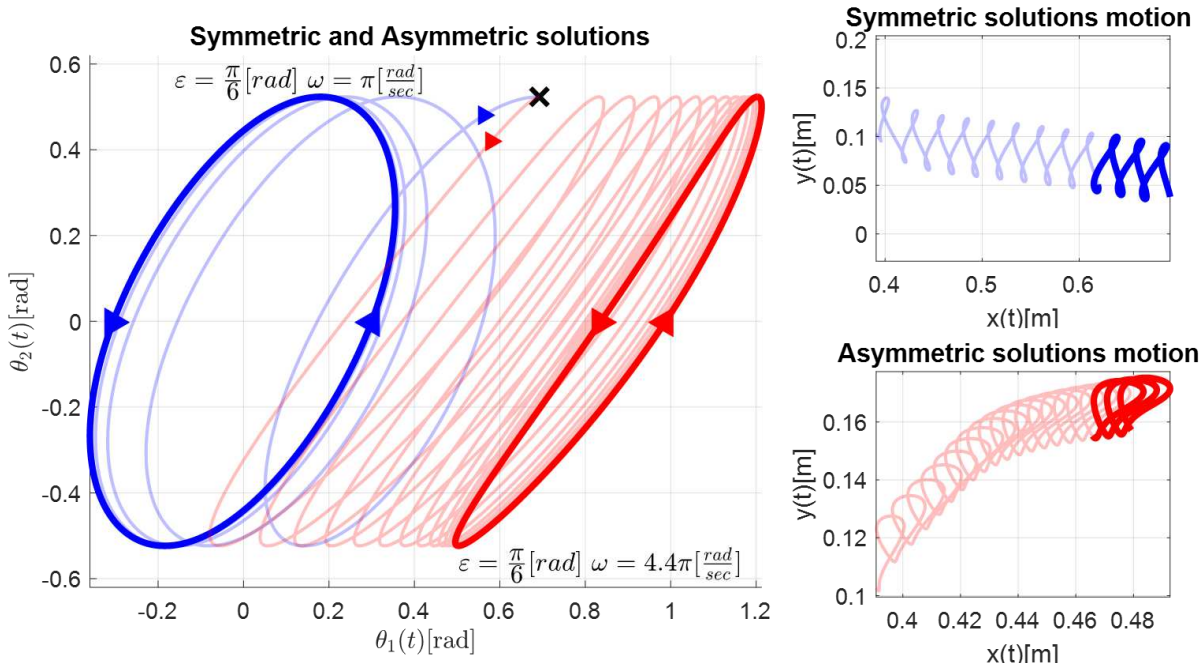

Figure 2: Transient simulations – Left: trajectories in joint-angles plane. Right: trajectories in x-y plane. Blue: symmetric solution, Red: asymmetric solution. Simulations with the same amplitude and initial condition and different frequencies result in significantly different solutions trajectories.

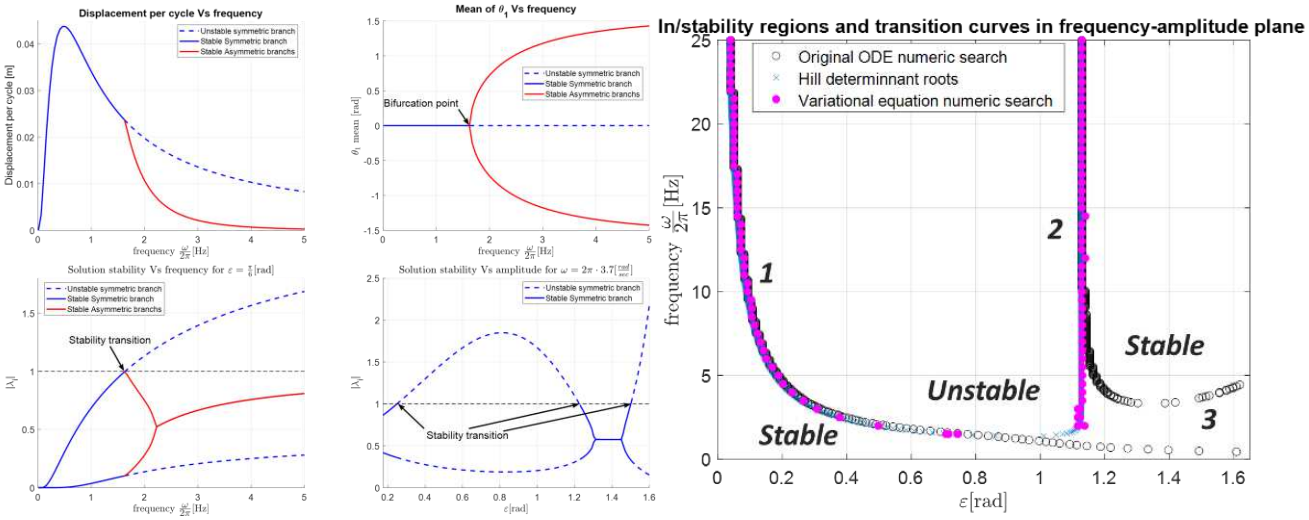

Figure 3: Steady state solution parameters in ω and ε – Optimal frequency is found where the net displacement per cycle is maximized. A bifurcation point depending on input's amplitude and frequency occurs, where the symmetric solution loses stability and a pair of stable asymmetric solutions evolve. Stability transitions involve Floquet multipliers crossing $|\lambda_i|$=1.

Figure 4: Stability and instability regions and transition curves in frequency-amplitude plane – The analytic stability transition condition of Hill's determinant predicts the first and second stability transitions. A third transition at higher amplitudes is not captured by the asymptotic analysis.

References

[1] B. Kwak and J. Bae, "Design of a robot with biologically-inspired swimming hairs for fast and efficient mobility in aquatic environment," IEEE Int. Conf. Intell. Robot. Syst., vol. 2016-Novem, pp. 4970–4975, Nov. 2016, doi: 10.1109/IROS.2016.7759730.

[2] G. Li, Y. Deng, O. L. Osen, S. Bi, and H. Zhang, "A bio-inspired swimming robot for marine aquaculture applications: From concept-design to simulation," Ocean. 2016 - Shanghai, Jun. 2016, doi: 10.1109/OCEANSAP.2016.7485691.

[3] E. Kanso, J. E. Marsden, C. W. Rowley, and J. B. Melli-Huber, "Locomotion of articulated bodies in a perfect fluid," J. Nonlinear Sci. 2005 154, vol. 15, no. 4, pp. 255–289, Aug. 2005, doi: 10.1007/S00332-004-0650-9.

[4] E. Virozub, O. Wiezel, and Y. Or, "Planar multi-link swimmers: experiments and theoretical investigation using 'perfect fluid' model," no. 2021776, 2017, [Online]. Available: http://arxiv.org/abs/1710.06645.

[5] R. Abrajan-Guerrero and S. D. Kelly, "Elastic compliance versus joint actuation in an articulated swimming robot," IFAC-PapersOnLine, vol. 51, no. 13, pp. 167–173, Jan. 2018, doi: 10.1016/J.IFACOL.2018.07.273.

[6] A. H. Nayfeh and D. T. Mook, Nonlinear Oscillations. 2008.

Effect of Piezoelectric Coupling on Dynamical Transitions of a Flexible Beam in Viscous Flow

Rajanya Chatterjee*, Chhote Lal Shah†, Sayan Gupta*, and Sunetra Sarkar †
*Department of Applied Mechanics, IIT Madras, India
†Department of Aerospace Engineering, IIT Madras, India

Summary. The effect of the piezoelectric coupling on the dynamical transition of a bimorph cantilever beam in free stream flow at low Reynolds number is numerically investigated in the present study. The results are simulated numerically by using an in-house three-way coupled Immersed Boundary Method (IBM)-based Fluid-structure Interaction (FSI) solver. The effect of piezoelectric coupling at low mass ratios is found to be negligible, as they exhibit periodic dynamics irrespective of the presence of piezoelectric. Without piezoelectric coupling effect, at higher mass ratio of 5.0, the system retains the periodic dynamics. Interestingly, when the piezoelectric coupling effect is introduced, the system transitions from periodic to aperiodic state at the same mass ratio. This study is of importance as it gives insights on the effects of mass ratio at which the efficient energy harvesting of such systems from the piezoelectric material can be possible.

Introduction

The recent advances in the research of alternate energy harvesters, in view of the global depletion of conventional energy resources, is not limited to the large scale solar power or wind energy harvesters. The small scale energy harvesters, powering micro electronic devices to automating small bio-mimetic robots have also been gaining attention from a range of research fields. The energy harvesting strategy from flow induced vibration of flexible flappers, using piezoelectric materials, is one such area, where the system requires a study in fluid structure interaction (FSI), vibration energy harvesters, as well as non linear dynamical characterization of the multiple parameters involved in it. A number of studies in the past and recent times, have contributed towards the development of these flow harvester models, from rigid cylinders with piezo patches in Zhu et al.[1] to more complex bluff body-flexible splitter plate models of Akaydin et al. [2]. In the current study, a flexible cantilever beam model, layered with PZT-5A on both sides (bimorph), has been placed in a viscous fluid, with an oncoming free stream velocity taking the beam to flutter for certain parametric regime. A study on the flutter condition by varying the stiffness and inertia parameters, for an FSI problem was presented in Akcabay et al.[3] and the energy harvesting potential was discussed. However, the authors have not commented on the effect of piezoelectric coupling in the dynamical transition of the system. Therefore, the present study intends to give a comparative analysis on the effect of the presence of piezoelectric coupling on the flutter conditions and energy harvesting capability.

Computational Methodology

A flexible beam layered with PZT-5A on both sides considered in the present study is inextensible where the length of the beam is $L_s = 1.0$. The leading-edge of the beam is fixed and the rest of the body is free to oscillate in the fluid. The non-dimensional governing equation of motion for the flexible beam is given by [3]

$$\beta\frac{\partial^2\mathbf{X}}{\partial t^2} = \frac{\partial}{\partial s}\left(T_s\frac{\partial\mathbf{X}}{\partial s}\right) - \frac{\partial^2}{\partial s^2}\left(\gamma\frac{\partial^2\mathbf{X}}{\partial s^2}\right) + \nu V\frac{d}{ds}\left[\delta(s) - \delta(s-L)\right] + \mathbf{F}, \tag{1}$$

where $\mathbf{X} = (X(s,t),\, Y(s,t))$ is the instantaneous position of the beam, s is the arc length, δ is a Dirac-Delta function, $\beta = \rho_s q/\rho_f L_s$ is the mass ratio (ρ_s, ρ_f and q are the structural density, fluid density and thickness of the beam, respectively). $\rho_f U_\infty^2 L_s$ is used to non-dimensionalize tension coefficient (T_s), $\rho_f U_\infty^2 L_s^3$ is used to non-dimensionalize bending stiffness (γ), t is the non-dimensional time, V is the voltage output non-dimensionalized by $L_s U_\infty(\rho_f/\epsilon)^{1/2}$, ν is the piezoelectric coupling term non-dimensionalized by $L_s U_\infty(\rho_f\epsilon)^{1/2}$ and $\mathbf{F}$ is the Lagrangian forcing acting on the solid body non-dimensionalized by $\rho_f U_\infty^2$. The non-dimensional energy equation for bimorph is given by,

$$\frac{1}{2}\frac{\partial V}{\partial t} + \frac{qq_p}{Rb}V(t) = -\int_0^1 \nu\frac{qq_p(1-q_p)}{2}\frac{\partial^3\mathbf{x}}{\partial t\partial s^2}, \tag{2}$$

where q_p is ratio of the thickness of one piezoelectric layer with the total thickness of the beam (piezo+substrate), Rb is the non dimensional resistance of the piezoelectric circuit. The structural equation (eq.1) and the energy equation (eq.2) have been discretized by using finite difference method (FDM), details of which can be found in [6]. The viscous flow around the flexible beam is governed by the unsteady Navier-Stokes equations. The momentum conservation and continuity equations in non-dimensional form can be written as,

$$\frac{\partial\mathbf{u}}{\partial t} + \nabla.(\mathbf{uu}) = -\nabla p + \frac{1}{Re}\nabla^2\mathbf{u} + \mathbf{f}; \tag{3}$$

$$\nabla.\mathbf{u} - q_s = 0. \tag{4}$$

Where $\mathbf{u}$ is the flow velocity vector non-dimensionalized by U_∞, $Re = \rho_f U_\infty L/\mu$ is the Reynolds number and pressure p is non-dimensionalized by $\rho_f U_\infty^2$. The momentum forcing term $\mathbf{f}$ is added throughout the solid domain to ensure no

slip and no penetration boundary condition is satisfied at the solid boundary and mass conservation is satisfied by adding a mass source/sink term (q_s) to the continuity equation [4]. The fluid, structure and energy equations are coupled in staggered manner where they exchange their information at every time-step.

Results and Discussions

The bimorph flexible beam has been kept in the free stream flow and the simulations are carried out for cases where, $\gamma = 10^{-2}$ and $Re = 200$ are kept constant. The model has been tested with and without piezoelectric coupling for a wide range of β values, and the case where the dynamical transitions due to electrical coupling is tangible, has been presented in this section. At the mass ratio of $\beta \in (0.05, 1.0)$, the system either settles to zero oscillation or shows a periodic flutter, which is unchanged with or without the piezoelectric coupling. However, for mass ratio as high as $\beta = 5.0$, the piezoelectric coupling plays a crucial role in the dynamical transitions. In the absence of piezoeletric coupling, the system exhibits periodic dynamics as shown in Figs. 1(a)-1(c). The tip displacement time history shows no modulation in the amplitude, signifying periodic dynamics (see Fig. 1(a)). The corresponding structural envelope shows mixed mode shape oscillations i.e. 1st and 2nd modes; see Fig. 1(b). The flow field shows the effect of periodic vibration giving rise to a $2p$ periodic vortex street (Fig.1(c)). However, the system transitions to an aperiodic state in the presence of piezoelectric

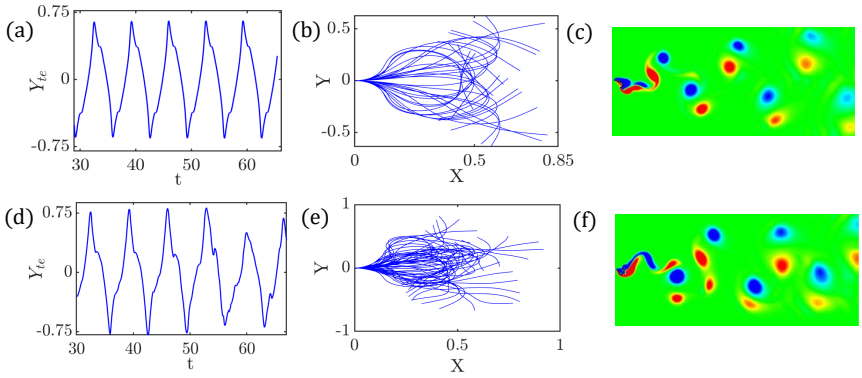

Figure 1: Time histories of beam-tip, beam envelopes and corresponding flowfields without piezo-coupling ((a)-(c)) and with piezo-coupling ((d)-(f)), respectively.

coupling as shown in Figs. 1(d)-1(f) where tip displacement time history shows modulation in the amplitude (Fig. 1(d)) and in the corresponding flow field the vortices are not well-organised (Fig. 1(f)), signifying the characteristics of aperiodic state. The irregular bending is also reflected in the the structural envelope (Fig. 1(e)). The effect of different coupling strengths (ν) are also being investigated currently in our group, to understand the effect of the different piezoelectric materials and will be presented in the the full length paper.

Conclusions

The effect of piezoelectric coupling in the dynamical transition of the three-way coupled FSI system is investigated in the present study. The system evinces periodic dynamics at the higher mass ratio of $\beta = 5.0$ in the absence of piezoelectric coupling. On the contrary, the system transitions to the aperiodic state in the presence of piezoelectric coupling. This study is of importance to identify the proper parametric regime in terms of mass ratio, piezoelectric coupling and bending rigidity in which the energy can be harvested efficiently. The authors are further investigating the effect of different dynamical state on the energy harvesting efficiency of the system.

Acknowledgement

We would like to thank Department of Science and technology (DST), India for funding this work, under the title of "Blade-less Wind Energy Harvesters" and the HPCE IIT Madras for providing with high performance computing facilities.

References

[1] Zhu H.,Zhang C., and Liu W.(2019) Wake-induced vibration of a circular cylinder at a low reynolds number of 100.*Physics of Fluids*.

[2] Akaydin HD. , Elvin N. , and Andreopoulos Y. (2012) The performance of a self-excited fluidic energy harvester. *Materials and Structures*

[3] Akcabay D. T., Young Y. L. (2012), Hydroelastic response and energy harvesting potential offlexible piezoelectric beams in viscous flow, Physics of Fluids 24 054106

[4] Majumdar D., Bose C., Sarkar S. (2020), Capturing the dynamical transitions in the flow-fieldof a flapping foil using immersed boundary method, J. Fluids Struct. 95 102999

[5] Shah, C. L., Majumdar, D., and Sarkar, S. (2020). Delaying the Chaotic Onset in the Flow-Field of Flapping Foil With Flexible Aft Tail. ASME International Mechanical Engineering Congress and Exposition, Vol. 84546, American Society of Mechanical Engineers, 2020, p. V07AT07A027.

[6] Huang W.X., Shin S. J., and Sung H.J. (2007), Simulation of flexible filaments in a uniform flow bythe immersed boundary method.Journal of Computational Physics, 226(2):2206–2228

Cantilevered Extensible Pipes Conveying Fluid: a Consistent Reduced-Order Modeling via the Extended Hamilton's Principle for Nonmaterial Volumes

Daniel de Oliveira Tomin*, Renato Maia Matarazzo Orsino† and Celso Pupo Pesce*
* *Offshore Mechanics Laboratory, Escola Politécnica, University of São Paulo, São Paulo, Brazil*
† *Mechanical Engineering Department, Mauá Institute of Technology, São Paulo, Brazil*

Summary. Applying the Extended Hamilton's Principle for nonmaterial volumes, a nonlinear reduced-order planar model of a cantilevered pipe conveying fluid is developed, consistently considering the effects of axial extensibility and conservation of mass associated to the internal flow. Unlike the corresponding inextensible pipe models, in which the term of transport of kinetic energy in the Extended Hamilton's Principle cancels out, in the present model such a term is not identically zero since the velocity of the flow along the pipe length is a function both of the generalized velocities and coordinates of the problem. The system dynamics is then investigated, assessing how extensibility and mass conservation affect dynamic bifurcations, by comparing root locus diagrams, and by simulating the resulting nonlinear model in some selected scenarios.

Introduction

One of the classical problems of Fluid-Structure Interactions (FSI) is the pipe conveying fluid, which is usually modeled as a flexible tube, with the use of the plug flow hypothesis for the velocity profile of the fluid. In general, the dynamic response is characterized by two types of motion depending on the internal flow velocity: stability around the static equilibrium position or dynamic Hopf bifurcations. As an open system, a proper mathematical formulation should be grounded on consistent variational principles, taking into account momentum and kinetic energy transport terms.
Benjamin [1] was responsible for the earlier investigations in this topic and considered the problem as a chain of articulated rigid pipes conveying fluid. He derived specific versions of Euler-Lagrange Equations and Hamilton's Principle for this system. Later, McIver [2] developed an extended form of Hamilton's Principle for open systems and confirmed Benjamin's work. In both studies, a term related to the transport of momentum appears.
Recently, the generalized forms of these principles were obtained by Irschik & Holl [3] and Casetta & Pesce [4]. In their derivation, an additional term related to the transport of the kinetic energy of the fluid through the nonmaterial surfaces appears, which was not present in McIver's formulation. When the inextensibility condition is assumed, the velocity of the internal plug flow relative to the pipe remains constant. Kheiri & Païdoussis [5] proved that, in this case, the term related to the transport of kinetic energy is identically zero, recovering McIver's formulation. However, when the axial extensibility of the pipe is considered, this term is not zero in the nonmaterial surface at the free end. Therefore, further discussion is needed to assess its theoretical and practical importance.
The present work proposes the formulation and analysis of a 2D reduced-order model for the cantilevered pipe conveying fluid, in which the extensibility is treated consistently, accounting for the conservation of fluid mass inside the pipe. Moreover, from Argand's type diagrams (root loci graphs) obtained through Lyapunov's indirect method, instabilities of the oscillatory modes are assessed. After these investigations, the nonlinear response in some selected scenarios is further analyzed through numerical simulations.
This introduction is followed by four sections, with the last of them bringing concluding remarks. The second section reviews the Extended Hamilton's principle for open systems. The third section describes the extensible pipe conveying fluid model, highlighting how the flow velocity expression is obtained by the application of the integral form of the conservation of mass, and deriving the equations of motion based on the definition of dimensionless variables and Galerkin's projection scheme. In the fourth section, some results are shown in the form of root loci diagrams obtained by a linearization around the static equilibrium, and on numerical integrations of the nonlinear equations of motion.

Hamilton's Principle for Open Systems or Nonmaterial Volumes

In the field of Continuum Mechanics, a material volume is understood as a volume whose closed boundary is moving with the material particles located in it. Because no transport of matter may occur, it can be also called a closed system. Whereas a nonmaterial volume - or a control volume in the terminology of Fluids Mechanics - is a fictional body which instantly coincides with a region defined by material particles; however, its control surface moves arbitrarily with respect to the material boundary, so that the particles accounted within the nonmaterial volume are not always the same, characterizing an open system. Although Hamilton's Principle and the Euler-Lagrange Equations are well formulated for material volumes or closed systems, the use of these variational approaches in problems where material transport exists is not straight-forward and needed further discussion.
According to Meirovitch [6], Hamilton's Principle for closed systems can be derived through the principle of virtual work for material volumes (D'Alembert's Principle). Assuming that δ denotes a variation in the context of Variational Calculus and $\frac{\mathrm{d}(\,)}{\mathrm{d}t}$ is the material derivative with respect to time t, it follows,

$$\delta T + \delta W - \frac{\mathrm{d}}{\mathrm{d}t}\int_V \rho\ (\mathbf{v}\cdot\delta\mathbf{p})\ \mathrm{d}V = 0, \tag{1}$$

where V is the the material volume and $T = \frac{1}{2}\int_V \rho(\mathbf{v}\cdot\mathbf{v})\,\mathrm{d}V$ is the kinetic energy associated with the material particles of mass density ρ, position $\mathbf{p}$ with virtual displacement $\delta\mathbf{p}$ - which satisfies any imposed constraints - and velocity $\mathbf{v} = \frac{\mathrm{d}\mathbf{p}}{\mathrm{d}t}$. δW is the virtual work of the conservative and nonconservative forces.
By integrating (1) over the time interval $t_1 \leq t \leq t_2$ and considering that the configuration of the system is prescribed at the limit points (thus, $\delta\mathbf{p}(t_1) = \delta\mathbf{p}(t_2) = \mathbf{0}$), Hamilton's Principle for material volumes is obtained

$$\int_{t_1}^{t_2} [\delta T + \delta W]\,\mathrm{d}t = 0. \tag{2}$$

McIver [2] was one of the first authors who derived an extended form of Hamilton's Principle for nonmaterial volumes by using Reynolds' transport theorem in the form below, developing the third term of Equation (1) in the form,

$$\frac{\mathrm{d}}{\mathrm{d}t}\int_V \rho\ (\mathbf{v}\cdot\delta\mathbf{p})\ \mathrm{d}V = \frac{\mathrm{d}}{\mathrm{d}t}\int_{V_u} \rho\ (\mathbf{v}\cdot\delta\mathbf{p})\ \mathrm{d}V_u + \int_{\partial V_u} \rho\ (\mathbf{v}\cdot\delta\mathbf{p})\,(\mathbf{v}-\mathbf{u})\cdot\mathbf{n}\,\mathrm{d}\partial V_u. \tag{3}$$

Consider V_u as the the nonmaterial volume whose surface ∂V_u, with external normal unit vector $\mathbf{n}$, is moving according to a velocity field $\mathbf{u}$. Thus, McIver's statement of the principle of virtual work for open systems is obtained and the corresponding Hamilton's Principle can be derived through a similar mathematical procedure as described for material volumes,

$$\int_{t_1}^{t_2} \left[\delta T_u + \delta W - \int_{\partial V_u} \rho\ (\mathbf{v}\cdot\delta\mathbf{p})\,(\mathbf{v}-\mathbf{u})\cdot\mathbf{n}\,\mathrm{d}\partial V_u\right]\ \mathrm{d}t = 0. \tag{4}$$

McIver revealed an extra term related to the transport of momentum through the open boundary which is not present in closed systems, as observed when compared to Equation (2). Also, the author implicitly utilized $\delta T = \delta T_u$ with $\delta T_u = \frac{1}{2}\int_V \rho(\mathbf{v}\cdot\mathbf{v})\,\mathrm{d}V$ as the kinetic energy of the material particles within the nonmaterial volume V_u.
Later, it was found out that McIver's derivation does not recover the extended Euler-Lagrange equations for open systems obtained by Irschik & Holl [3]. In their paper, the authors derived the extended equations using the abstract concept of fictitious particles, which was first introduced in Truesdell & Toupin [7] for the generalization of Reynolds' transport theorem. These fictitious particles have some of same properties of their material counterparts like kinetic energy density, but their velocity is $\mathbf{u}$, the same of the control surface ∂V_u. Consider that $\mathbf{r}$ represents their position and $\delta\mathbf{r}$ is the corresponding virtual displacement. Therefore, $\mathbf{u} = \frac{\mathrm{d}\mathbf{r}}{\mathrm{d}t}$. Further investigation of Hamilton's principle for nonmaterial volumes was then necessary.
This inconsistency was addressed in a paper by Casetta & Pesce [4]. Applying the concept of fictitious particles, the following mathematical statement can be proven

$$\begin{aligned}\delta T - \frac{\mathrm{d}}{\mathrm{d}t}\int_V \rho\ (\mathbf{v}\cdot\delta\mathbf{p})\ \mathrm{d}V = {}& \delta T_u + \int_{\partial V_u} \frac{1}{2}\,\rho\,(\mathbf{v}\cdot\mathbf{v})\,(\delta\mathbf{p}-\delta\mathbf{r})\cdot\mathbf{n}\,\mathrm{d}\partial V_u \\ & - \frac{\mathrm{d}}{\mathrm{d}t}\int_{V_u} \rho\ (\mathbf{v}\cdot\delta\mathbf{p})\ \mathrm{d}V_u - \int_{\partial V_u} \rho\ (\mathbf{v}\cdot\delta\mathbf{p})\,(\mathbf{v}-\mathbf{u})\cdot\mathbf{n}\,\mathrm{d}\partial V_u.\end{aligned} \tag{5}$$

Replacing the first and the third terms of Equation (1) with Equation (5), a consistent form of the principle of virtual work for open systems is written. By integrating with respect to t over $t_1 \leq t \leq t_2$, the appropriate Hamilton's Principle was derived and Irschik & Holl [3] extended Euler-Lagrange Equations could be obtained. In this case, Hamilton's Principle for nonmaterial volumes is written as follows, [4]:

$$\int_{t_1}^{t_2} \left[\delta T_u + \delta W - \int_{\partial V_u} \rho\ (\mathbf{v}\cdot\delta\mathbf{p})\,(\mathbf{v}-\mathbf{u})\cdot\mathbf{n}\,\mathrm{d}\partial V_\mu + \int_{\partial V_u} \frac{1}{2}\,\rho\,(\mathbf{v}\cdot\mathbf{v})\,(\delta\mathbf{p}-\delta\mathbf{r})\cdot\mathbf{n}\,\mathrm{d}\partial V_u\right]\ \mathrm{d}t = 0. \tag{6}$$

In contrast to Equation (4), not only a term for the transport of momentum appears, but also one related to the flux of kinetic energy through the control surface. Respectively, the third and fourth terms.
Whenever the last term of Equation (6) is equal to zero, McIver's form - Equation (4) - is recovered, which has been extensively utilized for the modeling of the pipe conveying fluid. In fact, take a system described by a set of a finite number of generalized coordinates q_i. Assume $\dot{(\,)} = \frac{\partial(\,)}{\partial t}$. The following identities are valid: $\delta\mathbf{p} = \frac{\partial\mathbf{p}}{\partial q_i}\delta q_i = \frac{\partial\mathbf{v}}{\partial\dot{q}_i}\delta q_i$ and $\delta\mathbf{r} = \frac{\partial\mathbf{r}}{\partial q_i}\delta q_i = \frac{\partial\mathbf{u}}{\partial\dot{q}_i}\delta q_i$. In the case of an extensible pipe, from those identities, it can be proved that the last term in Eq (6) is nonzero, as outlined in the next section.

Extensible Pipe Conveying Fluid

Imagine a cantilevered, slender, cylindrical and flexible pipe constituted by an elastic linear material, that is subjected to large displacements and small strains in a 2D plane. Therefore, it can be considered as a Euler-Bernoulli beam with geometric nonlinearities. Its undeformed configuration is vertical. An internal axial, steady and incompressible flow is

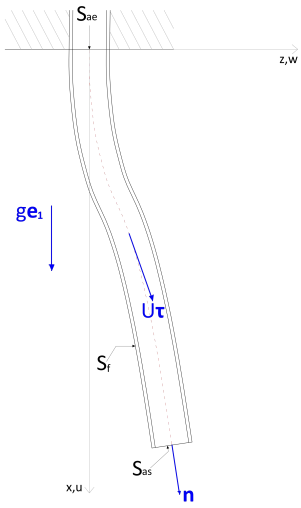

(a) Extensible pipe conveying fluid.

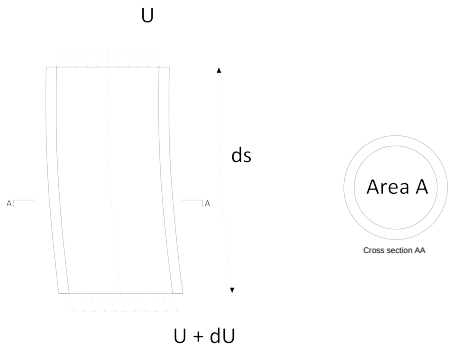

(b) Infinitesimal volume of the tube with length $\mathrm{d}s$.

Figure 1: The 2D model.

present and its velocity profile is modeled as a plug flow. No external fluid or hydrodynamic loads exist. The pipe is considered slender, so a singular position could be described by the centerline. The system is depicted in Figure 1a.
The fixed point of the centerline is adopted as the origin of a coordinate system (x, z) with corresponding unit vectors $(\mathbf{e_1}, \mathbf{e_2})$, defining an orthonormal basis. The x-coordinate is parallel to the length of the tube in the reference position and aligned with the local gravitational field. Thus, its undeformed configuration is denoted by $(x_0, z_0) = (x_0, 0)$, with $x_0 = 0$ being the fixed end and x_0 the free end. The associated position vector is $\mathbf{R} = (x, z)$, displacements are $u = x - x_0$ and $w = z - z_0 = z$, s is the arc length coordinate along the centerline and $\kappa = \left|\frac{\partial \mathbf{R}^2}{\partial s^2}\right|$ is the curvature.
The unstretched pipe length is L, its bending stiffness is EI, axial stiffness EA, Poisson's ratio ν (volume change rate $b = 1 - 2\nu$) and linear mass m. Consider E as the Young's modulus, A as the sectional area (A_i is the internal area) and I as the area moment of inertia around the z-axis. The fluid linear mass is M and the flow has a velocity $U\boldsymbol{\tau}$, in which $\boldsymbol{\tau} = \frac{\partial \mathbf{R}}{\partial s}$ is the instantaneous tangent unit vector. The gravitational acceleration is g. The nonmaterial volume is constituted by the open surfaces $S_{ae} \cup S_{as}$ and the closed boundary S_f.

On the modeling of the internal flow velocity

If the pipe is considered inextensible, the velocity field U is equal to the constant U_0. When the extensibility condition is utilized, Ghayesh, Païdoussis & Amabili [8] proposed an expression for U along the pipe length based on the conservation of the volumetric flow rate inside the pipe

$$U = U[q_i] = \frac{1 + \varepsilon[q_i]}{1 + b\varepsilon[q_i]} U_0, \tag{7}$$

where ε is the axial strain. As ε is a function of the generalized coordinates of the problem, so is U.
In the present work, the authors adopt the conservation of mass for incompressible flows applied in an infinitesimal volume of the tube (Fig. 1b) to obtain an generalized form for U. Consider that its length is $\mathrm{d}s$ and the velocities upstream and downstream are U and $U + \mathrm{d}U = U + \frac{\partial U}{\partial s}\mathrm{d}s$, respectively. Using the definition of $\frac{\partial U}{\partial s}\mathrm{d}s = \frac{\partial U}{\partial s}\frac{\partial s}{\partial x_0}\mathrm{d}x_0 = \frac{\partial U}{\partial x_0}\mathrm{d}x_0$, $\varepsilon = \frac{\mathrm{d}s - \mathrm{d}x_0}{\mathrm{d}x_0}$ and area variation due to Poisson effect through the volume change rate b, it can be proven that

$$U = U[\dot{q}_i; q_i] = U_0 - \int_0^{x_0} \frac{b(1 + \varepsilon[q_i])}{1 + b\varepsilon[q_i]} \frac{\partial \varepsilon[q_i]}{\partial t}\, \mathrm{d}x_0. \tag{8}$$

Notice that the expression above is a function of both the generalized coordinates and velocities of the problem.

Derivation of the equations of motion

The equations of motion in the continuum are formulated up to polynomial cubic-order terms with Equation (6) and discretized with Galerkin's method, originating ODEs. The kinetic energy T_u accounts for the tube and fluid particles, so

$$T_u = \frac{m}{2}\int_0^L \dot{\mathbf{R}} \cdot \dot{\mathbf{R}}\, \mathrm{d}x_0 + \frac{M}{2}\int_0^L \left(\dot{\mathbf{R}} + U\boldsymbol{\tau}\right) \cdot \left(\dot{\mathbf{R}} + U\boldsymbol{\tau}\right)\, \mathrm{d}x_0. \tag{9}$$

Suppose, for the sake of simplicity, that the work of the nonconservative forces is identically null, thus $W = -V$, in which V is the potential energy related to the deformation of the pipe and the gravitational field

$$V = \frac{EA}{2}\int_0^L \varepsilon^2 \,\mathrm{d}x_0 + \frac{EI}{2}\int_0^L (1+\varepsilon)^2\kappa^2 \,\mathrm{d}x_0 - (m+M)g\int_0^L x \,\mathrm{d}x_0. \tag{10}$$

Considering the nonmaterial volume, we can write $\mathbf{v} = \dot{\mathbf{R}} + U\boldsymbol{\tau}$ and $\mathbf{u} = \dot{\mathbf{R}}$, therefore, $\delta\mathbf{p} = \left(\frac{\partial\dot{\mathbf{R}}}{\partial\dot{q}_i} + \boldsymbol{\tau}\frac{\partial U}{\partial\dot{q}_i}\right)\,\delta q_i$ and $\delta\mathbf{r} = \frac{\partial\dot{\mathbf{R}}}{\partial\dot{q}_i}\,\delta q_i$. The transport terms are nonzero only if $x_0 = L$, so

$$\int_{\partial V_u} \rho\,(\mathbf{v}\cdot\delta\mathbf{p})\,(\mathbf{v}-\mathbf{u})\cdot\mathbf{n}\,\mathrm{d}\partial V_\mu = MU\left[\left(\dot{\mathbf{R}}+U\boldsymbol{\tau}\right)\cdot\left(\frac{\partial\dot{\mathbf{R}}}{\partial\dot{q}_i}+\boldsymbol{\tau}\frac{\partial U}{\partial\dot{q}_i}\right)\right](\boldsymbol{\tau}\cdot\boldsymbol{\tau})\,\delta q_i\Big|_{x_0=L}, \tag{11}$$

$$\int_{\partial V_u} \frac{1}{2}\,\rho\,(\mathbf{v}\cdot\mathbf{v})\,(\delta\mathbf{p}-\delta\mathbf{r})\cdot\mathbf{n}\,\mathrm{d}\partial V_u = \frac{M}{2}\frac{\partial U}{\partial\dot{q}_i}\left[\left(\dot{\mathbf{R}}+U\boldsymbol{\tau}\right)\cdot\left(\dot{\mathbf{R}}+U\boldsymbol{\tau}\right)\right](\boldsymbol{\tau}\cdot\boldsymbol{\tau})\,\delta q_i\Big|_{x_0=L}. \tag{12}$$

A discussion about the term related to the flux of kinetic energy - Eq. (12) - is also found in Kheiri & Païdoussis [5]. This term relies on the value of $\delta\mathbf{p} - \delta\mathbf{r} = \boldsymbol{\tau}\frac{\partial U}{\partial\dot{q}_i}\,\delta q_i$. If the pipe is ideally inextensible, $U = U_0$ and $\frac{\partial U}{\partial\dot{q}_i} = 0$. When the extensibility condition is utilized as in Ghayesh, Païdoussis & Amabili [8], Equation (7), the velocity U is not a function of the generalized velocities, therefore, it still cancels out. The present research proposes Equation (8) as an expression for U. Under this condition, $\frac{\partial U}{\partial\dot{q}_i} \neq 0$.

The polynomial cubic-order equations of motion in the continuum are derived following Variational Calculus techniques. Considering established dimensionless quantities well defined in the literature listed in Table 1, the PDEs can be rewritten and discretized via Galerkin's method.

Table 1: Dimensionless quantities.

Dimensionless parameter	**Symbol**	**Definition**
Undeformed coordinate	ξ	$\frac{x_0}{L}$
Axial coordinate and displacement	$\hat{x}$, $\hat{u}$	$\frac{x}{L}$, $\frac{u}{L}$
Transversal coordinate and displacement	$\hat{z}$, $\hat{w}$	$\frac{z}{L}$, $\frac{w}{L}$
Time	τ	$\left(\frac{EI}{M+m}\right)^{1/2}\frac{t}{L^2}$
Axial and flexural stiffness ratio	α	$\frac{EA}{EI}L^2$
Internal flow velocity	v	$\left(\frac{M}{EI}\right)^{1/2}U_0 L$
Quotient between linear masses	β	$\frac{M}{M+m}$
Gravitational and flexural stiffness ratio	γ	$\frac{M+m}{EI}gL^3$

For the proposed discretization, the ODEs are obtained assuming

$$\hat{u}[\xi;\tau] \cong \sum_{k=1}^{N}\psi_k[\xi]\hat{u}_k[\tau], \tag{13}$$

$$\hat{w}[\xi;\tau] \cong \sum_{k=1}^{N}\psi_k[\xi]\hat{w}_k[\tau], \tag{14}$$

in which ψ_k represents the family of projection functions

$$\psi_k[\xi] = \sqrt{2}\left(\frac{1-\cos\Lambda_k\xi}{\Lambda_k}\right). \tag{15}$$

Each value Λ_k results from the characteristic equation $\cos\Lambda_k = 0$. With these definitions, fixed end boundary conditions $\hat{u}[\xi=0;\tau]=0$, $\hat{w}[\xi=0;\tau]=0$ and $\frac{\partial\hat{w}}{\partial\xi}[\xi=0;\tau]=0$ are satisfied.

Results

Through a process of linearization of the corresponding nonlinear ODEs around the static equilibrium configuration - using v as a control parameter - root loci diagrams can be obtained and the stability of the system evaluated with the determination of the critical velocity v_{crit} by assessing the real part of the eigenvalues, following Lyapunov's indirect method. Numerical integration is utilized to verify the dynamic behavior observed in the Argand's type diagrams.
The nonlinear equations of motion of the inextensible pipe conveying fluid obtained by Semler, Li & Païdoussis [9] are also discretized with Equation (14) and analyzed. These results are compared with the proposed extensible model, which is consistent with the continuity equation, and the extensible system found in Ghayesh, Païdoussis & Amabili [8].
Two distinct scenarios of Table 3 are investigated with $N = 8$. The values are commonly used in the technical literature.

Table 2: Chosen scenarios.

Scenarios	β	α	ν	b	γ
S1	0.2	1000	0.5	0	0
S2	0.2	1000	0.5	0	100

It is important to note that the static equilibrium configuration for the transversal displacement is equal to zero because no external forces are assumed. For the extensible models, the axial static displacement is a function of γ and v, and is depicted with a graphic of $u \times v$ for some cross sections of the pipe; while the static displacement is identically zero in the inextensible case.

Root loci of the linearized models

The root loci diagrams show how each period T_i evolves with v, also displaying a color scale related to the value of the real part of the corresponding eigenvalue λ_i , i.e., characterizing the stability of the system in the neighborhood of the static equilibrium points. The eigenvalues and periods related to the transversal modes are shown in the inextensible diagrams. In the extensible ones, the associated axial quantities are perceived.
Figures 2 and 3 illustrate the stability analysis of **S1**. According to Figures 2, 3b and 3d, a Hopf bifurcation in the second transversal mode occurs at approximately the same value, defining the critical velocity $v_{crit} \approx 5.6$. The curves associated with the transversal modes are similar, with discrepancies for higher values of v in the post-critical interval, related to the order of the terms utilized in the derivation of each set of equations of motion and their linearizations. The axial periods present in the extensible diagrams remain almost constant. The main difference between the extensible models can be found in the axial static equilibrium configuration of Figures 3a and 3c: with the increase of v, a contraction is present in all the cross sections of the proposed extensible model, while in the results from Ghayesh, Païdoussis & Amabili [8], there is no static displacement.

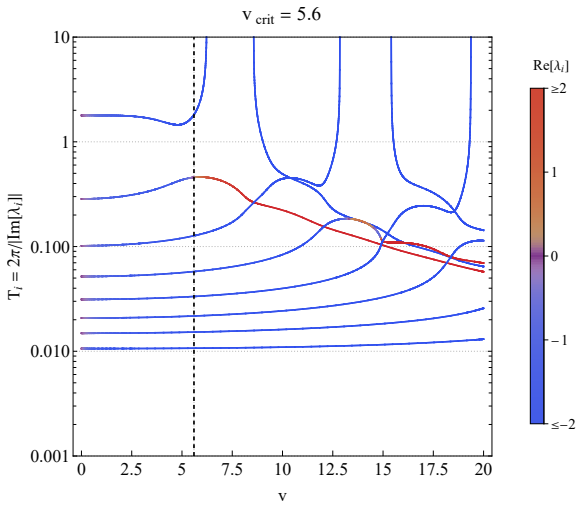

Figure 2: Root locus of the inextensible model for Scenario **S1**.

The stability analysis of Scenario **S2** is presented in Figures 4 and 5. The gravitational effects associated to $\gamma \neq 0$ are well documented in the literature, thus, a higher critical velocity is expected and noticed. In all the models, a Hopf bifurcation happens in the third transversal mode. For the inextensible model and the extensible model formulated in [8], Figures 4 and 5d, $v_{crit} \approx 10.5$, whereas in the proposed extensible model, Figure 5b, $v_{crit} \approx 11.3$, a significantly different value. The periods related to the axial modes are still relatively constant with v.

The behavior of the axial static configurations of Figures 5a and 5c are remarkably distinct: as $\gamma > 0$, there is a pipe elongation present in both of the graphs at $v = 0$, but a contraction in all the cross sections exists for the proposed extensible model and the elongation becomes higher in the case of the model based on [8].

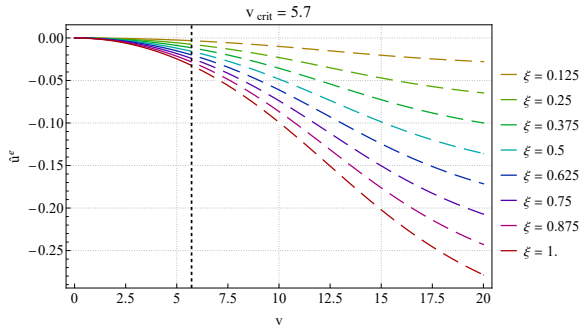

(a) Axial static equilibrium configuration of the proposed extensible model for some cross sections of the pipe.

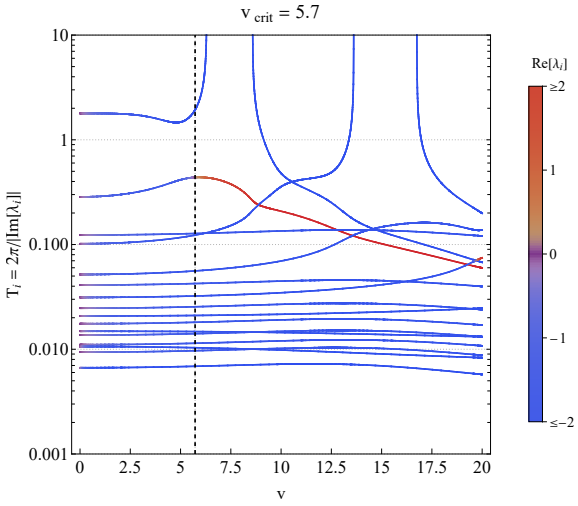

(b) Root locus of the proposed extensible model.

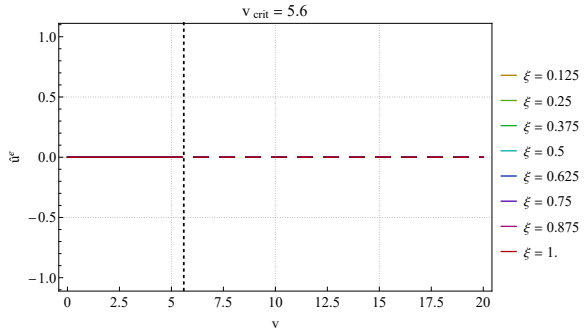

(c) Axial static equilibrium configuration of the model derived in [8] for some cross sections of the pipe.

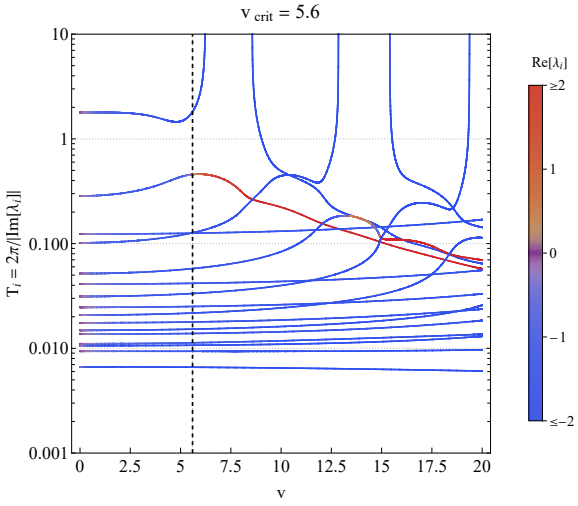

(d) Root locus of the model derived in [8].

Figure 3: Stability analysis of the extensible models for Scenario **S1**.

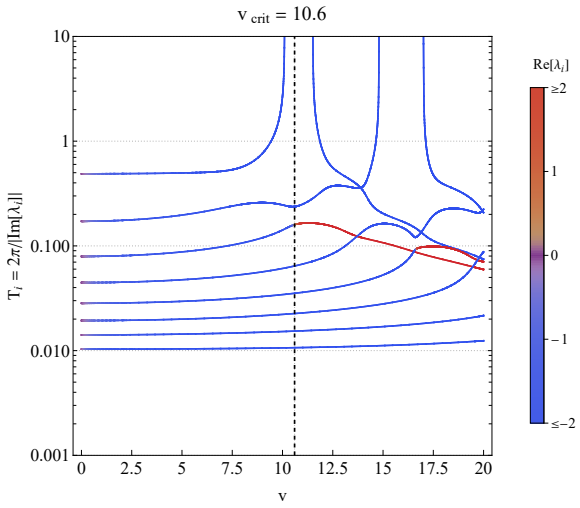

Figure 4: Root locus of the inextensible model for Scenario **S2**.

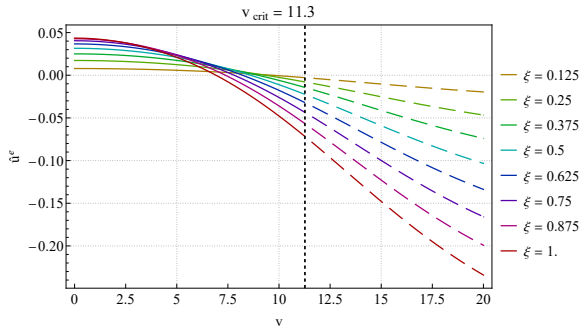

(a) Axial static equilibrium configuration of the proposed extensible model for some cross sections of the pipe.

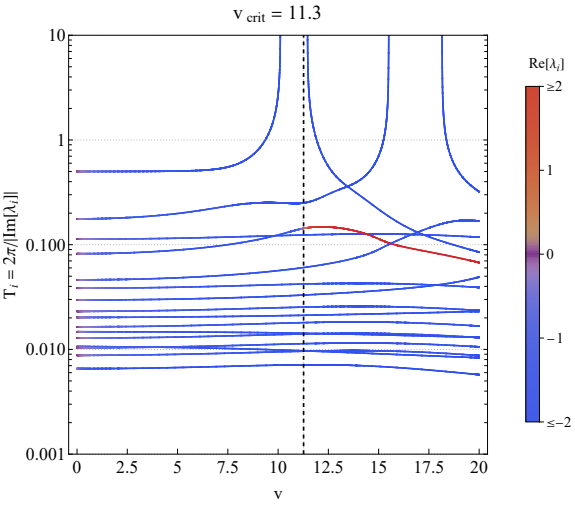

(b) Root locus of the proposed extensible model.

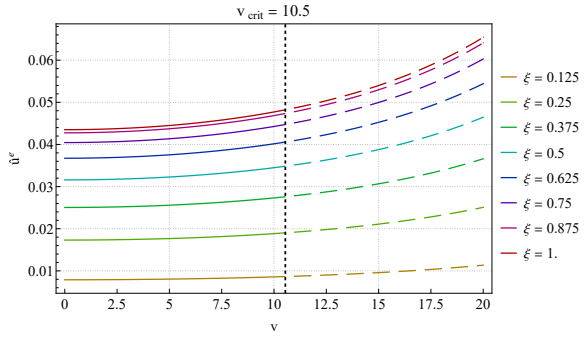

(c) Axial static equilibrium configuration of the model derived in [8] for some cross sections of the pipe.

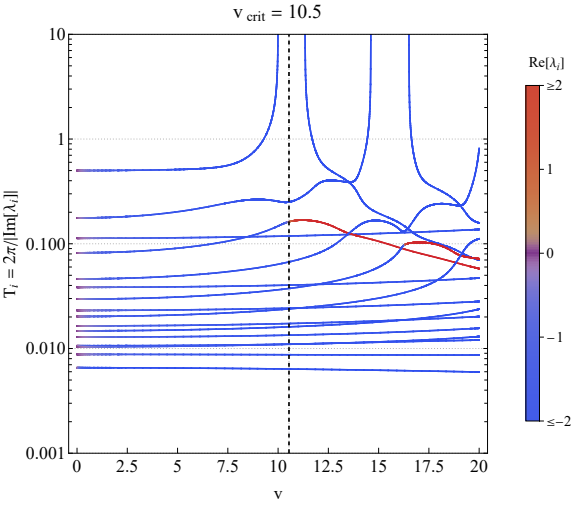

(d) Root locus of the model derived in [8].

Figure 5: Stability analysis of the extensible models for Scenario **S2**.

Numerical integration

Numerical integration of the nonlinear equations of motion of Scenario **S2** at $v = 11$ is done to verify the different behaviors foreseen from the root loci: for the ideally inextensible model and the extensible model of Ghayesh, Païdoussis & Amabili [8], there is a dynamic instability denoted by limit cycles; for the extensible model proposed in this work, the root loci indicate stability in the vicinity of the static equilibrium points. The free end ($\xi = 1$) axial and transversal displacements are shown in the Figures 6 and 7.

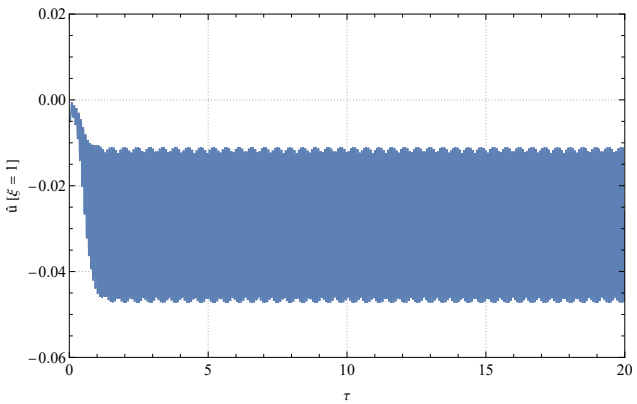

(a) $\hat{u}[\xi = 1; \tau] \times \tau$.

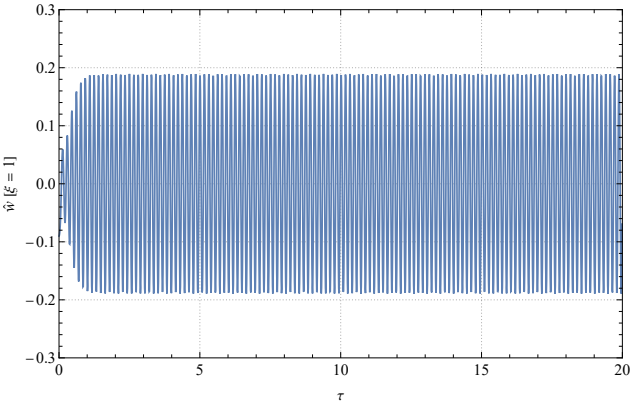

(b) $\hat{w}[\xi = 1; \tau] \times \tau$.

Figure 6: Numerical integration of Scenario **S2** at $v = 11$ of the inextensible model shows dynamic oscillatory instability.

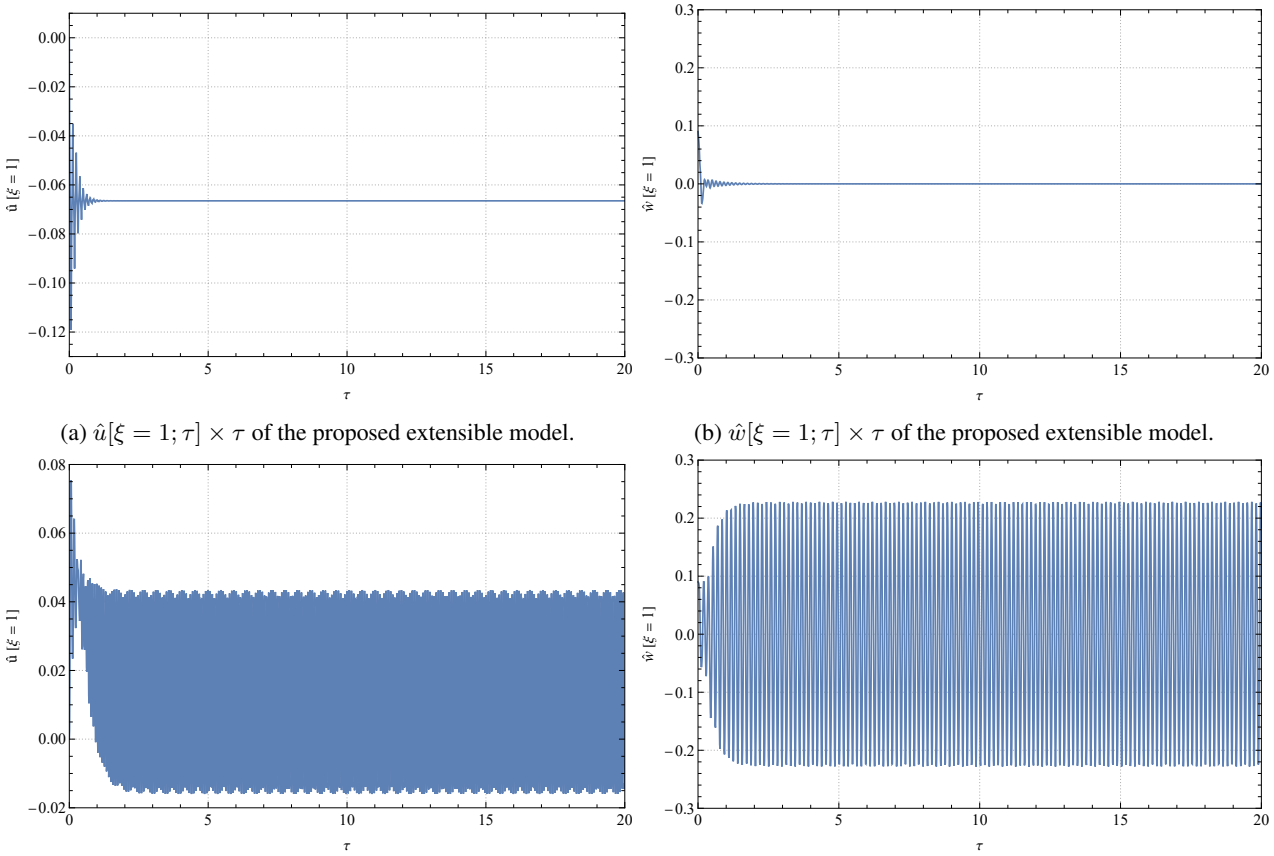

(a) $\hat{u}[\xi = 1; \tau] \times \tau$ of the proposed extensible model.

(b) $\hat{w}[\xi = 1; \tau] \times \tau$ of the proposed extensible model.

(c) $\hat{u}[\xi = 1; \tau] \times \tau$ of the model derived in [8].

(d) $\hat{w}[\xi = 1; \tau] \times \tau$ of the model derived in [8].

Figure 7: Numerical integration of Scenario **S2** at $v = 11$ of the proposed extensible model shows stability around the static equilibrium, while Ghayesh, Païdoussis & Amabili [8] extensible model displays a post-critical oscillatory regime.

The results obtained in time domain are consistent with those predicted by the linear analysis. Post-critical oscillatory regimes are noticed in the graphics of the inextensible and Ghayesh, Païdoussis & Amabili [8] models, whereas the proposed extensible model - which satisfies the conditions of the conservation of mass - shows stability.

Concluding Remarks

In this paper, a 2D reduced-order model for the cantilevered extensible pipe conveying fluid problem is proposed, in which the necessary conditions for conservation of mass (continuity equation) are satisfied. This model is obtained using the Extended Hamilton's Principle for nonmaterial volumes as formulated in Casetta & Pesce [4], with a cubic-order polynomial truncation and approximation followed by a discretization procedure based on Galerkin's method.

Although the formulation of the extensible model has similarities with nonlinear models of large displacements and small strains much discussed in the technical literature, the main difference is the consistent consideration of the conservation of mass in the internal flow. With such a hypothesis, a closed-form expression along the pipe length for the internal velocity U can be derived, which is a function of both the generalized coordinates and velocities of the problem (Eq. (8)). Previously, an extensible model discussed in Ghayesh, Païdoussis & Amabili [8] utilized Equation (7), in which the internal velocity U only depends on the generalized coordinates.

These distinct expressions for U have implications in the term related to flux of kinetic energy present in the Extended Hamilton's Principle, the fourth term of Equation (6). Under the assumption of an ideally inextensible pipe or Ghayesh, Païdoussis & Amabili [8] extensible model, this term is identically zero and the Hamilton's Principle for nonmaterial volumes is reduced to a form first obtained in McIver [2], Eq. (4). With the consideration of the proposed extensible model, the term associated with the transport of kinetic energy is nonzero and scenarios are investigated to study its influence on the dynamic response of the system.

Two tools are utilized for the comparison of the inextensible equations of motion of Semler, Li & Païdoussis [9], the extensible model described in this work and the extensible one obtained in Ghayesh, Païdoussis & Amabili [8]: (i) root loci diagrams calculated in the neighborhood of the static equilibrium configuration with v as control parameter and the characterization of the stability condition through Lyapunov's indirect method; (ii) numerical integration of the discretized nonlinear equations of motion to verify the dynamic behavior predicted by the root loci diagrams.

The analysis indicate a similar response for Scenario **S1** for all the models, with a Hopf bifurcation associated with the second transversal mode determining a critical velocity of $v_{crit} \approx 5.6$. The axial static equilibrium configuration of the

extensible models are distinct: for the proposed model, there is a contraction with the increasing of v, whereas for the extensible one derived in [8], the static displacement is zero.
For Scenario **S2**, a Hopf bifurcation occurs at the third transversal mode, but for the consistent extensible model $v_{crit} \approx 11.3$, and for the others, $v_{crit} \approx 10.5$. The root loci diagrams show a deviation of the present critical velocity with the numerical integration, confirming the expected response at $v = 11$ for the models. The axial static equilibrium remains different for the two extensible pipes.
Thus, extensibility effects may have substantial practical implications in the dynamics of this kind of system. The results obtained with the proposed extensible model reveal a higher critical velocity in a given scenario and different axial static configurations when compared to the cited previous models.

Acknowledgments

The São Paulo State Research Foundation (FAPESP) is gratefully acknowledged, for having supporting the whole development of the basic mathematical formalism, since 2012, through the Grants 2016/09730-0, 2013/02997-2 and 2012/10848-4, which set the fundamental grounds for this research to be successfully conducted, and for supporting the Conference attendance, Grant 2022/04072-5.
The authors also acknowledge Shell Brasil and ANP (Brazil's National Oil, Natural Gas, and Biofuels Agency) for the strategic support provided through the R&D levy regulation. D. Tomin and C. Pesce acknowledge CNPq - the Brazilian National Research Council, for a MSC scholarship, through the Graduate Program in Mechanical Engineering and for the Research Grant 308230/2018-3, respectively.

References

[1] Benjamin T.B. (1961) Dynamics of a system of articulated pipes conveying fluid - I.Theory. *Proc. R. Soc. London. Ser. A. Math. Phys. Sci.* **261**:457-486.

[2] McIver D.B. (1977) Hamilton's principle for systems of changing mass. *J. Eng. Math.* **7**:249-261.

[3] Irschik H., Holl H.J. (2002) The equations of Lagrange written for a non-material volume. *Acta Mech.* **153**:231-248.

[4] Casetta L., Pesce C.P. (2013) The generalized Hamilton's principle for a non-material volume. *Acta Mech.* **224**:919-924.

[5] Kheiri M., Païdoussis M.P. (2014) On the use of generalized Hamilton's principle for the derivation of the equation of motion of a pipe conveying fluid. *J. Fluids Struct.* **50**:18-24.

[6] Meirovitch, L. (1970) Methods of Analytical Dynamics. McGraw-Hill, NY

[7] Truesdell, C., Toupin, R.A. (1960) The classical field theories. In: Handbuch der Physik, vol. II/1: Prinzipien der klassischen Mechanik und Feldtheorie, pp. 226–793. Springer, Berlin

[8] Ghayesh M.H., Païdoussis M.P., Amabili M. (2013) Nonlinear dynamics of cantilevered extensible pipes conveying fluid. *J. Sound Vib.* **332**:6405-6418.

[9] Semler C., Li, M.X., Païdoussis M.P. (1994) The non-linear equations of motion of pipes conveying fluid. *J. Sound Vib.* **169**:577-599.

Thursday, July 21, 2022
08:30 - 10:30

MS-19 Fluid-Structure Interaction
Saint Clair 3B

Chair: Morten Brons

08:30 - 08:50
Freezing of Unsteady NonlinearWaves over an uneven bottom by Phase-Space Manipulation
EELTINK Debbie, BRANGER Hubert, LUNEAU Christopher, ARMAROLI Andrea, BRUNETTI Maura, KASPARIAN Jérôme, **GOMEL Alexis***
*University of Geneva (Bd. Carl Vogt 66, 1205 Geneva Switzerland)

08:50 - 09:10
Experimental Investigation of Flexible Cantilevered Pipes Aspirating Water under VIV
DEFENSOR Filho Wagner, **PESCE Celso***, FRANZINI Guilherme, VERNIZZI Guilherme, MACIEL Vitor, ORSINO Renato
*Celso Pupo Pesce (University of São Paulo Laboratorio de Mecanica Offshore Av. Prof. Lúcio Martins Rodrigues, Tr 4, n. 434 - 05508-020 São Paulo Brazil) - Escola Politécnica, University of São Paulo (Av. Prof. Mello Moraes 2231 05508-030 São Paulo, SP Brazil)

09:10 - 09:30
Flow-induced vibrations of two circular cylinders in tandem in a cross flow
ZHAO Jisheng, THOMPSON Mark, **HOURIGAN Kerry***
*Monash University (Department of Mechanical and Aerospace Engineering, 17 College Walk, Monash University Australia)

09:30 - 09:50
Fluid dynamics effect in large arrays
ANDE Raghu*
*Department of Mechanical Engineering, University of Canterbury (Ilam road, Christchurch, 8041 New Zealand)

09:50 - 10:10
Topology of exotic wakes
BRONS Morten*, NIELSEN Anne Ryelund, MATHARU Puneet, HEIL Matthias
*Technical University of Denmark (Lyngby Denmark)

Freezing of Unsteady Nonlinear Waves over an uneven bottom by Phase-Space Manipulation

A. N. Gomel*, D. Eeltink*, M. Brunetti*, J. Kasparian*,A. Chabchoub†, S.Trillo‡ and A.Armaroli§
*Institute of Environmental Science, University of Geneva, Bd. Carl Vogt 66, 1205 Geneva, Switzerland
†School of Civil Engineering, The University of Sydney, Australia
†Disaster Research Institute Hakubi Center for Advanced Research, Kyoto University, Japan
‡Deparment of Engineering, University of Ferrara, Via Saragat 1, Italy
§PhLAM,Université de Lille, 50 avenue Halley, Villeneuve d'Ascq, France

Summary. We develop two frameworks for "freezing" modulationally unstable wave packets of gravity waves over an uneven bottom modeled by a finite-depth third-order non-linear Schrödinger equation. We compare with experimental results in a 30 m wavetank featuring a sharp depth transition and propose a theoretical route for stabilizing of the modulated wave packets over an "adaibatic" depth variation.

Theoretical framework and experimental setup

We consider the stabilization of modulationally unstable wave packets within the framework of the nonlinear Schrödinger equation (NLS) in variable water depth [1].

$$i\frac{\partial U}{\partial \xi} + \alpha(kh)\frac{\partial^2 U}{\partial \tau^2} - \beta(kh)|U|^2 U = -i\mu_0 \frac{\partial(kh)}{\partial \xi} U \tag{1}$$

This is possible thanks to the simultaneous dependence of the parameters α and β in Eq. (1) on the adimentional depth (kh), and has also been verified in an optical fiber experiment [4], where there is even more freedom to change the parameters.
We provide two frameworks for the understanding and development of the stabilization, *or "freezing"*, of highly modulated waves. The first theoretical framework is to connect a solution related to modulationally unstable waves, such as the Akhmediev breather (AB), to a solution like the dnoidal function which is related to a stable wavepacket. The second consists in reducing the phase space to that of a carrier wave of frequency ω_0 and the first two sidebands at $\omega_0 \pm \Omega$ (the so-called three wave picture). In this context, "freezing" the wave packet corresponds to an expansion of a homoclinic orbit and its transformation into an elliptic fixed point through the simultaneous variation of the NLS parameters α and β. We experimentally demonstrate this process in a $30 \times 1\ m^2$ water wave tank with a fake bottom floor as shown in figure 1 (a), and provide a rigorous theoretical description of this process for a sharp change in bathymetry [3]. We also provide a stabilization route when the bathymetry change is very slow [2]. The theoretical predictions in the three-wave picture and the measurements show that the relative phase among the side-bands locks to π and their relative amplitude oscillates around a finite value (fig 1, panels on the right). As shown in figure 1, apart from a 10% conversion to higher-order side-bands, this implies that the breathing stage of modulation instability (MI) is indeed frozen. We confirm that this complex wave dynamics is robust and such control of MI processes is feasible in a realistic experimental system. Our results highlight the influence of topography and how waveguide properties can influence and manipulate the lifetime of nonlinear and extreme waves.

Conclusions

We study the nonlinear stage of evolution of modulational instability in surface gravity waves over a water body of increasing depth. We show that this stage can be stabilized and results in a uniform train of pulses on a background.
The initial condition does not need to be restricted to an exact NLS solution (as ABs), since we have shown that freezing occurs also in a three-wave system.
We have found a theoretical condition to dynamically stabilize unstable nonlinear waves. While the approach applies to any system described by the NLS equation, and could therefore be easily generalized to other dynamical models, we have experimentally confirmed our finding for the specific case of wave hydrodynamics. A sharp change in water depth simultaneously modifies the dispersion and nonlinearity experienced by surface gravity wave packets, thus dramatically modifying their dynamical behaviour. In the case of ABs, the separatrix expands and ends up enclosing the system trajectory, which is stabilized around an elliptic fixed point. This jump can be described as the optimal matching of an initial AB solution to a steady dnoidal solution of the universal NLS equation, illustrating the generality of this wave control process.
Although the flexibility available to vary parameters in the hydrodynamics of surface water-waves is much less than in other physical systems, such as optical fibers, our results help to clarify the possibility to dynamically control the breathing evolution of water wave-packets and to understand the impact of bathymetry on the persistence (or lifetime) of rogue waves.

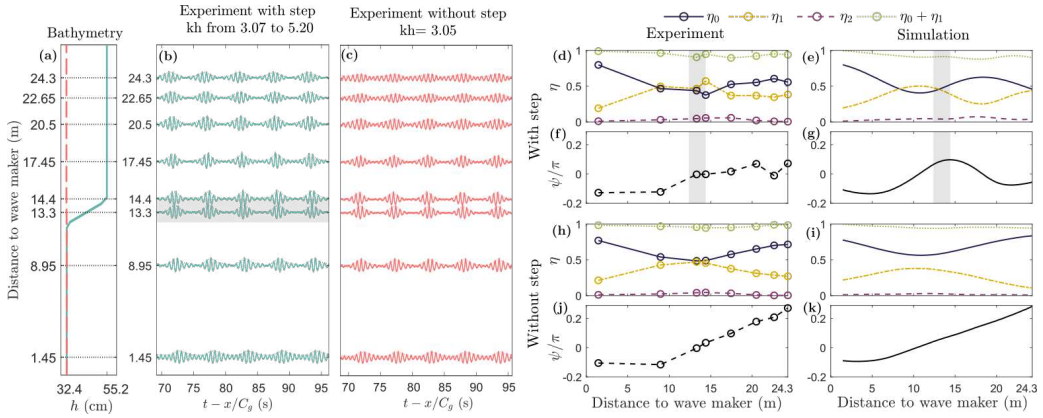

Figure 1: Left: (a) Water wave flume with artificial floor setup (cyan line), and the constant floor setup (dashed coral line). (b) Wave height at each recorded position for the experiment with variable bathymetry, multiplied by a factor 20; the gray stripe indicates the position of the step. (c) Wave height at each recorded position for the experiment with constant bathymetry, multiplied by a factor 20. (d)–(k) Sideband evolution of the AB-type surface water wave over the adopted bathymetry with the depth step (d),(e),(f),(g), and the constant flat bottom h_0 (h),(i),(j),(k). Here the initial condition for the envelope is of the form $U(\xi, \tau = 0) = u_0 e^{i\varphi_0} + u_1 e^{i\Omega\varphi_1} + u_{-1} e^{-i\Omega\varphi_{-1}}$, the sideband fraction $\eta_j = |u_j|^2/(|u_0|^2 + |u_1|^2 + |u_{-1}|^2)$ and the relative phase $\psi = (\varphi_1 + \varphi_{-1})/2 - \varphi_0$. (d)–(h) Sideband dynamics as identified from the eight gauge measurements, connected by a linear interpolation; (g)–(i) corresponding NLS equation-simulated evolution. (d),(e),(h),(i) Sideband fractions η_0, η_1, η_2 of modes at detuning 0 (carrier), Ω, and 2Ω, respectively. (f),(g),(j),(k) Phase ψ of first-order sidebands (modes at $\pm\Omega$) relative to the carrier frequency .

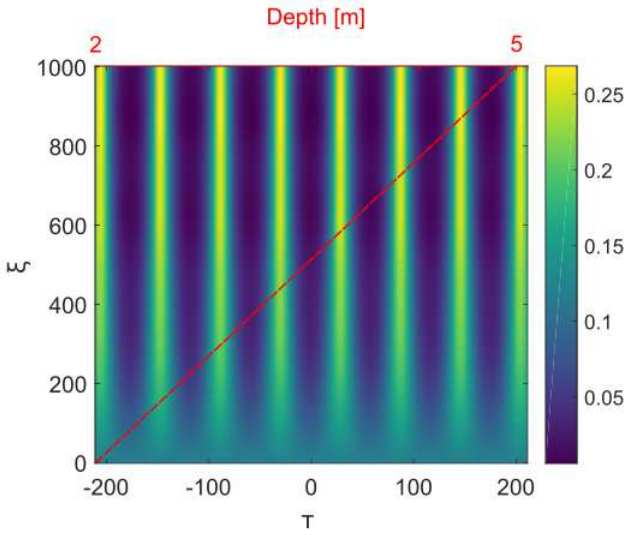

Figure 2: Evolution of the envelope amplitude (shown in meters on the colorbar) from a perturbated plane wave initial condition to a stabilized modulated wave packet over a constant slope from 2 m to 5 m.

References

[1] Djordjevic, V. and Redekopp, L., On the development of packets of surface gravity waves moving over an uneven bottom, ZAMP 29, 950-962 (1978)..

[2] Armaroli, A. et al., Stabilization of uni-directional water wave trains over an uneven bottom. 2021, Nonlinear Dynamics 101 , 1131-1145 (2021).

[3] Gomel, A. et al., Stabilization of Unsteady Nonlinear Waves by Phase-Space Manipulation, Physical Review Letters 126, 174501 (2021).

[4] Bendahmane, A. et al., Experimental dynamics of Akhmediev breathers in a dispersion varying optical fiber, Optics Letters 39, 4490-4493 (2014)

Experimental Investigation of Flexible Cantilevered Pipes Aspirating Water under VIV

Wagner Defensor, Celso Pesce, Guilherme Franzini, Guilherme Vernizzi, Vitor Maciel, Renato Orsino

Offshore Mechanics Laboratory, Escola Politécnica, University of São Paulo, Brazil

Summary. An innovative hydrodynamic campaign investigated three immersed flexible cantilevered aspirating pipes under VIV in a towing tank. Three experimental conditions have been considered: (i) aspirating flow; (ii) pure towing; (iii) combined aspirating and towing. Hopf bifurcations appeared in the aspirating case. Effects of supercritical internal flow on VIV were assessed and found small.

The experimental methodology and some results

The present extended abstract brings some experimental results concerning a hydrodynamic test campaign held at the Technological Research Institute (IPT) towing tank facility. The campaign showed 'weak' instabilities, of the Hopf bifurcation type, followed by fluttering of aspirating cantilevered flexible pipes, [1], [2], [3], and verified their small influence on VIV. Three flexible pipes, made of reinforced rubber hoses, with brass ballasts attached to the free end, were designed and built to respond, at the same towing speed, but each one at a distinct mode of vibration, the 1st, 2nd or 3rd (Figure 1, above, left). The motions of the pipes were tracked down by an underwater optical system. The *ballasted-hose* concept and the desired natural mode of vibration were identified by the acronyms BH-k; $k = 1,2,3$. An in-house mathematical model [3] was specially derived and implemented to guide the design. Argand's like diagrams predicted instabilities for all modes at very small internal aspirating flow velocities, (example for the BH-2 model in Figure 1, above-right). Aspirating flows up to $2v_{crit}$ were assessed, isolated and combined with towing (up to the modal reduced velocity $U^*_{ny} = U/f_{ny}D \approx 14$; $n = 1,2,3$). Data analysis employed Galerkin's projection techniques in time domain, with modal functions obtained in the deformed configurations (also provided by the in-house model), followed by an innovative filtering procedure that uses the Empirical Mode Decomposition ([4], [5]), to remove very low frequency contents outside VIV's range (Figure 2, charts below). Such slow motions occurred in the streamwise direction, as consequence of drag fluctuations due to the model deflection and the emission of tip vortices structures.

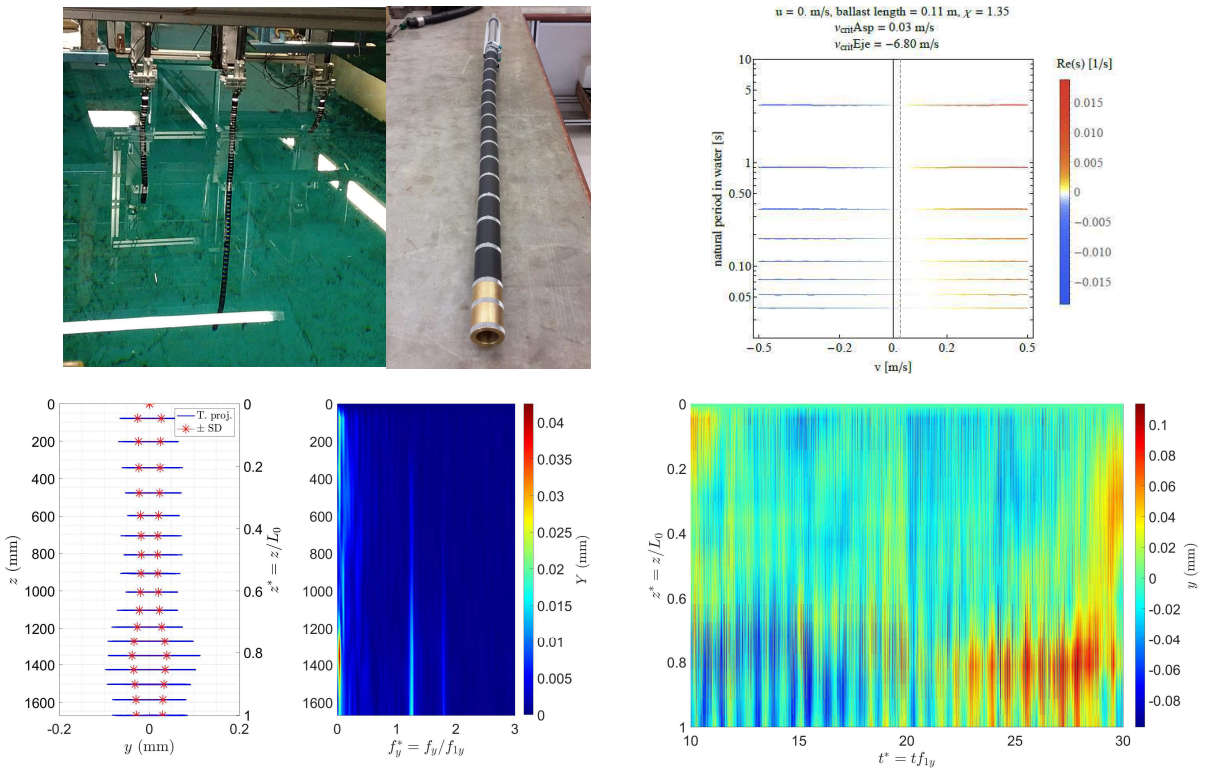

Figure 1: Above: left, ballasted-hose models; right, root-loci diagram, model BH-2. Below: aspirating case at $v = 2v_{crit}$.; left to right: spanwise trajectories projections, amplitude spectra and coordinate scalogram, in the crosswise direction w.r.t. towing.

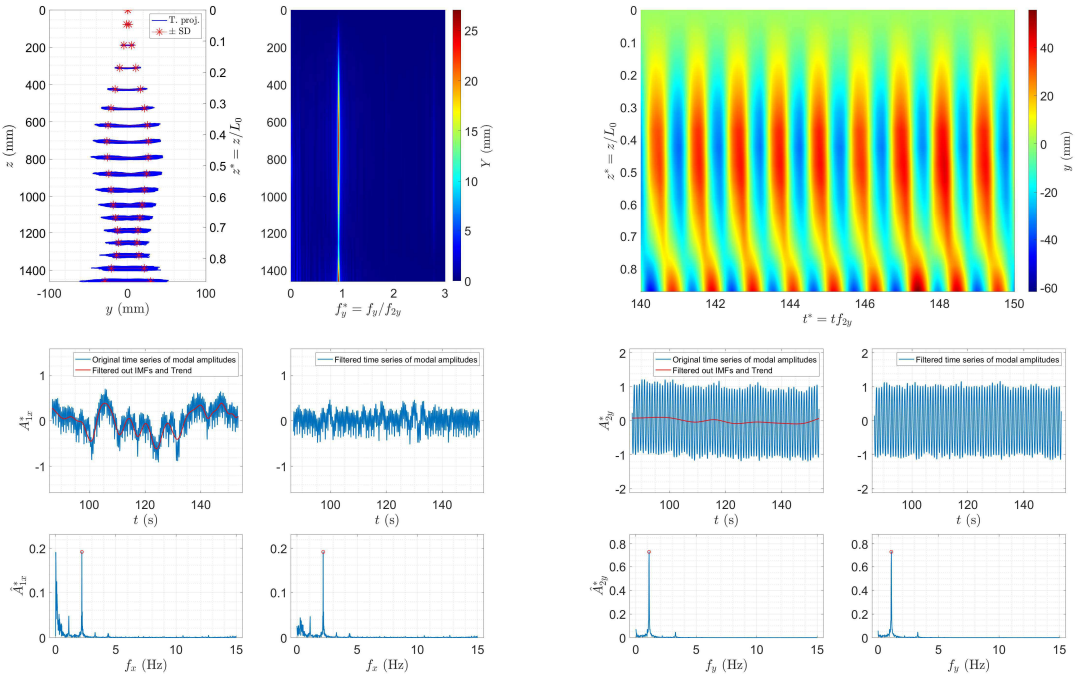

Figure 2: Model BH-2. Above, left to right: spanwise trajectories projections, amplitude spectra and coordinate scalogram, in crosswise direction. Below. EMD filtering of modal amplitude time series of the 1st and the 2nd mode shapes in streamwise (left) and crosswise (right) directions. Towing at modal reduced velocity $U_{2y}^* = 8.37$ ($U = 0.33$ m/s).

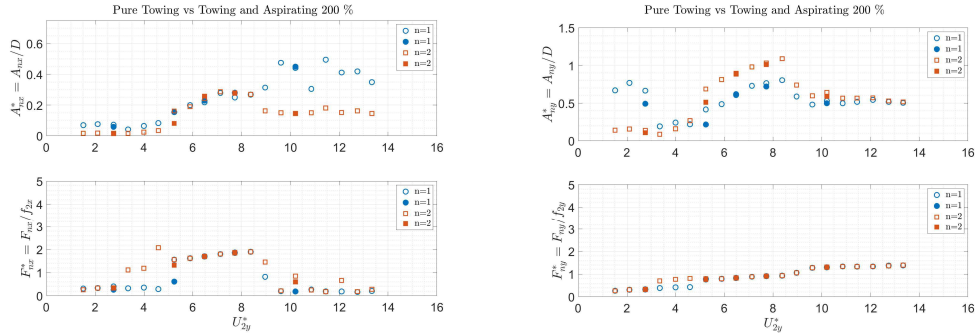

Figure 3: Model BH-2. Dimensionless modal amplitudes A_{nx}^* and A_{ny}^* and dimensionless dominant oscillation frequencies F_{nx}^* and F_{ny}^* of the nth vibration mode contributions, as function of modal reduced velocity U_{2y}^*, in streamwise (left) and crosswise (right) directions. Empty markers: towing only. Filled markers: towing and aspirating at $v = 2v_{crit}$.

In pure aspirating conditions, at $v = 2v_{crit}$, a 1st natural mode instability is depicted in the spanwise amplitude spectra at $f_y^* \approx 1.25$ and in the scalogram, coordinate shifting between positive and negative values along time (Figure 1, below, left and right, respectively). An expected behavior showed up in the pure towing case, the 2nd natural mode shape dominating the dynamics (Figure 2, above). An example of the EMD filtering procedure is presented in Figure 2 (below). VIV is practically not altered by the aspirating flow, even at $v = 2v_{crit}$ (Figure 3). Aside a small decrease in amplitudes and in the respective dominant frequency values, no significant differences in modal responses were observed, compared to the pure towing case. Moreover, the aspirating flow mitigated the low frequency content in the streamwise oscillation, possibly by changing the tip vortex field structure. A more detailed analysis shall be presented in the full paper.

Acknowledgements: To Shell Brazil, for the financial support through the ANP R&D levy regulation. To CAPES-PhD and FUSP DR-C project nº 3456 scholarships. To CNPq for the research grants 308230/2018-3 and 305945/2020-3. To IPT, for the use of the towing tank facility. To FAPESP for supporting the development of the basic mathematical formalism which set the fundamental grounds for this work (grants 2016/09730-0 and 2013/02997-2) and for supporting the Conference attendance, grant 2022/04072-5. To Prof. Dr. Gustavo Assi and Dr. Pedro C. de Mello.

References

[1] Michael P. Païdoussis (1999) *Aspirating pipes do not flutter at infinitesimally small flow*. Journal of Fluids and Structures **19**, 419-425.

[2] Dana B. Giacobbi, Stephanie Rinaldi, Christian Semler, Michael P. Païdoussis (2012) *The dynamics of a cantilevered pipe aspirating fluid studied by experimental, numerical and analytical methods*. Journal of Fluids and Structures **30**, 73-96.

[3] Renato M. M. Orsino, Celso P. Pesce, Fernando G. Toni, Wagner A. Defensor Filho, Guilherme R. Franzini (2021) *A 3D nonlinear Reduced-Order Model of a cantilevered aspirating pipe under VIV*. Proceedings of NODYCON-2021.

[4] Celso Pesce, L. K. Kubota, Andre Fujarra (2006) *The Hilbert-Huang Spectral Analysis Method Applied to VIV*. In Proceedings of the 25th International Conference on Offshore Mechanics and Artic Engineering, Hamburg, Germany.

[5] N. E. Huang, Z. Shen, S. Long, M. Wu, H. Shih, Q. Zheng, N. -C. Yen, C. Tung, H. Liu (1998) *The Empirical Mode Decomposition and the Hilbert Spectrum for Non-linear and Non-stationary Time Series Analysis*. Proc. R. Soc. Lond. A, 454, pp. 903-995.

Flow-induced vibrations of two circular cylinders in tandem in a cross flow

Jisheng Zhao*†, Mark C. Thompson† and Kerry Hourigan†
Fluids Laboratory for Aeronautical and Industrial Research (FLAIR),
Department of Mechanical and Aerospace Engineering,
Monash University, Clayton, Victoria 3800, Australia

Summary. This study reports on the dynamic response of two elastically-mounted circular cylinders in tandem undergoing transverse flow-induced vibration (FIV) in a free-stream flow. The results show that the FIV responses of the two cylinders are affected significantly by the cylinder-cylinder spacing ratio. This study suggests that there exist a variety of FIV response regimes as a function of the flow reduced velocity and the spacing ratio.

Introduction

The dynamics in flow-induced vibration (FIV) of structures is of substantial continuing interest, due to its intrinsic nature in science and importance in a large variety of engineering applications, such as offshore structures in ocean currents, and high-rise buildings and bridges in winds. In the past six decades, numerous studies have been motivated to fundamentally characterise FIV of bluff bodies and to provide insights into mechanisms of the fluid-structure interaction. This has led to a large body of work with a focus on FIV problems of a single body, e.g. two typical body oscillator phenomena of FIV, *vortex-induced vibration (VIV)* of a circular cylinder and *galloping* of a non-circular cylinder that is susceptible to an aerodynamic instability induced by the body movement (see [1]). On the other hand, considerable studies have also been conducted on flow past two fixed cylinders in tandem (see [2]), and transverse *wake-induced vibration (WIV)* of a free cylinder in the downstream of a fixed cylinder (e.g. [3]). These studies have shown that the spacing between two cylinders in tandem is a key parameter affecting the flow pattern and thus the fluid forcing on the bodies, resulting in complex nonlinear dynamics and structural response. However, much less work has been conducted on the FIV responses of two freely-vibrating cylinders in tandem; this is particularly so for cylinders with low mass ratio (the ratio between the total oscillating mass to the displaced fluid mass) at moderate Reynolds numbers. Thus, this study aims to gain a better understanding of the influence of the cylinder spacing on the FIV responses of two freely-vibrating cylinders in tandem in a free-stream flow, and to analyse the nonlinear dynamics of the fluid-structure interactions and the interaction between the two cylinders, through an experimental investigation of the fluid-structure system with low mass ratio at moderate Reynolds numbers.

Experimental method

The present FIV problem was modelled on two low-friction air-bearing systems (see [4]) in conjunction with the free-surface recirculating water channel of the *Fluids Laboratory for Aeronautical and Industrial Research (FLAIR)*, Monash University. This water channel facility has a test section of $600\,\mathrm{mm}$ in width, $800\,\mathrm{mm}$ in depth and $4000\,\mathrm{mm}$ in length.

The cylinders were vertically mounted onto two separated air-bearing systems. These cylinders, which were precision made from aluminium tubes and anodised against water corrosion, had an outer diameter of $D = 40 \pm 0.010\,\mathrm{mm}$ and an immersed length of $L = 614\,\mathrm{mm}$, giving an aspect ratio of $= L/D \approx 15.4$. For each cylinder, the total oscillating mass was $m = 1473.1\,\mathrm{g}$, and the displaced mass of the fluid was $m_d = 770.3\,\mathrm{g}$, giving a mass ratio of $m^* = m/m_d = 1.91$. The natural frequencies of the two hydro-elastic systems were measured by conducting free decay tests individually in air (f_{na}) and in quiescent water (f_{nw}). The structural damping ratio with consideration of the added masss (m_A) was determined by $\zeta = c/2\sqrt{k(m+m_A)}$, with $m_A = ((f_{\mathrm{na}}/f_{\mathrm{nw}})^2 - 1)\,m$. As shown in table 1, the natural frequencies were almost identical for the two circulars, while the difference in ζ was sufficiently small to have negligible effects. The FIV responses of the two cylinders were investigated for the spacing ratio (denoted by S^* as the streamwise spacing between the cylinder centres, S, normalised by the cylinder diameter, D, namely $S^* = S/D$) ranging from 1.25 to 15.0 over a wide reduced velocity range of $3 \leqslant U^* = U/(f_{\mathrm{nw}}D) \leqslant 30$ and a corresponding Reynolds number range of $1570 \leqslant Re = UD/\nu \leqslant 15\,700$, where U is the free-stream velocity, f_{nw} is the natural frequency in water of the upstream cylinder and ν is the kinematic viscosity. More experimental details can be found in [4].

Results and discussion

Figure 1 shows the normalised amplitude responses as a function of the flow reduced velocity for the two cylinders with various spacing ratios. The amplitude response is denoted by A^*_{10}, which represents the mean of the top 10% amplitude

Cylinder	m [g]	m_{d} [g]	m^*	f_{na} [Hz]	f_{nw} [Hz]	ζ
upstream	1473.1	770.3	1.91	0.432	0.343	2.02×10^{-3}
downstream	1473.1	770.3	1.91	0.430	0.345	1.78×10^{-3}

Table 1: The present experimental parameters of the two (upstream and downstream) cylinders in tandem.

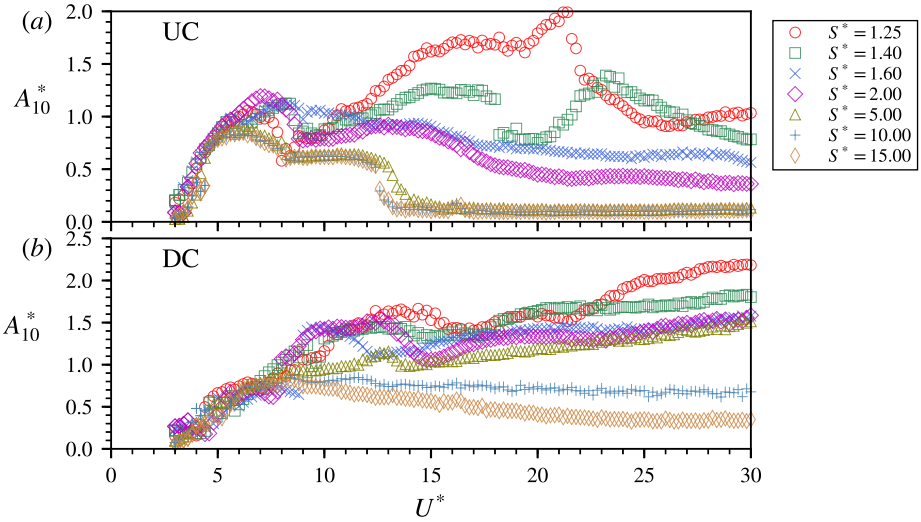

Figure 1: The normalised amplitude responses of the two cylinders in tandem as a function of the reduced velocity for various spacing ratios. The amplitude responses of the upstream and downstream cylinders (UC and DC) are plotted in (a) and (b), respectively.

peaks normalised by D.

As can be seen, the spacing ratio plays an important role affecting the amplitude responses of the two cylinders. For the cases of $S^* \leqslant 2.00$, the vibration of the upstream cylinder (UC) can be significantly enhanced in terms of the peak amplitude and also the U^* range exhibiting large body oscillation amplitude, as compared to that of a typical three-branch VIV response of a single circular cylinder (not shown here). For example, the A_{10}^* response of $S^* = 1.25$ displays an initial branch for low reduced velocities ($U^* < 5$), which is similar to that of the single cylinder case, but as U^* is further increased it exhibits a largely fluctuating variation to reach a peak value of $A_{10}^* \simeq 1.99$ at $U^* = 21.2$ (an increase of 234% against that observed in the VIV upper branch of the single cylinder case), prior to a gradual decrease trend to $A_{10}^* \approx 1.0$ for $U^* > 25$. As S^* is increased to 1.60, after reaching a peak value of $A_{10}^* \simeq 1.12$ at $U^* = 8.0$, the A_{10}^* response shows a gradual decrease trend with increasing U^*, distinctly different from those of the lower S^* cases. As S^* is further increase to 2.0, the A_{10}^* response exhibit a variation profile similar to the typical three-branch VIV response of a single cylinder, but with much larger vibration amplitudes. Furthermore, for the cases of $S^* \geqslant 5.00$, the A_{10}^* responses appear to be highly similar to the single cylinder case, indicating that the upper cylinder vibration is negligibly influenced by the perturbation of the downstream cylinder.

On the other hand, the A_{10}^* response of the downstream cylinder (DC) is also influenced significantly by S^*. As a result of the strong interaction between the two cylinders, the A_{10}^* response of the downstream cylinder tends to increase with U^*, but with large fluctuations at high reduced velocities ($U^* > 7$), for the cases of $S^* \leqslant 2.00$. As S^* is increased to 5.00, the A_{10}^* response sees a fairly stable increase trend for $U^* > 7$. However, for the cases of $S^* \geqslant 10.00$, the A_{10}^* response tends to decrease gradually with U^* increasing beyond 7.

Conclusions

The transverse FIVs of two circular cylinders in tandem have been investigated as a function of U^* for various spacing ratio of $1.25 \leqslant S^* \leqslant 15.00$. It was found that for $S^* \leqslant 2.00$ the FIV responses of the two cylinders exhibit complex variations due to their strong interaction, where their vibration could be largely enhanced as compared to VIV of a single cylinder. Enhancement of the A_{10}^* peak of the upstream cylinder diminished for $S^* \geqslant 5.00$, whereas the downstream cylinder displayed a decrease trend in A_{10}^* with increasing U^* beyond 7 for $S^* \geqslant 10.00$. The present results indicate that there exist a variety of FIV response regimes that would be of great interest for further investigations.

References

[1] Naudascher, E., Rockwell, D. 2005. Flow-Induced Vibrations: An Engineering Guide. Dover Publications.

[2] Zdravkovich, M. M. 1977. Review of flow interference between two circular cylinders in various arrangements. *Journal of Fluids Engineering* **19** (4), 618–633.

[3] Assi, G. R. S. and Bearman, P. W. and Meneghini, J. R. 2010. On the wake-induced vibration of tandem circular cylinders: the vortex interaction excitation mechanism. *Journal of Fluid Mechanics* **661**, 365–401.

[4] Zhao, J., Hourigan, K., Thompson, M. C. 2018. Flow-induced vibration of D-section cylinders: an afterbody is not essential for vortex induced vibration. *Journal of Fluid Mechanics* **851**, 317–343.

Fluid dynamics effect in large array

Ande Raghu, Mathieu Sellier and Stefanie Gutschmidt
Department of Mechanical Engineering, University of Canterbury, Christchurch, New Zealand

Summary. Fluid dynamics investigation of coupled oscillators and arrays of beams are important for several applications in biology, medicine, and especially and increasingly for MEMS and NEMS sensors. The most available literature on oscillators is either a single beam or small-sized arrays. Limited literature is available concerning the dynamics of large-sized arrays of beams. Our group has dedicated its research goals to understanding coupled MEMS oscillators and array dynamics to enhance technologies such as fast-scan AFM, nanometrology, and precision lithography. Some of these applications require knowledge of arrays in a fluidic environment. Before investigating fluid-structure interactions of such large-array a sound understanding of the fluid motion is required, which is the focus of this work. We investigate a large array of beams using the boundary integral technique, where the flow is governed by unsteady Stokes and Continuity equation. The analysis is performed for all beams that are equally excited in phase for different gap sizes between the beams at different Reynolds numbers, including the comparison of an increasing array size with the same and varying array lengths. Results include the onset of array effects, added mass, and viscous dissipation for a critical number of beams M, the gap between the beams and Reynolds numbers. The analysis suggests an increase in interactions between the neighbor and non-neighbor beams with an increase in array size at the same array length. The work guides for the design of arrays in fluids for different spacing and Reynolds numbers.

Background

Tuck [1] and Green [2] present an extensive work of dynamics for an individual beam, whereas Basak [3] and Manickavasagam [4] conducted investigations on small arrays of beams (number of beams less than five). Much lesser work can be found on a large array in general. No details are available for the large array of beams oscillating in fluids. In this work, we focus on the fluid dynamics of the large arrays [5].

Methodology

We base our analysis on the well established Boundary Integral Method (BIM) applied to unsteady Stokes and continuity equations. By applying the BIM, we have deduced the partial differential equations into integral form to calculate the fluid properties over the beams within the array using the analytical equation 1.

$$f(Re,x) = \frac{i}{Re}\left(\frac{1}{x} + (1i\cdot\sqrt{iRe}\cdot \mathrm{sgn}(x)\cdot K_1(\sqrt{iRe}\cdot \mathrm{abs}(x)\cdot(-1i)))\right) \tag{1}$$

The closed-form analytical equation is extended for M number of beams by following the technique used by Basak [3] and Manickavasagam [4]. We investigate the velocity configuration of all beams active in-phase, where x = (ξ'_j - ξ_k), ξ'_j is an node on the beam surface, ξ_k is the midpoint between any two nodes, $\xi_k = \frac{1}{2}(\xi_{j'} + \xi_{j'+1})$, Re is the corresponding Reynolds number and K_1 is the modified bessel function of first kind.

$$\xi'_j = (2+2\bar{g})m - (3+3\bar{g}) - \cos\left(\frac{\pi j}{N}\right) \qquad [m = 1,2,3,...,M], \tag{2}$$

To mitigate the singularities at the edges, the beam is discretized into unequal segments by using a generalized equation 2, which is applicable to all array of beams if the number of beams M in an array is greater than or equal to two as shown in Figure 1a and $\bar{g}$ is the nondimensional gap.

Analysis and Results

The following investigations are considered for a velocity configuration of all beams active with a gap between the beams $\bar{g}$ of 0.1 as shown in Figure 1a, which is below the critical gap theoretically [6] at Reynolds number 0.1. The input velocity of the beams and the matrix obtained from the analytical equation yields the hydrodynamic force over the array. Absolute, real, and imaginary hydrodynamic forces give us new insights into the large-array in fluids [5]. In Figures 1b to 1d horizontal axis presents the normalized beam number, the absolute A(F), imaginary I(F) (added mass), and real part R(F) (viscous dissipation) of the hydrodynamic force [7] are normalized corresponding to its respective width of the beam and plotted on the vertical axis.

From Figure 1b, it is observed that at the same array length and different array size there is an increment in the added mass and viscous dissipation which is due to the array effect which can be observed with an increase in the number of beams in an array, whereas with varying array length and increase in array size there is little effect on the dissipation as shown in the Figure 1c and drastic increment in the added mass due to increase in the array length as shown in the Figure 1d. The interaction between neighbor and non-neighbor increases with an increase in array size and at the same array length. If the distance between the beams is below a critical gap where the interaction of beams in an array is high due

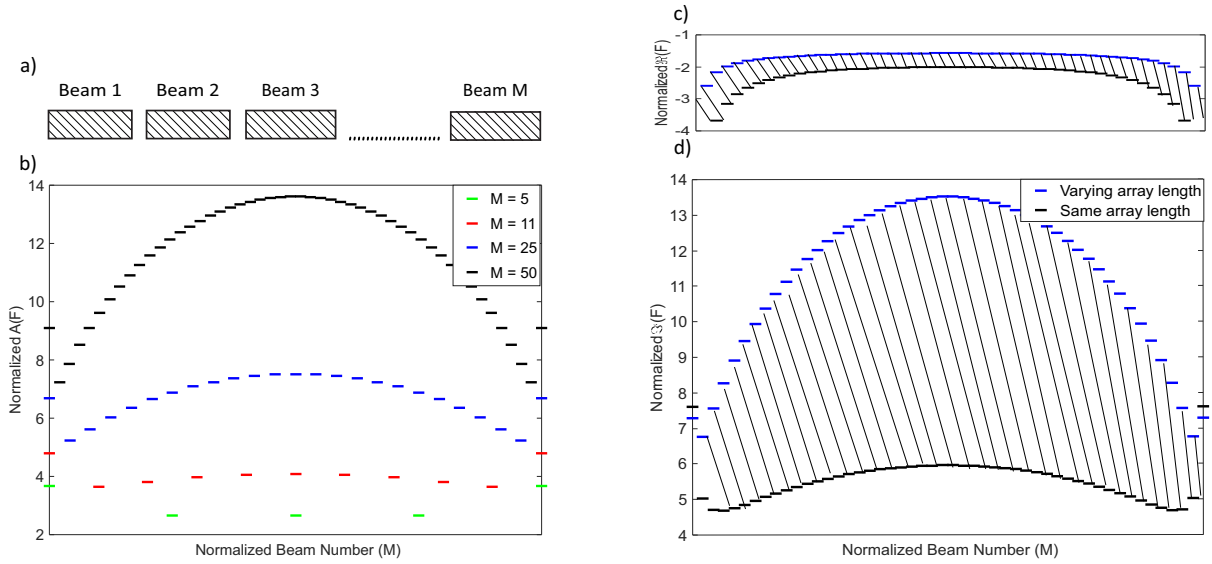

Figure 1: (a) Array of beams in non-viscous fluid (b) Absolute pressure for different array sizes (c) Real pressure and (d) Imaginary pressure for 50 beams array at $\bar{g} = 0.1$ and $Re = 0.1$.

to the overlapping of viscous layers, we can observe the array effect for varying the gaps between the beams for different Reynolds numbers. The hatched area in Figures 1c and 1d represents the increase in viscous dissipation and decrease in added mass with an increase in array size at the same array length.

Conclusions

It is important to understand the fluid dynamics of a large array of beams oscillating in the unbounded fluid environment to be able to accurately predict the full dynamics of such systems, and in turn to effectively develop future array technologies like AFM, lithography, and nano-metrology. In this work, we have extended the BIM of 2 beams by Basak [3] and small-sized arrays of beams by Manickavasagam [4] for any arbitrary number of beams to understand the associated array effects originating from the fluid environment. We have analyzed M equal to $5, 11, 25, 50$ beams exciting in-phase in a non-viscous fluid to calculate the hydrodynamic forces of large arrays of beams for different gaps between the beams and Reynolds numbers. New insights from A(F), I(F), and R(F) reveal critical design-relevant parameters for the development of future array technology. In addition, this work can be extended by oscillating the large array of beams close to a rigid surface and analyzing the influence of rigid surface on viscous damping and added mass.

References

[1] EO Tuck. Calculation of unsteady flows due to small motions of cylinders in a viscous fluid. *Journal of Engineering Mathematics*, 3(1):29–44, 1969.

[2] Christopher P Green and John E Sader. Small amplitude oscillations of a thin beam immersed in a viscous fluid near a solid surface. *Physics of Fluids*, 17(7):073102, 2005.

[3] Sudipta Basak and Arvind Raman. Hydrodynamic coupling between micromechanical beams oscillating in viscous fluids. *Physics of Fluids*, 19(1):017105, 2007.

[4] Arun Kumar Manickavasagam. Hydrodynamic coupling of arrays in fluids. 2020.

[5] Raghu Ande, Stefanie Gutschmidt, and Mathieu Sellier. Fluid dynamics investigation of a large array. *Physics of Fluids*, 33(7):073608, 2021.

[6] Chiang Mei and Guangda Li. Lecture 3.7: Oscillatory boundary layers. In *-Advanced Fluid Dynamics of the Environment–MIT Course No. 1.63*. Cambridge MA, 2002. MIT OpenCourseWare.

[7] LD Landau. D. & lifshitz, em 1959 fluid mechanics. *Reading: Addison-Wesley*, 1971.

Topology of exotic wakes

Morten Brøns*, Anne Ryelund Nielsen*, Puneet Matharu†, Matthias Heil†
*Department of Applied Mathematics and Computer Science, Technical University of Denmark, 2800 Lyngby, Denmark
†School of Mathematics, University of Manchester, Oxford Road, Manchester M13 9PL, UK

Summary. The formation of vortices in the flow around an oscillating cylinder is shown to be a complex set of topological bifurcations as the amplitude of the cylinder oscillations is varied. We show that the transition from a wake where two vortices are shed per cycle, to a configuration with three vortices are shed, goes through intermediate stages, where secondary vortices are created but disappear again.

Introduction

The wake behind a transversely oscillating cylinder allows a remarkable richness of flow structures. Vorticity created at the cylinder surface is advected downstream and organizes into distinct vortices. For a stationary cylinder in the periodic regime, two vortices of opposite circulation are shed per cycle forming the famous von Kármán vortex street. This is also denoted a 2S wake, where S means the shedding of a single vortex [6]. When the cylinder oscillates, this pattern may be modified depending on the frequency and amplitude of the forced oscillation. Patterns such as 2P, P+S, 2P+2S have been observed – here P means the shedding of a pair of vortices from the same side of the cylinder. These configurations are known as exotic wakes [5]. Bifurcation diagrams in the frequency-amplitude parameter plane (f, A) have been established, both experimentally and computationally, by many researchers, e.g. [6, 3].
The purpose of the present paper is to study the bifurcations which lead from one pattern to another. We primarily consider the case where the oscillation frequency of the cylinder is chosen as the Strouhal frequency, that is, the frequency of the vortex shedding for a fixed cylinder. For low values of the amplitude of the oscillating cylinder the wake is of type 2S, but for the dimensionless amplitude A around 1, the pattern changes into P+S. In the entire parameter range we consider the flow is periodic. The Reynolds number is 100, where it is reasonable to assume the flow is two-dimensional. Simulations are performed using the `oomph-lib` finite-element library [1].
In this study we characterize a flow configuration by the topology of the vorticity field, and define a vortex as a local extremum of vorticity. An extremal point of vorticity can be created together with a saddle point in a forward cusp bifurcation [2]. Similarly, an extremum and a saddle may merge and annihilate in a backward cusp bifurcation. We note that there are alternative definitions of a vortex, for instance the Q-criterion, which has also been of use in identifying creation and destruction of vortices [4].

Results

The results are summarized in Fig. 1. We focus on the negative vortices formed at the top of the cylinder. For the dimensionless amplitude A less than about 0.85, a positive and a negative vortex on each side of the cylinder are formed in the shear layers a few diameters downstream. Once created, the vortices persist and are advected downstream. This is a classical 2S wake. See Fig. 1(a) for a typical example. Increasing A to 1 as in Fig. 1(b), the filaments of vorticity (shear layers) emanating from the vortices may turn into individual vortices through a forward cusp bifurcation. These secondary vortices disappear again after a few cycles in a backward cusp bifurcation. This intermediary pattern cannot simply be described by the symbols P and S. Increasing A the secondary vortices persist for longer and longer times. For $A = 1.08$, Fig. 1(c), the secondary vortices never disappear again, and a full P+S wake is formed.
Hence, the transition process from a 2S to a P+S wake does not occur at a specific value of A, but is a sequence of bifurcations, possibly infinitely many, over a quite large interval of the parameter.

References

[1] A. Hazel and M. Heil. `oomph-lib` – an object-oriented multi-physics finite-element library. In M. Schäffer and H.-J. Bungartz, editors, *Fluid-Structure Interaction*, pages 19–49. Springer, 2006.

[2] M. Heil, J. Rosso, A. L. Hazel, and M. Brøns. Topological fluid mechanics of the formation of the Kármán-vortex street. *Journal of Fluid Mechanics*, 812:199–221, 2017.

[3] J. S. Leontini. Wake state and energy transitions of an oscillating cylinder at low Reynolds number. *Physics of Fluids*, 18(6):067101, 2006.

[4] A. R. Nielsen, M. Heil, M. Andersen, and M. Brøns. Bifurcation theory for vortices with application to boundary layer eruption. *Journal of Fluid Mechanics*, 865:831–849, 2019.

[5] F. Ponta and H. Aref. Numerical experiments on vortex shedding from an oscillating cylinder. *Journal of Fluids and Structures*, 22(3):327–344, 2006.

[6] C. H. K. Williamson and A. Roshko. Vortex formation in the wake of an oscillating cylinder. *Journal of Fluids and Structures*, 2(4):355–381, 1988.

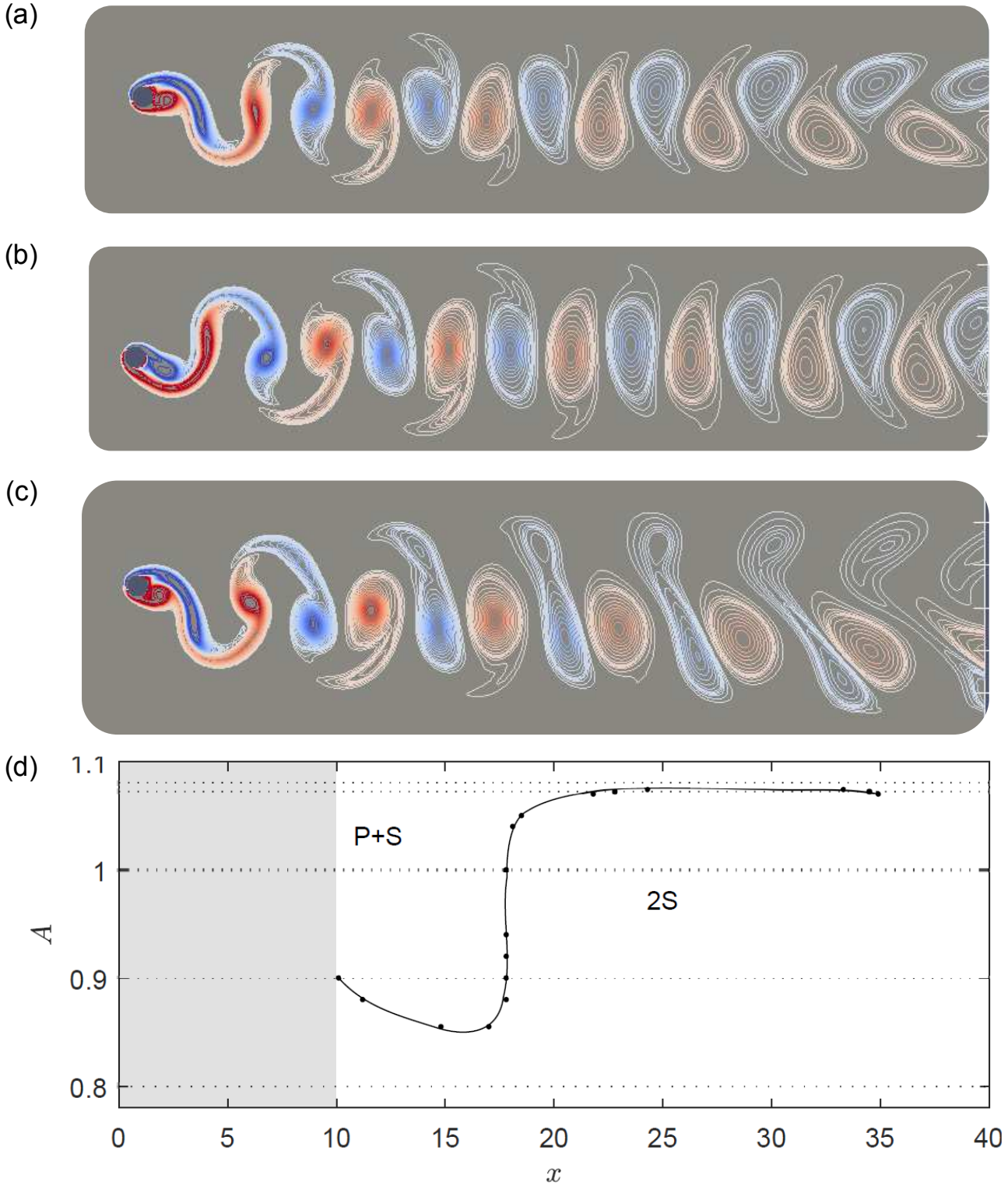

Figure 1: Snapshots of vorticity topologies for various values of the forcing amplitude A. (a): $A = 0.8$. (b): $A = 1$. (c): $A = 1.08$. (d): Bifurcation diagram showing the downstream distance x where forward or backward cusp bifurcations occur, at some time instant during the cycle. The shaded area shows the region where the shear layers are so thin that it is not possible to identify isolated extrema of vorticity.

Thursday, July 21, 2022
08:30 - 10:30

MS-17 Time-periodic systems
Saint Clair 3A

Chair: Fabia Bayer

08:30 - 08:50
Control optimization of digital hydraulic drive for knee exoskeleton
RITURAJ Rituraj*, SCHEIDL Rudolf
*Institute of Machine Design and Hydraulic Drives, Johannes Kepler University Linz (Johannes Kepler University Linz Altenberger Straße 69 4040 Linz, Austria Austria)

08:50 - 09:10
Non-linear Vibrations in a Coiling Process with Periodically Changing Radius
HOLL Helmut*
*Johannes Kepler University (Altenbergerstr. 69 A-4040 Linz Austria)

09:10 - 09:30
Nonlinear kinematics of a moored axisymmetric wave energy converter
GIORGI Giuseppe*, DAVIDSON Josh, HABIB Giuseppe, BRACCO Giovanni, MATTIAZZO Giuliana, KALMÁR-NAGY Tamás
*Politecnico di Torino [Torino] (Politecnico di Torino - Corso Duca degli Abruzzi, 24 10129 Torino Italy)

09:30 - 09:50
On periodic solutions and modal energy transfer of mechanical systems with state-dependent impulsive stiffness excitation
PUMHOESSEL Thomas*
*Johannes Kepler Universität Linz (Altenbergerstrasse 69, 4040-Linz Austria)

Control optimization of digital hydraulic drive for knee exoskeleton

Rituraj Rituraj [*], Rudolf Scheidl [*]
[*]*Institute of Machine Design and Hydraulic Drives, Johannes Kepler University, Linz, Austria*

Summary. A successful knee exoskeleton device must follow the periodic motion of the gait cycle in an energy efficient manner. This work investigates an optimal control strategy that can allow the periodic behavior of such a device with minimum error while also consuming minimum energy. Using a multi-objective optimization technique, a trade-off between the periodicity error and energy consumption is demonstrated. From the pareto front, an optimal control variable set is determined which allows an acceptable periodic behavior of the knee exoskeleton with negligible energy consumption.

Introduction

Exoskeletons are wearable devices that provide additional strength to the wearer's limbs. These devices are commonly used in physical rehabilitation to assist in the recovery of a limb's motion and strength. Furthermore, they are used by factory workers, military personnel, and firefighters for carrying heavy equipment over long distances. Most of these devices currently use electromechanical drives for motion actuation. However, in recent years, hydraulically driven exoskeleton devices have gained interest among the researchers [1–3] due to their capabilities of high force density, easy energy recuperation, motion locking, and damping. The advent of digital hydraulic technology in the last decade has strengthened the case for hydraulically driven exoskeleton devices due the added advantages of high energy efficiency, power density, precision, and robustness.
Inspired by these benefits, the authors have recently developed a novel design of digital hydraulically driven knee exoskeleton [4]. A novel control strategy is also proposed in an upcoming work [5]. However, a key challenge with this exoskeleton device is its motion repeatability over multiple gait cycles. The device should track the desired knee motion in the same periodic manner as observed in typical gait cycles. Furthermore, to keep the power source light, the device should consume as little energy per gait cycle as possible. In this work, a control optimization study is conducted to determine the optimal sets of control variables that can allow the desired periodic behavior of the knee exoskeleton device with minimal energy consumption.

Knee exoskeleton design and control strategies

Figure 1 shows the knee exoskeleton design, its hydraulic drive, and the control strategies in different phases of the gait cycle. The comprehensive details are present in [4,5]. In brief, the exoskeleton device is actuated by two hydraulic cylinders. The hydraulic chambers of each of the cylinders are connected to the pressure source and tank via 2/2-way valves. The motion control is achieved via three different control strategies during different phases of the gait cycle. In the stance phase, where an inverse relation between the knee angle and knee torque exists, an elastic control is employed, which allows the hydraulic chambers to act as elastic elements. Next, a simplified form of the model predictive control (MPC) strategy is used to ensure proper tracking of the knee motion. Finally, a pressurization control strategy is employed for a brief period where hydraulic chambers are pressurized to the appropriate levels needed for the next gait cycle.

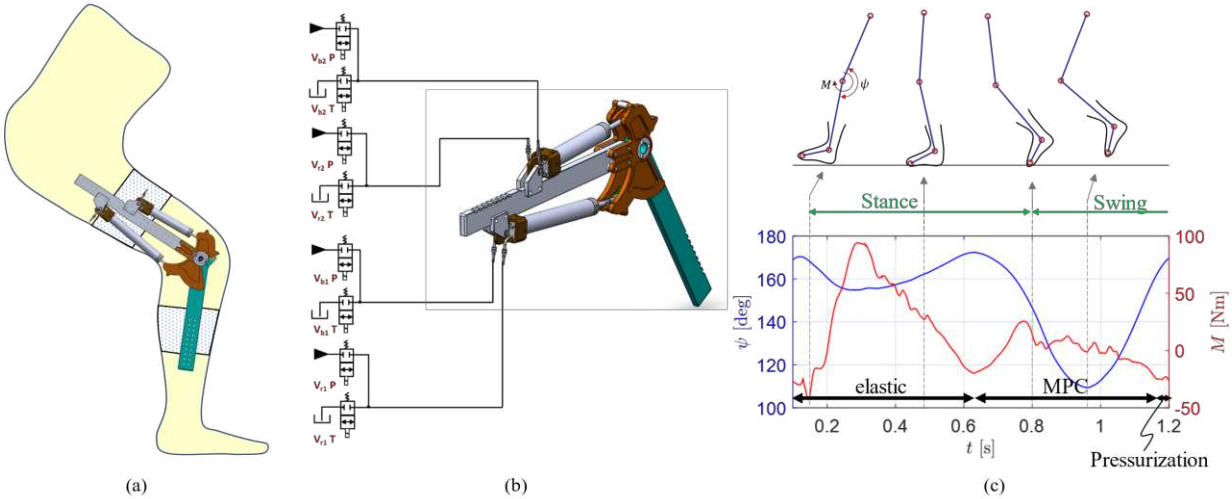

Figure 1: (a) Knee exoskeleton design, (b) hydraulic system, (c) phases in the gait cycle and control strategies used.

Control optimization study

The numerical simulations of the knee exoskeleton device show that the duration of each of the aforementioned control strategies and the time step involved in MPC significantly influence the accuracy of the periodic behavior of the device

motion over multiple gait cycles as well as the energy consumed per cycle. Thus, in the optimization study, the duration of the elastic control phase, the duration of the pressurization phase, and the time step in MPC algorithm are considered as the optimization variables.

The first optimization objective is to minimize the difference between the values of the state variables of the system at the beginning ($t = t_0$) and at the end of two gait cycles ($t = t_e$). The state variables are the knee angle (ψ), knee angle derivative ($\dot{\psi}$), and pressures in the four hydraulic chambers of the cylinders (p_i). Thus, the objective function is

$$\text{Minimize: } \epsilon = w_1 e_\psi + w_2 e_{\dot{\psi}} + w_3 \sum e_{p_i} \tag{1}$$

where, $e_\psi = |\psi_{t_0} - \psi_{t_e}|$, $e_{\dot{\psi}} = |\dot{\psi}_{t_0} - \dot{\psi}_{t_e}|$, $e_{p_i} = |p_{i,t_0} - p_{i,t_e}|$, and w_i are appropriately chosen weights.

The second objective is to minimize the energy consumed over two gait cycles. The energy consumption is determined as $E = V_p p_S$, where, V_p is the amount of fluid volume delivered by the pressure source and p_S is its pressure level.

This multi-objective optimization problem is solved using NSGA-II algorithm. The initial design space is populated with 1000 designs and the optimization algorithm is executed for 50 generations.

Results and discussion

Figure 2(a) shows the results obtained from the optimization study where the approximate pareto front is shown in red. Computational expensiveness limits the number of optimization generations and thus, the accuracy of the pareto front. Nevertheless, a trade-off between the periodicity error (ϵ) and the energy consumption (E) is observed. The negative energy consumption observed in the pareto front is the result of two factors. Firstly, the natural knee motion is inherently an energy delivering system over a complete gait cycle [6]. Secondly, several control variable sets save energy by supplying lower amount of high pressure fluid to the actuators. However, as observed in the figure, most of such sets exhibit high periodicity error.

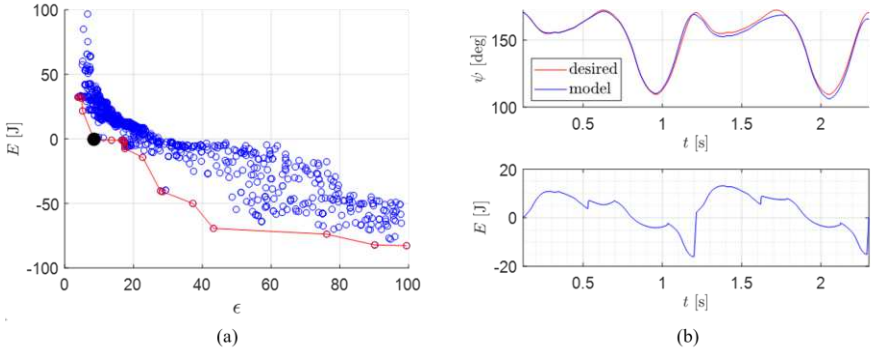

Figure 2: (a) Results from the optimization study with the pareto front shown in red, (b) Knee angle and energy consumption for a pareto optimal variable set (indicated as large black dot in Figure (a))

Figure 2(b) shows the simulation results obtained using a pareto optimal variable set (highlighted in large black dot in Figure 2(a)) for two gait cycles. The knee angle is tracked with reasonable accuracy and the energy consumption at the end of the gait cycle is almost zero. However, it is important to note that the losses due to internal friction were not considered in the energy calculation.

Conclusions

An investigation of the optimal control strategy for hydraulically driven knee exoskeleton is presented in this work. A multi-objective optimization study is conducted aimed at minimizing the error in the periodic behavior of the exoskeleton motion and the energy consumption per gait cycle. A trade-off between the two objectives is observed and using a pareto optimal variable set, it shown that a periodic behavior (with acceptable accuracy) could be achieved with theoretically zero energy consumption.

References

[1] A.B. Zoss, H. Kazerooni, A. Chu, Biomechanical design of the Berkeley Lower Extremity Exoskeleton (BLEEX), IEEE/ASME Transactions on Mechatronics. 11 (2006) 128–138. https://doi.org/10.1109/TMECH.2006.871087.

[2] W. Huo, S. Mohammed, J.C. Moreno, Y. Amirat, Lower Limb Wearable Robots for Assistance and Rehabilitation: A State of the Art, IEEE Systems Journal. 10 (2016) 1068–1081. https://doi.org/10.1109/JSYST.2014.2351491.

[3] H. Cao, Z. Ling, J. Zhu, Y. Wang, W. Wang, Design frame of a leg exoskeleton for load-carrying augmentation, in: 2009 IEEE International Conference on Robotics and Biomimetics, ROBIO 2009, IEEE, Guilin, China, 2009: pp. 426–431. https://doi.org/10.1109/ROBIO.2009.5420684.

[4] R. Rituraj, R. Scheidl, A novel design concept of digital hydraulic drive for knee exoskeleton, in: Proceedings of the ASME /BATH 2021 Symposium on Fluid Power and Motion Control FPMC2021, Online, 2021.

[5] R. Rituraj, R. Scheidl, Investigation of an optimal design and control of digital hydraulic drive for knee exoskeleton, in: The 13th International Fluid Power Conference, 13. IFK, Aachen, Germany, 2022.

[6] R. Scheidl, Digital Fluid Power for Exoskeleton Actuation - Guidelines, Opportunities, Challenges, in: The Ninth Workshop on Digital Fluid Power, Aalborg, Denmark, 2017.

Non-linear Vibrations in a Coiling Process with Periodically Changing Radius

Helmut J. Holl
Institute of Technical Mechanics, Johannes Kepler University, Linz, Austria

Summary. The mechanical model of a winding process has to consider the coupling of the vibrations of the strip and the coiling drum due to non-steady state operation conditions. In the mechanical model of this variable mass system additionally variable parameters are present and result in non-linear equations of motion. The longitudinal and transversal motion of the axially moving strip and the bending deflection of the coiling drum are considered by Rayleigh-Ritz approximations which involve the application of the extended equation of Lagrange. A periodically changing radius is a potential source of vibration excitation. A time integration algorithm with small time steps has to guarantee a converged solution for the long computation time. Simulation results of steady state and non-steady state operation conditions are computed and show the coupling of the vibrations and the excitation due to the periodic radius function.

Introduction

A suitable mechanical model is necessary for the simulation of the vibrations in a coiling process. In the coiling process an axially moving strip moves continuously towards a rotating drum where it is coiled. Between two successive coiling processes the strip passes through a Steckel mill where the thickness is reduced. The mechanical model starts at the exit of the Steckel mill and considers the axial motion of the strip with the transversal oscillations. Then the strip is coiled where the strip is attached on the drum, contributes to the bending stiffness and increases the mass of the drum. The resulting mechanical model is a non-linear dynamic model with varying mass and system parameters, which are defined by the variable outer radius of the drum, the variable bending stiffness of the drum and a variable eccentricity of the rotating drum. Due to the coiled material the mass of the coiling drum increases or decreases continuously. For the outer radius of the coiling drum an Archimedian Spiral and a periodic step function is assumed, which gives an outer radius and bending stiffness depending on the coiled strip length. For the simulation of the coiling process with the long computation time a integration algorithm was implemented. For the derivation of the equations of motion Rayleigh-Ritz approximations are used to get only a few degrees of freedom in the mechanical model. The application of the extended equations of Lagrange, see [1], is necessary as the mass in the system is not constant, which is a restriction for the well-known equations of Lagrange, see [2]. In the extended equations of Lagrange the control volume concept with the surface integrals with partial derivatives as a kernel are present. In [3] additionally some literature with examples on dynamic systems with variable mass is discussed. In [4] an alternative approach for the influence of the variable mass is considered using reactive forces, where also some examples are shown. The coupled vibrations are analysed and numerical studies are performed in order to increase the knowledge about the complicated variable mass non-linear dynamic system of the coiling drum with an outer radius involving a periodic excitation and the axially moving strip. For the dynamic system the initial and boundary conditions are defined and with the given operation conditions a time-integration algorithm computes the solution.

Mechanical modelling of the coiling drum and the moving strip

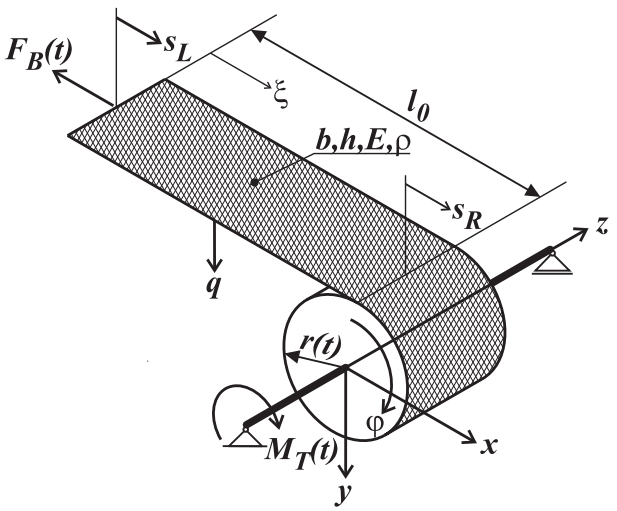

Figure 1: Mechanical model of the rotating drum with the axially moving strip

The mechanical model includes the coiling drum on elastic bearings and the moving strip, see Fig. 1. Rayleigh-Ritz approximations and the extended equations of Lagrange have been used for the derivation of the mechanical model. For the derivation of the equations of motion it is important to distinguish between the material control volume and the spatial control volume. The mechanical model has five degrees of freedom, the horizontal and vertical deflection x, y and the rotation angle φ of the coiling drum, the transversal deflection of the moving strip q and the entrance speed of the strip s_L. The strip tension force F_B is given as a predefined time-dependent value at the entrance of the system and the torque at the coiling drum M_T is computed. The coiling drum is modeled as a beam with different stiffness in longitudinal direction. The outer radius of the drum increases and an Archimedian spiral $r = r_0 + \dfrac{h\varphi}{2\pi}$ as well as a step-function $r = r_0 + h \text{ floor}\left(\dfrac{\varphi}{2\pi}\right)$ have been analysed. For the computation of the actual stiffness it is assumed that the coiled strip is attached to the drum and contributes to the stiffness.

The model of the coiling drum and the moving strip is described and derived in [5]. The coupling between the coiling drum and the moving strip is modelled considering the strain in the strip $\varepsilon_S = \varepsilon_{xx} - zw'' + \frac{1}{2}w'^2$. The horizontal motion of the strip in longitudinal direction at the right position where it touches the coiling drum considers the shortening effect of second order, see [5]. φ ist the rotation angle and x is the horizontal deflection of the center of the rotating drum.

Computed Results

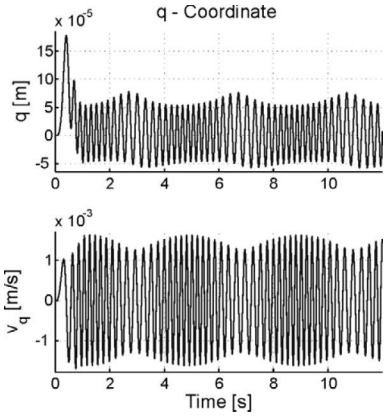

Figure 2: Amplitude and velocity of transversal motion of the strip

For the derived mechanical model the solution was computed and a parametric study has been performed. The parameters of the coiling drum based on the computations presented in this contribution are $L_0 = 5$m, $r_0 = 0.45$m, $h = 10$mm, $b = 0.5$m, $E = 105$kN/mm^2, $c_C = 10^7$kN/m, $\rho = 7800$kg/m^3, $m_0 = 1200$kg. For a strip tension force of $F_B = F_{B0}\left(1 + \frac{\sin(\pi t/2)}{2}\right)$ with $F_{B0} = 50$kN the computation is carried out. From the results of the amplitude of the transversal strip vibrations in Fig. 2 the non-linear coupling effect with the varying frequency and amplitude is shown.
When a step-function of the outer radius of the coiling drum is used, the computed resulting vibrations are shown in Fig. 3 and Fig. 4 for a constant strip tension force at the entrance of the system in Fig. 1. It can be seen that the effect of the step function in the outer radius gives an impact-like excitation which occurs after every revolution. For successive rotations the vibration amplitudes are computed with a small time step to get a convergent result as the step-function of the radius gives a modification in the kinematics of the system.

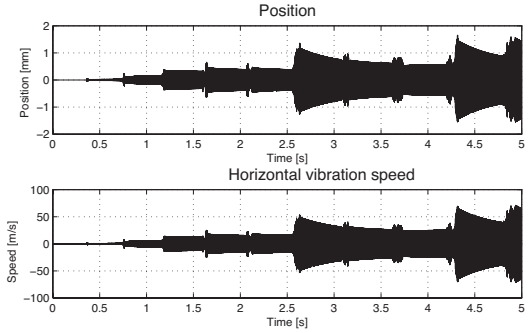

Figure 3: Horizontal Position and speed of the Center of the Coiling Drum

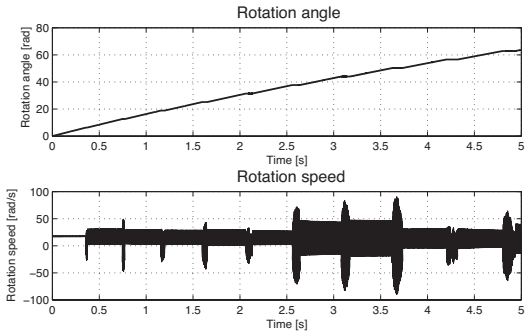

Figure 4: Rotation angle and speed of the coiling drum

Conclusion

A mechanical model with a variable mass and varying parameters and a periodic function for the outer radius of a coiling process was derived. The simulation results show a production process for a constant axial speed. For a defined variation of the strip tension force at the entrance the vibration amplitudes of the coordinates show non-linear coupled vibrations and the frequency and amplitude for the transversal strip oscillation depend on the strip tension force. For the step-function of the outer radius the computation needs a higher effort and shows an excitation after every revolution of the coiling drum.

Acknowledgement

The support of this work by the Linz Center of Mechatronics (LCM) in the framework of the Austrian Comet K2 program is gratefully acknowledged.

References

[1] Irschik, H., Holl, H.J. (2002) The Equations of Lagrange Written for a Non-Material Volume, Acta Mechanica, Vol.153 (3-4), 231-248.

[2] Ziegler, F. (1998): Mechanics of Solids and Fluids. 2nd ed, Springer Verlag.

[3] Irschik, H.; Holl, H.J. (2004) Mechanics of variable-mass systems - Part 1: Balance of Mass and Linear Momentum. Applied Mechanics Review 57(2), pp. 145-160.

[4] Cveticanin, L. (1998) Dynamics of Machines with Variable Mass. Gordon and Breach Science Publishers.

[5] Holl, H.J. (2019) Analysis of Variable Mass Rotordynamic Systems with Semi-Analytic Time-Integration. Proc. IFToMM 10th Int. Conf. Rotordynamics, Mechanisms and Machine Science **62**, eds.: Cavalca K. L. and Weber H. I. 412-425, Springer.

Nonlinear kinematics of a moored axisymmetric wave energy converter

Giuseppe Giorgi*, Josh Davidson†, Giuseppe Habib‡, Giovanni Bracco*, Giuliana Mattiazzo* and Tamas Kalmar-Nagy †

*Department of Mechanical and Aerospace Engineering, Polytechnic of Turin, Turin, Italy
†Department of Fluid Mechanics, Faculty of Mechanical Engineering, Budapest University of Technology and Economics, Hungary.
‡Department of Applied Mechanics, Faculty of Mechanical Engineering, Budapest University of Technology and Economics, Hungary.

Summary. Mathematical models for wave energy converters (WECs) are naturally germinated from the models in classical offshore engineering applications, where the assumption of linear kinematics and dynamics is commonplace. However, while the assumption of linear, small amplitude, motion fits traditional offshore problems (it is desirable to stabilize ships, boats and offshore platforms), it is not representative of the expected (and desired) motions of a WEC, since the main objective is to enhance the response and maximize power extraction. The inadequacy of linear models for many wave energy applications has led to an increasing number of publications and codes implementing nonlinear hydrodynamics. However, nonlinear kinematics has received little attention, since few models yet consider six degrees of freedom (DoFs) and large rotations. This paper implements a nonlinear kinematic model for one of the most well established WEC concepts: an axisymmetric heaving point absorber with single taut line mooring. The influence of the nonlinear kinematics are demonstrated and potential sources of numerical instability in yaw are discussed. Finally, the model is also used to articulate parametric resonance in roll/pitch.

Introduction

The kinematics and dynamics of floating bodies is traditionally related to offshore engineering problems, such as: naval applications and the design of large oil and gas platforms [1]. For these applications, the main objective is usually to stabilize the motion of the floating objects, therefore the resulting small amplitude motions are within the limits of where linear theory is sufficiently accurate for modelling the system. However, contrary to these conventional offshore applications, wave energy converters (WECs) are designed and controlled with the objective of enhancing the wave induced motion to maximize power absorption [2]. Therefore, it is often the case that linear models become inapt to accurately predict the behaviour of a WEC . The fidelity of mathematical models is crucial for a reliable estimation of the cost of electricity and for the effectiveness of model-based control strategy [3], which are essential for achieving economic viability [4, 5]. Including nonlinearities in energy-maximising control strategies is both essential and possible [6].
As the wave energy field grows in experience and maturity, the necessity of nonlinear models, for a comprehensive design of most WEC types, becomes increasingly apparent [7, 8, 9]. While fully-nonlinear models, such as the ones solving Navier-Stokes equations, achieve high accuracy, they are not computationally viable for control or optimization applications. Considering the more computationally convenient partially-nonlinear models based on potential theory, most of the research is focusing on nonlinear hydrodynamics, namely on the modelling of nonlinear Froude-Krylov, radiation, or diffraction forces, or on viscous effects [10, 11, 12, 13]. However, little effort is found towards modelling nonlinear kinematics [14].
The consideration of nonlinear kinematics is usually necesssary for systems with large amplitude motion and multiple, coupled degrees of freedom. The inclusion of nonlinear kinematics is shown to be important in applications such as biomechanics [15, 16], robotics [17, 18], transportation [19, 20], tracking control [21, 22] and design of manipulators [23, 24], to name a few. However, for wave energy applications, numerical models employed to simulate the dynamic behavious of WECs generally assume the motion to be planar, in the direction of wave travel, with up to 3 DoFs considered (horizontal translation, vertical translation and rotation in the resulting plane: surge, heave and pitch, respectively) [25]. Moreover, the rotational displacement and velocity are normally assumed to be small. Few nonlinear studies are performed in 6-DoFs, especially considering roll/pitch parametric resonance or yaw instability [26, 27]. Parametric resonance is usually detrimental, but the ability to model it can enable more efficient harvesting instead [28, 29].
This paper presents a nonlinear model relevant for wave energy applications, including both nonlinear kinematics and nonlinear hydrodynamics. Typical WEC modelling approaches are challenged, discussing potential issues arising from employing the usual simplifying assumptions. In particular, potential numerical instability may arise from neglecting the mooring line torsional stiffness and viscous dissipation.

Mathematical model for a moored axisymmetric floater

The case study, schematically shown in Figure 1, is the archetype of the popular WEC concept known as a “point absorber” (since its dimensions are small compared to the wavelength such that it can be virtually approximated by a single point). Consequently, a natural choice is to design point absorbers to be independent of the incoming wave direction, so they are normally axisymmetric. The energy extraction results from the relative movement between the buoy and a fixed point on the sea floor. The buoy is attached to the sea floor by a single taut mooring line.

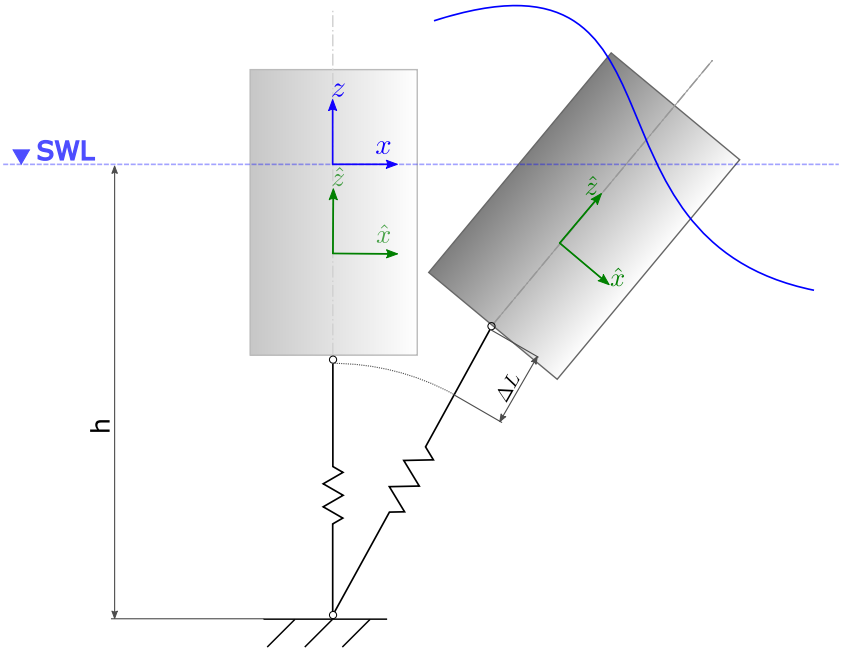

Figure 1: Cylindrical point absorber, with a single taut mooring line tethered to the sea floor (at depth h). Both the inertial frame (x, y, z) and the body-fixed frame $(\hat{x}, \hat{y}, \hat{z})$ have their origin at the still water level (SWL). The floater is shown at rest (in transparency) and displaced. The mooring line has axial stiffness K_{moor}, initial length L_0 and elongation ΔL. The device can rotate with respect to the mooring line.

Reference frames

Two right-handed frames of reference are defined, as schematically shown in Figure 1. The first one (x, y, z) is world-fixed, inertial, with the origin at the still water level (SWL) and on the centre of the buoy at rest, with the $x-$axis along and in the same positive direction of the wave propagation, and the $z-$axis pointing upwards. The inertial frame is used to describe the body displacements ($\boldsymbol{\zeta}$), divided into translations ($\mathbf{p}$) and rotations ($\boldsymbol{\Theta}$):

$$\boldsymbol{\zeta} = \begin{bmatrix} \mathbf{p} \\ \boldsymbol{\Theta} \end{bmatrix} \quad , \quad \mathbf{p} = \begin{bmatrix} x \\ y \\ z \end{bmatrix} \quad , \quad \boldsymbol{\Theta} = \begin{bmatrix} \phi \\ \theta \\ \psi \end{bmatrix}, \tag{1}$$

The second right-handed frame of reference is $(\hat{x}, \hat{y}, \hat{z})$, body-fixed, hence non-inertial, with the origin at the center of gravity of the floater. This is used for writing the dynamic equation of the system, since the inertial matrix remains constant. Therefore, both forces and velocities are represented in the body-fixed frame, along the axis of the buoy. Velocities ($\boldsymbol{\nu}$), divided into translation ($\mathbf{v}$) and rotations ($\boldsymbol{\omega}$), are defined as:

$$\boldsymbol{\nu} = \begin{bmatrix} \mathbf{v} \\ \boldsymbol{\omega} \end{bmatrix} \quad , \quad \mathbf{v} = \begin{bmatrix} u \\ v \\ w \end{bmatrix} = \begin{bmatrix} \dot{\hat{x}} \\ \dot{\hat{y}} \\ \dot{\hat{z}} \end{bmatrix} \quad , \quad \boldsymbol{\omega} = \begin{bmatrix} p \\ q \\ r \end{bmatrix}. \tag{2}$$

Kinematic mapping

It is worth remarking that forces and velocities are along time-varying axes, while displacements are along fixed axes. In linear hydrodynamic models there is no difference between such axes, based on the assumption of small displacements. However, in a nonlinear approach, a mapping from body- to world-frame velocities should be applied, at each time step, in order to obtain the correct displacements. One possible mapping is the following:

$$\dot{\boldsymbol{\zeta}} = \begin{bmatrix} \dot{\mathbf{p}} \\ \dot{\boldsymbol{\Theta}} \end{bmatrix} = \begin{bmatrix} \mathbf{R}_{\boldsymbol{\Theta}} & \mathbf{0}_{3\times3} \\ \mathbf{0}_{3\times3} & \mathbf{T}_{\boldsymbol{\Theta}} \end{bmatrix} \begin{bmatrix} \mathbf{v} \\ \boldsymbol{\omega} \end{bmatrix} = \mathbf{J}_{\boldsymbol{\Theta}} \boldsymbol{\nu}, \tag{3}$$

where $\mathbf{R}_{\boldsymbol{\Theta}}$ is the rotation matrix, depending on the Euler angles $\boldsymbol{\Theta}$, defined according to the 3-2-1 convention as:

$$\mathbf{R}_{\boldsymbol{\Theta}} = \mathbf{R}_{\hat{z},\psi} \mathbf{R}_{\hat{y},\theta} \mathbf{R}_{\hat{x},\phi} = \begin{bmatrix} c\psi & -s\psi & 0 \\ s\psi & c\psi & 0 \\ 0 & 0 & 1 \end{bmatrix} \begin{bmatrix} c\theta & 0 & s\theta \\ 0 & 1 & 0 \\ -s\theta & 0 & c\theta \end{bmatrix} \begin{bmatrix} 1 & 0 & 0 \\ 0 & c\phi & -s\phi \\ 0 & s\phi & c\phi \end{bmatrix}, \tag{4}$$

with c and s standing for $\cos()$ and $\sin()$ trigonometric operators, respectively. $\mathbf{R}_{\boldsymbol{\Theta}}$ is applied to translational velocities. $\mathbf{T}_{\boldsymbol{\Theta}}$ is applied to rotational ones, and is defined as follows:

$$\mathbf{T}_{\boldsymbol{\Theta}} = \begin{bmatrix} 1 & s\phi t\theta & c\phi t\theta \\ 0 & c\phi & -s\phi \\ 0 & s\phi/c\theta & c\phi/c\theta \end{bmatrix}, \tag{5}$$

where t stands for the $\tan()$ trigonometric operator. Note that the singularity of $\mathbf{T}_{\boldsymbol{\Theta}}$ in $\pm\pi/2$ is usually not an issue in wave energy applications, since the amplitude of the pitch angle is, by design, always expected to be smaller than $\pi/2$.

Coriolis and centripetal forces

Another consequence of using a body-fixed frame are Coriolis and centripetal forces, which are normally neglected under the assumption of small rotational velocities. Let us define, for convenience of notation, the skew-symmetric operator $\mathcal{S} : \mathbb{R}^3 \to \mathbb{R}^{3\times3}$ as

$$\mathcal{S} : \left\{ \boldsymbol{\lambda} \in \mathbb{R}^3 \,\middle|\, \mathcal{S}(\boldsymbol{\lambda}) \triangleq \begin{bmatrix} 0 & -\lambda_3 & \lambda_2 \\ \lambda_3 & 0 & -\lambda_1 \\ -\lambda_2 & \lambda_1 & 0 \end{bmatrix} \right\}. \tag{6}$$

Using such a notation, it is possible to define Coriolis and centripetal forces as:

$$\mathbf{F}_{Cor} = -\mathbf{C}_{Cor}\boldsymbol{\nu} = -\begin{bmatrix} M\mathcal{S}(\boldsymbol{\omega}) & -M\mathcal{S}(\boldsymbol{\omega})\mathcal{S}(\mathbf{r_g}) \\ M\mathcal{S}(\mathbf{r_g})\mathcal{S}(\boldsymbol{\omega}) & -\mathcal{S}(\mathbf{I}_r\boldsymbol{\omega}) \end{bmatrix} \begin{bmatrix} \mathbf{v} \\ \boldsymbol{\omega} \end{bmatrix}, \tag{7}$$

where M is the mass of the body, $\mathbf{r}_g$ is the vector from the origin of the body-fixed frame (reference point) to the centre of gravity, and $\mathbf{I}_r$ is the matrix of the moments of inertia with respect to the reference point. If the reference point is coincident with the center of gravity, then $\mathbf{r}_g$ is the null vector and $\mathbf{I}_r$ is a diagonal and minimal matrix, with I_x, I_y, and I_z on the diagonal. Consequently, the Coriolis and centripetal force in (7) becomes:

$$\mathbf{F}_{Cor} = -\begin{bmatrix} M\,(qw - rv) \\ M\,(ur - pw) \\ M\,(pv - qu) \\ qr\,(I_z - I_y) \\ rp\,(I_x - I_z) \\ pq\,(I_y - I_x) \end{bmatrix} \tag{8}$$

Hydrodynamic forces

The wave-structure interaction is modelled using the partially nonlinear hydrodynamic model detailed in [30]. This model decomposes the force from the fluid on the floater into several compoents: the Froude-Krylov (FK) force $\mathbf{F}_{FK}$, the diffraction force $\mathbf{F}_d$, the radiation force $\mathbf{F}_r$ and the viscous force $\mathbf{F}_v$. The model is labelled "partially nonlinear" since the diffraction and radiation forces are modelled linearly, whereas the viscous and FK force terms are nonlinear. The viscous force is described by an integral quadratic representation, and the nonlinear FK force is calculated by integrating the undisturbed pressure field from the incident wave over the instantaneous (updated at each time step) wetted surface of the floater. Full details of the nonlinear FK force representation are given in [31] for axisymmetric floaters, and in [32] for prismaric floaters. An open-source toolbox for the implementation of the nonlinear FK method is provided in [33].

Mooring force

The mooring system applies a force, $\mathbf{F}_m$, to the attachment point at the bottom center of the floater. The mooring force is modelled here as a linear spring.

Equation of motion

Finally, the dynamical equation in 6 DoFs for the floater becomes:

$$\begin{cases} \dot{\boldsymbol{\zeta}} = \mathbf{J}_{\boldsymbol{\Theta}}\boldsymbol{\nu} \\ \mathbf{M}\dot{\boldsymbol{\nu}} + \mathbf{F}_{Cor} = \mathbf{F}_{FK} + \mathbf{F}_d + \mathbf{F}_r + \mathbf{F}_v + \mathbf{F}_m \end{cases} \tag{9}$$

where $\mathbf{M}$ is the inertial matrix,

Coupling between DoFs

For the case of linear hydrodynamics, incoming unidirectional waves induce a planar external excitation on axisymmetric floaters (surge, heave and pitch). However, when considering nonlinear FK forces, a coupling can manifest under certain conditions, due to an internal excitation of the sway and roll DoFs [31]. In particular, when the excitation frequency is about twice the natural frequency in roll, a Mathieu-type of instability induces parametric resonance [34].
In these regions of parametric instability, a nonlinear FK model can provide 5 DoFs of excitation. Note, there is no means of exciting the yaw DoF. Even when considering the mooring system, the single mooring line does not provide any coupling between the excited DoFs and yaw [35]. However, if nonlinear kinematics effects are introduced, the Coriolis and centripetal forces, as well as the kinematic mapping $\mathbf{J}_{\boldsymbol{\Theta}}$, have the mathematical structure to provide a coupling with yaw. The following sections will show that, if these forces and the kinematic mapping are not appropriately taken into account, then the model can exhibit numerical instability.

Kinematic mapping

The last row of equation (3) represents the mapping from the body-fixed rotational velocities, $\boldsymbol{\omega}$, to the rate of change of the yaw displacement, $\dot{\psi}$:

$$\dot{\psi} = q\frac{\sin\phi}{\cos\theta} + r\frac{\cos\phi}{\cos\theta} \tag{10}$$

If ϕ is not exactly zero, Equation (10) shows that, $\dot{\psi}$ will be greater than zero. For the case of 3-DoF excitation (linear FK model or nonlinear FK model away from the parametric instability region), ϕ is not excited and simply decays from a small initial value ϕ_0; consequently $\dot{\psi} \approx 0$. On the other hand, when 5-DoF excitation occurs (nonlinear FK model in the parametric instability region), roll is internally excited and eventually the term $q\frac{\sin\phi}{\cos\theta}$ is non negligible, nor $\dot{\psi}$ anymore either.
Therefore, it results that the yaw DoF is coupled with other rotational DoFs, either weakly (in the 3-DoF case) or strongly (in the 5-DoF case). However, if there is no excitation of the yaw DoF, the yaw displacement is bounded, since $\dot{\psi}$ is of the same order of magnitude of q: $\dot{\psi} = \mathcal{O}(q)$. Nevertheless, under certain conditions, yaw may also be weakly excited by Coriolis and centripetal forces, potentially inducing the system to be unstable and generate an unbounded yaw response.

Coriolis and centripetal forces

As shown in Equation (8), the surge component of $\mathbf{F}_{Cor}$ is:

$$\mathbf{F}_{Cor}(1) = -M\,(qw - rv) \tag{11}$$

It is worth to notice that, in the simple 3-DoF case, the product $rv \approx 0$, so that $\mathbf{F}_{Cor}(1) \approx -Mqw$. Therefore, the mean of $\mathbf{F}_{Cor}(1)$ depends on the phase difference between pitch and heave, which are both externally excited. In particular, a zero mean is obtained if the phase difference is 90°, while strongly negative or positive means are obtained for phase differences of 0 or 180°, respectively. In a linear hydrodynamic model, the surge exciting force has zero mean, so that the resulting surge displacement is bounded to have the same sign of the mean of $\mathbf{F}_{Cor}(1)$, and magnitude depending on the mooring restoring force [35], since no hydrostatic force is present in surge. On the other hand, if a nonlinear hydrodynamic model is used, second order drift effects shift the mean of the surge exciting force to positive values, so that the resulting mean displacement is a combination of both the wave and the Coriolis and centripetal forces.
The yaw component of the $\mathbf{F}_{Cor}$ around the center of gravity, as shown in (8), is the following:

$$\mathbf{F}_{Cor}(6) = -pq\,(I_y - I_x) \tag{12}$$

Since pitch is externally excited, q is never zero. Since roll is either internally excited (5-DoF case) or in a simple decay (3-DoF case), p is either significantly large or relatively small, respectively, but never exactly zero. It follows that $\mathbf{F}_{Cor}(6)$ is exactly zero if and only if $I_x = I_y$.

Numerical yaw instability

Generally, both intuition and experience teach that no significant yaw response is expected from an axisymmetric system. Physically, the only restoring force in yaw is provided by moorings. For the mooring system shown in Figure 1, the restoring is provided by the torsional stiffness of the mooring line, which is normally small and usually neglected [36]. Consequently, no yaw restoring term is usually implemented in the numerical model. In addition, no dissipative mechanism are usually implemented in yaw, because radiation damping is ideally zero and viscous losses are reasonably negligible, due to the smooth axisymmetric geometry. However, neglecting dissipative and restoring terms in the yaw DoF can lead to unexpected yaw responses, and potentially generating conditions for numerical instability.

Initial conditions

Let us assume that the initial conditions, ($\boldsymbol{\zeta}_0$), are not exactly zero, but a small fraction of their expected steady state response, so that $\boldsymbol{\zeta}_0$ can be considered 'almost' zero. Such an assumption is consistent with the common application where, a mathematical model is coupled with a physical system, taking measured displacement and/or velocity signals as inputs (either in an experimental test-rig [37] or in real-sea deployment [38]). Furthermore, it is common practice to assume almost-zero initial conditions in nonlinear hydrodynamic models, in order to provide some initial energy to all DoFs and study the effect of instability [39, 40]. In absence of external-internal excitation or strong coupling, the small initial conditions rapidly decay. In the following discussion, the initial roll displacement, (ϕ_0), is slightly greater than zero (say, 0.5°), so that ϕ, $\dot{\phi}$, and p are non-zero.

Furthermore, let us assume that the initial yaw displacement ψ_0 is zero. Although this is an unnecessary assumption, it will highlight that a response in yaw (with no external nor internal hydrodynamic excitation) can appear solely due to the nonlinear kinematics.

Transversal moments of inertia

Theoretically, the two transversal moments of inertia, I_x and I_y, should be identical. However, numerically, the geometrical properties of the buoy will be reproduced with finite accuracy, thus I_x and I_y may be not exactly the same as each other. In this study, as an example, I_y has been considered to be $99.9\% I_x$.

Excitations

Table 1 summarizes all possible conditions that can arise.

Table 1: Characteristic of the yaw oscillatory response, ψ. Considering no viscous nor restoring terms in yaw and a small perturbation of the initial condition in roll and pitch. Two transversal moment of inertia cases are considered: ideal ($I_x = I_y$) and almost-ideal ($I_x \approx I_y$), in combination with two hydrodynamic excitation conditions: 3-DoF (linear FK model or nonlinear FK model away from the parametric resonance region) and 5-DoF (nonlinear FK model close to the parametric resonance region).

	Hydrodynamic excitation	
	3-DoF	**5-DoF**
$I_x = I_y$	Decay	Sustained, $\mathcal{O}(\theta)$
$I_x \approx I_y$	Unstable	Unstable

Let us consider the two hydrodynamic excitation conditions:

- 3-DoF excitation, where the excitation is external only.
- 5-DoF excitation, where 3-DoF are external excitation and 2 DoF are internal excitations present in the nonlinear FK model close to the parametric resonance region.

In the ideal case ($I_x = I_y$), there is no forcing term in yaw, so that the yaw response will follow roll and pitch angles, according to equation (10). In particular, in the 3-DoF excitation condition, yaw will follow the decay of roll; in the 5-DoF excitation condition, the oscillatory part of yaw will follow the pitch sustained response, modulated by the sine of the roll response. A slowly increasing mean of yaw is also present, due to the absence of a restoring force.

However, in the almost-ideal case ($I_x \approx I_y$), equation (12) shows that there is a forcing term of the yaw DoF, much smaller in a 3-DoF scenario than a 5-DoF scenario, but never exactly zero. Consequently, due to the lack of viscous and restoring terms, the yaw DoF is not restrained and becomes unstable, so that its response diverges at a rate proportional to the difference between I_x and I_y. Therefore, when implementing Coriolis and centripetal forces in a 6-DoF model, it is important to include a yaw restoring term, which prevents the numerical instability from appearing.

6-DoF response

A nonlinear 6-DoF model has been implemented, including nonlinear kinematics, Coriolis and centripetal forces, nonlinear Froude-Krylov forces, and 6-DoF quadratic viscous forces, as in [2]. The nonlinear hydrodynamics of this model is able to articulate parametric resonance in roll and pitch, which is a Mathieu-type of instability, arising when the period of the excitation force is about half the natural period in roll and pitch ($T_{n,5}$). Such an instability is mainly induced by the heave displacement causing, among other effects, a time-varying metacentric height (GM), thus hydrodynamic stiffness in roll and pitch.

In order to highlight such a behaviour, the floater, whose schematics is shown in Figure 1, is inspired by the cylinder studied in [41, 42], which is a renown example of parametrically unstable floater, due to the 2:1 ratio between natural periods in pitch/roll and heave. However, a notional single mooring line has been included, in order to consider the full 6-DoF model. For simplicity, the mooring restoring force has been assumed to be linear and with no coupling between DoFs. Note that, in order to avoid numerical instability in yaw, a torsional stiffness of the mooring line has been included. Furthermore, a 0.1% perturbation of one of the two transverse moments of inertia has been considered, in order to highlight the lack of instability thanks to the torsional stiffness.

Finally, note that all parameters and results here presented are normalized, enabling application to structures of varying size, such as the large spars in [41, 42], and to smaller WEC-like structures, as in [43]. The relevant common feature is to realize a 2:1 ratio between pitch and heave natural periods. Table 2 shows the ratio between the natural period in each DoF and $T_{n,5}$.

Table 2: Natural periods normalized by the pitch and roll natural periods [-].

Surge & Sway	**Heave**	**Roll & Pitch**	**Yaw**
7.7	0.5	1	5.1

Figure 2 shows the amplitude of the response to regular waves, as a function of wave periods (T_w) and wave heights (H_w). Periods are normalized by $T_{n,5}$, while the wave height and linear displacements are normalized by the metacentric height (GM). The dashed and dash-dotted red lines correspond to $T_w = \frac{1}{2}T_{n,5}$ and $T_w = T_{n,5}$, respectively. As expected, a roll and sway response is localized around an excitation period equal to $\frac{1}{2}T_{n,5}$. At the same period, there is a clear reduction of heave response, due to an internal exchange of energy between DoFs. Finally, under the 5-DoF excitation condition, there is a small response in the yaw DoF, made possible by the nonlinear kinematics and the perturbation of the transverse moment of inertia. However, due to the restoring term in yaw, numerical instability is avoided and the yaw response is contained below 1 degree.

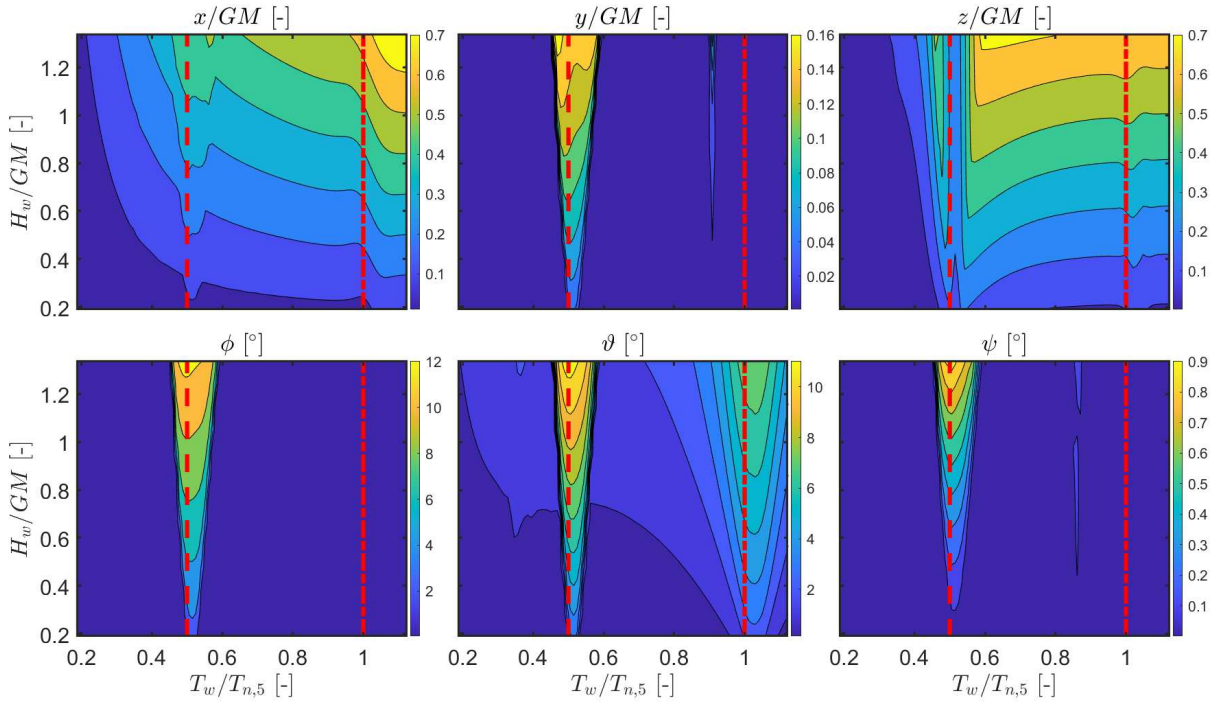

Figure 2: Amplitude of the response as a function of T_w and H_w. Periods are normalized by $T_{n,5}$, while the wave height and linear displacements are normalized by the metacentric height GM. The dashed and dash-dotted red lines correspond to $T_w = \frac{1}{2}T_{n,5}$ and $T_w = T_{n,5}$, respectively.

While Fig. 2 is obtained with a regular (monochromatic) waves, it is interesting to verify the development of parametric resonance and dynamic instability to more realistic irregular (panchromatic) waves. The most interesting condition is at the parametric resonance period, so that a peak period (T_p) of half $T_{n,5}$ is considered. Since the severity of the instability is proportional to the significant wave height (H_s) a medium-high value is considered, based on Fig.2, equal to GM. A typical Jonswap spectrum is considered, with the enhancing factor (γ) of 3.3. Figure 3 shows the dynamic response of the floater for a long realization of the resulting stochastic process. It is clear that the parametric resonance in roll is excited, but reaching a lower steady state amplitude than in the monochromatic condition, since the frequency-dependent instability is weaker.

Conclusions

This paper proposes a model in 6 degrees of freedom for axisymmetric floaters, including nonlinear kinematics, Coriolis and centripetal forces, and nonlinear Froude-Krylov forces. Although their physical impact is negligible, it is crucial to include damping and restoring terms in the yaw degree of freedom in the numerical model. In fact, if yaw is unrestrained, unstable and unbounded yaw responses may appear if there is a perturbation of the inertial properties of the system (likely

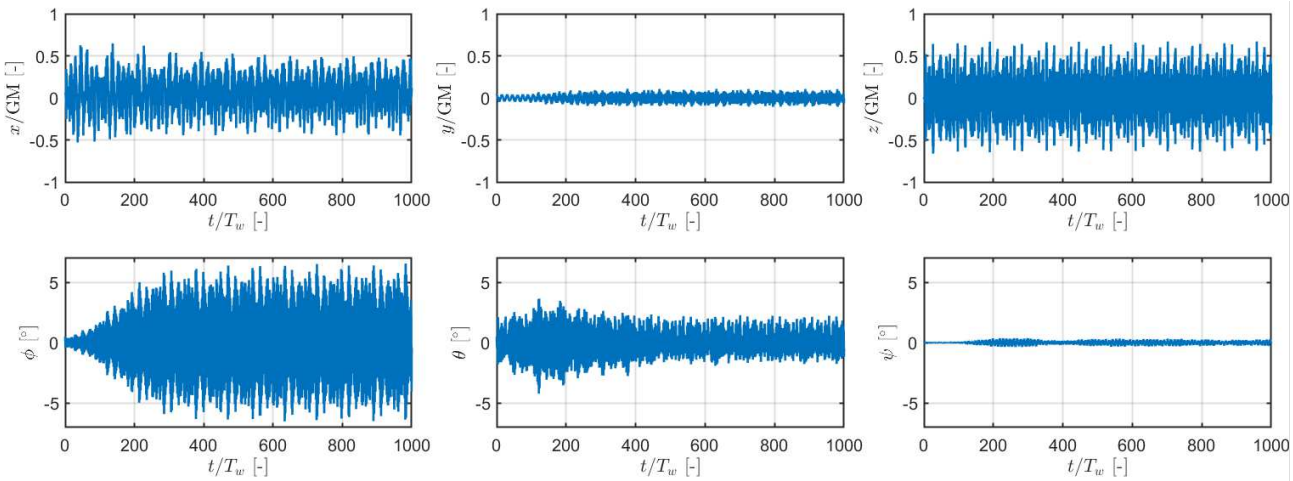

Figure 3: Dynamic response to a realization of a panchromatic wave with peak period $T_p = T_{n,5}/2$ and significant wave height $H_s = GM$.

if the mathematical model is coupled to a physical system). However, even with ideal inertial parameters, sustained bounded yaw response may be obtained if all other 5 DoFs are excited. This particular scenario arises due to parametric resonance conditions of the roll DoF, namely when the excitation force frequency is about twice the roll natural frequency. The proposed model, thanks to the nonlinear FK formulation, is also able to articulate parametric resonance.

Acknowledgement

This research has received funding from the European Research Council (ERC) under the European Union's Horizon 2020 research and innovation program under Grant No. 832140 and Grant No. 867453, and the Higher Education Excellence Program of the Ministry of Human Capacities in the frame of the Water Sciences & Disaster Prevention Research Area of BME (BME FIKP-VIZ), and in part by the National Research, Development and Innovation Fund through the Thematic Excellence Program under Grant TUDFO/51757/2019- ITM.

References

[1] J. N. Newman, L. Landweber, Marine Hydrodynamics, Vol. 45, The MIT Press, 1978. doi:10.1115/1.3424341.

[2] G. Giorgi, R. P. Gomes, J. C. Henriques, L. M. Gato, G. Bracco, G. Mattiazzo, Detecting parametric resonance in a floating oscillating water column device for wave energy conversion: Numerical simulations and validation with physical model tests, Applied Energy 276. doi:10.1016/j.apenergy.2020.115421.

[3] R. Genest, J. Davidson, J. V. Ringwood, Adaptive control of a wave energy converter, IEEE Transactions on Sustainable Energy 9 (4) (2018) 1588–1595.

[4] G. Bracco, M. Casassa, E. Giorcelli, G. Giorgi, M. Martini, G. Mattiazzo, B. Passione, M. Raffero, G. Vissio, Application of sub-optimal control techniques to a gyroscopic Wave Energy Converter, in: Renewable Energies Offshore, 2014, pp. 265–269.

[5] L. Genuardi, G. Bracco, S. A. Sirigu, M. Bonfanti, B. Paduano, P. Dafnakis, G. Mattiazzo, An application of model predictive control logic to inertial sea wave energy converter, in: Mechanisms and Machine Science, Vol. 73, Springer Netherlands, 2019, pp. 3561–3571. doi:10.1007/978-3-030-20131-9_351.

[6] N. Faedo, F. J. Dores Piuma, G. Giorgi, J. V. Ringwood, Nonlinear model reduction for wave energy systems: a moment-matching-based approach, Nonlinear Dynamics (2020) 1–23doi:10.1007/s11071-020-06028-0.

[7] A. S. Sirigu, F. Gallizio, G. Giorgi, M. Bonfanti, G. Bracco, G. Mattiazzo, Numerical and Experimental Identification of the Aerodynamic Power Losses of the ISWEC, Journal of Marine Science and Engineering 8 (49) (2020) 1–25. doi:10.3390/jmse8010049.

[8] M. Penalba, G. Giorgi, J. V. Ringwood, Mathematical modelling of wave energy converters: a review of nonlinear approaches, Renewable and Sustainable Energy Reviews 78 (2017) 1188–1207. doi:10.1016/j.rser.2016.11.137.

[9] J. Davidson, R. Costello, Efficient Nonlinear Hydrodynamic Models for Wave Energy Converter Design — A Scoping Study (2020) 1–65doi:10.3390/jmse8010035.

[10] F. Wendt, K. Nielsen, Y.-h. Yu, H. Bingham, C. Eskilsson, B. Kramer, A. Babarit, T. Bunnik, R. Costello, S. Crowley, G. Giorgi, S. Giorgi, S. Girardin, D. Greaves, Ocean Energy Systems wave energy modeling task : modeling , verification , and validation of wave energy converters, Journal of Marine Science and Engineering 7 (379) (2019) 1–22. doi:10.3390/jmse7110379.

[11] E. Ransley, S. Yan, S. Brown, D. Graham, P.-H. Musiedlak, C. Windt, J. Ringwood, J. Davidson, P. Schmitt, J. X. H. Wang, Q. Ma, Z. H. Xie, G. Giorgi, J. Hughes, A. Williams, I. Masters, Z. Lin, H. Chen, L. Qian, Z. Ma, D. Causon, C. Mingham, Q. Chen, H. Ding, J. Zang, J. van Rij, Y. Yu, N. Tom, Z. Li, B. Bouscasse, G. Ducrozet, H. Bingham, A blind comparative study of focused wave interactions with floating structures ({CCP-WSI Blind Test Series 3}), International Journal of Offshore and Polar Engineering 30 (1) (2020) 1–10. doi:10.17736/ijope.2020.jc774.

[12] M. Fontana, P. Casalone, S. A. Sirigu, G. Giorgi, Viscous Damping Identification for a Wave Energy Converter Using CFD-URANS Simulations, Journal of Marine Science and Engineering 8 (355) (2020) 1–26. doi:10.3390/jmse8050355.

[13] L. Letournel, C. Chauvigné, B. Gelly, A. Babarit, G. Ducrozet, P. Ferrant, Weakly nonlinear modeling of submerged wave energy converters, Applied Ocean Research 75 (March) (2018) 201–222. doi:10.1016/j.apor.2018.03.014.

[14] G. Giorgi, J. Davidson, G. Habib, G. Bracco, G. Mattiazzo, T. Kalmár-nagy, Nonlinear Dynamic and Kinematic Model of a Spar-Buoy : Parametric Resonance and Yaw Numerical Instability, Journal of Marine Science and Engineering 8 (504) (2020) 1–17. doi:10.3390/jmse8070504.

[15] S. H. Scott, D. A. Winter, Biomechanical model of the human foot: kinematics and kinetics during the stance phase of walking, Journal of biomechanics 26 (9) (1993) 1091–1104.

[16] U. H. Buzzi, N. Stergiou, M. J. Kurz, P. A. Hageman, J. Heidel, Nonlinear dynamics indicates aging affects variability during gait, Clinical biomechanics 18 (5) (2003) 435–443.

[17] A. J. Ijspeert, J. Nakanishi, S. Schaal, Movement imitation with nonlinear dynamical systems in humanoid robots, in: Proceedings 2002 IEEE International Conference on Robotics and Automation (Cat. No. 02CH37292), Vol. 2, IEEE, 2002, pp. 1398–1403.

[18] T. I. Fossen, S. I. Sagatun, Adaptive control of nonlinear systems: A case study of underwater robotic systems, Journal of Robotic Systems 8 (3) (1991) 393–412.

[19] T. D. Burton, A. M. Whitman, Nonlinear kinematics of wheel-rail contact.

[20] M. Kaminaga, M. Murata, Y. Tateishi, Factoring nonlinear kinematics into new suspension design: a CAE approach to vehicle roll dynamics, SAE transactions (1994) 1188–1198.

[21] H. J. Kim, D. H. Shim, S. Sastry, Nonlinear model predictive tracking control for rotorcraft-based unmanned aerial vehicles, in: Proceedings of the 2002 American Control Conference (IEEE Cat. No. CH37301), Vol. 5, IEEE, 2002, pp. 3576–3581.

[22] E. J. Clark, E. J. Griffith, S. Maskell, J. F. Ralph, Nonlinear kinematics for improved helicopter tracking, in: 2017 20th International Conference on Information Fusion (Fusion), IEEE, 2017, pp. 1–6.

[23] G. Naganathan, A. H. Soni, Coupling effects of kinematics and flexibility in manipulators, The International journal of robotics research 6 (1) (1987) 75–84.

[24] G. Naganathan, A. H. Soni, Nonlinear modeling of kinematic and flexibility effects in manipulator design, Journal of Mechanical Design.

[25] A. Babarit, J. H. Todalshaug, A. Kurniawan, M. Muliawan, T. Moan, J. Krokstad, The NumWEC Project: Numerical Esitmation of Energy Delivery from a Selection of Wave Energy Converters (December) (2011) 1–317. doi:10.13140/RG.2.1.3807.8885.

[26] J. Orszaghova, H. Wolgamot, S. Draper, P. H. Taylor, A. Rafiee, Onset and limiting amplitude of yaw instability of a submerged three-tethered buoy, Proceedings of the Royal Society A: Mathematical, Physical and Engineering Sciencesdoi:10.1098/rspa.2019.0762.

[27] H. Wang, A. Somayajula, J. Falzarano, Z. Xie, Development of a Blended Time-Domain Program for Predicting the Motions of a Wave Energy Structure, Journal of Marine Science and Engineering 8 (1) (2019) 1. doi:10.3390/jmse8010001.

[28] G. Giorgi, N. Faedo, Performance enhancement of a vibration energy harvester via harmonic time-varying damping: A pseudospectral-based approach, Mechanical Systems and Signal Processing 165 (2022) 108331. doi:10.1016/J.YMSSP.2021.108331.

[29] G. Giorgi, Parametric resonance exploitation due to periodic damping in an electromechanical energy harvester, International Journal of Mechanics and Control 22 (2021) 77–85.

[30] G. Giorgi, R. P. F. Gomes, G. Bracco, G. Mattiazzo, The effect of mooring line parameters in inducing parametric resonance on the Spar-buoy oscillating water column wave energy converter, Journal of Marine Science and Engineering 8 (1) (2020) 1–20. doi:10.3390/JMSE8010029.

[31] G. Giorgi, R. P. F. Gomes, G. Bracco, G. Mattiazzo, Numerical investigation of parametric resonance due to hydrodynamic coupling in a realistic wave energy converter, Nonlinear Dynamicsdoi:10.1007/s11071-020-05739-8.

[32] G. Giorgi, S. Sirigu, M. Bonfanti, G. Bracco, G. Mattiazzo, Fast nonlinear froude–krylov force calculation for prismatic floating platforms: a wave energy conversion application case, Journal of Ocean Engineering and Marine Energy 2021 7 (2021) 439–457. doi:10.1007/S40722-021-00212-Z.

[33] G. Giorgi, Nonlinear Froude-Krylov Matlab demonstration toolbox (2019). doi:10.5281/zenodo.4065202.

[34] T. I. Fossen, H. Nijmeijer, Parametric resonance in dynamical systems, Springer, 2012. doi:10.1007/978-1-4614-1043-0.

[35] J. Davidson, J. V. Ringwood, Mathematical modelling of mooring systems for wave energy converters - A review, Energies 10 (5). doi:10.3390/en10050666.

[36] B. Paduano, G. Giorgi, R. P. F. Gomes, E. Pasta, J. C. C. Henriques, L. M. C. Gato, G. Mattiazzo, Experimental Validation and Comparison of Numerical Models for the Mooring System of a Floating Wave Energy Converter, Journal of Marine Science and Engineering 8 (8) (2020) 565. doi:10.3390/jmse8080565.

[37] M. Bonfanti, G. Bracco, P. Dafnakis, E. Giorcelli, B. Passione, N. Pozzi, S. Sirigu, G. Mattiazzo, Application of a passive control technique to the ISWEC: Experimental tests on a 1:8 test rig, in: NAV International Conference on Ship and Shipping Research, no. 221499, 2018, pp. 60–70. doi:10.3233/978-1-61499-870-9-60.

[38] S. A. Sirigu, G. Bracco, M. Bonfanti, P. Dafnakis, G. Mattiazzo, On-board sea state estimation method validation based on measured floater motion, IFAC-PapersOnLine 51 (29) (2018) 68–73. doi:10.1016/J.IFACOL.2018.09.471.

[39] K. R. Tarrant, C. Meskell, Investigation on parametrically excited motions of point absorbers in regular waves, Ocean Engineering 111 (2016) 67–81. doi:10.1016/j.oceaneng.2015.10.041.

[40] G. Giorgi, J. V. Ringwood, Parametric motion detection for an oscillating water column spar buoy., in: Proceedings of the 3rd International Conference on Renewable Energies Offshore RENEW, Lisbon, 2018.

[41] Z. Jingrui, T. Yougang, S. Wenjun, A study on the combination resonance response of a classic spar platform, JVC/Journal of Vibration and Control 16 (14) (2010) 2083–2107. doi:10.1177/1077546309349393.

[42] E. Gavassoni, P. B. Gonçalves, D. M. Roehl, Nonlinear vibration modes and instability of a conceptual model of a spar platform, Nonlinear Dynamics 76 (1) (2014) 809–826. doi:10.1007/s11071-013-1171-6.

[43] R. Gomes, J. Henriques, L. Gato, A. Falcão, Time-domain simulation of a slack-moored floating oscillating water column and validation with physical model tests, Renewable Energy 149 (2020) 165–180. doi:10.1016/J.RENENE.2019.11.159.

On periodic solutions and modal energy transfer of mechanical systems with state-dependent impulsive stiffness excitation

Thomas Pumhössel
Institute of Mechatronic Design and Production, Johannes Kepler University Linz, Austria

Summary. In the present contribution, mechanical systems with impulsive stiffness excitation are investigated. It is shown that periodic solutions exist, which result in a repeated transfer of vibration energy from lower to higher modes and vice-versa. This allows that the structural damping of the mechanical system can be utilized more effectively, resulting in a faster decay of transient vibrations compared to the case where no impulsive excitation is present.

Introduction

The transfer of vibration energy, either in the modal space, or spatially to an attached system, allows to reduce transient vibrations after some initial disturbance. In the first case the enhanced damping properties of higher modes can be utilized more effectively, see. e.g. [1], whereas in the second case energy is transferred in a one-way, irreversible manner to a nonlinear coupled additional system, denoted as nonlinear energy sink (NES), see [2], for example.
In the present contribution, mechanical systems with state-dependent impulsive stiffness excitation are investigated. It is shown that, in the conservative case, periodic solutions exist which result in a periodic exchange of vibration energy across modes. By taking structural damping into account, the effect on the total energy content of mechanical systems is demonstrated.

Periodic solutions and energy transfer

In the following, mechanical systems with impulsive stiffness excitation described by equations of motion of the form

$$\mathbf{M}\ddot{\mathbf{x}}(t) + \mathbf{C}\dot{\mathbf{x}}(t) + (\mathbf{K} + \sum_{k=1}^{K} \varepsilon_k(\mathbf{x}_k, \dot{\mathbf{x}}_k)\mathbf{G}\delta(t - t_k))\mathbf{x}(t) = \mathbf{0}, \tag{1}$$

are investigated. Therein, $\mathbf{M}$, $\mathbf{C}$ and $\mathbf{K}$ represent the constant $(n \times n)$-dimensional mass-, damping- and stiffness-matrix. Impulsive parametric excitation is introduced at equidistant instants of time t_k by using Dirac-delta functions $\delta(t - t_k)$, where the state-dependent strength of the impulses is denoted as $\varepsilon_k(\mathbf{x}_k, \dot{\mathbf{x}}_k)$. It was shown in [3], that the state of the system $\mathbf{r}(t) = [\mathbf{x}(t)\ \dot{\mathbf{x}}(t)]^T$ just after an impulse at t_k, i.e. at $t_{k,+}$, can be related to the state after the preceding impulse at $t_{k-1,+}$ by

$$\mathbf{r}(t_{k,+}) = \mathbf{J}_k(\varepsilon_k)\boldsymbol{e}^{\mathbf{A}\Delta T}\mathbf{r}(t_{k-1,+}), \tag{2}$$

where

$$\mathbf{J}_k = \begin{bmatrix} \mathbf{I} & \mathbf{0} \\ -\varepsilon_k\mathbf{M}^{-1}\mathbf{G} & \mathbf{I} \end{bmatrix}, \quad \mathbf{A} = \begin{bmatrix} \mathbf{0} & \mathbf{I} \\ -\mathbf{M}^{-1}\mathbf{K} & -\mathbf{M}^{-1}\mathbf{C} \end{bmatrix}, \tag{3}$$

and $\Delta T = t_k - t_{k-1}$ holds. The matrix $\mathbf{J}_k$ was denoted as jump-transfer matrix by *Hsu*, see [3]. If the impulsive strength ε_k is selected to be state-dependent according to

$$\varepsilon_k = (\sum_{i=1}^{n} \mathbf{g}_i^T\mathbf{x}_{k-}\dot{x}_{i,k-})/(\frac{1}{2}\sum_{i=1}^{n}(\mathbf{g}_i^T\mathbf{x}_{k-})^2/m_i), \tag{4}$$

see [4], neither energy is extracted from, nor fed to the mechanical system by an impulse, i.e. the impulse is energy-neutral. In this case, $\mathbf{J}_k$ becomes a constant matrix and Eqn. (2) can be written in the form

$$\mathbf{r}(t_{k,+}) = \underbrace{\mathbf{J}\boldsymbol{e}^{\mathbf{A}\Delta T}}_{\mathbf{Q}(\Delta T)}\mathbf{r}(t_{k-1,+}) = \mathbf{Q}^k(\Delta T)\mathbf{r}_0 = \boldsymbol{\Psi}\boldsymbol{\Lambda}^k\boldsymbol{\Psi}^{-1}\mathbf{r}_0, \tag{5}$$

where $\mathbf{r}_0 = \mathbf{r}(t_0 = 0)$. The matrix $\boldsymbol{\Psi}$ is comprised of the eigenvectors of $\mathbf{Q}$, and $\boldsymbol{\Lambda} = \mathrm{diag}(\lambda_i),\ i = 1, 2, \ldots 2n$, of the corresponding eigenvalues. Following the notation in [5], a periodic solution with period R is given by a sequence of R distinct points $\mathbf{r}^*$ in the state-space according to

$$\mathbf{r}^*(t_{m+r,+}) = \mathbf{Q}^r\mathbf{r}^*(t_{m,+}), \quad r = 1, 2, \ldots R - 1, \tag{6}$$

$$\mathbf{r}^*(t_{m+R,+}) = \mathbf{Q}^R\mathbf{r}^*(t_{m,+}) = \mathbf{r}^*(t_{m,+}), \tag{7}$$

denoted as P-R solution. It can be seen from Eqn. (5), that the last condition (Eqn. (7)) is fulfilled if there exists a timespan ΔT between adjacent impulses, for which $\boldsymbol{\Lambda}^R = \mathbf{I}$ holds, where $\mathbf{I}$ represents the identity matrix. With a simple example, the existence of such cases is demonstrated in the following.
The investigated mechanical system comprises two masses connected by stiffness and damping elements and is pinned on one end, see Fig. (1), where the stiffness $k_{01} = \bar{k}_{01} + \varepsilon_k g_{01}\delta(t - t_k)$, i.e. consists of a constant and an impulsive part. At equidistant instants of time t_k, stiffness impulses with a strength according to Eqn. (4) are applied. Hence, the equations of motion are of the form of Eqn. (1). As system parameters $m_1 = 1$, $m_2 = 0.5$, $\bar{k}_{01} = 1$, $k_{12} = 2$, and a stiffness-proportional damping $\mathbf{C} = \alpha\mathbf{K}$, $\alpha = 0.01$, were used for the numerical calculations.

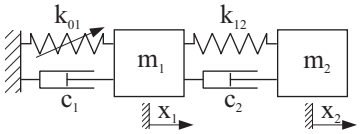

Figure 1: Sketch of investigated mechanical system.

Figure (2a) shows the eigenvalues λ_i, $i = 1, \dots 4$, of the mapping matrix $\mathbf{Q}$ in the undamped case ($\alpha = 0$), for different values of the timespan ΔT between adjacent impulses. One notes that within the investigated interval of ΔT, two real and two complex conjugate eigenvalues exist. Exemplarily, the case $\Delta T = 6.68672$ where $\lambda_{12} = \pm 1$ and $\lambda_{34} = \pm i$, see the dotted unit-circle in Fig. (2a), is investigated in more detail. Applying the mapping matrix $\mathbf{Q}$ four times gives $\lambda^R_{1,2} = 1$ and $\lambda^R_{3,4} = 1$, i.e. the mechanical system attains the initial state again after applying four impulses. Hence, we have a P-4 solution with a period of $4\Delta T_{P-4}$. Figure (2b) depicts the corresponding 4-periodic timeseries of the impulsive strength ε_k. The effect of the impulsive excitation on the modal coordinates y_1 and y_2 is shown in Fig. (2c). As a first mode deflection according to $\mathbf{y}(t=0) = [1\ 0]^T$ and $\dot{\mathbf{y}}(t=0) = [0\ 0]^T$ was used as initial condition, the mechanical system does not show any second mode vibrations initially. This changes with the application of the first impulse, as energy is transferred from the first to the second mode. In the following, the system exhibits first and second mode vibrations simultaneously, until after one period the energy content of the second mode vanishes again. Thereafter, one observes a periodic exchange of energy from the first to the second mode and vice-versa. Including structural damping ($\alpha = 0.01$) allows to exploit the enhanced damping properties of the second mode, see Fig. (2d). During the phases where the second mode contains vibration energy, the total energy content E of the mechanical system decreases faster compared to the phases where only first mode vibrations occur. This results in a globally faster decay of the vibration energy E compared to E_0 (energy content where no impulsive excitation is present).

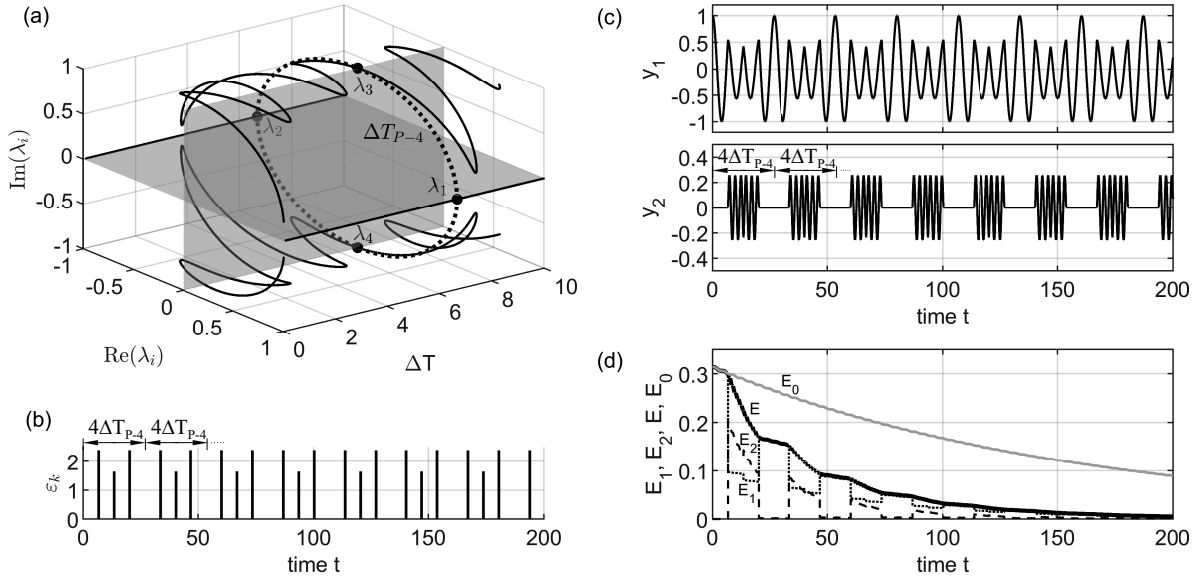

Figure 2: Eigenvalues λ_i, $i = 1, \dots 4$, of mapping matrix $\mathbf{Q}$ for different values of the timespan ΔT between adjacent impulses - undamped case $\alpha = 0$, (a). Impulsive strength (b), and modal displacements y_1 and y_2 (c) for the case $\Delta T = \Delta T_{P-4} = 6.68672$ and $\alpha = 0$. Modal energy contents E_1 (dotted) and E_2 (dashed), total energy content of the mechanical system E, and total energy content E_0 of system without impulsive excitation for the damped case (d).

Conclusions

It was demonstrated that conservative mechanical systems exhibited to impulsive stiffness excitation of energy-neutral kind can show a periodic behaviour, which can be utilized effectively to enhance the damping of transient vibrations.

References

[1] Al-Shudeifat M.A., Vakakis A.F., Bergman L.A. (2015) Shock mitigation by means of low- to high frequency nonlinear targeted energy transfers in a large scale structure. *ASME Journal of Computational and Nonlinear Dynamics* **11(2)**:021006-021006-11. doi:10.1115/1.4030540.

[2] Vakakis A.F., Gendelman O.V., Bergman L.A., McFarland D.M., Kerschen G., Lee Y.S. (2009) Nonlinear Targeted Energy Transfer in Mechanical and Structural Systems. Springer Netherlands.

[3] Hsu C.S. (1972) Impulsive Parametric Excitation: Theory. *ASME Journal of Applied Mechanics* **39(2)**:551-558.

[4] Pumhössel T. (2016) Energy-Neutral Transfer of Vibration Energy Across Modes by Using Active Nonlinear Stiffness Variation of Impulsive Type. *ASME Journal of Computational and Nonlinear Dynamics* **12(1)**:011001-011001-11. doi:10.1115/1.4034264.

[5] Hsu C.S., Cheng W.H. (1977) Steady-State Response of a Non-Linear System Under Impulsive Periodic Parametric Excitation. *Journal of Sound and Vibration* **50(1)**:95-116.

Thursday, July 21, 2022
08:30 - 10:30

MS-11 Systems with Time Delay
Saint Clair 2

Chair: Gabor Orosz

08:30 - 08:50
An alternative grinding wheel regenerative mechanism: distributed grit dullness
TOTH Mate*, CURTIS David, SIMS Neil
*The University of Sheffield (Western Bank, Sheffield S10 2TN United Kingdom)

08:50 - 09:10
An MID-based Control of a Vibrating Axisymmetric Membrane Using Piezoelectric Transducers
TLIBA Sami, BOUSSAADA Islam, NICULESCU Silviu-Iulian, **FALCON Ricardo***
*Laboratoire des signaux et systèmes (Plateau de Moulon 3 rue Joliot Curie 91192 GIF SUR YVETTE CEDEX France)

09:10 - 09:30
Analysis of Chatter Mechanisms in Cutting Process
WEREMCZUK Andrzej*, RUSINEK Rafal, WARMINSKI Jerzy
*Department of Applied Mechanics, Lublin University of Technology (Nadbystrzycka 38D, 20-618 Lublin Poland)

09:30 - 09:50
Bifurcation analysis at a degenerate parameter point of a non-collocated force control model
ZHANG Li, WANG Huailei, **STEPAN Gabor***
*Budapest University of Technology and Economics (Budapest Hungary)

09:50 - 10:10
Stabilizability Limits for the Inverted Pendulum with a Multiple-Delay Fractional-Order Controller
BALOGH Tamas*, INSPERGER Tamás
*Budapest University of Technology and Economics (Budapest, Muegyetem rkp. 3. Hungary)

An alternative grinding wheel regenerative mechanism: distributed grit dullness

Máté Tóth[*], David Curtis[**], and Neil D Sims[*]
[*]*Department of Mechanical Engineering, The University of Sheffield, Sheffield S1 3JD, UK*
[**]*Advanced Manufacturing Research Centre, Wallis Way, Rotherham S60 5TZ, UK*

Summary. This work focuses on the dynamics and stability of grinding operations. Surface regeneration, which is a well-known and widely accepted cause of regenerative chatter in machining, affects grinding in a unique way as it can occur not only on the workpiece but on the wheel as well. The vast majority of relevant publications consider only distributed radial wear or physical surface waves around the circumference of the grinding wheel in order to account for surface regeneration on the wheel. This research presents an alternative regenerative mechanism, namely the distributed dullness of the cutting edges captured by the specific energy, which is a fundamental quantity in grinding, similar to the cutting-force coefficient in conventional machining. The new chatter theory, which is validated experimentally, predicts stable grinding conditions with respect to wheel regeneration for a certain set of cutting parameters. This is atypical as far as the relevant literature is concerned, i.e., grinding is reported to be typically unstable with regard to wheel regeneration.

Introduction

Grinding is a widely used machining process with a significant 20-25% share of the manufacturing sector in developed countries [1]. The main difference between grinding and conventional machining lies in their respective cutting tools. While conventional processes (e.g. turning and milling) employ geometrically well-defined machine tools, grinding relies on a geometrically ill-defined wheel for material removal. Owing to its unique cutting tool, grinding has a number of advantages and disadvantages. Abrasive processes are known for producing excellent surface quality and dimensional accuracy, cutting difficult-to-machine materials with relative ease, and achieving high material removal rates. The downside of abrasive machining is excessive tool wear, significant heat generation, and – from a theoretical point of view – the complexity of process modelling and prediction due to the inherent randomness of the wheel geometry. This last disadvantage makes it especially complicated to accurately capture an already intricate phenomenon in grinding, which harmfully affects virtually all machining operations, namely regenerative machine tool vibration or chatter. The consequences of self-excited relative vibration between the workpiece and the cutting tool are serious: inadequate surface finish, inaccurate dimensions, reduced tool life, unpleasant noise, etc. Since machining under unstable conditions is highly unfavourable, chatter is to be avoided for the sake of product quality and manufacturing efficiency.

Literature review

Chatter modelling in conventional machining has been the topic of extensive research since Taylor published his famous work at the beginning of the 20th century, asserting that chatter is the most obscure of all machining problems, and there are probably no rules that can guide the machinist in maximising productivity and avoiding chatter at the same time [2]. Taylor's initial concerns have been allayed in the world of conventional processes by chatter theories that are capable of accurately predicting the onset of unstable vibrations [3,4]. However, grinding has been lagging behind the results of conventional theories, because the inherently random nature of its cutting tool makes regenerative chatter more difficult to model and predict. Nevertheless, grinding chatter has been the subject of active and diligent research since the middle of the 20th century [5,6].

Grinding is often a finishing operation responsible for the final surface quality and dimensional accuracy of the machined part. Therefore, in the case of grinding, unstable relative vibration between the wheel and the workpiece can be especially detrimental, because it can destroy a product on which a number of costly machining operations have already been performed. The uniqueness of grinding lies not only in its cutting tool but also in the fact that surface regeneration can occur not only on the workpiece but on the grinding wheel as well, introducing the possibility that the two phenomena happen simultaneously and influence one another in real time. This idea is often referred to as double regeneration in the literature, and has been meticulously studied ever since wheel-related instability was first measured in practice [7].

Surface regeneration on the grinding wheel has usually been modelled as distributed radial wear or physical surface waves around the circumference of the grinding wheel. While this is a perfectly reasonable approach to considering wheel-related instability, Li and Shin claimed that such a description is incomplete, as distributed radial wear alone cannot account for a number of experimental observations reported in the literature [8]. Therefore, they formulated a new theory based on a regenerative mechanism that combines distributed radial wear with distributed grit dullness (i.e. the distribution of the dullness of the cutting edges around the circumference of the grinding wheel). They characterised grit dullness by the specific energy, which quantifies the amount of grinding energy required to remove a unit volume of workpiece material, or equivalently, the amount of grinding power necessary to sustain a unit material removal rate. That is because a sharper/duller grain corresponds to a lower/higher specific energy, respectively. Therefore, Li and Shin considered not only physical surface waves but also specific energy waves on the grinding wheel.

Nevertheless, the current literature tends to model wheel regeneration as a result of uneven radial wear alone. The present study seeks to overcome this by investigating the approach taken by Li and Shin from an analytical and experimental perspective.

Model

A two-dimensional, single-degree-of-freedom model of single-pass surface grinding has been developed by the authors, where the distributed dullness of the cutting edges is quantified by the variation of the specific energy around the circumference of the wheel. The governing equation of motion of the system is linear in its primary variable, which is the specific energy (u), and contains two time delays – a point delay (T_g) and a distributed delay (τ, between 0 and $\tau_{c,0}$):

$$\ddot{u}(t) + 2\zeta\omega_n\dot{u}(t) + \omega_n^2 u(t) = \ddot{u}(t-T_g) + 2\zeta\omega_n\dot{u}(t-T_g) + \omega_n^2 u(t-T_g) - \frac{\mu_x\delta_0 w C_d v_w^2 \tau_g}{m\tau_{c,0}v_g}\int_0^{\tau_{c,0}} u(t-T_g+\tau_{c,0}-\tau)\,d\tau.$$

The point delay is equal to the rotation period of the grinding wheel, and the upper limit of the distributed delay describes the total time necessary for an individual grit to pass through the grinding zone. It can be seen that T_g is significantly larger than $\tau_{c,0}$ for practical values of the nominal depth of cut (δ_0). The mathematical complexities of the stability analysis introduced by these two time delays are dealt with in the frequency domain. Taking the Laplace transform of the equation of motion, the open-loop transfer function between the nominal depth of cut and the resulting wheel vibration reads

$$T_o(s) = \frac{\mu_x\delta_0 w C_d v_w^2 \tau_g e^{-T_g s}(e^{\tau_{c,0}s}-1)}{m\tau_{c,0}v_g s(1-e^{-T_g s})(s^2+2\zeta\omega_n s+\omega_n^2)}.$$

Having transformed the two time delays into a number of complex exponentials, it is possible to apply the Nyquist criterion to the open-loop transfer function above, in order to determine the stability properties of the system.

Results

The proposed theory predicts stable machining conditions for a certain, practically feasible set of grinding parameters (see black lines in Fig. 1). This is an unusual yet fascinating result, as grinding is reported to be typically unstable with respect to wheel regeneration in the literature [5,6]. Furthermore, a number of grinding trials have been performed by the authors as well, which present a strong case for the validity of the new model (see coloured circles in Fig. 1). The primary aspects of comparison were stability diagrams and, in the case of instability, chatter frequencies, which indicate a good correspondence between the theoretical predictions and the experimental data.

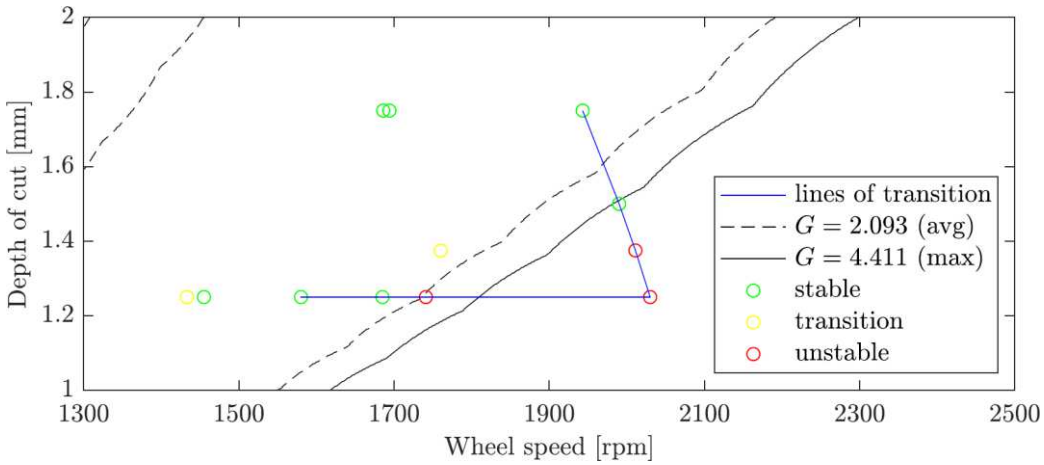

Figure 1: Comparison between theoretical and experimental stability boundaries with a good agreement between the two

Conclusions

The new chatter model proposed in this work is not only reliable in its own right, but also has a much broader area of application, calling for the alternative wheel regenerative mechanism of distributed grit dullness to be included in sophisticated grinding chatter models. Practically speaking, the new theory suggests that previously unknown regions of stability exist and can be utilised in the pursuit of avoiding chatter vibrations in grinding processes, which is the main and most promising outcome of this research.

References

[1] Malkin, S., & Guo, C. (2008). *Grinding technology: theory and application of machining with abrasives*. Industrial Press Inc.
[2] Taylor, F. W. (1906). *On the Art of Cutting Metals.* (Vol. 23). American society of mechanical engineers.
[3] Tobias, S. A. (1965). *Machine-tool vibration*. J. Wiley.
[4] Altintas, Y. (2012). *Manufacturing Automation*. Cambridge University Press.
[5] Snoeys, R., & Brown, D. (1970). Dominating parameters in grinding wheel—and workpiece regenerative chatter. In *Advances in Machine Tool Design and Research 1969* (pp. 325-348). Pergamon.
[6] Inasaki, I., Karpuschewski, B. A., & Lee, H. S. (2001). Grinding chatter–origin and suppression. *CIRP Annals*, *50*(2), 515-534.
[7] Landberg, P. (1956). *Experiments on grinding*. Technical University, Laboratory for Metal Processing.
[8] Li, H., & Shin, Y. C. (2006). Wheel regenerative chatter of surface grinding. *Journal of manufacturing science and engineering*, *128*(2), 393-403.

An MID-based Control of a Vibrating Axisymmetric Membrane Using Piezoelectric Transducers

Sami Tliba*, Islam Boussaada**,†, Silviu-Iulian Niculescu**,‡, and Ricardo Falcon *
*L2S, Université Paris-Saclay, CentraleSupélec, CNRS, 91190, Gif-sur-Yvette
**Inria Saclay-Île-de-France, Equipe DISCO
†IPSA, 63 Boulevard de Brandebourg, 94200 Ivry-sur-Seine, France
‡L2S, CNRS, CentraleSupélec, Université Paris-Saclay, 91190, Gif-sur-Yvette, France

Summary. In this paper, the problem of the active vibration control of a thin and flexible disc is addressed. The mechanical structure tackled here is equipped with two piezoelectric circular patches: one of them works as a sensor and the other is used as an actuator. Both are fixed on the disc, one on each side, and centered according to its axis of symmetry. The model of this system is obtained from a finite element analysis, leading to a linear state space model. The design of the proposed control scheme is based on delayed proportional actions. As a matter of fact, recent works emphasized the stabilizing effect of delayed feedback if a real multiple spectral occurs in the closed-loop called multiplicity-induced-dominancy (MID) property allowing to an assignment approach. The purpose of this work is to investigate the properties of the proposed MID-based output feedback controller in terms of vibration damping.

Introduction

This work focuses on the effect of multiplicity of spectral values on the exponential stability of a sixth-order retarded differential equation. An efficient way to study time-delay systems solution's stability is the frequency domain approach since in the Laplace domain, where a number of effective methods have been proposed, the stability analysis amounts to studying the distribution of the characteristic quasipolynomial function's roots, see for instance [10, 6, 7]. It is worth noting that the rightmost root for a quasipolynomial function corresponding to stable time-delay systems is actually the exponential decay rate of its time-domain solution, see for instance [9] for an estimate of the decay rate for stable linear delay systems. The dominancy induced from of a given multiple spectral value property called in the sequel *multiplicity-induced-dominancy* or MID for short is studied and analytically shown in scalar delay equations in [4], then in second-order systems controlled by a delayed proportional is proposed in [2] where its applicability in damping active vibrations for a piezo-actuated beam is proved. An extension to the delayed proportional-derivative controller case is studied in [3, 5] where the dominancy property is parametrically characterized and proven using the argument principle. Further, in [1] some sufficient conditions are established showing that such MID property holds for arbitrary-order dynamical system.

Problem statement

System description

The system considered here is described in Fig. 1. It is a composite membrane composed by a brass disc with a clamped circular edge. This disc is embedded into a mobile support moving only along the z axis. The moving support is subjected to an unknown acceleration, noted $w(t)$ in the sequel. This flexible membrane is equipped with two PZT-based piezoelectric patches: one used as an actuator and the other used as a sensor. The sensor's thickness is $0.7mm$. It is greater than the actuator's thickness which is $0.4mm$. An explanation about why should the thickness of a piezo-electric sensor must be greater than the actuator's one can be found in [11]. These circular patches are supposed to be rigidly bounded on the disc, one on each side, and centered according to the axis of symmetry. All the physical parameters of the materials used here can be found in [8].

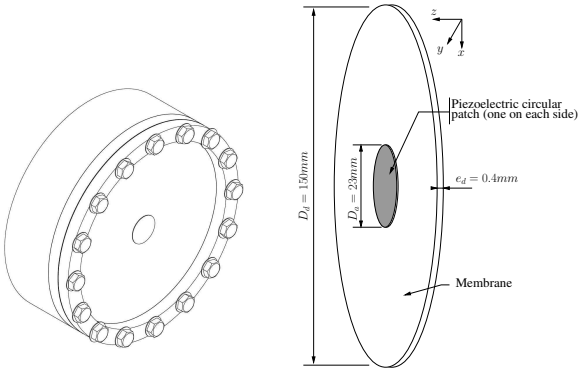

Figure 1: Axisymmetric composite membrane (dimensions on the right) inserted in the device which is subjected to vibrations (Computer Aided Design figure on the left)

The main dimensions of the composite membrane are given in Fig. 1. The controlled input noted $u(t)$ is the voltage applied across the piezoelectric actuator. The measured output noted $y(t)$ is the electric voltage delivered by the piezoelectric sensor. The disturbance input $w(t)$ is the total acceleration applied to the clamped circular edge of the structure. The controlled output that we consider, noted $z(t)$, is the z component of the acceleration of a point located at the center of the disc and on the upper side of the sensor.

The input-to-output transfer functions of finite order are derived from a Finite Element modelling of the axisymmetric membrane, following the steps described in [12].

Control approach

An interesting control objective is to damp the peaks of resonance of the first three bending modes, by using an *output feedback controller*, without affecting the vibrating modes that are neglected in the model considered here.

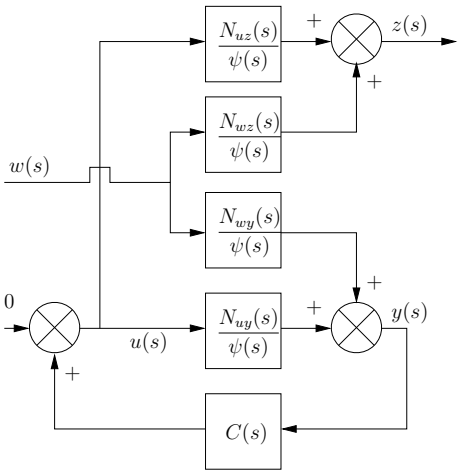

Figure 2: Feedback control structure.

By using the same notations as in [12], the piezo-actuated system is inserted in the output feedback control structure of Fig. 2, with a zero-reference signal and an input disturbance w corresponding to a rectangular impulse signal. The control problem consists in damping the vibrations due to the first three modes when the mobile support is subjected to a shock like disturbance. We define the output feedback control law $u(s) = C(s,\tau)\,y(s)$ involving the following Multiplicity-induced-dominancy (MID) controller given in Laplace domain by

$$C(s,\tau) := \frac{N(s,\tau)}{D(s,\tau)} \quad \text{where} \quad N(s,\tau) := n_0 + n_{r_0}\,e^{-\tau\,s} \quad \text{and} \quad D(s,\tau) := d_0 + d_{r_0}\,e^{-\tau\,s}. \tag{1}$$

By applying inverse Laplace transform, it can be easily shown that this control law is given in time domain by

$$u(t) = -\frac{d_{r_0}}{d_0}u(t-\tau) + \frac{n_0}{d_0}y(t) - \frac{n_{r_0}}{d_0}y(t-\tau) \tag{2}$$

which is an output feedback control law based on proportional actions plus delayed proportional actions.

Simulation results

The MID method gives the following numerical values for the parameters of the controller in (1) that assigns $\lambda_0 = -600$ as a rightmost root of multiplicity equal to 3: $n_0 \simeq 7.478025835$, $n_{r_0} \simeq 69.88393518$, $d_0 \simeq 1.626843813$, $d_{r_0} \simeq 5.858004955$ and $\tau \simeq 0.0001904171687$. To show the efficiency of the proposed MID-controller, we propose to compare, in Fig. 3, the time responses of both output signals in open-loop (blue) and in closed-loop (red) when the disturbance w is a rectangular impulse (black), say like a shock. We also put the time response of the control signal u that exhibits a peak of magnitude roughly equal to 12 V which is reasonable for this application.

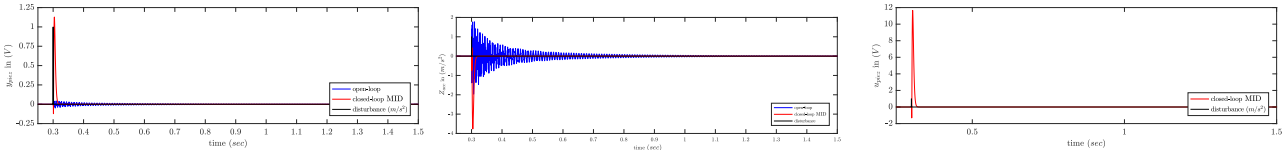

Figure 3: Time responses of the measured output y on the left, of the controlled output z on the middle and of the closed-loop control signal u on the right.

Conclusions

We have just shown a work dealing with the active vibration control of an axisymmetric membrane piezo-actuated, using closed-loop pole placement approach in order to design an efficient MID-based controller satisfying the control problem.

References

[1] Tamas Balogh, Tamas Insperger, Islam Boussaada, and Niculescu Silviu-Iulian. Towards an MID-based Delayed Design for Arbitrary-order Dynamical Systems with a Mechanical Application . working paper or preprint, 2020.

[2] I. Boussaada, S-I. Niculescu, S. Tliba, and T. Vyhlídal. On the coalescence of spectral values and its effect on the stability of time-delay systems: Application to active vibration control. *Procedia IUTAM*, 22(Supplement C):75 – 82, 2017.

[3] I. Boussaada, S-I. Niculescu, and K. Trabelsi. Toward a decay rate assignment based design for time-delay systems with multiple spectral values. In *Proceeding of the 23rd International Symposium on Mathematical Theory of Networks and Systems*, pages 864–871, 2018.

[4] I. Boussaada, H. Unal, and S-I. Niculescu. Multiplicity and stable varieties of time-delay systems: A missing link. In *Proceeding of the 22nd International Symposium on Mathematical Theory of Networks and Systems*, pages 1–6, 2016.

[5] Islam Boussaada, Silviu-Iulian Niculescu, Ali El Ati, Redamy Pérez-Ramos, and Karim Liviu Trabelsi. Multiplicity-Induced-Dominancy in parametric second-order delay differential equations: Analysis and application in control design. *ESAIM: Control, Optimisation and Calculus of Variations*, November 2019.

[6] J. K. Hale and S. M. Verduyn Lunel. *Introduction to functional differential equations*, volume 99 of *Applied Mathematics Sciences*. Springer Verlag, New York, 1993.

[7] W. Michiels and S-I. Niculescu. *Stability and stabilization of time-delay systems*, volume 12 of *Advances in Design and Control*. SIAM, 2007.

[8] E. Minazara-Erambert, D. Vasic, F. Costa, G. Poulin, and S. Tliba. Energy harvesting from vibration using a piezoelectric membrane. In *Proc. of Electro-Active Materials and Sustainable Growth (EMSG 2005), Journal de Physique IV*, volume 128, pages 187–193, EMSG Abbaye Les Vaux de Cernay, 23-25 mai 2005. EDP Sciences.

[9] T. Mori, N. Fukuma, and M. Kuwahara. On an estimate of the decay rate for stable linear delay systems. *International Journal of Control*, 36(1):95–97, 1982.

[10] G. Stépán. *Retarded Dynamical Systems: Stability and Characteristic Functions*. Pitman research notes in mathematics series. Longman Scientific and Technical, 1989.

[11] S. Tliba. *Contrôle actif des vibrations dans des structures mécaniques minces instrumentées de transducteurs piézoélectriques*. Thèse de doctorat (in french), École Normale Supérieure de Cachan, Cachan (94), France, Décembre 2004.

[12] Sami Tliba, Islam Boussaada, Fazia Bedouhene, and Silviu-Iulian Niculescu. Active vibration control through quasi-polynomial based controller. *IFAC-PapersOnLine*, 52(18):49 – 54, 2019. 15th IFAC Workshop on Time Delay Systems TDS 2019.

Analysis of Chatter Mechanisms in Cutting Process

Andrzej Weremczuk*, Rafal Rusinek * and Jerzy Warminski*
*Department of Applied Mechanics, Lublin University of Technology, Lublin, Poland

Summary. Analysis of a nonlinear two degree of freedom model of a cutting process is presented in the paper. Classical regenerative mechanism of chatter is enriched in an additional friction phenomenon which generates frictional chatter. A goal of the paper is to detect a mutual interaction between the regeneration and frictional effect. The nonlinear model is solved by means of the multiple time scale method. Stability of cutting process is checked in order to determine stability lobes diagrams and to find an influence of friction on the process. Nonlinear behaviour is also examined for different variants of stiffness ratio with the help of bifurcation diagrams where cutting velocity is chosen as the bifurcation parameters. Finally, the maps of chatter amplitudes are presented and new frictional stability lobe diagrams are proposed to analyse an influence of friction.

Introduction

Nowadays, cutting process is still one of the most popular manufacturing method. During machining operations, vibrations called chatter may occur between the workpiece and the tool. This phenomenon generates dimensional and geometrical inaccuracies, a poor surface finish, faster tool wear and reduction of spindle life. Therefore, it is necessary to understand and control chatter vibrations. The regenerative effect is related to the wavy workpiece surface generated by the previous cutting tooth pass. While, the frictional mechanism results from friction force occurring between the tool and the workpiece. Although, trace regeneration and friction are the most important in practical operations there are little papers which consider regenerative and frictional mechanisms together. Friction always exists in real cutting process therefore, excluding this phenomenon is rather a big simplification. Generally, chatter is a dynamic instability that can limit material removal rates, cause a poor surface finish and even damage the tool or the workpiece. Usually in the literature the problem of the regenerative and frictional chatter mechanisms are investigated separately, although friction phenomena exist always in case of a contact problem. Therefore, this approach describes the model of orthogonal cutting both with regenerative and frictional effect. The model of frictional chatter, presented in [3], is completed with regenerative effect. In order to get knowledge about an influence of frictional chatter on regenerative one and complete an mathematical approach, the mathematical model of cutting is developed and solved with the help of the method of the multiple time scales [1, 2]. An explanation of mutual interaction between frictional and regenerative mechanisms is the main purpose of the paper.

Mathematical model

To analyse regenerative and frictional mechanism of chatter, two degree of freedom model of orthogonal cutting is used (Fig.1a). Figure 1b presents the force distribution on the tool edge separately for the rake face and flank face. This is a quite new approach because classical analysis takes into account only the rake face forces or resultant force acting on the tool. Here, the resultant cutting force is distributed on the normal force on the rake N_1 and face N_2 force. The normal forces together with friction between the tool and the workpiece cause the friction force F_1 and F_2 on the rake and the flank face, respectively. This approach of cutting force distribution is presented more detailed in the paper [3]. The normal and the friction force are defined as follows:

$$\begin{aligned} N_1 &= Q_o\, a_p \left(c_1(v_r-1)^2+1\right) H(a_p)H(v_r), \quad N_2 = K_{con}\, a_p\, H(a_p), \\ F_1 &= N_1\mu_x\left(\mathrm{sgn}(v_f)-\alpha_x v_f+\beta_x {v_f}^3\right), \quad F_2 = N_2\mu_y\left(\mathrm{sgn}(v_r)-\alpha_y v_r+\beta_y {v_r}^3\right), \end{aligned} \tag{1}$$

where, Q_o represents the specific cutting force modulus, a_p is the instantaneous penetration of the tool into the workpiece (depth of cut), c_1 is a constant controlling the dependence of the cutting force on the relative velocity between the tool and the workpiece v_r, K_{con} is the contact stiffness and H represents the Heaviside function. Note that the $H(v_r)$ models the loss of contact between the tool and the chip while $H(a_p)$ accounts for the tool coming out of the workpiece. In the friction forces μ_x, μ_y denote the static coefficient of friction between the tool and the workpiece, and the tool and the chip, respectively, α_x, α_y, β_x, β_y are constants which regulate the nonlinear characteristics of the friction forces between the respective surfaces in contact. v_r and v_f are the relative velocities between the tool and the workpiece, and the tool and the chip, respectively and *sgn* represents the sign function. The instantaneous penetration of the tool into the workpiece or the cutting depth a_p can be written in terms of the specified depth of cut a_{po}, the tool motion y and the tool motion one rotation before $y(t-\tau)$ as:

$$a_p = a_{po} - y + \delta y(t-\tau), \tag{2}$$

where, δ equals *0* or *1* when the regenerative effect is switched off or on. Time delay τ is connected with a spindle or a workpiece speed Ω by equation $\tau=2\pi/\Omega$. The relative velocities between the tool and the workpiece v_r, and the tool and the chip v_f are related to the nominal cutting speed v_o, the shear angle of the workpiece material φ and the tool velocities by:

$$v_r = v_o - x', \quad v_f = v_r \tan\varphi - y'. \tag{3}$$

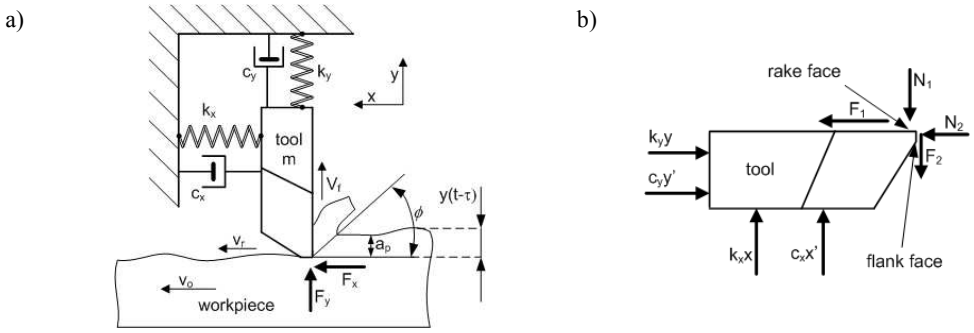

Figure 1: Two degrees of freedom model of orthogonal cutting (a), force distribution on tool edge (b) [3]

The non-dimensional equations of motion is defined in the form:

$$x'' + 2z_x x' + x = f_x, \qquad y'' + 2z_y\sqrt{\alpha}y' + \alpha y = f_y, \tag{4}$$

where:

$$\alpha = \frac{k_y}{k_x}, \quad \omega_x^2 = \frac{k_x}{m}, \quad \omega_y^2 = \frac{k_y}{m} = \alpha\,\omega_x^2, \quad z_x = \frac{c_x}{2m\omega_x}, \quad z_y = \frac{c_y}{2m\omega_y}, \tag{5}$$

and the forces are given by:

$$\begin{aligned} f_x &= q_o\, a_p \left(c_1(v_r-1)^2+1\right)H(a_p)H(v_r) + k_{con}\, a_p H(a_p)\,\mu_y\left(\mathrm{sgn}(v_r) - \alpha_y v_r + \beta_y {v_r}^3\right), \\ f_y &= k_{con}\, a_p H(a_p) + q_o\, a_p \left(c_1(v_r-1)^2+1\right)H(a_p)H(v_r)\,\mu_x\left(\mathrm{sgn}(v_f) - \alpha_x v_f + \beta_x {v_f}^3\right). \end{aligned} \tag{6}$$

Analytical and numerical results

The nonlinear model described by Eq.4 is solved by means of the multiple time scale method. Next to verified analytical result the numerical simulation was performed by using Matlab-Simulink software. Both results are presented as stability lobes diagrams (Fig.2), where cutting velocity v_o, proportional to the spindle speed Ω, is on the horizontal axis and on the vertical axis is cutting resistance q_o. Unstable areas (gray color in Fig.2a) were obtained analytically, while the amplitude value (gray scale in Fig.2b) was also numerically determined. In both cases, a characteristic stable area was observed in the middle of the graph.

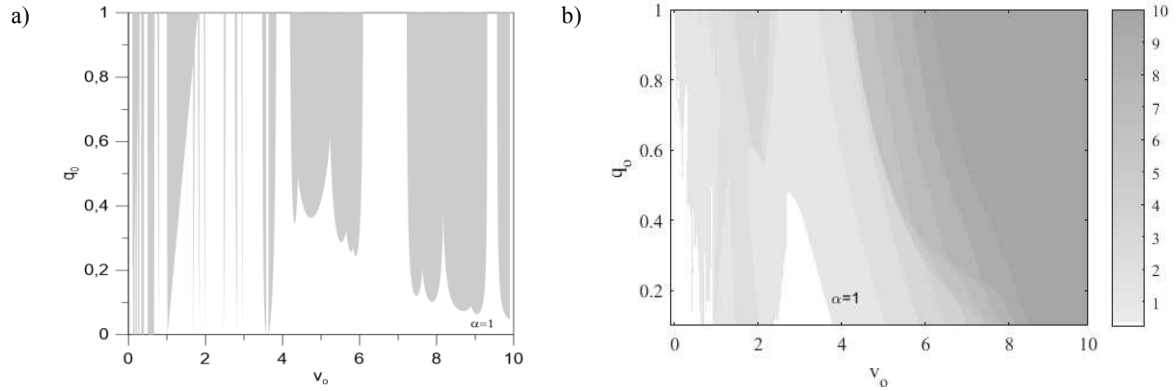

Figure 2: Stability lobes diagram obtained analytically (a) and numerically (b)

Conclusions

The paper presents the results of analytical and numerical analysis of a two degree of freedom nonlinear model. An analytical solution of the model near the primary resonances are obtained by using the method of multiple time scales. The frictional and regenerative mechanisms of chatter are important both acting together and separately. The regenerative effect is stronger for small velocities (rotational speeds) while the frictional one for higher velocities. However, it depends on the workpiece stiffness ratio as well. Friction causes a stabilising effect when regenerative chatter dominates. Regardless the chatter mechanisms the chatter free region can be found in the middle range of analysed velocities.

References

[1] Nayfeh A. H., Chin C. M., Pratt J. (1997) Perturbation Methods in Nonlinear Dynamics - Applications to Machining Dynamics. J. Manufacturing Science and Engineering 119:485-493.

[2] Rusinek R., Weremczuk A., Warminski J. (2011) Regenerative Model of Cutting Process with Nonlinear Duffing Oscillator. Mechanics and Mechanical Engineering 15:131-145.

[3] Rusinek R., Wiercigroch M, Wahi P. (2014) Modelling of Frictional Chatter in Metal Cutting. Int. J. of Mechanical Science 89:167–176.

Bifurcation analysis at a degenerate parameter point of a non-collocated force control model

Li Zhang[*], Huailei Wang[*] and Gabor Stepan[**]
[*]*College of Aerospace Engineering, Nanjing University of Aeronautics and Astronautics, Nanjing, China*
[**]*Department of Applied Mechanics, Budapest University of Technology and Economics, Budapest, Hungary*

Summary. Normal form analysis is carried out at a degenerate parameter point of the low degree-of-freedom non-collocated delayed force control model. It is shown that around the degenerate point where both the derivative of the real part of the eigenvalues and the first Lyapunov coefficient are zero, neutral stable periodic orbits arise and a specific transcritical bifurcation of limit cycles takes place.

Introduction

Force control is a relevant task of human motion control when an operator touches an object or the environment, and it is often studied as important part of the efforts for understanding human behavior. Due to the processing time of the sensory signals in the neural system, and also to the reaction time of the muscles, delay is one of the essential parameters in force control. This study will present bifurcation analysis at a degenerate parameter point of a non-collocated force control model in the presence of human reaction time delays.

Mechanical model

A basic model of delayed force control with non-collocated force sensor configuration is considered. A block of mass *m* is in contact with the rigid environment via a spring of stiffness k_1 along a horizontal axis as shown in Figure 1. The contact force can be obtained by a force sensor, which is a serially connected spring of large stiffness $k_2 (\gg k_1)$ located at the contact point to the rigid environment. The sensed signal is fed back to the control force *Q* of the human actuation. The governing equation takes the following form:

$$\begin{aligned} m\ddot{q}_1 &= Q - k_1(q_1 - q_2) \\ 0 &= k_1(q_1 - q_2) - k_2 q_2 \end{aligned} \tag{1}$$

where q_1 and q_2 are the absolute positions of the block and the end point of the spring that detects the force, respectively. With a simple control strategy and with saturation of the control force into consideration, the actual control force *Q* at time instant $\tilde{\tau}$ is given by

$$Q(\tilde{t}) = -F_S \tanh\left(\frac{1}{F_S} P(k_2 q_2(\tilde{t}-\tau) - F_d)\right) + k_2 q_2(\tilde{t}-\tau) \tag{2}$$

where P is the feedback gain, τ is the reaction time of the actuator, and F_S can describe the level of the actuator force saturation. By shifting $q_1(t)$ by the equilibrium position q_{10} of the block *m*, i.e., by introducing the coordinate $\tilde{x}(t) = q_1(t) - q_{10}$, using the assumption $k_2 \gg k_1$, and introducing the dimensionless coordinates $x = \tilde{x}/(F_S/k_1)$ and $t = \tilde{t}/\tau$, the Newtonian equation (1) is transformed to:

$$\ddot{x}(t) + (\omega_n \tau)^2 x(t) = (\omega_n \tau)^2 x(t-1) - (\omega_n \tau)^2 \tanh(Px(t-1)) \quad . \tag{3}$$

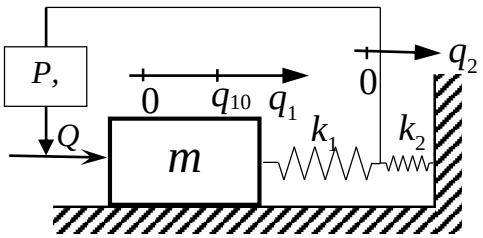

Figure 1: A basic model of non-collocated delayed force control

Linear Analysis

By means of analyzing the characteristic equation of the linear part of Equation (3), the stability chart in the parameter plane $(P, \omega_n \tau)$ is obtained as shown in Figure 2. The stability boundaries and regions are determined according to the number of characteristic roots with positive real parts.

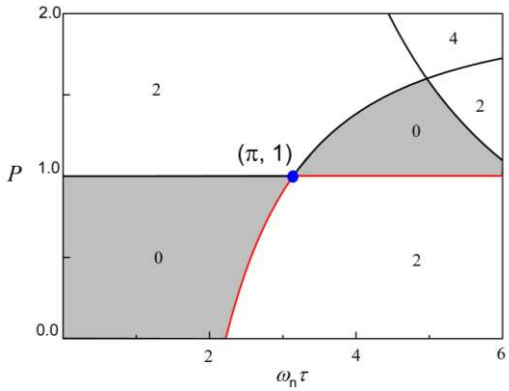

Figure 2: Stability chart in the parameter plane $(P, \omega_n\tau)$. Shaded regions refer to stability. Numbers indicate the number of characteristic roots with positive real parts. Black stability boundaries refer to supercritical Hopf bifurcations and red ones refer to subcritical Hopf bifurcations. The blue point at (π, 1) is the degenerate parameter point.

The 5th order Normal Form at the degenerate parameter point

According to [1], the black stability boundaries refer to supercritical Hopf bifurcations and the red stability boundaries refer to subcritical Hopf bifurcations in Figure 2. At the blue point (π, 1), the sense of Hopf bifurcations changes and the stability of the equilibrium swaps, which indicates that both the first Lyapunov coefficient and the derivative of the real part of the eigenvalues at the critical parameters are zero. To study this special degenerate parameter point, normal form up to the 5th order is carried out via symbolic calculation [2]. Let $P = 1+\mu$, then the normal form reads

$$\dot{y}_1 = i\omega_c y + S_1 y\mu + S_2 y\mu^2 + \Delta_1 y^2\bar{y} + S_3 y^2\bar{y}\mu + \Delta_2 y^3\bar{y}^2 \tag{4}$$

where $\mathrm{Re}(S_1) = 0$, $\mathrm{Re}(\Delta_1) = 0$, $\mathrm{Re}(S_2) = \pi^2/4$, $\mathrm{Re}(S_3) = -\pi^2/2$ and $\mathrm{Re}(\Delta_2) = \pi^2/4$. Therefore, the neutral stable bifurcated periodic vibration has amplitude ρ

$$\rho = 2\sqrt{1-\mu} \tag{5}$$

as shown in Figure 3.

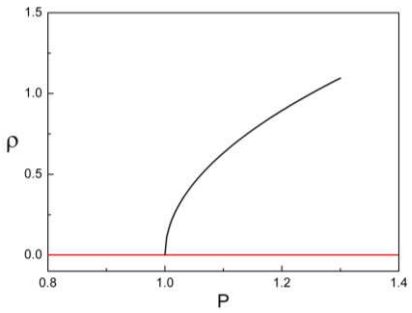

Figure 3: Bifurcation diagram of periodic motions with respect to feedback gain P at $\omega_n\tau = \pi$. Red line refers to unstable equilibrium.

Conclusion

The normal form up to the fifth order is obtained at the degenerate parameter point where both the derivative of the real part of the critical eigenvalues and the first Lyapunov coefficient at the critical parameters are zero for the simple non-collocated force control model. The nonlinear analysis shows that neutral stable periodic orbits arise around this point. This is not a standard fold bifurcation, but transcritical bifurcation of limit cycles, which happens around this degenerate parameter point.

Acknowledgement This research was supported by the Hungarian-Chinese Bilateral Scientific and Technological Cooperation Fund under grant no. 2018-2.1.14-TÉT-CN-2018-00008, the National Natural Science Foundation of China under Grants No. 11772151.

References

[1] Zhang L., Stepan G. (2019) Bifurcations in basic models of delayed force control. Nonlinear Dyn. https://doi.org/10.1007/s11071-019-05058-7.
[2] Zhang L., Wang H.L., Hu H.Y. (2012) Symbolic Computation of Normal Form for Hopf Bifurcation in a Neutral Delay Differential Equation and an Application to a Controlled Crane. Nonlinear Dyn. 70: 463-473.

Stabilizability Limits for the Inverted Pendulum with a Multiple-Delay Fractional-Order Controller

Tamas Balogh, Tamas Insperger
Department of Applied Mechanics, Budapest University of Technology and Economics and MTA-BME Lendület Human Balancing Research Group, Budapest, Hungary

Summary. In this study, we consider the PD$^\mu$ control of the inverted pendulum with different delays in the proportional and the fractional derivative terms. This concept gives a transition between several special cases already investigated in the literature. The main question is whether the critical delay can further be extended by employing fractional-order feedback combined with delay detuning.

Introduction

Time delay in state-feedback systems sets a strong limitation in the stabilization of unstable plants. If the feedback delay is larger than some critical value, then the system cannot be stabilized. This feature can well be demonstrated by the inverted pendulum paradigm [3, 4]. Stabilization of an inverted pendulum by proportional-derivative (PD) feedback is possible if and only if the feedback delay τ is smaller than a critical delay given by

$$\tau_{\mathrm{crit}}^{\mathrm{PD}} = \frac{T}{\pi\sqrt{2}}, \tag{1}$$

where T is the period of the oscillations of the pendulum hung downwards [4]. If $\tau > \tau_{\mathrm{crit}}$, then one cannot find proportional and derivative gains that stabilizes the inverted position of the pendulum.
The critical delay can be increased by employing control laws other than PD feedback. For instance, if the feedback involves acceleration (PDA feedback), then the critical delay can be increased to $\tau_{\mathrm{crit}}^{\mathrm{PDA}} = \sqrt{2}\,\tau_{\mathrm{crit,PD}}$ [3]. Alternatively, if the delay of the proportional and the derivative terms are detuned, then the critical delay increases to $\tau_{\mathrm{crit}}^{\mathrm{dPD}} \approx 1.47\,\tau_{\mathrm{crit}}^{\mathrm{PD}}$ [3]. Another alternative way to increase the critical delay is the application of fractional-order control: in case of PD$^\mu$ feedback, $\tau_{\mathrm{crit}}^{\mathrm{PD}^\mu} \approx 1.12\,\tau_{\mathrm{crit}}^{\mathrm{PD}}$ [1].
Introducing fractional-order derivative in the feedback loop allows us to exploit the time history starting from some initial time to the current time instant. This can be seen from the most frequently used definitions of fractional derivative: the Riemann-Liouville fractional derivative, the Caputo fractional derivative and the Grünvald-Letnikov fractional derivative. All of these definitions of the fractional derivative resembles a distributed delay term that converts into a point delay term if the order of the derivative is an integer [2].

Problem statement

The characteristic function of the system under investigation reads

$$D(s) = s^2 - a_0 + k_{\mathrm{p}}\mathrm{e}^{-s\tau_{\mathrm{p}}} + k_{\mathrm{d}}s^\mu\mathrm{e}^{-s\tau_{\mathrm{d}}}\,, \tag{2}$$

where $a_0 > 0$ is the open-loop system parameter, $\tau_{\mathrm{p}} > 0$ and $\tau_{\mathrm{d}} > 0$ are the feedback delays and $0 < \mu < 2$ is the order of the fractional derivative. This system can also be interpreted as a control system with a single latency τ with some additional delays (delay detunings) $\delta_{\mathrm{p}} \geq 0$ and $\delta_{\mathrm{d}} \geq 0$ in both terms such that $\tau_{\mathrm{p}} = \tau + \delta_{\mathrm{p}}$, $\tau_{\mathrm{d}} = \tau + \delta_{\mathrm{d}}$.
The D-subdivision method can also be applied to fractional-order systems. Substitution of $s = 0$ and $s = \pm\mathrm{i}\omega$, $\omega > 0$ into $D(s) = 0$ gives the D-curves

$$s = 0 \;:\quad k_{\mathrm{p}} = a_0\,,\quad k_{\mathrm{d}} \in \mathbb{R}\,, \tag{3}$$

$$s = \pm\mathrm{i}\omega, \omega > 0 \;:\quad \begin{cases} k_{\mathrm{p}} = \left(a_0 + \omega^2\right)\dfrac{\sin(\frac{\mu\pi}{2} - \tau_{\mathrm{d}}\omega)}{\sin\left(\frac{\mu\pi}{2} - (\tau_{\mathrm{d}} - \tau_{\mathrm{p}})\omega\right)}\,, \\ k_{\mathrm{d}} = \left(a_0 + \omega^2\right)\dfrac{\sin(\tau_{\mathrm{p}}\omega)}{\omega^\mu\sin\left(\frac{\mu\pi}{2} - (\tau_{\mathrm{d}} - \tau_{\mathrm{p}})\omega\right)}\,. \end{cases} \tag{4}$$

The D-curves bounds the parameter regions in the plane $(k_{\mathrm{p}}, k_{\mathrm{d}})$ where the number of unstable characteristic roots is constant. Stable regions (zero unstable characteristic roots) can be determined numerically using the argument principle. When the delays increase then the stable regions typically shrink and disappear. There is a critical delay $\tau_{\mathrm{crit}}^{\mathrm{dPD}^\mu}$: if $\min(\tau_{\mathrm{p}}, \tau_{\mathrm{d}}) > \tau_{\mathrm{crit}}^{\mathrm{dPD}^\mu}$ then the system cannot be stabilized by any triplet $(k_{\mathrm{p}}, k_{\mathrm{d}}, \mu)$. The goal of this study is to determine the stabilizability boundaries in the plane $(\tau_{\mathrm{p}}, \tau_{\mathrm{d}})$ and to find $\tau_{\mathrm{crit}}^{\mathrm{dPD}^\mu}$.

Special case: PD$^\mu$ controller with a single delay

Stabilizability was already investigated if the delays in the proportional and fractional derivative terms are the same ($\tau_{\mathrm{p}} = \tau_{\mathrm{d}} = \tau$). In the case of a PD$^\mu$ controller with a single delay, the stabilizable region was derived in [1] in the plane of the dimensionless parameters $a = a_0\tau^2$ and μ (see the left panel in Figure 1).

Using the D-subdivision technique, we can observe four types of loss of stabilizability. These geometric conditions can be directly translated into the multiplicity conditions shown in the right panel of Figure 1. This gives a more uniform description of the stabilizability boundaries compared to that of [1]. Conditions $\det \mathbf{J} = 0$ corresponds to the singularity of the Jacobian matrix of the other three (four) equations with respect to $k_\mathrm{p}, k_\mathrm{d}, \omega_1$ (and ω_2). The geometric interpretation of this condition is the tangency of D-curves at the limit of stabilizability.

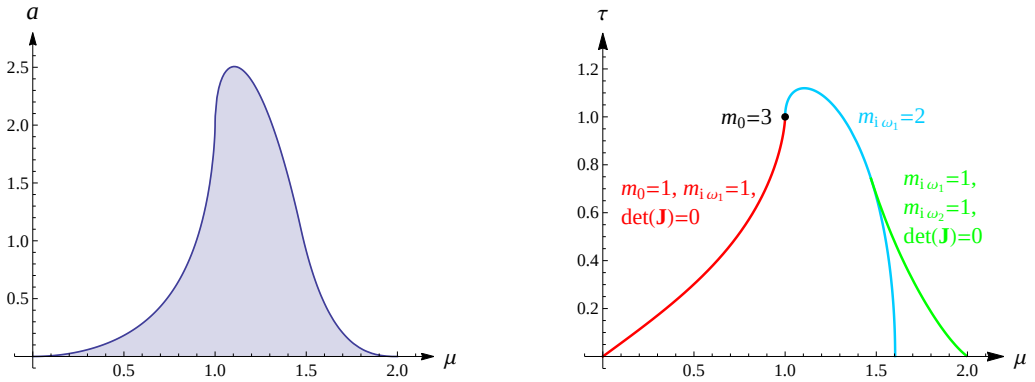

Figure 1: Stabilizable region of (2) if $\tau_\mathrm{p} = \tau_\mathrm{d} = \tau$ with $a = a_0\tau^2$ (left). The stabilizability boundaries and multiplicity conditions in the plane (μ, τ) if $a_0 = 2$ (right).

Main results: stabilizability diagrams in the plane $(\tau_\mathrm{p}, \tau_\mathrm{d})$

Using a similar technique described in the previous section, we can construct stabilizability diagrams for the case $\tau_\mathrm{p} \neq \tau_\mathrm{d}$. First, we need to detect the geometric conditions at the limit of stabilizability using D-subdivision. These geometric conditions can be translated into multiplicity conditions. From the multiplicity conditions, we obtain a nonlinear system of equations, which can be reduced after solving for k_p and k_d. Finally, the reduced equations can be solved using pseudo-arclength continuation.

Figure 2 shows the stabilizability boundaries in the plane $(\tau_\mathrm{p}, \tau_\mathrm{d})$ for different values of μ. The stabilizable region can be extended compared to the detuned PD controller ($\mu = 1$) by choosing an appropriate value of the fractional order μ. The largest admissible delay is obtained for $\mu = 0.999637$. In this case the critical delay is $\tau_\mathrm{crit}^{\mathrm{dPD}^\mu} = 1.00778\tau_\mathrm{crit}^{\mathrm{dPD}}$ (see the right panel of Figure 2). Hence, an extremely small but still finite extension of the critical delay can be achieved by employing detuned fractional-order control.

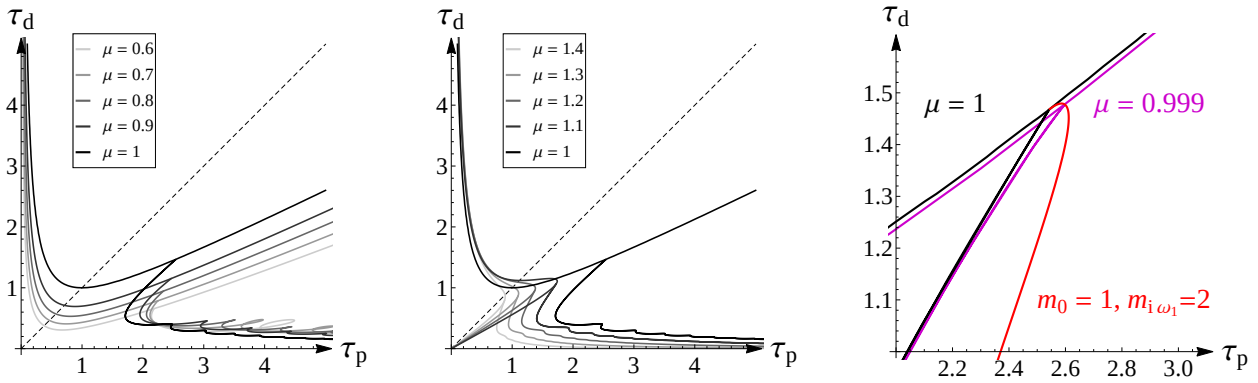

Figure 2: The stabilizability boundaries in the plane $(\tau_\mathrm{p}, \tau_\mathrm{d})$ if $\mu \leq 1$ (left) and $\mu \geq 1$ (middle) with $a_0 = 2$ (stabilizable regions are to the left of the curves). The path of the critical point associated with the maximal allowed delay in the plane $(\tau_\mathrm{p}, \tau_\mathrm{d})$ if $\mu \leq 1$ (right).

References

[1] Balogh T. and Insperger T. (2018) Extending the limits of stabilizability of systems with feedback delay via fractional-order PD controllers. *IFAC-PapersOnLine* **51(14)**:265-270.

[2] Podlubny I. (1999) Fractional differential equations. Academic Press, San Diego.

[3] Sieber J. and Krauskopf B. (2005) Extending the permissible control loop latency for the controlled inverted pendulum. *Dynamical Systems* **20(2)**:189-199.

[4] Stepan G. (2009) Delay effects in the human sensory system during balancing. *Philosophical Transactions of the Royal Society A: Mathematical, Physical and Engineering Sciences* **367(1891)**:1195-1212.

Thursday, July 21, 2022
08:30 - 10:30

MS-02 Asymptotic Methods
Saint Clair 1

Chair: Yu. Starosvetsky

08:30 - 08:50
A Reynolds' Limit Formula for the Shear Stress in Dorodnitzyn's Boundary Layer
VALENCIA Carla*
*Universidad Iberoamericana Ciudad de México (Prolongación Paseo de la Reforma No. 880, Lomas de Santa Fe, C.P. 01219, Ciudad de México Mexico)

08:50 - 09:10
Analysis of discrete breathers in the mass-in-mass chain in the state of acoustic vacuum
STAROSVETSKY Yuli*
*Department of Mechanical Engineering [Haifa] (Technion - Institute of Technology Haifa 32000 Israel Israel)

09:10 - 09:30
Asymptotic analysis of transient behavior of two coupled exciters
YÜZBASIOGLU Tunc*, FIDLIN Alexander
*Institute of Engineering Mechanics, Karlsruhe Institute of Technology (Kaiserstr. 10, 76131 Karlsruhe Germany)

09:30 - 09:50
Asymptotic formulation of bifurcation scenarios to post-buckling nonlinear vibrations in thermomechanically coupled plates
SETTIMI Valeria*, REGA Giuseppe
*Department of Structural and Geotechnical Engineering - Sapienza University of Rome (Via Gramsci, 53 - 00197 Rome, Italy Italy)

09:50 - 10:10
Axisymmetric, nonlinear capillary waves: dimple and jet formation
KAYAL Lohit*, BASAK Saswata, DASGUPTA Ratul
*Indian Institue of Technology Bombay (Powai, Mumbai, Maharashtra-400076 India)

A Reynolds' Limit Formula for the Shear Stress in Dorodnitzyn's Boundary Layer

Carla V. Valencia-Negrete*

* *Department of Physics and Mathematics, Universidad Iberoamericana, A. C., Mexico City, Mexico*

Summary. Shear Stress growth is an indicator of Boundary Layer separation. The main difficulty to obtain clear descriptions of its behavior lies in Navier-Stokes Equations' non-linearity. On the other hand, Dorodnitzyn stated a Gaseous Boundary Layer problem, valid in atmospheric conditions, and deduced a second-order quasi-linear problem for a transformation of the Shear Stress. This article presents a mathematical formalization of this last problem and a Reynolds' Limit Formula for it, deduced with Bayada and Chambat's change of variables. For general compressible Reynolds' equations, the problem was solved by Chupin and Sart in 2012. Undoubtedly, there is a mathematical formalization for Dorodnitzyn's model previous from the one that is given here, but the author has not been able to find it in the literature. In earlier work, the author verified his first step simplification. Now, the formalization is extended to Dorodnitzyn's second-order quasi-linear problem. Then, the small parameter problem is deduced, and a bound, independent of the parameter, is found in the corresponding Sobolev Space to prove the existence of a Reynolds' Limit Formula for Dorodnitzyn's Shear Stress problem.

Abstract

The Earth's Global Mean Temperature is going to increase by, at least, 1.5°C in the next 10 to 33 years [3, p. 6]. As a consequence, there will be an increment in the number of severe droughts and flooding [3, p. 9]. Its origin, atmospheric convection, could be studied as a boundary layer separation problem. To identify its sources and sinks, the suggestion is to study *shear stress* growth deduced from approximate gaseous boundary layer models in atmospheric conditions.

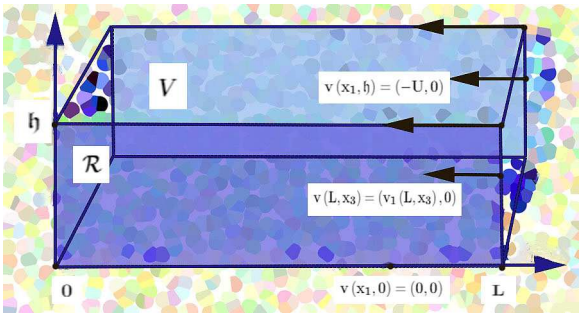

Figure 1: Dorodnitzyn's Rectangular Domain $\mathcal{R}= (0, L) \times (0, h) \in \mathbb{R}^2$

In 1942, Dorodnityzn stated a Gaseous Boundary Layer problem [2] in a rectangle $R = (0, L) \times (0, h) \subset \mathbb{R}^2$, where $L >> h > 0$ [2], of three simplified stationary Conservation of Mass, Conservation of Momentum, and Conservation of Energy laws, Eq. (1), (2) and (3),

$$\frac{\partial\,(\rho\,u)}{\partial x} + \frac{\partial\,(\rho\,v)}{\partial y} \;=\; 0\,; \tag{1}$$

$$\rho\left(u\,\frac{\partial u}{\partial x} + v\,\frac{\partial u}{\partial y}\right) \;=\; -\,\frac{\partial p}{\partial x} + \frac{\partial}{\partial y}\left(\mu\,\frac{\partial u}{\partial y}\right);\quad \text{y} \tag{2}$$

$$\rho\left[u\,\frac{\partial\,(c_p\,T)}{\partial x} + v\,\frac{\partial\,(c_p\,T)}{\partial y}\right] \;=\; \frac{\partial}{\partial y}\left[\kappa\,\frac{\partial T}{\partial y}\right] + \mu\left(\frac{\partial u}{\partial y}\right)^2 + \frac{\partial p}{\partial t}, \tag{3}$$

where one can assume that the *stationary density* $\rho \in L^2\,(R; (0, \infty))$; that the horizontal *velocity component* $u \in L^2\,(R)$ has *generalized derivatives* $\partial u/\partial x,\ \partial u/\partial y,\ \partial^2 u/\partial y^2 \in L^2\,(R)$; the vertical *velocity component* $v \in L^2\,(R)$; the *absolute temperature* $T \in L^2\,(R; (0, \infty))$ with $\partial T/\partial y,\ \partial^2 T/\partial y^2 \in L^2\,(R)$; the *dynamic viscosity* $\mu \in L^2\,(R)$, the *pressure* $p \in L^2\,(R)$, the *thermal conductivity* $\kappa \in L^2\,(R)$, all of them with first order generalized derivatives in $L^2\,(R)$; and both products $\rho\,u,\ \rho\,v \in L^2\,(R)$. This is, assume ρ, u, v, T, μ, p and κ are elements of the space $W^{1,2}\,(R)$, so that a *Leibnitz Rule* for product differentiation is valid in the non-empty open domain $R \subset \mathbb{R}^2$ when both factors and all the *generalized derivatives* involved are elements of $L^2(R)$ [4, p. 11]. The value c_p is the *specific heat at constant pressure for dry air*, and we have four Ideal Gas Thermodynamic Laws, Eq. (4), (5), (6), (7): the *Prandtl number* $Pr = 1$,

$$Pr \;=\; \frac{c_p\,\mu}{\kappa} = 1; \tag{4}$$

the *Equation of State* for the *Universal Gas Constant* R^*, a volume $V = \iiint_B dx\,dy\,dz$ of a ball $B(r, \mathbf{x_0}) \subset \mathbb{R}^3$ of positive radius $r > 0$ and center $\mathbf{x_0} = (x_0, y_0, z_0)$ such that $(x_0, y_0) \in R$ and $R \times \{0\} \subset B$, and the number of moles n of an ideal gas corresponding to the volume V,

$$p\,V \;=\; n\,R^*\,T; \tag{5}$$

the *adiabatic polytropic atmosphere* [7, p. 35] where $b = 1.405$ and c are constants,

$$p\,V^b \;=\; c; \tag{6}$$

and the *Power Law* [6, p. 46]

$$\frac{\mu}{\mu_h} \;=\; \left(\frac{T}{T_h}\right)^{\frac{19}{25}}. \tag{7}$$

The boundary conditions, Eq. (8), (9), (10), (11), (12), (13), are given by the *free-stream velocity* $U > 0$, the *no slip condition*,

$$(u,v)|_{\{(x,h)\colon 0\le x\le L\}} \;=\; (-U,0), \tag{8}$$
$$(u,v)|_{\{(x,0)\colon 0\le x\le L\}} \;=\; (0,0), \tag{9}$$

the *free-stream temperature* $T_h > 0$, the *free-stream dynamic viscosity* $\mu_h > 0$,

$$T|_{\{(x,h)\colon 0\le x\le L\}} \;=\; T_h > 0, \tag{10}$$
$$\mu|_{\{(x,h)\colon 0\le x\le L\}} \;=\; \mu_h > 0. \tag{11}$$

periodic conditions for all $y \in [0,h]$:

$$(u\,(0,y)\,,0) \;=\; (u\,(L,y)\,,0)\,; \tag{12}$$

and a Neumann condition:

$$\left.\frac{\partial T}{\partial y}\right|_{\{(x,0)\colon 0\le x\le L\}} \;=\; 0. \tag{13}$$

As Busemann previously did in 1935, Dorodnitzyn expressed T in terms of u, but considers the Conservation of Energy Law in terms of the *total energy per unit mass*, $E = c_p T + u^2/2$, in the form presented by Luigi Crocco in 1932. Additionally, he includes a pressure variation term, $\partial p/\partial x$, and so allows the possibility of a Boundary Layer separation. By a successive substitution of $T(u)$, this system of seven equations is reduced to a system of just two with inherited boundary conditions in terms of a *stream function* defined, in the formalisation, by means of a generalized *Green's Theorem* [5, p. 121] that is valid for elements of the Sobolev Spaces $W^{1,2}(R)$. Moreover, he defined a *diffeomorphism* $R \xrightarrow{\mathbf{s}} \Pi$ that allows writing von Kármán's Integral Formula for a compressible fluid in an incompressible form in a polygonal domain $\Pi = \mathbf{s}(R)$ where $(x,y) \overset{\mathbf{s}}{\longmapsto} (\ell, s)$, $\ell\,(\hat{x},\hat{y}) \longmapsto \int_0^{\hat{x}} p\,(x,\hat{y})\;dx$ and $s\,(\hat{x},\hat{y}) \longmapsto \int_0^{\hat{y}} \rho\,(\hat{x},y)\;dy$. This way, he opens the road to adapt Blasius' method to state the *stream function* problem as an Ordinary Differential Equation.

In order to do this, he applies a subsequent *diffeomorphism* $\Pi \xrightarrow{\mathbf{z}} S$ that takes the polygon Π into a strip band of infinite positive heights $S = \mathbf{z}(\Pi)$ with $(\ell, s) \overset{\mathbf{z}}{\longmapsto} (\ell, z)$ and $z\,(\ell, s) \longmapsto s/\sqrt{\ell}$. In terms of z, the *shear stress* $\tau = \mu\,\partial u/\partial y$ becomes $\tau_s(z) = (a\;x^{1/2}\;\tau) \circ \mathbf{s}^{-1} \circ \mathbf{z}^{-1}(z)$ for a constant a. If we denote $u_s(z) = u \circ \mathbf{s}^{-1} \circ \mathbf{z}^{-1}(z)$, $i_0 = c_p\;T_0$ and $\sigma_0 = 1 - \left(U^2/2i_0\right)$ where $T_0 = T_h + U^2/(2c_p)$ is the absolute temperature value at height $y = 0$ in R, then $(u, v, T, p, \rho, \mu, \kappa)$ is a *classical solution* of Eq. (1), (2), (3), (4), (5), (6), (7) with boundary conditions (8), (9), (10), (11), (12), (13) if and only if $\tau_s \in C^1(0,\infty)$ satisfies the second-order quasi-linear problem:

$$\tau_s\,\frac{\partial^2 \tau_s}{\partial u_s^2} = -\;A\;u_s\;\left(1 - \frac{u_s^2}{2i_0}\right)^{-6/25}, \tag{14}$$

with inherited boundary conditions and $A = 1/2 \cdot (n\;R^*\;T_0)/V \cdot\; T_0^{\frac{2b}{b-1}} \cdot \sigma_0^{1-\frac{b}{(b-1)}}$. Bayada and Chambat's change of variables $R \xrightarrow{\phi^\epsilon} R^\epsilon$ for $\epsilon = h/L > 0$ with $(x,y) \overset{\phi^\epsilon}{\longmapsto} (x/L, y/\,(L\epsilon))$ provides a small parameter problem [8] for the sequence $(\mathbf{v}^\epsilon)_\epsilon = (u^\epsilon, v^\epsilon)_\epsilon$ where $u^\epsilon = \frac{1}{L}\;u$ and $v^\epsilon = \frac{1}{L\epsilon}\;v$. This way, there is a inherent adimensional problem for the sequence (τ_s^ϵ) so that the existing bound found for (u^ϵ) in [8] is valid for (τ^ϵ), and we can derive a Reynolds' Limit Formula for Dorodnitzyn's Shear Stress problem.

References

[1] Bayada G. and Chambat M. (1986) The transition between the Stokes equations and the Reynolds equation: A mathematical proof. *Applied Mathematics and Optimization* **14.1**: 73-93 *Asymptotic Analysis* **76.3/4**: 193-231.

[2] Dorodnitzyn A. A. (1942) Laminar Boundary Layer in Compressible Fluid. *Comptes Rendus l'Académie des Sciences de l'URSS* **34.8**: 213-219.

[3] IPCC (2018) Global warming of 1.5°C: An IPCC Special Report on the impacts of global warming of 1.5°C above pre-industrial levels and related global greenhouse gas emission pathways, in the context of strengthening the global response to the threat of climate change, sustainable development, and efforts to eradicate poverty .

[4] Maz'ya V. G. Poborchi S. V. (1997) Differentiable functions on bad domains. World Scientific.

[5] Nečas J. (1967) Les Méthodes directes en théorie des équations elliptiques. Masson et Cie.

[6] Smits A. J. Dussauge J.-P. (2006) Turbulent Shear Layers in Supersonic Flow. Springer-Verlag, NY.

[7] Tietjens O. G. (1934) Fundamentals of Hydro- and Aerodynamics. Based on Lectures by L. Prandtl, Ph. D..

[8] Valencia-Negrete et al. C. V. (2018) Reynolds' Limit Formula for Dorodnitzyn's Atmospheric Boundary Layer In Convective Conditions. *International Journal of Applied Mathematics* **31.4.8**: 673-695.

Analysis of discrete breathers in the mass-in-mass chain in the state of acoustic vacuum

I. Koroleva (Kikot)[(2)], N. Breitman (Rayzan)[(1)], M. Kovaleva[(2)], Y. Starosvetsky[(1)]
[(1)] *Faculty of Mechanical Engineering,*
Technion Israel Institute of Technology,
Technion City, Haifa 32000, Israel
[(2)]*N. N. Semenov Institute of Chemical Physics,*
Russian Academy of Sciences,
Kosygin St. 4, Moscow 119991, Russia.

Summary Present study concerns the dynamics of special localized solutions emerging in the mass-in-mass anharmonic oscillatory chain in the state of acoustic vacuum. Each outer element of the chain incorporates an additional, purely nonlinear mass attachment. Analytical study of the later, revealed the distinct types of stationary discrete breather solutions. Along with the analytical description of their spatial wave profiles we also establish their zones of existence in the space of system parameters. Stability properties of these solutions are assessed through the linear analysis (Floquet). All analytical models are supported by the numerical simulations of the full model.

Introduction

Emergence of spatially localized, time-periodic solutions in the conservative nonlinear system, are known since the pioneering work by Ovchinnikov [1] at 1968. Special localized solutions which are usually referred to as discrete breathers (DBs) remain a subject of broad research interest in the various aspects of modern physics and mechanics. In fact DBs have a well-developed analytical methods when applied to the classical, nonlinear discrete models such as Discrete Klein-Gordon chains (DKGs), Fermi-Pasta Ulam (FPU) models, as well as the Discrete Nonlinear Schrodinger (DNLS) model [2].Formation of spatially localized solutions in all these classical nonlinear models has quite a broad range of applications, including Josephson junctions, nano-mechanical systems, Bose-Einstein condensates, carbon nanotubes, (see for example [3]). Of late, formation of localized excitations as well as nonlinear normal modes in highly nonlinear discrete models admitting a state of acoustic vacuum e.g. purely cubic FPU chains [4], uncompressed granular crystals [5-6], has become a subject of intense research.

Some recent studies, have considered both analytically and numerically the formation of DBs in the two different configurations of locally resonant granular crystals i.e. weakly nonlinear, compressed granular chain [31] as well as the uncompressed ones [32]. Both configurations comprised the chain of granular elements incorporating the internal, linear oscillating inclusions. These numerical and analytical studies unveiled the stationary and mobile DBs and presented a detailed analysis of their stability properties as well as the corresponding bifurcation structures. The system under consideration in the present study qualitatively differs from the previously considered ones by its internal nonlinear, local substructure as well as the special dynamical state of acoustic vacuum. In this study, we focus on the analytic description of stationary discrete breather solutions as well as the prediction of zones of their existence in the space of system parameters.

Model

System under consideration is an infinite, locally resonant chain of elements inter-coupled by linear springs. The governing non-dimensional equations of motion read:

$$\begin{aligned} &\varphi_n'' = (\varphi_{n-1}-\varphi_n)^3 - (\varphi_n-\varphi_{n+1})^3 - \alpha(\varphi_n-\psi_n)^3 \\ &\varepsilon\psi_n'' = \alpha(\varphi_n-\psi_n)^3 \end{aligned} \tag{1.1}$$

Analysis

Given the homogeneous structure of the system under consideration it is quite natural to study the dynamics and the bifurcation structure of the corresponding standing wave solutions by exploiting the well-known method of separation of variables $\varphi_n(\tau)=\hat{u}_n\eta(\tau),\ \psi_n(\tau)=\hat{v}_n\eta(\tau)$. Where $u=\{\hat{u}_n\}_{n\in Z}, v=\{\hat{v}_n\}_{n\in Z}$ are real sequences and $\eta(\tau)$ is a time-dependent modal coordinate. Introducing this change of coordinates in (1.1) and applying some trivial algebraic manipulations, we obtain the following system of algebraic equations

$$\begin{aligned} &(u_{n-1}+u_n)^3 + (u_n+u_{n+1})^3 = u_n - \varepsilon v_n \\ &\alpha(u_n+v_n)^3 = \varepsilon v_n \end{aligned} \tag{1.2}$$

In the present study we construct the analytical description of the spatial profiles of DBs and derive the parametric zones of their existence. These solutions assume the out-of-phase oscillations between the adjacent outer as well as the outer and inner elements. Apparently, analysis of DBs may become extremely cumbersome, if one tries to tackle the system (1.2) as a whole. However, system (1.2) can be considerably simplified if one manages to reduce it from the system involving the amplitudes of vibrations of outer and inner masses $\{u_n\}_{n\in\mathbf{Z}}, \{v_n\}_{n\in\mathbf{Z}}$ into the one containing only

the motion of the outer elements $\{u_n\}_{n\in\mathbf{Z}}$). Fortunately, any solution of system (1.2) can be effectively represented by the following reduced system

$$\begin{aligned}&(u_{n-1}+u_n)^3+(u_n+u_{n+1})^3=u_n-\varepsilon\left(t^{[m_n]}(u_n)\right)^3\\&t^{[m]}(u_i)=2\sqrt{\frac{\beta}{3}}\cos\left(\frac{1}{3}\arccos\left(-\frac{3u_i}{2\beta}\sqrt{\frac{3}{\beta}}\right)-\frac{2\pi m}{3}\right),\ m=0,1,2\end{aligned}\tag{1.3}$$

where $m=0,1,2$ corresponds to a certain branch assigned to each one of the cells. In the present study we present the asymptotic description of DBs and establish analytically their zones of existence. Passing to the quasi-continuum limit we obtain the following essentially nonlinear ODEs for each one of the branches,

$$u\left[u^2\right]_{xx}+\frac{8}{3}u^3+\frac{1}{6}\left\{\varepsilon\left(t^{[m]}(u)\right)^3-u\right\}=0,\ u\le u_{\max}\tag{1.4}$$

It can be easily shown that the out-of-phase oscillations, can be obtained on the two branches only, namely ($m=0,1$). Comparison of exact spatial wave profiles of DBs computed from (1.3) with these obtained from QCA (1.4) are presented in Fig. 1 (a) and (b) panels accordingly. In Fig. 1 (c) and (d) we illustrate their zones of existence obtained analytically.

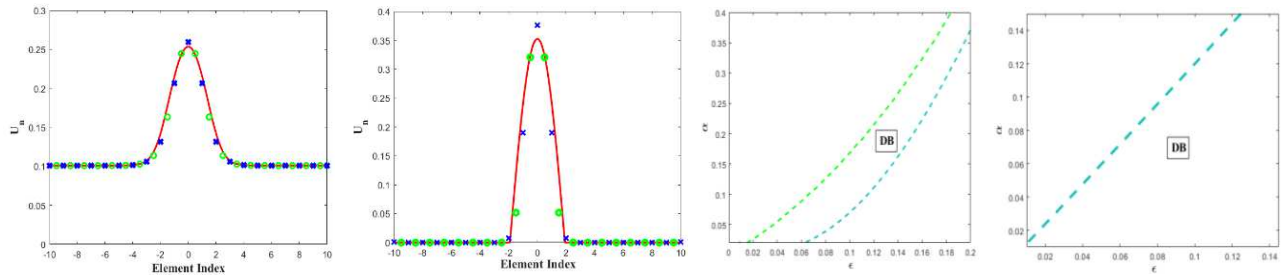

(a) **(b)** **(c)** **(d)**

Figure 1 (a, b) Spatial wave profiles of DBs corresponding to the homogeneous configurations. QCA is denoted with the bold solid line while exact solutions are denoted with 'cross' markers for site-centered breathers and 'o' markers for the bond-centered breathers. (**a**) $m=0$ (**b**) $m=1$. System parameters: $\varepsilon=0.1,\alpha=0.1$. (c, d) Zones of existence of a discrete breather (DB) corresponding to the homogeneous configurations i.e. m=0,1. **(c)** ($m=0$) **(d)** ($m=1$).

Conclusions

In the present study we analyze the special family of discrete breather solutions. Results of analytical study enable to describe the spatial wave profiles and establish their zones of existence. Separate linear stability analysis of DBs performed in this study revealed their stability zones in the plane of system parameters.

Acknowledgements

MK is thankful to the grant supported by Russian Foundation for Basic Research project no. 18-03-00716. YS acknowledges the financial support of Israeli Science Foundation, Grant No. 1079/16

References

[1] A. A. Ovchinnikov, Zh. Eksp. Teor. Fiz. 57, 263 (1969).
[2] S. Aubry, Physica D 103, 201 (1997).
[3] S. Flach and A. V. Gorbach, Phys. Rep. 467, 1 (2008).
[4] Y.S. Kivshar, Phys. Rev. E 48, R43(R) (1993)
[5] G. James , Math. Models Methods Appl. Sci., 21, 2335 (2011).
[6] G. James, P. G. Kevrekidis, and J. Cuevas, Physica D 251, 39 (2013).
[7] L. Liu, G. James, P. Kevrekidis, A. Vainchtein, Physica D 331 (2016) 27–47
[8] L. Liu, G. James, P. Kevrekidis, A. Vainchtein, Nonlinearity 29 (2016) 3496–3527

Asymptotic analysis of transient behavior of two coupled exciters

Tunc Yüzbasioglu*, Alexander Fidlin*
*Karlsruhe Institute of Technology (KIT), Institute of Engineering Mechanics, Karlsruhe, Germany

Summary. A model of two coupled exciters is considered to investigate transient behavior of self-synchronizing systems with non-negligible damping. An averaging method for partially strongly damped systems is used for asymptotic analysis. Stationary solutions of the system are derived. Attraction domains of different types of solutions are identified and depicted in phase space.

Introduction

Application of multiple exciters and utilization of self-synchronization in mechanical systems led to development of a new generation of vibratory machines including self-synchronous vibrating feeders, conveyors, screens, grinders and so on. Such systems replace kinematic connections like gears or chains with self-synchronization to generate required excitation forces. They also have the advantage of distributing and decreasing the load on bearings, if instead of just one big exciter, multiple smaller exciters are used.
The synchronization theory of mechanical exciters was first proposed by Blekhman [1]. Since then, many different synchronous systems are investigated. Previous works mostly just analyze synchronous solutions, their stability and existence with the assumption of negligible damping and that synchronization occurs far away from resonance. Goal of this work is to analyze transient behavior of synchronizing systems, examine different types of solutions in phase space and determine attraction domains of stable solutions.

Investigated model

Investigated model of two coupled exciters is shown in Fig. 1. It consists of a carrier of mass M, which is elastically suspended with a spring-damper element of stiffness c and damping d in horizontal direction. Two unbalanced rotors of mass m_i, moment of inertia J_i and eccentricity e_i, where $i = 1, 2$ is the index describing the number of rotors, are mounted on the carrier. They are driven in the same direction by induction or DC engines of limited power with a linearized torque characteristic given as $T_i = U_i(\omega_i^* - \dot{\varphi}_i)$. The parameter U_i describes the slope of motor characteristic and ω_i^* the nominal rotation speed. The equations of motion read

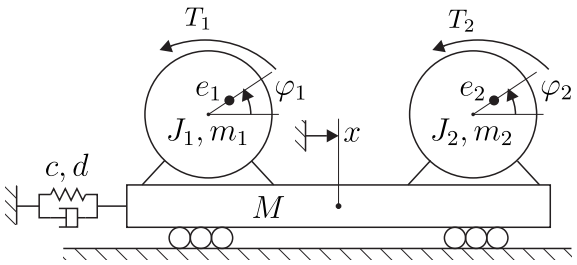

Figure 1: Investigated model

$$\xi'' + 2\sigma\xi' + \xi = \sum_{i=1}^{2} \mu_i\nu_i(\varphi_i'' \sin\varphi_i + \varphi_i'^2 \cos\varphi_i), \quad \varphi_i'' = \varepsilon\left(\frac{s_i}{\nu_i}\xi'' \sin\varphi_i + u_i(\lambda_i - \varphi_i')\right) = \varepsilon f_{\varphi_i}, \qquad i = 1, 2,$$

with the non-dimensional parameters and variables

$$\mu_i = \frac{m_i}{M^*}, \quad \nu_i = \frac{e_i}{e^*}, \quad \varepsilon s_i = \frac{1}{1 + J_i/m_i e_i^2}, \quad e^* = (e_1 + e_2)/2, \quad u_i = \frac{U_i s_i}{k m_i e_i^2}, \quad \lambda_i = \frac{\omega_i^*}{k},$$
$$\xi = \frac{x}{e^*}, \quad k^2 = \frac{c}{M^*}, \quad 2\sigma = \frac{d}{kM^*}, \quad M^* = M + m_1 + m_2, \quad \tau = kt.$$

The parameter ε is assumed to be small and the damping parameter σ is not small. The investigation is performed for a system with two identical rotors with different nominal speeds, which means that parameters of both rotors are identical except $\lambda_1 \neq \lambda_2$.

Asymptotic analysis

The averaging method for partially strongly damped systems is applied, see [2, 3]. Motion of the carrier can be replaced by its forced solution and the differential equation for ξ can be neglected in further analysis. Equations in standard form for a second order approximation with $\sqrt{\varepsilon}$ as the small parameter can then be acquired as

$$\frac{\mathrm{d}\delta}{\mathrm{d}\psi} = \frac{2\sqrt{\varepsilon}v}{p}, \qquad \frac{\mathrm{d}v}{\mathrm{d}\psi} = \frac{2\sqrt{\varepsilon}(f_{\varphi_2} - f_{\varphi_1})}{p}, \qquad \frac{\mathrm{d}p}{\mathrm{d}\psi} = \frac{2\varepsilon(f_{\varphi_2} + f_{\varphi_1})}{p}, \tag{1}$$

with the new variables $\omega_i = \varphi_i'$, $\psi = (\varphi_1 + \varphi_2)/2$, $\delta = \varphi_2 - \varphi_1$, $p = \omega_1 + \omega_2$, $v = (\omega_2 - \omega_1)/\sqrt{\varepsilon}$. By averaging these equations, a third-order system can be derived for the averaged variables $\bar{\delta}$, $\bar{v}$ and $\bar{p}$.

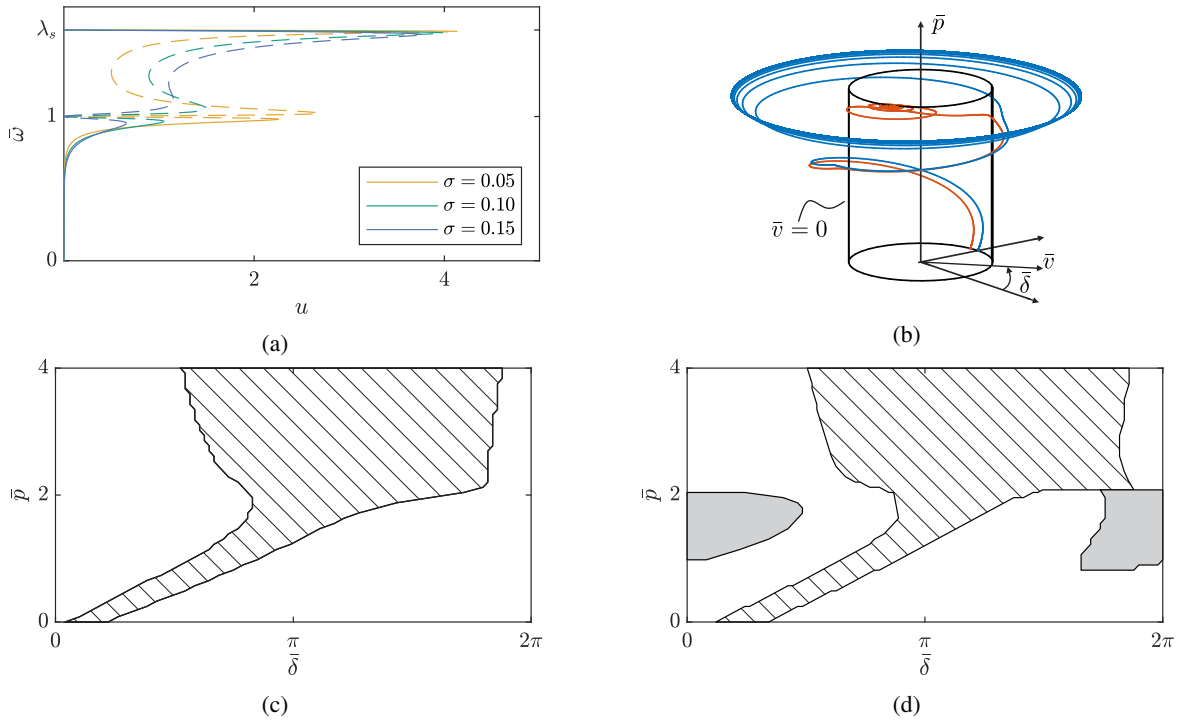

Figure 2: Results: (a) Stable (full) and unstable (dashed) stationary solutions of the averaged system for different values of damping, $\lambda_1 = 1.5$, $\lambda_2 = 1.7$, synchronization frequency $\lambda_S = 1.6$ derived according to [1]. (b) Two trajectories in cylindrical phase space. (c) A section of the phase space showing attraction domains of overcritical (white) and synchronous (hatched) solutions. (d) Same section of the phase space for smaller damping, where overcritical, synchronous and capture into resonance (grey) solutions all coexist.

Results

From the equation for $\bar{\delta}$ in Eq. (1) follows, that all stationary solutions of the system, which can be obtained under the assumptions made, are synchronous solutions ($\bar{v} = 0$, i.e. $\bar{\omega}_1 = \bar{\omega}_2 = \bar{\omega}$), including capture into resonance of both rotors. The stationary solutions as a function of parameter u ($u_1 = u_2 = u$) corresponding to the slope of motor characteristic and for different values of damping parameter σ are shown in Fig. 2a. First stable solution branch depicts capture into resonance, where both rotors cannot cross the resonance frequency of carrier ($\bar{\omega} = 1$). Second stable solution branch depicts synchronous solution at synchronization frequency λ_S. So Figure 2a can be interpreted as existence conditions of capture into resonance and self-synchronization as functions of engine power and damping. The overcritical solution, where both rotors reach their nominal speeds is not shown in Fig. 2a, because it is not a stationary solution.
To depict the phase space of the averaged system, cylinder coordinates are chosen, where $\bar{p}$ is the vertical, $\bar{v}$ is the radial and periodic variable $\bar{\delta}$ is the tangential coordinate. Since the variable $\bar{v}$ can become negative an arbitrary radius is chosen for $\bar{v} = 0$, see Fig. 2b. In the same Figure, two trajectories are shown, which start at resting position with different initial phase differences. One trajectory ends with self-synchronization, which is a point at $\bar{v} = 0$ and the other one converges to the overcritical periodic solution, which is a limit cycle in phase space. Lastly, sections of attraction domains of different solutions at the surface $\bar{v} = 0$ are shown in Fig. 2c,d. The trajectories in Fig. 2b can be explained with the attraction domains in Fig 2c. There is a narrow region, where the system can directly run-up to the synchronous solution form resting position. If the damping is chosen smaller, the three solution types (capture, synchronous and overcritical) can also coexist, see Fig 2d.

Conclusion

A model of two coupled exciters is investigated using an averaging method for partially strongly damped systems. Averaged equations of second order approximation in $\sqrt{\varepsilon}$ are analyzed. Stationary solutions and their existence conditions are discussed. Phase space of averaged system is described. Attraction domains of different types of solutions are exemplary depicted.

References

[1] Blekhman I. I. (1988) Synchronization in science and technology. ASME press

[2] Fidlin A., Thomsen J. J. (2008) Non-trivial effects of high-frequency excitation for strongly damped mechanical systems. *International journal of non-linear mechanics* **43.7**:569-578.

[3] Drozdetskaya O., Fidlin A. (2018) On the passing through resonance of a centrifugal exciter with two coaxial unbalances. *European Journal of Mechanics-A/Solids* **72**:516-520.

Asymptotic formulation of bifurcation scenarios to post-buckling nonlinear vibrations in thermomechanically coupled plates

Valeria Settimi*, Giuseppe Rega*
*Dipartimento di Ingegneria Strutturale e Geotecnica, Sapienza University of Rome, Rome, Italy

Summary. The nonlinear dynamics of composite plates with thermomechanical coupling is analytically addressed in order to describe the main dynamical phenomena triggering the involved pre- and post-buckling response scenario. The statical buckling occurrence, and two resonance conditions around the unbuckled and buckled equilibria are investigated by means of the asymptotic multiple scale method. The resulting modulation equations and the steady state mechanical and thermal responses are determined and compared with the numerical outcomes in order to verify the effectiveness of the adopted procedures.

Introduction

The nonlinear dynamical behavior of reduced order models of composite plates under different excitation conditions in a thermomechanical environment has been the subject of recent papers aimed at highlighting the role of multiphysics coupling and the main local and global features of the nonlinear response [1, 2]. The numerical analyses, carried out in strongly nonlinear regime and under different mechanical and thermal conditions, highlighted a rich and involved scenario characterized by multistability and possible chaos. Yet, the analytical treatment of the dynamical response can represent a useful tool to predict, describe and possibly modify the behavior of the coupled system. To this aim, three main response phenomena are detected in the weakly nonlinear regime, and the asymptotic multiple scale method [3] is applied in order to investigate existence and stability of the mechanical and thermal responses of the system.

Asymptotic analysis

With reference to a reduced model of rectangular laminated plate with von Kármán nonlinearities, third-order shear deformability and consistent cubic variation of the temperature along the thickness [4], the assumption of isothermal edges and free heat exchange on the upper and lower surfaces leads to obtain the following nondimensional equations of motion describing the plate dynamics around primary resonance:

$$\begin{aligned}
&\ddot{W}(t) + a_{12}\dot{W}(t) + (\Omega^2 - p)W(t) + a_{14}W(t)^3 + a_{15}T_{R1}(t) + a_{16}T_{R0}(t)W(t) - f\cos\Omega t = 0\\
&\dot{T}_{R0}(t) + a_{22}T_{R0}(t) + a_{23}\alpha_1 T_\infty + a_{24}W(t)\dot{W}(t) = 0\\
&\dot{T}_{R1}(t) + a_{32}T_{R0}(t) + a_{33}\dot{W}(t) = 0
\end{aligned} \tag{1}$$

in terms of the nondimensional reduced variables $W(t)$ (deflection of the center of the plate), $T_{R0}(t)$ (membrane temperature) and $T_{R1}(t)$ (bending temperature). The mechanical excitations consist of a uniform compressive force p on the plate edges and a distributed harmonic transverse mechanical excitation of amplitude f and frequency Ω. The thermal excitation is represented by the constant thermal difference between plate and environment T_∞, while a_{ij} are coefficients which incorporate the geometrical and physical properties of the model.

Local and global nonlinear dynamics of the presented model have been investigated by parametrically accounting for the single and combined presence of thermal and mechanical excitations. In particular, the transition to mechanically- or thermally-induced buckled responses has been analyzed, and a variety of rich multistable scenarios have been detected, as exemplarily shown in terms of numerical bifurcation diagrams as a function of the mechanical pretension in Fig. 1(a). With the aim to unveil the bifurcation phenomena triggering the development of such a rich scenario, identified in a strongly non-linear regime, a lower harmonic forcing amplitude has been applied to the system, with the relevant bifurcation diagram reported in Fig. 1(b). The results allow us to detect three main underlying dynamical features, i.e., a static pitchfork bifurcation inducing the mechanical buckling, and two resonance peaks occurring in the pre- and post-buckling branches. The first phenomenon occurs when the mechanical pretension p nullifies the linear mechanical stiffness, while the two peaks correspond to primary resonances of the pre- and post-buckling system frequencies with the external harmonic excitation.

The static buckling analysis is performed by obtaining the equilibria $\boldsymbol{e} = \{\boldsymbol{W_e}, \boldsymbol{T_{R0e}}, \boldsymbol{T_{R1e}}\}$ of the coupled system (1), which have the following expressions:

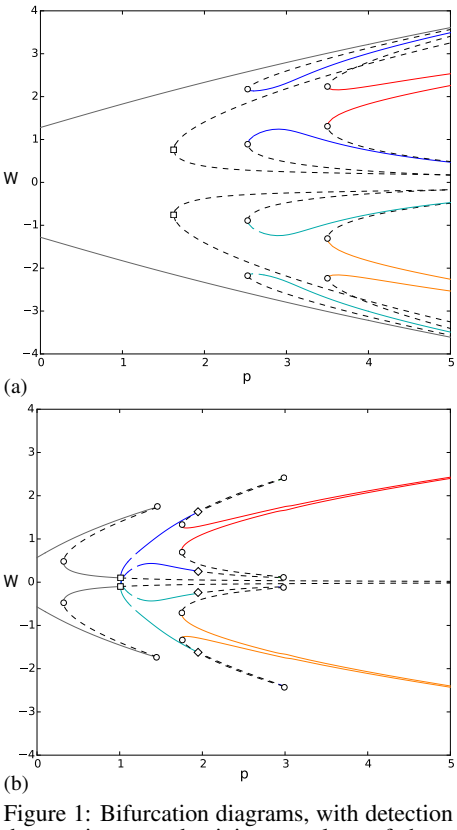

Figure 1: Bifurcation diagrams, with detection of the maximum and minimum values of the mechanical response as a function of p, at $\Omega = 1$, for $f = 1$ (a) and $f = 0.1$ (b).

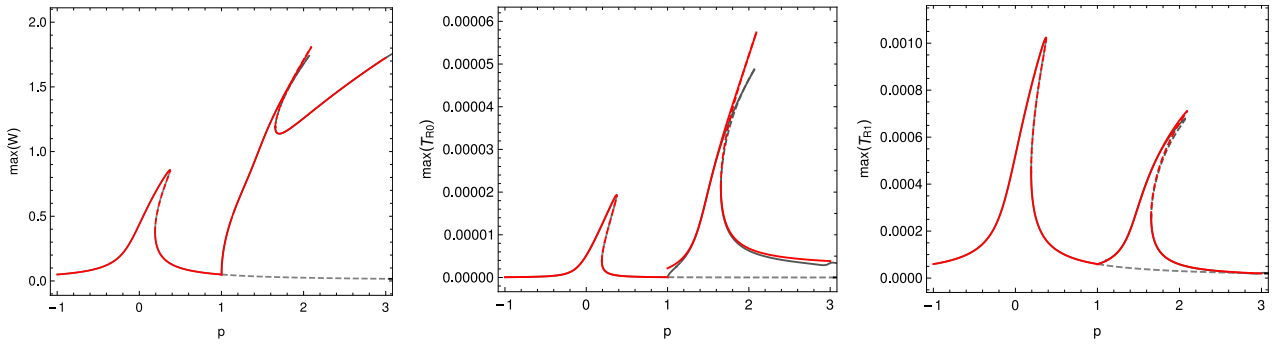

Figure 2: Comparison between numerical (gray) and analytical (red) bifurcation diagrams for $\Omega = 1$ and $f = 0.05$.

$$\boldsymbol{e_1} = \{0, -\frac{a_{23}\alpha_1 T_\infty}{a_{22}}, 0\}, \qquad \boldsymbol{e_{2,3}} = \{\pm\frac{\sqrt{a_{22}(p-\Omega^2) + a_{16}a_{23}\alpha_1 T_\infty}}{\sqrt{a_{14}a_{22}}}, -\frac{a_{23}\alpha_1 T_\infty}{a_{22}}, 0\} \tag{2}$$

The $\boldsymbol{e_1}$ equilibrium corresponds to the pre-buckling configuration representing the mechanical rest position, while $\boldsymbol{e_2}$ and $\boldsymbol{e_3}$ represent the two stable buckled non-trivial solutions arising after the pitchfork bifurcation. As already highlighted in some previous works [1, 2], expressions (2) show that the thermal excitation T_∞ plays the same role as the mechanical pretension in governing the mechanical equilibria, so that it is possible to reproduce exactly the diagrams of Fig. 1 by alternatively applying a properly scaled thermal excitation. The two resonance conditions are analytically investigated by means of the asymptotic method of multiple scales, in order to study the system nonlinear dynamics around the previously obtained $\boldsymbol{e_1}$ and $\boldsymbol{e_2}$ equilibria: $W(t) = W_e + \tilde{W}$, $T_{R0}(t) = T_{R0e} + \tilde{T}_{R0}$, $T_{R1}(t) = T_{R1e} + \tilde{T}_{R1}$. The perturbation equations around the pre-buckling equilibrium have the same structure of Eqs. (1) (with suppression of a_{23} term in the membrane thermal equation), with the system frequency (i.e., the time-independent linear stiffness) being $\omega^2 = \Omega^2 - p - a_{16}a_{23}\alpha_1 T_\infty / a_{22}$. Conversely, the analysis around the buckled position implies the presence of additional terms in the mechanical and membrane thermal equations:

$$\begin{aligned}
&\ddot{\tilde{W}} + a_{12}\dot{\tilde{W}} + \omega^2\tilde{W} + a_{14}\tilde{W}^3 + \frac{3\sqrt{a_{14}}}{\sqrt{2}}\omega\tilde{W}^2 + a_{15}\tilde{T}_{R1} + a_{16}(\frac{\omega}{\sqrt{2a_{14}}} + \tilde{W})\tilde{T}_{R0} - f\cos(\Omega t) = 0 \\
&\dot{\tilde{T}}_{R0} + a_{22}\tilde{T}_{R0} + a_{24}\dot{\tilde{W}}(\frac{\omega}{\sqrt{2a_{14}}} + \tilde{W}) = 0 \\
&\dot{\tilde{T}}_{R1} + a_{32}\tilde{T}_{R0} + a_{33}\dot{\tilde{W}} = 0
\end{aligned} \tag{3}$$

with $\omega^2 = 2(p + a_{16}a_{23}\alpha_1 T_\infty / a_{22} - \Omega^2)$. Consequently, the two asymptotic procedures require different choices in the scaling of variables and parameters, and different expansions to higher orders to account for the main effects (e.g., the occurrence of both quadratic and cubic nonlinearities, as in (3)). In both cases, anyway, they have been guided by the previous numerical analyses, which have pointed out the contemporary presence of slow (thermal) and fast (mechanical) dynamics, and have allowed to discuss the role of the coupling terms inside the three equations [5]. They result to be crucial into the thermal equations in order to determine the temperature response, while having a marginal effect on the mechanical equation, whose dynamics evolves much quicker than the coupled thermal one. The two procedures are developed separately, and the Amplitude Modulation Equations are obtained together with the reconstructed steady state mechanical and thermal responses. The outcomes reported in Fig. 2 show a good agreement between analytical (red) and numerical (gray) results, also in the post-buckling scenario where the mechanical response is moderately severe.

Conclusions

The analytical treatment through the multiple scale method is developed to describe the main dynamical phenomena underlying the rich multistable scenario characterizing the nonlinear behavior of thermomechanically coupled plates. The obtained modulation equations together with the reconstructed responses can be used to parametrically discuss the occurrence and stability of the main periodic unbuckled and buckled responses as a function of the main system parameters.

References

[1] Settimi V., Rega G., Saetta E. (2018) Avoiding/inducing dynamic buckling in a thermomechanically coupled plate: a local and global analysis of slow/fast response. *Proc. R. Soc. Lond., A*, **474(2213)**:20180206.

[2] Settimi V., Saetta E., Rega G. (2019) Nonlinear dynamics of a third-order reduced model of thermomechanically coupled plate under different thermal excitations. *Meccanica*, to appear.

[3] Nayfeh A.H., Mook D.T. (1979) Nonlinear oscillations. Wiley, NY.

[4] Saetta E., Rega G. (2017) Third-order thermomechanically coupled laminated plates: 2D nonlinear modeling, minimal reduction and transient/post-buckled dynamics under different thermal excitations. *Compos. Struct.*, **174**:420-441.

[5] Settimi V., Rega G. (2019) Thermomechanical coupling and transient to steady global dynamics of orthotropic plates. *in* Problems of Nonlinear Mechanics and Physics of Materials, Springer, pp:483-499.

Axisymmetric, nonlinear capillary waves: dimple and jet formation

Lohit Kayal and Saswata Basak and Ratul Dasgupta
Department of Chemical Engineering, IIT Bombay, Mumbai, India

Summary. We study axisymmetric, nonlinear capillary waves in confined cylindrical geometry. Extending our recent analytically and computational studies[5, 2], we present a third order theory [6] which can describe dimple formation in nonlinear axisymmetric capillary waves for moderately large values of the wave steepness parameter ϵ. For $\epsilon > 1.8$, we show that the dimple produces a jet which evolves self-similarly in a window of time and space. Analytical predictions are compared to numerical solutions.

Jet formation from an axisymmetric capillary wave

Jet formation from bursting bubbles have attracted persistent attention from the scientific community for more than half a century [3]. In addition to scientific curiosity, the phenomena is also of significant meterological interest as the bursting of bubbles on the open ocean surface (due to wave breaking) causes ejection of liquid droplets which are a source of sea-salt aerosols and can serve as cloud condensation nuclei. In a series of recent studies [5, 2] it was observed that similar jet ejection can also occur in apparently simpler conditions where the free-surface of quiescent liquid in a cylindrical container of radius R_0 is deformed as a an eigenmode of the linearised system viz. a Fourier-Bessel mode of the form $a_0 J_0(k_0 r)$. It was shown that [5, 2] that the resulting surface oscillation due to the restoring force of gravity and capillarity produces a trough whose subsequent evolution in time, closely resembles a collapsing cavity [4]. When the steepness parameter $\epsilon \equiv a_0 k$ is sufficiently large ($\mathcal{O}(1)$), a nonlinearity induced dimple like structure is produced at the base of the trough leading to the formation of a jet at the axis of symmetry [2, 5], much analogous to what is observed in the bursting of a bubble at a free-surface [8, 4]. While the $\mathcal{O}(\epsilon^2)$ non-linear theory presented in [2] was able to capture the inception of the dimple, it was unable to describe the same at later times. An important conclusion from [2] was that the lengthscale of the dimple rendered it completely dominated by capillary effects with the gravitational acceleration being insignificant. In this study, we lend further insight into this dimple formation focusing our attention on pure capillary waves (no gravity) [6]. A novel $\mathcal{O}(\epsilon^3)$ solution to the intial-value problem has been calculated [6] which significantly improves upon the second order calculation presented earlier in [2]. Fig. 1a depicts the initial axisymmetric, surface perturbation of the form $\eta(r,0) = \epsilon J_0(k_0 r)$ and fig. 1b shows the formation of the dimple for a moderately large $\epsilon = 0.8$, and is described quite accurately by our $\mathcal{O}(\epsilon^3)$ calculation. This is the solution to the initial-value problem using ϵ as a perturbation parameter and the Lindstedt-Poincaré technique. It has the form

$$\eta(r,\tau) = \epsilon \cos(\tau) \mathrm{J}_0(r) + \epsilon^2 \sum_{j=1}^{\infty} f^{(j)}(\tau) \mathrm{J}_0(\alpha_{j,p} r) + \epsilon^3 \left[\sum_{m=1}^{\infty} g^{(m)}(\tau) \mathrm{J}_0(r) + \sum_{j=1,\, j\neq p}^{\infty} h^{(j)}(\tau) \mathrm{J}_0(\alpha_{j,p} r) \right]$$

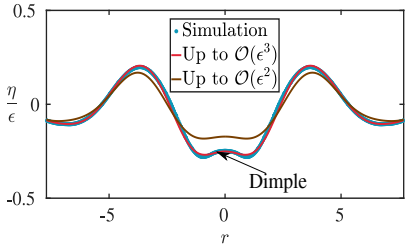

Figure 1: Comparison of the surface evolution of the interface at steepness $\epsilon = 0.8$. Numerical solution to the Euler's equation (•) using Basilisk [9], $\mathcal{O}(\epsilon^3)$ (—), $\mathcal{O}(\epsilon^2)$ (—). Third order theory captures the dimple very accurately. Here η is non dimensional interface and r is non-dimensional radial distance.

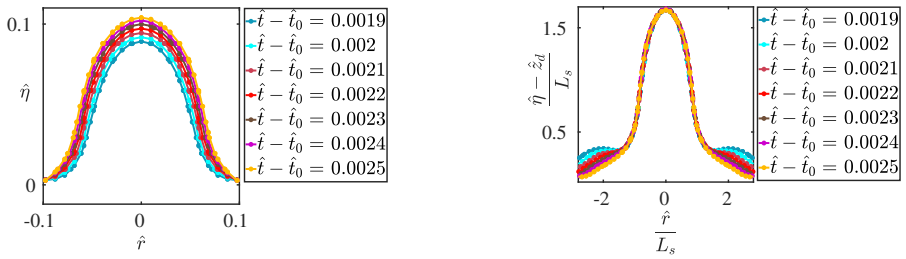

(a) A rising jet

(b) Self-similar behaviour of jet

Figure 2: Panel (a), (b): Self similar behaviour of the jet at $\epsilon = 2.0$ and cylinder radius $\mathrm{R}_0 = 2.936$ cm, where R_0 is the radius of the cylinder. Here $\hat{t}_0$ is the dimple formation time, $\hat{\eta}$ is dimensional interface and $\hat{r}$ is dimensional radial distance, $\hat{z}_d$ is the height of the jet base (all variables with hat are dimensional)

At larger values of $\epsilon = 2.0$, a clear jet emerges from the dimple as shown in fig. 2a. At large steepness($\epsilon > 1.8$), we

find that the jet evolution in time becomes self-similar. This is shown in fig. 2b where the length scale $L_s = \frac{(\hat{t}-\hat{t}_0)^{2/3}}{\left(\frac{\rho}{\mathrm{T}}\right)^{1/3}}$ [7, 10] has been used to scale the vertical and radial coordinate. Note that ρ, T are density and surface tension and $\hat{t}_0$ is the dimple formation time.

Modal analysis

In fig. 3, we plot the surface energy of the system from modal analysis [2]. The figure shows the Fourier-Bessel modes which are excited at the chosen instant of time. For the case $\epsilon = 2.0$, the time instant has been chosen to lie within the self-similar window shown earlier in fig. 2b. Comparing $\epsilon = 2.0$ with $\epsilon = 1.0$, it is clearly seen that a large number of modes are excited in the case of $\epsilon = 2.0$ compared to $\epsilon = 1.0$. Note that we have plotted $\left|\hat{H}(l_j)\right|$ which comes from the coefficient of the Dini series and provides an instantaneous measure of the potential energy contained in various wavenumbers [1] (l_j is the jth nontrivial root of the Bessel function $\mathrm{J}_1(\cdot)$).

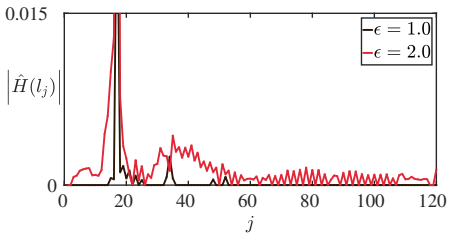

Figure 3: The potential energy between $\epsilon = 1.0$ (——) and $\epsilon = 2.0$ (——) are compared at the same time instant $\hat{t} = 0.0092$ s. At this instant the $\epsilon = 2.0$ simulation displays self similar collapse depicted earlier in fig. 2b. The simulation with $\epsilon = 1.0$ however does not show self similar behaviour at this instant or at later time.

Confinement and loss of self-similarity

We find that strong confinement (i.e. shrinking the radius of the container) leads to loss of self-similarity. This is shown in fig. 4(a) and (b) where both panels represent simulations with $\epsilon = 0.2$. In panel (a) the radius is small ($R_0 = 0.038$ cm) and the evolution of the jet is not self-similar in marked contrast to panel (b).

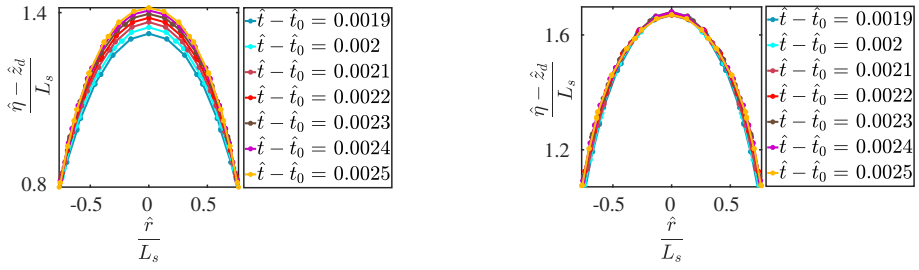

(a) R_0=0.038 cm (b) R_0=2.936 cm

Figure 4: Panel (a), (b): Effect of container radius on the self similar evolution of jet

Conclusions

We investigate dimple and jet formation from nonlinear capillary waves in axisymmetric cylindrical confined geometry. The initial value problem has been solved to $\mathcal{O}(\epsilon^3)$ using the Lindstedt Poincarè perturbation technique and it is found that the weakly nonlinear solution can predict the formation of the dimple quite well for moderately large value of ϵ. Using simulations, we have shown that for $\epsilon > 2.0$, the evolution of the jet happens in a self similar manner in a narrow window of space and time. The physical reasons for this self-similarity as well as the eventual loss of the same will be discussed at the meeting. All simulations have been performed using the open source Basilisk [9].

References

[1] V. G. Bagrov, A. A. Belov, V. N. Zadorozhyni, and A. Y. Trifonov. Methods of mathematical physics- special functions. `http://portal.tpu.ru:7777/SHARED/a/ATRIFONOV/eng/academics/Tab3/FTI_Bagrov_Belov_Zadorozhnyi_Trifonov_EMathPh-1e.pdf`, 2012.

[2] S. Basak, P. K. Farsoiya, and R. Dasgupta. Jetting in finite-amplitude, free, capillary-gravity waves. *Journal of Fluid Mechanics*, 909, 2021.

[3] D. C. Blanchard. The electrification of the atmosphere by particles from bubbles in the sea. *Progress in oceanography*, 1:73–202, 1963.

[4] L. Duchemin, S. Popinet, C. Josserand, and S. Zaleski. Jet formation in bubbles bursting at a free surface. *Physics of fluids*, 14(9):3000–3008, 2002.

[5] P. K. Farsoiya, Y. Mayya, and R. Dasgupta. Axisymmetric viscous interfacial oscillations–theory and simulations. *Journal of Fluid Mechanics*, 826:797–818, 2017.

[6] Kayal, Lohit and Basak, Saswata and Dasgupta, Ratul. Dimples, jets and self-similarity in nonlinear capillary waves (To be submitted).

[7] J. B. Keller and M. J. Miksis. Surface tension driven flows. *SIAM Journal on Applied Mathematics*, 43(2):268–277, 1983.

[8] C.-Y. Lai, J. Eggers, and L. Deike. Bubble bursting: universal cavity and jet profiles. *Physical review letters*, 121(14):144501, 2018.

[9] S. Popinet. Basilisk. *URl: http://basilisk. fr.(accessed: 10.21. 2019)*, 2014.

[10] B. W. Zeff, B. Kleber, J. Fineberg, and D. P. Lathrop. Singularity dynamics in curvature collapse and jet eruption on a fluid surface. *Nature*, 403(6768):401, 2000.

Thursday, July 21, 2022
08:30 - 10:30

MS-08 Nonlinear Phenomena in Mechanical and Structural Systems
Rhone 3B

Chair: Daniele Zulli

08:30 - 08:50
Modelling the nonlinear mechanical characteristics of a slack cable using Bouc-Wen model
ZAMANIAN Najafabadi Shima*, TURE Savadkoohi Alireza, LANGLOIS Sébastien
*University of Sherbrooke (2500, boul. de l'Université, Sherbrooke (Québec) J1K 2R1 Canada)

08:50 - 09:10
Nonlinear Analysis of the Snaking Motion of Towed Vehicles
HORVATH Hanna Zsofia*, TAKÁCS Dénes
*Department of Applied Mechanics, Budapest University of Technology and Ecomincs (3. Műegyetem rkp., Budapest 1111 Hungary)

09:10 - 09:30
Speed effects on vibration and collapse of slender structures under moving loads
VAN Der Heijden Gert*, ZHAO Xingwei
*University College London (Gower Street - London, WC1E 6BT United Kingdom)

09:30 - 09:50
Nonlinear Dynamics of a Shearable-Extensible Beam with an Elastic Longitudinal Support: Analytical Derivation, Numerical Simulation and Experimental Validation
KLODA Lukasz*, LENCI Stefano, WARMINSKI Jerzy
*Polytechnic University of Marche (via Brecce Bianche, 60131 Ancona, Italy Italy) - Department of Applied Mechanics, Lublin University of Technology (Nadbystrzycka 38D, 20-618 Lublin Poland)

09:50 - 10:10
Optimal design of impact based non-linear energy dissipation mechanism in pipeline systems
ALOSCHI Fabrizio*, ANDREOTTI Roberto, BURSI Oreste Salvatore, CERAVOLO Rosario
*IGF - Ingenieurgesellschaft Dr.-Ing.Fischbach mbH (An der Vogelrute 2 D-50374 Erftstadt-Lechenich Germany) - Department of Civil, Environmental and Mechanical Engineering, University of Trento (Via Mesiano 77, 38123, Trento Italy)

10:10 - 10:30
Nonlinear vibrations of nanoplates based double mode model and the nonlocal elasticity theory
MAZUR Olga*, AWREJCEWICZ Jan
*National Technical University "Kharkiv Polytechnic Institute" (Kyrpychova 2, 61002, Kharkiv Ukraine)

Modelling the nonlinear mechanical characteristics of a slack cable using Bouc-Wen model

Shima Zamanian Najafabadi*, Alireza Ture Savadkoohi† and Sébastien Langlois ‡
*Civil and Building Engineering Department, University of Sherbrooke, Canada.
†Univ Lyon, ENTPE, CNRS UMR5513, LTDS, France
‡Univ Sherbrooke, Civil and Building Engineering Department, Canada.

Summary. Slack cables are pieces of conductors that are used in bretelles and Stockbridge dampers, to mitigate the wind-induced vibration of overhead transmission lines. Under cyclic and dynamic excitations, inter-strand friction in slack cables makes their behavior nonlinear and hysteretic. On the other hand, due to the low tension, their mechanical behavior is different from stretched cables. Thus, it is important to develop a model that can predict their nonlinear behaviors under vibration. The main purpose of this study is to reproduce this nonlinear behavior using a linear Euler-Bernoulli beam coupled with a Bouc-Wen hysteresis model. The parameters of the Bouc-Wen model are identified based on the results of a characterization test on the slack cable of a Stockbridge damper, available in the literature. Using this method, the local bending behavior of the slack cable is well-reproduced.

Introduction

When a system exhibits hysteresis behavior, it means the response of the system depends not only on its current state, but also on the history of the previous states. Under cyclic loads, friction between the sliding wires of a slack cable makes their mechanical behavior nonlinear and hysteretic. This characteristic is important since it governs the energy dissipation of the system. In contrast to taut cables, the power dissipation of slack cables is significant, and they are used in bretelles and Stockbridge dampers to mitigate the aeolian vibration of overhead transmission lines. Aeolian vibration represents the major cause of fretting fatigue failure in transmission lines [1].

Due to hysteretic characteristics, the bending stiffness of a cable varies according to the curvature. In the literature, there are several models for the study of the nonlinear bending stiffness of taut cables. These models allow for predicting hysteresis load-deflection curves and calculation of the system energy dissipation. The model of Papailiou [2] describes the secants bending stiffness as a function of curvature taking into account the inter-layer slippage and friction force between the layers of a conductor. This model is validated through the results of quasi-static tests for high level of tensions. The bending stiffness was shown to transmit smoothly from EI_{max} to EI_{min}, which corresponds to the full-stick state and full-slip state, by the propagation of the wire slippage layer by layer towards the core. Dastous [3] converted the model of papailiou based on the tangent bending stiffness method and implemented it in a finite-element formulation. Hong [4] improved the model of Papailiou by reconsidering some simplifying assumptions, and introducing new criteria for wire slippage regarding the radial pressure transmission between the layers. Paradis [5] used the criteria of Hong [4], and developed a new model by considering the micro-slips in contact areas between the wires. Langlois [6] implemented the model of Paradis, and reproduced the variable bending stiffness of tensioned conductors through a finite element model.

To study specifically the hysteresis behavior of slack cables, Sauter [7] modeled the messenger cable of a Stockbridge damper as a linear beam coupled with the Masing hysteresis model to describe the local moment-curvature relationship. Parameters of the model were obtained locally, based on the results of quasi-static tests. It was shown that the behavior of the slack cable during the bending process, varies spatially along the cable and during the bending cycle based on the deformation history (loading-unloading). Foti et al. [8] reproduced the hysteresis moment-curvature of a damper cable using a bilinear elastic-plastic model coupled with the classic Bouc-Wen model. Langlois [9], developed a finite-element model of the messenger cable of a Stockbridge damper with variable bending stiffness by superimposing beam elements with material nonlinearity. The constitutive parameters of the model were identified from the characterization test on Stockbridge dampers such that the overall behavior was best reproduced. The model of damper later was added to a span of conductor to study the aeolian vibration amplitude of a system of conductor-damper.

Low tension in slack cables makes their behavior different from tensioned cables, and very few researches are available to study the nonlinear mechanical bending behavior of the slack cables. The main objective of this study is to develop a nonlinear model that predicts the hysteresis behavior of a slack cable under different amplitudes and frequencies. For this purpose, an analytical model of the slack cable by using a linear Euler-Bernoulli beam coupled with a nonlinear Bouc-Wen model is developed. Bouc-Wen model is a hysteresis model that is based on the continuous change of the stiffness with varying displacement, proposed by Bouc [10] and later improved by Wen [11]. The dynamic response of the system under a low-frequency sinusoidal load is obtained and the moment-curvature hysteresis loop at different locations along the slack-cable is calculated. The parameters of the Bouc-Wen model are obtained iteratively to reproduce the results of the characterization test performed by Sauter [7] on a rigidly clamped slack cable of a Stockbridge damper. This model can be coupled with a validated conductor model to predict the aeolian vibration amplitude of the system.

Figure 1: Stockbridge damper [12].

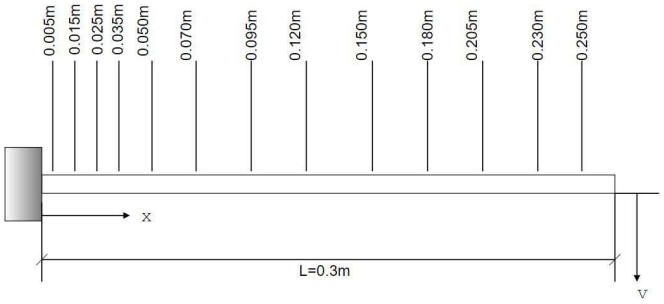

Figure 2: Sketch of the experimental test on the messenger cable.

Properties of the Slack Cable

Slack cables are used in Stockbridge dampers shown in Fig. 1. It consists of a clamp, a short messenger cable, and two inertial masses. This kind of damper is used to mitigate the aeolian vibration of transmission lines. The clamp of the damper is rigidly connected to the conductor, and as the vertical movement of the conductor happens, the masses vibrate and bend the messenger cable. This causes the relative movement of the wires of the messenger cable. Because of the friction between the wires, they exhibit hysteresis behavior. This phenomenon makes the relationship between the load and deflection rate dependent and hence, causes power dissipation in the system. This nonlinearity is shown in the load-deflection curves of messenger cable from experimental tests [13, 14]. Bending tests are usually done to characterize the dissipative behavior of the messenger cables. In these tests, a short length of messenger cable is clamped at one-end and free at the other end, and subjected to a transverse force at the tip monotonically or cyclically varying. The load-deflection curvature curves are usually obtained for different tip displacements.
In this study, the experimental validation of the models are done based on the characterization test of Sauter [7]. In this test, a short slack cable with the length of 0.3 m was rigidly clamp at one-end, and the free-end was subjected to a transverse cyclic displacement at a low frequency. The parameters measured are:

- The moment-curvature diagram at 25mm from the clamp end for cyclic transverse displacement of the free-end (5mm to 30mm peak-peak)
- The local moment-curvature diagram at different points along the cable under the transverse displacement of 25mm peak-peak.

The properties of the slack cable is presented in Table. 1. Figure 2 shows the setup of the test, and the locations for which the local hysteresis were measured.

Governing Equations of the System

In this study, the slack cable is modeled as a simple cantiliver beam (Fig. 2), coupled with a Bouc-wen model. The bending deflection $v(x,t)$ of a Euler-Bernoulli beam under a sinusoidal load $f(t)$ can be described by the following equation:

$$\frac{\partial^2}{\partial x^2}(EI(x)\frac{\partial^2 v(x,t)}{\partial x^2}) + f(t) = m\frac{\partial^2 v(x,t)}{\partial t^2} + c\frac{\partial v(x,t)}{\partial t} \tag{1}$$

where m is the mass per unit length, c is the damping, EI is the bending stiffness.
The boundary conditions for the cantiliver beam are:

$$\begin{aligned} v(0,t) &= 0, \forall t \\ v'(0,t) &= 0, \forall t \\ v''(l,t) &= 0, \forall t \\ v'''(l,t) &= 0, \forall t \end{aligned} \tag{2}$$

Where the prime denotes the derivative with respect to the space variable x, and l is the length of the slack cable.
As we are interested in the behavior of the system around the deformation of its first mode, the solution of the Eq. (1) can be expressed in the form of:

$$v(x,t) = \Gamma_1(x)g_1(t) \tag{3}$$

where $\Gamma_1(x)$ is the first natural mode of the system and $g_1(t)$ is the corresponding generalized coordinate. By solving the eigenvalue problem related to the free response of Eq. (1), the first vibration mode of the beam $\Gamma_1(x)$ could be obtained such that it satisfies the geometrical boundary conditions of the beam presented in Eq. (2).

Table 1: Mechanical Properties of the Slack Cable [7]

Total diameter (mm)	10.15
Number of layers except core	2
Number of wires	19
Wire diameter (mm)	2
Young modulus (GPa)	210
Mass per unit length (kg/m)	0.498

Thanks to the orthogonality of modes, the equation of motion in temporal state after addition of nonlinear Bouc-Wen model could be expressed as [10, 15, 16]:

$$\ddot{g_1}(t) + 2\xi\omega_1\dot{g_1}(t) + \alpha\omega_1^2 g_1(t) + (1-\alpha)\omega_1^2 z(t) = F(t) \tag{4}$$

$$\dot{z}(t) = \dot{g_1}(t)[1 - \mid \frac{z(t)}{g_y} \mid^n (\beta + \lambda sgn(z\dot{g_1}))] \tag{5}$$

Where the dots denotes the derivative with respect to time and ξ is the modal damping ratio, ω_1 is the first angular frequency, $F(t)$ is the modal force and $z(t)$ is the hysteresis parameter. The Bouc-Wen model is coupled with the equation of the beam in temporal state through a superposition of a linear elastic force $\alpha\omega_1^2 g_1(t)$ and a nonlinear hysteretic force $(1-\alpha)\omega_1^2 z(t)$. The Bouc-Wen parameters, α is the post-elastic to initial stiffness ratio, g_y is the generalized yield displacement and β, γ, n are model parameters. The response of the system is calculated by direct integration of Eq. (4) and Eq. (5) using "ode45" function in MATLAB. To be able to use this function, the Eq. (4) and Eq. (5) have to be transformed into a system of first order as below:

$$\begin{aligned} \dot{Y}(1) &= Y(2) \\ \dot{Y}(2) &= -2\xi\omega_1 Y(2) - \alpha\omega_1^2 Y(1) - (1-\alpha)\omega_1^2 Y(3) + F(t) \\ \dot{Y}(3) &= Y(2)[1 - \mid \frac{Y(3)}{g_y} \mid^n (\beta + \lambda sgn(Y(3)Y(2)))] \end{aligned} \tag{6}$$

The following initial conditions are considered for this system:

$$t = 0 \rightarrow \begin{cases} Y(1) = 0, & \dot{Y}(1) = 0 \\ Y(2) = 0, & \dot{Y}(2) = 0 \end{cases} \tag{7}$$

After obtaining the response of the system numerically, the moment-curvature relationship at each point throught the slack cable could be obtained as [17]:

$$M(t) = \alpha\omega_1^2\phi(t) + (1-\alpha)\omega_1^2 z(t) \tag{8}$$

Where $\phi(t)$ is the curvature, and it is calculated directy from the derivative of Eq. (3) with respect to displacement. The moment-curvature diagram is calculated for different excitation loads with a low frequency at the free-end of the slack cable. The force is adjusted to have the desired tip displacements. It has to be noted that this model allows us to predict the behaviour of the system for higher frequencies. The Bouc-Wen parameters of the model are adjusted through an iterative process such that the experimental results is best reproduced.

Model Parameter Identification

The parameters of a messenger cable modeled by the Bouc-Wen model are identified from the experimental data of Sauter [7]. The identification of the model was done iteratively using MATLAB. Five Bouc-Wen parameters, and the local bending stiffness of the system EI are identified. Table 2 shows the identified parameters of the system. Parameters λ and β control the shape and size of the hysteresis loops [11]. α is the post-elastic to initial elastic ratio, and g_y is generalizied yield displacement, and the parameter n is a nondimentional number that controls the transition from the elastic to inelastic part of the loop. Increasing this parameter to higher values can sharpen the transition [16]. This value is considered as 1 for all points.

Another parameter that has to be controlled is EI. Bending stiffness of a cable varies significantly with curvature during the bending, however it changes between two limits of EI_{min} and EI_{max} that are related to the full-slip and full-stick states, respectively. These parameters can be calculated as [1]:

$$\begin{aligned} EI_{min} &= \sum_i E_i I_{0i} = 2.83 N.m \\ EI_{max} &= \sum_i E_i (I_{0i} + A_i r_n^2 sin^2(\alpha_i)) = 67.1 N.m \end{aligned} \tag{9}$$

Table 2: Bouc-Wen parameters of the model

x (m)	α	β	λ	g_y	n
0.005	0.35	45	90	0.06	1
0.015	0.2	45	90	0.05	1
0.025	0.2	45	90	0.0045	1
0.035	0.2	45	90	0.0045	1
0.050	0.19	45	90	0.0045	1
0.070	0.19	45	90	0.0045	1
0.095	0.19	45	90	0.0048	1
0.12	0.19	45	90	0.0049	1
0.15	0.19	45	90	0.007	1
0.18	0.19	45	90	0.008	1
0.205	0.19	45	90	0.008	1
0.230	0.19	45	90	0.009	1
0.250	0.19	45	90	0.008	1

Where E_i is the modulus of elasticity, I_{0i} is the moment of inertia of each wire around its axis, A_i is the area of each wire, r_n is the distance of the center of each wire from the center of the cable, and α_i is the lay angle of each layer. Figure 3 demonstrates the local bending stiffness identified for the slack cable. In this model, the calculated value of EI for the points close to the clamp is more than EI_{max}. The reason could be due to the effect of the clamp on the cable. In the zones far from the clamp, EI decreases to EI_{min}, and from the middle to the tip it remains almost constant. All the wires of the cable far from the clamp slip so fast, however because of clamp effects most of the wires near the clamp stay in stick-state. This explains the variation of the local bending stiffness of the system.
Figures 4-7, show the results obtained from the Bouc-Wen model using the identified parameters (Table. 2) in comparison with experimental results. Figure 4 shows the moment-curvature results of a point 0.025m from the clamp under different tip displacements (5mm to 30mm, each 5mm). Figures 5-7, show the local moment-curvature loops for different points along the cable (Fig. 2) under a constant tip displacement of 25mm. Using the identified parameters, the experimental results are well reproduced in all cases.
As another validation, the displacement of the free end of the cable is measured under a given force. The results are compared to the experimental results in Fig. 8. It should be noted that to compare the global behavior of the slack cable, different sets of identified values are in the Table. 2 are tested, and the values for the point 35mm best reproduced the global behavior. The limitation of this method is that there is no possibility to use different sets of Bouc-Wen parameters at the same time for different points through the beam. However, by selecting a correct sets of values, correct global behavior can be obtained.

Conclusions

The mechanical behavior of a slack cable is modeled using a linear Euler-Bernoulli beam coupled with a hysteresis Bouc-Wen model. In this study, the response of the system is obtained based on the projection of the first mode. The validity of this model is shown by comparing the present results with the experimental results of the slack cable. At both local and global levels, this model reproduced the hysteresis behavior of the slack cable, adequately. The important advantage of this model is providity a fast tool that can describe and predict the nonlinear behavior of the slack cables, without systematic experimental tests. In addition, this model can be integrated into a conductor model, and it allows the assessment of the aeolian vibration amplitude of transmission lines.

References

[1] EPRI, Transmission Line Reference Book: Wind-Induced Conductor Motion. (2009) Palo Alto, CA, USA: Elect.

[2] Papailiou K. O. (1997) On the Bending Stiffness of Transmission Line Conductors. *IEEE Power Delivery*. vol. 12, no. 4, pp. 1576–1588.

[3] Dastous J.-B. (2005) Nonlinear finite-element analysis of stranded conductors with variable bending stiffness using the tangent stiffness method. *IEEE Power Delivery*. vol. 20, no. 1, pp. 328–338.

[4] Hong K.-J., Kiureghian A. D. , and Sackman J. L. (2005) Bending behavior of helically wrapped cables. *ASCE J. Eng. Mechan*., vol. 131, no. 5, pp. 500–511.

[5] Paradis JP. H, Legeron F.(2011) Modeling of the Free Bending Behavior of a Multilayer Cable Taking Into Account the Tangential Compliance of Contact Interfaces. *9th Int. Symp. Cable Dynam.*

[6] Langlois S. (2014) Time History Modeling of Vibrations on Overhead Conductors With Variable Bending Stiffnes. *IEEE Power Delivery*. vol. 29, no. 2, pp. 607-614.

[7] Sauter, D. (2003) Modeling the Dynamic Characteristics of Slack Wire Cables in Stockbridge dampers. *PhD Thesis*, Darmstadt, Germany.

[8] Foti F. (2018) Hysteretic Behavior of Stockbridge Dampers: Modelling and Parameter Identification. *Mathematical Problems in Engineering*.

[9] Langlois S. (2014) Prediction of Aeolian Vibration on Transmission-Line Conductors Using a Nonlinear Time History Model—Part I: Damper Model. *IEEE Power Delivery*. 29(3):1176–1183. ISSN 08858977. doi: 10.1109/TPWRD.2013.2291363.

[10] Bouc R., (1967) Forced Vibration of Mechanical Systems with Hysteresis. *Proceedings of the Fourth Conference on Nonlinear Oscillation* . Prague.

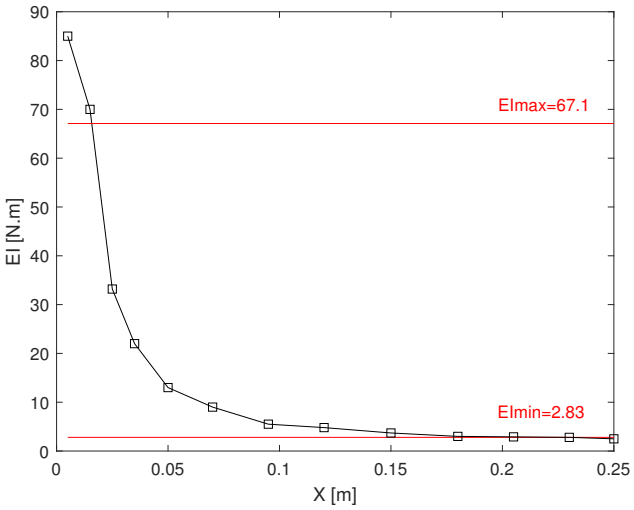

Figure 3: Identified local bending stiffness for the slack cable.

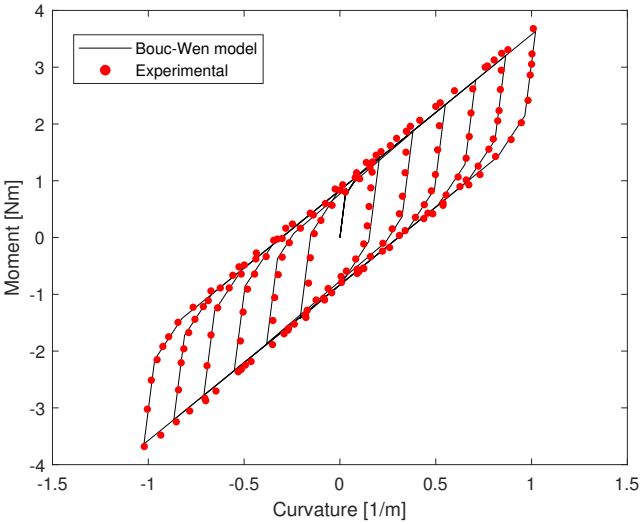

Figure 4: Moment-curvature hysteresis loops at 0.025m from the clamp for end displacement amplitudes (30mm to 5mm).

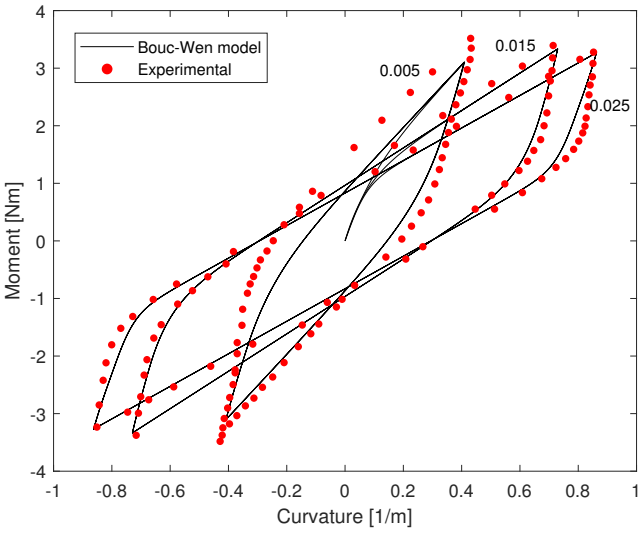

Figure 5: Moment-curvature hysteresis loops for end displacement amplitudes of 25mm at locations 0.005m, 0.015m and 0.025m from the clamp.

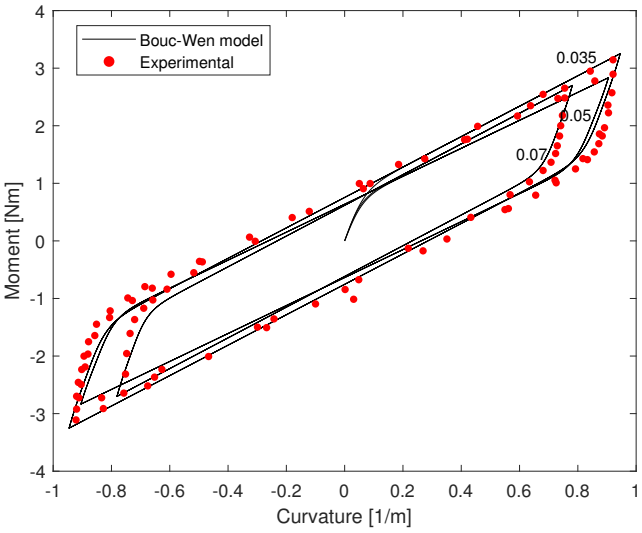

Figure 6: Moment-curvature hysteresis loops for end displacement amplitudes of 25mm at locations 0.035m, 0.05m and 0.07m from the clamp.

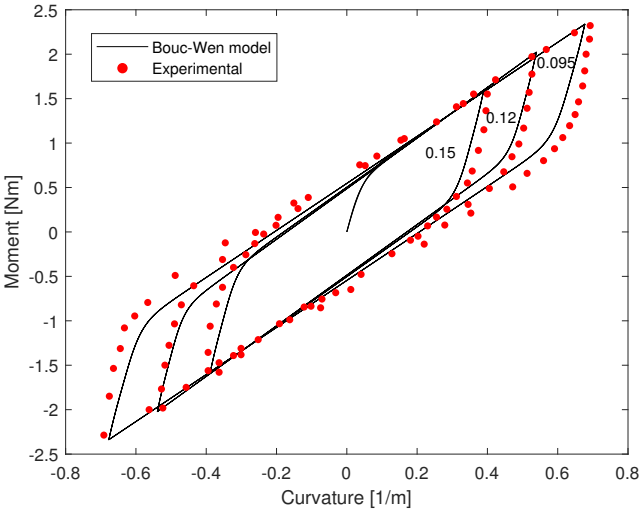

Figure 7: Moment-curvature hysteresis loops for end displacement amplitudes of 25mm at locations 0.095m, 0.15m and 0.15m from the clamp.

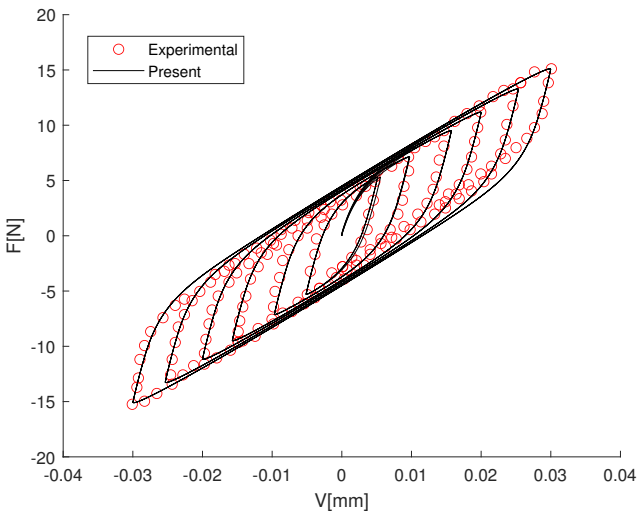

Figure 8: Validation of the force-displacement loops at the tip of the beam.

[11] Wen, Y.-K.(1980) Equivalent linearization for hysteretic system under random excitation, *Journal of Applied Mechanics*, 47:150-154.

[12] https://www.wikidata.org/wiki/Q1713773.

[13] Scanlan R. H. and Swart R. L. (1968) Bending stiffness and strain in stranded cables. Presented at the IEEE Winter Power Meeting, New York, Jan.

[14] Claren R. and Diana G.(1969) Dynamic strain distribution on loaded stranded cables. *IEEE Trans. Power App. Syst*. Vol. PAS-88, no. 11, pp. 1678–1690, Nov.

[15] Ture Savadkoohi A., Lamarque C. H., (2013) Dynamics of Coupled Dahl Type and Nonsmooth Systems at Different Scales of Time. *International journal of Bifurcation and Chaos*. vol. 23, no. 7, 1350114 (14 pages).

[16] Ikhouane F., Rodellar J., (2007) Systems with Hysteresis (John Wiley and Sons).

[17] Eleni Chatzi, K. Agathos, G. Abbiati (2017) Department of Civil, Environmental, and Geomatic Engineering (DBAUG) ETH Zürich. Lecture Notes: Method of Finite Elements II Modeling oHysteresis

Nonlinear Analysis of the Snaking Motion of Towed Vehicles

Hanna Zsofia Horvath* and Denes Takacs†
* *Department of Applied Mechanics, Budapest University of Technology and Economics, Budapest, Hungary*
† *MTA-BME Research Group on Dynamics of Machines and Vehicles, Budapest, Hungary*

Summary. A mechanical model is introduced in order to investigate the snaking/rocking motion of towed two-wheeled trailers. The sense of the Hopf bifurcations related to the linear stability boundaries of the rectilinear motion are investigated numerically. The center manifold reduction is also performed semi-analytically, by which the relevance of the pitch motion is identified.

Introduction

The instability of towed vehicles is a relevant safety risk on the roads. In case of a badly chosen towing velocity and/or a badly loaded trailer, the vehicle may start a so-called snaking motion [1, 2]. The trailer may even start rocking on its wheels, and the rollover of trailer can happen.
In-plane mechanical models of towed vehicles are deeply analyzed in the literature (see, for example, [3]) and it is established that the Hopf bifurcation is subcritical at the linear stability boundary located at small towing velocities. Here, the trailer is modeled with a spatial, 4 degrees-of-freedom (DoF) mechanical model given in [4], namely, the pitch and roll motions are also considered when the nonlinear vibrations (e.g. the rocking motion) are analyzed semi-analytically and numerically.

Mechanical Model

The mechanical model of the two-wheeled trailer can be seen in Fig. 1. The trailer is towed with constant velocity v in X direction at the king pin. The motion of the trailer is described with the yaw angle ψ, the pitch angle ϑ, the roll angle φ and the lateral displacement of the king pin u.

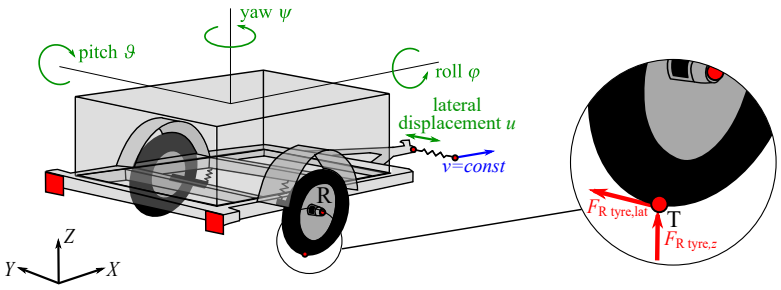

Figure 1: The mechanical model of the trailer with the generalized coordinates and the tyre forces.

Since there are only geometric constraints, the system is holonomic. Thus, the equations of motion can be derived from the Lagrange equation of the second kind (for details see [4]). The lateral tyre forces are considered as

$$F_{\mathrm{tyre,lat}} = \mu(\alpha) F_{\mathrm{tyre},z} \,, \tag{1}$$

where $F_{\mathrm{tyre},z}$ is the vertical load on the tyre and $\mu(\alpha)$ involves Pacejka's Magic Formula [6]. The side slip angle α is calculated by means of the longitudinal and lateral components of the velocity of the contact point T of the wheel:

$$\alpha = -\arctan\left(\frac{v_{\mathrm{T,lat}}}{v_{\mathrm{T,long}}}\right) . \tag{2}$$

Linear Stability Analysis and Bifurcation Analysis

Based on the linear stability analysis of the rectilinear motion, it can be concluded that the linearised system can be separated into two subsystems: the pitch motion can be decoupled as a 1 DoF subsystem, while remaining equations form a 3 DoF subsystem. Thus, the pitch motion does not affect the linear stability of the rectilinear motion. But, it has effect on the nonlinear vibrations.
Asymmetry is introduced into the system by the lateral tyre force characteristics formulated in (1). The vertical load $F_{\mathrm{tyre},z}$ on the tyres depends linearly on the pitch angle ϑ, as it can be seen in the left panel of Fig. 2. The coefficient $\mu(\alpha)$ is an even function (see the right panel of Fig. 2), thus, the lateral tyre force contains mixed second degree terms with respect to the generalized coordinates and velocities. When the bifurcation analysis is carried out with center manifold (CM) reduction, it can be identified that the pitch motion influences the sense of the Hopf bifurcation through these second degree terms.

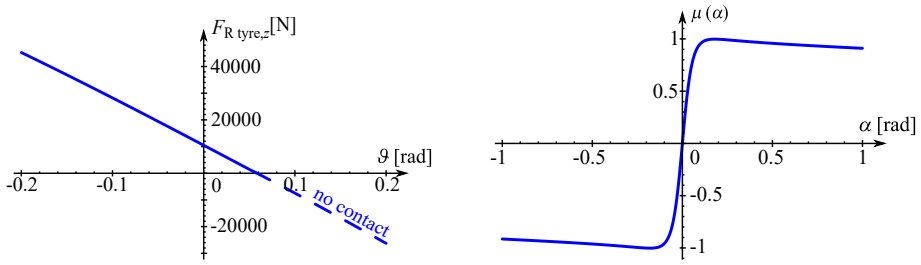

Figure 2: The characteristics of the vertical tyre forces and characteristics of the lateral force defined by the Magic Formula in $\mu(\alpha)$ [6].

The stability of the periodic orbits were also investigated by continuation in *DDE Biftool* [5]. It was confirmed that supercritical Hopf bifurcation exists at small velocities, while in-plane trailer models of the literature provides a subcritical one. To check our hypothesis on the effect of the pitch motion, a reduced model was also analyzed in which the pitch motion was blocked ($\vartheta \equiv 0$).

The nature of the periodic solutions, namely, the sense of the Hopf bifurcations can be seen in Fig. 3 for the spatial, 4 DoF model and for the reduced model. In the stability charts, the blue continuous and red dashed lines correspond to supercritical and subcritical bifurcations, respectively. In the figures, parameter f describes the vertical position of the center of mass. As it can be observed in the left panel, the periodic solution is stable at smaller critical speed in case of the 4 DoF model, thus, the bifurcation is supercritical. On the contrary, in the right panel, the periodic solution is unstable (subcritical Hopf bifurcation occurs) for the same critical speed when the reduced model is considered.

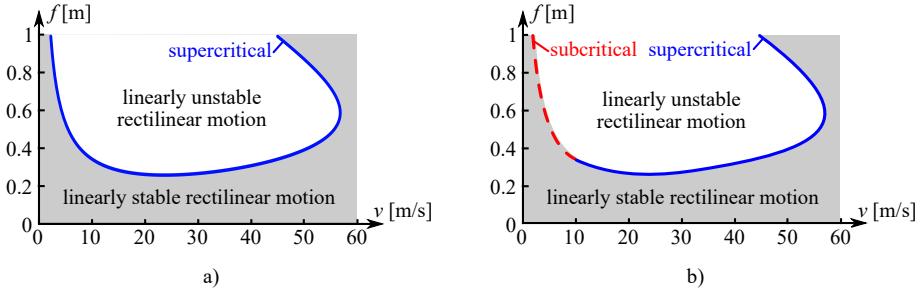

Figure 3: The stability of the periodic solutions a) for the spatial, b) for the reduced model.

Conclusions

Based on the semi-analytical bifurcation analysis, the effect of the pitch motion on the stability of the emerging periodic solutions is verified. It is shown that the in-plane trailer models of the literature can provide different results with respect to the sense of the Hopf bifurcation at small velocities.

Acknowledgements

This research was founded by the National Research, Development and Innovation Office under grant no. NKFI-128422. The publication of the work reported herein has been supported by ETDB at BME. The research reported in this paper was supported by the Higher Education Excellence Program of the Ministry of Human Capacities in the frame of Artificial intelligence research area of Budapest University of Technology and Economics (BME FIKP-MI).

References

[1] Troger, H., Zeman, K. (1984) A nonlinear-analysis of the generic types of loss of stability of the steady-state motion of a tractor-semitrailer. *Vehicle System Dynamics* **13**(4), pp. 161–172.

[2] Darling, J., Tilley, D., Gao, B. (2009) An experimental investigation of car-trailer high-speed stability. *Proceedings of the Institution of Mechanical Engineers, Part D: Journal of Automobile Engineering* **223** (4), pp. 471–484. http://dx.doi.org/10.1243/09544070jauto981

[3] Beregi, S., Takacs, D., Stepan, G. (2018) Bistability of straight-line motion of towed vehicles. *IUTAm Symposium 'Exploiting Nonlinear Dynamics for Engineering Systems': Book of Abstracts*. Novi Sad, Serbia: International Union for Theoretical and Applied Mechanics (IUTAM), pp. 45–46.

[4] Horvath, H.Zs., Takacs, D. (2019) Analogue Models of Rocking Suitcases and Snaking Trailers. *Proceedings of the International Nonlinear Dynamics Conference (NODYCON 2019), Volume I, Nonlinear Dynamics of Structures, Systems and Devices*. https://doi.org/10.1007/978-3-030-34713-0_12

[5] Sieber, J., Engelborghs, K., Luzyanina, T., Samaey, G., Roose, D. (2016) DDE-BIFTOOL v.3.1.1 Manual - Bifurcation analysis of delay differential equations. http://arxiv.org/abs/1406.7144.

[6] Pacejka, H.B. (2002) Tyre and Vehicle Dynamics, Elsevier Butterworth-Heinemann, Oxford.

[7] Carr, J. (1981) Application of Center Manifold, Spriner-Verlag, New York.

Speed effects on vibration and collapse of slender structures under moving loads

G.H.M. van der Heijden*, X.W. Zhao*
*Department of Civil, Environmental and Geomatic Engineering
University College London, Gower Street, London WC1E 6BT, UK

Summary. We study the nonlinear dynamics of one-dimensional slender structures such as beams and arches carrying a moving load. At resonant speeds the vibrations of curved beams are significantly suppressed, but large deformations are found to have a detuning effect. Arches are found to have different buckling (failure) modes depending on the depth of the arch and the speed of the traversing load.

Modelling

We study the nonlinear dynamics of one-dimensional slender structures such as beams and arches carrying a moving load. Geometrically-exact rod theory is used to model the structure, which is allowed to undergo arbitrary three-dimensional flexural and twisting deformations.

Results and conclusions

The exact natural frequencies ω_n (for symmetric or anti-symmetric modes) of a hinged curved horizontal beam with subtended angle α are given by

$$\omega_n = \mu_n \sqrt{\frac{EI}{\rho A L^4}}, \qquad \text{where} \qquad \mu_n = \frac{n\pi \left|(n\pi)^2 - \alpha^2\right|}{\sqrt{(n\pi)^2 + (1+\nu)\alpha^2}} \qquad (n = 1, 2, ...)$$

(ignoring rotational inertia). Here EI is the bending stiffness, A the cross-sectional area, ρ the density, ν Poisson's ratio and L the length of the beam. The critical resonance speed is defined as the speed at which the maximum midspan deflection occurs when the load leaves the beam. It is given by

$$v_{\text{crit}} = \frac{\omega_1 L}{\pi}$$

(i.e., the fundamental period is twice the passage time).

We find that nonlinearity due to large deformations has a detuning effect on resonances, as can be seen in midspan deflection plots for different values of α (see Figure 1).

At resonant speeds v we find cancellation of vibrations even at large deformations (see Figure 2).

Arches are found to have different buckling (failure) modes depending on the depth of the arch and the speed of the traversing load.

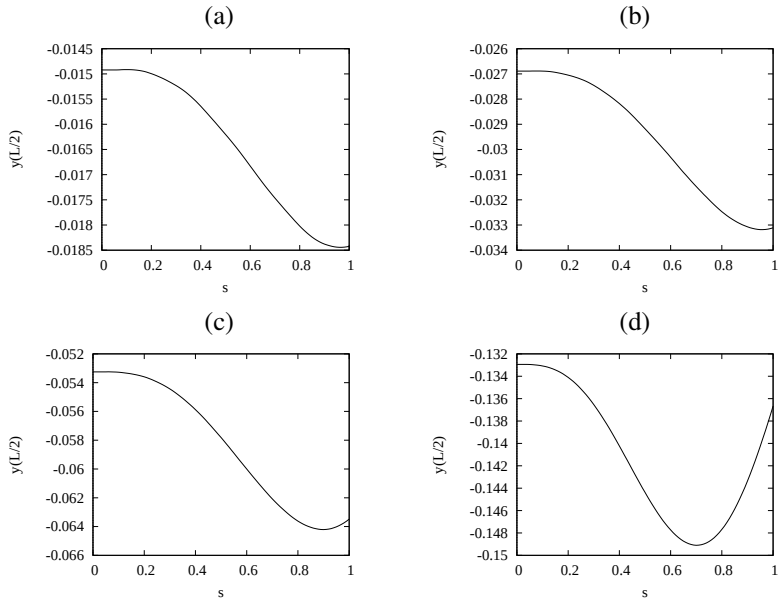

Figure 1: Detuning effect due to large deformations: (a) $\alpha = 50^\circ$, (b) $\alpha = 90^\circ$, (c) $\alpha = 120^\circ$, (d) $\alpha = 150^\circ$. The magnitude of the moving load is $F = 0.1$ (in units of EI/L^2). s is the instantaneous position of the load, normalised by L.

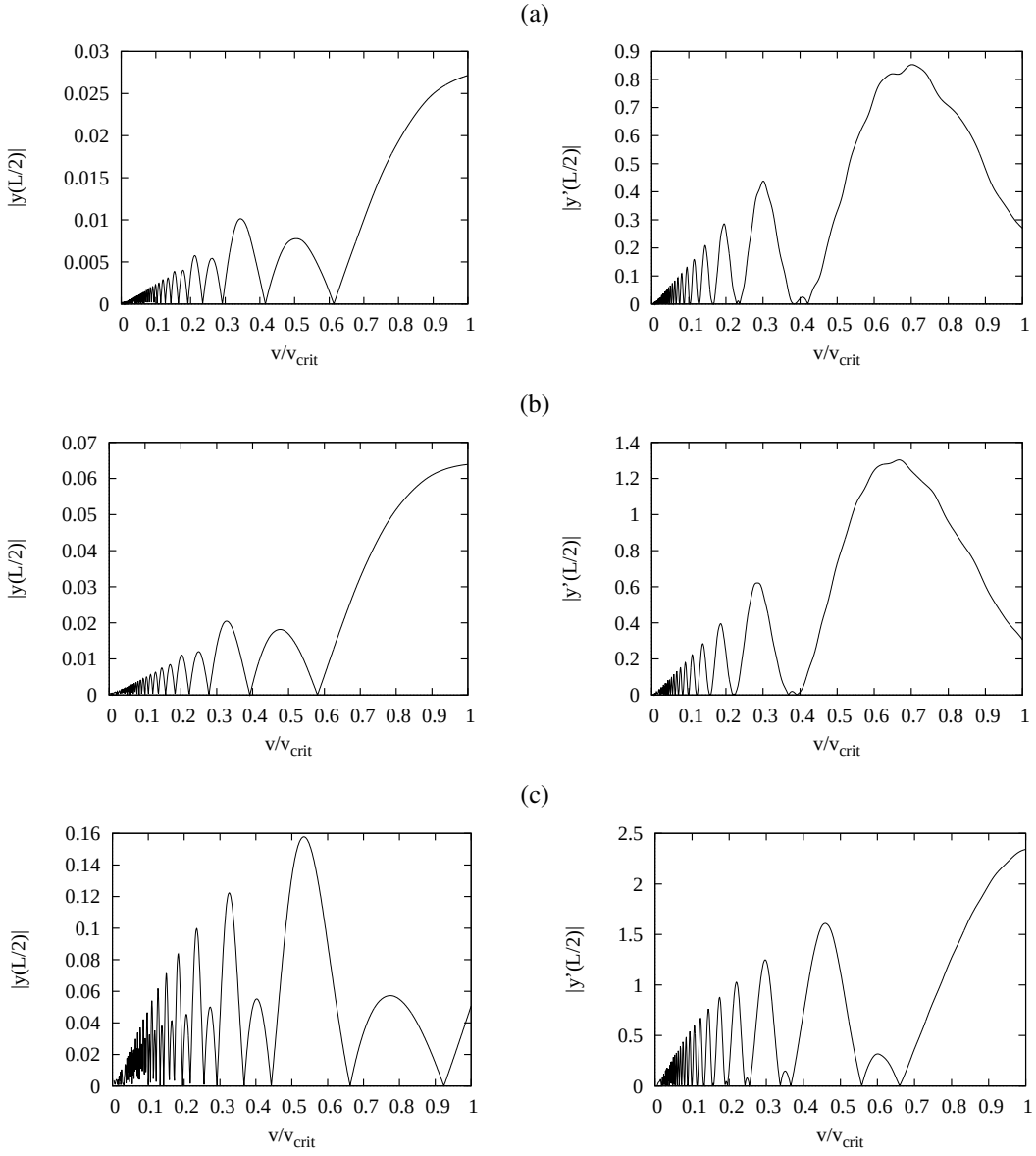

Figure 2: Cancellation of vertical midspan deflection (left) and velocity (right) of a horizontal curved beam with moving load $F = 1.0$ (in units of EI/L^2) at critical speeds v/v_{crit}. (a) $\alpha = 30^\circ$, (b) $\alpha = 90^\circ$, (c) $\alpha = 150^\circ$.

Nonlinear Dynamics of a Shearable-Extensible Beam with an Elastic Longitudinal Support: Analytical Derivation, Numerical Simulation and Experimental Validation

Lukasz Kloda*†, Stefano Lenci† and Jerzy Warminski*
*Department of Applied Mechanics, Lublin University of Technology, Lublin, Poland
†Department of Civil and Buildings Engineering and Architecture, Polytechnic University of Marche, Ancona, Italy

Summary. Coupled axial-transversal nonlinear oscillations of a simply supported beam with an axial spring are studied in the paper. The exact model of a planar beam with associated boundary conditions is derived, and then to analyze free and forced-damped dynamics of the structure the perturbation method up to cubic nonlinearity is used. Next, a finite element model of the beam-spring system is considered and then outcomes are compared. Experimental tests on a slender beam confirmed quantitatively analytical and numerical models.

Introduction

In the *classical beam theory* for vibrations only transverse inertia forces and bending moment are considered [1], and the shearing effect together with longitudinal deformations are neglected. Those assumptions are relatively correct for slender structures with axially restrained ends. Large amplitudes of a thick beam require the Timoshenko's shearing theory, and for the beam unrestrained in axial direction longitudinal inertia terms can not be neglected [2]. The inertia changes the dynamics of the structure, and as a consequence the simply supported beam has no longer a hardening nature but a softening behaviour. An axial spring subjected to the unrestrained end allows to passively control hardening/softening dichotomy [3, 4]. The goal of this paper is to investigate nonlinear dynamics of the beam-spring system and its sensitivity on boundary conditions by considering nonlinear coupling between transversal and longitudinal modes. For model validation a laboratory test is prepared.

Beam models

Analytic

In the paper two beam models are used, both of them assume linear elastic material properties as Young (E) and shear (G) modules (Eqs. (1)). It means that nonlinearities arise only from geometrical and inertia coupling. In the reference (rest) configuration the beam has length L and rectangular cross-section A. Normal, shearing and bending forces are proportional to elongation $\hat{e}$, shear strain γ and curvature k_g, respectively:

$$N = EA\hat{e}, \quad V = GA\gamma, \quad M = EJk_g. \tag{1}$$

Note that the beam is *extensible* . W is the longitudinal displacement, and U is the transversal one. The *geometrical* definition of curvature [5] is adopted in our study, see Eq. (2). θ describes the rotation of the beam's cross-section (Fig. 1a) which contains the slope angle φ and γ. The deformations are given by

$$\hat{e} = S' - 1, \quad S' = \sqrt{(1+W')^2 + U'^2}, \quad k_g = \frac{\theta'}{S'} = \frac{\theta'}{\sqrt{(1+W')^2 + U'^2}}, \quad \theta = \varphi + \gamma. \tag{2}$$

Decomposing strain forces into horizontal, vertical and rotational coordinates and supplementing them by inertia ($\rho A\ddot{W}$, $\rho A\ddot{U}$ and $\rho J\ddot{\theta}$), damping ($C_W\dot{W}$, $C_U\dot{U}$, $C_\theta\dot{\theta}$) and external forces (P_W, P_U, P_θ) the following balance equations are obtained

$$(N\cos\varphi + V\sin\varphi)' = \rho A\ddot{W} + C_W\dot{W} + P_W(Z,T), \tag{3}$$
$$(N\sin\varphi - V\cos\varphi)' = \rho A\ddot{U} + C_U\dot{U} + P_U(Z,T), \tag{4}$$
$$M' - VS' = \rho J\ddot{\theta} + C_\theta\dot{\theta} + P_\theta(Z,T), \tag{5}$$

where dots $\dot{()}$ are time derivative and primes $()'$ depict partial derivative with respect to the coordinate Z. The stiffness of the axial end spring k_s is responsible for change of boundary conditions only in the longitudinal direction:

$$U(0,T) = 0, \quad U(L,T) = 0, \quad M(0,T) = 0, \quad M(L,T) = 0, \quad W(0,T) = 0, \tag{6}$$
$$N(L,T)\cos\varphi + V(L,T)\sin\varphi + W(L,T)k_s = 0. \tag{7}$$

To solve the set of three equations (3)-(5) and associated boundary conditions (6)-(7) the multiple time scales method (*MTSM*) is applied, and after cumbersome computations, the frequency response curves are drawn for different $0 < k_s < \infty$ parameter [6].

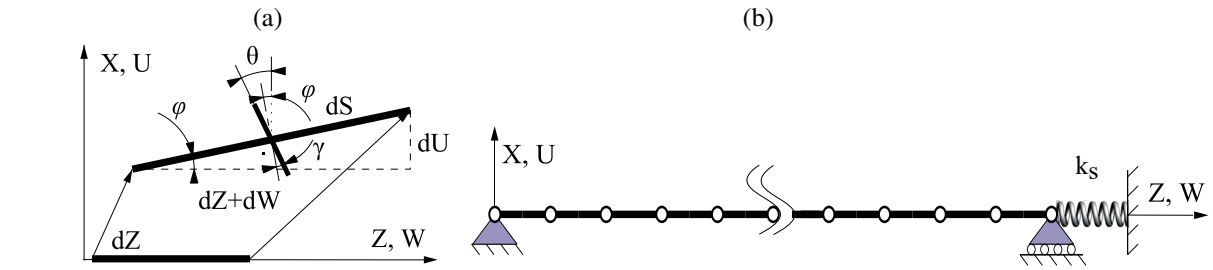

Figure 1: Kinematics of the beam segment in analytical approach (a) and finite element model of the hinged-simply supported beam (b).

Finite element

Numerical computations are made with the commercial software Abacus_CAE. Dynamical analysis is performed in two modules: *linear perturbation-frequency* and transient in time *dynamic explicit*. The finite element model (*FEM*) presented in Fig. 1(b) is composed of 100 segments *B21*-type plus one linear spring connector k_s. Boundary conditions are consistent with (6)-(7). Four different computational methods are applied: (i) linear modal analysis, (ii) free nonlinear dynamics, (iii) following-path and (iv) shooting method. All four methods complement each other and allow a deep study of any dynamical system for selected parameters to discover unexpected phenomena. However the computations in time domain are very time consuming.

Results and conclusions

Comparison of backbone curves obtained by *FEM* and *MTSM* is presented in Fig. 2(a). After passing the transient vibrations the simulation for steady states are in excellent agreement. For Timoshenko beam with partial tip reinforcement, the structure has hardening behaviour. Due to technical limitations experimental tests have been simplified to a kinematically excited slender beam presented in Fig. 2(c) and, then overlapped with numerical counterpart. The axially unrestrained case represents softening phenomenon and again results shown in Fig. 2(b) are in very good agreement. We conclude that analytical and numerical results are confirmed by experiments with excellent compliance.

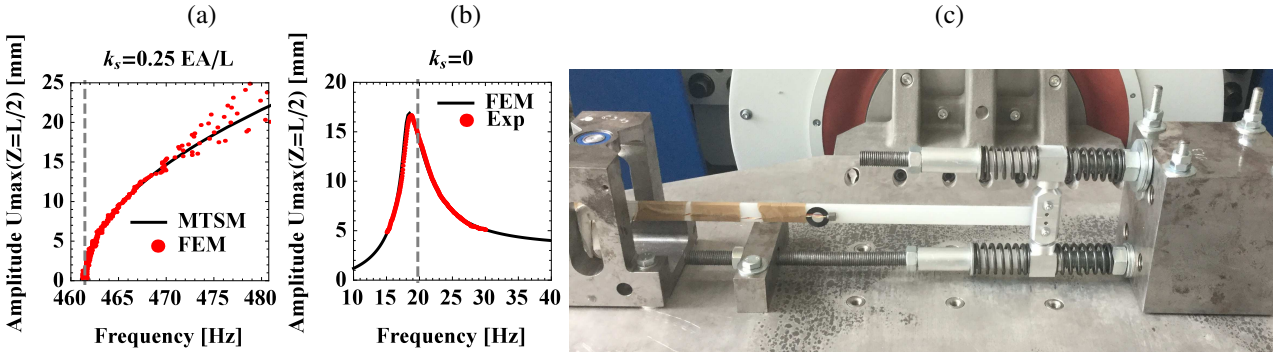

Figure 2: Free nonlinear oscillations (a), forced damped oscillations (b) and experimental setup - side view (c).

Acknowledgments

The work is financially supported by grant 2019/33/N/ST8/02661 from the National Science Centre, Poland.
This work is part of the collaboration between Polytechnic University of Marche and Lublin University of Technology, which is aimed at developing a Joined Doctoral Programme.

References

[1] Timoshenko S. (1991) History of strength of materials. Dover Publications, NY.

[2] Atluri S. (1973) Nonlinear Vibrations of a Hinged Beam Including Nonlinear Inertia Effects. *J. Appl. Mech.* **40**:121-126

[3] Lacarbonara W., Hiroshi Y. (2006) Refined models of elastic beams undergoing large in-plane motions: Theory and experiment. *Int. J. Solid Struct.* **17**:5066-5084.

[4] Shibata A., Ohishi S., Yabuno H. (2015) Passive method for controlling the nonlinear characteristics in a parametrically excited hinged-hinged beam by the addition of a linear spring. *J. Sound Vib.* **350**:111-122.

[5] Babilio E., Lenci S. (2017) On the notion of curvature and its mechanical meaning in a geometrically exact plane beam theory. *Int. J. Mechanical Science.* **128-129**:277-293.

[6] Kloda L., Lenci S., Warminski J. (2018) Nonlinear dynamics of a planar beam-spring system: analytical and numerical approaches. *Nonlinear Dyn.* **94**:1721-1738.

Optimal design of impact based non-linear energy dissipation mechanism in pipeline systems

Fabrizio Aloschi[*,**], Roberto Andreotti[*], Oreste S Bursi[*] and Rosario Ceravolo[***]
[*]*Department of Civil, Environmental and Mechanical Engineering, University of Trento, Trento, Italy*
[**]*IGF - Ingenieurgesellschaft Dr.-Ing. Fischbach mbH, Erftstadt, Germany*
[***]*Department of Structural and Geotechnical Engineering, Polytechnic of Turin, Turin, Italy*

Summary. Numerous techniques exist to control vibrations and dissipate energy in pipes that are supported by rack structures. Impacts are often used as a means of dissipating energy. In this research, we optimize two design parameters, gap and coefficient of restitution (COR), of a pipeline supported in a rack that is allowed to hit bumpers. For a given loading characteristic, indeed, the energy dissipation from such a non-linear system is dependent on the gap and the COR. The ratio of the total energy dissipated through impacts to the energy dissipated by material and structural damping of the pipe-rack is used as a measure of the energy dissipation efficiency. However, excessive number of impacts of the pipe against the bumper can damage or produce dents in the pipeline. The objective functions are therefore conflicting because it is to be ensured that the optimized system provides the least number of impacts while dissipating the maximum amount of energy. A kriging metamodel is used to interpolate the experimental points that are calculated for the values of gap and COR that are chosen after application of the central composite design (CCD). Finally, the Pareto front of the two response surfaces is calculated.

Introduction and problem statement

There are various mechanisms to dissipate energy and control the response of pipeline systems. The use of tuned mass damper is probably the most commonly adopted approach. In this work, impact is used as an energy dissipation mechanism. As an example, this kind of systems were previously used in the Trans-Alaskan pipeline systems which passes through major seismic faults [1]. During impact, a part of the input energy is dissipated in the form of heat, sound, plastic deformation of the material, etc. The COR is a measure of this dissipation.

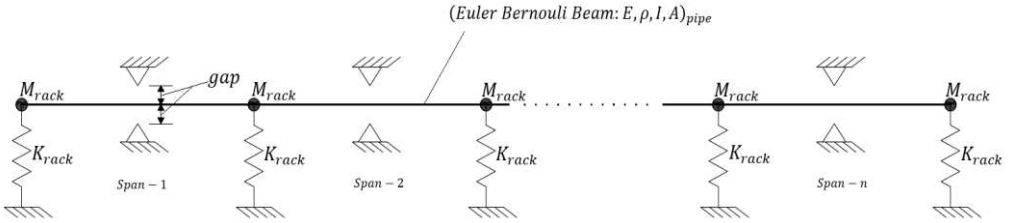

Figure 1: Analytical model of a pipe in a rack

In this study, a typical pipe-rack structure is analyzed and analytically modeled as shown in Figure 1. The pipe is allowed to hit bumpers placed at the center of each span. The energy dissipation in this case is dependent on two design variables, gap and COR.
Let $x \in \mathbb{R}^{n\,x\,1}$ and $\dot{x} \in \mathbb{R}^{n\,x\,1}$ be the displacement and velocity respectively of the pipe-rack system where n is the total number of degrees of freedom. For a given seismic excitation of duration t_d, a given gap and COR, the net energy dissipated by virtue of the internal structural damping (non-conservative) at time t_d is given by,

$$E_{damping}(t_d) = \sum_{t=0}^{t=t_d} dx_t{}^T . C . \dot{x}_{t_d}$$

where $C \in \mathbb{R}^{n\,x\,n}$ is the damping matrix of the system and $dx_t = x_t - x_{t-dt}$. The energy dissipated through impacts during this duration is given by,

$$E_{impact}(t_d) = \frac{1}{2}\sum_{i=1}^{N_d}\left(\dot{x}_{+_i}{}^T M \dot{x}_{+_i} - \dot{x}_{-_i}{}^T M \dot{x}_{-_i}\right)$$

where $\dot{x}_{+_i}$ and $\dot{x}_{-_i}$ is the velocity after and before the ith impact, which are related by the COR. M is the mass matrix of the system and N_d is the number of impacts in time t_d. At time t_d, two objective functions are defined for the design of the energy dissipation mechanism, as follows:

i. Ratio of total energy dissipated through impact to the energy dissipated by the internal damping of the structure, given as,

$$O_1 = \frac{E_{impact}}{E_{damping}}$$

ii. The number of impacts required for dissipating unit amount of energy,

$$O_2 = \frac{N_d}{E_{impact}}$$

In this study it is aimed to dissipate the maximum energy through impacts. However, when the number of impacts increases, there are more chances for the pipeline to suffer damage or dents. Hence, it is also aimed to achieve a desired energy dissipation with a minimum number of impacts. Thus, for a given seismic input, the function O_1 is maximized, or equivalently, $-O_1$ is minimized, whereas O_2 is minimized.

Methodology and preliminary results

Non-linear time history analyses are used to evaluate the objective functions O_1 and O_2 for a given input motion characteristic, and for given values of gap and COR. A CCD[2] provides the number of experiments that have to be carried out and also the corresponding values of gap and COR. The response surfaces, as shown in Figure 2, are subsequently evaluated by a surrogate kriging model that spatially interpolates the experimental outputs.

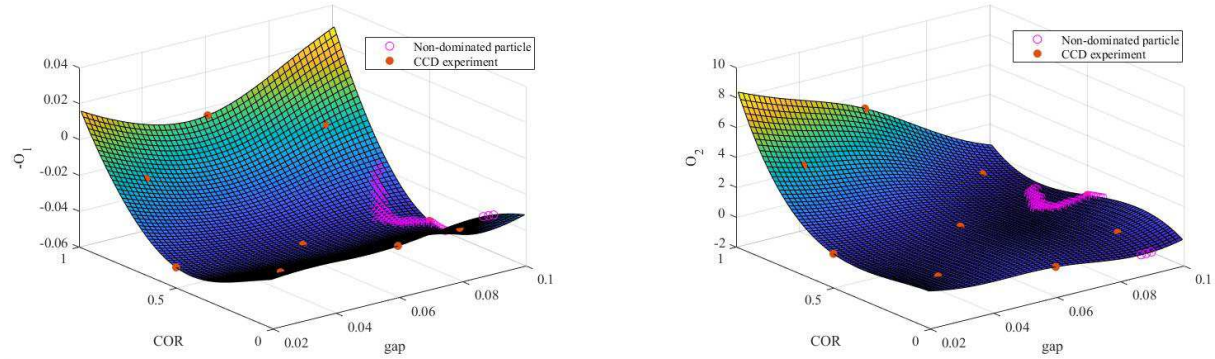

Figure 3: Response surfaces for (a) Objective function 1 and (b) Objective function 2

We finally find the Pareto front. The non-dominated particles, as shown in Figure 3, correspond to the solutions of this multi-objective optimization problem, for certain optimal values of gap and COR.

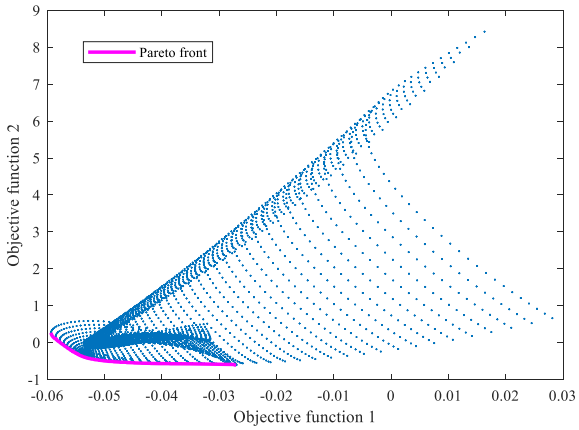

Figure 4: Representation of the Pareto frontier

References

[1] Douglas G. Honegger, Douglas J. Nyman, Elden R. Johnson, Lloyd S. Cluff, and Steve P. Sorensen. (2004) Trans-Alaska Pipeline System Performance in the 2002 Denali Fault, Alaska, Earthquake. Earthquake Spectra, 20(3), 707–738.

[2] Raymond H. Myers, Douglas C. Montgomery and Christine M. Anderson-Cook. Response Surface Methodology: Process and Product Optimization Using Designed Experiments, 4th Edition, ISBN: 978-1-118-91601-8, Wiley.

Nonlinear vibrations of nanoplates based double mode model and the nonlocal elasticity theory

Jan Awrejcewicz*, Olga Mazur**
* *Department of Automation, Biomechanics and Mechatronics, Lodz University of Technology, Lodz, Poland*
** *Department of Applied Mathematics National Technical University KhPI, Kharkiv, Ukraine*

Summary. Geometrically nonlinear vibrations of the rectangular simply supported nanoplates are investigated. The governing equations are employed in mixed form and used the nonlocal elasticity theory as well as Kirchhoff's hypotheses and the von Kármán theory. Application of the Bubnov-Galerkin method with a double mode model allows to reduce the governing system of partial differential equations (PDEs) to the system of the second-order ordinary differential equations (ODEs) . Analysing obtained ODEs the small-scale effects and force influence are studied.

Particular interest in the study of nanostructures is associated with their wide application in high-tech industry due to excellent mechanical, thermal, electrical properties. Theoretical and experimental research has allowed to observe the small-scale effects that were not detected within the classical theory. This fact led to the development of non-classical continuum theories for study the objects with sizes in nanoscale. The presented work is aimed at the study of geometrically nonlinear vibrations of the small-scale plates. The formulation of the problem is performed based on Kirchhoff's hypotheses, the von Kármán theory. In order to take into account the appearance of the small-scale effects in nanoplates the nonlocal theory of elasticity [1] is applied. It is based on the fact that the stress at a given point is a function of strains at all other points in the body. According to this theory the constitutive relation in differential form [2] has the following form

$$\left(1-\mu\nabla^2\right)\sigma=\sigma', \tag{1}$$

where σ', σ are local and nonlocal stress tensors, μ is nonlocal parameter, and ∇^2 is the Laplacian operator.
The nonlocal governing equations are taken in mixed form, introducing the Airy stress function F:

$$D\Delta^2 w=\left(1-\mu\nabla^2\right)\left(-N_1\frac{\partial^2 w}{\partial x^2}-N_2\frac{\partial^2 w}{\partial y^2}+L\left(w,F\right)-\rho h\frac{\partial^{2,} w}{\partial t^2}-\delta_0\frac{\partial w}{\partial t}+q\right), \tag{2}$$

$$(1-\mu\nabla^2)\frac{1}{E}\Delta^2 F=-\frac{h}{2}L\left(w,w\right), \tag{3}$$

where differential operators are defined as

$$L\left(w,F\right)=\frac{\partial^2 w}{\partial x^2}\frac{\partial^2 F}{\partial y^2}+\frac{\partial^2 F}{\partial x^2}\frac{\partial^2 w}{\partial y^2}-2\frac{\partial^2 w}{\partial x\partial y}\frac{\partial^2 F}{\partial x\partial y}, L\left(w,w\right)=2\left(\frac{\partial^2 w}{\partial x^2}\frac{\partial^2 w}{\partial y^2}-\left(\frac{\partial^2 w}{\partial x\partial y}\right)^2\right), \tag{4}$$

and $\Delta^2=(\frac{\partial^2}{\partial x^2}+\frac{\partial^2}{\partial y^2})^2$, $D=\frac{Eh^3}{12(1-\nu^2)}$ is flexural nanoplate rigidity, E is Young's modulus, ν is Poisson's ratio, w is deflection of the plate, N_1, N_2 are in-plane uniform forces, q is transverse force, ρ is density, h stands for thickness of the plate, whereas δ_0 is damping coefficient. It is assumed that the plate satisfies the simply supposed boundary conditions.
The proposed approach is based on two mode presentation of the deflection $w\left(x,y,t\right)$ of rectangular small-scale plate with sides a and b as follows [3]:

$$w\left(x,y,t\right)=w_1(t)\sin\frac{\pi x}{a}\sin\frac{\pi y}{b}+w_2(t)\sin\frac{2\pi x}{a}\sin\frac{2\pi y}{b}, \tag{5}$$

where w_1, w_2 are bi-modal amplitudes, $\sin\frac{\pi x}{a}\sin\frac{\pi y}{b}$ and $\sin\frac{2\pi x}{a}\sin\frac{2\pi y}{b}$ are shape functions, that satisfy the chosen boundary conditions. Substitution (5) into the equation (3) allows to obtain the stress function presentation:

$$F=f_1\cos\frac{2\pi x}{a}+f_2\cos\frac{2\pi y}{b}+f_3\cos\frac{4\pi x}{a}+f_4\cos\frac{4\pi y}{b}+f_5\cos\frac{3\pi x}{a}\cos\frac{\pi y}{b}+f_6\cos\frac{\pi x}{a}\cos\frac{3\pi y}{b}+p_1x^2+p_2y^2, \tag{6}$$

where coefficients depend on the small-scale parameter μ. Applying the Bubnov-Galerkin method, one can get the nonlocal system of ordinary differential equations. Size-dependent analysis of such system allows to study nonlinear vibrations regimes of the considered system. The numerical calculations are performed for graphene nanoplate with various excitation parameters.

References

[1] Eringen A.C. (1972) Linear theory of nonlocal elasticity and dispersion of plane waves. *International Journal of Engineering Science* **10**:425–435.

[2] Eringen A.C. (1983) On differential equations of nonlocal elasticity and solutions of screw dislocation and surface waves. *Journal of Applied Physics* **9**:4703–4710.

[3] Lai H. Y., Chen C. K., Yeh Y. L. (2002) Double-mode modeling of chaotic and bifurcation dynamics for a simply supported rectangular plate in large deflection. *International Journal of Non-Linear Mechanics* **37**:331–343.

Thursday, July 21, 2022
08:30 - 10:30

MS-12 Micro- and Nano-Electro-Mechanical Systems
Rhone 3A

Chair: S. Krylov

08:30 - 08:50
Engineering the Dynamic Range of Si3N4 Nonlinear String Resonators
LI Zichao*, XU Minxing, NORTE Richard, ARAGÓN Alejandro, VAN Keulen Fred, STEENEKEN Peter, ALIJANI Farbod
*Precision and microsystems engineering (Delft, The Netherlands) (Mekelweg 2, 2628 CD, Delft Netherlands)

08:50 - 09:10
Exploiting nonlinearities of mechanically-coupled microbeams for mass sensing: theoretical and experimental investigation
RABENIMANANA Toky, NAJAR Fehmi, WALTER Vincent, **KACEM Najib***, GHOMMEM Mehdi
*Univ. Bourgogne Franche-Comté, FEMTO-ST Institute (France France)

09:10 - 09:30
Frequency Stabilization of MEMS Oscillators Using Internal Resonance
SHOSHANI Oriel*, STRACHAN Scott, LOPEZ Daniel, CZAPLEWSKI David, SHAW Steven
*Ben Gurion University (Beer Sheva Israel)

09:30 - 09:50
Hopf Bifurcation in MEMS - (When) Do Such Exist?
GUTSCHMIDT Stefanie*, LENCI Stefano
*University of Canterbury, Mechanical Engineering Department (Christchurch 8140 New Zealand)

09:50 - 10:10
Internal Resonances in Magnetic Resonance Force Microscopy
GOTTLIEB Oded*, HACKER Evyatar
*Technion - Israel Institute of Technology [Haifa] (Technion City, Haifa 3200003 Israel)

10:10 - 10:30
Leveraging Rotating Frame Dynamics for Low-Power Chaos Generation in Nonlinear M/NEMS Resonators
HOURI Samer*, MINATI Ludovico, ASANO Motoki, YAMAGUCHI Hiroshi
*NTT – Basic Research Laboratories (NTT – Basic Research Laboratories 3-1, Morinosato Wakamiya Atsugi-shi, Kanagawa, Japan Japan)

Engineering the Dynamic Range of Si_3N_4 Nonlinear String Resonators

Zichao Li*, Minxing Xu*, †, Richard Norte*, †, Alejandro Aragón*,
Fred van Keulen*, Peter G. Steeneken*, † and Farbod Alijani*
*Department of Precision and Microsystems Engineering,
Delft University of Technology, Mekelweg 2, 2628 CD Delft, The Netherlands
†Kavli Institute of Nanoscience, Delft University of Technology,
Lorentzweg 1, 2628 CJ Delft, The Netherlands

Summary. Nanomechanical resonators are prone to nonlinear dynamic behavior at forces that are only a few nN. In this work, we introduce a novel design that allows us to engineer the dynamic range of a Si_3N_4 nonlinear string resonator using a pair of compliant supports. The design comprises a suspended string and two support beams that act as the compliant supports and form an H-shaped structure. By changing the support beams' width and length, we are able to tune the state of stress in the string and thus control its quality factor Q and Duffing constant γ. Our novel design allows engineering novel high-Q nonlinear resonators with large dynamic range.

Introduction

Although the Duffing nonlinearity has been frequently observed in nanomechanical systems, the engineering of it by geometric design has received little attention [1]. For studying and utilizing the nonlinear response of nano resonators, it is essential to precisely predict or tune their dynamic range in a simple and robust design. In this work, we decouple the stress-length dependence of high-stress Si_3N_4 nano strings [2] by introducing a pair of support beams. Our H-shaped structure offers new knobs for engineering nonlinearity in string resonators while maintaining dynamic similarity with doubly clamped strings. By changing the widths of support beams, we engineer the pre-stress of the string and thus control its Q factor and Duffing constant γ in a large frequency range.

Experimental procedure

Our samples are fabricated from 340nm thick high-stress Si_3N_4 with initial stress around 1.1GPa, which is deposited by low pressure chemical vapor deposition (LPCVD) on a silicon substrate. The scanning electron microscope (SEM) image of our H-shape structure is shown in Figure 1(a) and our measurement set-up is shown in Figure 1(b). A piezo actuator is used to drive the samples into resonance while a Polytec Laser Doppler Vibrometer is used to measure their out-of-plane deflection, as shown in Figure 1(c). The measurement is performed at room temperature and to minimize the air damping, the air pressure is pumped below 2×10^{-6} mbar.

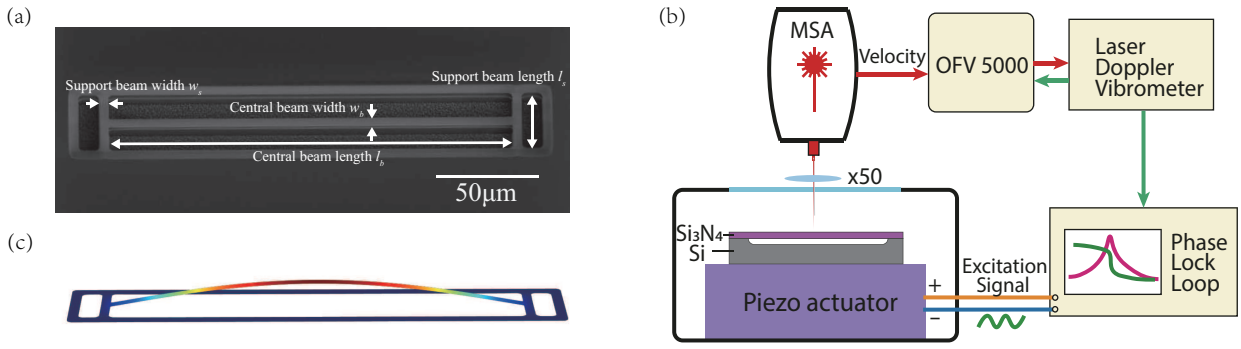

Figure 1: Experimental characterization of the H-shaped resonators. (a) Scanning electron microscope images of an H-beam with l_b=200μm, w_b=4μm, l_s=31μm, w_s=4.5μm. (b) Schematics of measurement set-up. (c) Fundamental mode shape of the H-beam in (a).

Modelling and the governing equation

Motion-induced tension modulation is the dominant source of nonlinearity in nanomechanical systems that gives rise to a cubic spring constant (Duffing term in the equation of motion) as follows [3]:

$$\ddot{x} + Q^{-1}\omega_0\dot{x} + \omega_0^2\left(x + \gamma x^3\right) = f\cos\omega t \tag{1}$$

Here, x is the generalized coordinate associated with the fundamental mode which is shown in Figure 1(c), Q is the mechanical quality factor, ω_0 is the fundamental eigenfrequency, γ is the Duffing coefficient, f is the force per unit mass acting on the nanoresonator of modal mass m and ω is the excitation frequency.
The critical vibration amplitude of the resonator associated with the onset of nonlinearity can be obtained as follows:

$$a_c = \left(\frac{64}{27}\right)^{0.25} \frac{1}{\sqrt{Q\gamma}} \tag{2}$$

We note that Q and γ in nanoresonators are functions of the pre-stress σ. Therefore, by controlling geometrical parameters of the support beams in our design, we can engineer the pre-stress σ in the central string resonator, tune Q and γ, and thus a_c of the resonator.

Control of quality factor Q and Duffing coefficient γ

Quality factor Q

For each resonator, we perform frequency sweeps in linear regime and record the resonant frequency of the fundamental out-of-plane mode by Lorentzian fits, as shown in Figure 2(a). After obtaining the fundamental resonant frequency, we perform ring-down measurements and obtain Q factors, also shown in Figure 2(a). In Figure 2(b), the simulated Q factors and the measurements on the H-beams with the same configuration are plotted against pre-stress σ in the string, which is tuned by the widths of the support beams.

Duffing coefficient γ

In this work, we extract γ by driving the string resonator in the nonlinear regime and sweeping the frequency in the spectral neighborhood of the fundamental resonance as shown in Figure 2c. By performing the experiments for multiple drive levels we find the "backbone" curve of the resonator and extract the Duffing constant γ using the following simple formula:

$$\omega^2_{backbone} = \omega_0^2 \left(1 + 0.75\gamma x^2_{max}\right) \tag{3}$$

For the design with l_b=200µm and w_b=4µm, we are able to tune Q factor down by 49% and tune γ down by 75% by varying w_s from 6µm to 1µm. With this combined effort, we can tune the critical vibration amplitude a_c of the resonator up to nearly 300% compared to simple doubly clamped string resonators. This shows the potential of the new design in enhancing the dynamic range of high-Q resonators, which is essential for sensing applications.

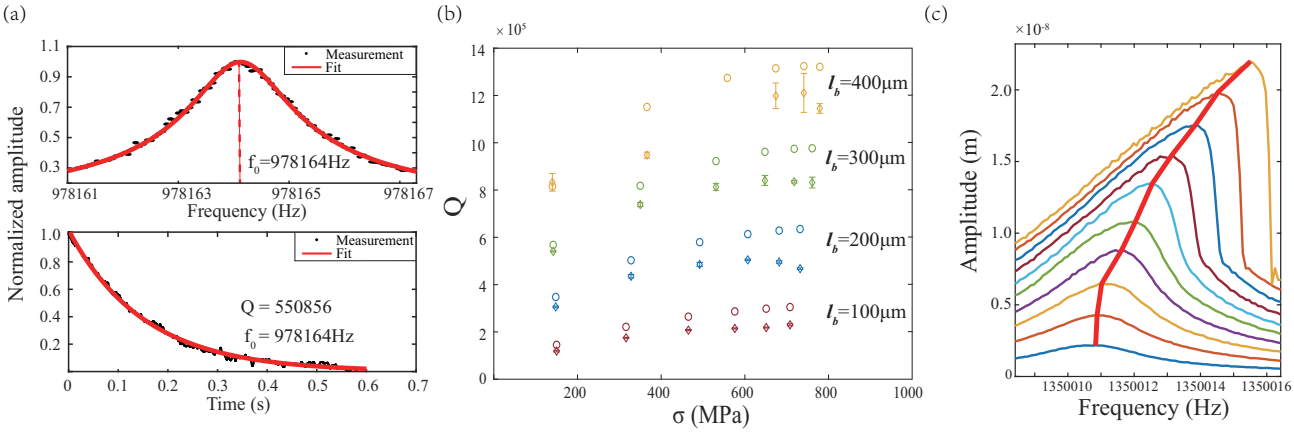

Figure 2: (a) The Lorentzian response of the H-beam showed in the Figure 1(a) excited in its fundamental mode under 1.25×10^{-5}mbar air pressure and the ring-down measurement of it. The y axis is the normalized to the maximum amplitude. (b) Variation of Q factor according to σ for H-beams with w_b=2µm and different l_b. Hollow circles and hollow diamonds with error bars are simulations and experimental results of Q factor respectively. (c) The Duffing effect of a doubly clamped beam with l_b=200µm and w_b=4µm excited by larger forces. The red line is the "backbone" curve.

Conclusions

We propose a new design for enhancing the dynamic range of high-Q Si_3N_4 string resonators by means of compliant supports. By tuning geometrical parameters at the boundaries, we are able to engineer the state of stress in the string from 0.1GPa to 1.0GPa. As a result, we can engineer the Q factor and Duffing constant γ of the resonator , and thus control its dynamic range.

References

[1] S. Dou, B. S. Strachan, S. W. Shaw, J. S. Jensen. (2015) Structural optimization for nonlinear dynamic response. *Philosophical Transactions of the Royal Society A: Mathematical, Physical and Engineering Sciences*, 373: 20140408.

[2] M. Bückle, Y. S. Klaß, F. B. Nägele, R. Braive, E. M. Weig. (2021) Universal length dependence of tensile stress in nanomechanical string resonators. *Physical Review Applied* , 15: 034063.

[3] I. Kozinsky, H.W. Ch. Postma, O. Kogan, A. Husain, M. L. Roukes. (2007) Basins of Attraction of a Nonlinear Nanomechanical Resonator. *Physical Review Letters* , 99: 207201.

Exploiting nonlinearities of mechanically-coupled microbeams for mass sensing: theoretical and experimental investigation

Toky Rabenimanana*, Fehmi Najar**, Vincent Walter*, Najib Kacem*, and Mehdi Ghommem***
*Univ. Bourgogne Franche-Comté, FEMTO-ST Institute, CNRS/UFC/ENSMM/UTBM, Department of Applied Mechanics, France
**Applied Mechanics and Systems Research Laboratory, Tunisia Polytechnic School, University of Carthage, B.P. 743, Al Marsa 2078, Tunis, Tunisia
***Department of Mechanical Engineering, American University of Sharjah, Sharjah 26666, UAE

Summary. In this work, we consider a MEMS device made of mechanically-coupled microbeams under electric actuation. We conduct an experimental study to identify the occurrence of veering and then investigate its dynamic response for different electric actuations. A slight change in the DC voltage bias from the veering point is observed to affect significantly the frequency response. Indeed, jump to large orbits occurred when perturbing the applied DC voltage while operating near the cyclic-fold bifurcation point. We also develop and validate a mathematical model to simulate the response of the device. The model showed similarities in the softening effect of the DC voltage bias and an added mass when matching their induced shift in the natural frequency. As such, one can exploit mode localization and the significant and abrupt jumps in the deflection of the coupled microbeams to enhance the sensitivity of mass sensors.

Introduction

The deployment of MEMS devices comprising electrically actuated vibrating micro-beams for mass sensing has gained significant interest in the last few years thanks to their outstanding dynamic features in response to small variations in their effective mass. MEMS mass sensor converts the presence of a tiny element (biological entities such as cells and viruses, gas molecules…) into a resolvable electrical signal via a transduction technique (capacitive, piezoelectric...). A new generation of MEMS mass sensors has been recently proposed based on adopting the concept of mode localization [1-4]. These devices have demonstrated significant improvement in terms of sensitivity by up to four orders of magnitude in comparison to their conventional counterparts. Yet, distinctive merits of mode localized mass sensors have been demonstrated over several research studies in the last decade [1]. However, there is still room for improvement of this kind of sensors, especially when exploiting and tuning their associated nonlinearities to increase further their sensitivity and extend their operating range. In this work, we consider a MEMS device made of mechanically-coupled microbeams subjected to electric actuation. We study unconventional nonlinear mass detection mechanisms and assessed their capabilities to enhance the performance of the mass sensors.

MEMS device description and experimental measurements

We consider a MEMS device comprising two mechanically coupled microbeams with slightly different lengths: $L_1 = 98\ \mu m$ and $L_2 = 100\ \mu m$ (see Figure 1). A coupling beam with a length of $L_c = 65\ \mu m$ is placed at a distance $x_c = 4.9\ \mu$m from the clamped end of the microbeams. The electrostatic actuation of the device is made by the application of combined DC and AC voltages via a stationary electrode placed underneath the short beam. The device was fabricated by using the Multi-User MEMS Processes (MUMPs®). The microbeams are composed of a polysilicon layer Poly2 reinforced by a second polysilicon layer Poly1 at the fixed end. The measured gap between the cantilevers and the bottom electrode (Poly0) is around g = 1.35 µm. The MEMS device is placed in a vacuum chamber at a pressure around 0.3 mbar to minimize the damping effect and the actuation voltage is applied with a micro probe. The quality factor Q is found equal to 900. To measure the vibrations at the tip of each cantilever beam, a single point laser Doppler vibrometer is used in order to experimentally confirm the feasibility of the operating principle of the sensor.

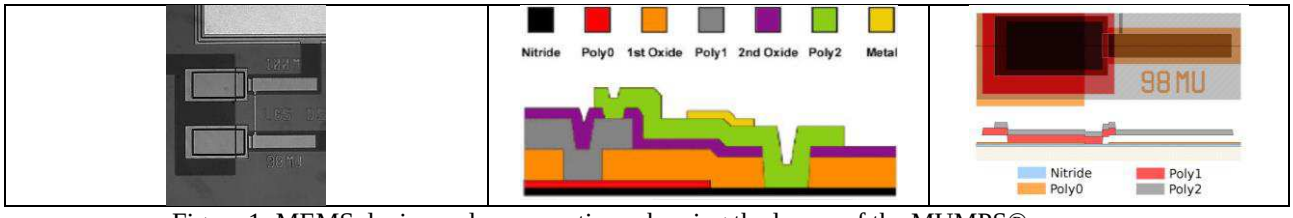

Figure 1: MEMS device and cross sections showing the layers of the MUMPS® process.

Results and discussion

We plot in Figure 2(a) the experimental frequency response of the MEMS device obtained at two different DC voltages. The results are shown for the short beam. We note that the electrostatic force is applied only to the short beam while operating at veering and setting the AC voltage at 30 mV. The needed DC voltage to reach veering is found experimentally equal to 7.73 V. Adding a DC voltage bias of 200 mV induces a significant jump in the beam deflection when operating at a suitable and a fixed excitation frequency near the cyclic-fold bifurcation, as indicated by the arrow at $\omega = 166.140$ kHz in Figure 2(a). This jump is illustrated further in the time response shown in Figure 2(b). A DC voltage bias of 200 mV is introduced at $t = 1$ s. The softening effect induced by the DC voltage is equivalent to that of an added mass

deposited on one of the microbeams as will be demonstrated next. As such, the observed jump to large orbits can be exploited for mass sensing purposes.

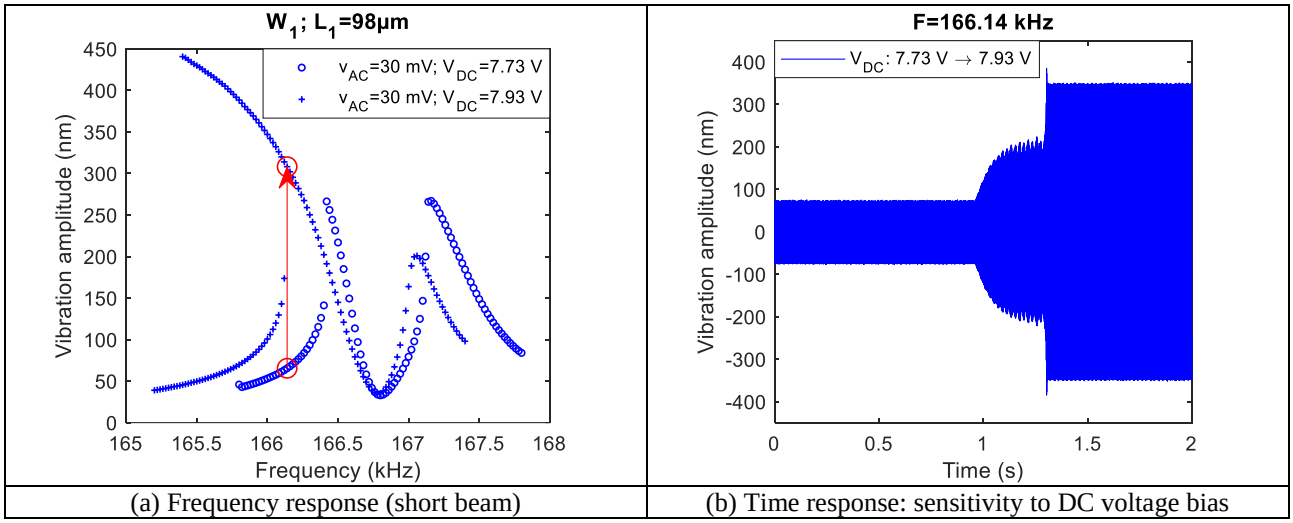

(a) Frequency response (short beam) | (b) Time response: sensitivity to DC voltage bias

Figure 2: Dynamic response of the MEMS device for different DC voltages (experimental results).

Following Euler-Bernoulli beam theory, we develop a nonlinear mathematical model governing the vibrations of the two mechanically coupled microbeams. The weak mechanical coupling is approximated by a torsional spring with rotational stiffness. We derive a reduced-order model using the Galerkin decomposition method [3]. In Figure 3(a), we compare the frequency response curves obtained using the developed nonlinear model (solid lines) against those measured experimentally (dotted lines). A good agreement between the numerical and experimental data is obtained. These simulation results demonstrate the capability of the nonlinear dynamic model to properly capture the dynamic response of the MEMS device. We show in Figure 3(b) the simulated frequency responses for different DC voltage biases (with respect to the veering DC voltage). We also plot the frequency response obtained when adding a mass of seven pg on the short beam. Of interest, the frequency response obtained for a DC voltage bias of 200 mV matches with that obtained for an added mass of seven pg. We note that increasing the applied DC voltage by 200 mV and adding a mass of seven pg lead to same shift in the natural frequency of the microsystem. As such, given these similarities, one can use the abrupt and significant jump to large orbits observed in mechanically coupled beams for mass sensing applications.

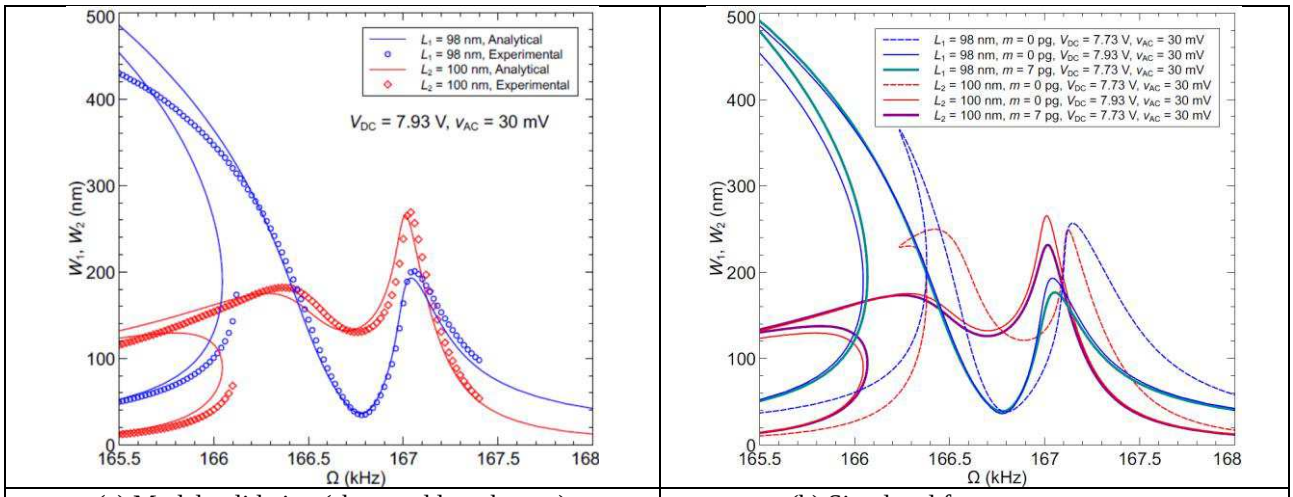

(a) Model validation (short and long beams) | (b) Simulated frequency responses

Figure 3: Frequency responses of the MEMS device: (a) numerical simulations (solid lines) vs. experiments (dotted lines), (b) Simulated frequency responses.

References

[1] Zhao, C., Montaseri, M. H., Wood, G. S., Pu, S. H., Seshia, A. A., & Kraft, M. (2016). A review on coupled MEMS resonators for sensing applications utilizing mode localization. *Sensors and Actuators A: Physical*, *249*, 93-111.

[2] Rabenimanana, T., Walter, V., Kacem, N., Le Moal, P., Bourbon, G., & Lardies, J. (2019). Mass sensor using mode localization in two weakly coupled MEMS cantilevers with different lengths: Design and experimental model validation. *Sensors and Actuators A: Physical*, *295*, 643-652.

[3] Alkaddour, M., Ghommem, M., & Najar, F. (2021). Nonlinear analysis and effectiveness of weakly coupled microbeams for mass sensing applications. *Nonlinear Dynamics*, *104*(1), 383-397.

[4] Rabenimanana, T., Walter, V., Kacem, N., Le Moal, P., Bourbon, G., & Lardiès, J. (2020). Functionalization of electrostatic nonlinearities to overcome mode aliasing limitations in the sensitivity of mass microsensors based on energy localization. *Applied Physics Letters*, *117*(3), 033502.

Frequency Stabilization of MEMS Oscillators Using Internal Resonance

Oriel Shoshani*, Scott Strachan**, Daniel Lopez¶, David Czaplewski† and Steven Shaw‡
*Ben-Gurion University of the Negev, Be'er-Sheva, Israel
**SiTime, Santa Clara, CA, USA
¶Pennsylvania State University, University Park, PA, USA
†Argonne National Laboratory, Lemont, IL, USA
‡Florida Institute of Technology, Melbourne, FL, USA

Summary. We study the frequency stabilization of a MEMS self-sustained oscillator operating in internal resonance. We show, both experimentally and theoretically, that coupling two vibrational modes with a frequency ratio of 1:3 through a nonlinear resonance makes it possible to stabilize the oscillation frequency of MEMS oscillators beyond any currently known frequency stabilization technique. Our analysis shows that this novel frequency stabilization stems from operation in a region of (nearly) zero frequency dispersion at large amplitudes. The large amplitude improves signal quality and the internal resonance provides both the zero dispersion as well as phase-locking between the modes, all of which are beneficial for noise reduction. Our findings provide a new strategy for engineering low-frequency noise oscillators capitalizing on the intrinsic nonlinear phenomena of micro- and nano-mechanical resonators.

Introduction

MEMS oscillators, which offer the potential for reduced power consumption, on-chip integration with CMOS, and a small footprint, are widely used for precision time keeping and as sensitive detectors. Therefore, their frequency stability is a key figure of merit. However, due to the small size of the mechanical vibrating structures in these MEMS oscillators, their vibrations are highly sensitive to noise and become nonlinear even for small amplitudes. Unlike linear vibrations, in nonlinear vibrations, the resonant frequency has a strong dependence on the oscillation amplitude (frequency dispersion), and therefore, amplitude fluctuations translate into frequency fluctuations. This amplitude-to-frequency (A-f) noise conversion considerably degrades the oscillator performance.

In this study, we show that a nonlinear resonance between a pair of modes that have a frequency ratio of 1:3 provides a zero-dispersion domain over which, local to the operating point, A-f effects are eliminated and the system regains some specific characteristics of linear vibrations, even though the operating point is well into the nonlinear regime. Moreover, the inter-modal phase locking of the nonlinear resonance produces a frequency stabilizing effect similar to that observed for pairs of synchronized oscillators. These effects both suppress frequency fluctuations in the primary mode, making the considered oscillator cleaner than its linear counterpart (which is ideally the cleanest oscillator).

Experimental method and observations

The resonator (i.e., the mechanical vibrating structure) of our MEMS oscillator is fabricated from single-crystal silicon and is composed of 3 beams connected at their centers to each other and to a pair of comb drives (see Refs. [1] for details). The resonantly interacting modes are the fundamental flexural mode (eigenfrequency ω_1) and the fundamental torsional mode (eigenfrequency $\omega_2 \approx 3\omega_1$); see the left panel of Fig. 1. The self-oscillation is achieved by a placing the resonator in a feedback loop with an amplifier and a phase shifter whose tuning both destabilizes the thermal vibrations and controls the amplitude and phase of the flexural mode. [4]

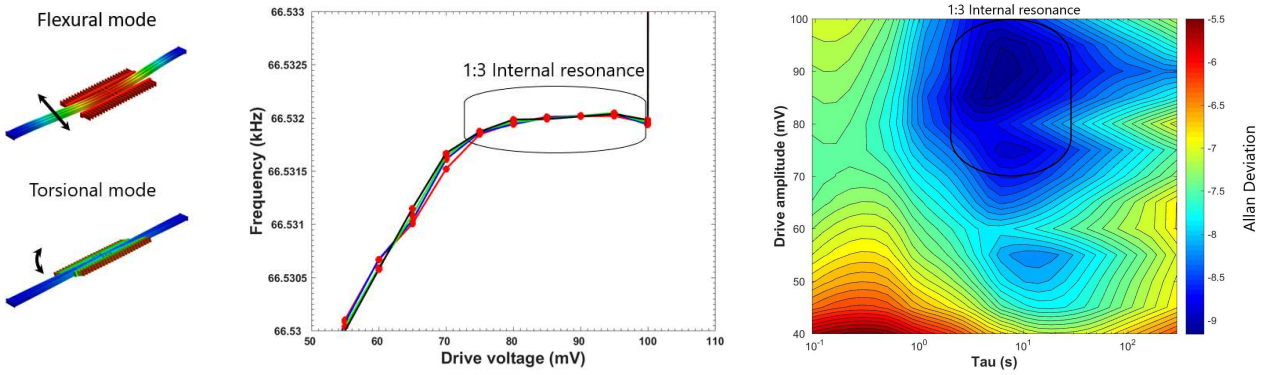

Figure 1: Device and experimental measurements. Left panel—the flexural (ω_1) and torsional (ω_2) modes from finite element models, which interact resonantly when $\omega_2/\omega_1 \approx 3$. Center panel—the operating frequency of the oscillator increases with the drive voltage, due to the Duffing nonlinearity, until it saturates with zero-dispersion in the vicinity of the 1:3 internal resonance. Right panel—at the internal resonance, the Allan deviation reduces dramatically, revealing the stabilizing effect of the nonlinear mode coupling.

The motion of the flexural (in-plane) mode is detected capacitively by one set of combs. The capacitance variation of the voltage-biased comb-drive electrode generates a current that is introduced into a current amplifier to produce a voltage output proportional to the oscillation amplitude of the flexural mode. This voltage is phase shifted and used to excite the beam through the other set of combs. The motion of the torsional (out-of-plane) mode is detected by an optical

interferometry method, with the laser spot focused on the outer-most position of the movable structure. The interference signal is then amplified to produce a voltage output proportional to the oscillation amplitude of the torsional mode. The frequency stability of the system was analyzed in terms of the Allan deviation from the signal of the flexural mode [2] $\sigma_y(\tau) = \sqrt{\frac{1}{2(N-1)}\sum_{i=1}^{N-1}(\langle y_{i+1}^{\tau}\rangle - \langle y_i^{\tau}\rangle)}$, where $\langle y_i^{\tau}\rangle$ are the relative frequency fluctuations averaged over the ith discrete time interval of τ. The center panel of Fig. 1 shows the zero dispersion by the flattening of the operating frequency as a function of amplitude, and the right panel clearly shows the attendant frequency stabilization obtained in the internal resonance by the reduction of the Allan variance at these amplitudes.

Analytical model and results

We consider the following closed loop system with a 1:3 internal resonance

$$\ddot{x}_1+2\Gamma_1\dot{x}_1+\omega_1^2(1+\eta_1)x_1+\gamma x_1^3+3\alpha x_1^2x_2 = S\cos(\omega_1 t+\phi_1+\Delta)+\xi_1,\;\; \ddot{x}_2+2\Gamma_2\dot{x}_2+\omega_2^2(1+\eta_2)x_2+\alpha x_1^3 = \xi_2,$$

where $\Gamma_{1,2}$ are the dissipation rates, $\omega_{1,2}$ are the modal eigenfrequencies ($\omega_2 \approx 3\omega_1$), S is the drive level (set by the amplifier), $\phi_1(t)$ represents the phase of the flexural mode, Δ is the imposed phase shift from the feedback loop, $\eta_{1,2}(t)$ are the frequency noises, and $\xi_{1,2}(t)$ are the additive thermal noises. We have assumed that the coupling stems from a single-term potential $U_{cpl} = \alpha x_1^3 x_2$, that the flexural mode nonlinearity is a simple Duffing type, γx_1^3, and the torsional mode operates in its linear range. Using the method of stochastic averaging [3], we derive a pair of Langevin equations for the phase sum $\phi = \phi_1+\phi_2$ and difference $\psi = 3\phi_1-\phi_2$ (ϕ_2 is the phase of the torsional mode). Near a stable operating point, it can be shown that diffusion of the phase difference remains constant and small. In contrast, the diffusion of the phase sum is always strong and associated with a variance that increases linearly in time ($\langle\varphi^2\rangle - \langle\varphi\rangle^2 = D_\varphi t$). However, in the zero-dispersion domain, D_φ reduces drastically due to elimination of the A-f noise conversion. Moreover, we can neglect the diffusion of ψ, which is considerably smaller than the strong diffusion of φ, and then approximate, using the relations $\phi_1 = (\varphi+\psi)/4$ and $\phi_2 = (3\varphi-\psi)/4$, the diffusion constants of the individual phases ($\langle\phi_{1,2}^2\rangle - \langle\phi_{1,2}\rangle^2 = D_{\mathrm{T}_{1,2}}t$) as $D_{\mathrm{T}_1} \approx (1/4)^2 D_\varphi$, $D_{\mathrm{T}_2} \approx (3/4)^2 D_\varphi$. Therefore, the phase-locking mechanism ($\dot{\psi} = 0$) of the internal resonance leads to a further reduction in the phase noise of the first mode (D_{T_1}). We note that the flexural mode is subjected to the noises of the feedback circuitry while the torsional mode is largely isolated from such noise sources. Thus, if the second mode (nearly purely mechanical) is significantly cleaner than the first mode, i.e., $D_{\xi_2} \ll D_{\xi_1} \ll$ and $D_{\eta_2} \ll D_{\eta_1}$, then the cleaner second mode, which has a threefold stronger influence, cleans the noisy first mode and its diffusion constant is reduced by a factor of 1/16, i.e., $D_{\mathrm{T}_1}|_{\text{Inside IR}} = (D_{\mathrm{T}_1}|_{\text{Outside IR}})/16$. This cleaning effect can be readily seen in Fig. 2, where in the zero-dispersion domain of the coupled-mode oscillator, the diffusion constant of the first mode is significantly lower than the diffusion constant of even the highly ideal single-mode linear oscillator. Note that without the phase cleaning effect, the diffusion constants would be (nearly) equal in the zero-dispersion domain.

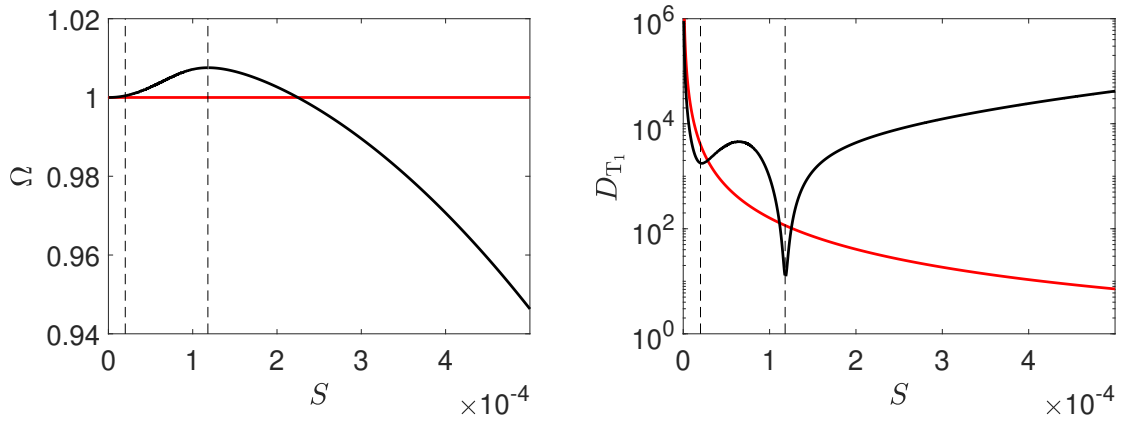

Figure 2: Operating frequency Ω (left panel) and total diffusion constant of the phase of the first mode (right panel) as functions of drive level for single-mode linear (red), and coupled-mode (black) closed-loop oscillators, with $\omega_1 = 1, \omega_2 = 3.06, \gamma = 3, \alpha = 10, \Gamma_1 = 10^{-3}, \Gamma_2 = 10^{-4} \Delta = \pi/2, D_{\eta_1} = 1, D_{\eta_2} = 0.1, D_{\xi_1} = 0.4$ and $D_{\xi_2} = 0.04$. Only the stable states in which $\Omega < \omega_2/3$ are shown. The diffusion constant of the linear oscillator decreases as S^{-2}, whereas the diffusion constant of the coupled-mode oscillator has a dual local minima (denoted by the dashed vertical lines), the lower of which is the usual operating point for a Duffing oscillator without zero dispersion. The cancellation of amplitude to frequency noise conversion at the zero-dispersion domain along with the phase constraint yield a diffusion constant for the coupled-mode oscillator that is even smaller than that of the linear oscillator.

References

[1] Czaplewski D.A., Chen C., López D., Shoshani O., Eriksson A.M., Strachan B.S., and S.W. (2018) Bifurcation generated mechanical frequency comb. *Phys. Rev. Lett.* **121**:244302.

[2] Levine, J. (1999) Nntroduction to time and frequency metrology. *Rev. Sci. Instrum* **70**:2567-2596.

[3] Stratonovich, R.L. (1967) Topics in the theory of random noise. CRC Press.

[4] Chen C., Zanette D.H., Guest J.R., Czaplewski D.A., López, D. (2016) Self-sustained micromechanical oscillator with linear feedback. *Phys. Rev. Lett.* **117**:017203.

Hopf Bifurcation in MEMS - (When) Do Such Exist?

Stefanie Gutschmidt* and Stefano Lenci†
*University of Canterbury, Christchurch, New Zealand
†Università Politecnica delle Marche, Ancona, Italy

Summary. When considering MEMS/NEMS not just as interesting dynamical systems theoretically, but also for technological applications, a Hopf bifurcation could be a desired property for e.g. increasing sensitivities of a sensor. However, MEMS/NEMS are not known to commonly experience a Hopf point. In this work we investigate a real MEMS system with integrated thermal actuation in passive and active operation modes and investigate this Hopf in MEMS/NEMS question. We show that when the system is operated actively, there are possible parameter ranges which include a Hopf bifurcation.

Background

MEMS are inherently nonlinear, which immediately provides additional properties to be exploited for technological implementation. These advantageous properties are associated with bifurcation points such as saddle-node, transcritical, pitch-fork and Hopf bifurcations. While the former three bifurcations are related to changes of fix-points (or real eigenvalue(s) of the Jacobian) of a system for a selected control parameter, the latter bifurcation is associated with a changing complex-conjugated pair of eigenvalues crossing the complex plane from negative to positive [1, 2]. Furthermore, the former bifurcations have been reported extensively in the literature (for example, the well-known pull-in phenomenon is associated with a saddle-node bifurcation) [3, 4], while the latter is less common, if not rare. For example, in the book by Younis [5] the occurrence of Hopf bifurcations in MEMS is not mentioned. The Hopf bifurcation is related to the damping properties of the system. A single degree-of-freedom (DOF) system (e.g. MEMS/NEMS in their first vibration mode) would therefore require negative damping properties. Furthermore, Gutschmidt and Gottlieb [6] and also Zehnder et al. [4] have observed Hopf (Neimark-Sacker) bifurcations in electrostatically coupled MEMS oscillators when operated near an internal resonance which is also known for parametrically excited systems in general [7] (for micro and macro-scale alike). From other macro-scale examples it is further known that other coupling can also introduce negative damping properties, especially when gyroscopic effects in addition to damping are present in a multi-DOF system. However, for more common MEMS geometries and configurations such scenario are rather rare or not existing.

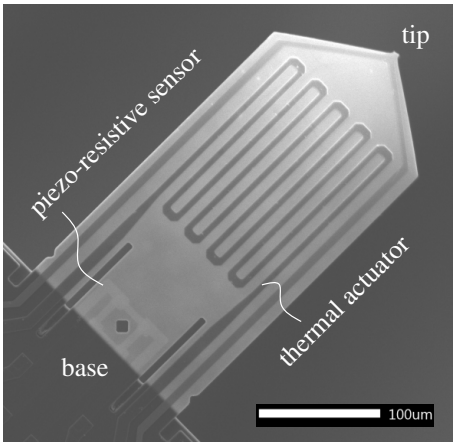

Figure 1: SEM image of the self-actuation, self-sensing cantilever (JEOL JSM-IT300).

In this work we consider such an otherwise typical MEMS (Fig. 1), but with the ability to be operated passively and actively. Unlike other MEMS devices, the considered system has self-sensing and self-actuating capabilities [8] with which a feedback scheme can be introduced and damping properties are altered.

Passive & Active MEMS Model and Dynamics

The motion of the cantilever is generated by the top layer of the composite structure being thermally actuated (see Fig. 1). The deflection of the cantilever tip is monitored by an integrated piezo-resistive sensor located near the supported end (base). Our analysis is based on our previous work [9] in which we derive the governing equations for this composite MEMS system from basic principles. In this work we radically simplify these equations by considering only the first vibration mode of the cantilever and dominating terms are as follows

$$\ddot{q}_w + \delta\dot{q}_w + q_w - \alpha q_\theta = \kappa_{ext}\,, \tag{1a}$$

$$\dot{q}_\theta + \beta q_\theta = \gamma i^2\,. \tag{1b}$$

q_w and q_θ are the nondimensionalised mechanical and thermal variables of the system representing the modal deflection of the cantilever and the response of temperature difference, respectively. Parameters α, β, γ, δ are classic integration constants originating from a modified Ritz discretization [9], wherein δ is related to the damping. The coupling between the mechanical and thermal systems is determined by the strength of the coupling parameter α. κ_{ext} is an external periodic stimulus. The integrated thermal actuation is modelled as Joule heating, through which the feedback mechanism is introduced with

$$i = i_{DC} + aq_w\,, \tag{2}$$

where i_{DC} is an off-set current with which to control equilibrium states and a is the feedback strength.

Analysis & Results

The analysis emphasizes on the existence of a Hopf bifurcation for equilibrium solutions. However, Hopf (Neimark-Sacker) bifurcations in the presence of external excitation of the system are also of interest. We consider the three following systems: passive (decoupled from the thermal actuation, only Eq. (1a)), thermally coupled but passive Eq. (1), and the actively operated system Eqs. (1) and (2), [10], with their Jacobian matrices accordingly being

$$J_{passive} = \begin{bmatrix} 0 & 1 \\ -1 & -\delta \end{bmatrix}, \qquad J_{coupled} = \begin{bmatrix} 0 & 1 & 0 \\ -1 & -\delta & \alpha \\ 0 & 0 & -\beta \end{bmatrix}, \qquad J_{active} = \begin{bmatrix} 0 & 1 & 0 \\ -1 & -\delta & \alpha \\ \epsilon & 0 & -\beta \end{bmatrix},$$

with $\epsilon = 2\gamma a i_{DC}$ from substituting (2) into (1b). Investigating the roots λ_i for $i = 1, 2, 3$ of these systems (Fig. 2) reveals the absence and existence of Hopf bifurcations. Figure 2a) depicts the roots of systems $J_{passive}$ and $J_{coupled}$, respectively.

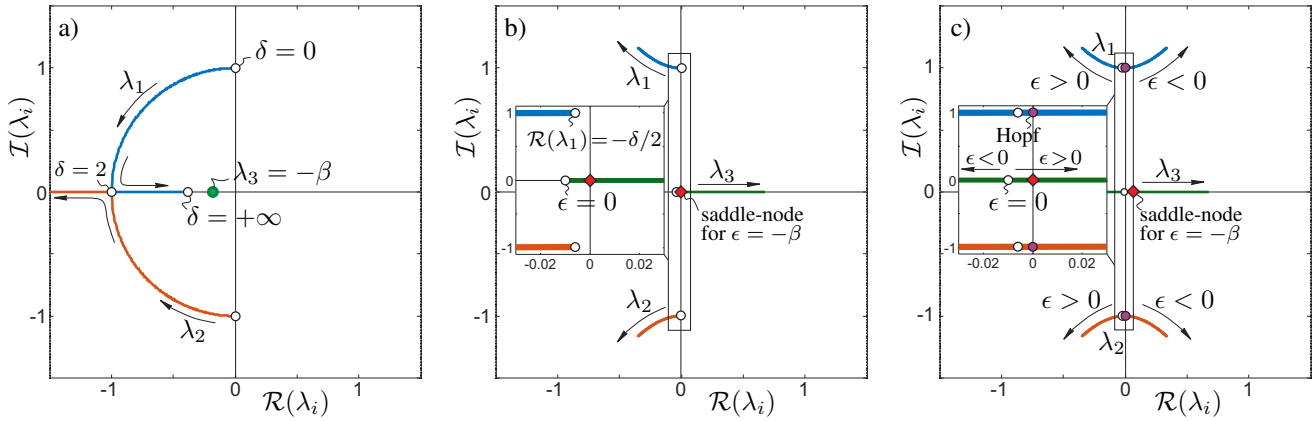

Figure 2: Roots of the MEMS for different operation modes; a) passive & passive coupled systems with all positive system parameters; b) active system with positive system and feedback parameters; c) active system with positive system and negative feedback parameters.

Note, the additional third root for system $J_{coupled}$ (green marker in Fig. 2a)). For positive values of δ (damping) there are no Hopf bifurcations present in either passive or coupled systems, as expected and observed in literature. Figure 2b) portraits the roots of the active system J_{active} (with feedback) for all system and feedback parameters having positive values. We observe a saddle-node bifurcation [10] but no Hopf! Only for negative values of the feedback parameter ϵ, a Hopf bifurcation is present which can be introduced by a negative off-set current i_{DC} or negative feedback strength a (see Eq. (2)).

Conclusions

In this work we investigate the existence of a Hopf bifurcation for equilibria of an ordinary MEMS structure as typically found in modern technological applications. The analysis includes passive and active operation modes, and reveals the existence of Hopf points for only the active operation mode and when feedback parameters include also the negative range. Although the emphasize is laid on Hopf bifurcations related to equilibria, the presentation will also include investigations of the system subject to external stimuli and the existence of Neimark-Sacker bifurcations.

References

[1] Nayfeh, A.H., Mook, D.T. (1979) Nonlinear Oscillations. John Wiley & Sons, Inc., Canada.

[2] Strogatz, S.H. (1994) Nonlinear Dynamics and Chaos. Perseus Books Publishing, LLC, Cambridge, MA.

[3] Rhoads, J.F., Shaw, S.W., Turner, K.L. (2010) Nonlinear Dynamics and Its Applications in Micro- and Nanoresonators. *Journal of Dynamic Systems, Measurement, and Control*, **132**(3).

[4] Zehnder, A.T., Rand, R.H., Krylov, S. (2018) Locking of electrostatically coupled thermo-optically driven MEMS limit cycle oscillators. *International Journal of Non-Linear Mechanics*, **102**: 92–100.

[5] Younis, M.I. (2011) MEMS Linear and Nonlinear Statics and Dynamics, Springer, New York.

[6] Gutschmidt, S., Gottlieb, O. (2012) Nonlinear dynamic behavior of a microbeam array subject to parametric actuation at low, medium and large DC-voltages. *Nonlinear Dynamics*, **67**(1): 1-36.

[7] Nayfeh, A.H. (2000) Nonlinear Interactions: Analytical, Computational, and Experimental Methods. Wiley, New York.

[8] Ivanov, T., Gotszalk, T., Grabiec, P., Tomerov, E., Rangelow, I.W. (2003) Thermally driven micromechanical beam with piezoresistive dedection readout. *Microelectronic Engineering*, **67-68**: 550-556.

[9] Roeser D., Gutschmidt S., Sattel T., Rangelow I.W. (2016) Tip Motion - Sensor Signal Relation for a Composite SPM Cantilever. *J. Microelectromech. Syst.*, **25**: 78-90.

[10] Lam, N., Hayashi, S., Gutschmidt, S. (2022) A novel MEMS sensor concept to improve signal-to-noise ratios. *International Journal of Non-Linear Mechanics*, **139**: 103863.

Internal Resonances in Magnetic Resonance Force Microscopy

Evyatar Hacker and Oded Gottlieb
Department of Mechanical Engineering, Technion - Israel Institute of Technology, Haifa, Israel

Summary. We investigate the existence of internal resonances in magnetic resonance force microscopy asymptotically and numerically and demonstrate the possible existence of energy transfer from a directly excited mode to its out-of-plane counterpart. The reconstitution multiple-scales method reveals the existence of non-stationary dynamics that yields coexisting periodic and quasiperiodic dynamics for small damping that may enable multi-functional detection of both electron spin and the sample magnetic properties.

.

Magnetic resonance force microscopy (MRFM) is an imaging technique that enables acquisition of three-dimensional magnetic images at nanometer scales, and has been adapted for detection of magnetic spin of a single electron [1]. It is based on combining the technologies of magnetic resonance imaging (MRI) with atomic force microscopy (AFM). In conventional MRI devices the electronic spins are detected by measuring their magnetic induction using an inductive coil as an antenna. However, in MRFM the detection is implemented mechanically using a cantilever to directly detect a modulated spin gradient force between the sample spins and a ferromagnetic particle attached to the tip of the cantilever. While MRFM systems are receiving a growing amount of interest, to date, a comprehensive theoretical treatment is still lacking. Existing models are based on simplistic lumped-mass reductions that include linear estimates of cantilever stiffness and damping complemented by a nonlinear approximation of the magnetic force [2] and are unable to resolve the spatio-temporal complexity of the magneto-elastic sensor.

We thus consistently formulate a nonlinear initial-boundary-value problem (IBVP) combining the three-dimensional motion of a viscoelastic micro-cantilever and the dynamic interactions of the spin magnetic moments (see Figure 1-left). The MRFM cantilever IBVP incorporates the generalizes forces defined by the total magnetic field which are augmented by the time-dependent spin magnetic moment components in a rotating system of coordinates described by the Bloch equations [3]. We reduce the IBVP to a seventh-order nonlinear dynamical system and investigate the three-dimensional motion of the MRFM cantilever tip corresponding to adiabatic and non-adiabatic conditions. We emphasize that periodic base excitation of the vertical MRFM configuration here is not sensitive to a global homoclinic escape bifurcation threshold [4] typical of the traditional horizontal configuration of the cantilever sensor which is limited to operation below a jump-to-contact condition.

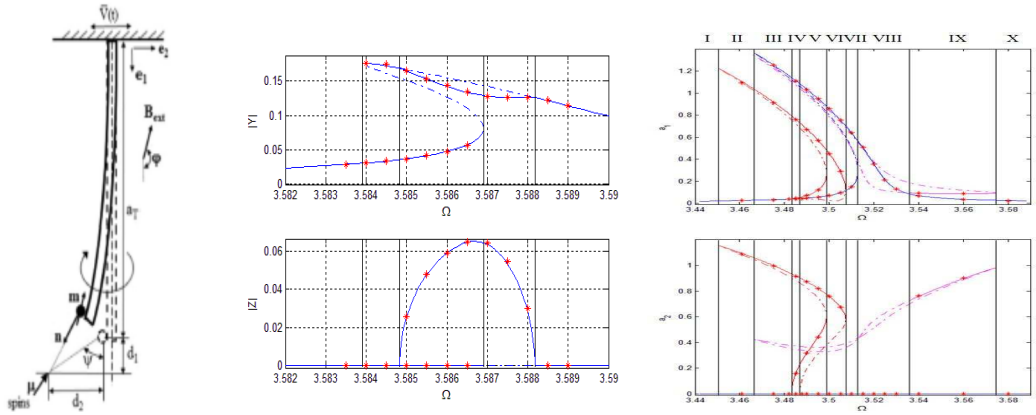

Figure 1 – MRFM model definition sketch (left), frequency response for the case of a 1:1 internal resonance (center) and for the case of a 2:1 internal resonance (right).

We use an asymptotic reconstitution multiple-scale analysis to accurately determine the MRFM system frequency response which enables estimation of the cantilever frequency shift corresponding to documented measurements. We investigate the stability of slowly varying evolutions for the conditions of both one-to-one (Figure 1-enter) and two-to-one internal resonances (Figure 1 – right) which reveal the existence coexisting periodic solutions and secondary Hopf bifurcations [5].

Numerical integration of the dynamical system for different values of system parameters near its two-to-one internal resonance reveal symmetry breaking of a fundamental period-doubled solution (Figure 2) which evolves to an asymmetric period three ultra-sub-harmonic and culminates with non-stationary solutions depicted by a dense power spectra and corresponding poincare' map**.**

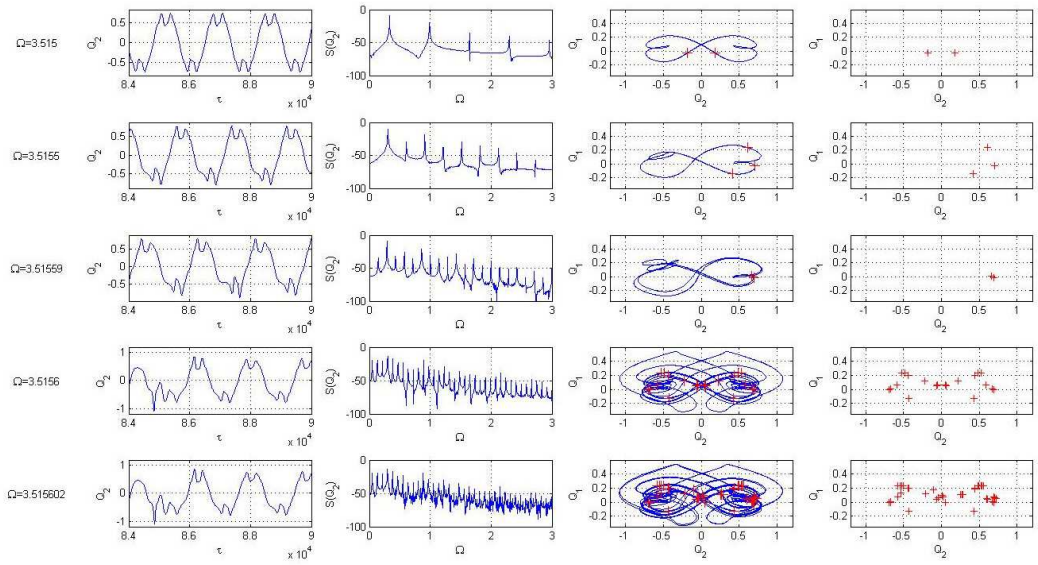

Figure 2 – Numerical response for a 2:1 internal resonance which exhibits complex periodic ultra-sub-harmonic solutions.

Numerical integration of the dynamical system for different values of system parameters near its one-to-one internal resonance (Figure 3) reveal quasiperiodic and chaotic like motion which in addition to identification of the spin gradient force may enable simultaneous multi-functional sensing of material properties of magnetized samples.

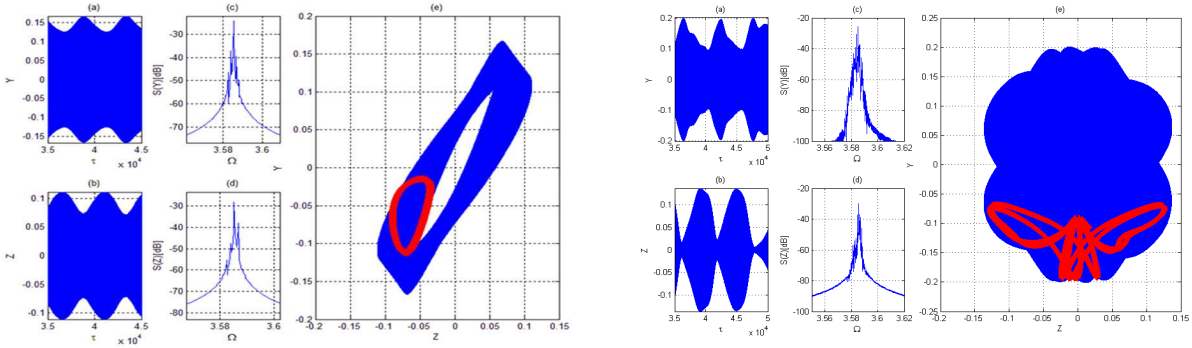

Figure 3 – Numerical response for a 1:1 internal resonance which exhibits a quasiperiodic torus (left) and a strange attractor (right).

References

[1] Rugar D., Budakian R., Mamin H.J., and Chui B.W., Single spin detection by magnetic resonance force microscopy, Nature 430, 329, 2004.
[2] Berman G.P., Borgonovi F., Gorshkov V.N., and Tsifriovich V.I., Magnetic Resonance Force Microscopy and Single-Spin Measurement, World Scientific, NJ 2006.
[3] Slichter C.P., Principles of Magnetic Resonance, Springer NY 1996.
[4] Hacker E. and Gottlieb O., Local and global bifurcations in magnetic resonance force microscopy, Nonlinear Dynamics, online 2019 doi.org/10.1007/s11071-019-05401-y.
[5] Hacker E. and Gottlieb O., Application of reconstitution multiple-scale asymptotics for a two-to-one internal resonance in magnetic resonance force microscopy, International Journal of Non-Linear Mechanics 94, 174-199 (2017).

Leveraging Rotating Frame Dynamics for Low-Power Chaos Generation in Nonlinear M/NEMS Resonators

Samer Houri*, Ludovico Minati†, Motoki Asano* and Hiroshi Yamaguchi*
*NTT Basic Research Laboratories, NTT Corporation, 3-1 Morinosato-Wakamiya, Atsugi-shi, Kanagawa 243-0198, Japan
†Tokyo Tech World Research Hub Initiative (WRHI), Institute of Innovative Research, Tokyo Institute of Technology, Yokohama 226-8503, Japan

Summary. This work presents an approach to chaos generation that both preserves and leverages the rotating frame approximation that is usually used to analyse nonlinear M/NEMS resonators. The approach relies on increasing the phase-space dimensions to meet the Poincaré-Bendixon condition. Chaos generation is further constrained within the parameter space by relying on arguments from Melnikov's method. Experimental validation is performed using a GaAs piezoelectric nonlinear MEMS resonator.

Introduction and Theory

The relatively low-loss and weakly nonlinear properties of M/NEMS resonators have made the use of perturbation based techniques to capture their dynamics a marking feature of this field of research. These perturbation techniques include multiple scale analysis and the rotating frame approximation, and assume that the dynamics take the form of a "slow-flow" envelope superimposed on an otherwise sinusoidal carrier. These same physical properties that make M/NEMS devices desirable and perturbations techniques possible are usually counterproductive when it comes to generating chaos, since this latter is not a perturbation phenomenon.
Mathematically this effect can be understood by looking at the governing Duffing equation, written in a non-dimensional form as:

$$\ddot{x} + \gamma\dot{x} + x + \alpha x^3 = F_1 cos(\omega_1 t) + F_2 cos(\omega_2 t) \tag{1}$$

where x is the displacement, γ and α correspond to the non-dimensional dissipation and nonlinearity terms, and F_1, F_2, ω_1 and ω_2 are the magnitudes and frequency of externally applied forcing terms. Note that for the rotating frame approximation to apply, the frequency difference between $(\omega_1 - \omega_2) \ll 1$
The application of the rotating frame approximation to equation (1) gives:

$$\begin{aligned} \dot{X} &= -\delta Y + \frac{3\alpha}{8}(X^2+Y^2)Y - \frac{1}{2}(F_2 sin(\Theta) + \gamma X) \\ \dot{Y} &= \delta X - \frac{3\alpha}{8}(X^2+Y^2)X + \frac{1}{2}(F_1 + F_2 cos(\Theta) - \gamma Y) \\ \dot{\Theta} &= \Omega = (\omega_2 - \omega_1)/\omega_0 \end{aligned} \tag{2}$$

where, $\delta = (\omega_1 - \omega_0)/\omega_0$, and X and Y are the rotating-frame quadratures.
Equation (2) explains why it is difficult to generate chaos within the range of applicability of the rotating frame approximation in the case of only one forcing term is applied, i.e. $F_2 = 0$. Since in such a case the system reduces to a two-dimensional system ($n = 2$), and does not possess the necessary dimensions, i.e. $n = 3$, for chaos generation.
The typical approach to chaos generation in nonlinear M/NEMS devices have been to operate the device beyond the regime where equation (2) is valid, usually by applying large driving amplitudes and using exotic nonlinearity [1, 2]. However, it is equally possible to generate chaos while remaining within the perturbation regime, by expanding the rotating frame dimensions from $n = 2$ to $n = 3$, which can be done by applying the second tone, i.e. $F_2 \neq 0$.
While increasing the rotating-frame dimensions from 2 to 3 is a necessary condition, it nevertheless does not define the area within the four-dimensional parameter-space (δ, Ω, F_1, F_2) where chaos can exist. Fortunately, the system of equation (2) is typically described by Melnikov's method [3], which imposes the existence of a homoclinic bifurcation as a precondition for chaos generation. The existence of a homoclinic orbit implies operating within the bistable regime. Thus, it is an equally necessary condition to have at least one of the two applied tones within the bistable area of operation shown in Fig. 1(a)-(c) as a function of the non-dimensional parameters.

Experimental Validation

Experimental validation is performed using a GaAs piezoelectric MEMS clamped-clamped beam resonator. Under low drive amplitudes (70 mV), the single-tone frequency response of the device shows a resonance frequency and quality factor of $f_0 = 1.559$ MHz and $Q = 1000$ respectively, Fig. 1(d). For large amplitude sweeps (2.8 V), the device exhibits a hardening-type Duffing nonlinearity, which is fitted to give an $\alpha = 16$, Fig. 1(d).
Upon the application of two tones, with one tone having 1 V amplitude and $\delta = 4$ kHz, while the other tone (2 V) is swept over a $\Omega = 10$ kHz interval. The system exhibits a frequency doubling bifurcation route to chaos once the high amplitude tone is within its respective bistability region. This effect holds for a bidirectional frequency sweep, as shown in Fig. 1(e). The spectral response as well as the phase-space plots corresponding to a rotating frame periodic motion, period-doubling motion, and chaotic motion are shown in Fig. 1(f)-(h), and Fig. 1(i)-(k), respectively.

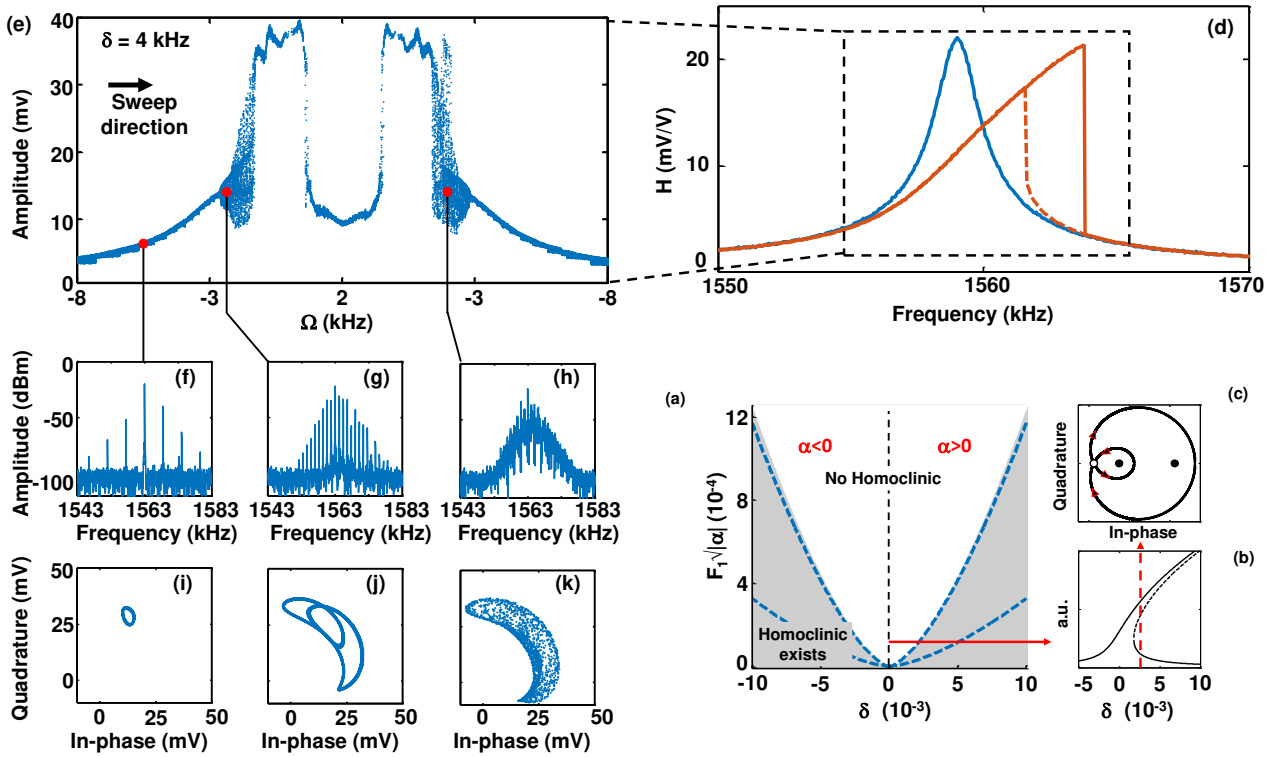

Figure 1: (a) Bistability map plotted as a function of non-dimensional force and detuning, showing the region of bistability for a lossless driven Duffing resonator (grey area), and for a low-loss (Q=1000) Duffing resonator (area within the dashed blue line). (b) Amplitude versus detuning response of a lossless Duffing taken for $F_1\sqrt{\alpha} = 1$. The corresponding phase-space plots for a detuning of $\delta = 2.5 \times 10^{-3}$ is shown in (c). The stable fixed points and the saddle point are shown as black and white dots respectively, as well as the homoclinic orbit. (d) Experimentally obtained frequency response sweep showing the linear regime (blue trace) and the Duffing regime (red trace). (e) Amplitude of the rotating-frame oscillations under the effect of a two-tone excitation, with one fixed tone ($\delta = 4$ kHz), and Θ swept between $[-8,\ 2]$ kHz, the frequency is swept in both directions with the forward and backward sweeps plotted side by side. The oscillations show Period 1, Period 2, and chaos, the spectral density and phase space plots of which examples are shown in (f)-(h), and (i)-(k), respectively.

Conclusions

In conclusion, this work presents an approach that leverages our understanding of the rotating frame approximation in order to generate chaos in nonlinear M/NEMS resonators using low power actuation. The chaos generation area within the parameter space is constrained using arguments from Melnikov's method, and the technique presented here is independent of the exact device design and scale, and therefore is generally applicable to low-loss nonlinear M/NEMS resonators.

References

[1] Bienstman J., Vandewalle J., Puers R. (1999) The autonomous impact resonator: a new operating principle for a silicon resonant strain gauge. *SENSOR ACTUAT A-PHYS* **66**:40-49.

[2] DeMartini B. E., Butterfield H. E., Moehlis J., Turner K. L. (2007) Chaos for a microelectromechanical oscillator governed by the nonlinear Mathieu equation. *J MICROELECTROMECH S*, **16**:1314-1323.

[3] Holmes P. (1979) A nonlinear oscillator with a strange attractor. *PHILOS T R SOC A*, **292**:419-448.

Thursday, July 21, 2022

08:30 - 10:30

MS-16 Random Dynamical Systems - Recent Advances and New Directions

Rhone 2

Chair: Rachel Kuske

08:30 - 08:50

Controlling the location of discrete breather formation in a nonlinear electrical lattice using random excitation

RAMAKRISHNAN Subramanian*, EDLUND Connor

*University of Dayton (Dayton, OH United States)

08:50 - 09:10

Long Time Trapping of Particles in a Rotating Sinai Billiards System

MITRA Saheli*, SAUGATA Bhattacharyya, PAKRASHI Vikram

*Laboratoire de physique des Solides, Université Paris Sud, Orsay, France (Université Paris Sud, Orsay, France France)

Controlling the location of discrete breather formation in a nonlinear electrical lattice using random excitation

Subramanian Ramakrishnan* and Connor Edlund†
*Department of Mechanical and Aerospace Engineering, University of Dayton, Dayton, USA
†Department of Electrical Engineering, University of Minnesota - Twin Cities, Minneapolis, USA

Summary. Emergence of *discrete breathers* (also known as Intrinsic Localized Modes) in nonlinear lattices, analogous to *solitons* in continuous media, is a uniquely nonlinear phenomenon wherein energy gets localized in specific nodes of the lattice. While extensively studied in various contexts including optical systems and MEMS arrays, the effects of random excitation on the formation and dynamics of breathers remains largely unexplored. In this talk, we will present our recent results which demonstrate that additive white noise excitation can aid the *controlled* formation and sustenance of discrete breathers in a nonlinear electrical lattice. In addition, we will present computational results that demonstrate that a temporary burst of random excitation of the white noise type can facilitate the change of location of a breather in a lattice. The results are expected to be of both theoretical interest as well as in several important applications involving discrete breathers, such as targeted energy transfer.

Overview and Analytical Framework

Discrete breathers (also known as Intrinsic Localized Modes) correspond to localization of energy at specific locations within perfectly periodic, nonlinear lattices. Manifest as sustained, stable oscillatory modes, the existence of breathers is predicated on the nonlinearity and discreteness of the lattice. Studies of discrete breathers may be traced back to investigations of the Fermi-Pasta-Ulam oscillator chain. Since then, the phenomenon has been observed in a broad spectrum of systems such as Josephson junctions, photonic crystals [2] and micro-cantilever (MEMS) arrays [3] thereby establishing its universality. In addition to being fundamentally important in theoretical studies of energy distribution in periodic nonlinear systems, breathers are of interest in applications such as targeted energy transfer and signal processing.
The dynamical scale of several systems in which breathers emerge point to the importance of stochastic effects. Furthermore, it is known that phenomena such as stochastic resonance that arise due the interplay between randomness and nonlinearity can be exploited to advantage in applications. However, the influence of randomness on the formation and dynamics of breathers is yet to be understood and motivates the present effort. In recent work, we found that random excitation (characterized by additive white noise of appropriate intensity) of even an arbitrarily chosen cell of a lattice for a short period of time can induce breather formation in a nonlinear electrical lattice [1]. Here, we specifically ask whether random excitation of a node at which a breather has emerged can induce a change of location of the breather. In other words, we ask whether random excitation can be used as a technique to manipulate and move breathers to different locations in a lattice.

Analytical Framework

The non-dimensional dynamic model equations for a unit cell "n" in the considered electrical lattice are given in Equations (1) and (2) [4]:

$$\frac{dv_n}{d\tau} = \frac{1}{c(v_n)}\left[y_n - i_D(v_n) - \frac{1}{\omega_0 C_0}\left(\frac{1}{R_I}+\frac{1}{R}\right)v_n + \frac{cos(\Omega\tau)}{RC_0\omega_0}\right] \tag{1}$$

$$\frac{dy_n}{d\tau} = \frac{L_2}{L_1}(v_{n+1} + v_{n-1} - 2v_n) - v_n \tag{2}$$

In these equations, $v_n = V_n/V_s$ is the non-dimensional node-voltage of cell n, $\tau = \omega_0 t$ is the non-dimensional time, $\Omega = \omega/\omega_0$ is the non-dimensional driving frequency with $\omega_0 = 1/\sqrt{L_2 C_0}$, $c(v_n) = C(V_n)/C_0$, and $i_D(v_n) = I_D(V_n)/w_0 C_0 V_s$. Note that the sinusoidal sources in each cell are identical in frequency Ω, amplitude V_s, and phase. R_l is an additional term added to account for the resistance of the inductors. It is considered to be parallel to L_2 and its value is dependent on the driving voltage amplitude V_s. In this case, where we have chosen $V_s = 4V$, R_l is equal to 5 $k\Omega$ [**?**].
To account for stochastic excitation, the modelling equations are recast as a vector-valued Ito stochastic differential equation given in Equation (3):

$$d\mathbf{x}(\tau) = f(\mathbf{x}(\tau), \tau)d\tau + \sigma\tilde{G}d\mathbf{W}(\tau) \tag{3}$$

where $d\mathbf{W}(t)$ is a Brownian motion increment that is drawn from the standard normal distribution and represents a white-noise Gaussian process. The noise intensity is represented by the scalar coefficient σ. The computational results are obtained by simulating the above equations using the standard Euler-Maruyama scheme for numerical solutions of stochastic differential equations.

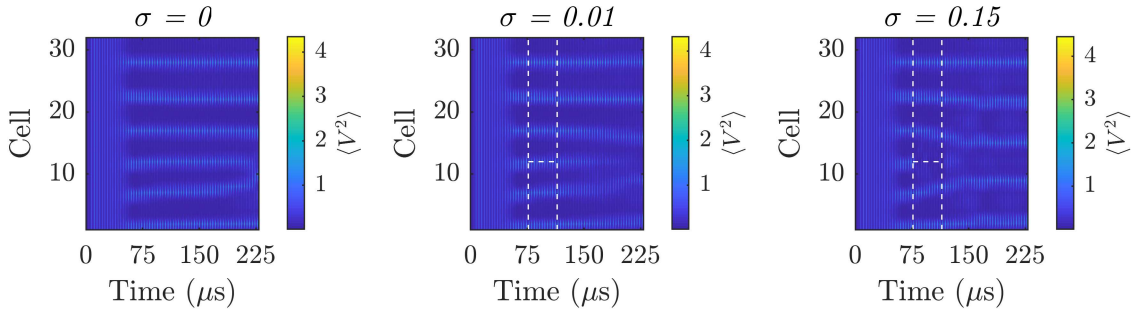

Figure 1: Averaged Results for Noise Burst at Cell 12

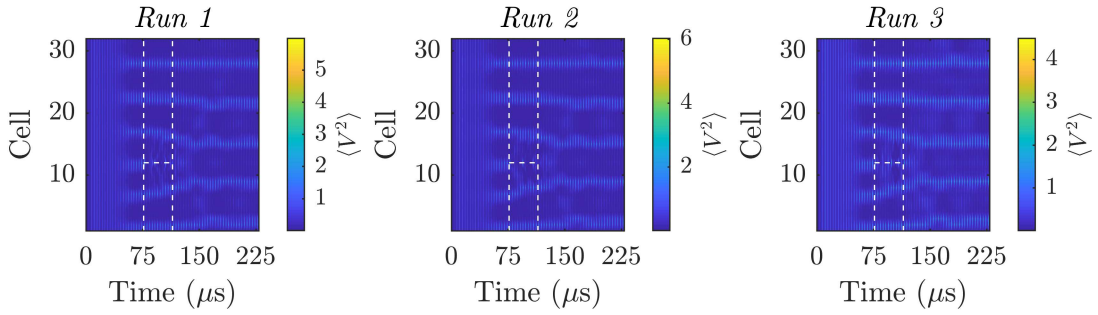

Figure 2: Individual Run Results for Noise Burst at Cell 12

Results

Breather formation spurred by small randomized initial voltage conditions at top node of cell in the range of 0 to 0.04 volts is observed. White noise is applied at cell 12 starting at 1/3 into the simulation, turned off again at the halfway point into the simulation. Figure 1 depicts the average of ten individual runs each using the same initial conditions but different noise profiles, with the dashed white lines indicating when and where noise is applied. As apparent, when $\sigma = 0.15$, the breather located at cell 12 is effectively eliminated. Individual run results pictured in Figure 2 further corroborate this. The ability to eliminate or shift breathers was found to depend on the initial condition profile used. For 2 of the 3 profiles used, including this one, it was possible to move or eliminate the breathers using a noise burst at its location. For the third profile tested, the breathers were too robust and reappeared after the noise burst in the same location. However, the effectiveness in the other two IC cases indicate that noise may be used to control the location of these breathers on average. The other cases suggest that appropriate choice of noise intensity is essential to successfully move the breathers.

Conclusions

The results indicate that random excitation characterized by additive white noise can induce a change of location of breathers in the lattice. This has not been reported in the literature and hence is a novel aspect with implications in applications where shepherding breathers across a lattice would be of interest. In addition, our recent results showing that discrete breather formation in a nonlinear electrical lattice may be controlled by random excitation will also be presented in the talk. Together, the results suggest that random excitation can be employed as a novel pathway towards controlling the emergence and dynamics of discrete breathers in nonlinear lattices.

References

[1] Edlund C., Ramakrishnan S. (2019) Creation of Discrete Breathers in a Nonlinear Electrical Lattice using Additive White Noise. *Phys. Rev. E.* (submitted).

[2] Sievers A.J., Takeno S. (1988) Intrinsic localized modes in anharmonic crystals. *Phys. Rev. Lett.* **61**:970–973.

[3] Ramakrishnan S., Balachandran B. (2010) Energy localization and white noise-induced enhancement of response in a micro-scale oscillator array. *Nonlinear Dynamics* **62**:1–16.

[4] English L.Q., et al. (2012) Generation of localized modes in an electrical lattice using subharmonic driving. *Phys. Rev. Lett.* **108**:084101.

Long Time Trapping of Particles in a Rotating Sinai Billiards System

Saheli Mitra, Saugata Bhattacharyya and Vikram Pakrashi
Laboratoire de physique des Solides, Université Paris Sud, Orsay, France
Department of Physics, Vidyasagar College, Calcutta University, India
UCD Centre for Mechanics, Dynamical Systems and Risk Laboratory, School of Mechanical and Materials Engineering, University College Dublin, Ireland
SFI MaREI Centre, University College Dublin, Ireland
UCD Energy Institute, University College Dublin, Ireland

Summary. We consider a rotating Sinai Billiards system in this paper and consider a square wall boundary with a circular scatterer. We subsequently consider the effects of rotation on this system for a number of particles. The question of ergodicity is considered from the point of view of whether or not in long time the particle can explore the complete phase space. The system is numerically simulated and tested for a range of rotational speed, indicating non-ergodic responses.

Introduction

A two-dimensional billiard with reflective square boundary and a single circular disk obstacle at the center is considered in this paper. In absence of external force, a point mass in this standard classical Sinai billiard system would have straight line trajectory until it collides either with the outer wall or the inner wall. Upon elastic collision it will change the direction of the velocity in accordance with angle of incidence is equal to angle of reflection. In this paper, the billiard system is considered under rotating conditions without an external force. Subsequently, we intend to investigate how non-ergodicity is manifested in the system as a function of rotational speed and the radius of the disk at the centre, the two main parameters governing the outcome of the system.

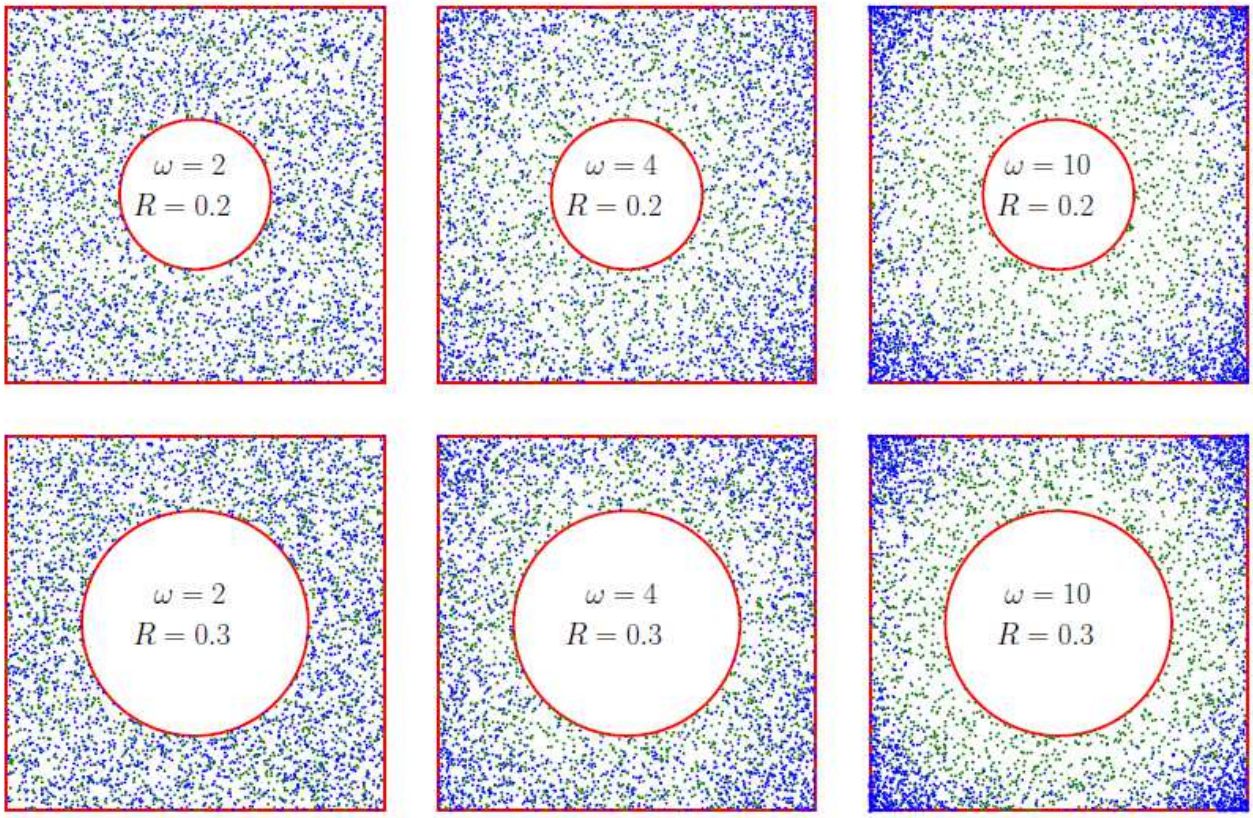

Fig.1. An ensemble of the initial and final positions of particles for different rotational speeds and disk radius. The green points indicate N=2000 initial positions of the mass point for N independent simulations. The blue points indicate their final positions after an equal amount of time has elapsed.

Results and discussions

Particle trajectories starting from different sets of initial conditions defined by position and velocity are simulated. The effect of increasing the rotational speed of the table for several cases of the radius of the circular disk on those trajectories are observed. For a certain set of rotational speed and radius of disk, 2000 initial conditions of location and velocity were considered drawing from uniformly distributed values between the inner and outer boundaries. After a sufficient time has elapsed (t = 10), the locations of the particles are noted for all of these independent runs, as observed in Fig 1.

From Fig.1, it is observed that as rotational speed increases, particles spend more time away from the disk and for high value of rotational speed the trajectories are trapped at the corners of the outer wall of the billiard making the system highly non-ergodic.

References

[1] Gelfreich, V., Rom-Kedar, V., Shah, K., and Turaev, D. (2011). "Robust exponential acceleration in time-dependent billiards." Physical review letters 106(7): 074101.

[2] Casati, G. and Prosen, T., 2012. Time irreversible billiards with piecewise-straight trajectories. Physical review letters, 109(17), p.174101.

[3] Robnik, M., 1983. Classical dynamics of a family of billiards with analytic boundaries. Journal of Physics A: Mathematical and General, 16(17), p.3971.

Thursday, July 21, 2022
08:30 - 10:30

MS-18 Control and Synchronization in Nonlinear Systems
Rhone 1

Chair: N. van de Wouw, B. Brogliato

08:30 - 08:50
Feedback control of propagating bubbles in Hele-Shaw channels
FONTANA Joao*, THOMPSON Alice
*The University of Manchester (Manchester M13 9PL United Kingdom)

08:50 - 09:10
Stabilizing reset control for motion systems with Stribeck friction
BEERENS Ruud, BISOFFI Andrea, ZACCARIAN Luca, HEEMELS Maurice, NIJMEIJER Henk, **VAN De Wouw Nathan***
*University of Minnesota (Minneapolis, MN United States) - Eindhoven University of Technology [Eindhoven] (Eindhoven Netherlands)

09:10 - 09:30
Finite time bias removal in multi-agent non-linear systems
VARMA Vineeth Satheeskumar*, MORARESCU Irinel Constantin, SRIKANT Sukumar
*CRAN-CNRS (Nancy France)

09:30 - 09:50
Hybrid formalism for consensus of nonholonomic robots with biased measurements
BORZONE Tommaso, MORARESCU Irinel Constantin, **JUNGERS Marc***, BOC Michael, JANNETEAU Christophe
*Université de Lorraine - CRAN CNRS UMR 7039 (2 Avenue de la Foret de Haye, Vandoeuvre les Nancy France)

09:50 - 10:10
Nonlinear vibration control of smart plates using nonlinear modified positive position feedback approach
CHAMAN Meymandi Saeideh*, SHOOSHTARI Alireza, MAHMOODI S. Nima
*Bu_Ali Sina University, Hamedan, Iran (Mechanical Engineering Department, Engineering Faculty, Bu_Ali Sina Un Ahmadi Roushan Blvd. Iran)

Feedback control of propagating bubbles in Hele-Shaw channels

João V. Fontana*, Alice B. Thompson*

*Manchester Centre for Nonlinear Dynamics and Department of Mathematics, University of Manchester, Oxford Road, Manchester, UK

Summary. We explore the capabilities of feedback control to stabilise and manipulate propagating bubbles in the confined geometry of a rectangular Hele-Shaw channel. Several steadily-propagating solution branches exist in this system, but only one is linearly stable. Subsequent branches featuring increasingly deformed bubble shapes and increasing numbers of unstable eigenmodes. Our aim is to use feedback control and control-based continuation to detect and stabilise at least the first of these unstable branches. This system is an appealing prototype for control: the low Reynolds number and strongly confined geometry means the system state is essentially encapsulated in the interface shape as viewed from above, recent experimental realisations of this system are in good agreement with depth-averaged models, and the system responds well to actuation via fluid injection, but nonetheless practical implementation of feedback control presents significant challenges. Here we use a depth-averaged model to explore how control would work in this system, including the design of a suitable feedback gain, the impact of control on the bifurcation structure, the complexities of controlling a propagating bubble moving past a fixed array of injection points, and how our idealised simulations relates to experimental reality.

Introduction

The study of nonlinear dynamics in soft matter systems often leads to a myriad of steady states. Stable states can be studied via both experimental and computational methods but experimental investigations at best transiently observe unstable states. Control based continuation (CBC) is a methodology that applies feedback control to the physical system using a target state as the control parameter. By choosing an unstable state as the target state and carefully choosing a feedback strategy it is possible to detect and stabilize the unstable solution without otherwise modifying it. This methodology enables tracking of bifurcation structures as well as experimental investigations of unstable behaviour [1, 2, 3]. Our aim is to use the CBC to investigate free-surface problems in fluid dynamics, both to understand the rich range of dynamical behaviour and to widen the range of possible applications of CBC in the future.

We study the propagation of an air bubble through a fluid filled rectangular Hele-Shaw channel at low Reynolds number. This system is a classical problem in fluid dynamics with known rich dynamics, which we have previously explored both via a depth-averaged model and also via laboratory experiments [4]. For steady propagation, the bubble system supports one stable solution (figure 1(a)) and an infinite number of multi-tipped unstable solutions that assume an increasing number of interface tips and unstable eigenvalues (figure 1(b,c)). Our aim is to develop and test an experimentally viable protocol for the stabilization of unstable solutions, to detect and stabilise at least the first unstable solution branch.

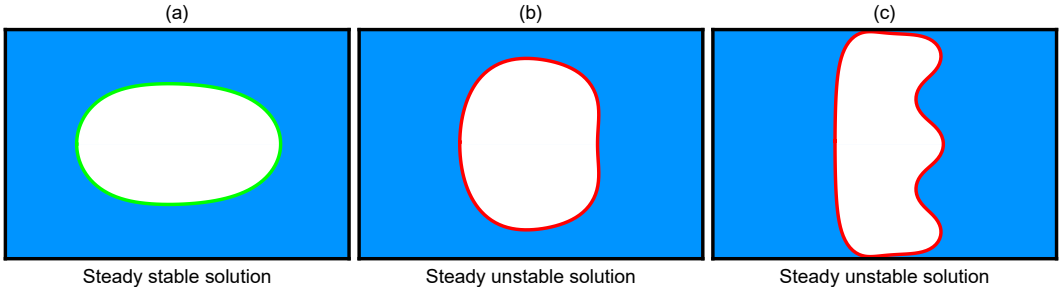

Figure 1: Three steady modes for a bubble propagating from left to right in a Hele-Shaw channel, calculated using our model.

Model

We take advantage of the shallowness of Hele-Shaw channels by using a depth-averaged approximation of the system, thus avoiding the computational complexity of the full 3D problem for bubble propagation. The problem domain is then two-dimensional, with the interface shape corresponding to the top view seen in experiments. The numerical simulations are implemented in C++ using the open-source object-oriented multi-physics finite element library oomph-lib (www.oomph-lib.org).

Our model is inevitably an approximation of the full experimental system and does not capture all details of the bifurcation structure in the experiments. Nonetheless, the model is in good qualitative agreement with experiments and in quantitative agreement in appropriate regimes. As a result, we have reason to believe that control strategies developed using this model would be effective, though not optimal, if applied in experiments.

Control via moving or fixed actuators

In order to actuate control, we inject fluid from specific points at the side walls with time-dependent amplitude $\mathbf{A}(t)$. The system can be generically represented as $\mathbf{F}(\mathbf{x}, \dot{\mathbf{x}}, \mathbf{A}) = \mathbf{0}$ where $\mathbf{x}(t)$ is a vector that describes the system state (the current interface shape) and $\mathbf{A}(t)$ describes the injection amplitude. The simplest case to analyse is when actuator position is fixed within the frame of the bubble, so actuator action is steady as perceived by the bubble. For simplicity we use a linear feedback control strategy $\mathbf{A(t)} = -\mathbf{K}(\mathbf{x(t)} - \mathbf{x_t})$ towards a target state $\mathbf{x}_T$. Various standard algorithms can be employed to choose a feedback gain $\mathbf{K}$ that (linearly) stabilizes the resulting steady solution.

We test our control strategies in nonlinear time-dependent simulations of the depth-averaged model. Choosing the unstable solution of the uncontrolled system (figure 1(b)) as the target state $\mathbf{x}_T$, the stable solution (figure 1(a)) as the initial condition, and using a pair of actuators placed a distance $d = 1$ (half the channel width) in front of the bubble centroid, we can successfully control the system towards the target solution, see figure 2(a). The transition between states is rapid and the bubble moves only a short distance along the channel.

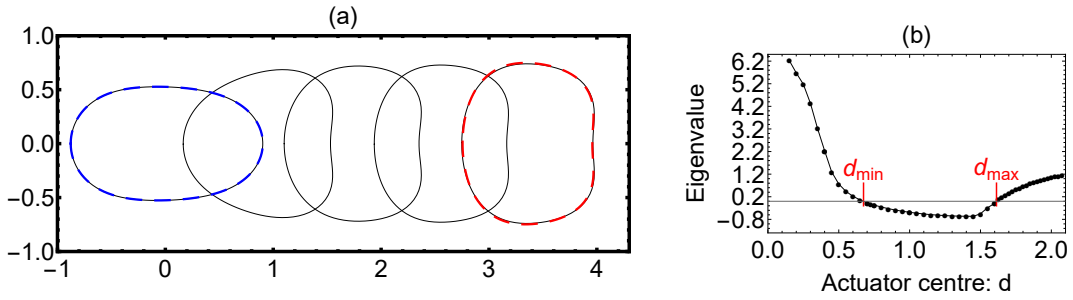

Figure 2: (a) Time evolution of a bubble, presented in the lab frame, starting with the stable solution as initial condition and evolving towards the unstable target solution. The actuator distance d is half of the channel width. The first and last interfaces are superposed with the stable and unstable solutions, in blue and red dashed lines respectively. (b) Eigenvalue plotted as a function of the actuator centre d. The steady state is successful stabilized for values of d between d_{min} and d_{max}.

A more realistic setup actuator setup is via an array of injection points fixed in the lab frame. In the frame of the bubble, this introduces time dependence in the control problem as the distance d between actuator and bubble depends on time. However, each fixed $\mathbf{K}$ has a window of d where the control is able to stabilize the equilibrium state (figure 2(b)). Hence by choosing actuator spacing within this range and switching the active actuators depending on the position of the bubble we are again able to stabilize bubbles in our simulations. Importantly for CBC, this piecewise constant $\mathbf{K}$ means that a low-dimensional parameterization of the target state is still sufficient for feedback control.

Outlook for experiments

Our analysis and simulations of control based on a depth-averaged model suggest that an unstable state can be successfully controlled via injection of fluid chosen in real time based on top view observations of the bubble. Compared to simulations, experiments present several new challenges, including noise and delay. CBC can in principle address the inevitable differences between experiment and model, as the model would be used to devise an effective control strategy which need not be optimal. It remains to be seen how closely the bifurcation structure, solution shapes and stability properties for unstable states in experiments corresponds to those predicted by the simplified model used here. We are currently developing an experimental setup to test and implement these control strategies in practice and will present experimental results for either static or moving bubbles if possible.

References

[1] D. A. W. Barton. Control-based continuation: Bifurcation and stability analysis for physical experiments. *Mech. Syst. Signal Pr.* **84**:54, 2017.

[2] J. Sieber, A. Gonzalez-Buelga, S. A. Neild, D. J. Wagg & B. Krauskopf. Experimental continuation of periodic orbits through a fold. *Phys. Rev. Lett.* **100**:244101, 2008.

[3] L. Renson, A. D. Shaw, D. A. W. Barton & S. A. Neild. Application of control-based continuation to a nonlinear structure with harmonically coupled modes. *Mech. Syst. Signal Pr.* **120**:449, 2019.

[4] A. Gaillard, J. S. Keeler, G. Le Lay, G. Lemoult, A. B. Thompson, A. L. Hazel & A. Juel. The life and fate of a bubble in a geometrically perturbed Hele-Shaw channel *J. Fluid Mech.* **914**:A34, 2021.

Stabilizing reset control for motion systems with Stribeck friction

Ruud Beerens[*], Andrea Bisoffi[***], Luca Zaccarian[****], Maurice Heemels[*], Henk Nijmeijer[*], Nathan van de Wouw[*,**]

[*]*Dept. of Mechanical Engineering, Eindhoven University of Technology, The Netherlands*
[**]*Dept. of Civil, Environmental and Geo-Engineering, University of Minnesota, Minneapolis, USA*
[***]*ENTEG, Univ. Groningen, The Netherlands* [****]*CNRS, France & Univ. Trento, Italy*

Summary. We present a reset control approach to achieve setpoint regulation of a PID-based motion system subject to Coulomb and velocity-dependent friction, including the velocity-weakening (Stribeck) effect. While classical PID control results in persistent oscillations around the setpoint (hunting), the proposed reset mechanism ensures asymptotic stability. Robustness for unknown static friction levels, and an unknown Stribeck contribution is obtained. The working principle of the controller is demonstrated experimentally on a motion stage of an electron microscope, showing superior performance over classical PID control.

Introduction

We present a reset integral control approach for stabilization of motion systems with unknown Coulomb and Stribeck friction. Friction is a performance-limiting factor in many high-precision motion systems, in the sense that it limits the achievable positioning accuracy and the settling times. Many different control techniques for frictional motion systems have been presented in the literature. Several control solutions rely on developing as-accurate-as-possible friction models, used for online compensation in a control loop, see, e.g., [1]. Also non-model-based solutions have been proposed, e.g., impulsive control (see [2]) or sliding-mode control.

Despite the availability of a wide range of control techniques for frictional systems, linear controllers are still used in the vast majority of industrial motion systems due to the existence of intuitive design and tuning tools. In the industry, the classical proportional-integral-derivative (PID) controller is most commonly used for motion systems with friction. In particular, the integrator action is capable of compensating the unknown static friction, due to the the control force increment arising from integrating the position error. However, PID control does not generally achieve stability in the presence of Stribeck friction, resulting in poor positioning accuracy. While the integrator action compensates for the static part of the friction, friction overcompensation occurs as the velocity increases due to the velocity-weakening effect. As a result, the system overshoots the setpoint and ends up in stick-slip oscillations (*hunting*). In order to eliminate these persistent oscillations, we propose a reset integral controller that induces asymptotic stability of the setpoint, despite the presence of *unknown* static friction, and an *unknown* velocity-weakening effect in the friction characteristic.

Reset controller design

Consider a single-degree-of-freedom mass m sliding on a horizontal plane with position z_1 and velocity z_2, subject to a control (force) input u and a friction force belonging to a set $\Psi(z_2)$, governed by the dynamics

$$\dot{z}_1 = z_2, \quad \dot{z}_2 \in \frac{1}{m}\left(\Psi(z_2) + u\right), \quad z_2 \rightrightarrows \Psi(z_2) := -F_s\,\mathrm{Sign}(z_2) - \alpha z_2 + f(z_2), \tag{1}$$

where F_s is the static friction, $\mathrm{Sign}(\cdot)$ is the set-valued sign function (i.e., with $\mathrm{Sign}(0) := [-1, 1]$), αz_2 the viscous friction contribution (where $\alpha \geq 0$ is the viscous friction coefficient), and f is a nonlinear velocity-dependent friction contribution, encompassing the Stribeck effect. Define the setpoint $(z_1, z_2) = (r, 0)$ for any constant position reference r. Let us first present a *classical* PID controller for input u in (1), i.e.,

$$u = -k_p(z_1 - r) - k_d z_2 - k_i z_3, \quad \dot{z}_3 = z_1 - r, \tag{2}$$

where z_3 is the integral state of the PID controller, and k_p, k_d, k_i represent the proportional, derivative and integral gains, respectively, satisfying $k_p > 0$, $k_i > 0$, and $k_p k_d > m k_i$. Finally, we embrace the (mild) assumption that the friction characteristic satisfies $|f(z_2)| \leq F_s$ for all z_2, that $z_2 f(z_2) \geq 0$ for all z_2, that f is globally Lipschitz with Lipschitz constant $L > 0$, and that, for some (potentially arbitrarily small) $\varepsilon_v > 0$ and $L_2 \in (k_d + \alpha, L]$, $f(z_2) = L_2 z_2$ for all $|z_2| \leq \varepsilon_v$.

In order to achieve closed-loop stability, we enhance the integrator in (2) with *resets*. The integrator performs two particular resets, where the key mechanism of these resets is to enforce that the integrator control force (given by $k_i z_3$) *always points in the direction of the setpoint*. To this end, we introduce a boolean state $b \in \{-1, 1\}$, characterizing whether the mass moves *towards* the setpoint (then $b = 1$), or *away from* the setpoint (then $b = -1$, typically after an overshoot of the position error). Then, the inequality $b z_2 (z_1 - r) \leq 0$ is always satisfied. The first reset that we propose entails a sign change of the integrator state z_3 at a zero-crossing of the position error $z_1 - r$. We also toggle b at this instant, because a zero-crossing of the position error marks the start of an overshoot phase, i.e.,

$$z_3^+ = -z_3, \quad b^+ = -b, \quad \text{when } z_1 - r = 0 \text{ and } b = 1, \tag{3}$$

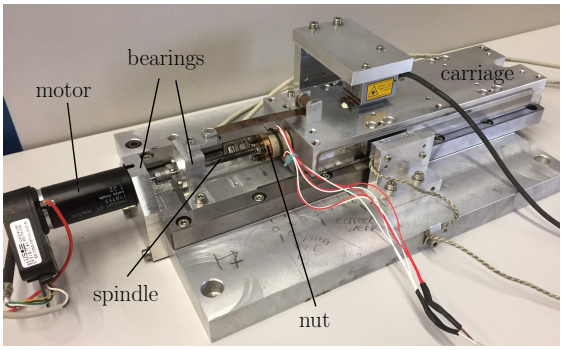

Figure 1: Experimental setup.

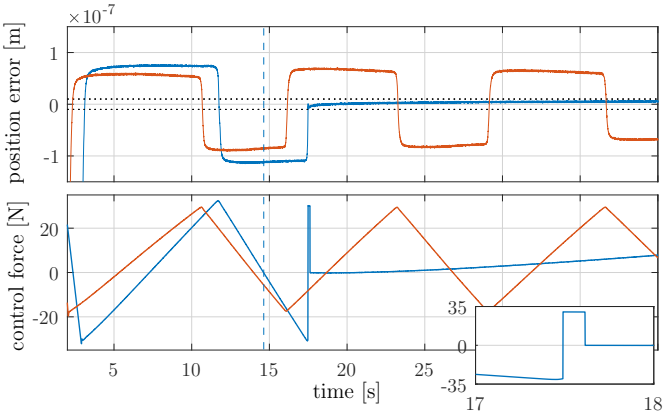

Figure 2: Position error response and experimental control force with the classical PID (red), and the reset PID (blue).

where the notation "x^+" represents the value of the considered state x after an instantaneous change, i.e., the controller reset. Besides recovering stability of the setpoint, the reset in (3) results also in some overshoot reduction. The second reset involves resetting to zero the integrator state z_3 when the velocity z_2 hits zero *after the overshoot*, i.e.,

$$z_3^+ = 0, \quad b^+ = -b, \qquad \text{when } z_2 = 0 \text{ and } b = -1. \tag{4}$$

The reset in (4) also results in a reduction of the duration of the stick phases occurring when the mass stops after the overshoot. Summarizing, the closed-loop system with the proposed reset PID controller is given by (1)-(4).
Closed-loop stability is analyzed as follows. First, we write the closed-loop system in the hybrid systems framework of [3], where we use a *hybrid* description of the Coulomb friction element in (1), as presented in [4]. We then prove that solutions to the closed-loop system (1)-(4) are also contained in said hybrid model. We then exploit the hybrid model to show that (under the aforementioned mild assumptions on the controller gains and friction characteristics) the setpoint is globally asymptotically stable, using a Lyapunov function and a recent hybrid invariance principle [5].

Experimental case study

We demonstrate the working principle and the effectiveness of the proposed reset controller on an industrial motion platform (a sample manipulation stage of an electron microscope), see Figure 1. A servo motor is connected via a spindle and a nut to a carriage, whose position is measured by a linear encoder. The goal is to position the carriage within a desired accuracy band of 10 nm. The main sources of friction are two bearings supporting the motor axis, and the contact between the spindle and the nut. We have implemented both the classical PID controller, and the proposed reset PID controller (with the same gains). For the latter one, we have designed suitable robustified conditions capable of triggering the controller resets (3), (4) also in the presence of measurement noise. Figure 2 shows the position error response and the control force for an experiment with the *classical* PID controller (red), and with the proposed *reset* PID controller (blue). The classical PID controller induces a persistent oscillation, limiting the achievable setpoint accuracy. For the reset controller experiment, the reset enhancements are activated at the time instant indicated by the blue vertical dashed line (up to this time instant, a classical PID controller is active). Then, the challenging desired accuracy band of 10 nm, indicated by the horizontal black dotted lines in the top subplot, is achieved after two controller resets. The corresponding control force is discontinuous due to the controller resets, visualized in the lower subplot and highlighted in the inset.

Conclusions

We proposed a reset PID control strategy for motion systems with unknown Coulomb and velocity-dependent friction, including the Stribeck effect. Our reset strategy recovers global asymptotic stability of the setpoint (lost by the hunting effect associated to the classical PID). The working principle and effectiveness of the controller are experimentally demonstrated on an industrial high-precision positioning device.

References

[1] B. Armstrong-Hélouvry, P. Dupont, C. Canudas de Wit, "A survey of models, analysis tools and compensation methods for the control of machines with friction", *Automatica*, vol. 30, no. 7, pp. 1083–1138, 1994.

[2] N. van de Wouw, R.I. Leine, "Robust impulsive control of motion systems with uncertain friction", *Int. J. of Robust and Nonlinear Control*, vol. 22, pp. 369–397, 2012.

[3] R. Goebel, R.G. Sanfelice, A.R. Teel, *Hybrid Dynamical Systems*, Princeton University Press, 2012.

[4] A. Bisoffi, R. Beerens, L. Zaccarian, W.P.M.H. Heemels, H. Nijmeijer, N. van de Wouw, "Hybrid model formulation and stability analysis of a PID-controlled motion system with Coulomb friction", *Proc. 11th IFAC Symposium on Nonlinear Control Systems (NolCos)*, pp. 116-121, 2019.

[5] A. Seuret, C. Prieur, S. Tarbouriech, A.R. Teel, L. Zaccarian, "A nonsmooth hybrid invariance principle applied to robust event-triggered design", *IEEE Trans. Autom. Control*, vol. 64, no. 5, pp. 2061–2068, 2019.

Finite time bias removal in multi-agent non-linear systems*

V.S. Varma*, S. Srikant† and I.-C. Morărescu*
*Université de Lorraine, CNRS, CRAN, F-54000 Nancy, France,
†IIT Bombay, India.

Summary. This work proposes some iterative procedures for estimating additive measurement biases in multi-agent non-linear systems. The bias is a constant additive offset in the relative measurement of states between agents. In contrast to existing literature which estimate biases asymptotically or does adaptive control to remove the impact of bias, we provide an iterative procedure that estimates the bias in a finite number of steps in the noiseless case.

Introduction

The multi-agent formalism enables treating problems that arise in many application domains such as engineering [3], sociology [5] or biology [9]. Consensus and synchronization were mainly studied for agents with linear dynamics interacting through a graph, see [6] for instance. However, there are also studies with nonlinear dynamics, see for example [8] which considers oscillators dynamics, or [3] on non-holonomic robots. However, the effect of measurement biases have not been well explored in this context. In [11], the authors develop an adaptive control to correct biases in a double integrator but it is not clear how this method can be adapted to general non-linear systems. In [2] and [7], the authors proposed algorithms to estimate sensor offsets in wireless sensor networks. These methods only partially compensate the offsets and never completely eliminate the bias. Recently, in [10], the authors propose a distributed bias removal strategy using a consensus type algorithm, however, the convergence of the estimate to the true bias is asymptotic.
Our main contribution is to provide a method of bias *removal in finite time* when dealing with nonlinear multi-agent systems subject to constant bias measurements. The method proposed here requires a limited number of communication instances and can be implemented either in a centralized manner through *cloud computing* or in a decentralized manner as long as *two interacting agents can measure the same reference point.*
Problem formulation: We consider a network of n interacting agents, where the interactions are described by a graph $G = (V, E)$. Each agent $i \in V$ is described by a state $x_i \in \mathbb{R}^{n_x}$. $\mathcal{N}_i = \{j \in V \mid (i, j) \in E\}$ specifies the neighborhood of agent i and represents the set of neighbors whose relative states can be measured by i. However, the measurements made by any agent i have a constant additive bias b_i which must be removed in order to accomplish the overall common goal. For any $j \in \mathcal{N}_i$, agent i has access to the measurement $z_{i,j}(t) = x_j(t) - x_i(t) + b_i$ and implements a distributed control $g(z_i)$ in order to achieve a cooperative task.
The agent dynamics is given by

$$x_i(t+1) = f_i(x_i(t), g(z_{i,j})). \tag{1}$$

We assume that the above algorithm performs well when the additive bias is 0. However, the presence of the additive bias leads to significant deterioration in performance and this must be corrected by taking $\bar{z}_{i,j} = z_{i,j} - \hat{b}_i(t)$, with $\hat{b}_i(t)$ assumed to be an estimate of the bias. Our objective is to estimate b_i for all i in finite time, using communication with a cloud or only among neighboring agents when a reference can be measured.

MAIN RESULTS

Estimating the additive biases without communication with neighbors is not possible since all the measurements have the same bias and this parameter can not be removed. In the following, we provide the assumptions on communication and on the graph structure so that bias can be estimated in a finite number of steps . .

Bias removal for non-bipartite connected graphs

Assumption 1 *We look at connected, undirected and non-bipartite graphs and assume that all agents can identify the tag of their neighbors and themselves.*

We use L^+ to denote the sign-less Laplacian which can be defined as having $L^+_{ij} = 1$ when $j \in N_i$, $L^+_{ij} = |N_i|$ if $i = j$ and 0 otherwise.

Lemma 1 ([4]) *The matrix L^+ is invertible when the graph is non-bipartite.*

We assume that all agents can communicate with the cloud which will then process all the information it has to estimate the bias. In the proposed procedure, all agents i will measure $z_{i,j}(0)$ for all its neighbors j and communicate this information to the cloud (synchronously or asynchronously). Once all agents have communicated their measurements to the cloud, it can use the following result to estimate all their biases.

*This work was partially funded by CEFIPRA under the grant 6001-A

Proposition 1 *Under Assumption 1, the cloud can estimate the bias for all agents as* $\hat{b} = (L^+)^{-1}\delta$ *where*

$$\delta_i = \sum_{j \in N_i} z_{i,j} + z_{j,i}. \tag{2}$$

From [1], we know that all non-bipartite graphs contain an odd-ring as a sub-graph. So the above procedure can work as long as the graph contains an odd-ring. In the absence of a cloud/central entity, the following distributed procedure may be used.

Remark 1 *When there is no central-cloud, if all agents have sufficient memory and can communicate with their neighbors, then all agents can estimate their bias in* N *steps. At each step all agents will communicate all the new information they have collected in the last step allowing them to aggregate all the information required to apply proposition 1.*

Distributed bias estimation with a reference

Assumption 2 *The graph is connected and there exist at least two neighboring agents* i, j *who can measure a common reference* r*.*

We use $z_{i,r}$ to denote the relative measurement of the reference with respect to agent i. In this case, we propose a distributed procedure for bias estimation in finite time. First, all agents i communicate $z_{i,j}(0)$ and $z_{i,r}(0)$ (if the reference can be measured by i) to all its neighbors.

Proposition 2 *Under Assumption 2, at least one agent* i *will be able to estimate*

$$\hat{b}_i = z_{i,r}(0) - (z_{j,r}(0) - z_{j,i}(0)). \tag{3}$$

after it receives communication from its neighbor j *which can also measure the reference.*

We propose the following distributed procedure for bias estimation in finite steps (at most N) for the remaining agents. The algorithm applied by any agent i can be described as follows.

Data: At time 0, measure and communicate $z_{i,j}(0)$ and $z_{i,r}(0)$ (if available) to all neighbors j.
if $z_{j,r}(0)$ *and* $z_{i,r}(0)$ *are known after receiving communication from neighbor* j **then**
  estimate $\hat{b}_i$ using proposition 2.
else
  $d_{i,j} \leftarrow z_{i,j}(0) + z_{j,i}(0)$
end
while $\hat{b}_i$ *is not estimated* **do**
  Wait for transmissions ;
  if *some neighbor* j *transmits* $\hat{b}_j$ **then**
    Estimate $\hat{b}_i \leftarrow d_{i,j} - \hat{b}_j$
  end
end
Transmit $\hat{b}_i$ to all neighbors.

Algorithm 1: Procedure of bias estimation

Since the graph is connected due to Assumption 2, the iterative procedure described above will have all agents estimating their own biases within N steps at most.

References

[1] Armen S Asratian, Tristan MJ Denley, and Roland Häggkvist. *Bipartite graphs and their applications*, volume 131. Cambridge university press, 1998.

[2] Saverio Bolognani, Simone Del Favero, Luca Schenato, and Damiano Varagnolo. Consensus-based distributed sensor calibration and least-square parameter identification in wsns. *International Journal of Robust and Nonlinear Control: IFAC-Affiliated Journal*, 20(2):176–193, 2010.

[3] Francesco Bullo, Jorge Cortes, and Sonia Martinez. *Distributed control of robotic networks: a mathematical approach to motion coordination algorithms*, volume 27. Princeton University Press, 2009.

[4] Dragoš Cvetković, Peter Rowlinson, and Slobodan K Simić. Signless laplacians of finite graphs. *Linear Algebra and its applications*, 423(1):155–171, 2007.

[5] Rainer Hegselmann, Ulrich Krause, et al. Opinion dynamics and bounded confidence models, analysis, and simulation. *Journal of artificial societies and social simulation*, 5(3), 2002.

[6] Ali Jadbabaie, Jie Lin, and A Stephen Morse. Coordination of groups of mobile autonomous agents using nearest neighbor rules. *IEEE Transactions on automatic control*, 48(6):988–1001, 2003.

[7] Byung-Hun Lee and Hyo-Sung Ahn. Distributed formation control via global orientation estimation. *Automatica*, 73:125–129, 2016.

[8] Irinel-Constantin Morărescu, Wim Michiels, and Marc Jungers. Effect of a distributed delay on relative stability of diffusely coupled systems, with application to synchronized equilibria. *International Journal of Robust and Nonlinear Control*, 26(7):1565–1582, 2016.

[9] Georgios A Pavlopoulos, Maria Secrier, Charalampos N Moschopoulos, Theodoros G Soldatos, Sophia Kossida, Jan Aerts, Reinhard Schneider, and Pantelis G Bagos. Using graph theory to analyze biological networks. *BioData mining*, 4(1):10, 2011.

[10] M. Shi, C. De Persis, P. Tesi, and N. Monshizadeh. *Bias estimation in sensor networks*. arXiv, 2019.

[11] Srikant Sukumar, Elena Panteley, Antonio Loría, and William Pasillas. On consensus of double integrators over directed graphs and with relative measurement bias. In *2018 IEEE Conference on Decision and Control (CDC)*, pages 4147–4152. IEEE, 2018.

Hybrid formalism for consensus of nonholonomic robots with biased measurements*

T. Borzone*,†, I.-C. Morărescu*, M. Jungers*, M. Boc† and C. Janneteau†
* *T. Borzone, I.-C. Morărescu and M. Jungers are with Université de Lorraine, CNRS, CRAN, F-54000 Nancy, France,*
† *T. Borzone, M. Boc and C. Janneteau are with CEA LIST (Commissariat à l'Energie Atomique et aux Energies alternatives - Communicating Systems Laboratory)*

Summary. This work focuses on the design of a control strategy for consensus of fleets of nonholonomic robots in presence of noisy measurements. The proposed strategy leads to a hybrid behaviour of the closed-loop dynamics of each robot. Precisely, the robots sporadically compute references that are kept constant until the next update. Between two updates of the reference the robots will apply a tracking controller allowing them to approach exponentially fast their targets. The main contributions are related to both the control design and the analysis of the resulting hybrid closed-loop dynamics. Simulations and real experiments will be presented at ENOC.

Introduction

During the last decades the design of control laws for nonholonomic robots received a lot of attention. This is mainly due to the fact that Brockett conditions [2] required for smooth stabilisation do not hold for this class of dynamics. To overcome the fact that smooth state-feedback controllers stabilizing the position and orientation of the robot do not exist, different discontinuous control laws have been proposed [5, 1]. We also point out that a control design for tracking a smooth trajectory has been also proposed for nonholonomic robots [4]. It is noteworthy that, all these strategies consider a stand-alone robot that is continuously controlled. *Our objective is to control a fleet of nonholonomic robots in a decentralized manner and in a harsh environment hampering continuous communications between robots.*
The main contribution of our work is twofold: first, the design of a hybrid control strategy for consensus of nonholonomic robots and second, the stability analysis of the closed-loop system providing minimum dwell-time conditions guaranteeing the overall system stability. As shown in the Figure 1 below, our strategy contains two loops. The external loop takes place in discrete time and uses local information related to neighbouring robots state in order to sporadically compute references of the robots. The internal loop takes place in continuous time, does not require communication with (or information from) other robots and uses a standard tracking (or point stabilization) controller such as the one proposed in [4].

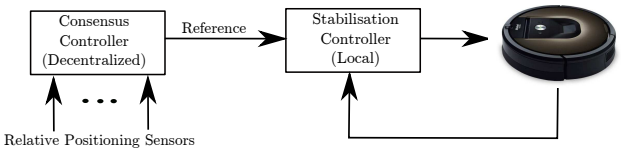

Figure 1: Control structure

Problem formulation

We consider a fleet of n nonholonomic robots that have to reach a consensus in the positions without requiring specific final orientation of the agents. For the sake of simplicity we remove the time argument t when it is not explicitly needed. We denote by $r_i = (r_{x_i}, r_{y_i})$ the 2D reference position for the robot i and we fix $r_{\theta_i} = 0$ its heading reference. The Cartesian coordinates of the center of mass of each vehicle with respect to the fixed inertial frame are denoted using vector $X_i = (x_i, y_i)$. Denoting $e_i = (e_{x_i}, e_{y_i}, e_{\theta_i})^\top$ the dynamics of the ith robot is described by the following differential equations

$$\dot{e}_i = g(e_i)u_i, \quad g(e_i) = \begin{bmatrix} \cos e_{\theta_i} & 0 \\ \sin e_{\theta_i} & 0 \\ 0 & 1 \end{bmatrix}, \quad u_i = \begin{bmatrix} v_i \\ \omega_i \end{bmatrix}. \tag{1}$$

where v_i is the linear velocity and ω_i is the angular velocity of the mobile robot; e_{x_i} and e_{y_i} are the Cartesian coordinates of the center of mass of the vehicle with respect to a frame positioned on the reference position r_i, and e_{θ_i} is the angle between the heading direction and the x-axis of this frame.
The point stabilization control considered in this work is the continuous piecewise smooth control law introduced in [3]. Basically, one considers a map $F : \mathbb{R}^3 \longmapsto \mathbb{R} \times (-\pi, \pi]$ relating $e_i \in \mathbb{R}^3$ to $z_i = (a_i, \alpha_i)^\top \in \mathbb{R} \times (-\pi, \pi]$. Taking $K, \gamma > 0$ the control law $u_i = \kappa(e_i) = (-\gamma b_1(e_i)a, -b_2(e_i)v - Ka)^\top$, where b_1, b_2 are explicitly defined in [3], exponentially stabilizes the origin of the planning reference frame $e_i = 0$. In the following, we denote $\varepsilon_i = (e_{x_i}, e_{y_i})$ the 2D Cartesian error coordinates *i.e.* $\varepsilon_i = X_i - r_i$.

Lemma 1 *Let us consider the closed loop dynamics $\dot{e}_i = g(e_i)\kappa(e_i)$ with $\kappa(e_i)$ defined above. Then, there exist positive constants c_ε and λ_ε such that $\forall t \geq t_0$ one has $\|\varepsilon_i(t)\|_\infty \leq \sqrt{n} c_\varepsilon \|\varepsilon_i(t_0)\|_\infty \mathrm{e}^{-\lambda_\varepsilon (t-t_0)}$, $\forall i \in \{1, \ldots, n\}$.*

*This work was partially funded by the Région Grand Est and CEA Tech Metz

As we previously said, the external loop designs references for each robot based on the sensing of relative positions of some neighbouring robots. These "interactions" are mathematically captured by a time-varying digraph (directed graph) $\mathcal{G}(t) = (\mathcal{V}, \mathcal{E}(t))$, where the vertex-set $\mathcal{V}$ represents the set of robots and the edge set $\mathcal{E}(t) \subset \mathcal{V} \times \mathcal{V}$ collects the interactions between robots at time t. A *path of length* p in a digraph $\bar{\mathcal{G}} = (\bar{\mathcal{V}}, \bar{\mathcal{E}})$ is a union of directed edges $\bigcup_{k=1}^{p}(i_k, j_k)$ such that $i_{k+1} = j_k$, $\forall k \in \{1, \dots, p-1\}$. The node j is *connected* with node i in $\bar{\mathcal{G}} = (\bar{\mathcal{V}}, \bar{\mathcal{E}})$ if there exists at least a path in $\bar{\mathcal{G}}$ from i to j (*i.e.* $i_1 = i$ and $j_p = j$). A *strongly connected digraph* is such that any of its two distinct elements are connected. In the sequel we consider the set of instants when at leat one robot updates its reference as $\mathcal{T} = \{t_k : t_k \in \mathbb{R}^+, t_k < t_{k+1}, \forall k \in \mathbb{N}, \lim_{k\to\infty} t_k = \infty\}$. Moreover, we define $\mathcal{T}_i \subset \mathcal{T}$ selecting the instants when robot i updates its reference (*i.e.* $\mathcal{T} = \bigcup_{i=1}^{n} \mathcal{T}_i$). At each instant $t_k \in \mathcal{T}$ a graph structure $\mathcal{G}(t_k) = (\mathcal{V}, \mathcal{E}(t_k))$ defines the interactions between neighbours. Let $\alpha \in (0, 1)$, $\beta \in (1/2, 1)$ be given. To each graph structure $\mathcal{G} = (\mathcal{V}, \mathcal{E})$ we uniquely associate a row stochastic matrix P satisfying the following properties: $P_{i,j} = 0$, if $(i, j) \notin \mathcal{E}$, $P_{i,i} > \beta$, $\forall i = \{1, \cdots, n\}$, $P_{i,j} > \alpha$, if $(i, j) \in \mathcal{E}$.

Assumption 1 (Connectivity) *The digraph $\mathcal{G} = \bigcup_{k\geq k_0} \mathcal{G}(t_k)$ is strongly connected for all $k_0 \in \mathbb{N}$.*

Assumption 2 (Bounded Intercommunication Interval) *If $(i, j) \in \mathcal{E}(t_k)$ infinitely often, then there is some $L \in \mathbb{N}$ such that, for all $t_k \in \mathcal{T}$, $(i, j) \in \mathcal{E}(t_k) \bigcup \mathcal{E}(t_{k+1}) \bigcup \cdots \bigcup \mathcal{E}(t_{k+L-1})$.*

Main results

The closed-loop hybrid dynamics associated with the i-th robot ($i \in \{1, \dots, n\}$) can be formulated as:

$$\begin{cases} \dot{r}_i(t) = 0, \qquad \dot{e}_i(t) = g(e_i(t))\kappa(e_i(t)) \quad \text{for } t \in \mathbb{R}^+ \setminus \mathcal{T}_i, \\ r_i(t_k) = \sum_{j=1}^{n} P_{i,j}(t_k)\varepsilon_j(t_k^-) + \sum_{j=1}^{n} P_{i,j}(t_k) r_j(t_k^-) + \delta_i(t_k), \quad \varepsilon_i(t_k) = \varepsilon_i(t_k^-) + r_i(t_k^-) - r_i(t_k) + \delta_i(t_k) \text{ for } t_k \in \mathcal{T}_i, \end{cases}$$

where $\delta_i(t_k)$ represents the measurement bias whose infinity norm is upper-bounded by $\bar{\delta} \in \mathbb{R}^+$. Our main objective is to analyse the ISS property of the overall dynamics of n robots defined above w.r.t the following set:

$$\mathcal{A} = \Big\{\varepsilon, r \in \mathbb{R}^{2n} \mid \varepsilon = 0,\ r_{x_i} = r_{x_i},\ r_{y_i} = r_{x_j}, \forall i, j \in \{1, \dots, n\}\Big\}.$$

Theorem 1 *Let Assumptions 1-2 hold. Then the overall dynamics of n systems defined above is ISS w.r.t. the set $\mathcal{A}$, if the time between any two consecutive updates of the reference for each robot is larger than τ^* with*

$$\tau^* = \frac{1}{\lambda} \ln \max \left\{ \frac{\eta_2 c N}{1-\eta_1} \sum_{l=0}^{2L-1} a^{\frac{2L-1-l}{2L-1}}, \frac{c(\eta_3(N-1)+1)}{(1-n(2L-1)\eta_3)a} \sum_{l=0}^{L-1} a^{\frac{2L-1-l}{2L-1}} \right\} > 0,$$

with $\eta_1 = 1 - \alpha^L, \eta_2 = 4 - 2\alpha, \eta_3 = 1 - \beta$ and $a = \frac{1+\eta_1}{2}$.

Remark 1

- *We note that theorem above does not fix the update instants but only provide a minimum dwell-time between updates of the reference of the same robot. Consequently, very frequent updates are forbidden.*
- *When $\bar{\delta} = 0$ (i.e. the sensors provide perfect measurements) the theorem above states that $\mathcal{A}$ is GUAS for the overall closed-loop dynamics of n nonholonomic robots.*

Conclusions

This work formulates a decentralized control strategy for fleets of nonholonomic robots with biased measurements. The control is designed as follows. In a first step, at sporadic time-instants the robots compute a reference based on measurements of relative postions of some neighbours. In a second step, the robots continuously apply a state-feedback tracking controller. This yields a hybrid behaviour of the closed-loop dynamics. We show that consensus can be achieved as far as a certain minimum dwell-time condition between the reference updates of each robot is respected. Simulations and real experiments will be presented at ENOC.

References

[1] A. Astolfi. Exponential stabilization of a wheeled mobile robot via discontinuous control. *Transactions-American Society of Mechanical Engineers Journal of Dynamic Systems, Measurement, and Control*, 121:121–125, 1999.

[2] R.W. Brockett. Asymptotic stability and feedback stabilization. *In Differential Geometric Control Theory*, (R.W. Brockett and R.S. Millman and H.J. Sussmann Eds):181–191, 1983.

[3] C. Canudas de Wit and O. J. Sordalen. Exponential stabilization of mobile robots with nonholonomic constraints. *IEEE Transactions on Automatic Control*, 37(11):1791–1797, 1992.

[4] E. Panteley, E. Lefeber, A. Loria, and H. Nijmeijier. Exponential tracking control of a mobile car using a cascaded approach. In *Proceedings of IFAC Motion Control*, pages 201–206, 1998.

[5] J.-B. Pomet. Explicit design of time-varying stabilizing control laws for a class of controllable systems without drift. *Systems & control letters*, 18(2):147–158, 1992.

Nonlinear vibration control of smart plates using nonlinear modified positive position feedback approach

Saideh Chaman Meymani[*]*,Alireza Shooshtari*[*]*,S.N. Mahmoodi*[**]
[*]*Mechanical Engineering Department, Bu_Ali Sina Department, Hamedan, Iran*
[**]*Alabama State University, United State of America*

Summary. In this paper, nonlinear vibration control of a plate is investigated using Nonlinear Modified Positive Position Feedback (NMPPF) method that is applied through a piezoelectric layer on the plate. NMPPF controller consists of a resonant second-order nonlinear compensator for vibration suppression at targeted resonance. In this model, transverse vibrations are studied and stimulations are performed for the primary resonance. Using time-space separation of the differential equations of the model and Galerkin method the temporal nonlinear equations governing the system have been found. Then, the free and forced vibrations of the structure with the NMPPF controller has been solved using Method of Multiple Scales to obtain an analytical solution. Results show that the NMPPF controller reduces the amplitude of the vibration by inducing an increase to the damping coefficient. In addition, the NMPPF controller provides a higher level of suppression in the overall frequency domain response by increasing the compensator gain. Finally, the results of the analytical solution for the closed-loop NMPPF controller are presented and compared with the result of the conventional Positive Position Feedback (PPF) controller and nonlinear integral resonant controller (NIRC).

Introduction

Controllers are one of the most effective ways to control linear and nonlinear vibrations. Hence, different control strategies have been presented and utilized [1]. One of the methods for nonlinear vibration control is to use of active control. The advantage of using active control is its real-time adjustment according to the condition of the system and alternations in the input disturbance force on the system. In order to have the highest level of suppression in the vibration control process, it is essential to design a controller compatible with the nonlinear characteristics of the system oscillations. Linear and nonlinear active vibration controllers typically employ piezoelectric actuators. Active vibration control is usually applied using piezoelectric ceramics as actuators and sensors, as an example, piezoelectric actuators are used in Atomic Force Microscopes to produce high-frequency vibrations. The purpose of this paper is to obtain the equations of nonlinear vibrations and controller system for elastic plate with a piezoelectric layer that follows the classical theory of Kirchhoff. In addition, Van Karman's nonlinear strains have been used to investigate geometrical nonlinear effects. This plate has a piezoelectric layer at its upper surface. This layer actually is utilized to actively suppress the vibrations of the plate. The external force applied to the piezoelectric layer is divided into two groups: 1) the control force ($F_c(t)$), the control force via the controller's compensator will be logged; and 2) the harmonic excitation force distributed uniformly on the plate as the disturbance. The constitutive equations for piezoelectric layer is utilized to implement the effect of applied voltage into the electromechanical model. Method of Multiple Scales is utilized for calculation of the frequency response of the system and the controller. The resulting modulation equations are, then, used to verify the effectiveness of the proposed controller. Having the solution for the controllers, results are graphically demonstrated and discussed. In order to understand the performance of the controllers in more detail, sensitivity analysis on the closed loop system responses is performed and the influence of each parameter on the control output have been investigated.

MATHEMATICAL MODELING OF THE STRUCTURE

In this section, the nonlinear dynamic model of the structure is investigated. The structure is composed of two layers of square plates, a substructure layer and a piezoelectric layer with the different thickness on top of the substructure, as shown in Fig. 1. It is assumed that the h_p and h_s are thicknesses of the piezoelectric layer and substructure, respectively. Also, as shown in Fig. 1, a is the side length of the plate. The origin of the coordinate system is placed on the corner of the middle plane of the substructure layer. The boundary conditions of the plate are considered as simply support and $u.v$ and w are the displacement of the plate in the $x.y$ and z directions respectively.

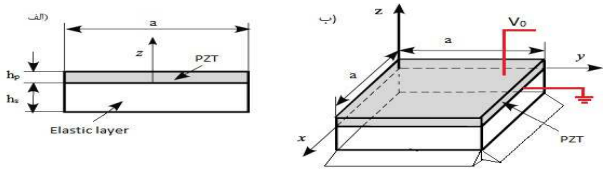

Figure 1. The symmetric unimorph piezoelectric plate.

Using Hamilton's principle, equations of motion of the plate based on classical theory and von Karman strain and then applying Galerkin method for simply suppotted B. C. in all edge of plate, nonlinear temporal equations can be expressed as:

$$\ddot{W}(t) + \omega_w^2 W(t) + \tilde{\alpha} W^3(t) + \tilde{\eta}_w \dot{W}(t) = \tilde{F}\, cos(\tilde{\Omega} t) \quad (1)$$

The control force, $F_c(t)$, will be added to the equation. Also, ω_w^2 consists of two parts of the natural frequency created in the sheet with the piezoelectric layer and a coefficient of the voltage created from the piezoelectric layer to the elastic

layer. The equation is created for the natural frequency of $\omega_w^2 = \omega^2 + s_1 V_e$ where s_1 is the constant coefficient of the voltage applied to the plate. The method of Multiple Time Scales is used to find a uniform nonlinear structure. The nonlinear system of Equation (1) under NMPPF controllers are defined as follows

$$\ddot{\bar{r}}(t) + \tilde{\eta}_r \dot{\bar{r}}(t) + \omega_r^2 \bar{r}(t) + \tilde{\delta} \overline{r^3}(t) = \tilde{k}_r U(t) \tag{2}$$

$$\dot{\bar{s}}(t) + \omega_s \bar{s}(t) = \tilde{k}_s U(t)$$

where $\bar{r}(t)$ *and* $\bar{s}(t)$ are compensatory first and second order state variables, respectively. k_r and k_s are the inputs of the control. The control law pertains to the modified positive position feedback controls system in the main system of Equation (1) as $F_c(t) = \tau_r r(t) + \tau_s s(t)$; that are τ_r and τ_s respectively, are first order compensator and second in a closed loop system. Using Multiple time scale method, the coupled equations obtained for the frequency are the response of the main system and the controller domain.

$$\left(\frac{\hat{f}}{2}\right)^2 = \left[\left(\frac{\hat{\eta}_u}{2} + \frac{\hat{\tau}_s \hat{k}_s}{2}\right)a + \frac{\hat{\tau}_r \hat{\eta}_r b^2}{2k_r a}\right]^2 + \left[\frac{3\hat{\alpha}}{8}a^3 + \frac{\hat{\tau}_s \hat{k}_s}{2}a - \frac{3\hat{\delta}\hat{\tau}_r}{8\hat{k}_r}\frac{b^4}{a} - \frac{\hat{\tau}_r}{\hat{k}_r}\left(\sigma_r - \sigma_f\right)\frac{b^2}{a} - \sigma_f a\right]^2 \tag{3}$$

$$\left[1 - \frac{\hat{\eta}_r^{\,2}}{\hat{k}_r^{\,2}}\frac{b^2}{a^2}\right]^{\frac{1}{2}} = \frac{3\hat{\delta}}{4\hat{k}_r}\frac{b^3}{a} + \frac{2}{\hat{k}_r}(\sigma_r - \sigma_f)\frac{b}{a}. \tag{4}$$

Results and discussions

This part has discussed the vibration range in the resonant frequency region and the performance of the controllers in controlling the vibration amplitude in the resonance region. The frequency response of main system is given in Fig. 2. Fig. 3 indicates the frequency response of the closed loop system with the PPF controller. Implementation of PPF controller reduces vibration range in the resonant frequency region $(\sigma_f = 0)$. This controller amplifies the production of two-peak amplitudes with relatively large amplitude around the frequency. Fig. 4 shows the frequency response of NMPPF controlled systems. In this Fig., the right peak has higher amplitude. Also, Fig. 5, shows the comparison of the effects of these nonlinear controllers on the frequency response of smart plate.

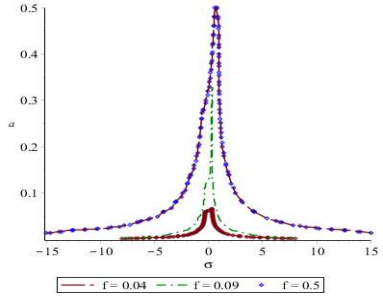

Fig 2. Frequency response of the uncontrolled system

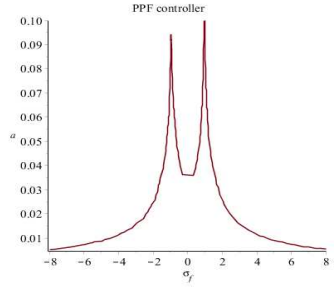

Fig 3. Frequency response of the PPF controlled

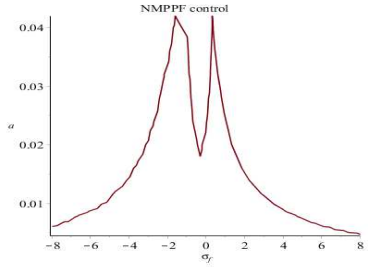

Fig 4. Frequency response of the NMPPF controlled system

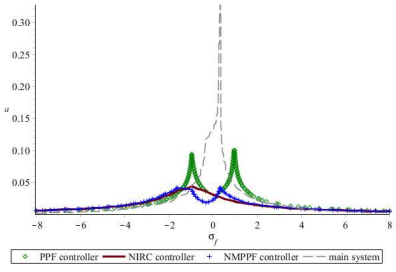

Fig 1. Comparison of the PPF, NIRC, and NMPPF controller performances

Conclusion

In this article, active nonlinear vibrations control of a simply supported smart plate using the NMPPF controller introduced. The system response also studied under NIRC and PPF control approaches. It is shown that the PPF controller had a weaker control effect than the other two controllers. Also, the NMPPF controller reduced the vibration amplitude on a large bandwidth in the frequency domain better than the other two methods.

References

[1] Omidi E and Mahmoodi S.N (2014) October. Nonlinear vibration control of flexible structures using nonlinear modified positive position feedback approach. In ASME (2014) *Dynamic Systems and Control Conference* (pp. V003T52A002-V003T52A002). American Society of Mechanical Engineers.

Thursday, July 21, 2022
08:30 - 10:30

MS-09 Nonlinear Dynamics in Engineering Systems
Auditorium Lumiere

Chair: Aubrey Beal - Antonio Zippo

08:30 - 08:50
Strongly Nonlinear Forced Damped Model for the Dynamics of the Valve Spring
GZAL Majdi*, GENDELMAN Oleg
*Technion - Israel Institute of Technology, Faculty of Mechanical Engineering, (Technion City, Haifa, 32000 Israel)

08:50 - 09:10
Tuned Mass System with a Hybrid Hysteresis Model
RATHORE Khogesh K*, BISWAS Saurabh
*Indian Institute of Technology, Jammu, India (IIT Jammu, Jagti 181221 India)

09:10 - 09:30
On the effects of meso-scale friction interface geometry on nonlinear dynamics of large mechanical structures
YUAN Jie*, SALLES Loic, SCHWINGSHACKL Christoph
*University of Strathclyde (16 Richmond St, Glasgow G1 1XQ United Kingdom)

09:30 - 09:50
The Basin Stability of a Bi-Stable Frictional Oscillator
STENDER Merten*, HOFFMANN Norbert, PAPANGELO Antonio
*Hamburg University of Technology (Am Schwarzenberg-Campus 1, 21073 Hamburg Germany)

09:50 - 10:10
Asymmetric oscillations of a shallow spherical cap under a harmonic pressure field: bifurcations and chaos
IARRICCIO Giovanni*, ZIPPO Antonio, PELLICANO Francesco
*InterMech MoRe Centre (Via Pietro Vivarelli 10 - int. 1 - 41125 Modena Italy) - Università degli Studi di Modena e Reggio Emilia, Dipartimento di Ingegneria Enzo Ferrari (V. P. Vivarelli 10 41125 Modena ITALY Italy)

Strongly Nonlinear Forced Damped Model for the Dynamics of the Valve Spring

Majdi Gzal and Oleg V. Gendelman
Faculty of Mechanical Engineering, Technion – Israel Institute of Technology, Haifa, Israel

Summary. The preloaded valve spring of an internal combustion engine is mathematically modeled as a one-dimensional finite non-homogenous forced-damped chain using the Hertzian contact law, and its strongly nonlinear dynamics is analytically studied. An approximated analytical single-frequency solution in the form of time-periodic and spatially localized state is derived. The theoretical results are confirmed by numerical simulations as well as experimental test results. This indicates that the strongly nonlinear chain allows a single-frequency approximate solution.

Introduction

The interplay between nonlinearity and discreteness supports time-periodic and spatially localized solutions, which are commonly referred to as discrete breathers (DBs) [1]. Exact solutions for symmetric discrete breathers were derived for the Hamiltonian model [2] and for the case of a homogenous external forcing with restitution coefficient less than unity [3]. Recently, we developed a discrete nonhomogeneous model for the nonlinear dynamics of the valve spring [4]. This model revealed two qualitatively different states of the periodic responses; we referred to them as propagating states and edge states. The propagating states are characterized by weak localization, and the edge states—by strong localization at the forced edge. To meet more realistic conditions of the valve train, in this study, we extend our previous model in two ways. First, using the Hertzian contact law to describe all the valve-valve seat interactions in each period of excitation. Second, we include the preload effect. This implies that in our model, both the precompression and the non-smooth behavior caused by the separation exist.

Model description and analytical treatment

Following our previous paper [4], the valve spring is mathematically described as a one-dimensional finite non-homogenous chain, as illustrated in Figure 1. The model includes a heavy mass, denoted by M, which represents the valve mass together with the mass of the upper element of the spring, and N light masses, each with mass m, i.e. the mass of one spring element. The masses are interconnected in series by linear springs and dampers, denoted by k and λ, respectively, resulting to total spring stiffness of k/N and total internal damping of the spring material of λ/N. In realistic settings of the valve train, the valve spring is preloaded by a static load of kd_0/N, resulting to total preload displacement of d_0 (as shown in Figure 1, middle). Then, the preloaded valve spring is closed by a rigid wall in such a way that the heavy mass interacts with the wall, as illustrated in Figure 1, right. We assume that this interaction is given by Hertzian contact law. This constraint on the displacement of the heavy mass represents the interaction between the valve and valve seat. Regarding the boundary conditions, the Nth light mass is fixed while the heavy mass is subjected to an external displacement $h(t)$, which represents the cam lobe profile, through a flexible connection called tappet, modeled by the spring k_c and damper λ_c.

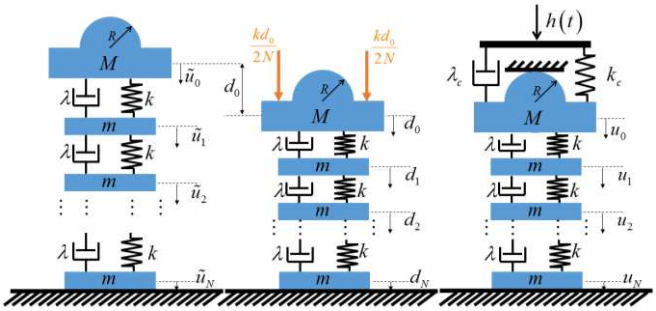

Figure 1: A mathematical model for the valve spring dynamics: free spring (left), preloaded spring in the static state (middle) and the forced spring with the contact constraint (right)

Let u_n denotes the dynamic displacement (relative to the preloaded state) of the nth mass. Thus, the equations of motion for the forced valve spring (Figure 1, right) are given as follows:

$$\begin{aligned} &n=0: \quad M\ddot{u}_0+\lambda\left(\dot{u}_0-\dot{u}_1\right)+k\left(u_0-u_1\right)+\lambda_c\dot{u}_0+k_c u_0=\alpha\left[\Delta-u_0\right]_+^{3/2}-\frac{kd_0}{N}+ \\ &\qquad +k_c a_0+\left[k_c a+\lambda_c\Omega b\right]\cos\left(\Omega t\right)+\left[k_c b-\lambda_c\Omega a\right]\sin\left(\Omega t\right) \qquad (1) \\ &1\le n<N-1: \quad m\ddot{u}_n+\lambda\left(2\dot{u}_n-\dot{u}_{n-1}-\dot{u}_{n+1}\right)+k\left(2u_n-u_{n-1}-u_{n+1}\right)=0 \\ &n=N: \quad u_N=0 \end{aligned}$$

Here in (1), the parameter Δ represents the equilibrium displacement induced by the preload force kd_0 / N, resulting to $\Delta = \left(kd_0 / \alpha N\right)^{2/3}$, α is a material parameter (depending on the elastic properties and the geometric characteristics of the heavy mass and the wall). The $(+)$ subscript is used to emphasize that the bracketed term is non-zero only if the term inside the bracket is positive and zero otherwise. The parameter Ω describes the frequency of the applied excitation, which was assumed to be given by the first harmonic approximation $h(t) = a_0 + a\cos(\Omega t) + b\sin(\Omega t)$. We assume that the response of each oscillator has a dominant harmonic component with the frequency equal to the frequency of the applied excitation, then, the following single-frequency solution is introduced:

$$u_n = U_0\left(1 - \frac{n}{N}\right) + C_n\cos(\Omega t) + S_n\sin(\Omega t) \tag{2}$$

Introducing the suggested solution (2) into (1) and expanding the non-smooth term into Fourier series to obtain static and dynamic components as follows:

$$\left[\Delta - U_0 - C_0\cos(\Omega t) - S_0\sin(\Omega t)\right]_+^{3/2} = \beta_0 + \sum_{r=1}^{\infty}\beta_r\cos(r\Omega t) + \sum_{r=1}^{\infty}\gamma_r\sin(r\Omega t) \tag{3}$$

For the first harmonics, one obtains:

$$\begin{aligned}
\beta_0 &= \frac{\sqrt{2}A^{3/2}}{3\pi}\left[\left(3\sigma^2 - 4\sigma + 1\right)\mathbf{K}(\bar{\sigma}) + 8\sigma\mathbf{E}(\bar{\sigma})\right] \\
\beta_1 &= \frac{2\sqrt{2}A^{3/2}\cos(\phi)}{5\pi}\left[\left(-\sigma^2 + 4\sigma - 3\right)\mathbf{K}(\bar{\sigma}) + 2\left(\sigma^2 + 3\right)\mathbf{E}(\bar{\sigma})\right] \\
\gamma_1 &= -\frac{2\sqrt{2}A^{3/2}\sin(\phi)}{5\pi}\left[\left(-\sigma^2 + 4\sigma - 3\right)\mathbf{K}(\bar{\sigma}) + 2\left(\sigma^2 + 3\right)\mathbf{E}(\bar{\sigma})\right]
\end{aligned} \tag{4}$$

Here we denote $\bar{\sigma} = \sqrt{2\sigma + 2}/2, \sigma = (\Delta - U_0)/A$, $\phi = \arctan(-S_0/C_0), A = -\sqrt{C_0^{\,2} + S_0^{\,2}}$, $\mathbf{K}(\bar{\sigma})$ represents the complete elliptic integral of the first kind, and $\mathbf{E}(\bar{\sigma})$ is the complete elliptical integral of the second kind.

Substituting equations (2), (3) and (4) into (1) and applying the harmonic balance method, one obtains a set of $(2N+3)$ nonlinear algebraic equations in the unknowns U_0, C_n and S_n, $n = 0,1,...,N$.

Conclusions

In this work, we introduce a strongly nonlinear mathematical model to describe the dynamics of the preloaded valve spring taking into account the valve-valve seat interaction, which has been described by the essentially nonlinear (nonlinearizable) Hertzian contact law. The dynamics of the chain is analytically studied under the assumption that the response of each oscillator has a dominant harmonic component with a frequency equal to the excitation frequency. Depending on the location of the applied frequency in the dispersion curve of the linear chain, the model under consideration reveals two different periodic responses, namely, propagating and edge breathers. The propagating breathers have main frequency in the propagation zone, and are characterized by weak localization, in which the energy can spread among all the masses. The edge breathers (we referred to them as edge states) possess frequency in the attenuation zone, these states are characterized by strong localization at the forced end of the chain, i.e. maximal concentration of energy in the excited mass against small-amplitude oscillations in the rest of the chain. This implies that in the edge states regime, the coupling between the zeroth and first masses can be removed, and the strongly nonlinear forced oscillator can be considered as a single DOF that excites the linear chain. Comparison of the analytical solution with numerical simulations and experimental test results yields close agreement.

References

[1] S. Flach, A. V. Gorbach (2008) Discrete Breathers: Advances in Theory and Applications. *Phys. Rep*. **467** (1) 1–116.
[2] O.V. Gendelman, L.I. Manevitch (2008) Discrete Breathers in Vibroimpact Chains: Analytic Solutions. *Phys. Rev. E* **78** (2) 026609.
[3] O.V. Gendelman (2013) Exact Solutions for Discrete Breathers in a Forced Damped Chain. *Phys. Rev. E* **87** (6) 062911.
[4] Gzal, M., Gendelman, O.V. (2020) Edge States and Frequency Response in Nonlinear Forced Damped Model of Valve Spring. *Nonlinear Dyn* **99**: 661–678.

Tuned Mass Systems with a Hybrid Hysteresis Model

Khogesh K Rathore and Saurabh Biswas
*Indian Institute of Technology Jammu, Jammu 181221, India

Summary. Tuned-mass-dampers are used in mechanical systems to reduce the dynamic response of the primary structures. The damping plays a significant role in a tuned-mass-damper system. In many engineering systems, damping is hysteretic in nature. Here, we study tuned mass systems with a hybrid version of hysteresis model with the Bouc-Wen model and a recently developed scalar hysteresis model. The sine sweep responses show two resonance peaks. The sine sweep responses indicate the amplitude vs. frequency of the systems. We compare the numerical results obtained for two different hysteresis models.

Introduction

Tuned mass dampers (TMD) are often used in practical systems to reduce the high amplitude vibrations. There have been extensive researches on TMDs and their applications to engineering problems. TMD devices are extensively used for vibration control, including long span cable bridges, tall buildings, tall water tanks, etc. Much researches have been done over the last several decades on the passive and active control of structures using TMD, see e.g., [1,2].

The damper of the TMD device plays a very important role. Both linear and nonlinear dampers are used in the TMD systems, see e.g., [3,4]. TMD systems with linear viscous damping are often analytically tractable. On the contrary, TMD systems with nonlinear damping models are mathematically challenging.

In many engineering systems, energy dissipation occurs in the form of rate-independent hysteresis. In general, rate-independent hysteresis introduces *signum* nonlinearities in systems. Several researchers used hysteretic dampers in the TMD systems, e.g., [5]. In [6], a hysteretic tuned mass damper is used for structural vibration reduction. In [7], the Bouc-Wen hysteresis model [8,9] is used as the damper in the TMD.

With the above motivation, we will study TMD systems with the Bouc-Wen model and a rate independent scalar hysteresis model developed in [10]. The hysteresis model of [10] is motivated by a study of an elastic plate with several frictional microcracks.

The above two models are briefly discussed below.

The Bouc-Wen hysteresis model is given by

$$\dot{f}(t) = \dot{z}(t)\left\{A - \left[\beta\,\mathrm{sgn}\left(\dot{z}(t)\,f(t)\right) + \gamma\right]|f(t)|^{n}\right\} \tag{1}$$

where $A > 0, \beta > 0,\ \gamma \in [-\beta, \beta]$ and $n > 0$ are the model parameters. Here, $z(t)$ is the given input and $f(t)$ is the corresponding hysteretic output of the system.

The rate-independent scalar hysteresis model of [10] is given by

$$\dot{\theta}(t) = \frac{\kappa}{|z(t)| + \in}\left\{\theta_a + \beta_0\,\mathrm{sgn}\left(z(t)\,\dot{z}(t)\right) - \theta(t)\right\}\cdot|\dot{z}(t)| \tag{2}$$

where $z(t)$ is the input displacement to the system and θ is an internal variable. Here, θ_a, κ, β_0 are model parameters and $\in$ is a small regularizing parameter. The hysteretic force is given by

$$f(t) = \theta(t)\cdot z(t) \tag{3}$$

We use the Bouc-Wen model and the scalar hysteresis model of [10] in parallel in TMD systems. We compare the numerical results obtained for both cases.

TMD with the Bouc-Wen hysteresis and the hysteresis model of [10] in parallel

Figure 1(left) shows a TMD system with the Bouc-Wen hysteresis model and the hysteresis model of [10] in parallel. Here, m_1 is the mass of the primary system, k_1 is the stiffness of the spring on which m_1 is mounted, m_2 is the mass of the secondary structure which is attached to the primary mass with a spring of stiffness k_2 and two hysteretic dampers in parallel indicated by h_1 and h_2. Here, the damper h_1 is governed by the hysteresis model of [10], and the damper h_2 is governed by the Bouc-Wen model. A harmonic force $F_0 \sin(\omega t)$ is applied to the primary mass.

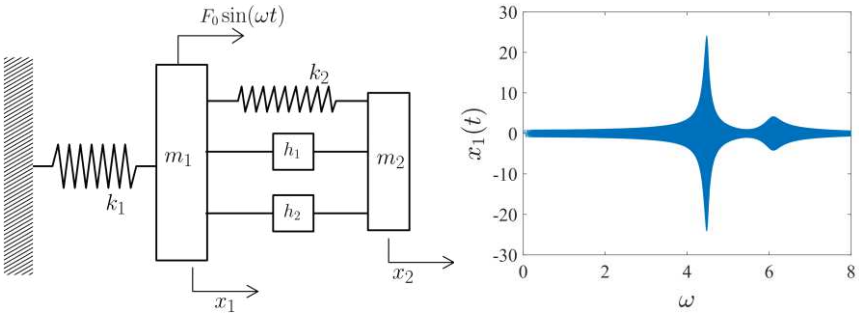

Fig. 1 Left: A tuned mass system with the Bouc-Wen hysteresis and the hysteresis model of [10] in parallel. Right: Response of the TMD with the Bouc-Wen and the model of [10] in parallel. Parameters used: $m_1 = 1$, $m_2 = 1/10$, $k_1 = 1$, $k_2 = 1/10$, $A = 1, n = 1, \beta = 0.5$, $\gamma = 0.1$, $\kappa = 4$, $\theta_a = 2$, $\beta_0 = 1.8$, $\in = 10^{-6}$, $F_0 = 1.2$, $\alpha = 0.01$, $\alpha_1 = 0.7$ and $\alpha_2 = 0.9$.

Equations of motion of the system are as follows:

$$m_1\ddot{x}_1 + (k_1 + k_2)x_1 - k_2x_2 - f = F_0\sin(\omega t) \tag{7}$$

$$m_2\ddot{x}_2 - k_2x_1 + k_2x_2 + f = 0 \tag{8}$$

$$\dot{\theta}(t) = \frac{\kappa}{|x_2(t) - x_1(t)| + \in}\{\theta_a + \beta_0\,\mathrm{sgn}[(x_2(t) - x_1(t))(\dot{x}_2(t) - \dot{x}_1(t))] - \theta(t)\}|\dot{x}_2(t) - \dot{x}_1(t)| \tag{9}$$

$$\dot{h}_2 = \alpha_2\left[|\dot{x}_2(t) - \dot{x}_1(t)|\left\{A - \left[\beta\,\mathrm{sgn}\left(h_2(t)(\dot{x}_2(t) - \dot{x}_1(t))\right) + \gamma\right]|h_2(t)|^n\right\}\right] \tag{10}$$

Here, $h_1 = \alpha_1 \cdot \theta \cdot (x_2(t) - x_1(t))$

and

$f = \alpha\left(h_1 + h_2\right)$

where α_1 and α_2 are scalar multipliers that control the level of damping. Note that, the input displacement to the dampers is $(x_2(t) - x_1(t))$.

We use a slowly time varying frequency $\omega = 10^{-5}t$ for the frequency sweep calculations. Figure 1(right) shows a frequency sweep response of the primary mass for the TMD with the Bouc-Wen hysteresis and the hysteresis model of [10] in parallel. Resonance peaks are seen in the frequency sweep response. In Figure 1(right), the frequency sweep responses indicate the amplitude vs. frequency of the primary mass. We can see the primary and secondary resonances of the TMDs. By tuning the parameters of the TMDs, we can get the desired resonant amplitudes for our systems.

Conclusions

In this paper, we have numerically studied tuned mass systems with the Bouc-Wen hysteresis model and the hysteresis model of [10] in parallel as the dampers. The net damping force is numerically controlled by two parameters. The goal of the paper was to numerically study the sine-sweep frequency responses of the TMDs. The sine-sweep response gives a clear idea of how the amplitude of the system varies with the frequency. The study helps to develop the idea to tune the model parameters in order to achieve desired resonant responses.

References

[1] Jangid R.S., Datta T. K. (1995) Seismic Behaviour of Base-Isolated Buildings: A State-of-the Art Review. *Proc. Institution of Civil Engineers-Structures and Buildings*. 110(2):186-203.

[2] Soto M.G., Adeli H. (2013) Tuned mass dampers. *Archives of Computational Methods in Engineering*. 20(4):419-31.

[3] Randall S.E. Halsted D.M., III, Taylor D.L. (1981) Optimum vibration absorbers for linear damped systems. *J. Mech. Des*. 103(4): 908-913.

[4] Starosvetsky Y, Gendelman O.V. (2009) Vibration absorption in systems with a nonlinear energy sink: nonlinear damping. *J. Sound Vib*. 324(3-5): 916-39.

[5] Gerges R.R., Vickery B.J. (2005) Design of tuned mass dampers incorporating wire rope springs: Part I&II: Dynamic representation of wire rope springs. Eng. Struct. 27(5):653-674.

[6] Carpineto N., Lacarbonara W., Vestroni F. (2014) Hysteretic tuned mass dampers for structural vibration mitigation. In: *J. Sound Vib*, 333, 1302-1318(2014).

[7] Lacarbonara W., Vestroni F. (2002) Feasibility of a vibration absorber based on hysteresis, In: *Proceedings of the Third World Congress on Structural Control*, Como, Italy.

[8] Bouc R. (1967) Forced vibration of mechanical systems with hysteresis. In: *Proceedings of the 4th Conference on Nonlinear Oscillation*, p. 315, Prague.

[9] Wen Y. (1976) Method for random vibration of hysteretic systems. *J. Eng. Mech. Div*. 102(2), 249–263.

[10] Biswas S., Jana P., Chatterjee A. (2016) Hysteretic damping in an elastic body with frictional microcracks. *Int. J. Mech. Sci*. 108, 61–71.

On the effects of meso-scale friction interface geometry on nonlinear dynamics of large mechanical structures

Jie Yuan*, Loic Salles† and Christoph Schwingshackl ‡
*Aerospace Centre of Excellence, University of Strathclyde, Glasgow, G1 1XQ, UK
†Skolkovo Institute of Science and Technology,Bol'shoy Bul'var, 30, Moscow, Russia, 121205
‡Vibration University Technology Centre, Imperial College London SW7 2AZ, London,UK

Summary. Friction interfaces can be almost found in all engineering structures which has major influence on their dynamical response. Previous experiments found that mesoscale geometrical characteristics of friction interfaces have a significant impact on the nonlinear modal properties of assembled systems but their effects on nonlinear dynamics has not numerically explored due to the complex coupling between tribology and dynamics. This work proposes an efficient multi-scale approach to investigate the influence of meso-scale interface geometry of friction interfaces. It is applied to a realistic "Dogbone" test rig designed to assess the effects of aero-engine blade root geometries in a fan blade system. The friction interface with different meso-scale profiles are effectively investigated.

Introduction

Friction interfaces have been widely used in assembled structures to connect components and transfer the mechanical loads. They are regarded as the main source of nonlinearities and uncertainties in an assembled structure. The relative motion occurring on friction interfaces often leads to a significant change of its dynamics such as reducing overall stiffness, shifting resonance frequencies and decreasing vibration amplitude through strong energy dissipation. A number of experiments have shown that the nonlinear dynamical behavior of the system is very sensitive to the geometry of friction interfaces [1, 2], which can greatly change the static and dynamic properties such as with crowning interface geometries. However, the effects of meso scale interface geometry on nonlinear dynamics has not been much investigated. However, there is a lack of efficient numerical approaches to design and analyse the influence of such meso-scale interface geometries on the nonlinear dynamical properties.

Methodology

This work proposes a multi-scale modelling framework to study the effects of meso-scale interface geometries on the nonlinear dynamics of complex dynamical systems with friction interfaces. The approach mainly consists in the integration of micro/meso-scale friction interfaces into macro-scale FE model. As shown in Eq.1, nonlinear static analysis (with a flat-on-flat contact interface) is firstly performed to evaluate overall contact loads on the friction interfaces under different pre-loadings. Then, based on overall contact loads from the nonlinear static analysis, a highly efficient semi-analytical solver based on the boundary element method shown in Eq.2 and 3 is performed to obtain the pressure and gap distribution from the contact interface with different geometrical characteristics [3]. The static pressure and gap distribution are then used as the input for a frequency domain nonlinear vibration solver to evaluate nonlinear vibration response of the whole assembled structures where the governing equation is shown in Eq.4. The detailed methodology for nonlinear dynamic analysis can refer to [4].

$$\mathbf{K}\, u(t) + \mathrm{F}_{nl}(u(t)) = \mathrm{F}_s(t) \tag{1}$$

$$u_z(x,y) = \frac{1-\nu^2}{\pi E} \int_{-\infty}^{+\infty}\int_{-\infty}^{+\infty} \frac{p(\xi,\eta)}{\sqrt{(\xi-x)^2+(\eta-y)^2}} d\xi d\eta \tag{2}$$

$$u_z(i,j) = K_{zz} \otimes p = \sum_{k=1}^{N_x}\sum_{l=1}^{N_y} p(k,l) K_{zz}(i-k, j-l) \tag{3}$$

$$\mathbf{M}\,\ddot{u}(t) + \mathbf{C}\,\dot{u}(t) + \mathbf{K}\,u(t) + \mathrm{F}_{nl}(u(t)) = \mathrm{F}_e(\gamma, \varphi, \Omega, t) \tag{4}$$

Test case and results

The test case for this study is based on a fan blade root test rig setup as shown in Fig.1 (a). The "Dogbone" rig consists of two main components: a set of identical solid root-block disks and a set of "bones" for different root designs [5]. Fig.1(b) shows the FE model representing the test rig which is performed in Hypermesh where matching mesh has been used on four friction interfaces. The 3D node to node contact element as shown in Figure 1(c) has been used to simulate the contact force. Different meso-scale interface geometries are considered including the different interface shapes including central bump, Y wise bump, edge wise radium. The geometry of the central bump is constructed using defined ellipse curves in both directions with maximum height in the central point similar to [2]. Figure 2 (a) shows the pressure distribution of the central bump contact interface with different maximum heights. With the increase of bumpiness of central bumper,

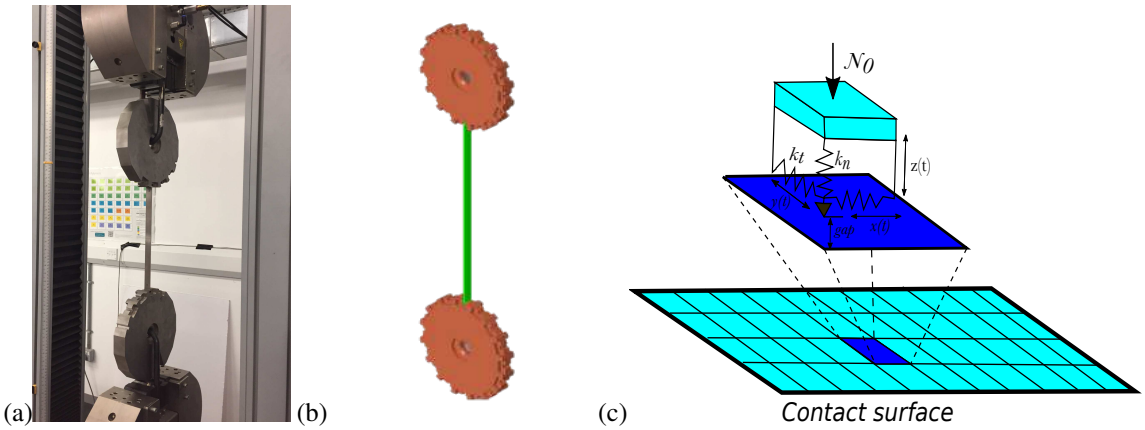

Figure 1: (a) Dogbone Test rig setup; (b) FE model of the Dogbone rig (c) Contact friction element

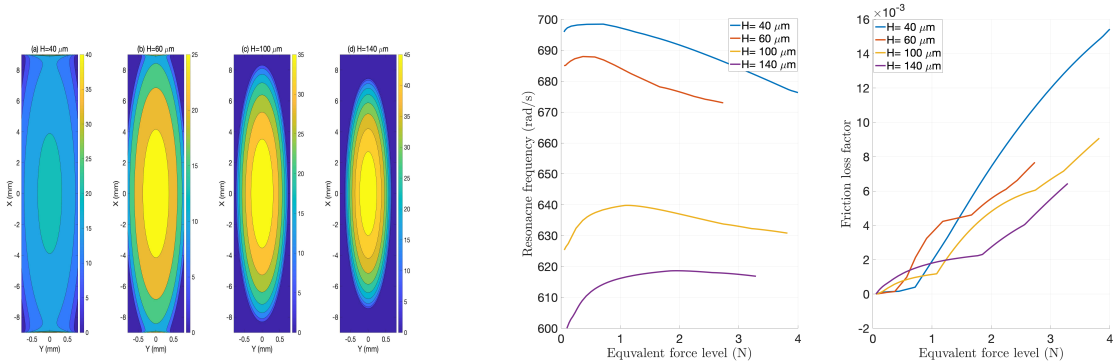

Figure 2: (a)Normal contact pressure and (b)Nonlinear modal properties of the Central Bump for diffident levels of bumpiness

the pressure distribution becomes more centralized in middle of the contact interface with higher stress amplitude. Figure 2 (b) shows the nonlinear modal properties of these central bump contact interfaces at different force levels. With the increasing bumpiness, it shows the stating resonance frequency is reduced from 700 to 600 rad/s mainly because of the increasingly reduced contact area making jointed friction interfaces become less and less stiff. With the increase of force level, for all the cases, the resonance frequency increases initially and then gradually decreases with further increase of energy levels.

Conclusions

This work presents a multi-scale-based approach to efficiently evaluate the effects of meso-scale interface geometries on the nonlinear dynamical response of structures with frictional interfaces. The proposed approach was applied to design and analysis of a blade root Dogbone test rig (similar to fan blade dovetail joints) to evaluate the effects of blade root geometries on the overall dynamic response of the system. Different meso-scale interface profiles including different shapes, level of bumpiness and edge radium were investigated. The studies show the proposed multi-scale approach can efficiently evaluate the influence of meso-scale interface profiles on the contact pressures at a much lower cost. The effects of meso-scale interface profiles on the damping and resonant frequency behavior are significant which should not be ignored in the design and analysis of jointed structures. The developed tool can also be used to design and optimize the friction interface for improved nonlinear dynamics.

References

[1] Beisheim, J. R., Sinclair, G. B. (2010). Improved three-dimensional crowning profiles for dovetail attachments. *Journal of Engineering for Gas Turbines and Power*, **132(6)**.

[2] Allara, M., Zucca, S., Gola, M. M. (2007). Effect of crowning of dovetail joints on turbine blade root damping. *In Key Engineering Materials* (Vol. 347, pp. 317-322). Trans Tech Publications Ltd.

[3] Armand, J., Salles, L., Schwingshackl, C.W., Süß, D., Willner, K. (2018) On the effects of roughness on the nonlinear dynamics of a bolted joint: a multiscale analysis. *Eur J Mech A Solid.* **70**, 44–57

[4] Yuan, J., Sun, Y., Schwingshackl, C., Salles, L. (2022). Computation of damped nonlinear normal modes for large scale nonlinear systems in a self-adaptive modal subspace. *Mechanical Systems and Signal Processing*, **162, 108082**.

[5] Schwingshackl, C.W., Zolfi, F., Ewins, D.J., Coro, A., Alonso, R. (2009) Nonlinear friction damping measurements over a wide range of amplitudes. In: *Proceedings of the international modal analysis conference XXVII*, Orlando

The Basin Stability of a Bi-Stable Frictional Oscillator

Merten Stender*, Norbert Hoffmann*,‡ and Antonio Papangelo †,*
* *Dynamics Group, Hamburg University of Technology, Hamburg, Germany*
† *Department of Mechanics Mathematics and Management, Politecnico di Bari, Bari, Italy*
‡ *Department of Mechanical Engineering, Imperial College London, London, United Kingdom*

Summary. The stability of steady-state solutions is typically assessed by means of local criteria. As an example, the eigenvalues' real parts indicate linear stability of an equilibrium position against small perturbations. However, realistic dynamical systems may exhibit multiple co-existing solutions. If the perturbations are not small, local stability measures have only a limited value for evaluating the effective probability of arriving at one of the multiple solutions. Therefore, global methods are required to evaluate the attractiveness of a state for finite perturbations. This work illustrates the concept of basin stability for a frictional oscillator that exhibits bi-stability. The results indicate how the global basin stability measure can complement conventional stability considerations.

Introduction

Dynamical systems are well-known to exhibit multistability, i.e. multiple stable states co-exist at a given system configuration. In this scenario, only the initial conditions and instantaneous perturbations dictate on which state the system will end up. For example, Gräbner et al. [1] report experimental observations of bi-stability in brake system vibrations. Recently, Jahn et al. [2] have discussed a friction-excited system that exhibits multistability via periodic orbits that compete with chaotic dynamics. Classical linearization-based approaches, such as eigenvalues or Lyapunov exponents, asses a state's stability by investigating the local behavior of small perturbations. The absolute values of those metrics quantify the rate of convergence (for stable states), or divergence (for unstable states), and classify the stability in a binary fashion. For example, the eigenvalue's real part indicates the growth of small perturbations in the vicinity of a fixed point, and hence the equilibrium is stable for a negative real part. However, local linear stability concepts cannot indicate the most desirable state amongst the multiple co-existing ones. This scenario is particularly unsatisfactory if some of the stable states are undesired for reasons of increased vibrations, noise, wear, or fatigue. The concept of basin stability [3] relates to the volume of the basin of attraction $\mathcal{B}$. The basin stability $S_\mathcal{B}$ of a particular state indicates the volumetric fraction of initial states that converge to the attracting set with respect to the overall state space volume. Therefore, it is a global nonlinear measure for the attractiveness of states, i.e. the basin stability can adequately assess the stability of a state under non-small perturbations. In practical system dynamics, the knowledge of multiple solutions and their stability, as typically displayed in bifurcation diagrams, is only one piece of information. The likelihood of the system arriving at one of those solutions may be of even greater importance during the operation of a mechanical structure or machine. This works strives to illustrate the concept of basin stability on the example of a bi-stable frictional oscillator.

Methods

We study the dynamics and stability of a single-degree-of-freedom system $m\ddot{x}+c\dot{x}+kx=F$, see Figure 1 (a), following

$$\begin{aligned} F &= -N\mu\left(v_\mathrm{rel}\right)\mathrm{sign}\left(v_\mathrm{rel}\right), \quad && v_\mathrm{rel}\neq 0, \quad v_\mathrm{rel}=\dot{x}-v_\mathrm{d} \\ |F| &< \mu_\mathrm{st}N, && v_\mathrm{rel}=0, \\ \mu(v_\mathrm{rel}) &= \mu_\mathrm{d}+\left(\mu_\mathrm{st}-\mu_\mathrm{d}\right)\exp\left(-\frac{|v_\mathrm{rel}|}{v_0}\right), \end{aligned} \tag{1}$$

that experiences friction-induced vibrations (FIV). The friction formulation features a velocity-dependent weakening-strengthening behavior that gives rise to an instability of the steady sliding solution, see Figure 1 (b). A self-excited stick-slip limit cycle exists for the parameter range $0 \leq \tilde{v}_\mathrm{d} \leq 1.84$ and, most importantly, co-exists with the steady sliding solution in the bi-stability regime $1.11 \leq \tilde{v}_\mathrm{d} \leq 1.84$ resulting from the subcritical Hopf bifurcation. Hence, in this parameter range, there exist two stable states in parallel, as depicted in Figure 1 (c). Depending on the initial condition or instantaneous perturbations, the system will either end up in the low-energy steady sliding state, or on the high-intensity stick-slip cycle.

Results

Conventionally, the stability of the equilibrium solution, i.e. the steady sliding state, is assessed by the eigenvalue's real part $\Re\left(\lambda\right)$. However, in realistic systems, it is often unknown what type of perturbations the system may experience during operation. In our model, the unstable periodic orbit (UPO) represents the separatrix between the basins of attraction ⌊ for the two stable states. A perturbation of $\tilde{x} < -0.65$ at $\tilde{v}_\mathrm{d} = 1.5$ would result in a jump from the steady sliding state to the limit cycle. The eigenvalue in Figure 2 (a) grows for a decline in belt velocity, indicating that the steady sliding state becomes less stable against perturbations up to $\tilde{v}_\mathrm{d} = 1.11$. However, the linear stability analysis is unable to show how fast the basin $\mathcal{B}$ of the steady sliding state shrinks for declining belt velocities $\tilde{v}_\mathrm{d}$. Hence, the eigenvalue analysis does not detect the critical transition at $\tilde{v}_\mathrm{d} = 1.84$ where the systems transits into the bi-stability regime. On the contrary, the basin

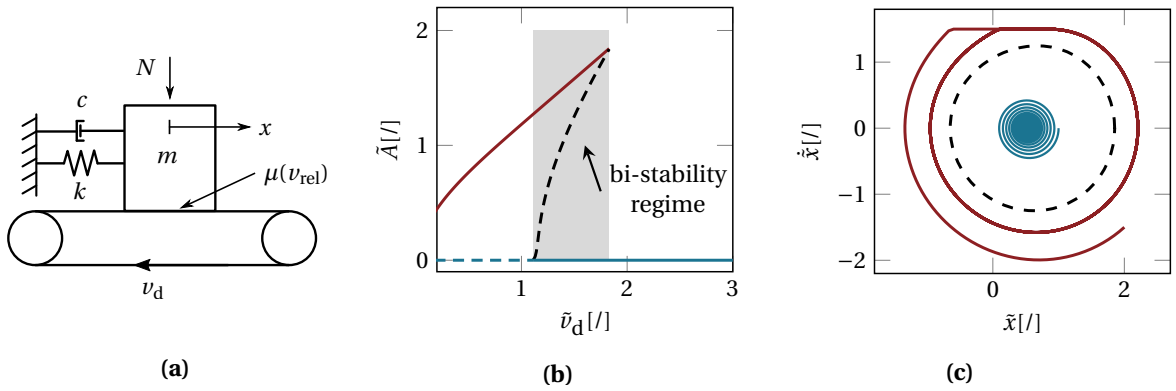

Figure 1: (a) single-degree-of-freedom frictional oscillator, (b) bifurcation diagram for the non-dimensional belt velocity $\tilde{v}_{\mathrm{d}}$, and (c) phase plane for $\tilde{v}_{\mathrm{d}} = 1.5$. Stable (unstable) solutions are indicated by solid (dashed)lines. The stable steady sliding state (blue spiral trajectory) co-exists with the unstable periodic orbit (black dashed line) and the stable stick-slip limit cycle (red trajectory). The non-dimensional system $(\tilde{\cdot})$ is evaluated for $\mu_{\mathrm{d}} = 0.5$, $\mu_{\mathrm{st}} = 1$, $\xi = 0.05$, $N = 1$ and $\tilde{v}_0 = 0.5$ following the work [4]

stability $S_{\mathcal{B}}$ in Figure 2 (b) indicates the *global degree of stability*, which changes quickly at the transition point. Here, $S_{\mathcal{B}}$ is a much more reliable proxy for detecting the critical transition of the steady sliding state. While the linear analysis states a negative eigenvalue at $\tilde{v}_{\mathrm{d}} = 1.5$, $S_{\mathcal{B}}$ indicates that the likelihood of converging to the steady sliding state is in fact only $S_{\mathrm{B}} = 0.255$. Hence, the system is three times more likely to exhibit stick-slip vibrations if the initial conditions or perturbations were randomly drawn from the given state space regime.

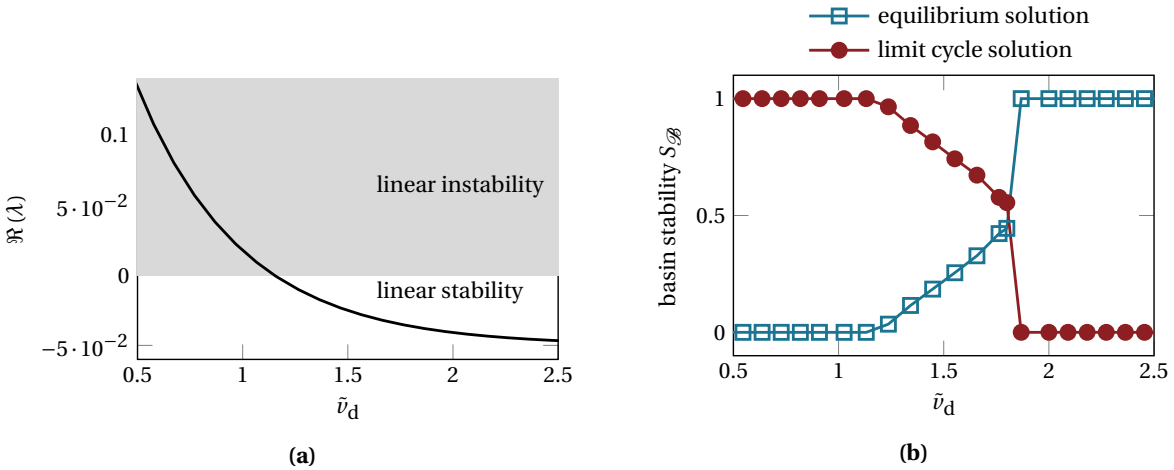

Figure 2: (a) eigenvalue's real part as a function of the belt velocity. The linearly unstable regime for $\Re(\lambda) > 0$, shaded in gray, is reached at $\tilde{v}_{\mathrm{d}} = 1.11$. (b) basin stability $S_{\mathcal{B}}$ of the steady sliding equilibrium and the stick-slip limit cycle. Initial conditions were drawn from $\tilde{x}_0 \in \{-2, 3\}$ and $\dot{\tilde{x}}_0 \in \{-2, 2\}$ using a uniform grid of 20×20 points.

Conclusions

The basin stability is studied as a measure for the state's relevance in a multistability scenario. While the (nonlinear) stability of this small oscillator is rather straight-forward, the basin stability seems to be a particularly useful stability measure for more complex, i.e. higher-dimensional, systems that feature a complicated multi-stability behavior [5]. Regarding the actual motion during operation, the basin stability is likely to contribute to higher prediction quality of numerical models of mechanical structures. As a second model, a frictional oscillator with multiple degrees of freedom and a more complicated dynamical behavior [2] will be studied in the full conference proceeding.

References

[1] Gräbner N., Tiedemann M., von Wagner U., Hoffmann N. (2014) Nonlinearities in friction brake nvh-experimental and numerical studies. *SAE Technical Paper* **2014**:2511.

[2] Jahn M., Stender M., Tatzko S., Hoffmann N., Grolet A., Wallaschek J. (2019) The extended periodic motion concept for fast limit cycle detection of self-excited systems. *Computers & Structures* **2019**:106-139.

[3] Menck P.J., Heitzig J., Marwan N., Kurths J. (2013) How basin stability complements the linear-stability paradigm. *Nature Physics* **9/2**:89-92.

[4] Papangelo A., Ciavarella M., Hoffmann N. (2017) Subcritical bifurcation in a self-excited single-degree-of-freedom system with velocity weakening–strengthening friction law: analytical results and comparison with experiments. *Nonlinear Dynamics* **90**:2037-2046.

[5] Nusse H.E., Yorke J.A., Kostelich E.J. (1994) Basins of attraction. *Applied Mathematical Sciences* **101**:269-314.

Asymmetric oscillations of a shallow spherical cap under a harmonic pressure field: bifurcations and chaos

Giovanni Iarriccio, Antonio Zippo and Francesco Pellicano
Dept. of Engineering "Enzo Ferrari", University of Modena and Reggio Emilia, Modena, Italy
Intermech Mo.Re Centre, Modena, Italy

Summary. The nonlinear vibrations of a homogeneous, isotropic, and shallow spherical cap under a harmonic pressure field are investigated. The problem is tackled using a semi-analytical method based on Novozhilov's nonlinear thin shell theory. The partial differential equations (PDEs) are reduced to a set of ordinary differential equations (ODEs) through the Rayleigh-Ritz approach and Lagrange equations. The final equations of motion are numerically solved using both continuation and direct integration techniques. Results depicted the activation of non-symmetric vibrational states, with the presence of multiple bifurcations and chaotically-modulated oscillations.

Introduction

The characterization of thin-walled structures under dynamic loads has always received considerable research attention due to the large number of applications in Engineering from macro to nanoscales (e.g. propellant tanks, micro-electro-mechanical systems, nanotubes).
This study proposes a method to analyze the dynamics of a homogeneous, isotropic, and thin-walled shallow spherical cap under a uniform, time-varying pressure distribution, see Figure 1.
Despite most of the previous studies on this topic being limited to the axisymmetric vibrations, which neglected the possible onset of non-symmetric vibrations, some authors suggest retaining asymmetric modes into the analysis to improve the matching among experimental and numerical results [1].
To this end, the formulation here presented uses Novozhilov's thin shell theory [2], a follower pressure to model the external load distribution [3], and it retains the asymmetric modes into the reduced-order model. Complete details regarding the present study are reported in Refs [4,5].

(a) (b)

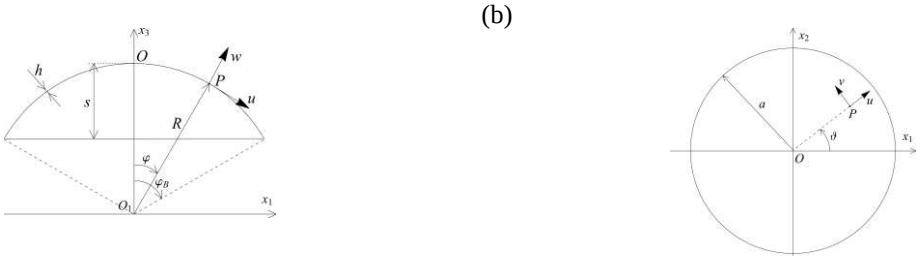

Figure 1: Spherical cap reference system: (a) side and (b) top view.

Results and Discussion

Following the analyses presented in Refs [4,5], a 38 dofs reduced-order model is considered. The structure is loaded by a uniform static pressure superimposed to a harmonic one. The frequency of the harmonic pressure varies about the first axisymmetric mode resonant frequency $\omega_{1,0}$. Using a continuation method to analyze the stability of periodic solutions, and directly integrating the equations of motion, a dynamic scenario characterized by multiple bifurcations and chaos is shown.
In Figure 2, the frequency-response diagram of the asymmetric modal coordinate $f_{w,1,2}^{(d)}$ is given. The continuation method (black-solid line) shows the presence of period-doubling bifurcations (PD) leading to the onset of asymmetric oscillations. The stability loss of the periodic responses (black-dotted line) agrees with the irregular response trend prompted by the direct integration of the equations of motion (red-dashed/blue-solid line).
Since an irregular frequency-response diagram suggests chaotic oscillations, Figure 3 shows the time response of $f_{w,1,2}^{(d)}$ for a normalized forcing frequency $\Omega = 1.09 \cdot \omega_{1,0}$. Two different phenomena could be observed: a slow dynamic, which module the oscillation amplitude, and a fast dynamic governed by rapid burst. This pattern has some periodicity, and the evolution of the Poincaré map clearly shows weekly chaotic vibrations: by reporting the section for an increasing number of periods n_P, the sparse cloud contour becomes regular, and a dense kernel becomes noticeable.

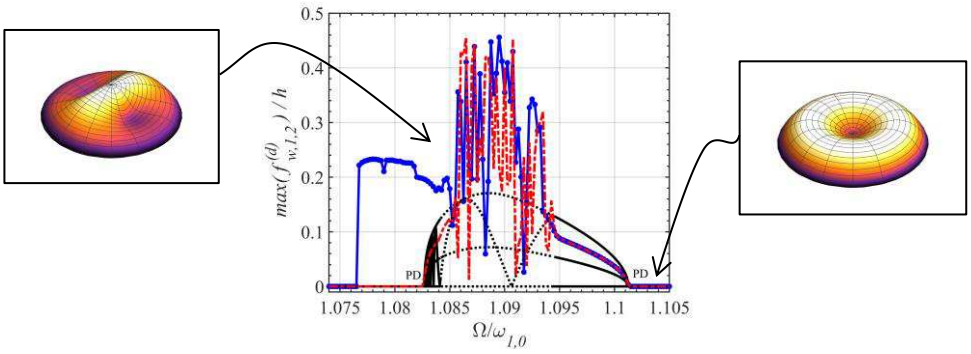

Figure 2: Asymmetric mode activation after period doubling bifurcation: continuation method VS direct time integration.

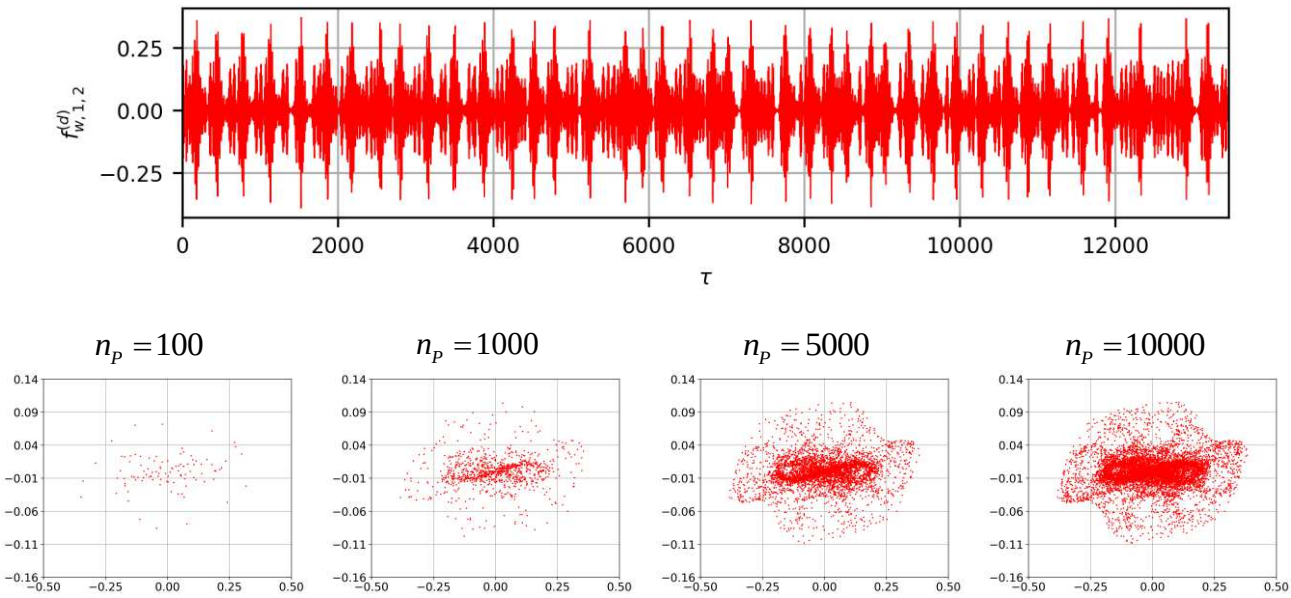

Figure 3: Chaotically-modulated oscillations with fast and weekly periodic burst: time history and progressive Poicaré map evolution of the asymmetric modal coordinate and its time derivative.

References

[1] Evensen, H. A., and Evan-Iwanowski, R. M. (1967) Dynamic response and stability of shallow spherical shells subject to time-dependent loading. *AIAA Journal*, 5(5), 969-976.

[2] Novozhilov, V.V. (1953) Foundations of the Nonlinear Theory of Elasticity. Graylock Press, Rochester, NY, USA (now available from Dover, NY, USA).

[3] Amabili, M., and Breslavsky, I. D. (2015) Displacement dependent pressure load for finite de-flection of doubly-curved thick shells and plates. International Journal of Non-Linear Mechanics, 77, 265-273.

[4] Iarriccio, G., and Pellicano, F. (2021) Nonlinear dynamics and stability of shallow spherical caps under pressure loading. *ASME J. Comput. Nonlinear Dynam.*, 16(2),021006.

[5] Iarriccio, G., Zippo, A., and Pellicano, F. (2022) Asymmetric vibrations and chaos in spherical caps under uniform time-varying pressure fields. *Nonlinear Dyn.* 107, 313–329.

Thursday, July 21, 2022
13:30 - 15:30

MS-17 Time-periodic systems
Saint Clair 3A

Chair: Zoltan Dombovari

13:30 - 13:50
Parameter identification of periodic systems by impulse dynamic subspace description
KISS Adam K.*, BACHRATHY Daniel, DOMBOVARI Zoltan
*MTA-BME Lendület Machine Tool Research Group, Department of Applied Mechanics, Budapest University of Technology and Economics (Budapest, Muegyetem rkp. 3. Hungary)

13:50 - 14:10
Test Rig with Drive Belt: Modelling and Simulation of Parametrically Excited Vibrations
MESSER Markus*, GASS Bernhard
*Technische Hochschule Mittelhessen, Fachbereich Maschinenbau, Mechatronik, Materialtechnologie (Wilhelm-Leuschner-Straße 13 61169 Friedberg Germany)

14:10 - 14:30
Parametric resonance in floating bodies - Comparing monochromatic and polychromatic input waves
DAVIDSON Josh, KARIMOV Mirlan, HABIB Giuseppe, **KALMÁR-NAGY Tamás***
*Department of Fluid Mechanics, Faculty of Mechanical Engineering, Budapest University of Technology and Economics (Bertalan Lajos 4-6, Budapest 1111 Hungary)

14:30 - 14:50
Stability of Stationary Solution of Time Periodic Nonlinear Single DoF Time Delayed System Based on Impulse Response Function
DOMBOVARI Zoltan*
*MTA-BME Lendület Machine Tool Research Group, Department of Applied Mechanics, Budapest University of Technology and Economics (Budapest, Muegyetem rkp. 3. Hungary)

14:50 - 15:10
Resonance analysis for a nonhomogeneous wave equation with a time-dependent coefficient in the Robin boundary condition
WANG Jing*, VAN Horssen Wim
*Delft University of Technology (Mekelweg 4, Delft, 2628 Netherlands) - Beijing Institute of Technology (5 South Zhongguancun Street, Haidian District, Beijing Postcode: 100081 China)

Parameter identification of periodic systems by impulse dynamic subspace description

Adam K. Kiss*, Daniel Bachrathy* and Zoltan Dombovari *
*MTA-BME Lendület Machine Tool Vibration Research Group, Department of Applied Mechanics, Budapest University of Technology and Economics, Budapest

Summary. In this contribution, a parameter identification technique is introduced for delayed time-periodic differential equation, which is based on the so-called impulse dynamic subspace (IDS). The description is tested on the delayed Mathieu equation. Then, a possible application is discussed for chatter detection technique in machine tool vibrations, and its limitation due to arising nonlinear behaviour is summarized.

Introduction

The main goal of this work is to characterize the dynamical behaviour of delayed periodic systems without substantial knowledge of the underlying model. Our assumptions are that the system is a linearized version of a nonlinear phenomenon and the time-period is known. The main idea is to capture the dominant spectral properties of the system from its impulse response. In order to achieve this, the so-called impulse dynamic subspace (IDS) is used [1]. This is an efficient description for possible automatic parameter fitting for mechanical structures. Originally, the method is developed for linear time-invariant systems. It is based on the evaluation of frequency response functions by using Green function representation of the homogeneous dynamics. However, in this work, we slightly modify the original ideas of the method to make it suitable for periodic systems. In this way, here, we apply this method for periodic non-autonomous systems and we characterize its the Floquet multipliers (characteristic multiplier), consequently, we characterize the stability properties of the underlying system without knowing its parameters. The method and its applicability is tested on a time-periodic delay-differential equation (DDE), the so-called delayed Mathieu equation by using time signal generated by numerical integration. Finally, one possible application field is discussed from the topic of machine tool vibrations, namely quantitative chatter detection and stability prediction method in milling operations [2].

Impulse dynamic subspace description for periodic non-autonomous case

The IDS can describe the relevant dynamics of a structure by means of the singular value decomposition applied on the Green function representation of the vibration signal $x(t)$ of a periodic non-autonomous system with time-period T. For detailed derivation on the IDS description, the reader is referred to [1]. The so-called block-Hankel matrix representation of the Green function for time-periodic system is

$$\mathbf{G} = \begin{bmatrix} \mathbf{x}_0 & \mathbf{x}_1 & \dots & \mathbf{x}_N \\ \mathbf{x}_1 & \mathbf{x}_2 & \dots & \mathbf{x}_{N+1} \\ \vdots & \vdots & \ddots & \vdots \\ \mathbf{x}_N & \mathbf{x}_{N+1} & \dots & \mathbf{x}_{2N} \end{bmatrix}, \tag{1}$$

where $\mathbf{x}_i$ is the discretized state vector along a period T. It form as

$$\mathbf{x}_i = [x(iT+\Delta t)\; x(iT+2\Delta t)\; \dots\; x(iT+(n-1)\Delta t)] = \mathrm{row}_{j=0}^{n-1} x(iT+j\Delta t), \tag{2}$$

where the number of sampled points in one period is n and the discretized time step is $\Delta t = T/n$. Note that in case of time-periodic systems, the blocks are shifted by 1 time-period in the Hankel matrix. By using singular value decomposition (SVD) of the Hankel matrix $\mathbf{G} = \mathbf{V}\mathbf{\Sigma}\mathbf{W}^{\mathrm{H}}$, the dominance of subsystems can be identified. Here $\mathbf{V}$ and $\mathbf{W}$ are the stroboscopic- and sampled-singular-responses (SR) (alike singular-IRF in [1]), respectively. By taking an appropriate singular set, as a result, using the truncated versions of the stroboscopic-SR $\tilde{\mathbf{V}}$, a discrete map can be defined as

$$\mathbf{B} = \tilde{\mathbf{V}}^{\mathrm{H}}\mathbf{S}\tilde{\mathbf{V}}, \tag{3}$$

where $\mathbf{S}$ is a shift matrix with non-zero elements $S_{i,i} = 1$. The eigenvalues of $\mathbf{B}$ are the Floquet multipliers of the periodic non-autonomous (time-variant) system.

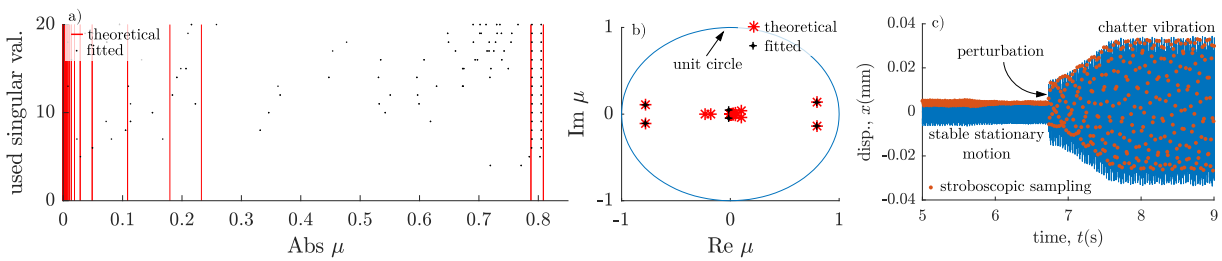

Figure 1: Effect of truncation on fitted multipliers (a), dominant multipliers in the complex plane (b); bistabe machining process (c).

Test case

In this section, the time periodic DDEs are detailed, on which IDS description was applied. The general form of the delayed Mathieu equation reads

$$\ddot{x}(t) + a_1\dot{x}(t) + (\delta + \varepsilon\cos t)\, x(t) = b_0 x(t-\tau)\ . \tag{4}$$

where the time-period is $T = 2\pi$. Here, the special case will be investigated, when the time delay is just equal to the principal period ($\tau = T$). For periodic systems, the stability condition is provided by the Floquet theory.
In order to validate the description by IDS, we test it on the delayed Mathieu equation, where the fitted dominant multipliers are compared directly to the theoretically ones calculated by the semidiscretization method (SDM) [3]. The IDS description is applied on numerically generated time signal, with parameters $\delta = 3.1605,\ \epsilon = 1,\ a_1 = 0,\ b_0 = -0.6246$ and initial function $[x_0\ \ \dot{x}_0]^\top = \mathbf{0}$ if $t \in [-\tau, 0)$ and $[x_0\ \ \dot{x}_0]^\top = [0\ \ 1]^\top$ if $t = 0$. The number of the simulated periods are $2N = 120$ and the discretized number of points during 1 period is $n = 100$. Consequently, the size of the Hankel matrix is $N \times n\, N$. The size of the problem is decreased by truncating the Hankel matrix squarely, thus, considering only $N \times N$ elements. Then, the IDS description is applied with several truncated versions of the stroboscopic-SR $\tilde{\mathbf{V}}$, also (see Eq. 3).
The magnitude of the fitted multiplier are plotted in Fig. 1a with black dots together with the theoretical values (red vertical lines) as a function of the truncation of $\tilde{\mathbf{V}}$. For a few considered stroboscopic-SR, the IDS description can capture 2 complex conjugate pair of multipliers with large magnitude with good accuracy. On the other hand, taking into account more stroboscopic-SR, the fitted multipliers start to scatter. To select the appropriate number of stroboscopic-SR, the singular values of the Hankel matrix can be analysed, see more details in [1]. In this case, we select 6, since all the other singular values were merely close to zero. This case is illustrated in the complex plane in Fig. 1b. As shown in the figure, the IDS description is not only able to capture the magnitude of the multipliers, but its imaginary and real components as well. However, as cons of the proposed method, it could not identify multipliers with small magnitude, since solution segments relating to these terms are decaying very fast. Nevertheless, from the practical point of view, those are usually not relevant in engineering applications.

Stability prediction in machining

One possible application of the described method can be used in the operational stability prediction in milling processes [2]. During machining, an undesired phenomenon, the so-called chatter vibration can lead to unacceptable surface quality and possible damage in the machine components. Therefore, avoidance, or at least, the prediction of these vibrations is necessary.
During the operational stability prediction technique, the stability of the machining process can be characterized through the Floquet multipliers. They can be determined during machining by applying the above discussed method. By changing technological parameters, the variation of the modulus of the Floquet multipliers can be monitored, by which, precise stability limit can be extrapolated while the manufacturing parameters remain in the safe region.
On the other hand, according to practical observations, usually there is a bistable region near the linear stability boundary due to unmodelled nonlinear effects. This is also unsafe zone since two attractive motions coexist: stable cutting and large amplitude chatter, which are separated by an unstable periodic motion [4, 5]. In this range, the vibration can jump from the linear attraction zone to the chatter motion due to a large-enough perturbation, as shown in Fig. 1c. Consequently, one cannot excite a stable stationary solution in this range and thus one cannot determine the multipliers of the linearized system.

Acknowledgement Supported by the ÚNKP-19-3 New National Excellence Program of the Ministry for Innovation and Technology. This paper was supported by the Hungarian Scientific Research Fund OTKA FK-124462 and PD-124646.

References

[1] Z. Dombovari (2016) Dominant modal decomposition method. *Journal of Sound and Vibration* **392**:56-69.

[2] A.K. Kiss, D. Hajdu, D. Bachrathy, G. Stepan, Operational stability prediction in milling based on impact tests. *Mechanical Systems and Signal Processing*, **103**:327-339, 2018

[3] T. Insperger, G. Stepan, Semi-discretization for time-delay systems, vol. 178. New York: Springer, 2011

[4] H.M. Shi, S.A. Tobias, Theory of finite-amplitude machine-tool instability. *Int J Mach Tool Manu.* **24**(1):45–69, 1984

[5] Z. Dombovari, A. Iglesias , T.G. Molnar, G. Habib, J. Munoa, R. Kuske, G. Stepan, Experimental observations on unsafe zones in milling processes *Philosophical Transactions of the Royal Society A* **377**(2153), 20180125

Test Rig with Drive Belt: Modelling and Simulation of Parametrically Excited Vibrations

Markus H. E. Messer and Bernhard Gass
Fachbereich Maschinenbau, Mechatronik, Materialtechnologie (Mechanical Engineering), Technische Hochschule Mittelhessen (University of Applied Sciences), Friedberg, Germany

Summary. This paper deals with the modelling and simulation of parametrically excited vibrations in a test rig with a drive belt. The structure is modelled as a dynamical system with time-periodic coefficients and four degrees of freedom (two rotational and two translational degrees of freedom). Stiffness parameters are obtained from experimental load-displacement diagrams, and mass parameters are calculated by hand or by CAD software. The system's proportional damping parameters are derived from measured damping ratios of the structure. Finally, the parametrically excited vibrations are studied numerically by using fourth-order Runge-Kutta method. The simulation results are considered to be very valuable for the upcoming measurements and the analysis of experimental data.

Introduction

Machines with drive belts often exhibit parametrically excited vibrations [1]. The test rig in figure 1 uses a V-ripped L-profile drive belt. For the most part, the drive belt consists of vulcanized rubber material. In addition to that, the drive belt contains a load-carrying tension member (high strength fibres) for transmitting the longitudinal forces. This type of drive belt can be found in many different machines, e.g. sheet-fed offset printing machines. Recent work of one of the authors showed, that the drive belt can be modelled as a spring with time-periodic stiffness. This parametric stiffness excitation leads to numerical results that match very well with measured vibrations [2].

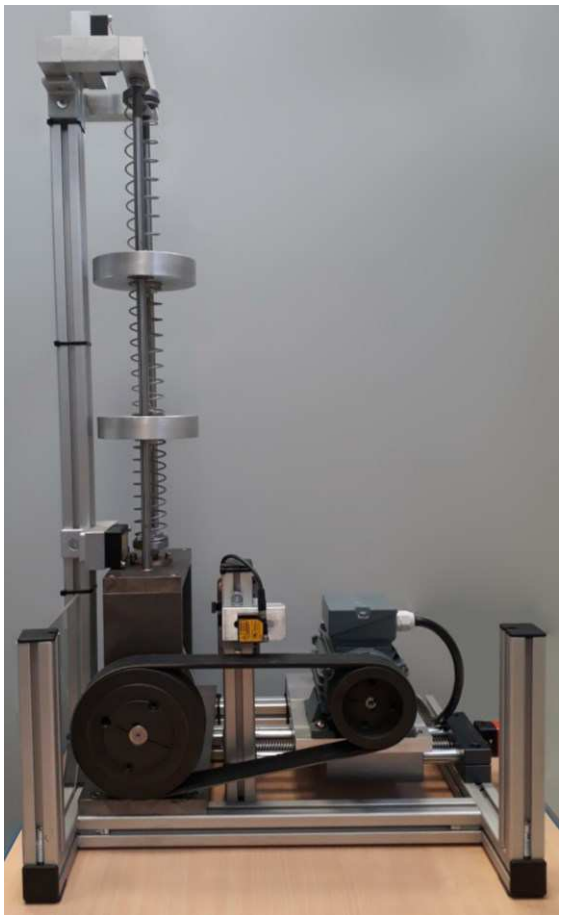

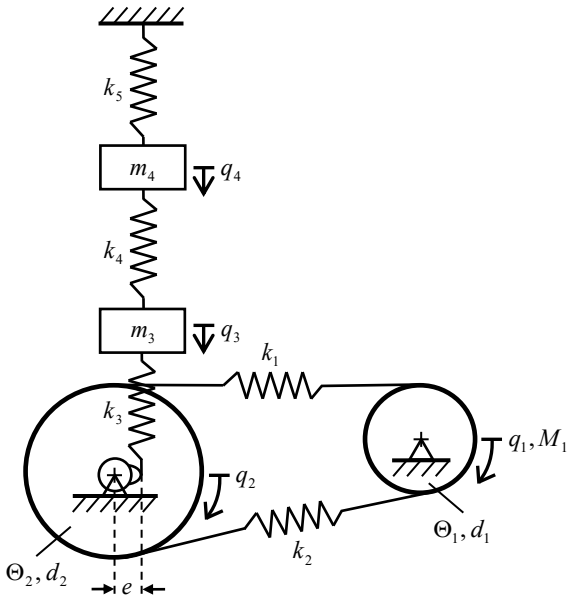

Parameters:
$\Theta_1 = 1.64 \cdot 10^{-3}$ kg m^2, $\Theta_2 = 2.21 \cdot 10^{-2}$ kg m^2,
$m_3 = m_4 = 1.25$ kg, $d_1 = 0.104$ m, $d_2 = 0.164$ m,
$e = 0.005$ m, $k_3 = k_4 = k_5 = 492$ N/m,
$\alpha = 2.45$ s^{-1}, $\beta = 8.37 \cdot 10^{-4}$ s

Drive belt's geometry and stiffness:
$L = 0.991$ m, $h = 0.007$ m, $b = 0.038$ m,
$k_1 = k_2 = 6.78 \cdot 10^5$ N/m $\cdot \left[1 + 0.175 \cdot \cos\left(\frac{\dot{q}_1 \pi d_1 t}{L}\right)\right]$

Figure 1 (left): Photograph of the test rig. Figure 2 (right): Sketch and parameters of the dynamical system.

Dynamical system

Figure 2 displays a sketch of the dynamical system. The rotational degrees of freedom of the two belt pulleys are denoted by q_1 and q_2. The two masses m_3 and m_4 have translational degrees of freedom (q_3 and q_4). An asynchronous motor fed from a frequency converter delivers the drive torque M_1 to the small belt pulley. According to [3], the drive belt's stiffness can be different for tight span (k_1) and slack span (k_2). k_3, k_4 and k_5 represent helical compression springs.

Applying Newton's Second Law yields the following equations of motion:

$$\Theta_1\ddot{q}_1 + (k_1 + k_2)\frac{d_1^2}{4}q_1 - (k_1 + k_2)\frac{d_1 d_2}{4}q_2 - M_1 = 0 \quad (1)$$

$$\Theta_2\ddot{q}_2 + (k_1 + k_2)\frac{d_2^2}{4}q_2 - (k_1 + k_2)\frac{d_1 d_2}{4}q_1 + k_3 e^2 \sin(q_2)\cos(q_2) - k_3 e\cos(q_2)q_3 = 0 \quad (2)$$

$$m_3\ddot{q}_3 + (k_3 + k_4)q_3 - k_4 q_4 - k_3 e\sin(q_2) = 0 \quad (3)$$

$$m_4\ddot{q}_4 + (k_4 + k_5)q_4 - k_4 q_3 = 0 \quad (4)$$

Kammer experimentally acquired the linear load-displacement diagram for the helical compression springs used in the test rig [4]. This leads to $k_3 = k_4 = k_5 = 492$ N/m. Furthermore, the authors' colleagues Pyttel and Wiesner carried out a tensile test of the drive belt [5]. The measured load-displacement relationship is nonlinear, but linearizing the progressive (hardening) curve at the operating point (belt tension: 278 N) leads to: $k = 6.78 \cdot 10^5$ N/m. In accordance with recent work of one of the authors, the drive belt is modelled as a spring with time-periodic stiffness as follows [2].

$$k_1 = k_2 = k \cdot [1 + \varepsilon \cdot \cos(\omega_{PE} t)] \quad (5)$$

Neglecting slip, the parametric excitation frequency ω_{PE} relates to the drive belt's length L as follows:

$$\omega_{PE} = \frac{\dot{q}_1 \pi d_1}{L} \quad (6)$$

For $\dot{q}_1 = \dot{q}_2 = 0$ (non-rotating belt pulleys) Kammer measured free vibrations of m_3 and m_4 and identified eigenfrequencies (20 rad/s, 34 rad/s) and corresponding damping ratios (0.07, 0.05) [4]. Consistent with [2], proportional damping ($\underline{D} = \alpha\underline{M} + \beta\underline{K}$) is assumed, and α and β are chosen to yield the system's above-mentioned damping ratios.

Simulation of parametrically excited vibrations

Since the drive torque M_1 hasn't been measured yet, the dynamical system is simulated for the scenario $\dot{q}_1 = \text{const}$. Figure 3 shows simulation results for $\varepsilon = 0.175$, which is in line with [2]. Maximum amplitudes in figure 3 occur at order $0.33 = \pi d_1/L$ (first drive belt order). Simulation results will be compared with impending measurements.

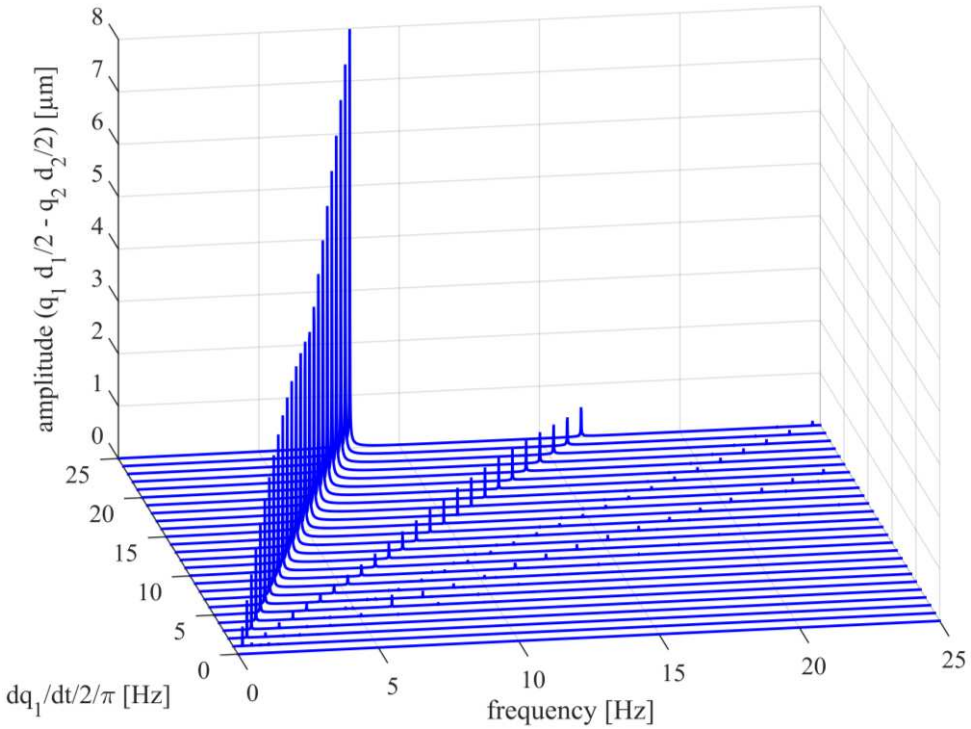

Figure 3: Simulated parametrically excited vibrations

References

[1] Dresig, H., and Fidlin, A. (2014) Schwingungen mechanischer Antriebssysteme. Third edition. Springer-Verlag Berlin Heidelberg, Germany.
[2] Messer, M. H. E. (2017) Parametric Excitation of Vibrations in Printing Machines. *International Journal of Acoustics and Vibration* **22(4)**:448-455.
[3] Dresig, H., and Holzweißig, F. (2016) Maschinendynamik. Twelfth edition. Springer-Verlag Berlin Heidelberg, Germany.
[4] Kammer, S. (2016) Inbetriebnahme eines Versuchsstands mit Keilrippenriemen und experimentelle Untersuchung parametererregter Schwingungen. Master's Thesis, Fachbereich Maschinenbau, Mechatronik, Materialtechnologie, Technische Hochschule Mittelhessen, Friedberg, Germany.
[5] Pyttel, T., and Wiesner, D. (2019) Tensile test (4 November 2019): Load and displacement data. Fachbereich Maschinenbau, Mechatronik, Materialtechnologie, Technische Hochschule Mittelhessen, Friedberg, Germany.

Parametric resonance in floating bodies - Comparing monochromatic and polychromatic input waves

Josh Davidson*, Mirlan Karimov*, Giuseppe Habib† and Tamas Kalmar-Nagy*
*Department of Fluid Mechanics, Faculty of Mechanical Engineering, Budapest University of Technology and Economics
† Department of Applied Mechanics, Faculty of Mechanical Engineering, Budapest University of Technology and Economics

Summary. Parametric resonance in floating bodies is well known for large amplitude pitch and roll oscillations with a slower period than the wave induced motions. The pitch and roll dynamics exhibit characteristics of the damped Mathieu equation, due the restoring torque being dependent on the heave postion, which is oscillating in response to the input waves. Therefore, when ocean waves are approximated as a sinusoid, the monochromatic input wave can cause parametric resonance to occur in the system when the input frequency is around twice the pitch/roll natural frequency. However, in reality ocean waves contain a spectrum of frequencies. This paper examines the motion of floating bodies subject to input waves represented by sinusoids and by standard ocean wave spectra. The occurance of parametric resonance is compared for these two cases. A test case, considering a spar-type heaving cylinder from the literature, is presented, showing the resulting parametrically induced pitch and roll motions for the different input waves.

Parametric resonance in floating bodies

Parametric resonance is caused by the time-varying changes in the parameters of a dynamical system, resulting in an exponential increase in oscillation amplitude [1]. Parametric resonance is known to cause large amplitude pitch and roll oscillations in floating bodies. This phenomena was first noted by Froude in 1861 [2], where large amplitude roll motions were observed for a ship when the input wave frequency was half the roll frequency. Parametric pitch/roll is relevant in a number of fields, such as shipping [3], spar-buoy platforms [4], marine based wireless sensor networking [5] and offshore renewable energy [6].

Dynamics

The pitch and roll dynamics of a floating body (we consider a heaving, spar-type cylinder as depicted in Figure 2-(b)) can be well approximated by the Damped Mathieu Equation [1]:

$$\ddot{x}(t) + b\dot{x}(t) + a(t)x(t) = 0. \tag{1}$$

Mechanically, this equation describes the motion, $x(t)$, of a mass-spring-damper system with a time-varying spring stiffness term, $a(t)$. For harmonic variation of the parameter, $a(t)$, the system is known to become unstable at certain frequencies and amplitude thresholds. For a floating body, the spring stiffness in the pitch and roll degrees of freedom, depends on the heave position, which varies in time due to wave induced oscillations. Therefore, the wave induced heave motion of a floating body can trigger parametric resonance in the pitch and roll modes of motion. This is depicted in Figure 1, showing the heave and pitch motions of a floating cylinder subjected to a sinusoidal input wave with a frequency twice the pitch natural frequency.

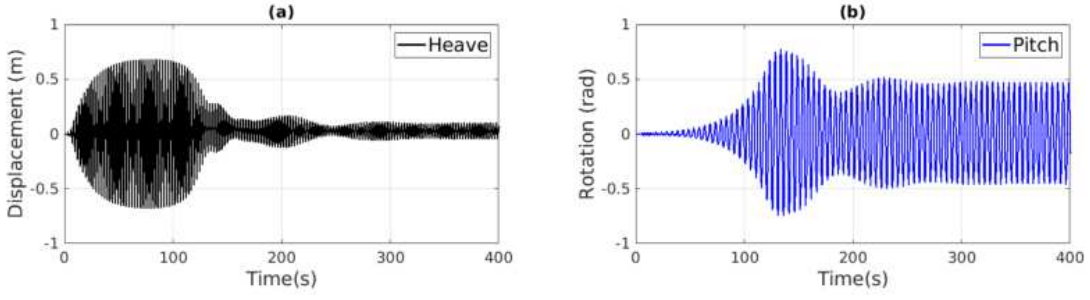

Figure 1: The heave and pitch response of a floating cylinder, subject to an input sinusoidal wave, showing the transfer of energy from heave to pitch

Ocean waves

While the analysis of parametric resonance and Mathieu instability is well known for sinusoidal waves, real ocean waves are stochastic [7]. For engineering purposes, ocean waves are often approximated by Fourier analysis, described by a wave spectrum, with the sea surface well represented by a linear superposition of harmonic components. Figure 2-(a) shows standard wave spectra, JONSWAP and Pierson-Moskowitz, whose shape and bandwidth depends on the wind speed and fetch distance over which the wind blows.

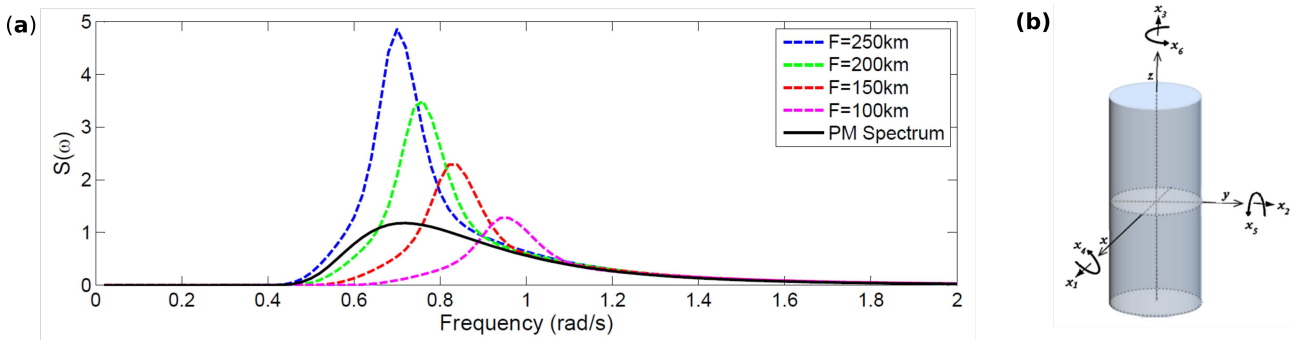

Figure 2: (a) Comparison of the JONSWAP spectrum for varying fetch, F, distance (dashed lines) against the Pierson-Moskowitz (PM) spectrum for a 12m/s wind speed (from [5]) (b) Schematic of the generic spar-type structure in the test case (from [9]).

Test case

As an illustrative example, we consider a heaving, spar-type cylinder, as depicted in Figure 2-(b), whose dynamic instability was previosuly examined in [8, 9, 10]. The pitch/roll natural frequency of the cylinder is twice the pitch/roll natural frequency which makes the cylinder particularly prone to parametric resonance. Numerical simulations of the cylinder motion are presented, considering a range of monochromatic and polychromatic wave inputs and the occurance of parametric resonance in the different wave regimes compared. We compare the occurance of parametric resonance in floating bodies, for experiments considering single frequency or multi-frequency input waves. For the multi-frequency spectra, the effect of the bandwidth is also investigated, comparing narrowband with broadband spectra.

Acknowledgement

The research reported in this paper was supported by the Higher Education Excellence Program of the Ministry of Human Capacities in the frame of the Water Sciences & Disaster Prevention research area of BME (BME FIKP-VÍZ). The research reported in this paper has been supported by the National Research, Development and Innovation Fund(TUDFO/51757/2019-ITM, Thematic Excellence Program). This project has received funding from the European Union's Horizon 2020 research and innovation programme under the Marie Sklodowska-Curie grant agreement No 867453.

References

[1] Fossen, T. and Nijmeijer, H. (2011) Parametric resonance in dynamical system, *Springer*.

[2] Froude, W. (1861). On the rolling of ships, *Institution of Naval Architects*.

[3] Galeazzi, R. (2009). Autonomous supervision and control of parametric roll resonance, *Ph.D. thesis, Technical University of Denmark, Department of Naval Architecture and Offshore Engineering*.

[4] Neves, M.A., Sphaier, S.H., Mattoso, B.M., Rodriguez, C.A., Santos, A.L., Vileti, V.L., and Torres, F. (2008). On the occurrence of mathieu instabilities of vertical cylinders. *27th International Conference on Offshore Mechanics and Arctic Engineering.*

[5] Davidson J., Energy Harvesting for Marine Based Sensors (2016) PhD Thesis *James Cook University*.

[6] Davidson J., Kalmar-Nagy T., Giorgi G. and Ringwood J.V. (2018) Nonlinear Rock and Roll - Modelling and Control of Parametric Resonance in Wave Energy Converters. *MATHOD*.

[7] Tucker, M.J. and Pitt, E.G. (2001) Waves in Ocean Engineering. *Elsevier*.

[8] Jingrui, Z., Yougang, T., and Wenjun, S. (2010). A study on the combination resonance response of a classic spar platform. *Journal of vibration and control*.

[9] Gavassoni, E., Goncalves, P.B., and Roehl, D.M. (2014) Nonlinear vibration modes and instability of a conceptual model of a spar platform. *Nonlinear Dynamics*, 76(1), 809-826.

[10] Karimov, M., Davidson, J., Habib, G., and Kalmar-Nagy, T. (2020) Parametric Excitation Suppression in a Floating Cylinder via Dynamic Vibration Absorbers: a Comparative Analysis. *Journal of Marine Science and Engineering*.

Stability of Stationary Solution of Time Periodic Nonlinear Single DoF Time Delayed System Based on Impulse Response Function

Zoltan Dombovari[*,‡]
[*]*MTA-BME Lendület Machine Tool Vibration Research Group, Budapest, Hungary*
[‡]*Dynamics and Control Department, Ideko, Elgoibar, Spain*

Summary. An extension of the semidiscretization method to impulse dynamic subspace (IDS) is summarized. This domain is the eigenspace of a measured impulse response function (IRF), which is commonly used in the industry. By considering the special properties of the measurement the stability of a single degree of freedom (DoF) milling model is presented as a representative example. Convergences are shown for Hopf and Period Doubling (PD) induced instabilities.

Introduction

In the verge of the new technological revolution more and more automatized solutions will appear in the daily life and very much in the manufacturing sector. One of the most difficult processes to be automatized are the ones that rely on human pattern recognition like understanding traffic situations. Dynamic characterization of machine tools are one of these problems, due to the special parameter identification techniques and selection methodologies used nowadays in the industry. In order to avoid that the impulse dynamic subspace (IDS, [1]) is used for carrying dynamic information.
In this work, a modeling technique is presented where the determination of model parameters is avoided and the process is directly described in the IDS. The main aim is to show that it is possible to derive theoretically the stability properties of a time-periodic milling process by only using the measurable IRF. The time-periodic nature of the milling process induces a stationary solution, which is always apparent and it directly determines the surface quality. However, this stationary solution can loose its stability by setting 'wrong' parameters, and can lead to a high amplitude, limiting oscillation. This limiting oscillation is mathematically stable, although the engineering jargon calls this as chatter instability [2], which refers mathematically to the unstable nature of the stationary time-periodic solution.
The main reason of this oscillation is the regenerative effect, when the consecutive tooth of the milling cutter cuts the surface left by the previous teeth. Since then many methods have been developed in time- and frequency- domain for determining stability of the corresponding stationary solution. Frequency domain solutions, like zeroth order approximation (ZOA, [2]) and multi-frequency (MF, [2]) solution, based on D-subdivision, and Hill's infinite determinant method, can include the measured frequency response functions (FRFs). However, this advantage comes with a huge disadvantage, namely, these methods only provide the critical (non-hyperbolic) limits and not actually the stability boundaries. Also to define the 'measure of stability' (distance from the border) is not straightforward in this case. One needs extremely specialized theorems to perform optimization. Time-domain methods like semidiscretization, time-finite element, collocation methods and spectral element methods, provide the Floquet-multipliers [3], whose magnitude are excellent to 'measure' stability for optimization purposes. However, all these methods rely on time-consuming modal parameter fitting, which computation time adds to the already slow extensive scanning of the parameter space constructing a given stability chart. In order to help on this disadvantage a method is proposed here by performing process modeling based on the IDS [4], which essentially a good candidate for avoiding manual fitting. Moreover by using time-domain based methods the 'measure' of stability is also granted by the magnitude of the multipliers.

Stationary Solution

There are plenty of papers dealing with modeling of regenerative milling processes [2, 5, 1]. In general, the milling process is not only time-periodic, but also nonlinear due to the degressive characteristic of the specific cutting force $f_{tra}(h)\,(\mathrm{N/m})$ [6] given in (tra) (figure $1a$) coordinate system. In milling, each ith ($i = 1, ..., Z$) tooth cuts different thickness of the workpiece h_i material during the rotation of the tool with angular velocity Ω. On the other hand, the chip thickness is also state dependent due to the regeneration [2], that is, $h_i(t) := h_i(t, x_t(\xi))$ ($\xi \in [-\tau, 0]$, $x_t(\xi) = x(t + \xi)$). In general, the resultant cutting force is time-periodic in its coefficients ($F_x(t, \bullet) = F_x(t + T, \bullet)$) and has the form (more detail in [6])

$$F_x(t, x_t(\xi)) := F_x(t, f_{tra}(h_i(t, , x_t(\xi)))) = F_{x,0}(t) + \Delta F_x(t, x_t(\xi)) + g_x(t, x_t(\xi)), \tag{1}$$

where the stationary part of the force is $F_{x,0}(t) = F_x(t, \overline{x}_t(\xi))$, while the linear variational part and the higher order terms are $\Delta F_x(t, x_t(\xi))$ and $g_x(t, x_t(\xi))$, respectively. The structural behavior of the machine tool is supposed to be linear, thus, it can be represented with an IRF as $h(\theta) = (\mathcal{F}^{-1}\{H(\omega)\})(\theta)$ subjected to the causality $h(\theta \leq 0) = 0$. If that is true, the response behaviour for a zero initial value can be represented by the Duhamel's integral as $\overline{x}_t(\theta) := \int_0^\theta h(\theta - \vartheta) F_x(t + \vartheta)\,\mathrm{d}\vartheta$. Since the stationary solution is time-periodic $\overline{x}_t(\theta) = \overline{x}_{t+T}(\theta) = \overline{x}_t(\theta + T)$, Duhamel's representation actually works for the nonlinear state-dependent forcing case too, if the stationary solution is considered frozen for the time period T in the interval $\theta \in [0, T]$. The stationary solution is then shifted with a sufficient enough transient time T_t to ensure periodicity and the boundary problem is solvable in both time and frequency domain with

$$\overline{x}_0(\theta) = \int_{-\infty}^{\theta} h(\theta - \vartheta) F_x(\vartheta, \overline{x}_\vartheta(\xi))\,\mathrm{d}\vartheta = \int_0^{T_\mathrm{t}+T} h(\theta + T_\mathrm{t} - \vartheta) F_x(\vartheta, \overline{x}_0((\xi + \vartheta) \bmod T))\,\mathrm{d}\vartheta. \tag{2}$$

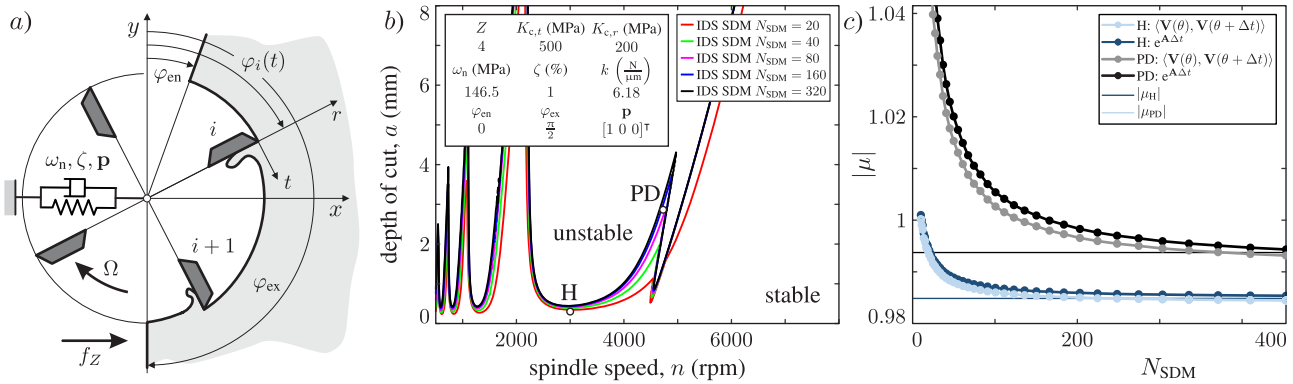

Figure 1: *a*) sketch of the milling model, *b*) stability charts with Hopf (H) and flip (PD) curves. Convergence for the solutions is checked in *c*) by varying the discretisation resolution N_{SDM} at H and PD points depicted in *b*).

Linear Stability of Stationary Solution

Perturbation is introduced around the time periodic stationary solution as $x = \overline{x} + u$. By neglecting the nonlinear terms g_x in (1), the linear variational system can be expressed in the following linear form

$$u_t(\theta) = \int_0^\infty G(\theta,\vartheta)\Delta F_u^-(t-\vartheta)\mathrm{d}\vartheta + \int_0^\theta h(\theta-\vartheta)\Delta F_x^+(t+\vartheta, u_{t+\vartheta}(\xi))\mathrm{d}\vartheta, \;\Rightarrow\; u_t(\theta) = u_{\mathrm{IF},t}(\theta) + u_{\mathrm{F0},t}(\theta, u_t(\xi)). \quad (3)$$

The first term u_{IF} of (3) represents the response for initial (variational) forcing ΔF_u^- (IF, alternative to initial condition), while the second term u_{F0} describes the solution for actual forcing $\Delta F_x(t, u_t(\xi)) = a\,K_{\mathrm{c}}A_x(t)(u(t)-u(t-\tau))$ (see (1)) combined with the transient solution for zero initial condition (F0). In the first term the so-called Green function can be replaced with the IRF as $G(\theta,\vartheta) := h(\theta+\vartheta) = \mathbf{V}(\theta)\mathbf{\Sigma}\,\mathbf{W}^{\mathsf{H}}(\vartheta)$, whose two left-singular-IRF for a single DoF system $\mathbf{V}(\theta) = [V_1(\theta)\; V_2(\theta)]$ can be used to introduce the new IDS as a result of SVD explained in [4]

$$u(t+\theta) = \mathbf{V}(\theta)\mathbf{q}(t), \quad \Rightarrow \quad \dot{\mathbf{q}}(t) = \mathbf{A}\,\mathbf{q}. \quad (4)$$

By defining the product $\langle \mathbf{a}(\xi), \mathbf{b}(\xi)\rangle := \int_0^\infty \mathbf{a}^{\mathsf{H}}(\xi)\mathbf{b}(\xi)\mathrm{d}\xi$ the system matrix can be derived as $\mathbf{A} = \langle \mathbf{V}(\theta), \mathbf{V}'(\theta)\rangle$ (using $\mathbf{V}'(\theta) = \langle G'(\theta,\vartheta), \mathbf{W}(\vartheta)\rangle\,\mathbf{\Sigma}^{-1}$, $G'(\theta,\vartheta) := h'(\theta+\vartheta), h'(\theta) := (\mathcal{F}^{-1}\{\mathrm{i}\omega H(\omega)\})(\theta)$, [4]). Describing the behavior in the IDS ($\mathbf{q}_i = \mathbf{q}(t_i)$, $t_i = i\,\Delta t$, $\Delta\theta = \Delta t$) and considering that only physical displacement space $u_i = u(t_i)$ is needed for the calculation of the process force, the size of the problem can be significantly decreased. Thus

$$\mathbf{q}_{i+1} = \mathrm{e}^{\mathbf{A}\,\Delta t}\mathbf{q}_i + \langle \mathbf{V}(\theta), u_{\mathrm{F0},i+1}(\theta, u_i, \sigma_t(u_{i-l}))\rangle\,, \quad l = 0,1,2,...,r, \quad r = \left\lceil \tfrac{\tau}{\Delta\theta} - \tfrac{1}{2}\right\rceil + \left\lfloor \tfrac{p}{2}\right\rfloor, \quad (5)$$

where $u_{\mathrm{IF},i+1}(\theta) := u_{\mathrm{IF},t_i+\Delta t}(\theta) = \mathbf{V}(\theta+\Delta t)\mathbf{q}_i$, $u_{\mathrm{F0},i+1}(\theta, u_t(0), u_t(-\tau)) := u_{\mathrm{F0},t_i+\Delta t}(\theta, u_t(\xi)) = aK_{\mathrm{c}}\int_0^{\Delta t} h(\theta-\vartheta)A_x(t+\vartheta)(u_{t+\vartheta}(0) - u_{t+\vartheta}(-\tau))\mathrm{d}\vartheta$ and $u_t(0) := u_i$, $u_t(-\tau) \approx \sigma_t(u_{i-l}) = \sum_{k=0}^{p} P_k(t)\,u_{i-r+k}$. Using the homogeneous solution operator (exponential term in (5)) as $\mathrm{e}^{\mathbf{A}\,\Delta t} = \langle \mathbf{V}(\theta), \mathbf{V}(\theta+\Delta t)\rangle$ [4] the following semidiscretization map can be derived

$$\left.\begin{aligned} \mathbf{q}_{i+1} = \langle \mathbf{V}(\theta), \mathbf{V}(\theta+\Delta t)\rangle\,\mathbf{q}_i + \mathbf{D}_i\,u_i + ... + \mathbf{D}_{i-r+1}\,u_{i-r+1} + \mathbf{D}_{i-r}\,u_{i-r}, \\ u_{i+1} = \mathbf{V}(\Delta t)\mathbf{q}_i, \end{aligned}\right\}$$
$$\mathbf{D}_{i-l} = -aK_{\mathrm{c}}\left\langle \mathbf{V}(\theta), \textstyle\int_0^{\Delta t} h(\theta-\vartheta)A_x(t_i+\vartheta)P_{r-l}(t_i+\vartheta)\mathrm{d}\vartheta\right\rangle, \quad P_r(t) = -1. \quad (6)$$

Conclusion

The map presented in (6) can be used to approximate the monodromy operator of the time-periodic milling system in order to calculate stability properties (figure 1*c*) of the corresponding stationary solution $\overline{x}$. This converging solution (figure 1*c*) uses the IDS which actually originated from measured IRF by using a well posed SVD on the homogeneous core of the dynamics ($G(\theta,\vartheta)$ at (3)). This theoretical framework can be extended for the entire period by facilitating larger portion of the corresponding IRF function by using nested convolutions.

References

[1] Dombovari, Z., Munoa, J., and Stepan, G., 2012. "General milling stability model for cylindrical tools". *Procedia CIRP*.

[2] Altintas, Y., 2012. *Manufacturing Automation: Metal Cutting Mechanics, Machine Tool Vibrations, and CNC Design*. Cambridge University Press.

[3] Lehotzky, D., and Insperger, T., 2016. "A pseudospectral tau approximation for time delay systems and its comparison with other weighted residual type methods". *Int. J. Numer. Meth. Eng.,* ***108***(6), pp. 588–613.

[4] Dombovari, Z., 2017. "Dominant modal decomposition method". *Journal of Sound and Vibration,* ***392***, pp. 56–69.

[5] Altintas, Y., and Kilic, Z., 2013. "Generalized dynamic model of metal cutting operations". *CIRP Annals - Manufacturing Technology,* ***62***(1), pp. 47–50.

[6] Dombovari, Z., and Stepan, G., 2015. "On the bistable zone of milling processes". *Phil. Trans. R. Soc. A,* ***373***(2051), p. 20140409.

Resonance analysis for a nonhomogeneous wave equation with a time-dependent coefficient in the Robin boundary condition

Jing Wang[†*], Wim T. van Horssen[†]

[†] *Department of Mathematical Physics, Delft Institute of Applied Mathematics, Delft University of Technology, Mekelweg 4, Delft, 2628CD, Netherlands*

[*] *School of Mathematics and Statistics, Beijing Institute of Technology, Beijing, 100081, PR China*

Summary. This work is devoted to how the frequency of an external force effects the resonances in a one-dimensional initial-boundary value problem for a nonhomogeneous wave equation involving a Robin type of boundary condition with a time-dependent coefficient. By setting the frequency of the external force equal to ω, and the time-dependent boundary coefficient in the boundary condition equal to $k(t)$, different kinds of resonances can be obtained by numerical simulations. Next, by using the method of d'Alembert and wave reflections, we can calculate the solution $u(x,t)$ by dividing the time domain into finite intervals of length 2. Finally, the resonance results can be analyzed by the map of the solution from $t = 2n$ to $t = 2(n+1)$, which are in agreement with those obtained by using a numerical method.

Statement of the problem

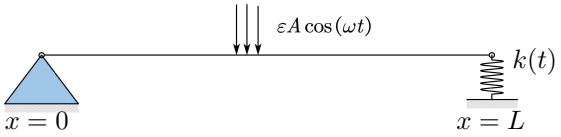

Figure 1: The transverse vibrating string with a time-varying spring-stiffness support at x=L.

In this paper we study resonance for a nonhomogeneous wave equation (see Figure 1), where one end is attached to a spring for which the stiffness properties change in time (due to fatigue, temperature change, and so on). By using Hamilton's principle, the system can be written as:

$$\rho u_{tt}(x,t) - P u_{xx}(x,t) = \varepsilon cos(\omega t), \quad 0 < x < L, \quad t > 0, \tag{1}$$

where ρ is the mass density, P is the axial tension which is assumed to be constant, L is the distance between the supports, and u describes the lateral displacement of the string. $\varepsilon cos(\omega t)$ is an external force acting on the whole string, where ε and ω are constants. The boundary conditions are:

$$u(0,t) = 0, \quad P u_x(L,t) + k(t) u(L,t) = 0, \quad t > 0, \tag{2}$$

where $k(t)$ is the time-varying stiffness of the spring at $x = L$. The boundary condition at $x = 0$ is a Dirichlet type of boundary condition, and the boundary condition at $x = L$ is a Robin type of boundary condition with a time-dependent coefficient $k(t)$. Based on the Buckingham Pi theorem,the governing equation (1), the boundary conditions (2), and the initial conditions can be transformed to the following non-dimensional form:

$$\begin{cases} u_{tt}(x,t) - u_{xx}(x,t) = \varepsilon cos(\omega t), \quad 0 < x < 1, \quad t > 0, \\ u(0,t) = 0, \quad u_x(1,t) + k(t) u(1,t) = 0, \quad t > 0, \\ u(x,0) = f(x), \quad u_t(x,0) = g(x), \quad 0 < x < 1. \end{cases} \tag{3}$$

Numerical example of Resonance

This section is devoted to presenting some numerical simulations on the dynamical resonance behavior of system (3) for two cases. Let us first assume that $\varepsilon = 1$ and the following initial conditions are given:

$$f(x) = sin^2(1.7155x), \quad g(x) = 0, \quad 0 < x < 1. \tag{4}$$

Case 1: k(t) is constant

Choosing $k(t) = 2$ and setting $\omega = \lambda_1$ (λ_i satisfies the transcendental equation $-\frac{1}{k}\lambda_i = tan(\lambda_i)$) the solution of the nonhomogeneous wave equation (3) can be obtained, and is given as in Figure 2-1 (where a resonance arises).

Case 2: k(t) is not constant ($k(t) = \frac{1}{at+1}$)

Let $k(t) = \frac{1}{at+1}$. We know the eigenvalues λ satisfy approximately $-(at+1)\lambda = tan(\lambda)$ (see Figure 3). By giving fixed values for "ω" and "a", different solution shapes can be obtained as time increases (see Figure 2-2 to 2-4). Resonances might occur (or not) depending on the choices for "ω" and "a".

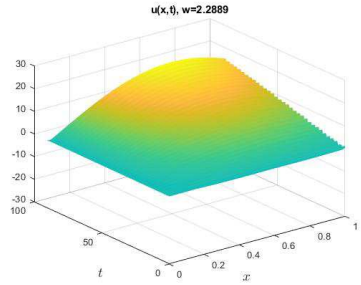

Figure 2-1: The solution $u(x,t)$ with k=2, ω=2.2889.

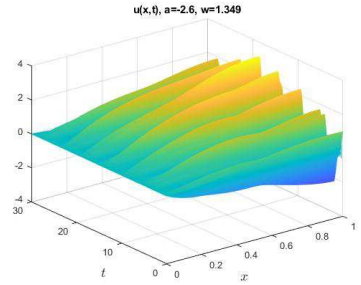

Figure 2-2: $\omega = 1.329$, resonance zone is around (2,16).

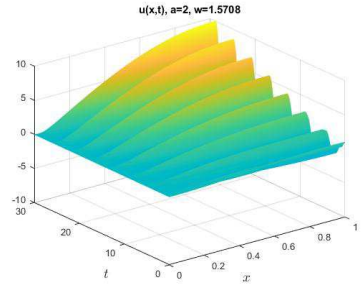

Figure 2-3: Resonance arises when $\omega = \frac{\pi}{2}$.

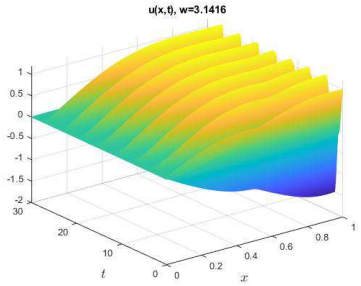

Figure 2-4: No resonance when $\omega = \pi$.

Resonance (unbounded solution) analysis

The analytical solution based on the method of d'Alembert

According to the method of d'Alembert (see [1]), the general solution to Eq.(3) is given by

$$u(x,t) = \frac{1}{2}[f(x-t) + f(x+t)] + \frac{1}{2}\int_{x-t}^{x+t} g(s)ds + \varepsilon \int_0^t (t-\tau)cos(\omega\tau)d\tau.$$

It should be noted that the functions f and g are only defined on the interval [0,1]. To extend f and g on the whole domain $(-\infty, +\infty)$, the boundary conditions should be considered.

The nonhomogeneous wave equation we considered above in Eq.(3) has a propagation speed of 1, which implies that the vibration information at the point $x = x_i$ and $t = 0$ will propagate into two different directions with speed 1, and the information will be back to the position x_i at $t = 2$ as shown Figure 4-1. Furthermore, Figure 4-2 shows the domain of dependence. Then by treating the state at $t = 2$ as a new initial condition and using the same extension procedures, the information needed to calculate the solution of the equation up to every time can be obtained (for details see [2]).

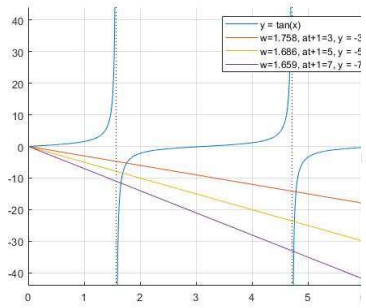

Figure 3: The resonance produced by different values of ω.

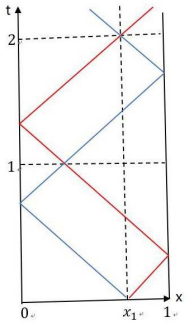

Figure 4-1: Wave reflections.

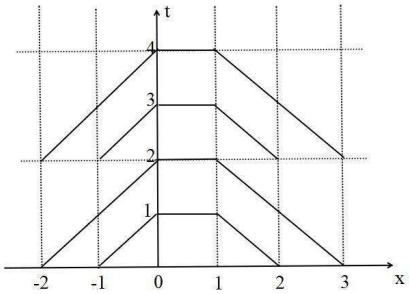

Figure 4-2: Domain of dependence.

Solution and mapping

The resonance results can be analyzed by the map of the solution based on the proposed method (the method of d'Alembert), from $t = 2n$ to $t = 2(n+1)$, which turns out to be in complete agreement with those obtained by using a numerical method.

References

[1] J. d'Alembert, (1747) Researches sur la courbe que forme une corde tendue mise en vibrations (Researches on the curve that a tense cord forms when set into vibration). *Hist. l'Académie R. Des Sci. Belles Lettres*, **3**:214-249.

[2] Wim T. van Horssen, Yandong Wang, Guohua Cao, (2018) On solving wave equations on fixed bounded intervals involving Robin boundary conditions with time-dependent coefficients. *Journal of Sound and Vibration*, **424**:263-271.

Thursday, July 21, 2022
13:30 - 15:30

MS-11 Systems with Time Delay
Saint Clair 2

Chair: Giuseppe Habib

13:30 - 13:50
Calculation of feedback delay during human balancing on rolling balance board
MOLNÁR Csenge Andrea*, INSPERGER Tamás
*MTA-BME Lendület Human Balancing Research Group (1016 Budapest, Gellérthegy u. 30-32 Hungary) - Department of Applied Mechanics, Budapest University of Technology and Economics (1111 Budapest, Műegyetem rkp. 5. Hungary)

13:50 - 14:10
Conservative solitons and reversibility in time delayed systems
JAVALOYES Julien, **SEIDEL Thomas***, GUREVICH Svetlana
*Westfälische Wilhelms-Universität Münster (Universität Münster Schlossplatz 2 48149 Münster Germany)

14:10 - 14:30
Destabilizing effect of back electromotive force along the cyclic coordinate in case of a digitally controlled Furuta pendulum
VIZI Mate*, STEPAN Gabor
*Department of Applied Mechanics, Budapest University of Technology and Economics (Muegyetem rkp. 5., 1111 Budapest, Hungary Hungary)

14:30 - 14:50
Dynamics of Temporal Localized States in Time-Delayed Optically Injected Kerr Gires-Tournois Interferometers
SEIDEL Thomas, JAVALOYES Julien, **GUREVICH Svetlana***
*Institute for Theoretical Physics, University of Münster (Universität Münster Schlossplatz 2 48149 Münster Germany)

14:50 - 15:10
Entrainment of Self-Organized Synchronized States in Delay-Coupled Oscillators
PROUSALIS Dimitrios*, JÜLICHER Frank, WETZEL Lucas
*Max Planck Institute for the Physics of Complex Systems (Max Planck Institute for the Physics of Complex Systems Nöthnitzer Straße 38 01187 Dresden Germany Germany)

15:10 - 15:30
Human positioning of a planar pendulum
SZAKSZ Bence*, STEPAN Gabor
*Department of Applied Mechanics, Budapest University of Technology and Economics (1111 Budapest, Muegyetem rakpart 5 Hungary)

Calculation of feedback delay during human balancing on rolling balance board

Csenge A. Molnar* and Tamas Insperger*
*Budapest University of Technology and Economics, Faculty of Mechanical Engineering, Department of Applied Mechanics and MTA-BME Lendület Human Balancing Research Group, Budapest, Hungary

Summary. Human balancing on rolling balance board in the sagittal plane is analyzed by a two-degree-of-freedom mechanical model. Human body is modeled by an inverted pendulum. The geometry of the balance board can be adjusted: the radius of the wheels and the elevation between the top of the wheel and the board can be changed. The central nervous system is modeled by a delayed proportional-derivative (PD) controller, where the constant feedback delay corresponds to the human reaction time. A critical delay can be defined for each setting of the balance board geometry: if the reaction time is larger than the critical delay, then there are no control gains that can stabilize the system. The critical time delays were determined by a numerical method for four balance board geometry with different radii. Balancing trials by a human subject were analyzed and the reaction time was estimated by comparing the theoretical and experimental results. In this particular balancing task, the reaction time was estimated to be 170 ms.

Introduction

Stabilization of the human body around an unstable equilibrium is controlled by the central nervous system (CNS). The sensory organs obtain information about the spatial position and velocity of the body and the CNS determine the corrective movement in order to maintain equilibrium. This process requires certain amount of time, therefore the balancing task can be modeled as a delayed control system, where the feedback delay is identical to the reaction time. In this study, CNS is assumed to obtain information about the angular position and angular velocity of the balance board and the human body, therefore delayed PD controller with constant time delay τ is used in the model. Nowadays, more and more accidents are caused by loss of balance during everyday activities, especially in the elderly societies. One of the main reasons of falls is the increased reaction time. Understanding the control concept and the effect of increasing feedback delay, therefore may help to predict and prevent falls.

Mechanical model

Human balancing on rolling balance board with adjustable geometry is analyzed in this work. The radius R of the wheels and the elevation h between the top of the wheel and the board can be changed, which highly influence the difficulty of balancing. Previous experiments showed that ankle strategy is dominant during balancing on rolling balance board in the sagittal plane, and oscillations at the hip are negligible compared to that at the ankle. Therefore, human body was modeled as an inverted pendulum which connects to the balance board through the ankle joint as can be seen in Fig. 1a. The control torque

$$T(t) = P_\varphi \varphi(t-\tau) + D_\varphi \dot{\varphi}(t-\tau) + P_\vartheta \vartheta(t-\tau) + D_\vartheta \dot{\vartheta}(t-\tau) \tag{1}$$

is applied at the ankle, where $P_\varphi, P_\vartheta, D_\varphi, D_\vartheta$ are the proportional and derivative control gains with respect to the generalized coordinates, which are the angle φ of the human body and angle ϑ the balance board measured from the equilibrium. Following [2], the passive stiffness s of the ankle is determined using the mass m_h and height l of the balancing subject as

$$s = 0.91 m_h g \frac{l}{2}. \tag{2}$$

The position of the ankle are described by parameter e and f as shown in Fig. 1a. The center of gravity, mass m_h and mass moment of inertia I_h of the human body were determined based on the literature [1]. The same parameters for the balance board (l_b, m_b, I_b) were calculated using the actual geometry.

Stability analysis

After deriving the governing equations of motion of the system, and linearization about the equilibrium, the mathematical model is obtained as a system of delay differential equations of the retarded type. Stability is analyzed in the four-dimensional space of the control gains $P_\varphi, P_\vartheta, D_\varphi, D_\vartheta$ for a fixed delay τ. If the value of the delay is increased, then the size of the stable domain of gains decreases and it completely disappears at a specific value, which is called critical delay (τ_{crit}). Stability analysis was performed over a non-uniform grid in the four-dimensional space $(P_\varphi, P_\vartheta, D_\varphi, D_\vartheta)$ such that $\pm 10\%$ inaccuracy was allowed the control gains. The critical delay was determined numerically using the Walton-Marshall method [3] above the four-dimensional grid for four different radius of the balance board ($R = 125,\ 100,\ 75,\ 50$ mm). The board elevation $R - h$ was the same in all cases, such that the board was adjusted to the lowest position of the wheel. The calculated critical delays are shown in Fig. 2. It is assumed that if the reaction time of the balancing subject is lower than the critical delay obtained based on the mechanical model, then the subject is able to stand on the balance board.

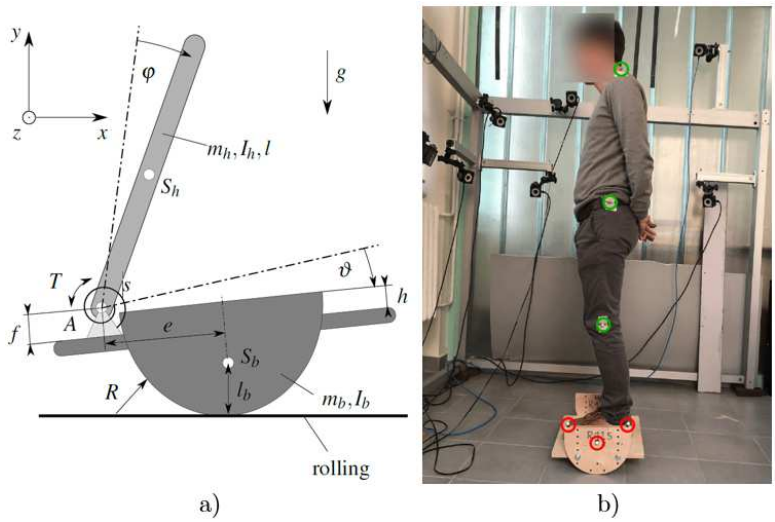

Figure 1: a) Mechanical model of human balancing on rolling balance board in the sagittal plane. b) Measurement setup.

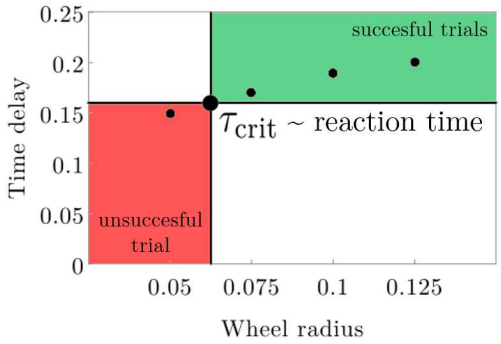

Figure 2: Estimation of reaction time based on experimental and numerical results.

Experimental analysis

The numerical results of the mechanical model were compared with actual balancing trials. A balancing subject was asked to stand on the balance board with radius 125, 100, 75, and 50 mm. The task was to stand at least 60 s long with stretched legs and open eyes. The arms had to be hold at the back as shown in Fig. 1b. Standing on the balance board with radius 125, 100, and 75 mm was successful, however, the subject was not able to stand on the balance board associated with 50 mm radius as indicated by green and red colors in Fig. 2. This means that the reaction time is between the critical delays obtained for 50 and 75 mm, which gives approximately 170 ms.

Conclusion

The reaction time can be estimated by comparing experimental and numerical results of a balancing task. The reaction time of the subject is 170 ms, which is in the range of the values that can be found in the literature [4, 5]. In the future, the calculations and experiments will be repeated involving larger number of participants.

Acknowledgment

This work was supported by the UNKP-20-3 New National Excellence Program of the Ministry for Innovation and Technology from the source of the national research, development and innovation fund.

References

[1] P. De Leva (1996) Adjustments to Zatsiorsky-Seluyanov's segment inertia parameters. *Journal of Biomechanics*, **29**(9):1223-1230.

[2] I. D. Loram, and M. Lakie (2002) Direct measurement of human ankle stiffness during quiet standing: the intrinsic mechanical stiffness is insufficient for stability. *The Journal of Physiology*, **545**(3):1041-1053.

[3] K. Walton, J.E. Marshall (1987) Direct method for tds stability analysis. *IEE Proceedings D - Control Theory and Applications*, **134**(2):101-107.

[4] T. Kiemel, Y. Zhang, and J.J. Jeka (2011) Identification of neural feedback for upright stance in humans: stabilization rather than sway minimization. *Journal of Neuroscience*, **31**(42):15144-15153.

[5] A.D. Goodworth, R.J. Peterka (2010) Influence of Stance Width on Frontal Plane Postural Dynamics and Coordination in Human Balance Control. *Journal of Neurophysiology*, **104**:1103-1118.

Conservative solitons and reversibility in time delayed systems

Julien Javaloyes*, Thomas G. Seidel†,‡ and Svetlana V. Gurevich ‡
* *Departament de Física & Institute of Applied Computing and Community Code (IAC-3), Universitat de les Illes Baleares, C/ Valldemossa km 7.5, 07122 Mallorca, Spain*
† *Institute for Theoretical Physics, University of Münster, Wilhelm-Klemm-Str. 9, D-48149 Münster, Germany*
‡ *Center of Nonlinear Science (CeNoS), Westfälische Wilhelms-Universität Münster, Corrensstrasse 2, 48149 Münster, Germany*

Summary. Time-delayed dynamical systems (TDSs) materialize in situations where distant, point-wise, nonlinear nodes exchange information that propagates at a finite speed. They are akin in their complexity to spatially extended *dissipative and diffusive* systems. However, they are considered devoid of dispersive effects, which are known to play a leading role in pattern formation and wave dynamics. It explains why the existence of nonlinear conservative TDSs remains an open problem. In this work we show how dispersion may appear naturally in a wide class of delayed systems that can lead to conservative dynamics. We exemplify our result considering a dispersive micro-cavity containing a Kerr medium coupled to a distant external mirror. At low energies and in the long delay limit, a multi-scale analysis shows the equivalence with the nonlinear Schrödinger equation.

Introduction

Delayed dynamical systems describe a large number of phenomena in nature and they exhibit a wealth of dynamical regimes such as localized structures, fronts and chimera states [1, 2, 3, 4, 5]. The presence of delayed terms is connected with the finite propagation speed of signals, hence delayed systems are widely used to model, e.g., networks, map lattices or optical systems. A fertile perspective lies in their interpretation as spatially extended *diffusive* systems which holds in the limit of long delays [6]. This correspondence enables a direct interpretation of purely temporal phenomena in terms of diffusive, dissipative spatio-temporal dynamics. It was shown recently[7] that a more general class of singularly perturbed TDSs allows to cancel this generic diffusive behavior which lead to a dispersive response and the purely imaginary eigenvalue spectrum typical of reversible systems. However, the question whether conservative solitons can be obtained in such TDSs remains open. In this contribution, we demonstrate the existence, that remained elusive so far, of nonlinear, time-reversible, conservative TDSs leading to conservative solitons.

Results

We consider a micro-cavity containing a nonlinear Kerr medium coupled to an external mirror as depicted in Fig. 1 (a). Our theoretical approach follows the method developed in [8] and the dynamical model for the slowly varying electromagnetic field envelopes in the micro-cavity E and the external cavity Y reads

$$\dot{E} = \left(-1 + i\,|E|^2\right) E + hY\,, \tag{1}$$

$$Y = r_e e^{i\varphi}\left[E(t-\tau) - Y(t-\tau)\right]\,. \tag{2}$$

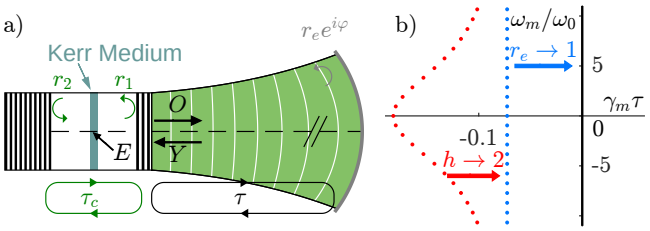

Figure 1: a) A schematic of a micro-cavity enclosed by two distributed Bragg mirrors with reflectivities $r_{1,2}$. It is coupled to a long external cavity with round-trip time τ which is closed by a mirror with reflectivity r_e. E is the sum of the forward and backward propagating fields that interfere upon the Kerr medium while Y is the field impinging upon the top mirror. b) The eigenvalue spectrum of Eqs. (3,4) for different values of h and r_e. For $h < 2$ and $r_e < 1$ (red dots) the spectrum resemble an inverted parabola. When $h \to 2$ (blue dots) it flattens as $\gamma_m\tau = \ln r_e$. For $r_e \to 1$, the spectrum converges to the imaginary axis.

We scale time to the photon lifetime in the micro-cavity and the cavity enhancement is scaled out allowing E and Y to be of the same order of magnitude leading to a simpler input-output relation: The cavity output $O = E - Y$ is the combination of the intra-cavity photons transmitted by the micro-cavity and those reflected. Finally, the field intensities are scaled by the intra-cavity enhanced Kerr saturation parameter. The coupling between the fields E and Y is given in Eq. (2). Due to the absence of the time derivative, the latter is a Delay Algebraic Equation (DAE) that takes into account all the multiple reflections in the external cavity. The field is re-injected after a round-trip τ with the attenuation factor $r_e\, e^{i\varphi}$, where r_e is the external-mirror reflectivity and the phase φ contains both the propagation phase as well as that of the external mirror. The light coupling efficiency in the cavity is given by the factor $h = (1 + |r_2|)(1 - |r_1|)/(1 - |r_1 r_2|)$, where $|r_{1,2}|$ are the upper and lower distributed Bragg mirror reflectivities (cf. Fig. 1 (a)). In particular, for a perfectly lossless bottom mirror $|r_2| = 1$ yields $h = 2$, which corresponds to the Gires-Tournois regime [9]. Second- and third-order dispersion are naturally captured by Eqs. (1,2) as was shown in [7].

The system (1,2) possesses infinitely many degrees of freedom and its eigenvalue spectrum is a countably infinite set. In the long delay limit $\tau \to \infty$ the spectrum becomes quasi-continuous [10] and the real part of the eigenvalues, obtained

around the $(E, Y) = (0, 0)$ solution, $\lambda_m = \gamma_m + i\omega_m$ can be expressed as a function of its imaginary part as [7]

$$\gamma_m = \frac{1}{\tau}\left(\ln r_e + \frac{h-2}{1+\omega_m^2}\right), \tag{3}$$

$$\omega_m\tau + 2\arctan\omega_m = \frac{h-2}{1+\omega_m^2}\omega_m + 2\pi m, \tag{4}$$

with $m \in \mathbb{Z}$, see the red dots in Fig. 1 (b). Note that for $h = 2$ the real part γ_m does not depend on ω_m yielding a vertical, yet lossy, spectrum which is shifted from zero by $\ln r_e/\tau$ (blue dots). In what follows we consider the lossless cavity limit that corresponds to $(r_e, h) = (1, 2)$ and where λ_m converges towards *the unitary spectrum* presented in solid black in Fig. 1 (b). In itself, a unitary spectrum is rather surprising in the context of TDSs since it implies the possibility to integrate linear perturbations backward in time without any particular problem.
The link between Eqs. 4(1),(2) and the nonlinear Schrödinger (NLS) equation can be clarified by performing a multi-scale. We introduce the two time representation by defining $\sigma \in [0, \tau]$ and $\theta \in \mathbb{N}$ so that time can be expressed a $t[\sigma, \theta] = \sigma + \theta\tau$. Assuming a field with carrier frequency δ as $E(t) = A(t)\exp(i\delta t)$ one obtains the following amplitude equation

$$i\left(\partial_\theta + \upsilon\partial_\sigma\right)A + \tilde{\varphi}A - \frac{\beta_2}{2}\partial_\sigma^2 A - i\frac{\beta_3}{6}\partial_\sigma^3 A + \gamma|A|^2 A = 0, \tag{5}$$

that is, the NLS equation with third order dispersion. Changing the carrier frequency allows to modify the sign and even cancel the second order dispersion coefficient β_2 which corresponds to the transition from anomalous to normal dispersion while third order dispersion β_3 can also cancel for some particular value of the carrier frequency $\delta_\pm = \pm 1/\sqrt{3}$. In this case Eq. (5) is equivalent to the classical NLS equation up to fourth order. From this equivalence, we observed that in the anomalous dispersion regime the Eqs. (1),(2) allows for the exisistence of bright hyperbolic secant solitons while we also observed dark solitons for normal dispersion. Our results were confirmed using the continuation package ddebiftool [11]. Finally, one can rewrite the Eqs. (1),(2) as a Neutral Differential Delayed Equation (NDDE)

$$E + \dot{E} - i|E|^2 E = \left(E_\tau - \dot{E}_\tau + i|E_\tau|^2 E_\tau\right)e^{i\varphi}. \tag{6}$$

The Eq. (6) is a so-called bilateral NDDE which preserves its type under time inversion. This property, as well as the presence of a purely imaginary nonlinearity that corresponds to the Kerr effect allows to demonstrate the reversibility in time of the dynamics under the parity-conjugation symmetry.

Conclusions

We discussed how second and third order dispersion can be implemented in delayed dynamical systems using delay algebraic equations and how this particular form of dynamical systems appears naturally as a boundary conditions on a partially reflecting micro-cavity. Using a realistic photonic example, we have demonstrated that nonlinear reversible TDSs exist and that they can host conservative solitons in the long delay limit, thereby bridging the gap with the results known for dissipative TDSs. The essential structure consists of a bilateral NDDE with an imaginary cubic nonlinearity which preserves the solution smoothness upon forward and backward propagation and may generate a unitary spectrum. The normal form identifies with the NLS equation, thereby allowing for bright and dark solitons. We believe that bilateral NDDEs open an avenue for the potential realization of conservative nonlinear dynamics in TDSs, such as, e.g., the Fermi-Pasta-Ulam-Tsingou [12] recurrence or the observation of the Korteweg-de-Vries solitons.

References

[1] Giovanni Giacomelli, Francesco Marino, Michael A. Zaks, and Serhiy Yanchuk. Nucleation in bistable dynamical systems with long delay. *Phys. Rev. E*, 88:062920, Dec 2013.

[2] Laurent Larger, Bogdan Penkovsky, and Yuri Maistrenko. Virtual chimera states for delayed-feedback systems. *Phys. Rev. Lett.*, 111:054103, Aug 2013.

[3] M. Marconi, J. Javaloyes, S. Barland, S. Balle, and M. Giudici. Vectorial dissipative solitons in vertical-cavity surface-emitting lasers with delays. *Nature Photonics*, 9:450–455, 2015.

[4] B. Garbin, J. Javaloyes, G. Tissoni, and S. Barland. Topological solitons as addressable phase bits in a driven laser. *Nat. Com.*, 6, 2015.

[5] Serhiy Yanchuk and Giovanni Giacomelli. Pattern formation in systems with multiple delayed feedbacks. *Phys. Rev. Lett.*, 112:174103, May 2014.

[6] G. Giacomelli and A. Politi. Relationship between delayed and spatially extended dynamical systems. *Phys. Rev. Lett.*, 76:2686–2689, Apr 1996.

[7] C. Schelte, P. Camelin, M. Marconi, A. Garnache, G. Huyet, G. Beaudoin, I. Sagnes, M. Giudici, J. Javaloyes, and S. V. Gurevich. Third order dispersion in time-delayed systems. *Phys. Rev. Lett.*, 123:043902, Jul 2019.

[8] C. Schelte, A. Pimenov, A. G. Vladimirov, J. Javaloyes, and S. V. Gurevich. Tunable Kerr frequency combs and temporal localized states in time-delayed Gires-Tournois interferometers. *Opt. Lett.*, 44(20):4925–4928, Oct 2019.

[9] F. Gires and P. Tournois. Interferometre utilisable pour la compression d'impulsions lumineuses modulees en frequence. *C. R. Acad. Sci. Paris*, (258):6112–6115, 1964.

[10] Serhiy Yanchuk, Leonhard Lücken, Matthias Wolfrum, and Alexander Mielke. Spectrum and amplitude equations for scalar delay-differential equations with large delay. *Discrete and Continuous Dynamical Systems*, 35(1):537–553, 2015.

[11] K. Engelborghs, T. Luzyanina, and D. Roose. Numerical bifurcation analysis of delay differential equations using dde-biftool. *ACM Trans. Math. Softw.*, 28(1):1–21, March 2002.

[12] Enrico Fermi, John Pasta, and Stanislaw M. Ulam. Studies of nonlinear problems. i. Technical Report LA-1940, may 1955.

Destabilizing effect of back electromotive force along the cyclic coordinate in case of a digitally controlled Furuta pendulum

Mate Benjamin Vizi and Gabor Stepan
Department of Applied Mechanics, Budapest University of Technology and Economics, Budapest, Hungary

Summary. Two usually neglected effects are considered in the mechanical model of the Furuta pendulum: the additional viscous damping caused by back electromotive force and the sampling delay caused by the digital control. These effects have relevant influence on the choice of the control algorithm and on the stability properties of the upward position of Furuta pendulum.

Introduction

The Furuta pendulum [1] is a relatively simple two degree of freedom mechanical device (see the left panel of Figure 1), which has became a commonly used equipment for demonstrating various control algorithms applied on a highly nonlinear dynamical system. The arm is usually driven by an electric DC motor and the pendulum hangs freely, so this system is underactuated. The contol signal is the input voltage of the motor, and its calculation by means of a digital controller requires the consideration of both the sampling delay and the additional viscous damping caused by the back electromotive force appearing in the real system. This work considers these two often neglected effects; the consequences on stability and possible control algorithms are discussed.

Governing equations

The nonlinear equations of motion of the Furuta pendulum can be obtained by means of the Lagrangian equations of the second kind in the form of:

$$(J_\mathrm{a} + J_\mathrm{p}\sin^2\theta)\ddot{\varphi} - (m_2 r l\cos\theta)\,\ddot{\theta} + 2J_\mathrm{p}(\sin\theta\cos\theta)\,\dot{\theta}\dot{\varphi} + (m_2 r l\sin\theta)\,\dot{\theta}^2 = M\,, \tag{1}$$

$$J_\mathrm{p}\ddot{\theta} - (m_2 r l\cos\theta)\,\ddot{\varphi} - J_\mathrm{p}(\sin\theta\cos\theta)\,\dot{\varphi}^2 - m_2 g l\sin\theta = 0\,, \tag{2}$$

where θ is the pendulum angle, φ is the arm angle, $J_\mathrm{p} = m_2 l^2 + J_2$ and $J_\mathrm{a} = m_1(r/2)^2 + m_2 r^2 + J_1$ are corresponding mass moments of inertia; the other mechanical parameters are shown in Figure 1. The control torque M applied on the arm is usually provided by a DC motor, for which the output torque can be determined based on the governing equations of the electric motor as a function of the input voltage U_in and the motor angular speed which is proportional to the arm angular velocity $\dot{\varphi}$ of the Furuta pendulum:

$$M = NU_\mathrm{in} - K\dot{\varphi}. \tag{3}$$

The constants N and K are the motor parameters related to the input voltage and back electromotive force, respectively. Note that substituting this into the equation of motion, the back electromotive force is analogous to a viscous damping force applied at the arm. Considering that the input voltage is determined by a digital microcontroller, sampling delay appears in the feedback loop in the following form

$$U_\mathrm{in}(t) = -P_1\theta(t_{j-1}) - D_1\dot{\theta}(t_{j-1}) + D_2\dot{\varphi}(t_{j-1}), \quad t\in[t_j, t_{j+1}), \tag{4}$$

where P_1, D_1, D_2 are the control gains; $t_j = j\tau$, $j\in\mathbb{Z}$ is the jth sampling instant, and τ is the sampling time, which is assumed to be constant. Alternatively, if the angular velocity $\dot{\varphi}$ cannot be measured, then the application of an integral term can be considered in the feedback loop:

$$U_\mathrm{in}(t) = -P_1\theta(t_{j-1}) - D_1\dot{\theta}(t_{j-1}) - I_1\tau\sum_{i=0}^{j-1}\theta(t_i), \quad t\in[t_j, t_{j+1}), \tag{5}$$

In what follows, we discuss the case of Equation (4).

Results

The sampling delay causes stability problems in the control systems as shown in [3, 4]. Based on the linearized system model, the critical sampling time can be calculated; this is the maximal sampling time of the digital control for which the pendulum can be stabilized with appropriate control gains. The minimal value of $D_{2,\min} > 0$ control gain can also determined, which means the simplest $\mathrm{P_1D_1}$ controller (with $D_2 = 0$) cannot stabilize the system. In other words, the upward pendulum position $\theta = 0$ is unstable for any P_1, D_1 control gains without feedback of the arm angular velocity (or the integral of the pendulum angle, see (5)). This instability is caused by the back electromotive force of the DC motor, which is similar to the viscous damping along the cyclic coordinate, while the inverted pendulum is underactuated

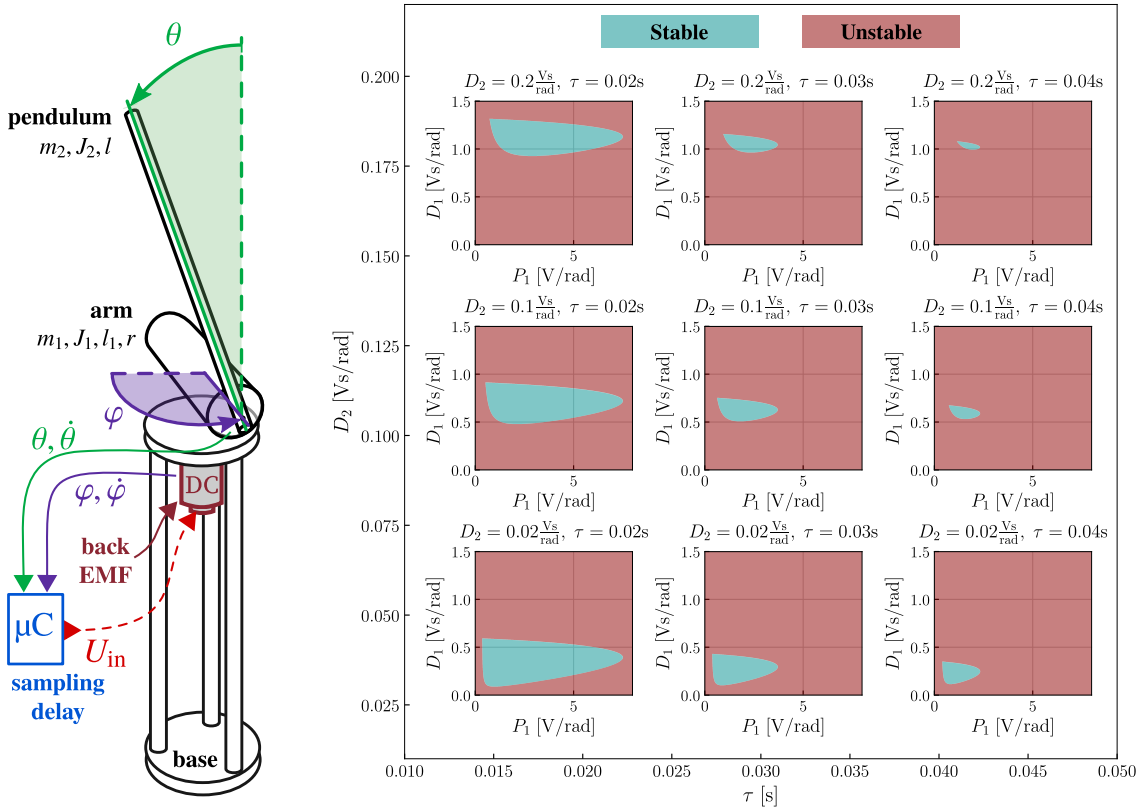

Figure 1: The Furuta pendulum (left) and the four dimensional stability chart of the Furuta pendulum which takes into account the back electromotive force of the DC motor and the sampling delay of the feedback loop (right).

due to the control force applied along the cyclic coordinate only. In case of standard positioning tasks of fully actuated systems, the back electromotive force does not cause such kind of instability, moreover, it is often considered useful because of its extra damping effect. In case of the underactuated control task like the Furuta pendulum, the presence of back electromotive force makes the system inherently unstable in case of classical PD control, this is the reason why an improved control law is needed to achieve stable system behavior: either the feedback of the arm (motor) angular velocity $\dot{\varphi}$ with a $D_2 > D_{2,\min}$ control gain is needed, or an integral gain has to be used with respect to the pendulum angle θ. The results of the corresponding calculations are represented by stability charts in the right panel of Figure 1, in the space of four parameters: the sampling time τ and the three control gains P_1, D_1, D_2. It can be seen, that the size of the stable parameter region becomes smaller with increasing sampling time τ and it completely vanishes at the identified critical values. The effect of the parameter D_2 is similar: the stable regions disappear above maximal and below minimal gain values. The stability charts are similar if the integral gain I_1 is applied as shown in Equation (5).

Conclusions

It was found that the simple P_1D_1 control law applied on the pendulum angle θ and angular speed $\dot{\theta}$ is insufficient in the presence of cyclic viscous damping or back electromotive force; an improved control algorithm is necessary, by extending the P_1D_1 controller with an extra derivative term D_2 applied on the angular speed $\dot{\varphi}$ or with an extra integral term I_1 applied on the pendulum angular position θ. The critical sampling times of the digital control loops can also be determined, which are identified also by laboratory experiments on the Furuta pendulum.

Acknowledgments

The research reported in this paper has been supported by the National Research, Development and Innovation Fund (TUDFO/51757/2019-ITM, Thematic Excellence Program).

References

[1] Furuta, K., Yamakita, M., Kobayashi, S. (1992). Swing-up control of inverted pendulum using pseudo-state feedback. *Proceedings of the Institution of Mechanical Engineers, Part I: Journal of Systems and Control Engineering, 206*(4), 263-269.

[2] Cazzolato, B. S., Prime, Z. (2011). On the dynamics of the Furuta pendulum. *Journal of Control Science and Engineering, 2011*, 3.

[3] Enikov, E., Stépán, G. (1994). Stabilizing an inverted pendulum-alternatives and limitations. *Periodica Polytechnica Mechanical Engineering, 38*(1), 19-26.

[4] Enikov, E., Stepan, G. (1998). Microchaotic motion of digitally controlled machines. *Journal of Vibration and control, 4*(4), 427-443.

Dynamics of Temporal Localized States in Time-Delayed Optically Injected Kerr Gires-Tournois Interferometers

Thomas Seidel*, Julien Javaloyes† and Svetlana V. Gurevich*,†
*Affiliation: Institute for Theoretical Physics, University of Münster, Wilhelm-Klemm-Str. 9, 48149 Münster, Germany
†Affiliation: Departament de Física, Universitat de les Illes Baleares, C/Valldemossa km 7.5, 07122 Mallorca, Spain

Summary. We study theoretically the formation and dynamics of phase-locked temporal localized states (TLSs) and frequency combs that can be generated from a high finesse Fabry-Perot microcavity containing a Kerr medium that is coupled to a external cavity in the presence of optical injection. These TLSs possess a strongly asymmetrical oscillating tail which results from third order dispersion induced by the cavity. Using a first principle model based on delay algebraic equations and applying a combination of direct numerical simulations and path continuation methods, we disclose sets of multistable dark and bright TLSs coexisting on their respective bistable homogeneous backgrounds. In particular, we show that the detuning of the injection with respect to the microcavity resonance controls the region of existence of TLSs and its change can lead to a period-doubling route to chaos. Further we discuss a transformation of the original delay model to a normal form given by a partial differential equation using a rigorous multiple time scale analysis and a functional mapping approach.

Introduction

Time-delayed systems (TDS) describe a large number of phenomena in nature and they proposed for hosting localized structures, fronts and chimera states [1, 2, 3, 4, 5, 6, 7]. They also have been analyzed from the perspective of their equivalence with spatial extended systems [8]. In general, the expansion of a delayed term leads to drift and diffusion. However, it was shown [9] that considering a more general class of singularly perturbed TDS allows to cancel the generic diffusive behavior which leads to a dispersive response. Here, an example of TDS giving rise to second and third order dispersion (TOD), which combined with Kerr effect and optical injection is able to generate temporal localized states (TLSs), as well as molecules induced by third order dispersion [10].

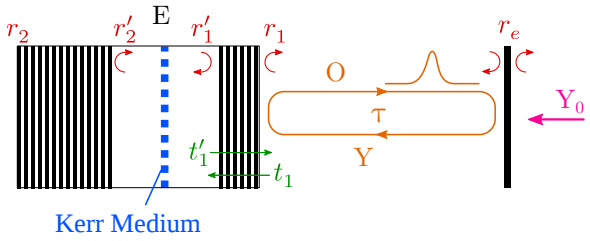

Figure 1: A schematic of the coupled cavity configuration. E denotes the field amplitude in the Kerr region. The output and injection fields in the external cavity are represented by O and Y, respectively. The round-trip time is τ

Model

Our schematic setup is depicted in Fig. 1 in which we show i) the intra-cavity field E and ii) the external cavity field Y. We follow the approach of [11] that consists in solving the field propagation in the linear sections of the micro-cavity. That way one obtains a dynamical model linking the two fields E and Y. Their coupling is achieved considering the transmission and reflection coefficients of the top Distributed Bragg Mirror (DBR). After normalization, one obtains the rate equations for the fields E and Y

$$\frac{dE}{dt} = \left[-1 + i\left(\gamma\left|E\right|^2 - \delta\right)\right]E + hY \quad , \quad Y = \eta\left[E\left(t-\tau\right) - Y\left(t-\tau\right)\right] + \sqrt{1-\left|\eta\right|^2}Y_0\,. \tag{1}$$

The field cavity enhancement can be conveniently scaled out using Stockes relations allowing E and Y to be of the same order of magnitude. This leads to the simple input-output relation $O = E - Y$. The cavity-enhanced complex nonlinear coefficient is $\gamma = \gamma_r + i\gamma_i$, where γ_r stands for the self-phase modulation and γ_i models the two-photon absorption. The effects of the external mirror and signal extraction (e.g., a beam-splitter or transmission through the mirror itself) are combined in the attenuation factor $\eta = r_e \exp\left(i\varphi\right)$. The coupling between the intra-cavity and the external cavity fields E and Y is given in Eqs. (1) by a delay-algebraic equation (DAE). The latter takes into account all the multiple reflections in a possibly high finesse external cavity for which $|\eta| \lessapprox 1$ [9]. Note that in the limit of a very low external mirror reflectivity $\eta \ll 1$, one would obtain $Y = \eta E\left(t-\tau\right) + \mathcal{O}\left(\eta^2\right)$ leading to the so-called Lang-Kobayashi model [12].

Results

In **[SCH19]**, the DAE system (1) was successfully used to prove the existence of multistable dark and bright TLS coexisting on their respective bistable homogeneous continuum wave (CW) backgrounds for fixed parameter values, see Fig. 2

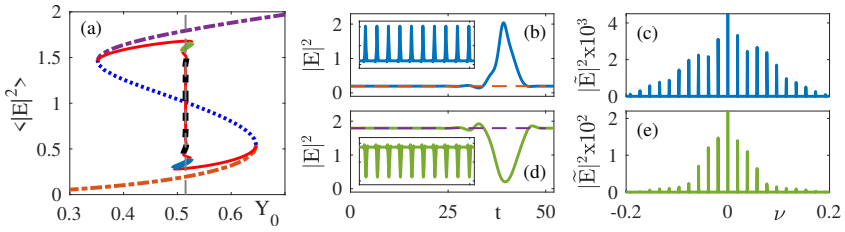

Figure 2: (a) Bistable cavity response under CW injection (dotted line). The lower and upper snaking branches (full lines) correspond to the trains of bright (b) and dark (d) TLSs observed as a function of time t. The inset shows the dynamics over many roundtrips. The respective frequency combs are depicted in panels(c) and (e), where the injection frequency was cut for clarity.

Here, we conduct extensive direct numerical simulations of DAEs (1) in the combination with path continuation methods. In particular, the influence of the detuning δ is analyzed in details. We show that it controls the region of existence of TLSs and its change can lead to a period-doubling route to chaos.

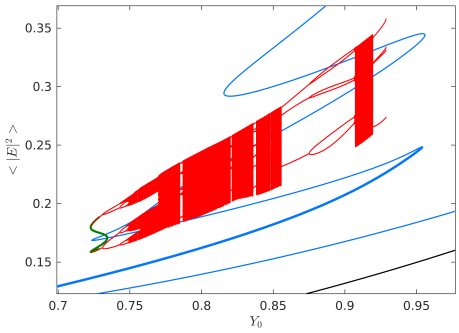

Figure 3: A part of the branch of the TLS (blue) of DAEs (1) as a function of the injection Y_0, obtained with the contunuation methods together with the results of the direct numerical simulations (red). A period-doubling route to chaos is visible. Green line indicate a branch of period-doubled solutions.

Further, the influence of attenuation factor η will be studied. In particular, the regimes of low and high η will be assessed. We demonstrate that in the so-called good cavity limit ($\eta \to 1$), the dynamics is dominated by TOD leading to a wide region of multistability between bright and dark TLS.
Finally we discuss a transformation of the original DAE model (1) to a normal form at the onset of optical bistability given by a partial differential equation using a rigorous multiple time scale analysis and a functional mapping approach.

References

[1] Giovanni Giacomelli, Francesco Marino, Michael A. Zaks, and Serhiy Yanchuk. Nucleation in bistable dynamical systems with long delay. *Phys. Rev. E*, 88:062920, Dec 2013.

[2] Laurent Larger, Bogdan Penkovsky, and Yuri Maistrenko. Virtual chimera states for delayed-feedback systems. *Phys. Rev. Lett.*, 111:054103, Aug 2013.

[3] Francesco Marino, Giovanni Giacomelli, and Stephane Barland. Front pinning and localized states analogues in long-delayed bistable systems. *Phys. Rev. Lett.*, 112:103901, Mar 2014.

[4] M. Marconi, J. Javaloyes, S. Barland, S. Balle, and M. Giudici. Vectorial dissipative solitons in vertical-cavity surface-emitting lasers with delays. *Nature Photonics*, 9:450–455, 2015.

[5] B. Garbin, J. Javaloyes, G. Tissoni, and S. Barland. Topological solitons as addressable phase bits in a driven laser. *Nat. Com.*, 6, 2015.

[6] Serhiy Yanchuk and Giovanni Giacomelli. Dynamical systems with multiple long-delayed feedbacks: Multiscale analysis and spatiotemporal equivalence. *Phys. Rev. E*, 92:042903, Oct 2015.

[7] Serhiy Yanchuk and Giovanni Giacomelli. Pattern formation in systems with multiple delayed feedbacks. *Phys. Rev. Lett.*, 112:174103, May 2014.

[8] G. Giacomelli and A. Politi. Relationship between delayed and spatially extended dynamical systems. *Phys. Rev. Lett.*, 76:2686–2689, Apr 1996.

[9] C. Schelte, P. Camelin, M. Marconi, A. Garnache, G. Huyet, G. Beaudoin, I. Sagnes, M. Giudici, J. Javaloyes, and S. V. Gurevich. Third order dispersion in time-delayed systems. *Phys. Rev. Lett.*, 123:043902, Jul 2019.

[10] C. Schelte, A. Pimenov, A. G. Vladimirov, J. Javaloyes, and S. V. Gurevich. Tunable Kerr frequency combs and temporal localized states in time-delayed Gires-Tournois interferometers. *Opt. Lett.*, 44(20):4925–4928, Oct 2019.

[11] J. Mulet and S. Balle. Mode locking dynamics in electrically-driven vertical-external-cavity surface-emitting lasers. *Quantum Electronics, IEEE Journal of*, 41(9):1148–1156, 2005.

[12] R. Lang and K. Kobayashi. External optical feedback effects on semiconductor injection laser properties. *Quantum Electronics, IEEE Journal of*, 16(3):347 – 355, mar 1980.

Entrainment of Self-Organized Synchronized States in Delay-Coupled Oscillators

Dimitrios Prousalis, Frank Jülicher and Lucas Wetzel
*Max Planck Institute for the Physics of Complex Systems, Nöthnitzer Straße 38, 01187 Dresden, DE

Summary. This work presents how synchronized states that self-organize in networks of mutually coupled oscillators can be entrained by an external reference oscillator. A second-order Kuramoto model with time-delayed coupling is used to predict the phase-differences in the network and the stability of the entrained states. The model predictions are then verified by experimental measurements.

Introduction

Synchronization is important for well-defined and concerted operations and provides the means to establish and keep time-synchronization in networks of spatially distributed clocks [1]. In technical applications synchronization is usually achieved by entraining an oscillator with a periodic signal of a high quality reference oscillator [2]. In natural systems self-organized synchronization is prevalent and based on a mutual coupling between, e.g., cellular oscillators. In this manuscript we study the complex dynamics in finite system of inert, mutually delay-coupled oscillators when subject to an external forcing. The theoretical results for the minimal case, where a reference entrains a network of two mutually delay-coupled oscillators, are verified by experiments with electronic phase-locked loop (PLL) oscillators [4]. We discuss the experimental results taking into account the basins of attraction of the synchronized states that are studied.

Model for Studying the Entrainment of Networks of Mutually Delay-Coupled Oscillators

The dynamics in networks of inert, delay-coupled oscillators can be studied using a second-order Kuramoto model [3, 4]

$$m_k\,\ddot{\theta}_k(t)+\dot{\theta}_k(t)=\omega_k+\frac{K_k}{n_k}\sum_{l=1}^{N}c_{kl}\,h\left(\theta_l(t-\tau_{kl})-\theta_k(t)\right), \tag{1}$$

where $k=1,\ldots,N$ indexes the N oscillators, $\omega_k\in\mathbb{R}$ denotes the intrinsic frequencies, $h(\cdot)$ a periodic coupling function, $K_k\geq 0\in\mathbb{R}$ the coupling strength, $m_k\geq 0\in\mathbb{R}$ an inertial parameter, $n_k\geq 0\in\mathbb{N}_0$ the number of inputs of oscillator k, $\theta_i(t)\in S^1$ for $i=\{k,l\}$ the phases of the oscillators' output signals with $\dot{\theta}(t)$ and $\ddot{\theta}(t)$ denoting their first and second time derivatives, $c_{kl}=\{0,1\}$ the components of the network's adjacency matrix, and $\tau_{kl}\in\mathbb{R}$ denotes the cross-coupling time delays. The ansatz to study synchronized states and their linear stability is

$$\theta_k(t)=\Omega t+\beta_k+\epsilon q_k(t), \tag{2}$$

where Ω denotes the global frequency of a synchronized state, $\epsilon q_k(t)$ a small perturbation ($\epsilon\ll 1$), and β_k a phase-offset.

Network of mutually delay-coupled oscillators: frequency and phase differences of synchronized states
Using the ansatz (2) in Eqs. (1) and expanding $h(\cdot)$ to first order with respect to ϵ, we obtain the properties of synchronized states from $\mathcal{O}(\epsilon^0)$: $\Omega=\omega_k+K\,h\left(-\Omega\tau_{kl}+\beta_{kl}\right)$, where $\beta_{kl}=\beta_k-\beta_l$, e.g., equal to 0 or π for identical oscillators. The linear stability of these states depends on the the oscillator's parameters and the properties of the synchronized states [4].

Individual oscillator entrained by a reference: phase difference with respect to reference oscillator
Here, the frequency of the synchronized state is determined by the reference $\Omega=\omega_R$. The phase difference is $\beta=-h^{-1}\left[(\omega_R-\omega)/K\right]-\omega_R\tau$. The stability depends only on the detuning of the frequencies and the coupling strength [5].

Networks of mutually delay-coupled oscillators entrained by a reference: phase differences
Here, we consider a network of heterogeneous oscillators, making the ansatz (2) for $\Omega=\omega_{\mathrm{R}}$. The entrainment is accounted for by assigning the reference oscillator with $k=1$ and setting $c_{1l}=0\,\forall\,l$. The $N-1$ phase differences can then be obtained from

$$\omega_R=\omega_k+\frac{K_k}{n_k}\sum_{l=1}^{N}c_{kl}\,h\left[-\omega_R\tau_{kl}-\beta_{kl}\right]. \tag{3}$$

Example of a Minimal Entrained Network and Experimental Verification

We study a network of two mutually coupled oscillators one of which is forced by an external reference, see Fig. 1. From Eq. (3) the phase differences between the mutually coupled oscillators $\beta_{23}=\omega_R\tau_{32}+h^{-1}\left[(\omega_R-\omega_3)/K_3\right]$ and that to the reference $\beta_{R2}=\omega_R\tau_{R2}+h^{-1}\left[2\left(\omega_R-\omega_2\right)/K_2-h\left[-\omega_R\tau_{23}-\beta_{23}\right]\right]$ are obtained. The theoretical predictions and the experimental results β_{23} and β_{R2} of the synchronized states are shown as a function of the reference frequency in Fig. 2c. The range of reference frequencies for which synchronized states are linearly stable is shown in green. In experiments however, we only find stable synchronized states in a smaller range than predicted. This can be explained by the basins of attraction obtained from time-series simulations shown in Figs. 2a, 2b. They show the basins for different initial phase histories for $t\in[-\tau,\,0]$. In Fig. 2a all oscillators are initially free-running, as can be realized in the experimental setup.

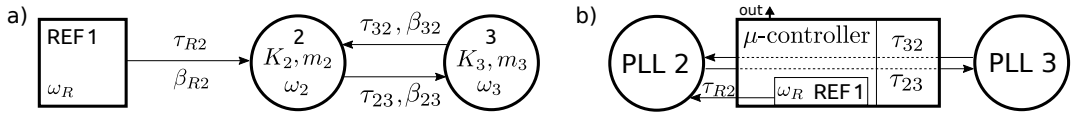

Figure 1: a) Sketch of entrainment of a network of two mutually delay-coupled oscillators. b) The experimental setup consists of a microcontroller that organizes the delay-coupling between the two mutually coupled PLLs and the entrainment by a virtual reference derived from its internal clock. For details about the experimental setup see reference [4].

In Fig. 2b, the simulation starts in the entrained synchronous state, similarly to linear stability analysis. Their x- and y-axis represent the phase differences $\phi_1 = \theta_3(0) - \theta_2(0)$ and $\phi_2 = \theta_3(0) - \theta_1(0)$ between the oscillators at $t = 0$, respectively. The color encodes the asymptotic value of the order parameter for any combination (ϕ_1, ϕ_2), obtained from a time series simulation of the oscillator network using the Eqs. (1). The order parameter has been modified such that it is equal to one if the phase configuration of the entrained synchronous state under investigation is achieved [3]. From Fig. 2a it can be understood that the basin of attraction has zero volume close to the boundaries of linear stability. Hence, we cannot find entrained synchronous states with the experimental setup (Fig. 1b) that always starts from an initially free-running state.

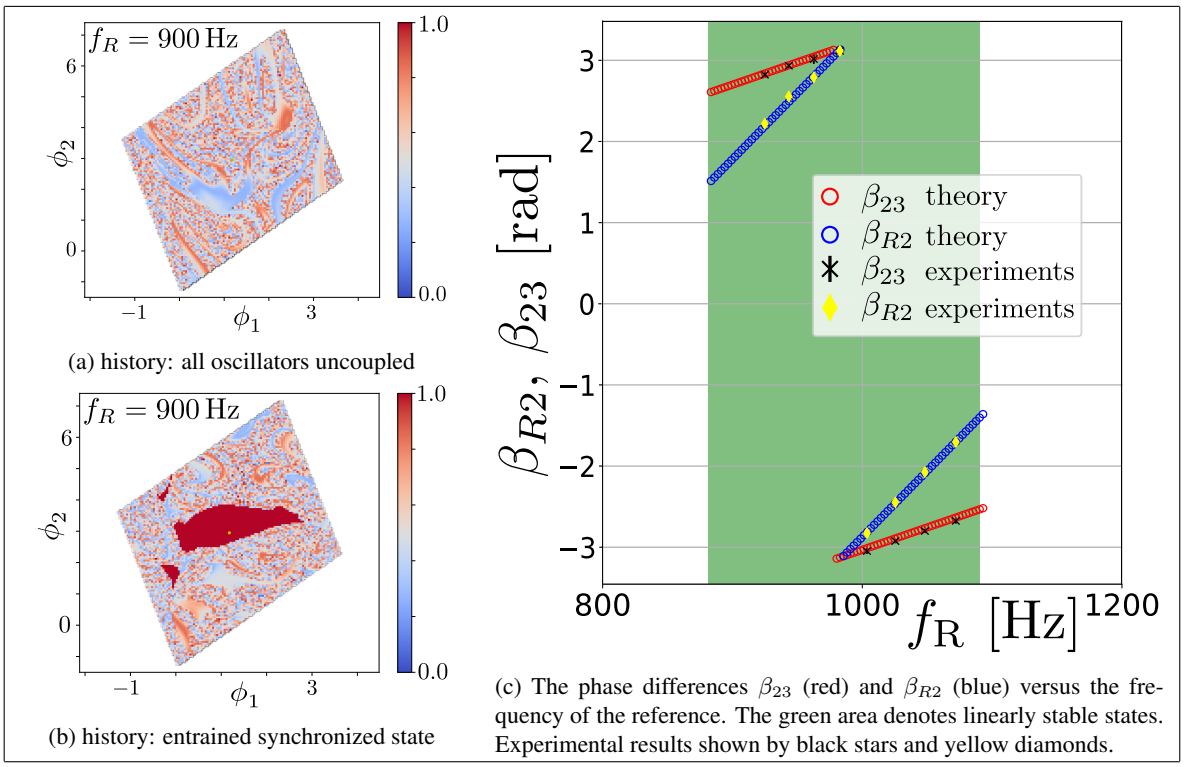

(a) history: all oscillators uncoupled

(b) history: entrained synchronized state

(c) The phase differences β_{23} (red) and β_{R2} (blue) versus the frequency of the reference. The green area denotes linearly stable states. Experimental results shown by black stars and yellow diamonds.

Figure 2: Parameters: $\omega_2 = 1004 \cdot 2\pi$ Hz, $\omega_3 = 996 \cdot 2\pi$ Hz, $K_2 = 423 \cdot 2\pi$ Hz, $K_3 = 408 \cdot 2\pi$ Hz, and $\tau_{R1} = \tau_{12} = 0.265$ s.

Conclusions

This work studies the entrainment of self-organized synchronous states. Our phase oscillator model takes into account time-delays in the coupling and inert oscillator response. It predicts the properties of entrained synchronous states as verified here by experimental results obtained from electronic oscillators. Self-organized synchronous states can be viewed as an effective oscillator that has emerged over a network of mutually coupled oscillators. This effective oscillator is characterized by its quiescent frequency Ω and the frequency range within which it can lock to a reference. Both properties affect the linear stability of entrained synchronous states and depend on the delays within the mutually coupled oscillators. The delay between reference and network only affects the phase differences of the entrained synchronized states.

References

[1] Pikovsky, A., Rosenblum, M. G. and Kurths, J. (2001) Synchronization, A Universal Concept in Nonlinear Sciences, Cambridge University Press.

[2] Lindsey, W. C., Ghazvinian, F., Hagmann, W.C. and Dessouky, K. (1985) Network Synchronization, *Proceedings of the IEEE* **73**:1445-1467.

[3] Rodrigues, F. A., Peron, T. K., Ji, P., Kurths, J. (2016) The Kuramoto model in complex networks, *Physics Reports* **610**:1-98.

[4] Wetzel, L., Jörg, D. J., Pollakis, A., Rave, W., Fettweis, G., Jülicher, F. (2017) Self-organized synchronization of digital phase-locked loops with delayed coupling in theory and experiment, *PLOS ONE* **12**:1-21.

[5] Riaz, R. F., Prousalis, D., Hoyer, C., Wagner, J., Ellinger, F., Jülicher, F., and Wetzel, L. (2020) Stability and Transient Dynamics of PLLs in Theory and Experiments, *2020 European Conference on Circuit Theory and Design (ECCTD)*.

Human positioning of a planar pendulum

Bence Szaksz and Gabor Stepan
Department of Applied Mechanics, Budapest University of Technology and Ec., Budapest, Hungary

Summary. The human positioning of a planar pendulum is investigated. The system is modelled with two particles which are connected with a rope. Collocated proportional-derivative control acts with human reaction delay at the suspension point of the pendulum that can only move horizontally. The Hopf bifurcation analysis of the system is executed which leads to closed form algebraic expressions for the Poincaré-Lyapunov coefficient and for the amplitude of oscillation.

Introduction

The motion of a planar pendulum is examined at its downward position considering human position control. The human intervention is modelled with a proportional-derivative (PD) controller subjected to constant reaction delay, which leads to a system of delay differential equations (DDEs). The inclusion of the time delay implies that the stability region in the PD-plane will be bounded and sub- and supercritical Hopf bifurcations appear along the stability boundary.
The stability and amplitude of the periodic solutions close to the bifurcation point are calculated analytically leading to closed form algebraic equations. We follow the algebraic procedures of Hopf bifurcation calculation as given in [1, 2, 3].

Mechanical model

The coupled hand-held pendulum system is modelled with two point masses connected with a rope as shown in Fig. 1. The human hand is modelled with the mass m_1 on which the control force F acts; this is the pivot point of the planar mathematical pendulum with mass m_2 and length l. The controlled mass can slide in a linear guide so that it can only move along the x axis. The horizontal displacement of the hand and the bottom point of the pendulum are denoted with x_1 and x_2, respectively. The equations of motion of the system are derived with respect to the two generalized coordinates

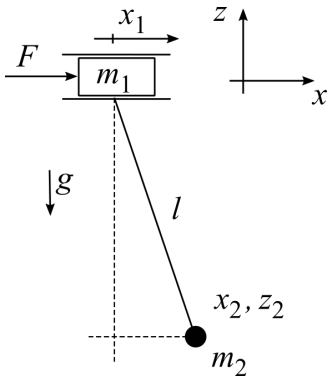

Figure 1: In-plane model of the coupled hand-pendulum system

x_1 and x_2 [4]. These expressions are highly nonlinear, therefore, their Taylor series are calculated up to third order in x_1 and x_2 leading to the governing equations:

$$\ddot{x}_1 = \frac{F}{m_1} + \frac{m_2}{m_1}\frac{g}{l}(x_2 - x_1) - \frac{m_2}{m_1}\left(\left(\frac{m_2}{m_1} + \frac{1}{2}\right)\frac{g}{l^3}(x_2 - x_1)^3 - \frac{1}{l^2}(x_2 - x_1)(\dot{x}_2 - \dot{x}_1)^2 + \frac{F}{m_1 l^2}(x_2 - x_1)^2\right), \quad (1)$$

$$\ddot{x}_2 = -\frac{g}{l}(x_2 - x_1) + \left(\frac{m_2}{m_1} + \frac{1}{2}\right)\frac{g}{l^3}(x_2 - x_1)^3 - \frac{1}{l^2}(x_2 - x_1)(\dot{x}_2 - \dot{x}_1)^2 + \frac{F}{m_1 l^2}(x_2 - x_1)^2, \quad (2)$$

where the time derivative is denoted by dot. The control force can be chosen in different ways. In this study, a collocated PD control is investigated which means that the human operator acts based on the displacement and velocity of his/her hand:

$$F(t) = -Px_1(t - \tau) - D\dot{x}_1(t - \tau). \quad (3)$$

Here, τ stands for the delay caused by the reaction time, while P and D are the proportional and derivative gain parameters, respectively.

Stability analysis

Introduce the dimensionless distances $\tilde{x}_i = x_i/l$ (for $i = 1, 2$) and the dimensionless time $\tilde{t} = t/\tau$, furthermore, the transformed characteristic exponents and angular frequencies $\tilde{\lambda} = \tau\lambda$ and $\tilde{\omega} = \tau\omega$, respectively. By abuse of notation we

drop the tildes and introduce the dimensionless parameters: $\mu = m_2/m_1$, $\alpha = \tau\sqrt{g/l}$, $p = P\tau^2/m_1$, and $d = D\tau/m_1$. Then the characteristic equation assumes the form:

$$D(\lambda) = \lambda^4 + d\lambda^3 e^{-\lambda} + \alpha^2(1+\mu)\lambda^2 + p\lambda^2 e^{-\lambda} + \alpha^2 d\lambda e^{-\lambda} + \alpha^2 p e^{-\lambda} = 0. \tag{4}$$

When the real characteristic exponent crosses the origin at $\lambda = 0$, saddle-node bifurcation appears at $p = 0$. Hopf bifurcation occours when a pair of complex conjugate roots lies on the imaginary axis at $\lambda = \mathrm{i}\omega$, which yields the stability boundary curve:

$$p_{cr} = \left(1 - \frac{\mu\alpha^2}{\omega^2 - \alpha^2}\right)\omega^2 \cos\omega, \quad d_{cr} = \left(1 - \frac{\mu\alpha^2}{\omega^2 - \alpha^2}\right)\omega \sin\omega. \tag{5}$$

Let the proportional gain p be the bifurcation parameter. Then the real part of the root tendency $\lambda' = \mathrm{d}\lambda(p_{cr})/\mathrm{d}p$ assumes the form:

$$\Re(\lambda') = \frac{\omega}{4(a^2+b^2)}\left(\sin\omega + \omega\cos\omega + \mu\alpha^2\frac{\omega^2+\alpha^2}{(\omega^2-\alpha^2)^2}\sin\omega - \frac{\omega\mu\alpha^2}{\omega^2-\alpha^2}\cos\omega\right), \tag{6}$$

where a and b can be expressed as

$$a = \frac{1}{2}\omega\left(1 - \frac{\mu\alpha^2}{\omega^2-\alpha^2}\right)\left(\frac{1}{2}\sin(2\omega) - \omega\right), \quad b = \omega + \frac{\omega\mu\alpha^4}{(\omega^2-\alpha^2)^2} - \frac{1}{2}\left(1 - \frac{\mu\alpha^2}{\omega^2-\alpha^2}\right)\sin^2\omega^2. \tag{7}$$

The Poincaré-Lyapunov coefficient Δ and the amplitude of oscillation A are obtained in the form:

$$\Delta = \frac{\mu}{8(a^2+b^2)}\left(\frac{\omega^2}{\omega^2-\alpha^2}\right)^4\left(1 - \frac{\mu\alpha^2}{\omega^2-\alpha^2}\right)\left(\frac{1}{4}\omega\sin(2\omega) - \frac{1}{2}\omega^2\right)\left(2\omega^2 - \frac{3}{2}\alpha^2\right), \tag{8}$$

$$A = \sqrt{-\frac{\Re(\lambda')}{\Delta}(p-p_{cr})} = \left(\frac{\omega^2-\alpha^2}{\omega^2}\right)^2\sqrt{-\frac{2}{\mu}\frac{\sin\omega\left(1+\mu\frac{\omega^2\alpha^2+\alpha^4}{(\omega^2-\alpha^2)^2}\right) + \omega\cos\omega\left(1-\mu\frac{\omega\alpha^2}{\omega^2-\alpha^2}\right)}{\left(1-\mu\frac{\alpha^2}{\omega^2-\alpha^2}\right)\left(\frac{1}{4}\omega\sin(2\omega) - \frac{1}{2}\omega^2\right)\left(2\omega^2 - \frac{3}{2}\alpha^2\right)}(p-p_{cr})}. \tag{9}$$

The first two terms of Eq. 8 are nonnegative, therefore the last three terms determine the sign of Δ and so the sense of the bifurcation. Fig. 2 shows the saddle node and Hopf bifurcation curves of the system indicating the sub- or subcritical nature as well. The boundary of the stable region is always supercritical.

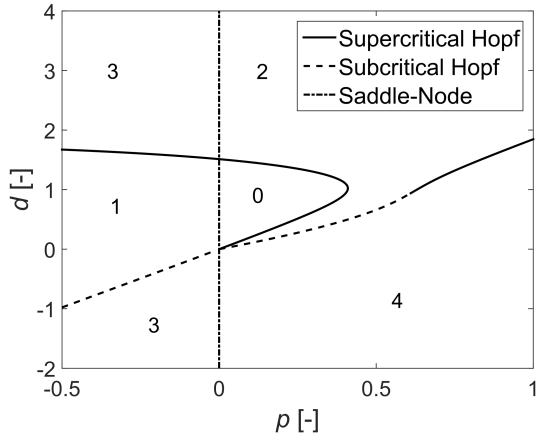

Figure 2: Stability chart in the PD plane. The numbers indicate the number of unstable characteristic exponents. ($\mu = 1/30$, $\alpha = 1.1437$)

Conclusions

The model can explain why hand-held pendulums often oscillate in spite of the intention of the human operator.

References

[1] Hassard B. D., Kazarinoff N. D., Wan Y.-H. (1981) Theory and Applications of Hopf Bifurcation, *London Mathematical Society Lecture Note Series*, vol. 41. Cambridge University Press, Cambridge

[2] Stepan G. (1989) Retarded Dynamical Systems: Stability and Characteristic Functions, *Pitman Research Notes in Mathematics*, vol. 210. Longman, Essex

[3] Orosz G. (2004) Hopf bifurcation calculations in delayed systems, *Periodica Polytechnica Ser. Mech. Eng.* **48**:189-200

[4] Chin C., Nayfeh A. H., Abdel-Rahman E. (2001) Nonlinear dynamics of a boom crane, *Journal of Vibration and Control* **7**:199-220

Thursday, July 21, 2022
13:30 - 15:30

MS-02 Asymptotic Methods
Saint Clair 1

Chair: Roman Starosta

13:30 - 13:50
Small and large amplitude, free oscillations of a pinned spherical interface
DHOTE Yashika*, GOSWAMI Partha, DASGUPTA Ratul
*Indian Institute of Technology Bombay (Powai, Mumbai, Maharashtra-400076 India)

13:50 - 14:10
Forced vibration of spring pendulum with nonlinear springs connected in series
SYPNIEWSKA-KAMINSKA Grażyna*, STAROSTA Roman, AWREJCEWICZ Jan
*Poznań University of Technology, Institute of Applied Mechanics (Jana Pawła II 24, 60-965 Poznań, Poland Poland)

14:10 - 14:30
Stabilisation of Rayleigh-Plateau modes on a liquid cylinder
PATANKAR Sagar*, BASAK Saswata, DASGUPTA Ratul
*Indian Institute of Technology [Bombay] (Powai, Mumbai - 400076, INDIA India)

14:30 - 14:50
On solving one-dimensional wave equations subject to nonclassical and to nonlinear boundary conditions
VAN Horssen Wim*
*Delft University of Technology / Delft Institute of Applied Mathematics (Van Mourik Broekmanweg 6, 2628 XE Delft Netherlands)

Small and large amplitude, free oscillations of a pinned spherical interface

Yashika Dhote, Partha S. Goswami and Ratul Dasgupta
Department of Chemical Engineering, IIT Bombay, Mumbai, India

Summary. We investigate using linearised theory and numerical solution to the incompressible Euler equation, the effect of density ratio and perturbation amplitude on shape oscillations of a pinned spherical interface. The interface in the base state is a spherical cap separating quiescent fluids and may be pinned at any angle lying in the interval $[0, \pi]$. The linearised analysis presented in [1] which takes into account the density of fluid inside the spherical cap only, is further extended to account for the density of fluids inside($\rho^{\mathcal{I}}$) as well as outside($\rho^{\mathcal{O}}$). The limits of linearised theoretical predictions are tested via numerical simulations by exciting the first eigenmode of the system at various pinning angles(α). For sufficiently small perturbation amplitude, the agreement with linearised predictions found to be quite good. A systematic nonlinear correction to frequency is observed as the perturbation amplitude is increased, becoming particularly discernable after the first few oscillations. The simulations are carried out using the open source code Gerris [8] and we quantify the effect of non-linearity and droplet ejection is observed due to increasing perturbation amplitude. We investigate the bubble limit and the droplet limit respectively where density of fluid inside the cap is negligible compared to that outside and vice versa.

Inviscid oscillations of a pinned interface

Natural and forced oscillations of a pinned spherical cap due to surface tension is of interest in numerous applications both in engineering as well as in the natural sciences and remains a topic of active research interest [2]. The frequency spectrum of small amplitude free oscillations of an inviscid free drop of unperturbed radius R_0 and density $\rho^{\mathcal{I}}$ due to the restoring force of surface tension T was first obtained by Rayleigh [9]. The effect of the second fluid on the spectrum was studied by Lamb [5] lead to the classical dispersion relation for shape oscillations of liquid drops ($\rho^{\mathcal{I}} >> \rho^{\mathcal{O}}$) and bubbles ($\rho^{\mathcal{O}} >> \rho^{\mathcal{I}}$):

$$\omega_0^2 = \frac{T}{R_0^3}\frac{l(l+1)(l-1)(l+2)}{\rho^{\mathcal{I}}(l+1)+l\rho^{\mathcal{O}}} \tag{1}$$

where l is a positive integer arising from the spherical harmonic $\mathbb{Y}_l^m(s,\psi)$. In many engineering applications like vibration induced atomisation [4], it is necessary to know the modification to the Rayleigh-Lamb frequency spectrum (eqn.1) due to the droplet resting on a substrate. While a number of studies have investigated this problem under the assumption of a hemispherical cap [6], the first study which systematically studied the modification to the spectrum for the case of a droplet pinned at an arbitrary angle α was by Steen [1]. As a part of the present study, we extend the analysis of of their work to take into account the density of the second fluid on the shape oscillation of pinned bubbles. For this, we closely follow the analysis by Steen employing two spherical coordinate systems as shown in fig.1(a). It maybe shown that in the inviscid, irrotational approximation [3, 7] the perturbation velocity potential ϕ and the surface perturbation η can be expressed in the standing wave form [3].

$$\eta(s,\psi,t) = a(t)y(s)\exp(il\psi),\ \phi^{\mathcal{I}}(\rho,\theta,\psi,t) = \dot{a}(t)\ \Phi^{\mathcal{I}}(\rho,\theta)\exp(il\psi),\quad \phi^{\mathcal{O}}(\rho,\theta,\psi,t) = \dot{a}(t)\ \Phi^{\mathcal{O}}(\rho,\theta)\exp(il\psi) \tag{2a,b,c}$$

Here, $\dot{a} \equiv \frac{da}{dt}$ and it maybe be further shown that $a(t)$ satisfies the simple harmonic oscillator equation $\ddot{a}+\omega_0^2 a(t) = 0$. The pinned frequency ω_0^2 is calculated by solving a generalised eigenvalue problem employing the Green function formalism suggested in [1] and additionally also taking into account both densities [3]. We test predictions made in the droplet and in the bubble limits using the open-source code Gerris [8] and these are described below in fig. 2, 3 and 4.

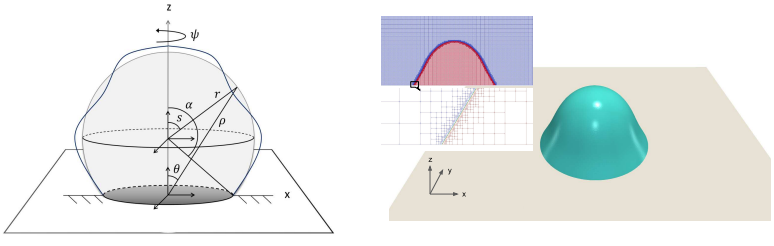

(a) Geometry (b) Initial condition in numerical simulation

Figure 1: (a) A cartoon representation of a spherical cap (in the base state) pinned at an angle α on a substrate [1]. In close analogy to the linearised analysis by [1], we employ two spherical coordinates systems viz. one centred on the substrate with scaled coordinates (ρ,θ,ψ) and another centred at the spherical cap with scaled coordinates (r,s,ψ). The density of the fluid inside is taken as $\rho^{\mathcal{I}}$ while that outside is $\rho^{\mathcal{O}}$. (b) The initial deformation is obtained from linear theory by computing the eigenmodes which may be represented as $r = R_0 + a_0\eta(s,\psi)$. Shown here is the lowest axisymmetric eigenmode for a pinning angle of $80°$. For consistency and to justify the neglect of gravity, R_0 is chosen to be much smaller than the capillary length scale. Grid density of 2048x2048 is used near the interface and 512x512 is used away from the interface.

Droplet Limit $(\rho^{\mathcal{O}}/\rho^{\mathcal{I}} \to 0)$: Axisymmetric modes and comparison of linear theory with simulations

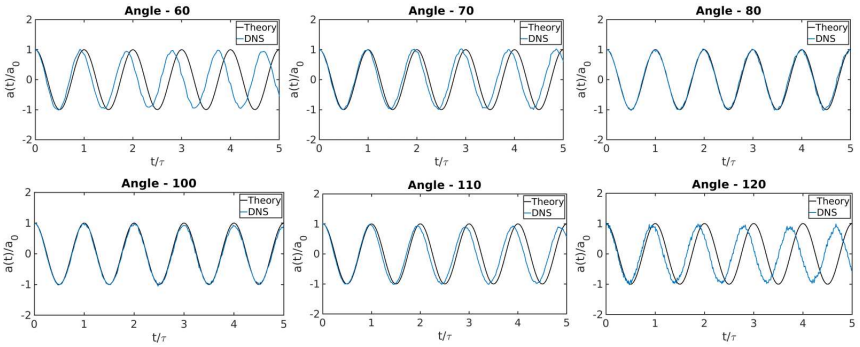

Figure 2: Time signal from oscillatory response of the interface obtained from numerical solution to the incompressible Euler equation (labelled as DNS in the plots) with surface tension $(72dyne/cm)$. We distort the spherical cap at the indicated pinning angle using the axi-symmetric eigenmodes with zero perturbation velocity as shown in fig.1b. In the droplet case, these eigenmodes are provided in [1] and correspond to the droplet limit. $(R_0 = 0.1cm, \rho^{\mathcal{O}}/\rho^{\mathcal{I}} = 0.001$. The time signals are measured at the interface at a location slightly off the apex of the spherical cap and compared to a sinusoidal signal with the frequency obtained by solving a generalised eigenvalue problem in Matlab [1, 3]. Note that the time t is non-dimensionalised by the time period τ predicted from linear theory [1]. A good agreement with linear predictions is seen in simulations with small disagrement in the predicted frequency around $\alpha = 60^\circ$ and $\alpha = 120^\circ$.

Bubble Limit $(\rho^{\mathcal{O}}/\rho^{\mathcal{I}} \to \infty)$: axisymmetric modes and comparison with simulations

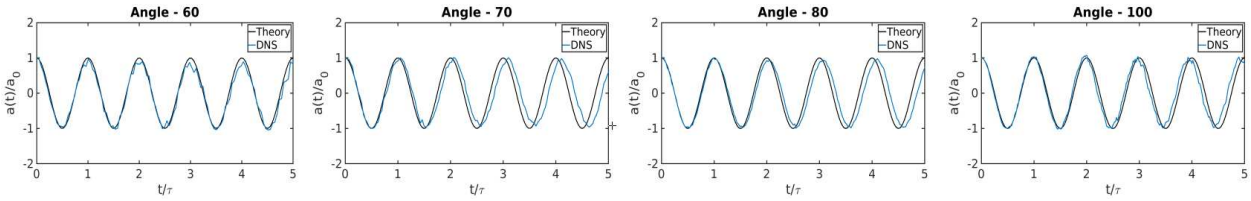

Figure 3: Oscillatory response obtained from numerical simulations in the bubble limit$(\rho^{\mathcal{O}}/\rho^{\mathcal{I}} = 1000)$ and comparison with linearised predictions [3]. A resonably agreement is seen in all cases for comparison of linear theory with simulations.

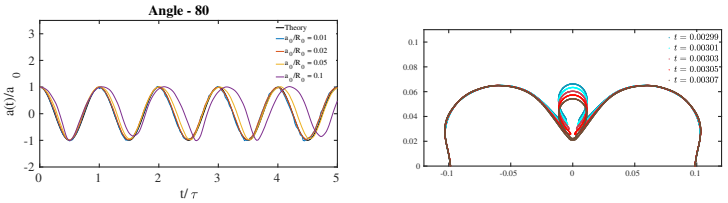

(a) Effect of changing perturbation amplitude(b) Droplet ejection during oscillation for $a_0/R_0 = 0.3$

Figure 4: Effect of change of perturbation amplitude for a spherical cap pinned at 80°.

Fig. 4(a) shows the effect of increase of the perturbation amplitude a_0. It is seen that the time signal becomes distinctly non-sinusoidal with a frequency which increases with increasing a_0. Panel (b) of the same figure shows a large amplitude simulation where a droplet is (nearly) detached from the spherical cap as a result of large amplitude deformation. Systematic comparisons of nonlinear effects for free and pinned droplets will be discussed at the meeting.

Conclusions

We extend the theoretical formalism developed in [1] to include the effect of internal as well as external (linearised) fluid inertia for pinned spherical interfaces. For sufficiently small amplitude, we find good agreement with linearised theoretical predictions both in the droplet as well as the bubble limit. For perturbation amplitude exceeding about 10 percent of the spherical cap radius, discernable nonlinear effects are seen in the numerical simulations and in the large amplitude regime, droplet ejection is observed.

References

[1] J. Bostwick and P. Steen. Dynamics of sessile drops. part 1. inviscid theory. *Journal of fluid mechanics*, 760:5–38, 2014.

[2] J. Bostwick and P. Steen. Stability of constrained capillary surfaces. *Annual Review of Fluid Mechanics*, 47:539–568, 2015.

[3] Dhote, Yashika and Goswami, Partha Sarathi and Dasgupta, Ratul. Shape oscillations of a pinned spherical interface, 2021. In preparation.

[4] A. James, B. Vukasinovic, M. K. Smith, and A. Glezer. Vibration-induced drop atomization and bursting. *Journal of Fluid Mechanics*, 476:1–28, 2003.

[5] H. Lamb. *Hydrodynamics*. University Press, 1924.

[6] D. Lyubimov, T. Lyubimova, and S. Shklyaev. Non-axisymmetric oscillations of a hemispherical drop. *Fluid Dynamics*, 39(6):851–862, 2004.

[7] S. Patankar, P. K. Farsoiya, and R. Dasgupta. Faraday waves on a cylindrical fluid filament–generalised equation and simulations. *Journal of Fluid Mechanics*, 857:80–110, 2018.

[8] S. Popinet. The gerris flow solver. *http://gfs. sf. net*, 2007.

[9] L. Rayleigh et al. On the capillary phenomena of jets. *Proc. R. Soc. London*, 29(196-199):71–97, 1879.

Forced vibration of spring pendulum with nonlinear springs connected in series

Jan Awrejcewicz[*], Roman Starosta[**], Grażyna Sypniewska-Kamińska[**]
[*] *Technical University of Łódź, Department of Automatics and Biomechanics, Łódź, Poland*
[**] *Poznań University of Technology, Institute of Applied Mechanics, Poznań, Poland*

Summary. An attempt to solve the problem and to conduct a qualitative analysis of the forced vibration of the spring pendulum containing nonlinear springs connected in series is made in the paper. The method of multiple scales in time domain (MMS) has been employed in order to carry out the analytical computations. The MMS allows one, among others, to predict the resonances which can appear in the systems. The approximate solution of analytical form has been obtained for vibration at main resonance.

Introduction

Elastic elements arranged in various kinds of connections (in serial, in parallel or in branching) are widely applied in many mechanisms, mechatronic devices and more and more often in micromechanical systems [1], [7]. When the massless springs are connected in series or in branching, modelling of them as massless elastic links, commonly used in discrete approach, leads to the mathematical model equations among which there are algebraic equations beside the differential ones. The algebraic equations describe then the equilibrium of the nodes at which the springs connect with each other. In the linear case, spring connections of such types create no greater difficulties. Depending on the degree of complexity of the connection, the equivalent spring constant can be introduced or one can retain in the mathematical model the algebraic equations that are linear, which results in a positive semi-definite mass matrix [2]. In nonlinear systems, the principle of superposition does not apply, which is a source of certain computational difficulties. It should be emphasized the serial springs connections increase the whole system pliancy, thus its nonlinear character manifests itself even more.
Various nonlinear oscillators with serially connected springs were investigated by many authors mostly numerically. An approximate analytical approach to the free vibration of oscillators with two nonlinear springs or one linear and another nonlinear spring is used among other in papers [4-5] and [3], [6] respectively. The free vibration of two mechanical systems with springs connected in series is studied using MSM in [5].

Mathematical model

The pendulum with two serially connected springs, presented in Fig. 1, is constrained to the motion on the vertical plane. Z_1 and Z_2 stand for the total elongation of the springs whereas L_{0i} denotes the length of the *i*th non-stretched spring. The springs nonlinearity is of the cubic type, i.e. $F_i = k_i(Z_i + \Lambda_i Z_i^3)$ for $i = 1,2$, and the nonlinear contributions to the whole elastic force are assumed to be small. There are two purely viscous dampers in the system. The system is loaded by the torque of magnitude $M(t) = M_0 \cos(\Omega_2 t)$ and by the force **F** whose magnitude changes also harmonically i.e. $F(t) = F_0 \cos(\Omega_1 t)$. Although the system has two degrees of freedom, its state is unambiguously determined by three time functions: the elongations Z_1 and Z_2 and the angle Φ.

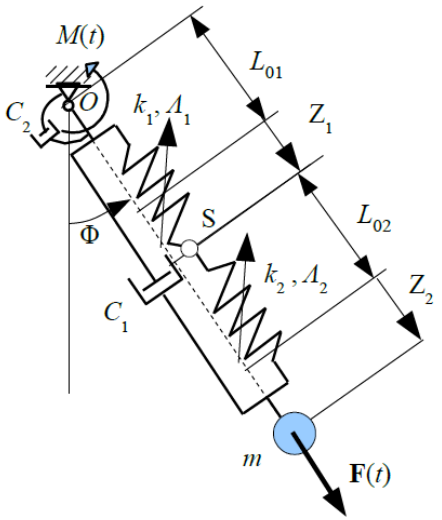

Figure 1: Forced and damped spring pendulum with two nonlinear springs

Two equations of motion, obtained using the Lagrange formalism, and the equilibrium equation of the join *S* govern the dynamic behaviour of the pendulum. They are as follows:

$$\left(1+\frac{dZ_1}{dZ_2}\right)^2(m\ddot{Z}_2+C_1\dot{Z}_2)+m\left(1+\frac{dZ_1}{dZ_2}\right)\dot{Z}_2^2\ddot{Z}_1+k_2Z_2(1+\Lambda_2Z_2^2)+$$
$$k_1Z_1(1+\Lambda_1Z_1^2)\frac{dZ_1}{dZ_2}-m\left(1+\frac{dZ_1}{dZ_2}\right)\left((L_0+Z_1+Z_2)\dot{\Phi}^2+g\cos\Phi-f_0\cos(\Omega_1 t)\right)=0, \quad (1)$$

$$m(L_0+Z_1+Z_2)^2\ddot{\Phi}+C_2\dot{\Phi}+2m(L_0+Z_1+Z_2)\left(1+\frac{dZ_1}{dZ_2}\right)\dot{Z}_2\dot{\Phi}+$$
$$mg(L_0+Z_1+Z_2)\sin\Phi-M_0\cos(\Omega_2 t)=0, \quad (2)$$

$$k_2Z_2(1+\Lambda_2Z_2^2)=k_1Z_1(1+\Lambda_1Z_1^2), \quad (3)$$

where: $L_0=L_{01}+L_{02}$.
Equations (1) – (3) are supplemented by the initial conditions of the following form

$$Z_1(0)+Z_2(0)=Z_0,\ \dot{Z}_1(0)+\dot{Z}_2(0)=v_0,\quad \Phi(0)=\Phi_0,\quad \dot{\Phi}(0)=\omega_0, \quad (4)$$

where $Z_0,\ v_0, \Phi_0, \omega_0$ are known quantities.
The derivative $\frac{dZ_1}{dZ_2}$ one can calculate taking into account Eq. (3) which simplifies significantly the governing equations.
The method of multiple scales in time domain with three time variables is applied to solve the considered problem. Because of the algebraic-differential character of the motion equations the use of the method requires an appropriately modified approach. Omitting the details of the adaptation, it is worth noting that at each subsequent approximation there is an additional algebraic equation that after differentiating allows one to determine the relationship between the derivatives of the mutually dependent coordinates Z_1 and Z_2. The approximate solution obtained allowed for prediction of the resonance conditions. Then, the governing equations have been modified appropriately in order to describe the main resonance. The solution to the resonant vibration problem has semi-analytical form, because of the equations of modulation of the amplitudes and phases are solved in numerical manner.

Conclusions

The dynamics of the 2-dof system containing two serially connected nonlinear springs has been studied. The mathematical model consists of the differential and algebraic equations. The approximate solution to the governing equations, up to the third order, has been obtained using MMS with three time scales. The forced vibration of the pendulum have been analysed for two cases: far from resonance and in the resonance conditions. The analytical or semi-analytical form of the solution is the main advantage of the applied approach giving the possibility of the qualitative and quantitative study of the pendulum dynamics in wide spectrum.

Acknowledgments

This paper was financially supported by the grant of Ministry of Science and Higher Education 02/21/DSPB/3544.

References

[1] Andrzejewski R., Awrejcewicz J. (2005) Nonlinear Dynamics of a Wheeled Vehicle. Springer, Berlin.
[2] Bishop R.E.D, Gladwell G.M.L, Michaelson S. (2008) The matrix analysis of vibration. Cambridge University Press, London.
[3] Lai S.K., Lim C.W. (2007) Accurate approximate analytical solutions for nonlinear free vibration of systems with serial linear and nonlinear stiffness. *J. Sound Vib* **307**:72-736.
[4] Sanmiguel-Rojas E., Hidalgo-Martinez M., Jimenez-Gonzales J.I., Martin-Alcantara A. (2015) Analytical approaches to oscillators with nonlinear springs in parallel and series connections. *Mech Mach Theory* **93**: 39-52.
[5] Starosta R., Sypniewska-Kamińska G., Awrejcewicz J. (2017) Quantifying non-linear dynamics of mass-springs in series oscillators via asymptotic approach. *Mech Syst Signal Pr* **89**:149 – 158.
[6] Telli S., Kopmaz O. (2006) Free vibrations of a mass grounded by linear and nonlinear springs in series. *J. Sound Vib* **289**: 689-710.
[7] Wang Y.J., Chen C.D., Lin C.C., Yu, J.H. (2015) A nonlinear suspended energy harvester for a tire pressure monitoring system. *Micromachines* **6**: 312 – 327.

Stabilisation of Rayleigh-Plateau modes on a liquid cylinder

Sagar Patankar, Saswata Basak and Ratul Dasgupta
Department of Chemical Engineering, IIT Bombay, Mumbai, India

Summary. We show stabilisation of unstable Rayleigh-Plateau(RP) modes on a liquid cylinder by subjecting it to a radial oscillatory body force. The proposed stabilsation was short lived as shown earlier in our inviscid study [5]. Viscous analysis is performed which has importance for this stabilisation. Linear stability predictions are obtained via Floquet analysis [3]. We also solve the linearised, viscous initial-value problem for free-surface perturbations obtaining an integro-differential equation governing the amplitude of Fourier mode. This equation represents the cylindrical analogue of its Cartesian counterpart [1]. Present study [4] shows that RP stabilisation can be extended longer in time using radial oscillatory forcing. Predictions from the numerical solution to this equation demonstrates RP mode stabilisation upto several hundred forcing cycles and shows excellent agreement with direct numerical simulations(DNS) of the incompressible, Navier-Stokes equations using Basilisk [7]. An expanded version of present study is under review in a journal for publication.

Dynamic stabilisation of RP modes - Linear inviscid theory

Liquid filaments, jets or annular fluid films coating the rods are susceptible to breakup into droplets via classical Rayleigh-Plateau (RP hereafter) instability [6, 8]. In our earlier inviscid study [5], Faraday waves on a liquid cylinder where dynamic stabilisation of RP modes was predicted but found to be extremely short-lived in inviscid simulations. Figure 1, shows an infinitely long, quiescent liquid cylinder of density ρ, surface-tension T, kinematic viscosity ν and radius R_0 being subject to a radial, oscillatory body force $\mathcal{F}(r,t)$. Interface perturbation is expressed as $\eta(\theta,z,t) = a_m(t;k)\cos(m\theta)\cos(kz)$, where k and m represents axial and azimuthal wavenumber.

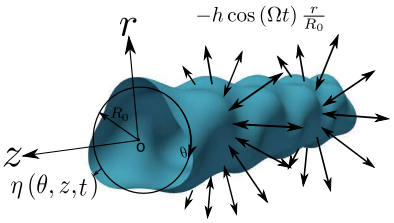

Figure 1: A schematic representation of surface perturbation on a viscous liquid cylinder of radius R_0 subject to a radial body force $\boldsymbol{\mathcal{F}}(r,t) = -h\left(\frac{r}{R_0}\right)\cos(\Omega t)\hat{\mathbf{e}}_r$, where h and Ω are imposed forcing strength and frequency respectively.

Under the linearised, inviscid, irrotational approximation, the equation governing amplitude $a_m(t;k)$ of Faraday waves on the free surface is shown to be Mathieu equation[5],

$$\frac{d^2a_m}{dt^2} + \frac{\mathrm{I}_m'(kR_0)}{\mathrm{I}_m(kR_0)}\left[\frac{T}{\rho R_0^3}kR_0\left(k^2R_0^2+m^2-1\right) + kh\cos(\Omega t)\right]a_m(t;k) = 0, \tag{1}$$

Figure 2a and 2b shows the inviscid stability chart and stabilisation of RP modes through DNS being short lived due to nonlinearity.

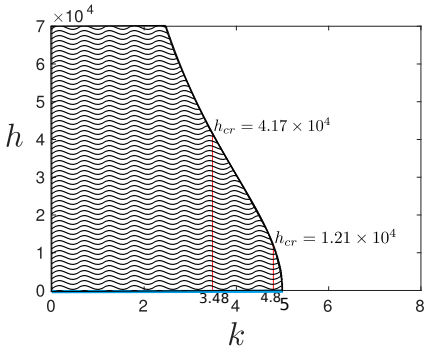

(a) Inviscid stability chart

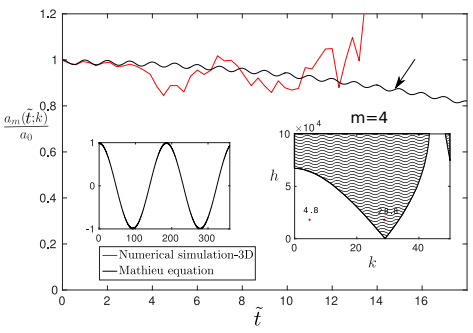

(b) DNS for $k = 4.8, h = 1.8 \times 10^4$cm/s^2

Figure 2: Shaded and white indicate unstable and stable regions respectively. **Panel (a)** Inviscid stablity chart from equation 1 showing critical forcing strength h_{cr} above which RP unstable mode $k_0 = 4.8$ cm^{-1} will be stablised. Parameters: $\Omega = 600\pi$ rad/s (f=300 Hz), $R_0 = 0.2$ cm, $\rho = 0.957$ gm/cm^3, $T = 20.7$ dynes/cm. **Panel (b)** (Red curve) Time signal from inviscid 3D-DNS [7], ($k_0 = 4.8$ cm$^{-1}, m_0 = 0$) excited at $t = 0$. (Black curve) Solution to equation 1, (Left inset) Zoomed out view of solution to equation 1, (Right inset) Stability chart for $m = 4$ showing unstable non-axisymmetric Fourier mode ($k = 28.8 = 6k_0, m = 4$) at $\tilde{t} \approx 14$ s causing destabilisation.

Dynamic stabilisation of RP modes - Linear viscous theory

In the *viscous* analysis presented here [4] we performed Floquet analysis following [3] to obtain viscous stability chart and solve the initial-value problem (IVP) following toroidal-poloidal decomposition [2] on a cylinder. We finally obtain an integro-differential equation (2) for $a_m(t;k)$ which has a damping and two memory terms incomparison to Mathieu equation 1. It is shown that, by carefully tuning the strength and frequency of (radial) forcing, RP modes accessible to the system maybe rendered stable thus stabilising the cylinder for long time (many forcing time periods).

$$\frac{d^2a_m}{dt^2} + 2\nu k^2 \frac{\mathrm{I}_m''(kR_0)}{\mathrm{I}_m(kR_0)} \frac{da_m}{dt} + \int_0^t \hat{\mathbf{L}}^{-1}\left(\tilde{\chi}(s)\right) \frac{\mathrm{I}_m'(kR_0)}{\mathrm{I}_m(kR_0)} \left[\frac{T}{\rho R_0^3} kR_0 \left(k^2R_0^2 + m^2 - 1\right) + hk\cos\left[\Omega(t-\tau)\right] \right] a_m(t-\tau)d\tau + 4\nu k \frac{\mathrm{I}_m'(kR_0)}{\mathrm{I}_m(kR_0)} \int_0^t \hat{\mathbf{L}}^{-1}\left[\zeta(s)\right] \frac{da_m}{dt}(t-\tau)d\tau = 0 \tag{2}$$

Stablisation of RP modes: viscous stability chart and DNS comparison

Case	Fluid	$a(0)$	m_0	k_0	$\rho^{\mathcal{I}}$	$\rho^{\mathcal{O}}$	$\mu^{\mathcal{I}}$	$\mu^{\mathcal{O}}$	R_0	h	Ω	T
1	Silicone oil	0.01	0	4.8	0.957	0.001	0.1	0.001	0.2	1.8×10^4	600π	20.7

Table 1: Parameters for stability chart and DNS (CGS units)

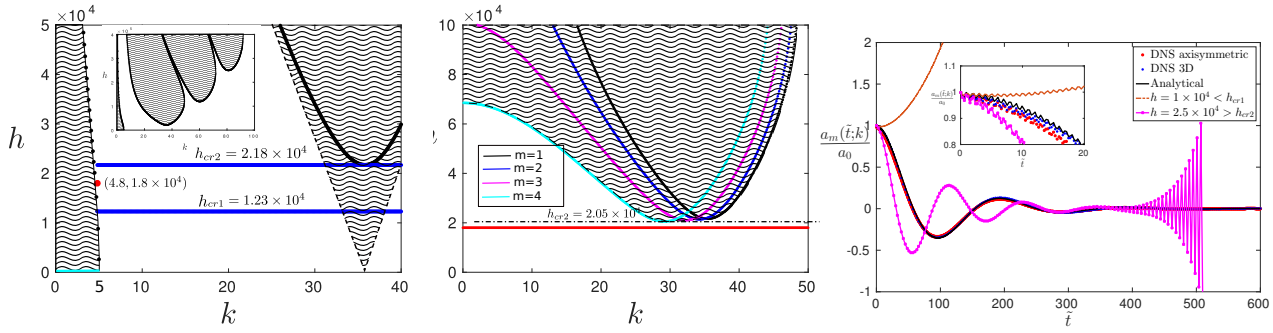

(a) m=0 (b) m=1,2,3,4 (c) DNS comparison

Figure 3: **Panel a)** Stability chart ($m = 0$) and **panel (b)** non-axisymmetric ($m = 1, 2, 3, 4$) modes with Case 1 parameters in table 1. Figure 3a shows bold black lines $\rightarrow$ viscous tongue, black dashed line$\rightarrow$ inviscid tongue. (Inset) complete chart. The mode ($k_0 = 4.8, m_0 = 0$) is stabilised when $h_{\mathrm{cr1}} < h < h_{\mathrm{cr2}}$ with $h_{\mathrm{cr2}} = 2.05 \times 10^4$ cm/s^2 from $m = 4$ (see figure 3b). We select $h = 1.8 \times 10^4$ (red dot and solid red line in figure 3a and 3b respectively) for stabilisation. **Panel (c)** DNS time signal for case1 with parameters in table 1: (Red and blue dots) from DNS shows excellent agreement with solution to equation 2(refered as Analytical in figure 3c) upto 600 forcing cycles ($\tilde{t} \equiv t\Omega/2\pi$). (Orange line) Destabilisation seen in axisymmetric DNS when $h < h_{\mathrm{cr1}}$ and when (Pink line) $h > h_{\mathrm{cr2}}$. Note that inviscid simulation in figure 2b where for the same k_0, stabilisation is seen for only three forcing cycles.

Conclusions

We solved the initial-value problem (IVP) leading to a novel integro-differential equation governing the (linearised) amplitude of three-dimensional Fourier modes on the viscous liquid cylinder extending our earlier inviscid study. It is demonstrated that by suitably tuning the frequency of forcing and choosing strength $h_{\mathrm{cr1}} < h < h_{\mathrm{cr2}}$, RP mode ($k_0$) can be stabilised with all axisymmetric and three-dimensional modes that may be generated by nonlinear effects, can be prevented from destabilising the cylinder. DNS comparison have shown excellent aggreement with theoretical predictions demonstrating RP stabilisation upto hundreds of forcing cycles.

References

[1] J. Beyer and R. Friedrich. Faraday instability: linear analysis for viscous fluids. *Physical Review E*, 51(2):1162, 1995.

[2] P. Boronski and L. S. Tuckerman. Poloidal–toroidal decomposition in a finite cylinder. i: Influence matrices for the magnetohydrodynamic equations. *Journal of Computational Physics*, 227(2):1523–1543, 2007.

[3] K. Kumar and L. S. Tuckerman. Parametric instability of the interface between two fluids. *Journal of Fluid Mechanics*, 279:49–68, 1994.

[4] S. Patankar, S. Basak, and R. Dasgupta. Dynamic stabilisation of rayleigh-plateau modes on a liquid cylinder. *(Under review)*, 2021.

[5] S. Patankar, P. K. Farsoiya, and R. Dasgupta. Faraday waves on a cylindrical fluid filament–generalised equation and simulations. *Journal of Fluid Mechanics*, 857:80–110, 2018.

[6] J. A. F. Plateau. *Statique expérimentale et théorique des liquides soumis aux seules forces moléculaires*, volume 2. Gauthier-Villars, 1873.

[7] S. Popinet. Basilisk. http://basilisk.fr, 2014.

[8] L. Rayleigh. Xvi. on the instability of a cylinder of viscous liquid under capillary force. *The London, Edinburgh, and Dublin Philosophical Magazine and Journal of Science*, 34(207):145–154, 1892.

On solving one-dimensional wave equations subject to nonclassical and to nonlinear boundary conditions

Wim T. van Horssen
Delft Institute of Applied Mathematics, Delft University of Technology, Delft, The Netherlands

Summary. In this paper it will be shown how characteristic coordinates, or equivalently how the well-known formula of d'Alembert can be used to solve initial-boundary value problems for wave equations on semi-infinite intervals or on fixed, bounded intervals involving non-classical and nonlinear boundary conditions. It will be shown that solutions or approximations of solutions for wave-problems can be constructed for a much larger class of problems than generally is assumed. In this paper linear and nonlinear mass-spring-damper systems will be considered at the boundary, and it will be shown how (approximations of) solutions can be constructed.

Introduction and overview

The study of a one-dimensional wave equation such as

$$u_{tt} - u_{xx} = 0 \quad , \quad t > 0, -\infty < x < \infty \, , \tag{1}$$

goes back to the middle of the 18th century when d'Alembert solved an initial value problem for Eq. (1) on an infinite interval (that is, on $-\infty < x < \infty$) by using characteristic coordinates. In Eq. (1) $u = u(x,t)$ is a displacement (usually a lateral displacement of a string), x is a space coordinate, and t is time. When the initial displacement, and the initial velocity are given by

$$u(x,0) = f(x), \text{ and } u_t(x,0) = g(x) \, , \tag{2}$$

respectively, one obtains as solution the well-known formula of d'Alembert

$$u(x,t) = \tfrac{1}{2} f(x+t) + \tfrac{1}{2} f(x-t) + \tfrac{1}{2} \int_{x-t}^{x+t} g(s)\, ds. \tag{3}$$

On a semi-infinite interval (that is, for instance on $x > 0$) this formula (3) can also be used to solve an initial value problem for a wave equation. For a Dirichlet type of boundary condition at $x = 0$, or for a Neumann type of boundary condition at $x = 0$, it is also well-known that the functions in the classical formula of d'Alembert should be extended as odd, or as even functions in x, respectively. How the functions should be extended for a Robin type of boundary condition (with constant coefficients) at $x = 0$, is less well-known, but is was already discovered at the end of the 19th century by Bryan. Recently in [1] and [2] the extension procedures on semi-infinite intervals for problems with a linear mass-spring-damper boundary condition at $x = 0$, were presented for a string equation and for an axially moving string equation, respectively.

On a bounded interval (that is for instance on $0 < x < L < \infty$) the classical formula of d'Alembert can also be used to solve an initial value problem for a wave equation. In the literature only the cases where one has Dirichlet and/or Neumann boundary conditions, are solved by using the formula of d'Alembert, and leads to odd and/or even periodic extensions of the functions in the formula of d'Alembert. For other boundary conditions the formula of d'Alembert is not used, most likely, because it is not (well) known how to extend the functions in the formula of d'Alembert for other boundary conditions than those of Dirichlet type or of Neumann type.

Usually the method of separation of variables, or the (equivalent) Laplace transform method is used to solve initial value problem for a wave equation on a bounded interval for various types of boundary conditions with constant coefficients. However, when a Robin boundary condition with a time-dependent coefficient is involved in the problem, then the aforementioned methods are not applicable. In [3] it has been shown how characteristic coordinates or equivalently, how the classical formula of d'Alembert can be used to solve an initial value problem for a wave equation on a bounded, fixed interval with at one endpoint a Dirichlet type of boundary condition, and at the other end a Robin type of boundary condition with a time-dependent coefficient. The Robin boundary condition with a time-dependent coefficient is an interesting one to study from the applicational (and from the mathematical) point of view. When one considers the transversal vibrations of a string which at one end is attached to a spring for which the stiffness properties change in time (due to fatigue, temperature change, and so on), then a Robin type of boundary condition is obtained with a time-varying coefficient. But also in the study of longitudinal vibrations of axially moving strings with time-varying lengths (as simple models for vibrations of elevator or mining cables), one obtains, after some transformations as a first order approximation of the problem, a wave equation for which at one end a Robin type of boundary condition with a time-varying coefficient has to be satisfied.

For nonlinear or weakly nonlinear boundary conditions not so many results are known. The reader is referred to [4] (and the references in [4]) for some recent and historical approaches that have been used. In this paper a problem for a wave equation on a semi-infinite domain will be discussed. The boundary condition is assumed to be weakly nonlinear and it will be explained how a multiple time-scales perturbation method can be applied to construct approximations of the solution of the problem.

In this paper our recent results on the applicability of the formula of d'Alembert (as discussed above) will be presented. For details the reader is referred to our recent publications [1, 2, 3].

Four classes of problems

In this paper four classes of problems will be explained in detail. In the first class the vibrations of a semi-infinite string (that is, equation (1) with $x > 0$) will be studied with a spring-damper system attached at $x = 0$, that is, a boundary condition like

$$Tu_x(0,t) = ku(0,t) + \alpha u_t(0,t) \tag{4}$$

will be considered, where T is the tension in the string, k the stiffness of the spring, and α the damping coefficient of the dashpot. By using characteristic coordinates or equivalently, by using d'Alembert's formula (3) it will be shown that the extensions of the functions f and g in (3) for negative arguments in the functions f and g, have to satisfy nonhomogeneous, first order ordinary differential equations (ODEs). The solutions of these ODEs can readily be obtained, and so, reflected waves and energy dissipation can be determined.

In the second class of problems the vibrations of a semi-infinited string will be studied with a mass-spring-damper system attached at $x = 0$, that is, a boundary condition like

$$mu_{tt}(0,t) = Tu_x(0,t) - ku(0,t) - \alpha u_t(0,t) \tag{5}$$

will be considered, where m is the mass in the attached system at $x = 0$. In this case the extensions of the functions of f and g have to satisfy nonhomogeneous, second order ODEs with constant coefficients. Again reflected waves and damping properties can be determined.

In the third class of problems the vibrations of a finite string (that is, equation (1) with $0 < x < L < \infty$) will be studied with a fixed end at $x = 0$ and a spring (with a time-varying stiffness $k(t)$) attached at $x = L$, that is, with the boundary conditions

$$\begin{aligned} u(0,t) &= 0, \\ Tu_x(L,t) &= -k(t)u(L,t). \end{aligned} \tag{6}$$

It will be shown that the method of separation of variables can not be applied, but d'Alembert's formula (3) can be used. It will turn out that the extensions of the functions f and g (outside the interval $[0, L]$) have to satisfy nonhomogeneous first order ODEs and have to satisfy a certain iteration process. Again properties of the solutions can be obtained from d'Alembert's formula (3).

In the fourth class of problems the vibrations of a semi-infinite string will be studied for $x > 0$ with a (weakly) nonlinear mass-spring-damper system attached at $x = 0$, that is, a boundary condition like

$$mu_{tt}(0,t) = Tu_x(0,t) - k_1u(0,t) - k_3u^3(0,t) - \alpha u_t(0,t) \tag{7}$$

will be considered, where k_1 and k_3 are constants. When the displacement $u(x,t)$ is small, or when k_3 is small, perturbation methods like the two time-scales perturbation method can be used to construct accurate approximations of the solution, which are valid on a long time scale.

Conclusions and future work

In this paper it has been shown that the formula of d'Alembert can be applied to a much larger class of problems than is generally assumed. This also implies that a larger class of weakly nonlinear problems for wave equations can be studied by means of characteristic coordinates (see also recent work in [5, 6]).

References

[1] Akkaya T., van Horssen W. T., (2015) Reflection and damping properties for semi-infinite string equation with non-classical boundary conditions. *Journal of Sound and Vibration*, Vol. 336, pp. 179-190.

[2] Gaiko N. V., van Horssen W. T., (2016) One wave reflections and energetics for a semi-infinite traveling string with a nonclassical boundary support. *Journal of Sound and Vibration*, Vol. 370, pp. 336-350.

[3] Van Horssen W. T., Wang Y., Cao G., (2018) On solving wave equations on fixed bounded intervals involving Robin boundary conditions with time-dependent coefficients. *Journal of Sound and Vibration*. Vol. 424, pp. 263-271.

[4] Tang B., Brennan M. J., Manconi E., (2018) On the use of the phase closure principle to calculate the natural frequencies of a rod or beam with nonlinear boundaries. *Journal of Sound and Vibration*. Vol. 433, pp. 461-475.

[5] Malookani R. A., van Horssen W. T., (2016) On the asymptotic approximation of the solution of an equation for a non-constant axially moving string. *Journal of Sound and Vibrations*, Vol. 367, pp. 203-218.

[6] Malookani R. A., van Horssen W. T.,(2017) On parametric stability of a nonconstant axially moving string near resonances. *Journal of Vibration and Acoustics*, Vol. 139 (1), 011005 (12 pages).

Thursday, July 21, 2022
13:30 - 15:30

MS-12 Micro- and Nano-Electro-Mechanical Systems
Rhone 3A

Chair: S. Krylov

13:30 - 13:50
Modeling non-conventional vibrational modes of micro-plates in viscous fluids
LOCH Gesing Andre*, PLATZ Daniel, SCHMID Ulrich
*Institute of Sensor and Actuator Systems - Vienna University of Technology (Gusshausstrasse 27, 1040 Vienna, Austria Austria)

13:50 - 14:10
Modeling of Frequency Locking in a Differential Vibrational Beam Accelerometer
HALEVY Omer, **KRYLOV Slava***
*School of Mechanical Engineering, Faculty of Engineering (Tel Aviv University, Tel Aviv, Israel 69978 Israel)

14:10 - 14:30
Multi-Gas Sensing Design based on Nonlinear Coupled Micromachined Resonators
FANG Zhengliang*, HAJJAJ Amal, THEODOSSIADES Stephanos
*Wolfson School of Mechanical, Electrical and Manufacturing Engineering (Wolfson School of Mechanical, Electrical and Manufacturing Engineering, Loughborough, LE11 3TU, UK United Kingdom)

14:30 - 14:50
Nonlinear dynamics of 2D materials
ALIJANI Farbod*, STEENEKEN Peter G.
*Precision and microsystems engineering (TU Delft, The Netherlands) (Mekelweg 2 2628 CD Delft Netherlands)

14:50 - 15:10
Resonance frequency measurement of stress-engineered nanomechanical resonator and its lower limit of frequency uncertainty
WANG Mingkang, ZHANG Rui, ILIC Robert, LIU Yuxiang, **VLADIMIR Aksyuk***
*National Institute of Standards and Technology [Gaithersburg] (100 Bureau Drive, Stop 1070, Gaithersburg, MD 20899-1070 United States)

15:10 - 15:30
Period Tripling States and Non-Monotonic Energy Dissipation in MEMS with Internal Resonance
WANG Mingkang, PEREZ-MOLERO Diego, LOPEZ Daniel, **AKSYUK Vladimir***
*National Institute of Standards and Technology [Gaithersburg] (100 Bureau Drive, Stop 1070, Gaithersburg, MD 20899-1070 United States)

Modeling non-conventional vibrational modes of micro-plates in viscous fluids

Andre Loch Gesing*, Daniel Platz* and Ulrich Schmid*
*Institute of Sensor and Actuator Systems, TU Wien, Gußhausstraße 27, 1040 Vienna, Austria

Summary. Micro-plates exhibit extraordinarily low losses in viscous fluids when vibrating in the non-conventional roof tile-shaped modes. However roof tile-shaped modes are commonly not considered for micro-sensors due to the lack of methods to predict these modes' dynamic response in viscous fluids. We developed a numerical method to calculate the spectral displacement of micro-plates oscillating in viscous fluids with which we can predict both conventional and non-conventional vibrational modes. The method is based on the Kirchhoff-Love plate equation, which we solve with a continuous-discontinuous approach to the Galerkin Method, with the method of fundamental solutions for the linearized Navier-Stokes equations. We show-case our method with the analysis of a silicon micro-plate immersed in water. With the spectral displacement curve it is straight forward to categorize peaks correspondent to beam bending modes, torsional modes and roof tile-shaped modes. Furthermore, we calculate the fluid flow field associated to each vibrating mode of the micro-plate. Our method thus provides a crucial understanding of the flow field around an oscillating micro-plate, which may enable novel device architectures for resonantly operated micro-sensors in viscous fluids.

Introduction

Commonly micro electro-mechanical systems (MEMS) devices exploit as key building block the Euler-Bernoulli (EB) flexural bending modes, or torsional modes, of narrow beams. These modes are chosen because methods to predict their dynamic response and thermal calibration in viscous fluids are well established and straightforwardly implemented [1]. Higher order bending modes of beams in viscous fluids are subject to high viscous losses. High order roof tile-shaped modes of micro-plates, on the other hand, exhibit extraordinarily low losses in viscous fluids [2]. However numerical methods for the prediction of the dynamic response of micro-plates in viscous fluids, and thus for roof tile shaped modes, are missing. Thus, a method for the prediction of the dynamic response of micro-plates in viscous fluids is of utmost importance to improve device performance even further.

Numerical Method

Micro-plates immersed in viscous fluids is a multi-scale problem, which means its solution via traditional numerical techniques - e.g. computational fluid dynamics and finite differences - is not straight forward. Our approach is to solve the Kirchhoff-Love (KL) plate equation combined with the method of fundamental solutions for the linearized Navier-Stokes (LNS) equations. KL plate theory is based on a fourth order partial differential equation (PDE), which can't be solved with out-of-the-box Finite Element Method (FEM). We solve the KL PDE with a continuous/discontinuous method called interior penalty (IP). IP method enables us to use Lagrange-type continuous elements (C0 continuous) while minimizing discontinuities in first order derivatives (obtaining thus C1 continuity) and weakly enforcing clamped and free-end boundary conditions. For comparison purposes we also implemented the IP method for the EB beam equation. To solve the fluid-structure interaction, we assume the non-slip condition at the plate's surface and assume that the fluid velocity in the longitudinal direction of the plate is small in comparison to the other components. With this simplification, there is a fundamental solution for the LNS that relates pressure at the plate surface and the plate's transverse displacement at each cross-section [3]. Evaluation of the fundamental solution at top and bottom surfaces of the plate results in a complex pressure jump over the plate which is linearly and non-locally dependent on the plate's transverse displacement.

Results

As an application example we consider a $300 \times 300 \times 5\ \mu\mathrm{m}^3$ silicon micro-plate immersed in water. The micro-plate is clamped on one side and free on the three others, and is excited by an external force at one of the free corners. Fig. 1 shows the displacement spectrum per unit excitation force ϕ/F of the free corner of the plate where the force is applied. Note that some of the peaks in the displacement spectrum are predicted by both KL and EB models. These peaks correspond, evidently, to flexural bending modes. The second peak in KL displacement spectrum corresponds to the first torsional mode. First beam bending mode and first torsional mode are shown in Figs. 2a and 2b, respectively. Roof tile modes in water occur at frequencies 237.4 kHz and 651.8 kHz and are shown in Figs. 2c and 2d. Naturally, note that these modes are predicted only with the KL method. Once the plate spectral displacement is calculated, we can predict the velocity field at any point of the fluid domain by applying once again the fundamental solutions for the LNS. The results of this procedure are shown in Fig. 3, where the velocity field is shown for the plate's vibrational modes shown in Fig. 2. Velocity field associated with the first bending mode exhibits two vortices at the edges of the plate's cross section with opposite directions, with the fluid near the middle being dominated by a normal component. For the torsional mode we see the vortices with opposite directions at the edges, and the fluid moves across the plate's surface dominated by a tangential component. For roof tile modes the fluid moves back and forth across the plate's surface with a pattern that varies with the number of nodal lines of the vibrating mode. Note also that for roof tile modes the velocity field can reach higher velocities near the middle of the plate than at its edges.

Conclusions

We showed that with the KL method we can model non-conventional modes of micro-plates in viscous fluids besides the traditional bending and torsional modes. What is more, we are able to calculate the fluid flow associated to each vibrational mode, which in turn enable novel strategies to further decrease energy losses to the fluid. Future developments include implement 3D fundamental solutions for the LNS and comparison to experimental data.

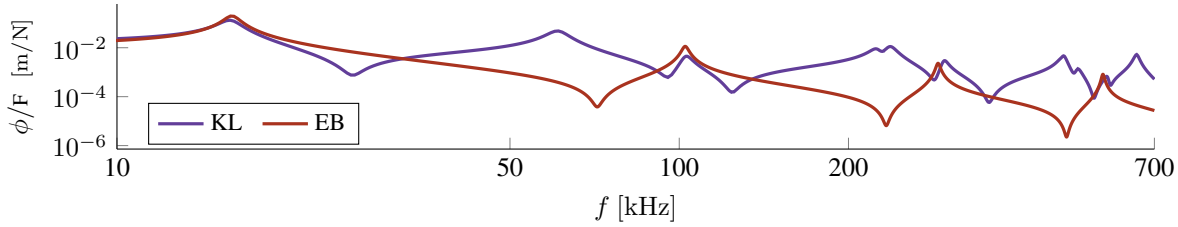

Figure 1: Displacement of a corner of the plate per unit excitation force calculated with KL and EB methods.

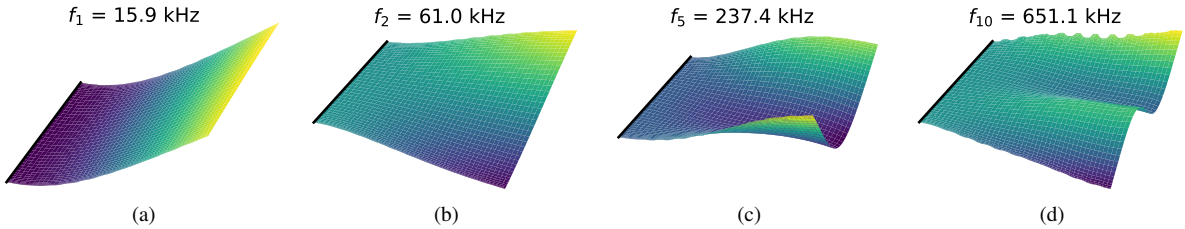

Figure 2: (a) First flexural, (b) first torsional, (c) first and (d) second roof tile-shaped vibrating modes.

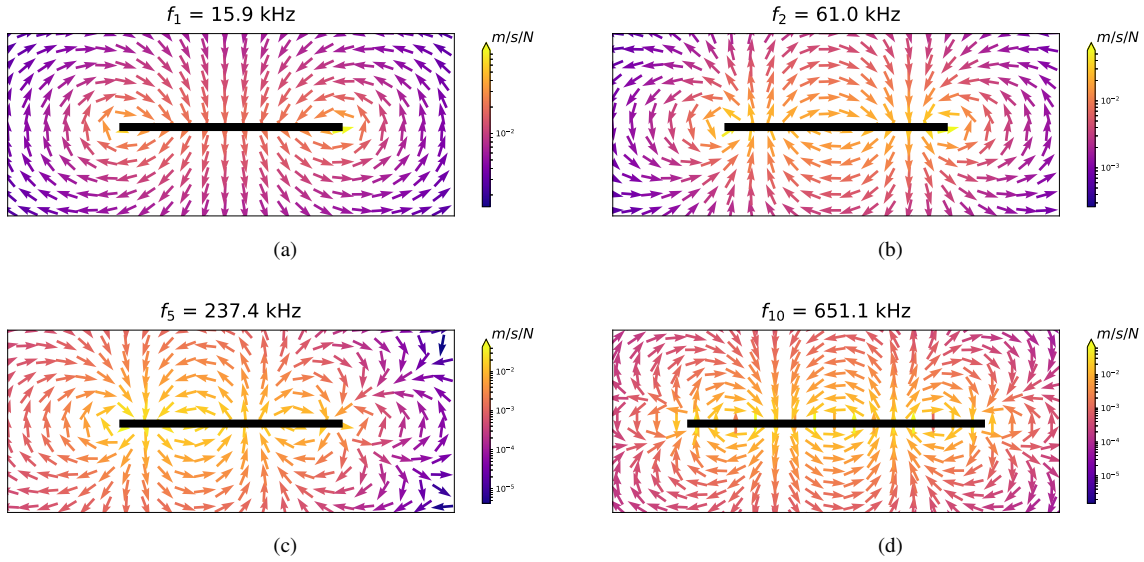

Figure 3: Fluid flow associated to the plate's different mode shapes.

References

[1] J. E. Sader, "Frequency response of cantilever beams immersed in viscous fluids with applications to the atomic force microscope," *Journal of Applied Physics*, vol. 84, no. 1, pp. 64–76, 1998.

[2] M. Kucera, E. Wistrela, G. Pfusterschmied, V. R. Díez, J. L. S. Rojas, J. Schalko, A. Bittner, and U. Schmid, "Characterisation of multi roof tile-shaped out-of-plane vibrational modes in aluminium-nitride-actuated self-sensing micro-resonators in liquid media," *Applied Physics Letters*, vol. 107, no. 5, pp. 1–5, 2015.

[3] E. O. Tuck, "Calculation of unsteady flows due to small motions of cylinders in a viscous fluid," *Journal of Engineering Mathematics*, vol. 3, no. 1, pp. 29–44, 1969.

Modeling of Frequency Locking in a Differential Vibrational Beam Accelerometer

Omer HaLevy and Slava Krylov
School of Mechanical Engineering, Faculty of Engineering, Tel Aviv University, Ramat Aviv, Tel Aviv, Israel 69978

Summary. Nonlinear dynamic behavior of a generic differential vibrating beam accelerometer is studied numerically and analytically with the emphasize on the frequency locking phenomenon. The device incorporates two tuning fork oscillators attached to a proof mass and described as a weakly nonlinear Kirchhoff beam driven through the self-excitation loop. Our numerical results obtained using the reduced order (RO) Galerkin model indicate that the influence of the geometric nonlinearity and inertial coupling on the locking is minor while the role of the structural coupling is dominant. An analytical prediction of the acceleration range where the locking occurs is obtained by considering two coupled Van der Pol oscillators and is found to be in a good agreement with the numerical results.

Introduction

Microelectromechanical (MEMS) accelerometers are among the most widely implemented and commercially successful micro devices. New challenges imposed by emerging applications continue to stimulate intensive research in the inertial sensors area. Among the approaches allowing performance enhancement are resonant accelerometers, which exploit the dependence of the sensing element natural frequency on the inertial (acceleration) force acting on the proof mass. A large variety of resonant accelerometer designs were reported, including beams directly stretched by an inertial force [1], as well as sensors implementing force amplification or electrostatic softening.

In this work, to explore device's dynamics and modeling approaches, we consider the most generic architecture of a vibrating beam accelerometer (VBA). The device consists of two beam-type tuning fork oscillators attached to a proof mass, Fig. 1(a) [1]. Inertial force acting on the mass results in the increase/decrease of the frequencies of the left (L)/right(R) pairs of the beams $f_{L/R} = f_0\sqrt{1 \pm \gamma Ma/N_E} \approx f_0(1 \pm \gamma Ma/(2N_E))$. Here f_0 is the reference frequency of the unloaded beam, γ is the correction coefficient, M is the proof mass, a is the acceleration and $N_E \gg \gamma Ma$ is the Euler's buckling force. The acceleration is extracted from the measurement of the difference between the two frequencies $\Delta f = (f_L - f_R)$. In the case of nominally identical and uncoupled L and R beams Δf should be zero at $a = 0$. However, as was observed in experiments [2], at small a frequency locking occurs, when two beams oscillate at the same frequency and phase. This phenomenon leads to a "blind zone" in the scale factor curve, limiting the minimal measurable a. As a result, the differential sensing, implemented in these devices to reduce the negative influence of thermal and other environmental effects, cannot be used. Locking (also referred as synchronization) is a well-known phenomenon and the literature on the subject is voluminous [3, 4]. In the MEMS/NEMS area where synchronization can be beneficial, most of the works were focused on the approaches allowing to achieve rather than avoid locking (e.g., see [5] and references therein). However, there is only a limited amount of publications dealing with the modeling of locking in resonant accelerometers [2].

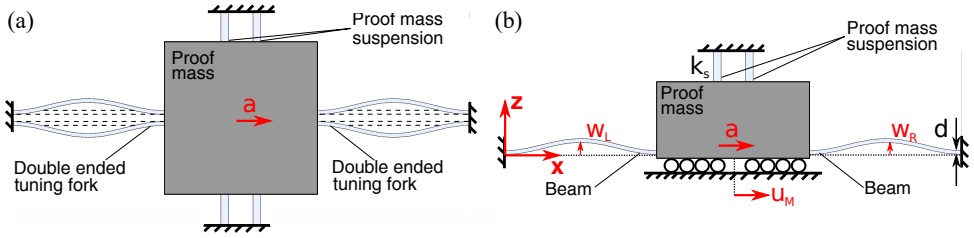

Figure 1: (a) Schematics of a generic vibrational beam accelerometer (VBA). (b) The half-model used in this work.

Model of the device

Due to symmetry only one half of the device is considered, Fig. 1(b). Each of the (assumed to be identical) beams (ties) is clamped at one end and is attached to a proof mass at the other end. The mass moving in the x direction is anchored through the suspension beams. The ties are described in the framework of the nonlinear Kirchhoff beam model, which accounts for a deflection-dependent stretching. By implementing the single-term Galerkin approximation, the beams are described as single DOF oscillators. The dynamics of the device are governed by three coupled nonlinear differential equations in terms of the L and R beams deflections q_L, q_R and the mass displacement u_M

$$\begin{cases} \ddot{q}_L + c\,\dot{q}_L + (1+\sigma u_M)q_L + k_{nl}q_L^3 + \alpha\,(q_L - q_R) = F_L \text{sign}\,(\dot{q}_L) \\ \ddot{u}_M + c_M\dot{u}_M + k_M u_M = a + \mu\left((q_R)^2 - (q_L)^2\right) \\ \ddot{q}_R + c\,\dot{q}_R + (1-\sigma u_M)q_+ k_{nl}\,(q_R)^3 + \alpha\,(q_R - q_L) = F_R \text{sign}\,(\dot{q}_R) \end{cases} \tag{1}$$

Here c, c_M are the damping coefficients of the beams and proof mass, σ is the inertial force coefficient, k_{nl} is the nonlinear stiffness coefficient, μ is the inertial coupling coefficient [3], k_M is the effective stiffness of the mass suspension and F

is the driving force amplitude. The overdot represents time derivative. The structural coupling coefficient α is extracted from the results of a three-dimensional finite elements modal analysis. Namely, $f_L,\ f_R$ were calculated for the beams with slightly detuned parameters and α was obtained by fitting the veering frequency curves in the vicinity of $a = 0$.

Results

Equations (1) completed by zero initial conditions were solved numerically using Runge-Kutta solver. The beam's frequencies were extracted from the steady-periodic time-history using FFT and zero crossing approaches. The phase between the beams was obtained using Hilbert transform. The results presented here correspond to the following parameters: $c = 2.85 \times 10^{-5},\ c_m = 2.55 \times 10^{-8},\ k_{nl} = 6.75,\ k_M = 0.0115,\ \alpha = 5.75 \times 10^{-5}, \sigma = 2.95 \times 10^{-5}, \mu = 1320, F = 6.68 \times 10^{-8}$. The relative frequency shifts $\Delta f^{rel}_{L/R} = (f_{L/R} - f_0)/f_0$ are shown in Fig. 2(a). In certain range of a the locking occurs and the curves are indistinguishable. The curve representing the maximal phase difference $\Delta\phi$ between the oscillators, Fig. 2(b), indicates that the locking region (in terms of a) is subdivided into two sub-regions - the strong locking where $\Delta\phi$ is close to zero and the weak locking, where a certain phase difference is apparent. Within the locking region the difference in the amplitudes of the two beams (the "mode localization" effect) is more pronounced than outside of the locking area, Fig. 2(c). Our numerical results suggest that for typically small (compared to the beam's width d) values of vibrational amplitudes, the influence of the geometric nonlinearity and of the nonlinear inertial coupling on the locking region is minor. This allows to consider the deflection of the proof mass as quasi-static, and to reduce the problem to two equations of motion which are coupled only through the stiffness coefficients. An additional simplification, which was made due to a periodic character of motion, is to replace the sign function in the driving force such that $\text{sign}(\dot{q}) \approx \arctan(\dot{q}) \approx \dot{q}(1-\dot{q}^2/3) \approx \dot{q}(1-q^2/3)$. As a result, Eqs. (1) are reduced to two coupled Van der Pol equations

$$\begin{cases} \ddot{q}_L + \left[c - F_L\left(1 - q_L^2/3\right)\right]\dot{q}_L + \left(1 + \tilde{\sigma}\, a\right) q_L + \alpha\left(q_L - q_R\right) = 0 \\ \ddot{q}_R + \left[c + F_R\left(1 - q_R^2/3\right)\right]\dot{q}_R + \left(1 - \tilde{\sigma}\, a\right) q_R + \alpha\left(q_R - q_L\right) = 0 \end{cases} \tag{2}$$

where $\tilde{\sigma}$ is the new acceleration force coefficient. The results based on the asymptotic analytical solution of these equations obtained using averaging [6] are shown in Fig. 2(d). Comparison between the analytically predicted locking region (obtained for the realistic device parameters) and the numerical results showed good agreement between the two. Our modeling approach can be useful also for the analysis of other resonant electrostatically or piezoelectrically actuated accelerometers including tilting devices, devices implementing mechanical force amplification or electrostatic softening.

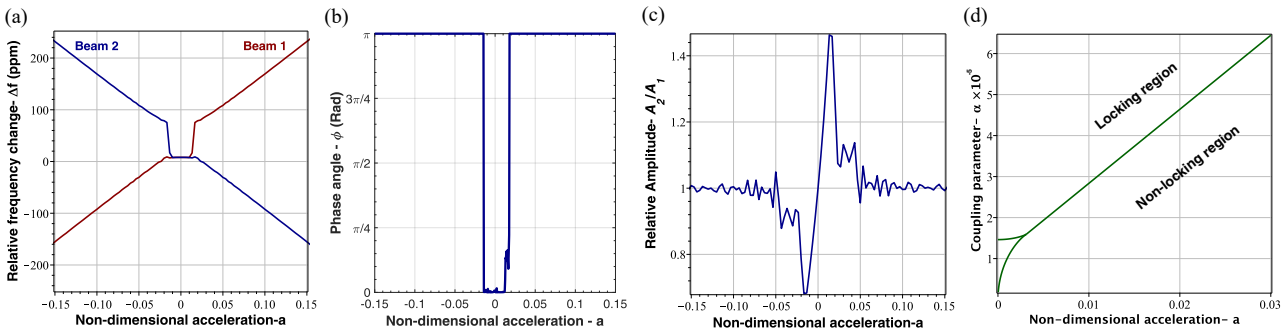

Figure 2: Numerical results obtained by solving Eq. (1) (a) The relative frequency shifts of the each of the beams as a function of the acceleration. In incense of locking the frequency-acceleration dependence curves for each of the beams should cross at $a = 0$. (b) The maximal phase difference between the oscillators as a function of the acceleration. (c) The ratio between the amplitudes of the L and the R beams. (d) Analytical solution - a boundary separating the locked and unlocked regions in the acceleration (detuning)-coupling plane.

References

[1] Hopkins, R., et al. (2006). The silicon oscillating accelerometer: A high-performance MEMS accelerometer for precision navigation and strategic guidance applications. Technology Digest, 4.

[2] Le Traon, O., et al. (2005). Monolithic differential vibrating beam accelerometer within an isolating system between the two resonators. In SENSORS, 2005 IEEE (pp. 4-pp). IEEE.

[3] Bennett, M., et al. (2002). Huygens's clocks. Proc. of the Royal Society of London. Series A: Mathematical, Physical and Engineering Sciences, 458, 563–579.

[4] Pikovsky, A., Rosenblum, M., Kurths. J. (2001). Synchronization. A universal concept in nonlinear sciences, Cambridge Nonlinear Science Series 12, Cambridge Univ. Press.

[5] Zehnder, A. T., Rand, R.H., Krylov. S.(2018). Locking of electrostatically coupled thermo-optically driven MEMS limit cycle oscillators. Int. J. of Non-Lin. Mech. 102, 92–100.

[6] Rand, R. H. (2012). Lecture notes on nonlinear vibrations. Cornell University. Available at

Multi-Gas Sensing Design based on Nonlinear Coupled Micromachined Resonators

Zhengliang Fang, Amal Z. Hajjaj and Stephanos Theodossiades
Wolfson School of Mechanical, Electrical and Manufacturing Engineering, Loughborough, LE11 3TU, UK

Summary. Micro-electromechanical (MEMS) gas sensors receive increasing interest thanks to the high demand for environmental monitoring, air quality measurement, chemical process control, and personal safety. Extensive research has been conducted to improve the selectivity and sensitivity of gas sensors. However, there is still no comprehensive study on multi-gas sensing despite its potential. This work proposes a new prototype of gas sensors that can simultaneously detect the concentration of two different surrounding gases using a single structure based on a weakly coupled resonator. This study presents a thorough theoretical investigation on the dynamics of coupled cantilever and bridge resonators to prove its potential for multi-gas sensing. The sensing scheme relies on mass (due to gas absorption) and stiffness (due to cooling/heating) alteration of the cantilever and bridge resonators, respectively. A nonlinear theoretical model is developed using the Euler-Bernoulli beam theory while accounting for the geometric and electrostatic nonlinearities. The sensor's dynamic is explored using the Reduced-Order model and one-mode Galerkin discretization, showing its richness. The results suggest the potential of the nonlinear coupled resonator in performing muti-gas detection.

Manuscript

Over the past decades, several gas-sensing mechanisms have been developed, including resistive/chemical-resistive, electro-chemical, work function, thermal conductivity, optical and surface acoustic wave [1]. One of the most widely used sensor designs is based on sensors coating. These conventional gas sensors rely on special coating materials for selective and sensitive detection [2]. Alternatively, the thermal conductivity-based gas sensors show comparable sensing performance and gains lots of interests. These sensors rely on the thermal energy dissipation of a heated structure due to the alteration of the surrounding gas concentration [3]. This research will present a sensor that combines the thermal conductivity-based gas sensor technique and coating surfaces with micro-electromechanical systems (MEMS) technology. This generates a new kind of multi-gas sensing technology based on micro-gravimetric sensing by mass absorption and the thermal conductivity sensor design. The new sensing approach shows the potential to detect numerous gases and analyze the binary gas mixture.

On the other hand, electrostatically driven MEMS based mass (gas) sensors showed an excellent capability in various potential applications thanks to their easy implementation [4]. A mechanically coupled resonant device is designed to provide a stable sensing performance, as shown in Figure 1. The sensor comprises a weakly coupled resonator including a cantilever and bridge resonators. A thin coupling beam weakly couples both resonators. By changing the coupling position, the moment of inertia and the length of the coupling beam, the coupling strength could be controlled [5]. Both cantilever and the bridge resonators are driven electrostatically by a DC polarization voltage V_{DC} and an AC harmonic voltage of amplitude V_{AC}. The system geometry is optimized to ensure that both the first and second modes are similar.

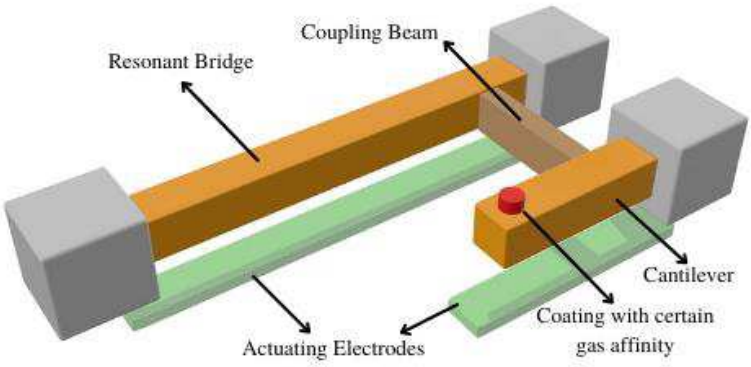

Physical Parameter (Units)	Value
Gap between the electrodes of bridge, $d_1(\mu m)$	7
Gap between the electrodes of cantilever, $d_2(\mu m)$	7
Length of coupling beam, $L_c(\mu m)$	10
Length of bridge, $L_1(\mu m)$	700
Thickness of all microbeams, $h(\mu m)$	3
Widths of bridge and cantilever, $b(\mu m)$	10
Position of the coupling beam, $X_c(\mu m)$	20
Mass adsorption position, $X_m(\mu m)$	250
Bridge actuating DC voltage, V_{dc1}	50
Bridge actuating AC voltage, V_{ac1}	20
Cantilever actuating DC voltage, V_{dc2}	50
Cantilever actuating AC voltage, V_{ac2}	20

Figure 1: 3D schematic of the weakly coupled micromachined resonator for gas sensing application

Table 1: Geometric parameters of the sensor structure

The multiple gas sensing methodology is demonstrated in two aspects in this sensor structure. The bridge resonator will be heated electrothermally, experiencing convective cooling (or heating) from the ambient gas. The thermal expansion will change the bridge's stiffness and hence its resonance frequency. This technique is promised to detect gases with significant differences in thermal conductivity compared to the air (26.2 mW/mK in 300K), such as Hydrogen (186.9mW/mK in 300K) or Carbon dioxide (16.8 mW/mK in 300K) [3]. At the same time, the cantilever will be coated with a specific material having an affinity to absorb Ammonia (which has a similar thermal conductivity of 24.4 mW/mK with air), causing a mass perturbation and hence frequency shift. Through simultaneous tracking of multiple modes of vibration of the coupled resonator, the change in the surrounding gases' thermal conductivity and the mass perturbation (i.e., due to gas absorption) are shown accurately in the shift in the resonance frequency of the systems.

Results and Discussion

The analytical study is based on nonlinear Euler-Bernoulli beam theory while accounting for the geometric and electrostatic nonlinearities. To simulate the dynamics of the studied system, a reduced-order model and one-mode Galerkin discretization (for each resonator) were used. The geometric parameters of both beams are carefully designed: by adjusting the length of the cantilever, two beams' resonant frequencies are balanced (Figure 2(a)). The theoretical results of eigenvalue problems reveal how mass/stiffness perturbation influences two resonant frequencies (Figure 2(b), 2(c)). The frequency response of two beams' deflection (Figure 2(d), 2(e)) shows several non-linear phenomena of hysteresis and jumps, hence providing the possibilities of high-sensitivity sensing. The results for both stiffness and mass perturbation simulations (Figure 2(f), 2(g), 2(h), 2(i)) present rich dynamics, further prove the influence of both kinds of perturbations on resonant frequencies, which suggests the potential of the proposed design to perform multi-sensing.

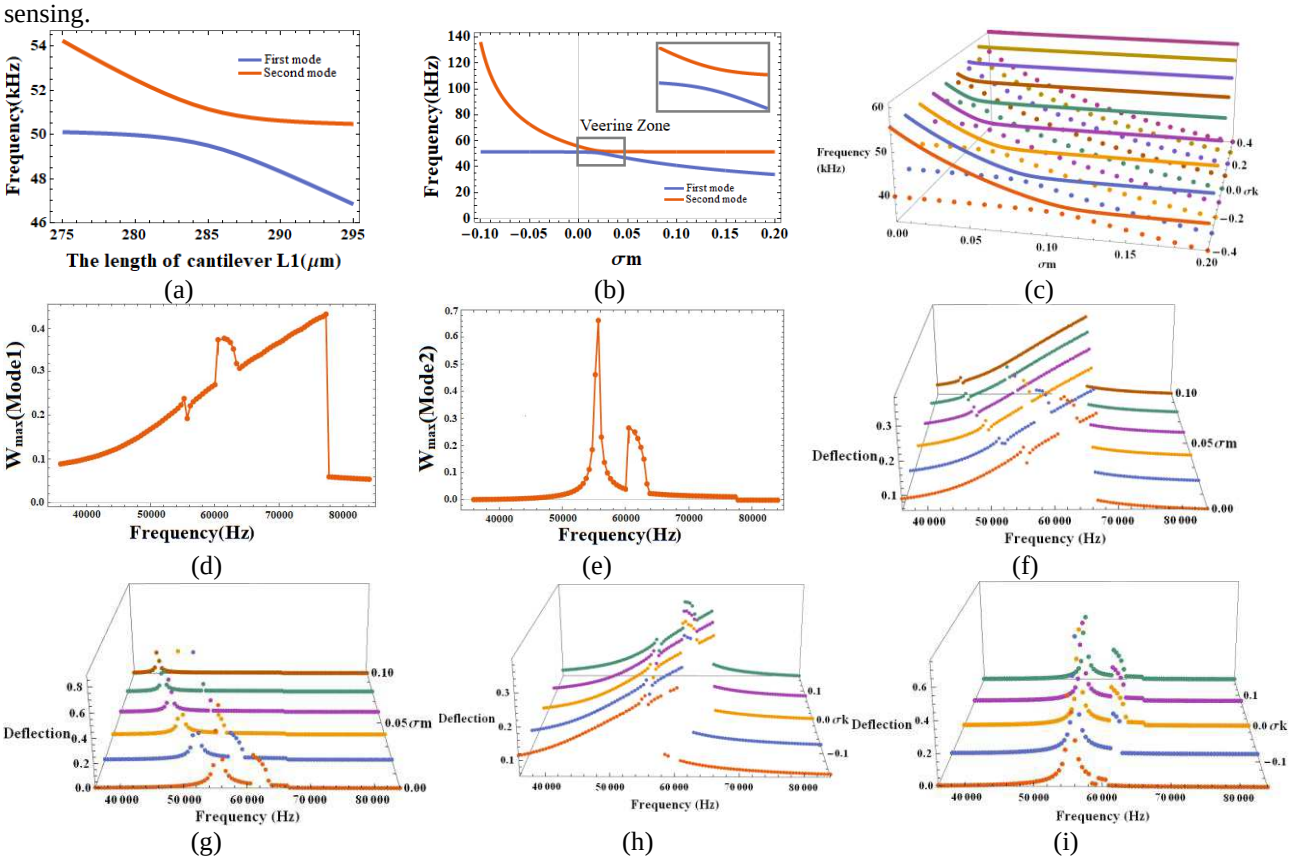

Figure 2: (a) Length of cantilever versus two resonant frequencies. Eigenvalue problems for single mass perturbation (b) and both mass and stiffness perturbation (c). The inset of (b) presents the enlarge view of veering zone.
With the actuating of $V_{dc1} = 50V$, $V_{ac1} = 20V$ on bridge resonator, the frequency response of max deflection for bridge and cantilever without perturbation (d) and (e); with mass perturbation (f) and (g); with stiffness perturbation (h) and (i).

Conclusions

We designed a potential sensor prototype for multi-gas sensing that combined micro-gravimetric sensing technique and thermal conductivity sensing techniques. The dynamics of the proposed design are simulated theoretically and showed promising results for accurate detection of two different surrounding gases simultaneously. The obtained results encourage further experimental and theoretical investigation of the dynamic of the proposed weakly coupled system. This work could reveal a new-generation answer for multi-gas sensing and show potential on different applications.

References

[1] Yaqoob, U., & Younis, M. (2021). Chemical Gas Sensors: Recent Developments, Challenges, and the Potential of Machine Learning—A Review. Sensors, 21(8), 2877. https://doi.org/10.3390/s21082877

[2] Umesh, S., Balachandra, T., & Usha, A. (2018). Design and Simulation of MEMS Gas Sensor Topologies for Detection of Inert Gases. Materials Today: Proceedings, 5(10), 21355-21362. https://doi.org/10.1016/j.matpr.2018.06.540

[3] Hajjaj, A., Jaber, N., Alcheikh, N., & Younis, M. (2020). A Resonant Gas Sensor Based on Multimode Excitation of a Buckled Microbeam. IEEE Sensors Journal, 20(4), 1778-1785. https://doi.org/10.1109/jsen.2019.2950495

[4] Rabenimanana, T., Walter, V., Kacem, N., Le Moal, P., Bourbon, G., & Lardiès, J. (2019). Mass sensor using mode localization in two weakly coupled MEMS cantilevers with different lengths: Design and experimental model validation. Sensors And Actuators A: Physical, 295, 643-652. https://doi.org/10.1016/j.sna.2019.06.004

[5] Li, L., Liu, H., Shao, M., & Ma, C. (2021). A Novel Frequency Stabilization Approach for Mass Detection in Nonlinear Mechanically Coupled Resonant Sensors. Micromachines, 12(2), 178. https://doi.org/10.3390/mi12020178

Nonlinear dynamics of 2D materials

Farbod Alijani, Peter G. Steeneken
*Department of Precision and Microsystems Engineering, TU Delft, The Netherlands

Summary. Two-dimensional (2D) materials such as graphene are model systems for investigating nonlinear dynamics at the nanoscale. They exhibit phenomena such as intermodal coupling and stochastic switching already at amplitudes that are only a few nanometers with potential applications that are yet to be harnessed. In this talk, I will give an overview of the recent advancements in nonlinear dynamic studies of 2D materials with particular focus on methods for utilizing nonlinearity in ultra-thin mechanical systems.

Introduction

Nanomechanical systems are ubiquitous in a variety of applications in modern technology. The advent of 2D materials, and the ability to fabricate one-atom thick membranes, have made it possible to reach the ultimate sensing capabilities that not so long ago were only dreamed of. But this revolutionary downscaling has been associated with constraints on the linear dynamic range of these mechanical systems since signatures of nonlinearity already emerge at amplitudes that are only a few nanometers [1].
Although the field of nonlinear dynamics dates back several centuries, its implications in atomically thin membranes have remained largely unexplored. In this talk, we present methods and experiments for understanding and utilizing nonlinear dynamic phenomena in 2D material membranes. Our aim is to shed light on the intricate modal couplings and the strong interplay between noise and nonlinearity and discuss the means to harness these effects.

Results

Our experiments are performed on multilayer graphene nanodrums with a diameter of 5 μm, which are transferred over a cavity etched in a layer of SiO_2 with a depth of 285 nm. We use a blue laser to opto-mechanically modulate the tension of the membrane, and a red laser to detect the motion, using interferometry. To control the static deflection of the drum, in some of our experiments we also place a local electrode at the bottom of the cavity. The presence of this electrode will allow us to controllably deflect the membrane downwards and use that as an electromechanical knob to tune the tension and thus resonance frequencies of the drum. Moreover, to reduce the damping from the surrounding air we perform the experiments in a vacuum chamber. A schematic of the setup is shown in Fig. 1a together with microscopic image of the graphene drum in Fig. 1b.

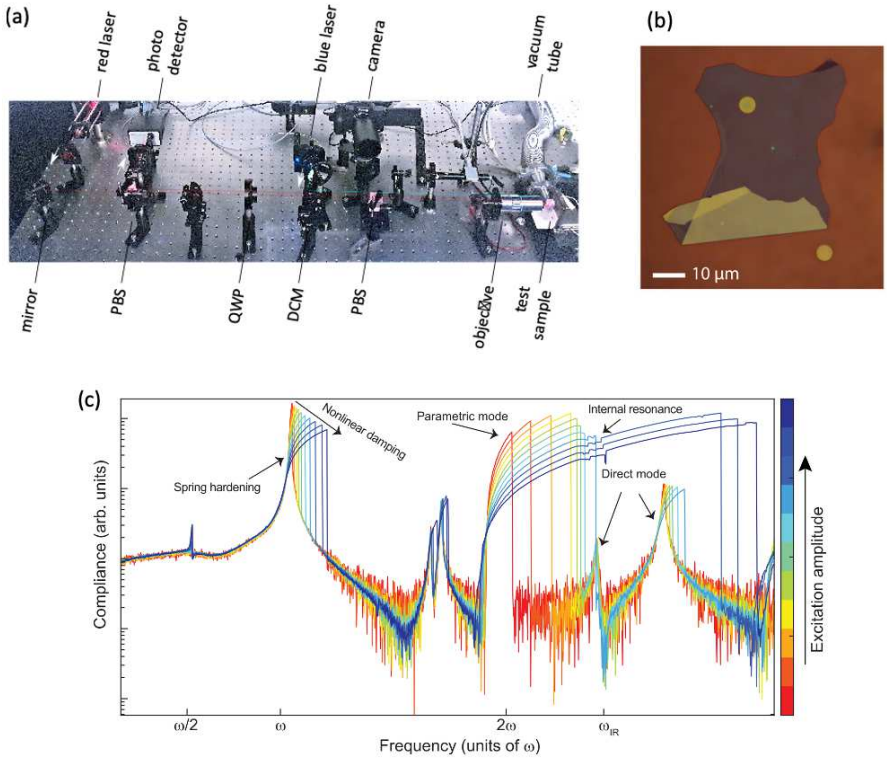

Figure 1: (a)The opto-mechanical set-up for actuating and detecting the motion of the graphene membranes; (b) Microscopic image of the graphene drum [2]; (c) Measurement of the nonlinear dynamic response as a function of the excitation amplitude [3].

By increasing the power of the blue laser, we detect a plethora of nonlinear dynamic phenomena over a wide frequency range. This includes the presence of spring hardening nonlinearity already at forces that are only a few pN, the emergence of nonlinear damping, parametric resonance, parametric -direct internal resonance [2] and a range of direct-direct 2:1 internal resonance. We show that it is possible to make use of these nonlinear effects. For instance, by adding random fluctuations to the drive level, it is possible to obtain stochastic switching rates of 4 kHz between the stable states of the graphene Duffing resonator that are 100 times faster than current state-of-the-art, at effective temperatures 3000 times lower (See Figure 2a and 2b), providing the possibility to transduce weak signals through stochastic resonance. Moreover, by tuning the tension of the membrane using a back gate, we can control internal resonance conditions, obtain quasiperiodic oscillations and thus generate mechanical frequency combs (see Figure 2c).

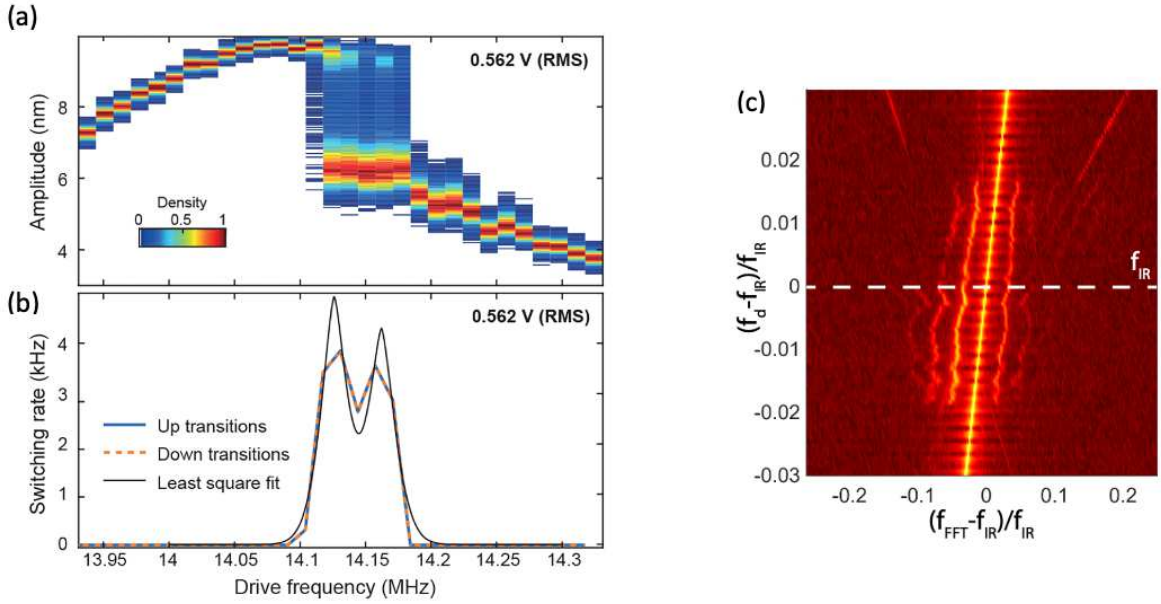

Figure 2: (a) stochastic switching in a graphene resonator close to room temperature [4]; (b) Up and down switching rates as a function of fixed drive frequency [4]; (c) Emergence of frequency combs at internal resonance.

Conclusions

In conclusion we showed that 2D material resonators exhibit a wealth of nonlinear dynamic phenomena and discussed the means to detect them. We showed that these atomically thin membranes provide a platform for investigating a range of modal interactions and the strong interplay between fluctuations and nonlinearities, thus paving the way towards new opportunities for utilizing nonlinear dynamics at smallest length scales and very fast (MHz frequency) time scales.

References

[1] Davidovikj D, et al. (2017) Nonlinear dynamic characterization of two-dimensional materials. *Nature communications* 8.1: 1-7.
[2] Keşkekler A, et al. (2021) Tuning nonlinear damping in graphene nanoresonators by parametric–direct internal resonance. *Nature communications* 12.1: 1-7.
[3] Steeneken P, et al. (2021) Dynamics of 2D Material Membranes. *arXiv preprint arXiv:2105.07489*.
[4] Dolleman R, et al. (2019) High-frequency stochastic switching of graphene resonators near room temperature. *Nano letters*19.2: 1282-1288.

Resonance frequency measurement of stress-engineered nanomechanical resonator and its lower limit of frequency uncertainty

Mingkang Wang[*, **], Rui Zhang[***], Robert Ilic[*], Yuxiang Liu[***], and Vladimir Aksyuk[*]
*Microsystems and Nanotechnology Division, National Institute of Standards and Technology, Gaithersburg, MD 20899 USA
**Institute for Research in Electronics and Applied Physics, University of Maryland, College Park, MD 20742, USA
***Department of Mechanical Engineering, Worcester Polytechnic Institute, Worcester, MA 011609 USA

Summary. In this work, we experimentally measure a relative frequency stability below 10^{-6} for a stress-engineered ≈ 28 MHz nanomechanical resonator by detecting and analyzing its thermodynamic fluctuations at room temperature, without external excitation. We devive the Cramer-Rao lower bound (CRLB) thermodynamic limit for resonance frequency measurement precision for a classical harmonic oscillator subject to dissipation, thermodynamic noise, detection uncertainty and with or without external excitation. We propose a general statistically efficient frequency estimator and experimentally show frequency uncertainty reaching the CRLB on the cavity-optomechanically detected ≈ 1 pg resonator data for up to ≈ 0.1 s averaging. The stress-engineered nanomechanical resonator with high frequency-Quality factor ($fQ \approx 10^{12}$) and considerable frequency stability could be used for frequency-readout displacement sensors with no excitation required.

Introduction and Novelty

The work is related to an earlier report about passive frequency stabilization [1] which uses the same type of high fQ tuning fork resonator [4]. Resonance frequency variance is critical to the performance of nanoresonators. With sufficient motion detection precision, frequency measurement is fundamentally limited by the thermodynamic fluctuations. Lower measured frequency variance is achieved by increasing the driven amplitude. However, as the thermodynamic uncertainty is lowered, the variance becomes limited by frequency drift at ever shorter time scales. Here, we study the frequency variance of a stress-engineered nanomechanical resonator with an effective mode mass of ≈ 1 pg. First, without external excitation, the relative frequency stability is reaching below 10^{-6}, which is better than the average performance of state-of-the-art driven NEMS in such mass range [2]. Second, more importantly, we derive rigorous CRLB, establishing the theoretically lowest limit for the resonance frequency estimation variance. It is applicable to any linear harmonic resonator, including the Micro- and Nano-electron-mechanical systems. Our undriven and driven devices perform at those limits up to the averaging times of ≈ 0.1 s without any extra stabilization [3]. Finally, we present a computationally-fast and statistically efficient frequency estimator–a formula for converting motion records into frequencies with imprecisions at the CRLB. The presented general analysis is applicable to any undriven or harmonically-driven M/NEMs in the linear regime and may be extendable to the nonlinear regime by considering a nonlinear equation of motion, such as a duffing oscillator.

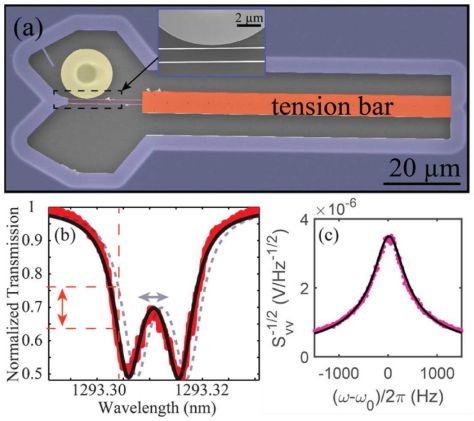

Figure 1: Experimental system introduction. (a) False-colored SEM image of the stress-engineered nanomechanical resonator. (b) Measured optical resonance and the operating principle of the optomechanical detection. (c) Mechanical vibration power spectral density in a vacuum.

Results and Discussion

In this work, stress engineering is applied to increase fQ products of nanoscale Si_3N_4 tuning forks, reaching 10^{12} to 10^{13} range. A false-colored SEM image of the device with a stress tuning bar is shown in Fig. 1(a). The mechanical motion of

the tuning fork modulates the optical resonance frequency of an adjacent microdisk resonator (Fig. 1(b)), generating time-varying optical transmission signals proportional to mechanical displacement. Fig 1(c) shows the mechanical power spectral density of the thermodynamically fluctuating tuning fork mode.

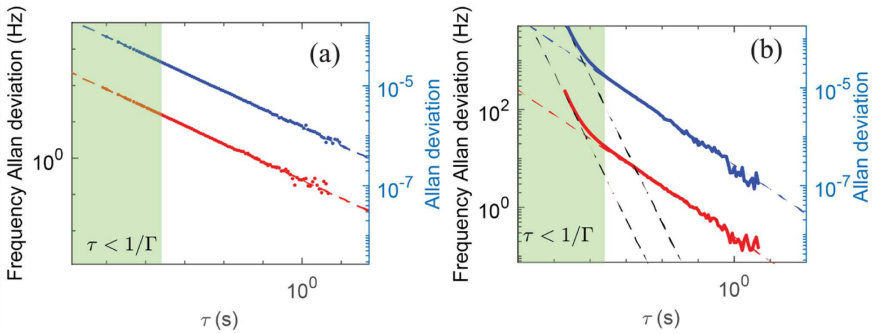

Figure 2: ADEV for simulated data(solid lines) with (a) negligible motion detection noise and (b) experimentally-realistic detection noise added. ADEV without (blue) and with (red) external excitation agrees with theoretical CRLB (dashed lines)

To verify the validity of the derived CRLB and the efficiency of the derived frequency estimator, we first apply the estimator to a simulated motion trace of a fluctuating resonator and calculate the resulting frequency Allan deviation (ADEV). Following the expected $\propto \tau^{-1/2}$, the ADEV quantitaively agrees with the CRLB without any adjustable parameters on all time scale for both the driven and non-driven cases, provided detection noise is negligible (Fig. 2(a)). The maximum-likelihood frequency estimator includes the contributions from both the phase and the phase derivative for the frequency estimation. When artificial motion-detection noise is added to the simulation, the ADEV becomes detection noise limited at the shortest time scales (widest bandwidth), following $\propto \tau^{-3/2}$. The ADEV follows $\propto \tau^{-1/2}$ and quantitatively agrees with the CRLB for the longer time scales, where our CRLB is valid (Fig. 2(b)).

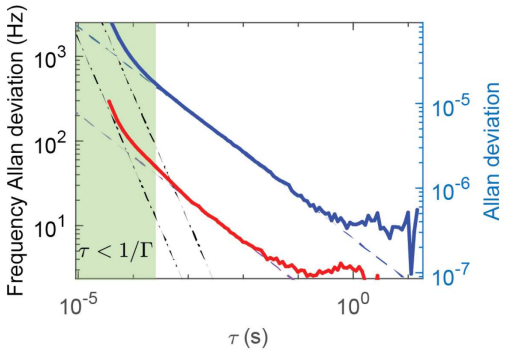

Figure 3: ADEV (solid lines) for experimental data without (blue) and with (red) external excitation. Dashed lines are corresponding theoretical CRLB $\propto \tau^{-1/2}$. Dot-dash lines $\propto \tau^{-3/2}$ are the theoretically expected *limits from the detection noise.*

The ADEV for experimental data presented in Fig. 3 shows similar features to the simulated data with detection noise, and quantitatively agrees with CRLB without adjustable parameters for $\tau <$ 0.1 s. At longer averaging the resonance frequency drift becomes apparent. Remarkably, the resonator without any applied excitation (blue line) shows a low frequency ADEV at the thermodynamic limit of ≈ 7 Hz/Hz$^{0.5}$ below 1 s and (relative) stability of ≈ 10 Hz (≈ 0.40×10^{-6}) above 1 s averaging. The undriven and driven devices perform at CRLB up to averaging times of about 1 s and 0.1 s.

Conclusions

In conclusion, we present a statistically efficient resonance frequency estimator and the thermodynamic limit of resonance frequency measurement uncertainty applicable to linear resonator subjects to harmonic drive, thermal fluctuations, and detection uncertainty, on all time scales. After validating them with simulated data, we have implemented the frequency estimator on a stress-engineered nanomechanical resonator. Remarkably, the resonator remained at the thermodynamic limit even for fairly long averaging times, and better than part per million frequency stability has been measured, even though the resonator was driven solely by thermal fluctuations. The stress-engineered nanomechanical resonator with high frequency-Quality factor and considerable frequency stability may be used for developing frequency-readout displacement sensors requiring no excitation.

References

[1] Zhang, R., Ilic, R., & Liu, Y. *Solid-State, Actuators, and Microsystems Workshop* (2018)
[2] Sansa, M., Sage, E., Bullard, E. C., Gély, M., Alava, T., Colinet, E., ... & Jourdan, G. (2016). Nature nanotechnology, 11(6), 552.
[3] Gavartin, E., Verlot, P., & Kippenberg, T. J. (2013). Nature communications, 4, 2860.
[4] Zhang, R., Ti, C., Davanço, M., Ren, Y., Aksyuk, V., Liu, Y., & Srinivasan, K. (2015, June). In Integrated Photonics Research, Silicon and Nanophotonics (pp. IT4B-5). Optical Society of America.

Period Tripling States and Non-Monotonic Energy Dissipation in MEMS with Internal Resonance

Mingkang Wang[*,**], Diego J. Perez-Morelo[*,**], Daniel Lopez[***,*] and Vladimir A. Aksyuk[*]
[*]*Microsystems and Nanotechnology Division, National Institute of Standards and Technology, Gaithersburg, MD 20899 USA*
[**]*Institute for Research in Electronics and Applied Physics, University of Maryland, College Park, MD 20742, USA*
[***]*Materials Research Institute, Penn State University, University Park, PA 16802, USA*

Summary. We study free ringdown dynamics of a MEMS system with two modes near a 1:3 internal resonance. By separately preparing initial states and measuring the motion of both modes, we demonstrate that dependent on the initial relative phase the modes can either bypass or enter a phase-locked state, which can persist several times longer than the dissipation timescales. The sustained energy transfer between modes in the phase-locked state leads to non-monotonic energy dependence for one of the modes and overall lower dissipation rate for the system. The observations are accurately modeled by the coupled equations of motion, and can be understood by considering the low frequency mode as entering or bypassing a period tripling state under the influence of the periodic force from the high-frequency mode.

Persistent phase-locked state is described by a PTS model.

Nonlinearity in MEMS resonators is widely used in frequency stabilization [1], dissipation engineering [2], and improvement of resonance-based sensing [3] to achieve performance not available in the linear regime. Here, we thoroughly studied the nonlinear dynamics of two coupled MEMS resonators during free ringdown. The two resonators are designed with commensurate 1:3 eigenfrequencies to facilitate fast energy flow at internal resonance (IR). Remarkably, the two modes can get locked during ringdown and persist in this phase-locked state for extended periods of time, much longer than their intrinsic dissipation timescales. During relaxation, the low-frequency mode exhibits striking non-monotonic energy dissipation and negative modal energy dissipation rate (transient energy gain). The rich dynamics observed in the experiment are well explained by an intuitive model that regards the low-frequency mode at period-tripling states (PTS) created by the high-frequency mode, similar to the period-two states in parametric oscillators. In contrast to works at steady states [1,4,5], we demonstrate for the first time the phase lock at the transient states, the non-monotonic dissipation rate, and we provide an intuitive PTS model to describe it, simultaneously and independently from [5]. The observation and the model pave the way to engineering efficient energy flow between coupled nonlinear MEMS, which can be used for frequency stabilization and dissipation engineering.

Results

The two coupled modes are the fundamental in-plane mode (mode1) and torsional mode (mode2) of a clamp-clamp beam, as shown in Figure 1. The two modes are driven electrically with driving frequency $\omega_{1,osc}$ and $\omega_{2,osc}$ via the side gates. The modes are measured electrically and optically by an oscilloscope and a vibrometer, respectively. The eigenfrequencies of mode1 and mode2 are $\omega_1/2\pi \approx 64.6$ kHz and $\omega_2/2\pi \approx 199.9$ kHz ($\omega_1 \approx \omega_2/3$). When the driving force is strong, they exhibit spring hardening and softening effects, respectively, as shown in Figure 2. The dip on mode1's spectrum (orange) corresponds to the IR frequency of $\omega_{1,osc} = \omega_2/3$ where the model coupling is the strongest. In the experiment, we drive the two modes separately to their initial amplitude $A_{1,0}$ and $A_{2,0}$, labeled as red dots. At time t = 0, we turn off their drive simultaneously to let them ring down. Following their Duffing trajectory (black arrows in Figure 2), their frequencies shift due to the exponentially decaying amplitude (Fig. 3) and finally get locked at IR (black dots in Figure 2). The locking duration is ≈ 3× of the system intrinsic dissipation time ≈ $1/\Gamma_2$ where $\Gamma_2/2\pi \approx 3.3$ Hz is the intrinsic dissipation rate of mode2. The two modes persist in this state by spontaneously transferring energy from mode2 to mode1, indicated by the energy gain and rapid energy loss of mode1 and mode2 in Fig. 3(b). Their energies are calibrated to the same scale and fitted (black line) based on energy conservation in this system. The coupled two modes system can be regarded as a parametric resonator at PTS (mode1) subject to a period-three harmonic drive (mode 2). Repeating the same ringdown-locking experiment, we find the system exhibits discrete relative phase $n\times 2\pi/3$ shown in Figure 4, similar to period-two parametric oscillators. Following this logic, the non-monotonic and negative energy dissipation rate of mode1 (Γ_1) shown in the inset of Figure 3(b)) can be explained by the opposite Duffing coefficients of the two modes: (1) Spring softening effect of mode2 leads to increasing ω_2 during ringdown. (2) Locked by mode2, mode1's amplitude increases at higher frequency following its spring hardening spectrum.

Discussion

More generally, the gain or loss of mode1 can be engineered by altering mode2's Duffing coefficient, i.e. mode1 can either perform gain or rapid loss depending on mode2's parameters. The findings of phase-locking states and tunable dissipation rates are useful for energy dissipation engineering, such as for fast switches or low-dissipation timing/sensing devices. The proposed intuitive model provides a picture to understand the complicated dynamics in coupled nonlinear resonators. More details can be found in our preprint [6].

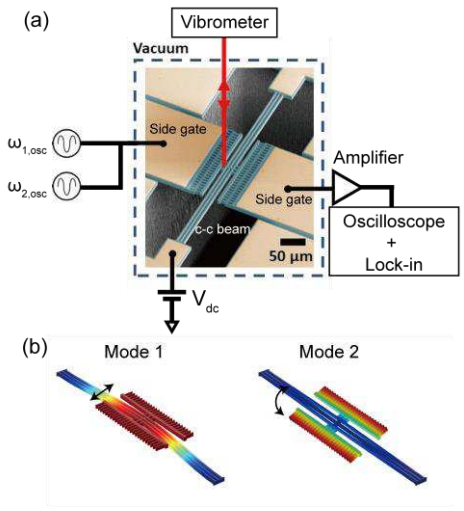

Figure 1: (a) Measurement schematics and false-colored SEM micrograph of the clamp-clamp beam MEMS. Optical and electrical measurements are performed, simultaneously. (b) Simulated mode shape of the two coupled modes.

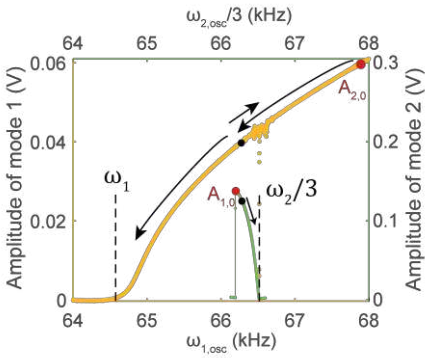

Figure 2. Spectrums of mode1 and mode2 are labeled by yellow and green dots. The oscillating frequency of mode2 is divided by 3. The two modes have opposite Duffing coefficients. In ringdown experiments, we set the initial conditions at $A_{1,0}$ and $A_{2,0}$ (red dots), respectively, and turn off the drive simultaneously. They evolve to equilibrium following the black arrows. After locked at the black dots, mode1 experiences frequency and amplitude increase shown as the short black arrow.

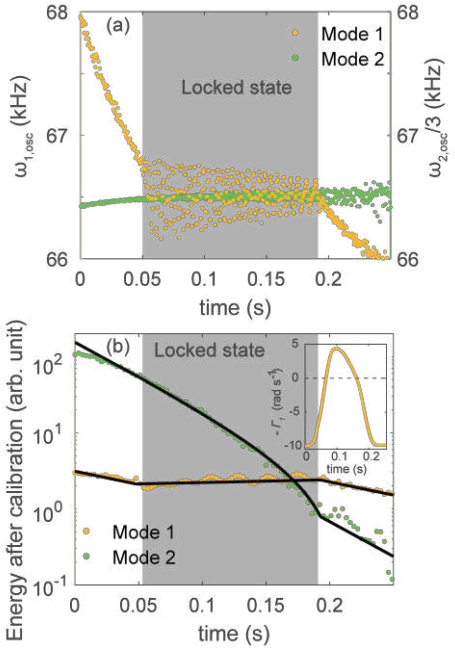

Figure 3. Oscillating frequencies and energy of the two modes are presented in (a) and (b), respectively. The yellow and green dots correspond to mode1 and mode2, respectively. The inset of (b) shows the minors of the measured effective dissipation rate of mode1 ($-\Gamma_1$). It indicates that mode1 shows a non-monotonic and negative dissipation rate during locking.

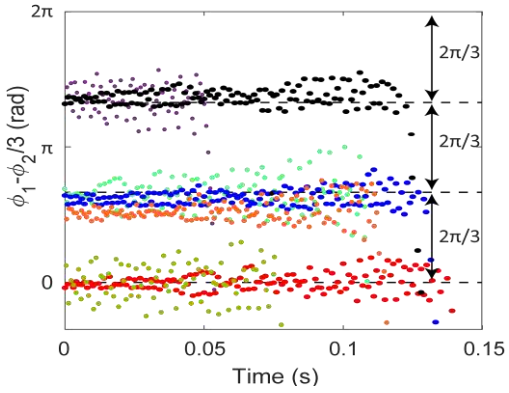

Figure 4. Relative phase of mode1 (φ_1) and mode2 (φ_2) in 7 repeating experiments. φ_1-$\varphi_2/3$ exhibits discrete values of (0, $2\pi/3$, $4\pi/3$) as expected in period tripling states.

References

[1] Antonio D., Zanette D. H, López D. (2012) Frequency stabilization in nonlinear micromechanical oscillators. *Nature* communications **3**(1), 1-6.

[2] Güttinger J., et al, (2017) Energy-dependent path of dissipation in nanomechanical resonators. *Nature nanotechnology* **12**(7), 631-636.

[3] Huang, L., et al, (2019) Frequency stabilization and noise-induced spectral narrowing in resonators with zero dispersion. *Nature* communications **10**(1), 1-10

[4] Czaplewski D. A., et al, (2018) Frequency comb generation in a nonlinear resonator through mode coupling using a single tone driving signal. *Technical digest-Solid-State Sensor, Actuator, and Microsystems Workshop*

[5] Yan Y., et.al. (2022) Energy Transfer into Period-Tripled States in Coupled Electromechanical Modes at Internal Resonance. *PRX* in press, arXiv:2206.0163

[6] Wang M., et al, (2022) Persistent nonlinear phase-locking and non-monotonic energy dissipation in micromechanical resonators. arXiv: 2206.01089

Thursday, July 21, 2022
13:30 - 15:30

MS-18 Control and Synchronization in Nonlinear Systems
Rhone 1

Chair: N. Van de Wouw, B. Brogliato

13:30 - 13:50
Online Control-Based Continuation of Nonlinear Structures Using Adaptive Filtering
ABELOOS Gaëtan*, RENSON Ludovic, COLLETTE Christophe, KERSCHEN Gaëtan
*Aerospace and Mechanical Engineering Department [Liège] (1, Chemin des Chevreuils Sart Tilman 4000 Liège Belgium)

13:50 - 14:10
Optimal Control of Spin Coating on a Spherical Substrate
SHEPHERD Ross*, BOUJO Edouard, SELLIER Mathieu
*University of Canterbury (20 Kirkwood Avenue, Upper Riccarton, Christchurch 8041 New Zealand)

14:10 - 14:30
Non-smooth inverted pendulum swing-up control optimization using a novel, Fourier series based numerical method
BALCERZAK Marek*, ZARYCHTA Sandra, DENYSENKO Volodymyr, STEFANSKI Andrzej
*Lodz University of Technology (1/15 Stefanowskiego Street, 90-924 Lodz Poland)

14:30 - 14:50
PID-based learning control for frictional motion systems
HAZELEGER Leroy, BEERENS Ruud, **VAN De Wouw Nathan***
*University of Minnesota, Department of Civil, Environmental and Geo-Engineering (Minneapolis MN 55455 United States) - Technische Universiteit Eindhoven, Department of Mechanical Engineering (P.O box 513 5600 MB Eindhoven Netherlands)

14:50 - 15:10
Simulation of an OWMS PLL network for clock signal distribution using parallel computing
BUENO Atila*, MACIEL Elvio, BATISTA Matheus, PANZO Eduardo, DERMENDJIAN Fabio, BATISTELA Cristiane, PIQUEIRA José, BALTHAZAR José
*Instituto de Ciência e Tecnologia - Universidade Estadual Paulista (Av. Três de março, 511, Sorocaba - SP Brazil)

Online Control-Based Continuation of Nonlinear Structures Using Adaptive Filtering

Gaëtan Abeloos*, Ludovic Renson†, Christophe Collette*‡ and Gaëtan Kerschen *
*Dept. of Aerospace & Mechanical Engineering, University of Liège, Liège, Belgium
†Dept. of Mechanical Engineering, Imperial College London, London, UK
‡Dept. of Bio, Electro and Mechanical Systems, Université Libre de Bruxelles, Brussels, Belgium

Summary. Control-Based Continuation uses feedback control to follow stable and unstable branches of periodic orbits of a nonlinear system without the need for advanced post-processing of experimental data. CBC relies on an iterative scheme to modify the harmonic content of the control target and obtain a non-invasive control signal. This scheme currently requires to wait for the experiment to settle down to steady-state and hence runs offline (i.e. at a much lower frequency than the feedback controller). This paper proposes to replace this conventional iterative scheme by adaptive filters. Adaptive filters can directly synthesize the control target adequately and can operate online (i.e. at the same frequency as the feedback controller). This novel approach is found to significantly accelerate convergence to non-invasive steady-state responses to the extent that the structure response can be characterized in a continuous amplitude sweep. Importantly, the stabilizing effect of the controller is not affected.

State of the art of Control-Based Continuation

A common way to characterize the steady-state behavior of a nonlinear structure consists in identifying its orbits under a monoharmonic excitation. Nonlinear structures can reach different periodic orbits under identical excitation, each one with its own response amplitude, stability and harmonic content. Some of the responses are unstable and cannot be observed experimentally without diverging towards another periodic orbit. Control-Based Continuation (CBC) is an experimental method that stabilizes the structure using feedback control of the displacement to generate the excitation signal and reach these unstable response branches [1][2]. Characterizing the unstable branches is useful to uncover potential hidden branches that, even though stable, cannot be reached by performing standard uncontrolled experiments such as frequency sweeps [3].
Non-fundamental harmonic content of the displacement x is fed back through the controller and must be taken into account to ensure monoharmonic excitation, synonymous with non-invasiveness of the controller [4]. Current implementations of CBC shown in Fig. 1a iterate (e.g. using Newton or fixed-point iterations) on the harmonics of the non-fundamental component of the control target x_{nf}^* until the non-fundamental harmonics of the excitation signal are below tolerance [5][6]. The fundamental component of the target x_{f}^* determines the fundamental amplitude of the response. Such a method necessitates waiting for steady-state to perform the harmonic decomposition before each target update.

Control-Based Continuation with adaptive filtering

Adaptive filters have been used for online harmonic elimination in the literature [7]. In this work, they are used to estimate the non-fundamental harmonics of the response and synthesize the non-fundamental control target x_{nf}^*. The now fully online strategy is shown in Fig. 1b. No offline iteration is needed to ensure a non-invasive controller. Two continuation procedures can be considered: finite steps like the state of the art lead up to 25% of experimental time reduction; continuous sweep of the target amplitude lead up to 50% time reduction, but high sweep rate can induce transient effects in the system's dynamics, decreasing accuracy. When using an adaptive filter in closed-loop, the structural and filter dynamics are coupled. More research is needed to predict the effect of such a coupling. However, the convergence time of the adaptive filter in open-loop is significantly shorter than the structural transient time.

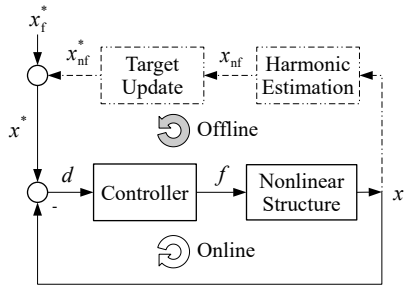

(a) Offline iterations on the non-fundamental target x_{nf}^*; the dashed-dotted line is performed offline, i.e. at a much lower frequency (state of the art)

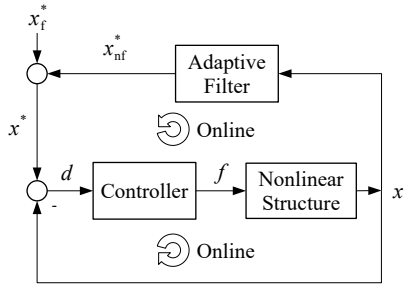

(b) Fully online strategy to synthesize the non-fundamental target x_{nf}^*

Figure 1: Two methods canceling high harmonic content in the excitation signal f by ensuring that the non-fundamental target x_{nf}^* equals the non-fundamental part of the response x_{nf}, making d monoharmonic; the fundamental target x_{f}^* drives the amplitude of response

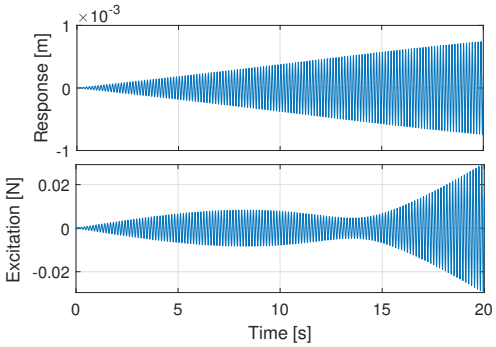

(a) Time series of the target sweep at 7 Hz

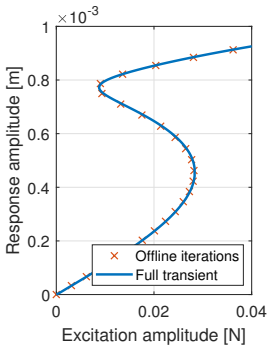

(b) S-curve at 7 Hz

Figure 2: The relationship between excitation and response amplitudes (S-curve) can be obtained by sweeping the target amplitude

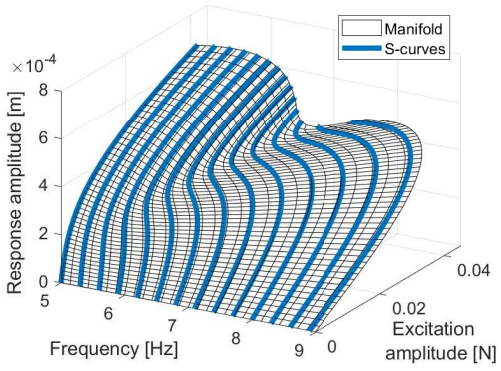

(a) S-curves and interpolating manifold in 3D space

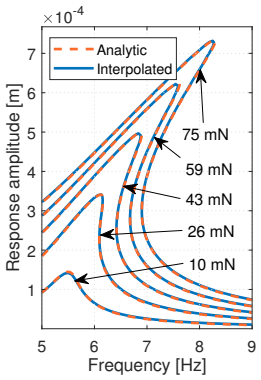

(b) Frequency response curves

Figure 3: S-curves are measured for different frequencies and the manifold is interpolated using a B-spline surface; the interpolated frequency response curves are obtained by slicing the surface in the frequency-response plane for constant excitation amplitudes

The proposed strategy is demonstrated numerically using a Duffing oscillator; the resulting time series and the corresponding S-curves at 7 Hz are shown in Fig. 2. By performing sweeps at different frequencies, the manifold characterizing the structural dynamics can be interpolated, as shown in Fig. 3a. The frequency response curves can then be extracted, they are shown in Fig. 3b.

Conclusion

An online method that identifies stable and unstable periodic orbits of nonlinear mechanical systems is proposed. To ensure non-invasiveness of the controller, an adaptive filter is used to synthesize a target which renders the controller's output monoharmonic. This strategy removes the need for offline iterations on the control target. Therefore, identifying complete frequency response curves with fully-transient sweeps is within reach, significantly accelerating the experimental characterization of nonlinear systems.

Acknowledgements

G.A. is funded by the FRIA grant of the Fonds National de la Recherche Scientifique (FNRS), L.R. is funded by a Research Fellowship from the Royal Academy of Engineering (RF1516/15/11). They gratefully acknowledge the financial support of the Royal Academy of Engineering and the FNRS.

References

[1] Sieber J., Krauskopf, B. (2008) Control based bifurcation analysis for experiments. *Nonlinear Dynam* **51**:356–377

[2] Sieber J. et al. (2008) Experimental continuation of periodic orbits through a fold. *Phys Rev Lett* **100**:244101

[3] Renson L., Shaw A.D., Barton D.A.W., Neild S.A. (2019) Application of control-based continuation to a nonlinear structure with harmonically coupled modes. *Mech Syst Signal Pr* **120**:449–464

[4] Barton D.A.W., Sieber J. (2013) Systematic experimental exploration of bifurcations with noninvasive control. *Phys Rev E* **87**:52916

[5] Renson L. et al. (2016) Robust identification of backbone curves using control-based continuation. *J. Sound Vib* **367**:145–158

[6] Renson L., Barton D.A.W., Neild S. A. (2017) Experimental tracking of limit-point bifurcations and backbone curves using control-based continuation. *Int J. Bifurcat Chaos* **27**:1730002

[7] Glover, J. R. (1977). Adaptive Noise Canceling Applied to Sinusoidal Interferences. *IEEE T. Acoust. Speech*, **25**:484-–491.

Optimal Control of Spin Coating on a Spherical Substrate

Ross G. Shepherd*, Edouard Boujo† and Mathieu Sellier*
*Department of Mechanical Engineering, University of Canterbury, Christchurch 8140, New Zealand
†Laboratory of Fluid Mechanics and Instabilities, École Polytechnique Fédérale de Lausanne, CH1015 Lausanne, Switzerland

Summary. We consider the optimal control of spin coating on a convex spherical substrate. We present a lubrication model for the flow a thin fluid film on the surface of a rotating sphere, and derive a corresponding adjoint problem to calculate the effects of changes in spin speed on the thickness profile of films produced by spin coating. This was used to determine an optimal time-varying angular velocity throughout the spin coating process in order to produce a uniform coating over section of the substrate. With this we demonstrate that there are circumstances in which spinning can allow for greater control of coating thickness than gravitational draining, but even the best performance achieved by optimal spinning showed up to a 10% deviation from the desired coating thickness.

Introduction

Spin coating has been used in a wide range of industrial applications since the early 20th century as a technique to deposit thin liquid films onto flat substrates [1]. Today, it is used to apply functional and protective coatings in the manufacturing of printed circuit boards, solar panels, light-emitting diode displays, chemical sensors, and optical components [2]. Current spin coating methods are limited, however, to flat substrate geometries and cannot reliably produce uniform thin films over curved substrates. A novel spin coating process for curved substrates could enable the development of new technologies in consumer electronics, medicine, and optics, among many other fields. Building on the seminal work of Emslie et al. [3], spin coating on flat substrates has been extensively studied, however the problems associated with coating curved surfaces have received relatively little attention despite being identified as early as this original paper. Feng and Sun [4], Chen et al. [5], and Liu et al. [6] have all developed models for spin coating on spherical substrates and validated these against experimental measurements, but the question of how to improve coating performance on curved substrates has yet to be addressed. Here, we investigate whether the spin speed used throughout the process can be manipulated to improve coating performance on a convex spherical substrate.

Model Development

We consider the flow of an axisymmetric thin liquid film on the surface of a rotating spherical substrate, parameterised by the zenith angle ϕ from the top of the sphere. Let h be the film thickness measured normal to the substrate, let R be the substrate radius, and let Ω be the angular velocity of the substrate around the vertical axis. Choosing the average film thickness $\bar{h}$ and drainage time $t_\mathrm{d} = \mu_0\bar{h}/\varepsilon\gamma$ as characteristic length and time scales (where $\varepsilon = \bar{h}/R$ and μ_0, γ are the initial viscosity and surface tension of the fluid), we derive a dimensionless 4th-order partial differential equation (PDE) describing the evolution of the film, with hats denoting rescaled dimensionless variables and subscripts denoting partial derivatives:

$$0 = \frac{\partial \hat{h}}{\partial \hat{t}} + \frac{1}{\sin\phi}\left(\frac{\hat{h}^3}{3\hat{\mu}}\sin\phi\left[\varepsilon^2\hat{\kappa}_\phi + Bo\left(\sin\phi - \varepsilon\hat{h}_\phi\cos\phi + \varepsilon Ga\hat{\Omega}^2\left(\sin\phi\cos\phi + \varepsilon\hat{h}_\phi\sin^2\phi\right)\right)\right]\right)_\phi. \tag{1}$$

Here, $Bo = \rho g\bar{h}^2/\gamma$ is the Bond number, $Ga = \gamma^2/{\mu_0}^2\bar{h}g$ is the Galileo number characterising the relative strength of gravity and centrifugal force, and $\hat{\kappa}_\phi = \hat{h}_{\phi\phi\phi} + \hat{h}_{\phi\phi}\cot\phi + \hat{h}_\phi(2 - \csc^2\phi)$ is the derivative of the dimensionless curvature of the free surface. We incorporate the effects of increases in viscosity due to curing or evaporation following the method of Lee et al. [7] by introducing the coefficient:

$$\hat{\mu}(t) = \begin{cases} \exp(\beta t), & t \le t_\mathrm{c} \\ \hat{\mu}_1 t^\alpha, & t > t_\mathrm{c} \end{cases} \tag{2}$$

so that the time-varying viscosity may be written as $\mu = \mu_0\hat{\mu}(t)$, with a characteristic curing time t_c after which the film becomes essentially solid. Here, $\hat{\mu}_1 = \exp(\beta t_\mathrm{c}){t_\mathrm{c}}^{-\alpha}$ is chosen to ensure continuity. An example film evolution under the effects of gravity alone is shown in figure 1 (left panel) using the same fluid properties and substrate dimensions as [7]. We see that beginning from a non-uniform initial condition concentrated around the top of the sphere, the fluid drains over the entire upper half before hardening, leaving a non-uniform coating with thickness of approximately $\hat{h} \approx 2.5$.

Optimal Control Methodology

We now wish to determine how the angular velocity $\hat{\Omega}$ can be changed as a function of time throughout the spin-coating process in order to achieve a more even coating. We begin by choosing (as a proof of concept) the region of the substrate surface $\phi \in D = [0, \pi/4]$ over which we want a produce a uniform coating. We also choose $\hat{h}_\mathrm{opt} = 2$ as a desired coating

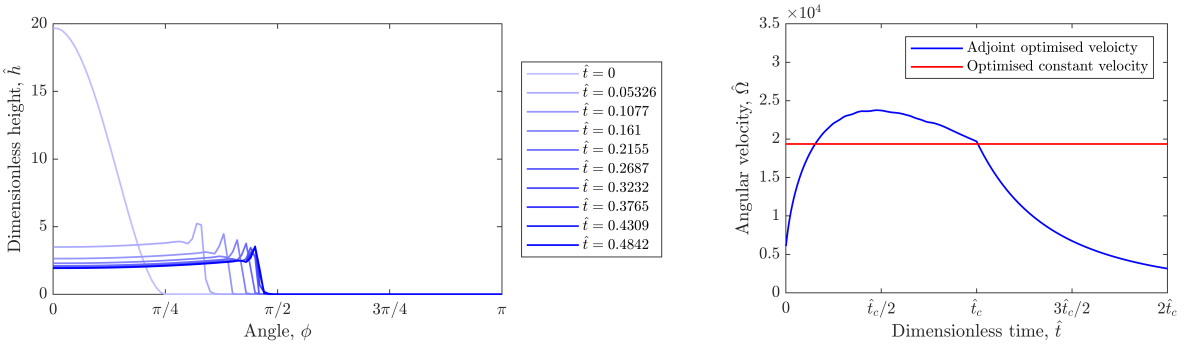

Figure 1: (Left panel) Example evolution of a film under gravitational draining alone with $\hat{\Omega} = 0$, $Bo = 5.7\times10^{-3}$, $Ga = 6.9\times10^{-10}$, $\varepsilon = 2.6\times10^{-3}$, and $\hat{t}_c = 0.2421$ in order to match [7]. (Right panel) The optimal angular velocity distribution over time by the adjoint method with the same parameters, compared with an optimal constant angular velocity with comparable performance.

thickness, corresponding to the thickness of a uniform coating over the entire upper-half sphere. The uniformity of the final film $\hat{h}_\mathrm{f} = \hat{h}(\phi, \hat{t}_\mathrm{f})$ at the time $\hat{t}_\mathrm{f} = 2\hat{t}_\mathrm{c}$ can then be characterised by:

$$\mathcal{J}(\hat{h}, \hat{\Omega}^2) = \int_D (\hat{h}_\mathrm{f} - \hat{h}_\mathrm{opt})^2 \sin\phi \,\mathrm{d}\phi, \tag{3}$$

where small values of $\mathcal{J}$ correspond to good coating performance. We determine the optimal $\hat{\Omega}(\hat{t})$ using the same method as Boujo and Sellier [8] by considering the constrained minimisation of (3) subject to (1). We then introduce an adjoint variable λ as a Lagrange multiplier for $\hat{h}$ and derive a terminal value PDE which can be solved for λ. The adjoint variable then allows for the calculation of the gradient $\mathrm{d}\mathcal{J}/\mathrm{d}\hat{\Omega}$ and the use of a simple gradient-descent optimisation algorithm.

Results and Conclusions

The optimal control methodology described above was implemented using COMSOL Multiphysics and MATLAB for two cases: (i) with no restrictions on the angular velocity distribution over time $\hat{\Omega}(\hat{t})$, and (ii) with the additional constraint that $\hat{\Omega}$ is constant over time, similar a typical speed profile currently used in spin coating. The angular velocity profiles resulting from the optimisation are shown in figure 1 (right panel). We see that the optimal angular velocity is greatest early in the coating process, then decreases as the viscosity increases and the film hardens. The final film uniformities produced using adjoint optimised and constant angular velocities are $\mathcal{J}_\mathrm{adjoint} = 7.55 \times 10^{-4}$ and $\mathcal{J}_\mathrm{constant} = 8.17 \times 10^{-4}$, respectively, compared to $\mathcal{J}_0 = 0.0159$ if the film drains under gravity alone ($\hat{\Omega} = 0$). However, following optimal spinning the final film thickness still varied by up to 10% from $\hat{h}_\mathrm{opt}$ over the domain $D = [0, \pi/4]$. This shows that spin coating offers significantly improved control of film thickness over simple gravitational draining, but a constant angular velocity is able to achieve almost the same coating performance as the optimal time-varying velocity profile. We can conclude from this that spin coating cannot, in general, be used to uniformly coat a curved substrate even with optimised angular velocity. We also see that the use of an adjoint-optimised time-varying angular velocity cannot produce a significantly more uniform coating than the constant speeds typically used in spin coating. This suggests that new coating processes designed specifically for curved surfaces will be required if we wish to produce uniform spin-coated films on non-planar substrates.

References

[1] Norrman, K., Ghanbari-Siahkali, A., and Larsen, N. B. (2005) Studies of spin-coated polymer films. *Annual Reports on the Progress of Chemistry – Section C* **101**:174–201.

[2] Cohen, E. and Lightfoot, E. J. (2011) "Coating Processes" in *Kirk–Othmer Encyclopedia of Chemical Technology*. Wiley, NJ.

[3] Emslie, A. G., Bonner, F. T., and Peck, L. G. (1958) Flow of a Viscous Liquid on a Rotating Disk. *J. App. Phys.* **29**(5):858–862.

[4] Feng, X.-g. and Sun, L.-c. (2005) Mathematical model of spin-coated photoresist on a spherical substrate. *Optics Express* **13**(18):7070–7075.

[5] Chen, L. J., Liang, Y. Y., Luo, J. B., Zhang, C. H., and Yang, G. G. (2009) Mathematical modeling and experimental study on photoresist whirl-coating in convex-surface laser lithography. *Journal of Optics A: Pure and Applied Optics* **11**(10).

[6] Liu, H., Fang, X., Meng, L., and Wang, S. (2017) Spin Coating on Spherical Substrate with Large Central Angles. *Coatings* **7**(8).

[7] Lee, A., Brun, P. T., Marthelot, J., Balestra, G., Gallaire, F., and Reis, P. M. (2016) Fabrication of slender elastic shells by the coating of curved surfaces. *Nat. Comm.* **7**.

[8] Boujo, E. and Sellier, M. (2019) Pancake making and surface coating: Optimal control of a gravity-driven liquid film. *Phys. Rev. Fluids* **4**(6).

Non-smooth inverted pendulum swing-up control optimization using a novel, Fourier series based numerical method

Marek Balcerzak[*], Sandra Zarychta[*], Volodymyr Denysenko* and Andrzej Stefanski[*]
[*]*Division of Dynamics, Lodz University of Technology, Lodz, Poland*

Summary. Swing-up control of an inverted pendulum is one of the classical tasks in dynamics and control theory. Optimization of the pendulum's trajectory and the corresponding control function is not trivial, particularly when the controlled object is non-smooth (for example, due to presence of dry friction). This short paper contains a concise description of a novel, Fourier series based numerical method of control optimization, which is able to successfully solve such problem. It is expected that this algorithm will enable progress in control optimization of systems, for which typical approaches cannot be utilized.

Introduction

Optimal control is the one that minimizes the cost of performing a desired action [1]. In the case of systems described by a set of ordinary differential equations (ODEs), the necessary conditions for control optimality have been described by Pontryagin [2] in terms of variational calculus. Another classical approach to solving optimal control problems is the dynamic programming method, introduced by Bellman et al. [3]. However, the former cannot be utilized in non-smooth and discontinuous systems, whereas the latter requires significant computing power even in simple cases [1]. Therefore, there is a need for a simple method which solves optimal control problems in non-smooth systems. In this paper authors present a novel, Fourier series based numerical algorithm [4] applied in optimization of the swing-up control of an inverted pendulum [5] with a dry friction discontinuity.

System description

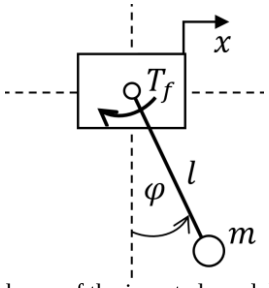

Figure 1: Scheme of the inverted pendulum system

The inverted pendulum system [5], whose scheme is presented in Fig. 1, consists of the controlled cart, able to move along the x axis, with a mathematical pendulum of the mass m and the length l attached to it. Dry and viscous friction torque in the pendulum's bearing is taken into account, i.e. $T_f = c_v\dot{\varphi} + c_d \operatorname{sgn}\dot{\varphi}$. The swing-up control means moving the cart in such a manner that the pendulum stands up from the initial state $\varphi = \dot{\varphi} = x = \dot{x} = 0$ (pendulum hanging vertically downwards) to the final one $\varphi = \pi, \dot{\varphi} = x = \dot{x} = 0$ (pendulum standing vertically upwards). Defining the dimensionless time $\tau = \omega t$ with $\omega = \sqrt{\frac{g}{l}}$, transforming the derivatives $\dot{\varphi} = \frac{d\varphi}{d\tau}\frac{d\tau}{dt} = \varphi'\omega,\ \ddot{\varphi} = \omega^2\varphi'',\ \ddot{x} = \omega^2 x''$ and introducing dimensionless parameters $z = \frac{x}{l}, \zeta = \frac{c_v}{2m\omega l^2}, \mu = \frac{c_d}{m\omega^2 l^2}$ yield the following dimensionless form of the model.

$$\varphi'' = -\sin\varphi - z''\cos\varphi - 2\zeta\varphi' - \mu \operatorname{sgn}\varphi'$$

The quantity $u = z' = \frac{\dot{x}}{\omega l}$, a dimensionless counterpart of the cart's velocity, is the controlled variable in the system. Obviously, velocity and acceleration of any physical drive are bounded. Moreover, the space in which the cart moves may be restricted. Therefore, the following constraints are assumed: $-z_{max} \le z \le z_{max},\ -v_{max} \le z' \le v_{max},\ -a_{max} \le z'' \le a_{max}$, where $z_{max} > 0,\ v_{max} > 0,\ a_{max} > 0$.

Optimization method

Assume that the goal is to minimize two factors in parallel, motion time T and drive usage - the integral of u'^2. Therefore, the cost functional can be defined as follows: $J = \int_0^T (\lambda + u'^2)d\tau$, where λ is a positive, real parameter. The proposed optimization method assumes that the control function $u(\tau)$ to be optimized is described using a finite number of harmonics of the Fourier series.

$$u(\tau) = \frac{a_0}{2} + \sum_{i=1}^{K} [a_i \cos(i\omega\tau) + b_i \sin(i\omega\tau)]$$

Bearing in mind that $u(\tau) = z'$ and taking into account the boundary conditions $z(0) = z'(0) = z(T) = z'(T) = 0$, it can be easily shown that $a_0 = 0$, $a_K = -\sum_{i=1}^{K-1} a_i$, $b_K = -\sum_{i=1}^{K-1} \frac{b_i}{i}$. Consequently, the control function $u(\tau)$ depends on $(2K-2)$ independent parameters, which can be collected in a vector $\boldsymbol{H} = [a_1, b_1, a_2, b_2, \dots, a_{K-1}, b_{K-1}] \in \mathbb{R}^{2(K-1)}$. Taking a large enough value K enables to approximate $u(\tau)$ with arbitrarily high accuracy. Now an important fact must be noticed: the *direction* of the vector $\boldsymbol{H}$ in $\mathbb{R}^{2(K-1)}$ is responsible for the *shape* of the function $u(\tau)$, i.e. signs of its derivatives of all degrees, locations of local extrema and inflection points etc., whereas the *length* of $\boldsymbol{H}$ determines the *span*, i.e. the set of values and the global extrema of $u(\tau)$ [4]. Therefore, the *shape* of the function $u(\tau)$ for a fixed ω can be uniquely defined by a *direction* $\mathbb{R}^{2K-2}$, which in turn can be described by a point on a unit hypersphere immersed in $\mathbb{R}^{2K-2}$, i.e. on S^{2K-3}, a $(2K-3)$ −dimensional one. Location of any point on such hypersphere depends on $2K-3$ angular coordinates, which uniquely define the *shape* of $u(\tau)$ [4]. Assume that this *shape* is already known. Now, as the continuous function $z' = u(\tau)$ is constrained by $-z_{max} \le z \le z_{max}$, $-v_{max} \le z' \le v_{max}$, $-a_{max} \le z'' \le a_{max}$, there exists the smallest number $Q > 0$ such that at least one of the constraints is violated by $q * u(\tau)$ if $q > Q$. Consequently, as the shape of $u(\tau)$ is fixed, then $p * Q * u(\tau)$ with a parameter $p \in (0, 1]$ define all the admissible functions $u(\tau)$ of the shape defined by a point on S^{2K-3}. Summing up, K-harmonics approximation of any Dirichlet control function $f: [0, T] \subset \mathbb{R} \to [-v_{max}, v_{max}] \subset \mathbb{R}$ can be described using $(2K-3)$ angular coordinates on S^{2K-3} and the parameters ω, p. Global optimization of all these parameters, for example using Differential Evolution method [6], leads to optimization of the control function $u(\tau)$ itself. When the proposed approach is utilized, smoothness of the controlled system is not required as long as the required trajectories exist and are unique.

Results and conclusions

The shape of the function $u(\tau)$ was optimized for $K \in \{2, 3\}$ parametrized in terms of spherical coordinates on S^{2K-3} along with the parameters $\omega \in [0.1, 10], p \in (0, 1]$ using the Differential Evolution method [6]. The results are presented in the graphs below.

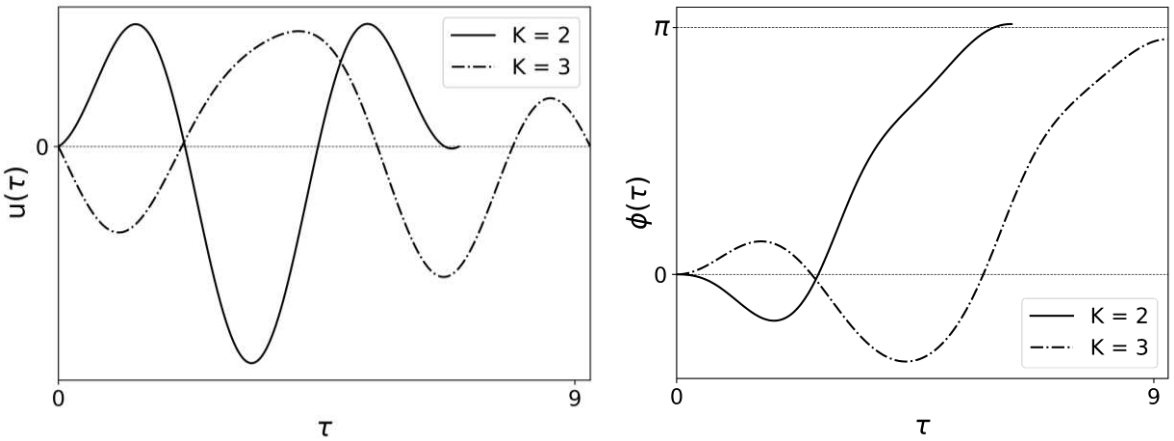

Figure 2: Results of optimizing the control function $u(\tau)$ with respect to the cost functional J.

The optimized values of the cost functional $J = \int_0^T (\lambda + u'^2) d\tau$ were approximately equal 13.93 (optimization with 2 harmonics, i.e. $K = 2$) and 12.62 (optimization with 3 harmonics, i.e. $K = 3$). Therefore, it can be noticed that increasing number of harmonics in the optimized function $u(\tau)$ from $K = 2$ to $K = 3$ increases accuracy of control optimization. It is expected that larger values of K lead to better approximations of the optimal control. As it can be noticed, the method works successfully in the discontinuous system. Authors hope that this algorithm will enable progress in control optimization of systems, for which typical approaches cannot be utilized.

***Acknowledgements**: This study has been supported by the National Science Centre, Poland, PRELUDIUM Programme (Project No. 2020/37/N/ST8/03448). This study has been supported by the National Science Centre, Poland under project No. 2017/27/B/ST8/01619. This paper has been completed while the second author was the Doctoral Candidate in the Interdisciplinary Doctoral School at the Lodz University of Technology, Poland.*

References

[1] Kirk, D. E. (2004). Optimal control theory: an introduction. Courier Corporation.
[2] Pontryagin, L. S., Boltyanskii, V. G., Gamkrelidze, R. V., & Mishchenko, E. F. (1962). The mathematical theory of optimal processes, translated by KN Trirogoff. New York.
[3] Bellman, R., & Kalaba, R. E. (1965). Dynamic programming and modern control theory (Vol. 81). New York: Academic Press.
[4] Zarychta, S., Sagan, T., Balcerzak, M., Dabrowski, A., Stefanski, A., & Kapitaniak, T. (2021). A novel, Fourier series based method of control optimization and its application to a discontinuous capsule drive model. arXiv preprint arXiv:2108.10611.
[5] Yoshida, K. (1999, June). Swing-up control of an inverted pendulum by energy-based methods. In Proceedings of the 1999 American Control Conference (Cat. No. 99CH36251) (Vol. 6, pp. 4045-4047). IEEE.
[6] Storn, R., & Price, K. (1997). Differential evolution–a simple and efficient heuristic for global optimization over continuous spaces. Journal of global optimization, 11(4), 341-359.

PID-based learning control for frictional motion systems

Leroy Hazeleger*, Ruud Beererns* and Nathan van de Wouw * †
*Deparment of Mechanical Engineering, Eindhoven University of Technology, P.O. Box 513, Eindhoven 5600 MB, The Netherlands
†Department of Civil, Environmental and Geo-Engineering, University of Minnesota, Minneapolis, MN 55455, USA

Summary. Classical PID control is exploited widely in industrial motion systems suffering from dry friction. This is motivated by the easy-to-use design tools available. However, friction-induced limit cycling (i.e., *hunting*) is observed when integral control is employed on frictional systems that suffer from the Stribeck effect, thereby compromising setpoint stability. In addition, the resulting time-domain behavior, such as, e.g., rise-time, overshoot, settling time, and positioning accuracy, highly depends on the particular frictional characteristic, which is typically unknown or uncertain. On the other hand, omitting integral control can lead to constant non-zero setpoint errors (i.e., *stick*). To achieve superior setpoint performance for frictional motion systems in a repetitive motion setting, we propose a PID-based feedback controller with a *time-varying* integrator gain design. To ensure optimal setpoint positioning accuracy, a data-based sampled-data extremum-seeking architecture is employed to obtain the optimal time-varying integrator gain design. The proposed approach does not rely on knowledge on the friction characteristic. The effectiveness of the proposed approach is evidenced experimentally by application to an industrial nano-positioning motion stage set-up of a high-end electron microscope.

Introduction

The vast majority of the high-precision industry employs classical PID control, since control practitioners are often well-trained in linear control design (loop-shaping). Moreover, it is well-known that integral action in PID control is capable of compensating for *unknown* static friction in motion systems. However, friction-induced limit cycling (i.e., *hunting*, see [1]) is observed when integral control is employed on systems where the friction characteristic includes the velocity-weakening (Stribeck) effect, so that stability of the setpoint is lost. Even if stability can be warranted, rise-time, overshoot, settling time (see [2]), and positioning accuracy depend on the particular friction characteristic, which is highly uncertain in practice. Hence, despite the popularity of the PID controller in industry, friction is a performance- and reliability-limiting factor in PID-controlled motion systems.
In this work, we propose a PID-based learning controller in order to achieve a high setpoint accuracy for repetitive tasks in motion systems subject to unknown static and velocity-dependent friction, including the Stribeck effect. The PID-based learning controller consists of two elements. First, a PID control architecture with a *time-varying integrator gain* design is proposed, facilitating a tailored design such that friction-induced limit cycles can be avoided, and high accuracy repetitive setpoint positioning can be achieved instead. In addition, similar robustness properties as for the classical PD control at the desired setpoint can be achieved. Second, a sampled-data extremum-seeking architecture (see [3]) is proposed, in order to iteratively find the optimal time-varying integrator gain, in the presence of unknown friction. The effectiveness of the proposed approach is evidenced experimentally by application to an industrial nano-positioning motion stage set-up of a high-end electron microscope

Control problem formulation for frictional motion systems

Consider a single-degree-of-freedom motion system, consisting of a mass m sliding on a horizontal plane, with measurable position x_1, velocity x_2, control input u_c, and subject to a friction force F_f. The friction force F_f takes values according to the set-valued mapping of the velocity $x_2 \rightrightarrows \Phi(x_2)$. The set-valued friction characteristic Φ consists of a Coulomb friction component with (unknown) static friction F_s, a viscous contribution γx_2 (where $\gamma \geq 0$ is the viscous friction coefficient), and a (unknown) nonlinear velocity-dependent friction component f, encompassing the Stribeck effect, i.e.,

$$F_f \in \Phi(x_2) := -F_s \text{Sign}(x_2) - \gamma x_2 + f(x_2), \tag{1}$$

The dynamics are governed by the following differential inclusion:

$$\dot{x}_1 = x_2,\ m\dot{x}_2 \in \Phi(x_2) + u_c. \tag{2}$$

We focus on achieving high-accuracy positioning for frictional motion systems that perform a T*-repetitive* motion. We consider, for the position x_1, a desired repetitive reference r, defined on the time interval $[0, T]$, where the system starts and ends at rest and define two particular time intervals; 1) the interval $t \in [0, T_B)$ during which the system is allowed to move from 0 to r, and 2) the interval $t \in [T_B, T]$, during which standstill at r is required. The time interval $[T_B, T]$ is typically used by the industrial machine, of which the motion system is part, to perform a certain machining operation, for which accurate positioning is required. We address the following setpoint control problem: *Design a PID-based control strategy for motion systems of the form* (2), (1)*, that perform a repetitive motion profile and are subject to unknown static and velocity-dependent friction, such that high-accuracy setpoint positioning during the standstill time window is achieved*.

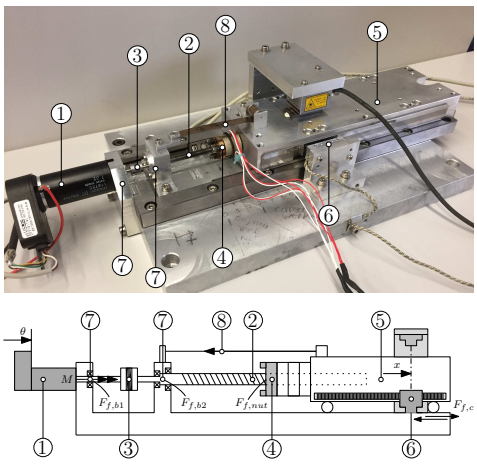

Figure 1: Nano-positioning motion stage set-up: ① Maxon RE25 DC servo motor, ② spindle, ③ coupling, ④ nut, ⑤ carriage, ⑥ linear Renishaw encoder, ⑦ bearings, ⑧ coiled spring.

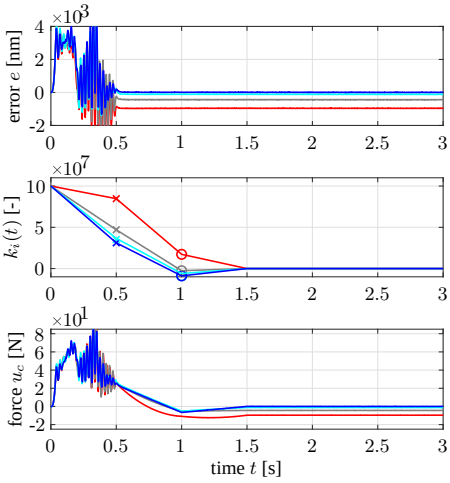

Figure 2: Experimental results that show the error and corresponding $k_i(t)$ and u_c after the initial parameter setting $u_0 = [0.85,\ 0.175]^\top \cdot 10^8$ (—), the 2nd (—), 4th (—), and 7th (—) extremum seeking controller update, leading to an achieved setpoint accuracy of about $4-6$ nm.

A time-varying integrator gain design for PID-based control of frictional motion systems

Limit-cycle behavior present in the case of PID control with *constant* integrator gain is caused by the build-up of integrator action (during transients and the stick phase) in interplay with the friction characteristic, see, e.g., [1]. This observation motivates the design of a novel *time-varying* integrator gain $k_i(t)$ for point-to-point motion, namely: 1) the presence of integrator action still allows the system to escape undesired stick phases, 2) overcompensation of friction due to, e.g., a severe Stribeck effect, can be avoided, by altering $k_i(t)$ during the slip phase, and 3) zero integral action can be enforced at the setpoint when standstill of the system is required, such that robustness against other force disturbances is provided by the static friction. The resulting controller is then given by $u_c = k_p e + k_d \dot{e} + k_i(t) x_3,\ \dot{x}_3 = \varsigma(t) e$, with $\varsigma(t) \in \{0, 1\}$ a to-be-designed switching function that prevents uncontrolled growth of x_3. We are able to 1) escape undesired stick phases by enabling $k_i \neq 0$ and $\varsigma(t) = 1$ during $t \in [0, T_B]$, and 2) create robustness to other force disturbances close to the setpoint, by enforcing $k_i = 0$ and $\varsigma = 0$ during $t \in [T_B, T]$. Thereto, we parametrize $k_i(t) = \sum_{j=1}^{6} [v^{(j)}\ v^{(j+1)}] \Psi^{(j)}(t)$ by linear spline basis functions $\Psi^{(j)}(t)$, with $v^\top = [1 \cdot 10^8\ u_0^\top\ 0^{1\times 4}]$, and u_0 a to-be-optimized parameter vector.

PID-based learning control for an industrial nano-positioning motion stage

The working principle and the effectiveness of the proposed PID-based controller are demonstrated on an industrial nano-positioning stage, representing a sample manipulation stage of an electron microscope, exhibiting significant and unknown frictional effects. The experimental setup and a schematic representation are presented in Fig. 1. A sampled-data extremum-seeking architecture (see, [3]) is used to iteratively find a time-varying integrator gain design $k_i(t)$, ultimately leading to a position error in the range of $4-6$ nm, depicted by (—) in Fig. 2. In contrast, the classical PID controller for this particular set-up yields an absolute error of about 100 nm on the same time interval, and does not provide robustness during the standstill time window. This clearly illustrates the performance benefits of the proposed PID-based learning controller in terms of the ability to cope with Stribeck friction and achieving superior setpoint positioning accuracy.

Conclusions

We have presented a novel time-varying integrator gain design for motion systems with unknown Coulomb and velocity-dependent friction, capable of achieving a high positioning accuracy, in contrast to classical PID control, which often leads to limit cycling. The optimal time-varying integrator gain is iteratively obtained by employing a sampled-data extremum-seeking architecture. The superior performance of the proposed control architecture over classical PID control is experimentally demonstrated on a nano-positioning stage of an electron microscope.

References

[1] R.H.A. Hensen, M.J.G. van de Molengraft, M. Steinbuch, Friction induced hunting limit cycles: A comparison between the LuGre and switch friction model. *Automatica*, 39(12):2131–2137, 2003.

[2] R. Beerens, A. Bisoffi, L. Zaccarian, W.P.M.H. Heemels, H. Nijmeijer, H. N. van de Wouw, Reset integral control for improved settling of PID-based motion systems with friction. *Automatica*, vol. 107:483–492, 2019.

[3] L. Hazeleger, R. Beerens, N. van de Wouw, A sampled-data extremum-seeking approach for accurate setpoint control of motion systems with friction. *Proc. 11th IFAC Symposium on Nonlinear Control Systems (NolCos, Vienna, 2019).*

Simulation of an OWMS PLL network for clock signal distribution using parallel computing

E. A. Maciel[1], M. S. Batista[1], E. C. Panzo[1], F. H. Dermendjian[2], C. M. Batistela[3], J. R. C. Piqueira[3], J. M. Balthazar[2] and A. M. Bueno[1]
[1]*Institute of Science and Technology, São Paulo State University - UNESP, Sorocaba - SP, Brazil*
[2]*School of Engineering, São Paulo State University - UNESP, Bauru - SP, Brazil*
[3]*Polytechnique School, São Paulo University - USP, São Paulo - SP, Brazil.*

Summary. The development of electronics in general, in particular integrated circuits, allowed accurate and stable clock signal - or phase and frequency - distribution. The PLL is the fundamental component of clock signal distribution networks, and consists of a closed-loop control system that synchronizes a local oscillator, or clock, to a reference signal. The Phase-Locked Loop (PLL) is the basic element of clock signal distribution networks that is a fundamental part of digital communications networks. In many cases One-Way Master-Slave (OWMS) chain networks is used for clock signal distribution due to its reliability and low cost. Due to the nonlinear behavior of PLLs the design of the networks is a difficult problem, therefore, numerical simulations play important role. In this paper, a parallel computing strategy is used do simulate OWMS chain networks aiming to develop a more efficient simulation strategy, and to study the nodes interaction effects on the network due to parallel computing and distribution of the clock signal.

Index Terms — Clock distribution, phase-locked loop, synchronization, OWMS chain networks and parallel computing.

Introduction

PLLs (Phase-Locked Loops) are part of numerous applications in Electrical Engineering, control systems, and especially in communication networks. A time synchronization signal distribution network is defined by the connection of a certain clock oscillators whose purpose is to organize a temporal coordination. Synchronization networks are characterized by the fact that several oscillators (clocks) operate with the same frequency and phase. The basic element in these networks are PLL circuits [1, 2]. The PLL is a control system that synchronizes a local oscillator to an input signal. If properly designed the PLL tracks the input signal and filter phase and frequency fluctuations (jitter and wander) [3, 4, 5, 6].
The PLL block diagram shown in Fig. 1 is composed of a Phase Detector (PD), of a Low-Pass Filter (LPF) and of a Voltage Controlled Oscillator (VCO). The multiplier type PD compares the input signal v_i (Eq. 1) with the output v_o (Eq. 2) of the VCO and generates the phase error signal v_d with the same sign of the phase difference. The LPF filters the phase and frequency fluctuations and also provide the control signal v_c that controls the VCO frequency and phase (Eq. 3) around the free-running frequency ω_M.

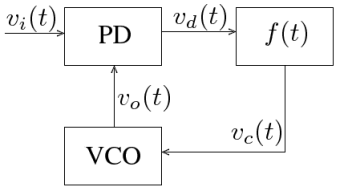

Figure 1: PLL block diagram.

$$v_i(t) = \mathrm{v}_i \sin(\omega_M t + \theta_i(t)) \tag{1}$$
$$v_o(t) = \mathrm{v}_o \cos(\omega_M t + \theta_o(t)) \tag{2}$$

$$\frac{d}{dt}\theta_o(t) = k_o v_c(t), \tag{3}$$

Considering a multiplier type PD in Fig. 1 with the input and output signals in Eqs. 1 and 2, and that the VCO control signal 3, the mathematical model of a PLL is given by

$$L\left[\theta_o(t)\right] + GQ\left[\sin\left(\theta_o(t) - \theta_i(t)\right)\right] = GQ\left[\sin\left(2\omega_M t + \theta_i(t) + \theta_o(t)\right)\right], \tag{4}$$

where $G = \frac{1}{2}k_m k_o \mathrm{v}_i \mathrm{v}_o$ is the loop gain and the operators L and Q depend on the LPF transfer function. In addition, the nonlinear differential equation in 4 is of order $p+1$ given that the LPF order is p [1, 5].

Network Synchronization

The clock signal distribution in synchronous networks requires that the frequencies and phases are common to all network elements. Many methods have been proposed for synchronization of spatially distributed clocks, such as mutually connected networks or master-slave networks. In mutually connected networks, see Fig. 2(a), all the PLLs (clocks) contribute to the phase and frequency scales. On the other hand, in Master-Slave networks, see Fig. 2(b), the master clock dictates

the phase and frequency scales. Due to simplicity and low cost, the Master-Slave strategy is frequently used for clock signal distribution. In OWMS (One-Way Master-Slave) networks, the master node has its own time base and is independent the others while slave nodes have their time base depends on a single node, may come from the master node or from another slave node. The master clock has its own and independent time basis. Slave clocks have their basis depending on a unique node, the master or another slave. Besides, these networks are classified according to the topology in chain and star.

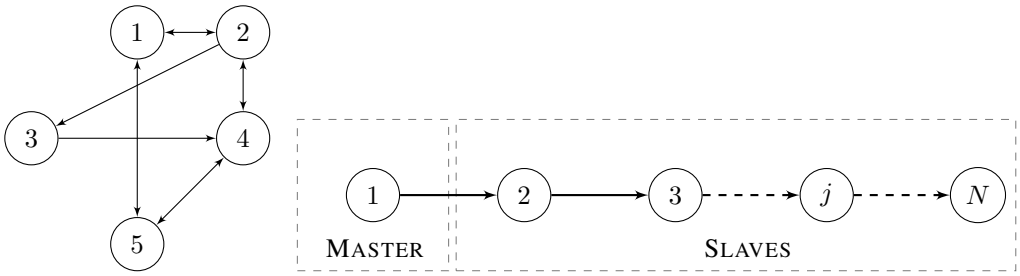

(a) PLL network. (b) OWMS network.

Figure 2: Clock signal distribution networks.

Considering an OWMS network with N nodes, as shown in Fig. 2(b), and the PLL model of the previous section, the OWMS network model of the slave nodes is given by

$$L^{(j)}\left[\theta_o^{(j)}(t)\right] + G^{(j)}Q^{(j)}\left[\sin\left(\theta_o^{(j)}(t) - \theta_o^{(j-1)}(t)\right)\right] = G^{(j)}Q^{(j)}\left[\sin\left(2\omega_M t + \theta_o^{(j-1)}(t) + \theta_o^{(j)}(t)\right)\right] \tag{5}$$

for $j = 2, 3, \cdots, N$. As it can be noticed, the master clock's phase and frequency scales do not instantaneously spread throughout the network given that it depends on the dynamics of each slave node. In addition, noise, jitter and wander impair the quality of the clock signal distribution. The nonlinear and interaction of the slave nodes generate complex dynamics, and in this case numerical simulation is an important tool to study the qualitative behavior of the synchronization.

Parallel Programming

With the development of computational resources and multicore processors, it is possible to buid faster computational systems with higher precision and stability using parallel programming techniques [7]. A program is considered sequential programming when it is viewed as a series of sequential instructions that must be executed on a single processor. A program is considered parallel programming when it is seen as a set of parts that can be solved concurrently. Each part also consists of a series of sequential instructions, which together can be executed simultaneously on several cores of the multicore processor, as depicted in Fig 3. Traditionally, parallel programming was motivated by the resolution of fundamental engineering problems of great scientific and economic relevance, called Grand Challenge Problems (GCPs). Typically, GCPs simulate phenomena that cannot be measured by experimentation, such as: climatic, physical, chemical and biological phenomena and in telecommunications, mainly in the propagation of signals. Two main reasons for using parallel programming are: to reduce the time needed to solve a problem and to solve more complex and larger issues [7].

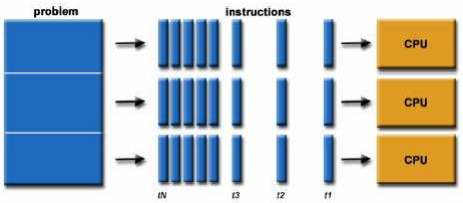

Figure 3: Instructions will be executed simultaneously on multiple processor cores [7].

Today, applications that require the development of faster and faster computers are everywhere. These applications require a lot of computing power or require the processing of large amounts of information. Same idea can be applied for the simulation of synchronization networks. A computer program is considered parallel when it organized as a set of parts that can be solved concurrently, reducing the time needed for complex computational solutions. Each part is also composed of a series of sequential instructions, but as a whole they can be executed simultaneously in several processors or processing cores, as depicted in Fig. 4.

In this paper the parallel programming is used to build and simulate the nodes of OWMS network. The target is developing an efficient simulation strategy, that allows to study the interaction of the nodes running in parallel in a distributed computation system.

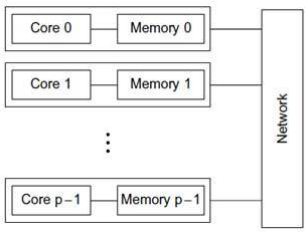

Figure 4: Distributed processing system for a network [7].

Parallel Programming in Matlab

With parallel computing, Matlab can help solve large computing problems in different ways. The software provides an interactive programming environment where it can vectorize tasks and use parallel computing support through distributed matrices, allowing you to perform multiple calculations simultaneously. Big problems can often be broken down into smaller ones, which are then solved at the same time (in sync) The main reasons to consider parallel computing in Matlab are: optimization of simulation time when distributing tasks with simultaneous execution, solving big data problems and simulating signal propagation in telecommunications and electronics [8].
Workers in Matlab are the cores of the multicore processor and are thought of as computational engines that automatically execute smaller tasks (threads) in the background when triggered by parallelism commands. Here, the PARFOR loop was used, which executes the sequence of instructions of the loop in parallel, analogously synchronous counter.

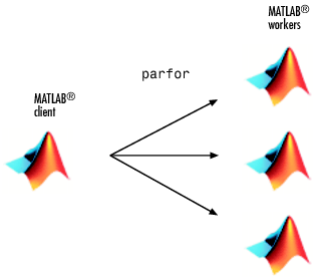

Figure 5: Interactively run a loop in parallel using PARFOR [9].

Each loop execution is an iteration where the workers perform in any order and independently of each other. If the number of workers is equal to the number of iterations of the loop, each one performs one iteration, as depicted in Fig. 5. If there are more iterations than cores, some will run more than one, receiving multiple threads at once to reduce processing time. When using parallelism commands, consideration must be given to the parallel overhead, which includes the parameterization of the processor cores, the time required for communication, coordination and data transfer (sending and receiving data) [9].

Steps to simulate a OWMS chain network

To design the mathematical simulation some steps were followed:
1 - Simulation parameters: number of PLLs, start and end time, integration math step, time vector and number of integration points;
2 - PLL parameters: input and output sinusoids amplitudes, phase detector and VCO gains, free-running angular frequency and excitation signal input;
3 - Declaration of 2 auxiliary variables to handle parallel processing. Its necessary cause the processing output of each core is given by a matrix that indexes each line corresponds to a processor core;
4 – Designing the OWMS network: making a selector to identify the condition of PLL1 (Master) and the others PLLs (Slaves), that identify the blocks that should receive feedback signal (previous PLL);
5 – Run the Network in parallel processing (PARFOR Loop);
6 - Receive the calculated values from the simulating, compile results and call the graphics function.

Simulation graphics

The simulation was performed with 4 PLLs OWMS chain network and phase angle step excitation input θ_i(t) = u(t).
Let vi(t): input signal, vo(t): output signal; vd(t): output of detector phase; vc(t): control signal; θ_i(t): reference phase and θ_o(t): ouput phase (or lagged phase).

First PLL node (Master)

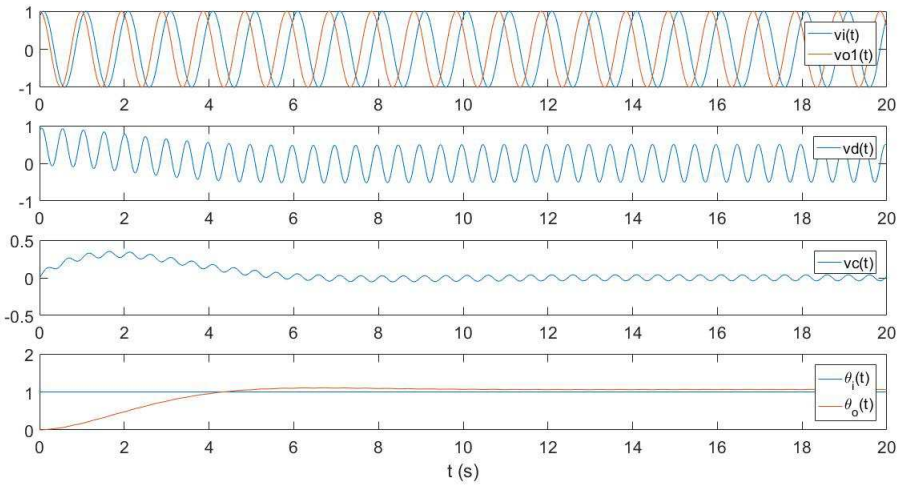

Figure 6: The output signal is lagged 90 degree (π/2 rad) of input signal, according to Eqs. 1 and 2.

Second PLL node (1º Slave)

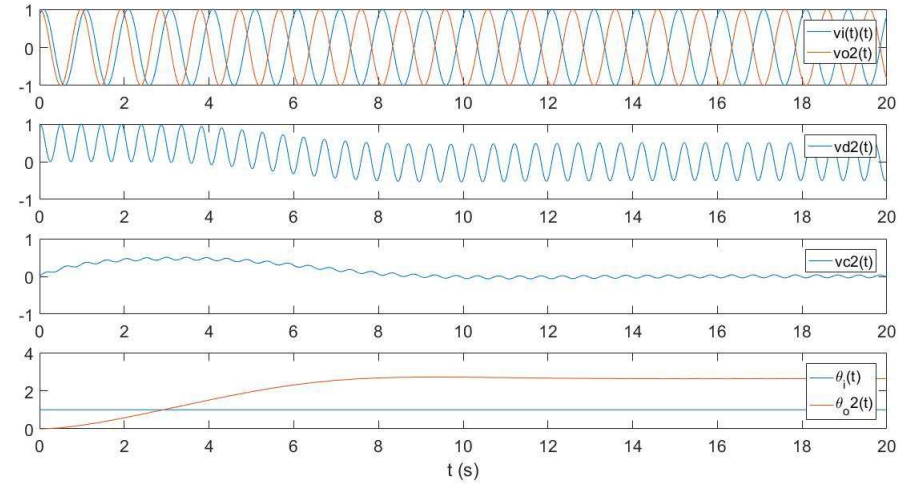

Figure 7: The output signal is lagged 180 degree (π rad) of input signal

Third PLL node (2º Slave)

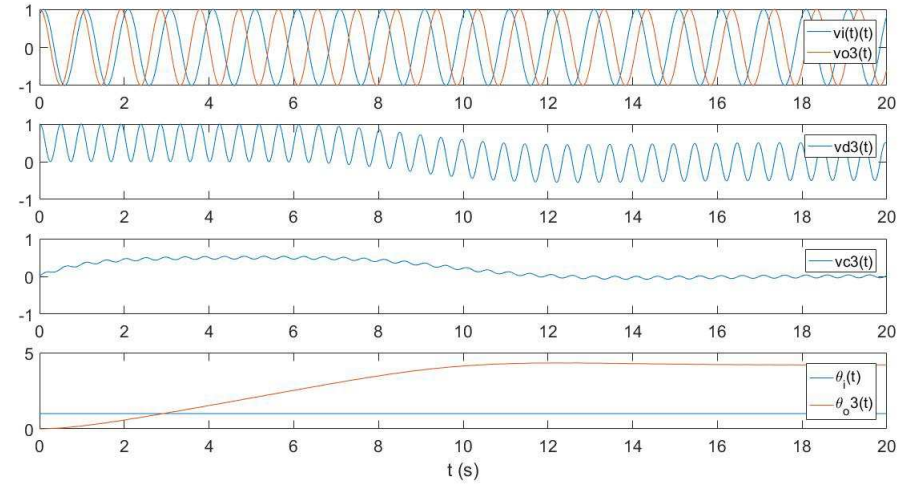

Figure 8: The output signal is lagged 270 degree (3π/2 rad) of input signal

Fourth PLL node (3º Slave)

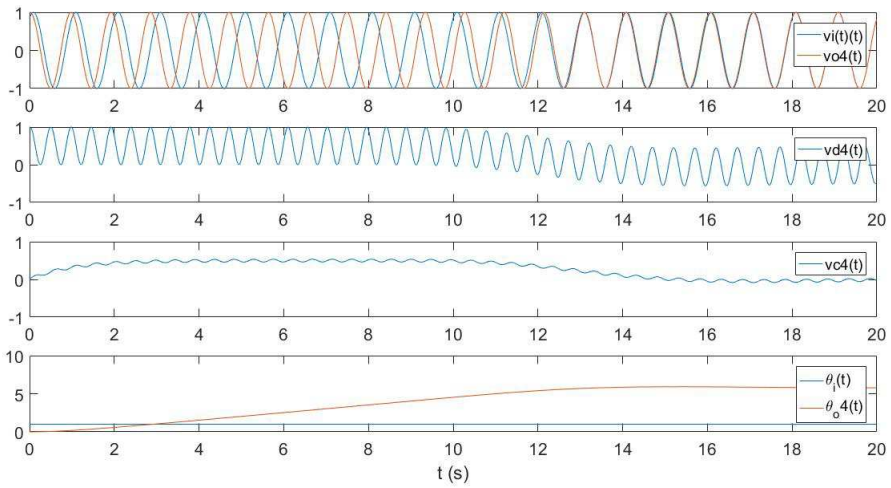

Figure 9: The output signal is lagged 360 degree (2π rad) of input signal (1 delay cicle, in phase).

Comparison between input and output phase

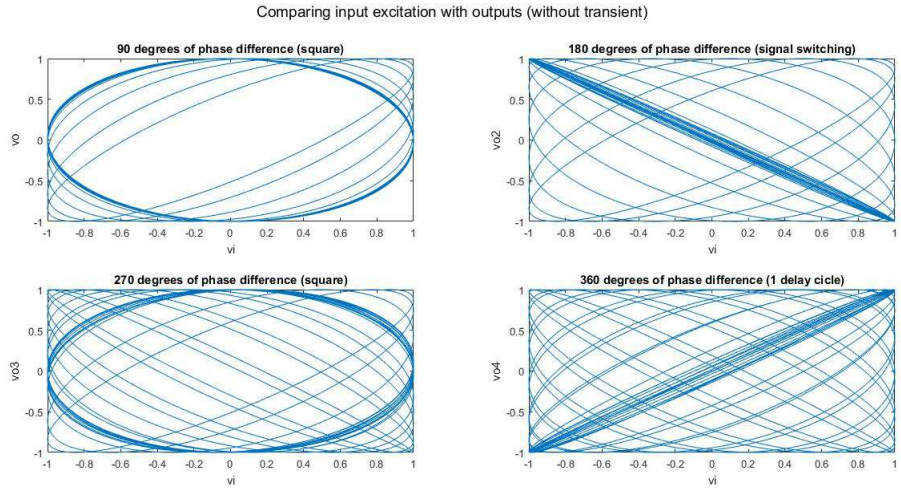

Figure 10: After the transient the trajectory of the system presents a closed orbit around of a point in lissajous.

Conclusions

Dynamic Systems Simulation is a very useful tool for this type of problem, providing conditions of existence and stability for the synchronous state of networks, relating circuit parameters, delays and deviations. An OWMS chain network was modeled with order P + 1 PLLs as slave nodes, taking into account the jitter from the phase detector. Notes that if it is not properly mitigated, network performance can be seriously degraded. It was shown that amplitude on the control signal depends on the node gain and on the filter frequency response. Using several processing cores to build a synchronization network gives flexibility to the simulation, however, parallel interactions of the nonlinear nodes, including jitter and wander dynamics, can lead to complex dynamics and, probably, to a more realistic model of synchronization networks. While parallel computing can be more complex and have a higher upfront cost, the advantage of being able to solve a problem more quickly outweighs any difficulties.

References

[1] W. C. Lindsey, F. Ghazvinian, W. C. Hagmann, and K. Dessouky. Network synchronization. *Proceedings of the IEEE*, 73(10):1445–1467, 1985.

[2] G. C. Lopes, Á. M. Bueno, and J. M. Balthazar. Elastic beam vibration control with phase-locked loop. *Volume 4B: Dynamics, Vibration, and Control*, Nov 2014.

[3] ITU-T. *Timing Characteristics of Primary Clocks - Recomendation G.811 ITU-T*, 1997.

[4] ITU-T. *Timing Requirements of Slave Clocks Suitable for Use as Node Clocks in Synchronization networks - Recomendation G.812 ITU-T*, 1997.

[5] A. M. Bueno, A. A. Ferreira, and J. R. C. Piqueira. Modeling and filtering double-frequency jitter in one-way master slave chain networks. *Circuits and Systems I: Regular Papers, IEEE Transactions on*, 57(12):3104–3111, Dec. 2010.

[6] R. O. Felix, A. M. Bueno, D. P. F. Correa, and J. M. Balthazar. Analysis of double-frequency jitter on time-delayed oscillators networks and perturbations adjustment in clock. *The European Physical Journal Special Topics*, 230(18):3603–3608, 2021.

[7] P. Pacheco. *An Introduction to Parallel Programming*. Elsevier Science, 2011.

[8] A. Zaid. *Introduction to Parallel Computing using Matlab*. Lambert Academic Publishing, 2015.

[9] MATHWORKS: Parallel Computing Fundamentals web site, https://www.mathworks.com/help/parallel-computing/parallel-computing-fundamentals.html

[10] M. Szymczyk, and P. Szymczyk. Matlab and parallel computing. *Image Processing and Communications*, 17(4), 207, 2012.

[11] P. Luszczek. Parallel programming in MATLAB. *The International Journal of High Performance Computing Applications*, 23(3), 277-283, 2009.

[12] J. R. C.Piqueira, S. A. Castillo-Vargas, L. H. A. MONTEIRO. *Two-way master-slave double-chain networks: limitations imposed by linear master drift for second order PLLs as slave nodes.* IEEE Communications Letters, v. 9, n. 9, p. 829-831, 2005.

[13] J. R. C.Piqueira. *Master-Slave Topologies with Phase-Locked Loops.* Wireless Communications and Mobile Computing, v. 2020, 2020.

[14] J. R. C.Piqueira and A. C. B. de Godoi. *Clock signal distribution with second order nodes: Design hints.* ISA transactions, v. 115, p. 124-142, 2021.

Thursday, July 21, 2022

13:30 - 15:30

MS-14 Nonlinear Dynamics for Engineering Design

Rhone 2

Chair: Pedro Ribeiro

13:30 - 13:50
Nonlinear oscillations of a beam-like model of pipe with deformable cross-sections
CASALOTTI Arnaldo, **ZULLI Daniele**[*], LUONGO Angelo
[*]University of L'Aquila (Piazzale Ernesto Pontieri 1, 67100 Loc. Monteluco, L'Aquila Italy)

13:50 - 14:10
Analysis of parametric instabilities of two-oscillator bi-linear model through the resonant order reduction in the vicinity of similar nonlinear normal modes
KUMAR Anish, **STAROSVETSKY Yuli**[*]
[*]Technion - Israel Institute of Technology (Department of Mechanical Engineering, Technion-IIT, Haifa, Israel Israel)

14:10 - 14:30
On the Nonreciprocal Dynamics of Bilinearly Coupled Oscillators
KOGANI Ali, ZOKA Hooman, **YOUSEFZADEH Behrooz**[*]
[*]Concordia University (1455 De Maisonneuve Blvd. W., EV 4.139 Montreal, QC, H3G 1M8 Canada)

14:30 - 14:50
Parametric excitation of an asynchronous Ziegler's column with a piezoelectric element
MAZZILLI Carlos[*], FRANZINI Guilherme
[*]Escola Politécnica, University of São Paulo (Av. Prof. Almeida Prado 83 CEP 05508-900 São Paulo Brazil)

Nonlinear oscillations of a beam-like model of pipe with deformable cross-sections

Arnaldo Casalotti and Daniele Zulli and Angelo Luongo
Department of Civil, Construction-Architectural and Environmental Engineering, University of L'Aquila, Italy

Summary. Nonlinear dynamics of a beam-like model of pipe are considered here. The mechanical model allows change in shape of the cross-sections of the pipe under bending, through a nonlinear and coupled response function for the hyperelastic materials, which is outcome of a homogenization procedure. The coupling between global bending and change in shape of the cross-sections is addressed, and large amplitude vibrations are analyzed under harmonic loading, including different internal resonance conditions.

Introduction

Pipes are widely used structures in civil and industrial applications, and the evaluation of their strength represents a key point for structural engineers to be addressed in the design process. Usually, their thin-walled nature introduces some peculiar features to be considered during structural analysis, like possible occurrence of local effects as well as change in the transversal shape. In this framework, the use of beam-like models for their analysis can, on the one hand, allow one to deal with (moderately) handy equilibrium or dynamic equations; on the other hand, they may not avoid to include specific aspects which are commonly discarded for slender beams, like cross-section change in shape and warping. For instance, it is well known that ovalization of the cross-section, taking places when pipes are bent over, may lead to instability phenomena, with consequent loss of carrying capacity of the whole structure. This phenomenon is explained by the occurrence of a limit point in the bending moment-curvature relationship, as a consequence of the softening nature of such a law, and is known as Brazier effect [1]. This specific effect is analyzed in [2] in case of anisotropic materials. In case of multi-layered structures, a one-dimensional beam-like, which is derived from a corresponding three-dimensional continuum, is proposed in [3], distinguishing the case of open and closed cross-sections and accounting for the Vlasov theory. Theories of multi-layered beams and cross-sectional models are addressed in [4], where use of the Variational Asymptotic Method is made to obtain the equations of motion. In [5], a homogeneous beam-like coarse model is adopted to describe the mechanics of thin-walled beams with possibility of cross-section distortion. In [6], static and free dynamic analysis of a homogeneous beam-like model is performed, after an identification procedure from a companion three-dimensional continuum. The same model is then extended in [7], where further parameters are introduced in order to take into account shear deformations in the multi-layered case, and in [8], where inertial contributions are identified in order to take into account dynamical effects.

In some cases, a soft core realized with structural foam may be introduced to improve the performance of the pipes under bending. For instance, in [9], the contribution of soft elastic cores is analyzed in thin-walled cylindrical structures, letting inspiration from nature where, e.g., plant stems or hedgehog spines have their mechanical efficiency increased by soft cores. In [10] the optimum design of thin-walled cylindrical shells with compliant cores, subjected to uniaxial compression and bending, is theoretically addressed and experimentally proved. In [11], an internally constrained beam model is proposed to deal with foam filled tubes, and equilibrium analysis is then performed in order to forecast and reproduce typical phenomena.

Here, the one-dimensional non-standard beam-like model presented in [7, 8] is used to address nonlinear oscillations under specific internal resonance conditions between global (bending) and local (ovalization) modes, also in presence of a resonant external load which expends work on cross-section flattening.

Equations of motion

A nonlinear beam-like model is used to analyze nonlinear dynamics of an elastic pipe. The beam model is shown in Fig. 1a, where the axis-line, spanned by the abscissa s running from 0 to l, and the generic cross-section are sketched. Besides the classical kinematic descriptors of planar Timoshenko beams, which are the longitudinal and transversal displacements of the axis line (u, v) and the cross-section bending rotation (ϑ), two further s- and time-functions are used, referred to as a_p and a_w and related to the cross-section change in shape, in its plane and out of its plane, respectively. The kinematic equations are posed and the dynamic equilibrium equations of the beam evaluated from the consequential use of the virtual power theorem. The constitutive relations are evaluated by means of a process of homogenization from a corresponding 3D model, shown in Fig. 1b, where the pipe is assumed as realized by longitudinal rods and transversal ribs. For the homogenization purposes, the change in shape of the cross-section is described as in the GBT theory [12], namely the kinematic variables a_p and a_w multiply assumed functions, as shown in Fig. 1c. The equations of motion are written

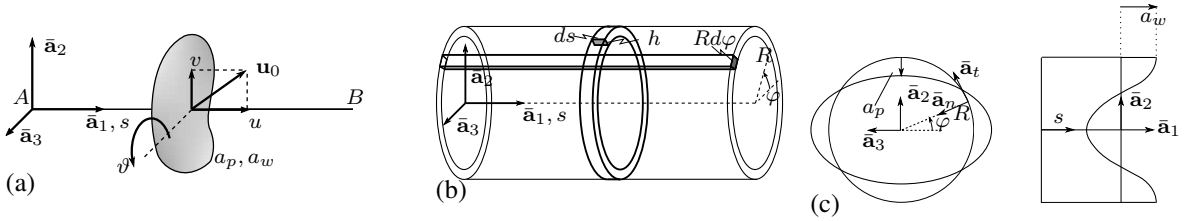

Figure 1: (a) The one-dimensional beam-like model; (b) the three-dimensional model with fibers and ribs; (c) the assumed functions and amplitudes for the change in shape of the cross-section.

below, where the nonlinear terms are related to elastic and inertial contributions:

$$\left[c_1\left(v'-\vartheta-\left(\frac{\vartheta^2}{2}-\vartheta v'\right)\vartheta+\frac{1}{6}(\vartheta^3-3\vartheta^2 v')\right)-\frac{1}{2}c_1 a_w\vartheta'\right]'+p_v-m_1\ddot{v}$$
$$-\left\{\frac{c_1(v'-\vartheta)\vartheta^2}{2}-\vartheta\left[c_1(v'-\vartheta)\vartheta+\int_s^l\left(p_u-m_1\int_0^\xi\left(\frac{\vartheta^2}{2}-\vartheta v'\right)^{\bullet\bullet}d\zeta\right)d\xi\right]\right\}'=0 \tag{1}$$

$$\left[c_2\vartheta'+c_3 a_p\vartheta'+c_4 a_p^2\vartheta'-\frac{1}{2}c_1 a_w(v'-\vartheta)+\frac{1}{2}c_1 a_w^2\vartheta'\right]'+c_1\left(v'-\vartheta-\left(\frac{\vartheta^2}{2}-\vartheta v'\right)\vartheta+\frac{1}{6}(\vartheta^3-3\vartheta^2 v')\right)$$
$$-\frac{1}{2}c_1 a_w\vartheta'+(\vartheta-v')\left(c_1(v'-\vartheta)\vartheta+\int_s^l\left(p_u-m_1\int_0^\xi\left(\frac{\vartheta^2}{2}-\vartheta v'\right)^{\bullet\bullet}d\zeta\right)d\xi\right)+c$$
$$-m_2\ddot{\vartheta}-m_3\dot{a}_p\dot{\vartheta}-m_3 a_p\ddot{\vartheta}-m_4\dot{a}_p a_p\dot{\vartheta}-m_1 a_w\dot{a}_w\dot{\vartheta}-m_5 a_p^2\ddot{\vartheta}-m_6 a_w^2\ddot{\vartheta}=0 \tag{2}$$

$$[c_7 a_w+c_8 a_w^3+\frac{1}{4}c_1 a_p']'-c_5 a_p-c_4 a_p\vartheta'^2-c_6\vartheta'^2+q_p-m_4\ddot{a}_p+\frac{5}{8}m_6 a_p\dot{\vartheta}^2-m_7\dot{\vartheta}^2=0 \tag{3}$$

$$c_{12}a_w''-c_9 a_w-c_7 a_p'-c_{11}a_w^2 a_p'-\frac{1}{2}c_1 a_w\vartheta'^2-c_{10}a_w^3+\frac{1}{2}c_1(v'-\vartheta)\vartheta'+q_w-m_6\ddot{a}_w+m_6 a_w\dot{\vartheta}^2=0 \tag{4}$$

Boundary conditions are combined to Eqs. (1)-(4), prime indicates s-derivative and dot t-derivative, whereas p_v, c, q_p and q_w are external load components. It is worth noticing that the bending problem (variables v, ϑ) and the cross-section problem (variables a_p, a_w) are uncoupled in their linear part, while coupling occurs only due to nonlinear terms. Solutions are obtained both via perturbation methods and pure numerical approach, in case of internal resonance conditions among modes involving the bending and cross-section problems. Discussion on the effect of change in shape of the cross-sections during bending vibrations is provided, highlighting the resulting softening behavior related to reduction of bending stiffness of the pipe due to the cross-section flattening.

Conclusions

Nonlinear dynamics of a thin pipe is analyzed here. A homogeneous beam-like model is used, where specific kinematic functions describe the change in shape of the cross-section. Dynamic interaction between bending of the beam and change in shape of the cross-sections is addressed, leading to a softening behavior of the cantilever and related to the reduction of the bending stiffness as the cross-sections flatten.

References

[1] L. Brazier (1927), On the flexure of thin cylindrical shells and other 'thin' sections, *Proc. Royal Society of London A*, **116** 104–114.

[2] D. Harursampath, D. Hodges (1999), Asymptotic analysis of the non-linear behavior of long anisotropic tubes, *International Journal of Non-linear Mechanics*, **34** 1003–1018.

[3] L. Librescu, O. Song (2006), Thin-walled Composite Beams. Theory and applications, Springer-Verlag.

[4] D. Hodges (2006), Nonlinear Composite Beam Theory, American Institute of Aeronautics and Astronautics.

[5] S. Gabriele, N. Rizzi, V. Varano (2016), A 1D nonlinear TWB model accounting for in plane cross-section deformation, *International Journal of Solids and Structures*, **94-95** 170–178.

[6] A. Luongo, D. Zulli (2014), A non-linear one-dimensional model of cross-deformable tubular beam, *International Journal of Non-Linear Mechanics*, **66** 33–42.

[7] D. Zulli (2019), A one-dimensional beam-like model for double-layered pipes, *International Journal of Non-Linear Mechanics*, **109** 50–62.

[8] A. Casalotti, D. Zulli, A. Luongo (2021), Dynamic response to transverse loading of a single-layered tubular beam via a perturbation approach, *International Journal of Non-Linear Mechanics*, **139** 103822.

[9] M. Dawson, L. Gibson (2007), Optimization of cylindrical shells with compliant cores, *International Journal of Solids and Structures*, **44** (3) 1145–1160.

[10] G. Karam, L. Gibson (1995), Elastic buckling of cylindrical shells with elastic cores-I. Analysis, *International Journal of Solids and Structures*, **32** (8) 1259–1283.

[11] A. Luongo, D. Zulli, I. Scognamiglio (2018), The Brazier effect for elastic pipe beams with foam cores, *Thin-Walled Structures*, **124** 72–80.

[12] R. Gonçalves, M. Ritto-Corrêa, D. Camotim (2010), A large displacement and finite rotation thin-walled beam formulation including cross-section deformation, *Computer Methods in Applied Mechanics and Engineering*, **199** (23-24) 1627–1643.

Analysis of parametric instabilities of two-oscillator bi-linear model through the resonant order reduction in the vicinity of similar nonlinear normal modes

Anish Kumar* and Yuli Starosvetsky†
*Department of Mechanical Engineering, JK Lakshmipat University, Jaipur, Rajsthan, India
†Department of Mechanical Engineering, Technion-Israel Institute of Technology, Haifa, Israel

Summary. Present study is devoted to analysis of fundamental problem of parametric instability of damped-driven bi-linear two-oscillator model, given to the low-amplitude parametric forcing. Assuming the resonant excitation in the vicinity of similar NNMs, we derive the reduced order model. Further, applying the method of isolated resonance we analyze asymptotically the most significant family of sub-harmonic (m:1) resonance regions which reveal their peculiar properties.

Introduction

Response of bi-linear oscillatory systems subject to various types of forcing has become a subject of immense theoretical and experimental research. These models are broadly applied for mathematical modeling of the response of various engineering problems such as mooring towers [1], interlocking structures [2], suspension bridges [3], beams with breathing cracks [4] and many more. Numerous analytical and numerical works have been devoted to the analysis of externally forced, single bi-linear oscillator. Shaw and Holmes [5] were the first to develop the semi-analytical methods for the analysis of stability and bifurcation structure of periodic orbits emerging in the harmonically forced piece-wise linear oscillator (PWLO). In the same year, a thorough computational study of sub-harmonic orbits, bifurcations of periodic solutions and chaotic motion of harmonically forced piece-wise linear oscillator has been reported by Thomson et al. [6]. Some initial experimental work by Shaw [8] has shown the superharmonic and sub-harmonic steady state regimes in the experimental setup, mimicking the damped-forced response of piece-wise linear oscillator. We bring here some most fundamental theoretical works which considered the parametric instability phenomena arising in the various damped-driven piece-wise linear setups [9, 10, 11].

Model

In the present study we consider the damped-driven system of two coupled identical, bi-linear oscillators which assume the parametric excitation on the first oscillator. The non-dimensional equations of motion of the system under consideration read,

$$\xi_1^{''} + \epsilon\lambda\xi_1^{'} + [1 + \alpha\mathcal{H}(-\xi_1)]\,\xi_1 + \beta\,(\xi_1 - \xi_2) + \epsilon P\cos(\Omega t)\xi_1 = 0\ , \tag{1a}$$

$$\xi_2^{''} + \epsilon\lambda\xi_1^{'} + [1 + \alpha\mathcal{H}(\xi_2)]\,\xi_2 + \beta\,(\xi_2 - \xi_1) = 0\ , \tag{1b}$$

. Here ϵ is a formal, small non-dimensional system parameter. Where λ, P, α, β stand for the damping, forcing, bi-linear nonlinearity and coupling parameters. The formal small system parameter $0 < \epsilon << 1$ is introduced for scaling the magnitude of damping and forcing terms. This system can model the low amplitude vibrations of two linearly coupled, damped pendulums where one out of the two pendulums, performs the prescribed vertical oscillatory motion on its point of suspension.

It can be easily seen that OP NNN belongs to the special family of NNMs of similar type. Further setting the OP NNM to be the resonating mode, we define the two auxiliary coordinates $\xi_1 - \xi_2 = \eta$ and $\xi_1 + \xi_2 = \zeta$. It is reasonable to assume that in the resonant motion of the system being parametrically excited in the resonant region of OP NNM, the newly defined η variable, dominates over ζ. Applying some rather simple algebraic manipulation and using the same resonant assumption, one readily arrives at the following, reduced order model (ROM) i.e. the damped-driven, bi-linear oscillator which recovers the entire resonance structure of resonating OP NNM.

$$\eta^{''} + \epsilon\lambda\eta^{'} + (1 + \alpha\mathcal{H}(-\eta) + 2\beta)\,\eta + \epsilon\frac{P}{2}\cos((m\Omega_N + \epsilon\sigma)t)\eta = 0\ . \tag{2}$$

Results

We rewrite Eq. (2) in the phase space form, as follows:

$$q^{'} = p, \quad p^{'} = -\epsilon\lambda p - (1 + \alpha\mathcal{H}(-q) + 2\beta)\,q + \epsilon\frac{P}{2}\cos((m\Omega_N + \epsilon\sigma)t)q\ , \tag{3}$$

It is worthwhile noting that the asymptotic analysis applied in the present work is valid up to $\mathcal{O}(\epsilon)$ order. Therefore, the terms of the higher asymptotic order are omitted in the following part of analysis. To derive the asymptotic approximation for transition curves corresponding to the special family of (m:1) resonant tongues, we introduce the action-angle variables [11, 12]

$$I(E) = \frac{1}{2\pi}\oint p(q,E)dq\ , \quad \text{and} \quad \Theta = \frac{\partial}{\partial I}\int_0^q p(q,I)dq\ . \tag{4}$$

and using the method of isolated resonance derive the averaged flow in the neighborhood of (m:1) resonance tongues.Further analysis of the averaged flow, reveals the closed form asymptotic approximations for the transition curves for different resonance conditions (see e.g. [12]). Please note that $\epsilon\sigma$ stands for the small detuning parameter, while the excitation frequency in the vicinity of m:1 resonant neighborhood is taken as $\Omega = m\Omega + \epsilon\sigma$. Here Ω_N is a natural frequency of the out-of-phase NNM. In Figure. 1 we present the stability charts for the three resonant cases. It can be readily seen that the analytical approximation of transition curves (shown by black solid lines) are in very good agreement with the results of numerical simulations of the full model (Eqs. (1a) and (1b)). In Figure.2 (left panel) we present the evolution of transition curve w.r.t damping. In the limiting case of zero damping transition curves become straight lines whose slopes change w.r.t the system parameter α. As is shown in 2 (right panel) the width of the instability regions, varies w.r.t the change in the parameter of non-linearity, such that the well-known, fundamental, 2:1 parametric resonance tongue can become narrower than the 1:1 tongue.

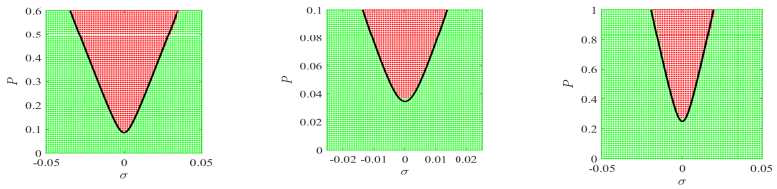

(a) (b) (c)

Figure 1: Stability chart for resonance conditions (a) $1:1$, (b) $2:1$, and (c) $3:1$. Here green and red colours represent stable and unstable regions, respectively obtained numerically from exact model in Eqs. (1a) and (1b) and black solid lines represent instability boundaries obtained using A-A method. Parameters are $\alpha = 2$, $\beta = 0.5$, $\lambda = 0.005$ and $\epsilon = 0.1$.

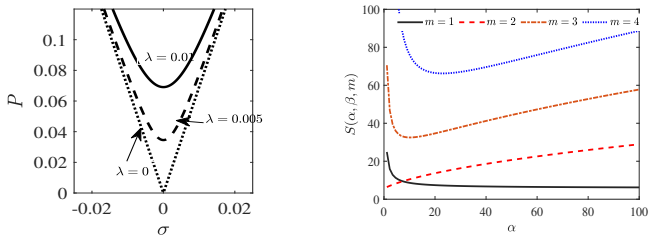

(a) (b)

Figure 2: (a) Variations of the instability tongues with damping coefficient λ for resonance condition $2:1$. (b) Variations of the slope corresponding to each resonance condition with α.

Concluding Remarks

Present study has concerned the resonant parametric excitation of the symmetric system of two coupled bi-linear oscillators. To derive the relatively simple analytical approximation to transition curves, we derive the reduced order model which mimics the response of resonantly excited two-oscillator model in the vicinity of out-of-phase NNM. Boundaries of the transition regions emerging in the original, parametrically forced system are approximated asymptotically. Transition curves emerging from the analysis of effective bi-linear, parametric oscillator are in very good agreement with numerical results of the original system. In this talk, we will also present the alternative analytical treatment for the case of resonant system reduction in the vicinity of NNMs of the general type. This part of the talk is currently a work in progress.

References

[1] M. Gerber, L. Engelbrecht (1993) Mooring tower *Ocean Eng.* **20 (2)**:113–133

[2] Dyskin A. V., Pasternak E., Estrin Y. (2012) Mortar;ess structures. *Front. Strut. Civ. Eng.* **6(2)**:188-197.

[3] Lazer A. C., McKenna P. J. (1990) Suspension bridges.*SIAM Rev.* **32(4)**:537-578.

[4] Chati M., Rand R., Mukharjee S. (1997) Cracked beam. *J. Sound Vib.*, **207(2)**:249-270.

[5] Shaw S. W., Holmes P. J. (1983) A periodically forced piecewise linear oscillator. *J. Sound Vib.*, **121(1)**:117-126.

[6] Thompson T. M. J., Bokaian A. R., (1983) Bilinear Oscillator. *IMA J. Appl. Math.*, **31**:207-234.

[7] Natsiavas S. (1990) Oscillator with bilinear damping and spring. *Int. J. Non-linear Mech.*, **25(5)**:535-554.

[8] Shaw S. W. (1985) Beam with one sided amplitude constraint. *J. Sound Vib.*, **99(2)**:199-212.

[9] Babitsky V. I., Krupenin V. I. (2001) Vibration of Strongly Nonlinear Discontinuous Systems. *first ed. Springer*.

[10] Marathe A, Chatterjee A. (12006) Asymmetric Mathieu equation. *Proc.R. Soc. A* , **462**:1643-1659.

[11] Jayaprakash K. R., Starovetsky Y. (2020) Bi-linear Mathieu equation. *Nonlinear Dynam.*, **101**:2615-2627.

[12] Kumar A., Starovetsky Y. (2021) Bi-linear coupled oscillators. *J. Sound Vib.*., **515**:116435.

On the Nonreciprocal Dynamics of Bilinearly Coupled Oscillators

Ali Kogani, Hooman Zoka and Behrooz Yousefzadeh
Department of Mechanical, Industrial and Aerospace Engineering,
Concordia University, Montreal, QC, Canada

Summary. This work explores nonreciprocity in the dynamic response of oscillators that are coupled by a bilinear elastic force and subject to external harmonic drive. The conditions for breaking reciprocity and the influence of different parameters on the steady-state nonreciprocal dynamics of the system are described. The manifestation of nonreciprocity in the time profile of the response is discussed in terms of the amplitudes of oscillation, phase differences and time-independent shifts. While the main focus is on the frequency-preserving response regime, the nonreciprocal response beyond the weakly nonlinear regime is also addressed.

Introduction

There has been an incredible interest in the recent years to explore scenarios in which reciprocity theorems do not hold [1]. A main motivation is that deviation from reciprocity can lead to asymmetric propagation of elastic waves for opposite directions. Reciprocity theorems generally apply to linear, time-invariant systems [2]. The breakdown of reciprocity may take place, for example, in systems with time-dependent (active) [3] or nonlinear (passive) [4] material properties.
The focus of this work is on nonreciprocity caused by nonlinearity. In particular, the nonreciprocal dynamics that results from bilinear elasticity is studied. A bilinear spring exhibits two different values of stiffness with a transition occurring at a critical strain. Bilinear stiffness is used, among other problems, for modeling systems involving contact and friction. A system with bilinear elasticity, due to its non-smooth character, can exhibit complex nonlinear dynamic behavior [5].
This work studies the conditions that lead to the emergence of nonreciprocal dynamics in bilinearly coupled oscillators subject to external harmonic excitation.

Bilinearly Coupled Oscillators

The following normalized equations govern the dynamics of the system considered here

$$\begin{cases} \ddot{x}_1 + c\dot{x}_1 + x_1 + k_c(x_1 - x_2) = F_1\cos(\Omega t) \\ (1+\mu)\ddot{x}_2 + c\dot{x}_2 + x_2 + k_c(x_2 - x_1) = F_2\cos(\Omega t) \end{cases}, \quad k_c = \begin{cases} 1+b\,, & x_1 - x_2 > d \\ 1\,, & x_1 - x_2 < d \end{cases} \tag{1}$$

where d is the offset above which bilinearity is triggered. The steady state dynamic response is computed as the periodic orbits of Eq. (1) using the numerical continuation software package AUTO [6]. The bilinear stiffness is regularized using a hyperbolic tangent function to maintain smoothness. A very large coefficient is used for regularization to ensure the results are representative of the bilinear system.
To investigate reciprocity, two configurations need to be considered: (i) *forward*, where $F_1 = P$, $F_2 = 0$ and the steady response of x_2 is monitored; (ii) *backward*, where $F_1 = 0$, $F_2 = P$ and the steady response of x_1 is monitored. A reciprocal response is characterized by $x_2^f = x_1^b$, where the superscripts f and b denote the response in the forward and backward configurations, respectively. To better analyze the results, the steady time-periodic response of each oscillator is decomposed into a constant (time-independent) and oscillating component: $x_i(t) = C_i + y_i(t)$, where $C_i = (1/T)\int_0^T x_i(t)dt$ with T denoting the period of oscillations. Furthermore, the amplitude of oscillations is defined as A_i, where $A_i^2 = (2/T)\int_0^T y_i^2(t)dt$. A difference norm M is used as a quantitative measure of nonreciprocity: $M = (1/T)\int_0^T (x_2^f - x_1^b)^2 dt$.

Nonreciprocal Dynamics

Fig. 1 shows the steady response of the system for $\mu = 1$ and $b = 1$. A damping coefficient of $c = 0.008$ is chosen. A non-zero value of $d = 0.1$ is chosen for the offset; accordingly, the response of the system is linear for very small values of the driving amplitude. The driving amplitude $P = 0.0015$ is just high enough to trigger the transition into bilinearity (i.e., $x_1 - x_2 > d$) for one of the configurations. Panel (a) shows the normalized amplitude of oscillations $\log_{10}(A_i/P)$ as a function of Ω for the forward and backward configurations. As expected, the first appearance of nonlinear behavior occurs near the out-of-phase mode because $(x_1 - x_2)$ has a larger value there. The inspection of A_i near this resonance in panel (b) shows that while the system is behaving linearly in the backward configuration, the response of the forward configuration has clearly entered the nonlinear regime. The initial effect of bilinearity is to increase the frequency of the second mode (because $b > 0$). Panel (c) shows the difference norm M for the same frequency range as in panel (b). The time profile of three points are shown in panels (d)-(f), with the corresponding points marked by a triangle, square and circle in panels (b) and (c). Panel (d) corresponds to the peak oscillation amplitude of the backward configuration. Panel (e) corresponds to equal oscillation amplitudes for the forward and backward configuration. Note, however, that it corresponds to a large phase difference between the two configurations, which is responsible for the large value of M; see [7] for a detailed discussion. Panel (f) corresponds to the peak oscillation amplitude of the forward configuration. The backward configuration is off-resonance at this point, explaining the large difference between the amplitudes.

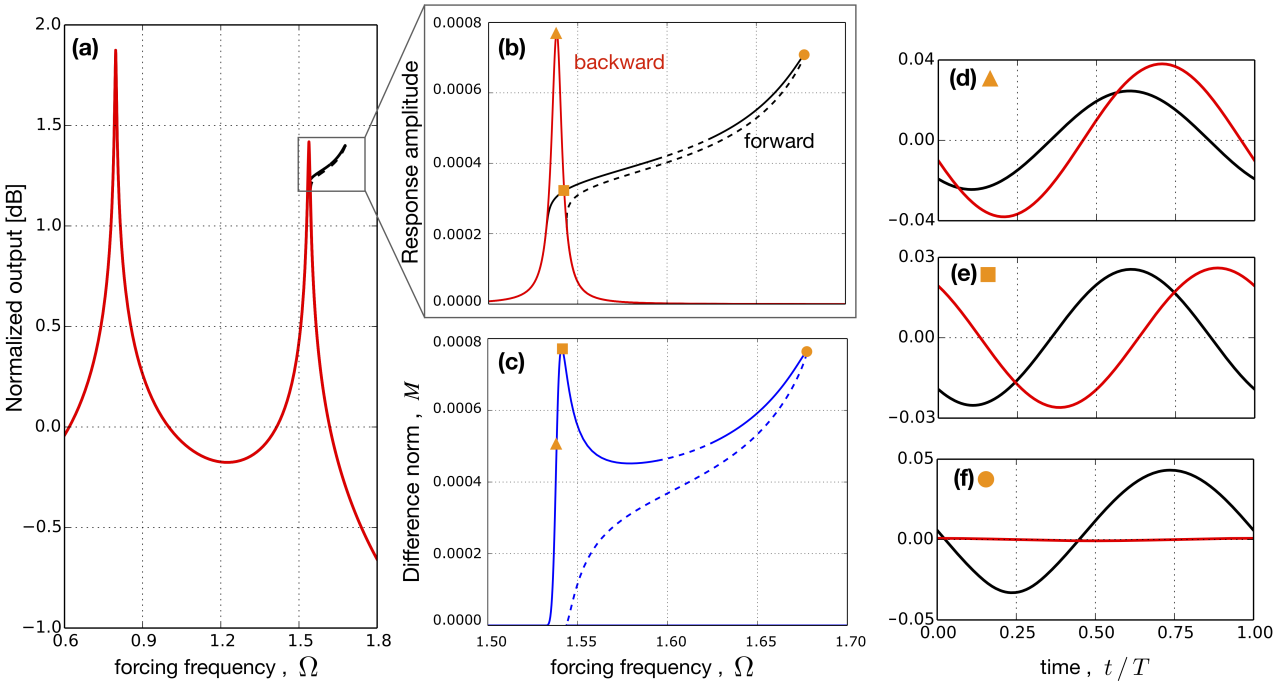

Figure 1: The steady-state dynamic response of the system for $\mu = 1$ and $b = 1$.

The bilinear nature of the coupling force causes nonreciprocity in the system, manifested by a large difference in the amplitude of oscillations (panel (f)), as well as a significant phase difference between the backward and forward configurations (panel (e)). The bilinear response may also exhibit a time-independent component (a DC shift). In particular, the shift in the response is different for the forward and backward configurations, contributing to the nonreciprocity of the response. This shift can be seen in panel (f) for the forward configuration. In the weakly nonlinear regime, the DC shift in the response is less significant than the shift in the resonance frequencies (i.e., it appears in a higher order of correction).
It is important to note the significant influence of b and μ on nonreciprocity. b controls the degree of nonlinearity and its type (softening or hardening). In the limit of very large b, the coupling force is effectively modeling an impact problem [5]. Having a non-zero value for μ is essential for violating reciprocity because it is the parameter than breaks the symmetry; nonlinearity and asymmetry are both needed for breaking reciprocity in a passive dynamical system. The values used here for b and μ (as well as for c and d) can be realized in experiments.
At larger driving amplitudes (equivalently, at higher values of b or lower values of d), the backward configuration also exhibits nonlinear behavior in the out-of-phase mode. Beyond the weakly nonlinear response, we also observe some of the typical bifurcations in a bilinear system such as period doubling and subharmonic resonances. A period-doubling bifurcation is already detectable in Fig. 1(b), though it is not further explored here. As expected, these nonlinear behaviors are more readily accessible through the out-of-phase mode of the system.

Conclusions

Bilinearly coupled oscillators can exhibit steady nonreciprocal dynamics when subject to external harmonic drive. The nonreciprocal regime can be reached at relatively small values of driving amplitude, degree of bilinearity and asymmetry, making the mechanical system a good candidate for experiments. The nonreciprocal behavior manifests in the time domain as different amplitudes of oscillation, phases and time-independent shifts. Typical instabilities such as period-doubling bifurcations may be observed and further exploited for nonreciprocity. This work highlights the potential of bilinear elasticity in realizing passive nonreciprocity in mechanical systems.

References

[1] Nassar H., Yousefzadeh B., Fleury R., Ruzzene M., Alù A., Daraio C., Norris A.N., Huang G., Haberman M.R. (2020) Nonreciprocity in acoustic and elastic materials. *Nat. Rev. Mater.* **5**: 667-685.

[2] Achenbach J.D. (2006) Reciprocity and related topics in elastodynamics. *Appl. Mech. Rev.* **59**: 13-32.

[3] Lurie K.A. (2007) An introduction to the mathematical theory of dynamic materials. Springer. New York.

[4] Blanchard A., Sapsis T.P., Vakakis A.F. (2018) Non-reciprocity in nonlinear elastodynamics. *J. Sound Vib.* **412**: 326-335.

[5] di Bernardo M., Budd C., Champneys A.R., Kowalczyk P. (2008) Piecewise-smooth dynamical systems: Theory and applications. Springer. London.

[6] Doedel E.J., Oldeman B.E. (2012) AUTO-07P: Continuation and bifurcation software for ordinary differential equations. Concordia Univ. Montreal.

[7] Yousefzadeh B. (2022) Computation of nonreciprocal dynamics in nonlinear materials *J. Comp. Dyn.* **9**.

Parametric excitation of an asynchronous Ziegler's column with a piezoelectric element

Carlos Mazzilli and Guilherme Franzini
Department of Structural and Geotechnical Engineering, Escola Politécnica, University of São Paulo, São Paulo, Brazil

Summary. The paper addresses the use of a piezoelectric element for energy-harvesting purposes in a 2 DOF Ziegler's column subjected to a harmonically varying follower force. Hence, two different destabilizing mechanisms are potentially present in this problem, namely the follower-force-driven flutter and the parametric instability. The system parameters are chosen in such a way that the column is tuned into the principal parametric resonance with respect to an asynchronous vibration mode. The initial voltage applied to the piezoelectric element is a key variable which either favours vibration control – as a result of the structural stiffening associated to the inverse effect, inherent to piezoelectric coupling – or energy harvesting. For brevity reasons, only small initial voltages will be considered herewith, focusing the case of enhanced vibrations to a stable post-critical steady state, which is suitable for energy harvesting. Due to the similarity of this problem to that of pipes carrying fluids or gases in harmonic flows, it is expected that similar behaviour could also appear there.

Introduction

The 2 DOF model of a column with a follower force P, forming an angle θ_2 with the vertical direction, as represented in Fig. 1, is the classic model studied in [1,2]. In this paper, it is further assumed that the follower force varies harmonically with time, so that $P(t) = P_0 + P_1 \cos \Omega t$. When $L_1 = L_2 = L$, $M_1 = 2M_2 = 2M$, $K_1 = K_2 = K$, $C_1 = C_2 = 0$ and also $\bar{p} = \frac{P_0 L}{K} = 2$, the system displays a stable asynchronous (in the sense it is *localised*) vibration mode $\mathbf{u}_1 = \{\theta_1 \quad \theta_2\}^T = \{0 \quad 1\}^T$ with natural frequency $\omega_{10} = \frac{1}{L}\sqrt{\frac{K}{M}}$. By the way, this value of $\bar{p} = 2$ is *slightly smaller* than the critical load $\bar{p}_{cr0} = \frac{7-2\sqrt{2}}{2}$ that causes instability of the trivial solution for the undamped model, as seen in [3]. At $\bar{p}_{cr0}$ a supercritical Hopf bifurcation takes place and a stable periodic attractor appears. It is worth noting that there is also a subcritical Hopf bifurcation at $\bar{p}_{cr0}$, indicating that if $\bar{p} < \bar{p}_{cr0}$, which happens to be the case, the basin of attraction of the stable trivial solution is very small due to the proximity to the critical load. It is further known that even an infinitesimal damping $C_1 = C_2 = \mu$ is capable of finitely reducing the critical load of the model to $\bar{p}_{cr\mu} = \frac{41}{28}$, as seen in [3]. Hence, the load $\bar{p} = 2$ that tunes the system into a *stable* asynchronous mode, which is *smaller* than the critical load for the undamped system, becomes *larger* than the critical one for the damped one.

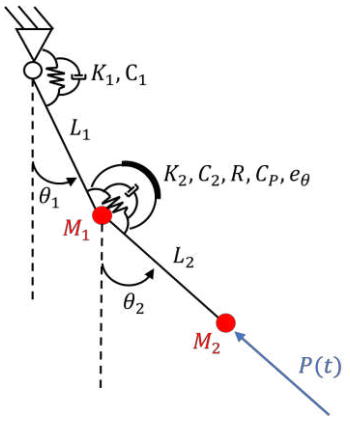

Figure 1: 2 DOF Ziegler column with follower force

A single piezoelectric element is inserted in parallel with spring K_2, with the following constitutive properties: electro-mechanical coupling term e_θ and capacitance C_P. Two dimensionless quantities associated with the piezoelectric parameters are introduced, namely $\sigma_1 = \frac{e_\theta^2}{C_P M L^2 \omega^2}$ and $\sigma_2 = \frac{1}{RC_P\omega}$, $\omega = \frac{1}{L}\sqrt{\frac{K}{M}}$ being the chosen reference frequency. The energy harvesting circuit is composed of an electrical resistance R. It is worth mentioning that if a new modal analysis is performed for the enlarged 3 DOF electro-mechanical model, in which the piezoelectric element voltage v is added as the third generalized coordinate, the previously found structural vibration mode $\mathbf{u}_1$ will not be practically affected, i.e. it will be *nearly-asynchronous*, provided σ_1 and σ_2 are *small*, which happens to be the case for $\sigma_1 = \sigma_2 = 0.01$. Yet, a slightly different natural frequency appears for the nearly-asynchronous mode, namely $\omega_1 = 1.02\frac{1}{L}\sqrt{\frac{K}{M}}$. Further, a free-body mode $\mathbf{u}_0 = \{\theta_1 \quad \theta_2 \quad v\}^T = \{-0.817 \quad -0.408 \quad 0.108\}^T$ will also appear, coinciding with the quasi-static deformed configuration due to an applied initial voltage to the piezoelectric element, known as the *inverse effect*.

Parametric excitation

In addition to the follower force scenario, already explained, parametric excitation is applied to the column by means of a harmonic variation of load $P(t) = P_0 + P_1 \cos \Omega t$, with $\Delta p = \frac{P_1 L}{K} = 0.20$ about $\bar{p} = \frac{P_0 L}{K} = 2$. The forcing frequency Ω is assumed to be twice the natural frequency $\omega_1 = 1.02 \frac{1}{L}\sqrt{\frac{K}{M}}$ of the nearly-asynchronous mode, so that the system is subjected to the *principal parametric instability* of the trivial configuration. Nevertheless, due to the kinematic and piezoelectric nonlinearities, it may be stabilised in a post-critical fluttering pattern. The piezoelectric element plays the role of an energy harvester. Fig. 2 illustrates the time histories for $\theta_1(t)$, $\theta_2(t)$ and $v(t)$ for a mechanically undamped ($\zeta = \frac{\mu}{2\sqrt{ML^2K}} = 0$) or a damped system ($\zeta = \frac{\mu}{2\sqrt{ML^2K}} = 0.01$). The assumed initial conditions were $\theta_1(0) = 0$, $\theta_2(0) = 0.01$ and $v(0) = 0$.

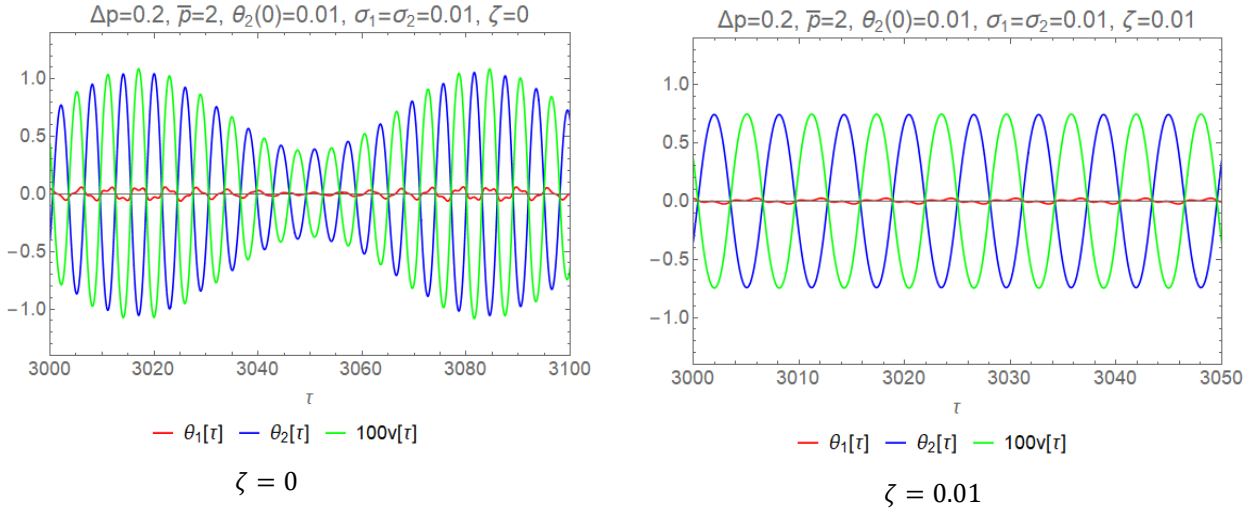

Figure 2: time histories for $\theta_1(t)$, $\theta_2(t)$ and $v(t)$

Although the follower-force-driven pattern alone *is not* characterised by localised vibrations, the parametric-instability pattern *does favour* localisation. It is seen that, for sufficiently large values of Δp, which happens to be the case here, the parametric instability pattern *prevails*, as seen in Fig.2, since $\theta_1(t) \approx 0$. The undamped case leads to a *post-critical amplitude-modulated nearly-asynchronous response*, whereas the damped one indicates a well-defined *stable periodic steady state nearly-asynchronous response*, in which $\theta_2(t)$ and $v(t)$ are in *anti-phase*.

Conclusions and final remarks

The two mechanical DOF Ziegler column model has been addressed in a scenario characterised by the coupling of four phenomena, namely: follower-force-driven flutter, parametric instability, modal asynchronicity and energy harvesting using a piezoelectric element. The paper is still the result of on-going research. The high system-parameter-space dimension didn't allow yet for an exhaustive study of all possible response regimes, such as those related to vibration control and the influence of the inverse-effect phenomenon provided by the piezoelectric constitutive properties. Future work will also look at the three mechanical DOF model of the Ziegler's column and the continuous model of the Beck's column. As already mentioned, the problem of pipes carrying fluids or gases in harmonic flows, due to common characteristics with the model studied herewith is of the author's interest.

Acknowledgement

The first author acknowledges the support of CNPq (Brazilian National Council for Scientific Development) under grant 301050/2018-0.

References

[1] Ziegler H. (1952) Die Stabilitätskriterien del Elastomechanik, Ing.-Arch. 20, 49-56.
[2] Hagedorn P. (1970) On the destabilizing effect of non-linear damping in non-conservative systems with follower forces. Int. J. Non-Lin. Mech. 5(2), 341-358.
[3] Mazzilli C.E.N. (1988) Nonlinear dynamics and stability: a formulation for systems subjected to support excitation and/or non-conservative loadings. Habilitation Thesis (in Portuguese), Escola Politécnica, University of São Paulo.

Thursday, July 21, 2022

13:30 - 15:30

MS-09 Nonlinear Dynamics in Engineering Systems

Auditorium Lumiere

Chair: Francesco Pellicano - Giovani Iarricio

13:30 - 13:50

A machine learning perspective on frictional contacts and self-excited vibrations.

THEVENOT Mael*, STENDER Merten, BRUNEL Jean-François, GEIER Charlotte, DUFRÉNOY Philippe, HOFFMANN Norbert

*Univ. Lille, CNRS, Centrale Lille, UMR 9013 - LaMcube - Laboratoire de Mécanique Multiphysique Multiéchelle, F-59000, Lille, France (Bâtiment ESPRIT, avenue Paul Langevin 59650 Villeneuve-d'Ascq France)

13:50 - 14:10

[visio] Free vibration analysis of functionally graded plates with crack or slit by the R-functions method

SHMATKO Tetyana, AWREJCEWICZ Jan, **KURPA Lidiya***, SHMATKO Aleksandr

*National Technical University "Kharkiv Polytechnic Institute" (Kyrpychov Str., 2, Kharkiv, Ukraine, 61002 Ukraine)

14:10 - 14:30

Methods for decreasing order and dimension in mechanics of solids

KRYSKO-JR. Vadim*, AWREJCEWICZ Jan

*Łódź University of Technology (116 Żeromskiego Street90-924 Lodz Poland)

14:30 - 14:50

[visio] Nonlinear vibrations of sandwich shells with additive manufactured flexible honeycomb core interacting with supersonic gas flow

AVRAMOV Konstantin*, USPENSKY B

*Podgorny Institute for Mechanical Engineering (61046, Kharkiv, 2/10 Dm. Pozharskoho St. Ukraine)

14:50 - 15:10

[visio] Self-sustained Vibrations and Dynamic Instability of Functionally Graded Carbon Nanotubes Reinforced Composite Shells

AVRAMOV Konstantin*, CHERNOBRYVKO Marina, USPENSKY Boris

*Podgorny Institute for Mechanical Engineering (61046, Kharkiv, 2/10 Dm. Pozharskoho St. Ukraine)

15:10 - 15:30

[visio] Resonance Steady State and Transient in the Non-Ideal System having the Pendulum Absorber

MIKHLIN Yuri*, LEBEDENKO Yana

*National Technical University Kharkiv Polytechnic Institute (NTU "KhPI" 2, Kyrpychova str., 61002, Kharkiv, Ukraine Ukraine) - Yuri V. Mikhlin (Dept. of Applied Mathematics National Technical University "KhPI"2 Kyrpychev str. Kharkov 61002 Ukraine Ukraine)

A machine learning perspective on frictional contacts and self-excited vibrations.

Maël Thévenot*[1], Merten Stender[2], Jean-François Brunel[1], Charlotte Geier[2], Philippe Dufrénoy[1] and Norbert Hoffmann [2,3]
[1]*Univ. Lille, CNRS, Centrale Lille, UMR 9013 - LaMcube - Laboratoire de Mécanique Multiphysique Multiéchelle, F-59000, Lille, France*
[2]*Hamburg University of Technology, Dynamics Group, Hamburg, Germany*
[3]*Imperial College London, Department of Mechanical Engineering, London, United Kingdom*

Summary. Braking systems of modern cars require a high speed contact between a rotating and a stationary part, with material flows taking place in between for optimal functioning. During those situations, self-excited vibrations can lead to squeals phenomena which can be of high intensity. A high speed contact test rig was developed to recreate various contact conditions occurring in a road profile. Thermal and mechanical instrumentation were used in each test, coupled with surface observations and numerical modeling. Establishing an understanding of thermo-mechanical phenomena and tribological behavior of the contact to guide machine learning models allows to develop a more accurate, physics-based estimation of the squeal occurrence in a frictional contact.

Pin-on-disk interaction

The self-excitation of friction-induced vibrations has a long history in tribology and vibrations research, and still today lacks a full-explanatory framework of mechanisms, driving factors and instability conditions [1, 2]. Most uncertainty stems from the frictional interface, which is notoriously difficult to access, measure and characterise in practice [3]. However, data retrieved from the interface carry information representative of the whole system (state of materials, vibrations from all scales...). In this work an experimental study of frictional contact between a pin and a rotating disk is conducted (Fig. 1), with self-excited vibrations and squeal sound emissions. The set-up is heavily-instrumented at the system and contact scales. Particularly, along thermomechanical characterization from sensors on the pin and disk, surface observations such as profilometry are realised on both parts between solicitations to track the interface evolution. Cross-checking those pieces of information allows for the deduction of which phenomena will be in play during the contact and to establish a better understanding of their influence on vibrations and squeal. Tests are realised with various contact parameters (in term of normal load, rotating speed of the disc, contact duration and duration between each contact) to represent different road profiles.

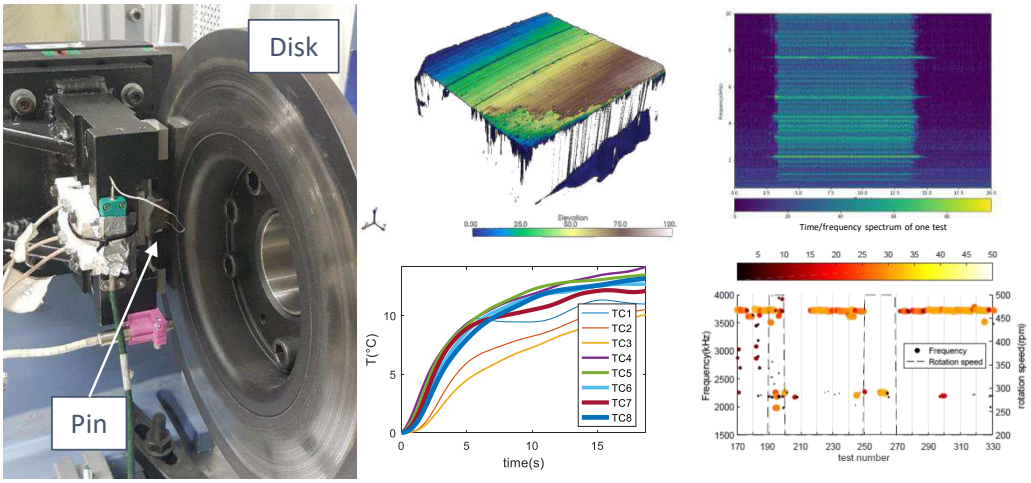

Figure 1: Pin and disk assembled on the test bench - sample recordings of temperatures, frequencies and surface observation.

Data analysis

The aim of this work is to establish the relation between phenomena involved at the interface and the propensity of high-amplitude self-excited vibrations for the system at hand. In order to further reveal the relation of effect and cause, a data analytics perspective is taken. Machine learning models are set up to replicate the dynamical system in the sense of a digital twin model, and recognize patterns in the high-dimensional space of loading conditions acting in the interface and the structural response [4]. Based on the extensive experimental measurements and with the help of appropriate processing algorithms the study of correlations between physics expected to be responsible of self-excited vibrations and squeal occurrence is investigated [5]. Deep learning methods, namely recurrent and convolutional neural architectures, are employed to approximate the functional relationship of external loads (frictional contact loads), internal states (interface

temperatures and friction), and the vibrational response of the structure at hand. A multivariate sequence classification task is set up to predict a binary target indicating linear instability and the resulting nonlinear high-amplitude vibrations. Neural architecture search is performed upfront for selecting proper model hyperparameters and results are reported in terms of binary classification metrics with an intentional correction of imbalanced data sets. Correlations are identified, for example, between heating and squealing events, which are signs of variations in load-bearing area [6] and in the contact interface morphology.

Conclusion

Post-mortem observations of the surfaces (profilometry, camera) allows the identification of various material flows through the contact, which are used to establish a phenomenological model of the third body at the interface. Thermo-mechanical characterisation realised during tests allows to better understand the mechanisms underlying those material flows and to locate them in time and place. The influence of contact parameters is investigated to guide machine learning models, which highlight the relationships between the identified phenomena and the occurence of self-excited vibrations. The treatments also show the importance of considering the history effects corresponding to the evolution of the tribological situation. This study shows the contribution of machine learning models in the prediction of non-linear vibrations from frictional contact.

References

[1] Singla N. (2020) Experiment to Investigate the Relationship Between the Third-Body Layer and the Occurrence of Squeals in Dry Sliding Contact. *Tribology Letters* (volume 68)

[2] Duboc M. (2020) Experimental set-up and the associated model for squeal analysis. *Mechanics and Industry* (volume 21)

[3] Lai V.-V. (2022) Squeal occurrence related to the tracking of the bearing surfaces on a pin-on-disc system. *Mechanical Systems and Signal Processing* (volume 165)

[4] Stender M. (2021) Deep learning for brake squeal: Brake noise detection, characterization and prediction. *Mechanical Systems and Signal Processing* (volume 149)

[5] Stender M. (2019) Determining growth rates of instabilities from time-series vibration data: Methods and applications for brake squeal. *Mechanical Systems and Signal Processing* (volume 129)

[6] Lai V.-V. (2020) Multi-scale contact localization and dynamic instability related to brake squeal. *Lubricants* (volume 8)

Free Vibration Analysis of Functionally Graded Plates with Crack or Slit by the R-Functions Method

Jan Awrejcewicz[*], Lidiya Kurpa[**], Tetyana Shmatko[**], Aleksandr Shmatko[**]
[*] *Lodz University of Technology, Poland*
[**] *National Technical University "KhPI", Kharkov, Ukraine*

Summary. The proposed approach applies the Ritz method combined with the R-functions theory to analyze the free vibrations of cracked functionally graded material (FGM) plates of an arbitrary planform and different boundary conditions. Material properties are assumed to be temperature-independent and varying along the thickness direction according to Voigt's law. The paper proposes a new set of admissible functions in order to describe the effect of cracks on the frequencies and mode shapes of vibrations. The admissible functions constructed by the R-functions theory take into account discontinuous of deflection. A comparison of the obtained results with available ones for rectangular plates confirms validation of the proposed approach. The present method is employed to obtain the frequencies and mode shapes for FGM plates with complex form and internal cracks, having various locations and length. Effects of the gradient index, crack location, crack length and orientation on frequencies and mode shapes of FGM plates are studied.

Introduction

Free vibration analysis of cracked functionally graded materials (FGM) plates with complex planform is a difficult mathematical problem, but it is very important for investigation of the nonlinear dynamical behavior of many modern thin walled construction. Number of publications devoted to this problem is quite limited and concerns only rectangular plates [1-3]. In this study we propose to apply the R-functions theory to construct the corresponding admissible functions which take into account the discontinuous behavior of the deflection of FGM plates with complex planforms. The developed approach is tested on linear vibration problems, what is important for solving nonlinear vibration problems.

Problem formulation

Assume that a plate is made from a mixture of ceramics (top of the plate) and metal (bottom). Below a power-law distributions (Voigt's model) of the volume fractions of the metal and ceramics is employed. Then the effective material properties $P_{ef}(z)$ such as Young's modulus E, Poisson's ratio ν, and mass density ρ can be expressed as [1-4]:

$$P_{ef}(z) = (P_c(T) - P_m(T))\left(\frac{z}{h} + \frac{1}{2}\right)^k + P_m(T). \tag{1}$$

Mechanical characteristics of ceramic P_c and metal P_m depend on temperature T. This dependence is defined by known formula presented in work [4]. Stress and strain resultants in matrix form are as follows:

$$\{N\} = [A]\{\varepsilon^0\} + [B]\{\chi\}, \quad \{M\} = [B]\{\varepsilon^0\} + [D]\{\chi\}, \tag{2}$$

where $\{N\} = \{N_{11}, N_{22}, N_{12}\}^T$ are forces per unit edge length in the middle surface of a plate, $\{M\} = \{M_{11}, M_{22}, M_{12}\}^T$ are bending and twisting moments per unit edge length, whereas the components of the vectors $\{\varepsilon^0\} = \{\varepsilon_{11}^0, \varepsilon_{22}^0, \varepsilon_{12}^0\}^T$ and $\{\chi\} = \{\chi_{11}, \chi_{22}, \chi_{12}\}^T$ are defined in the following way

$$\varepsilon_{11}^0 = u_{,x} \quad \varepsilon_{22}^0 = v_{,y} \quad \varepsilon_{12}^0 = u_{,y} + v_{,x}, \quad \varepsilon_{13} = \delta(w_{,x} + \psi_x), \quad \varepsilon_{23} = \delta(w_{,y} + \psi_y),$$
$$\chi_{11} = \delta\psi_{x,x} - (1-\delta)w_{,xx}, \quad \chi_{22} = \delta\psi_{y,y} - (1-\delta)w_{,yy}, \quad \chi_{12} = \delta(\psi_{x,y} + \psi_{y,x}) - 2(1-\delta)w_{,xy}. \tag{3}$$

where u, v are middle surface displacements along the axes Ox and Oy respectively, w is the transverse deflection of the plate along the axis Oz, ψ_x, ψ_y are angles of rotations of the normal to the middle surface about the axes Ox and Oy. Symbol $\delta = 1$ stands for first order shear deformation theory (FSDT) and $\delta = 0$ is associated with the classical theory (CLT). Elements of the matrixes $[A], [B], [D]$ have the following form:

$$([A], [B], [D]) = \int_{-\frac{h}{2}}^{\frac{h}{2}} E(z)[C](1, z, z^2)\,dz, \quad [C] = \frac{1}{1-\nu^2}\begin{bmatrix} 1 & \nu & 0 \\ \nu & 1 & 0 \\ 0 & 0 & \frac{1-\nu}{2} \end{bmatrix}. \tag{4}$$

The proposed method of investigation of free vibration of FGM plates is based on an application of the R-functions theory and the Ritz method [5, 6]. Variational statement of the vibration problem is reduced to determine the stationary point of the following functional

$$J = U - \omega^2 P, \tag{5}$$

where U and P are maximum potential and kinetic energies [3] relatively:

$$U = \frac{1}{2}\iint_{\Omega}\left(N_{11}\varepsilon_{11} + N_{22}\varepsilon_{22} + N_{12}\varepsilon_{12} + M_{11}\chi_{11} + M_{22}\chi_{22} + M_{12}\chi_{12}Q_x\varepsilon_{13} + Q_y\varepsilon_{23}\right)d\Omega\,, \tag{6}$$

$$P = \frac{1}{2}\iint_{\Omega} I_0\left(\dot{u},_t^2 + \dot{v},_t^2 + \dot{w},_t^2\right) + 2I_1\left(\dot{u},_t\,\dot{\psi}_x,_t + \dot{v}_t\dot{\psi}_y,_t\right) + I_2\left(\dot{\psi}_x,_t^2 + \dot{\psi}_y,_t^2\right)dxdy\,, \tag{7}$$

where

$$\left(I_0, I_1, I_2\right)\int_{-\frac{h}{2}}^{\frac{h}{2}}\rho(z)\left(1, z, z^2\right)dz\,. \tag{8}$$

Construction of admissible functions

Let us construct admissible functions for FGM plates clamped on part of the border and free on remain part of the border. Suppose that a crack or a slit is located on the straight line directed from the free plate part to inside domain. Equation of the clamped part of the border $\omega_1(x,y)=0$ can be constructed by the R-functions theory. Normalized equation of the crack or slit $\omega_2(x,y)=0$ can be also constructed using tools of the R-functions theory. If crack or slit lies on the line *l* with the normalized equation $l=0$ and the function $\varphi(x,y)\geq 0$ describes the area, separating the part of the line coinciding with length and position of the crack or slit, then the function $\omega_2(x,y)=0$ takes the following form

$$\omega_2(x,y) = \sqrt{l^2 \vee_0 \overline{\varphi}}\,, \tag{9}$$

where $\vee_0$ is a sign of the R-disjunction [6]. The R-function theory allows to construct an equation of the free part of the border $\omega_3(x,y)=0$. It is possible to prove that solution structure with an account of crack on free part of the boundary plate has the following form

$$W = \frac{\omega_1^2}{\omega_1^2 + \omega_3}\left(\Phi_1 q_1 + \Phi_2 q_2 + (1+\omega_3)\Phi_1\right), \tag{10}$$

where Φ_1, Φ_2, Φ_3 are indefinite components of the solution structure. Functions $q_1(x,y), q_2(x,y)$ are defined as

$$q_1(x,y) = \left(1 + D_1^{(l)}\omega_2(x,y)\right)/2, \quad q_2(x,y) = \left(1 - D_1^{(l)}\omega_2(x,y)\right)/2\,, \tag{11}$$

where $D_1^{(l)}\omega_2 = l,_x\,\omega_2,_x + l,_y\,\omega_2,_y$. It is possible to show that $D_1^{(l)}\omega_2 = \pm 1 + O(\omega_2)$.

The corresponding structures can be constructed for the functions *u*, *v* and $\psi_x\ \psi_y$ in a similar way. In order to get admissible functions, indefinite components Φ_1, Φ_2, Φ_3 are expanded into series over some complete system of functions $\left\{\varphi_i^{(k)}\right\}$, $k = 1,2,3.$

Conclusions

A new approach is proposed to study free vibrations of FG plates with cracks or slits. System of basic functions, which takes into account the shape of a crack and the discontinuous behavior of the deflection, is constructed by the R-functions theory. The proposed approach is validated against available results for the linear frequencies of cracked isotropic and FGM plates with various boundary conditions and rectangular planform. The comparison was made for simply supported square plate with center crack and cantilevered plate with a side crack. The obtained results are found to be in a good agreement with the known solutions. In order to demonstrate the possibilities of the proposed method and developed software, we have analyzed influence of the location, crack length on natural frequencies of the FGM plates with complex planform.

References

[1] Natarajan S., Baiz P.M, Bordas S. et all (2011) Natural frequencies of cracked functionally graded material plates by extended finite element method. *J.Compos Struct* **93**: 3082-3092.

[2] Huang C.S., Leissa A.W., Chan C.W. (2011) Vibrations of rectangular plates with internal cracks or slits. *Int.J Mech Sci* **53**:436-445.

[3] Huang C.S., Leissa A.W. (2009) Vibration analysis of rectangular plates with side cracks via the Ritz method. *J.Sound & Vibr* **323**: 974-988.

[4] Shen H.S. (2009) Functionally Graded M of plates and Shells. CRC Press, Florida.

[5] Awrejcewicz J., Kurpa L., Shmatko T. (2015) Investigating geometrically nonlinear vibrations of laminated shallow shells with layers of variable thickness via the R-functions theory. *J.Compos Struct* **125**: 575-585.

[6] Rvachev V.L. (1982) The R-Functions theory and its some application. Naukova Dumka, Kiev (in Russian).

Methods for decreasing order and dimension in mechanics of solids

V.A. Krysko- jr.* J. Awrejcewicz*

**Department of Automation, Biomechanics and Mechatronics, Lodz University of Technology,*

1/15 Stefanowskiego St., 90-924 Lodz, POLAND; (vadimakrysko@gmail.com)

Summary: The paper gives further development of methods for reducing a system of partial differential equations (PDEs) to a system of ordinary differential equations (ODEs). Iterative methods are proposed which at each loading step for static problems and at each time step employ suitable approximating functions. The Bubnov-Galerkin method was considered as a basis for further consideration. The effectiveness of the developed methods were demonstrated by solving the problems of the theory of plates and shells. The proposed approaches allow us to solve a wide class of problems in linear/nonlinear formulation for both full-sized and nanoscale structures. The problems were solved taking into account the temperature field, geometric and physical nonlinearities, contact interaction between structures, as well as the Casimir and Van der Waals effects. The convergence theorems of solutions for some iterative methods were proved. Software packages for solving problems of statics/dynamics were developed. The exact solutions regarding plates were given taking into account the nanoscale parameter and constant load. Then exact solution was compared with solutions obtained by two iterative methods.

Introduction

Such problems are usually solved using the following methods: finite difference methods (FDM), finite element method (FEM) and in result a system of linear or nonlinear algebraic equations is obtained, which bounds application of these methods.

Mathematical models and solution methods

Iterative methods for reducing PDEs to a system of ODEs were constructed. These methods are based on the Bubnov-Galerkin method, and the method of Kantorovich–Vlasov (MKV) [1] . The latter method, by its ideology, match the Fourier method (MF) based on the variables separation and the Bubnov-Galerkin method (MBG), which gave impetus to a number of modifications (Fig. 1) including the following modifications: the Vaindiner method (MV)[2], the variational iteration method (MVI) [3] or extended Kantorovich method (EKM) [4], the Agranovsky – Baglai – Smirnov method (MABS) [5-6] and their combinations [7-10]. These articles provide evidence of convergence and a comparative analysis of the results can be applicable for full-sized structures. The method of variational iterations (MVI) eliminates the need to construct a system of approximating functions in the procedure of employment of the Bubnov-Galerkin method. The functions initially specified in an arbitrary way (obviously satisfying certain well-known smoothness conditions) were refined in the process of calculations by MVI based on the solutions of the original system of PDEs. The resulting system of functions was given and the Bubny-Galerkin method was used to obtain a system of ODEs with respect to another variable. This iterative process continues to obtain a solution with a given accuracy. In this paper, these methods are implemented to solve a class of problems in the mechanics of a continuous deformable medium. The nanostructures are described using the modified couple stress theory [11] and the classical theory of shallow shells. Contact interaction is investigated using the theory of Kantor. Physical nonlinearity is taken into account according to the deformation theory. The temperature field is determined from the solution of a three-dimensional heat PDE. The relationship between the strain fields and temperature is not taken into account

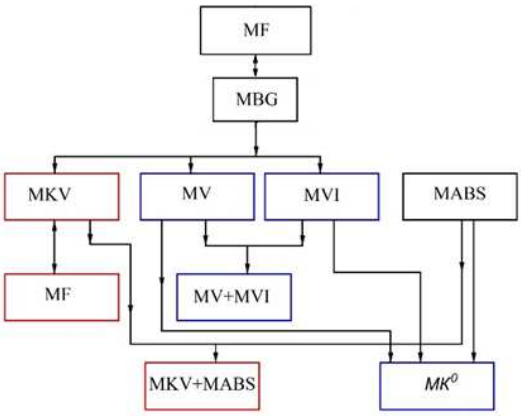

Fig.1 Interrelation of the Bubnov-Galerkin method, the Fourier method, the method of Kantorovich-Vlasov and their modifications

The effects of Casimir [12], Van der Waals are taken into account as well as a geometric non-linearity based on the von Kármán theory. The governing partial differential equations, boundary and initial conditions are obtained from the Hamilton principle and the calculus of variations. For a number of approaches (Fig. 1), theorems were formulated and proved for the existence and uniqueness of solution for the equations of nanostructures of rectangular shells in terms of geometric nonlinearity.

Results

As a numerical example, the results of a study of the static problem of a square in terms of a nanoplate are presented. The load is uniformly distributed over the plate area. Plate material is isotropic and elastic with Poisson's ratio ν=0.3. The solution is obtained for two types of boundary conditions. The problems are solved in a linear formulation for a size dependent parameter γ=0 and γ=0.5. Exact solutions have been obtained.

Table 1.

Boundary condition	Exact solution	γ	MVI	MVI+MABS
Hinge	0.2028	γ=0	0.2030	0.2028
Rigid jamming	0.0661		0.0653	0.0661
Hinge	0.1064	γ=0.5	0.1073	0.1065
Rigid	0.0381		0.0376	0.0383

The solutions are obtained by a combination of MVI and MVI + MABS. These solutions practically coincide with the exact solution of the considered problems. This indicates the effectiveness of these methods. These two approaches have their advantages: there was no need to build an initial approximation that satisfies the given boundary conditions of the problem. The methods (MV) and (MV+MABS) have the same property. To analyze the problems of nonlinear dynamics, the methods of the theory of differential equations are used including analyses of signals, phase portraits, Fourier power spectra and wavelets. In addition, the Lyapunov exponents are numerically estimated using the Wolf, Kantz, and Rosenstein methods. Static problems are obtained from dynamic solutions using the set up method.

Remark. The approach proposed in Fig. 1 applies to elliptic equations. It is possible to extend it to linear and nonlinear hyperbolic equations. Then the solution can be represented as a product of three functions, each of which depends on one variable *t*,*x*,*y*. B Reducing the PDE's to ODE's regarding *t* at each time step, it was proposed to use the methods described in Fig. 1.

Acknowledgements

This work has been supported by the Polish National Science Centre under the Grant PRELUDIUM 16 No. 2018/31/N/ST8/00707.

References

[1] Kantorovich L., Krylov V.L. (1958) Approximate method of higher analysis. New York, Interscience.
[2] Vaindiner A.I. (1969) The convergence of a direct method. USSR Computational Mathematics and Mathematical Physics, 8:4:285-293.
[3] Kirichenko V. F., Krysko V. A. (1981) Substantiation of the variational iteration method in the theory of plates, Soviet Applied Mechanics, 17:4:366-370.
[4] Kerr A. D. (1978) An extension of the Kantorovich method. Quarterly of Applied Mathematics 26:219-229.
[5] Agranovskii M. L., Baglai R. D. Smirnov K. K. (1978) Identification of a class of non-linear operators. USSR Computational Mathematics and Mathematical Physics. 18:2:7-15
[6] Baglai R. D. Smirnov K. K. (1975) The computer processing of two-dimensional signals. USSR Computational Mathematics and Mathematical Physics, 15:1:234-241
[7] Krysko A.V., Awrejcewicz J., Pavlov S.P., Zhigalov M.V., Krysko V.A. (2014) On the iterative methods of linearization, decrease of order and dimension of the Karman-type PDEs, The Scientific World Journal.
[8] Krysko A.V., Awrejcewicz J., Zhigalov M.V., Krysko V.A. (2016) On the contact interaction between two rectangular plates. Nonlinear Dynamics, 84:4:2729-2748.
[9] Awrejcewicz J., Krysko V.A., Zhigalov M.V., Krysko A.V. (2018) Contact interaction of two rectangular plates made from different materials with an account of physical non-linearity. Nonlinear Dynamics: An International Journal of Nonlinear Dynamics and Chaos in Engineering Systems, 85:1191–1211
[10] Awrejcewicz J., Krysko-Jr. V.A., Kalutsky L.A., Zhigalov M. V., Krysko V. A. (2021) Review of the Methods of Transition from Partial to Ordinary Differential Equations: From Macro- to Nano-structural Dynamics. Arch Computat Methods Eng, 28:4781–4813.
[11] Yang F., Chong A.C.M., Lam D.C.C., Tong P. (2002) Couple stress based strain gradient theory for elasticity, Int. J. Sol. Struct., 39:2731–2743.
[12] Casimir H.B. (1948) On the attraction between two perfectly conducting plates, Proc. Kon. Ned. Akad. Wet. 51:7:793.

Nonlinear vibrations of sandwich shells with additive manufactured flexible honeycomb core interacting with supersonic gas flow

Konstantin Avramov[*,**,***], Borys Uspensky[*]

[*]*National Academy of Science of Ukraine, Podgorny Institute for Mechanical Engineering, Department of Vibrations, 2/10 Pozharskogo St., 61046, Kharkiv, Ukraine*

[**]*National Aerospace University N.Ye. Zhukovsky "KhAI", Department of Aircraft Strength, Kharkov, Ukraine*

[***]*Department of Technical Systems, Kharkiv National University of Radio Electronics, Kharkov, Ukraine*

Summary. The sandwich conical shell with three layers is considered. The middle layer of the structure consists of honeycomb core, which is manufactured by FDM additive technology from ULTEM 9085 material. Top and bottom faces are produced from the carbon fiber-reinforced composite. The self-structure vibrations are observed due to structure interactions with supersonic gas flow. The assumed mode method is used to obtain the system of nonlinear ordinary differential equations for the structure motions. The combination of the shooting technique and the continuation algorithm is used to study the structure periodic vibrations. The periodic and quasiperiodic self-sustained vibrations are discussed. The quasiperiodic vibrations are born due to the Naimark-Sacker bifurcation.

Introduction

Honeycomb sandwich structures are commonly used in aircrafts and launch vehicle structures because of their superior strength and stiffness. Honeycomb sandwich shell can be used to make rocket and missile head shell, engine tail nozzle, spacecraft fairing, solar cell shell and so on. Therefore, many efforts were made to study the mechanical properties of the honeycomb sandwich structures. Now the nonlinear vibrations of the honeycomb sandwich structures are treated. The nonlinear vibrations of smart viscoelastic composite doubly curved sandwich shell with flexible core and magnetorheological layer with different distribution patterns are treated in [1]. The nonlinear vibration analysis of composite sandwich doubly curved shell with a flexible core integrated with a piezoelectric layer is considered in [2]. The nonlinear dynamic behavior of the double curved shallow shells with negative Poisson's ratios in auxetic honeycombs on elastic foundations subjected blast is treated in [3]. A geometrically nonlinear forced vibration analysis of circular cylindrical sandwich shells with cellular core using higher-order shear deformation theory is presented in [4]. The paper [5] studies the nonlinear free and forced vibration of the sandwich cylindrical panel on Pasternak foundations in thermal environment under the action of blast load. The sandwich cylindrical panel consists of the auxetic honeycombs core and two carbon nanotube reinforced composite face sheets. The nonlinear dynamics of a double curvature sandwich shell with honeycomb are studied in [6].

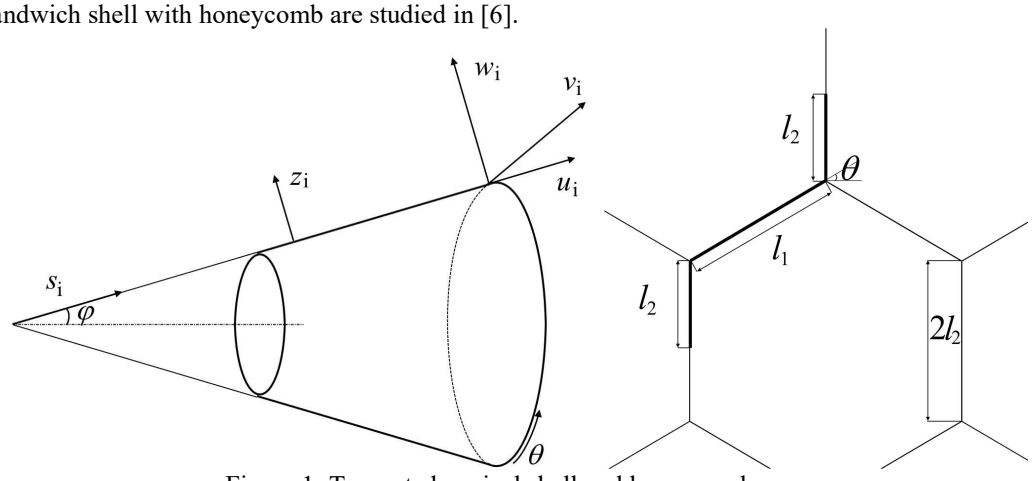

Figure 1: Truncated conical shell and honeycomb core

Problem formulation and main equations

The sandwich conical shell with three layers is shown on Fig.1. The middle layer of the structure consists of honeycomb core, which is manufactured by FDM additive technology (Fig.1) from ULTEM 9085 material. Top and bottom faces are produced from the carbon fiber-reinforced composite. The main geometrical parameters of the honeycomb cell (Fig.1) are the following: l_1, l_2, h_c, ψ, where h_c is thickness of the cells.

The dynamic instability and the self-sustained vibrations of the sandwich conical shell are treated. These nonlinear vibrations are take place due to interaction of the supersonic gas flow with the sandwich conical shell. The growth of

vibrational amplitudes of thin-walled structures is observed due to the system dynamic instability. Then the geometrical nonlinearity contributes essentially to the nonlinear mathematical model of the sandwich structure. This geometrical nonlinearity limits of the vibrational amplitudes grow. This limitation results in the self-sustained vibrations. Therefore, the geometrical nonlinearity is taken into account. The faces composite material and the honeycomb materials satisfy the Hooke's law. The shell initial imperfections are not accounted here.

As the sandwich structure self-sustained vibrations are expanded by the eigenmodes, the linear vibrations of the sandwich structure are considered in this paper too.

The stress-strain state of the sandwich conical shell is studied in the curvilinear coordinate system. Three curvilinear coordinate systems, which are connected with the layers middle surfaces, are used. The curvilinear coordinate systems of the top, core and bottom layers are denoted as: $(s_t, \theta, z_t), (s_c, \theta, z_c), (s_b, \theta, z_b)$, where s_t, s_c, s_b are longitudinal coordinates directed along the generating line of the layer middle surface; θ is curvilinear coordinate (Fig.1); z_t, z_t, z_t are lateral coordinates of the layers.

Results of numerical analysis

The data of the self-sustained vibrations numerical simulations, which are observed due to interaction of supersonic gas flow with the sandwich conical shell is considered accounting geometrical nonlinear deformations. The nonlinear autonomous dynamical system of the structure vibrations has 21 degrees-of-freedom. This dynamical system is analyzed numerically by the algorithm, which combines the shooting technique and the continuation approach. Fig. 2 shows the result of the dynamical systems steady states. The dependences of the vibrational amplitudes $\max(q_1/h_c)$ on the pressure p_∞ is shown on the figure. The stable and unstable steady states are shown by solid lines and dotted lines, respectively.

The dynamical behavior of the structure, which are shown on Fig.2, are considered. The trivial equilibriums, which are described by the straight line (AB) (Fig.2), are observed at any value of p_∞. The Hopf bifurcation is taken place in the H point. The stable equilibriums (AH) are transformed into the unstable equilibriums (HB) and the stable self-sustained vibrations are born. These vibrations are described by the curve (HN_s). The Naimark-Sacker bifurcation is observed in the point N_s. Then the stable self-sustained vibrations are transformed into unstable ones and stable quasiperiodic vibrations are born. The amplitudes of such quasiperiodic vibrations are shown by the curve $(N_S D)$.

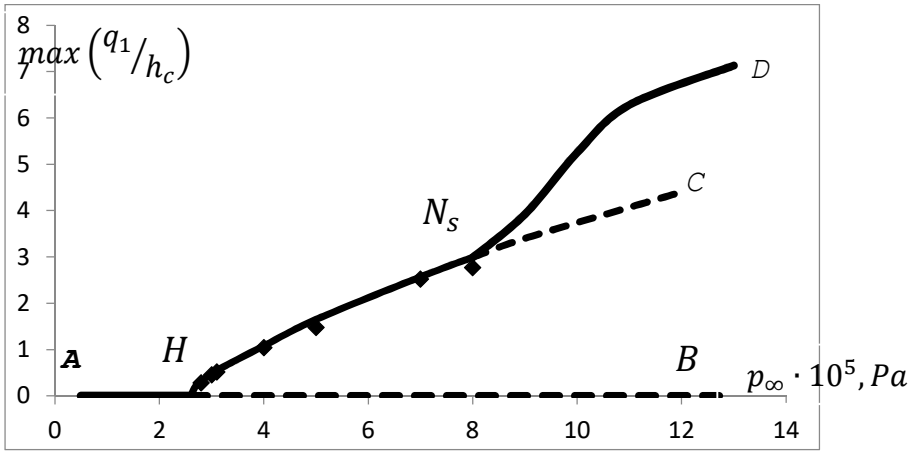

Figure 2: Bifurcation diagram of cantilever conical shell self-sustained vibrations at M=1.5

Acknowledgements

This study was funded by National Research Foundation of Ukraine (grant number 128/02.2020) and by National Academy of Science of Ukraine (grant 0120U101241).

References

[1] Karimiasl M., Ebrahimi F. (2019) Large amplitude vibration of viscoelastically damped multiscale composite doubly curved sandwich shell with flexible core and MR layers. *Thin-Walled Struct* **144**: 106128.

[2] Karimiasla M., Ebrahimia F., Maheshb V. (2019) Nonlinear forced vibration of smart multiscale sandwich composite doubly curved porous shell. *Thin-Walled Struct* **143**: 106152.

[3] Cong P. H., Khanh N. D., Khoa N. D., Duc N. D. (2018) New approach to investigate nonlinear dynamic response of sandwich auxetic double curves shallow shells using TSDT. *Comp Struct* **185**: 455–465.

[4] Yadav A., Amabili M., Panda S. K., Dey T., Kumar R. (2021) Forced nonlinear vibrations of circular cylindrical sandwich shells with cellular core using higher-order shear and thickness deformation theory. J of Sound and Vibr **510**: 116283.

[5] Van Quyen N., Thanh N.V., Quan T.Q., Duc N.D. (2021) Nonlinear forced vibration of sandwich cylindrical panel with negative Poisson's ratio auxetic honeycombs core and CNTRC face sheets. Thin-Walled Struc **162**: 107571.

[6] Zhang Y., Li Y. (2019) Nonlinear dynamic analysis of a double curvature honeycomb sandwich shell with simply supported boundaries by the homotopy analysis method. *Comp Struct* 221: 110884.

Self-sustained Vibrations and Dynamic Instability of Functionally Graded Carbon Nanotubes Reinforced Composite Shells

Konstantin Avramov[*,**,***], Boris Uspensky[*], Marina Chernobryvko[*],
[*]*National Academy of Science of Ukraine, Podgorny Institute for Mechanical Engineering, Department of Vibrations, 2/10 Pozharskogo St., 61046, Kharkiv, Ukraine*
[**]*National Aerospace University N.Ye. Zhukovsky "KhAI", Department of Aircraft Strength, Kharkov, Ukraine*
[***]*Department of Technical Systems, Kharkiv National University of Radio Electronics, Kharkov, Ukraine*

Summary. Dynamic models of geometrical nonlinear deformations of functionally graded carbon nanotubes reinforced composite thin-walled structures are obtained. Reddy higher- order shear deformation theory is used to derive this model. The nonlinear system of high dimension ordinary differential equations, which describes the structure nonlinear vibrations, is obtained using the assumed-mode method. The linear piston theory is used to describe the supersonic flow. The losses of the cylindrical shell dynamic stability owing to the Hopf bifurcations are analyzed. The self- sustained vibrations, which describe the circumferential traveling waves flutter, occur due to this bifurcation. The harmonic balance method is applied to analyze these self-sustained vibrations. The properties of the circumferential traveling waves are analyzed. The dynamic instability of conical- cylindrical thin-walled nanocomposite structure is treated.

1. Introduction

Intensive researches in advanced materials, which have been widely used in aerospace engineering, are carried out in recent years. The extraordinary stiffness and tensile strength of carbon nanotubes (CNTs) make them well-suited as reinforcing components of composites. Computational approaches play a significant role in the development of the CNT reinforced composites by providing simulations results, which help to understand the behavior of nanocomposite structures. Effective elastic properties of CNTs are obtained in [1]. These properties are used to obtain effective elastic parameters of nanocomposites by the Mori-Tanaka methods. The effective mechanical properties of CNT reinforced composites are evaluated by 3D nanoscale representative volume element method by Liu, Chen [2]. The technique for developing constitutive models of CNTs reinforced polymer composite materials is proposed by Odegard and others [3].

The mechanical characteristics of the nanocomposites are analyzed experimentally by several researchers. The tensile tests of dog-bone shaped specimens were performed by Allaoui and others [4]. They obtained, that the Young's modulus and the yield strength have been doubled and quadrupled for composites with respectively 1 and 4 wt.% CNT in comparison with the pure resin matrix samples. Ci and Bai [5] systematically evaluate the stiffness of nanocomposite, when the CNTs reinforcement is used. The ultimate stresses experimental analysis of rubbery epoxy with CNTs reinforcement is treated by Richard and others [6].

The geometrical nonlinear vibrations of functionally graded CNTs reinforced composite cylindrical shell is analyzed by using the higher- order shear deformation theory. The self- sustained vibrations of the cylindrical shell interacted with the supersonic flow are analyzed numerically. The piston theory is applied to describe the supersonic flow.

The assumed-mode method is used to analyze the nonlinear vibrations of functionally graded CNTs reinforced composite cylindrical shell. The high dimension nonlinear system of the ordinary differential equations is obtained. The harmonic balance method with monoharmonic approximation of the self-sustained vibrations is applied to analyze the self-sustained vibrations. The system of the nonlinear algebraic equations with respect to the self-sustained vibrations amplitudes is derived.

The dynamic instability of the shell with different types of composite CNTs reinforcement is analyzed. As follows from the numerical analysis, the type of composite reinforcement affects essentially on the system parameters, when the flutter occurs. If the type of composite reinforcement is changed, the system parameters of the flutter origination can be changed twice.

The effect of the composite reinforcement type on the self-sustained vibrations is investigated. As follows from the data of the numerical simulations, the CNTs reinforcements of the composite shell affect essentially on the amplitudes of the self-sustained vibrations.

2. Problem formulation and main equations

The cylindrical shell with constant thickness h in supersonic flow is treated. The dynamic stress-strain state of the cylindrical shell is analyzed in curvilinear coordinate system (x, θ, z). Three projections of the middle surface displacements and rotations of the middle surface normal are chosen as the main unknowns. The dynamic instability of the cylindrical shell in supersonic flow is analyzed. This instability results in an increase of the vibrations amplitudes. In

this case, the shell geometrical nonlinear deformations occur. This growth of the amplitudes is limited due to the shell geometrical nonlinear behavior. Then three projections of the middle surface displacements u, v, w are moderate and shell strains are small. The Hooke's law is true.

The material of the shell is functionally graded CNTs reinforced composite. CNTs are assumed to be uniaxially aligned. Five types of CNTs reinforced are considered. UD denotes uniform CNTs reinforced in the transverse direction of the cylindrical shell. The rest types of CNTs reinforced are FGV, FG**Λ**, FGX and FGO. They have variable CNTs dispersion. The shell material is functionally graded. The part of the volume for uniform distribution, which is occupied by CNTs, is denoted by V^*_{CNT}.

As the shell material is functionally graded and composite, shear is taken into account. The shear modulus takes the form: $G_{13}(z) = G_{12}(z);\ G_{23}(z) = G_{12}(z)$. The Hooke's law is the following:

$$\begin{bmatrix}\sigma_{XX}\\ \sigma_{\theta\theta}\end{bmatrix} = \begin{bmatrix}Q_{11}(z) & Q_{12}(z)\\ Q_{12}(z) & Q_{22}(z)\end{bmatrix}\begin{bmatrix}\varepsilon_{XX}\\ \varepsilon_{\theta\theta}\end{bmatrix}; \quad (1)$$

$$\sigma_{\theta Z} = G_{23}(z)\gamma_{\theta Z};$$
$$\sigma_{XZ} = G_{13}(z)\gamma_{XZ};$$
$$\sigma_{X\theta} = G_{12}(z)\gamma_{X\theta}.$$

The projections of the shell points displacements, which are placed on the z distance from the middle surface, are denoted by $u_x(x,\theta,t,z), u_\theta(x,\theta,t,z)$ and $u_z(x,\theta,t,z)$. The higher- order shear deformation theory is used to describe the shell displacements:

$$u_x(x,\theta,t,z) = u(x,\theta,t) + z\phi_1(x,\theta,t) + z^2\psi_1(x,\theta,t) + z^3\gamma_1(x,\theta,t); \quad (2)$$

$$u_\theta(x,\theta,t,z) = \left(1+\frac{z}{R}\right)v(x,\theta,t) + z\phi_2(x,\theta,t) + z^2\psi_2(x,\theta,t) + z^3\gamma_2(x,\theta,t);$$

$$u_z(x,\theta,t,z) = w(x,\theta,t),$$

where R is radius of the cylindrical shell; ϕ_1 and ϕ_1 are the rotations of the middle surface normal about the θ and x axes, respectively.

3. Results and discussions

As a result of the numerical analysis, the bifurcation diagram is calculated (Fig.1). The self-sustained vibrations are originated as a result of the Hopf bifurcation. The influence of the types of CNTs reinforced is analyzed.

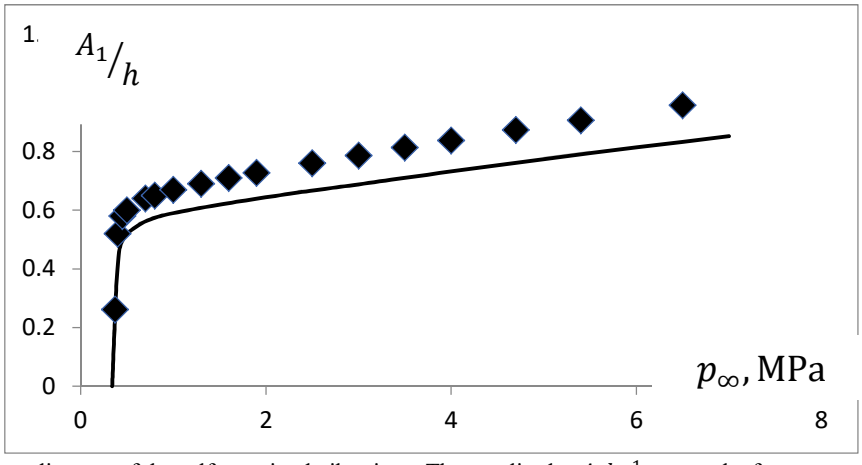

Figure 1: The response diagram of the self-sustained vibrations. The amplitudes $A_1 h^{-1}$ versus the free stream static pressure p_∞ is shown

This study was funded by National Research Foundation of Ukraine (grant number 128/02.2020) and by National Academy of Science of Ukraine (grant 0120U101241).

References

[1] Seidel G.D., Lagoudas, D.C. (2006) Micromechanical analysis of the effective elastic properties of carbon nanotube reinforced composites. *Mech. of Mater* **38** 884–907

[2] Liu Y.J., Chen X.L. (2003) Evaluations of the effective material properties of carbon nanotube-based composites using a nanoscale representative volume element. *Mech. of Mater* **35** 69–81

[3] Odegard G.M., Gates, T.S., Wise, K.E., Park, C., Siochi, E.J. (2003) Constitutive modeling of nanotube–reinforced polymer composites. *Comp. Sc. and Techn*. **63** 1671–1687

[4] Allaoui, A., Bai, S., Cheng, H.M., Bai, J.B. (2002) Mechanical and electrical properties of a MWNT/epoxy composite. *Comp. Sc. and Tech*. **62** 1993–1998

[5] Ci L., Bai J.B. (2006) The reinforcement role of carbon nanotubes in epoxy composites with different matrix stiffness. *Comp. Sc. and Techn.* **66** 599–603

[6] Richard P., Prasse T., Cavaille J.Y., Chazeau L., Gauthier C., Duchet, J. (2003) Reinforcement of rubbery epoxy by carbon nanofibres. *Mater. Sc. and Engin*. **A352**, 344-348

Resonance Steady State and Transient in the Non-Ideal System having the Pendulum Absorber

Yuri V. Mikhlin* and Yana O. Lebedenko*
Dept. of Applied Mathematics, National Technical University "KhPI", Kharkiv, Ukraine

Summary. Resonance behavior of the system with a limited power-supply (or non-ideal system) having the pendulum as absorber is considered. The multiple scales method is used to describe the system dynamics near the resonance. It is shown that the essential reduction of the resonance vibration amplitudes can be obtained by choose of the system parameters. Transient in the non-ideal system under consideration is effectively constructed using the rational Padé approximation. Tending of the transient to the resonance steady state is shown. It is shown that the amplitudes of resonant oscillations of the elastic subsystem can be essentially reduced by choosing some system parameters.

Introduction. The basic model.

The systems with limited power supply are characterized by interaction of the source of energy and elastic sub-system which is under action of the source. Such systems are named also as non-ideal systems (NIS). For the NIS the external excitation depends on the excited elastic sub-system dynamics. The most interesting effect appearing in non-ideal systems is the Sommerfeld effect [1], when in the elastic sub-system the large amplitude resonance regime is appeared, and the big part of the vibration energy passes from the energy source to the resonance behavior. Resonance dynamics of the systems with limited power supply is first analytically described by V.Kononenko [2]. Then investigations on the subject were continued by Kononenko [3] and other authors [4-7]. Reviews of numerous studies of the NIS dynamics can be found in [8-10]. We can note that different types of the NIS behaviour were considered, including forced and parametric oscillations, self-oscillations, transient, chaotic oscillations, interaction of the NIS with energy sources of different physical characteristics, and so on.
It is known that nonlinear vibration absorbers can significantly reduce the amplitudes of resonant elastic vibrations. We consider here the resonant behaviour of the non-ideal system with three DOF (Fig.1), having the pendulum-type absorber, by the multiple scales method. Both the resonance steady state and the transient are constructed. The transient is effectively presented using the rational Padé approximants [11] containing exponents. It is shown that amplitudes of the resonant oscillations of the elastic subsystem can be reduced by changing some system parameters.

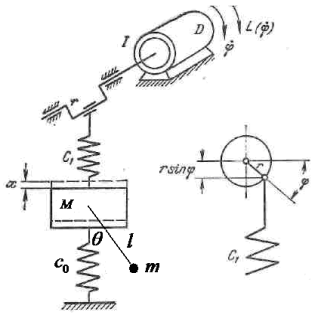

Figure. 1. The model under consideration

Resonance steady state solution. Influence of the system parameters to resonance dynamics of the system

Equations of motion of the system under consideration with respect to variables x, φ and θ are the following:

$$\begin{cases} (M+m)\ddot{x}+(c_0+c_1)x = c_1 r\sin\varphi - ml\left(\ddot{\theta}\cos\theta-\dot{\theta}^2\sin\theta\right); \\ I\ddot{\varphi} = a-b\dot{\varphi}+c_1 r\left(x-r\sin\varphi\right)\cos\varphi; \\ ml\left(l\ddot{\theta}+g\sin\theta+\ddot{x}\cos\theta\right)=0. \end{cases} \tag{1}$$

Here I is the moment of inertia of rotating masses; (c_0+c_1) is the rigidity of the elastic subsystem having the mass M; the combination $L=a-b\dot{\varphi}$ describes both the driving moment of the energy source and the moment of the forces of resistance to the rotation that is the so-called characteristics of the engine. From equations (1) it is seen that the moment $c_1 r x\cos\varphi$ is the part of the motor excitation that depends on the oscillations of the elastic subsystem.

Construction of a stationary resonant solution.

In the first place, we use some transformations. Namely, the functions $\cos\theta$ and $\sin\theta$ are expanded in the McLaren series, and terms remain to the third degree. Then a small parameter ε, introduced into the equations of motion, characterizes the small mass of the absorber with respect to the mass of the elastic part of the system, $m \to \varepsilon m$, and the smallness of vibration components in variability in time of the angle φ velocity with respect to its main constant component. Terms $\varepsilon h\dot{x}$ and $\varepsilon h\dot{\theta}$ describe the small dissipation. Considering a region of the resonance between frequencies of the motor rotation and the elastic sub-system vibrations, we introduce the small frequency detuning as $\varepsilon\Delta = \omega_x^2 - \dot{\varphi}^2$, where $c_0 + c_1 = M\omega_x^2$. We also assume that in the resonance region the external excitation of the elastic subsystem is small. A relatively not large nonlinear part of the elastic subsystem response is represented by the term $\varepsilon\tau x^3$, which is included in the first equation of the system (1). As a result, we consider the following equations of motion instead of the equations (1):

$$\begin{cases} (M+\varepsilon m)\ddot{x} + \omega_x^2 x + \varepsilon h\dot{x} + \varepsilon\tau x^3 = \varepsilon c_1 r\sin\varphi - \varepsilon ml\left(\ddot{\theta}\left(1-\frac{1}{2}\theta^2\right) - \left(\theta - \frac{\theta^3}{6}\right)\dot{\theta}^2\right) \\ I\ddot{\varphi} = \varepsilon\left(a - b\dot{\varphi} + c_1 r\left(x - r\sin\varphi\right)\cos\varphi\right) \\ \varepsilon ml\left(l\ddot{\theta} + g\left(\theta - \frac{\theta^3}{6}\right) + \ddot{x}\left(1-\frac{1}{2}\theta^2\right)\right) + \varepsilon h\dot{\theta} = 0 \end{cases} \tag{2}$$

The multiple scales method [12] is used to describe the behaviour of the system in the field of resonance. According to this method, we write the following representations of solutions:

$$x(t,\varepsilon) = x\left(t, \varepsilon t, \varepsilon^2 t, ...; \varepsilon\right); \quad \varphi(t,\varepsilon) = \varphi\left(t, \varepsilon t, \varepsilon^2 t, ...; \varepsilon\right); \quad \theta(t,\varepsilon) = \theta\left(t, \varepsilon t, \varepsilon^2 t, ...; \varepsilon\right) \tag{3}$$

In addition, the following transformations are used:

$$\begin{aligned} \frac{d}{dt} &= \frac{\partial}{\partial T_0} + \varepsilon\frac{\partial}{\partial T_1} + \varepsilon^2\frac{\partial}{\partial T_2} + ... \\ \frac{d^2}{dt^2} &= \frac{\partial^2}{\partial T_0^2} + 2\varepsilon\frac{\partial}{\partial T_0}\frac{\partial}{\partial T_1} + \varepsilon^2\left(\frac{\partial^2}{\partial T_1^2} + 2\frac{\partial}{\partial T_0}\frac{\partial}{\partial T_2}\right) + ... \end{aligned} \tag{4}$$

Here $T_0 = \omega t$, $T_1 = \varepsilon\omega t$ and $\omega = \omega_x$. The representations (3) are decomposed in the form of the power series by the small parameter. Substituting the power series into the system (2), we distinguish the terms of zero and first degrees by the small parameter. As a result, the following system of differential equations can be obtained:

$$\varepsilon^0 : \frac{\partial^2 x_0}{\partial T_0^2} + \Omega^2 x_0 = 0, \tag{5}$$

$$\frac{\partial^2\varphi_0}{\partial T_0^2} = 0, \tag{6}$$

$$\begin{aligned} &\varepsilon^1 : 2M\frac{\partial^2 x_0}{\partial T_0\partial T_1} + M\frac{\partial^2 x_1}{\partial T_0^2} + m\frac{\partial^2 x_0}{\partial T_0^2} + \Delta M x_0 + M\Omega^2 x_1 + h\frac{\partial x_0}{\partial T_0} + r\tau x_0^3 = c_1 r\sin\left(\Omega T_0\right) - \\ &-ml\frac{\partial^2\theta_0}{\partial T_0^2} + \frac{1}{2}ml\frac{\partial^2\theta_0}{\partial T_0^2}\cdot\theta_0^2 + ml\theta_0\left(\frac{\partial\theta_0}{\partial T_0}\right)^2 - ml\frac{\theta_0^3}{6}\cdot\left(\frac{\partial\theta_0}{\partial T_0}\right)^2 \quad , \end{aligned} \tag{7}$$

$$2\frac{\partial^2\varphi_0}{\partial T_0\partial T_1} + \frac{\partial^2\varphi_1}{\partial T_0^2} = K - N\Omega\frac{\partial\varphi_0}{\partial T_0} + qx_0\cos\varphi_0 - \frac{qr}{2}\sin 2\varphi_0, \tag{8}$$

$$l\frac{\partial^2\theta_0}{\partial T_0^2} + g\theta_0 - g\frac{\theta_0^3}{6} + \frac{\partial^2 x_0}{\partial T_0^2} - \frac{\theta_0^2}{2}\frac{\partial^2 x_0}{\partial T_0^2} + \tilde{h}\frac{\partial\theta_0}{\partial T_0} = 0 \tag{9}$$

Here $\tilde{h} = h/(ml)$, Ω is the frequency of the motor rotation, depending on the time scale T_1. The solutions of equations of the zero approximation by the small parameter (5) and (6) are presented as follows:

$$\begin{cases} x_0 = A\cos(\Omega T_0) + B\sin(\Omega T_0) \\ \varphi_0 = \Omega T_0 \end{cases} \tag{10}$$

We assume that in the resonance between the engine speeds and the oscillations of the elastic subsystem, the amplitudes of the pendulum oscillations are small. Therefore, we assume that in equation (9) all members with a degree greater than one have the order of the small parameter ε. As a result, from equation (9) we have the following:

$$\theta_0 = C\cos\Omega T_0 + D\sin\Omega T_0, \quad \text{where} \quad C = \frac{A\Omega^2}{g - l\Omega^2}, \quad D = \frac{B\Omega^2}{g - l\Omega^2}. \tag{11}$$

The solution of the zero approximation (10) is substituted to the equation (7). To avoid the appearance of secular terms the following modulation equations are obtained:

$$2\frac{\partial A}{\partial T_1}\Omega + \mu B\Omega^2 - \Delta B + \frac{hA\Omega}{M} - \frac{3\tau A^2 B}{4M} - \frac{3\tau B^3}{4M} + \sigma + \mu lD\Omega^2 = 0, \tag{12}$$

$$-2\frac{\partial B}{\partial T_1}\Omega + \mu A\Omega^2 - \Delta A - \frac{hB\Omega}{M} - \frac{3\tau AB^2}{4M} - \frac{3\tau A^3}{4M} + \mu lC\Omega^2 = 0, \tag{13}$$

$$\left(\mu = \frac{m}{M}, \sigma = \frac{c_1 r}{M}\right)$$

To avoid the appearance of secular terms in the solution of the equation (8) we use the following relation:

$$-2\frac{\partial\Omega}{\partial T_1} + K - N\Omega^2 + \frac{qA}{2} = 0, \quad \text{where} \quad K = \frac{a}{I\omega_x^2}, \quad N = \frac{b}{I\omega_x}, \quad q = \frac{c_1 r}{I\omega_x^2}. \tag{14}$$

Together, all three equations (12-14) give variables *A, B* and Ω, which correspond to the resonant state. Considering the steady state, we assume that the values of *A, B* and Ω are constant. In this case, equations (12-14) are transformed into a system of nonlinear algebraic equations for these values, which is solved by the Newton's numerical method. Thus, constants can be obtained for a stationary solution $\tilde{A}_0, \tilde{B}_0, \tilde{\Omega}_0$. In particular, from equation (14) we have that

$$\tilde{\Omega}_0 = \pm((2a + c_1 r\tilde{A}_o)/2b)^{1/2} \tag{15}$$

Note that in the resonance region, the frequencies Ω and ω_x differ by an order of magnitude of the small parameter ε. Thus, if in the coefficients *K, N* the variable frequency Ω changes by ω_x, then we can find the following solution of equation (14):

$$\Omega = \tilde{\Omega}_0 + \rho(\eta + 1), \quad \text{where} \quad \rho = C_2 = \frac{\tilde{\Omega}_0}{10}, \quad \eta = e^{-\frac{N}{2}T_1} - 1. \tag{16}$$

The last relation shows the approach of the motor frequency to the stationary value of $\tilde{\Omega}_0$ with increasing time.

Construction of the transient using the Padé approximants.

The expression (16) is substituted to equations (12) and (13), preserving the terms of zero and first degree by the variable η. To solve the obtained differential equations, the following representations of functions *A* and *B* in the form of the following power series:

$$A = A_o + A_1\eta + A_2\eta^2 + \cdots \quad , \quad B = B_o + B_1\eta + B_2\eta^2 + \cdots \tag{17}$$

Here the magnitudes A_0 and B_0 selected to match the corresponding values for stationary mode, namely, the values $\tilde{A}_0, \tilde{B}_0$. Next, we need to select equations that contain members of the order $\eta^0, \eta, \ldots$ The zero approximation solutions with respect to η, which is not presented here, permits to obtain A_1 and B_1, namely

$$A_1 = \frac{\mu B_0 \Omega_0}{2\beta} + \frac{\mu B_0 \rho}{2\beta} - \frac{\omega_x^2 B_0}{2\beta(\Omega_0 + \rho)} + \frac{B_0 \Omega_0}{2\beta} + \frac{B_0 \rho}{2\beta} + \frac{hA_0}{2\beta M} - \\ - \frac{3\tau A_0^2 B_0}{8\beta M(\Omega_0 + \rho)} - \frac{3\tau B_0^3}{8\beta M(\Omega_0 + \rho)} + \frac{\sigma}{2\beta(\Omega_0 + \rho)} + \frac{\mu l B_0 (\Omega_0 + \rho)^3}{2\beta G}; \tag{18}$$

$$B_1 = -\frac{\mu A_0 \Omega_0}{2\beta} - \frac{\mu A_0 \rho}{2\beta} + \frac{\omega_x^2 A_0}{2\beta(\Omega_0 + \rho)} - \frac{A_0 \Omega_0}{2\beta} - \frac{A_0 \rho}{2\beta} + \frac{hB_0}{2\beta M} + \\ + \frac{3\tau B_0^2 A_0}{8\beta M(\Omega_0 + \rho)} + \frac{3\tau A_0^3}{8\beta M(\Omega_0 + \rho)} - \frac{\mu l A_0 (\Omega_0 + \rho)^3}{2\beta G}. \tag{19}$$

Here $\beta = \frac{N}{2}, G = g - l(\Omega_0 + \rho)^2$. From the equations of the first approximation, i.e. equations containing members of the order η, the constants A_2 and B_2 can be found, which are not presented here. Then we introduce the following expansions of functions A and B in power series:

$$A = A_{0in} + A_1\eta + A_2\eta^2 + \ldots \quad B = B_{0in} + B_1\eta + B_2\eta^2 + \ldots \tag{20}$$

Here (A_{0in}, B_{0in}) these are here arbitrary values of the amplitudes of oscillations, which are determined by the initial conditions. For further research, we also introduce the following parameter:

$$\psi = \frac{e^{-\beta T_1} - 1}{e^{-\beta T_1}} = \frac{\eta}{\eta + 1}, \quad \text{then} \quad \eta = \frac{\psi}{1 - \psi} \tag{21}$$

Substituting the relationship (21) to the power series (20) and decomposing these expressions into McLaren series by the parameter ψ, corresponding to the case $T_1 \to 0$, one has the following:

$$A = A_{0in} + A_1\psi + (A_1 + A_2)\psi + \ldots \\ B = B_{0in} + B_1\psi + (B_1 + B_2)\psi + \ldots \tag{22}$$

We introduce the Padé approximants for values ψ, varying it from zero to infinity, corresponding to change of the time scale T_1 also from zero to infinity, as:

$$A_p = \frac{\alpha_0 + \alpha_1\psi + \alpha_2\psi^2}{1 + \beta_1\psi + \beta_2\psi^2}; \\ B_p = \frac{\tilde{\alpha}_0 + \tilde{\alpha}_1\psi + \tilde{\alpha}_2\psi^2}{1 + \tilde{\beta}_1\psi + \tilde{\beta}_2\psi^2}. \tag{23}$$

Then we compare expressions (23) with series (22). In addition, to describe the approximation of the transition process to the stationary regime, we consider the boundary of expressions (23) when $\psi \to \infty$ (that is, when $T_1 \to \infty$) and equate this limit to the values of the amplitudes $\widetilde{A_0}$ and $\widetilde{B_0}$, previously obtained for stationary mode, i.e. $\frac{\alpha_2}{\beta_2} = \tilde{A}_0, \quad \frac{\tilde{\alpha}_2}{\tilde{\beta}_2} = \tilde{B}_0$. All this makes it possible to obtain coefficients of the Padé approximants (23) from a system of linear algebraic equations.

Comparative characteristics of the transition and stationary modes. Resonant behaviour of the system when changing system parameters.

Here we consider a comparison of the stationary solution and the transient of the system at small and time values. Then we consider also the influence of the system parameters on the amplitude of elastic oscillations in the resonant region.

This applies to the change of the parameters of the pendulum mass *m* and the parameter of nonlinearity in the elastic force τ. The corresponding numerical simulation was performed for the basic system (2) using the 4th order Runge-Kutta procedure. Change of the driving moment coefficient a and the length of the pendulum l leads to a slight decrease in the amplitude of elastic oscillations, thus graphical representations corresponding to changes in these parameters are not given. From numerical simulations it can be concluded that the amplitudes of resonant elastic oscillations can be significantly reduced with the parameters *m* and τ. We will consider the solutions at different time intervals, as at small values of time, $t \in (0; 5)$, and for significant values of time, $t \in (220; 225)$. Note that in the pictures a),c) the variable *x(t)*, and in the pictures b),d) the variable $\theta(t)$ are presented. In all Figs. the following fixed parameters are given: $= 0{,}37261;\ \ l = 1$. In Fig. 2 the comparison of the stationary solution and the transient at $t \in (0; 5)$ is presented for $\tau = 0{,}05$. In Fig. 2. a,b the parameter $m = 0.07$ and in Fig. 2. c,d one has $m = 0.11$. Fig. 3 shows the comparison of the stationary solution and the transient at $t \in (220; 225)$ for the same fixed parameters $a,\ l,\ \tau$ as in Fig. 2. In Fig. 3a,b the parameter $m = 0.07$, and in Fig. 3c,d one has $m = 0.11$. Fig. 4 presents the comparison of the stationary solution and the transient at $t \in (0; 5)$, for $m = 0.05$. In Fig. 4a,b the parameter $\tau = 0{,}01$, and on Fig. 4c,d one has $\tau = 0{,}05$. In Fig. 5 the comparison is shown at $t \in (220; 225)$ for the same fixes parameters $a,\ l,\ \tau$ as in Fig. 4. In Fig. 5a,b the parameter $\tau = 0{,}01$, and in Fig. 5c,d one has $\tau = 0{,}05$.

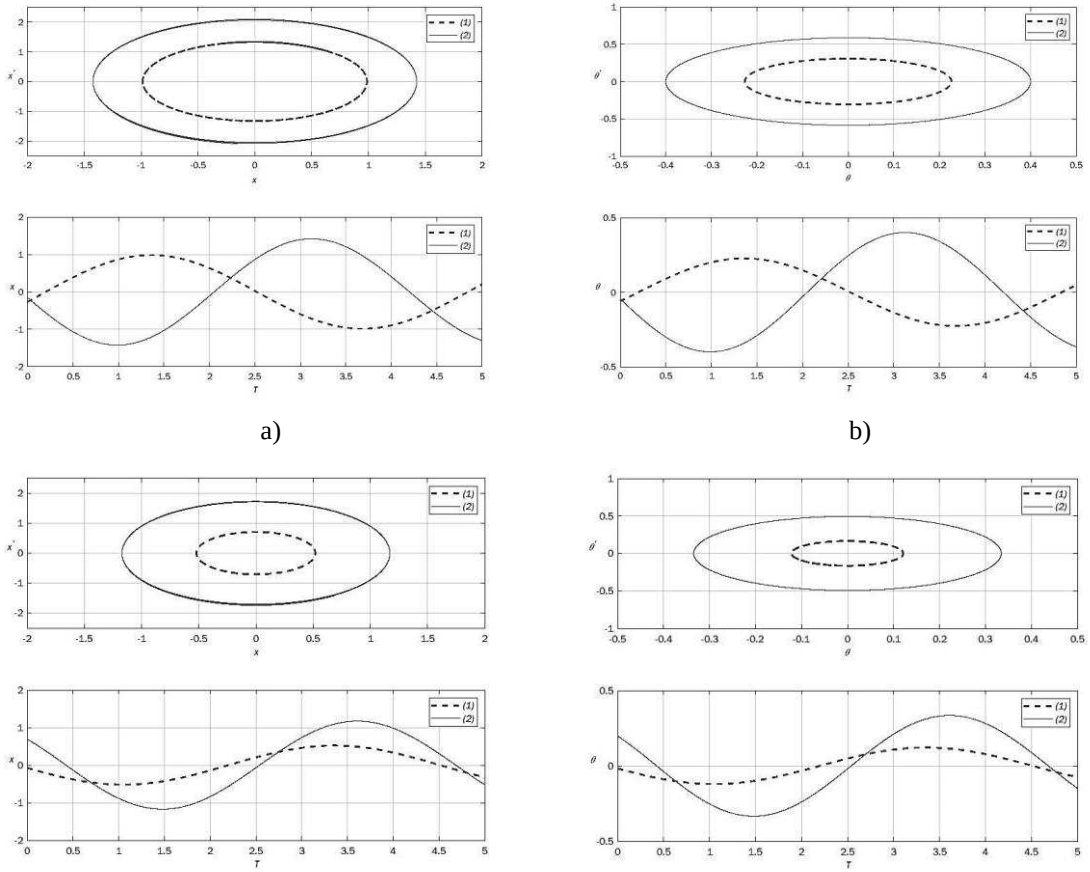

Figure 2. Comparison of the stationary solution (1) and the transient (2) at $t \in (0; 5)$: a) variable *x* for $m = 0.07$; b) variable θ for $m = 0.07$; c) variable *x* for $m = 0.11$; d) variable θ for $m = 0.11$.

Conclusions

Analyzing the obtained results, we can obtain the following conclusions. First, it is fashionable to obtain the resonance steady state effectively by the multiple scales method. Secondly, we can see a good coincidence of the transient represented by the Padé approximants to the stationary regime with increasing time values. Thus, the proposed Padé approximants having exponents are very effective for the transient presentation. Finally, the numerical simulation demonstrates a significant decrease in the amplitudes of elastic oscillations with increasing the pendulum mass and the nonlinearity in the elastic force.

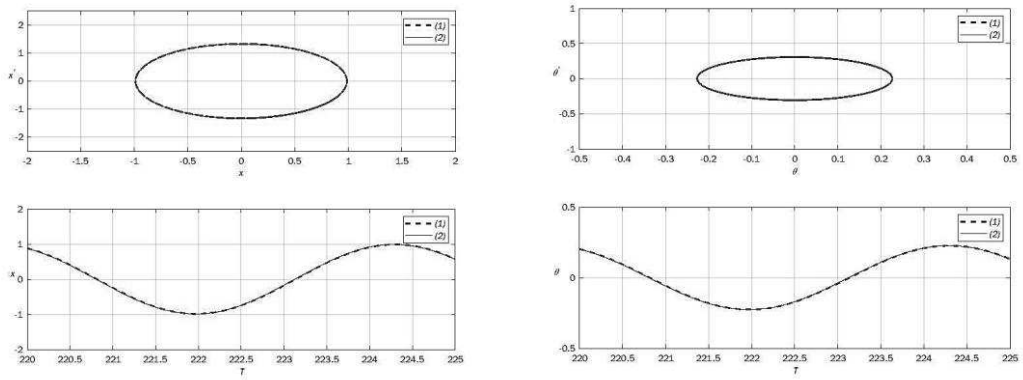

a) b)

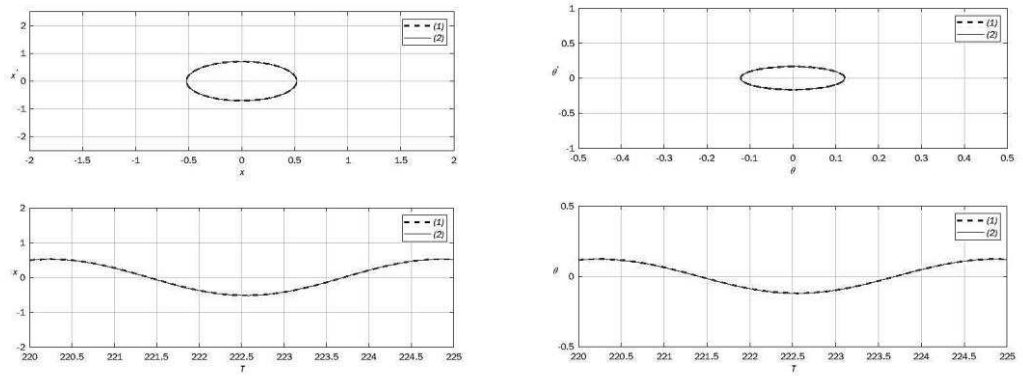

c) d)

Figure 3. Comparison of stationary solution (1) and transient (2) at $t \in (220; 225)$: a) variable *x* for $m = 0.07$; b) variable θ for $m = 0.07$; c) variable *x* for $m = 0.11$; d) variable θ for $m = 0.11$.

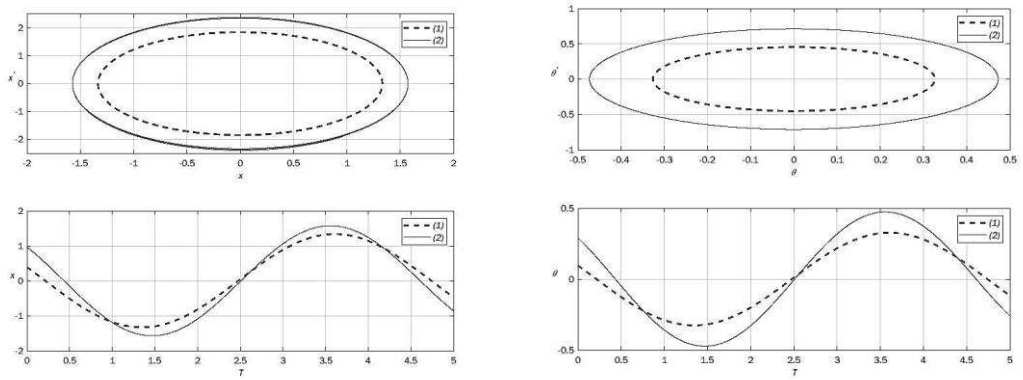

a) b)

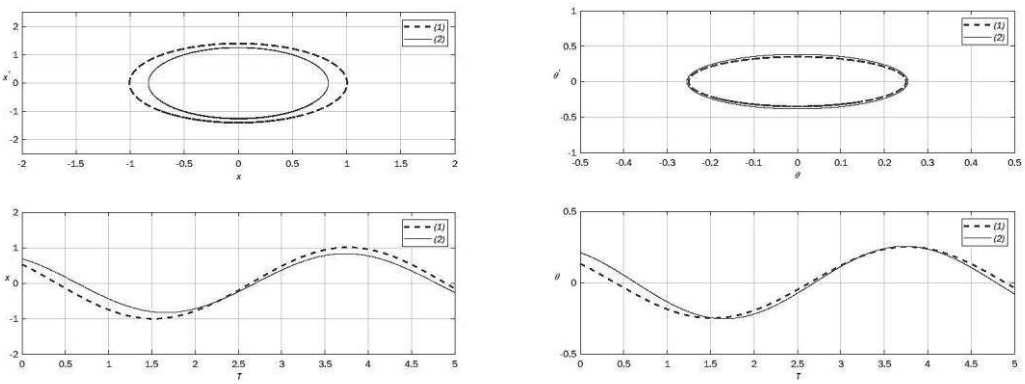

c) d)

Figure 4. Comparison of the stationary solution (1) and the transient (2) at $t \in (0; 5)$: a) variable *x* for $\tau = 0{,}01$; b) variable θ for $\tau = 0{,}01$; c) variable *x* for $\tau = 0{,}05$; d) variable θ for $\tau = 0{,}05$.

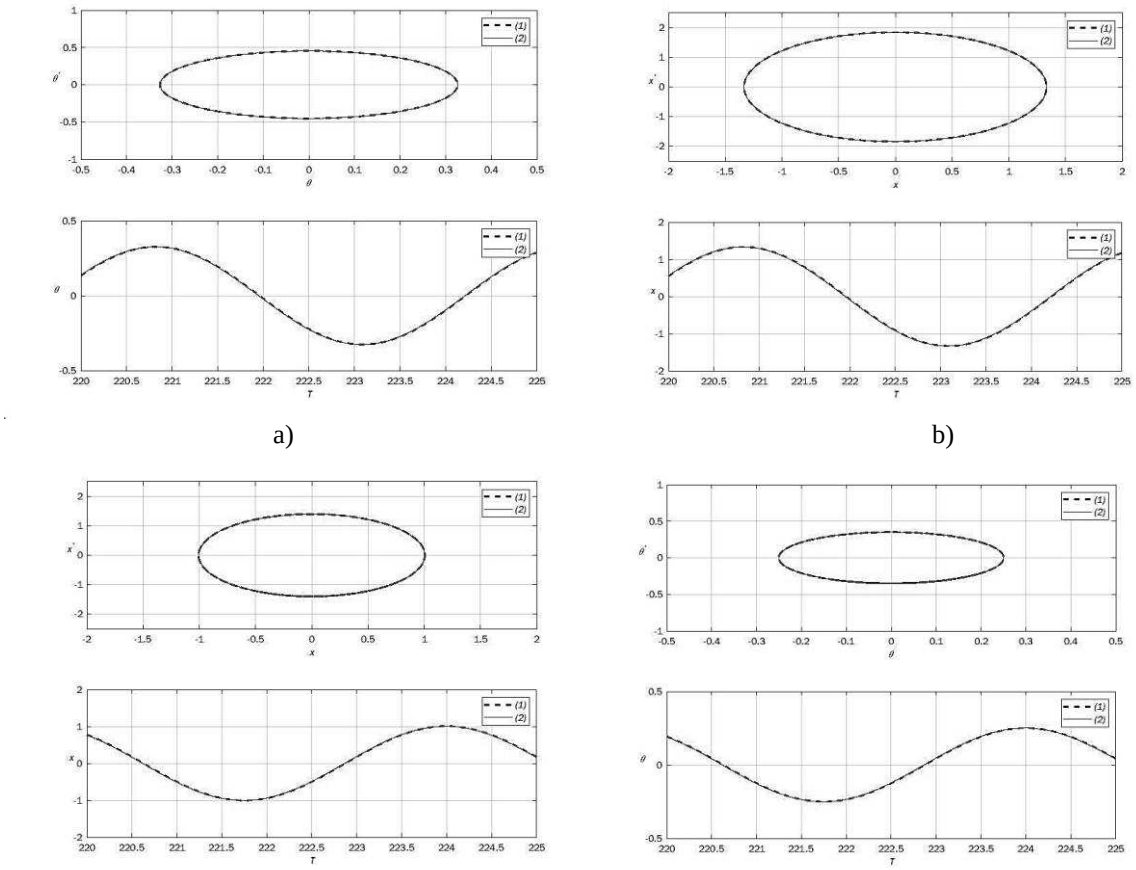

a) b)

c) d)

Figure 5. Comparison of the stationary solution (1) and the transient (2) at $t \in (220; 225)$: a) variable *x* for $\tau = 0{,}01$; b) variable θ for $\tau = 0{,}01$; c) variable *x* for $\tau = 0{,}05$; d) variable θ for $\tau = 0{,}05$.

References

[1] Sommerfeld A. (1902) Beiträge zum dynamischen ausbau der festigkeitslehe. *Phys. Z.* 166-186.
[2] Kononenko V.O. (1969) Vibrating Systems with Limited Power Supply. Illife Books, London.
[3] Kononenko, V.O., Kovalchuk P.S. (1973) Dynamic interaction of mechanisms generating oscillations in nonlinear systems. *Mech. Solids (USSR)* **8**, 48-56 .
[4] Goloskokov E.G., Filippov A.P. (1977) Unsteady oscillations of deformable systems. Naukova dumka, Kyiv (1977).
[5] Alifov A.A., Frolov K.V. (1990) Interaction of Nonlinear Oscillatory Systems with Energy Sources. Taylor & Francis Inc., London.
[6] de Souza et al. (2005) Impact dampers for controlling chaos in systems with limited power supply. *J. Sound and Vibration* **279** (3-5), 955–967.
[7] Felix, J.L.P., Balthazar, J.M (2009) Comments on a nonlinear and non-ideal electromechanical damping vibration absorber, Sommerfeld effect and energy transfer. *Nonlinear Dynamics* 55(1), 1–11.
[8] Eckert M. (1996) The Sommerfeld effect: theory and history of a remarkable resonance phenomenon. *Eur. J. Phys.* **17**(5), 285-289.
[9] Balthazar J.M. et al. (2018) An overviewon the appearance of the Sommerfeld effect and saturation phenomenon in non-ideal vibrating systems (NIS) in macro and mems scales. *Nonlinear Dynamics* **93**(1): 19–40.
[10] Cveticanin, L., Zukovic, M., Balthazar, J.M. (2018) Dynamics of Mechanical Systems with Non-Ideal Excitation. Springer, Cham.
[11] Baker G.A., Graves-Morris P. (1981) Padé Approximants. Addison-Wesley, London.
[12] Nayfeh A.H., Mook D.T. (1979) Nonlinear Oscillations. Wiley, NY.

Thursday, July 21, 2022

13:30 - 15:30

MS-08 Nonlinear Phenomena in Mechanical and Structural Systems

Rhone 3B

Chair: Emil Manoach

13:30 - 13:50
The effect of additional masses on the dynamic buckling of a like-beam structure
ALAOUI-TAHIRI Amine*
*Institut des Sciences de la mécanique et Applications industrielles (828 bd des maréchaux 91762 Palaiseau cedex Franceanciennement LAMSID UMR 8193 France)

13:50 - 14:10
The Bifurcation Structure of a Self-Excited Inertia Wheel Double Pendulum
LEVI Yuval*, GOTTLIEB Oded
*Technion - Israel Institute of Technology [Haifa] (Israel)

14:10 - 14:30
Switching from primary to subharmonic resonances in nonlinear systems
RAZE Ghislain*, HOURI Samer, KERSCHEN Gaëtan
*Aerospace and Mechanical Engineering Department, University of Liège (Quartier Polytech 1 (B52/3) Allée de la Découverte 9 Liege, B-4000, Belgium Belgium)

14:30 - 14:50
[visio] Nonlinear Normal Modes in the pendulum system under magnetic excitation
MIKHLIN Yuri, **SURHANOVA Yuliia***
*Dept. od Applied Mathematics, National Technical University "KhPI" (2 Kyrpychov str., Kharkiv 61002 Ukraine Ukraine)

14:50 - 15:10
[visio] Nonlinear Dynamics of a Body with Two Elastic Supports on an Inclined Rough Plane
DOSAEV Marat*, SAMSONOV Vitaly
*Institute of Mechanics, Lomonosov Moscow State University (119192, 1 Michurinskiy pr-t, Moscow, Russia Russia)

15:10 - 15:30
The Role of Dynamics in Face sheet/Core Interface Debonding of Sandwich Panels
BURLAYENKO Vyacheslav*, DIMITROVA Svetlana
*National Technical University 'Kharkiv Polytechnic Institute' (2 Kyrpychova Str., 61002, Kharkiv Ukraine)

The effect of additional masses on the dynamic buckling of a like-beam structure

Amine Alaoui-Tahiri[*,**], Claude Stolz[*,**], Pierre Badel[*,**], Mathieu Corus[*,**]
[*]*IMSIA, UMR-CNRS 9219, 828 Bd des Maréchaux, Palaiseau, France*
[**]*EDF R&D, Dpt ERMES, 7 Bd Gaspard Monge, 91120 Palaiseau, France*

Summary. A mechanical model of a beam subjected to impact velocity is analyzed. It consists of a beam with additional mass-spring systems. We investigate the distribution of the axial stress along the beam, and the effect of different parameters (masses and their distribution, spring's stiffness) on the stability of the beam.

Introduction

In industrial safety, dynamic buckling is one of the most important considerations to design structures subjected to sudden loadings. For instance, spacer grids in nuclear fuel assembly should have sufficient buckling strength in case of major accidents as earthquakes. Several studies using finite elements models with experimental validation for static buckling and post-buckling of spacer grids were conducted [1]. In literature, most studies focus only on inner characteristics of the spacer grid components without a fully dynamic analysis of the fuel rods movements [2]. Dynamic buckling of structural elements (columns, plates, shells...) under impulsive axial loading has been studied using different approaches. It has been widely investigated for imperfection-sensitive structures with neglected axial inertia forces [3]. For nearly perfect structures, other studies have shown that the axial inertia forces must be considered, particularly in the case of high impact velocities [4].

Mechanical model

We propose a simplified beam model to reproduce the effect of fuel rods, as lumped masses, on the dynamic buckling of the spacer grid. In the present study, we conduct a stability analysis based on eigenvalues evolution for the systems shown in figure 1 and figure 2. The occurrence of buckling and its characteristics (time to buckling, evolution of eigenvalues) are affected by additional masses due to axial stress waves. This effect is illustrated through the impact response of the system with an initial velocity for different configurations. Each configuration is defined by a specific distribution of mass-spring systems and by their frequencies.

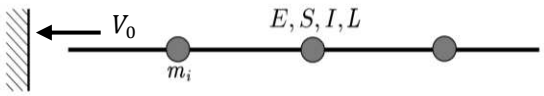

Figure 1: Model of a beam with additional masses

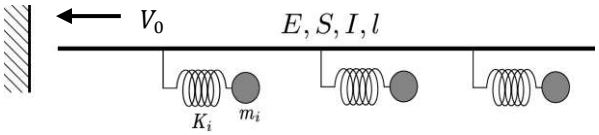

Figure 2: Model of a beam with additional mass-spring systems

To predict a potential buckling of the beam, we solve the wave equation by considering the additional masses

$$\mathrm{E}\,\frac{\partial^2 \mathrm{u}}{\partial \mathrm{x}^2} = \rho\,\frac{\partial^2 \mathrm{u}}{\partial \mathrm{t}^2} \tag{1}$$

To obtain the geometric stiffness matrix at each time step, we consider the first nonlinear term in transverse direction in the axial strain of the beam

$$\mathrm{E\,I}\,\frac{\partial^4 \mathrm{v}}{\partial \mathrm{x}^4} + \frac{\partial}{\partial \mathrm{x}}\left(\mathrm{E\,A}\,\frac{\partial \mathrm{u}}{\partial \mathrm{x}}(\mathrm{x},\mathrm{t}).\frac{\partial \mathrm{v}}{\partial \mathrm{x}}\right) + \rho\,\mathrm{A}\,\frac{\partial^2 \mathrm{v}}{\partial \mathrm{t}^2} = 0 \tag{2}$$

Then an eigenvalue problem is obtained at each time step

$$[\mathrm{K_{elas}} + \mathrm{K_{geom}}(\mathrm{t})].\,\mathrm{X} + \mathrm{M}.\ddot{\mathrm{X}} = 0 \tag{3}$$

In fact, the system is instable if one eigenvalue of the system is positive.

Results

The study is carried out for several configurations with multiple distributions of the masses or the mass-spring systems. Herein we present the results obtained for two configurations. The first configuration consists of a beam with three masses characterized by the mass ratio: $r_m = \frac{m_i}{M_{beam}}$, with M_{beam} is the beam's mass. The second one consists of a beam with three mass-spring systems characterized by the frequency ratio: $r_f = \frac{f_i}{f_{beam}}$ where f_{beam} is the first natural longitudinal frequency of the beam and f_i is the frequency of the mass-spring system. The distribution of the axial stress along the beam at each time step is shown in figures 3 and 4 for the first and the second configurations, respectively. As shown in figure 5 the beam tends to buckle for heavy additional masses. Furthermore, for a given additional mass, the frequency of the mass-spring system needs to be smaller than the natural frequencies of the beam to avoid buckling (figure 6).

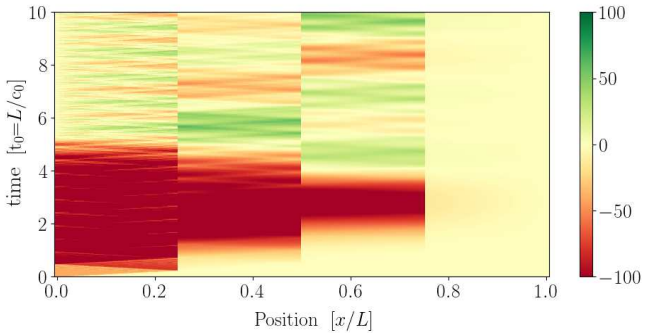

Figure 3: axial stress in the beam with masses for $r_m = 1$

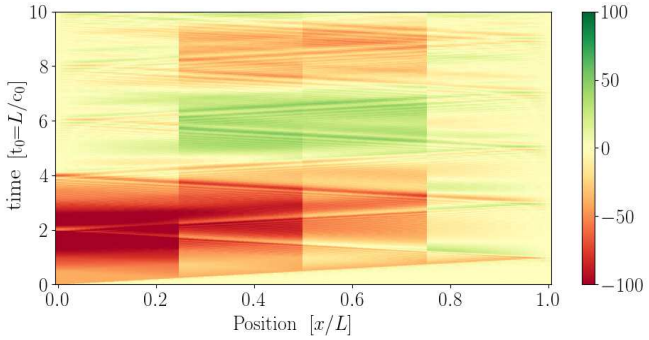

Figure 4: axial stress in the beam with mass-spring systems for $r_f = 1$

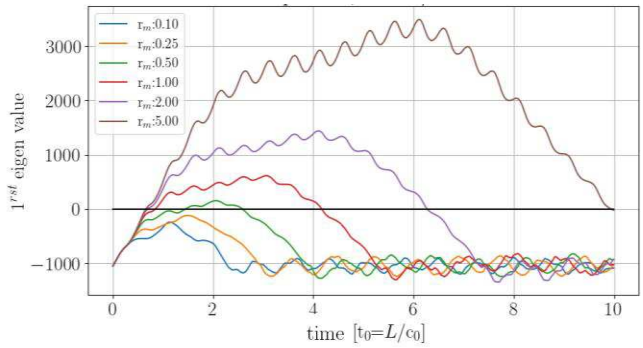

Figure 5: Evolution of the maximum real part of eigenvalues of the beam with masses for different mass ratios

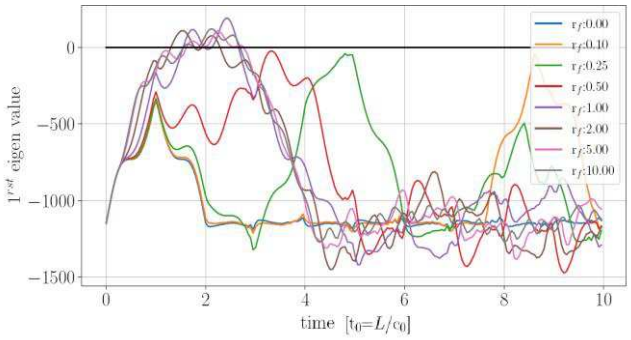

Figure 6: Evolution of the maximum real part of eigenvalues of the beam with mass-spring systems for different frequency ratios

Conclusion and comparison with experimental data

In this study we highlight the importance of considering the compression wave in the prediction of the buckling of a beam with an impact velocity. A further study considering non-linear springs is currently carried out to investigate their effect on the axial wave motion.

For the beam model with mass-springs, the validation of this analysis is considered by setting up a prototype of a structure with rigid point mass inclusions and an adapted experimental protocol under impact conditions.

References

[1] Yoo, Y.I., Park, N.G., Kim, K.J., Suh, J.M. "Static buckling analysis of the partial spacer grid of the nuclear fuel assembly". Proceedings of ANSYS Conference and 32nd CADFEM Users' Meeting, 2014.

[2] Yoo, Y., Kim, K., Lee, S. "Finite element analysis of the mechanical behaviour of a nuclear fuel assembly spacer grid". Nuclear Engineering and Design. 2019.

[3] H, Lindberg., A, Florence., "Dynamic Pulse Buckling: Theory and Experiment" M. Nijhoff, Boston, 1987.

[4] J. Wooseok, A,Waas. "Dynamic bifurcation buckling of an impacted column". International Journal of Engineering Science. 46: 958-967,2008.

The Bifurcation Structure of a Self-Excited Inertia Wheel Double Pendulum

Y. Levi and O. Gottlieb
Department of Mechanical Engineering, Technion-Israel Institute of Technology, Haifa, Israel.

Summary. We construct the bifurcation structure of a self-excited inertia wheel double pendulum. The dynamical system exhibits stable equilibria, periodic limit cycle oscillations and nonstationary rotations. We investigate several configurations documented in literature which exhibit internal resonances and compare their bifurcation structure demonstrating similarities in periodic oscillations and distinct differences in patterns of chaotic rotations.

Introduction

Self-excitation of restrained and freely oscillating rigid bodies are encountered in a variety of engineering applications including friction induced vibration, aeroelastic limit cycle oscillations and fluid-structure interaction. Stabilization of limit cycle oscillations has been proposed by several approaches including boundary feed forward control of a multi-tethered lighter-than-air sphere [1] and digital delayed feedback control of an aero-pendulum [2]. Of particular importance is the capability of an inertia wheel (or reaction wheel) with linear and nonlinear feedback to obtain stable and robust limit-cycle oscillations in underactuated dynamical systems [3,4]. We thus investigate the self-excited dynamics of an autonomous dynamical system which consists of a planar double pendulum augmented with a rotating inertia wheel (see Fig.1-left). We consider double pendulum configurations documented in literature which exhibit conditions near a 1:1 [5], 2:1 [6] and 3:1 [7] internal resonances. Stability analysis of the zero-angle equilibrium position under a partial-state feedback scheme yields a stability map of feedback gains (Fig.1-right) that includes a distinct region (green) of possible self-excited limit cycles that is bounded by Hopf and Saddle-Node bifurcations denoting the transitions from stable equilibria to periodic limit-cycle oscillations (solid blue line) and the transition to rotations (dashed red line), respectively.

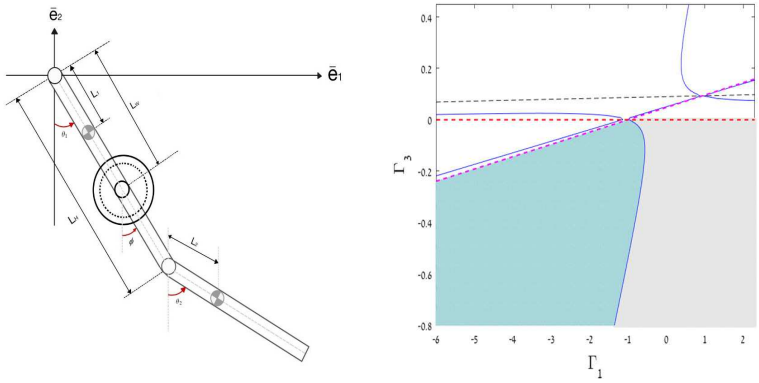

Figure 1. Definition sketch (left) and stability map of the inertia wheel feedback gains for a 2:1 configuration depicting regions of stable zero equilibrium (grey), possible limit-cycles (green) and rotations (white).

Results

We perform a numerical investigation of the dynamical system near a 1:1 internal resonance where the states include the angles (X1, X3) and angular velocities of the pendula and wheel (X2, X4, X5), respectively. The bifurcation diagram (Fig.2-left) depicts the maximal state oscillation amplitude as a function of the wheel velocity feedback gain (Γ_3) and includes two regions of periodic oscillations (about the stable zero equilibrium and about the unstable upper equilibrium) and two regions of nonstationary oscillations and rotations. Examples of a periodic limit cycle (Fig.2-center) and a chaotic rotation (Fig.2-right) include state space projections of the system conjugate momenta (P_i, i=1,2,3) and the bottom pendulum position (Y(X) overlaid with their corresponding Poincare' maps (sampled every positive zero crossing of the bounded wheel velocity).

Discussion

We numerically integrate the dynamical system using the conditions of the above noted 2:1 and 3:1 internal resonances and normalize their bifurcation structures by their respective Hopf thresholds (Γ_3/Γ_{3Hopf}). We portray the normalized bifurcation strucutres (Fig.3-left) demonstrating a distinct similarity of the periodic

self-excited limit cycles between the configurations of the 1:1 (blue), 2:1 (red) and 3:1 (green) internal resonances.) However, the Poincare' maps of the nonstationary rotations for the 2:1 (Fig.3-center) and 3:1 (Fig.3-right) configurations reveal a distinctly different chaotic pattern than the one obtained for the configuration near a 1:1 internal resonance (Fig.2-right). Furthermore, while all the considered cases reveal similar behavior of the inertia wheel velocity (X5), the velocities of the two pendulum elements (X2, X4) exhibited a distinctly different behavior between the region of periodic limit cycle oscillations and nonstationary rotations.

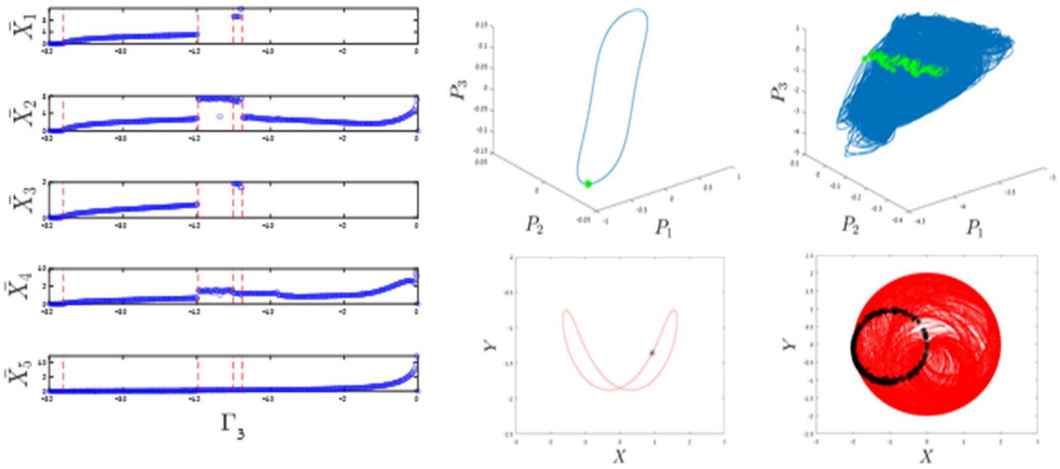

Figure 2. Bifurcation diagram (left), and overlaid state space with Poincare' map for periodic limit cycle oscillations (center) and nonstationary rotations (right)**.**

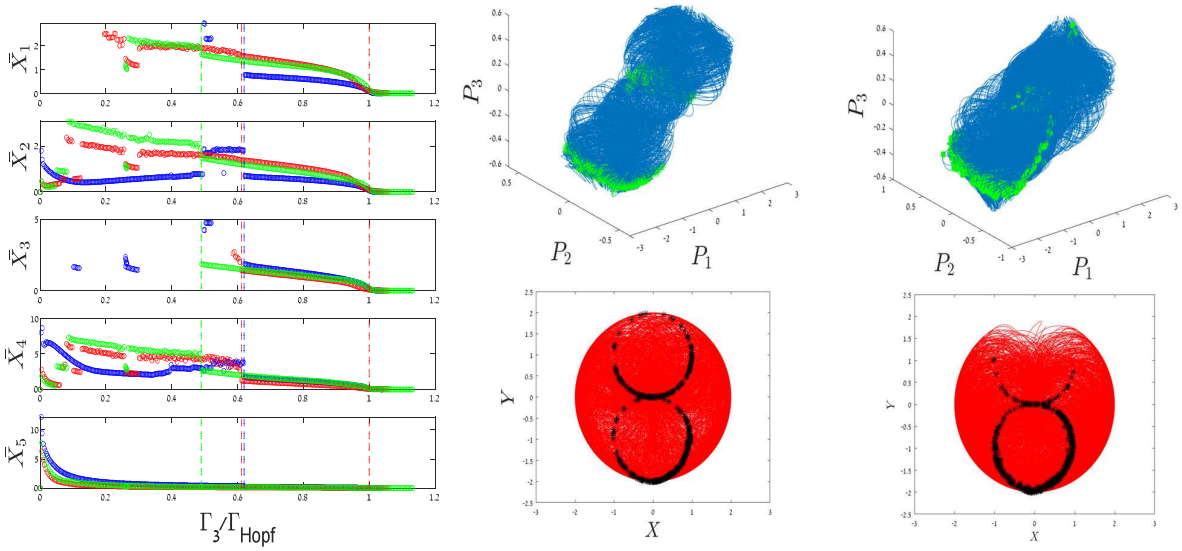

Figure 3. Normalized bifurcation diagram (left) depicting the configurations of the 1:1 (blue), 2:1 (red) and 3:1 (green) internal resonances and overlaid state space and Poincare' map for nonstationary rotations of the 2:1 (center) and 3:1 (right) internal resonances.

References

[1] Mi L. and Gottlieb O., Nonlinear Dynamics, 93: 1353–1369, 2018.
[2] Habib G., Miklos A., Enikov E.T., Stepan G., and Rega G., In. J. Dynamics and Control, 5: 629-643, 2017.
[3] Alonso D.M., Paolini E.E., and Moiola J.L., Nonlinear Dynamics, 40: 205–225, 2005
[4] Haddad, N.K., Belghith, S, Gritli, H. and Chemori, A. Int. J. Bifurcation and Chaos, 27: 1750104, 2017.
[5] Dudkowsky D., Wojewoda J., Czolczynski K. and Kapitaniak T., Nonlinear Dynamics, 102: 759–770, 2020.
[6] Levien, R.B, Tan S.M, American J. Physics, 61: 1038-1044, 1993.
[7] Vadai G., Gingl Z., Mellar J., European J. Physics, 33: 907-920, 2012.

Switching from primary to subharmonic resonances in nonlinear systems

Ghislain Raze*, Samer Houri* and Gaëtan Kerschen*
*Aerospace and Mechanical Engineering Department, University of Liège, Liège, Belgium

Summary. This work proposes a simple method to switch between the primary and subharmonic resonances of nonlinear systems. For a primary resonance harmonically excited at a specific forcing amplitude, there exists another forcing amplitude at an integer multiple of the fundamental frequency allowing for the excitation of the corresponding subharmonic resonance having the same amplitude and frequency. Using an energy analysis, it is possible to determine the necessary forcing amplitude change to switch to the targeted subharmonic resonance. The proposed method is numerically illustrated with a transition from a 1:1 to a 1:3 resonance of a Duffing oscillator.

Introduction

Nonlinear systems feature rich dynamics, such as multistability, modal interactions, isolated responses, quasiperiodic oscillations under harmonic forcing, and chaos. Furthermore, the nonlinearities of the system generate harmonics of the forcing frequency. This leads to the appearance of different families of resonances in addition to the primary one, such as superharmonic, subharmonic, ultra-subharmonic and combination resonances [1]. Among theses, subharmonic resonances are unique in that they occur when the excitation frequency is an integer multiple of a resonance frequency.
Subharmonic resonances have attracted attention in various physics and engineering research areas, such as energy harvesting [2, 3], micro-electromechanical systems [4] and metamaterials [5]. An inherent difficulty associated with their characterization is that they usually appear as isolated branches with respect to the main nonlinear frequency response [1, 6]. Exciting them thus generally requires time-consuming stochastic approaches to bring the state of the system under test into the basin of attraction of the sought resonance [3].
This work proposes a method to excite subharmonic resonances when the corresponding primary resonance is known. If the system is excited at one of its primary resonances, and we wish to seamlessly transition to a subharmonic resonance while maintaining the same motion in terms of amplitude, frequency and phase, then an explicit relation between the forcing amplitudes in these two cases can be derived using an energy method. By performing an adequate change in excitation frequency and amplitude, it is thus possible to change a primary resonance into a subharmonic one.

Energy analysis of resonances

The following equations of motion are considered:

$$\mathbf{M}\ddot{\mathbf{x}}(t) + \mathbf{C}\dot{\mathbf{x}}(t) + \mathbf{K}\mathbf{x}(t) + \mathbf{f}_{nl}(\mathbf{x}(t), \dot{\mathbf{x}}(t)) = f_\nu \mathbf{f}_{ext} \sin(\nu\omega t), \tag{1}$$

where $\mathbf{M}$, $\mathbf{C}$ and $\mathbf{K}$ are structural mass, damping and stiffness matrices, respectively, $\mathbf{f}_{nl}$ is the vector of nonlinear forces, and f_ν and $\mathbf{f}_{ext}$ are the external forcing amplitude and spatial distribution, respectively. It is assumed that the structure responds periodically with an angular frequency ω to the external forcing at angular frequency $\nu\omega$ (with ν a strictly positive integer number). The response can thus be expressed by the Fourier series

$$\mathbf{x}(t) = \frac{\mathbf{x}_{c0}}{\sqrt{2}} + \sum_{n=1}^{\infty} \mathbf{x}_{sn} \sin(n\omega t) + \mathbf{x}_{cn} \cos(n\omega t). \tag{2}$$

We now look for the conditions under which a primary resonance $\mathbf{x}_{1:1}(t)$ can be switched to a subharmonic one $\mathbf{x}_{1:\nu}(t)$, where $\mathbf{x}_{1:1}(t)$ and $\mathbf{x}_{1:\nu}(t)$ represent the solution of Equation (1) for $\nu = 1$ and $\nu \neq 1$, respectively. It is thus assumed that $\mathbf{x}(t) := \mathbf{x}_{1:1}(t) \approx \mathbf{x}_{1:\nu}(t)$. A justification of this hypothesis can be found in [6] if lightly-damped systems are considered, because primary and subharmonic resonances can both be seen as perturbations of the same periodic orbit of the underlying conservative system. The premultiplication of Equation (1) by $\dot{\mathbf{x}}^T(t)$ (where superscript T denotes transposition) and subsequent integration over one period of motion T feature the dissipation $\mathcal{D}$ and the work done by the external forcing over one period $\mathcal{W}_{ext,\nu}$

$$\mathcal{D} = \int_0^T \dot{\mathbf{x}}^T(t) \left(\mathbf{C}\dot{\mathbf{x}}(t) + \mathbf{f}_{nl}(\mathbf{x}(t), \dot{\mathbf{x}}(t))\right) dt = \int_0^T \dot{\mathbf{x}}^T(t) f_\nu \mathbf{f}_{ext} \sin(\nu\omega t)\, dt = \mathcal{W}_{ext,\nu} = -\nu\pi \mathbf{x}_{c\nu}^T \mathbf{f}_{ext} f_\nu, \tag{3}$$

where the last equality is obtained thanks to Equation (2). $\mathcal{D}$ depends only on the motion $\mathbf{x}(t)$ and is therefore identical for the primary and subharmonic resonances by assumption. It then follows that $\mathcal{W}_{ext,1} = \mathcal{W}_{ext,\nu}$, and hence from Equation (3) the forcing amplitudes of the primary (f_1) and subharmonic (f_ν, $\nu \neq 1$) resonances must satisfy a relation given by

$$f_\nu = \frac{\mathbf{x}_{c1}^T \mathbf{f}_{ext}}{\nu \mathbf{x}_{c\nu}^T \mathbf{f}_{ext}} f_1. \tag{4}$$

This suggests that a subharmonic resonance may simply be excited by initiating the structure to its primary resonance, and by subsequently performing a multiplication of the forcing frequency by ν and a change in amplitude according to Equation (4). The factor in this equation can readily be computed either numerically or experimentally, as it only requires to monitor the first and ν^{th} cosine Fourier coefficients of the response at the forcing location ($\mathbf{x}_{c1}^T \mathbf{f}_{ext}$ and $\mathbf{x}_{c\nu}^T \mathbf{f}_{ext}$).

Illustration with a Duffing oscillator

To illustrate the proposed approach, we consider a Duffing oscillator governed by the equation of motion

$$m\ddot{x}(t) + c\dot{x}(t) + kx(t) + k_{nl}x^3(t) = f(t), \tag{5}$$

with parameters $m = 1$ kg, $c = 0.01$ kg/s, $k = 1$ N/m and $k_{nl} = 1$ N/m^3.
The structure is excited at its primary (phase) resonance with a harmonic forcing of amplitude 0.047 N at frequency $\omega = 2.14$ rad/s. A jump to the 1:3 subharmonic resonance is initiated by multiplying the forcing frequency by 3 and changing its amplitude to 0.49 N, this new amplitude being computed from Equation (4). The time simulation results (obtained with a Runge-Kutta time integration scheme) are depicted in Figure 1. In spite of the strong change in forcing featured in Figure 1a, nearly no transient is observed in the motion, and the forcing is effectively able to sustain a motion with threefold period. Figure 1b indicates that this regime is sustained after the transients died out, which confirms that this subharmonic motion is a stable attractor of the system.

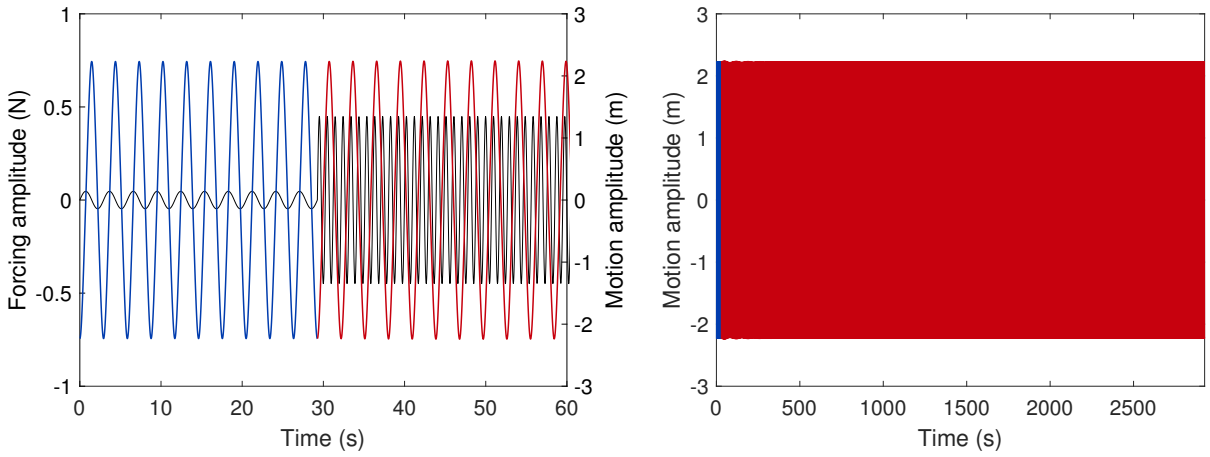

(a) (b)

Figure 1: Time simulation of a Duffing oscillator undergoing a transition from a 1:1 to a 1:3 resonance: forcing $f(t)$ (—) and motion $x(t)$ before (—) and after (—) the change in forcing; close-up on the transition time (a) and full time simulation (b).

Conclusion

An approach to excite subharmonic resonances of nonlinear systems was proposed in this work. Based on the assumption that the resonant motions and the work provided by the external forcings are both identical for the primary and subharmonic resonances, an explicit relation was derived between the two forcing amplitudes. This allows for the transition from a primary to a subharmonic resonance through a suitable change in forcing amplitude and frequency. The proposed method was numerically demonstrated with a Duffing oscillator. This method is simple and holds great promises to find and predict subharmonic resonances of more complex nonlinear systems from the knowledge of their associated primary resonance, both numerically and experimentally.

References

[1] Nayfeh A. H., Mook D. (1995) Nonlinear Oscillations. Wiley, NY.

[2] Anh N. D. et al. (2020) Efficiency of mono-stable piezoelectric Duffing energy harvester in the secondary resonances by averaging method. Part 1: Sub-harmonic resonance *Int. J. Non. Linear. Mech.* **126**:103537.

[3] Huguet T., Badel A., Druet O., Lallart M. (2018) Drastic bandwidth enhancement of bistable energy harvesters: Study of subharmonic behaviors and their stability robustness *Appl. Energy* **226**:607-617.

[4] Nayfeh, A. H., Younis M. I. (2005) Dynamics of MEMS resonators under superharmonic and subharmonic excitations *J. Micromechanics Microengineering* **15**:1840-1847.

[5] Zega V., Silva P. B., Geers M. G. D., Kouznetsova V. G. (2020) Experimental proof of emergent subharmonic attenuation zones in a nonlinear locally resonant metamaterial *Sci. Rep.* **1**:12041.

[6] Cenedese M., Haller G. (2020) How do conservative backbone curves perturb into forced responses? A Melnikov function analysis *Proc. R. Soc. A Math. Phys. Eng. Sci.* **2234**:20190494.

Nonlinear Normal Modes in the pendulum system under magnetic excitation

Yuri V. Mikhlin*, Yuliia E. Surhanova*
*Dept. of Applied Mathematics, National Technical University "KhPI", Kharkiv, Ukraine

Summary. Dynamics of two coupled pendulums under magnetic excitation is considered. Inertial components of the pendulums are essentially different, and a ratio of masses is chosen as a small parameter. Padé approximants is used to for the magnetic forces approximation. The small parameter method and the method of multiple scales are used to construct nonlinear normal modes (NNMs), one of them is localized one. Influence of the initial values and the system parameters, including the pendulum masses, change to the NNMs is studied.

Introduction. The basic model.

The system containing two pendulums under the electromagnetic motor influence is studied in few papers [1-3] where some corresponding mathematical models are constructed, and their validation is discussed after comparison of the numerical simulation and experimental results. Then some important aspects of the system dynamics are analyzed. Here we consider a similar system of two pendulums under magnetic force when inertial characteristics of these pendulums are essentially different. In this case, a localization of energy on the small mass pendulum is possible. To describe the system dynamics, the nonlinear normal modes (NNMs) theory is used. Different theoretical aspects of the NNMs theory and applications of the theory are presented in numerous publications, in particular, in reviews [4,5].
The Padé approximant and the nonlinear least squares method are used for analytical presentation of the magnetic force; such approximation demonstrates a good correspondence with experimental results presented in [2,3] as is shown in Fig.1.

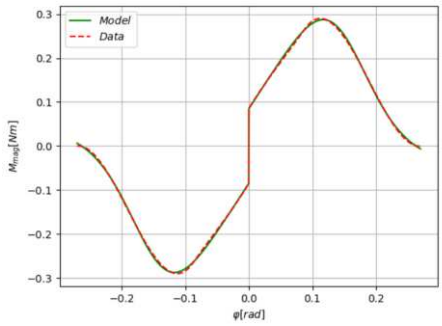

Fig.1. Comparison of the magnetic force Padé approximation with experimental result [2,3].

Equations of motion of the system under consideration with respect to the pendulum angles are the following:

$$\begin{cases} \varepsilon I\ddot{\varphi}_1 = \varepsilon M_{mag_1} - \varepsilon mgs\sin\varphi_1 - k_l(\varphi_1 - \varphi_2), \\ I\ddot{\varphi}_2 = \varepsilon M_{mag_2} - mgs\sin\varphi_2 - k_l(\varphi_2 - \varphi_1), \end{cases} \tag{1}$$

Here I is the inertia moment of the big mass pendulum, rotating masses, $k_l(\varphi_1 - \varphi_2)$ is the moment of the torsional deformation, s is a distance between the pendulum centrum of masses and the axes of rotation. Later $\sin(\varphi) \cong \varphi - \frac{\varepsilon}{6}\varphi^3$. The small parameter ε characterizes the pendulum masses ratio. Then the small parameter method is used. In zero approximation, the relation $\varphi_{10} = \varphi_{20}$ is obtained for the coupled (in phase) vibration mode, and the relation $\varphi_{20} = 0$ is obtained for the localized vibration mode after the following time transformation: $\boldsymbol{t=\varepsilon\tau}$. Without the magnetic influence in a wide range of changes in the system parameters, the error of the analytical solution is insignificant over sufficiently long time intervals and slowly increases with the growth of t up to the values of the pendulum initial angle deviations of the order 0.8727 rad (50°). Numerical simulations show a good exactness of the obtained analytical solution for relatively small values of the parameter ε. But with increasing of the parameter ε there is a gradual transition from the localized vibration mode to the out-of-phase one.

Influence of the initial deviations and the system parameters to the connected and localized nonlinear normal vibration modes under magnetic excitation

Considering numerical simulation of the connected and/or localized NNMs in the system under magnetic excitation we can conclude that at small angles, the influence of the magnetic force is greater, which means that the shape of the NNMs should not be preserved, although a localization of vibration is saved. At the same time, for large angles (for

high energies), the both stable NNMs take place. But, if the modulated magnetic effect itself is small, the in-phase mode will be observed even with small values of the initial deviations of the pendulums. The localized NNM for small and relatively large values of initial deviations is presented in Fig. 2б where the simulation is made for the following system parameters: $m = 0.5\ kg, k_l = 0.5\frac{Nm}{rad}, s = 2.5\ m.$

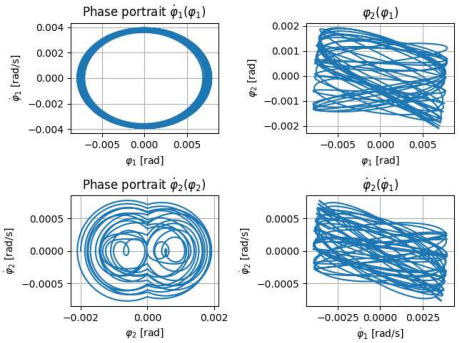

Fig. 2a: $\varphi_1(0) = 0.007 rad, \varepsilon = 0.22, \varphi_2(0) = -0.002$ rad

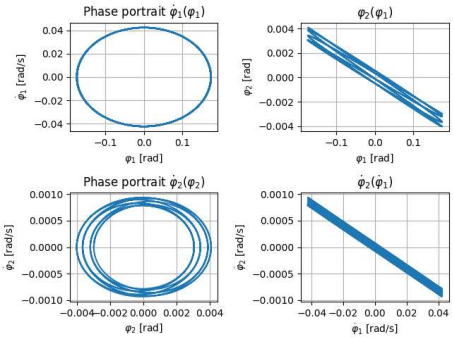

Fig.2b: $\varphi_1(0) = 0.175\ rad, \varepsilon = 0.02, \varphi_2(0) = -0.003\ rad$

Fig.2. Localized NNM for small and relatively large values of the initial angles.

With the moderate increase of the parameter ε, the connected mode shape is observed with small deviations of the trajectories, but with further increase of ε, the deviations increase significantly for both pendulums, and some divergences from the connected mode shape is observed.

With increase of the coupling, the sharps of the in-phase and localized modes becomes more defined. It is true for a system with both a large magnetic effect and a small one.

Increase of the distance from the center of mass of the pendulum to the axis of rotation under both small and large initial conditions, as well as at small and large coupling coefficients, always leads to the clear manifestation of the connected (in-phase) mode. But if the initial angle of deflection of the pendulum is small, and the connection is small, both for a small magnetic effect and for a large magnetic one, then increasing the distance from the center of mass of the pendulum to the axis of rotation *s* does not contribute to the emergence of a stable localized shape.

A change in the distance from the center of mass to the axis of rotation with not too large values of the small parameter (ε <0.2 and with a large value of the coupling coefficient), does not significantly affect the localized shape of the oscillations. With a small connection and a large distance from the center of mass of the pendulum to the axis of rotation, there are significant wanderings of trajectories around the localized mode

Conclusions

An analytical and numerical study of nonlinear vibration modes in a system consisting of two connected pendulums under the influence of electromagnetic forces is carried out, and here the masses of the pendulums differ significantly (*the masses ratio is characterized by the small parameter* ε), which leads to the appearance of a localized vibration mode. Both vibration modes are constructed by the small parameter method. Influence of the system parameters to the connected and localized NNMs is analyzed. In particular, we can conclude that both NNMs are clearly manifested for not small values of the initial angles. With a very small initial angle, the localized mode does not manifest itself.

References

[1] Siahmakoun A., French V., Patterson J. (1997) Nonlinear dynamics of a sinusoidally driven pendulum in a repulsive magnetic field. *Am J Phys.* **65,** 393–400.

[2] Gajek J., Awrejcewicz J.(2018) Mathematical models and nonlinear dynamics of a linear electromagnetic motor. *Nonlinear Dyn.* **94,**:377–396.

[3] Wojna M., Wijata A., Wasilewski G. et al. (2018). Numerical and experimental study of a double physical pendulum with magnetic interaction. *J. of Sound and Vibration* **430**, 214–230.

[4] Mikhlin Yu.V., Avramov K.V. (2010) Nonlinear normal modes for vibrating mechanical systems. Review of theoretical developments. *Appl. Mech. Rev.* **63,** 4–20.

[5] Avramov K.V., Mikhlin, Yu.V. (2013) Review of applications of nonlinear normal modes for vibrating mechanical systems. *Appl. Mech. Rev.* **65** (2) (20 pages).

Nonlinear Dynamics of a Body with Two Elastic Supports on an Inclined Rough Plane

Marat Dosaev, Vitaly Samsonov
Institute of Mechanics, Lomonosov Moscow State University, Moscow, Russia

Summary. The features of behavior of a dynamically asymmetric heavy body with two elastic supports on an inclined rough plane are studied. The classical Coulomb model of dry friction is used. The supports can move without friction along parallel guides fixed in the body and interact with the body by means of elastic springs. It is shown that the equilibrium position of the system is isolated. There is no stagnation zone by the tilt angle of the guides. Depending on the relationship between friction and the angle of inclination of the plane, the body can slide on one or both supports. The equations of motion represent a dynamic system of variable structure. The range of inclination angles of the supporting plane close to the critical one is considered. For inclination angle values smaller than the critical one, the body on rigid supports does not start sliding from rest along the given inclined plane; for angle values greater than the critical one, the body on rigid supports starts sliding from rest. For elastic supports, it is shown that if the initial position of the body is not equilibrium, then, starting from a state of rest, the center of mass of the system acquires a non-zero longitudinal velocity even if the angle of inclination of the supporting plane is less than the critical one.

Introduction

To ensure the stability of building structures when supported on a rough foundation, it is necessary to take into account various factors: deviations in the dimensions of finished structures from design ones, compliance of structures, deviation of the supporting surface from the horizontal, etc. In particular, it is of interest to model the behavior of structures for a case of various additional disturbances, such as an earthquake (see, for example, [1]). The difficulties of modeling mechanical systems with dry friction were actively considered at the end of the 19th century ([2]). At the beginning of the 20th century, the phenomenon of "friction impact" was substantiated ([3]).

Modeling the interaction of dry friction with elastic forces leads to the formation of dynamic systems of variable structure. Such systems, even after the linearization of the equations, have properties characteristic of nonlinear systems. Such equations have several singular points depending on the mode of motion. In [4], the sliding of a flat rigid body supported on a horizontal rough plane by two elastic telescopic supports was considered. The alternation of body sliding on one and two supports is described depending on the coefficient of friction.

In this paper, some effects of the behavior of a dynamically asymmetric heavy body on two elastic supports on an inclined rough plane are considered. The equations of plane-parallel motion of the system are obtained for the cases of sliding of one or two supports. The equilibrium position has been found. Conditions for falling one of the supports into a friction cone are obtained. A numerical calculation of motion from a state of rest in a position close to equilibrium has been carried out. It is shown that the center of mass of the system acquires a non-zero longitudinal velocity even when the angle of inclination of the reference plane is less than that required for the beginning of sliding of a solid (inelastic) body.

Problem statement

Consider a heavy body $ABCD$ with mass m (Fig. 1a) supported by supports AA_1 and BB_1 on an inclined rough plane. We assume that the angle α between the plane and horizontal H_1H_2 is small. For simplicity, we assume that the body is rectangular ($AB = 2a$, $AD = 2b$).The support rods can slide along parallel guides without friction. To simulate the compliance of the supports, we introduce identical springs of sufficiently high rigidity between the body and the rods. When the springs are not stressed, $AA_1 = BB_1 = l_0$, $l_0 < b < a$. The center of gravity G_1 of the rectangle is displaced from the center of the rectangle G along the straight line DC by a distance d. Consider $d > 0$, the right support is more loaded than the left one. Support springs act on the body by forces $F_{el1} = -k(l_1 - l_0), F_{el2} = -k(l_2 - l_0)$, where k is the spring stiffness coefficient, l_1 is the length of the left support AA_1, l_2 is the length of the right support BB_1.

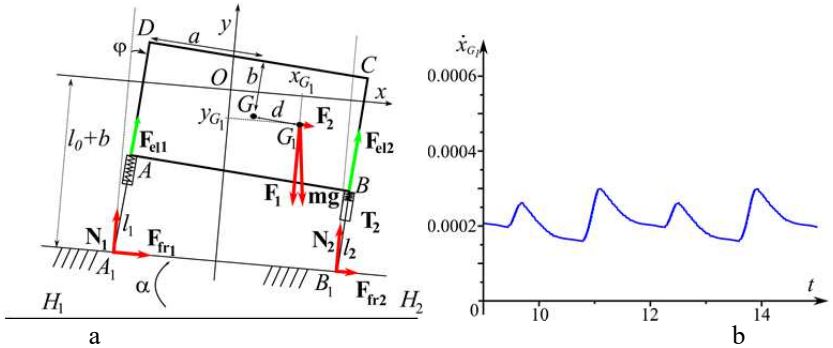

Figure 1: The body on a rough inclined plane. a) Mechanical system in consideration; b) Time dependence of the longitudinal velocity $\dot{x}_{G_1}$ of the center of mass in the steady regime of motion for the angle of inclination $\alpha < \alpha_crit$.

The following external forces act on the system: gravity **mg**, normal $\mathbf{N_1}, \mathbf{N_2}$ and tangential $\mathbf{F_{fr1}}, \mathbf{F_{fr2}}$ support reactions. The values of normal reactions at the support points are determined from the following relationships: $N_1 = F_{el1}\cos\varphi$, $N_2 = F_{el2}\cos\varphi$. In the case of sliding of the supporting legs, the reactions of the supports are interconnected according to the Coulomb law. In the case when the supporting leg is at rest, the value of the corresponding tangential reactions $F_{fr1} = F_{fr1stat}, F_{fr2} = F_{fr2stat}$ is determined from other motion characteristics.

Let us introduce a coordinate system *Oxy*. The axis *Ox* is parallel to the support plane and is at a distance $l_0 + b$ from it. The axis *Oy* is directed along the normal to the support plane. For convenience, we decompose the force of gravity into two components $\mathbf{mg} = \mathbf{F_1} + \mathbf{F_2}$, where $\mathbf{F_1}, \mathbf{F_2}$ are the projections of the force of gravity on the *Oxy* axes.

As generalized coordinates, we choose the coordinates of the center of mass x_{G_1}, y_{G_1} and the angle φ between the vertical and the sides of the rectangle. We distinguish between longitudinal (along the inclined plane) $\dot{x}_{G_1}$ and transverse $\dot{y}_{G_1}$ velocities of the center of mass.

The equilibrium position $\{\varphi^*, y^*_{G_1}\}$ of the system does not depend on the presence of tangential reactions and can be obtained from the following equations:

$$\begin{cases} y_{G_1} = (F_2 sin\varphi cos\varphi - F_1 cos^2\varphi)/(2k) + (b + l_0)(cos\varphi - 1) - d sin\varphi \\ 2F_2F_1 cos^5\varphi + ((F_1^2 - F_2^2)sin\varphi - (2((b+l_0)F_2 + F_1 d))k)cos^4\varphi - \\ -(2k(-F_2 d + F_1(b+l_0)))sin\varphi + F_2F_1)cos^3\varphi - 2F_2 akcos\varphi sin\varphi + 4a^2k^2 sin\varphi = 0 \end{cases}$$

In the region of small values φ^*, the dependences $\varphi^*(d), y^*_{G_1}(d)$ are single valued. The equilibrium position is isolated. There is no stagnation zone in the angle φ of inclination of the support guides.

Obviously, if friction is absent or sufficiently small, then both points of support slide during motion. If during some time period the point B_1 is motionless, then the number of degrees of freedom has decreased by one, the dynamical system must contain two equations of the second order. The immobility of the point is verified by the inequality: $\Delta = \mu N_2 - abs(F_{fr2stat})$. As the initial conditions we choose the position of rest, at which the guides of the supports are perpendicular to the supporting plane: $\varphi = 0$, $(x_{G_1}, y_{G_1}) = (d, -F_1/2k)$, $\dot{\varphi} = 0, \dot{x}_{G_1} = 0, \dot{y}_{G_1} = 0$. Then the inequality takes the following form: $\mu > \mu_2 = \dfrac{2\left|md(l_0 + b - 0.5F_1/k) - ((a-d)^2 m + J)F_2/(mg)\right|}{(J + m((a-d)^2 + (l_0 + b - 0.5F_1/k)^2)}$, J is the central moment of inertia of the body. If the inequality is satisfied, then the right support does not slide. For $\mu < \mu_2$ both supports start sliding. Similar reasoning can be carried out in the case of stopping the supporting point A_1.

Let us single out the value of the angle of inclination $\alpha = \alpha_crit$ of the plane such that the force F_2 is equal in magnitude to the maximum value of the friction force of rest of the same body with rigid supports: $F_2_crit = \mu F_1 = \mu$. For smaller inclination angles, the body on rigid supports does not slip. It turned out that for the considered case of elastic supports, the body slides from a state of rest even if the angle of inclination of the plane is less than the critical one. Residual internal oscillations lead to a change in the normal pressure and, accordingly, to a change in the friction forces in the supports. In the final motion, the body has a variable non-zero longitudinal velocity. The time dependence of the longitudinal velocity $\dot{x}_{G_1}$ of the center of mass in the steady regime of motion is shown in Fig. 1b for $F_2 = 0.00199, \mu = 0.002$. Such a regime, in particular, is possible due to the fact that the rear supporting point A_1 from time to time makes an instantaneous stop, and then slides in the opposite direction.

Conclusions

Plane motion of a heavy body supported by two elastic supports on a rough inclined plane is considered. The equations of motion are obtained, which are the dynamic system of variable structure. The isolated equilibrium position is found. It is numerically shown that from the state of rest, the center of mass of the system, can obtain a non-zero longitudinal velocity even if the angle of inclination of the supporting plane is less than the critical one required to start sliding of a rigid (inelastic) body.

The work is partially supported by Russian Science Foundation (project 22-21-00303).

References

[1] Selyutskiy Y., Garziera R., Collini L.(2017) On dynamics of a rigid body on a moving rough plane. *Archive of Applied Mechanics* **87**: 829–839.
[2] Painlevé P. (1895) Leçon sur le frottement, Hermann.
[3] Bolotov Ye.A. (1906) The motion of a plane material under constraints with friction. *Mat. Sbornik* **25 (4)**:562-708.
[4] Dosaev M., Samsonov V. (2021) Singularities in Dynamic Systems Involving Elastic Elements and Dry Friction. *Mechanics of Solids* **56 (8)**:1473–1481.

The Role of Dynamics in Face sheet/Core Interface Debonding of Sandwich Panels

Vyacheslav N. Burlayenko*, Svetlana D. Dimitrova†
*Department of Applied Mathematics, National Technical University 'KhPI', Kharkiv, Ukraine
†Department of Higher Mathematics, National Technical University 'KhPI', Kharkiv, Ukraine

Summary. The current research addresses the study of debonding the face sheet from the core in a sandwich structure in dynamic regime by means of the use of a cohesive zone model accounting for contact and friction nonlinear effects. The finite element method within the ABAQUS environment is used for modeling and simulations of the dynamic debonding propagation problem. By numerical examples, the influence of different parameters, such as the adhesive properties in terms of the interface strength and toughness and the type of traction separation law and types and rates of the imposed loading, in relation to the double cantilever beam test are estimated. The obtained results demonstrate the relevance of both the adhesive properties and loading conditions, the changes of which may notably modify the stress state near the interface crack tip and the debonding evolution in the sandwich specimen in dynamics.

Introduction

The use of lightweight sandwich composites as primary structural components has been considered as one of the means for designing structures with increasing stiffness and strength at minimal increasing in their weight. However, sandwich structures are very susceptible to debonding of the face sheet from the core. Dynamic loading is relevant for many applications of sandwich structures. In dynamics, the debonding growth and eventual structural failure may happen even at a load level significantly lower than the predetermined critical one [1]. Therefore, sandwich composites to be safely exploited should be developed to withstand the debonding propagation at a certain level of dynamic loading.
In the present study, the cohesive element formulation is used to model the debonding behaviour along the face sheet/core interface of sandwich panels in dynamic regimes. First, the finite element formulation is outlined and the constitutive relationships for the cohesive element are introduced. Finally, the numerical calculations related to the finite element model of the double cantilever sandwich beam (DCB) test are carried out and the results are discussed in details.

Formulation and method of solution

A dynamic framework of the finite element method (FEM) combined with cohesive zone approach is considered. By assuming infinitesimal deformations, neglecting body forces, but accounting for cohesive and contact forces for a body occupying a space V and containing crack modeled by cohesive elements at the surface $\partial V_c = \partial V_c^+ \cup \partial V_c^-$, the principle of virtual work states as follows [2]:

$$\int_{V\setminus\partial V_c} (\boldsymbol{\sigma} : \nabla\delta\mathbf{u} + \rho\ddot{\mathbf{u}}\cdot\delta\mathbf{u})\, dV + \int_{\partial V_c} \mathbf{T}\cdot\delta\boldsymbol{\Delta} dA + \int_{\partial V_c} (t_N\delta g_N + \mathbf{t}_T\cdot\delta\mathbf{g}_T)\, dA - \int_{\partial V_t} \overline{\mathbf{t}}\cdot\delta\mathbf{u} dA = 0 \qquad (1)$$

for all kinematically admissible displacement fields $\delta\mathbf{u}$ and given displacements $\bar{\mathbf{u}}$ at a boundary ∂V_u and a traction vector $\overline{\mathbf{t}}$ at ∂V_t. Herein, ρ is the density of material; $\boldsymbol{\sigma}$ is the Cauchy stress tensor associated with a displacement field $\mathbf{u}$, and $\ddot{\mathbf{u}}$ stands for an acceleration field; $\boldsymbol{\Delta}$ is the displacement jump across and $\mathbf{T} = \boldsymbol{\sigma}\cdot\mathbf{n}_c$ are cohesive forces along ∂V_c oriented by the normal $\mathbf{n}_c$; $\mathbf{t}_N = t_N\mathbf{n}_c$ and $\mathbf{t}_T$ are normal and tangential components of the contact traction which are interrelated with normal g_N and tangential $\mathbf{g}_T$ gap functions [3]. It is assumed that a bilinear traction separation law (TSL) governs the fracture behaviour. The TSL has the following form for each fracture mode $(i = I, II, III)$ [4]:

$$T = \begin{cases} k_i\Delta_i, & \Delta_i \le \Delta_i^0 \\ (1-D_i)k_i\Delta_i, & \Delta_i^0 \le \Delta_i \le \Delta_i^f \\ 0, & \Delta_i \ge \Delta_i^f, \end{cases} \qquad (2)$$

where $D_i = \left(\Delta_i^f(\Delta_i - \Delta_i^0)\right) / \left(\Delta_i(\Delta_i^f - \Delta_i^0)\right)$ is a damage variable. Herewith, damage initiates based on the quadratic stress criterion, whereas the damage evolves when the Benzeggagh-Kenane fracture criterion is met.
The impenetrability and friction constraints are stated in the form of Karush–Kuhn–Tucker conditions as follows:

$$t_N \le 0, \quad g_N \ge 0, \quad t_N g_N = 0 \quad \text{and} \quad \|\mathbf{t}_T\| \le \tau_{crit}, \quad \|\mathbf{g}_T\| \ge 0, \quad (\|\mathbf{t}_T\| - \tau_{crit})\,\|\mathbf{g}_T\| = 0 \qquad (3)$$

In the case of the Coulomb friction model, $\tau_{crit} = \mu t_N$, where μ is the coefficient of friction.
Following the FEM framework, the discrete system of dynamic equations of motion at time t takes the form:

$$[M]\{\ddot{U}\}_t + \{R_{int}\}_t + \{R_{coh}\}_t + \{R_{cont}\}_t = \{R_{ext}\}_t\,, \qquad (4)$$

where $\{U\}$, $\{R_{int}\}$, $\{R_{ext}\}$, $\{R_{coh}\}$ and $\{R_{cont}\}$ are the vectors attributed to the nodal displacements, and the nodal internal, external, cohesive and contact forces, respectively; $[M]$ is the mass matrix. The system (4) is solved using either central difference explicit or Hilber-Hughes-Taylor implicit time-stepping schemes available in ABAQUS [5].

To estimate the stress state close to the crack tip appeared along the surface ∂V_c, the interaction integral method is used to calculate the components of stress intensity factors as follows:

$$K_i = \frac{H}{2K_i^{aux}} J_{int}^i, \quad \text{where} \quad H = (2\cosh^2 \pi\epsilon)/(1/\bar{E}_1 + 1/\bar{E}_2), \tag{5}$$

where (*aux*) stands for auxiliary factors known from the asymptotic Williams type' solutions of the corresponding material system; $\bar{E}_k = E_k$ for in plane stress and $\bar{E}_k = E_k/(1-\nu_k)$ for in plane strain, $k = 1, 2$; and ϵ is the bi-material oscillation index. Herewith, the interaction integral is defined as

$$J_{int}^i = \lim_{\Gamma \to 0} \int_{\mathcal{C}+\mathcal{C}_+ + \Gamma + \mathcal{C}_-} \mathbf{m} \cdot \left\{ \boldsymbol{\sigma} : (\boldsymbol{\varepsilon})_i^{aux} \mathbf{I} - \boldsymbol{\sigma} \cdot \left(\frac{\partial \mathbf{u}}{\partial x_1} \right)_i^{aux} - (\boldsymbol{\sigma})_i^{aux} \frac{\partial \mathbf{u}}{\partial x_1} \right\} \cdot \mathbf{q} d\Gamma, \tag{6}$$

where $\mathbf{q}$ is a weighting function within the region enclosed by a contour $\mathcal{C} \cup \Gamma \cup \mathcal{C}_+ \cup \mathcal{C}_-$; $\mathbf{q} = \mathbf{q}_1$ on Γ and $\mathbf{q} = 0$ on $\mathcal{C}$; $\mathbf{m}$ is the outward normal. The line integral (6) is computed based on the domain integral formulation [6].

Results and conclusions

A 2-D finite element model of the DCB specimen is developed using eight-node reduced integration plane strain finite elements (`CPE8R`) available in ABAQUS. The mesh contained a refinement around the crack-tip.
The effect of impulsive loading on the transient dynamic SIFs of the DCB with stationary debonding is demonstrated in Figure 1. One can see that the DSIFs exceed their static counterparts for all the cases of loading. Also, the forms of impulse remarkably affect the time histories of the DSIFs. Herewith, unlike the stationary loading, the transient loads generate a high enough value of the mode II component.

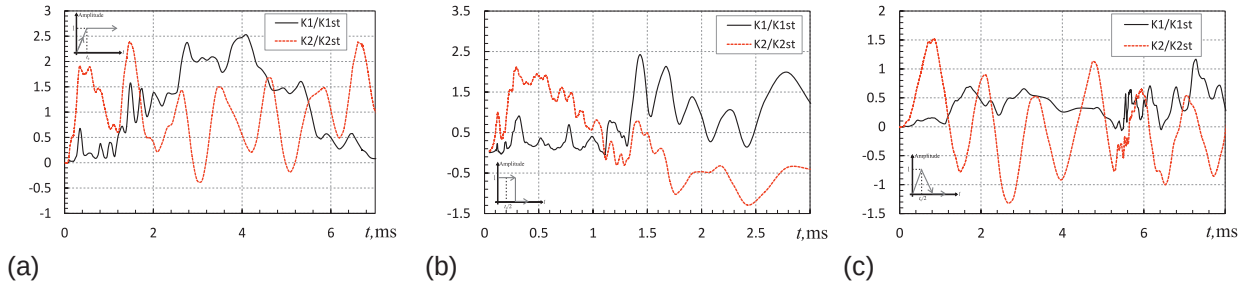

Figure 1: Dynamic SIFs with a ramp time $t_0 = 1$ ms due to: (a) step loading; (b) rectangular pulse; (c) triangular pulse.

Four-node cohesive elements (`COH2D4`) satisfying the TSL (2) were inserted into the finite element mesh of the DCB model to simulate fracture of the specimens under dynamic loading. The debonding growth under impulse loads of different durations and the harmonic load at a ceratin driving frequency is shown in Figure 2.

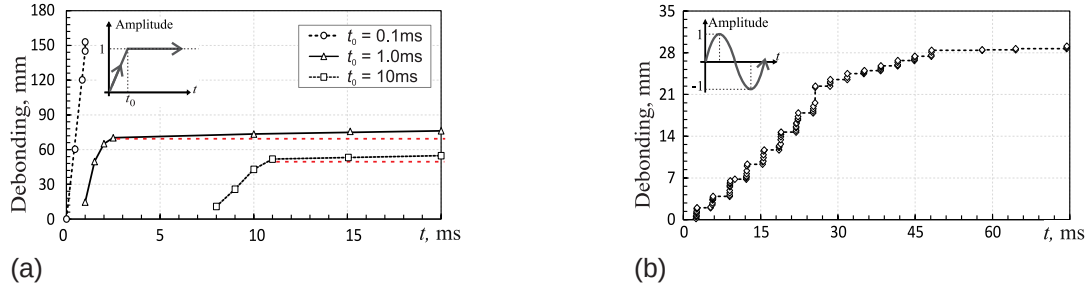

Figure 2: Debonding propagation versus time under: (a) impulsive step loading; (b) harmonic loading

The calculations revealed that there is a large dynamic effect in the DCB test, primarily due to stress waves from both the loading and crack face contact. Such waves interact with the crack tip and strongly affect the fracture parameters and the debonging behaviour of the DCB sandwich specimen.

References

[1] Funari M.F., Greco F., Lonetti P. (2018) Sandwich panels under interfacial debonding mechanisms. *Compos Struct* **203**:310–320.

[2] Burlayenko V.N., Sadowski T. (2014) Simulations of post-impact skin/core debond growth in sandwich plates under impulsive loading *J. Appl Nonlin Dyn* **3**(4):369–379.

[3] Burlayenko V.N., Sadowski T. (2018) Linear and nonlinear dynamic analyses of sandwich panels with face sheet-to-core debonding. *Shock Vibr* **2018**:Article ID 5715863.

[4] Camanho P.P., Dávila C.G., de Moura M.F. (2003) Numerical simulation of mixed-mode progressive delamination in composite materials. *J. Compos Mater* **37**(16):1415–1438.

[5] ABAQUS User's Manual ver. 2016. (2016) Dassault Systmes Simulia Corp., Providence, RI.

[6] Shih C.F., Asaro R.J. (1988) Elastic-plastic analysis of cracks on bimaterial interfaces: Part I—Small scale yielding. *J. Appl Mech* **55**(2):299–316.

Thursday, July 21, 2022
13:30 - 15:30

MS-19 Fluid-Structure Interaction
Saint Clair 3B

Chair: Andrei Metrikine

13:30 - 13:50
Linear stability analysis of fluid-structure interactions with an Immersed-Boundary method
TIRRI Antonia*, NITTI Alessandro, SIERRA Ausin Javier, DE Tullio Marco Donato, GIANNETTI Flavio
*Politecnico di Bari (Via Edoardo Orabona, 4, 70126 Bari BA, Italy Italy)

13:50 - 14:10
Membrane flutter induced by radiation of surface gravity waves on a uniform flow
KIRILLOV Oleg, **LABARBE Joris***
*Northumbria University (Northumbria University Mathematics, Physics and Electrical Engineering Ellison Building, D219 Newcastle upon Tyne NE1 8ST United Kingdom)

14:10 - 14:30
Passive fluidic control of flow around a circular cylinder
RAMSAY James, **SELLIER Mathieu***, HO Wei Hua
*University of Canterbury (University of Canterbury Private Bag 4800, Christchurch 8140 New Zealand)

14:30 - 14:50
Stability transitions of flexible nano-swimmer under rotating magnetic field
CHAPNIK Zvi*, HARDUF Yuval, WU Jiaen, JANG Bumjin, NELSON Bradley, PANÉ Salvador, OR Yizhar
*Department of Mechanical Engineering, Technion - Institute of Technology Haifa 32000 Israel (Technion - Institute of Technology Haifa 32000 Israel Israel)

14:50 - 15:10
Stochastic resonance in a parametrically perturbed aeroelastic system.
H. S. Varun*, ASWATHY M. S., SARKAR Sunetra
*Indian Institute of Technology [Madras] (Chennai 600036 India)

Linear stability analysis of fluid-structure interactions with an Immersed-Boundary method

Antonia Tirri*, Alessandro Nitti*, Javier A. Sierra †, Marco D. de Tullio * and Flavio Giannetti ‡
*Department of Mechanics Mathematics and Management, Polytechnic University of Bari, Bari, Italy
†Institut de Mécanique des Fluide de Toulouse, Toulouse, France
‡Department of Industrial Engineering, University of Salerno, Fisciano, Italy

Summary. In this paper a novel time-stepping approach for the linear stability analysis of elastic structures interacting with incompressible viscous flows is presented. The method is based on the coupling of an iterative Krylov-subspace algorithm for the solution of large eigenvalue problems within an Immersed-Boundary (IB) framework, to obtain a matrix-free global stability solver which extracts the necessary information directly from Direct Numerical Simulation (DNS).
In this work, the proposed approach is explained and validated with respect to test cases involving elastically-mounted rigid bodies immersed in open flows.

Introduction

The interactions of elastic structures with incompressible flows have been the subject of numerous works in recent years, due to their dynamically reach and complex behaviour. Despite the non-linear nature of these phenomena, the onset of the transition from a state of the system to another one can be predicted via a linear stability analysis. However, even with high-performing numerical tools, the global stability analysis of a fluid–structure system remains a prohibitive task due to considerable implementation difficulties; in particular, the linearisation of interface terms is often cumbersome.
This work presents an approach to perform the linear stability analysis of fluid-structure configurations which is incorporated into a validated FSI solver based on a Moving-Least-Squares Immersed boundary [1]. This technique has been largely used to explore the behaviour of fully coupled FSI applications involving large displacements, while linear stability analyses, on the other hand, are usually performed using mesh-deforming techniques. Although the latter methods are often chosen for two-dimensional cases, their implementation is often too expensive in three-dimensional applications. Furthermore, the extension to complex multi-body configurations is non trivial.
In this work, we adopt the approach followed by Mack and Schmid [2] for the global stability analysis of compressible flows and extend it to the coupled physics problem.

Methodology

We investigate the dynamics of elastically-mounted rigid bodies immersed in a Newtonian viscous fluid with homogeneous density. The flow is governed by the Navier-Stokes equations, here written in an Immersed-Boundary formulation,

$$\begin{cases} \dfrac{\partial \boldsymbol{u}}{\partial t} + \boldsymbol{u}\cdot\nabla\boldsymbol{u} = -\nabla p + \dfrac{1}{Re}\Delta\mathbf{u} + \mathbf{f}, \quad \text{in} \quad \Omega \\ \nabla\cdot\boldsymbol{u} = 0, \quad \text{in} \quad \Omega \end{cases} \tag{1}$$

where $\boldsymbol{u}$ and p denote the fluid velocity and pressure respectively, Ω is the physical region occupied by the fluid and $\mathbf{f}$ is the volume force arising from the IB treatment. The immersed bodies are modeled as mass-spring-damper systems,

$$\boldsymbol{M}\ddot{\boldsymbol{x}} + \boldsymbol{C}\dot{\boldsymbol{x}} + \boldsymbol{K}\boldsymbol{x} + \boldsymbol{F}_{nl}(\boldsymbol{x}, \dot{\boldsymbol{x}}) = \boldsymbol{F}(t), \tag{2}$$

where $\boldsymbol{x}$ is displacement vector, $\boldsymbol{M}$, $\boldsymbol{C}$ and $\boldsymbol{K}$ are the lumped mass, damping and stiffness matrix respectively, and $\boldsymbol{F}_{nl}$ takes into account the non-linear contributions. The forcing vector $\boldsymbol{F}(t)$ provides the resultant force on the body which, in the absence of gravity and other volume force components, reduce to the hydrodynamic load on the immersed surfaces. Collecting fluid and solid variables into the state vector $\boldsymbol{q}$, the coupled problem can be reformulated as

$$\frac{\partial \boldsymbol{q}}{\partial t} = \boldsymbol{R}(\boldsymbol{q}), \tag{3}$$

where $\boldsymbol{q}$ is the state vector, containing all the degrees of freedom of the problem, and $\boldsymbol{R}$ is the nonlinear evolution operator. The stability of the system in the vicinity of a steady steady solution of (3), $\boldsymbol{q}_b$, is given by a generalized eigenvalue problem for the Jacobian operator $\boldsymbol{J}$, who is an unknown quantity in the general case. Therefore, following Eriksson and Rizzi [3], we linearise the system numerically, approximating the evolution in time of a small perturbation $\boldsymbol{q}_p$ via the second-order accurate finite difference

$$\boldsymbol{q}_p(t_0 + n\Delta t) = \frac{\boldsymbol{q}_+ - \boldsymbol{q}_-}{2\epsilon}, \tag{4}$$

where $\boldsymbol{q}_+$ and $\boldsymbol{q}_-$ are outcomes of two disjoint advancement carried out by the DNS-IB solver:

$$\boldsymbol{q}_+ = \boldsymbol{F}(\boldsymbol{q}_b + \epsilon \boldsymbol{q}_p(t_0), n\Delta t), \tag{5}$$
$$\boldsymbol{q}_- = \boldsymbol{F}(\boldsymbol{q}_b - \epsilon \boldsymbol{q}_p(t_0), n\Delta t). \tag{6}$$

Recalling that the evolution of a small perturbation $\boldsymbol{q}'$ of the base state is given by

$$\boldsymbol{q'}(t_0 + T) = e^{\boldsymbol{J}T}\boldsymbol{q'}(t_0), \tag{7}$$

we recognize that the finite difference (4) approximates the action of the exponential transformation of the Jacobian matrix on the perturbation vector. Thus, we can compute a set of the least stable eigenvalues of the system by means of an iterative algorithm such as those belonging to the general class of Krylov subspace methods.
In the present work, the approximation of the leading eigenvalues of the system is computed by using the *Implicity Restarted Arnoldi Method* (IRAM) as implemented in the ARPACK open source package [4]. The steps of the algorithm are listed below:

1. The base flow is computed via the *BoostConv* [7] stabilization procedure;
2. Arnoldi iterations are performed until convergence is reached: $(k = 1, 2, ...)$
   (a) Vector $\boldsymbol{q}_p^k$ is generated
   (b) Reverse communication to the DNS-IB solver gives $\boldsymbol{q}_p^k(n\Delta t) = \frac{q^+ - q^-}{2\epsilon}$
   (c) Convergence of the desired Ritz pairs is checked
3. A logarithmic transformation is performed to recover the eigenvalues of the Jacobian matrix.

Results and discussion

The presented methodology has been validated with respect to several literature cases involving rigid bluff bodies interacting with flows with low Reynolds numbers. As a proof of concept, figure 1 shows the growth rate and frequency of the first two eigenvalues for the case of a elastically-mounted circular cylinder, undergoing vortex-induced vibrations in a flow with $Re = 60$. The cylinder is allowed to move only in the direction orthogonal to the unperturbed flow.
Given its matrix-free and Immersed-Boundary formulation, the method is capable of coping with complex geometries,

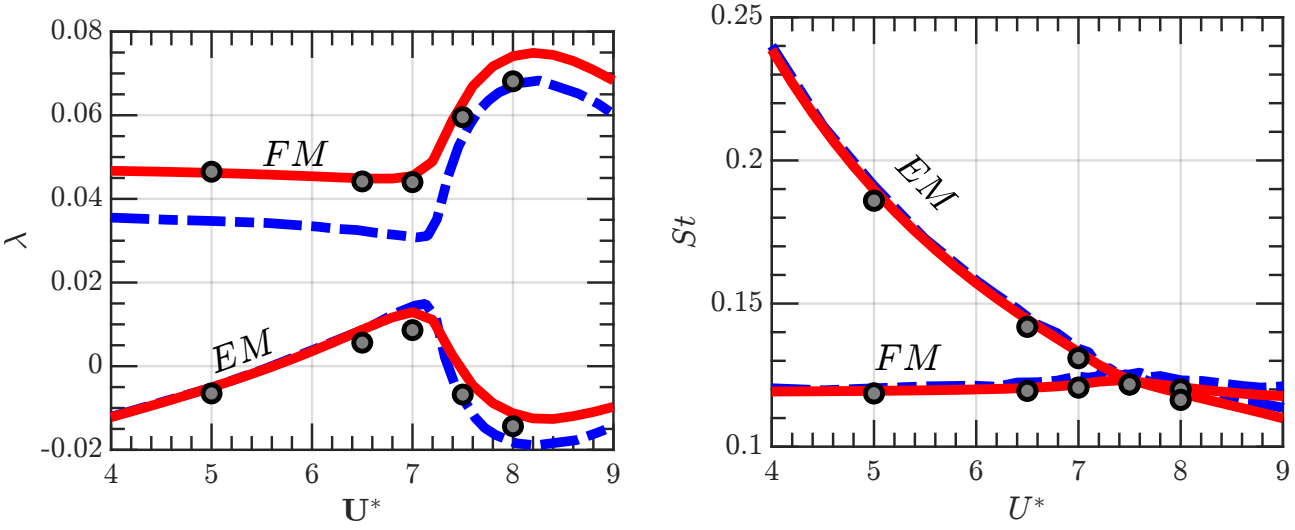

Figure 1: Results of the linear stability analysis of the VIV cylinder with $Re = 60$ and $m^* = 20$. Left figure: growth rate of the two least stable eigenmodes with U^*; Right figure: Strouhal number variation of the same eigenvalues with U^*. Red line: results from [6]; blu dotted line: results from [5]; black circles: present results.

multibody systems and large-scale inhomogeneous three-dimensional flows.

References

[1] Nitti A., Kiendl J., Reali A., de Tullio M. (2020) An immersed-boundary/isogeometric method for fluid–structure interaction involving thin shells. *Comput. Methods Appl. Mech. Eng.* **364**:112977.

[2] Mack C.J., Schmid P.J. (2010) A preconditioned Krylov technique for global hydrodynamic stability analysis of large-scale compressible flows. *J. Comput. Phys.* **229**:541-560.

[3] Eriksson L.E., Rizzi A. (1985) Computer-aided analysis of the convergence to steady state of discrete approximations to the euler equations. *J. Comput. Phys.* **57**:90-128.

[4] Lehoucq R.B., Sorensen D.C., Yang C. (1998) ARPACK Users' Guide: Solution of Large-Scale Eigenvalue Problems with Implicitly Restarted Arnoldi Methods. ISBN: 978-0-89871-407-4.

[5] Navrose, Mittal S. (2016) Lock-in in vortex-induced vibration. *J. Fluid Mech.* **794**:565–594.

[6] Sabino D., Fabre D., Leontini J.S., Lo Jacono D. (2020) Vortex-induced vibration prediction via an impedance criterion. *J, Fluid Mech.* **890**.

[7] Citro V., Luchini P., Giannetti F., Auteri F. (2017) Efficient stabilization and acceleration of numerical simulation of fluid flows by residual recombination. *J. Comput. Phys.* **344**:234–246.

Membrane flutter induced by radiation of surface gravity waves on a uniform flow

Joris Labarbe*, Oleg Kirillov*
*Northumbria University, NE1 8ST Newcastle upon Tyne, UK

Summary. We consider stability of an elastic membrane being on the bottom of a uniform horizontal flow of an inviscid and incompressible fluid of finite depth with free surface. The membrane is simply supported at the leading and the trailing edges which attach it to the two parts of the horizontal rigid floor. The membrane has an infinite span in the direction perpendicular to the direction of the flow and a finite width in the direction of the flow. For the membrane of infinite width we derive a full dispersion relation that is valid for arbitrary depth of the fluid layer and find conditions for the flutter of the membrane due to emission of surface gravity waves. We describe this radiation-induced instability by means of the perturbation theory of the roots of the dispersion relation and the concept of negative energy waves and study its relation to the anomalous Doppler effect.

Membrane flutter as a radiation-induced instability

Flutter of membranes is a classical subject for at least seven decades. Membranes submerged in a compressible gas flow and their flutter at supersonic speeds have been considered already in the works [1, 2]. Recent works on the membrane flutter are motivated by such diverse applications as stability of membrane roofs in civil engineering [3], flutter of traveling paper webs [4] and aerodynamics of sails and membrane wings of natural flyers [5, 6].

Surface gravity waves on a motionless fluid of finite depth is a classical subject as well, going back to the seminal studies of Russell and Kelvin [7]. Numerous generalizations are known taking into account, for instance, a uniform or a shear flow and surface tension [8], flexible bottom or a flexible plate resting on a free surface [9]. The latter setting has a straightforward motivation in dynamics of sea ice and a less obvious application in analogue gravity experiments [7].

Remarkably, another phenomenon that is being analysed from the analogue gravity perspective is super-radiance [7] and its particular form, discovered by Ginzburg and Frank [10], known as the anomalous Doppler effect (ADE) [11, 12]. In electrodynamics, the ADE manifests itself when an electrically neutral overall particle, endowed with an internal structure, becomes excited and emits a photon during its uniform but superluminal motion through a medium, even if it started the motion in its ground state; the energy source is the bulk motion of the particle [11].

Anomalous Doppler effect in hydrodynamics was demonstrated for a mechanical oscillator with one degree of freedom, moving parallel to the boundary between two incompressible fluids of different densities [13]. It was shown that the oscillator becomes excited due to radiation of internal gravity waves if it moves sufficiently fast. In [14] the ADE for such an oscillator was demonstrated due to radiation of surface gravity waves in a layer of an incompressible fluid.

Nemtsov [15] was the first who considered flutter of an elastic membrane being on the bottom of a uniform horizontal flow of an inviscid and incompressible fluid as an anomalous Doppler effect due to emission of long surface gravity waves. In the shallow water approximation, he investigated both the case of a membrane that spreads infinitely far in both horizontal directions and the case when the width of the membrane in the direction of the flow is finite whereas the span in the perpendicular direction is infinite. Nevertheless, the case of the flow of arbitrary depth has not been studied in [15] as well as no numerical computation supporting the asymptotical results has been performed. Another issue that has not been addressed in [15] is the relation of stability domains for the membrane of the finite width to that for the membrane of the infinite width.

Vedeneev studied flutter of an elastic plate of finite and infinite widths on the bottom of a uniform horizontal flow of a compressible gas occupying the upper semi-space. He performed analysis of the relation of stability conditions for the finite plate with that for the infinite plate using the method of global stability analysis by Kulikovskii [16, 17]. However, no connection has been made to the ADE and the concept of negative energy waves.

In the present work we reconsider the setting of Nemtsov in order to address the finite height of the fluid layer, find flutter domains in the parameter space, analyze them using perturbation of multiple roots of the dispersion relation, find the domains of absolute and convective instability and investigate dependence of the flutter onset on the width of the membrane including the limit of infinite width. We will explain the instabilities via the interaction of positive and negative energy waves by finding an appropriate G-Hamiltonian formulation and relate them to the anomalous Doppler effect.

References

[1] Benjamin T. B. (1963) The threefold classification of unstable disturbances in flexible surfaces bounding inviscid flows. *J. Fluid Mech.* **16**: 436–450.

[2] Bolotin V. V. (1963) *Nonconservative Problems of the Theory of Elastic Stability.* Pergamon Press, Oxford.

[3] Sygulski R. (2007), Stability of membrane in low subsonic flow. *Int. J. Non-Linear Mech.*, **42**(1): 196–202.

[4] Banichuk N., Barsuk A., Jeronen J., Tuovinen T., Neittaanmäki P. (2019) *Stability of Axially Moving Materials*, Springer, Berlin.

[5] Newman B. G., Paidoussis M. P. (1991) The stability of two-dimensional membranes in streaming flow. *J. of Fluids and Struct.* **5**: 443–454.

[6] Tiomkin S., Raveh D. E. (2017) On the stability of two-dimensional membrane wings. *J. Fluids Struct.*, **71**: 143–163.

[7] Carusotto I., Rousseaux G. (2013) The Cerenkov Effect Revisited: From Swimming Ducks to Zero Modes in Gravitational Analogues. In: Faccio D., Belgiorno F., Cacciatori S., Gorini V., Liberati S., Moschella U. (eds) Analogue Gravity Phenomenology. Springer, Cham.

[8] Maissa P., Rousseaux G., Stepanyants Y. (2016) Negative energy waves in a shear flow with a linear profile. *Eur. J. Mech. B/Fluids*, **56**: 192–199.

[9] Das S., Sahoo T., Meylan M. H. (2018) Dynamics of flexural gravity waves: from sea ice to Hawking radiation and analogue gravity. *Proc. R. Soc. A* **474**: 20170223.

[10] Ginzburg V. L., Frank I. M. (1947) On the Doppler effect at the superluminal velocity. *Dokl. Akad. Nauk SSSR* **56**: 583–586.

[11] Bekenstein J. D. , Schiffer M. (1998) The many faces of superradiance. *Phys. Rev. D* **58**: 064014.

[12] Nezlin M. V. (1976) Negative-energy waves and the anomalous Doppler effect. *Sov, Phys. Uspekhi* **19**: 946–954.

[13] Gaponov-Grekhov A. V., Dolina I. S., Ostrovskii L. A. (1983) The anomalous Doppler effect and the radiation instability of oscillator motion in hydrodynamics, *Doklady Akad. Nauk SSSR* **268**(4): 827–831. In Russian.

[14] Abramovich B. S., Mareev E. A., Nemtsov B. E. (1986) Instability in the oscillations of a moving oscillator while it radiates surface and internal waves. *Fluid Dynamics* **21**(1): 147–149.

[15] Nemtsov B. E. (1986) Flutter effect and emission in the region of anomalous and normal Doppler effects. *Radiophys. Quant. Elect.*, **28**(12): 1076–1079.

[16] Doaré O., de Langre E. (2006) The role of boundary conditions in the instability of one-dimensional systems, *Eur. J. Mech. B/Fluids*, **25**: 948–959.

[17] Vedeneev V. V. (2016) On the application of the asymptotic method of global instability in aeroelasticity problems. *Proc. Steklov Inst. Math.* **295**: 274–301.

Passive Fluidic Control of Flow around Circular Cylinder

James Ramsay*, Mathieu Sellier* and Wei Hua Ho†
*Department of Mechanical Engineering, University of Canterbury, Christchurch, New Zealand
† School of Mechanical, Industrial & Aeronautical Engineering, University of Witwatersrand, Johannesburg, South Africa

Summary. Suction of the boundary layer is an effective means of delaying separation and reducing drag on external flows. However, if a pumping system is required to generate the suction, the weight and power consumption of the system can undo that benefit. 'Autogenous' (self-generating) suction control is a type of flow control that utilises the energy already within a flow (notably the pressure gradients) to drive the suction, thereby requiring no further energy to the system. This paper describes numerical studies that were performed on the flow around the circular cylinder in the 2D laminar range: $Re = 40$ (steady) and $Re = 120$ (unsteady). Suction and blowing control were implemented by imposed velocity boundary conditions. These controls were then modified using optimisation methods to generate arrangements of suction and blowing that can be passively generated by their pressure differential (i.e. $P_s \geq P_b$). Steady and unsteady simulations were performed. It was found that at both $Re = 40$ and $Re = 120$ drag-reducing arrangements could be produced. At $Re = 120$ a reduction in drag of 4.3% was found while maintaining a positive pressure differential from the suction to blowing loci. This approach for developing passive suction control can be applied to other bluff body flows and higher Reynolds numbers to design efficient optimised flow control.

Introduction

Boundary layer suction has a long history as an effective means of flow control. The first recorded use of suction to control a fluid flow was by Ludwig Prandtl to test his boundary layer theory (1). It has been shown by many experimental (2; 3; 4) and numerical (5; 6; 7; 8) studies that suction control is extremely effective at reducing drag, subduing vortex shedding, or improving lift in external flows. Additionally, optimised non-uniform suction can be much more efficient and effective than uniform suction or slot suction (9). In some applications, suction control is effective not by its influence on the boundary layer, but by its body force imposed on the flow, for example when suction is applied on the already separated wake behind an object (10).

On the other hand, to generate the suction flow, an appropriate pressure gradient is required. This pressure gradient must be sufficient to overcome porous and viscous losses through any suction ducting, and depending on the strength of suction desired, must also overpower the momentum of fluid outside the boundary layer. This is the case whether the suction is applied through slots or with a porous surface. In practice, this is typically achieved using a pump or compressor (11; 3). The energy required to power this pump may exceed the savings in energy from drag reduction. Additionally, the weight of the pump and suction system will increase the mass needed to accelerate for transportation applications. Due to this and other considerations, while suction control may be extremely effective, it may be inefficient (12).

One alternative to a pump system is to use the pressure gradients already within a flow to drive a suction/blowing through the bounding surface. This was coined 'autogenous suction control' by Atik and van Dommelen, meaning 'self-generating' (13). By connecting a region of high pressure to a region of low pressure, a secondary flow can naturally develop. Autogenous suction was first explored behind shocks (14; 15; 16), but Atik and van Dommelen were the first to explore its potential in subsonic and laminar flows.

In their numerical study, it was shown that autogenous suction control was possible for a thin airfoil and could delay separation over a range of angles of attack (13)). The autogenous suction control was achieved by applying suction over a distributed area downstream of the location of minimum pressure (and separation point) while exhausting the fluid removed by suction upstream. The numerical approach by Atik and van Dommelen was limited in that it solved the boundary layer equations rather than the full Navier-Stokes equations, which was appropriate for their idealised airfoil but is unlikely to be so for other flow cases. Additionally, their study was intentionally idealised, and many considerations of a physical implementation were ignored or set to arbitrary values (e.g. viscous and porous losses, the effect of tangential pressure gradients). However, a type of autogenous suction control device was patented by inventor Pradip Parikh and assigned to Boeing, to delay separation over an aircraft wing (17).

The paper by Atik and van Dommelen demonstrated the potential for autogenous suction to beneficially control the flow around an aerodynamic shape (delayed separation), while the patent held by Boeing demonstrates how it might be used for a real-world application (13; 17). However, it has not been shown whether autogenous suction control can reduce drag on a body, and whether other arrangements – such as suction upstream of the minimum pressure location – would be beneficial. Therefore, in this study, autogenous suction control was developed on a canonical flow with the objective to minimise drag and develop a methodology for designing autogenous suction control using the Navier-Stokes equations. A bluff body was chosen as the geometry in order to supplement the work of Atik and van Dommelen on a streamlined shape, hence, the flow around the circular cylinder in the 2D laminar range ($Re \leq 188.5$) was modelled numerically. Parameterised boundary conditions were used to impose the suction and blowing flows, which were then optimised with constraints so as to be autogenous.

Methodology

Computational Domain & Governing Equations

The flow around the circular cylinder was modelled numerically for $Re = 40$ and $Re = 120$ using COMSOL Multiphysics, a commercial Finite Element software package. The governing equations are the incompressible isothermal Navier-Stokes equations:

$$\frac{\partial \mathbf{u}}{\partial t} + (\mathbf{u}\cdot\nabla)\,\mathbf{u} - \nu\nabla^2\mathbf{u} + \frac{1}{\rho}\nabla p = \mathbf{f}, \tag{1}$$

$$\nabla\cdot\mathbf{u} = 0, \tag{2}$$

where $\mathbf{u}$ and p are the velocity vector and scalar pressure fields respectively (the dependent variables), $\nu = \mu/\rho$ is the kinematic viscosity, ρ is the fluid density, and $\mathbf{f}$ is the vector for all external forcing terms (in this case, zero). Both steady-state and unsteady simulations were employed in this study, and in the former case the time-derivatives vanish (first term of Equation (1)).

The computational domain is shown in Figure 1. This is the same as in (9), where the model was extensively validated against experimental data for drag and separation angle from the literature (18; 19; 20; 21). The flow around the circular cylinder is commonly studied, and its characteristics are well known (22). The flow is characterised by its Reynolds number, $Re = \frac{\rho U D}{\mu}$, where the characteristic length is the cylinder diameter, D. For $Re \leq 188.5$ the flow is 2D and wholly laminar, but for $Re \geq 47$ the flow is unsteady.

With 31,640 elements and a time-step of $dt = \frac{1}{30}T = \frac{1}{30}\frac{D}{USt}$, where T is the vortex shedding period and St is the Strouhal number, the model is sufficiently mesh and time independent for $Re \leq 180$ (see (9)). Here, the control was ramped up over $1T$ on a fully-developed solution of the uncontrolled flow. The simulation was run until the flow was fully-developed again (usually $10T$). The unsteady studies always commenced using a fully-developed uncontrolled flow as the initial condition.

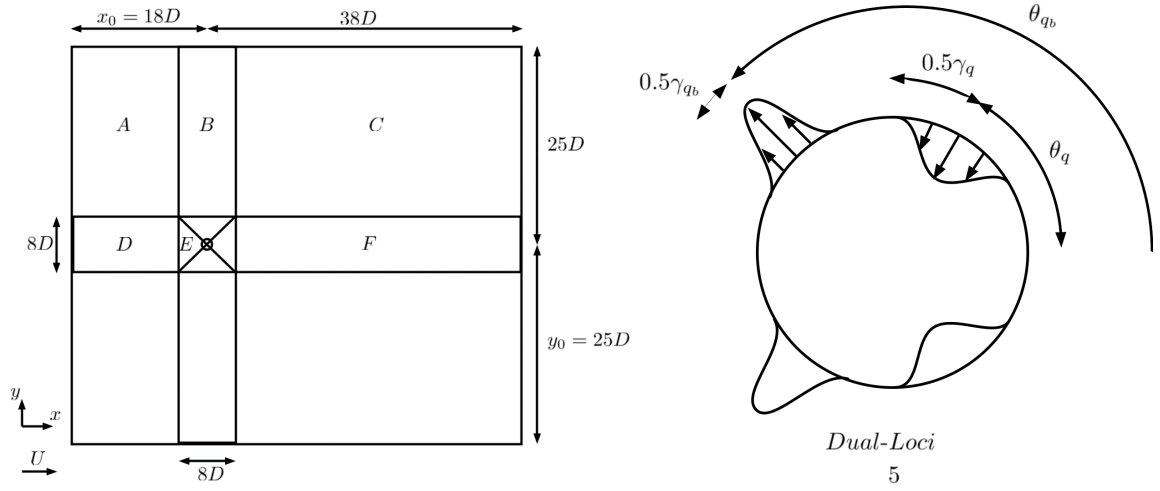

Figure 1: Computational domain for simulations (a); Schematic illustrating the key parameters for the dual-loci control. The subscript 'b' denotes a blowing control parameter, while no subscript indicates suction (b).

Boundary Conditions

The numerical boundary conditions consist of a uniform inlet on the left, lower and upper boundaries, $u = U = \frac{Re\nu}{D}$, $v = 0$. A zero relative pressure outlet is defined on the right boundary. The boundary on the cylinder was defined with a prescribed velocity Dirichlet condition. Suction and blowing profiles were implemented through this boundary condition as a function of angle from the trailing edge, θ. Theoretically infinite suction/blowing profiles could be implemented, however it was found in (9) that optimal suction in this range typically consisted of a single locus of suction. A bell-shaped (cubic) profile was effective. Hence, in this work varieties of this 'single locus' profile for the suction and blowing profiles were considered, and with suction/blowing in the normal direction only ($\mathbf{u} = (u_n, u_t) = (u_n, 0)$ at the cylinder wall).

The suction/blowing profiles on the cylinder were defined to have one area (locus) of suction and one locus of blowing. This is called the 'dual-loci' approach in this paper. Each control locus utilises the 'single locus' profile from (9) which defines a smooth cubic profile with zero derivatives at its centre and edge. Three parameters are needed to define the profile: the location of the locus centre as measured from the trailing edge (TE), θ_q, the spread of the locus measured as an angle, γ_q, and the maximum strength (which is applied at the centre, $c_{q_{max}}$. These are illustrated in Figure 1. By superimposing two single locus profiles – one for blowing, one for suction – the dual-loci control is achieved. The control applied is mirrored across the streamwise axis of the cylinder.

Outline of Studies

The results of two studies on autogenous suction control are presented here:

1. Q-balanced control: flow-rates of the suction and blowing loci must be equal ($Q_s = Q_b$), but no pressure requirement is imposed.
2. P-Q-balanced control: Flow-rates must be equal and the pressure gradient negative from suction to blowing ($Q_s = Q_b$, $P_s - P_b \geq 0$).

The first represents a case where a pump or other device must be used in order to produce the suction/blowing, whereas the second is the autogenous case.

Optimisation Approach

Control Parameters

In each model there were five independent control parameters and one dependent control parameter as summarised in Table 1. As Q_s must equal Q_b to maintain continuity, the sixth control parameter ($c_{q_{max_b}}$) is dependent on the rest.

Table 1: Control Parameters

Parameter Name	Suction Parameter	Blowing Parameter
Control angle (°)	$0 \leq \theta_q \leq 180$	$0 \leq \theta_{q_b} \leq 180$
Control spread (°)	$0 \leq \gamma_q \leq 90$	$0 \leq \gamma_{q_b} \leq 90$
Control peak strength	$0 \leq c_{q_{max}} \leq 1$	$c_{q_{max_b}} = \frac{\gamma_{q_s}}{\gamma_{q_b}} c_{q_{max}}$

Objectives and Constraints

The major control objective in each study was to minimise the total drag on the cylinder as evaluated by integrating the stream-wise normal and shear forces:

$$J_{d_t} = C_{d_t} = C_{d_p} + C_{d_f} = \frac{1}{\frac{1}{2}\rho U^2 D} \oint \left(-p\left(\theta\right) + \mu \frac{-\partial u_t\left(\theta\right)}{\partial r} \right) \cos\left(\theta\right) R d\theta, \tag{3}$$

where R the radius of the cylinder, and θ the angle measured anti-clockwise from the trailing edge.

For the autogenous control studies (Model III), an additional objective that the averaged suction pressure must be greater than the averaged blowing pressure was included:

$$J_{auto} = \Delta P = P_s - P_b \geq 0. \tag{4}$$

The suction and blowing parameters were optimised with a nested approach, as shown in Figure 2. I.e. the suction control parameters are selected by the control algorithm, then a secondary optimisation occurs to arrange the blowing locus such that the drag is minimised and pressure drop maximised for that particular suction arrangement. The major optimisation then evaluates how well this combined suction/blowing control achieves the total objectives. The inner (minor) optimisations had a maximum of 50 model evaluations each time it was called.

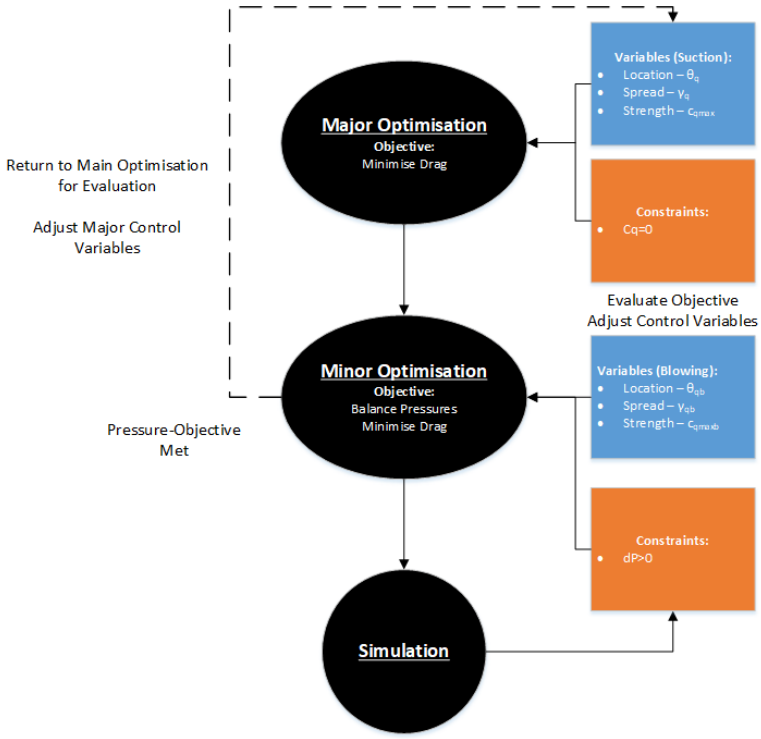

Figure 2: Flow-chart of P-Q-Balanced Dual-Loci optimisation (autogenous suction control).

An additional constraint was also implemented, preventing the suction and blowing loci from overlapping in order to generate realisable controls.

Results & Discussion

Optimisation of Non-Autogenous Dual-Loci Control

Optimisation of the Q-balanced dual-loci control resulted in suction/blowing control which reduced drag by up to 13% at $Re = 40$ and 22% at $Re = 120$. The control parameters and key results for the optimised control summarised in Table 2 and Table 3 while the velocity and pressure contours are shown in Figure 3. The improvement in drag is strong at both Re, but more potent at the higher Reynolds number of $Re = 120$. However, when the pressure differential between the suction and blowing loci are considered ($-dP = -1.5387\& - 1.4143$), it can be seen that this control would require substantial power to run due to the strong APG between the suction and blowing loci.

The optimised control profiles feature suction upstream and blowing near the trailing edge of the cylinder. The suction removes the low momentum fluid and entrains higher momentum which delays the separation. Consequently the pressure drag is greatly reduced, while there is a smaller increase in skin friction drag due to the now higher velocity gradient at the wall. At both Reynolds numbers there is a narrow spread for the suction and a wider spread for blowing. This reflects the previous findings shown in (9) where the drag is very sensitive to the location of suction - with clearly advantageous locations. Therefore, the most efficient control targets these locations. Similarly, it appears that the trailing edge is the best location for blowing control. This helps to increase the base pressure.

Table 2: Key control parameters for drag-optimised Q-balanced dual-loci control compared to its unbalanced variety.

Parameter	$Re = 40$	Re=120
θ_q	97.898°	78.897°
γ_q	31.676°	43.607°
$c_{q_{max}}$	0.987	0.569
θ_{q_b}	31.501°	27.835°
γ_{q_b}	63.001°	55.669°
$c_{q_{max_b}}$	-0.496	-0.446
C_q	0	0

Table 3: Key results for optimised Q-balanced control compared to uncontrolled case.

	$Re = 40$		$Re = 120$	
Parameter	No Control	Q-Balanced	No Control	Q-Balanced
C_{d_t}	1.6321	1.4158	1.0860	0.8486
C_{d_p}	1.0760	0.4365	0.8177	0.1998
C_{d_f}	0.5561	0.9793	0.2683	0.6487
θ_s	54.107°	37.809°	68.826°	32.612°
dP	-	-1.5387	-	-1.4143

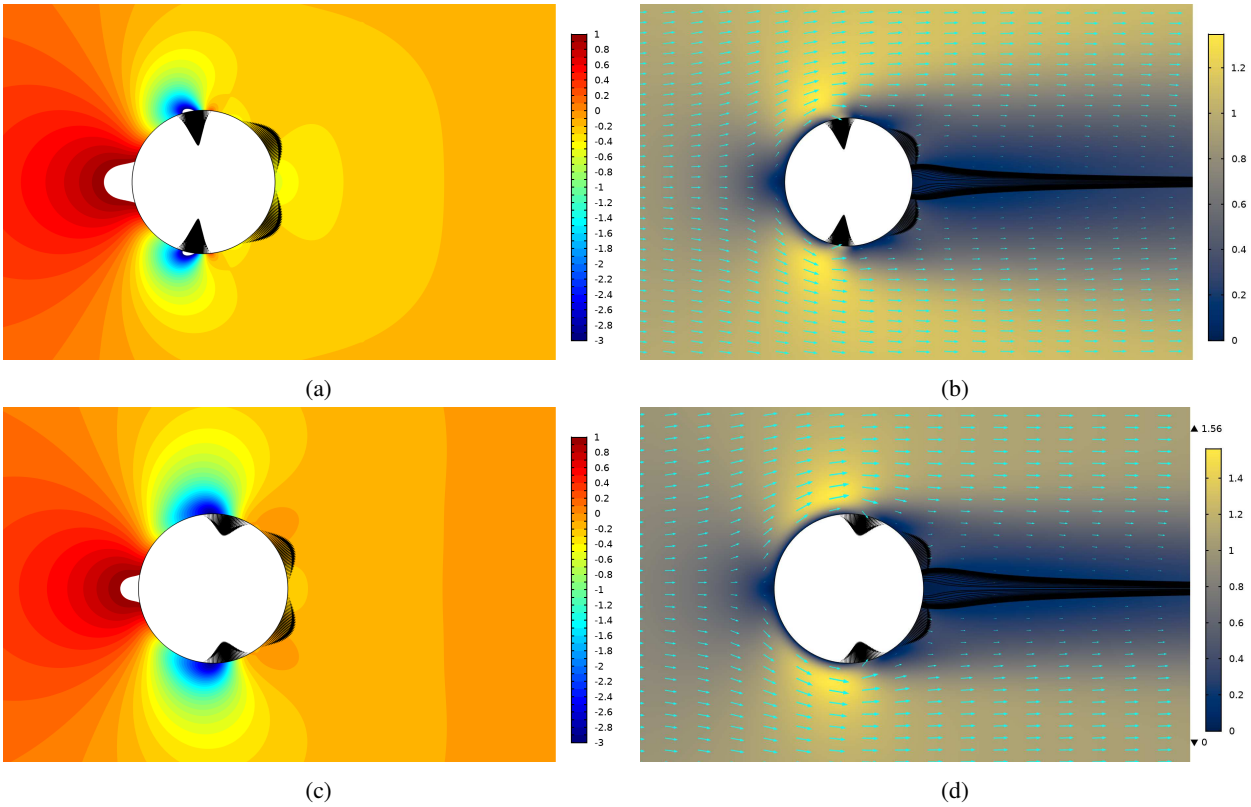

(a) (b) (c) (d)

Figure 3: Velocity surface (a,c) and pressure contours (b,d) for optimised Q-balanced dual-loci controlled flow at $Re = 40$ (a,b) and $Re = 120$ (c,d).

Time-Dependent Simulation Verification

Time-Dependent Simulation Verification

The key results for best non-autogenous control from the optimisation study at $Re = 120$ are shown in Table 4. This optimised control is strong enough to fully stabilise the flow, therefore the results from the steady-state simulations match perfectly with the time-dependent simulations. However, since this control should be compared against the drag for the time-dependent case, the improvement is now seen to be 38.7%. The data in Table 6 clearly indicates that this massive improvement comes from the large reduction in pressure drag, while the skin friction drag has almost doubled. The control arrangement is still highly unfavourable for autogenous control, and its actual efficiency would be low given the large adverse pressure gradient (APG) that the control flow has to overcome. However, it is encouraging to see that the dual-loci control can be extremely effective on unsteady flows. The pressure and velocity contours are not shown for this simulation as they match in practically every aspect, those in Figure 3.

Table 4: Key results for optimised Q-balanced dual-loci control verified on time-dependent simulations at $Re = 120$.

Parameter	No Control (SS)	No Control (TD)	Q-Opti (SS)	Change from No Control SS (%)	Q-Opti TD	Change from No Control TD (%)
C_{d_t}	1.086	1.3851	0.8486	-21.90%	0.8486	-38.70%
C_{d_p}	0.8177	1.0585	0.1998	-75.60%	0.1997	-81.10%
C_{d_f}	0.2683	0.3266	0.6487	141.80%	0.6489	98.70%
dP	-	-	-1.414	-	-1.415	-

Optimisation of Autogenous Dual-Loci Control
Steady-State Optimisation

Using the two-optimisation process, the dual-loci control was successfully optimised to minimise drag while enforcing the constraint on pressure drop between the suction and blowing loci.The optimised control parameters and key results are shown in Tables 6 to 8.

The improvement in drag is much weaker when the autogenous constraint is imposed compared to the Q-balanced approach above. Nevertheless, the drag on the cylinder was reduced while maintaining a positive pressure gradient from the suction to blowing loci. In other words, autogenous suction control was effective for this flow. It was found that the optimised control was quite sensitive to the initial control parameter values for this flow, so two sets of initial values were used at both Re - IV1 and IV2 as described in Table 5. For IV1, at $Re = 40$ the drag was reduced by 5.45% while at $Re = 120$ a more modest 3.68% improvement was achieved while the improvements from the IV2 case were even lower.

Table 5: Initial values of control parameters for P-Q-balanced dual-loci optimisation.

Control parameter	**Initial Values (IV1)**	**Alternative Initial Values (IV2)**
θ_q	150°	120°
γ_q	20°	40°
$c_{q_{max}}$	0.1	0.1
θ_{q_b}	90°	80°
γ_{q_b}	10°	10°
$c_{q_{max_b}}$	-0.2	-0.4

In both cases, the drag improvement was through a combination of the pressure drag and skin friction drag. This is unlike for the case of suction only or Q-balanced control, where the pressure drag is substantially improved but the skin friction worsened to produce a net benefit. At both Reynolds numbers, a quite different control flow was utilised to achieve the drag objective. This was to produce a suction and blowing very close to each other on the front half. This is effective at manipulating the C_f and C_p profiles over the front half, reducing the pressure and skin friction, rather than delaying separation or improving the base pressure.

This dramatically different control arrangement appears to be a factor of the initial values provided for the control. When alternative initial values – IV2 – were used, the resulting control was quite different. The final optimised controls were very similar to their initial conditions which suggests that there are other local optima that may be found also.

Table 6: Optimised control values for different dual-loci settings.

	$Re = 40$		$Re = 120$	
Parameters	P-Q-Balanced	Q-Balanced	P-Q-Balanced	Q-Balanced
θ_q	165.520°	97.898°	165.260°	78.897°
γ_q	26.015°	31.676°	27.158°	43.607°
$c_{q_{max}}$	0.381	0.987	0.162	0.569
θ_{q_b}	144°	31.501°	146°	27.835°
γ_{q_b}	10°	63.001°	4.410°	55.669°
$c_{q_{max_b}}$	-0.99	-0.496	-1	-0.446
C_q	0	0	0	0

Table 7: Optimised control values for different dual-loci settings.

Parameter	$Re = 40$			$Re = 120$		
	No Control	Q-Balanced	P-Q-Balanced	No Control	Q-Balanced	P-Q-Balanced
C_{d_t}	1.6321	1.4158	1.5432	1.086	0.8196	1.046
C_{d_p}	1.076	0.4365	1.03	0.8177	0.1265	0.8013
C_{d_f}	0.5561	0.9793	0.51316	0.2683	0.6931	0.2447
θ_s	54.107°	37.809°	176.08	68.826°	29.392°	147.74
dP	-1.6333	-1.5387	0.3403	-	-1.4143	0.4928

Table 8: Change in optimised result depending on initial values for control at $Re = 40$ and $Re = 120$.

Parameters	IV1	Re=40 Opti	Re=120 Opti	IV2	$Re = 40$ Opti	$Re = 120$ Opti
θ_q	150°	165.52°	165.26°	120°	119.96°	121.91°
γ_q	20°	26.015°	27.158°	40°	42.566°	51.7°
$c_{q_{max}}$	0.1	0.3807	0.16239	0.1	0.111	0.053
θ_{q_b}	90°	144°	146°	80°	24.313°	39.5°
γ_{q_b}	10°	10°	4.4102°	10°	47.125°	23.5°
$c_{q_{max_b}}$	-0.2	-0.9904	-1	-0.4	-0.1002	-0.1176
dP	-	0.3403	1.046	-	0.0277	1.077
C_{d_t}	-	1.5432	0.8013	-	1.6083	0.7716

The pressure contour and velocity surfaces are shown for the best optimised P-Q-Balanced dual-loci control (IV1 case) below at $Re = 40$ & 120 in Figure 4. The control is concentrated on the front-half and improves both the skin friction and pressure drag modestly. This control arrangement is highly dependent on the initial values used for the optimisation study.

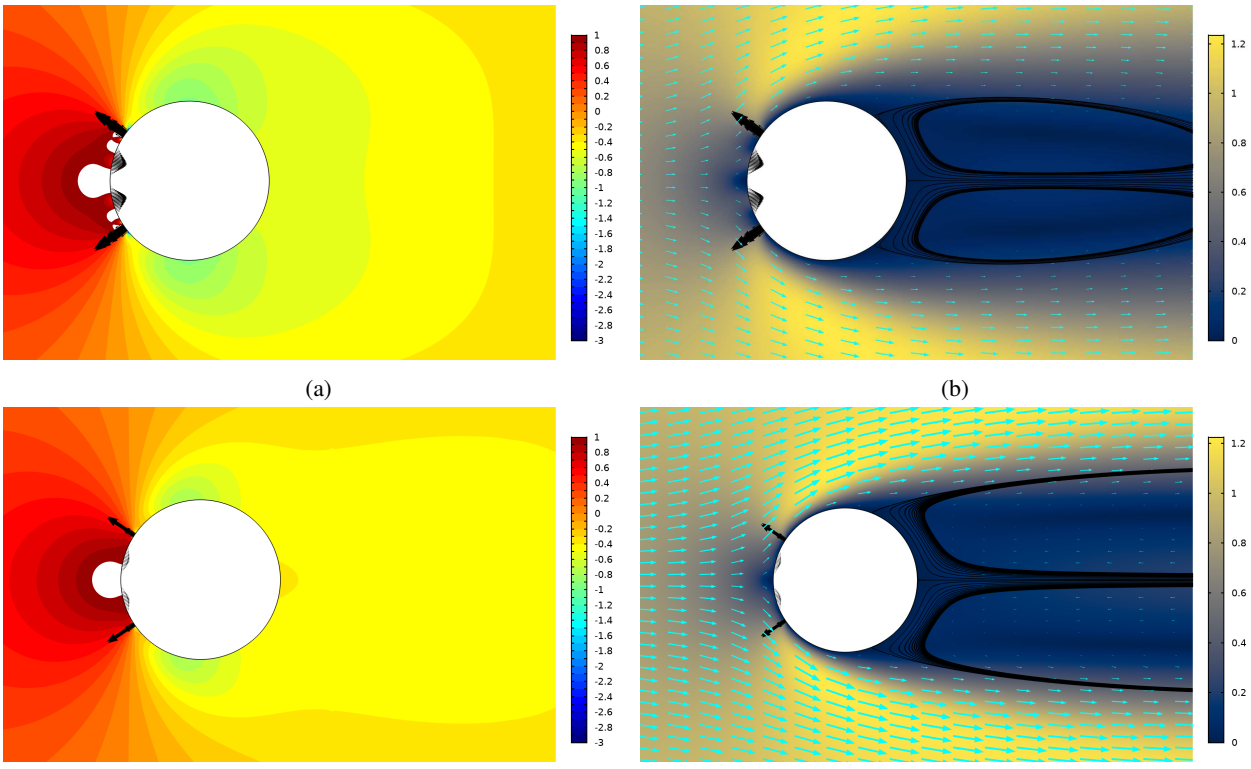

Figure 4: Velocity surface (a,c) and pressure contours (b,d) for optimised P-Q-balanced dual-loci controlled flow round cylinder at $Re = 40$ (a,b) and $Re = 120$ (c,d).

Overall, the major research question of "can autogenous suction control theoretically be used to reduce drag for bluff body flows?" has been found to be true. Certainly for $Re = 40$, whereas the flow at $Re = 120$ should be resolved with

an unsteady simulation to confirm.

Time-Dependent Verification

As for the non-autogenous Q-balanced control, to verify whether these results are feasible for the true unsteady flow at $Re = 120$, time-dependent simulations were carried out with the optimised control parameter. These simulations were successful and found that the optimised controls still satisfied the pressure-drop requirements in both time-dependent cases. Unlike for the Q-balanced control, the optimised autogenous control does not stabilise the flow at $Re = 120$ and therefore the steady-state simulations are flawed. The time-averaged values (over one vortex-shedding period), and their fluctuation are given for the key parameters of the first P-Q-balanced design compared to the steady-state values in Table 9. The key parameters for both P-Q-balanced designs are provided in Table 10.

As expected, the drag coefficient values are quite different from the steady-state values, but the reaction to the control is consistent in the TD simulations. For the first optimised arrangement (with the suction and blowing situated at the front of the cylinder), the improvement in drag is dulled. An average 2.5% improvement was produced compared to the 3.7% predicted by the steady-state study. Importantly, the positive pressure gradient between the suction and blowing loci remains, and in fact is greater for the TD case (0.5764 vs. 0.4928). This makes sense as the pressure profile is steeper and has a larger fluctuation for the unsteady case, even for the uncontrolled flow, which is beneficial for the autogenous constraint.

The most interesting result is the dramatic change in performance for the second P-Q-balanced design (produced using the second set of initial values in the optimisation). Where the steady-state result suggested a reduction in drag of only 0.83%, the actual result when applied to the unsteady cylinder flow was actually 4.3%. This is not just better than the SS estimate, but it is a greater improvement than the first P-Q-balanced design. While the first design reduces both skin friction and pressure drag modestly, the second design uses the same mechanisms as suction-only control to minimise total drag by greatly reducing the pressure drag at the cost of slightly increasing the skin friction drag. The design of this control fits better with previous findings that suction near the 90° mark with blowing situated near the rear produces the best drag-reduction but is difficult to achieve with autogenous pressure gradients (5).

Table 9: Key results for SS-optimised P-Q-balanced dual-loci control applied to time-dependent simulation compared to the steady result and uncontrolled values. SS= steady-state, TD= time-dependent.

Parameter	SS No Control	SS P-Q Opti	TD No Control Average	TD P-Q Average	TD P-Q Fluctuation (±)	% Change
C_{d_t}	1.086	1.046	1.3851	1.3517	0.0169	-2.50%
C_{d_p}	0.8177	0.8013	1.0585	1.0485	0.0155	-1.00%
C_{d_f}	0.2683	0.2447	0.3266	0.3032	0.0017	-7.70%
dP	-	0.4928	-	0.5764	0	-

Table 10: Comparison of the two optimised P-Q-Balanced dual-loci control in full time-dependent simulation.

Parameter	TD No Control Average	TD Fluctuation (±)	IV1 TD P-Q Average	IV1 TD P-Q Fluctuation (±)	IV2 TD P-Q Average	IV2 TD P-Q Fluctuation (±)
C_{d_t}	1.3851	0.0171	1.3517	0.0169	1.3274	0.0096
C_{d_p}	1.0585	0.0156	1.0485	0.0155	0.9715	0.0088
C_{d_f}	0.3266	0.0017	0.3032	0.0017	0.356	0.0008
dP	-	-	0.5764	0	0.0747	0.0027

This second arrangement of the autogenous suction control is particularly promising for a variety of reasons. Firstly, the control flow rates are much lower. While the relationship between the control flow rate and the necessary pressure to drive it has mostly been ignored in the present study, it is likely that large control flows will require larger pressure drops. The peak suction strength is only $c_{q_{max}} = 0.053$ which is more like the level of suction seen for early boundary layer studies (23, p. 383). Secondly, the flow-path for the control is better. While the optimisation procedure accounts for the effects of blowing control on the boundary layer and the second-order impact on the pressure profile, it seems logical to have the flow exhausted out the rear of the cylinder. This prevents the boundary layer from being blown away, and does not have to produce a dramatic change in the momentum direction of the control flow. Finally, the second control arrangement appears to dampen the dynamics of the flow. The fluctuations of the drag coefficients are all reduced from the uncontrolled case. The time-averaged flow fields are shown for the two controlled and uncontrolled cases in Figure 5.

The changes to the flow are subtle so there is little to remark on except the small morphing of the reversed flow region in the wake from the blowing in the second case.

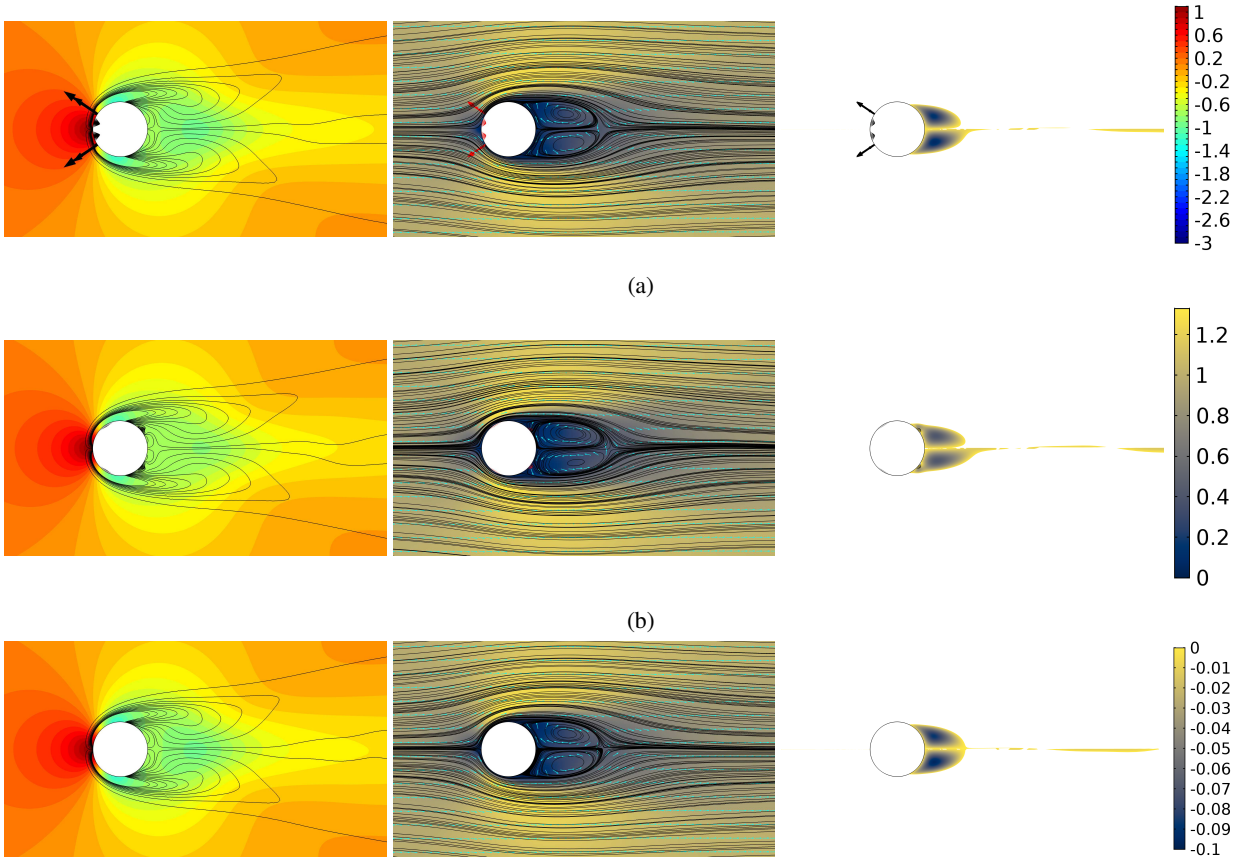

Figure 5: Pressure contours with vorticity streamlines (left), velocity surface with streamlines (middle) and reversed flow surfaces for the time-averaged flow round the cylinder for the IV1 optimised control (a), IV2 optimised control (b) and no control (c). Flow field is averaged over 1 vortex shedding period of the uncontrolled flow. The colour bars for the pressure, velocity and reversed flow surfaces are shown in the final column (in descending order).

Conclusions

Numerical studies were carried out on laminar flow around a circular cylinder to develop autogenous suction control. Dual-loci control - consisting of a locus of suction and one of blowing - was imposed using velocity outlet condition on the cylinder. The parameters of this control were optimised to minimise total drag at $Re = 40$ and $Re = 120$. To impose autogenous control, a constraint that the average pressure of the suction locus is greater than or equal to that of the blowing locus. Steady-state and unsteady simulations were performed.

The optimised autogenous control was able to successfully reduce drag while maintaining the pressure gradient needed to be self-generating at both Reynolds numbers. The optimal control arrangements featured suction on the front half and blowing on the leeward half. This arrangement results in the pressure being reduced on the front half and a modest increase on the rear, resulting in a reduced pressure drag. This comes at the cost of slightly higher skin friction drag, however. Total drag was reduced by up to 4.3% at $Re = 120$ using dual-loci control with a positive pressure gradient from the suction to blowing locations, and 5.45% for $Re = 40$.

Overall the results are encouraging for the development and use of autogenous suction control in real flows. The numerical results showed improvement over the uncontrolled case, and this increased with Reynolds number. On the other hand, more work is needed. The pressure constraint is idealised - not accounting for any losses in internal ducting. The investigation successfully extended the findings of Atik and van Dommelen to show that autogenous suction control is viable for bluff body flows also.

References

[1] Prandtl, L. (1905). Über Flüssigkeitsbewegung bei sehr kleiner Reibung. Verhandlungen des III. Internationalen Mathematiker-Kongresses, Heidelberg. LPGA, 2, 575-584.

[2] Huang, L. R., Cox, E. C., Austin, R. H., & Sturm, J. C. (2004). Continuous particle separation through deterministic lateral displacement. *Science* **304(5673)**: 987-990.

[3] Fransson, J. H., Konieczny, P., & Alfredsson, P. H. (2004). Flow around a porous cylinder subject to continuous suction or blowing. *Journal of Fluids and Structures* **19(8)**:1031-1048.

[4] Gao, D., Chen, G., Chen, W., Huang, Y., & Li, H. (2019). Active control of circular cylinder flow with windward suction and leeward blowing. *Experiments in Fluids* **60(2)**: 1-17.

[5] Min, C., & Choi, H. (1999). Suboptimal feedback control of vortex shedding at low Reynolds numbers. *Journal of Fluid Mechanics* **401**:123-156.

[6] Li, Z., Navon, I. M., Hussaini, M. Y., & Le Dimet, F. X. (2003). Optimal control of cylinder wakes via suction and blowing. *Computers & Fluids* **32(2)**:149-171.

[7] Sohankar, A., & Najafi, M. (2018). Control of vortex shedding, forces and heat transfer from a square cylinder at incidence by suction and blowing. *I*nternational Journal of Thermal Sciences **129**:266-279.

[8] Ramsay, J., Sellier, M., & Ho, W. H. (2020). Eliminating Boundary Layer Separation on a Cylinder with Nonuniform Suction. *International Journal of Aerospace Engineering* **2020**.

[9] Ramsay, J., Sellier, M., & Ho, W. H. (2020). Non-uniform suction control of flow around a circular cylinder. *International Journal of Heat and Fluid Flow* **82**: 108559.

[10] Lorite-Díez, M., Jiménez-González, J. I., Pastur, L., Cadot, O., & Martínez-Bazán, C. (2020). Drag reduction on a three-dimensional blunt body with different rear cavities under cross-wind conditions. *Journal of Wind Engineering and Industrial Aerodynamics* **200**:104145.

[11] Braslow, A. L. (1999). A history of suction-type laminar-flow control with emphasis on flight research (No. 13). NASA History Division, Office of Policy and Plans, NASA Headquarters.

[12] Choi, H., Jeon, W. P., & Kim, J. (2008). Control of flow over a bluff body. *Annu. Rev. Fluid Mech.* **40**:113-139.

[13] Atik, H., van Dommelen, L. (2008). Autogenous suction to prevent laminar boundary-layer separation. *Journal of fluids engineering* **130(1)**: 011201–1.

[14] Bahi, L., Ross, J., & Nagamatsu, H. (1983). Passive shock wave/boundary layer control for transonic airfoil drag reduction. In 21st Aerospace Sciences Meeting (p. 137).

[15] Nagamatsu, H., & FICARRA, R. (1985, January). Supercritical airfoil drag reduction by passive shock wave/boundary layer control in the Mach number range. 75 to. 90. In 23rd Aerospace Sciences Meeting (p. 207).

[16] Nagamatsu, H., Trilling, T., & Bossard, J. (1987). Passive drag reduction on a complete NACA 0012 airfoil at transonic Mach numbers. In 19th AIAA, Fluid Dynamics, Plasma Dynamics, and Lasers Conference (p. 1263).

[17] Parikh, Pradip G. "Passive removal of suction air for laminar flow control, and associated systems and methods." U.S. Patent 7,866,609, issued January 11, 2011.

[18] Wieselsberger, C. (1922). New data on the laws of fluid resistance (No. NACA-TN-84).

[19] Tritton, D. J. (1959). Experiments on the flow past a circular cylinder at low Reynolds numbers. *Journal of Fluid Mechanics* **6(4)**:547-567.

[20] Henderson, R. D. (1995). Details of the drag curve near the onset of vortex shedding. *Physics of Fluids* **7(9)**:2102-2104.

[21] Wu, M. H., Wen, C. Y., Yen, R. H., Weng, M. C., & Wang, A. B. (2004). Experimental and numerical study of the separation angle for flow around a circular cylinder at low Reynolds number. *Journal of Fluid Mechanics* **515**:233-260.

[22] Zdravkovich, M. M. (1997). Flow around circular cylinders: Volume 2: Applications (Vol. 2). Oxford university press.

[23] Schlichting, H. (1987). Boundary layer theory. New York: McGraw-Hill.

Stability transitions of flexible nano-swimmer under rotating magnetic field

Zvi Chapnik[*], Yuval Harduf[*], Jiaen Wu[**], Bumjin Jang[**],
Bradley J. Nelson[**], Salvador Pané[**] and Yizhar Or[*]
[*]*Faculty of Mechanical Engineering, Technion – Israel Institute of Technology, Haifa, Israel.*
[**]*Multi-Scale Robotics Lab, Institute of Robotics and Intelligent Systems, ETH Zurich, Switzerland*

Summary. Micro-nano-robotic swimmers have a promising potential for future biomedical tasks such as targeted drug delivery and minimally-invasive diagnosis. An efficient method for controlled actuation of such nano-swimmers is applying a time-varying external magnetic field. While rigid helical nano-structures that move in corkscrew motion under a rotating magnetic field are hard to fabricate, we recently found that two nano-rods (magnetized nickel and a rhodium tail) connected by a soft polysaccharide hinge may also exhibit helical motion under a rotating magnetic field. We also discovered interesting mode transitions depending on the actuation frequency. In low frequency regime, the nano-swimmer tumbles in plane, while larger frequencies lead to out-of-plane helical motion, optimum of peak speed, followed by step-out loss of synchronization. In this work, we analyzed these effects by formulating the spatial dynamics of 3D rotating nano-swimmer compose of two links connected by a passive rotary joint with a torsion spring representing the flexible hinge. Assuming quasi-steady Stokes drag acting on the links, numerical simulations and analysis of the nano-swimmer's nonlinear dynamics reveal the stability transitions of possible synchronized solution, as well as bifurcations with respect to actuation frequency. The results highlight the importance of simple low-dimensional models of nonlinear dynamics and their utility in predicting and optimizing motion of magnetically-actuated nano-swimmers.

Introduction

Inspired by the motion of bacteria and other microorganisms, researchers have developed artificial helix-shaped micro- and nano-structures that can perform corkscrew motion and helical-path swimming upon a suitable stimulation with external energy sources. These small-scale helical devices attract much interest because of their great potential for disease diagnosis, minimally invasive surgery, telemetry, targeted therapies, or plasmonic-based nanorheology. The most common strategy consists of actuating magnetically responsive structures comprising helical components that revolve around their long axis when they are actuated using rotating magnetic fields resulting in corkscrew locomotion.
In this work (recent paper [1]), we show that incorporating a complex helical body shape in swimmers' architectures is not necessary to enable helical swimming. This is an advantageous feature of the presented hinged swimmers, especially in terms of fabrication, adjusting the length of hinges and rods becomes easier. In this contribution, we show for the first time that a highly integrated multifunctional nonhelical nano-swimmer is capable of helical klinotactic swimming when stimulated by purely rotating magnetic fields.

Modeling

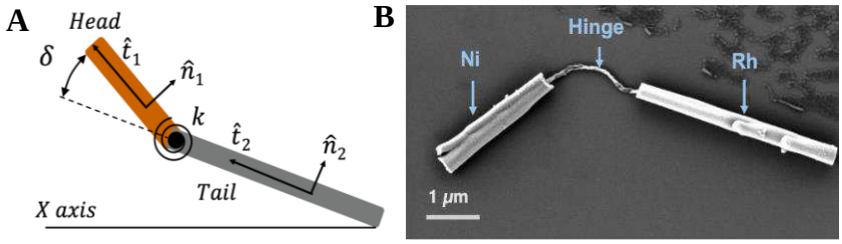

Figure 1: (A) Simplified Theoretical model; (B) A SEM image of the finalized structure of nano-swimmer

The nano-swimmer consists of two cylindrical rigid metallic links (nickel and rhodium) joined by a soft polymeric hinge (Figure 1B). The ferromagnetic nickel link serves as the magnetically responsive motile head component. The non-ferromagnetic rhodium segment acts as a tail, while the polymeric hinge functions as a flexible joint to promote the swimmer's motion by deformation. In the experiments [1], we observed different motion phases, as shown in previous helical nanobots' papers [2,3], at low frequency tumbling, low-speed movements, at a higher frequency, moving forward in a helical path, in further frequency increase we obtain asynchronous swimming.
In order to systematically understand the theoretical mechanism of the spatial dynamic motion of the swimmers, a theoretical model was developed. The theoretical model of the two-link nano-swimmer comprises two rigid slender cylinders connected by a point-size revolute joint, with a relative angle δ of rotation about a body-fixed axis perpendicular to the link's longitudinal direction (Figure 1 A). The flexibility of the revolute joint represented by a linear torsion spring with stiffness k, the torque at the joint is given by $\tau_k = -k\delta$. The head link made of ferromagnetic material, its magnetization vector $\mathbf{m}$ directed along the link's longitudinal axis $\hat{\mathbf{t}}_1$. While being actuated by a rotating magnetic field. The external magnetic field B(t) is rotating in the Y-Z plane by $\boldsymbol{B}(t) = [0 \quad sin(\omega t) \quad cos(\omega t)]b$, where b is the magnetic field's intensity and ω is its rotational frequency.
Assuming a spatially uniform magnetic field, it induces a pure torque $\boldsymbol{\tau}^m$ on the magnetized head link, which depends on its orientation and the time-varying field B(t) as $\boldsymbol{\tau}^m = \mathbf{m} \times \mathbf{B}$ .The nano-swimmer submerged in a viscous fluid. The Stokes drag forces and torques acting on each of the two links $\boldsymbol{f}_i, \boldsymbol{\tau}_i$ depend linearly on their angular velocity vectors $\mathbf{v}_i, \boldsymbol{\Omega}_i$. Neglecting hydrodynamic interactions between the links implies linear drag resistance relations.

The vector of generalized coordinates describing the swimmer's spatial pose is $\mathbf{q}=(x,y,z,\phi,\theta,\psi,\delta)^T$, where (x,y,z) denote the position of the head link's center, (ϕ,θ,ψ) are Euler angles describing its spatial orientation (ZXZ convention), and δ is the joint angle. Formulating the links' linear and angular velocities $\mathbf{v}_i,\boldsymbol{\Omega}_i$ in terms of orientation and generalized velocities, $\mathbf{q}$ and $\dot{\mathbf{q}}$. Static equilibrium balance of forces and torques on the two links, including viscous drag terms $\begin{pmatrix}\boldsymbol{f}_i\\ \boldsymbol{\tau}_i\end{pmatrix}=-\begin{pmatrix}\boldsymbol{\xi}_i & \boldsymbol{\mathcal{B}}_i\\ \boldsymbol{\mathcal{B}}_i^T & \boldsymbol{\kappa}_i\end{pmatrix}\begin{pmatrix}\mathbf{v}_i\\ \boldsymbol{\Omega}_i\end{pmatrix}$, where $\boldsymbol{\xi}_i,\boldsymbol{\mathcal{B}}_i,\boldsymbol{\kappa}_i$ are the translational, rotational and coupling viscous resistance tensor as notated in [2], magnetic torque $\boldsymbol{\tau}^m$ and elastic joint torque $\boldsymbol{\tau}_k$, leads to a system of first-order nonlinearly coupled ordinary differential equations of the form $\dot{\mathbf{q}}=\mathbf{g}(\mathbf{q},t)$.

Results

This system is integrated numerically using MATLAB's ODE15s function, under initial conditions $\mathbf{q}(0)=0$ of straightened links aligned with X-axis. The swimmer's motion is extracted from solutions of $\mathbf{q}(t)$ after convergence to steady-state synchronized periodic motion, whenever it exists. Beyond the step-out frequency, such synchronized motion no longer exists, and we observe quasi-periodic oscillations.

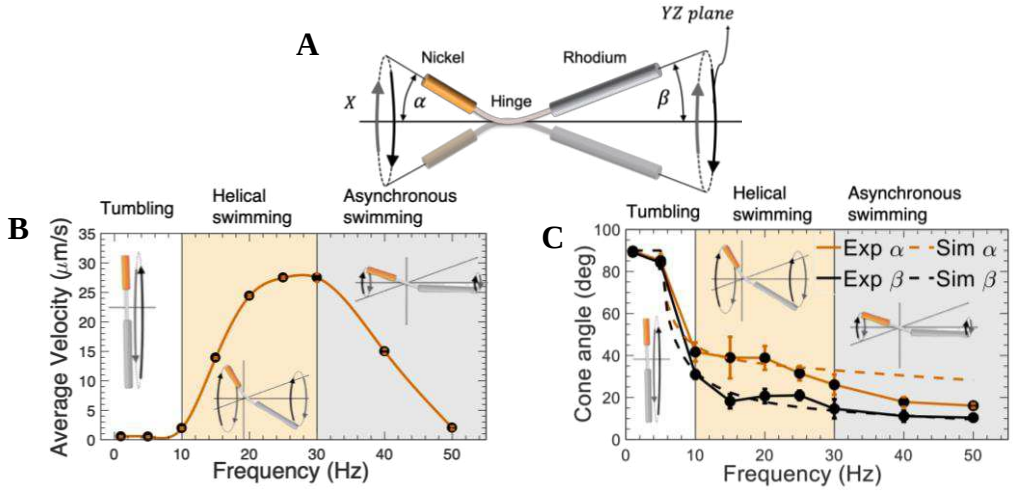

Figure 2: (A) schematic diagram of nano-swimmer illustrating precession angles and XYZ coordinate. (B) Simulation's values of the average speed of a flexible hinged nano-swimmer as a function of rotating magnetic frequency. (C) Mean precession cone angles α and β as a function of the external rotating magnetic field frequency in the experiment.

In order to study the locomotion behavior of nano-swimmers, we define the following parameters shown in Figure 2A. YZ plane corresponds to the plane of the magnetic field rotation. α is the maximum angle between the magnetic head and the X-axis, and β is the maximum angle between the tail link and the X-axis. For the analysis of nano-swimmers' locomotion characteristics, magnetic fields of 15 mT and rotational frequencies of up to 50 Hz with steps of 5 Hz investigated. At low frequency below 10 Hz, the nano-swimmer's movement speed was relatively low at around 0.5 μm/s. The nano-swimmer was bent a little and rotated in YZ plane. From 10 Hz to 30 Hz, it started to move forward in a helical path. The speed increased almost linearly up to 27.49 μm/s in the frequency region of 10 – 25 Hz. At the frequency range of 25 – 30 Hz, the speed curve shows an inflection point corresponding to a maximum speed of around 28 μm/s. A further increase in the frequency results in a decrease in the speed towards zero.

We classify the precession behavior into three different motion phases: tumbling, helical and asynchronous swimming, based on the speed and precession angles of the swimmer, as shown in Figures 2B and 2C. The transformation of the nano-swimmer's locomotion from tumbling to helical motion is supported by the fact that the precession angle α and β dramatically decrease as the rotational magnetic frequency increases. The simulation results in [1] were in good agreement with the experimental results.
The different dynamic behavior by in-plane tumbling or spatial helical klinotactic swimming can be switched by changing the magnetic field frequency and strength. The effects of the magnetic field strength, the Ni head length, and the hinge length on locomotion behavior were investigated by numerical simulation and experiments in [1], were in good fit. We will also present new analytical results of the system's periodic solutions, their existence and stability conditions, for specific limit cases.

References

[1] Wu, J., Jang, B., Harduf, Y., Chapnik, Z., Bartu Avci, Ö., Chen, X., Puigmartí-Luis, J., Ergeneman, O., Nelson, B. J., Or Y. & Pané S. (2021) Helical Klinotactic Locomotion of Two-Link Nano-swimmers with Dual-Function Drug-Loaded Soft Polysaccharide Hinges, to appear in *Advanced Science*, DOI: 10.1002/advs.202004458.
[2] Morozov, K. I., & Leshansky, A. M. (2014). The chiral magnetic nanomotors. *Nanoscale*, 6(3), 1580-1588.
[3] Ghosh, A., Mandal, P., Karmakar, S., & Ghosh, A. (2013). Analytical theory and stability analysis of an elongated nanoscale object under external torque. *Physical Chemistry Chemical Physics*, *15*(26), 10817-10823.

Stochastic resonance in a parametrically perturbed aeroelastic system

Varun H. S.*, M. S. Aswathy* and Sunetra Sarkar*
*Department of Aerospace Engineering, Indian Institute of Technology Madras, Chennai, India

Summary. In this work, we investigate the effect of parametric noise on a classical two degree-of-freedom pitch-plunge aeroelastic system and study the manifestation of stochastic resonance in the same. The non-dimensional form of the governing equations are studied, considering nonlinear soft-springs. The reduced velocity of the flow is modelled as a stochastically varying parameter by the Ornstein-Uhlenbeck (OU) process. This parametric noise significantly changes the qualitative dynamics of the system. One such new qualitative dynamics that we observe is noise induced intermittency, where the system hops between two attractors– $\vec{0}$ fixed point and a stable limit cycle oscillation (LCO). Next, we fix the mean reduced velocity near the onset of bifurcation and examine effect of noise intensity. We see that the signal to noise ratio (SNR) of the system responses reaches a maxima for an optimum value of the noise intensity. This characteristic feature in the aeroelastic system perturbed by parametric noise indicates the phenomenon of stochastic resonance.

Introduction

The response of an elastic structure in a fluid flow is a very important research area as the applications range from aeroelastic system design to design of tall buildings, bridges [1]. The design of these structures requires careful consideration as there is interplay between three kinds of forces — inertial, elastic and aerodynamic forces. The interaction between the three forces can cause the structure to exhibit LCOs, which is undesirable as it can cause fatigue failure in the structure [2]. These self-excited LCOs of the structure is termed as the flutter phenomena. Recently, a lot of importance is being given to the role played by parametric noise in such engineering systems [3, 4]. Noise is known to bring drastic qualitative changes in the dynamical behaviour of such systems. One important feature in physical and biological systems subjected to noise is the phenomenon of stochastic resonance [9, 10], which manifests due to a change in noise intensity. It is known that such systems attain a maximum SNR at an optimum noise intensity. Inspired from these works, we make an attempt to study the effect of parametric noise and the role played by the noise intensity on a classical pitch-plunge aeroelastic system.

Methodology

The aeroelastic system is modelled as an airfoil undergoing motion in the pitch and plunge degrees-of-freedom under a steady, uniform incoming flow and is based on the model by Lee *et al* [6, 7]. The non-dimensional governing equations of motion are given in Equation 1.

$$\begin{aligned} \epsilon'' + x_\alpha \alpha'' + 2\zeta_\epsilon \left(\frac{\bar{\omega}}{U}\right) \epsilon' + \left(\frac{\bar{\omega}}{U}\right)^2 (\epsilon + \beta_\epsilon \epsilon^3) &= -\left(\frac{1}{\pi\mu}\right) C_L(\tau) \\ \left(\frac{x_\alpha}{r_\alpha^2}\right) \epsilon'' + \alpha'' + 2\left(\frac{\zeta_\alpha}{U}\right) \alpha' + \left(\frac{1}{U^2}\right)^2 (\alpha + \beta_\alpha \alpha^3) &= \left(\frac{2}{\pi\mu r_\alpha^2}\right) C_M(\tau) \end{aligned} \tag{1}$$

where $x_\alpha b$ is the distance between the elastic axis and the centre of mass of the airfoil, $r_\alpha b$ is the radius of gyration of the airfoil, b is the semi-chord length of the airfoil. $'$ denotes differentiation with respect to non-dimensional time, ϵ is the non-dimensional plunge of the elastic axis, α is the pitch of the elastic axis, U is the reduced velocity, $\bar{\omega}$ is the ratio of uncoupled natural frequencies in the plunge to the pitch mode, μ is the mass ratio, β_α and β_ϵ denote the coefficients of the cubic term of stiffness in the pitch and plunge modes respectively, ζ_α and ζ_ϵ are the damping ratios in the pitch and plunge modes respectively. C_L and C_M are the lift and moment coefficients respectively, which are derived based on the Wagner function formulation [5]. The springs are assumed to be soft springs (β_α is $-ve$).

Noise model

The reduced velocity U in Equation 1 is stochastically modelled as an OU process, which is generated by the Stochastic Differential Equation (SDE) given in Equation 2

$$dU = \lambda(U_m - U)\, dt + \sigma\, dW \tag{2}$$

where U_m is the mean reduced velocity, λ is the inverse of the correlation time, σ is the noise intensity – parameters of the OU process, W represents the standard brownian motion. The generated process has a correlation $R_{UU}(\Delta\tau) = \exp(-\lambda\Delta\tau)$ with variance $\sigma^2/(2\lambda)$. The entire system when cast in state space form looks like Equation 3

$$\begin{aligned} d\vec{X} &= \mathbf{f}(\vec{X}, U, \tau)\, d\tau \\ dU &= \lambda(U_m - U)\, d\tau + \sigma\, dW \end{aligned} \tag{3}$$

where $\vec{X}$ consists of the system and auxillary variables (see [6, 7]). The Equations in 3 are interpreted as an Itô SDE and are integrated by using the Euler-Maruyama method [8, 9].

Results and Discussions

Firstly, the bifurcation behaviour of the deterministic system is studied by varying reduced velocity (U). The system undergoes a sub-critical Hopf bifurcation (flutter point, $U = 6.29$) beyond which it gets attracted to a stable LCO. The unstable LCO takes a turn and becomes the stable LCO branch (turning point, $U = 5.93$). Now we investigate how these responses get altered in the presence of parametric noise. Figure 1 (a) and (b) show time histories of $U(\tau)$, $\alpha(\tau)$ respectively for $\sigma = 0.37$ and Figure 1 (c) and (d) shows the same for $\sigma = 0.27$. For $U_m = 6.25$ the system starts to display hopping dynamics (Figure 1 (b) and (d)), wherein it intermittently switches between the $\vec{0}$ fixed point and the LCO. This effect is solely due to the presence of parametric noise in the system and is dubbed as noise induced intermittency in the literature [3, 11]. Next, we fix $U_m = 6.25$ and vary the noise intensity σ. As σ is increased, the SNR value of

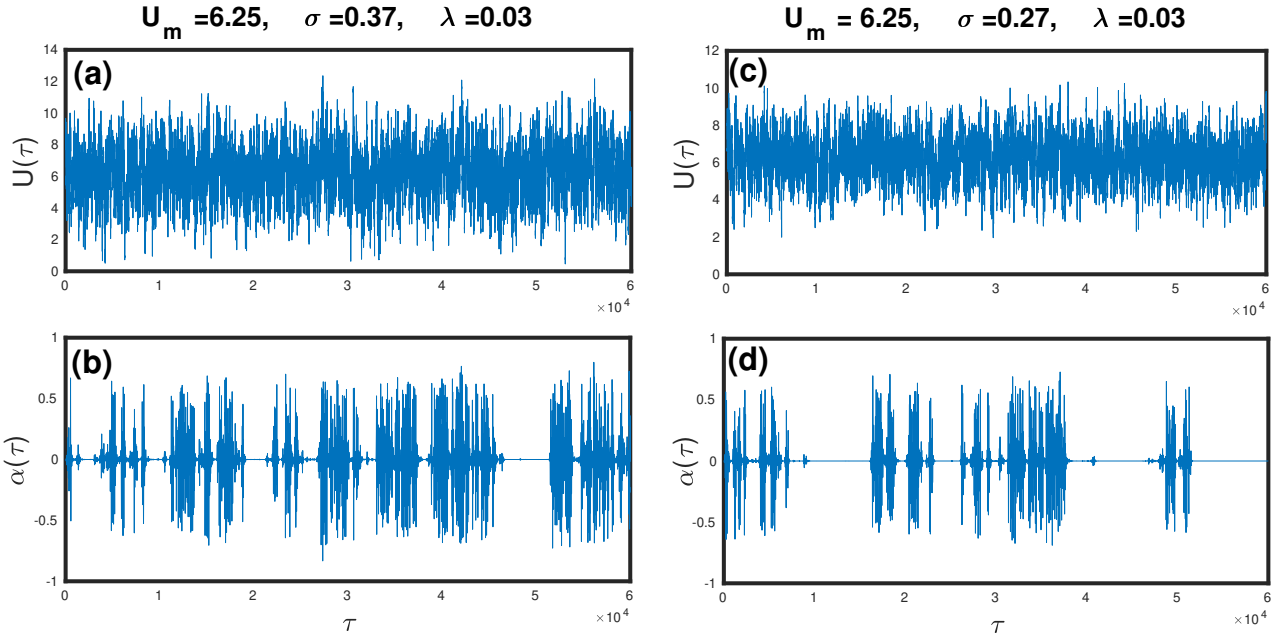

Figure 1: Time histories for $\alpha(\tau)$ and $U(\tau)$. (a) and (b): $\sigma = 0.37$, (c) and (d): $\sigma = 0.27$

the response increases as the system starts spending greater amounts of time in the LCO attractor. Further increase in σ leads to a decrease in the value of SNR due to frequent switching between the attractors and the dynamics gets dictated by the noise. This is further confirmed by plotting the power spectra and mean residence times of the responses. This phenomenon where the SNR reaches a maxima for an optimum value of intensity of the noise is termed as stochastic resonance [9, 10] and is being reported in the aeroelastic system for the first time.

Conclusions

We have investigated the effects of parametric noise on the considered aeroelastic system. The introduction of parametric noise in U, modelled as an OU process brings about drastic changes in the system dynamics. The system starts hopping between the two attractors and displays a new state of intermittent oscillations. The phenomenon of stochastic resonance is observed when the noise intensity σ is varied. These changes in the system dynamics and the manifestation of stochastic resonance brought on due to the parametric noise presents new challenges during design and use of aeroelastic systems.

References

[1] Hodges D. H., Pierce G. A. (2011) Introduction to Structural Dynamics and Aeroelasticity. Cambridge University Press .

[2] Schijve J. (2009) Fatigue damage in aircraft structures, not wanted, but tolerated? *Int. J. Fatigue* **31**:998-1011.

[3] Venkatramani J., Krishna S. K., Sarkar S., Gupta S. (2017) Physical mechanism of intermittency route to aeroelastic flutter. *J. Fluids Struct* **75**:9-26.

[4] Aswathy M. S., Sarkar S. (2019) Effect of stochastic parametric noise on vortex induced vibrations. *Int. J. Mech Sci* **153-154**:103-118.

[5] Fung Y. C. (1955) An Introduction to the theory of Aeroelasticity. John Wiley and Sons, New York.

[6] Lee B. H. K., Gong L., Wong Y.S. (1997) Analysis and Computation of Nonlinear Dynamic Response of a Two-Degree-of-Freedom System and its Application in Aeroelasticity. *J. Fluids Struct* **11**:225-246.

[7] Lee B.H.K., Jiang L.Y., Wong Y.S. (1999) Flutter of an Airfoil with Cubic Restoring Force. *J. Fluids Struct* **13**:75-101.

[8] Higham D.J. (2001) An Algorithmic Introduction to Numerical Simulation of Stochastic Differential Equations. *SIAM Rev.* **43**:525-546.

[9] Rajasekar S., Sanjuan M.A.F. (2016) Nonlinear Resonances. Springer International

[10] Dykman M., McClintock P. (1999) Stochastic Resonance. *Sci Prog* **82**:113-134.

[11] Krishna S. K., Sarkar S., Gupta S. (2019) Multiplicative noise induced intermittency in maps. *Int. J. Nonlin Mech* **117**:103251

Thursday, July 21, 2022

16:00 - 18:00

Poster Session

Foyer Lumiere

???

16:00 - 18:00
Influence of friction damping on frequency lock-in in cyclic structure
BYRTUS Miroslav*, DYK Stepan
*University of West Bohemia [Plzeň] (Univerzitní 2732/8, 306 14 Plzeň 3 Czech Republic)

16:00 - 18:00
Computation of Damped Nonlinear Normal Modes Using Force Appropriation Technique and Efficient Path Following Method
JELVEH Meisam, **SADR Mohammad Homayoune***, MUSAVI Seyyed Mojtaba
*Amirkabir University of Technology (424 Hafez Ave, Tehran, Iran, 15875-4413 Iran)

16:00 - 18:00
Bifurcations and stability transitions in nonlinear dynamics of a planar undulating magnetic microswimmer
PAUL Jithu*, OR Yizhar, GENDELMAN Oleg
*Technion - Israel Institute of Technology [Haifa] (Haifa Israel)

16:00 - 18:00
Stability of Nonlinear Normal Modes under Stochastic Excitation
MIKHLIN Yuri*, RUDNYEVA Gayane
*National Technical University Kharkiv Polytechnic Institute (NTU "KhPI" 2, Kyrpychova str., 61002, Kharkiv, Ukraine Ukraine)

16:00 - 18:00
SIR model for rumor propagation
PIQUEIRA José, **BATISTELA Cristiane***, MEDINA Cabrera Manuel, GODOI Antonio
*Escola Politecnica da Universidade de Sao Paulo [Sao Paulo] (Av. Prof. Luciano Gualberto, 380 - Butantã, São Paulo - SP, 05508-010 Brazil)

16:00 - 18:00
Dynamics and minimalistic control of a flexible structure containing bi-stable elements
GERON Yamit*, GIVLI Sefi, OR Yizhar
*Technion - Israel Institute of Technology [Haifa] (Haifa Israel)

16:00 - 18:00
Optomechanical cavities: from synchronization to mode locking
BUKS Eyal*
*Technion (Haifa, Israel Israel)

16:00 - 18:00
Analytical study of interfacial three dimensional gravity waves in presence of current
SALMI Soraya*, ALLALOU Nabil
*Université M'Hamed Bougara de Boumerdes (Département de physique, Faculté des sciences, Route de la gare Ferroviaire, Boumerdes 35000 Algeria)

16:00 - 18:00
Control-Oriented Modeling of a Planar Cable-Driven Parallel Robot with Non-Straight Cables
SAADAOUI Rima*, PICCIN Olivier, OMRAN Hassan, BARA Iuliana, LAROCHE Edouard
*Université de Strasbourg (4 Rue Blaise Pascal, 67081 Strasbourg France)

16:00 - 18:00
Experimental verification of the crossover between the time-fractional and standard diffusion in a hierarchical porous

material
ZHOKH Alexey*, STRIZHAK Peter
*L.V. Pisarzhevskii Institute of Physical Chemistry of National Academy of Sciences of Ukraine (Nauki Avenue, 31, Kiev 03028 Ukraine)

16:00 - 18:00
Investigation of vibro-impact dynamics in PILine® ultrasonic motors
KAPELKE Simon*, HARTENBACH Felix, SEEMANN Wolfgang
*Physik Instrumente (PI) GmbH & Co. KG (Auf der Roemerstrasse 1 76228 Karlsruhe Germany)

16:00 - 18:00
Model order reduction approach for problems with moving discontinuities
BANSAL Harshit*, RAVE Stephan, IAPICHINO Laura, SCHILDERS Wil, WOUW Nathan
*Eindhoven University of Technology (5612 AZ Eindhoven Netherlands)

16:00 - 18:00
Numerical investigation on storage tank buckling near the liquid level under seismic loading
COLLIGNON Christophe*
*FRAMATOME (10, Rue Juliette Récamier, 69006 Lyon France)

16:00 - 18:00
Nonlinear Dynamics of a Ring-Type MEMS Gyroscope
ASOKANTHAN Samuel, **GEBREL Ibrahim***, WANG Ligang
*The University of Western Ontario (London, ON N6A 5B9 Canada)

16:00 - 18:00
On the solution of the Mathieu equation with multiple harmonic stiffness, parametric amplification for constant and harmonic forcing
ABBOUD Eddy*, THOMAS Olivier, GROLET Aurelien, MAHÉ Hervé
*Valeo Transmissions, Centre d'Étude des Produits Nouveaux (Espace Industriel Nord, Route de Poulainville, 80009 Amiens Cedex 1 France) - Laboratoire d'Ingénierie des Systèmes Physiques et Numériques (Arts et Metiers Institute of Technology, LISPEN, HESAM Université, F-59000 Lille, France France)

16:00 - 18:00
Optimization Process for Ride Quality of a Nonlinear Suspension Model Based on Newton-Euler's Augmented Formulation
BELHORMA Mohamed*, BOUCHIKHI Aboubakar
*University of Sidi Bel Abbes (BP 89, Cite Ben M'hidi, University of Sidi Bel Abbes, Sidi Bel Abbes 22000, Algeria Algeria)

16:00 - 18:00
Passive suppression of parametric excitation of cables using a nonlinear vibration absorber
KOLB Pauline*
*Department Civil Engineering (Technische Universitat D-64277 Darmstadt Germany) - Universidade de São Paulo (Cidade Universitaria - 05508-090 São Paulo Brazil)

16:00 - 18:00
TWMS synchronization network simulation with parallel computing
BATISTA Matheus*, BUENO Atila, BATISTELA Cristiane, MACIEL Elvio, PANZO Eduardo, DERMENDJIAN Fabio, BALTHAZAR José, PIQUEIRA José
*Instituto de Ciência e Tecnologia - Universidade Estadual Paulista (Av. Três de março, 511, Sorocaba - SP Brazil)

16:00 - 18:00
Stability Analysis of Rotary Drilling Systems Associated with Multiple State-Dependent Delays
ZHANG He*, DETOURNAY Emmanuel
*University of Minnesota (500 Pillsbury Dr. S.E., Minneapolis, MN, 55455 United States)

16:00 - 18:00
Two-stroke single-cylinder engine with elastic hinges with preset force characteristics
ZOTOV Alexey*, SVIRIDOV Alexey, TOKAREV Artem
*Ufa State Petroleum Technological University (Kosmonavtov Street 1, Ufa, The Republic of Bashkortostan, Russian Federation, 450062 Russia)

16:00 - 18:00
When friction and vibro-impact make music: physical model of the tromba marina

ABLITZER Frédéric*, GILBERT Joël, GAUTIER François
*Laboratoire d'Acoustique de l'Université du Mans, CNRS UMR 6613, Le Mans, France (Avenue Olivier Messiaen 72085 LE MANS CEDEX 9 France)

Influence of friction damping on frequency lock-in in cyclic structure

Miroslav Byrtus* and Štěpán Dyk *
**Department of Mechanics, University of West Bohemia, Pilsen, Czech Republic*

Summary. The paper deals with modelling and investigation of lock-in phenomena in bladed cyclic structure which is further influenced by friction damping couplings. The investifation is focused on how the friction can affect the unstable behaviour during frequency lock-in regimes.

Introduction

The fliud-structure interaction (FSI) phenomenon arises when an elastic structure interacts with the embracing fliud flow. A particular case of FSI in which an alternate shedding of vortices forms the vibration of the structure is Vortex-Induced Vibration (VIV). The natural vortex shedding frequency is dependent on the velocity of the flow. The vortex sheddding exerts a periodic unsteady force on the body. As the vortex shedding frequency approaches the the natural frequency of the body, the two frequencies lock-in for a small range of the velocity flow [2]. Experimental characterization of lock-in is performed in [1].
The FSI plays significant role in modern aerofoils and turbine blades which are designed for higher efficiencies and higher power under higher operational temperatures and flow rates. Higher operational safety and economical demands force the designers to be more precise during phase of design with respect to operational condition laying out of the area with loss of stability [3, 4, 5]. The fluid-induced forces create an aero-elastic couplings between the aerofoils and the fluid flow. Moreover, in the case of periodical structures (gas or steam turbine blades in bladed disks) the aero-elastic coupling influences not only the single blade but the adjacent blades as well. There are many experimental works investigating experimentally the conditions of instability origin, e.g. [7, 8]. The paper deals with the modelling and dynamical analysis of a periodic blade system influenced by VIV and friction-damping in inter-blade couplings.

Cyclic structure of blade profiles influenced by VIV

Further, it is assumed the cyclic structure formed by a bladed disk has N_B blades which are created by identical airfoil profiles. Each blade is modelled by the approach presented in the previous section, i.e. it comprises two degrees of freedom (bending and torsion) and moreover these two motion are mutually coupled by so called bending-torsion coupling, see [6]. Usually, in steam turbine applications, the bladed disks are equipped with different kinds of shrouding, which causes that the system of blades mounted on a rotating disk become more stiff, especially with respect to axial flow direction.
The time-varying vortex force due to the alternating sheddin of vortices in the wake causing the VIV is modeled by the van der Pol equation. The van der Pol model has two significant properties: i) self-sustained stable limit cycle oscillation and ii) the lock-in with the frequency of external forcing [2].
In Fig. 1, the blade cascade of a bladed disk is depicted in a plane view. The axis of rotational symmetry designates the axis of rotor symmetry which is the bladed disk attached to. Further, it is assumed that the flow direction is parallel with the blade chords. The shrouding is supposed to be mounted at tips of the blades and it is modelled by means of two lumped springs representing bending k_{shb} and torsional k_{sht} stiffness of each shrouding section between two adjacent blades.

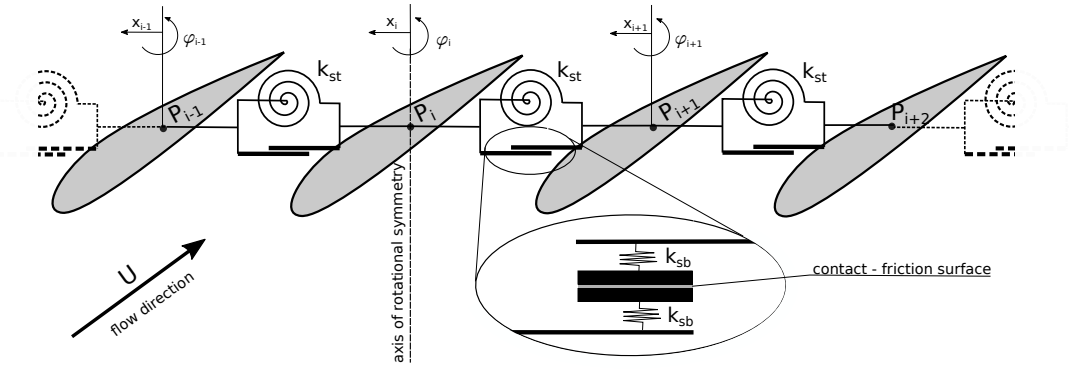

Figure 1: Bladed cascade section with contact-friction shrouding coupling modelling.

The derivation of the linearized mathematical model of a bladed disk with the influence VIV is based on the methodology presented in [2]. Here, it is extended for a cyclic structure and completed by the influence of interblade damping-friction forces which are incopororated in shrouding coupling. It can be advantageously written in matrix form

$$\mathbf{M}_{BD}\ddot{\mathbf{q}}_{BD} + \mathbf{C}_{BD}\dot{\mathbf{q}}_{BD} + \mathbf{K}_{BD}\mathbf{q}_{BD} = \mathbf{f}_{BD}^{E} + \mathbf{f}_{BD}^{FC}, \tag{1}$$

where $\mathbf{M}_{BD}$, $\mathbf{C}_{BD}$ and $\mathbf{K}_{BD}$ are rectangular of order $3N_B$ mass, damping and stiffness matrices of a complex bladed disk model. Right hand side of (1) contains force vectors of friction coupling $\mathbf{f}_{BD}^{FC}$. Vector of generalized coordinates is of following form $\mathbf{q}_{BD} = [\ldots, x_i, \varphi_i, q_i, \ldots]^T \in \mathbb{R}^{3N_B}$, where index $i = 1, \ldots, N_B$ designates the particular blade. The coordinate q_i is governed by van der Pol equation which is used for the wake dynamics.

Lock-in in the cyclic structure

The figures below show multiple frequency lock-in reagarding different mode shapes of the structure (left). Real parts of the eigen values witness of the stability. It is clear that when the frequency lock-in happens, the system exhibit can unstable vibration.

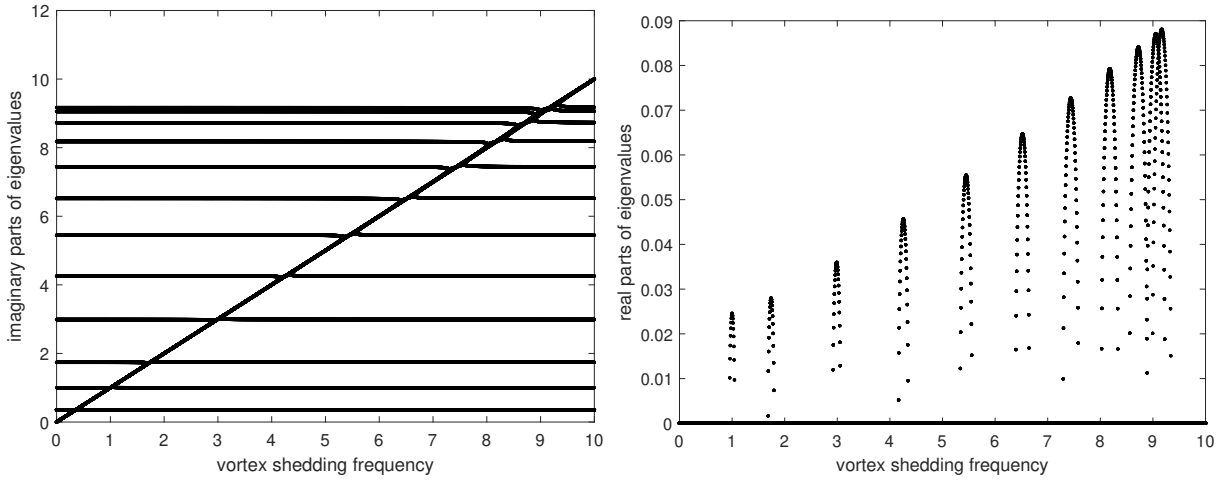

Figure 2: Frequency lock-in areas and stability charts for cyclic structure created of identical air-foil profile connected by shrouding.

Conclusions

The paper presents phenomenological model of vortex-induced vibration in a cyclic structure which is formed by blade profiles. The attention is paid on the investigation of lock-in phenomenon using linearized model, which will further completed by nonlinear friction terms based on LuGre friction model. There is obvious in the presented results, that the system losses its stability during the lock-in phases. The future aim is to propose suitable damping mechanism which is based on friction dampers and complete the analyses with experimental data.

Acknowledgement: This work was supported by the GA CR project No. 20-26779S "Study of dynamic stall flutter instabilities and their consequences in turbomachinery application using mathematical, numerical and experimental methods".

References

[1] Giannini O., Sestieri A. (2016) Experimental characterization of veering crossing and lock-in in simple mechanical systems, *Mechanical Systems and Signal Processing* **72-73**:846-864.

[2] Hoskoti L., Dinesh A.A., Ajay M. (2020) Frequency lock-in during nonlinear vibration of an airfoil coupled with van der Pol Oscillator, *Journal of Fluids and Structures* **92**:102776.

[3] Fung Y.C. (1993) An Introduction to the theory of aeroelasticity, Dover Publications, Inc.

[4] Hodges D.H., Pierce G.A. (2002) Introduction to structural dynamics and aeroelasticity, Cambridge University Press.

[5] Tondl A., Ruijgrok T., Verhulst F., Nebergoj R. (2000) Autoparametric Resonance in Mechanical Systems, Cambridge University Press.

[6] Hayat K. et al. (2016) Flutter performance of bend-twist coupled large-scale wind turbine blades, *Journal of Sound and Vibration* **370**:149-162.

[7] Ertveldt J., Lataire J., Pintelon R., Vanlanduit S. (2012) *Flutter speed prediction based on frequency-domain identification of a time-varying system*, Proceedings of ISMA2012-USD2012, 3013-3024.

[8] Hobeck J.D., Inman D.J. (2016) *Dual cantilever flutter: Experimentally validated lumped parameter modeling and numerical characterization*, Journal of Fluid and Structures **61**:324-338.

[9] Byrtus M., Hajzman M., Dupal J., Polach P. (2016) *Dynamic phenomena of a blade system with aero-elastic coupling*, Proceedings of ISMA2016-USD2016, 3013-3024.

[10] di Bernardo M., Budd C.J., Champneys A.R., Kowalczyk P. (2008) Picewise-smooth dynamical systems (Theory and Applications), Springer-Verlag London Limited.

Computation of Damped Nonlinear Normal Modes Using Force Appropriation Technique and Efficient Path Following Method

Meisam Jelveh[*], Seyyed Mojtaba Musavi [*] and Mohammad Homayoune Sadr[**]
[*]*Ph.D candidate, Faculty of Aerospace Engineering, Amirkabir University of Technology, Tehran, Iran*
[**]*Associated professor, Faculty of Aerospace Engineering, Amirkabir University of Technology, Tehran, Iran*

Summary. In this paper a new method is presented for computation of nonlinear normal modes (NNMs) of damped nonlinear systems. Pseudo arc length continuation of periodic solution method is well accepted as a strong tool for computation of NNMs and in many literature is used as reference solution. However, this method is limited to conservative systems and its application to damped nonlinear systems is still an open field of problem and very few attempts were made to solve that. In this article a new algorithm based on combination of force appropriation technique and a modified version of pseudo arc length continuation method called efficient path following method (EPFM) is presented to compute NNMs of damped nonlinear system. In order to investigate the capability of the algorithm, NNMs of a two D.o.Fs damped mass-spring system was calculated. It was observed that the results were in very good agreement to those obtained in other references.

Introduction

In recent decade, NNMs have attracted many researchers and comprehensive article reviews are published on the concept, theory and application of them. Nowadays, there are two common definitions for NNMs: a) periodic motion of nonlinear autonomous system b) two dimensional invariant manifold in phase space. As Renson et al. mentioned, The role played by damping in the dynamics of nonlinear structures is not yet completely uncovered and its effect on the modal interactions and invariant manifolds are largely unanswered [5].
Pseudo arc length continuation is used to compute NNMs based on periodic motion definition of them. However in general autonomous motions of damped systems are not periodic. This makes it difficult to use pseudo arc length continuation for computation of damped NNM. Kuether and Allen used combination of Force appropriation technique, complex Fourier expansion and numerical continuation to compute NNMs of damped systems [3]. They compute NNMs up to moderate levels of energy, but they couldn't capture internal resonances. Krack added an artificial damping proportional to mass matrix to the equation of motion of the system with suitable sign to cancel the effect of system's damping[2]. By adding this artificial damping, he made the solution of the system periodic and used pseudo arc length continuation for computation of NNMs. This method was limited to low damped systems and he didn't capture any modal interactions.
In this paper a novel method is presented based on force appropriation technique and EPFM. EPFM is a modified version of pseudo arc length continuation method which Sadr et al. showed that, it is up to 70% faster than similar algorithms [4]. This new method is capable to compute damped NNMs and their interactions with no limitation on energy level. In order to use this algorithm

Theory and application

One of the most important properties of NNMs is that force resonances occur near them. The governing equation of motion under harmonic force in state space is written as equation (1) in which z is vector of state variables defined as $Z^T = [\dot{x}^T \quad x^T]$ where $\dot{x}$ is velocity vector and x is vector of displacements. F_0 is the amplitude of external force, V_F is the shape of external force and ω is frequency of external force which could be defined as $\omega = \frac{2\pi}{T}$ where T is the period of the external force.

$$\dot{Z} = g(Z) + F_0 V_F \sin(\omega t) \quad (1)$$

The shooting function would be defined as follow:

$$H(Z_0.T.F_0) = Z(T) - Z_0 \quad (2)$$

So the Tylor expansion of H and correction vector of initial guess maybe found by formula of equation (4). The matrix $\frac{\partial H}{\partial Z_0}$ and $\frac{\partial H}{\partial T}$ are computed according to [4] and $\frac{\partial H}{\partial F_0}$ is computed by means of finite difference method.

$$H(Z_0.T.F_0) + \frac{\partial H}{\partial Z_0}\Delta Z_0 + \frac{\partial H}{\partial T}\Delta T + \frac{\partial H}{\partial F_0}\Delta F_0 + HOT = 0 \quad (3)$$

$$\frac{\partial H}{\partial Z_0}\Delta Z_0^k + \frac{\partial H}{\partial T}\Delta T^k + \frac{\partial H}{\partial F_0}\Delta F_0^k = -H^k \quad (4)$$

$$Z_0^{k+1} = Z_0^k + \Delta Z_0^k \; ; \; T^{k+1} = T^k + \Delta T^k ; \; F_0^{k+1} = F_0^k + \Delta F_0^k \quad (5)$$

Among all possible periodic solution of forced vibration, solutions satisfying phase quadrature lag criterion are NNMs of the nonlinear systems. It means that each harmonic in the excitation must be 90 degrees out of phase with each harmonic in the response. From energy point of view, phase quadrature lag criterion is defined as equation (6)[1].

$$\int_0^T \dot{x}^T C\dot{x}\, dt = \int_0^T \dot{x}^T F(t)\, dt \quad (6)$$

Because the periodic solution of the system is invariant wrt linear shift of time origin, a phase condition equation may be used. In pseudo arc length continuation method, to make the convergence faster, the correction vector is forced to be perpendicular to the prediction vector. So the correction vector is calculated from following set of equations in which j is the continuation index and k is the iteration index in each step of continuation. Prediction vector of each continuation step is defined as $P = \begin{bmatrix} P_{Z_0 j} & P_{T_j} & P_{F_j} \end{bmatrix}$.

$$\begin{bmatrix} \frac{\partial H}{\partial Z_0} & \frac{\partial H}{\partial T} & \frac{\partial H}{\partial F} \\ h(Z_0) & 0 & 0 \\ P_{Z_0 j} & P_{T_j} & P_{F_j} \end{bmatrix} \begin{Bmatrix} \Delta Z_0^k \\ \Delta T^k \\ \Delta F^k \end{Bmatrix} = \begin{Bmatrix} -H \\ 0 \\ 0 \end{Bmatrix} \quad (7)$$

In order to implement the algorithm, forced response of the system at two near constant force amplitude are calculated using method developed by Sadr et al. and solutions satisfying energy condition defined by equation (8) are selected. ε is the acceptable tolerance. Then prediction vector is constructed using these tow point. Then continuation procedure is applied as stated before.

$$E_{err} = \left| \frac{\int_0^T \dot{x}^T C \dot{x}\, dt - \int_0^T \dot{x}^T F(t)\, dt}{Mechanical\ energy} \right| < \varepsilon \quad (8)$$

Results

The method is applied to a two D.o.Fs Damped cubic nonlinear mass spring system and its first NNM is investigated. As stated in many references, NNMs of very lightly damped systems are similar to that of corresponding conservative systems. As seen in the results, when the damping is very low, the NNM is very close to conservative NNM. As the damping increases the modal interaction tong gets shorter and wider. It is observed that, the obtained solutions completely satisfy energy condition of equation4.

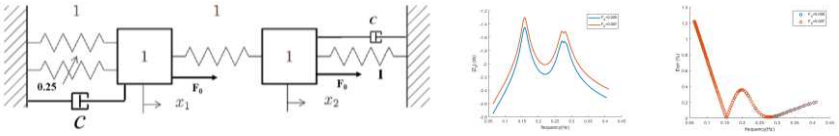

(a) (b) (c)

Figure 1: (a) damped cubic nonlinear mass spring system (b) forced response of the system at constant amplitude of force (c)energy condition of the forced response

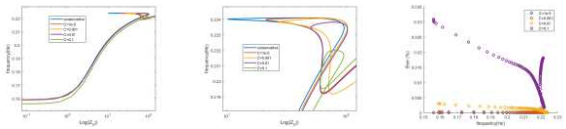

(a) (b) (c)

Figure 1: (a) FEP of First NNM for different values of damping (b) Detail view of first NNM (c)energy condition for obtained results

conclusion

in this paper a new method based on force appropriation technique and pseudo arc length continuation is presented for computation of damped NNMs of nonlinear system. The method applied to a two D.o.Fs system. As observed the accuracy of results was very good. The method can capture the modal interactions without any difficulties. It was seen from the results as the damping of the system increases, the FEP tongs becomes shorter and wider.

References

[1] M. GERADIN and D. J. RIXEN, Mechanical Vibrations Theory and Application to Structural Dynamics, Wiley, 2015.
[2] M. KRACK, Nonlinear modal analysis of nonconservative systems: Extension of the periodic motion concept, Computers & Structures, 154 (2015), pp. 59-71.
[3] R. J. KUETHER and M. S. ALLEN, Computing Nonlinear Normal Modes Using Numerical Continuation and Force Appropriation, 2012, pp. 329-340.
[4] S. M. MOUSAVI, M.-H. SADR and M. JELVEH, Forced vibration analysis of nonlinearsystems using efficient path followingmethod, Journal of Vibration and Control (2019).
[5] L. RENSON, G. KERSCHEN and B. COCHELIN, Numerical computation of nonlinear normal modes in mechanical engineering, Journal of Sound and Vibration, 364 (2016), pp. 177-206.

Bifurcations and stability transitions in nonlinear dynamics of a planar undulating magnetic microswimmer

Jithu Paul*, Yizhar Or* and Oleg Gendelman*

*Faculty of Mechanical Engineering, Technion–Israel Institute of Technology, Haifa, Israel

Summary. A microswimmer, motivated from biological microorganisms or cells motion, which has two links representing a tail and a magnetized head is studied. The links are connected by a passive elastic joint and the microswimmer is actuated by an external time – periodic magnetic field. This simple system is very rich in dynamics and we identified that there exists co-existing periodic solutions- symmetric as well as asymmetric, and stability transitions with pitchfork bifurcations. There is optimum observations for the displacement and velocity of the swimmer with respect to the system parameters, may enable significantly improving the design aspects of the robotic microswimmer.

The micro swimmers are motivated by biology [1], and their dynamics is always interesting . Among the simplest and most efficient techniques for actuation of robotic microswimmers , is by applying time-varying external magnetic fields [2]. One of the important milestones in the field of magnetically actuated microswimmer is given in by Dreyfus et. al [3]. Inspired from the classical work of Purcell [4], a very simple model of two-link swimmer has been presented by Gutman et. al [5], with an external magnetic actuation on the head as shown in Fig. 1. The external magnetic field, $B(t) = [\gamma, \beta \sin(\omega t)]^T$ has an oscillating component in y direction and a constant x component, γ. The same model with paramagnetic excitation is studied in [6] with interesting observations on bistability and analogy of tilted Kapitza pendulum. We revisit the model in [5] and explore co-existence of periodic solutions as well as their bifurcations, stability transitions, and symmetry-breaking.

The system in Fig. 1 has four coordinates: body position (x,y) and two angles θ and ϕ, which represent body orientation angle and relative angle between the links, respectively. Invariance with respect to x and y enables reduction of the system into two dimensional state equations in two variables, θ and ϕ only. The stiffness of the torsional spring at the passive elastic joint is given by k. Coming to the major assumptions, the swimmer is submerged in a Newtonian fluid and it remains neutrally buoyant (no effect due to gravity). The micron size of the swimmer allows assuming low Reynolds number hydrodynamics where viscous forces dominate while inertial effects are negligible. The resistive force theory for slender bodies governs the net forces and torques acting at the links' centers due to viscous drag. In the work of Gutman et. al [5], fixed, $\gamma = 1$ and small $\beta \ll \gamma$ are assumed, and focused only on symmetric periodic solutions with mean $(\theta, \phi) = (0,0)$.

Here, as an extension to [5], as shown in Fig. 2, we extracted other co-existing solutions, symmetric around mean $(\theta, \phi) = (\pi, 0)$, as well as asymmetric, and their stability transitions (Fig. 2(a)) and bifurcation (Fig. 2(b)). Upon varying the actuation parameters (β, γ, ω), the results are obtained by numerical analysis using the MATLAB tools ODE45 and fsolve. There are also optimum plots (for stable region) for X, net displacement in x versus β , amplitudes of excitation (Fig. 2(c)) and V, mean velocity versus ω, frequency (Fig. 2(d)), where all the parameters are in experimentally relevant region. It can be analytically studied since there exists small amplitudes for θ, ϕ for $\gamma \ll 1$. These stable optimum regions and indications towards stability transitions can improve designing a simple efficient two link robotic microswimmer, which can be used for a wide range of applications.

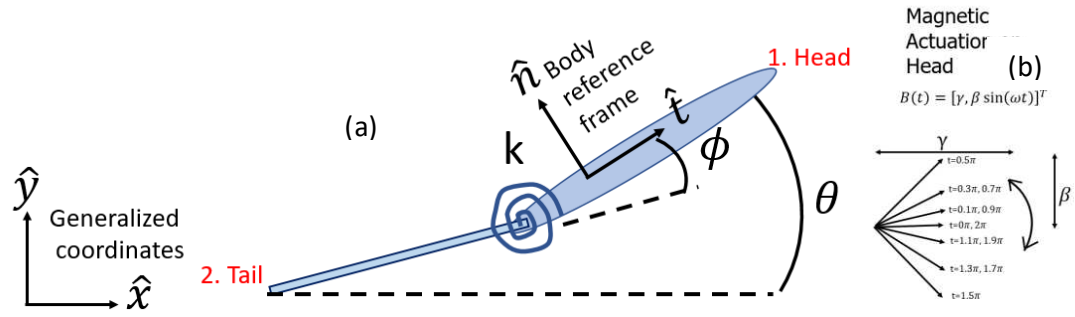

Fig. 1. Model system, (a) shows two link microswimmer which are connected by torsional spring and its head receives magnetic actuation. (b) shows the details of magnetic actuation

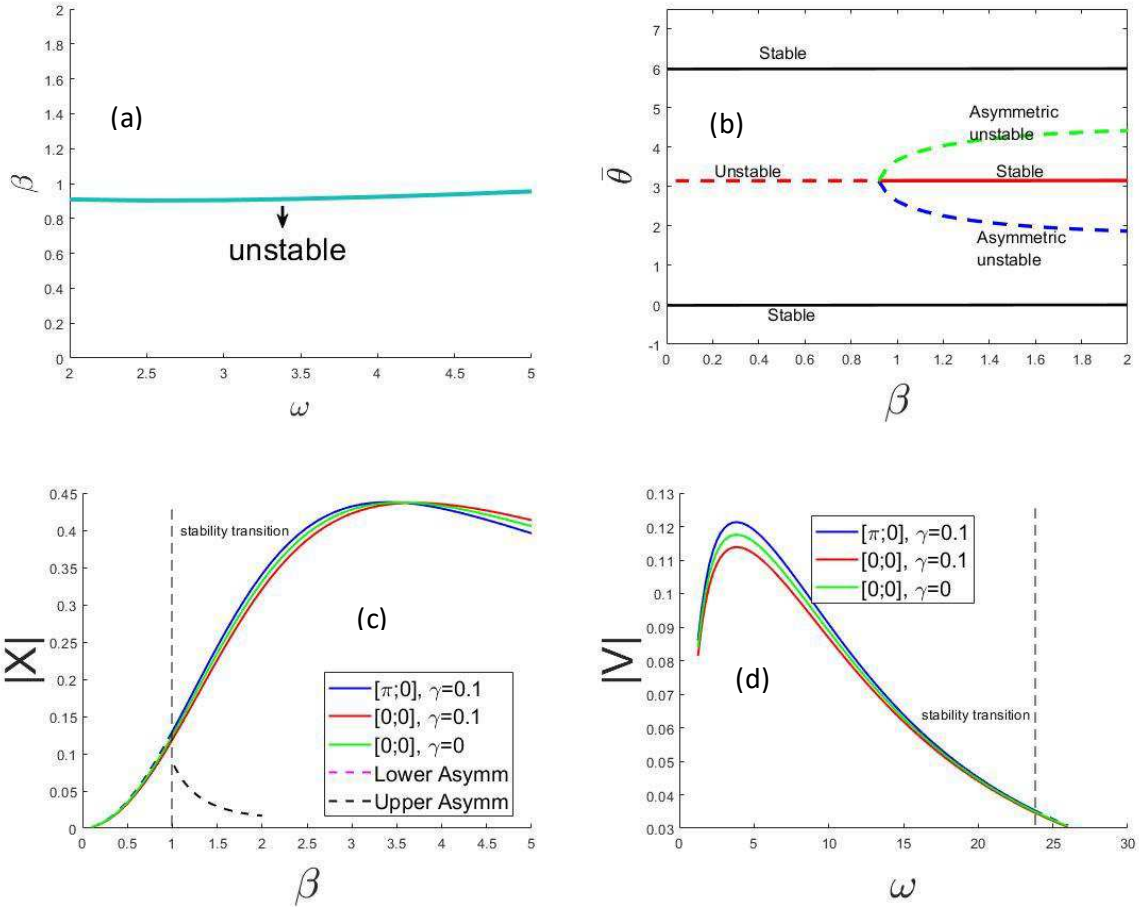

Fig. 2. (a) shows Stability transition in $\beta - \omega$ plane at $\gamma = 0.1$, (b) shows possibility of a subcritical pitchfork bifurcation at the stability transition where $\omega = 2, \gamma = 0.1$, (c) shows optimum displacement plot with respect to amplitude of actuation oscillations β and (d) shows the optimum velocity plot versus frequency ω.

References

[1] B. J. Nelson, I. K. Kaliakatsos, and J. J. Abbott, *Microrobots for Minimally Invasive Medicine*, Annu. Rev. Biomed. Eng. **12**, 55 (2010).

[2] K. E. Peyer, L. Zhang, and B. J. Nelson, *Bio-Inspired Magnetic Swimming Microrobots for Biomedical Applications*, Nanoscale **5**, 1259 (2013).

[3] R. Dreyfus, J. Baudry, M. L. Roper, M. Fermigier, H. A. Stone, and J. Bibette, *Microscopic Artificial Swimmers*, Nature **437**, 7060 (2005).

[4] E. M. Purcell, *Life at Low Reynolds Number*, Am. J. Phys. **45**, 3 (1977).

[5] E. Gutman and Y. Or, *Simple Model of a Planar Undulating Magnetic Microswimmer*, Phys. Rev. E **90**, 013012 (2014).

[6] Y. Harduf, D. Jin, Y. Or, and L. Zhang, *Nonlinear Parametric Excitation Effect Induces Stability Transitions in Swimming Direction of Flexible Superparamagnetic Microswimmers*, Soft Robot. **5**, 389 (2018).

Stability of Nonlinear Normal Modes under Stochastic Excitation

Yuri V. Mikhlin* and Gayane V. Rudnyeva*
*National Technical University "Kharkiv Polytechnic Institute", Kharkiv, Ukraine

Summary. Two-DOF nonlinear system under white noise excitation is considered. It is assumed that the system allows from two up to four nonlinear normal modes (NNMs) with rectilinear trajectories in the system configuration space. Influence of the random excitation to the NNMs stability is analyzed by using the analytical-numerical test, which is an implication of the well-known Lyapunov stability criterion. Boundary of the stability/ instability regions is obtained in place of two parameters, namely, a connection between partial oscillators, and the excitation intensity. Stability of the NNMs under deterministic chaos excitation is also considered.

Introduction

Investigation of nonlinear normal modes (NNMs) is an important part of general analysis of dynamical systems. Different theoretical aspects of the NNMs theory and applications of the theory are presented in numerous publications, in particular, in review [1]. NNMs having rectilinear trajectories in configuration space (so-called similar nonlinear normal modes) were first found in some essential nonlinear systems by Rosenberg [2].

Numerous publications are dedicated to investigation of behavior of dynamical systems under stochastic excitation. In this regard, different theoretical and numerical procedures are developed. We cite here only few publications on the subject, namely, books [3-5]. In [6] the dynamics of aerospace vehicles and/or other structures subject to random excitation is investigated using a reduced order model in terms of its nonlinear normal modes. Evolution of NNMs is studied by the continuation algorithm and presented in the plot "energy-frequency".

Here some numerical-analytical test [7] which is a consequence of the well-know Lyapunov criterion of stability is used to analyze a stability of NNMs in two-DOF nonlinear system under white noise excitation. We assume that the system allows from nonlinear normal modes with rectilinear trajectories in the system configuration space. We analyze also a stability of the NNMs under deterministic chaos excitation.

Principal model under consideration

The following two-DOF nonlinear system under stochastic excitation is considered:

$$\begin{cases} \ddot{x}_1 + x_1^3 + \gamma\left(x_1 - x_2\right)^3 = \varepsilon\xi_1(t), \\ \ddot{x}_2 + x_2^3 + \gamma\left(x_2 - x_1\right)^3 = \varepsilon\xi_2(t), \end{cases} \tag{1}$$

where ε is the small parameter, and the functions $\xi_1(t)$, $\xi_2(t)$ represent stochastic excitation. When $\varepsilon=0$ the system allows so-called similar NNMs in the form $x_2 = cx_1$, where c is the modal constant. We can note that the equations (1) always allow two similar NNMs, where $c_{1,2} = \pm 1$. The solution $c_1 = +1$ corresponds to the in-phase nonlinear normal mode, and the solution $c_2 = -1$ corresponds to the out-of-phase (anti-phase) one. We consider the external excitations which save the in-phase and out-of-phase NNMs but can change their stability and point of bifurcation.

Test of stability as implication of the Lyapunov stability criterion

Consider the well-known Lyapunov definition of stability which can be presented in the simplest variant as the following: the solution $y = 0$ is stable if for any positive ε there a positive δ exists such that for all $y_0 \in N_\delta(0)$ and $t \geq 0$ we have the following: $y(t) \in N_\varepsilon(t)$ where stated neighborhoods can be determined using norms in some functional space. Here the variable y has meaning of variation with respect to the solution studied for stability. Later a modulus of the function is used as the norm. One introduces a relation between the quantity ε and the initial value of the variable y; it corresponds to a sense of the definition by Lyapunov when the initial variations must not tend to zero. Let

$$\varepsilon = \rho\left|y_0\right| \leq \rho\delta \quad (\rho = const) \tag{2}$$

We can note that a value of δ is not arbitrarily small; it corresponds to essence of the Lyapunov definition because in this definition the initial values of variations cannot tend to zero. One has from the Lyapunov stability definition that $\left|y(t)\right| \leq \rho\left|y(0)\right|$ for a case of stability.

We introduce the following test for the system under consideration [6]: Instability of the solution $y = 0$ is fixed if

$$\left|y(t)\right| \geq \rho \ \left|y(0)\right| \qquad (0 \leq t \leq T). \tag{3}$$

In contrast to the Lyapunov definition a time of numerical calculations T is limited in the test (3). It is necessary to discuss a choice of values of ρ and T. There is some arbitrariness in a choice of the value ρ. In fact, in the instability region the variations leave the solution ε-neighborhood under increase of t for any choice of the parameter ρ. We can choose, for example, $\rho = 10$. One discusses now a choice of the constant T. Note that all concrete calculations are realized by using the standard Runge-Kutta procedure. These calculations are made at points on some chosen mesh of

the system parameter space. Calculations are conducted as long as boundaries of stability/instability regions in a chosen scale on the system parameter space are variable. This is a principal criterion for the choice of the calculation time T [7]. Taking into account a specific character of the stability problem under stochastic excitation, we are introduced some important modification to the proposed test (3). Namely, we can observe that in the last case some variations can leave the ε-neighborhood and then return back to one. Thus, we will allow that some small part of variations (not more than 10 percent) is out of the neighborhood during each fixed interval of time.

Stability of the similar NNMs: results of simulation

To investigate the stability/instability of the in-phase and out-of-phase nonlinear normal modes, we pass to the systems in variations by means of change of variables in (1), namely:

for the out-of-phase NNM $x_1 = (u-v)/\sqrt{2},\ x_2 = (u+v)/\sqrt{2}\ ,\ u = 0+\Delta u, v = v_0+\Delta v,\ \ \xi_2 = -\xi_1;$

for the in-phase NNM $x_1 = (u-v)/\sqrt{2},\ x_2 = (u+v)/\sqrt{2}\ \ ,\ u = u_0+\Delta u, v = 0+\Delta v,\ \xi_2 = \xi_1\ .$

Some results of numerical simulation for the presented NNM stability problem by using the stability criterion (3) are presented. Figs. 1 and 2 demonstrate boundaries of stability/instability of the out-of-phase nonlinear normal mode for different values of parameters. Figs. 3 and 4 show a behavior in time of the out-of-phase NNM simulated for different values of the connection parameter: γ=0.24 and γ=0.26, correspondingly. Fig.5 shows boundaries of the stability/ instability regions in the place (γ,ε). Note that such results are obtained for four different kinds of stochastic excitation.

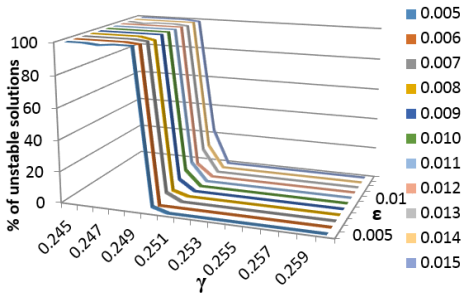

Figure 1

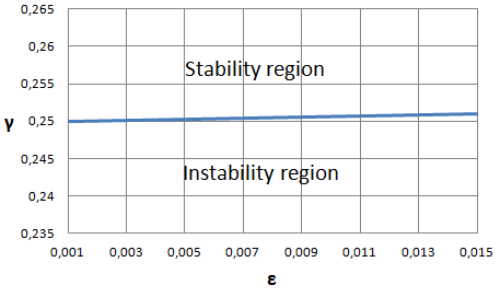

Figure 2

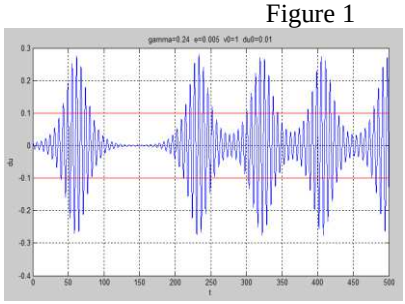

Figure 3

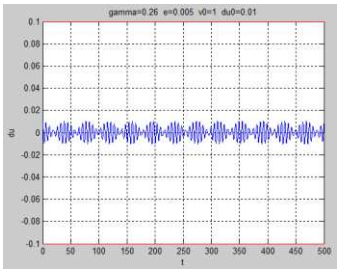

Figure 4

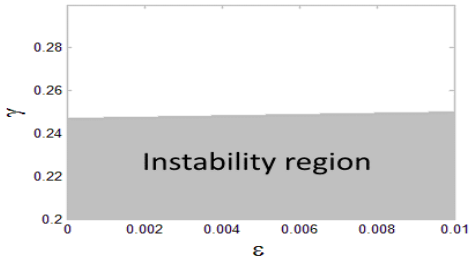

Figure 5

Stability of NNMs under excitation in the form of determined chaos

Determined chaotic excitation can be obtained, in particular, by solution of the non-autonomous Duffing equation for some values of the equation parameters. Numerical simulation shows that excitation in the form of the determined chaos does not influence to stability of the NNMs in the system under consideration.

Conclusions

It is shown that the analytical-numerical test, which is an implication of the Lyapunov stability criterion, can be successfully used in analysis of stability of NNMs in two-DOF system under white noise excitation. Boundary of the stability/ instability regions is obtained in place of the system parameters, including parameter of the excitation intensity. It is shown also that the deterministic chaos excitation does not affect to the NNMs stability.

References

[1] Mikhlin Yu.V., Avramov K.V. (2010) Nonlinear normal modes for vibrating mechanical systems. Review of theoretical developments, *Appl. Mech. Rev*. **63**: 4–20.
[2] Rosenberg, R. (1966) Nonlinear vibrations of systems with many degrees of freedom. *Adv. Appl. Mech*. **9:** 156–243.
[3] Schuss Z. (2010) Theory and Applications of Stochastic Processes, Vol. 170 of Applied Mathematical Sciences. Springer, NY.
[4] Roberts J. B., Spanos P. D. (2003) Random vibration and statistical linearization, Dover Publications.
[5] Li J., Chen J. (2009) Stochastic dynamics of structures. Wiley, NY.
[6] Schoneman J.D., Allen M.S. (2017) Relationships between nonlinear normal modes and response to random inputs. *Mechanical Systems and Signal Processing* **84:** 184-199.
[7] Mikhlin Yu.V., Shmatko T.V., Manucharyan G.V. (2004) Lyapunov definition and stability of regular or chaotic vibration modes in systems with several equilibrium positions. *Computer & Structures* **82:** 2733–2742.

SIR model for rumor propagation

Cristiane M. Batistela*, Manuel A. M. Cabrera*, Antonio C. B. Godoi* and José R. C. Piqueira*
* *Control Engineering Department, São Paulo University, São Paulo, Brazil*

Summary. Similarities exist between rumor propagation and disease spreading. In analogy with the SIR (Susceptible-Infected-Removed) epidemiological model, the ISS (Ignorant-Spreader-Stifler) rumor model has been developed. Here, the SIR model was modified with the new compartment, originating the ISSV (Ignorant-Spreader-Stifler-Verifier) rumor model. In this work, the model is presented and how its parameters are related to network characteristics is explained. This paper presents a system of differential equations that describes the spreading of a rumor in a new model, with a novel compartment, the verifier. By using concepts from Dynamical Systems Theory, equilibrium point is calculated, the stability and bifurcation conditions are derived. According parameters and initial conditions, the model is validated with numerical experiments. The relations among the model parameters in the several bifurcation conditions allow a rumor propagation design minimizing risks.

Introduction

With the rapid development of the Internet, the way to acquire information changed. There are a lot of platforms for this, as a typical example, social networks and they have been widely recognized. The media commonly releases their latest information through social networks, consequently can bring efficiency to daily life and information exchange, but it also results in gradual prevalence of online rumor.

Rumor, as a part of everyone is daily life, has often been defined as a type of social phenomenon with which some unconfirmed elaboration or annotation of the public interested events or issues spread on a large scale within a relatively short period of time through various channels, whether it is true or false [3].

People disseminate rumors as a mean of increasing awareness, orienting society, slandering others and so on. The spread of rumors can shape the public opinion and impact finantial markets and change population behavior [10].

The research on rumor propagation models started with development the stochastic rumor propagation proposed by Daley-Kendall, wich divided people into classes: ignorant, spreaders and stiflers, based on the infectious disease research method [1]. Maki-Thompson believed that rumors were disseminated through the two-way contact between the disseminators and other people in the crowd based on Markov chain [11]. Zanette first studied the dynamic behavior of rumor propagation in small world networks, and similarly to disease models he obtained the spreading threshold [17].

Based on the fact that social behavior and biological diseases are a result of interaction between individuals, many researchers have studied the dynamics of social systems by applying epidemiological models.

The epidemiological model proposed by Kermack and McKendrick, the SIR (Susceptible-Infected-Removed) compartmental model [7, 8, 9], has been used in several areas and modifications of this work allowed Daley and Kendall (DK) to propose a rumor spread model [1], the ISS (Ignorant-Spreader-Stifler) model wich shares commons characteristics with epidemic model [2], being important mark in rumor propagation.

The equations that model are similar with the ignorant and spreading populations from ISS model being analogous to susceptible and infected populations of the SIR model, respectively. The main difference between in the models, is that, in ISS, the stifler population plays a different role from the removed population because they does not propagation the rumor and remains in a constant state. In the other way, in SIR models, the removed individuals can be transformed into susceptible ones.

Based on the DK model, in which the participants were divided into three groups: one group of people who never heard the rumor (ignorant), one knowing and spreading the rumor (spreader), and one knowing the rumor but never spreading it (stifler). Afterwards, the rumor spreading model was refined with consideration of the forgetting mechanism [14] and by incorporating the effects of remembering mechanism in complex networks [18].

Various mathematical models for the propagation of a rumour within a population have been developed: the rumor spreading process with denial and skepticism [5], rumor spreading model with skepticism mechanism in social networks, epidemiological approach to model viral meme propagation [16], deterministic models for rumor transmission with constant and variable rumor in an age-independent population, models considering limited information exchange, which two types of rumors spread simultaneously among the crowd, stochastic rumor propagation model [6]. Recently, based on the classical SIR rumor propagation model, a new Susceptible-Infected-Hibernator-Removed model by adding a direct link from ignorants to stiflers and a new group hibernator [18].

Here, assuming an ISS model as a generalization of DK model and with analogies with the SIR model, the rumor spreading is studied, considering a new compartment, the verifier, ISSV (Ignorant-Spreader-Stifler-Verifier). The different dynamical propagation behaviors are possible, depending on how the nodes are connected. Furthermore, the model is studied under the assuming homogeneous distribution of social network that gives plausive qualitative results.

First, the differential equations representing the ISSV model are presented, followed by the stability analysis of the equilibrium points and the possibility of the bifurcation. Numerical experiments are performed to validade the analytical results. Finally, we present our conclusions and discuss some implications of the results.

ISSV Model: hypothesis and equations

The model proposed here is based on the original SIR model with analogies in epidemiologic models. A quantitative version of this model associated with compartmental model was analised by Moreno et al. [13].
By using concepts from Dynamics Systems Theory and assuming the ISS (Ignorant-Spreader-Stifler) models as generalization of DK model, the rumor spreading representation was studied, the several asymptotic behaviors are discussed and the possible bifurcations are shown by Piqueira [15] with the total population (T), divided into three groups: ignorants (I), spreaders (S) and stiflers (R).
Here, the proposed models have a new compartmant and each of the elements of the network can be one of the four different states: the first class are ignorants, and represents those individuals that never heard the rumor and are susceptible to be informed (I); the second group contains the individuals that are spreading the rumor, the spreaders (S); the third compartment, the verifier (V), can verify the rumor and finally, stiflers are those who know the rumor but that are no longer spreading it (R). This model is shown in Figure 1.

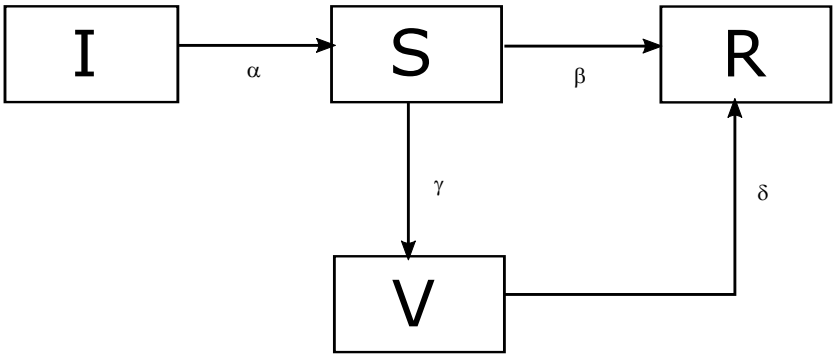

Figure 1: ISSV model.

The dynamical behavior of the spreading process depends on the way the individuals encounter each other. When a spreader meets an ignorant, the latter becomes a new spreader with probability α. Similar to the SIR model, the decay of the spreading process could be either when a spreader meets a stifler and contacts are supposed to have a probability equal to β or became verifier with the rate coefficient γ; in addition, verifier transform into stiflers with the rate coefficiente δ.
The dynamic equation for the populations I, S, V and R are:

$$\begin{cases} \dot{I} &= -\alpha IS; \\ \dot{S} &= \alpha IS - \gamma S - \beta S; \\ \dot{V} &= \gamma S - \delta V; \\ \dot{R} &= \beta S + \delta V. \end{cases} \tag{1}$$

The initial conditios are assumed to be $S(0) \geq 0$, $I(0) \geq 0$, $V(0) \geq 0$ and $R(0) \geq 0$. It is noticed that, for the model represented by (1), the total population $T = I + S + V + R$ remains constant and one of the equations can be expressed by a linear combination of the other three.

Bifurcation of the equilibrium states

In order to explore the influence of the verifiers during the rumor propagation, the dynamic system can be studied considering the equilibrium point of the model represented by (1).
The local stability of these points is analysed using Hartman-Grobman Theorem and the Jacobian derivative is calculated for each equilibrium points and the eigenvalues is calculated.
Examining the dynamical equation for the model, it is possible to determine that there is no spreader equilibrium point, i.e., equilibrium with spreaders nodes. This equilibrium states, spreader-free, corresponding to the absence the spreaders ($S = 0$) and the models in study presented one equilibrium condition, $P = (I, S, V, R) = (I^*, 0, 0, R^*)$.
To analyze the stability of this point, the general Jacobian (J), for the model (1), is constructed as:

$$J = \begin{bmatrix} -\alpha S & -\alpha I & 0 & 0 \\ \alpha S & \alpha I - \gamma - \beta & 0 & 0 \\ 0 & \gamma & -\delta & 0 \\ 0 & \beta & \delta & 0 \end{bmatrix}.$$

The Jacobian calculated in the equilibrium point P is reduced to:

$$J_P = \begin{bmatrix} 0 & -\alpha I & 0 & 0 \\ 0 & \alpha I - \gamma - \beta & 0 & 0 \\ 0 & \gamma & -\delta & 0 \\ 0 & \beta & \delta & 0 \end{bmatrix}.$$

Using MATLAB R2013a [12], the eigenvalues can be calculated: $\lambda_1 = 0$, $\lambda_2 = \alpha I - \gamma - \beta$, $\lambda_3 = -\delta$ and $\lambda_4 = 0$.
Considering the eigenvalues in J_P, for $\lambda_1 = 0$ and $\lambda_4 = 0$, one zero eigenvalue corresponds to the fact that the order of the dynamical system is three and other represent the central manifold [4] represented by the degenerated equilibrium.
The eingenvalue $\lambda_2 = \alpha I - \gamma - \beta$, suggesting the detailed analyses because of the bifurcation possibility.
Examing the eigenvalue $\lambda_2 = \alpha I - \gamma - \beta$ and considering $T = I + R$ for the equilibrium point, the λ_2 can be rewritten as $\lambda_2 = \alpha T - \gamma - \beta$.
Analysing the signal of the second eigenvalue, the equilibrium point is asymptotically stable if $T < (\gamma + \beta)/\alpha$ and if $T > (\gamma + \beta)/\alpha$, the equilibrium point is unstable.

Numerical Experiments

To quantitative analyze the influence of verification nodes on the rumor network, numerical simulations of the model are performed considering the unitary total population ($T = I + S + V + R = 1$). Thus, the instantaneous values of the populations I, S, V, and R are expressed in percentage.
By using the Simulink tool from MATLAB R2013a [12], model simulations were performed to confirm the analytical results, showing the possible behaviors of the dynamical system when verifier compartments are present. The chosen parameters must be corrected to reproduce the results for different population sizes.
In order to simulate the stability of equilibrium point, the parameters must respect the condition $T < (\gamma + \beta)/\alpha$. Then, for $\alpha = 0.5$, β is chosen equal 0.3, $\gamma = 0.25$ and $\delta = 0.5$.
Starting with a condition with at least one percent spreader, the asymptotically stable equilibrium, P, is reachable and the rumor is not propagated. Figure 2 shows the time evolution of the model starting with $I_0 = 0.99$ and $S_0 = 0.01$. The spreaders become stiflers as well as a small percentage of ignorant. The resulting time evolution obtained and ending at the spreader-free equilibrium P.

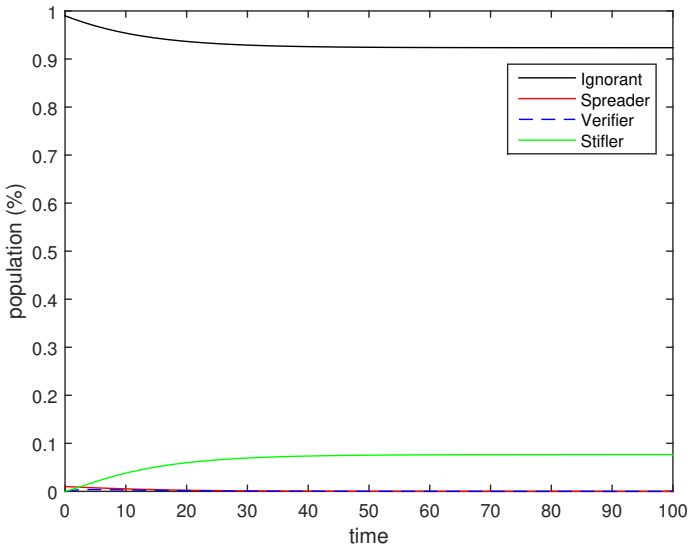

Figure 2: Simulating near stable equilibrium ($\alpha = 0.5$; $\beta = 0.3$; $\gamma = 0.25$; $\delta = 0.5$).

Remaining with the same parameter values and changing the initial conditions, the Figure 3 shows the spreader-free equilibrium P being reached for the initial conditions $I_0 = 0.89$, $S_0 = 0.10$ and $V_0 = 0.01$. In this situation, the spreaders and verifeirs become stiflers and some ignorants came to know the rumors.
Satisfying the condition $T < (\gamma+\beta)/\alpha$, the rumor is contained and decreasing the parameter α or increasing the parameter γ or β, rumor propagation dynamics are not changed.
In order to study the dynamics of the rumor propagation by varying the parameters, the initial condition is considered $I_0 = 0.99$ and $S_0 = 0.01$ and the β value was changed to 0.03. Then, for $\alpha = 0.5$, γ is chosen equal 0.25 and $\delta = 0.5$.
Even decreasing the transformation rate of spreaders into stiffler, the rumor propogation occured by the increase of the stiflers. Figure 4 shows part of the ignorats become stifflers and in this situation $T > (\gamma + \beta)/\alpha$.

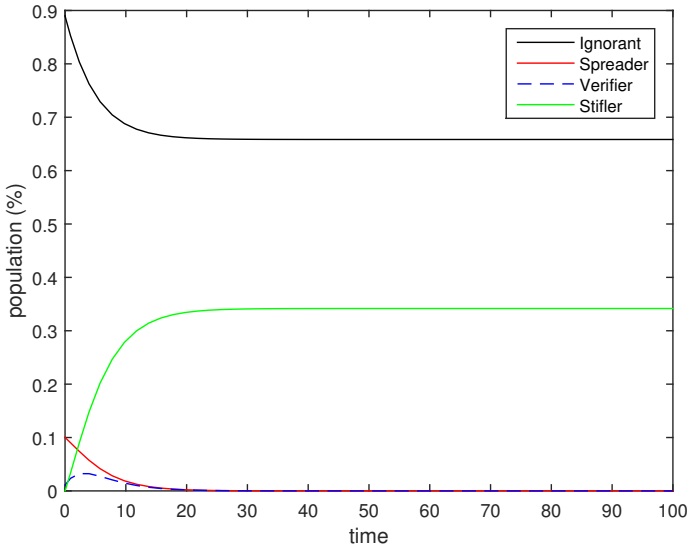

Figure 3: Simulating near stable equilibrium changing the initial percentage of spreader.

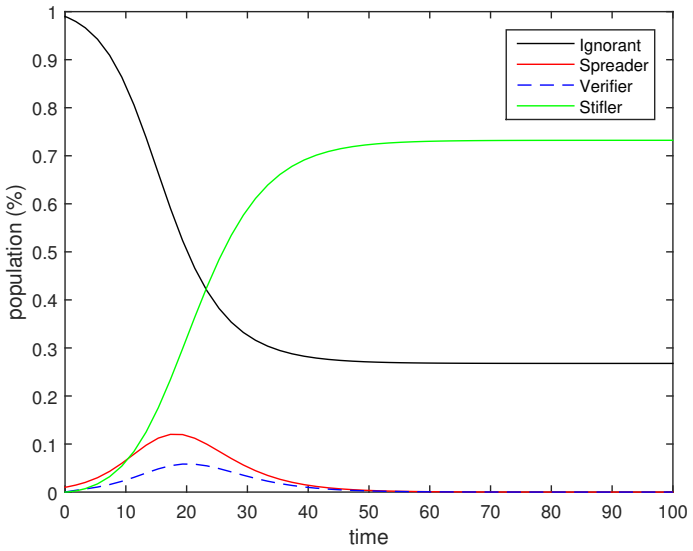

Figure 4: Changing β ($\alpha = 0.5$; $\beta = 0.03$; $\gamma = 0.25$; $\delta = 0.5$).

Changing the parameter α and considering the initial condition $I_0 = 0.98$, $S_0 = 0.01$ and $V_0 = 0.01$, Figure 5 shows the unstability of the equilibrium point P. The parameters are: $\alpha = 5$; $\beta = 0.03$; $\gamma = 0.25$; $\delta = 0.5$ and in this situation all the population become stiflers.
Considering $\delta = 0.05$ and the initial condition $I = 0.98$, $S = 0.01$ and $V = 0.01$, Figure 6 shows the influence of this parameter in the dynamics of the rumor propagation. The others parameters are: $\alpha = 5$; $\beta = 0.03$; $\gamma = 0.25$; $\delta = 0.05$ and in this situation all the population become stiflers. With the decreasing of this rate, the time evolution is changed but the qualitative behavior is the same.

Conclusions

The analysis of the ISSV model shows that, for a given total population, T, the main control parameters are probabilities α, β and γ measuring the efficient communication ignorant-spreader (α), spreader-stifler (β) and spreader-verifier (γ), respectively.
Perturbing near the equilibrium point with at least one spreader, for any combination the parameters, satisfying the condition $T > (\gamma + \beta)/\alpha$, the steady state is composed of a few ignorants, a lot of stiflers, and no spreaders, meaning that almost all the population heard the rumor.
Under the same initial conditions but satisfying the condition $T < (\gamma+\beta)/\alpha$, the equibrium point is not changed meaning that the rumor is not propagated.

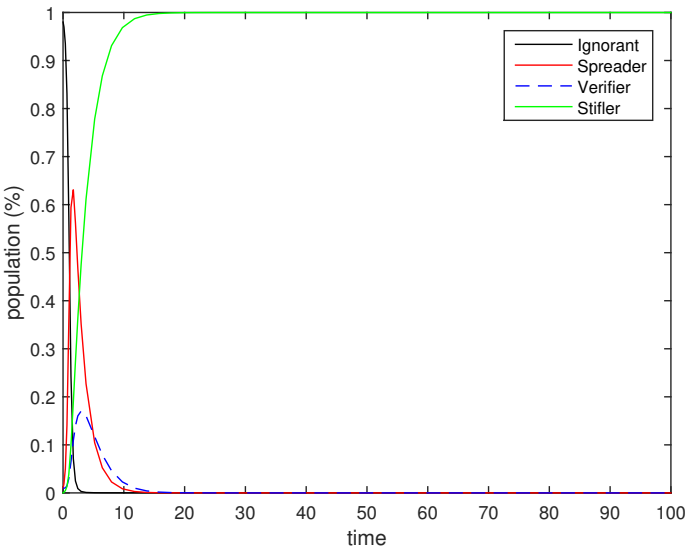

Figure 5: Changing α ($\alpha = 5$; $\beta = 0.03$; $\gamma = 0.25$; $\delta = 0.5$).

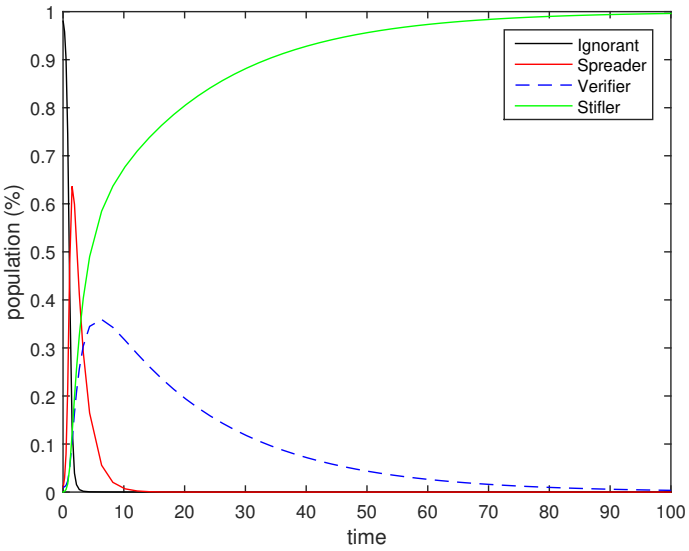

Figure 6: Changing α ($\alpha = 5$; $\beta = 0.03$; $\gamma = 0.25$; $\delta = 0.05$).

Changing the δ parameter, wich transform verifier into stifler, does not change the qualitative behavior associated with the spread of rumors.

References

[1] Daley, D. J., Kendall, D. G. (1964) Epidemics and rumours. *Nature* **204(4963)**: 1118-1118.

[2] Dietz, K. (1967) Epidemics and rumours: A survey. *Journal of the Royal Statistical Society: Series A (General)* **130(4)**: 505-528.

[3] Galam, S. (2003). Modelling rumors: the no plane Pentagon French hoax case. *Physica A: Statistical Mechanics and Its Applications* **320**: 571-580.

[4] Guckenheimer, J. Holmes, P. (1983) Nonlinear Oscillations, Dynamic Systems and Bifurcation of Vector Fields. Springer, NY.

[5] Huang, W. (2011) On rumour spreading with skepticism and denial. *Working paper*.

[6] Jia, F., Lv, G. (2018). Dynamic analysis of a stochastic rumor propagation model. *Physica A: Statistical Mechanics and its Applications* **490**: 613-623.

[7] Kermack, W. O., McKendrick, A. G. (1927) Contributions to the mathematical theory of epidemics. *Proceedings of the Royal Society Series A* **115(772)**: 700-721.

[8] Kermack, W. O., McKendrick, A. G. (1932) Contributions to the mathematical theory of epidemics. *Proceedings of the Royal Society Series A* **138(834)**: 55-83.

[9] Kermack, W. O., McKendrick, A. G. (1933) Contributions to the mathematical theory of epidemics. *Proceedings of the Royal Society Series A* **141(843)**: 94-122.

[10] Kimmel, A. J. (2004) Rumors and the financial marketplace. *The Journal of Behavioral Finance* **5(3)**: 134-141.

[11] Maki, D. P., Thompson, M. (1973). Mathematical models and applications: with emphasis on the social life, and management sciences. Prentice-Hall, Englewood Cliffs, NJ.

[12] Moler, C.B.(2004) Numerical Computing with MATLAB. SIAM, Philadelphia, PA.

[13] Moreno, Y., Nekovee, M., Pacheco, A. F. (2004) Dynamics of rumor spreading in complex networks.*Physical Review E* **69(6)**: 066130.

[14] Nekovee, M., Moreno, Y., Bianconi, G., Marsili, M. (2007) Theory of rumour spreading in complex social networks. *Physica A: Statistical Mechanics and its Applications* **374(1)**: 457-470.

[15] Piqueira, J. R. C. (2010) Rumor propagation model: An equilibrium study. *Mathematical Problems in Engineering* **2010**.

[16] Wang, L., Wood, B. C. (2011) An epidemiological approach to model the viral propagation of memes.*Applied Mathematical Modelling* **35(11)**: 5442-5447.

[17] Zanette, D. H. (2001). Critical behavior of propagation on small-world networks. *Physical Review E* **64(5)**: 050901.

[18] Zhao, L., Wang, J., Chen, Y., Wang, Q., Cheng, J., Cui, H. (2012). SIHR rumor spreading model in social networks. *Physica A: Statistical Mechanics and its Applications* **391(7)**: 2444-2453.

Dynamics and minimalistic control of a flexible structure containing bi-stable elements

Yamit Geron*, Sefi Givli*, Yizhar Or *
*Faculty of Mechanical Engineering, Technion - Israel Institute of Technology, Haifa, Israel.

Summary. This study aims to design and analyze a system of mechanically-coupled bistable elements such that transitions between states (different equilibrium branches) take place in a desirable order by controlling a single degree of freedom. Such systems may be useful in a range of applications, e.g. soft robots or foldable structures, where a complex sequence of movements or configurations needs be achieved by minimal control. The theoretical part involves analytical and numerical investigation of the non-linear dynamic response of an array of bistable elements connected in series. The model accounts for the non-linear behavior of the bistable elements assuming linear damping and negligible inertia where the only control input is the displacement at the end of the chain (u_0). The quasi-static and dynamic response of a chain of two elements is studied. Focus is put on the multiplicity of equilibrium states, stability, and conditions for transition between stable states. Special attention is given to identifying critical rates that separate between different transition sequences, and how they are influenced by the properties of the bistable elements and the variability between them. We show, and demonstrate experimentally, that by clever design of the bistable elements, one can robustly control the order of transitions between states by merely varying the rate (speed) of the applied overall extension.

Introduction

A bi-stable mechanical element has two stable equilibrium states for the same external load and allows transition between states. The behavior of a chain of bistable elements has been studied extensively in various contexts. For example, in [1] the quasi-static behavior and stability of equilibrium configurations of a chain of identical bistable elements was investigated. Recently, robotic systems with bistable elements have been proposed for achieving controlled transitions using minimalistic control [2]. In another recent work [3], such concept was demonstrated on a system of identical hyper-elastic thin-walled balloons connected in series, where a desirable state is attained by a sequence of quasi-static inflations and deflations using a single flow control input.

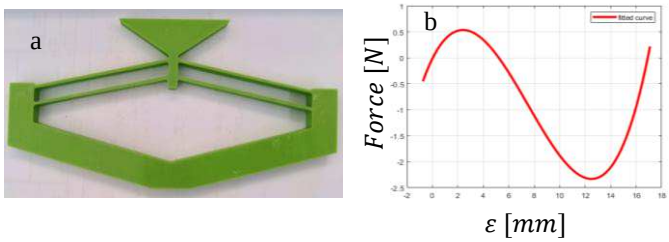

Figure 1: **(a).** A 3D-printed bistable element made of ABS material. **(b).** The measured force–elongation relation of the 3D-printed bistable element.

Results

The dynamic equations of a system comprising two bistable elements connected in series were formulated by assuming linear damping and negligible inertial forces. A thorough investigation revealed that the sequence of transitions between stable equilibrium branches can be dictated by merely controlling the input (elongation) speed.

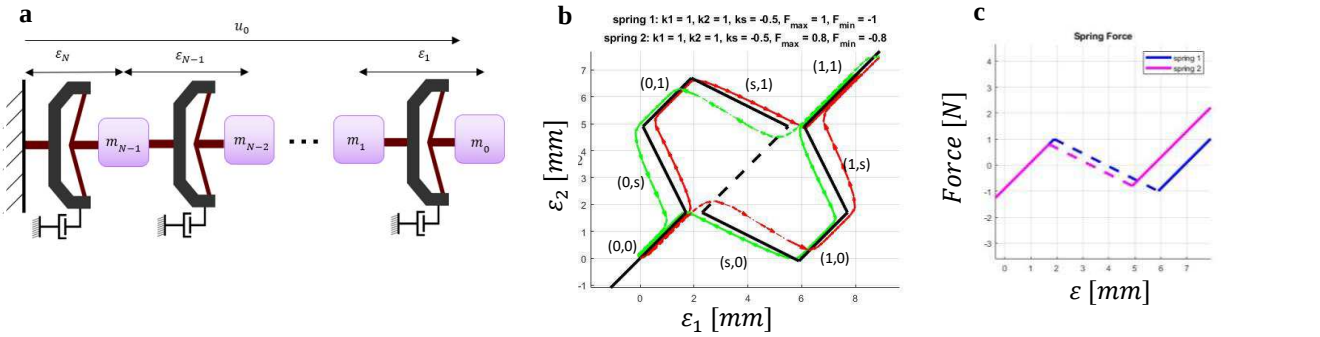

Figure 2: **(a).** Dynamic model; u_0 is the input control and ε_i is the elongation of element i. **(b).** Equilibrium curves (dashed – unstable) and dynamic trajectories on the map of the elongation of the elements. **(c).** The force – elongation relation of the elements in the system.

For example, during stretching, the condition for generating a sequence of transition events that differs from that of the quasi-static (or slow) loading is that the first element reaches the negative-stiffness branch (right of the red vertical line in Fig. 3b) before the second element does (above the horizontal gray line in Fig. 3b).

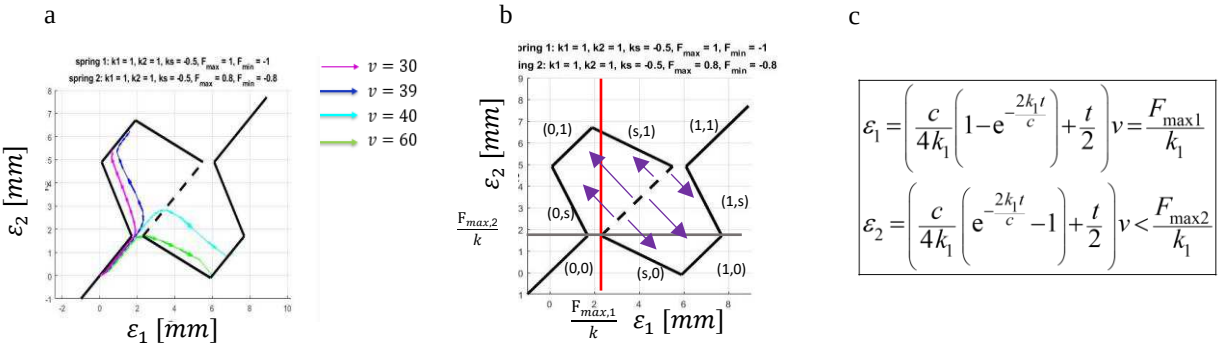

Figure 3: **(a).** It can be seen in the graph that there is a critical speed which changes the trajectory of the movement from the trivial trajectory to the non-trivial trajectory. **(b).** Shows the requirements for the transition to the non-trivial route on a force – elongation profile. **(c).** Algebraic transition conditions according to the conditions in graph b.

Let us define the following non-dimensional parameters: $\tau = \frac{k_1}{c}t, \bar{u} = \frac{cv}{2(F_{\max 1}+F_{\max 2})}, \beta = \frac{(F_{\max 1}-F_{\max 2})}{(F_{\max 1}+F_{\max 2})}$. The condition for changing transition sequence is $\beta + \bar{u}\left(e^{-\frac{1}{\bar{u}}} - 1\right) > 0$. We find that for relatively small values of β, even up to β=0.18, the critical speed may be well approximated by $v > \frac{2(F_{\max 1}-F_{\max 2})}{c}$.

To test the theoretical predictions, we designed and built an experimental setup. The bistable elements were manufactured by 3D-printing, and the details of their bistable behavior (including the desired difference between the two) were tailored by careful design of the geometry of the parallel bending beams. Damping was introduced by strong magnets attached to each element and hovering over a copper plate (see Fig. 4).

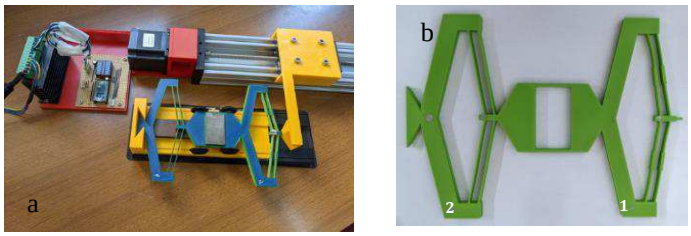

Figure 4: **(a).** Experimental system. **(b).** Two bistable elements are printed on a 3D printer made of ABS material.

The dynamic response was recorded using a digital camera and then analyzed by means of standard image processing tools. The experimental results, in terms of elongation of each of the two bistable elements, are shown in Fig. 5, and display a very good agreement with the theoretical predictions.

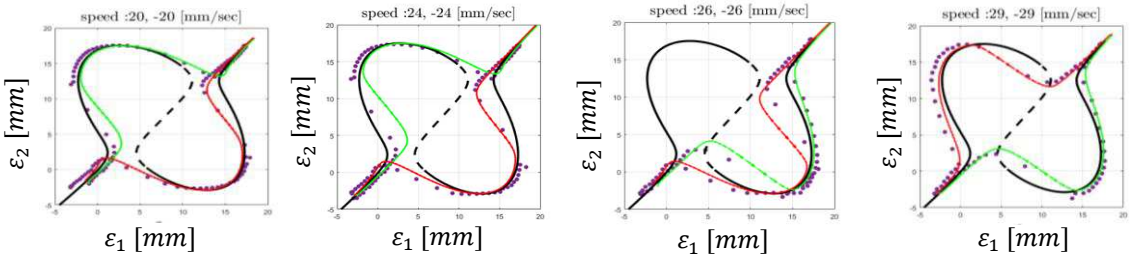

Figure 5: Comparison of the results of the experiment measured in image processing to the results of the simulation. Purple dots (experiment results), red line (stretching simulation) green line (compression simulation), dashed line black (unstable equilibrium), black line (stable equilibrium).

References

[1] I. Benichou and S. Givli, "Structures undergoing discrete phase transformation," *J. Mech. Phys. Solids*, vol. 61, no. 1, pp. 94–113, 2013, doi: 10.1016/J.JMPS.2012.08.009.

[2] E. Ben-Haim, L. Salem, Y. Or, and A. D. Gat, "Single-Input Control of Multiple Fluid-Driven Elastic Actuators via Interaction between Bistability and Viscosity," *Soft Robot.*, vol. 7, no. 2, pp. 259–265, Apr. 2020, doi: 10.1089/soro.2019.0060.

[3] D. Melancon, B. Gorissen, C. J. García-Mora, C. Hoberman, and K. Bertoldi, "Multistable inflatable origami structures at the metre scale," *Nat.* |, vol. 592, p. 545, 2021, doi: 10.1038/s41586-021-03407-4.

Optomechanical cavities: from synchronization to mode locking

Eyal Buks*
*Andrew and Erna Viterbi Department of Electrical Engineering, Technion, Haifa 32000 Israel

Summary. We experimentally study a fiber-based optical ring cavity integrated with a mechanical resonator mirror and an optical amplifier. The device exhibits a variety of intriguing nonlinear effects including synchronization and self-excited oscillation. Passively generated optical pulses are observed when the frequency of the optical ring cavity is tuned very close to the mechanical frequency of the suspended mirror. The optical power at the threshold of this process of mechanical mode locking is found to be related to quantum noise of the optical amplifier.

Analytical study of interfacial three dimensional gravity waves in presence of current

Soraya Salmi[*, **], Nabil Allalou [***]

[*]*Département de physique, Faculté des sciences, Université M'Hamed Bougara de Boumerdes, Route de la gare Ferroviaire, Boumerdes 35000, Algeria.*

[**]*Laboratoire revêtements, Matériaux et Environnement, Université M'Hamed Bougara de Boumerdes, Avenue de l'indépendance, Boumerdes 35000, Algeria.*

[***] *Faculté de physique, Laboratoire mécanique des fluides théoriques et appliqués, Université des Sciences et de la Technologie Houari Boumediene, B.P.32 El Alia, Alger 16111, Algeria.*

Summary. Analytical study of short crested interfacial gravity waves propagating between two infinite fluids layers has been carried out. These waves are the simplest form of three dimensional waves and are obtained through a reflection of a 2D wave train into a vertical wall. The fluids have different densities and the upper is moving relative to the lower with horizontal and uniform velocity U. The fluids are taken to be incompressible and inviscid and the motion assumed to be irrotational. Using a perturbation method, the forth order solutions was obtained. Using this method attention was focused for the determination of the harmonic resonance of short-crested interfacial waves.

Introduction

For several years efforts have been devoted to the study of the two dimensional interfacial gravity waves in the presence of current. The most interesting approach to this issue has been proposed by Saffman [1], where he identified the critical current which limiting the existence of steady solutions. However, modeling some aspects of three dimensional interfacial gravity waves in the presence of current is essential for more realistic descriptions. Applying this modeling to appropriate cases of practical interest is the main goal of the present work. Most of the work published for three dimensional waves often deals with short crested waves which represent the simplest form, that is why, in our study we focused in this wave form. Using perturbation method an analytical approach has been presented up to the fourth order for the case of interfacial waves between two infinite fluid layers with different densities.

System of equations.

Considering Cartesian coordinate composed of the horizontal plane (x-y) of propagation's interfacial three dimensional wave between two infinite fluid layers (fig.1.a). Herein, short crested-wave field generated from the nonlinear interaction of two wave trains propagating to each other's having the same amplitude and wavelength. L is the wavelength of the incident wave, θ is the angle between the direction of incidence and the normal to the wall. U is the uniform current paralleling to the direction of propagation on the upper layer as shown in (fig.1.b).

(a) (b)

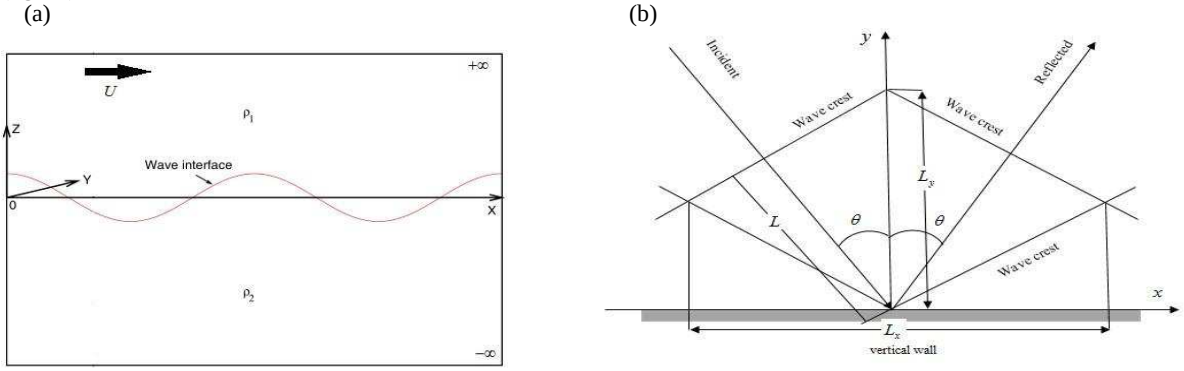

Figure.1: schematic presentation of a short crested wave in presence of current.

The two fluids with densities ρ_1 and ρ_2 are assumed to be inviscid, incompressible and the motion is irrotational. However, with this assumptions the fluid motion can be described by the velocity potential $\phi_1(X, Y, Z)$ and $\phi_2(X, Y, Z)$, which satisfy the dimensionless Laplace's equation in the two fluid layers domain.

$$\Delta\phi_1 = 0 \quad for \quad 0 < Z < +\infty, \tag{1}$$

$$\Delta\phi_2 = 0 \quad for \quad +\infty < Z < 0. \tag{2}$$

And due to the presence of a current on the upper layer, herein, the total velocity potential can be expressed by:

$$\phi_{1T}(X, Y, Z) = pUX + \phi_1(X, Y, Z). \tag{3}$$

Solutions of equations (1) and (2) are obtained using some boundary conditions for each layer of fluid, they are summarized in dimensionless form as below:

Kinematic boundary conditions at the interface: $(pU - \omega)\eta_X + p^2\eta_X\phi_{1X} + q^2\eta_Y\phi_{1Y} - \phi_{1Z} = 0$, (4)

$$-\omega\eta_X + p^2\eta_X\phi_{2X} + q^2\eta_Y\phi_{2Y} - \phi_{2Z} = 0, \tag{5}$$

Dynamic boundary condition resulting from the Bernoulli's theorem where C is the Bernoulli's constant:

$$\mu\left\{(pU-\omega)\phi_{1X}+\eta+\frac{1}{2}(p^2\phi_{1X}^2+q^2\phi_{1Y}^2+\phi_{1Z}^2)\right\}+\omega\phi_{2X}-\eta-\frac{1}{2}(p^2\phi_{2X}^2+q^2\phi_{2Y}^2+\phi_{2Z}^2)+C=0, \quad (6)$$

Bottom boundary conditions: $\phi_{1Z}=0 \quad at \quad Z\to+\infty,$ (7)

$$\phi_{2Z}=0 \quad at \quad Z\to-\infty. \quad (8)$$

Perturbation method

The problem is solved by the perturbation method. Such an analysis assumes that the non linearities present a small corrections to linear wave theory. The parameters of the problem are developed in power series based on a small parameter h:

$$\phi=\sum_{r=1}^{\infty}h^r\phi_i^r(X,Y,Z),\ \eta=\sum_{r=1}^{\infty}h^r\eta_i^r(X,Y),\ \omega=\sum_{r=1}^{\infty}h^r\omega_r, \quad (9)$$

Where the wave steepness defined by $h=\frac{1}{2}\left(\eta(0,0)-\eta(0,\pi)\right)$.

In the first order, we retain only the linear terms. Thus, the linear solution is:

$$\begin{cases}\phi_1^{(1)}=(pU-\omega_0)\sin X\ \cos Y e^{-Z},\\ \phi_2^{(1)}=\omega_0\sin X\ \cos Y e^{Z},\\ \eta^{(1)}=\cos X\ \cos Y,\\ \omega_0=\mu pU+\sqrt{-\mu^2-\mu p^2U^2+1}\Big/\mu+1,\end{cases} \quad (10)$$

The dispersion relation for the linear interfacial wave can be expressed by: $\mu(pU-\omega_0)^2+\omega_0^2=1-\mu,$ (11)

From this relation the value of the critical current is given by: $U_{cl}=\sqrt{-\mu(\mu^2-1)}\Big/\mu p$. (12)

As $U>U_{cl}$ the three-dimensional waves cannot be observed in regular form, in other words steady solutions no longer exist and the wave profile becomes unphysical.

In the higher order, the linearization of kinematic and dynamic equations is carried out by performing a Taylor series expansion of the potential velocities in the neighbourhood of $\eta=0$. After solving the system of equations, the following solutions are obtained in each order:

$$a_{mn}^{(r)}=-\frac{m(\mu pUf_{1,mn}^{(r)}-\mu\omega_0 f_{1,mn}^{(r)}-\omega_0 f_{2,mn}^{(r)})-\alpha_{mn}F_{mn}^{(r)}}{m^2(\mu p^2U^2-2\mu\omega_0 pU+\mu\omega_0^2+\omega_0^2)+\alpha_{mn}(\mu-1)}, \quad (13)$$

$$b_{mn}^{(r)}=\frac{(pU-\omega_0)m^2\omega_0 f_{2,mn}^{(r)}+(pU-\omega_0)mF_{mn}^{(r)}\alpha_{mn}+(m\omega_0+\mu\alpha_{mn}-\alpha_{mn})f_{1,mn}^{(r)}}{\alpha_{mn}\left[m^2(\mu p^2U^2-2\mu\omega_0 pU+\mu\omega_0^2+\omega_0^2)+\alpha_{mn}(\mu-1)\right]}, \quad (14)$$

$$c_{mn}^{(r)}=-\frac{(\mu pU-\omega_0)m^2\omega_0 f_{1,mn}^{(r)}-\omega_0 mF_{mn}^{(r)}\alpha_{mn}+(p^2U^2+2pU\omega_0+\omega_0^2)\mu m^2 f_{2,mn}^{(r)}+(\mu-1)\alpha_{mn}f_{2,mn}^{(r)}}{\alpha_{mn}\left[m^2(\mu p^2U^2-2\mu\omega_0 pU+\mu\omega_0^2+\omega_0^2)+\alpha_{mn}(\mu-1)\right]}, \quad (15)$$

A secular term appears when the denominator of the coefficients becomes zero. This condition is called harmonic resonance. The appearance of secular terms is characteristic of nonlinear short crested waves. Roberts [2] was the first to discover the phenomenon of harmonic resonance of short crested surface waves, and then extended by Allalou, Debiane and Kharif [3] for 3D interface waves in finite depth. When the resonance occurs, we have:

$$m^2(\mu p^2U^2-2\mu\omega_0 pU+\mu\omega_0^2+\omega_0^2)+\alpha_{mn}(\mu-1)=0. \quad (16)$$

Relationship (16) is considered an extension of Allalou's, study in the presence of a uniform current.

Conclusions

In this work, we presented the internal three-dimensional gravity waves in the presence of a parallel current. The latter gave an original aspect to this study. Based on previous work mainly that carried out by N. Allalou & al. [3] it was found that our results were in good agreement. We presented all the physical aspects of the internal three-dimensional wave and we were able to extend our analytical results to the fourth order. We deduced the values of the critical velocity that did not exceeded throughout the study. Moreover, we were able to determine the neighbourhood of the harmonic resonance, and the observation of the wave profile was made by varying several parameters**.**

References

[1] SAFFMAN, P. G. & YUEN, H. C. 1982 Finite-amplitude interracial waves in the presence of a current.J. Fluid Mech. 123, 459-476.

[2] A. J. Roberts. Highly nonlinear short-crested water waves. J. Fluid. Mech., 135-301–321, 1983.

[3] N Allalou, M Debiane, and C Kharif. Three-dimensional periodic interfacial gravity waves: Analytical and numerical results, European Journal of Mechanics-B/Fluids, 371-386, 2011.

Control-Oriented Modeling of a Planar Cable-Driven Parallel Robot with Non-Straight Cables

Rima Saadaoui[*†], Olivier Piccin[*‡], Hassan Omran[*†], Iuliana Bara[*†], and Edouard Laroche[*†]
[*]*ICube, engineering science, computer science and imaging laboratory, Strasbourg, France*
[†]*University of Strasbourg, France*
[‡]*INSA of Strasbourg, France*

Summary. This communication deals with the control-oriented modeling of cable-driven parallel manipulators when the cables are not considered as straight but show transverse deflections due to fast movements of the platform. The model has been derived from Euler-Lagrange equations with multipliers in order to deal with the kinematic constraints (DAE model). The number of generalized coordinates have been reduced by performing a transformation of the DAE model to an ODE model. The ODE model has been linearized and an $\mathscr{H}_\infty$ controller has been synthesized to control the cable tension and enable the platform to track a reference trajectory.

Introduction

Cable-driven parallel robots (CDPR) are composed of a platform attached to fixed points by cables. The movement of the platform is obtained by winding the cables. One usually distinguishes fully-constrained robots where the number of cables exceeds the number of degrees of freedom and suspended robots. Notwithstanding the commercially available CableCam system[1], CDPR are considered in a number of research projects for applications such as aircraft and ship construction, building facade cleaning and rescue in open air [1].

We are interested here in the modeling of cable robots taking into account cables deflections. More precisely, we take into account the cables inertial effects on the transverse displacements. A planar robot model with three cables made it possible to assess the effects of transverse displacements and the limits of a conventional control strategy [2]. The model was developed from the Lagrangian calculation by approximating the transverse displacements of the cables by parabolic functions.

Albeit this model allows to evaluate the system in simulation, it cannot be readily used to determine the stability properties and properly assess the system performance during a path-following task due to a lack of controllability. This communication discusses three possible methods to obtain such a control-oriented model from a model derived from the laws of physics, taking the example of the planar CDPR.

CDPR description and model

A planar robot with three cables holding a point mass is considered. The dynamic model has been obtained with the Lagrange method with multipliers that suit for dynamic systems with kinematic constraints. Each of the three cables is considered without elongation as depending on three variables: its length l_k (for the cable #k), its transverse displacement (only one mode is considered, corresponding to a parabolic transverse displacement equal to $\frac{w_k}{l_k}x^2$ for cable #k and $x \in [0; l_k]$) and its orientation at the attachment point. The x and y coordinates of the platform are also included, thus yielding a geometric representation based on 11 variables stacked in the generalized coordinates vector q. The three loop-closure equations of the parallel robot provide six kinematic constraint equations $A(q)\,\dot{q} = 0$. This model, described in details in [2], is given as

$$\begin{bmatrix} M(q) & -A^{\mathrm{T}}(q) \\ A(q) & 0 \end{bmatrix} \begin{bmatrix} \ddot{q} \\ \lambda \end{bmatrix} = \begin{bmatrix} F(q,\dot{q},\Gamma) \\ -\dot{A}\,\dot{q} \end{bmatrix} \tag{1}$$

where λ is the multiplier vector, Γ is the vector of the winder torques, M is the kinetic energy matrix and F is the generalized force vector.

From the laws of physics to a control model

Whether based on the Hamiltonian or the Lagrangian [9], the methods of analytical mechanics render possible to determine models of poly-articulated systems with continuous displacements [3]. In addition to the dynamic equations, the model often includes algebraic equations, resulting in a system of differential-algebraic equations (DAE). This is generally the case for parallel robots (including CDPR) when we consider the geometric and kinematic constraints linking the displacements of cables and those of the platform [2, 4].

The control methods allow to study the stability and performance of systems governed by dynamic equations, with the advantage of providing results that are independent from a considered trajectory, thus allowing to reduce the number of simulations to be made in a validation step. Powerful methods allow to evaluate the stability and the performance of ODE

[1] See `http://cablecam.fr`.

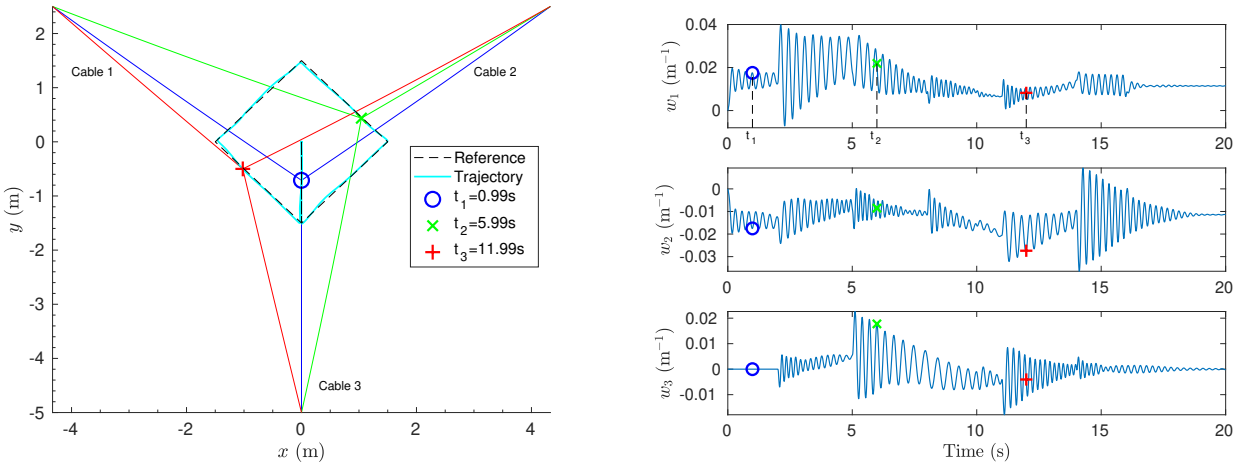

a. CDPR configuration at three different times

b. Modal coordinates for the displacements of the cables

Figure 1: Simulation results

systems with uncertainties on parameters. However, a basic prerequisite is that the model is both controllable and observable [5]. Properties can be established globally, for example using methods based on Lyapunov functions which mimic energy functions [6], or more simply locally in which case a linear model, approaching the behavior in a neighborhood of an equilibrium point, is enough [7].

Starting from the nonlinear DAE model, several ways can be followed in order to get a model suitable for control:

A1. The left-hand side matrix in the model (1) can be inverted in order to reveal a second order ODE model $\ddot{q} = f(q, \dot{q}, \Gamma)$ depending on 11 state variables. But it was not possible to conclude on the controllability of the resulting model: the tests on its linearized version failled due to ill-conditioned matrices of the state-space representation. Moreover, standard tools were not able to provide a controllable and observable reduced-order model.

A2. Rather than making the linearization after inversion of the left-hand side matrix as described in A1, model (1) can be directly linearized so as to obtain a linear descriptor model for which analysis and controller synthesis methods are available [8]. However, the linearized descriptor system was also found uncontrollable and unobservable.

A3. When possible, algebraic equations $A(q)\,\dot{q} = 0$ could be solved in order to obtain a description based on a reduced generalized position vector $\tilde{q}$. This leads to a fewer number of equations of higher complexity (transformation of the DEA model to an ODE model).

Controller synthesis

Approach A3 has been implemented and has lead to a model depending on only 5 generalized coordinates. This ODE linear model was found controllable and observable and an $\mathscr{H}_\infty$ control synthesis has been performed in order to control the cables mean tension and the end-effector position (x, y) (refer to [10] for details on the control strategy). Considering a 1 kg platform and a linear density of cables is 0.17 kg/m, the performance of the $\mathscr{H}_\infty$ closed-loop non linear ODE model for a square reference trajectory at a speed of about 1 m/s has been depicted in Fig. 1. The results show a good trajectory tracking and disturbance rejection.

References

[1] Gosselin C. (2013) Cables-driven parallel mechanisms: state of art and perspectives. *Mechanical Engineering Reviews*. **1**:1-17.

[2] Ayala Cuevas J. I., Laroche E., Piccin O. (2018) Assumed-mode-based dynamics model for cable robots with non-straight cables, *In Mechanisms and Machine Series*. **53**.

[3] Shi P., McPhee J., Heppler G. R. (2001) A deformation field for Euler–Bernoulli beams with applications to flexible multibody dynamics, *Multibody System Dynamics* **5**:79–104.

[4] Du J., Agrawal S. K. (2015) Dynamics modeling of cables-driven parallel manipulators with distributed mass flexible cables, *Journal of Vibration and Acoustics*, **137**(2).

[5] Zhou K., Doyle J. C., Glover K. (1996) Robust and Optimal Control. *Prentice Hall*.

[6] Khalil H. K., (2001) Nonlinear systems, **3rd ed**, *Pearson new international edition*.

[7] Bacciotti A. (2019) Stability and control of linear systems, *Studies in Systems, Decision and Control*, *Springer* **185**.

[8] Duan G. R. (2010) Analysis and design of descriptor linear systems, *Advances in Mechanics and Mathematics Springer*. **23**.

[9] Goldstein H., Poole C., Safko J. (2001) Classical Mechanics, **3rd ed**, *Addison Wesley*.

[10] Saadaoui R. et al. (2021) $\mathscr{H}_\infty$ Synthesis for a Planar Flexible Cable-Driven Robot, *European Control Conference*, Rotterdam, Netherlands.

Experimental verification of the crossover between the time-fractional and standard diffusion in a hierarchical porous material

Alexey Zhokh* and Peter Strizhak*
*L.V. Pisarzhevskii Institute of Physical Chemistry of the National Academy of Sciences of Ukraine, Kiev, Ukraine

Summary. A transport process may cross over from the standard to anomalous diffusion. Herein, we experimentally verify the relevant changes of the diffusion regimes via an analysis of the diffusion concentration profiles in a hierarchically porous material. It is shown that at relatively short times the transport process experiences anomalous diffusion, whereas the standard Fickian diffusion is obeyed at relatively long times. The anomalous diffusion is described by the time-fractional diffusion equation with the superdiffusive anomalous diffusion exponent. The observed transitions seem to be associated with the transport in different components of a porous material.

Objectives

The transitions between the diffusion regimes in a porous medium are fairly typical. In a geometrically restricted environment, e. g. microchannels, an increase in the width of a channel governs the change of the diffusion regime from the single-file to the standard Fickian. This phenomenon has been experimentally verified for the transport process in single-wall carbon nanotubes [1]. Moreover, the analytic approaches for evaluation of the transition time have been established [2]. The effect of the pore size may not be the only reason for the diffusion regime transitions. The crossover between different diffusion regimes may also depend on the evolving time. The experimental investigation on the diffusion of silicon atoms in bulk germanium demonstrated the change in the diffusion kinetics from the anomalous superdiffusion to the standard Fickian versus observation time [3]. To this end, investigating the transport peculiarities through a porous material at various time scales is important for better understanding the fundamentals of the anomalous transport.

Linearized solutions of the standard and time-fractional diffusion equations

The experimental configuration is subjected to the following initial and boundary conditions: $C(x, 0) = C_0 = const$, $\partial C(0, t)/\partial x = 0$, $-D \cdot \partial C(L, t)/\partial x = \gamma \cdot C(L, t)$. The relevant linearized solutions of the standard and time-fractional diffusion equations, which are suitable for medium and long times, may be expressed as follows [4]:

$$\ln\left[\ln a - \ln\left[\frac{C(L,t)}{C_0}\right]\right] = \ln\left[\frac{D \cdot \pi^2}{4 \cdot L^2}\right] + \ln t \quad (1)$$

$$\ln\left[\frac{C(L,t)}{C_0}\right] = \ln\left[\frac{4 \cdot L^2 \cdot a}{\pi^2 \cdot K \cdot \Gamma[m-\alpha]}\right] - \alpha \cdot \ln t \quad (2)$$

Herein, L is the thickness of a solid porous particle, γ is the penetration coefficient, D and K are the standard and time-fractional diffusion coefficients, respectively, a is a coefficient defined by the initial and boundary conditions, α is a fractional order, m is 1 for $0 < \alpha < 1$, and m is 2 for $1 < \alpha < 2$, $\Gamma(z)$ is the Euler gamma function. For the standard diffusion, the corresponding solution (eq. (1)) is linearized in the bi-logarithmic coordinates with slope that equals unity. In contrast, the solution of the time-fractional diffusion equation (eq. (2)) admits linearization in the logarithmic coordinates possessing the slope directly proportional to the time-fractional order. To this end, if the slope of the experimental data under the relevant bi-logarithmic transformations deviates from unity, the standard diffusion equation fails to describe the experimental transport kinetics.

Experimental procedure

To identify different transport regimes, a combined porous material with hierarchical porous structure was used. The used porous solid consisted of ZSM-5 zeolite and alumina with zeolite/alumina ratio equal to 1/1 by mass. The porous material was prepared using extrusion technique. The as-prepared porous material was characterized by the low-temperature nitrogen adsorption-desorption isotherm. The textural properties estimated from the isotherm data are as follows: BET surface area is 272 m^2/g; pore volume is 0.22 cm^3/g; BJH pore diameter is 3.9 nm; external surface area is 21 m^2/g; micropore volume is 0.04 cm^3/g; mesopores surface area is 177 m^2/g. The X-ray diffraction revealed the presence of the crystalline phase relevant to ZSM-5 zeolite and γ-alumina. The latter demonstrated rather low amount of crystalline phase.

Methyl alcohol was utilized as a diffusing agent. The methanol transport through the porous solid material was studied using commercial LHM-72 gas chromatograph with the flame ionization detector equipped by the diffusion cell instead of the chromatograph column. The detailed description of the diffusion cell design, as well as the experimental procedure, may be found in our previous report [5]. The mass transfer was investigated under the following experimental conditions. The purge flow rate (argon) was 30 cm^3/min; the temperature inside the diffusion cell was kept 120 °C. The methanol amount injected into the diffusion cell using the syringe for gas chromatography was 0.4 µl. The thickness of the porous zeolite/alumina particle was 2 mm.

Results

Fig. 1a demonstrates the relative methanol concentration decaying in time obtained in the experiment. At relatively small times, i.e. $C(L, t)/C_0 < 0.30$, the standard diffusion equation fails to describe the experimental data because the experimental slope in the bi-logarithmic coordinates significantly deviate from unity (Fig. 1b). At these times, the time-fractional diffusion equation may be successively utilized (Fig. 1c). The decrease of the relative concentration at the starting point of the calculation from 0.30 to 0.15 results in the change of the diffusion regime from the time-fractional to the standard Fickian (Fig. 1d). Therefore, the transport process studied in the current paper exhibits the anomalous time-fractional diffusion at shorter time crossing over to the standard diffusion at a long time. This phenomenon may be associated with the fact that the standard diffusion equation admits the infinite propagation velocity, which is physically unreliable. To eliminate this issue, the Cattaneo-type diffusion equation has been proposed. The Cattaneo diffusion equation implies finite propagation velocity, which is recovered by introducing a relaxation time τ. The time-fractional Cattaneo diffusion equation is given by:

$$\tau^{\alpha} \cdot \frac{\partial^{\alpha+1} C}{\partial t^{\alpha+1}} + \frac{\partial C}{\partial t} = D \cdot \frac{\partial^2 C}{\partial x^2} \tag{3}$$

The relaxation time is individual for each diffusing substance and porous material. The higher is the crystallinity of a material, the lower is the relaxation time. The solid porous particle used in the present study consists of the two phases, particularly, the crystal phase of ZSM-5 zeolite and the partially amorphous phase of the alumina. To this end, the relaxation times may be different in different parts of the porous material, e.g. in the micropores of zeolite crystallites and the mesopores of the amorphous alumina matrix. In this respect, the diffusion in zeolite micropores seems to be characterized by smaller relaxation time compared to the diffusion in the alumina mesopores. The pores may be also formed by the cavities between the amorphous alumina globes and zeolite crystallites. In these pores, the relaxation time may be different from the relaxation times in either zeolite micropores or alumina mesopores.

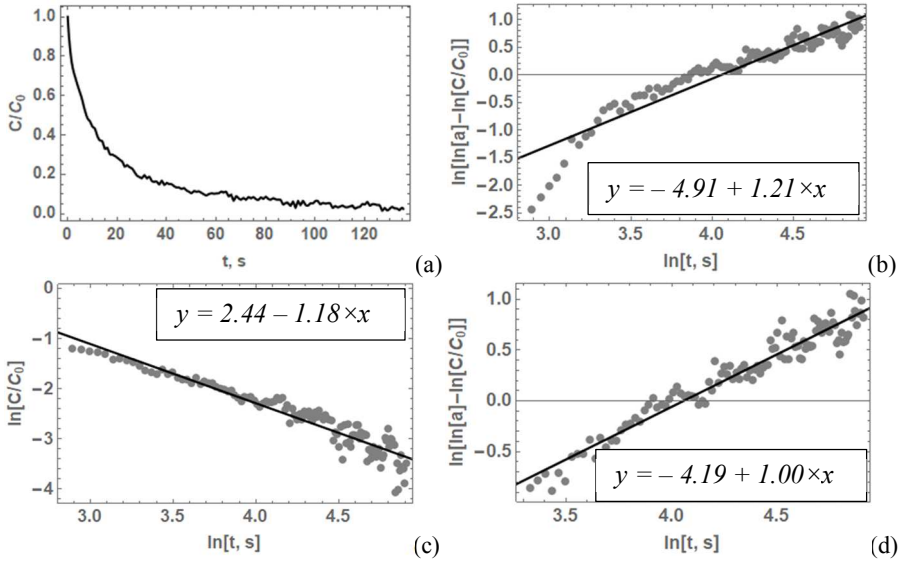

Figure 1: Concentration evolution versus time (a), short time, i.e. $C/C_0 < 0.30$ (b) and (c), and longtime, i.e. $C/C_0 < 0.15$ (d) analysis

Conclusions

Investigation of the mass transfer in a hierarchically porous material consisting of crystalline and amorphous parts provides experimental evidence of the crossover between the anomalous diffusion at relatively short times and the standard diffusion at long times. The time-fractional diffusion equation is successively applied to describe the mass transfer kinetics at relatively short times. Unequal relaxation times in crystalline and amorphous parts of a combined porous material allows obeying either time-fractional or the normal diffusion behavior.

Acknowledgments. This research received funding from the National Research Foundation of Ukraine (grant 2020.02/0050).

References

[1] Chen Q., Moore J. D. et al (2010) Transition from single- file to Fickian diffusion for binary mixtures in single-walled carbon nanotubes. *J. Chem. Phys.* **133**:094501.

[2] Ahmadi S., Bowles R. K. (2017) Diffusion in quasi-one-dimensional channels: a small system n, p, T, transition state theory for hopping times. *J. Chem. Phys*. **146**:154505.

[3] Balogh Z., Erdélyi Z. et al (2008) Transition from anomalous kinetics toward Fickian diffusion for Si dissolution into amorphous Ge. *Appl. Phys. Lett.* **92**:143104.

[4] Zhokh A., Strizhak P. (2018) Non-Fickian Transport in Porous Media: Always Temporally Anomalous? *Transp. Porous Media* **124**: 309.

[5] Zhokh A., Trypolskyi A., Strizhak P. (2019) A diffusion cell for the mass transfer investigation in the solid porous media. *Int. J. Chem. React. Eng*. **17**: 5.

Investigation of vibro-impact dynamics in PILine® ultrasonic motors

Simon Kapelke*, Felix Hartenbach* and Wolfgang Seemann**
*Physik Instrumente (PI) GmbH & Co. KG, Karlsruhe, Germany
**Institute of Engineering Mechanics, Karlsruhe Institute of Technology (KIT), Karlsruhe, Germany

Summary. PILine® ultrasonic motors belong to the group of standing wave ultrasonic motors and, as common for this kind of drives, use certain eigenmodes of a piezoelectric actuator to generate motion. The motion of the actuator is transmitted to a moving slider by means of friction using a coupling element, which performs a high-frequency oblique or elliptical motion. Within this contribution, the possible onset of impact oscillations in standing wave ultrasonic motors is investigated. After introducing a basic motor structure, corresponding experimental results are presented accounting for low-frequency dynamics. Subsequently, a simple mechanical model for normal oscillations of the piezoelectric actuator is evaluated by means of numerical integration. The derived results are compared qualitatively to experimental observations and provide good insight into the relevant dynamics.

Introduction

Piezoelectric motors are commonly used in several commercial, industrial or research related applications. Depending on the specific driving principle, piezoelectric motors can be divided into different categories, such as ultrasonic, stepping or inertia type drives. Ultrasonic motors, and in particular standing wave ultrasonic motors, are known for their high dynamics and accuracy in motion and positioning while providing long travel ranges and self-locking capabilities at rest. These basic properties are achieved by exciting certain eigenmodes of one or more piezoelectric actuators, such that a coupling element attached to the piezoelectric actuator performs a high-frequency oblique or elliptical motion, which is transmitted to a linear or rotational slider by means of friction [1].
The underlying dynamic processes are highly non-linear and, among others, include electro-mechanical coupling, vibro-impact dynamics and friction. Nevertheless, some effort has been spent in the past in order to establish mathematical descriptions of the corresponding dynamics [2, 3]. While most publications assume quasi-static behaviour of the piezoelectric actuator, the exceptional role of actuator inertia properties and, accordingly, the possible onset of impact oscillations has been pointed out recently [4].
Within this contribution, both experimental and model-based investigations related to vibro-impact dynamics of standing wave ultrasonic motors are carried out. Based on the schematic structure of PILine® ultrasonic motors and corresponding experimental observations, a simple mathematical model is presented accounting for vibro-impact dynamics. The model can be investigated either by separating slow and fast system dynamics or in terms of direct numerical integration and, together with the experimental observations, gives good insight into relevant dynamic processes.

Basic motor structure and experimental observations

The basic structure of PILine® ultrasonic motors is depicted in Fig. 1 and contains a rectangular piezoelectric actuator (1) and the attached coupling element (2). Due to electrical excitation of the piezoelectric actuator, the coupling element performs an elliptical motion, which is transmitted to the slider (3) with horizontal guiding by means of dry friction. The actuator has a pre-stressed elastic foundation, while transverse motion is suppressed by a corresponding suspension (4).
Under certain driving conditions, many ultrasonic motors show undesired vibrations in the audible range, although typical driving frequencies can easily exceed 100 kHz. Among undesired noise phenomena, this behaviour can even cause a loss of performance and is mostly handled by using advanced driving or control techniques [5]. However, in terms of system modelling and for improved control design, deeper understanding of the corresponding dynamics is required.
A recent publication has pointed out the possible onset of impact oscillations resulting from the high-frequency motion of the piezoelectric actuator in combination with the non-linear contact mechanics between coupling element and slider [4].

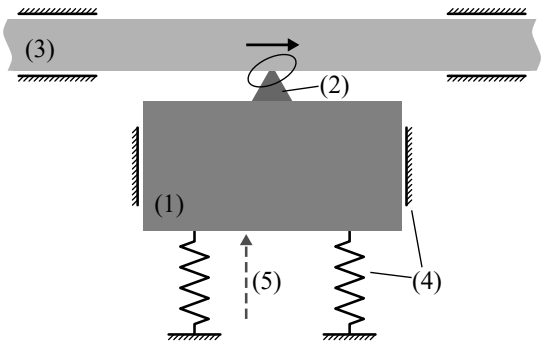

Figure 1: Schematic PILine® motor structure (1–4) and vibrometer measurement beam (5)

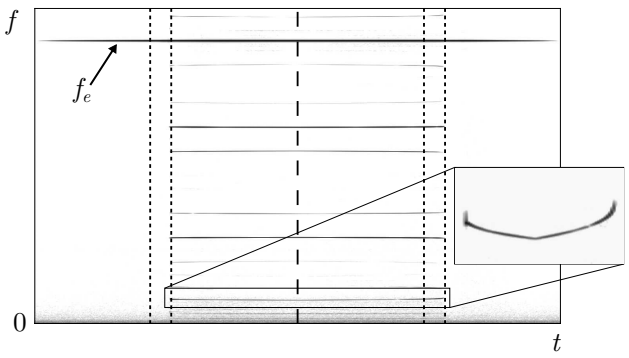

Figure 2: Experimental results for linearly increasing (first half) and decreasing (second half) excitation amplitude

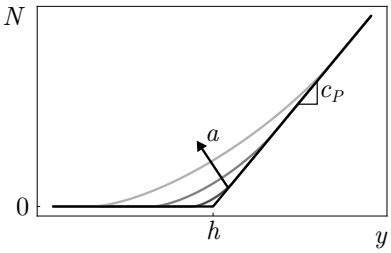

Figure 3: Average normal contact force for different excitation amplitudes

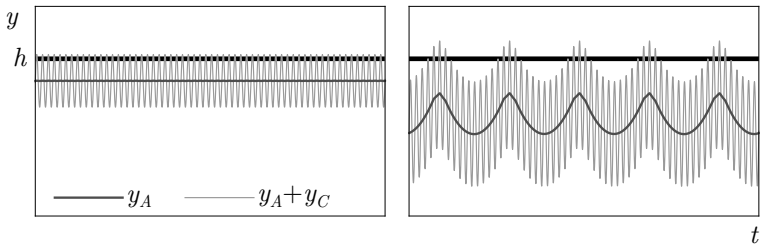

Figure 4: Exemplary solutions for different excitation amplitudes: floating type (left) and period-n solution (right)

Corresponding experimental results, where the normal motion of the piezoelectric actuator has been investigated using a *Polytec VibroFlex Xtra* laser vibrometer (5), are shown in Fig. 2. Herein, the frequency content of the normal actuator motion has been recorded, while increasing and decreasing the excitation amplitude at fixed driving frequency. Apart from the basic driving frequency f_e, the results contain several lower frequencies and other non-linear characteristics, which can be used to validate model-based approaches. Important observations are related to bifurcations, co-existing stable solutions, amplitude-dependent frequencies and the non-linear amplitude evolution.

Modelling approach and first numerical results

In order to simplify the mathematical description and focus on normal oscillations of the actuator, normal and tangential components are investigated separately. This approach appears suitable, since the friction type coupling of normal and tangential motion is mainly unilateral. According to the basic structure of the ultrasonic motor introduced before, the equation for normal actuator motion can be stated as

$$m\ddot{y}_A + d\dot{y}_A + c_A y_A + N = 0 \qquad \text{with} \qquad N = \begin{cases} c_P(y_A + y_C - h), & \text{contact} \\ 0, & \text{separation} \end{cases} . \tag{1}$$

Herein, y_A is the normal displacement of the actuator, m is the corresponding mass and d, c_A are damping and stiffness coefficients of the foundation. N is the normal contact force with local contact stiffness c_P, $y_C = a \sin \omega t$ is the high-frequency motion of the coupling element and h corresponds to the location of the slider.
The system can be investigated by using separate descriptions for slow and fast system dynamics. This approach results in a compact formulation for the slow dynamics and allows for further (semi-)analytical investigations, e. g. smoothing of the normal contact force as depicted in Fig. 3 or evaluation of the corresponding amplitude-dependent natural frequency. However, for a first qualitative comparison between model-based results and experimental observations, simple numerical evaluation appears more suitable. Fig. 4 shows two exemplary solutions of the system depending on the chosen parameters and initial conditions: The first one is a typical floating type solution without low-frequency motion and one contact phase per period of the excitation. This kind of solution is commonly regarded as the desired mode of operation of standing wave ultrasonic motors. The second solution is obtained for the same model parameters and initial conditions, but with increased excitation amplitude. The resulting motion can be referred to as a period-n solution of the system showing large low-frequency oscillations together with the high-frequency excitation. Herein, long separation phases can be observed and the interval between two contact phases is mainly determined by the low-frequency actuator motion.

Conclusions and outlook

The given results can be regarded as a first local analysis of the presented model showing possible mechanisms for the non-linear system behaviour observed experimentally. However, further investigations require a global analysis of the modelling approach and improved experimental validation. First results as well as practical experience indicate the importance of considering further compliant properties of the slider. Otherwise, many of the previously observed phenomena are limited to transient behaviour or minor basins of attraction. Nevertheless, the presented results give good insight into relevant dynamic processes and their impact on the basic driving principle of standing wave ultrasonic motors.

References

[1] Spanner, K., Koc, B. (2016) Piezoelectric Motors, an Overview. *Actuators* **5**: 6.

[2] Li, X., Yao, Z., Lv, Q., Liu, Z. (2016) Modeling stick-slip-separation dynamics in a bimodal standing wave ultrasonic motor. *Journal of Sound and Vibration* **382**: 140–157.

[3] Tsai, M.-S., Lee, C.-H., Hwang, S.-H. (2003) Dynamic modeling and analysis of a bimodal ultrasonic motor. *IEEE Transactions on Ultrasonics, Ferroelectrics, and Frequency Control* **50**: 245–256.

[4] Kapelke, S. (2021) A vibro-impact approach to PILine® ultrasonic motors. *ACTUATOR, International Conference and Exhibition on New Actuator Systems and Applications 2021*: 93–96

[5] Delibas, B., Koc, B. (2020) A method to realize low velocity movability and eliminate friction induced noise in piezoelectric ultrasonic motors. *IEEE/ASME Transactions on Mechatronics* **25**: 2677-2687.

Model order reduction approach for problems with moving discontinuities

Harshit Bansal*, Stephan Rave†, Laura Iapichino*, Wil Schilders* and Nathan van de Wouw ‡,††
*Department of Mathematics and Computer Science, TU Eindhoven, The Netherlands
†Applied Mathematics, University of Muenster, Germany
‡Department of Mechanical Engineering, TU Eindhoven, The Netherlands
††Department of Civil, Environmental and Geo-Engineering, University of Minnesota, U.S.A.

Summary. We propose a new model order reduction (MOR) approach to obtain effective reduction in the context of transport-dominated problems or hyperbolic partial differential equations. The main ingredient is a novel decomposition of the solution into *(i)* a function that tracks the evolving discontinuity and *(ii)* the residual part that is devoid of shock features. This decomposition strategy is then combined with Proper Orthogonal Decomposition which is applied to the residual part only to develop an efficient reduced-order model representation for problems with multiple moving and possibly merging discontinuous features. Numerical case-studies show the potential of the approach in terms of computational accuracy compared with standard MOR techniques.

Problem Description

Hyperbolic partial differential equations (PDEs) are ubiquitous in science and engineering. Applications encompassing the fields of chemical industry, nuclear industry, drilling industry, etc., fall within this class. Moving discontinuities (such as shock-fronts) are representative features of this class of problems and pose a major hindrance to obtain effective reduced-order model representations [1]. As a result, standard Model Order Reduction techniques [2] do not fit the requirements for real-time estimation and control or multi-query simulations for such problems. This motivates us to investigate and propose efficient, advanced and automated approaches to obtain reduced models, while still guaranteeing the accurate approximation of wave propagation (and wave interaction) phenomena.
The main contribution of the work is to propose a new decomposition ansatz that decomposes the solution into *(i)* a basis function that tracks the evolving discontinuity (wave front) and *(ii)* the residual part that is expected to be devoid of shock features. This decomposition renders the residual part to be amenable for efficient basis generation. We, then, use these generated bases to apply Proper Orthogonal Decomposition (POD) on the residual part and later reconstruct the solution by lifting it to the high-dimensional problem space. We finally assess the combined performance of decomposition, reduction and reconstruction approach (as opposed to conventional reduction and reconstruction approach) in the scope of transport-dominated problems with moving and interacting discontinuities.

Mathematical Formulation

We discuss the proposed decomposition ansatz and outline the whole procedure in order to obtain a reduced-order model.

Decomposition step

We consider a scalar 1D conservation equation of the form:

$$\partial_t u(x,t) + \partial_x f(u(x,t)) = 0, \;\; u(x,0) = u_0(x). \tag{1}$$

We assume that $u(x,0) = u_0(x)$ already has S number of shocks at locations $x_1(0), ..., x_S(0)$ with values $u^-(x_s(0),0)$, $s = 1, ..., S$ from the left and values $u^+(x_s(0),0), \quad s = 1, ..., S$ from the right. We associate a single basis function $\sigma_s(x - x_s(t))$ to each discontinuity at their respective locations. This basis function has a jump of height 1, i.e., $\sigma_s^+(0) - \sigma_s^-(0) = 1$, at the location of the discontinuity. We now decompose the solution, u, in the following way:

$$u(x,t) = \sum_{s=1}^{S} j_s(t)\sigma_s(x - x_s(t)) + u_r(x,t),$$

$$j_s(t) = u^-(x_s(t),t) - u^+(x_s(t),t). \tag{2}$$

When $x_s(t)$ exactly matches the location of the shocks and (2) is exactly fulfilled, then $u_r(x,t)$ represents a function without any shocks (discontinuities) and hence is amenable to a low-rank approximation.
The time-stepping scheme can be defined in the following manner. In each time step, we first compute updated shock locations $x_s(t^{n+1})$, jumps $j_s(t^{n+1})$ and then compute the residual part $u_r(x,t^{n+1})$ from

$$u_r(x,t^{n+1}) - u_r(x,t^n) = \sum_{s=1}^{S} j_s(t^n)\sigma_s(x - x_s(t^n)) - \Delta t \partial_x f(u(x,t^n)) - \sum_{s=1}^{S} j_s(t^{n+1})\sigma_s(x - x_s(t^{n+1})). \tag{3}$$

Reduced Order Model

The standard way to construct a reduced-order model (ROM) is to reduce (1) by applying Galerkin projection on u. Instead, we apply POD on the residual part, i.e., we reduce (3) via Galerkin projection onto $V_N \subseteq V_h$ (where V_N is a

reduced space and V_h is a high-fidelity space). Upon considering the projection operator $P_N : V_h \rightarrow V_N$, the reduced scheme on the residual part is:

$$u_{r,N}^{k+1} = u_{r,N}^{k} + P_N\Big(\sum_{s=1}^{S} j_{s,N}(t^k)\sigma_s(x - x_{s,N}(t^k)) - \Delta t \partial_x f(P_N^{'} u_N^k) - \sum_{s=1}^{S} j_{s,N}(t^{k+1})\sigma_s(x - x_{s,N}(t^{k+1}))\Big), \quad (4)$$

where k indicates the time-instant, $u_{r,N}^k \in V_N$, $u_{r,N}^0 = P_N(u_r^0)$ with u_N^k defined as:

$$P_N^{'} u_N^k = \sum_{s=1}^{S} j_{s,N}(t^k)\sigma_s(x - x_{s,N}(t^k)) + P_N' u_{r,N}^k. \quad (5)$$

Numerical Experiments

We reduce the Burgers equation given by: $\partial_t u + \partial_x(\frac{u^2}{2}) = 0, x \in [0, L]$, for illustrating the potential of the proposed approach. The case studies under consideration assume that the shock is already present in the initial data, which for single and multiple wavefront scenarios, is respectively given by:

$$u(x,0) = u_0(x) = \begin{cases} x, & 0 \leq x \leq 1, \\ 0, & \text{otherwise} \end{cases} \quad \text{and} \quad u(x,0) = u_0(x) = \begin{cases} x-2, & 2 \leq x \leq 4, \\ (x-5)/2, & 5 \leq x \leq 7, \\ 0, & \text{otherwise.} \end{cases}$$

We consider the spatial domain to be of length $L = 10$ and use an upwind finite volume scheme for the spatial discretization and a first-order Forward Euler for the time-stepping. We take 8000 steps in time for the scenarios under consideration i.e., $t \in [0, 4]$ with a timestep of 0.0005. We consider three different spatial mesh resolutions (spatial step size of 0.005, 0.002 and 0.001) to assess the performance of the standard (POD without decomposition) and the proposed approach.

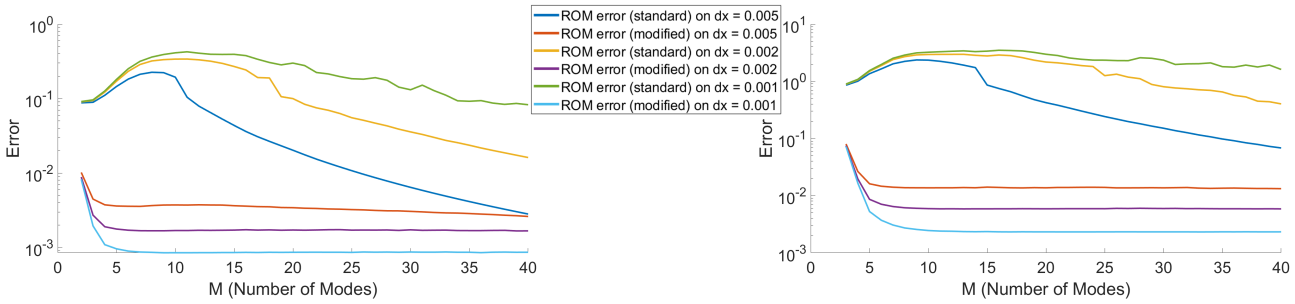

Figure 1: ROM error for the single wavefront scenario (left) and multiple wavefront scenario (right) under different mesh sizes.

We consider that $j_{s,N} = j_s$ and $x_{s,N} = x_s$ and use these jumps and shock locations during the ROM time-stepping. We, further, use the computed residual part to generate the bases and build a ROM. Figure 1 demonstrates the decay of the 'L^2 in space and L^2 in time' (absolute) error (between the full-order model governed by (1) and the reconstruction given by (5)) for the scenarios of interest. Firstly, the initial error incurred via the proposed approach is lower than that of the standard approach. This is attributed to the fact that our decomposition approach associates a basis function corresponding to the travelling discontinuity. Secondly, the rate of decay of the error is better for the proposed approach compared to the standard approach. Moreover, the ROM error for the proposed approach stagnates later for finer mesh-sizes. It is also observable that the mesh refinement reduces the ROM error obtained via proposed approach in contrast to the ROM error obtained via standard approach. The difference in the order of magnitude of the ROM error (at a certain number of basis function) computed via standard and proposed approach is even more pronounced for fine mesh-sizes.

Conclusions

We have proposed a decomposition ansatz for problems with moving discontinuities and combined it with POD applied to the residual part only. We have show-cased the performance of the proposed approach on the Burgers equation. The proposed approach is able to resolve the discontinuities and also offers reduction in ROM error by using much less number of basis functions. We will perform numerical experiments on many other mathematical models (falling within the class of transport-dominated problems) in the near future.

References

[1] M. Ohlberger and S. Rave, Reduced basis methods: Success, limitations and future challenges," Proceedings of the Conference Algoritmy, 2016.

[2] A. Quarteroni and G. Rozza, edts. Reduced Order Methods for Modeling and Computational Reduction. Springer International Publishing, Cham, 2014.

Numerical investigation on storage tank buckling near the liquid level under seismic loading

Christophe Collignon

Mechanical Engineer, structural analysis, Framatome, Lyon (France) - christophe.collignon@framatome.com

ABSTRACT

In Nuclear Power Plants, storage tanks are used to contain a large volume of borated water which can be injected into the reactor pool and the spent fuel pool cooling system. Considering they are subjected to the hydrostatic pressure only in normal service conditions, these components are usually designed as thin-wall large shell, which presents the characteristic of being more sensitive to dynamic excitation loads, such as the ones arising from earthquakes.

The most common damages caused to steel tanks of industrial facilities in recent earthquakes are the “elephant foot” buckling and the “diamond shape” buckling, both phenomena are located at the lower part of the cylindrical shell, close to the anchorage. These two kinds of buckling are well-known and usually analyzed within the engineering practice. Nevertheless, the current design standards do not cover another type of instability which is sometimes observed after an earthquake: the shell buckling at the upper part of the cylindrical wall, near the liquid free level, due to the sloshing motion.

The present paper describes the numerical investigations performed on a typical storage tank of the nuclear industry to assess whether the upper shell buckling can lead to a severe damage or not (collapse, cracks). The EUROPLEXUS software is used for the modelling and computation considering its very efficient fluid-structure interaction algorithms and liquid-gas flow models. As a first step, the EUROPLEXUS explicit time integration scheme capability of simulating sloshing motion for a long duration (typically up to 30 s) is validated reproducing the Hinatsu’s experimental tests. As a second step, several simulation tests are run on a full 3D model of the tank to analyze the structure post-buckling states during and after the seismic event.

The numerical results show that the vibration amplitudes on the shell buckling modes are small enough to keep the structure globally in the elastic range, even for strong earthquake with a Peak Ground Acceleration of 0.5g. Only low plastic strains confined near the liquid free level are calculated. It is noted that the deformed shapes at the end of the computation are consistent with the post-seismic observations on actual tanks.

Nonlinear Dynamics of a Ring-Type MEMS Gyroscope

Ibrahim F. Gebrel[*], Ligang Wang [**] and Samuel F. Asokanthan[*]
[*] *Dept. of Mech. and Matls. Engineering, The University of Western Ontario, London, ON N6A5B9, Canada*
[**] *Dept. of Mathematica, Harbin University, Harbin, Heilongjiang 150001,China*

Summary. This paper investigates the nonlinear dynamic behavior of a rotating ring that forms an essential element in MEMS ring-based vibratory gyroscopes that utilize oscillatory nonlinear electrostatic forces. Mathematical model that incorporates geometric nonlinearities for the MEMS ring structure as well as a model that represents nonlinear electrostatic forces that act on the ring structure are formulated. Galerkin's procedure is employed to reduce the equations of motion to a set of ordinary differential equations. Understanding the effects of nonlinear actuator dynamics is considered important for characterizing the dynamic behavior of such devices. For investigating the dynamic response behavior of a ring-type vibratory angular rate, the equations of motion are simplified by ignoring the extensional vibrations, since the second resonant flexural mode is excited in this class of applications. Dynamic responses in the driving and the sensing directions are examined via time responses, phase diagram, and Poincare' map plots when the input angular motion and the nonlinear electrostatic force are considered simultaneously. The analysis is envisaged to aid fabrication of this class of devices as well as for providing design improvements in MEMS-based Ring-type Gyroscopes.

Concept and Modeling

In the present paper, nonlinear dynamic behavior of rotating thin circular rings for use in vibratory angular rate sensors have been investigated via numerical simulations. A homogenous, isotropic ring is chosen for the angular rate sensor. Cho [1] developed mathematical models for rotating ring based angular rate sensors for the purpose of investigating linear as well as nonlinear dynamic behavior and dynamic stability of angular rate sensors which are subjected to external excitation. In the past, Huang and Soedel [2] and Natasiavas [3], among others, have also studied the nonlinear dynamic behaviour of rotating thin circular rings. Dynamic response behavior of rotating thin circular rings for use in vibratory angular rate sensors was investigated by Gebrel et al [4] via numerical simulations by employing the linearized model considering the second mode. In this study, a suitable theoretical model is developed for the purposes of representing the nonlinear electromagnetic actuation forces that are used for exciting the ring from two positions to obtain improved device sensitivity. Figure 1(a) illustrates the geometry and parameters used in the present study while Figure 1(b) illustrates the two degenerate modal configurations associated with the second flexural mode, and are separated by 45 degrees. The schematic of the rotating ring geometry used in present study have been described in detail in [1, 4].

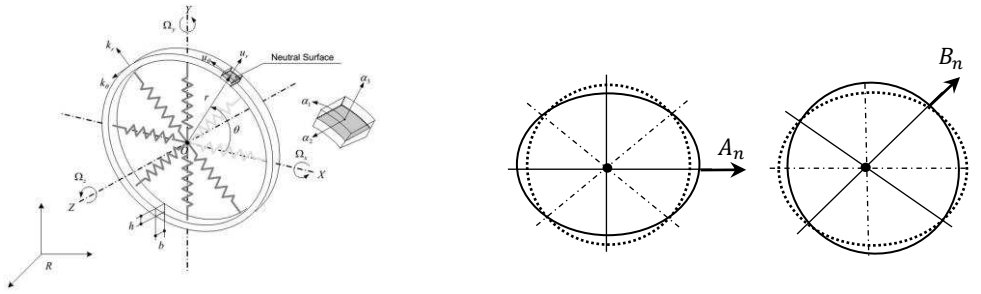

(a) (b)

Figure 1: (a) schematic of the rotating ring geometry, and (b) Visualization of second flexural modes of ring

In the present paper, the nonlinear equations of motion in terms of the generalized coordinates associated with the flexural coordinates A_n and B_n [1, 5] are developed for the purposes of illustrating the dynamic behavior. The discretized equations of motion that govern the dynamics with suitable nonlinear harmonic electrostatic forces are derived:

$$\left[\rho h\pi + 2\rho h\pi\left(\frac{n\gamma}{2r}\right)^2 A_n^2\right]\ddot{A_n} + 2\rho h\pi\left(\frac{n\gamma}{2r}\right)^2 A_n B_n \ddot{B_n} + 2\zeta\omega_0\dot{A_n} + \left[\frac{EI}{br^4}(n^2-1)n^2 + \rho h\Omega^2(n^2-2) + k_r\right]\pi A_n +$$

$$\left[\frac{EA}{br^2} + k_r\right]\left(\frac{n\gamma}{2r}\right)^2 [A_n^2 + B_n^2]\pi A_n + 2\rho h\pi\left(\frac{n\gamma}{2r}\right)^2 \left[\dot{A}_n^2 + \dot{B}_n^2\right]A_n - \rho h\pi\dot{\Omega}\frac{1}{n}B_n - 2\rho h\pi\Omega\frac{1}{n}\dot{B_n} = f_{Nes}(A_n, B_n, \theta_i)cos(\omega t) \quad (1)$$

$$\left[\rho h\pi + 2\rho h\pi\left(\frac{n\gamma}{2r}\right)^2 B_n^2\right]\ddot{B_n} + 2\rho h\pi\left(\frac{n\gamma}{2r}\right)^2 A_n B_n \ddot{A_n} + 2\zeta\omega_0\dot{B_n} + \left[\frac{EI}{br^4}(n^2-1)n^2 + \rho h\Omega^2(n^2-2) + k_r\right]\pi B_n +$$

$$\left[\frac{EA}{br^2} + k_r\right]\left(\frac{n\gamma}{2r}\right)^2 [A_n^2 + B_n^2]\pi B_n + 2\rho h\pi\left(\frac{n\gamma}{2r}\right)^2 \left[\dot{A}_n^2 + \dot{B}_n^2\right]B_n + \rho h\pi\dot{\Omega}\frac{1}{n}A_n + 2\rho h\pi\Omega\frac{1}{n}\dot{A_n} = 0 \quad (2)$$

where ρ is mass density, EI represents flexural rigidity, A is the cross sectional area of ring, b denotes axial thickness of ring, h is radial thickness, r is the mean radius of the ring, and k_r support spring stiffness in the radial direction. The

quantification of the nonlinear terms are governed by the parameter γ. Oscillatory external nonlinear electrostatic actuator force that acts along the A_n direction is considered to have a magnitude f_{Nes} and frequency ω , while input angular velocity and acceleration, respectively, are denoted by Ω and $\dot{\Omega}$. The area moment of inertia of the ring cross section about its neutral axis is expressed as $I = bh^3/12$. The parameter ζ represents the mechanical damping ratio, and n denotes the number of modes which is taken to be 2 in the present study. The angular positions of electrostatic forces that excite the ring in the primary direction is denoted by θ_i , $i = 1,2,3,4$. In order to represent the oscillatory electrostatic force, a suitable theoretical formulation is employed:

$$f_{Nes} = \sum_{i=1}^{4}(\cos(n\theta_i) - \left(\frac{n\gamma}{2r}\right)A_n) * \left[\frac{\varepsilon_0 V^2 a}{2\left\{d - A_n\cos(n\theta_i) - B_n\sin(n\theta_i) + \frac{n\gamma}{4R}[A_n^2 + B_n^2]\right\}^2}\right] \quad , \tag{3}$$

where the parameter ε_0 represents the permittivity of air, V represents the applied voltage between the electrode and the ring, a represent the electrode width which represents the space between electrode and the surface of the ring, d is the distance between electrode and ring

Results and Discussion

For the purposes of predicting the nonlinear response characteristic of MEMS ring-type gyroscope, equations (1) and (2) have been solved numerically. Parameters associated with a typical MEMS ring-type gyroscope are considered. The following ring design parameters: radius of 500 μm, thickness of 12.5 μm , and a height of 30 μm with Young's modulus of 210 Gpa and the density of 8800 Kg/m^3 have been chosen. At a nominal input angular rate of $2\,\pi\, rad/sec$ and a typical device high quality factor of 1×10^5 , the resulting frequencies have been evaluated as $\omega_1 = 2.1422 \times 10^5\ (rad/sec)$, and $\omega_2 = 2.1428 \times 10^5\ (rad/sec)$. The generalized coordinates $q_1 = A_n/h, q_2 = B_n/h$ have been used for the non-dimensional equations. For an input angular velocity $\Omega = 2\,\pi\ (rad/sec\ )$, under nonlinear oscillatory electrostatic excitation, the time response of the ring in the sensing direction in the presence of geometric nonlinear terms is depicted in Figure 2(a). Figure 2(b) depict the phase portrait based on the steady-state response in the sensing direction. The effects of nonlinearities due to the nonlinearities of the system as well as nonlinear electrostatic force are evident from the plots. Furthermore, nonlinearity can be seen in the Poincare' map results as shown in Figure 2(c), where the Poincare' maps appear as a cloud of unorganized points in the phase plane in Figure 2(b) due to the influence of nonlinear terms in the model as well as nonlinear actuator. Internal resonance behavior is not analyzed in this study since the natural frequencies are close to each other and cannot be equal in the typical device operating range.

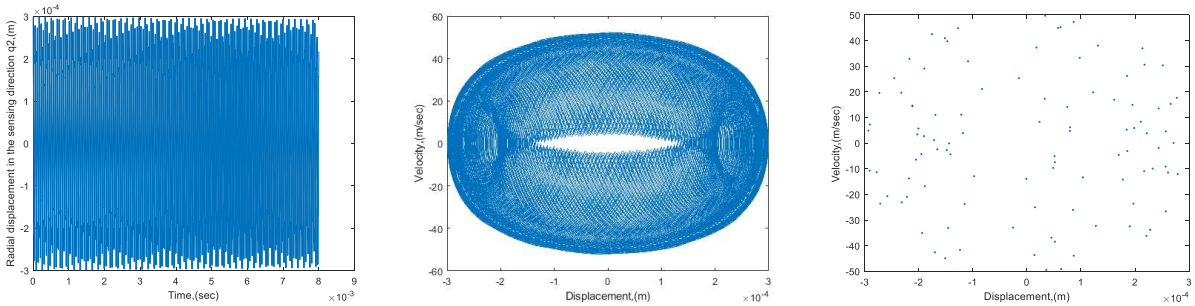

(a) (b) (c)

Figure 2: (a) Time Response , (b) Phase diagram, and (c) Poincare' map.

Conclusions

Nonlinear dynamic behavior of a MEMS-scale ring-type vibratory gyroscope has been examined via numerical simulations. The device exhibits nonlinearity in the presence of geometric nonlinear term in the model which may be attributed to high vibration amplitudes. In addition, nonlinearities due to electrostatic actuation have also been incorporated. Results on the dynamic response obtained via time-response, Phase portraits and Poincare' maps indicate significant influence of geometric nonlinearities on the resulting steady state behavior. The analysis is envisaged to aid fabrication of this class of devices as well as for providing design improvements in MEMS Ring-based Gyroscopes.

References

[1] Cho, J., Asokanthan, S.F. (2009) Nonlinear Instabilities in Ring-Based Vibratory Angular Rate Sensors. PhD. Thesis, Department of Mechanical Engineering, University of Western at London ON.

[2] Huang. S. D., Soedel, W. (1987) Effects of Coriolis Acceleration on the Free and Forced In-plane Vibrations of Rotating Rings on Elastic Foundation, *J.Sound and Vibration*. 115(2), 253-274.

[3] Natsiavas. S. (1994) Dynamics and Stability of Non-linear Free Vibration of Thin Rotating Rings, *J. Sound and Vibration*, 29(1), 31-48.

[4] Gebrel, I.F., Wang, L., Asokanthan, S.F. (2018) Dynamics of a Ring-Type Macro Gyroscope under Electromagnetic External Actuation Forces. *Proc. ASME International Design Engineering Technical Conferences* IDETC/CIE, Quebec, Canada, 86334, pp.V008T10A028.

[5] Evensen, D. A. (1966) Nonlinear Flexural Vibrations of Thin Circular Rings. *J. Applied Mechanics*, 33, pp. 553-560

On the solution of the Mathieu equation with multiple harmonic stiffness: parametric amplification for constant and harmonic forcing.

Eddy Abboud[*,†], Aurélien Grolet[†], Hervé Mahe [*] and Olivier Thomas[†]

[†]*Arts et Metiers Institute of Technology, LISPEN, HESAM Université, F-59000 Lille, France*
[*]*Valeo Embrayages, 81 Avenue Roger Dumoulin, 80009 Amiens Cedex 1, France*

Summary. In this abstract, we focus on the study of a single degree-of-freedom Mathieu-type differential equation, which can be found in engineering examples such as in the modelling of geared systems. We consider that the variable part of the stiffness is composed of several harmonic components and that the forcing terms contain a constant component along with an harmonic component. The phenomenon of parametric amplification is described in the case of a single harmonic force, as well as in the case of a purely constant force. The combination of both forces is also considered in the study

Introduction

This abstract presents a study of a Mathieu type equation arising, for example, when modelling the meshing of two gears mounted on rigid shafts [1] or when studying a pendulum attached to a moving point [2]. The equation represents the motion of a (damped and forced) single degree-of-freedom attached to the ground through a periodically time varying stiffness and is given by the following:

$$\ddot{x} + \mu\dot{x} + [\omega_0^2 + g(t)]x = h(t), \tag{1}$$

where $x(t)$ represents the variable under interest, μ is the damping coefficient, ω_0 is the natural angular frequency, $g(t)$ is the periodic time varying stiffness (with zero mean) and $h(t)$ is the external force.
In the following, we will assume that the stiffness $g(t)$ is periodic with fundamental pulsation Ω, such that it can be represented by its Fourier series: $g(t) = \sum_{p\neq 0} \widehat{\chi}_p e^{ip\Omega t}$, where $\widehat{\chi}_p \in \mathbb{C}$ is the complex amplitude of the p-th harmonic of the stiffness. The external force $h(t)$ will be considered to be the sum of a constant part h_0 and an harmonic part $h_n(t)$ at a given order $n \in \mathbb{N}$: $h(t) = h_0 + (\widehat{h}_n e^{in\Omega t} + c.c.)$, where $\widehat{h}_n \in \mathbb{C}$ is the complex amplitude of the n-th harmonic of the external force, and $c.c.$ stands for complex conjugate.
After introducing some scaling using a small parameter ϵ, the multiple scale method [3] can be used to derive approximated solutions to Eq.(1) under the form $x(t) = x_0(t) + \epsilon x_1(t) + ...$ In this study, one supposes that the damping coefficient (μ), the variable part of the stiffness (g) and the variable part of the force (h_n) are of order ϵ (all the other terms remaining at order 1). The application of the multiple scale method up to order one, leads to two linear differential equations for x_0 and x_1, and the cancellation of the secular terms inside the second equations allows to identify the coupling that can occurs between the different harmonics of the stiffness and the force, along with the computation of the approximated solution $x_0(t)$.
In this study, we consider the solution to Eq.(1) for three different kinds of forcing: i) harmonic forcing only ($h_0 = 0$)), ii) constant forcing only ($h_n = 0$) and iii) combination of constant and variable forcing. In each cases, we describe the phenomenon of parametric amplification exposed by the multiple scale method and we use numerical methods to validate our results. Note that in this study, one will consider that the damping coefficient μ is sufficiently high to avoid parametric instabilities.

Results

Harmonic forcing only

Here we first consider that the system is forced harmonically ($h_0 = 0$ and $\widehat{h}_n \neq 0$) close to its resonance ($n\Omega \approx \omega_0$). The cancellation of the secular terms shows that, at first order in ϵ, the $p = 2n$-th harmonic of the stiffness interacts with the (n-th) harmonic of the force, leading to the following form for the approximated solution:

$$x(t) \approx \left(\frac{\widehat{N}(\Omega)\widehat{h}_n + \widehat{h}_n^* \widehat{\chi}_{2n}}{D(\Omega)} e^{in\Omega t} + c.c. \right), \tag{2}$$

with $\widehat{N}(\Omega) \in \mathbb{C}$ and $D(\Omega) \in \mathbb{R}$. It can be seen that, for a given Ω (e.g. $n\Omega = \omega_0$), the amplitude of the solution can be made maximum (resp. minimum) if the phase between the complex numbers $\widehat{N}(\Omega)\widehat{h}_n$ and $\widehat{h}_n^*\widehat{\chi}_{2n}$ is zero (resp. is π). This phenomenon is known as the parametric amplification effect: by choosing conveniently the complex amplitude $\widehat{\chi}_{2n}$ on can create an amplification, or an attenuation of the vibration amplitude for a given excitation frequency (usually around resonance) [4, 5].

Constant forcing only

Here, we consider that the system is only statically forced ($h_0 \neq 0$ and $\widehat{h}_n = 0$), and that the fundamental pulsation of the periodic stiffness is such that $p\Omega \approx \omega_0$ (for a given $p \in \mathbb{N}$ such that $\widehat{\chi}_p \neq 0$). The cancellation of the secular terms shows

that, at first order in ϵ, the p-th and the $2p$-th harmonic of the stiffness interacts together, leading to the following form for the approximated solution:

$$x(t) \approx \frac{h_0}{\omega_0^2}\left[1 + \left(\frac{\widehat{N}(\Omega)\widehat{\chi}_p + \widehat{\chi}_p^*\widehat{\chi}_{2p}}{D(\Omega)} e^{ip\Omega t} + c.c.\right)\right], \tag{3}$$

again with $\widehat{N}(\Omega) \in \mathbb{C}$ and $D(\Omega) \in \mathbb{R}$. It can be seen that, for a given Ω (e.g. $p\Omega = \omega_0$), the amplitude of variable part of the solution can be made maximum (resp. minimum) if the phase between the complex numbers $\widehat{N}(\Omega)\widehat{\chi}_p$ and $\widehat{\chi}_p^*\widehat{\chi}_{2p}$ is zero (resp. is π). This phenomenon appears to be very similar to the parametric amplification effect presented before: adjusting the phase between the p-th and $2p$-th harmonic of the stiffness can lead to amplification or attenuation of the vibration level (see Fig.1). To our knowledge, this phenomenon is not often refereed to (one explanation might be that, most of the time, researchers consider Mathieu's equation with only a single harmonic variable stiffness along with an harmonic forcing only), and we think it might be useful to understand and/or design gear systems.

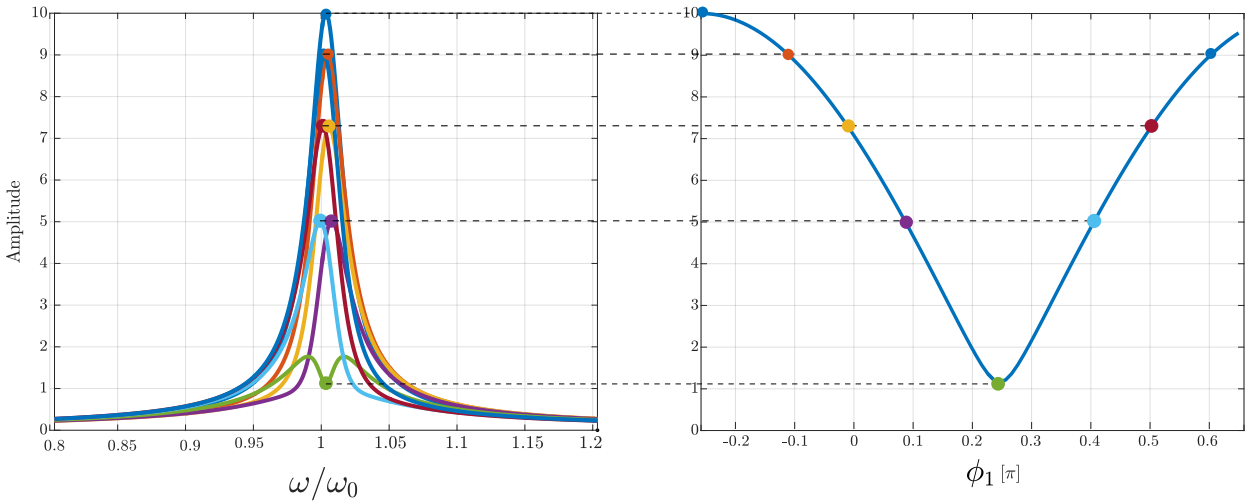

Figure 1: Constant forcing only. Left plot: amplitude of the variable part of the solution in Eq.(3) for different value of the phase between the p-th and $2p$-th harmonic of the stiffness. Right plot: Amplitudes at the resonance as a function of the phase difference, an amplification takes place at $\phi_1 = -\frac{\pi}{4}$ and an attenuation at $\phi_1 = \frac{\pi}{4}$. In this example $p = 1$ and $\phi_2 = 0$ (the second harmonic of the stiffness is the origin for the phase)

Constant and Harmonic forcing

Here, we consider that the system is statically and harmonically forced ($h_0 \neq 0$ and $\widehat{h}_n \neq 0$) around its resonance ($n\Omega \approx \omega_0$) and that $\widehat{\chi}_p \neq 0$ and $\widehat{\chi}_{2p} \neq 0$. Due to the linearity of Eq.(1), the solution to this case can be obtained by summing the results of Eq.(2) and Eq.(3). This leads to interactions between the harmonics of the force and/or the stiffness resulting in parametric amplification or attenuation effect, depending on the relative phase between $\widehat{h}_n$, $\widehat{\chi_n}$ and $\widehat{\chi}_{2n}$, that will be described in the presentation.

Conclusions

In this study, we have shown that parametric amplification in Mathieu's oscillators is possible for in the case of an harmonic forcing as well as in the case of a pure constant forcing. The parametric amplification is due to interaction between harmonics of the stiffness and/or of the forcing. This can be interesting for various fields of applications where the modification of the phases between the harmonics of the stiffness may cause a reduction in vibration levels. In particular, we think that this phenomenon might be of interest for understanding and/or designing geared systems.

References

[1] N.Sainte-Marie. A transmission-error-based gear dynamic model: Applications to single-and multi-mesh transmissions. PhD thesis, INSA Lyon, 2016.

[2] L.Ruby. Applications of the mathieu equation. American Journal of Physics, 1996.

[3] A. Nayfeh and D. Mook. Nonlinear oscillations. John wiley & sons, 1997.

[4] D.Rugar and P.Grutter. Mechanical parametric amplification and thermomechanical noise squeezing. Physical Review Letters, 1991.

[5] O.Thomas, F.Mathieu, W.Mansfield, C.Huang, S.Trolier-McKinstry, and L.Nicu. Efficient parametric amplification in micro-resonators with integrated piezoelectric actuation and sensing capabilities. Applied Physics Letters, 2013.

Optimization Process for Ride Quality of a Nonlinear Suspension Model Based on Newton-Euler's Augmented Formulation

Mohamed Belhorma*, and Aboubakar S. Bouchikhi*
*The Mechanics of structures and solids Laboratory, BP 89, Cite Ben M'hidi, University of Sidi Bel Abbes, Sidi Bel Abbes 22000, Algeria.

Summary. This paper addresses modeling a Double A-Arm suspension, a three-dimensional nonlinear model has been developed using the multibody systems formalism. Dynamical study of the different components responses was done, particularly for the wheel assembly including the tire body and the knuckle. To validate those results, a similar model was constructed and simulated by RecurDyn; a professional multibody dynamics simulation software. The model has been used as an Objectif function that generate an optimization algorithm for ride quality improvement.

Introduction

Modern systems are often very complex and consist of many components interconnected by joints and force elements. These systems are commonly called multibody systems (MBS). Vehicles can be considered as MBS and the dynamic equations that govern their motion are highly nonlinear which in most cases cannot be solved analytically. One must resort to the numerical solution of the resulting dynamic equations. Nikravesh work in [1] can be considered as an interesting reference about the Newton-Euler equations and its most suitable forms.
The aim of this study is the implementation of the augmented formulation in a dynamical model of the double A-Arms suspension. This system contains two lateral control arms to hold the wheel where the length between the upper and lower arms is not the same [2]. The upcoming sections represent a suspension mathematical model witch can be used as an Objectif function that generate an optimization algorithm for ride quality improvement.

Dynamic Equations of motion

From [1], The equation of motion for the mass center of a rigid body is directly obtained from Newton's second law as

$$\mathbf{M}.\ddot{\mathbf{q}} = \mathbf{h} \tag{1}$$

For a system of n_b constrained bodies, we must revise Equation 1 by including the reaction (constraint) forces

$$\mathbf{M}.\ddot{\mathbf{q}} = \mathbf{h} \quad \rightarrow \quad \mathbf{M}.\ddot{\mathbf{q}} = \mathbf{h} + {}^{(c)}\mathbf{h} \tag{2}$$

Assume that the position constraints between the n_b bodies form n_c constraint equations that are expressed in general form as

$$\mathbf{\Phi}(\mathbf{q}) = 0 \tag{3}$$

The velocity and acceleration constraints are expressed as

$$\dot{\mathbf{\Phi}} = \mathbf{\Phi}_q.\dot{\mathbf{q}} = 0 \tag{4}$$

$$\ddot{\mathbf{\Phi}} = \mathbf{\Phi}_q.\ddot{\mathbf{q}} - \boldsymbol{\alpha} = 0 \tag{5}$$

Where $\mathbf{\Phi}_q$ is the Jacobian matrix. According to the method of Lagrange multipliers, the array of reaction forces ${}^{(c)}\mathbf{h}$ can be presented as

$${}^{(c)}\mathbf{h} = \mathbf{\Phi}_q^T.\boldsymbol{\lambda} \tag{6}$$

$\boldsymbol{\lambda}$ is a vector of n_c Lagrange multipliers. Then Equation 2 is rewritten as

$$\mathbf{M}.\ddot{\mathbf{q}} = \mathbf{h} + \mathbf{\Phi}_q^T.\boldsymbol{\lambda} \tag{7}$$

This system contains n_b equations and n_b+n_c unknowns, accelerations and Lagrange multipliers.

THREE-DIMENSIONAL NONLINEAR MODEL OF DOUBLE A-ARM SUSPENSION

To well understand the selected approach, three-dimensional nonlinear model of double A-Arm suspension will be presented. The system contains four (04) moving bodies that are connected with each other by kinematic joints and driven by a set of forces, Figure 1. With this formulation the number of unknowns is $n + m$, since not only $\boldsymbol{q}$ but also $\boldsymbol{\lambda}$ needs to be calculated.

$$\mathbf{q} = (\mathbf{q}_1 \;\; \mathbf{q}_2 \;\; \mathbf{q}_3 \;\; \mathbf{q}_4)^T \tag{8}$$

where

$$\mathbf{q}_i = (x_i \;\; y_i \;\; z_i \;\; \gamma_i \;\; \beta_i \;\; \varphi_i)^T \tag{9}$$

For validation, RecurDyn software is used. It provides realistic simulation of multibody dynamics.

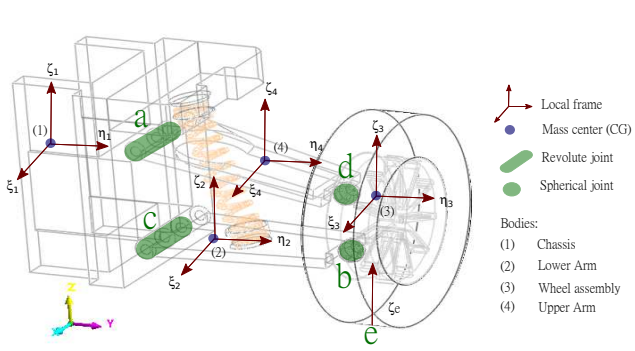

Figure 1: Three-Dimensional Double A-Arm Suspension system

Type of joint	Notation	body$_i$-body$_j$	Constraints Eqts = 0
Translational	$\mathbf{\Phi}^{(2tr,3rot)}_{CoG_1}$	GRF-1 along Z-axis	$\begin{pmatrix} x_1 & y_1 & \gamma_1 & \beta_1 & \varphi_1 \end{pmatrix}^T$
Revolute in c	$\mathbf{\Phi}^{(3tr,2rot)}_{c}$	1-2 about x-axis	$\mathbf{\Phi}^{3tr}(c_1,c_2)$ $\mathbf{\Phi}^{2rot}_1(\vec{u}_1,\vec{u}_2)$ or $\mathbf{\Phi}^{2rot}_2(\vec{u}_2,\vec{u}_1)$
Spherical in b	$\mathbf{\Phi}^{(3tr)}_{b}$	2-3	$\mathbf{\Phi}^{3tr}(b_2,b_3)$
Spherical in d	$\mathbf{\Phi}^{(3tr)}_{d}$	3-4	$\mathbf{\Phi}^{3tr}(d_3,d_4)$
Cylindrical in a	$\mathbf{\Phi}^{(2tr,2rot)}_{a}$	4-1 $\begin{cases}\text{along x}-\text{axis}\\ \text{about x}-\text{axis}\end{cases}$	$\mathbf{\Phi}^{2tr}(a_4,a_1)=0$ $\mathbf{\Phi}^{2rot}_4(\vec{u}_4,\vec{u}_1)$ or $\mathbf{\Phi}^{2rot}_1(\vec{u}_1,\vec{u}_4)$
Driving in e	$\mathbf{\Phi}^{1D}_{A}$	3-A in Z-direction	$z_A - f(t)$

Table 1: Constraints configuration of the double A-arm system.

OPTIMIZATION PROCESS

The chassis vertical acceleration is minimized, while the design constraints on the suspension working space and dynamic tire load should be satisfied. The RMS of the acceleration of a sprung mass $\ddot{Z}1$ is frequently used to evaluate the riding quality of a vehicle. A rider's comfort improves as the acceleration decreases. Ride comfort is chosen to be the design criterion. The design optimization problem can be described as: Minimize $\ddot{Z}1(m_1, m_2, m_3, m_4, K_s, N_s, K_t, N_t)$.
We choose the *fmincon* function in MATLAB to execute this simple optimization process which .

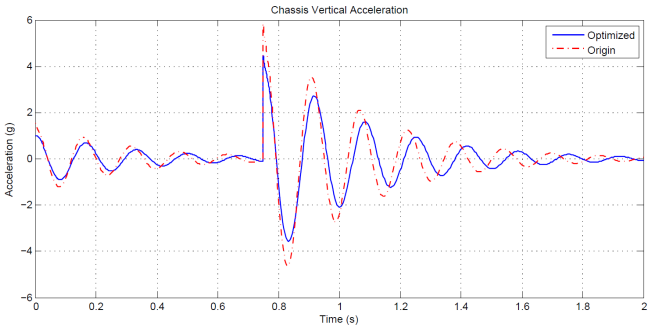

Figure 2: Optimized and origin vertical accelerations.

Conclusions

This paper has focused on the vertical motion of the Nonlinear planar model of the Double A-Arm suspension. The comparison between the responses of the three-Dimensional nonlinear model and the one in the simulation software shows that a precise setting in the multibody modeling of mechanical systems can offer great results in short period of time with low processing capacity requirements.
As a final step in the process, this model was transformed to an Objectif function. The use of this function allowed us to generate an optimization algorithm capable of calculating the optimal suspension to improve vehicle ride quality. The vertical acceleration of the chassis was reduced but the process has some difficulties because of the set of the differential-algebraic equations and the constraints violation

References

[1] Nikravesh, P.E. (1988) Computer-Aided Analysis of Mechanical Systems. Prentice-Hall, New Jersey.
[2] Reza, N.J. (2014) Vehicle Dynamics, Theory and Application. Second Edition. Springer, New York.

Passive suppression of parametric excitation of cables using a nonlinear vibration absorber (NVA)

Pauline Kolb*, Vitor Schwenk† and Guilherme Rosa Franzini †
*Institute of Structural Mechanics and Design, Technische Universität Darmstadt, Darmstadt, Germany
†Universidade de São Paulo, Escola Politécnica, LMO, Brazil

Summary. The usage of non-linear vibration absorbers is a rather new but practical way to prevent a fatigue failure of a structure exposed to especially broad banded dynamic loading. In this work, a non-linear vibration absorber will suppress the response of a flexible rod under parametric excitation. Therefore, a mathematical model is derived using the extended Hamilton's principle. A reduced-order model (ROM) is obtained after the application of the Galerkin's method and is numerically integrated aiming at observing the Mathieu's instability and its suppression. This excitation scenario is common in offshore engineering where parametric excitation appears on risers of TLP tethers, slender structures linked to the seabed and the floating unit. Nonlinear vibration absorbers can be designed, built and installed with a relatively small effort compared to other methods and provide a positive effect on the sustainability of the rod [1]. The results show a suppression of the oscillation is possible to a certain degree, when the NVA reaches a sufficient mass ratio.

Introduction

Besides the academic interest, the studies of parametric excitation have a technological importance on off-shore and ocean engineering. Especially for the dynamic of risers and tendons of TLPs (Tension Leg Platforms), buoyant platforms held in place by a mooring system as can be seen in figure 1. Even though the considered structures are always under tension, the value varies with time due to the vertical movement of the platforms and the change of lifting force.

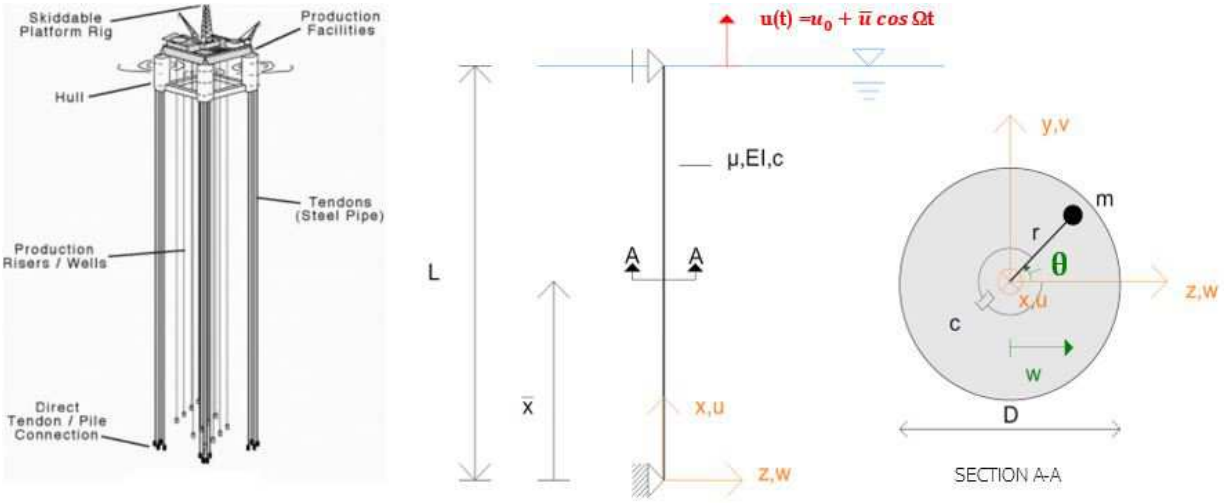

Figure 1: TLP [4] and system of flexible cable with NVA at x = $\bar{x}$

Parametric excitation

In contrast to external excitation, parametric excitation leads to *homogenous* differential equations with a parameter depending only on time on the left side. Of significance is that even a small parametric excitation produces a large response when the frequency of excitation Ω resembles twice the natural frequency ω of the system (*principle parametric resonance*)[2]. Therefore, an efficient suppression device is to be designed.

Non-linear suppression

A non-linear vibration absorber (NVA) as can be seen in figure 1 has the advantage to be able to react to a broad band loading. Due to the absence of a linearizable natural frequency, the NVA uses internal resonances for a spacial transfer of energy and its dissipation. This process is known as energy pumping, or TET (Targeted Energy Transfer). Further information can be found in papers by Lee [3] and Vakakis [5].

Mathematical model

Consider a flexible cable with a diameter D, mass per unit length μ and the structural damping ratio c. A rotative NVA (mass m, radius r) is attached to the cable at the height $\bar{x}$ by a dashpot (c_Θ), as can be seen in figure 1. The kinetic energy T and the potential energy V with $\epsilon = u' - zw'' + \frac{1}{2}w'^2$ are regarded for the Lagrangian, as well as the virtual work

for extended Hamilton's principle. Using Galerkin's method by considering one degree of freedom (1-DOF) and placing the NVA at midspan, the non-dimensional equations of motion can be written as seen in equation 1 for the system and equation 2 for the NVA.

$$(\frac{1}{2}+\hat{m})\ddot{A}_1+\zeta_s\dot{A}_1+K_3\dot{A}_1|\dot{A}_1|+[K_0+\bar{K}cos\eta\tau]A_1+K_2A_1^3=\hat{r}\hat{m}(\ddot{\Theta}sin\Theta+\dot{\Theta}^2cos\Theta) \tag{1}$$

$$\ddot{\Theta}-\frac{1}{\hat{r}}sin\Theta\ddot{A}_1+2\zeta_\Theta\dot{\Theta}=0 \tag{2}$$

Results and discussion

After a numerical Runge-Kutta based integration with MATLAB, the behaviour of structure and NVA can be observed. In figure 2 the time histories can be divided in three main sections, where A and B show the typical behaviour of energy pumping, while C describes a more or less steady oscillation. Figure 2 also shows that depending on given parameters a NVA might also lead to an increase of the main amplitude. To give an overview over the choice of parameters $\hat{m}$ and $\hat{r}$,

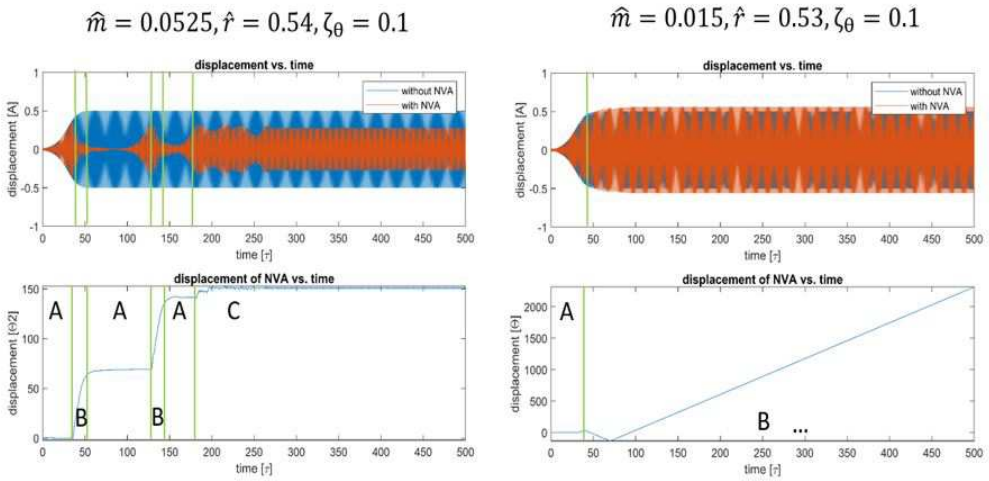

Figure 2: Time history and NVA sections with $\hat{m} = \frac{\text{mass NVA}}{\text{mass cable}}$, $\hat{r} = \frac{r}{D}$

the ratio of standard deviations with and without NVA can be seen in figure 3, where red areas show an increase and blue areas a significant reduction of the main structures vibration.

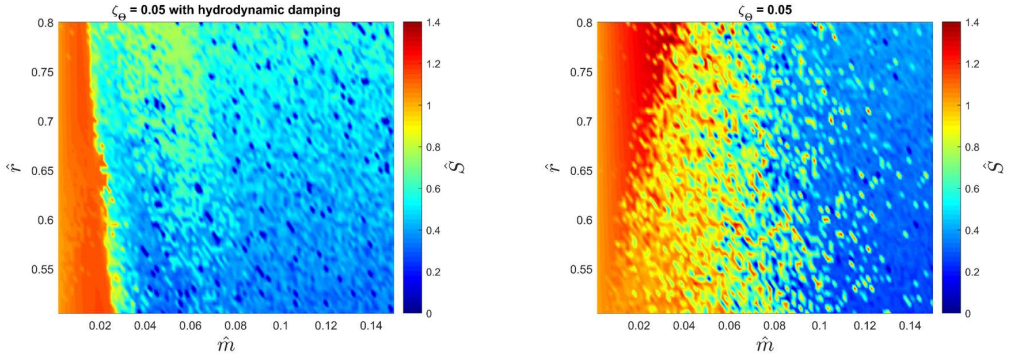

Figure 3: Maps

References

[1] G. R. Franzini, G. R. Campedelli, and C. E. N. Mazzilli. A numerical investigation on passive suppression of the parametric instability phenomenon using a rotative non-linear vibration absorber. *International Journal of Non-Linear Mechanics*, 105(January):249–260, 2018.

[2] G. R. Franzini and C. E. Mazzilli. Non-linear reduced-order model for parametric excitation analysis of an immersed vertical slender rod. *International Journal of Non-Linear Mechanics*, 80:29–39, 2016.

[3] Y. S. Lee, A. F. Vakakis, L. A. Bergman, D. M. McFarland, G. Kerschen, F. Nucera, S. Tsakirtzis, and P. N. Panagopoulos. Passive non-linear targeted energy transfer and its applications to vibration absorption: A review. *Proceedings of the Institution of Mechanical Engineers*, 2008.

[4] J. Pike. Tension Leg Platform (TLP), 2011.

[5] A. F. Vakakis. Intentional utilization of strong nonlinearity in structural dynamics. *Procedia Engineering*, 199:70–77, 2017.

TWMS synchronization network simulation with parallel computing

M. S. Batista[1], E. A. Maciel[1], E. C. Panzo[1], F. H. Dermendjian[2], C. M. Batistela[3], J. R. C. Piqueira[3], J. M. Balthazar[2] and A. M. Bueno[1]
[1]*Institute of Science and Technology, São Paulo State University - UNESP, Sorocaba - SP, Brazil*
[2]*School of Engineering, São Paulo State University - UNESP, Bauru - SP, Brazil*
[3]*Polytechnique School, São Paulo University - USP, São Paulo - SP, Brazil.*

Summary. Synchronization networks play important roles in Engineering and Physical systems, allowing information distribution and exchange between the components of computation, communication and complex dynamical systems. In the recent decades the growing need for data communication led to the development of a world wide communication and data transmission network. The clock signal distribution network is an important part of these networks. The Phase-Locked Loop (PLL) is the circuit that synchronizes the local oscillator (clock) to a reference signal (phase and frequency scale). Usually, the PLL networks are build in Mutually-Connected or in Master-Slave topologies. In many cases the Master-Slave is used due to its simplicity and low cost. The nonlinear behavior of PLLs makes the design of clock signal distribution networks a difficult task, therefore, numerical simulation is an important tool. In this work, a Two-Way Master-Slave network is build using parallel computation, aiming to develop a more efficient simulation strategy, and to study the effects of the interacting PLLs running in a parallel computation system.

Introduction

Complex systems can be thought as a set of a large number of connected, usually simple, elements, exchanging signal (information), and producing new behaviors difficult to predicted from the components or boundary conditions. The study of dynamical systems arise from the need to understand phenomena, and to build mechanisms or circuits, such as the complex systems. Synchronization networks are complex systems with growing interest given the need for global communication systems [1, 2, 3].
The PLL is the fundamental component of clock signal distribution networks, and consists of a closed-loop control system that synchronizes a local oscillator, or clock, to a reference signal. The PLL block diagram, shown in Fig. 1, is composed of a Phase Detector (PD), of a Low-Pass Filter, and of a Voltage-Controlled Oscillator (VCO) [4].

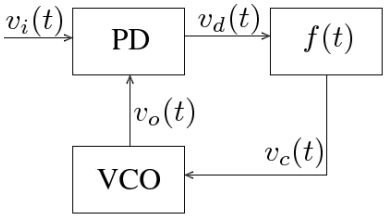

Figure 1: PLL block diagram.

Given the input and output signals in Eqs. 1 and 2, the multiplier type PD generates an error signal $v_d(t)$ with the same sign of the phase difference $\theta_i(t) - \theta_o(t)$.

$$v_i(t) = \mathrm{v}_i \sin(\omega_M t + \theta_i(t)) \tag{1}$$
$$v_i(o) = \mathrm{v}_o \cos(\omega_M t + \theta_o(t)) \tag{2}$$

The LPF controls the VCO phase and frequency, according to the relation in 3, around the free-running frequency ω_M, tracking the input phase $\theta_i(t)$ and filtering noise, jitter and wander frequency fluctuations [2, 5, 6].

$$\frac{d}{dt}\theta_o(t) = k_o v_c(t) \tag{3}$$

Considering the foregoing relations the PLL mathematical model is given by Eq. 4,

$$L\left[\theta_o(t)\right] + GQ\left[\sin\left(\theta_o(t) - \theta_i(t)\right)\right] = GQ\left[\sin\left(2\omega_M t + \theta_i(t) + \theta_o(t)\right)\right], \tag{4}$$

where $G = \frac{1}{2}k_m k_o \mathrm{v}_i \mathrm{v}_o$ is the loop gain and the operators L and Q depend on the LPF transfer function [1, 2].

TWMS PLL network

There are many strategies for synchronization of clocks. Each strategy depend on the choice for the network topology. In Mutually-Connected networks all the nodes (PLLs) contribute to the phase and frequency scale of the network, however, in Master-Slave networks, the master clock dictates the phase and frequency scales for the whole network. In most cases the Master-Slave strategy is used due to its simplicity and low cost [2, 7].

In One-Way Maste-Slave network the master node alone dictates the phase and frequency scales for the whole network. On the other hand, in the Two-Way Master-Slave strategy, the slave nodes also contribute to the determination of the phase and frequency scales of the network. In Fig. 2(a) the PLL block diagram for a TWMS network is shown. Differently from Fig. 1, the error signal depends on the average phase between the previous and of following nodes, as it shown in Fig. 2(b).

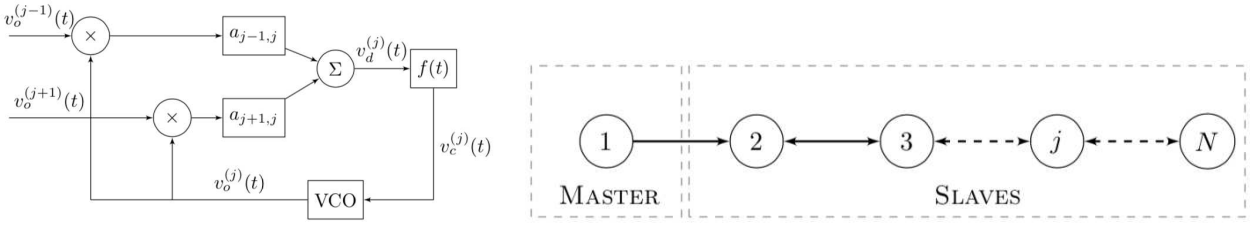

(a) TWMS PLL.

(b) TWMS network.

Figure 2: TWMS Clock signal distribution networks.

Following a procedure similar to the previous section the mathematical model of the slave-nodes in a TWMS network is given by

$$L^{(j)}\left[\theta_o^{(j)}(t)\right] + Q^{(j)}\left[\sum_{\substack{\ell=j-1\\ \ell\neq j}}^{j+1} G^{(j,\ell)}\sin\left(\theta_o^{(j)}(t)-\theta_o^{(\ell)}(t)\right)\right] = Q^{(j)}\left[\sum_{\substack{\ell=j-1\\ \ell\neq j}}^{j+1} G^{(j,\ell)}\sin\left(2\omega_M t+\theta_o^{(\ell)}(t)+\theta_o^{(j)}(t)\right)\right] \tag{5}$$

where $j = 2, 3, \cdots, N$, $G^{(j,\ell)} = \frac{1}{2}a_{\ell,j}k_m^{(j)}k_o^{(j)}\mathrm{v}_o^{(j)}\mathrm{v}_o^{(\ell)}$ is the loop gain and the operators $L^{(j)}$ and $Q^{(j)}$ depend on each slave node LPF transfer function.

As it can be noticed from Fig. 2, the phase and frequency scales for the slave nodes depend on the master clock and on the parallel interaction of the slave nodes. Although this is a MS strategy, there is a mutual connection of the slave nodes. The nonlinear and simultaneous interactions generate complex dynamic behaviors. In this case parallel computing is helpful to study and to build more realistic synchonization networks models.

Parallel Programming

Parallel computation consists of solving parts of the system concurrently, that is, in parallel, and in different processors (or cores), in order to reduce the simulation time. In addition, this technique gives more flexibility to build the network [8].

MATLAB's Parallel Computing Toolbox (PCT) allows the developer to work with memory sharing and distributed memory architecture. Within this tool, the development of the "local" infrastructure is built inside a multi-core computer [9]. Generally speaking, hardware architectures are commonly two-, four-, or eight-core versions.

PCT delivers functions to MATLAB such as parallel loop execution, creation and/or manipulation as well as enabling the construction of animal arrays of parallel logic. PCT allows you to use even the cores of the machine on which they all run as they enable interactive development and debugging of code in parallel logic. As a possibility of expanding the work developed on this platform, the largest developed can scale to a number of cores using the MATLAB Distributed Computing Server [10] . Fig. 3 shows a division of the sections into desktop system and cluster computer.

Using MATLAB's PCT, a program with parallel logic can be expressed in three different ways [11]:

1. by the *parfor* feature, which executes a for loop in parallel;
2. by the *spmd* feature, which creates a synchronous process of cooperation;
3. by the *task* feature, which creates multiple, independent programs.

Among the PCT functions, *parfor* (parallel for)-loop stands out, which is very useful in situations that require several iterations in a loop, with a simple function being executed between these iterations, such as Monte Carlo simulations and image processing. In order to run the *parfor*, it is necessary to use PCT, adapting the original code to the new commands of that toolbox [12].

The iterations that run in *parfor* are independent and run in independent instances of MATLAB, running them separately from the operating system process. That way, the function that will be executed at each iteration cannot depend on results that are found in that loop. This is due to the construction of *parfor* inside the PCT, which does not share memory during execution. The application of this solution is feasible for different computers connected via the network because the PCT is able to transform each core of this network into a processing unit of *parfor* iterations [9, 12, 13].

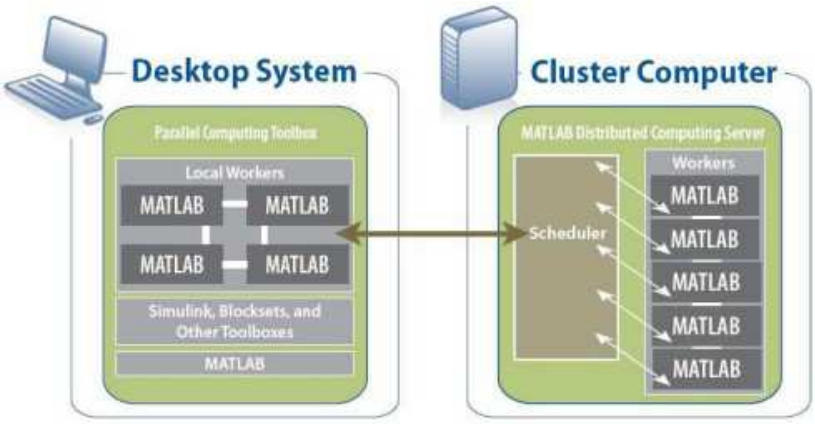

Figure 3: The Parallel Computing Toolbox and MATLAB Distributed Computing Server [10].

Proposed Algorithm

For the development of the work, the necessary calculation steps for the execution of the PLL were followed. Thus, in the first moment, the phase comparison of the input signal and the output signal of the VCO of the PLL itself was performed. This signal is called VD and it feeds the LPF filter of the PLL, in which the fourth-order Runge-Kutta integrative method is used, in which the implementation was based on [14]. Finally, the output signal from the LPF, called VC, is directed to the VCO, closing the loop. The proposed algorithm for running the simulations has three main sections:

1. Definition of initial and simulation parameters – the following questions are answered: What is the input signal; What is the size of the network; What is the start time, end time and sample rate of the simulation; What are the filter parameters;

2. TWMS network simulation – the calculations referring to the constructed TWMS network are performed, in which the calculation of the LPF output is performed in parallel;

3. Construction and presentation of the results obtained – creation of an output file with the simulation results and graphs of the system's behavior.

In this work, the development of parallelism via TPC was chosen through the function *parfor*. Basically in the PLL integration loop, the repetitive structure that advances in time according to the sample rate is a *for* structure. This structure directs the "round" the system is in, that is, it manages the integration step. In this case, we call it the main program.
Within the main program, due to the LPF operation, we need an integration, so that the control signal for the VCO (which in this case is the LPF output) is found. In this step, the *parfor* was applied, that is, the calculation of all PLLS of the TWMS network is performed simultaneously.

Simulation features

The simulated TWMS network is formed by a PLL Master, a PLL Slave, called Slave 1, whose input signal $v_i(t)$ depends on both the Master and Slave 2, and another PLL Slave, called Slave 2, whose signal depends only on the output signal $v_o(t)$ of Slave 1,as described in [15].

Results to step

The simulated TWMS network contains a PLL Master, Slave 1 (having its input signal dependent on the output signals of the PLL Master and Slave 2) and Slave 2 (having its input signal dependent only on Slave 1). The simulations followed the models found in [4, 15, 16, 17].
When analyzing Fig. 4, we see that the PLL Master and Slave 2 are in sync with the input signal because the phase error of θ_o with respect to θ_i is zero. This fact is confirmed by observing Fig. 5 which are results of the steady state of the network. In this case, the Lissajous figure in the post-transient regime demonstrates that the PD input ($v_i(t)$) and the VCO output ($v_o(t)$) of Master and Slave 2 are signals periodic, with the same frequency and quadrature phase, implying synchronization.
Slave 1, in the studied interval, does not reset the phase error of the output in relation to the input. This fact evidenced by Fig. 4 and 5. The signal of Slave 1, when looking at the Lissajous graph, the behavior of the PD input ($v_i(t)$) and the VCO output ($v_o(t)$) Slave 1 has $\theta_o(t)$ equal to 180º, thus being out of phase in relation to $\theta_i(t)$, implying non-synchronization.

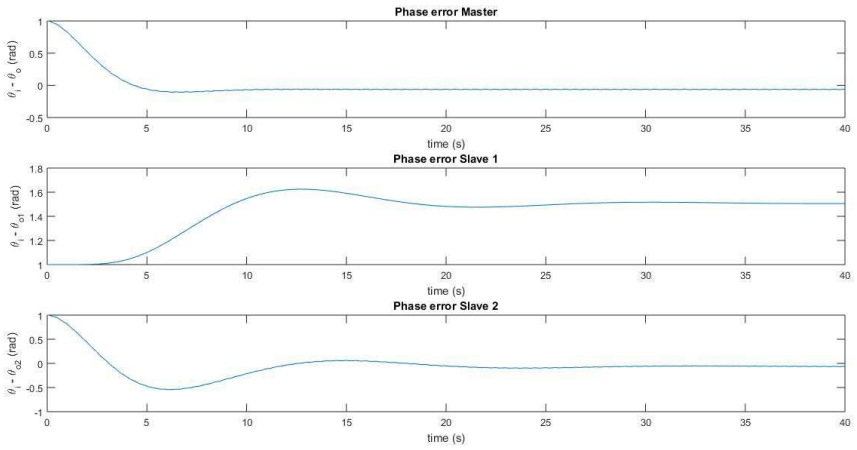

Figure 4: TWMS: Phase error of the step response.

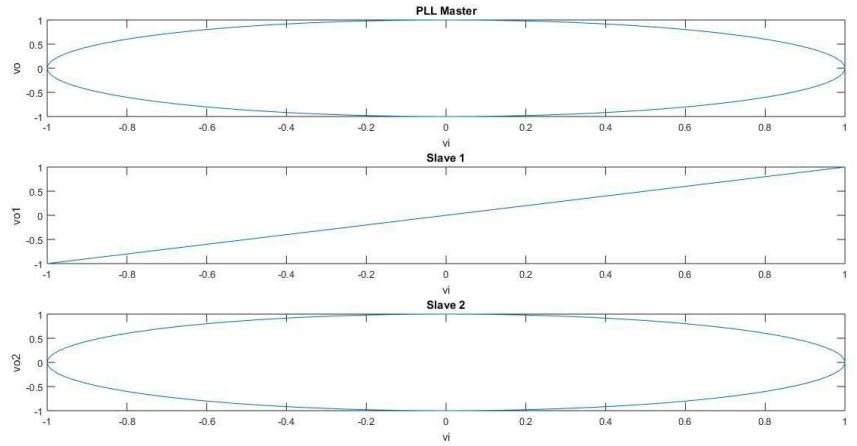

Figure 5: TWMS: Lissajous of the step response.

Results to ramp

When we apply a ramp to the network and observe the behavior of the network, we see that in the TWMS model that the phase of θ_o in relation to θ_i follows the ramp. In Fig 9, we notice that the Master, Slave 1 and Slave 2 replicate the ramp applied to the PD ($v_i(t)$), causing the VCO output ($v_o(t)$) has the same behavior, not synchronizing any of the network PLLs.

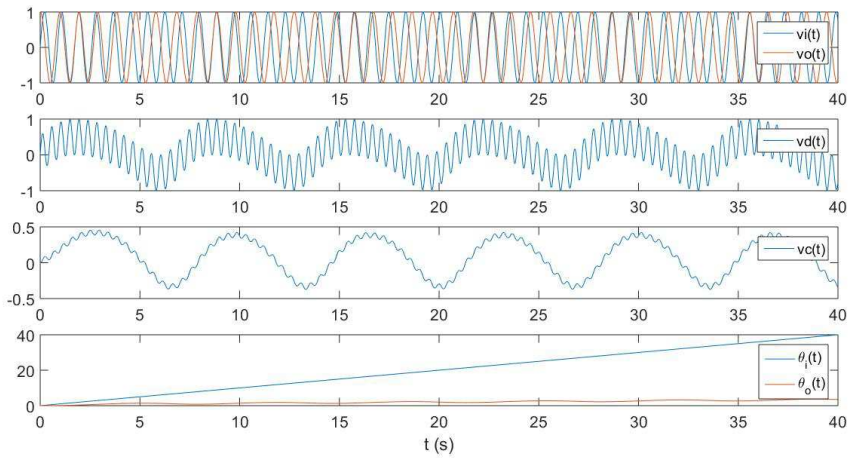

Figure 6: TWMS: Master's response to ramp.

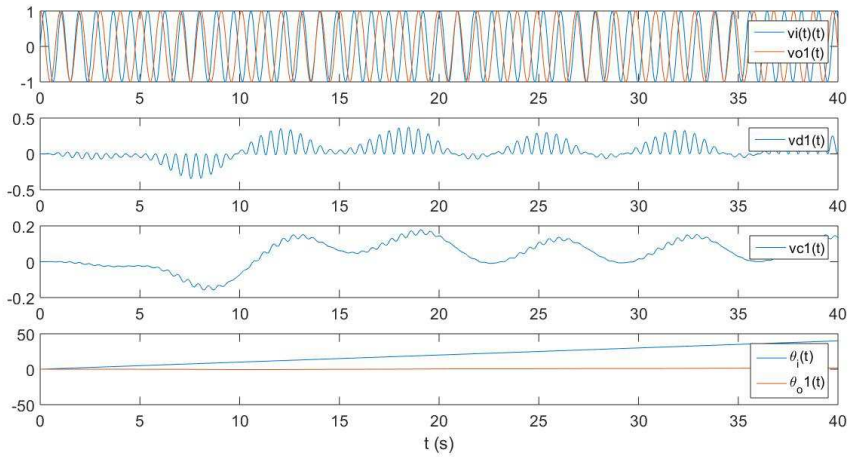

Figure 7: TWMS: Slave 1's response to ramp.

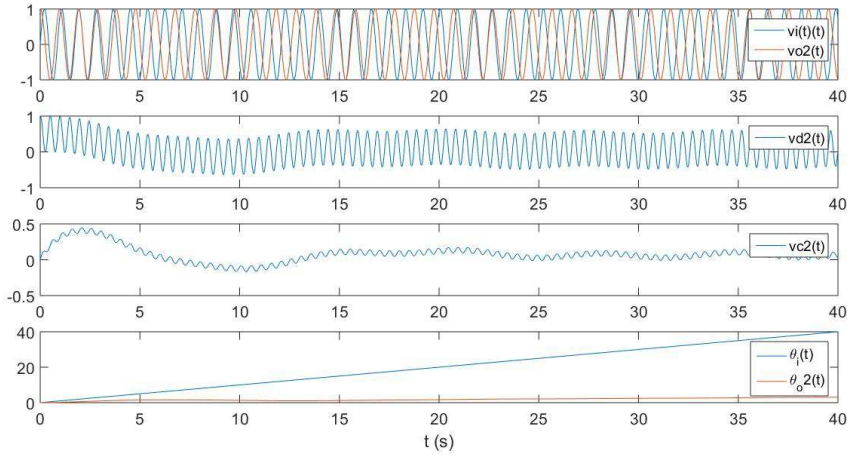

Figure 8: TWMS: Slave 2's response to ramp.

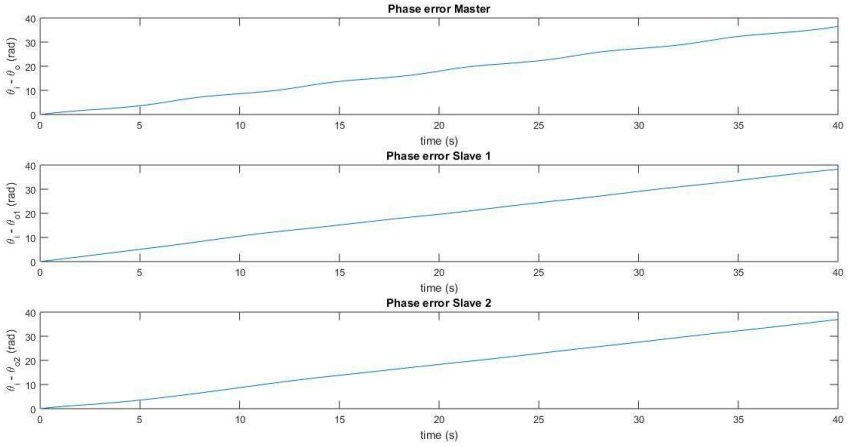

Figure 9: TWMS: Phase error of the ramp response.

Conclusion

In the TWMS network, composed of 3 PLLs, when we apply a step to the input signal phase, we notice that through the phase error and the Lissajous figures that the Master and Slave 2 synchronize with this signal, having a jitter due to the

characteristics of the simulated system. Slave 1 has as a response the non-synchronization with the input signal, a fact observed in the phase error and also by its Lissajous, whose arrangement indicates a phase delay in the order of 180º, as shown in [17].
When applying a ramp to the input phase, it is noted that both the Master and Slaves do not find a control voltage capable of tuning the output signal with the input applied. As shown in [15, 17], the ramp signal causes synchronization failures in all PLLs.

References

[1] W. C. Lindsey, F. Ghazvinian, W. C. Hagmann, and K. Dessouky. Network synchronization. *Proceedings of the IEEE*, 73(10):1445–1467, 1985.

[2] A. M. Bueno, A. A. Ferreira, and J. R. C. Piqueira. Modeling and filtering double-frequency jitter in one-way master slave chain networks. *Circuits and Systems I: Regular Papers, IEEE Transactions on*, 57(12):3104–3111, Dec. 2010.

[3] R. S. Sánchez, J. C. Piqueira, and Á. M. Bueno. Comparing phase detectors in analog phase-locked loops. *The European Physical Journal Special Topics*, 230(18):3609–3614, 2021.

[4] A. M. Bueno, A. G. Rigon, A. A. Ferreira, and J. R. C. Piqueira. Design constraints for third-order pll nodes in master-slave clock distribution networks. *Communications in Nonlinear Science and Numerical Simulation*, 15(9):2565–2574, 2010.

[5] ITU-T. *Timing Characteristics of Primary Clocks - Recomendation G.811 ITU-T*, 1997.

[6] ITU-T. *Timing Requirements of Slave Clocks Suitable for Use as Node Clocks in Synchronization networks - Recomendation G.812 ITU-T*, 1997.

[7] A. M. Bueno, A. A. Ferreira, and J. R. C. Piqueira. Fully connected pll networks: How filter determines the number of nodes. *Mathematical Problems In Engineering*, 2009(Article ID 256765):13 pages, 2009.

[8] P. Pacheco. *An Introduction to Parallel Programming*. Elsevier Science, 2011.

[9] D. N. Varsamis, C. Talagkozis, P. A. Mastorocostas, E. Outsios and N. P. Karampetakis. *The performance of the MATLAB Parallel Computing Toolbox in specific problems*. In: Federated Conference on Computer Science and Information Systems (FedCSIS), Wroclaw, Poland. 2012. p. 587-593.

[10] A. Krishnamurthy, S. Samsi and V. Gadepally. *Parallel MATLAB Techniques*. InTech, 2009.

[11] M.Szymczyk and P. Szymczyk. *Matlab and parallel computing.* Image Processing & Communications, v. 17, n. 4, p. 207, 2012.

[12] P. Luszczek. *Parallel programming in MATLAB*. The International Journal of High Performance Computing Applications, v. 23, n. 3, p. 277-283, 2009.

[13] Mathworks. *Parallel Computing Fundamentals web site,* https://www.mathworks.com/help/parallel-computing/parallel-computing- fundamentals.html

[14] D. Tan and Z. Chen. *On a general formula of fourth order Runge-Kutta method*. Journal of Mathematical Science & Mathematics Education, v. 7, n. 2, p. 1-10, 2012.

[15] J. R. C.Piqueira, S. A. Castillo-Vargas, L. H. A. MONTEIRO. *Two-way master-slave double-chain networks: limitations imposed by linear master drift for second order PLLs as slave nodes.* IEEE Communications Letters, v. 9, n. 9, p. 829-831, 2005.

[16] J. R. C.Piqueira. *Master-Slave Topologies with Phase-Locked Loops.* Wireless Communications and Mobile Computing, v. 2020, 2020.

[17] J. R. C.Piqueira and A. C. B. de Godoi. *Clock signal distribution with second order nodes: Design hints.* ISA transactions, v. 115, p. 124-142, 2021.

Stability Analysis of Rotary Drilling Systems Associated with Multiple State-Dependent Delays

He Zhang* and Emmanuel Detournay†
*Department of Civil, Environmental, and Geo-Engineering, University of Minnesota, Minneapolis, MN, USA, 55414;

Summary. This paper presents an algorithm to conduct numerical linear stability analyses of rotary drilling systems equipped with a realistic Polycrystalline Diamond Compact (PDC) bit. The interaction between a PDC bit and the rock introduces up to 100 state-dependent delays into the differential equations governing the rotary drilling system, here represented by a discrete multiple degrees of freedom model. A bit trajectory function is proposed to convert the time delays into their corresponding angular delays that are embedded in the PDC bit design. The proposed algorithm has the potential to be used for optimizing PDC bit design with the goal of postponing the occurrence of torsional stick-slips.

Introduction

Torsional stick-slip vibrations are destructive dynamic phenomena encountered during rotary drilling of oil and gas wells. The torsional stick-slips are characterized by alternating stick phases with the bit at rest for a period of time and slip phases, during which the angular velocity of the tool increases up to two times the nominal angular velocity. The root cause of the torsional stick-slip oscillations lies in the nature of bit-rock interaction as both laboratory and field measurement data have shown that PDC bit design has a significant influence on the torsional stick-slips. However, it is a challenging problem to model the interaction between a realistic PDC bit and the rock, which is associated with two major sources of nonlinearities: (i) the regenerative rock cutting process introduces up to 100 state-dependent delays due to the complex layout of PDC cutters; (ii) the unilateral nature of the frictional contact process introduces a discontinuity in the boundary conditions [1]. The search for the numerous state-dependent delays in numerical simulations is, however, CPU intensive, which renders the computational efficiency of conventional solution strategies unacceptable.

This difficulty has recently been overcome by Tian et al [1], who employed a bit trajectory function [2, 3], to reformulate the time delay-related variables. In this way, the state-dependent time delays are converted into the corresponding angular delays that are known from the PDC bit designs. The evolution of the bit trajectory function is governed by a partial differential equation (PDE), which is coupled by the system of ordinary differential equations (ODEs) that governs the dynamics of the discretized drillstring. By the application of the Galerkin method, the coupled system of PDE-ODEs are transformed into a system of ODEs, which can be efficiently integrated. The drillstring in [1] is, however, simplified as a low-dimensional (LD) discrete model that solely consists of two degrees of freedom (DOFs). This LD drillstring model considers only one torsional DOF, which is thus unable to capture the higher modes of torsional resonance that are usually responsible for the occurrence of torsional stick-slips [3].

This paper extends the LD drillstring model in [1] to a high-dimensional model (HD) with multiple DOFs. Instead of pursuing the time simulation of the HD model with strong nonlinearities, this paper focuses on its linear stability analysis, which provides useful information regarding the growth rate of torsional vibrations into stick-slip oscillations by the examination of unstable poles. The linear stability analysis thus has the potential application in the optimization of PDC bit designs in terms of postponing the occurrence of torsional stick-slips due to its high computational efficiency.

Numerical Stability Analysis

The PDC bit-rock interaction model is adopted from [1], while the HD drillstring model is the same as that in [3]. A combination of both leads to a system of nonlinear coupled PDE-ODEs governing the dynamics of the HD model. The reader is referred to the references [1, 3] for a full description of the derivation. Linearization of this nonlinear system is carried out around the equilibrium point by imposing small perturbations to the steady-state variables. The system of linear coupled PDE-ODEs that governs the perturbation of bit trajectory $\tilde{h}\,(\theta,\,\tau)$ function and state variables reads

$$\frac{\partial \tilde{h}}{\partial \tau} + \omega_0 \frac{\partial \tilde{h}}{\partial \theta} + \dot{\varphi}_b \frac{v_0}{\omega_0} = 0, \tag{1}$$

$$\hat{\boldsymbol{I}}\ddot{\boldsymbol{u}} + \hat{\boldsymbol{C}}_{\boldsymbol{a}}\dot{\boldsymbol{u}} + \hat{\boldsymbol{K}}_{\boldsymbol{a}}\boldsymbol{u} = \hat{\boldsymbol{W}}, \tag{2}$$

$$\hat{\boldsymbol{I}}\ddot{\boldsymbol{\varphi}} + \hat{\boldsymbol{C}}_{\boldsymbol{t}}\dot{\boldsymbol{\varphi}} + \hat{\boldsymbol{K}}_{\boldsymbol{t}}\boldsymbol{\varphi} = \hat{\boldsymbol{T}}, \tag{3}$$

where $v_0\,(\omega_0)$ is the non-dimensional nominal axial (torsional) velocity; $\dot{\varphi}_b$ is the perturbed bit angular velocity; $\hat{\boldsymbol{I}}$ is the unit diagonal matrix; $\hat{\boldsymbol{C}}_{\boldsymbol{a}}\left(\hat{\boldsymbol{C}}_{\boldsymbol{t}}\right)$ and $\hat{\boldsymbol{K}}_{\boldsymbol{a}}\left(\hat{\boldsymbol{K}}_{\boldsymbol{t}}\right)$ are the dimensionless damping and stiffness matrices for axial (torsional) motion; $\boldsymbol{u}$, $\boldsymbol{\varphi}$, $\hat{\boldsymbol{W}}$, $\hat{\boldsymbol{T}}$ represent, respectively, the vectors of dimensionless axial and angular displacement, external axial force and torque. The perturbed bit trajectory function $\tilde{h}\,(\theta,\tau)$ can be approximated by

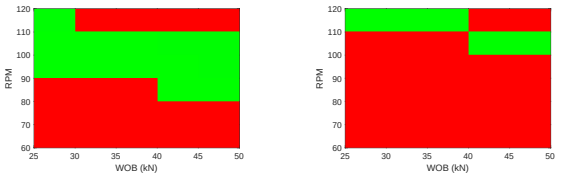

(a) (b)

Figure 1: Stability map in the space of the operating parameters (weight-on-bit and rotary speed) for two PDC bit designs: (a) bit A and (b) bit B. The red color denotes the region of operating parameters with large real parts, while the green color represents the region with smaller real parts.

$$\tilde{h}\left(\theta,\tau\right)=\tilde{a}_0\left(1-\frac{\theta}{2\pi}\right)+\tilde{a}_1\frac{\theta}{2\pi}+\sum_{k=1}^{N-1}\tilde{a}_{k+1}\sin\left(\frac{k\theta}{2}\right),\quad\theta\in\left[0,2\pi\right), \tag{4}$$

Substituting the approximation (4) into the linearized PDE (1) and invoking the Galerkin method to minimize the resulting residual $\tilde{\mathcal{R}}$ yields a system of first-order ODEs that governs the evolution of the perturbed coefficients

$$\int_0^{2\pi}\tilde{\mathcal{R}}\frac{\theta}{2\pi}d\theta=0,\ \int_0^{2\pi}\tilde{\mathcal{R}}\sin\left(\frac{m\theta}{2}\right)d\theta=0,\ m=1,...,N-1. \tag{5}$$

This systems of ODEs together with the system of ODEs in (2)-(3) can be written in the matrix-vector form as

$$\boldsymbol{A}\dot{\tilde{\boldsymbol{X}}}+\boldsymbol{B}\tilde{\boldsymbol{X}}=\boldsymbol{0} \tag{6}$$

where $\boldsymbol{A}$ and $\boldsymbol{B}$ are coefficient matrices and $\tilde{\boldsymbol{X}}$comprises the perturbed state variables and coefficients $\tilde{a}_i,\ i=1,2,...,N$. The linear stability analysis of the system of coupled PDE-ODEs (1)-(3) has thus been replaced by the equivalent stability analysis of the linear system of ODEs (6). If the system is stable, the perturbed vector $\tilde{\boldsymbol{X}}$ converges to the null vector; otherwise, $\tilde{\boldsymbol{X}}$ grows exponentially. The instability of the linear system of ODEs (6) is indicated by positive real part of the eigenvalues of the matrix $\boldsymbol{A}^{-1}\boldsymbol{B}$.

Numerical results

Surface rotary speed (RPM) and weight-on-bit (WOB) are two operating parameters that are commonly adjusted to alleviate drillstring vibrations. Preliminary linear stability analyses have shown that the drillstring system is unstable within the practical ranges of the operating parameters (weight-on-bit and rotary speed). This indicates that the torsional vibrations will always degenerate into stick-slips given enough time.

Extensive simulation results have shown that the most unstable pole with the maximum real part of the system (6) corresponds to the axial dynamics of the drillstring. The magnitude of the real part of the most unstable pole determines the rate at which the axial dynamics evolves eventually to the axial stick-slips. Therefore, the values of the operating parameters that lead to smaller real parts of the most unstable poles will delay the occurrence of axial stick-slips. Figure 1 presents the distributions of maximum real parts of the eigenvalues for different combinations of operating parameters for two PDC bit designs. It is observed that different PDC bit designs have different optimum pairs of the operating parameters.

Furthermore, the unstable axial dynamics influences the torsional dynamics via the coupling caused by the bit-rock interaction. It is observed from the time simulation results that the axial stick-slips always precede torsional stick-slips. Therefore, the occurrence of torsional stick-slips can be possibly delayed by selecting PDC bit designs for which the most unstable pole has the smallest real part for prescribed values of the operating parameters.

Conclusions

This paper presents an algorithm for the stability analysis of a high-dimensional drillstring model in conjunction with PDC bit-rock interaction. It is shown that PDC bit designs affect the stability of the drillstring. By recognizing that the most unstable pole corresponds to the axial dynamics and that the axial stick-slips always precede torsional stick-slips, it is possible to delay the occurrence of torsional stick-slips by optimizing PDC bit design that leads to the smallest real part of the most unstable pole. The validity of this approach is currently being verified by time domain simulations.

References

[1] Tian K., Detournay E., Zhang H. (2022) An Alternative Formulation for Modeling Self-Excited Vibrations of Drillstring with PDC Bits. *Journal of Computational and Nonlinear Dynamics* (in press).

[2] Zhang H., Detournay E. (2020) An alternative formulation for modeling self-excited oscillations of rotary drilling systems. *Journal of Sound and Vibration* **474**: 115241.

[3] Zhang H., Detournay E. (2022) A High-Dimensional Model to Study the Self-Excited Oscillations of Rotary Drilling Systems. *submitted to Communications in Nonlinear Science and Numerical Simulation*.

Two-stroke single-cylinder engine with elastic hinges with preset force characteristics

A.N. Zotov, A.S. Sviridov, A.P. Tokarev
Ufa State Petroleum Technological University, Kosmonavtov Street 1, Ufa, 450062, Russian Federation

Abstract. The work is devoted to balancing a two-stroke single-cylinder engine by installing two elastic hinges with a given characteristic (the dependence of the restoring moment on the angle of rotation) between the strut and the crank and between the crank and the connecting rod. The hinge is an elastic element (spring or pneumatic spring) that moves between the guides of the calculated shape. The characteristic of the elastic hinge between the crank and the connecting rod is such that the lateral force acting on the piston decreases many times during engine operation. With certain parameters of the engine under consideration with a hinge between the crank and the connecting rod, the lateral force acting on the piston is zero at any angle of rotation of the crank. The characteristic of the elastic hinge between the strut and the crank is such that the angular velocity of the crank will be constant. In this case, you can either completely abandon the flywheel in the engine design or significantly reduce its weight. Flywheel inertia can now account for up to 80 percent of all moving parts in an engine. Such parameters of the proposed two-stroke single-cylinder engine are selected, at which it becomes fully balanced. At the moment, the considered problem has been solved for a certain constant angular velocity of the crank. For a different angular velocity, a different characteristic of the elastic hinge will be required. A possible solution to this problem can be the use of a pneumatic spring as an elastic element of the proposed hinges. By changing the pressure in the pneumatic spring in an appropriate way with a change in the angular velocity of the crank, it is possible to achieve the proper coefficient of uneven operation of the considered two-stroke engine. The approach proposed here for balancing a two-stroke single-cylinder engine can also be applied to balancing four-stroke engines.

The problem of balancing internal combustion engines (ICE) based on a crank mechanism (CM) has been the subject of many works, for example [1-4]. This work is devoted to a two-stroke single-cylinder engine (TSSCE) with two elastic hinges with preset force characteristics [5] located between the crank and connecting rod at point A (with characteristic $M_{12}(\varphi)$) and between the crank and connecting rod at point 0 with characteristic $M_1(\varphi)$ (Fig. 1, *(a)*). The dependence $M_{Cr.}(\varphi)$ on the TSSCE crank shaft was taken from [6] and was approximated by the analytical function (1), where φ is in degrees.

$$\begin{aligned} M_{Cr.}(\varphi) = {} & -2{,}693510959090909 \cdot 10^7 + 1009131{,}066530486 \cdot (\varphi \cdot \pi/180) - \\ & -16831{,}236170949003 \cdot (\varphi \cdot \pi/180)^2 + 164{,}56930773216035 \cdot (\varphi \cdot \pi/180)^3 - \\ & -1{,}0445902415421795 \cdot (\varphi \cdot \pi/180)^4 + 0{,}004497285554988163 \cdot (\varphi \cdot \pi/180)^5 - \\ & -0{,}000013297457442994316 \cdot (\varphi \cdot \pi/180)^6 + 2{,}665200570792428 \cdot 10^{-8} \cdot (\varphi \cdot \pi/180)^7 - \\ & -3{,}463864860887725 \cdot 10^{-11} \cdot (\varphi \cdot \pi/180)^8 + 2{,}636647972125913 \times 10^{-14} \cdot (\varphi \cdot \pi/180)^9 - \\ & -8.947485203612654 \cdot 10^{-18} \cdot (\varphi \cdot \pi/180)^{10} + (2{,}693510959090909 \cdot 10^7 - \\ & -1008993{,}066791191 \cdot (\varphi \cdot \pi/180) + 16823{,}278538256654 \cdot (\varphi \cdot \pi/180)^2 - \\ & 164{,}3809582389641 \cdot (\varphi \cdot \pi/180)^3 + 1{,}0422601817406472 \cdot (\varphi \cdot \pi/180)^4 - \\ & -0{,}0044809411801945455 \cdot (\varphi \cdot \pi/180)^5 + 0{,}00001323216876702 2518 \cdot (\varphi \cdot \pi/180)^6 - \\ & -2{,}651459239985029 \cdot 10^{-8} \cdot (\varphi \cdot \pi/180)^7 + 3{,}452203947414538 \cdot 10^{-11} \cdot (\varphi \cdot \pi/180)^8 - \\ & -2{,}636647972125913 \cdot 10^{-14} \cdot (\varphi \cdot \pi/180)^9 + 8{,}947485203612654 \cdot 10^{-18} \cdot (\varphi \cdot \pi/180)^{10}) \cdot \mathrm{Sign}[180 - \varphi]. \end{aligned} \quad (1)$$

In this formulation of the problem, a CM with a counterweight on the connecting rod is considered. We consider that the weight of the counterweight is P_4, and its length is ℓ_0. Rod weight AC_4 was not taken into account (Fig. 1).

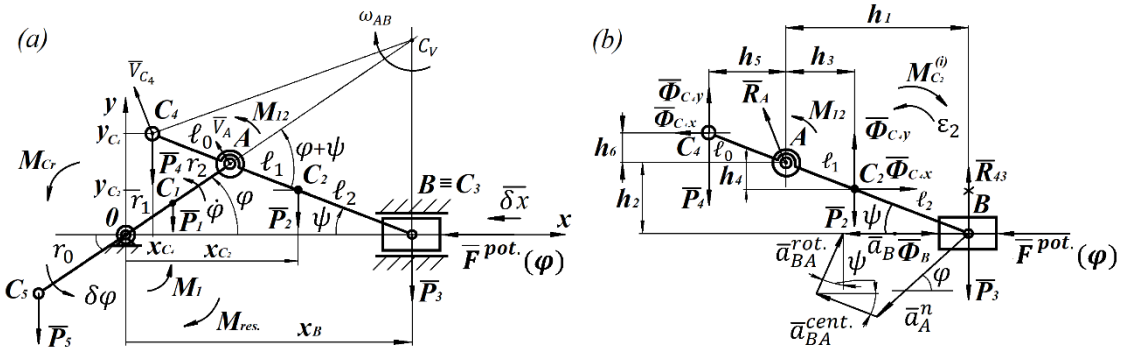

Fig. 1.

To determine the dependence $M_{12}(\varphi)$ in steady state, taking into account the operating resistance $M_{res.}$, the horizontal force $F^{pot.}$ acting on the piston from condition (2) was determined.

$$F^{pot.}(\varphi)dx = M_{Cr.}^{pot.}(\varphi)d\varphi, \tag{2}$$

where $M_{Cr.}^{pot.}(\varphi) = M_{Cr.}(\varphi) - \int_0^{2\pi} M_{Cr.}(\varphi)d\varphi/2\pi$ - potential component of the moment on the shaft of the ICE ($\int_0^{2\pi} M_{Cr.}^{pot.}(\varphi)d\varphi = 0$) in the steady state of the engine, taking into account the resistance (Fig. 1, *(a)*).

It is assumed that dependence (1) and, consequently, dependence (2) can be determined for any TSSCE. Figure 2 shows the dependencies $M_{Cr.}(\varphi)$ (dependence 1 according to formula (1)) and $M_{Cr}^{pot.}(\varphi)$ (dependence 2) at one turn of the crank.

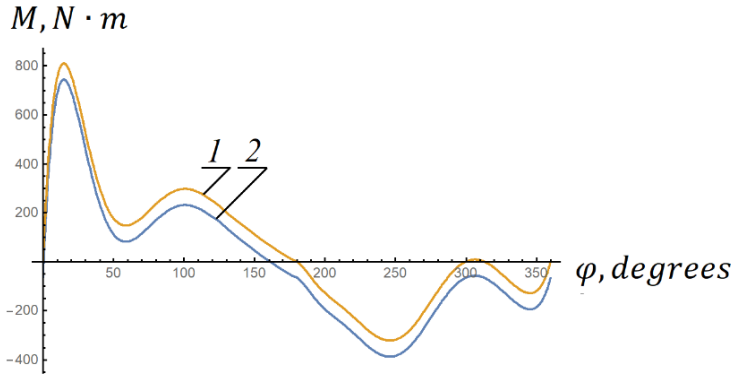

1 - $M_{Cr.}(\varphi)$; 2 - $M_{Cr}^{pot.}(\varphi)$.

Fig. 2.

Omitting calculations for dependence (2), we write an expression for $F^{pot.}(\varphi)$ ($\oint F^{pot.}dx = 0$).

$$F^{pot.} = M_{Cr.}^{pot.}/((r_1 + r_2) \cdot \sin\varphi \cdot \left(1 + \lambda\frac{\cos\varphi}{\sqrt{1-\lambda^2 \cdot sin^2\varphi}}\right)), \tag{3}$$

where r_1 – distance from point 0 to the center of mass of the crank; $(r_1 + r_2)$ – crank length; $\lambda = \frac{(r_1+r_2)}{(\ell_1+\ell_2)}$; ℓ_1 – distance from point A to the center of gravity of the connecting rod AB; $(\ell_1 + \ell_2)$ – crank length AB.

To determine the dependence $M_{12}(\varphi)$ (4), in which the lateral force R_{43} acting on the piston is equal to 0 at any angle of rotation of the crank (Fig. 1, *(b)*), the sum of the moments of active forces (P_2, P_3, P_4, $F^{pot.}$), inertia forces ($P_3 \cdot \ddot{x}_B/g$, $P_2 \cdot \ddot{x}_{C2}/g$, $P_2 \cdot \ddot{y}_{C2}/g$, $P_4 \cdot \ddot{x}_{C4}/g$, $P_4 \cdot \ddot{y}_{C4}/g$), torque inertia of the connecting rod ($I_{C2}^{(2)} \cdot \varepsilon_2$) relative to point A. It was assumed that the angular velocity of the crank φ is constant. The direction of rotation of the crank is counterclockwise (Fig. 1, *(a)*).

$$M_{12} = -P_4 \cdot h_5 + P_3 \cdot h_1 + P_2 \cdot h_3 + I_{C2}^{(2)} \cdot \varepsilon_2 + \frac{P_3}{g} \cdot \ddot{x}_B \cdot h_2 + F^{pot.} \cdot h_2 +$$

$$+ \frac{P_2}{g} \cdot \ddot{x}_{C2} \cdot h_4 + \frac{P_2}{g} \cdot \ddot{y}_{C2} \cdot h_3 - \frac{P_4}{g} \cdot \ddot{x}_{C4} \cdot h_6 - \frac{P_4}{g} \cdot \ddot{y}_{C4} \cdot h_5, \quad (4)$$

where $h_1 = (\ell_1 + \ell_2) \cdot (1 - 0{,}25\lambda^2 + 0{,}25\lambda^2 \cdot \cos 2\varphi)$; $h_2 = (\ell_1 + \ell_2) \cdot \lambda \cdot \sin\varphi$; $h_6 = \ell_0 \cdot \lambda \cdot \sin\varphi$;

$h_3 = \ell_1 \cdot (1 - 0{,}25\lambda^2 + 0{,}25\lambda^2 \cdot \cos 2\varphi)$; $h_4 = \ell_1 \cdot \lambda \cdot \sin\varphi$ $h_5 = \ell_0 \cdot (1 - 0{,}25\lambda^2 + 0{,}25\lambda^2 \cdot \cos 2\varphi)$;

$\varepsilon_2 = \lambda \cdot \dot{\varphi}^2 \cdot \sin\varphi \cdot (1 - (\lambda \cdot \cos\varphi / (1 - 0{,}25\lambda^2 + 0{,}25\lambda^2 \cdot \cos 2\varphi))^2) / (1 - 0{,}25\lambda^2 + 0{,}25\lambda^2 \cdot \cos 2\varphi)$;

$\ddot{x}_B = -(r_1 + r_2) \cdot \dot{\varphi}^2 \cdot (\cos\varphi + \lambda \cdot \cos 2\varphi)$; $\ddot{x}_{C_2} = -(r_1 + r_2) \cdot \cos\varphi \cdot \dot{\varphi}^2 - \ell_1 \cdot \lambda^2 \cdot \cos 2\varphi \cdot \dot{\varphi}^2$;

$\ddot{y}_{C_2} = -\ell_2 \cdot \lambda \cdot \dot{\varphi}^2 \cdot \sin\varphi$; $\ddot{x}_{C_4} = -(r_1 + r_2) \cdot \cos\varphi \cdot \dot{\varphi}^2 + \ell_0 \cdot \lambda^2 \cdot \cos 2\varphi \cdot \dot{\varphi}^2$;

$\ddot{y}_{C_4} = -(r_1 + r_2 + \ell_0 \cdot \lambda) \cdot \sin\varphi \cdot \dot{\varphi}^2$.

In the absence of an elastic hinge at point *A*, the lateral force R_{430} will be determined by the dependence (5).

$$R_{430} = M_{12} / ((\ell_1 + \ell_2) \cdot (1 - 0{,}25 \cdot \lambda^2 + 0{,}25 \cdot \lambda^2 \cdot \cos 2\varphi)) \quad (5)$$

Dependence (4) turned out to be such that $\int_0^{2\pi} M_{12}(\varphi) d\varphi \neq 0$. It should be noted that $\int_0^{2\pi} M_{12}(\varphi) d\varphi$ does not depend on the angular velocity of the crank. To obtain such dependence $M_{12}^{pot.}(\varphi)$ that $\int_0^{2\pi} M_{12}^{pot.} d\varphi = 0$, dependence (6) can be used.

$$M_{12}^{pot.} = M_{12} - \int_0^{2\pi} M_{12} d\varphi \,/ 2\pi \quad (6)$$

When the elastic hinge is located with characteristic (6), the lateral force acting on the piston $R_{43}(\varphi)$ (Fig. 1, *(b)*), is determined by the following expression.

$$R_{43} = \int_0^{2\pi} M_{12} d\varphi \,/ (2\pi \cdot (\ell_1 + \ell_2) \cdot (1 - 0{,}25 \cdot \lambda^2 + 0{,}25 \cdot \lambda^2 \cdot \cos 2\varphi)) \quad (7)$$

Fig. 3 shows the dependencies $M_{12}(\varphi)$, $M_{12}^{pot.}$, $R_{430}(\varphi)$, $R_{43}(\varphi)$ obtained by dependences (4), (5), (6), (7), respectively. Options *(a)* and *(c)* were obtained with $P_4 = 0$ and $\ell_0 = 0$. Variants *(b)* and *(d)* were obtained with such values of P_4 and ℓ_0 ($P_4 = 20$ N, $\ell_0 = 0.4\ m$) that the center of mass of the system "counterweight at point C_4-rod-piston" is at point A.

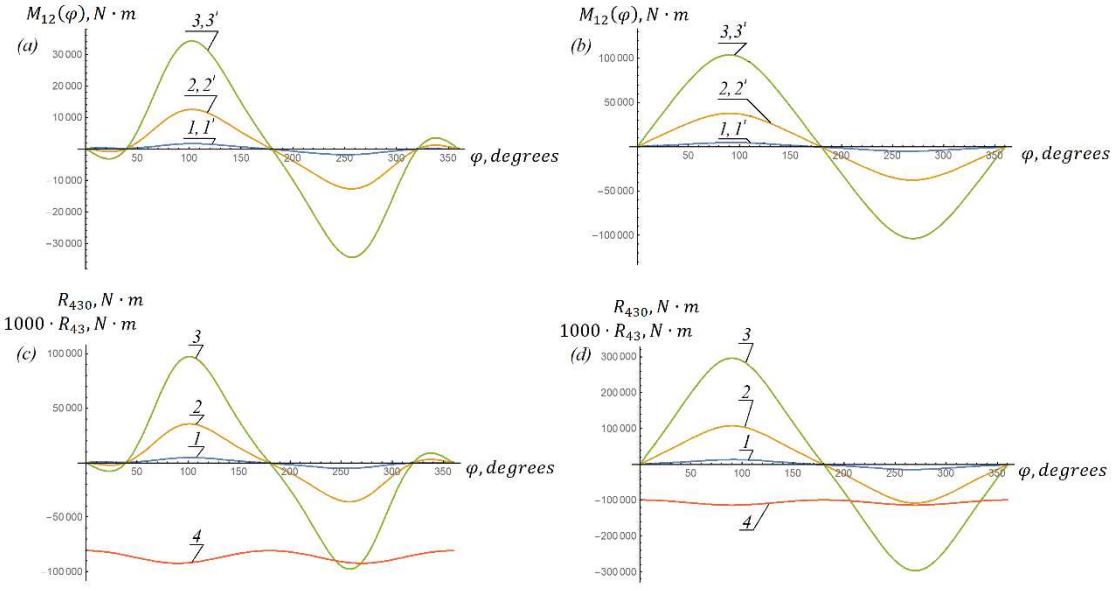

$r_1 = 0{,}1\ m$; $r_2 = 0{,}1\ m$; $\ell_1 = 0{,}2\ m$; $\ell_2 = 0{,}2\ m$; $P_2 = 10\ N$; $P_3 = 15\ N$;

1 - $\dot{\varphi} = 100\ s^{-1}$; 2 - $\dot{\varphi} = 300\ s^{-1}$; 3 - $\dot{\varphi} = 500\ s^{-1}$; 4 – dependence $R_{430}(\varphi)$ according to (5).

Fig. 3.

As can be seen from Figure 3, the dependences $M_{12}(\varphi)$ (without a prime) and $M_{12}^{pot.}$ (with a prime) practically coincide. Installing an elastic hinge with a given characteristic between the crank and the connecting rod reduces the lateral force acting on the piston $R_{43}(\varphi)$ hundreds of times. It should be noted that the reaction R_43 (φ) is practically independent of the angular velocity of the crank for these parameters. It was possible to select such parameters of the system under consideration, in which the lateral force $R_{43}(\varphi)$ is equal to zero at any angle of rotation of the crank. Figure 4 shows such dependencies. Option *(a)* obtained with $P_4 = \ell_0 = 0$. Option *(b)* with $P_4 = 10\ N$ и $\ell_0 = 0.1$ m. For the case when the center of mass of the system "counterweight at point C_4-rod-slider" is at point A, select such parameters for which $R_{43}(\varphi) = 0$ at any angle φ, failed.

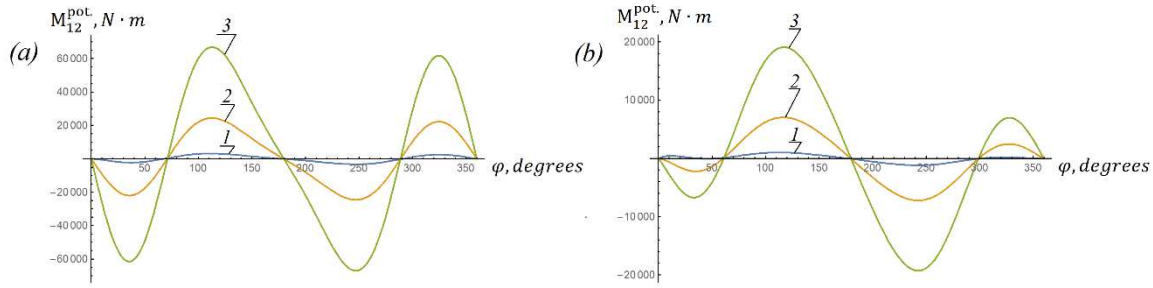

$r_1 = 0{,}1\ m$; $r_2 = 0{,}1\ m$; 1 - $\dot{\varphi} = 100\ s^{-1}$; 2 - $\dot{\varphi} = 300\ s^{-1}$; 3 - $\dot{\varphi} = 500\ s^{-1}$;

a) $\ell_1 = 0{,}2\ m$; $\ell_2 = 0{,}2\ m$; $P_2 \approx 54{,}40\ N$; $P_3 = 79\ N$;
b) $\ell_1 = 0{,}4\ m$; $\ell_2 = 0{,}4\ m$; $P_2 = 10\ N$; $P_3 \approx 18{,}16\ N$.

Fig. 4.

The case was considered when the angular velocity of the crank is constant. To determine the characteristics of the elastic hinge at point 0 ($M_1(\varphi)$, Fig. 1, *(a)*) the Lagrange equation of the second kind was compiled.

$$\frac{d}{dt}\left(\frac{\partial T}{\partial \dot{\varphi}}\right) - \frac{\partial T}{\partial \varphi} = Q_{\delta\varphi}, \tag{8}$$

where $T = \frac{1}{2} I_{giv.} \cdot \dot{\varphi}^2$ – kinetic energy of the mechanism in Fig. 1, *(a)*);

$$I_{giv.} = I_0^{(1)} + \frac{P_2}{g} \cdot (r_1 + r_2)^2 \cdot [(\sin\varphi - \frac{\ell_1 \cdot \lambda}{2(\ell_1 + \ell_2)} \cdot \sin 2\varphi)^2 + \frac{\ell_2^2 \cdot \cos^2\varphi}{(\ell_1 + \ell_2)^2}] + I_{C2}^{(2)} \cdot \frac{\lambda^2 \cdot \cos^2\varphi}{(1 - \frac{1}{4}\lambda^2 + \frac{1}{4}\lambda^2 \cos 2\varphi)^2} +$$

$$+ \frac{P_3}{g} \cdot (r_1 + r_2)^2 \cdot (\sin\varphi + \frac{1}{2}\lambda \cdot \sin 2\varphi)^2 + \frac{P_4}{g} \cdot \frac{\lambda^2 \cdot \cos^2\varphi}{(1 - \frac{1}{4}\lambda^2 + \frac{1}{4}\lambda^2 \cos 2\varphi)^2} \cdot ((\ell_0 + \ell_1 + \ell_2)^2 +$$

$$+ 2(\ell_0 + \ell_1 + \ell_2) \cdot ((r_1 + r_2) \cdot cos\varphi + (\ell_1 + \ell_2) \cdot (1 - \tfrac{1}{4}\lambda^2 + \tfrac{1}{4}\lambda^2 cos 2\varphi)) \cdot tg\varphi \cdot \lambda \cdot \sin\varphi) + \tfrac{P_5}{g} \cdot r_0^2;$$

$I_{giv.}$ – reduced moment of inertia of the mechanism in Fig. 1, *(a)*);

$$\frac{\partial T}{\partial \varphi} = \left(\frac{1}{2}\dot{\varphi}^2\right) \cdot [-\frac{2I_{C2}^{(2)} \cdot \lambda^2 \cdot \cos\varphi \cdot \sin\varphi}{(1 - 0{,}25\lambda^2 + 0{,}25\lambda^2 \cdot \cos 2\varphi)^2} + \frac{\left(I_{C2}^{(2)} \cdot \lambda^4 \cdot \cos\varphi^2 \cdot \sin 2\varphi\right)}{(1 - 0{,}25\lambda^2 + 0{,}25\lambda^2 \cdot \cos 2\varphi)^3} +$$

$$+ \frac{(2P_3 \cdot (r_1 + r_2)^2 \cdot \cos\varphi + \lambda \cdot \cos 2\varphi) \cdot (\sin\varphi + 0{,}5\lambda \cdot \sin 2\varphi)}{g} -$$

$$- \frac{1}{g} \cdot P_2 \cdot (r_1 + r_2)^2 \cdot (((2I_{C2}^{(2)} \cdot \cos\varphi \cdot \sin\varphi)/(\ell_1 + \ell_2)^2) + 2(\cos\varphi - \frac{\lambda \cdot \ell_1 \cdot \cos 2\varphi}{(\ell_1 + \ell_2)}) \times$$

$$\times (sin\varphi - \frac{\lambda \cdot \ell_1 \cdot \sin 2\varphi}{2(\ell_1 + \ell_2)})) - (2\lambda^2 \cdot P_4 \cdot \cos\varphi \cdot \sin\varphi \cdot ((\ell_0 + \ell_1 + \ell_2)^2 + 2\,\lambda \cdot (\ell_0 + \ell_1 + \ell_2) \cdot ((r_1 + r_2) \times$$

$$\times \cos\varphi + (\ell_1 + \ell_2) \cdot (1 - 0{,}25\lambda^2 + 0{,}25\lambda^2 \cdot \cos 2\varphi)) \cdot \sin\varphi \cdot tg\varphi))/(g \times$$

$$\times \cdot (1 - 0{,}25\lambda^2 + 0{,}25\lambda^2 \cdot \cos 2\varphi)^2) + (\lambda^4 \cdot P_4 \cdot (\cos\varphi)^2 \cdot \sin 2\varphi \cdot ((\ell_0 + \ell_1 + \ell_2)^2 + 2\lambda \cdot (\ell_0 + \ell_1 + \ell_2) \times$$

$$\times ((r_1 + r_2) \cdot \cos\varphi + (\ell_1 + \ell_2) \cdot (1 - 0{,}25\lambda^2 + 0{,}25\lambda^2 \cdot \cos 2\varphi)) \cdot \sin\varphi \cdot tg\varphi))/(g \times$$

$$\times (1 - 0{,}25\lambda^2 + 0{,}25\lambda^2 \cdot \cos 2\varphi)^3) + (\lambda^2 \cdot P_4 \cdot (\cos\varphi)^2 \cdot (2\lambda \cdot (\ell_0 + \ell_1 + \ell_2) \cdot ((r_1 + r_2) \cdot \cos\varphi +$$

$$+(\ell_1 + \ell_2) \cdot (1 - 0{,}25\lambda^2 + 0{,}25\lambda^2 \cdot \cos 2\varphi)) \cdot \sin\varphi + 2\lambda \cdot (\ell_0 + \ell_1 + \ell_2) \cdot ((r_1 + r_2) \cdot \cos\varphi +$$

$$+(\ell_1 + \ell_2) \cdot (1 - 0{,}25\lambda^2 + 0{,}25\lambda^2 \cdot \cos 2\varphi)) \cdot \sec\varphi \cdot tg\varphi + 2\lambda \cdot (\ell_0 + \ell_1 + \ell_2) \cdot \sin\varphi \cdot (-(r_1 + r_2) \times$$

$$\times \sin\varphi - 0{,}5\lambda^2 \cdot (\ell_1 + \ell_2) \cdot \sin 2\varphi) \cdot tg\varphi))/(g \cdot (1 - 0{,}25\lambda^2 + 0{,}25\lambda^2 \cdot \cos 2\varphi)^2)];$$

$$\frac{d}{dt}\left(\frac{\partial T}{\partial \dot{\varphi}}\right) = \dot{I}_{giv.} \cdot \dot{\varphi} + I_{giv.} \cdot \ddot{\varphi};$$

$$\dot{I}_{giv.} = -(\frac{2\mathrm{I}_{C2}^{(2)} \cdot \lambda^2 \cdot \cos\varphi \cdot \sin\varphi \cdot \dot{\varphi}}{1 - 0{,}25(\lambda^4 + 0{,}25(\lambda^2 \cdot \cos 2\varphi)^2} + \frac{(\mathrm{I}_{C2}^{(2)} \cdot \lambda^4 \cdot (\cos\varphi)^2 \cdot \sin 2\varphi \cdot \dot{\varphi})}{(1 - 0{,}25\lambda^2 + 0{,}25\lambda^2 \cdot \cos 2\varphi)^3} -$$

$$-(2\lambda^2 \cdot P_4 \cdot \cos\varphi \cdot \sin\varphi \cdot ((\ell_0 + \ell_1 + \ell_2)^2 + 2\lambda \cdot (\ell_0 + \ell_1 + \ell_2) \cdot ((r_1 + r_2) \cdot \cos\varphi +$$

$$+(\ell_1 + \ell_2) \cdot (1 - 0{,}25\lambda^2 + 0{,}25\lambda^2 \cdot \cos 2\varphi)) \cdot \sin\varphi \cdot tg\varphi) \cdot \frac{\dot{\varphi}}{g \cdot (1 - 0{,}25\lambda^2 + 0{,}25\lambda^2 \cdot \cos 2\varphi)^2} +$$

$$+(\lambda^4 \cdot P_4 \cdot (\cos\varphi)^2 \cdot \sin 2\varphi \cdot ((\ell_0 + \ell_1 + \ell_2)^2 + 2\lambda \cdot (\ell_0 + \ell_1 + \ell_2) \cdot ((r_1 + r_2) \cdot \cos\varphi +$$

$$+(\ell_1 + \ell_2) \cdot (1 - 0{,}25\lambda^2 + 0{,}25\lambda^2 \cdot \cos 2\varphi)) \cdot \sin\varphi \cdot tg\varphi) \cdot \varphi)/((1 - 0{,}25\lambda^2 + \dot{0}{,}25\lambda^2 \cdot \cos 2\varphi)^3) +$$

$$+(1/g) \cdot 2P_3 \cdot (r_1 + r_2)^2 \cdot (\sin\varphi + 0{,}5\lambda \cdot \sin 2\varphi) \cdot (\cos\varphi \cdot \dot{\varphi} + \lambda \cdot \cos\varphi \cdot \dot{\varphi}) + (1/g) \cdot P_2 \cdot (r_1 + r_2)^2 \times$$

$$\times (-\left(\frac{2\ell_2^2 \cdot \cos\varphi \cdot \sin\varphi \cdot \dot{\varphi}}{(\ell_1 + \ell_2)^2}\right) + 2(\sin\varphi - \frac{\lambda \cdot \ell_1 \cdot \sin\varphi}{2(\ell_1 + \ell_2)}) \cdot (\cos\varphi \cdot \dot{\varphi} - (\lambda \cdot \ell_1 \cdot \cos\varphi \cdot \dot{\varphi})/(\ell_1 + \ell_2))) +$$

$$+(\lambda^2 \cdot P_4 \cdot (\cos\varphi)^2 \cdot (2\lambda \cdot (\ell_0 + \ell_1 + \ell_2) \cdot \left((r_1 + r_2) \cdot \cos\varphi + (\ell_1 + \ell_2) \cdot \lambda^2 + 0{,}25\lambda^2 \cdot \cos 2\varphi\right)) \cdot \sin\varphi \cdot \dot{\varphi} +$$

$$+2\lambda \cdot (\ell_0 + \ell_1 + \ell_2) \cdot ((r_1 + r_2) \cdot \cos\varphi + (\ell_1 + \ell_2) \cdot (1 - 0{,}25\lambda^2 + 0{,}25\lambda^2 \cdot \cos 2\varphi)) \cdot \sec\varphi \cdot tg\varphi \cdot \dot{\varphi} +$$

$$+2\lambda \cdot (\ell_0 + \ell_1 + \ell_2) \cdot \sin\varphi \cdot tg\varphi \cdot (-(r_1 + r_2) \cdot \sin\varphi \cdot \dot{\varphi} - 0{,}5\lambda^2 \cdot (\ell_1 + \ell_2) \cdot \sin\varphi \cdot \dot{\varphi})))/(g \cdot (1 -$$

$$-0{,}25\lambda^2 + 0{,}25\lambda^2 \cdot \cos 2\varphi)^2)$$

$$Q_{\delta\varphi} = F^{pot.} \cdot \left((r_1 + r_2) \cdot sin\varphi + \frac{(r_1+r_2)^2 \cdot sin2\varphi}{2 \cdot (\ell_1+\ell_2)}\right) + M_1 - P_1 \cdot r_1 \cdot Cos\varphi + P_5 \cdot r_0 \cdot \mathrm{Cos}\,\varphi - \frac{P_2\delta y_{C_2} + P_4\delta y_{C_4} + M_{12}\delta(\varphi+\psi)}{\delta\varphi};$$

P_1, P_2, P_4, P_5 – the weights respectively of the crank, connecting rod, counterweight at point C_4 and counterweight at point C_5;

r_1 is the coordinate that determines the position of the center of mass of the crank;

r_0 is the coordinate that determines the position of the counterweight at point C_5;

y_{C_2}, y_{C_4} – ordinates of points C_2 and C_4 respectively (Fig. 1); $\delta y_{C2} = \ell_2 \cdot \lambda \cdot cos\varphi\delta\varphi$;

$\delta y_{C4} = (r_1 + r_2) \cdot cos\varphi\delta\varphi + \ell_0 \cdot (r_1 + r_2)/(\ell_1 + \ell_2) \cdot cos\varphi\delta\varphi$;

$\delta\psi = (r_1 + r_2) \cdot cos\,\varphi\,\delta\varphi/(\ell_1 + \ell_2) \cdot (1 - 0{,}25 \cdot (\frac{r_1+r_2}{\ell_1+\ell_2})^2 + 0{,}25 \cdot (\frac{r_1+r_2}{\ell_1+\ell_2})^2 \cdot cos2\varphi)$;

$$Q_{\delta\varphi} = F^{pot.} \cdot \left((r_1 + r_2) \cdot sin\varphi + \frac{(r_1 + r_2)^2 \cdot sin2\varphi}{2 \cdot (\ell_1 + \ell_2)}\right) - P_1 \cdot r_1 \cdot cos\varphi +$$

$$+P_5 \cdot r_0 \cdot cos\,\varphi + M_1 - P_2 \cdot \ell_2 \cdot \frac{r_1 + r_2}{\ell_1 + \ell_2} \cdot cos\varphi - P_4 \cdot ((r_1 + r_2) \cdot cos\varphi +$$

$$+\ell_0 \cdot \frac{r_1 + r_2}{\ell_1 + \ell_2} \cdot cos\varphi) - M_{12} -$$

$$-M_{12}\cdot\frac{(r_1+r_2)\cdot cos\,\varphi}{(\ell_1+\ell_2)\cdot(1-0{,}25\cdot(\frac{r_1+r_2}{\ell_1+\ell_2})^2+0{,}25\cdot\left(\frac{r_1+r_2}{\ell_1+\ell_2}\right)^2\cdot cos2\varphi)};$$

Let us rewrite equation (8) in the following form.

$$\dot{I}_{giv.}\cdot\dot{\varphi}+I_{giv.}\cdot\ddot{\varphi}-\frac{1}{2}\dot{\varphi}^2\cdot\frac{\partial I_{giv.}}{\partial\varphi}=Q_{\delta\varphi}. \tag{9}$$

From equation (9) we obtain the dependence of the moment on the crank on its angle of rotation ($\ddot{\varphi}=0$).

$$M_1=\dot{I}_{giv.}\cdot\dot{\varphi}-\frac{1}{2}\dot{\varphi}^2\cdot\frac{\partial I_{giv.}}{\partial\varphi}-F^{pot.}\cdot\left((r_1+r_2)\cdot sin\varphi+\frac{(r_1+r_2)^2\cdot sin2\varphi}{2\cdot(\ell_1+\ell_2)}\right)+$$

$$+P_1\cdot r_1\cdot cos\varphi-P_5\cdot r_0\cdot cos\,\varphi+P_2\cdot\ell_2\cdot\frac{r_1+r_2}{\ell_1+\ell_2}\cdot cos\varphi+P_4\cdot((r_1+r_2)\cdot cos\varphi- \tag{10}$$

$$-\ell_0\cdot\frac{r_1+r_2}{\ell_1+\ell_2}\cdot cos\varphi)+M_{12}+$$

$$+M_{12}\cdot(r_1+r_2)\cdot cos\,\varphi/(\ell_1+\ell_2)\cdot(1-0{,}25\cdot(\frac{r_1+r_2}{\ell_1+\ell_2})^2+0{,}25\cdot\left(\frac{r_1+r_2}{\ell_1+\ell_2}\right)^2\cdot cos\ 2\varphi).$$

Variants were considered in which $M_{12}=M_{12}^{pot.}$, that is, in the presence of an elastic hinge with the characteristic $M_{12}^{pot.}(\varphi)$ between the crank and the connecting rod. It turned out that not for all parameters of the considered system $\int_0^{2\pi}M_1d\varphi=0$. For example, for the data on which Fig. 3, *(b)*, $\int_0^{2\pi}M_1d\varphi\approx 14193.2\ J$ under the condition of vertical balancing (Fig. 5, *(a)*, - according to equation (10)). Vertical balancing of the CM in Fig. 1, *(a)* was determined by the following equation

$$P_5\cdot r_0\cdot sin\,\varphi=P_1\cdot r_1\cdot sin\,\varphi+P_2\cdot\ell_2\cdot sin\,\psi+P_4\cdot(\ell_1+\ell_2+\ell_0)\cdot sin\,\psi. \tag{11}$$

The weight P_5 from equation (11) is given by the following expression

$$P_5=\left(P_1\cdot r_1+P_2\cdot\ell_2\cdot\frac{r_1+r_2}{\ell_1+\ell_2}+P_4\cdot(\ell_1+\ell_2+\ell_0)\cdot\frac{r_1+r_2}{\ell_1+\ell_2}\right)/r_0 \tag{12}$$

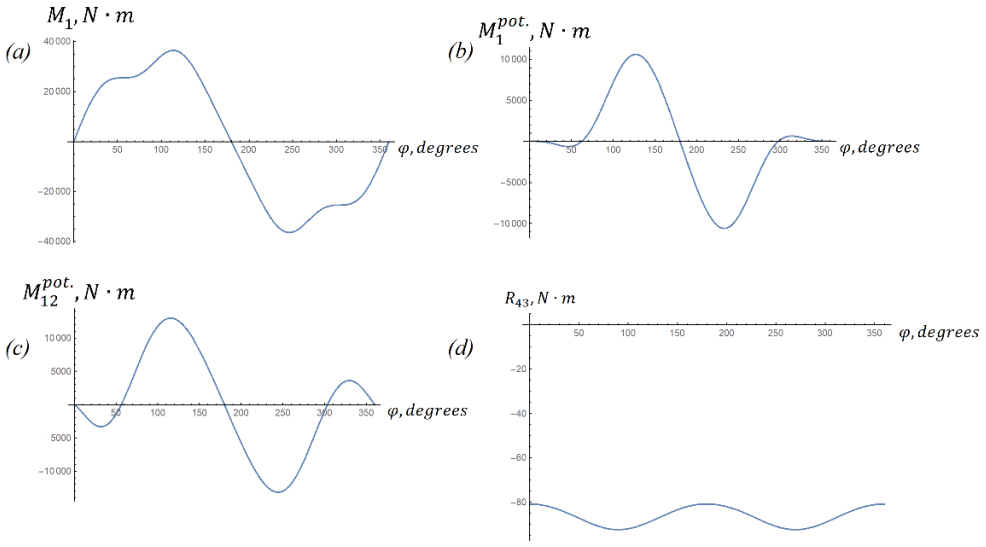

$\dot{\varphi}=300\ s^{-1}$; $I_0^{(1)}=0{,}2\ kg\cdot m^2$; $r_1=0{,}1\ m$; $r_2=0{,}1\ m$;

a) $r_0=0{,}1\ m$ $\ell_0=0{,}4\ m$; $\ell_1=0{,}2\ m$; $\ell_2=0{,}2\ m$;

$P_1=5\ N$; $P_2=10\ N$; $P_3=15\ N$; $P_4=20\ N$; $P_5=47{,}50\ N$;

b), c), d) $r_0=0{,}4\ m$; $\ell_0=0{,}2\ m$; $\ell_1=0{,}4\ m$; $\ell_2=0{,}45\ m$;

$P_1=20\ N$ $P_2=30\ N$; $P_3=30\ N$; $P_4=30\ N$; $P_5=31{,}47\ N$.

Fig. 5.

For option *(b)* $\int_0^{2\pi} M_1 d\varphi = 0$, while $\int_0^{2\pi} M_{12}^{pot.} d\varphi = 0$ (*(c)*, - according to (4)). As can be seen from the figure 5, the lateral force acting on the piston (*(d)*, - according to (7)), is quite small.

The condition for finding the center of mass of the system in fig. 1, *(a)* at point 0 the following

$$P_5 = \big((P_2 + P_3 + P_4) \cdot (r_1 + r_2) + P_1 \cdot r_1\big)/r_0, \tag{13}$$

where $P_4 = (P_3 \cdot (\ell_1 + \ell_2) + P_2 \cdot \ell_1)/\ell_0$ (the condition for finding the central mass of the system "counterweight at point C_4-rod-posun" at point A, Fig.1).

Figure 6, *(a)* shows the dependence $M_1(\varphi)$ in the case when the center of mass of the system in Fig.1, *(a)* is at point 0 (condition (13) is satisfied). Figure 6, *(b)* shows the dependence of the lateral force acting on the piston on the angle of rotation (in the presence of an elastic hinge at point A, Fig. 1, *b*).

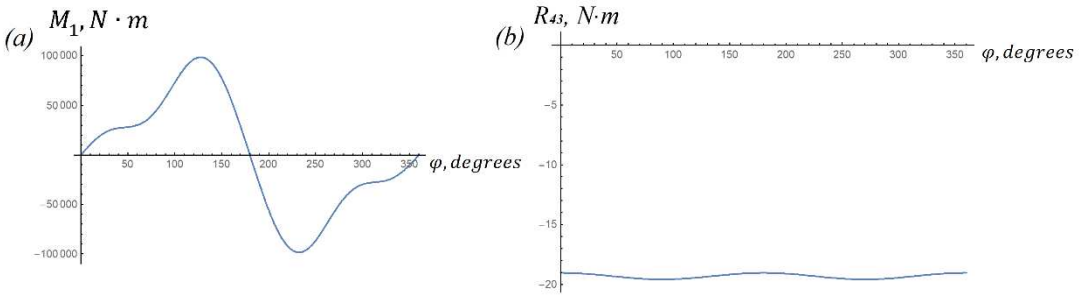

$r_0 = 0{,}4\ m;\ r_1 = 0{,}1\ m;\ r_2 = 0{,}1\ m;\ \dot{\varphi} = 300\ s^{-1};\ \ell_0 = 0{,}2\ m;\ \ell_1 = 0{,}4\ m;\ \ell_2 = 0{,}45\ m;$

$I_0^{(1)} = 0{,}2\ kg \cdot m^2;\ P_1 = 20\ N;\ P_2 = 30\ N;\ P_3 = 30\ N;\ P_4 = 187{,}50\ N;\ P_5 = 128{,}75\ N.$

Fig. 6.

An elastic hinge with a given characteristic is an elastic element, a spring or a pneumatic spring, moving between the guides of the given form (Fig. 7). For option *(a)*, the elastic element is a spring; for option *(b)* the elastic element is a pneumatic spring. The shape of the guides is such that the reactions N_1 and N_2 create a calculated restoring moment depending on the angle of rotation of the elastic element relative to the guides α. For an elastic hinge at point 0, the angle α is equal to the angle of rotation of the crank φ. For a hinge at point A: $\alpha = \varphi + \psi$, or $\alpha = \varphi + \arcsin(\lambda \cdot sin\varphi)$. The method for calculating the shape of the guides of an elastic hinge is presented in the article [7]. At first, the guides are calculated assuming that the radius of the rollers in contact with the guides is zero. Then equidistant guides are built to the obtained ones, taking into account the radius of the rollers. For example, according to the dependences $M_{12}^{pot.}(\varphi)$ and $M_1(\varphi)$ derived in this article, it is possible to calculate the guides of the elastic hinges, which will be located between the crank and the connecting rod and between the strut and the crank, respectively. For the steady-state operation of the engine at different constant angular velocities of the crank, elastic hinges with different characteristics are required. From this point of view, elastic hinges are preferable, in which a pneumatic spring is used as an elastic element. Then, with a small change in the magnitude of the angular velocity of the crank, it is possible to achieve the proper coefficient of uneven operation of the considered engine by calculating the pressure change in the air spring [7].

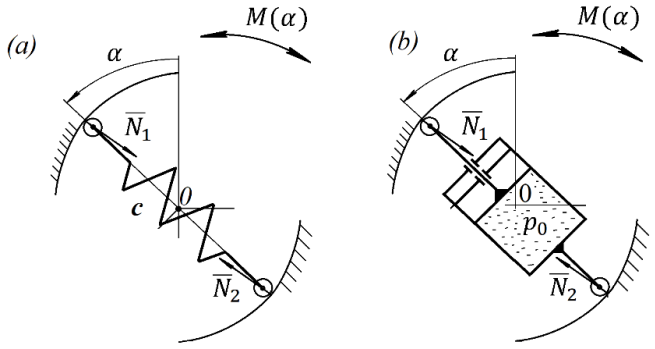

Fig. 7.

Conclusions.

1. Installation of an elastic hinge with a given characteristic between the crank and the TSSCE connecting rod can reduce the lateral force acting on the piston by hundreds of times. For certain parameters of the system under consideration, the lateral force acting on the piston during the operation of the TSSCE is equal to zero at any angle of rotation of the crank.

2. Installation of an elastic hinge with a given characteristic between the strut and the crank, in the presence of an elastic hinge between the crank and the connecting rod, makes it possible to obtain a constant angular velocity of the TSSCE crank with a minimum lateral force acting on the piston.

3. For CM with counterweights on the connecting rod and crank with elastic hinges located between the strut and the crank and between the crank and the connecting rod, it is possible to obtain a fully balanced TSSCE with a constant angular velocity of the crank

REFERENCES

[1] V. Arakelian, S. Briot, «Simultaneous Inertia Force/Moment Balancing and Torque Compensation of Slider-Crank Mechanisms,» Mechanics Research Communications, Elsevier, 37 (2), 2010, pp.265-269.

[2] R. S. Berkof, «Complete force and moment balancing of inline four-bar linkages,» Mechanism and Machine Theory 8, 1973, pp. 397-410.

[3] D. Groza, C. Antonya, «Dynamically Spring Balanced Slider-Crank Mechanism for Reciprocating Machines,» SSRG International Journal of Mechanical Engineering (SSRG – IJME) – Volume 2 Issue 6 – June 2015.

[4] Jih-Lian Haa, Rong-Fong Fungb, Kun-Yung Chenb, Shao-Chien Hsien, «Dynamic modeling and identification of a slider-crank mechanism,» Journal of Sound and Vibration 289 (2006) 1019–1044.

[5] A.N. Zotov, A.S. Sviridov «A Crank Mechanism with Elastic Joints Having Preset Characteristics,» Journal of Machinery Manufacture and Reliability, 2021, Vol. 50, No. 5, pp. 388–395.

[6] V.A. Stopin «Ship's main power equipment. Shipboard diesel engines,» Textbook for course and diploma design, Severodvinsk: Sevmashvtuz, 2003. – p. 64.

[7] A.N. Zotov, A.R. Valeev, A.S. Sviridov « Stabilization of the Torque on the Shaft of a Statically Balanced Crank Mechanism,» 2020 International Conference on Dynamics and Vibroacoustics of Machines (DVM), Samara, Russia, 2020, pp. 1-7.

When friction and vibro-impact makes music: physical model of the tromba marina

Frédéric Ablitzer, Joël Gilbert, François Gautier
Laboratoire d'Acoustique de l'Université du Mans, CNRS UMR 6613, Le Mans, France

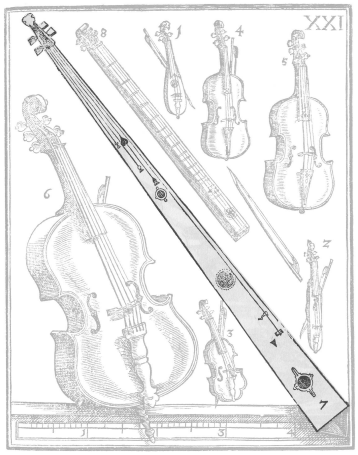

Figure 1: Representation of a tromba marina (adapted from [1]).

The tromba marina (Fig.1) is a bowed string ancient instrument able to imitate the sound of a brass instrument [2, 3]. The functioning of the instrument takes advantage of two non-linear phenomena: dry friction, which allows the emergence of self-sustained oscillations, and vibro-impact mechanism, which makes the "brassy" sound. In this study, a physical model of tromba marina is developed to investigate the phenomenon of spectral enrichment caused by the collisions between one foot of the bridge and the soundboard.

The model consists of a perfectly flexible string fixed at both extremity, vibrating in the plane parallel to the soundboard (Fig. 2a). The string is coupled to a soundboard through the bridge (Fig. 2b). The foot of the bridge located under the string is considered rigidly linked to the soundboard, whereas the other foot is free to move independently of the soundboard, except when they are in contact. The dynamic behavior of the assembly is represented by a set of $N_s + N_b$ modal equations. The N_s modes of the string are known analytically, whereas the N_s modes of the body (soundboard and bridge) are obtained with a finite element model.

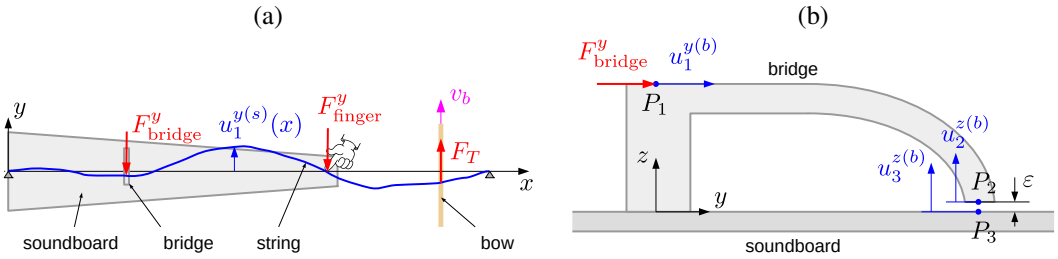

Figure 2: (a) Top view of the simplified instrument. (b) Front view of the bridge. P_1 is the coupling point with the string. P_2 and P_3 are the points likely to enter into contact during playing.

The contact law used to produce the vibro-impact mechanism is the Hunt & Crossley model [4]. The model contains three parameters (stiffness coefficient k, non-linear power exponent n and damping coefficient λ) and expresses the contact force as

$$F_c = \begin{cases} k\delta^p + \lambda\delta^p\dot{\delta} & \text{if } \delta > 0 \\ 0 & \text{if } \delta \leq 0 \,, \end{cases} \tag{1}$$

where $\delta = u_3^{z(b)} - u_2^{z(b)} - \varepsilon$ is the indentation between the two bodies in contact (ε is a control parameter which represents the initial gap between the bridge foot and the soundboard, see Fig. 2b). The friction law describing the interaction between the bow and the string assumes that the string perfectly sticks to the bow during sticking phases and that the friction coefficient during sliding phases depends on the relative velocity as

$$\mu(\Delta v) = \mu_d + \frac{\mu_s - \mu_d}{1 - \Delta v / v_0} \,, \tag{2}$$

where Δv is the relative velocity between the bow and the string, μ_s is the coefficient of static friction, μ_d the asymptotic coefficient of dynamic friction and v_0 a parameter controlling the shape of the friction curve.

Time-domain simulations are performed using an explicit numerical scheme of the form

$$\mathbf{x}(t_{i+1}) = \mathbf{A}\mathbf{x}(t_i) + \mathbf{B}\mathbf{f}(t_i) \,, \tag{3}$$

where $\mathbf{x}$ is a vector containing all modal coordinates and their time derivatives and $\mathbf{f}$ is a vector containing the modal forces. The coefficients in $\mathbf{A}$ and $\mathbf{B}$ are obtained using a piecewise constant approximation of the right-hand side of modal equations. At each time step, the contact force F_c is calculated using the available solution at t_i. The other unknown forces (coupling force F^y_{bridge} between the string and the body, reaction force F^y_{finger} of the finger stopping the string, friction force F_T exerted by the bow on the string) are obtained by enforcing constraints: continuity of displacement

between the string and the body, zero displacement at finger location, sticking or sliding condition. Finally, the pressure radiated by the soundboard is calculated using Rayleigh integral, assuming that it is surrounded by an infinite baffle.

To highlight the phenomenon of spectral enrichment, a *crescendo* is simulated by bowing the open string with linear increase of the bow speed, after a short phase intended to establish a periodic regime, the Helmholtz motion [5, 6]. Figure 3 illustrates the results of the simulation. During a first phase of the simulation, no collision occurs. After $t = 1.6$ s, the body response has sufficient amplitude so that the free foot of the bridge enter into contact with the soundboard. Figure 4a shows the sound pressure radiated by the instrument for the same gesture and Figure 4b the corresponding spectrogram. As expected, the occurrence of collisions from $t = 1.6$ s is accompanied by a strong spectral enrichment. To highlight this, the evolution of the spectral centroid is shown on the same figure. The emergence of high rank harmonics during the *crescendo*, making the sound perceived as "brassy", is a common feature with brass instruments. However, the effect appears suddenly in the case of the tromba marina, as seen by the abrupt increase in spectral centroid at $t = 1.6$ s, whereas a progressive spectral enrichment is typically observed when a *crescendo* is played on a brass instrument. This significant difference is due to the fact that different physical phenomena are at the origin of the spectral enrichment: non-linear wave propagation in the air column contained in the brass instrument [7], vibro-impact mechanism for the tromba marina.

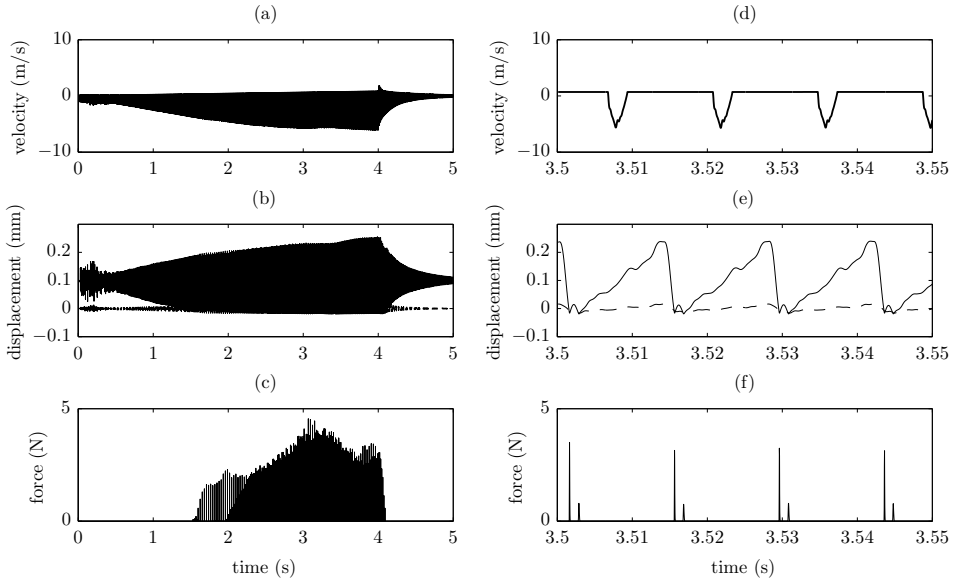

Figure 3: (a)-(d) Velocity of the string at bowing point, (b)-(e) displacement of point P_2 and P_3 (see Fig. 2b), (c)-(f) contact force F_c.

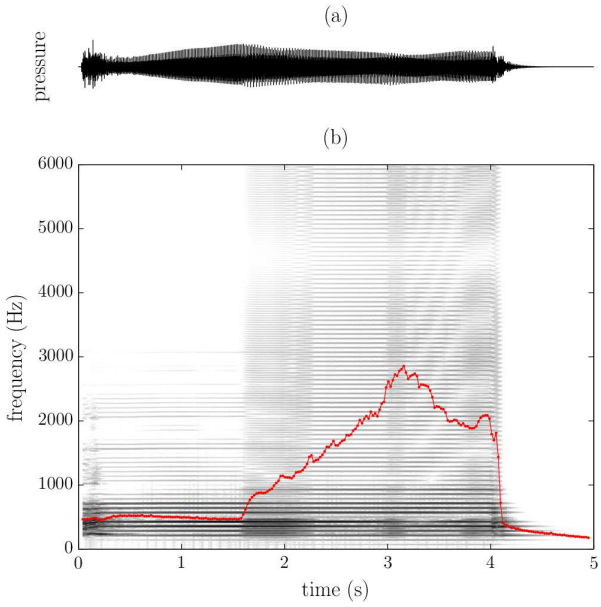

Figure 4: (a) Sound pressure (normalized) radiated during a *crescendo* and (b) its spectrogram. The superimposed red curve is the spectral centroid.

References

[1] M. Praetorius, *Syntagma Musicum* Vol. 2, Wolfenbüttel, 1619.

[2] A. Padilla and V. Gibiat, *The "trumpet marine", an instrument between a trumpet and a violin*, Proceedings of Forum Acusticum, Budapest, 2005.

[3] S. Willemsen, S. Serafin, S. Bilbao, M. Ducceschi, *Real-time implementation of a physical model of the tromba marina*, Proceedings of the Sound and Music Computing Conference, Torino, 2020.

[4] K.H. Hunt and F.R.E. Crossley, *Coefficient of restitution interpreted as damping in vibroimpact*, J. Appl. Mech. 42(2), 440-445, 1975.

[5] L. Cremer, *The physics of the violin*, MIT Press, 1985.

[6] A. Chaigne and J. Kergomard, *Acoustics of Musical Instruments*, Springer, 2016.

[7] M. Campbell, J. Gilbert, A. Myers, The Science of Brass Instruments, Springer, 2021.

Friday, July 22, 2022

08:30 - 10:30

MS-11 Systems with Time Delay

Saint Clair 2

Chair: Gabor Stepan

08:30 - 08:50

Parametric study of a switching control model of stick balancing

NAGY Dalma J.*, BENCSIK László, INSPERGER Tamás

*MTA-BME Lendület Human Balancing Research Group, Budapest University of Technology and Economics (1111 Budapest, Muegyetem rkp. 5. Hungary) - Department of Applied Mechanics, Budapest University of Technology and Economics (1111 Budapest, Muegyetem rkp. 5. Hungary)

08:50 - 09:10

Bistability in nonlinear elastic robotic arms subject to delayed feedback control

HABIB Giuseppe, BARRIOS Asier, **BARTFAI Andras***, DOMBOVARI Zoltan

*MTA-BME Lendület Machine Tool Research Group, Department of Applied Mechanics, Budapest University of Technology and Economics (Budapest, Muegyetem rkp. 3. Hungary)

09:10 - 09:30

Multifrequency dynamics in an excitable microlaser with delayed optical feedback

TERRIEN Soizic*, KRAUSKOPF Bernd, BRODERICK Neil G. R., BARBAY Sylvain

*Department of Mathematics, The University of Auckland (38 Princes Street, Auckland CBD, Auckland 1010 New Zealand) - Dodd-Walls Centre for Photonic and Quantum Technologies (Dodd-Walls Centre University of Otago PO Box 56 Dunedin 9056 New Zealand New Zealand)

09:30 - 09:50

Multiplicity-induced-dominancy for some retarded differential equations

BENARAB Amina*, MAZANTI Guilherme, BOUSSAADA Islam, NICULESCU Silviu-Iulian

*Laboratoire des Signaux et Systèmes (91190, Gif-sur-Yvette France)

09:50 - 10:10

Playing dominoes with lasers: Excitability and pulsed solutions of the Yamada model for a semiconductor laser with saturable absorber and delayed optical feedback

RUSCHEL Stefan*, KRAUSKOPF Bernd, BRODERICK Neil G. R.

*Department of Mathematics [Auckland] (The University of Auckland Private Bag 92019 Auckland 1142 New Zealand)

10:10 - 10:30

Ploughing-limited post-critical dynamics under chatter in turning. Harmonic balance based investigation

GUSKOV Mikhail*

*Procédés et Ingénierie en Mécanique et Matériaux [Paris] (151 Boulevard de l'Hôpital, 75013 Paris France)

Parametric study of a switching control model of stick balancing

Dalma J. Nagy[*,†], László Bencsik[†,‡] and Tamás Insperger [*,†]
[*]*Department of Applied Mechanics, Budapest University of Technology and Economics, Budapest, Hungary*
[†]*MTA-BME Lendület Human Balancing Research Group, Budapest, Hungary*
[‡]*MTA-BME Research Group on Dynamics of Machines and Vehicles, Budapest, Hungary*

Summary. We are interested in understanding the control mechanism employed by the central nervous system during stick balancing on the fingertip. Although this is a relatively simple balancing task, the underlying control law is still not yet fully understood. In this research, predictor feedback is applied in the mechanical model of stick balancing by taking into account the dead zone of human perception of the stick's state and the reaction delay. Using these assumptions, we derive a switched control model whose behaviour is then investigated as the function of the system parameters.

Introduction

In recent years, the interest on studying human balancing from an engineering point of view is constantly growing [1]. The results of this research can be beneficial in helping people living with balance disorders and in the therapeutic motor control development of children. Stick balancing on the fingertip represents the key features of dynamic balancing, namely, an unstable equilibrium should be stabilized in the presence of reaction time delay and sensory uncertainty. Therefore, in this paper the stick balancing task is studied by developing the mechanical model and performing numerical analysis using the semidiscretization method for time-delay systems [2]. There are several control concepts to model the balancing mechanism, e.g. delayed PD controller [3], PDA controller [4], intermittent controller [5]. Measured time signals of stick balancing tasks suggest that nonlinearities due to switching-type control may be a key feature of human balancing [6]. Here, a switching-type predictor controller is applied to model the control force exerted by human subjects.

Mechanical model and applied controller

Our research group has developed a device, in order to have a simplified measurement setup, where planar stick balancing can be carried out by human subjects. The stick is mounted on a cart via a pin joint and the cart is only allowed to move along a 1-meter-long rail. Subjects sit in a chair so their shoulders are parallel to the rail, therefore, the balancing occurs in the subject's medio-lateral plane [7]. It is assumed, that humans move only their forearm in this balancing task and not their upper arm. The mechanical model of the system is shown in Fig. 1a), where the forearm of the subject is modelled by a truncated cone [8]. The inertia of the forearm and hand can be modelled by a cart of equivalent mass m_a which is added to the mass of the cart m_c and thus, the system is reduced to a two-degree-of-freedom pendulum-cart model shown in Fig. 1b), where $m_\mathrm{e} = m_\mathrm{a} + m_\mathrm{c}$.

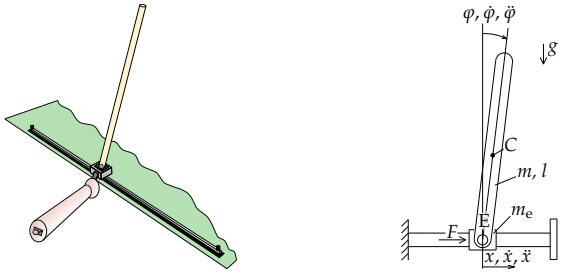

Figure 1: a) Schematic 3D figure of the stick balancing task. The cart is linearly driven on a rail and the stick is pinned onto the cart via a planar joint. The subject controls the cart with their hand using a handle that is rigidly fixed to the cart. b) Reduced mechanical model of the stick balancing task.

By taking the generalised coordinates x - the position of the cart - and φ - the angular deviation of the stick -, the equation of motion can be derived for the 2 DoF system. However, x is a cyclic coordinate, and therefore can be eliminated from the equation. After linearisation, the equation of motion reads

$$\ddot{\varphi}(t) = \frac{6g}{c\,l}\,\varphi(t) - \frac{6F(t)}{(m+m_\mathrm{e})c\,l}, \tag{1}$$

where $c = 4 - 3m/(m+m_\mathrm{e})$, m is the mass of the stick, l is the length of the stick, m_e is the equivalent mass of the cart, g is the gravitational acceleration and $F(t)$ is the control force applied by the human. When applying predictor feedback, it is assumed that the internal model of the human is exact, that is it matches the actual system parameters as a result of a

long enough learning process. In this case, the feedback of the predicted state eliminates the delay from the control loop [4] and the control force of the switching-type model predictor feedback is:

$$F(t) = \begin{cases} 0 & \text{if} |\varphi(t-\tau)| < \Pi_\varphi \text{ and } |\dot{\varphi}(t-\tau)| < \Pi_{\dot{\varphi}}, \\ P\varphi(t) & \text{if} |\varphi(t-\tau)| \geq \Pi_\varphi \text{ and } |\dot{\varphi}(t-\tau)| < \Pi_{\dot{\varphi}}, \\ D\dot{\varphi}(t) & \text{if} |\varphi(t-\tau)| < \Pi_\varphi \text{ and } |\dot{\varphi}(t-\tau)| \geq \Pi_{\dot{\varphi}}, \\ P\varphi(t) + D\dot{\varphi}(t) & \text{if} |\varphi(t-\tau)| \geq \Pi_\varphi \text{ and } |\dot{\varphi}(t-\tau)| \geq \Pi_{\dot{\varphi}}, \end{cases} \tag{2}$$

where it is assumed, that the angular deviation and the angular velocity of the stick is sensed by the human perception and the prediction is made based on these measured values. The human sensory dead zone is also accounted for in the model of the control force, hence the switching. Different sensory dead zones are applied for the angle and angular velocity of the stick denoted by Π_φ and $\Pi_{\dot{\varphi}}$, respectively. The switching of the control force occurs with a time delay τ, since it takes a finite time for the human to detect that the stick is out of the dead zone, which is equal to the reaction delay of the subject. Substituting $F(t)$ into Eq. (1) gives a nonlinear model of human balance control.

Numerical study

A numerical study on the stability of the system is carried out using the semidiscretization method [2] as a function of the system parameters P, D and τ. The values of $m_e = 1.73$ [kg], $m = 0.1$ [kg] and $l = 0.9$ [m] are held constant during the analysis. The equivalent mass is determined by anthropometric data from [9] and by measuring $m_c = 0.12$ [kg]. Because of the model predictor feedback, the discrete map corresponds to a sampled output system without any feedback delay, where the stability diagram depends on the sampling time Δt. The sampling time was set to $\Delta t = 0.01$ [s]. Fixed value of sensory dead zone is applied for the angle $\Pi_\varphi = 1$ [deg] and the sensory threshold for the angular velocity is varied between $\Pi_{\dot{\varphi}} = 0.02...2$ [deg/s].

Conclusions

The parametric study leads to the detection of solutions converging to pseudo-equilibria that lies on the switching line determined by the size of the dead zone for the angle if the sensory dead zone of the angular velocity is sufficiently small and $\tau = 0$ [s]. However, if the size of the dead zone of the angular velocity is large, a stable periodic orbit determined by both sensory dead zones can be observed for the parameter combination $P = 30$ [N], $D = 5$ [Ns] and $\tau = 0$ [s]. Nevertheless, $\tau = 0$ [s] is not physiologically feasible for the case of human balancing. For a feasible value of time delay a stable symmetric orbit with a long period is found for the control gains $P = 30$ [N], $D = 5$ [Ns], and $\tau = 0.3$ [s].

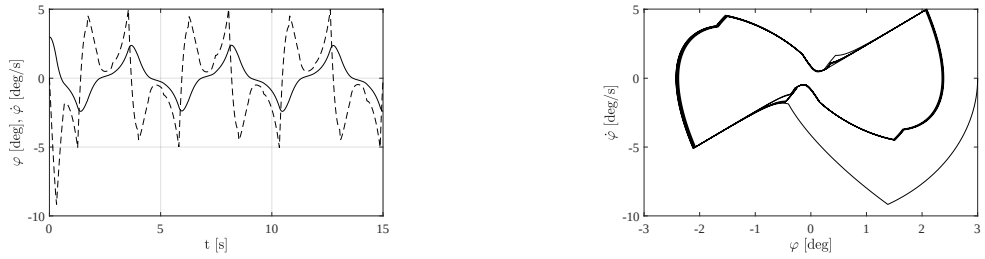

(a) (b)

Figure 2: a) Numerical solution for control parameters $\tau = 0.3$ [s], $P = 30$ [N], $D = 5$ [Ns]. b) Stable symmetric orbit in phase plane for the numerical solution.

References

[1] P. Kowalczyk, P. Gledinning, M. Brown, G. Medrano-Cerda, H. Dallali, J. Shapiro (2012) Modelling human balance using switched systems with linear feedback control. *J. R. Soc. Interface* **9**:234-245.

[2] T. Insperger, G. Stepan (2011) Semi-Discreatization for Time-Delay Systems - Stability and Engineering Applications. Springer NY.?

[3] B. Mehta, S. Schaal (2002) Forward models in visuomotor control. *Journal of Neurophysiology* **88**:942-953.

[4] T. Insperger, J. Milton, G. Stepan (2014) Sensory uncertainty and stick balancing at the fingertip. *Biological Cybernetics* **108**(1):85-101.

[5] P. Gawthrop, K.-L. Lee, N. O'Dwyer, M. Halaki (2013) Human stick balancing: an intermittent control explanation. *Biological Cybernetics* **107**:637-652

[6] D. J. Nagy, L. Bencsik, T. Insperger (2019) Experimental estimation of tactile reaction delay during stick balancing using cepstral analysis. *Mechanical Systems and Signal Processing* submitted manuscript

[7] M. Nordin, V. H. Frankel (1989) Basic biomechanics of the musculoskeletal system. Lea & Febiger.

[8] E. P. Hanavan (1964) A Mathematical Model of the Human Body. *Technical Report*, Aerospace Medical Research Laboratory Wright-Patterson Air Force Base, Ohio

[9] P. de Leva (1996) Adjustments to Zatsiorsky-Seluyanov 's segment inertia parameters. *Journal of Biomechanics* **29**(9):1223-1230

Bistability in nonlinear elastic robotic arms subject to delayed feedback control

Giuseppe Habib*, Asier Barrios‡, Andras Bartfai*, Zoltan Dombovari*
*MTA-BME Lendület Machine Tool Vibrations Research Group, Department of Applied Mechanics, Budapest University of Technology and Economics, Budapest, Hungary
‡Dynamics and Control Department, Ideko, Elgoibar, Spain

Summary. Stability and bifurcation analysis of a non-rigid robotic arm controlled with a time delayed feedback loop is addressed in this work. The study aims at revealing the dynamical mechanisms leading to the appearance of limit cycle oscillations existing in the stable region of the trivial solution of the system, which are related to the combined dynamics of the robot control and its structural nonlinearities. An analytical study of the bifurcations occurring at the loss of stability enables the development of strategies to eliminate this undesired bistable phenomenon by the implementation of special additional nonlinearities in the control force.

Introduction

Robots are increasingly adopted in modern manufacturing facilities, thanks to their versatility and relatively low cost [1]. Milling operation is one of the operations robots are intended to be used for, where complicated tool trajectories can be realized in a large workspace, with a relatively low cost. The relative vibrations between workpiece and tool are a troublesome phenomenon in milling that is mainly caused by the so-called regenerative vibration. The main solution to avoid them is to increase stiffness and damping and try to disturb time delays introduced by the regenerative effect [2]. Generally, increasing the stiffness is hardly achievable, since robotic arms are naturally slender and not especially stiff structures [3]. This makes them particularly prone to vibrations. The main method to mitigate these vibrations should consists of implementing an active controller working collaboratively in the robot original feedback loop. This envisioned controller online reads the acceleration of the end effector (EE, see Fig. 1a) as input and sends a proportional signal to the robot controller in order to counteract and suppress the arising oscillations. This signal is combined to the signal of the position controller of the robot required to make the robotic arm follow the prescribed path during machining.
Although this procedure is rather straightforward to be implemented, there are several aspects that can undermine the effectivity of such combined system if the followings are not properly accounted for: (i) Robotic arms are naturally slender and they cannot be assumed to be rigid, especially if they are subject to strong periodic forces, as in the case of machining. (ii) Since the actuators are placed at the joints of the arm, the system is underactuated. Depending on the position of the sensors, either near the motor or near the EE, the system can be considered as collocated or non-collocated, which have relevant consequences on the system stability [4, 5]. (iii) Robot configuration changes continuously during operation and the drive components of the robot generate non-negligible nonlinearities; as we will illustrate in this study, these nonlinearities might have important consequences on the system robustness. (iv) Robot's controller is unavoidably subject to time delay in the feedback loop. Although this is often negligible, if large control gains are required to counteract strong forces, time delay can still generate instabilities.
This study is motivated by the appearance of unexpected vibrations in a real industrial robotic arm in milling operation. This robot is equipped with a built-in controller (most probably a proportional-derivative controller) for its correct positioning and with an additional controller proportional to the EE acceleration, to counteract machining vibrations (Fig. 1a). Although the control parameters of the system were set such that the system was stable (Fig. 1b), when subject to very small external forcing, in some occasions the robotic arm exhibited either large or small oscillations, which suggests that it was in bistable conditions (see Fig. 1c). The objective of this work is to define and study a general simplified model of this system in order to understand the origin of the bistability and define methods to avoid it. From a broader prospective, this seed research aim at providing a reliable modelling of robotic manufacturing.

Mathematical model

The mathematical model adopted is a two degrees of freedom (DoF) system (Fig. 1a), consisting of two lumped masses m_1 and m_2, connected by a linear damper c, and a nonlinear spring k_{nl}. The two DoF of the system represent the two dominant DoFs measured for the actual robotic arm in a certain frequency bandwidth. The nonlinearity models a stiffness nonlinearity observed during measurement, most probably originated in the joints. This simplified equivalent mechanical model captures the most important features of the real robotic arm considered in the study. The model is equivalent since during a simple dynamic measurement on the EE the source of the stiffness, damping and nonlinearities are hard to be traced. A prescribed reference trajectory x_{d} is programmed, such that, in ideal circumstances, an identical constrained motion x_{r} is imposed to m_1 via a spring of stiffness k with a certain time delay τ_r. This enables the robot to follow the prescribed path. The equations of motion has the following form:

$$\begin{aligned} m_1\ddot{x}_1 + c\left(\dot{x}_1 - \dot{x}_2\right) + k_{\text{nl}}(\Delta x)\left(x_1 - x_2\right) + kx_1 &= kx_{\text{r}}, \\ m_2\ddot{x}_2 + c\left(\dot{x}_2 - \dot{x}_1\right) + k_{\text{nl}}(\Delta x)\left(x_2 - x_1\right) &= 0, \end{aligned} \tag{1}$$

where $k_{\text{nl}}(\Delta x) = k_2 + \kappa\Delta x^2$ ($\Delta x := x_2 - x_1$). Apart from the position controller integrated in the robot, an additional signal x_{f}, proportional to the acceleration of the EE, is added to x_{r}. This generates a final constrained motion $x_{\text{r}}(t) =$

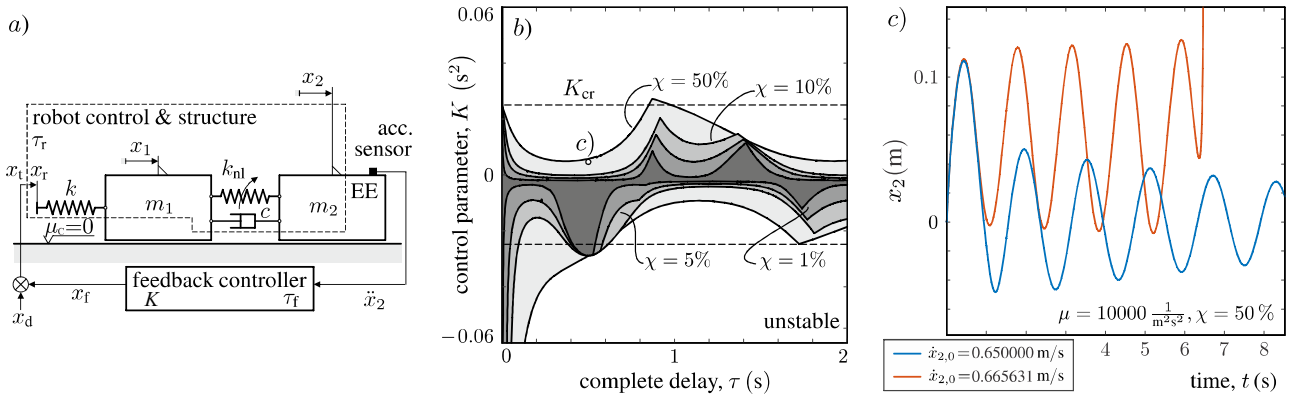

Figure 1: a) shows the sketch of the 2 DoF model with the additional acceleration feedback control ; b) stability chart in the (τ, K) space for $\omega_1 = \omega_2 = 2\pi$ rad/s, $r = 1$, $\chi =: (50,\ 10,\ 5,\ 1)\,\%$, $K_{\mathrm{cr}} = 0.0253\,\mathrm{s}^2$, c) time evolutions for different initial conditions.

$x_{\mathrm{d}}(t-\tau_{\mathrm{r}}) + K\ddot{x}_2(t-\tau_{\mathrm{r}}-\tau_{\mathrm{f}})$, where τ_{f} is the delay of the acceleration feedback. In order to focus on the instabilities generated by the acceleration feedback control, in this work we assume constant desired position, that is, $x_{\mathrm{d}}(t) := x_{\mathrm{d}}$, which results in the equilibrium $(\overline{x}_1, \overline{x}_2) = (x_{\mathrm{d}}, x_{\mathrm{d}})$. By introducing the perturbations $x_1 := \overline{x}_1 + u_1$ and $x_2 := \overline{x}_2 + u_2$, the stability of the local equilibrium can be studied. Via a standard non-dimensionalization procedure, the equations of motion around the equilibrium are reduced to the equation, where $r := m_2/m_1$, $\omega_1^2 := k_1/m_1$, $\omega_2^2 := k_2/m_2$, $\chi := c/(2m_2\omega_2)$, $\mu := \kappa/m_2$, $\ddot{u}_{2\tau} := \ddot{u}_2(t-\tau)$ and $\tau := \tau_{\mathrm{r}} + \tau_{\mathrm{f}}$.

$$\begin{aligned} &\ddot{u}_1 + 2\chi r\omega_2\left(\dot{u}_1 - \dot{u}_2\right) + \omega_2^2 r\left(u_1 - u_2\right) + \mu r(u_1 - u_2)^3 + \omega_1^2 u_1 = \omega_1^2 K\ddot{u}_{2\tau}, \\ &\ddot{u}_2 + 2\chi\omega_2\left(\dot{u}_2 - \dot{u}_1\right) + \omega_2^2\left(u_2 - u_1\right) + \mu(u_2 - u_1)^3 = 0, \end{aligned} \tag{2}$$

Stability and bistable behavior

By linearising (2) and setting $\chi := 0$, the linear stability of the corresponding neutral equation can be investigated (see Fig. 1b). A naive necessary condition of stability for neutral equation is to have the neutral coefficient (here $\omega_1^2 K$) less than one in its magnitude with $|K_{\mathrm{cr}}| \leq \omega_1^{-2}$. However, the investigated robotic arm is non-collocated; therefore, the neutral condition is always fulfilled, thus, the stability domains overtakes K_{cr} . In the case of small damping, repeating lobe structure significantly erodes the stable region, which is limited to a narrow region around $K = 0$.
Apart from the local stability of the trivial solution, time simulations show that the nonlinearity of the system has significant impact on its global stability. In particular, if the system is subject to a stiffening nonlinearity ($\mu > 0$) simulations for parameter values within the stable region tend to diverge if initial conditions are sufficiently large. This phenomenon is caused by the subcritical characteristic of the bifurcations occurring at the stability limit and it is probably directly related to the bistable behaviour observed in real robotic arms. The detailed analysis of the bifurcation behaviour of the system enables us to design additional nonlinearities to be included in the control force algorithm to enforce supercritical behaviour; therefore, eliminating the bistable behavior in the stable region.

Conclusions

The stability and bifurcation analysis of a simplified model of the robotic arm subject to acceleration feedback was performed. Results illustrated that the stability chart is characterized by a critical value of the control gain, which is a necessary condition to guarantee stability, and by a repeating stability limit pattern, which strongly depends on the time delay and on system damping. The mechanism connecting bistable behavior and hardening nonlinearity was also identified. The full understanding of this mechanism enables the development of a control algorithm, based on nonlinear functions, which forces the bifurcation to be supercritical, suppressing bistable behaviour in the stable region.

References

[1] Hagele M. (2016) Robots Conquer the World [Turning Point]. *IEEE Robot Autom Mag* **23**:120-118.

[2] Munoa J., Beudaert X., Dombovari Z., Altintas Y., Budak E., Brecher C., Stépán G. (2016) Chatter suppression techniques in metal cutting. *CIRP Annals* **65**(2):785-808.

[3] Mousavi S., Gagnol V., Bouzgarrou B.C., Ray P. (2018) Stability Optimization in Robotic Milling through the Control of Functional Redundancies. *Robot Com-Int Manuf* **50**:181-192.

[4] De Luca A., Schroder D., Thummel M. (2007) An Acceleration-Based State Observer for Robot Manipulators with Elastic Joints. *Proc IEEE Int Conf Robot Autom*:3817-3823.

[5] Habib G., Rega G., Stépán G. (2015) Stability Analysis of a Two-degree-of-freedom Mechanical System Subject to Proportional-Derivative Digital Position Control. *J Vib Control* **21**:1539-1555.

[6] Stépán, G. (1989) Retarded Dynamical Systems: Stability and Characteristic Functions. Longman Scientific & Technical, London.

Multifrequency dynamics in an excitable microlaser with delayed optical feedback

Soizic Terrien[1], Bernd Krauskopf[1] Neil G.R. Broderick[2] and Sylvain Barbay[3]
[1]*Department of Mathematics, University of Auckland, Auckland, New Zealand.*
[2]*Department of Physics, University of Auckland, Auckland, New Zealand.*
[3]*Centre de Nanosciences et de Nanotechnologies, CNRS, Université Paris-Sud, Université Paris-Saclay, Palaiseau, France.*

Summary. We investigate theoretically the multi-frequency dynamics observed experimentally in an excitable microlaser subject to delayed optical feedback. We perform a bifurcation analysis of a suitable mathematical model using advanced numerical methods. This demonstrates that the modulated dynamics can be interpreted as quasiperiodic oscillations on a stable torus and hat it originates in the interplay between the delay time and the internal slow timescales of the microlaser.

As sources of short, high-amplitude light pulses, self-pulsing lasers are central to many applications, including telecommunications and neuromorphic photonic computing. We consider a semiconductor micropillar laser with integrated saturable absorber subject to delayed optical feedback [2]. The solitary microlaser is excitable [1]: it is in its non-lasing state, but displays an all-or-none response to external perturbations, in the form of a short, high-amplitude light pulse, depending on whether or not the perturbation amplitude exceeds the so-called excitable threshold [3]. In the presence of a feedback loop, recent theoretical and experimental work demonstrated that a first excitable pulse can regenerate itself when reinjected in the laser after the delay time [5, 4]. As such, a single external perturbation can trigger a train of pulses whose repetition rate is close to the delay time. It has recently been shown [4] that several pulse trains can be triggered and sustained simultaneously: in such a case, a very slow convergence is typically observed towards a pulsing pattern where the pulses are equidistant in the laser cavity. In other words, the system is slowly attracted towards one of the stable pulsing periodic solutions with periods close to submultiples of the delay time.
Here, we show theoretically and experimentally that the delayed feedback can also induce complex multifrequency dynamics. In particular, we provide experimental evidence of the existence of pulsing regimes with a strong modulation of the pulse amplitude on a slow timescale compared to the delay time.

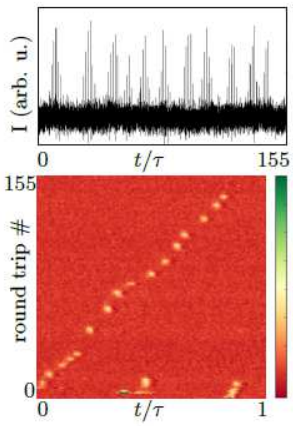

Figure 1: Experimental intensity time series, represented over reduced time (top) and in the pseudo-space (bottom) where the x-axis represents one delay time and the y-axis represents the number of roundtrips in the laser external (feedback) cavity.

We focus on the theoretical investigation of such multifrequency dynamics and perform a numerical bifurcation analysis of the Yamada model with feedback. This system of three delay-differential equations (DDEs) for the gain G, the absorption Q and the intensity I is written as follows in the dimensionless form:

$$\begin{aligned} \dot{G} &= \gamma_G(A - G - GI); \\ \dot{Q} &= \gamma_Q(B - Q - aQI); \\ \dot{I} &= (G - Q - 1)I + \kappa I(t - \tau). \end{aligned} \tag{1}$$

Here, A is the pump parameter, B is the non-saturable absorption, a is the saturation parameter and γ_G and γ_Q are the carrier recombination rates in the gain and absorber media, respectively. The values of γ_G and γ_Q are typically small, and the model (1) is then a slow-fast dynamical system with two slow variables (the gain G and the absorption Q) and one fast variable (the laser field intensity I). The optical feedback is described by the delayed term in the intensity equation, where κ is the feedback strength and τ is the feedback delay. This model has been shown to describe accurately the dynamics observed experimentally [6, 4].

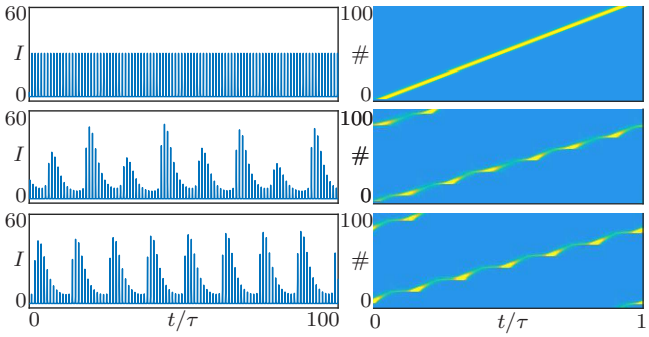

Figure 2: Simulated intensity time series represented over reduced time (left) and in the pseudo-space (right), for $\kappa = 0.39$ (top), $\kappa = 0.3805$ (middle), and $\kappa = 0.38$ (bottom). The delay is $\tau = 965$.

Time domain simulations of the Yamada model with feedback, in figure 2, demonstrates its ability to reproduce the modulated pulsing dynamics observed in the experiment. We perform an in-depth bifurcation analysis of the model (1) with advanced numerical methods [7], considering both the feedback strength κ and feedback delay τ as bifurcation parameters. It demonstrates that the modulated dynamics can be interpreted as quasiperiodic oscillations on a stable torus. The bifurcation analysis unveils an interplay between the delay time and the internal timescales of the microlaser (related to the carrier recombination rates in the gain and absorber sections) as the main reason behind the emergence of such multifrequency dynamics. Moreover, time-domain simulations of the Yamada model with delay show that chaotic dynamics exists in small regions of the parameter space.

Overall, our results provide a better understanding of pulsing dynamics in an excitable laser with delayed feedback. As such, they constitute a step toward an all-optical control of pulse trains, which may prove useful for optical memories or neuromorphic photonic computing. Despite its simplicity, the Yamada model with feedback describes accurately the complex dynamics observed in the experiment and displays complex dynamics, including chaotic behaviour. Importantly, the only ingredients, excitability and feedback, are very general [1]. Therefore, we believe our results may be of interest beyond the scope of laser dynamics.

References

[1] Izhikevich, E. M., and Moehlis, J. (2008). Dynamical Systems in Neuroscience: The geometry of excitability and bursting. *SIAM review*, **50**(2), 397.

[2] Elsass, T., Gauthron, K., Beaudoin, G., Sagnes, I., Kuszelewicz, R., and Barbay, S. (2010). Control of cavity solitons and dynamical states in a monolithic vertical cavity laser with saturable absorber. *The European Physical Journal D*, **59**(1), 91-96.

[3] Barbay, S., Kuszelewicz, R., and Yacomotti, A. M. (2011). Excitability in a semiconductor laser with saturable absorber. *Optics letters*, **36**(23), 4476-4478.

[4] Terrien, S., Krauskopf, B., Broderick, N. G., Braive, R., Beaudoin, G., Sagnes, I., and Barbay, S. (2018). Pulse train interaction and control in a microcavity laser with delayed optical feedback. *Optics letters*, **43**(13), 3013-3016.

[5] Terrien, S., Krauskopf, B., and Broderick, N. G. (2017). Bifurcation analysis of the Yamada model for a pulsing semiconductor laser with saturable absorber and delayed optical feedback. *SIAM Journal on Applied Dynamical Systems*, **16**(2), 771-801.

[6] Selmi, F., Braive, R., Beaudoin, G., Sagnes, I., Kuszelewicz, R., and Barbay, S. (2014). Relative refractory period in an excitable semiconductor laser. *Physical review letters*, **112**(18), 183902.

[7] Engelborghs, K., Luzyanina, T., and Roose, D (2002) Numerical bifurcation analysis of delay differential equations using DDE-BIFTOOL. *ACM Transactions on Mathematical Software (TOMS)*, **28**(1), 1-21.

Multiplicity-induced-dominancy for some retarded differential equations

Amina Benarab*†, Islam Boussaada*†, Guilherme Mazanti*, and Silviu-Iulian Niculescu*
*Université Paris-Saclay, CNRS, CentraleSupélec, Inria, Laboratoire des signaux et systèmes, 91190, Gif-sur-Yvette, France. E-mails: {first name.last name}@l2s.centralesupelec.fr
†Institut Polytechnique des Sciences Avancées (IPSA) 63 boulevard de Brandebourg, 94200 Ivry-sur-Seine, France.

Summary. The stability analysis of generic retarded differential equations is a difficult question since their asymptotic behavior depends on a non-trivial way on parameters and delays. From a control point of view, the main difficulty is that one has infinitely many spectral roots but only finitely many parameters in the system. A natural question is then to design techniques of assigning a finite number of roots guaranteeing that the rightmost root is among the ones assigned. One such a technique is to place roots of maximal multiplicity, which are often also dominant, a property known as *multiplicity-induced-dominancy* (MID). This paper proves that the MID property holds for some classes of systems by using a priori bounds on the imaginary part of roots on the right half-plane, a suitable factorization of the characteristic equation in integral form, and the analysis of crossing imaginary roots.

Introduction

This paper is interested in linear time-invariant differential equations with delays which can be written under the form

$$y^{(n)}(t) + \sum_{j=0}^{N} \sum_{k=0}^{n-1} \alpha_{j,k} y^{(k)}(t - \tau_j) = 0, \tag{1}$$

where n and N are positive integers, $\alpha_{j,k} \in \mathbb{R}$, and $\tau_j \geq 0$. With no loss of generality, we assume $0 = \tau_0 < \tau_1 < \cdots < \tau_N$. Equation (1) is said to be *retarded* since the highest order derivative only appears in the non-delayed term $y^{(n)}(t)$. The stability analysis of time-delay systems has attracted much research effort and is an active field [4, 5, 8, 9, 11]. The asymptotic behavior of (1) can be studied through spectral methods by considering the complex roots of the corresponding characteristic function $\Delta : \mathbb{C} \to \mathbb{C}$ defined for $s \in \mathbb{C}$ by

$$\Delta(s) = s^n + \sum_{j=0}^{N} e^{-s\tau_j} \sum_{k=0}^{n-1} \alpha_{j,k} s^k. \tag{2}$$

Functions such as Δ that can be written under the form $Q(s) = \sum_{j=0}^{\ell} P_j(s) e^{\lambda_j s}$ for some non-zero polynomials with real coefficients $P_0, \ldots, P_\ell$ and pairwise distinct real numbers $\lambda_0, \ldots, \lambda_\ell$ are called *quasipolynomials*. The integer $D = \ell + \sum_{j=0}^{\ell} d_j$ is called the *degree* of Q, where d_j denotes the degree of P_j. A classical result on quasipolynomials provided in [10, Problem 206.2] implies that the multiplicity of any root of Q does not exceed D.
A root s_0 of Δ is said to be *(strictly) dominant* if every other root of Δ has a real part (strictly) smaller than $\operatorname{Re} s_0$. It has been observed in several works that real roots of maximal multiplicity tend to be dominant, a property known as *multiplicity-induced-dominancy* (MID) (see, e.g., [1, 3] for the case $N = 1$ and $n = 2$ using approaches based on factorization and Cauchy's argument principle). The interest in considering multiple roots does not rely on the multiplicity itself, but on its connection with dominance and its implications for stability analysis and control design.

Main results

The main results of this paper prove that the MID property holds for some classes of systems under the form (1).

Theorem 1 *Consider the quasipolynomial Δ given by* (2) *in the case $N = 1$. Let $s_0 \in \mathbb{R}$. The number s_0 is a root of multiplicity $2n$ of Δ if and only if, for every $k \in \{0, \ldots, n-1\}$,*

$$\begin{cases} \alpha_{0,k} = \binom{n}{k} (-s_0)^{n-k} + (-1)^{n-k} n! \displaystyle\sum_{j=k}^{n-1} \binom{j}{k} \binom{2n-j-1}{n-1} \frac{s_0^{j-k}}{j! \tau_1^{n-j}}, \\ \alpha_{1,k} = (-1)^{n-1} e^{s_0 \tau_1} \displaystyle\sum_{j=k}^{n-1} \frac{(-1)^{j-k} (2n-j-1)!}{k!(j-k)!(n-j-1)!} \frac{s_0^{j-k}}{\tau_1^{n-j}}. \end{cases} \tag{3}$$

Moreover, if (3) *is satisfied, then s_0 is a strictly dominant root of Δ.*

Thanks to the change of variables $z = \tau_1(s - s_0)$ transforming $\Delta(s)$ into $\hat{\Delta}(z) = \tau^n \Delta(s_0 + \frac{z}{\tau_1})$, it suffices to prove Theorem 1 in the case $s_0 = 0$ and $\tau_1 = 1$. Its first part can be obtained by solving the system of linear equations $\hat{\Delta}^{(\ell)}(0) = 0$ for $\ell \in \{0, \ldots, 2n-1\}$. As for the second part, when (3) is satisfied and $z = 0$ is a root of multiplicity $2n$ of $\hat{\Delta}$, one can factorize $\hat{\Delta}$ as $\hat{\Delta}(z) = z^{2n} I(z)$, where $I(z)$ is an entire function which can be written as an integral, for

instance $I(z) = \int_0^1 t(1-t)^2 e^{-zt}\,\mathrm{d}t$ when $n = 2$. A direct study of I, making use of the a priori information that roots z of $\hat{\Delta}$ in the closed right half-plane $\mathbb{C}_+$ must satisfy $|\mathrm{Im}\, z| \leq 2\pi$, shows that it cannot have roots in $\mathbb{C}_+$. A detailed proof is provided in [6].

Theorem 2 *Consider the quasipolynomial Δ given by* (2) *in the case $N = 1$ and $n = 2$. Let $s_0 \in \mathbb{C}$, $\sigma_0 = \mathrm{Re}\, s_0$, and $\theta_0 = \mathrm{Im}\, s_0$ and assume that $\theta_0 \neq 0$. The numbers s_0 and $\overline{s}_0$ are roots of multiplicity 2 of Δ if and only if*

$$\begin{cases} \alpha_{0,0} = \sigma_0^2 + 2\sigma_0\theta_0 \dfrac{\tau_1\theta_0 - \sin(\tau_1\theta_0)\cos(\tau_1\theta_0)}{\tau_1^2\theta_0^2 - \sin^2(\tau_1\theta_0)} + \theta_0^2 \dfrac{\tau_1^2\theta_0^2 + \sin^2(\tau_1\theta_0)}{\tau_1^2\theta_0^2 - \sin^2(\tau_1\theta_0)}, \\ \alpha_{0,1} = -2\sigma_0 - 2\theta_0 \dfrac{\tau_1\theta_0 - \sin(\tau_1\theta_0)\cos(\tau_1\theta_0)}{\tau_1^2\theta_0^2 - \sin^2(\tau_1\theta_0)}, \\ \alpha_{1,0} = 2\theta_0 e^{\sigma_0\tau_1}\left(\sigma_0 \dfrac{\sin(\tau_1\theta_0) - \tau_1\theta_0\cos(\tau_1\theta_0)}{\tau_1^2\theta_0^2 - \sin^2(\tau_1\theta_0)} - \dfrac{\tau_1\theta_0^2\sin(\tau_1\theta_0)}{\tau_1^2\theta_0^2 - \sin^2(\tau_1\theta_0)}\right), \\ \alpha_{1,1} = 2\theta_0 e^{\sigma_0\tau_1} \dfrac{\tau_1\theta_0\cos(\tau_1\theta_0) - \sin(\tau_1\theta_0)}{\tau_1^2\theta_0^2 - \sin^2(\tau_1\theta_0)}. \end{cases} \tag{4}$$

Moreover, if (4) *is satisfied, then s_0 and $\overline{s}_0$ are a pair of strictly dominant roots of Δ.*

Similarly to Theorem 1, one may reduce the proof of Theorem 2 to the case $\sigma_0 = 0$ and $\tau_1 = 1$, with (4) being again proved by solving a linear system of equations. As $\theta_0 \to 0$, (4) converges (3) with $n = 2$, and one can thus prove dominance of the complex conjugate pair $\pm i\theta_0$ by proving that, as θ_0 increases from 0, no roots of $\hat{\Delta}$ may lie on the imaginary axis other than $\pm i\theta_0$, and hence no roots can cross to the right half-plane. See [7] for a detailed proof.

Theorem 3 *Consider the quasipolynomial Δ given by* (2) *in the case $N = 2$ and $n = 1$. Let $s_0 \in \mathbb{R}$. The number s_0 is a root of multiplicity $2n$ of Δ if and only if*

$$\alpha_{0,0} = -s_0 - \frac{1}{\tau_1} - \frac{1}{\tau_2}, \qquad \alpha_{10} = e^{s_0\tau_1}\frac{\tau_2}{\tau_1(\tau_2 - \tau_1)}, \qquad \alpha_{20} = -e^{s_0\tau_2}\frac{\tau_1}{\tau_2(\tau_2 - \tau_1)}. \tag{5}$$

Moreover, if (5) *is satisfied, then s_0 is a strictly dominant root of Δ.*

One obtains (5) using the same arguments from Theorems 1 and 2. The second part of the statement can be proved by considering the limit $\tau_2 \to \tau_1$ and proving that s_0 is dominant for the limiting quasipolynomial and that, as τ_2 increases, no roots other than s_0 may have real part s_0, excluding the possibility of any other root becoming dominant.

Conclusion

We further explored the MID property for generic single-delay retarded systems of arbitrary order, showing that a real spectral value with maximal multiplicity is necessarily dominant. For a scalar equation with two delays, it is shown that the MID property still applies. Further, in the second-order case, we contributed by extending the MID property for complex conjugate pairs of spectral values.
In recent studies, the applicability of the MID property in reduced-complexity delayed controller design was shown, where the attenuation of the dominant vibrating modes of flexible mechanical structures was considered [2]. In future work, the MID property will be further exploited in the problem of vibration quenching.

References

[1] I. Boussaada, S.-I. Niculescu, A. El Ati, R. Perez-Ramos, and K. L. Trabelsi. Multiplicity-induced-dominancy in parametric second-order delay differential equations: Analysis and application in control design. *ESAIM Control Optim. Calc. Var.*, to appear.

[2] I. Boussaada, S.-I. Niculescu, S. Tliba, and T. Vyhlídal. On the coalescence of spectral values and its effect on the stability of time-delay systems: Application to active vibration control. *Procedia IUTAM*, 22:75–82, 2017.

[3] I. Boussaada, S. Tliba, S.-I. Niculescu, H. U. Ünal, and T. Vyhlídal. Further remarks on the effect of multiple spectral values on the dynamics of time-delay systems. Application to the control of a mechanical system. *Linear Algebra Appl.*, 542:589–604, 2018.

[4] J. Chen, G. Gu, and C. N. Nett. A new method for computing delay margins for stability of linear delay systems. *Systems Control Lett.*, 26(2):107–117, 1995.

[5] K. Gu, V. L. Kharitonov, and J. Chen. *Stability of time-delay systems*. Control Engineering. Birkhäuser Boston, Inc., Boston, MA, 2003.

[6] G. Mazanti, I. Boussaada, and S.-I. Niculescu. Multiplicity-induced-dominancy for delay-differential equations of retarded type. *J. Differential Equations*, 286:84–118, 2021.

[7] G. Mazanti, I. Boussaada, S.-I. Niculescu, and T. Vyhlídal. Spectral dominance of complex roots for single-delay linear equations. *IFAC-PapersOnLine*, 53(2):4357–4362, 2020. 21st IFAC World Congress.

[8] W. Michiels and S.-I. Niculescu. *Stability and stabilization of time-delay systems: An eigenvalue-based approach*, volume 12 of *Advances in Design and Control*. Society for Industrial and Applied Mathematics (SIAM), Philadelphia, PA, 2007.

[9] N. Olgac and R. Sipahi. An exact method for the stability analysis of time-delayed linear time-invariant (LTI) systems. *IEEE Trans. Automat. Control*, 47(5):793–797, 2002.

[10] G. Pólya and G. Szegő. *Problems and theorems in analysis. I*. Classics in Mathematics. Springer-Verlag, Berlin, 1998. Series, integral calculus, theory of functions, Translated from the German by Dorothee Aeppli, Reprint of the 1978 English translation.

[11] R. Sipahi, S.-I. Niculescu, C. T. Abdallah, W. Michiels, and K. Gu. Stability and stabilization of systems with time delay: limitations and opportunities. *IEEE Control Syst. Mag.*, 31(1):38–65, 2011.

Playing dominoes with lasers: Excitability and pulsed solutions of the Yamada model for a semiconductor laser with saturable absorber and delayed optical feedback

Stefan Ruschel[*,†], Bernd Krauskopf[*,†] and Neil G. R. Broderick [‡,†]
[*]*Department of Mathematics, The University of Auckland, New Zealand*
[†]*Dodd-Walls Centre for Photonic and Quantum Technologies, New Zealand*
[‡]*Department of Physics, The University of Auckland, New Zealand*

Summary. We are concerned with the generation of periodic light pulses in semiconductor lasers with saturable absorber through delayed re-injection of the pulse via a reflecting mirror. More specifically, we consider the Yamada model with delayed feedback and study the generation of periodic pulse trains via repeated self-excitation after passage through the delayed feedback loop. We employ numerical continuation and analytical methods for delay differential equations to characterize these periodic solution and their bifurcations.

Surely everyone is familiar with chain reactions of falling domino tiles. After careful preparation of upright rectangular tiles along some path and in close proximity to one another, toppling the first tile leads to a chain reaction that hopefully causes all dominoes to fall. Such setups shall serve as an analogy for directed networks of delay-coupled excitable systems. Here, a sufficiently large perturbation (toppling the first tile) is capable of producing an excitation, in the form of a pulse, a spike or some kind of localized change in a physical quantity (momentum in the case of dominoes), which propagates to a subsequent node in the network and itself serves as a perturbation. If this perturbation is again large enough, a secondary excitation is created and the process continues. The speed of this propagation is finite and can be modeled via time delays between the nodes. Specific examples of this kind of relay are networks of semiconductor lasers with saturable absorber; another is the human brain consisting of millions of connected neurons, which are hard to study both experimentally and analytically.

Motivated by experiments with a micropillar semiconductor laser with saturable absorber and a reflecting mirror [1], we are concerned with the simplest network motif allowing for sustained re-excitation: a single node with delayed self-coupling. We modify the Yamada model [2] for an excitable or self-pulsating laser to incorporate delayed optical self-feedback [3]. Although seemingly simple, this setup allows for the generation of periodic light pulses that constitute the basis for modern telecommunication, material processing and high energy physics.

Here, we present an analytical tool that characterizes the onset and termination of such light pulses as a bifurcation in this system of delay differential equations (DDE). In dimensionless form, the model reads

$$G'(t) = \gamma\left(A - G(t)[1 + I(t)]\right), \tag{1}$$
$$Q'(t) = \gamma\left(B - Q(t)[1 + aI(t)]\right), \tag{2}$$
$$I'(t) = \left[G(t) - Q(t) - 1\right] I(t) + \kappa I(t - \tau). \tag{3}$$

Equations (1)–(3) describe the time evolution of the laser output intensity $I(t)$, as well as the gain $G(t)$ and absorption $Q(t)$ of photons in the laser cavity. The parameter A is the pump strength (the amount of energy provided to the laser), $B, a, \gamma > 0$ describe physical properties of the laser; and they differ from device to device. The time delay τ reflects the distance from the mirror to the laser cavity and the feedback strength κ accounts for the losses along that feedback loop. We fix parameters $A = 6.5, B = 5.8, a = 1.8$, and $\gamma = 0.04$ as in [4] and refer the interested reader to [1, 2] for the physical details.

The excitability of Eqs. (1)–(3) is governed by a homoclinic bifurcation [4]. For the considered parameter values, the stable manifold of a steady state locally separates the state space of the system [5]. The laser is essentially off, yet a sufficiently large perturbation that brings the system above this manifold, causes a fast increase in I that is followed by fast relaxation. Such an orbit is referred to as a pulse in the context of lasers; see Fig. 1(a, black) for an example. At the homoclinic bifurcation, the stable and unstable manifold of the equilibrium intersect transversally and give rise to a periodic orbit [4].

In the following, we focus on the full system (1)–(3) and study the effects of delayed feedback to the system in the excitable configuration. A detailed bifurcation analysis of Eqs. (1)–(3) has been carried out earlier by some of the authors [6], and we present here a refined analysis with regard to periodic orbits that are generated by sustained self-excitation after one delayed feedback loop. To illustrate our results, we fix $\tau = 5000$ and $\kappa = 0.52$ and prepare the pulse in Fig. 1(a) as the initial condition for system (1)–(3). We observe sustained pulsation: each pulse travels along the delayed feedback loop and triggers a subsequent pulse after approximately one delay interval. Remarkably, the pulsed solution reached from this initial condition has a higher peak intensity than the original pulse of the solitary system, and we observe a different profile; see Fig. 1(b, blue). Our formal analysis reveals that these solutions correspond to different periodic orbits, which coexist for the chosen parameter values. In fact, there is a third type of small pulsed solution present for the chosen parameter values; see Fig. 1(c, red).

We employ numerical continuation to reveal that these solutions correspond to different branches (black, blue, red) of periodic orbits when the time delay is varied as a parameter; see Fig. 1(d). The branches of periodic orbits share a

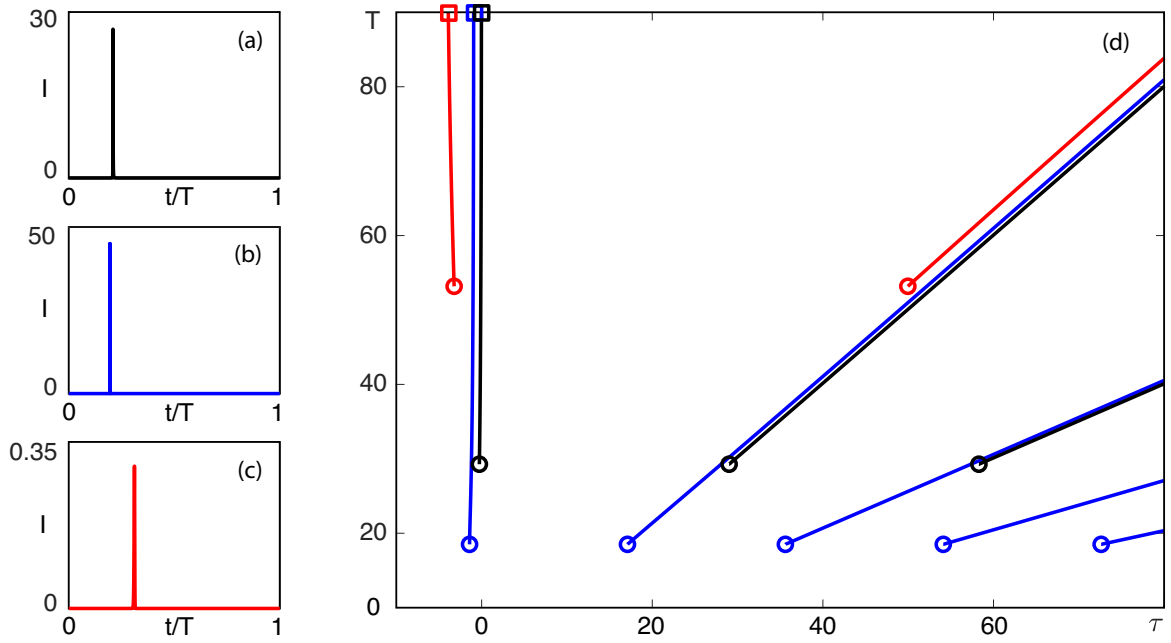

Figure 1: Panels (a)-(c) show the I-component of coexisting pulsed solutions with large period for large delay $\tau = 5000$. Panel (d) is the corresponding bifurcation diagram for small values of the delay; shown are the period of the periodic orbits (solid curves), points of Hopf bifurcations (circles), and indicated loci of Homoclinic bifurcations (squares). Other parameters are $A = 6.5, B = 5.8, a = 1.8, \gamma = 0.04$, and $\kappa = 0.52$.

remarkable property: their period scales effectively linearly with the delay. More precisely, the period T along a given family satisfies $T = \tau + \delta$, where $\delta \ll \tau$ and $\delta/\tau = T/\tau - 1 \to 0$ as $\tau \to \infty$. The intuition is clear: the I-component of the pulsed solutions is close to zero throughout most of their period. Therefore, a pulse that is emitted at time t, travels the length of the delay loop and only affects the system at time $t + \tau$. Additionally, there is a certain response time δ of the system to build up in intensity and to produce a subsequent pulse. Such periodic solutions are also referred to as Temporal Dissipative Solitons (TDS) in DDEs [7]. Each branch of pulsed periodic orbits in system (1)–(3) corresponds to a family of periodic solutions of the so-called profile equation, given by Eqs. (1)–(2) and

$$I'(t) = [G(t) - Q(t) - 1]\, I(t) + \kappa I(t + \delta), \tag{4}$$

which undergoes a homoclinic bifurcation. Figure 1(d) shows that for each branch of periodic orbits (black, blue, black) with $T > \tau$, for $\tau > 0$, there is a branch (red, blue, black) of periodic orbits with $\tau < 0$ exhibiting a homoclinic bifurcation. This correspondence can be seen by using the concept of reappearance of periodic orbits for DDEs [8].
Hence, we study the pulsed solutions of Eqs. (1)–(3) indirectly via bifurcations and codimension-two points of homoclinic orbits in Eqs. (1),(2) and (4). We show that the onset and termination of such pulse trains correspond to a bifurcation of countably many saddle-node periodic orbits with infinite period; moreover, we show these bifurcations coincide with codimension-two points along the family of homoclinic orbits as κ is varied as a parameter. This approach allows us to compute the corresponding critical coupling strengths that give rise to pulsed solutions in Eqs. (1)-(3). Our methodology is relevant for the rigorous analysis of delay-coupled excitable systems in general. Future applications will include recurrent networks of lasers and neurons, which are in a similar excitable configuration when at rest.

References

[1] Barbay S., Kuszelewicz R., Yacomotti A. M. (2011) Excitability in a semiconductor laser with saturable absorber. *Optics Lett.* **36**:4476.

[2] Yamada M. (1992) A Theoretical Analysis of Self-Sustained Pulsation Phenomena in Narrow-Stripe Semiconductor Lasers. *IEEE J. Quantum Electron.*, 29(5):1330–1336.

[3] Krauskopf B., Walker J. J. (2012) Bifurcation Study of a Semiconductor Laser with Saturable Absorber and Delayed Optical Feedback. *Nonlinear Laser Dyn. From Quantum Dots to Cryptogr.*, Wiley-VCH Verlag GmbH & Co. KGaA, Weinheim, Germany, 161–181.

[4] Dubbeldam J., Krauskopf B. (1999) Self-pulsations of lasers with saturable absorber: dynamics and bifurcations *Optics Comm.* **159**:325–338.

[5] Otupiri R., Krauskopf B., Broderick N. G. R. (2019) The Yamada model for a self-pulsing laser: bifurcation structure for non-identical decay times of gain and absorber. *arXiv:* 1911.01835.

[6] Terrien S., Krauskopf B., Broderick N. (2017) Bifurcation Analysis of the Yamada Model for a Pulsing Semiconductor Laser with Saturable Absorber and Delayed Optical Feedback *SIAM J. Appl. Dyn. Syst.* **16**:771-801.

[7] Yanchuk S., Ruschel S., Sieber J., Wolfrum M. (2019) Temporal dissipative solitons in time-delay feedback systems *Phys. Rev. Lett.* **123**:053901.

[8] Yanchuk S., Perlikowski P. (2009) Delay and Periodicity *Phys. Rev. E* **79**:046221.

[9] Sieber J., Engelborghs K., Luzyanina T., Samaey G., and Roose D. (2014) DDE-BIFTOOL Manual - Bifurcation analysis of delay differential equations. *arXiv:* 1406.7144.

Ploughing-limited post-critical dynamics under chatter in turning. Harmonic balance based investigation

Mikhail Guskov*
*PIMM, Arts et Metiers Institute of Technology, CNRS, Cnam, HESAM University, 151 boulevard de l'Hopital, 75013 Paris (France)

Summary. At chatter onset, as many works show, vibrations magnitudes grow until the tool exits the continuous cutting. Another magnitude limitation mechanism, namely ploughing is investigated in the present contribution, in a harmonic balance + continuation framework

Chatter problematics

Regenerative chatter instability in metal cutting processes such as turning is known to possess subcritical behaviour [1], inducing bistable regions in the vicinity of the bifurcation. Investigations of post-critical vibrations have shown growing magnitude until the tool exit [2]. Once the cut becomes intermittent due to tool exit, the dynamics are much more complex due to the interrupted surface regeneration. Nevertheless, in some cases magnitude is limited by other mechanisms, such as ploughing [3]. In the present work we investigate post-critical dynamics of a 1 degree of freedom (DOF) with a piecewise linear ploughing model via a harmonic balance method (HBM) framework coupled with arclength continuation.

1DOF cutting system

The investigation is carried out on a system schematized on Fig. 1, giving place to the following equation of motion:

$$m\ddot{X} + c\dot{X} + kX = F_c(h) + F_p(\dot{X}), \tag{1}$$

$$F_c = -F_{c0}\left(\frac{h}{f}\right)^{\alpha}, \qquad h = f + X - X_D, \quad X_D = X(t-D), \tag{2}$$

$$F_p = -H(\Delta\Gamma)\,F_{p0}\,\Delta\Gamma, \qquad \Delta\Gamma = \frac{\dot{X}}{V_c} - \Gamma, \tag{3}$$

with m mass, c damping, k stiffness, f feed, V_c cutting velocity, D delay period, F_c and F_p cutting and ploughing force, F_{c0}, F_{p0}, α, Γ respective tool-workpiece interaction parameters, H Heaviside step function.
Cutting force definition (2) is based on the assumption of uninterrupted cut. The ploughing force model (3) features a unilateral penalty term corresponding to a closure of effective clearance angle $\Delta\Gamma$ at high magnitude oscillations.

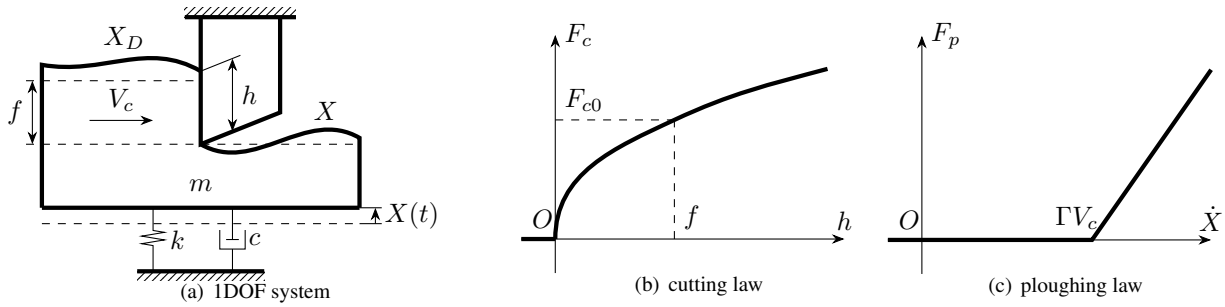

(a) 1DOF system (b) cutting law (c) ploughing law

Figure 1: Cutting system model illustration

By introducing, for a given oscillation frequency ω, time and length scaling $\tau = \omega t$ and $x = X/f$, the equation (1) can be rewritten in adimensional form:

$$\Omega^2 x'' + 2\Omega\zeta x' + x + \kappa\,(x - x_D + 1)^{\alpha} + Z_p\Pi_p(\Omega x' - \phi) = 0, \qquad \Pi_p = H(\Omega x' - \phi) \tag{4}$$

In the present work, the system is based on a case described in literature [4], with chatter onset parameters $\zeta = 0.01$, $\Omega = \omega/\sqrt{k/m} = \sqrt{1-2\zeta}$, $\omega D = 3\pi/2$, $\alpha\kappa_0 = 0.02$, the cutting law being a power law with exponent $\alpha = 3/4$.

HBM approach with continuation

The HBM approach used in this work is a variant of trigonometric collocation [5]. The solution is sought in the form of a trigonometric polynomial or order N (N-truncated Fourier series):

$$x(\tau) = \mathbf{T}(\tau)\mathbf{x}, \qquad \mathbf{T} = \left[\frac{1}{2}, \cos\tau, \sin\tau, ..., \cos N\tau, \sin N\tau\right], \qquad \mathbf{x} = [a_0,\, a_1,\, b_1, ...,\, a_N,\, b_N]^T \tag{5}$$

In the case of chatter, constituting an auto-oscillation of a priori unknown frequency Ω, a phase condition is used ($b_1 = 0$). For variation of κ in the vicinity the chatter onset configuration at a given delay D, the following continuation condition ("arclength") is used for neighbouring points:

$$\|\Delta \mathbf{x}\|^2 + \Delta\Omega^2 + \Delta\kappa^2 = s^2 \tag{6}$$

with s a given (small) step distance.

Investigation of ploughing parameters

The postcritical oscillations were analyzed in a range $\kappa \in [0,\ 2\kappa_0]$ for a wide set of ploughing parameters Z_p and ϕ was simulated, with $N = 7$ and time discretization of 1024 points. The response is essentially mono-harmonic and thus are shown as the magnitude of the fundamental component on fig. 2. As for other variables, it can be noticed that Ω remains very close to 1 and the static component a_0 shows a slight variation with κ.
The upper limits of the plots are due to the cut interruption. The left branch of the plots, especially in cases of high ploughing thresholds $\phi \geq 0.7$, corresponds to a "no ploughing" behavior. The ploughing term comes in at $a_1 \approx \phi/\Omega$. As a general trend, the oscillation magnitudes tend be lower for higher ploughing coefficient Z_p and for small ϕ. In particular, for the lowest values of Z_p combined with big ϕ, the tool gets to exit the cutting process in the given range of κ (top limits of the plots). At the extreme opposite, one can notice for $Z_p \geq 3$ a quasi-constant oscillation magnitude is maintained.

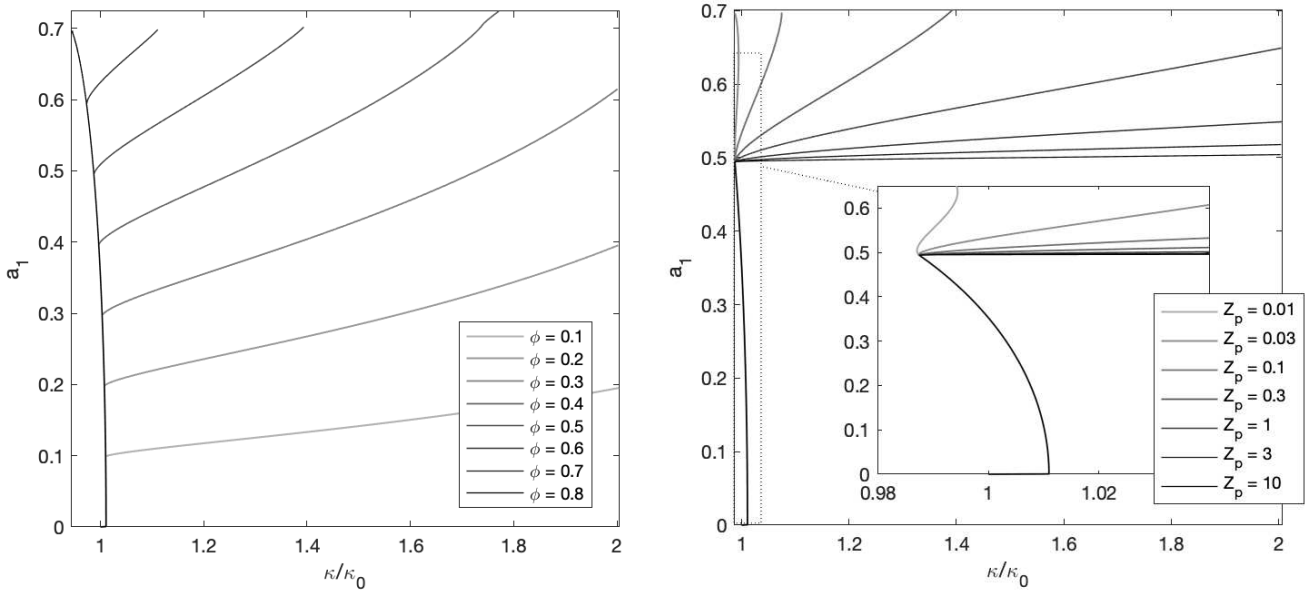

(a) $Z_p = 0.1$ (b) $\phi = 0.5$

Figure 2: Postcritical response of (4) for $\kappa \in [0, 2\kappa_0]$

References

[1] Hanna, NH, and SA Tobias. (1969) The Non-Linear Dynamic Behaviour of a Machine Tool Structure. *International Journal of Machine Tool Design and Research* **9**, no. 3: 293–307.

[2] Dombovari, Zoltan, David A. W. Barton, R. Eddie Wilson, and Gabor Stepan (2011) On the Global Dynamics of Chatter in the Orthogonal Cutting model. *International Journal of Non-Linear Mechanics* **46**, no. 1: 330–38.

[3] Gerasimenko, A., M. Guskov, P. Lorong, J. Duchemin, and A. Gouskov (2016) Experimental Investigation of Chatter Dynamics in Thin-Walled Tubular Parts Turning, *HSM16 conference, Metz, France*.

[4] Altintas, Yusuf (2012) Manufacturing Automation: Metal Cutting Mechanics, Machine Tool Vibrations, and CNC Design. *Cambridge University Press*.

[5] Nataraj, C., and H. D. Nelson (1989) Periodic Solutions in Rotor Dynamic Systems With Nonlinear Supports: A General Approach. *Journal of Vibration, Acoustics, Stress, and Reliability in Design***111**, no. 2: 187–93.

Friday, July 22, 2022
08:30 - 10:30

MS-09 Nonlinear Dynamics in Engineering Systems

Auditorium Lumiere

Chair: Yuri Mikhlin - Konstantin Avramov

Friday, July 22, 2022

08:30 - 10:30

MS-18 Control and Synchronization in Nonlinear Systems

Rhone 1

Chair: A. Pavlov, B. Brogliato

08:30 - 08:50

Suppression of synchronous spiking in two interacting populations of excitatory and inhibitory quadratic integrate-and-fire neurons

PYRAGAS Kestutis*, FEDARAVIČIUS Augustinas, PYRAGIENĖ Tatjana

*Center for Physical Sciences and Technology (Savanorių pr. 231, LT-02300 Vilnius Lithuania)

08:50 - 09:10

Synchronization of a Sef-Excited Inertia Wheel Pendula Array

YAKIR Gilad*, GOTTLIEB Oded

*Technion - Israel Institute of Technology (Mechanical Engineering, Technion City, Haifa 320003 Israel)

09:10 - 09:30

Synchronization of networks of dynamical systems by nonlinear integral couplings and sequential decoloring of the network graph

PAVLOV Alexey*, STEUR Erik, VAN De Wouw Nathan

*Norwegian University of Science and Technology [Trondheim] (NO-7491 Trondheim Norway)

09:30 - 09:50

Vibration control of underactuated 3-DOF systems inspired by tuned vibration absorbers: the non-linear Euler-Lagrange controller

JUCHEM Jasper*, LOCCUFIER Mia

*Ghent University (Technologiepark 125, 9052 Zwijnaarde Belgium)

Suppression of synchronous spiking in two interacting populations of excitatory and inhibitory quadratic integrate-and-fire neurons

Kestutis Pyragas, Augustinas P. Fedaravičius, and Tatjana Pyragienė
Department of Fundamental Research, Center for Physical Sciences and Technology, Vilnius, Lithuania

Summary. Collective oscillations and their suppression by external stimulation are analyzed in a large-scale neural network consisting of two interacting populations of excitatory and inhibitory quadratic integrate-and-fire neurons. In the limit of an infinite number of neurons, the microscopic model of this network can be reduced to an exact low-dimensional system of mean-field equations. Bifurcation analysis of these equations reveals three different dynamic modes in a free network: a stable resting state, a stable limit cycle, and bistability with a coexisting resting state and a limit cycle. We show that in the limit cycle mode, high-frequency stimulation of an inhibitory population can stabilize an unstable resting state and effectively suppress collective oscillations. We also show that in the bistable mode, the dynamics of the network can be switched from a stable limit cycle to a stable resting state by applying an inhibitory pulse to the excitatory population. The results are confirmed by numerical simulation of the microscopic model.

Introduction

Synchronization processes in large populations of interacting dynamical units are the focus of intense research in physical, technological and biological systems. In neural networks, synchronization can play a dual role. Under normal conditions, synchronization is responsible for cognition and learning, while excessive synchronization can cause abnormal brain rhythms associated with neurological diseases such as Parkinson's disease, epilepsy, and others. Various algorithms have been developed to suppress unwanted synchronized network oscillations. A therapeutic procedure clinically approved for the treatment of Parkinson's disease is a high-frequency (HF) deep brain stimulation (DBS). The mechanism of action of DBS is still poorly understood. Clinical observations show that the effects of lesions and DBS of the same target area are similar. This suggests that HF stimulation suppresses neuronal activity in the target area. In this context, the effect of HF stimulation can be explained in terms of stabilization of neuron's resting state [1]. However, there is no clear theoretical understanding of how HF stimulation affects synchronization processes in neural networks.

Recent advances in dynamical systems theory have allowed us to better understand the effects of synchronization in large-scale oscillatory networks. A major breakthrough in these studies was achieved by Ott and Antonsen [2], who showed that the microscopic model equations of globally coupled heterogeneous phase oscillators (Kuramoto model) can be reduced to a low-dimensional system of ordinary differential equations that accurately describe the macroscopic evolution of the system in the infinite-size (thermodynamic) limit. Later this approach was extended to a particular class of heterogeneous neural networks composed of all-to-all pulse-coupled quadratic integrate-and-fire (QIF) neurons [3]. In thermodynamic limit, a low-dimensional system of mean-field equations was derived for biophysically relevant macroscopic quantities: the firing rate and the mean membrane potential. The approach has been further developed in recent publications to analyze the occurrence of synchronized macroscopic oscillations in networks of QIF neurons with a realistic synaptic coupling [4], in the presence of a delay in couplings [5] and in the presence of noise [6].

Here, we demonstrate that mean-field equations are useful not only for understanding the occurrence of collective oscillations in large-scale neural networks, but also for understanding the effect of stimulation on synchronization processes [7]. As an example, we consider a network of two interacting populations of excitatory and inhibitory QIF neurons.

Microscopic model and low-dimensional mean-field equations in the thermodynamic limit

The microscopic state of the QIF network is determined by the set of $2N$ neurons' membrane potentials $\{V_j^{(E,I)}\}_{j=1,\dots,N}$, which satisfy the following system of $2N$ ordinary differential equations:

$$\tau \dot{V}_j^{(E,I)} = (V_j^{(E,I)})^2 + \eta_j^{(E,I)} + \mathcal{I}_j^{(E,I)}, \;\; \text{if} \;\; V_j^{(E,I)} \geq V_p \;\; \text{then} \;\; V_j^{(E,I)} \leftarrow V_r. \tag{1}$$

Here, τ is the membrane time constant and $V_j^{(E,I)}$ is the membrane potential of neuron j in either the excitatory (E) or the inhibitory (I) population. For simplicity, we set the number of neurons N and the time constant τ the same for both populations. The heterogeneous parameter of excitability $\eta_j^{(E,I)}$ is a current that specifies the behavior of each isolated neuron and the term $\mathcal{I}_j^{(E,I)}$ defines the synaptic coupling between neurons as well as external stimulation. The isolated neurons ($\mathcal{I}_j^{(E,I)} = 0$) with the negative value of the parameter $\eta_j^{(E,I)} < 0$ are at rest, while the neurons with the positive value of the parameter $\eta_j^{(E,I)} > 0$ generate instantaneous spikes, which are approximated by the Dirac delta function. The spikes are emitted at the moments when the membrane potential $V_j^{(E,I)}$ reaches a peak value V_p. Immediately after the spike emission the membrane potential is reset to a value V_r. We assume $V_p = -V_r \to \infty$. The values of the heterogeneous parameter $\eta_j^{(E,I)}$ for both populations are independently taken from the Lorentzian distributions: $g_{E,I}(\eta) = \Delta_{E,I}/\{\pi[(\eta - \bar{\eta}_{E,I})^2 + \Delta_{E,I}^2]\}$, where $\Delta_{E,I}$ and $\bar{\eta}_{E,I}$ are respectively the width and the center of the

distribution for the excitatory (E) and inhibitory (I) populations. The last term $\mathcal{I}_j^{(E,I)}$ in Eqs. (1) describes synaptic coupling and an external stimulation. For the excitatory and inhibitory populations, this term respectively is

$$\mathcal{I}_j^{(E)} = -J_{IE}S_I(t) + I_E(t), \quad \mathcal{I}_j^{(I)} = J_{EI}S_E(t) - J_{II}S_I(t) + I_I(t). \tag{2}$$

Here, $S_E(t)$ and $S_I(t)$ determine the mean synaptic activation of E and I populations:
$S_{E,I}(t) = \frac{\tau}{N}\sum_{j=1}^{N}\sum_{k\setminus(t_j^k)_{E,I}<t}\delta(t-(t_j^k)_{E,I})$, where $(t_j^k)_{E,I}$ is the time of the kth spike of the jth neuron in either E or I population and $\delta(t)$ is the Dirac delta function. The positive parameters J_{EI}, J_{IE} and J_{II} define synaptic weights. The current $-J_{IE}S_I(t)$ inhibits E neurons due to synaptic activity of I population, while the current $J_{EI}S_E(t)$ excites I neurons due to synaptic activity of E population. The term $-J_{II}S_I(t)$ determines recurrent inhibition of neurons within I population. The currents $I_E(t)$ and $I_I(t)$ represent external homogeneous stimulation of the excitatory and the inhibitory populations, respectively.
In the thermodynamic limit $N \to \infty$, the microscopic model (1) can be reduced to the exact system of four ODEs [3]:

$$\tau\dot{r}_E = \Delta_E/\pi + 2r_Ev_E, \quad \tau\dot{v}_E = \bar{\eta}_E + v_E^2 - \pi^2r_E^2 - J_{IE}r_I + I_E(t), \tag{3a}$$

$$\tau\dot{r}_I = \Delta_I/\pi + 2r_Iv_I, \quad \tau\dot{v}_I = \bar{\eta}_I + v_I^2 - \pi^2r_I^2 + J_{EI}r_E - J_{II}r_I + I_I(t), \tag{3b}$$

where $r_{E,I}(t)$ and $v_{E,I}(t)$ are respectively the spiking rates and the mean membrane potentials of E and I populations.

Results and conclusions

Relatively simple mean field Eqs. (3) make it possible to conduct a thorough bifurcation analysis of various dynamic modes of a free network and to reveal the mechanisms of action of various stimulation algorithms. We performed a bifurcation analysis of a free network depending on the coupling strengths J_{EI} and J_{IE} of the bidirectional interaction between excitatory and inhibitory populations and the coupling strength J_{II}, which determines the interaction within the inhibitory population. We also built a bifurcation diagram in the plane of the parameters $(\bar{\eta}_I, \bar{\eta}_E)$, which determine the centers of the distributions $g_{E,I}(\eta)$ of the excitability parameter η for I and E populations. As a result of this analysis, three different modes were established. Depending on the values of the parameters, the system can have a single stable fixed point, a single stable limit cycle, or be in a bistable mode with these two coexisting attractors.
As the next step in our analysis, we looked at the problem of controlling network synchronization. Some neurological diseases are successfully treated with high-frequency stimulation. Here, we tested the effectiveness of the HF algorithm for suppressing synchronous spiking in the network of excitatory and inhibitory QIF neurons. We have shown that HF stimulation of the inhibitory population is very effective, whereas HF stimulation of the excitatory population cannot suppress the oscillations. The mechanism of action of HF stimulation is explained using mean-field equations averaged over the stimulation period. The averaged mean-field equations are equivalent to the free mean-field equations, but with a modified parameter $\bar{\eta}_I$ or $\bar{\eta}_E$, depending on which inhibitory or excitatory population is stimulated. When HF stimulation is applied to the inhibitory population, changing the $\bar{\eta}_I$ parameter increases the proportion of spiking neurons in that population. This leads to the stabilization of the state of rest of the network. The averaged mean-field equations made it possible to obtain an analytical expression for the threshold amplitude of HF stimulation, which stabilizes the resting state. This amplitude is proportional to the frequency of stimulation.
HF stimulation of the excitatory population is ineffective, since changing the $\bar{\eta}_E$ parameter increases the proportion of spiking neurons in the excitatory population and cannot stabilize the resting state of the network. Nevertheless, stopping the network oscillation by controlling the excitatory population can still be achieved if the system parameters are in the bistable area. By applying a rectangular inhibitory pulse to this population, the network state can be switched from the stable limit cycle to the stable state of rest.
To test the performance of the above stimulation algorithms for finite-size networks, we numerically simulated the equations of the microscopic model. Modeling networks with 2000 excitatory and 2000 inhibitory QIF neurons gave results that are in good agreement with the results obtained from the mean-field equations. Based on our research, we believe that mean-field equations derived from the microscopic dynamics of interacting QIF neurons can serve as an effective tool for developing various stimulation algorithms to control synchronization processes in large-scale neural networks.

References

[1] Pyragas K., Novičenko V., Tass P. A. (2013) Mechanism of suppression of sustained neuronal spiking under high-frequency stimulation. *Biol. Cybern.* **107**:669-684.

[2] Ott E., Antonsen, T. M. (2008) Low dimensional behavior of large systems of globally coupled oscillators. *Chaos* **18**:037113.

[3] Montbrió E., Pazó D., Roxin A. (2015) Macroscopic Description for Networks of Spiking Neurons. *Phys. Rev. X* **5**:021028.

[4] Ratas I., Pyragas K. (2016) Macroscopic self-oscillations and aging transition in a network of synaptically coupled quadratic integrate-and-fire neurons. *Phys. Rev. E* **94**:032215.

[5] Ratas I., Pyragas K. (2018) Macroscopic oscillations of a quadratic integrate-and-fire neuron network with global distributed-delay coupling. *Phys. Rev. E* **98**:052224.

[6] Ratas I., Pyragas K. (2019) Noise-induced macroscopic oscillations in a network of synapt ically coupled quadratic integrate-and-fire neurons. *Phys. Rev. E* **100**:052211.

[7] Pyragas K., Fedaravičius A. P., Pyragienė T. (2021) Suppression of synchronous spiking in two interacting populations of excitatory and inhibitory quadratic integrate-and-fire neurons. *Phys. Rev. E* **104**:014203.

Synchronization of a Self-Excited Inertia-Wheel Pendula Array

Gilad Yakir and Oded Gottlieb
Dept. of Mechanical Engineering, Technion – Israel Institute of Technology, Haifa, 32000, Israel

Summary. We investigate synchronization of a self-excited inertia wheel pendula array. The dynamical system exhibits asymptotically stable equilibria, periodic limit cycle oscillations, and non-stationary rotations. The analysis reveals that synchronous periodic oscillators are in-phase whereas quasiperiodic oscillators are out-of-phase. Furthermore, the non-stationary rotations exhibit combinations of oscillations and rotations of the individual elements which are asynchronous.

Introduction

Self-excited synchronous oscillations in multibody dynamical systems have been documented since the middle of the seventeenth century with the observation of Christiaan Huygens that two pendulum clocks hanging from a common flexible support swung together periodically approaching and receding in opposite motions[1]. Examples of synchronization in rigid-body and continuous dynamical systems have been documented for coupled mechanical metronomes[2], coupled pendula suspended from a moving beam[3], and a nano mechanical cantilever array[4]. We examine the complexity of coexisting synchronous and asynchronous self-excited oscillations in an array of three planar pendula augmented with rotating inertia wheels governed by a linear feedback mechanism. We formulate the dynamical system using a Lagrangian approach (Fig. 1 left). A linear stability map analysis of the zero equilibria yields a transition from an asymptotically stable region (Fig. 1 right-red) to a region of self-excited oscillations (Fig. 1 right-blue), culminating with a region of rotations (Fig. 1 right-white). We note that the saddle-node bifurcation $(\Gamma_3 = 0)$ for both a stationary array $(x \in \mathbb{R}^5)$ is identical to that of a moving array $(x \in \mathbb{R}^{11})$. However, the Hopf bifurcation between a stable zero equilibria and periodic oscillations reveals a slightly larger region of self-excited limit cycles (Fig. 1 right-dashed).

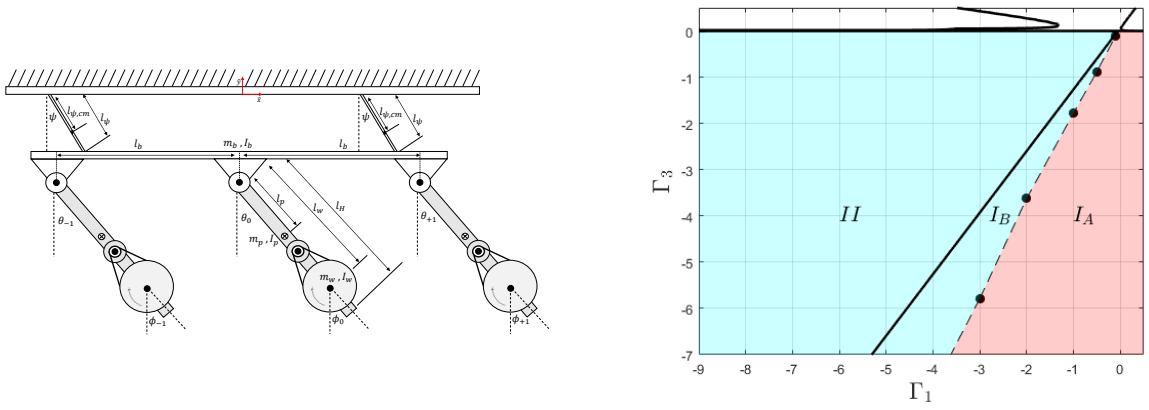

Figure 1: Definition sketch (left), stability map (right) of the inertia wheel feedback gains $\left(\Gamma_3(\Gamma_1)\right)$ for a stationary (solid) and moving (dashed) array

Results

By enforcing the analytical constraints[7] we find the Hopf threshold (Fig. 1 right-solid) of the stationary array. The Hopf threshold of the moving pendulum array is obtained numerically for varying values of the gain Γ_1 (Fig. 1 right-circles). Area I_A yields asymptotic stability for the moving array, and area I_B together with I_A yields asymptotic stability for the stationary array. We simulate the dynamics of the array for gain values Γ_3 both near and far from the Hopf threshold $\Gamma_{3H}(\Gamma_{1H})$ for an arbitrary constant gain parameter $\Gamma_1 = const$. For gains Γ_3 near the Hopf threshold we obtain periodic motion of the array elements which reveals in-phase synchronization (Fig. 2 left). As the gain Γ_3 increases we obtain quasiperiodic dynamics of the individual elements and out-of-phase synchronization (Fig. 2 center). The quasiperiodic motion leads to asynchronous chaotic oscillations (Fig. 2 right). The behavior of the dynamical system was examined through Poincaré maps (Fig. 2 bottom) portrayed by the system conjugate momenta $(p_\psi, p_{\theta i}, p_{\phi i})$ and sampled every positive zero crossing of the central inertia wheel velocity which is bounded.

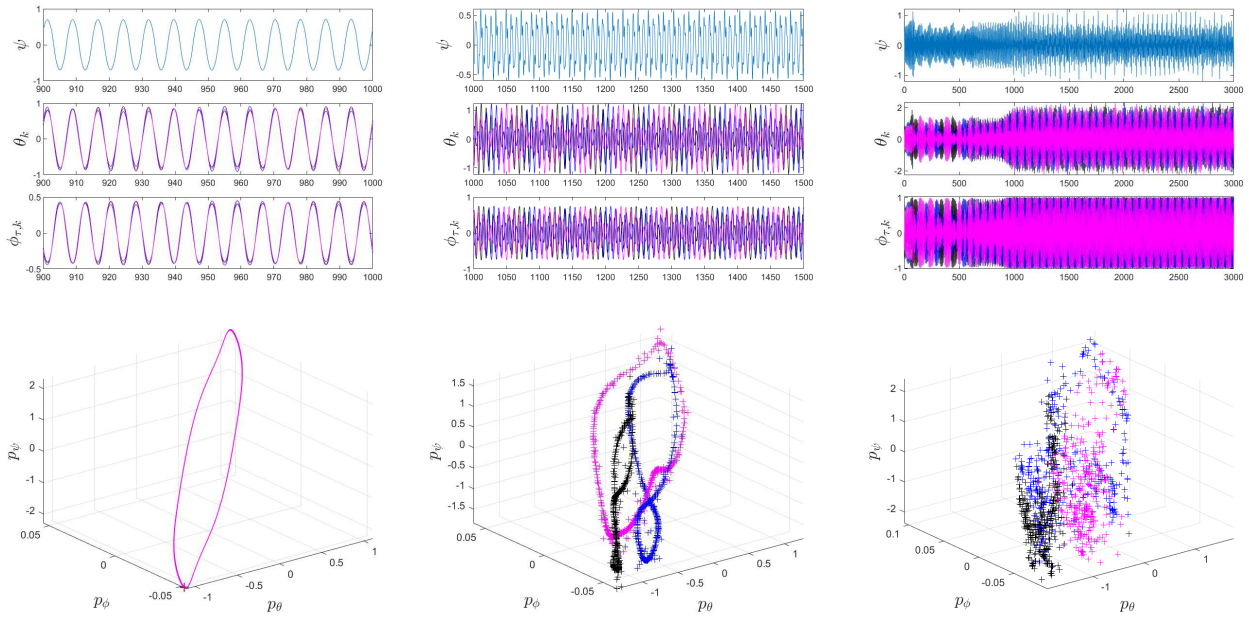

Figure 2: Time histories (upper) and conjugate momenta Poincaré maps (lower) for an in-phase periodic response (left) and an out-of-phase quasiperiodic response (center), and asynchronous chaotic oscillations (right)

Discussion

Non-stationary rotations occur first in the periphery pendula (Fig. 3 left), while the center pendulum exhibits chaotic oscillations. After a threshold gain value $\hat{\Gamma}_{3R}$ all three pendula rotate while the base oscillates chaotically (Fig. 3 center). The chaotic oscillations of the base culminate with rotations of all system elements (Fig. 3 right). We note that the linear feedback governing inertia wheel dynamics was synchronized with the pendula array periodic (out-of-phase) and quasiperiodic/chaotic (in-phase) oscillations, the non-stationary rotations were found to be asynchronous.

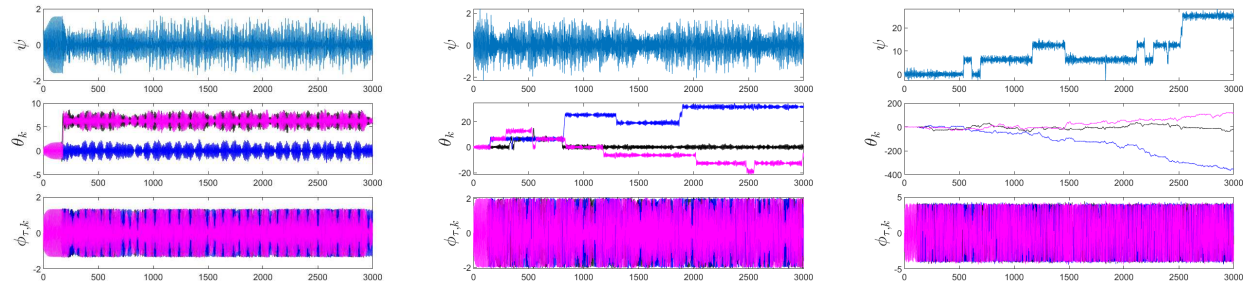

Figure 3: Time histories for non-stationary rotations combined with oscillations of the array elements (left) and (center), and non-stationary rotations of all elements (right)

References

[1] Ramirez, J. P., Olvera, L. A., Nijmeijer, H., and Joaquin, A (2016) The sympathy of two pendulum clocks: beyond Huygens' observations. *Scientific Reports* **6**:23580.

[2] Ulrichs, H., Mann, A. and Parlitz, U. (2009) Synchronization and Chaotic Dynamics of Coupled Mechanical Metronomes. *Chaos* **19**:043120.

[3] Koluda, P., Brzeski, P. and Perlikowski, P. (2014) Dynamics of n Coupled Double Pendula Suspended to the Moving Beam. *International Journal of Structural Stability and Dynamics* **14**:1440028.

[4] Kambali, P., Torres, F., Barniol, N., and Gottlieb, O. (2019) Nonlinear Multi-Element Interactions in an Elastically Coupled Microcantilever Array Subject to Electrodynamic Excitation. *Nonlinear Dynamics* **98**:3067-3094.

[5] Alonso, M. D., Paolini, E. E. and Moiola, L. J. (2005) Global Bifurcation Analysis of a Controlled Underactuated Mechanical System. *Nonlinear Dynamics* **98**:205-225.

[6] Haddad, N. K., Belghith, S., Gritli, H., and Chemori, A. (2017) From Hopf Bifurcation to Limit Cycles Control in Underactuated Mechanical Systems. *International Journal of Bifurcation and Chaos* **27**:1750104.

[7] Guckenheimer, J., Mark, M., Gritli, H., and Bernd, S. (1997) Computing Hopf Bifurcations I. *SIAM Journal on Numerical Analysis* **34**:1-21.

Synchronization of networks of dynamical systems by nonlinear integral couplings and sequential decoloring of the network graph

Alexey Pavlov*, Erik Steur† and Nathan van de Wouw †‡
* *Dept. of Geoscience and Petroleum, NTNU, Trondheim, Norway*
† *Dept. of Mechanical Engineering, Eindhoven Univ. of Tech., The Netherlands*
‡ *Dept. of Civil, Environmental, and Geo- Engineering, Univ. of Minnesota, USA*

Summary. In this work we present a method for controlled synchronization of networked nonlinear systems based on nonlinear integral couplings. For a class of nonlinear systems and network topologies, this method allows one to design synchronizing nonlinear couplings with noticeably lower coupling gains (understood in a nonlinear sense) than for the case of linear diffusive couplings. This results in lower control values and energy consumption needed for synchronization as well as lower sensitivity to measurement noise. The method is illustrated by application to synchronization of Hindmarsh-Rose oscillators.

Synchronization and nonlinear integral couplings

In this abstract we consider N identical nonlinear systems of the form

$$\dot{x}_i = f(x_i) + Bu_i, \;\; y_i = Cx_i, \;\; i = 1, \dots N, \tag{1}$$

with $x_i \in \mathbb{R}^n$, $y_i, u_i \in \mathbb{R}$, C^1 function $f(x)$ and matrices B and C of appropriate dimensions. The problem of controlled synchronization considered in this abstract is to find control laws for each u_i such that for any initial conditions of the closed-loop system, state vectors $x_i(t)$, $i = 1, \dots, N$ are bounded and

$$|x_i(t) - x_j(t)| \to 0, \;\; \text{as} \;\; t \to \infty, \;\; \forall i, j. \tag{2}$$

For each system i, u_i is allowed to depend on the system's output y_i and on the outputs y_j of the systems $j \in \mathcal{N}_i$, where $\mathcal{N}_i$ is the set of systems that can communicate to system i. The sets $\mathcal{N}_i$ specify the communication graph $\mathcal{G}$ for the network (there is an edge from node j to node i if $j \in \mathcal{N}_i$). It is required that for identical outputs $y_1 = y_2 = \ldots = y_N$, the controls satisfy $u_1 = u_2 = \ldots = u_N = 0$, such that in exact synchrony the systems exhibit dynamics of the unforced (with zero input) system (1).
In this work we propose synchronizing control laws u_i in the form of nonlinear integral couplings:

$$u_i = \sum_{j \in \mathcal{N}_i} \int_{y_i}^{y_j} \lambda(s) ds, \;\; i = 1, \dots, N, \tag{3}$$

where $\lambda(s) \geq 0$, $\forall s$, is a nonlinear coupling gain—the main design parameter in this scheme. Note that (3) is a generalization of conventional linear diffusive coupling, which is obtained from (3) with constant $\lambda(s) \equiv C$.
Contrary to the linear diffusive coupling, nonlinear integral coupling (3) allows one to differentiate the coupling strength depending on the location of the system's outputs in space, applying higher coupling gains only where the systems' nonlinearities counteract synchronization, while employing lower (or even zero) coupling gains where the nonlinearities do not have significant negative effects on synchronization. From the closed-loop performance point of view, the immediate consequences of this flexibility can be lower average synchronizing gains, lower coupling actions and energy needed to achieve and maintain synchronization and, consequently, lower sensitivity to measurement noise in outputs y_i. From the analysis point of view, this can provide better estimates of what should be the minimal coupling needed for synchronization. As couplings in physical, engineering and biological networked systems can have nonlinear nature (with their linear approximation studied in diffusive coupling), such estimates can shed more light on how synchronization is or can be achieved in such systems.

Main result

Let us first formulate notions and assumptions that delineate the considered class of systems (1) and the class of network topologies. The first assumption specifies the class of systems (1).

Assumption 1 *There exist $P = P^T > 0$, $R = R^T > 0$ and a scalar continuous function $\gamma(s)$ such that*

$$P\frac{\partial f}{\partial x}(x) + \frac{\partial f}{\partial x}^T(x)P - 2C^T C\gamma(Cx) \leq -R, \quad PB = C^T, \quad \forall x \in \mathbb{R}^n, \tag{4}$$

These conditions are satisfied for a class of incrementally minimumphase nonlinear systems [1]. Next, we formulate conditions on the communication graph $\mathcal{G}$. The conditions are linked to the notion of relaxed balanced coloring of the nodes of $\mathcal{G}$.

Definition 1 *A coloring of the nodes with $k \in \{1, \dots, N\}$ colors $c_1, \dots, c_k$ is called a* relaxed balanced coloring *if each node is assigned a color, and every c_i-colored node receives an equal number of edges from c_j-colored nodes for all $j \in \{1, 2 \dots, k\} \backslash \{i\}$.*

A communication graph can be colored according to relaxed balanced coloring in multiple ways. The two trivial colorings are given by a) assigning each node an individual color and b) by assigning all nodes the same color. We call the graph *sequentially decolorable* if there exists a sequence of $N-1$ relaxed balanced colorings, starting from the coloring a) and ending with coloring b), such that each coloring is obtained from the previous one by taking two groups of nodes with two different colors are assigning them the same color. Examples of sequentially decolorable graphs include graphs with two nodes with bi- and unidirectional couplings; bi-directionally coupled rings with 3 and 4 nodes, a graph with N nodes with all-to-all couplings. There are algorithms that allow one to verify whether a graph is sequentially decolorable in a computationally efficient way. Now we can formulate our main result.

Theorem 1 *Consider N systems of the form* (1) *satisfying Assumption 1 and interconnected through nonlinear integral coupling* (3) *with a sequentially decorolable communication graph $\mathcal{G}$. Suppose the coupling gain function $\lambda(s)$ satisfies*

$$\lambda(s) \geq max(0, \gamma(s)), \quad \forall s \in \mathbb{R}, \quad \int_{-\infty}^{+\infty} \lambda(s) ds \leq +\infty. \tag{5}$$

Then all solutions of the closed-loop system (1)*,* (3) *are bounded and satisfy* (2)*.*

Remark: The condition (5) can be relaxed by taking into account quantitative characteristics of communication graph. For example, for a graph with N nodes and all-to-all interconnections, the first condition in (5) can be substituted by $\lambda(s) \geq max(0, \gamma(s)/N)$.

Synchroniztion of Hindmarsh-Rose oscillators

We demonstrate our results with synchronization of Hindmarsh-Rose oscillators, which represent a simplified model of neuron dynamics [2]:

$$\dot{z}_1 = c - dy^2 - z_1, \quad \dot{z}_2 = \varepsilon(m(y + y_0) - z_2), \quad \dot{y} = -ay^3 + by^2 + z_1 - z_2 + I + u, \tag{6}$$

where y, z_1 and z_2 represent various states of a neuron and external stimulation is provided by input u. All other parameters are positive constants. Analysis of synchronization in a network of such oscillators with *linear* coupling is presented in [3]. For numerical simulations we choose the following values of system parameters: $a = 1$, $b = 3$, $c = 1$, $d = 5$, $m = 4$, $I = 2.8$, $y_0 = 1.618$, $\varepsilon = 0.005$ [3]. In this abstract, we consider 4 systems interconnected in the following way: $\mathcal{N}_1 = \{2, 4\}$, $\mathcal{N}_2 = \{3\}$, $\mathcal{N}_3 = \{2, 4\}$, $\mathcal{N}_4 = \{1\}$. System (6) satisfies Assumption 1 with some $P = P^T > 0$, $R = R^T > 0$ and $\gamma(s) = \epsilon - 3as^2 + 2bs + \frac{(1-\delta ds)^2}{2(\delta - \epsilon)}$, for any sufficiently small $\epsilon > 0$ and, for the chosen system parameters, with $\delta = 0.2$, [1]. Thus, if we select $\lambda(s) = max(0, \gamma(s))$, the function $\lambda(s)$ will satisfy (5) and, by Theorem 1 synchronization will be achieved. Simulations results are shown in Figure 1. The results demonstrate the synchronizing system states y_i, z_{1i}, z_{2i} and control inputs u_i, $i = 1, \dots 4$. The last plot shows variable gain $g_{12}(t)$ of the nonlinear integral coupling defined as $g_{12}(t) = \int_{y_1(t)}^{y_2(t)} \lambda(s) ds / (y_2(t) - y_1(t))$, [1]. According to the simulations, the gain varies from 3 down to 0. The higher coupling gain is applied whenever it is needed to achieve synchronization. It is reduced and even set to zero in accordance with system's dynamics while maintaining synchronization. The average gain over the simulation of 500s equals 1.09 (shown as red dashed line in Figure 1). The lower coupling gains (instantaneous and average) is a distinctive feature of the proposed method over linear diffusive couplings. The best estimate of the linear diffusive coupling gain that we are aware of is 3, which can be computed using the results of [4].

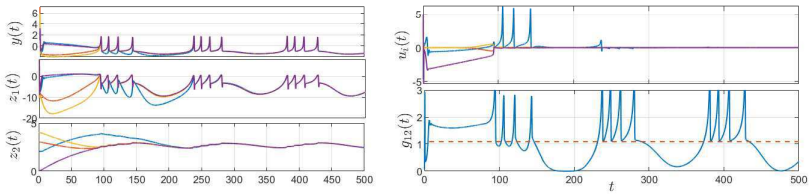

Figure 1: Synchronization of 4 Hindmarsh-Rose oscillators.

References

[1] A. Pavlov, E. Steur, and N. van de Wouw. Controlled synchronization via nonlinear integral coupling. In *Proc. 48th IEEE Conf. Decision and Control, Shanghai, China*, 2009.

[2] J.L. Hindmarsh and R.M. Rose. A model for neuronal bursting using three coupled differential equations. *Proc. R. Soc. Lond.*, B 221:87–102, 1984.

[3] I. Castanedo-Guerra, E. Steur, and H. Nijmeijer. Synchronization of "light-sensitive" Hindmarsh Rose neurons. *Communications in Nonlinear Science and Numerical Simulation*, 57:322–330, 2018.

[4] I. Belykh, M. Hasler, M. Lauret, and H. Nijmeijer. Synchronization and graph topology. *Int. J. of Bifurcations and Chaos*, 15(11), 2005.

Vibration control of underactuated 3-DOF systems inspired by tuned vibration absorbers: the non-linear Euler-Lagrange controller

Jasper Juchem* and Mia Loccufier*
*Department of Electromechanical, Systems and Metal Engineering, Ghent University, Ghent, Belgium

Summary. The concept of the non-linear Euler-Lagrange controller aims to combine the advantages of passive and active vibration control. The flexibility and adaptability of active control is combined with the intuitive design of a passive tuned vibration absorber. To verify this statement, an intuitive tuning procedure, which is inspired by the tuned vibration absorber, is stated. An energy-inspired approach is used to proof (asymptotic) stability using Lyapunov's direct method. A three-link planar manipulator with one actuator at the base is controlled to mitigate vibrations in the unactuated links. The controller contains a non-linear damper. Finally, some different experiments should give insight whether it is necessary to capture all modes, with the disadvantage that the number of controller parameters increases drastically. Also, a non-linear damper is compared to a linear one.

System description

The system that needs to be controlled, also referred to as the process, is a planar three-link manipulator. The joints are assumed to be frictionless. Between the links a spring creates a restoring force. At the base of the first link no spring is attached. The equation of motion is given by the general differential equation:

$$D(q)\ddot{q} + C(q,\dot{q})\dot{q} + K(q) = -Mu \tag{1}$$

with the generalized coordinates the relative angles between the links $q = \begin{bmatrix} q_1 & q_2 & q_3 \end{bmatrix}'$ and $\cdot'$ the transpose. The inertia matrix $D(q) = D(q)' > 0 \in \mathbb{R}^{n_p \times n_p}$ with $n_p = 3$ the number of generalized coordinates of the process, $C(q,\dot{q}) \in \mathbb{R}^{n_p \times n_p}$ the coriolis/gyroscopic and damping terms, stiffness matrix $K(q) \in \mathbb{R}^{n_p}$, and $u \in \mathbb{R}^{n_p}$. The matrices for this system can be found in [3].
The controller consists of two blocks that are placed in parallel: a proportional controller $u_1 = K_p M' q$ and an Euler-Lagrange controller

$$\begin{cases} D_0\ddot{z} + \frac{\partial F}{\partial \dot{z}}(\dot{z}) + K_0(z) = -N_1 M' q - N_2 M' \dot{q} \\ u_2 = \nu_1 z + \nu_2 \dot{z} \end{cases} \tag{2}$$

with $z \in \mathbb{R}^{n_c}$ the generalized coordinates of the controller, $D_0 \in \mathbb{R}^{n_c \times n_c}$ the inertia matrix, $\partial F/\partial \dot{z} \in \mathbb{R}^{n_c}$ non-linear damping function, $K_0(z) \in \mathbb{R}^{n_c}$ stiffness matrix of the controller, $N_1, \nu_1' \in \mathbb{R}^{n_c \times n_p}$ the amplification of the position coupling with the process in the input and output equation respectively, and $N_2, \nu_2' \in \mathbb{R}^{n_c \times n_p}$ the amplification of the velocity coupling with the process in the input and output equation respectively.
The controller effort in (1) is then given by $u = u_1 + u_2$. Notice the similarity with adding a mechanical structure to the system. However, the difference with adding a tuned vibration absorber is the way of connecting the controller and the process. Furthermore, in the differential equations $M = diag(\{0,1\}) \in \mathbb{R}^{n_p \times n_p}$ forces a collocated control strategy.
For the compound system to be an Euler-Lagrange system, the following must hold: $\nu_1 = N_1'$.

Asymptotic stability: Lyapunov's direct method

The stability is proven using Lyapunov's direct method. Let x_e be an equilibrium point for

$$\dot{x}(t) = f(x(t)) \tag{3}$$

where $f : D \to \mathbb{R}^n$ is a locally Lipschitz map from a domain $D \subset \mathbb{R}^n$ into $\mathbb{R}^n$, with $x_e \in D$. Let $V_L : D \to \mathbb{R}$ be a continuously differentiable function, such that

$$V_L(x_e) = 0, V_L(x) > 0 \text{ in } D \setminus \{x_e\}, \dot{V}_L(x) \leq 0 \text{ in } D, \text{ and } \dot{V}_L(x) < 0 \text{ in } D \setminus \{x_e\} \tag{4}$$

with $\dot{V}_L(x) = \frac{\partial V_L(x)}{\partial x} f(x)$. Then x_e is asymptotically stable.
Here, the Hamiltonian $\mathcal{H}$ is chosen to be the Lyapunov function. This leads to four conditions for the controller parameters that need to be fulfilled:

1. $\frac{dK_0}{dz}$ should be continuous, invertible and positive definite,
2. $\frac{dK(q)}{dq} + MK_p - M\nu_1 \frac{dK_0(z)}{dz}^{-1} \nu_1' M' > 0$,
3. $\nu_2' = -N_2$, and
4. $\left(\frac{\partial F}{\partial \dot{z}}\right)' \dot{z} \geq 0$.

Controller tuning

This research focusses on mitigating vibrations due to impulse impacts on the third link. After impact, the open-loop system will vibrate infinitely, as there is no damping present. It is not possible to apply a controlled torque to the second or third joint, what complicates diminishing these vibrations. The topology of the controller allows the introduction of tuning techniques from passive vibration control. One can try to make the controller sensitive to the main system, such that easy energy transfer occurs from the process to the controller. Once the energy is transferred, it can be dissipated in this controller [1].

Eigenfrequency matching

To facilitate an easy energy flow from the process to the controller, eigenfrequency matching is well-known strategy [2]. In this work, this is done in two steps. Firstly, the eigenfrequencies of the substructures are matched by tuning K_p in the case that $\nu_1 = \nu_2 = \mathbf{0}$. Secondly, the eigenfrequency of the process and controller are matched. Let $\Omega^2 = diag(\omega_1^2, \omega_2^2, \omega_3^2)$ with ω_i an eigenfrequency of the process. Now, the controller is tuned to have the same eigenfrequency

$$K_0(z) = D_0 \Omega^2 z \tag{5}$$

Notice that depending on n_p the number of modes that are captured can be altered. To achieve stability, $\omega_i \neq 0$, as all conditions on $\frac{dK_0}{dz}$ are then fulfilled. The second condition leads to the expression $k_{p,1} - \nu_{111}^2/\omega_1 - \nu_{112}^2/\omega_2 - \nu_{113}^2/\omega_3 > 0$ with $K_p = diag(k_{p,1}, k_{p,2}, k_{p,3})$ and $\nu_1 = \begin{bmatrix} \nu_{111} & \nu_{112} & \nu_{113} \\ \nu_{121} & \nu_{122} & \nu_{123} \\ \nu_{131} & \nu_{132} & \nu_{133} \end{bmatrix} = \begin{bmatrix} \nu_{111} & \nu_{112} & \nu_{113} \\ 0 & 0 & 0 \\ 0 & 0 & 0 \end{bmatrix}$, which is equivalent as only the first link can be actuated.

Optimization

Without loss of generality it can be assumed that D_0 is an identity matrix [4]. This leaves us with three unknown matrices: ν_1, ν_2, and $\frac{\partial F}{\partial \dot{z}}$. As ν_2 introduces a conservative coriolis force and due to non-linear damping, the analysis is too complex to be carried out analytically [5, 6]. Therefore, the remaining parameters will follow from an optimization. The optimization algorithm will use four objective functions:

$$f_1 = T_{s,1}\omega_1; f_2 = T_{s,2}\omega_1; f_3 = T_{s,3}\omega_1; f_4 = \int \frac{\mathcal{H}(t)}{\max \mathcal{H}} dt \tag{6}$$

with settling time $T_{s,i}$ of link i the time after which the time signal stays within 5% of the maximal deviation around equilibrium, and ω_1 the slowest eigenfrequency.
As mentioned before, the controller's damping will be a non-linear function

$$\frac{\partial F}{\partial \dot{z}} = c_1 \dot{z} + c_2 \arctan\left(\frac{c_0 - c_1}{c_2} \dot{z}\right) \approx \begin{cases} c_0 \dot{z} & \text{if } \dot{z} \approx 0 \\ c_1 \dot{z} + cst & \text{if } |\dot{z}| \to \infty \end{cases} \tag{7}$$

with $c_i > 0$. Then $\left(\frac{\partial F}{\partial \dot{z}}\right)' \dot{z} > 0$ if $c_0 > c_1$.

Results

In this section different controllers are compared. First of all, increasing the number of generalized coordinates of the controller, n_c, leads to capturing all modes of the process. However, it also increases the number of controller parameters drastically, thus increasing the optimization time. Next to that, a non-linear Euler-Lagrange controller will be compared to a linear one. All simulations will be the result of an impulse on the tip of the third link.

Conclusions

A planar underactuated three-link manipulator will be controlled with a non-linear Euler-Lagrange controller. Next to stability, a tuning strategy based on tuned vibration absorbers will be validated. The number of generalized coordinates of the controller (n_c) will be varied from one to three to observe whether the increase in tuning parameters leads to an significantly improved result. Also, the difference between linear and non-linear damping is examined.

References

[1] Yang F., Sedaghati R., Esmailzadeh E. (2021) Vibration suppression of structures using tuned mass damper technology: a state-of-the-art review. *J Vib Control* **0**(0):1-25.

[2] Den Hartog J.P. (1985) Mechanical Vibrations. Dover Publications Inc., NY.

[3] Fantoni I., Lozano R. (1973) Non-Linear control for underactuated mechanical systems. Springer-Verlag, London.

[4] Arnold V.I., Kozlov V.V., Neishtadt A.I. (1988) Dynamical Systems III, *Encyclopedia of Mathematical Sciences, vol. 3*. Springer-Verlag, Berlin.

[5] Qian J., Lin W.W. (2007) A numerical method for quadratic eigenvalue problems of gyroscopic systems. *J Sound Vib* **12**(10):1337-1342.

[6] Starosvetsky Y., Gendelman O.V. (2009), Vibration absorption in systems with a nonlinear energy sink: Nonlinear damping. *J Sound Vib* **324**(3-5):916-939.

Friday, July 22, 2022

08:30 - 10:30

MS-14 Nonlinear Dynamics for Engineering Design

Rhone 2

Chair: Jerzy Warminski

08:30 - 08:50
Estimating the fractality of a basins of attraction using basin entropy method and sample based approach.
LESZCZYNSKI Maciej*
*Lodz University of Technology (Politechnika Łódzka Wydział Mechaniczny Katedra Dynamiki Maszyn 90-537 Łódź, ul. Stefanowskiego 1/15 Poland)

08:50 - 09:10
Dynamics and Control of a Rotating Beam with Active Element
WARMINSKI Jerzy*, MITURA Andrzej, KLODA Lukasz
*Department of Applied Mechanics, Lublin University of Technology (Nadbystrzycka 38D, 20-618 Lublin Poland)

09:10 - 09:30
Utilizing Noise to Manipulate Energy Localization in a Circular Oscillator Array
ACAR Gizem, ALOFI Abdulrahman, BALACHANDRAN Balakumar, **BREUNUNG Thomas***
*Eidgenössische Technische Hochschule Zürich (Switzerland)

09:30 - 09:50
Evaluating the Resistant Force of a Vibro-Impact Self-Propelled Capsule Moving in the Small Intestine
LIU Yang*, TIAN Jiyuan, YAN Yao, GUO Bingyong
*University of Exeter (North Park Road, Exeter United Kingdom)

09:50 - 10:10
Work-loop techniques for optimising nonlinear forced oscillators
PONS Arion*, BEATUS Tsevi
*Hebrew University of Jerusalem (Giv'at Ram, Jerusalem Israel)

10:10 - 10:30
A novel lubricated friction model for describing underdamped free responses of a spring ? sliding mass oscillator
PERRET-LIAUDET Joel*, MAJDOUB Fida
*Laboratoire de Tribologie et Dynamique des Systèmes (Ecole Centrale de Lyon. 36 avenue Guy de Collongue. 69134 ECULLY cedex France)

Estimating the fractality of a basins of attraction using basin entropy method and sample based approach.

Maciej Leszczyński*, Przemysław Perlikowski*, Tomasz Burzyński*, Tomasz M. Kowalski**, Piotr Brzeski*

*Division of Dynamics, Lodz University of Technology, Stefanowskiego 1/15, 90-924 Lodz, Poland

**Institute of Applied Computer Science, Lodz University of Technology, Lodz 90-924, Poland

Summary. Two sampled based methods, i.e. the basin stability and basin entropy used to describe the dynamics of multistable systems will be presented. Both methods are based on integrating the system's equations of motion for a large set of different initial conditions and classifying the solutions based on final attractors. The main difference between the two approaches is the different sample methods of initial conditions for each trial. In the first one, we use the random initial conditions. In contrast, for the second one, the phase space should be uniformly divided into boxes of equal size. We show under which conditions it is possible to calculate the basin entropy using random samples of initial conditions. Moreover, the basin entropy method assumes the identical size of the investigated box in all directions of multi-dimensional phase space. In many real-life systems, it is impossible to achieve; hence we introduce the scaling of the box to overcome this problem. To summarize, we show under which conditions we can accomplish the reliable value of basin entropy using random initial conditions and rescaled size of the box.

Introduction

Non-linear ODEs describing dynamical systems can be solved analytically, but it often requires simplifying equations or imposing strong assumptions on the solution. Hence, nowadays, most non-linear ODEs are tackled with numerical methods. The are several approaches that allow to investigate of the multi-stability of the systems. The problem appears for higher dimensional systems, where we can present only two-dimensional cross-sections of multidimensional phase space. Again, it is possible to overcome that, with a method proposed by Menck et al. [1] called basin stability. It can be used to characterize the volume of basins of attraction in the multidimensional phase space. To estimate the basin stability measure, one has to perform a large number of Bernoulli trials each time, drawing initial conditions randomly and checking which attractor is reached. This method is rather new, but was already successfully applied in a numerous different scenarios. The main advantages of this method are that it can be applied to all types of systems, and it is a straightforward procedure, thus a person who is not an expert on non-linear dynamics can use it to estimate the risk of unwanted behaviour. In 2017, the experimental validation of the basin stability approach has been performed [2] and results proved that the accuracy of basin stability approach is comparable with classical methods.

The disadvantage of the basin stability approach, is that it does not take into consideration the structure of the analysed basins. In 2016 Daza et al. [3] proposed a new method that include the information about the structure of the phase space. It is called a basin entropy measure and it provides information about the unpredictability of the dynamical system. To obtain basin entropy, one has to build a grid on the phase space and, in each part, estimate basin stability. Then, this value is used to obtain Gibbs entropy for every part of the grid. Summing the entropies, leads to a quantitative measure of the uncertainty associated with the state space.

The motivation is to combine these two metrics for an analysis of a dynamical system. The aim is to show, that it is possible to estimate the basin entropy accurately without distinct simulation for every part of the grid. To prove that, we will show that the basin entropy calculated using the data obtained during the estimation of basin stability is a good approximation of the one calculated classically.

Basin stability

Basin stability is defined for a n-dimensional dynamical system with N attractors in an analysed region of the state space $\Omega \subset R^n$. Then, integrating the system equation of the motion multiple times with random initial conditions from Ω allows to estimate the probability of reaching each attractor. The proportion of initial conditions that reach certain attractor to the overall number of trials is the estimation how the attractor is stable, and called basin stability $B_s(A)$ of attractor A. The application of the method is presented on an archetypal model of externally excited oscillator, the Van der Pol-Duffing system:

$$\ddot{x} - \alpha(1 - x^2)\dot{x} + x^3 = Fsin(\omega t),$$

where α, F and ω are positive constants.

Basin entropy

Basin entropy is defined for a n-dimensional dynamical system with N attractors in an analysed region of the state space $\Omega \subset R^n$. We then cover Ω with $k \in N$ disjoint n-dimensional hypercubes of linear size ε in each dimension. Each of

these boxes, in principle contains infinitely many trajectories. Moreover, each of such trajectory lead to one of N attractors mentioned before. For such a formulation, the basin entropy is given by

$$S_b = \frac{1}{N}\sum_{i=1}^{k} S_i = \frac{1}{N}\sum_{i=1}^{k}\sum_{j=1}^{N_A} p_{i,j}\, log\left(\frac{1}{p_{i,j}}\right)$$

Where $p_{i,j}$ is the basin stability of a j-th attractor numbered $j \in \{1, \dots N_A\}$ calculated in i-th box. The application of the method is again presented on the Van der Pol-Duffing system. Furthermore, it is shown that the value of basin entropy is not affected by scaling the state space. This is helpful in the cases, where the ranges of initial values for some state variables differ significantly from the other ones.

Estimating basin entropy with sample based methods

Basin entropy requires the initial conditions to be distributed over the state space, so that every box created during the calculation of basin entropy contains the same amount of trials. On the other hand, the basin stability initializes all trials at random, thus it cannot be ensured that the basin entropy calculated on such data matches the one equally distributed. The analysis of the relative error of basin entropy for a single multidimensional box was performed, followed by the comparison of basin entropy calculated with three different types of input data: two types of equal distribution of points per box (25 points and 100 points) and random sampling using 4,000,000 trials. It is summarized that one can accurately estimate the value of basin entropy using the random sampling method.

Trial based basin entropy for a double pendulum model

The idea behind basin stability type metrics, is to evaluate the asymptotic behaviour of a general system, where one cannot in principle visualize the results. Hence, in this section we present previously discussed metrics for a double pendulum model which is a paradigmatic example in nonlinear dynamics. We based on the real experimental rig which has been designed, constructed and tested in our laboratory. This rig was also used to experimentally validate the basin stability approach [2]. The physical model of the system is shown in Figure 1

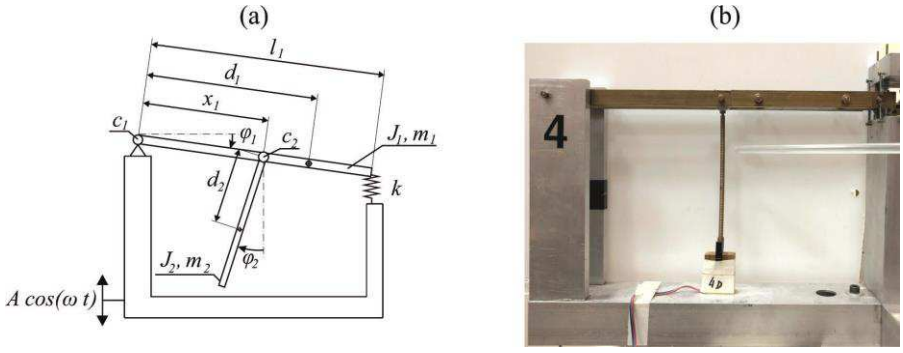

Figure 1: The physical model of the double pendulum system and its realization in laboratory.

Conclusions

The basin stability and the modified basin entropy was then used to analyse the double pendulum system. Due to the described modifications, we were able to calculate the basin entropy on the scaled state space, using the randomized trials obtained with the procedure of calculating basin stability. To choose the proper number of simulations, we performed the analysis of entropy for randomized subsets of the state space. The values of basin stability for the main attractors of the system were also presented. We detected two most stable periodic attractors, both with period 1. Finally, we calculated the basin entropy, concluding that the analysed basins are neither fractal, nor regular.

References

[1] Peter J. Menck, Jobst Heitzig, Norbert Marwan, and Jürgen Kurths. How basin stability complements the linearstability paradigm. Nature Physics, 9(2):89-92, 2013.

[2] P. Brzeski, J. Wojewoda, T. Kapitaniak, J. Kurths, and P. Perlikowski. Sample-based approach can outperform the classical dynamical analysis - experimental confirmation of the basin stability method. Scientific reports, 7:6121, Jul 2017

[3] Alvar Daza, Alexandre Wagemakers, Bertrand Georgeot, David Guéry-Odelin, and Miguel A. F. Sanjuán. Basin entropy: a new tool to analyze uncertainty in dynamical systems. Scientific Reports, 6(1):31416, 2016.

Dynamics and Control of a Rotating Beam with Active Element

Jerzy Warminski*, Andrzej Mitura*, Lukasz Kloda*
*Department of Applied Mechanics, Lublin University of Technology, Lublin, Poland

Summary. Dynamics of a rotating flexible beam with an embedded active element is studied in the paper. The beam model is based on Bernoulli-Euler theory but it is extended taking into account beam's extensionality and large transversal deformations with nonlinear curvature. The macro fibre composite (MFC) embedded into the structure is applied to control or reduce externally excited vibrations. The model of MFC element is considered in a few variants of simplifications. The complete model takes into account electromechanical properties of MFC element including hysteresis and also properties of a voltage amplifier. The influence of the MCF model simplifications on the effective vibration control is presented.

Introduction

Rotating structures are of interest in many engineering applications. One of the classical examples are rotors of helicopters [1], drones or wind turbines. The blades of such rotors can be subjected to various loadings, for example can be excited by aerodynamic forces leading to flutter oscillations, and then large amplitude vibrations may arise. In order to avoid unwanted vibrations a special design of blades is proposed. The good possibility to obtain specific properties of the blade can be achieved by application of modern composite materials which enable creating specific mechanical features of the blade as presented in paper [2]. An additional option of a vibration reduction is to apply actuators embedded into the rotating blade which may reduce unwanted vibrations by use of dedicated control algorithms. The effectiveness of selected linear and nonlinear algorithms tested numerically and experimentally for a cantilever composite beam with active Macro Fibre Composite (MFC) elements was presented in paper [3]. The nonlinear saturation control and the positive position feedback control were demonstrated as the most powerful methods to suppress beam vibrations. However, the methods were tested for a fixed (non-rotating) structure. The proportional (P) and derivative (D) control method for the rotating beam was proposed in [4]. A pair of piezoelectric actuaturs/sensors were used to reduced vibrations of the structure. The analysis showed that typical P control method did not reduce vibration but only PD algorithm enhanced vibration damping of the rotating beam. The goal of this paper is to study dynamics of a rotating structure which takes into account more precise nonlinear model of the rotating beam (the plant) together with nonlinear properties of the emended MFC actuator. Then, the model will be used to propose and test a proper control algorithm, including linear and nonlinear control strategies.

Model formulation and results

A model of the rotating structure is composed of a rigid hub and a flexible blade oscillating in the rotating frame (x, y) which has position defined by a preset angle θ measured from the axis Z_0 of the rotating hub (Fig. 1a). A lumped mass m_t is added to the beam tip which allows to study more general case with dynamic boundary conditions. The beam with a rectangular cross-section is made of material having isotropic and linear properties. The beam is assumed to be thin and its model is based on Bernoulli–Euler beam theory. However, due to possible large deformations a nonlinear curvature and furthermore its extensionality is taken into account which, in case of rotating structure may play an important role. At the present study it is assumed that the hub rotates with constant angular speed $\dot{\psi}(t) = \Omega$ and, in addition, the beam is excited periodically by periodic loading distributed along the beam's spam.

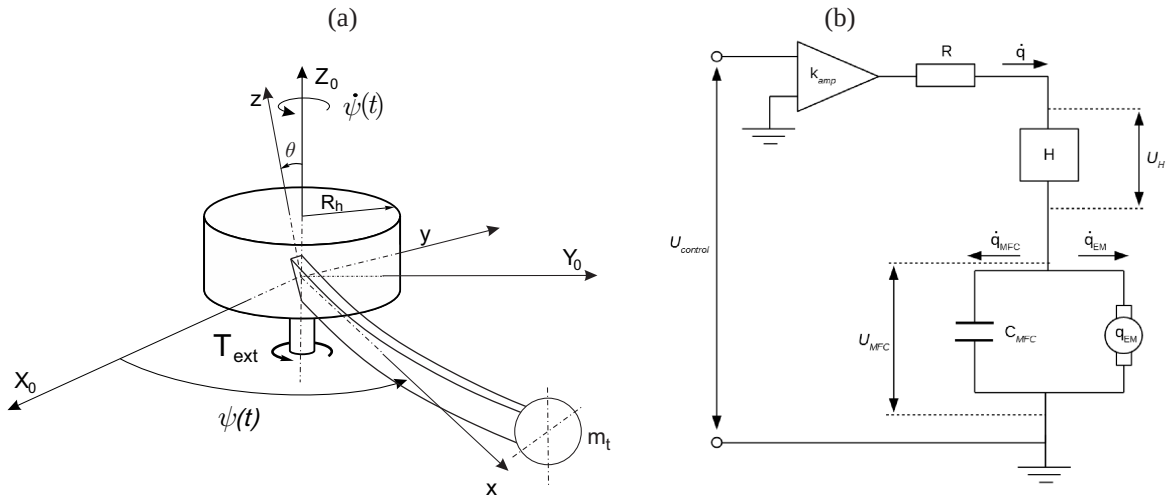

Figure 1: Model of the rotating hub–beam structure with tip mass (a) and schematic model of the MFC actuator (b).

The equations governing the beam dynamics are given as a set of partial differential equations (PDE) with associated

dynamic boundary conditions. The equations have been solved analytically by the multiple time scale method. The resonance curves obtained analytically for the first and the second bending mode are presented in Fig. 2. The curves are computed for rotating structure for $\Omega = 10$ rad/s and selected preset angles $\theta = 30^0$, $\theta = 45^0$ and $\theta = 60^0$. The rotating beam demonstrates nonlinear beahaviour with hardening effect for the first mode (Fig. 2a) and softening for the second (Fig. 2b). The first resonance curve is sensitive for varied preset angle while the influence for the second is minor, almost invisible.

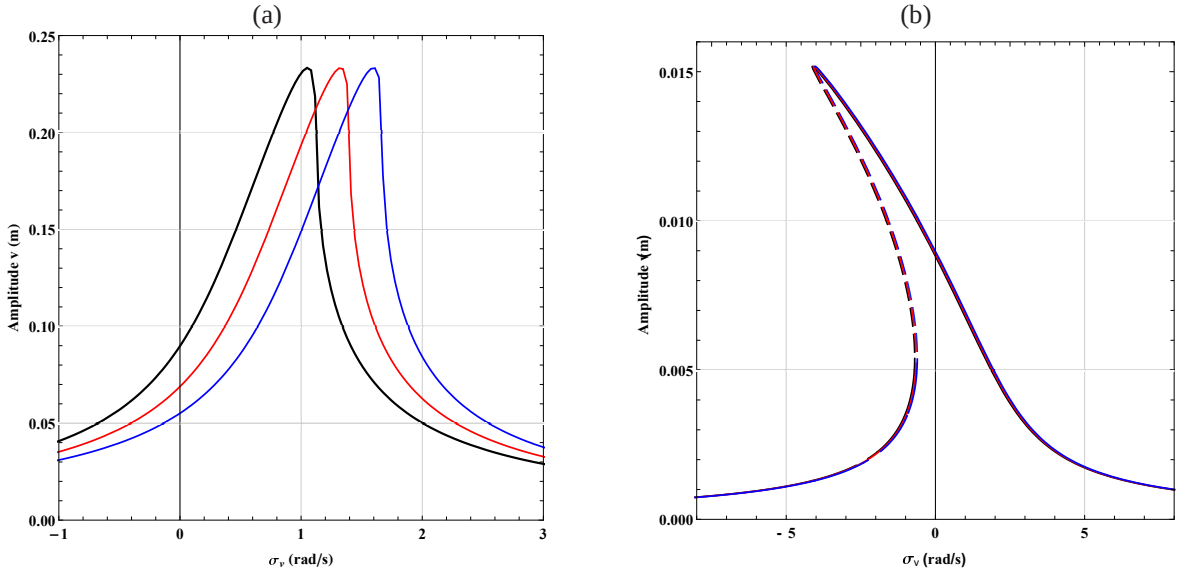

Figure 2: Resonance curves against frequency detuning parameter σ_v around the first (a) and the second (b) bending mode. Angular velocity $\Omega = 10$ rad/s and preset angle: $\theta = 30^0$ - black, $\theta = 45^0$ - red, $\theta = 60^0$ - blue.

To control the rotating beam and reduce vibrations the active MFC elements are embedded into the beam structure. The model of piezoelectric MFC element and its amplifier is presented schematically in Fig. 1b. In the scheme two elements k_{amp} and R describe amplifier properties. The gain k_{amp} is related to voltage $U_{control}$, resistor R models the output resistance of the amplifier. The piezoelectric actuator is represented by a capacitor with capacity C_{MFC}. The direct and indirect (converse) piezoelectric effect transform the actuator deformation into charge q_{EM} and actuator voltage U_{MFC} into mechanical force F_{EM}, respectively. The model also takes into account nonlinear properties of the piezoelectric actuator including the hysteresis phenomenon which schematically is represented by H element. The nonlinear and hysteretic piezo-element is added to the main structure (the plant) and the obtained combined electro-mechanical system is studied in order to select the most effective control algorithm enabling active vibration suppression for selected resonance states. Linear and nonlinear control strategies are tested and some of them are verified in laboratory.

Conclusions

The developed model of the nonlinear rotating beam which takes into account influence of angular velocity and preset angle is studied in the paper. Due to nonlinear geometrical nonlinearities hardening or softening effects are observed for the first and the second bending modes, respectively. It has been shown that varied preset angle affects mainly the first mode resonance observed by a shift of the resonance zone. The second mode resonance is almost not affected, just a very minor change is present. Apart from the nonlinear rotating beam model (the plant) also the model of active MFC element is proposed. The model takes into account two-way electromechanical coupling as well as hysteresis of the active element. The control strategy for active vibration damping with linear and nonlinear control algorithms is analysed.

Acknowledgements

The work is financially supported by grant 2016/23/B/ST8/01865 from the National Science Centre, Poland.

References

[1] Crespo da Silva M. R. M. and Glynn C. C. (2007) Nonlinear flexural-flexural-torsional dynamics of inextensional beams. I. Equations of motion. *Journal of Structural Mechanics*, **6**:437–448.

[2] Latalski J. and Warminski J. (2019) Nonlinear vibrations of a rotating thin-walled composite piezo-beam with circumferentially uniform stiffness (CUS). *Nonlinear Dynamics* https://doi.org/10.1007/s11071-019-05175-3.

[3] Warminski J., Bochenski M., Jarzyna W., Filipek P. and Augustyniak M. (2011) Active suppression of nonlinear composite beam vibrations by selected control algorithms. *Communications in Nonlinear Science and Numerical Simulation* **16**: 2237–2248.

[4] Lin S.-M. (2008) PD control of a rotating smart beam with an elastic root. *Journal of Sound and Vibration* **312**:109–124.

Utilizing Noise to Manipulate Energy Localization in a Circular Oscillator Array

Gizem Dilber Acar*, Abdulrahman Alofi* and Balakumar Balachandran *
*Department of Mechanical Engineering, University of Maryland, College Park, 20742, USA

Summary. In this work, energy localization in an array of Duffing oscillators with periodic boundary conditions is studied. Each oscillator in this array can exhibit multi-stable behavior, and the localized mode of the forced array exists in a certain frequency range. For a specific excitation frequency, Gaussian noise is applied in addition to the harmonic forcing to move the system response from the localized mode to a low-amplitude mode. Through this study, the authors shed light on how noise can be used to design the desired dynamics of coupled oscillator arrays, such as a circular array of rotor blades.

Introduction

Coupled oscillator arrays represent numerous mechanical systems including multi-bladed rotors and micro- electro- mechanical resonators [1]. Understanding nonlinear behavior of oscillator arrays is important for designing such systems. Energy localization is a nonlinear phenomenon that can be observed in oscillator arrays, wherein the system's energy is spatially focused in one or more oscillators. Although spatial energy localization can happen in discrete systems due to imperfections, it can be observed in homogeneous discrete systems due to nonlinearity [2]. Depending on the application, spatial localization of energy can be desirable or harmful.
Cyclically symmetric, discrete systems can exhibit localization behavior when the coupling between the discrete elements is weak [3]. In this study, the responses of an array subjected to a harmonic forcing and harmonic forcing with noise are numerically examined. The system exhibits multi-stable behavior in a particular frequency range, and depending on the initial conditions, one of these responses can correspond to energy localization. The array has a circular configuration (i.e., periodic boundary conditions), and each oscillator is coupled with two neighbors. Furthermore, energy can flow through the boundaries without interruptions. Here, the system is excited with a harmonic forcing so as to excite a localized mode. Then, Gaussian noise is added to the harmonic forcing in order to steer the system to a non-localized response. By using the numerical studies, the authors show that the Gaussian input can be used to move the system from the localized mode to a low-amplitude mode, wherein all the oscillator move with the same amplitude, and the energy is uniformly distributed across the array. For different noise intensities, the authors explore the possibility of using noise to destroy energy localization.

Numerical Experiments

A circular array of six identical hardening Duffing oscillators are considered, wherein each oscillator has associated linear stiffness, cubic stiffness, and linear damping. Each oscillator is coupled with the neighbors through linear springs, as shown in Figure 1a. The system is cyclically symmetric with periodic boundary conditions. The localized mode of the system is found using the anti-continuous limit method [4], according to which the localized mode is first found for the system with zero coupling stiffness. Then, by gradually increasing the coupling in small steps, and using the numerical shooting method at each step, the localized mode of the coupled system is found. The array is excited with a harmonic forcing that can induce energy localization in the system. A representative amplitude profile of the localized mode is shown in Figure 1b. The localized mode is symmetric about the high-amplitude oscillator, and each oscillator moves out-of-phase with its two neighbors. In this analysis, the authors chose the 3rd oscillator for the localization. It is noted that with a different choice of initial conditions, the system energy can be localized in another oscillator. Although energy localization can be observed in systems with smaller numbers of degrees of freedom, the authors analyzed an array with six oscillators to show that the amplitude of oscillations varies drastically around the localization, and it decreases as one moves away from the high-amplitude oscillator. For arrays with larger numbers of oscillators, the amplitude profile may become more uniform across the oscillators that are away from the high-amplitude oscillator.
In order to analyze the system behavior under noise, a Gaussian input is added to the harmonic forcing, as shown below.

$$\ddot{x}_n + c\dot{x}_n + k_1 x_n + k_3 x_n^3 + k_c(2x_n - x_{n-1} - x_{n+1}) = F_0 \cos(\omega t) + \sigma \dot{W}(t), \tag{1}$$

for $n = 1, \ldots, N$, where the periodic boundary conditions imply that the N + 1 oscillator coincides with the first oscillator. The incremental noise is represented with $\sigma \dot{W}(t)$. In this study, each oscillator is excited with the same forcing function to avoid inducing asymmetry into the system through forcing. The system equations with noise are put into Langevin form, and the Euler Maruyama method is used to numerically integrate the noise-influenced system equations [5]. For three different noise intensity levels, the obtained energy distribution in the oscillator array is shown in Figure 2. For each chosen noise intensity, the energy distribution plots are provided by using an average of the responses of the oscillator array to 400 different noise vectors. Although depending on the noise vector, it might take longer or shorter for the noise to suppress localization, the averaged dynamics show that for higher noise intensities ($\sigma = 0.01$ and $\sigma = 0.006$), the Gaussian input can destroy the energy localization, and push the system to a state with uniform energy distribution. However, for a smaller noise intensity ($\sigma = 0.002$), one is not able to use the noise to the unison amplitude mode, and the localization persists.

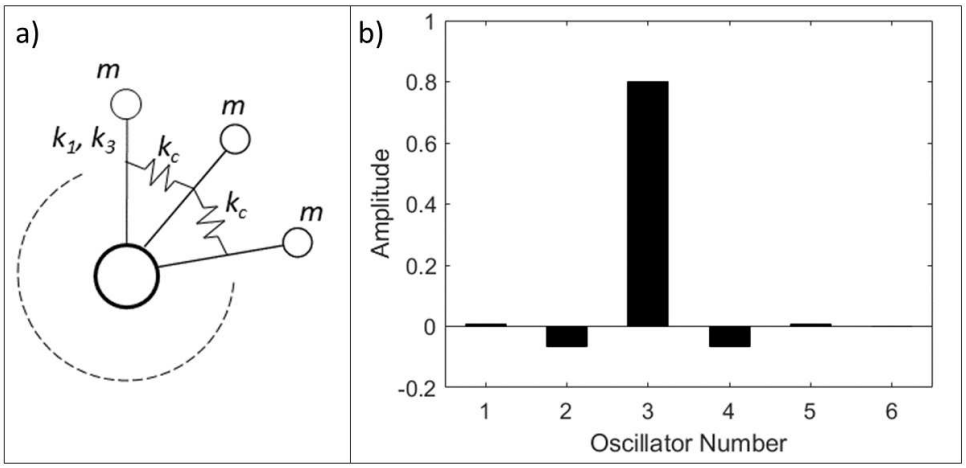

Figure 1: a) Coupled circular Duffing oscillator array with periodic boundary conditions. b) Amplitude profile of the localized mode: The energy is localized in the 3rd oscillator, and the amplitude profile is symmetric about the oscillator with the highest amplitude.

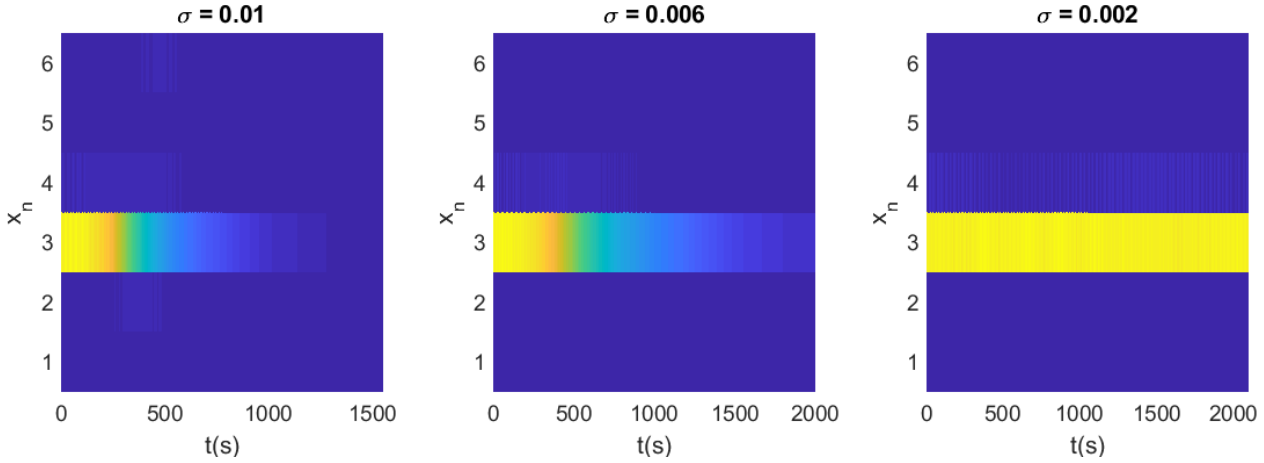

Figure 2: Energy distribution in a circular Duffing oscillator array averaged over 400 simulations. In all three cases, the energy is localized in the 3rd oscillator in the beginning. Addition of noise with intensity $\sigma = 0.01$ and $\sigma = 0.006$ can suppress the energy localization, and lead to a uniform energy distribution in the array. However, a lower noise intensity ($\sigma = 0.002$) is found to be inadequate for pushing the system to the unison-amplitude mode.

Conclusions

In this study, energy localization in a circular array of hardening Duffing oscillators with weak, linear coupling was investigated. The system was first excited with a harmonic forcing frequency, for which the array can oscillate in a localized mode. Then, various levels of Gaussian noise were applied along with the harmonic forcing, to explore the effects of noise on energy localization. Through numerical studies, it was found that above a certain noise level, the localization can be suppressed. The findings may provide a basis for suppressing energy localization in arrays of turbine blades. The studies will be extended to larger systems in order to explore the effects of number of oscillators on the noise required to drive the system between solutions with different energy distributions.

Acknowledgment

The authors are grateful for the support received from the U.S. National Science Foundation, through grant CMMI-1760366.

References

[1] Dick A. J., Balachandran B., Mote C. D. (2008) Intrinsic localized modes in microresonator arrays and their relationship to nonlinear vibration modes. *Nonlinear Dynamics* **54.1-2**: 13-29.

[2] Sievers A.J., Takeno S. (1988) Intrinsic localized modes in anharmonic crystals. *Physical Review Letters* **61.8**: 970.

[3] Vakais Alexander F., Cetinkaya C. (1993) Mode localization in a class of multidegree-of-freedom nonlinear systems with cyclic symmetry. *SIAM Journal on Applied Mathematics* **53.1**: 265-282.

[4] Marin J. L., Aubry S. (1996) Breathers in nonlinear lattices: numerical calculation from the anticontinuous limit. *Nonlinearity* **9.6**: 1501.

[5] Higham D. J. (2010) An algorithmic introduction to numerical simulation of stochastic differential equations. *SIAM review* **43.3**: 525-546.

Evaluating the Resistant Force of a Vibro-Impact Self-Propelled Capsule Moving in the Small Intestine

Yang Liu* Jiyuan Tian* Yao Yan† and Bingyong Guo‡
*College of Engineering, Mathematics and Physical Sciences, University of Exeter, Exeter, UK
†School of Aeronautics and Astronautics, University of Electronic Science and Technology of China, Chengdu, China
‡School of Marine Science and Technology, Northwestern Polytechnical University, Xi'an, China

Summary. In this work, we study a mathematical model for evaluating the resistant force of a vibro-impact capsule self-propelling in the small intestine with a consideration of its anatomy. Circular fold is the main source of intestinal resistance that needs to be overcome during the endoscopic procedure. Our model is able to calculate the resistance of such folds in different dimensions. Finite element analysis and experimental testing are presented to validate the proposed model. Our investigation shows that the resistance reaches its maximum immediately after the capsule is driven against the fold, and drops off gradually during the crossing motion.

Introduction

Diseases of surface lining of the small intestine are highly challenging to diagnose and treat. To develop new endoscopic devices capable of self-propelling in the small intestine, endoscopic engineers need to take the complex anatomy of the small intestine into account, in particular the circular fold of the small intestine, when evaluating the performance of their designs. The purpose of the present work is to develop a mathematical model for accurately predicting the resistant force of the capsule-type devices moving in the small intestine and use the model to test the vibro-impact self-propelled capsule developed in the Applied Dynamics and Control Lab at the University of Exeter [1, 2].

According to the movement of the small intestine, most of the research works (e.g., [5, 4]) assume that the capsule distends the intestine in the radial direction when assessing the intestinal resistance. However, this assumption is only valid for a very short time interval during the intestinal movement. For most of the time of diagnosis, the capsule is in one-sided contact with the intestinal wall, so the resistance from the hoop pressure does not apply. For this reason, Guo et al. [7, 8] estimated the intestinal resistance for a self-propelled capsule by considering both partial and full capsule-intestine contacts. In the present work, we use the cylindrical capsule as an example and take the circular fold of the small intestine into consideration to study the required driving force for self-propulsion and the capsule's dynamics in clinical scenario.

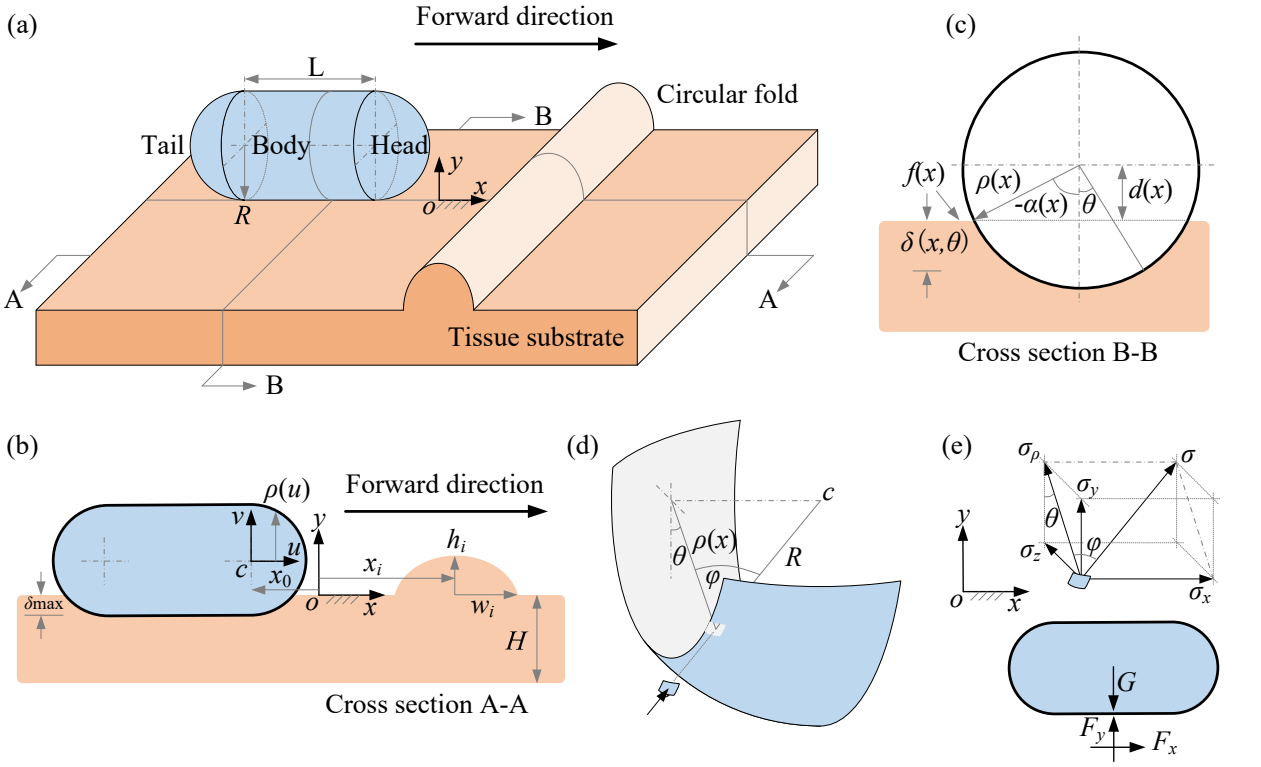

Figure 1: (a) 3D schematic of an endoscopic capsule moving towards a circular fold on a flat tissue substrate. (b) Cross section A-A shows the horizontal and vertical location of the capsule by x_0 and $\delta_{\max}$, and the location, width and height of the ith fold by x_i, w_i and h_i. (c) Cross section B-B shows the capsule-substrate contact angle, $\theta \in [-\alpha(x), \alpha(x)]$. (d) The stress, $\sigma(x, \theta)$, is exerted on the capsule shell as a normal pressure. (e) Integrating the x and y components of the pressure yields the horizontal and vertical reactions, where F_y is balanced by the capsule's gravity, G, and F_x resists the capsule's motion.

Mathematical modelling and validation

The interaction between the capsule and a tissue substrate is schematically illustrated in Fig. 1. As seen, the capsule's hemispheric head and tail is connected by a cylindrical body with a length of L and a radius of R. When the capsule moves horizontally in x-direction, it engages with the circular fold of the small intestine, resulting in complex interactive forces and capsule motion. The detailed modelling procedure can be found in [9].

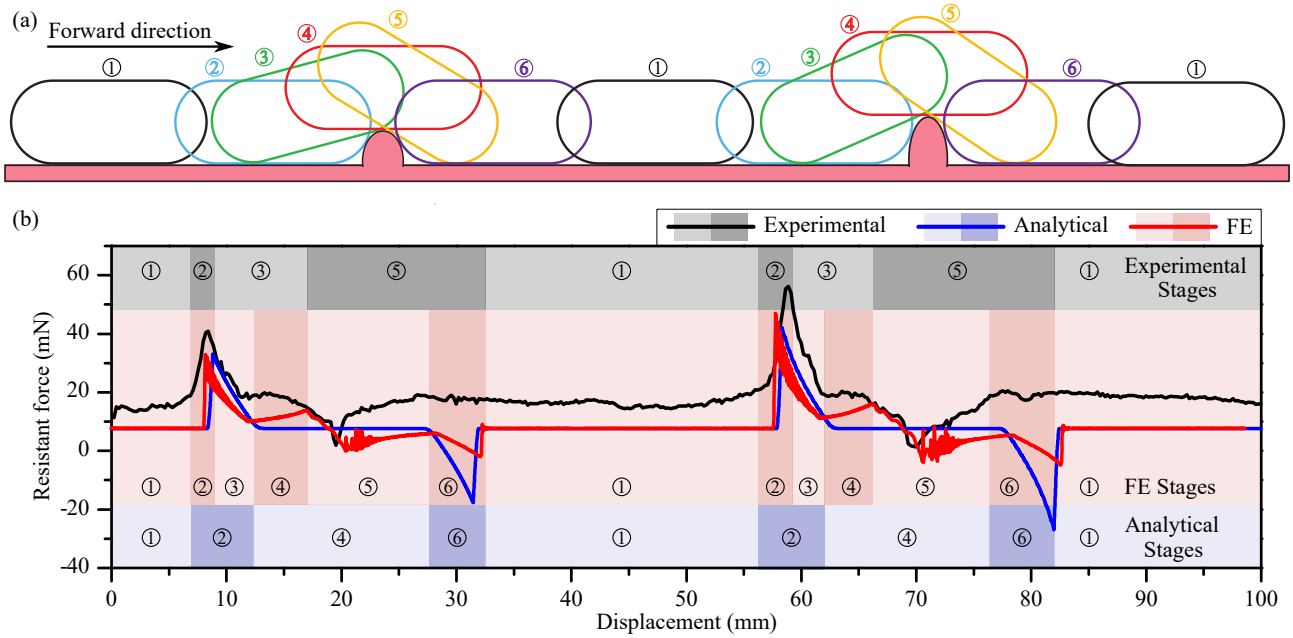

Figure 2: (Colour online) Resistant force acting on the capsule as a function of capsule's displacement when the capsule was pulled on a cut-open synthetic small intestine consisting of two different circular folds in a constant speed of 8 [mm/s] obtained from the mathematical model (blue line), the FE model (red line) and the experiment (black line). FE model can capture all of the six stages of the capsule's motion. Due to the limitations, experiment missed Stages ④ and ⑥, and the mathematical model cannot capture Stages ③ and ⑤. Parameters for the mathematical and FE models were chosen as $E = 100$ [kPa], $G = 33.96$ [mN], $\mu = 0.2293$, $R = 5.50$ [mm], $L = 15$ [mm], $H = 0.69$ [mm], $x_1 = 12.66$ [mm], $h_1 = 1.67$ [mm], $w_1 = 1.665$ [mm], $x_2 = 62.66$ [mm], $h_2 = 2.34$ [mm] and $w_2 = 1.545$ [mm], which were identified from the experimental setup in [8].

In order to validate the analysis, the mathematical and finite element (FE) models adopted the parameters corresponding to the experimental setup described in [8]. Under the same position, the one-to-one correspondence between the capsule's posture and the resistant force is shown in Fig. 2. According to the FE result, the process of capsule's crossing over a circular fold can be divided into six stages. Although some stages were missed by the mathematical model and the experiment due to their limitations, here we are interested with the maximum resistant force experiencing by the capsule when it crosses over the fold.

Conclusions

In conclusion, the FE model captured all of the crossing stages, but the computation was so time-consuming that we only adopted a 2D FE model to sacrifice its accuracy. Nonetheless, all these three (analytical, FE and experimental) methods yielded consistent results for evaluating the maximum resistant force.

References

[1] Liu Y., Guo B., Prasad S. (2019) Resonance Enhanced Self-Propelled Capsule Endoscopy for Small Bowel Examination. *Gut* **68**:A31-A31.

[2] Liu, Y., Páez Chávez, J., Zhang, J., Tian, J., Guo, B., Prasad, S. (2020) The Vibro-Impact Capsule System in Millimetre Scale: Numerical Optimisation and Experimental Verification. *Meccanica* **55**:1885–1902.

[3] Yan, Y., Zhang, B., Liu, Y., Prasad, S. (2021) Dynamics of a Vibro-Impact Self-Propelled Capsule Encountering a Circular Fold in the Small Intestine. *Meccanica*, under review.

[4] Wang, Z., Ye, X., Zhou, M. (2013) Frictional Resistance Model of Capsule Endoscope in the Intestine. *Tribol. Lett.* **51**:409-418.

[5] Woo, S., Kim, T., Mohy-Ud-Din, Z., Park, I., Cho, J. (2011) Small Intestinal Model for Electrically Propelled Capsule Endoscopy. *Biomed. Eng. Online* **10**:108.

[6] Sliker, L., Ciuti, G., Rentschler, M., Menciassi, A. (2016) Frictional Resistance Model for Tissue-Capsule Endoscope Sliding Contact in the Gastrointestinal Tract. *Tribol. Int.* **102**:472-484.

[7] Guo, B., Liu, Y., Prasad, S. (2019) Modelling of Capsule–Intestine Contact for a Self-Propelled Capsule Robot via Experimental and Numerical Investigation. *Nonlinear Dyn.* **98**:3155-3167.

[8] Guo, B., Ley, E., Tian, J., Zhang, J., Liu, Y., Prasad, S. (2020) Experimental and Numerical Studies of Intestinal Frictions for Propulsive Force Optimisation of a Vibro-Impact Capsule System. *Nonlinear Dyn.* **101**:65-83.

[9] Yan, Y., Guo, B. Tian, J., Zhang, J., Zhang, B., Ley, E., Liu, Y., Prasad, S. (2021) Evaluating the Resistant Force of an Endoscopic Capsule Moving in the Small Intestine. *Tribol. Int.* under review.

Work-loop techniques for optimising nonlinear forced oscillators

Arion Pons [*] [**] [†], and Tsevi Beatus [*] [**] [‡]
[*] *Institute of Life Sciences, Hebrew University of Jerusalem, Israel*
[**] *School of Computer Science and Engineering, Hebrew University of Jerusalem, Israel*

Summary. Linear and nonlinear resonant states can be restrictive: they exist at particular discrete states in frequency and/or elasticity, under particular (*e.g.*, simple-harmonic) waveforms. In forced oscillators, this restrictiveness is an obstacle to system design and control modulation: altering the system elasticity, or modulating the response, would both appear to necessarily incur a penalty to efficiency. In this work, we describe an approach for bypassing this obstacle. Using novel work-loop techniques, we prove and illustrate how certain classes of resonant optimisation problem lead to non-unique solutions. In a structural optimisation context, several categories of energetically-optimal elasticity are non-unique. In an optimal control context, several categories of energetically-optimal frequency are non-unique. For these classes of non-unique optimum, we can derive simple bounds defining the optimal region. These novel theoretical results have practical implications for the design and control of a range of biomimetic propulsion systems, including flapping-wing micro-air-vehicles: using these results, we can generate efficient forms of wingbeat modulation for flight control.

1. Introduction

A wide range of biological and engineering systems utilize nonlinear structural elasticity to shape and control an oscillatory forced response. Insects rely on strain-hardening thoracic elasticity to modulate flight motor muscular actuation [1, 2]. Micro-mechanical energy harvesters utilise nonlinear elasticity to improve harvesting efficiency [3–5]. Compliant bipedal robots utilise distributed elasticity to improve walking efficiency [6]. Among the multifaceted roles that nonlinear elasticity can play in such systems, energetic roles are often central: structural elasticity can absorb inertial loads and/or mitigate inertial power requirements, thereby increasing system efficiency. However, there is a sense in which the pursuit of efficiency can be restrictive. Energetically-optimal states tend to be discrete: located at particular states of elasticity (*e.g.*, the resonant elasticity); or at particular discrete frequencies (*e.g.*, the resonant frequencies), and particular (*e.g.*, symmetric, harmonic) waveforms. For instance: as per classical analysis, linear resonance occurs at discrete frequencies, and under simple-harmonic forcing; and in nonlinear systems, such as the Duffing oscillator, frequency response magnitude peaks are also typically discrete. In both cases, deviating from the energetically-optimal frequency-elasticity match, or resonant state, incurs a penalty in efficiency.

Here, we describe a novel technique for bypassing this efficiency penalty in some contexts. Using work-loop analysis techniques – showing several parallels with phase portrait techniques – we can illustrate and prove several key optimality results. These techniques allow us to prove how several classes of forward- and inverse-problems for energetic optimality necessarily lead to non-unique solutions; and to derive simple bounds defining this region of non-unique optimal solutions. These new theoretical results have significant implications for the use of nonlinear dynamics in engineering design. They describe ways to introduce nonlinear elasticities into a system to ensure energetic optimality, and illustrate how, for certain classes of energetic optimality, a whole space of optimal nonlinear elasticities exists. The choice of nonlinear elasticity within this space is a design tool that can be used to control other aspects of system behaviour. These results also describe methods for modulating the frequency of a resonant response, and/or breaking its symmetry, while maintaining energetic optimality. Improving the energetic optimality of these forms of response modulation is crucial to several forms of bio-inspired locomotion system: modulating the frequency of bipedal walking can govern the transition to running [7]; and modulating the wingstroke offset of a flapping-wing micro-air-vehicle (FW-MAV) can lead to body pitch control [8]. In this way, these theoretical techniques lead to new design and control principles for a range of engineering systems.

2. Energy resonance in the time-domain

In linear and nonlinear systems, the phenomenon of resonance is complex and multifaceted: representing a range of distinct, and often mutually-exclusive, states of optimality [9, 10] and interaction phenomena [11]. Energy, or global, resonance is one such resonant phenomenon that has key relevance to the design and operation of efficient resonators (biolocomotive systems, energy harvesters, *etc.*) [3–5, 9, 12]. Consider, for instance, a general nonlinear time-invariant single-degree-of-freedom (1DOF) parallel elastic actuation (PEA) system (Fig. 1):

$$D(x, \dot{x}, \ddot{x}, \dots) + F_s(x) = F(t). \tag{1}$$

[†] arion.pons@mail.huji.ac.il
[‡] tsevi.beatus@mail.huji.ac.il

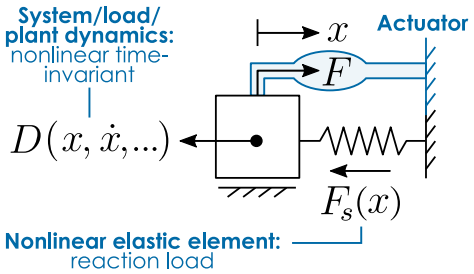

Figure 1: Schematic of a general nonlinear time-invariant 1DOF PEA system

with general system (*i.e.*, plant, or load) dynamics $D(x, \dot{x}, \ddot{x}, \dots)$, linear or nonlinear elastic element $F_s(x)$, and actuator load input $G(t)$. The state of energy resonance in this system is easy to define, but hard to locate – it is the state:

$$F(t)\dot{x}(t) \geq 0, \forall t. \tag{2}$$

That is, the actuator power consumption should always be positive: power should flow from the actuator to the system, and never vice-versa. This unidirectionality of power flow represents both an intuitive state of energetic optimality, and a formal one. Intuitively, if we desire the largest possible system response, then we should seek always to use the actuator, $F(t)$, to feed energy into the system – rather than draw energy out of the system. Unidirectional power flow defines the condition that all of the actuator power consumption is directed towards increasing the total energy in the system.

Formally, energy resonant states are optimal with respect to elasticity. Consider an energy resonant state for Eq. 1 at some $F_s(x)$, and some $x(t)$ and $F(t)$ that are periodic with common period T. The overall actuator mechanical power consumption at this state can be defined in multiple ways, for instance:

$$\begin{aligned}
&\text{the net power:} && \overline{\mathrm{P}}_{\mathrm{net}} = \int_0^T F(t)\dot{x}(t)\, dt, \\
&\text{the absolute power:} && \overline{\mathrm{P}}_{\mathrm{abs}} = \int_0^T |F(t)\dot{x}(t)|\, dt, \\
&\text{the positive-only power:} && \overline{\mathrm{P}}_{\mathrm{pos}} = \int_0^T F(t)\dot{x}(t)[F(t)\dot{x}(t) > 0]_I\, dt,
\end{aligned} \tag{3}$$

where $[\,\cdot\,]_I$ is the Iverson bracket, $[\lambda]_I = 1$ for λ true, $[\lambda]_I = 0$ for λ false [13]. This difference between these metrics lies in their treatment of negative power, $F\dot{x} < 0$. The net power represents the mechanical power throughput of the system – the power dissipated to the system or plant, $D(\cdot)$. It does not represent the mechanical power consumption of the actuation except in the case where the actuator is intrinsically capable of absorbing negative power, and storing this power for future use – for instance, in certain configurations of electrical actuator with power electronics. The absolute power represents the mechanical power consumption of the actuator if the actuator itself is responsible for drawing power out of the system – for instance, a rocket or jet engine, which must consume fuel to produce thrust, irrespective of the direction this thrust is oriented (whether to produce negative or positive power). The positive-only power represents the mechanical power consumption of the actuator if an additional dissipative braking system is responsible for generating negative power – for instance, in a vehicle with a dissipative braking system. A dissipative braking system can relieve the actuator from a responsibility to generate negative power, but cannot store this energy for future use.

Note that further, more generalised, negative-power penalties can be defined, *e.g.*, to represent the behaviours of biological muscles [12, 14, 15]. However, the penalty detail matters not: it is clear that, only under the energy resonant condition, Eq. 2, will the power throughput (net power) equal the actuator power consumption (absolute, positive-only, *etc.*). In any non-energy resonant state, the actuator power consumption will be greater than the net power; the difference in power representing wasted negative power. A key corollary of this is that, at an energy resonant state, there exists no other elasticity, $F_s(x)$, that could reduce the actuator power consumption (absolute, positive-only, *etc.*) required to generate $x(t)$. This can be demonstrated in the following way. The elasticity, $F_s(x)$, cannot alter the net power required to generate a specified $x(t)$ – this can be confirmed by evaluating the net power integral:

$$\int_0^T F(t)\dot{x}(t)\, dt = \int_0^T D(x, \dot{x}, \ddot{x}, \dots)\dot{x}(t)\, dt + \int_{x(0)}^{x(T)} F_s(x)\, dx = \int_0^T D(x, \dot{x}, \ddot{x}, \dots)\dot{x}(t)\, dt. \tag{4}$$

It is also impossible for the actuator power consumption to be less than the net power – this is a property of the definitions in Eq. 3. Therefore, there exists no elasticity $F_s(x)$, that could further minimise the actuator power consumption (absolute, positive-only, *etc.*) required to generate the output, $x(t)$, of an energy resonant state. In this sense, energy resonant states are energetically-optimal.

3. Energy resonance in work-loop planes

Work loops are an analysis tool used frequently in applied contexts, but have not yet seen significant theoretical application. Their defining characteristic is that they display a metric of force against a metric displacement, and therefore have an area that is synonymous with work, *i.e.*, energy. In biomechanics, work loops are used to visualise, and characterise the behaviour of muscle groups undergoing periodic motion – *e.g.*, muscles within the insect flight motor [16–18]. In materials science, they are one of many forms of hysteresis loop, used to characterise viscoelastic and other hysteretic material behaviour [19]. Work-loop techniques can be applied to the dynamical system of Eq. 1: given some pair of $x(t)$ and $F(t)$ for Eq. 1, it is possible to visualise this pair in the plane of F against x (Fig. 2). We denote this plane x-F (abscissa-ordinate). If $x(t)$ and $F(t)$ are periodic, with common period, then this pair will trace out a closed loop in the x-F place: a work loop. This work loop may take many shapes. For instance, any linear PEA system undergoing steady-state simple-harmonic motion shows an elliptical work loop (Fig. 2a). That is, for a system of the form:

$$\ddot{x} + 2\zeta\omega_0\dot{x} + \omega_0^2 x = F(t), \tag{5}$$

with $x = \hat{x}\cos(\Omega t)$, we can establish that:

$$F^2 - 2F(\omega_0^2 - \Omega^2)x + ((\omega_0^2 - \Omega^2)^2 + 4\zeta^2\omega_0^2\Omega^2)x^2 = 4\zeta^2\omega_0^2\Omega^2\hat{x}^2, \tag{6}$$

describing an ellipse. However, categories of dynamical system do not directly translate to consistent work loop shapes. For instance, as we add additional harmonics to the motion of a linear system, the work loop rapidly becomes inexpressible in closed form.

In our analysis, we will consider a system which is simultaneously more general and more restrictive than the nonlinear PEA system of Eq. 1. We consider a work loop that is a closed simple curve (*i.e.*, no self-intersections), and is no more than bivalued at any x (Fig. 2). Other than this, the shape of the loop can be arbitrary. Such a loop could arise from systems considerably more complex than Eq. 1, including, *e.g.*, computational fluid dynamics (CFD) models. For instance, Fig. 2b illustrates a work loop arising from CFD analysis of *Drosophila melanogaster* wingbeat oscillation, derived from [20–22]. But, conversely, even the linear PEA system, Eq. 5, is capable of generating work loops which are more than bivalued at any x – for instance, very simply, in cases where the output, $x(t)$, is not composed of two monotonic half cycles.

In cases where the work loop is a closed simple curve, as specified, it is representable as an upper and lower curve: $F^+(x)$ and $F^-(x)$ (Fig. 2a). These curves represent the two monotonic half-cycles of $x(t)$, and, as such, are each associated with a particular sign of the velocity ($\dot{x}$). For a dissipative work loop (net power > 0), over F^+, $\dot{x} > 0$, and over F^-, $\dot{x} < 0$. Going further, if we distinguish between the system's elastic load, $F(t)$, and inelastic load, $G(t)$, as altered by a parallel (PEA) elasticity – that is, in the particular case of Eq. 1, as:

$$\begin{aligned} &\text{inelastic load, } G(t): && D(x, \dot{x}, \ddot{x}, \dots) = G(t), \\ &\text{elastic load, } F(t): && D(x, \dot{x}, \ddot{x}, \dots) + F_s(x) = G(t) + F_s(x) = F(t), \end{aligned} \tag{7}$$

– then we can define work-loop equations of motion for this general PEA system:

$$G^{\pm}(x) + F_s(x) = F^{\pm}(x). \tag{8}$$

These work-loop equations of motion describe not only Eq. 1, but also the load-requirement dynamics of a more complex system (*e.g.*, the CFD model in Fig. 2b): elasticity, $F_s(x)$ alters the load, $F^{\pm}(x)$, required to generate the output response associated with the desired output, $G^{\pm}(x)$. In simple cases, Eq. 7-8 can be expressed entirely in closed form. For instance, the linear PEA system undergoing simple-harmonic motion (Eq. 5):

$$\begin{aligned} &G^{\pm}(x) = \Omega^2 x \pm 2\zeta\omega_0\Omega\sqrt{\hat{x}^2 - x^2} \\ &F^{\pm}(x) = (\omega_0^2 - \Omega^2)x \pm 2\zeta\omega_0\Omega\sqrt{\hat{x}^2 - x^2} \\ &\textit{i.e.}, \; G^{\pm}(x) + \omega_0^2 x = F^{\pm}(x). \end{aligned} \tag{9}$$

The work-loop equations of motion, Eq. 8, permit a definition of the energy resonant condition, Eq. 2, in the work-loop plane. We seek to define the condition $F\dot{x} \geq 0$ (Eq. 2), and we know that over F^+, $\dot{x} > 0$, and over F^-, $\dot{x} < 0$, therefore, for energy resonance:

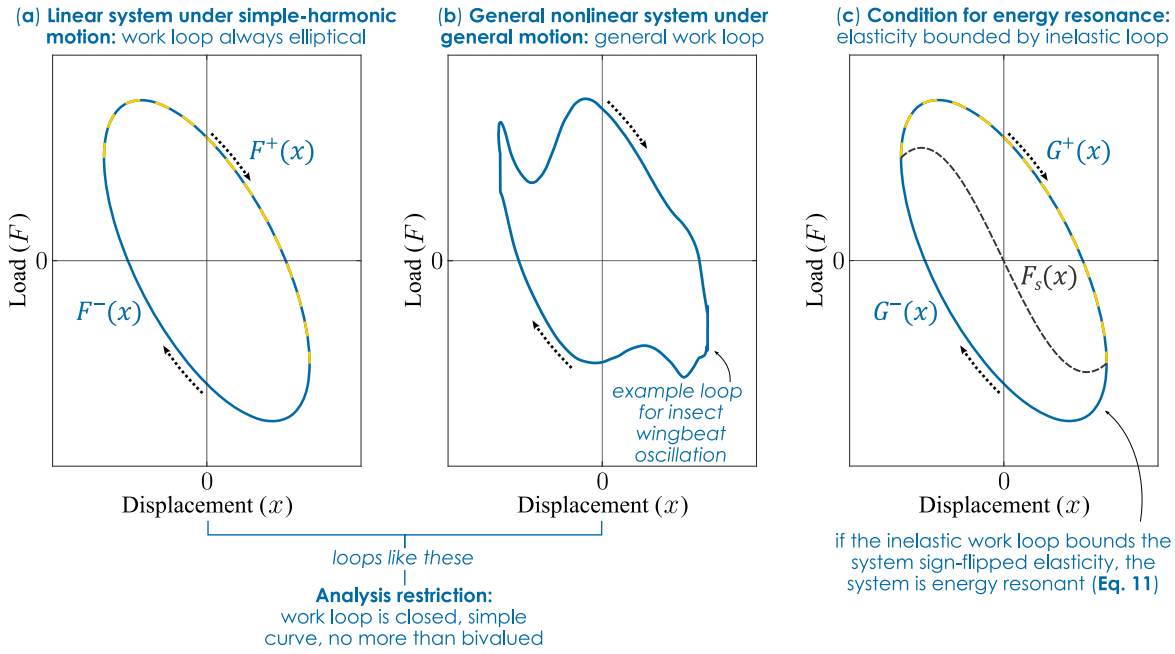

Figure 2: Schematic of work loops for (**a**) linear and (**b**) general systems, alongside (**c**) the conditions for energy resonance, in $F_s(x)$ and $G^{\pm}(x)$.

$$F^+(x) \geq 0 \text{ and } F^-(x) \leq 0. \tag{10}$$

Or, via Eq. 8, for energy resonance:

$$G^-(x) \leq -F_s(x) \leq G^+(x), \tag{11}$$

as illustrated in Fig. 2c. Eq. 11 is the elastic-bound condition for this general PEA system, describing the relationship between elasticity, $F_s(x)$, and the inelastic system work loop, $G^{\pm}(x)$ (a function only of the plant dynamics and desired output) that must exist in order for an energy resonant state to exist. Eq. 11 is an inequality condition, describing a continuum of states – whether in $F_s(x)$, or $G^{\pm}(x)$ – that are energy resonant. Notably, however, this condition contains within it a pair of equality condition. At $\max x$ and $\min x$ ($\pm\hat{x}$ for simple-harmonic motion), $G^-(x) = G^+(x)$, by virtue of the fact that the work loop is closed. Therefore, at these values, the inequality in Eq. 12 becomes an equality:

$$\begin{aligned} G^-(\max x) &= -F_s(\max x) = G^+(\max x), \\ G^-(\min x) &= -F_s(\min x) = G^+(\min x). \end{aligned} \tag{12}$$

Physically, peak inertial loads (inelastic loads at the x-extrema, where $\dot{x} = 0$) must always match peak elastic loads (elastic loads at the x-extrema). This equality condition, Eq. 12, is a useful commonality between the continuum of energy resonant states defined by Eq. 11 – we will illustrate its utility in Sections 4-5.

4. Work-loop analysis for structural optimisation

4.1. Elastic-bound optimisation principle

Practical applications of work-loop analysis arise in a range of physical and analytical contexts. One such analytical context is that of structural optimisation in nonlinear oscillators – for instance, the optimisation of oscillator structural properties so as to generate a desired forced oscillatory response at maximum efficiency. Structural optimisation problems of this form arise in a range of physically-relevant oscillatory systems: for instance, flapping-wing micro-air-vehicles, involving the design of drivetrain elastic elements to ensure maximum efficiency [23–25]; and micro-mechanical energy harvesters, involving the design of oscillators for maximum energy absorption [3–5]. The elastic-bound conditions, Eq. 11, are directly applicable in a structural optimisation context. Consider a nonlinear oscillator, of the form $D(x, \dot{x}, \ddot{x}, \ldots) + F_s(x) = G(t)$ (Eq. 8), with some structural elasticity, $F_s(x)$, that we have design control over. If we specify some desired system output, a periodic $x(t)$, then, given some $F_s(x)$, we know the actuator load, a periodic $F(t)$, that is required to generate this desired output. The optimisation problem then is to select $F_s(x)$ such that this load requirement, $F(t)$, is optimal in some way. If we are interested in energy-efficiency, then a key metric to optimise is the mechanical power consumption associated

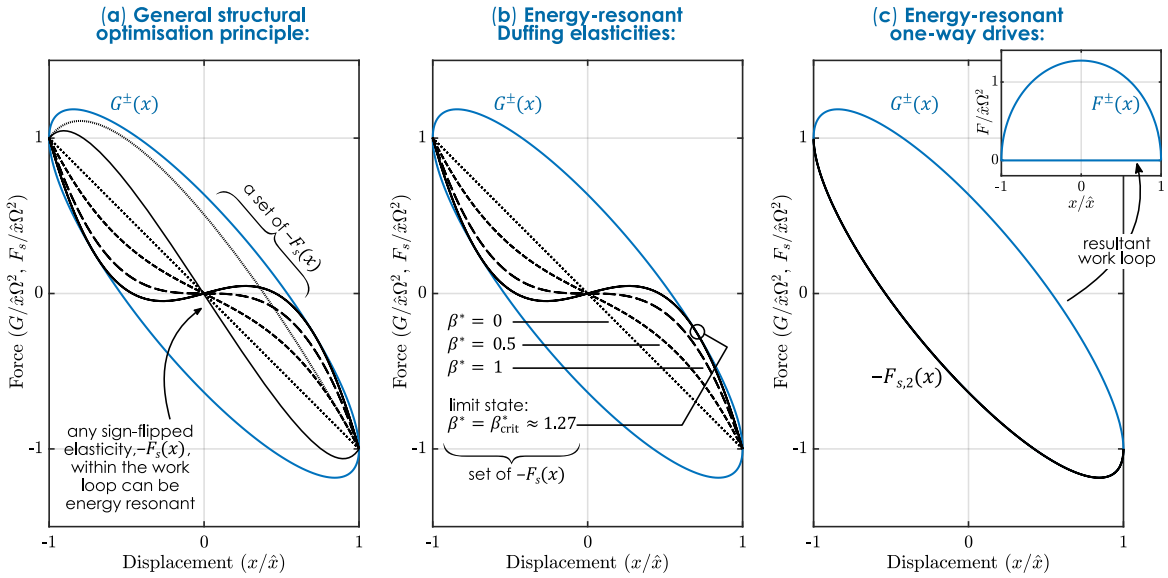

Figure 3: Work loop analysis and energy resonance in a structural optimization context. (**a**) The general structural optimisation principle (Section 4.2); (**b**) a set of energy-resonant Duffing elasticities (Section 4.2); (**c**) and energy-resonant one-way-drive elasticity (Section 4.3). The Duffing oscillator inelastic parameters are $\delta = 4$, $\omega = 2\pi$, $\hat{x} = 1$.

with $F(t)$: for instance, the absolute power, $\overline{\mathrm{P}}_{\mathrm{abs}}$, or positive-only power, $\overline{\mathrm{P}}_{\mathrm{pos}}$, as per Eq. 3[§]. In either case, the elastic-bound conditions provide a direct solution to this optimisation problem: it is the elasticities, $F_s(x)$, satisfying Eq. 11, that ensure that $\overline{\mathrm{P}}_{\mathrm{abs}}$ and $\overline{\mathrm{P}}_{\mathrm{pos}}$ take their minimum values with respect to $F_s(x)$. This is a highly-general principle, applicable to any PEA system that generates a closed, simple, bi-valued work loop, under the specified $x(t)$ (*cf.* Section 3). Fig. 3a illustrates this principle, alongside the two more specific cases studied below.

4.2 Structural optimisation of a Duffing oscillator

As an example of the work-loop structural optimisation process, consider the Duffing oscillator:

$$\ddot{x} + \delta\dot{x} + \alpha x + \beta x^3 = F(t) \tag{13}$$

with damping $\delta > 0$, linear stiffness α, cubic stiffness β, and input loading $F(t)$ which, in our analysis, may not necessarily be simple-harmonic. The energy-minimisation structural optimisation problem in this oscillator is to compute the elastic parameters, α and β, such that this specified output can be generated at a state of energy resonance, by some $F(t)$. As such, in a work-loop context, we can split Eq. 13 into an inelastic load, $G(t)$, and an elastic profile, $F_s(x)$:

$$\ddot{x} + \delta\dot{x} = G(t), \qquad F_s(x) = \alpha x + \beta x^3 \tag{14}$$

More specifically, consider a steady-state simple-harmonic output, $x = \hat{x}\cos(\Omega t)$. In this case, the inelastic work loop is given by the elliptical profile:

$$G^{\pm}(x) = -\Omega^2 x \pm \delta\Omega\sqrt{\hat{x}^2 - x^2}. \tag{15}$$

The elastic-bound equality conditions (Eq. 12) translate to conditions on the stiffness parameters, α and β:

$$-F_s(\hat{x}) = G^{\pm}(\hat{x}) \;\therefore\; \Omega^2\hat{x} = \alpha\hat{x} + \beta\hat{x}^3 \;\therefore\; \alpha = \Omega^2 - \beta\hat{x}^2 \tag{16}$$

which is to say, the Duffing stiffnesses, $F_s(x)$ that can generate this simple-harmonic output at a state of energy resonance are necessarily of the form

$$\frac{F_s(x)}{\Omega^2} = (1 - \beta^*\hat{x}^2)x + \beta^* x^3 \tag{17}$$

where $\beta^* = \beta/\Omega^2$ is a free parameter. Note that the equality condition, yielding Eq. 17, is necessary for the existence of an energy resonant state, but no sufficient. We anticipate, based on the full elastic-bound conditions,

[§] Note that, even if the net power, $\overline{\mathrm{P}}_{\mathrm{net}}$, were to be relevant to the actuator under consideration, $\overline{\mathrm{P}}_{\mathrm{net}}$ is independent of $F_s(x)$: the structural optimisation problem associated with $\overline{\mathrm{P}}_{\mathrm{net}}$ is irrelevant. This is further illustration of how $\overline{\mathrm{P}}_{\mathrm{abs}}$ and $\overline{\mathrm{P}}_{\mathrm{pos}}$ are more relevant metrics of actuator mechanical power consumption.

that Eq. 17 should describe an energy-resonant state only over some range of β^*. We may compute this range via the full elastic-bound conditions. Consider that, at the point at which the elastic-bound conditions fail, there exists the critical state:

$$G^+(x) = F_s(x) \text{ or } G^-(x) = F_s(x), \text{ for some } x \neq \pm\hat{x}. \tag{18}$$

That this state necessarily exists is a property of the smoothness of this system. Again, with the elliptical inelastic work loop profile, Eq. 15, we can describe x such that Eq. 18 is satisfied, as the roots of the quartic polynomial:

$$x^4 - x^2\hat{x}^2 + \frac{\delta^2}{\beta^{*2}\Omega^2} = 0. \tag{19}$$

Eq. 19 is a quadratic polynomial in x^2, and, as such, we can determine that the critical x will exist (as a real number) if and only if the discriminant of this quadratic is positive. This leads to the condition:

$$-\beta^*_{\text{crit}} \leq \beta^* \leq \beta^*_{\text{crit}}, \qquad \beta^*_{\text{crit}} = \frac{2\delta}{\hat{x}^2\Omega} \tag{20}$$

For the constrained Duffing elasticity, Eq. 19, to be capable of generating an energy-resonant simple-harmonic output, under some periodic forcing. The actual periodic forcing required is trivial to define – it is given by Eq. 13 – though note that chaotic effects may necessitate a control system to maintain a steady-state output (and may even mean that such control is impractical). Nevertheless, Eq. 17 and 20 define the Duffing stiffnesses that are required for an energetically-optimal simple-harmonic output. Other non-simple-harmonic outputs can be optimised via the same work-loop analysis process, though numerical techniques may be required to compute both the form of the optimal elasticity (Eq. 17) and the range over which it is valid (Eq. 20)

4.3 Special cases of energy-resonant structure

In Section 4.2, we considered the optimisation of an elastic element of prescribed structure: the cubic elasticity of the Duffing oscillator. However, in a broader systems-design context, there may be no particular reason to restrict oneself to prescribed structures – considering elasticities with particular energy-resonant properties, irrespective of structure, may also be worthwhile. Work-loop analysis is a tool for identifying energy-resonant elasticities with special properties. As a notable example of this, consider again the elastic-bound conditions, Eq. 11. These conditions include, as an extremal case, the elasticities lying on the upper and lower boundaries of the loop:

$$\begin{aligned} F_{s,1}(x) &= -G^+(x), \\ F_{s,2}(x) &= -G^-(x). \end{aligned} \tag{21}$$

By definition, these elasticities generate a resultant work loop, $F^{\pm}(x)$, that has one half-cycle at zero load (Eq. 9, Fig. 3c):

$$\begin{aligned} F_{s,1}(x) = -G^+(x) \;\therefore\; F^-(x) = G^-(x) - G^+(x), \;\; F^+(x) = 0, \\ F_{s,2}(x) = -G^-(x) \;\therefore\; F^+(x) = G^+(x) - G^-(x), \;\; F^-(x) = 0. \end{aligned} \tag{22}$$

It follows also, that the other half-cycle will be at a state of unidirectional load: $G^+(x) - G^-(x)$ can never change sign, if $G^+(x) \geq G^-(x)$ as per our condition for no self-intersection of the work loop. The result is an energy-resonant state requiring only unidirectional actuation: we term this, a one-way-drive state. An additional property of this state is that it the duty cycle of the actuator is reduced: over the region of zero load requirement, the actuator need not be activated or energised. With the proper selection of one-way-drive elasticity, the actuator duty cycle can be reduced to 50% or less, for any appropriate work loop [12]. Both these properties make one-way-drive states systems ideal for certain classes of actuator: those which are capable of generating large intermittent loads in a single direction – such as combustion cylinders, explosive actuators, and solenoid actuators [26, 27]. Combustion cylinders, in particular, are more energy-dense than many forms of electromechanical actuator: utilising combustion cylinders to generate one-way-drive energy resonant oscillations in a flapping-wing aircraft may be an avenue to increasing the range and endurance of these aircraft.

5. Work-loop analysis for optimal control

5.1. Elastic-bound optimal control principle

Another practical application of work-loop analysis arises in the context of optimal control. In contrast with structural optimisation, which deals variable system structural properties, optimal control problems typically relate to a fixed system structure, and consider variable responses within this structure – with the aim to locate output responses (and, input forces) that are optimal in some sense. Work loop analysis is particularly relevant to optimal control problems that are concerned with optimising power consumption, or energetic efficiency, as it allows an easy description, and visualisation, of the location and properties of energy-resonant states. One of the interesting properties of energy resonance is that, even in the simplest linear systems, energy resonance is a non-unique state. As per Section 4, the energy-resonant structural elasticity for a system undergoing a specified output is non-unique

– there exists a continuum of energy-resonant elasticities. So also, the energy-resonant output for a system with fixed elasticity is non-unique – there exists a continuum of energy-resonant outputs. This continuum of energy-resonant outputs is defined directly by the elastic-bound conditions: for fixed elasticity $F_s(x)$, we seek $G^{\pm}(x)$ such that Eq. 11 is satisfied – $G^{\pm}(x)$ depending only on the desired output, $x(t)$, and the inelastic dynamics of the system, $D(\cdot)$[**]. We note that these different work loops may represent outputs at different amplitudes, frequencies, and symmetric or asymmetric waveforms. If then, as part of our control problem, we desire to modulate the frequency of our system output response, while maintaining a state of energy resonance (*i.e.*, optimality in mechanical power consumption), then work-loop analysis techniques provide a strategy for doing so. We refer to this energy-resonant frequency modulation as frequency-band resonance, and note that other forms of energy resonant modulation (*e.g.*, offset-band resonance, involving symmetry-breaking modulation [12]) are also available.

5.2. Optimal frequency control of a Duffing oscillator

Consider again the general Duffing oscillator, Eq. 14. As per our structural optimisation results (Eq. 16), the frequency, ω_e, at which a simple-harmonic output is energy resonant in this general system is:

$$\omega_e^2 = \alpha + \beta\hat{x}^2. \tag{23}$$

As per our optimal control analysis, the question arises: can one maintain energy resonance while deviating from this energy-resonant frequency? As one instance of a deviation from a simple-harmonic output, consider the multiharmonic output given by:

$$\begin{aligned} x(t) &= \hat{x}(1-\rho)\cos(\Omega t) + \hat{x}\rho\cos(3\Omega t), \\ \dot{x}(t) &= -\Omega\hat{x}(1-\rho)\sin(\Omega t) - 3\Omega\hat{x}\rho\sin(3\Omega t), \\ \ddot{x}(t) &= -\Omega^2\hat{x}(1-\rho)\cos(\Omega t) - 9\Omega^2\hat{x}\rho\cos(3\Omega t), \end{aligned} \tag{24}$$

for small ρ, this multiharmonic wave is qualitatively sinusoidal. More precisely: for the window $-0.125 \leq \rho \leq 1$, computed numerically, the global displacement extrema of $x(t)$ are $\pm\hat{x}$ ($\max x = \hat{x}$ and $\min x = -\hat{x}$), and are located at $t = 0,\ T/2,\ T,\ \ldots$, where $T = 2\pi/\Omega$. For the more restrictive window $-0.125 \leq \rho \leq 0.25$, also computed numerically, $x(t)$ is composed of two monotonic half-cycles (velocity reversal, where $\dot{x} = 0$, exists only at $t = 0,\ T/2,\ T,\ \ldots$). We require both these conditions to be true – thus limiting ourselves to the more restrictive of these windows.

As part of a frequency-band analysis, we seek $\rho(\Omega)$ such that $x(t)$ is energy resonant at Ω. Note that, at the energy-resonant frequency, ω_e, a simple-harmonic wave is energy resonant (Section 4.2), and thus $\rho(\omega_e) = 0$. To compute the rest of $\rho(\Omega)$, note that the elastic-bound conditions necessitate:

$$G^{\pm}(\hat{x}) = F_s(\hat{x}), \text{ and } G^{\pm}(-\hat{x}) = F_s(-\hat{x}), \tag{25}$$

where we have assumed that $\max x = \hat{x}$ and $\min x = -\hat{x}$; an assumption we know to be valid over $-0.125 \leq \rho \leq 1$. Over this window we know, in addition, that these extrema will be located at $= 0,\ T/2,\ T,\ \ldots$, where $T = 2\pi/\Omega$. We can therefore translate Eq. 25 into a condition in the time-domain:

$$\begin{aligned} G(0) = G(T) &= F_s(\hat{x}) = \alpha\hat{x} + \beta\hat{x}^3, \\ G(T/2) &= F_s(-\hat{x}) = -\alpha\hat{x} - \beta\hat{x}^3, \end{aligned} \tag{26}$$

which, combining with load profile:

$$\begin{aligned} G(t) = \ddot{x} + \delta\dot{x} = &-\Omega^2\hat{x}(1-\rho)\cos(\Omega t) - 9\Omega^2\hat{x}\rho\cos(3\Omega t) \\ &- \delta\Omega\hat{x}(1-\rho)\sin(\Omega t) - 3\delta\Omega\hat{x}\rho\sin(3\Omega t), \end{aligned} \tag{27}$$

yields the condition:

$$G(0) = G(T) = -G(T/2) = -\Omega^2\hat{x}(1+8\rho) = -F_s(\hat{x}) = -\alpha\hat{x} - \beta\hat{x}^3. \tag{28}$$

From Eq. 28 we deduce that the relationship $\rho(\Omega)$ is:

$$\rho(\Omega) = \frac{1}{8}\left(\frac{\alpha + \beta\hat{x}^2}{\Omega^2} - 1\right) = \frac{1}{8}\left(\frac{\omega_e^2}{\Omega^2} - 1\right). \tag{29}$$

This relationship ensures that the elastic-bound equality conditions (Eq. 12) will be satisfied in the Duffing oscillator. Again, we expect that this relationship will satisfy the full elastic-bound conditions (Eq. 11) only over a certain window of ρ and Ω. The properties of this window are determined by the Duffing parameters α, β, δ,

[**] Note that this is the same as saying that we seek $F^{\pm}(x)$ such that Eq. 10 is satisfied. This latter formulation does not necessitate that the system be split into 'elastic' and 'inelastic' components.

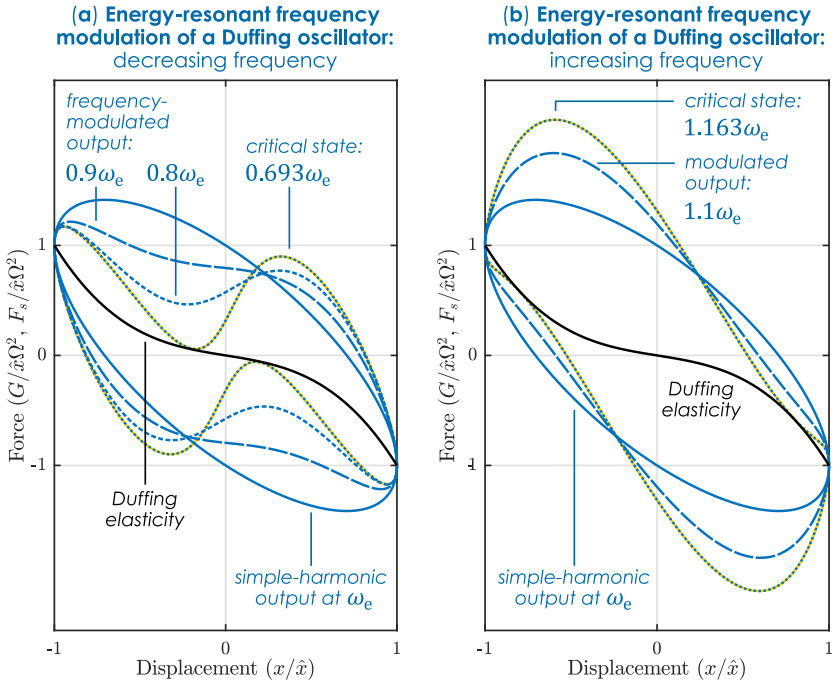

Figure 4: Work loop analysis and energy resonance in an optimal control context: frequency modulation of a Duffing oscillator, involving (**a**) decreasing and (**b**) increasing output frequency.

and $\hat{x}$, but they are difficult to define analytically. The critical states defining the boundaries of this window are given as the solution of:

$$G(t) = -F_s(x), \tag{30}$$

with $x(t)$ as per Eq. 24, and $\rho(\Omega)$ as per Eq. 29. We compute these critical states numerically. For instance, for $\alpha = 1$, $\beta = 3$, $\delta = 2$, and $\hat{x} = 1$, we estimate, conservatively, that frequency-band resonant states exist within $0.693\omega_e < \Omega < 1.163\omega_e$, for which $-0.0650 < \rho < 0.0441$. This range is illustrated in Fig. 4. This demonstration of frequency-band resonance raises the possibility of energetically-optimal frequency modulation in a range of physical systems – we refer, in particular, to insects and FW-MAVs, for which wingbeat frequency modulation can be an important form of lift and thrust control. This illustrates the phenomenon that energetically-optimal (*i.e.*, energy resonant) operation of linear and nonlinear systems is not restricted to a single resonant frequency, but is, in fact, available over a window of frequencies. Not that this effect is not a result of nonlinearity (it exists, for instance, when $\beta = 0$), but is a result of the damping in the system (δ: the width of the work loop in the elastic-bound conditions, *cf.* Eq. 15). Damping allows energy-resonant behaviour over a range of frequencies – a remarkable physical phenomenon.

7. Conclusion

In this work we present several novel techniques of work-loop analysis, and demonstrate their theoretical and practical significance. Utilising them, we prove new optimality results for a wide class of nonlinear system, with implications for optimal system design and optimal control modulation in a range of engineering systems, including FW-MAVs. These optimality results have a range of implications in structural optimisation and optimal control – defining new designs for optimal biolocomotion system, and new principles for biolocomotive optimal control. They also illustrate a remarkable phenomenon. Energy-resonant states are not discrete, *e.g.*, restricted to particular frequencies, but in fact, are available in windows of frequency. The existence of these windows is due not to system nonlinearity, but to system damping – damping allows energetically-optimal frequency modulation.

References

1. Jankauski, M.A.: Measuring the frequency response of the honeybee thorax. Bioinspir. Biomim. 15, 046002 (2020). https://doi.org/10.1088/1748-3190/ab835b
2. Gau, J., Gravish, N., Sponberg, S.: Indirect actuation reduces flight power requirements in *Manduca sexta* via elastic energy exchange. J. R. Soc. Interface. 16, 20190543 (2019). https://doi.org/10.1098/rsif.2019.0543
3. Ma, T., Zhang, H.: Reaping the potentials of nonlinear energy harvesting with tunable damping and modulation of the forcing functions. Appl. Phys. Lett. 104, 214104 (2014). https://doi.org/10.1063/1.4879846

4. Zhang, H., Ma, T.: Roles of the Excitation in Harvesting Energy from Vibrations. PLOS ONE. 10, e0141299 (2015). https://doi.org/10.1371/journal.pone.0141299
5. Zhang, H., Corr, L.R., Ma, T.: Issues in vibration energy harvesting. J. Sound Vib. 421, 79–90 (2018). https://doi.org/10.1016/j.jsv.2018.01.057
6. Reher, J., Ma, W.-L., Ames, A.D.: Dynamic Walking with Compliance on a Cassie Bipedal Robot. In: 2019 18th European Control Conference (ECC). pp. 2589–2595. IEEE, Naples, Italy (2019)
7. Srinivasan, M., Ruina, A.: Computer optimization of a minimal biped model discovers walking and running. Nature. 439, 72–75 (2006). https://doi.org/10.1038/nature04113
8. Whitehead, S.C., Beatus, T., Canale, L., Cohen, I.: Pitch perfect: how fruit flies control their body pitch angle. J. Exp. Biol. 218, 3508–3519 (2015). https://doi.org/10.1242/jeb.122622
9. Pons, A., Beatus, T.: Distinct forms of resonant optimality within insect indirect flight motors. J. R. Soc. Interface. in press, (2022). https://doi.org/10.1098/rsif.2022.0080
10. Thomsen, J.J.: Vibrations and Stability: Advanced Theory, Analysis, and Tools. Springer, Berlin, Germany (2021)
11. Kartashova, E.: Nonlinear resonance analysis: theory, computation, applications. Cambridge University Press, Cambridge, UK (2011)
12. Pons, A., Beatus, T.: Elastic-bound conditions for energetically optimal elasticity and their implications for biomimetic propulsion systems. Nonlinear Dyn. (2022). https://doi.org/10.1007/s11071-022-07325-6
13. Graham, R.L., Knuth, D.E., Patashnik, O.: Concrete mathematics: a foundation for computer science. Addison-Wesley, Reading, MA (1994)
14. Ruina, A., Bertram, J.E.A., Srinivasan, M.: A collisional model of the energetic cost of support work qualitatively explains leg sequencing in walking and galloping, pseudo-elastic leg behavior in running and the walk-to-run transition. J. Theor. Biol. 237, 170–192 (2005). https://doi.org/10.1016/j.jtbi.2005.04.004
15. Alexander, R.M.: A model of bipedal locomotion on compliant legs. Philos. Trans. R. Soc. Lond. B. Biol. Sci. 338, 189–198 (1992). https://doi.org/10.1098/rstb.1992.0138
16. Tu, M., Dickinson, M.: Modulation of negative work output from a steering muscle of the blowfly Calliphora vicina. J. Exp. Biol. 192, 207–224 (1994). https://doi.org/10.1242/jeb.192.1.207
17. Josephson, R.K., Malamud, J.G., Stokes, D.R.: Power output by an asynchronous flight muscle from a beetle. J. Exp. Biol. 203, 2667 (2000). https://doi.org/10.1242/jeb.203.17.2667
18. Dudley, R.: The Biomechanics of Insect Flight. Princeton University Press, Princeton, NJ (2002)
19. Brinson, H.F., Brinson, L.C.: Polymer Engineering Science and Viscoelasticity: An Introduction. Springer, New York, NY (2015)
20. Shen, C., Liu, Y., Sun, M.: Lift and power in fruitflies in vertically-ascending flight. Bioinspir. Biomim. 13, 056008 (2018). https://doi.org/10.1088/1748-3190/aad212
21. Meng, X.G., Sun, M.: Aerodynamics and vortical structures in hovering fruitflies. Phys. Fluids. 27, 031901 (2015). https://doi.org/10.1063/1.4914042
22. Meng, X., Liu, Y., Sun, M.: Aerodynamics of Ascending Flight in Fruit Flies. J. Bionic Eng. 14, 75–87 (2017). https://doi.org/10.1016/S1672-6529(16)60379-7
23. Baek, S.S., Ma, K.Y., Fearing, R.S.: Efficient resonant drive of flapping-wing robots. In: 2009 IEEE/RSJ International Conference on Intelligent Robots and Systems. pp. 2854–2860. IEEE, St. Louis, MO, USA (2009)
24. Zhang, C., Rossi, C.: A review of compliant transmission mechanisms for bio-inspired flapping-wing micro air vehicles. Bioinspir. Biomim. 12, 025005 (2017). https://doi.org/10.1088/1748-3190/aa58d3
25. Bolsman, C.T., Goosen, J.F.L., van Keulen, F.: Design Overview of a Resonant Wing Actuation Mechanism for Application in Flapping Wing MAVs. Int. J. Micro Air Veh. 1, 263–272 (2009). https://doi.org/10.1260/175682909790291500
26. van den Broek, D.M., Elwenspoek, M.: Explosive Micro-Bubble Actuator. In: TRANSDUCERS 2007 - 2007 International Solid-State Sensors, Actuators and Microsystems Conference. pp. 2441–2444. IEEE, Lyon (2007)
27. Shepherd, R.F., Stokes, A.A., Freake, J., Barber, J., Snyder, P.W., Mazzeo, A.D., Cademartiri, L., Morin, S.A., Whitesides, G.M.: Using explosions to power a soft robot. Angew. Chem. Int. Ed. 52, 2892–2896 (2013). https://doi.org/10.1002/anie.201209540

A novel lubricated friction model for describing underdamped free responses of a spring – sliding mass oscillator

Joël Perret-Liaudet[*], Fida Majdoub[**]
[*]*Ecole centrale de Lyon, UMR CNRS 5513, LTDS, France*
[**]*ECAM, LabECAM, France*

Summary. A novel friction model is introduced in order to describe lubricated sliding contact under unsteady or transient dynamic conditions. It is based on a state variable friction model consisting on a friction force equation and a state ones. Effective film thickness is introduced as the internal variable. Relaxation behaviour to reach the steady state film thickness is introduced via a first order differential equation. To obtain friction force, film thickness is interpreted as a sharing effect between solid interaction or confined lubricant and the lubricant film itself. Experimental results consisting on free dynamic responses of a sliding oscillating system under lubrication confirm the phenomenon captured by the proposed theoretical approach.

Introduction

Friction is a nonlinear phenomenon that occurs in a lot of mechanical systems including contacts. This is in particular the case of mechanisms which are often making use of contacting surfaces in relative motion (gears, cam and cam follower systems, rolling bearings, piston ring/cylinder liner contact, universal joints, etc.) for transforming input forces and motion. In order to simulate and analyze the dynamic behavior of such systems, it is necessary to choose friction law that can be able to describe and model it. A classical way to describe friction is to use the Coulomb friction or viscous friction models, or the combination of both [1]. Such friction models are very useful thanks to their simplicity. However, in many circumstances, they cannot accurately describe tribological behaviors. In the case of lubricated contacts, other models have been used to reproduce the well-known Stribeck behavior, but they usually ignore the dynamic effects [2]. In this context, the principal aim of this study is to introduce a novel approach which can describe lubrication in a relative simple way, and capture the dynamic lag effect of the film thickness settling [3]. Finally, comparisons between numerical and experimental results obtained from an original dynamic tribometer has been reported in this study.

The suggested friction model

The proposed model is based on introduction of an internal state variables in the constitutive friction law. In this approach, modelling consists on a friction force equation coupled to a state equation, which can be formally written as

$$\begin{cases} T = & \mathcal{F}(v,y) \\ \dot{y} = & \mathcal{G}(v,y) \end{cases} \tag{1}$$

where y is the internal state variable and $\mathcal{F}(\cdot)$ and $\mathcal{G}(\cdot)$ are two nonlinear functions to be precise. The well-known rate-and-state-variable friction law [4] which is formulated in term of an average contact lifetime as the internal state variable is a good example of this kind of formulation. In our novel model, we heuristically suggest to introduce the instantaneous film thickness as the internal state variable y. Indeed, this is the key to interpret transition between boundary and full film hydrodynamic regimes revealed by the popular Stribeck curve [5]. For the state equation, we propose a simple relaxation process governed by the following differential equation

$$\dot{y} = (Y_{ss}(v) - y)/\tau \tag{2}$$

where $Y_{ss}(v)$ represents the film thickness to be reached. In this way, it corresponds to the steady state film thickness associated to the instantaneous sliding velocity $v(t)$. In addition, τ is the relaxation time associated to the exponential decay introduced by the equation (2). Concerning the friction equation, we introduced a mixed law given by

$$T = (1-\alpha)T_{BL} + \alpha T_{HL} \tag{3}$$

Thus, the total friction force is assumed to be sharing between friction force T_{HL} associated to the lubricant film itself and friction force T_{BL} associated to solid interaction through surface roughness. In agreement with the Stribeck curve interpretation, the weight function $\alpha = \alpha(y)$ introduces the effect of the film thickness y. Basically, it consists on a sigmoid function which increases monotonically from 0 to 1. Finally, the friction force component T_{BL} is assumed to be constant, i.e. $T_{BL} = \mu N \text{sign}(v)$, and the friction force component T_{HL} is assumed to be velocity-dependent through a power law $T_{HL} = \eta N |v|^p \text{sign}(v)$. N represents the applied normal load and μ, η are two constants.

The dynamic transient oscillating response under study

As reported in previous works [1,6,7], we have designed and built a dynamic tribometer in order to quantify general trends of friction as a function of the sliding velocity. This experimental setup, described in Figure 1, is based on the measurement of transient responses $x(t)$ of an underdamped frictional single-degree-of-freedom mass-spring oscillator. In the principle, a

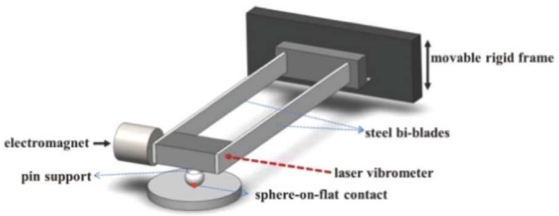

Figure 1: Scheme of the dynamic oscillating tribometer

moving mass m slides in contact with the tribological system under study.
The governing equation of motion can be written as follows

$$m\ddot{x} + kx = -T \tag{4}$$

where k is the spring stiffness. By considering the proposed friction model, it follows the first order equations

$$\begin{cases} \dot{x} = & v \\ \dot{v} = & -kx - T(v,y) \\ \dot{y} = & (Y_{ss}(v) - y)/\tau \end{cases} \tag{5}$$

with the friction force $T(v,y)$ defined by equation (3). In order to integrate equations (5), we have used a Runge Kutta numerical scheme of order 4.

Results

Figure 2 (a) shows example of an experimental velocity response. We can observe that it begins with a convex envelop and finish by a concave one. As shown in Figure 2 (b), this behavior is well captured by our model. From Figure 2 (d), this particular envelope can be interpreted by a transition from a full lubricant film force contribution to a dominant solid force contribution. This interpretation is confirmed by measurement of the electrical contact resistance (ECR) presented in Figure 2 (c). At the beginning, the separation between solids is total (the ECR is very high) and at the end full electrical contact is observed (the ECR has a low value).

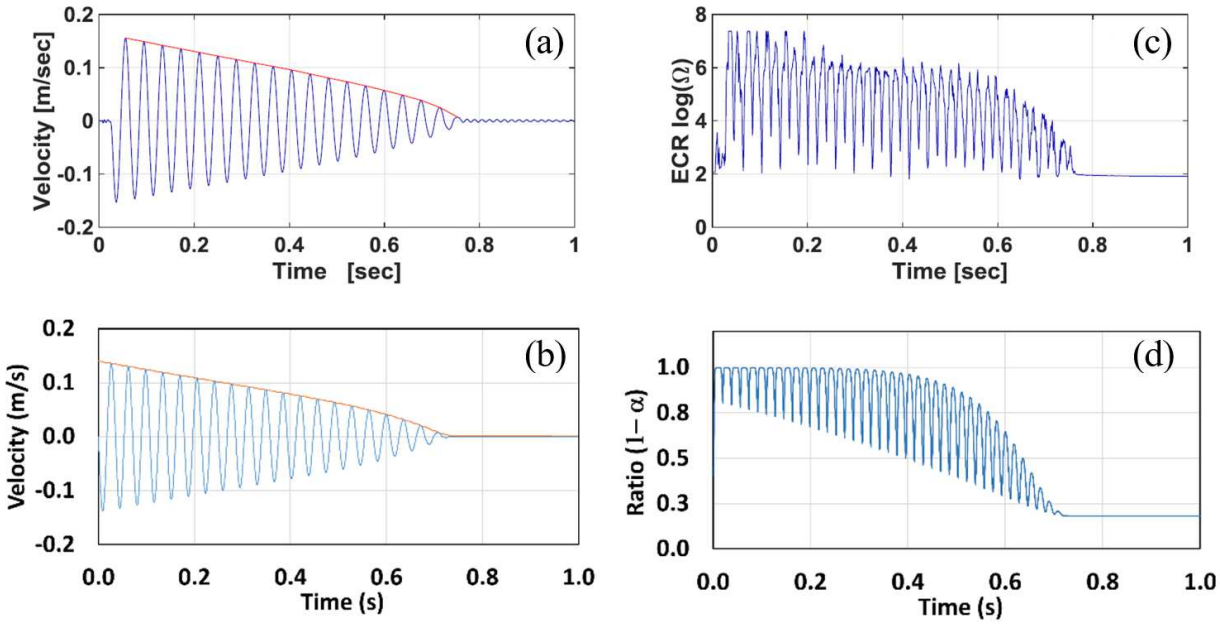

Figure 2: (a) Experimental and (b) simulated velocity responses; (c) experimental contact resistance; (d) ratio $(1-\alpha)$ of the lubricant film force contribution.

Conclusions

The relevance of the proposed model is demonstrated in the light of comparison between numerical results and experimental ones. In particular, our new model can capture the transition related to the instantaneous film thickness which separates the two sliding surfaces, including the lag effect of the thickness dynamics. Now, ongoing work is conducted in order to relate the model parameters to the physical properties of the tribological contact.

References

[1] Rigaud E., Perret-Liaudet J., Belin M. *et al*., (2010) A dynamical tribotest discriminating friction and viscous damping, *Tribol. Int.* 43.
[2] Juel Thomsen J., Fidlin A. (2003) Analytical approximations for stick–slip vibration amplitudes, *Int. J. Non-Linear Mech.* 38.
[3] Myant C., Fowell M., Cann P. (2014) The effect of transient motion on Isoviscous-EHL films in compliant point contacts, *Tribol. Int.* 72.
[4] Gu J.-C., Rice J.R., Ruina A.L. *et al*. (1984) Slip motion and stability of a single degree of freedom elastic system with rate and state dependent friction, *J. Mech. Phys. Solids.* 32.
[5] Dowson D. (1998) History of tribology, 2nd ed., Professional Engineering Publishong, London and Bury St Edmunds, UK.
[6] Majdoub F., Belin M., Martin J.M., *et al*. (2013) Exploring low friction of lubricated DLC coatings in no-wear conditions with a new relaxation tribometer, *Tribol. Int.* 65.
[7] Majdoub F., Perret-Liaudet J., Belin M., et al. (2015) Decaying law for the free oscillating response with a pseudo-polynomial friction law: Analysis of a superlow lubricated friction test, *J. Sound Vib.* 348.

Friday, July 22, 2022

08:30 - 10:30

MS-12 Micro- and Nano-Electro-Mechanical Systems

Rhone 3A

Chair: S. Krylov

08:30 - 08:50
Nonlinear damping in graphene resonators undergoing internal resonance
KEŞKEKLER Ata*, SHOSHANI Oriel, STEENEKEN Peter, ALIJANI Farbod
*TU Delft (Department of Precision and Microsystems Engineering, Delft University of Technology, Mekelweg 2, 2628 CD, Delft Netherlands)

08:50 - 09:10
Parametric resonance of a shallow arch microbeam for sensing applications
OUAKAD Hassen*, NAJAR Fehmi
*SULTAN QABOOS UNIVERSIY (Al Khoudh, MUSCAT, OMA Oman)

09:10 - 09:30
Nonlinear Damping in MEMS Bridge Resonators
FAROKHI Hamed*, ROCHA Rodrigo, HAJJAJ Amal, YOUNIS Mohammad
*University of Northumbria at Newcastle (Newcastle City Campus, 2 Ellison Pl, Newcastle upon Tyne NE1 8ST, United Kingdom United Kingdom)

09:30 - 09:50
Drag Forces in Non-Uniform Cantilever Beam Oscillating in Viscous fluid
DEVSOTH Lalsingh*, PANDEY Ashok
*Indian Institute of Technology [Hyderabad] (Indian Institute of Technology HyderabadKandi, Sangareddy - 502285Telangana India)

09:50 - 10:10
Data driven identification of tip-sample interaction in atomic force microscopy
CHANDRASHEKAR Abhilash, **BELARDINELLI Pierpaolo***, BESSA Miguel, STAUFER Urs, ALIJANI Farbod
*DICEA, Polytechnic University of Marche (DICEA, Polytechnic University of Marche, Italy)

Nonlinear damping in graphene resonators undergoing internal resonance

Ata Keşkekler[1], Oriel Shoshani[2], Peter Steeneken[1] and Farbod Alijani[1]
[1]*Precision and Microsystems Engineering, TU Delft, Delft, The Netherlands*
[2]*Department of Mechanical Engineering, Ben-Gurion University of the Negev, Beer-Sheva, Israel*

Summary. We study the nonlinear damping of a nanomechanical graphene drum resonator. Laser interferometry is used to measure and optothermally actuate the resonator near an internal resonance condition. An unconventional nonlinear damping behavior is observed at the internal resonance frequency. A multimodal analytical model is constructed to understand the nature of this phenomenon and to relate the observed nonlinear damping to the physics of the system.

Introduction

Micro/Nano-mechanical systems are utilized in many technologies and often have been used for their sensing capabilities. An ideal framework for sensitive nanomechanical devices is 2-D materials, and especially graphene, due to its exceptional mechanical, electrical and thermal properties. By their atomically thin nature, these systems are fundamentally nonlinear. In addition to the geometric nonlinearities, graphene membranes also have nonlinear energy decay mechanisms[1]. Nonlinear damping in these devices is a fundamental limitation to their sensing capabilities yet its full understanding is an open question. Among different dissipation mechanisms, an important factor that is hypothesized to affect damping properties of graphene nanodrums is the intermodal couplings[2]. In this work, we study the nonlinear dynamics of a nanomechanical graphene resonator near its internal resonance condition to amplify the intermodal effects and uncover the physics between nonlinear damping and mode coupling.

Experimental method and observations

Experiments were conducted by optothermally actuating a graphene nanodrum while measuring its motion using laser interferometry. Optothermal actuation results in modulation of membrane tension, effectively creating a parametric excitation to the fundamental mode of the membrane that has an eigenfrequency ω_1 and direct excitation to a secondary mode of the membrane that has an eigenfrequency $\omega_2 \approx 2\omega_1$. We take advantage of this to investigate the effects of intermodal couplings and internal resonance on the nonlinear damping by exciting the membrane with an actuation frequency of $\omega_F \approx 2\omega_1$, which drives both modes resonantly. We experimentally study the membrane frequency response curves (Figure 1). By increasing the excitation level, we utilize the hardening type geometric nonlinearity of the system to match the internal resonance condition between these two modes. At the vicinity of internal resonance, we observe frequency "locking" at higher drive powers, where the increase in resonance peak with respect to the excitation amplitude is almost zero. We found that forcing the system even further breaks the "locking" barrier, causing a dramatic increase in amplitude and frequency of the parametric resonance, which we refer as "shooting".

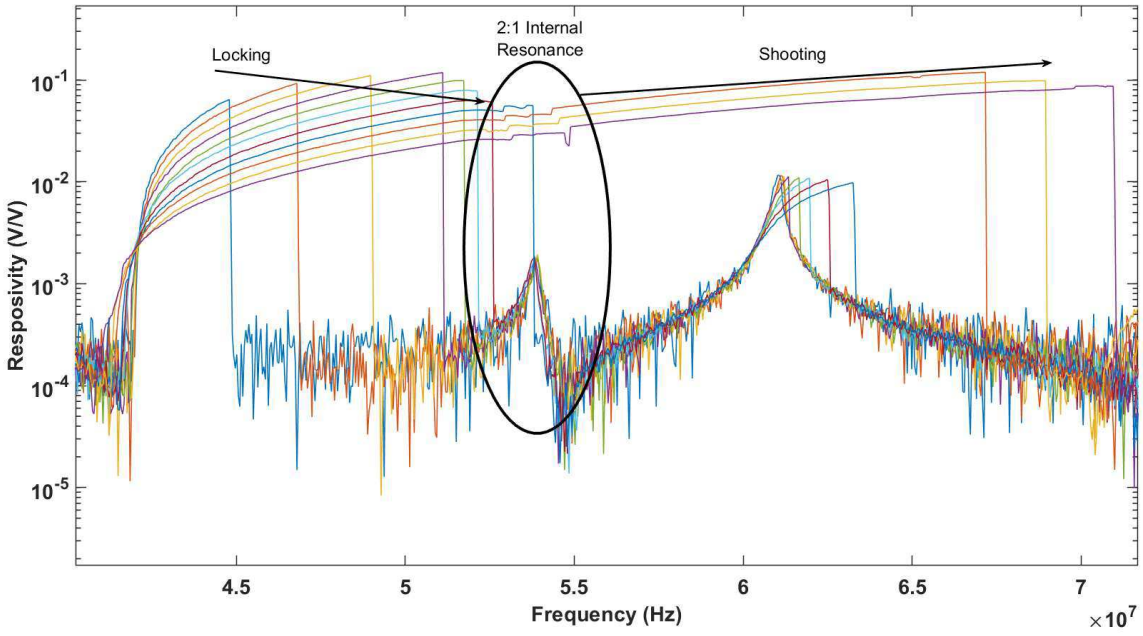

Figure 1: Experimentally measured frequency response curves of the membrane with increasing excitation levels, in the vicinity of internal resonance conditions.

Analytical model and results

Parametric resonance of nanomechanical systems is commonly modelled by using a single Mathieu-van der Pol-Duffing equation [3]. This model is only viable for nonlinear dynamic characterization far from the internal resonance as it will imply a varying intrinsic nonlinear damping for high driving powers in the vicinity of internal resonance, which has no physical foundations. This is clearly because of the intermodal effects, that necessitate multimodal modelling of the system. To capture the dynamics at the vicinity of internal resonance, we add to the Mathieu-van der Pol-Duffing single-mode model, a secondary linear oscillator that is directly driven by the excitation. We couple two modes by terms that arise from the nonlinear potential of 2:1 internal resonance $U_{cpl} = \alpha x_1^2 x_2$ (i.e., the coupling terms are: $-\partial U_{cpl}/\partial x_1$ for the primary mode, and $-\partial U_{cpl}/\partial x_2$ for the secondary mode):

$$\ddot{x}_1 + \omega_1^2 x_1 + \gamma x_1^3 + 2\alpha x_1 x_2 = F_1 x_1 \cos(\omega_F t) - 2\dot{x}_1(\tau_1 + \tau_{nl} x_1^2)$$
$$\ddot{x}_2 + \omega_2^2 x_2 + \alpha x_1^2 = F_2 \cos(\omega_F t) - 2\tau_2 \dot{x}_2$$

where γ is the Duffing coefficient, α is the intermodal coupling strength, F_1 is the parametric excitation level, F_2 is the corresponding direct forcing level and τ_l, τ_{nl} are the linear and nonlinear damping coefficients respectively. By analyzing the slow dynamics of the system, we reveal the modification of system parameters due to modal coupling, near the internal resonance condition ($2\omega_1 \approx \omega_2$). Using the intrinsic parameters of the modes for analysis, characterized by analyzing the uncoupled nonlinear response measurements, it is possible to see that the biggest effect of modal coupling is on the nonlinear damping. Additionally, the nature of the dramatic amplitude increase after the internal resonance is discovered by the bifurcation analysis of stationary solutions. The stationary (steady-state) solutions of the equations cease to exist in the vicinity of the internal resonance (see Figure 2) due to saddle-node bifurcation points. The annihilation of the bifurcation points connects two solutions branches, triggering the "shooting" phenomenon and can be used to characterize the coupling strength between the modes.

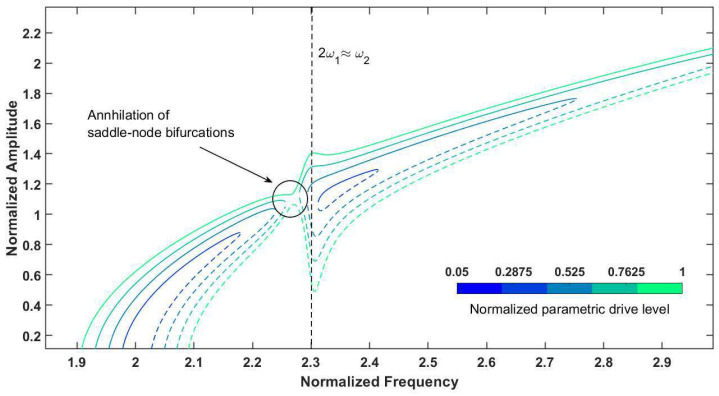

Figure 2: Steady state frequency response of the analytical model revealing the source of "shooting" behavior observed in the experiments, which is annihilation of saddle-node bifurcations.

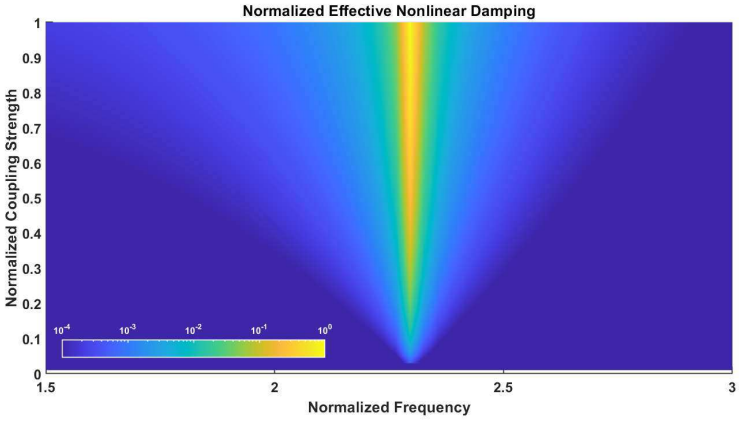

Figure 3: Effective nonlinear damping with respect to intermodal coupling strength and excitation frequency. Nonlinear damping is maximum at the internal resonance condition.

Conclusion

We report on nonlinear damping variation via 2:1 internal resonance in graphene nanomechanical resonators. We observe a massive increase in damping in the vicinity of internal resonance that is followed by a bifurcation causing a dramatic increase of amplitude and resonance frequency. To understand this phenomenon, the resonator has been modeled by a two-modes dynamical system undergoing a 2:1 internal resonance, which successfully explained the observations. This work shows a possible nonlinear dynamics methodology to characterize the intermodal coupling of nonlinear resonators by operating them in an internal resonance condition.

References

[1] A. Eichler, J. Moser, J. Chaste, M. Zdrojek, I. Wilson-Rae and A. Bachtold, "Nonlinear damping in mechanical resonators made from carbon nanotubes and graphene," Nature Nanotechnology, vol. 6, no. 6, pp. 339-342, 2011.

[2] D. Midtvedt, A. Croy, A. Isacsson, Z. Qi and H. S. Park, "Fermi-Pasta-Ulam Physics with Nanomechanical Graphene Resonators: Intrinsic Relaxation and Thermalization from Flexural Mode Coupling," Physical Review Letters, vol. 112, no. 14, p. 145503, 2014.

[3] R. J. Dolleman, S. Houri, A. Chandrashekar, F. Alijani, H. S. J. v. d. Zant and P. G. Steeneken, "Opto-thermally excited multimode parametric resonance in graphene membranes," Scientific Reports, vol. 8, no. 1, p. 9366, 2018.

Parametric resonance of a shallow arch microbeam for sensing applications

Hassen M. OUAKAD* and Fehmi NAJAR ‡
*Mechanical & Industrial Engineering Department, Sultan Qaboos University, P.O Box 33, AlKhod 123, Muscat, Sultanate of Oman
‡Applied Mechanics and Systems Research Laboratory, Tunisia Polytechnic School, University of Carthage, B.P. 743, Al Marsa 2078, Tunis, Tunisia.

Summary. In this work a clamped-guided shallow arch microbeam is considered. The actuation of the microbeam is both through a transverse and axial electrostatic forces. The considered equation of motion takes into account the initial rise of the microbeam and the sliding degree of freedom at the guided side. The static and free vibration problems are solved using the Differential Quadrature Method. The results are validated with previously published experiments found in the literature. The model is able to reproduce experimental findings regarding fundamental resonance and parametric resonance of the first mode.

Introduction

Parallel-plate based MEMS actuators are limited by the occurrence of pull-in in the static and dynamic regimes. An example of design improvement was proposed by Abu-Salih and Elata [1], where they introduced a curved microbeam obtained by buckling. Ouakad and Younis [2] proposed to analyze the nonlinear dynamics of curved microbeam using perturbation techniques. They concluded that the initial deflection of the curved beam strongly affects its behavior. Therefore, it can be used as control parameter to tune the response of the device. Recently, Ramini et al. [3] developed and experimentally tested a design in which the initial gap of the arched microbeam can be tuned using a transverse electrostatic parallel plate actuator. The design allows also the introduction of a parametric excitation through the applied axial force. Excitations at secondary resonances generate large stroke actuation generally unachievable by classical MEMS actuators. The device fabricated and tested by Alcheikh et al. [4], depicted high tunability up to 160% for the first and third mode shapes. Ouakad et al. [5] demonstrated that three-to-one and one-to-one internal resonance are achievable by controlling the initial rise of the arched microbeam. The proposed work aim to model an arched microbeam with an applied electrostatic axial force. The proposed mathematical model should reproduce the experimental finding of the previously fabricated shallow arch microbeams.

Problem Formulation

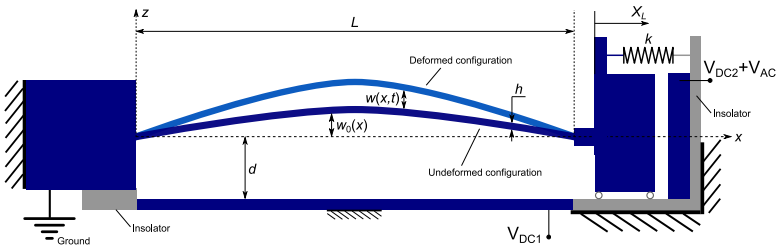

Figure 1: Clamped-guided shallow arch microbeam with transverse and axial excitations.

We consider a clamped-guided shallow arch given by Figure 1, of initial shape $w_0(x)$, width b, thickness h, length L, modulus of elasticity E, cross sectional are $A = bh$, moment of inertia I, mass density ρ and M and k are the mass and stiffness of the moving side electrode. The axial displacement is denoted by $u(x,t)$ and the transverse displacement is denoted by $w(x,t)$ and assumed to be around the initial curvature $w_0(x)$ (Figure 1). Using the Euler-Bernoulli beam theory and the von Karman nonlinear strain, the extended Hamilton's principle is used to derive the governing equations and boundary conditions. They are given as follows:

$$\rho A\ddot{w} + EIw'''' + c\dot{w} = N_L\left(w'' + w_0''\right) + \frac{\epsilon b V_1^2}{2(d + w + w_0)^2} \tag{1}$$

$$M\,\ddot{X}_L + kX_L = \frac{\epsilon A_{pp}(V_2 + V_{AC}\cos(2n\pi ft))^2}{2(g - X_L)^2} - N_L \tag{2}$$

$$w(0,t) = 0, \quad w'(0,t) = 0, \quad w(L,t) = 0, \quad w'(L,t) = 0 \tag{3}$$

$$N_L(t) = \frac{EA}{L}\left[X_L + \frac{1}{2}\int_0^L \left(w'^2 + 2w'w_0'\right)dx\right] \tag{4}$$

where $n = 1$ or 2 for the fundamental and parametric excitations, respectively.
Equations 1 to 4 are solved using the Differential Quadrature Method (DQM) for the space derivative and then the Finite Difference Method (FDM) is used to calculate limit cycle solution [6].

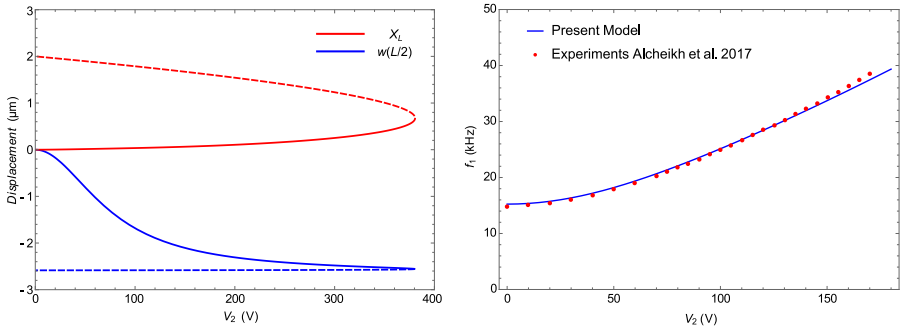

Figure 2: (a) Variation of the static deflection $w(L/2)$ with respect to V_2 for $d_0 = 2.6\mu$m. (b) Variation of the first natural frequency for $d_0 = 2.6\mu$m.

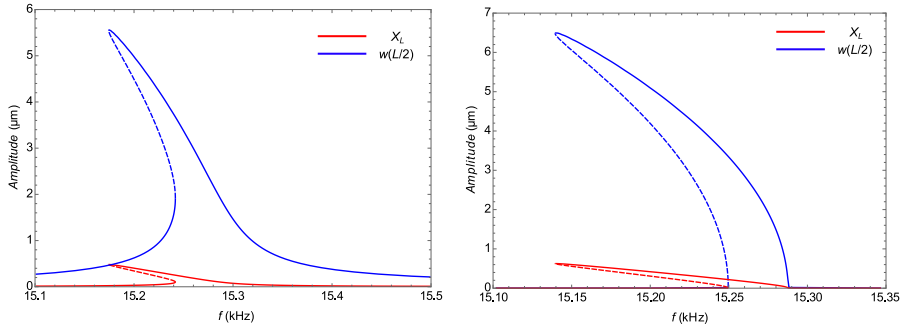

Figure 3: Frequency-response curves of the midspan transverse deflection and axial displacement for $V_2 = 3$V and $V_{AC} = 5$V when $d_0 = 2.6\mu$m and $f_1 = 15.27$kHz. (a) Fundamental resonance, (b) Principal parametric resonance of the first mode.

Static and free vibration of the microbeam

The static response of the microbeam is shown in Figure 2-a. Only the effect of the side voltage V_2 has been considered here. As shown, the static response of the transverse deflection at midspan $w(L/2)$ is highly constrained when the microbeam recover a straight position at $w(L/2) = d_0$. The axial displacement at $x = L$, expressed by X_L, is responding as a classical electrostatic parallel plate actuator. The dashed branches denote unstable solutions. The free vibration problem is also solved under the effect of the applied side voltage V_2. The results shown in Figure 2-b are compared with those obtained experimentally by Alcheikh et al. [4]. As shown, very good agreement is obtained.

Fundamental resonance and parametric resonance of the first mode

The frequency-response curves for the fundamental resonance are shown in Figure 3-a for the midspan transverse deflection and axial displacement. A softening behavior is deduced from the simulations. A similar behavior is observed for the parametric resonance of the first mode in Figure 3-b. Also here, dashed branches denote unstable solutions.

Conclusions

We proposed a nonlinear dynamic analysis of a clamped-guided shallow arch microbeam. The governing equations and associated boundary conditions are derived and the solved using a combination of Differential Quadrature Method, for the space derivative, and the Finite Difference Method for the limit-cycle solutions. The static and free vibration responses have been simulated for the transverse and side displacements. The variation of the fundamental frequency with respect to the applied side voltage is compared and validated with published experimental results. The frequency-response curves showed that both fundamental and parametric resonances are possible in accordance with previously reported experimental analyses.

References

[1] Abu-Salih S. S. and Elata D. (2006) Experimental Validation of Electromechanical Buckling. *J. Microelectromech Sys* **15**:1656-1663.

[2] Ouakad H. M. and Younis M. I. (2010) The Dynamic Behavior of MEMS Arch Resonators Actuated Electrically. *I. J. Non-Linear Mech* **45**:704-713.

[3] Ramini A., Alcheikh N., Ilyas S. and Younis M. I. (2016) Efficient Primary and Parametric Resonance Excitation of Bistable Resonators. *AIP Advances* **6**:095307.

[4] Alcheikh N., Ramini A., Hafiz M. A. A. and Younis M. I. (2017) Tunable ClampedâĂŞGuided Arch Resonators Using Electrostatically Induced Axial Loads. *Micromachines* **8**:14.

[5] Ouakad H. M., Sedighi H. M., Younis M. I. (2017) One-to-One and Three-to-One Internal Resonances in MEMS Shallow Arches. *J. Comp Nonlinear Dyn* **12**:051025.

[6] Ben Sassi S. and Najar F. (2018) Strong Nonlinear Dynamics of MEMS and NEMS Structures Based on Semi-Analytical Approaches. *Comm Nonli Sci Num Sim* **61**:1-21.

Nonlinear Damping in MEMS Bridge Resonators

Hamed Farokhi[1], Rodrigo T. Rocha[2], Amal Z. Hajjaj[3], Mohammad I. Younis[2,4]
[1]*Department of Mechanical and Construction Engineering, Northumbria University, UK*
[2]*Physical Sciences and Engineering Division, KAUST, Saudi Arabia*
[3]*Wolfson School of Mechanical, Electrical and Manufacturing Engineering, Loughborough, UK*
[4]*Department of Mechanical Engineering, State University of New York at Binghamton, USA*

Summary. This study investigates the nonlinear damping in in-plane micromachined electromechanical resonators theoretically and experimentally. More specifically, precise experiments are performed on an electrically actuated micromachined bridge resonator and the response of the system in the primary resonance region is captured at various AC voltage levels. For the theoretical part, a nonlinear Euler-Bernoulli beam theory is utilised taking into account the geometric, electrostatic, and damping nonlinearities. A general cubic damping model and a Kelvin-Voigt model are considered in the theoretical model. A high-dimensional discretisation is carried out by retaining 10 modes in the Galerkin discretisation. Extensive comparisons are conducted between the experimental data and the theoretical results at different AC voltage levels. It is shown that the resonator exhibits strong nonlinear damping. Different damping models are compared to examine the performance of each model in capturing the damping nonlinearity.

Introduction

Nonlinearly driven micro-electromechanical (MEMS) resonators have drawn increasing attention in the recent decades by wide-spreading potential applications, such as frequency stabilization, filtering, and sensing [1]. Nonlinear vibration of these movable structures has been intensely investigated theoretically and experimentally, chiefly for the electrostatically driven MEMS resonators. A key property affecting the nonlinear vibration of MEMS resonators is damping, in which a variety of physical mechanisms could contribute (e.g., thermoelastic, squeeze film damping, nonlinear mode coupling, and linear viscous damping) [2,3]. As driven the system nonlinearly, the energy dissipation tends to deviate from the linear viscous dissipation and start to vary nonlinearly. Despite the deep study of the nonlinear energy dissipation (or nonlinear damping) in the recent decades [4,5], there is still no comprehensive study on nonlinear damping in MEMS resonators electrostatically driven with relatively large gaps. The present study thoroughly investigates the nonlinear damping in micromachined electromechanical resonators using carefully conducted experiments and an accurate nonlinear theoretical model.

Experimental set-up and theoretical model

In this study, a clamped-clamped in-plane microbeam made of silicon is considered, which is of length L, width b, cross-sectional area A, second moment of area I, Young's modulus E, mass density ρ, and material damping coefficient η,. The microbeam is excited by a stationary electrode separated from the microbeam with a large transduction gap, Fig.1(a). To minimize the effect of squeeze film damping, the microbeam is placed in a vacuum chamber with a pressure of 950mTorr set throughout the experiments. Hence the squeeze film damping effect will be neglected in the theoretical study. The nonlinear equation of motion for the MEMS resonator under consideration is derived using the Euler-Bernoulli beam theory and utilising a Kelvin-Voigt model, resulting in a nonlinear damping mechanism. Apart from the Kelvin-Voigt damping, a general nonlinear cubic damping mechanism (for the transverse motion w) is modelled as well. The equation of motion can be derived as

$$\rho A\partial_{tt}w + c_1\partial_t w + c_2\partial_t w|\partial_t w| + c_3(\partial_t w)^3 + EI\partial_{xxxx}w + \eta I\partial_{txxxx}w - \frac{EA}{2L}\partial_{xx}w\int_0^L(\partial_x w)^2\,\mathrm{d}\,x$$
$$-\frac{\eta A}{2L}\partial_{xx}w\int_0^L 2\partial_x w\partial_{tx}w\,\mathrm{d}\,x - \frac{\varepsilon b[V_{\mathrm{DC}} + V_{\mathrm{AC}}\cos(\omega t)]^2}{2(d-w)^2} = 0, \tag{8}$$

in which c_1, c_2, and c_3 are damping coefficients and d is the MEMS gap width.

The equation of motion is first recast into nondimensional form and then discretised into a set of nonlinearly coupled ordinary differential equations via use of Galerkin technique, considering 10 degrees of freedom. The resultant set is solved using a continuation technique.

Results and Discussion

In this section, the nonlinear resonance response of the MEMS resonator is examined in detail and thorough comparisons are conducted between the theoretical predictions and experimental data. Different linear and nonlinear damping models are examined to determine which model better predict the dissipation in the system. All models are calibrated once and then the damping coefficients are kept fixed as the AC excitation level is increased. Four cases are examined, namely the linear viscous damping model, Kelvin-Voigt damping, cubic nonlinear model (c_1 and c_3) and general quadratic-cubic model. In the results shown in Figs.1(b)-(e), ω_1 denotes the primary nondimensional natural frequency of the microbeam, Ω stands for the nondimensional frequency of excitation, and w_d indicates the nondimensional midpoint transverse oscillation amplitude (with respect to d), measured from the deflected configuration. In all the theoretical results, solid and dashed lines denote stable and unstable periodic solutions, respectively.

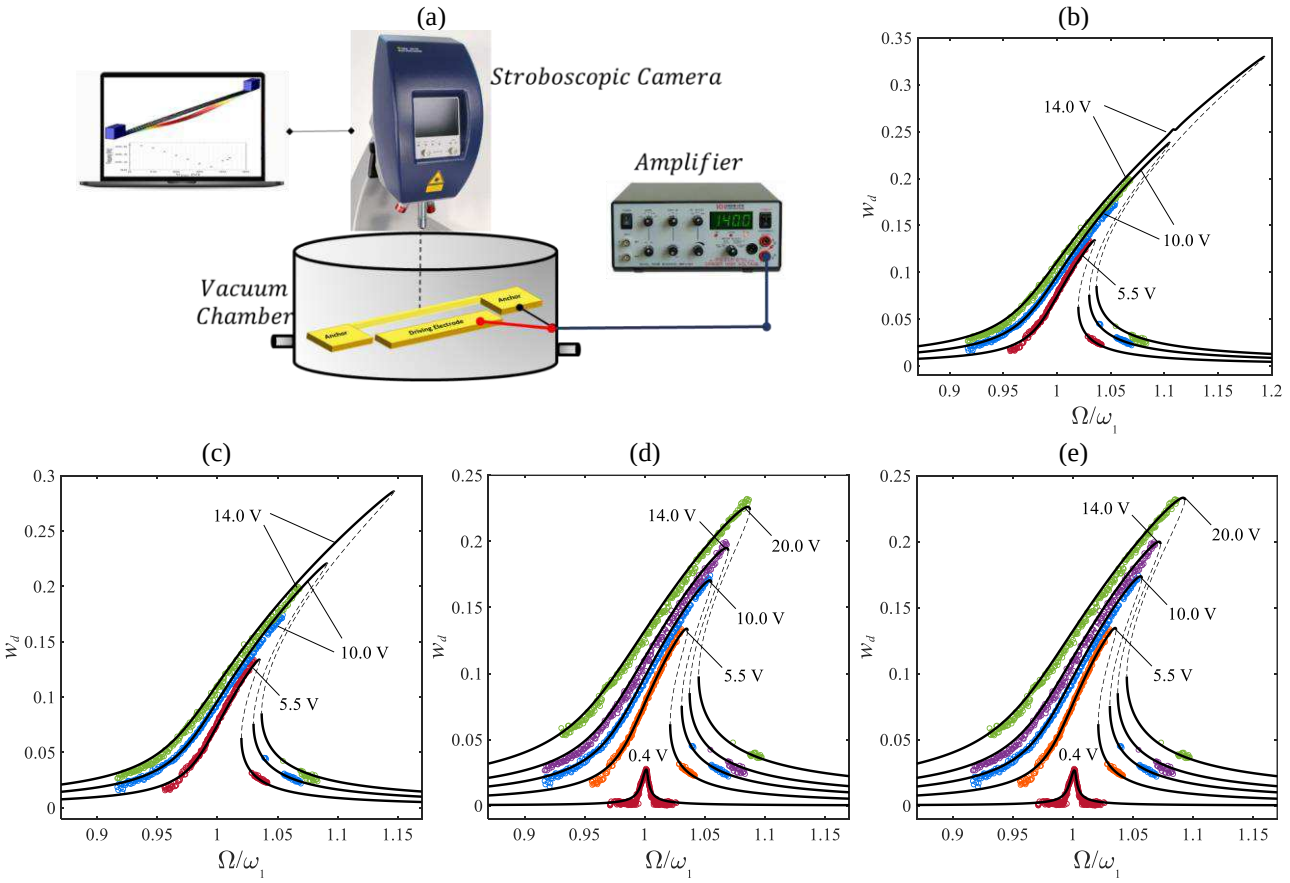

Figure 1: (a) Experimental setup with 3D schematic of the microbeam with length 800 µm, thickness 2.9 µm, width 25 µm, and transduction gap 8 µm. (b, c) Frequency responses of the MEMS resonator at $V_{\mathrm{DC}} = 5$ V and three AC voltages (shown on the curves) based on linear and Kelvin-Voigt damping models, respectively. (d, e) Frequency responses of the MEMS resonator at $V_{\mathrm{DC}} = 5$ V and various AC voltages (denoted on the curves), based on cubic and general quadratic-cubic models, respectively.

Figs.1(b) and (c) correspond to linear and Kelvin-Voigt damping, respectively. For both cases, the frequency response for $V_{\mathrm{AC}} = 5.5$ V is used to calibrate the damping coefficient which is then kept fixed as the AC voltage is increased to larger magnitudes. As seen, both damping models overestimate peak oscillation amplitudes for both AC excitation levels. The results for the cubic damping model are shown in Fig.1(d); for this damping model, the coefficients c_1 and c_3 are calibrated using the two lower-amplitude frequency responses, i.e. those for 0.4 and 5.5 V. The damping coefficients are then kept fixed and the frequency responses at other AC voltages are obtained and compared to the experimental data. It is seen that the cubic model captures the nonlinear damping in the system with a good accuracy; however, it slightly underestimates the peak amplitude, and this becomes more visible at higher AC voltage levels. The final model examined is the general quadratic-cubic damping model and the result for this case is shown in Fig.1(e). This model requires three frequency responses for calibration of three damping coefficients. As seen, this model has the best accuracy in predicting the primary resonance response amplitudes at various AC voltages among all damping models examined.

Conclusions

This study conducted a theoretical-experimental investigation on the nonlinear damping in in-plane MEMS resonators. It was shown that both linear and Kelvin-Voigt models overestimate the peak amplitude at higher excitation levels. The general quadratic-cubic damping model showed excellent agreement with experimental data and worked best among different models.

References

[1] A.Z. Hajjaj, N. Jaber, S. Ilyas, F.K. Alfosail, M.I. Younis, Linear and nonlinear dynamics of micro and nano-resonators: Review of recent advances, Int. J. Non. Linear. Mech. 119 103328. https://doi.org/10.1016/j.ijnonlinmec.2019.103328.

[2] E. Kazemnia Kakhki, S.M. Hosseini, M. Tahani, An analytical solution for thermoelastic damping in a micro-beam based on generalized theory of thermoelasticity and modified couple stress theory, Appl. Math. Model. 40 (2016) 3164–3174. https://doi.org/https://doi.org/10.1016/j.apm.2015.10.019.

[3] F. Najar, M. Ghommem, A. Abdelkefi, A double-side electrically-actuated arch microbeam for pressure sensing applications, Int. J. Mech. Sci. 178 (2020) 105624. https://doi.org/https://doi.org/10.1016/j.ijmecsci.2020.105624.

[4] M. Amabili, Derivation of nonlinear damping from viscoelasticity in case of nonlinear vibrations, Nonlinear Dyn. 97 (2019) 1785–1797. https://doi.org/10.1007/s11071-018-4312-0.

[5] A. Keşkekler, O. Shoshani, M. Lee, H.S.J. van der Zant, P.G. Steeneken, F. Alijani, Tuning nonlinear damping in graphene nanoresonators by parametric–direct internal resonance, Nat. Commun. 12 (2021) 1–7.

Drag Forces in Non-Uniform Cantilever Beam Oscillating in Viscous fluid

Lalsingh Devsoth and Ashok Kumar Pandey
Indian Institute of Technology Hyderabad, Kandi, Sangareddy, Telangana,502285.

Summary. Sensitiveness of the micro-mechanical cantilever beams strongly depends on the fluid damping such as damping due to drag and squeeze film. There have been many studies associated with drag force computation in uniform cantilever beam oscillating in isolation. In this work, we are presenting drag force computation in non-uniform cantilever beam with linear and quartic converging and diverging widths. Finally, we find the variation of added mass effect and quality factor based on drag force as a function of degree of non-uniformity, i.e., tapering parameter. It is found that the quality factor increases for converging beam and decreases for diverging beam. The effect is found to be more in quartic varying beam.

Introduction

Micro-Electro-Mechanical Systems (MEMS)/ Nano-Electro-Mechanical Systems (NEMS) such as biosensors, atomic force microscope, etc., generally operate in fluid. Therefore it is essential to compute drag forces due to fluid and structure interaction [1]. To compute drag forces in uniform cantilever beam, there exist formulas to compute fluid damping and added mass effect of a rigid circular cylinder oscillating with certain frequency in air [2]. To generalize the formula for arbitrary cross-section, Tuck [3] had developed formulation to compute drag forces and added mass effect. Although, generalized formula is written in terms of unknowns pressure and vorticity it appears little complex. However, he also extended it to a thin ribbon having zero thickness. To further include the effect of mode shape and rectangular section, Sader [4] modified hydrodynamic function for cantilever beam with rectangular section by modifying the hydrodynamic function of circular cylinder given in [2]. Zhang et al. [5] obtained more explicit form of drag force and add-mass effect in cantilever beam. However, all the previous study are limited to uniform cantilever section with circular or thin-rectangular sections. In this study, we compute the drag forces in non-uniform cantilever beam based on the mode-shapes and frequencies of corresponding converging and diverging beams and compare it with that of uniform beam.

Theoretical model for non-uniform beam

The oscillations of a cantilever beam in a viscous fluid is governed by a linearized unsteady Stokes equation $-i\omega\rho\mathbf{v} = -\nabla p + \mu\nabla^2\mathbf{v}, \nabla.\mathbf{v} = 0$. Fourier transformed unsteady Stokes equation is solved using the stream function [3], where, ω frequency of oscillation, velocity $\mathbf{v}$ and pressure p is obtain by transforming above equation into vorticity equation and pressure harmonic equation $\nabla^2 p = 0$ [3]. Assuming the velocity of vibrating beam in z-direction with velocity, $u = u_0 e^{i\omega t}$[1], where, u_0 is the maximum amplitude of the vibration, the hydrodynamic function is found by integrating pressure along beam width in terms of Reynold's number ($\mathtt{Re} = \frac{\rho\omega \mathtt{b}^2}{\mu}$, where, b is the width of beam) [3]. Subsequently, damping coefficient at each section of the beam is found from imaginary component of hydrodynamic function and then the modal damping. To compute the force for a thin beam with converging and diverging widths, we use the corresponding frequencies and mode shapes obtained by Sajal et al.[7]. Here, the beam width is taken as $b = b_0(1 + \alpha\frac{x}{L})^n$, where,$n = 1$(linear),$n = 4$(quartic), α is tapering parameter varying from -0.5 to 0.5. For converging beam, it is negative and for diverging beam it is positive. The mode shape of non-uniform beam is given by $w(x) = \frac{v(x)}{\sigma(x)}$, where, $v(x)$ is the exact mode shape of the uniform beam, $\sigma(x)$ is function to capture non-uniform effect which is taken for linear variation in width as $\sigma(x) = \sqrt{1 + \alpha\frac{x}{L}}$ and for the quadratic as $\sigma(x) = (1 + \alpha\frac{x}{L})^2$ [7]. The area and area moment of inertia of the beam section also vary with width. The different modal frequencies $\omega = (\frac{\lambda}{l})^2\sqrt{\frac{EI}{\rho_b A}}$ of the non-uniform beam are obtained by solving the characteristic equation of the beam [7, 6], where, λ for linearly tapered beam are 4.3119, 4.0978, 3.922, 3.7710, 3.6420, 3.5160, 3.4129, 3.3208, 3.2368, 3.162, 3.0958 for tapering parameter are -0.5, -0.4, -0.3, -0.2, -0.1, 0, 0.1, 0.2, 0.3, 0.4, 0.5. The corresonding λ for quartic case are 7.558, 6.2981, 5.3361, 4.5882, 3.9940, 3.516, 3.1241, 2.7989, 2.5259, 2.294, 2.0961. Finally, quality factor (i.e $\mathtt{Q} = \frac{\mathtt{mass}\times\omega}{\mathtt{C_{davg}}}$) and the modal damping coefficient $C_{davg} = \frac{\int_0^L c_{dx} w^2(x)dx}{\int_0^L w^2(x)dx}$ are computed.

Results and Discussion

For a non-uniform microbeam as shown in Figure 1(a) undergoes vibration in ambient air of viscosity of $1.8 \times 10^{-5}\frac{kg}{m-s}$) which induces fluid damping and added mass. To compute these quantities, we take a microbeam of density $\rho = 2300kg/m^3$, elastic modulus, $E = 62.5$Gpa, width at fixed end as $b_0 = 40\mu m$, length $L = 200\mu m$, and thickness $h_0 = 0.965\mu m$. To compare the influence of drag forces and added mass, we plot the hydrodynamic function per velocity for free end width corresponding to tapering parameters of ($\alpha = -0.5, 0, 0.5$) as shown in Fig 1(b)-(e) for both linear and quartic converging diverging beam. Figure 1(b) and Fig 1(c) represent the added-mass and damping effect, respectively, for a linear converging diverging beam. The trend of both the curve show decrease in their value as Re increase. Similarly, for the quartic converging diverging beam, Fig 1(d) and Fig 1(e) show that the added-mass and damping effect similar trend. However the effect is more pronounced in quartic beams. For validation, we have also compared the results of uniform beam ($\alpha = 0$) results with circular cylinder case mentioned in [2]. Subsequently, for frequency variation as shown in Fig 1(f) from [7], Fig 1(g) and Fig 1(h) show variation of damping coefficient and added-mass of non-uniform beam with different tapering parameters for linear and quartic varying beams. As the tapering ratio increases,

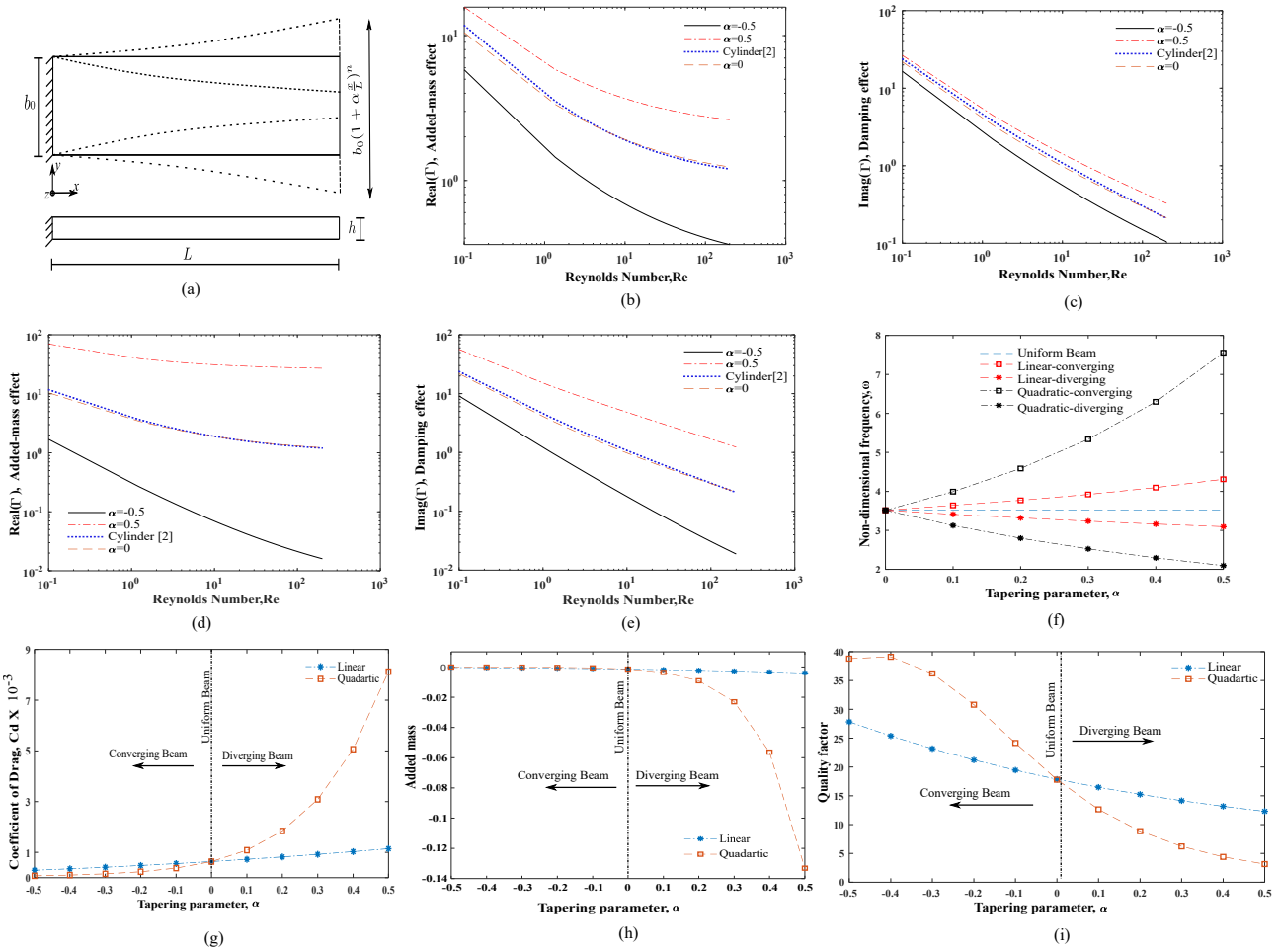

Figure 1: (a) A typical cantilever beam; Variation of hydrodynamic function with Re for $\alpha = -0.5, 0, 0.5$ to capture (b)added-mass and (c)damping coefficient of linearly varying beam, and (d) added-mass and (e) damping coefficient of quartic varying beam. Variation of (f) non-dimensional frequency, (g) coefficient of drag, (h) added mass, (i) Quality factor of converging-diverging beam with tapering ratio α.

overlaping/wet area increases which lead to increase in damping and reduction in added mass effect. Finally, the variation of quality factor for liearly and quartic beam are shown in Fig 1(i). It shows that quality factor increases for converging beam and decreases for diverging in both types non-uniform beam. The results presented here will be useful in designing non-uniform beam based mass sensors [8].

Conclusions

We have computed damping coefficient and added mass effect due to drag forces in non-uniform cantilever beam based on semi-analytical method. For free-end width of non-uniform beam corresponding to $\alpha = -0.5$, 0, 0.5, we compare the hydrodynamic functions corresponding to damping and added mass effect per unit length. Subsequently, we find modal damping coefficient and modal added mass effect linear and quartic varying beam with $\alpha = -0.5, 0, 0.5$. It is found that damping effect increases with increases in tapering parameter. The corresponding quality factor increases with decrease in tapering parameter. Such variation can be useful in optimizing the performance of non-uniform cantilever sensor.

References

[1] Landau, L. D., & Lifshitz, E. M. (1987). Fluid mechanics.

[2] Lighthill, M. J., & Rosenhead, L. (1963). Laminar boundary layers. Clarendon Press, Oxford

[3] Tuck, E. O. (1969). Calculation of unsteady flows due to small motions of cylinders in a viscous fluid. Journal of Engineering Mathematics, 3(1), 29-44.

[4] Sader, J. E. (1998). Frequency response of cantilever beams immersed in viscous fluids with applications to the atomic force microscope. Journal of applied physics, 84(1), 64-76.

[5] Zhang, W., & Turner, K. L. (2006). Fluid Damping and Loading Effects of MEMS Flexural Resonators: Theory and Applications.

[6] Singh, S. S., Pal, P., & Pandey, A. K. (2015). Pull-in analysis of non-uniform microcantilever beams under large deflection. Journal of Applied Physics, 118(20), 204303.

[7] Sagar Singh, S., Pal, P., & Kumar Pandey, A. (2016). Mass sensitivity of nonuniform microcantilever beams. Journal of Vibration and Acoustics, 138(6).

[8] Ashok, A., Kumar, P. M., Singh, S. S., Raju, P., Pal, P., & Pandey, A. K. (2018). Achieving wideband micromechanical system using coupled non-uniform beams array. Sensors and Actuators A: Physical, 273, 12-18.

Data driven identification of tip-sample interaction in atomic force microscopy

Abhilash Chandrashekar*, Pierpaolo Belardinelli†, Miguel A. Bessa‡, Urs Staufer*, and Farbod Alijani*

*Precision and Microsystems Engineering, TU Delft, Delft, The Netherlands

†DICEA, Polytechnic University of Marche, Ancona, Italy

‡Materials Science and Engineering, TU Delft, Delft, The Netherlands

Summary. Dynamic AFM is transitioning from a high-resolution imaging tool to a nanomechanical probe that can perform precise quantification of matter in fields as varied as microbiology, molecular metrology, and material science. To date, this has been achieved by estimating the nanoscale forces that exist between the probe and the sample, using empirical models that are merely approximations of the true probe-sample interaction physics. Here, we go beyond such approximations by making use of the recent advances in data-science and machine learning to distil nonlinear governing equations of dynamic AFM, and thus predict tip-sample forces directly from experimental raw deflection data. Our data-driven algorithm obtains physics-based models from experiments and is able to estimate time-resolved nanoscale interactions with sub-microsecond resolution.

Introduction

Dynamic atomic force microscopy (AFM) has become an indispensable tool for resolving mechanical, chemical and biological properties of samples at nanoscale. The precise quantification of materials at the nanoscale is achieved with accurate estimation of the tip-sample interaction force. However, dynamic AFM in contrast to its name does not measure directly the interaction force while imaging in any of its modalities. Instead, the interaction force is often reconstructed indirectly by combining different information channels like the frequency, amplitude and phase of the oscillating cantilever, while modulating the height of the probe above the sample surface [4]. The existing reconstruction techniques in dynamic AFM posses several drawbacks such as inability to resolve instantaneous tip-sample force, requiring a priori knowledge on the transfer function of the cantilever or large number of harmonics, which makes them cumbersome and inefficient to study the fast processes encountered in biological and chemical systems [3]. Thus a generalized approach for dynamic AFM that allows direct access to time-resolved surface forces irrespective of the chosen probe-sample configuration is currently missing.

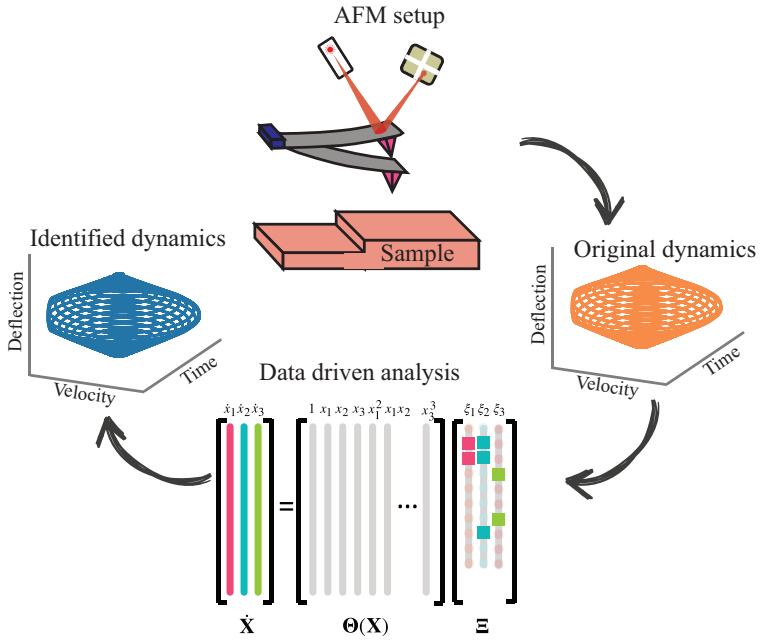

Figure 1: Schematic of the identification process. The data (orange trajectories) from the AFM setup is used as input to the sparse identification algorithm. The algorithm determines the governing model of the system and predicts the corresponding dynamics as shown by the blue phase space trajectories.

In this regard, here we demonstrate that data-driven identification applied to dynamic AFM experiments can provide physically interpretable models and simultaneously estimate the time-resolved interaction forces. We make use of the recent advances in sparse identification [1] and machine learning [2] techniques to identify the governing equations directly from the experimental measurements. In contrast to existing methods, the data-driven approach has no inherent assumptions on the type of interactions or mathematical models but relies solely on the measurements and thus can be generalized to any cantilever-sample configuration. Furthermore, based on the identified governing equations, our method also quantifies

the tip-sample force with a sub-microsecond resolution. We showcase this experimentally by using the data-driven algorithm on the temporal data obtained from a silicon cantilever interacting with a two-component polymeric sample made up of Polystyrene (PS) and Low-Density-Polyethylene (LDPE). The results and insights obtained from the identification procedure are in excellent agreement with the expected tip-sample interaction mechanism in polymers. In particular, we showcase the variation in contact duration, peak loading forces in stiff and compliant materials as well as highlight the ability of the technique to probe transient surface forces and capture the hysteresis phenomenon. A schematic of such an identification is shown in Fig. 1.

Methods and Results

In order to characterize the tip-sample force in experimental scenario, we first begin by training the algorithm on several standard AFM models such as Derjaguin-Muller-Toporov (DMT), Johnson, Kendall and Roberts (JKR) and Lennard-Jones (LJ) among others. This step allows us to expand the library of functions which is used to reconstruct the tip-sample nonlinearities from polynomials, trigonometric terms to specific nonlinear functions that are capable of describing the nano-scale forces encountered in dynamic AFM. We present in Fig.2 the identification results on synthetic data obtained from DMT model. Here, Fig.2(a) shows the identified dynamics (Orange) and the original dynamics (blue) of the system in a 2D phase-space portrait. Whereas, Fig.2(b) shows the identified versus the original co-efficients of the dynamical system governed by DMT tip-sample interaction force. The difference in the identified co-efficients is attributed to the noise added to the synthetic data to mimic the experimental conditions. By utilizing the co-efficients of the identified system, the tip-sample force is re-constructed with sub-microsecond resolution.

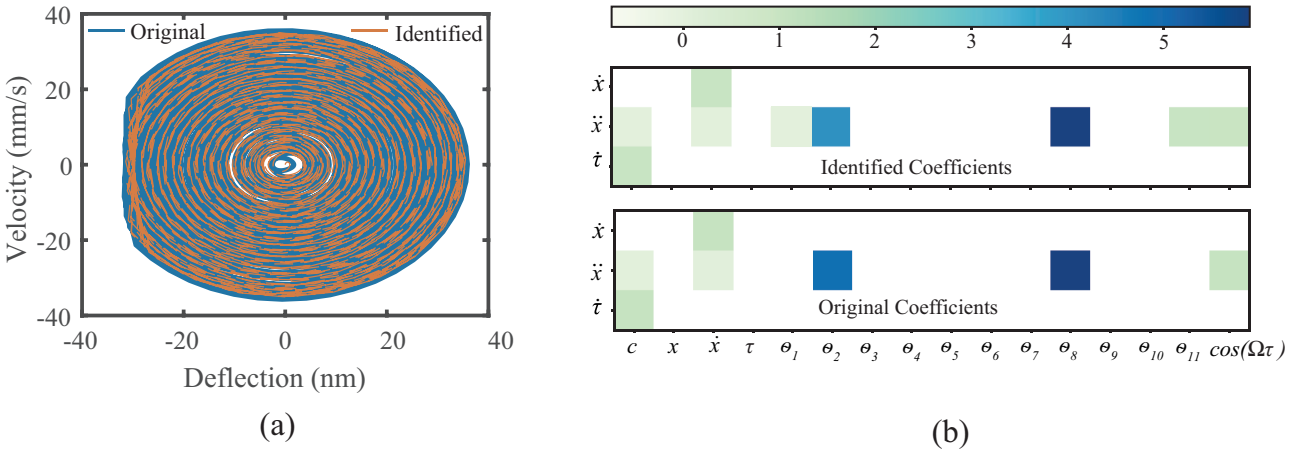

Figure 2: Identification of DMT model dynamics. (a) Identified (orange) trajectories from data driven analysis superimposed on the original trajectories (blue) obtained from simulations. (b) Map showing the strength of identified versus the original coefficient values used in the simulations.

Conclusion

We report here a novel approach at identifying the governing equations of motion and the associated tip-sample force in dynamic AFM using machine learning and data science techniques. The data driven algorithm based on sparse identification is trained on standard AFM models and a condensed library of functions capable of identifying experimental tip-sample interaction mechanics is determined. To highlight the capability of the technique, numerical simulations with noise corrupted synthetic data and experiments on polymer materials are performed. The analysis of the results show that the technique is able to obtain the dynamical trajectory of the underlying system without any prior assumption on the nature of tip-sample interaction. The method thus opens a completely new window into using machine learning algorithms in AFM nano-characterization with real-time data as well in developing novel feedback architectures and high-speed imaging.

References

[1] Steven L. Brunton, Joshua L. Proctor, and J. Nathan Kutz. Discovering governing equations from data by sparse identification of nonlinear dynamical systems. *Proceedings of the National Academy of Sciences*, 113(15):3932–3937, 2016.

[2] K. Champion, P. Zheng, A. Y. Aravkin, S. L. Brunton, and J. N. Kutz. A unified sparse optimization framework to learn parsimonious physics-informed models from data. *IEEE Access*, 8:169259–169271, 2020.

[3] Adrian P. Nievergelt, Niccolo Banterle, Santiago H. Andany, Pierre Gonczy, and Georg E. Fantner. High-speed photothermal off-resonance atomic force microscopy reveals assembly routes of centriolar scaffold protein sas-6. *Nature Nanotechnology*, 13(8):696–701, 2018.

[4] Amir F. Payam, Daniel Martin-Jimenez, and Ricardo Garcia. Force reconstruction from tapping mode force microscopy experiments. *Nanotechnology*, 26(18):185706, 2015.

Friday, July 22, 2022

08:30 - 10:30

MS-08 Nonlinear Phenomena in Mechanical and Structural Systems

Rhone 3B

Chair: Stefano Lenci

Friday, July 22, 2022

08:30 - 10:30

MS-02 Asymptotic Methods

Saint Clair 1

Chair: Wei Lin - C.H. Lamarque

08:50 - 09:10

[visio] Asymptotic solutions of singular perturbed system of transport equations with small mutual diffusion in the case of many spatial variables

NESTEROV Andrey*

*Russian University of Economics. G. V. Plekhanov (36 Stremyanny pereulok, Moscow, 117997, Russian Federation Russia)

09:10 - 09:30

[visio] Dynamic of the wind powered walking vehicle

GARBUZ Mikhail*, KLIMINA Liubov, SAMSONOV Vitaly

*Institute of Mechanics, Lomonosov Moscow State University (119192 Moscow, Michurinskiy prosp., 1 Russia)

09:30 - 09:50

[visio] Methods of perturbation theory and their applications in nonlinear fracture mechanics and continuum damage mechanics

STEPANOVA Larisa*

*Samara University (Moskovskoe shosse, 34, Samara 443086 Russia)

09:50 - 10:10

[visio] Energy model of free vibrations and resonance in elastic bodies

ALYUSHIN Yuriy*

*National University of Science and Technology MISIS (Leninskiy Prospekt 4, NUST MISIS, Moscow, RU, Moscow Russia Russia)

10:10 - 10:30

Non-stationary dynamics of the sine-lattice consisting of three pendulums (trimer)

KOVALEVA Margarita*, MANEVITCH Leonid

*Federal Research Center for Chemical Physics, Russia Academy of Sciences (119991, 4 Kosygin street, Moscow Russia)

Asymptotic solutions of singular perturbed system of transport equations with small mutual diffusion in the case of many spatial variables

Nesterov Andrey
[*] *PLEKHANOV Russian University of Econonics, Moscov, Russia*

Summary. We construct an asymptotic expansion on a small parameter of the solution of the Cauchy problem for a singularly perturbed system of transport equations with small nonlinearity and mutual diffusion describing the transport in a multiphase medium for many spatial variables. The asymptotic expansion of the solution is constructed as a series in powers of a small parameter and contains a functions of the boundary and inner layers. The main part of the asymptotics is described by one equation, which under certain requirements on the nonlinearity and diffusion terms is a generalization of the equation Burgers -Korteweg-de Vries in the case of many spatial variables.

Statement of the problem

The asymptotic expansion (AE) of the solution of the Cauchy problem for a singularly perturbed system of transport equations with small nonlinearity and diffusion is constructed

$$\varepsilon^2(U_t+\sum_{i=1}^{m}D_iU_{x_i})=AU+\varepsilon F(U)+\varepsilon^3\sum_{i=1}^{m}B_{ij}(U)U_{x_ix_j},|\bar{x}|<\infty,t>0,$$
$$U(\bar{x},0)=H\omega\left(\frac{\bar{x}}{\varepsilon}\right). \qquad (1)\text{-}(2)$$

Here $U=\{u_1,...,u_n\}$ is the solution, $0<\varepsilon<<1$ is a small positive parameter, D_i is a diagonal constant matrix, the function $F(U)$ and the matrix $B_{ij}(U)$ are smooth enough, smooth function $\omega(x)$ is rapidly decreasing together with all derivatives. Matrix A has a single zero eigenvalue, which corresponds to the eigenvector h_0 , vector h^*_0 - eigenvector of the matrix A^T, corresponding to the zero eigenvalue, non-zero eigenvalues of the matrix A is imposed condition $Re\,\lambda<0$. Below, without limiting generality, we put $(h_0,h_0^*)=1$. Additionally, it is required that

$$\left(F(Z),h^*_0\right)=0,\ \left(B_{ij}(Z)\right)^T h^*_0=0\forall\ Z,i,j=1,...,m,\mathrm{Re}\,\lambda>0\forall\lambda\neq 0. \qquad (3)$$

Such systems of equations can describe the transfer of substances in multiphase media.
The AE of the solution up to order N (determined by the smoothness of the input data) is constructed by the method of boundary functions [4] and has the form

$$U(\bar{x},t)=\sum_{i=0}^{N}\varepsilon^i(s_i(\bar{\zeta},t)+\pi_i(\bar{\xi},\tau))+R_N=U_N+R_N,$$
$$\bar{\zeta}=(\bar{x}-\bar{V}t)/\varepsilon,\bar{\xi}=\bar{x}/\varepsilon,\tau=t/\varepsilon^2,\bar{V}=\{(D^ih_0,h_0^*)/(h_0,h_0^*),i=1,...,m\}. \qquad (4)$$

The construction of AE members is described in detail in [1], [2], [3] and others. In accordance with the boundary layer method of A. V. Vasilyeva and V. F. Butuzov [4] we present nonlinear function $F(U)$ in the form

$$F(U)=F(\bar{U}+S+\Pi+R)=F(\bar{U})+(F(\bar{U}+S)-F(\bar{U}))+\ (F(\bar{U}+\Pi)-F(\bar{U}))+$$
$$+(F(\bar{U}+S+\Pi+R)-F(\bar{U}+S)-F(\bar{U}+\Pi)+F(\bar{U}))=\bar{F}+SF+\Pi F+RF.$$

A similar representation is made for $B(U)$

$$B(U)=\bar{B}+SB+\Pi B+RB.$$

Construction of asymptotic expansion of the solution

Construction regular part AE
Regular part AE have the form

$$\bar{U}(\bar{x},t)=\sum_{i=0}^{N}\varepsilon^i\bar{u}_i(\bar{x},t). \qquad (5)$$

The term $\bar{U}$ plays a supporting role.
Substitute the expantion (5) in the system (6)

$$\varepsilon^2(\bar{U}_t+\sum_{i=1}^{m}D_i\bar{U}_{x_i})=A\bar{U}+\varepsilon F(\bar{U})+\varepsilon^3\sum_{i,j=1}^{m}B_{ij}(\bar{U})\bar{U}_{x_ix_j},|x_i|<\infty,1\le i\le m,\ t>0, \qquad (6)$$

and we obtain the equations for the terms of the expansion [4]:

$$\begin{cases} \varepsilon^0 : A\bar{u}_0 = 0, \\ \varepsilon^1 : A\bar{u}_1 = -F(\bar{u}_0), \\ \varepsilon^2 : A\bar{u}_2 = \bar{u}_{0,t} + \sum_{i=1}^{m} D_i \bar{u}_{0,x_i} - F_u'(\bar{u}_0)\bar{u}_1 \\ \dots \end{cases}$$

The equation at ε is solvable by condition (3).
Hence

$$\begin{cases} \bar{u}_0(x,t) = u_0(x,t)h_0 \\ \bar{u}_1(x,t) = u_1(x,t)h_0 - GF(\bar{u}_0), \end{cases}$$

Here G is a pseudo-inverse to A operator, u_0 and u_1 are some scalar functions.
We write down the condition of solvability of the equation at ε^2:

$$(\bar{u}_{0,t} + \sum_{i=1}^{m} D_i \bar{u}_{0,x_i} - F_u'(\bar{u}_0)\bar{u}_1, h^*_0) = 0.$$

From condition (3) follows $(F_u'(Z)\delta, h^*_0) = 0 \forall \delta.$

Therefore the solvability condition gives the equation for u_0

$$u_{0,t} + \sum_{i=1}^{m} V_i u_{0,x_i} = 0, V_i = (D_i h_0, h_0^*). \tag{7}$$

From the regular part of initial conditions $u_0(\bar{x},0) = 0$ it follows $u_0(\bar{x},t) \equiv 0 \forall \bar{x}, t.$
Similarly, all other u_i are zero. The values V_i will be used below.

Construction S function

S function have the form

$$S(\bar{\zeta},t) = \sum_{i=0}^{N} \varepsilon^i s_i(\bar{\zeta},t), \quad \zeta_i = (x_i - V_i t)/\varepsilon, i = 1,\dots,m. \tag{8}$$

V_i defined by the formula (7).
Function S is the solution of the system

$$\varepsilon^2 (S_t + \sum_{i=1}^{m} D_i S_{x_i}) = AS + \varepsilon SF + \varepsilon^3 \sum_{i,j=1}^{m} SB_{ij} S_{x_i x_j}, |\bar{\zeta}| < \infty, t > 0. \tag{9}$$

Moving to the variables $(\bar{\zeta},t)$ taking into account $\bar{U} = 0,$ we get

$$\varepsilon^2 S_t + \varepsilon \sum_{i=1}^{m} \Psi_i S_{\zeta_i} = AS + \varepsilon F(S) + \varepsilon^3 \sum_{i,j=1}^{m} B_{ij}(S) S_{\zeta_i \zeta_j},$$
$$\Psi_i \equiv D_i - V_i. \tag{10}$$

Than we obtain the equations for the terms of the expansion [4]

$$\begin{cases} \varepsilon^0 : As_0 = 0, \\ \varepsilon^1 : As_1 = \sum_{i=1}^{m} \Psi_i s_{0,\zeta_i} - F(s_0) - \sum_{i,j=1}^{m} B_{ij}(s_0) s_{0,\zeta_i \zeta_j} \equiv Q_1, \\ \varepsilon^2 : As_2 = s_{0,t} + \sum_{i=1}^{m} \Psi_i s_{1,\zeta_i} - F_u'(s_0)s_1 - \sum_{i,j=1}^{m} B_{ij}(s_0) s_{1,\zeta_i \zeta_j} \equiv Q_2, \\ \dots \end{cases}$$

From here, taking into account the condition (3), we get

$$s_0(\bar{\zeta},t) = \varphi_0(\bar{\zeta},t)h_0,$$
$$s_1(\bar{\zeta},t) = \varphi_1(\bar{\zeta},t)h_0 + GQ_1.$$

We write down the solvability conditions of the equation at ε^2:

$$(Q_2, h^*_0) = (s_{0,t} + \sum_{i=1}^{m} \Psi_i s_{1,\zeta_i} - F_u'(s_0)s_1 - \sum_{i,j=1}^{m} B_{ij} s_{1,\zeta_i \zeta_j}, h^*_0) = 0.$$

Substituting here the expression for s_1 and taking into account the conditions (3) as well as equality $(\Psi_i h_0, h^*_0) = ((D_i - V_i)h_0, h^*_0) = 0,$

we obtain equation for determining φ_0 . Let's introduce notation

$$M_{ij} = (\Psi_i G \Psi_j h_0, h^*_0) + (\Psi_j G \Psi_i h_0, h^*_0) \forall i \neq j, M_{ii} = (\Psi_i G \Psi_i h_0, h^*_0),$$

$$F_{i,eff}(\varphi_0) = -(\Psi_i G F(\varphi_0 h_0), h^*_0),$$

$$B_{ijk,eff}(\varphi_0) = -(\Psi_k G B_{ij}(\varphi_0 h_0) h_0, h^*_0).$$

Then the equation for determining φ_0 can be rewritten as

$$\varphi_{0,t} + \sum_{i,j=1}^{m} M_{ij} \varphi_{0,\zeta_i \zeta_j} + \sum_{i=1}^{m} (F_{i,eff}(\varphi_0))'_{\zeta_i} + \sum_{i,j,k=1}^{m} (B_{ijk,eff}(\varphi_0) \varphi_{0,\zeta_i \zeta_j})'_{\zeta_k} = 0. \tag{11}$$

In the expanded form the equation has the form

$$\varphi_{0,t} + \sum_{i,j=1}^{m} M_{ij} \varphi_{0,\zeta_i \zeta_j} + \sum_{i=1}^{m} F'_{i,eff}(\varphi_0) \varphi_{0,\zeta_i} +$$

$$+ \sum_{i,j,k=1}^{m} (B_{ijk,eff}(\varphi_0) \varphi_{0,\zeta_i \zeta_j \zeta_k} + B_{ijk,eff}{}'(\varphi_0) \varphi_{0,\zeta_i} \varphi_{0\zeta_k}) = 0. \tag{12}$$

We will impose an additional condition

$$\sum_{i,j=1}^{m} M_{ij} z_i z_j \leq 0 \forall \sum_{i=1}^{m} z_i^2 > 0.$$

To obtain the equation for s_n, $n \geq 1$, we write the expansion terms of order ε^n, ε^{n+1} and ε^{n+2} :

$$\varepsilon^j : A s_j = s_{j-2,t} + Q_j, \; j = n, n+1, n+2,$$

where Q_1 is defined above, and Q_p for $p>1$ is expressed in terms of previously found s_{p-1}

$$Q_p = \sum_{i=1}^{m} \Psi_i s_{p-1,\zeta_i} - F'_u(s_0) s_{p-1} - \sum_{i,j=1}^{m} B_{ij} s_{p-1,\zeta_i \zeta_j}, \; p = 2, 3, \ldots$$

From the relations for $j=n,n+1$ it follows that

$$s_j = h_0 \varphi_j(\bar{\zeta}, t) + G Q_j, \; j = n, n+1,$$

where φ_n, φ_{n+1} are as yet unknown functions.

Writing the solvability condition $\left(s_{n,t} + Q_{n+2}, h^*_0\right) = 0$ of the equation for s_{n+2}

after exception of s_{n+1} , we obtain the equation for s_n . Adding a designation

$$F1_{i,eff} = -(\Psi_i G F'(\varphi_0 h_0) h_0, h^*_0),$$

taking into account the notations introduced earlier, the linear equation for φ_n can be rewritten as

$$\varphi_{n,t} + \sum_{i,j=1}^{m} M_{ij} \varphi_{n,\zeta_i \zeta_j} + \sum_{i=1}^{m} (F1_{i,eff} \varphi_n)_{\zeta_i} + \sum_{i,j,k=1}^{m} (B_{ijk,eff}(\varphi_0) \varphi_{n,\zeta_i \zeta_j})_{\zeta_k} +$$

$$+ \sum_{i,j,k=1}^{m} ((B_{ijk,eff}(\varphi_0))' \varphi_n \varphi_{0\zeta_i \zeta_j})_{\zeta_k} = \Phi_n(\bar{\zeta}, t), \quad n \geq 1. \tag{13}$$

where Φ_n is expressed by the previously found φ_j, $j<n$.

Construction Π function

To satisfy the initial conditions the function Π is constructed.

Π function have the form

$$\Pi(\bar{\xi}, \tau) = \sum_{i=0}^{N} \varepsilon^i p_i(\bar{\xi}, \tau), \quad \bar{\xi} = \bar{x} / \varepsilon, \tau = t / \varepsilon^2, \tag{14}$$

produced as standard [4]. Function Π is the solution of the system

$$\Pi_\tau + \varepsilon \sum_{i=1}^{m} D_i \Pi_{\xi_i} = A\Pi + \varepsilon \Pi F + \varepsilon \sum_{i,j=1}^{m} B \Pi_{ij} \Pi_{\xi_i \xi_j}, \left|\bar{\xi}\right| < \infty, \tau > 0, \tag{15}$$

together with satisfies the initial conditions and is a boundary layer function

$$S(\bar{\zeta}, 0) + \Pi(\bar{\xi}, 0) = H\omega\left(\frac{\bar{x}}{\varepsilon}\right), \Pi(\bar{\xi}, \tau) \underset{\tau \to \infty}{\to} 0.$$

The main term is defined as the solution of the system

$$p_{0,\tau} = Ap_0, \left|\bar{\xi}\right| < \infty, \tau > 0. \tag{16}$$

The initial conditions for φ_0 and p_0 are defined together, with the addition of the constraint condition p_0 at $\tau \to \infty$:

$$p_0 + \varphi_0\big|_{t=0} = U(\bar{x},0) = H\omega\left(\frac{\bar{x}}{\varepsilon}\right), \left|p_0(\bar{\xi},\infty)\right| < \infty. \tag{17}$$

From conditions (17), we obtain the initial conditions for φ_0 and p_0 .The solution of problem (16) with initial condition (17) and condition at infinity exists and satisfies the estimate

$$\left\|p_0(\bar{\xi},\tau)\right\| < C\exp(-\kappa\tau), \kappa > 0. \tag{18}$$

The remaining p_i are defined as solutions of linear inhomogeneous ODES and satisfy similar estimates:

$$p_{i,\tau} = Ap_i + P_i, i \geq 1, \left|\bar{\xi}\right| < \infty, \tau > 0.$$
$$\left\|p_i(\bar{\xi},\tau)\right\| < C\exp(-\kappa\tau), \kappa > 0. \tag{19}$$

Here P_i is expressed through previously found p_j, $j<i$.

The initial conditions for the functions φ_i and p_i are obtained together from the conditions

$$\sum_{i=1}^{\infty} \varepsilon^i (s_i(\bar{\zeta},0) + p_i(\bar{\xi},0)) = 0, \sum_{i=1}^{\infty} \varepsilon^i p_i(\bar{\xi},\tau) \underset{\tau\to\infty}{\to} 0,$$

what gives

$$s_i(\bar{\zeta},0) + p_i(\bar{\xi},0) = 0, p_i(\bar{\xi},\tau) \underset{\tau\to\infty}{\to} 0 \quad \forall i > 0. \tag{20}$$

From conditions (21) we obtain the initial conditions for the functions φ_i and p_i.

Evaluation of the residual member

The residual term is estimated by the residual term in the problem.

The question of the existence of a solution and exponential estimates of the solution of equations (1)-(2), (11)-(17) under rapidly decreasing initial conditions for the variable ζ not considered here.

The residual term was estimated by residual.

Let the function $\omega(z)$ have derivatives up to $N+3$rd order, the function $F(z)$ have derivatives up to $N+3$rd order in the domain $||U|| < C$, $C>0$, and let $||U(x,0)|| < C-\delta$, $\delta>0$.

Theorem. The solution of the problem (1) - (2) is represented as

$$U(\bar{x},t) = \sum_{i=0}^{N} \varepsilon^i (s_i(\bar{\zeta},t) + p_i(\bar{\xi},\tau)) + R_N = U_N + R_N, \tag{21}$$

where $U_N = S_N + \Pi_N$ is the constructed AE, and the residual term R_N satisfies the Cauchy problem

$$\varepsilon^2 (R_t + \sum_{i=1}^{m} D_i R_{x_i}) = AR + \varepsilon RF + \varepsilon^3 \sum_{i,j=1}^{m} RB_{ij} R_{x_i x_j} + r, \left|\bar{x}\right| < \infty, t > 0,$$
$$R(\bar{x},0) = 0, r = O(\varepsilon^N).$$

Conclusion

1. The solution of the problem (1) - (2) at $t > t_0$, where $t_0 > 0$ is some fixed (independent of ε), has the form

$$U(\bar{x},t) = \sum_{i=0}^{N} \varepsilon^i (s_i(\bar{\zeta},t) + p_i(\bar{\xi},\tau)) + R_N = s_0(\bar{\zeta},t) + O(\varepsilon) = \varphi_0(\bar{\zeta},t)h_0 + O(\varepsilon),$$

where the principal term AE $\varphi_0(\zeta, t)$ is the solution of the equation

$$\varphi_{0,t} + \sum_{i,j=1}^{m} M_{ij} \varphi_{0,\zeta_i\zeta_j} + \sum_{i=1}^{m} (F_{i,eff}(\varphi_0))'_{\zeta_i} + \sum_{i,j,k=1}^{m} (B_{ijk,eff}(\varphi_0)\varphi_{0,\zeta_i\zeta_j})'_{\zeta_k} = 0$$

(generalized Burgers – Korteweg – de Vries equation). For a quadratic function $F(u)$ and constant matrics $B(u)$, equation (13) is a generalization of the Burgers - Korteweg – de Vries equation [5] to the multidimensional case:

$$\varphi_{0,t} + \sum_{i,j=1}^{m} M_{ij} \varphi_{0,\zeta_i\zeta_j} + \sum_{i=1}^{m} k_i \varphi_0 \varphi_{0,\zeta_i} + \sum_{i,j,k=1}^{m} B_{ijk,eff} \varphi_{0,\zeta_i\zeta_j\zeta_k} = 0.$$

For the case of a single spatial variable, the equation (13) differs from the BKdF equation only in the numerical values of the coefficients

$$\varphi_{0,t} + M\varphi''_{0,\zeta\zeta} + k\varphi_0\varphi'_{0,\zeta} + B\varphi'''_{0,\zeta\zeta\zeta} = 0.$$

2. Very interesting properties of the spatial part (the relationship between the degree of degeneracy of the parabolic part of the operator and the dimension of the system (1) are obtained in [1],[3].

3. For the dissipativity of the equation (11), the condition is sufficient

$$M(\bar{z}) = \sum_{i,j=1}^{m} M_{ij} z_i z_j \le 0 \forall \sum_{i=1}^{m} z_i^2 > 0. \qquad (22)$$

It is shown in [1] that the set of matrices *A* that satisfies the conditions imposed above and satisfies the condition (22) is not empty.

4. When *B (U) =0*, the system (1) becomes a system of transfer equations, i.e. a hyperbolic type system.
In this case, the equation (11) that defines the main AE term has the form

$$\varphi_{0,t} + \sum_{i,j=1}^{m} M_{ij}\varphi_{0,\zeta_i\zeta_j} + \sum_{i=1}^{m} (F_{i,eff}(\varphi_0))'_{\zeta_i} = 0, \qquad (23)$$

In [1], a class of matrices *A* is allocated for which the quadratic form $M(\bar{z})$,defining the spatial part of the equation, is sign-positive, and the equation (23) i.e. becomes a parabolic equation (such as the Burgers equation). The nature of the evolution of the principal term of the AE can be described as the movement with some "effective speed" V_{eff}

$$\bar{V}_{eff} = \{V_i = (D_i h_0, h_0^*), i = 1,...,n\}$$

with simultaneous pseudodiffusion, the nature of which is determined by the coefficients M_{ij} , which is influenced by nonlinearity.
The spatial part with the second derivatives is determined by the symmetric matrix *M*. In [1] it is obtained that the quadratic form $M(\bar{z})$ can be degenerate, and the degree of degeneration depends on the ratio of the number of equations n and the number of spatial variables m. For a class of matrices *A* allocated in [1], for m=3 (three spatial variables) and for n=2, the matrix *M* has two zero eigenvalues and one negative, for n=3 - one zero and two negative, for n=4 and more , all eigenvalues of the matrix M become negative.
Figure 1 shows the evolution of the main AE member for m=3 and n=2, n=3.

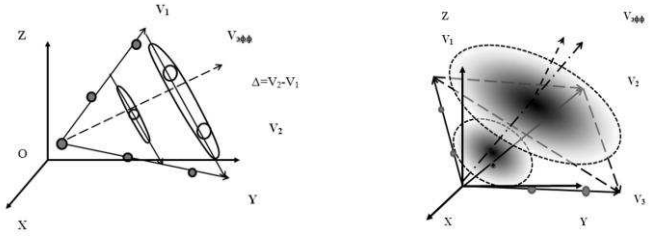

Figure 1. n=2, n=3.

In the case of three-dimensional space, the picture of the solution evolution of the principal term of the AE will have the following view. In a two-phase environment, pseudodiffusion processes develop along one axis (the direction of which is given by the vector $\Delta = \bar{V}_1 - \bar{V}_2$). Accordingly, the initial local perturbation will move in space with an "effective" average speed Veff and simultaneously deform, diffusing into a "cloud" extended in the direction of the vector Δ. In the case of three phases (a system of three equations), the initial perturbation will move to the Pro-
travel with the averaged speed and diffuse in the plane of vectors $\bar{V}_1 - \bar{V}_2, \bar{V}_1 - \bar{V}_3$, forming a flat "cloud".
In the case of four or more phases (a system of 4 or more equations), the initial perturbation will move at the effective velocity V_{ef} and diffuse over all three axes.

5. For the case of *B(U) =0* and a slightly different type of nonlinearity, an AE of a similar problem is constructed in [1]. When a number of additional conditions are imposed, it is possible to prove the estimate of the residual term of the constructed AE in the norm *C*.

6. The obtained result (11) allows us to identify non-obvious patterns of behavior of the solution of the Cauchy problem for singularly perturbed systems of type (1), as well as to identify non-obvious patterns of transfer processes in multiphase media in the case of rapid exchange between phases.
7. The numerical solution of the Cauchy problem for equation (11) requires significantly less computational resources than the solution of the original problem (1), due to the fact that equation (11) is not singularly perturbed.

References

[1] Nesterov A.V. (2016) On the structure of the solution of one class of hyperbolic systems with several spatial variables in the far zone. Compt. Math. and Math. Phys, v. 56, №4, c. 639-649.
[2] Nesterov A.V., Shuliko O. V. (2010) On the asymptotic of the solution of a singularly perturbed system of parabolic equations in the critical case. Compt. Math. and Math. Phys, v. 50, №2, c. 268-275.
[3] T.V. Pavlyuk, A.V. Nesterov, (2014), On the Asymptotics of the Solution to a Singularly Perturbed Hyperbolic System of Equations with Several Spatial Variables in the Critical Case. Compt. Math. and Math. Phys, 2014, v. 54, № 3, pp. 462–473.
[4] Vasilyeva A. B., Butuzov V. F. (1978) Singularly perturbed equations in critical cases. Moscow state University publishing House.
[5] Wisam George. Linear and nonlinear waves. Moscow, Mir, 1977.
[6] Ladyzhenskaya O. A., Solonnikov V. A., Uraltseva N. N.(1967) Linear and quasi-linear parabola equationschesky type. Moscow: Nauka.

Dynamic of the wind powered walking vehicle

Mikhail Garbuz [*], Liubov Klimina[*] and Vitaly Samsonov[*]
[*] *Institute of Mechanics, Lomonosov Moscow State University, Moscow, Russia*

Summary. This paper presents the modelling of novel walking vehicle which aims to move against the wind flow using only the energy of the wind. The vehicle consist of the body, four legs, and wind propeller installed on it. When it is situated in a wind flow, propeller begins to rotate and transmits the energy to the main crank of the legs.
A mathematical model of the system is constructed. Aerodynamics of the propeller is described using a quasi-steady approach basing on available experimental data. It is shown that for certain values of parameters the apparatus can perform motion in upwind direction. Sufficient conditions of existence of periodic regimes are obtained. It is shown that the system can possess two types of periodic regimes corresponding to upwind motion. The average velocity of the body depending on the geometrical parameters is investigated. Evolution of attracting and repelling regimes of motion is analyzed. To demonstrate the possibility of motion against the wind, the plastic prototype of the vehicle is constructed and tested.

Introduction

The problem statement of a straight motion against the flow due to the energy of this flow for walking robots is unique. Nowadays Theo Jansen's mechanical devices are widely known, which are able to walk and get energy from the wind [1, 2]. Such mechanisms can perform motion in downwind direction with a help of sails, or in perpendicular to the wind direction, using a propeller.
In present work, we introduce the novel wind powered walking vehicle based on the Chebyshev plantigrade machine [3,4]. To realize the upwind motion, we upgraded mechanical scheme and supplemented a wind propeller on the body.

Description of the mechanical system

Scheme of the mechanical system is represented in Fig.1. The base of the walking mechanism consists of the body and four legs which are installed on it. This base is equipped with a wind turbine so that the shaft of the propeller is connected with the main shaft of legs by a warm gear. We suppose that this vehicle is located in the horizontal steady wind flow with the speed v_0. The vehicle moves straight along the wind over an absolutely rough plane in the gravity field.

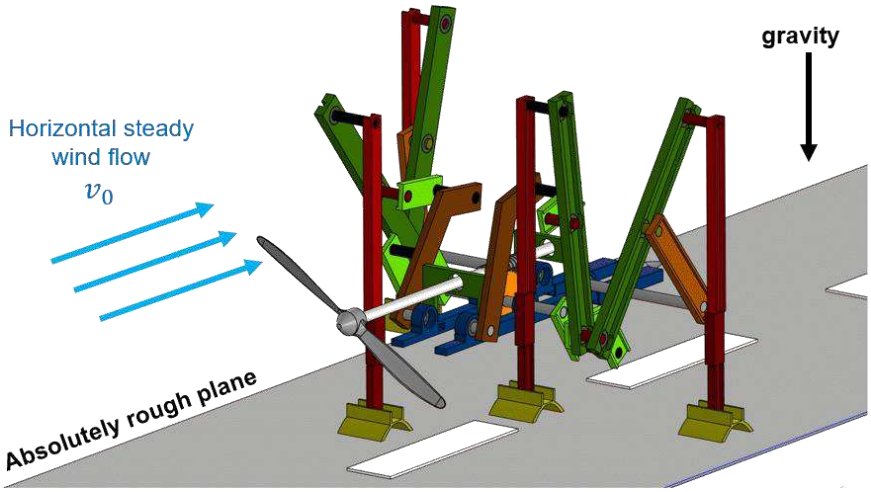

Figure 1: The scheme of the mechanism.

We assume that there is no slipping of the supporting legs and there is no tilting of the body. With these assumptions, the vehicle has one degree of freedom. The angle φ of rotation of the leg's crank shaft is chosen as a generalized coordinate. Equations of motion of the system are derived using the Lagrange formalism:

$$\frac{d}{dt}\left(\frac{\partial L}{\partial \dot{\varphi}}\right) - \left(\frac{\partial L}{\partial \varphi}\right) = n \cdot M_{aero} - \frac{v}{\dot{\varphi}}\left(F_{aero} + k(v + v_0)\right).$$

Here $L(\varphi, \dot{\varphi})$ is the Lagrange function, n is a gear ratio between propeller and cranks, v is a horizontal velocity of the body, k is the aerodynamic drag coefficient of the body. M_{aero} and F_{aero} are the aerodynamic torque and the drag force acting on the propeller, correspondently. These functions are described according a quasi-steady model and have the following form:

$$M_{aero} = \frac{1}{2}\rho_a S \cdot r_a (v + v_0)^2 C_T(\lambda), \qquad F_{aero} = \frac{1}{2}\rho_a S \cdot (v + v_0)^2 C_D(\lambda),$$

where $\lambda = n r_a \dot{\varphi}\,(v + v_0)^{-1}$ is a tip speed ratio of the propeller, ρ_a is the air density, S and r_a are the characteristic area and the radius of the propeller. $C_T(\lambda)$ and $C_D(\lambda)$ are non-dimensional coefficients of torque and drag force, correspondingly. These coefficients are approximated using experimental data [5].

Right hand side of the system is π-periodic with respect to φ. Therefore, the phase space of the system is cylindrical. An attracting limit cycle with a positive value of $\dot{\varphi}$ enclosing the phase cylinder corresponds to desired upwind motion regime.
The following parameter is introduced: $\varepsilon =$. It is supposed to be a small value. This means that characteristic values of aerodynamic loads are significantly smaller than characteristic values of inertial forces.

Main results

We obtained sufficient conditions of existence of periodic upwind motion regimes using the Andronov-Pontryagin asymptotic method [6]. This method involves the averaging procedure. Notice that averaging is widely used in most powerful and demanded approaches of nonlinear dynamics [7, 8]. We performed analysis of limit cycles depending on parameters of the vehicle. The attraction properties of the regimes are studied.

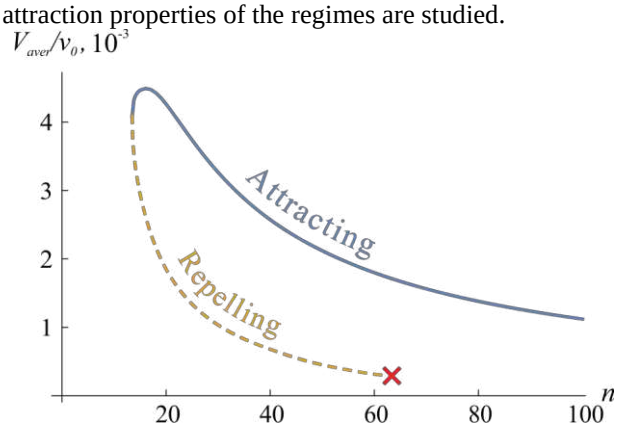

Figure 2: Bifurcation diagram for periodical trajectories.

An example of bifurcation diagram is shown in Fig. 2 for the case $\varepsilon \to 0$ with other parameters of the system corresponding to the laboratory prototype constructed and tested in the Institute of Mechanics of Lomonosov Moscow State University. The description of the prototype and the video of its upwind motion are available [9]. In particular, the total length of the prototype is 225 mm. Fig. 2 illustrates how the average velocity the body depends on gear ratio n. Upper branch of diagram corresponds to attracting trajectories, and lower to repelling ones. Red cross corresponds to the bifurcation when a repelling periodic trajectory enclosing a phase cylinder merges with a separatrix and is destroyed as a result. Accuracy of asymptotic bifurcation diagram was checked by direct numerical integration of the system for the case $\varepsilon = 0.76$. In particular, the value of parameter n for which repelling trajectory is destroyed is determined with 6% precession.

Conclusion

The mathematical model of a wind powered walking vehicle is constructed. Results of parametrical analysis of the model are used to adjust constructive parameters of the first prototype. Experimental testing of the prototype demonstrated the possibility of motion against the wind for a walking mechanism.

The work was carried out within the framework of the research project “Development of methods for the study of controlled mechanical systems interacting with a continuous medium” (AAAA-A19-119012990123-0).

References

[1] GIESBRECHT D, WU CQ, SEPEHRI N: Design and optimization of an eight-bar legged walking mechanism imitating a kinetic sculpture, “wind beast”. Transactions of the Canadian Society for Mechanical Engineering 2012, 36(4):343-355.
[2] NANSAI S, ELARA MR, IWASE M: Dynamic analysis and modeling of Jansen mechanism. Procedia Engineering 2013, 64:1562-1571.
[3] OTTAVIANO E, GRANDE S, CECCARELLI M: A biped walking mechanism for a rickshaw robot. Mechanics based design of structures and machines 2010, 38(2):227-242.
[4] PAVLOVSKY V: For elaboration of walking machines. Keldysh Institute Preprints 2013, 101:1-32.
[5] ADARAMOLA M, KROGSTAD P: Experimental investigation of wake effects on wind turbine performance. Renewable Energy 2011, 36(8):2078-2086.
[6] PONTRYAGIN L: On dynamical systems close to hamiltonian. Zh. Eksp. Teor. Fiz. 1934, 4, 234–238.
[7] BOGOLYUBOV N, MITROPOLSKII Y : Asymptotic methods in the theory of nonlinear oscillations. Moscow: State Publishing House for Tachnical Theoretical Literatute, 1955. 449 p.
[8] AWREJCEWICZ J, ANDRIANOV I, MANEVITCH L: Asymptotic approaches in nonlinear dynamics: New trends and applications. Springer 1998. DOI:10.1007/978-3-642-72079-6
[9] WALKING MECHANISM MOVING AGAINST THE WIND FLOW. Virtual museum. URL: https://mgarbuz.github.io/plantigrade-site/

Methods of perturbation theory and their applications in nonlinear fracture mechanics and continuum damage mechanics

Larisa Stepanova*

*Department of Mathematical Modeling in Mechanics, Samara University, Samara, 443086, Russia

Summary. Perturbation theory techniques and their applications in nonlinear fracture mechanics (NFM) are discussed. This study summarizes an overview of the state of the art on the asymptotic description of fracture of nonlinear and damaged materials. The asymptotic stress, strain and damage fields near the crack tip for power-law materials and the influence of the damage accumulation processes on the stress-strain state in the vicinity of the crack tip are analyzed. The paper gives a detailed review of the fundamental results obtained in NFM by means of asymptotic methods and perturbation theory approaches. The main attention is paid to power-law materials and asymptotic stress and strain fields in the vicinity of the crack in both non-damaged materials and damaged materials under mixed mode loadings. The paper analyses the development of the asymptotic elastic-plastic crack-tip fields derived by Hutchinson, Rice and Rosengren as a singular dominant term of the asymptotic expansion for the stress and strain fields in a power-law hardening material and shows the current state of the asymptotic methods and their applications in NFM and continuum damage mechanics.

Introduction

Asymptotic methods have several essential advantages: universality, the analytical form of the solutions obtained and simplicity of further qualitative analysis. The asymptotic methods and perturbation theory are promising and effective approach of the derivation of approximate or even closed form solutions. Nowadays the perturbation theory techniques are applied to a wide variety of static and dynamic solid mechanics problems. Asymptotic methods have also been used with success in various nonlinear problems of fracture mechanics. The asymptotic analysis of the stress and strain distributions in the vicinity of the wedge-shaped domain is one of the most fundamental problems both in linear fracture mechanics and NFM. Thus, in linear fracture mechanics very important results have been obtained by use of the methods of asymptotic analysis. An excellent review of the most considerable contributions in this field is provided by A. Carpinteri and M. Paggi in their work [1]. The present study is aimed at analysis of the results recently obtained in NFM and continuum damage mechanics for power-law constitutive equations and the power-law damage evolution equation by means of asymptotic methods and perturbation theory.

Asymptotic solutions to problems of NFM

Crack-tip stress and strain singularities for pure power law material response $\varepsilon/\varepsilon_0=\alpha\left(\sigma/\sigma_0\right)^n$, where α is a material constant, σ_0 is the reference yield strength, n is the strain hardening exponent, $\varepsilon_0=\sigma_0/E$ is the reference yield strain, are investigated in [2-4]. The crack tip fields can be derived in the separable form [2-4]

$$\sigma_{ij}(r,\theta)=\sigma_0\left(\frac{J}{k_n r}\right)^{1/(n+1)}\tilde{\sigma}_{ij}(\theta,n),\ \varepsilon_{ij}(r,\theta)=\alpha\varepsilon_0\left(\frac{J}{k_n r}\right)^{n/(n+1)}\tilde{\varepsilon}_{ij}(\theta,n),\ u_i(r,\theta)=\alpha\varepsilon_0\left(\frac{J}{k_n r}\right)^{n/(n+1)}r^{1/(n+1)}\tilde{u}_i(\theta,n), \tag{1}$$

where J is the path-independent integral, I_n is the dimensionless J -integral (an integration constant depending on n), $k_n=\alpha\sigma_0\varepsilon_0 I_n$. The asymptotic fields (1) are referred to as the Hutchinson-Rice-Rosengren (HRR) fields in the vicinity of the crack tip in power-law materials. The asymptotic solution (1) was sought in the separable form $\chi\left(r,\theta\right)=r^{\lambda+1}f(\theta)$. where $\chi\left(r,\theta\right)$ is the Airy stress function: $\sigma_{\theta\theta}=\chi_{,rr}$, $\sigma_{rr}=\Delta\chi-\sigma_{\theta\theta}$, $\sigma_{r\theta}=-r^{-1}\left(r^{-1}\chi_{,\theta}\right)_{,r}$. The resulting nonlinear ordinary differential equation following from the compatibility equation is homogeneous in $f(\theta)$:

$$\begin{aligned}
&f_e^2 f^{IV}\left\{(n-1)\left[\left(1-\lambda^2\right)f+f''\right]^2+f_e^2\right\}+(n-1)(n-3)\left\{\left[\left(1-\lambda^2\right)f+f''\right]\left[\left(1-\lambda^2\right)f'+f'''\right]+4\lambda^2 ff''\right\}^2\left[\left(1-\lambda^2\right)f+f''\right]+\\
&+(n-1)f_e^2\left\{\left[\left(1-\lambda^2\right)f'+f'''\right]^2+\left[\left(1-\lambda^2\right)f+f''\right]\left(1-\lambda^2\right)f''+4\lambda^2\left(f''^2+ff'''\right)\right\}\left[\left(1-\lambda^2\right)f+f''\right]+2(n-1)f_e^2\times\\
&\times\left\{\left[\left(1-\lambda^2\right)f+f''\right]\left[\left(1-\lambda^2\right)f'+f'''\right]+4\lambda^2 ff''\right\}\left[\left(1-\lambda^2\right)f'+f'''\right]-C_2 f_e^4\left[\left(1-\lambda^2\right)f+f''\right]+f_e^4\left(1-\lambda^2\right)f''+\\
&+C_1(n-1)f_e^2\left\{\left[\left(1-\lambda^2\right)f+f''\right]\left[\left(1-\lambda^2\right)f'+f'''\right]+4\lambda^2 ff''\right\}f'+C_1 f_e^4 f''=0,\quad f_e^2=\left[\left(1-\lambda^2\right)f+f''\right]^2+4\lambda^2 f'^2
\end{aligned} \tag{2}$$

where the following notations are adopted: $C_1=4\lambda\left[(\lambda-1)n+1\right]$, $C_2=(\lambda-1)n\left[(\lambda-1)n+2\right]$.

The fourth order nonlinear differential equation (2) with traction-free boundary conditions

$$f\left(\theta=\pm\pi\right)=0,\quad f'\left(\theta=\pm\pi\right)=0 \tag{3}$$

defines a nonlinear eigenvalue problem in which λ is the eigenvalue and $f(\theta)$ is the corresponding eigenfunction. Thus, the eigenfunction expansion method results in the nonlinear eigenvalue problem: it is necessary to find eigenvalues leading to nontrivial solutions of Eq. (2) satisfying the boundary conditions (3). The eigenvalue corresponding to the HRR problem (1) is well known $\lambda=n/(n+1)$. The further development of NFM required analysis of eigenspectra and orders of singularity at a crack tip for power-law materials [5 – 8]. In [6] the necessity of introducing higher or lower order

singular terms to more correctly describe the asymptotic fields of crack tip is shown. The coordinate perturbation technique is employed to study the eigenspectra of creeping body. To attain eigensolutions a numerical scheme is worked out and the results obtained provide the information including the number of singularities, and their orders, as well as the angular distributions of stresses. The present study discusses different approaches to solve nonlinear eigenvalue problems arising in NFM for power-law materials. The main attention is paid to perturbation techniques to solve nonlinear eigenvalue problems (2), (3). Eqs. (2) and (3) form a nonlinear eigenvalue problem, where the unknown eigenvalue λ and the eigenfunction $f(\theta)$ depend on the boundary conditions and the hardening exponent. An analytical expression for the eigenvalues of the nonlinear equation can be derived by applying the perturbation method. For this purpose, the eigenvalue is split into $\lambda = \lambda_0 + \varepsilon,$ where λ_0 refers to the "undisturbed" linear problem and ε is the deviation on account of the nonlinearity. The hardening exponent n and the stress function $f(\theta)$ are represented as power series

$$n = n_0 + \varepsilon n_1 + \varepsilon^2 n_2 + \varepsilon^3 n_3 + ... = \sum_{j=0}^{\infty} \varepsilon^j n_j,\ f(\theta) = f_0(\theta) + \varepsilon f_1(\theta) + \varepsilon^2 f_2(\theta) + \varepsilon^3 f_3(\theta) + ... = \sum_{j=0}^{\infty} \varepsilon^j f_j(\theta),$$

where $n_0 = 1$ and $f_0(\theta)$ are referred to the linear solution. This method allows us to find the closed form solution.

Conclusions

Recent activity is surveyed in the analysis of crack-tip stress and strain fields for stationary and growing cracks in power-law materials. Some of the main subjects to further progress are discussed. In the study the detailed review of solutions for crack problems obtained for power law constitutive equations is presented. In NFM, one often needs to solve nonlinear differential equations about eigenfunction and eigenvalue. Many nonlinear eigenvalue equations have multiple solutions. Boundary value problems of these problems are not easy to gain by means of numerical techniques such as the shooting method. The perturbation and asymptotic approximations of nonlinear problems often break down as nonlinearity becomes strong [9, 10]. Therefore, they are only valid for weakly nonlinear ordinary differential equations and partial differential equations in general. The homotopy analysis method (HAM) is an analytic approximation method for highly nonlinear problems. Unlike perturbation techniques, the HAM is independent of any small/large physical parameters at all. The HAM provides us a convenient way to guarantee the convergence of solution series so that it is valid even if nonlinearity becomes rather strong. Thus, in fracture mechanics HAM may play a significant role in solving nonlinear eigenvalue problems. The book [9] shows the great potential and validity of the for highly nonlinear eigenvalue equations with multiple solutions and singularity. The HAM will provide us one of the promising approaches for nonlinear eigenvalue problem arising in fracture mechanics. The present review shows that asymptotic solutions of fracture mechanics problem will be connected with derivation of multi-term asymptotic series expansions for the crack-tip fields using effective computer algorithms and procedures [7,8]. The further development of NFM and continuum damage mechanics will evidently be connected with experimental determination of active damage accumulation zone in the vicinity of the crack tip via interference-optic methods [11], tomographic scanning techniques [12], acoustic emission methods [13] and, undoubtedly, with using highly accurate current perturbation theory and homotopy techniques [14].

Acknowledgments

The work is supported by the Russian Science Foundation (project 21-11-00346).

References

[1] Carpinteri A., Paggi M. (2009) Asymptotic analysis in Linear Elasticity: From the pioneering studies by Wieghardt and Irwin until today. *Engineering Fracture Mechanics* **76:**1771-1784.
[2] Hutchinson J. W. (1968) Singular behaviour at the end of a tensile crack in a hardening material. *J Mech Phys Solids* **16**:13-31.
[3] Rice J. R., Rosengren G. F. (1968) Plain strain deformation near a crack tip in a power-law hardening material. *J Mech Phys Solids* **16:**1-12.
[4] Hutchinson JW (1968) Plastic stress and strain fields at a crack tip. J Mech Phys Solids **16**:337-347.
[5] Hui C.Y. (1986) The mechanics of self-similar crack growth in an elastic power-law creeping material. *Intern J of Solids and Structures* **22(4)**: 357-372.
[6] Meng L, Lee S.B. (1998) Eigenspectra and orders of singularity at a crack tip for a power-law creeping medium. *International Journal of Fracture* **92**:55-70.
[7] Stepanova L.V., Yakovleva E.M. (2015) Asymptotic stress field in the vicinity of a mixed-mode crack under plane stress conditions for a power-law hardening material. *Journal of Mechanics of Materials and Structures* **10(3)**:367-393
[8] Stepanova L.V., Yakovleva E.M. (2016) Stress-strain state near the crack tip under mixed-mode loading: Asymptotic approach and numerical solutions of nonlinear eigenvalue problems. *AIP Conference Proceedings* **1785**:030030.
[9] Liao S. (2011) Homotopy Analysis Method in Nonlinear Differential Equations. Springer, Berlin.
[10] Liao S. (1992) The proposed Homotopy Analysis Technique for the Solution of Nonlinear Problems. *PhD dissertation,* Shanghai Jiao Tong University, Shanghai.
[11] Stepanova L., Roslyakov P. (2016) Complete Williams asymptotic expansion of the stress field near the crack tip: Analytical solutions, interference-optic methods and numerical experiments. *AIP Conf. Proceedings* **1785**:030029.
[12] Tian W, Han N (2019) Analysis on meso-damage processes in concrete by X-ray computed tomographic scanning techniques based on divisional zones. *Measurement* **140**:382-387.
[13] Arumugam V., Saravanakumar K., Santulli C. (2018) Damage characterization of stiffened glass-epoxy laminates under tensile loading with acoustic emission monitoring. *Composites Part B: Engineering* **147**:22 -32.
[14] Wang A.-Y., Xu H. (2022) Highly accurate wavelet-homotopy solutions for mixed convection hybrid nanofluid flow in an inclined square lid-driven cavity. Computers and Mathematics with Applications 108: 88-108.

Energy model of free vibrations and resonance in elastic bodies

Yuriy Alyushin
National University of Science and Technology MISIS, Moscow, 119991, Russia

Mechanics based on the concepts of space, time, and energy with a single elastic modulus and a new average stress scale that takes into account the energy of particles in the initial state is used to analyze the energy features of free vibrations and resonance. When describing motion in the Lagrange form, the elastic energy is determined by the quadratic invariant of the tensor, whose components are partial derivatives of Euler variables with respect to Lagrange variables. The increment of the invariant due to elastic deformation is represented as the sum of two scalars, one of which depends on the average value of the relative lengths of the edges of particles in the form of an infinitesimal parallelepiped, the second is equal to the standard deviation of these lengths from the average value. It is shown that each of the scalars can be represented as two dimensionless kinematic analogs of elastic energy that participate in the implementation of the law of conservation of energy in different ways. One part of the elastic energy passes into kinetic energy and participates in the implementation of the law of conservation of energy for the body as a whole, taking into account external forces. The second part is not converted to kinetic energy, leads to a change in the deformed state of the particles in accordance with the equations of motion, while maintaining the same level of the elastic energy of the particles used for this purpose. Kinematic analogues differ from the corresponding types of energy by a multiplier equal to the elastic modulus, which is directly proportional to the density and heat capacity of the material and inversely proportional to the volume compression coefficient. Transverse, torsional, and longitudinal vibrations are considered in free and resonant conditions. A mechanism for converting forced vibrations into their own after the termination of external influences is proposed. Resonance occurs due to the superposition of free and forced vibrations with the same or similar frequency with the formation of a new free wave on each cycle with an increase in the amplitude and energy involved in the vibrations, which occurs mainly due to internal sources, and not external forces.

Non-stationary dynamics of the sine-lattice consisting of three pendulums (trimer)

Margarita Kovaleva[*], Leonid Manevitch[*]
[*]*N.N. Semenov Federal Research Center for Chemical Physics, Russian Academy of Sciences, Moscow, Russia*

Summary. We present an analysis of both low- and high-amplitude oscillations of nonlinearly coupled trimer, even when the quasi-linear approximation cannot be applied. The described models are fundamental for many areas of Mechanics and Physics (paraffin crystals, DNA molecules etc.). We obtained the conditions of stability of basic stationary solutions corresponding to nonlinear normal modes (NNMs). Supposing the NNMs resonant interaction we introduce a "slow" time-scale which determines a characteristic time of the energy exchange between the pendulums. Introducing the angle variables, we reduce the considered phase space.

Introduction

Dynamics of coupled nonlinear oscillators attracts the growing interest of scientific community because of its fundamental meaning and various applications.

We will focus on the large-amplitude oscillations but not rotations of the pendulums. In current paper, in contrast to many works devoted to interacting nonlinear oscillators, non-linearity of both the pendulums and the coupling between them are not assumed to be small. Thus, research methods that involve quasi-linearity and the presence of a small parameter characterizing nonlinearity and/or coupling are not applicable. To overcome this difficulty a semi-inverse method was proposed [1]. Using this method and LPT concept the system of two identical linearly and strongly nonlinearly coupled pendulums was examined under different oscillation amplitudes [2]. Stationary and non-stationary transitions leading to a qualitative change in the dynamic behavior of the system were analytically described. This work continues the previous investigations for the more complex case, when the coupling between the pendulums cannot be assumed, and the number of degrees of freedom is equal three.

The model and asymptotic procedure

Hamiltonian of the system of three identic pendula coupled via cosine potential in the dimensionless form can be represented in the following form:

$$H=\sum_{j=1,2,3}\left(\frac{1}{2}\left(\frac{dq_j}{dt}\right)^2+\left(1-\cos(q_j)\right)\right)+\beta\left(1-\cos(q_2-q_3)\right)+\beta\left(1-\cos(q_2-q_1)\right) \tag{1}$$

We suppose that NNMs frequencies are close to each other, and the motion of the system happens with the frequency which is also close to those of Nonlinear Normal Modes (NNMs) of the system. The assumption of the closeness of the motion to the resonance with single frequency allows application of the semi-inverse approach, which was already used in our earlier works. Closeness to resonance allows us to introduce a small parameter and further apply a multi-scale procedure. In the slow time-scale we obtain a system of equations with new form of non-linearity:

$$\begin{aligned}
&i\frac{d}{d\tau_1}\varphi_1+\mu\left(-\frac{\omega}{2}\varphi_1+\frac{1}{\sqrt{2\omega}}J_1\left(\sqrt{\frac{2}{\omega}}|\varphi_1|\right)\frac{\varphi_1}{|\varphi_1|}\right)+\frac{\beta_0}{\sqrt{2\omega}}J_1\left(\sqrt{\frac{2}{\omega}}|\varphi_1-\varphi_2|\right)\frac{\varphi_1-\varphi_2}{|\varphi_1-\varphi_2|}=0,\\
&i\frac{d}{d\tau_1}\varphi_2+\mu\left(-\frac{\omega}{2}\varphi_2+\frac{1}{\sqrt{2\omega}}J_1\left(\sqrt{\frac{2}{\omega}}|\varphi_2|\right)\frac{\varphi_2}{|\varphi_2|}\right)+\frac{\beta_0}{\sqrt{2\omega}}J_1\left(\sqrt{\frac{2}{\omega}}|\varphi_2-\varphi_1|\right)\frac{\varphi_2-\varphi_1}{|\varphi_j-\varphi_{3-j}|}+\frac{\beta_0}{\sqrt{2\omega}}J_1\left(\sqrt{\frac{2}{\omega}}|\varphi_2-\varphi_3|\right)\frac{\varphi_2-\varphi_3}{|\varphi_2-\varphi_3|}=0,\\
&i\frac{d}{d\tau_1}\varphi_3+\mu\left(-\frac{\omega}{2}\varphi_3+\frac{1}{\sqrt{2\omega}}J_1\left(\sqrt{\frac{2}{\omega}}|\varphi_3|\right)\frac{\varphi_3}{|\varphi_3|}\right)+\frac{\beta_0}{\sqrt{2\omega}}J_1\left(\sqrt{\frac{2}{\omega}}|\varphi_3-\varphi_2|\right)\frac{\varphi_3-\varphi_2}{|\varphi_3-\varphi_2|}=0,
\end{aligned} \tag{2}$$

where J_1 is Bessel function of the first kind. Using such reptresentation we can obtain analytical description of the NNMs' frequencies in the system. We see a very good agreement for the initial excitation up to Q=9/10π. As we expected the frequency of the oscillations decreases with the increase of the initial excitation (due to the 'soft' nonlinearity effect). We should also emphasize that our assumption on the closeness of the NNMs frequencies appears to be valid for a wide range of the parameters and initial conditions.

Non-stationary dynamics: Poincaré maps study

To proceed with the study of the phase space we intend to reduce the dimensionality of the model. Similarly to the system of two pendula [2] asymptotic system (2) possesses an additional integral of motion

$$X=\sum_{k=1}^{3}|\varphi_k|^2$$

It allows us to introduce spherical coordinates

$$\begin{cases} \varphi_1 = \sqrt{X}\cos\theta\cos\varphi\, e^{i\delta_1} \\ \varphi_2 = \sqrt{X}\sin\theta\, e^{i\delta_2} \\ \varphi_3 = \sqrt{X}\cos\theta\sin\varphi\, e^{i\delta_3} \end{cases} \tag{3}$$

and using the fact that only the relative phases have physical meaning we reduce the system's dimentionality: $\Delta_{12} = \delta_1 - \delta_2$, $\Delta_{23} = \delta_2 - \delta_3$. The systems Hamiltonian:

$$H_{4D} = \mu\left(\frac{1}{4}Q^2\omega^2 - J_0(Q\sin\theta) - J_0(Q\cos\theta\cos\varphi) - J_0(Q\cos\theta\sin\varphi)\right) - \beta_0 J_0\left(Q\sqrt{S_1}\right) - \beta_0 J_0\left(Q\sqrt{S_2}\right). \tag{4}$$

System (8) is four-dimensional, and its dimensionality can be reduced using Hamiltonian (9), but the system remains non-integrable even in the slow time scale. However, the Poincaré sections analysis of the reduced system can be provided. The section plane was defined as $\theta = 1.53$, Δ_{23} was defined from (4) as $H = h(\beta_0)$.

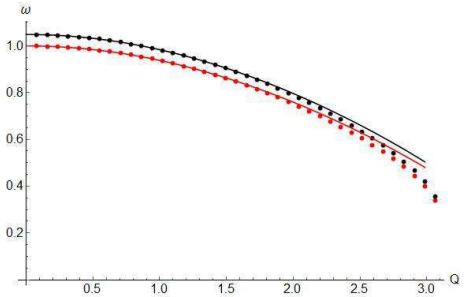

Figure 1: NNMs of the asymptotic system (solid lines) and comparison with the numerical results of the full system (dotted lines)

We have constructed Poincaré maps for different values of the coupling parameter β. For low values of coupling the dynamics is regular; there are two stationary points on the map C_1 and C_2, which correspond to quasiperiodic dynamical regimes with energy localization on one of the side-oscillators (see Fig 2a). If the coupling increases the chaotic regimes occupy the most of the phase space, then a new periodic regime C_3 of regular energy transport from one side-element to another appears in the chaotic region (see Fig 2b). We remind that this regime is called LPT, which is a phase trajectory that shows the possibility of the intensive regular energy exchange between the two edges of the short chain.

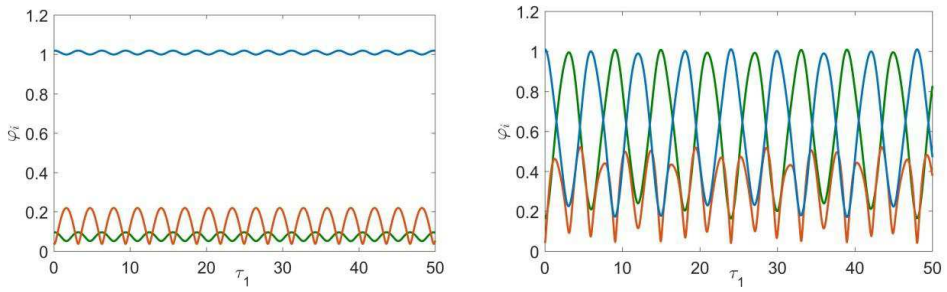

Figure 2: Time-evolutions of different regimes of system (4): θ=1.53, ε=0.1, μ=10, a) β0 = 0.5, initial conditions correspond to C1; b) β0 = 2, initial conditions correspond to C3

Conclusions

We report the study of the non-stationary dynamics in the system of three pendulums coupled by cosine potential. In the earlier works the intensive beatings were reported in the systems with more than two degrees of freedom with the periodic boundary conditions but they characterize the energy exchange not between the coherent domains. Present work extends the phenomenon of the intensive periodic energy exchange between the two ends of the short oscillatory chains with more than two degrees of freedom. The physical meaning of the regime with excitation mostly localized on the side-element is similar to that of the discrete breather in the long chain of nonlinear oscillators

Acknowledgements

This work was supported by Russian Science Foundation according to the research project no. 16-13-10302

References

[1] Manevitch LL., Smirnov VV (2016) Semi-inverse Method in Nonlinear Dynamics, in Proceedings of 5th International Conference "Nonlinear Dynamics", Kharkov, 28-37.

[2] Kovaleva M.A., Smirnov V.V., Manevitch LI. Stationary and nonstationary dynamics of the system of two harmonically coupled pendulums Rus. J. Nonlin. Dyn., 2017, vol. 13, no. 1, pp. 105–115 (Russian)

[3] Kovaleva M, Smirnov V., Manevitch L. I. Nonstationary dynamics of the sine lattice consisting of three pendula (trimer) // Physical Review E - Statistical, Nonlinear, and Soft Matter Physics. 2019. Vol. 99. No. 012209. P. 012209-1-012209-12.

Friday, July 22, 2022

08:30 - 10:30

MS-17 Time-periodic systems

Saint Clair 3A

Chair: Daniel Bachrathy

08:30 - 08:50

Period approximation for nonlinear oscillators with Carleman linearization

HUBAY Csanád Árpád*, KALMÁR-NAGY Tamás

*Budapest University of Technology and Economics, Department of Fluid Mechanics [Budapest] (Bertalan Lajos Street 4-6, 1111 - Budapest Hungary)

08:50 - 09:10

Time integration based stability calculation for delayed periodic system with linear time complexity

BACHRATHY Daniel*, KRISTOF Nagy

*MTA-BME Lendület Machine Tool Research Group, Department of Applied Mechanics, Budapest University of Technology and Economics (Budapest, Muegyetem rkp. 3. Hungary)

09:10 - 09:30

Uni-directional wave propagation in time-modulated inerter-based lattice

KARLICIC Danilo*, CAJIC Milan, PAUNOVIC Stepa, ADHIKARI Sondipon

*Mathematical institute of the Serbian Academy of Sciences and Arts, Belgrade, Serbia (Kneza Mihaila 36, Belgrade Serbia)

09:30 - 09:50

Energy flow characteristics of periodical orbits of nonlinear dynamical systems

XING Jing Tang*

*University of Southampton (Maritime, FEPS, Boldrewood Campus, University of Southampton, Burgess Road, Southampton SO16 7QF United Kingdom)

09:50 - 10:10

New simple oscillator model describing ice-induced vibrations of an offshore structure

ABRAMIAN Andrei*, VAKULENKO Sergei

*Institute for Problems in Mechanical Engineering RAS (V.O., Bolshoj pr., 61 St. Petersburg, 199178 Russia Russia)

Period approximation for nonlinear oscillators with Carleman linearization

Csanád Árpád Hubay and Tamás Kalmár-Nagy
Department of Fluid Mechanics, Faculty of Mechanical Engineering, Budapest University of Technology and Economics, Budapest, Hungary

Summary. A method for period approximation of nonlinear oscillators using Carleman linearization is presented. The approximation of the amplitude-dependent period of a given nonlinear oscillator is calculated and compared to exact period values.

Introduction

Calculation of the period of a nonlinear oscillator is an important engineering problem. In this paper, a versatile tool, the so-called Carleman linearization [1] is used to obtain the solutions of nonlinear oscillator $\ddot{x} + f(x,\, \dot{x}) = 0$ and its exact amplitude-dependent period is approximated. An example of such nonlinear oscillator is

$$\ddot{x} + (1 + \dot{x}^2)x = 0, \quad x(0) = A, \quad \dot{x}(0) = 0. \tag{1}$$

Mickens et al. [2] derived the formula of the exact period of the oscillator (1):

$$T_{exact}(A) = 4A \int_0^1 \frac{\mathrm{d}z}{\sqrt{\exp(A^2(1-z^2)) - 1}}. \tag{2}$$

An approximation of the exact period in case of small values of A is given in [3] as

$$T_{approx}(A) \approx 2\pi \left(1 - \frac{1}{8}A^2 + \frac{1}{256}A^4 + \frac{5}{6144}A^6 - \frac{7}{262144}A^8 + \dots\right). \tag{3}$$

Small and large amplitude periodic orbits of Eq. (1) were investigated by Kalmár-Nagy and Erneux in [4].

Carleman linearization and period approximation

Eq. (1) can be written as

$$\begin{aligned} \dot{x}_1 &= x_2, \\ \dot{x}_2 &= -(1 + x_2^2)x_1. \end{aligned} \tag{4}$$

By introducing the notation

$$\mathbf{x}^{[j]} = (x_1^j,\, x_1^{j-1}x_2,\, x_1^{j-2}x_2^2,\, \dots,\, x_1^2x_2^{j-2},\, x_1x_2^{j-1}, x_2^j)^{\mathrm{T}}, \quad j = 1,\, \dots,\, n, \tag{5}$$

and applying Carleman linearization [1] Eq. (4) is recast as

$$\underbrace{\frac{\mathrm{d}}{\mathrm{d}t}\begin{pmatrix} \mathbf{x}^{[1]} \\ \mathbf{x}^{[2]} \\ \mathbf{x}^{[3]} \\ \vdots \\ \mathbf{x}^{[n-2]} \\ \mathbf{x}^{[n-1]} \\ \mathbf{x}^{[n]} \end{pmatrix}}_{\dot{\mathbf{y}}_n} = \underbrace{\begin{pmatrix} \mathbf{B}_{1,1} & \mathbf{0} & \mathbf{B}_{1,3} & \dots & \mathbf{0} & \mathbf{0} & \mathbf{0} \\ \mathbf{0} & \mathbf{B}_{2,2} & \mathbf{0} & \ddots & \mathbf{0} & \mathbf{0} & \mathbf{0} \\ \vdots & \vdots & \ddots & \dots & \vdots & \vdots & \vdots \\ \mathbf{0} & \mathbf{0} & \mathbf{0} & \dots & \mathbf{B}_{n-2,n-2} & \mathbf{0} & \mathbf{B}_{n-2,n} \\ \mathbf{0} & \mathbf{0} & \mathbf{0} & \dots & \mathbf{0} & \mathbf{B}_{n-1,n-1} & \mathbf{0} \\ \mathbf{0} & \mathbf{0} & \mathbf{0} & \dots & \mathbf{0} & \mathbf{0} & \mathbf{B}_{n,n} \end{pmatrix}}_{\mathbf{C}_n} \underbrace{\begin{pmatrix} \mathbf{x}^{[1]} \\ \mathbf{x}^{[2]} \\ \mathbf{x}^{[3]} \\ \vdots \\ \mathbf{x}^{[n-2]} \\ \mathbf{x}^{[n-1]} \\ \mathbf{x}^{[n]} \end{pmatrix}}_{\mathbf{y}_n}, \tag{6}$$

$$\mathbf{y}_0(A) = \left(A,\, 0,\, A^2,\, 0,\, 0,\, A^3,\, 0,\, 0,\, 0, \dots,\, A^n,\, \dots,\, 0\right)^{\mathrm{T}},$$

where $\mathbf{C}_n$ denotes the Carleman matrix of order n and $\mathbf{y}_0$ is the vector of initial conditions. The matrices $\mathbf{B}_{j,j}$, $j = 1,\, \dots,\, n$ and $\mathbf{B}_{k,k+2}$, $k = 1,\, \dots,\, n-2$ are constructed as follows

$$\mathbf{B}_{j,j} = \begin{pmatrix} 0 & -j & & & \\ 1 & 0 & -j+1 & & \mathbf{0} \\ & 2 & 0 & \dots & \\ & & \dots & 0 & -2 \\ & \mathbf{0} & & j-1 & 0 & -1 \\ & & & & j & 0 \end{pmatrix}, \quad \mathbf{B}_{k,k+2} = \begin{pmatrix} 0 & 0 & 0 & 0 & \dots & 0 & 0 \\ 0 & 0 & -1 & 0 & \dots & 0 & 0 \\ 0 & 0 & 0 & -2 & \dots & 0 & 0 \\ \vdots & \vdots & \vdots & \vdots & \ddots & \vdots & \vdots \\ 0 & 0 & 0 & 0 & \dots & -k & 0 \end{pmatrix}. \tag{7}$$

The approximation of the solution of Eq. (4) is written as

$$\widehat{x}_1(t) = \mathbf{e}_1^{\mathrm{T}} e^{\mathbf{C}_n t}\mathbf{y}_0(A), \quad \widehat{x}_2(t) = \mathbf{e}_2^{\mathrm{T}} e^{\mathbf{C}_n t}\mathbf{y}_0(A), \tag{8}$$

where $\mathbf{e}_1$ and $\mathbf{e}_2$ are standard basis vectors. The approximate solution $\widehat{x}_2(t)$ can be written as power series of A, i.e.,

$$\widehat{x}_2(t) = \sum_{k=1}^{n} \tilde{x}_{2,k}(t) \frac{A^k}{k!}. \tag{9}$$

The period $T(A)$ of system (4) is approximated based on [5] as

$$T(A) = 2\pi + \Delta T(A) = 2\pi + \sum_{k=1}^{n} A^k \widetilde{T}_k. \tag{10}$$

The coefficients $\tilde{x}_{2,k}(t)$ in Eq. (9) at the period $T(A)$ are expressed as

$$\tilde{x}_{2,k}(T(A)) = \tilde{x}_{2,k}(2\pi + \Delta T(A)) = \tilde{x}_{2,k}(2\pi) + \sum_{m=1}^{n} \tilde{x}_{2,k}^{(m)}(2\pi) \frac{\Delta T(A)^m}{m!}, \tag{11}$$

where $\tilde{x}_{2,k}^{(m)}$ denotes the mth derivative. Since Eq. (4) is a conservative system [4], $\widehat{x}_2(T(A)) = 0$ must hold . Balancing the terms

$$\begin{aligned} A &: 0 = \tilde{x}_{2,1}(2\pi), \\ A^2 &: 0 = \tilde{x}_{2,2}(2\pi) + \tilde{x}'_{2,1}(2\pi)\widetilde{T}_1, \\ A^3 &: 0 = \tilde{x}_{2,3}(2\pi) + \tilde{x}'_{2,2}(2\pi)\widetilde{T}_1 + \tilde{x}'_{2,1}(2\pi)\widetilde{T}_2 + \tilde{x}''_{2,1}(2\pi)\frac{\widetilde{T}_1^2}{2!}, \\ &\vdots \end{aligned} \tag{12}$$

where the primes mean derivation. System (12) is solved for the unknown $\widetilde{T}_k$'s.
Using the Carleman linearization of order $n = 9$ of system (4) the approximation of the period reads as

$$T(A) \approx 2\pi \left(1 - \frac{1}{8}A^2 + \frac{1}{256}A^4 + \frac{5}{6144}A^6 - \frac{7}{262144}A^8\right), \tag{13}$$

the same as in Eq. (3). The following table shows some numerical results in case of $n = 5,\ 7,\ 9$ order Carleman matrices.

		$n=5$		$n=7$		$n=9$	
A	$T_{exact}(A)$	$T(A)$	Rel. error [%]	$T(A)$	Rel. error [%]	$T(A)$	Rel. error [%]
0.01	6.2831	6.2831		6.2831		6.2831	
0.1	6.2753	6.2753		6.2753		6.2753	
1	5.5272	5.5223	0.088	5.5274	0.004	5.5273	0.001
1.5	4.6903	4.6403	1.065	4.6985	0.176	4.6942	0.085
2	3.7613	3.5343	6.036	3.8615	2.644	3.8186	1.522
2.2	3.4131	3.0568	10.44	3.6366	6.547	3.5445	3.850

Conclusions

A new way of calculation for the period of a nonlinear oscillator was introduced. Approximate period values of a given oscillator were calculated and compared to exact ones. We conclude, in the case of small amplitudes, Carleman linearization can be used for approximation of the period of a nonlinear oscillator.

Acknowledgements

The research reported in this paper was supported by the Higher Education Excellence Program of the Ministry of Human Capacities in the frame of the Water Science & Disaster Prevention research area of Budapest University of Technology and Economics (BME FIKP-VÍZ). The research reported in this paper has been supported by the National Research, Development, and Innovation Fund (TUDFO/51757/2019-ITM, Thematic Excellence Program). This project was supported by the UNKP-19-3-II New National Excellence Program of the Ministry of Human Capacities of Hungary.

References

[1] Hubay C.Á., Kalmár-Nagy T. (2019) Computing Poincaré-Lyapunov Constants via Carleman Linearization. *Volume 6: 15th International Conference on Multibody Systems, Nonlinear Dynamics, and Control*.

[2] Mickens R.E. (2006) Investigation of the properties of the period for the nonlinear oscillator $\ddot{x} + (1 + \dot{x}^2)x = 0$. *Journal of Sound and Vibration* **292(3-5):**1031-1035.

[3] Beléndez A., Hernandez A., Beléndez T., Neipp C., Márquez A. (2007) Asymptotic representations of the period for the nonlinear oscillator. *Journal of Sound and Vibration* **299(1-2):**403-408.

[4] Kalmár-Nagy T., Erneux T. (2008) Approximating small and large amplitude periodic orbits of the oscillator $\ddot{x} + (1 + \dot{x}^2)x = 0$. *Journal of Sound and Vibration* **313(3-5):**806-811.

[5] Kuznetsov N. V., Leonov G. A. (2008) Computation of Lyapunov quantities. *6th EUROMECH Nonlinear Dynamics Conference* **(3)**.

Time integration based stability calculation for delayed periodic system with linear time complexity

Daniel Bachrathy*,Kristof Nagy*
* *MTA-BME Lendület Machine Tool Research Group, Department of Applied Mechanics, Budapest University of Technology and Economics*

Summary. In this work, the implicit subspace iteration method is combinded with direct time integration of linear periodic delay differential equations. The linear time complexity of the proposed method is shown for different DDE solvers with higher order convergence. The propoesed method is really efficinet for dynamical system with large time period.

Semi-Discretization Method

There have been many algorithms [1, 5, 6, 7] developed during the last 20 years for systems where the time-delay effect is coupled with parametric excitation. The semi-discretization method (SDM) is one of the efficient ways to the analyze stability [1, 2]. The basic idea of the SDM is the numerical discretization of the delayed terms only above the delay-time interval. Consequently, the governing DDE becomes an ordinary differential equation (ODE) that can be solved in closed form in linear cases for each time step within these discrete delay-intervals, and a linear discrete map is constructed that describes the connection of the discretized state as a large vector over the discrete time instants within the delay interval. The size of this mapping depends on the resolution of the delay discretization.
If explicit time-periodicity also appears due to the parametric excitation, the time-periodic coefficients (or even the delays) should also be discretized in time over the time period, and the above procedure leads to different linear mappings at each sampled instant of the time period:

$$\mathbf{z}_{i+1} = \mathbf{G}_i \mathbf{z}_i \quad i = 0, 1, \dots n-1 \tag{1}$$

Here, $\mathbf{G}_i$ denotes the coefficient matrix connecting states $\mathbf{z}_i$ and $\mathbf{z}_{i+1}$, which are the vectors of the discretized states sampled at the discrete time intervals at subsequent time instants. A discrete map can be defined between the initial delay-discrete state $\mathbf{z}_0$ and the one $\mathbf{z}_m$ a principal period later:

$$\mathbf{z}_n = \mathbf{G}_{m-1} \dots \mathbf{G}_2 \mathbf{G}_1 \mathbf{G}_0 \mathbf{z}_0 = \mathbf{\Phi} \mathbf{z}_0, \tag{2}$$

where the transition matrix $\mathbf{\Phi}$ is a finite-dimensional approximation of the infinite-dimensional monodromy operator. Thus, the stability analysis is reduced to the problem whether the absolute values of all the eigenvalues of $\mathbf{\Phi}$ are less than one: $|\mu_i| < 1$. In order to improve numerical accuracy, the delay resolution, the order of semi-discretization, and the time periodicity resolution can be increased.

Implicit Subspace Iteration

Consider the general eigenvalue problem [4] $\mathbf{\Phi S} = \mathbf{S}\boldsymbol{\mu}$, where $\mathbf{\Phi}$ is an $\mathbb{R}^{n\times n}$ square matrix, $\boldsymbol{\mu}$ is a diagonal matrix of size $\mathbb{R}^{n\times n}$ containing the eigenvalues of $\mathbf{\Phi}$ on its main diagonal, and matrix $\mathbf{S}$ of size $\mathbb{R}^{n\times n}$ consists of the eigenvectors of $\mathbf{\Phi}$ in its columns. A set of $N_s < n$ dominant eigenvectors corresponding to the first N_s eigenvalues of the largest absolute values can be approximated in an iterative way. Let $\mathbf{S}_j$ of size $\mathbb{R}^{n\times N_s}$ denote the matrix of the N_s dominant eigenvectors after the jth iteration step. Starting from a random set of initial conditions $\mathbf{S}_0$ and taking an iteration, a new set $\mathbf{V}_j$ of size $\mathbb{R}^{n\times N_s}$ can be calculated according to the following iteration [4]

$$\mathbf{V}_j = \mathbf{\Phi} \mathbf{S}_j \tag{3}$$

$$\mathbf{V}_j \approx \mathbf{S}_j \mathbf{H}_j \;\rightarrow \mathbf{H}_j = \left(\mathbf{S}_j^{\mathrm{H}} \mathbf{S}_j\right)^{-1} \mathbf{S}_j^{\mathrm{H}} \mathbf{V}_j \tag{4}$$

$$\mathbf{H}_j = \mathbf{G}_j \boldsymbol{\lambda}_j \mathbf{G}_j^{-1} \tag{5}$$

$$\mathbf{S}_{j+1} = \mathbf{V}_j \mathbf{G}_j \tag{6}$$

where $\mathbf{G}_j$ is the matrix formed by the eigenvectors of $\mathbf{H}_j$ and $\boldsymbol{\lambda}_j$ is a diagonal matrix of eigenvalues of $\mathbf{H}_j$. Note, that in a numerical implementation, the approximated eigenvectors should be normalized after each iteration steps.
If $\mathbf{S}_j$ is obtained after a sufficient number of iteration steps, it will converge to the dominant eigenvectors, and the basis formed by the column vectors in both $\mathbf{S}_j$ and $\mathbf{V}_j$ span approximately the same space. Therefore, an approximate matrix $\mathbf{H}_j$ of size $\mathbb{R}^{N_s\times N_s}$ connecting $\mathbf{S}_j$ and $\mathbf{V}_j$ can be obtained using a pseudo-inverse calculation from the relation. After several iteration steps, the eigenvalues of $\mathbf{H}_j$ provide a good approximation for the dominant eigenvalues of $\mathbf{\Phi}$. This way, it is enough to compute the eigenvalues of a significantly reduced N_s-sized matrix $\mathbf{H}_j$ instead of the large n-sized matrix $\mathbf{\Phi}$. The details of this iteration process can be found in [3, 4].
In this form, the Implicit Subspace Iteration iteration is just an iterative method to find the eigenvalues of a known matrix $\mathbf{\Phi}$, however, the calculation of this matrix itself is the most time consuming operation if the time period is long $m \gg n$.

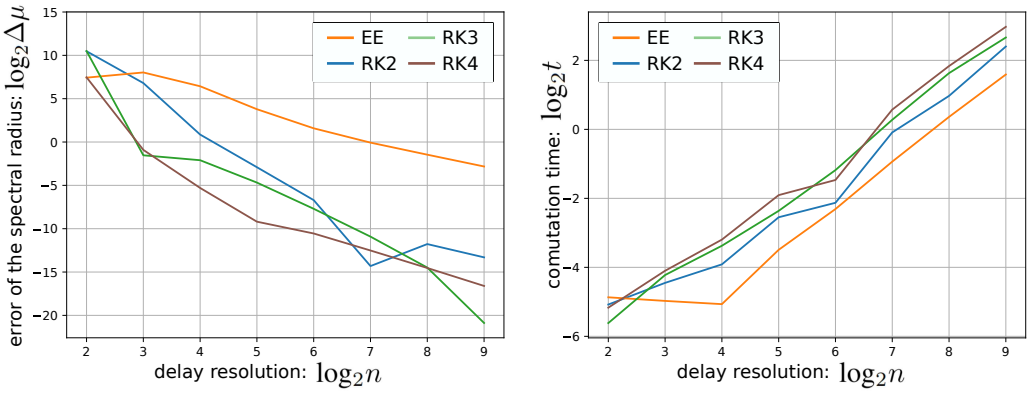

Figure 1: Convergence of thee spectral radius for the tradition SDM and for Implicit Sub Space Iteration combined with time integration with Explicit Euler (EE) method and higher-order Runge-Kutta methods

Dute to the m number of matrix multiplication in Eq.(2), the time complexity is proportional to $\mathcal{O}(mn^3)$, if a spares representation of $\mathbf{G}_i$ is used then it can tend to $\mathcal{O}(mn^2)$ [8, 9]. To decrease the computational need one can reduce the stepsize (m and n together) and increase the order of semi-discretization, however, it is complicated to increase it above 2 [2].

Direct time integration

It is also possible to determine the mapping in Eq.(3) without calculating the whole matrix $\mathbf{\Phi}$. The vector $\mathbf{V}_j$ can be calculated directly by means of the time integration of the equations of motion of the given system with $\mathcal{O}(m)$ time complexity. Thus, the advantage of implementing the ISIM is that the transition matrix $\mathbf{\Phi}$ does not have to be calculated. During the time integration process, one can use the same approximation as in the SDM (constant coefficients within the time step), then the final results for the eigenvalues will be identical.
However, if we apply time integration, then any advanced higher-order fixed-time-step computation scheme can be used to increasre the reat of convergence of the eigenvalues, while the time complexity will be the same. This is presented for the well-known delayed Mathieu equation:

$$\ddot{x}(t) + \kappa\dot{x}(t) + (\delta + \epsilon cos(\omega t))\, x = bx(t-\tau). \tag{7}$$

In Fig.1 the error of the largest multiplier is shown for paramteres $\kappa = 0.01, \delta = 5, \epsilon = 1, b = 1, \tau = 2\pi, \omega = 0.01$ (note, that $m = 100n$). The reference values for the eigenvalues is computed of $n = 2^15$.

Conclusions

The combination of the IISI with fixed-step-time-integration have only a linear time complexity and the convergence rate of the eigenvalues is the same as the order of the integration scheme. The next research goal is to the implement integrators with variable step size, which will have a great advantage in the case when the change of the coefficients of the governing equation are not smooth, however, the non-uniform steps size leads to a difficulty in the computation of $\mathbf{H}_j$ in Eq.(4).

Acknowledgement

This paper was supported by the Hungarian Scientific Research Fund OTKA FK-124462 and PD-124646.

References

[1] T. Insperger, Full-discretization and semi-discretization for milling stability prediction: Some comments, *Int. J. Mach. Tool Manu.* (2010) **50**:658-662

[2] T. Insperger, G. Stepan, J. Turi, On the higher-order semi-discretizations for periodic delayed systems. *J. Sound Vib.* (2008) **313**:334-341

[3] M. Zatarain, Z. Dombovari, Stability analysis of milling with irregular pitch tools by the implicit subspace iteration method, Springer-Verlag, Berlin, 2014

[4] M. Zatarain, J. Alvarez, I. Bediaga, J. Munoa, Z. Dombovari, Implicit subspace iteration as an efficient method to compute milling stability lobe diagrams, *Int. J. Adv. Manuf. Technol.* (2015) **77**:597-607

[5] G. M. Hulbert, Time Finite Element Methods for Structural Dynamics, *Int. J. Num. Meth. in Eng.* (1992) **33**:307-331

[6] E. Budak, Y. Altintas, Analytical prediction of chatter stability conditions for multi-degree of systems in milling, *Transactions of ASME Journal of Dynamic Systems Measurement and Control*, (1998) **120**:22-30

[7] P. V. Bayly, J. E. Halley, B. P. Mann, Davies, M. A. Stability of interrupted cutting by temporal finite element analysis. *Journal of Manufacturing Science and Engineering*, (2003) **125**(2):220-225

[8] C. Henninger, P. Eberhard, Improving the computational efficiency and accuracy of the semi-discretization method for periodic delay-differential equations. *European Journal of Mechanics A/Solids* (2008) **27**:975âĂŞ985

[9] T. Insperger, and G. Stepan, Semi-discretization for time-delay systems: stability and engineering applications. *Springer Science Business Media*, 2011. **178**

Uni-directional wave propagation in time-modulated inerter-based lattice

Danilo Karličić *, Milan Cajić †, Stepa Paunović * and Sondipon Adhikari ‡
* *Mathematical institute of the Serbian Academy of Sciences and Arts, Belgrade, Serbia*
† *College of Engineering, Swansea University, United Kingdom*
‡*James Watt School of Engineering,University of Glasgow, Glasgow, UK*

Summary. In this work, we investigate the uni-directional wave propagation in elastic locally resonant mechanical metamaterials with inerter elements, where mass and stiffness properties are simultaneously modulated as periodic functions of time. Time-modulated properties of inerter elements are adopted in order to highlight the effect of time-dependent inertia amplification on mass properties. By considering the Bloch theorem and Fourier expansion, the system of Hill equations is reduced to the eigenvalue problem that gives dispersion relations with asymmetric frequency band structures.

Formulation of the problem

Let us consider the mass-spring-inerter systems representing the locally resonant mechanical metamaterial (LRMM) lattice as shown in Figure 1. The model consists of the periodically repeated mass-spring-inerter blocks connected into an infinite chain. The local resonators are represented by small inner masses inside the host outer masses. The local resonators are introduced into the lattice due to the well know properties of generating low-frequency band gaps in the metamaterial structures. Bloch wave propagation analysis is performed for the corresponding unit cell by applying the proper periodic boundary conditions. Figure 1 illustrates the n-th unit cell of the LRMM lattice, which is bounded by red dashed rectangle and it consists of three identical mass-in-mass subsystems connected through time-modulated springs and inerters. Moreover, each mass-in-mass subsystem is connected to the ground through pairs of time-modulated springs and inerters. Note that internal resonators are also connected to the host mass through a time-modulated spring.

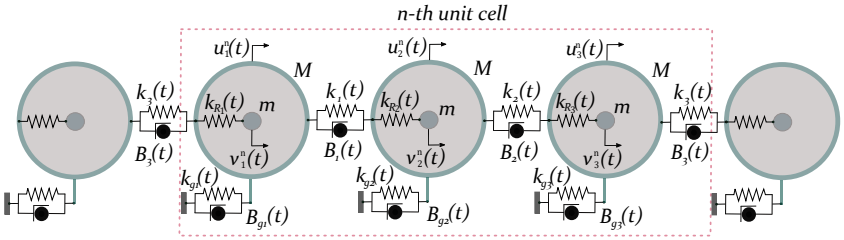

Figure 1: The unit cell of the inerter-based LRMM lattice.

Mathematical model

The governing equations of the locally resonant lattice with time varying stiffness and inerter properties for the n-th unit cell (Figure 1) can be expressed, in a general case, as a system of ordinary differential equations with time dependent coefficients, known as Hill equations [1], as follows

$$M\ddot{u}_r^n + k_{r-1}(t)(u_r^n - u_{r-1}^n) + k_r(t)(u_r^n - u_{r+1}^n) + k_{gr}(t)u_r^n + k_{Rr}(t)(u_r^n - v_r^n) + B_{r-1}(t)(\ddot{u}_r^n - \ddot{u}_{r-1}^n) + \tag{1}$$
$$B_r(t)(\ddot{u}_r^n - \ddot{u}_{r+1}^n) + B_{gr}(t)\ddot{u}_r^n + \dot{B}_{r-1}(t)(\dot{u}_r^n - \dot{u}_{r-1}^n) + \dot{B}_r(t)(\dot{u}_r^n - \dot{u}_{r+1}^n) + \dot{B}_{gr}(t)\dot{u}_r^n = 0,$$
$$m\ddot{v}_r^n + k_{Rr}(t)(v_r^n - u_r^n) = 0, \tag{2}$$

where $r = 1, ..., R$, R is the number of masses in the n-th unit cell.
In order to study the uni-directional wave propagation in the time-modulated one-dimensional lattice structure we limit our analysis to the case when $R = 3$. The differential equation (1) describes the motion of the r-th point mass in the n-th unit cell, and differential equation (2) describes the motion of the internal resonator.

Solution procedures

Plane wave method is applied by considering the Fourier series expansion of displacement vector and time-dependent mass and stiffness matrices. We assume that mass and stiffness matrices are modulated with the velocity $v_m = \frac{\lambda_m}{T_m}$. The terms λ_m and T_m are related to the spatial wave length and temporal period of modulation, respectively. By considering the inverse method explained in [2], the plane wave solution of the time-varying lattice model presented in equations (1) and (2) can be assumed in Bloch-Fourier form [3] as

$$\mathbf{u}_n(t) = e^{i(-n\mu+\omega t)} \sum_{p=-\infty}^{\infty} \mathbf{a}_p e^{ip\omega_m t}, \tag{3}$$

where $\mathbf{a}(t) = \mathbf{a}(t + T_m)$ is the vector of periodic amplitude function in time and $\mu = \lambda_m \kappa$ is the non-dimensional wavenumber. Considering the truncated expansion from equation (3), the system of differential equations is reduced to

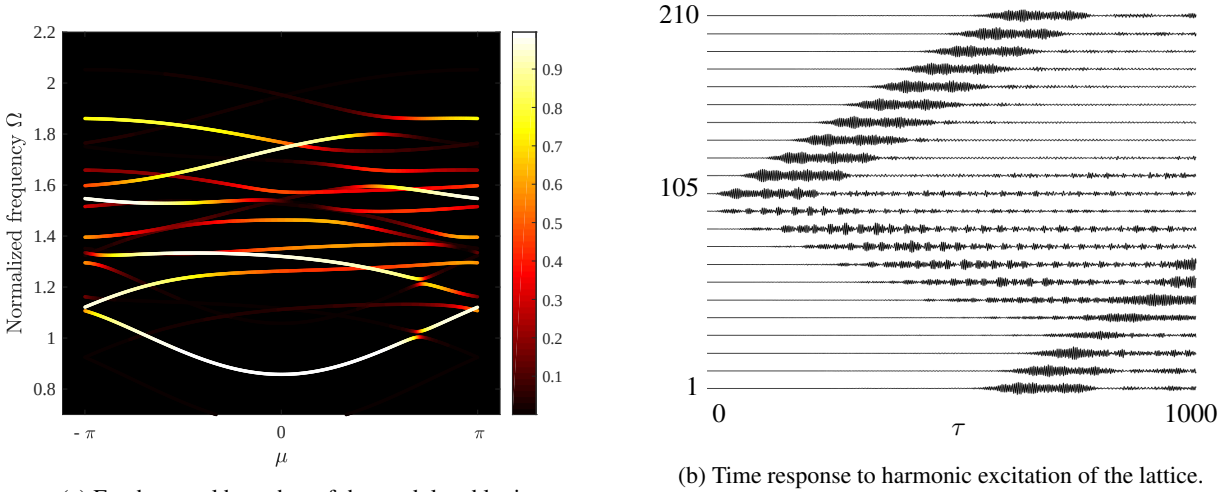

(a) Fundamental branches of the modulated lattice.

(b) Time response to harmonic excitation of the lattice.

Figure 2: The local resonant structure with time varying inerter and stiffness properties.

the system of $(R + N_r)(2P + 1)$ algebraic equations. Therefore, by taking the values of $P = 1$ and $Q = 2$ in equation (3) the system (1) is reduced to the following quadratic eigenvalue problem

$$(\Omega^2 \mathbf{A}_1 + \Omega \mathbf{A}_2 + \mathbf{A}_3)\mathbf{a} = \mathbf{0}, \tag{4}$$

where $\Omega = \omega/\omega_0$ and $\mathbf{a}$ are eigenvalues and eigenvectors of the system, respectively.

Numerical results

The aim of the numerical study is to verify the applicability of the above proposed method based on the Bloch-Fourier expansion and to perform the dispersion analysis of the time-modulated periodic elastic lattice with local resonators given in the form of one-dimensional chain with inerters (Figure 2a). Moreover, the uni-directional wave propagation is observed based on the solution of the system of equations using the finite difference method for a specified excitation frequency (Figure 2b).

By considering the simultaneous time-modulation of stiffness and inertia properties, the dispersion characteristic of the lattice is presented in Figure 2a. The diagrams show many crossings and folding of dispersion branches within, and at the edges of the first Brillouin zone. The fundamental branches are obtained by using the weighting and threshold process. Moreover, the asymmetric band gaps can be observed for the presented configuration, from which we can find specter of frequencies which can lead to asymmetric or uni-directional wave propagation. Finally, to demonstrate the uni-directional wave propagation we apply the harmonic excitation on the center mass of the finite chain with the picked frequency $\Omega = 1.7$. The finite chain has 70 unit cells and Born–von Karman boundary conditions are applied at the ends of the chain. We observe only the displacement amplitudes of outer masses of the chain. The spatial profile in Figure 2b indicates one way traveling of the primary wave in the positive direction $+x$. However, it can be noticed that a small portion of wave energy is traveling in the opposite direction, which can be attributed to the fact that the corresponding asymmetric band gap is influenced by internal resonators of the LRMM lattice.

Conclusions

In this study, we numerically demonstrate how uni-directional wave propagation can occur in time-modulated elastic and locally resonant metamaterial lattices with inerters. We successfully included inerter elements in the lattice structure demonstrating the shift of dispersion frequencies to lower values due to the inertia amplification effect. The Bloch-Fourier based procedure is suggested to analyze the dispersion characteristics of systems with simultaneous time-modulation of stiffness and mass properties. Dispersion characteristic is used to confirm the existence of asymmetric band gaps and then applied as a basis for transient analysis and demonstration of uni-directional wave propagation.

References

[1] Richards, John A. Analysis of periodically time-varying systems. Springer Science & Business Media, 2012.

[2] Hussein, Mahmoud I and Leamy, Michael J and Ruzzene, Massimo. Dynamics of phononic materials and structures: Historical origins, recent progress, and future outlook. *Applied Mechanics Reviews*, 66(4), 2014.

[3] Vila, Javier and Pal, Raj Kumar and Ruzzene, Massimo and Trainiti, Giuseppe. A bloch-based procedure for dispersion analysis of lattices with periodic time-varying properties. *Journal of Sound and Vibration*, 406 : 363-377, 2017.

Energy flow characteristics of periodical orbits of nonlinear dynamical systems

Jing Tang Xing
Maritime Engineering, Faculty of Engineering & Physical Sciences, Boldrewood Campus, University of Southampton, Southampton SO16 7QF, UK

Summary. Based on energy flow theory, it is revealed that a necessary sufficient condition for nonlinear dynamical systems (NDS) $\dot{\mathbf{y}} = \mathbf{f}(\mathbf{y}, t)$ to have periodical orbits is that there exist a non-zero spin matrix and one closed orbit with a corresponding period *T*, along which the time averaged flows of generalised potential energy (GPE) and generalised kinetic energy (GKE) vanish. For autonomous systems, a necessary condition to have periodical orbits is the energy flow characteristic factors (EFCFs) must not be semi-positive or semi-negative. Three examples are given to support the above revealed characteristics.

Keywords: Nonlinear dynamics, Periodical orbits, Energy flow matrices, Spin matrices, Generalised potential / kinetic energies.

Introduction

NDS investigated herein are generally sufficient to regard a second order differential equation with its initial conditions in a non-dimensional form, as discussed by [1-5], which can be transformed into the first order differential equation

$$d\mathbf{y}/dt \equiv \dot{\mathbf{y}} = \mathbf{f}(t, \mathbf{y}), \qquad \mathbf{y}(0) = \mathbf{y}_0. \tag{1}$$

We consider that $\mathbf{y} = \mathbf{y}(t) \in R^n$ is a vector valued function of an independent variable $t \in I = (t_1, t_2) \subseteq R$ and $\mathbf{f}: U \to R^n$ is a smooth function of variable t and vector $\mathbf{y}$ defined on some subset $U \subseteq R^n$, an *n*-dimensional phase space, and we seek a solution $\boldsymbol{\varphi}(\mathbf{y}_0, t)$ such that

$$\boldsymbol{\varphi}(\mathbf{y}_0, 0) = \mathbf{y}_0. \tag{2}$$

The solution $\boldsymbol{\varphi}(\mathbf{y}_0, \cdot): I \to R^n$ defines a solution curve, trajectory or orbit of Eq.1 based at $\mathbf{y}_0$ as shown by Fig. 1(a). According to the basic local existence and uniqueness theorem [6], there exist no intersections of the trajectories of Eq.1 in the solution space except at its fixed points. The solution curves $\boldsymbol{\varphi}_t(U)$ generate the flow shown by Fig. 1(b).To investigate the behaviors of NDS, Xing [5] developed an energy flow theory, which has discovered that i) GPE automatically plays a role of Lyapunov function for stability at fixed points of NDS, ii) generalised energy conservation law of chaotic motions [5,7], iii) behaviors of friction-induced vibrations [8]. This paper aims to tackle the periodical solutions of NDS to reveal its energy flow characteristics.

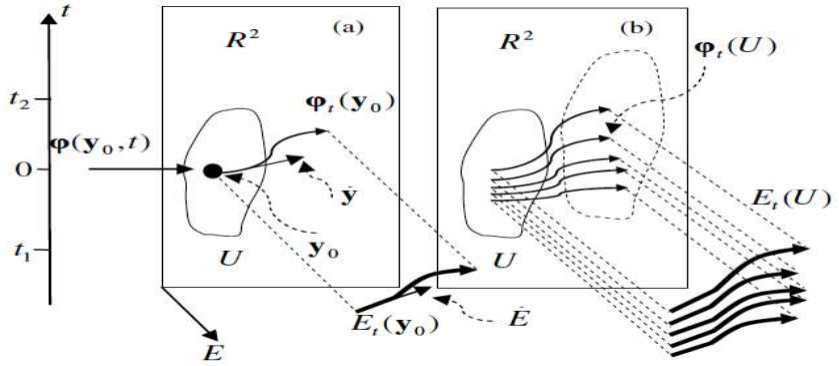

Figure 1: (a) a solution curve $\boldsymbol{\varphi}_t(\mathbf{y}_0)$ with its energy flow curve $E_t(\mathbf{y}_0)$, of which their tangent vectors at a point $\mathbf{y}$ are $\dot{\mathbf{y}} = \mathbf{f}$ and $\dot{E}$, respectively; (b) the flow $\boldsymbol{\varphi}_t(U)$ and the energy flow $E_t(U)$ in R^n (Xing [5, 7]).

Fundamentals of energy flow analysis

Energy flow variables, matrices, and equations

In the energy flow theory, the following energy flow variables based on Eq.1 in phase space are defined,

$$\text{GPE: } E = 0.5\mathbf{y}^T\mathbf{y}; \qquad \text{GKE: } K = 0.5\dot{\mathbf{y}}^T\dot{\mathbf{y}}; \quad \text{Force power: } P = \mathbf{y}^T\mathbf{f}, \tag{3}$$

of which the time averaged GPE and GKE as well as the time averaged GPE-flow (GPEF) and the time averaged GKE-flow (GKEF) during a period $(0, T)$ are respectively defined by

$$\langle E \rangle = \int_0^T 0.5\mathbf{y}^T\mathbf{y}\, dt/T, \qquad \langle K \rangle = \int_0^T 0.5\dot{\mathbf{y}}^T\dot{\mathbf{y}}\, dt/T, \qquad \langle P \rangle = \int_0^T \mathbf{y}^T\mathbf{f}\, dt/T,$$
$$\langle \dot{E} \rangle = \int_0^T \dot{E}\, dt/T = [E(T) - E(0)]/T = \int_0^T P\, dt/T = \langle P \rangle, \tag{4}$$

$$\langle \dot{K} \rangle = \int_0^T \dot{K}\, dt/T = [K(T) - K(0)]/T = \int_0^T \dot{\mathbf{y}}^T \dot{\mathbf{f}}\, dt/T\ .$$

The corresponding energy flow equilibrium equations take the forms

$$\dot{E} = \dot{P}, \quad E_0 = 0.5\mathbf{y}_\mathbf{0}^T\mathbf{y}_\mathbf{0}, \quad \mathbf{J} = \partial\mathbf{f}/\partial\mathbf{y}^T, \quad \mathbf{E} = 0.5(\mathbf{J} + \mathbf{J}^T), \quad \mathbf{U} = 0.5(\mathbf{J} - \mathbf{J}^T),$$

$$\dot{K} = \dot{\mathbf{y}}^T\ddot{\mathbf{y}} = \dot{\mathbf{y}}^T\dot{\mathbf{f}} = \dot{\mathbf{y}}^T(\partial\mathbf{f}/\partial t + \mathbf{J}\dot{\mathbf{y}}) = \dot{\mathbf{y}}^T\,\partial\mathbf{f}/\partial t + \dot{\mathbf{y}}^T\mathbf{E}\dot{\mathbf{y}} = \partial K/\partial t + \dot{\mathbf{y}}^T\mathbf{E}\dot{\mathbf{y}}, \tag{5}$$

where **J** is *Jacobian* matrix, the partial derivative of vector **f** with respect to vector $\mathbf{y}^T$ [5]. For autonomous NDS from Eq. 5 we have

$$\dot{\mathbf{y}} = \mathbf{f}(\mathbf{y}), \qquad \dot{K} = \dot{\mathbf{y}}^T\mathbf{E}\dot{\mathbf{y}}, \qquad \langle \dot{K} \rangle = \tfrac{1}{T}\textstyle\int_0^T \dot{\mathbf{y}}^T\mathbf{E}\dot{\mathbf{y}}\, dt, \tag{6}$$

since $\partial K/\partial t = 0$. Here **E** is a real symmetrical *energy flow matrice* while **U** is a real skew-symmetrical *spin matrix*, so that $\mathbf{y}^T\mathbf{U}\mathbf{y} = \mathbf{0} = \dot{\mathbf{y}}^T\mathbf{U}\dot{\mathbf{y}}$**.** Geometrically, GPE relates the position **y** of a point in phase space, while GKE involves the velocity or tangent vector $\dot{\mathbf{y}}$ of solution curve, and the generalised force power *P* gives the energy flow, the time change rate of GPE.

Energy flow characteristic factors

The energy flow matrix **E** is a real symmetrical matrix, of which the eigenvalues and the corresponding eigenvectors are real, and its characteristic equation

$$\mathbf{E}\boldsymbol{\varepsilon} = \lambda\boldsymbol{\varepsilon}, \qquad |\mathbf{E} - \lambda\mathbf{I}| = 0, \tag{7}$$

can give the eigenvalue λ_I and its corresponding eigenvector $\boldsymbol{\psi}_I$ satisfying the orthogonal relationships

$$\boldsymbol{\Psi}^T\mathbf{E}\boldsymbol{\Psi} = \boldsymbol{\Lambda} = \mathbf{diag}(\lambda_I), \quad \boldsymbol{\Psi}^T\boldsymbol{\Psi} = \mathbf{I}, \quad \boldsymbol{\Psi} = [\boldsymbol{\psi}_1 \quad \boldsymbol{\psi}_2 \quad \cdots \quad \boldsymbol{\psi}_n]. \tag{8}$$

Normally, the eigenvectors with different eigenvalues span a complete subspace in the neighbor of the point where the matrix **E** defined, so that the vector $\boldsymbol{\varepsilon}$ can be represented as

$$\boldsymbol{\varepsilon} = \boldsymbol{\Psi}\boldsymbol{\zeta}, \tag{9}$$

which, when substituted into the term $\boldsymbol{\varepsilon}^T\mathbf{E}\boldsymbol{\varepsilon}$ and by using the orthogonal relationships in Eq.8, gives

$$\boldsymbol{\varepsilon}^T\mathbf{E}\boldsymbol{\varepsilon} = \boldsymbol{\zeta}^T\boldsymbol{\Psi}^T\mathbf{E}\boldsymbol{\Psi}\boldsymbol{\zeta} = \boldsymbol{\zeta}^T\boldsymbol{\Lambda}\boldsymbol{\zeta} = \textstyle\sum_{I=1}^n \lambda_I\,\zeta_I^2. \tag{10}$$

This result implies that the value of $\boldsymbol{\varepsilon}^T\mathbf{E}\boldsymbol{\varepsilon}$ about a point is totally determined by the eigenvalues and eigenvectors of energy flow matrix. We respectively call λ_I and $\boldsymbol{\psi}_I$ as the energy flow characteristic factors (EFCFs) and the energy flow characteristic vectors (EFCVs) of NDS.

Spin matrix

The spin matrix **U** is a real skew-symmetric matrix and therefore its non-zero eigenvalues κ_I must be conjugate purely imaginaries with the complex eigenvector matrix **Y** satisfying the following orthogonal relationships

$$\mathbf{Y}^{*T}\mathbf{U}\mathbf{Y} = \mathbf{diag}(\kappa_I), \qquad \mathbf{Y}^{*T}\mathbf{Y} = \mathbf{I}, \tag{11}$$

Here * denotes a conjugate of complex number.

Curl of a vector field

The curl of a vector field **f**, denoted by curl**f**, or $\nabla \times \mathbf{f}$, at a point *O* is defined in terms of its projection onto various lines through the point. As shown in Fig.2, if **ν** is a unit vector, the projection of the curl**f** onto **ν** is defined as a limited value of a closed-curve integral in a plane orthogonal to **ν**, divided by the area *A* enclosed by the closed curve. Here, the path *C* of integration is constructed around the point *O*, so that, when Eqs. 1 and 3 are introduced, we have

$$(\nabla \times \mathbf{f})_\nu = \lim_{A\to 0}\left\{\oint_C \mathbf{f}\cdot d\mathbf{y}/A\right\} = \lim_{A\to 0}\left\{\oint_C \dot{\mathbf{y}}\cdot\dot{\mathbf{y}}/A\right\} = \lim_{A\to 0}\left\{\oint_C 2K dt/A\right\}. \tag{12}$$

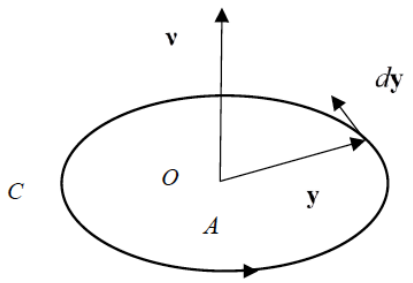

Figure 2: Circulation integration of path *C* with its positive direction obeying the right-hand rule to define the curl of vector field **f**.

For 3-dimensional space, the curl**f** can be denoted in a tensor form

$$(\nabla \times \mathbf{f})_i = e_{ijk} f_{k,j}, \tag{13}$$

where e_{ijk} is the permutation tensor [9,10]. The curl**f** is a dual vector of a skew-symmetrical matrix **U**, spin matrix, satisfying the following relationship

$$(\mathbf{U})_{ij} = U_{ij} = -0.5 e_{ijk}(\nabla \times \mathbf{f})_k = -0.5 e_{ijk} e_{krs} f_{s,r} = -0.5\left(\delta_{ir}\delta_{js} - \delta_{is}\delta_{jr}\right) f_{s,r} = 0.5\left(f_{i,j} - f_{j,i}\right) = 0.5(\mathbf{J} - \mathbf{J}^T)_{ij}. \tag{14}$$

Periodical orbits

For NDS, a periodical orbit is defined as a closed path governed by Eq. 1 in phase space, along which the phase point $\mathbf{y}(t)$ with its velocity $\dot{\mathbf{y}}(t)$, starting from a position $\mathbf{y}(\hat{t})$ at time $\hat{t}$, moves to the same position $\mathbf{y}(\hat{t}+T) = \mathbf{y}(\hat{t})$ with the same velocity $\dot{\mathbf{y}}(\hat{t}+T) = \dot{\mathbf{y}}(\hat{t})$ after a period *T*, and the motion repeats again, such as $\hat{t} = 0$ shown in Fig.3. If we assume that dS denotes a differential line element with its unit outside normal vector ν_i and unit tangent vector τ_i at a point on the closed curve in Fig.3, so that

$$\boldsymbol{\tau} dS = \dot{\mathbf{y}}|d\mathbf{y}|/|\dot{\mathbf{y}}| = \dot{\mathbf{y}}|\dot{\mathbf{y}}dt|/|\dot{\mathbf{y}}| = \dot{\mathbf{y}}dt, \tag{15}$$

based on which the integrals along the curve in the next section hold.

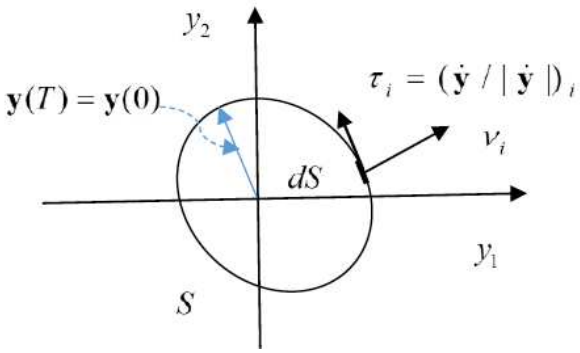

Figure 3: The periodical orbit and the unit normal / tangent vectors of line element dS on orbit.

This definition implies that for a periodical orbit, its position vector should be a periodical function of time. Generally, this periodical function can be represented by a Fourier series of period *T*. For simplifying mathematic formulations but not losing generality, as an example, we consider this function is a sinusoidal function

$$\mathbf{y}(t) = \hat{\mathbf{y}} \sin(\omega t + \hat{\phi}), \qquad \dot{\mathbf{y}}(t) = \hat{\mathbf{y}}\omega \cos(\omega t + \hat{\phi}), \qquad \omega = \frac{2\pi}{T}, \tag{16}$$

where $\hat{\mathbf{y}}$ and $\hat{\phi}$ denote the amplitude and phase angle, ω is a frequency corresponding to the period. From Eq. 16, it follows that GPE and GKE respectively are

$$E = \frac{1}{2}\sin^2(\omega t + \hat{\phi})\,\hat{\mathbf{y}}^T\hat{\mathbf{y}} = 2\hat{E}\sin^2(\omega t + \hat{\phi}), \qquad \hat{E} = \frac{\hat{\mathbf{y}}^T\hat{\mathbf{y}}}{4}, \tag{17}$$
$$K = \frac{1}{2}\cos^2(\omega t + \hat{\phi})\,\hat{\mathbf{y}}^T\hat{\mathbf{y}}\omega^2 = 2\hat{K}\sin^2(\omega t + \hat{\phi}), \qquad \hat{K} = \frac{\hat{\mathbf{y}}^T\hat{\mathbf{y}}}{4}\omega^2 = \omega^2\hat{E}.$$

Energy flow characteristics of periodical orbits of NDS

Based on the definition of periodical orbits governed by Eq. 1, if there exists a periodical orbit, the following energy flow characteristics must hold.

Time averaged GPE

$$\langle E \rangle = \frac{1}{T}\oint_S E dt = \hat{E}, \tag{18}$$

where $\hat{E}$ is a positive constant representing the averaged distance of phase points on the orbit to the origin since *E* is positive and the motion repeats along the closed orbit.

Time averaged GPEF

$$\langle \dot{E} \rangle = \frac{1}{T}\int_{\hat{t}}^{T+\hat{t}} \dot{E}\, dt = \frac{E(T+\hat{t}) - E(\hat{t})}{T} = 0 = \frac{1}{T}\int_{\hat{t}}^{T+\hat{t}} \mathbf{y}^T\mathbf{f}\, dt, \tag{19-1}$$

since for the periodical orbit *S*, $\mathbf{y}(\hat{t}+T) = \mathbf{y}(\hat{t})$. If the vector field **f** takes a form

$$\mathbf{f} = \mathbf{B}(\mathbf{y})\mathbf{y} = (\bar{\mathbf{E}} + \bar{\mathbf{U}})\mathbf{y}, \quad \bar{\mathbf{E}} = (\mathbf{B} + \mathbf{B}^T)/2, \qquad \bar{\mathbf{U}} = (\mathbf{B} - \mathbf{B}^T)/2, \tag{19-2}$$

Eq. 19-1 requires the EFCFs of matrix $\bar{\mathbf{E}}$ not always being semi-positive or semi-negative in the period *T*.

Time averaged GKE

$$\langle K\rangle = \frac{1}{T}\oint_S Kdt = \widehat{K} = \frac{1}{2T}\oint_S \dot{\mathbf{y}}\cdot\dot{\mathbf{y}}dt = \frac{1}{2T}\oint_S \dot{\mathbf{y}}\cdot\boldsymbol{\tau}dt, \tag{20}$$

where $\widehat{K}$ is a positive constant, sine GKE is not negative. From this result, when Eq.12 noticed, it follows that curl**f** must not vanish, so that Eq. 14 implies

$$\mathbf{U} \neq 0. \tag{21}$$

In a reverse case if Eq.21 holds, then Eq. 20 holds. Therefore, Eq. 21 is a necessary and sufficient condition for Eq. 20.

Time averaged GKEF

$$\langle \dot{K}\rangle = \frac{1}{T}\int_{\hat{t}}^{T+\hat{t}} \dot{K}\,dt = \frac{K(T+\hat{t})-K(\hat{t})}{T} = 0 = \frac{1}{T}\int_{\hat{t}}^{T+\hat{t}} (\frac{\partial K}{\partial t} + \dot{\mathbf{y}}^T\mathbf{E}\dot{\mathbf{y}})\,dt, \tag{22-1}$$

For autonomous NDS, $\partial K/\partial t = 0$, from Eq. 10, it follows

$$\langle \dot{K}\rangle = \frac{1}{T}\int_{\hat{t}}^{T+\hat{t}} (\dot{\mathbf{y}}^T\mathbf{E}\dot{\mathbf{y}})\,dt = \frac{1}{T}\int_{\hat{t}}^{T+\hat{t}} (\boldsymbol{\zeta}^T\boldsymbol{\Lambda}\boldsymbol{\zeta})\,dt = \frac{1}{T}\int_{\hat{t}}^{T+\hat{t}} (\sum_{I=1}^{n}\lambda_I\zeta_I^2)\,dt = 0, \tag{22-2}$$

holds, implying that the EFCFs of NDS must not always be semi-positive or semi-negative in the period *T*.

Above equations are valid if exsisting periodical orbits of NDS, so that they are necessary conditions. Considering GPE geometrically involves the distance of a phase point to the origin, we can confirm that for a periodical oribit curve, of which each point has its positive distance to the origin, so that Eq. 18 always is valid. Moreover, as discussed above, the condition in Eq. 21 can replace the Eq. 20, which implies that non-zero spin matrix of NDS is a necessary condition for its periodical orbits.

Theorem A necessary sufficient condition for NDS, governed by Eq. 1, having periodical orbits is that its spin matrix $\mathbf{U} \neq 0$ and there exists at least one closed curve with a corresponding period *T*, along which the time averaged GPEF and GKEF vanish. For autonomous NDS, the condition of time averaged GKEF can be replaced by that its EFCFs of energy flow matrix **E** are always not semi-positive or semi-negative in the period *T*.

Examples

A linear system

As an example, we consider a system with one degree of freedom governed by equation

$$\ddot{x} + \alpha\dot{x} + x = f\cos t, \tag{23-1}$$

which can be rewritten in the form of phase space

$$\begin{bmatrix}\dot{x}\\ \dot{y}\end{bmatrix} = \begin{bmatrix}0 & 1\\ -1 & -\alpha\end{bmatrix}\begin{bmatrix}x\\ y\end{bmatrix} + \begin{bmatrix}0\\ f\cos t\end{bmatrix}, \tag{23-2}$$

with its Jacobian, energy flow, spin matrices and energy flow equation respectively as follows

$$\mathbf{J} = \begin{bmatrix}0 & 1\\ -1 & -\alpha\end{bmatrix} = \mathbf{B}, \bar{\mathbf{E}} = \begin{bmatrix}0 & 0\\ 0 & -\alpha\end{bmatrix}, \bar{\mathbf{U}} = \begin{bmatrix}0 & 1\\ -1 & 0\end{bmatrix}, \dot{E} = -\alpha y^2 + yf\cos t\,,\ \dot{K} = \frac{\partial K}{\partial t} - \alpha y^2 = -\alpha y^2 - \dot{y}f\sin t. \tag{23-3}$$

The time averaged GPEF and GKEF of the system are respectively given by

$$\langle \dot{E}\rangle = \frac{1}{2\pi}\int_0^{2\pi}(-\alpha y^2 + yf\cos t)dt, \qquad \langle \dot{K}\rangle = \frac{1}{2\pi}\int_0^{2\pi}(-\alpha y^2 - \dot{y}f\sin t)dt. \tag{23-4}$$

It is not difficult to obtain the EFCFs of the system

$$\bar{\lambda}_1 = -\alpha, \qquad \bar{\lambda}_2 = 0, \tag{23-5}$$

implying they are semi-positive for $\alpha < 0$, semi-negative for $\alpha > 0$, and vanish when $\alpha = 0$. Based on the above results, we discuss its two cases as follows.

Non-forced case $f = 0$

For this case, the time averaged GPEF and GKEF have the values

$$\langle \dot{E}\rangle = \langle \dot{K}\rangle = \begin{cases} > 0, & \alpha < 0,\\ < 0, & \alpha > 0,\\ = 0, & \alpha = 0.\end{cases} \tag{23-6}$$

As shown in Fig. 4, from this result it follows that the system is a divergence one when $\alpha < 0$, due to time averaged GPEF and GKEF are always increasing and the orbit tends to infinite; while it is a converged one when $\alpha > 0$, the orbit tends to the origin of phase space. There are no periodical orbits for non-zero values of parameter α although the spin matrix of the system is not zero. Also, EFCFs are semi-positive or semi-negative which do not satisfy the conditions in

Theorem. When $\alpha = 0$ the system has its periodical orbit of radius $\rho = \sqrt{x_0^2 + y_0^2}$ depending on the initial condition (x_0, y_0) shown in Fig.4.

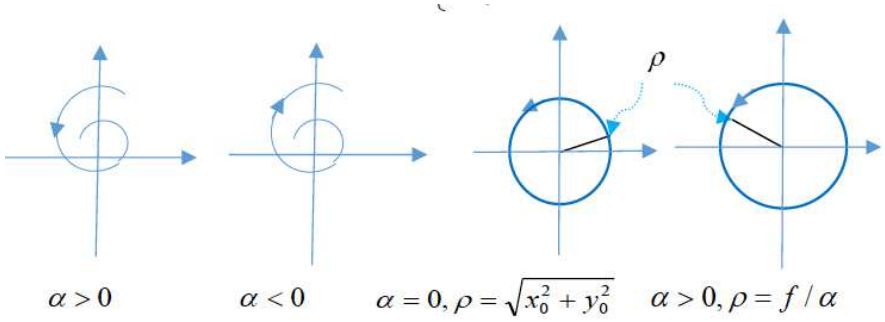

Figure 4: The orbits of 1-DOF system affected by the damping parameter α and external force *f*.

Forced case $f \neq 0, \alpha > 0$
For this case, since the system is linear, we know the solution of system is

$$x = \rho \sin t, \quad y = \rho \cos t, \tag{23-7}$$

so that its time averaged GPEF and GKEF calculated by using Eq. 23-4 are

$$\langle \dot{E} \rangle = \frac{1}{2\pi}\int_0^{2\pi}(-\alpha\rho^2 \cos^2 t + \rho f \cos^2 t)dt = \frac{-\alpha\rho^2+\rho f}{2} = \langle \dot{K} \rangle = \frac{1}{2\pi}\int_0^{2\pi}(-\alpha\rho^2 \cos^2 t + \rho f \sin^2 t)dt. \tag{23-8}$$

Therefore, both GPEF and GKEF vanish when $\rho = f/\alpha$, in which the work done by the external force is dissipated by the damping of the system and the system undergoes a periodical motion with radius $\rho = f/\alpha$ shown in Fig. 4.

Van der Pol's equation
Van der Pol's equation provides an example of an oscillation with nonlinear damping, its energy dissipated at large amplitude but generated at low amplitude. The governing equation of Van der Pol's system is given by

$$\begin{bmatrix}\dot{x}\\ \dot{y}\end{bmatrix} = \mathbf{B}\begin{bmatrix}x\\ y\end{bmatrix}, \quad \mathbf{J} = \begin{bmatrix}0 & 1\\ -1-2xy & -(x^2-1)\end{bmatrix}, \quad \mathbf{B} = \begin{bmatrix}0 & 1\\ -1 & -(x^2-1)\end{bmatrix}, \tag{24-1}$$

from which, when Eq. 5 used, it follows

$$\mathbf{E} = \begin{bmatrix}0 & -xy\\ -xy & -(x^2-1)\end{bmatrix}, \ \mathbf{U} = \begin{bmatrix}0 & 1+xy\\ -1-xy & 0\end{bmatrix}, \ \dot{E} = -(x^2-1)y^2, \ \dot{K} = \dot{\mathbf{y}}^T\mathbf{E}\dot{\mathbf{y}} = -2xy\dot{x}\dot{y} - \dot{y}^2(x^2-1). \tag{24-2}$$

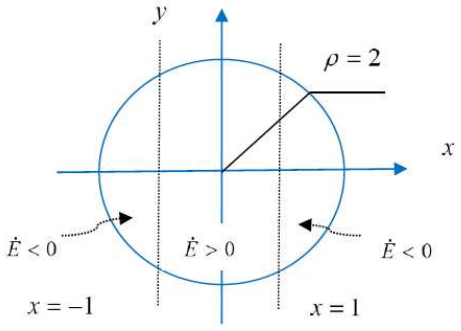

Figure 5: the periodical orbit of Van der Pol's equation**.**

To check if the time averaged GPEF and GKEF vanish in a possible closed orbit, we assume that

$$x = \rho \sin t, \quad y = \rho \cos t, \tag{24-3}$$

so that we obtain

$$\langle \dot{E} \rangle = \frac{1}{2\pi}\int_0^{2\pi}[-(\rho^2 \cos^2 t - 1)\rho^2 \sin^2 t)dt = -\frac{\rho^2}{2}\left(\frac{\rho^2}{4} - 1\right), \tag{24-4}$$

$$\langle \dot{K} \rangle = \frac{1}{2\pi}\int_0^{2\pi}[2\rho^4 \sin^2 t \cos^2 t - \rho^2 \sin^2 t(\rho^2 \sin^2 t - 1)]\,dt = -\frac{\rho^2}{2}\left(\frac{\rho^2}{4} - 1\right).$$

Therefore, when $\rho = 2$, the GPEF and GKEF vanish, which gives a periodical orbit. For matrix **E**, its EFCFs are

$$\lambda_{1,2} = \{-(x^2-1) \pm \sqrt{(x^2-1) + 4x^2y^2}\}/2, \tag{24-5}$$

of which one positive and another negative. These results satisfy the conditions in theorem. As shown in Fig. 5, the periodical orbit is a circle of radius $\rho = 2$, along which on the domain with $|x| > 1$, the energy flow $\dot{E} < 0$, while on the domain with $|x| < 1$,the energy flow $\dot{E} > 0$, and on the full circle the averaged energy flow vanishes.

A planar system

We investigate a planar system governed by

$$\dot{x} = xy, \qquad \dot{y} = -y + x^2/2, \tag{25-1}$$

of which its Jacobian, energy flow and spin matrices respectively as

$$\mathbf{J} = \begin{bmatrix} y & x \\ x & -1 \end{bmatrix} = \mathbf{E}, \qquad \mathbf{U} = 0, \tag{25-2}$$

so that there are no periodical orbits due to spin matrix vanishes. We can calculate the energy flow of the system, i.e.

$$\dot{E} = 3yx^2/2 - y^2, \tag{25-3}$$

of which its zero energy flow curves are

$$y = 0, \qquad y = 3x^2/2\ , \tag{25-4}$$

as shown in Fig.6. Using the Eq. 24-3, the time averaged GPEF is calculated as follows

$$\langle \dot{E} \rangle = \frac{\rho^2}{2\pi} \int_0^{2\pi} (\frac{3\rho}{2} \cos^2 t \sin t - \sin^2 t) dt = -\frac{\rho^2}{2} \neq 0, \tag{25-5}$$

which indicates periodical orbits are impossible.

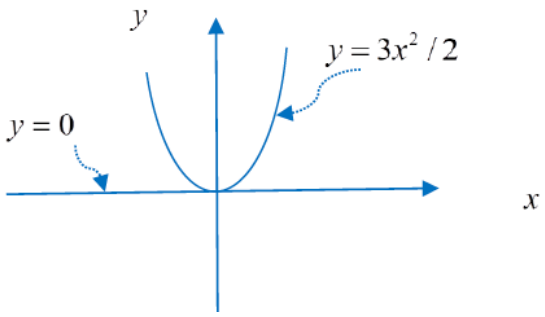

Figure 6: The zero energy flow curves of system shown by Eq. 25-1.

Conclusions

Energy flow theory with two scalars, GPE and GKE as well as the real symmetrical energy flow matrix **E** and the real skew-symmetrical spin matrix **U** is effectively used to investigate NDS in phase space. It is revealed that a necessary sufficient condition for NDS $\dot{\mathbf{y}} = \mathbf{f}(t, \mathbf{y})$ having periodical orbits is that there exist a non-zero spin matrix and a closed orbit with a corresponding period *T*, along which the time averaged GPEF and GKEF vanish. For autonomous systems with energy flow matrix **E** the necessary condition for periodical orbits is its EFCFs not being semi-positive or semi-negative. Three examples, a damping / forced linear system, the Van der Pol's system, and a planar one, are presented to illustrate the revealed characteristics. The developed energy flow theory provides an important means to explore dynamic characteristics of various NDS.

References

[1] Guckenheimer, J., Holmes, P. (1983) Nonlinear oscillations, dynamical systems, and bifurcations of vector fields. Springer-Verlag, NY.
[2] Thompson J. M. T., Stewart H. B. (1986) Nonlinear dynamics and chaos, geometrical methods for engineers and scientists. John Wiley, Chichester.
[3] Chen Y., Tang Y., Lu Q., Zheng Z., Xu J., Ouyang Y. (1992) Modern analysis methods in nonlinear dynamics (in Chinese). Science Press, Beijing.
[4] Yang S., Cao Q., Zhang W. (2011) Some theories and applications of nonlinear dynamics and controls (in Chinese). Science Press, Beijing.
[5] Xing J. T. (2015) Energy flow theory of nonlinear dynamical systems with applications. Springer, Heidelberg.
[6] Hirsch M. W., Smale S. (1974) Differential equations, dynamical systems, and linear algebra. Academic Press, NY.
[7] Xing J. T. (2019) Generalised energy conservation law for chaotic phenomena, *Acta Mechanica Sinica* 35(6):1257–1268.
[8] Qin, L., Qin, H., Xing, J.T. (2021) Energy flow characteristics of friction-induced nonlinear vibrations in a water-lubricated bearing-shaft coupled system. *Acta Mechanica Sinica* 37(4): 679-704.
[9] Fung Y.C. (1977) A first course in continuum mechanics. Prentice-Hall, Englewood Cliffs, NJ.
[10] Xing J.T. (2019 /2021) Fluid-solid interaction dynamics, theory, variational principles, numerical methods, and applications. Elsevier Academic Press, NY (2019) & Higher Education Press, Beijing (2021).

New simple oscillator model describing ice-induced vibrations of an offshore structure

A. K. Abramian*, S. A. Vakulenko†
*Institute for Problems in Mechanical Engineering RAS, Saint Petersburg, Russia
†Institute for Problems in Mechanical Engineering RAS, Saint Petersburg, Russia

Summary. In this paper a new simple oscillator model is considered describing ice induced vibrations of upstanding, water surrounded, and bottom-founded offshore structures. Existing models are extended by taking into account deformations of an ice floe, and a moving contact interaction between an ice rod, which is cut out from the floe, and the oscillator which represents the offshore structure. Special attention is paid to a type of ice-induced vibrations (IIV) of structures, known as frequency lock-in, and characterized by having the dominant frequency of the ice forces near a natural frequency of the structure. The instability onset,induced by resonance for the oscillator and generated by the ice rod structure interaction, is studied in detail.

Statement of the problem

Vertically-sided, bottom-founded offshore structures occasionally experience sustained vibrations due to drifting ice sheets crushing against them. Usually, three regimes of interaction are distinguished: intermittent crushing, frequency lock in, and continuous brittle crushing. In this paper, we introduce a mathematical model for a special type of ice- induced vibrations (IIV) of structures, known as frequency lock-in, and characterized by having the dominant frequency of the ice forces near a natural frequency of the structure. In this paper, we propose a model extending the previous ones, in particular, those suggested in [1, 2, 3, 4]. A novelty with respect to the previous investigations is that we study the ice deformations in more detail including nonlinear deformation. We describe deformations of the ice rod taking into account possible viscous ice behaviour, and a moving contact between the structure and the ice. Following [1, 2, 3, 4] we consider an offshore structure as a one-degree-of- freedom oscillator and the ice floe as a system of ice rods, whose properties include local failure. In particular, we consider a simple oscillator, which interacts with one of such rods. Considering only one rod we take into account the connections of this rod with the others following the approach suggested in [5]. In order to simulate the behavior of the structure during the frequency lock-in regime the condition was set that the ice should always be in contact with the structure. On the basis of this requirement the equation describing the simple oscillator dynamics is given by:

$$q_{tt} + \Omega^2 q + \alpha q_t = \mu, \tag{1}$$

where $q = q(t)$ is the oscillator displacement, $\Omega^2 = \frac{G}{M}$, where Ω is the oscillator frequency, and M and G are the mass and rigidity of the oscillator respectively, and $\alpha > 0$ is a positive damping coefficient. For (1) the following initial conditions are used:

$$q(0) = 0, \quad q_t(0) = 0. \tag{2}$$

The term μ in (1) defines a force which is acting on the oscillator due to the ice rod, and has the form

$$\mu = \frac{EF}{M}(u_x + \frac{\delta_0}{E}u_{xt} + u_x^2)|_{x=q(t)}, \tag{3}$$

where $u = u(x,t)$ is the longitudinal ice rod displacement, E is an ice Young's modulus, F is the ice rod cross sectional area, and δ_0 is the ice internal, structural damping coefficient. The term u_x in the right hand side of (3) defines the contribution of linear deformations, and the term u_{xt} is the ice viscosity. The following equation describes the dynamics of the ice rod, which is defined on the semi-infinite domain $I_q = \{x : q < x < \infty\}$.

$$ru_{xx} - mu_{tt} + \delta_0 u_{xxt} = Q, \tag{4}$$

$$Q = -\beta(s_t - u_t) - k_0(s - u), \tag{5}$$

where $u(x,t)$ is the unknown ice rod displacement, m is the ice rod mass per unit length, Q is a force occurring in the rod due to its side-surface contact with others ice rods in the space around the rod in the ice floe that is considered in (4). The ice floe is drifting along the x-axis. The parameters β,r,δ_0, and k_0 are positive. The coefficient β is the ice friction coefficient during its side-surface contact, the coefficient r is the coefficient relating the shearing stress and the strain in the ice floe, and thus defines "the load spreading capacity of the foundation" according to [5]. The parameter k_0 characterizes the rod compression which is caused by stresses due to the ice rod compression in the transverse direction by other ice rods. In other words, the ice floe behavior can be modelled by a generalized spring and a generalized dashpot. The function $s(t)$ describes the shift of the ice rod, and $s(t)$ is defined by $s(t) = -vt + \rho(t)$, where $v > 0$ is the relative ice velocity, and $\rho(t) = \sum_{n=1}^{\infty} d_n H(t - t_n)$.
Here t_n are time moments when the ice rod crushes at $x = q(t)$; d_n are the lengths of ice blocks that split off, and $H(z)$ stands for the Heaviside step function. The time moments t_n are defined by the condition

$$p(t_n) = p_c, \tag{6}$$

that is, the pressure p in the ice periodically attains a critical level p_c. We introduce the following boundary conditions

$$u(q(t),t) = q(t), \quad u(x,t) \to 0, \ for\ x \to +\infty. \tag{7}$$

The first one is a contact relation between the ice rod and the oscillator, and the second one is a radiation condition at infinity. The initial conditions are given by

$$u(x,0) = \phi_0(x), \quad u_t(x,0) = \phi_1(x), \quad x \in (q(0),\infty), \tag{8}$$

where $\phi_j(x)$ are fast decreasing functions in x for $x \to \infty$.

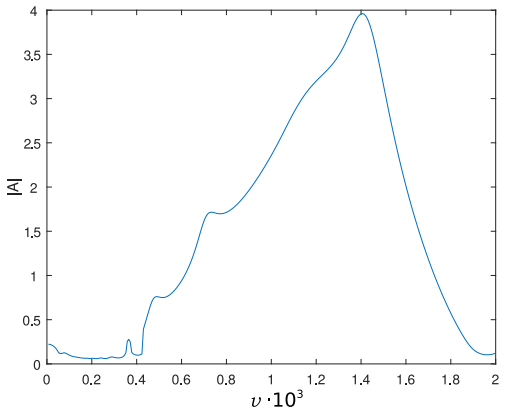

Figure 1: The dependence of the equilibrium amplitude A on the ice rod speed v for the dimensionless parameters $k_0 = 25$, $d = 1$, $\beta = 0.2$, $\bar{\alpha} = 4$, and $\delta_0 = 0.1$.

Conclusions

In this paper, a new model is proposed to describe the interaction between an ice-rod and an oscillator. This model takes into account deformations of the ice floe. The model is analytically investigated by asymptotic methods.It is shown that the contact interaction between the oscillator and the ice rod leads to resonances. The main resonance between the oscillator and the external load occurs when the natural frequency Ω of the oscillator is close to the external load frequency ω. We also find a new mechanism for the oscillator's behavior which can be described by a resonance between the external load, the oscillator, and the part of the ice rod (boundary layer) inducing an oscillator-ice rod interaction during the rod's motion with speed v. We show that ice rod deformation patterns arise which are generated by an interaction between the oscillator and the rod. This ice rod deformation is exponentially decreasing along the ice rod length. We obtain a plot describing how the oscillator's amplitude A depends on the ice velocity v. For some parameter choices this plot shows a significant peak for the amplitude A. For small rod-speeds v we have a small oscillation amplitude A, as well as for large v. The height and width of the peak depend on the system parameters.

References

[1] Matlock, H., Dawkins, W.P., and Panak, J.J. (1971) Analytical Model for Ice Structure Interaction. ASCE Journal of the Engineering Mechanics Division, EM 4, *J. Fluid Mech* **1083**:1083-1092.

[2] Sodhi, D.S.: A theoretical model for Ice-Structure Interaction, Proc. of the OMAE-94 conference, ASME, New York, Vol. IV, pp. 29–34.

[3] G.Huang and P.Liu (2008) A dynamic model for Ice-Induced Vibrations of Structures. Journal of Offshore Mechanics and Arctic Engineering , **011501**: 011501-011506.

[4] H. Hendrikse, A. Metrikine (2015) Interpretation and prediction of ice induced vibrations based on contact area variation. International Journal of Solids and Structures 75 **336** 336-348.

[5] V.Z. Vlasov, N.N. Leont'ev: Beams,plates and shells on elastic foundations, Israel Program for Scientific Translation, Jerusalem, Israel, 1966.

Friday, July 22, 2022

08:30 - 10:30

MS-19 Fluid-Structure Interaction

Saint Clair 3B

Chair: Vasily Vedeneev - Andrei Metrikine

08:50 - 09:10

[no show] Vibrations of a vertical flexible riser in sheared flow

KURUSHINA Victoria*, PAVLOVSKAIA Ekaterina

*Newcastle University [Newcastle] (Newcastle upon Tyne NE1 7RU United Kingdom) - Industrial University of Tyumen (38 Volodarskogo Street, Tyumen, 625000 Russia)

09:30 - 09:50

Stochastic Dynamics of Inclined Risers Induced by Pulsating Internal Fluid Flow

ALFOSAIL Feras*, CUNHA Americo, YOUNIS Mohammad

*King Abdullah University of Science and Technology (King Abdullah University of Science and Technology P.O.Box 55455 Jeddah 21534, Saudi Arabia Saudi Arabia) - Saudi Aramco (P.O. Box 5000 Dhahran 31311 Saudi Arabia)

09:50 - 10:10

Solitary wave-like solutions in hyperelastic tubes conveying inviscid and viscous fluid

VEDENEEV Vasily*

*Lomonosov Moscow State University (GSP-1, Leninskie Gory, Moscow, 119991, Russian Federation Russia)

Vibrations of a vertical flexible riser in sheared flow

Victoria Kurushina[*,†] and Ekaterina Pavlovskaia[‡]
[*]*Centre for Perspective Research and Innovative Development, Industrial University of Tyumen, Tyumen, 625000, Russia*
[†]*School of Engineering, Newcastle University, Newcastle, NE1 7RU, United Kingdom*
[‡]*Centre for Applied Dynamics Research, University of Aberdeen, King's College, Aberdeen, AB24 3UE, United Kingdom*

Summary. Vortex-induced vibrations of a flexible pipe, with pinned-pinned ends and straight initial configuration, are considered in this work in a number of linear and nonlinear velocity profiles, varying along the length of structure. Krenk-Nielsen [1] and Van der Pol wake oscillators are employed in order to simulate fluctuations of the fluid forces, while the structure is modelled using the Euler-Bernoulli beam. Trajectories, time histories, multi-mode lock-in are studied using the case parameters, previously investigated by [2].

Introduction

Vibrations of flexible structures remain a vital problem for the safety of oil and gas subsea production systems. Application of fluid oscillators is one of the modern ways to improve the current prediction capabilities and study the complex multi-mode vibration mechanism. The focus of this work is on the near-resonant velocity profiles and resulting behaviour of the vertical flexible structure.

Flexible riser model

The structure with pinned-pinned ends, previously studied in uniform flow in 2D in [3], is subjected to sheared flow, and the approximate solution is obtained using the method described in [4]. Approximation for sheared flow is developed using integration of the velocity profile along the length of the riser. The reduced order non-dimensional model for *i*th mode is as follows:

$$\ddot{X}_i + 2a\sum_{n=1}^{N}\dot{X}_n\Theta_{ni} + \omega_{rn}^2 X_i = \frac{W_w}{Lm_*\omega_0^2}\sum_{n=1}^{N}X_n\Phi_{ni} + \frac{a}{2\pi St}\Lambda_i + \frac{b}{4\pi St}\sum_{n=1}^{N}w_n\Gamma_{ni} - b\sum_{n=1}^{N}\sum_{m=1}^{N}w_n\dot{X}_m\Delta_{nmi} + \tag{1}$$
$$+\frac{c}{2}\sum_{n=1}^{N}\sum_{m=1}^{N}q_n\dot{Y}_m\Delta_{nmi} + 2\pi Sta\sum_{n=1}^{N}\sum_{m=1}^{N}\dot{X}_n\dot{X}_m\Pi_{nmi} + \pi Sta\sum_{n=1}^{N}\sum_{m=1}^{N}\dot{Y}_n\dot{Y}_m\Pi_{nmi};$$
$$\ddot{Y}_i + a\sum_{n=1}^{N}\dot{Y}_n\Theta_{ni} + \omega_{rn}^2 Y_i = \frac{W_w}{Lm_*\omega_0^2}\sum_{n=1}^{N}Y_n\Phi_{ni} - \frac{b}{2}\sum_{n=1}^{N}\sum_{m=1}^{N}w_n\dot{Y}_m\Delta_{nmi} + \frac{c}{4\pi St}\sum_{n=1}^{N}q_n\Gamma_{ni} -$$
$$-c\sum_{n=1}^{N}\sum_{m=1}^{N}q_n\dot{X}_m\Delta_{nmi} + 2\pi Sta\sum_{n=1}^{N}\sum_{n=1}^{m}\dot{X}_n\dot{Y}_m\Pi_{nmi};$$
$$\ddot{w}_i - 2\varepsilon_{x1}\sum_{n=1}^{N}\dot{w}_n\Theta_{ni} + 2\varepsilon_{x2}\sum_{n=1}^{N}\sum_{m=1}^{N}\sum_{l=1}^{N}\dot{w}_n w_m w_l\Xi_{nmli} + 2\varepsilon_{x3}\sum_{n=1}^{N}\sum_{m=1}^{N}\sum_{l=1}^{N}\dot{w}_n\dot{w}_m\dot{w}_l B_{nmli} + 4\sum_{n=1}^{N}w_n\Gamma_{ni} = A_x\ddot{X}_i;$$
$$\ddot{q}_i - \varepsilon_y\sum_{n=1}^{N}\dot{q}_n\Theta_{ni} + \varepsilon_y\sum_{n=1}^{N}\sum_{m=1}^{N}\sum_{l=1}^{N}\dot{q}_n q_m q_l\Xi_{nmli} + \sum_{n=1}^{N}q_n\Gamma_{ni} = A_y\ddot{Y}_i,$$

where

$$X(\zeta,\tau) = \sum_{n=1}^{N}X_n(\tau)\widetilde{X}_n(\zeta); \quad Y(\zeta,\tau) = \sum_{n=1}^{N}Y_n(\tau)\widetilde{Y}_n(\zeta); \quad w(\zeta,\tau) = \sum_{n=1}^{N}w_n(\tau)\widetilde{w}_n(\zeta); \quad q(\zeta,\tau) = \sum_{n=1}^{N}q_n(\tau)\widetilde{q}_n(\zeta).$$

Here, τ is non-dimensional time, $\zeta = \frac{z}{L}$ is location of considered cross-section of the beam (where z represents the axial coordinate), $\widetilde{X}_n(\zeta), \widetilde{Y}_n(\zeta), \widetilde{w}_n(\zeta), \widetilde{q}_n(\zeta)$ are sinusoidal functions, X_i and Y_i constitute in-line and cross-flow displacements multipliers, w_i and q_i are wake coefficients multipliers, Ω_R is vortex shedding frequency, St is Strouhal number, $\varepsilon_{x1}, \varepsilon_{x2}, \varepsilon_{x3}, \varepsilon_y$ are dimensionless wake oscillator damping coefficients, A_x, A_y are empirical coupling coefficients, a, b, c are dimensionless coefficients depending on the initial drag, fluctuating drag and lift coefficients respectively, N is total number of modes considered, ω_{ni} is the *i*th natural frequency, ω_0 is reference frequency, m_* is mass per unit length (including structural mass and fluid added mass), W_w is weight of structure per unit length. Dimensionless coefficients Λ_i, Θ_{ni}, Φ_{ni}, Γ_{ni}, Δ_{nmi}, Π_{nmi}, B_{nmli}, Ξ_{nmli} represent interaction of modes with numbers n, m, l. Among them, Λ_i, Θ_{ni}, Γ_{ni}, Δ_{nmi}, B_{nmli}, Ξ_{nmli} constitute the difference with the uniform flow model [3] and account for the velocity/vortex shedding frequency profile integrated along ζ, e.g. $\Theta_{ni} = 2\int_0^1 \Big[sin(n\pi\zeta)sin(i\pi\zeta)StU_R(\zeta)\Big]d\zeta$. In this work, the dynamics of the vertical flexible structure is studied using 5 mode approximation, where reduced velocity is defined based on the first natural frequency measured in [2].

Results

Five sheared flow velocity profiles were considered in the current study where the flow velocities lie in the proximity of the first few natural frequencies of the flexible structure, including reduced velocities $U_R = 5.0$ and $U_R = 10.0$, as shown in Fig. 1a. In this example, constant velocity profile with $U_R = 5.0$ results in the highest in-line and cross-flow displacement amplitudes observed in the bottom part of the structure, as illustrated in Figs 1c and 1d. Structural motion under this constant uniform velocity and under the parabolic profile with the maximum reduced velocity $U_R = 5.0$ show response of 4 modes. The parabolic profile with the maximum reduced velocity $U_R = 10.0$ leads to the most symmetric displacement amplitudes, relatively $\zeta = 0.50$ with three more significant medium peaks. Linearly varying profiles result in the increased displacements in the cross-sections subjected to the increased flow velocity, however, the profile with the velocity growing towards the top of structure leads to higher maximum amplitudes in both in-line and cross-flow directions. Fig. 1b provides two samples of multi-frequency cross-flow displacement signals at the cross-section of $\zeta = 0.33$ with the largest amplitudes demonstrated under the flow of constant velocity.

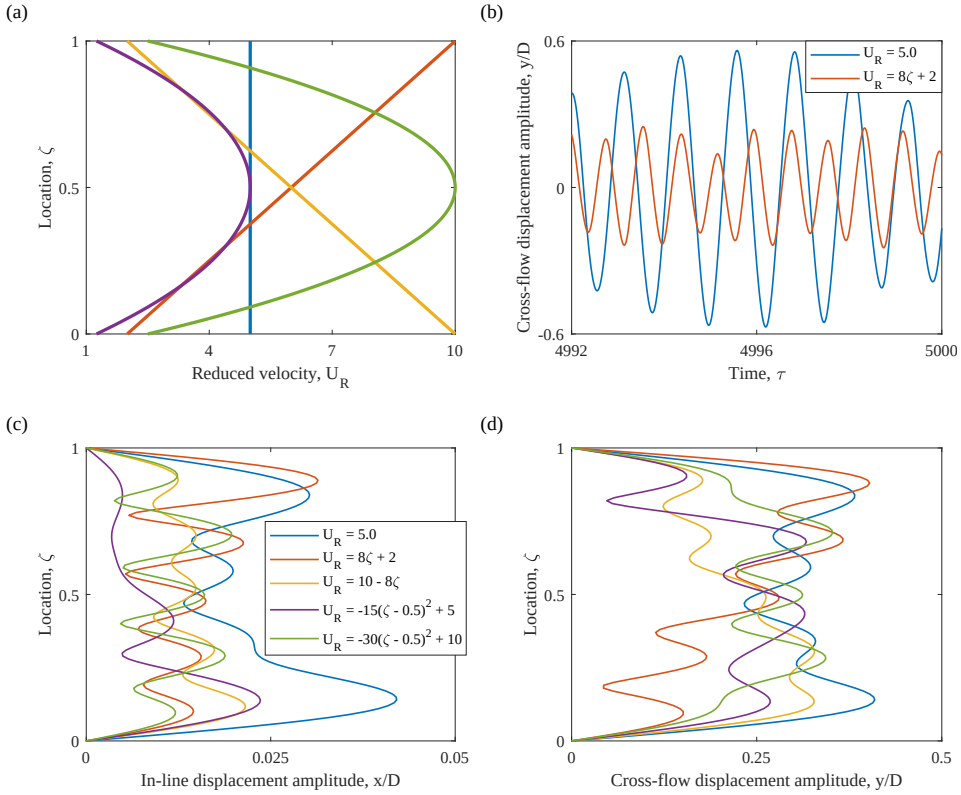

Figure 1: Dynamics of a vertical flexible structure predicted by the 5 mode approximation: (a) five considered velocity profiles shown in terms of the reduced velocity and the length of structure; (b) time histories of the largest and smallest cross-flow displacement amplitudes at $\zeta = 0.33$; (c) in-line and (d) cross-flow displacement amplitude variation along the length of structure.

Conclusions

Results of the flexible structure dynamics simulations for a number of linear and nonlinear sheared flow profiles are presented in this work, using 5 mode approximation obtained in a similar way as was done in the previous studies for uniform flows [3, 4]. The novelty of this model formulation is in the coefficients representing mode interaction and the integrated velocity profile. Multi-mode lock-in is considered in details, and the highest displacement amplitudes are predicted to occur under the influence of linear velocity profiles including the limited cases of uniform flows.

References

[1] Krenk S., Nielsen, S.R.K. (1999) Energy balanced double oscillator model for vortex-induced vibrations. *Journal of Engineering Mechanics* **125(3)**:263-271.

[2] Sanaati B., Kato N. (2012) A study on the effects of axial stiffness and pre-tension on VIV dynamics of a flexible cylinder in uniform cross-flow. *Applied Ocean Research* **37**:198-210.

[3] Kurushina V., Pavlovskaia E., Wiercigroch M. (2019) VIVs of flexible structure in 2D uniform flow. *Under Review.*

[4] Pavlovskaia E., Keber M., Postnikov A., Reddington K., Wiercigroch M. (2016) Multi-modes approach to modelling of vortex-induced vibration. *International Journal of Non-Linear Mechanics* **80**: 40-51.

Stochastic Dynamics of Inclined Risers Induced by Pulsating Internal Fluid Flow

Feras Alfosail[*,**], Americo Cunha Jr[***], Mohammad I. Younis[*]
[*]*King Abdullah University of Science and Technology, Thuwal 23955-9600, Saudi Arabia*
[**]*Consulting Services Department, Saudi Aramco, Dhahran 31311, Saudi Arabia*
[***] *Rio de Janeiro State University, UERJ*

Summary. In this work, we numerically explore the stochastic dynamics of inclined marine risers subjected to pulsating internal fluid flow. The presence of geometric nonlinearities with static deflection makes the response of the inclined riser different from conventional top tension risers when subjected to pulsating flows. At first, the riser model is solved via Galerkin method and validated using perturbation approaches. Then, we study the propagation of uncertainties i.e. amplitude and frequency of pulsations in the stochastic model revealing rich and complex dynamics features.

Introduction

Pulsating flow is a phenomenon that affects the oil and gas industries. It occurs due to abrupt perturbations and fluctuations in the internal fluid flow of the riser pipe which in return can affect and influence the vibrational motion of the structure. It occurs due to several reasons such as the nature of the multi-phase flow and sudden geometric changes [1]. Because the value of the excitation amplitude and frequency of fluctuation of the flow are uncertain i.e. stochastic, the influence of the flow can be sever especially if the frequency of these flows are near structural resonances of the riser making them prone to failure by fatigue.

Problem Formulation

The inclined riser to be analyzed in this work is under mid-plane stretching and subjected to static deflection [2] and pulsating internal fluid flow. Then, the equation that describes the motion of the riser in dimensionless form can be written as

$$\begin{aligned}&\frac{\partial^2 y_d}{\partial t^2}+\frac{\partial^4 y_d}{\partial x^4}+2\sqrt{\beta}v\frac{\partial^2 y_d}{\partial x\partial t}+\sqrt{\beta}\frac{\partial v}{\partial t}(1-x)\frac{\partial^2 y_d}{\partial x^2}+c\frac{\partial y_d}{\partial t}+c_d\frac{\partial y_d}{\partial t}\left|\frac{\partial y_d}{\partial t}\right|+\left(v^2-T+\sigma(1-x)\right)\left(\frac{\partial^2 y_d}{\partial x^2}\right)-\sigma\left(\frac{\partial y_d}{\partial x}\right)\\&-\left(\eta\left(\int_0^1\left(\frac{dy_s}{dx}\right)^2dx+\int_0^1\left(\frac{\partial y_d}{\partial x}\right)^2dx+\int_0^1 2\frac{dy_s}{dx}\frac{\partial y_d}{\partial x}dx\right)\left(\frac{\partial^2 y_d}{\partial x^2}\right)-\eta\left(\int_0^1 2\frac{dy_s}{dx}\frac{\partial y_d}{\partial x}dx+\int_0^1\left(\frac{\partial y_d}{\partial x}\right)^2dx\right)\left(\frac{d^2 y_s}{dx^2}\right)=0\end{aligned}\tag{1}$$

where y_d is the deflection of the riser along position x and time t, β is fluid mass parameter, σ is self-weight parameter, v is internal fluid flow velocity, η is nonlinear geometric parameter, c is structural damping, c_d is external fluid damping and T is the applied top tension. Due to flow fluctuations, the internal velocity is assumed to have the form $v=V(1+\gamma\cos(\Omega t))$ where V is the magnitude of the internal velocity, γ is a detuning parameter between 0 and 1 and Ω is the excitation frequency. Equation (1) is solved via Galerkin method utilizing the procedures prescribed in [3] and [4] and validated using perturbation method defined in [5-7]. Next, we consider a probabilistic frame of work in which the amplitude γ and the excitation frequency Ω are random variables. Then, we study the influence of type of different probability distributions (PDF) on the dynamic response of the structure using Monte Carlo (MC) simulations with 2^{13} samples.

Numerical Results

At first, the deterministic model is analyzed. Due to the quadratic nature of the internal fluid flow, the excitation frequency is expected to occur at Ω and 2Ω because of the nature of the parametric excitation. The dynamic response of the lowest three modes is depicted in Fig.1

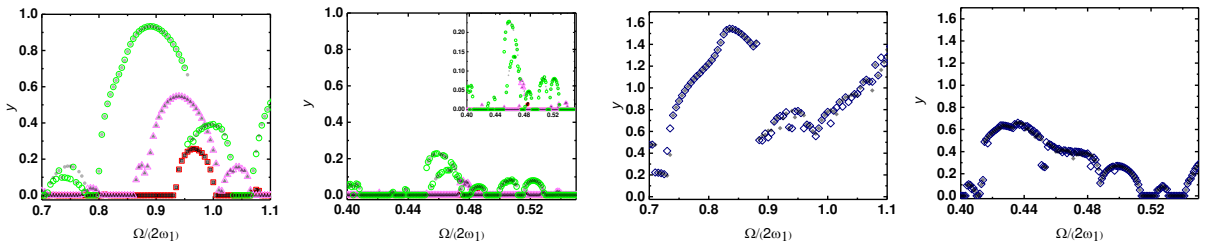

Figure 1: Multi-modal Frequency response curves around the first mode of vibrations for $V=\sqrt{\sigma}$, $c_d=0.416$ at x=0.48. (a,b) Backward Sweep (□) $\gamma=0.25$, (△) $\gamma=0.50$, (○) $\gamma=0.75$. The inset is magnified results for case (b). (c,d) (◇) $\gamma=1$. Filled shapes denotes forward sweep.

We observe, in Fig. 1, the influence of the different components that exists in the system as a result of the interaction. The influence of the softening nonlinearity is less apparent due to the competing effects between the first mode and contributions from other modes that exist in the response. This is observed very well in Fig. 1b in comparison to other cases. In addition, the interaction of other resonances with the response of the solution near Ω and 2Ω become more visible at higher fluctuating velocity as the solution demonstrate chaotic behavior.

Next, we consider the stochastic response of the riser. The results from the MC method are divided into ten categories considering the two excitation frequency ranges and the combination of the distributions for the amplitude utilizing Beta and uniform distributions where they are applicable. As an example, we demonstrate the response of the riser under Beta distribution for excitation at a frequency of $\Omega/2\omega_1 = 0.464$ in Fig.2

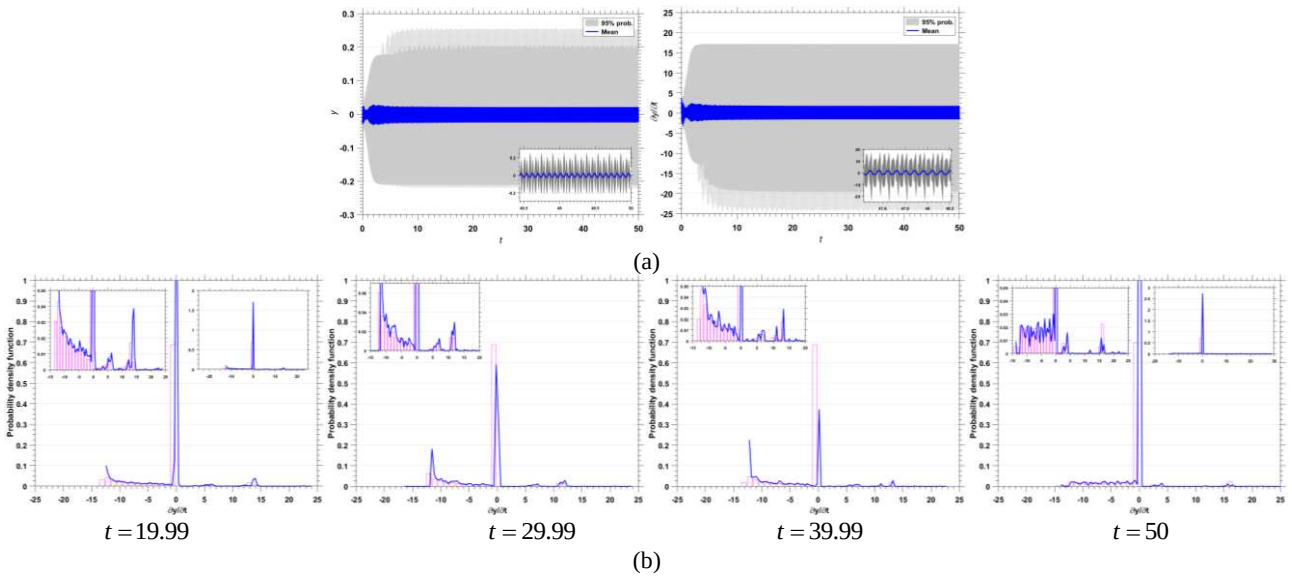

Figure 2: $\Omega/2\omega_1 = 0.464$ (a) Illustration of the nominal value (Blue line) and the 95 % envelop (grey shadow) of the displacement (left) and the velocity (right) of the riser. The box in each figure is a magnified response of the riser. (b) Evolution of the normalized probability density function as a function of the rise velocity at different times. The box in each figure is a magnified distribution of the probability density function.

The response of the riser displacement is exhibited on the left Fig. 2a and we plot the velocity in order to have a better representation of the riser response. The distribution influences type of response because at this frequency the riser excite not only secondary terms due to quadratic nonlinearity but also primary due the squaring of terms. Due to this fact, the mean value is observed to be superseded by different excitation amplitudes constituting the envelope. The propagation of the probability density function at different time interval demonstrate that it is stationary. The main feature is attributed to the primary excitation of the riser structure.

Conclusions

In this work, the stochastic dynamics of inclined risers is studied considering the influence of pulsating internal fluid flow. The presence of static deflection under the influence of geometric nonlinearity causes multiple resonances to exist. This influences the stochastic response of the riser examined under different distributions. As a result, the response of the riser in the Monte Carlo simulations revealed interesting complex and rich dynamic features

References

[1] M. P. Paidoussis, *Fluid-Structure Interactions* vol. 1. Oxford: Academic Press, 2014.
[2] F. K. Alfosail, A. H. Nayfeh, and M. I. Younis, "An analytic solution of the static problem of inclined risers conveying fluid," *Meccanica*, vol. 52, pp. 1175-1187, 2016.
[3] F. K. Alfosail, A. H. Nayfeh, and M. I. Younis, "Natural frequencies and mode shapes of statically deformed inclined risers," *International Journal of Non-Linear Mechanics*, 2016.
[4] G. Franzini and C. Mazzilli, "Non-linear reduced-order model for parametric excitation analysis of an immersed vertical slender rod," *International Journal of Non-Linear Mechanics*, vol. 80, pp. 29-39, 2016.
[5] A. H. Nayfeh and P. F. Pai, *Linear and nonlinear structural mechanics*: John Wiley & Sons, 2008.
[6] R. H. Plaut, J. J. Gentry, and D. T. Mook, "Non-linear structural vibrations under combined multi-frequency parametric and external excitations," *Journal of Sound and Vibration*, vol. 140, pp. 381-390, 1990/08/08/ 1990.
[7] R. H. Plaut, J. J. Gentry, and D. T. Mook, "Non-linear oscillations under multifrequency parametric excitation," *International Journal of Non-Linear Mechanics*, vol. 25, pp. 187-198, 1990.

Solitary wave-like solutions in hyperelastic tubes conveying inviscid and viscous fluid

Vasily Vedeneev*
*Lomonosov Moscow State University, Moscow, Russia

Summary. We study possible steady states of an infinitely long tube made of a hyperelastic membrane and conveying either an inviscid, or a viscous fluid with power-law rheology. The tube model is geometrically and physically nonlinear; the fluid model is limited to smooth changes in the tube's radius. For the inviscid case, we analyse the tube's stretch and flow velocity range at which standing solitary waves of both the swelling and the necking type exist. For the viscous case, we show that a steady-state solution exists only for sufficiently small flow speeds and that it has a form of a kink wave; solitary waves do not exist. For the case of a semi-infinite tube (infinite either upstream or downstream), there exist both kink and solitary wave solutions. For finite-length tubes, there exist solutions of any kind, i.e. in the form of pieces of kink waves, solitary waves, and periodic waves.

Introduction

Nonlinear waves in fluid-filled elastic tubes play an important role in problems of the cardiovascular system [1,7]. Solitary wave solutions are used for the analysis of pulse waves as well as for the study of the formation of aneurysms [3,4]. As a rule, such solutions are theoretically analysed without consideration of the fluid viscosity [2,5]. The goal of this study is to include the viscosity into account and to study its effect on solitary-wave-like solutions.

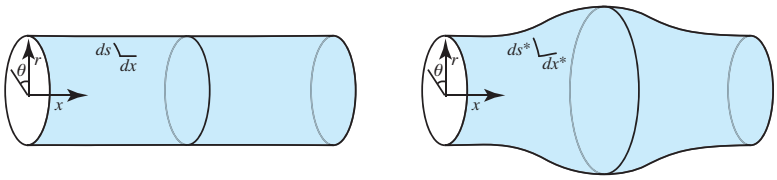

Figure 1: Cylindrical membrane tube in the initial and the deformed state.

Problem formulation and results

Governing equations

We consider a cylindrical membrane tube with a circular cross-section with a thickness of h and a radius of R, made of incompressible hyperelastic Gent material (Fig. 1). The ratio h/R is sufficiently small for the bending stresses to be neglected compared to the membrane stresses. The tube conveys a non-Newtonian viscous fluid whose rheology obeys a power law. We restrict ourselves to axisymmetric motion. In [2], a self-contained derivation of the exact equations of motion for the case of an inviscid fluid was given. We re-derive these equations and upgrade it by the viscous fluid forces taken into account. The fluid equations are considered in the formulation [9, 10]. With these assumptions, closed system of four differential equations is derived.

Analysis: inviscid fluid

If the fluid viscosity is neglected and the velocity is constant at each cross-section, the system of equation has four first integrals, as shown in [2]. We prove that the existence of these integrals retains if the velocity distribution is non-constant, but the viscosity is still neglected. The system of first integrals is reduced to a two-dimensional dynamic system, which is analysed by its phase plane (Fig. 2).

It is known [6] that for a quiescent fluid (or, equivalently, if a constant pressure is set in the tube) in a tube that is axially unstretched at infinity (axial stretch $\lambda_{10} = 1$), a standing solitary wave in the form of a localised swelling exists for a range of far-field circumferential stretches $1.18 < \lambda_{20} < 1.69$. We show that in the case of a moving fluid, there is a range of velocities ($0.063 \le v_{f0} \le 0.58$ for far-field radial stretch $\lambda_{20} = 1.5$), in which there exists, simultaneously with

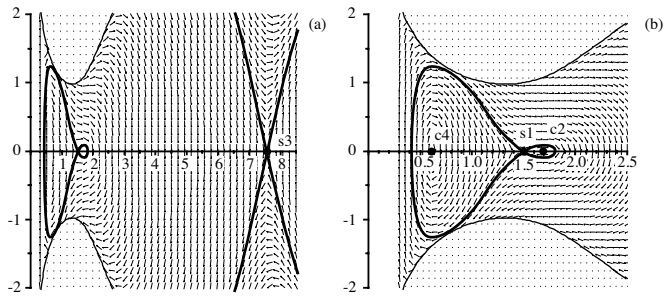

Figure 2: Vector field and separatrices of the stationary saddle points for $\lambda_{10} = 1$, $\lambda_{20} = 1.5$, and $v_{f0} = 0.4$. General view (a), enlarged view in the area of the separatrix loops (b).

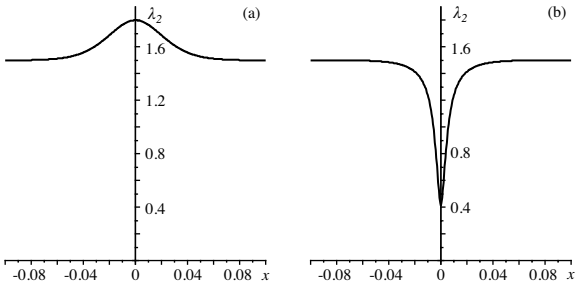

Figure 3: Swelling (a) and necking (b) solitary waves $\lambda_2(x)$ for $\lambda_{10} = 1$, $\lambda_{20} = 1.5$, and $v_{f0} = 0.4$.

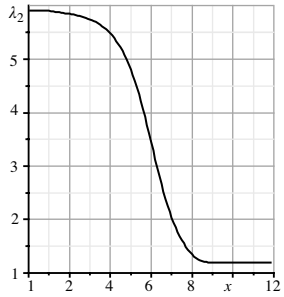

Figure 4: Kink-like solution $\lambda_2(x)$ for infinite-length tube conveying viscous fluid.

the standing swelling solitary wave, a standing necking solitary wave. At a lower fluid velocity, there is only a swelling solitary wave; for larger velocities, no solitary waves exist. Note that in a model of a geometrically and physically linear tube, in which only the nonlinearity of the flow was taken into account [8], there always exists, for any nonzero flow velocity, only a standing necking solitary wave. Thus, both the existence of a standing swelling solitary wave and the limited range of fluid velocities for which a standing necking solitary wave exists are consequences of the physical and geometrical nonlinearities of the tube model.

Analysis: viscous fluid

When a viscous fluid moves, only two of the four first integrals exist, and the motion of the trajectory on the phase plane is accompanied by a simultaneous change of the vector field. First, we prove that there are limit stretch states of the tube as $x \to -\infty$ and $x \to +\infty$, with the stretches λ_1 and λ_2 tending to constants but the stresses tending to infinities to compensate for the fluid pressure and the longitudinal stress caused by the fluid viscosity, which are infinitely growing upstream and infinitely decreasing downstream. The transition between these limit states occurs in the central section of the tube and exists only if the fluid velocity is sufficiently small. In this case there is a unique solution linking the states at infinity in the form of a monotonic decrease in the radius downstream, i.e. a kink-like solution. Localised swelling or necking solutions for a tube that is infinitely long in both directions do not exist. However, such solutions exist if the tube is infinitely long in only one direction, either downstream or upstream. But solutions in which a semi-infinite tube has multiple neckings or swellings do not exist. For finite-length tubes, there exist 'pieces' of both swelling and necking solitary waves, as well as close-to-solitary-wave solutions with a finite number of successive swellings or neckings.

This work was supported by a grant of the Russian Foundation for Basic Research No. 18-29-10020.

References

[1] Cao Y., Zheng Y., Li G-Y., Jiang Y. (2019) Elastodiagnosis of diseases: A review. *Extreme Mech. Letters* **27**:102–123.

[2] Epstein M., Johnston C.R. (2001) On the exact speed and amplitude of solitary waves in fluid-filled elastic tubes. *Proc. R. Soc. Lond. A* **457**:1195–1213.

[3] Dehghani H., Desena-Galarza D., Jha N.K., Reinoso J., Merodio J. (2019) Bifurcation and post-bifurcation of an inflated and extended residually-stressed circular cylindrical tube with application to aneurysms initiation and propagation in arterial wall tissue. *Finite Elem. Anal. Des.* **161**:51–60.

[4] de Gelidia S., Bucchia A. (2019) Comparative finite element modelling of aneurysm formation and physiologic inflation in the descending aorta. *Comp. Meth. Biomech. Biomed. Eng.* **22(15)**:1197–1208.

[5] Il'ichev A.T., Shargatov V.A., Fu Y.B. (2020) Characterization and dynamical stability of fully nonlinear strain solitary waves in a fluid-filled hyperelastic membrane tube. *Acta Mech.* **231**:4095–4110.

[6] Pearce S.P., Fu Y.B. (2010) Characterization and stability of localized bulging/necking in inflated membrane tubes. *IMA J. Appl. Math.* **75**:581–602.

[7] Pedley T.J. (2003) Arterial and Venous Fluid Dynamics. In Cardiovascular fluid mechanics (ed. G. Pedrizzetti and K. Perktold), chap. 1. Springer.

[8] Poroshina A.B., Vedeneev V.V. (2018) Existence and uniqueness of steady state of elastic tubes conveying power law fluid. *Russian Journal of Biomechanics* **22(2)**:169–193.

[9] Vedeneev V.V., Poroshina A.B. (2018) Stability of an elastic tube conveying a non-Newtonian fluid and having a locally weakened section. *Proc. Steklov Inst. Math* **300**:34–55.

[10] Yushutin V.S. (2012) Stability of flow of a nonlinear viscous power-law hardening medium in a deformable channel. *Moscow Univ. Mech. Bull.* **67 (4)**:99–102.

List of authors

(STEVANOVIÉ) Hedrih Katica, 618

ABBASI Mohammad Hossein, 406, 536
ABBOUD Eddy, 1054
ABELE Eberhard, 773
ABELOOS Gaëtan, 978
ABLITZER Frédéric, 272, 1055
ABRAMIAN Andrei, 1179
ACAR Gizem, 1133
ACARY Vincent, 228, 556
ADHIKARI Sondipon, 250, 1179
AHMED Alaa, 289
AHSAN Zaid, 179
AKAY Mehmet, 726
AKHAVAN Hamed, 503
AKSYUK Vladimir, 965
AL-SHUDEIFAT Mohammad, 155
AL-SHUDEIFAT Mohammed, 663
ALAOUI-TAHIRI Amine, 1020
ALCORTA Roberto, 179
ALEKSANDRS Ipatovs, 164
ALEVRAS Panagiotis, 478
ALEXANDER Keith, 204
ALFOSAIL Feras, 1194
ALIJANI Farbod, 891, 965, 1153
ALLALOU Nabil, 1053
ALOFI Abdulrahman, 1133
ALOSCHI Fabrizio, 875
ALYUSHIN Yuriy, 1165
AMS Alfons, 478
ANANIEVSKI Igor, 571
ANDE Raghu, 826
ANDONOVSKI Nemanja, 453
ANDREOTTI Roberto, 875
ANDRIANOELY Marie-Ange, 603, 726
ANTALI Mate, 556
ANTRETTER Thomas, 792
ANTUNES Ana Margarida, 503
ANTUNES José, 272
ANZOLEAGA Grandi Alvaro, 792
AOUALI Kaouthar, 26
AOUSTIN Yannick, 36
ARAGÓN Alejandro, 891
ARIBOWO Arviandy, 228
ARIFIN Davin, 496
ARMAROLI Andrea, 826
ARTEMYEV Anton, 584
ASANO Motoki, 891
ASOKANTHAN Samuel, 514, 1054
ASWATHY M. S., 1033
AVRAMOV Konstantin, 1002
AVRUTIN Viktor, 556
AWREJCEWICZ Jan, 875, 955, 1002
AXÅS Joar, 536
AYALA Helon, 11
AYDOGDU Yusuf, 319

BABILIO Enrico, 164
BACHRATHY Daniel, 677, 931, 1179
BACIGALUPO Andrea, 120
BADEL Adrien, 388
BAGUET Sébastien, 179, 514
BAJAJ Anil, 304
BALACHANDRAN Balakumar, 1133
BALCERZAK Marek, 63, 978
BALOGH Tamas, 852
BALTHAZAR José, 978, 1054
BANSAL Harshit, 1054
BARA Iuliana, 1053
BARAKAT Ahmed, 792
BARAKAT Ahmed A., 496
BARBAY Sylvain, 1110
BARRIOS Asier, 1110
BARTELT Perry, 36
BARTFAI Andras, 1110
BARTON David, 11, 289
BASAK Saswata, 863, 955
BASROUR Skandar, 496
BATISTA Matheus, 978, 1054
BATISTELA Cristiane, 439, 978, 1053, 1054
BAUDIN Sophie, 726
BAUER Ulrich, 179
BAYER Fabia, 792
BAZZANI Armando, 89
BEAL Aubrey, 649
BEATUS Tsevi, 1133
BEERENS Ruud, 909, 978
BELARDINELLI Pierpaolo, 1153
BELHORMA Mohamed, 1054
BELLIZZI Sergio, 26
BELMOKHTAR Mohamed, 773
BENACCHIO Simon, 105
BENAICHA Youness, 649
BENARAB Amina, 1110
BENCSIK László, 1110
BEREGI Sandor, 289
BERGEOT Baptiste, 26
BERGER Sébastien, 26
BERGHAUS Tomer, 808
BERGMAN Lawrence, 375, 663
BERTHE Loïc, 536
BERTRAND Charlélie, 228
BESSA Miguel, 1153
BESSELINK Bart, 406
BIDET Jean-Paul, 453
BILAL Nasir, 304
BILBAO Stefan, 692
BILGEN Onur, 754
BIRCH Robert, 134
BISOFFI Andrea, 909
BISWAS Saurabh, 920
BLAHOS Jiri, 739
BLANCHARD Antoine, 76
BOC Michael, 909
BOGOSLAVSKII Ivan, 571
BOLOTNIK Nikolay, 571
BORISENKOV Bogdan, 636
BORZONE Tommaso, 909

BOUCHIKHI Aboubakar, 1054
BOUDY Bastien, 453
BOUHADDI Noureddine, 26
BOUJO Edouard, 978
BOUSSAADA Islam, 852, 1110
BRØNS Marie, 164
BRACCO Giovanni, 837
BRANGER Hubert, 826
BRASIL Reyolando, 134
BREUNUNG Thomas, 677, 1133
BRIEND Yvon, 726
BRODERICK Neil G. R., 1110
BROGLIATO Bernard, 228, 556
BRONS Morten, 826
BRUGNOLI Andrea, 76
BRUNEL Jean-François, 1002
BRUNETTI Matteo, 11
BRUNETTI Maura, 826
BRZESKI Piotr, 63
BUCHER Izhak, 272
BUDAI Csaba, 627
BUDD Chris, 105
BUENO Atila, 978, 1054
BUKS Eyal, 439, 1053
BURLAYENKO Vyacheslav, 1020
BURLION Laurent, 754
BURSI Oreste Salvatore, 875
BURZYŃSKI Tomasz, 63
BYRTUS Miroslav, 603, 1053

CADOU Jean-Marc, 358
CAJIC Milan, 250, 525, 618, 1179
CALBRIX Leopold, 358
CAPOANI Federico, 89
CAPOBIANCO Giuseppe, 36
CARBONI Biagio, 289
CARDOSO-RIBEIRO Flávio Luiz, 272
CARRION Juan, 663
CARTMELL Matthew, 773
CASALOTTI Arnaldo, 993
CATARCI Stefano, 289
CAVALLO Miriam, 164
CENEDESE Mattia, 503, 536
CERAVOLO Rosario, 875
CHAMAN Meymandi Saeideh, 909
CHANDRASHEKAR Abhilash, 1153
CHAPNIK Zvi, 1033
CHARLES Alexandre, 556
CHARLEUX Ludovic, 388
CHASALEVRIS Athanasios, 453
CHATELET Eric, 726
CHATTERJEE Rajanya, 808
CHATZI Eleni, 388
CHAUMETTE Serge, 618
CHAUNSALI Rajesh, 120
CHAWLA Rohit, 677
CHEN Huai-Pu, 636
CHERNOBRYVKO Marina, 1002
CHERNOUSKO Felix, 571
CHEVALIER Christophe, 773
CHONDROGIANNIS Kyriakos Alexandros, 388
CHOUVION Benjamin, 536
CHRISTIANSEN Peter, 195
CHRISTOPHE Giraud-Audine, 26, 420
CHUNG Soon-Jo, 663
COCHELIN Bruno, 134, 272, 420
COLLETTE Christophe, 289, 978
COLLIGNON Christophe, 1054
COMISSIONG Donna, 338
COSTA Dimitri, 155
COUINEAUX Audrey, 272
CSERNÁK Gábor, 739
CUNHA Americo, 1194
CURTIS David, 852
CZAPLEWSKI David, 891

DA Silveira Zanin Camila, 514
DACK Alex, 349
DALMONT Jean-Pierre, 692
DANKOWICZ Harry, 76, 179
DASGUPTA Ratul, 863, 955
DATLA Raju, 289
DAVIDSON Josh, 837, 931
DE Cesare Irene, 338
DE La Cuadra Patricio, 420
DE Tullio Marco Donato, 1033
DEÜ Jean-François, 304
DEAN Robert, 649
DEBEURRE Marielle, 134
DEBUT Vincent, 272
DEFENSOR Filho Wagner, 826
DEFOORT Martial, 496
DEGENFELD-SCHONBURG Peter, 63
DEKEMELE Kevin, 636
DENIS Vivien, 420
DENYSENKO Volodymyr, 978
DERMENDJIAN Fabio, 978, 1054
DERTIMANIS Vasilis, 388
DETOURNAY Emmanuel, 228, 1054
DEVSOTH Lalsingh, 1153
DHOTE Yashika, 955
DI Nino Simona, 319
DI Stasio Jean, 105
DIAS Rodrigues José, 503
DIGNATH Florian, 204
DIMITROVA Svetlana, 1020
DOLEV Amit, 272
DOMBOVARI Zoltan, 931, 1110
DONEVA Simona, 503, 603
DOSAEV Marat, 571, 1020
DOSTAL Leo, 120, 349
DRAUSCHKE Fenja, 754
DUCCESCHI Michele, 692
DUFFY Michael, 663
DUFOUR Régis, 514, 603, 726
DUFRÉNOY Philippe, 1002
DUREISSEIX David, 105
DYK Stepan, 603, 1053

EBERHARD Peter, 204
EDELMANN Johannes, 195
EDLUND Connor, 904
EELTINK Debbie, 826
EHLERS Tobias, 228

EICHINGER Katharina, 478
EL Haddad Fadi, 739
ELLIOTT Stephen, 649
ENGEL Amit, 155
ERTURK Alper, 63
EZRA Tal, 155

FĂRĂGĂU Andrei, 120, 388, 603
FABRE Benoît, 420
FALCON Ricardo, 852
FANG Zhengliang, 965
FAROKHI Hamed, 63, 1153
FEDARAVIČIUS Augustinas, 1124
FEHR Joerg, 204
FENDLEY Casey, 649
FEY Rob, 406
FIDLIN Alexander, 155, 584, 863
FIGURINA Tatiana, 571
FILIPPOVA Tatiana, 571
FITER Christophe, 754
FLOSI Jean, 375
FONTANA Joao, 909
FORMALSKII Alexander, 36, 571
FRÉOUR Vincent, 420
FRADDOSIO Aguinaldo, 164
FRANGI Attilio, 63, 76, 304, 726
FRANZINI Guilherme, 26, 503, 636, 826, 993
FRISWELL Michael, 726

GAILLARD Antoine, 11
GARBUZ Mikhail, 1165
GARZERI Flavio, 134
GASS Bernhard, 931
GAUTIER François, 272, 692, 1055
GAVALAS Ioannis, 453
GEBAI Sarah, 636
GEBREL Ibrahim, 514, 1054
GEIER Charlotte, 1002
GENDA Attila, 584
GENDELMAN Oleg, 105, 120, 155, 375, 584, 603, 663, 920, 1053
GEORGES Gabriel, 105
GERON Yamit, 1053
GHANIPOOR Farhad, 525
GHOMMEM Mehdi, 891
GIANNETTI Flavio, 1033
GILBERT Joël, 692, 1055
GIORGI Giuseppe, 837
GIOVANNOZZI Massimo, 89
GIRAUD-AUDINE Christophe, 105
GIRAULT Gregory, 358
GIVLI Sefi, 1053
GIVOIS Arthur, 304
GNANN Manuel, 478
GODOI Antonio, 1053
GOGOI Ankush, 63
GOMEL Alexis, 826
GOSS Victor, 439
GOSWAMI Partha, 955
GOTTLIEB Oded, 808, 891, 1020, 1124
GOURDON Emmanuel, 514
GOVAERTS Willy, 358
GRÄBNER Nils, 514
GRAHAM Bradley, 503
GRAVOUIL Anthony, 105
GRENAT Clément, 179
GRIFFITH Cody, 105
GRIZANS Juris, 164
GROLET Aurelien, 134, 304, 627, 1054
GUILLOT Louis, 420
GUNN Ben, 478
GUO Bingyong, 1133
GUO Tieding, 536, 663
GUPTA Sayan, 808
GUREVICH Svetlana, 942
GUSKOV Mikhail, 603, 1110
GUTSCHMIDT Stefanie, 204, 891
GYEBRÓSZKI Gergely, 739
GZAL Majdi, 375, 663, 920

H. S. Varun, 1033
HÖHNE Joshua, 349
HÖVEL Philipp, 63
HÉLIE Thomas, 420
HABIB Giuseppe, 179, 837, 931, 1110
HACKER Evyatar, 891
HAGEDORN Peter, 496, 792
HAJJ Muhammad, 289
HAJJAJ Amal, 965, 1153
HALEVY Omer, 965
HALLER George, 319, 503, 536, 677
HANNES Eschmann, 204
HARDUF Yuval, 1033
HARTENBACH Felix, 1054
HAZEL Andrew, 11
HAZELEGER Leroy, 978
HAZRA Budhaditya, 63
HEDRIH Andjelka, 439, 618
HEEMELS Maurice, 909
HEGEDŰS Ferenc, 792
HEIL Matthias, 826
HELIE Thomas, 420
HENDERSON Michael, 76
HETEL Laurentiu, 754
HEYSER Dennis, 773
HIEN David, 179
HO Wei Hua, 1033
HOFFMANN Norbert, 134, 920, 1002
HOHL Andreas, 726
HOLL Helmut, 837
HOLLM Marten, 120, 349
HOMOLLE Thomas, 105
HORVÁTH Dávid András, 304
HORVATH Hanna Zsofia, 875
HOURI Samer, 891, 1020
HOURIGAN Kerry, 826
HUANG Yu-Hsi, 636
HUBAY Csanád Árpád, 1179
HUNNEKENS Bram, 754
HUSSEIN Mahmoud, 250

IAPICHINO Laura, 406, 536, 1054
IARRICCIO Giovanni, 649, 663, 920
IGNÁCIO Da Silva José Augusto, 375

IGNACIO Ortega-Piwonka, 89
IHEANACHO Chukwuma Victor, 164
ILIC Robert, 965
INSPERGER Tamás, 852, 942, 1110

JÜLICHER Frank, 942
JABER Nizar, 304
JAIN Shobhit, 319, 503
JAMES Guillaume, 228
JAMSHIDI Rasa, 289
JANG Bumjin, 1033
JANNETEAU Christophe, 909
JARDON Hildeberto, 195
JAVALOYES Julien, 89, 942
JEFFREY Mike, 556
JELVEH Meisam, 627, 1053
JENKINS Alejandro, 571
JOB Stéphane, 164
JOHNSTON Daniel, 773
JONGENEEL Maarten, 228
JOSSIC Marguerite, 420
JOVANOVIC George, 439
JOVIC Srdjan, 525
JUCHEM Jasper, 1124
JUEL Anne, 11
JUNGE Oliver, 179
JUNGERS Marc, 909
JURISITS Richard, 792
JUST Wolfram, 76

K R Jayaprakash, 388, 603
KÖVECSES József, 556, 627
KÁDÁR Fanni, 525
KACEM Najib, 26, 891
KACZMARCZYK Stefan, 525
KADRI Usama, 584, 692
KALMÁR-NAGY Tamás, 837, 931, 1179
KAMBALI Prashant, 406
KANDALA Shanti Swaroop, 388
KAPELKE Simon, 1054
KARGL Arnim, 204
KARIMOV Mirlan, 931
KARLIČIĆ Danilo, 250
KARLICIC Danilo, 525, 618, 1179
KAROUI A. Yassine, 89
KASPARIAN Jérôme, 826
KAST Mariella, 406
KAUFMANN Andreas, 792
KAYAL Lohit, 863
KEŞKEKLER Ata, 1153
KEELER Jack, 11
KERSCHEN Gaëtan, 739, 978, 1020
KESSELS Bas, 406
KHAJEHTOURIAN Romik, 250
KHAN Kamil, 228
KHEIRI Mojtaba, 636
KIRILLOV Oleg, 36, 1033
KISER Shawn, 603
KISS Adam K., 931
KLEYMAN Gleb, 134, 228
KLIMINA Liubov, 571, 1165
KLODA Lukasz, 875, 1133
KNOWLES James, 503
KOGAN Eugene, 250
KOGANI Ali, 993
KOGELBAUER Florian, 677
KOLB Pauline, 1054
KORNFELD Matthias, 792
KORVER Julian, 406
KOUTRAS Evangelos, 76
KOVACIC Ivana, 773
KOVALEVA Margarita, 663, 1165
KRÄHLING Péter, 792
KRACK Malte, 406, 603
KRAUS Zacharias, 792
KRAUSKOPF Bernd, 89, 358, 584, 1110
KRAVETC Pavel, 105
KRISTOF Nagy, 1179
KRIVTSOV Anton, 636
KRYLOV Slava, 965
KRYSKO-JR. Vadim, 1002
KUEHN Christian, 195, 478
KULKE Vincent, 726
KUMAR Anish, 993
KURPA Lidiya, 1002
KURUSHINA Victoria, 525, 1194
KUSKE Rachel, 105, 155, 349, 478
KUZNETSOV Yuri, 358

LABARBE Joris, 1033
LABETOULLE Aurélie, 514
LACARBONARA Walter, 289
LACHMAYER Roland, 228
LAMARQUE Claude-Henri, 228, 375, 514, 636, 773
LANGFIELD Peter, 584
LANGLOIS Sébastien, 636, 875
LAROCHE Edouard, 1053
LATALSKI Jaroslaw, 726
LAUTERBORN Werner, 792
LAZARUS Arnaud, 792
LEBEDENKO Yana, 1002
LEE Kyoung Hyun, 11
LEENEN Tom, 406
LEFÈVRE Laurent, 272
LEGRAND Franck, 726
LEGRAND Mathias, 105, 228, 556
LEINE Remco, 36, 89, 453, 792
LELKES János, 304
LENCI Stefano, 164, 503, 875, 891
LENK Claudia, 63
LENTZ Lukas, 514
LEPIDI Marco, 120
LEROUX Matthieu, 636
LESZCZYNSKI Maciej, 1133
LEVI Yuval, 1020
LI Haiqin, 692
LI Mingwu, 179, 319
LI Xiaofu, 649
LI Zichao, 891
LIN Hoang-Yan, 636
LIU Ruofeng, 155
LIU Xuefeng, 134
LIU Yang, 375, 439, 1133
LIU Yuxiang, 965

LIU Zihan, 406
LO Feudo Stefania, 164
LOCCUFIER Mia, 636, 1124
LOCH Gesing Andre, 965
LOPEZ Daniel, 891, 965
LU Guang, 36
LU Tianzheng, 228
LUNEAU Christopher, 826
LUONGO Angelo, 319, 993

MÜLLER Florian, 603
MACIEL Elvio, 978, 1054
MACIEL Vitor, 826
MAHÉ Hervé, 627, 1054
MAHE Vincent, 627
MAHJOUB Mohamed, 603
MAHMOODI S. Nima, 909
MAJDOUB Fida, 1133
MANEVITCH Leonid, 1165
MANIN Lionel, 603
MANOACH Emil, 503, 603
MARCEL Aron, 792
MARQUES Flávio, 375
MARTIN Adrien, 76, 726
MARUCCI Lucia, 338
MASRI Sami, 289, 388
MASUDA Hideyuki, 420
MATHARU Puneet, 826
MATIGNON Denis, 76, 272, 420, 618
MATLACK Kathryn, 250
MATTÉOLI Rémi, 692
MATTEI Pierre-Olivier, 134
MATTIAZZO Giuliana, 837
MAUGEAIS Sylvain, 692
MAVROS Georgios, 503
MAZANTI Guilherme, 1110
MAZUR Olga, 875
MAZZILLI Carlos, 993
MCWILLIAM Stewart, 496
MEDINA Cabrera Manuel, 1053
MEHNER Jan, 63
MEIJER Hil, 358
MEINERS Alexander, 179
MELCHIOR Pierre, 618
MELOT Adrien, 649
MENAND Stephane, 603
MESSER Markus, 931
METRIKINE Andrei, 120, 388, 584, 603
METTIN Robert, 792
MI Jia, 289
MICHON Guilhem, 319
MIKHLIN Yuri, 1002, 1020, 1053
MILOH Touvia, 808
MINATI Ludovico, 891
MISCHAIKOW Konstantin, 179
MITRA Saheli, 904
MITURA Andrzej, 11, 1133
MOHAJERIN Esfahani Peyman, 525
MOJAHED Alireza, 120, 375
MOLNÁR Csenge Andrea, 942
MORARESCU Irinel Constantin, 909
MOREL Adrien, 388
MORSY Ahmed, 406
MOUFID Ilyes, 618
MOUSAVI Seyed Mojtaba, 627
MOUSSALLAM Nadim, 453
MUCCHIELLI Paul, 63
MURGUIA Carlos, 525
MUSAVI Seyyed Mojtaba, 1053
MUSOKE Elle, 89

NABHOLZ Ulrike, 63
NADERI Lordejani Sajad, 406
NAGY Dalma J., 1110
NAJAR Fehmi, 891, 1153
NAMACHCHIVAYA Navaratnam Sri, 319
NAMBIAR Amal, 155
NATARAJ C., 406
NATSIAVAS Sotirios, 76
NEILD Simon, 289
NEIRYNCK Niels, 358
NELSON Bradley, 1033
NESIC Nikola, 525
NESTEROV Andrey, 1165
NGUYEN Khac Long, 603
NICULESCU Silviu-Iulian, 852, 1110
NIEDERGESÄSS Björn, 134
NIELSEN Anne Ryelund, 826
NIJMEIJER Henk, 105, 909
NIKLAS Meyer, 289
NITTI Alessandro, 1033
NORTE Richard, 891
NOVELIA Alyssa, 319

OCHIAI Koki, 134
OIKAWA Yuki, 134
OMELCHENKO Iryna, 754
OMRAN Hassan, 1053
OOMEN Tom, 754
OPRENI Andrea, 63, 76, 304, 726
OR Yizhar, 105, 808, 1033, 1053
ORSINO Renato, 808, 826
OSINGA Hinke, 358
OSINGA Hinke M., 89, 584
OSTERMEYER Georg-Peter, 726
OUAKAD Hassen, 726, 1153
OULDRIDGE Thomas, 349
OVSEEVICH Alexander, 571

PĘKAL Marcin, 36, 204
PAKRASHI Vikram, 63, 677, 773, 904
PANÉ Salvador, 1033
PANAGIOTOPOULOS Ilias, 76
PANDEY Ashok, 1153
PANDEY Manoj, 155
PANZO Eduardo, 978, 1054
PAPAFRAGKOS Panagiotis, 453
PAPANGELO Antonio, 920
PARASKEVOPOULOS Elias, 76
PARKER Robert, 773
PARLITZ Ulrich, 792
PATANKAR Sagar, 955
PATIL Ganesh, 250
PAUL Jithu, 375, 1053
PAULS Vitaly, 164

PAUNOVIĆ Stepa, 250, 618
PAUNOVIC Stepa, 1179
PAVLOV Alexey, 536, 1124
PAVLOVSKAIA Ekaterina, 525, 1194
PELAT Adrien, 692
PELLICANO Francesco, 649, 663, 920
PENG Linyu, 134
PEREZ-MOLERO Diego, 965
PERKINS Edmon, 649
PERLIKOWSKI Przemysław, 63
PERRET-LIAUDET Joël, 649
PERRET-LIAUDET Joel, 11, 349, 1133
PESCE Celso, 808, 826
PHANI A. Srikantha, 375
PICCIN Olivier, 1053
PICCIONI Mario Daniele, 164
PIERRE Christophe, 105
PIKUĻINS Dmitrijs, 164
PILIPCHUK Valery, 195, 627
PIOT Estelle, 618
PIQUEIRA José, 978, 1053, 1054
PIRES Macedo Oliveira Dos Santos Ingrid, 11
PLÖCHL Manfred, 195
PLATZ Daniel, 965
PLESA Tomislav, 349
POGROMSKY Alexander, 536
PONS Arion, 1133
PONTHUS Nicolas, 349
PRABEL Benoit, 179
PRASAD Shyam, 439
PRIEUR Christophe, 228
PROFIZI Paul, 556
PROTIÈRE Suzie, 792
PROUSALIS Dimitrios, 942
PUMHOESSEL Thomas, 837
PYRAGAS Kestutis, 1124
PYRAGIENĖ Tatjana, 1124

QUAEGEBEUR Samuel, 536
QUINN Courtney, 358

RABENIMANANA Toky, 891
RACHINSKII Dmitrii, 105
RACKAUCKAS Christopher, 677
RAFAL Rusinek, 453
RAMAKRISHNAN Subramanian, 904
RAMSAY James, 1033
RANC Nicolas, 603
RAOOFIAN Ali, 556
RAPTOPOULOS Ioannis, 453
RASMUSSEN Anders, 195
RATHORE Khogesh K, 920
RAVE Stephan, 1054
RAVICHANDRAN Thambirajah, 319
RAZE Ghislain, 1020
REBILLAT Marc, 603
REGA Giuseppe, 536, 663, 863
REINDERS Joey, 754
RENAULT Alexandre, 627
RENSON Ludovic, 11, 338, 978
REZGUI Djamel, 289
RIBEIRO Pedro, 503
RICHARD Jean-Pierre, 754
RICKETTS Evan, 692
RIGAUD Emmanuel, 11, 649
RILL Georg, 36
RITURAJ Rituraj, 837
ROCCA Alexandre, 556
ROCHA Rodrigo, 1153
ROEVEN Luke, 204
ROMEO Francesco, 11
RONCEN Rémi, 618
ROSENBERG Sahar, 319
ROUNAK Aasifa, 677
ROUX Émile, 388
ROZE David, 420
RUDERMAN Michael, 754
RUDNYEVA Gayane, 1053
RUFER Libor, 496
RUIZ Kendric, 618
RUSCHEL Stefan, 1110
RUSINEK Rafal, 338, 852

SØRENSEN Mads, 195
SAADAOUI Rima, 1053
SACCO Elio, 164
SACCON Alessandro, 228
SADR Mohammad Homayoune, 627, 1053
SAILER Simon, 453
SAINT-MARTIN Camille, 388
SALLES Loïc, 304
SALLES Loic, 304, 726, 739, 920
SALLES Rafael, 808
SALMI Soraya, 1053
SAMAEY Giovanni, 739
SAMSONOV Vitaly, 1020, 1165
SANCHES Leonardo, 319, 375
SAPSIS Themistoklis, 76
SARBINOWSKI Filip, 26
SARKAR Sunetra, 808, 1033
SAUGATA Bhattacharyya, 904
SAWICKI Jakub, 754
SCHÖLL Eckehard, 754
SCHEEL Maren, 406
SCHEIBERT Julien, 349
SCHEIDL Jakob, 773
SCHEIDL Rudolf, 388, 837
SCHIENI Rick, 754
SCHILDER Frank, 76
SCHILDERS Wil, 406, 536, 1054
SCHMID Patrick, 204
SCHMID Ulrich, 965
SCHMIDT Franziska, 773
SCHNEIDER Georg, 204
SCHWEIZER Bernhard, 773
SCHWENCK Franco Maciel Vitor, 636
SCHWINGSHACKL Christoph, 920
SEDIGHI Hamid, 726
SEEMANN Wolfgang, 1054
SEIDEL Thomas, 942
SEIFRIED Robert, 289, 349
SELLIER Mathieu, 978, 1033
SELYUTSKIY Yury, 571
SENSI Mattia, 89

SEPYAN Gregory, 808
SERDUKOVA Larissa, 478
SERGEJS Tjukovs, 164
SETTIMI Valeria, 120, 863
SHAH Chhote, 808
SHAKIB Mohammad Fahim, 536
SHALABY Ahmed, 289
SHAMI Zein Alabidin, 26, 134
SHAW Alexander, 726
SHAW Steven, 891
SHEN Yichang, 304
SHEPHERD Ross, 978
SHMATKO Aleksandr, 1002
SHMATKO Tetyana, 1002
SHOOSHTARI Alireza, 909
SHOR Roman, 388
SHOSHANI Oriel, 319, 891, 1153
SHOUGAT Md Raf E Ul, 649
SHUKLA Amit, 105
SIEBER Jan, 76, 179, 358
SIERRA Ausin Javier, 1033
SILVA Fabrice, 272
SIMONOVIC Julijana, 338
SIMS Neil, 852
SIMSEK Mehmet, 754
SNIJDERS Max, 179
SOARES Filipe, 272
SOKOLOV Aleksei, 636
SONG Yingkai, 228
SOOKNANAN Joanna, 338
SOROKIN Sergey, 164
SPENCER Bill, 663
SPILIOTIS Konstantinos, 338
SRIKANT Sukumar, 909
STARKE Jens, 76, 338
STAROSTA Roman, 26, 955
STAROSTIN Eugene, 439
STAROSVETSKY Yuli, 388, 663, 863, 993
STAUFER Urs, 1153
STEENEKEN Peter, 891, 1153
STEENEKEN Peter G., 965
STEFANO Lenci, 453, 663
STEFANSKI Andrzej, 978
STEINDL Alois, 195
STENDER Merten, 920, 1002
STEPAN Gabor, 525, 627, 852, 942
STEPANOVA Larisa, 1165
STEUR Erik, 754, 1124
STRACHAN Scott, 891
STRIJBOSCH Nard, 105
STRIZHAK Peter, 1054
STROZZI Matteo, 120
SUGIURA Toshihiko, 134
SURHANOVA Yuliia, 1020
SVIRIDOV Alexey, 1054
SYKORA Henrik, 289, 349, 677
SYPNIEWSKA-KAMINSKA Grażyna, 955
SZAKSZ Bence, 942
SZMIT Zofia, 453

TAFUNI Alessandro, 164
TAKÁCS Dénes, 677, 875
TALEBI Bidhendi M. Reza, 375
TANAYS Rémy, 319
TATZKO Sebastian, 134, 228
TAYEBI Sajad, 677
TEICHMANN Marek, 556
TERRIEN Soizic, 420, 1110
THEOCHARIS Georgios, 120
THEODOSSIADES Stephanos, 478, 965
THEVENOT Mael, 1002
THOMAS Jijju, 754
THOMAS Olivier, 26, 105, 134, 304, 420, 627, 1054
THOMPSON Alice, 11, 909
THOMPSON Mark, 826
THOMSEN Jon, 164
THOUVEREZ Fabrice, 536
TIAN Jiyuan, 439, 1133
TIRRI Antonia, 1033
TISO Paolo, 406
TLIBA Sami, 852
TOHIDI Hadi, 627
TOKAREV Artem, 1054
TOMIN Daniel, 808
TOTH Mate, 852
TOUZÉ Cyril, 63, 76, 304, 692, 726
TOUZE Cyril, 304
TOVI Elon, 808
TRAN Quang Thinh, 603
TSETAS Athanasios, 584
TSOUVALAS Apostolos, 584
TURE Savadkoohi Alireza, 228, 375, 514, 636, 773, 875

UECKER Hannes, 179
URMAN David, 556
USPENSKY B, 1002
USPENSKY Boris, 1002

VÖRÖS Illés, 677
VAINCHTEIN Dmitri, 584
VAKAKIS Alexander, 120, 375, 603, 663
VAKULENKO Sergei, 1179
VALENCIA Carla, 863
VAN Dalen Karel, 120, 388, 603
VAN De Wouw Nathan, 228, 406, 525, 536, 754, 909, 978, 1124
VAN Der Esch Anton, 603
VAN Der Heijden Gert, 439, 875
VAN Horssen Wim, 931, 955
VAN Keulen Fred, 891
VAN Torre Patrick, 636
VAN Wezel Richard, 358
VARKONYI Peter, 105, 556
VARMA Vineeth Satheeskumar, 909
VED Kalpan, 63
VEDENEEV Vasily, 1194
VELTMAN Yuval, 375
VERED Yoav, 649
VERGEZ Christophe, 272, 420, 692
VERNIZZI Guilherme, 503, 826
VETYUKOV Yury, 773
VICTOR Stephane, 618
VIZI Mate, 942

VIZZACARRO Alessandra, 304, 739
VIZZACCARO Alessandra, 63, 76, 304, 726
VLADIMIR Aksyuk, 965
VO Van Nam, 228
VOLVERT Martin, 739
VOLZ Marcel, 773
VON Wagner Utz, 514
VOROTNIKOV Kirill, 228

WALLASCHEK Jörg, 134
WALTER Vincent, 891
WANG Chenxin, 773
WANG Huailei, 852
WANG Jing, 931
WANG Ligang, 514, 1054
WANG Mingkang, 965
WANG Yuqing, 76
WANG Zepeng, 439
WARMINSKI Jerzy, 11, 453, 503, 603, 726, 852, 875, 1133
WEBB Craig, 692
WEBER Hans, 11
WEDIG Walter, 478
WEREMCZUK Andrzej, 852
WETZEL Lucas, 942
WIDMANN David, 677
WIJNAND Marc, 420
WILDEMANS Roeland, 228
WOJTYRA Marek, 36, 204
WOLFGANG Müller, 636
WONG Nelson, 358
WOOLLEY Thomas, 338
WOUW Nathan, 228, 406, 536, 1054
WU Jiaen, 1033

WYNNE Bradley, 773

XIA Yiwei, 63
XING Jing Tang, 1179
XU Minxing, 891

YÜZBASIOGLU Tunc, 863
YAKIR Gilad, 1124
YAMAGUCHI Hiroshi, 891
YAN Yao, 1133
YOUNIS Mohammad, 1153, 1194
YOUSEFZADEH Behrooz, 993
YUAN Jie, 920
YURCHENKO Daniil, 155, 349, 478

ZABLOTNI Robert, 338
ZACCARIAN Luca, 909
ZAGAR Philipp, 388
ZAMANIAN Najafabadi Shima, 875
ZARYCHTA Sandra, 978
ZHANG He, 1054
ZHANG Jiangyi, 603
ZHANG Li, 852
ZHANG Rui, 965
ZHANG Xiaojia, 584
ZHAO Jisheng, 826
ZHAO Xingwei, 875
ZHOKH Alexey, 1054
ZIEGLER Martin, 63
ZIPPO Antonio, 649, 663, 920
ZOKA Hooman, 993
ZOTOV Alexey, 1054
ZOUABI Chaima, 349
ZULLI Daniele, 993
ZUO Lei, 289